

# ISAF '94

## PROCEEDINGS

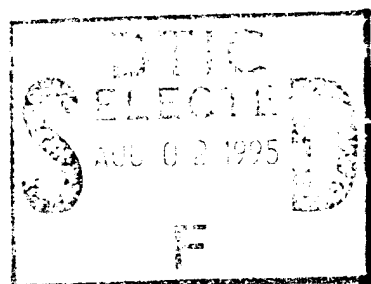
of the  
Ninth  
IEEE

DISTRIBUTION STATEMENT A

Approved for public release

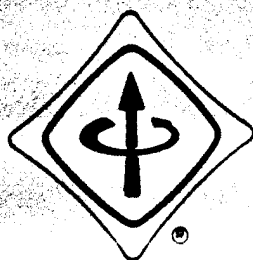
and Distribution Unlimited

International Symposium on  
Applications of Ferroelectrics



Editors:

R. K. Pandey  
Michael Liu  
Ahmad Safari



Penn State Scanticon Conference Center  
The Pennsylvania State University  
University Park, Pennsylvania  
USA

August 7 - August 10, 1994

IEEE Catalog Number 94CH3416-5

19950731 003

DTIC QUALITY INSPECTED 8



Dr. L. Eric Cross  
Evan Pugh Professor  
of Electrical Engineering

Telephone (814) 865-1181  
Fax No. (814) 863-7846  
e-mail: [tmcl@alpha.mrl.psu.edu](mailto:tmcl@alpha.mrl.psu.edu)

187 Materials Research Laboratory  
The Pennsylvania State University  
University Park, PA 16802-4800

July 17, 1995

Defense Technical Information Center  
Building 5, Cameron Station  
Alexandria, VA 22314

RE: Grant No. N00014-94-1-0584  
"The Ninth IEEE International Symposium on the  
Applications of Ferroelectrics (ISAF 94)"

To Whom This May Concern,

Please accept the enclosed copy of the ISAF 94 Abstract Book and  
ISAF 94 Conference Proceedings as the final report that we are required  
to send to you per Symposium Grant guidelines.

Should you require any other information pertaining to this funded project  
please feel free to contact me.

Thank you for your support.

Yours faithfully,

L. Eric Cross  
Evan Pugh Professor  
of Electrical Engineering

LEC:tmc  
Enclosures (2)  
cc: L.A. Hipple  
A.S. Bhalla



# ISAF '94

## PROCEEDINGS

of the  
Ninth  
IEEE

International Symposium on  
Applications of Ferroelectrics

Editors:

R. K. Pandey  
Michael Liu  
Ahmad Safari



Penn State Scanticon Conference Center  
The Pennsylvania State University  
University Park, Pennsylvania  
USA  
August 7 - August 10, 1994

IEEE Catalog Number 94CH3416-5

Accession For	
NTIS CRA&I	<input checked="checked" type="checkbox"/>
DTIC TAB	<input type="checkbox"/>
Unannounced	<input type="checkbox"/>
Justification	
By <i>N00014-94-1-0584</i>	
Distribution /	
Availability Codes	
Dist	Avail and/or Special
<i>A-1</i>	

## 1994 IEEE 9th INTERNATIONAL SYMPOSIUM ON APPLICATIONS OF FERROELECTRICS

Copyright and Reprint Permission: Abstracting is permitted with credit to the source. Libraries are permitted to photocopy beyond the limit of U.S. copyright law for private use of patrons those articles in this volume that carry a code at the bottom of the first page, provided the per-copy fee indicated in the code is paid through Copyright Clearance Center, 27 Congress Street, Salem, MA 01970. Instructors are permitted to photocopy isolated articles for non-commercial classroom use without fee. For other copying, reprint or republication permission, write to IEEE Copyrights Manager, IEEE Service Center, 445 Hoes Lane, P.O. Box 1331, Piscataway, NJ 08855-1331. All rights reserved. Copyright ©1990 by the Institute of Electrical and Electronics Engineers, Inc.

IEEE Catalog Number: 94CH3416-5

ISBN: 0-7803-1847-1 (Softbound)

ISBN: 0-7803-1858-7 (Casebound)

ISBN: 0-7803-1848-X (Microfiche)

Library of Congress: 94-75165

Additional copies of this publication are available from

IEEE Service Center  
445 Hoes Lane  
Piscataway, NJ 08854-4150

1-800678-IEEE

---

# THE NINTH INTERNATIONAL SYMPOSIUM ON THE APPLICATIONS OF FERROELECTRICS

---

*Aug. 7 - 10, 1994, Penn State Scanticon Conference Center  
The Pennsylvania State University  
University Park, Pennsylvania, USA*

The Ninth International Symposium on the Applications of Ferroelectrics (ISAF '94) was held at the Penn State Scanticon Conference Center, the Pennsylvania State University, University Park, Pennsylvania, during August 7-10, 1994.

The Symposium program contained 377 scientific papers on various aspects of ferroelectrics and their applications. The program was put together by the program coordinating committee chaired by A. S. Bhalla, R. Guo, and L. E. Cross. There were 116 oral (42 invited) and 261 poster papers presented in three parallel oral sessions and in the poster sessions each day over the three days of the meeting. The meeting covered major advances in the areas of piezoelectrics, dielectrics, thin film ferroelectrics, actuators, smart materials, pyroelectrics, nonlinear optical ferroelectrics, photorefractive materials, and their applications. The conference was attended by international scientists representing 21 countries. The geographical distribution of the papers, international and national, is represented in the accompanying table and graphs.

The meeting also commemorated several milestones in the history of ferroelectricity. Two special history sessions were organized to mark these events:

- Centennial of "Observation of the First Dielectric Anomaly with Temperature in Rochelle Salt (1894)"
- 75th Year of the Discovery of Ferroelectricity (1920)
- The Golden Anniversary of the "Discovery of the First Most Widely Used Ferroelectric  $\text{BaTiO}_3$ "

The conference highlighted and honored the achievements and contributions of several pioneer researchers who worked in the early development of ferroelectrics in the forties, fifties and early sixties.

Mr. Akira Murata was presented the Certificate of Recognition by the Ferroelectrics Committee at the conference. The presentation was made during the symposium banquet by Professor L. Eric Cross and received on behalf of Akira Murata by Dr. Kikuo Wakino of Ritsumeikan University and Murata Manufacturing Co.. The citation reads: "*Founder and Chairman of the Board of Murata Manufacturing Company Ltd. as a Pioneer in the Development and Application of Ferroelectric Ceramics.*"

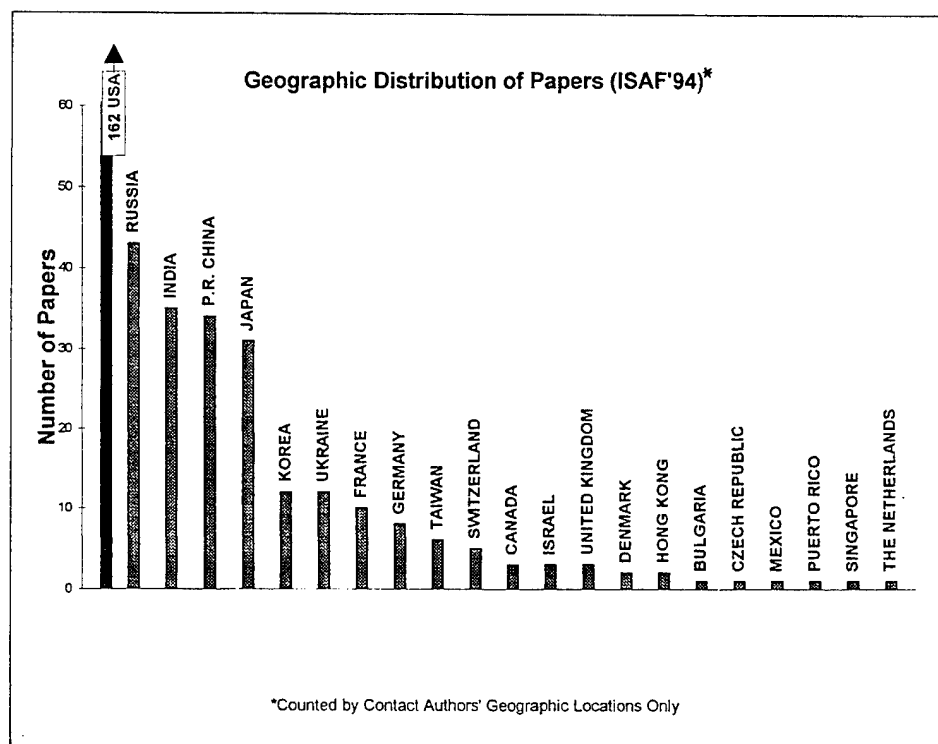
Organizing committee is thankful to the sponsoring organizations: The Institute of Electrical and Electronic Engineers (IEEE), Ultrasonic, Ferroelectrics and Frequency Control Society (UFFC), and several government agencies whose financial support made this conference a successful one and made it possible for many national and international scientists and students to attend and to publish proceedings of the conference. We acknowledge gratefully the financial assistance of Advanced Research Projects Agency (ARPA), Army Research Office (ARO), International Science Foundation (ISF), National Science Foundation (NSF), and Office of Naval Research (ONR). We extend our thanks to Murata Manufacturing Co., Ltd., who provided the support to organize special events and the history sessions at the meeting.

*A. S. Bhalla*  
General Chair, and  
*The Organizing Committee*  
ISAF '94

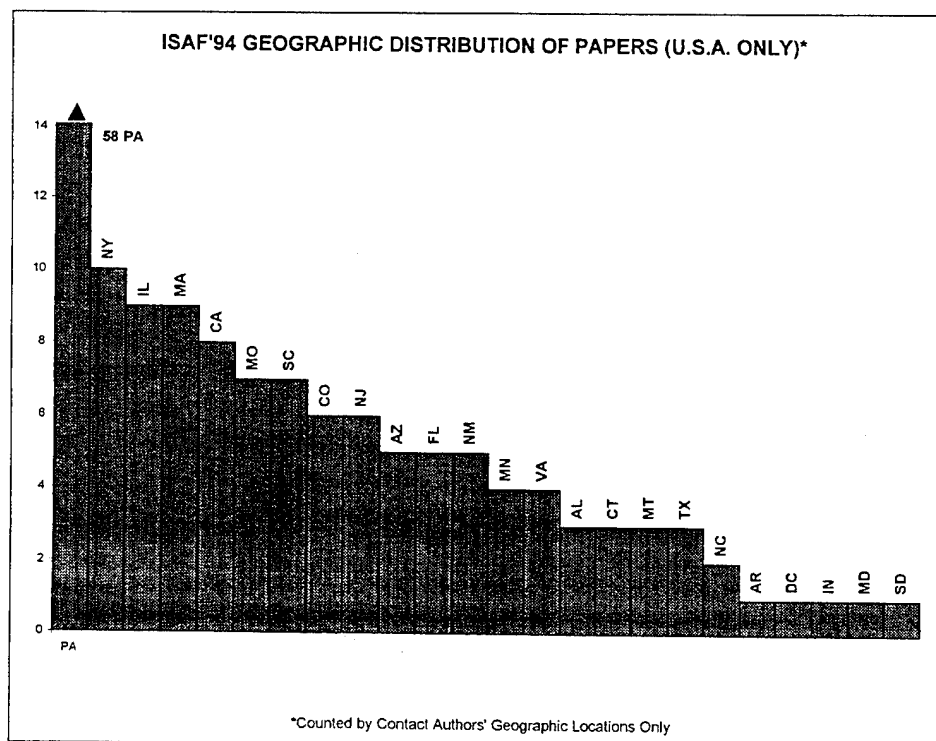
# Geographic Distribution of Invited and Contributed papers

(Counted by Contact Author's Origin)

United States	162
Russia	43
India	35
P.R. China	34
Japan	31
Korea	12
Ukraine	12
France	10
Germany	8
Taiwan	6
Switzerland	5
Canada	3
Israel	3
United Kingdom	3
Denmark	2
Hong Kong	2
Bulgaria	1
Czech Republic	1
Mexico	1
Puerto Rico	1
Singapore	1
The Netherlands	1
<b>Subtotal</b>	<b>(Non-U.S.) 215 (U.S.) 162</b>
<b>Total</b>	<b>377</b>



(42 invited presentations);  
 116 oral presentations;  
 261 poster presentations;  
 1281 authors.



# THE NINTH INTERNATIONAL SYMPOSIUM ON THE APPLICATIONS OF FERROELECTRICS (ISAF '94)

*Aug. 7 - 10, 1994, Penn State Scanticon Conference Center  
The Pennsylvania State University, University Park, PA 16802 USA*

**Amar S. Bhalla**

CONFERENCE GENERAL CHAIR

Materials Research Laboratory, The Pennsylvania State University, University Park, PA 16802, USA.  
Tel. (814) 865-9232, FAX: (814) 865-2326, e-mail: ASB2@psuvm.psu.edu.

**TECHNICAL PROGRAM COORDINATORS:** *Amar S. Bhalla*, Materials Research Laboratory, Penn State University; *Ruyan Guo*, Materials Research Laboratory, Penn State University.

**TREASURER:** *Tom Catchen*, The Institute of Electrical and Electronic Engineers.

**PUBLICATION:** *R. K. Pandey*, Texas A&M University, College Station, Texas; *S. T. Liu*, Honeywell Corp.; *Ahmad Safari*, Rutgers University, Piscataway, New Jersey.

## INTERNATIONAL ADVISORY COMMITTEE:

*L. Eric Cross*, Penn State University, University Park, Pennsylvania, USA.  
*R. E. Newnham*, Penn State University, University Park, Pennsylvania, USA.  
*T. Takenaka*, Science University of Tokyo, Tokyo, Japan.  
*Yao Xi*, Xi'an Jiaotong University, Xi'an, The People's Republic of China.  
*Nava Setter*, EPHL, Lousanne, Switzerland.  
*Frank Ainger*, United Kingdom.  
*G. W. Taylor*, Princeton Resources, New Jersey, USA.  
*Gene Haertling*, Clemson University, South Carolina, USA.  
*R. C. Pohanka*, Office of Naval Research, Virginia, USA.  
*D. C. Dube*, Indian Institute of Technology, Delhi, India.

## ORGANIZING COMMITTEE:

*Amar S. Bhalla*, Materials Research Laboratory, Penn State University.  
*L. Eric Cross*, Materials Research Laboratory, Penn State University.  
*Wallace A. Smith*, Office of Naval Research.  
*Lucilla Cross*, Companion hospitality program, State College.  
*Tina M. Confer*, Materials Research Laboratory, Penn State University.  
*Debora Shay*, Materials Research Laboratory, Penn State University.  
*Monica M. Vacca*, Conference Planner, Continuing and Distance Education, Penn State University.

## PROGRAM COMMITTEE:

*L. Eric Cross*, Materials Research Laboratory, Penn State University.  
*Ruyan Guo*, Materials Research Laboratory, Penn State University.  
*Edward Sharp*, Army Research Laboratory.  
*David Skatrud*, Army Research Office.  
*Sei-Joo Jang*, Materials Research Laboratory, Penn State University.  
*Jane Alexander*, Advanced Research Projects Agency.  
*R. R. Neurgaonkar*, Rockwell International Science Center.  
*S. B. Krupanidhi*, Materials Research Laboratory, Penn State University.



## TABLE OF CONTENTS

### History of Ferroelectricity

Joseph Valasek and the Discovery of Ferroelectricity - Jan Fousek .....	1
200 Years of Research on Boracites - A. G. Castellanos-Guzman .....	6
History of Ferroelectric Ceramics in Japan - Kiyoshi Okazaki .....	10
Grain Size Effects in Barium Titanate - Revisited - A. J. Bell .....	14

### Concurrent Session 1A - Piezoelectric

Morphotropic Phase Boundary and Microstructure of Low-Temperature Sintered PZT Ceramics with $\text{BiFeO}_3$ and $\text{Ba}(\text{Cu}_{0.5}\text{W}_{0.5})\text{O}_3$ - Kenji Murakami, Nagaya Okada, Dunzhuo Dong and Shoji Kaneko .....	19
Development of New Piezoelectric Ceramics with Bismuth Perovskites - Tadashi Takenaka, Masotoshi Yamada and Takeo Okuda .....	21

### Concurrent Session - 2A: Thin Films

A Simple Unified Analytical Model for Ferroelectric Thin Film Capacitor and Its Applications for Nonvolatile Memory Operation - Deng-Yuan Chen, Masamichi Azuma, Larry D. McMillan and C. A. Paz de Araujo .....	25
Stress in $\text{Pt/Pb}(\text{Zr}_1\text{Ti})\text{O}_3$ /Pt Capacitors for Integrated Ferroelectric Devices - G.A.C.M. Spierings, G.J.M. Dormans, W.G.J. Moors, M.J.E. Ulenaers and P.K. Larsen ...	29

### Concurrent Session - 3A: Dielectrics

A New Proposal on Mixing Rule of the Dielectric Constant of Mixture - Kikuo Wakino	33
A Numerical Approach to Analyze the Internal Electrical Response of Dielectric Ceramics with Arbitrary Shaped Inclusion - M. E. Azimi and P. K. Ghosh .....	39

### Concurrent Session - 1B: Piezoelectrics

Local Structure of PLZT - S. Telsic and T. Egami .....	43
Dielectric and Brillouin Scattering Anomalies in $\text{An Na}_{1/2}\text{Bi}_{1/2}\text{TiO}_3$ (NBT) Relaxor Ferroelectric Crystals - V. H. Schmidt, C.-S. Tu, and I. G. Siny .....	45
Processing of Porous and Dense PZT Thick Films on $\text{Al}_2\text{O}_3$ Substrates - J. F. Fernandez, E. Nieto, C. Moure, and P. Duran .....	49

### Concurrent Session - 2B: Thin Films

Preparation and Properties of Lanthanum Modified $\text{PbTiO}_3$ Thin Films by rf-Magnetron Sputtering - Kenji Iijima, Takayuki Takeuchi, Nobuaki Nagao, Ryouichi Takayama and Ichiro Ueda .....	53
---	----

Ferroelectric MIM and MOS Structure of Laser Deposited ( $\text{Sr}_{0.2}\text{Ba}_{0.8}$ ) $\text{TiO}_3$ Thin Films - Hsiu-Fung Cheng and I.N. Lin	59
Micropatterning Process of Ferroelectric Oxides by Irradiation of an Electron Beam on Metal Naphthenate Films - S. Okamura, A. Kakimi S. R. Zhang, C. W. Zhong, Y. Yagi, K. Mori and T. Tsukamoto	62
Imprint of Ferroelectric PLZT Thin-Film Capacitors with Lanthanum Strontium Cobalt Oxide Electrodes - J. M. Benedetto, M. L. Roush, I. K. Lloyd and R. Ramesh	66
Analysis of Ferroelectric Thin Films Deposited by Pulsed Laser Deposition on Oxide and Fluoride Substrates - S. Sengupta, L. C. Sengupta, S. Stowell, E. Ngo and W. E. Kosik	70
Characterization of Sputter-Deposited ( $\text{Ba,Sr}$ ) $\text{TiO}_3$ Thin Films on the Sidewalls of Fine- Patterned Electrodes - S. Yamamichi, K. Takemura, T. Sakuma, H. Watanabe, H. Ono, K. Tokashiki, E. Ikawa and Y. Miyasaka	74

### Concurrent Session - 3B: Dielectrics

A Model for Describing Current-Voltage Characteristics of $\text{SrTiO}_3$ Capacitors Under Low Electric Fields - Yukio Fukuda, Ken Numata, Katsuhiko Aoki and Akitoshi Nishimura	79
Relating Local Electric Field in A Ferroelectric Capacitor to Externally Measurable Voltages - Francis K. Chai, J. R. Brews, R. D. Schrimpf, and Sungchul Lee	83
Fine Grain Barium Titanate: Ferroelectric Domains and X-Ray Diffraction Diagram - F. Batllo, N. Floquet, M. Maglione, M. Mesnier, J. C. Niepce, P. Perriat, P. Sarrazin and C. M. Valot	87
The Domain Mechanism of Aging and Degeneration of Ferroelectric Material - A. S. Sidorkin	91

### Poster Session P1: Piezoelectrics

Fine PMN Powders Prepared from Nitrate Solutions - Yoshio Yoshikawa	95
Phase T, $x$ -Diagram of $\text{Pb}_{1-x}\text{Ca}_x\text{TiO}_3$ Single Crystals - V. V. Eremkin, V. G. Smotrakov, L. E. Balyunis, S. I. Shevtsova, A. T. Kozakov	97
Effect of Calcia Additions on the Electromechanical Properties of Samarium-Modified Lead Titanate Ceramics - W. R. Xue, P. W. Lu and W. Huebner	101
Effects of Lanthanum Doping on The Grain Size and Piezo-Electric Properties of Lead Titanate Ceramics - P. Talwar, R. P. Tandon and Abhai Mansingh	105
Structural and Thermal Study of $\text{Pb}(\text{Zr}, \text{Ti}, \text{Ce})\text{O}_3$ Ceramics - E. Ching-Prado, W. Perez, R. S. Katiyar, Ajay Garg and D. C. Agrawal	108
The Influence of Processing Parameters on the Physical Characteristics of Doped Lead Titanate Ceramics - A. Ahmad, T. A. Wheat, M. Hirsch and A. G. McDonald	111
PZT Ceramics from Hydrothermally Synthesized Powders - C. H. Lin, T. S. Chin, S. C. Pei, J. Y. Huang and C. H. Li	115
Fabrication of High Density, Fine-Grained PZT Ceramics Using a Post Sintering HIP Treatment - C. E. Millar, B. Andersen, E. Ringg�ari, W. Wolny, J. Ricote and L. Pardo	118



A Study of the Sintering Mechanism of PZT-Based Piezoceramics - P. W. Lu, W. R. Xue and W. Huebner	122
Electric Field Assisted Hot Forging of Bismuth Titanate - P. A. Fuierer and A. Nichtawitz	126
Spray Pyrolysis Synthesis of Lead Magnesium Niobate Relaxor Ferroelectric Powders - J. G. Marx and W. Huebner	130
Investigations of the Phase Diagram of The $\text{PbTiO}_3$ - $\text{BiFeO}_3$ System - P. W. Lu, W. M. Zhang, W. R. Xue, X. F. Wang and W. Huebner	134
Effect of Processing on Surface Acoustic Wave Properties of a Modified Lead Titanate Ceramic - C. E. Millar, L. Pedersen, L. Pardo, J. Ricote, C. Alemany, B. Jimenez, G. Feuillard and M. Lethiecq	138
Piezoceramic Materials with Very Large Anisotropy of Piezoelectric Coefficients: Physical Aspects of the Problem - A. V. Turik and V. Yu. Topolov	142
Averaging Physical Constants and the Problem of Connection Between Piezoelectric Properties of Single-Crystal and Ceramic Ferroelectrics - A. V. Turik, V. Yu. Topolov and A. I. Chernobabov	144
Electromechanical Properties of Rainbow Devices - E. Furman, G. Li and G. H. Haertling	146
Microstructural Effects on the Electromechanical Properties of PZT-BF Ceramics - W. Huebner, W. R. Sue and P. W. Lu	150
Evaluation of Barium Doped PZT Ceramics for Underwater Hydrophone Applications - K. Trinath, B. S. Sarma, N. S. Prasad and A. Bhanumathi	154
Increased Operating Temperature Range in La-Modified $(\text{Pb}(\text{Mg}_{1/3}\text{Nb}_{2/3})\text{O}_3 - \text{PbTiO}_3$ Relaxor Ferroelectric-Based Transducers - J. T. Fielding, Jr, T. R. Shrout and S. J. Jang	158
Sample Aspect Ratio Influence on the Shear Coefficients Measurements of a Piezoelectric Bar - N. Aurelle, D. Roche, C. Richard and P. Gonnard	162
On Elastic Dipoles in Li Metaniobate Ceramics - L. A. Reznitchenko, E. I. Bondarenko and A. N. Klevtsov	166
Temperature Stability of Resonance Frequency of Filter Materials Obtained by Different Techniques - S. V. Gavril'yatchenko, A. Ya. Dantsiger, L. A. Reznitchenko, O. N. Razumovskaja and A. N. Klevtsov	168
Data Bank on Properties and Applications of Ferro- Piezoelectrics Materials - A. Ya.Dantsiger, L. A. Reznitchenko, O. N. Razumovskaja, S. I. Dudkina, N. V. Dergunova, S. V. Gavril'yatchenko, R. U. Devlikanova and A. P. Naumov	170
High-Efficiency Transducers for Acoustic Diagnostics on the Basis of Novel Anisotropic Piezoelectric Materials - V. M. Shikhman and L. D. Grineva	172
High-Efficiency Ferro-Piezoceramics PCR-Type Materials for Various Applications - A. Ya. Dantsiger, O. N. Razumovskaya, L. A. Reznitchenko, L. D. Grineva, S. I. Dudkina, S. V. Gavril'yatchenko and N. V. Dergunova	175
Piezoceramic Materials for Filters with Large Guaranteed Decay - S. V. Gavril'yatchenko and A. Ya. Dantsiger	178
On the Specific Features of Anisotropy in Piezoelectric Properties of High-Temperature Ferroelectric Ceramics - L. A. Reznitchenko and E. I. Bondarenko	179

The Origins of Electromechanical Response in Polyurethane Elastomers - H. Wang, Q. M. Zhang, L. E. Cross, R. Ting, C. Coughlin and K. Rittenmyer . . . . .	182
Theoretical Equations for Dielectric, Elastic and Piezoelectric Constants of Diphasic Composite Changing its Connectivity From 3-0 to 0-3 Via 3-3 - Hisao Banno . . . . .	186
Piezoelectric Composites: Thermal Stabilization and Improvement of Properties - L. N. Syrkin, E. T. Kancherova and N. N. Feoktistova . . . . .	190
Piezoelectric Properties of 1-3 Composites of PZT in P(VDF-TrFE) Copolymer - K. W. Kwok, H. L. W. Chan and C. L. Choy . . . . .	194
Study of PZT4/VF <sub>2</sub> /VF <sub>3</sub> Piezoelectric 0-3 Composites - H. L. W. Chan, Y. Chen and C. L. Choy . . . . .	198
Characterization of PZT Hollow-Sphere Transducers - J. T. Fielding, Jr., D. Smith, R. Meyers, Jr., S. Troler McKinstry and R. E. Newnham . . . . .	202
Fabrication of 2-2 Connectivity PZT/Thermoplastic Composites for High Frequency Linear Arrays - W. Huebner, M. R. Reidmeyer, J.W. Stevenson and L. Busse . . . . .	206
Rochelle Salt Nanocrystals Embedded in Porous Glasses - E. K. Jang, J. W. Woo and I. Yu . . . . .	210
Lead Zirconate Titanate-Lead Silicate Piezoelectric Glass-Ceramics - Boen Houng and Michael J. Haun . . . . .	214
Electric Properties and Domain Structures in Ba(Ti,Sn)O <sub>3</sub> Ceramics - Ki-Young Oh, Kenji Uchino and L. Eric Cross . . . . .	218
Influence of Proton-Exchange Conditions on Ferroelectric Domain Inversion Caused in LiTaO <sub>3</sub> Crystals - Ailie Tourlog and Kiyoshi Nakamura . . . . .	222
HREM Studies of Ordered Superstructure in PMN and PLMN Ceramics - Liu Yinmei, Song Chengyu and Wen Baosong . . . . .	226
Controlled Chaos in Ferroelectric Systems - R. Habel, S. Blochwitz and H. Beige . . . . .	229
Thinned Ferroelectric Crystals and Ceramics - Susan Troler-McKinstry . . . . .	233
Brillouin Scattering in Single Crystals of Rb <sub>1-x</sub> (ND <sub>4</sub> ) <sub>x</sub> D <sub>2</sub> AsO <sub>4</sub> - Chi-Shun Tu and V. Hugo Schmidt . . . . .	237
Ferroelectric Transition in the Ternary System of Pb(Mg <sub>1/3</sub> Nb <sub>2/3</sub> )O <sub>3</sub> - La(Mg <sub>2/3</sub> Nb <sub>1/3</sub> )O <sub>3</sub> - PbTiO <sub>3</sub> - T. B. Wu, K. S. Liu and J. L. Chen . . . . .	241
Dielectric and Piezoelectric Properties of Ceramics in the Lead Indium Niobate-Lead Scandium Tantalate Solid Solution - Edward F. Alberta and Amar S. Bhalla . . . . .	245
An Evaluation of Lead-Zirconate Based Ceramics for Use as Non-Volatile Ferroelectric Memory Devices - Edward F. Alberta and Amar S. Bhalla . . . . .	249
Ferroelectric Ceramics in the Na <sub>0.5</sub> Bi <sub>0.5</sub> TiO <sub>3</sub> - K <sub>0.5</sub> Bi <sub>0.5</sub> TiO <sub>3</sub> , Na <sub>0.5</sub> Bi <sub>0.5</sub> TiO <sub>3</sub> - PbTiO <sub>3</sub> and K <sub>0.5</sub> Bi <sub>0.5</sub> TiO <sub>3</sub> -PbTiO <sub>3</sub> Systems - O. Elkechai and J. P. Mercurio . . . . .	253
Ferroelectric Properties of the Mixed Aurivillius Phase Bi <sub>7</sub> Ti <sub>4</sub> NbO <sub>21</sub> - R. Maalal, M. Manier, J. P. Mercurio and B. Frit . . . . .	257
Enhanced Densification of SrTiO <sub>3</sub> Perovskite Ceramics - Kuo-Shung Liu and I-Nan Lin . . . . .	261
Phase Transition of Ferroelectric (Na <sub>1/2</sub> Bi <sub>1/2</sub> )TiO <sub>3</sub> - Seung-Eek Park and Su-Jin Chung . . . . .	265
Microstructural Studies of Modified SBN Ceramics - S. Narayanan Murty, S. Bangar Raju, A. Bhanumathi, G. Padmavathi and K. Linga Murty . . . . .	269
Frequency Response of MgO:LiNbO <sub>3</sub> Crystals - B. M. Jin, A. S. Bhalla, I. W. Kim and B. C. Park . . . . .	273

Lithium Niobate Single Crystals with Improved Sound Speed Resistant to the Light Influence - N. I. Deriugina and M. K. Sheinkman . . . . .	277
Growth and Characterization of $\text{MgO}:\text{LiNbO}_3$ Crystals - I. W. Kim, B. M. Jin, A. S. Bhalla and J. W. Kim . . . . .	279
Studies on Ag and Pb Doped Bi-Sr-Ca-Cu-O Superconductors - V. Syamalamba, S. Narayanan Murty, G. Padmavathi, K. V. Ramana Murthy and Ch. V. V. Satyanarayana . . . . .	283
Dielectric and Piezoelectric Properties of Stacked and Plated PVDF, P(VDF/TeFE), P(VDF/TrFE) and Ceramic/Rubber Composite Thick Films - Philip E. Bloomfield . . . . .	287

#### **Concurrent Session - 1C: Piezoelectrics**

Development of 1-3 PZT-Polymer Composite for Low Frequency Acoustical Applications - C. Richard, R. Y. Ting and C. Audoly . . . . .	291
Fine-Scale, Large Area Piezoelectric Fiber/Polymer Composites for Transducer Applications - V. F. Janas, S. M. Ting, S. Livneh, F. R. Walker, R. Schaeffer, T. F. McNulty and A. Safari . . . . .	295
3-3 Composite Hydrophones from Distorted Reticulated Ceramics - Matthew J. Creedon, Sodhakar Gopalakrishnan and Walter A. Schulze . . . . .	299

#### **Concurrent Session - 2C: Thin Films**

Comparison of the Properties of $\text{Pb}(\text{Zr,Ti})\text{O}_3$ Thin Films Obtained by MOCVD Using Different Source Materials - Tadashi Shiosake and Masaru Shimizu . . . . .	303
Physical Vapor Deposition of Antimony Sulpho-Iodide ( $\text{SbSI}$ ) Thin Films and Their Properties - Narayanan S. and R. K. Pandey . . . . .	309

#### **Concurrent Session - 4A: Actuators and Electrostriction**

Compositional Study of PLZT Rainbow Ceramics for Piezo Actuators - Gene H. Haertling . . . . .	313
Piezoelectric Actuators/Ultrasonic Motors - Their Development and Markets - Kenji Uchino . . . . .	319
Fatigue Behavior of Multilayer Piezoelectric Actuators - B. Zickgraf, G. A. Schneider and F. Aldinger . . . . .	325

#### **Concurrent Session - 1C: Piezoelectrics**

Ultrasonic Piezoceramic-Polymer Composite Transducer---Dynamic Behavior and Effects of Heterogeneous Structure - Q. M. Zhang, X. Geng, Y. Shui, Wenwu Cao and L. E. Cross . . . . .	329
High Pressure Applications of Ferroelectric Polymers - Francois Bauer . . . . .	333
High Frequency Dielectric and Electromechanical Properties of Ferroelectric Nylons - L. F. Brown, J. I. Scheinbeim and B. A. Newman . . . . .	337

Dependence on Supramolecular Structure and on Charge Injection Conditions of Ferroelectric Switching of PVDF and its Blends with PMMA - A. Becker, M. Stein and B.-J. Jungnickel .....	341
--	-----

#### **Concurrent Session - 2C: Thin Films**

Characteristics of NDRO Ferroelectric FETs with a Poly-Si Floating Gate - Takashi Nakamura, Yuichi Nakao, Akira Kamisawa and Hidemi Takasu .....	345
Ferroelectric Thin Film Bismuth Titanate Prepared from Acetate Precursors - Yanxia Lu, Walter Schulze, David Hoelzer, Bruce Tuttle and B. G. Potter .....	348

#### **Concurrent Session - 4A: Actuators/Electrostriction**

Electrostriction Measurements in Diffuse Phase Transition Materials and Perovskite Glass Ceramics - V. Sundar, R. E. Newnham, D. McCauley, K. Wa Gachigi and K. A. Markowski .....	353
Electro-Mechanical Coupling in 8/65/35 PLZT- Christopher S. Lynch .....	357
Incommensuration in "Dirty" Antiferroelectrics - Z. Xu, Xunhu Dai and Dwight Viehland .....	361
Field-Induced Piezoelectric Materials for 100kHz - 10MHz Transducers Applications - J. T. Fielding, Jr., S. J. Jang and T. R. Shrout .....	363

#### **Concurrent Session - 3C: Dielectrics**

The Application of Microwave Ceramics - Takashi Okawa .....	367
Investigation of Aging Effects From High Voltage Profiles in Ceramic Phase-Shifter Materials - S. Stowell, L. C. Sengupta, E. Ngo, M. E. O'Day and R. Lancto ..	372

#### **Concurrent Session - 1D: Piezoelectrics**

Electro-Mechanical Characteristics of Lead-Zirconate-Titanate Ceramics Under Vibration-Level Change - Sadayuki Takahashi, Seiji Hirose, Kenji Uchino and Ki-Young Oh .....	377
Typical Characteristics of a Piezoelectric Ceramic Material for Squeeze Igniters - D. Audigier, L. Eyraud, P. Eyraud, F. Eyraud, N. Glissa, P. Gonnard, M. Troccaz and M. Sprumont .....	383
Investigation on Piezoelectric Ceramics with High $d_{33}$ , $d_{31}$ for a New Type of Rotational Stepper Motor - Zhilun Gui, Wei Zhong, Shuxiang Dong, Longtu Li and Xiaowen Zhang .....	387
The Dielectric Piezoelectric and Hydrostatic Properties of PLZT Based Rainbow Ceramics - S. Sherit, H. D. Widerick, B. K. Mukherjee and G. H. Haertling .....	390
Nonlinear Stress-Strain Behavior of Piezoelectric Ceramics Under Tensile Loading - Toshio Tanimoto, Kohji Yamamoto and Tohru Morii .....	394

### Concurrent Session: 2D: Thin Films

Sol-Gel Barium Titanate Thin Films on Nickel Alloy Electrodes - T. Ogawa, S. Saitoh, O. Sugiyama, A. Kondoh, T. Mochizuka and H. Masuda . . . . .	399
Rapid Thermal Processing of Sol-Gel Derived PZT 53/47 Thin Layers - Charles D. E. Lakeman, Zhenkui Xu and David A. Payne . . . . .	404
The Formation of a Fine-Patterned Ferroelectric Thin Film from a Sol-Gel Solution Containing a Photo-Sensitive Water-Generator - Nobuyuki Soyama, Go Sasaki, Tsutomu Atsuki, Tadashi Yonezawa and Katsumi Ogi . . . . .	408
PZT-Film Compositional Development and Physical Properties - H. Schönecker, H.-J. Gesemann, S. Merklein, W. Grond, K. Franke and M. Weihnacht . . . . .	412
Antiferroelectric to Ferroelectric Phase Switching Thin Films in the Lead Zirconate Titanate Solid Solution System - C. J. Gaskey, K. R. Udayakumar, H. T. Chen and L. E. Cross . . . . .	416

### Poster Session - P2: Thin Films

Structure and Optical Properties of $\text{PbTiO}_3$ - $\text{SiO}_2$ Nanocomposites Through Sol-Gel Technique - Qifa Zhou, Jinxiu Zhang, Liangying Zhang and Xi Yao . . . . .	419
Precursor Dependent Properties of $\text{Ba}_{1-x}\text{Sr}_x\text{TiO}_3$ Thin Films Fabricated by Sol-Gel Method - J. Kim, S.-I. Kwuan and J.-G. Yoon . . . . .	423
Sol-Gel Preparation of Barium Strontium Titanate Thin Films - D. Tahan, A. Safari and L. C. Klein . . . . .	427
Pulsed Laser Deposition (PLD) of Ferroelectric Thin Films in Conjunction with Superconducting Oxides - S. Sengupta, L. C. Sengupta and W. E. Kosik . . . . .	431
Lower Temperature Crystallization and Ordering in Sol-Gel Derived $\text{Pb}(\text{Sc}_{0.5}\text{Ta}_{0.5})\text{O}_3$ Powders and Thin Layers - Donhang Liu and David A. Payne . . . . .	435
Preparation of Epitaxial $\text{LiNbO}_3$ Films by the Sol-Gel Method - Kazuya Terabe, Nobuo Iyi, Hisayoki Suematsu, Yoshio Matsui, Kenji Kitamura and Shigeuki Kimura . . . . .	439
Preparation and Characterization of Manganese Doped Lead Titanate Films by Sol-Gel Techniques - R. P. Tandon, V. Raman, Ramadhar Singh and Amarjeet K. Narula . . . . .	443
Effects of Sol-Gel PZT Film Thickness and Electrode Structure on the Electrical Behavior of Pt/PZT/Pt Capacitors - E. A. Kneer, D. P. Birnie III, G. Teowee and J. C. Podlesny . . . . .	446
Electrical Properties of PZT Thin Films Derived From Sol-Gel Solution Containing Photo-Sensitive Water-Generator - Yuichi Nakao, Takashi Nakamura, Akira Kamisawa, Hidemi Takasu, Nobuyuki Soyama, Go Sasaki, Tsutomu Atsuki, Tadashi Yonezawa and Katsumi Ogi . . . . .	450
Mechanisms Controlling Phase Formation in PZT Thin Films - S. B. Majumder, D. C. Agrawal, Y. N. Mohapatra and V. N. Kulkarni . . . . .	454
Sol-Gel Processed Ferroelectric Barium Titanate Thin Films and Ceramics - H. Basantakumar Sharma and Abhai Mansingh . . . . .	457
Process/Structure/Property Relations of Barium Strontium Titanate Thin Films Deposited by Multi-ion-Beam Sputtering Technique - C.-J. Peng and S. B. Krupanidhi . . . . .	460

Study of $\text{Ba}_{1-x}\text{SrTiO}_3$ (100) Epitaxial Thin Films Prepared by Laser Deposition - Naijuan Wu, He Lin, Kan Xie, X. Y. Li, Jia Li and Alex Ignatiev	464
Processing and Characterization of Ferroelectric Thin Films in the $\text{Pb}_5\text{Ge}_3\text{O}_{11}$ - $\text{PbZr}_{0.5}\text{Ti}_{0.5}\text{O}_3$ System - Steven M. Landin and Michael J. Hann	468
Paraelectric Properties of PLT (28) Reactively Sputtered by Multi-Element Metal Target - H. H. Kim, K. S. Sohn, L. M. Casas, R. L. Pfeffer and R. T. Lareau	472
Ferroelectric Properties of $(\text{Pb},\text{La})\text{TiO}_3$ Thin Films by Multiple Cathode Sputtering - Hiroshi Maiwa, Noboru Ichinose and Kiyoshi Okazaki	476
Properties of $\text{PbTiO}_3$ Grown by Multiple Magnetron Sputtering Method - R. C. Hoffmann, Krishnan K. Deb and D. A. Jackson	480
Annealing Effects on the Polarity of Stored Charge of $\text{BaTiO}_3$ Films on Si - L. H. Chang and W. A. Anderson	482
Preparation of $\text{Bi}_4\text{Ti}_3\text{O}_{12}$ Thin Films by Reactive Magnetron Sputtering Using Metal Target and Their Evaluations - T. Tamamoto and H. Matsuoka	485
RF-Sputtered $\text{LiNbO}_3$ Films for Piezoelectric Applications - Azamat Bakirov, Aron Margolin, Larisa Reznichenko, Evgeny Sviridov and Vladimir Dudkevich	488
The Growth Behavior of Pb-Containing Perovskite Thin Films Using Pulsed Laser Deposition Technique - I-Nan Lin, Kuo-Shung Liu, Shun-Lih Tu and Sheng-Jenn Yang	491
Development and Electrical Characterization of Lead Zirconate Titanate Thick Films on Silicon Substrates - H. D. Chen, K. R. Udayakumar, L. E. Cross, J. J. Bernstein and L. C. Niles	495
The Structural Phase Transition in PZT Ferroelectric Films - Lev Sapozhnikov, Irina Sem, Irina Zakhazchenko, Evgeny Sviridov, Vladimir A. Alyoshin and Vladimir Dudkevich	499
The Control of Ferroelectric Film Texture upon RF Sputtering - Azamat Bakirov, Evgeny Sviridov and Vladimir Dudkevich	502
Low Frequency AC Conduction and Dielectric Relaxation in PVDF Films - Ramadhar Singh, R. P. Tandon, R. D. P. Sinha and Subhas Chandras	504
Effect Post Deposition Annealing on Sputtered Zinc Oxide Film - Vinay Gupta and Abhai Mansingh	508
Processing and Characterization of Samarium and Manganese Modified Lead Titanate Thin Film - Chen-Lung Fan and Wayne Huebner	512
Relationships Between Thermal Treatment and Properties of PLT Thin Films - Yun Liu, Liangying Zhang and Xi Yao	516
Piezoelectric Response of PZT Thin Film Actuated Micromachined Silicon Cantilever Beams - K. G. Brooks, D. Damjanovic, N. Setter, Ph. Luginbuhl, G. A. -Racine and N. F. de Rooij	520
Fatigue and Retention Behaviors of Pt-PZT-Metal Capacitors with Various Top Metallizations - G. Teowee, C. D. Baertlein, J. M. Boulton, E. L. Quackenbush and D. R. Uhlmann	523
Electrode Stress Effects on Electrical Properties of PZT Thin Film Capacitors - Isub Chung, I. K. Yoo, W. Lee, C. W. Chung and J. K. Lee	527
Breakdown in Lead Zirconate Titanate (PZT) Thin Film Capacitors - In Kyeong Yoo and Seshu Babu Desu	531

Heat Flow and $D^*$ of Multilayer Thin Film Pyroelectric Detector - Q. Kang, W. G. Liu, L. Y. Zhang and X. Yao	535
Nucleation Crystallization Behavior of MOD Derived PZT Thin Film - Si-Bei Xiong, Xiao-Qing Wu, Liang-Ying Zhang and Xi Yao	539
The Structural and Acoustic Properties of Sputtered Aluminum Nitride on Silicon - F. S. Hickernell and H. M. Liaw	543
Electrical Properties of PZT Thin Films with Ir and $\text{IrO}_2$ Electrodes - Takashi Nakamura, Yuichi Nakao, Akira Kamisawa and Hidemi Takasu	547
Electrical Conduction and Dielectric Behaviour of $\text{Ge}^{4+}$ -Substituted Magnesium Ferrites - D. R. Sagar, S. N. Chatterjee, Chandra Prakash and Pran Kishan	551
Dielectric Properties and D. C. Resistivity of Magnesium-Substituted Lithium Ferrites - Sumitra Phanjoubam, Deepika Kothari, Chandra Prakash and Pran Kishan	554

### Poster Session P3: Dielectrics

Investigation of $\text{Bi}_{0.5}\text{Na}_{0.5}\text{TiO}_3$ - $\text{PbTiO}_3$ System for High Temperature Dielectrics - S. Kuharungrong and W. A. Schulze	559
Supercritical Drying of Barium Titanate Alcogels - G. D. Pethybridge, P. J. Dobson and R. J. Brook	562
Parametric Small Signal Amplification Near Bifurcations - M. Diestelhorst, H. Beige and R. P. Kapsch	564
Pore-Dependent Dielectric and Electrical Properties of Barium Titanate Ceramic - Kyeong Ho Cho and Hee Young Lee	566
Degradation Behavior of Ca-Doped Barium Titanate Ceramic Capacitors - Min Huh, Kyeong Ho Cho, Hyo-Duk Nam and Hee Young Lee	572
Dielectric Breakdown in PLZT 9.5/65/35 Ceramics - E. Furman and L. E. Cross	577
Correlation of Wettability and Interfacial Reaction to the Densification and Dielectric Properties of Fluxed- $\text{BaTiO}_3$ - Sea Fang Wang, Wayne Huebner and Joseph P. Dougherty	581
Low-Firing $\text{Pb}(\text{Mg}_{1/3}\text{Nb}_{2/3})\text{O}_3$ - $\text{PbTiO}_3$ - $\text{Pb}_5\text{Ge}_2\text{SiO}_{11}$ Compositions for Thick-Film Capacitor Applications - Y. D. Kim, S. M. Landin, I. A. Cornejo and M. J. Huan	585
Transmission Electron Microscopy Observation of an Incommensurate-Commensurate Transformation in Tin-modified Lead Zirconate Titanate - Z. Xu, Dwight Viehland, and D. A. Payne	589
Reaction Sequence of Perovskite Formation Process in PFW-PFN System by B-Site Precursor Method - Kyung Ki Min and Nam Kyoung Kim	591
Transmission Electron Microscopy Study of Strontium Barium Niobate Relaxors - Z. Xu, Weng-Hsing Huang, Dwight Viehland and R. R. Neurgaonkar	595
The Effect of High Temperature HIPing and Annealing on the Dielectric Properties of Modified Lead Titanate Ceramics - M. R. Cockburn, D. A. Hall and C. E. Millar	597
Loosely Associated Ion Interaction in the Oxide and Oxyfluoride Pyrochlores - Xiukai Cai, Liangying Zhang and Xi Yao	601
The Structure and Dielectric Properties of New Oxyfluorides - Xiukai Cai, Liangying Zhang and Xi Yao	604

Dielectric Properties and Low Temperature Relaxation Studies of Doped TGS Single Crystals - B. M. Jin, S. Erdei and A. S. Bhalla . . . . .	607
Non-Linear Dielectric Properties of $\text{KTa}_{1-x}\text{Nb}_x\text{O}_3$ - R. K. Pattnaik and J. Toulouse . . .	611
Dielectric Permittivity in Paraelectric/Ferroelectric Coexistence Region in Several Proton Glasses - F. L. Howell, I. L. Fundaun and S. Stadler . . . . .	614

### Poster Session P3MD/S: Microwave Dielectrics

Effect of Perovskite Impurity Addition on Microwave Dielectric Properties of $\text{Ba}(\text{Mg}_{1/3}\text{Ta}_{2/3})\text{O}_3$ - $\text{Ba}(\text{Ni}_{1/3}\text{Ta}_{2/3})\text{O}_3$ Ceramics - Shin-Young Kim, Hee Young Lee, Cheul-Kee Yang, Jeong-Joo Kim, Tae Hong Kim and Tae Goo Choy . . . . .	617
Fabrication & Characterization of Barium Strontium Titanate and Non-Ferroelectric Oxide Composites for Use in Phased Array Antennas and Other Electronic Devices - L. C. Senupta, E. Ngo, M. E. O'Day, S. Stowell and R. Lancto . . . . .	622
Microwave Dielectric Properties of $\text{BaO-TiO}_2\text{-WO}_3$ Ceramics Sintered with Glasses - Takahiro Takada, Sea Fue Wang, Shoko Yoshikawa, Sei-Joo Jang and Robert E. Newnham . . . . .	626
Dielectric Properties of Strontium and Lead Based Complex Perovskite Ceramics - S. A. Gridnev, N. G. Pavlova, S. P. Rogova, L. N. Korotkov and V. V. Zaentsev . . . . .	630

### Concurrent Session - 5A: Photorefractives

The Use of Applied Electric Fields on the Photorefractive Tungsten Bronze Ferroelectrics - Nianyu Bei, Galen C. Durce, Gregory J. Salamo, Rakesh Kapoor, Edward J. Sharp and Ratnaker R. Neurgaonkar . . . . .	633
Ce:Fe:LiNbO <sub>3</sub> Photorefractive Crystal: Material Properties and Applications - F.T.S. Yu, A. S. Bhalla, S. Yin, F. Zhao, Z. Wu and D. M. Salerno . . . . .	636

### Concurrent Session - 6A: Pyroelectrics

Uncooled Infrared Focal Plane Arrays - Paul W. Kruse . . . . .	643
Ferroelectric Ceramics and Thin Films for Uncooled Thermal Imaging Arrays - A. Patel, P. C. Osbond, N. M. Shorrocks, R. C. Twiney, R. W. Whatmore and R. Watton . . . . .	647
High Performance Infrared Detector Array Using Thin Film Microstructures - B. Cole, R. Horning, B. Johnson, K. Nguyen, P. W. Kruse and M. C. Foote . . . . .	653
Uncooled Pyroelectric Thermal Imaging - Charles Hanson and Howard Beratan . . . . .	657

### Concurrent Session - 2E: Thin Films

Dielectric Response of Ferroelectric Films - A. Mansingh and M. Sayer . . . . .	663
Switching in Ferroelectric Thin Films: How to Extract Information About Domain Kinetics from Traditional Current Data - V. Ya. Shur, E. L. Romyantsev, S. D. Makarov and V. V. Volegov . . . . .	669



Ferroelectric Materials for Thin-Film and Membrane Resonators - Arthur Ballato, John G. Gualtieri and John A. Kosinski . . . . .	674
--	-----

#### **Concurrent Session - 5A: Photorefractives**

Mutually Pumped Phase Conjugation with High Spatial Resolution - Jan M. Yarrison-Rice, Edward J. Sharp, Gary L. Wood, Gregory J. Salamo, Richard J. Anderson, Ratnakar R. Neurgaonkar and Robert Klanck . . . . .	681
Large Electrooptic Modulation Using Ferroelectric Thin Films in a Fabry-Perot Cavity - Feiling Wang and Gene H. Haerting . . . . .	683
Liquid Delivery CVD of PLZT Thick Films for Electro-Optic Applications - J. F. Roeder, S. M. Bilodeau, P. C. Van Buskirk, V. H. Ozguz, J. Ma and S. H. Lee . . . . .	687

#### **Concurrent Session - 6A: Pyroelectrics**

PbTiO <sub>3</sub> Thin Films for Pyroelectric Detection - A. Bell, Y. Huang, O. Paul, P. Ryser and M. Forster . . . . .	691
Effect of Simultaneous Organic and Inorganic Dopants on the Characteristics of Triglycine Sulfate (TGS) Crystals - R. B. Lal, S. Etminan and A. K. Batra . . . . .	695
Pyrotransistor - GaAs FET with a "Pyroelectric Wafer" Gate - Y. M. Poplavko, V. A. Moskalyuk, V. I. Timofeyev, and Y. V. Prokopenko . . . . .	698

#### **Concurrent Session - 2E: Thin Films**

Antiferroelectric/Ferroelectric Composite Thin Films - D. E. Dausch, F. Wang and G. H. Haertling . . . . .	701
--	-----

#### **Concurrent Session - 4B/1E: Electrostriction/Piezoelectrics**

Composite Transducers and Actuators - Robert E. Newnham and Kelley A. Markowski	705
Nonlinear Dynamics and Ferroelectric Materials - S. Blochwitz, R. Habel, M. Diestelhorst and H. Beige . . . . .	709
Study on Characteristics of Standing Wave Motors - Longtu Li, Shuxiang Dong, Zhilun Gui, Wei Pan and Xiaowen Zhang . . . . .	713
Mixing and Detection of Electrical Signals from 10 Hz to 20 GHz in an Electrostrictive Fiber Optic Sensor - S. T. Vohra and L. Fabiny . . . . .	717

#### **Concurrent Session - 5B/6B: Photorefractives/Pyroelectrics/Electrooptics**

Optically Induced Ferroelectric Domain Gratings in SBN: Theory and Applications to Quasi-Phase Matching and Optical Data Storage - Anthony S. Kewitsch, Mordechai Segev, Akio Saito, Amnon Yariv, Gregory J. Salamo, Terrence W. Towe, Edward J. Sharp and Ratnakar R. Neurgaonkar . . . . .	719
--	-----

The Design, Processing, Evaluation and Characterization of Pyroelectric PVDF Copolymer/Silicon Mosfet Detector Arrays - Philip E. Bloomfield, Francisco Castro and Roy M. Goeller . . . . .	725
---	-----

#### Poster Session P4: Actuators and Electrostriction

PTCR Characteristics of Single Grain Boundaries in Barium Titanate Ceramics - M. Kuwabara, K. Morimo, S. Takahashi, H. Shimooka and T. Matsunaga . . . . .	729
A Stress-Sensing Ceramic Device Based on PTCR Barium Titanate - Joseph S. Capurso and Walter A. Shulze . . . . .	731
The Development of High Sensitivity NTC Thermistors - Hiroshi Yamamoto, Akira Shibata, Keibunn Hajime, Fumio Takao, Katsuhiko Sugisawa, Yoshiyuki Niwatsukino, Hideki Shishiba and Shu-ichi Takeda . . . . .	735
Study on Piezoelectric Ceramic/Metal Composite Thin Plate of Driving Stator for Travelling- Wave Motor - Shuxiang Dong, Longtu Li and Xiaowen Zhang . . . . .	739
Photo-Acoustic Devices Using (Pb,La)(Zr,Ti)O <sub>3</sub> Ceramics - Sheng-Yuan Chu and Kenji Uchino . . . . .	743
Design Low Frequency Ultrasonic Transducers by 1-3 Tubular Piezocomposite - J. Chen, Q. M. Zhang, L. E. Cross and Michael Trottier . . . . .	746
Destruction Mechanism and Destruction Detection Technique for Multilayer Ceramic Actuators - Hideaki Aburatani, Kenji Uchino, Atushi Furuta and Yoshiaki Fuda . . . . .	750
Electrostrictive Properties of PbZrO <sub>3</sub> - K <sub>0.5</sub> Bi <sub>0.5</sub> TiO <sub>3</sub> Ceramics - S. A. Gridnev, N. G. Pavlova, and S. P. Rogova . . . . .	753
Optical Two Channel Elongation Measurement of PZT Piezoelectric Multilayer Stack Actuators - A. Wolff, D. Cramer, H. Hellebrand, I. Probst and K. Lubitz . . . . .	755
PTCR Characteristics in Undoped Barium Titanate Ceramics with Core-Shell Type Duplex Microstructure - M. Kuwabara, E. Matsuyama, S. Takahashi, H. Shimooka and Y. Urakawa . . . . .	758
Electrically-Induced Shape Changes in Cement-based Materials - Hua Ai, Jie-Fang Li and Dwight Viehland . . . . .	760
The Role of Statistical Design in the Development of Electrostrictive Materials S. E. Prasad, S. Varma, T. Hoang, T. A. Wheat and A. Ahmad . . . . .	762
High-Power Characteristics of Piezoelectric Materials - Seiji Hirose, Sadayuki Takahashi, Manabu Aoyagi and Yoshiro Tomikawa . . . . .	766
Flexi-Distortional Piezoelectric Sensor Results - W. B. Carlson, S. M. Pilgrim, W. A. Schulze, Y. S. Kato and J. M. Frommelt . . . . .	770

#### Poster Session P5: Photorefractives

Photorefractive Properties of Cr/Mo Co-Doped SBN:60 - Gary L. Wood, Brian P. Ketchel and R. R. Neurgaonkar . . . . .	773
Flux Growth of Bulk Photorefractive Barium Titanate Crystals - M. D. Aggarwal, W. S. Wang and J. Choi . . . . .	775

Growth and Properties of Tungsten-Bronze Ferroelectric Potassium Lithium Niobate Single Crystals for Optical Applications - Masatoshi Adachi, Zhiming Chen and Akira Kawabata . . . . .	778
Anisotropy of Speckle-Field in Barium-Sodium Niobate Crystals - S. V. Ivanova . . . .	781
Effects of Applied Stress on the Dielectric Properties of PLZT Thin Films - William E. Paradise, F. Wang and G. H. Haertling . . . . .	784
Electro-Optic Switching Behaviour of a Noval Shortpitch Ferroelectric Liquid Crystal Mixture - K. K. Raina and H. J. Coles . . . . .	788
Suspended Particle Flat Panel Displays Using Colloidal Particles - T. Li, T. Kido and J. H. Adair . . . . .	791
Microstructural and Optical Properties of Potassium Niobate Thin Films - Alice F. Chow, Daniel J. Lichtenwalner, T. M. Graettinger, James R. Busch, O. H. Auciello and A. I. Kingon . . . . .	794
Quantum Size Effects and Nonlinear Optical Properties of ZnS and CdS Semiconductor-Doped Silica Glasses Prepared by Sol-Gel Process - Qingchun Zhao, Chunliang Liu, Hongling Liu, Liangying Zhang and Xi Yao . . . . .	797

#### Poster Session P6: Pyroelectrics

Influence of $\gamma$ -ray Irradiation on the Thermochromic Phase Transition in Diethylammoniumtetrachlorocuprate - V. Kapustianik, S. Sveleba, Ya. Ozhybko, R. Tchukvinskyi, V. Soldatov, I. Polovinko and V. Mokryi . . . . .	801
Fabrication of Pyroelectric Thin Film Ceramics by Tape Casting Method - S. R. Zhang, C. W. Zhong, R. B. Liu, S. W. Lin, C. F. Qu, C. H. Yao, and Y. H. Jin . . . . .	804
Dielectric, Piezoelectric and Pyroelectric Properties of Barium-Modified Lead Magnesium Tantalate-Lead Titanate Ceramics - S. W. Choi and J. M. Jung . . . . .	806
Dielectric, Piezoelectric and Pyroelectric Properties of the $\text{Pb}(\text{Mg}_{1/3}\text{Ta}_{2/3})\text{O}_3$ - $\text{PbTiO}_3$ - $\text{PbZrO}_3$ Solid Solution System - H. Y. Weon, Y. J. Kim and S. W. Choi . . . . .	808
Dielectric, Piezoelectric and Pyroelectric Properties of Sr-Doped PMT-PT Solid Solution Ceramics - J. M. Jung, Y. H. Park and S. W. Choi . . . . .	810
Series Pyroelectric Ceramics Used for Small Area IR Detector - R. B. Liu, S. W. Lin, C. F. Qu, C. H. Yao, Y. H. Jin, Y. S. Lin and Y. R. Zhang . . . . .	812
Pyroelectric Ceramics with Low Resistivity - R. B. Liu, S. W. Lin, C. F. Qu, C. H. Yao and Y. H. Jin . . . . .	815
Pyroelectric and Dielectric Properties of Dry and Moist TGS-Gelatin Films - V. E. Khutorsky and Sydney B. Lang . . . . .	817
Inhomogeneity Study of Alanine and Valine-Doped TGS Crystal Using Micro-Probe Raman Spectroscopy - B. M. Jin, S. Erdei and A. S. Bhalla . . . . .	821
Pyroelectric Measurements on Various Kinds Doped TGS Single Crystals - B. M. Jin, S. Erdei and A. S. Bhalla . . . . .	825
Author's Index . . . . .	829
Attendees List . . . . .	835

# History Session

# Joseph Valasek and the Discovery of Ferroelectricity

Jan Fousek

Institute of Physics, Academy of Sciences  
of the Czech Republic, Na Slovance 2, 18040 Prague 8

**Abstract** - In 1921 Joseph Valasek recognized for the first time ferroelectric properties in a crystal, namely in Rochelle salt. In this lecture we review the story of this discovery, of Valasek's origin and career.

Ladies and gentlemen,

the field of our research is much alive. The programme of this very Symposium is a clear proof of this state-ment. To document the impressive activities going on in ferroelectricity and closely related subjects, we sometimes refer to the graph showing the number of publications devoted to ferroelectric research over the last seventy years, as reproduced in Fig.1 [1]. Certainly the slope is impressive. But rather than to comment on this, we wish to focus on the first peak on the curve. It extends over a few years after 1921. It is my honour as well as a pleasant task to say a few words about the scientist and also about the man whose name is intimately connected with this first significant mark in the history of ferroelectricity.

## VALASEK THE STUDENT

In 1919 the student Joseph Valasek begins his graduate work at the University of Minnesota in Minneapolis. Professor W. F. G. Swan, a physicist known e.g. by his theoretical work in cosmic rays physics but also known to have a wide overview in many other directions, suggests that Valasek studies physical properties of Rochelle salt single crystals.

Why Rochelle salt? Surely not because of its rather exotic structure and even less for its properties for work in the laboratory: a soft material, not very pleasant for sample preparation, very sensitive to humidity. On the positive side was the relative easiness of growing crystals. The decisive factor, however, was that it was already known to show piezoelectricity - stronger than quartz - and in addition it revealed other interesting properties such as pyroelectricity and optical activity. It must be recognized that the selection of compounds which were known to exhibit interesting properties and at the same time could be prepared in single crystalline form was very limited. Valasek himself, in his article [2] "Early history of ferroelectricity", describes the circumstances that led to the selection of Rochelle salt for a targeted research project:

- anomalous electro-optical properties were known, discovered by Pockels;
- it was known that under some conditions electromechanical properties were much stronger than those of quartz,
- but at the same time several unpleasant features were found: properties depended on temperature and electric field, but also on previous history of electrical and mechanical treatment and, of course, also on humidity;
- there was a need for sensitive electromechanical transducers for military purposes: submarine detection, location of large guns etc.

Looking at the last mentioned point, indeed one cannot escape a feeling of historical irony: has not the same aim been a driving force of concentrated research in ferroelectric ceramics at the time of the cold war?

Professor Swan realized that some effects observed in Rochelle salt resembled magnetic properties of iron. He proposed to develop methods of preparation of crystalline samples of Rochelle salt, and to study their properties with the aim of mastering their erratic behaviour and constructing a sensitive piezoelectric seismometer.

At that time, in 1919, Valasek was already to some extent experienced. Born on April 27, 1897 in Cleveland, Ohio, he got his bachelor's degree in physics at Case Institute of Technology where Prof. D. C. Miller started him on a career in physics. His first employment was at the National Bureau of Standards in Washington D.C., where he did research on the annealing of optical glass. In 1919 he came to the University of Minnesota as a graduate teaching assistant.

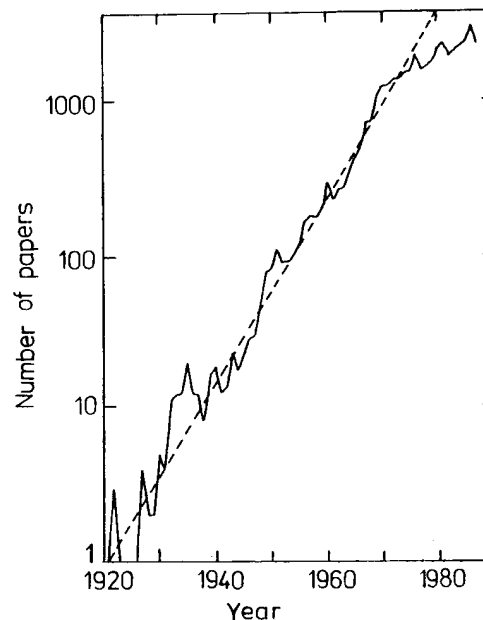


Fig.1 Number of publications concerning ferroelectricity [1].

Under Swan's supervision, Valasek works hard and soon proves his experimental skills. He obtains two large crystals of Rochelle salt from W. R. Whitney of General Electric Company. He masters techniques for very accurate sample preparation and constructs an apparatus for controlling humidity. In the two coming years he builds a number of set-ups for measuring diverse macroscopic properties: linear dielectric response, nonlinear dielectric properties, piezoelectric properties, dilatometry, very accurate refractive index measurements, pyroelectric phenomena. It is the nonlinear and slightly hysteretic dielectric response and the pyroelectric effect which build the bridge to ferroelectricity.

Its date and place of birth are April 23, 1920 and the Meeting of American Physical Society in Washington. Here Valasek presents a report [3] in which he states: "...the dielectric displacement  $D$ , electric intensity  $E$ , and polarization  $P$  ... are analogous to  $B$ ,  $H$ , and  $I$  in the case of magnetism." The data ... "is due to a hysteresis in  $P$  analogous to magnetic hysteresis. This would suggest a parallelism between the behavior of Rochelle salt as a dielectric and steel, for example, as a ferromagnetic substance. Bearing out this idea, typical hysteresis curves were obtained for Rochelle salt, analogous to the  $B$ ,  $H$  curves of magnetism." He also observed that the piezoelectric response vs.  $E$  behaves as susceptibility vs.  $E$ , being maximum where the slope of the hysteresis is large. Obviously, this was the consequence of stress-induced shifts of domain walls and resulting changes of average polarization. Thus already this first paper gave proof of simultaneous existence of ferroelectricity and ferroelasticity in Rochelle salt.

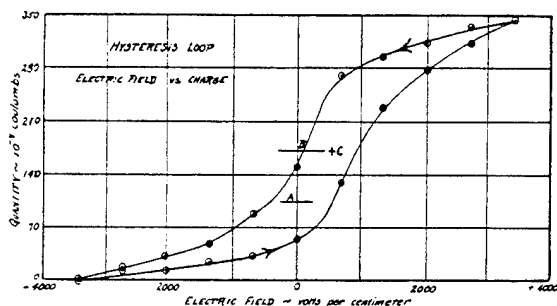


Fig 2 The first published hysteresis curve. Taken from Ref. 4.

The full version of this presentation was submitted to Physical Review in December 1920, entitled "Piezoelectric and allied phenomena in Rochelle salt" [4]. It marks two milestones. Here Valasek stated for the first time that "permanent polarization is the natural state" of Rochelle Salt. First hysteretic dependences of charge vs. electric field are given (cf. fig.2). In the same year he becomes Master of Arts.

Valasek's PhD Thesis "Piezo-electric activity of Rochelle salt under various conditions" is dated 1922. I found a copy of it in the University Library in Prague (fig. 3). Except for the title page the Dissertation is directly reprinted from the article in Physical Review [5]. Here the author gives new results on dielectric and piezoelectric properties, on the influence of electrode materials and on fatigue effects. He continues to fight serious moisture problems. Perhaps the history-making graph is that of the temperature dependence of piezoelectric response, indicating the existence of a relatively narrow temperature range of high piezoelectric activity, in fact indicating the existence of two phase transitions (fig.4). Indeed Valasek speaks here for the first time about the existence of two Curie points in Rochelle salt.

#### THE PAPER WHICH COULD SERVE AS A TEXT-BOOK ON CRYSTAL PHYSICS

However, the best publication, to my opinion, is still to come. It appears in Physical Review [6] the same year 1922 under the title "Properties of Rochelle salt related to the piezoelectric effect". Fig. 5 shows Valasek's photograph taken at this time.

This paper is a true textbook of crystal physics of that time. Here are presented precise measurements of refractive indices (with an accuracy of  $10^{-5}$ ) and their dispersion, fitted to the five-constants formula, as well as their temperature coefficients. Valasek built a dilatometer using the Fizeau method and measured thermal expansion along all axes. He studied temperature dependence of electric conductivity. He showed the validity of the Lorentz formula connecting density and refractive indices. He further measured optical activity of the water solution of Rochelle salt and also the Pockels effect. To measure electro-optic properties in the longitudinal geometry, transparent electrodes were needed. Valasek solved the problem by using alcohol electrodes not solving the crystal but having enough conductivity. Another section concerns the pyroelectric effect which was measured using an electrometer compensating system in a slow heating regime. An obvious maximum was found in the region of the upper Curie point.

## Piezo-Electric Activity of Rochelle Salt Under Various Conditions

BY  
J. VALASEK



A THESIS

SUBMITTED TO THE FACULTY OF THE GRADUATE SCHOOL OF THE UNIVERSITY OF MINNESOTA IN PARTIAL FULFILLMENT OF THE REQUIREMENTS FOR THE DEGREE OF DOCTOR OF PHILOSOPHY.

Reprinted from PHYSICAL REVIEW, Vol. XIX, No. 5, May, 1922.

Fig.3 Title page of Valasek's Thesis.

In the last chapter, Valasek discusses in detail the obvious discrepancy between his findings, i.e. the existence of piezoelectricity and pyroelectricity, and the symmetry of Rochelle Salt as revealed by the habitus of the crystals. The latter does not show any polar symmetry while the properties do. This would be a violation of Neumann's principle. A closer examination of the second crystal out of the two he had at his disposal indicated some polarity in its external form. Then, Valasek realizes, the symmetry would be lower and much more work would be needed to determine all tensorial properties allowed by symmetry. He suggests an X-ray analysis but finds it difficult for this type of organic crystalline compound.

This extensive publication shows Valasek at his best; as an ingenious and careful experimentalist who can devise complicated setups and think about the meaning and significance of the obtained data. We could only wish that our present PhD students, in addition to spending so much time in front of a computer reanalyzing and rescaling data collected automatically, would also show such devotion to what might be called "hard-ware experimenting" in the laboratory, including solving electrode or moisture problems.

One of Valasek's most prominent graduate students in the 1930's was Ray Pepinsky, later professor at Penn State where he discovered an impressive number of ferroelectric crystals. In his recollection on Valasek [7] he writes: "... He is a thoughtful and thorough scholar, a splendid experimentalist."

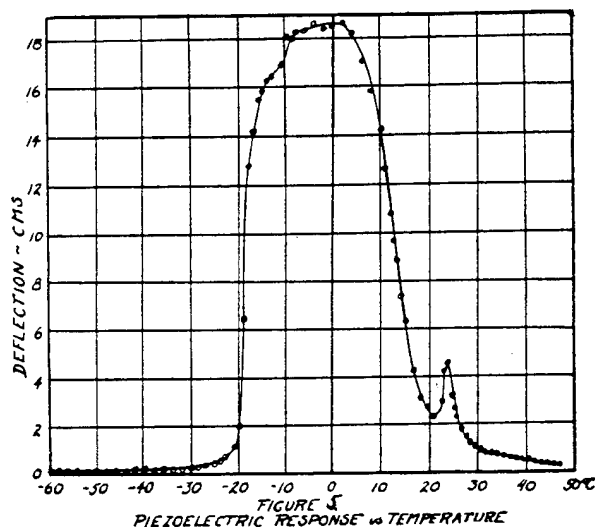


Fig.4 Piezoelectric activity of Rochelle salt vs. temperature indicates the existence of two phase transitions. Taken from ref. 5.

From the point of view of our present knowledge, it is tempting to speculate how further research would have been influenced if Valasek had done what every experimentalist does today when investigating a new material: if he had looked on a plate of Rochelle salt crystal in a polarizing microscope, in particular when tracing the hysteresis loop. The domains and their movement in this material are very easy to see. Such an observation could have considerably accelerated the development of our field. At that time even the ferromagnetic domains was a mere speculation and only in 1931 did Bitter [8] show the existence of a powder pattern on the surface of a ferromagnetic material. But as it happened, we had to wait for the concept of ferroelectric domains for quite a time and many strange phenomena occurring in the ferroelectric phases remained a mystery.

#### THE CONCEPT OF FERROELECTRICITY: SCHRÖDINGER, VALASEK OR MUELLER?

Altogether, Valasek published 6 papers in Physical Review on basic properties of Rochelle salt (cf. ref. 2). He did not work in a vacuum. His first papers became very soon widely cited and stimulated further research of Rochelle salt. He returned to the subject once more in 1934 when he initiated an infrared absorption study which led to the correct conclusion that molecules of crystalline water play no essential role in the large polarizability of the crystal.

No doubt that Valasek deserves our highest appreciation for the role he played in the first stages of ferroelectric research. The first points in fig. 1 are connected with his name. He was the first to state clearly [4] that "...the dielectric displacement  $D$ , electric intensity  $E$  and the polarization  $P$  are analogous to  $B$ ,  $H$  and  $I$  in the case of magnetism. Rochelle Salt shows an electric hysteresis analogous to the magnetic hysteresis in the case of iron". He was the first to use the concepts of spontaneous polarization and Curie points in connection with dielectrics.



Fig.5 Joseph Valasek in 1922.  
By courtesy of Mr. Josef Valášek, Sobětuš, Czech Republic.

Yet it is interesting to observe that he never used the word ferroelectricity. He probably was not aware of the fact that already in 1912 the famous Erwin Schrödinger proposed this concept [9] in his Habilitation Thesis "Studien über Kinetik der Dielektrika, den Schmelzpunkt, Pyro- und Piezoelektrizität" in connection with the idea that polar liquids might become spontaneously electrified when solidifying. "Man kann nämlich im ersten Augenblick glauben, daß nach dieser Auffassung des festen Zustandes alle Festkörper "ferroelektrisch" (s.v.v.) sein müßten." Please pay attention to the abbreviation s.v.v. It stands for Latin "sit venia verbo", meaning "let the word be allowed" or simply "with your permission". In this way Schrödinger emphasizes that he is coining a new concept. However, in the following sentence Schrödinger waives aside the existence of such ferroelectrics: "Wir werden sehen, daß dies nicht der Fall ist und die einzige Analogie zum Ferromagnetismus in der Piezo- und Pyroelektrizität finden."

Schrödinger's proposal was not known among true ferroelectricians. In the early post-Valasek era, mainly marked by the theoretical work in Russia and the establishment of the Zurich

school which led to the discovery of KDP as a ferroelectric, the name "Seignette-electricity" was frequently used, derived from Seignette Salt as an alternative name for Rochelle salt. It was only much later that Hans Mueller from MIT in his brilliant papers in which he showed the interrelations between different anomalies in Rochelle salt, introduced the term as we know it today. In 1935 [10] he first speaks modestly about the "ferro-dielectric state". It seems that at MIT a laboratory jargon developed since in the following Mueller's publication [11], in 1940, the concept of "ferroelectric temperature range" is used unhesitatingly without any comment. Quoting Helene Megaw [12]: "...perhaps the real reason for its [i.e. of the name Seignette-electricity] rejection ... is its failure to fit comfortably into the English language. As an adjective, >ferroelectric< is euphonious, while >Seignette-electric< grates on the ear".

#### VALASEK'S FURTHER CAREER

Let us now have a short look at the subsequent career of Joseph Valasek [13]. After becoming Doctor of Philosophy in 1922 he joins the School of Physics and Astronomy, University of Minnesota as an assistant professor and in 1928 he is promoted to associate professorship. At the end of the twenties he spends one year as a visiting scientist at the University of Uppsala in Sweden. Together with Prof. M. Siegbahn he works in X-ray spectroscopy.

It is this topic which remains in the foreground of his next activities. Within the period 1935 to 1965 he publishes a number of papers on X-ray spectroscopy. In 1941 he becomes full Professor at the University of Minnesota. His pedagogic activities are documented by two textbooks on optics he wrote. In 1965 he retires as the Professor emeritus of Physics.

When preparing this lecture I looked up recent volumes of the Scientific Citation Index. Under Joseph Valasek I found a number of citations. In addition to papers on Rochelle Salt some of his other publications are still referred to - those on X-ray emission spectra of sulphides and sulphates, alkali halides etc.

Professor Valasek died on October 4, 1993.

#### VALÁŠEK'S TIES TO CZECHOSLOVAKIA

During the stay of my wife Anna and myself at Penn State in 1967 we visited Professor Valasek and his wife in their home at Minneapolis. We received a very warm reception. Even before this visit I was especially challenged by the Valasek's name which sounds very much Czech. In the telephone directory of Prague you will find more than 60 persons of this name out of which 10 are Josephs. We write the name as Valášek, to make it sound long and soft: Valaashek. (Note: Valášek = small Valach. Valach = Moravian shepherd.)

My guess proved correct. His parents came from Sobětuš, a small village in a flat agricultural countryside about 100 km east of Prague, where the family owned a farm. On my recent visit of the place I found that the farm still exists. More than that: the family is still there and the present owner is Mr. Josef Valášek whose father was the physicist Valasek's cousin. In the family, rich correspondence is kept adding details to our story. Valasek-the-physicist's father belonged to a group of Czech students involved in political activities favouring independent cultural and political life of Czech intellectuals in the Austrian-Hungarian Monarchy. He even contributed to illegal Czech periodicals under the pen-name Karel Borecký. He emigrated to the United States in 1894 after being charged with insulting Emperor Franz-Josef of Austria-Hungary. Living in Cleveland, he became the editor of the periodical "Květy americké" published for the Czech minority. The father of his wife,

Josef Pytlík, was the principal of a school in the small town of Vodňany in Southern Bohemia. His major subjects were mathematics and physics; quoting Joseph Valasek [13]: "I suppose that I inherited my inclination toward physics from him."

In 1982 he wrote [13]: "I feel fond ties to Czechoslovakia being the son of Czech parents... I read Czech (my mother tongue) fairly well but speak and write it with difficulty, largely because of its complicated grammar but also because of my limited vocabulary." However, letters kept at the Sobětuš farm and those addressed to me show his good knowledge of the Czech language. Fig. 6 offers an

*Přejeme Vám zdraví a radost  
na vánoce a vždycky.*

*Leila a Josef Valášek*

*Postscript: -*

*Dear Jan: Dec. 8, 1981*

*I just received five volumes of Ferroelectrics containing the Proceedings of the 5th International Meeting. I am impressed by the growth of interest in ferroelectricity since the 1920's and 30's. You deserve much credit for starting and contributing to the planning of these international meetings. It is a great achievement.*

*Sincerely,  
Joseph Valasek*

Fig.6 Facsimile of Valasek's letter to the author, dated December 1981.

illustration: "Přejeme Vám zdraví a radost na vánoce a na vždycky" i.e. We wish you health and joy for Christmas and for ever. Here he also expresses his satisfaction by the growth of interest in ferroelectricity.

He visited the country of his origin only once. In 1929 he went to Sobětuš and also to Prague. Here he was in contact with Professors Dolejšek and Posejpal who were well known because of their investigations of X-ray spectra, and also Dr. Heyrovský who later became the Nobel Prize winner for the invention of polarography.

#### FULL RECOGNITION

Has the scientific community acknowledged Valasek's contribution to establishing a branch of physics to which in each text-book of solid state physics an independent chapter is devoted? In 1940 Hans Mueller wrote [14]: "The significance of Valasek's discovery was not realized for a number of years." However, the recognition has come. I quote from a letter I received in May 1981: "I was honored at a session of the Solid State Division of the American Physical Society on February 5, 1971, in New York, commemorating the 50th anniversary of the discovery of Ferroelectricity. Dr. W. P. Mason of Columbia University was the guest speaker. Then on May 19, 1971, the School of Physics at the University of Minnesota held a Colloquium in my honor at which Prof. Raymond Pepinsky was the guest speaker. A congratulatory letter by Prof. John. H. Van Vleck of Harvard University was read. This was followed by a dinner at the Minnesota Club in St. Paul. This recognition of my discovery was very pleasant and sufficient. I ask for no more."



The last two sentences correspond exactly to what Valasek's former student Professor Pepinsky wrote [7]: "Professor Valasek is a gentle, modest rather shy man, always kind and sensitive to others."

Even more recognition, however, was to come: In 1983 the University of Minnesota conferred upon Valasek the honoris causa degree of doctor of science (fig.7).

In the last letter I received from Prof. Valasek, dated June 1992, he expresses satisfaction with the warm character of the celebrations of his 95th birthday in which not only his family but also physicists from his University took part.



## JOSEPH VALASEK

Resident of Minnesota; graduate of Case Institute of Technology with a bachelor of science degree in 1917; graduate of the University of Minnesota with master of arts and doctor of philosophy degrees in physics in 1920 and 1921; National Research Council Fellow in 1921; faculty member in the School of Physics and Astronomy at the University of Minnesota from 1922, when he started as an assistant professor, until his retirement in 1965 as professor emeritus of physics; author of numerous research publications and two textbooks; pioneering researcher in the fields of piezoelectricity and ferroelectricity; distinguished scholar, whose discovery in 1920 of the ferroelectricity of Rochelle salts has had a continuing impact on the understanding of a new and important area of physics; universally recognized discoverer of the fundamental physical phenomenon of ferroelectricity, which was believed to be a rarity in nature until theoretical breakthroughs were made in the 1960s—

Because your discovery is one of the most important ever made in physical science at the University of Minnesota; because you have been a scientist ahead of your time; because of the great impact of your work on science and technology; because of your lifetime contributions to the excellence of the physics program at the University—

The regents of the University of Minnesota, upon recommendation of the faculties, confer upon you, Joseph Valasek, the degree of doctor of science, honoris causa.

Conferred June 11, 1983.

*Alvan K. Hansen*  
SECRETARY

*C. Bar Magnett*  
PRESIDENT

Fig.7 Facsimile of the Diploma conferring upon Joseph Valasek the degree of Doctor of Science, honoris causa.

### BACK TO THE FIRST STEP IN 1921

Speaking from the 1994 point of view, Rochelle salt is forgotten as far as applications are concerned, but it still attracts attention in the realm of basic research, partly because of the microscopic origin of ferroelectricity, partly as an example of those compounds in which the text-book sequence of phases >>parent phase - ferroelectric phase << is disturbed by the existence of another nonpolar phase at low temperatures.

But except for Rochelle salt, how far did we go since 1921? A part of the answer is encoded in Fig.1. Very far indeed. This graph does not reflect the high degree of our understanding of ferroelectricity. Nor does it show the technical importance of these materials. The interrelations between ferroelectricity and electromechanical properties are still in the foreground of present day research. The spectrum of technical devices in which ferroelectrics are employed has become incredibly wide and is still growing.

Certainly Valasek's high level work shaped the beginning of the ferroelectric story. What if he had chosen another professor or if Swan had had directed his activity in some other direction and the idea of comparing the properties of Rochelle salt with those of iron would not have occurred? Considering that the establishment of the Zurich school was stimulated by and based on Valasek's discovery (cf. Busch's narrative in refs. 15, 16) we can speculate that solid state physics would have had to wait till World War II for the discovery of the first ferroelectric, barium titanate. Luckily, however, history knows no "ifs" and thus we were fortunate to have the right man on the right spot at the right time: Joseph Valasek.

### REFERENCES

- [1] By courtesy of K. Deguchi. See also Landolt Börnstein, New Series, Vol. 28a. Springer-Verlag, Berlin, 1990
- [2] J. Valasek, "The early history of ferroelectricity", *Ferroelectrics*, vol. 2, pp. 239-244, 1971.
- [3] J. Valasek, "Piezoelectric and allied phenomena in Rochelle salt", *Phys. Rev.*, vol. 15, pp. 537-538, 1920.
- [4] J. Valasek, "Piezo-electric and allied phenomena in Rochelle salt", *Phys. Rev.*, vol. 17, pp. 475-481, 1921.
- [5] J. Valasek, "Piezo-electric activity of Rochelle salt under various conditions", *Phys. Rev.*, vol. 19, pp. 478-491, 1922.
- [6] J. Valasek, "Properties of Rochelle salt related to the piezo-electric effect", *Phys. Rev.*, vol. 20, pp. 639-664, 1922.
- [7] R. Pepinsky, quoted by I. Lefkowitz and G.W. Taylor, "Editorial", *Ferroelectrics*, vol. 2, p. 237, 1971.
- [8] F. Bitter, "On inhomogeneities in the magnetization of ferromagnetic materials", *Phys. Rev.*, vol. 38, p. 1903, 1931.
- [9] E. Schrödinger, "Studien über Kinetik der Dielektrika, den Schmelzpunkt, Pyro- und Piezoelektrizität", *Sitzungsberichten der Kaiserl. Akademie der Wissenschaften in Wien. Mathem.-naturw. Klasse; Bd. CXXI. Abt.IIa*, pp. 1-36, November 1912.
- [10] H. Mueller, "Properties of Rochelle salt", *Phys. Rev.*, vol. 47, pp. 175-191, 1935.
- [11] H. Mueller, "Properties of Rochelle salt", *Phys. Rev.*, vol. 57, pp. 829-839, 1940.
- [12] H. D. Megaw, *Ferroelectricity in Crystals*. London: Methuen & Co., Ltd., 1957, p.2..
- [13] Some of the facts given here have been obtained from the correspondence of Joseph Valasek with his relatives at Sobětuš, with the author and with Dr. Březina from the same Institute.
- [14] H. Mueller, "The dielectric anomalies of Rochelle salt", *Annals of the New York Academy of Sciences*, vol. 40, pp. 321-356, 1940.
- [15] G. Busch, "How I discovered the ferroelectric properties of KH<sub>2</sub>PO<sub>4</sub>", *Ferroelectrics*, vol. 71, pp. 43-47, 1987.
- [16] G. Busch, "Early history of ferroelectricity", *Ferroelectrics*, vol. 74, pp. 267-284, 1987.

# 200 Years Of Research On Boracites

A. G. Castellanos-Guzmán  
Laboratorio de Investigación en Materiales  
Dirección de Vinculación y Transferencia de Tecnología  
Universidad de Guadalajara  
Apdo. Postal 2-638  
44281 Guadalajara Jal. México

**Abstract-** The boracite family has attracted the attention of researchers for more than 200 years not only due to its peculiar physical properties but because these compounds display unusual property coefficients including a large figure of merit for IR detection and pyroelectric applications. The purpose of this brief paper is to point out some of the main characteristics of this family that make them potential candidates for a certain number of applications.

## Introduction

It is not my intention here to recapitulate or improve on those excellent accounts on boracites available in the literature which have been written by Nemes [1], Schmid [2] and Burzo [3] among others, but only to extend the overview a little to the more recent times as well as to stress the need to investigate the physical properties of more members of this interesting ferroelectric family.

A.G. Werner, one of the early German crystallographers gave the name of "boracite" to the mineral  $\text{Mg}_3\text{B}_7\text{O}_{13}\text{Cl}$  (a magnesium chloroborate currently found in sedimentary deposits of anhydrite, gypsum and halite in different regions of Germany, France and USA [4,5]), but long before that the children of the German town of Lüneburg already used to play at dice with their "Würfelstein" made of "kubische" boracite [6]. They were probably the discoverers of this mineral. The term "boracite" is presently given to a large number of synthetic compounds all with general formula  $\text{Me}_3\text{B}_7\text{O}_{13}\text{X}$  where Me stands for one of the divalent metals such as Mg, Cr, Mn, Fe, Co, Ni, Cu, Zn or Cd and X is generally a halogen Cl, Br, or I. Occasionally Me can be monovalent Li and it has been found that X can be F, OH, S, Se, Te or  $\text{NO}_3$  [1,7]. However, as compared with halogen boracites very little is yet known about the properties of these compositions [8] thus here the attention will be focused entirely on boracites where  $\text{X}=\text{Cl}$ , Br or I. Besides Mg-Cl (in what follows we will refer to a boracite by giving the symbols of the metal and halogen only) two other members of the family are found in Nature: Ericaite (Fe-Cl) and Chambersite (Mn-Cl) [9].

Although the entry of boracites into the area of Solid State Physics has been dated as 1880 [1] because in that year the Curie brothers and Friedel observed for the first time the piezoelectric effect in natural boracite [10], it is known that Haüy had already explored Pyroelectricity in Mg-Cl as early as 1791 [5].

## Crystal Growth and Structural Studies

In a period of time that started in 1860 and has apparently ended in 1980 [11] the synthetic boracites have been prepared by four basic techniques: sintering flux method [1,2], vapour transport method [2], hydrothermal method [7], and "pressure reaction" method [11]. With the aid of these methods all possible combinations of halogen boracites have been

synthesized, with the exception of Cu-I that was obtained until 1985 using high pressure applied to condensed phases [12]. The vapour transport method of Schmid is still the most widely used technique for synthesis of boracites in single crystal form.

Most halogen boracites transform from a cubic high temperature phase (point group  $\bar{4}3m$ ) to one or to a sequence of phases with point groups  $mm2$ ,  $m$  and  $3m$  [13], with the exception of Cr-Br, Cr-I and Cu-I that remain cubic down to 10 K. Recently Ye et al. [14] found a new tetragonal phase (point group  $\bar{4}2m$ ) in Cr-Cl that is followed by an orthorhombic  $mm2$  polar phase. This case is unique among boracites.

The cubic-orthorhombic phase transition is especially noted since it is of the improper type [1,2,15]. The transition temperature varies according to composition from 60 to 800 K but for any given metal it falls in the sequence  $\text{Cl} \rightarrow \text{Br} \rightarrow \text{I}$ .

Structural studies on halogen boracites started in 1951 well before the resurgence of interest in the boracites happened, when Ito et al. [1,2] determined the cubic and orthorhombic structures of a natural Mg-Cl crystal. Structural work done between 1951 and 1974 has been described and compared in detail by Nemes [1], since then the structure of the cubic phase has been determined in Cr-Cl [16], Cr-Br [17], Cr-I [18], Cu-Cl [17], Cu-Br [19], Cu-I [12], Co-I [19] and Ni-I [3]. These structures have been found to be essentially the same as that of cubic Mg-Cl as described by Nemes [1]. The structure of the orthorhombic phase is known for Fe-I [20], Co-Br [21], Ni-Cl [21], Ni-Br [22], and Cu-Cl [3], while that of the trigonal phase has only been determined in Fe-Cl [23] and Zn-Cl [24]. The structure of the new tetragonal phase in Cr-Cl was determined in 1991 [25]. No structure of the monoclinic phase has yet been made. In a space-limited contribution like this it is not possible to quote all the references related with boracites so a limited selection has been made. The extensive structural study of Nemes and co-workers in halogen boracites has been published in a series of six papers in the Journal of Physics C (1974-1981) [19]. Recent structural determinations made by the groups of the University of Geneva are to be found in Acta Cryst. B and C as well as in Ferroelectrics [21,24]. These studies have revealed displacements of the boron and oxygen framework [1] at the cubic-orthorhombic phase transition of the same order of magnitude as those of the metal and halogen atoms, contradicting initial assumptions of a quasi static boron and oxygen framework [1, 21]. It was also shown that as the size of the halogen ion increases the difference between the metal-halogen distance diminishes. Except in Cu and Cr boracites which show smaller differences. This may explain the absence of phase transitions in chromium bromine and iodine and in copper iodine boracites, where the transition-metal atoms seem to occupy stable positions between the halogen atoms [20].

Accurate determination of the structure of boracites is complicated by the formation of ferroelectric/ferroelastic domains in the transition to the low temperature phase, particularly by fine lamella twins that can not be detected easily

under the polarized light microscope, unless one has at hand a spindle stage in order to rotate the sample in all possible directions. In some cases, however, it is possible to obtain a single domain crystal from a twinned crystal by mechanical pressure[21] a rather delicate operation due to the small size of the samples used in x-ray work.

### Physical Properties and Applications

Halogen boracites present unusual physical properties [1,26] which re-attracted increasing attention for a period of about 25 years (from 1966 onwards). Ferroelectricity in a synthetic boracite (Ni-Cl) was experimentally demonstrated by Ascher et al. in 1964[27] thus ending a matter of controversy that had lasted for 30 years[1]. In 1965 Schmid succeeded in growing single crystals of most halogen boracites of a suitable size for physical characterization [2], just a year later Ascher et al [28] found in Ni-I the occurrence of both ferroelectricity and weak ferromagnetism and the coupling between spontaneous polarization and magnetization at low temperatures. These papers were followed by an explosion of work on boracites[1]: the improper character of the cubic-orthorhombic phase transition was confirmed through studies of the permittivity behaviour in several boracites as a function of temperature. These studies also showed striking differences among their dielectric anomalies. In most boracites  $\epsilon_r$  as temperature is decreased from the high symmetry phase  $\epsilon_r$  increases slightly and at the transition to the orthorhombic low temperature phase  $\epsilon_r$  jumps abruptly downwards. However, in four compounds (Mn-I, Ni-I, Cu-Cl and Mn-Br) the jump of  $\epsilon_r$  at the transition is upwards[26].

The dielectric behaviour at the cubic-orthorhombic phase transition in boracites has been theoretically analyzed by Kobayashi, Dvorak, Dvorak and Petzelt, Gufan and Sakhnenko, Levanyuk and Sannikov, Toledano et al. (See for example the list of references in Toledano et al.[26, 29]), but as summarized by these authors none of these models have been able to account successfully for the entire set of experimental data of boracites.

In a recent and very comprehensive review on Ferroelectricity, Fousek [30] has remarked that the key force pushing the research on these materials ahead has been the interest of using the unique features of ferroelectric materials in technical applications. Something springs up to the eye when one sees Table 2 of such an excellent paper: boracites are very promising for almost every application mentioned in it. For example, the low values of the dielectric constant (typically 8 to 10 at room temperature) and the absence of dielectric divergence made boracites, as well as other improper ferroelectrics like gadolinium molybdate (GMO), good candidates for pyroelectric detection of infrared radiation and thermal imaging. It is convenient, when comparing the properties of pyroelectric materials to define appropriate "figures of merit". One of these figures involves the ratio of the pyroelectric coefficient to the product of the permittivity and the volume specific heat since it determines the maximum responsivity bandwidth product obtainable for a small-area (point) detector [31]. Some boracites were investigated in order to determine their figures of merit, they compared well with other materials[32, 33]. Considerable amounts of work have been done in this direction by industrial laboratories (Plessey

Research Ltd.in England, Philips Laboratories in USA, Batelle in Geneva) as well as by our host in this meeting; the Materials Research Laboratory. from Penn. State[34].

A certain number of works were devoted to the study of the pyroelectric properties of boracites[6]. After the initial observations of Häüy [4,5] Hankel studied in detail this effect in natural boracite[5]. The temperature dependence of the pyroelectric coefficient has been determined by dynamical and quasi static methods in Mg-Cl[6], Cr-Cl[35], Mn-Cl, Mn-Br, and Mn-I[36], Fe-Br[3], Fe-I[37], Co-Cl, Co-I and Ni-I[6], Cu-Cl[37], Cu-Br[6]. All data available from 1957 to 1977 were reviewed in reference 6. This analysis also showed a serious discrepancy between published data of the spontaneous polarization of boracites. The current  $P_s$  value in boracites is of the order of  $1$  to  $4 \times 10^{-2}$  C/m<sup>2</sup> however many of collected  $P_s$  data fall short by one to four orders of magnitude. Schmid and Tippmann suggested that the origin of these differences was the lack of simultaneous visual control of the domain state in the sample throughout the entire range of measurement. This seems to have been confirmed in Cr-Cl boracite for which an astonishingly small and temperature independent spontaneous polarization had been reported[6], four orders of magnitude smaller as compared with the recent value found by Ye et al. [14] in measurements with visual control of the domain state of the sample.

The isobaric molar heat capacity,  $C_p$ , has been evaluated for at least 16 boracites at the structural and magnetic transitions[3]. Large upper bound values of the enthalpy of transition,  $\Delta H$ , and of the entropy of the transition,  $\Delta S$ , suggest that the transition is of the first order, as required by the form of the free energy in phenomenological theories [1,15,29]. Typical  $C_p$  values near the cubic-orthorhombic phase transition run from 580 up to 1200 J/mole/K. From x-ray diffuse scattering experiments, Felix et al.[1] concluded that the first-order character of the phase transition decreases with a decrease in the mass and size of the halogen, however,  $C_p$  measurements performed on Mn-X boracites [3] showed that the transition in Mn-I is close to being of second order, thus contradicting Felix's expectations. Another phenomenon observed in calorimetric measurements on boracites is the occurrence at the phase transition of multiple peaking in the heat capacity of Ni-Br, Cr-Cl, Mn-Br and Mn-I, for example[3]. In some cases, the multiple peaking is attributed to internal stresses within the crystals, stresses which can be eliminated by a thermal treatment. However, in Mn-Br and Mn-I the thermal treatment proved to be ineffective, so the origin of the peaks in  $C_p$  has been attributed to growth sectors [1,3] occurring usually together in the one "single" crystal. Each growth sector would then have a slightly different transition temperature giving rise to the peaking of  $C_p$ . In spite of the great influence that growth sectors can have on physical and chemical properties of boracites[1], no other studies than those mentioned by Nelmes have been carried on this phenomenon.

The peculiar optical properties of boracites were the center of controversy for about 70 years[5,6]. Detailed optical field effects studies carried on by Schmid's groups (both at Batelle Geneva and since 1978 at the University of Geneva)[38] showed that since boracites belong to the symmetry species  $\bar{4}3mFmm2$ (fully ferroelectric/fully ferroelastic)[39] the polarization vector and optical indicatrix are differently oriented in every domain, hence the coupling between

ferroelasticity and optical indicatrix is complete. This offers the possibility of using single crystals or epitaxial layers for technical applications. Scrutiny of all encompassed electrical-optical effects made by Schmid and Schwarzmüller[38] showed that boracites have an equally favorable optical performance as GMO. However to date, the possibilities of boracites in these truly ferroelectric applications have not been further explored nor the studies extended to many of these compositions.

Magnetic properties have been investigated in 11 boracites and were remarkably reviewed in references[1,3,13,26]. The magnetoelectric coefficients are known for Co-I, Ni-Cl, Ni-Br, Ni-Cl and Cu-Cl [3], and a full theory on magnetic transitions was recently laid down by Toledano et al.[26]. However, in spite that the unusual magnetic behaviour of boracites is of considerable interest for technical applications the phenomenon remains unexploited.

Chemical and physical feasibility studies have also shown that a number of properties of boracites may be exploited technologically, but in the last few years the number of publications about applications of boracites has been reduced drastically though this is not the case for basic research on these materials[3].

The usually rose argument against boracites is that crystals of large size free of fractures are very difficult to grow but the possibility to grow sufficiently large, chemically stable and defect-free crystals of these compounds has been opened with new techniques[11,40] that seem to improve not only quality but reduce production costs. It should also be noted that the recent resurgence of interest in ferroelectric thin films opens new possibilities for the application of boracites in this field. To our knowledge only Ni-Cl epitaxial layers on a Cr-Cl substrate are known[3] so it seems worthwhile to develop processing techniques for thin films of boracites.

In spite that a number of boracites have been thoroughly studied[1,3,6,] a relative paucity of accurate physical information is still noted for many new members of this large family. Perhaps it is the case that these materials have followed the "curve of history" as described by Newnham et al.[34] but it is our believe that by exploring physical properties of more of these compounds more interesting phenomena would be found and the "best" boracite could also be found for real applications.

#### Acknowledgments

A major part of this contribution was done during my research visit at the Mineralogisches Institut of the University of Kiel. I would like to thank Prof. Dr. Wulf Depmeier and to his collaborators for hospitality and the inspiring atmosphere they have created at that Institute. Thanks are also due to DAAD- Germany for economical support and to Professors J. Fousek, H. Schmid and A. Levasseur for letting me have some reprints that were not easily accessible to me.

#### References

- [1] R. J. Nelmes, "Structural studies of boracites. A review of the properties of boracites" *J. Phys. C*, vol.7, pp.3840-3854, 1974.
- [2] Hans Schmid "The synthesis of boracites with the aid of transport reactions" *J. Phys. and Chem. of Solids*, vol. 26, pp.973-988, 1965 (Translated by E. A. Johnson Translation No. 498 Royal Radar Establishment 1975).
- [3] Landolt-Börnstein, *Numerical Data and Functional Relationships in Science and Technology*, Berlin: Springer, 1993 vol.27h, pp. 128-204 Berlin: Springer-Verlag, 1993.
- [4] Carl Hintze, *Handbuch der Mineralogie* Berlin: Walter De Gruyter Co. 1933, vol.4, pp. 104-128.
- [5] Charles Palache, Harry Berman and Clifford Frondel, *The Dana's System of Mineralogy*. New York: John Wiley, 1947, vol.II, pp. 378-381.
- [6] H. Schmid and H. Tippmann, "Spontaneous birefringence in boracites measurements and applications" *Ferroelectrics*, vol.20, pp.21-36, 1978.
- [7] C. Fouassier, A. Levasseur, J.C. Joubert, J. Muller et P. Hagenmuller, "Les Systemes B<sub>2</sub>O<sub>3</sub>-MO-MS, Boracites M-S (M= Mg, Mn, Fe, Cd) et sodalites M-S (M=Co, Zn), *Zeitschrift für Anorganische Chemie*, vol.375, pp.202-212, 1970.
- [8] R.O. Gould, R.J. Nelmes and S.E.B. Gould "Structural studies of boracites: VII. Cadmium sulphur boracite" *J. Phys. C*, vol.14, pp. 5259-5267, 1981.
- [9] Russell M. Honea and Frank R. Beck, "Chambersite. A new mineral" *The American Mineralogist*, vol.47, pp.665- 671, 1962.
- [10] Jacques Curie, Pierre Curie et M. Friedel "Développement, par pression, de l'électricité polaire dans les cristaux hémiedres à faces inclinées" *C.R.- Acad.Sci. Paris*, vol.91, pp.294-295, 1880.
- [11] M. Delfino, G.M. Loiacono and P.S. Gentile, "Preparation and Mechanistic Studies of Halogen Boracites" *Inorg. Chimica Acta*, vol.43, pp.59-63, 1980.
- [12] G. Berset, W. Depmeier, R. Boutellier and Hans Schmid, "Structure of Boracite Cu<sub>3</sub>B<sub>7</sub>O<sub>13</sub>I" *Acta Cryst. C*, vol. 41, pp 1694-1696, 1985.
- [13] Hans Schmid "On a magnetoelectric classification of materials" *Int. J. Magnetism*, vol.4 pp. 337-361, 1973.
- [14] Zuo-Guang Ye, Jean-Pierre Rivera and Hans Schmid, "A new tetragonal 42m phase and related phase sequence in Cr-Cl boracite" *Ferroelectrics*, vol.106, pp. 87-92, 1990.
- [15] V. Dvorak, "A thermodynamic theory of the cubic-orthorhombic phase transition in boracites" *Czech.J.Phys*, vol .B21, pp.1250-1261, 1971.
- [16] R. J. Nelmes and F. R. Thornley "Structural studies of boracites. The cubic phase of chromium chlorine boracite, Cr<sub>3</sub>B<sub>7</sub>O<sub>13</sub>Cl" *J. Phys. C*, vol.7, pp. 3855-3874, 1974.
- [17] M. Yoshida, K. Yvon, F. Kubel and H. Schmid "Cubic-structure of chromium-bromine boracite at 298 and 113 K" *Acta Cryst. B*, vol. 48, pp. 30-32, 1992.
- [18] A. Monnier, G. Berset, H. Schmid and K. Yvon "Cubic structure of chromium iodine boracite" *Acta. Cryst. C*, vol. 43, pp.1243-1245, 1987.
- [19] R.J. Nelmes and W. J. Hay, "Structural studies of boracites: VI. The cubic phase of cobalt iodine Co<sub>3</sub>B<sub>7</sub>O<sub>13</sub>I, and of copper bromine boracite, Cu<sub>3</sub>B<sub>7</sub>O<sub>13</sub>Br" *J. Phys. C*, vol.14, pp. 5247-5257, 1981.
- [20] F. Kubel and A. -M. Janner "Structure of the fully ferroelectric/fully ferroelastic orthorhombic room temperature phase of iron iodine boracite, Fe<sub>3</sub>B<sub>7</sub>O<sub>13</sub>I", *Acta Cryst. C*, vol. 49, pp. 657-659, 1993.

- [21] F. Kubel, S.Y. Mao and H. Schmid "Structure of the fully ferroelectric/fully ferroelastic orthorhombic room-temperature phase of Cobalt-Bromine boracite  $\text{Co}_3\text{B}_7\text{O}_{13}\text{Br}$ , and Nickel-Chlorine boracite  $\text{Ni}_3\text{B}_7\text{O}_{13}\text{Cl}$ ", *Acta Cryst. C*, vol.48, pp.1167-1170, 1992.
- [22] S. C. Abrahams, J. L. Bernstein and C. Svensson "Orthorhombic phase of nickel bromine boracite,  $\text{Ni}_3\text{B}_7\text{O}_{13}\text{Br}$ : room temperature ferroelectric-ferroelastic crystal structure" *J. Chem. Phys.*, vol. 75, pp. 1912-1918, 1981.
- [23] M.-E.Mendoza-Alvarez, K. Yvon, W.Depmeier and H.Schmid "Structure refinement of trigonal iron-chlorine boracite" *Acta Cryst. C*, vol.41, pp. 1551-1552, 1985.
- [24] S.Y.Mao, M.-E.Mendoza-Alvarez, W.Depmeier, F. Kubel, H.Schmid and K.Yvon "Structure refinement of trigonal Zinc-Chlorine boracite from single-crystal and powder x-ray diffraction" *Ferroelectrics*, vol.115, pp.91-96,1991.
- [25] S.Y.Mao, F. Kubel, H. Schmid and K. Yvon, "Tetragonal Ferroelastic/Antiferroelectric Chromium-Chlorine,  $\text{Cr}_3\text{B}_7\text{O}_{13}\text{Cl}$  boracite from x-ray diffraction on a single-domain crystal at 230 K" *Acta Cryst. B*, vol. 47, pp.692-696, 1991.
- [26] P.Toledano, H.Schmid, M.Clin and J.-P. Rivera, "Theory of the low- temperature phases in boracites: Latent antiferromagnetism, weak ferromagnetism, and improper magneto structural couplings" *Phys. Rev.B*, vol. 32, pp.6006-6038, 1985.
- [27] E. Ascher, H. Schmid and D. Tar, "Dielectric Properties of boracites and evidence for Ferroelectricity", *Solid State Commun.* vol.2, pp.45-49, 1964.
- [28] E. Ascher, H. Rieder, H. Schmid and H. Stossel, "Some properties of ferromagnetoelectric Nickel-Iodine boracite" *J. Appl. Phys.* vol.37, pp. 1404-1405, 1966.
- [29] P. Toledano, H.Schmid, M. Clin and J.-P-Rivera, "Structural transitions in boracites: one or two order-parameters?" *Jpn. J.Appl.Phys.Suppl.* vol. 24, pp.1379-1381, 1985.
- [30] Jan Fousek, "Ferroelectricity: remarks on historical aspects and present trends", *Ferroelectrics*, vol.113, pp.3-20,1991.
- [31] A. Shaulov, W.A. Smith, G.M. Loiacono, M.I. Bell and Y.H. Tsuo, "Improper Ferroelectrics for Pyroelectric Detection of Infrared Radiation", *Ferroelectrics*, vol. 27, pp. 117-121, 1980.
- [32] R. W. Whatmore, J. M. Herbert and F. W. Ainger, "Recent developments in Ferroelectrics for Infrared Detectors", *Phys. Stat. Sol. (a)*, vol. 61, pp. 73-80, 1980.
- [33] A. G. Castellanos-Guzman, J. Campa-Molina, M. Barcena-Soto and J. Reyes-Gomez, "Properties of improper ferroelectrics for IR detection and optical applications" in *Proceedings of the International Workshop on Optoelectronic Materials and their Applications*, 1993, pp. 255-258.
- [34] R. E. Newnham, D. P. Skinner, K. A. Klicker, A. S. Bhalla, B. Hardiman and T. R. Gururaja, "Ferroelectric Ceramic-Plastic Composites for Piezoelectric and Pyroelectric Applications" *Ferroelectrics*, vol.27, pp. 49-55, 1980.
- [35] Z. G. Ye, J.-P. Rivera, E. Burkhardt and H. Schmid "Spontaneous birefringence and polarization studies on boracite  $\text{Cr}_3\text{B}_7\text{O}_{13}\text{Cl}$ " *Phase Transitions*, vol. 36, pp. 13-25, 1991.
- [36] A. G. Castellanos-Guzman, J. C. Burfoot, H. Schmid and P. Tissot, "Dielectric properties of orthorhombic  $\text{Mn}_3\text{B}_7\text{O}_{13}\text{Cl}$ ,  $\text{Mn}_3\text{B}_7\text{O}_{13}\text{Br}$ , and  $\text{Mn}_3\text{B}_7\text{O}_{13}\text{I}$  boracites", *Ferroelectrics*, vol. 36, pp. 411-414, 1981.
- [37] H. Schmid, P. Genequand, G. Pouilly and P. Chan, "Pyroelectricity of Fe-I and Cu-Cl boracites", *Ferroelectrics*, vol. 25, pp. 535-541, 1982.
- [38] H.Schmid and J. Schwarzmuller, "Review of ferroelectric materials usable for passive electro-optic alpha numeric display devices" *Ferroelectrics* vol.10 pp. 283-293, 1978.
- [39] Hans Schmid, "Polarized Light Microscopy (PLM) of Ferroelectric-Ferroelastic Domains in Transmitted and Reflected Light", in *Ferroelectric Ceramics*: Basel:Birkhäuser Verlag, 1992, pp. 107-126.
- [40] Y. Uesu, Y. Murase, D. Hirasawa and T. Ishigaki, "Crystal growth and optical second harmonic generation of Ni-Br boracite", *Ferroelectrics*, vol. 36, pp. 33-36, 1989

# HISTORY OF FERROELECTRIC CERAMICS IN JAPAN -GLIMPSE OF HISTORICAL FERROELECTRIC CERAMIC TECHNOLOGY- IN JAPAN BEFORE 1955

Kiyoshi Okazaki

Dept. of Materials Science and Ceramic Technology,  
Shonan Institute of Technology, Fujisawa 251, Japan

1 Hessho and Stemag in Germany started the production of  $\text{TiO}_2$  capacitors and steatite insulators around 1935. Just before the world war II, Ito<sup>1)</sup> who was a student of Barkhausen and a leader of Japanese Navy lader brought back several samples of Hessho and Stemag to Japan from Germany. A German book on technical development of high frequency insulators and temperature compensating(TC) capacitors in was translated into Japanese<sup>2)</sup> in 1940.

## 高周波絶縁物

イー・アルベールズ・シ・ンベルグ著

日本無線電信電話株式会社技師

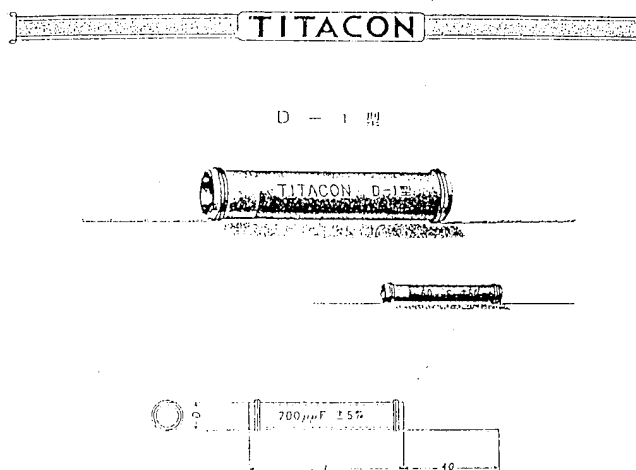
船 曳 春 吉 譯



Fig. 1 Translation book of "High Frequency Insulator" 1939 Berlin, edited by Ernst Albert-Schonberg, translated by H. Funabiki, 1940 March Yushodo, Tokyo

2 Around 1935, the research of electronic ceramics started at the Electric Laboratory(now, NTT). The dielectric properties  $\text{MgO-Al}_2\text{O}_3\text{-SiO}_2$  by Moriyasu<sup>3)</sup> was the representative paper for the insulator applications. In 1939, he was invited by Kawabata Co. (now, KCK) and he developed the production of steatite and  $\text{TiO}_2$  ceramic capacitors in 1940. Figure 2 is the first catalog of Kawabata "TITACON".

3 Around 1939, Ogawa and Waku<sup>4)</sup> started the research for improvement of  $\text{TiO}_2$  ceramic capacitors with zero TC in the ternary system of  $\text{MgO-TiO}_2\text{-alkalioearth oxides}$  and they first found a high dielectric constant of 1000-1200 and the Curie peak of 60 °C. In 1943, they found an almost pure  $\text{BaTiO}_3$  with a room temperature dielectric constant of 1000 and the Curie peak dielectric constant of 4000 at 110 °C.



D - 1 型 定 価 表

級 別	容 量 確 度	試 験 電 圧	A 級		B 級	
			主 5%以内		主 10%以内	
寸 法	法 則	容 量 (μF)	1,000V (A.C.)		1,000V (A.C.)	
			容 量 定 価	容 量 定 価	容 量 定 価	容 量 定 価
12	50	500 ~ 1,000			500 ~ 1,000	
8	12	200 ~ 500			200 ~ 500	
8	50	100 ~ 200			100 ~ 200	
4	40	100 ~ 200			100 ~ 200	
4	80	50 ~ 100			50 ~ 100	

図面上の寸法は寸法の単位に準じます

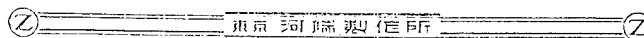


Fig. 2 The first catalog of Kawabata "TITACON" in 1940

## 物 性 論 研 究

6

1947年7月

部分は想像線である。

$\text{TiO}_2 = 100$ の所に

$\epsilon > 100$  があるのは金

紅石磁石の  $\epsilon$  が 110 程

度であるからである。

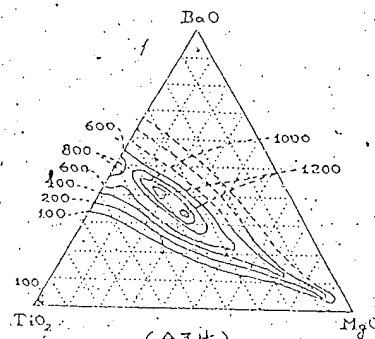
3.3. 誘電率の周

波数特性

酸化チタン磁石の誘

電率は一般に低周波で

の値が高周波で値より



(分子比)

第3図

$\text{TiO}_2\text{-MgO-BaO}$ 系磁石の誘電率  $< 10^3$  値、室温

Fig. 3 The ternary system of  $\text{MgO-TiO}_2\text{-BaO}$  and [Busseron Kenkyu]<sup>5)</sup>

4 In 1947, [busseiron kenkyu] on ferroelectric materials was published by a study group of physics. This includes the discovery of  $\text{BaTiO}_3$  during the world war II by Ogawa, anomaly of dielectric properties of  $\text{BaTiO}_3$  by Takahashi and Nakamura, phase transition of  $\text{BaTiO}_3$  by Miyake and Ueda, specific heat and thermal expansion of  $\text{BaTiO}_3$  by Sawada and Shirane and others. Also, "High Dielectric Constant Ceramics"<sup>6)</sup> by Hippel was referred.

5 In 1947, Murata make a small cylindrical Hi-K capacitor sample of 5000 pF with a composition of  $(\text{Ba}_{0.7}\text{Sr}_{0.29})\text{TiO}_3$  as same as Hippel composition.

6 After the war, many scraped US military communication equipments appeared on the black market. Okazaki<sup>7)</sup> collected the electronic components including ERIE capacitors from the equipments. It is noticed that the US equipment made in 1943 used  $\text{BaTiO}_3$  ceramic capacitors. The typical American  $\text{BaTiO}_3$  cylindrical capacitors were 1 1/16 inch in length, 5/16 inch in diameter and 0.6 mm in thick. The capacity was 0.005  $\mu\text{F}$  and the working voltage was 300 V, dc. The chemical composition is illustrated in Table 1.

Table 1 The chemical composition of American  $\text{BaTiO}_3$  capacitors, probably made in 1943<sup>7)</sup>

BaO	64.73 wt %
TiO <sub>2</sub>	31.32
SiO <sub>2</sub>	1.02
Al <sub>2</sub> O <sub>3</sub>	2.5
Total	99.56

#### ERIE HI-K TUBULAR CERAMICONS

##### ERIE HI-K-12 AND HI-K-35 CERAMICONS

The curve in Figure 14 shows the effect of temperature on capacity of HI-K-12 Ceramicons and series GP2 Ceramicons above 100 MMF. Figure 15 shows the same characteristics for HI-K-35 material. These charts show typical results and are not intended as guaranteed limits. Specifications for HI-K-12 and HI-K-35 Ceramicons are given on the next page. These specifications also apply to GP2 Ceramicons, which are described on pages 13 and 14.

It should be noted that power factor of Erie HI-K-12 and HI-K-35 Ceramicons decreases as temperature is increased. This phenomenon provides an added advantage where operation above room temperature is required.

Leakage resistance may be expected to drop off somewhat at elevated temperatures. However, as a rule initial leakage resistance is many times higher than the specified 7500 megohms. This means that in most cases resistance will be safely above 7500 megohms even at 85°C.

HI-K-35 material is recommended where space requirements are limited and effects of temperature are not critical.

ERIE STYLES	CAPACITY IN MMF			
	HI-K-12		HI-K-35	
A, K, 331	100	1,000	1,000	1,800
B, L, 332	1,100	1,500	2,000	4,300
C, M, 333	1,600	5,100	4,700	13,000
D, 334	6,000	8,000	*	*
E, 335	8,100	12,000	*	*
F, 336	13,000	16,000	*	*
S, 337	1,600	4,100	4,300	7,500
T, 338	1,100	2,000	*	*

\*Not available.

Tolerances available:

HI-K-12—100-1500 MMF  $\pm 10\%$  or  $\pm 20\%$

HI-K-12—greater than 1500 MMF  $\pm 20\%$  only

HI-K-35— $\pm 20\%$  or  $\pm 100\%$ —0%

Maximum Working Voltage—500 volts D.C.

For descriptions of Erie Styles, see page 2.

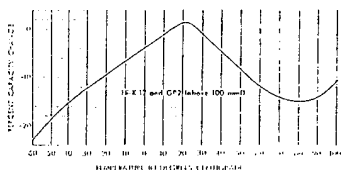


Figure 14

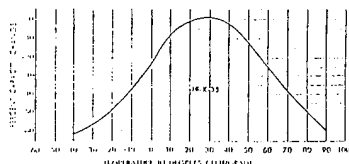


Figure 15

Fig. 4 Erie Catalog in 1947 in Japan

Fig. 5 First Catalog of Murata Capacitors (designed by Michiko Okazaki)

6 In May 1948, Okazaki measured  $\text{BaTiO}_3$  cylindrical capacitors of 10000, 7000, 5000 and 1000 pF made in Toshiba Co. The Curie peaks were 85-95 °C. Murata also tried to produce Hi-K capacitors with the Curie peaks of 120 °C and room temperature. In the end of 1959, Okazaki made the first catalog including two types of Hi-K with the Curie peaks of 120 °C and 30 °C, and the TC capacitors of P100, N750, N1400 using  $\text{CaTiO}_3$  and N3300 using  $(\text{Sr}, \text{Ba})\text{TiO}_3$ .

7 Abe<sup>8)</sup> who was in MIT with Hippel in 1937-39 and Tanaka<sup>9)</sup> of Dept. of Electrical Engineering at Kyoto Univ. started the research on  $(\text{Ba}, \text{Sr})\text{TiO}_3$  system and they presented the temp. and freq. dependences of dielectric properties in the fall of 1948.

8 In 1949, Tanaka<sup>10)</sup> measured electrostriction of Erie  $\text{BaTiO}_3$  cylindrical capacitors using a hand made apparatus as shown in Fig. 6 and Abe and Tanaka<sup>10)</sup> tried to develop piezoelectric applications. After the successful sintering of  $\text{BaTiO}_3$  discs with a diameter of 50 mm and a thickness of 5 mm at Murata in 1950 May, they developed a Langevin-type  $\text{BaTiO}_3$  vibrator as a new electro-acoustic transducer as shown in Fig. 7. The first practical test for a fish finder was conducted Suruga Bay in 1951 March with corporation of Murata, Japan Radio Co. (JRC) and Sanken Co. The first trial manufacture of phonograph pick up was presented at a meeting in 1951 April. In 1951 Nov., the late Showa Emperor came to Kyoto Univ. At that time, Abe showed the Langevin-type fish finder and the phonograph pick up to His Majesty.

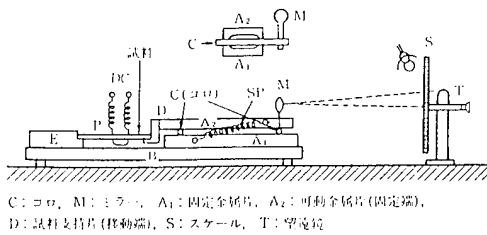


図3 微小ひずみの観測装置

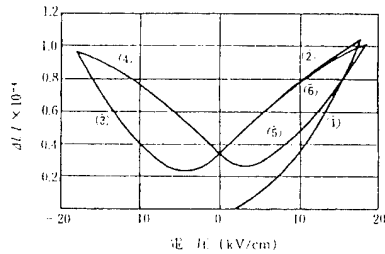


図4 ひずみの電圧特性

Fig. 6 Had made electrostriction measuring apparatus by Tanaka and the result

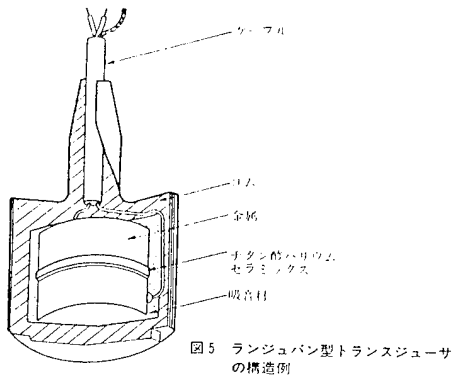


Fig. 7 Langevin-type BaTiO<sub>3</sub> vibrator as a new electro-acoustic transducer

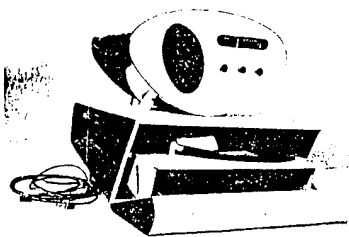
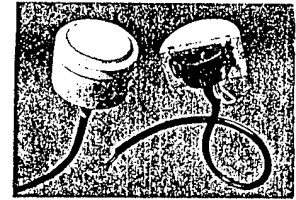
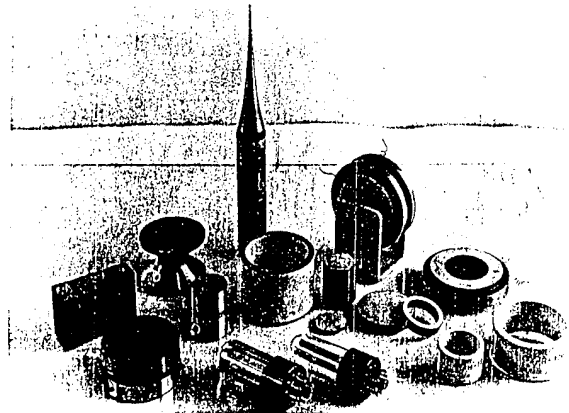


Fig. 8 Phonograph pick up in Murata in 1951

昭和26年、昭和天皇京都大学  
行幸の時天覧頂いたチタバリ  
ピックアップとレコードプレー  
ヤーとラジオ



ゴムモールドしたチタバリ・  
ランジュバン型超音波振動子



初期の圧電製品のいろいろ

応用製品写真 405

Fig. 9 Piezoelectric products in Murata in 1956.

Table 3 The first composition of BaTiO<sub>3</sub> for a piezoelectric vibrator for fish finder in MURATA in 1951-1952.

B-12 (the first successful firing, 1950 March)	
BaCO <sub>3</sub> ·TiO <sub>2</sub>	100 g
TiO <sub>2</sub>	2 (Tochigi Chemical, now Fuji Titanium Co. including a small amount of MnO <sub>2</sub> )
PbO	2
CaF <sub>2</sub>	2
clay	2 (Motoyama clay)

two pieces of 50 mm φ, 3 mm in thick, one piece goes to

Tohoku Univ. through Fujishima and the motional impedance was measured.

B-15 (The first fish finder experiment, 1951 March)	
BaCO <sub>3</sub>	710 wt
TiO <sub>2</sub>	290 (Tochigi Chemical, including a small amount of MnO <sub>2</sub> )
Pb <sub>3</sub> O <sub>4</sub>	20
CaF <sub>2</sub>	20
clay	20 (Motoyama clay)

V-2 (standard after 1952 for piezoelectric applications)	
BaCO <sub>3</sub>	718 wt (Sakai Chemical)
TiO <sub>2</sub>	282 (Chitan kogyo, without a small amount of MnO <sub>2</sub> )
clay	20 (Motoyama clay)
MnO <sub>2</sub>	2



9 After the great success of the fish finder experiment, Ito proposed to organize "Study Group of Ferroelectrics in Japan" chaired by Abe, with Tanaka, Nakajima(JRC) who was Telefunken before the world war I, Hoshiai(Tokyo Univ.), Matsudaira(Tohoku Univ.), Saneyoshi (TIT) and the very small company Murata. This Study Group was a great driving force of practical applications of ferroelectric ceramics in Japan for 40 years.


10 The basic technology of the capacitor production of TC and Hi-K and the quality control were almost established in 1951-53 by solving the technical problems on humidity and life tests using a small amount of  $MnO_2$  additives.

11 Robert first investigated an anomaly of dielectric properties of  $PbZrO_3$ <sup>11)</sup>. Takagi first presented the anti-ferroelectrics at the fall meeting of Jpn. Phys. Soc. in Nov. of 1950 in Osaka with a system  $PbZrO_3$  including 3-7 at % of  $PbTiO_3$ . This was the first announcement of anti-ferroelectrics before Kittel<sup>12)</sup>.

12 Sawada and Nomura investigated  $(Ba,Pb)TiO_3$  and other binary systems including  $BaTiO_3$  with Takagi, Shirane, Sawaguchi and others. This cooperated research accomplished a famous PZT phase diagram. Unfortunately, Sawaguchi forgot to measure the PZT piezoelectric properties. B. Jaffe' PZT patents were shocking affects to Japanese ceramic industries.

A U S G A B E 1969

Abbildungen und Werte gelten nur bedingt als Unterlagen für Bestellungen. Rechtsverbindlich ist jeweils die Auftragsbestätigung.  
Änderungen, die den Fortschritt dokumentieren, vorbehalten.

Exporteur: **HEIM  ELECTRIC**  
Export- und Importgesellschaft m.b.H.  
DDR-104 Berlin, Luiseustraße 46

Kombinat  
VEB Keramische Werke Hermsdorf - DDR-653 Hermsdorf/Thüringen

Drahtwort: Kaweha Hermsdorfthür  
Fernsprecher: Sa-Nr. 411 und 501  
Telex: 058 246

III/18/2-14124 Ag 26/12/69

Fig. 10 Catalog of later Hessho in East Germany in 1973.

13 TC capacitors for Japan Military force developed by Wakino in Murata in 1953.  $BaTiO_3$  Feed through capacitor for microwave relay station of NTT developed by Saburi in 1953. In 1955, Okazaki joined at The National Defence Academy. In 1956,  $BaTiO_3$  disc capacitors for TV use started a great growth in Murata, TDK, Taiyo Yuden and others.

#### References

- 1 Party of in Honor the Publication: Condolence of Dr. Yoji Ito, 1955.
- 2 Ernst Albert-Schonberg ed: "High Frequency Insulator" 1939 Berlin, Translation book translated by H. Funabiki, 1940 March Yushodo, Tokyo
- 3 S. Moyiyasu: NTT Research Report, No. 401. 1936, 12.
- 4 S. Waku; presented at Special Seminar on Ferroelectric Research, 1974, Aug. 1, at NTT.
- 5 T. Ogawa, H. Takahashi, T. Nakamura, T. Miyake and Ueda, Sawada, G. Shirane and others: "Busseiron kenkyuu" 1947, 7.
- 6 A. Von Hippel: "High Dielectric Constant Ceramics", J. Ind. Eng. Chem., 28, (1946) 1097.
- 7 K. Okazaki: Ceramic Engineering For Dielectrics, 1st ed. 1964, Gakkensha, translated into Russian, 4th ed. published in 1992.
- 8 K. Okazaki: Condolence for Emeritus Professor Kiyoshi Abe, Father of Application of Ferroelectric Materials in Japan, Ferroelectrics, 1980, Vol. 29, pp. 1-2.
- 9 T. Tanaka, K. Okazaki and N. Ichinose ed: Piezoelectric Ceramic Materials, Gakkensha, 1973, in Japanese.
- 10 Murata Co. Ltd.: Memory Publication of Murata. Co. 45 years, "Kyo-no Chitabari" 1990, Maruzen, Tokyo.
- 11 T. Takagi: presented at fall meeting of Jpn. Phys. Soc., Nov. 1950.
- 12 C. Kittel: Introduction to Solid State Physics, 2nd ed, 1956.

# Grain Size Effects in Barium Titanate - Revisited

A.J. Bell

Laboratoire de Céramique, EPFL, 1015 Lausanne, Switzerland

**Abstract** — The effects of grain size on the dielectric properties of barium titanate ceramics are reviewed from a historical perspective. The problem has been studied for 40 years, and great insight concerning the characteristics of fine grained materials has been gained. Nevertheless, the story has still to reach a satisfactory conclusion.

## INTRODUCTION

It is now forty years since the observations of Kneipkamp and Heywang [1] revealed a rather significant dependence of the dielectric permittivity of barium titanate ceramics on their grain size. Today, perhaps the largest application of ferroelectric materials is as high permittivity dielectrics with moderate temperature stability (X7R type), the majority of which are dependent upon this effect to achieve the required combination of properties for use in multilayer capacitors [2]. However, despite its present-day importance and the time elapsed since its discovery, a large number of studies of the grain size effect have failed to reach satisfactory agreement concerning the origin of the phenomenon.

In the context of the historical perspective of the 9th ISAF, a chronology of studies concerning the grain size effect is presented, followed by a discussion of the most important issues. For brevity, data concerning size effects in powders [3, 4, 5, 6 and 7] have been omitted from the review.

## A SUMMARY OF THE SIZE EFFECTS

For the sake of clarity, the most important experimental observations, are first summarised without speculating on their origin. References are omitted from this section but can be found within the chronology itself.

### Room Temperature Permittivity

The one experimental result virtually common to all studies is that the room temperature relative permittivity of coarse grained ceramics of barium titanate (grain size  $\geq 10 \mu\text{m}$ ) lies in the range from 1500 to 2000, whilst that of fine grained ceramics (grain size  $\leq 1 \mu\text{m}$ ) is much larger, with values in the range 3500 to 6000 being reported. The coarse grained permittivity has been shown to be consistent with that expected from the single crystal values ( $\epsilon_{11} = 4500$ ,  $\epsilon_{33} = 250$ ) and contributions from domain walls, whilst the values for fine grained materials are much higher than may be expected by simple averaging. The permittivity reaches a maximum for grain sizes in the range 0.4 to 0.8  $\mu\text{m}$  and then again decreases for smaller grain sizes.

### Permittivity at the Ferroelectric Phase Transition

In a number of studies of fine grained ceramics, the transition from the cubic paraelectric to the tetragonal ferroelectric phase, normally at a

temperature between 120 and 130°C, appears to lose its first order character and become more diffuse. This is apparent as a suppression and, for the finest grain sizes, a broadening of the peak in permittivity at the transition temperature. Shifts in the tetragonal-orthorhombic and orthorhombic-rhombohedral transition temperatures as a function of grain size have also been observed.

## CHRONOLOGY

**1954** Kneipkamp and Heywang [1] report a value of permittivity for fine-grained barium titanate of 3500, twice that of coarse grained material.

**1955** Egerton and Koonce [8] carried out fast-firing studies, allowing them to achieve ceramics with 95% density by firing at 1270°C for 15 minutes with very little grain growth and resulting in a permittivity of 3400. Coarse grained ceramics fired at  $> 1300^\circ\text{C}$  exhibited permittivities of 1800. A tentative explanation suggested that there was a preferred orientation of the crystallite 'a' axes parallel to the measurement direction.

**1956** Marutake [9] publishes methods for calculating the relative permittivity of single domain polycrystalline barium titanate from the single crystal values. A simple treatment produces a result identical to that of Bruggeman [10] with a value of 2500, however including terms due to "piezoelectric clamping" of the grains produces a value of 1500.

**1960** Anan'eva [11] reports a value of room temperature permittivity of 6000 for ceramics prepared from a "chemically pure" powder.

**1962** Jonker and Noorlander [12] observed a tetragonal ratio for fine grained barium titanate ceramics which was less than that of equivalently sized powder.

**1966** Following unpublished observations at the Sprague Electric Company that in comparison to coarse grained material, the occurrence of stress relieving, 90° twins was very much reduced in fine grained barium titanate Buessem, Cross and Goswami [13] proposed that the internal stress in fine-grained material must be greater than that in coarse grained ceramics. Using the Devonshire version of Landau theory as applied to ferroelectrics [14], in which the free energy of the system is expanded in terms of polarisation, and including the electrostrictive coupling terms between stress and polarisation, Buessem considered a stress system consisting of a uniform compression along the c-axes and equal tensions along the a-axes of single domain crystallites. The resulting logarithmically averaged polycrystalline permittivity was 3000 for an internal stress of  $640 \text{ kg cm}^{-2}$  (63 MPa) and 6000 for a value of  $800 \text{ kg cm}^{-2}$  (78.4 MPa). The former level of internal stress was shown to be consistent with a reduction in the c/a ratio of 15%, in apparent agreement with the X-ray data of Jonker [12].

In an accompanying publication [15] the same authors used the same model to show that the observed differences in permittivity of coarse and fine grained ceramics subjected to two dimensional compressive stresses could be accounted for by the presence of internal stress, of the above-mentioned type, in the fine grained material.

**1972** Micheron [16] interpreted the apparent diffuseness of the ferroelectric phase transition in barium titanate ceramics as the consequence of a distribution of internal stresses acting on the crystallites. Again using the Devonshire treatment, he assumed a Gaussian distribution of internal stresses centred around zero and showed that on fitting to experimental data, the RMS value of internal stress increased by a factor of 2 as the grain size decreased from 100 to 5  $\mu\text{m}$ .

**1974** Martirena and Burfoot [17] argued that the model proposed by Buessem et al. [13] was flawed, in that the level of internal stress predicted by the model would imply a reduction in the phase transition temperature by 30 to 40°C. The model was regarded as having "failed"

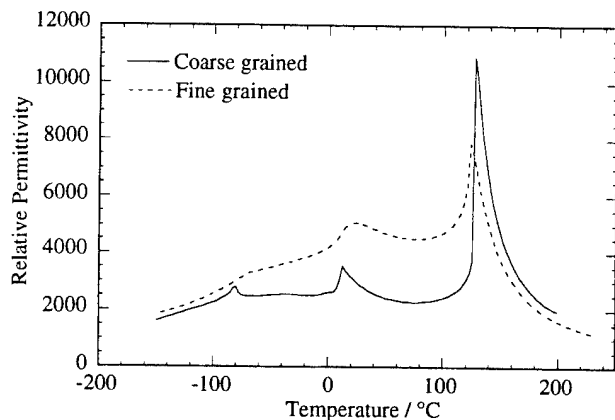


Figure 1. Typical example of the relative permittivity as a function of temperature for coarse and fine grained barium titanate.

because it did not account for the diffuseness of the ferroelectric-paraelectric transition in terms of a distribution of stresses. The authors attempted to show that the earlier model of Diamond [18] for calculation of the permittivity due to an ensemble of grains with a Gaussian distribution of transition temperatures could account for both the diffuseness of the phase transition and the high permittivity at room temperature in fine-grained materials.

Sharma and McCartney [19] found an exponential dependence of permittivity with decreasing grain size.

Simpson [20] published a method, based on the variational theory of Hashin and Shtrikman [21] for the calculation of the upper and lower bounds of permittivity of a polycrystalline body in which a unique microscopic geometry cannot be defined. The upper and lower limits for barium titanate were calculated as 2430 and 865 respectively.

**1976** Pohanka and co-workers [22] measured the fracture strength of barium titanate ceramics at room temperature and at 150°C, i.e. 20°C above the cubic-tetragonal phase transition. They found that, independent of grain size, from 2 to 200 µm, the flexure strength at room temperature was 60 MPa less than above the transition. This was interpreted as implying the presence of an internal stress at room temperature of 60 MPa, which would add to the applied stress and reducing that required to cause failure. The value of 60 MPa is in good agreement with the internal stress model of Buessem et al. [13], but the grain size independence is not. This latter point was accounted for by assuming that the internal stress in coarse grained materials is localised at the grain boundaries, the probable origin of fracture. Such a stress would contribute to the fracture strength for all grain sizes but would be of significance to the dielectric properties for the smallest of grain sizes only.

Some of the most unambiguous experimental data concerning the grain size effects came from the laboratories of NTT in Japan. Kinoshita and Yamaji [23] measured dielectric properties for ceramics with grain sizes in the range 1.1 to 53 µm showing a monotonic increase of permittivity at room temperature with decreasing grain size. It was shown that there were virtually no observed effects of the grain size upon the dielectric properties around the cubic-tetragonal phase transition; the transition temperature, the Curie constant and maximum permittivity are virtually independent of grain size. In addition the data are collinear above the transition. The authors also reported that the temperatures of the tetragonal-orthorhombic and orthorhombic-rhombohedral phase transitions both increase by 10°C with grain size decreasing from 53 to 1.1 µm.

**1977** The same group published more detailed data for a second set of fine-grained ceramics which exhibited similar trends in their properties [24]. In this case the fine grain size was achieved by doping with Dy<sup>3+</sup> in concentrations up to 1.2 at %. They showed that both grain size and spontaneous strain decreased with Dy concentration as room temperature permittivity increased. For a sample with mean grain size of 1.5 µm, the frequency of occurrence of 90° domains was determined as a function of the size of grain by scanning electron microscopy of etched replicas. Domains were identified in 70% of grains of diameter 3.25 µm, but in less than 5 % of grains with diameter 0.75 µm. This observation appears to support the original inspiration for the internal stress model, i.e. that the occurrence of domains in fine grained materials is very much diminished in comparison to coarse specimens. It is tempting to speculate therefore that the behaviour of the observed dielectric properties and spontaneous strain are a consequence of the size effect, caused by internal stress, rather than a direct change in the lattice response due to the incorporation of Dy<sup>3+</sup>. This view is supported by the observation that the cubic-tetragonal transition temperature, the Curie constant, and the cubic cell parameter and its temperature dependence above the transition, are all virtually independent of the Dy concentration. As in their previous study of pure materials [23], the systematic variation of dielectric properties occurs only in the ferroelectric phases.

**1978** In order to explain the gradual increase in room temperature permittivity as a function of decreasing grain size the NTT group invoked a model [25] inspired by the localised stress interpretation of Pohanka's strength measurements [21]. They showed that the assumption of each grain consisting of two regions, an unstressed core ( $\epsilon_r = 1300$ ) and a stressed shell ( $\epsilon_r = 5000$ , thickness 0.3 µm), resulted in a match to the experimentally observed dependence of permittivity on grain size.

Further fracture experiments were carried out by Pohanka, Freiman and Bender [26] in which the fracture toughness was measured on

centre-grooved, double cantilever beam specimens as a function of grain size, both above and below the cubic-tetragonal phase transition. An increase in fracture toughness was observed with increasing grain size in the ferroelectric state; no corresponding variation was seen in the paraelectric state, in which the fracture energy was independent of grain size and equal to that of the fine-grained ceramic at room temperature. These observations were interpreted as an increase in the fracture energy in the ferroelectric state due to stress relief and energy dissipation at the crack tip due to the motion of 90° domain walls and/or twin nucleated parasitic cracking. Such an explanation would be consistent with the diminished occurrence or mobility of 90° domain walls in fine-grained ceramics. An internal stress for fine-grained ceramics was estimated to be approximately 70 MPa.

**1980** Arlt and Sasko [27] described the dominant domain configurations observed in large grained barium titanate ceramics.

Multani and Palkar [28] suggest that the reduction of permittivity as a function of grain size at ferroelectric transitions is a consequence of the cut-off of the soft-mode frequency by the finite size of the grain.

**1981** Dudkevich et al. [29] noted for barium titanate thin films a correlation between the room temperature permittivity and the size of coherently scattering regions, as measured by X-ray line broadening. The film permittivity increased from < 100 to > 1000 as the coherent region size increased from 200 to 600 Å. They attributed this effect to the same cut-off in the low frequency phonon modes described by Multani [28], but with the coherently diffracting region acting as the "grain". They estimated an upper limit for the "critical size" for the appearance of this effect as 250 to 300 Å.

**1983** A similar analysis of the interaction between soft-modes and grain size was presented by Srinivasan and co-workers [30]. The effect on the dielectric properties of the grain size limit to the phonon spectrum was shown to occur for particle sizes below 0.1 µm, but was only significant for sizes below 150 Å. The calculated behaviour appears as an overall reduction in the permittivity, both at room temperature and at the phase transition, rather than as an increase in the diffuseness of the transition as a function of decreasing size.

Taking the existing description of domain configurations in barium titanate [27], Arlt and Peusens [31] calculated the volume contribution to the permittivity of coarse grained material to be approximately 1000. They assumed that the difference between this and measured values,  $\Delta\epsilon_r \approx 650$ , is due to the contribution from 90° domain wall motion.

Strength measurements made using controlled flaw sizes, performed by Cook et al. [32] again indicated the presence of internal stress below the phase transition temperature as the induced flaw size coincided with the grain size of the ceramic.

**1984** Buessem's phenomenological calculations of the internal stress dependence of relative permittivity [13] were extended by Bell [33] to encompass all ferroelectric phases of the materials and the paraelectric-ferroelectric transition. The internal stress was entered into the free energy expression as a strain-dependent, and hence, polarisation-dependent term, with the result that the relationships between internal stress, phase transition shifts and relative permittivity were demonstrated to be similar to the experimental observations [22].

**1985** Arlt and co-workers [34] made observations of domain structures and dielectric measurements on ceramics with grain sizes in the range 0.2 to 100 µm. They found that the room temperature relative permittivity was a maximum for grain sizes around 0.7 µm, below which there was a rapid decrease in permittivity with decreasing grain size and a suppression of the peak at the phase transition. Scanning and transmission electron microscopy revealed that 90° domains could still be identified for grain sizes as low as 0.5 µm and that the domain width was proportional to the square root of the grain size. This latter finding was supported by theoretical analysis of the minimum energy condition for a single grain containing 90° domains. It was also suggested that domains would not occur for grain sizes less than 0.4 µm. Arlt concluded that the internal stress model was invalidated by the observation of increasing numbers of stress-relieving domains with decreasing grain size and showed that the high permittivity for fine grained materials could be explained in terms of a very large contribution from the 90° domain walls, 5 or 6 times greater than that in coarse grained ceramics and 3 to 4 times greater than the intrinsic volume contribution. It was also noted that between 1 µm and 0.5 µm grain size there was a reduction in the spontaneous strain by a factor of 2, coincident with the introduction of orthorhombic-type peaks in the X-

**1989** Shaikh et al. [35] made similar dielectric observations to Arlt [34] down to grain sizes of 0.3  $\mu\text{m}$ , noting a maximum in the permittivity at about 0.4  $\mu\text{m}$ . In addition, they noted a strong reduction in the spontaneous polarisation with decreasing grain size below 1  $\mu\text{m}$  consistent with previous spontaneous strain measurements [34]. In attempting to model the permittivity as a function of grain size, the authors assumed that the original internal stress model applies for grain sizes < 0.4  $\mu\text{m}$ , whilst for grain sizes > 0.4  $\mu\text{m}$  stresses are completely compensated by 90° domains, the permittivity contributions from which are proportional to the reciprocal of the square root of grain size. In addition, the concept of an amorphous grain boundary phase of low dielectric constant and zero spontaneous polarisation is introduced. The increasing importance of the grain boundary phase, with decreasing grain size, acts to reduce the total permittivity and polarisation. In the numerical calculation, the fit to the observed data involves four parameters which include a diffusion coefficient and activation energy for the growth of the amorphous phase. The model provides a good fit to the data, with the outcome that the thickness of the amorphous phase, with a relative permittivity of 90, increases from 1 nm for a 15  $\mu\text{m}$  grain size to 9 nm for 0.3  $\mu\text{m}$  grains.

**1990** Arlt [36 & 37] reviewed in greater detail the calculation of domain width as a function of grain size, finding a lower limit of domain width of 40 nm. The ability of 90° domains to fully compensate homogeneous stresses and the creation of inhomogeneous stresses close to the grain boundary are emphasised.

**1991** Arlt and Pertsev [38] derived an expression for the restoring force constant of 90° domain walls, finding an inverse proportionality to the domain width. Hence the domain walls of smaller domains are more difficult to move than those of large domains, in apparent contradiction of the model previously proposed by Arlt [34] to explain the high permittivity in fine grained ceramics. For coarse grained ceramics the contribution to the permittivity from domain wall movement is estimated as approximately 600, in agreement with previous estimates [31]. Included in the derivation of mobility is a term due to the inhomogeneous stresses at the grain boundaries. As these stresses are reduced by movement of the domain wall, they have a positive contribution to the mobility. Inclusion of this term for grain sizes of 1  $\mu\text{m}$  increases the domain wall contribution to permittivity by only 25 %, but this is observed to be clearly insufficient to account for the established experimental data. However, there is speculation that the domain wall motion might be softened by the reduction in spontaneous strain and polarisation observed in fine grained materials and hence further increase the domain wall contribution.

**1992** Wu and Schulze [39 & 40] compared the ageing and a.c. field dependence of permittivity of fine and coarse grained ceramics. The ageing in fine grain ceramics is slower and less temperature and frequency sensitive. Both the relative permittivity and  $\tan \delta$  of coarse grained ceramics were observed to be constant up to a.c. measurement fields of approximately 200 V  $\text{cm}^{-1}$  above which they increased strongly with increasing applied field - the so-called non-linear effect. For fine grained ceramics, although the weak field permittivity is, as expected, higher than that of the coarse grained materials, the subsequent increase in permittivity with ac field was much smaller, with a less pronounced threshold field for the onset of non-linearity. Similarly, the increase in  $\tan \delta$  was much less significant for the fine grained ceramic, and notably the weak field  $\tan \delta$  of fine and coarse grained materials were equal.

Two groups [41 & 42] reported grain size effects in strontium barium titanate ceramics with strontium substitutions up to 30%. Similar grain size effects were seen as in pure barium titanate.

Criado et al. [43] noted a correlation of the size of coherently diffracting domains in X-ray line broadening measurements to the dielectric properties of fine grained ceramics, similar to that noted for thin films [29]. The permittivity decreased at all temperatures for decreasing diffracting domain size in the range 100 to 10000 Å.

**1993** Bell [44] proposed that the above observation [43] may be explained, in part, by the spatially uniform thermal fluctuations of small coherently polarising domains leading to a distribution of spontaneous polarisation and permittivity over an ensemble of domains. Calculations showed, however, that the upper domain size limit for which such effects become important was approximately 150Å.

It was more than 10 years after the first reports of the anomalous effects of grain size on the permittivity that an acceptable, quantitative model was proposed. In the following 20 years evidence in the form of the results of fracture mechanics investigations supported the internal stress model of Buessem, Cross and Goswami [13] with remarkable consistency concerning the quantitative estimates of the stress [22]. Attempts to explain both the room temperature effect and the "diffuseness" of the phase transition through a distribution of phase transition temperatures were not convincing. The results of Martirena and Burfoot [17] did not fit existing data satisfactorily; a distribution width of 140°C is consistent with a room temperature permittivity of 3000, but the peak at the cubic-tetragonal transition is rendered non-existent. Their dismissal of Buessem's model was perhaps a little misguided as: (i) it was never explicitly assumed that the proposed internal stress was independent of temperature, (indeed it was more logical to assume that the stress decreased with increasing temperature, as does the spontaneous strain, and so is unlikely to result in a large reduction in the phase transition temperature), and (ii) the model was not proposed to account for the diffuseness of phase transitions. In this respect the data from the NTT laboratories provided important clarification [23-25]. The data allow two important conclusions to be made: (i) the high permittivity in the ferroelectric phases is certainly a consequence of ferroelectricity and not of the ceramic microstructure alone (e.g. grain boundary phases), and (ii) the diffuseness of the cubic-tetragonal transition, reported by a number of observers, is not of the same origin as the elevated room temperature permittivity and must be attributed to another mechanism, most probably process dependent. Bearing in mind the correlation of properties with sub-grain, defect related, features, it is likely that the phenomena referred to by Dudkevich [29], Srinivasan [30] and Bell [44], may well play a role in the suppression of permittivity at the phase transition, particularly for ceramics that have been exposed to minimal thermal treatments.

By 1984, therefore, the internal stress model was well established and it seemed that, with confirmation of its consistency with observed shifts in phase transition temperatures [33], there was little to question its veracity. However, in 1985, the observations of the increasing density of domains with decreasing grain size [34] completely contradicted one of the original influences for the development of the internal stress model, i.e. the observation that the occurrence of 90° domains diminished with decreasing grain size, which was cited in Buessem's paper [13] and later supported by independent data from NTT [24]. There followed half a dozen years in which it seemed impossible to reconcile the two schools of thought, — the existence of domain walls implied insignificant levels of the internal stress and the increasing density of domain walls could account for the increase in permittivity with decreasing grain size. However, the calculations by Arlt [38] of the domain wall mobility as a function of grain size, cast doubt on his own model. The reduction of mobility for decreasing domain and hence grain sizes appeared to indicate that the domain walls could not provide the contribution necessary to raise the permittivity to values between 4000 and 6000. Even considering the extra softening mechanisms referred to by Arlt,

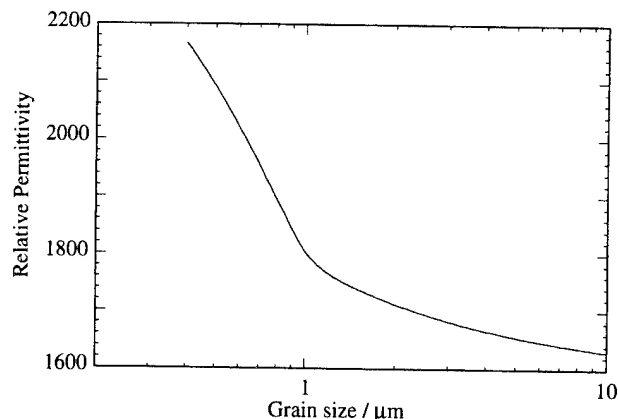


Figure 2. Relative permittivity as a function of grain size calculated for domain wall contributions, and including the softening terms described by Arlt and Pertsev [38].

due to the reduction in spontaneous strain and polarisation for grain sizes of less than 1  $\mu\text{m}$ , the domain wall contribution, calculated here, still falls a factor of 5 below that necessary to match experimental data (Figure 2).

More recently further doubt was cast upon the domain wall contribution model by the measurements of Wu and Schulze [39 & 40]. Both ageing and non-linear dielectric effects in ferroelectric ceramics have been attributed to the movement of 90° domain walls [45]. The virtual absence of non-linear effects and low  $\tan \delta$  in fine grained barium titanate suggests that in these materials, either the domain walls are anhysteretic and make almost their full contribution at very low measurement fields, or that the domain walls are clamped, contributing little to the dielectric properties. The very low ageing rates in these materials are perhaps more consistent with the latter.

Superficially it might seem as though both of the established models are now fatally flawed and that one must look elsewhere for an explanation of the anomalous room temperature effect. However, it seems possible that the observations of increasing occurrence of domains with decreasing grain size are not contradictory to the internal stress model. Arlt acknowledged the increasing importance of the stresses at the grain boundaries with decreasing grain size [38] and the existence of an inhomogeneous stress component was recognised experimentally in 1976 [26]. However, are these factors consistent with the anomalous permittivity and the decrease in spontaneous strain/polarisation below 1  $\mu\text{m}$ ? This is certainly a question with which to inspire the next generation of Ph.D. candidates who address the problem of grain size effects in barium titanate.

One of the more puzzling aspects of this story is that the study of domain occurrence as a function of grain size published in 1985 [34] produced results completely opposite to those of previous work. Perhaps this is most easily attributable to the improvement in microscopy techniques in the intervening years. The studies at NTT were carried out using scanning electron microscopy of replicas of etched specimens. It is quite believable that the resolution of this technique could be quite limited, with respect to sub-micron domains.

In concluding it is interesting to reflect on other changes that have occurred in experimental technique during the past forty years and to speculate on the influence they may have had on the development of this topic. In terms of the materials preparation, it would seem that little has changed. Although we now find a host of references in the literature to novel preparation methods, the great majority of the materials referred to in this study were based on oxalate-derived powders, a process that has been used since the mid-1950's. Hot-pressing and fast-firing were used in some of the earliest studies of the effect and are not a modern development. Certainly, instrumentation for the measurement of dielectric properties has changed over the last forty years, but this seems to have had very little impact on the quality of data obtained. Perhaps it is somewhat easier now, than it was 40 years ago, to measure the a.c. field dependence of properties, but this was not attempted in the majority of studies. The quantity of data has increased, a factor which can be attributed to automation of experiments. The major benefit, perhaps, has been to increase the number of data points per unit temperature, providing a clearer picture of the behaviour at the phase transition. Similarly, the increased availability of fast, desk-top computers and user-friendly maths applications has reduced the development time for numerical simulations, but without, necessarily, a commensurate improvement in the quality of the underlying physical models.

#### Acknowledgement

The author thanks M. Demartin and A. Glazounov of the Ceramics Laboratory, EPFL, for the data in Figure 1.

#### REFERENCES

- H. Kneipkamp and W. Heywang, "Depolarisation effects in polycrystalline  $\text{BaTiO}_3$ " *Zeit. Angew. Phys.* **6**, 385 (1954)
- D. Hennings and G. Rosenstein, "Temperature-stable dielectrics based on chemically inhomogeneous  $\text{BaTiO}_3$ " *J. Am. Ceram. Soc.* **67**, 249, (1984)
- M. Anliker, H.R. Brugger and W. Känzig, "Study of fine powder ferroelectrics II: Barium Titanate  $\text{BaTiO}_3$ " *Helv. Phys. Acta.* **27** 99 (1954)
- M. Shojiet Brit. *J. Appl. Phys.* **15** 719 (1964)
- A.J. Mountvala *J. Am Ceram. Soc.* **54** 544 (1971)
- K. Uchino, E. Sadanaga and T. Hirose "Dependence of the crystal structure on particle size in barium titanate", *J. Am. Ceram. Soc.* **72** 1555 (1989)
- Y.G. Wang, W.-L. Zhong and P.L. Zhang "Size driven phase transition in ferroelectric particles" *Solid State Comm.* **90** 329 (1994)
- L. Egerton and S.E. Koonce "Effect of firing cycle on structure and some dielectric and piezoelectric properties of barium titanate ceramics." *J. Am. Ceram. Soc.* **38** 412 (1955)
- M. Marutake "A calculation of physical constants of ceramic barium titanate" *J. Phys. Soc. Jpn.* **11** 807 (1956)
- D.A.G. Bruggeman, "Calculation of various physical constants of heterogeneous substances" *Ann. Phys.* **24** 636 (1935)
- A.A. Anan'eva, B.V. Strizkov and M.A. Ugrymova "Some anomalous properties of chemically pure barium titanate" *Bull. Acad. Sci. U.S.S.R. Phys. Sci (English Translation)* **24** 1395 (1960)
- G.H. Jonker and W. Noorlander in *Science of Ceramics* vol.1, p 255, ed. G.H. Stewart, Academic Press, New York (1962)
- W.R. Buessem, L.E. Cross and A.K. Goswami, "Phenomenological theory of high permittivity in fine-grained barium titanate", *J. Am. Ceram. Soc.* **49**, 33 (1966)
- A.F. Devonshire "Theory of barium titanate, Part I", *Phil. Mag.* **40** 1040 (1949)
- W.R. Buessem, L.E. Cross and A.K. Goswami, "Effect of two dimensional stress on the permittivity of fine- and coarse-grained barium titanate", *J. Am. Ceram. Soc.* **49**, 36 (1966)
- F. Micheron "Influence des contraintes internes sur les propriétés statiques et dynamiques des matériaux ferroélectriques polycristallins", *Rev. Tech. Thomson-CSF* **4** 5 (1972)
- H.T. Martirena and J.C. Burfoot "Grain size effects on properties of some ferroelectric ceramics", *J. Phys. C: Solid State Phys.* **7** 3182 (1974)
- H. Diamond "Variation of permittivity with electric field in perovskite-like ferroelectrics" *J. Appl. Phys.* **32** 909 (1961)
- N.C. Sharma and E.R. McCartney "The dielectric properties of pure barium titanate as a function of grain size" *J. Aus. Ceram. Soc.* **10** 16 (1974)
- G. Simpson "The dielectric constants of a ferroelectric ceramic" *Ferroelectrics* **6** 283 (1974)
- Z. Hashin and V. Shtrikman, *Phys. Rev.* **130** 129 (1963)
- R.C. Pohanka, R.W. Rice and B.E. Walker, Jr., "Effect of internal stress on the strength of  $\text{BaTiO}_3$ " *J. Am. Ceram. Soc.* **59** 71 (1976)
- K. Kinoshita and A. Yamaji "Grain-size effects on the dielectric properties in barium titanate ceramics" *J. Appl. Phys.* **47** 371 (1976)
- A. Yamaji, Y. Enomoto, K. Kinoshita and T. Murakami "Preparation, characterisation and properties of Dy-doped small-grained  $\text{BaTiO}_3$  ceramics" *J. Am. Ceram. Soc.* **60** 97 (1977)
- A. Yamaji, Y. Enomoto, K. Kinoshita and T. Tetsuro "Piezoelectric properties and stress distribution in Dy-doped small grained  $\text{BaTiO}_3$  ceramics" *Proc. of 1st Meeting on Ferroelectric Materials and their Applications* 269 (1978)
- R.C. Pohanka, S.W. Freiman and B.A. Bender, "Effect of the phase transformation on the fracture behaviour of  $\text{BaTiO}_3$ " *J. Am. Ceram. Soc.* **61** 72 (1978)
- G. Arlt and P. Sasko "Domain configuration and equilibrium size of domains in  $\text{BaTiO}_3$  ceramics" *J. Appl. Phys.* **51** 4957 (1980)
- M.S. Multani and V.R. Palkar "Grain-size dependent properties of polycrystalline ferroelectrics" *phys. stat. sol (a)* **58** K29 (1980)
- V.P. Dudkevich, V.M. Mukhortov, Y.I. Golovko, V.A. Bukreev, V.M. Mukhortov, Y.G. Sindeev and E.G. Fesenko "Dependences of dielectric properties of condensed  $\text{BaTiO}_3$  films on the size of coherent scattering regions" *Sov. Phys. Solid State* **23** 347 (1981)
- M.R. Srinivasan, M.S. Multani, P. Ayub and R. Vijayaraghavan "Soft modes and grain size effects in ferroelectric ceramics" *Ferroelectrics* **51** 137 (1983)
- G. Arlt and H. Peusens "The dielectric constant of coarse grained  $\text{BaTiO}_3$  ceramics" *Ferroelectrics* **48** 213 (1983)
- R.F. Cook, S.W. Frieman, B.R. Lawn and R.C. Pohanka "Fracture of ferroelectric ceramics" *Ferroelectrics* **50** 593 (1983)
- A.J. Bell, Ph.D. Thesis, University of Leeds (1984)
- G. Arlt, D. Hennings and G. de With "Dielectric properties of fine-grained barium titanate dielectrics" *J. Appl. Phys.* **58** 1619 (1985)
- A.S. Shaikh, R.W. Vest and G.W. Vest "Dielectric properties of ultrafine grained  $\text{BaTiO}_3$ " *IEEE Trans. Ultrasonics, Ferroelectrics and Frequency Control* **36** 407 (1989)
- G. Arlt "Twining in ferroelectric and ferroelastic ceramics: stress relief" *J. Mat. Sci.* **25** 2655 (1990)
- G. Arlt "The influence of microstructure on the properties of ferroelectric ceramics" *Ferroelectrics* **104** 217 (1990)
- G. Arlt and N.A. Pertsev "Force constant and effective mass of 90° domain wall in ferroelectric ceramics" *J. Appl. Phys.* **70** 2283 (1991)
- K. Wu and W.A. Schulze "Effect of the ac field level on the aging of the dielectric response in polycrystalline  $\text{BaTiO}_3$ " *J. Am. Ceram. Soc.* **75** 3385 (1992)
- K. Wu and W.A. Schulze "Aging of the weak-field dielectric response in fine- and coarse-grain ceramic  $\text{BaTiO}_3$ " *J. Am. Ceram. Soc.* **75** 3390 (1992)
- U. Kumar, S.F. Wang, S.R. Varanasi and J.P. Dougherty "Grain size effects on the dielectric properties of strontium barium titanate", *Proc. 8th ISAF*, p.55 (1992)
- H.-W. Wang and D.A. Hall "The effect of dysprosium on the microstructure and dielectric properties of  $(\text{Ba}_{1-x}\text{Sr}_x)\text{TiO}_3$  ceramics" *Proc. 8th ISAF*, p.51 (1992)
- J.M. Criado M.J. Dainez F. Gotor, C. Real, M. Mundi, S. Ramos and J. Del Credo "Correlation between synthesis conditions, coherently diffracting domain size and cubic phase stabilisation in barium titanate", *Ferro. Lett.* **14** 79 (1992)
- A.J. Bell "Calculations of finite size effects in barium titanate" *Ferro. Lett.* **15** 133 (1993)
- S. Li, W. Cao and L.E. Cross "The extrinsic nature of nonlinear behaviour observed in lead zirconate titanate ferroelectric ceramic" *J. Appl. Phys.* **69** 7219 (1991)



# **Concurrent Session - 1A: Piezoelectrics**

# Morphotropic Phase Boundary and Microstructure of Low-Temperature Sintered PZT Ceramics with $\text{BiFeO}_3$ and $\text{Ba}(\text{Cu}_{0.5}\text{W}_{0.5})\text{O}_3$

Kenji Murakami, Nagaya Okada, \*Dunzhuo Dong and \*\*Shoji Kaneko

Research Institute of Electronics, Shizuoka University, \*Graduate School of Electronic Science and Technology, Shizuoka University and \*\*Department of Materials Science and Technology, Shizuoka University  
3-5-1, Johoku, Hamamatsu, Shizuoka 432, JAPAN

**Abstract** - The sintering temperature of the 0.5 wt%  $\text{MnO}_2$ -added  $\text{Pb}(\text{Zr}_{0.53}\text{Ti}_{0.47})\text{O}_3$  ceramics was successfully lowered down to 935 °C by the addition of the complex oxides,  $\text{BiFeO}_3$  and  $\text{Ba}(\text{Cu}_{0.5}\text{W}_{0.5})\text{O}_3$ . This addition may cause a shift of the morphotropic phase boundary (MPB) at which the  $\text{Pb}(\text{Zr,Ti})\text{O}_3$  ceramics shows excellent piezoelectric and dielectric properties. Indeed, the XRD studies reveal that the MPB of the ceramics with additives shifts toward the Ti-rich composition. Thus, the electrical properties are affected by this shift of the MPB and the optimum Zr/Ti ratio of 52/48 is determined. Furthermore, the microstructural analyses by using SEM indicate that the additives seem to form stable grain boundaries and the most stable boundaries are obtained with the corresponding composition.

## INTRODUCTION

Lowering the sintering temperature of  $\text{Pb}(\text{Zr,Ti})\text{O}_3$  ceramics has been attempted to avoid the volatilization of  $\text{PbO}$  component which causes the compositional fluctuation and the environmental contamination. Smith et al. [1] have shown that the  $\text{BiFeO}_3$ - $\text{Pb}(\text{Zr,Ti})\text{O}_3$  system was hot-pressed at a temperature between 750°C and 900°C. It has been also reported that another perovskite-type additive,  $\text{Ba}(\text{Cu}_{0.5}\text{W}_{0.5})\text{O}_3$  was used to reduce the sintering temperature of  $\text{Pb}(\text{Fe}_{0.5}\text{Nb}_{0.5})\text{O}_3$  ceramics as well as to improve the dielectric properties [2].

The authors have attempted a combined use of two additives,  $\text{BiFeO}_3$  (abbreviated as BF) and  $\text{Ba}(\text{Cu}_{0.5}\text{W}_{0.5})\text{O}_3$  (BCW) in 0.5wt%  $\text{MnO}_2$ -added  $\text{Pb}(\text{Zr}_{0.53}\text{Ti}_{0.47})\text{O}_3$  (PZT) ceramics and succeeded to lower its sintering temperature down to 935°C [3,4]. The macroscopic characterizations have already suggested an existence of the transient liquid phase in the ceramics which is caused from the addition of the complex oxides. The lowering of the sintering temperature seems to be related to this transient phase.

On the other hand, the highest piezoelectric coupling as well as the maximum dielectric susceptibility have been found for the morphotropic phase boundary (MPB) of the  $\text{Pb}(\text{Zr,Ti})\text{O}_3$  ceramics. The addition of the complex oxides to  $\text{Pb}(\text{Zr,Ti})\text{O}_3$  ceramics may cause a shift of this MPB, which results in the deterioration of electrical properties. The XRD studies have indicated clearly the coexistence region of tetragonal and rhombohedral phases for the MPB in the case of PZT-BF-BCW ceramics[5].

In this paper, we have investigated the relations between the composition ratio of Zr/Ti and the electrical properties within the coexistence region to obtain the optimal composition for the best properties. Furthermore, microscopic analyses of grain boundaries have been carried out by using TEM and SEM.

## EXPERIMENTAL

### Sample Preparation

The samples were prepared by using a conventional method of ceramic preparation. Commercially available  $\text{Pb}_3\text{O}_4$ ,  $\text{ZrO}_2$ ,  $\text{TiO}_2$ ,  $\text{BaCO}_3$ ,  $\text{CuO}$ ,  $\text{WO}_3$ ,  $\text{Bi}_2\text{O}_3$ ,  $\text{Fe}_2\text{O}_3$  and  $\text{MnO}_2$  (>99.9% purity) were used, and PZT and BCW were separately synthesized by pulverization. PZT, BCW,  $\text{Bi}_2\text{O}_3$  and  $\text{Fe}_2\text{O}_3$  were weighed out according to the formula  $0.92\text{PZT}-0.05\text{BF}-0.03\text{BCW} + 0.08$  wt%  $\text{CuO}$  (PZT-C') and the components were mixed. Disk samples 10 mm in diameter and 3 mm in thickness were formed at the pressure of 800 kg/cm<sup>2</sup> and sintered isothermally with a heating rate of 5 °C/min at temperatures for PZT-C' and 1250 °C for PZT for 30 min.

### XRD Measurements

A detailed XRD profile was obtained using a Rigaku RINT 1100 X-ray diffractometer with  $\text{CuK}\alpha$  radiation to determine the crystalline phase of the ceramics. The behavior of MPB was observed from the XRD profiles of (002) and (200) planes for the tetragonal phase, and the (200) plane for the rhombohedral phase in the diffraction angles (2 $\theta$ ) from 43° to 46°. The lattice constants,  $a$  and  $c$ , of the tetragonal phase were calculated from the profiles of (002) and (200) planes using (220) diffraction profile of Si as an internal standard. The lattice spacing of the (100) plane,  $d_{100}$ , was chosen to determine the lattice constant,  $a$ , of the rhombohedral phase since the rhombohedral angle,  $\alpha$ , falls between 89.6° and 89.7°; therefore, the value of  $a$  is nearly equal to that of  $d_{100}$ [6].

### Electrical Measurements

In order to measure the electrical properties, electrical contacts were made with a silver paste. The silver coating was made on both sides of the sample and subsequently fired at 780°C for 20 min. The dielectric properties (1 kHz) and piezoelectric properties of samples were measured using an impedance analyzer (YHP-4194A) after being poled under 3 kV/mm bias at 120°C in a silicone oil bath for 15 min.

### Characterization

The morphology and composition of the ceramics were observed by JEOL JSM-T330A SEM (scanning electron microscope) and Shimadzu EPMA-8705 EPMA (electron probe micro analyzer), respectively. The microstructure and the composition around grain boundaries of the ceramics were analyzed by JEOL JEM-2000FX II TEM (transmission electron microscope).

## RESULTS AND DISCUSSION

### XRD Analyses

In order to determine the MPB in the  $\text{PbZrO}_3$ - $\text{PbTiO}_3$  solid



solution, the XRD profiles were obtained for the PZT and PZT-C' ceramics of various composition with different ratios of Zr/Ti. Figure 1 plots the change of calculated lattice constants from the XRD profiles. The result clearly indicates that the coexistence region on the MPB was observed between  $x(=Zr/Zr+Ti)=0.52$  and  $x=0.67$  for PZT, while the region becomes narrow ( $x=0.51\sim0.53$ ) and shifts toward the Ti-rich region of the composition for PZT-C'. It was found from the calculation of the unit cell volume and the  $c/a$  ratio that the unit cell volume of PZT-C' is larger than that of PZT, while the  $c/a$  ratio of PZT-C' is smaller than that of PZT for all Zr/Ti ratios studied. The radius of  $Ba^{2+}$  (1.36 Å) is larger than that of  $Pb^{2+}$  (1.26 Å), and that of  $Cu^{2+}$  (0.73 Å) is larger than those of  $Zr^{4+}$  (0.72 Å) and  $Ti^{4+}$  (0.61 Å). Therefore, the increase in the unit cell volume suggests the substitutions of  $Ba^{2+}$  for  $Pb^{2+}$  and  $Cu^{2+}$  for  $(Zr,Ti)^{4+}$ , respectively. Furthermore, the substitution of  $Ba^{2+}$  for more readily polarized  $Pb^{2+}$  probably leads to the reduction in the  $c/a$  ratio. Similarly, Ikeda and Okano have reported that the solid solution of  $BiFeO_3$  into  $Pb(Zr,Ti)O_3$  led to a decrease in the  $c/a$  ratio[7].

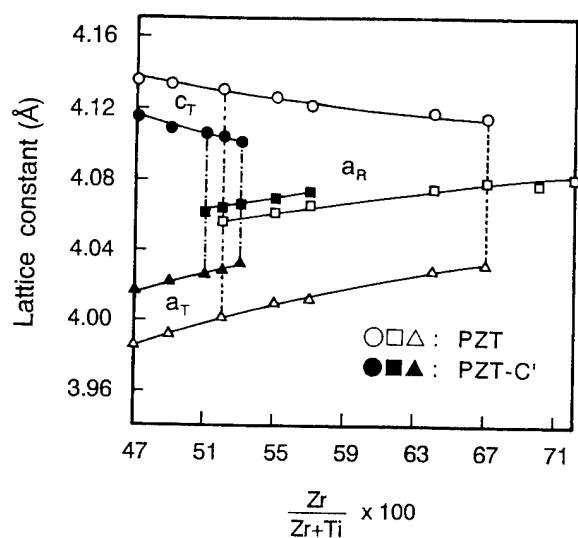


**Figure 1.** Variation of lattice constants of PZT and PZT-C' with Zr/Ti ratio. The coexistence region on the MPB is indicated by a broken line for PZT and by a dot-dashed line for PZT-C'.

### Electrical Properties

The above results suggest that the addition of complex oxides shifts the coexistence region on the MPB toward the Ti-rich region of the composition. This shift may lead to the deterioration of the electrical properties. It was obtained from the electrical measurements that the dissipation factor,  $\tan \delta$ , increases almost linearly with the ratio and that the relative dielectric constant,  $\epsilon_{33}^T/\epsilon_0$ , and the electromechanical coupling factor,  $K_p$ , initially increase with the ratio and then decrease beyond a certain ratio, while the mechanical quality factor,  $Q_m$ , initially decreases with an increase in the ratio and then increases beyond a certain ratio. These results are similar to the case of  $Pb(Zr,Ti)O_3$  ceramics without any additives[8]. The measurements clearly proven that some electrical properties of PZT-C' are deteriorated at the ratio of 53/47 compared with PZT, but that the properties are recovered with the Ti-rich ratios in the shifted coexistence region;  $Q_m$  of PZT-C' is larger than that of PZT,  $K_p$  and  $\epsilon_{33}^T/\epsilon_0$  are slightly smaller due presumably to the reduction in  $c/a$  ratio, and  $\tan \delta$  is almost the same[5]. The results suggest that the

electrical properties of PZT-C' are strongly associated with the shift of the MPB due to the addition of the complex oxides to PZT, namely the shift of the MPB toward the Ti-rich region of the composition induces a corresponding shift of the properties.

### Microstructural Analyses

In order to clarify the influence of the addition of complex oxides to PZT on the microstructure of the ceramics, structural and compositional analyses were carried out by using TEM in the vicinity of the grain boundaries of the ceramic compact[9]. The results revealed that the isolated microstructures exist at the grain boundaries, the lead ion segregates there and that the segregation is more pronounced in the case of the ceramics with the complex oxide additives.

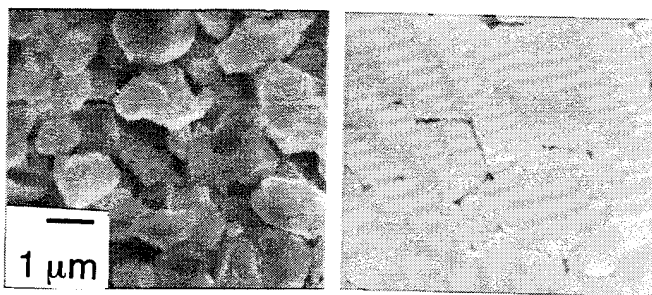


**Figure 2.** SEM micrographs of PZT (left) and PZT-C' (right) chemically etched for 150 s.

For further clarification of the effect of the complex oxide additives, the ceramics was chemically etched with conc. HCl solution, followed by morphological analysis of the grain boundaries with SEM. Figure 2 shows the SEM micrographs of PZT and PZT-C' etched for 150 s. It is clearly revealed that the grains of the ceramics without the complex oxide additives (PZT) are etched more deeply than those with the additives (PZT-C'). The result suggests that the grain boundaries of the PZT-C' ceramics are chemically more stable than those of the PZT ceramics. Even for the PZT-C' ceramics, this chemical stable grain boundaries are observed in the coexistence region on the MPB and the PZT-C' ceramics with the optimum composition of Zr/Ti of 52/48 shows the most stable grain boundaries. Above analyses strongly suggest that the addition of complex oxide to PZT forms the chemically stable grain boundaries resulting in no deterioration of the electrical properties even for the ceramics sintered at lower temperature.

### REFERENCES

- [1] R.T. Smith, G.D. Achenbach, R. Gerson and W. James, *J. Appl. Phys.*, vol. 39, pp. 70-74, 1968.
- [2] K. Handa, T. Watanabe, Y. Yamashita and M. Harata, *IEEE Trans. Consum. Electron.*, vol. CE-30, pp. 342-347, 1984.
- [3] D. Dong, M. Xiong, K. Murakami and S. Kaneko, *Ferroelectrics*, vol. 145, pp. 128-135, 1993.
- [4] D. Dong, K. Murakami, S. Kaneko and M. Xiong, *J. Ceram. Soc. Jpn.*, vol. 101, pp. 1090-1094, 1993.
- [5] D. Dong, K. Murakami, N. Okada and S. Kaneko, *Jpn. J. Appl. Phys.*, in press.
- [6] K. Kakegawa, J. Mohri, S. Shirasaki and K. Takahashi, *J. Am. Ceram. Soc.*, vol. 65, pp. 515-519, 1982.
- [7] T. Ikeda and T. Okano, *Jpn. J. Appl. Phys.*, vol. 2, pp. 63-64, 1963.
- [8] D. Berlincourt, C. Cmolik and H. Jaffe, *Proc. IRE*, vol. 48, pp. 220-229, 1960.
- [9] D. Dong, K. Murakami, N. Okada and S. Kaneko, in *Proc. RIM-PAC '93*, Honolulu, Hawaii, pp. 161-168, 1994.

# Development of New Piezoelectric Ceramics with Bismuth Perovskites

Tadashi Takenaka, Masatoshi Yamada and Takeo Okuda  
Faculty of Science and Technology, Science University of Tokyo,  
Noda, Chiba-ken 278, JAPAN

A new solid solution,  $(1-x)\text{Bi}(\text{Ni}_{0.5}\text{Ti}_{0.5})\text{O}_3 - x(\text{Pb}_a\text{Ba}_b)\text{TiO}_3$  ( $a+b=1$ ) (NTPB [100x-100a/100b]), are studied on the dielectric, ferroelectric, piezoelectric and mechanical properties as a new group of piezoelectric ceramics. One of the end member of the solid solution, BINT ( $a=b=0$ ,  $x=0$ ) is a mixture of a bismuth layered structure consisting of  $\text{Bi}_4\text{Ti}_3\text{O}_{12}$ ,  $\text{NiO}$  and  $\text{Bi}_2\text{O}_3$ . When  $x$  is increased, the crystal structure changes from a mixture of bismuth layered and perovskite structures to a single phase of the perovskite structure at  $x=0.2\sim 0.25$ , being independent of the ratio of  $\text{PbTiO}_3$  to  $\text{BaTiO}_3$ . The crystal phase with  $x \geq 0.25$  of the solid solution is a perovskite structure. The electrical properties are mainly investigated for the specimens of the perovskite structure ( $x \geq 0.25$ ) with 0.02wt% added  $\text{MnCO}_3$ . The electromechanical coupling factors  $k_{33}$ ,  $k_t$  and  $k_p$  of NTPB[40-100/0] + Mn (0.02 wt%) are 0.51, 0.47 and 0.32, respectively. The mechanical bending strength of NTPB[44.5-100/0] + Mn (0.02wt%) is about 150 MPa.

## 1. Introduction

Recently solid solutions based on bismuth perovskite compounds have been investigated as a new family of piezoelectric ceramics different from  $\text{PbZrO}_3$ - $\text{PbTiO}_3$  (PZT) system. The advantage over PZT system is that the atmosphere control to avoid  $\text{PbO}$  evaporation is not necessary because they are free or low content of  $\text{PbO}$ . The other feature is that these ceramics show higher mechanical strength than those of PZT ceramics.

The solid solutions in this group are mainly bismuth sodium titanate,  $(\text{Bi}_{1/2}\text{Na}_{1/2})\text{TiO}_3$  [BNT]<sup>1,2)</sup>-based solid solutions, namely,  $(\text{Bi}_{1/2}\text{Na}_{1/2})_{1-x}(\text{Sr}_a\text{Pb}_b\text{Ca}_c)_x\text{TiO}_3$  ( $a+b+c=1$ ) [BNTX]<sup>3,4)</sup>,  $(\text{Bi}_{1/2}\text{Na}_{1/2})_{1-x}(\text{Pb}_a\text{Ba}_b)_x\text{TiO}_3$  ( $a+b=1$ ) [BNPB]<sup>5,6)</sup>, and  $(\text{BNT})_{1-x}(\text{KNbO}_3)_x$  [BNTKN]<sup>7)</sup>.

A rhombohedral ( $F_R$ ) - tetragonal ( $F_T$ ) morphotropic phase boundary (MPB) in BNTX and BNPB systems enhances the piezoelectric properties. For example, electromechanical coupling factors and piezoelectric strain constants for MPB compositions of BNPB are  $k_{33} \approx 0.55$ ,  $k_{31} \approx 0.20$  and  $d_{33} \approx 120$ ,  $d_{31} \approx 40$  ( $\times 10^{-12}$  C/N). The three-point bending strength of BNT-based piezoelectric ceramics is  $\sigma \approx 200$  MPa which is about twice than those of commercial PZT ceramics. However, the working temperature range of BNT-based ceramics is narrow at higher temperatures because of the ferroelectric to antiferroelectric phase transition at low temperature of  $T_a = 100 \sim 200^\circ\text{C}$ .

To improve the narrow working temperature-range, a new solid solution based on bismuth lead nickel titanate,  $\text{Bi}_{1-x}\text{Pb}_x(\text{Ni}_{(1-x)/2}\text{Ti}_{(1+x)/2})\text{O}_3$ , was proposed and reported<sup>8-10)</sup> on the dielectric and ferroelectric properties.

In this paper, dielectric, piezoelectric and mechanical properties of a new solid solution,  $(1-x)\text{Bi}(\text{Ni}_{0.5}\text{Ti}_{0.5})\text{O}_3 - x(\text{Pb}_a\text{Ba}_b)\text{TiO}_3$

( $a+b=1$ ) (abbreviated to NTPB[100x-100a/100b]), are studied with an eye to finding new piezoelectric ceramics having high mechanical strength. These ceramics will be of interest to new piezoelectric devices because of wide working temperature and high mechanical strength.

## 2. Sample Preparation and Experiments

Solid-solution NTPB piezoelectric ceramics were prepared according to the conventional ceramic sintering technique. Reagent-grade metal oxide or carbonate powders with 99% + purity of  $\text{Bi}_2\text{O}_3$ ,  $\text{PbO}$ ,  $\text{BaCO}_3$ ,  $\text{NiO}$ ,  $\text{TiO}_2$  and  $\text{MnCO}_3$  were used as the starting materials. The oxides and carbonates mixed by ball milling for 10 h were calcined at  $800^\circ\text{C}$  for 1~2 h. After calcining, the mixtures were ground and ball-milled for 20 h in a polyethylene jar with 2 mmφ-zirconia-balls in acetone medium to obtain ceramic powders with mean-particle-size less than 1  $\mu\text{m}$ . The powders were pressed into discs 20mm in diameter and about 2 mm in thickness. The disks were finally sintered at  $1000 \sim 1150^\circ\text{C}$  for 2 h in air. The crystal phase of the sintered ceramics was checked using an X-ray diffractometer.

The electrodes were made of fired-on silver paste for the dielectric, ferroelectric and piezoelectric measurements. Electrical properties were measured by the usual evaluation techniques. Temperature dependence of the dielectric constant  $\epsilon_s$  and loss tangent  $\tan\delta$  of unpoled samples were measured for the determination of the Curie temperature  $T_C$  at 1 MHz using an automated dielectric measurement system with a multifrequency LCR meter (YHP 4275 A). Resistivity  $\rho$  was measured by a three-terminal method with a high-resistance meter (YHP 4329A). D-E hysteresis loops were observed by a standard Sawyer-Tower circuit at 50 Hz.

Specimens for piezoelectric measurements were poled at  $70^\circ\text{C}$  in a stirred silicone oil bath by applying a dc electric field of 3 kV/mm for 30 min for the (33) mode and 4 kV/mm for 5 min for thickness and planar modes. Piezoelectric properties were measured by the resonance-antiresonance method on the basis of IEEE standards using an impedance analyzer (YHP 4192 A).

Mechanical strength was measured by a three-point bending strength test. The bending strength  $\sigma$  was calculated using

$$\sigma = (3 \cdot F \cdot l) / (2 \cdot w \cdot t^2) \text{ [Pa]},$$

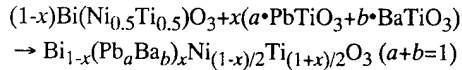
where  $F$  is the maximum load [N],  $l$  the separation between supporting points,  $w$  the sample width and  $t$  the sample thickness: in this case,  $l=7$  mm,  $w=3$  mm and  $t=1$  mm.

## 3. Results and Discussion

To control the  $\text{PbO}$  atmosphere during the sintering process of this solid solution is not necessary due to the low evaporation of  $\text{PbO}$ , which is not the case with conventional PZT or PZT-based

ceramics. Then it was very easy to sinter the NTPB ceramics with more than 93% measured density ratio to theoretical density.

The new solid solution consists of  $\text{Bi}(\text{Ni}_{0.5}\text{Ti}_{0.5})\text{O}_3$  (BINT),  $\text{PbTiO}_3$  (PT) and  $\text{BaTiO}_3$  (BT) as follows.



However, one of the end members of the solid solution, BINT, cannot be fabricated into a perovskite structure in the ceramic form by the conventional sintering process. The X-ray powder diffraction pattern for  $\text{Bi}(\text{Ni}_{0.5}\text{Ti}_{0.5})\text{O}_3$  (BINT) sintered at 1000 °C shows that the crystal phase does not have the perovskite structure but a mixture of a bismuth layered structure consisting of  $\text{Bi}_4\text{Ti}_3\text{O}_{12}$ ,  $\text{NiO}$  and  $\text{Bi}_2\text{O}_3$ , namely,  $6\text{Bi}(\text{Ni}_{0.5}\text{Ti}_{0.5})\text{O}_3 \rightarrow \text{Bi}_4\text{Ti}_3\text{O}_{12} + 3\text{NiO} + \text{Bi}_2\text{O}_3$ .

Figure 1 shows the X-ray powder diffraction patterns for (A) NTPB[100x-100/0] ( $x=0.17, 0.2, 0.22$ ), (B) NTPB[100x-50/50] ( $x=0.15, 0.2, 0.25$ ) and (C) NTPB[100x-0/100] ( $x=0.10, 0.15, 0.2$ ), respectively. The patterns of the systems show that the crystal phase is a mixture of bismuth layered and perovskite structures at  $x \leq 0.2$ ; on the other hand, a single phase of perovskite type at  $x > 0.2$ .

We previously reported<sup>9)</sup> that the NTPB[100x-100/0] system has the morphotropic phase boundary (MPB) where the crystal phase changes from the rhombohedral phase to tetragonal phase at  $x=0.445$ . However, the MPB does not exist in the NTPB[100x-50/50] or NTPB[100x-0/100] system ( $x \leq 0.5$ ).

The resistivity  $\rho$  of the NTPB system is about  $10^7 \sim 10^9 \Omega \cdot \text{cm}$  at room temperature (about 25 °C), depending on the materials, which is too low to be poled for piezoelectric ceramics. Therefore we try to improve it by adding Mn ions. Figure 2 shows the resistivity  $\rho$  and the loss tangent  $\tan \delta$  at 30 °C of NTPB[40-100/0] as a function of the amount of doped  $\text{MnCO}_3$ . The resistivity reaches its maximum value of about  $10^{13} \Omega \cdot \text{cm}$  at 0.02 wt%  $\text{MnCO}_3$ . Hereafter, we report the electrical properties of specimens with 0.02wt% added  $\text{MnCO}_3$ .

Figure 3 shows temperature dependence of the dielectric constant,  $\epsilon_s$ , and loss tangent,  $\tan \delta$ , of (A) NTPB[100x-100/0], (B) NTPB[100x-50/50] and (C) NTPB[100x-0/100] with 0.02wt% added  $\text{MnCO}_3$ , respectively. The  $T_C$  of NTPB[40-100/0] was 390 °C. It is considered that the peak at about 300~390 °C is caused by the Curie point  $T_C$  of the perovskite structure. On the other hand, the  $\epsilon_s$ - $T$  curves of the compositions ( $0.15 \leq x \leq 0.2$ ) near the mixture of bismuth layer and perovskite structures shows the other peak at about 670 °C which is caused by the  $T_C$  of the bismuth layered structure. As the content of Pb ions ( $x$ ) increases, the peak of the perovskite structure becomes sharp and the peak of the bismuth layered structure becomes flat. It seems that the crystal structure gradually changes from a mixture of bismuth layered and perovskite structures to the single phase of the perovskite structure at about  $x=0.2$ .

Figure 4 shows the D-E hysteresis loop of NTPB[40-100/0] with 0.02wt% added  $\text{MnCO}_3$  at room temperature. The loop has a large remanent polarization,  $P_r = 33.7 \mu\text{C}/\text{cm}^2$  and a coercive field,  $E_c = 18.8 \text{ kV}/\text{cm}$ . The  $P_r$  is larger than that of BNT-based solid solutions. The large  $P_r$  of NTPB[100x-100/0] seems to be enhanced for piezoelectric ceramics. Data on the remanent polarization  $P_r$  of the unpoled NTPB[100x-100/0] system with 0.02wt% added  $\text{MnCO}_3$  at room temperature as a function of the amount ( $x$ ) of modified Pb ions indicated that the  $P_r$  becomes

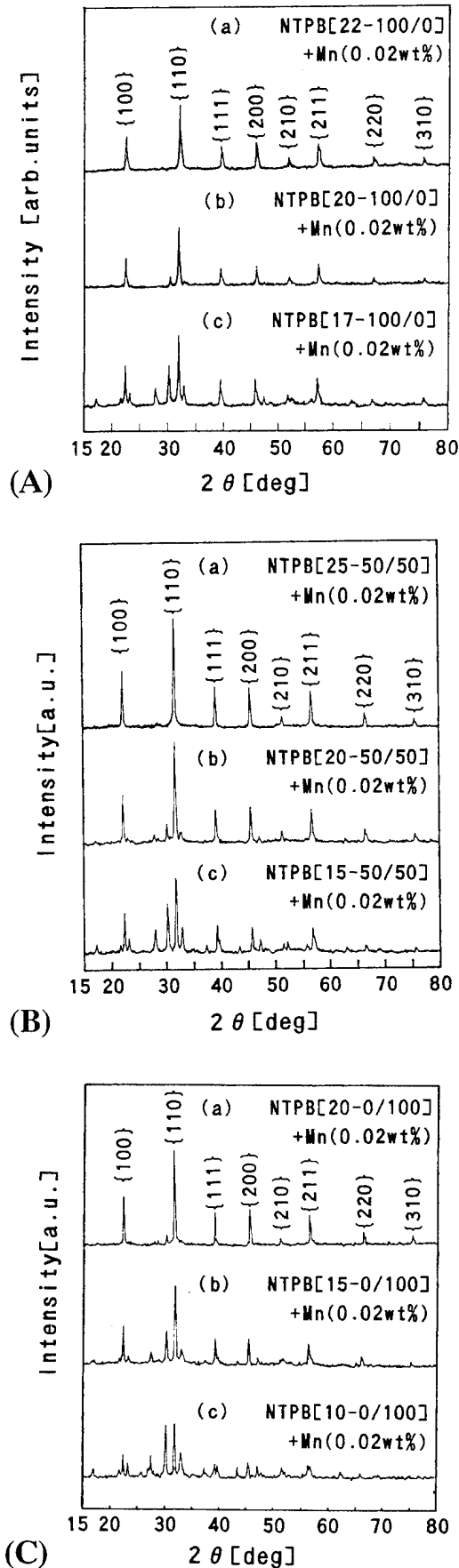


Fig. 1 X-ray powder diffraction patterns for (A) NTPB[100x-100/0] ( $x=0.17, 0.2, 0.22$ ), (B) NTPB[100x-50/50] ( $x=0.15, 0.2, 0.25$ ) and (C) NTPB[100x-0/100] ( $x=0.10, 0.15, 0.2$ ).

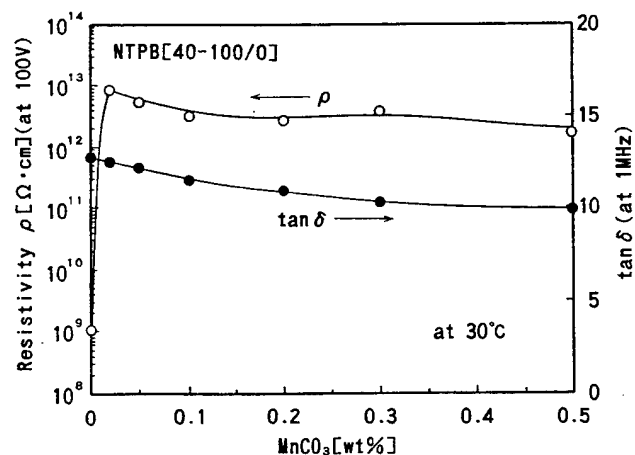


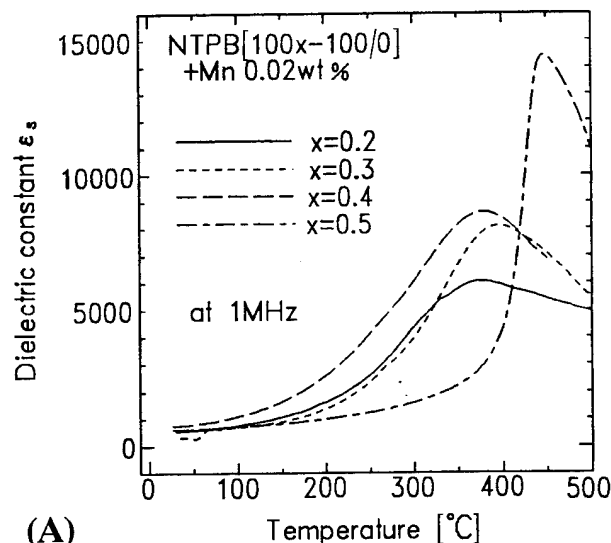
Fig. 2 The resistivity  $\rho$  and the loss tangent  $\tan\delta$  at 30 °C of NTPB[40-100/0] as a function of the amount of doped  $\text{MnCO}_3$ .

maximum ( $33.7 \mu\text{C}/\text{cm}^2$ ) at  $x=0.4$ . Therefore NTPB[40-100/0] with 0.02wt% added  $\text{MnCO}_3$  is expected to have active piezoelectric properties.

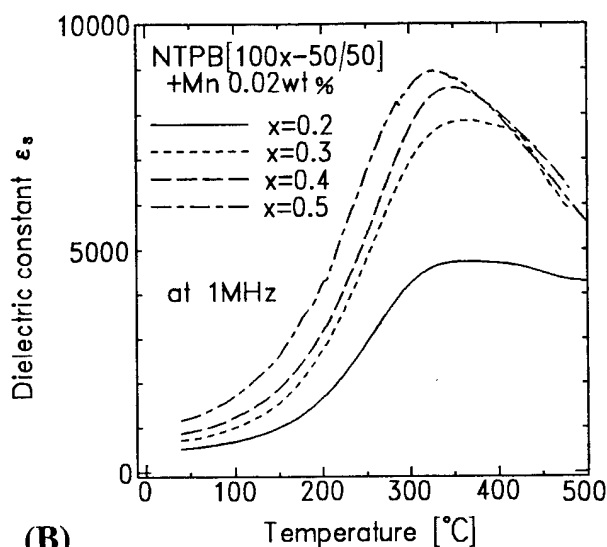
Figure 5 shows the electromechanical coupling factors  $k_t$ ,  $k_p$  and  $k_{33}$  in the thickness, planar and longitudinal modes, respectively, of the NTPB[100x-100/0] system with 0.02wt% added  $\text{MnCO}_3$  as a function of the amount ( $x$ ) of modified Pb ions. In all modes, the coupling factors  $k$  of this system become maximum at  $x=0.4$ ; the values of  $k_t$ ,  $k_p$  and  $k_{33}$  are 0.47, 0.325 and 0.515, respectively. These values are almost the same as those of the  $\text{PbTiO}_3$ -based high- $T_C$  piezoelectric ceramics, but are slightly lower than the values expected from their large  $P_r$ . The reason why the coupling factors are small may be that voltage high enough to fully pole NTPB[100x-100/0] with 0.02wt% added  $\text{MnCO}_3$  could not be applied due to its low breakdown voltage. The frequency constants  $N_t$ ,  $N_p$  and  $N_{33}$  of NTPB[40-100/0] with 0.02wt% added  $\text{MnCO}_3$  are 2007, 2366 and 1936  $\text{Hz}\cdot\text{m}$ , respectively. The strain constant  $d_{33}$  of the NTPB[100x-100/0] system with 0.02wt% added  $\text{MnCO}_3$  becomes maximum at  $x=0.445$  ( $192 \times 10^{-12} \text{ C/N}$ ).

Figure 6 shows the Weibull plot of the 3-point bending strength  $\sigma$  and the probability of survival  $S$  of NTPB[100x-100/0] with 0.02wt% added  $\text{MnCO}_3$  at  $x=0.3, 0.35, 0.4, 0.445$  and  $0.5$  before poling. As the amount of Pb ions ( $x$ ) increases, the bending strength of this system ( $0.3 \leq x \leq 0.5$ ) tends to become high. The bending strength of NTPB[44.5-100/0] with 0.02wt% added  $\text{MnCO}_3$  was about 150 MPa.

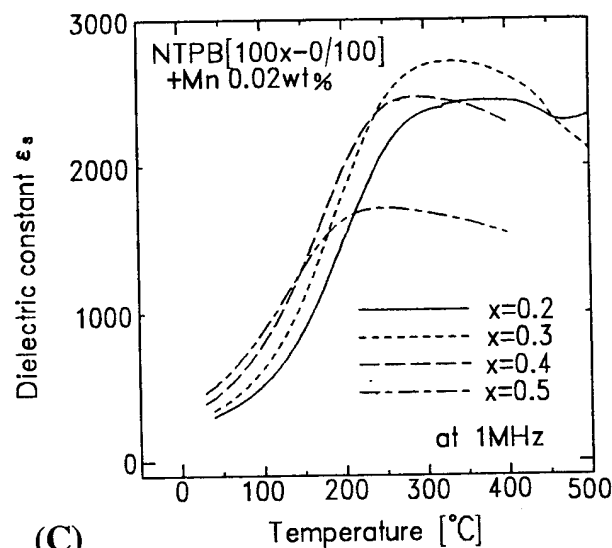
NTPB[100x-100/0] piezoelectric ceramics with 0.02wt% added  $\text{MnCO}_3$  ( $0.3 \leq x \leq 0.5$ ) may be superior for piezoelectric actuator devices or automobile sensors, since they have high Curie temperature and high mechanical strength. The relationship between piezoelectric and mechanical properties should be investigated on the ratios of Pb/Ba in the NTPB solid-solution system.



(A)



(B)



(C)

Fig. 3 Temperature dependence of the dielectric constant,  $\epsilon_s$ , and loss tangent,  $\tan\delta$ , of (A) NTPB[100x-100/0], (B) NTPB[100x-50/50] and (C) NTPB[100x-0/100] with 0.02wt% added  $\text{MnCO}_3$ .

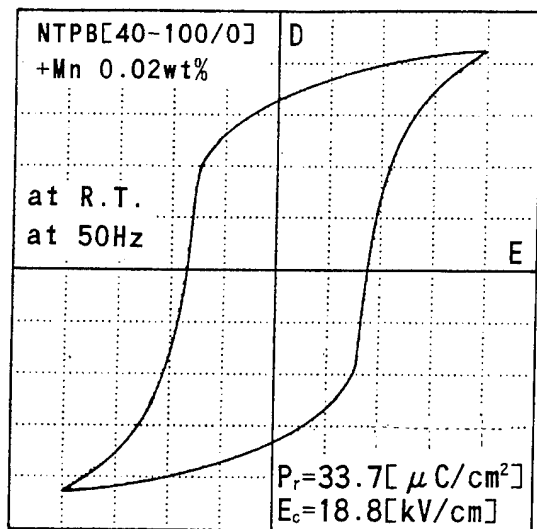


Fig. 4 The D-E hysteresis loop of NTPB[40-100/0] with 0.02wt% added  $\text{MnCO}_3$  at room temperature at 50 Hz. (X: 10.0 kV/cm/div, Y: 9.6  $\mu\text{C}/\text{cm}^2/\text{div}$ )

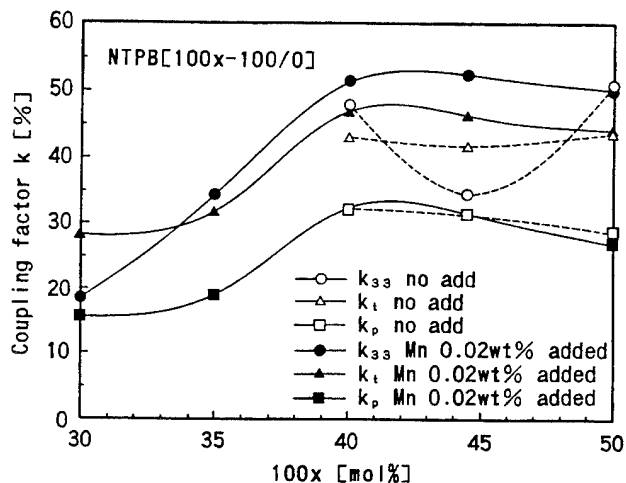


Fig. 5 The electromechanical coupling factors  $k_t$ ,  $k_p$  and  $k_{33}$  of the NTPB[100x-100/0] system with 0.02wt% added  $\text{MnCO}_3$  as a function of the amount (x) of modified Pb ions.

#### 4. Conclusions

Dielectric, ferroelectric, piezoelectric and mechanical properties of new compositions in bismuth solid solution series,  $\text{Bi}_{1-x}(\text{Pb}_a\text{Ba}_b)_x\text{Ni}_{(1-x)/2}\text{Ti}_{(1+x)/2}\text{O}_3$  (NTPB[100x-100a/100b]) ( $a+b=1$ ) ( $0 \leq x \leq 0.5$ ), were investigated as a new group of piezoelectric ceramics.

The  $T_C$  of NTPB[40-100/0] is 390 °C. The  $P_r$  of the NTPB[100x-100/0] system with 0.02wt% added  $\text{MnCO}_3$  becomes maximum (33.7  $\mu\text{C}/\text{cm}^2$ ) at  $x=0.4$  where the  $k_{33}$  is 0.515. Also the maximum  $d_{33}$  is  $192 \times 10^{-12}$  C/N at  $x=0.445$ .

NTPB[100x-100/0] (+0.02wt%  $\text{MnCO}_3$ ) seem to be favorable for piezoelectric sensor materials and piezoelectric actuator applications, due to their relatively high mechanical strength. Future work must be undertaken to study why bismuth perovskites, including BNT-based and NTPB piezoceramics, have higher mechanical strength than those of PZT systems.

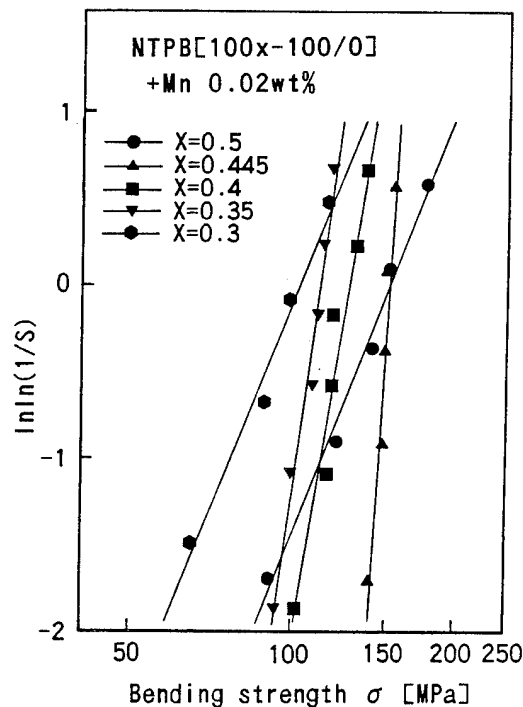


Fig. 6 Weibull plots of the 3-point bending strength  $\sigma$  and the fracture probability  $F (=1-S)$  of NTPB[100x-100/0]+Mn(0.02 wt%) before poling.

#### References

- [1] G. A. Smolensky, V. A. Isupov, A. I. Agranovskaya and N. N. Krainik, "New Ferroelectrics of Complex Composition. IV", *Soviet Physics- Solid State*, vol. 2, pp.2651-2654, May, 1961.
- [2] C. F. Buhrer, "Some Properties of Bismuth Perovskites", *J. Chem. Phys.*, vol. 36, pp.798-803, February, 1962.
- [3] T. Takenaka and K. Sakata, "New Piezo- and Pyroelectric Sensor Materials of  $(\text{BiNa})_{1/2}\text{TiO}_3$ -based Ceramics", *Sensors and Materials*, vol. 1, pp.123-131, 1988.
- [4] T. Takenaka, K. Sakata and K. Toda, "Piezoelectric Properties of  $(\text{Bi}_{1/2}\text{Na}_{1/2})\text{TiO}_3$ -Based Ceramics", *Ferroelectrics*, vol. 106, pp.375-380, 1990.
- [5] T. Takenaka, Y. Naitou, N. Takahashi and K. Sakata, " $(\text{Bi}_{1/2}\text{Na}_{1/2})\text{TiO}_3$ - $\text{PbTiO}_3$ - $\text{BaTiO}_3$  Solid Solution for Piezoelectric Ceramics", *Proc. 1990 IEEE 7th International Symposium on Applications of Ferroelectrics* (IEEE, 1991) pp.313-316.
- [6] T. Takenaka, U. Naitou and K. Sakata, "Piezoelectric Ceramics of  $(\text{Bi}_{1/2}\text{Na}_{1/2})\text{TiO}_3$ - $\text{PbTiO}_3$ - $\text{BaTiO}_3$  System", *Electrical Engineering in Japan*, vol.112, No.7, pp.92-101, 1992.
- [7] T. Takenaka, A. Hozumi, T. Hata and K. Sakata, "Mechanical Properties of  $(\text{Bi}_{1/2}\text{Na}_{1/2})\text{TiO}_3$ -based Piezoelectric Ceramics", *Silicates Industries - Ceramic Science and Technology*, vol. 58, No.7-8, pp.136-142, 1993.
- [8] T. Takenaka and M. Yamada, "Ferroelectric Properties of  $(\text{Bi}_{1/2}\text{Pb}_{1/2})(\text{Ni}_{1/4}\text{Ti}_{3/4})\text{O}_3$  for New Piezoelectric Ceramics", *Jpn. J. Appl. Phys.*, vol. 32, Part 2, No.7A, pp.L928-L931, July, 1993.
- [9] T. Takenaka and M. Yamada, "Solid-Solution  $(\text{Bi}_{1-x}\text{Pb}_x)(\text{Ni}_{(1-x)/2}\text{Ti}_{(1+x)/2})\text{O}_3$  for New Piezoelectric Ceramics", *Jpn. J. Appl. Phys.*, vol.32, Part 1, No.9B, pp.4218-4222, 1993.
- [10] T. Takenaka, M. Yamada and T. Okuda, "Dielectric and Piezoelectric Properties of Bismuth Nickel Titanate-based Ceramics", *Ferroelectrics*, 1994 (to be published).

# Concurrent Session - 2A: Thin Films

# A Simple Unified Analytical Model for Ferroelectric Thin Film Capacitor and Its Applications for Nonvolatile Memory Operation

Deng-Yuan Chen (1), Masamichi Azuma (2), Larry D. McMillan (3), Carlos A. Paz de Araujo (4)  
 (1) Ramtron International Corp., 1850 Ramtron Dr., Colorado Springs, CO 80921  
 (2) Electronics Research Lab., Matsushita Electronics Corp., Osaka, Japan  
 (3) Symetrix Corp., Colorado Springs, CO 80918  
 (4) Microelectronics Research Lab., University of Colorado, Colorado Springs, CO 80933-7150

**Abstract** - A simple unified analytical ferroelectric model has been developed based on an effective field assumption and statistical physics, which covers ferroelectric hysteresis, switching, and phase transitions including first and second order phase transitions as well as Curie-Weiss Law. The model parameters may be extracted from measured data using commercial customizable optimization tools such as SmartSpice's Optimizer. The model can be used for modeling, simulation and statistical process control for ferroelectric nonvolatile memory design and fabrication.

## INTRODUCTION

Driven by the improvements in thin-film technology, ferroelectric device for nonvolatile memory application has been investigated extensively again because of its nonvolatility, radiation hardness, high speed, high density, low power, physical robustness, and compatibility with silicon and gallium arsenide fabrication [1][2].

The foundation of device physics for ferroelectric memory, however, has not been well established. Although there are some well-known classical theories and models such as phenomenological theory and nucleation domain theory [3], none of them may cover all of the ferroelectric fundamental phenomena and related device phenomena, shown in Table 1.

The phenomenological theory has been successful for ferroelectric phase transitions but it fails to model ferroelectric hysteresis and switching current analytically [3]. On the other hand, the ferroelectric switching models based on the microscopic domain nucleation theory [4] has been successful for ferroelectric switching current but it falls short in describing the entirety of hysteresis. For example, it is not able to predicate the temperature effect (phase transitions) on polarization. In addition, most the model parameters are not measurable, which makes difficulty for model extraction and statistical process control.

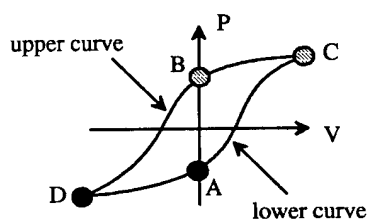


Fig. 1 Ferroelectric polarization reversal (switching) on hysteresis

In fact, ferroelectric phase transition or switching property may be predicted from its hysteresis property analytically because there must be a relationship between them. This lack of unity in consensus of the

underlying physics has foiled the development of this discipline into a well-organized body of knowledge for many years.

The purpose of this work is to propose a unified analytical theory for the ferroelectric device physics, covering all fundamental device phenomena, and its application for nonvolatile memory operations.

## MODEL DERIVATION

### Fundamental Assumptions and Ferroelectric Hysteresis

The effective field was first proposed by P. Weiss to explain the ferromagnetic phase transitions. Because the ferroelectric phase transitions are completely analogous to the ferromagnetic transitions, the effective field approach can also be used in the case of uniaxial systems with rigid elementary dipoles reorientable in either of two opposite (up and down) directions [5]. The effective field,  $E_{eff}$ , is given by

$$E_{eff} = E + E_{CP} \quad (1)$$

where  $E$  is the external field,  $E_{CP}$  is the cooperative field due to partially ordered system of dipoles, which is given by  $\beta P$  classically. Where  $\beta$  is a generalized Lorentz factor depending on the geometry of the dipole lattice and  $P$  is the polarization per unit volume [5]. However, our assumption for the cooperative field is given by [6]

$$E_{eff} = \begin{cases} E - E_C(E, T, S) & \text{for lower curve} \\ E + E_C(E, T, S) & \text{for upper curve} \end{cases} \quad (2)$$

where the lower and upper curves are indicated in Fig. 1.  $E_C(E, T, S)$  is the coercive field of ferroelectric, which is a function of previously applied field ( $E$ ), the temperature ( $T$ ) and mechanic stress ( $S$ ). For simplicity, only temperature effect for ferroelectric with single critical temperature is assumed in this paper, given by

$$E_C(T) = \begin{cases} E_{CO}(T_C - T)^\theta & \text{for } T \leq T_C \\ 0 & \text{for } T > T_C \end{cases} \quad (3)$$

where  $T_C$  is the critical temperature,  $E_{CO}$  and  $\theta$  are model parameters, which could be extracted from the measured data of coercive field at different temperature.

Based on the statistical physics, the relation between polarization and field can be derived [6], or

$$P = \begin{cases} P_{SO} \tanh \left[ \frac{\mu(E - E_C)}{kT} \right] & \text{for lower curve} \\ P_{SO} \tanh \left[ \frac{\mu(E + E_C)}{kT} \right] & \text{for upper curve} \end{cases} \quad (4)$$

where  $\mu$  is the elementary dipole moment,  $k$  is Boltzmann constant,  $T$  is temperature,  $E$  is the field,  $P_{SO} = N\mu$  is the saturation polarization and  $N$  is the number of total dipoles per volume. It is noticed that the real polarization (hysteresis) curve does not saturate at high field, the

	Typical Characterization	Example
Ferroelectric Related Fundamental Phenomena	Polarization vs. Electric Field	Hysteresis
	Polarization vs. Time	Switching
	Polarization vs. Temperature	Phase Transitions, Pyroelectric, Curie-Weiss Law
	Polarization vs. Pressure (Mechanic Stress)	Piezoelectric
	Polarization vs. Light Wavelength or Intensity	Electro-Optical, Photovoltaic
Ferroelectric Other Device Phenomena	Ferroelectric Device Capacitance vs. Bias	MFM C-V, Shifted MFS C-V
	Ferroelectric Device Current vs. Bias	MFM TVS I-V, Shifted MFSFET I-V, etc.
Ferroelectric Device Failure Phenomena	Ferroelectric Device Leakage Current vs. Bias	Leakage, Interface, Electrode, Defect, Breakdown
	Ferroelectric Polarization vs. Time or Cycle	Fatigue or Endurance, Retention, etc.

Table 1 Ferroelectric device phenomena

saturation polarization has so-called external field effect (better known as space charge effect) given by [6]

$$P_{SO} \approx P_O(1 + \alpha E) \quad (5)$$

where  $\alpha$  is the parameter contributing to this effect,  $P_O = N\mu_O$  and  $\mu_O$  are the saturation polarization and elementary dipole moment, respectively, at  $T=0$  and  $E=0$ . It is noticed that the hysteresis (and  $E_C$  and  $P_R$ ) here means the major hysteresis loop. The initial curve and minor hysteresis loops will be discussed later.

### Phase Transitions

Based on the new hysteresis model, the model for phase transitions can be derived analytically. The relationship between remanent polarization and coercive field is given by

$$P_R(T) = P(E=0) = P_O \tanh \frac{\mu_O E_C(T)}{kT} \quad (6)$$

The pyroelectric model is given by

$$P(T) = P_R(T) = P_O \tanh \left[ \frac{\mu_O E_C(T)}{kT} \right] \quad (7)$$

The susceptibility model is given by

$$\chi(T) = \frac{1}{\epsilon_O} \left. \frac{dP(T)}{dE} \right|_{E=0} = \frac{\mu_O P_O}{\epsilon_O kT} \text{sech}^2 \left[ \frac{\mu_O E_C(T)}{kT} \right] \quad (8)$$

The dielectric constant model is given by

$$\epsilon(T) = 1 + \chi(T) = 1 + \frac{\mu_O P_O}{\epsilon_O kT} \text{sech}^2 \left[ \frac{\mu_O E_C(T)}{kT} \right] \quad (9)$$

Finally, Curie-Weiss law is derived, or given by

$$\frac{1}{\chi} \Big|_{T > T_C} = \frac{\epsilon_O kT}{\mu_O P_O} = \frac{\epsilon_O kT_C}{\mu_O P_O} + \frac{\epsilon_O k}{\mu_O P_O} (T - T_C) = \frac{1}{\chi_O} + \frac{1}{C} (T - T_C) \quad (10)$$

$$\frac{1}{\chi} \Big|_{T < T_C} = \frac{\epsilon_O kT}{\mu_O P_O} + \frac{\epsilon_O \mu_O E_C^2}{2kT P_O} (T_C - T)^{2\theta} \approx \frac{1}{\chi_O} + \frac{\mu_O^2 E_C^2}{2k^2 C T_C} (T_C - T)^{2\theta} \quad (11)$$

where  $\chi_O$  is the susceptibility at  $T_C$  and  $C$  is Curie constant.

### Polarization Switching Current and Non-switching Current

The P-E model of hysteresis can be converted to P-V model or

$$P = \begin{cases} P_O(1 + \alpha V) \tanh \left[ \frac{V - V_C}{2V_O} \right] & \text{for lower curve} \\ P_O(1 + \alpha V) \tanh \left[ \frac{V + V_C}{2V_O} \right] & \text{for upper curve} \end{cases} \quad (12)$$

where

$$V_O = \frac{V_C}{\ln \left( \frac{1 + \frac{P_R}{P_O}}{1 - \frac{P_R}{P_O}} \right)} \quad (13)$$

$$V_C = d_f E_C \quad (14)$$

where  $d_f$  is ferroelectric thickness and

$$\mu_O = \frac{kT d_f}{2V_C} \ln \left( \frac{1 + \frac{P_R}{P_O}}{1 - \frac{P_R}{P_O}} \right) \quad (15)$$

which implies that the elementary dipole moment can be obtained from hysteresis measurement.

Ferroelectric polarization reversal or switching on hysteresis is shown in Fig. 1. If the initial state of a polarized ferroelectric is A and the voltage bias on the film is increased from zero, the polarization state will be changed to C, which is switched. On the other hand, if the initial state is B and the bias is increased from zero, the final state will be C, which is not switched. The non-switching current representing polarization path B-C may be given by

$$i_{ns}(t) = A_f \frac{dD}{dt} = A_f \left( \frac{\epsilon_O}{d_f} + \frac{dP_{BC}}{dV} \right) \frac{dV}{dt} \quad (16)$$

the full switching current representing polarization path A-C may be given by

$$i_{fs}(t) = A_f \left( \frac{\epsilon_O}{d_f} + \frac{dP_{AC}}{dV} \right) \frac{dV}{dt} \quad (17)$$

and the relative switching current is given by

$$i_{sw}(t) = i_{fs}(t) - i_{ns}(t) = A_f \left( \frac{dP_{AC}}{dV} - \frac{dP_{BC}}{dV} \right) \frac{dV}{dt} \quad (18)$$

where  $A_f$  is device area and  $D$  is the displacement. Therefore, the switched charge is obtained

$$Q_{sw} = \int i_{sw}(t) dt = 2A_f P_R + A_f P_O (1 + \alpha V_m) \Delta(V) \leq 2A_f P_R \quad (19)$$

where

$$\Delta(V) = \left[ \tanh \left( \frac{V_m - V_C}{2V_O} \right) - \tanh \left( \frac{V_m + V_C}{2V_O} \right) \right] \leq 0 \quad (20)$$

where  $V_m$  is the maximum value of bias voltage. Eq. (19) suggests that the maximum value of bias must be higher enough to get the accurate remanent polarization for major loop.

The hysteresis (energy) loss can be obtained from the new model, or,

$$W_{ACB} = \frac{1}{2} A_f \int_A^B \vec{D} \cdot d\vec{E} \quad (21)$$

or

$$W_{ACB} = \frac{1}{2} A_f \left\{ \epsilon_O V_m^2 + 2P_O V_O d_f \ln \left[ \frac{\cosh \left( \frac{V_m - V_C}{2V_O} \right) \cosh \left( \frac{V_m + V_C}{2V_O} \right)}{\cosh \left( \frac{-V_C}{2V_O} \right) \cosh \left( \frac{V_C}{2V_O} \right)} \right] \right\} \quad (22)$$

where  $W_{ACB}$  is the energy loss for the polarization path A-C-B,  $E$  is the field,  $\alpha$  is assumed to be zero for mathematical simplicity.

The commonly used test circuit for ferroelectric switching current characterization is shown in Fig. 2. Its circuit equation is given by

$$V_{in}(t) = V_F(t) + R \cdot A_f \cdot \left( \frac{\epsilon_O}{d_f} + \frac{dP}{dV_F} \right) \cdot \frac{dV_F}{dt} \quad (23)$$

where  $V_{in}(t)$  is input signal,  $R$  is the load resistance,  $V_F(t)$  is the potential on the ferroelectric as function of time, and  $P$  is the ferroelectric polarization as function of  $V_F(t)$  given by the hysteresis model equation. By solving  $V_F(t)$ , the non-switching current, full switching current, relative switching current, and the switched charge can be obtained.

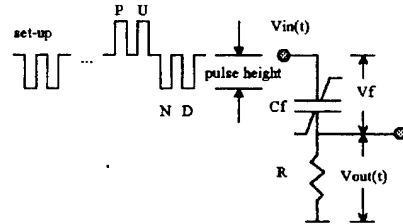


Fig. 2 RC circuit for ferroelectric switching (PUND) measurement where P and U are positive switched and unswitched pulse, respectively; N and D are negative switched and unswitched pulse; Cf is a ferroelectric capacitor; R is a resistor.

### Ferroelectric C-V and TVS I-V

Ferroelectric capacitance as function of bias may be given by

$$C_F(V_F) = A_f \cdot \frac{dD}{dV_F} = A_f \cdot [C_{FO} + C_{FV}(V_F)] \quad (24)$$

where

$$C_{FO} = \frac{\epsilon_O}{d_f} \quad (25)$$

$$C_{FV}(V_F) = \frac{dP(V_F)}{dV_F} =$$

$$\begin{cases} P_O \alpha \tanh \left( \frac{V_F - V_C}{2V_O} \right) + \frac{P_O}{2V_O} (1 + \alpha V_F) \text{sech}^2 \left( \frac{V_F - V_C}{2V_O} \right) & \text{for L} \\ P_O \alpha \tanh \left( \frac{V_F + V_C}{2V_O} \right) + \frac{P_O}{2V_O} (1 + \alpha V_F) \text{sech}^2 \left( \frac{V_F + V_C}{2V_O} \right) & \text{for H} \end{cases} \quad (26)$$

where L and H represent lower and upper curves on hysteresis, respectively. The triangular sweep voltage current vs. voltage (TVS I-V) is then given by

$$i_F(V_F) = C_F(V_F) \cdot \frac{dV_F}{dt} \quad (27)$$



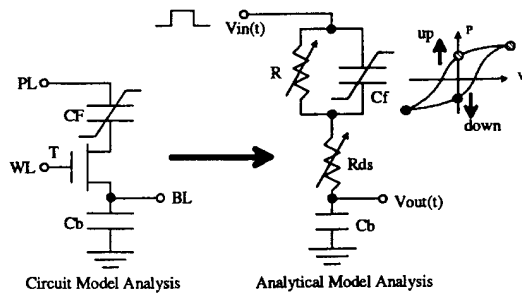


Fig. 3 Circuit model for high density 1T-1C ferroelectric RAM, where PL, WL and BL are pulsed plate line, word line and bit line. CF, Cf and Cb are the real ferroelectric capacitor, ideal ferroelectric capacitor and equivalent bit line capacitor, respectively. T is n-channel MOSFET.

### MODEL APPLICATION FOR MEMORY

Since the ferroelectric polarization characteristic, i.e., hysteresis, is the foundation for ferroelectric device, the ferroelectric nonvolatile memory operation can be described by the polarization state on hysteresis curves [6]. Fig. 3 shows the READ operation for 1T-1C ferroelectric memory cell, whose circuit equations are given by

$$V_{in}(t) = V_F(t) + V_{DS}(t) + V_{out}(t) \quad (28)$$

$$V_{DS}(t) = \left[ \frac{V_F}{R} + A_f \left( \frac{\epsilon_o}{d_f} + \frac{dP}{dV_F} \right) \frac{dV_F}{dt} \right] R_{ds} \quad (29)$$

$$V_{out}(t) = C_b \int \left[ \frac{V_F}{R} + A_f \left( \frac{\epsilon_o}{d_f} + \frac{dP}{dV_F} \right) \frac{dV_F}{dt} \right] dt \quad (30)$$

where  $V_{in}(t)$  is the READ pulse, Cf is the ferroelectric capacitor, R is the resistance contributing to ferroelectric leakage current, Rds is the channel resistant of n-channel MOSFET (T). By solving  $V_F(t)$  and  $V_{out}(t)$  for

initial up and down states, respectively, from above equations, the reference voltage may be designed in the middle of these two values. Therefore,  $V_{out}(t)$  for initial up state or down state may be sensed as "0" and "1", when compared with the reference.

### RESULTS AND DISCUSSIONS

By modeling  $E_c$ ,  $\mu$ ,  $P_o$  and  $\alpha$  as functions of history, i.e., the previously maximum applied field, the ferroelectric hysteresis curves including initial curve, minor and major loops can be simulated analytically, shown in Fig. 4.

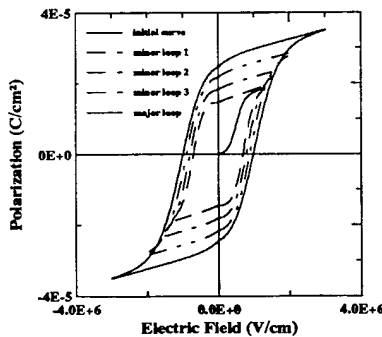


Fig. 4 Simulation of ferroelectric hysteresis loops

The simulation result compared with experimental data is shown in Fig. 5. The simulation result of temperature effect on hysteresis is shown in Fig. 6. It shows that the hysteresis loop becomes smaller as temperature goes up. When the temperature is at or above the critical temperature, the hysteresis loop will disappear. The simulation results for ferroelectric phase transitions are shown in Figs. 7 and 8. The results imply that there is no absolute boundary between first order and second order phase transitions, which was discussed by H. Megaw [7]. The phase transitions for ferroelectric with multiple critical temperatures may also be simulated

by modeling its coercive field as function of temperature. The electric field effect on the phase transitions, which is shown in classical ferroelectric books such as [8], may also be simulated analytically, shown in Fig. 9. The simulation results of the ferroelectric switching current from PUND testing setup are shown in Fig. 10. Finally, the simulation for ferroelectric thin film C-V and TVS I-V are shown in Fig. 11.

Similar to the standard device model development for integrated circuit, the ferroelectric model parameters may be extracted from the measured data using optimization tool such as SmartSpice's Optimizer or PSpice's Device Equation Options or HSpice, which could interpret the source codes or macro models containing device equations during simulation or model parameter extraction. The parameters  $P_o$  and  $\alpha$  may be extracted, while  $P_r$  (or  $\mu$ ) and  $V_c$  (or  $E_c$ ) may be measured directly from hysteresis or RC switching current measurement. The temperature model may also be extracted from measurement data for hysteresis at different temperature. In fact, based on the data, the temperature model for coercive field (or voltage) could be improved more accurately. Therefore, the model parameters could be used for statistical process control and yield improvement for ferroelectric RAM production.

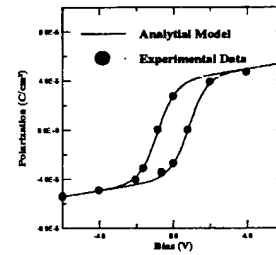


Fig. 5 Ferroelectric (PZT) hysteresis simulation result compared with experimental data, where  $P_o = 40 \mu\text{C}/\text{cm}^2$ ,  $P_r = 27.34 \mu\text{C}/\text{cm}^2$ ,  $V_c = 0.8 \text{ V}$ ,  $\alpha = 0.06 \text{ 1/V}$ ,  $d_f = 650 \text{ \AA}$ ,  $A_f = 40\mu\text{m} \times 40\mu\text{m}$  [9].

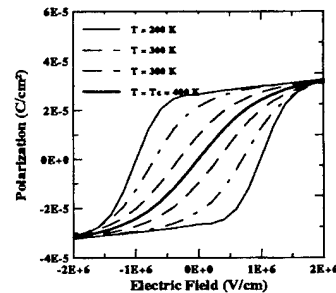


Fig. 6 Simulation of temperature effect on the hysteresis, where  $T_c = 400 \text{ K}$ ,  $E_{\infty} = 7 \times 10^4 \text{ V/cm}$ ,  $P_o = 27 \mu\text{C}/\text{cm}^2$ ,  $\alpha = 10^{-7} \text{ cm/V}$ ,  $\theta = 0.5$ ,  $T = 200 \text{ K}, 300 \text{ K}, 350 \text{ K}, 380 \text{ K}, \text{ and } 400 \text{ K}$ , respectively.

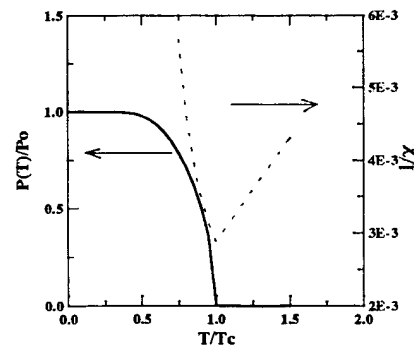


Fig. 7 (a) and (b) Simulation of ferroelectric second order phase transition and Curie-Weiss Law, where  $\mu_o = 6.3 \times 10^{-27} \text{ J cm/V}$ ,  $P_o = 27 \mu\text{C}/\text{cm}^2$ ,  $E_{\infty} = 7 \times 10^4 \text{ V/cm}$ ,  $\theta = 0.5$ , and  $T_c = 400 \text{ K}$

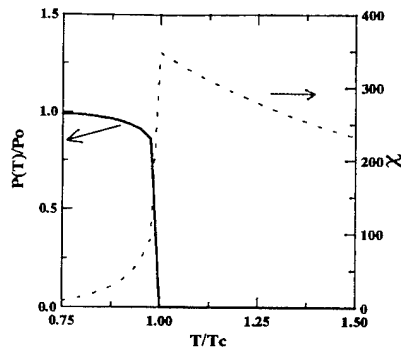


Fig. 8 Simulation of ferroelectric first order phase transition, where  $\mu_0 = 6.3 \times 10^{-27}$  J cm/V,  $P_0 = 27$   $\mu$ C/cm<sup>2</sup>,  $E_{co} = 7 \times 10^5$  V/cm,  $\theta = 0.2$ , and  $T_c = 400$  K

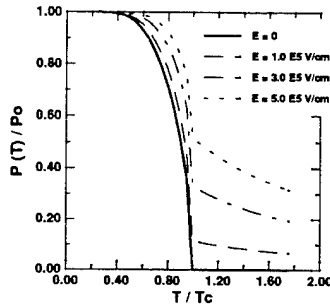


Fig. 9 Simulation of electric field effect on the phase transitions, where  $\mu_0 = 6.3 \times 10^{-27}$  J cm/V,  $P_0 = 27$   $\mu$ C/cm<sup>2</sup>,  $\theta = 0.5$ ,  $T_c = 400$  K,  $E_{co} = 7 \times 10^5$ , and  $E = 0, 1 \times 10^5, 3 \times 10^5, 5 \times 10^5$  V/cm, respectively.

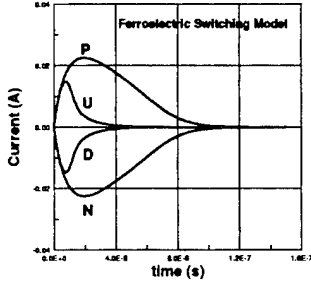


Fig. 10 Simulation of switching current for the RC testing circuit using P, U, N, and D pulses, where  $P_0 = 40$   $\mu$ C/cm<sup>2</sup>,  $V_c = 0.8$  volts,  $K_p = P_r / P_0 = 0.8$ ,  $P_r = K_p P_0 = 32$   $\mu$ C/cm<sup>2</sup>;  $A_t = 40$   $\mu$ m  $\times$   $40$   $\mu$ m,  $d_t = 1000$  Å,  $\alpha = 0.07$  /V,  $R = 50$   $\Omega$ , pulse height  $V_m = 2.0$  volts; and the rise time  $t_r = 10$  ns of square pulse with exponential rise edge [6].

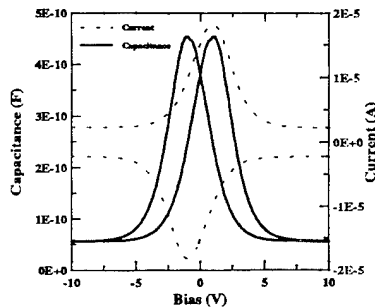


Fig. 11 Simulation result of ideal metal ferroelectric metal capacitor's C-V and TVS I-V curves, where  $P_0 = 50$   $\mu$ C/cm<sup>2</sup>,  $V_c = 0.8$  volts,  $K_p = P_r / P_0 = 0.4$ ,  $P_r = K_p P_0 = 20$   $\mu$ C/cm<sup>2</sup>;  $A_t = 40$   $\mu$ m  $\times$   $40$   $\mu$ m,  $d_t = 1000$  Å,  $\alpha = 0.07$  /V, and  $dV/dt = \pm 4 \times 10^4$  V/s.

## CONCLUSIONS AND SUGGESTIONS

A unified analytical model for ferroelectric device is proposed, which covers ferroelectric hysteresis, phase transition and polarization reversal (switching). The model may be used as a tool for device design and process integration towards the development of nonvolatile ferroelectric memories. In the same way as electric (and temperature) effect on the ferroelectric polarization was modeled, the piezoelectric effect and ferroelectric photovoltaic effect may be modeled, respectively, by modeling the coercive field as function of mechanic stress and light wavelength (or intensity). The modeling methodology may also be used for ferromagnetic device modeling.

## ACKNOWLEDGMENT

Most of this work is based on D.-Y. Chen's Ph. D. work, which was mainly supported by Symetrix Corp. and Defense Nuclear Agency (DNA) contract. Part of this paper was done during the time when Chen was working for the Advanced Process Development of AT&T Global Information Solutions Microelectronics Products Division (NCR MPD) at Colorado Springs. A great deal of thanks is also due Ramtron Corp. for financial support for the presentation of this paper.

- [1] J. F. Scott and C. A. Araujo, "Ferroelectric Memories", Science 246, pp. 1400-1405, 1989.
- [2] C. A. Araujo and G. W. Taylor, "Integrated Ferroelectrics", Ferroelectrics, Vol. 116, pp. 215-228, 1991.
- [3] M. E. Lines and A. M. Glass, Principles and Applications of Ferroelectrics and Related Materials, Clarendon Press, Oxford, 1977.
- [4] e.g., Y. Ishibashi and Y. Takagi, "Note on Ferroelectric Domain Switching", J. Phys. Soc. of Jpn., Vol. 31, No. 2, pp. 506-510, 1971.
- [5] J. A. Gonzalo, Effective Field Approach to Phase Transitions and Some Applications to Ferroelectrics, World Scientific Lecture Notes in Physics, Vol. 25, World Scientific, New Jersey, 1991.
- [6] D.-Y. Chen, Phenomena and Device Modeling of Ferroelectric on Semiconductor, Ph. D. Dissertation, University of Colorado, Colorado Springs, 1993.
- [7] H. D. Megaw, Ferroelectricity in Crystals, Methuen & Co. Ltd., London, 1957.
- [8] J. C. Burfoot, Ferroelectrics: An Introduction to the Physical Principles, D. Van Nostrand Co. Ltd., London, 1967.
- [9] B. P. Maderic, L. E. Sanchez and S. Y. Wu, Ferroelectrics, 116, 65 (1991)

# Stress in Pt/Pb(Zr,Ti)O<sub>3</sub>/Pt Capacitors for Integrated Ferroelectric Devices

G.A.C.M. Spierings, G.J.M. Dormans, W.G.J. Moors,  
M.J.E. Ulenaers and P.K. Larsen.

Philips Research Laboratories,  
Prof. Holstlaan 4, 5656 AA Eindhoven, The Netherlands

**Abstract** -- Stresses were studied in a ferroelectric capacitor consisting of Pt bottom and top electrodes and a Pb(Zr,Ti)O<sub>3</sub> (PZT) film during and after its processing. The Pt electrodes were deposited by sputtering. The PZT film was made by a sol-gel technique. Stress measurements after each deposition step, during annealing treatments and after etching steps made it possible to follow the stress evolution in the capacitor.

The largest stress effects are found in the Pt-electrodes. After sputter-deposition these have a large intrinsic compressive stress which is changed into a large thermal tensile stress after a temperature treatment exceeding 500 °C. The stress in the PZT film is small and is influenced by the deposition of the top electrode. An analysis shows that it is mainly of thermal nature. Thermal cycling shows that after the top electrode is annealed the as grown poling direction which has a large component in the plane of the substrate is changed to a poling direction perpendicular to the substrate. This results in a large improvement of the switching behavior of the PZT film.

## INTRODUCTION

The piezoelectric nature of ferroelectric materials can be expected to lead to stress-related effects on the properties of a thin film integrated ferroelectric capacitor [1]. In addition, excessive stresses in the stack may result in cracking or delamination of the thin films [2].

Stresses in ferroelectric thin films and effects on some properties have been subjects of recent investigations. Desu showed that for BaTiO<sub>3</sub> films the hysteresis curve deteriorates when the film is compressively stressed [3] while Tuttle et al. related the properties of Pb(Zr,Ti)O<sub>3</sub> (PZT) films deposited on silicon and MgO to thermal stress effects [4].

In this paper the evolution of stress during processing of a ferroelectric capacitor prepared with Pt bottom and top electrodes and a PbZr<sub>x</sub>Ti<sub>1-x</sub>O<sub>3</sub> film on an oxidized Si substrate is reported. First the stress behavior during deposition and annealing is determined. Secondly the influence of interactions between the different layers of the capacitor stack is discussed on the basis of stress data obtained from a step by step removal of the films. Finally the effects of stresses in the PZT film prior and after the top electrode anneal on the switching behavior is treated.

## EXPERIMENTAL METHODS

**Thin film deposition and etching:** The bottom electrodes consisting of a 4 nm adhesion promoting Ti layer and a 70 nm Pt film were deposited by sputtering on 100 mm diameter oxidized silicon wafers without substrate heating. A Nordiko NS2050 sputter system was used; the electrode properties have been described in detail in ref. 5. PZT films with compositions near the morphotropic phase boundary ( $x \approx 0.5$ ) were deposited by a sol-gel technique [6]. The top electrode (70 nm Pt, 7 nm Ti) was also sputter-deposited. Here, the Ti film on top of the Pt electrode serves as an adhesion promoter for the dielectric layer to be deposited at a later stage in the processing [7]. Etching of the capacitor films was carried out by ion-beam milling for Pt [8] and by wet-chemically for PZT.

**Stress measurement:** Stress in a thin film results in a circular warpage of the substrate. A commercial stress analyzer (Tencor FLX-2900) was used to measure this warpage with a laser-reflection system. This analyzer has the possibility to measure the warpage in-situ during heating to 900 °C. From the difference in the radii of curvature before ( $R_0$ ) and after ( $R$ ) each processing step (deposition, anneal), the stress  $\sigma$  in the film can be calculated using the Stookey formula:

$$\sigma = \frac{E_s}{6(1-\nu_s)} \frac{t_s^2}{t_f} \left( \frac{1}{R} - \frac{1}{R_0} \right) \quad (1)$$

where  $t_f$  is the film thickness and  $E_s$ ,  $\nu_s$  and  $t_s$  are the elastic modulus, Poisson ratio and thickness of the substrate respectively. Negative values for  $\sigma$  indicate a compressive stress and positive ones a tensile stress.

The application of Eq. 1 requires that the substrate and other films (e.g. previously deposited) are not affected during deposition and further (anneal) treatment of a specific film. However, it is very likely that such effects occur, e.g. by recrystallization, interdiffusion, reaction or plastic deformation processes. A possibility for investigating such influences is to compare the stress condition before and after removal of the different layers of the capacitor. In this way the stress contribution of each individual film in the completed stack is determined without interference from changes in the stresses of the other films, except for possible effects related to the etching process.

## STRESS MEASUREMENTS DURING PROCESSING

In general two types of stresses can be distinguished: Internal stress and thermal stress [2]. Internal stress, or growth stress, is the result of the accumulation of flaws that are built into the film during the deposition process. It is to a large degree determined by the sputter-deposition conditions. The thermal stress originates from the difference in thermal expansion between the substrate and the thin film material. The relevant properties of the materials with respect to this are given in Table I. When films are annealed the internal stresses are reduced by e.g. interdiffusion and recrystallization. However, on subsequent cooling (to room temperature) a thermal stress is introduced. When there is no interaction between the films such as interdiffusion or chemical reactions, the total stress in a multiple stack is the sum of the stresses in each film. In addition to film stresses interfacial stresses may also be present which are the result of elastic interface deformation [9].

### Stresses in the Pt bottom electrode

The stress in Ti/Pt bottom electrode can be varied over a wide range, from tensile to compressive, by modifying the sputter conditions, particularly by the pressure and power. In this work a Pt electrode sputtered at 800 W and 20 mTorr is as a standard material. This film is highly compressive ( $\sigma = -700$  to  $-750$  MPa). An anneal of it in N<sub>2</sub>/O<sub>2</sub> up to 750 °C prior to deposition of the sol-gel PZT is found to be very beneficial for the formation of the PZT film. This is related to the hillock formation during the annealing. The hillocks

Table I

Young moduli, Poisson ratio and thermal expansion coefficients of Pt [10], unpoled polycrystalline PZT [11] and Si [12].

	$E_s$ (GPa)	$\nu_s$	$\alpha$ (25-100 °C) (K <sup>-1</sup> )
Pt	170	0.39	$9.0 \times 10^{-6}$
PZT	72	0.30	$1.7 \times 10^{-6}$
Si	130	0.28	$2.8 \times 10^{-6}$

serve as nucleation sites for the sol-gel PZT [5].

**Stress development during thermal cycling:** The platinized wafer was heated in the furnace of the stress analyzer at a rate of 15 °C/min in a nitrogen atmosphere to a temperature of 700 °C and subsequently cooled to room temperature. During this thermal cycle the stress was determined at regular time intervals. The results are shown in Fig. 1.

Initially upon heating the compressive strength increases due to a larger thermal expansion of platinum compared to the silicon wafer. Above 200 °C a stress relaxation starts, but between 370 and 500 °C the compressive stress increases presumably caused by the diffusion of Ti into the Pt film. Above 500 °C a stress relaxation process is observed due to recrystallization within the Pt film and the compressive stress decreases to a relatively small value.

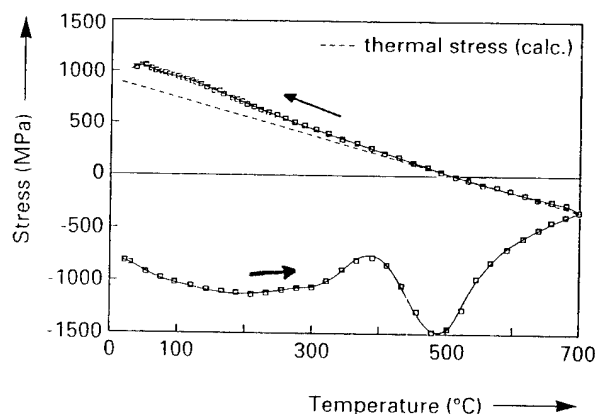


**Figure 1** Stress in a 4nmTi/70nmPt film on an oxidized silicon wafer during a thermal cycle in N<sub>2</sub>. Also shown is the theoretical thermal stress calculated from the thermal expansion of Si [12] and Pt [10].

After cooling to room temperature a large tensile stress has developed due to the larger thermal expansion of platinum as compared to silicon. A completed thermal cycle changes the stress from 700 MPa compressive to 1000 MPa tensile. A repeated heating gives results similar to the upper curve of Fig. 1.

**Standard anneal treatment:** The standard anneal treatment of the bottom electrode is 30 min. at 650 °C in N<sub>2</sub>/O<sub>2</sub>. This treatment results in an electrode which, as mentioned above, is covered with small hillocks. The thin Ti film is oxidized and it has partly diffused to the surface [5]. The stress found after this anneal is 950 MPa tensile which is very similar to the value found after the thermal cycling in N<sub>2</sub>.

#### Stresses in the PZT film

The sol-gel PZT film was deposited on the annealed bottom electrode and it consisted of three spin-coated layers with thicknesses of 90 nm, 65 nm and 65 nm respectively. After deposition of each layer a bake-out treatment was applied. This was a 30 min. heat treatment in N<sub>2</sub>/O<sub>2</sub> at 550 °C for the

Table II

The stress at room temperature after deposition and bake-out of each of the three PZT layers as well as integrated over the complete stack and after the final anneal.

	thickness (nm)	Stress (MPa)
PZT-layer 1	90	-128
PZT-layer 2	65	51
PZT-layer 3	65	191
PZT-total	220	18
PZT-annealed	220	113

first layer and at 600 °C for the other two layers. The deposition was completed with a final anneal (650 °C, N<sub>2</sub>/O<sub>2</sub>, 30 min.). The orientation of the PZT is predominantly (111) and to a lesser degree (100). The curvatures of the wafer were measured after each spin-coating step (incl. the bake-out) and after the final annealing. From the curvature the stress in each layer was calculated using eq. 1. The results are given in Table II.

The stress in the PZT film is smaller than that in the Pt electrode and this reflects a much smaller difference in thermal expansion coefficient of the PZT film and the substrate than of the Pt film and the substrate. The first PZT layer is compressive and the two subsequent layers are increasingly tensile. This indicates the presence of both internal and thermal stresses after the bake-out treatments. On the basis of the thermal expansion coefficients given in Table I one expects a compressive thermal stress. The increased tensile stress resulting from increasing the PZT film thickness and from the final anneal must therefore be caused by an internal stress in the PZT film.

The stress in the PZT film as a function of temperature was determined by the thermal cycling of an already film. This was done in N<sub>2</sub>, since stress measurement in an oxygen ambient was not possible at higher temperatures. The results of these measurements are shown in Fig. 2. A maximum is observed at about 425 °C. This behavior can be understood on the basis of the thermal expansion coefficient ( $\alpha_{PZT}$ ) as measured by Cook Jr. et al. [11]. For poled PZT ( $x = 0.52$ )  $\alpha_{PZT}$  is very anisotropic being smaller than that of Si below the Curie temperature ( $T_C$ ) and this is reversed at higher tem-

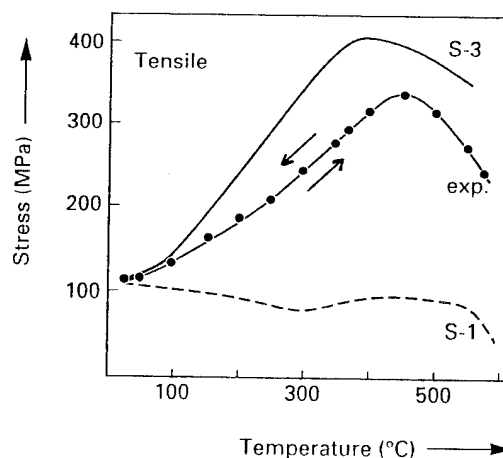


**Figure 2** Stress for a 220 nm PZT film prepared by sol-gel as a function of temperature during thermal cycling compared with the thermal stress calculated from thermal coefficient data of bulk polycrystalline PZT [11] with the direction parallel to the poling (S-3) and perpendicular to the poling (S-1).

peratures. For the direction parallel to the polarization the thermal expansion coefficient is negative with a minimum at about 365 °C while for the direction perpendicular to the polarization a positive thermal expansion coefficient not very different from that of Si was found. Using the data in ref. 11 the thermal stress in a 220 nm thick PZT film was calculated for two polarization directions, parallel and perpendicular to the substrate surface, respectively. The results are shown in Fig. 2. It is clear that the thermal stress measured here is qualitatively very similar to that calculated for bulk PZT with the polarization parallel to the film surface. Therefore the as-grown films are poled with a polarization having a large component in the plane of the film. The decrease of tensile stress above 425 °C is caused by an increase of  $\alpha_{\text{PZT}}$  to a value exceeding that of Si. If it is assumed that this temperature corresponds to the Curie point, it is substantially higher than what is expected for bulk PZT ( $x=0.52$  and 1%  $\text{Nb}_2\text{O}_5$  with  $T_C = 386^\circ\text{C}$  [1]). A comparable increase of  $T_C$  has been observed by Kwok and Desu [13] which was attribute to the intrinsic tensile stress shifting the volume-decreasing ferroelectric to paraelectric transition, i.e. the Curie point, to a higher temperature.

### Stress in the Pt top electrode

The as-deposited top electrode has a compressive stress ( $\sigma = -520$  MPa). This value is somewhat smaller than the value for the bottom electrode and it could indicate a changed microstructure. Thermal cycling of the top electrode shows a similar stress behavior as found for the bottom electrode (see Fig. 1). The stress in the top electrode at room temperature has changed to 940 MPa tensile after an anneal treatment (5 mins. in  $\text{O}_2$  at 500 °C). This is again comparable to the values found for the bottom electrode after the temperature cycling in  $\text{N}_2$  as well as the anneal in  $\text{O}_2$ . Such an anneal treatment of processed, i.e. structured ferroelectric capacitors are found to give a substantial improvement of the electrical properties [7].

### STRESS ANALYSIS BY REMOVAL OF CAPACITOR LAYERS

The total stress in the completed capacitor stack is the sum of the stresses in each film. When the stress of a film is measured after each processing step, the effect of this step on all the underlying films is also included in the curvature. This can give rise to an erroneous interpretation of the measurements. In order to eliminate such effects stress measurements were carried out in combination with removal of the different films. In that case the change in curvature of the wafer can be attributed to the stress present in the removed film.

### Stress in the processed ferroelectric stack

In Table III stress values obtained by the film removal method for the case of as-deposited as well as annealed top electrodes are given. The value for the bottom electrode has to be compared with the value of 950 MPa before PZT deposition. It can be concluded that the stress in the bottom electrode has hardly been influenced by the subsequent deposition, annealing and etching process steps carried out during the processing of the ferroelectric stack. By selectively etching the Pt bottom electrode an oxidized Ti film remains on the thermal oxide layer. The stress in the  $\text{TiO}_2$  film is  $\sigma \approx -900$  MPa, assuming a thickness of 8 nm after Ti oxidation.

For the PZT film Table III shows a significant difference between the stresses in the case of an as-deposited and an annealed top electrode. A comparison with the value before the deposition of the top electrode ( $\sigma = 113$  MPa, see Table II) also clearly demonstrates the shift towards a more compressive stress of the PZT film induced by the top electrode.

Table III

*The stress in the films within a fully processed stack as determined by the film removal method for as-deposited and annealed top electrodes.*

Film	As-deposited (MPa)	Annealed (MPa)
Top electrode	-530	930
PZT	80	-37
Bottom electrode	$\approx 900$	895

### Stress state of PZT film

The stress of the PZT film becomes more compressive by the deposition and especially by the annealing of the top electrode. One would expect this on the basis of the large tensile stress observed in both the bottom and top electrodes after annealing treatments. In order to further investigate the stress state of the PZT film as it is in the complete Pt/PZT/Pt stack we have measured the dependence of the stress on a thermal cycling after removal of the top electrode. This has been done for the two cases of an as-deposited and an annealed top electrode. The results are shown in Fig. 3. In both cases the stresses during heating and cooling are different with by far the largest change in the case of the annealed top electrode. The stress curves during cooling are in both cases qualitatively in agreement with the thermal stress behavior from Fig. 2. Thus, the heat treatment of the PZT film without Pt on top restores the stress situation that was present before the top electrode deposition and anneal treatment.

### ELECTRICAL RESULTS

We have investigated the switching properties of structured ferroelectric capacitors for the as-deposited and the annealed top electrode. The processing of the capacitors has been described elsewhere [7]. In Fig. 4 the switched and non-switched polarizations ( $\Delta P_s$  and  $\Delta P_{ns}$ ) are shown as a function of the pulse amplitude ( $V_p$ ). The measurements were done using single pulse switching and were carried out for the virgin capacitors ( $N=1$ ) and after poling with 1000 pulses at  $V_p = 8\text{V}$ .

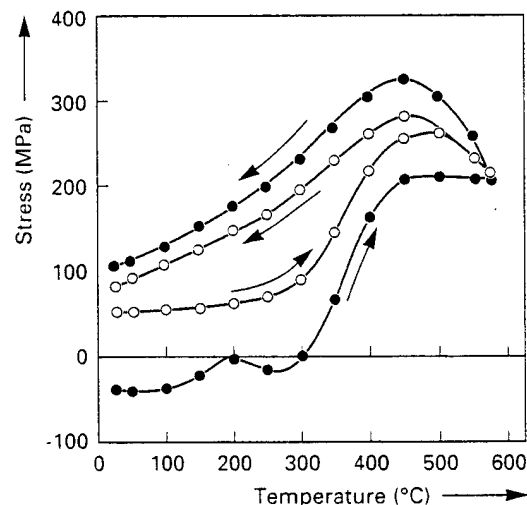


**Figure 3** Stress in PZT after deposition and etching of the top electrode. The film is thermally cycled to 575 °C with a heating rate of 15 °C/min. The stress development is shown for the case where the top electrode is not annealed (○) and annealed for 5 min. at 500 °C in  $\text{O}_2$  (●).

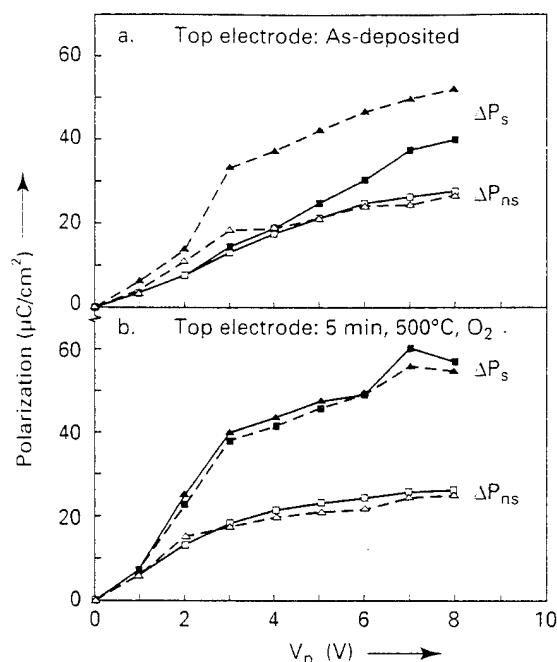


**Figure 4**  $\Delta P_s$  (closed symbols) and  $\Delta P_{ns}$  (open symbols) as a function of  $V_p$  for a  $2000 \mu\text{m}^2$  ferroelectric capacitor for a virgin capacitor (solid line) and after poling with 1000 pulses at 8V (broken line) in the case of as-deposited (a) and annealed top electrodes (b).

The unannealed capacitor shows for  $N=1$  a poor switching behavior with, almost no difference between  $\Delta P_s$  and  $\Delta P_{ns}$  below 4V and only a small difference above this voltage. Furthermore it is seen that the poling with 1000 pulses of 8V greatly improves the switching behavior. For the annealed samples there is little difference between the curves for  $N=1$  and  $N=1000$ , i.e. the capacitor in its virgin state is already poled.

## DISCUSSION AND CONCLUSIONS

The fully processed ferroelectric capacitor consists of a PZT film with a low compressive stress sandwiched between two platinum electrodes which both do have a large thermal tensile stress of about 1 GPa. However, prior to the anneal of the top electrode the PZT is tensively stressed while the top electrode does have a large as-deposited compressive stress.

It is well established that stresses in PZT ceramics influence properties such as permittivity,  $\tan\delta$  and piezoelectric coefficients [14]. These effects are most pronounced for compressive stresses applied parallel to the polar axis. PZT can react to an applied stress by  $90^\circ$  reorientation for the tetragonal and  $109^\circ$  or  $71^\circ$  reorientation for the rhombohedral phase [11]. This indicates the possibility of stress induced effects in the switching behavior of a PZT film.

After its deposition processing is finished by an annealing treatment and after the deposition of the top electrode the stress in the PZT film is tensile. The stress as a function of temperature during thermal cycling (Figs. 2 and 3) indicates that for these PZT films a large fraction of the crystallites have a large poling component in the plane of the substrate. This polar orientation explains the observed switching behavior of the unannealed capacitors (Fig. 4). In the virgin state relatively few domains are directed parallel to the substrate and only after 1000 pulses of 8 V a large fraction has undergone a  $90^\circ$  reorientation which has improved switching.

After the anneal treatment of the top electrode, the stress in the PZT at room temperature has become compressive. A heating of the PZT film with the top electrode removed shows a stress which is hardly influenced up to about  $300^\circ\text{C}$  (Fig. 3). If one compares these stress levels with the calcu-

lated curves S-1 and S-3 in Fig. 2 it is striking that the heating curves of Fig. 3 up to about  $300^\circ\text{C}$  qualitatively are much more comparable to the S-3 curve than the S-1 curve. This strongly indicates that for a large part the poling direction is perpendicular to the substrate. The electrical switching behavior showing a high switchable polarization in a virgin state of the film, is in agreement with this orientation. At temperatures above  $300^\circ\text{C}$  there is a marked increase in tensile stress with temperature and the influence of the (removed) top electrode disappears.

In conclusion: The improvement of the switching properties of a ferroelectric capacitor, in particular the behavior of virgin capacitors, by an anneal treatment is caused by a reorientation of the poling direction from parallel to perpendicular to the substrate. In this way fully functional capacitors can be obtained without the need for an additional poling treatment.

## REFERENCES

- [1] D. Berlincourt, "Piezoelectric ceramics: Characteristics and Applications," *J. Acoust. Soc. Am.*, vol. 70, pp. 1586-1595, 1981.
- [2] J.A. Thornton and D.W. Hoffman, "Stress-related effects in thin films," *Thin Solid Films*, vol. 117, pp. 5-31, 1989.
- [3] S.B. Desu, "Influence of stresses on the properties of ferroelectric  $\text{BaTiO}_3$  thin films," *J. Electrochem. Soc.* vol. 140, 2981-2987, 1993.
- [4] B.A. Tuttle, J.A. Voigt, T.J. Garino, D.C. Goodnow, R.W. Schwartz, D.L. Lamppa, T.J. Headley and M.O. Eatough, "Chemically prepared  $\text{Pb}(\text{Zr,Ti})\text{O}_3$  thin films: The effect of orientation and stress," in *Proceedings of the IEEE 8th International Symposium on Applied Ferroelectrics*, 1992, pp. 344-348.
- [5] G.A.C.M. Spierings, J. van Zon, P.K. Larsen and M. Klee, "Influence of platinum-based electrodes on the microstructure of sol-gel and MOD prepared lead zirconate titanate films," *Integrated Ferroelectrics*, vol. 3, pp. 283-292, 1993.
- [6] M. Klee, R. Eusemann, R. Waser and H. van Hal, "Processing and electrical properties of  $\text{Pb}(\text{Zr,Ti}_{1-x})\text{O}_3$  ( $x = 0.2 - 0.75$ ) films: Comparison of metal-organic decomposition and sol-gel processing" *J. Appl. Phys.*, vol. 71, 1566-1576, 1992.
- [7] G.J.M. Dormans, P.K. Larsen, G.A.C.M. Spierings, J. Dikken, M.J.E. Ulenlaers, R. Cuppens, D.J. Taylor and R.D.J. Verhaar, "Processing and performance of integrated ferroelectric and CMOS test structures for memory applications," *Integrated Ferroelectrics*, (in press).
- [8] J.J. van Glabbeek, G.A.C.M. Spierings, M.J.E. Ulenlaers, G.J.M. Dormans and P.K. Larsen, "Reactive ion etching of Pt/PZT/Pt integrated ferroelectric capacitors," *Mat. Res. Soc. Symp. Proc.*, vol. 310, pp. 127-132, 1993.
- [9] J.A. Ruud, A. Witvrouw and F. Spaepen, "Interface stress in artificial multilayers," *Mat. Res. Soc. Symp. Proc.*, vol. 209, pp. 737-740, 1990.
- [10] L. Holborn and A.L. Day, "Über die Ausdehnung einiger Metalle in hoher Temperatur," *Ann. Phys.*, vol. 4, 104-122, 1901.
- [11] W.R. Cook Jr, D.A. Berlincourt and F.J. Scholz, "Thermal expansion and pyroelectricity in lead titanate zirconate and bariumtitanate," *J. Appl. Phys.*, vol. 34, pp. 1392-1398, 1963.
- [12] T. Soma and H. Matsuo Kagayo, "Thermal Expansion coefficient of Si," in *Properties of Silicon*. London: Inspec, 1988, Ch. 1.12, pp. 33-34.
- [13] C.K. Kwok and S.D. Desu, "A novel method for determining the Curie temperature of ferroelectric films," *Mat. Res. Soc. Symp. Proc.*, vol. 310, pp. 429-433, 1993.
- [14] H.H.A. Krueger, "Stress Sensitivity of Piezoelectric Ceramics," *J. Acoust. Soc. Am.*, vol. 42, pp. 636-645, 1967; vol. 43, pp. 576-582, 583-591, 1968.

# Concurrent Session - 3A: Dielectrics

# A New Proposal on Mixing Rule of the Dielectric Constant of Mixture

Kikuo Wakino \*

Institute of Science and Engineering, Ritsumeikan University,  
1916, Nojicho, Kusatsu-shi, Shiga-prefecture, 525, Japan

**Abstract** — We proposed a new equation for predicting the apparent dielectric constant of two materials compound in the Journal of American Ceramic Society last year. This equation was derived using the Monte Carlo and finite element methods with the assumption of a non aspect and randomly dispersed mixture of two different materials. We found that, in the high concentration range of the higher dielectric constant material, calculated value of the dielectric constant showed a parallel model like tendency. On the contrary, in the low concentration range of higher dielectric constant material, the compound showed a serial model like behavior. Around 35% content of the higher dielectric constant material, it exhibited results similar to the logarithmic mixing rule. In this work we tried to introduce the order parameter  $n$  and  $S$  which closely relates to the aspect ratio of dispersing material and aligning angle with respect to the applied electric field.

## INTRODUCTION

Several types of equations predicting the dielectric constant of a compound of different materials, either theoretical or experimental, have been proposed by many researchers[1--15].

Maxwell-Wagner's equation is well known as an analytical solution for a dispersion of spherical shape particle, but this model is too ideal and deviates considerably from actual cases. The following equation is the most well known general empirical equation for the calculation of the dielectric constant of a compound.[2, 5].

$$\varepsilon_r^\alpha = \sum_i V_i \varepsilon_{ri}^\alpha \quad (1)$$

where,  $\varepsilon_r$  is the calculated relative dielectric constant of the compound,  $V_i$  and  $\varepsilon_{ri}$  are the volume fraction and relative dielectric constant of  $i$ -th material, and  $\alpha$  is a constant. The value of the constant  $\alpha$  determines the type of the mixing rule.

$\alpha$	type of mixing rule
1	parallel model
0	logarithmic mixing rule
-1	series model

Parallel and series models are the two extreme cases and do not represent a compound composed of finely divided components. The logarithmic mixing rule which has been most widely used for the wide composition ratio application, is also not sufficiently exact for practical use. Several

experimental equations giving better predictions were proposed, but in some cases, these equations omit the influence of the infringement of the electric flux due to discontinuity at the boundary regions of constituents and also these experiments were performed in a restricted range of mixing ratio. As a result, sometimes the agreement between predicted dielectric constant value and the measured one is applicable only in a limited range of composition.

In our preceding work, simulation of the apparent dielectric constant of a compound of two different non aspect materials using the Monte Carlo and the finite element methods was attempted by taking into account the effects of infringing electric flux at the boundary region of two different materials. Based on the results of extensive simulation works, the following equations were proposed.[17]

$$\varepsilon_r^{(V_1-V_c)} = V_1 \varepsilon_{r1}^{(V_1-V_c)} + V_2 \varepsilon_{r2}^{(V_1-V_c)} \quad (2)$$

or, as an explicit expression for  $\varepsilon_r$

$$\varepsilon_r = \exp\{\ln[V_1 \varepsilon_{r1}^{(V_1-V_c)} + V_2 \varepsilon_{r2}^{(V_1-V_c)}] / (V_1 - V_c)\} \quad (2')$$

where,  $\varepsilon_r$ ,  $\varepsilon_{r1}$ , and  $\varepsilon_{r2}$  are the relative dielectric constants of the compound, material 1 and material 2 respectively, and  $V_1$  and  $V_2$  are the volume fractions of material 1 and 2. Further,  $V_c$  is the critical volume fraction at the point where the curves of dielectric constant predicted by the new equation and the logarithmic mixing rule intercept each other. It was concluded that the value of  $V_c$  would be 0.35 after extensive calculation, and it was confirmed that the fit between measured and calculated (by equation (2')) dielectric constant is by far the best among the other equations reported till that time.

\* Corporate Adviser : Murata Manufacturing Co., Ltd.  
2-26-10, Tenjin, Nagaokakyo-shi, Kyoto, 617, Japan



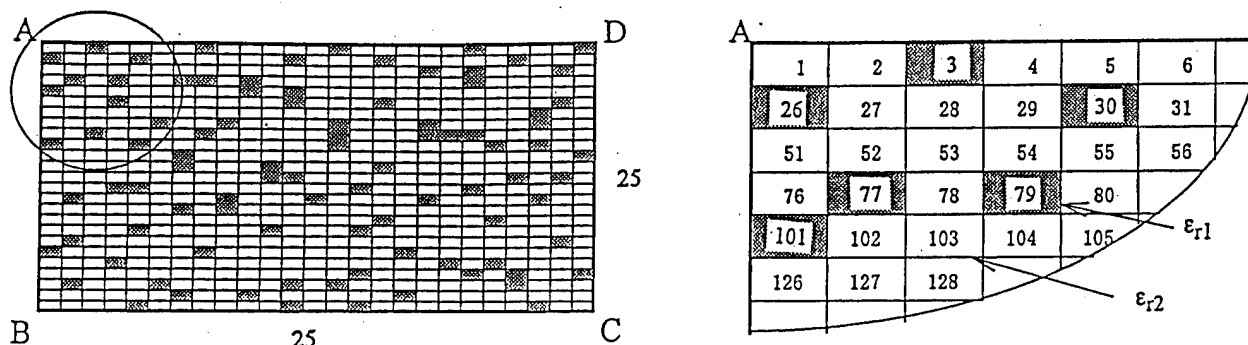


Fig. 1. The rectangle is divided into  $25 \times 25$  subcells and each subcell is assigned to material 1 or 2 randomly.

In the preceding work, the critical volume fraction  $V_c$  was derived through computational experiment. As an extension of preceding work, in this work, the empirical factor,  $(1 - |S|^n) \cdot V + \{S - [\frac{1}{2}(1 - S^2)]^{\frac{1}{2}}\}$ , was introduced instead of  $(V_1 - V_c)$ , where  $n$  and  $S$  are the parameters.  $S$  takes the value between  $-1$  and  $+1$ . The cases of the value of  $S$  equal to  $-1$ ,  $0$  and  $+1$  correspond to serial, non aspect random and parallel model respectively. The results of Monte Carlo and finite element method obtained by changing the aspect ratio of mixing cells showed good coincidence with the results of the calculated value of  $\epsilon_r$  by changing the sign and magnitude of the parameter  $S$ .

### SIMULATION PROCEDURE

The rectangle ABCD was divided into the serially numbered  $25 \times 25$  sub cells of equal sizes as shown in Fig. 1. The value of the aspect ratio  $R$ , ( $R = AB/AD$ ), was chosen as  $5:1$ ,  $3:1$ ,  $2:1$ ,  $1:1$ ,  $1:2$ ,  $1:3$ , and  $1:5$ . From these 625 cells,  $V_1 \times 625$  number of cells were chosen randomly using a random number generator applying on the set of  $[1 - 625]$ , without duplication, where the mixing ratio of material 1 to 2

is given by the ratio  $V_1 : V_2$  ( $V_1 + V_2 = 1$ ). The relative dielectric constant of material 1,  $\epsilon_{r1}$ , was assigned to the selected cells and  $\epsilon_{r2}$  for material 2 was assigned to the remaining cells, as shown in the same figure. Here, we assume  $\epsilon_{r1}$  is larger than  $\epsilon_{r2}$  in our calculation.

The apparent relative dielectric constant  $\epsilon_r$  was then calculated using the two dimensional finite element method. The simulation process was repeated 1000 times on each compound using mixing ratios of  $1.0$ ,  $0.9$ ,  $0.8$ , ...,  $0.1$  and  $0.0$ . One thousand different  $\epsilon_r$  values were obtained after each calculation depending on the one thousand scattering patterns of the selected cells. Then the mean value of  $\epsilon_r$  and standard deviation of each mixing rate compound was calculated as the most probable expected value  $\langle \epsilon_r \rangle$ . Although, a more accurate  $\langle \epsilon_r \rangle$  and a narrower standard deviation will be obtained with a larger number of divisions, we confirmed that the  $25 \times 25$  grid is accurate enough for this simulation work, as described in the preceding report.

### RESULTS OF SIMULATION

In Figs. 2(a) through 2(c), the patterns of the electric flux distribution for most typical cases on 90%, 50% and 20% of

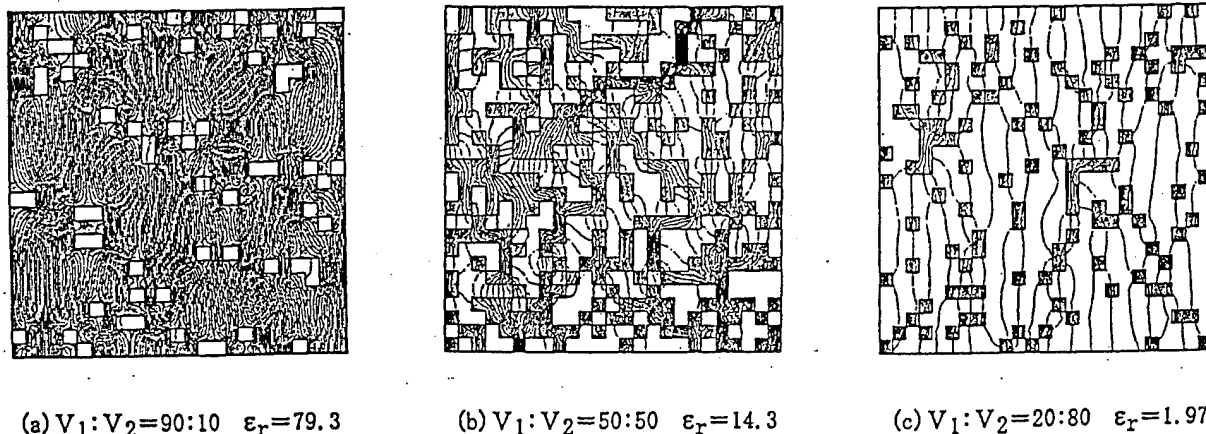
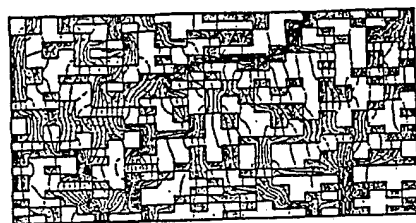
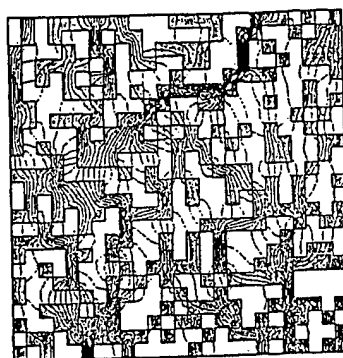


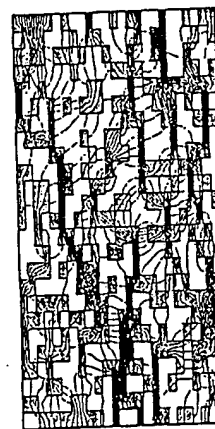
Fig. 2. Dielectric flux distribution patterns simulated by the finite element method for non aspect and 90, 50 and 20 vol% of material 1 compound. The strength of one flux line is proportional to  $(\epsilon_r)^{1/2}$ . ( $\epsilon_{r1} = 100.0$ ,  $\epsilon_{r2} = 1.0$ )



(a)  $R = 0.5 \quad \epsilon_r = 9.64$



(b)  $R = 1.0 \quad \epsilon_r = 14.3$



(c)  $R = 2.0 \quad \epsilon_r = 23.5$

Fig. 3. Dielectric flux distribution patterns simulated by the finite element method for 50 vol% of material 1 compound. The strength of one flux line is proportional to  $(\epsilon_r)^{1/2}$ . ( $\epsilon_{r1} = 100.0$ ,  $\epsilon_{r2} = 1.0$ )

non aspect mixture are shown. In Figs.3(a) through 3(c), similar figures for the cases of aspect ratios 2 : 1, 1 : 1 and 1 : 2 on 50 % mixture are shown. It can be seen from these figures that :

At the higher content range of material 1 and/or the larger aspect ratio of cell parallel to the electric field, the appearance of the electric flux flow pattern is closer to that of the parallel model. Because the impedance through the higher K (relative dielectric constant) sub-cells is lower than through the lower K sub-cell, the electric flux stream along the applied electric field has a tendency to flow mainly passing through higher K sub-cells. When the density of higher K material is high or the longer axis of the cell align along the applied field, the electric flux connecting two electrodes has a higher probability to pass through the higher K sub cells, which is close to the parallel model.

On the contrary, at the lower content range of material 1 and/or the smaller aspect ratio of cell, the appearance of the electric flux flow pattern is closer to that of the serial model. The number of chains of lower K sub cells crossing the electric flux is larger for the diluted compound, which leads to higher impedance and, consequently a lower  $\epsilon_r$ . This situation further emphasized when longer axis of lower K cells are aligned perpendicular to the electric field (i.e. lower aspect ratio case).

However, for the non aspect mixture and at the critical volume mixing region, the pattern of the electric flux is rather complicated. In rare cases, these patterns were similar to the parallel model or to the serial model, but in the most cases, the cluster like (localized complex combinations of the patterns for the parallel and serial

model) configuration was dominant.

## CONSIDERATION

First, we reconsider briefly the non aspect ratio case [17]. In Fig. 4, the curves of  $\epsilon_{r\text{sim}}$  simulated by Monte Carlo Method for the non aspect compound, the dielectric constants calculated by parallel model, serial model, logarithmic mixing rule and Maxwell-Wagner Model are plotted.

The dielectric constant value curve of non aspect mixture by Monte Carlo simulation intercepts the line of the logarithmic mixing rule curve at around  $V_f = 0.35 (=V_c)$ , and it can be recognized that the curve of dielectric constant simulated by Monte Carlo method shows the convex shape which is similar to parallel model in higher concentration region and shows the concave shape which is similar to the

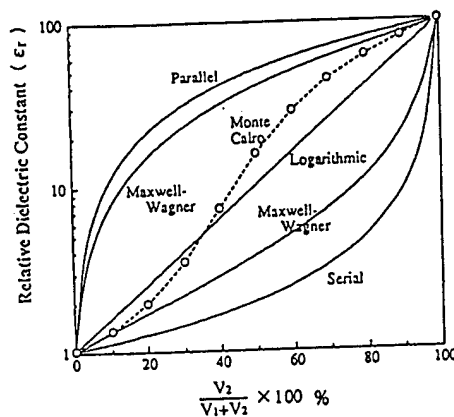


Fig. 4. Comparison between relative dielectric constant calculated by several predictive equations and Monte Carlo simulated value with respect to composition.

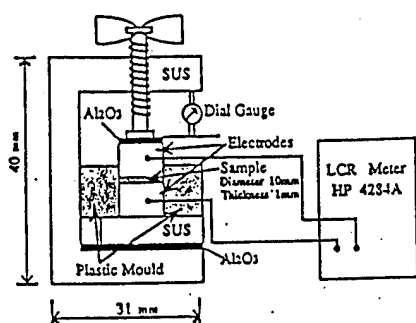


Fig. 5. Schematic drawing of measuring fixture of apparent relative electric constant of pressed powder including pore.

serial model in the dilute region. In the critical mixing range, it shows similar result as the logarithmic mixing rule.

Considering the relations between the values of  $\alpha$  and the mixing rules, for the non aspect mixture, we found that in the Taylor Expansion approximation around  $\alpha = 0$  of eq. (1), when  $\alpha = V_I - V_C$ , we could achieve the best fit of the calculated value obtained by the new equation with that by the Monte Carlo method. When  $V$  varies from 0 to 1, the value of  $(V - V_C)$  varies from negative to positive through 0 at  $V = V_C$ . These conclusions would be reasonable and also in good accordance with the results of the electric flux distribution patterns which were mentioned in the preceding section.

### Experimental Verification

CaTiO<sub>3</sub> (CT) powder, crushed and sieved between 1.0 to 3.0  $\mu\text{m}$ , was pressed into the disk shape of several packing densities using capacitor die jig as shown in Fig. 5. The pore ratio was calculated from the weight of CT which was fed into die, the theoretical density of CT and the geometry of the die cavity. The apparent capacitance value of specimen

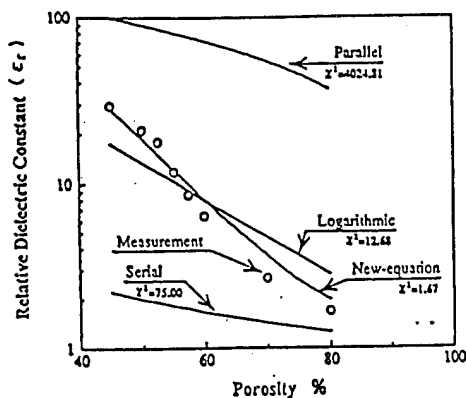


Fig. 6. Relative dielectric constant of pressed CaTiO<sub>3</sub> powder with respect to its porosity.

was measured using HP-4284 Impedance Analyzer at 1 MHz to eliminate several undesired effects at low frequencies. The actual capacitance value of specimen was calculated from the capacitance values of empty and powder filled die jig by subtracting the stray capacitance due to the edge effect. The effective relative dielectric constant of porous specimen was calculated using actual capacitance value and geometry of the mold.

The data for the above are shown in Fig. 6. The  $\chi^2$  values in figure are statistical fitness parameter between the reference (or ideal) value and actual values. The smaller  $\chi^2$  value indicates better fitness. We can see best consistency with the equation (2').

### Verification using the Reported Data

For further evaluation of the equation (2'), we compared the fitness of the new equation and most popular equations using reported measured values in several papers and publications [7, - 15], and found that the fit is always best with the equation (2'). One example is shown in Fig. 7. As can be seen in this figure, equation (2') best fits the published data among several other equations.

### COMPUTATIONAL EXPERIMENT WITH CHANGING ASPECT RATIO

Since equation (2') is applicable only on the mixture of non aspect and randomly dispersed case, the derivation of a new type equation for needle, flake and cluster type mixtures will be useful for actual applications.

After several consideration, an exponential factor defined by following equation was derived as the replacement of  $(V - V_C)$  in the preceding report.

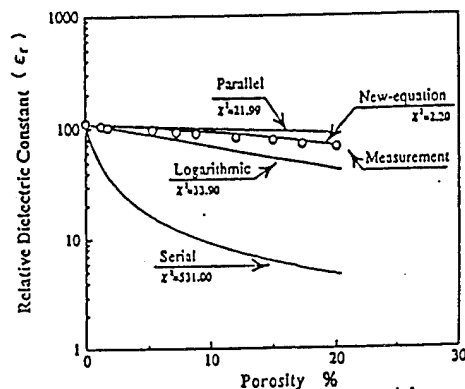


Fig. 7. Fitness check of several predictive equations and the equation proposed in preceding report.

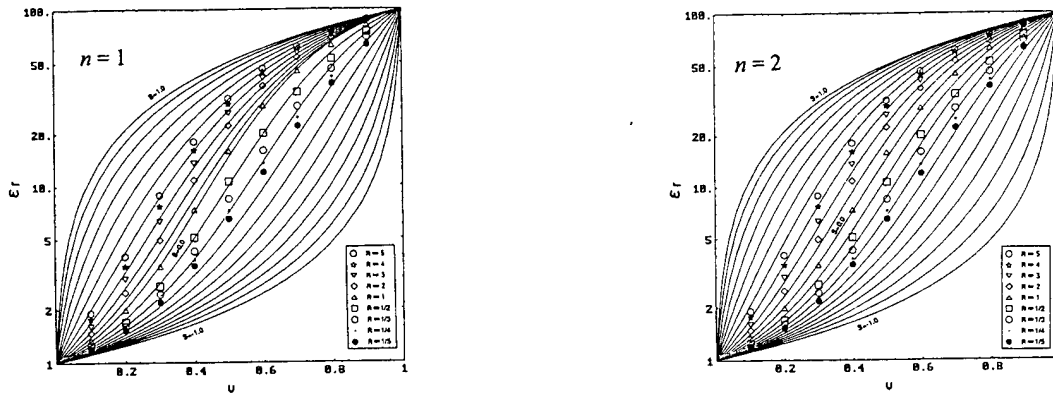


Fig. 8. A line plot of the new equation and point plot of  $\epsilon_r$  simulated by Monte Carlo and finite element method with respect to the mixing ratio.

$$(1 - |S|^n) \cdot V + \{S - [\frac{1}{2}(1 - S^2)]^2\} = B(V, n, S) \quad (3)$$

where  $n$  and  $S$  are the parameters related to the aspect ratio and ordering, and the following is the final equation for  $\epsilon_r$ .

$$\epsilon_r = \exp\{\ln[V\epsilon_{r1}^{B(V,n,S)} + (1-V)\epsilon_{r2}^{B(V,n,S)}] / B(V,n,S)\} \quad (4)$$

As it is easily calculated, the values of  $S$ , +1, 0 and -1, lead the exponential factor to the value of +1,  $(V - 0.35) = (V - V_c)$  and -1 regardless of  $n$ .

Since it is difficult to get reproducible and correct data of the influence of the parameter  $n$  and  $S$  by actual experiments, we performed the computational experiment by changing the aspect ratio of the shape of the specimen and sub cells as described in the section of simulation procedure. Fig.8 shows the line plots of calculated  $\epsilon_r$  by eq. (4) and the point plots of  $\epsilon_r$  calculated by Monte Carlo simulation with changing the aspect ratio  $R$  of cell. Among several plots with changing values of  $n$ , the data for  $n = 2$  gave the best coincidence between  $\epsilon_r$  by eq. (4) and simulation. As it is seen in Fig. 8,  $\epsilon_r$  by eq. (4) of larger  $R$  is closer to parallel model, smaller  $R$  is closer to series model and  $R = 0$  coincides with the non aspect random dispersion case. This conclusion agrees well with the result of the electric flux pattern in Figs.2 and 3. Although it is difficult to postulate quantitative explanation based on the physical image of the relation between  $S$ , aspect ratio  $R$  and calculated value of dielectric constant, but the qualitative conclusion shown in the following table would be reasonably justified.

R	S	mixing rule
large	+1	parallel model
1	0	logarithmic mixing rule
small	-1	series model

## CONCLUSION

As a result of the boundary conditions set up in the finite element method calculation, the effects of polarization and infringement of electric flux at the discontinuity at the boundary region were considered automatically. Rectangular or square geometry approximations are not realistic in actual case, but it is expected that when the number of divisions into sub cell and trials are increased greatly, the simulated value would tend to the actual one.

Although a clear physical scheme or image was not defined, qualitative explanation on the relationship between the aspect ratio of parallel or perpendicularly aligned mixture of the needle like or flake like compound and the value of order parameter  $S$  was presented. For the general case,  $n$  and  $S$  would relate to the several complicated phenomena and it is almost impossible to show quantitative justification for each physical reason separately. But in some extreme case of almost perfectly aligned compound such as extruded or forged compounds, this idea of parameter  $n$  and  $S$  would be useful to apply for prediction of electric parameter in total.

Due to the computational limit of computer in this work, the apparent dielectric constant of compound was simulated on a two dimensional model, but the result of this scheme can be extended to three dimensional case without significant changes.

Because of the complexity of situation and difficulty of the simulation on the case of oblique alignment cells, we omitted the simulation work on the dependency of aligning angle. The necessity of the parameter  $n$  which seems to be most dependent to the aligning angle to the electric field, is not clear, but for the actual application, two parameters related to the aspect ratio and alignment could be necessary.

## ACKNOWLEDGMENT

The author would like to express his thanks to Mr. Tsutomu Okada and Norio Yoshida of Murata Manufacturing Co. Ltd., for performing the tedious computing work and for their valuable discussion.

## REFERENCES

- [1] K. W. Wagner, Arch. Electrotech., 2, pp. 371, (1914).
- [2] A. R. von Hippel, "Dielectrics and Waves": John Willey & Sons, New York, (1954).
- [3] W. R. Bussem, "Ceramic Problems for the Consideration of Solid State physicist": The Physics and Chemistry of Ceramics, Edited by C.Klingsberg, Goldon and Breach Science Pub. Inc., pp. 22-29, (1963).
- [4] A. R. von Hippel, "Dielectric Materials and Applications"; MIT Press, Cambridge, pp. 301, (1966).
- [5] W. D. Kingery, H.K.Bowen, and D.R.Uhlmann, "Introduction to Ceramics": pp. 686-759, (1967).
- [6] A. Buchner, Wiss. Veroeff. Siemens-Werken, 18, 84 (1939).
- [7] G. Economos, "Ceramic Fabrication Processes": Edited by W.D.Kingery, John Willey & Sons, N.Y. pp. 201, (1958).
- [8] G. Partridge, "Lead-through seals incorporating a foamed glass ceramic": Glass Technology, 24, pp. 293, (1983).
- [9] R. E. Newnham, D. P. Skinner and L. E. Cross, "Connectivity and Piezoelectric-Pyroelectric Composites": Mat. Res. Bull., 13, pp. 525-536, (1978).
- [10] K. Okazaki and K. Nagata, "The Effect of Density and Grain Size of Piezoelectric Ceramic Influencing upon the Electrical Properties,": Denki-gakkai-shi (Trans. IECE), 53-C [11] pp. 815, (1970), (in Japanese).
- [11] H. Igarashi, "Effects of Porosity and Grain Size on the Magnetic Properties of NiZn Ferrite,": J. Amer. Ceram. Soc., 60 pp. 51-54 (1977).
- [12] H. Igarashi, "Control of Microstructure of Dielectric Ceramics and Their Properties,": Seramikusu ( Ceramics Japan ), 12 [2] pp. 126-131, (1977) (in Japanese).
- [13] H. Banno, "Theoretical Equations for Dielectric and Piezoelectric Properties of Ferroelectric Composites Based on Modified Cubes Model,": Jpn. J. Appl. Phys., 24, Suppl., [24-2] pp. 445-447, (1985).
- [14] T. Furukawa, K. Ishida and E. Fukada, "Piezoelectric Properties in the Composite Systems of Polymers and PZT Ceramics,": J. Appl. Phys., 50 [7] pp. 4904 (1979).
- [15] P. Sliva, L. E. Cross, T. R. Gururaja and B. E. Scheetz, "Relative Dielectric Permittivity of calcium aluminate Cement-Glass Microsphere Composites": Mat. Letters 4, pp. 475-480, (1986).
- [16] P. P. Silvester and R. L. Ferrari, "Finite Element for Electrical Engineers": Cambridge University Press (1983).
- [17] K. Wakino, T. Okada, N. Yoshida and K. Tomono, " A New Equation for Predicting the Dielectric Constant of Mixture": J. Amer. Ceram. Soc., 76

# A Numerical Approach to Analyze the Internal Electrical Response of Dielectric Ceramics With Arbitrary Shaped Inclusion

M.E. Azimi and P.K. Ghosh

Department of Electrical and Computer Engineering  
Syracuse University  
Link Hall, Syracuse, NY 13244

## ABSTRACT

Multicomponent dielectric ceramic structures are becoming more desirable for their capability to satisfy the growing need for better sensitivity and selectivity of modern devices. Theoretical analysis of these multicomponent dielectric ceramic structures is rather complicated. Most of the reported analytical methods are generally limited to isotropic mixtures with spheretical and in some cases elliptical inclusions. We believe that the inherent limitation in the analytical approach makes it difficult to get a closed form solution for arbitrary shaped inclusions. We have developed a rather simple and accurate numerical method which enables one to predict the internal electrical environment within the dielectric ceramics with arbitrary shaped inclusions. This method was used to calculate the potential distribution, the polarization and the effective permittivity. Discussion will also include the effect of the inclusion's shape on these properties.

## INTRODUCTION

The primary objective of this paper is to obtain the field distribution and the polarization of the multicomponent ceramic structures. Most simulation techniques are two-dimensional and are limited to isotropic mixture [1-4]. In this paper, a numerical method [5] is used as a means of obtaining realistic three-dimensional simulations of field distribution within multicomponent ceramic structures. The ceramic structures are made of many dielectrics and conductors. In addition, dielectric inclusions could be of arbitrary shape and orientation. After deriving the integral equation for the internal electric field we proceeded to solve the equations numerically by the method of moments [6]. Effects of the shape and the orientation of each inclusion was included in the calculation. Finally, the polarization of the inclusion was found numerically to estimate the effective permittivity of the composite structure.

## DESCRIPTION OF THE METHOD

Consider a multicomponent three-dimensional structure with embedded multiple dielectrics ( $\epsilon_i$ ) and conductors (C). We assume that each conductor is an equipotential surface and could be of either infinitesimal or finite cross section, as shown in fig. 1. To compute the field distribution we, first, create an equivalent environment such that the field distribution remains unchanged. In this environment dielectrics and conductors are replaced by free space and proper sources (electric charge or current) are placed on the interfaces. Let, there are  $N_c$  conductor-to-dielectric interfaces and  $N_d$  dielectric-to-dielectric interfaces. On each conductor-to-dielectric interface, the total charge  $\sigma_T$  is the sum of the free charge and the polarization charge. On each dielectric-to-dielectric interface, the total charge is the polarization charge. Each charge density layer was discretized into a set of planar triangular patches and assumed a constant charge density on any given patch.

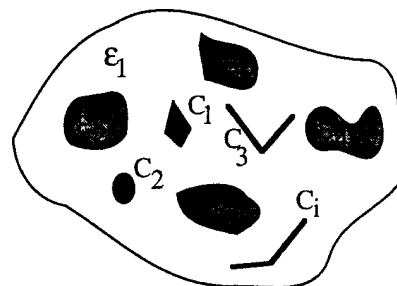


Fig. 1 Assumed composite structure for numerical development.

At any point  $r$ , the potential is due to the combination of  $\sigma_T$  on all patches. From the potential one can easily find the electric field and as  $r$  approaches to an interface the electric field can be expressed as [5]

$$E^{\pm}(r) = \frac{1}{4\pi\epsilon_0} \sum_{j=1}^{N_c+N_d} \int_{S_j} \sigma_T(r') \left[ \frac{r-r'}{|r-r'|^3} \right] ds' \pm \bar{n} \frac{\sigma_T(r)}{2\epsilon_0} \quad \dots (1)$$

where  $S_j$  is the surface area of the  $j$ th patch,  $ds'$  is the differential element area at  $r'$  on  $S_j$  and  $\bar{n}$  is the unit vector normal to  $S_j$  at  $r$ . The side of  $S_j$  toward which  $\bar{n}$  points is referred to as the positive side of  $S_j$  and the other side of  $S_j$  is referred to as the negative side of  $S_j$ .  $E^+(r)$  and  $E^-(r)$  are the electric field on the positive and the negative side of  $S_j$ . Next applying the boundary conditions so that (a) the normal component of the displacement vector is continuous across each dielectric-to-dielectric interface and (b) on each conductor-to-dielectric interface the potential is constant, one obtains a set of  $N_c+N_d$  integral equations for the unknown total charge  $\sigma_T$  on the interface whose patches are on  $S_j$  [5]. These integral equations are then converted to matrix equations using the method of moments [6]. Resultant matrix are then solved numerically. Using this method, calculation of the potential, the charge distribution on interfaces and the effective permittivity of a particular composite structure has been reported by the authors [7].

In this paper we extend our theory to include the effect of randomly oriented arbitrarily shaped multiple inclusions as shown in Fig. 2.

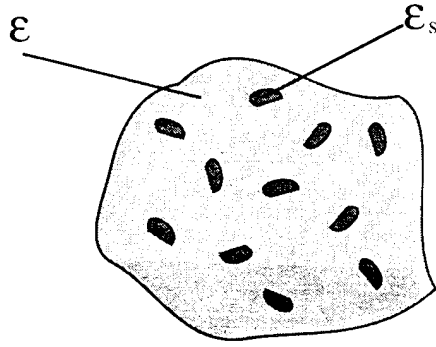


Fig. 2 Dielectric composite with multiple inclusions.

The local electric field ( $E^c$ ) on each inclusion will be different from the average field ( $E$ ) in composite and they are related by [8,9]

$$E^c = E + \frac{1}{\epsilon_a} \bar{L} \cdot \langle P \rangle \quad (2)$$

where  $\epsilon_a$  is the apparent permittivity "seen" by each inclusion in composite and  $\langle P \rangle$  is the average polarization in the neighborhood of an inclusion. Now, if  $\Omega$  represents three angle parameters which describe orientation of any inclusion and  $\omega_0(\Omega)$  is the orientation distribution function of inclusions, the average polarization  $\langle P \rangle$  can be expressed as

$$\langle P \rangle = \int_{4\pi} \omega_0(\Omega) P(\Omega) \quad (3)$$

Now if we assume the inclusions are oriented randomly and the total volume fraction of inclusion is  $f$  then,

$$\omega_0(\Omega) = \frac{f}{4\pi} \quad (4)$$

and,

$$f = \int_{4\pi} d\Omega \omega_0(\Omega) \quad (5)$$

Combining the above equations with the well-known permittivity expressions, the effective permittivity of a composite structure of Fig. 2 with multiple inclusions can be written as

$$\bar{\epsilon}_{eff} = \epsilon \bar{I} + \frac{f}{4\pi} \left( \bar{I} - \frac{f}{4\pi \epsilon_a} \int_{4\pi} d\Omega \bar{\alpha} \cdot \bar{L} \right)^{-1} \cdot \int_{4\pi} d\Omega \bar{\alpha} \quad (6)$$

where  $\bar{I}$  is the unit dyadic and  $\bar{\alpha}$  is the polarizability of each inclusion.

To calculate the  $\bar{\epsilon}_{eff}$  one needs to find  $\bar{L}$ ,  $\epsilon_a$  and polarizability  $\bar{\alpha}$ .

The depolarization dyadic  $\bar{L}$  is a symmetric dyadic which only depend on the geometrical shape of the inclusions and can be expressed by [8,9]

$$\bar{L} = \int_{S'} \frac{\bar{n} \bar{e}_R}{R^2} ds' \quad (7)$$

where  $\bar{n}$ ,  $\bar{e}_R$ ,  $R$  and  $S'$  are illustrated in Fig. 3. The polarizability  $\bar{\alpha}$  can be calculated in closed form for certain shapes like sphere or ellipsoid but in general it should be calculated numerically. For our calculation we have assumed a system, as shown in Fig. 4, in which a cubic dielectric is immersed in a "approximately uniform" electric field created by the potential applied to the conductor plates. Fig. 5 shows the normalized dipole moment per unit volume as a function of the inclusion's permittivity. As expected for  $\theta=0$  the dipole moment is along Z-axis and its value is less than a sphere of same volume. Fig. 6 shows the effective permittivity of a composite structure as a function of the volume fraction of the inclusion. In this calculation we have assumed the inclusion and the matrix permittivity to be of 12 and 2 respectively. Again, as expected the effective permittivity for spherical inclusion is greater than that for cubic inclusion of same volume.

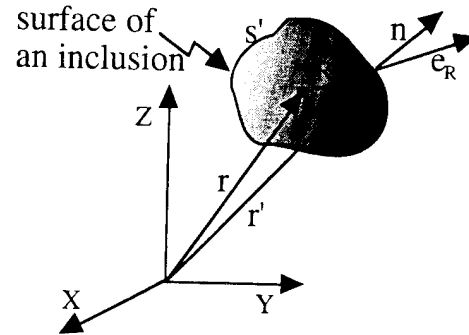


Fig. 3 Notation associated with an inclusion to define the depolarization dyadic  $\bar{L}$ .

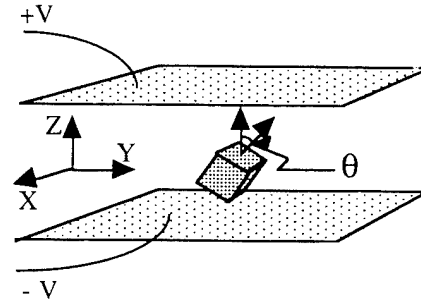


Fig. 4 Simulated arrangement for calculating the polarizability of cubic inclusion.

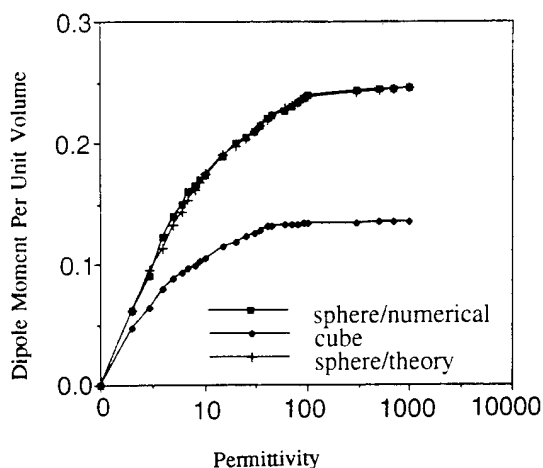


Fig. 5 Comparison between dipole moment per unit volume,

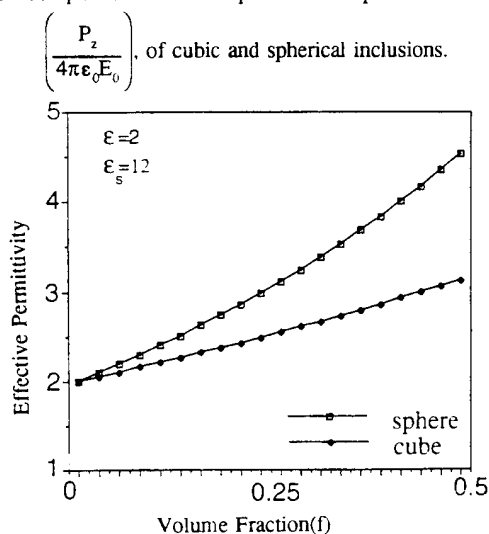


Fig. 6 Calculated effective permittivity of mixture as a function of volume fraction of the inclusion, for two different shapes.

#### SUMMARY

A numerical method has been developed to obtain the field distribution within three-dimensional multicomponent structures. The numerical method was employed to calculate the polarizability including the shape and the orientation effects of inclusions. The calculated polarizabilities then were used to estimate the effective permittivity of mixtures with spherical and cubical inclusions. This method is general in nature and can be extended to estimate the electrical properties of many other composites.

#### REFERENCES

- [1] J.C. Maxwell-Garnett, "Colours in Metal Glasses and in Metal Films," *Philos., R. Soc., London*, Vol. 203, pp. 385-420 (1904).
- [2] L.K.H. VanBeek, "Dielectric Behavior of Heterogeneous Systems," *Progress in Dielectrics*, Lond., Vol. 7, pp. 76-77, 92-101, (1967).
- [3] L.E. Nielsen, "The Permittivity of Suspensions and Two Phase Mixtures," *J. Phys., D: Appl. Phys.*, Vol. 7, pp. 1549-1555, (1974).

- [4] A.H. Sihvola, "Self Consistency Aspects of Dielectric Mixing Theories," *IEEE Trans. GeoSci. and Remote Sen.*, Vol. 27, No. 4, pp. 403-415, (1989).
- [5] S.M. Rao, T.K. Sarkar and R.F. Harrington, "The Electrostatic Field of Conducting Bodies in Multiple Dielectric Media," *IEEE Trans. on MTT*, Vol. 32, No. 11, pp. 1441-1448, (1984).
- [6] R.F. Harrington, *Field Computation by Moment Methods*, Krieger, Melbourne, Florida, (1982).
- [7] M.E. Azimi and P.K. Ghosh, "Numerical Calculation of the Electrostatic Environment Within a Dielectric Composite Using Boundary Charge Method," *Modeling and Sim. in Mat. Sci. and Eng.*, (in press).
- [8] A. Yaghjian, "Electric Dyadic Green's Functions in the Source Region," *Proc. IEEE*, Vol. 68, No. 2, pp. 248-263, (1980).
- [9] A. Yaghjian, "Maxwellian and Cavity Electromagnetic Fields Within Continuous Sources," *Am. J. Phys.*, Vol. 53, No. 9, pp. 859-863, (1985).





# Concurrent Session - 1B: Piezoelectrics

# Local Structure of PLZT

S. Teslic and T. Egami

Department of Materials Science and Engineering,  
Laboratory for Research on the Structure of Matter,  
University of Pennsylvania, Philadelphia, PA 19104-6272

**Abstract** - The local structure of PLZT has been examined by the means of neutron-powder-diffraction derived pair-distribution function (PDF). We find that atoms are displaced from the average periodic structure by a significant amount. The directions and magnitudes of the atomic displacements in PLZT are very similar to those found in PMN. The short- and intermediate-range structural changes between ferroelectric, relaxor and antiferroelectric PLZT phases were compared.

## INTRODUCTION

Relaxor ferroelectrics are characterized by a diffuse ferroelectric phase transformation occurring over tens of degrees centigrade, with strong dielectric dispersion in this temperature region. Compositional fluctuations have long been believed to be responsible for the diffuse phase transformation leading to ferroelectric microregions with a distribution of Curie temperatures which effectively "diffused" the macroscopic transition [1]. While the evidence in favor of this approach is extensive it is not direct and is rather limited to some systems. On the other hand, local atomic displacements are found to be large in ferroelectric solids, especially in mixed ferroelectrics. Since they are not correlated over long distances they contribute only to diffuse scattering without leading to any extra peaks in the diffraction profile. Diffraction profile refinements, which ignore the diffuse scattering, cannot extract this structural information and will just refine large thermal factors on these sites. When averaged over the whole crystal, this local order will appear just as an uncharacterized uncertainty in atom position.

In this paper we address the question on the nature of atomic displacements and their short range correlations in relaxor ferroelectrics. The real space method for powder diffraction, or the atomic pair-distribution function (PDF) analysis allows us to have direct information on local atomic correlations without assuming long-range order. The PDF is a representation of the distribution of interatomic distances present in a material. It is determined from both the Bragg and diffuse scattering intensities without an assumption made regarding long-range periodicity. Thus information on short-range order is preserved. For this reason the PDF analysis has been able to differentiate between random and short-range correlated atom displacements.

If diffuse ferroelectric phase transformations are caused by compositional fluctuations, it might be expected that they are common in many multi-component materials. Since that is not the case the role of compositional fluctuations in diffuse ferroelectric phase transformation should be investigated with a great care. In perovskites  $ABO_3$  with ions of different valency on B sites  $Pb(Mg_{1/3}Nb_{2/3})O_3$  (PMN) this role seems to be pronounced, but not for conventional ferroelectric  $Pb(Zr_xTi_{1-x})O_3$  (PZT) with ions of the same valency on B sites. Lanthanum doped solid solution of PZT,  $(Pb_{1-x}La_x)(Zr_yTi_{1-y})_{1-x/4}O_3$  (PLZT) shows relaxation behavior for an interval of atom percent of La [2], and presents particularly suitable system for study.

## REAL-SPACE STRUCTURAL ANALYSIS

Neutron powder diffraction measurements were carried out using the special environment powder diffractometer (SEPD) instrument at the Intense Pulsed Neutron Source (IPNS) at Argonne National Laboratory. The powder-diffraction spectrum was corrected for absorption, multiple-scattering, the scattering intensities from background, the vanadium sample container, and the Plazcek shift to obtain the total diffraction intensity. After correction the intensity of neutrons scattered from a col-

lection of atoms is given by

$$I(Q) = \left\langle \sum_{\alpha, \alpha'} b_{\alpha} b_{\alpha'} \exp[iQ(r_{\alpha} - r_{\alpha'})] \right\rangle \quad (1)$$

where  $Q$  is the scattering vector ( $=4\pi \sin \Theta / \lambda$ , where  $\Theta$  is the diffraction angle and  $\lambda$  is the wavelength of incident neutrons),  $b_{\alpha}$  and  $b_{\alpha'}$  are the neutron-scattering lengths of the  $\alpha$ th and  $\alpha'$ th atoms, respectively, at positions  $r_{\alpha}$  and  $r_{\alpha'}$ . The brackets  $\langle \rangle$  denote a time average. It is convenient to define a structure function  $S(Q)$  which depends only on the structure of the sample. Thus,

$$S(Q) = \frac{I(Q)}{\langle b(Q) \rangle^2} + \frac{\langle b(Q) \rangle^2 - \langle b^2(Q) \rangle}{\langle b(Q) \rangle^2} \quad (2)$$

The pair density, or distribution function (PDF) is obtained by Fourier-transforming the spherically averaged  $S(Q)$ ,

$$\rho(r) = \rho_0 + \frac{1}{2\pi^2 r} \int Q(S(Q) - 1) \sin(Qr) dQ \quad (3)$$

where  $\rho_0$  is the average atomic density. In order to include all the available structural information, and at the same time to reduce the termination error which is introduced by the finite range of integration in Eq. (3), the Fourier transformation has been carried out up to  $30 \text{ \AA}^{-1}$ .

The PDF PLZT with the composition 8/65/35 (x/y/1-y) at  $T=300\text{K}$  obtained by pulsed neutron scattering at the SEPD is shown in Figure 1. Also shown, by a dashed curve, is the PDF calculated for an ideal perovskite structure. In calculating the model PDF we assumed a lattice constant of  $4.08 \text{ \AA}$  and the vibrational amplitude of  $0.05 \text{ \AA}$ , expected from the Debye temperature. The first peak of calculated PDF corresponds to the Zr/Ti-O distance, the second peak to the Pb/La-O and O-O distances which are equal, the third to the Pb/La-Zr/Ti, and the fourth to the lattice periodicity. The experimental PDF is significantly different from the calculated PDF, indicating that the real structure in this solid is grossly departed from the crystallographic lattice structure. Since the Zr/Ti-O correlation is well preserved it is most likely that the integrity of the Zr/Ti-O<sub>6</sub> octahedra is reasonably well maintained. At the same time the first peak is shifted from ideal distance Zr/Ti-O  $2.04 \text{ \AA}$  to  $2.12 \text{ \AA}$ .

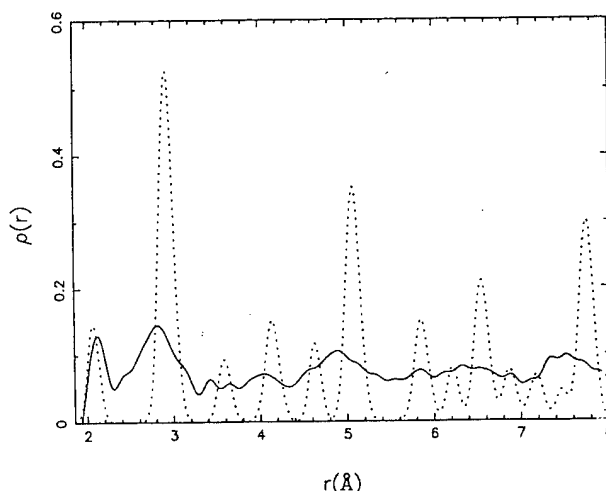


Figure 1. Comparison of experimental PDF for 8/65/35 PLZT (solid line) and the PDF calculated for an undistorted perovskite structure.

The most natural way to explain this significant increase in the Zr/Ti-O distance from a half of lattice constant is the tilting of the Zr/Ti-O<sub>6</sub> octahedra. If we assume uniform tilt of octahedra for the same angles around all principle axes then we predict that tilt angles are about 12°.

Calculated peak at 2.88 Å describes both Pb/La-O and O-O distances. Corresponding experimental peak is shifted toward shorter interparticle distances and its irregular shape implies that it consists of a few overlapping peaks. We speculate that Pb/La-O distance is reduced and split due to non-uniform oxygen octahedra tiltings and that the O-O distance is preserved.

The Rietveld profile analysis was used by Glazer *et al.* [3] to describe the structure of room temperature ferroelectric phase. The distortion of ideal perovskite structure was observed and described using a number of unit cell parameters. The tilt angle about [111] axes was 5.42° and thermal factors were unphysically large. These values are used for PDF shown in Figure 2. Agreement is obviously still very poor indicating that the description of the PLZT in terms of a periodic structure does not yield correct short and intermediate-range structural features.

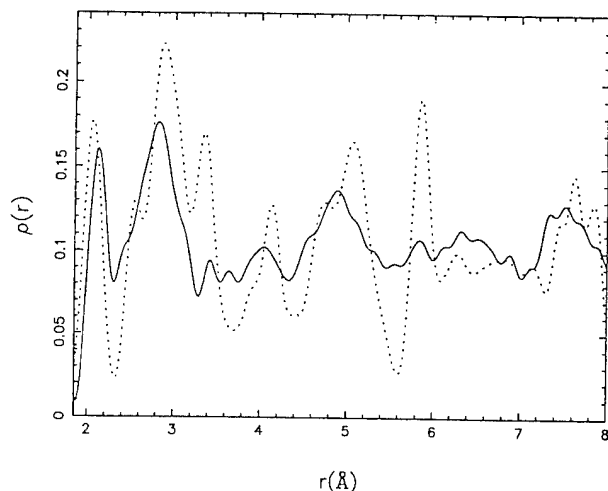


Figure 2. Comparison of experimental PDF (solid line) and the Rietveld-refined model PDF (dashed line) for 8/65/35 PLZT.

The detailed model of short and intermediate range atomic structure in PMN was developed by Rosenfeld *et al.* [4] using both crystallographic and pair-distribution function analysis of atomic structure. Vibrational amplitudes in this model were less than 0.07 Å, cation displacements about 0.2 Å and oxygen octahedra tilt angles about 13°. In Figure 3, the experimental PDF of PLZT is compared to that of PMN. Overall agreement is very good implying that the directions and magnitudes of the atomic displacements from ideal cubic lattice sites in PLZT are very similar to those found in PMN.

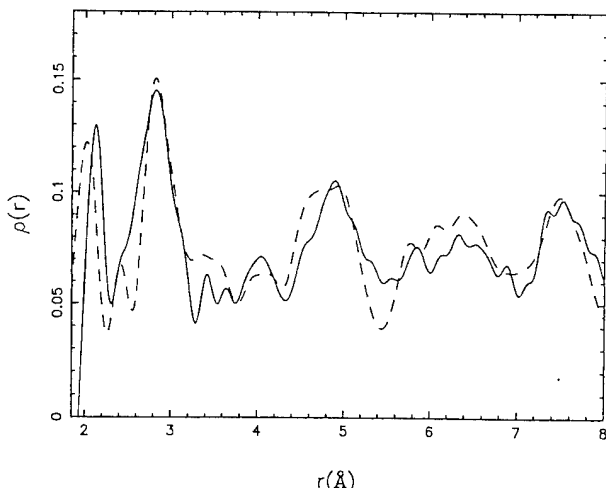


Figure 3. Room-temperature experimentally observed PDF's for 8/65/35 PLZT (solid line) and PMN (dashed line).

In order to investigate the short- and intermediate-range structural changes between ferroelectric, relaxor and antiferroelectric phases PDF's of 8/65/35, 10/65/35, and 12/65/35 PLZT concentrations were compared. Although changes are subtle and detailed simulation are needed, some conclusions may already be made. First peaks for all three compositions are shown in Figure 4. The peak of intermediate 10/65/35 concentration, which is in relaxation region, is the lowest and broadest implying the most random distribution of Zr/Ti-O distances. The lattice periodicity peak for ferroelectric phase 8/65/35 is low and broad, but almost Gaussian in shape, Figure 4. On the other hand, for relaxor 10/65/35 that peak is clearly split in two, and for 12/65/35 it again takes the Gaussian shape, although non-symmetrical.

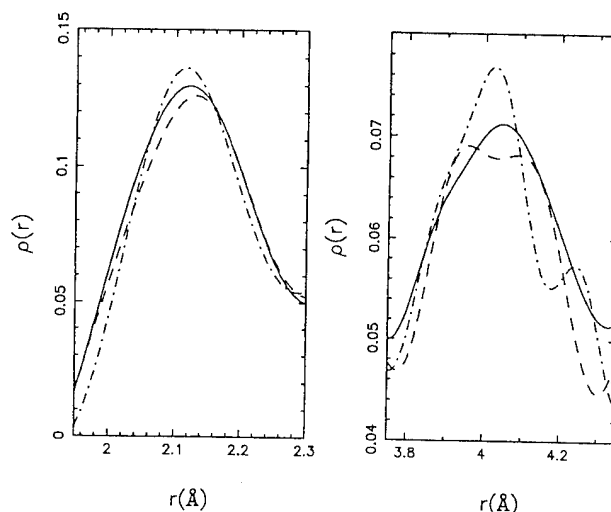


Figure 4. Compositional dependence of Zr/Ti-O peak (left) and lattice periodicity peak (right) of PDF for PLZT for: 12/65/35 (chained curve), 10/65/35 (dashed curve), and 8/65/35 (solid curve).

## CONCLUSIONS

In mixed ferroelectric solids exhibiting a relaxor behavior atoms are found to be locally displaced from the average periodic structure by a significant amount. The directions and magnitudes of the atomic displacements in PLZT are very similar to those found in PMN. The short- and intermediate-range structural changes between ferroelectric, relaxor and antiferroelectric PLZT phases were compared. Although changes are subtle, additional degree of randomness is observed in relaxor phase.

## ACKNOWLEDGEMENTS

Work at the University of Pennsylvania was supported by the Office of Naval Research through N001491-J-1036. The intense Pulsed Neutron Source is operated as a user facility by the U. S. Department of Energy, Division of Materials Science, under contract W-31-109-Eng-38.

## REFERENCES

- [1] G.A. Smolenskii, A.I. Agranovskaya, *Soviet Physics Solid State* 1, pp. 1429, 1959.
- [2] G.H. Haertling and C.E. Land, "Hot-Pressed (Pb,Lu)(Zr,Ti)O<sub>3</sub> Ferroelectric Ceramics for Electrooptic Applications", *J. Amer. Ceram. Soc.*, 54 (1), pp. 1-11, 1971
- [3] A. M. Glazer, A. A. Mabud, and R. Clarke, "Powder Profile Refinement of Lead Zirconate Titanate at Several Temperatures. I Pb(Zr<sub>0.9</sub>Ti<sub>0.1</sub>)O<sub>3</sub>", *Acta Cryst.* B34, pp. 1060-1065, 1978.
- [4] H. D. Rosenfeld and T. Egami, "A Model of Local Atomic Structure in the Relaxor Ferroelectric Pb(Mg<sub>1/3</sub>Nb<sub>2/3</sub>)O<sub>3</sub>", *Ferroelectrics*, vol.150, pp. 183-197, 1993.

V. H. Schmidt, C.-S. Tu, and I. G. Siny<sup>1</sup>

Physics Department, Montana State University, Bozeman, MT 59717, USA

<sup>1</sup>Now returned to A.F. Ioffe Physical Technical Institute, RAS, St. Petersburg 194021, Russia

(abstract) We investigated dielectric and hypersonic properties of NBT over a wide temperature range. The dielectric permittivity and loss measured from 20 Hz to 300 kHz agree at lower temperature with previous results. At higher temperature in and near the tetragonal phase the lower frequencies show a very large permittivity peak with considerable dispersion and large loss. This behavior is very similar to that found in other perovskite crystals and ceramics, in some cases far above  $T_c$ . We attribute it to extrinsic bulk conductivity. The phase shift giving nonzero  $\sigma''$  in  $\sigma = \sigma' + j\sigma''$  may be caused by a spread in mobility activation energy. The Brillouin scattering data at 514.5 nm show a very broad dip in sound velocity and a very large and broad attenuation peak, both centered in the tetragonal phase temperature range. This behavior is attributed to hybridization of order parameter and cluster fluctuation contributions.

## INTRODUCTION

Sodium bismuth titanate (NBT, formula  $\text{Na}_{1/2}\text{Bi}_{1/2}\text{TiO}_3$ ) is a relaxor ferroelectric with unusual dielectric, optical and other properties.[1] The  $\text{Na}^+$  and  $\text{Bi}^{3+}$  ions randomly occupy the "A" cation sites. This random ion placement broadens the phase transitions and changes the nature near the transitions of the anomalies in permittivity and in sound velocity and attenuation determined by Brillouin scattering.

In this paper we first describe our Brillouin scattering and lower-temperature dielectric results. Most of the paper is devoted to the large low-frequency permittivity peak seen by us[1] at high temperature in NBT. This peak and associated loss resemble behavior of other perovskite crystals and ceramics.[2-5] We explain these phenomena in terms of extrinsic bulk conductivity with a spatial distribution of mobility activation energies.

## BRILLOUIN SCATTERING RESULTS

Our Brillouin scattering results are summarized in Fig. 1. Only the background intensity shows an obvious anomaly right at a transition, namely the jump at the trigonal-tetragonal transition. The dip in Brillouin shift, and the peaks in linewidth and background intensity, all appear in the tetragonal phase between its transitions to the trigonal and cubic phases. We believe the usual anomalies caused by Landau-Khalatnikov-type (order parameter) variations are absent because of the presence of large fluctuations which must cause "hybridization" mixing of the fluctuation and Landau-Khalatnikov contributions.[6] We attribute the location of the anomalies between two transitions to an interaction between the two types of fluctuations associated with these two transitions. Further details of the Brillouin experiment and results, and comparison with results for other relaxor ferroelectrics, have been submitted for publication elsewhere.

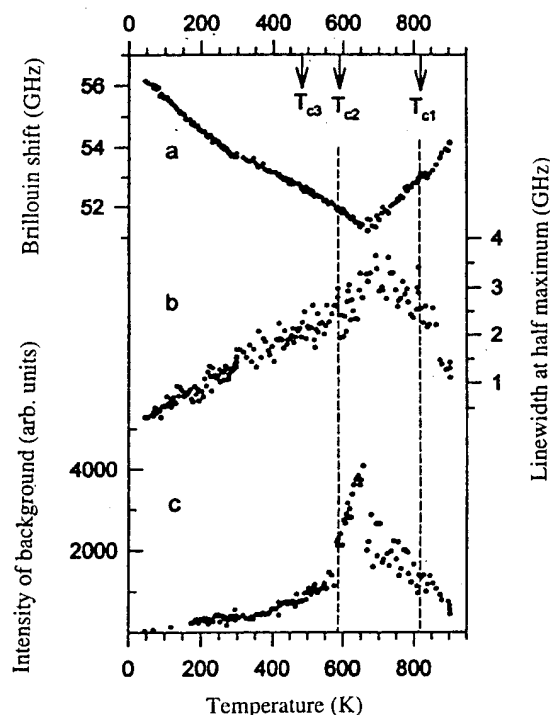


Figure 1. Brillouin scattering results for NBT.  $T_{c1}$  and  $T_{c2}$  represent the transitions from the orthorhombic to the cubic and trigonal phases respectively.  $T_{c3}$  denotes the transition from the antiferroelectric to the ferroelectric phase as temperature decreases.

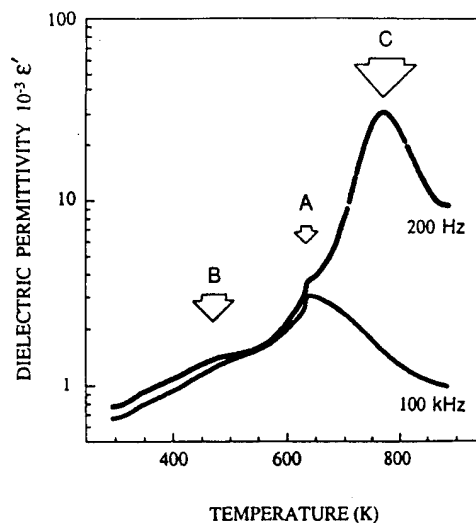


Figure 2. (from Ref. 1) The dielectric permittivity of NBT upon heating. A and B correspond to  $T_{c2}$  and  $T_{c3}$  of Fig. 1 respectively. C represents a peak whose temperature is frequency-dependent.

\*Work supported by NSF Grant DMR-9017429, an NRC CAST Grant, and DOE Equipment Grant FG05-91ER79046.

## DIELECTRIC RESULTS AT LOWER TEMPERATURES

These results, going upward from room temperature as shown in Fig. 2, begin with a steady increase in permittivity. The only indication of the transition at  $T_{c3}$  near 550 K is disappearance of the weak dispersion. The slope then increases to a cusp at  $T_{c2}$ . The phase between  $T_{c3}$  and  $T_{c2}$  is antiferroelectric or antiferroelectric incommensurate. Our results agree with those of others to an extent determined by crystal quality variations. Comparison and further interpretation of these results appears elsewhere.[1]

The 100 kHz permittivity is quite large just above  $T_{c2}$  in the tetragonal phase. It decreases gradually as temperature increases, but shows no anomaly at  $T_{c1}$ .

A striking feature of Fig. 2 is the huge permittivity peak (C) at 200 Hz in the tetragonal phase. At this low frequency also, there is no anomaly at  $T_{c1}$ . We previously[1] attributed this peak to superparaelectric clusters whose switching is related to the conductivity mechanism. Very recently we learned of such peaks far inside the cubic phase for other perovskites. The remainder of this paper is devoted to our new explanation for such peaks.

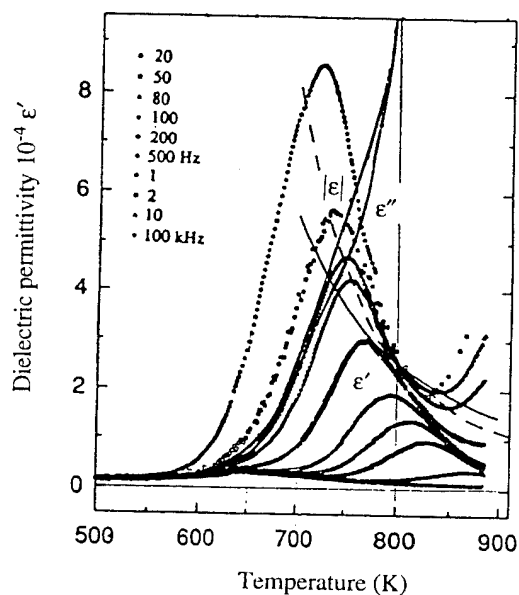


Figure 3. (from Ref. 1) Permittivity  $\epsilon'$  vs. temperature for NBT, with scale chosen to emphasize the large low-frequency peaks. The upturns at the right may be artifacts resulting from the very much larger  $\epsilon''$  values at high temperature. The solid and dashed lines indicate fits to a model we no longer consider applicable.

## THE HIGH-TEMPERATURE DIELECTRIC BEHAVIOR IN VARIOUS PEROVSKITES

The strong dispersion associated with the largest (C) permittivity peak in NBT is illustrated in Fig. 3. An important feature, discussed later, is the overlap envelope on the high-temperature side. Two other important features are that both the peak height and peak frequency approximately obey the Arrhenius law. Although these permittivity peaks are high, the lossy component  $\epsilon''$  of the permittivity at each peak is even higher.

The physical nature of the dielectric loss  $\epsilon''$  is better understood by plotting it logarithmically as  $\sigma'$ , using the relation  $\sigma' = 2\pi f \epsilon_0 \epsilon''$ , where  $f$  is frequency and  $\epsilon_0$  is the MKS constant  $8.85 \times 10^{-12} \text{ C}^2/\text{Nm}^2$ . This plot appears in Fig. 4. There are two distinct envelopes where curves for different frequencies overlap. The upper one is the ac conductivity limit, and the lower one the dc conductivity limit. Both envelopes obey the Arrhenius law, with the

dc envelope having the higher activation energy. A kink appears in the ac envelope at  $T_{c2}$  near 640 K, and a rounded bend occurs in the ac and dc envelopes at  $T_{c1}$  near 820 K.

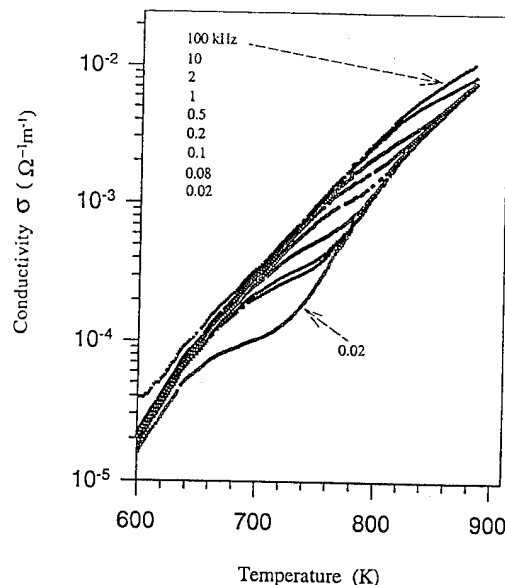


Figure 4. Electrical conductivity  $\sigma$  vs. temperature for NBT for several frequencies.

Figure 5 shows similar behavior found by Stumpe *et al.*[2] for a 0.24 mm thick  $\text{SrTiO}_3$  crystal (but plotted as  $\rho$  vs.  $1/T$ ). Both our results and theirs show ac and dc conductivity envelopes which tend toward convergence at finite temperature. The permittivity plot[2] for their 1.02 mm thick  $\text{SrTiO}_3$  crystal is similar to our Fig. 3. For their 0.24 mm crystal this dispersive behavior is superimposed on broad permittivity humps peaking near 950 K and showing little dispersion. This may be a surface effect appearing only in the thinner crystal, which may cause the S-type upward distortion of resistivity with decreasing temperature in Fig. 5. Unfortunately they provided no resistivity data for their 1.02 mm crystal.

Similar permittivity behavior to ours was seen by Kuwabara *et al.*[3] in a ceramic sample of  $\text{Pb}_{1-x}\text{La}_{2x/3}\text{TiO}_3$  (PLT10) with  $x=0.10$ , as shown in Fig. 6. The lowest-frequency peaks are distorted by the proximity of the ferroelectric transition at 378 °C (651 K; pure  $\text{PbTiO}_3$  has  $T_c=490$  °C). For  $x=0.05$  they observed broad nondispersive peaks centered near 462 °C which may be locked onto the ferroelectric transition.

The NBT,  $\text{SrTiO}_3$ , and PLT10 samples are compared in Fig. 7 where the  $\sigma'$  and  $\sigma''$  components of the conductivity  $\sigma = \sigma' + j\sigma''$  are plotted at the temperatures for which the  $\epsilon'$ (or  $\sigma''$ ) peaks occur. Striking similarity is noted for these results from quite different samples. The  $\sigma'$  values always exceed the  $\sigma''$  values, supporting the idea that a phase-shifted conductivity is being observed. The  $\sigma'$  values obey the Arrhenius law, while the  $\sigma''$  values show curvature.

Large and dispersive permittivity peaks were also observed by Bidault *et al.*[5] in  $\text{BaTiO}_3$  single crystals far above  $T_c$ . The peak height increased for reduced samples, and decreased for oxidized samples. Similar behavior was noted for a  $\text{CaTiO}_3$  single crystal and various PLT ceramics. Ujma and Dmytrów[4] found dispersive peaks above the ferroelectric (233 °C and antiferroelectric (225 °C) transition sequence in  $\text{PbZrO}_3$  single crystals and ceramics. Neither group[4,5] provided conductivity data for their samples.

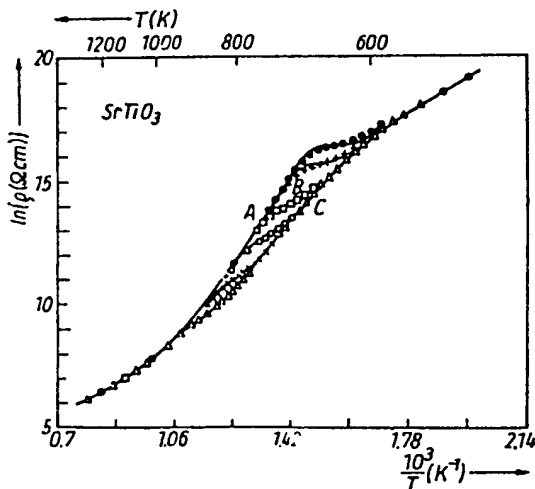


Figure 5. (from Ref. 2) Logarithm (to base e) of resistivity of 0.24 mm thick SrTiO<sub>3</sub> single crystal vs. inverse temperature for frequencies 0.1 kHz (filled circles), 0.2, 1, 4, 20 kHz, and 100 kHz (open triangles).

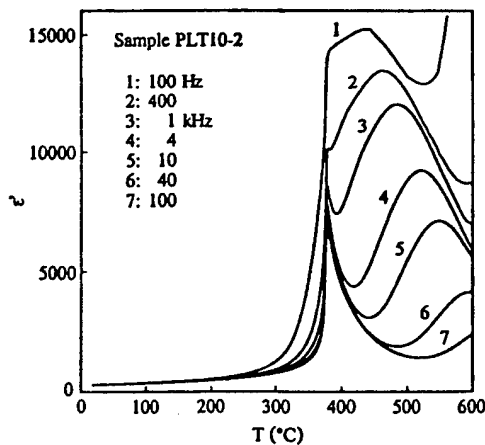


Figure 6. Temperature dependence of permittivity  $\epsilon'$  vs. temperature for various frequencies for a lead lanthanum titanate ceramic sample with 90% lead.

#### CONDUCTIVITY MODEL FOR HIGH-TEMPERATURE DIELECTRIC PEAK

This model for the very large low-frequency permittivity and loss was reached by a process of elimination. First, any model based on microdomains[3] or superparaelectric clusters[1] seems ruled out, because such ordered regions should not exist in the 700 to 900 K range in the quantum paraelectric strontium titanate,[2] or hundreds of degrees above  $T_c$  in barium titanate,[5] in which similar large peaks were found. Given that the basic dielectric behavior is not anomalous for these two materials in this temperature range, and noting that the lossy part of the permittivity shows thermal activation, we are led to consider the phenomena as electrical conductivity phase-shifted enough to provide the permittivity  $\epsilon'$  peaks.

Given that conductivity is important, are we dealing with a bulk or a surface-modified effect? Stumpe *et al.*[2] and Bidault *et al.*[5] attributed the phenomenon to a high-impedance surface layer. We followed Stumpe in describing the bulk as a parallel RC circuit, in series with another parallel RC circuit representing the two surfaces. We provided both R's with thermal activation, but kept the C's independent of temperature as required, to approximate such

materials as SrTiO<sub>3</sub> and BaTiO<sub>3</sub>. This model reproduces, for some parameter choices, the shoulder in  $\epsilon''$  representing upward deviation from an Arrhenius law, as seen in Fig. 8. However, Fig. 8 also shows only a plateau in  $\epsilon'$  could be achieved, and not a peak. The plateau level is independent of frequency whereas experimentally the peak amplitude increases rapidly with falling temperature. The failure to reproduce this characteristic peak behavior seems to rule out the blocking surface interpretation.

We are thus led to consider the behavior as a bulk conductivity phenomenon, but not of the usual type for which  $\sigma''=0$  and  $\sigma'$  lacks frequency dependence. The only evident way of causing such dependence is to assume a spatial distribution of mobility barrier heights. We decide on the basis of the following discussion whether this distribution starts at zero energy. The conductivity (Figs. 4 and 5) shows a dc limit envelope where data at some frequencies overlap, and a higher ac limit envelope with lower activation energy where data for other frequencies overlap. The difference between the ac and dc slopes corresponds to a rather small activation energy, several times  $kT$  but much smaller than the overall conductivity activation energy.

One might attribute this small difference to mobility activation energy resulting from a spatial distribution of relatively small barriers, and attribute the major part of the activation energy to the carrier concentration  $n$ . This assumption fails because it would require the permittivity peaks to occur at much higher frequencies than observed. The conductivity instead appears to be extrinsic, with a fixed number of carriers and a high mobility activation energy which has a relatively small spatial spread to account for the nonzero  $\sigma''$ .

The conductivity is related to sample preparation and treatment, as seen in relation to oxidation or reduction of barium titanate.[5] Both the extrinsic carrier concentration and the barrier distribution can be affected.

We accordingly are led to a model with extrinsic conductivity. The large conductivity activation energy is associated with the high barrier for the carrier to hop from one site to the next. This energy is comparable to that for diffusion of metal ions in NaCl, for instance.[7] The required distribution in barrier heights is caused by crystal imperfections. The nature of the distribution and its effects will require considerable analysis. We present here only a first attempt at such analysis.

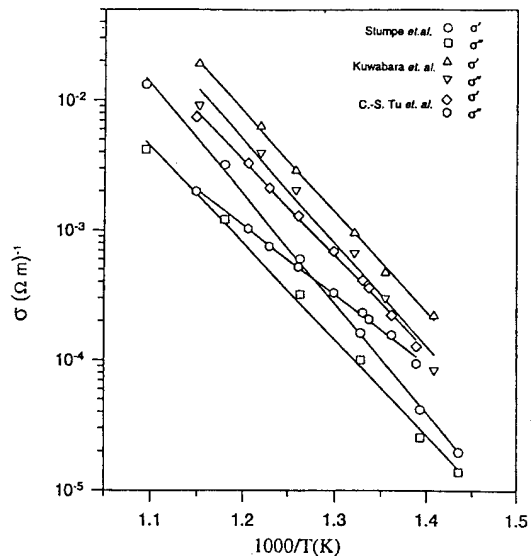


Figure 7. Semilogarithmic plot of real ( $\sigma'$ ) and imaginary ( $\sigma''$ ) conductivities vs. inverse temperature at the temperatures for which the  $\epsilon'$  (or  $\sigma''$ ) peaks occur, for the NBT (Ref. 1), SrTiO<sub>3</sub> (Ref. 2), and PLT10 (Ref. 3) samples described in the text.

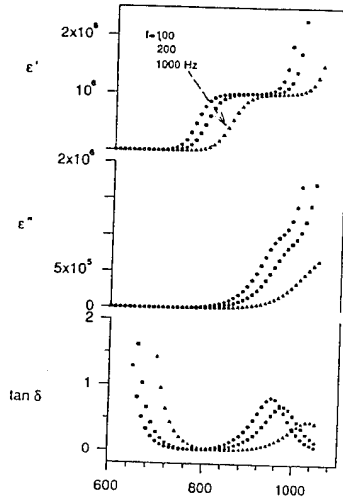


Figure 8. Plots of real and imaginary parts of permittivity for a crystal and its surface modelled by two parallel RC circuits in series, with thermally activated R's and temperature-independent C's. Parameters are  $d_{\text{bulk}}=1$  mm,  $d_{\text{surf}}=10^{-4}$  mm,  $W_{\text{bulk}}=20000$  K,  $W_{\text{surf}}=30000$  K,  $\epsilon'_{\text{bulk}}=\epsilon'_{\text{surf}}=100$ ,  $\sigma_0=10^7$  (ohm-m) $^{-1}$ .

We assume a spatial power law for the distribution of barrier heights about the mean height  $B$ . We force the distribution to reach a maximum value  $B_0$  by writing it as

$$U(r)=B+B_0[r/(R+r)]^\gamma \quad (1)$$

In this paper we apply this model and the above distribution only to the SrTiO<sub>3</sub> data,[2] because these are farthest from complicating effects of phase transitions. This is not a perfect test case, because these data may be shifted by surface impedance effects, as discussed both above and below. We will try to fit the SrTiO<sub>3</sub> ac and dc conductivity envelopes and the permittivity envelope discussed above.

The ac conductivity envelope should have the activation energy  $B$  in Eq. (1). We take the  $f=4$  kHz curve which departs from the ac envelope at  $T=700$  K in Fig. 5, use  $B/k=15960$  K as the measured slope of that envelope, and assume an attempt frequency  $\nu=3 \times 10^{12}$  Hz. At this departure point the relation

$$\nu^{-1} \exp(B/T)=1/2\pi f \quad (2)$$

should hold. If  $B$  is taken as the unknown in Eq. (2), we actually get  $B=12730$  K.

If we assume hopping conductivity with steps of  $a_0=0.4$  nm (one lattice constant) obeying the equation  $\sigma=\nu \exp(-B/kT) e^2 a_0^2 / kT$ , we can solve for the (assumed temperature-independent) carrier concentration and obtain (for  $\sigma=1.24 \times 10^{-4}$  ohm $^{-1}$ m $^{-1}$  and  $B=12730$  K) the value  $n=7.71 \times 10^{27}/\text{m}^3$ . This value is somewhat large, because the unit cell concentration is only  $(4 \text{ nm})^{-3}=1.56 \times 10^{28}/\text{m}^3$ . Either the activation energy  $B$  must be lower, or the mobility must be higher, as it could be if electrons rather than ions are the carriers.

The  $f=4$  kHz curve joins the dc envelope at  $T=800$  K, and the measured slope of that envelope is  $(B+B_0)/k=20080$  K. Employing the same attempt frequency in the analog to Eq. (2) yields  $B+B_0=14880$  K. The agreement both for  $B$  and for  $B+B_0$  is only fair, but as mentioned above, the measured envelopes in Fig. 5 may be too steep because of surface impedance. The important point is that this model qualitatively reproduces the curves of Fig. 5, with low frequencies as observed at the ac to dc envelope crossovers.

Obtaining the permittivity envelope for the barrier height distribution of Eq. (1) is a difficult problem. As an initial

approximation we assume that at the temperature  $T$  at which the permittivity peak at frequency  $f$  occurs, the effect of the barriers is the same as that of an infinite barrier at a radius  $r_b$  where from Eq. (1)  $U(r_b)=B+B_0-kT$ . The motivation for this assumption is that the carriers in one period can just diffuse to the radius where thermal motion is sufficient to let them drift without appreciable additional trapping. This radius is given by

$$r_b/R=[(1-kT/B_0)^{-1/\gamma}-1]^{-1} \quad (3)$$

The dipole moment  $p$  per carrier is  $e^2 E r_b^2 / 5kT$  for this spherical radius. A reasonable fit using  $\epsilon''=np/\epsilon_0 E$  to the peak  $\epsilon'$  amplitudes at various frequencies is obtained by choosing  $\gamma=1/3$ ,  $B_0$  smaller than found above, only 1200 K,  $B=13000$  K near the value found above, and  $R=30$   $\mu\text{m}$ . This  $\gamma$  value gives  $r_b$  strong temperature dependence, as seen in Fig. 9. Such strong dependence gives the observed strong temperature dependence of the peak  $\epsilon'$  values.

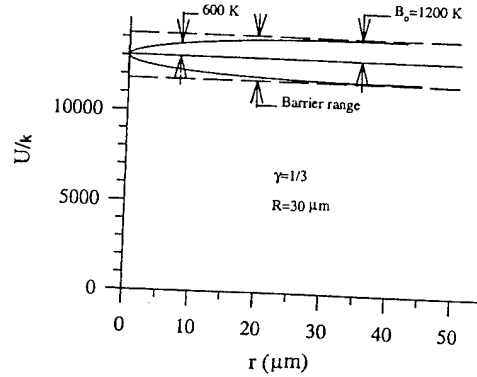


Figure 9. Shape of the mobility barrier height distribution of Eq. (1) for parameters given in the text.

## CONCLUSIONS

The relaxor ferroelectric nature of NBT is evident in the unusual Brillouin scattering and lower-temperature dielectric behavior. The large ac dielectric peaks and their dispersive behavior in the 700 to 900 K range are a common feature of perovskite crystals and ceramics, and appear to result from a phase-shifted conductivity. A spatial distribution of mobility barriers for extrinsic bulk conductivity seems the likeliest origin of the phase shift.

- [1] C.-S. Tu, I. G. Siny, and V. H. Schmidt, "Sequence of dielectric anomalies and high-temperature relaxation behavior in  $\text{Na}_{1/2}\text{Bi}_{1/2}\text{TiO}_3$ ," *Phys. Rev. B*, vol. 49, pp. 11550-11559, May 1994.
- [2] R. Stumpe, D. Wagner, and D. Bäuerle, "Influence of bulk and interface properties on the electric transport in  $\text{ABO}_3$  perovskites," *Phys. Stat. Sol. (a)*, vol. 75, pp. 143-154, 1983.
- [3] M. Kuwabara, K. Goda, and K. Oshima, "Coexistence of normal and diffuse ferroelectric-paraelectric phase transitions in  $(\text{Pb},\text{La})\text{TiO}_3$  ceramics," *Phys. Rev. B*, vol. 42, pp. 10012-10015, Dec. 1990.
- [4] Z. Ujma and D. Dmytrów, "Low-frequency dielectric dispersion in  $\text{PbZrO}_3$  with oxygen vacancies," *Ferroelectrics*, vol. 150, pp. 351-362, Dec. 1993.
- [5] O. Bidault, P. Goux, M. Kchikech, M. Belkaumi, and M. Maglione, "Space-charge relaxation in perovskites," *Phys. Rev. B*, vol. 49, pp. 7868-7873, March 1994.
- [6] R. A. Ferrell and J. K. Bhattacharjee, "Critical ultrasonic attenuation in superfluid helium: Mixing of order-parameter and fluctuation contributions," *Phys. Rev. B*, vol. 23, pp. 2434-2437, March 1981.
- [7] W. Jost, *Diffusion*. New York: Academic Press, 1960, ch. 4, p. 202.



# Processing of Porous and Dense PZT Thick Films on Al<sub>2</sub>O<sub>3</sub> Substrates

J. F. Fernandez, E. Nieto, C. Moure, P. Duran  
Electroceramics Department. Instituto de Ceramica y Vidrio, CSIC,  
28500 Arganda del Rey, Madrid, SPAIN.

**Abstract** -- The processing of porous PZT thick film ceramics on Al<sub>2</sub>O<sub>3</sub> has been studied. The films were screen-printed from a thixotropic ink of PZT with a 58% solids content. The thick films were sintered between 1000°C and 1100°C for 2 hours. The sintered films show a 10 µm thickness and a average pore diameter ranging from 1 to 1.6 µm. The PZT forms a continuous skeleton that can be filled with the desired polymer. Dense and continuous PZT films were fabricated by screen-printing PZT ink on previously electroded Al<sub>2</sub>O<sub>3</sub> substrates with Ag/Pd 70/30 paste. Densification of the PZT was obtaining by sintering near the liquidus temperature of the Ag-Pd system.

## INTRODUCTION

PZT/polymer composites and porous PZT ceramics have been extensively investigated up to the present since Newnham et al [1], first reported the importance of connectivity in piezoelectric composites. The fabrication of piezoelectric composites requires careful replacement of a portion of the piezoelectric ceramic with a polymer. This replacement allows the reduction of the acoustic impedance of the piezoelectric ceramics for application in an acoustic system containing water and a living body. In recent years the research efforts in this field have been directed towards the material fabrication techniques, finite element modeling and the use of electrostrictive ceramics.

In 3-3 composites, each of the constituent phases is continuously self-connected in three dimensions to give two interlocking skeletons in intimate contact with one another. Skinner et al [2] prepared 3-3 type composite materials consisting of porous PZT ceramics with coral skeleton structures, duplicated by the "replamine form" process, into which silicon rubber was injected. Shrout et al [3] developed a more readily produced type of porous ceramics using burned-out plastic spheres and PZT powder in an inorganic binder. When carefully sintered a porous PZT skeleton is formed, which is later backfilled with polymers to form a 3-3 composite. Hayashi et al [4] investigated the processing of porous 3-3 type PZT ceramics with a controlled porosity by using capsule-free O<sub>2</sub>-HIP. That method allows little densification of porous PZT sintered bodies after treatment, that results in an increase of the contact areas of PZT interparticles without changing the pore volume and distribution. The HIPed porous ceramic possessed a large permittivity and small depolarizing factor of about half those of normally sintered porous PZT bodies. Waller et al [5] used a replication process to fabricate woven PZT/polymer matrix composites with finely spaced structures. This process involves using a carbon fiber material which determines the form of the PZT ceramic phase.

The greater part of the piezocomposites reported in the literature shows an interconnected porosity with pore size ranging from 50 to 600 µm [2-4]. In modified Ca-PbTiO<sub>3</sub> ceramics of the same porosity, the smaller pore size samples had better properties than the large pore size ones [6]. In these materials, the increase in dielectric properties with increasing porosity was related to their good pore-interconnection which promoted stress transfer to the skeleton more effectively [6].

Porous ceramics are also interesting for a variety of applications as sensors, bioceramics, membranes, etc. This study focuses on the processing of porous 3-3 type PZT thick film ceramics with a controlled porosity. The porous ceramics were developed on Al<sub>2</sub>O<sub>3</sub> substrates. From these porous ceramics, dense PZT film could also be sintered by using a electrode interlayer between the substrate and the PZT ceramic.

## EXPERIMENTAL PROCEDURE

Pb(Zr<sub>0.53</sub>Ti<sub>0.47</sub>)O<sub>3</sub> (hereafter PZT) ceramic powders were prepared following a modified conventional route oxide process starting from analytical reagent grade oxides [7]. In this process TiO<sub>2</sub> and ZrO<sub>2</sub> adequate amounts were put in 1:1 ratio of isopropyl alcohol to water. Oxalic acid was added to the suspension. The suspension was heated and continuously stirred. The stoichiometric amount of lead oxide was added. The dried powders were amorphous and were calcined at 700°C for 4 hours and attrition milled with zirconia balls. The thermal treatment crystallized the powders into tetragonal perovskite phase plus zirconia and lead oxides that remained partially unreacted.

PZT ink was prepared by ultrasonic dispersion of the ceramic powders [8] in  $\alpha$ -terpineol and 2-2 (Buthoxyethoxy) ethyl acetate. The as prepared paste was milled with ethyl cellulose that give the thixotropic characteristic required to the inks used in screen-printed processes. The ink was screen-printed on 5.2x5.2 cm<sup>2</sup> 99% Al<sub>2</sub>O<sub>3</sub> substrates with a roughness of 0.3 µm (Rubalit 710, HOESCHT). The substrates were laser pre-cut in order to achieve samples of 2.5x1 cm<sup>2</sup>. A stainless steel 45° oriented 320 mesh screen was used. Some substrates were previously electroded with 70/30 Ag/Pd paste (6142D, DUPONT). The electrode was sintered at 850°C in a typical electrode sintering cycle of 1 hour. The screen-printed films were dried at 150°C for 15 minutes, and the organic vehicle was burn-out at 500°C. The samples were sintered in high purity alumina crucibles at a heating rate of 3°C/min. A lead-rich atmosphere was maintained by placing PbZrO<sub>3</sub>+5 wt% ZrO<sub>2</sub> powders near the samples. The porosity distribution of the sintered thick films were evaluated by a mercury porosimeter (Autopore II 9220) with a mercury filling pressure from 4x10<sup>-3</sup> MPa up to 400 MPa. In order to assure that the stem volume used reached an adequate value, several samples were used each time. The microstructure of the as sintered samples and transverse polished cross section were examined by Scanning Electron Microscopy (Zeiss DSM 950).

## RESULTS AND DISCUSSION

### Porous PZT thick films.

Figure 1 shows the pore diameter distribution for selected sintering temperatures and Figure 2 shows the microstructure of these sintered samples. The porosity of the alumina substrates in this range, <10 µm, is negligible compared to the porosity of the sintered PZT thick films. The alumina substrates exhibited a range of ore diameters from 8 to 120 µm (not shown) that is attributed to the drills and the fracture surfaces of the laser pre-cut substrates. The pore size curves show different contributions to the whole porosity volume. The porosity ranges from 0.1 to 3 µm. All of the porosity could be attributed to interparticle porosity, or interaggregate porosity [9].

The microstructure of the samples sintered at 1000°C and 1050°C for 2 hours shows a similar structure. The PZT particles form chains of grains. Small aggregates consisting of a couple of grains and discontinuities in the skeleton ceramic structure can be found. The sample sintered at 1100°C for 2 hours presented an interconnected well densified 3-3 ceramic/pore structure. The chain of grains sintered to form bigger grains that are connected almost grain to grain. Few small particles remained in aggregates or in the surface of the bigger ones.

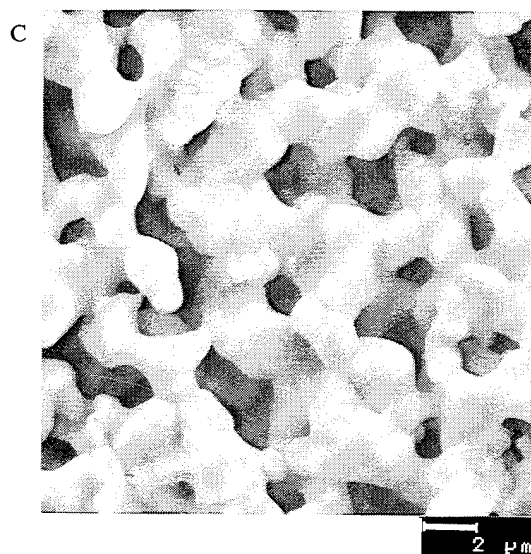
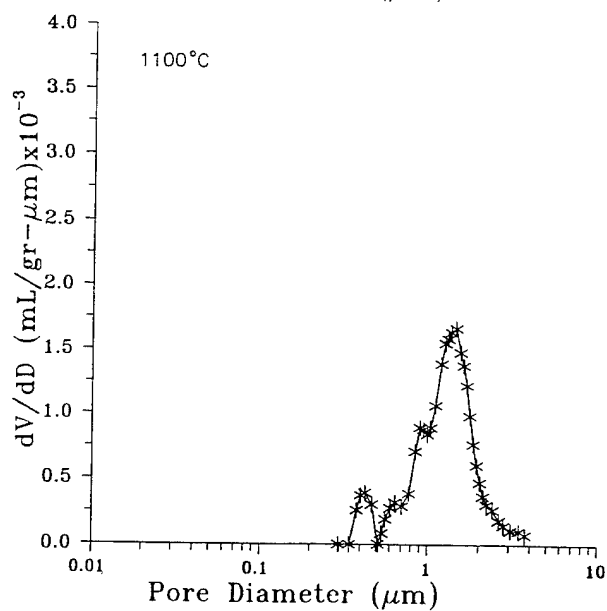
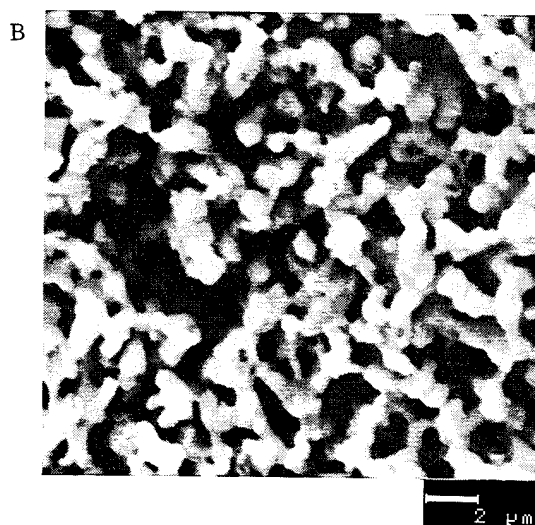
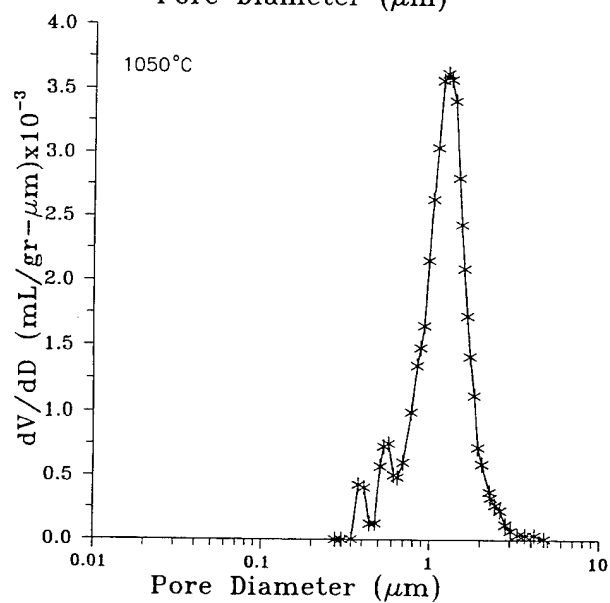
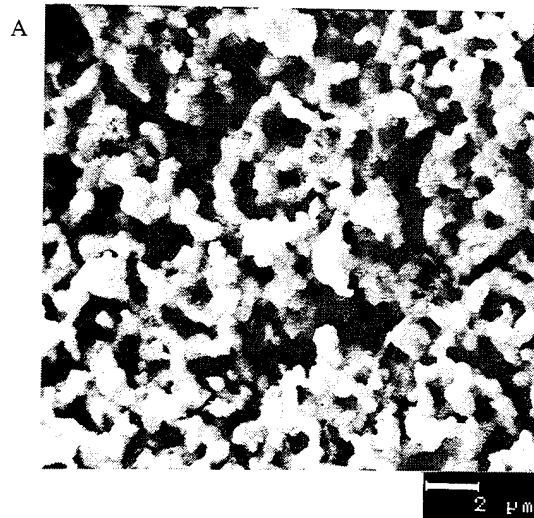
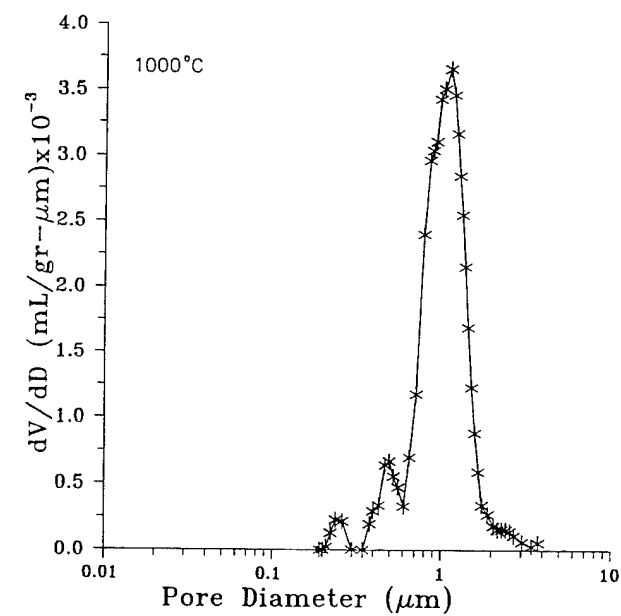


Figure 1. Porosity curves of the samples sintered at different temperatures.

Figure 2. SEM micrographs of samples sintered at: a) 1000°C, 2h, b) 1050°C, 2h and, c) 1100°C, 2h.

Taking into account the microstructure and the porosity curves, three different contributions to the porosity could be proposed: 1) Low interparticle porosity: This type of porosity ranged below  $\sim 0.7 \mu\text{m}$ , its contribution to the whole porosity is very low and could be attributed to both the interparticle porosity of the aggregates and to the pores formed during the sintering of the small particles that are not completely eliminated. 2) Main interparticle porosity: this porosity type is the most important in volume and shows a narrow pore size distribution that indicates the high degree of homogeneity, and, 3) High interparticle porosity: these pores are the tail above  $2 \mu\text{m}$  that corresponds to the discontinuities in the ceramic skeleton structure. The discontinuities are attributed to both the burn out process and to the presence of organic agglomerates that were not completely eliminated during the paste preparation, mainly ethyl cellulose agglomerates.

The porosity decreased when the grain growth took place. The  $1100^\circ\text{C}$  for 2 hours sintered thick film ceramics show the low porosity. At this sintering temperature the average area pore size is  $1.42 \mu\text{m}$  (Figure 3). The average pore size increase almost linearly with the sintering temperature, however the main pore size maximum increased more rapidly than the average pore size for temperatures below which grain growth took place; that could be attributed to the coalescence process of the pores. The pore size distribution does not change significantly even when the particles lost their initial shape, and at this sintering stage the pore size does not increase. That means that the sintering of the PZT takes place without significantly modifying the skeleton structure. The initial dispersion of the powders has a very important role in the sintering mechanism. The small particles that form aggregates sintered and bigger particles resulted. These new bigger size particles were surrounded by both particles and pores. The number of contact points between particles decreased and the probability of formation of new sintering necks decreased with the grain growth increase.

The as sintered thick films show a  $\sim 10 \mu\text{m}$  thickness and good 3-3 connectivity (figure 4). The epoxy resin filled adequately the porous structure. Both the thickness and the good pore connectivity are the reasons for such behavior.

#### Dense PZT films

Figure 5.a shows the microstructure of dense as sintered PZT thick films. The microstructure is a duplex one with most of the porosity located at the triple point junctions. The big grains are typically faceted perovskite grains. The thickness of the film is  $\sim 5 \mu\text{m}$  (figure 5.b). In this case the thickness reduction favors the adequate elimination of the pores and the densification of the ceramic films. The driving forces for the sintering are assisted for the sintered bottom film of Ag/Pd 70/30.  $1100^\circ\text{C}$  is a temperature near the liquidus temperature of the Ag/Pd system. The substrate seems to react slightly with the electrode and that gives good adhesion properties of the film on the  $\text{Al}_2\text{O}_3$  substrate.

#### CONCLUSIONS

A method for processing porous and dense thick PZT films has been developed. The initial distribution of dispersed PZT particles in an organic medium gives a final skeleton structure with 3-3 pattern connectivity. The porous PZT thick films could be easily filled with polymer. By adjusting the process parameters a  $1/2\lambda$  thickness (half wavelength of a desirable resonant frequency)[10] thick film piezocomposite could be fabricated. This method adapted very well to curved surfaces and it allows the piezocomposite to be focused without additional and expensive treatments. This process could serve as an integrating step between the electroceramics materials and the hybrid circuit technologies.

#### ACKNOWLEDGEMENTS

The authors wish to express their gratitude to the Spanish Science Ministry Commission for the financial support of this work (CICYT MAT-1386-E) and to Dr. Rubio for Porosimeter facilities.

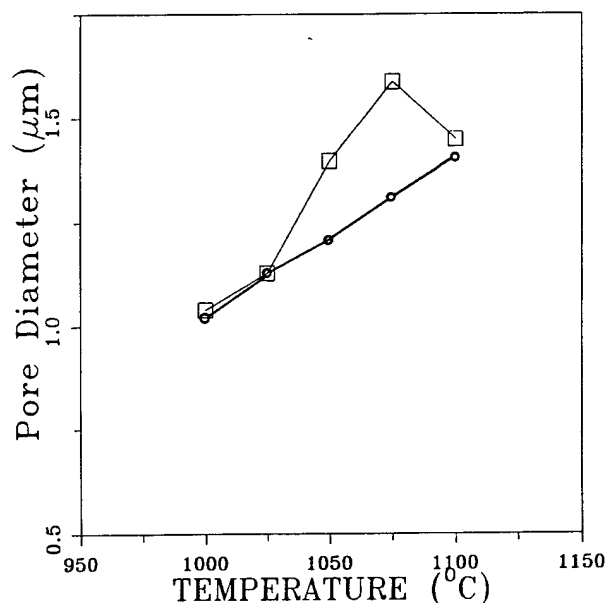


Figure 3 Average pore size (○) and main pore size maximum (◻) for different sintering temperatures.

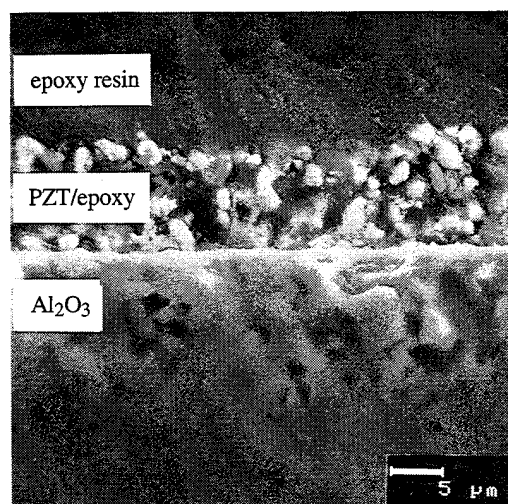


Figure 4. SEM micrograph of polished cross section of PZT thick film sintered at  $1100^\circ\text{C}$ , 2h and filled with epoxy resins.

## REFERENCES

- [1] R. E. Newnham, D. P. Skinner and L. E. Cross, "Connectivity and Piezoelectric-Pyroelectric Composites", *Mater. Res. Bull.*, 13,525-36(1978).
- [2] D. P. Skinner, R. E. Newnham and L. E. Cross, "Flexible Composite Transducer", *Mater. Res. Bull.*, 13,599-607(1978).
- [3] T. R. Shrout, W. A. Schulze and J. V. Biggers, "Simplified Fabrication of PZT/polymer Composites", *Mater. Res. Bull.*, 14,1553-59(1979).
- [4] T. Hayashi, S. Sugihara and K. Okazaki, "Processing of Porous 3-3 PZT Ceramics Using Capsule-Free O<sub>2</sub>-HIP", *Jap. Journal Applied Physics*, 30,9B,22432246(1991).
- [5] D. J. Waller, A. Safari and R. J. Card, "Woven PZT Ceramic/Polymer Composites for Transducer Applications", *Proceeding of the IEEE International Symposium on Applications on Ferroelectrics 1990*, pp82-85.
- [6] K. H. Yoon and M. J. Lee, "Piezoelectric Properties of Interconnected Porous Pb<sub>0.76</sub>Ca<sub>0.24</sub>Ti<sub>0.96</sub>(Co<sub>0.5</sub>W<sub>0.5</sub>)<sub>0.04</sub>O<sub>3</sub> Ceramics", *Ferroelectrics* 119,53-60(1991).
- [7] E. Nieto, J. F. Fernandez, C. Moure, P. Duran. Presented at 8th CIMTEC Florence June 1994.
- [8] T. Chartier, E. Jorge and P. Boch, "Ultrasonic Deagglomeration of Al<sub>2</sub>O<sub>3</sub> and BaTiO<sub>3</sub> for Tape Casting", *J. Physics III*, 1,689-95(1991).
- [9] W. F. M. Groot Zevert, A. J. A. Winnubst, G. S. A. Theunissen and A. J. Burgraaf, "Powder Preparation and Compacting Behavior of Fine Grained Y-TZP", *J. Mater. Sci.* 25, 3449-55(1990).
- [10] M. H. Slayton, H. S. N. Setty, "Single Layer Piezoelectric-Epoxy Composite", *Proceedings of the IEEE International Symposium on Application on Ferroelectrics 1990*, pp. 90-92.

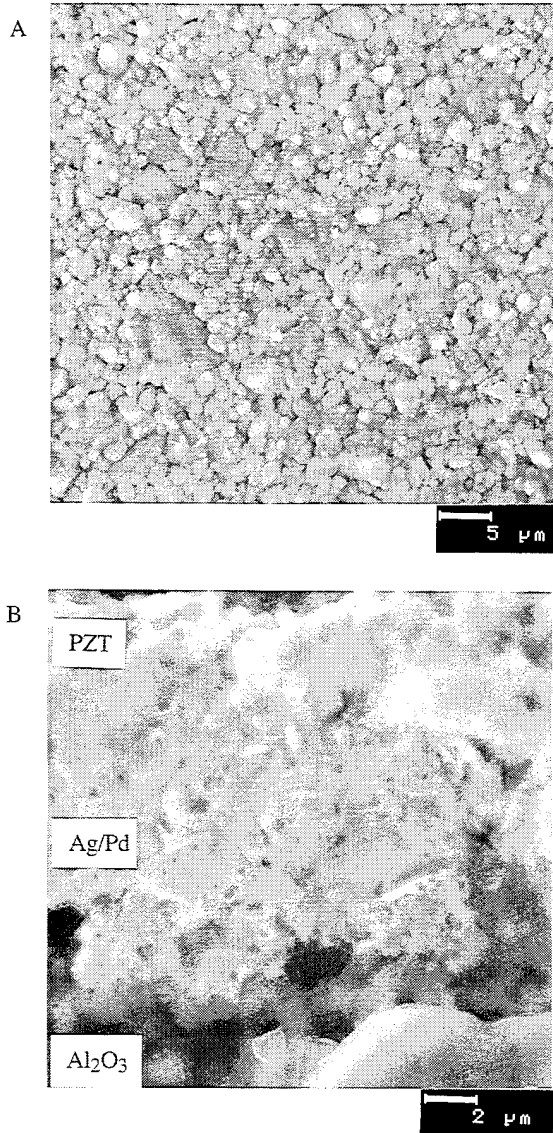


Figure 5. SEM micrographs of dense PZT thick film sintered at 1100°C, 2h a) as sintered surface and, b) polished cross section of the thick film.

# Concurrent Session - 2B: Thin Films

# Preparation and Properties of Lanthanum Modified $\text{PbTiO}_3$ Thin Films by *rf*-Magnetron Sputtering

K.Iijima, T.Takeuchi, N.Nagao, R.Takayama and I.Ueda  
Central Research Laboratories, Matsushita Electric Industrial Co. Ltd.,  
Seika-cho, Kyoto 619-02, JAPAN

**Abstract**—Highly *c*-axis oriented  $\text{Pb}_{1-x}\text{La}_x\text{Ti}_{1-x/4}\text{O}_3$  (PLT) thin films were prepared by *rf*-magnetron sputtering on (100)MgO and (100)Pt/MgO substrate. These films were characterized by X-ray and electron diffraction and electron microscope. Thin film growth manner and *c*-axis orientation mechanism was discussed. Dielectric measurement revealed the phase transition behavior of PLT thin films. PLT thin film of  $x=0.15$  shows an extremely large pyroelectric coefficient of  $9.5 \times 10^{-8}$  C/cm<sup>2</sup>K and low dielectric constant of 330.

## INTRODUCTION

A pyroelectric infrared sensor has a merit of a room temperature operation and a wavelength independent responsivity and it is expected to provide the sensing system which is highly sensitive, lightweight, small size, maintenance-free, and inexpensive.

The output voltage of a pyroelectric sensor is proportional to the figure of merit,  $F_v$ :  $F_v = \gamma / (\epsilon_r \cdot C_v)$ , where  $\gamma$ ,  $\epsilon_r$ , and  $C_v$  is pyroelectric coefficient, relative dielectric constant and volume specific heat, respectively.  $\text{PbTiO}_3$  ceramics has a large  $\gamma$  and a relatively small  $\epsilon_r$  and is widely used as a single element sensor in various field[1]. However, when considering about the remote sensing system for such as a person and an environment, a more sensitive linear or area sensor with fast response is strongly required. For that purposes, it is necessary to develop a new pyroelectric material and a new type of sensor structure.

Single crystal or polarization axis oriented Pb based ferroelectric thin films, especially PLT thin films, will meet the demands mentioned above, because it might have a large pyroelectric coefficient. Development of high quality single crystal thin film of Pb-based ferroelectrics has been a major issue of our thin film research to obtain new or advanced properties unattainable in ceramic form with randomly oriented grain structure. The difficulties to produce high quality thin films of Pb-based ferroelectrics are mainly due to the high volatility of PbO. Recent progress of thin film technology make it possible to grow a high quality thin films[2-3]. We have reported the preparation and properties of Pb-based ferroelectric thin films[4-8]. However, the growth mechanism and *c*-axis orientation mechanism of the sputtered Pb-based ferroelectric thin film is still not clear.

In this paper, we are reporting the preparation and the properties of PLT thin films. The electron microscopic observation revealed the detail structure of the film and the early stage of thin film growth on the substrate. Highly *c*-axis oriented PLT thin film demonstrated an excellent pyroelectric properties.

## PREPARATION OF THE FILMS

The selection of the substrate is very important to obtain a high quality thin film ; that is the single crystal which has a similar oxygen arrangement in the surface as that of PLT and has a good lattice matching. From this view point, the substrates used were (100)MgO ( $a=0.4213\text{nm}$ ) and (100) oriented Pt ( $a=0.3923\text{nm}$ ) thin film(100nm of thickness) deposited on MgO.

The compositions of sputtering target powders were given by the formula:  $(1-Y)\text{Pb}_{1-x}\text{La}_x\text{Ti}_{1-x/4}\text{O}_3 + Y\text{PbO}$  where  $x=0.0-0.30$  and  $Y=0.2$ . The films were deposited at substrate temperatures between 500 and 650°C in a sputtering gas ( $\text{Ar}/\text{O}_2 = 9/1$ ) and the sputtering gas pressure around  $10^{-2}$ Torr. The deposition rate of the films was typically 6nm/min.

## RESULTS AND DISCUSSION

### 1.Characterization of the films

The films were examined by electron and X-ray (Cu  $K\alpha$ ) diffractometry and electron microscopy. The evaluation of the films was made by the degree of *c*-axis orientation  $\alpha$ ;  $\alpha = I_{001} / (I_{100} + I_{001})$ , where  $I_{100}$  and  $I_{001}$  represent the diffraction intensities of 100 and 001 reflections, respectively.

The *c*-axis oriented PLT thin film is important for infrared sensors, because the *c*-axis is the polarization axis. The films having the  $\alpha > 0.9$  were obtained in the entire compositional range in this study on both the MgO and Pt/MgO substrate. Figure 1 shows the typical X-ray diffraction pattern of the *c*-axis oriented PLT( $x=0.15$ ) thin film. The  $\alpha$  of this film is 0.97 and 001 reflection of perovskite structure are mainly observed. The *h*00 reflections are very weak.

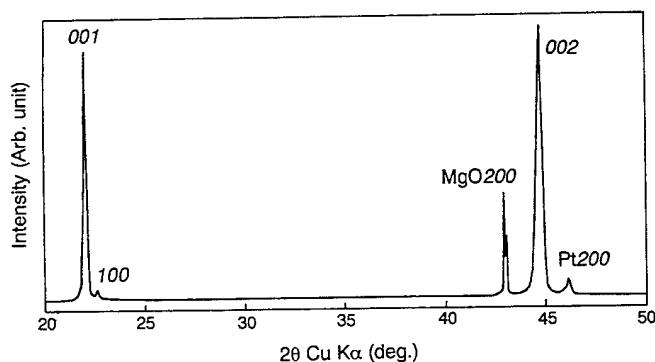


Fig. 1 X-ray diffraction pattern of PLT( $x=0.15$ ) thin film deposited on (100)Pt/MgO.

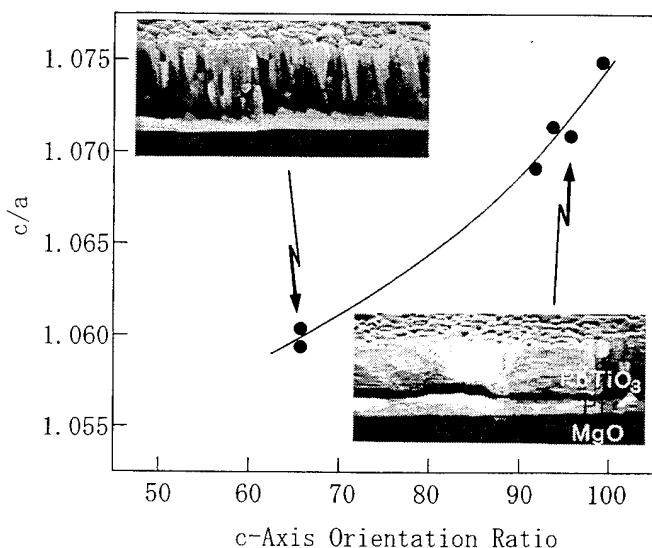


Fig. 2 The  $c/a$  axial ratio of  $\text{PbTiO}_3$  thin film as a function of the  $c$ -axis orientation rate  $\alpha$ . SEM photographs for the film with  $\alpha$  of 0.65 and 0.95 are also shown in this figure.

X-ray diffraction measurement showed that the  $c$ -axis oriented films were elongated along the  $c$ -axis. Figure 2 shows the tetragonality  $c/a$  of  $\text{PbTiO}_3$  film plotted as a function of the  $\alpha$ . The  $c/a$  ratio correlate closely with the  $\alpha$  and the  $c/a$  axial ratio increases with increasing the  $\alpha$ . The  $c/a$  axial ratio of the film of  $\alpha=0.98$  is 1.075 and is about 1.2% larger than that for bulk  $\text{PbTiO}_3$ . As shown in Fig. 2, scanning electron microscope (SEM) photographs revealed that the films having low  $\alpha$  and normal  $c/a$  shows inhomogeneous columnar texture, whereas the films with uniform and dense texture have large  $\alpha$  and large  $c/a$ . These results indicate the existence of a large two dimensional compressive stress in the film.

It is believed that two dimensional stress in the PLT film can be effective in aligning the  $c$ -axis perpendicular to the substrate[4]. We measured the stress in the PLT ( $x=0$ ) film deposited on MgO substrate preparing the cantilever by etching the MgO substrate after the deposition as shown in Fig. 3. The stress was calculated was made using the displacement of the cantilever by the following equation, (1),

$$\sigma = Eb^2\delta/[3(1-\nu)L^2d] \quad (1),$$

where

$E=2.5 \times 10^6 \text{ kgf/cm}^2$  : Young's modulus of MgO,

$b=30 \mu\text{m}$  : thickness of substrate,

$\delta=0.14 \text{ cm}$  : displacement of cantilever,

$\nu=0.2$  : Poisson's ratio of MgO

$L=0.63 \text{ cm}$  : cantilever length

$d=6.6 \mu\text{m}$  : film thickness.

The internal compressive stress of  $\text{PbTiO}_3$  thin film of  $6.6 \mu\text{m}$  deposited on MgO substrate was extremely large and about 490MPa. This internal stress is almost the same as that of  $\text{PbTiO}_3$  thin film deposited on  $\text{SrTiO}_3$  single crystal[9].

To investigate the  $c$ -axis orientation mechanism, the change of domain population in the film was observed by using high temperature X-ray diffraction. Figure 4(a)

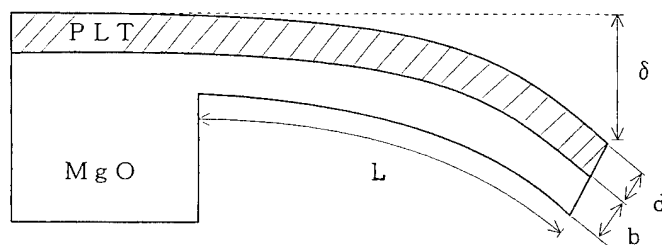


Fig. 3 Schematic drawing of  $\text{PbTiO}_3/\text{MgO}$  composite cantilever which is prepared by etching the MgO substrate.

shows the temperature dependence of the  $\alpha$  on cooling from high temperature cubic phase. The film, just below the Curie point,  $T_c$ , is  $a$ -axis oriented one and then the  $\alpha$  increases with increasing temperature. The  $\alpha$  is still increasing even near the room temperature. The growth kinetics of  $c$ -domain was examined by keeping the temperature at just below the Curie temperature,  $T_c$ . The  $c$ -domain was not grown by keeping the temperature as shown in Fig. 4(b). These results show that  $c$ -axis orientation of the film is caused by a ferroelastic nature of PLT and is attained by introducing the compressive stress which is increasing on cooling process. Therefore, the preparation of highly dense and epitaxial thin film is necessary to obtain the PLT thin films with large  $\alpha$ .

Both the  $\text{PbTiO}_3$  thin films deposited on MgO and  $\text{SrTiO}_3$  substrate have almost the same internal stress. The origin of this large compressive stress can not be explained by the difference of the thermal expansion coefficient between the substrate ( $13 \times 10^{-6}/\text{deg}$  and  $10 \times 10^{-6}/\text{deg}$  for MgO and  $\text{SrTiO}_3$ ) and the film ( $12$ – $13 \times 10^{-6}/\text{deg}$  for  $\text{PbTiO}_3$   $a$  axis below  $T_c$ ). This study is still continuing and will be published in near future.

In order to investigate the film quality as well as to reveal the interface structure, the PLT films were examined by transmission electron microscope (TEM).

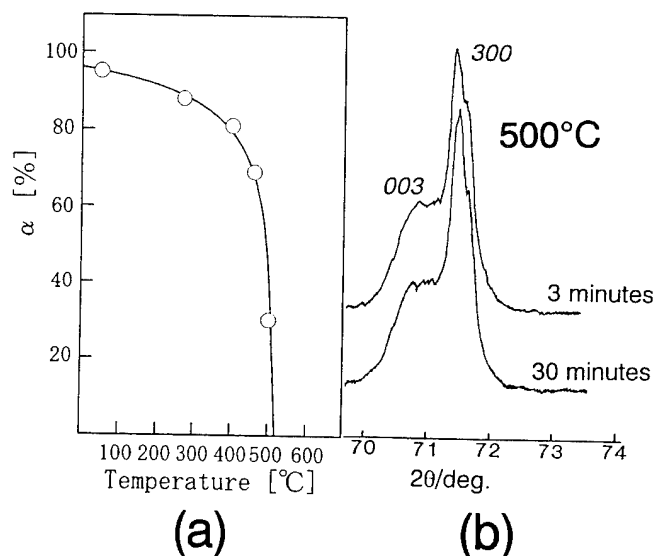
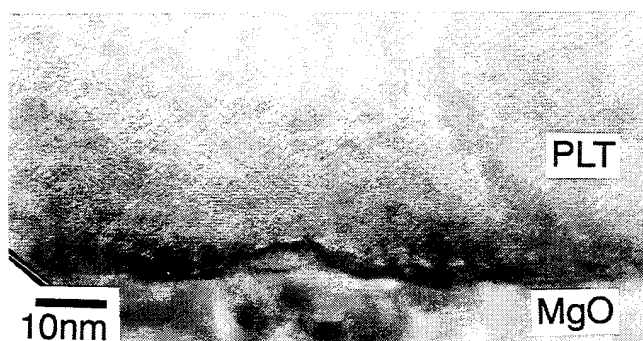
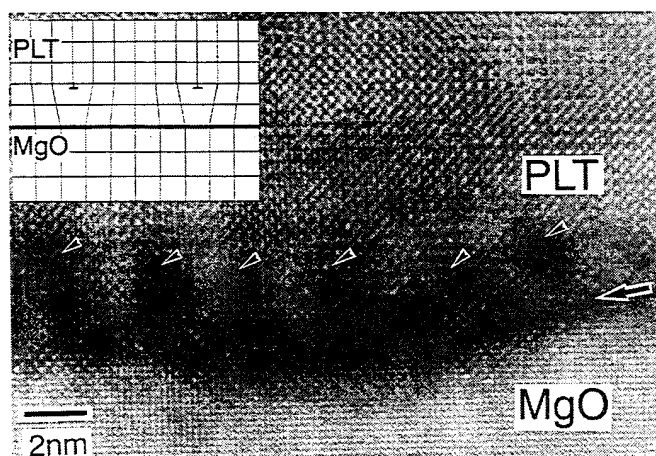


Fig. 4 (a) Temperature dependence of the  $\alpha$  obtained from high temperature X-ray measurement. (b) Annealing effect to the peak profile around 300 and 003 peak of  $\text{PbTiO}_3$  film.

TEM photographs of the cross section of the PLT ( $x=0.15$ ) film deposited on the MgO substrate are shown in Fig. 5. Figure 5(a) shows a low magnification image of the film in which no crack and no grain boundary is observed and the film seems to be homogeneous. The diffraction pattern of this area shows that the film is a single crystal and the film is constructed by mainly the  $c$ -domain ( $c$ -axis of the film is perpendicular to the substrate) and small portion of  $a$ -domain ( $c$ -axis is almost parallel to the substrate). The periodic dark contrasts are observed at the interface of the film to the substrate. High resolution TEM photograph (Fig. 5(b)) shows that the PLT film grew epitaxially on the MgO substrate and the connection of the atomic rows in the  $[001]$  direction going from the MgO substrate into the PLT film is clearly observed. The dark periodic contrasts are clearly observed in the PLT film near the interface to the MgO substrate. The period of the contrast is about 3nm ( $=[a_p/(a_M-a_p)] \times a_p/2$ , where  $a_p$  and  $a_M$  represent a lattice constant of PLT and MgO, respectively) and correspond to mismatch dislocation introduced in PLT thin film as shown in Fig. 5(b). The dislocations are not observed at the interface of the film and the substrate but in the PLT film about 2nm apart from the surface. Although the lattice mismatch between PLT and MgO is very large and about 8%, the PLT seems to accommodate its crystal lattice to that of MgO.



(a)



(b)

Fig. 5 (a) A low magnification TEM image of (001)PLT ( $x=0.15$ ) on (100)MgO. (b) A high resolution TEM image of the PLT/MgO interface.

## 2. Growth mechanism

The early stages of sputtered thin film formation on single crystal surface are very interesting from the view point of the heteroepitaxial growth with large lattice mismatch. Figures 6 show the reflection high energy electron diffraction (RHEED) photographs for the 4nm thick  $\text{PbTiO}_3$  thin films deposited on (100)MgO surface and (100)Pt surface, respectively. These RHEED patterns show that  $\text{PbTiO}_3$  grow on the substrate epitaxially from the beginning of the film growth.

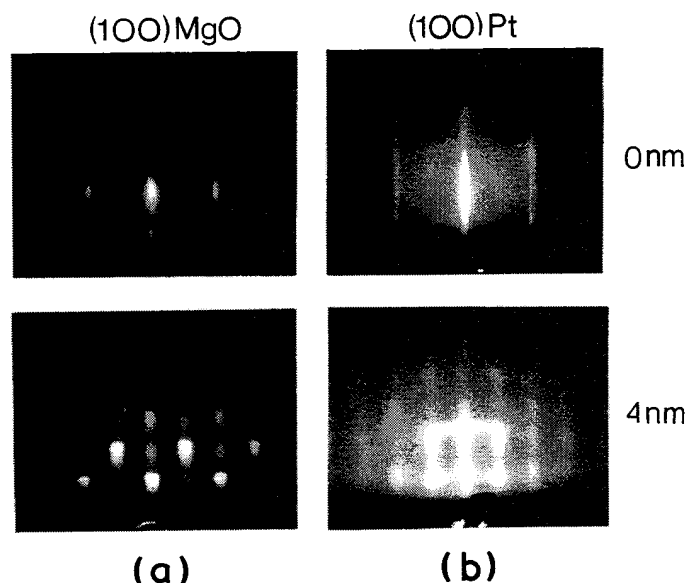


Fig. 6 RHEED patterns for the substrate and 4nm thick PLT thin film. (a)(00)MgO substrate and (b)(100)Pt/MgO substrate. The azimuth of electron beam incidence is  $[010]$ .

Figure 7 shows SEM photographs for the  $\text{PbTiO}_3$  films deposited on (100)MgO surface. These films were deposited with very low deposition rate of 1nm/min and deposited 45 minutes (a) and 60 minutes (b), respectively. In Fig. 7(a), there observed a lot of small island or particles of about 100–200nm in diameter on the surface of MgO substrate indicating that  $\text{PbTiO}_3$  grow in three dimensional Volmer–Weber growth mode on MgO surface. From the results of RHEED observations these islands are single crystal and keep epitaxial relationships with respect to the substrate. The nucleation density on the surface seems to be very low and migration length of sputtered atoms on the surface is fairly long and estimated about a hundred nanometer.

After one hour deposition, in Fig. 7(b), the number of islands are decreased and their size becomes larger than that observed in Fig 7(a). Some of them are becoming a rod-shape. These rod-shape islands are directed their rod axis to  $\langle 110 \rangle$  direction of the MgO substrate. Few of them aligned to  $\langle 100 \rangle$  direction of the MgO substrate. These islands also a single crystal and keep epitaxial relation to the substrate, judging from RHEED photographs. Furthermore, on (100)Pt surface,  $\text{PbTiO}_3$  grow almost the same manner as on the (100)MgO substrate as shown in SEM photograph of Fig. 7(c).

From these observation, the growth process of  $\text{PbTiO}_3$  on MgO and Pt surface is considered as follows: After the



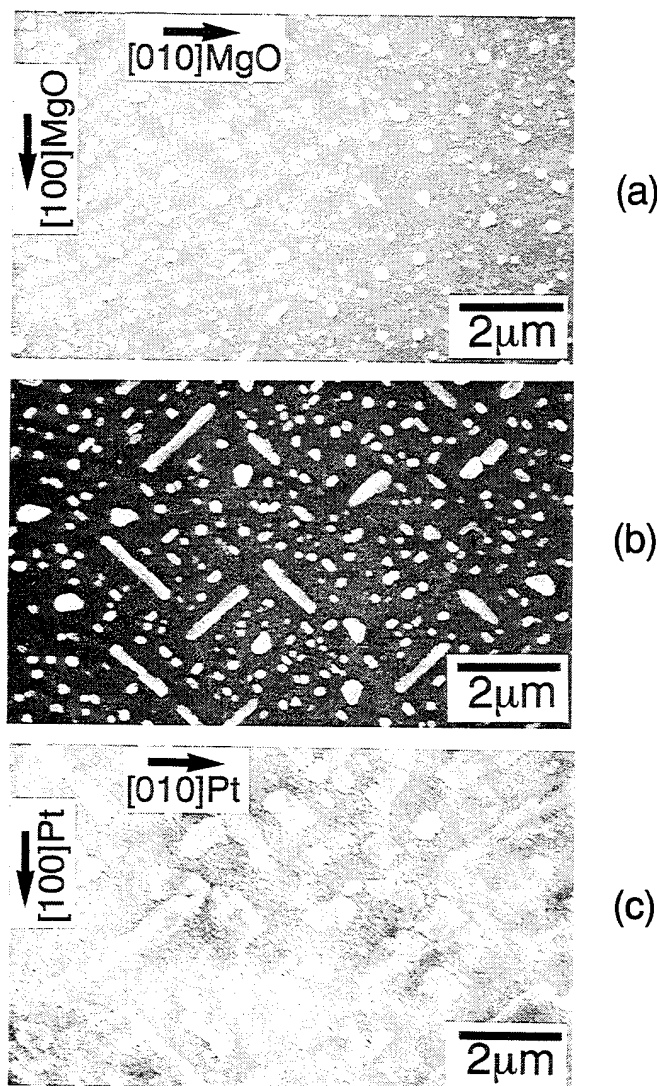


Fig. 7 SEM photographs of the early stages of thin film growth. After 45 minutes (a) and 60 minutes (b) for MgO substrate and after 60 minutes (c) for Pt/MgO substrate. These films were deposited with very low deposition rate of 1nm/min

nucleation process, crystal island grow on the substrate and the small island also can migrate on the surface. These particles are in epitaxial relation with the substrate, already. The size of the island are increased by a continuous supply of materials from the target. When the particle size becomes about 200nm or more, the island coalescent each other and change the shape to rod-like one. These larger particles also in the epitaxial relation with MgO substrate. After the coalescence process, the particles make a continuous film covering the surface of the substrate. Although  $\text{PbTiO}_3$  does not grow in two dimensional layer by layer mode, the obtained film are dense and continuous on an atomic scale and there observed no grain boundary in SEM and TEM photographs. These process are described in Fig.8 schematically.

### 3. Electric properties of the films

Dielectric constant,  $\epsilon_r$ , and dielectric loss factor,  $\tan\delta$ , were measured at 1kHz applying about 25kV/cm by

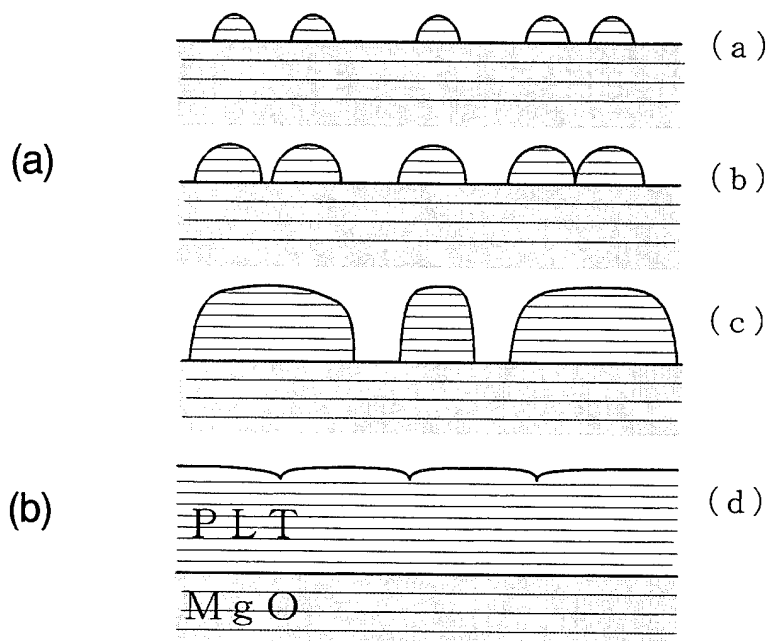


Fig. 8 Schematic drawing of growth manner of PLT thin film.

multifrequency LCR meter. D-E hysteresis loops were observed using a Sawyer-Tower circuit with sinusoidal wave of 100Hz. Pyroelectric coefficient,  $\gamma$  was obtained from the temperature gradient of pyroelectric current measured by a pico-ammeter. These measurements were performed without a poling treatment. Nevertheless, significant pyroelectric currents were detected on all the thin films. Usually, pyroelectric currents cannot be observed on ferroelectric polycrystalline ceramics and single crystal without a poling treatment. This phenomenon is named "self-polarization" and is shown in Fig. 9 schematically.

Figure 10 shows  $\epsilon_r$  and  $\gamma$  of  $\text{PbTiO}_3$  films as a function of the  $c$ -axis orientation rate  $\alpha$ .  $\epsilon_r$  decreases and  $\gamma$  increases with increasing  $\alpha$ . Figure 11 shows coercive force  $E_c$  and remanent polarization  $P_r$  of  $\text{PbTiO}_3$  thin film as a function of the  $\alpha$ .  $E_c$  is almost constant, whereas  $P_r$  increases with increasing the degree of  $c$ -axis orientation  $\alpha$ . These behavior can be explained by the fact that  $\epsilon_r$  along the  $c$ -axis is smaller than that perpendicular to the  $c$ -axis, and the  $c$ -axis is the polarization axis. The film with  $\alpha=0.8$  shows an  $\epsilon_r$  of 97 and  $\gamma$  of  $2.5 \times 10^{-8} \text{C/cm}^2\text{K}$ .  $\epsilon_r$  is smaller and  $\gamma$  is larger

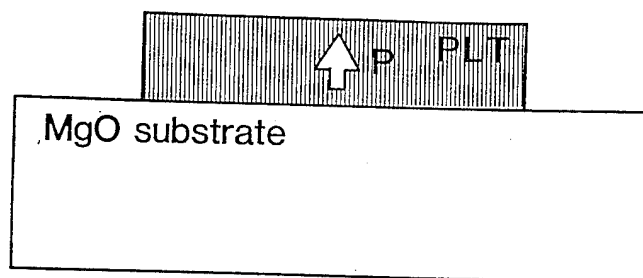


Fig. 9 Schematic drawing of  $c$ -axis oriented PLT thin film which have polarization without poling treatment.

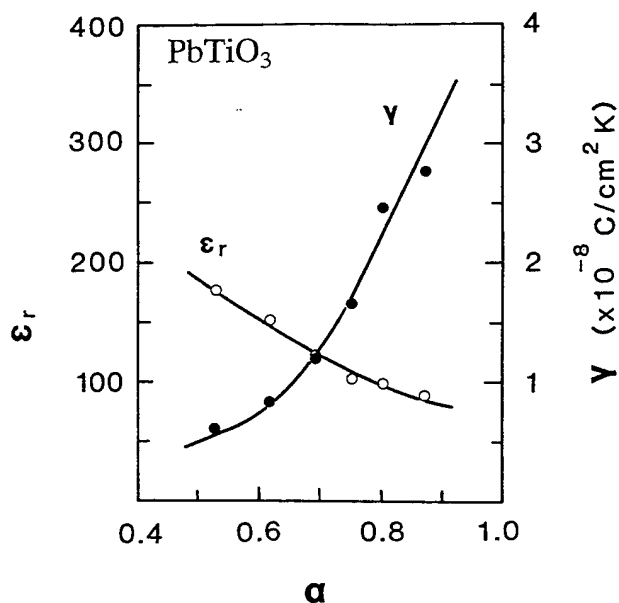


Fig. 10 Relation between pyroelectric coefficient  $\gamma$ , dielectric constant  $\epsilon_r$  and  $c$ -axis orientation rate  $\alpha$  for  $\text{PbTiO}_3$  film.

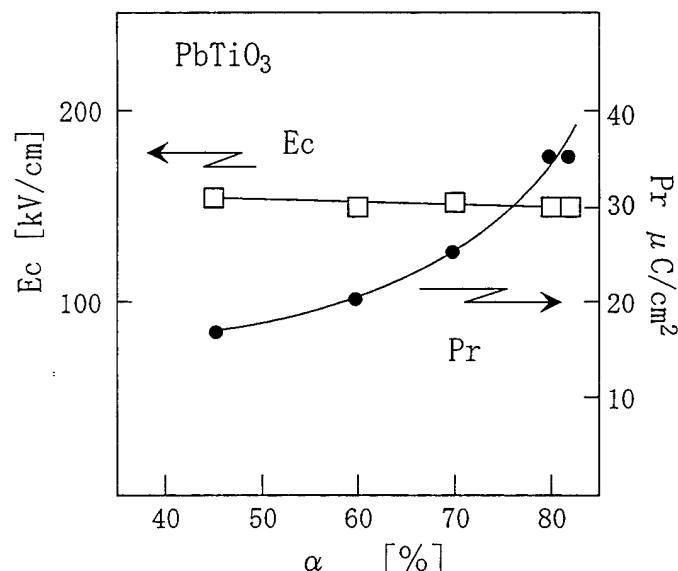


Fig. 11 Relation between coercive force  $E_c$  and remanent polarization  $P_r$  and  $c$ -axis orientation rate  $\alpha$  for  $\text{PbTiO}_3$  thin film.

than those of  $\text{PbTiO}_3$  ceramics ( $\epsilon_r=190, \gamma=1.8 \times 10^{-8} \text{ C/cm}^2\text{K}$ ).

Figure 12 shows  $\epsilon_r$  and  $\gamma$  of the films as a function of La content.  $\epsilon_r$  increase with increasing La content.  $\gamma$  increased with increasing La and shows its maximum at  $x=0.15$  and then decreased with increasing La. As we mentioned above, we measure the pyroelectric properties without poling treatment. This results show that although the  $\alpha$  of the films are high, self-polarization of the films is disappearing in a region containing La more than 15 at%. To investigate the behavior of phase transition, temperature dependence of  $\epsilon_r$  was measured and results are shown in Fig. 13 for the samples containing La more than 15%. This figure shows that all the samples exhibit a characteristic peak of the dielectric constant at around their Curie point, varying consistently with composition.

It is evident that the phase transition behavior of the films changes with composition from normal phase transition characterized by a sharp peak of the dielectric constant to diffused phase transition characterized by a broad peak with increasing La content.

$\epsilon_r$ -temperature characteristics for ferroelectric materials above the Curie point have been reported to be described by the equation  $(1/\epsilon - 1/\epsilon_m)^{1/n} = (T - T_m)/C'$ , where  $\epsilon_m$  is the maximum dielectric constant of a material,  $T_m$  is the temperature giving  $\epsilon_m$  and  $n$  and  $C'$  are constants changing with the composition[10]. It is also known that  $n=1$  for normal phase transition materials and  $n=2$  for diffused phase transition materials[10]. The  $n$ -values were obtained from the replot of the data on a  $\log(1/\epsilon - 1/\epsilon_m)$  versus  $\log(T - T_m)$  plot. The result are shown in Fig. 14 as a function of the La content. In this figure, it is obvious that the diffuseness of the phase transitions in the PLT continuously varies with the composition and it is increased with increasing La.

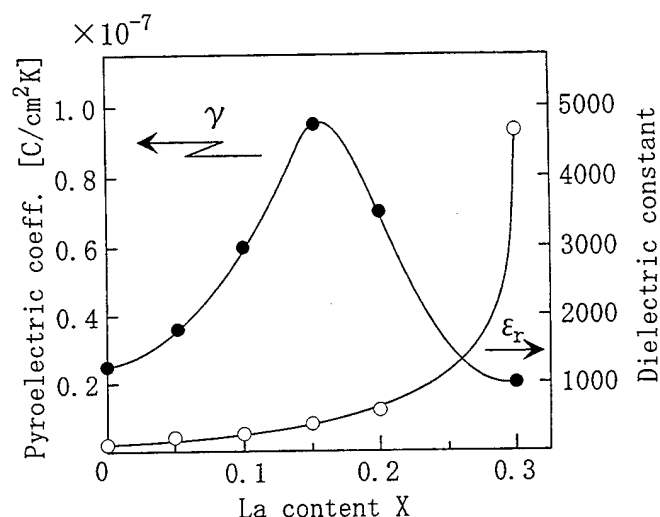


Fig. 12 Dielectric constant  $\epsilon_r$  and pyroelectric coefficient  $\gamma$  as a function of the La content,  $x$ .

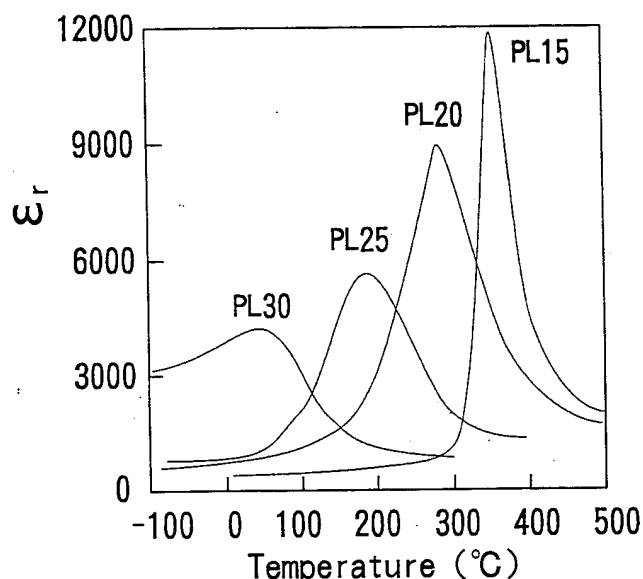


Fig. 13 Dielectric constant of PLT ( $x=0.15, 0.20, 0.25, 0.30$ ) as a function of temperature for 1kHz.

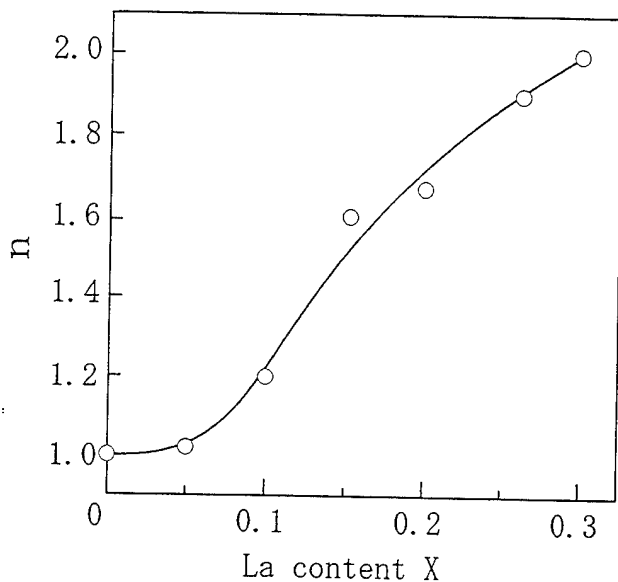


Fig. 14 Variation of  $n$  plotted as a function of La content  $x$ .

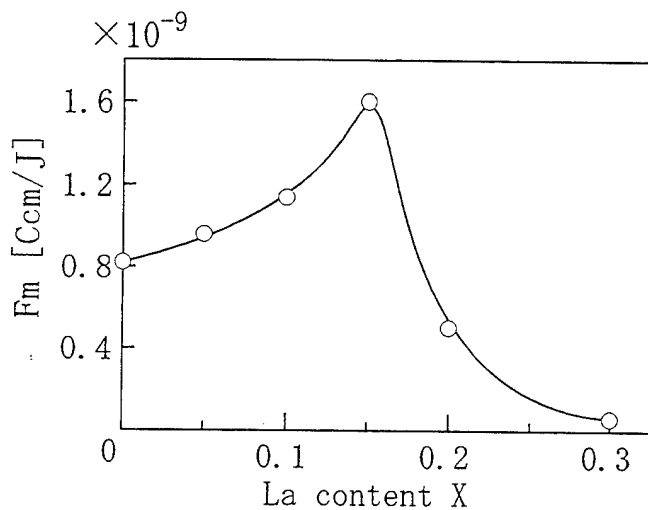


Fig. 15 Figure of merit,  $F_m$ , for specific detectivity as a function of La content  $x$ .

The dielectric properties of relaxer is understood by the microscopic composition fluctuation[11]. In the PLT case, a defect structure incorporated in PLT by the exchange of  $Pb^{2+}$  to  $La^{3+}$  ion is strongly related to the fluctuation. It is considered that such fluctuation and/or the exchange of  $Pb^{2+}$  to  $La^{3+}$  is weakening the long-range ordering of  $Ti^{4+}$  ions in the materials and consequently, self-polarization disappeared in La-rich PLT thin films.

The figure of merit of detectivity  $D^*$  for infrared sensor was calculated using the obtained  $\epsilon_r$ ,  $\tan\delta$  and  $\gamma$  by the equation:  $F_m = \gamma / (C_v \cdot (\tan\delta \cdot \epsilon_r)^{1/2})$  and the results are shown in Fig. 15 as a function of La content.  $F_m$  increase with increasing La content up to  $x=0.15$  because of the increase of pyroelectric coefficient and show maximum at  $x=0.15$ . The results are summarized in Table I with the data of common pyroelectric materials.  $F_m$  of the PLT( $x=0.15$ ) is about 4 times larger than that of  $PbTiO_3$  ceramics and is considered to be a good material for infrared sensor.

Highly sensitive linear array sensors were fabricated using PLT thin films[7]. The  $D^*$  of this sensor is considerably large and  $6 \times 10^8 \text{ cmHz}^{1/2}/\text{W}$  is attained.

This type of sensor using PLT thin film with 8 elements have been carried on the air-conditioner to instantly identify the number, location and postures – standing or sitting – of people in a room, expecting the sensor help to provide more adequate air-conditioning by making the room more comfortable for all occupants.

TABLE I

	$\epsilon_r$	$\gamma$ [C/cm <sup>2</sup> K]	$F_m$ [Ccm/J]	$T_c$ [°C]
PLT thin film	330	$9.5 \times 10^{-8}$	$16 \times 10^{-9}$	330
$PbTiO_3$ ceramics	190	1.8	4	490
PZT ceramics	380	5.0	8	220
$LiTaO_3$ single crystal	54	2.3	9	620

## CONCLUSION

Highly  $c$ -axis oriented PLT thin films with excellent pyroelectric properties were obtained. X-ray diffraction study, internal stress analysis, and SEM observations revealed that  $c$ -axis orientation is due to the compressive stress in the film and this compressive stress is attained by preparing the highly dense epitaxial thin films. The PLT thin films ( $x=0.15$ ) showed an excellent pyroelectric properties.

Dielectric measurement demonstrated that phase transition behavior of PLT changes from normal to diffused phase transition with increasing La content. The self-polarization disappeared in the film of diffused phase transition composition.

**Acknowledgement**– The authors would like to thank Dr.K.Kugimiya for stimulus discussion and also thank to Mr.Y.Daito and Prof. Y.Bando of Kyoto University for taking the TEM photographs.

## REFERENCES

- [1]S.Ikegami, I.Ueda and T.Nagata, J. Acoust. Soc. Am., 50, Pt1, 1060 (1971), T.Ishigaki, K.Nakamura and E.Yamaka, National Tech. Rept., 24, 453 (1978).
- [2]M.Okuyama, T.Usuki, Y.Hamakawa and T.Nakagawa, Appl. Phys., 21, 339 (1980).
- [3]M.Okada, K.Tominaga, T.Araki, S.Katayama and Y.Sakashita, Jpn. J. Appl. Phys., 29, 718 (1990).
- [4]K.Iijima, Y.Tomita, R.Takayama and I.Ueda, J. Appl. Phys., 60, 361 (1986).
- [5]K.Iijima, R.Takayama, Y.Tomita and I.Ueda, *ibid*, 60, 2914 (1986).
- [6]K.Iijima, I.Ueda and K.Kugimiya, Jpn. J. Appl. Phys., 30, 2149 (1991).
- [7]R.Takayama, Y.Tomita, K.Iijima and I.Ueda, J. Appl. Phys., 63, 5868 (1988).
- [8]R.Takayama, Y.Tomita, K.Iijima and I.Ueda, *ibid*, 61, 411 (1987).
- [9]G.A.Rossetti, L.E.Cross, and K.Kushida, Appl. Phys. Lett., 59, 2524 (1991).
- [10]M.Kuwabara, S.Takahashi, K.Goda, K.Oshima and K.Watanabe, Jpn.J.Appl.Phys., 31, 3241 (1992)
- [11]H.B.Krause, J.M.Cowley and J.Wheathley, Acta Crystallogra., A35, 1015 (1979).

# FERROELECTRIC MIM AND MOS STRUCTURE OF LASER DEPOSITED $(\text{Sr}_{0.2}\text{Ba}_{0.8})\text{TiO}_3$ THIN FILMS

\*H. F. Cheng, Phys. Dept., NTNU; I. N. Lin, MSC, NTHU;

\*Phys. Dept. NTNU, 88 Sec. 4, Ting-Chou Road, Taipei, Taiwan, R.O.C.

## Abstract

The laser ablation technique has been applied to synthesize the  $(\text{Sr}_{0.2}\text{Ba}_{0.8})\text{TiO}_3$  thin films. Substrate temperature and chamber oxygen pressure were observed to affect the characteristics of the films most prominently. The metal-insulator-metal (MIM) structure of the films deposited on Pt-coated Si-substrates, possesses better ferroelectric properties than those of the metal-oxide-semiconductor (MOS) structure, as demonstrated by hysteresis loops of remanence  $P_r=1.56 \mu\text{C}/\text{cm}^2$  and coercivity  $E_c=13.5 \text{ kV}/\text{cm}$ . The ferroelectricity of MIM structure is also indicated by butterfly C-V characteristics while that of MOS structure is depicted by hysteresis C-V curves. The charge-discharge test reveals that the effective dielectric constant of the ferroelectric  $(\text{Sr}_{0.2}\text{Ba}_{0.8})\text{TiO}_3$  thin films can reach a value as high as  $\epsilon_r=788$ .

The development of high density dynamic random access memories (DRAM) requires large charge storage capacity in a very small area<sup>(1)</sup>. Utilizing the ferroelectric materials in place of the low dielectric constant  $\text{SiO}_2$  ( $\epsilon_r=3.8$ ) films provides another possibility to improve the charge storage capacity of the memory cells. The  $\text{BaTiO}_3$  materials are ferroelectrics which possess high dielectric constant near the Curie temperature ( $120^\circ\text{C}\sim 130^\circ\text{C}$ ). They have been successfully synthesized by R.F. sputtering<sup>(2-3)</sup>, activated reactive evaporation<sup>(4)</sup>, metalorganic chemical vapor deposition<sup>(5)</sup>, sol-gel<sup>(6)</sup> and pulsed laser ablation<sup>(7,8)</sup> techniques. Among these processes, the pulsed laser ablation method possesses overwhelmingly advantages. The ferroelectric properties of the Sr-modified  $\text{BaTiO}_3$  films prepared by using pulsed laser ablation technique will be presented in this paper. The influence of substrate materials on the characteristics of these films will be described.

The apparatus used for synthesizing the modified  $\text{BaTiO}_3$  films was described elsewhere<sup>(9)</sup>. Ultraviolet beams (308 nm) from XeCl excimer laser (Lambda Physik; LPX 200) were introduced onto rotating  $(\text{Sr}_{0.2}\text{Ba}_{0.8})\text{TiO}_3$  target to generate a plume consisting of Sr, Ba, and Ti ions and neutral atoms. The  $(\text{Sr}_{0.2}\text{Ba}_{0.8})\text{TiO}_3$  film was then deposited onto the substrate placed at the tip of plume and heated by halogen lamp. The substrate temperature was controlled at  $650^\circ\text{C}$  and the oxygen pressure of the chamber was maintained at 1 mbar. The substrates used for growing the  $(\text{Sr}_{0.2}\text{Ba}_{0.8})\text{TiO}_3$  films include bare n-type silicon (100), platinum coated silicon(100), amorphous glass and MgO (100) single crystal. The crystal structure of the films was examined using x-ray diffractometer (Rigaku). The ferroelectric hysteresis loops (D-E curves) were measured using Sawyer-Tower circuit. The charge storage capacity of

the films was estimated from the charge-discharge curves of the films in response to the applied square pulse signal.

The X-ray diffraction patterns of the  $(\text{Sr}_{0.2}\text{Ba}_{0.8})\text{TiO}_3$  films deposited on various kinds of substrates, at 1 mbar oxygen pressure and  $650^\circ\text{C}$  substrate temperature, are shown in Figs.1a~1d to indicate that all the films are of the same

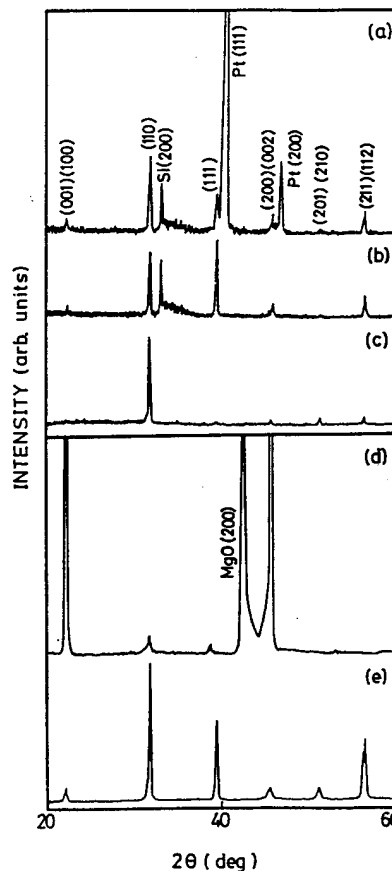


Fig.1 The x-ray diffraction patterns of  $(\text{Sr}_{0.2}\text{Ba}_{0.8})\text{TiO}_3$  thin films deposited under  $650^\circ\text{C}/1 \text{ mbar}$  on (a) Pt (Si), (b) n-type Si, (c) glass and (d) MgO (100) single crystal and (e) that of the target materials.

perovskite crystal structure as that of the target (Fig.1e). The substrate materials have significantly influenced the texture characteristics of the films. Both of the surfaces on the Pt/Si substrate and n-type silicon substrate can effectively trigger the heterogeneous nucleation of the  $(\text{Sr}_{0.2}\text{Ba}_{0.8})\text{TiO}_3$  grains such that randomly oriented films were resulted (Figs.1a & 1b). The surface of the glass substrate has enhanced the growth of the (110) grains (Fig.1c), while that of the MgO substrate has facilitated the deposition of the (200)/(002) family grains (Fig.1d).

The electrical properties of the  $(\text{Sr}_{0.2}\text{Ba}_{0.8})\text{TiO}_3$  films were characterized by measuring the charge storage capacity of the films, which was evaluated by applying the

square shaped pulse to the samples and measuring the charge or discharge behavior across a seriesly connected resistance, shown as the inset in Fig.2. The charge-discharge behaviors for the films deposited on Pt(Si), which is of metal-insulator-metal structure (MIM), are the same no matter whether the applied pulses are positive or negative (Fig.2c). The estimated dielectric constant  $\epsilon_r=788$ . On the other hand, when the same signals were applied to the films deposited on bare silicon, which is of metal-oxide-semiconductor (MOS) structure, large charge-discharge response can be obtained only when the negative pulses were applied. In other words, the response was large when the n-Si was forwardly biased and was small when it was reversely biased (Fig.2b). The charge-discharge signals of MOS structure is significantly lower than those of the MIM structure. It implies that there exists a low dielectric constant layer beneath the  $(\text{Sr}_{0.2}\text{Ba}_{0.8})\text{TiO}_3$  film, such that the seriesly connected capacitance value is lowered markedly.

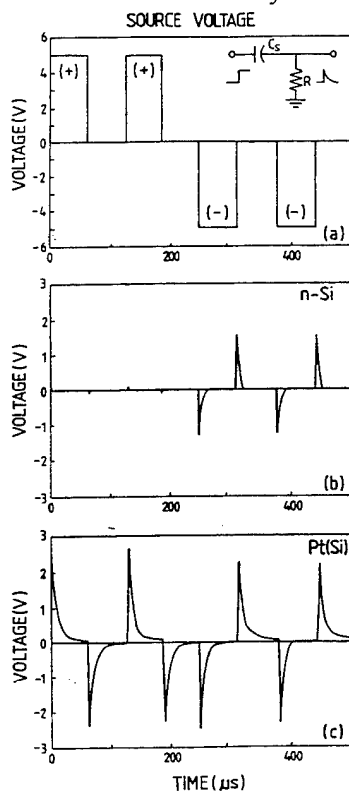


Fig.2 The charge-discharge behavior of  $(\text{Sr}_{0.2}\text{Ba}_{0.8})\text{TiO}_3$  thin films; (a) the applied pulse signal and the response of (b) MOS and (c) MIM structure for films deposited, respectively, on bare-Si and Pt coated Si.

The ferroelectric properties of the  $(\text{Sr}_{0.2}\text{Ba}_{0.8})\text{TiO}_3$  films were characterized by the electric field (E) dependence of the displacement (D), using Sawyer-Tower circuit. The results are shown in Fig.3a for the films deposited on Pt(Si). The films behave as linear dielectric in small applied signal. The hysteresis loops were observed for large enough applied signal but were distorted when the applied electric field exceeded certain limit. The remanance ( $P_r$ ) and coercivity ( $E_c$ ) estimated from the saturated hysteresis loops are, respectively,  $P_r=1.56 \mu\text{C}/\text{cm}^2$  and  $E_c=13.5 \text{ kV}/\text{cm}$ . The remanence of the films is smaller than that of the bulk

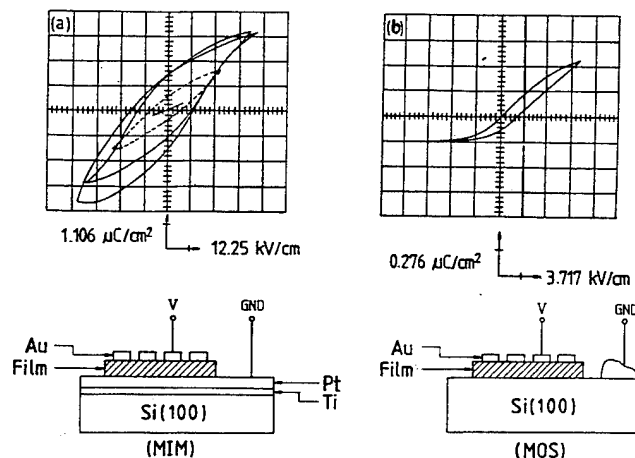


Fig.3 The displacement-electric field (D-E) relationship of the  $(\text{Sr}_{0.2}\text{Ba}_{0.8})\text{TiO}_3$  films deposited on (a) Pt (Si) substrate and (b) n-Si substrate.

samples ( $P_r=6.56 \mu\text{C}/\text{cm}^2$ ), while the coercivity of the films is larger than that of the ceramic samples ( $E_c=1.56 \text{ kV}/\text{cm}$ ). The phenomenon that the hysteresis loops were distorted when the applied field exceeded some limit, is probably due to (i) the asymmetry in the electrodes or (ii) the asymmetry in residual strain. The former is caused by the fact that the bottom electrode is of large area ground plane, while the top electrode is only a dot of diameter 0.5 mm. The latter is resulted from the lattice mismatch between the film and substrate. The D-E curves of the films deposited on n-Si is slim and asymmetric with respect to applied voltage (Fig.3b). This is ascribed to the existence of low dielectric constant layer at film-substrate interface and the formation of depletion region under reversed biased situation.

In summary, the characteristics of  $(\text{Sr}_{0.2}\text{Ba}_{0.8})\text{TiO}_3$  thin films deposited on various substrates at  $650^\circ\text{C}$  and 1 mbar depositing oxygen pressure have been studied. The films deposited on MgO and glass substrates are, respectively, textured in (200) and (110) orientation. Those deposited on either Pt-coated Si or n-type Si are randomly oriented polycrystalline. The charge-discharge characteristics reveal that the MIM structure of the films deposited on Pt coated silicon possesses better charge storage capacity and effective dielectric constant than the MOS structure of the films grown on bare silicon. The best result of dielectric constant is  $\epsilon_r=788$ . The ferroelectric properties of the  $(\text{Sr}_{0.2}\text{Ba}_{0.8})\text{TiO}_3$  films are confirmed by the existence of D-E hysteresis curves. The best ferroelectric parameters are  $P_r=1.56 \mu\text{C}/\text{cm}^2$  and  $E_c=13.5 \text{ kV}/\text{cm}$ , respectively.

#### Acknowledgement

The work is supported by NSC 83-0416-E-003-002 and NSC 84-2112-M-003-001.

#### References

- [1]. L.H. Parker and A.F. Tasch, "Ferroelectric materials for 64 Mb and 256 Mb DRAMs", IEEE Circuits and Devices Magazine, January, 17-26, 1990.
- [2]. K. Screenvias and Abhai Mansingh, "Preparation and

- characterization of RF sputtered BaTiO<sub>3</sub> thin films", IEEE, 602-605, 1986.
- [3]. I.H. Pratt and S. Firestone, "Fabrication of RF-sputtered Barium Titanate thin films", J. Vac. Sci. Vol 8(1), 256-260, 1989.
  - [4]. K. Iijima, T. Terashima, K. Yamamoto, K. Hirata and Y. Bando, "Preparation of ferroelectric BaTiO<sub>3</sub> thin films by activated reactive evaporation", Appl. Phys. Lett, 56(6), 527-529, 1990.
  - [5]. B.S. Kwak and K. Zhang, "Metalorganic chemical vapor deposition of BaTiO<sub>3</sub> thin films", J. Appl. Phys., 69(2), 767-772, 1991.
  - [6]. M.N. Kamalasanan and Subhas Chandra, "Structural and optical properties of Sol-Gel-processed BaTiO<sub>3</sub> ferroelectric thin Films", Appl, Phys. Lett., 59(27), 3547-3549, 1991.
  - [7]. G.M. Davis and M.C. Gower, "Epitaxial growth of thin films of BaTiO<sub>3</sub> using excimer Laser ablation", Appl. Phys. Lett., 55(2), 112-114, 1989.
  - [8]. K. Nashimoto and D.K. Fork, "Epitaxial growth of MgO on GaAs (001) for growing epitaxial BaTiO<sub>3</sub> thin films by pulsed laser deposition", Appl. Phys. Lett., 60, (9), 1199-1201, 1992.
  - [9]. H.F. Cheng, M.H. Yeh, K.S. Liu and I.N. Lin, "The characteristics of BaTiO<sub>3</sub> films prepared by pulsed laser deposition", Jpn. J. Appl. Phys. Vol 32 part1, No.12, 5656-5660, 1993.

# Micropatterning Process of Ferroelectric Oxides by Irradiation of an Electron Beam on Metal Naphthenate Films

Soichiro Okamura, Atsushi Kakimi, Yukie Yagi\*, Katsumi Mori\* and Takeyo Tsukamoto

Department of Applied Physics, Faculty of Science, Science University of Tokyo,

1-3 Kagurazaka, Shinjuku-ku, Tokyo 162, JAPAN

\* Yamaguchi College, Science University of Tokyo,

1-1-1 Daigaku-dori, Onoda, Yamaguchi 756, JAPAN

**Abstract** - Fine micropatterns with linewidth of 0.35  $\mu\text{m}$  were fabricated by irradiation of an electron beam on metal naphthenate films being precursors of ferroelectric oxide and development with a solvent. Relatively large patterns were crystallized into the single phase  $\text{Bi}_4\text{Ti}_3\text{O}_{12}$  with *c*-axis orientation by successive heat-treatment at 800  $^{\circ}\text{C}$ . Micropatterns with linewidth of 1  $\mu\text{m}$  were crystallized into single crystals and their volume was reduced to 15 % by the heat-treatment. PZT and  $\text{Bi}_4\text{Ti}_3\text{O}_{12}$  thin films formed by the dipping pyrolysis method, which is the base of this patterning process, exhibited good ferroelectric properties; the remanent polarization  $P_r$  and the coercive field  $E_c$  were 24  $\mu\text{C}/\text{cm}^2$  and 39  $\text{kV}/\text{cm}$  for PZT, and 1.6  $\mu\text{C}/\text{cm}^2$  and 24  $\text{kV}/\text{cm}$  for  $\text{Bi}_4\text{Ti}_3\text{O}_{12}$ , respectively.

## I. INTRODUCTION

FERROELECTRIC thin films on silicon wafers have a great potential for an application to electronic devices such as high-density dynamic random access memories (DRAMs) and nonvolatile memories [1]. There is also possibility as second harmonic generators (SHGs) and optical switches in optoelectronic devices. Therefore, over the past few years, numerous studies to form ferroelectric thin films have been made by several methods such as metalorganic chemical vapor deposition (MOCVD), sol-gel method, rf-sputtering and the laser ablation.

Micropatterning of ferroelectric materials is one of the most important technologies for application of them to silicon-based integrated circuits (ICs). In ordinary semiconductor process, silicon and silicon dioxide ( $\text{SiO}_2$ ) are patterned by dry etching with resist patterns. It is, however, difficult to etch ferroelectric oxides without reactive gases because of their hardness. Only a few attempts on micropatterning of ferroelectric oxides have been made so far. M. A. Title *et al.* [2] and M. R. Poor *et al.* [3] patterned PLT or PLZT films by dry etching with HCl and/or  $\text{CF}_4$ . Y. Nakao *et al.* [4] and N. Tohge *et al.* [5] made PZT micropatterns by using photo-sensitive sol-gel solutions.

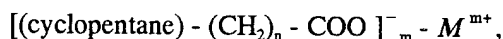
We have proposed a micropatterning process for composite oxides  $\text{YBa}_2\text{Cu}_3\text{O}_{7-x}$  using an electron beam in 1992 [6]. In this process, at first, an electron beam is irradiated on metal naphthenate films, then unirradiated area is removed by development with a solvent. The precursor micropatterns are pyrolyzed and crystallized into target oxides by successive heat-treatment. In the heat-treatment of sub-micron micropatterns, it is expected that the precursor micropatterns may be crystallized into single crystals. It is possible to apply this process to ferroelectric oxides. We have reported the fabrication of bismuth titanate  $\text{Bi}_4\text{Ti}_3\text{O}_{12}$  micropatterns by this process [7][8].

This paper describes the formation of lead zirconate-titanate (PZT) and  $\text{Bi}_4\text{Ti}_3\text{O}_{12}$  thin films by the dipping pyrolysis method, which is the base of this patterning process, and fabrication of ferroelectric micropatterns by an electron beam irradiation and successive heat-treatment.

## II. EXPERIMENTAL

### A. Dipping Solutions

Metal naphthenates consist of cyclopentanes or cyclohexanes, methylene chains  $-(\text{CH}_2)_n-$ ,  $-\text{COO}-$  and metals. They have mainly following structure;



where,  $M$  is a metal atom. They are stable in air and sticky liquid at room temperature. In this study, titanium, bismuth, lead and zirconium naphthenates were used as starting materials to prepare dipping solutions. Metal contents of these naphthenates were estimated to be 3.6, 5.1, 25 and 7.8 wt%, respectively.

Two kinds of dipping solutions for PZT and  $\text{Bi}_4\text{Ti}_3\text{O}_{12}$  were prepared by mixing the metal naphthenates with  $\text{Pb}:\text{Zr}:\text{Ti} = 1.05:0.52:0.48$  and  $\text{Bi}:\text{Ti} = 4:3$  in molar ratio, respectively. They were diluted with toluene to realize appropriate viscosity for the spin-coating. All the operations were carried out in air.

### B. Formation of Ferroelectric Oxide Thin Films

Platinum (Pt) plates were used as substrates. The substrates were spin-coated with the dipping solutions at a rate of 4000 rpm for 20 s and dried in air at 110  $^{\circ}\text{C}$  for 10 min. Then, they were calcined in air at 500  $^{\circ}\text{C}$  for 5 min. The drying and calcination temperatures were determined from results of thermogravimetry-differential thermal analysis (TG-DTA) for the dipping solutions [7]. Film thickness was adjusted by repetition of the spin-coating and the calcination. Finally, they were crystallized into ferroelectric oxides by sintering at 600  $\sim$  800  $^{\circ}\text{C}$  for 30 min in  $\text{O}_2$  atmosphere.

Film thickness was measured by observation of cross-section using a scanning electron microscope (SEM). Crystal structure was confirmed by X-ray diffraction analysis (XRD) with  $\text{CuK}\alpha$ . Surface morphology was observed by an SEM.

To evaluate electric properties, Au dots of 1 mm  $\phi$  deposited on the film surface by vacuum evaporation were

used as top electrodes and Pt plates were used as bottom ones. Dielectric constants and losses were measured by an LCR meter at 1 kHz. *D-E* hysteresis loops were observed by means of the Sawyer-Tower circuit with a sinusoidal field.

### C. Fabrication of Ferroelectric Oxide Micropatterns

Fig. 1 shows micropatterning process of ferroelectric oxides. At first, substrates were spin-coated with the dipping solutions to form homogenous precursor thin films at a rate of 1000 rpm for 10 s. After they were dried in air at 110 °C for 10 min, an electron beam was irradiated on the precursor films. Fig. 2 shows an electron beam drawing system constructed by modifying a conventional SEM. Drawing patterns inputted to the personal computer consisted of three primitive elements; horizontal lines, vertical ones and squares. The electron beam accelerated at a voltage of 30 kV was scanned according to the given pattern by the computer which controls vertical and horizontal deflecting voltage, and blanking signal. Irradiation time for each point was 5 ms. Metal naphthenate films have negative exposure characteristics for the electron beam and the sensitivity is  $2.5 \times 10^{-3} \text{ C/cm}^2$  [7]. It seems that energized electrons cause a bridge-building reaction in the films and make them insoluble in toluene [8]. Total dose was adjusted by the repetition of scanning. Size of whole patterns was controlled by changing the magnitude in the SEM. Spot size of the electron beam was appropriately adjusted to the requested size of the patterns. Probe current was measured by a pA meter inserted between the sample and the ground. In typical conditions for drawing patterns with 1  $\mu\text{m}$  order, the spot size and the probe current of the electron beam were 10 nm  $\phi$  and 12 pA, respectively.

After the electron beam drawing, the samples were developed with toluene to remove the unirradiated area. In this moment, the precursor micropatterns were formed on

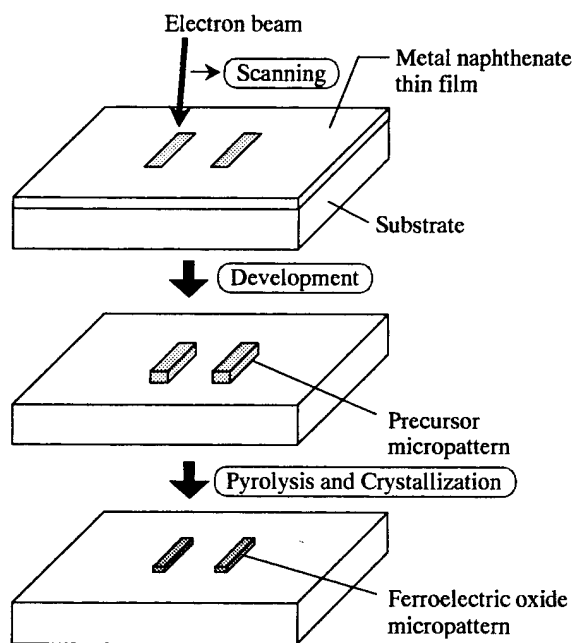


Fig.1 Micropatterning process of ferroelectric oxides by irradiation of an electron beam on metal naphthenate films and development.

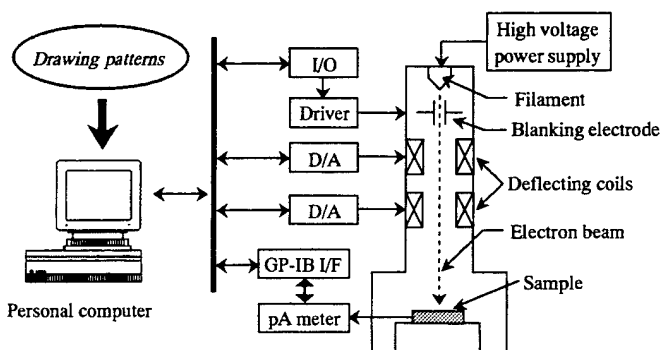


Fig.2 Schematic diagram of the electron beam drawing system.

substrates. They were crystallized into ferroelectric oxides by successive heat-treatment.

The crystal structure of patterns formed on Pt plates was confirmed by XRD. Aspects of the micropatterns before and after sintering were observed by an SEM.

## III. RESULTS AND DISCUSSION

### A. PZT Thin Films

PZT thin films were formed on Pt plates by calcination at 500 °C. The film thickness was estimated to be 500 nm. Fig. 3(a) shows an XRD pattern of the PZT film. It is confirmed that the film was crystallized into the  $\text{Pb}(\text{Zr}_{0.52}, \text{Ti}_{0.48})\text{O}_3$

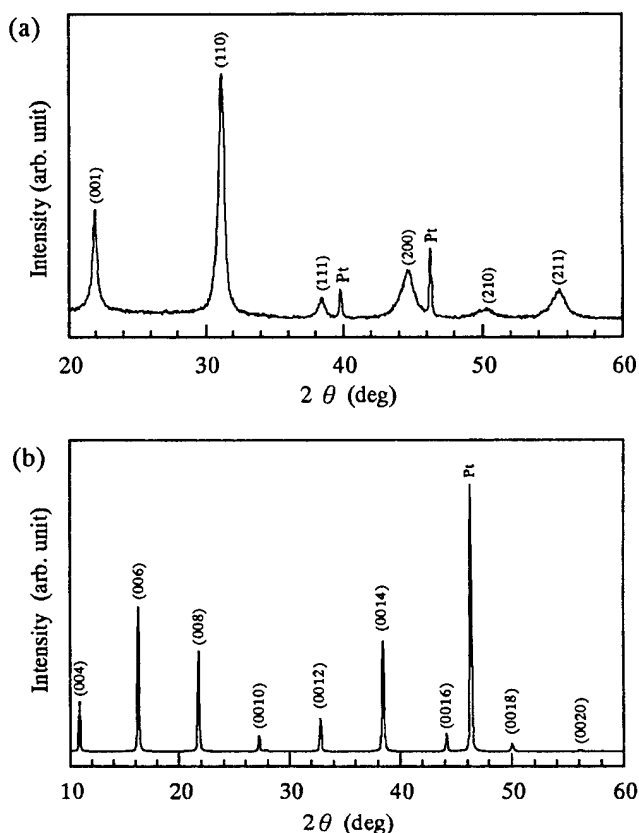


Fig.3 XRD patterns of (a) the PZT thin film and (b) the  $\text{Bi}_4\text{Ti}_3\text{O}_{12}$  thin film.



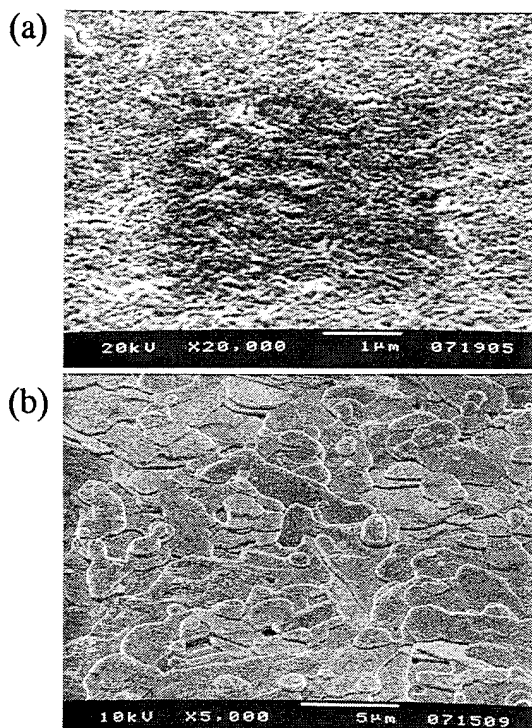


Fig.4 Surface morphologies of (a) the PZT thin film and (b) the  $\text{Bi}_4\text{Ti}_3\text{O}_{12}$  thin film.

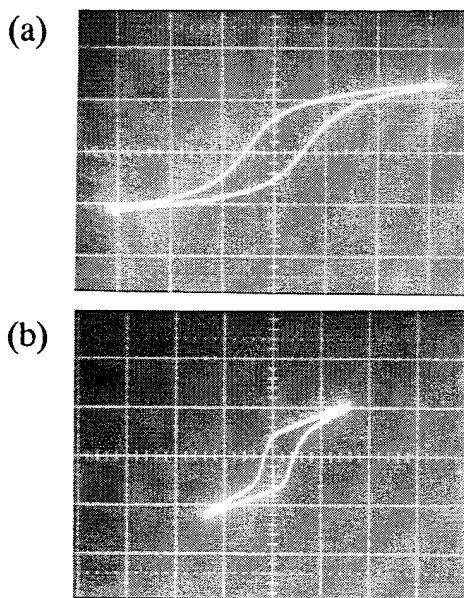


Fig.5  $D$ - $E$  hysteresis loops of (a) the PZT thin film ( $P_r = 24 \mu\text{C}/\text{cm}^2$ ,  $E_c = 39 \text{ kV}/\text{cm}$ ) and (b) the  $\text{Bi}_4\text{Ti}_3\text{O}_{12}$  thin film ( $P_r = 1.6 \mu\text{C}/\text{cm}^2$ ,  $E_c = 24 \text{ kV}/\text{cm}$ ).

phase. Heat-treatment above  $550^\circ\text{C}$  made no change in XRD patterns. Surface morphology of the film was shown in Fig. 4(a). It is found that small grains of  $20 \sim 50 \text{ nm}$  close each other.

Fig. 5(a) shows a  $D$ - $E$  hysteresis loop of the PZT film observed at  $10 \text{ kHz}$ . From this figure, it was estimated that the remanent polarization  $P_r$  and the coercive field  $E_c$  were  $24 \mu\text{C}/\text{cm}^2$  and  $39 \text{ kV}/\text{cm}$ , respectively. Dielectric constant

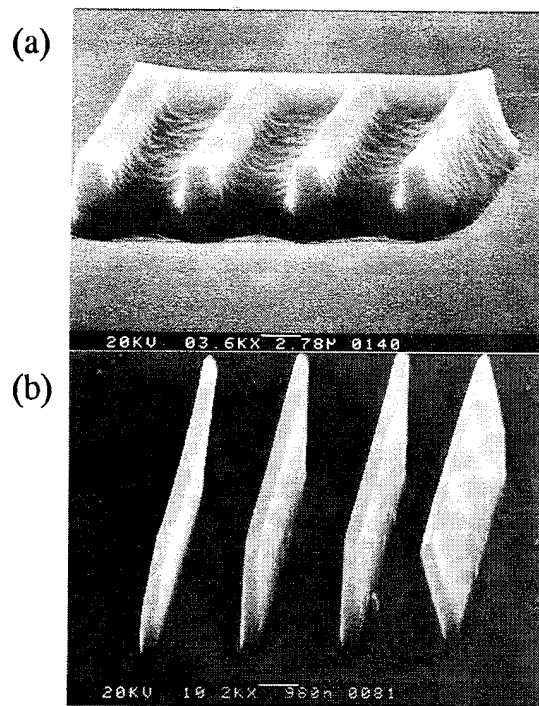


Fig.6 SEM photographs of (a) micropattern formed on precursor film with  $5 \mu\text{m}$  in thickness and (b) fine precursor micropattern with linewidth of  $0.35 \mu\text{m}$ .

and loss were estimated to be 309 and 0.06, respectively. These values agree with those reported by Shimizu *et al.* [9].

#### B. $\text{Bi}_4\text{Ti}_3\text{O}_{12}$ Thin Films

$\text{Bi}_4\text{Ti}_3\text{O}_{12}$  thin films were formed on Pt plates by calcination at  $500^\circ\text{C}$  and sintering at  $800^\circ\text{C}$ . The film thickness was estimated to be  $500 \text{ nm}$ . Fig. 3(b) shows an XRD pattern of the film. It is confirmed that the film was crystallized into the single  $\text{Bi}_4\text{Ti}_3\text{O}_{12}$  phase with  $c$ -axis orientation. Surface morphology of the film was shown in Fig. 4(b). Platelike crystals were piled up on the substrate.

Fig. 5(b) shows a  $D$ - $E$  hysteresis loop of the  $\text{Bi}_4\text{Ti}_3\text{O}_{12}$  film observed at  $150 \text{ Hz}$ . From this figure, the remanent polarization  $P_r$  and the coercive field  $E_c$  were estimated to be  $1.6 \mu\text{C}/\text{cm}^2$  and  $24 \text{ kV}/\text{cm}$ , respectively. Dielectric constant and loss were estimated to be 48 and 0.02, respectively. These values are comparable with those reported by Toyoda *et al.* [10].

#### C. Fabricated Precursor Micropatterns

It seems that the aspect of micropatterns was affected by the thickness of precursor films. To estimate the film thickness of which the electron beam could make fine patterns, drawing to precursor films with different thickness was carried out. Fig. 6(a) shows a PZT precursor pattern formed on a film with  $5.5 \mu\text{m}$  in thickness. In this case, although lines are separated at film surface, they broaden to the substrate and connect each other at near the substrate surface due to the scattering of electrons in the film. It suggests that there is limitation in the thickness of precursor films to form fine micropatterns by the electron beam drawing.

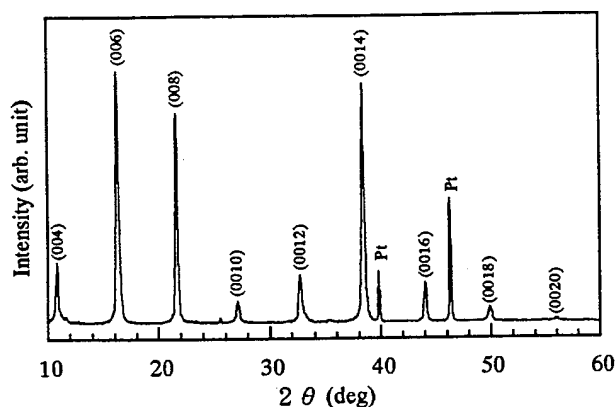


Fig.7 An XRD pattern of the square  $\text{Bi}_4\text{Ti}_3\text{O}_{12}$  pattern sintered at 800 °C.

The aspect of PZT precursor micropatterns formed on a film with 2.5  $\mu\text{m}$  in thickness is shown in Fig. 6(b). It is found that fine micropatterns with linewidth of 0.35  $\mu\text{m}$  and aspect ratio of 7 are fabricated.

#### D. Crystallization of $\text{Bi}_4\text{Ti}_3\text{O}_{12}$ Precursor Micropatterns

An XRD pattern of the  $3 \times 4 \text{ mm}^2$  square pattern of bismuth titanate fabricated on the Pt plate by irradiation of the electron beam and successive heat-treatment at 800 °C is shown in Fig. 7. It is confirmed that the pattern was crystallized into single phase  $\text{Bi}_4\text{Ti}_3\text{O}_{12}$  with  $c$ -axis orientation as well as thin films. It means that the electron beam never causes the composition change of films. However, ferroelectric properties for this pattern were not observed because of the high conductivity.

To observe the crystallization of  $\text{Bi}_4\text{Ti}_3\text{O}_{12}$  micropatterns,  $1 \times 2 \mu\text{m}^2$  patterns were formed and then sintered in  $\text{O}_2$  at 800 °C for 5 min. Fig. 8(a) and 8(b) show micropatterns of  $\text{Bi}_4\text{Ti}_3\text{O}_{12}$  before and after heat-treatment, respectively. Patterns with 1  $\mu\text{m}$  width and 0.6  $\mu\text{m}$  height changed to ones of 0.5  $\mu\text{m}$  width and 0.3  $\mu\text{m}$  height, respectively. The volume was reduced to 15% by the heat-treatment. It seems that they are crack-free single crystals.

#### IV. CONCLUSIONS

Ferroelectric PZT and  $\text{Bi}_4\text{Ti}_3\text{O}_{12}$  oxide thin films were formed by dipping pyrolysis of metal naphthenates. The PZT thin film exhibited the remanent polarization  $P_r$  of 24  $\mu\text{C}/\text{cm}^2$  and the coercive field  $E_c$  of 39 kV/cm. The  $\text{Bi}_4\text{Ti}_3\text{O}_{12}$  thin film with  $c$ -axis orientation exhibited the remanent polarization  $P_r$  of 1.6  $\mu\text{C}/\text{cm}^2$  and the coercive field  $E_c$  of 24 kV/cm.

Fine precursor micropatterns with linewidth of 0.35  $\mu\text{m}$  were fabricated by irradiation of the electron beam on metal naphthenate films and development with toluene. The pattern on thicker precursor films broadens to the depth direction due to electron beam scattering in the films.

The relatively large bismuth titanate pattern was crystallized into single phase  $\text{Bi}_4\text{Ti}_3\text{O}_{12}$  with  $c$ -axis orientation by heat-treatment at 800 °C. It seems that precursor micropatterns with linewidth of 1  $\mu\text{m}$  were crystallized into single crystals. Properties of each microblock in the patterns are now in progress.

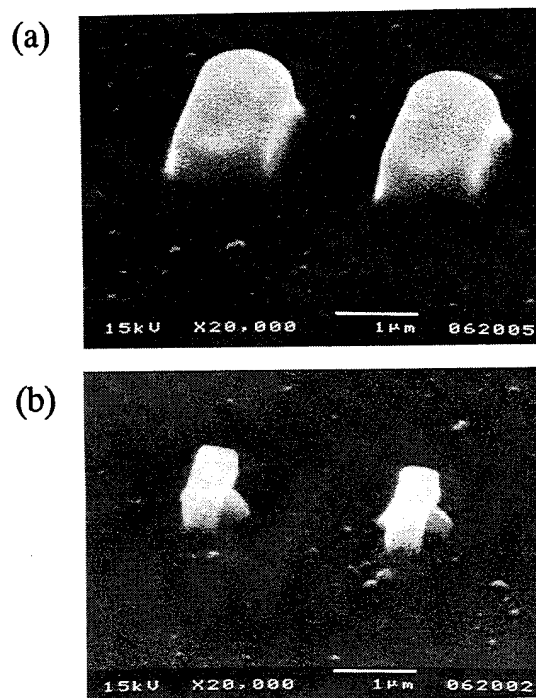


Fig.8 Aspects of the micropatterns (a) before and (b) after heat-treatment.

#### REFERENCES

- [1] J. F. Scott and C. A. Araujo, "Ferroelectric Memories," *Science*, vol. 246, pp. 1400-1405, 1989.
- [2] M. A. Title, L. M. Walpita, W. X. Chen, S. H. Lee and W. S. C. Chang, "Reactive ion beam etching of PLZT electrooptic substrates with repeated self-aligned masking," *Applied Optics*, vol. 25, pp. 1508-1510, 1986.
- [3] M. R. Poor, A. M. Hurd, C. B. Fleddermann and A. Y. Wu, "Plasma Etching of PLT Thin Films and Bulk PLZT Using Fluorine- and Chlorine- Based Gases," *Mater. Res. Soc. Symp. Proc.*, vol. 200, pp.211-216, 1990.
- [4] Y. Nakao, T. Nakamura, K. Hoshiba, K. Sameshima, A. Kamisawa, K. Abe, N. Soyama and K. Ogi, "Micro-patterning of  $\text{PbZr}_{1-x}\text{Ti}_x\text{O}_3$  Thin Films Prepared by Photo Sensitive Sol-Gel Solution," *Jpn. J. Appl. Phys.*, vol. 32, pp.4141-4143, 1993.
- [5] N. Tohge, K. Shinmou and T. Minami, "Patterning of PZT thin films by the photolysis of chemically modified metal-alkoxides," *Proc. Annu. Meet. Ceramic Society of Japan*, Nagoya, April, p. 512, 1994 [in Japanese].
- [6] K. Mori and S. Okamura, "Electron-Beam-Induced Structuring of Composite Oxides by means of Dipping Pyrolysis of Metal Naphthenate Films," *Jpn. J. Appl. Phys.*, vol. 31, pp. L1143-L1145, 1992.
- [7] S. Okamura, A. Kakimi, K. Yoshimura, Y. Yagi, K. Mori and T. Tsukamoto, "Fabrication of ferroelectric  $\text{Bi}_4\text{Ti}_3\text{O}_{12}$  thin films by dipping-pyrolysis of metal naphthenates and micro patterning process using an electron beam," *Trans. Mater. Res. Soc. Jpn.*, vol. 14B, 1994 in press.
- [8] A. Kakimi, S. Okamura, Y. Yagi, K. Mori and T. Tsukamoto, "Fabrication of Ferroelectric  $\text{Bi}_4\text{Ti}_3\text{O}_{12}$  Thin Films by Dipping Pyrolysis of Metal Naphthenates and Micropatterns by an Electron Beam," *Jpn. J. Appl. Phys.*, vol. 33, no. 9B, 1994 in press.
- [9] M. Shimizu, T. Katayama, M. Sugiyama and T. Shiosaki, "Thin Film Growth of  $\text{Pb}(\text{Zr},\text{Ti})\text{O}_3$  by Photoenhanced Metalorganic Chemical Vapor Deposition Using  $\text{NO}_2$ ," *Jpn. J. Appl. Phys.*, vol. 32, pp. 4074-4077, 1993.
- [10] M. Toyoda, Y. Hamaji, K. Tomono and D. A. Payne, "Synthesis and Characteriation of  $\text{Bi}_4\text{Ti}_3\text{O}_{12}$  Thin Films by Sol-Gel Processing," *Jpn. J. Appl. Phys.*, vol. 32, pp. 4158-4162, 1993.

# Imprint of Ferroelectric PLZT Thin-Film Capacitors with Lanthanum Strontium Cobalt Oxide Electrodes

J. M. Benedetto<sup>1,2</sup>, M. L. Roush<sup>2</sup>, I. K. Lloyd<sup>2</sup>, and R. Ramesh<sup>3</sup>

<sup>1</sup>Army Research Laboratory, Adelphi, MD 20783

<sup>2</sup>University of Maryland, College Park, MD 20742

<sup>3</sup>Bell Communication Research, Red Bank, NJ 07701

## Abstract

Ferroelectric imprint is measured on thin-film PLZT capacitors with lanthanum strontium cobalt oxide top and bottom electrodes. The data show a significant amount of imprint with a combined elevated temperature and alternating (unipolar) voltage stress. No imprint was observed on samples that were temperature stressed without external bias.

## Introduction

Imprint of ferroelectric (FE) thin-films is generally considered to be an asymmetrical retention phenomena that is manifested by the tendency of a FE capacitor element in a non-volatile memory to spontaneously (without the application of an external electric field) switch (partially or fully) to a preferential state. For imprint to occur, a preferential state has to be developed either by some operational stress on the capacitor element (e.g., bias temperature stress), or as a "built-in" preferential state that may develop during film growth or other process-related steps. For this work we use the term "imprint" to describe any asymmetrical retention characteristics of the FE capacitor element. This work discusses the results of imprint testing on lead lanthanum zirconate titanate (PLZT) FE capacitors with

lanthanum strontium cobalt oxide (LSCO) electrodes using a measurement and analysis technique to determine the degree of imprint of FE capacitor elements as a function of time after the write pulse. The results of these measurements will be shown and the implications to memory failure due to imprint will be briefly discussed.

The imprint characteristics of these particular thin-film heterostructures are of interest because of their excellent fatigue and retention characteristics ( $>10^{12}$  cycles with only minimal polarization loss) [1]. Because of this excellent fatigue behavior this type of heterostructure may be a candidate for FE nonvolatile memories in the near future.

## Measurement Technique

The imprint measurement used for this work consists of a voltage pulse technique which uses square voltage pulses for both writing and reading data bits to FE capacitors [2]. Figure 1 shows the pulse configurations and the resulting digitized data from an oscilloscope for the two positive read conditions (Fig. 1a) and the two negative read conditions (Fig. 1b). This measurement approach attempts to simulate the same write/read conditions that a FE capacitor cell would experience in a

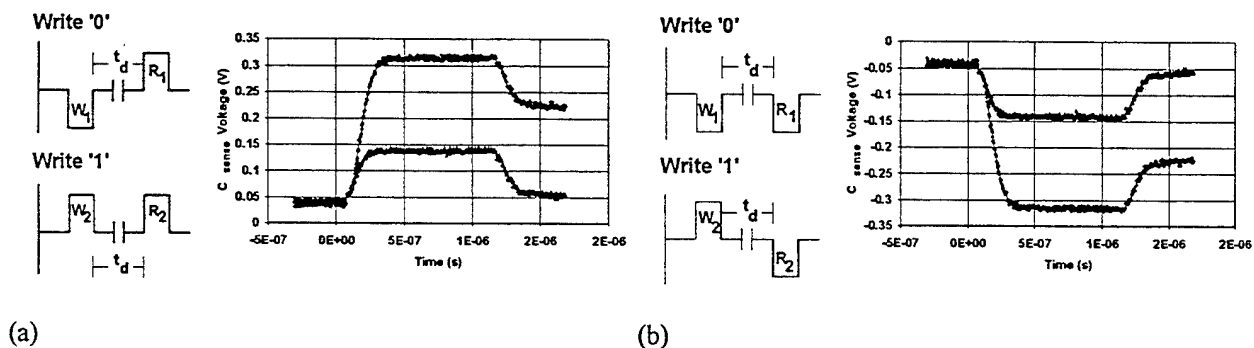


Figure 1: Oscilloscope trace of switched and non-switched polarizations, (a) positive reads and (b) negative reads.

This work partially supported by the Advanced Research Projects Agency.

nonvolatile memory (i.e., relatively short write/read pulses and variable delay times between write and read pulses).

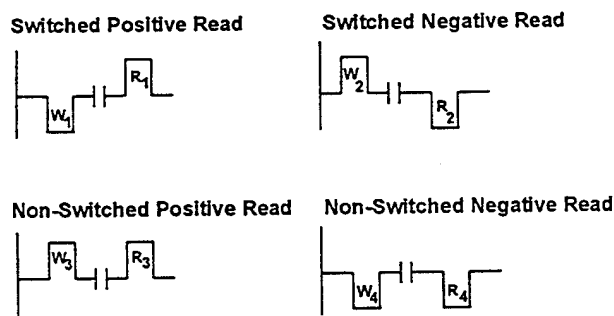


Figure 2: All possible pulse configurations for a destructive read out memory.

Figure 2 shows all four possible voltage pulse pair configurations a capacitor can experience (with variable write/read delay) in a destructive readout (DRO) memory. These four cases are: (a) write down/read up (switched polarization, positive read), (b) write up/read down (switched polarization, negative read), (c) write up/read up (non-switched polarization, positive read), and (d) write down/read down (non-switched polarization, negative read). Note that in the first two cases the polarization state is being switched, hence these cases are referred to as switched positive read, and switched negative read, respectively. In the last two cases the polarization state is being read in the same direction as the write therefore the polarization state is not switched and these cases are referred to as non-switched positive read, and non-switched negative read, respectively.

It should be noted at this point that for a FE capacitor element which contains no asymmetrical retention loss (or imprint) the write up/read down polarization has to exactly equal the write down/read up polarization (by our earlier definition of imprint) and similarly for the non-switched polarization cases write up/read up equals write down/read down. If these polarizations are not equal then, by definition, the device contains an asymmetrical retention characteristic and can be said to show some imprint or preferential state.

### Imprint Tests

All the capacitors tested were packaged in ceramic 16-pin dual in-line packages (DIPs) at the Army Research Laboratory (ARL) Semiconductor and Electronic

Materials Test Facility prior to testing. The parts were packaged to facilitate the bias temperature stressing used to "imprint" the samples. The samples were screened and their retention characteristics recorded from 1  $\mu$ s to 100 s write/read delay time prior to bias temperature stressing.

All the "imprint" stressing was performed at 100°C. The samples were heated to temperature with the top and bottom electrodes tied to ground (to mitigate any pyroelectric fields). Once at temperature the voltage portion of the imprint stress was applied. Four different voltage stress were studied:

- (1) No bias-the capacitors were poled with a -5 V pulse and the bias removed prior to heating,
- (2) A 0 to +5 Vac 100-Hz 50% duty cycle waveform,
- (3) A 0 to -5 Vac 100-Hz 50% duty cycle waveform, and
- (4) A 0 to +2.5 Vac 100-Hz 50% duty cycle waveform.

Post-stress retention was measured at room temperature (the samples were allowed to cool with top and bottom electrodes tied to ground for 2 hours prior to the retention measurements) after each stress interval. The stress intervals were 100, 200, 500, and 1000 s.

### Results

Figure 3 shows the retention characteristics for a LSCO/PLZT/LSCO sample prior to any bias temperature stressing. The ordinate is the voltage measured across the integrating capacitor and is related to polarization by a constant. The abscissa is the time

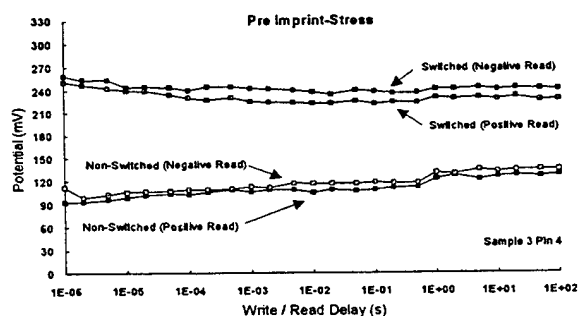


Figure 3: Pre imprint-stress retention characteristics.

delay between the write and read pulses. As mentioned above, these measurements attempt to simulate, as closely as possible, the conditions a capacitor used as a

memory element could experience in an actual memory device. Note in this figure that there is only a very small difference between the switched positive read and switched negative read and similarly between the non-switched cases. This implies that, as grown, these samples do not have a significant preferential state.

Figure 4 shows the retention characteristics of the same sample shown in figure 3, but now the capacitor has been stressed at 100°C for 1000 s with a 0 to +5 V 100-Hz 50% duty cycle waveform. Note that the two

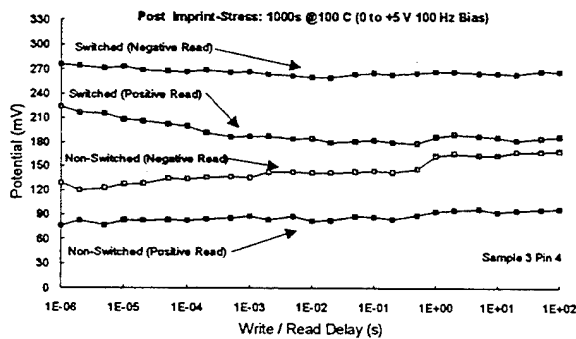


Figure 4: Post imprint-stress retention characteristics (0 to +5 V 100 Hz 50% duty cycle stress waveform).

switched polarizations and the non-switched polarizations have separated by a significant amount. This sample now shows an asymmetrical retention characteristic with the switched positive read polarization decreasing in magnitude and the non-switched negative read polarization increasing in magnitude. Note also that the switched (positive read) and non-switched (negative read) come together at long write/read delay times.

Figure 5 shows another sample taken from the same substrate as the sample shown in figures 3 and 4. This figure shows the sample after 1000 s of bias temperature

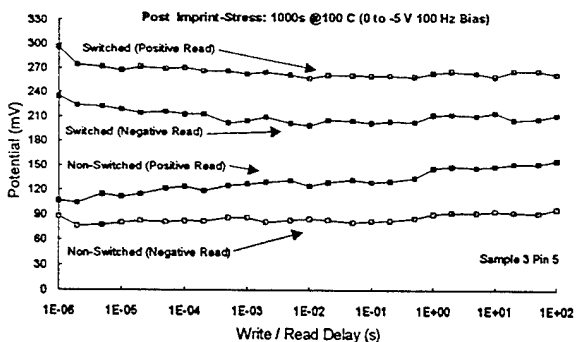


Figure 5: Post imprint-stress retention characteristics (0 to -5 V 100 Hz 50% duty cycle stress waveform).

stressing at 100°C with a 0 to -5 V 100-Hz 50% duty cycle waveform. Under these stressing conditions the switched (negative read) and non-switched (positive read) polarizations move somewhat closer together (indicating a negative preferential state). Unlike the previous case (0 to +5 V stressing) the switched (positive read) and non-switched (negative read) polarizations remain apart by a significant margin.

Figure 6 shows another sample after 1000 s at 100°C with no applied external bias. The sample was poled negative prior to the temperature stressing, but the bias

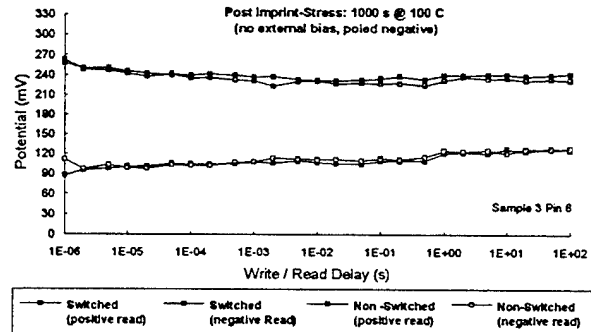


Figure 6: Post imprint-stress retention characteristics (no external bias, poled negative).

was removed before heating the sample. The data indicate that no preferential state (i.e., asymmetrical retention characteristic) is developed by thermal stressing alone.

For length considerations the data from the 0 to 2.5 V imprint stressing measurement is not shown. However the data is consistent with figure 4, except the degree of post-stress asymmetry is less.

## Discussion

The data in figures 4 and 5 show a strong asymmetrical retention characteristic brought about by external bias temperature stressing. Figure 4 shows a reduction in the switched charge (positive read) and an increase in the non-switched charge (negative read). There is also very little change in the switched charge (negative read) and non-switched charge (positive read). Similar results are seen in figure 5, except in this case, with BT stressing with a negative going unipolar pulse, there is a significant decrease in the switched charge (negative read) and an increase in the non-switched charge (positive read). It is interesting to note, however, that

here remained a significant "window" between the respective switched and non-switched polarizations.

For many destructive readout non-volatile memory applications only a single read direction would be used—i.e., either a positive or negative read pulse. From an examination of the data in figures 4 and 5 it may appear that for any single polarity read pulse application imprint might not be a significant problem because the difference between the switched charge and non-switched charge does not change significantly for a given read pulse direction. In other words, after 1000s of BT stressing the difference between the switched and non-switched charge for the positive read pulse case is approximately 100 mV (figure 4). The difference between the switched and non-switched charge for the negative read pulse case is approximately 110 mV (figure 4) (at 2-ms write/read delay time). This would imply that it is always possible to determine the switched charge from the non-switched charge and therefore possible to tell a stored '0' from a stored '1' in a NV memory element.

However, what is not known when querying a memory element is in which direction (if at all) a bit may have been imprinted. From the data in figures 4 and 5 we see that the switched polarization decreases when the read pulse is in the same polarity as the imprint stress polarity. Similarly, the non-switched polarization increases when the read pulse is in the opposite direction from the imprint stress polarity. The switched (read pulse polarity opposite imprint polarity) and the non-switched (read pulse polarity same as imprint polarity) polarizations do not change significantly.

From figure 3 we see that if a voltage of approximately 250 mV appears across the integrating capacitor during a read pulse we know the capacitor polarization has been switched. On the other hand, if a voltage of 120 mV appears on the integrating capacitor then we know the polarization was not switched. From this we can determine directly whether a '0' or a '1' was stored. Now referring to figure 4 we see that if a voltage of approximately 160 mV appears across our integrating capacitor we cannot determine whether we have a switched polarization (in the imprint direction) or a non-switched polarization (opposite the imprint direction). This could lead to an ambiguous reading for a sense amplifier in a FE non-volatile memory which would default randomly to '1' or a '0'. About half the time the default state will be incorrect and an imprint failure will have occurred.

## Conclusions

This work has demonstrated several key aspects about imprint in LSCO/PLZT/LSCO structures. It has been shown that:

1. Imprint can be measured on individual capacitors and the results at the capacitor level should extend to the memory level.
2. These capacitors could be imprinted either in the positive or negative direction, and
3. Imprint occurs under bias temperature stressing but not with temperature alone (for these samples and within the time frame of these measurements).

## References

1. R. Ramesh, H. Gilchrist, T. Sands, V. G. Keramidas, R. Haakenaasen, and D. K. Fork, "Ferroelectric La-Sr-Co-O/Pb-Zr-Ti-O/La-Sr-Co-O Heterostructures on Silicon Via Template Growth," *APL* 63, p. 3592 (1993).
2. J. M. Benedetto, R. A. Moore, and F. B. McLean, "Fast Decay Component of the Remanent Polarization in Thin-Film PZT Capacitors," *Integrated Ferroelectrics*, 1, p. 195 (1992).

# ANALYSIS OF FERROELECTRIC THIN FILMS DEPOSITED BY PULSED LASER DEPOSITION ON OXIDE AND FLUORIDE SUBSTRATES

S. Sengupta, L.C.Sengupta, S. Stowell, E. Ngo, and W. E. Kosik  
U.S. Army Research Laboratory, Materials Directorate, Ceramics/Metals Division  
Watertown, MA 02172

and  
D.K. Vijay  
Virginia Polytechnic Institute  
Department of Materials Science and Engineering  
Blacksburg, VA 24061

**Abstract:** This work has been carried out as part of an ongoing investigation in which thin film ferroelectric phase shifters are being constructed, tested, and optimized. The phase shifters will be incorporated into multi-element phased array antennas. The beam steering material used here was  $\text{Ba}_{0.6}\text{Sr}_{0.4}\text{TiO}_3$  (BSTO) and BSTO with 1 wt% oxide additive. Thin films of BSTO have been deposited by pulsed laser deposition (PLD) onto various oxide and fluoride substrates. These include oxide substrates such as magnesium oxide (MgO), sapphire ( $\text{Al}_2\text{O}_3$ ), lanthanum aluminate ( $\text{LaAlO}_3$ ), neodymium gallate ( $\text{NdGaO}_3$ ), and fluoride substrates such as rubidium manganese fluoride ( $\text{RbMnF}_3$ ). These substrates were selected for their relatively low dielectric constants and good lattice matches to the ferroelectric thin film compound ( $a = 3.94 \text{ \AA}$ ). The substrate / film interfaces, areal film thicknesses and compositional variation have been studied using Rutherford Backscattering Spectroscopy (RBS), and physical thicknesses have been measured using a profilometer. The orientation of the thin films was investigated using glancing angle x-ray diffraction. Various electrodes have been used in order to optimize the electronic properties of the films. These electronic properties were tested at 30 KHz using an HP 4194A impedance analyzer. The measured electronic properties include the dielectric constant, and the tunability (change in the dielectric constant with applied electric field). The electronic properties have been correlated to the results derived from RBS and x-ray data and will be discussed in terms of substrate and electroding optimization.

## INTRODUCTION

Phased array antennas can steer transmitted or received signals either linearly or in two dimensions without mechanically oscillating the antenna. These antennas are currently constructed using ferrite phase shifting elements. Due to the circuit requirements necessary to operate these antennas, they are costly, large and heavy. Therefore, the use of these antennas has been limited primarily to military applications which are strategically dependent on such capabilities. In order to make these devices available for many other commercial and military uses, the basic concept of the antenna must be improved. If ferroelectric materials could be used for the phase shifting element instead of ferrites, phased array antennas could be significantly improved.

A ceramic Barium Strontium Titanate,  $\text{Ba}_{1-x}\text{Sr}_x\text{TiO}_3$ , (BSTO), phase shifter using a planar microstrip construction has been demonstrated [1]. In order to meet the required performance specifications, maximum phase shifting ability, the electronic properties in the low frequency (KHz) and microwave regions (GHz) must be optimized. As part of this optimization process, various composites of BSTO and non-ferroelectric oxides have been formulated.

In order to obtain higher operating frequencies and to decrease the voltage requirements, thin film fabrication of the above candidate materials is necessary. This paper outlines preliminary work on the PLD of undoped and modified BSTO on various substrates. The substrate / film interface and the compositional analysis of the films have been obtained using RBS. Glancing angle x-ray diffraction has been used to determine the orientation of the

films. Various electroding combinations were used in order to optimize the electronic properties of the films and these properties were measured for some of the films using an HP 4194A impedance analyzer. The results of these measurements will be discussed and correlated to the RBS and x-ray diffraction data.

## EXPERIMENTAL

The PLD was accomplished using a krypton-fluoride excimer laser with a wavelength of 248 nm and a repetition rate of 10 Hz. The average pulse energy was 300 mJ with a 20 ns pulse width. The oxygen partial pressure in the chamber was 150 mT and the substrate temperature was  $520^\circ\text{C}$ , which was monitored by a thermocouple clamped between the heater and the substrate. The substrate was parallel to target and their separation distance was maintained at 48 mm. The ceramic targets were prepared according to a description published previously [2].

The lattice parameters and dielectric constants of the substrates used in this experiment are listed in Table 1. Prior to PLD, the substrates underwent a cleaning cycle which included an ultrasonic cycle of TCE followed by two methanol ultrasonic cycles. The samples were then rinsed with methanol and air dried.

**Table 1.** Relevant physical parameters of the single crystals used as substrates

	SUBSTRATE				
	MgO	$\text{Al}_2\text{O}_3$	$\text{LaAlO}_3$	$\text{NdGaO}_3$	$\text{RbMnF}_3$
Lattice parameter ( $\text{\AA}$ )	4.21	4.76	3.79	3.84	4.24
Dielectric constant (300K)	10	11	23	20	15

The targets chosen for this report were  $\text{Ba}_{0.6}\text{Sr}_{0.4}\text{TiO}_3$  (BSTO), BSTO with 1 wt.% alumina and BSTO with 1 wt.% of an additive oxide, referred hereafter as oxide III. A Dektak-200 profilometer was used to measure the films thickness which was approximately 5000  $\text{\AA}$  on all the substrates.

In order to measure the electronic properties of the films, two different ground plane electrodes were used. For the first system, the Ti/Pt electrode were sputtered sequentially with a Xe ion Zymet Z-100 ion implantation unit. A target angle of  $30^\circ$  with respect to the incident beam was used. The thickness of the sputtered Ti layer was 1000  $\text{\AA}$  and the thickness of the overlying Pt layer was 1500  $\text{\AA}$ . For the second system, Ruthenium oxide ( $\text{RuO}_2$ ) was sputtered onto the substrates at a substrate temperature of  $200^\circ\text{C}$  and a  $\text{O}_2/\text{Ar}$  ratio of 1:4 with a total pressure of 10 mT. The Ruthenium oxide films were 3000  $\text{\AA}$  thick. The resistivity of the as-deposited films were in the order of 160  $\mu\text{ohms-cm}$ . They were annealed at  $600^\circ\text{C}$  for 30 minutes to lower the resistivity and were cooled by furnace quenching. The resistivity of the annealed films were measured to be 110  $\mu\text{ohms-cm}$ . The thicknesses of the top electrodes were measured to be

approximately 3000 Å using a Dektak-200 profilometer. The metallized films used for the electrical measurements were: (1) Sapphire / Ti/Pt / BSTO with 1 wt% alumina / Au, (2) Sapphire / RuO<sub>2</sub> / BSTO / Au and (3) Sapphire / RuO<sub>2</sub> / BSTO with 1 wt% oxide III / Au. The thickness of film (1) was measured to be 8000 Å while the thickness of combinations (2) and (3) was measured to be about 6000 Å.

The RBS technique used involve the acceleration of He<sup>+</sup> ions to 2 MeV by a National Electrostatics Corporation (NEC) tandem pelletron accelerator. This He<sup>+</sup> ion beam is collimated to a 1 mm diameter beam which is incident upon the film/crystal substrate. The scattered helium ions were detected at a backscattering angle of 170° with a surface barrier detector with a system energy resolution of 20 to 25 KeV. The energy detection system is calibrated with a standard prior to data acquisition. The elements in the crystal are determined from the detected energies of the backscattered ions which are related to the mass of the atoms. The composition of the films/crystals were obtained by utilizing the software program RUMP to fit the data [3].

The glancing angle x-ray measurements were performed using a Rigaku RU 200 rotating anode x-ray diffractometer. The entrance slit had a width of 0.2° and the angle of incidence of the Cu Kα (λ=1.5415 Å) beam was set at 1°. The sample interval was 0.02° and the scan rate was 9°/minute.

The dielectric constants (ε') and % tunability were determined for all thin film/substrate combination. The % tunability of a material is determined using the following equation:

$$\% \text{ tunability} = \{ \epsilon'(0) - \epsilon'(\text{Vapp}) \} / \{ \epsilon'(0) \} \quad (1)$$

The tunability measurements were taken with an applied electric field which ranged from 0 to +/- 8.0 V/micron (μm). The electronic properties were measured at a frequency of 30 KHz. Capacitance versus voltage (C-V) measurements for the films were taken using an HP4194 impedance / phase gain analyzer. The voltage was applied internally through the HP 4194A and was varied from -8.0 V to +8.0 V.

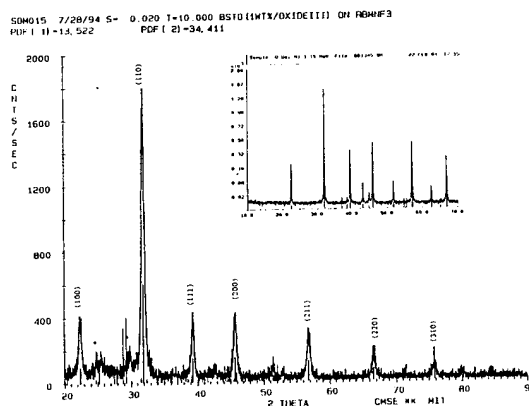
## RESULTS AND DISCUSSION

### Glancing Angle X-ray Results

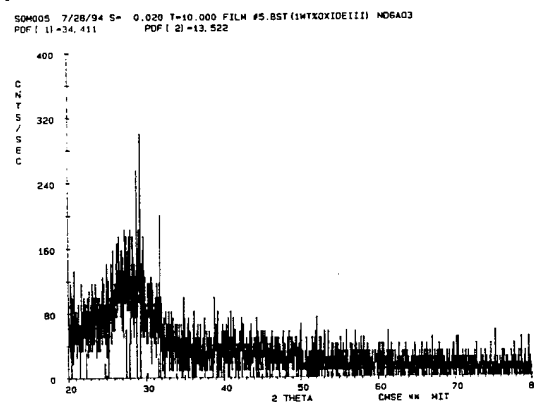
**Bare Substrates:** The glancing angle x-ray diffraction pattern (GAXRD) for the BSTO / 1wt% oxide III film deposited on RbMnF<sub>3</sub> is shown in Figure 1. As shown in the figure, all of the x-ray peaks match the peaks of the of the target material, which is shown in the inset. However, there is evidence of the presence of a small amount of a secondary Ba-rich (Ba<sub>1.91</sub>Sr<sub>0.09</sub>TiO<sub>4</sub>) phase. The preferred (110) orientation of the film is indicated by the relative intensity of the (110) peak as shown in the x-ray pattern.

Fig. 2 shows the GAXRD of BSTO/1 wt% oxide III deposited on NdGaO<sub>3</sub>. The pattern does not show a good match with the target material and is indicative of an amorphous film. We observed the same type of amorphous film quality for the BSTO / Oxide III deposited on LaAlO<sub>3</sub>.

**Metallized Films:** Fig. 3 shows the GAXRD pattern for the BSTO (with 1 wt.% alumina) film deposited on the platinized sapphire substrate. The inset shows the powder diffraction pattern of the target material. It was observed from the x-ray pattern of the target that a secondary phase (Ba<sub>3</sub>Al<sub>10</sub>TiO<sub>20</sub>) is present. As shown in the figure the dominant peak for the pattern is the (220) peak. The slight systematic shift in the position of the peaks may be attributed to the change in the lattice parameter of the material due to the dopant.



**Figure 1.** Glancing angle x-ray diffraction pattern of BSTO / 1wt.% oxide III film deposited on RbMnF<sub>3</sub>. Inset shows x-ray pattern of the target material.



**Figure 2.** Glancing angle x-ray diffraction pattern of BSTO / 1wt.% oxide III film deposited on NdGaO<sub>3</sub>.

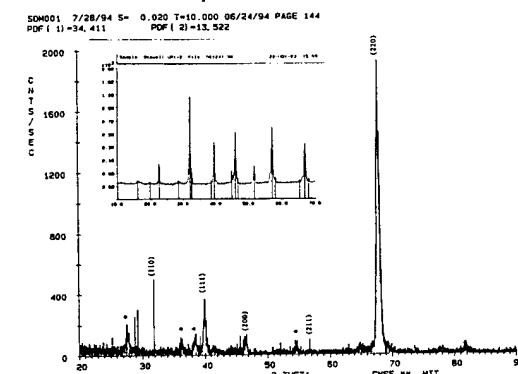


**Figure 3.** Glancing angle x-ray diffraction pattern for the BSTO (with 1 wt.% alumina) film deposited on the platinized sapphire substrate. The inset shows the powder diffraction pattern of the target material.



In Fig 4, the GAXRD pattern of the BSTO (with 1 wt.% oxide III) film deposited on the  $\text{RuO}_2$ /sapphire substrate is shown. The inset is the x-ray pattern of the BSTO target material. The pattern does not indicate the presence of any secondary phase. The peaks located at  $28.1^\circ$  and  $54.2^\circ$   $2\theta$  positions are those of  $\text{RuO}_2$ .

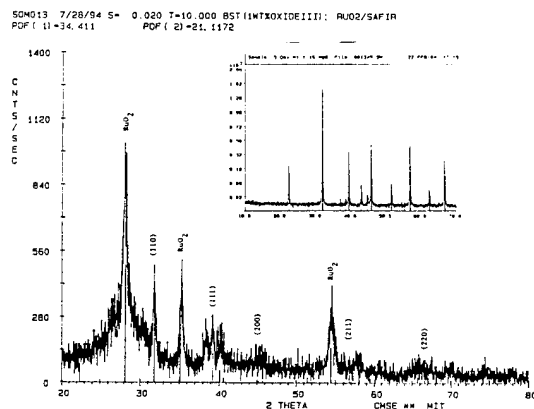


**Figure 4.** Glancing angle x-ray diffraction pattern of the BSTO (with 1 wt.% oxide III) film deposited on the  $\text{RuO}_2$ /sapphire substrate is shown. The inset is the x-ray pattern of the ceramic target.

#### SEM EDS Results

The presence of a secondary phase in the films evident from the x-ray patterns discussed above were confirmed by SEM/EDS results. The secondary Ba-rich phase in the BSTO/oxide III film deposited on  $\text{RbMnF}_3$  is evident from the light areas in the SEM micrograph shown in Fig. 5. The x mark shows the location of this Ba-rich phase confirmed by EDS. Figure 6 contains the SEM micrograph of the BSTO/Alumina thin film deposited on platinized sapphire. The presence of a secondary phase in the material is revealed in the micrograph by the small light regions. EDS performed on these areas also indicated the presence of a Ba-rich phase as well as the presence of a segregated strontium deficient titanate phase. This type of segregation was also observed in the bulk ceramic used as the ablation target.

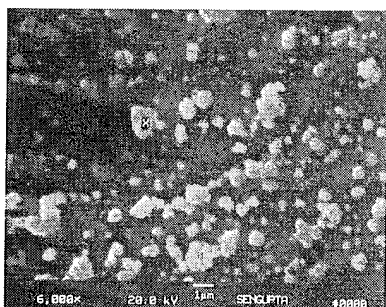


**Figure 5.** SEM micrograph of BSTO/1 wt.% oxide III film deposited on  $\text{RbMnF}_3$ .

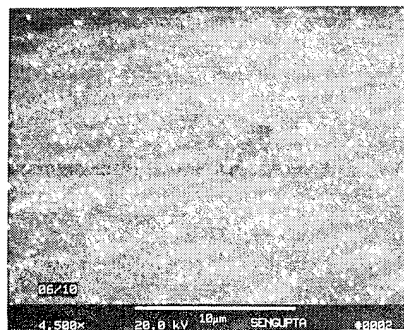


**Figure 6.** SEM micrograph of BSTO/1 wt.% alumina film deposited on platinized sapphire.

#### RBS Results

Fig. 7, shows the RBS spectrum of BSTO / 1 wt.% oxide III film deposited on  $\text{NdGaO}_3$ . The dotted line is the experimental data, while the solid line represents the theoretical fit to the data using RUMP simulation code. The data was fit by subtracting the RBS spectrum of the substrate from the spectrum of the BSTO/ 1 wt.% oxide III film deposited on the substrate and by assuming a composition of  $\text{Ba}_{0.6}\text{Sr}_{0.4}\text{TiO}_3$  (1wt.% oxide III) for the film. The goodness of the fit indicates that the film has a composition close to that of the ceramic target which was  $\text{Ba}_{0.6}\text{Sr}_{0.4}\text{TiO}_3$  (1wt.% oxide III). However, GAXRD shown in Fig. 2 reveals that the film is noncrystalline.

The RBS spectra of the BSTO films deposited on the other substrates also show close agreement of the thin film elemental composition with that of the original ceramic target.

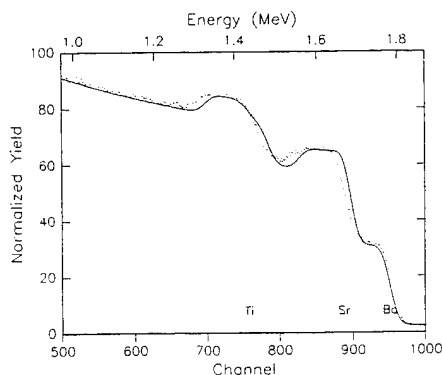


**Figure 7.** RBS spectrum of BSTO / 1 wt.% oxide III film deposited on  $\text{NdGaO}_3$ , [Experimental data (dotted line) and RUMP fit (solid line)].

#### Electronic Measurements

Fig. 8, shows the capacitance versus voltage characteristics for the BSTO (undoped) film deposited on  $\text{RuO}_2/\text{MgO}$ . The curve shows a symmetric capacitance-voltage relationship which is characteristic of paraelectric films. The dielectric constant at zero bias was calculated to be 1474 and the tunability is 88 % at a field of  $7.5 \text{ V}/\mu\text{m}$ . The bulk undoped material has a dielectric constant of 3300 and a tunability of 20 % at  $0.73 \text{ V}/\mu\text{m}$ . It has been previously shown that the dielectric constant in ferroelectric

films are inherently less than the bulk ceramics due to oxygen defects at the electrode/ film interface [4]. Also any porosity and/or leakage current in the films will tend to decrease the dielectric constants obtained.

The C-V curve for the BSTO/ 1wt.% alumina film deposited on platinized sapphire is shown in Fig. 9. The curve shows a typical paraelectric behavior, (i.e. a symmetric capacitance), with positive and negative bias applied. The dielectric constant at zero voltage calculated from this curve is 189. The tunability obtained up to 6.3 V/ $\mu\text{m}$  was 40%. The value for the dielectric constant found in the bulk ceramic target of BSTO/ 1 wt.% alumina was 2607 and a tunability of 46% at 2.7 V/ $\mu\text{m}$ . The low value for the dielectric constant in the film relative to that in the bulk ceramic target may be attributed to the porosity of the film, the presence of leakage current (on the order of  $10^{-5}$  A) and also to the segregation of the secondary phase as was shown in Fig. 6.

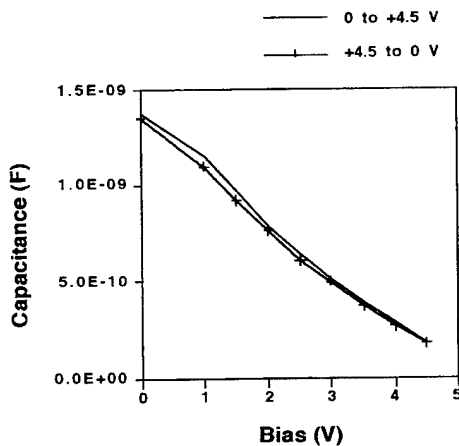


Figure 8. Capacitance versus voltage for BSTO (undoped) deposited on  $\text{RuO}_2$  /  $\text{MgO}$  with Pt top electrode.

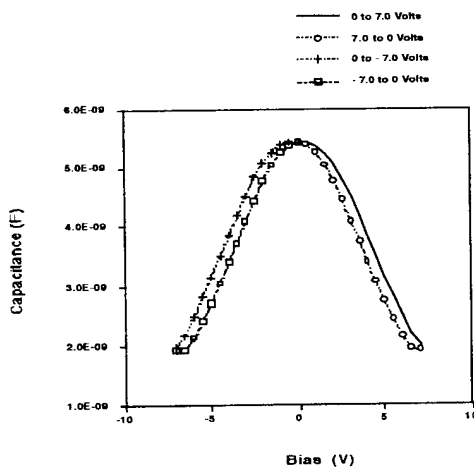


Figure 9. Capacitance versus voltage for BSTO / 1 wt.% alumina deposited on platinized sapphire with Au top electrode.

The capacitance versus voltage for the BSTO/1 wt.% oxide III film deposited on  $\text{RuO}_2$ /sapphire is shown in Fig. 10. This curve also shows the typical paraelectric behavior of symmetric

capacitance versus voltage behavior. The value for the zero voltage dielectric constant is 398 and the tunability is 79% at 2.0 V/ $\mu\text{m}$ . The bulk ceramic dielectric constant was 1276 and the tunability was 16% with 2.3V/ $\mu\text{m}$ . The decreased value of the dielectric constant in the film is again attributed to the porosity of the film and the leakage current observed in the film.

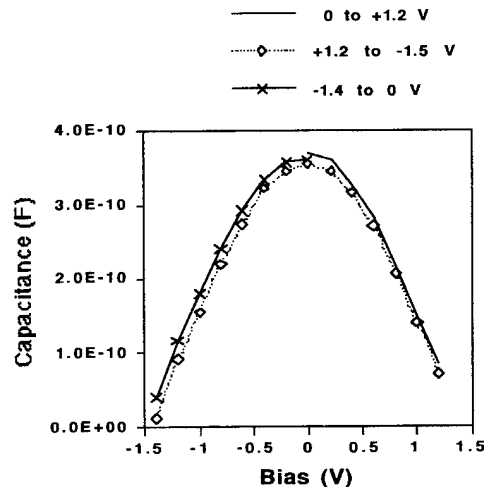


Figure 10. Capacitance versus voltage for BSTO / 1 wt.% oxide III deposited on  $\text{RuO}_2$  / sapphire with Au top electrode.

#### CONCLUSION

Thin films of both undoped and oxide modified BSTO have been deposited by PLD onto oxide and fluoride substrates. It was shown that in case of  $\text{RbMnF}_3$  the film was preferentially oriented and contained a secondary phase. The film deposited on  $\text{NdGaO}_3$  was amorphous; however, RBS confirmed a good agreement of film composition relative to the target materials. The BSTO/1wt.% alumina film deposited on the platinized substrate showed similar phase segregation as the ceramic material. The oxide modified film deposited on  $\text{RuO}_2$ /sapphire substrate did not show any evidence of a secondary phase. The electronic properties of the undoped and oxide modified BSTO thin films exhibited similar behavior relative to the bulk material. The dielectric constant and the tunability of the undoped BSTO film are higher than that of the doped films.

We have shown that the tailoring of the electronic properties of BSTO thin films is possible through the incorporation of metal oxides. Further investigation of such tailoring through the incorporation of other oxides is underway.

#### ACKNOWLEDGMENTS

The authors would like to thank A. Kirkpatrick of Epion Corp., Bedford, MA, N. Sonnenburg of CPRL, M.I.T., A. Cassanho, CMSE, M.I.T., R. Shehagian of Implant Sciences, Wakefield, MA and P.Wong of ARL, for their help.

#### REFERENCES

- [1] R.W. Babbitt, T. E. Kosica, and W.E. Drach, "Planar Microwave Electro-optic Phase Shifters," *Microwave Journal*, vol. 35, pp. 63-79, June 1992.
- [2] L.C. Sengupta, S. Stowell, E. Ngo, M.E. O'Day and R. Lancto, *J. of Integrated Ferroelectrics*, in press, (1994).
- [3] L.R. Doolittle, *Nuclear Instru. Meth.*, vol B9, p. 334 (1985).
- [4] C.J. Brennan, *Integrated Ferroelectrics*, vol. 2, pp.73-82 (1992).

# CHARACTERIZATION OF SPUTTER-DEPOSITED (Ba,Sr)TiO<sub>3</sub> THIN FILMS ON THE SIDEWALLS OF FINE-PATTERNED ELECTRODES

Shintaro Yamamichi, Koichi Takemura, Toshiyuki Sakuma, Hirohito Watanabe\*,  
Haruhiko Ono\*, Ken Tokashiki\*, Eiji Ikawa\* and Yoichi Miyasaka

Fundamental Research Laboratories, NEC Corporation  
4-1-1 Miyazaki, Miyamae-ku, Kawasaki, 216 Japan

\*ULSI Device Development Laboratories, NEC Corporation

\*1120 Shimokuzawa, Sagamihara, 229 Japan

## ABSTRACT

The dielectric properties of high dielectric constant thin films on the electrode sidewalls were evaluated for the first time, and sputter-deposited (Ba,Sr)TiO<sub>3</sub> thin films were characterized on the sidewalls of RuO<sub>2</sub> electrodes patterned down to submicron sizes. A fairly large step coverage around 50 % was obtained for (Ba,Sr)TiO<sub>3</sub>. The  $\epsilon_r$  value for (Ba,Sr)TiO<sub>3</sub> films on the sidewalls was the same as that for the films on the top surface, but the leakage current was larger. The (Ba,Sr)TiO<sub>3</sub> films on the sidewalls were found to be well-crystallized, however, the grain size was smaller, and a porous structure was observed by TEM analysis.

## INTRODUCTION

Recently, high dielectric constant materials, such as SrTiO<sub>3</sub>, (Ba,Sr)TiO<sub>3</sub> (BST), and (Pb,Lu)(Zr,Ti)O<sub>3</sub> have attracted great interest for application to cell capacitors of dynamic random access memories (DRAMs). Because of their higher dielectric constant ( $\epsilon_r$ ) than SiO<sub>2</sub> or Si<sub>3</sub>N<sub>4</sub>, the cell capacitor structure could be simplified from a complex three-dimensional structure to a flat one, which is easier to fabricate. The dielectric properties of high  $\epsilon_r$  thin films with a flat structure have been widely reported, and in some reports, real capacitor structures have also been proposed<sup>1</sup>. Films with SiO<sub>2</sub> equivalent thicknesses less than 0.5 nm and low leakage current characteristics have also been reported<sup>2-5</sup>. However, for gigabit generation DRAMs, the storage capacitance density obtained with a flat structure will not be sufficient, unless an SiO<sub>2</sub> equivalent thickness less than 0.1 nm is obtained. Presently, the capacitance density is limited because of the thickness dependence of  $\epsilon_r$ , that is,  $\epsilon_r$  decreases with decreasing film thickness. As the sidewall surface of storage electrodes will become larger than the top surface for an electrode height more than 100 nm in Gigabit-scale DRAMs, it is also very important to investigate the feasibility of fabricating a three-dimensional structure with high  $\epsilon_r$  thin films.

Before considering the total three-dimensional structure, we should first characterize high  $\epsilon_r$  thin films on the electrode sidewalls. For this purpose, it is necessary to make conductive bottom electrodes, which are thick enough and patterned finely enough to evaluate the influence of the sidewalls. Platinum is often selected as the electrode material, however, etching of platinum thicker than 100 nm without residues, which usually cause an increase in the leakage current, is very difficult. In this study, we selected ruthenium oxide (RuO<sub>2</sub>) as bottom electrodes, because we found that it can easily be patterned by electron cyclotron resonance (ECR)

plasma etching, as shown in Fig. 1. As the details of RuO<sub>2</sub> etching will be reported elsewhere, only two important points are reported here. One is that RuO<sub>2</sub> is reactively etched with a gas mixture of oxygen and an halogen. Therefore, no residues are observed, and the etching is well controlled so that we can stop the etching in the middle of the RuO<sub>2</sub> layer. By patterning

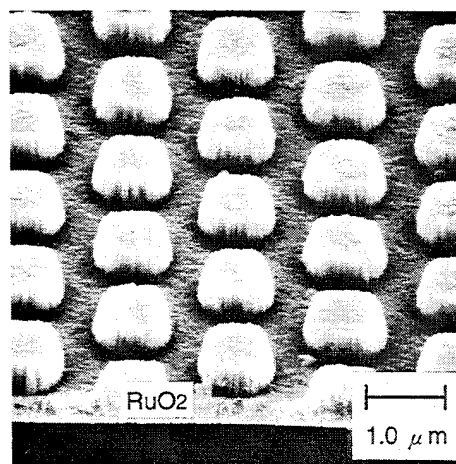


Fig. 1. SEM micrograph of the RuO<sub>2</sub> patterned surface

RuO<sub>2</sub> to submicron sizes, the sidewall area can be increased relatively to the top surface area. The other point is that RuO<sub>2</sub> sidewalls are slightly tapered after the etching is stopped in the middle of the RuO<sub>2</sub> layer. Therefore we expect that a good lateral step coverage can be obtained even for BST films prepared by sputtering. In this paper, the characterization of BST thin films on RuO<sub>2</sub> electrode sidewalls is described.

## EXPERIMENTAL

The sample has a metal-insulator-metal structure as shown in Fig. 2. First, RuO<sub>2</sub>(1000 nm)/TiN(50 nm) double layers were deposited on Si(100) substrates by dc magnetron sputtering at room temperature and 200 °C, respectively. Then, a resist was deposited and patterned to four sizes of 0.6×0.6, 0.8×0.8, 1.0×1.0, and 2.0 μm ×2.0 μm squares on one wafer by photolithography. The number of square patterns was also changed on one wafer from 2025 to 7400 for each capacitor area. Next, by stopping the RuO<sub>2</sub> etching at a depth of 650 nm, patterned electrodes were fabricated. A large flat area of RuO<sub>2</sub> remained on the same wafer in order to fabricate capacitors with a flat structure. The RuO<sub>2</sub> etching rate was very large more than 200 nm/min, almost twenty times larger than previously reported values<sup>6</sup>, and very good reproducibility and

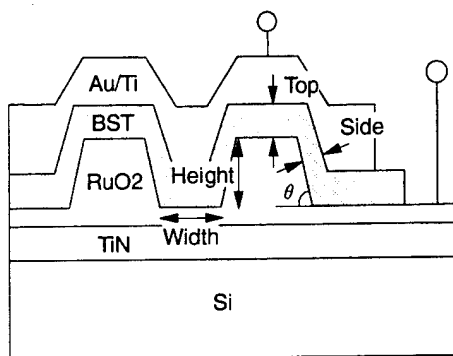


Fig. 2. Schematic view of the sample.

uniformity of the  $\text{RuO}_2$  etching depth were obtained. After removing the resist, BST thin films were deposited by rf magnetron sputtering. The detailed conditions have already been reported in a previous publication<sup>7</sup>. The target was a powder of  $(\text{Ba}_{0.5}\text{Sr}_{0.5})\text{TiO}_3$ , and the substrate temperature was kept at 650 °C during deposition. The BST thicknesses on the  $\text{RuO}_2$  top surface were 100, 150, and 200 nm. Finally, the top electrode was deposited by dc magnetron sputtering, and patterned to the projected area of 0.029 mm<sup>2</sup> by wet etching. The electrical measurements and structural analysis were performed with Au(300 nm)/Ti(150 nm) and Al(750 nm)/TiN(150 nm) electrodes, respectively. For electrical measurements, BST was removed in some part of the wafer by wet etching to expose the  $\text{RuO}_2$  surface as the bottom electrode, as shown in Fig. 2.

Two parameters were defined as follows: the aspect ratio was defined as the ratio of the  $\text{RuO}_2$  step height to the pattern width, and the lateral step coverage was defined as the ratio of the BST thickness on  $\text{RuO}_2$  sidewalls to that on  $\text{RuO}_2$  top surface. Both parameters were evaluated on cross sectional SEM pictures. Attentions should be paid when calculating the sidewall area, because the initial  $\text{RuO}_2$  height of 650 nm is not the effective electrode step height. It should rather be the result of subtraction of the BST deposited thickness from the initial step height. Capacitance and  $\tan\delta$  values were measured in the 100-Hz to 10-MHz frequency range with a Hewlett-Packard 4194A impedance analyzer. The dielectric constant was calculated from the capacitance value at 10 kHz. Current-voltage characteristics were measured with a Keithley 617 electrometer.

## RESULTS AND DISCUSSION

A cross-sectional SEM micrograph is shown in Fig. 3.

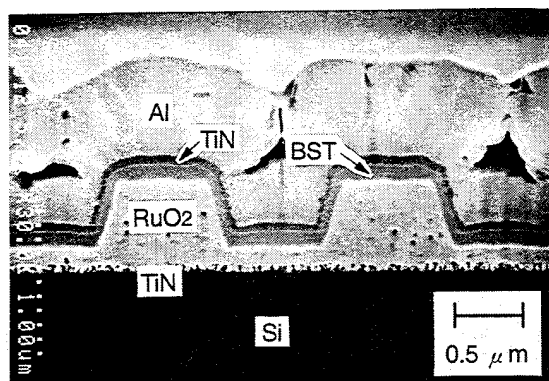


Fig. 3. Cross-sectional SEM micrograph

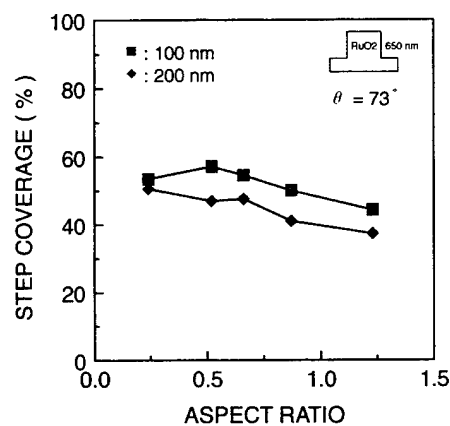


Fig. 4. Step coverage as a function of the aspect ratio

Fine etching of  $\text{RuO}_2$  and good step coverage of BST were successfully obtained. Hereafter in this paper, BST films on the top/bottom and the sidewall surfaces of the patterned  $\text{RuO}_2$  electrodes are referred as top-BST and side-BST, respectively. BST films in the capacitors with a flat structure are called flat-BST.

The step coverage is shown in Fig. 4 as a function of the aspect ratio for 100 and 200 nm thick BST. Though it slightly decreases with increasing aspect ratio, fairly large values from 40 to 55 % are obtained for BST films prepared by sputtering. This is partly because  $\text{RuO}_2$  sidewalls have a tapered angle of 73°, which is constant for an aspect ratio from 0.25 to 1.25.

The frequency dependence of the capacitance and  $\tan\delta$  for both flat and patterned structures is shown in Fig. 5. The top-BST thickness is 200 nm. The top and bottom  $\text{RuO}_2$  surfaces had the same value of 0.029 mm<sup>2</sup> for both structures, and the patterned structure had a total electrode area of 0.040 mm<sup>2</sup> by adding the sidewall area of 0.011 mm<sup>2</sup>. There is no frequency dispersion for the capacitance, and  $\tan\delta$  is low, below 0.1. The increase in  $\tan\delta$  at a frequency higher than 1 MHz is only due to the contact resistance between the probe and electrode. The increase in the capacitance, which is due to the contribution of the capacitance of side-BST, is clearly observed. The capacitance measured at 10 kHz is shown in Fig.

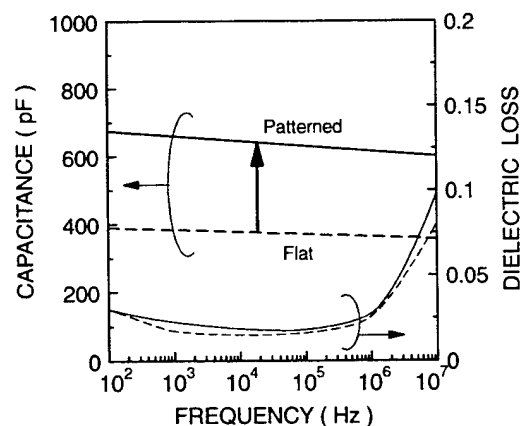


Fig. 5. Frequency dependence of the capacitance and  $\tan\delta$

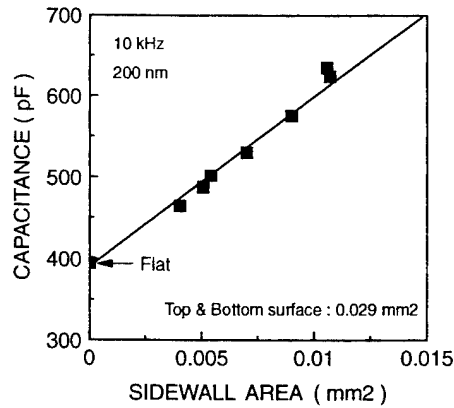


Fig. 6. Measured capacitance as a function of the sidewall area

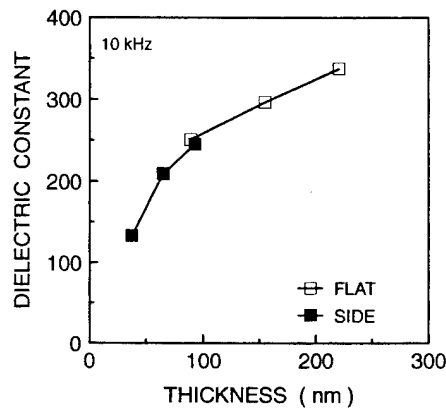


Fig. 7. Thickness dependence of  $\epsilon_r$  for top- and side-BST

6 as a function of the sidewall area for this sample. The top and bottom  $\text{RuO}_2$  surface area was also kept at  $0.029 \text{ mm}^2$ . As the capacitance and sidewall area show a good linear relationship, it is considered again that the measured capacitance increases because of the contribution of side-BST. From Fig. 6, we can evaluate the  $\epsilon_r$  value for side-BST, independently of that for top-BST. We call this  $\epsilon_r(\text{side})$ . As it can be considered that flat-BST and top-BST have the same thickness and same  $\epsilon_r$  value, we call the  $\epsilon_r$  value for top-BST  $\epsilon_r(\text{flat})$ . First, we calculated the capacitance difference between the flat and patterned structures for each value of the sidewall area, and then, calculated  $\epsilon_r(\text{side})$  according to the following formula:

$$C(\text{patterned}) - C(\text{flat}) = \epsilon_0 \cdot \epsilon_r(\text{side}) \cdot S / d$$

,where  $S$  is the sidewall area, and  $d$  is the side-BST thickness

Finally, we determined  $\epsilon_r(\text{side})$  by calculating the average value. Three  $\epsilon_r(\text{side})$  values were calculated for side-BST with thicknesses of 50, 75, and 100 nm, which were half the values of flat-BST thicknesses of 100, 150, 200 nm, respectively. Both  $\epsilon_r(\text{side})$  and  $\epsilon_r(\text{flat})$  values are plotted in the same graph, as shown in Fig. 7. At the thickness of 100 nm,  $\epsilon_r(\text{side})$  and  $\epsilon_r(\text{flat})$  show the same large values of 250. A continuous

thickness dependence is obtained for both  $\epsilon_r$  values, and the overall dependence is similar to that obtained for BST on the flat structure. These results clearly show that high  $\epsilon_r$  BST thin films can be fabricated on the electrode sidewalls.

However, the leakage current was larger for the patterned structure. The current-voltage characteristics for the flat and patterned structures are shown in Fig. 8. To compare the leakage currents, the flat-BST and side-BST thickness have the same values of 100 nm. The leakage currents are low about  $1 \times 10^{-8} \text{ A/cm}^2$  at less than 0.8 V for both structures, but the current for the patterned structure increases at a lower voltage than that for the flat structure. There are two possible reasons why the leakage current increases. One is because side-BST itself is leaky. The other is because some particular points due to the patterned structure, such as the top or bottom corner of  $\text{RuO}_2$ , exist as a major path of the leakage current. To investigate the degradation mechanism for the patterned

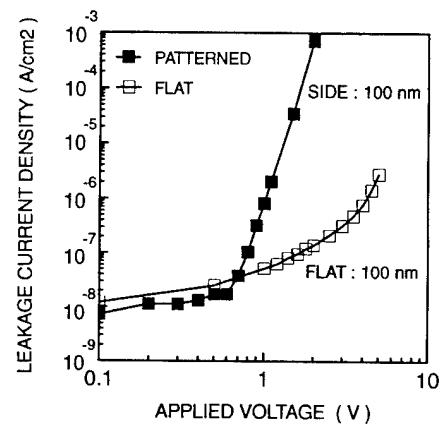


Fig. 8. I-V characteristics for the flat and patterned

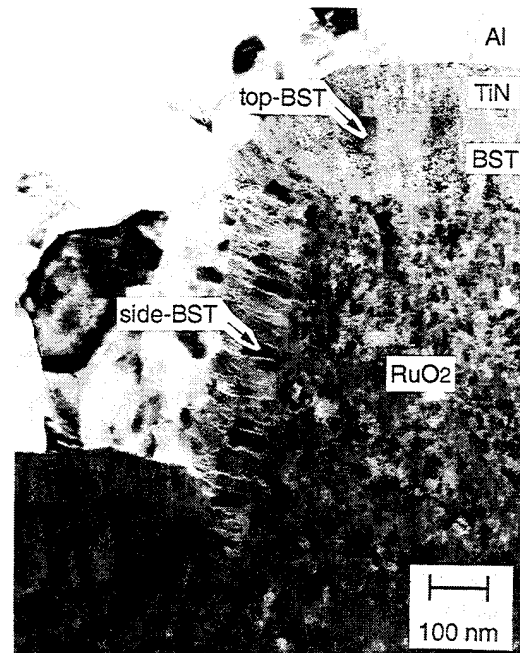


Fig. 9. Cross-sectional TEM micrograph for BST

structure, the leakage current was plotted as a function of the sidewall area, and it increased linearly with increasing sidewall area. This relationship supports the first explanation, however, further investigation of the structural effects is necessary.

The high resolution TEM micrograph of BST films on the patterned RuO<sub>2</sub> is shown in Fig. 9. It is found that side-BST is as well crystallized as top-BST, however, the grain size is around 25 nm, smaller than the 50 nm observed for top-BST. The most important point is that side-BST has a porous structure, although top-BST has a dense structure. From Figs. 6, 7, and 8, we can conclude that side-BST is well crystallized and each side-BST grain has an  $\epsilon_r$  value as high as for top-BST grains, but the leakage current is larger because of the porous structure. It is necessary to investigate more suitable deposition conditions in order to obtain high quality side-BST with a dense structure.

#### CONCLUSION

We extracted and evaluated the dielectric properties of high  $\epsilon_r$  thin films on electrode sidewalls for the first time, and characterized sputter-deposited (Ba,Sr)TiO<sub>3</sub> thin films on RuO<sub>2</sub> sidewalls patterned down to submicron sizes. A fairly large step coverage around 50 % was obtained for BST. The  $\epsilon_r$  value for side-BST was the same as that for flat-BST, but the leakage current increased. The side-BST was found to be well-crystallized, however, it had smaller grain size and a porous structure by TEM analysis.

#### ACKNOWLEDGMENTS

The authors would like to thank Dr. R. Lang, Dr. M. Kamoshida, Dr. N. Shohata, Dr. A. Ishitani, and Dr. N. Endo for their continuous encouragements. The authors also thank Dr. M. Yoshida, Dr. P-Y. Lesaichere, H. Yamaguchi, S. Sone, K. Amanuma, T. Hase, and H. Yabuta for valuable discussions and S. Adachi, J. Sone, M. Noguchi, M. Seki, K. Sato, N. Tawarayama, and A. Yamamichi for sample preparation and electrical measurements.

#### REFERENCES

- [1] A lot of papers have been presented, for example:  
K. Koyama, T. Sakuma, S. Yamamichi, H. Watanabe, H. Aoki, S. Ohya, Y. Miyasaka, and T. Kikkawa, "A Stacked Capacitor with (Ba<sub>x</sub>Sr<sub>1-x</sub>)TiO<sub>3</sub> for 256M DRAM", IEDM Tech. Dig., pp823-826, 1991,  
  
E. Fujii, Y. Uemoto, S. Hayashi, T. Nasu, Y. Shimada, A. Matsuda, M. Kibe, M. Azuma, T. Otsuki, G. Kano, Mo. Scott, L. D. McMillan, and C. A. Paz de Araujo, "ULSI DRAM Technology with Ba<sub>0.7</sub>Sr<sub>0.3</sub>TiO<sub>3</sub> Film of 1.3 nm Equivalent SiO<sub>2</sub> Thickness and 10<sup>-9</sup> A/cm<sup>2</sup> Leakage Current", IEDM Tech. Dig., pp267-270, 1992
- [2] T. Eimori, Y. Ohno, H. Kimura, J. Matsuhisa, S. Kishimura, A. Yoshida, H. Sumitani, T. Maruyama, Y. Hayashide, K. Moriizumi, T. Katayama, M. Asakura, T. Horikawa, T. Shibano, H. Itoh, K. Sato, K. Namba, T. Nishimura, S. Satoh, and H. Miyoshi, "A newly

Designed Planar Stacked Capacitor Cell With High dielectric Constant Film for 256M DRAM, IEDM, Tech. Dig., pp631-634, 1993

- [3] Y. Ohno, T. Horikawa, H. Shinkawata, K. Kashihara, T. Kuroiwa, T. Okudaira, Y. Hashizume, K. Fukumoto, T. Eimori, T. Shibano, K. Arimoto, H. Itoh, T. Nishimura, and H. Miyoshi, "A Memory Cell Capacitor with Ba<sub>x</sub>Sr<sub>1-x</sub>TiO<sub>3</sub> (BST) Film for Advanced DRAMs", Symp. on VLSI, Tech. Dig., pp149-150, 1994
- [4] J. Kim, R. Khamankar, C. Sudhama, B. Jiang, J. Lee, P. Maniar, R. Moazzami, R. Jones, C. J. Mogab, "La Doped PZT Films for Gigabit DRAM Technology", Symp. on VLSI, Tech. Dig., pp151-152, 1994
- [5] S. Hayashi, M. Huffman, M. Azuma, Y. Shimada, T. Otsuki, G. Kano, L. D. McMillan, and C. A. Paz de Araujo, "Gigabit-Scale DRAM Capacitor Technology with High Dielectric Constant thin Films by A Novel Conformal Deposition Technique", Symp. on VLSI, Tech. Dig., pp153-154, 1994
- [6] S. Saito and K. Kuramasu, "Plasma Etching of RuO<sub>2</sub> Thin Films", Jpn. J. Appl. Phys., vol.31, pp135-138, 1992
- [7] K. Takemura, T. Sakuma, and Y. Miyasaka, "High dielectric constant (Ba,Sr)TiO<sub>3</sub> thin films prepared on RuO<sub>2</sub>/sapphire", Appl. Phys. Lett., vol.64, No.22, pp2967-2969, 1994



# Concurrent Session - 3B: Dielectrics



# A MODEL FOR DESCRIBING CURRENT-VOLTAGE CHARACTERISTICS OF SrTiO<sub>3</sub> CAPACITORS UNDER LOW ELECTRIC FIELDS

Yukio Fukuda, Ken Numata, Katsuhiro Aoki and Akitoshi Nishimura  
ULSI Development & Productization  
Texas Instruments Japan Ltd.  
2350 Kihara, Mihomura, Inashikigun 300-04 Japan.

## Abstract

It is now widely accepted that the well-fabricated SrTiO<sub>3</sub> (STO) thin-film capacitors with high-work-function metallic electrodes show excellent low leakage characteristics. However, the magnitude of the leakage current in the low electric fields shows strong dependences on the measurement conditions, namely the values of voltage-step  $\Delta V$  and delay-time  $t_d$  in the conventional staircase current-voltage ramps. This anomalous effect is attributed to the dielectric relaxation phenomena of the STO capacitor structures. In this paper, we propose a model which describes the relationship between such measurement conditions and observed current-voltage characteristics.

The absorption current due to the dielectric relaxation of the Debye-type relaxation species can be formulated as

$$I(V = j\omega \Delta V) = \Delta V \sum_{i=1}^n (C_i / \tau_i) \exp(-j\omega t_d / \tau_i),$$

where  $C_i$  and  $\tau_i$  respectively denote the capacitance and the relaxation time constant of the  $i$ -th relaxation species. The unknown parameters in the equation,  $C_i$  and  $\tau_i$ , can be determined by applying a multiple nonlinear least squares method to the current-time measurements.

The model was applied to characterize the sputter-deposited STO capacitors which exhibited apparent leakage currents of less than 10 nA/cm<sup>2</sup> for the electric field strengths of less than 1 MV/cm. We observed three kinds of relaxation species for such capacitors. The current-voltage curves calculated based on these relaxation species fit very well with the measured values obtained under the various measurement conditions.

## Introduction

Recently, perovskite-structured oxides such as SrTiO<sub>3</sub> (STO), (Ba<sub>x</sub>Sr<sub>1-x</sub>)TiO<sub>3</sub> and Pb(Zr<sub>x</sub>Ti<sub>1-x</sub>)O<sub>3</sub> have attracted much attention for the charge storage capacitor of ultra large scale integrated circuit memory. Among them, STO is of particular interest because of its paraelectricity even at very low temperatures [1]. The SiO<sub>2</sub> equivalent thickness of as low as 0.9 nm has been achieved for the 53-nm-thick STO film whose dielectric constant is 230 [2]. Additional advantage of the STO film is its low leakage current characteristics. The leakage current density of this film is less than 10 nA/cm<sup>2</sup> at up to 2 V.

To date, there have been a number of published papers which deal with the preparation and dielectric properties of the STO thin films. However, there are very few papers which clearly mentioned the leakage current mechanism [3-6]. This paper describes the current-voltage characteristics of the STO thin films prepared on the Pt electrode by electron-cyclotron-resonance (ECR) sputtering. We will especially focus our efforts on the leakage characteristics and their modeling in the low electric fields where the current-voltage (I-V) characteristics show anomalous phenomena depending on the measurement conditions.

## Experimental

STO thin films were deposited by ECR-sputtering. A cylindrical ceramic target with a stoichiometric composition was used. Sputtering was performed at 0.1 Pa pressure with 50 % Ar and 50 % O<sub>2</sub> gas composition. Supplied rf (13.56 MHz) and microwave (2.45 GHz) powers were 200 W and 400 W, respectively. These conditions resulted in a deposition rate of 2.3 nm/min. The substrate used in this

study was Pt (200 nm) / Ti (50 nm) / SiO<sub>2</sub> (100 nm) / Si. Both Pt and Ti films were deposited on thermally grown SiO<sub>2</sub> coated Si substrate by dc-sputtering. Substrate temperature was kept constant at 400 °C which was monitored with a thermocouple attached to the substrate surface. We confirmed that the Pt and Ti layers were stable at this temperature and their intermetallic reaction or oxidation reaction of Ti were not observed [7].

For electrical measurements, Au electrode with an area of  $9.4 \times 10^{-4}$  cm<sup>2</sup> was deposited on the STO surface through a metal shadow mask by thermal evaporation. I-V characteristics were measured by HP-4142B with staircase voltage ramps. It will be shown that the values of the voltage-step  $\Delta V$  and the measurement delay-time  $t_d$  after applying each voltage-step greatly influence the measurement results. Unless otherwise mentioned, electrical measurements were performed at 25 °C.

## Experimental results

Figure 1 shows a typical I-V characteristic obtained from a 68-nm-thick STO with a positive bias to the Au electrode. Values of  $\Delta V$  and  $t_d$  were 0.1 V and 1 s, respectively. It is shown that there are two regions where the leakage current is almost proportional to the electric field which is lower than about 1 MV/cm, and is proportional to the square root of the electric field in the higher-electric-field region. This result indicates that the I-V characteristics of the STO capacitor can be explained in terms of ohmic conduction [3] in the low-electric-field region, and by Schottky emission [5,8] or Poole-Frenkel conduction [3,4] in the high-electric-field region. However, as described below, it was found that this ohmic-like leakage characteristics changed drastically depending on the measurement parameters  $\Delta V$  and  $t_d$ .

Figures 2(a) and 2(b) respectively show dependences of the leakage characteristics on  $\Delta V$  with  $t_d = 1$  s and on  $t_d$  with  $\Delta V = 0.1$  V. Figure 2(a) shows that the leakage current increases almost linearly with increase in  $\Delta V$ . On the other hand, Fig. 2(b) shows that the leakage current decreases with increase in  $t_d$ . These results indicate that the measured leakage currents were not those in the equilibrium state, and special care should be taken in the leakage current measurements.

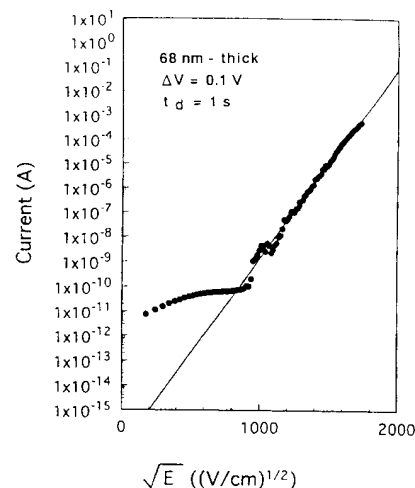


Fig.1. Current vs square root of electric field ( $\sqrt{E}$ ) for 68-nm-thick SrTiO<sub>3</sub> film. Measurement parameters  $\Delta V$  and  $t_d$  are 0.1 V and 1 s, respectively.

Figure 3 shows temperature dependences of the current-time (*I-t*) characteristics measured with an applied voltage  $V_{app}$  of 1 V. It can be seen that the currents decay monotonously with time and do not show any apparent saturation, especially when the temperature is lower than 100°C. This strongly suggests that if the leakage mechanism is considered simply in terms of the temperature dependence of the leakage current without taking account of its time dependence, there is a great possibility of obtaining erroneous conclusion.

The Schottky emission current density  $J$  is expressed as

$$J = A^* T^2 \exp \left[ -q \left( \phi_B - \sqrt{qE/4\pi\epsilon_i} \right) / kT \right], \quad (1)$$

where  $A^*$  is the effective Richardson constant,  $T$  the absolute temperature,  $q$  the elementary charge,  $\phi_B$  the barrier height,  $E$  the electric field strength,  $\epsilon_i$  the insulator dynamic permittivity, and  $k$  the Boltzmann constant [9]. Figure 4 shows the Schottky plots for the currents at a time of 150 s in Fig. 3. Reflecting the nonsaturable characteristics of the leakage currents at lower temperatures, the data deviate from a straight line with decrease in the temperature.  $A^*$  and  $\phi_B$  estimated from the fitted straight line in the figure are 0.49 A/(cm<sup>2</sup> · K<sup>2</sup>) and 0.98 eV, respectively. This barrier height is equal to the value for the applied voltage of 1 V and that for zero bias will be slightly larger if we consider barrier height lowering due to the Schottky effect [9] and the work-function difference between Pt and Au [8]. The barrier height for zero bias can be estimated from the intersection of the fitted straight line in Fig.1 and the effective Richardson constant

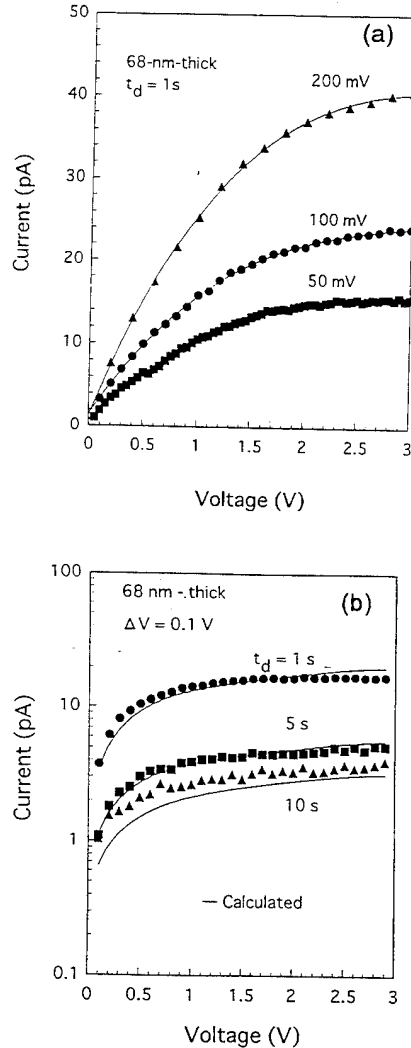


Fig.2. Dependences of leakage characteristics of 68-nm-thick SrTiO<sub>3</sub> film on (a)  $\Delta V$  with  $t_d = 1$  s and on (b)  $t_d$  with  $\Delta V = 0.1$  V. Solid curves shown in (b) are theoretical results obtained for each  $t_d$ .

estimated above. The result is 1.1 eV which agrees well with the barrier height of the Pt / STO interface reported by Abe and Komatsu [5] who used another approach.

The Schottky emission current at 1 V and 25 °C calculated from obtained  $A^*$  and  $\phi_B$  is  $2 \times 10^{-15}$  A. This coincides well with the value of  $8 \times 10^{-15}$  A which was obtained by extrapolating the currents in the high-electric-field region to the corresponding electric field strength of 0.15 MV/cm in Fig.1. This agreement suggests that the overall leakage characteristics are governed by the Schottky emission from the Pt electrode. However, the value of the relative dielectric constant, obtained from the slope of  $\log(I)$  vs  $\sqrt{E}$  in the high-electric-field region in Fig.1, is 0.7. Thus, further investigation should be required to conclude the leakage mechanism. In any case, the ohmic-like leakage current observed in the low-electric-field region may not be a true dc leakage current.

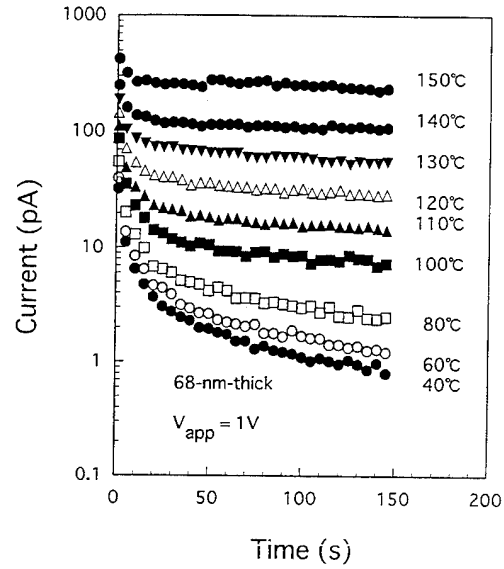


Fig.3. Temperature dependences of current-time characteristics of 68-nm-thick SrTiO<sub>3</sub> film measured with  $V_{app}$  of 1V.

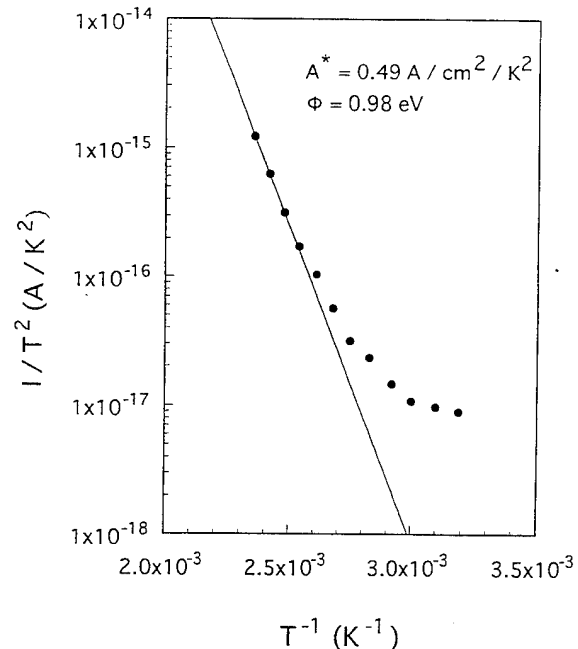


Fig.4. Schottky plots of currents at a time of 150 s in Fig. 3.

Fig.5 shows the  $V_{app}$  dependences of the I-t characteristics obtained from different capacitors. The values of  $V_{app}$  are 1, 2 and 3V, respectively. It is shown that the measured current is almost proportional to  $V_{app}$ , independent of the time.

Fig.6 shows the I-t characteristics of the same capacitor at  $V_{app}=1V$ , where open circle shows the result of the first measurement and the closed circle the result obtained after being retained for ten minutes after the first measurement under the open-circuit condition. It is interesting to note that the monotonously decayed I-t characteristics by the first measurement can be restored by open-circuit retention even at 25 °C, and this result suggests that observed I-t characteristics

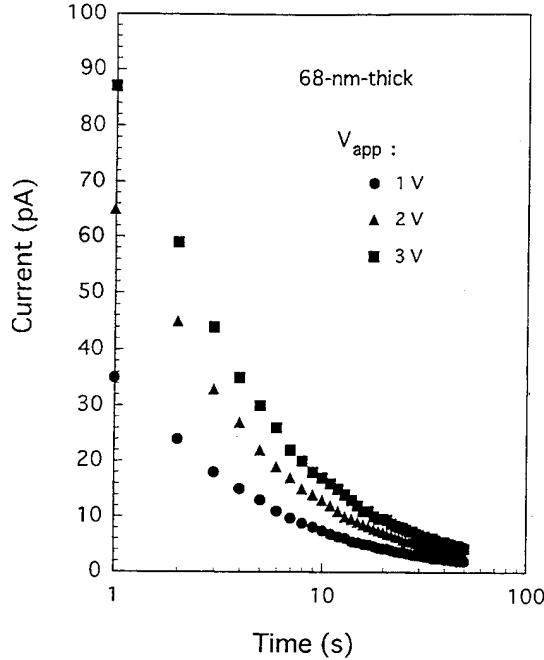


Fig.5.  $V_{app}$  dependences of current-time characteristics obtained from different capacitors.

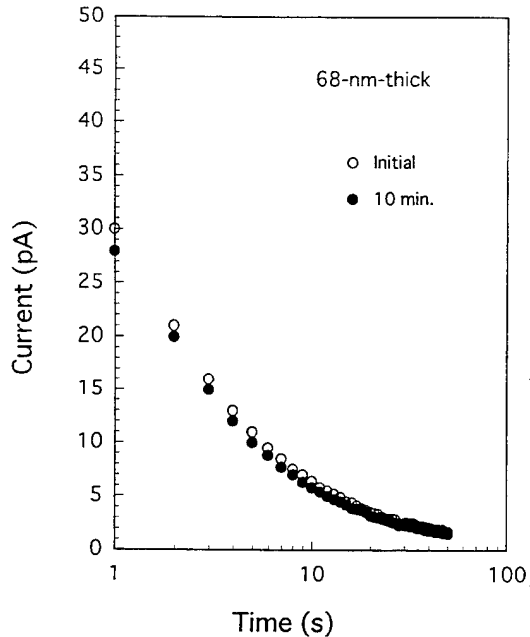


Fig.6 Current-time characteristics of the same capacitor with  $V_{app}$  of 1V. Open circle shows the result of the first measurement and closed circle the result obtained after being retained for ten minutes after the first measurement under the open-circuit condition.

may not be due to built-up of the internal field caused by charge-trapping of the carriers injected into the STO film from the Pt electrode.

Linear-dependences of the leakage characteristics on  $V_{app}$  and their restoration characteristics strongly suggest that the leakage currents observed in the low electric fields are due to the dielectric relaxation phenomenon of the capacitor. More direct evidence which supports this assumption is to observe charging and discharging absorption currents. Fig.7 shows the I-t characteristics of the capacitor when  $V_{app}$  of 1 V was first applied for fifty seconds, then 0 V was applied for the continuous fifty seconds. Almost equivalent amounts of charging and discharging absorption currents were observed.

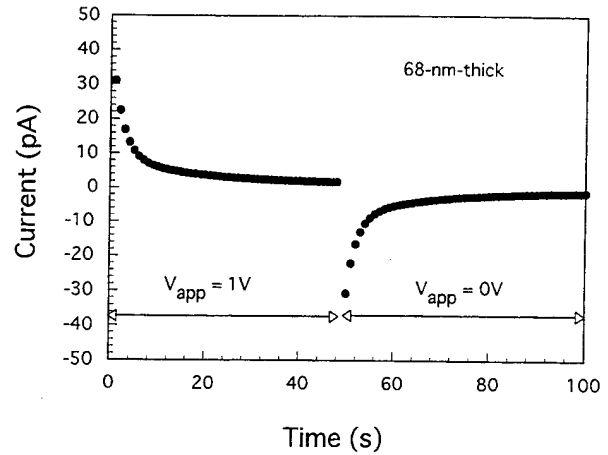


Fig.7 Current-time characteristics of capacitor when  $V_{app}$  of 1 V was first applied for fifty seconds, then 0 V was applied for the continuous fifty seconds.

#### Modeling of I-V characteristics under low electric fields

When the stair-case voltage ramp is applied to the capacitor, the absorption current  $I_{ac}$  due to the dielectric relaxation of the Debye-type relaxation species can be formulated as [10]

$$I_{ac}(V) = j \times \Delta V \sum_{i=1}^m \sum_{j=1}^n (C_i / \tau_i) \exp(-j \times t_d / \tau_i), \quad (2)$$

where  $C_i$  and  $\tau_i$  respectively denote the capacitance and the relaxation time constant of the  $i$ -th relaxation species, and  $\Delta V$  and  $t_d$  represent the measurement parameters described above. The unknown parameters  $C_i$  and  $\tau_i$  in this equation can be determined by applying a multiple nonlinear least squares method to the I-t measurements according to the relation

$$I(t) = V_{app} \sum_{i=1}^m (C_i / \tau_i) \exp(-t / \tau_i). \quad (3)$$

Figure 8 shows a result of this fitting to the I-t measurement of the 68-nm-thick capacitor with  $V_{app}=1V$ . We extracted three kinds of relaxation species from this fitting: (a)  $C_1=290$  pF,  $\tau_1=166$  s, (b)  $C_2=114$  pF,  $\tau_2=14.7$  s and (c)  $C_3=75.2$  pF,  $\tau_3=2.16$  s. The measurement parameter dependences of the absorption current can be calculated by substituting these values into eq.(2). The solid curves shown in Fig.2(b) are the calculation results for each value of  $t_d$ . The experimental results and the theory described here show very good agreements. The proportional relationship between the leakage current and  $\Delta V$  observed in Fig. 2(a) seems to be obvious because the absorption current is a linear function of  $\Delta V$ , as expressed in eq.(2).

Next, we discuss why the absorption current shows an ohmic-like I-V characteristics.  $\Delta I$ , the difference in the absorption current between  $j=n-1$  and  $n$  in eq.(2) becomes

$$\Delta I(j=n-1, n) = \Delta V \sum_{i=1}^m (C_i / \tau_i) [\exp(-t_d / \tau_i)]^n. \quad (4)$$

If we measure a leakage current under the condition of  $t_d \ll \tau_i$ , the term  $[\exp(-t_d / \tau_i)]^n$  is  $\sim 1$ , thus  $\Delta I$  becomes constant. Since the relaxation time constants of the Debye-type species (a) and (b) are fairly longer than  $t_d$ , this explanation for the observed ohmic-like I-V characteristics in the low-electric-field seems to be plausible.

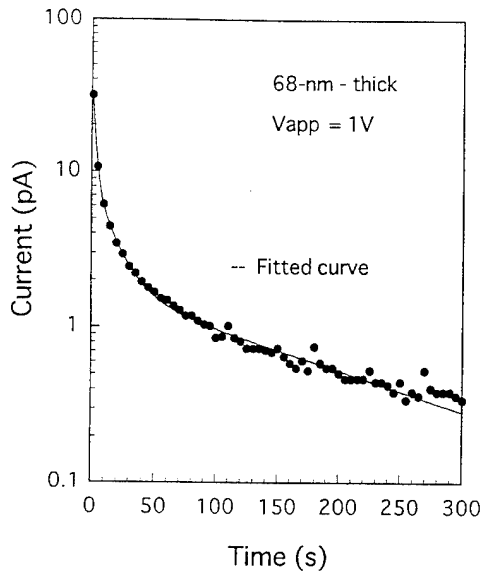


Fig.8. Current-time characteristics of 68-nm-thick SrTiO<sub>3</sub> film with  $V_{app}$  of 1 V. Solid curve is a result of curve fitting of eq.(3) in the text.

### Conclusions

I-V characteristics of SrTiO<sub>3</sub> thin film capacitors prepared by ECR-sputtering have been studied. It was found that the leakage current characteristics of the films show an ohmic-like conduction for electric field strengths lower than 1 MV/cm. These ohmic-like leakage characteristics showed strong dependences on the measurement conditions, the values of the voltage-step and the measurement

delay-time in the staircase I-V ramps. This effect was found to be attributed to the absorption current due to the dielectric relaxation phenomena of the SrTiO<sub>3</sub> capacitors. Theoretical I-V curves derived based on the Debye-type dielectric relaxation species fit very well with the experimental results obtained under the various measurement conditions.

### Acknowledgement

The authors express their great thanks to Dr. S. Hasegawa for his continuous support and encouragement.

### References

- [1] K. H. Hellwege and A. M. Hellwege (Ed.), Landolt-Bornstein Numerical Data and Functional Relationships in Science and Technology, New Series vol. 16. New York: Springer-Verlag, 1981, pp. 308-312.
- [2] S. Yamauchi, T. Sakuma, K. Takemura and Y. Miyasaka, "SrTiO<sub>3</sub> thin film preparation by ion beam sputtering and its dielectric properties," Jpn. J. Appl. Phys., vol.30, pp.2193-2196, September 1991.
- [3] T. Kuroiwa, T. Honda, H. Watarai and K. Sato, "Electrical properties of SrTiO<sub>3</sub> thin films prepared by rf sputtering," Jpn. J. Appl. Phys., vol.31, pp.3025-3028, September 1992.
- [4] W. B. Pennebaker, "Rf sputtered strontium titanate films," IBM J. Res. Develop., pp.686-695, November 1969.
- [5] K. Abe and S. Komatsu, "Epitaxial growth of SrTiO<sub>3</sub> on Pt electrodes and their electrical properties," Jpn. J. Appl. Phys., vol.31, pp.2985-2988, September 1992.
- [6] K. Abe and S. Komatsu, "Dielectric constant and leakage current of epitaxially grown and polycrystalline SrTiO<sub>3</sub> thin films," Jpn. J. Appl. Phys., vol.32, pp.4186-4189, September 1993.
- [7] K. Numata, K. Aoki, Y. Fukuda and A. Nishimura, "Annealing effects to electrode Pt/Ti for PZT," in Proceedings of the Mat. Res. Soc. Symp., 1994, pp.659-664.
- [8] J. E. Cames and A. M. Goodman, "Evaporated metallic contacts to conducting strontium titanate single crystals," J. Appl. Phys., vol.38, pp.3091-3096, July 1967.
- [9] S. M. Sze, Physics of Semiconductor Devices (2nd ed.). New York: John Wiley and Sons, 1981, p.402.
- [10] Y. Inuishi, T. Nakajima, K. Kawabe and M. Ieda, Yuudentai Gensyounon (Dielectric Phenomenology). Tokyo: Ohmsha, 1973, pp.95-98.

# Relating Local Electric Field in a Ferroelectric Capacitor to Externally Measurable Voltages

Francis K. Chai, J.R. Brews, R.D. Schrimpf, D.P. Birnie III<sup>†</sup>

University of Arizona  
Department of Electrical and Computer Engineering

<sup>†</sup>Department of Materials Science and Engineering  
Tucson, AZ. 85721

## Abstract

The field-dependent polarization model is a commonly proposed model to describe the hysteresis loop of a ferroelectric material. The electric field in the model refers to the local field which varies with position within the ferroelectric film. However, the parameters in the field-dependent polarization are usually extracted based on the macroscopic experimentally averaged field, i.e., applied voltage divided by film thickness. In this work physical quantities such as field, potential, electric displacement and polarization inside the ferroelectric capacitor are obtained by assuming that the capacitor is wholly depleted. The resultant electric field distribution demonstrates the significant difference between the local electric field and the macroscopic average field, indicates that extension of some modeling works is necessary. For the assumption of complete depletion to be valid, a constraint is required upon the film thickness at a given value of doping. A design curve is constructed that shows the maximum allowable film thickness for typical PZT film doping levels in order for the assumption of complete depletion to be valid. The technique presented in this work provides a simple and direct way of relating the macroscopic properties of the capacitor to the actual electric field and potential distribution in the ferroelectric film, furthermore, it will serve as a basis for the C-V modeling of ferroelectric capacitors.

## I. Introduction

The interest in ferroelectrics has increased because of the potential applications in memory devices. Compared with silicon dioxide, ferroelectrics have better charge storage capability per unit area[1], making thin-film ferroelectric devices physically smaller than conventional metal-oxide-semiconductor

(MOS) devices[2]. In addition, ferroelectric devices can be used as nonvolatile memory elements that do not require energy to maintain their memory state[3-4]. These attractive properties make ferroelectrics a promising candidate material for memories.

The important property of ferroelectrics for application to nonvolatile memory devices is their hysteresis behavior. However, the hysteresis behavior of ferroelectrics is not well understood. To obtain insight for designing circuits with ferroelectric devices, quantitative models need to be developed to fully describe the electrical properties of ferroelectrics. One approach for analyzing the hysteresis loop quantitatively is the field-dependent polarization or field-dependent dielectric constant model[5-7]. A common ambiguity in these models is the confusion between the local electric field inside the ferroelectric thin film and the averaged field, which is the applied voltage divided by the thickness of the film. In the process of extracting parameters for these quantitative models, the local field is actually treated as the macroscopic average field. The purpose of this work is to distinguish between the local field and the averaged field.

In this work, the field-dependent polarization model is reviewed and parameters in the model are extracted by fitting the model to the hysteresis loop measured from a Sawyer-Tower circuit. The issue of local versus averaged field is pointed out. The local electric field is derived and related to the averaged wholly depleted. Finally, the wholly depleted assumption is examined and design curve is constructed.

## II. Field-Dependent Polarization Model and the Confusion

S.L. Miller et al. proposed a quantitative model to simulate the hysteresis loop of ferroelectric capacitors[5] and applied the model in a modified Sawyer-Tower circuit to predict the electrical properties. Due to the convenient mathematical properties of the model, it is taken as a tool to simulate the hysteresis behavior in this work.

The proposed field-dependent polarization for the right half of the hysteresis loop is

$$P_d^+(E) = P_s \tanh\left(\frac{E - E_c}{2\delta}\right), \quad (1)$$

where  $E$  is the local field in the PZT film,  $E_c$  is the coercive field, and the parameter  $\delta$  is a function of

the remanent polarization,  $P_r$ , the saturation polarization,  $P_s$ , and  $E_c$ . The left half of the hysteresis loop can be obtained by changing the sign of the coercive field.

To simulate the experimental hysteresis loop, the total polarization is expressed as the sum of the linear and the switching polarization

$$P_{total}(E) = P_{linear}(E) + P_{switching}(E), \quad (2)$$

where

$$P_{linear}(E) = \epsilon_0(\epsilon_f - 1)E \quad (3)$$

and

$$P_{switching}(E) = P_d^+(E). \quad (4)$$

The total, switching, and linear polarization are plotted in Fig. 1 for illustration.

The electric field in the hysteresis measurement refers to the macroscopic average field, i.e., applied voltage divided by the thickness of the capacitor. The electric field  $E$  in equation (1) is actually the local field which varies with position; however, the unknown parameters  $\epsilon_f$ ,  $P_s$ ,  $P_r$ , and  $E_c$  are going to be extracted by fitting the total polarization  $P_{total}$  in equation (4) to the experimental hysteresis measurement. Thus, the local electric field  $E$  in equation (1) is treated as the macroscopic average field. The objective of this modeling work is to relate the local field to the experimentally measurable voltage.

### III. Derivation of the Field as a Function of Position in the PZT Thin Film

To obtain the field as a function of position, Poisson's equation is solved taking into account the field-dependent polarization model with the parameters  $\epsilon_f$ ,  $P_s$ ,  $P_r$ , and  $E_c$  extracted by fitting equation (3) to the experimental hysteresis loop. It is assumed that the PZT thin film has a constant doping level and is wholly depleted. An example of the result of calculation is shown in Fig.1-4. The PZT capacitor is not biased in this case and was assumed to have a doping level of  $N_A = 3 \times 10^{18} \text{ cm}^{-3}$  and a film thickness of  $0.76 \mu\text{m}$ .

Fig.2 shows an example of the calculated electric displacement, field, polarization, and potential as functions of position in the PZT thin film. As can be seen in Fig.2, due to the assumed constant doping, the electric displacement is linear with position. In Fig.3, the electric field in a PZT film, in a regular dielectric with constant doping, and in a charge-free capacitor are plotted together for comparison. The shape of the field in the PZT film is a result of the

field-dependent polarization model. Note that at the surface of the PZT film, the field is as high as  $300 \text{ kV/cm}$ . Due to the lack of switching polarization, the total polarization of a regular dielectric has only the linear component and thus is proportional to the electric field. With an identical dielectric constant  $\epsilon_f$  as the ferroelectrics, the calculated field in a regular dielectric film is linear with position. Since the capacitor is not biased, the averaged field (field in a charge-free capacitor) is zero throughout. The actual field as a function of position is indeed very different from the averaged field in both the PZT and the regular dielectric film.

Polarization and its components as functions of position are shown in Fig.4. Total polarization, which is the sum of switching and linear polarization, is linear with position in the film due to the constant doping. The linear polarization is proportional to the electric field and thus has the same shape as the field. The switching polarization saturates close to the electrodes because of the large electric field in the region.

The potential as a function of position is shown in Fig.5. The potential is zero at both  $x = 0$  and  $0.76 \mu\text{m}$ , indicating that the ferroelectric capacitor is not biased.

### IV. Design Curve

The criterion for the wholly depleted assumption is set to be that the maximum concentrations of electron and hole are 1% of the doping level of the PZT film, i.e., the film is at least 99% depleted of mobile carriers. The maximum and minimum possible Fermi levels are then calculated. As the thickness of the film increases, the range of possible Fermi levels gets smaller. When the maximum and minimum Fermi levels merge, the film is at the maximum allowable thickness which just satisfies the assumption of complete depletion. The calculated maximum allowable thickness is plotted versus PZT doping in Fig.6. The design curve shows the maximum allowable film thickness in order for the assumption of complete depletion to be valid. Any film with thickness smaller than the maximum allowable thickness (at a given doping shown in the design curve) is a valid film for the application of this model.

One noteworthy point is that the typical film thickness for PZT thin films is  $0.2$  to  $0.8 \mu\text{m}$ , this range is marked within dashed lines in the design curve. It can be seen that the valid region covers

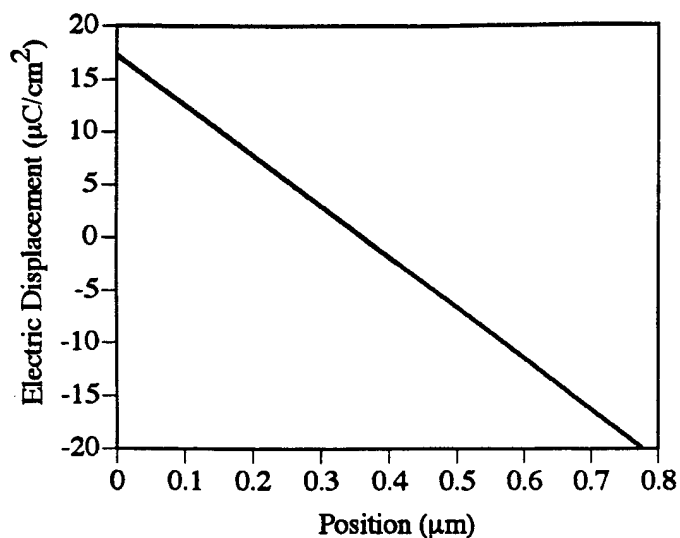


Fig.2 The electric displacement as a function of position.

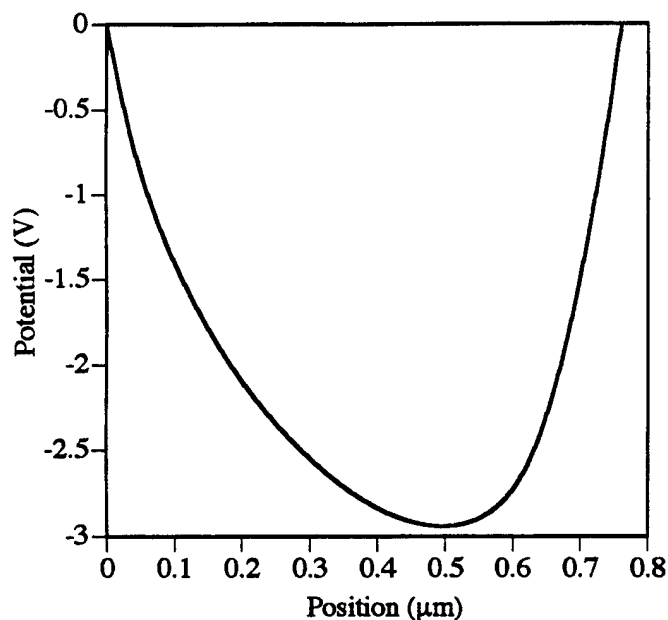


Fig.5 The potential as a function of position.

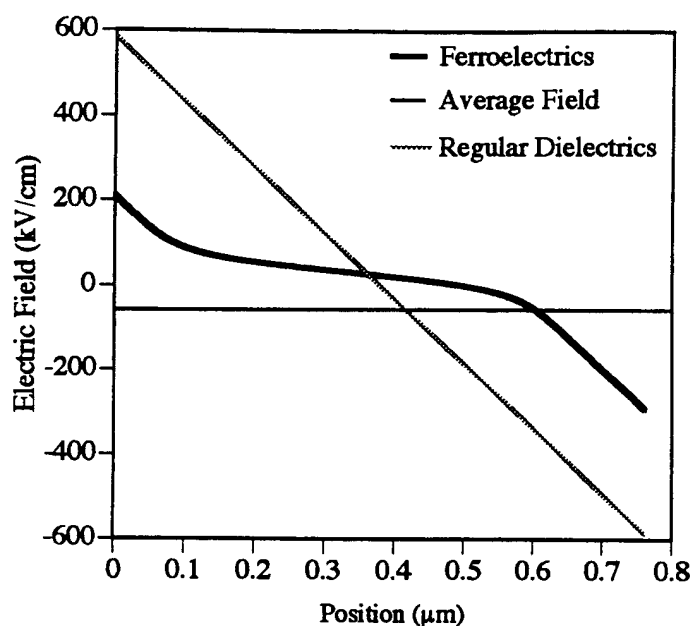


Fig.3 The electric field as a function of position.

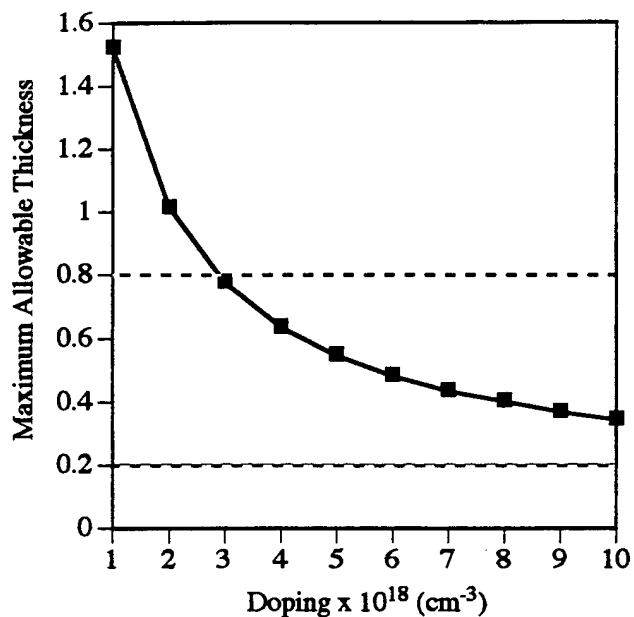


Fig.6 Design curve of the presented model.

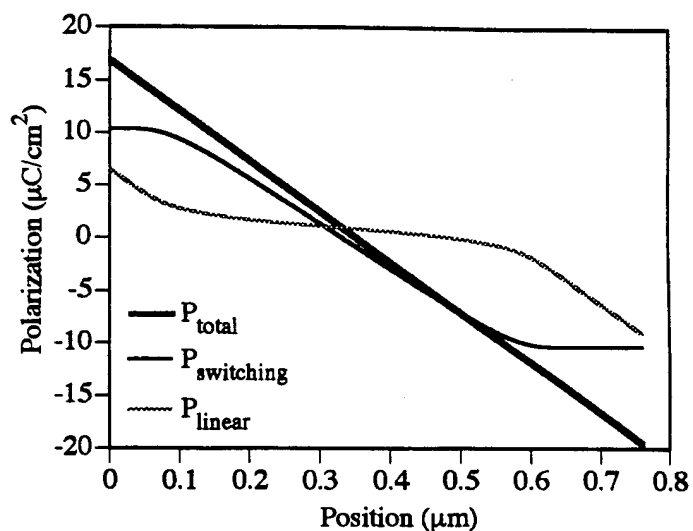


Fig.4 The total, switching, and linear polarization as functions of position.

most of the typical PZT film doping range, indicating that the model has wide applicability.

## V. Result and Discussion

It can be seen that though different approach is taken, the results shown here are similar to a previous work by Brennan[8], which solves from the free energy expansion. Note that even though the capacitor is not biased, the potential is not a symmetrical function with position. For a regular dielectric, the unbiased potential as a function of position is symmetrical (a parabola). The asymmetry of potential for the PZT is a characteristic of ferroelectrics and is an indication of a nonzero coercive field. Energy band diagram can be constructed by inverting the potential profile. Biased cases can be calculated in the same way by matching the magnitude of potential at the top and bottom electrodes.

## VI. Conclusion

Based on the macroscopically extracted parameters, electric displacement, total polarization, and the linear and switching components of the polarization are calculated as functions of position by assuming that the PZT thin film has a constant doping and is wholly depleted. The results show that the oversimplified average field is very different from the actual electric field in the PZT thin film. Design curve is constructed based on the wholly depleted criterion for typical PZT doping levels ( $10^{18}$  to  $10^{19} \text{ cm}^{-3}$ ) and the result indicates that for typical PZT thin film thickness and doping, the applicable range of this model is wide.

## Acknowledgments

This work was supported in part by the U.S. Navy under contract no. N00014-90-C-2130. The authors would like to thank J. Ramsey, R. Pugh, J. Henderson, and C. J. Brennan for constructive suggestions.

## References

- [1] R. Moazzami, C. Hu, and W.H. Shepherd, "Electrical Characteristics of Ferroelectric PZT Thin Films for DRAM Application," *IEEE Tran. ED.*, vol. 39, no. 9, pp. 2044-2049, 1992.
- [2] G. Rohrer, S. Narayan, L. McMillan, and A. Kulkarni, "A New Technique for Characterization of Thin-Film Ferroelectric Memory Devices," *J. Vac.*

*Sci. Technol.*, A vol. 6, no. 3, pp. 1756-1758, 1988.

[3] S.S. Eaton, D.B. Butler, M. Parris, D. Wilson, and H. McNeillie, "A Ferroelectric Nonvolatile Memory," *Proc. of IEEE International Solid-State Circuits Conference*, pp. 130-131, 1988.

[4] J.T. Evans and R. Womack, "An Experimental 512-bit Nonvolatile Memory with Ferroelectric Storage Cell," *IEEE Journal of Solid-State Circuit*, vol. 23, no. 5, pp. 1171-1175, 1988.

[5] S.L. Miller, R.D. Nasby, J.R. Schwank, M.S. Rodgers, and P.V. Dressendorfer, "Device Modeling of Ferroelectric Capacitors," *J. Appl. Phys.* vol. 68, no. 12, pp.6463-6471, 15 December, 1990.

[6] Sungchul Lee, "Characterization of Lead Zirconate-Titanate (PZT) Thin Films for Ferroelectric Memory Applications", 1993, Ph.D. dissertation, Department of Electrical and Computer Engineering, University of Arizona.

[7] N. Bar-Chaim, M. Brunstein, J. Grünberg, and A. Seidman, "Electric Field Dependence of the Dielectric Constant of PZT Ferroelectric Ceramics," *J. Appl. Phys.* vol. 45, no.6, pp. 2398-2405, June, 1974.

[8] C. J. Brennan., "Analysis of Electric Fields. Space Charges, and Polarization of Thin-Film Ferroelectric Capacitors Based on Landau Theory," *Ferroelectric Thin Films II Symposium*, pp.141-146, 1992.

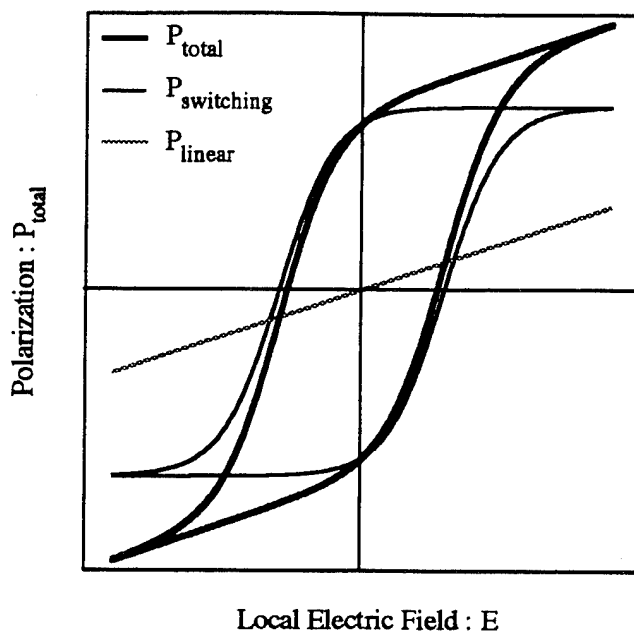


Fig.1 The field-dependent polarization model.



# Fine Grain Barium Titanate: Ferroelectric Domains and X-Ray Diffraction Diagram

F. Batllo, N. Floquet, M. Maglione, M. Mesnier, J.C. Niepce, P. Perriat, P. Sarrazin and C.M. Valot.

Laboratory "Reactivité des Solides"  
URA CNRS 23  
University of Burgundy  
BP 138  
21004 DIJON Cedex (France)

**Abstract:** Through three different studies, using various kinds of BaTiO<sub>3</sub> samples:  
- as a powder while heating over the Curie temperature,  
- as a green ceramic as a function of the forming pressure,  
- as a ceramic while applying a D.C. field,  
it is shown how X-Ray diffraction is able to give information about the evolution of the 90° ferroelectric domain microstructure.

## INTRODUCTION

Barium titanate is the main component of the dielectric of type 2 ceramic capacitors. The actual objectives of the ceramic capacitor industry are oriented towards decreasing both the price and the volume of the capacitor while increasing the dielectric properties of the material. As shown in previous studies (1)(2) the dielectric properties of BaTiO<sub>3</sub> are strongly grain size dependent and in order to meet the objectives stated above, materials with finer and finer grains are required. As the dielectric properties are related to the crystalline structure, X-Ray diffraction analysis has been used, for a long time, in order to improve the understanding of the material as a function of the grain size (3,4,5,6). However, all the crystalline characteristics of BaTiO<sub>3</sub> which are grain size dependent are not able to explain, alone, the full X-Ray diffraction diagram as a function of the grain size. For a full interpretation of the diffraction diagram, it has been necessary to introduce a contribution of the 90° ferroelectric domain microstructure (7).

At the present time, the theoretical approach is rather simplistic. A few years ago, Caboche et Al.(7) proposed a model taking into account the contribution of the association of two 90° adjacent ferroelectric domains to the diffracted intensity in the vicinity of the 002 and 200 diffraction lines. Although this model was simplistic, an important result was drawn up: *the size of the domain which is diffracting coherently the X-ray beam is largely greater than the size of the 90° ferroelectric domains.* A more complete model, able to explain the full diagram is now in progress.

In the present paper, new experimental results are presented; they are interpreted taking into account the consequences from the coherent diffraction between two 90° adjacent ferroelectric domains.

## EXPERIMENTAL

### Samples

**The initial powder:** A coarse grained BaTiO<sub>3</sub> powder, with a narrow grain size distribution has been used in order to get well separated 002 and 200 diffraction lines.

**The green ceramics:** After a slip drying and granule preparation, thick disks of 8 mm diameter were formed by die pressing. The forming pressure range was from 100 to 1000 MPa.

**The sintered ceramics:** The sintering conditions ( air, 1250°C, 16 hours ) were chosen in order to obtain well densified thick disks with no grain growth.

### Data recording

Most of the XRD diagrams were recorded using a  $\theta$ - $\theta$  horizontal axis goniometer allowing a motionless sample and a curved position sensitive detector (INEL CPS 120). A curved quartz monochromator was providing the copper K $\alpha_1$  radiation.

#### *In situ XRD versus electric field:*

An electric field applied on the samples was provided by a DC generator. Gold was vapour deposited on each side of the samples to form the electrodes. The layer had to be sufficiently thick to insure a good electrical contact and sufficiently thin to induce a negligible adsorption of the X-ray beam.

#### *In situ XRD versus temperature:*

The powder diffraction patterns were collected with a synchrotron radiation in LURE (Orsay, France). The parameters of the device D23 were :  $\lambda=1,4$  Å; step scan = 0,006 (°2 $\theta$ ) ; counting time = 16s ; monitor = 800 000 cts)

This study required an XRD set up with a very high and well known resolution, in order to detect very slight changes in the line broadening. The resolution of the apparatus (device D23) were about 0.02 (°2 $\theta$ ); The XRD diagrams were recorded at different temperatures: from room temperature up to 150°C

(above  $T_c \approx 120^\circ\text{C}$ ), then at  $450^\circ\text{C}$  and finally cooled down to room temperature after the thermal treatment.

### INFORMATION ON THE FERROELECTRIC MICROSTRUCTURE IN THE X-RAY DIFFRACTION DIAGRAM

#### *Ferroelectric domains in Barium Titanate*

At room temperature, the  $\text{BaTiO}_3$  grains are usually divided in ferroelectric domains; "180° domains" in which the polarization vectors are antiparallel and "90° domains" in which the polarization vectors are rectangular. This division allows a minimization of the overall deformation and polarization induced during the paraelectric to ferroelectric transition. A ferroelectric domain wall is the boundary between two domains.

#### *The Williamson and Hall analysis*

A Williamson and Hall (W-H) diagram allows qualitative data on the crystallite size and lattice microdistortions of the material by the measurement of the XRD line broadening. The W-H diagram consists of a straight line with the origin ordinate (OO) leading to the mean apparent crystallite size and the slope (S) to the mean apparent defect ratio in the direction perpendicular to the hkl planes considered.

#### *The W-H plot in case of ferroelectric $\text{BaTiO}_3$*

In the case of  $\text{BaTiO}_3$  polycrystalline materials, the origin ordinate and the slope of the W-H straight lines are also depending on the ferroelectric microstructure. The slope S depends on both the amount of lattice distortions but also on the amount of domain walls, since a 90° domain wall and a dislocation has a very similar effect on the line broadening.

The effect of the ferroelectric domain microstructure is depending on the considered diffraction lines.

In the present work two kinds of lines have been considered: the hhh lines, on the one hand, and the 00h and h00 lines, on the other hand (Figure 1).

The relative intensities of 002 and 200 lines are a function of the polarization of the material.

The 002-200 line widths are related to the ferroelectric domain size. A particular contribution to the diffracted intensity is observed in the area between these two lines(7).

On the contrary, the subdivision into ferroelectric domains modifies the 111 line profile differently. From a WH plot using the hhh lines, the size effect on the origin ordinate is only the grain size (here grain = crystallite) but not the 90° domain size while the distortion effect on the slope is due to both the true lattice distortions and the apparent distortions associated to the 90° domain walls.

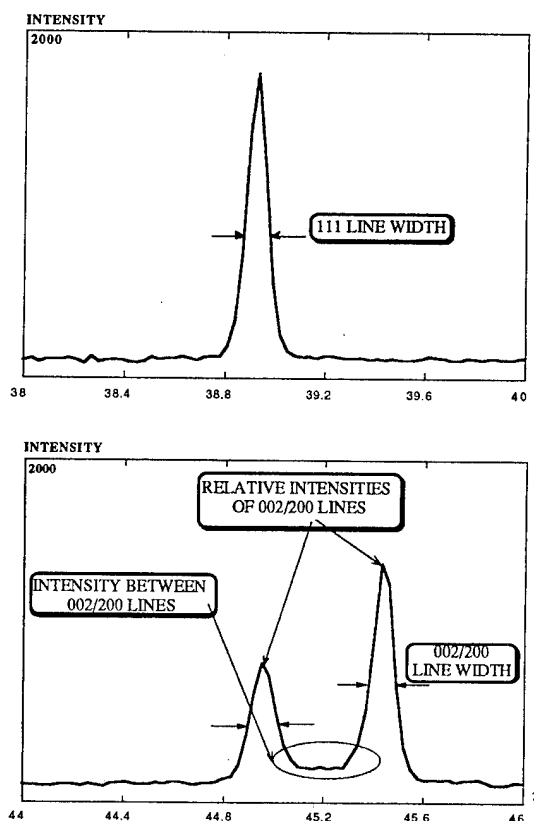


Figure 1 : Main characteristic parameters of the 111, 002 and 200 diffraction lines of polycrystalline  $\text{BaTiO}_3$ .

### HEATING A POWDER OVER THE CURIE TEMPERATURE

The results are presented in a W-H plot of the hhh lines as a function of the temperature (Figure 2).

As the temperature increases close to the phase transition temperature  $T_c$ , the slope S decreases. For temperatures above  $T_c$  ( $T_c < T < 450^\circ\text{C}$ ), there is no more evolution of S.

At low temperatures ( $T < T_c$ ), the decrease of the broadening is not likely to be due to a classical lattice distortion relaxation. It is most likely due to the reduction of the domain wall contribution which finally disappears at  $T_c$  when  $\text{BaTiO}_3$  lattice becomes cubic.

For  $T_c < T < 450^\circ\text{C}$ , there is no more ferroelectric domains and the value of the slope S represents only classical microdistortions. Moreover, when the powder is cooled back to room temperature, the slope S and the apparent defect ratio due to the domain walls, as well, come back to their initial values.

Note that in this study, the origin ordinate OO is remaining approximately equal to zero and has no

real significance. This is due to the large grain size; thus the approximation of the infinite size crystal is valid all along this study.

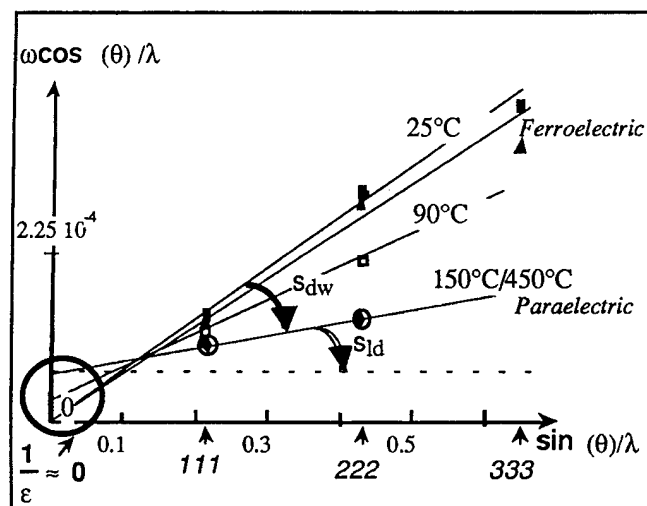


Figure 2 : Experimental proof of the ferroelectric domain wall contribution to the broadening of the hhh lines by a behaviour similar to lattice distortions in a Williamson-Hall plot.

■ : 25°C before heating    ▲ : 25°C after heating  
 $s_{dw}$  : domains walls contribution to the slope  
 $s_{ld}$  : lattice distortions contribution to the slope

### INFLUENCE OF THE FORMING PRESSURE ON GREEN CERAMICS

#### Evolution of the diffracted intensity profile around the 002-200 lines

Figure 3 shows the typical modifications of the 002-200 lines involved by the pressing : both the 002 and 200 line widths and the diffracted intensity between the two peaks increase with forming pressure.

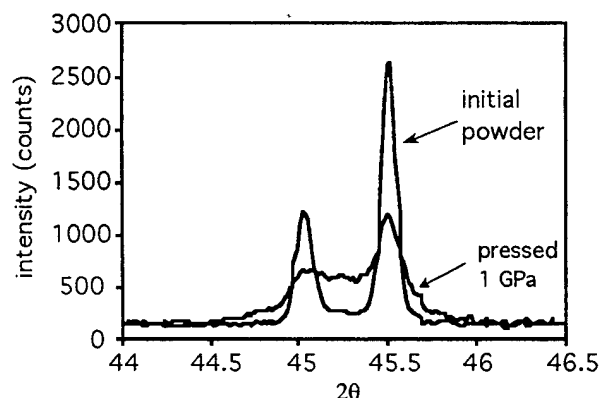


Figure 3 : 002-200 line profiles of the initial powder and of a green sample after pressing (1GPa)

#### Evolution of the broadening of the 111 and 222 lines

A Williamson and Hall analysis has been performed on the 111 and 222 lines of each sample (Figure 4). The broadening of the 111 and 222 lines is only due to a lattice distortion effect. Therefore, the modifications of the structure involved by the forming are seen as an increase in the lattice defects along the [111] axis without any variation of the size of the coherence domains.

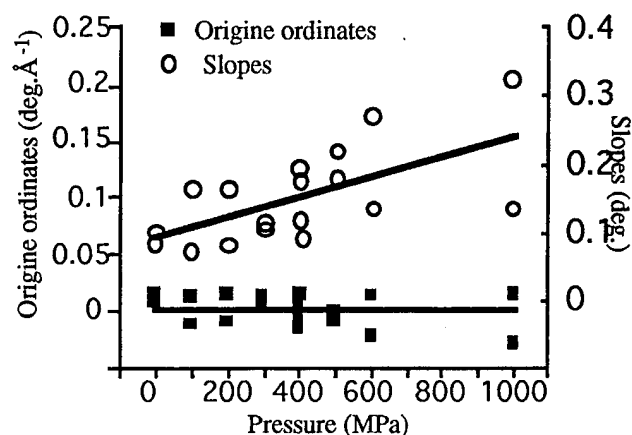


Figure 4 : Origin ordinate and slope of the Williamson & Hall straight lines obtained with the hhh lines of BaTiO<sub>3</sub> green samples versus the forming pressure.

#### Discussion

The increase of the apparent amount of lattice defects when increasing the forming pressure has to

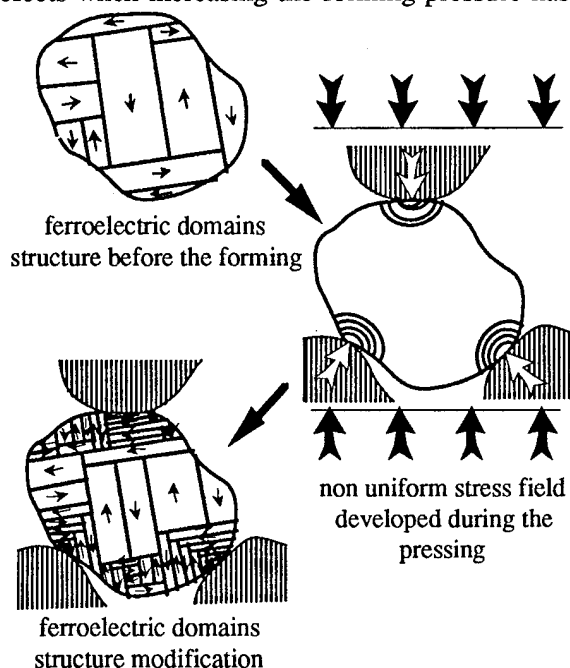


Figure 5: Proposed mechanism to explain the die pressing effect on the 90° ferroelectric domain structure.

be seen as an increase of the amount of 90° domain walls.

It is related to a reduction of the domain size induced by the pressing. A mechanism, presented in Figure 5, has been proposed to explain this phenomenon : a fragmentation of the ferroelectric domains allows the minimization of the mechanical energy of the material.

### INFLUENCE OF A DC FIELD ON A CERAMIC

The application of an electric field is a direct way to modify the ferroelectric domain microstructure. A special device was set up, allowing to record the X-ray diffraction diagram while applying an electric field perpendicular to a ceramic disk (9).

The experimental results reveal a change of the 002 and 200 line relative intensities ( $I_{002}/I_{200}$ ). When increasing the electric field,  $I_{200}$  decreases while  $I_{002}$  increases. Consequently the {001} plane families proportion grows at the expense of the {100} plane families. In a well densified ceramic no reorientation of the grains in order to modify the relative intensities is possible; only the ferroelectric domain walls are supposed to move in order to extend the domains having the polarization vector the closest to the electric field.

The relative intensities of the 002 and 200 lines characterize the polarization state. The curve  $R=f(E)$  (Figure 6), obtained from the diffracted intensity measurements, has been compared to the schematic first polarization curve.

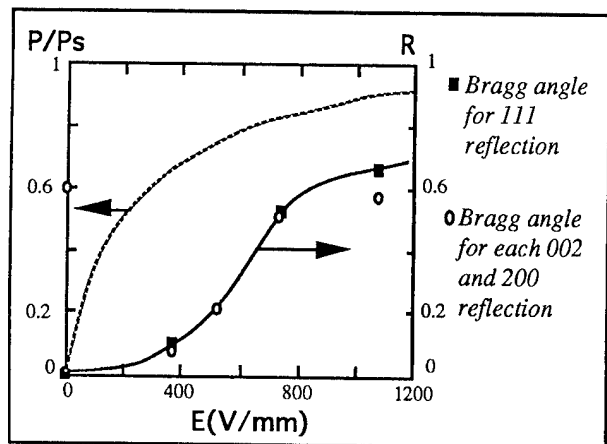


Figure 6 : Comparison between a diagrammatic relative polarization curve  $P/P_s$  and the  $R$  curve obtained by the X-Ray diffraction measurements.

$P$ : Polarization,  $P_s$ : Saturation polarization,  
 $R = (I_{002} - (I_{002})_{uc}) / (I_{002} + I_{200} - (I_{002})_{uc})$   
 $I_{002}$ ,  $I_{200}$ ,  $(I_{002})_{uc}$ : Intensities of the 002 and 200 diffraction lines and of the 002 line in the unpoled ceramic respectively.

Electrical polarization measurement and X-ray diffraction do not analyse the polarization state on the same way:

- the electric polarization considers the whole sample volume, with all the grains (whatever their orientation), with all the domains (each domain contributes to the polarization)
- the X-ray diffraction consider only the surface (a few  $\mu\text{m}$ ) and only some grains (that are in diffraction angular position) and two anti-parallel domains cannot be distinguished.

The comparative interpretations of the  $R$  curve and of the first polarization curve allow to characterize the domain wall motion under the influence of the electric field. The 180° domain wall motion occurs for a very low value of the electric field for which  $R=0$ . Whereas, the 90° domain walls move for an higher value of the electric field corresponding to  $R>0$  (on the contrary of that is said in (10)).

### CONCLUSION

All the presented experimental results exhibit various aspects of the contribution of the 90° ferroelectric domain microstructure of a ferroelectric material such as barium titanate to its X-Ray diffraction diagram when considered as a polycrystalline material. However all these results are at the present time only qualitative or semi-quantitative. In order to obtain a better knowledge of the ferroelectric material from its X-Ray diffraction diagram, a more realistic model is in progress.

### REFERENCES

- (1) K.Kinoshita and A.Yamaji, *J.Appl.Phys.* **47**, 371-373 (1976)
- (2) G.Arlt,D.Hennings and G. de With *J. Appl. Phys.* **58**, 1619-1625 (1985)
- (3) W. Kanzig *Phys. Rev.* **98**, 549-550 (1955)
- (4) K. Uchino, E. Sadanaga and T. Hirose *J. Amer. Ceram. Soc.* **72**, 1555-1558 (1989)
- (5) S. Malbe, J.C. Mutin and J.C. Niepce *J.Chim. Phy.* **89**, 825-843 (1992)
- (6) G. Caboche, F. Chaput, J. P. Boilot and J.C. Niepce *Silic. Ind.* **58**, 103-107 (1993)
- (7) G Caboche, J.F. Berar, M.T.Mesnier, J.C.Niepce, J.Pannetier and M.F.Ravet *Silic. Ind* **58**, 239-243 (1993)
- (8) G.K. Williamson and W.H. Hall *Acta. Met.* **1**, 22-... (1953)
- (9) C.M. Valot, J.F. Berar, C. Courtois, M. Maglione, M.T. Mesnier, J.C. Niepce, *Ferroelectrics Letters*, **17**, 5-12 (1994)
- (10) Y.S. Ng and A.D. McDonald *Ferroelectrics* **62**, 167-178 (1985)

# THE DOMAIN MECHANISM OF AGING AND DEGENERATION OF FERROELECTRIC MATERIAL

A.S. Sidorkin

Voronezh State University  
Voronezh, 394693 Russia

The mechanism of interactions of domain boundaries in ferroelectric-ferroelastic crystals with different (uncharge, charge and elastic types) defects are investigated. The diffusion of defects to boundaries and the processes of the motion of domain walls interacting with defects are studied. The values of domain contribution in dielectric permeability and the coercitive field determined by the storage time and the number of switching cycles for the material with initial random defect distribution are calculated.

## INTRODUCTION

The processes of aging and degeneration (i.e. worsening of operating properties in the usage process) of ferroelectric monocrystal materials is mainly determined by processes on the electrodes, by domain-defect interactions and in ceramic materials by the additional diffusion processes occurring along the intergrain boundaries [1,2].

The aim of the present work is the study of the contribution of domain-defect interaction in the aging and degeneration processes in monocrystal as in ceramic materials. The mechanisms of the mentioned effects are connected with the decrease of the total energy of real ferroelectric material in case when defects lie at the domain boundaries. It results in the diffusion of the defects to the domain boundaries (the aging process) on the one hand, and to the additional lock-on to defects by moving domain boundaries during the switching process (degeneration process) on the other hand. In the result the number of points of domain walls fixing by defects increases and so the contribution of the domain boundaries in dielectric permeability decreases and the value of coercitive field increases respectively with the increase of storage time and of number of switching cycles (i.e. of operation time).

## MECHANISMS OF DOMAIN WALL-DEFECT INTERACTION

Let us consider the principal mechanisms of domain wall-defect interaction in ferroelectrics and ferroelectrics-ferroelastics. Here we limit ourselves with the defects classified as point charged and elastic ones as well as with a non-ferroelectric inclusion. In reality they represent practically all possible imperfections of crystalline lattice with atomic dimensions: the implantation and substitution impurities, vacancies, pores and others. The interaction of any concrete defect with the domain wall may be caused simultaneously by several mechanisms.

The mechanism of interaction of point charge defect with the domain wall is shown at Fig.1a. The pressure on the wall from the electric field is connected with the difference in energy of dipoles of neighbouring domain in

that field. Unlike the homogeneous field the charge defect one is asymmetrical along the polar axis relative to normal to the boundary passing through the defect. It causes the pressure on the wall from this field having a different sign in the regions upper and lower of the normal. Being displaced here by the electric field in opposite directions, the boundary finally sags near the point with  $z=0$ . The sign of the bound charge arising on the sagging boundary is always opposite to one of initial charge defect. The interaction between the domain wall and initial charge is the result of one between the indicated charges. So for any sign of initial charge its interaction with domain wall has always an attraction character.

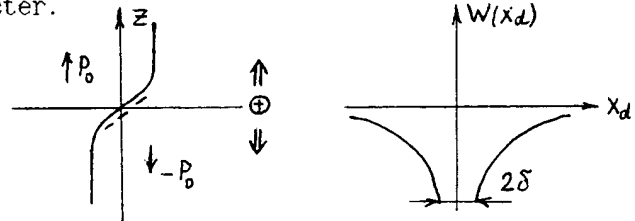


Fig.1. The character of the displacement of the domain wall near the point charge defect - a) and the energy of their interaction as a function of the distance between the initial position of the domain wall and defect.

The details of such interaction are described by the system of equations (1), first of which is the equation of equilibrium of the domain wall and second - the Poisson equation that connects the domain wall displacement  $u$  with their accompanied electric field with the potential  $\varphi$  [3,4]:

$$\begin{cases} \epsilon_c \frac{\partial^2 \varphi}{\partial z^2} + \epsilon_a \left( \frac{\partial^2 \varphi}{\partial y^2} + \frac{\partial^2 \varphi}{\partial x^2} \right) = 8\pi P_0 \delta(x) \frac{\partial u}{\partial z} - 4\pi z e \delta(z - z_d), \\ -\gamma \left( \frac{\partial^2 u}{\partial z^2} + \frac{\partial^2 u}{\partial y^2} \right) + 2P_0 \frac{\partial \varphi}{\partial z} \Big|_{x=0} = 0 \end{cases} \quad (1)$$

Here  $P_0$  is the spontaneous polarization,  $\epsilon_c, \epsilon_a$  - dielectric permeabilities of monodomain crystal along and perpendicular to the polar axis,  $\gamma$  - the surface density of energy of domain wall.

The cooperative solution of the equations of system (1) allows to describe the profile of interacting domain wall, to obtain the potential of indicated charges on the wall and in the result the energy of interaction of defect and boundary as a function of the distance between them. Omitting the unwieldy calculations we note that the last one is easily calculated if one takes into account that in neglecting the surface tension of the boundary, i.e. by the increase of its length at the sag, the domain wall in the equilibrium position is an equipotential surface. So the in-

interaction of indicated charges is the interaction between the initial charge and image charge with the energy

$$W(\chi_d) = Ze\varphi_{ind}(\chi_d) = \frac{Z^2 e^2}{2\sqrt{\epsilon_0 \epsilon_a} \chi_d} \quad (2)$$

In ferroelectric-ferroelastic crystal domains represent not only electrical twinning but mechanical ones distinguished in simplest case by the sign of the shift spontaneous deformation. The plane of the domain wall coincides here as a rule with the invariant one where the atomic positions remain unchanged at the process of crystalline structure reconstruction at phase transition. At each point of such boundary the deformations are compatible and the medium continuity is conserved. At the deviation of the domain wall from the invariant plane the gaps of continuity arise which depend on the direction of the wall displacement and can be presented by the edge and screw twinning dislocations. At the interaction with domain wall in elastic crystal of elastic nature defect similar to the previous case of charge defect the domain boundary aspires to flex and to destroy the elastic stresses which cause the pressure on the domain wall from the defect. In the result the interaction of initial elastic defect and induced by the wall sag twinning dislocations here always has the attraction character too. The concrete form of sagging wall and the energy of interaction of wall and defect are determined in ferroelectric-ferroelastic material by the system of equations:

$$\begin{cases} -2P_0 \frac{\partial \varphi}{\partial z} \Big|_{x=0} + 2\epsilon_0 \epsilon_{12} \Big|_{x=0} = 0, \\ \epsilon_{ij, \kappa\kappa} + \frac{m}{m+1} (\epsilon_{\kappa\kappa, ij} - \epsilon_{\kappa\kappa, \ell\ell} \delta_{ij} + f_{ij, j} - f_{\ell\ell, i} \delta_{ij}) = 2\mu \eta_{ij} \\ \epsilon_{ij} \frac{\partial^2 \varphi}{\partial x_i \partial x_j} = 8\pi P_0 \delta(x) \frac{\partial u}{\partial x} \end{cases} \quad (3)$$

Here  $\epsilon_0$  is spontaneous deformation,  $\epsilon_{ij}$  is the tensor of elastic stresses, third equation is non-compatibility of strains one where  $f(\vec{r})$  is the volume density of forces corresponding to defect,  $m = 2(\mu + \lambda)/\lambda$ ,  $\mu$ ,  $\lambda$  - are Lamé coefficients,  $\eta_{ij}$  is non-compatibility tensor. This equation allows to connect the concrete sags of the wall with their accompanied elastic stresses. The solution of the system (3) in the case of interaction of domain boundary with dilatation center (the mathematical model of point elastic defect) shows the following energy of interaction of center with boundary [5]

$$W(\chi_d) = \frac{\mu \epsilon_0^2}{36\pi \chi_d^3} \frac{(3\lambda + 2\mu)^2}{(\lambda + \mu)^2} \frac{1}{[\sqrt{\omega} + \sqrt{\beta + 1} \sqrt{\omega}]} \quad (4)$$

Here  $\omega = 2(\lambda + \mu)/(\lambda + 2\mu)$ ,  $\beta = 8\pi P_0^2 / 2\mu \epsilon_0^2 \tilde{\epsilon}$ ,  $\tilde{\epsilon} \equiv \epsilon_c = \epsilon_a$ ,  $\epsilon_0$  is the change of crystal volume caused by existence of a defect in it. As it is seen from (4) the value of  $W(\chi_d)$  doesn't depend on the sign of  $\Omega_0$ . The dependence of  $W$  on  $\chi_d$  here is essentially more stronger than in (2). The profile of interacting with dilatation center domain wall is complicated enough and is described by the Fig.2.

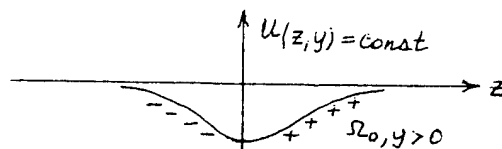
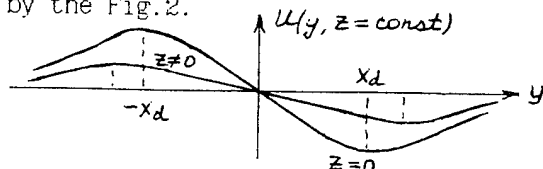


Fig.2. The displacement of domain wall in ferroelectric-ferroelastic interaction with dilatation center.

The interaction of non-ferroelectric inclusion with the domain boundary is caused by at least two factors. On the one hand the impact of such an inclusion with the boundary decreases its area (Fig.3a) and so far as the energy of boundary is positive, the interaction has the attraction character here [6]. Evidently this interaction is a short-distance one as it can be observed only in case of a direct impact of the defect with the boundary and its maximum value as equal to

$$W_c = \gamma \pi R^2 \quad (5)$$

Here  $R$  is the radius of the inclusion. On the other hand the impact of the defect with the boundary decreases the energy of bound charges of the spontaneous polarization arising on the pore surface (Fig.3b) [7]. This process is similar to the decrease of the depolarized field energy occurring at the splitting of the finite form crystal into domains. The last interaction is a short-distanced one too and its maximum value is:

$$W_c = \frac{\pi P_0^2}{\sqrt{\epsilon_c \epsilon_a}} R^3 \quad (6)$$

Fig.3. The domain wall-inclusion interaction caused by a) the decrease of the domain surface area, b) the decrease of depolarized field energy of pore.

#### THE CHANGE IN THE AGING PROCESS OF DIELECTRIC PERMEABILITY AND COERCITIVE FIELD.

The special experiment shows [8,9] that dielectric properties of ferroelectric materials at least of those not near  $T_c$  are determined by the motion of domain boundaries. Their contribution in the value of  $\epsilon$  is defined by the extent of displacement of domain boundaries in a given field. In the defect material the main controlling factor is the obstacle to the domain walls motion created by the defects. It was shown earlier [10] that the domain walls sags in the process of their displacement in the defect pinning region turn out to be very distinctly located. As a result the difference between the average displacement of the wall and its maximum value is not practically observed. The value of displacement of the wall itself is proportional here to force influencing the wall and so may be obtained in the frames of quasi-elastic approximation from condition  $k\ell/\ell^2 = 2P_0 E$  of equality of pressure on the boundary from resetting force to pressure from the side of external field  $E$ , where  $\ell$  is the mean distance bet-

ween defects and coefficient of quasi-elasticity  $k$  in particular for pure ferroelectrics is equal to

$$k = \frac{4\pi p_0 \sqrt{8a}}{\sqrt{\epsilon_0 \epsilon} a} \quad (7)$$

Hence it follows that

$$\bar{U} = \frac{E e^2 \sqrt{\epsilon}}{2\sqrt{2} \pi \sqrt{8a}} \quad (8)$$

( $a$  is radius of the range of interaction of boundary with defect). The domain conclusion in the value of dielectric permeability

$$\epsilon = \frac{8\pi p_0}{E} \frac{\bar{U}}{d} = \frac{4p_0 e^2 \sqrt{\epsilon}}{\sqrt{2} d \sqrt{8a}} \quad (9)$$

where  $d$  is the mean width of domains.

For comparison with the experiment it is necessary to define the mean distance between the wall pinning defects by means of their volume concentration  $n$ . The connection between the values mentioned depends apparently on the distribution of defects over the sample volume. In a newly made (not aging) material the distribution of defects over the sample it is natural to consider as homogeneous one. Taking into account that already in initial state (i.e. before the applying of electric field) the domain boundary is deformed in certain form [10] at the expense of lock-on to nearby defects, the bond between values and here we shall obtain from the relation  $n_0 \bar{U} = 1/\ell^2$ , where  $\bar{U}$  is maximum distance from defect to the plane of mean orientation of the wall when defect locks-on to boundary. The value of  $\bar{U}$  in its turn is calculated from condition  $k\bar{U}^2/2 = w_0$ , where  $w_0$  is maximum energy of interaction of boundary with defect, and in view of (7) is found as

$$\bar{U} = \left( \frac{w_0 \sqrt{\epsilon}}{2\sqrt{2} \pi p_0 \sqrt{8a}} \right)^{1/2} \quad (10)$$

Substituting in (9)  $\ell^2$  expressed through  $n_0$  from the condition  $\ell^2 = 1/n_0 \bar{U}$  with the account of (10) we obtain finally

$$\epsilon(t=0) = \frac{8p_0 \sqrt{p_0} \bar{\epsilon}^{1/4}}{(\delta a)^{1/4} n_0 w_0^{1/2} d} \quad (11)$$

As it is seen from (11) the value of  $\epsilon(t=0)$  here is inversely proportional to the defect concentration that quite corresponds to the experiment [9].

To account of the aging effect it is necessary to take into consideration the enrichment with defect in time the crystal region neighboring with domain boundary and so to take into account the effect of increase of number of pinning points of wall with time. Let us use for this reason the usual kinetics equation

$$\frac{dn(x,t)}{dt} = - \frac{n - n_\infty(x,t)}{\tau} \quad (12)$$

where  $\tau$  is relaxation time and  $n_\infty(x,t)$  is the equilibrium defect concentration. In the case of unmoving boundary the value of  $n_\infty$  doesn't depend on  $t$  and the solution of (12) has simple form

$$n(x,t) = n(x,t=0) e^{-\frac{t}{\tau}} + n_\infty(x) (1 - e^{-\frac{t}{\tau}}) \quad (13)$$

In our case  $n(x,t=0) = n_0$  and dependence of  $n_\infty(x)$  with the account of the effect of deformability of the wall at its lock-on to defects is

$$n_\infty(x) = n_0 \cdot e^{-\frac{W(x)}{\tau}} = \begin{cases} n_0 \cdot e^{-\frac{W_0 - kx/2}{\tau}}, & x \leq \bar{U} \\ n_0, & x > \bar{U} \end{cases} \quad (14)$$

The condition determining the bound of  $n_0$  and  $\ell^2$  is now

$$\int_0^{\bar{U}} n(x) dx = 1/\ell^2 \quad (15)$$

Substituting here  $n(x)$  in the form (13-14) we obtain the indicated bond as following

$$n_0 \bar{U} [e^{-\frac{k}{2\tau}} + (1 - e^{-\frac{k}{2\tau}}) \frac{\sqrt{\bar{U}}}{\sqrt{2}} \sqrt{\frac{\tau}{w_0}} e^{\frac{w_0}{\tau}} \text{erf}(w_0/\tau)] = 1/\ell^2 \quad (16)$$

Changing now in initial relation for  $\epsilon$  (9)  $\ell^2$  through last one with account of expression for  $\bar{U}$  we obtain the expression for change with time of dielectric permeability in aging ferroelectric

$$\epsilon = \frac{\epsilon(t=0)}{[e^{-\frac{k}{2\tau}} + (1 - e^{-\frac{k}{2\tau}}) \frac{\sqrt{\bar{U}}}{\sqrt{2}} \sqrt{\frac{\tau}{w_0}} e^{\frac{w_0}{\tau}} \text{erf}(w_0/\tau)]} \quad (17)$$

As it is seen from (17) the aging effect itself is determined only by the mobility of defects and by energy of their interaction with domain boundary.

The other important character defining the dielectric properties of ferroelectric is the coercitive field  $E_c$  which in model of lateral motion of domain wall may be determined from the condition  $2p_0 E_c = F_m$  where  $F_m$  is maximum force of interaction of boundary with defects.

The value

$$F(\bar{U}) = \int \frac{\partial W(x-\bar{U})}{\partial x} n(x,t) dx = \int \frac{\partial W(x)}{\partial x} n(x+\bar{U},t) dx \quad (18)$$

The substitution here  $W$  and  $n(x,t)$  give us

$$F(\bar{U}) = \frac{n_0 e^{-\frac{t}{\tau}} k}{2} [2\bar{U}\bar{U} - \bar{U}^2] + 2n_0 (1 - e^{-\frac{t}{\tau}}) \cdot \tau \cdot e^{-\frac{k\bar{U}^2}{2\tau}} \cdot \delta h \left( \frac{k\bar{U}}{\tau} \right) \cdot \bar{U} \quad (19)$$

Avoiding unwieldy expressions we shall obtain the value  $E_c$  separately in an unaging ( $E_c^u$ ) and in an aging ( $E_c^a$ ) sample. In first case determining the maximum of  $F(\bar{U})$  and comparing it to value  $2p_0 E_c$  we obtain

$$E_c^u = \frac{n_0 w_0}{2p_0} \quad (20)$$

in the second analogously

$$E_c^a = \frac{n_0 \tau}{p_0} \cdot e^{w_0/\tau} \quad (21)$$

Here we state a certain increase with time of the value of  $E_c$  although its particular changes depend strongly on the relation between  $w_0$  and  $\tau$ .

During the process of exploitation of ferroelectric material in a small amplitude field by analogy with the process of aging the enrichment with defect occurs now in boundaries of all region where quasi-cycled domain wall moves. Besides, it leads to additional pinning of bounds with defects and, therefore, to de-

crease of its contribution to the value of  $\epsilon$ . The character of defect distribution in the region of moving domain wall and, therefore, the value of resulting effect depend on the frequency and amplitude of operating field.

#### REFERENCES

- [1]. Q.Y.Jiang, L.E.Cross, "Effect of porosity on electric fatigue behaviour in PLZT and PZT ferroelectric ceramics", J. Material Science, vol.28, pp.4536-4543, 1993.
- [2]. C.J.Brennan, R.D.Parrella, D.E.Larsen, "Temperature dependent fatigue rates in thin-film ferroelectric capacitors", presented at the 8th Intern.Meet on Ferroelectricity, Gaithersburg, Maryland, August 8-13, 1993.
- [3]. B.M.Darinskii, V.N.Nechaev, V.N.Fedosov, "The interaction Energy between a charge and Ferroelectric Domain Wall", Phys.Stat. Sol.(a), vol.59, pp.701-705, 1980.
- [4]. A.S.Sidorkin and B.M.Darinskii "The structure of domain boundary in ferroelectric with point charge defects", Fizika tverdogo tela, vol.28, pp.285-288, 1986.
- [5]. A.S.Sidorkin and A.A.Shevchenko "The interaction of domain wall in ferroelectric-ferroelastic crystal with dilatation center", Ferroelectrics, vol.141, pp.235-242, 1993.
- [6]. S.V.Vonsovsky, Magnetism. Moskow: "Nauka", 1971, pp.786-804.
- [7]. A.P.Lazarev, V.N.Fedosov, "Depolarizing field of inclusion with finite size in ferroelectrics. Kristallographiya, vol.29, pp.1182-1184.
- [8]. N.A.Burdanina, L.N.Kamysheva, S.A.Gridnev and others "Dielectric and mechanical loss of KH<sub>2</sub>PO<sub>4</sub> crystal with specially added defects", Mechanisms of relaxation phenomena in solid bodies", Kaunas, 1974, pp.239-244.
- [9]. L.N.Kamysheva, N.A.Burdanina, O.K.Zhukov "About dielectric properties of KDP crystal with chromium additions", Kristallographiya, vol.14, pp.940-943, 1969.
- [10]. B.M.Darinskii, A.S.Sidorkin, A.P.Lazarev "The structure and the motion of the domain boundaries of ferroelectrics-ferroelastics", Ferroelectrics, vol.98, pp.245-252, 1989.



# Poster Session P1: Piezoelectrics

# Fine PMN Powders Prepared from Nitrate Solutions

Yoshio Yoshikawa

College of Engineering, Nihon University  
Koriyama, Fukushima 963, Japan

**Abstract** - A partial coprecipitation method was developed in order to synthesize lead magnesium niobate  $\text{Pb}(\text{Mg}_{1/3}\text{Nb}_{2/3})\text{O}_3$  (PMN) powders from nitrate solutions. To obtain a niobium precursor compatible with the chemical routes, peroxo-niobium complex solutions were prepared by dissolving hydrated niobia precipitates in a dilute nitric acid solution with hydrogen peroxide. Fine PMN powders were prepared from these nitrate solutions by two-stage hydrolysis. During calcination, these amorphous powders began to crystallize simultaneously to both a cubic pyrochlore phase and a cubic perovskite phase at about  $400^\circ\text{C}$ .

## INTRODUCTION

Recently, lead magnesium niobate (PMN)-based ceramics prepared from mixed oxides by hot-pressing [1] or hot-isostatic pressing [2] have been investigated for possible use in electrooptic applications. The electrooptic and other dielectric properties of the final ceramic depend on variables related to several processes such as purity, stoichiometry, pyrochlore phase, grain size, etc. The most reported conventional method of PMN powder processing is calcining powder mixtures of  $\text{PbO}$ ,  $\text{MgO}$ , and  $\text{Nb}_2\text{O}_5$  [3,4,5] or mixtures of  $\text{PbO}$  and  $\text{MgNb}_2\text{O}_6$  [6] using solid state techniques. Some problems that have arisen are the dispersability and reactivity of  $\text{MgO}$  powder, eliminating the pyrochlore phase, and  $\text{PbO}$  volatilization at high temperature. There are many experimental procedures with respect to the solid state reaction sequence that have been proposed by different research groups. The differences in the sequences are caused by the reaction kinetics dependency on various processing parameters, such as particle size and surface area of starting materials, and heating rates [6]. It has also been observed that high-energy milling techniques and/or addition of excess  $\text{MgO}$  could improve the kinetic properties and promote the formation of perovskite phase. However, this process yield some contaminations and nonstoichiometric powders.

In general, chemical powder processing is an excellent technique to synthesize high-purity multicomponent materials as it offers good chemical homogeneity on the nanometer-scale. The chemical synthesis of PMN powders, however, has been limited by difficulties in the availability of a niobium precursor compatible with chemical routes. The chemical methods reported previously are sol-gel [8,9,10], aqueous solution [11,12,13], and hydrothermal [14]. The powders from the alkoxide precursors are very expensive and must be prepared under a controlled environment. In this study, a partial coprecipitation method was developed using nitrate salts and niobium oxalate as a niobium source.

## EXPERIMENTAL

**Preparation of niobium precursor solutions:** The solubility of metal oxalates in water are strongly dependent on solution acidity. By acidifying with nitric acid, one can prepare a clear aqueous PMN solution from lead and magnesium nitrates and niobium oxalate. However, coprecipitation by hydrolysis with ammonia solution is restricted by preferential precipitation of lead oxalate. Thus, oxalato-free niobium precursor solutions were prepared from aqueous niobium oxalate solutions by hydrolysis with ammonia solution. After filtering and washing, the hydrated niobia was dissolved in 0.1 M/L- $\text{HNO}_3$  with hydrogen peroxide. Nb content in the precursor solutions was determined by quantitative chemical analysis.

The addition of hydrogen peroxide increased the solubility of the hydrated niobia, and decreased the required time for dissolution. Through this research, practical techniques are suggested to determine the appropriate amount of hydrogen peroxide to attain an acceptable molar ratio of  $\text{H}_2\text{O}_2/\text{Nb}$ . These ratios varied from 1.0 to 10.0. Clear yellow-colored solutions were obtained respectively, indicating that niobium oxalate converted into peroxo-niobium complexes. The effects of hydrogen peroxide contents on precipitated composition from the niobium precursor solutions were characterized by X-ray diffraction (XRD).

**Preparation of PMN Powders:** A flow diagram of the preparation of PMN powders is shown in Fig.1. 0.024 M/L-PN solution was prepared from lead nitrates and the niobium precursor solution. The hydrogen peroxide content in the niobium precursor solution had a 1.65 molar ratio of  $\text{H}_2\text{O}_2/\text{Nb}$ . An amount of excess lead nitrate (10wt%) was added in order to promote the reaction and/or to compensate for the loss of lead oxide during calcination. 15 M/L- $\text{NH}_4\text{OH}$  was poured into the PN solution while continuously stirring the solution. The final pH of the solutions containing the coprecipitates were on the order of 10.5-10.8. Coprecipitates were then washed with water, dispersed in water, and then magnesium nitrate was dissolved in the liquid. Again 15 M/L- $\text{NH}_4\text{OH}$  was poured into the liquid to hydrolyze the magnesium nitrate at about pH11. The precipitates were dried overnight at  $80^\circ\text{C}$ .

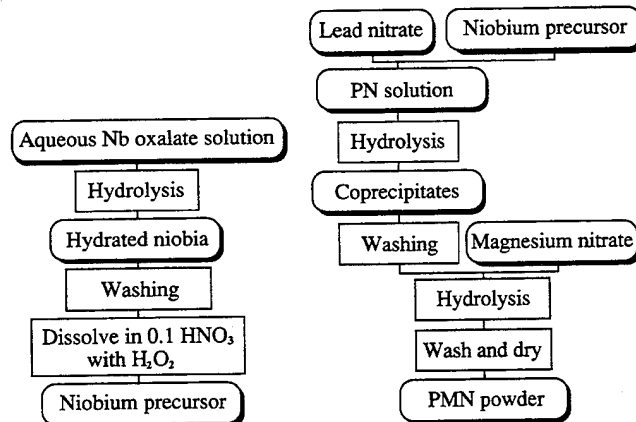


Fig. 1 Flow diagram of the preparation of PMN powder.

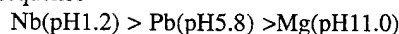
## RESULTS AND DISCUSSION

Niobium precursor solutions prepared with hydrogen peroxide were clear yellow solutions. Niobium exists in these solutions as some peroxo-complexes. It is believed that several kinds of peroxo-niobium complexes exist in aqueous solutions. However, the structure of these complexes have not been reported to my knowledge. As the molar ratio of  $\text{H}_2\text{O}_2/\text{Nb}$  exceeded 5, precipitates from the precursors changed in composition and phase from a gel to a crystalline ammonium perorthoniobate  $(\text{NH}_4)_3\text{NbO}_8$  as shown in Table 1. To achieve sufficient coprecipitate homogeneity in the multicomponent system, a niobium precursor solution, which will precipitate those crystalline compounds by hydrolysis, should be avoided. In this study the niobium precursor solution with 1.65

Table 1. Effect of hydrogen peroxide on precipitates phase

mole ratio of H <sub>2</sub> O <sub>2</sub> /Nb	major precipitates
1.0	gel (hydrated niobia)
2.5	gel (hydrated niobia)
5.0	crystalline (NH <sub>4</sub> ) <sub>3</sub> NbO <sub>8</sub>
10.0	crystalline (NH <sub>4</sub> ) <sub>3</sub> NbO <sub>8</sub>

H<sub>2</sub>O<sub>2</sub>/Nb was used for the PMN powder processing. Preliminary experiment revealed that the relative ease of precipitation in individual solutions corresponding to the 0.008M/L-PMN composition follows the sequence



Considering the mobility of each cations in solid state for the formation of perovskite structure, homogeneous mixing of B-site atoms (Mg and Nb) is very important for low calcination temperatures. Unfortunately, the pH range where precipitation occurs is so different between magnesium and niobium nitrate solutions that homogeneous coprecipitation at molecular level is difficult to attain.

XRD analysis revealed that the gelatinous, yellow precipitates obtained by present method are amorphous. When lead nitrate was hydrolyzed separately, crystalline Pb<sub>3</sub>(NO<sub>3</sub>)(OH)<sub>5</sub> precipitated from the aqueous solution in the pH range of 9 - 11 [15], and crystalline Pb(NO<sub>3</sub>)OH and Pb<sub>7</sub>(NO<sub>3</sub>)<sub>4</sub>(OH)<sub>10</sub> from nitric acidified solutions in the pH range of 6 - 10. Addition of hydrogen peroxide to these solutions prior to hydrolysis, a fine, reddish-yellow, amorphous precipitate (3PbO.2PbO<sub>2</sub>.3H<sub>2</sub>O) was obtained as a result of oxidation of the crystalline lead hydroxides [15]. The hydrogen peroxide, which was introduced by niobium precursor solution oxidized the crystalline lead hydroxides. It is favorable to obtain homogeneous precipitates. The morphology of as-dried powders was determined by scanning electron microscopy. The powder consisted of agglomerates of small particles ranging in diameter from 20 to 30 nm.

Thermogravimetric analysis curve shows a 10 % weight loss below 400°C due to the physical desorption of water and dehydration of precipitates. Differential thermal analysis curve has an endothermic peak at 370°C, corresponding to the dehydration of magnesium hydroxide, and an exothermic peak at 435 °C. The exothermic peak was associated with the crystallization, which was confirmed with the results of XRD.

Figure 2 show the XRD patterns of powders calcined at 410°C. During calcination, these amorphous powders began to crystallize simultaneously to both a cubic pyrochlore phase and a cubic perovskite phase at about 400°C. Pyrochlore and perovskite phases with broad peaks at about 400°C indicate that small size crystallites could form in the fine powders. The pyrochlore phase grew up with increasing temperature and periods, while the perovskite phase did not grow with increasing temperature until at temperature (700°C) was reached where the pyrochlore converted to the perovskite rapidly. Considering the fact that most of crystallization temperatures reported for mixed oxide methods were around 800°C, such lower crystallization temperature reveals that the powders have high reactivities and compositional homogeneities. This reaction sequence differs from those of the sol-gel powders [8,9] and mixed oxide powders [3,4,5] which include several intermediate products in their formation of perovskite phase. T. Fukui et al. [10] reported such direct crystallization of the perovskite phase from their sol-gel powders. Some precipitation conditions and chemical bonds in amorphous precipitates cause the formation of perovskite at low temperatures. It shows the possibility of low temperature calcination for single phase perovskite PMN powders. A beneficial effect of excess PbO on the formation of perovskite structure was observed at 700°C. The excess PbO not only compensates the loss of lead oxide during calcination, but acts as a mineralizer for phase transition.

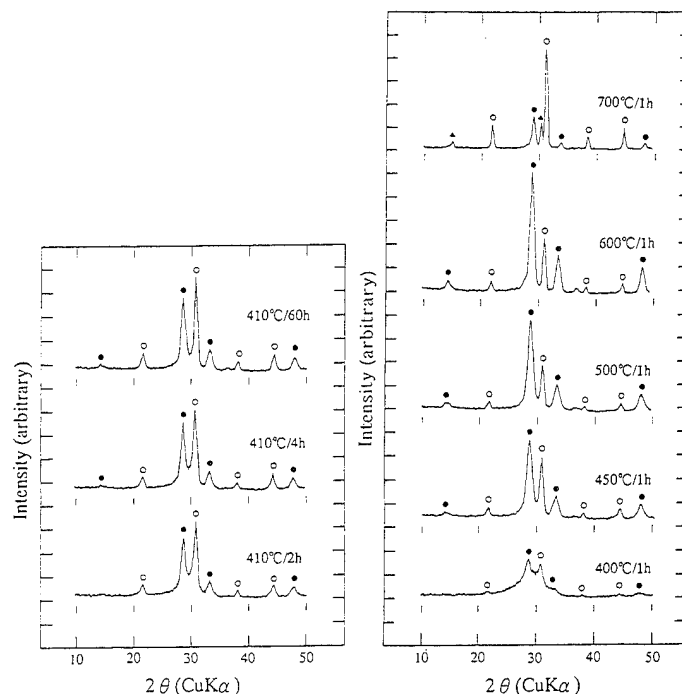


Fig. 2 XRD patterns of powders calcined : (○) perovskite; (●) pyrochlore.

## CONCLUSIONS

A partial coprecipitation method was developed to synthesize Pb(Mg<sub>1/3</sub>Nb<sub>2/3</sub>)O<sub>3</sub> powders from nitrate solutions. Niobium precursor solutions which consisted of oxalato-free, peroxo-complexes, were prepared from niobium oxalate with hydrogen peroxide as the niobium source. Fine PMN powders were synthesized from nitrate solutions by two-stage hydrolysis with ammonia. As-dried powders were 20-30 nm in diameter and crystallized to both a cubic pyrochlore and perovskite phase at about 400 °C.

## REFERENCES

- [1] D. A. Mchenry, J. Giniewicz, S-J. Jang, A.Bhalla and T. R. Shrout, *Ferroelectrics*, 93, 351-359, 1989.
- [2] N. Kim, D. A. Mchenry, S-J. Jang, and T. R. Shrout, *J. Am. Ceram.Soc.*, 73, 923-28, [4], 1990.
- [3] F. Imoto and H. Iida, *Yogyo-Kyokai-Shi*, 80, 197-203, 1972.
- [4] M. Lejeune and J. P. Boilot, *Ceramic International*, 8, 99-103, [3], 1982.
- [5] M. Dambekalne, I. Brante and A. Sternberg, *Ferroelectrics*, 99, 1-14, 1989.
- [6] S. L. Swartz and T. R. Shrout, *Mat. Res. Bull.*, 17, 1245-50, 1982.
- [7] T. R. Shrout and S. L. Swartz, *ibid.*, 18, 663-667, 1983.
- [8] F. Chaput, J-P. Boilot, M. Lejeune, R. Papiernik, and L. G. Hubert-Pfalzgraf, *J. Am. Ceram. Soc.*, 72, 1335-57, [8], 1989.
- [9] P. Ravindranathan, S. Komarneni and R. Roy, *ibid.*, 73, 1024-25, [4], 1989.
- [10] T. Fukui, C. Sakurai and M. Okuyama, *J. Non-Cryst. Solids*, 134, 293-95, 1991.
- [11] H. S. Horowitz, *J. Am. Ceram. Soc.*, 71, C-250-C-251, [5], 1988.
- [12] G.G.-Martel, M. A. Aegerter and P. Barboux, "Better Ceramics Though Chemistry V", *MRS*, 1992, 121-126.
- [13] D. Mohan, *J. Mat. Sci. Letters*, 12, 564-566, 1993.
- [14] T. Yamamoto, Y. Shimizu and M. Watanabe, *J. Ceram. Soc. Japan*, 98, 776-80, 8, 1990.
- [15] Y. Yoshikawa and K. Tsuzuki, *J. Euro. Ceram. Soc.*, 6, 227-235, 1990.

# PHASE T,x-DIAGRAM OF $\text{Pb}_{1-x}\text{Ca}_x\text{TiO}_3$ SINGLE CRYSTALS

V.V. Eremkin, V.G. Smotrakov, L.E. Balyunis,

S.I. Shevtsova and A.T. Kozakov

Institute of Physics, Rostov State University, Stachki

Avenue 194, Rostov-on-Don 344104, Russia

**Abstract** - Phase T,x-diagram of the  $\text{Pb}_{1-x}\text{Ca}_x\text{TiO}_3$  ( $0 \leq x \leq 0.62$ ) solid solution system has been constructed in the range from room temperature to 770 K using data of single crystal optical studies and x-ray microanalysis. Besides the typical for  $\text{PbTiO}_3$  ferroelectric tetragonal and paraelectric cubic phases, two ferro- and non-ferroelectric ones having the pseudomonoclinic unit cell distortions also as two additional tetragonal phases, at least one of which is confidently non-ferroelectric, have been found and their exact stability limits have been determined.

## INTRODUCTION

The  $\text{Pb}_{1-x}\text{Ca}_x\text{TiO}_3$  solid solution system is noticeable for the excellent high anisotropy of piezoelectric properties. Modern ceramic materials based on this system contain up to 34 mol.% of  $\text{CaTiO}_3$ , that is in a neighbourhood of the range where the ferroelectric and "tilted"-type phases may co-exist. Unfortunately, the problems of phase formation and phase equilibrium in the central part of the  $\text{Pb}_{1-x}\text{Ca}_x\text{TiO}_3$  solid solutions have not received any development recently. The majority of the known phase  $\text{Pb}_{1-x}\text{Ca}_x\text{TiO}_3$  T,x-diagrams was constructed in 50th years [1-3]. This works contain some contrarieties and can not be considered as complete ones.

At present it is known that rising of  $\text{CaTiO}_3$  content in the solid solution causes the smooth decrease of the spontaneous deformation in  $\text{PbTiO}_3$  tetragonal unit cell and lowering of the Curie temperature [1-5]. According to the most opinions, at room temperature the boundary between the ferroelectric tetragonal phase and the paraelectric cubic one is disposed near  $x=0.5$  [1, 4, 5]. At the same time there are the different values of it position  $x=0.38$  [2] and  $x=0.60 - 0.62$  [3] in the literature. It is also assumed that two non-ferroelectric phases, which are typical

for pure  $\text{CaTiO}_3$ , exist in the solid solutions with the large content of calcium [1,2]. One of them is tetragonal and other is orthorhombic, having the pseudomonoclinic distortion of the prototype unit cell. Unfortunately the exact limits of their existence were not determined.

The concentration interval  $0.40 \leq x \leq 0.50$  deserves of a special attention. Some of the authors suppose, that the symmetry of  $\text{Pb}_{1-x}\text{Ca}_x\text{TiO}_3$  with  $x > 0.40$  is not tetragonal in spite of the ferroelectric property conservations up to  $x=0.50$  [6,7]. According to other information in this composition region the symmetry stays tetragonal, but regulating of a mutual disposition of the calcium and lead ions is appeared in the solid solution [5]. Despite of such statement, authors [5] could not find the  $90^\circ$  domains, which are typical for a ferroelectric tetragonal phase, in the samples with the calcium content from  $x=0.42$  to  $x=0.50$ .

All stated above points to the necessity of additional studies of phase formations in the  $\text{Pb}_{1-x}\text{Ca}_x\text{TiO}_3$  solid solutions particularly in the concentration range of  $0.40 \leq x \leq 0.50$ . We also suppose that in this case, in the conditions of small lattice distortions and at the presence of non-ferroelectric phases, optical studying of single crystals would be more suitable for the determination of phases and phase transitions than x-ray and neutron diffraction methods as well as measurements of dielectric permittivity.

## EXPERIMENTAL PROCEDURE

### Crystal growth

The  $\text{Pb}_{1-x}\text{Ca}_x\text{TiO}_3$  single crystals were grown by the flux method from high temperature solutions in the  $\text{PbO-CaO-TiO}_2\text{-B}_2\text{O}_3$  system. The optimum melt compositions, given in molar ratio, were varied from 0.55 PbO - 0.04 CaO - 0.13

$\text{TiO}_2 - 0.28 \text{ B}_2\text{O}_3$  ( $x=0.04$ ) to  $0.43 \text{ PbO} - 0.20 \text{ CaO} - 0.12 \text{ TiO}_2 - 0.25 \text{ B}_2\text{O}_3$  ( $x=0.62$ ). Further rising of CaO portion in the melt caused it liquation and resulted in the growth of forcedly shaped crystals on the melt surface. Since an existence of another phase transitions besides the "tilted"-type ones was hardly probable in the solid solutions with greater  $\text{CaTiO}_3$  content, we refused from attempts to select a more suitable solvent.

The starting mixtures were placed into the covered Pt crucibles with the volume  $75 \text{ cm}^3$  and heated up to  $1320-1330 \text{ K}$ . After 3-4 hours of homogenization melts were cooled down to  $1260-1270 \text{ K}$  at rates 3-5 K/h. Then the liquid remained was removed from the crucible and it was cooled down to room temperature in thermal insulation. The crystals obtained had a yellow colour and isometric or plate-like form with the sides parallel to the  $\{100\}$  planes of perovskite prototype lattice. The typical edge dimensions were about 1-3 mm.

#### Optical study

For optical studies we selected the transparent plate-like single crystals with thickness from 30 to  $100 \mu\text{m}$ . Any special treatment of crystal surfaces was not performed. The optical studies were carried out in transmitted polarized light using MIN-8 microscope with a heating chamber having a temperature gradient about  $0.01-0.02 \text{ K/cm}$  and a rate of both heating and cooling from  $1.8 \text{ K/h}$  to  $180 \text{ K/h}$ . Phase transitions were stated on an appearance of phase boundaries, on twinning changes and on birefringence jumps.

#### Determination of chemical composition

The determination of chemical composition of every studied single crystal was carried out on the electron probe x-ray microanalyzer "Camebax-Micro" (France) using the standard method of correction (ZAF).  $\text{PbTiO}_3$  and  $\text{CaTiO}_3$  single crystals served as comparison samples. It was found that  $\text{Pb}_{1-x}\text{Ca}_x\text{TiO}_3$  as well as the earlier studied  $\text{PbZr}_{1-x}\text{Ti}_x\text{O}_3$  single crystals [8] showed the appearance of the  $\text{PbTiO}_3$ -enriched layer, which was generated on crystal surfaces during the flux removal. The thick-

ness of this layer for  $\text{Pb}_{1-x}\text{Ca}_x\text{TiO}_3$  did not exceed  $5 \mu\text{m}$ . Electron probe x-ray microanalysis was held after a previous treatment of every crystal sample, namely after a mechanical removal of the surface layer and sputtering of a thin carbon electroconducted film. This method is characterized by local measurements ( $\sim 1 \mu\text{m}^3$ ). For every sample the composition was measured in 5-10 random local areas on the crystal surface, then this data were statistically treated. The accuracy of chemical composition determination did not exceed 1-1.5 mol.%.

### RESULTS AND DISCUSSION

The  $\text{Pb}_{1-x}\text{Ca}_x\text{TiO}_3$  phase T,x-diagram ( $0 \leq x \leq 0.62$ ) resulted from the performed at heating optical studies has the form, given in Fig. 1. There exist six phases in all. Phase I is the ferroelectric tetragonal one analogous to the ferroelectric phase of  $\text{PbTiO}_3$ , phase II is the paraelectric cubic phase. Phases III and IV have a tetragonal symmetry. For phases V and VI it is characteristic that one of the axes of the optical indicatrix coincides in the direction with an edge of crystal facet and two other axes lie at  $45^\circ$  to respective edges. This orientation of the optical indicatrix is typical for orthorhombic crystals with perovskite structure showing the pseudomonoclinic unit cell distortions. The exact phase boundaries, oriented nearly in parallel to  $\{100\}$ -type planes of perovskite unit cell, were observed during all the phase transitions besides the III  $\rightleftharpoons$  IV one.

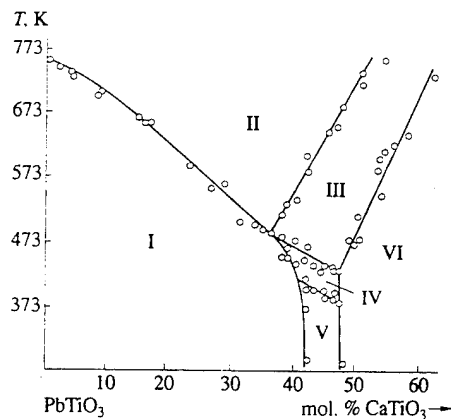


Fig. 1. Phase T,x-diagram of  $\text{PbTiO}_3$ - $\text{CaTiO}_3$  system

The phase transitions were also attended with the noticeable leaps of birefringence values as well as the changes in a domain structure. According to this, it may be supposed that all the phase transitions mentioned above are the first order ones. At the same time any exact phase boundary was not appeared at the transition between the phases III and IV. This phase transition was accompanied by smooth varying in birefringence values together with reconstructions of a domain structure. We are assuming that the phase transition III  $\rightleftharpoons$  IV is at least similar to the second order ones.

The conclusions on a nature of the obtained phases were made on a base of the literary data analysis. The phases III, VI are non-ferroelectric and the phase transitions II  $\rightarrow$  III, III  $\rightarrow$  VI may be concerned to the "tilted"-type ones. It is confirmed by the sharp growth of the transition temperatures at increasing of  $\text{CaTiO}_3$  content as well as by the absence of noticeable dielectric permittivity anomalies within the respective ranges of temperatures and compositions in earlier works. According to [9], during heating this phases are stable in pure  $\text{CaTiO}_3$  in such succession: the orthorhombic structure of  $\text{CaTiO}_3$  undergoes to the tetragonal phase at 1373 K and then to the cubic phase at 1473 K.

Ferroelectric properties of  $\text{Pb}_{1-x}\text{Ca}_x\text{TiO}_3$  solid solutions in the orthorhombic phase V are corroborated by the presence of the dielectric hysteresis loops up to  $x=0.50$  [5,7]. According to our results, at room temperature the boundary divided the tetragonal and orthorhombic ferroelectric phases is disposed at  $x=0.42$ , that is in a good agreement with the values  $x=0.40$  and  $0.38$ , where the authors [7] and [2] ascertain the disappearance of unit cell tetragonality. The presence of this phase boundary can explain the maximum of electromechanical coupling coefficient  $K_p$  and the anomalies on the composition dependences of dielectric permittivity and spontaneous polarization, which were earlier found at  $x=0.40-0.42$  [5].

According to our data, the boundary between the ferro- and non-ferroelectric orthorhombic phases is located at  $x=0.48$ , which slightly differs from the generally accepted value  $x=0.50$ , where the Curie point decreases to ro-

om temperature [1,4,5]. The appearance of double dielectric hysteresis loops, which were marked in [6,7] for  $\text{Pb}_{0.5}\text{Ca}_{0.5}\text{TiO}_3$  ceramics, is probably connected with the field induced phase transition from the non-polar orthorhombic phase to the ferroelectric one and not with the aging processes accompanied by an exfoliation of the starting ferroelectric phase on several others, as it was supposed earlier.

Since some information devoted to the phase IV is absent in a literature, the problem of its nature may be finally solved only as a result of additional studies. However, because the phase transition IV  $\rightleftharpoons$  III is similar to the second order phase transitions, in a case of a ferroelectric state we had to detect the noticeable anomaly on the dependence of dielectric permittivity from temperature. At the same time the Curie point versus composition dependence, given in the work [5], corresponds in the whole to the phase transition line V  $\rightarrow$  IV, but not to the line IV  $\rightarrow$  III, at our phase diagram in the interval from  $x=0.42$  to  $x=0.48$ . Besides the Curie maxima, another were not obtained on the dielectric permittivity versus temperature curves in that work too.

#### SUMMARY AND CONCLUSIONS

The transparent single crystals of  $\text{Pb}_{1-x}\text{Ca}_x\text{TiO}_3$  ( $0 \leq x \leq 0.62$ ) suitable for optical studies were grown from a  $\text{PbO-B}_2\text{O}_3$  flux. The temperature and compositional limits were determined for six phases appeared in the  $\text{Pb}_{1-x}\text{Ca}_x\text{TiO}_3$  solid solutions. Two phases, the ferroelectric tetragonal and paraelectric cubic phases, are typical for  $\text{PbTiO}_3$ ; two others, the non-ferroelectric tetragonal and non-ferroelectric orthorhombic phases, were found earlier for pure  $\text{CaTiO}_3$ . The existence of the ferroelectric orthorhombic phase with the pseudomonoclinic perovskite cell distortion and the second non-ferroelectric tetragonal phase was established for the first time.

#### REFERENCES

- [1]. T. Ikeda, "Some studies on the ternary system  $(\text{Ba-Pb-Ca})\text{TiO}_3$ ", J. Phys. Soc. Japan, vol. 13, pp. 335-340, April 1958.

- [2] M. McQuarrie, "Studies in the system (Ba, Ca, Pb)TiO<sub>3</sub>", J. Amer. Ceram. Soc., vol. 40, pp. 35-41, February 1957.
- [3] M. Dery, "Untersuchungen über seignette-elektrische mischtitanate", Period. Polytechn. Chem. Engug, vol. 4, pp. 307-328, April 1960.
- [4] S.A. Fedulov and Yu. N. Venevtsev, "Studies of the systems PbTiO<sub>3</sub>-CaSnO<sub>3</sub> and PbTiO<sub>3</sub>-CaZrO<sub>3</sub>", Kristallografiya, vol. 9, pp. 358-362, May-June 1964.
- [5] T. Yamamoto, M. Saho, K. Okazaki and Ed. Goo, "Electrical properties and microstructure of Ca modified PbTiO<sub>3</sub> ceramics", Japan J. Appl. Phys., vol. 26, pp. 57-60, February (Suppl. 26-2) 1987.
- [6] E. Sawaguchi, T. Mitsuma and Z. Ichi, "Double hysteresis loop of (Pb<sub>λ</sub>Ca<sub>1-λ</sub>)TiO<sub>3</sub> ceramics", J. Phys. Soc. Japan, vol. 11, p. 1298, December 1956.
- [7] E. Sawaguchi and M.L. Charters, "Aging and the double hysteresis loop of Pb<sub>λ</sub>Ca<sub>1-λ</sub>TiO<sub>3</sub> ceramics", J. Amer. Ceram. Soc., vol. 42, pp. 157-164, April 1959.
- [8] E.G. Fesenko, V.V. Eremkin, V.G. Smotrakov, S.G. Shmalko and A.T. Kozakov, "Crystal growth and study of PbZr<sub>1-x</sub>Ti<sub>x</sub>O<sub>3</sub> phase x,T-diagram", Kristallografiya, vol. 32, pp. 1049-1052, July-August 1987.
- [9] M. McQuarrie, "Structural behavior in the system (Ba, Ca, Sr)TiO<sub>3</sub> and its relation to certain dielectric characteristics", J. Amer. Ceram. Soc., vol. 38, pp. 444-449, December 1955.

# EFFECT OF CALCIA ADDITIONS ON THE ELECTROMECHANICAL PROPERTIES OF SAMARIUM-MODIFIED LEAD TITANATE CERAMICS

W.R. Xue and P.W. Lu

Nanjing Institute of Chemical Technology  
Nanjing, Jiangsu 210009  
P.R.C.

W. Huebner

Department of Ceramic Engineering  
University of Missouri - Rolla  
Rolla, MO 65401

## ABSTRACT

Modified lead titanate ceramics with a composition of  $(\text{Pb}_{0.88-x}\text{Ca}_x\text{Sm}_{0.08})(\text{Ti}_{0.98}\text{Mn}_{0.02})\text{O}_3$ ;  $x = 0.11, 0.13, 0.15$  and  $0.17$  were prepared. Simultaneous doping of samarium and calcium resulted in normal ferroelectric behavior, i.e. the dielectric properties changed in a manner typically associated with isovalent shifting of the Curie temperature. However, the unique attribute of this system appeared for the  $x=0.13$  and  $0.15$  compositions, which exhibited  $k_t$ 's  $\geq 57\%$ .

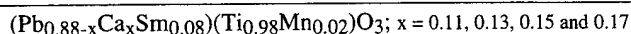
## INTRODUCTION

In recent years polycrystalline lead titanate ( $\text{PbTiO}_3$ ) has received a great deal of attention due to several characteristics, including:

- ♦ highly anisotropic piezoelectric properties [1-10]
- ♦ a lower dielectric constant, which results in a larger piezoelectric voltage coefficient,  $g_{ij}$
- ♦ a high Curie temperature,  $T_c$
- ♦ a high spontaneous polarization,  $P_s$
- ♦ a low aging rate
- ♦ a relatively low mechanical quality factor,  $Q_m$

These attributes make  $\text{PbTiO}_3$ -based materials attractive for many bulk, thin film, composite, and single crystal applications. For example,  $\text{PbTiO}_3$  modified with an alkaline-earth element on the A-site results in a relatively large longitudinal piezoelectric coefficient,  $d_{33}$ , and a low transverse coefficient,  $d_{31}$ . This yields a large ratio of the thickness to lateral electromechanical coupling coefficient ( $k_t/k_p$ ). As such, it can be used for high frequency transducer geometries [11,12] in which the lateral dimensions of the element are similar to the thickness, with minimal noise associated with coupled lateral vibrations. Additional applications include pyroelectric detectors [13-14], hydrophones [15], and 0-3 composites [16].

Many studies have focused on the influence of both isovalent and aliovalent doping on the properties of  $\text{PbTiO}_3$  [1-10, 17-19]. It is well known that of the isovalent alkaline earth additives,  $\text{Ca}^{2+}$  results in the highest anisotropy of the  $k_t/k_p$ , although small additions of  $\text{Sr}^{2+}$  or  $\text{Ba}^{2+}$  can increase the dielectric constant without affecting the piezoelectric properties [19]. Donor doping with rare-earths, or manganese on the B-site also improve the properties, although their impact on the defect structure remains in question. In this paper we have extended the compositional range of previous studies, exploring the system:



This compositional range was chosen to address whether simultaneous Ca and Sm additions result in properties similar or superior to  $(\text{Pb}_{0.85}\text{Sm}_{0.10})(\text{Ti}_{0.98}\text{Mn}_{0.02})\text{O}_3$ , or  $(\text{Pb}_{0.76}\text{Ca}_{0.24})[(\text{Co}_{1/2}\text{W}_{1/2})_{0.04}\text{Ti}_{0.97}]\text{O}_3$ , which have been previously shown to exhibit the overall best combination of dielectric and piezoelectric properties. The primary goal was to further improve the thickness electromechanical coupling coefficient,  $k_t$ , without affecting the anisotropy.

## EXPERIMENTAL PROCEDURE

Figure 1 overviews in detail the processing steps used to prepare the  $\text{PbTiO}_3$ -based ceramics used in this study. Compositional homogeneity was checked using X-ray diffraction (XRD - Scintag X-ray diffractometer). Dielectric measurements were performed on plane parallel disks approximately 1 to 2 mm thick. Gold electrodes were sputtered onto the surface in a vacuum through a mask. Dielectric properties were measured as a function of temperature and frequency using a General Radio GR1689 RLC Digibridge and a muffle tube furnace. Measurements were taken during heating at  $4^\circ\text{C}/\text{min}$  from 25 to  $450^\circ\text{C}$ , at 1, 10 and 100 kHz.

Experimental Procedure		
Raw Materials:	♦ PbO	99%
	♦ $\text{Sm}_2\text{O}_3$	99.9%
	♦ $\text{CaCO}_3$	99%
	♦ $\text{TiO}_2$	99%
	♦ $\text{MnO}_2$	99%
Mixing	♦ Batch: $\text{ZrO}_2$ media:alcohol = 1:4:0.8 (by weight)	
	♦ Polyethylene jar	
	♦ 24 h	
Calcination:	♦ $900^\circ\text{C}$ - 2h; covered $\text{Al}_2\text{O}_3$ crucibles	
Milling	♦ Aggregates broken up with an agate mortar & pestle	
	♦ Milled again as above	
Pressing:	♦ 8 wt% of a PVA solution (5% PVA in $\text{H}_2\text{O}$ )	
	♦ Granulation	
	♦ Uniaxial pressing; 1000 $\text{kg}/\text{cm}^2$	
	[green density: 55% T.D.]	
Sintering:	♦ $650^\circ\text{C}$ -1 h (binder burnout)	
	♦ $1250^\circ\text{C}$ - 2.5 h	
	♦ Covered $\text{Al}_2\text{O}_3$ crucibles; lead source of the same composition	
Poling:	♦ Ground / polished with SiC paper	
	♦ Sputtered gold electrodes	
	♦ $T=150^\circ\text{C}$ ; $E = 60\text{kV}/\text{cm}$ ; $t = 10$ min	

Figure 1: Overview of the processing steps used to prepare the  $\text{PbTiO}_3$ -based ceramics.



After poling, a Berlincourt  $d_{33}$  meter was used to measure the  $d_{33}$  coefficient, and resonance measurements were performed with an impedance analyzer (Hewlett-Packard 4194A Impedance Analyzer with a 41941A Impedance Probe and 16092A Test Fixture).

## RESULTS AND DISCUSSION

Figure 2 exhibits the powders and fired surfaces of the  $(\text{Pb}_{0.78-x}\text{Ca}_x\text{Sm}_{0.08})(\text{Ti}_{0.98}\text{Mn}_{0.02})\text{O}_3$  ceramics. All starting powders were equiaxed, unaggregated, and  $\approx 0.3 - 0.5 \mu\text{m}$  in size. These powder characteristics consistently allowed for high green densities ( $\geq 55\%$  theoretical) and uniform microstructures. XRD patterns revealed no discernible second phases. After sintering, all ceramics were  $\geq 98\%$  theoretical density, which is a must to withstand the high electric fields ( $\geq 50 \text{ kV/cm}$ ) necessary to pole  $\text{PbTiO}_3$ -based systems. The SEM micrographs of Figure 2 reveal uniform microstructures with equiaxed grains of slightly cubic morphology, and grain sizes on the order of  $2-3 \mu\text{m}$ . No effects of the different Ca-doping levels were noted.

Figures 3 through 7 exhibit the temperature dependence of the dielectric properties, and Table I summarizes the dielectric and piezoelectric properties. For each Ca-doping level, the dielectric properties exhibited normal ferroelectric behavior, with a distinct anomaly in the dielectric constant at  $T_c$ . As expected, increasing the  $\text{Ca}^{2+}$  doping level decreased the  $T_c$ , ranging from  $298^\circ\text{C}$  for  $x=0.11$  down to  $251^\circ\text{C}$  for  $x=0.17$ . This can be more clearly seen in Figure 7, which exhibits the dielectric constant at  $100\text{kHz}$  for all four compositions. The phase transition appears to be second order. Increasing the  $\text{Ca}^{2+}$  content also increased the room temperature

dielectric constant from 212 for  $x=0.11$ , up to 288 for  $x=0.17$ . These values are higher than  $(\text{Pb}_{0.85}\text{Sm}_{0.10})(\text{Ti}_{0.98}\text{Mn}_{0.02})\text{O}_3$  which has a  $K \approx 180$ , or  $(\text{Pb}_{0.76}\text{Ca}_{0.24})[(\text{Co}_{1/2}\text{W}_{1/2})_{0.04}\text{Ti}_{0.97}]\text{O}_3$  which has a  $K \approx 190$  [8], but lower than values recently reported for Sr and Ba-doped systems [19]. This is not remarkable, however, since in almost all cases the room temperature dielectric constant of  $\text{PbTiO}_3$ -based systems simply depends upon  $T_c$ . The ability to manipulate the dielectric constant without affecting the piezoelectric properties is desirable in terms of impedance matching for a transducer.

At room temperature the dielectric loss was  $\leq 0.2\%$  for all compositions. With increasing temperature the dielectric loss became dispersive, although losses were acceptably low for  $T < T_c$ . Higher  $\text{Ca}^{2+}$  content compositions exhibited lower dielectric losses for  $T < T_c$ , although all became lossy at higher temperatures. The highly dispersive  $\tan \delta$  at  $T > T_c$  is clearly indicative of an increasing ionic or electronic conduction.

Table I summarizes the room temperature piezoelectric properties. The  $d_{33}$  coefficient is similar to other modified lead titanates, however the  $k_t$  for the  $x=0.13$  and  $0.15$  compositions is  $\geq 57\%$ . This is  $\approx 7\%$  higher than previously reported for any modified lead titanate. Resonance measurements exhibited no trace of a lateral vibrational mode, hence  $k_p = 0$ . Damjanovic [8] showed that under the appropriate processing conditions, a minimum in  $k_p$  can be explained by a change in sign of the piezoelectric coefficient,  $d_{31}$ . The compositions studied here are most likely exhibiting this behavior, although a full set of measurements to determine the real and imaginary components of the piezoelectric coefficients as a function of temperature are currently being performed. The  $Q_m$  is also low for this system, which minimizes ringdown and improves the axial resolution of a transducer.

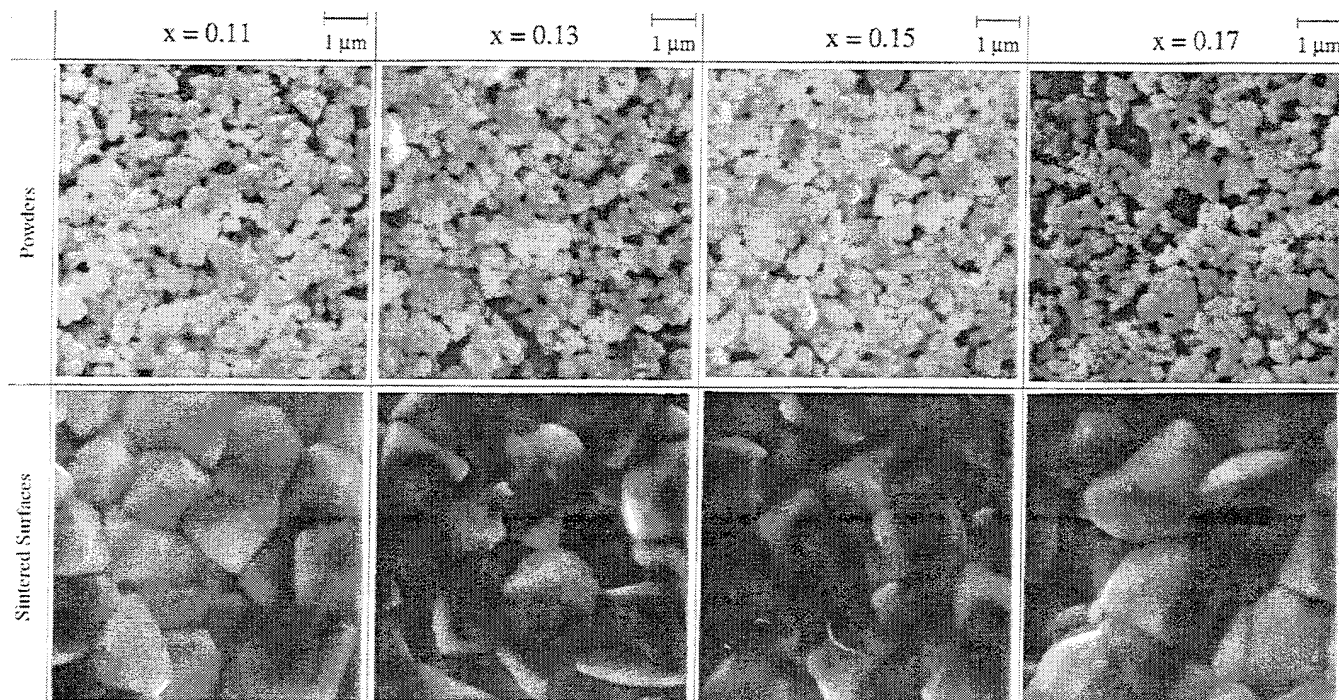


Figure 2: SEM micrographs of the powders and sintered surfaces of the  $(\text{Pb}_{0.88-x}\text{Ca}_x\text{Sm}_{0.08})(\text{Ti}_{0.98}\text{Mn}_{0.02})\text{O}_3$  ceramics.

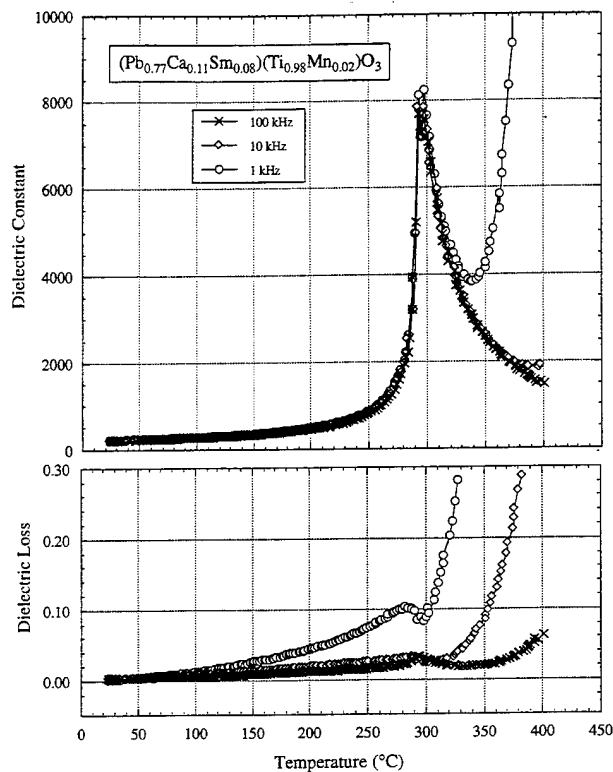


Figure 3: Temperature dependence of the dielectric constant and loss of  $(\text{Pb}_{0.77}\text{Ca}_{0.11}\text{Sm}_{0.08})(\text{Ti}_{0.98}\text{Mn}_{0.02})\text{O}_3$ .

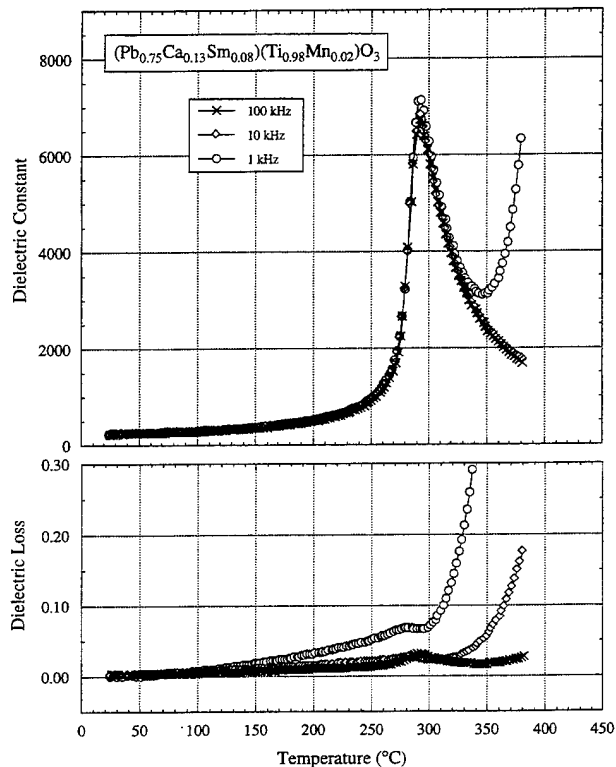


Figure 4: Temperature dependence of the dielectric constant and loss of  $(\text{Pb}_{0.75}\text{Ca}_{0.13}\text{Sm}_{0.08})(\text{Ti}_{0.98}\text{Mn}_{0.02})\text{O}_3$ .

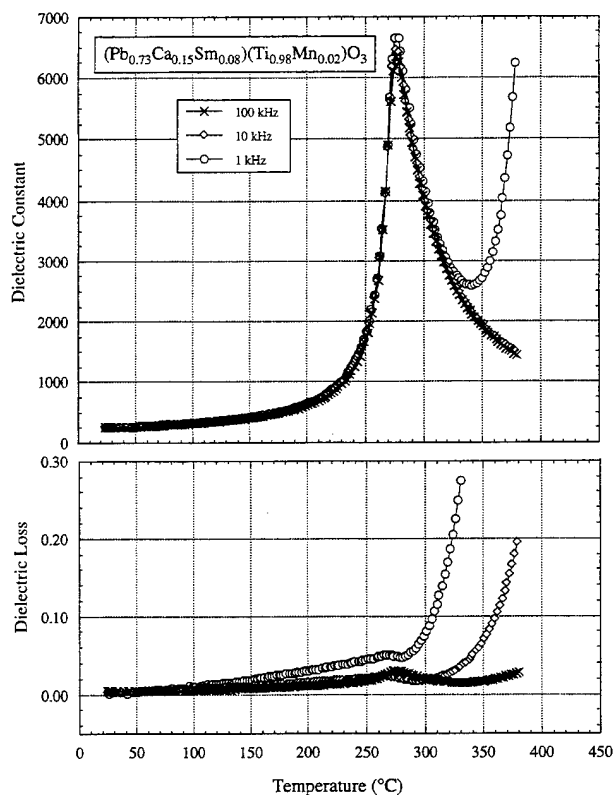


Figure 5: Temperature dependence of the dielectric constant and loss of  $(\text{Pb}_{0.73}\text{Ca}_{0.15}\text{Sm}_{0.08})(\text{Ti}_{0.98}\text{Mn}_{0.02})\text{O}_3$ .

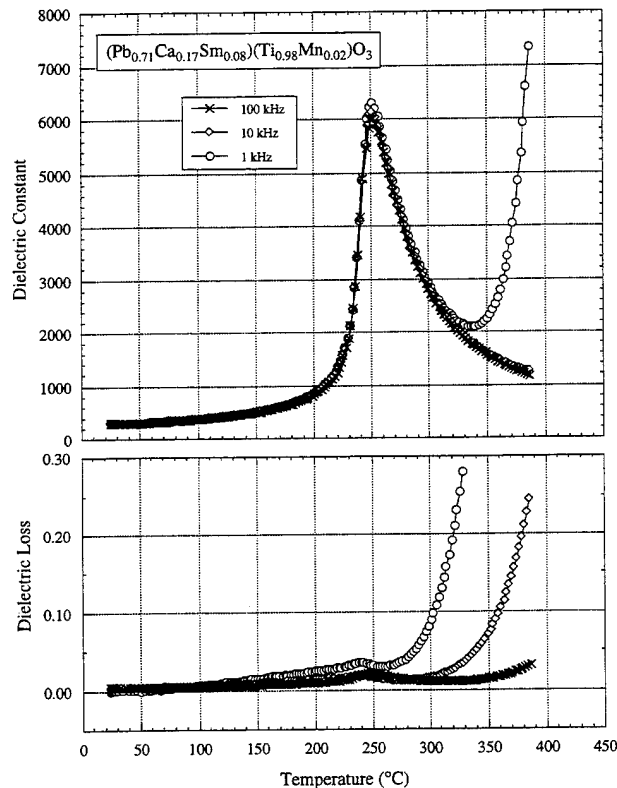


Figure 6: Temperature dependence of the dielectric constant and loss of  $(\text{Pb}_{0.71}\text{Ca}_{0.17}\text{Sm}_{0.08})(\text{Ti}_{0.98}\text{Mn}_{0.02})\text{O}_3$ .

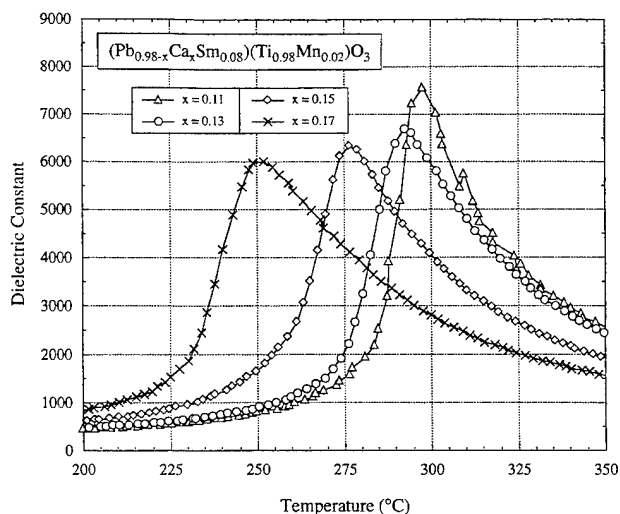


Figure 7: Temperature dependence of the dielectric constant ( $\omega=100\text{kHz}$ ) of  $(\text{Pb}_{0.78-x}\text{Ca}_x\text{Sm}_{0.08})(\text{Ti}_{0.98}\text{Mn}_{0.02})\text{O}_3$ ;  $x=0.11, 0.13, 0.15$  and  $0.17$ .

Table I

Electrical Properties of  $(\text{Pb}_{0.88-x}\text{Ca}_x\text{Sm}_{0.08})(\text{Ti}_{0.98}\text{Mn}_{0.02})\text{O}_3$

	% Ca			
	11	13	15	17
Density ( $\text{g/cm}^3$ )	7.19	7.13	7.09	7.04
$\epsilon$ ( $\omega=1\text{kHz}$ , $T=25^\circ\text{C}$ )	212	228	251	288
$\tan \delta$ ( $\omega=1\text{kHz}$ , $T=25^\circ\text{C}$ )	0.16%	0.10%	0.17%	0.10%
$T_c$	298	294	278	251
$d_{33}$ ( $\text{pC/N}$ )	64	67	72	81
$k_t$ , %	47.6	57.0	57.2	54.8
$k_p$ , %	$\approx 0$	$\approx 0$	$\approx 0$	$\approx 0$
$Q_m$	82	29	39	29
$N_t$ (MHz-mm)	2.259	2.168	2.156	2.237

## CONCLUSIONS

Modified lead titanate compositions were prepared with the purpose of determining whether simultaneous Ca and Sm additions result in desirable piezoelectric and dielectric properties similar or superior to previously-prepared systems. Results showed that the  $(\text{Pb}_{0.88-x}\text{Ca}_x\text{Sm}_{0.08})(\text{Ti}_{0.98}\text{Mn}_{0.02})\text{O}_3$ ;  $x = 0.11, 0.13, 0.15$  and  $0.17$  system exhibits normal ferroelectric behavior, with most properties similar to other modified lead titanates. The unique attribute of this system appeared for the  $x=0.13$  and  $0.15$  compositions, which exhibited  $k_t$ 's  $\geq 57\%$ . Further studies are underway to understand why.

## Acknowledgment

This work was sponsored by the Office of Naval Research under Grant N00014-92-J-1469.

## REFERENCES

- [1] I. Ueda and S. Ikegami, "Piezoelectric Properties of Modified  $\text{PbTiO}_3$  Ceramics," *Jap. J. Appl. Phys.*, **7**, 236-242 (1968).
- [2] S. Ikegami, I. Ueda, and T. Nagata, "Electromechanical Properties of  $\text{PbTiO}_3$  Ceramics Containing La and Mn," *J. Acoust. Soc. Amer.*, **50**[4], 1060-1066 (1971).
- [3] I. Ueda, "Effect of Additives on Piezoelectric and Related Properties of  $\text{PbTiO}_3$  Ceramics," *Jap. J. Appl. Phys.*, **11**[4], 450-462 (1972).
- [4] Y. Yamashita, K. Yokoyama, H. Honda, and T. Takahashi, " $(\text{Pb,Ca})[(\text{Co}_{1/2}\text{W}_{1/2})\text{Ti}]\text{O}_3$  Piezoelectric Ceramics and Their Applications," *Jap. J. Appl. Phys.*, **20**, 183-187 (1981).
- [5] H. Takeuchi, S. Jyomura, E. Yamamoto and Y. Ito, "Electromechanical Properties of  $(\text{Pb,Ln})(\text{Ti,Mn})\text{O}_3$  Ceramics," *J. Acoust. Soc. Amer.*, **72**[4], 1114-1120 (1982).
- [6] J. Mendiola, M.L. Pardo and L.D. Olmo, "Electric Poling Effect on Piezoelectricity of Calcium-Modified Lead Titanate Ceramics," *Ferroelectrics*, **29**, 1249-1252 (1988).
- [7] K. Takeuchi, D. Damjanovic, T.R. Gururaja, S.J. Jang and L.E. Cross, "Electromechanical Properties of Calcium-Modified Lead Titanate Ceramics," pp. 402-405 in *Proc. of the Sixth International Symposium on Applications of Ferroelectrics*, IEEE, New York (1986).
- [8] D. Damjanovic, T.R. Gururaja, and L.E. Cross, "Anisotropy in Piezoelectric Properties of Modified Lead Titanate Ceramics," *Am. Ceram. Soc. Bull.*, **66**[4], 699-703 (1987).
- [9] W.R. Xue, J.N. Kim, S.J. Jang, L.E. Cross and R.E. Newnham, "Temperature Behavior of Dielectric and Electromechanical Coupling Properties of Samarium-Modified Lead Titanate Ceramics," *Jap. J. Appl. Phys.*, **24**, 718-720 (1985).
- [10] P. Duran, J.F. Fdez, F. Capel, and C. Moure, "Large Electromechanical Anisotropic Modified Lead Titanate Ceramics," *J. Mater. Sci.*, **23**, 4463-4469 (1988).
- [11] H. Takeuchi, Y. Ishikawa and E. Yamamoto, "A 7.5 MHz Linear Array Ultrasonic Probe Using Modified Lead Titanate Ceramics," pp. 849-853 in *Proc. of the IEEE Ultrasonics Symposium*, San Diego, CA (1982).
- [12] H. Honda, Y. Yamashita, and K. Uchida, "Array Transducer using Modified Lead Titanate Ceramics," pp. 845-848 in *Proc. of the IEEE Ultrasonics Symposium*, San Diego, CA (1982).
- [13] K. Iijima, "Epitaxial Growth and the Crystallographic, Dielectric, and Pyroelectric Properties of Lanthanum-Modified Lead Titanate," *J. Appl. Phys.*, **60**[8], 2914-2919 (1986).
- [14] A. Ahmad, T.A. Wheat, S. Sherit and B.K. Mukherjee, "Microstructural, Dielectric, Piezoelectric and Pyroelectric Properties of Chemically-Derived Modified Lead Titanate," pp. 520-524 in *Proc. of the Eighth International Symposium on Applications of Ferroelectrics*, IEEE, New York (1992).
- [15] K. Rittenmeyer and R.Y. Ting, "Piezoelectric and Dielectric Properties of Calcium- and Samarium-modified Lead Titanate Ceramics for Hydroacoustic Applications," *Ferroelectrics*, **110**, 171-82 (1990).
- [16] H. Banno, "Recent Progress in Science and Technology of Flexible Piezoelectric Composites in Japan," pp. 67-72, *Proc. of the Seventh International Symposium on Applications of Ferroelectrics*, IEEE, New York (1990).
- [17] W.R. Xue, P.W. Lu, K.P. Liu, G.F. Fu, and Y.L. Wang, "Domain Structure of Modified Lead Titanate Ceramics," pp. 321-323, *Proc. of the Seventh International Symposium on Applications of Ferroelectrics*, IEEE, New York (1990).
- [18] A. Ahmad, T.A. Wheat, J.D. Canaday, A.K. Kuriakose, S.E. Prasad and S. Varma, "Processing and Characterization of Ca, Ce, and Na-Ion Doped Lead Titanates," pp. 516-519 in *Proc. of the Eighth International Symposium on Applications of Ferroelectrics*, IEEE, New York (1992).
- [19] L.M. Troilo, D. Damjanovic, and R.E. Newnham, "Modified Lead Calcium Titanate Ceramics with a Relatively Large Dielectric Constant for Hydrophone Applications," *J. Amer. Ceram. Soc.*, **77**[3], 857-859 (1994).

# EFFECTS OF LANTHANUM DOPING ON THE GRAIN SIZE AND PIEZO- ELECTRIC PROPERTIES OF LEAD TITANATE CERAMICS.

P.Talwar, R.P. Tandon\* and Abhai Mansingh  
Department of Physics and Astrophysics ,University of Delhi,  
Delhi (India),

\*National Physical Laboratory, New Delhi.

## ABSTRACT:

Modified lead titanate ceramics were prepared using mixed oxide route. A fixed amount of (1 mol %) iron (Fe) was added to get highly dense ceramics. Addition of 1 mol % tungsten (W) greatly enhanced the grain size. Lanthanum (La) concentration was changed from 2 to 25 mol %, keeping the concentration of Fe and W fixed at 1 mol %. The Curie temperature and tetragonality decreased with increasing La content. The dielectric constant showed a systematic increase with increasing La content. The piezoelectric coefficient were determined and it was found that the thickness coupling coefficient ( $k_t$ ) showed a marked increase with increasing La content reaching a peak value of 0.60 around 15 mol % while planar coupling coefficient ( $k_p$ ) was found to be almost independent of composition and having a value around 0.1. The hydrostatic figure of merit of about 1400 was achieved for 15 mol % of La which is one of the highest reported values even for hot pressed ceramics.

## INTRODUCTION:

Lead titanate ceramics modified by rare earth elements and alkaline earth elements can be conveniently fabricated. These ceramics hold a lot of promise for various piezoelectric applications due to the presence of large electro-mechanical anisotropy in the coupling factors along and transverse to the direction of polarization. These modified materials are very good candidates for high temperature and high frequency applications [1]. Yamamoto et. al. [2] have reported that by an additional doping by 1 mol%  $\text{MnO}_2$  in a composition having 10 mol %  $\text{La}_2\text{O}_3$  the electro-mechanical thickness coupling factor is increased by 20 to exhibit a higher  $k_t$  value of 0.60. This suggests that by mixed modifications, the La doped ceramics can also be

tailored to exhibit improved piezoelectric and electro-mechanical properties. The ceramic series investigated by Yamamoto et.al. were prepared by hot pressing technique. The present studies were aimed at finding suitable additive to get high piezoelectric coupling coefficient for cold pressed and sintered La modified PZT ceramic. This has been achieved by adding 1 mol % Fe and 1 mol % W in addition to La.

## EXPERIMENTAL

The constituent chemicals (AR Grade) were weighed in proper proportions. While the ceramics contained a fixed amount of Fe and W (1mol %), the quantity of La was varied between 2 to 25 mol %. Additional 2-3 mol% lead was

added [3,4] to compensate the lead losses occurring during sintering. The powders were mixed by ball milling. The ground powders were calcined and sintered at 1200 °C in air atmosphere. Sintered samples were polished and provided with silver electrodes before poling them using high fields at 120 °C. The dielectric properties were measured using GR 1615 capacitance bridge and d-constants were evaluated by Belincourt's  $d_{33}$  meter.  $g_{31}$  was calculated by the relation,  $g_{31} = d_{33} / 2d_{31}$ . Other piezoelectric co-efficients were evaluated as per IRE method [5].

## RESULTS AND DISCUSSION

The grain size in lead titanate depends on the type and the content of the additives and is one of the most important factors influencing the dielectric and piezoelectric properties. The grain size is seen to sharply increase with increasing La content. The minimum grain size exhibited by 3 mol % La composition is 3.3 microns and increases to 9.7 microns for 25 mol% composition (Fig.1). The c/a ratio which is a measure of crystal tetragonality is seen to decrease with increasing La content (Fig.2). c/a ratio is

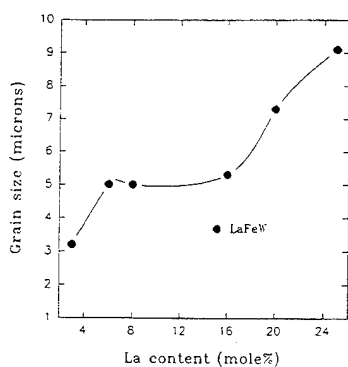


Figure 1. Effect of La content on grain size

found to decrease from 1.0498 to 1.0075 in going from 3 to 25 mol % of La. Pure lead titanate ceramics which crumble at Curie temperature during the cooling process, because of its large spontaneous stress, now upon La addition, do not crumble due to reduced anisotropy.

Due to varying amounts of La modifications, the crystal structure of various compositions does not maintain

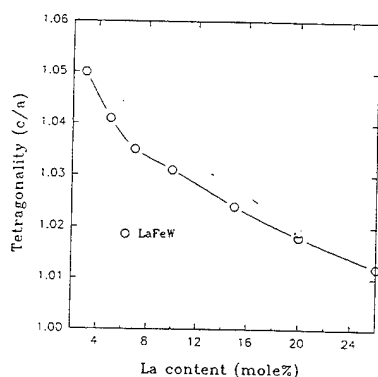


Figure 2. c/a ratio as function of La addition

the same lattice parameters, resulting in different Curie temperatures at which the crystal changes its symmetry along with the unit cell parameters. A linear decrease in the Curie temperature with decreasing c/a ratio is reported by Yamamoto et. al. [2]. for the La modified lead titanate ceramics. Kiyoshi Okazaki [6] has also reported that as the internal stress decreases with decreasing c/a ratio, the Curie temperature is also lowered. The internal stress decreases as  $T_c$  fall below room temperature and finally drops to zero in the cubic region. It can be seen

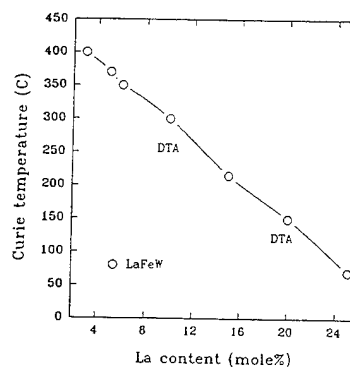


Figure 3. Curie temperature as function of La content

from Fig. 3 that the Curie temperature of LaFeW series exhibit a systematic decrease with increasing La incorporation. The decrease is observed to be linear with slope of 15°C/mol%. i.e. according to the following relation:

$$T_c(x) = T_c(0) - ax$$

where  $a = 15^\circ\text{C/mol}\%$

However, the rate of decrease of  $T_c$  observed in the present case is different from the reported rate at which  $T_c$  falls for only La incorporation in lead titanate ceramics. The observed lower values of Curie temperature in the present case of LaFeW ceramics and interestingly, that too inspite of the presence of a lower rate of  $T_c$  decrease clearly indicates that there must exist an inherent shift in  $T_c$  to the lower temperatures. This basically reflects that the influence of the additional modifiers in the form of Fe and W, is to lower the Curie temperature.

The electromechanical coupling factor of the planar ( $k_p$ ) and thickness dilational mode ( $k_t$ ) are found to show a dependence on the additive content with the former showing only a slight variation, the latter greatly influenced by La concentration. It achieves a maximum value of 0.59 at 15 mol% of La and then drops off rapidly for LaFeW 25. A similar behaviour of coupling factors have also been reported by Yamamoto et. al. (2) also for only La doped lead titanate ceramics.

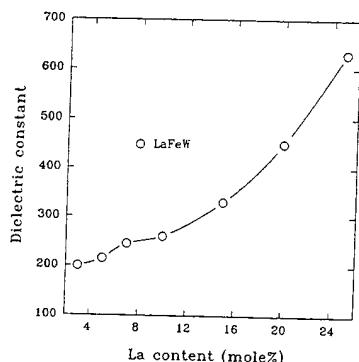


Figure 4. Variation of dielectric constant as a function of La

The variations of dielectric constant with La contents has been shown in Fig.4. The dielectric constant increases with La contents. The dielectric loss tangent (Fig.5) does not show a systematic behaviour and is found to be very sensitive to the processing conditions.

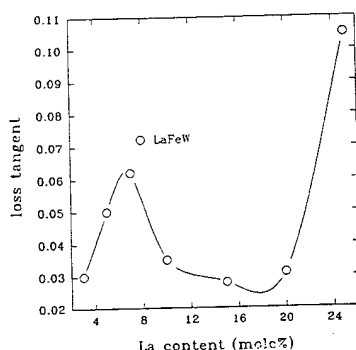


Figure 5. Effect of La on dielectric loss tangent

The hydrostatic charge coefficients are found to exhibit a gradual increase initially as increasing amount of lanthanum replaces lead from its crystal lattice. This effect can be best recognised if one calculates the figure of merit ( $g_h d_h$ ) which is a measure of the performance of a material as hydrophone. These results for LaFeW have been shown in Fig.6 from which it is evident that it shows a peak around 15 mol% La. The value of  $g_h d_h$  is around 300 at lower La contents and a maximum value of 1291 has been seen for LaFeW 15. This value results from the large  $d_{33}$  co-efficient. Although this value is smaller than calcium modified ceramics, it is still among the best reported figure of merit capable of commercial exploitation.

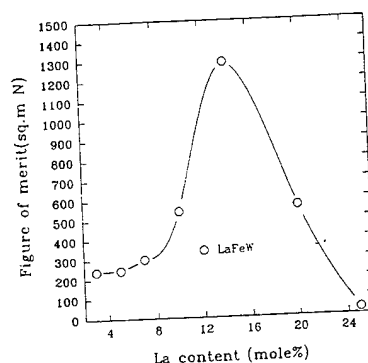


Figure 6. Variation of figure of merit with La addition

## CONCLUSIONS:

Addition of 1 mol% Fe increases the densification and 1 mol% W increases the grain size of lead titanate ceramics. Increasing content of lanthanum decreases tetragonality and increases grain size. At an optimum level of 15 mol% of La, high  $k_p$ , low  $k_r$  and high values of hydrostatic coefficients have been achieved.

The authors wish to acknowledge David Barrow for his assistance in preparing this manuscript.

## REFERENCES:

1. T. Takahashi, Ceramic Bull. **69**(4), 691 (1990)
2. T. Yamamoto, H. Igarashi and K. Okazaki, J. Amer. Ceram. Soc. **66**(5), 363 (1983)
3. S. Takahashi, Ferroelectrics, **41**, 143 (1982)
4. L. Wu, T. Wu, C. Wei and H. Lui, A. Appl. Phys. C, Solid State Phys. **16**, 2823 (1983)
5. Proc. IRE **49**, 1161 (1961)
6. K. Okazaki, Ceram. Bull. **63**(9), 1150 (1984)

# Structural and Thermal Study of $\text{Pb}(\text{Zr}, \text{Ti}, \text{Ce})\text{O}_3$ Ceramics

E.Ching-Prado, W. Perez, R.S. Katiyar, Ajay Garg\*, and D.C. Agrawal\*

Department of Physics, University of Puerto Rico  
San Juan, PR 00931-3343

\*Indian Institute of Technology, Kanpur, India

## Abstract

Solid solution having compositions  $\text{Pb}[\text{Zr}_{x-y}\text{Ce}_y\text{Ti}_{1-x}]\text{O}_3$  with  $y = 0.0, 0.001, 0.00125$ , and  $0.02$  were studied. The samples were prepared from sintered oxides. XRD measurements indicate a mixture of rhombohedral and tetragonal phases in all the samples, where the tetragonal phase increases with increasing  $\text{CeO}_2$  concentration. Also, the  $c/a$  ratio of the tetragonal structure was found to increase with increasing  $\text{CeO}_2$  content. Precipitation of cerium oxide was observed for the sample with  $y=0.02$ , showing that the solubility of  $\text{CeO}_2$  in lead zirconate is lower than 2%. Raman Scattering measurements confirm that all the samples are perovskite in structure, but inhomogeneities were found. The strong line around  $465\text{ cm}^{-1}$ , corresponding to  $F_{2g}$  symmetry, shows the presence of cerium oxide in the sample with  $y=0.02$ . Finally, DSC measurements show that the Curie temperature decreases with increasing  $\text{CeO}_2$  content.

## Introduction

Ferroelectric materials, characterized by anomalous dielectric, optical, and piezoelectric properties are good candidates for a large number of applications, such as non-volatile memories, infrared sensors, optical shutters, etc[1]. A group of these materials are the oxygen octahedral class ( $\text{BaTiO}_3$ ,  $\text{LiNbO}_3$ , etc).  $\text{PbZr}_x\text{Ti}_{1-x}\text{O}_3$  (PZT) is one of these materials that have received increasing attention. PZT is a solid solution of lead zirconate and lead titanate with a morphotropic phase boundary (MPB) from a tetragonal phase to a rhombohedral phase for  $x \sim 0.535$ [2]. Some studies in powders form have shown that the MPB takes place at a specific ratio of Zr to Ti in the PZT solid solution, while others investigators have reported that there is coexistence of tetragonal and rhombohedral phases over a wide range of composition around MPB. Compositional modifications, such as isovalent substitutions, have been studied in order to improve physical properties. Some of these systems are  $\text{Pb}_{1-x}\text{La}_x(\text{Zr}, \text{Ti})\text{O}_3$ ,  $\text{Pb}(\text{Hf}, \text{Zr})\text{TiO}_3$ , and  $\text{Pb}(\text{Sn}, \text{Zr})\text{TiO}_3$ [3].

In this paper we performed x-ray diffraction, Raman scattering and differential scanning calorimetric measurements on PZT ceramics with 0.0, 0.1, 0.125, and 2 mole % of  $\text{CeO}_2$ .

## Sample Preparation

Samples having compositions  $\text{Pb}(\text{Zr}_{x-y}\text{Ce}_y\text{Ti}_{1-x})\text{O}_3$  with  $y = 0.0, 0.001, 0.00125$ , and  $0.02$  were studied. Powders of  $\text{PbO}$ ,  $\text{ZrO}_2$ ,  $\text{TiO}_2$ , and  $\text{CeO}_2$  were ball milled in a plastic jar for 5 hours using alumina balls and triple distilled water. The ball milled slurry was dried and then sieved in a 100 mesh. The

powder was then calcined at  $960^\circ\text{C}$  for 4 hours. The calcined powder was pressed into 12 mm dia. x 4 mm high pellets at 550 MPa. Pellets were then sintered at  $1200^\circ\text{C}$  for 4 hours. The calcined powder was pressed into 1 mm thick discs. The sintered density was measured by measuring the dry weight and the weight in water. The phases and the lattice parameters were obtained by X-ray diffraction from the sintered discs using a diffractometer (Rich Seiter, Iso Debyelex 2002, Germany).

The Raman measurements were performed using a Raman Microprobe (from Instrument S.A). The excitation source was the 514.5 nm line from an Argon ion laser (INNOVA 90-6), and the 588 nm line from a CR-599 dye laser, both manufactured by Coherent Inc. The spectra were measured in the back scattering geometry with 100x microscope objective. Finally, Thermal measurements were made using a differential scanning calorimeter (DSC), from Shimadzu Scientific Instruments.

## Results and Discussions

Fig.1 shows the x-ray diffractograms from samples in the range  $43^\circ < 2\theta < 46^\circ$ . In the unsubstituted sample, the phase present is mostly rhombohedral with small amount of the tetragonal phase. The intensity of the tetragonal peaks increases with increasing  $\text{CeO}_2$  content. Both rhombohedral and tetragonal phases are, however, present at all the compositions. The  $c/a$  value of the tetragonal phase increases on addition of  $\text{CeO}_2$  (Table I). Figure 2 shows that free  $\text{CeO}_2$  is present in 2% samples, i.e. the solid solubility of  $\text{CeO}_2$  in lead zirconate titanate is  $< 2\%$ . The precipitation of the  $\text{CeO}_2$  particles was also observed in the SEM micrographs. The piezoelectric coefficients were found to maximize at 0.1 mole % of  $\text{CeO}_2$ [4].

Also, in Table I appears the Curie temperature values obtained by DSC measurements. The Curie temperature is observed to decrease with increasing  $\text{CeO}_2$  content. Curie temperature extrapolation, from Cerium oxide dependence, for the sample with 2% of  $\text{CeO}_2$  indicates that cerium ions corresponding to 0.145% of  $\text{CeO}_2$  is found in substitutional sites. A previous work of one of the authors shows that the solubility of  $\text{CeO}_2$  is less than 1%[5]. In addition, only the thermal measurements of the sample with 2% of  $\text{CeO}_2$  presents a strong exothermic peak around  $480^\circ\text{C}$ , which can be associated with a second phase predicted as  $(\text{Ce}, \text{Zr})\text{O}_2$  solid solution[6].

Figure 3 show the Raman spectra of the samples. Most of the peaks are similar to those found in  $\text{PbTiO}_3$ [7]. However, the broad band around  $550\text{ cm}^{-1}$  contain contributions of different orientation of the phonon polarization with respect to

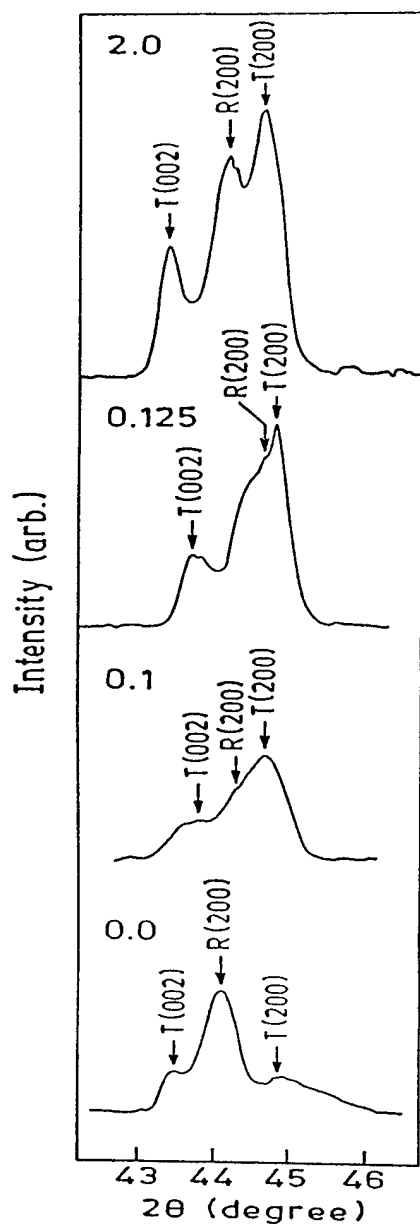


Fig. 1: X-ray diffractograms of sintered sample; the numbers indicate the mole %  $\text{CeO}_2$  in the sample.

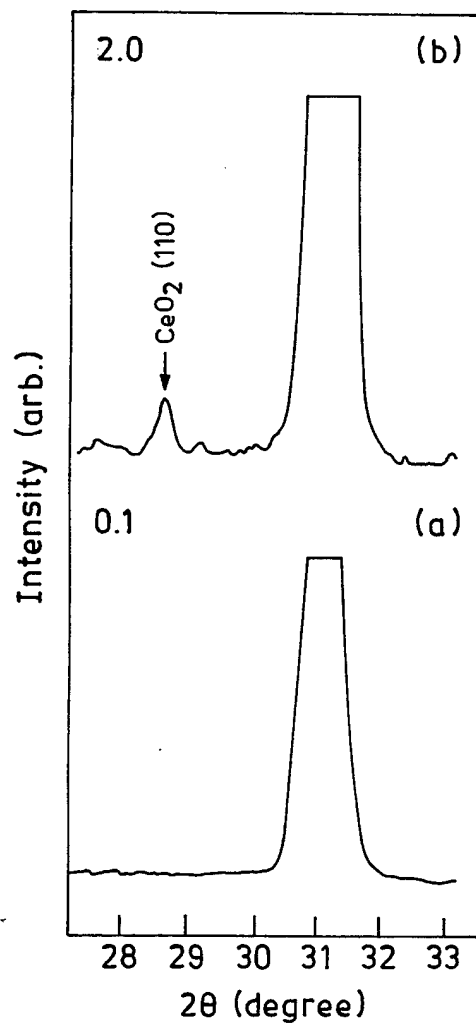


Fig. 2: X-ray diffractograms sintered sample containing (a) 0.1 mole % and (b) 2 mole %  $\text{CeO}_2$ . Note the presence of free  $\text{CeO}_2$  peak in (b).

Table I: Phases,  $c/a$  ratio of the tetragonal phase, and  $T_c$  with the variation of  $\text{CeO}_2$  in PZT.

Mole % Ceria	Phase	$c/a$	$T_c(^{\circ}\text{C})$
0	Rhom + Tet	1.0139	381
0.1	Rhom +Tet	1.015	378.3
0.125	Rhom + Tet	1.0151	373.6
2	Rhom +Tet	1.0155	368.7

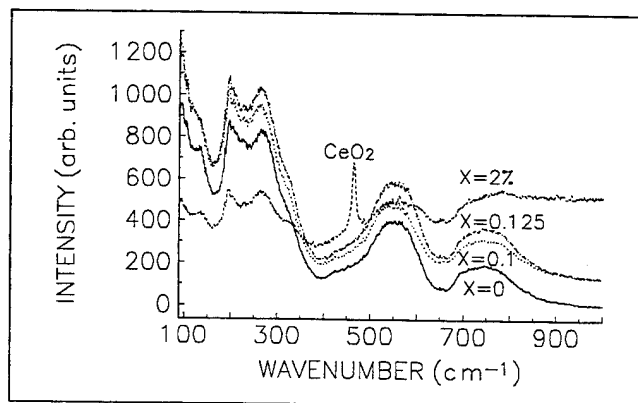


Figure 3: Raman spectra of sintered samples. X indicates the concentration of  $\text{CeO}_2$ .



the  $k$  vector that can lead to a large variation in its frequency. The phonon frequency of this band can change from  $E(\text{TO})$  to  $A_1(\text{TO})$  mode, depending on the orientation in the scattering area of the samples. Similar behavior is found in the broad band around  $750\text{ cm}^{-1}$ , which involve  $E(\text{LO})$  and  $A_1(\text{LO})$  modes[2]. A strong change is observed in the sample with  $y=2\%$ . The background in the low frequency region was lower when compared with the other samples. In addition, a well defined  $A_1(\text{TO})$  peak around  $330\text{ cm}^{-1}$  is found. In agreement with x-ray diffraction, this sample showed residue of  $\text{CeO}_2$ , which is evidenced by the presence of a strong sharp peak around  $465\text{ cm}^{-1}$  corresponding to a  $F_{2g}$  mode[8].

X-ray study of  $\text{PbZr}_x\text{Ti}_{1-x}\text{O}_3$ , around MPB, indicates that the composition in coexistence between the tetragonal and the rhombohedral phases depend upon the amount of substitutional Zr ions[9]. Thus, the X-ray spectra of our PZT samples with different  $\text{CeO}_2$  contents seem similar to PZT samples with  $x$  between 0.53 and 0.59[9]. Our Raman spectra seem consistent with this result. Because, it has been found that in PZT the bands are broadening when  $x$  increase from 0.43 to 0.65. Particularly, the band around  $330\text{ cm}^{-1}$ , associated with an  $A_1(\text{TO})$  mode, where a well defined peak is observed for  $x \leq 0.52$ . While for  $0.65 > x > 0.52$  there is a strong overlap between this band and those centered around  $194\text{ cm}^{-1}$  and  $270\text{ cm}^{-1}$ . So that no clear  $330\text{ cm}^{-1}$  band can be observed[7]. However, the lattice constants of the tetragonal and rhombohedral structures in PZT are practically constant between  $x=0.49$  and  $x=0.64$ , which is not the case in our samples. The  $a$  and  $c$  lattice parameters in the tetragonal phase in our samples increase with the substitution of Ce ions. This result could be understood if the  $\text{CeO}_2$  occupy PZT lattice sites.

The ionic radio of  $\text{Ce}^{+3}$  and  $\text{Ce}^{+4}$  are  $1.01\text{\AA}$  and  $0.87\text{\AA}$ , respectively. Thus, the Ce ions are capable of occupying **A** and **B** sites ions in the  $\text{ABO}_3$  perovskite lattice. When two of the **A** sites are occupied by  $\text{Ce}^{+3}$  in the solubility limit, a Pb vacancy is created in the lattice in order to maintain electroneutrality. Therefore, it is expected that the lattice constants decrease with increasing  $\text{CeO}_2$  content. On the other hand, when the  $\text{Ce}^{+4}$  occupy **B** sites, the lattice constant changes only due to the difference of ionic sizes between  $\text{Ce}^{+4}$  and  $\text{Zr}^{+4}$ , where Zr- ionic radius is  $0.79\text{\AA}$ . So that it is expected that the lattice constants increase with increasing  $\text{CeO}_2$  content[6]. Thus, the Ce ions are occupying the **B** lattice sites.

### Conclusion

We studied  $\text{CeO}_2$  added PZT. Structural measurements indicate a mixture of rhombohedral and tetragonal phases, where the tetragonal phase increase with increasing  $\text{CeO}_2$  concentration. In addition, the Curie temperature was found to decrease with increasing  $\text{CeO}_2$  content. Precipitation of cerium oxide was observed for 2 mole % of  $\text{CeO}_2$ .

### Acknowledgements

This work was supported in part by EPSCoR-NSF Grant EHR-9108775, DOD-ONR Grant N00014-93-1266 and ARO Grant DAAH04-93-2-0008.

### References

- [1] A. Mansingh "Fabrication and Applications of Piezo and Ferroelectric Films", *Ferroelectrics*, Vol.102, pp. 69-84, 1990.
- [2] D.C. Agrawal, S.B. Majumder, Y.N. Mohapatra, S. Sathiah, H.D. Bist, R.S. Katiyar, E. Ching-Prado, and A. Reynes, " Micro-Raman Spectroscopy of Sol-Gel Derived PZT Thin Films", *Journal of Raman Spectroscopy*, Vol. 24, pp.459-462, 1993.
- [3] B. Jaffe, W.R. Cook, and H. Jaffe, "Piezoelectric Ceramics", New York, Academic Press, 1970.
- [4] D. C. Agrawal, and Ajai Garg (To be Published).
- [5] S.K. Nag, D.C. Agrawal, "Piezoelectric and Mechanical Properties of Ceria-Doped Lead Zirconate Titanate Ceramics", *J. Mater. Sci.*, Vol. 27, pp. 4125-4130, Aug. 1992.
- [6] K. Y. Kim, W. S. Kim, Y.B. Son, and S. J. Yoon, "Microwave Dielectric Properties of  $\text{CeO}_2$  Added PCZ Ceramic System", *Ferroelectrics*, Vol. 145, pp.135-141, 1993.
- [7] D. Bauerle, W.B. Holzapfel, A. Pinczuk, and Y. Yacoby, "Temperature and Hydrostatic Pressure Dependence of Vibrational Modes in PZT", *Phys. Stat. Sol.*, Vol. 83, pp. 99-107, 1977.
- [8] W.H. Weber, K.C. Hass, and J.R. McBride, "Raman Study of  $\text{CeO}_2$ ", *Physical Rev. B*, Vol. 48, pp. 178-185, July 1993.
- [9] P. Ari-Gur, and L. Benguigui, "Direct determination of the Coexistence region in the Solid Solutions PZT", *J. Phys. D*, Vol. 8, pp. 1856-1862, 1975.

# THE INFLUENCE OF PROCESSING PARAMETERS ON THE PHYSICAL CHARACTERISTICS OF DOPED LEAD TITANATE CERAMICS

A. Ahmad, T.A. Wheat, M. Hirsch, and A.G. McDonald  
Mineral Sciences Laboratory, CANMET  
Natural Resources Canada  
555 Booth Street  
Ottawa, Ontario, K1A 0G1, Canada

S.E. Prasad and S. Varma  
Sensor Technology Ltd. (B.M. Hi-Tech Division)  
P.O. Box 97  
Collingwood, Ontario, L9Y 3Z4, Canada

**Abstract** -- A series of doped lead calcium titanate based ceramic compositions has been synthesized using a conventional attrition milling process. The influence of dopants and the powder processing conditions on the density, microstructure, dielectric and piezoelectric properties of the products is presented.

## INTRODUCTION

Lead titanate (PT) is a potential candidate for high temperature, high frequency device applications such as ultrasonic transducer elements for non destructive evaluation of materials, medical diagnostics, SAW devices, infrared sensors, hydrophones, etc. (1-3). Compared to PZT, lead titanate based ceramic array transducers can be operated at higher frequencies, thus providing a better image resolution. This is due to the very small lateral or planar mode coupling coefficient of PT allowing the width-to-thickness ratio of the transducer element to be greater than one ( $w/t > 1$ ). This is in contrast to the order of magnitude larger planar mode coupling factor of PZT that restricts  $w/t$  to  $< 1$  to avoid lateral vibrations from affecting the acoustic beam. This makes it difficult for PZT to be used for high frequency array transducers. Due to this dimensional limitation and subsequent difficulties in machining plates into a large number of small elements, the operating frequency of commercially available array transducers is limited to the 5MHz region (4-5).

Unfortunately, a large spontaneous strain and thermal expansion anisotropy of the tetragonal phase in pure lead titanate cause the mechanical fracture of lead titanate ceramics as they are cooled from the sintering temperature through the cubic to tetragonal phase transition at the Curie temperature  $\approx 490^\circ\text{C}$  (6). The lattice constants for lead titanate at room temperature are  $a = 3.904 \text{ \AA}$  and  $c = 4.152 \text{ \AA}$  (7). This gives a  $c/a$  ratio of 1.063 as opposed to 1.01 in isomorphous barium titanate. This large anisotropy in crystal structure often results in the formation of macro and micro-cracks in the sintered body, thus rendering it useless for device applications. In addition, the loss of lead during sintering increases the conductivity of the lead titanate which together with the high coercive field makes poling of these ceramics very difficult resulting in poor dielectric and piezoelectric properties.

It has been shown that highly dense materials having superior dielectric and piezoelectric properties can be produced by doping lead titanate with a variety of alkaline-earth and rare-earth oxides (8-15). Sintering temperatures can also be reduced by adding transition metal oxides along with tungsten oxide as a mineralizer. Furthermore, the addition of MnO increases the insulation resistance, and improves the sinterability and poling conditions of lead titanate. A calcium modified lead titanate ceramic,  $(\text{Pb}, \text{Ca})(\text{Co}_{0.05}\text{W}_{0.05})\text{TiO}_3$  introduced by Yamashita et. al (14), offers a combination of dielectric and piezoelectric properties particularly suitable for high frequency ultrasonic transducers applications.

In our earlier publications (16-19) we reported the development of lead calcium titanate based ceramics containing various A sites dopants. This study gives preliminary data on the influence of various donor dopants on the B site of a modified lead calcium titanate composition.

## MATERIALS AND METHODS

The compositions of various modified lead calcium titanate materials used in this work can be described by the general formula:



where Me represents Nb, W, Mo, V or Ta metal-oxide ions. The following is a list of the intended elemental composition of each powder:

Powder	Composition
A	$\text{Pb}_{0.725}\text{Ca}_{0.275}(\text{Mn}_{0.015}\text{Fe}_{0.01}\text{Nb}_{0.02}\text{Ti}_{0.955})\text{O}_3$
B	$\text{Pb}_{0.725}\text{Ca}_{0.275}(\text{Mn}_{0.015}\text{Fe}_{0.01}\text{W}_{0.02}\text{Ti}_{0.955})\text{O}_3$
C	$\text{Pb}_{0.725}\text{Ca}_{0.275}(\text{Mn}_{0.015}\text{Fe}_{0.01}\text{Mo}_{0.02}\text{Ti}_{0.955})\text{O}_3$
D	$\text{Pb}_{0.725}\text{Ca}_{0.275}(\text{Mn}_{0.015}\text{Fe}_{0.01}\text{V}_{0.02}\text{Ti}_{0.955})\text{O}_3$
E	$\text{Pb}_{0.725}\text{Ca}_{0.275}(\text{Mn}_{0.015}\text{Fe}_{0.01}\text{Ta}_{0.02}\text{Ti}_{0.955})\text{O}_3$

Powders were prepared from high purity commercial raw materials in the form of oxides or carbonates. Batches of 300-400g were initially dry mixed in a rotary tumbler followed by wet attrition milling for two to four hours in a 1-L jar having high purity, 3-mm diameter zirconia milling media and water containing 0.55wt% of 'Darvan C' deflocculant. Water was removed from the slurries by either filtration (if the reagents were insoluble) or rotary evaporation (if soluble components were present). For rotary evaporation, slurries were placed in a 2-L round-bottomed flask and evaporated down to a small volume at room temperature and 15-20mm pressure. A calculated amount of isopropyl alcohol was added to remove the remaining water azeotropically and the slurry was evaporated to dryness. The recovered material from filtration or rotary evaporation was dried overnight at  $120^\circ\text{C}$ .

Batches of 50-100 g of powder were calcined in a zirconia crucible covered with platinum foil placed in a muffle furnace and heated at  $800^\circ\text{C}$  for 2 hours. The calcined batches were re-attrition milled for 2 hours to break up any agglomerates formed during calcination. Re-attrition milled powders were dried by filtration or vacuum evaporation. The powders were pressed into 19 mm diameter discs each weighing between 3.5 and 4.0 g by adding a small amount of polyvinyl alcohol (PVA) as a binder and pressing at 20,000 psi for 30 s.

Before sintering, PVA was removed by heating at  $5^\circ\text{C}/\text{min}$  to  $300^\circ\text{C}$  and holding for 1 h, followed by raising the temperature at

15°C/min from 300° to 600°C and holding for 2 h. The discs were sintered by heating to 600°C at 15°C/min and then to their respective sintering temperatures at 5°C/min.

Sintered discs were lapped with 600 grit silicon carbide to ensure the two faces were parallel and finished with 2/0 and 3/0 SiC abrasive paper on a rotary polisher to give a smooth surface for electroding. Silver electrode paint (Dupont #4731) was applied to each face, allowed to dry and then fired on by heating at 15°C/min to 660°C and soaking for 15 minutes. Two coats were applied.

For piezoelectric measurements, samples were poled at 25 kV/cm in a silicone oil bath at 100°C for 10 minutes. The piezoelectric properties were determined on samples 24 hours after poling using a method similar to that described in IRE standard (20). The thickness mode coupling coefficient ( $K_t$ ) was calculated from the ratio of the overtone frequency  $f_2$  to the fundamental frequency  $f_1$ , of the thickness mode series resonance and using Table 2, in the work of Onoe et al. (21).

## RESULTS AND DISCUSSION

A typical example of the x-ray diffraction patterns of the calcined powders and sintered materials is shown in Fig.1. In all cases, materials sintered at temperatures  $\geq 1000^\circ\text{C}$  produced a single phase  $\text{PbTiO}_3$  type (perovskite) crystal structure. However, trace amounts of  $\text{PbO}$  and  $\text{CaTiO}_3$  phases were present in all compositions calcined at  $800^\circ\text{C}$ . X-ray diffraction patterns of calcined and sintered materials were indexed as a tetragonal phase in all cases. The diffraction patterns clearly showed the effect of dopants on the d-spacings in the material. Unit cell volumes and tetragonality ( $c/a$ ) were calculated by indexing the powder diffraction patterns of the sintered materials and obtaining "a" and "c" values using a program developed at CANMET. Theoretical densities calculated using lattice parameters were used to determine optimum sintering conditions. Sample densities were calculated from the masses and dimensions of lapped, polished discs. Data from the XRD studies, optimum sintering temperatures and observed sintered densities for the above compositions are summarised in Table. 1. The lattice constants for lead titanate at room temperature are  $a = 3.904 \text{ \AA}$  and  $c = 4.152 \text{ \AA}$  (7). This gives a unit cell tetragonality ratio ( $c/a$ ) of 1.063 for undoped lead titanate. Compared to undoped material, the modified lead titanate compositions exhibit a strong reduction of the 'c' parameter (Table 1).

On the other hand, no significant change was observed in the 'a' parameter. As a consequence, the tetragonality of the modified lead titanate compositions is significantly lower than the undoped  $\text{PbTiO}_3$ . The lower tetragonality ( $c/a$  ratio) is a desirable feature as the materials showing less tetragonality are less susceptible to thermal shock. The explanation for this is that large differences in lattice dimensions result in large differences between the rates of thermal expansion along different axes. These differences set up mechanical stresses in randomly oriented poly-crystalline material that result in macro or micro cracking of the ceramic body while cooling through the Curie temperature.

The large anisotropy in the crystal structure is the reason why

pure  $\text{PbTiO}_3$  fractures on cooling and must be doped in order to obtain a useable product. Lower  $c/a$  also facilitates successful poling of the ceramic at high electric fields. As the tetragonal  $c/a$  ratio decreases, the  $90^\circ$  domains can orient more easily with the

Table 1. Unit Cell Parameters and Densities of Various Samples

Property	Composition				
	A	B	C	D	E
a (Å)	3.8893	3.8913	3.8890	3.8910	3.8915
c (Å)	4.0543	4.0390	4.0494	4.0379	4.0499
c/a	1.0424	1.0379	1.0412	1.0377	1.0407
Unit Cell Volume (Å) <sup>3</sup>	61.328	61.099	61.244	61.132	61.330
$\rho$ (Theoret.) (g/cc)	6.986	7.066	7.001	6.985	7.038
$\rho$ (Observed) (g/cc)	6.72	6.95	6.16	6.89	6.88
% Theoret. Density	96.25	98.40	88.0	98.70	97.8
Optimum Sint Temp °C	1175	1175	1210	1000	1175

applied field. Lowering of unit cell tetragonality has also previously been reported (9-14) for other doped lead titanates. With the exception of composition C, all other compositions had sintered densities that were greater than 96% of the theoretical values. The initial powder composition also appears to have a strong influence on the sintering/densification behaviour of the materials, Fig.2. Powders containing 0.02 moles of vanadium ions (composition D) could be sintered to densities approaching 99% of the theoretical value at a temperature of  $1000^\circ\text{C}$ . However composition C containing 0.02 moles of molybdenum ions could not be sintered to  $>88\%$  of the theoretical value, even at sintering temperatures above  $1200^\circ\text{C}$ . The optimum sintering temperatures and sintered densities for these materials are also given in Table 1.

The microstructures of the fractured surfaces were examined using scanning electron microscopy. The sample composition also

appears to have a significant effect on the fracture behaviour of the materials sintered at optimum sintering conditions, Fig.3(a-e). Sample A displayed intra-granular fracture. The material appears to be dense, having only a few pores that range from 1 to  $4\mu\text{m}$  in size. Whereas sample B exhibited inter-granular fracture having pseudo cubic particles ranging from  $1-3\mu\text{m}$  in size. The material is highly dense and possesses a fairly uniform grain size distribution. This confirms the observed high density ( $>98\%$ ) for sample B. Sample C showed predominantly inter-granular fracture. There is some evidence of bimodal grain size distribution with some grains exceeding  $10\mu\text{m}$  in size. The material also appears to be highly porous, having a pore size ranging from 3-

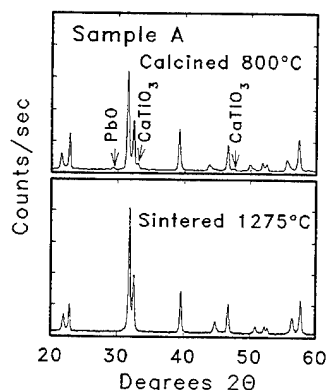


Fig. 1 - Typical XRD Pattern of Calcined and Sintered Material

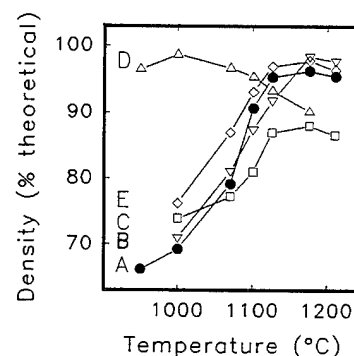


Fig. 2 - Variation of Sintered Density with Temperature

10 $\mu$ m in size. This confirms the observed low density ( $\leq 88\%$  of the theoretical) for sample C. Sample D displayed both inter and intra-granular fracture behaviour. The material is highly dense and possesses a submicron pore size. Many grains appear to have a thin layer on them suggesting the possibility of a liquid phase present during the sintering stage. It should be noted that these materials could be sintered to  $\approx 99\%$  of the theoretical value at

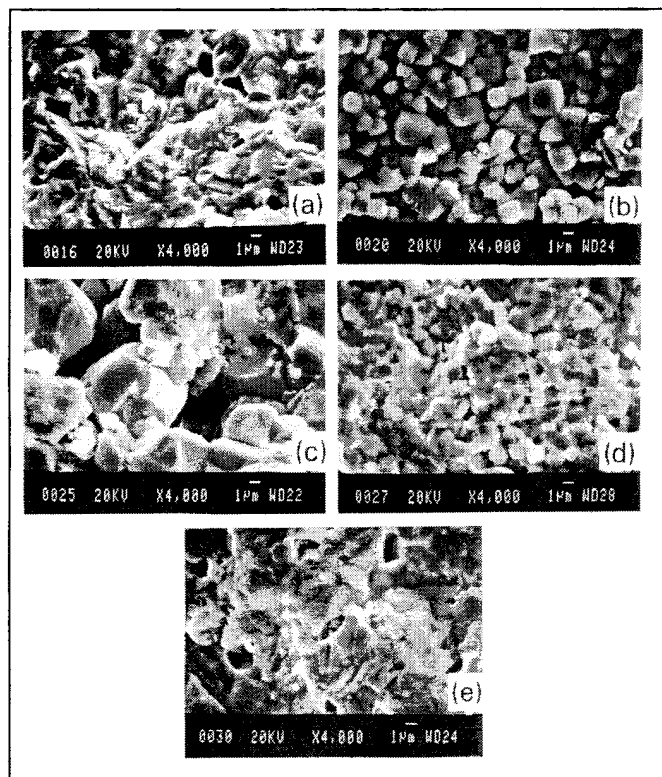


Fig. 3 - SEM Micrographs of Fracture Surfaces

relatively lower sintering temperatures of  $\approx 1000^\circ\text{C}$ . Sample E also exhibited intra-granular fracture that was similar to sample A. The sample is fairly dense, having a pore size ranging from 1-3 $\mu$ m in size.

Data from the dielectric and piezoelectric property measurements are given in Table 2. An examination of the data indicates that both dielectric and piezoelectric properties of the sintered discs are strongly influenced by the powder compositions. Except for sample C that has the lowest dielectric constant ( $\epsilon = 149$ ), all other samples exhibited dielectric constants that were similar to that of pure  $\text{PbTiO}_3$  ( $\epsilon \approx 200$ ). The above characteristics make these materials very promising for high frequency applications.

The lower dielectric constant for sample C could be due to the observed low density and relatively higher porosity in this material. The dielectric loss ( $\tan\delta$ ) in these materials was also found to be composition dependent. Sample C doped with 0.02 mole of molybdenum displayed the highest dielectric loss ( $\tan\delta = 0.084$ ), whereas, sample A and sample E exhibited the lowest values for the dielectric loss ( $\tan\delta = 0.017$ ). In most cases dielectric losses were substantially reduced upon poling the samples at 25 kV/cm. However, because of the initial high dielectric loss values and higher ac conductivity, samples C and sample D could not be poled at electric fields higher than 30 kV/cm. Compared to room temperature values, the ac conductivities for samples A, B and E were increased by about an order of magnitude upon heat treatment of the samples to 150 $^\circ\text{C}$ . However, samples C and D did not exhibit such large increases

upon heat treatment. This suggests that the high temperature conduction mechanisms for these two sets of samples may be different.

The Curie temperature for these samples ranged from 230-260 $^\circ\text{C}$ . No correlation could be derived between the Curie temperature and the cell tetragonality ( $c/a$ ) of the materials. The piezoelectric properties e.g., planar and thickness mode coupling coefficients ( $K_p$  and  $K_t$ ), the ratio  $K_t/K_p$ , longitudinal piezoelectric constant  $d_{33}$  as well as the mechanical quality factor calculated for the thickness mode  $Q_m$  showed strong dependence on the initial powder compositions. Samples A and E exhibited lower  $K_p$ , higher  $K_t$  and larger  $K_t/K_p$  ratio and  $d_{33}$  values. These features enable efficient coupling between the transducer and the medium without

Table 2. Dielectric and Piezoelectric Properties

Property	Composition				
	A	B	C	D	E
$\epsilon(25^\circ\text{C})$ unpoled	182	226	149	200	185
Loss-1kHz 25 $^\circ\text{C}$	0.048	0.017	0.084	0.054	0.017
Loss-poled 25 $^\circ\text{C}$	0.019	0.013	0.064	0.026	0.016
$\sigma_{ac}$ 25 $^\circ\text{C}$ ( $\Omega\text{cm}$ ) $^{-1}$	$1.70 \times 10^9$	$1.90 \times 10^9$	$1.93 \times 10^8$	$9.20 \times 10^9$	$1.65 \times 10^9$
$\sigma_{ac}$ 150 $^\circ\text{C}$ ( $\Omega\text{cm}$ ) $^{-1}$	$1.24 \times 10^8$	$1.0 \times 10^8$	$3.3 \times 10^8$	$4.12 \times 10^8$	$1.30 \times 10^8$
Curie Temp. ( $^\circ\text{C}$ )	253	232	257	261	250
$K_p$	0.042	0.115	0.092	0.080	0.037
$K_t$	0.46	0.34	0.33	0.12	0.47
$K_t/K_p$	10.95	2.96	3.59	1.5	12.70
$Q_m$	414	50	49	291	256
$N_p(\text{Hz m})$	2833	2810	2501	2772	2973
$N_t(\text{Hz m})$	2261	2189	2008	2251	2230
$d_{33} \times 10^{-12}$ (C/N)	61	42	38	14	66

interference from undesirable modes, providing improved resolution (larger signal to noise ratio), hence greater detectability for non-destructive testing (NDT) applications. Samples B, C and D displayed higher  $K_p$  and lower  $K_t$  making them less attractive for NDT transducer applications. It should be indicated that all of the materials investigated were poled at 100 $^\circ\text{C}$  for 10 minutes using an electric field of 25 kV/cm. The poling conditions for these samples have not yet been optimized. It is known (10) that poling of lead calcium titanate based ceramics at higher electric fields results in lowering of  $K_p$  and increase in the  $K_t$  values. Thus the piezoelectric properties presented in Table 2. do not represent the optimum values. It is interesting to note that there appears to be no simple correlation between crystal anisotropy and piezoelectric properties as reported in the literature (10) for similar materials.

## SUMMARY

Donor dopants on the B site in modified lead calcium titanate appear to have a strong influence on the density, crystal structure, microstructure as well as both dielectric and piezoelectric properties of the materials investigated. Except for composition C doped with molybdenum oxide, all other materials could be sintered to high densities ( $> 96\%$ ). Compared to pure lead

titanate, all of the compositions studied displayed lower crystal tetragonality (c/a ratio ref. Table 1). Similar results have been previously reported for other modified lead titanate compositions (9-14). Materials doped with vanadium and tungsten oxides exhibited the lowest crystal anisotropy and also exhibited the highest sintered densities. Scanning electron micrographs showed that small amounts of dopant can substantially influence the fracture behaviour as well as microstructure of the sintered specimens. Samples A and E displayed intra-granular fracture, whereas, samples B and C exhibited inter-granular fracture. On the other hand, sample D exhibited both inter- and intra-granular fracture. SEM studies also confirmed the observed high densities for samples A, B, D and E, and the higher porosity in sample C.

Both the dielectric and piezoelectric properties in these materials are strongly influenced by the sample composition. Doping with vanadium and molybdenum ion produces more conductive and lossy materials resulting in electrical breakdown of the samples during poling at electric fields higher than 30 kV/cm. Of all the materials studied, A and E showed the most favourable piezoelectric properties, having a thickness coupling coefficient of  $\approx 0.47$ , a planar coupling coefficient of  $\approx 0.040$  and a  $d_{33} > 60$ . These characteristics make them promising candidates for use as transducer elements for non-destructive testing of materials and similar device applications.

### ACKNOWLEDGEMENTS

The authors would like to thank P. Carrière, D.R. Owens and Dr. J.T. Szymanski of CANMET, for the XRD and SEM data.

### REFERENCES

1. Y. Yamashita, K. Yokoyama, H. Honda and T. Takahashi, "(Pb,Ca)  $(\text{Co}_{1/2}\text{W}_{1/2})\text{TiO}_3$  Ceramics and their Applications"; *Jap. J. Appl. Phys.* vol. 20 (Suppl. 20-4), pp. 183-187; 1981.
2. Y. Ito, H. Takeuchi, K. Nagatsuma, S. Jyomura and S. Ashida, "Surface Acoustic Wave Properties of  $(\text{Pb,Ln})(\text{Ti,Mn,In})\text{O}_3$  Ceramics (Ln = La and Nd)", *J. Appl. Phys.* vol. 52(5), pp. 3223-3228, 1981.
3. N. Ichinose, "Electronic Ceramics for Sensors", *Amer. Ceram. Soc. Bull.* vol. 64(12), pp. 1581-1585, 1985.
4. Takeuchi, H., Ishikawa, Y., Yamamoto, E. "A 7.5 MHz Linear Array Ultrasonic Probe Using Modified Lead Titanate Ceramics" in *Proceedings of the IEEE Ultrasonic Symposium*, San Diego, CA. Institute of Electrical and Electronic Engineers, 1982, pp. 849-853.
5. Honda, H., Yamashita, Y. and Uchida, K. "Array Transducer Using Modified Lead Titanate Ceramics", *ibid.*, pp. 845-848.
6. Matsuo Y., Fujimura M. and Sasaki H., "Lead Titanate Ceramics Doped with Manganese Oxide", *J. Amer. Ceram. Soc.* vol. 48, pp. 111-112, 1965.
7. Shirane, G., Pepinsky, R. and Frazer, B.C., "X-Ray and Neutron Diffraction Study of Ferroelectric  $\text{PbTiO}_3$ ", *Acta Cryst.* pp.131-, 1956.
8. Ueda, I. "Effect Of Additives on Piezoelectric and Related Properties of  $\text{PbTiO}_3$  Ceramics"; *Japanese J. of Appl. Phys.* vol. 11(4), pp.450-462, 1972.
9. Ikegami, S., Ueda, I. and Nagata, T. "Electromechanical Properties of  $\text{PbTiO}_3$  Ceramics Containing La and Mn"; *The J. Acoust. Soc. of America* vol. 50(4) (Part 1), pp. 1060-1066, 1971.
10. Duran, P., Falez Lazano, J.F., Capel, F. and Moure, C. "Large Electromechanical Anisotropic Modified Lead Titanate Ceramics", *J. Mater. Sci.* vol. 24, pp.447-452, 1988.
11. Ueda, I. and Ikegami, S. "Piezoelectric Properties of Modified  $\text{PbTiO}_3$  Ceramics", *Jap. J. Appl. Phys.* vol. 7(3), pp.236-242, 1968.
12. Yamashita, Y., Yoshida, S. and Takahashi, T. "Effect of MnO Additive on Piezoelectric Properties of Modified  $(\text{Pb,Ca})\text{TiO}_3$  Ferroelectric Ceramics" in *Proceedings of the 4th Meeting on Ferroelectric Materials and Their Applications*, Kyoto, 1983. Also *Jap. J. Appl. Phys.* vol. 22, Supplement 22-2, pp.40-42, 1983.
13. Ahmad, A., Wheat, T.A., Kuriakose, A.K., Quon, D.H.H. and Berry, R. "The Effect of Processing Parameters on the Properties of Modified Lead Titanate", *Division Report MSL-88-19(OP)*, CANMET, EMR, Canada, 1988.
14. Yamashita, Y., Yokoyama, K., Honda, H. and Takahashi, T. "(Pb,Ca)(( $\text{Co}_{1/2}\text{W}_{1/2}$ ), Ti) $\text{O}_3$ ) Piezoelectric Ceramics and Their Applications", *Jap. J. Appl. Phys.* vol. 20(Supplement 20-4), pp. 183-187, 1981.
15. Ahmad, A., Mikhail, S., Chehab, S., Owens, D.R., and Turcotte, A.M., "Microstructure and Thermophysical Characteristics of  $\text{PbTiO}_3$ -Based Ceramics", *J. Mater. Sci.* vol. 27, pp. 1772-1780, 1992.
16. Ahmad, A., Besso, K., Chehab, S., Wheat, T.A., and D. Napier, "Chemical Processing of Modified Lead Titanate", *J. Mater. Sci.* vol. 25, pp. 5298-5302, 1990.
17. Ahmad, A., Kuriakose, A.K., Canaday, J.D., Wheat, T.A. and Chehab, S.F., "Alkaline-earth and Rare-earth Doped Lead Titanates", *Jour. Can. Ceram. Soc.* vol. 60(1), pp. 56-60, 1991.
18. Ahmad, A., Canaday, J.D., Wheat, T.A., Kuriakose, A.K., Prasad, S.E. and Varma, S., "Processing and Characterization of Ca, Ce, and Na-ion doped Lead Titanates" in *Proceedings of the 8th International Symposium on the Applications of Ferroelectric Ceramics*, IEEE Catalog Number, 92 CH 3080-9, pp. 516-519, 1992.
19. Ahmad, A., Wheat, T.A., Sherrit, S. and Mukherjee, B.K., "Microstructure, Dielectric, Piezoelectric and Pyroelectric Properties of Chemically Derived Lead Titanate" in *Proceedings of the 8th International Symposium on the Applications of Ferroelectric Ceramics*, IEEE Catalog Number, 92 CH 3080-9, pp. 520-523, 1992.
20. "IRE Standard on Piezoelectric Crystals: Measurements of Piezoelectric Ceramic, 1961", *Proc. Inst. Radio Engineering*, vol. 49(7), pp. 1161-69, 1961.
21. Onoe, M., Tietstien, H.F., and Meitzler, A.J., "Shift in the Location of Resonant Frequencies by Large Electromechanical Coupling in Thickness-Mode Resonators", *J. Acoust. Soc. Am.*, vol. 35(1), pp. 36-42, 1963.

# PZT Ceramics from Hydrothermally Synthesized Powders

C.H. Lin, T.S. Chin, and S. C. Pei

Department of Materials Science, National Tsing Hua University, Hsinchu, Taiwan

J.Y. Huang and C.H. Li

Institute of Electro-Optical Engineering, Chiao-Tung University, Hsinchu, Taiwan

**Abstract**—PZT ( $\text{PbTi}_{1-x}\text{Zr}_x\text{O}_3$ ,  $x=0.52$  to  $0.64$ ) powders were hydrothermally produced at  $200^\circ\text{C}$  for 24 hrs, from a solution containing  $\text{Ti}(\text{OH})_4 \cdot x\text{H}_2\text{O}$ ,  $\text{ZrOCl}_2$ ,  $\text{Pb}(\text{CH}_3\text{COO})_2$ , and  $\text{NaOH}$ . PZT ( $x=0.52$ ) powder was also produced by the solid-state sintering method. The powders from both the hydrothermal method and the solid-state reaction method were pressed and subsequently sintered at  $1250^\circ\text{C}$  for 2 hrs. The characteristic difference of the ceramics produced from both powders were compared with each other.

The hydrothermal PZT powders are chemically homogeneous, and around  $0.2 \mu\text{m}$  in particle size (numerical average). The solid-state reacted powder is a mixture of tetragonal  $\text{PbTiO}_3$ , rhombohedral  $\text{PbZrO}_3$ , unreacted  $\text{TiO}_2$ , and unreacted  $\text{PbO}$ .

The PZT ceramics from hydrothermal powders become softer, i.e., lower  $E_c$  and higher  $P_r$ , as more Zr is added in PZT (higher  $x$  value). The  $K$ ,  $Q$ , and  $K_p$  values reach maximum when  $x=0.54$ . The  $Q$  value monotonously increases with the  $x$  value and the  $K_p$  value linearly increase with the grain size of the ceramics.

The ceramics from the hydrothermal method have higher density, grain size, dielectric constant,  $K_p$ , and lower  $D$  and  $Q_m$ . The hydrothermal powders are much more sinterable than powders produced by the solid-state reaction method.

## INTRODUCTION

PZT powders used for producing PZT ceramics are conventionally produced by solid-state reaction method. Sol-gel method is sometimes used to produce high quality PZT powders. However, this process is tedious and expensive because of scarce raw materials used. Hydrothermal method<sup>[1-4]</sup> was reported to be capable of producing PZT powders. The advantages of hydrothermal method are: that (1) powders produced by this method are homogeneous in chemical composition and particle size, (2) presintering can be avoided, and (3) low sintering temperature is possible because of finer particle size. Few reports have investigated the properties of PZT ceramics produced from the hydrothermal powders. In this study, a comparison was made of the difference between PZT ceramics produced from the hydrothermal powders and those from the solid-state reaction method. Both the hydrothermal method and solid-state reaction method were used to produce PZT powders, thereby, producing PZT ceramics from these powders. A composition of  $x=0.52$  to  $0.64$  in  $\text{PbTi}_{1-x}\text{Zr}_x\text{O}_3$  was selected in this study, because there is a rhombohedral-tetragonal phase boundary change between these compositions and PZT ceramics demonstrate significant features at these compositions<sup>[4]</sup>.

## EXPERIMENTAL

PZT( $\text{PbTi}_{1-x}\text{Zr}_x\text{O}_3$ ,  $x=0.52$  to  $0.64$ ) powders were hydrothermally produced at  $200^\circ\text{C}$  for 24 hrs, from a slurry solution containing  $\text{Ti}(\text{OH})_4 \cdot x\text{H}_2\text{O}$ ,  $\text{ZrOCl}_2$ ,  $\text{Pb}(\text{CH}_3\text{COO})_2$ , and  $\text{NaOH}$ . PZT( $x=0.52$ ) powder were also produced by solid-state reaction method by reacting  $\text{PbO}$ ,  $\text{ZrO}_2$ , and  $\text{TiO}_2$  together at  $800^\circ\text{C}$  for 4 hrs. The powders from both the hydrothermal method and the solid-state reaction method were pressed at  $1.75 \text{ ton/cm}^2$  and subsequently sintered at  $1250^\circ\text{C}$  for 2 hours.

Laser particle size analyzer, STEM, X-ray diffractometer, and impedance analyzer were used to examine the characteristics of PZT powders and ceramics. Detailed preparation processes and examination procedures of PZT powders and ceramics have been reported elsewhere<sup>[5-6]</sup>.

## RESULTS AND DISCUSSION

Electron micrographs in Figure 1 and X-ray diffraction patterns in Figure 2 revealed that the hydrothermal PZT powders ( $\text{PbTi}_{1-x}\text{Zr}_x\text{O}_3$ ,  $x=0.52$  to  $0.64$ ) produced from the hydrothermal method are all cubic and the PZT powder ( $x=0.52$ ) produced from the solid state reaction method at  $800^\circ\text{C}$  is a mixture of tetragonal  $\text{PbTiO}_3$ , rhombohedral  $\text{PbZrO}_3$ , unreacted  $\text{TiO}_2$ , and unreacted  $\text{PbO}$ . After the powders were pressed and sintered, the structure of the powders have changed. X-ray diffraction patterns in Figure 3 indicated that the structure of sintered PZT ceramics produced from the hydrothermal method was changed to tetragonal, which was the stable form<sup>[4]</sup>, if  $x=0.52$  or  $0.54$ , and rhombohedral if  $x=0.56$ ,  $0.60$ , or  $0.64$ . The structure of sintered PZT ceramics produced from solid-state reacted powder was changed to rhombohedral, which was the stable form at this composition<sup>[4]</sup>.

The particle size of the hydrothermal powders in Figure 4a is around  $0.2 \mu\text{m}$  in numerical average and decreased with increasing  $x$  value. The density of the sintered PZT in Figure 4b was found to be independent of  $x$  value. The grain size of the sintered PZT ceramics reached maximum when  $x=0.54$  (Figure 4c), which corresponds to rhombohedral-tetragonal phase change boundary.

The P-E curves of the PZT ceramics in Figure 5 show that the hysteresis loop gradually became narrower and taller, i.e., the material became softer as  $x$  value increased from  $0.52$  to  $0.64$ . The  $E_c$  value (Coercive field) and  $P_r$  value (remanent polarization), as respectively shown in Figures 6a and 6b, are obtained from the hysteresis loops of Figure 5. The decrease of  $E_c$  value and the increase of  $P_r$  value imply that the electrical moments of the PZT ceramics become more likely to flop when it was subject to a reverse field. This fact is agreeable with the literature<sup>[4]</sup> that this material will become softer as more Zr is added. The  $K$  value (dielectric constant),  $Q$  value (dissipation factor), and  $K_p$  value (electro-mechanical coupling factor) of the PZT ceramics (as respectively shown in Figure 6c and 6d) reach maximum when  $x=0.54$ .



Figure 1 Electron micrograph of hydrothermal  $\text{PbTi}_{1-x}\text{Zr}_x\text{O}_3$  powders reacted at  $200^\circ\text{C}$  for 24 hrs,  $x=0.52$ .

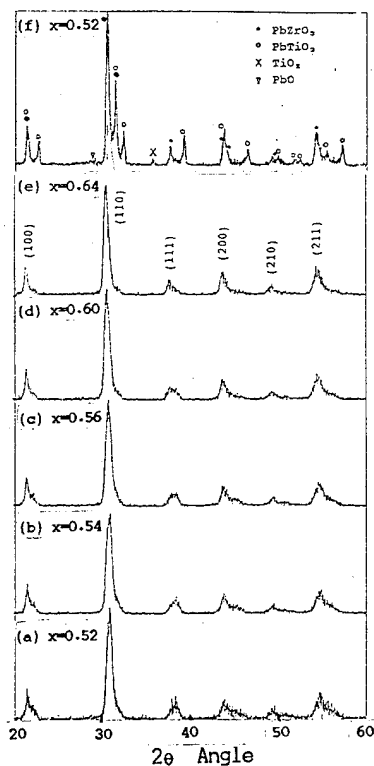


Figure 2 X-ray diffraction patterns of  $\text{PbTi}_{1-x}\text{Zr}_x\text{O}_3$  powders. (a) to (e) by hydrothermal method reacted at  $200^\circ\text{C}$  for 24 hrs. (f) by solid-state reaction method at  $800^\circ\text{C}$  for 4 hrs.

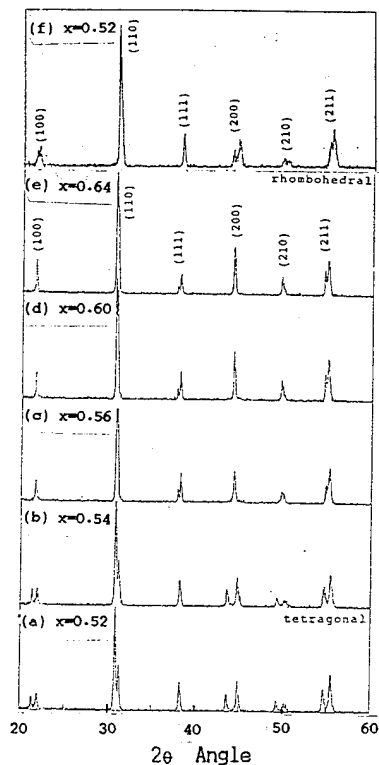


Figure 3 X-ray diffraction patterns of  $\text{PbTi}_{1-x}\text{Zr}_x\text{O}_3$  ceramics sintered at  $1250^\circ\text{C}$  for 2 hrs. (a) to (e) are from hydrothermal powders, and (f) is from solid-state reacted powder.

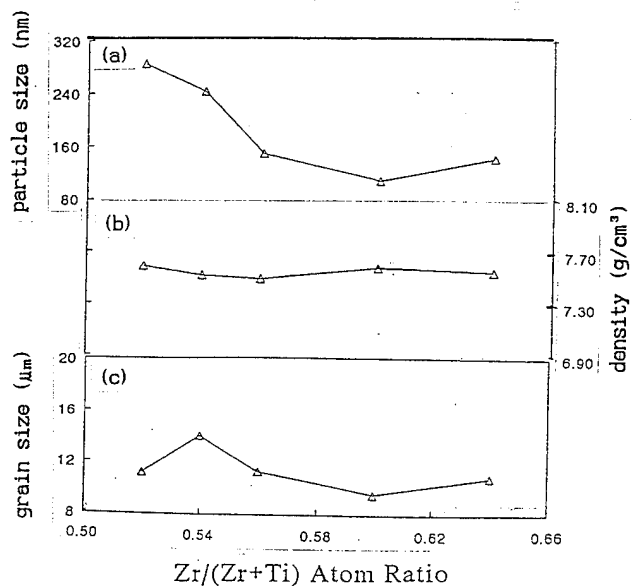


Figure 4 Relationships between  $x$  value of  $\text{PbTi}_{1-x}\text{Zr}_x\text{O}_3$  with (a) particle size, (b) density, (c) grain size of hydrothermal ceramics.

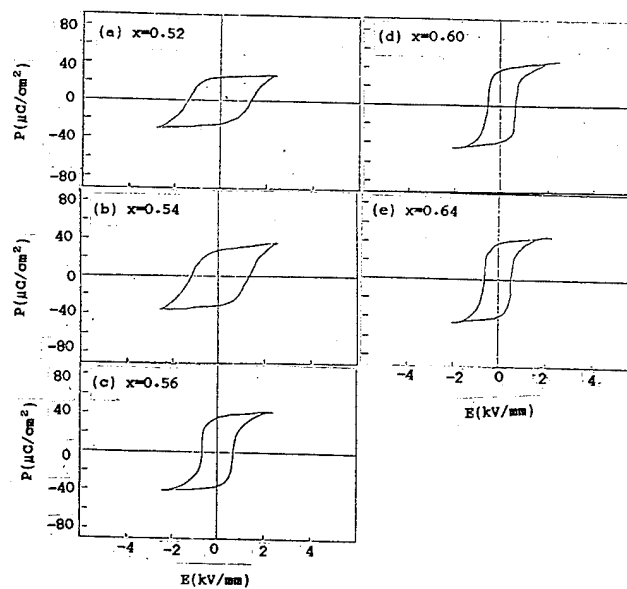


Figure 5 P-E Hysteresis loops of hydrothermal  $\text{PbTi}_{1-x}\text{Zr}_x\text{O}_3$  ceramics.

Table 1 Characteristics of PZT ceramics from different powders

	density $\text{g/cm}^3$	grain size, $\mu\text{m}$	K	D %	Kp	Qm
hydrothermal	7.52	13.50	947	1.69	0.57	130
solid-state	7.40	7.93	855	2.46	0.48	204

The  $Q_m$  value (mechanical quality) of the ceramics monotonously increases with  $x$  value. A combination of the data of Figure 4c with 6e reveals that the  $K_p$  value in Figure 7 linearly increased with the grain size of the ceramics.

A Comparison was next made of the microstructure of ceramics produced from the hydrothermal powders with that from the solid-state-reacted powder at the same sintering temperature (1250°C). The larger grain size in Figure 8 indicated that the hydrothermal powders were more active and sinterable.

The PZT ceramics from the hydrothermal powders in Table 1 were observed to have higher density, grain size, dielectric constant and surprisingly have a lower dissipation factor. Furthermore, the PZT ceramics from the hydrothermal powders have higher  $K_p$  and lower  $Q_m$  values because a larger grain size would enhance  $K_p$  value but induce a loss.

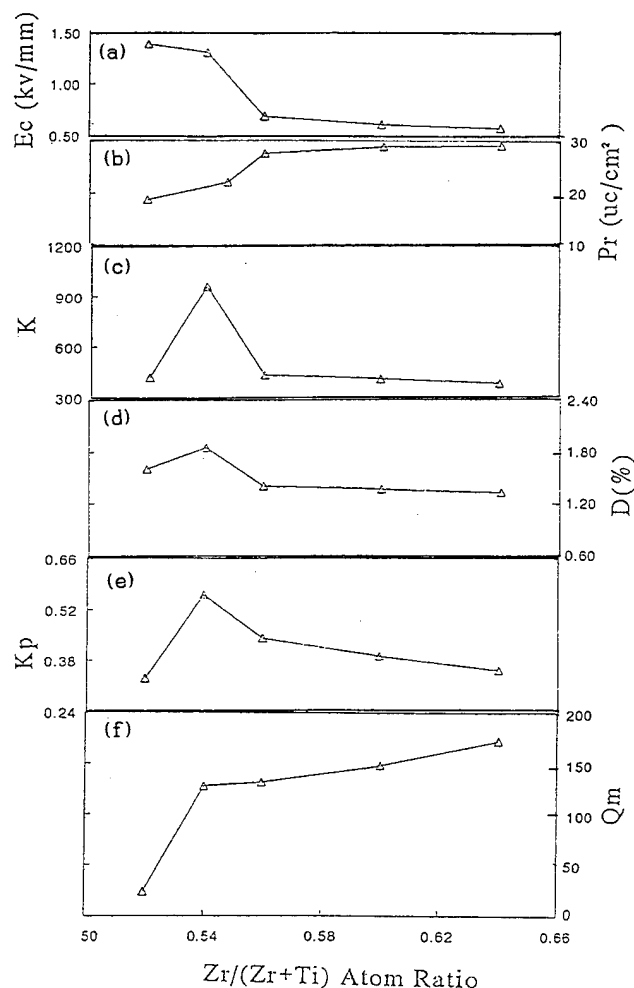


Figure 6 Relationships between  $x$  value of hydrothermal  $PbTi_{1-x}Zr_xO_3$  ceramics with (a)  $E_c$ , (b)  $P_r$ , (c)  $K$ , (d)  $D$ , (e)  $K_p$ , and (f)  $Q_m$ .

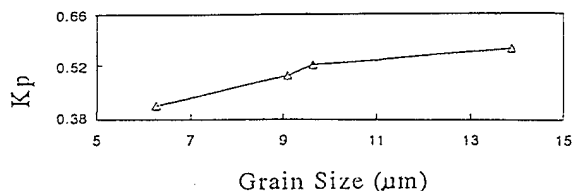


Figure 7 Relationships between  $k_p$  value and grain size of hydrothermal  $PbTi_{1-x}Zr_xO_3$  ceramics,  $x=0.54$ .

## CONCLUSIONS

PZT powders produced from the hydrothermal method are all cubic in external shape and crystal structure, while PZT powder from the solid-state reaction method at  $x=0.52$  is tetragonal in crystal structure. PZT ceramics produced from hydrothermal powders are tetragonal if  $x$  value is 0.52 or 0.54, and rhombohedral if the ratio is 0.56, 0.60, or 0.64. PZT ceramics produced from solid-states reacted powder was quite close to rhombohedral at  $x=0.52$ . The particle size of the hydrothermal powders is around  $0.2 \mu m$  and decreases with the  $x$  value. Also The grain size reaches maximum at  $x=0.54$ .

The electrical properties of the PZT ceramics produced from the hydrothermal powders become softer as the  $x$  value increases.  $K$ ,  $D$ , and  $K_p$  values of the PZT ceramics reaches maximum at  $x=0.54$ , which is very close to  $x=0.52$  for PZT ceramics produced from the solid-state reacted powder.

The hydrothermal powders are much more sinterable than the solid-state reacted powder. The hydrothermal powders are suitable to produce PZT ceramics requiring higher  $K$ ,  $K_p$ , and low  $Q$  values.

A hydrothermal method has been successfully developed to produce PZT powders for high quality PZT ceramics. The operation of this process is rather simple and only inexpensive chemical reagents were used.

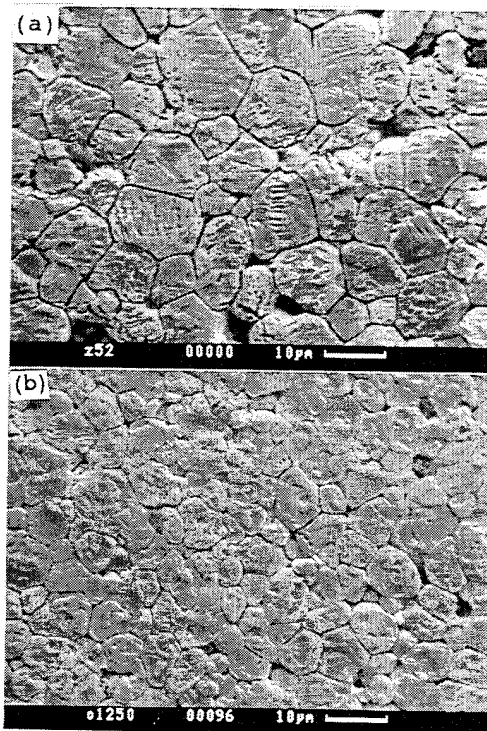


Figure 8 Microstructures of  $PbTi_{1-x}Zr_xO_3$  ceramics from (a) hydrothermal powders, and (b) solid-state reacted powder sintered at 1250°C for 2 hrs.

## REFERENCES

1. T.R.N. Kutty and R. Balachandran, "Direct Predipitation of Lead Zirconate Titanate by Hydrothermal Method," *Materials Research Bulletin*, **19**, 1479, (1984).
2. K.C. Beal, "Precipitation of Lead Zirconate Titanate Solid Solutions under Hydrothermal Conditions," in *Advances in Ceramics*, Vol. 21, P.33, ed. by G.L. Messing, K.S. Mazdhyasni, J. W. Mauley and R.A. Haber, The American Ceramic Society, Inc., ISBN 0-916094-83-9, 1987.
3. W.J. Dawson, "Hydrothermal Synthesis of Advanced Ceramic Powders," *Ceramic Bulletin*, **10**, 1673(1988).
4. B. Jaffe, etc., "Piezoelectric Ceramics," Academic Press, 1971.
5. C.H. Lin, S.C. Pei, T.S. Chin, "Hydrothermal Synthesis of  $PbTi_{1-x}Zr_xO_3$  Ceramic Powders," in *Ceramics Transactions Vol. 32, Dielectric Ceramics: Processing, Properties, and Applications*, P.261-274(1993), ISBN 0-944904-60-2.
6. C.H. Lin and S.C. Pei, "PLZT Ceramics from Hydrothermally produced Powders," *Proceedings of International Union of MRS International Conference in Asia, China, Sept. 6-10, 1993, Yantze Gorges, China*.



# Fabrication of High Density, Fine-grained PZT Ceramics using a Post-sinter HIP Treatment

C. E Millar<sup>†</sup>, B. Andersen<sup>†</sup>, E. Ringgård<sup>†</sup>, W. Wolny<sup>†</sup>, J. Ricote<sup>‡</sup>, & L. Pardo<sup>‡</sup>

<sup>†</sup> Ferroperm A/S, Hejreskovvej 6, 3490 Kvistgård, Denmark.

<sup>‡</sup> Instituto de Ciencia de Materiales (Sede A). CSIC, Serrano, 144, 28006 - Madrid, Spain

**Abstract,** For many applications, such as medical array transducers, the frequency of use of ceramics is limited by their grain size and porosity content. Here, the microstructure of two commercial soft PZT ceramics (with  $\epsilon_r$  of 1800 and 4000) is optimised through a combined sintering and HIP study. The study includes the effect of sintering temperature ( $T = 1100$  to  $1260^\circ\text{C}$ ) and HIP conditions ( $T = 1000^\circ\text{C}$ ,  $P = 50$  to  $200$  MPa and  $t = 1$  to  $4$  h) on the microstructure and dielectric and piezoelectric properties. The properties obtained are compared with those of the conventionally prepared ceramics.

## INTRODUCTION

Lead zirconate titanate ceramics are used in a wide variety of applications. However the porosity and grain size imposes limits for certain applications, and pore free, fine-grained ceramics are desirable. For example, such ceramics would allow the frequency range of medical imaging transducers to be extended and for finer structures to be produced for medical arrays or inkjet printers.

Here two PZT ceramics are studied. The first is a standard soft PZT material (Pz-27 - Ferroperm). The other is a PZT composition (Pz-21 - Ferroperm) with high dielectric constant, which has advantages for high frequency and array transducers, as it has a lower impedance, giving improved electrical matching. The aim of this paper was to optimise the microstructure using powders prepared by a conventional solid state reaction. The powders were milled for 72 hours to reduce the particle size and produce a more reactive starting powder, thus allowing sintering to be carried out at a lower temperature. A sintering study was completed to determine the conditions required to produce ceramics with suitable density and fine grain size. The optimum sintering temperature was then selected, and the effect of three post-sintering hot isostatic pressing (HIP) treatments on the microstructure and properties is investigated and related to the HIP conditions used. Finally, the properties of the fine-grained, high density ceramics are compared with those of ceramics produced commercially.

## EXPERIMENTAL PROCEDURE

Two commercial soft PZT compositions were studied (Ferroperm, Pz-21 and Pz-27). The calcined powders were milled for 72 hours to obtain a particle size of  $0.4\ \mu\text{m}$ . After adding a binder, the powders were pressed into discs using a pressure of 98 MPa. The discs were sintered at 1100, 1140, 1180, 1220 or  $1260^\circ\text{C}$  for 1 hour.

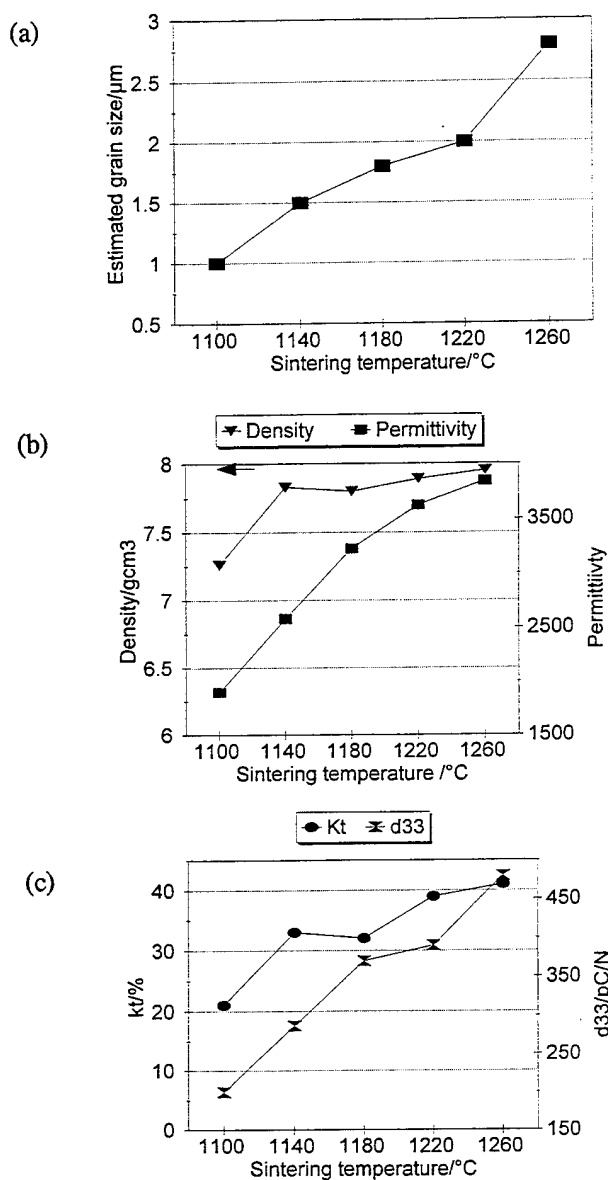
On the basis of the results obtained for the sintering study (see results section) a sintering temperature was selected for each of the two materials and used for the remainder of the study. Samples sintered at these temperatures were hot isostatically pressed without encapsulation, using 3 different conditions:  $T = 1000^\circ\text{C}$ , with a pressure of 50 MPa for 1 or 4 hours (HIP-1 and 2) and  $T = 1000^\circ\text{C}$  with a pressure of 200 MPa for 1 hour (HIP-3). The atmosphere was mixture of 20%  $\text{O}_2$  and 80% Ar. Heating and cooling rates were  $600^\circ\text{C}/\text{hour}$ .

The porosity content of as-sintered and HIP-1 to HIP-3 ceramics were examined using optical microscopy and image analysis (IA). As-sintered and HIP-2 samples were characterised more fully, including both grain size and porosity measurements. Porosity measurements were made on polished surfaces and the grain size distributions were determined from thermally etched samples. Measurements were made using software based on IMCO 10 system (Kontron Elektronik GmbH 1990) on, typically, 10 images for porosity measurements and on a total number of 1000 grains for grain size determination. The grain size was calculated as equivalent diameters to a circular shape from the measured areas. For calculation of the mean values and standard deviations, the distributions were considered as Gaussian.

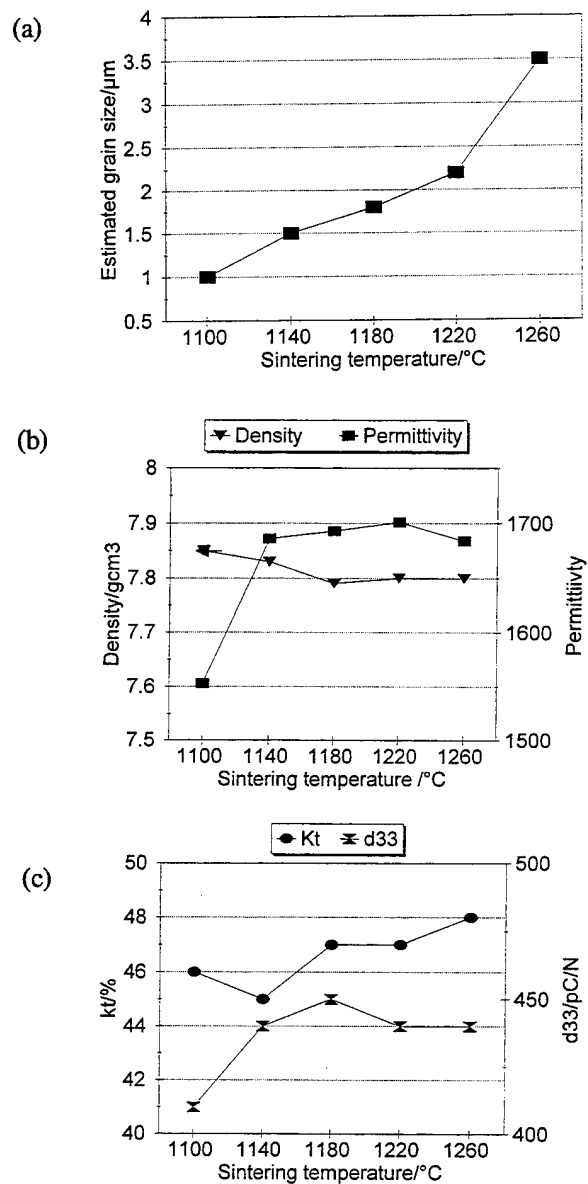
For characterisation of the dielectric and piezoelectric properties, the discs were lapped to give a diameter/thickness ratio  $> 20$  and then electroded. Poling was carried out at  $130^\circ\text{C}$  for 2 minutes with a field of 20 kV/cm. The relative permittivity,  $\epsilon_{33}^T$  and dielectric loss at 1 kHz were measured using an LCR meter. Thickness and planar electromechanical coupling coefficients,  $k_t$  and  $k_p$ , were calculated according to IEEE Standards<sup>[1]</sup> from resonance data. The piezoelectric  $d_{33}$  coefficient was measured using meter similar to the Berlincourt meter. All measurements were made at least 24 hours after poling.

## RESULTS AND DISCUSSION

The properties of Pz-21 and Pz-27 ceramics as a function of sintering temperature are shown in Figures 1(a) to (f). It can be seen that for Pz-21, the grain size, density, permittivity and the piezoelectric properties,  $d_{33}$  and  $k_t$  all increased with increasing sintering temperature. For Pz-27, the density of the ceramics remained fairly constant as the sintering temperature increased, whereas the grain size, permittivity and piezoelectric properties tended to increase, suggesting that the properties were dependent on grain size. Mattirena



Figures 1 (a) to (c) properties of Pz-21 as a function of sintering temperature



Figures 1 (d) to (f) properties of Pz-27 as a function of sintering temperature

Table 1 Summary of ceramic microstructure parameters

Sample	HIP			Porosity %	pore area/ $\mu\text{m}$	
	T/ $^{\circ}\text{C}$	t/h	P/MPa		Ave.	STD. Dev.
Pz-21						
As-sintered (1220 $^{\circ}\text{C}$ )				3.0	14.2	23
HIP-1	1000	1	50	1.0	11.4	18
HIP-2	1000	4	50	0.2	7.2	11
HIP-3	1000	1	200	1.9	15.6	36
PZ-27						
As-sintered (1180 $^{\circ}\text{C}$ )				1.8	7.8	13
HIP-1	1000	1	50	0.5	7.0	9
HIP-2	1000	4	50	0.3	6.2	9
HIP-3	1000	1	200	0.6	6.7	11

Table 2 Characterisation of grain size by image analysis

Sample	Grain size / $\mu\text{m}$		
	Average	STD Dev.	Max
Pz-21			
as sintered	1.8	0.9	5.2
HIP-2	1.9	0.9	5.3
Pz-27			
as sintered	1.7	0.8	5.4
HIP-2	1.7	0.9	5.7

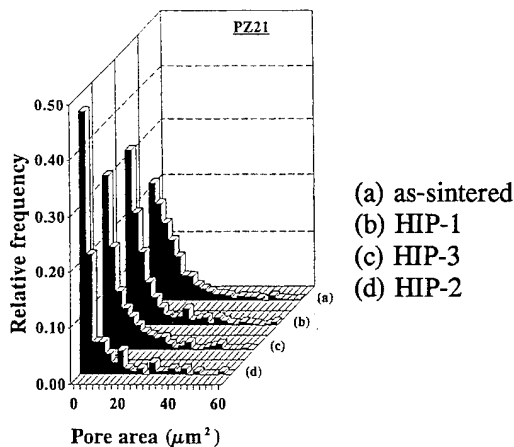


Figure 2(a) Histogram of pore size distribution Pz-21

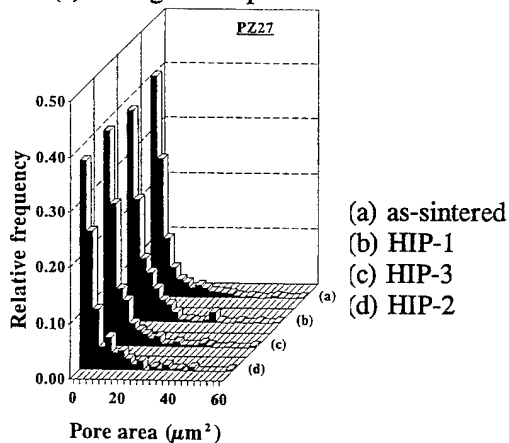


Figure 2(b) Histogram of pore size distribution Pz-27

and Burfoot<sup>[2]</sup> attributed the effect of grain size on permittivity of PZT type materials to the reduction in mobility of 90° domain walls in small grains due to pinning. In addition, they suggested that this reduces the proportion of 90° domains switched during poling and thus their contribution to the increase in permittivity usually found after poling, and the piezoelectric properties.

By examining the properties obtained, sintering temperatures were selected for each material for which reasonable density and properties, as well as fine grain size was obtained. The temperatures selected were 1220°C for Pz-21 and 1180°C for Pz-27.

The porosity parameters obtained by image analysis for the selected as-sintered and corresponding HIP materials are given in Table 1 and pore area distributions shown in Figures 2 (a) and (b). It can be seen that HIP-1 reduces the porosity content from 3 to 1 % for Pz-21 and from 1.8 to 0.5 % for Pz-27. This reduction in porosity is accompanied by a reduction in the mean value of the pore area and width of the pore area distribution, with the greatest effect being on the large pores (see Figure 2).

Increasing the time from 1 to 4 hours, reduced the porosity content further to 0.2 and 0.3 % for Pz-21 and Pz-27 respectively. Thus indicating that the densification is time dependent and is influenced, to some extent, by the type and size of porosity present in the starting ceramics. This can be seen in Figure 2 (a), in which the size distribution of the Pz-21 ceramics is reduced by increasing the HIP time to 4 hours. This effect, although present for Pz-27, is not so great as the sintered ceramics contained lower porosity and the average pore area was smaller.

Using a higher pressure, 200 MPa, HIP-3, the porosity content of both materials was higher than for HIP-1. For Pz-21 the increase was significant, 1.9 %, and the ceramics contained cracks and tended to be mechanically weak. This is thought to be due to the high pressure contained in the remaining porosity, which causes stresses during decompression. The results obtained here, indicate that this effect was only large for the Pz-21-HIP-3 materials. The

Table 3 Dielectric and piezoelectric properties

HIP run	Porosity from IA (%)	$\epsilon_r$	$\tan\delta$	$k_t$ %	$k_p$ %	$d_{33}$ pC/N <sup>-1</sup>	$N_t$ Hzm
Pz-21							
as-sintered	3.0	3730	0.020	38	48	468	1955
HIP-1	1.0	4020	0.019	42	44	517	2057
HIP-2	0.2	4100	0.018	41	56	523	2091
Pz-27							
as-sintered	1.8	1690	0.016	46	58	452	1900
HIP-1	0.5	1800	0.017	45	62	478	2040
HIP-2	0.3	1760	0.017	44	64	488	2050
HIP-3	0.6	1560	0.016	50	55	421	1900

Table 4 Comparison of standard, fine grained and HIP-2 materials

Material	Porosity %	grain size $\mu\text{m}$	$\epsilon_r$	$\tan\delta$	$k_t$ %	$k_p$ %	$d_{33}$ $\text{pC}\cdot\text{N}^{-1}$	$N_t$ Hzm
Pz-21								
as-sintered (1220°C)	3.0	1.8	3730	0.020	38	48	468	1955
HIP-2	0.2	1.9	4100	0.018	41	56	523	2091
Conventional	~ 3	~ 6	4200	0.019	44	56	503	2030
Pz-27								
as-sintered (1180°C)	1.8	1.7	1690	0.016	46	58	452	1900
HIP-2	0.3	1.7	1760	0.017	44	64	488	2050
Conventional	~ 2	~ 5	1800	0.016	46	59	447	200

reasons for this may be the higher content of large pores in Pz-21 ceramics.

The grain sizes of the as-sintered ceramics and HIP-2 materials is shown in Table 2. Both materials had an average grain size of  $< 2\mu\text{m}$ . There was little change in the mean value of grain size or distribution of either ceramics during the HIP process, revealed by image analysis of SEM micrographs. The as-sintered and HIP distributions can be considered statistically equal. As this was the longest of the HIP runs, similar results are expected for HIP-1 and HIP-3 ceramics.

The dielectric and piezoelectric properties of the as-sintered and HIP ceramics are given in Table 3. For both Pz-21 and Pz-27, the reduction in the porosity content of HIP-1 ceramics leads to an improvement in the properties. For example, the permittivity, piezoelectric coefficients and frequency constants are all higher. In addition, the dielectric loss remains unchanged. The increases in properties are close to 10 %, which is consistent with other authors for HIP materials<sup>[3]</sup>.

Increasing the HIP time to 4 hours and corresponding reduction in porosity, improved the properties still further, and these materials had the highest dielectric and piezoelectric properties.

For HIP-3 ( $P=200\text{ MPa}$ ) only values for Pz-27 are given here. The values are lower than for either HIP-1 and HIP-2 ceramics, and in some cases are lower than for the as-sintered materials. For these materials the porosity of the ceramics was reduced and the little change in properties may be related to the increase in internal stresses in the ceramics, created during decompression.

The properties obtained for the fine-grained ceramics, as-sintered and after HIP-2 are compared with those of conventionally prepared materials, Table 4. It can be seen that although the density was similar, the as-sintered materials had lower dielectric and piezoelectric properties than conventionally prepared materials (grain size  $5\mu\text{m}$ ). It is likely that this is due to grain size effects. As discussed

earlier, it is well known that both dielectric and piezoelectric properties decrease as grain size decreases. This may also explain the difference in  $k_t/k_p$  between the materials. The effect of HIP-2 was to increase the properties by approximately 10%, overcoming the reduction in properties due to reduction in grain size and thus, the properties were similar to those for conventionally processed materials, whilst having advantages of finer grain size and very low porosity. These ceramics are more easily machined and less susceptible to electrical breakdown for the fabrication of fine structures or high frequency parts.

## CONCLUSIONS

Fine-grained, high density ceramics were prepared from two PZT compositions using standard powder processing routes followed by a post-sintering HIP treatment. The powder was milled to  $<0.5\mu\text{m}$ , which allowed the sintering temperature to be reduced and ceramics with a grain size of  $< 2\mu\text{m}$  to be obtained. An increase in HIP time from 1 to 4 hours, led to better results, with ceramics containing  $<0.3\%$  porosity.

The dielectric and piezoelectric properties were found to depend on grain size, and were lower for the fine-grained ceramics. However, after a suitable HIP treatment, the decrease in porosity led to an improvement in properties, and properties similar to those of conventionally prepared materials were obtained. The fine-grained, high density materials offer advantages for the preparation of high frequency and fine structure applications

## REFERENCES

- [1] IEEE Standards on Piezoelectricity ANSI/IEEE Std 176 (1987)
- [2] H. Martrena and J. C. Burfoot " Grain size effects on properties of some ferroelectric ceramics" *J. Phys. Solid State Physics* vol. 7, pp. 3183-92, 1974
- [3] L. Bowen, W. A. Schulze and J. V. Biggers " Hot-isostatic pressing of PZT materials" *Powder Met. Int.* vol. 12, pp. 92-5 1980.

# A STUDY OF THE SINTERING MECHANISM OF PZT-BASED PIEZOCERAMICS

P.W. Lu and W.R. Xue

Nanjing Institute of Chemical Technology  
Nanjing, Jiangsu 210009  
P.R.C.

W. Huebner

Department of Ceramic Engineering  
University of Missouri - Rolla  
Rolla, MO 65401

## ABSTRACT

The densification behavior a PZT-based composition with additions of BiFeO<sub>3</sub> as a flux was studied. Two different PZT powders were studied with varying initial particle sizes. Results clearly showed that BiFeO<sub>3</sub> forms a low temperature liquid that aids in the densification behavior, with 3 mole% being optimum. Fine particle sizes substantially improved the density at low temperatures, with the net result that ceramics could be densified in air without the aid of a lead source. The corresponding electromechanical properties were typical of a hard PZT formulation.

## INTRODUCTION

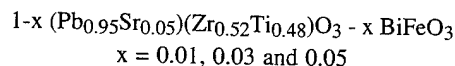
One of the key parameters which affects the microstructural evolution and electromechanical properties of Pb(Zr,Ti)O<sub>3</sub> (PZT) - based ceramics is control over the lead activity,  $a_{Pb}$ . It is well known that the vapor pressure of lead above PZT at temperatures well below the sintering temperature is high [1-4], and that the associated lead loss has a detrimental affect on the piezoelectric properties [5]. In practice, this problem is overcome by sintering in the presence of a lead source, such as PbZrO<sub>3</sub>, which has a higher vapor pressure than the PZT, and also batching excess PbO. The latter dictates annealing of the PZT after sintering in order to remove any second phases in the grain boundary.

An effective strategy to minimize this problem is to lower the sintering temperature through the use of ultrafine powders [6], and/or liquid phase sintering. To obtain materials which retain good piezoelectric properties, a key step is to tailor the flux composition to produce densification with limited grain growth. During grain growth, dissolution of the additive ions from the flux into the ceramic is assisted by solution-precipitation processes, hence these additive ions should serve as the aliovalent or isovalent dopants desired to manipulate the piezoelectric properties. An additional requirement is for the flux to be either totally soluble in the piezoelectric, i.e. transient liquid phase sintering, or volatilize in order to minimize the presence of intergranular phases and porosity. Therefore the flux composition, melting temperature, reactions between the flux and the piezoelectric, and microstructural evolution during liquid phase sintering are all very important parameters to characterize and understand in any attempt to precisely control piezoelectric properties.

In this study we present results on the use of BiFeO<sub>3</sub> as a sintering aid for a PZT-based composition. BiFeO<sub>3</sub> was chosen on the basis of its incongruent melting temperature of  $\approx 930^\circ\text{C}$  [7], and since Bi<sup>3+</sup> and Fe<sup>3+</sup> are both soluble onto the lattice, BiFeO<sub>3</sub> can yield desirable piezoelectric properties [8-10]. Additionally, the  $T_c$  for BiFeO<sub>3</sub> is  $\approx 850^\circ\text{C}$ , and hence, in the interest of higher temperature piezoelectric applications, may increase  $T_c$  of the system [10].

## EXPERIMENTAL PROCEDURE

Figure 1 overviews in detail the processing steps used to prepare the following three compositions:



Note that the mixed oxide approach was used to make the compositions, and that the PZT and BF were pre-calcined. Figure 2 shows the PZT powders calcined at 780°C and 840°C for 2 h. This 60°C difference made a large difference in the powder characteristics; the 780°C powder had a surface area of 1.65 m<sup>2</sup>/g, and the 840°C powder 0.47 m<sup>2</sup>/g. This corresponds to equivalent spherical diameters of 0.47 and 1.69  $\mu\text{m}$ , respectively. Both powders are equiaxed, and exhibit little aggregation. X-ray diffraction analyses on the pre-calcined PZT and BF verified the compositions.

All of the sintering studies were performed in air, without a lead source or excess PbO additions. Remember our goal is learn how to densify PZT ceramics without control over the lead activity.

Room temperature electrical measurements were performed on plane parallel disks approximately 1 to 2 mm thick. Gold electrodes were sputtered onto the surface in a vacuum through a mask. The dielectric properties were measured using a General Radio GR1689 RLC Digibridge. After poling, a Berlincourt d<sub>33</sub> meter was used to measure the d<sub>33</sub> coefficient, and resonance measurements were performed with an impedance analyzer (Hewlett-Packard 4194A

Raw Materials:	♦ PbO 99%	♦ TiO <sub>2</sub> 99%
	♦ SrCO <sub>3</sub> 99.9%	♦ ZrO <sub>2</sub> 99%
	♦ Fe <sub>2</sub> O <sub>3</sub> 99.8%	
Mixing	♦ Batch:ZrO <sub>2</sub> media:alcohol = 1:4:0.8	
	♦ Polyethylene jar	
	♦ 24 h	
Calcination:	♦ Bi <sub>2</sub> O <sub>3</sub> and Fe <sub>2</sub> O <sub>3</sub> pre-calcined: 680°C - 3h → BiFeO <sub>3</sub>	
	♦ (Pb <sub>0.95</sub> Sr <sub>0.05</sub> )(Zr <sub>0.52</sub> Ti <sub>0.48</sub> )O <sub>3</sub> : 780°C - 2h; 840°C - 2h	
Milling	♦ Aggregates broken up with an agate mortar & pestle	
	♦ Milled again as above	
Pressing:	♦ 8 wt% of a 5% PVA solution	
	♦ Granulation	
	♦ Uniaxial pressing; 1000 kg/cm <sup>2</sup> [green density: 55% T.D.]	
Sintering:	♦ 650°C-4 h (binder burnout)	
	♦ Dilatometry: 10°C/min to 1300°C	
	♦ Isothermal dilatometry: 850 & 1100°C	

Figure 1: Overview of the processing steps used to prepare the PZT-BF ceramics.

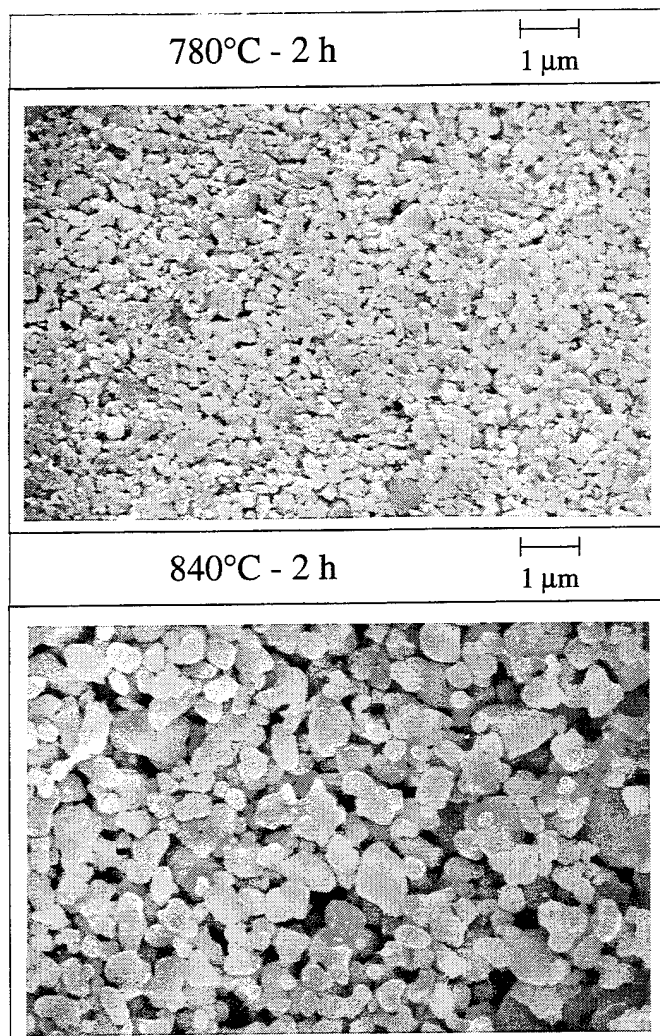


Figure 2: SEM micrographs of the PZT powder calcined at 780 and 840°C for 2 h.

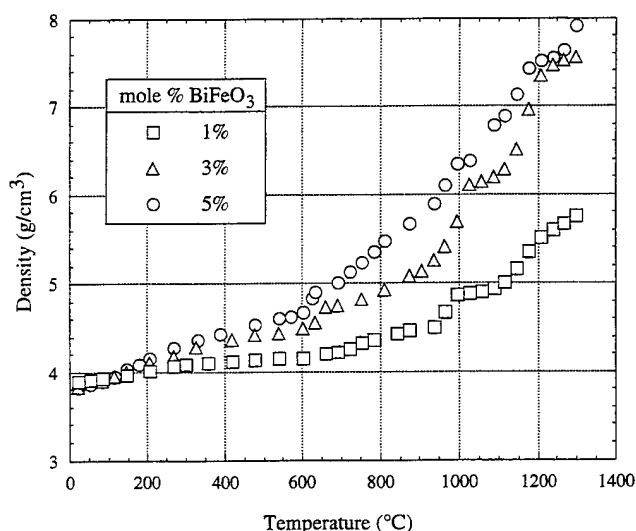


Figure 3: Densification behavior of the PZT-BF ceramics as a function of %BF.

Impedance Analyzer with a 41941A Impedance Probe and 16092A Test Fixture) to determine  $k_t$  and  $k_p$ .

## RESULTS AND DISCUSSION

The main results presented in this paper deal with the influence of starting powder characteristics and %BF on the densification behavior, coupled with electromechanical properties.

Figure 3 exhibits the influence of the %BF, in all three cases using the 780°C calcined powder. Clearly 1% additions are insufficient to densify the ceramic, resulting in  $\approx 73\%$  T.D at 1300°C. Increasing to 3% BF improved the densification behavior, resulting in a density of 95% theoretical. Note in this behavior that the densification rate increases substantially at  $\approx 900^\circ\text{C}$ , which is close to the melting temperature of the BF. The situation is further improved by the addition of 5% BF, and the densification rate increases sharply at a lower temperature of 600°C. The density at 1300°C is similar to that of the 3% composition,  $\approx 95\%$  T.D.

Figure 4 exhibits fired surface SEM micrographs of the three compositions. The presence of a residual liquid phase is evident in the 5% BF composition. The grain sizes of all three were  $\approx 1\ \mu\text{m}$ . DTA analyses on both the 780°C and 840°C powders with 3% BF additions are shown in Figure 5. The low temperature exotherm is associated with alcohol removal. Only the 780°C powder exhibited a reaction at  $\approx 600^\circ\text{C}$ , which is 300°C lower than the temperature at which the densification rate changed sharply for this composition. The DTA curve for the 5% composition was nearly identical, hence it is likely that even though a liquid phase is forming in the 3% BF composition at  $\approx 600^\circ\text{C}$ , that the amount of the liquid phase is insufficient to result in significant particle rearrangement.

Using the 3% BF composition, further studies on the influence of the starting powder characteristics on the densification rate were performed. Figure 6 exhibits a comparison of the 780°C and 840°C powders. The impact of starting particle size is clear. Although the final density is nearly the same, the rate is substantially higher at low temperatures for the 780°C powder. The isothermal studies at 850°C and 1100°C shown in Figures 7 and 8 reinforce these results. Replotting this data with as a function of  $t^{1/3}$  (indicative of a solution-precipitation mechanism) results in linear plots, but at this stage more data is needed to confirm the sintering mechanism.

The electromechanical properties of the PZT-3% BF ceramics after sintering at 1300°C are shown in Table I. Both ceramics exhibit behavior typical of a hard PZT ( $\text{Fe}^{3+}$ -doping), but the ceramics prepared using the 780°C powders are superior.

## CONCLUSIONS

The densification behavior a PZT-based composition with additions of  $\text{BiFeO}_3$  as a flux were studied. Two different PZT powders were studied with varying initial particle sizes. Results clearly showed that  $\text{BiFeO}_3$  forms a low temperature liquid that aids in the densification behavior, with 3 mole% being optimum. Fine particle sizes substantially improved the density at low temperatures, with the net result that ceramics could be densified in air without the aid of a lead source.

## Acknowledgment

This work was sponsored by the Office of Naval Research under Grant N00014-92-J-1469.

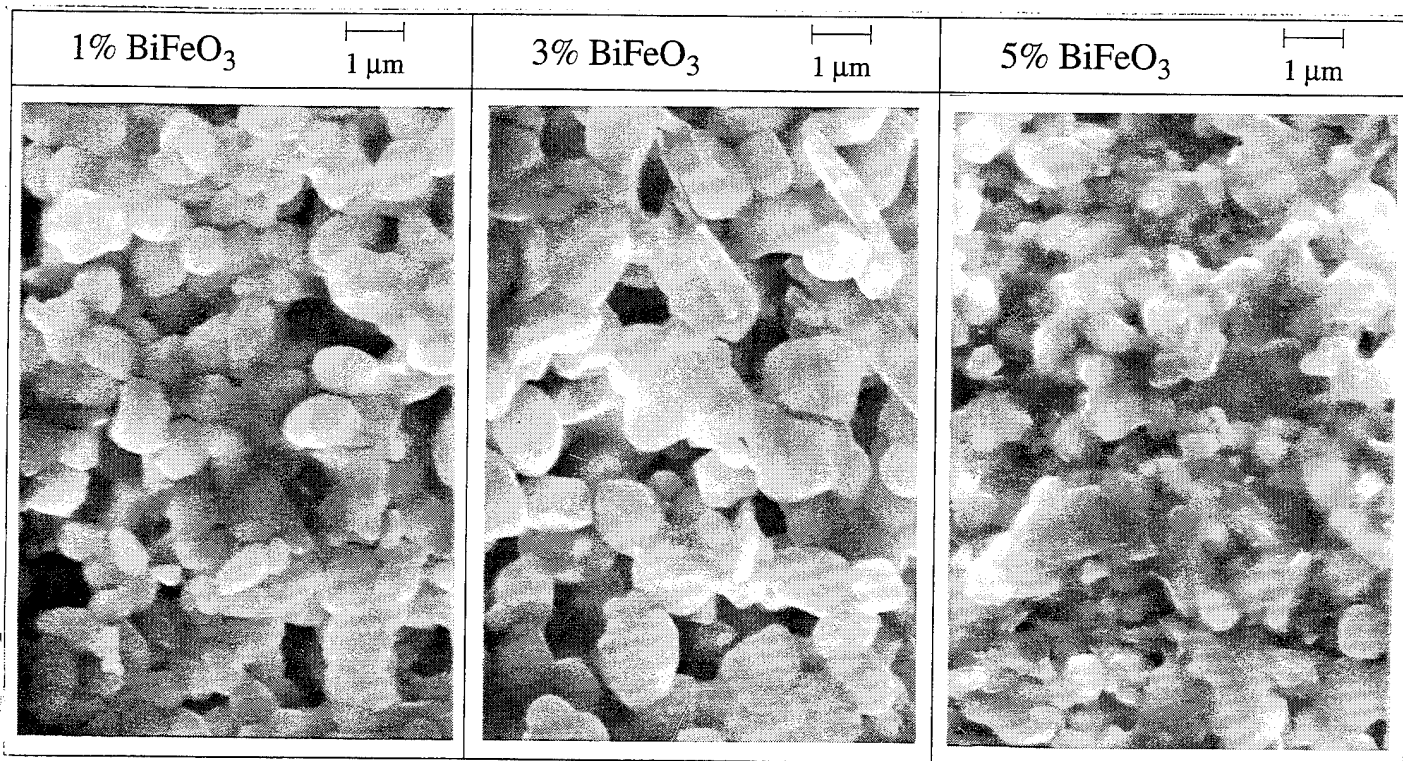


Figure 4: SEM micrographs of the PZT-BF ceramics after sintering to 1300°C.

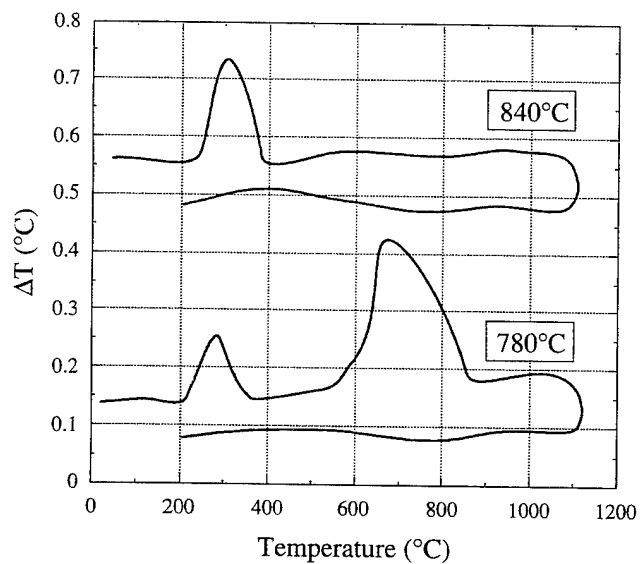


Figure 5: DTA analyses of the 780°C and 840°C powders with 3% BF additions.

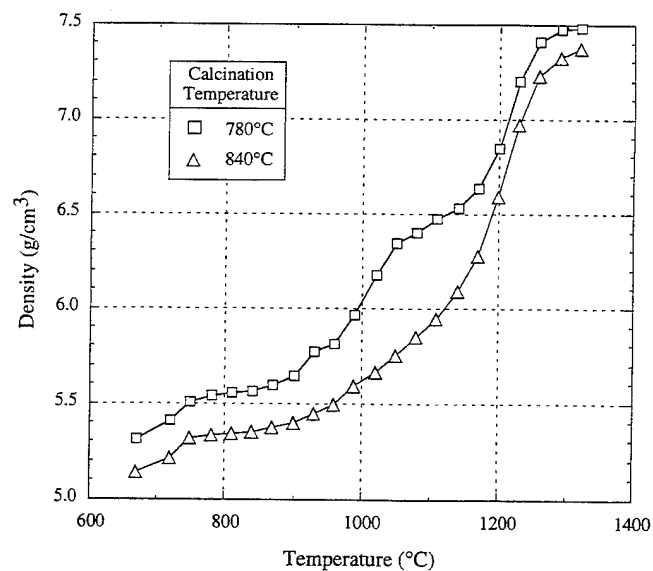


Figure 6: Densification behavior of the PZT-BF ceramics as a function of the powder calcination temperature.

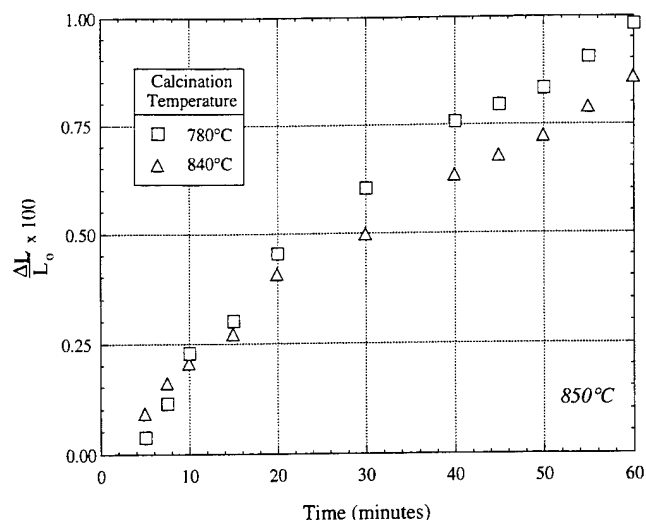


Figure 7: Isothermal shrinkage at 850°C of the PZT-3%BF powders calcined at 780°C and 840°C for 2 h.

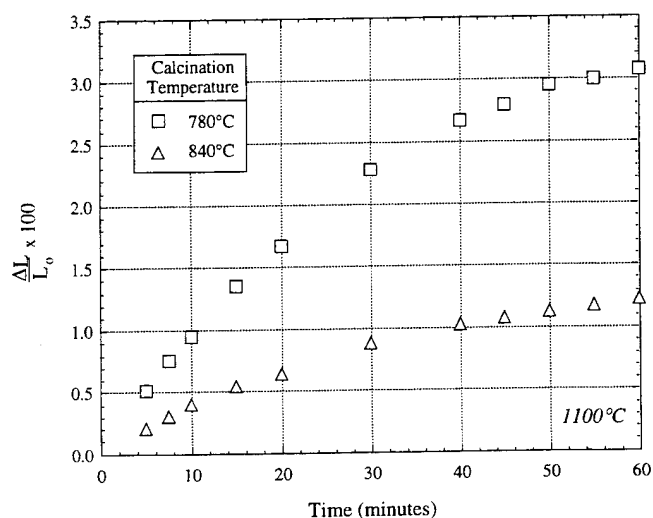


Figure 8: Isothermal shrinkage at 1100°C of the PZT-3%BF powders calcined at 780°C and 840°C for 2 h.

TABLE I

EFFECT OF CALCINATION TEMPERATURE ON THE ELECTROMECHANICAL PROPERTIES OF PZT-3% BF

Property	780°C - 2 h	840°C - 2h
$\epsilon_{33}/\epsilon_0$	1157	1325
$\tan \delta$ (%)	0.49	0.79
$d_{33}$ (pC/N)	285	256
$k_p$ (%)	54.1	48.7
$k_t$ (%)	47.3	41.4
$Q_m$	128	75

## REFERENCES

- [1] R.B. Atkin and R.M. Fulrath, "Point Defects and Sintering of Lead Zirconate Titanate," *J. Amer. Cer. Soc.*, **54**[5], 265-70 (1971).
- [2] K.H. Hardtl and H. Rau, "PbO Vapour Pressure in the  $\text{Pb}(\text{Zr}_{1-x}\text{Ti}_x)\text{O}_3$  System," *Solid State Communications*, **7**, 41-45 (1969).
- [3] D.A. Northrop, "Vaporization of Lead Zirconate Titanate Materials," *J. Amer. Cer. Soc.*, **50**[9], 441-445 (1967).
- [4] P.G. Lucuta, F. Constantinescu and D. Barb, "Structural Dependence on Sintering Temperature of Lead Zirconate-Titanate Solid Solutions," *J. Amer. Cer. Soc.*, **68**[5], 533-37 (1985).
- [5] A.H. Webster, T.B. Weston, and N.H. Bright, "Effect of PbO Deficiency on the Piezoelectric Properties of Lead Zirconate Titanate Ceramics," *J. Amer. Cer. Soc.*, **50**[9], 490-91 (1967).
- [6] C.D. Near, W.J. Dawson, and S.L. Swartz, "Novel Methods of Powder Preparation and Ceramic Forming for Improving Reliability of Multilayer Ceramic Actuators," presented at the 1993 conference on Smart Structures and Materials, Albuquerque, NM.
- [7] *Phase Diagrams for Ceramists, 1969 Supplement*, ed. E.M. Levin, C.R. Robbins and H. McMurdie, p. 99, American Ceramic Society, Columbus, Ohio (1969).
- [8] R.T. Smith, G.D. Achenbach, R. Gerson and W.J. James, "Dielectric Properties of Solid Solutions of  $\text{BiFeO}_3$  with  $\text{Pb}(\text{Zr,Ti})\text{O}_3$  at High Temperature and High Frequency," *J. Appl. Phys.*, **39**, 70 (1968).
- [9] T.R. Weston, A.H. Webster and V.M. McNamara, "Lead Zirconate-Lead Titanate Piezoelectric Ceramics with Iron Oxide Additions," *J. Amer. Cer. Soc.*, **52**[5], 253-257 (1969).
- [10] R.B. Atkin, R.L. Holman, and R.M. Fulrath, "Substitution of Bi and Nb Ions In Lead-Zirconate-Titanate," *J. Amer. Cer. Soc.*, **54**[2], 113-115 (1971).



# Electric Field Assisted Hot Forging of Bismuth Titanate

P. A. Fuierer and A. Nichtawitz  
Materials Engineering Department  
New Mexico Institute of Mining and Technology  
Socorro, NM 87801

**Abstract** - An electric field applied across a specimen during the forging process is expected to affect the kinetics of grain growth and orientation. In addition, just as a field can align molecules in a nematic liquid with the axis of greatest polarizability in the direction of the applied field, it is possible that the polar axis in a crystallite may also be aligned during the high temperature densification process. This may improve the electric or piezoelectric properties of certain low symmetry ferroelectric materials. The idea is to combine crystallographic alignment, densification and poling all into one step, and approach single crystal-like properties in a polycrystalline ceramic. Electric fields (both DC and AC) were applied transverse to the forging direction of the low symmetry ferroelectric  $\text{Bi}_4\text{Ti}_3\text{O}_{12}$ . The AC field was found to have little influence on crystallographic orientation. The DC field was found to have a profound effect; aligning the polar axis during forging, and yielding further anisotropy in the ferroelectric hysteresis.

## INTRODUCTION

The structures of bismuth titanatum oxides, first described by Aurivillius some forty years ago and later by others [1], consist of  $\text{Bi}_2\text{O}_2$  layers interleaved with perovskite-like layers, giving the crystals a micaceous habit (Figure 1). Since the discovery of ferroelectricity in  $\text{Bi}_4\text{Ti}_3\text{O}_{12}$  (BIT), improvements in composition and processing have led to the use of bismuth layer structure ferroelectrics (BLSF) in certain high-Q and high temperature piezoelectric applications [2]. However, polycrystalline ceramics have much lower piezoelectric activities than do single crystals due to the two-dimensional restriction on the permissible rotations of the spontaneous polarization.

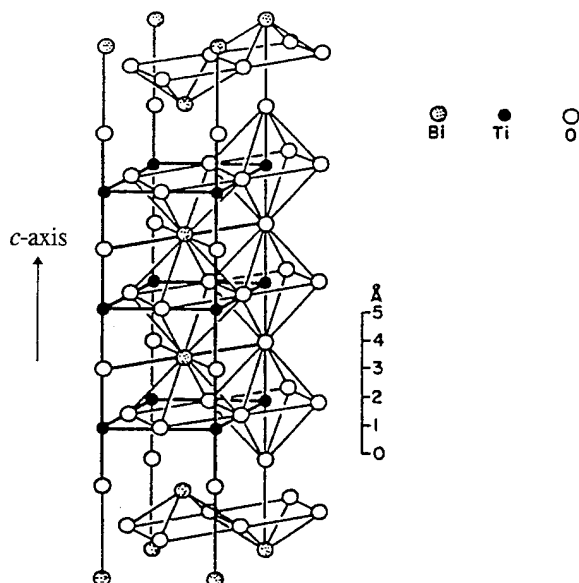


Fig. 1. Prototype structure of  $\text{Bi}_4\text{Ti}_3\text{O}_{12}$ , illustrating the perovskite-like layers separated by  $\text{Bi}_2\text{O}_2$  layers [1].

Hot-working of ceramics with anisotropic crystal structures such as bismuth titanate, barium ferrite and others has been applied for several years. Starting in about 1977, Takenaka and Sakata [3-5] used hot-forging to achieve a high degree of preferred orientation in BIT type ceramics, with correspondingly enhanced ferroelectric and piezoelectric properties. Despite the high degree of grain orientation, though, single-crystal like remanent polarization, and therefore piezoelectricity, is still impossible due to the radial distribution of the polar  $b$ -axis. It is the intent of our work to introduce a second orienting force during the high temperature forming process besides just the uniaxial force; that being an applied electric field transverse to the pressing direction. The process is termed electric field assisted hot forging (EFAHF).

## SAMPLE PREPARATION

A stoichiometric mixture of bismuth and titanium oxide powders was calcined ( $850^\circ\text{C}$ ) to form single phase  $\text{Bi}_4\text{Ti}_3\text{O}_{12}$  and pressed into tall cylinders. These cylinders were then presintered at  $925^\circ\text{C}$  to impart some mechanical strength for forging. Figure 2 shows the set up for the EFAHF process.

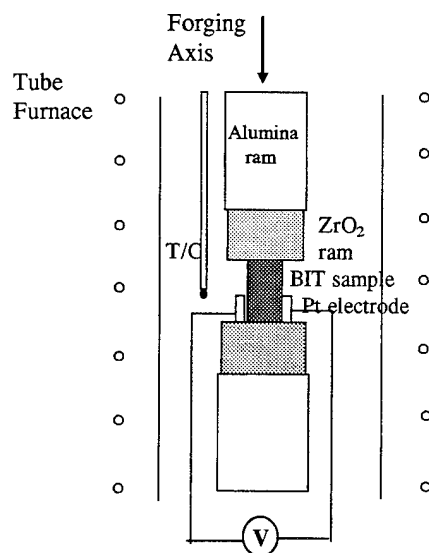


Fig. 2. Electric field assisted hot forging (EFAHF) setup.

Forging was carried out at a temperature of  $1100^\circ\text{C}$ , using a maximum load of 200 lbs on a final pellet diameter of 1 inch. Ceramic stops were used in order to forge each sample to the same thickness (3mm). Platinum electrode plates (3mm tall by 15mm long) with Pt leads were connected to a voltage source in order to apply the transverse electric field (either AC or DC). "Flats" were ground into opposite sides of the cylinder sample in order to get an intimate contact between electrodes and sample. The electrodes were allowed to move laterally as the material

forged and deformed outward so as to provide a continuous voltage or current to the sample. Figure 3 illustrates the temperature, loading and applied voltage schedule. Three samples were made for this study: i) simple hot-forged with no applied field, ii) DC-field assisted hot forged with 115 V initial, 20V final applied potential (constant 275mA leakage current), and iii) AC-Field assisted with a 60Hz, 120V potential.

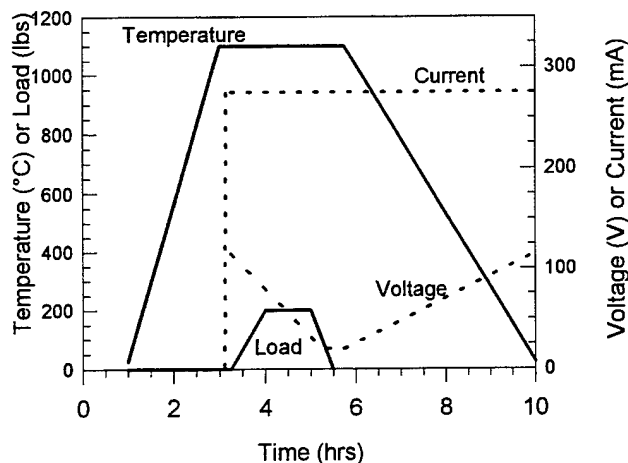


Fig. 3. Typical DC EFAHF schedule showing temperature, applied load, applied voltage and leakage current through the sample.

Simple hot forged ceramics belong to the Curie Group  $\infty/mm$ , and require only two cuts, one parallel ( $||$ ) and one perpendicular ( $\perp$ ) to the forging axis, to describe the physical properties. On the other hand, E-field assisted and/or poled hot forged ceramics belong to orthorhombic point group  $mm2$ , and three sample cuts are required to define the physical properties (of second rank). These cuts are defined with respect to the FA and applied E-field as in Figure 4. The different cuts were used to analyze the samples by x-ray diffraction, SEM, and dielectric and ferroelectric measurements.

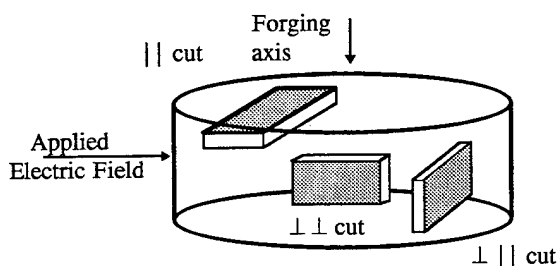


Fig. 4. Three different cuts needed to characterize an electric field assisted hot forged sample. The shaded surfaces represent the measurement electrodes.

#### CRYSTALLOGRAPHIC ORIENTATION & MICROSTRUCTURE

Figure 5 shows the XRD pattern for  $Bi_4Ti_3O_{12}$  powder, along with patterns taken from the  $||$  cuts of normal hot-forged ceramic, and EFAHF ceramic. Note the  $c$ -axis orientation in the forged samples. The degree of orientation is calculated from peak intensities using the Lotgering Orientation factor,  $f$ :

$$f = \frac{(p-p_0)}{(1-p_0)} \quad \text{where,} \quad p = \frac{\sum I_{(00l)}}{\sum I_{(hkl)}}$$

and  $p_0$  is the value for the random orientation powder pattern [6]. Calculations show sample (b) to have 26% ( $f=0.26$ ) orientation at approximately 0.3mm from the surface. (From the authors' experience, this factor increases as one proceeds to the interior of the sample.) In contrast, a typical fully forged ceramic will have about 85%  $c$ -orientation at this depth. The E-field assisted samples reported here were forged to the same extent, that is the same thickness contraction, as sample (b). This partial forging was done as an initial study of the effect of the electric field, and so as to end up with a relatively thick sample with which to work. The field assisted forging resulted in orientations of 38% for DC (Fig. 5(c)) and 31% for AC at a depth of 3mm. The DC field in particular seemed to give increased texturing.

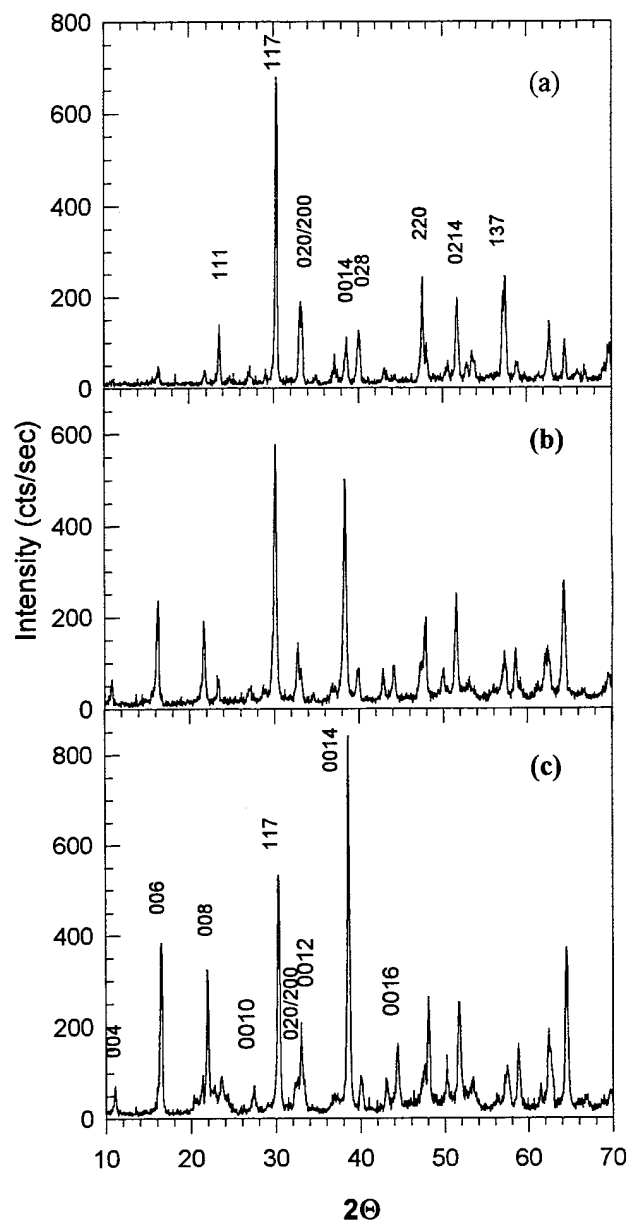


Fig. 5. X-ray diffraction patterns for  $Bi_4Ti_3O_{12}$ : (a) calcined powder; (b) normal partially hot-forged ceramic; (c) DC field assisted partially hot-forged ceramic. Patterns indexed according to an orthorhombic unit cell.

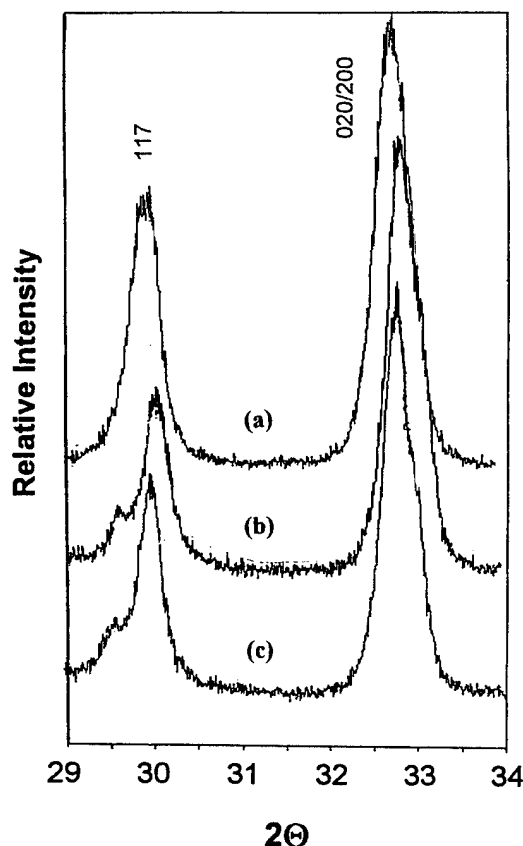


Fig. 6. The dominant (200)/(020) peak observed on perpendicular cuts from hot-forged BIT. (a) is the  $\perp$  cut from a normal forged sample. (b) is the  $\perp\perp$  and (c) the  $\perp||$  cut from the AC field assisted forged sample. The peak shows no splitting, suggesting little distortion of the unit cell parameters.

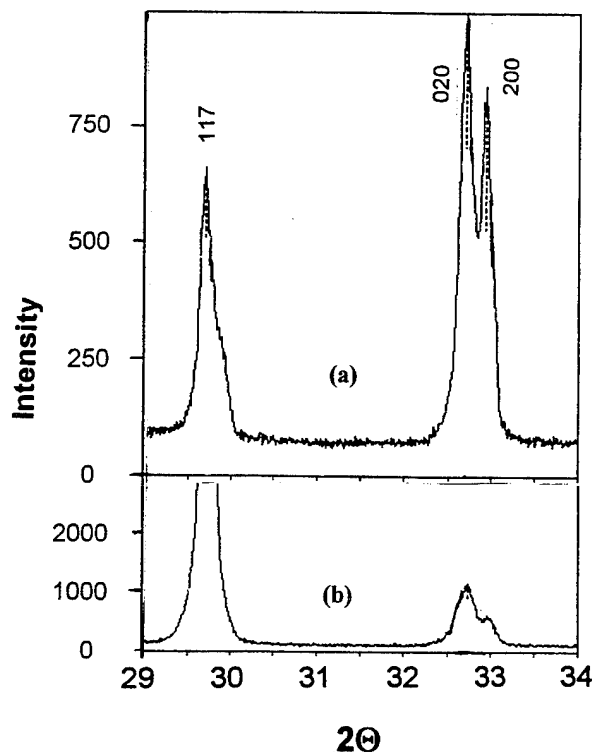


Fig. 7. The  $\perp$  cuts from the DC field assisted forged BIT also show  $a$  and  $b$  axis orientation. In addition, the  $\perp||$  cut (b) has a more dominant (020) reflection, than does the  $\perp\perp$  cut (a), due to some alignment of the polar  $b$  axis. (Note the different intensity scales.)

Of most interest in this work is the diffraction pattern of the cross-sectional plane. Selected angle x-ray scans are shown in Figure 6 and 7 for the three different samples. Neither the simple forged sample (Fig. 6(a)) or the AC-field assisted sample (Fig. 6(b&c)) show splitting of the (020)/(200) peaks. The DC-field assisted, on the other hand, exhibits distinct separation of these peaks (Figure 7), suggesting:

1. a greater difference in  $a$  and  $b$  lattice parameters
2. some degree of poling

Moreover, the relative heights of the (020) and (200) peaks differ for the two cross-sectional cuts. The (020) peak height is twice that of the (200) for the  $\perp||$  cut, while the ratio is only 1.16 for the  $\perp\perp$  cut. This result suggests that the DC field was successful in orienting the polar axis ( $b$ -axis) in the direction of the applied field and/or in poling of the ceramic. The reason for the difference in the (117) peak height is unclear.

SEM revealed the same alignment of plate-like grains as previously reported for BIT [5] and other hot-forged layered structure ferroelectrics [7,8]. The applied electric field appeared to have little effect on the microstructure.

### ELECTRICAL CHARACTERIZATION

The dielectric constants were calculated from capacitance measurements (HP 4192A Impedance Analyzer) made on the various cuts. These are tabulated below:

Table I  
Dielectric Constants (1MHz, room temp.) for  
Hot Forged  $\text{Bi}_4\text{Ti}_3\text{O}_{12}$

	$K_{  }$	$K_{\perp\perp}$	$K_{\perp  }$
Simple HF (this work)	122	147	
Simple HF (ref 5)	133	149	
Simple HF, poled (ref 5)	114	131	129
DC HF (this work)	110	133	124
AC HF (this work)	129	140	136

The measurements show that the low permittivity direction is along the long  $c$ -axis of the structure, and dielectric values agree quite well with previous work [5]. The slightly higher values reported by Takenaka are due to a small (0.2 wt%) Mn addition to the base composition. For the field assisted samples, the highest permittivity direction is perpendicular to both the forging axis and the applied field. Again, this suggests the possibility of alignment of the polar axis. The lower value of  $K_{\perp||}$  is because it is in a poled state where the low field permittivity is small.

Ferroelectric hysteresis results are very interesting. The normal hot-forged sample gives loops just as expected from previous work [5]. Parallel to the forging axis, polarization and coercive field are quite small. This direction contains the  $c$ -component of the canted polarization vector. Perpendicular to the FA, the loop is quite large with large polarization and coercive field. This direction includes the  $b$ -component of the canted polarization vector. Now look at the loops in the three directions for the DC-assisted hot forged sample in Figure 10. Parallel to the FA, the loop is essentially the same as in simple HF, small and square. The important point is the difference between the  $\perp||$  and the  $\perp\perp$  samples. The fact that there is a

difference in hysteresis character suggests some effect of the DC field on crystallographic orientation. The  $\perp\perp$  loop was very difficult to open, resulting in a very thin loop, almost linear in nature in some samples. This suggests a predominance of the non-polar  $a$  axis in this direction. The  $\perp||$  loop on the other hand exhibits a very square loop with high polarization and coercive field, suggesting a predominance of the polar  $b$ -axis in this direction. In fact, the squareness ( $P_r/P_s$ ) of this loop is greater than for the simple hot-forged. This is strong evidence for coupling between the applied field and the polar crystallographic axis during processing, which was of course the goal of this experiment.

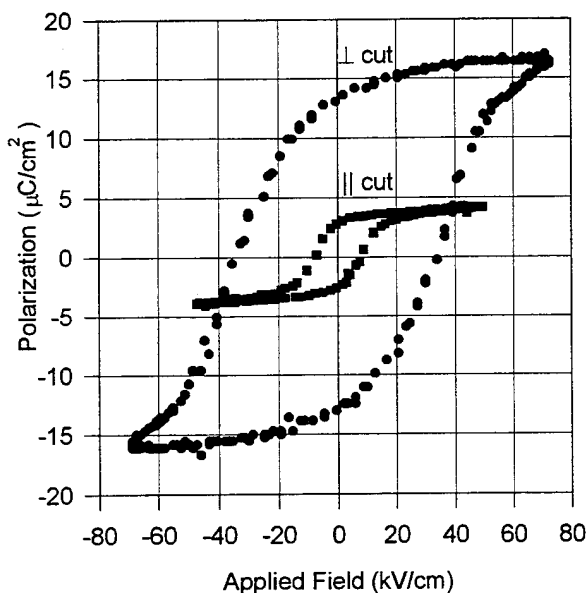


Fig. 8. Hysteresis loops for normal hot-forged  $\text{Bi}_4\text{Ti}_3\text{O}_{12}$  measured parallel and perpendicular to the forging axis.

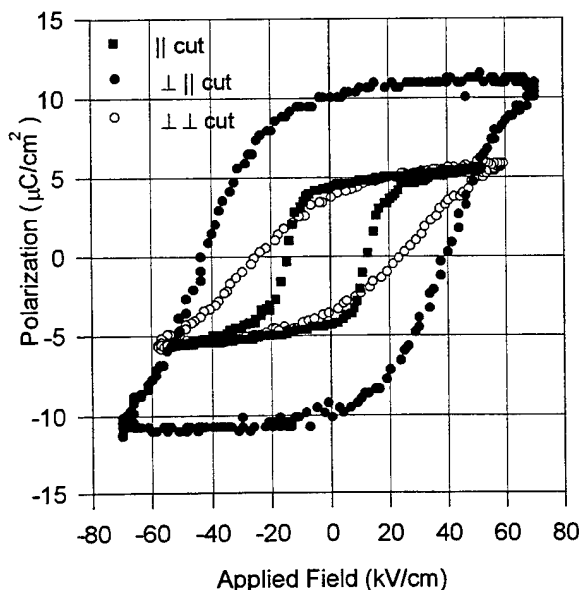


Fig. 9. Hysteresis loops for DC-field assisted hot-forged  $\text{Bi}_4\text{Ti}_3\text{O}_{12}$  illustrating the anisotropy in three directions.

Piezoactivity was determined via the resonance method. As expected, the simple forged and AC-assisted samples displayed a piezoelectric resonance only when subjected to a poling procedure of 50KV/cm for 20min at 150°C. A piezoelectric resonance was found in the DC-assisted without an additional poling step. Piezoelectric measurements are preliminary at this stage, and will be reported in a future communication.

## CONCLUSIONS

X-ray diffraction, dielectric and ferroelectric hysteresis measurements have shown that a transverse DC field applied during the hot-forging process can influence the crystallographic alignment in ferroelectric ceramics. The mechanism is not clear at this point, since the processing was done above the Curie point of bismuth titanate. The hysteresis measurements in particular provide strong evidence for the potential of this novel EFAHF process to eliminate the radial distribution of the polar axis in forged polycrystalline ferroelectrics. It remains to be seen whether the process can be used to increase the piezoactivity of polycrystalline bismuth layered structures, as well as other ferroelectrics like  $\text{Sr}_2\text{Nb}_2\text{O}_7$  which have interesting possibilities for high temperature transducers.

## ACKNOWLEDGMENT

The authors would like to acknowledge the funding of this work by the Sandia National Laboratories Educational Initiative in Materials and Mechanics.

## REFERENCES

- [1] R.E. Newnham, R.W. Wolfe and J.F. Dorian, "Structural Basis of Ferroelectricity in the Bismuth Titanate Family", *Mat.Res. Bull.*, vol.6, 1029-1033, 1971.
- [2] Keramos Inc., Indianapolis, IN, USA. General Catalog, 1991.
- [3] K. Sakata, T. Takenaka and K. Shoji, "Hot-Forged Ferroelectric Ceramics of Some Bismuth Compounds with Layer Structure," *Ferroelectrics*, vol. 22, pp. 825-826, 1978.
- [4] T. Takenaka and K. Sakata, "Grain Oriented and Mn-doped  $(\text{NaBi})_{(1-x)/2}\text{Ca}_x\text{Bi}_4\text{Ti}_4\text{O}_{15}$  ceramics for Piezo and Pyrosensor Materials," *Sensors and Materials*, vol. 1, pp.35-46, 1988.
- [5] T. Takenaka, "Hot-Forged Bismuth Layer Structure Ferroelectrics", PhD Thesis, The Science University of Tokyo, Tokyo, 1984.
- [6] F.K. Lotgering, "Topotactical Reactions With Ferrimagnetic Oxides Having Hexagonal Crystal Structures-I," *J. Inor. Nucl. Chem.*, vol. 9, pp.113-123, 1959.
- [7] P.A. Fuierer and R.E. Newnham, " $\text{La}_2\text{Ti}_2\text{O}_7$  Ceramics," *J. Am. Ceram. Soc.*, vol.75 [11], pp. 2876-81 (1991).
- [8] P.A. Fuierer, T.R. Shrout and R.E. Newnham, "Physical, Electrical and Piezoelectric Properties of Hot-forged  $\text{Sr}_2(\text{NbTa})_2\text{O}_7$  Ceramics," in *Smart Materials Fabrication and Materials for Micro-Electro-Mechanical Systems, MRS Symposium Proceedings*, vol. 276, pp. 51-57, 1992.

# SPRAY PYROLYSIS SYNTHESIS OF LEAD MAGNESIUM NIOBATE RELAXOR FERROELECTRIC POWDERS

J. G. Marx and W. Huebner  
Department of Ceramic Engineering  
University of Missouri-Rolla  
Rolla, MO 65401

## Abstract

The spray pyrolysis method was applied to the synthesis of Lead Magnesium Niobate (PMN). This synthesis method offers several advantages over conventional processing for this material. These advantages include the ability to produce unagglomerated spherical particles, and to systematically control the particle size. Sub micron powders were produced by the atomization of an aqueous polymeric precursor, and passing the aerosol through a multi-zone furnace. Powders in the composition range  $\text{XPb}(\text{Mg}_{1/3}\text{Nb}_{2/3})\text{O}_3 - (1-\text{X})\text{PbTiO}_3$  were produced. Phase development during synthesis was investigated, and the sintering behavior of these powders studied.

## Introduction

Recent developments in transducer and electrostrictive actuator research have indicated the utility of using Relaxor Ferroelectrics. This family of materials offer numerous advantages over "normal" piezoelectrics including higher dielectric constants, electrostrictive strains, induced piezoelectric coefficients, and also sensitivity which can be actively modulated by an electric field. For composite transducers this yields the potential for dynamic shading and/or element selection. A major drawback of these materials, in particular in the  $\text{Pb}(\text{Mg}_{1/3}\text{Nb}_{2/3})\text{O}_3$  (PMN) system, is difficulty with reproducible synthesis due to the formation of a stable pyrochlore phase[1,2,3]. Spray pyrolysis synthesis was chosen because it offered the possibility of eliminating the reproducibility/phase formation problems. Spray pyrolysis is a synthesis technique where a precursor solution is atomized and the resulting aerosol is passed through a furnace. In the furnace the solvent is evaporated and the resulting precursor particle decomposed to form oxide[5,6,7]. The goals of this research include the synthesis of perovskite PMN powders, and the preparation and characterization of monoliths and composites with tailored microstructure using these powders.

## Experimental Procedure

Solutions for this work were of a polymeric precursor with Citric Acid and Ethylene Glycol added to chelate the cations and form a polymeric gel which encourages atomic scale mixing of cations. The cation sources used were reagent grade lead nitrate, magnesium nitrate, niobium oxalate, and titanium isopropoxide. Cation citrate solutions were prepared from both the Niobium and Titanium sources, and aqueous solutions of nitrates were prepared. All solutions were standardized gravimetrically. The data given in this paper was prepared using 1/32 M solutions based on final oxide. Powders were prepared with the compositions of  $\text{Pb}(\text{Mg}_{1/3}\text{Nb}_{2/3})\text{O}_3$  (PMN) and 0.9PMN - 0.1  $\text{PbTiO}_3$  (PT). Phase development was investigated as a function of spray pyrolysis temperature, post calcination conditions, and excess lead and magnesium content. Spray pyrolysis was carried out using the apparatus shown in figure 1. Atomization was performed using a modified ultrasonic humidifier. The furnace utilized a fused silica tube with an outside diameter of four inches, and a length of nine feet. The furnace consists of four separately controlled zones with a total hot zone length of seven feet. The first two zones use Kanthal wound elements, and the two final zones are heated by SiC bar elements. For all runs, the first two zones were set at 100°C and 200°C respectively. The final zone was set at the high temperature listed in discussions, and the third zone was maintained at 200°C below the high temperature. Powders were collected on a Gore Tex™ membrane filter on a Nomex™ felt backing. Back pressure was maintained on the filter using a common heating system squirrel cage fan.

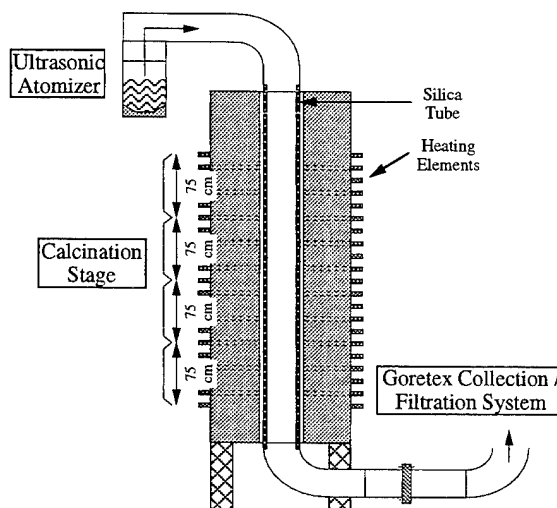
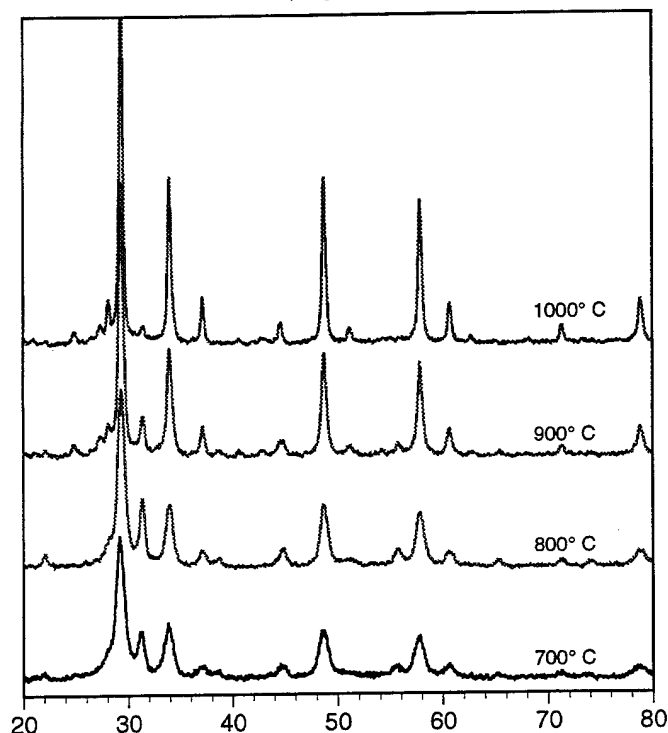


Figure 1. Schematic of Spray Pyrolysis Apparatus at U.M.R.

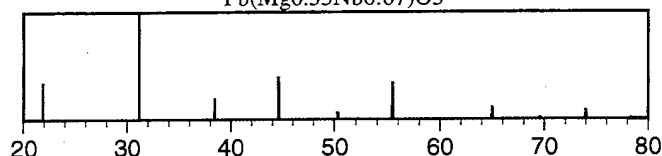
## Results & Discussion

Powders were prepared of PMN and PMN-PT both with and without additions of excess lead or magnesium. The effects of thermal profile on the phase development were investigated. Figure 2 shows the X-ray diffraction patterns of stoichiometric PMN as a function of spray pyrolysis temperature. Crystallinity increases with increasing spray pyrolysis temperature as expected. The amount of pyrochlore increases with temperature, and the amount of perovskite increases up to 800° C where it begins to decrease with temperature. With stoichiometric PMN a maximum of 27% perovskite (remainder pyrochlore) by XRD could be formed by spray pyrolysis. PMN with 10%  $\text{PbTiO}_3$  (PT) was also prepared and the results were very similar with regard to phase formation. The bottom of figure 2 contains representations of the JCPDF standard X-ray patterns for perovskite PMN and Shroot's composition pyrochlore ( $\text{Pb}_{1.83}\text{Mg}_{0.29}\text{Nb}_{1.71}\text{O}_{6.39}$ ) which is the most commonly seen phase impurity in the PMN system[4].

XRD of stoichiometric PMN  
as a function of spray pyrolysis temperature



Perovskite PMN JCPDF 27-1199  
 $\text{Pb}(\text{Mg}_{0.33}\text{Nb}_{0.67})\text{O}_3$



Pyrochlore PMN JCPDF 33-769  
 $\text{Pb}_{1.83}(\text{Mg}_{0.29}\text{Nb}_{1.71})\text{O}_{6.39}$

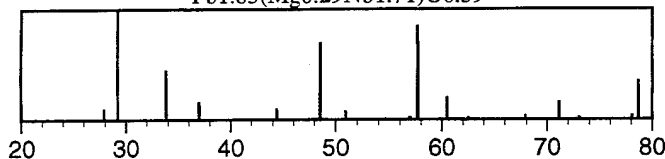


Figure 2. XRD of PMN as a function  
of spray pyrolysis temperature

In order to increase the amount of perovskite phase in the as sprayed powders, batches of powder were prepared with excess lead or magnesium.[1,3] The effect of both additions was an increase in the relative amount of perovskite phase. The magnitude of the improvement was similar for both additions, but due to space limitations only lead additions will be discussed in this paper. Figure 3 is a plot of the XRD patterns of spray pyrolyzed PMN powders with three different lead contents. The three powders contained 0, 2, and 5 mol percent excess lead above the stoichiometric amount. As can be seen, additions of lead improve the ratio of perovskite to pyrochlore formed. All powders for this set of experiments were spray pyrolyzed under identical conditions with the exception of lead stoichiometry. The best result achieved through manipulation of spray pyrolysis temperature and lead content was 77% perovskite phase with 5 mol percent excess lead with a spray pyrolysis temperature of 850°.

Phase development of PMN as a function of excess  
lead content for powders spray pyrolyzed at 900° C

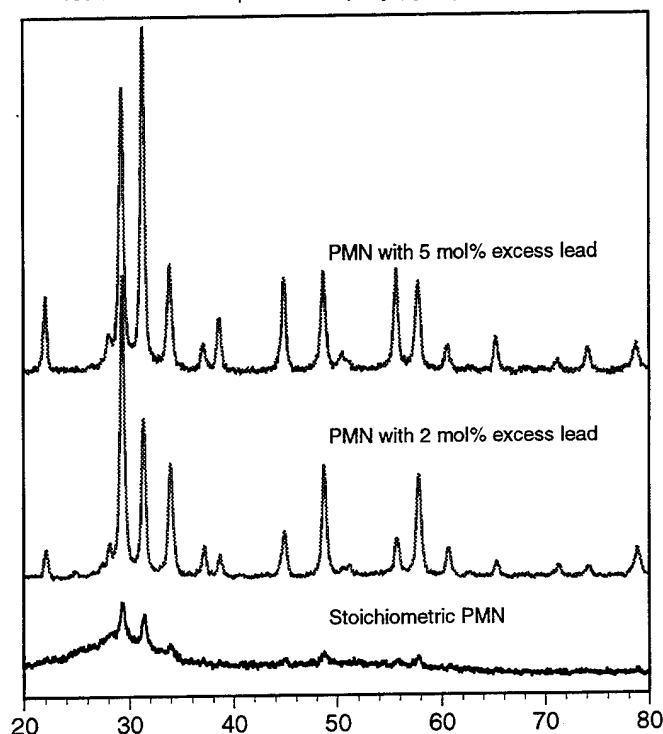


Figure 3. XRD of PMN as a function of Pb content

Fully perovskite powders were not obtained directly from spray pyrolysis, which is most likely due to the extremely short residence time at temperature (less than 5 seconds). Subsequently, a calcination study was done. Powders produced by spray pyrolysis at 1000° C were calcined in closed crucibles for differing times at 800° C with a 3 hour ramp. The relative amounts of perovskite and pyrochlore in the resulting powders were determined qualitatively by X-ray diffraction. The results of these investigations for PMN with 0, 2, and 5 mol percent excess lead are summarized in figure 4. Full transformation to perovskite was achieved only with 5% excess lead, and a calcination time of only 15 minutes was required. Similar results were obtained with PMN-PT spray pyrolyzed powders with the same quantities of excess lead.

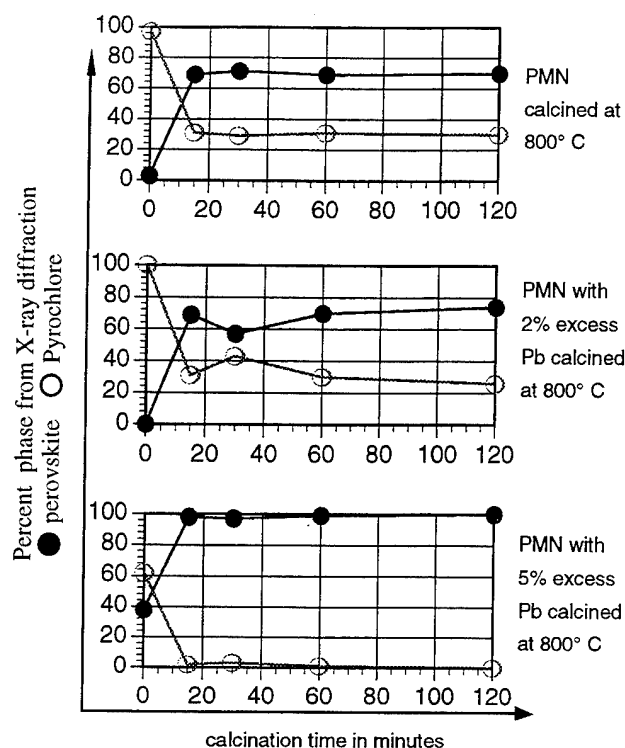
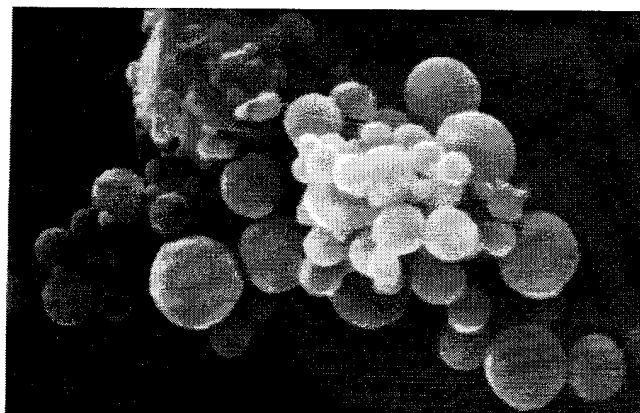


Figure 4. Phase transformation plot

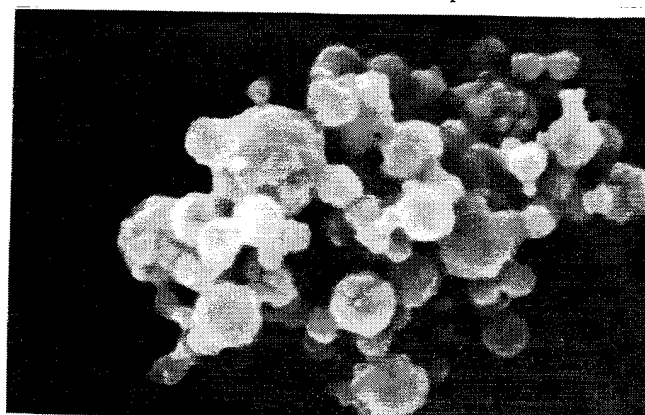
Figure 5 exhibits a SEM photomicrograph of PMN powder with 5 mol percent excess lead after spray pyrolysis at a maximum temperature of 1000° C. This powder is spherical, and unagglomerated with nearly all particles having diameters below 1  $\mu\text{m}$ . The particle size can be systematically controlled with the spray pyrolysis method to yield particles from tens of nanometers up to ~10  $\mu\text{m}$ . This powder has the composition  $\text{Pb}_{1.05}(\text{Mg}_{1/3}\text{Nb}_{2/3})\text{O}_3$ , but due to the short residence time in the furnace it is not fully crystallized in the perovskite form. The lower micrograph in figure 5 is a micrograph of the same powder after calcination at 800° C for 15 minutes. This heat treatment was sufficient to effect complete transformation to the desired perovskite phase. As can be seen in the second micrograph, there is a dramatic change in the morphology which occurs without an accompanying size change. As can be seen, some minor neck growth between particles has occurred.

Powder Micrographs of PMN with 5% excess Lead



1  $\mu\text{m}$

As sprayed at 800° C maximum temperature



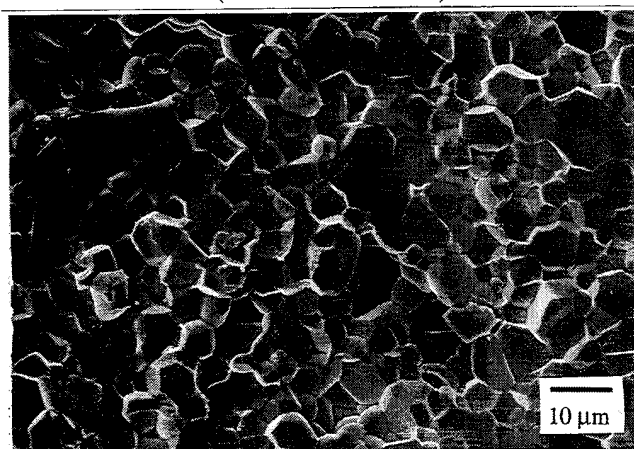
1  $\mu\text{m}$

Sprayed at 800° C and calcined at 800° C for 15 minutes

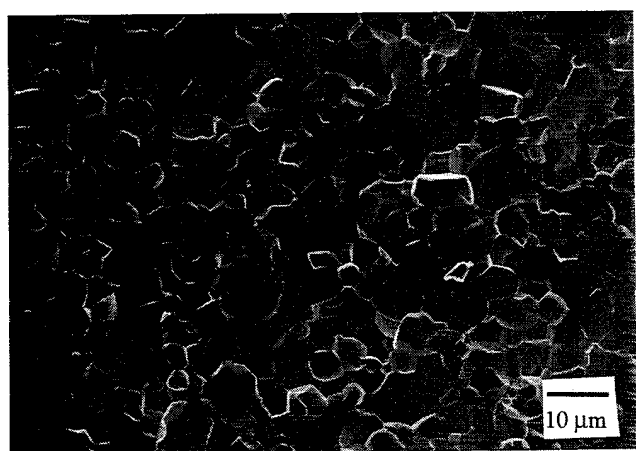
Figure 5. Powder micrographs of spray pyrolyzed PMN powders

Two spray pyrolyzed PMN powders were pressed uniaxially into pellets with PVA binder and fired. The two powders were both PMN with 5% excess lead. The first was as sprayed at 800° C and the second was sprayed at 800° and calcined at 800° C to fully perovskite phase. The following micrographs are fracture cross sections of pellets fired at 1250° C for 30 minutes. Both pellets are 100% perovskite by XRD after firing, as the first pellet transformed fully to perovskite upon firing. Both microstructures are fairly homogeneous with equiaxed grains and densities above 90% of theoretical. The grain size of the uncalcined pellet is slightly larger, and the density slightly less. This can be attributed to a volumetric expansion upon formation of the perovskite phase. This expansion has been used to advantage in other synthesis techniques commonly called "reactive calcination," [2] but necessitates calcination before firing in the case of spray pyrolysis synthesis.

Micrographs of PMN with 5% excess Lead fired at 1250° C for 30 minutes (fracture cross sections)



Fired as sprayed at 800° C maximum temperature



Sprayed at 800° C and calcined at 800° C for 15 minutes before firing

Figure 6. Fired microstructures of spray pyrolyzed PMN powders

### Conclusions

Powders were made in the composition range  $\text{XPb}(\text{Mg}_{1/3}\text{Nb}_{2/3})\text{O}_3 - (1-\text{X})\text{PbTiO}_3$  by the spray pyrolysis synthesis method. Powders can be produced which are spherical, unaggregated, and sub-micron. The addition of excess lead or magnesium was found to increase the relative amount of the perovskite phase that formed. Due to the short residence time in the spray pyrolysis furnace, phase pure perovskite powders could not be produced directly. With the addition of 5 mol percent excess lead, 100% perovskite phase (by XRD) can be produced by calcination at 800° C for 15 minutes following spray pyrolysis. Fine grained ( $<10\mu\text{m}$ ), dense homogeneous microstructures could be produced by uniaxial pressing and sintering at 1250° C for 30 minutes.

### References

- [1] S.L. Swartz and T.R. Shrout, "Fabrication of Perovskite Lead Magnesium Niobate," *Mat. Res. Bull.*, Vol 17, 1245-1250 (1982)
- [2] T.R. Shrout, P. Papet, S. Kim, and Gye-Song Lee, "Conventionally Prepared Submicrometer Lead-Based Perovskite Powders by Reactive Calcination," *J. Am. Ceram. Soc.*, 73 [7] 1862-67 (1990)
- [3] J.P. Guha, and H.U. Anderson, "Preparation of Perovskite  $\text{Pb}(\text{Mg}_{1/3}\text{Nb}_{2/3})\text{O}_3$  Using  $\text{Pb}_3\text{Nb}_2\text{O}_8$  and  $\text{MgO}$ ," *J. Am. Ceram. Soc.*, 69 [11] C-287-C-288 (1986)

- [4] T.R. Shrout, and L.L. Swartz, "Dielectric Properties of Pyrochlore Lead Magnesium Niobate," *Mat. Res. Bull.*, Vol. 18, 663-667 (1983)
- [5] Gary L. Messing, Shi-Chang Zhang, and Gopal V. Jaanthi, "Ceramic Powder Synthesis by Spray Pyrolysis," *J. Am. Ceram. Soc.* 76 [11] 2707-26
- [6] Shi Chang Zhang, G. L. Messing, and W. Huebner, "YBa<sub>2</sub>Cu<sub>3</sub>O<sub>7-x</sub> Superconductor Powder Synthesis by Spray Pyrolysis of Organic Acid Solutions," *J. Aerosol Sci.*, 22 [5] 585-599 (1991)
- [7] Y. Kanno, and T. Suzuki, "Estimation of Formation Mechanism of Spherical Fine ZrO<sub>2</sub>-SiO<sub>2</sub> Particles by Ultrasonic Spray Pyrolysis," *J. Mat. Sci.* 23 3067-72 (1988)



# INVESTIGATIONS OF THE PHASE DIAGRAM OF THE PbTiO<sub>3</sub> - BiFeO<sub>3</sub> SYSTEM

P.W. Lu, W.M. Zhang, W.R. Xue, and X.F. Wang

Nanjing Institute of Chemical Technology  
Nanjing, Jiangsu 210009  
P.R.C.

W. Huebner

Department of Ceramic Engineering  
University of Missouri - Rolla  
Rolla, MO 65401

## ABSTRACT

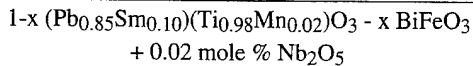
The phase diagram of the (Pb<sub>0.85</sub>Sm<sub>0.10</sub>)(Ti<sub>0.98</sub>Mn<sub>0.02</sub>)O<sub>3</sub> - BiFeO<sub>3</sub> system was studied by measuring the dielectric behavior as a function of temperature, coupled with room temperature XRD and measurements of d<sub>33</sub>, k<sub>t</sub>, and k<sub>p</sub>. A morphotropic phase boundary exists for between the tetragonal and rhombohedral phases for a BiFeO<sub>3</sub> content of ~55 mole%. Some of the studied compositions exhibit electromechanical properties suitable for transducer applications.

## INTRODUCTION

Lead titanate (PbTiO<sub>3</sub>) exhibits many interesting characteristics including highly anisotropic piezoelectric properties, a high piezoelectric voltage coefficient due to its lower dielectric constant, a high Curie temperature, a high spontaneous polarization, a low aging rate, and a relatively low mechanical quality factor. It is rarely used in its pure form, as doping with isovalent alkaline-earth elements on the A-site [1-4], donor dopants [5-8], or both [9-14] results in a relatively large longitudinal piezoelectric coefficient, d<sub>33</sub>, and a low transverse coefficient, d<sub>31</sub>. This yields a large ratio of the thickness to lateral electromechanical coupling coefficient (k<sub>t</sub>/k<sub>p</sub>).

When used as the filler in 0-3 composites, PbTiO<sub>3</sub> is modified with BiFeO<sub>3</sub> (50 mole%), which increases the c/a ratio to ≥1.10 [15-18], and improves the composite piezoelectric properties. BiFeO<sub>3</sub> is a perovskite with T<sub>c</sub>≈850°C [19]. Studies on the PbTiO<sub>3</sub>-BiFeO<sub>3</sub> (PT-BF) phase diagram [20-21] show that a morphotropic phase boundary (MPB) exists between the tetragonal and rhombohedral phases at ~70-75m% BF. At this boundary the c/a ratio of the tetragonal phase is 1.18, which is very high. Dielectric properties along the phase diagram [21] show that the properties do not exhibit a maximum near the MPB, although measurements were made at 0.53 GHz to remove effects associated with the high electrical conductivity of this system. The T<sub>c</sub> increased steadily with m% BF from 490°C to 850°C [21].

In this study we chose to explore the phase diagram and electromechanical properties along a modified-PT-BF system:



This PT-based composition exhibits superior electromechanical properties, and the Nb<sup>5+</sup> donor dopant is expected to decrease the conductivity as BF is added [21].

## EXPERIMENTAL PROCEDURE

Figure 1 overviews in detail the processing steps used to prepare the 1-x (Pb<sub>0.85</sub>Sm<sub>0.10</sub>)(Ti<sub>0.98</sub>Mn<sub>0.02</sub>)O<sub>3</sub> - x BiFeO<sub>3</sub> + 0.02 m% Nb<sub>2</sub>O<sub>5</sub> ceramics used in this study. Detailed microstructural development studies showed that the sintering temperature, T<sub>sint</sub>, steadily decreased with BF additions, which is not surprising considering the incongruent melting temperature of BiFeO<sub>3</sub> at ~930°C. The T<sub>sint</sub> (°C - for 2 h) and measured densities, ρ (g/cm<sup>3</sup>), for the system were:

x →	0.00	0.10	0.20	0.30	0.40	0.425	0.45	0.475
T <sub>sint</sub> →	1250	1200	1190	1180	1170	1160	1140	1130
ρ →	7.71	7.70	7.64	7.64	7.69	7.75	7.73	7.75

x →	0.50	0.525	0.55	0.575	0.60	0.70	0.80	1.00
T <sub>sint</sub> →	1080	1080	1070	1060	1040	1030	1020	850
ρ →	7.81	7.83	7.93	7.92	7.92	8.02	8.11	7.36

Figure 2 exhibits the fired surfaces of the PT-BF system. In all instances the grains were equiaxed, and for x≤0.55 the grains were of mostly cubic morphology. Grain sizes were on the order of 2-5 μm, with a steady decrease exhibited with increasing BF content. Fracture surfaces showed a small amount of closed porosity (≤2 vol%) was present, yet this did not impede poling.

Compositional analyses and lattice parameters were determined using X-ray diffraction (Scintag X-ray diffractometer). Dielectric measurements were performed on plane parallel disks approximately 1 to 2 mm thick. Gold electrodes were sputtered onto the surface in a vacuum through a mask. Dielectric properties were measured as a function of temperature and frequency using a General Radio GR1689 RLC Digibridge and a muffle tube furnace. Measurements were taken during heating at 4°C/min from 25 to 450°C, at 1, 10 and 100 kHz.

After poling, a Berlincourt d<sub>33</sub> meter was used to measure the d<sub>33</sub> coefficient, and resonance measurements were performed with an impedance analyzer (Hewlett-Packard 4194A Impedance Analyzer with a 41941A Impedance Probe and 16092A Test Fixture) to determine k<sub>t</sub> and k<sub>p</sub>.

## RESULTS AND DISCUSSION

The lattice parameters of the modified PT-BF system are shown in Figure 3. For x=0.00 the c/a ratio is 1.048, which is less than that of pure PbTiO<sub>3</sub> (c/a=1.063) due to the addition of the Sm<sub>2</sub>O<sub>3</sub>. As BF is added, the tetragonality steadily increases up until x=0.55, at which point c/a=1.072. Careful observations of the (200) and (111) peaks over this range clearly indicated no rhombohedral phase was present. For 0.575 ≤ x ≤ 0.60 both

<b>Raw</b>	• PbO 99%	• TiO <sub>2</sub> 99%
<b>Materials:</b>	• Sm <sub>2</sub> O <sub>3</sub> 99.9%	• MnO <sub>2</sub> 99%
	• Bi <sub>2</sub> O <sub>3</sub> 99%	• Fe <sub>2</sub> O <sub>3</sub> 99.8%
<b>Mixing</b>	• Batch:ZrO <sub>2</sub> media:alcohol = 1:4:0.8	
	• Polyethylene jar	
	• 24 h	
<b>Calcination:</b>	• Bi <sub>2</sub> O <sub>3</sub> and Fe <sub>2</sub> O <sub>3</sub> pre-calcined: 680°C - 3h → BiFeO <sub>3</sub>	
	• (Pb <sub>0.85</sub> Sm <sub>0.10</sub> )(Ti <sub>0.98</sub> Mn <sub>0.02</sub> )O <sub>3</sub> : 900°C - 2h	
<b>Milling</b>	• Aggregates broken up with an agate mortar & pestle	
	• Milled again as above	
<b>Pressing:</b>	• 8 wt% of a 5% PVA solution	
	• Granulation	
	• Uniaxial pressing: 1000 kg/cm <sup>2</sup> [green density: 55% T.D.]	
<b>Sintering:</b>	• 650°C-4 h (binder burnout)	
	• Sintering temperature: 1250°C ≤ T ≤ 850°C	
	• Covered Al <sub>2</sub> O <sub>3</sub> crucibles; PbZrO <sub>3</sub> lead source	

Figure 1: Overview of the processing steps used to prepare the modified PT-BF ceramics.

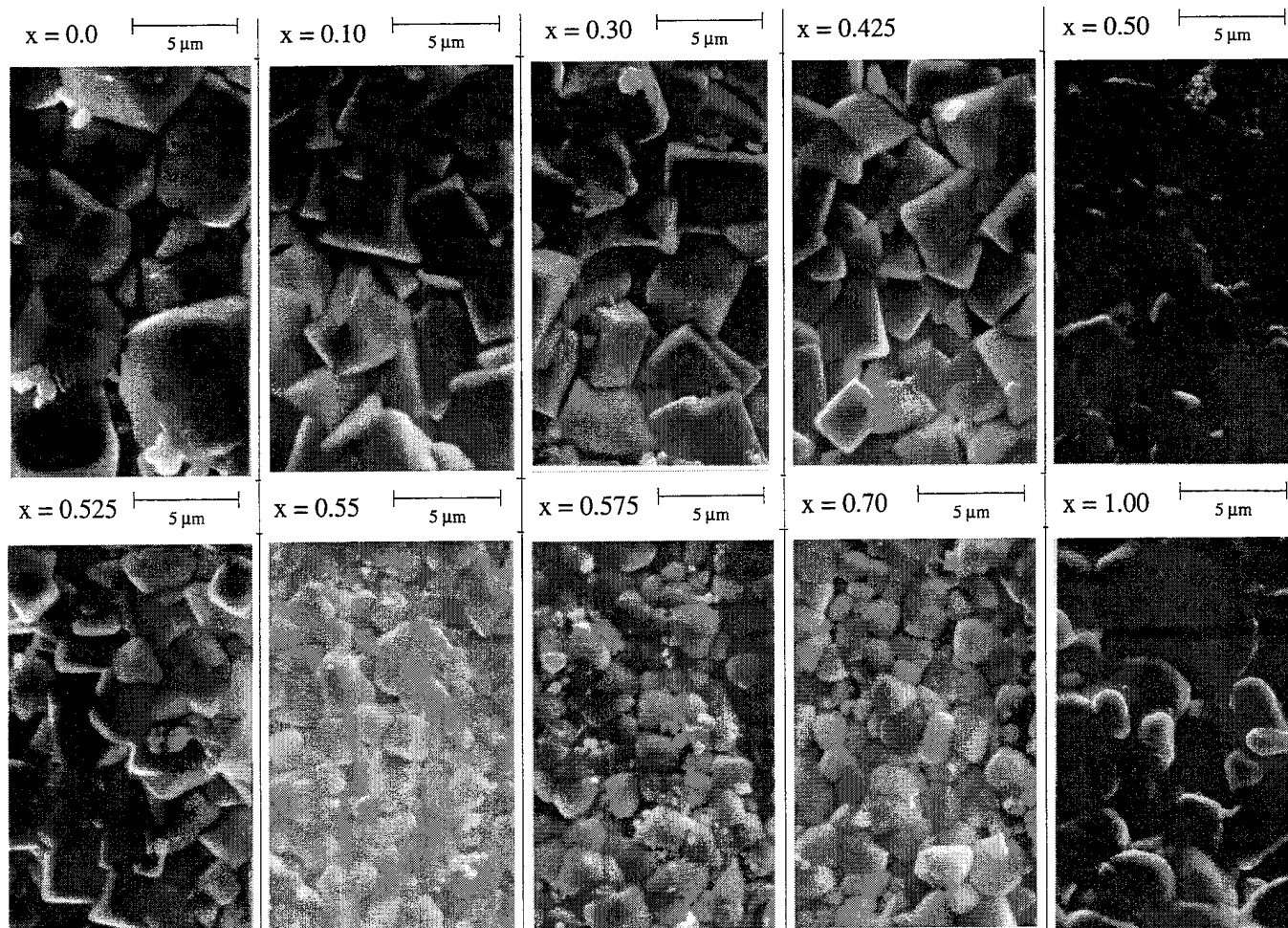


Figure 2: SEM micrographs of the sintered surfaces of the modified PT-BF ceramics.

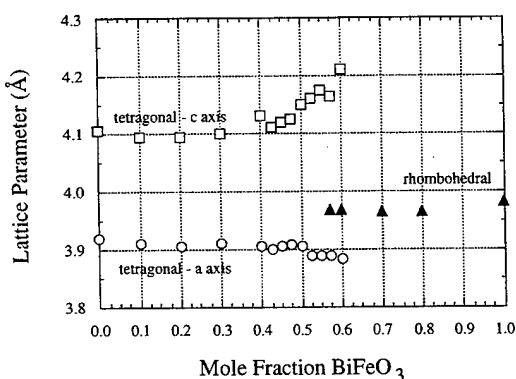


Figure 3: Lattice parameters of the modified  $\text{PbTiO}_3$ - $\text{BiFeO}_3$  binary.

rhombohedral and tetragonal phases were present;  $c/a=1.085$  for the tetragonal phase at  $x=0.60$ . These results are similar to pure PT-BF, which exhibits a tetragonal-rhombohedral mixed phase region between  $\approx 67.5$  to 75 mol% BF [20,21]. For  $x>0.6$  only a rhombohedral phase was observed, although more compositions between  $x=0.60$  and 0.70 should be prepared to more accurately define the region.

In general, all of the compositions exhibited a high resistivity at low temperatures, but as the temperature approached  $\approx 200$ - $300^\circ\text{C}$ , the conductivity became sufficient such that a strong dispersion of the dielectric properties appeared. Figure 4 shows a typical plot of

$K'$  and  $K''$  vs. temperature, in this case for a BF content = 45 mol%. The low frequency behavior is typical for a lossy dielectric. However, the higher frequency data (100 kHz) exhibited a sufficiently low  $K''$  such that meaningful interpretations of the dielectric behavior could be made for  $T<350^\circ\text{C}$ . A previous study on the undoped PT-BF system [21] could only generate meaningful dielectric data at 0.53 GHz. The presence of a second order transition is clearly seen, as reflected by the peak in  $K'$  and the corresponding decrease in  $K''$  at  $\approx 330^\circ\text{C}$ .

Figures 5-7 exhibit the temperature dependence of the dielectric properties for the entire PZT-BF system measured at 100 kHz, and Figure 8 plots the corresponding  $K'$  vs. mol% BF. These results correlate well with the phase stability regimes of Figure 3. At  $25^\circ\text{C}$  the  $K'$  exhibits a maximum at  $x=0.55$ , which falls within the MPB. The MPB as determined from Figure 8 is constant up until  $250^\circ\text{C}$ , then bends towards the PT-rich side. At  $275^\circ\text{C}$  the maximum occurs for  $x=0.50$ , and at  $300^\circ\text{C}$  for  $x=0.45$ . For  $x=0.60$  the  $K'$  vs.  $T$  response still exhibits the hint of a phase transition due to the inflection near  $\approx 400^\circ\text{C}$ , but the  $x=0.70$  composition exhibits a much lower  $K'$  and no anomalies at all.

No systematic changes in the phase transition associated with  $K_{\text{max}}$  were observed with increasing BF content. This is contrary to the pure PT-BF system, which has been reported to exhibit a continuous change in  $T_c$  all the way up to  $850^\circ\text{C}$  for pure BF. This suggests that the samarium doping is dominating the observed phase transition. Indeed, the MPB of this modified PT-BF system occurs for a BF content  $\approx 10$  mol% less than the undoped system.

Room temperature measurements of  $k_t$ ,  $k_p$  and  $d_{33}$  also exhibit maxima at the MPB (Figure 9), which is similar to the  $\text{Pb}(\text{Zr},\text{Ti})\text{O}_3$  system. For  $x\leq 0.3$  the planar resonance was virtually absent. The reason for the minima of  $k_t$  at low  $x$  is unknown.

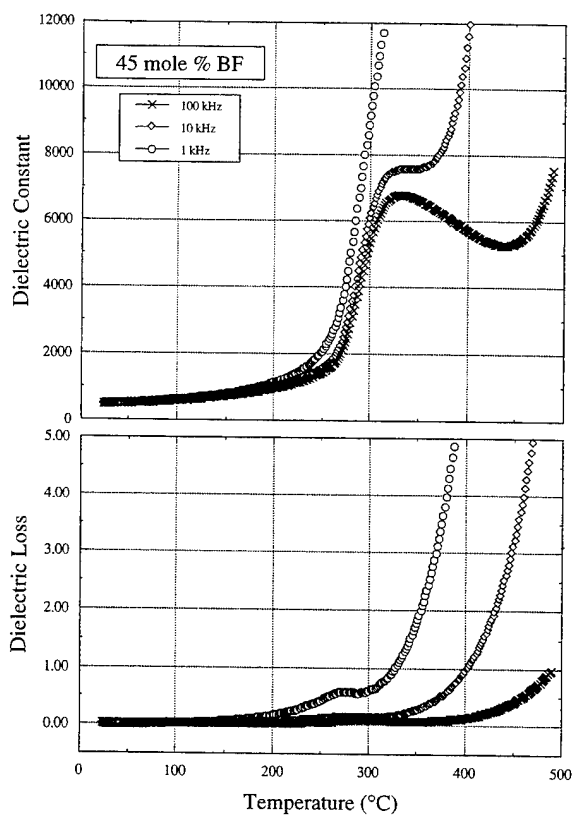


Figure 4: Temperature and frequency dependence of the dielectric constant and loss of the 45 mol% BF composition.

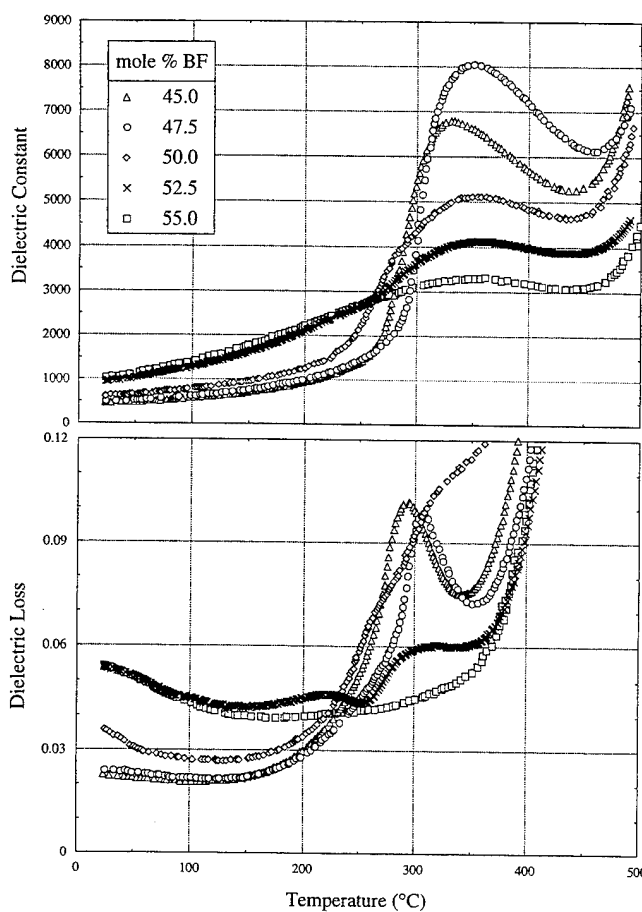


Figure 6: Temperature dependence of the dielectric constant and loss for compositions with  $0.45 \leq x \leq 0.55$ .

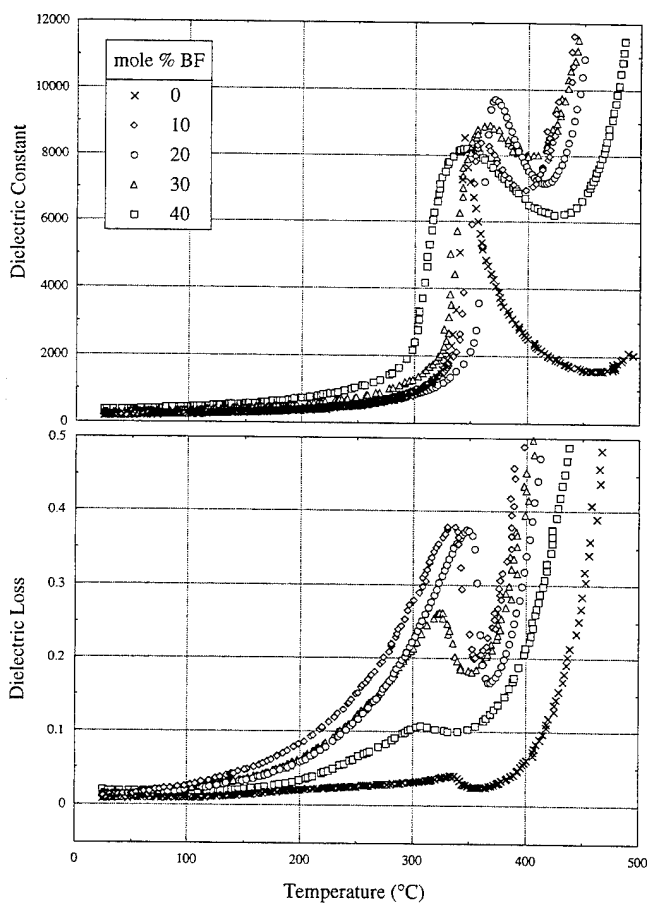


Figure 5: Temperature dependence of the dielectric constant and loss for compositions with  $0.00 \leq x \leq 0.40$ .

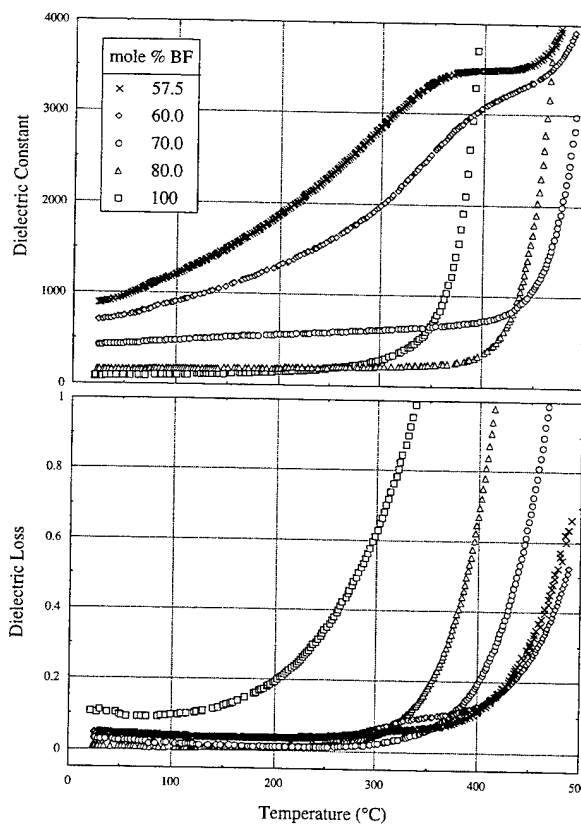


Figure 7: Temperature dependence of the dielectric constant and loss for compositions with  $0.575 \leq x \leq 1.00$ .

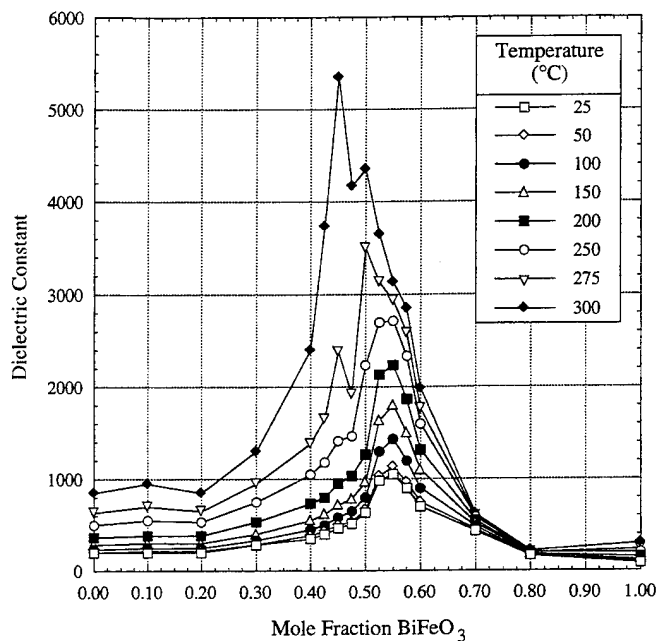


Figure 8: Dielectric constant of the modified  $\text{PbTiO}_3$ - $\text{BiFeO}_3$  binary at different temperatures.

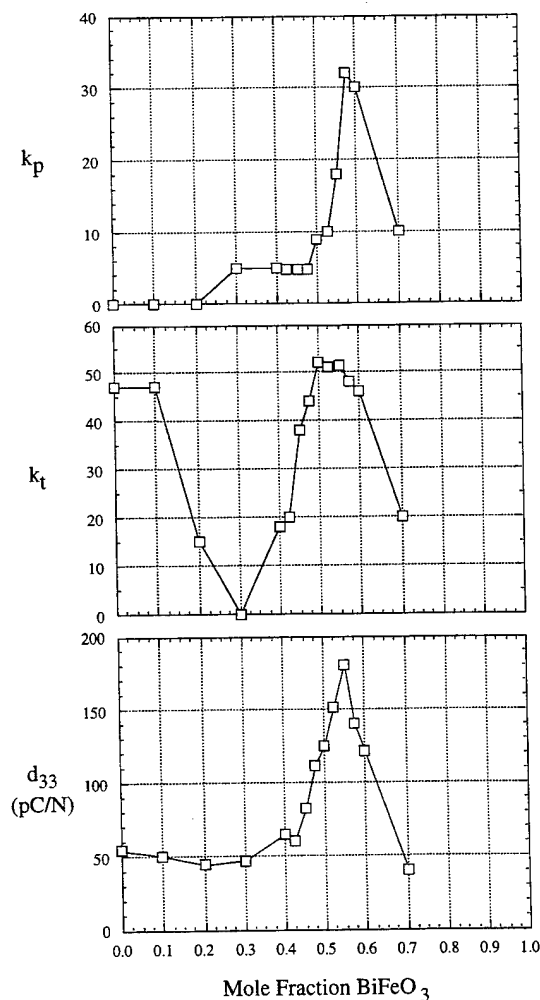


Figure 9: Electromechanical properties of the modified  $\text{PbTiO}_3$ - $\text{BiFeO}_3$  binary.

## CONCLUSIONS

The phase diagram of the  $(\text{Pb}_{0.85}\text{Sm}_{0.10})(\text{Ti}_{0.98}\text{Mn}_{0.02})\text{O}_3$  -  $\text{BiFeO}_3$  system was studied by measuring the dielectric behavior as a function of temperature, coupled with room temperature XRD and measurements of  $d_{33}$ ,  $k_t$ , and  $k_p$ . A solid solution forms over a wide range between the modified PT and the BF, with a mixed phase region occurring between 57.5 and 60%. Further studies should be performed to more finely define this region. The maximum  $K'$ ,  $k_t$ ,  $k_p$  and  $d_{33}$  were exhibited in this MPB region. Some of the studied compositions exhibit electromechanical properties suitable for transducer applications, over a compositional range where the  $K'$  varies widely.

## Acknowledgment

This work was sponsored by the Office of Naval Research under Grant N00014-92-J-1469.

## REFERENCES

- [1] I. Ueda and S. Ikegami, "Piezoelectric Properties of Modified  $\text{PbTiO}_3$  Ceramics," *Jap. J. Appl. Phys.*, **7**, 236-242 (1968).
- [2] J. Mendiola et. al, "Electric Poling Effect on Piezoelectricity of Ca-Modified  $\text{PbTiO}_3$  Ceramics," *Ferroelectrics*, **29**, 1249-1252 (1988).
- [3] K. Takeuchi et. al, "Electromechanical Properties of Calcium-Modified Lead Titanate Ceramics," pp. 402-405 in *Proc. of the 6th Intl. Symp. on Applications of Ferroelectrics*, IEEE, New York (1986).
- [4] A. Ahmad, T.A. Wheat, J.D. Canaday, A.K. Kuriakose, S.E. Prasad and S. Varma, "Processing and Characterization of Ca, Ce, and Na-Ion Doped Lead Titanates," pp. 516-519 in *Proc. of the Eighth Intl. Symp. on Applications of Ferroelectrics*, IEEE, New York (1992).
- [5] S. Ikegami, I. Ueda, and T. Nagata, "Electromechanical Properties of  $\text{PbTiO}_3$  Ceramics Containing La and Mn," *J. Acoust. Soc. Amer.*, **50**[4], 1060-1066 (1971).
- [6] H. Takeuchi, S. Jyomura, E. Yamamoto and Y. Ito, "Electromechanical Properties of  $(\text{Pb,Ln})(\text{Ti,Mn})\text{O}_3$  Ceramics," *J. Acoust. Soc. Amer.*, **72**[4], 1114-1120 (1982).
- [7] W.R. Xue et. al, "Temperature Behavior of Dielectric and Electromechanical Coupling Properties of Samarium-Modified Lead Titanate Ceramics," *Jap. J. Appl. Phys.*, **24**, 718-720 (1985).
- [8] K. Iijima, "Epitaxial Growth and the Crystallographic, Dielectric, and Pyroelectric Properties of Lanthanum-Modified Lead Titanate," *J. Appl. Phys.*, **60**[8], 2914-2919 (1986).
- [9] I. Ueda, "Effect of Additives on Piezoelectric and Related Properties of  $\text{PbTiO}_3$  Ceramics," *Jap. J. Appl. Phys.*, **11**[4], 450-462 (1972).
- [10] Y. Yamashita, K. Yokoyama, H. Honda, and T. Takahashi, " $(\text{Pb,Ca})[(\text{Co}_{1/2}\text{W}_{1/2})\text{Ti}]\text{O}_3$  Piezoelectric Ceramics and Their Applications," *Jap. J. Appl. Phys.*, **20**, 183-187 (1981).
- [11] D. Damjanovic, T.R. Gururaja, and L.E. Cross, "Anisotropy in Piezoelectric Properties of Modified Lead Titanate Ceramics," *Am. Ceram. Soc. Bull.*, **66**[4], 699-703 (1987).
- [12] P. Duran et. al, "Large Electromechanical Anisotropic Modified Lead Titanate Ceramics," *J. Mater. Sci.*, **23**, 4463-4469 (1988).
- [13] K. Rittenmeyer and R.Y. Ting, "Piezoelectric and Dielectric Properties of Calcium- and Samarium-modified Lead Titanate Ceramics for Hydroacoustic Applications," *Ferroelectrics*, **110**, 171-82 (1990).
- [14] L.M. Troilo et. al, "Modified Lead Calcium Titanate Ceramics with a Relatively Large Dielectric Constant for Hydrophone Applications," *J. Amer. Ceram. Soc.*, **77**[3], 857-859 (1994).
- [15] H. Banno, "Recent Progress in Science and Technology of Flexible Piezoelectric Composites in Japan," pp. 67-72, *Proc. of the Seventh Intl. Symp. on Applications of Ferroelectrics*, IEEE, New York (1990).
- [16] J. Giniewicz, " $(\text{Pb,Bi})(\text{Ti,Fe})\text{O}_3$  / Polymer Composite Materials for Hydrophone Applications," M.S. Thesis, Penn State, 1985.
- [17] D.M. Reed, T.T. Srinivasan, Q.C. Xu, and R.E. Newnham, "Effect of Particle Size on the Dielectric and Piezoelectric Properties of  $\text{PbTiO}_3$ -Polymer Composites," pp. 324-327, *Proc. of the Seventh Intl. Symp. on Applications of Ferroelectrics*, IEEE, New York (1990).
- [18] K.H. Han, R.E. Riman and A. Safari, "Dielectric and Piezoelectric Properties of Flexible 0-3 Piezoelectric Composites Prepared by Coprecipitated  $(\text{Pb}_{0.5}\text{Bi}_{0.5})(\text{Ti}_{0.5}(\text{Fe}_{1-x}\text{Mn}_x)_{0.5})$  ( $x=0.00-0.02$ ) Ceramic Powders," pp. 591-594, *Proc. of the 7th Intl. Symposium on Applications of Ferroelectrics*, IEEE, New York (1990).
- [19] S.A. Fedulov et. al, "High Temperature X-ray and Thermal Analysis Results for Bismuth Ferrite," *Sov. Phys. Cryst.*, **6**, 640-641 (1961).
- [20] S.A. Fedulov et. al, "Complete Phase Diagram of the  $\text{PbTiO}_3$ - $\text{BiFeO}_3$  System," *Sov. Phys. - Solid State*, **6**[2], 375-378 (1964).
- [21] R.T. Smith et. al, "Dielectric Properties of Solid Solutions of  $\text{BiFeO}_3$  with  $\text{Pb}(\text{Ti,Zr})\text{O}_3$  at High Temperatures and High Frequency," *J. Appl. Phys.*, **39**[1], 70-74 (1968).

# Effect of Processing on Surface Acoustic Wave Properties of a Modified Lead Titanate Ceramic

C.E. Millar<sup>1</sup>, L. Pedersen<sup>1</sup>, L. Pardo<sup>2</sup>, J. Ricote<sup>2</sup>, C. Alemany<sup>2</sup>, B. Jimenez<sup>2</sup>, G. Feuillard<sup>3</sup> and M. Lethiecq<sup>3</sup>.

<sup>1</sup> Ferroperm A/S, Hejreskovvej 6, 3490 Kvistgård, Denmark.

<sup>2</sup> Instituto de Ciencia de Materiales (Sede A). CSIC, Serrano, 144, 28006 - Madrid, Spain

<sup>3</sup> GIP Ultrasons, Fac. Médecine, 37032 Tours, France

**Abstract** - Piezoceramic substrates are of interest for many surface acoustic wave (SAW) applications, such as chemical and biological sensors and TV filters. For these applications the reproducibility of the SAW properties is important. Here, the effect of a variety of ceramic processing conditions on the microstructure and SAW properties of the ceramics is examined to determine the sensitivity of the properties to processing. The study includes, the influence of milling time, sintering conditions and a post sintering HIP treatment. Microstructure, bulk and SAW properties are characterised and processing-microstructure-property relations examined.

## INTRODUCTION

Piezoceramics have potential for SAW device applications due to the ability to modify the composition to achieve a desirable combination of properties, including high surface coupling coefficient and surface velocity with a low temperature coefficient of delay time. However, the use of piezoceramics in SAW devices has been limited by their high propagation losses and poor reproducibility compared to single crystals.

A variety of compositions have been examined in the literature, such as PZT<sup>[1]</sup> and modified lead titanate<sup>[2]</sup>. Much of the work has concentrated on the effect of composition to produce a low or zero coefficient of delay time and little attention has been paid to the effect of processing and/or microstructure on the surface properties. Jyomura et. al. examined the effect of grain size on the propagation losses<sup>[3]</sup> and Shapiro et. al. investigated the effect of hot pressing PZT ceramics on the surface velocity and coupling coefficients<sup>[4]</sup>, but neither presented a full set of SAW data. Previous work done by the authors<sup>[5]</sup> showed that substrates fabricated from powders prepared by hydrothermal synthesis had much lower temperature coefficients of delay time than substrates prepared by the mixed oxide route. This paper examines the effect of processing, including milling time, sintering temperature and hot isostatic pressing (HIP) on the SAW properties, with emphasis on the temperature coefficient of delay time. The resulting microstructures, bulk and SAW properties are characterised and reactions between them discussed. Finally, the effect on processing on achieving reproducible ceramics is examined.

## EXPERIMENTAL PROCEDURE

A modified lead titanate powder, with composition  $(\text{Pb}_{0.88}, \text{Sm}_{0.04}, \text{La}_{0.04})(\text{Ti}_{0.98}, \text{Mn}_{0.02})\text{O}_3$  was processed by a conventional mixed oxide method.

After calcination the powder was milled for 8 hours and used for the sintering and HIP study. A second batch of powder

was milled for 48 hours, in an attempt to reduce the particle size.

After addition of a binder, the powders were pressed into plates with dimensions; 30 x 20 x 1.5 mm, for SAW measurements, and discs with a diameter of 16 mm and thickness 0.8 mm, for bulk measurements, using a pressure of 98 MPa. The plates and discs were sintered from 1220 to 1280°C for 2 hours, with 20°C intervals. After sintering some of the plates and discs, sintered at 1240, 1260 and 1280°C, were hot isostatically pressed at 1100°C for 1 hour with a pressure of 200 MPa (using a 20%O<sub>2</sub>/80%Ar atmosphere). Before poling, the plates were lapped to obtain parallel faces and one side of each plate was polished to a mirror finish, for which surface roughness, (Ra) values were < 0.1 µm. The plates and discs were electroded and poled in a heated oil bath at 100°C with a field of 6 kV/mm for 10 minutes.

The microstructures of a selection of the ceramics prepared were characterised using image analysis. For this, ceramics were polished, metallised with gold and examined using either optical and scanning electron microscopy. The pore area distributions were determined from polished surfaces and the grain size distributions were determined from thermally etched samples. Measurements were made using software based on IMCO 10 system (Kontron Elektronik GMBH 1990) on, typically, 10 images with a total number of 1000 measured objects. The grain size was calculated as equivalent diameters to a circular shape from the measured areas. Mean values and standard deviations were calculated from the distributions considered as Gaussian.

The dielectric permittivity,  $\epsilon_{33}^T$  and dielectric loss at 1 kHz were measured using an LCR meter. Thickness and planar electromechanical coupling coefficients,  $k_t$  and  $k_p$ , and the elastic coefficient,  $c_{33}^D$ , of the discs were calculated according to IEEE Standards<sup>[6]</sup> from resonance data. The bulk dielectric and piezoelectric properties of the plates were measured before removing the electrodes, to test their polarisation level (this data is not given).

To characterise the SAW properties of the ceramics, aluminium electrode patterns, (0.3 µm thick) in the form of interdigital transducers with a periodicity of 100 µm, were applied onto the polished surface using the "lift off" photolithographic process. The permittivity,  $\epsilon_s$ , free surface velocity,  $v_o$ , and surface coupling coefficient,  $k_{2s}$ , were obtained at 25 MHz using an unapodised, single electrode SAW transducer, by curve fitting the electrical impedance of the transducer with theoretical curves generated using a model based on Morgan's analysis<sup>[7]</sup>.

The propagation losses and the temperature coefficient of delay time were measured using the SAW delay line shown in Figure 1. The input transducers had the same characteristics as the transducer described above, but with a finger length of 5 mm. The output transducer comprised two, 1.5 mm long receivers connected in parallel. The two transducers were placed at 4 mm and 8.75 mm from the input. The surface propagation losses,  $\alpha$ , was calculated using:

$$\alpha = \frac{-20 \log_{10} \left( \frac{V_2}{V_1} \right)}{L} \quad (1)$$

where,  $V_1$  and  $V_2$  are the measured voltages of the first and second receivers, and  $L$  is the distance between the 2 receivers.

The temperature coefficient of delay time, CTF was determined from measurements of time of flight,  $t$ , between the input and output transducer ( $t_0$  is the time of flight at room temperature) over the temperature range,  $T = 0$  to  $60^\circ\text{C}$ , using the following equation:

$$CTF = \frac{1}{t_0} \frac{dt}{dT} \quad (2)$$

where,  $t$  is the time of flight of the surface acoustic wave between the input and output transducers, and  $T$  is temperature.

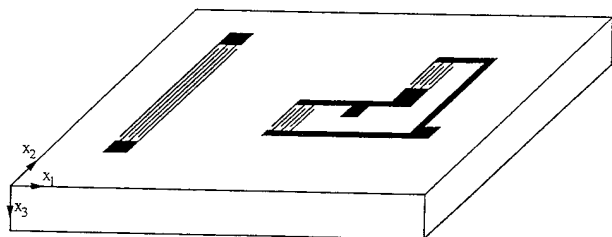


Figure 1. SAW Delay Line

## RESULTS

A summary of the microstructural parameters of a selection of the materials is given in Table 1. The ceramic milled for 8 hours and sintered at  $1260^\circ\text{C}$  for 2 hours had a low porosity content (1.9 %) and fine grain size ( $1 \mu\text{m}$ ). Carrying out a post-sintering HIP process on this material further reduced the porosity to 0.4 %, without increasing the grain size. In addition, examination of the pore area distribution (Figure 2(a) and maximum pore area (given in Table 1) shows that the HIP process was most effective on the large pores.

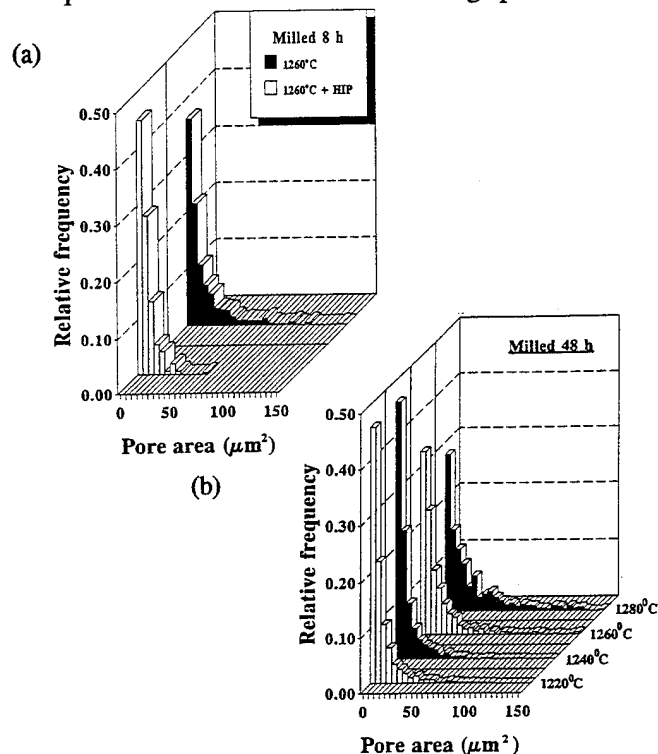


Figure 2. Histograms of pore area distribution for (a)  $1260^\circ\text{C}$  and  $1260^\circ\text{C} + \text{HIP}$  (milled 8 h) ceramics and (b) ceramics (milled 48 h) sintered 1220 to  $1280^\circ\text{C}$ .

It can be seen that increasing the sintering temperature from 1220 to  $1280^\circ\text{C}$  for materials prepared by milling for 48

Table 1 Summary of ceramic microstructure parameters

Processing	Milled 8 hours		Milled 48 hours			
Sintering conditions	1260	1260 + HIP	1220	1240	1260	1280
Porosity (%)	1.9	0.4	2.4	2.3	2.7	3.2
Average pore area ( $\mu\text{m}^2$ )	17	8	12	12	18	29
Maximum pore area ( $\mu\text{m}^2$ )	233	61	187	204	264	540
Standard Deviation ( $\mu\text{m}^2$ )	24	8	17	18	28	29
Average grain size ( $\mu\text{m}$ )	1.0	1.0	1.0	1.1	1.1	1.4
Standard Deviation. ( $\mu\text{m}$ )	0.4	0.5	0.5	0.5	0.6	0.7

hour, the average grain size increases from 1.0 to 1.4  $\mu\text{m}$ , and the porosity increased from 2.4 to 3.2 %. The increase in porosity was accompanied by an increase in pore area (from an average pore area of 12 to 29  $\mu\text{m}^2$ ), maximum pore area (from 187 to 507  $\mu\text{m}^2$ ) and width of the distribution, shown in Figure 2(b). Above 1240°C, the microstructure deteriorates with the growth of porosity. A similar effect was found for materials prepared by milling for 8 hours, in this case deterioration of the microstructure occurred above 1260°C. Ceramics sintered at 1280°C had porosity of 2.8%, an average pore area of 36  $\mu\text{m}^2$  and a standard deviation of 56, all considerably larger than those for the materials sintered at 1260°C.

Milling the powders for 48 hours instead of 8 hours reduced the optimum sintering temperature, thus for the same sintering temperatures, materials milled for 48 hours will have a larger grain size and greater porosity, in the range of temperatures studied here. This is demonstrated by the samples sintered at 1260°C for 2 hours in Table 1.

The bulk properties of the materials are given in Table 2. All of the sintered materials had densities 97 - 98 % of the theoretical density. Increasing the sintering temperature for both sets of materials did not change the properties significantly. Any changes in properties can be related to changes in porosity content, so that  $\epsilon_{33}^T$ ,  $k_p$ ,  $c_{33}^D$  and  $Q_m$  all reduced slightly as the sintering temperature and porosity increased. The difference between the materials milled for 8 and 48 hours can be attributed to the shift in temperature of the optimum sintering conditions to lower temperatures for the materials milled for the longer time. The HIP materials had improved properties, higher permittivity, coupling coefficients and elastic properties, corresponding to the increase in density (>99%), and lower  $\tan\delta$

The SAW properties are given in Table 3. Apart from the material sintered at 1280°C, most of the samples had similar surface properties. Typically, with surface permittivity between 220 and 250, velocity between 2550 and 2600 m/s and surface coupling between 1.4 and 2, attenuation of 0.3 dB/mm and CTF around 70 ppm/°C.

Again changes in the properties can be related to changes in the porosity content, so that, increasing the sintering temperature (and thus porosity content) decreased the permittivity and velocity. The surface coupling and losses were independent of sintering temperature. The CTF value for materials sintered at 1280°C showed the largest change in properties, reducing from >70 to 57 ppm/°C. Milling time had little effect on the surface properties, except that the CTF value for the 1260°C materials was lower than that milled for 8 hours, again most likely due to the increase in porosity.

For the HIP ceramics, very homogeneous surface properties were obtained, irrespective of the sintering temperature. Comparing the values with those obtained for the as-sintered materials, in general all of the properties are improved, higher permittivity, velocity, coupling coefficient and lower propagation losses. The CTF value was similar to the materials sintered at 1260°C

## DISCUSSION

The changes in the surface properties can be related to changes in the microstructure of the ceramics. The higher velocity of the HIP materials (2600 m/s) correspond to an increase of the rigidity constants due to the reduction in porosity. This can be seen by comparing the  $c_{33}^D$  of the as sintered and HIP materials, which increases from  $16 \times 10^{10}$  to  $18 \times 10^{10}$  N/m<sup>2</sup>, whilst the density increases from 98 to >99%. This can also be seen to a lesser extent for the as-

Table 2 Bulk piezoelectric properties of discs.

Heat treatment	Density % Th.	$\epsilon_{33}^T$	$\tan \delta$ %	$k_t$ %	$k_p$ %	$Q_m$ (planar)	$c_{33}^D$ $\times 10^{10}$ Nm <sup>-2</sup>
Milled 8 hours							
1220	98	217	1.1	41	8.6	1383	16.6
1240	98	208	1.0	45	8.0	1715	17.0
1260	98	208	1.0	45	7.5	1717	16.9
1280	97	196	1.1	46	6.6	1430	16.1
1240 + HIP	>99	222	0.6	47	10.0	2034	18.5
1260 + HIP	>99	219	0.7	46	9.5	1869	18.1
1280 + HIP	>99	217	0.7	46	8.5	1938	18.4
Milled 48 hours							
1220	97	213	1.2	44	8.2	1452	17.0
1240	97	208	1.0	45	7.5	1627	16.9
1260	97	206	1.1	43	7.3	1510	16.5
1280	97	198	0.9	45	6.6	1498	16.2



Table 3. A comparison of SAW properties

Material	$\epsilon_s$	$v_o$ m/s	$k_s^2$ %	$\alpha$ dB/cm	CTF ppm/°C
Milled 8 hours					
1220	240	2565	1.7	0.63	75
1240	237	2555	1.43	0.36	79
1260	231	2550	1.93	0.1	71
1280	217	2550	1.71	0.46	57
1240 + HIP	248	2595	1.97	0.19	77
1260 + HIP	246	2600	2.09	0.17	75
1280 + HIP	240	2600	2.06	0.19	77
Milled 48 hours					
1220	238	2555	1.56	0.38	81
1260	178	2550	1.81	0.39	66

sintered materials, for which the higher values at low sintering temperatures correspond to lower porosity contents. The surface permittivity decreased with increasing the sintering temperature, in a similar way to that of the bulk permittivity, again due to the increase in porosity.

Discussion of  $k_s$  is more complicated, as it depends on a combination of the bulk thickness and planar coefficient as well as the shear coefficient. First considering the effect of sintering temperature, the thickness coupling coefficient increases, whilst the planar coupling coefficient decreases, which may explain the lack of trend in properties for this coefficient. For the HIP materials, both  $k_t$  and  $k_p$  increase, giving an increase in  $k_s$ .

The differences in the propagation losses reflect the changes in  $\tan\delta$  and  $Q_m$ . The HIP materials have low  $\tan\delta$  and high  $Q_m$ , again corresponding to the reduction in porosity of the materials.

CTF showed the most important effect of microstructure. For the materials sintered at 1220 to 1260°C (2 to 2.5 % porosity) and the HIP materials (<1% porosity), similar values, 70 to 75 ppm/°C, were obtained, indicating for these porosity values, the CTF value is predominately due to composition and microstructure has little effect. However, the material sintered at 1280°C had significantly lower CTF values (57 ppm/°C), suggesting that for these materials, the porosity or perhaps the size of porosity, contributes to the CTF value. This is confirmed by the 1280 + HIP material, for which the CTF value was increased to 77 ppm/°C. It has already been noticed that the porosity and not the grain size changed during the HIP process.

The HIP process had a two fold effect on the properties, giving rise to improvements in the values, as well as homogenising the properties between the different sintering temperatures. Thus indicating the microstructure has an important effect on the SAW properties, particularly the temperature coefficient. Secondly, the results indicate that the

properties prepared using a post sintering HIP treatment will be more reproducible than those of sintered ceramics.

## CONCLUSIONS

The results show that processing and its effect on microstructure influence all of the SAW properties, but particularly the temperature coefficient of delay time. It may therefore be possible to adjust the microstructure of the ceramics to reduce the temperature coefficient of delay time.

To obtain reproducible SAW properties careful control of the processing conditions must be carried out. The porosity content should be less than 2 % and homogeneously distributed. Using a suitable post-sintering HIP treatment, uniform properties can be achieved. In addition, the HIP ceramics had improved properties, higher velocity, coupling coefficient and lower propagation losses.

## REFERENCES

- [1] H. Iwasaki, T. Takahashi, H. Ohkuma and N. Ichinose, "Temperature-stable Ferroelectric Ceramics for Surface Acoustic Wave Devices" *Ferroelectrics*, vol. 10, pp. 135-8, 1976.
- [2] Y. Ito, H. Takeuchi, S. Jyomura, K. Nagatsuma and S. Ashida "Temperature Compensated PbTiO<sub>3</sub> Ceramics for Surface Acoustic Wave Applications" *J. Appl. Phys.* 35 pp. 595-7 (1979)
- [3] S. Jyomura, K. Nagatsuma and H. Takeuchi "SAW Propagation loss mechanisms in Piezoelectric Ceramics" *J. Appl. Phys.* 52 pp. 4472-6 (1981)
- [4] G. Sapiro, K. El-Assal, M. Sayer, C. K. Jen "Piezoelectric Ceramics for Surface Acoustic Wave Applications" *Proc. IEEE. Int. Symp. Appl. Ferroelectrics*. 1986, pp. 451-4.
- [5] C. E. Millar, W. Wolny, L. Pardo, J. Ricote, R. Sirera, G. Feuillard and M. Lethiecq, "Processing of Piezoceramics for SAW Applications, *Proc 3<sup>rd</sup> Euro-Ceramics Conf.* 1993 pp. 187-92.
- [6] IEEE Standards on Piezoelectricity ANSI/IEEE Std 176 (1987)
- [7] G. Feuillard, M. Lethiecq, Y. Amazit, D. Certon, C. E. Millar & F. Patat "Experimental Determination of the SAW properties of new Fine Grained Ceramics" *J. Appl. Phys.* vol 1, pp.71 (1993)



# Piezoceramic Materials with Very Large Anisotropy of Piezoelectric Coefficients: Physical Aspects of the Problem

A.V. TURIK and V.YU. TOPOLOV  
Rostov State University, 344104 Rostov-on-Don, Russia

**Abstract** - This work contains a review of the authors' up-to-date papers devoted to the topical problem of the large anisotropy of the piezoelectric coefficients  $d_{33}^*/|d_{31}^*|$  in ferroelectric ceramic materials. The principal physical factors responsible for this effect in  $\text{PbTiO}_3$ -based materials have been analysed.

The need for improvement of technical parameters of piezoelectric ceramic materials determines the great interest to the problem of creation of materials with a large anisotropy of piezoelectric coefficients (PC's)  $d_{33}^*/|d_{31}^*| \gg 1$ . The present report contains a review of the principal theoretical results obtained by us [1]-[4] and devoted to this problem in  $\text{PbTiO}_3$ -based polarized ferroelectric ceramic (FC) materials.

In  $\text{PbTiO}_3$  as well as in other perovskite-type ferroelectrics the piezoelectric effect shows as a linearized electrostriction. Therefore PC's  $d_{ij}$  of single-domain crystal are proportional to the dielectric permittivities of stress-free crystal  $\varepsilon_{ii}^0$  and to the spontaneous polarization  $P_s$  [5]

$$d_{31} = 2Q_{12}P_s\varepsilon_{33}^0, d_{33} = 2Q_{11}P_s\varepsilon_{33}^0, d_{15} = Q_{44}P_s\varepsilon_{11}^0 \quad (1)$$

where  $Q_{kl}$  are the electrostrictive constants. In the case of FC the analogous relations become more complicated due to determination of PC's  $d_{ij}^*$  by averaging piezoelectric, dielectric and elastic constants of corresponding single-domain and polydomain crystals [5], [6]. The large anisotropy  $d_{33}^*/|d_{31}^*|$  in  $\text{PbTiO}_3$  FC has been firstly interpreted in [1] that contains the principal results being corroborated by the subsequent investigations (see e.g. [7], [8]).

Turik et al. [1] showed that the principal cause for the large PC anisotropy in  $\text{PbTiO}_3$ -based FC is associated with a small anisotropy of dielectric permittivities  $\varepsilon_{11}^0/\varepsilon_{33}^0 \leq 1.3$  of stress-free single-domain crystals. Owing to this fact the relative contribution by PC  $d_{15}$  of single-domain crystals forming FC into  $d_{31}^*$  is decreased. An unusual instability in the sign and value of  $d_{31}^*$  may be seen from Equations (1) and formulae [5] for PC's of FC

$$d_{33}^* = \frac{1}{4}(d_{33} + d_{31} + d_{15}), d_{31}^* = \frac{1}{8}(d_{33} + 3d_{31} - d_{15}) \quad (2)$$

which have been obtained by direct averaging PC's of

single-domain crystals on condition that all the possible  $180^\circ$  domain reversals have achieved during the polarization of ceramics. The PC  $d_{15}$  is included

into Equations (2) for  $d_{33}^*$  and  $d_{31}^*$  as an item with the different signs, and as a result following from Equations (1) and [1], there is  $d_{31}^* \rightarrow 0$  without an essential variation of  $d_{33}^*$  due to the small anisotropy of dielectric permittivities  $\varepsilon_{11}^0/\varepsilon_{33}^0 \rightarrow 1$ . Such behavior leads to reversing the sign of  $d_{31}^*$  by the variations of the temperature, domain structure, microstructure or by the appropriate modifying FC composition.

Our papers [2]-[4] contain the results of the theoretical investigations regarding the influence of the temperature, domain structure and modifying an initial composition on the physical properties and, in particular, on the piezoelectric anisotropy of  $\text{PbTiO}_3$ -based polydomain crystals and FC. The investigations carried out were based on methods [9], [10].

We showed that, besides dielectric permittivities  $\varepsilon_{11}^0, \varepsilon_{33}^0$  and volume concentrations  $m$  and  $1 - m$  of  $90^\circ$  domains, the value of the ratio  $Q_{11}/|Q_{12}|$  of electrostrictive constants had the large influence on the PC  $d_{31}^*$  of FC; according to different estimates based on experimental data for  $\text{PbTiO}_3$ ,  $Q_{11}/|Q_{12}|$  changed from 5.3 [11] to 4.0. By means of these estimates we were able to establish some values of the volume concentration of  $90^\circ$  domains  $m^*$  and of the temperature  $T^*$  satisfying the condition  $d_{31}^*(m^*, T^*) = 0$ . The important feature of our estimates was significant difference in the temperatures  $T^*$  at  $m^* = \text{const}$  but at different  $Q_{11}/|Q_{12}|$ . This fact testifies to the large sensitivity of the PC  $d_{31}^*$  and the anisotropy  $d_{33}^*/|d_{31}^*|$  to the change in the spontaneous strain of crystal.

$90^\circ$  domain structure of the real polarized grains of  $\text{PbTiO}_3$  corresponds apparently to the domain volume concentrations within the range between  $m_1 = 0.5$  (equal-width periodical lamellar domains) and  $m_2 = 0.76$  (corresponds to the condition for elastic matching the paraelectric and ferroelectric phases close by the Curie point  $T_c \approx 765$  K [12]). Realization of condition  $d_{31}^*(m^*, T^*) \rightarrow 0$  close by the room temperature is possible for  $m_1 \leq m^* \leq m_2$  and

$Q_{11}/Q_{12} \approx 5.3$  that leads to  $d_{33}^*/d_{31}^* \rightarrow \infty$  and is in well agreement with known data [13] on modified  $\text{PbTiO}_3$ -based FC. In the case of  $Q_{11}/Q_{12} \approx 4.0$  behavior of  $d_{31}^*(m, T)$  is similar to the experimental dependences for pure  $\text{PbTiO}_3$  FC.

Studying the influence of modifying  $\text{PbTiO}_3$  by Ca, Sr, Ba or Zr ions on the piezoelectric anisotropy showed that  $|d_{ij}^*(m, x)|$  and  $|d_{ij}^*(m, y)|$  dependences for all  $(\text{Pb}_{1-x}\text{M}_x)\text{TiO}_3$  and  $\text{Pb}(\text{Zr}_{1-y}\text{Ti}_y)\text{O}_3$  compositions are monotonously increasing with increase of  $x$  and with decrease of  $y$  at  $m = \text{const}$ . An only exception represents a group of  $d_{31}^*(m, x)$  dependences for FC with  $M = \text{Ca}$  (i.e. by the small-radius ion substitution for Pb) which have diffused maxima (minima of  $|d_{31}^*|$ ) close by  $x = 0.25$  leading to maxima of the piezoelectric anisotropy  $d_{33}^*/d_{31}^*$ . As in the case of the pure  $\text{PbTiO}_3$ , especially small  $|d_{31}^*| \rightarrow 0$  and the large PC anisotropy are realized in FC with the polydomain grains at  $m \approx 0.5$ . An important feature of the investigated  $(\text{Pb}_{1-x}\text{M}_x)\text{TiO}_3$  compositions lies in the fact that their PC  $d_{31}^*(m, x)$  and anisotropy  $d_{33}^*(m, x)/d_{31}^*(m, x)$  dependences at  $m = \text{const}$  are in agreement with  $Q_{12}(x)$  dependences calculated by us for corresponding single-domain crystals. The display of this fact is connected with maxima of  $d_{31}^*(0.5, x)$ ,  $d_{33}^*(0.5, x)/d_{31}^*(0.5, x)$  and  $Q_{12}(x)$  dependences close by the same value  $x = 0.25$  for  $M = \text{Ca}$  and with the monotone character of all these dependences on  $x$  for  $M = \text{Ba}$ ; Sr. As in the pure  $\text{PbTiO}_3$ , the small anisotropy of  $\epsilon_{ii}^0$  has the significant influence on the PC anisotropy.

Our estimates for the contribution  $\Delta d_{31}^*$  by the reversible  $90^\circ$  domain-wall displacements to PC  $d_{31}^*$  of  $(\text{Pb}, \text{Ca})\text{TiO}_3$  FC show that  $\Delta d_{31}^*$  are commensurable with the total PC values  $d_{31, \text{tot}}^* = d_{31}^* + \Delta d_{31}^*$ . Reversing the sign and passing  $\Delta d_{31}^*$  contribution through maximum in the vicinity of  $x = 0.25$  cause  $d_{31, \text{tot}}^* \rightarrow 0$ .

So the principal factors for the achievement of the large anisotropy  $d_{33}^*/d_{31}^*$  of  $\text{PbTiO}_3$ -based FC are following:

- (i) the small anisotropy of dielectric permittivities  $\epsilon_{11}^0/\epsilon_{33}^0$  of single-domain crystals constituting FC;
- (ii) substitution of Pb ion by the small-radius ion;
- (iii) the domain-structure features (approximate

equality of the volume concentrations of  $90^\circ$  domains);

(iv) optimization of the polarization rate of ceramics and the working temperature.

## REFERENCES

- [1] A.V. Turik, E.G. Fesenko, V. G. Gavril'yachenko, and G.I. Khasabova, "Anisotropy of the dielectric and piezoelectric properties of lead titanate," *Sov. Phys. Crystallogr.*, vol. 19, pp. 677-678, 1975.
- [2] V.Yu. Topolov, E.I. Bondarenko, A.V. Turik, and A.I. Chernobabov, "The effect of domain structure on electromechanical properties of  $\text{PbTiO}_3$ -type ferroelectrics," *Ferroelectrics*, vol. 140, pp. 175-181, 1993.
- [3] A.V. Turik, V.Yu. Topolov, A.I. Chernobabov, and E.I. Bondarenko, "On the nature of the anisotropy of piezoelectric moduli of lead titanate," *Izv. RAN Ser. Fiz.*, vol. 57, no. 6, pp. 82-85, 1993.
- [4] V.Yu. Topolov, A.V. Turik and A.I. Chernobabov, "On the piezoelectric anisotropy in modified  $\text{PbTiO}_3$  ceramics," in *Program Summary and Abstract Book IMF 8, Gaithersburg, MD*, p.161, 1993, to be published in *Ferroelectrics*.
- [5] L.P. Kholodenko, *Thermodynamic Theory of Ferroelectrics of Barium Titanate Type*. Riga: Zinatne Press, 1971, ch.7 (in Russian).
- [6] A.V. Turik and A.I. Chernobabov, "On the orientation contribution to the dielectric, piezoelectric and elastic constants of ferroelectric ceramics," *Zh. Tekhn. Fiz.*, vol.47, pp. 1944-1948, 1977.
- [7] M.J. Haun, E. Furman, S.J. Jang, and L.E. Cross, "Modeling of the electrostrictive, dielectric and piezoelectric properties of ceramic  $\text{PbTiO}_3$ ," *IEEE Trans. Ultrason., Ferroelec., and Freq. Contr.*, vol. 36, pp. 393-401, 1989.
- [8] W. Wersing, K. Lubitz and J. Mohaupt, "Anisotropic piezoelectric effect in modified  $\text{PbTiO}_3$  ceramics," *ibid.*, pp. 424-433.
- [9] A.V. Turik, "The elastic, piezoelectric and dielectric properties of  $\text{BaTiO}_3$  single crystals with the laminar domain structure," *Fiz. Tverd. Tela*, vol.12, pp. 892-899, 1970.
- [10] M. Marutake, "A calculation of physical constants of ceramic barium titanate," *J. Phys. Soc. Jap.*, vol.11, pp. 807-814, 1956.
- [11] G. Shirane, S. Hoshino and K. Suzuki, "X-ray study of the phase transition in lead titanate," *Phys. Rev.*, vol. 80, pp. 1105-1106, 1950.
- [12] A.V. Turik, A.I. Chernobabov and V.Yu. Topolov, "Internal stress-relaxation and thermodynamics of phase transitions in ferroelectrics," *Fiz. Tverd. Tela*, vol. 26, pp. 3618-3621, 1984.
- [13] D. Damjanovic, T.R. Gururaja, S.J. Jang, and L.E. Cross, "Possible mechanisms for the electro-mechanical anisotropy in modified lead titanate ceramics," presented at IEEE Ultrason. Symp., Williamsburg, VA, November 17-19, 1986.

**Abstract-** This paper is devoted to the analysis of different methods for averaging the physical constants of ferroelectric crystals as well as to the calculation of the piezoelectric coefficients  $d_{ij}^*$  and their anisotropy  $d_{33}^*/|d_{31}^*|$  for  $\text{PbTiO}_3$ -type ceramics being under the polarization electric field.

Last years an attention of many researchers is given to the problem of a large anisotropy of the piezoelectric coefficients (PC's)  $\zeta = d_{33}^*/|d_{31}^*|$  and corresponding electromechanical coupling factors in modified  $\text{PbTiO}_3$  ferroelectric ceramics (FC).  $\text{PbTiO}_3$ -based FC are actively studied for the acoustic-wave applications, in particular for creating transducers with an improved direction diagram and with only one working thickness mode. The physical nature of the large piezoelectric anisotropy and related phenomena is a subject of the numerous experimental [1]-[3] and theoretical [4]-[7] investigations.

The polarization process is one of the obligatory and important factors for optimization of the piezoelectric anisotropy, therefore it would be necessary to study an effect of the electric field on the electromechanical properties of  $\text{PbTiO}_3$ -based FC. This paper is devoted to solving some important questions within the limits of this problem.

The simplest theory of the electromechanical properties of FC [8],[9] is based on an assumption that FC PC's may be determined by direct averaging the single-domain crystal constants. The corresponding FC PC's

$$\begin{aligned} d_{31}^* &= \frac{1}{8}(1 + \cos\vartheta)[4d_{31} + (d_{33} - d_{31} - d_{15})\sin^2\vartheta], \\ d_{33}^* &= \frac{1}{4}(1 + \cos\vartheta)[2d_{33} - (d_{33} - d_{31} - d_{15})\sin^2\vartheta], \\ d_{15}^* &= \frac{1}{4}(1 + \cos\vartheta)[2d_{15} + (d_{33} - d_{31} - d_{15})\sin^2\vartheta] \end{aligned} \quad (1)$$

are expressed by PC's of single-domain crystal  $d_{ij}$  and the maximum angle  $\vartheta$  between the direction of the polarization electric field  $E_p$  and the domain polar axes. Direct averaging the single-domain PC tensor components  $d_{ij}$  of  $\text{PbTiO}_3$  by use of Equations (1) for  $\vartheta = 90^\circ$  (i.e. at  $180^\circ$  domain reversals only) has shown [10] a peculiar instability in the sign and value of PC  $d_{31}^*$  that demonstrates a possibility of  $d_{31}^* \rightarrow 0$ . As a result, the very large anisotropy of PC's may be realized owing to changes in the temperature, domain structure or to appropriate modifying the

initial  $\text{PbTiO}_3$  composition.

In this paper for the first time we use effective-medium method for a description of the effect of the polarization on the piezoelectric properties and the anisotropy of PC's of  $\text{PbTiO}_3$ -based FC. According to our model presentations, the grain is split into  $90^\circ$  domains of two types having the volume concentrations  $m$  (for the domains with the polar axes located closer to the direction of the electric field strength vector  $E_p$ ) and  $1 - m$ . The physical constants of the polydomain grain are determined by method [11]. The spontaneous polarization of this grain is determined by the vector  $P = mP_{s1} + (1 - m)P_{s2}$  where  $P_{si}$  are the spontaneous polarization vectors of the separate domain types. A change in the orientation angle  $\vartheta$  between  $P_s$  and  $E_p$  vectors which occurs by the polarization of tetragonal FC due to increasing the external electric field strength  $E_p$  is realized within the range from

$180^\circ$  to a limit value [8]  $\vartheta_0 = \arcsin\sqrt{2/3} \approx 55^\circ$  that corresponds to the complete  $180^\circ$  and  $90^\circ$  domain reversals. The values of the elastic, piezoelectric and dielectric constants of single-domain  $\text{PbTiO}_3$  crystal and  $(\text{Pb}_{1-x}\text{Ca}_x)\text{TiO}_3$  (PCT) one close by  $x = 0.25$  were determined at the room temperature in [6] and [7], respectively.

The dependences  $d_{33}^*(\vartheta)$  and  $d_{15}^*(\vartheta)$  calculated by effective-medium method for various  $0.5 \leq m \leq 1$  are the monotonously decreasing functions. Of particular interest are PC's  $d_{31}^*$  (Fig. 1) displaying in some cases a nonmonotonic dependence on  $\vartheta$  in spite of results [9]. The orientation dependences of PC  $d_{31}^*(\vartheta)$  for  $m = 1$  (see Equations (1)) and for  $m = 0.5$  being a result of direct averaging the physical constants of  $\text{PbTiO}_3$  and PCT crystals are shown in Fig.

1 for a comparison. PC's of polydomain crystal with  $m = 0.5$  are determined in accordance with formulae [11]. The comparison between the dependences  $d_{31}^*(\vartheta)$  and  $d_{31}^*(\vartheta)$  for both FC shows that the achievement of  $d_{31}^* = 0$  and  $\zeta \rightarrow \infty$ , respectively, is very sensitive to a choice of single-domain crystal initial constants and, undoubtedly, to the changes in  $Q_{11}/|Q_{12}|$  ratio. The choice of the volume concentrations of  $90^\circ$  domains close by  $m = 0.5$  (the equal-width lamellar domains with the regular arrangement) is most favourable for  $d_{31}^* \rightarrow 0$ . The sufficiently small anisotropy of dielectric permittivities of stress-free single-domain

crystal  $\varepsilon_{11}^0/\varepsilon_{33}^0 \rightarrow 1$ , which is characteristic of both the compositions, is the necessary condition but the insufficient one to obtain the large anisotropy of FC PC's.

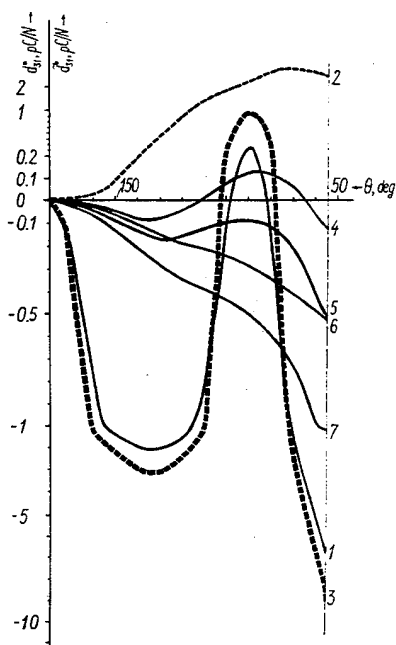


Fig. 1. The orientation dependences of the averaged piezoelectric coefficients  $d_{31}^*$  (curves 1, 3 for  $m = 1$  and 2 for  $m = 0.5$ ) and  $d_{31}^*$  (curves 4, 6 for  $m = 0.5$  and 5, 7 for  $m = 0.6$ ) of ferroelectric ceramics: 1, 2, 4, 5 -  $\text{PbTiO}_3$ ; 3, 6, 7 -  $(\text{Pb}_{1-x}\text{Ca}_x)\text{TiO}_3$  at  $x \approx 0.25$ .

The estimates of a contribution  $\Delta d_{31}^*$  of the reversible  $90^\circ$  domain-wall displacements into PC  $d_{31}^*$  of FC have been carried out using method [12]. Taking into account the volume concentration of the domains  $m = 0.5$  we found  $\Delta d_{31}^* = 3.00$  pC/N and  $0.58$  pC/N for  $\text{PbTiO}_3$  and PCT FC, respectively. Therefore close by  $\theta = 90^\circ$  the total value of PC  $d_{31,\text{tot}}^* = d_{31}^* + \Delta d_{31}^*$  may equal approximately  $3.1$  pC/N and  $0.30$  pC/N for  $\text{PbTiO}_3$  and PCT FC, respectively. In that way, in the case of both  $\text{PbTiO}_3$  and PCT, a transition of  $d_{31,\text{tot}}^*$  through the zero value and  $\zeta \rightarrow \infty$  are possible that correspond sufficiently well to the experimental dependence  $d_{31}^*(E_p)$  of  $\text{PbTiO}_3$  - based FC [1].

Thus it has been established by us that when decreasing  $\theta$  (increasing  $E_p$ ) the  $d_{31}^*$  value can pass through a minimum and a maximum and reverse the sign that leads to the large piezoelectric anisotropy ( $\zeta \rightarrow$

$\infty$ ). The possible reasons of such nonmonotonic behavior are connected with the features of the electrostrictive constants behavior and with the small anisotropy of single-domain dielectric permittivities.

#### REFERENCES

- [1] D. Damjanovic, T.R. Gururaja, S.J. Jang, and L.E. Cross, "Possible mechanisms for the electromechanical anisotropy in modified lead titanate ceramics," presented at IEEE Ultrason. Symp., Williamsburg, VA, November 17-19, 1986.
- [2] N. Ichinose, Y. Fuse, Y. Yamada, and R. Sato, "Piezoelectric anisotropy in the modified  $\text{PbTiO}_3$  ceramics," *Jap. J. Appl. Phys.*, vol. 28, suppl. 28-2, pp. 87-90, 1989.
- [3] L. Pardo, J. Mendiola, A. Gonzalez, and J. de Frutos, "Role of  $90^\circ$  domains in the electromechanical anisotropy of Ca-modified  $\text{PbTiO}_3$  ceramics," *Ferroelectrics*, vol. 94, pp. 189-194, 1989.
- [4] M.J. Haun, E. Furman, S.J. Jang, and L.E. Cross, "Modeling of the electrostrictive, dielectric and piezoelectric properties of ceramic  $\text{PbTiO}_3$ ," *IEEE Trans. Ultrason., Ferroelec. and Freq. Contr.*, vol. 36, pp. 393-401, 1989.
- [5] W. Wersing, K. Lubitz and J. Mohaupt, "Anisotropic piezoelectric effect in modified  $\text{PbTiO}_3$  ceramics," *ibid.*, pp. 424-433.
- [6] V.Yu. Topolov, E.I. Bondarenko, A.V. Turik, and A.I. Chernobabov, "The effect of domain structure on electromechanical properties of  $\text{PbTiO}_3$  - based ferroelectrics," *Ferroelectrics*, vol. 140, pp. 175-181, 1993.
- [7] V.Yu. Topolov, A.V. Turik and A.I. Chernobabov, "On the piezoelectric anisotropy in modified  $\text{PbTiO}_3$  ceramics," in *Program Summary and Abstract Book IMF 8*, Gaithersburg, MD, p.161, 1993, to be published in *Ferroelectrics*.
- [8] L.P. Kholodenko, *Thermodynamic Theory of Ferroelectrics of Barium Titanate Type*. Riga: Zinatne Press, 1971, ch.7 (in Russian).
- [9] L.A. Shuvalov, "The dielectric and piezoelectric properties of polarized  $\text{BaTiO}_3$  ceramics in different ferroelectric phases," *Kristallografiya*, vol. 2, pp. 119-129, 1957.
- [10] A.V. Turik, E.G. Fesenko, V.G. Gavrilachenko, and G.I. Khasabova, "Anisotropy of the dielectric and piezoelectric properties of lead titanate," *Sov. Phys. Crystallogr.*, vol. 19, pp. 677-678, 1975.
- [11] A.V. Turik, "The elastic, piezoelectric and dielectric properties of  $\text{BaTiO}_3$  single crystals with the laminar domain structure," *Fiz. Tverd. Tela*, vol. 12, pp. 892-899, 1970.
- [12] E.I. Bondarenko, V.Yu. Topolov and A.V. Turik, "The role of  $90^\circ$  domain wall displacements in forming physical properties of perovskite ferroelectric ceramics," *Ferroelectrics. Lett. Sec.*, vol. 13, pp. 13-19, 1991.

# Electromechanical Properties of Rainbow Devices

E. Furman, G. Li and G. H. Haertling

The Gilbert C. Robinson Department of Ceramic Engineering  
Clemson University, Clemson, South Carolina 29634-0907

**Abstract** — A stress-biased, domed, electromechanical bender called a Rainbow was recently developed. Displacement characteristics for Rainbow devices based on piezoelectric PLZT compositions were studied in the frequency range far below the fundamental resonant mode frequency. Experimentally obtained field-induced displacements were compared with those predicted by a finite element model. The model underestimated the observed displacements. Low frequency relaxation of the displacements was observed experimentally.

## INTRODUCTION

There are a number of applications including pumps, speakers, laser deflectors, optical scanners, and relays for which displacements well above those obtained using linear actuators are desirable. For these applications, piezoelectric benders have traditionally been used [1-4]. Benders are based on a bimorph or unimorph structure. Bimorphs contain two electromechanically active layers, and unimorphs have an active and a constraining layer. In both cases, layers must have good bonding since bending occurs as a result of field-induced lateral strain being nonuniform in different parts of a structure. To accommodate this strain, the sample bends, producing vertical displacement. The key parameter for these devices is the piezoelectric  $d_{31}$  or electrostrictive  $Q_{12}$  coefficient, which should be maximized.

Recently, a new type of bender called a RAINBOW (Reduced And Internally Biased Oxide Wafer) was developed with promising characteristics [5]. Rainbow devices with maximum displacements of 3 mm and sustaining point loads up to 10 kg were demonstrated [6]. The trade-off between the displacement and load-bearing capabilities was established.

In this paper the electromechanical properties of Rainbow devices well below the fundamental resonance mode frequency will be described and compared to those predicted by a finite element model (FEM).

## RAINBOW ACTUATORS

Rainbow actuators consist of an electromechanically active layer and a constraining layer, similar to conventional unimorphs. Unlike the unimorph, however, the Rainbow is a monolithic structure. The constraining layer is formed by exposing one side of a lead-containing ceramic to a reducing atmosphere at high temperature produced by placing a ceramic in contact with a carbon block. The reduction of lead lanthanum zirconate titanate (PLZT) ceramics occurs as a result of oxidation of the solid carbon block, first to carbon monoxide and then to carbon dioxide gases [7]. The reduced layer is no longer piezoelectric, and is, in fact, a good electrical conductor due to a presence of a large amount of lead. The reduced layer functions as the electrode and the constraining part of the bender.

Rainbows also differ from unimorph benders by the presence of large internal stresses developed during the process of reduction and cooling to room temperature. Because of the volume decrease during the reduction step and the higher thermal expansion of the reduced layer compared to the oxide layer, the stress-free equilibrium dimensions of the reduced layer are smaller than for the oxide layer. To retain continuity at the interface between the oxide and the reduced layers and to minimize stored elastic energy, the sample develops curvature. For the Rainbows with a large reduced/oxide layer thickness ratio, the oxide layer is in compression throughout its volume. For a sufficiently small reduced/oxide layer thickness ratio, the neutral axis is in the oxide layer with the oxide material close to the interface being in compression and further away in tension.

## EXPERIMENTAL PROCEDURE

Batches with various PLZT compositions were prepared using the mixed oxide method. The powders were calcined at 925 °C for two hours in closed alumina crucibles. The samples were either sintered at 1250 °C for 6 hours in oxygen or hot pressed at 1200 °C for 6 hours at 14 MPa. For the reduction process, a lapped sample was placed on a graphite block and introduced into a preheated furnace held at 975 °C for approximately one hour, and then removed from the hot furnace. Silver electrodes were used throughout the testing [6].

Field-induced displacement was determined using LVDT-based apparatus. Displacements were determined for the forward-biased case and for the complete loop cycling. For the forward-biased case a Rainbow was poled at room temperature with approximately 900 volts applied until the displacement stabilized, and then the displacement was measured in the poling direction quasi-statically from zero volts to the poling voltage. The procedures for determinations of the thermal expansion coefficients and elastic constants will be published elsewhere [8].

## MODELING

Finite-element modeling of complicated piezoelectric structures has been used successfully [9]. For this study the ABAQUS commercial FEM package (Hibitt, Karlsson & Sorenson, Inc., version 5.2) was used to simulate thermo-mechanical and electromechanical properties for the Rainbow devices. The model uses linear piezoelectric, dielectric, and elastic properties of the oxide and reduced layers.

The constituent equations for the piezoelectric media used in the modeling are:

$$S_i = s_{ij}^E T_j + d_{ij}^T E_j \quad (1)$$

$$D_i = d_{ij} T_j + \epsilon_{ij}^T E_j \quad (2)$$

where  $S_i$  is the strain,  $D_i$  is the polarization,  $T_j$  is the stress,

$E_j$  is the electric field,  $s_{ij}^E$  is the elastic compliance,  $\epsilon_{ij}^T$  is the dielectric permittivity, and  $d_{ij}$  is the piezoelectric compliance.

Modeling of Rainbow devices includes three major parts: 1) the definition of material properties and sample geometry, 2) the modeling of the cool down from the reducing temperature to room temperature, and 3) the determination of the response to the specified set of boundary conditions.

For the modeling of the cool down step nonlinear analyses were used to account for the considerable stiffening of the Rainbow structure during this step. The model permits linear analyses of the piezoelectric properties. Currently, nonlinear piezoelectric effects and electrostrictive properties cannot be modeled. For the calculation of the field-induced displacements a structure based on 60 elements gave satisfactory results for the modeling of the quasi-static field-induced displacements.

## RESULTS AND DISCUSSION

In the case of piezoelectric ceramics there are three piezoelectric, two dielectric, and five elastic coefficients which are permitted by symmetry to be nonzero. The complete set of these values are known for only a few ceramics. Fortunately, for PZT 5 all of the above properties have been characterized [10]. PZT 5 is a soft PZT, and it should have values similar to those of PLZT ceramics with low lanthanum content. Piezoelectric, dielectric, and elastic constants of PZT 5 were used in the model. In addition, Young's modulus, Poisson's ratio, densities, and thermal expansion coefficients for the reduced layer formed from PLZT 5.5/57/43 (La/Zr/Ti) ceramics have been experimentally determined [8]. The data used in the modeling work are shown in Table 1. A rate of formation of the reduced layer of 127  $\mu\text{m}/\text{hour}$  was used in the model.

To verify the model, a comparison was made between the predicted displacement from the FEM model and the analytical model of the cantilevered bimorph [3]. For one bimorph, the FEM predicted a field-induced displacement of 61 microns compared to the 50 microns predicted by the analytical model. The FEM correctly predicted the field-induced displacement to be proportional to the length of the cantilever squared, again in good agreement with the analytical model.

There was reasonable agreement between the experimentally determined spontaneous displacements measured at the center of a Rainbow after cool down and the modeling predictions as is shown in Table 2. Rainbow devices were found to be partially poled during the cool down which lowers their spontaneous displacement (Rainbow devices become flatter when poled).

Table 1. (a) PZT 5 data used for the oxide layer modeling, and (b) experimental data for the reduced layer prepared from PLZT 5.5/57/43.

Material	Property	Magnitude
(a) PZT 5	$c_{11}^E$	$12.1 \cdot 10^{10} \text{ N/m}^2$
	$c_{12}^E$	$7.54 \cdot 10^{10} \text{ N/m}^2$
	$c_{13}^E$	$7.52 \cdot 10^{10} \text{ N/m}^2$
	$c_{33}^E$	$11.1 \cdot 10^{10} \text{ N/m}^2$
	$c_{44}^E$	$2.11 \cdot 10^{10} \text{ N/m}^2$
	$d_{33}$	$374 \cdot 10^{-12} \text{ C/N}$
	$d_{31}$	$-171 \cdot 10^{-12} \text{ C/N}$
	$d_{15}$	$584 \cdot 10^{-12} \text{ C/N}$
	$\epsilon_{11}^T / \epsilon^0$	1730
	$\epsilon_{33}^T / \epsilon^0$	1700
(b) Reduced Layer	Density	$8.00 \text{ gm/cm}^3$
	Young's modulus	$6.86 \cdot 10^{10} \text{ N/m}^2$
	Poisson's ratio	0.381
	Thermal Expansion	$\sim 10 \cdot 10^{-6} \text{ }^\circ\text{C}^{-1}$

The experimentally obtained displacements are significantly higher than those predicted by the model (Table 2). There are appreciable variations from sample to sample in the ratio of total displacement to the forward biased displacement. The larger experimental displacement compared to the model may be accounted for by considering additional nonlinear contributions from the non-180° domain walls and phase boundaries [11] and higher linear piezoelectric coefficients.

The model was used to compare the effects of the reduced/oxide layer thickness ratio on a Rainbow's field-induced and cool down displacements. The magnitude of the displacement on cool down is determined by the difference in the effective thermal expansion coefficients between the oxide and reduced layers, the geometry of a sample, and the elastic constants. Figure 1 shows that the maximum predicted spontaneous displacement should occur for the reduced/oxide layer thickness ratio of approximately one. This result is in qualitative agreement with Timoshenko's model of the bi-metal thermostat [12], which also predicts maximum displacement near the layer thickness ratio of one for the two layers having properties of the oxide and reduced layers. As is also shown in Figure 1, the maximum field-induced and cool down displacements occur at the same Rainbow geometry. This result is applicable if the magnitude of the electric field is kept constant in the oxide layer as the geometry changes, which was done in the case described in Figure 1. For the case of constant voltage across the oxide

Table 2. Experimental results and FEM predictions of electromechanical properties.

Oxide Layer Composition	Reduction Temperature/ Time ( $^\circ\text{C}$ / minutes)	Total Rainbow Thickness ( $\mu\text{m}$ )	Full Cycle Voltage (Volts)	Experimental Full Cycle Displacement ( $\mu\text{m}$ )	Experimental Forward Bias Displacement ( $\mu\text{m}$ )	Calculated Forward Bias Displacement ( $\mu\text{m}$ )	Experimental Cool Down Displacement ( $\mu\text{m}$ )	Calculated Cool Down Displacement ( $\mu\text{m}$ )
1.0 / 53 / 47	975 / 105	762	$\pm 1026$	301	116	40	547	789
6.0 / 59.5 / 40.5	975 / 90	635	$\pm 912$	177	78	42	759	844
6.0 / 59.5 / 40.5	975 / 105	864	$\pm 912$	150	35	27	742	705
6.0 / 57 / 43	975 / 60	508	$\pm 1026$	357	129	51	1067	828
6.0 / 56 / 44	975 / 75	508	$\pm 912$	307	140	53	668	884

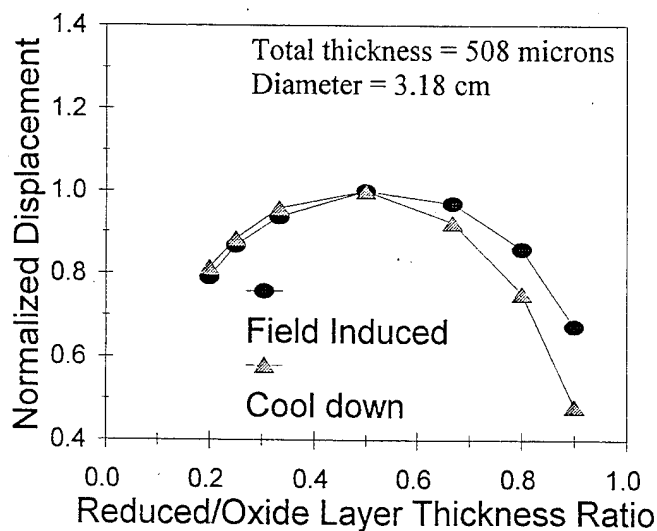


Figure 1. Normalized displacements induced by cool down and application of voltage.

layer the displacement continues to increase with the reduction of the oxide layer thickness. This is consistent with the electrical energy stored in the oxide layer being inversely proportional to its thickness, permitting greater field-induced lateral strain which increases the degree of bending of a Rainbow.

The shapes of the Rainbow samples having different diameters before and after the electric field application are shown in Figure 2. The flatter samples have no applied voltage; the more curved Rainbows bend up as a result of voltage applied in the opposite direction to the poling direction (the magnitude of movement is exaggerated). For the thicker Rainbows, there is less flattening in the middle portions. The model predicts this shape as a result of the nonlinear cool down step. Because FEM predicts that the

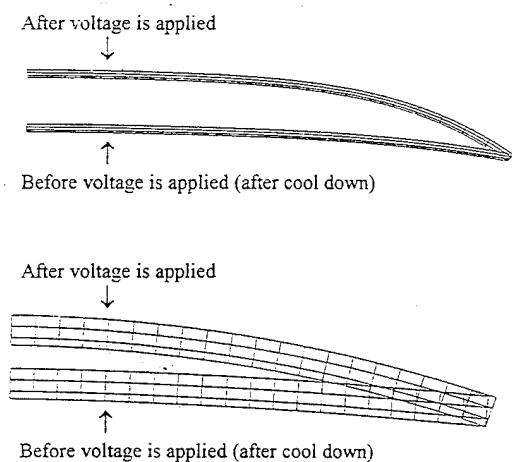


Figure 2. Shapes of Rainbows with diameter 6.35 cm (top) and 1.59 cm (bottom) before and after voltage is applied. Reduced/oxide layer thickness ratio: 1:3, thickness: 508  $\mu\text{m}$ , applied voltage: 500 V for both samples.

curvature of a Rainbow is nonuniform, it is not compatible with the predictions of linear models, mentioned above, which ignore nonlinear effects. In particular, the model predicted smaller displacement than the diameter squared dependence of the field-induced displacement.

Rainbow samples are capable of significant load-bearing capability. As is shown in Figure 3, there is excellent reproducibility in field-induced strain for a sample with up to 500 grams point load applied to the center of the sample.

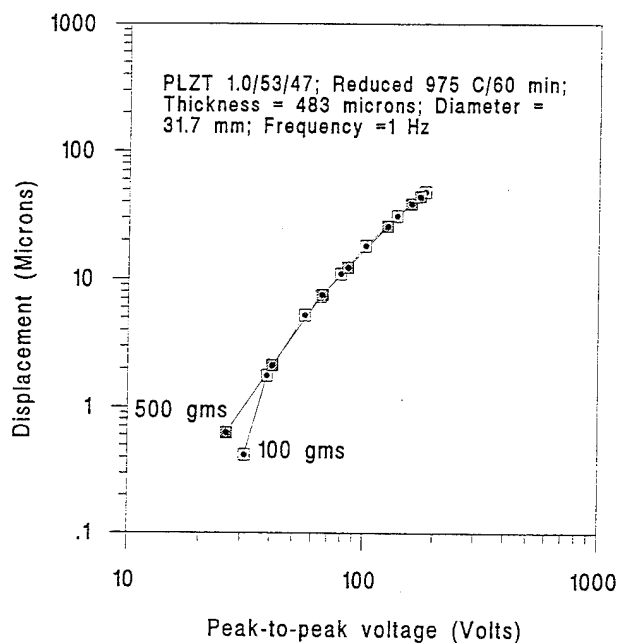


Figure 3. Field-induced displacements as a function of voltage for different loading conditions.

Rainbow samples have pronounced low frequency relaxation of the field-induced strain. It usually is manifested strongly for only one polarity. The response is relatively fast for the other polarity. An example of the low frequency contribution to the Rainbow displacement is shown in Figure 4. This sample was poled at 800 volts, and the field-induced displacements were measured at  $\pm 53$  volts. It can be observed that the field-induced displacement fits a straight line on semilog paper, indicating that the displacement becomes especially large at low frequencies.

The intriguing possibility to consider is whether the strong frequency-dependence of displacements and displacements exceeding the FEM's predictions are enhanced in Rainbow devices compared to conventional benders. Because Rainbows have large internal stresses it is reasonable to expect greater density of ferroelastic domain walls compared to ferroelectric devices without the macro-scale internal stresses, which could lead to enhanced displacements. Another possible contributing factor to the large displacements observed in Rainbow devices is unique to its structure.

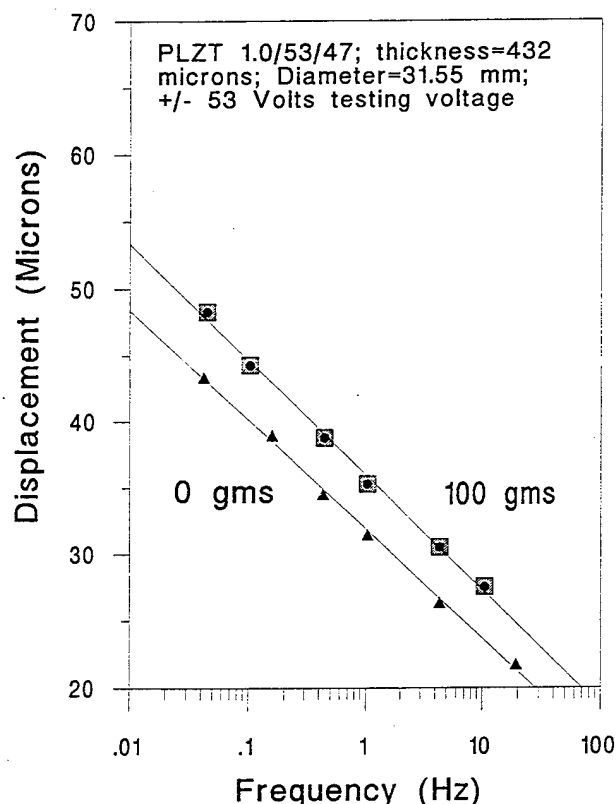


Figure 4. Field-induced displacements as a function of frequency for different loading conditions.

Because of the gradual change in the stress level in the oxide layer, different domain orientations are favored in different parts of the sample. Free charges may be trapped to compensate for polarization discontinuity at high temperature where conductivity is relatively high. As the sample is cooled down rapidly to room temperature it remains partially poled, and there may be net trapped charge in the bulk of the sample. Slow migration of charges during the domain switching may account for low frequency enhanced displacements. Finally, since a greater volume fraction of the oxide layer is in compression, higher switchable polarization should be available compared to the unstressed bender, as was shown for thin films in compression [13].

#### CONCLUSIONS

Electromechanical properties of Rainbow devices were studied at low frequencies and the results were compared to the FEM. The distinguishing characteristic of Rainbow devices is large and nonuniform stress on a macroscopic scale. Possible reasons for larger than expected displacements and frequency-dependent properties were discussed, and are believed to be related to a unique Rainbow structure.

#### ACKNOWLEDGMENT

This work is supported by NASA under grant No. NAG-1-1301 and by ONR under grant No. N0014-94-1-0563.

- [1] J. van Randeraat and R. E. Settrington (Ed.), *Piezoelectric Ceramics*. N. V. Philips' Gloeilampenfabrieken, Eindhoven, The Netherlands, 1974.
- [2] A. G. Kuzin, N. Mirgorodskii, V. Pikarnikov and V. Soroka, "Piezoelectric Light Beam Deflectors. I. Theory of Bimorph Deflectors and Experimental Tests," *Sov. Phys. Tech. Phys.*, vol. 21, pp. 1128-1130, 1976.
- [3] M. R. Steel, F. Harrison and P. G. Harper, "The Piezoelectric Bimorph: An Experimental and Theoretical Study of its Quasistatic Response," *J. Phys. D.: Appl. Phys.*, vol. 11, pp. 979-989, 1978.
- [4] J. K. Lee and M. M. Marcus, "The Deflection-Bandwidth Product of Poly(vinylidene Fluoride) Benders and Related Structures," *Ferroelectrics*, vol. 32, pp. 93-101, 1981.
- [5] G. H. Haertling, "Rainbow Ceramics - A New Type of Ultra-High-Displacement Actuator," *Am. Cer. Soc. Bull.*, vol. 73, pp. 93-96, 1994.
- [6] G. H. Haertling, "Chemically Reduced PLZT Ceramics for Ultra-High Displacement Actuators," *Ferroelectrics*, vol. 154, pp. 101-106, 1994.
- [7] G. H. Haertling, "Reduction/Oxidation Effects in PLZT Ceramics," pp. 699-711 in *Proceedings of the 4th International SAMPE Electronics Conference*, pp. 699-711, 1990.
- [8] E. Furman, G. Li and G. H. Haertling, "An Investigation of the Resonance Properties of Rainbow Devices," accepted for publication in *Ferroelectrics*.
- [9] R. Learch, "Simulation of Piezoelectric Devices by Two- and Three-Dimensional Finite Elements," *IEEE Trans. Ultrasonics, Ferroel., and Frequency Control*, vol. 37, pp. 233-247, 1990.
- [10] D. A. Berlincourt, D. R. Curran and H. Jaffe, "Piezoelectric and Piezomagnetic Materials and Their Function in Transducers," in *Physical Acoustics*, vol. 1 Part A, New York: Academic Press, 1964, Ch. 3.
- [11] S. Li, W. Cao, R. E. Newnham and L. E. Cross, "Electromechanical Nonlinearity of Ferroelectric Ceramics and Related non-180° Domain Wall Motions," *Ferroelectrics*, vol. 139, pp. 25-49, 1993.
- [12] S. Timoshenko, "Analyses of Bi-Metal Thermostats," *J.O.S.A. & R.S.I.*, vol. 11, pp. 233-251, Sept. 1925.
- [13] B. Tuttle, et. al., "Chemically Prepared Pb(Zr,Ti)O<sub>3</sub> Thin Films: the Effects of Orientation and Stress," in *Proc. of IEEE 8th Int. Symp. on Appl. of Ferroelectrics*, 1992, pp. 344-348.



# MICROSTRUCTURAL EFFECTS ON THE ELECTROMECHANICAL PROPERTIES OF PZT-BF CERAMICS

W. Huebner

Department of Ceramic Engineering  
University of Missouri - Rolla  
Rolla, MO 65401

W.R. Xue and P.W. Lu

Nanjing Institute of Chemical Technology  
Nanjing, Jiangsu 210009  
P.R.C.

## ABSTRACT

In this study microstructure $\leftrightarrow$ property relationships were explored for piezoelectric ceramics with a composition of  $0.97[(\text{Pb}_{0.95}\text{Sr}_{0.05})(\text{Zr}_{0.514}\text{Ti}_{0.484})\text{O}_3] - 0.03\text{BiFeO}_3$ . Very minor changes in the sintering temperature (1290 - 1310°C) or soak time (1.5 - 3.5 h) resulted in large differences in the electromechanical properties. Specifically, higher sintering temperatures resulted in no residual grain boundary phases, but larger grain sizes and/or variations in the defect structure resulted in lower permittivities, piezoelectric coefficients, and lower mechanical Q's. The sintering time exhibited an optimal value; too short or too long resulted in poor performance. This study points clearly illustrates the difficulty in performing systematic compositional studies when the role of the microstructure can be dominant.

## INTRODUCTION

In recent years numerous "high performance" applications for piezoelectric ceramics have emerged which require smaller geometries and features, and at the same time higher mechanical and electrical performance. Applications such as ultrasonic motors, smart structures, ink jets, multilayer actuators, and ultrasonic transducers all face performance or reliability limitations due to the piezoelectric ceramic. Microstructurally, in all cases the desire is have a fully dense ceramic with a fine grain size, typically  $\leq 1\text{-}2\text{ }\mu\text{m}$ . The specific application will dictate the requisite electrical properties, but in general it is desirable to have high (and anisotropic) piezoelectric coefficients, a variable dielectric constant for impedance matching, resistance to depoling through control over the coercive field and Curie temperature, and a low dielectric loss.

In this study microstructure $\leftrightarrow$ property relationships for  $0.97[(\text{Pb}_{0.95}\text{Sr}_{0.05})(\text{Zr}_{0.514}\text{Ti}_{0.484})\text{O}_3] - 0.03\text{BiFeO}_3$  (PZT-BF) were evaluated. Strontium increases the dielectric constant [1], the Zr/Ti ratio is along the morphotropic phase boundary (MPB), and  $\text{Bi}^{3+}$  and  $\text{Fe}^{3+}$  serve as donor and acceptor dopants, respectively [2,3]. The aliovalent dopants were added in the form of  $\text{BiFeO}_3$  due to its melting temperature of  $\approx 930^\circ\text{C}$  [4], and hence we anticipated it may serve as a transient liquid phase to aid in densification. Additionally, the  $T_c$  for  $\text{BiFeO}_3$  is  $\approx 850^\circ\text{C}$ , and hence may increase  $T_c$  of the system [5].

## EXPERIMENTAL PROCEDURE

Figure 1 overviews in detail the processing steps used to prepare the PZT-BF ceramics used in this study. Compositional homogeneity was checked using X-ray diffraction (XRD - Scintag X-ray diffractometer). Dielectric measurements were performed on plane parallel disks approximately 1 to 2 mm thick. Gold electrodes were sputtered onto the surface in a vacuum through a mask. Dielectric properties were measured as a function of temperature and frequency using a General Radio GR1689 RLC Digibridge and a muffle tube furnace. Measurements were taken during heating at  $4^\circ\text{C}/\text{min}$  from 25 to  $450^\circ\text{C}$ , at 1, 10 and 100 kHz.

After poling, a Berlincourt  $d_{33}$  meter was used to measure the  $d_{33}$  coefficient, and resonance measurements were performed with an impedance analyzer (Hewlett-Packard 4194A Impedance Analyzer with a 41941A Impedance Probe and 16092A Test Fixture).

## RESULTS AND DISCUSSION

Studies focused on the influence of sintering temperature (1290, 1300, and  $1310^\circ\text{C}$  - 2.5 h), and soak time ( $1290^\circ\text{C}$  - 1.5, 2.0, 2.5, 3.0 and 3.5 h) on the microstructure and properties. Figures 2 and 3 exhibit the fracture surfaces. In all cases, the microstructures were uniform with equiaxed grains. Densities were all  $\geq 97\%$  theoretical. The influence of only a  $20^\circ\text{C}$  change in sintering temperature was pronounced; the grain size increased from  $1\text{-}2\text{ }\mu\text{m}$  for the  $1290^\circ\text{C}$ , up to  $3\text{-}5\text{ }\mu\text{m}$  at  $1310^\circ\text{C}$ . Importantly, the fracture surface changed from a mixed mode of transgranular and intergranular crack propagation to strictly intergranular. A similar effect is seen in Figure 3 with soak time, although the grain size remains constant.

The general form of the dielectric response for all 6 variations was similar; Figure 4 exhibits  $K$  and  $\tan \delta$  vs. temperature for the  $1290^\circ\text{C}$  - 2.5 h sample. The dielectric behavior exhibits a room temperature  $K \approx 1160$ , and a  $\tan \delta = 0.49\%$ . Minimal dispersion is exhibited at low temperatures, but all compositions exhibited distinctive relaxor behavior in  $K$  near  $T_c$ . In this case  $K$  decreased from  $\approx 15,000$  at 1 kHz down to 11,000 at 100 kHz. While the second order transition is not unusual for PZT-based systems at the MPB, the relaxor behavior at this low dopant concentration is. The loss decreases with increasing frequency for  $T < T_c$ , which is unlike a relaxor, but the magnitude and dispersive behavior of  $\tan \delta$  at  $T_c$  is insufficient to account for  $K$ . Perhaps chemical inhomogeneity has resulted from sintering with  $\text{BiFeO}_3$ , but the dispersive behavior did not change with increases in the sintering temperature or time,

Experimental Procedure				
Raw	♦	PbO	99%	♦ TiO <sub>2</sub> 99%
Materials:	♦	SrCO <sub>3</sub>	99.9%	♦ ZrO <sub>2</sub> 99%
	♦	Bi <sub>2</sub> O <sub>3</sub>	99%	♦ Fe <sub>2</sub> O <sub>3</sub> 99.8%
Mixing	♦	Batch: ZrO <sub>2</sub> media: alcohol = 1:4:0.8		
	♦	Polyethylene jar / 24 h		
Calcination:	♦	Bi <sub>2</sub> O <sub>3</sub> and Fe <sub>2</sub> O <sub>3</sub> pre-calcined @ $680^\circ\text{C}$ → BiFeO <sub>3</sub>		
	♦	Remaining oxides calcined at $780^\circ\text{C}$ -2 h		
Milling	♦	Aggregates broken up with an agate mortar & pestle		
	♦	Milled again as above		
Pressing:	♦	8 wt% of a 5% PVA solution		
	♦	Granulation		
	♦	Uniaxial pressing; 1000 kg/cm <sup>2</sup>		
Sintering:	♦	Covered alumina crucibles; Pb source of the same composition		
	♦	$650^\circ\text{C}$ -1 h (binder burnout)		
	♦	1290, 1300, $1310^\circ\text{C}$ : 2.5 h		
	♦	$1290^\circ\text{C}$ : 1.5 - 3.5 h		
Poling:	♦	Ground / polished with SiC		
	♦	Sputtered gold electrodes		
	♦	$T = 100^\circ\text{C}$ ; $E = 30\text{ kV/cm}$ ; $t = 10\text{ min}$		

Figure 1: Overview of the processing steps used to prepare the PZT-BF ceramics.

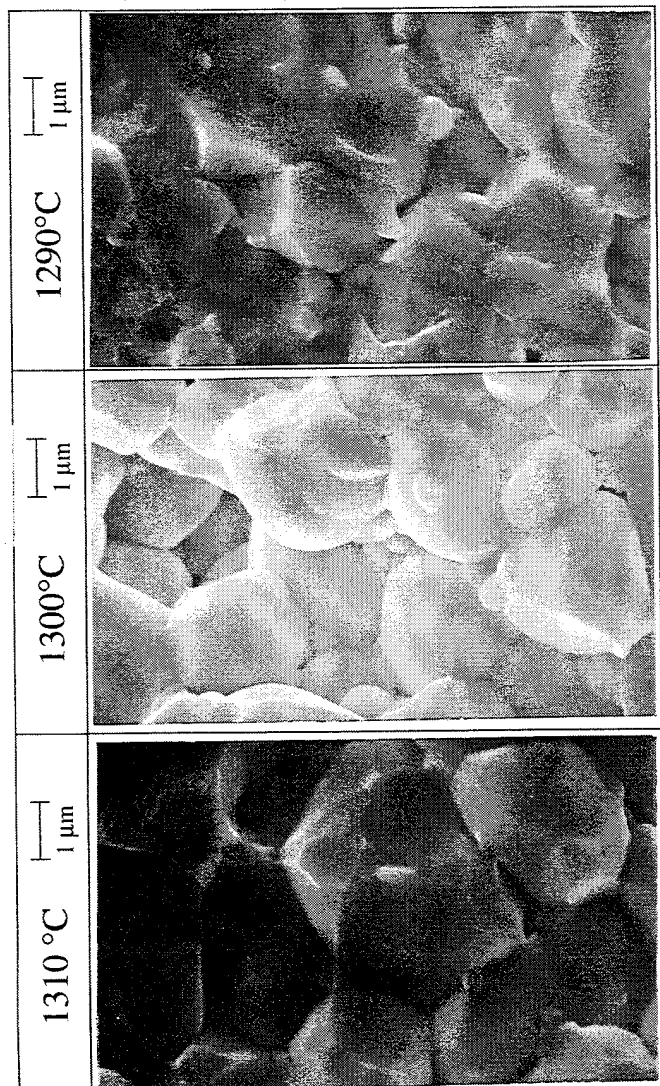


Figure 2: SEM micrographs of the PZT-BF ceramics sintered at various temperatures for 2.5 h.

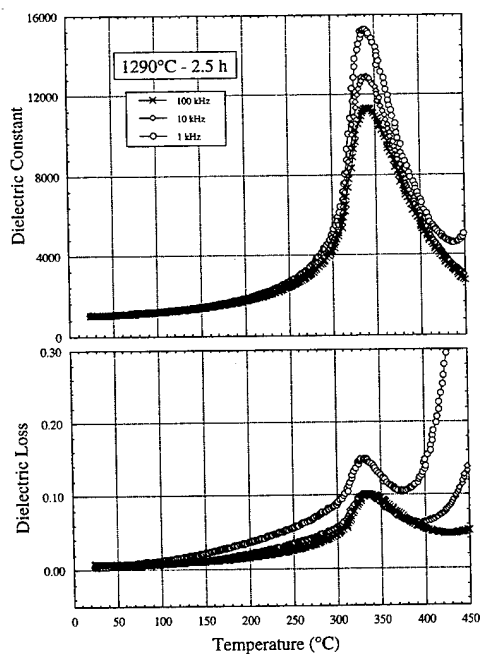


Figure 4: Temperature dependence of the dielectric constant and loss of PZT-BF sintered at 1290°C for 2.5 h.

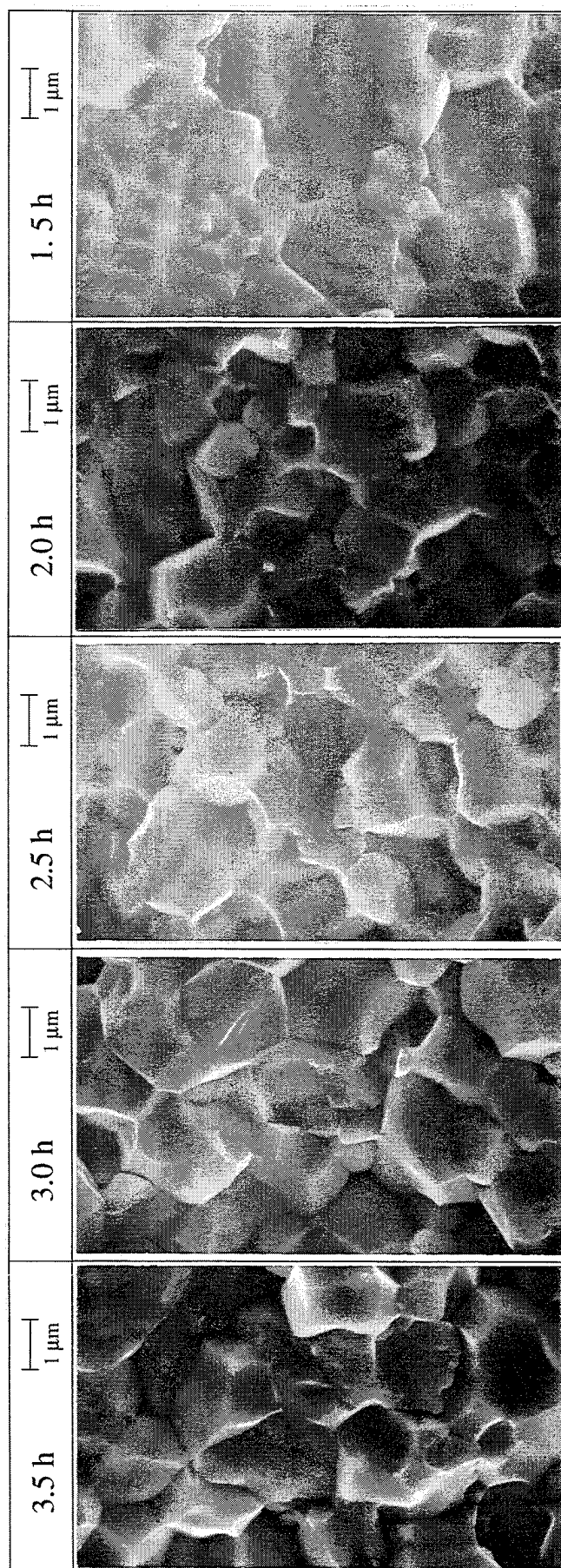


Figure 3: SEM micrographs of the PZT-BF ceramics sintered at various times at 1290°C.

suggesting an equilibrium state has been achieved within the grains. Ongoing TEM analyses will address this issue.

The influence of sintering temperature on the electromechanical properties is shown in Figure 5, and summarized in Table I. Clearly the best properties are exhibited by the 1290°C sample. The dielectric constant is higher over the entire temperature range, and the  $\tan \delta$  and conductivity are a minimum. The same is true of the piezoelectric properties, exhibiting the maximum value of the  $d_{33}$ ,  $k_p$ , and  $Q_m$ . Correlating this data with the microstructures of Figure 3, we note that the minimum grain size exhibited the best properties. This is unusual, in that it is generally considered that the best piezoelectric properties are exhibited for a grain size on the order of 3-5  $\mu\text{m}$ . Certainly the state of the grain boundary is playing a dominant role, as the higher sintering temperatures resulted in intergranular fracture; i.e. a weaker grain boundary. Whether this is associated with a different defect chemistry of the grain boundary associated with Pb volatilization is unclear, although one would anticipate that the removal of a second phase in the grain boundaries would improve the properties, not degrade them.

The influence of soak time on the properties of samples sintered at 1290°C are shown in Figure 6 and Table II. Since the grain size remained constant over this range, the effect of the grain boundary is most likely dominant. The trend is for the dielectric properties to be optimum at a given soak time, in this case coincident with 2.5 h. The dielectric constant is lower by 10-15% for shorter or longer times. Similar behavior is exhibited by the other properties, with the exception that the short soak time resulted in a higher  $Q_m$  and lower  $\tan \delta$ . At short soak times any residual grain boundary phase must result in a stronger grain boundary, albeit at the expense of the electrical properties. The shift in the peak dielectric constant is unusual, but was not further addressed in this study.

It is well-recognized that Pb vaporizes with time [6], and that Pb losses from the bulk are detrimental to the overall properties [7]. Previous studies [8,9] have also shown the importance of sintering temperature, time and atmosphere (PbO activity) on the densification and grain growth behavior, but didn't correlate this behavior to the electrical properties. The results from this study do not conflict with these previous studies, but simply reinforce the concept that annealing is an important factor in optimizing properties, i.e. some volatilization of lead is necessary, but too much is detrimental. These results on the PZT-BF system clearly show the pronounced sensitivity, and point out the care which must be taken when investigating the influence of composition on properties.

## CONCLUSIONS

Microstructure $\leftrightarrow$ property relationships were explored for piezoelectric ceramics with a composition of  $0.97[(\text{Pb}_{0.95}\text{Sr}_{0.05})(\text{Zr}_{0.514}\text{Ti}_{0.484})\text{O}_3] - 0.03\text{BiFeO}_3$ . Minor changes in the sintering temperature or soak time resulted in large differences in the electromechanical properties. Specifically, higher sintering temperatures resulted in no residual grain boundary phases, but larger grain sizes and/or variations in the defect structure resulted in lower permittivities, piezoelectric coefficients, and lower mechanical Q's. The sintering time exhibited an optimal value; too short or too long resulted in poor performance. This study clearly illustrates the difficulty in performing systematic compositional studies when the role of the microstructure can be dominant.

## Acknowledgment

This work was sponsored by the Office of Naval Research under Grant N00014-92-J-1469.

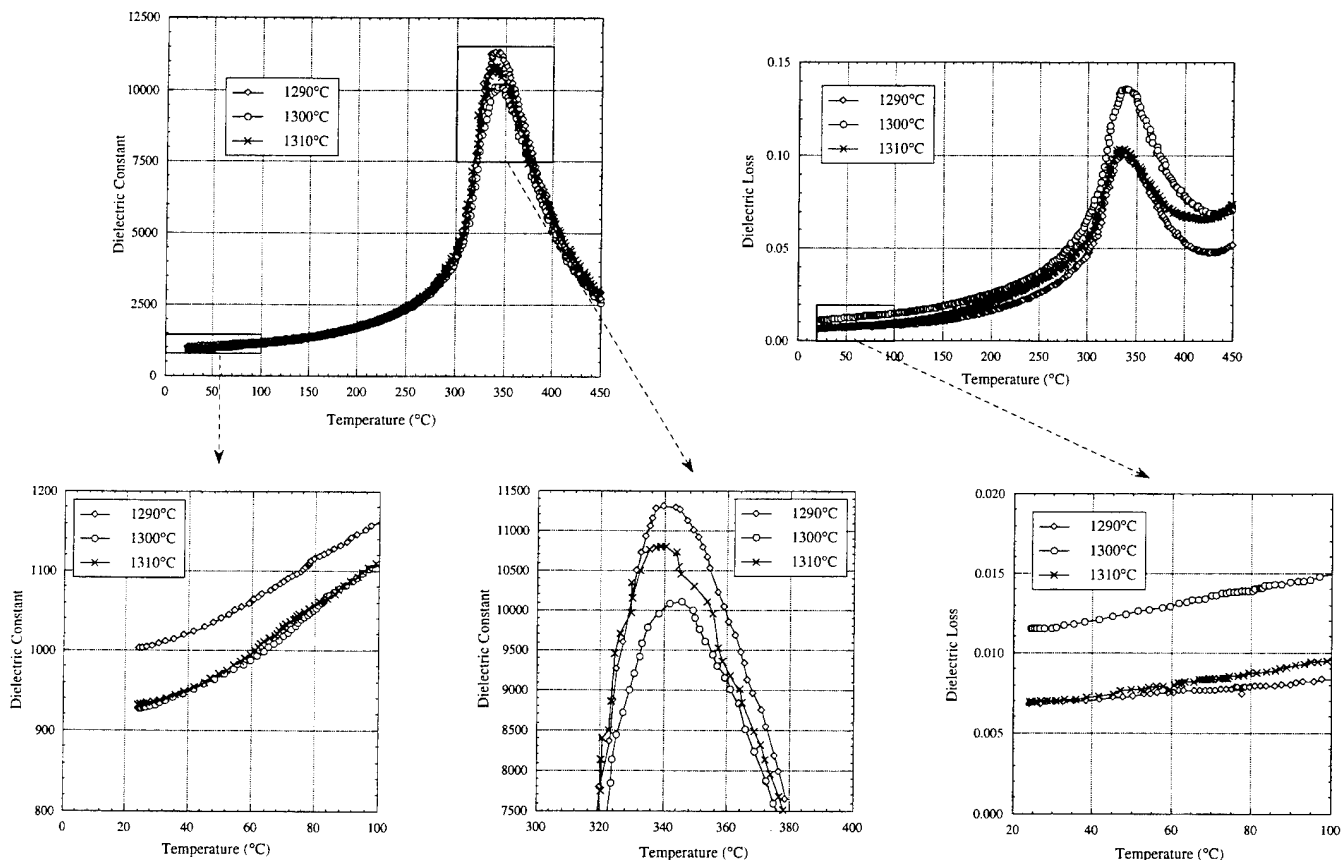


Figure 5: Temperature dependence of the dielectric constant and loss at 100 kHz for PZT-BF sintered for 2.5 h at 1290, 1300 and 1310°C.

## REFERENCES

- [1] F. Kulcsar, "Electromechanical Properties of Lead Titanate Zirconate Ceramics with Lead Partially Replaced by Calcium or Strontium," *J. Amer. Cer. Soc.*, **42**[1], 49-51 (1959).
- [2] R.B. Atkin, R.L. Holman, and R.M. Fulrath, "Substitution of Bi and Nb Ions In Lead-Zirconate-Titanate," *J. Amer. Cer. Soc.*, **54**[2], 113-115 (1971).
- [3] T.R. Weston, A.H. Webster and V.M. McNamara, "Lead Zirconate-Lead Titanate Piezoelectric Ceramics with Iron Oxide Additions," *J. Amer. Cer. Soc.*, **52**[5], 253-257 (1969).
- [4] Phase Diagrams for Ceramists, 1969 Supplement, ed. E.M. Levin, C.R. Robbins and H. McMurdie, p. 99, American Ceramic Society, Columbus, Ohio (1969).
- [5] R.T. Smith, G.D. Achenbach, R. Gerson and W.J. James, "Dielectric Properties of Solid Solutions of  $\text{BiFeO}_3$  with  $\text{Pb}(\text{Zr,Ti})\text{O}_3$  at High Temperature and High Frequency," *J. Appl. Phys.*, **39**, 70 (1968).
- [6] D. Northrop, "Vaporization of Lead Zirconate-Lead Titanate Materials," *J. Amer. Cer. Soc.*, **50**[8], 441-45 (1967).
- [7] A.H. Webster, T.B. Weston and F.H. Bright, "Effect of  $\text{PbO}$  Deficiency on the Piezoelectric Properties of Lead Zirconate-Titanate Ceramics," *J. Amer. Cer. Soc.*, **50**[8], 490-91 (1967).
- [8] R.B. Atkin and R.M. Fulrath, "Point Defects and Sintering of Lead Zirconate Titanate," *J. Amer. Cer. Soc.*, **54**[5], 265-70 (1971).
- [9] P.G. Lucuta, F. Constantinescu and D. Barb, "Structural Dependence on Sintering Temperature of Lead Zirconate-Titanate Solid Solutions," *J. Amer. Cer. Soc.*, **68**[5], 533-37 (1985).

Table I

Effect of Sintering Temperature on the Electromechanical Properties

Property	Sintering Temperature ( $^{\circ}\text{C}$ ) - 2.5 h		
	1290	1300	1310
$\epsilon_{33}/\epsilon_0$	1157	1068	979
$\tan \delta$ (%)	0.49	0.85	0.99
$d_{33}$ (pC/N)	285	261	258
$k_p$ (%)	54.1	53.0	52.5
$k_t$ (%)	47.3	44.2	47.8
$Q_m$	128	98	98
Density ( $\text{g}/\text{cm}^3$ )	7.78	7.72	7.63
$I_L$ ( $\mu\text{A}$ ; 4kV/mm; 100 $^{\circ}\text{C}$ )	1.2	7.2	18

Table II

Effect of Soak Time on the Electromechanical Properties

Property	Soak Time (hours)				
	1.5	2.0	2.5	3.0	3.5
$\epsilon_{33}/\epsilon_0$	920	930	1020	905	845
$\tan \delta$ (%)	0.44	0.85	0.68	0.84	0.86
$d_{33}$ (pC/N)	238	285	285	274	270
$k_p$ (%)	49.2	53.9	54.1	52.8	52.2
$k_t$ (%)	45.5	47.8	47.3	48.2	48.9
$Q_m$	301	174	128	78	78
Density ( $\text{g}/\text{cm}^3$ )	7.86	7.80	7.78	7.76	7.73
$I_L$ ( $\mu\text{A}$ ; 4kV/mm; 100 $^{\circ}\text{C}$ )	0.9	1.2	1.2	2.0	2.6

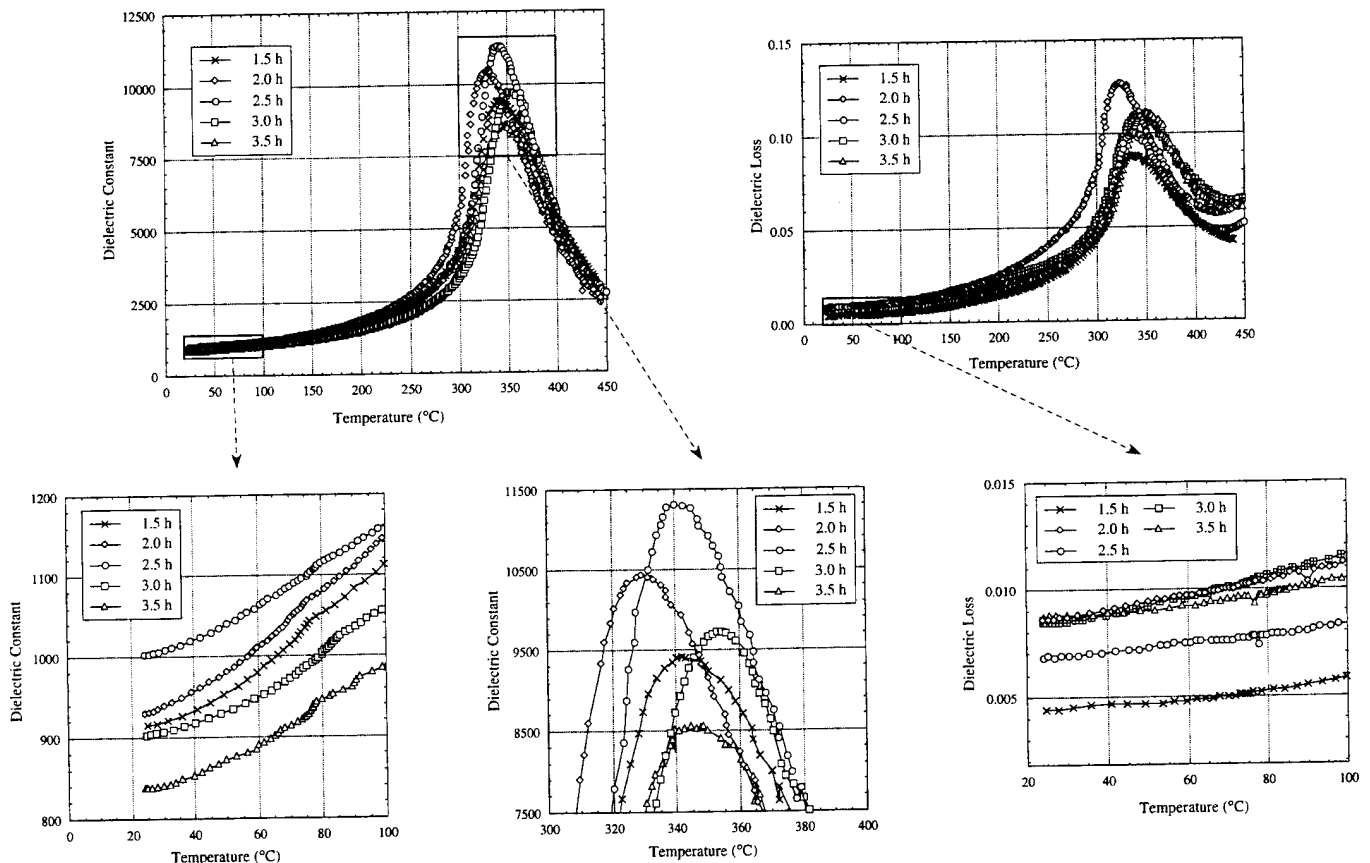


Figure 6: Temperature dependence of the dielectric constant and loss at 100 kHz for PZT-BF sintered at 1290 $^{\circ}\text{C}$  for 1.5, 2.0, 2.5, 3.0 and 3.5 h.

# Evaluation of Barium Doped PZT Ceramics for Underwater Hydrophone Applications

K.Trinath, B.S.Sarma, N.S.Prasad and A.Bhanumathi \*

Naval Science & Technological Laboratory  
\* Andhra University, Dept. of Physics  
Visakhapatnam  
India.

**Abstract :** Ferroelectric and piezo-electric properties of barium doped PZT are investigated for various concentrations of barium. Planar coupling coefficient  $k_p$  of 0.5 was obtained.  $d_{33}$  values are in the range of 300 - 500 pC/N. The results obtained show that the PZTs developed by us can be used for underwater hydrophones.

## INTRODUCTION

An ideal hydrophone material shall possess a high dielectric permittivity along with high charge constant. The material should offer highest capacitance per unit volume. It should have higher coupling coefficients, curie temperature and time stability. Towards achieving the above objectives several researchers tried various dopants for PZTs [1-3]. In this study we investigated the effect of barium doping on PZTs. Hysteresis behaviour and variation of dielectric constant with temperature are studied. Another variable that was used during the study was the sintering temperature. X-ray diffraction results are also presented.

## EXPERIMENTAL PROCEDURE

### Material Preparation

PZT ceramics with formula  $(\text{Pb}_{1-x}\text{Ba}_x\text{Zr}_y\text{Ti}_{1-y})\text{O}_3$  were prepared by conventional sintering. High purity reagent grade oxides, weighed according to their stoichiometric proportions were mixed in the presence of methanol. Calcination was done at 850°C for 2-3 hours. Some of the pellets were sintered at 1260°C and the others were sintered at 1320°C for 3-4 hours.

### Poling

The sintered samples were poled in silicon oil bath at a temperature of 100°C for 60 to 90 minutes under a DC field of 15 - 20 kV/cm. [4].

### Dielectric and Piezoelectric Measurements

Variation of dielectric constant with temperature was measured using HP Low Impedance Analyser Model 4192 A. Dissipation factor was also noted. The same instrument is used for computing coupling coefficients by measuring resonance and anti-resonance frequencies.  $d_{33}$  was measured using computer aided Berlincourt Piezo d-meter model CADT. Value of  $g_{33}$  was computed using standard

formula [5].

### Hysteresis Behaviour

Hysteresis behaviour was studied by using Hysteresis Loop Tracer (HLT) of Digital Systems.[6].

### X-Ray Diffraction Studies

The ceramic compositions were characterised by powder X-ray diffraction studies by using Philips X-ray Diffractometer operating at 25-30 KV and 15-20 mA current with Cu  $K_\alpha$  radiation and Ni filter. All the samples displayed tetragonal splitting.[7]. The XRD pattern for one of the samples is shown in the figure.

## RESULTS AND DISCUSSION

Nine compositions are studied. They are shown in Table.1. The parameters measured and computed are shown in Tables.2,3 & 4. In the first set of measurements, by keeping Zr/Ti ratio constant, as Pb/Ba decreases, dielectric constant increases.

But for a higher sintering temperature there is a decrease in dielectric constant probably due to loss of lead at higher temperatures. Curie temperature decreases from 339°C to 210°C. There is not much change in  $d_{33}$  value and  $k_p$  is slightly decreased. As concentration of Ba increases  $P_r$  and  $E_c$  decrease.

In the second set of measurements with Pb/Ba ratio equal to 0.9/0.1, as Zr/Ti ratio approaches the value of morphotropic phase boundary (MPB), both  $d_{33}$  and  $k_p$  are maximum. Dielectric constant is also maximum near MPB for sample F.  $k_t$  is almost constant. For same Ba content as Zr increases,  $E_c$  decreases. Sample G which is rhombohedral has minimum  $E_c$ . Sample E which is tetragonal has high  $E_c$  value. For tetragonal systems, due to the increase in strain involved for rotation of 90° domains  $E_c$  is high.

In the third set of measurements with Pb/Ba ratio equal to 0.85/0.15 as Zr/Ti increases  $d_{33}$  increases dramatically from 342 to 521 as Zr/Ti ratio approaches MPB. The values of  $k_p$ ,  $k_t$  and dielectric constant also increase.

## CONCLUSIONS

Samples B and F which exhibit high  $d_{33}$  values also have low dissipation factors. Hence these will be suitable for hydrophones.

Table.1

	SAMPLE	Pb	Ba	Zr	Ti
SET-1 : (Zr/Ti ratio is kept constant at 0.525/0.475 and Pb/Ba ratio is gradually decreased)	A	0.950	0.050	0.525	0.475
	B	0.900	0.100	0.525	0.475
	C	0.850	0.150	0.525	0.475
	D	0.800	0.200	0.525	0.475
SET-2 : (Pb/Ba ratio is 0.9/0.1 and Zr/Ti ratio is gradually increased)	E	0.900	0.100	0.515	0.485
	F	0.900	0.100	0.525	0.475
	G	0.900	0.100	0.535	0.465
SET-3 : (Pb/Ba ratio is 0.85/0.15 and Zr/Ti ratio is increased)	H	0.850	0.150	0.515	0.485
	I	0.850	0.150	0.535	0.465

Table.2 : Piezoelectric Data

Sintering Temp. 1260°C					Sintering Temp. 1320°C			
Sample	$d_{33}$ pC/N	$g_{33} \times 10^3$ V-M/N	$k_p$	$k_t$	$d_{33}$ pC/N	$g_{33} \times 10^3$ V-M/N	$k_p$	$k_t$
A	409	25.76	0.536	0.353	285	25.8	0.358	0.342
B	436	23.47	0.535	0.367	406	24.4	0.512	0.342
C	404	22.32	0.464	0.316	415	20.5	0.508	0.299
D	367	19.08	0.388	0.234	430	19.1	0.489	0.233
E	333	23.33	0.450	0.333	305	22.7	0.43	0.311
F	435	27.79	0.490	0.316	413	25.1	0.49	0.339
G	401	31.77	0.510	0.416	453	29.8	0.52	0.334
H	325	23.92	0.410	0.311	342	21.6	0.44	0.331
I	493	27.25	0.490	0.397	521	25.0	0.51	0.441

Table.3 : Hysteresis Data

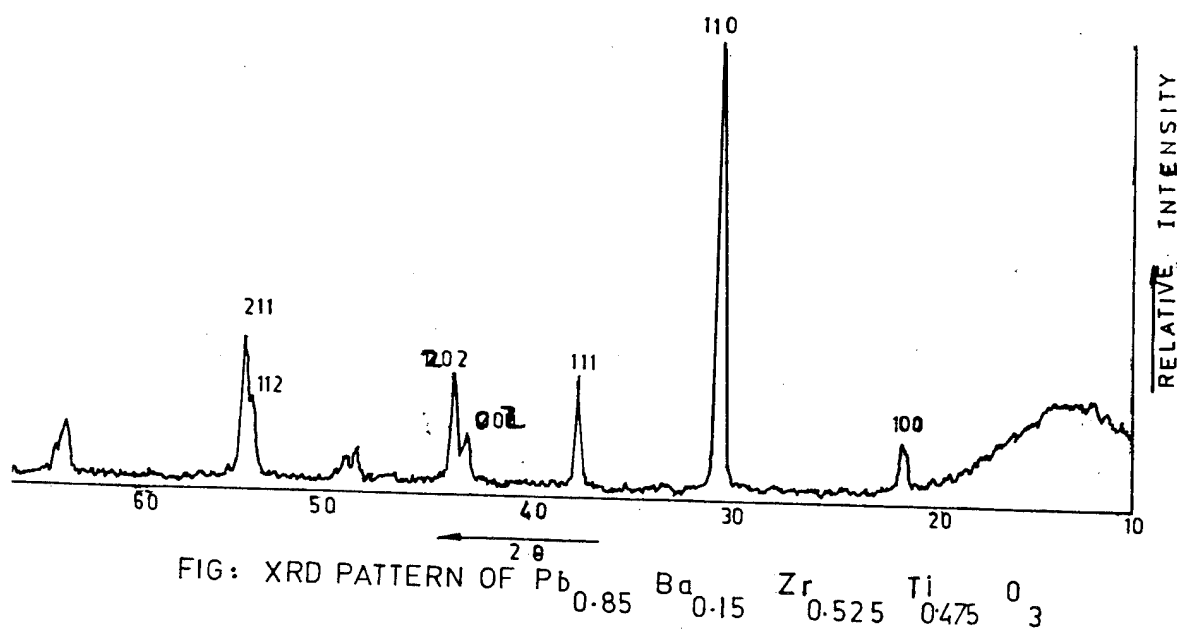
Sintering Temp. 1260°C			Sintering Temp. 1320°C		
Sample	Pr $\mu C/cm^2$	Ec kV/cm	Sample	Pr $\mu C/cm^2$	Ec kV/cm
C	23.86	12.0	A	27.80	15.4
			B	23.86	13.53
			C	21.90	12.66
			D	18.33	12.65
E	23.85	16.9	E	13.33	17.56
F	18.33	16.55	F	23.0	11.3
G	20.0	11.53	G	21.66	11.32
H	21.0	10.0	H	11.66	16.21
			I	20.0	12.24

Table.4 : Dielectric Data at 1 kHz.

Sample	$\epsilon_{RT}$	$D_{RT}$	$\epsilon_{CT}$	$D_{CT}$	CT $^{\circ}$ C
A	1823	0.023	28615	0.034	339
B	1900	0.017	21518	0.0255	280
C	1994	0.0396	21380	0.098	262
D	2219	0.0401	16674	0.078	210
E	1611	0.023	25661	0.030	290
F	1769	0.022	25156	0.0361	240
H	1456	0.034	20309	0.058	240

[ Note :

1. Samples A,C,D,E,F & H are sintered at 1260 $^{\circ}$ C and samples B & G are sintered at 1320 $^{\circ}$ C.
2.  $\epsilon_{RT}$ ,  $D_{RT}$  are dielectric constant and dissipation factor at room temperature.
3.  $\epsilon_{CT}$ ,  $D_{CT}$  are dielectric constant and dissipation factor at curie temperature.
4. CT is curie temperature.]



# ACKNOWLEDGEMENTS

The authors are thankful to Dr. K.V.Reddy Principal Scientific Officer, CIL, University of Hyderabad for providing facilities for XRD studies and to Dr. A.V.N.R.Rao, Mr. K.V.S.Ramam and Mr. N.Srinivasa Rao for their help during measurements. Thanks are also due to Mr. C.V.K.Sastry, and Dr. K.Satyanarayana, for their guidance for doing this work. The authors are grateful to Rear Admiral R.S.Chaudhry, AVSM, VSM, Director, Naval Science & Technological Laboratory, for the encouragement and for giving permission to publish this paper.

# REFERENCES

- [1] Hiromu Ouchi et al., "Piezoelectric properties of  $\text{Pb}(\text{Mg}_{1/3}\text{Nb}_{2/3})\text{O}_3 - \text{PbTiO}_3 - \text{PbZrO}_3$  solid solution ceramics", Journal of the American ceramic society, vol. 48, No. 12, pp. 630-635, Dec.1965.
- [2] Hiromu Ouchi et al., "Piezoelectric properties of  $\text{Pb}(\text{Mg}_{1/3}\text{Nb}_{2/3})\text{O}_3 - \text{PbTiO}_3 - \text{PbZrO}_3$  ceramics modified with certain additives", Journal of the American ceramic society, vol.49, No. 11, pp.577-582, Nov.1966.
- [3] G.Li and G. Haertling, "The electrostrictive and related properties of  $(\text{Pb}_{1-x}\text{Ba}_x)_{1-y}\text{Bi}_y(\text{Zr}_{1-y}\text{Ti}_y)\text{O}_3$  ceramic system", in Proceedings of the IEEE International symposium on applications of ferroelectrics, 1992, pp.569-572.
- [4] J.H.Belding and M.G.Mciaren, American ceramic society bulletin, vol.49, pp. 1025, 1970.
- [5] Sensor Technology Ltd. (BM Hi-Tech Division, Ontario, Canada, "Piezoelectric ceramics - Application Notes" 1991.
- [6] Digital Systems, Laxmi Industrial Estate, New Link road, Andheri (W), Bombay - 400 058, India.
- [7] P.Ari-Gur and L.Benguigui, "X-Ray Study of the PZT solid solutions near the Morphotrophic phase transition", Solid State Communications, vol.15, pp.1077-1079, 1974.
- [8] Don Berlincourt, "Piezoelectric ceramic compositional development", Journal of Acoustical society of America, Vol. 91(5), pp.3034-3040, May 1992.



# Increased Operating Temperature Range In La-Modified $\text{Pb}(\text{Mg}_{1/3}\text{Nb}_{2/3})\text{O}_3$ - $\text{PbTiO}_3$ Relaxor Ferroelectric-Based Transducers

J. T. Fielding, Jr., T. R. Shrout, and S. J. Jang

Materials Research Laboratory, The Pennsylvania State University, University Park, PA 16802

**Abstract**-The large E- field induced strains and electromechanical coupling in PMN-based relaxors have been utilized in actuator and transducer applications. The effect of  $\text{La}^{3+}$  modifications on the field-dependent dielectric and piezoelectric properties was investigated for several  $(1-x)\text{PMN}$ - $(x)\text{PT}$  compositions with transition regions near room temperature. The effect of  $\text{La}^{3+}$  modifications, increasing the width of the micro-macro polar transition range ( $\Delta T$ ), defined as the difference between the temperature of maximum permittivity ( $T_{\text{max}}$ ) and the depolarization temperature ( $T_d$ ), results in a broader temperature range for obtaining large induced electromechanical coupling factors with negligible hysteresis.

## INTRODUCTION

Electrostrictive materials have been extensively investigated for actuator applications. [1] There has been recent interest in utilizing the field-induced piezoelectric effect in electrostrictive materials for transducer applications such as biomedical imaging [2]. Several families of perovskite-based electrostrictors have been investigated as potential candidates for high frequency transducer applications. [3]

One of the advantages of using certain classes of electrostrictors, such as relaxors, is the anhysteretic strain-field response. This behavior is observed in normal ferroelectrics at temperatures greater than  $T_c$  or in relaxors at greater than the depolarization temperature,  $T_d$ . The breadth of the micro-macro transition region ( $\Delta T$ ), the difference between the temperatures of dielectric maxima ( $T_{\text{max}}$ ) and depolarization ( $T_d$ ), indicates a much broader operating temperature range for potential devices. Additionally, the field dependence of the dielectric, piezoelectric and elastic properties allows the tuning of the electromechanical coupling  $k_{ij}$  and mechanical  $Q$ . Also, the induced electromechanical coupling vanishes upon removal of the electric field, reducing spurious noise, which is important in several transducer applications.

The primary criteria, to induce a large piezoelectric effect, can be achieved by selecting materials in which a large polarization can be produced by the application of an external electric field. The piezoelectric charge coefficient  $d_{ijk}$  is defined as follows:

$$d_{ijk} = 2 \chi_{mk} \epsilon_0 Q_{ijmn} P_n \quad (\text{Eqn. 1})$$

where  $\chi_{mk}$ ,  $Q_{ijmn}$ , and  $P_n$  are the dielectric susceptibility, electrostrictive coefficient and total polarization, respectively. Other desirable performance criteria for selecting materials for transducer applications include reproducible piezoelectric coefficients, low losses, rapid response time and a wide operating temperature range.

The relaxor ferroelectric lead magnesium niobate-lead titanate  $(1-x)\text{Pb}(\text{Mg}_{1/3}\text{Nb}_{2/3})\text{O}_3$ - $(x)\text{PbTiO}_3$  (PMN-PT) is interesting due to the large polarizations and maximum permittivities, broad anomaly in the dielectric response, and anhysteretic strain-electric field behavior available over a broad range of temperatures reported.

The effects of  $\text{La}_2\text{O}_3$  and  $\text{PbTiO}_3$  modifications on the dielectric properties have been previously reported. [4,5,6] The temperature of the dielectric maxima,  $T_{\text{max}}$ , was reduced approximately  $25^\circ\text{C}/\text{atom}\%$  La. The micro- to macro-polar transition region,  $\Delta T$ , was observed to increase with increasing  $\text{La}^{3+}$  additions. The permittivity was also reduced. These effects were thought to be related to an increase in non-stoichiometric ordering of Mg and Nb cations. [4,5]

Additions of PT resulted in a gradual disappearance of non-stoichiometric cation ordering near the morphotropic phase boundary (MPB). [6] The sharpness of the dielectric anomaly, transition temperature  $T_{\text{max}}$  and depolarization temperature  $T_d$  increase with increasing PT content. The maximum dielectric permittivity  $K_{\text{max}}$  was observed to increase with increasing PT content up to values of  $x \sim 0.30$ - $0.33$ , achieving levels  $>30,000$  (@ 1 kHz). [7] The maximum dielectric loss is  $\sim 0.10$  at 1 kHz and decreases rapidly to values  $\leq 0.01$  at temperatures  $>T_{\text{max}}$ .  $\Delta T$  were observed to decrease with increasing PT content, exhibiting a sharp dielectric transition for values of  $x > 0.33$  and indicating a change in the relaxor nature with increasing additions of a normal ferroelectric.

In this study, several compositions in each of the families were processed. The field dependent dielectric, piezoelectric and elastic properties were evaluated at frequencies between 100 kHz and 5 MHz and at temperatures in the various polarization regimes of interest.

## EXPERIMENTAL

$(1-x)\text{PMN}$ - $(x)\text{PT}$  powders with 0 and 1 atom% La modifications were prepared using reagent grade oxides. The columbite precursor method was utilized to maximize pyrochlore formation. [9] Batches were formulated and mixed using vibratory milling using deionized  $\text{H}_2\text{O}$  and ammonium polyelectrolyte dispersant. After drying, powders were crushed, using mortar and pestle, and calcined for 4 hours at  $700^\circ\text{C}$ . X-ray diffraction analysis was used to ensure proper phase formation. Pyrochlore content measured using XRD was less than 3%. To break up aggregates and reduce particle size, compositions were milled overnight in deionized  $\text{H}_2\text{O}$  with dispersant and dried. 3 wt% acrylic binder (Rohm and Haas Acryloid B-7) was added and powder was sieved -80 mesh prior to uniaxial pressing. Disks with 1.27 and 2.54 cm diameters were pressed at 150 MPa. Binder was removed by heating at  $3^\circ\text{C}/\text{min}$ . to  $300^\circ\text{C}$  and  $5^\circ\text{C}/\text{min}$ . to  $550^\circ\text{C}$ .

Disks were sintered on Pt foil in high density  $\text{Al}_2\text{O}_3$  crucibles for 2 hours at  $1150$ - $1200^\circ\text{C}$  using a  $\text{PbZrO}_3$  source powder for controlling  $\text{PbO}$  volatility. Weight loss and geometric densities were calculated. Specimens were precision lapped to 0.5 mm thickness to produce a dilatational thickness mode resonance  $\sim 4.5$ - $5$  MHz.

Dielectric property measurements included characterization of the field and temperature dependence of the relative dielectric permittivity and dielectric loss, performed over the frequency range from 0.1 kHz to 100 kHz using capacitance bridges (HP 4274 and 4275) and from 1 to  $>5$  MHz using complex impedance data obtained from an impedance analyzer (HP3577A). Additionally, the polarization versus electric field behavior was examined and compared between families, using P vs. E measurements at several temperatures performed using a Sawyer-Tower circuit. Measurements of the pyroelectric current as a function of temperature was performed using the static Byer-Roundy technique to determine the pyroelectric coefficient, remanent polarization levels and effects of external electric fields on the depolarization temperature  $T_d$  in relaxor and normal ferroelectrics.

High frequency field-induced electromechanical coupling factor were obtained from measurements of the series ( $f_s$ ) and parallel ( $f_p$ ) resonances, performed using a HP3577A network analyzer with HP35677A S-parameter test set configured for a one-port input reflection technique. Typical applied d.c. bias levels used for the measurements were between 1 and 15 kV/cm. The radial coupling

factor  $k_p$  was calculated using a polynomial curve fitting equation.[18]. The dilatational thickness mode coupling factor  $k_t$  was calculated using the following equation: [18]

$$k_t^2 = \frac{\pi}{2} \frac{f_s}{f_p} \text{TAN} \frac{\pi}{2} \frac{(f_s - f_p)}{f_p} \quad (\text{Eqn. 2})$$

Several temperature regions were selected for measurement, depending on the material family. For relaxor ferroelectrics, resonance measurements were made over a range from the micro-polar region ( $T > T_{\max}$ ) to well below the depolarization temperature  $T_d$ .

## RESULTS AND DISCUSSION

### Dielectric Properties

Large small signal permittivities were observed in unmodified and La-modified PMN-PT compositions. The low frequency dielectric constant and polarization behavior is shown for a 0.90PMN-0.10PT composition in Figure 1a. The temperature dependence of the permittivity and loss for several 1 atom% La-modified compositions is shown in Figure 1b. Values for  $K_{\max}$  (@ 1 kHz) were 27-36,000 for the PMN compositions investigated. At temperatures above  $T_{\max}$ , all the families exhibited low losses at 1 kHz. A summary of the dielectric properties for the various families investigated is presented in Table I.

Large polarizations were measured for the Pb-based relaxor families. The micro-macro transition region,  $\Delta T$ , was 25-45 °C for the PMN-PT relaxor families. The pyroelectric response for several 1 atom% La-modified compositions is shown in Figure 2. The effect of La additions on P and  $\Delta T$  for varying PT contents is shown in Figure 3. La additions reduced the polarization and increased the micro-macro transition region for the PT contents evaluated.

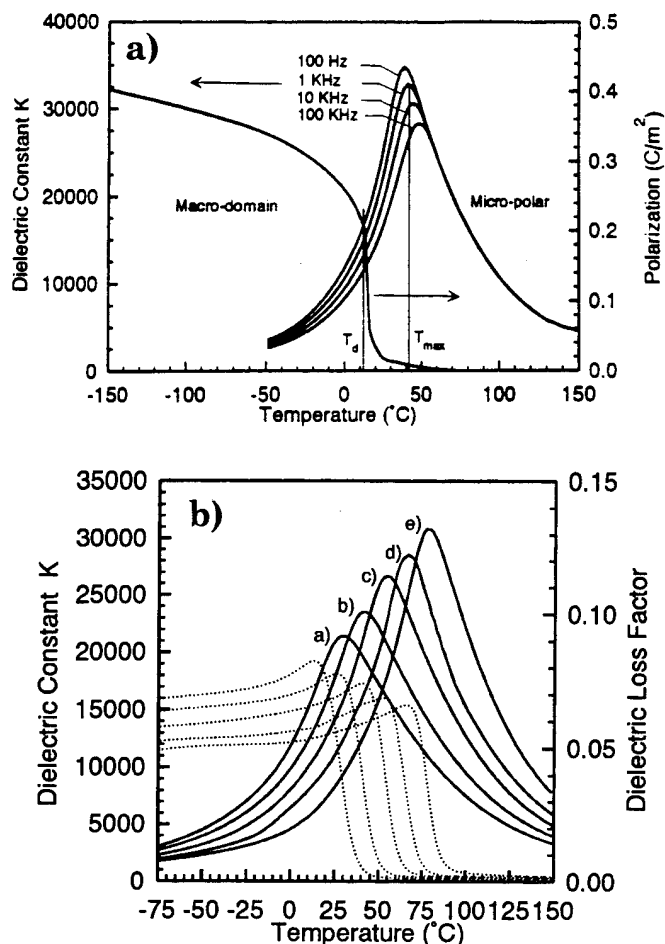


Figure 1. a) Polarization and dielectric constant as function of temperature for 0.90PMN-0.10PT. b) Dielectric constant and loss factor for 1 atom% La-modified (1-x)PMN-(x)PT compositions with x=a) 0.125; b) 0.15; c) 0.175; d) 0.20; e) 0.225.

Table I. Summary of dielectric measurements for several PMN-PT and 1 mol% La compositions.

x=	1 kHz				100 kHz		1 MHz			5 MHz		
	$T_{\max}$ (°C)	$K_{\max}$	D.F. max.	(@)	$K_{\max}$	D.F. $T > T_{\max}$	$K_{\max}$ 0 kV/cm	$K_{\max}$ 10 kV/cm	D.F. $T > T_{\max}$	$K_{\max}$ 0 kV/cm	$K_{\max}$ 10 kV/cm	D.F. $T > T_{\max}$
w/ 0 mole% $\text{La}_2\text{O}_3$												
0.10	40	32,800	0.092	28	28,280	<0.003	26,600	8,700	<0.004	25,200	8,500	<0.005
0.125	52	32,100	0.073	35	28,230	<0.003	26,800	9,000	<0.003	25,600	8,650	<0.004
0.15	68	36,530	0.063	50	32,890	<0.003	30,800	8,500	<0.003	29,600	8,300	<0.004
w/ 1 mole% $\text{La}_2\text{O}_3$												
0.125	30	21,430	0.082	12	18,930	<0.006	17,650	8,750	<0.006	16,500	7,600	<0.008
0.15	41	23520	0.078	27	20,760	<0.005	19,450	9,100	<0.005	18,300	8,400	<0.008
0.175	55	26,670	0.074	40	23,430	<0.005	23,500	9,450	<0.005	21,700	8,900	<0.008
0.20	66	28,550	0.069	53	25,380	<0.004	24,600	9,800	<0.005	22,300	9,160	<0.007
0.225	78	30,860	0.066	65	27,170	<0.004	26,400	10,100	<0.005	24,100	9,300	<0.007

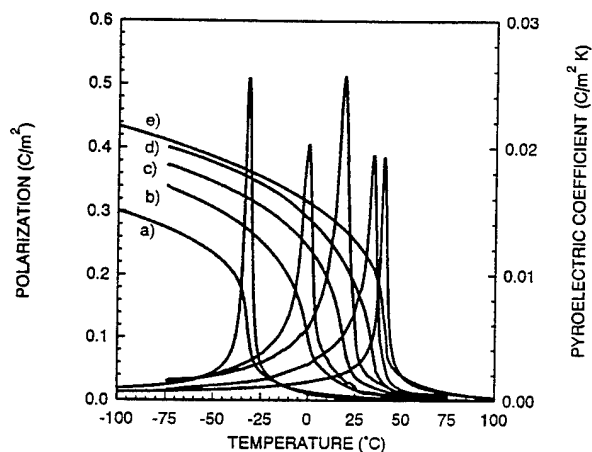


Figure 2. Pyroelectric coefficient and polarization for 1 atom% La-modified (1-x)PMN-(x)PT compositions with x=a) 0.125;b) 0.15;c) 0.175;d) 0.20;e) 0.225.

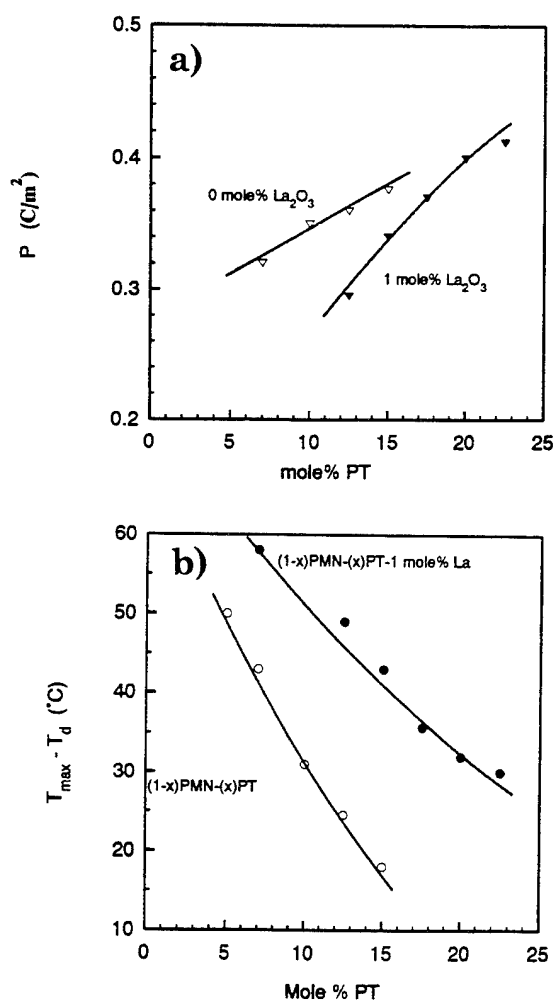


Figure 3. Effect of PT on polarization and  $\Delta T$  for 0 and 1 %La modified PMN-PT ceramics.

#### Electromechanical Properties

Large field-induced coupling factors were obtained for PMN-PT compositions evaluated. The field dependence of the coupling factor for a 0.85PMN-0.15PT-1%La specimen at two temperatures, 50°C ( $T \sim T_{\max}$ ), and 75°C ( $T > T_{\max}$ ), is shown in Figure 4. There was no remanent  $k_t$  observed after field removal for temperatures  $> T_d$ . The E-field dependence of  $k_t$  correlates fairly well with  $P_{\text{ind}}$  behavior at the measurement temperatures.

The temperature dependence of the field-induced thickness coupling factor  $k_t$  is shown in Figure 5 for 0.875PMN-0.125PT and 0.85PMN-0.15PT-1%La at several d.c. bias levels. The La-modified compositions were able to maintain larger electromechanical effect at higher temperatures for comparable E-field levels. The temperature range for inducing large  $k_t$ 's without remanence was increased due to the downward shift of  $T_d$  with 1 atom% La additions. The induced  $k_t$  values at 10 kV/cm field levels and remanent  $k_t$ , normalized to  $T_{\max}$ , for the  $x = 0.125$  and 0.15-1%La compositions, shown in Figure 6, illustrate the effect of La additions.

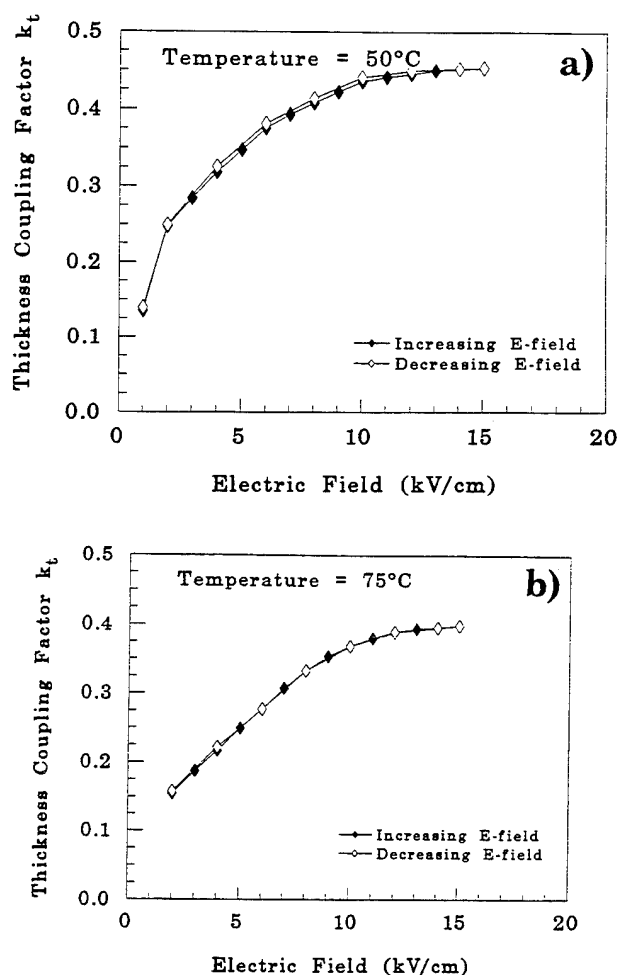


Figure 4. Field-dependence of induced thickness coupling factor  $k_t$  for temperatures a) 50°C and b) 75°C.

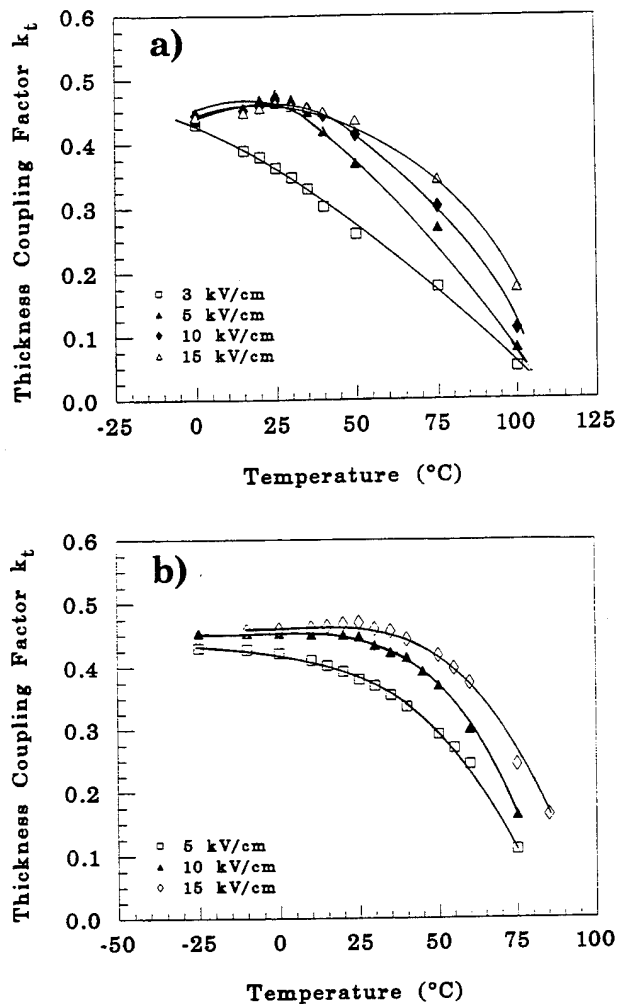


Figure 5. Temperature dependence of induced  $k_t$  at several field levels for a) 0.875PMN-0.125PT and b) 0.85PMN-0.15PT-1%La specimen.

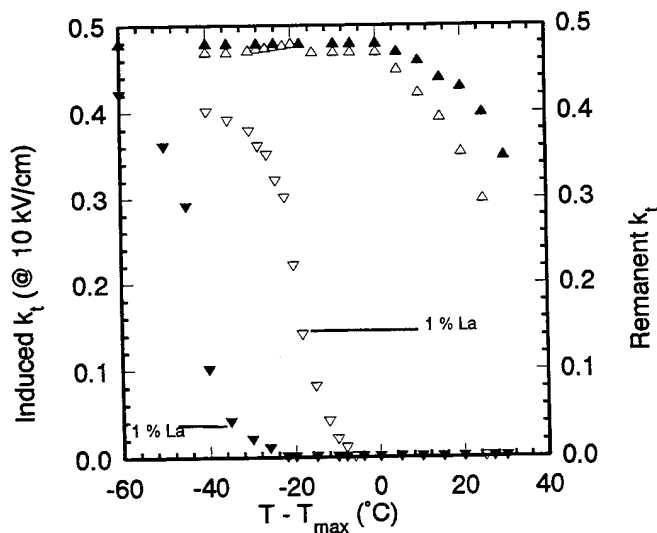


Figure 6. Induced (@ 10 kV/cm) and remanent  $k_t$  values as function of temperature for (1-x)PMN-(x)PT samples with x=0.125 and x=0.15-1%La.

## CONCLUSIONS

The effect of La additions to increase the width of the micro-macro transition region in PMN-PT relaxors was investigated. The range for achieving large induced polarizations and electromechanical coupling factors ( $k_t$ 's 0.47-0.50) increased with 1 atom%  $\text{La}^{3+}$  additions. The large, tunable  $k_t$  values obtained were comparable to those of conventional poled piezoceramics such as PZT.

PMN-PT relaxors offer large  $K$ 's, low losses, and adjustable induced piezoelectric and elastic properties. However, the strong frequency dependence of the dielectric properties of relaxors may reduce the other advantages in some fixed frequency transducer applications.

## REFERENCES

- [1] K. Uchino, "Electrostrictive Actuators: Materials and Applications," *Am. Ceram. Bull.*, **65** [4], pp. 647-652 (1986).
- [2] H. Takeuchi, H. Masuzawa, and C. Nakaya, "Relaxor Ferroelectric Transducers," *Proceedings of 1990 Ultrasonics Symposium*, 697 (1990).
- [3] J. T. Fielding, Jr., "Field-Induced Piezoelectric Materials for High Frequency Transducer Applications," Ph.D. Thesis, The Pennsylvania State University, (1993).
- [4] N. Kim, "The Role of Lanthanum Modification on the Fabrication and Properties of Lead Magnesium Niobate-Lead Titanate Ceramics," M.S. Thesis, The Pennsylvania State University (1990).
- [5] J. Chen and M. Harmer, "Ordering Structure and Dielectric Properties of Undoped and La/Na doped  $\text{Pb}(\text{Mg}_{1/3}\text{Nb}_{2/3})\text{O}_3$  Ceramics," *J. Am. Ceram. Soc.*, **72**, 593 (1989).
- [6] A. D. Hilton
- [7] S. W. Choi, T. R. Shrout, S. J. Jang and A. S. Bhalla, "Dielectric and Pyroelectric Properties in the PMN:PT System," *Ferroelectrics*, **100**, 29 (1989).
- [8] IEEE Standard on Piezoelectricity, ANSI/IEEE Std 176-1978, The Institute of Electrical and Electronic Engineers, Inc., New York (1978).
- [9] S. L. Swartz and T. R. Shrout, "Fabrication of Perovskite Lead Magnesium Niobate," *Mat. Res. Bull.*, **17**, 1245-1250 (1982).

# SAMPLE ASPECT RATIO INFLUENCE ON THE SHEAR COEFFICIENTS MEASUREMENTS OF A PIEZOELECTRIC BAR

N. Aurelle, D. Roche, C. Richard and P. Gonnard

Laboratoire de Génie Electrique et Ferroélectricité  
INSA, Bat.504, 69621 VILLEURBANNE Cédex

**Abstract :** The variation of the shear related coefficient measurements of a piezoelectric bar with respect to the sample aspect ratio is investigated. This study is carried out with PZT P188 and PZT P189 prismatic rods. The inter-electrodes distance is  $t$  and  $L$  is the length along the polar axis. Samples with aspect ratio  $t/L$  lying between 0.04 and 20 have been characterised using a resonance method. The  $k_{15}$  coefficient is then derived with either a constant field model (high  $t/L$ ) or a constant induction model (small  $t/L$ ). The dependencies of  $k_{15}$ ,  $d_{15}$  and  $\varepsilon_{11}^T$  on the aspect ratio are given. The derived  $d_{15}$  constants are compared with a direct measurement, made in a quasi-static mode using a Laser Doppler Vibrometry technique, and with ATILA F.E.M. simulations. For low  $t/L$  ratios, a clamping of the bar is shown. Moreover,  $\varepsilon_{11}^T$  is strongly dependent on the aspect ratio. For high  $t/L$  ratios, no clamping is observed and the permittivity is roughly constant. Finally, the use of a constant field model is justified. The best agreement between the different analyses is obtained for  $t/L$  ratios higher than 8.

## Introduction

According to the different references found in the literature [1], a large disparity between the different approaches of the shear mode study of a piezoelectric element can be noticed. In fact, in order to determine the piezoelectric coefficient  $d_{15}$ , different shapes of specimen are proposed. But, discrepancies on the  $d_{15}$  values, that can reach up to 30% between two samples, have been experimentally found. That is why it is important to investigate this type of vibration so to choose the better test specimen and normalise it.

The following notations will be used in this paper (Fig.1) :

- $\{ L$  : length along the polar axis,
- $\{ t$  : inter - electrodes distance,
- $\{ w$  : third dimension.

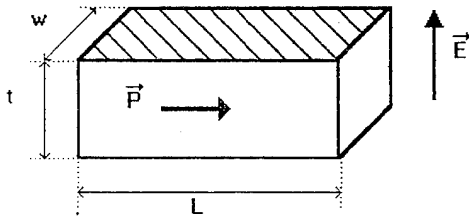


Fig. 1 : Sample dimension notations.

This study is divided into two parts. The first one, theoretical, presents a constant field model (corresponding to samples with high  $t/L$  ratio) and a constant induction model (corresponding to samples with small  $t/L$ ). Both these formulations are based on Mason's theory [2].

The second part presents experimental measurements, based on the resonance method, that give the dependence of the coupling factor  $k_{15}$ , piezoelectric constant  $d_{15}$  and permittivity  $\varepsilon_{11}^T$  on the aspect ratio  $t/L$ . These results are then compared with ATILA Finite Element Method (F.E.M.) simulations [3] and with a direct measurement of the  $d_{15}$  constant made by a Laser Doppler Vibrometry (L.D.V.) technique.

Finally, some rules for the choice of a shear mode sample are proposed.

## Theoretical analysis

The shear strain is defined by an angle  $\alpha$  in the plane formed by the polarisation vector  $\vec{P}$  and the electric field  $\vec{E}$  (Fig.2). According to reference [4],  $S_5 = \tan \alpha = \frac{\partial u_3}{\partial x_1} + \frac{\partial u_1}{\partial x_3}$ .

We can see, from this expression, that the shear motion has two components. In order to separate one shear wave from the other one, suitable dimensions of the piezoelectric sample have to be determined.

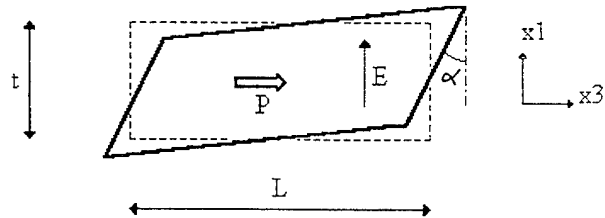


Fig. 2 : Shear strain definition.

## Constant induction model

If  $L \gg t$ , then the shear motion is parallel to the polar axis and the shear wave propagates under constant induction. In this case, the shear strain  $S_5$  and the induction  $D_1$  are the independent variables in the piezoelectric equations :

$$\begin{cases} T_5 = c_{55}^D \cdot S_5 - h_{15} \cdot D_1 \\ E_1 = h_{15} \cdot S_5 + \beta_{11}^S \cdot D_1 \end{cases} \quad (1)$$

$$\text{where } S_5 \approx \frac{\partial u_3}{\partial x_1} \text{ and } c_{55}^D = c_{44}^D = \frac{1}{s_{44}^D}$$

$$\text{The Newton law is : } \frac{\partial^2 u_3}{\partial t^2} = \frac{c_{55}^D}{\rho} \frac{\partial^2 u_3}{\partial x_1^2} = (v_s^D)^2 \frac{\partial^2 u_3}{\partial x_1^2} \quad (2)$$

$$\text{where } v_s^D = \sqrt{c_{55}^D / \rho} \text{ is the wave velocity .}$$

The solution of equation (2) is assumed to be :

$$u_3 = \left( A \sin\left(\frac{\omega x_1}{v_s^D}\right) + B \cos\left(\frac{\omega x_1}{v_s^D}\right) \right) \exp(j\omega t) \quad (3)$$

where A and B are constants.

$$\text{Assuming the boundary conditions : } \begin{cases} \text{at } x_1 = 0, T_5 = 0 \\ \text{at } x_1 = t, T_5 = 0 \end{cases} \quad (4),$$

the mechanical displacement  $u_3$  is :

$$u_3 = \frac{v_s^D h_{15} D_1}{\omega c_{55}^D} \left( \sin\left(\frac{\omega x_1}{v_s^D}\right) - \tan\left(\frac{\omega t}{2v_s^D}\right) \cos\left(\frac{\omega x_1}{v_s^D}\right) \right) \quad (5).$$

The sample admittance is then calculated according to :

$$Y = \frac{I}{V} = \frac{j\omega w L D_1}{\int_0^t E_1 dx_1}$$

$$\text{Thus, } Y = j\omega C \left[ 1 - k_{15}^2 \frac{\tan\left(\frac{\omega t}{2v_s^D}\right)}{\frac{\omega t}{2v_s^D}} \right]^{-1} \quad (6)$$

where  $C = \epsilon_{11}^S wL/t$  is the clamped capacitance,

$\epsilon_{11}^T = C_{bf} t/wL$  is the material permittivity derived from the sample capacitance measurement at 1 kHz,

$k_{15}^2 = d_{15}^2 / \epsilon_{11}^T s_{44}^E$  is the shear coupling coefficient.

The anti resonance frequency,  $f_n$ , corresponding to  $Y = 0$  is  $f_n = v_s^D/2t$  while the resonance frequency,  $f_m$ , calculated for infinite

$$Y, \text{ is defined by } k_{15}^2 = \pi f_m / 2 f_n \cdot \cotan(\pi f_m / 2 f_n) \quad (7).$$

### Constant field model

If  $t \gg L$  then the shear motion is parallel to the electric field : the shear wave propagates along an equipotential surface, under constant field. As we saw in the previous part, the piezoelectric equations and the equation of the shear motion for a shear displacement  $u_1$  are given as follows :

$$\begin{cases} T_5 = c_{55}^E S_5 - e_{15} E_1 \\ D_1 = e_{15} S_5 + \epsilon_{11}^S E_1 \\ u_1 = \frac{v_s^E e_{15} E_1}{\omega c_{55}^E} \left( \sin\left(\frac{\omega x_3}{v_s^E}\right) - \tan\left(\frac{\omega L}{2v_s^E}\right) \cos\left(\frac{\omega x_3}{v_s^E}\right) \right) \end{cases} \quad (8)$$

where  $c_{55}^E = c_{44}^E = \frac{1}{s_{44}^E}$ ,  $S_5 \approx \frac{\partial u_1}{\partial x_3}$  and the wave velocity is

$$v_s^E = \sqrt{c_{55}^E / \rho}.$$

The derived sample admittance is :

$$Y = j\omega C \left[ 1 + \frac{k_{15}^2}{1 - k_{15}^2} \frac{\tan\left(\frac{\omega L}{2v_s^E}\right)}{\frac{\omega L}{2v_s^E}} \right] \quad (9).$$

Consequently, the resonance frequency is :  $f_m = v_s^E/2L$  and the anti resonance frequency is calculated from :

$$k_{15}^2 = \left[ 1 - \tan(\pi f_n / 2 f_m) / (\pi f_n / 2 f_m) \right]^{-1} \quad (10).$$

### Experimental results and discussion

Experiments have been realised on several piezoelectric ceramic compositions. In order to get results valid for a wide range of ceramic types, soft (P188) and hard (P189) PZT made by Quartz & Silice (Saint-Gobain, France) have been investigated.

The study was carried out with prismatic rods. All the different samples have been cut in the same piece of ceramic so to avoid variations related to a change of composition. Similarly it is preferred to pole one ceramic block first and cut the specimens into it afterwards. The first measurements, performed with PZT P188 rods individually poled showed a dispersion in the results that indicates a non homogeneous polarisation of the different samples (especially, the  $d_{33}$  coefficient was often varying).

In this study, two series of measurements with samples corresponding to the constant field model or to the constant induction model, have been carried out. So, two sets of samples have been tested whose dimensions are :

$$\begin{cases} - 0.04 < t/L < 1 \\ \text{and} \\ - 1 < t/L < 20 \end{cases}$$

For each specimen, the capacitance at low frequency (1 kHz), the maximum admittance frequency  $f_m$  and the minimum admittance frequency  $f_n$  have been measured using an impedance analyser HP 4194A.

From these experimental results,  $\epsilon_{11}^T$ ,  $k_{15}$  and  $d_{15}$  are derived as functions of the aspect ratio  $t/L$ .

### Permittivity ( $\epsilon_{11}^T$ )

Figure 3 shows the influence of the sample aspect ratio  $t/L$  on the permittivity  $\epsilon_{11}^T$ . Both piezoceramics P188 and P189 present the same trends : on the low  $t/L$  ratios side ( $t/L < 0.5$ ), the permittivity fluctuates a lot and decreases as  $t/L$  approaches zero whereas on the large  $t/L$  ratios side, smoother variations are observed, saturating as  $t/L$  increases.

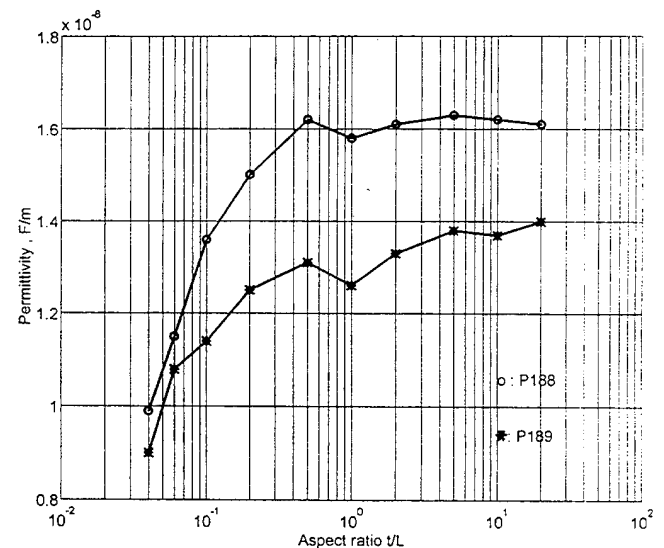


Fig.3 : Permittivity evolution.

It is important to note that this permittivity fluctuation on the low  $t/L$  side is responsible for an important  $d_{15}$  piezoelectric coefficient variation. This shows how critical it is to choose a shear mode sample, to avoid disparities such as observed in the literature.

### Coupling coefficient $k_{15}$ and piezoelectric shear coefficient $d_{15}$

The impedance analyser shows an isolated pure mode, without any spurious mode, in the three following cases:  $t/L \approx 1$ ,  $t/L$  lower than 0.2 and  $t/L$  higher than 5.

- The first case ( $t/L \approx 1$ ) is quite complicated. A 2D plane strain F.E.M. simulation shows a two dimensional deformation (Fig 4). This means that there is a coupling of two shear waves, one longitudinal propagating along the polar axis and the other one transversal propagating parallelly to the electric field. It is thus necessary to develop a two dimensional analytical model for this sample, which does not come within the scope of this paper.

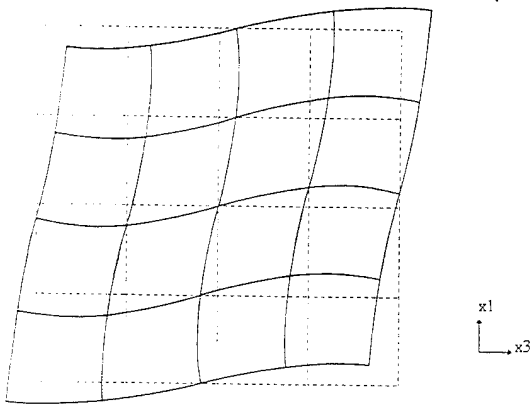


Fig.4 : 2D plane strain F.E.M. modelling for  $t/L = 1$ .

- For low aspect ratio, the unidimensional constant induction model defined previously is used. The dependencies of  $k_{15}$  and  $d_{15}$  on the aspect ratio are given, respectively on figures 5 and 6. It is observed that, for  $t/L$  values where the constant induction model is valid ( $t/L < 0.2$ ),  $d_{15}$  and  $k_{15}$  are constantly dependent on the aspect ratio.

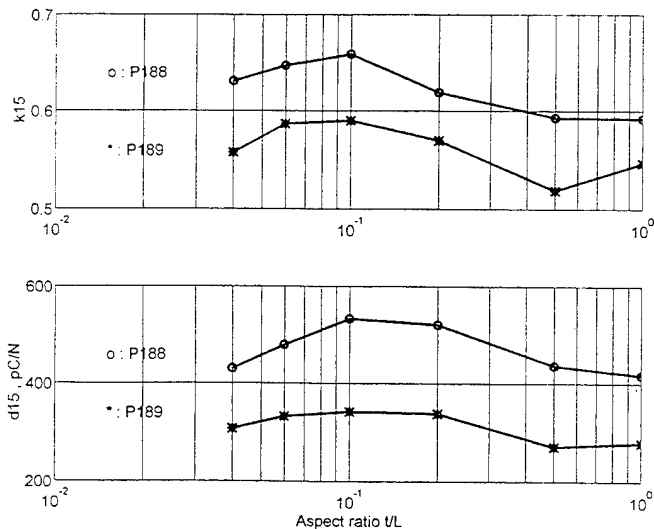


Fig 5 and 6 : Shear coefficients evolution for constant induction model.

For a  $t/L$  ratio lying between 0.2 and 1, there is an interference of several modes, that are the fundamental of the longitudinal shear mode and harmonics of the transversal one. For  $t/L$  ratios lower than 0.2, the continuous decrease of the permittivity  $\epsilon_{11}^T$ , shown in figure 3, leads to an erroneous and constantly varying  $d_{15}$ . Moreover, F.E.M. simulations show a clamping effect at both ends of the sample, certainly affecting the coupling coefficient  $k_{15}$  (Fig.7).

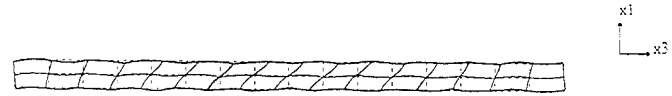


Fig.7 : 2D plane strain F.E.M. modelling for  $t/L = 0.05$ .

- For high  $t/L$  ratios, the unidimensional constant field model is used. Figures 8 and 9, representing the variations of  $k_{15}$  and  $d_{15}$  as a function of the aspect ratio, show a non monotonous region for  $t/L$  lower than 5 : there is an interference of the transversal shear mode and harmonics of the longitudinal one. For  $t/L$  ratios higher than 5, a large asymptotic plateau is observed. In contrast with the previous case, the permittivity,  $d_{15}$  and  $k_{15}$  are constant.

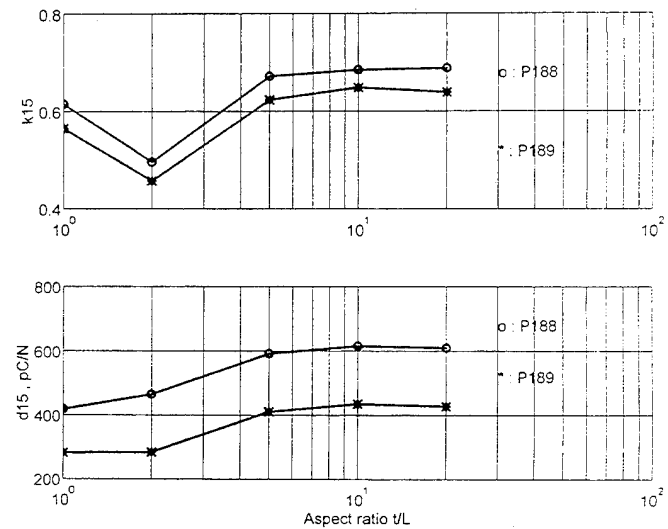


Fig.8 and 9 : Shear coefficients evolution for constant field model.

As shown in figure 10, no more clamping is observed, resulting in a quite pure shear mode with a higher  $k_{15}$  coupling.



Fig.10 : 2D plane strain F.E.M. modelling for  $t/L = 20$ .

### Direct $d_{15}$ measurement

The derived  $d_{15}$  constants have finally been compared with a direct measurement made in quasi-static mode using a Laser Doppler Vibrometry technique. Figure 11 shows the experimental set-up. A cubic PZT ceramic, with 5 mm sides, is fixed on a duralumin wall with a cyanoacrylate adhesive. It is driven by a 100 Vrms, 1 kHz sinusoidal signal. A lock-in amplifier allows the measurement of the small vibration speed obtained.

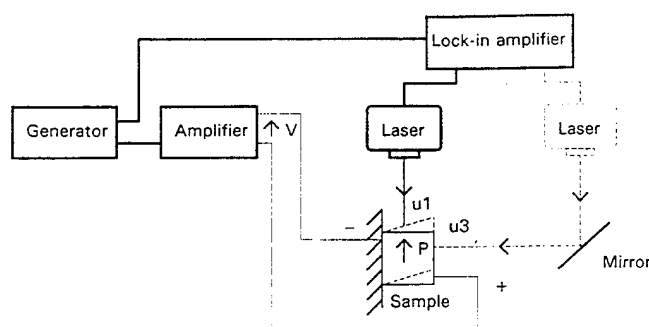


Fig. 11 : Experimental set-up for direct  $d_{15}$  measurement.

Both the upper and vertical faces displacements are measured and plotted on figure 12. As expected, no horizontal motion is detected and the vertical face slips parallelly to the wall. The slope of the vertical elongation of the upper face gives the shear angle and thus the  $d_{15}$  coefficient :

$$d_{15} = \frac{S_5}{E_1} = \frac{dl}{V} = 630 \text{ pC/N for the PZT P188}$$

$$= 410 \text{ pC/N for the PZT P189}$$

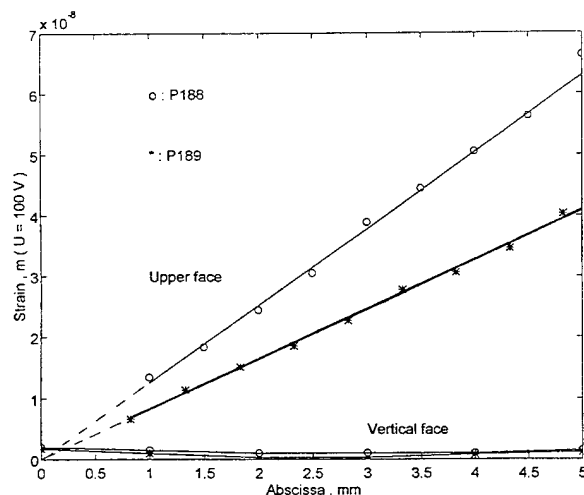


Fig. 12 : Shear strain measurements.

A good agreement, better than 5%, between the resonance method and the quasi-static measurement is obtained for aspect ratios higher than 8.

### Conclusion

The variations of the shear coefficients for PZT prismatic rods have been investigated as a function of the sample aspect ratio  $t/L$ . It is shown that two shear waves coexist that can be separated if appropriate dimensions  $t$  and  $L$  are chosen. Pure modes are achieved for  $t/L$  ratio higher than 5 and lower than 0.2. For  $t/L$  ratios lying between 0.2 and 5, two shear waves are strongly interconnected and a two dimensional model has to be used to derive the shear coefficient.

For low  $t/L$  ratios, an unidimensional constant induction model can be used. Unfortunately, this sample size leads to results varying strongly with the aspect ratio. This is due to the continuous fluctuation of the permittivity with the aspect ratio and to a clamping effect at both ends of the bar.

For high  $t/L$  ratios, the unidimensional constant field model can be applied. The permittivity stays constant with the aspect ratio, F.E.M. analysis show pure shear modes and experimental measurements show an asymptotic variation of shear coefficients as  $t/L$  increases. Moreover, these measurements corroborate results obtained in quasi static mode with the L.D.V. technique.

Consequently, the appropriate sample used to characterise the shear mode must have an aspect ratio  $t/L$  greater than 8.

### Acknowledgements

The authors are grateful to R. VIGNAT for his assistance in the samples preparation. This research was supported by the CERDSM-DCN of Toulon.

### References

- [1] "Guide to dynamic measurements of piezoelectric ceramics with high electromechanical coupling", I.E.C. Standard, First edition, 1976.
- [2] D.A.Berlincourt, D.R.Curran and H.J.Jaffe, *Physical Acoustics*, New-York : Academic Press, 1964, Ch.3, Vol.1A, pp.169-270.
- [3] B.Dubus, "ATILA Finite Element Code for Piezoelectric and Magnetostrictive Transducer Modelling", Version 5.02, User's manual, Lille, ISEN, 1991.
- [4] "IEEE Standard on Piezoelectricity", ANSI/IEEE Standard 176, 1987.



# On Elastic Dipoles in Li Metaniobate Ceramics

L.A. Reznitchenko, E.I. Bondarenko and  
A.N. Klevtsov

Rostov State University, Institute of Physics,  
Stachki St., 194, Rostov-on-Don, 344104, Russia .

**Abstract** - It was established that in contrast to triaxial BaTiO<sub>3</sub>-type ferroelectrics (FE) the unnormally large values of elastic compliance  $S_{11}^E$  (unnormally small values of elastic modulus  $C_{33}^D$ ) are characteristic for ceramic uniaxial Li metaniobate (LMN) while retaining the usual (corresponding to the averaged values of single-domain crystal constants) values of dielectric permittivity. It was suggested that the additional contribution to the strain and elastic compliances of the LMN ceramics is due to the existence of two-minimum asymmetrical potential of Li ions in sonic mechanically strained unit cells inside crystallites that because of the interaction of Li ions with the surrounding lattice leads to the appearance of elastic dipole moments (elastic dipoles) distributed in random way and capable of reorientation in the field of mechanical stress of the acoustic wave. The conclusion that FE crystals with multi-minimum single-particle potential have the specific mechanism of redistribution of incompletely ordered Li ions, induced by mechanical stresses. These stresses lead to essential increase of elastic compliances in comparison with mean ones for corresponding monocrystals. This circumstance causes decrease of the speed of propagation of acoustic waves in ceramics in comparison with theoretically obtainable speeds.

We continue our studying the physical properties of Li metaniobate ferroceramics LiNbO<sub>3</sub>. This study was begun in papers [1,2], where dielectric and piezoelectric properties of this ceramics were studied. The specimens of LiNbO<sub>3</sub> ceramics had the shape of large-dimensioned blocks and they were made with using the technique, described in [2]. The specimens to be tested represented polarized disks whose diameter and thickness were equal to  $10 \cdot 10^{-3}$  m and  $1 \cdot 10^{-3}$  m respectively. The longitudinal sonic speeds  $V_R^E$  and  $V_3^D$  to be

used for obtaining the magnitudes of elastic compliance  $S_{11}^E$  and of elastic modulus  $C_{33}^D$  were measured by the standard technique, based upon resonance frequency of radial oscillations and upon antiresonance one of thickness oscillations.

The summary of measured (mean for 4-6 specimens) and of calculated by Marutake method ceramics constants is given in table. The calculations by Marutake method used the constants of single-domain LiNbO<sub>3</sub> crystals. In this calculations the density of ceramics was assumed to be equal to roentgen one  $\rho = 4.63 \cdot 10^3$  kg/m<sup>3</sup>.

The significant scatter (up to 30-40%) of elastic constants was observed both for specimens of thoroughly purified ceramics and for specimens of alloyed by small (up to 1 mol.%) quantity of copper and titanium ions at practically unchanged permittivities  $\epsilon$ .

It follows from Tab. 1 that the large difference obtained from experiment and calculated elastic constants  $S$  and  $C$  is a characteristics of LiNbO<sub>3</sub> ceramics. The magnitudes of  $S$ , obtained from experiment are greater than calculated ones. The magnitudes of  $C$ , obtained from experiment, are less than calculated ones. This situation is typical for BaTiO<sub>3</sub> ceramics [4], but the magnitudes of permittivities, obtained by experiment are greater than calculated magnitudes for BaTiO<sub>3</sub>, whereas the corresponding  $\epsilon^E$  are very close in fact for LiNbO<sub>3</sub> ceramics. The several difference is caused by incomplete polarization of LiNbO<sub>3</sub> ceramics (see [2]).

Two reasons may be responsible for so unusual behaviour of elastic constants of LiNbO<sub>3</sub> ceramics.

1st. There is a contribution into elastic constants at the expense of reversible reorientations of mechanical (not being 180 out of phase) dipoles. These dipoles may appear because of one of one of the numerous low-temperature phase transitions, observed in LiNbO<sub>3</sub> [6].

Table 1.

The density  $\rho$ , the speeds of longitudinal sonic waves  $V_R^E$  and  $V_3^D$ , elastic compliance  $S_{11}^E$ , elastic modulus  $C_{33}^D$ , permittivities  $\epsilon_{33}^E/\epsilon_0$  of mechanically free and of clamped ceramics LiNbO<sub>3</sub> at 25 C.

Ceramics	$\rho \cdot 10^{-3}$ , kg/m <sup>3</sup>	$V_R^E$ , m/sec	$V_3^D$ , m/sec	$S_{11}^E \cdot 10^{12}$ , m <sup>2</sup> /N	$C_{33}^D \cdot 10^{-11}$ , N/m <sup>2</sup>	$\epsilon_{33}^E/\epsilon_0$	$\epsilon^E/\epsilon_0$
LiNbO <sub>3</sub>	4.38	4500	4760	11.70	0.99	47.0	40.0
LiNbO <sub>3</sub> (alloyed)	4.56	4900	5100	9.40	1.19	53.3	48.5
Theor. values	4.63	6440	7000	5.51	2.27	50.4	45.5

This contribution should significantly fall and even vanish when applying sufficiently high mechanical stress to specimen, conjugate to the corresponding mode of oscillation, i.e. radial compression of specimen when measuring  $S_{11}$ . But measurements, conducted with usage of special type holder of specimen to permit loading specimen with radial stress  $\sigma \sim 10^7$  Pas revealed no changes of  $S_{11}$ . That's why the orientational mechanism of increasing  $S_{11}$  (decreasing  $C_{33}$ ) is unlikely to be possible.

2nd. The contribution into elastic constants is due to incomplete ordering Li ions in crystallites, being constitutives of ceramics. As for our opinion, this mechanism is the most probable reason of abnormally large magnitudes of elastic compliance of ceramics. Let us consider it detail.

According to [7], the disposition on Li ions in paraelectric phase of crystals of  $\text{LiTaO}_3$  and  $\text{LiNbO}_3$  is out of order. The ions have two-minimum single-particle potential in the direction of C axis. They occupy the positions at the distance of  $\pm(0.04-0.05)$  nms from the centresymmetric position in the centre of common side of two oxygen octahedrons with equal probability.

The transition into ferroelectric phase is caused by the displacement of heavy ions of Nb(Ta) and of O. It is due to elastic response of matrix. In this matrix the appearance and anisotropic growth of crystals of ferroelectric phase occur at para-ferroelectric phase transition (Curie temperature is equal to  $1210^\circ\text{C}$ , the symmetry of ferroelectric phase is  $R3c$ ). The phenomena referred to are followed by posterior cooling the  $\text{LiNbO}_3$  ceramics down to room temperature. It is observable, that such a response is reduced to uniaxial compression of crystallite along C axis accompanied by biaxial tension in directions, perpendicular to C axis. It would lead to increase of elastic energy of crystal-matrix system (see [8]).

The incomplete ordering the disposition of Li ions is one of ways of decreasing elastic energy. In crystallites, where Li ions are displaced in directions, contravert to one of spontaneous polarization  $P_s$ , the values of  $P_s$  and spontaneous electrostriction  $\zeta_s \sim P_s^2$  are decreased, i.e. the reason of elastic crystallity-matrix interaction is partially removed.

Thus, the Li ions have two states of equilibrium in elementary cell. The

probability of occupying one of them is defined by correlation between internal electric field, depending upon  $P_s$ , and stresses, implied by matrix. The periodic changes of stresses, acting upon crystallite (especially acting along polar axis) cause change of probability of Li ions occupying different positions. These changes of stresses of occur at acoustic wave propagation and, thus, cause redistribution of local minimums of single-particle potential. It is also a reason of the additional electrostrictional contribution to strains and to elastic complians of ceramics.

Thus, ferroelectric crystals with multi-minimum single-particle ion potential have especial mechanism of redistribution of incompletely orderedions, exited by stressed. This mechanism would lead to essential increase of elastic compliances of ceramics compared with the mean ones of crystallites' constitutives. This circumstance causes the fall of sonic speed for waves, propagating in ceramics in comparison with theoretically predicted speeds.

#### References

- [1] E.G. Fesenko, V.A. Chernyshkov, L.A. Reznitchenko et al., *Journal Technicheskoy Physiki*, vol. 54, No. 2, pp. 412-415, in Russian.
- [2] L.A. Reznitchenko, L.A. Turik, G.I. Hasabova et al., *Journal Technicheskoy Physiki*, vol. 56, No. 7, pp. 1407-1409.
- [3] M. Marutake, *J. Phys. Soc. Japan*, vol. 11, No. 8, pp. 807-814.
- [4] A.V. Turik, A.I. Chernobabov, *Jurnal Technicheskoy Physiki*, vol. 47, No. 9, pp. 1944-1948, 1977, in Russian.
- [5] I.A. Dan'kov, E.F. Tokarev, G.S. Kudryashov et al., *Izv. AN SSSR, Ser. Neorg. Mater.*, vol. 19, No. 7, pp. 1165-1171, 1983, in Russian.
- [6] I.G. Ismailadze, V.I. Nesterenko, F.A. Mirijuli, *Crystallographia*, vol. 13, No. 7, pp. 33-37, 1968, in Russian.
- [7] M. Lines, A. Glass, *Ferroelectrics and allied materials*. Moscow: Izd. Mir, 1981, translated into Russian.
- [8] A.V. Turik, A.I. Chernobabov, V.Yu. Topolov, *Physika Tvyordogo Tela*, vol. 25, No. 9, pp. 2839-2841, 1983, in Russian.

# Temperature Stability of Resonance Frequency of Filter Materials Obtained by Different Techniques

S.V. Gavrilyatchenko, A.Ya. Dantsiger, L.A. Reznichenko, O.N. Razumovskaja and A.N. Klevtsov.  
Rostov State University, Institute of Physics,  
Stachki St., 194, Rostov-on-Don, 344104, Russia .

**Abstract** - The influence of the various techniques on the character of microstructure and temperature stability of resonance frequency for piezoelectric materials PCR-62 and PCR-63 has been considered. It is noted that temperature stability has high magnitudes at transition from hot pressing to traditional sintering. It is connected with an increase of field of bulk charge when the density of ceramics decreases.

The problem of controlling the mechanism of stabilization of ferroelectric solid solutions is of great importance. The main factors, influencing the temperature stability of resonance frequency ( $f_r$ ) in solid solutions of  $PbTiO_3$ - $PbZrO_3$ - $PbB_{1-x}^{II}B_x^{IV}O_3$ - $PbB_{1-x}^{III}B_x^{IV}O_3$  - type are the character of chemical bond (see [1]), the character of domain tie and microstructure (see [2]). The influence of various techniques of sintering on microstructure and temperature stability is investigated in this paper. The solid solutions, sintered by traditional ceramic technology (TT), by hot pressing (HP), in oxygen atmosphere ( $O_2$ ) are investigated. The piezoelectric materials PCR-62 and PCR-63 are chosen as objects for investigation. These materials, obtained in the Institute of Physics at RGU are intended for applications in stepwise filters of medium frequency. The parameters of PCR-62 and PCR-63 materials, sintered by various techniques are given in Tables 1 and 2.

The sintering temperature range  $T_s=1110^\circ\text{C}$ - $1150^\circ\text{C}$  is optimum for hot pressed PCR-62. The sintering temperature range  $T_s=1100^\circ\text{C}$ - $1140^\circ\text{C}$  is optimum for PCR-62, sintered by traditional ceramic technique. The sintering temperature range  $T_s=1120^\circ\text{C}$ - $1150^\circ\text{C}$  is optimum for PCR-62 sintered in  $O_2$  atmosphere. The certain decrease of electromechanical coupling factor  $K_p$  is a distinctive feature of sintering in  $O_2$  atmosphere. Thus, the PCR-62 is well reproduced by all three sintering methods. It is an evidence of its hightechnologicalness. The behaviour of PCR-63 differs by some details. It well-sintered by HP in wide temperature range  $T_s=1130$ - $1180^\circ\text{C}$ . But is incompletely reproduced by magnitude of  $\epsilon_{33}/\epsilon_0$  when sintered by TT and in  $O_2$  atmosphere. It follows from tables that high values of  $Q_M$  and of temperature stability of  $f_r$  remain both in high-densed finegrained ceramics and in low-densed coarsegrained ceramics. It is shown in [3] that the increase of grain size is accompanied by increase of doubling. This doubling is followed by decrease of internal stresses. This results the decrease of switching field and also the decrease of mechanical quality, because mechanical losses increase as number of domain walls increases. In addition, according to [2] the increase of number of domain walls leads to fall of stability of  $f_r$ . One may explain these regularities by influence of bulk charge

Table 1.  
The parameters of PCR-62 material sintered by different methods .

Method	$T_s, ^\circ\text{C}$	$\epsilon/\epsilon_0$	$\epsilon_{33}/\epsilon_0$	$K_p$	$Q_M$	$\delta f_r/f_r, \%$ -25÷85 $^\circ\text{C}$	$\bar{D}, \text{mcm}$	$\rho \cdot 10^{-3},$ kg/m <sup>3</sup>
HP	1070	610	660	0.30	1800	0.27	-	8.00
	1090	620	670	0.32	2200	0.25	1-2	8.00
	1110	590	660	0.32	1200	0.21	2-3.6	8.00
	1130	590	660	0.32	2700	0.13	3.6-5	8.00
	1150	580	670	0.32	2900	0.15	3.6-5	8.00
TT	1060	610	650	0.29	2000	0.39	2.0	7.59
	1060	610	670	0.31	2500	0.20	2-3.6	7.77
	1100	570	650	0.29	2800	0.14	5.7	7.78
	1120	560	620	0.31	3100	0.15	5.0	7.76
	1140	540	600	0.30	2900	0.17	5.0	7.72
	1160	530	590	0.28	2800	0.16	8.7	7.69
	1180	480	550	0.26	2600	0.15	9.2	7.64
	1200	490	540	0.25	1500	0.17	16.4	7.50
$O_2$	1120	510	580	0.29	2000	0.08	15.5	7.78
	1130	530	600	0.28	2800	0.18	8.5	7.94
	1140	500	560	0.26	2500	0.14	10.0	7.98
	1150	490	560	0.26	2300	0.15	10.2	7.94
	1160	470	520	0.21	1700	0.27	12.6	7.67

Table 2.

The parameters of PCR-63 material sintered by different methods .

Method	$T_c, ^\circ C$	$\epsilon/\epsilon_0$	$\epsilon_{33}^T/\epsilon_0$	$K_p$	$Q_M$	$\delta f_r/f_r, \%$ -25+85 $^\circ C$	$\bar{D}, mcm$	$\rho \cdot 10^{-3},$ kg/m <sup>3</sup>
HP	1120	800	1010	0.31	1100	-	-	8.0
	1130	950	1140	0.36	1300	0.10	7.1	8.0
	1140	990	1170	0.37	1100	0.13	7.6	8.0
	1150	860	1110	0.34	1100	0.10	5.0	8.0
	1160	960	1140	0.35	1000	0.10	5.0	8.0
	1180	950	1140	0.35	1100	0.10	5.0	8.0
TT	1120	750	830	0.23	400	0.46	-	6.03
	1140	760	830	0.27	800	0.22	5-7	6.86
	1160	770	830	0.26	600	0.30	13.5	7.04
	1180	810	870	0.25	600	0.17	15.0	7.07
	1200	850	880	0.20	1100	0.28	16.0	7.29
	1220	700	750	0.18	900	0.21	>20	7.11
	1240	700	760	0.24	800	0.17	>20	7.15
O <sub>2</sub>	1120	810	870	0.21	500	0.51	16.0	6.84
	1130	820	870	0.22	700	0.34	15.0	7.00
	1140	680	750	0.18	800	0.34	14.6	7.82
	1150	800	900	0.22	1000	0.17	14.5	7.33
	1160	800	900	0.24	1400	0.25	15.8	7.06

field, appearing at the bounds of crystals (see [4]). According to the proposed model the ferroceramics consists of the set of ferroelectric grains and layers of the frontier material. The lattice's vacancies, dashing atoms, held in intergranular bounds are one of sources of bulk charge, influencing on the state of domain structure in ceramics. In the finegrained ceramics (particle size < 5 mcm) the surface effects become significant. The ferroelectric polarization is screened by the layer of bulk charge at these effects. These effects influence the switching domains in ceramics.

The size of crystals increases whereas the stability of  $f_r$  keeps high values for ceramics sintered by TT. In this case the field of bulk charge increases at the expence of decreasing ceramics' density. It fits the conclusions, made in paper [4]: it is expected that the increase of ceramics' density would be accompanied by decrease of the field of bulk charge, because this field is depressed by bulk charges of neighbouring grains easier than in "porous" ceramics.

Thus it may be concluded that the temperature stability of  $f_r$  increases as the grain size and ceramics' density decrease due to increase of the field of bulk charge. This

increase causes decreasing mobility of domain bounds.

#### References

- [1] L.D. Grineva, S.V. Gavril'yatchenko, A.Ya. Dantsiger et al., "The dependance of temperature stability of resonance frequency of ferroelectric perovskite-type materials on the specific characteristics of their constitutive cations," *Izv. AN SSSR, Ser. Neorg. Mater.*, vol. 22, pp.270-272, 1986, in Russian.
- [2] E.G. Fesenko, A.Ya. Dantsiger et al., "The investigation of complex oxides," *Izv. AN SSSR, Ser. Neorg. Mater.*, vol. 16, pp.2247-2250, 1980, in Russian.
- [3] W.R. Buessem, L.E. Gross, R. Goswami, "Effect of twodimensional pressure on the permittivity of fine- and coarsegrained barium titanate," *J. Am. Ceram. Soc.*, vol. 49, pp. 36-39, 1966.
- [4] K. Okasaki, K. Nagata, "Effects of grain size and porosity on electrical and optical properties of PLZT ceramics," *J. Amer. Ceram. Soc.*, vol. 56, pp.82-86, 1973.

# Data Bank on Properties and Applications of Ferro-Piezoelectric Materials .

A.Ya. Dantsiger, L.A. Reznitchenko, O.N. Razumovskaja,  
S.I. Dudkina, N.V. Dergunova , S.V. Gavril'yatchenko,  
R.U. Devlikanova and A.P. Naumov.  
Rostov State University, Institute of Physics,  
Stachki St., 194, Rostov-on-Don, 344104, Russia .

**Abstract** - The works on the formation of the data bank on FPCM developed at the Institute of Physics (Rostov State University) are under way. The bank contains electrophysical, elastic, structural parameters of materials, their chemical composition and technological characteristics and the fields of applications. FPCM of different groups possess various parameters: very high and extremely low values of permittivity and mechanical quality, low dielectric losses; high values of piezoelectric response; temperature stability of resonance frequency and Curie point. There is a wide spectrum of FPCM applications: low - and high-frequency devices, high sensitive and high-temperature transducers, devices with high specific power, filter devices and others. The use of above mentioned data bank will make it possible to proceed to a new step of analyzing and generalizing the results of investigations of FPCM. The analytical dependences relating the composition of materials with their properties will allow one to predict and to design the materials with prescribed properties.

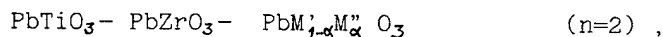
The large volume of data on properties of materials and on technologies of making them in the field of creating ferro-piezoelectric materials has been accumulated for many years in the Institute of Physics at Rostov State University. But part of data sometimes is lost and becomes unavailable. That's why the problem of creating the informational software for inquiries on the basis of the contemporary informational technology is of great importance.

The data bank on high-efficiency ferro-piezoelectric materials has been composed in the Institute of Physics. This data bank contains the main electrophysical parameters (for several compositions), the structural and technological characteristics, chemical contents and fields of application of these materials.

The materials presented in data bank have been obtained by investigation of multicomponent systems of complex oxides, based upon lead zirconate-titanate, binary and ternary component solid solutions, based upon niobated oxides, the substances with structure of tetragonal bronze of kalium-tungsten, the bismuth - containing substances of layered structure, lead titanate. The ferro-piezoceramics of different groups have the various parameters: very high and ultimately low magnitudes of permittivity and of mechanical quality respectively, of temperature stability of resonance frequency and of Curie point. The wide variety of fields of applications is presented in this

data bank, e.g. LF and RF transducers, ultrasonic emitters, piezoengines, piezotransformers, accelerometers, defectoscopes, the medical diagnostic devices, high-temperature transducers.

Using the database available allows one to proceed to the new stage of analyzing and generalizing the results of investigations of ferro-piezoelectric materials. The correlations between the electrophysical ( $\epsilon_{33}^T/\epsilon_0$ ,  $K_p$ ,  $d_{31}$ ), crystallochemical and structural parameters of solid solutions of multicomponent systems:



where M' is one of Nb, Ta, Sb, W; M'' is one of Li, Mg, Zn, Ni, Co, Mn; and  $\alpha=1/3$  or  $\alpha=1/2$  depend on elements' valencies. The summary electronegativity of M' and M'' elements with an account of their degrees of oxidation and concentrations in solid solutions is chosen as a main crystallochemical parameter describing the state of chemical bond M-O. The mean values of electronegativity for the elements, possessing the variable valency are taken for degrees of oxidation, possible at material making conditions. The data for calculating dependences have been obtained from data bank by conditional queries and are passed to the programs for calculating the summary electronegativity. The results of computation are analyzed by the use of graphic subroutines package by approximation of experimental points with polynomials using the least squares method. The graphic dependences of  $\epsilon_{33}^T/\epsilon_0$ ,  $K_p$  and  $d_{31}$  versus summary electronegativity of M' and M'' at fixed ratio of atomic portions Ti/Zr=1.04-1.11 which defines the relative to morphotropic area position of solid solutions are presented on Figs. 1-3. It is observed that the increase of electronegativity is accompanied by parameters' decrease with their passing through maximum point. Their initial ascent may be associated with the increase of orientational polarization's contribution, and posterior fall may be associated with the increase of ferrohardness of solid solutions, which impedes orientational processes. The direct dependence of spontaneous strain characterized by the uniform strain parameter  $\delta$  (see [1]) upon electronegativity of M and the dependences referred to may allow one to estimate the structure and electrophysical properties of solid solutions on the basis of their contents and also to define their contents on the basis of their properties.

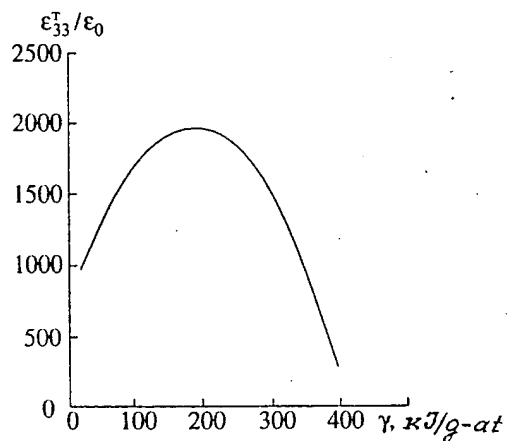


Figure 1. The dependance of permittivity upon the summary electronegativity of M' and M" elements at ratio Ti/Zr=1.04-1.11(at. portions)

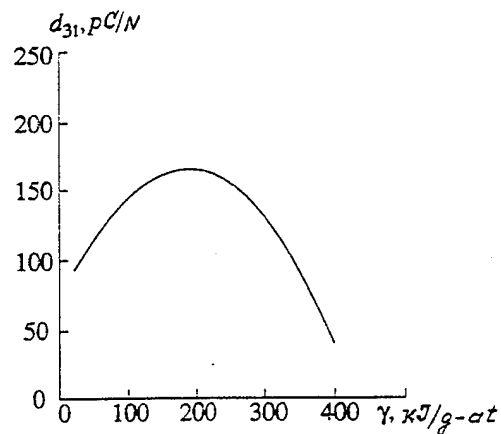


Figure 3. The dependance of  $d_{31}$  upon summary electronegativity of M' and M" elements at ratio Ti/Zr=1.04-1.11(at. portions)

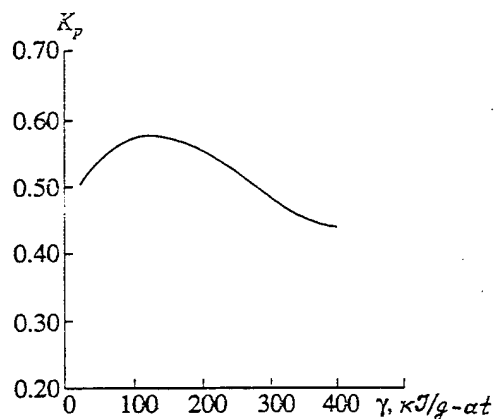


Figure 2. The dependance of electromechanical coupling factor upon summary electronegativity of M' and M" elements at ratio Ti/Zr=1.04-1.11(at. portions)

#### References.

- [1] A.Ya. Dantsiger , N.V. Dergunova , S.V. Dudkina , O.N. Razumovskaja , A.Ya. Shilkina "The prognosis of the properties of ferroelectric solid solutions on the basis of their contents and structure," Izv. AN SSSR , Ser. Phys., vol. 54, No. 4, pp.717-720

## High - Efficiency Transducers for Acoustic Diagnostics on the Basis of Novel Anisotropic Piezoelectric Materials

V.M. Shikhman, L.D. Grineva,  
Rostov State University, Institute of Physics,  
Stachki St., 194, Rostov-on-Don, 344104, Russia .

**Abstract** - A major source of the improvement in acoustic means of technical diagnostics is the use of high-efficiency piezoelectric materials in primary information pickups (transducers). The most optimum relation of characteristics is ensured by a new group of so called anisotropic piezoelectric materials possessing a high anisotropy of piezoelectric properties. The  $\text{PbTiO}_3$  - based PCR - 70 and PCR - 72 piezoceramics developed by our Institute belong to this group: they are characterized by the high  $K_t$ , the high piezoelectric response ( $g_{33} > 50 \text{ mV} \cdot \text{m/N}$ ), the very low mechanical quality ( $Q_M(t) < 10$ ) and a practically zero value of  $K_p$ . The transducer characteristics were studied in a receiving mode during the operation on a massive plate surface. Special steps were taken to remove reverberations. The above properties of piezoelectric materials ensure the high response ( $1 \dots 4 \cdot 10^9 \text{ V/N}$ ), a small duration of transient processes and a high selectivity to longitudinal (normal to the operating surface) vibrations for transducers. A combination of the obtained characteristics makes the developed transducers competitive with the best known analogues.

### Introduction.

The one of the most important directions for improvement and development of the acoustic methods for diagnosing the constructive materials and products is working up high-efficiency specialized receiving transducers. The methods mentioned above are such as: acoustic emission, acoustic spectroscopy etc. These transducers must give an adequate and sufficient information about the wavefield parameters, needed to adopt the decision whether the defects is available. The general requirements to the transducers for acoustic diagnostics are:

high sensitivity, the least distortion of the wavefield characteristics, the selectivity to certain types of oscillations.

### The Novel Materials' Characteristics.

The conformity to the above mentioned requirements and the ways of improving the transducers are significantly dependant upon the active element piezomaterial's parameters. The unique characteristics and the most optimum correlation of transducer's parameters are provided by novel piezomaterials PCR-67... PCR-72 (see [1,2]). The fact that planar piezomodulus of them is more than of 1st order less than longitudinal one is a characteristic feature of these materials. This planar piezomodulus is almost equal to zero for several modifications of materials referred to. The Tab. 1 presents the characteristics of some anisotropic ceramics.

The characteristics of the industrial-made ceramics PZT-19 are given in this table for comparison. The  $K_p$  and  $K_t$  are planar and thickness electromechanical coupling factors respectively,  $d_{33}$  and  $d_{31}$  are piezomoduli,  $g_{33}$  is a piezoconstant,  $Q_M(t)$  is a mechanical quality of the thickness oscillation mode,  $T_c$  is a Curie temperature. Besides the high degree of anisotropy of piezoelectric parameters, the novel materials are featured by extremely high magnitudes of  $g_{33}$  and also extremely low  $Q_M(t)$ . Such a combination of parameters implies wide transmission band and shortened pulse characteristics whereas high sensitivity remains. The almost complete absence of radial resonance and selectivity to the longitudinal (normal to working surface) oscillations is due to planar piezomodulus's being equal to zero. The anisotropic piezoceramics is sintered by the use of the traditional ceramic technique in oxygen atmosphere. The strong dependance of materials' physical properties

Table 1.  
The characteristics of the most perspective anisotropic materials.

Material	$T_c, ^\circ\text{C}$	$\epsilon_{33}/\epsilon_0$	$K_t$	$K_p$	$Q_M(t)$	$d_{33}$ pC./N	$g_{33}$ mV·m/N
PCR-68	288	157	0.59	~0	12	135	97
PCR-70	324	120	0.64	~0	5	130	122
PCR-71	337	140	0.59	~0	7	140	112
PCR-72	277	153	0.67	~0	4	100	73
PZT-19	290	1725	0.50	0.47	67	200	13

Table 2.  
The dependance of physical parameters of PCR-70 piezoceramics on piezoelement's thickness.

$h$ , mm	$f_r(t)$ MHz	$\epsilon_{33}/\epsilon_0$	$K_t$	$K_p$	$d_{33}$ , pC./N	$g_{33}$ mV·m/N	$Q_M(t)$
0.55	2.25	110	0.6	~0	80	90	4
1.1	0.95	136	0.57	~0	114	94	7
2	0.56	125	0.51	~0	90	80	15
3.2	0.42	160	0.55	~0	85	60	20
4	0.4	170	0.49	0.05	115	76	30
5	0.34	180	0.43	0.05	105	65	40

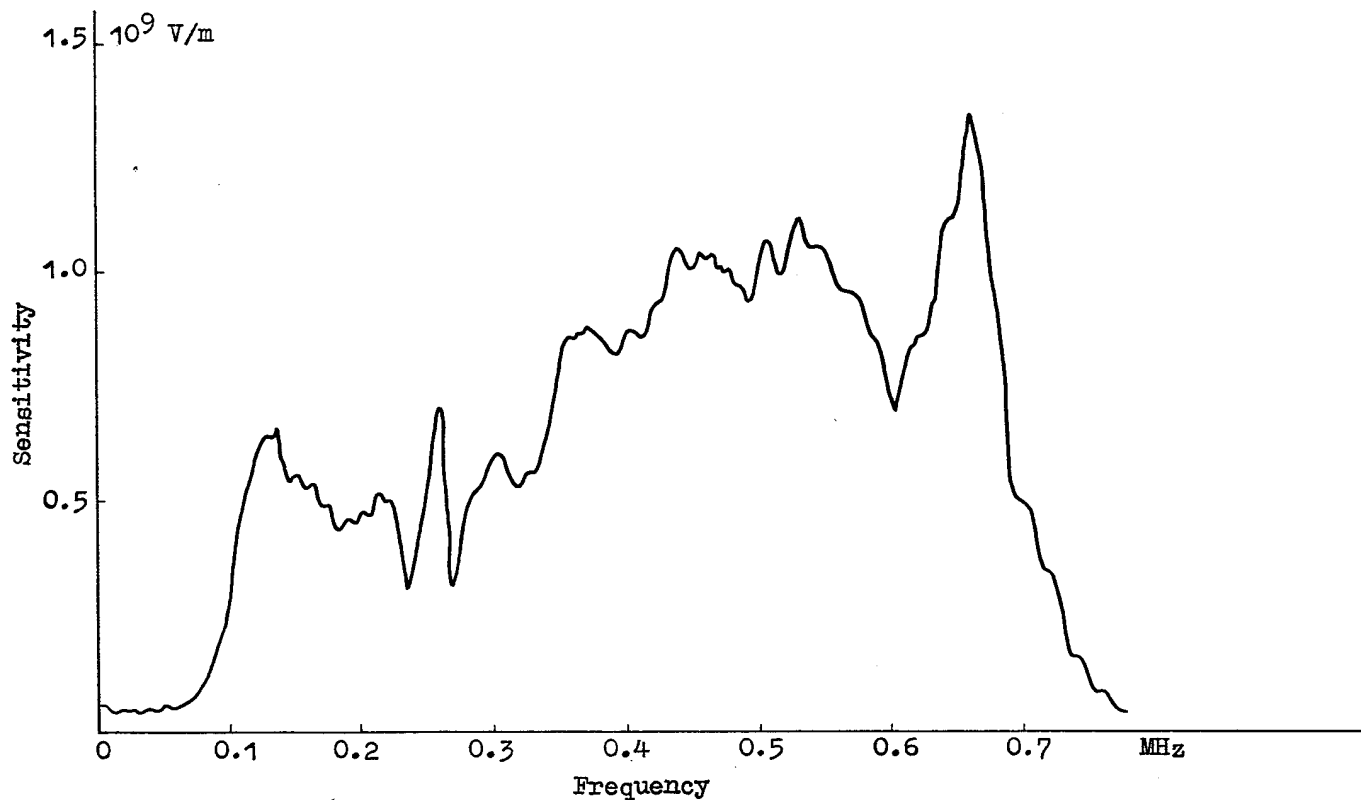


FIGURE 1. Gain-frequency characteristics of the transducer, made of the PCR-70 piezoceramics for the frequency band 0.1 ... 0.7 MHz



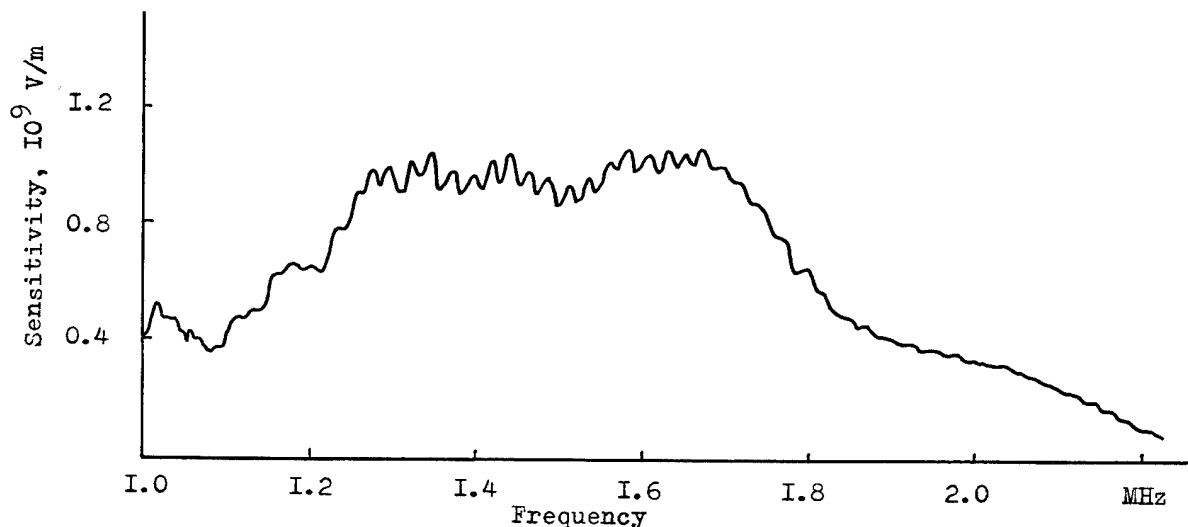


FIGURE 2. Gain-frequency characteristics of the transducer, made of the PCR-70 piezoceramics for the frequency band 1.0 ... 1.8 MHz

upon the magnitude of polarizing field is an important feature of these materials.

There is a non-linear character of dependence of several X-ray structural parameters on increasing polarizing field. These parameters are: the degree of residual 90 domain reorientation, microstrains, coherent dissipation areas. The parameters ( $K_t, K_p, d_{33}, Q_M(t)$ ) and strength non-linearly depend upon polarizing field too. It is due to non-stationarity of forming and growing microcracks 'cause of their interaction with rebuilding domain structure and with the defects (see [1,2]). The investigation of dependence of physical parameters on piezoelement's thickness (see Tab.2) is interest too. The values of  $\epsilon_{33}$  and  $Q_M(t)$  increase when thickness increases.

#### The Transducers' Characteristics

The method of calibration on the massive steel block with damped bounds was used for investigation of the gain-frequency characteristics (GFC) of transducer's sensitivity. The displacement field of set amplitude was obtained in the working zone on the block's surface by the use of wide-band piezoelectric emitter. The transducer to be investigated was moved into the working zone onto the layer of lubricant. The frequency-scanning voltage of the constant amplitude was input to the emitter. The output registered voltage was proportional to the gain-frequency characteristics of transducer's sensitivity. The fact that transducer was loaded to the solid body was an advantage of the calibration technique. This body may be chosen as corresponding to the controlled product by material and geometry. The Fig. 1 and Fig. 2 present the GFC of two variants of transducers, based upon PCR-70 piezoceramics. The operating frequency bands of these transducers are: 0.1...0.7 MHz and 1.2...1.8 MHz. The working temperature range for them is up to 150°C.

#### Summary

Thus, having created the novel class of the anisotropic low-quality piezomaterials helped to solve a series of problems in working up acoustic diagnostic transducers, i.e. the achievement of high sensitivity, the improvement of the gain-frequency characteristics, the achievement of selectivity to certain types of oscillations.

#### References

- [1] L. D. Grineva, V. P. Zatsarinny, V. A. Alyoshin, V. A. Servouli, R. A. Molchanova, "The investigation of the polarizing field influence on strength of anisotropic piezoceramics  $PbTiO_3$ ," *Problemy prochnosti*, No. 4, pp. 34-39, 1993.
- [2] L. D. Grineva, V. A. Alyoshin, V. A. Servouli, V. D. Komarov, E. S. Miroshnichenko, "The electric field influence on the properties of polycrystalline solid solutions based upon  $PbTiO_3$ ," *Izv. AN SSSR, ser. Phys.*, vol. 54, No. 4, pp. 772-775.

# High-Efficiency Ferro-Piezoceramic PCR-Type Materials for Various Applications .

A.Ya. Dantsiger, O.N. Razumovskaja, L.A. Reznitchenko,  
L.D. Grineva, S.I. Dudkina, S.V. Gavril'yatchenko,  
N.V. Dergunova,  
Rostov State University, Institute of Physics,  
Stachki St., 194, Rostov-on-Don, 344104, Russia .

**Abstract** - The piezoceramic materials, possessing the wide variety of properties, have been designed. They may be used effectively in the various fields of science and of technics .

High-efficiency piezoelectric materials with various combinations of parameters are divided into several groups depend on their properties and purposes. These groups are such:

- materials, that are stable to electric and mechanical influences for devices, working in power modes, e.g. ultrasonic emitters, piezoengines, piezotransformers etc;
- materials, having high, medium and low magnitudes of permittivity, applicable for LF, MF and RF transducers correspondingly;
- high-sensitive materials, including anisotropic ones, applicable for accelerometers, defectoscopes, medical diagnostic devices;
- materials, characterized by high stability of resonance frequency, applicable for filter devices;
- materials, characterized by high pyroelectric coefficient, applicable for pyroelectric receivers of radiant (heat) energy;
- materials, characterized by high Curie point, applicable for high-temperature transducers, which are used in atomic energetics and in cosmic technics etc;

The properties of some of groups above listed are described in paper [1]. Nevertheless, the new materials, featured by parameters, close to limit ones, have been obtained recently. These materials promote to improve the characteristics of the corresponding devices .

The hot pressing technique, as well as the traditional ceramic technique are used in making PCR-type materials. The abbreviation PCR means Piezoelectric Ceramics of Rostov .

The most characteristic parameters of listed materials are presented in Tables 1-6. The assessment of these parameters is given too. The ceramics, obtained in last years and not listed in [1], are given essential consideration.

The materials, shown in Tab. 1, are divided into ferrohard, e.g. PCR-8, PCR-77, PCR-78 and midferrohard, e.g. PCR-22, PCR-86. The advantages of PCR-8 and of PCR-22 over industrial-made materials are shown in [1]. Materials, obtained recently, have greater advantages. For example, the PCR-77 and PCR-78 materials have higher piezoelectric parameters and lower dielectric losses in comparison with PCR-88 (see Tab. 1). The advantages of PCR-86 over PCR-22 are of same character. Moreover, PCR-77 and PCR-78 have the top values of Curie point in this group.

It calls forth a fair temperature stability of their piezomoduli. All these advantages promote an opportunity to improve the operating characteristics of power mode devices.

The materials, shown in Tab. 2, are related to two groups. The first one includes the materials with high permittivity, namely, PCR-7M, PCR-73. The second one includes the materials with medium permittivity, namely, PCR-66, PCR-88, PCR-89. They are applicable for LF and MF transducers respectively. The PCR-88 and PCR-89 materials are well-sintered when the traditional ceramic technique is in use.

The materials of 1st group are featured with high magnitudes of piezomoduli, especially PCR-73, which has no industrial-made analogues. Using it in vibroexciting devices of displacement is very efficient.

All the materials of these groups possess very high magnitudes of  $d_{ij}/\sqrt{\epsilon_{33}/\epsilon_0}$  which are proportional to specific sensitivity of of ultrasonic receiver, and excel well-known industrial-made analogues, such as PZT-5H (see [2]), ZTSNW-1, PZT-19 (see [3]).

High-sensitive (see Tab. 3) materials are characterized, first of all, by higher sensitivity to mechanical stress, characterized by g-factor. They may be used with an efficiency in accelerometers, ultrasonic defectoscopes, medical diagnostic devices etc. PCR-1 material combines high  $K_{15}$  (0.7) with enough low magnitude of  $\epsilon_{11}^T/\epsilon_0$ . It's applied in serially made ultrasonic delay lines for coloured TV sets .

The PCR-40, PCR-69 and PCR-70 materials are well-sintered by the hot pressing, as well as by using the traditional ceramic technology . They are featured by high anisotropy of piezoelectric parameters in combination with low permittivity, especially two late, having very low mechanical quality. The given advantages promote improving operational characteristics of indestructive control RF devices and of medical equipment, i.e. they increase sensitivity and resolution.

The materials, shown in Tab. 4, are intended for using them in filters. They are listed in decreasing order of electromechanical coupling factor  $K_p$ , i.e. in order of decreasing the corresponding filter pass band. All these materials have high stability of resonance frequency, excelling native-made analogues . Moreover, most of them have essentially higher mechanical quality, than well-known analogues have . PCR-84 has the highest  $Q_m(12000)$ , that, perhaps, will permit to use it instead of quartz for frequency stabilizing.

The PCR-74 material has high degree of anisotropy of elastic constants ( $C_{44}^D/C_{44}^E=6$ ) and may be used on thickness oscillations with energy capture.

Table 1.  
The parameters of piezoceramic materials, stable to electric influences and mechanical ones.

Material	tc, °C	$\epsilon_{33}^T/\epsilon_0$	K <sub>p</sub>	d <sub>31</sub>  , pC/N	tgδ·100, 50V/cm   1kV/cm		Q <sub>m</sub>
PCR-8	325	1400	0.58	130	0.35	0.70	2000
PCR-77	345	1350	0.62	140	0.30	0.40	1200
PCR-78	350	1250	0.60	130	0.30	0.60	1000
PCR-22	240	2100	0.57	155	0.35	0.90	1800
PCR-86	235	2300	0.60	170	0.35	0.60	1250

Table 2.  
The parameters of piezoceramic materials, with high and medium permittivity

Material	tc, °C	$\epsilon_{33}^T/\epsilon_0$	K <sub>p</sub>	d <sub>31</sub>  , pC/N	d <sub>33</sub> , pC/N	tgδ·100, 50V/cm	Q <sub>m</sub>
PCR-7M	175	5000	0.71	350	760	2.0	60
PCR-73	155	6000	0.70	380	860	2.9	35
PCR-66	280	2800	0.68	245	535	1.2	70
PCR-88	315	2200	0.65	210	470	1.4	70
PCR-89	320	1900	0.67	205	460	1.6	75

Table 3.  
The parameters of high sensitive, including anisotropic, piezoceramic materials

Material	tc, °C	$\epsilon_{33}^T/\epsilon_0$	K <sub>p</sub>	K <sub>t</sub>	d <sub>31</sub>  , pC/N	d <sub>33</sub> , pC/N	g <sub>31</sub>  , mV·m N <sup>-1</sup>	g <sub>33</sub> , mV·m N <sup>-1</sup>	Q <sub>m</sub>
PCR-1	355	650	0.62	0.50	95	220	16.5	38	90
PCR-37	345	1400	0.68	0.46	170	375	13.7	30.3	105
PCR-40	440	180	0.07	0.44	5.0	52	3.2	33	2000
PCR-69	350	170	0.04	0.57	3.5	90	2.3	60	50
PCR-70	324	120	0	0.64	0	114	0	108	8

Table 4.  
The parameters of piezoceramic materials with high stability of resonance frequency

Material	tc, °C	$\epsilon_{33}^T/\epsilon_0$	K <sub>p</sub>	K <sub>t</sub>	δf <sub>0</sub> /f <sub>r</sub> , %(-60÷85 °C)	tgδ·100, 50V/cm	Q <sub>m</sub>
PCR-21	310	1400	0.53	0.45	≤ 0.25	0.7	300
PCR-74	365	850	0.52	0.47	≤ 0.20	1.6	400
PCR-63	235	1170	0.37	0.38	≤ 0.15	2.0	1100
PCR-80	310	800	0.36	-	≤ 0.25	0.6	4000
PCR-62	300	660	0.32	0.35	≤ 0.15	1.4	2700
PCR-28	325	600	0.28	-	≤ 0.25	0.5	2000
PCR-83	360	400	0.26	-	≤ 0.15	0.6	4000
PCR-84	360	180	0.10	0.25	≤ 0.15	0.2	12000

\* The measures were carried out by thickness mode

Table 5.  
The parameters of piezoceramic materials with low permittivity

Material	tc, °C	$\epsilon_{33}^T/\epsilon_0$	K <sub>p</sub>	K <sub>45</sub> (K <sub>s</sub> )	d <sub>31</sub>  , pC/N	Q <sub>m</sub>	V <sub>R</sub> , km/sec
PCR-53	240	260	0.20	(0.16)	16	4500	4.20
PCR-3	280	350	0.38	-	37	2000	3.95
PCR-20	315	510	0.54	0.72	70	700	3.6
PCR-35	370	120	0.22	0.31	12	1000	5.90
PCR-34	420	460	0.42	0.60	45	150	5.40

Table 6.

The parameters of high temperature piezoceramic materials

Material	$t_c$ , °C	$t_{work}$ , °C	$\epsilon_{33}^T/\epsilon_0$	$K_p$	$K_t$	$d_{33}$ , pC/N	$Q_m$
PCR-26	400	300	455	0.32	—	90	200
PCR-45	420	350	380	0.26	0.46	100	3000
PCR-40	440	350	180	0.07	0.44	52	2000
PCR-50	670	500	150	0.04	0.32	25	4000
PCR-61	1200	950	48	0.015	0.29	12	100

The most of this group's materials are sintered by the traditional ceramic technology.

The group of ceramics represented in Tab. 5 is intended for use in RF acoustic-electric transducers. The value of sonic speed for PCR-35 and for PCR-34 is 1.5 times greater than for other ones. It allows one to simplify RF element making technology. Besides that, the low values of their densities promote using them in devices, strongly dependant on weight characteristics.

When using materials in ultrasonic delay lines on bulk waves the high  $K_{15}$  factor is of great importance at relatively low  $\epsilon_{11}^T/\epsilon_0$  and  $Q_m$ . The PCR-20 and PCR-34 possess mentioned combination of parameters. The PCR-53 has the best combination of parameters for devices on surface acoustic waves (SAW), 'cause it has low temperature dependence factor ( $50 \cdot 10^{-6} K^{-1}$ ) and high  $K_s$ . The most of materials, belonging to the group under consideration have high pyrocoefficients  $\gamma$  and  $\gamma\epsilon_0/\epsilon_{33}^T$  factors, proportional to the Volt-Watt sensitivity of pyroreceiver. The use of one of them (PCR-3) instead of the industrial-made material has increased the sensitivity and fast response of pyroreceiver two times.

High temperature materials (see Tab. 6) are featured by high magnitudes of Curie points and of working temperatures. They may be used with an efficiency for indestructive control of heated bodies, for control indicators of processes, occurring in various industrial energetics plants, and in other high temperature devices. The materials are listed in increasing order of their Curie temperatures. They all have fallen or low magnitudes of permittivity, that makes them fit for use in RF devices. The PCR-40, PCR-50 and PCR-61 possess high anisotropy of piezoelectric parameters, which promotes depressing undesirable oscillations. The material, named PCR-61 ( $T = 1200^\circ C$ ) has the top working temperature and extremely low permittivity. It excels the native-made analogues TNW-1 by all the parameters. PCR-61 may be used as a base of high-precision generator type piezoindicators of rapidly changing pressure for systems, controlling objects at extreme external influences ( $t > 950^\circ C$ ,  $p > 200$  MPa).

#### References

- [1] E.G. Fesenko, A.Ya. Dantsiger, O.N. Razumovskaja, *New Piezoceramic materials*. Rostov-on-Don: Izd. RGU, 1983.
- [2] G. Jaffe, D.A. Berlincourt, "Piezoelectric materials for transducers," *TIIER*, vol. 53, No. 10, pp. 1552-1567, 1965.
- [3] "Piezoceramic materials. Technical conditions," *OST 11 0444-87*, group E10, January 1, 1988.

# Piezoceramic Materials for Filters With Large Guaranteed Decay

A.Ya. Dantsiger, S.V. Gavril'yatchenko  
Rostov State University, Institute of Physics,  
Stachki St., 194, Rostov-on-Don, 344104, Russia .

**Abstract** - The ferroelectric materials PCR-62, PCR-63 for narrow-band and midband filters with large guaranteed decay have been obtained.

The high ratio of static capacities  $C_2/C_1 \approx 20$  of piezoelements for arms of stepwise filter scheme is required for making filters with large guaranteed decay.

The  $C_2/C_1$  ratio may vary at the expense of changing both dimensions of piezoelements as permittivities  $(\epsilon_{33})_1$  and  $(\epsilon_{33})_2$ .

The significant difference between permittivities must permit to obtain the needed ratio at lower differences of element's dimensions. It would simplify the filters construction, i.e. would decrease dimensions and the number of piezoelements. Besides that, the material with less  $(\epsilon_{33})_1$  should possess greater factor of electromechanical coupling factor  $(K_p)_1$ . This requirement is dictated by the fact that the element of material with less  $\epsilon_{33}/\epsilon_0$  must have significantly less diameter of one of electrodes to obtain

minimum capacity. It causes the fall of relative resonance range  $\Delta f_r/f_r$ , i.e. causes lessening  $K_p$ . But the combination of less  $\epsilon_{33}/\epsilon_0$  of filter material with greater  $K_p$  is hardly attainable.

It was shown (see [1]) that solid solutions (SS) on the Pb zirconate-titanate (PZT) with high temperature stability of resonance frequency ( $f_r$ ) belonged to tetragonal phase on phase diagram. The analysis of concentrational dependance of relative change of resonance frequency of radial oscillations in operating temperature interval, which characterizes the stability of  $f_r$  showed that in T-phase the region of SS referred to was at distance of 5-10 mol.% of  $PbTiO_3$  from the morphotropic region (MR).

The decrease of permittivity is accompanied by the fall of  $K_p$  as the distance from MR increases. It is also confirmed by thermodynamic correlation  $K_p \sim \sqrt{\epsilon_{33}} \cdot P_r$ .

The parameters of worked up materials are presented in Table 1.

Table 1.  
The parameters of piezoceramic materials PCR-62, PCR-63, PCR-13M .

Material	$\epsilon_{33}^T / \epsilon_0$	$K_p$	$Q_M$	$\delta f_\theta / f_r, \%$
PCR-62 TT, $T_s=1120^\circ\text{C}$	600	0.30	2000	0.13
PCR-63 TT, $T_s=1200^\circ\text{C}$	900	0.22	1000	0.17
PCR-63 HP, $T_s=1260^\circ\text{C}$	1170	0.37	1100	0.13
PCR-13M TT, $T_s=1140^\circ\text{C}$	800	0.40	1900	0.25

The optimum magnitudes for pair of materials PCR-62 and PCR-63 are obtained by according to traditional ceramic technology (TT). The sintering temperatures are  $1120^\circ\text{C}$  and  $1200^\circ\text{C}$  respectively for each material.

The mentioned materials have the 1.5 times distinction in  $\epsilon_{33}/\epsilon_0$  magnitude. The greater magnitudes of  $K_p$  correspond to less  $\epsilon_{33}/\epsilon_0$ . These materials are applicable for narrow-band filters.

The couple of materials PCR-63 / PCR-13M possesses the optimum parameters combination when sintering PCR-13 by TT ( $T=1260^\circ\text{C}$ ) and when sintering PCR-64 by hot pressing (HP) ( $T=1140^\circ\text{C}$ ). The fall of  $K_p$  down to 0.2-0.25 for PCR-62 is attained by polarization conditions: the field falls down to  $\sim 1\text{kV/mm}$ , the polarizing time is equal to 25 min,

whereas optimum mode is of following kind:  $E_{p01} \approx 3.5\text{ kV/mm}$ ,  $t_{p01}=40\text{ min}$ . It should be noted that  $\epsilon_{33}/\epsilon_0$  of specimens, polarized at such the regimes is less by about 10% than  $\epsilon_{33}/\epsilon_0$  at maximum polarization.

The materials obtained have also high magnitudes of mechanical quality and a small variety of resonance frequency values in the temperature range of  $-20^\circ\text{C}$  to  $85^\circ\text{C}$ .

## References

- [1] E.G. Fesenko, A.Ya. Dantsiger et al. "The investigation of complex oxides," *Izv. AN SSSR, Ser. Neorgan. Mater.*, vol. 16, pp. 2247-2250, 1980, in Russian.

# On the Specific Features of Anisotropy in Piezoelectric Properties of High-Temperature Ferroelectric Ceramics .

L.A. Reznitchenko and E.I. Bondarenko  
Rostov State University, Institute of Physics,  
Stachki St., 194, Rostov-on-Don, 344104, Russia .

**Abstract** - The most known representatives of ferroelectric ceramics(FC) with very different values of piezoelectric coefficients for different types of vibrations ,i.e., with a high degree of their anisotropy are the compositions based on lead titanate(PT) . Recently, it has been found that other FC compounds and their solid solutions belonging to the structural families other than PT: Ba- and Pb niobates(tetragonal-tungsten-bronze type), Bi titanates and niobates(layered perovskite-like), Li niobate and tantalate (pseudoilmenites) also possess a pronounced anisotropy in piezoelectric properties (PPA) . All of these compounds have the same high value of the Curie point temperature( $T_c$ ): with increasing the latter there is a tendency of PPA to increase, especially at  $T > T_c = 400^\circ\text{C}$ . It was shown that such a variation in PPA is due to the absence of low-temperature phase transitions in the FE region in corresponding compositions and, as a result, the decreased anisotropy in dielectric properties(DPA). Using the thermodynamic approach to the connection between PPA and DPA and the phase state of FC was considered.

ferroelectric ceramics(FC) with very different values of piezoelectric coefficients for different types of vibrations ,i.e., with a high degree of their anisotropy are the compositions based on lead titanate(PT) . Recently, it has been found that other FC compounds and their solid solutions (SS) belonging to the structural families other than PT:Ba- and Pb niobates(tetragonal - tungsten - bronze-type), Bi titanates and niobates( layered perovskite-like), Li niobate and tantalate (pseudoilmenites)) also possess a pronounced anisotropy in piezoelectric properties (PPA). All of these compounds have the same high value of the Curie point temperature( $T_c$ ): with increasing the latter there is a tendency of PPA to increase, especially at  $T > T_c = 400^\circ\text{C}$ . The piezomoduli ratio  $d_{33}/d_{31}$  is a main criterion characterizing this behaviour. The rare (by the 1st order) increasing PPA near  $400^\circ\text{C}$  is observed too . These tendencies must reflect an obvious correlation between the structure of compounds(and their SS) and  $T_c$ . The analysis of structural types (see Table ) has shown that decrease of symmetry of paraelectric(PE) phase is observed as  $T_c$  falls. The absence of phase transitions in

The most known representatives of

Table 1

The change of spatial symmetry at phase transitions in compounds to be studied.

FE-phase		PE-phase
LiNbO <sub>3</sub>	Li niobate(LN)	
Trigonal R3c(=c <sub>3v</sub> )	1210 °C	Trigonal R3c(=D <sub>3d</sub> <sup>6</sup> )
Bi <sub>4</sub> Ti <sub>3</sub> O <sub>12</sub>	Bi titanate(BT)	
Rhombic F <sub>mm</sub> 2(=c <sub>2v</sub> <sup>18</sup> )	675 °C	Tetragonal 4/mmm(=D <sub>nn</sub> )
PbNb <sub>2</sub> O <sub>6</sub>	Lead mataniobate(PMN)	
Rhombic C <sub>mm</sub> 2(=c <sub>2v</sub> <sup>11</sup> )	570 °C	Tetragonal P4/mbm
PbTiO <sub>3</sub>	Lead titanate(PT)	
Tetragonal P4 <sub>mm</sub> (=c <sub>4v</sub> <sup>4</sup> )	490 °C	Cubic Pm <sub>3m</sub> (=O <sub>n</sub> <sup>4</sup> )

the range from  $T_c$  down to room temperature follows from this correlation. The last fact is confirmed by dependance of permittivity  $\epsilon_{33}/\epsilon_0$  of ceramics upon  $T_c$ : at  $T_c \leq 400^\circ\text{C}$  (the region of faint PPA) the values of  $\epsilon_{33}^T/\epsilon_0$  are greater by the 1st order than ones at  $T \gg 400^\circ\text{C}$ . Initially the increase of  $T_c$  implies sharp fall of  $\epsilon_{33}^T/\epsilon_0$ , then this increase leads to its smooth small (from  $\sim 200$  down to 50) decrease in the high-temperature (h.t.) region. This behaviour of  $\epsilon_{33}^T/\epsilon_0$  is in concordance to thermodynamic principles, in assumption that there are no phase transitions in FE-phase at temperatures  $400^\circ\text{C}$ . The large value of  $\epsilon_{33}^T/\epsilon_0$  at  $T_c \leq 400^\circ\text{C}$  is probably due to low-temperature phase transitions, namely, rhombic(R), rhombohedral(RH) in lead zirconate-titanate (PZT) and tetragonal(T) in Ba-Pb-titanate(BT). As it is noted in [1] when investigating the BT monocrystals, such transitions are accompanied by orientation of spontaneous polarization vector  $P_s$  and by abrupt growth of  $\epsilon_{11}$ -component of permittivity, perpendicular to polar axis at relatively small change of  $\epsilon_{33}$ , directed along the polar axis, i.e. by observable anisotropy of dielectric properties  $\epsilon_{11}/\epsilon_{33}$  (DPA). The absence of low-temperature phase transitions in compounds with  $T_c \gg 400^\circ\text{C}$  probably causes the small values of  $\epsilon_{33}^T/\epsilon_0$  and of DPA that conforms to the conclusion of authors of paper [2] on the reasons of the small permittivity in the PT-crystals. That's why one may suppose that in FC with  $T_c \gg 400^\circ\text{C}$  the faint DPA, caused by the absence of phase transition in FE region may cause the large PPA.

To consider the contribution of DPA in forming PPA let us express the ceramics' piezomoduli  $d_{ijk}$  in the terms of monocrystal's piezomoduli  $d_{ijn}$ . The simplest way to do it is using the method of averaging by all possible orientations of crystals:

$$d_{ikk}^* = \int_0^{2\pi} \int_0^{2\pi} \int_0^\pi d\theta d\psi d\varphi \sin\varphi f(\varphi) \alpha_{ij} \alpha_{kl} \alpha_{kn} d_{ijn}$$

$f(\varphi)$  here is a difference of distribution of polar axes of crystals,  $\alpha_{ij}$  are direction cosines. If we consider only  $180^\circ$  reorientations of domains induced by polarizing field then it will be possible to obtain the distribution function as being of such kind:

$f(\varphi) = 2$  if  $0 \leq \varphi \leq \varphi_0$ ;  $f(\varphi) = 1$  if  $0 \leq \varphi \leq \pi - \varphi_0$ ;  $f(\varphi) = 0$  if  $\pi - \varphi_0 \leq \varphi \leq \pi$ . It is valid both for uniaxial FC having no  $90^\circ$  reorientations and for multiaxial ones in which the portion of these reorientations is small. In this case we have

$$\begin{aligned} d_{31}^* &= d_{31} P(1-aP), \\ d_{33}^* &= d_{33} P(1-bP) \end{aligned} \quad (1)$$

In (1)  $a = (d_{33} - d_{31} - d_{15}) / (-2d_{31})$ ;  $b = a - (2d_{31} / d_{33})$ ;  $P = P^* / P_s$  where

$P^* = P_s \int_0^{2\pi} \int_0^{2\pi} \int_0^\pi d\theta d\psi d\varphi \sin\varphi f(\varphi) d_{33} = 0.5P_s (1 - \cos^2 \varphi_0)$ ;  $P_s$  is a spontaneous polarization,  $P$  characterizes the degree of polarizability of specimen and is minimum when  $P = 0.5P_s$  and  $P = 0.5$  that corresponds to 100% reorientation. According to (1) the piezomoduli's dependance on  $P$  is

non-monotonous: when  $P$  increases the values of  $d_{31}^*$  and of  $d_{33}^*$  increase achieving the maximum values at  $P = 0.5/a$  and  $0.5/b$  then decrease and become equal to zero at  $P = 1/a$  and  $P = 1/b$ . The existing difference between the values of  $a$  and  $b$  defines the specifics of the behaviour of the piezomoduli in any case. In TB  $a$  and  $b$  are negative ( $a = -3.9, b = -3.2$ ) and this leads only to increase of  $d_{31}^*$  and of  $d_{33}^*$  as the degree of polarization of specimen increases. In PT both these values are positive ( $a = 2.5, b = 0.8$ ). That's why  $d_{31}^*$  and  $d_{33}^*$  fall after initial growth until the maximums at  $P = 0.5/a = 0.2$  and  $P = 0.5/b = 0.625$  down to zero at  $P = 0.4$  and  $P = 1.25$ . So far as  $P$  cannot be greater than 0.5  $d_{33}^*$  will increase as polarization increases whereas  $d_{31}^*$  having achieved maximum at realization of 40% of all  $180^\circ$  reorientations becomes equal to zero in the region of enough strong polarizing fields, providing 80% of all  $180^\circ$  switchings, i.e. when almost all possible switchings have been finished (the portion of  $90^\circ$  of them is faint in the PT) [3]. Such a dependence of  $d_{31}^*$  upon the degree of specimen's polarization completely fits the experimental data on PT-based ceramics. On assigning  $d_{33} = 2Q_{33}P_s\epsilon_{33}\epsilon_0$ ,  $d_{31} = 2Q_{31}P_s\epsilon_{33}\epsilon_0$ ,  $d_{15} = Q_{55}P_s\epsilon_{11}\epsilon_0$ ,  $\epsilon_{33}^* = (\epsilon_{33} + 2\epsilon_{11})/3$  in (1) where  $Q_{ik}$  are electrostrictive constants,  $\epsilon_{33}$  is an averaged ceramics' permittivity we obtain

$$\begin{aligned} a &= (Q_{33} - Q_{31} - 0.5Q_{55}\epsilon_{11}/\epsilon_{33}) / (-2Q_{31}) \quad (3) \\ d_{31}^*/d_{33}^* &= 0.75\epsilon_{33}^*PQ_{55} - \epsilon_{33}[P(Q_{33} - Q_{13} + 0.25Q_{55}) + 2Q_{31}] \end{aligned}$$

Since  $\epsilon_{33}$  changes faintly at transitions from one type of ceramics to another one, i.e. at changing  $T_c$  in comparison with  $\epsilon_{33}$ , for example, in the monocrystals of BT  $\epsilon_{33} = 160$ , in PT  $\epsilon_{33} = 115$ , in lead metaniobate (PMN)  $\epsilon_{33}$  is equal to 130, in Li niobate  $\epsilon_{33} \approx 30$  then, according to (2) it is expectable that dependence  $d_{31}^*(T_c)$  will be defined in the whole by the dependence  $\epsilon_{33}(T_c)$ . Indeed, there is a correlation between dependences referred to, which leads to linear dependence  $d_{31}^* \sim \epsilon_{33}^*$  in the complete accordance with (3). Consequently, it is necessary to decrease  $\epsilon_{33}$  in order to attain faint, close to zero magnitudes of  $d_{31}^*$ . The magnitude of latter is defined, first of all, by the DPA: the greater  $\epsilon_{11}$  in comparison with  $\epsilon_{33}$  (the stronger DPA) the greater  $\epsilon_{33}^*$  in comparison with  $\epsilon_{33}$  (see (2)) and the greater  $d_{31}^*$  (see (3)) and, thus, the less DPA. That's why in the region  $T_c \gg 400^\circ\text{C}$ , where the values of  $\epsilon_{33}$  are small, one may expect the small values of  $d_{31}^*$ , and as a result the large DPA. The threshold value of  $\epsilon_{33}$  exists and is equal to 250. It means that the faint difference between  $\epsilon_{33}^*$  and  $\epsilon_{33}$  would be available for appearance of PPA observable, i.e. as it follows from (2) the small DPA is needed. The analysis of expression (3) with an account of (1) has shown that it's necessary to conform to condition  $a > 1$ , possible at small value of  $\epsilon_{11}/\epsilon_{33}$ . When increasing the DPA the value of  $a$  becomes negative (as for BT), that is followed by increase of  $d_{31}^*$  and decrease of PPA. Thus, the low DPA, being usual for materials with high  $T_c$  may lead to high PPA because of absence of phase transitions for these materials in FE region of states.

# References

- [1] F. Iona, D. Shirane, *Ferroelectric crystals*, Moscow: Izd. Mir, 1965.
- [2] A.V. Turik, N.V. Shevchenko, S.V. Gavril'yatchenko, E.G. Fesenko, "On the nature of dielectric permittivity of  $\text{PnTiO}_3$  single-crystals," *Phys. Status Solidi*, vol. 94, No. 2, pp. 525-528.
- [3] A.D. Feronov, V. V. Kuleshov, V.P. Dudkevich, E.G. Fesenko, "The properties of dense chemically pure  $\text{PbTiO}_3$  ceramics," *Journal Technicheskoy Fiziki*, vol. 50, No. 3, pp. 630-632, in Russian.



# The Origins of Electromechanical Response in Polyurethane Elastomers

H. Wang, Q. M. Zhang, L. E. Cross, R. Ting\*, C. Coughlin\*, and K. Rittenmyer\*

Materials Research Laboratory  
The Pennsylvania State University  
University Park, PA 16802

\* Underwater Sound Reference Detachment  
Naval Research Laboratory  
Orlando, FL 32856

**Abstract** --- Electric-field-induced strains of polyurethane elastomers have been measured. The mechanical constraints and flexure motion of the samples which can cause large experimental error were excluded from the measured strain signals. The longitudinal and transverse strain coefficients are evaluated as functions of frequency. The dielectric and elastic properties and their temperature and frequency dependencies have also been studied. The experimental results show that strain larger than 2% can be obtained and that the sample processing conditions can affect the strain level. The contributions from Maxwell stress effect and electrostriction to the strain responses are examined. The results suggest that Maxwell stress effect plays an important role in electromechanical response of the materials.

## INTRODUCTION

Piezoelectric polymers such as polyvinylidene fluoride (PVDF) and its copolymers with trifluoroethylene (TrFE) have been widely utilized in transducers and electromechanical devices [1-3]. These polymers possess several merits over inorganic ceramics. For example, they have high piezoelectric voltage constants ( $g$ ) and low density, and they are flexible and easy to be made. However, the low piezoelectric strain coefficients ( $d$ ) [4] and low electromechanical coupling constants [5] of these piezoelectric polymers are undesirable in some applications. Recently, it has been found that large electric field induced strain and a large  $d$  constant can be obtained in polyurethane elastomers. The quadratic relationship between induced strain and applied field indicates that the effect may originate from electrostriction and/or Maxwell stress effect. In this paper, the dielectric and elastic properties and electric-field-induced strain responses of polyurethane elastomers will be presented. Using thermodynamic relationships relating the strain to dielectric constant, elastic constant, and the electrostrictive coefficients, the contributions from Maxwell stress effect and electrostriction are examined. The results suggest that Maxwell stress effect plays an important role in electromechanical response of the materials.

## EXPERIMENTAL DETAILS

### Sample Preparation

Two different polyurethanes, 2103-80AE and PE193, were employed for this study. The 2103-80AE samples were prepared by casting and injection molding, and the PE193 samples were prepared by casting and calendering. Both 2103-80AE and PE193 are polyurethane block copolymers consisting of soft segment and hard segment. All samples together with processing methods and sample thicknesses are tabulated in Table I.

Table I Processing conditions and sample thickness of polyurethanes

Sample	Processing Condition	Thickness (mm)	Symbol
2103-80AE	Casting	0.153	80CF-1
	(filtered)	0.65	80CF-2
	Casting	0.184	80CN-1
	(nonfiltered)	1.30	80CN-2
	Injection Molding	1.70	80IM-1
PE193	Calendering	0.69	193CD-1
	Casting	0.93	193CT-1

Samples were cut into different sizes for various measurements. For longitudinal strain measurement, the area of the samples was

limited to less than  $3 \times 5 \text{ mm}^2$  to avoid flexure motions, and for transverse strain measurement, the length to width ratio of the samples was greater than 6.

### Strain Measurement

A laser interferometer was used to measure electric-field-induced strains of the polyurethanes. Because polyurethane elastomers were elastically much softer than PVDF and ceramics and some samples were made into very thin films to achieve a high electric field level, great care must be taken in the strain measurements of polyurethanes to ensure the accuracy of the data. For such soft film-like materials flexure motion and mechanical clamping of a sample are two major causes of the errors in the strain measurements by a laser interferometer. To exclude bending motions from measured displacements, we used the interferometer in double-beam form. By adjusting two probing spots of the laser beams at the same position on two opposite surfaces of a sample, the error caused by flexure motion can be eliminated. All strain measurements were repeated at different positions of a sample to further assure no bending effect was included in the results. To avoid mechanical clamping, a careful sample mounting is needed. Sample mountings for longitudinal and transverse displacement measurements are shown in Figs. 1 (a) and (b), respectively. For longitudinal measurement, the bonding length on the bottom edge of a sample was limited to less than one seventh of the whole length of the edge, while for the transverse measurement, the bonding area was limited to less than one tenth of the whole area of a sample. In this way, samples were considered almost mechanical free in response to a driving field.

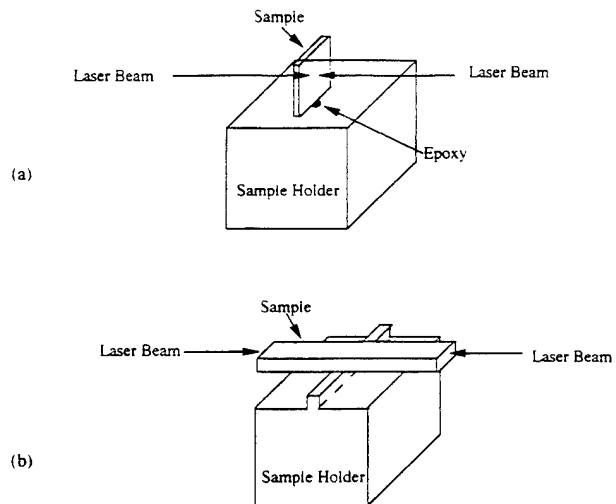


Fig. 1 Sample mounting for strain measurement.  
(a) longitudinal; (b) transverse.

The data of strain measurements can also be affected by resonance of the sample. The occurrence of resonance in a sample strongly depends on sample dimension, sample mounting (boundary condition) and driving frequency. Near resonance frequencies, the amplitude of the displacement increases rapidly, forming a peak, while the phase angle shifts  $180^\circ$ . By a proper sample-mounting, most of the resonance peaks were eliminated. In all measurements of the strain coefficients, a frequency scan was first carried out to ensure the

measuring frequencies were far away from sample resonance peaks to avoid this error.

### Dielectric Property Measurement

Dielectric constant ( $K$ ) and loss tangent ( $D$ ) of the polyurethane elastomers were measured by a Multi-Frequency LCR Meter (Hewlett Packard 4274A) (1-100 kHz) and an Impedance Analyzer (Hewlett Packard 4194A) (100 Hz-10MHz). The change of sample capacitance under hydrostatic pressure were measured by a high precision capacitance bridge (General Radio, Model 1616) while the samples were placed in a high pressure chamber.

## RESULTS

### Dielectric and Elastic Properties

Room temperature dielectric constants and loss tangents of all polyurethane samples measured at 1 kHz are summarized in Table II. Polyurethanes are polar in nature and are, to certain degree, hydrophilic which results in the absorption of moisture when exposed to the atmosphere. The moisture content of a sample strongly affects its dielectric properties, including both dielectric constant and loss tangent, and this effect becomes more significant with the decrease of frequency. The results presented in Table II were acquired on samples dried in a desiccator for more than 48 hours.

Table II Room temperature dielectric and elastic properties

Sample	K	D	Y ( $\times 10^7$ Pa)	$\tan \delta$	$s_{11}$ ( $\times 10^{-8} \text{ m}^2/\text{N}$ )
80CF-1	5.9	0.0300			
80CF-2	6.58	0.0383	2.97	0.10	3.37
80CN-1	6.5	0.0322			
80CN-2	6.17	0.0339			
80IM-1	6.30	0.0307	1.74	0.10	5.75
193CD-1	5.63	0.0335	0.98	0.114	10.2
193CT-1	5.63	0.0315			

Shown in Fig. 2 are dielectric constants and losses of 80CF-1 as functions of temperature at frequency 1, 10, and 100 kHz. Similar results were obtained for 80CN-1. From the results, it can be seen that the glass transition is around  $-15^\circ\text{C}$  for both filtered and non filtered samples. The room temperature dielectric properties of 80CF-1 as functions of frequency are depicted in Fig. 3.

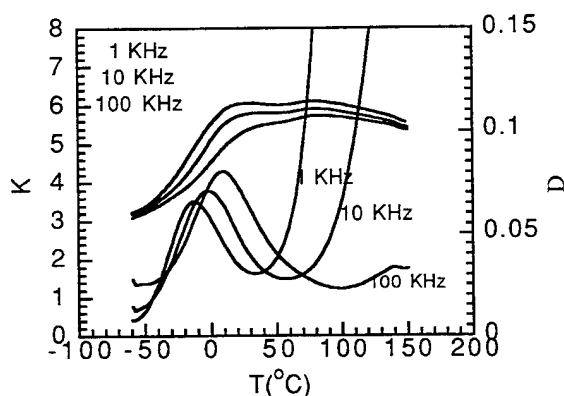


Fig. 2 Temperature spectra of the dielectric properties of 80CF-1

The temperature and frequency dependencies of Young's modulus of 80IM-1 are presented in Figs. 4 and 5, respectively. Listed in Table II are also Young's modulus  $Y$ , loss tangent  $\tan \delta$  and elastic compliance  $s_{11}$  ( $= 1/Y$ ) of these samples measured at room temperature ( $25^\circ\text{C}$ ).

### Strain Coefficients

Using the double-beam laser interferometer, strain-field

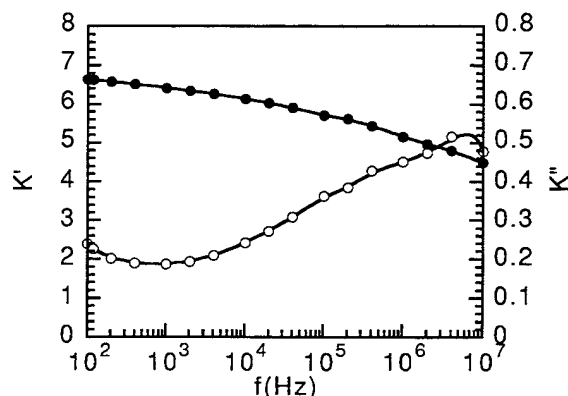


Fig. 3 Room temperature frequency spectra of the dielectric properties of 80CF-1

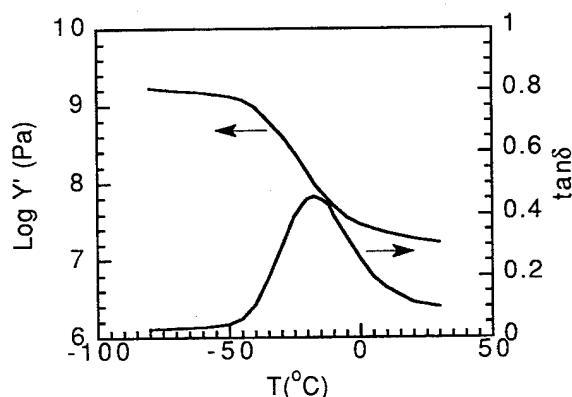


Fig. 4 Temperature spectra of the Young's modulus of 80IM-1

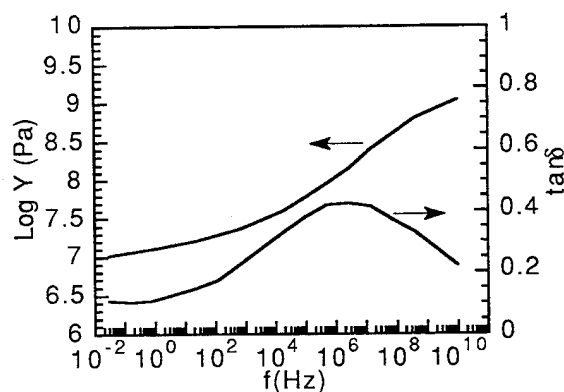


Fig. 5 Frequency spectra of Young's modulus of 80IM-1

relationship was explored on all samples listed in Table I including both longitudinal and transverse effects. Typical quadratic curves were obtained. Illustrated in Figs. 6 (a) and (b) are longitudinal and transverse strain responses to the driving fields of 80CN-1 and 193CD-1, respectively. As seen from the results, strains are proportional to the square of the driving electric field as follows:

$$x_3 = R_{33} E_3^2 \quad (1a)$$

$$x_1 = R_{13} E_3^2 \quad (1b)$$

where direction 3 is perpendicular to the sample surface and direction 1 is parallel with the sample surface.

Longitudinal and transverse strain coefficients  $R_{33}$  and  $R_{13}$  of all samples determined by Eqs. (1a) and (1b) are tabulated in Table III.

Table III Longitudinal and transverse strain coefficients of polyurethanes measured at room temperature and 50 Hz

Sample	Thickness (mm)	R <sub>33</sub> (x10 <sup>-18</sup> m <sup>2</sup> /V <sup>2</sup> )	R <sub>13</sub> (x10 <sup>-18</sup> m <sup>2</sup> /V <sup>2</sup> )
80CF-1	0.153	-1.16 (83 Hz)	
80CF-2	0.65	-0.90	0.43
80CN-1	0.184	-3.78	
80CN-2	1.30	-0.90	0.44
80IM-1	1.70	-1.96	0.52
193CD-1	0.69	-4.5	0.95
193CT-1	0.93	-2.64	1.20

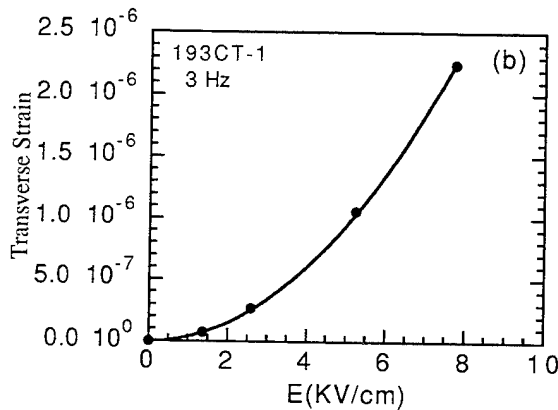
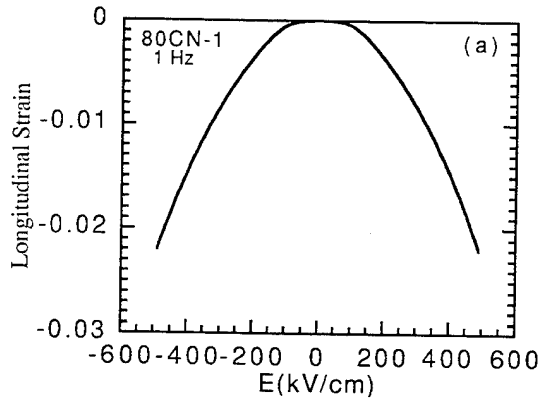


Fig. 6 Strain response to a driving field. (a) longitudinal; (b) transverse.

All coefficients were measured at room temperature and a frequency of 50 Hz unless otherwise noted. For the convenience of discussion, the sample thicknesses are also listed. As seen from the table, the strain coefficients of polyurethanes depend upon the composition, the processing condition, and sample thickness. For 80CF and 80CN samples, longitudinal coefficient R<sub>33</sub> increases remarkably when sample thickness decreases.

#### Frequency Dependence of R<sub>33</sub> and R<sub>13</sub>

Coefficients R<sub>33</sub> and R<sub>13</sub> as functions of frequency are depicted in Fig. 7 for cast samples and in Fig. 8 for injection-molded and calendered samples, respectively. As can be seen from the diagrams, both longitudinal and transverse R constants are strongly frequency dependent. Over the corresponding frequency range, transverse coefficients R<sub>13</sub> are approximately half of the longitudinal coefficients for all cast samples, while for injection-molded and calendered samples they are significantly less than half of the corresponding longitudinal coefficients.

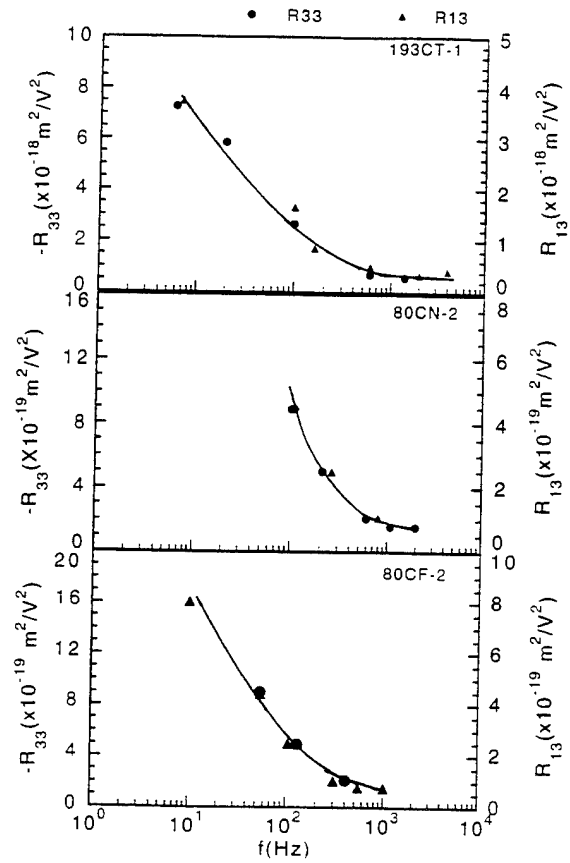


Fig.7 Frequency dependence of strain coefficients of three cast samples

#### Hydrostatic Properties

Under hydrostatic pressure, the capacitance (C) of a parallel-plate capacitor varies due to the converse effect of electrostriction and the change of its dimensions. For soft materials like polyurethanes, the change of capacitance caused by the sample dimension change under hydrostatic pressure can be quite significant. This capacitance change is related to electrostriction coefficient and elastic constants as follows:

$$\frac{1}{C} \frac{\partial C}{\partial p} = -2\epsilon_0 K_{33} Q_h - (s_{11} + 2s_{12}) \quad (2)$$

where p is hydrostatic pressure, Q<sub>h</sub> is the hydrostatic electrostriction constant of the material. For polyurethane elastomers studied here it is reasonable to assume that the Poisson's ratio  $\sigma_{12} = -\frac{s_{12}}{s_{11}}$  is 0.5 for isotropic materials. Under this condition, Eq. (2) can be further simplified into:

$$\frac{1}{C} \frac{\partial C}{\partial p} = -2\epsilon_0 K_{33} Q_h \quad (3)$$

For a material with symmetry of point group 422, the expression of the relative change of the capacitance is:

$$\frac{1}{C} \frac{\partial C}{\partial p} = -2\epsilon_0 K_{33} Q_h + (s_{33} - 2s_{11} - 2s_{12}) \quad (4)$$

The change of capacitance with hydrostatic pressure were measured for 80CF-1 and 193CD at 100 Hz. The values of relative change of capacitance with hydrostatic pressure of 80CF-1 and 193CD-1 are  $1.95 \times 10^{-10} \text{ m/N}^2$  and  $2.48 \times 10^{-9} \text{ m/N}^2$ , respectively. 80CF-1 was made by casting, while 193CD was made by calendering. Therefore, 80CF-1 is mechanically isotropic, while 193CD may possess, to certain degree, mechanical anisotropy in the

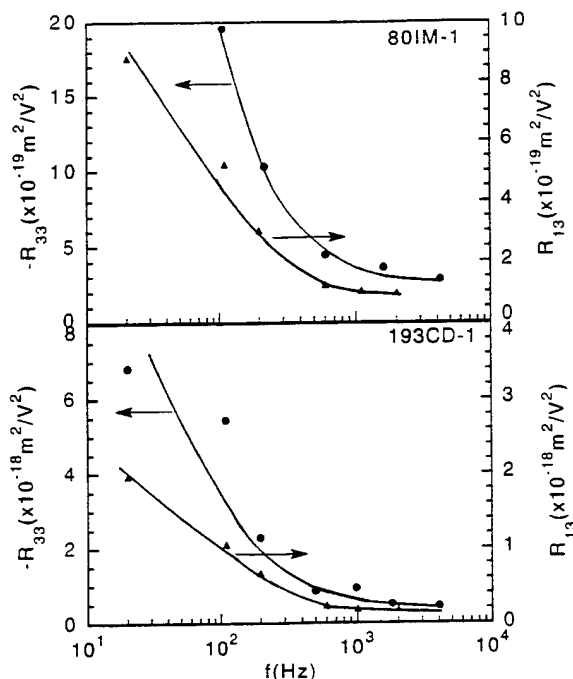


Fig. 8 Frequency dependence of strain coefficients of injection molded and calendered samples

direction normal to the sample surface, or the symmetry 422. Using Eq. (3), the hydrostatic electrostriction coefficient ( $Q_h$ ) of 80CF-1 is  $-1.64 \text{ m}^4/\text{C}^2$ . Assuming the same electrostriction constant for 193CD, it is concluded that mechanical anisotropy ( $s_{33}-2s_{11}-2s_{12}$ ) strongly affects hydrostatic dependence of the capacitance of a sample.

## DISCUSSION

The field-induced strain of polyurethane elastomers can originate from two contributions, i.e. electrostriction and Maxwell stress. The expressions of the strains of these two effects as functions of the applied field are:

$$x_i^e = \epsilon_0^2 K_{33}^2 Q_{i3} E^2 \quad (5a)$$

$$x_i^M = \frac{1}{2} \epsilon_0 K_{33} s_{i3} E^2 \quad (5b)$$

where  $x_i^e$  and  $x_i^M$  are electrostrictive strain and Maxwell stress induced strain, respectively;  $i = 1$  and  $3$  for transverse and longitudinal strains, respectively.  $Q_{i3}$  is the electrostriction constant. Strain coefficients of a polyurethane elastomer, therefore, include two contributions:

$$R_{33} = \epsilon_0^2 K_{33}^2 Q_{33} - \frac{1}{2} \epsilon_0 K_{33} s_{33} \quad (6a)$$

$$R_{13} = \epsilon_0^2 K_{33}^2 Q_{13} - \frac{1}{2} \epsilon_0 K_{33} s_{13} \quad (6b)$$

### Contribution from Electrostriction

In the previous section, from experimental data, the hydrostatic electrostriction constant of 80CF-1 is estimated by using Eq. (4). Compared with the electrostriction coefficients of other polymers, e.g.  $Q_{33} = 2.1 \text{ m}^4/\text{C}^2$  for PVDF [6], it is assume that, for polyurethane elastomers,  $Q_{33}$  is, at most, ten times of  $Q_h$ , or,  $Q_{33} = 10Q_h = -16.4 \text{ m}^4/\text{C}^2$ . Using this data, for 193CD, the electrostriction contribution ( $\epsilon_0^2 K_{33}^2 Q_{33}$ ) to  $R_{33}$  is  $-0.06 \times 10^{-18} \text{ m}^2/\text{V}^2$  (at 50 Hz). Compared with the measured  $R_{33}$  ( $-4.5 \times 10^{-18} \text{ m}^2/\text{V}^2$ ) of this material, this contribution is only about 1.5% of the total  $R$  constant.

### Contribution from Maxwell Stress Effect

Electrostrictive strain is independent of elastic properties, while Maxwell stress induced strain is proportional to the elastic compliance of the sample. For isotropic elastomer studied, the Poisson's ratio is about 0.5. The fact that the transverse strain constants are nearly half of the longitudinal constants for all cast sample suggests the major contribution to the field induced strain is more likely from the Maxwell stress effect. The smaller transverse coefficients of injection-molded samples and calendered samples are attributed to the mechanical anisotropy introduced by material processing.

Since the dielectric constant  $K_{33}$  of all samples and the elastic compliance  $s_{11}$  of 80CF-1, 80IM-1, and 193CT-1 have been measured, the contribution from the Maxwell stress can also be estimated if the materials are assumed to be isotropic ( $s_{33} = s_{11}$ ) and uniform. Table V presents the results of the estimations for the three samples. For each sample, material parameters involved in calculations were of the same frequency since all these parameters were frequency dependent. Low frequency  $R$  constants were obtained by extrapolating their frequency dependence curves. From the table, it appears that the term  $\frac{1}{2} \epsilon_0 K_{33} s_{33}$  accounts for less than 50% of coefficient  $R_{33}$  for all three samples.

Table V Estimation of Maxwell stress contribution to strain coefficient

Sample	f(Hz)	$s_{11}$ ( $\times 10^{-8}$ $\text{m}^2/\text{N}$ )	$K_{33}$	$-\frac{1}{2} \epsilon_0 K_{33} s_{11}$ ( $\times 10^{-18} \text{ m}^2/\text{V}^2$ )	$R_{33}$ ( $\times 10^{-18}$ $\text{m}^2/\text{V}^2$ )
80CF-2	1	3.37	8.94	-1.33	-3.2
80IM-1	10	5.75	7.73	-1.96	-4.3
193CD	10	10.2	7.13	-3.22	-6.8

### Enhancement of Strain Response by Sample Non-uniformity

The estimation of the contributions from electrostriction and Maxwell stress effect is based on the condition that the materials are uniform. The fact that the estimation only accounts about half of the measured  $R$  constants may be explained by the non-uniformity of the samples. Examination of the strain coefficients of the polyurethanes presented in Table III indicates that  $R_{33}$  is strongly sample-thickness dependent. For both 80CF and 80CD samples,  $R_{33}$  increases significantly when the thickness of a sample decreases which indicates that the materials are not uniform. That is, the surface region of a sample is different from the interior region in the response to a driving field. When the total thickness of a sample decreases, this effect becomes more significant. Since the Maxwell stress induced strain depends on the dielectric and elastic properties of a sample, this strain can be significantly enhanced if the dielectric constant of the surface region is smaller than that of the interior region while the elastic compliance of the surface is greater than that of the interior region. Even if the dielectric and elastic properties are uniform through a sample a interface can exist between the electrodes and the polymer due to the space charge [7], and the electric field induced strain can also be enhanced.

## REFERENCES

- [1] H. R. Gallantree, "Review of transducer applications of polyvinylidene fluoride," *IEEE Proceedings*, vol. 130, pp. 189-194, 1983.
- [2] T. Furukawa, "Recent advances in ferroelectric polymers," *Ferroelectrics*, vol. 104, pp. 229-240, 1990.
- [3] T. T. Wang, J. M. Herbert and A. M. Glass, "The Applications of Ferroelectric Polymers," New York: Chapman and Hall, 1988.
- [4] H. Wang, Q. M. Zhang, L. E. Cross and A. O. Sykes, "Piezoelectric, dielectric, and elastic properties of poly(vinylidene fluoride/trifluoroethylene)," *J. Appl. Phys.*, vol. 74, pp. 3394-3398, 1993.
- [5] H. Ohigashi, "Electromechanical properties of polarized polyvinylidene fluoride films as studied by the piezoelectric resonance method," *J. Appl. Phys.*, vol. 47, pp. 949-955, 1976.
- [6] T. Furukawa and N. Seo, "Electrostriction as the origin of piezoelectricity in ferroelectric polymers," *Jpn. J. Appl. Phys.*, vol. 29, pp. 675-680, 1990.
- [7] Y. Li and T. Takada, "Observation of charge behavior in multiply low-density polyethylene," *J. Appl. Phys.*, vol. 74, pp. 2725-2703, 1993.

# THEORETICAL EQUATIONS FOR DIELECTRIC, ELASTIC AND PIEZOELECTRIC CONSTANTS OF DIPHASIC COMPOSITE CHANGING ITS CONNECTIVITY FROM 3-0 TO 0-3 VIA 3-3.

Hisao Banno

NTK Technical Ceramics Div., NGK Spark Plug Co., Ltd.  
14-18, Takatsuji-cho, Mizuho, Nagoya 467-91, Japan.

## Abstract

Theoretical equations for dielectric, elastic and piezoelectric constants of diphasic composite changing its connectivity from 3-0 (or 0-3) to 3-3 are obtained based on a model combining cubes (3-0 or 0-3) and 3-3 models. This theory is applied to the experimental results for dielectric constant of  $\text{Pb}(\text{Mg}_{1/3}\text{Nb}_{2/3})\text{O}_3$ -pyrochlore phase mixture and for dielectric, elastic and piezoelectric constants of porous PZT ceramics, where a good agreement between experimental and theoretical results is observed.

## Introduction

Variation of dielectric constant in PMN ( $\text{Pb}(\text{Mg}_{1/3}\text{Nb}_{2/3})\text{O}_3$ )-pyrochlore diphasic mixture has been experimentally investigated as a function of volume fraction of pyrochlore phase by J.Chen et al. and also has been explained by the Lichtenecker and Wiener's rules for mixture.[1]-[3]

K-I.Huh et al. have investigated the variation of dielectric constant in PMN ( $\text{Pb}(\text{Mg}_{1/3}\text{Nb}_{2/3})\text{O}_3$ )-pyrochlore diphasic mixture as functions of grain size and volume fraction of pyrochlore phase and have suggested that the experimental results could be explained by microstructural changes in the PMN-pyrochlore diphasic mixture (i.e. connectivity[4] of the diphasic mixture changes from 3-0 to 0-3 via 3-3), which have not yet been theoretically discussed.[5]

Effects of pore structure and porosity on dielectric, elastic and piezoelectric constants of porous ceramics with closed and open pores have been theoretically discussed based on 3-0 (modified cubes) and 3-3 models by the author.[6][7] As to a structure of porous ceramics, he has also proposed a model combining cubes (3-0) and 3-3 models, which changes connectivity of two-phase from 3-0 to 3-3. Based on this model, theoretical equations for dielectric, elastic and piezoelectric constants of porous ceramics have been obtained.[8]

As to properties of two-phase composite, theoretical equations for dielectric, elastic and piezoelectric constants of 3-0 (or 0-3) composite have been obtained based on modified cubes model [10][11], but those of composite changing its connectivity from 3-0 (or 0-3) to 3-3 have not yet been obtained based on the model combining cubes (3-0) and 3-3 models.

In this paper, a new model for diphasic composite changing its connectivity from 3-0 to 0-3 via 3-3 are

proposed, which combined 3-0 (0-3) and 3-3 models. Dielectric, elastic and piezoelectric constants of diphasic composite changing its connectivity from 3-0 to 0-3 via 3-3 are derived as a function of volume fraction of phase 1 based on the model. These results are compared with the experimental data on PMN-pyrochlore mixture and highly porous PZT ceramics.

## Theory

### Modified 3-3 model

Figure 1 shows schematically a new model for diphasic composite changing its connectivity from cubes (3-0 or 0-3) to 3-3, which is cited as modified 3-3 model, where  $a$  and  $c$  are assumed. The composite structure, from cubes to 3-3, can be treated with the selection of a ratio  $r$  ( $=c/a$ ). That is,  $r = 0$  and  $1$  correspond to simple cube and 3-3 models, respectively, and the intermediate state stands for the modified 3-3 model.

### Diphasic composite changing its connectivity from 3-0 to 3-3

Assuming that the unit cell of the model is divided into seven parts, as shown in Fig.2(a) for the Z-axis direction and in Fig.2(b) for the X-(or Y-) axis direction, one can derive the theoretical equations for dielectric, elastic and piezoelectric constants, as a function of volume fraction of phase 1, based on this geometry and by combining the theoretical equations from series and parallel models.[4][6][9] (Errata were found in the equations for dielectric loss tangent ( $\tan \delta$ ), which were reported in the previous paper.[6] The corrected equations are shown in Appendix A.) The

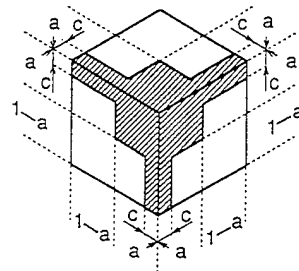


Fig.1. A model combining cubes (3-0 or 0-3) and 3-3 models for diphasic composite changing its connectivity from 3-0 (or 0-3) to 3-3.

notation used in this paper is similar to Newnham's [4] and the previous papers.[6]

Theoretical equations for the constants of the diphasic composite are obtained as follows.

For dielectric properties

$$\bar{\epsilon}_{33} = A_a + B_a + C_a + D_a \quad (1)$$

where

$$A_a = a^2 (1-r^2) / [a^{1/2} \epsilon_{33} + (1-a)^{1/2} \epsilon_{33}] \quad (1-1)$$

$$B_a = 2ar(1-a) / [ar^{1/2} \epsilon_{33} + (1-ar)^{1/2} \epsilon_{33}] \quad (1-2)$$

$$C_a = (1-a)(1+a-2ar)^{1/2} \epsilon_{33} \quad (1-3)$$

$$\text{and } D_a = (ar)^{2 \cdot 1} \epsilon_{33} \quad (1-4)$$

$$\tan \delta_{33} = (A_b + B_b + C_b + D_b) / \bar{\epsilon}_{33} \quad (2)$$

where

$$A_b = a^2 (1-r^2) \{ a^{1/2} \tan \delta_{33} / \epsilon_{33} + (1-a)^{1/2} \tan \delta_{33} / \epsilon_{33} \} / [a^{1/2} \epsilon_{33} + (1-a)^{1/2} \epsilon_{33}]^2 \quad (2-1)$$

$$B_b = 2ar(1-a) \{ ar^{1/2} \tan \delta_{33} / \epsilon_{33} + (1-ar)^{1/2} \tan \delta_{33} / \epsilon_{33} \} / [ar^{1/2} \epsilon_{33} + (1-ar)^{1/2} \epsilon_{33}]^2 \quad (2-2)$$

$$C_b = (1-a)(1+a-2ar)^{1/2} \tan \delta_{33} \epsilon_{33} \quad (2-3)$$

$$\text{and } D_b = (ar)^{2 \cdot 1} \tan \delta_{33} \epsilon_{33} \quad (2-4)$$

$\bar{\epsilon}_{11}$  (or  $\bar{\epsilon}_{22}$ ) and  $\tan \delta_{11}$  (or  $\tan \delta_{22}$ ) can be obtained by substituting  $\epsilon_{11}$  (or  $\epsilon_{22}$ ) and  $\tan \delta_{11}$  (or  $\tan \delta_{22}$ ) for  $\epsilon_{33}$  and  $\tan \delta_{33}$  in eqs.(1) and (2), respectively.

For elastic properties

$1/\bar{s}_{33}$  (or  $1/\bar{s}_{11}$  and  $1/\bar{s}_{22}$ ) and  $\tan \delta_{33}$  (or  $\tan \delta_{11}$  and  $\tan \delta_{22}$ ) can be obtained by substituting  $1/s_{33}$  (or  $1/s_{11}$  and  $1/s_{22}$ ) for  $\epsilon_{33}$  and  $\tan \delta_{33}$  in eqs.(1) and (2), respectively.

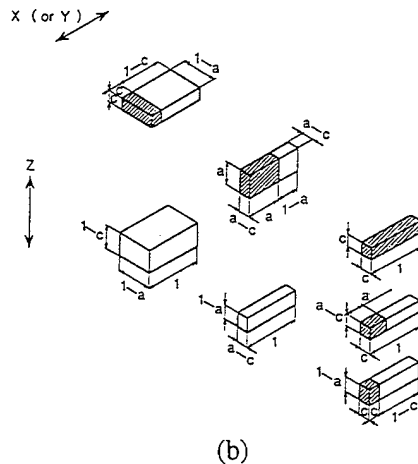
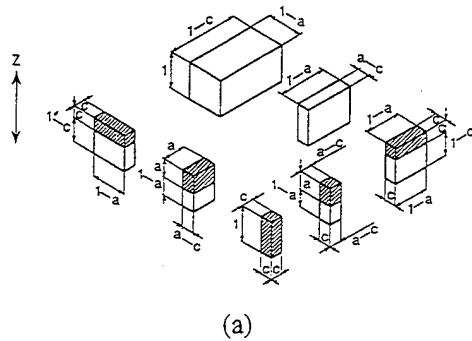


Fig.2 Schematic representation of a model, combining cubes and 3-3 models, which is divided into seven parts for (a) Z-axis direction and (b) X- (or Y-) axis direction as an assumption to derive theoretical equations.

$$\bar{\sigma}_{31} = A_c + B_c + C_c + D_c \quad (3)$$

where

$$A_c = a^2 (1-r^2) [a^{1/2} \sigma_{31} / \epsilon_{33} + (1-a)^{1/2} \sigma_{31} / \epsilon_{33}] / [a^{1/2} \epsilon_{33} + (1-a)^{1/2} \epsilon_{33}] \quad (3-1)$$

$$B_c = 2ar(1-a) [ar^{1/2} \sigma_{31} / \epsilon_{33} + (1-ar)^{1/2} \sigma_{31} / \epsilon_{33}] / [ar^{1/2} \epsilon_{33} + (1-ar)^{1/2} \epsilon_{33}] \quad (3-2)$$

$$C_c = (1-a)(1+a-2ar)^{1/2} \sigma_{31} \quad (3-3)$$

$$\text{and } D_c = (ar)^{2 \cdot 1} \sigma_{31} \quad (3-4)$$

$\bar{\sigma}_{12}$  can be obtained by substituting  $s_{11}$  and  $\sigma_{12}$  for  $s_{33}$  and  $\sigma_{31}$ , respectively.

For piezoelectric properties

$$\bar{d}_{33} = (A_d + B_d + C_d + D_d) \cdot \bar{s}_{33} \quad (4)$$

where

$$A_d = a^2 (1-r^2) \{ a^{1/2} d_{33} / \epsilon_{33} + (1-a)^{1/2} d_{33} / \epsilon_{33} \} / [a^{1/2} \epsilon_{33} + (1-a)^{1/2} \epsilon_{33}] \quad (4-1)$$

$$B_d = 2ar(1-a) \{ ar^{1/2} d_{33} / \epsilon_{33} + (1-ar)^{1/2} d_{33} / \epsilon_{33} \} / [ar^{1/2} \epsilon_{33} + (1-ar)^{1/2} \epsilon_{33}] \quad (4-2)$$

$$C_d = (1-a)(1+a-2ar)^{1/2} d_{33} \epsilon_{33} \quad (4-3)$$

$$\text{and } D_d = (ar)^{2 \cdot 1} d_{33} \epsilon_{33} \quad (4-4)$$

$$\bar{d}_{31} = (A_e + B_e + C_e + D_e + E_e + F_e + G_e) \cdot \bar{s}_{11} \quad (5)$$

where

$$A_e = a^2 (1-r^2) \{ a^{1/2} d_{31} / \epsilon_{33} \} / [a^{1/2} \epsilon_{33} + (1-a)^{1/2} \epsilon_{33}] \quad (5-1)$$

$$B_e = ar(1-a) \{ ar^{1/2} d_{31} / \epsilon_{33} \} / [ar^{1/2} \epsilon_{33} + (1-ar)^{1/2} \epsilon_{33}] \quad (5-2)$$

$$C_e = a(1-a)(1-r)^{1/2} d_{31} \{ a / [a^{1/2} \epsilon_{33} + (1-a)^{1/2} \epsilon_{33}] \} \quad (5-3)$$

$$D_e = (1-a)(1-ar)^{1/2} d_{31} \{ ar / [ar^{1/2} \epsilon_{33} + (1-ar)^{1/2} \epsilon_{33}] \} \quad (5-4)$$

$$E_e = (ar)^2 \{ (1-a)^{1/2} d_{31} / \epsilon_{33} \} / [a^{1/2} \epsilon_{33} + (1-a)^{1/2} \epsilon_{33}] \quad (5-5)$$

$$F_e = ar(1-a) \{ (1-a)^{1/2} d_{31} / \epsilon_{33} \} / [ar^{1/2} \epsilon_{33} + (1-ar)^{1/2} \epsilon_{33}] \quad (5-6)$$

$$\text{and } G_e = (ar)^2 \{ (1-a)^{1/2} d_{31} / \epsilon_{33} \} / [a^{1/2} \epsilon_{33} + (1-a)^{1/2} \epsilon_{33}] \quad (5-7)$$

$$A_f = a^2 (1-r^2) \{ a^{1/2} d_{31} / \epsilon_{33} \} / [a^{1/2} \epsilon_{33} + (1-a)^{1/2} \epsilon_{33}] \quad (5-8)$$

$$B_f = ar(1-a) \{ ar^{1/2} d_{31} / \epsilon_{33} \} / [ar^{1/2} \epsilon_{33} + (1-ar)^{1/2} \epsilon_{33}] \quad (5-9)$$

$$C_f = a(1-a)(1-r)^{1/2} d_{31} \{ a / [a^{1/2} \epsilon_{33} + (1-a)^{1/2} \epsilon_{33}] \} \quad (5-10)$$

$$D_f = (1-a)(1-ar)^{1/2} d_{31} \{ ar / [ar^{1/2} \epsilon_{33} + (1-ar)^{1/2} \epsilon_{33}] \} \quad (5-11)$$

$$E_f = (ar)^2 \{ (1-a)^{1/2} d_{31} / \epsilon_{33} \} / [a^{1/2} \epsilon_{33} + (1-a)^{1/2} \epsilon_{33}] \quad (5-12)$$

$$F_f = ar(1-a) \{ (1-a)^{1/2} d_{31} / \epsilon_{33} \} / [ar^{1/2} \epsilon_{33} + (1-ar)^{1/2} \epsilon_{33}] \quad (5-13)$$

$$G_f = (ar)^2 \{ (1-a)^{1/2} d_{31} / \epsilon_{33} \} / [a^{1/2} \epsilon_{33} + (1-a)^{1/2} \epsilon_{33}] \quad (5-14)$$

$$H_f = a^2 (1-r^2) \{ a^{1/2} d_{31} / \epsilon_{33} \} / [a^{1/2} \epsilon_{33} + (1-a)^{1/2} \epsilon_{33}] \quad (5-15)$$

$$I_f = ar(1-a) \{ ar^{1/2} d_{31} / \epsilon_{33} \} / [ar^{1/2} \epsilon_{33} + (1-ar)^{1/2} \epsilon_{33}] \quad (5-16)$$

$$J_f = a(1-a)(1-r)^{1/2} d_{31} \{ a / [a^{1/2} \epsilon_{33} + (1-a)^{1/2} \epsilon_{33}] \} \quad (5-17)$$

$$K_f = (1-a)(1-ar)^{1/2} d_{31} \{ ar / [ar^{1/2} \epsilon_{33} + (1-ar)^{1/2} \epsilon_{33}] \} \quad (5-18)$$

$$L_f = (ar)^2 \{ (1-a)^{1/2} d_{31} / \epsilon_{33} \} / [a^{1/2} \epsilon_{33} + (1-a)^{1/2} \epsilon_{33}] \quad (5-19)$$

$$M_f = ar(1-a) \{ (1-a)^{1/2} d_{31} / \epsilon_{33} \} / [ar^{1/2} \epsilon_{33} + (1-ar)^{1/2} \epsilon_{33}] \quad (5-20)$$

$$N_f = (ar)^2 \{ (1-a)^{1/2} d_{31} / \epsilon_{33} \} / [a^{1/2} \epsilon_{33} + (1-a)^{1/2} \epsilon_{33}] \quad (5-21)$$

$$O_f = a^2 (1-r^2) \{ a^{1/2} d_{31} / \epsilon_{33} \} / [a^{1/2} \epsilon_{33} + (1-a)^{1/2} \epsilon_{33}] \quad (5-22)$$

$$P_f = ar(1-a) \{ ar^{1/2} d_{31} / \epsilon_{33} \} / [ar^{1/2} \epsilon_{33} + (1-ar)^{1/2} \epsilon_{33}] \quad (5-23)$$

$$Q_f = a(1-a)(1-r)^{1/2} d_{31} \{ a / [a^{1/2} \epsilon_{33} + (1-a)^{1/2} \epsilon_{33}] \} \quad (5-24)$$

Volume fraction of phase 1 is expressed as

$$V = a^3 + 3a^2(1-a)r^2, \quad 0 < a < 1, \quad (6)$$

where  $r$  is expressed as

$$r = c/a. \quad (7)$$

### Diphasic composite changing its connectivity from 0-3 to 3-3

As phases 1 and 2 of 0-3 composite correspond to phases 2 and 1 of 3-0 composite respectively, theoretical equations for the constants of 0-3 composite can be obtained by substituting constants of phases 1 and 2 for those of phases 2 and 1 in eqs. (1)-(7), respectively.

Equations (1) and (7), for example, become as follows;

$$\bar{\epsilon}_{33} = A_r + B_r + C_r + D_r \quad (8)$$

where

$$A_r = a^2 (1-r^2) / [a^{1/2} \epsilon_{33} + (1-a)^{1/2} \epsilon_{33}] \quad (8-1)$$

$$B_r = 2ar(1-a) / [ar^{1/2} \epsilon_{33} + (1-ar)^{1/2} \epsilon_{33}] \quad (8-2)$$

$$C_r = (1-a)(1+a-2ar)^{1/2} \epsilon_{33} \quad (8-3)$$

$$\text{and } D_r = (ar)^{2 \cdot 2} \epsilon_{33}. \quad (8-4)$$

$$^2v = a^3 + 3a^2(1-a)r^2, \quad 0 < a < 1, \quad (9)$$

$$\text{and } ^1v = 1 - ^2v = 1 - a^3 - 3a^2(1-a)r^2. \quad (10)$$

### Results and Discussion

In the case where  $[r = 0]$  and  $[r = 1]$ , the model is reduced to cubes (3-0 or 0-3) and 3-3 models, respectively.

Theoretical equations for dielectric, elastic and piezoelectric constants of diphasic composite based on cubes model are obtained as a special case of  $[\ell = m = n = 1]$  in the equations reported in the previous paper.[10][11] The theoretical equations for the constants of porous ceramics have been obtained in the previous paper.[7][8]

The above-mentioned equations should be involved in the equations (1)-(7).

To verify the equations (1)-(7) for a general solution, those were applied to a special case such as  $[r = 0]$ ,  $[r$

$$= 1, \quad ^2\varepsilon \gg ^1\varepsilon = \varepsilon_0, \quad 1/s = 0, \quad ^1\tan\delta = ^1\tan\delta_m = 0 \text{ and } ^1\sigma = 0] \text{ and } [^2\varepsilon \gg ^1\varepsilon = \varepsilon_0, \quad 1/s = 0, \quad ^1\tan\delta = ^1\tan\delta_m = 0 \text{ and } ^1\sigma = 0]. [10][7][8]$$

Thus, we achieved the same theoretical expressions as the above-mentioned equations except the equations for dielectric loss tangent based on cubes model.[10][11] This is due to the errata in the equations for dielectric loss tangent based on series and parallel models. The corrected equations are shown in Appendix B, which become at  $[\ell = m = n = 1]$  the same expressions as the equation (2) at  $[r = 0]$ .

Now, let us discuss the variation of dielectric

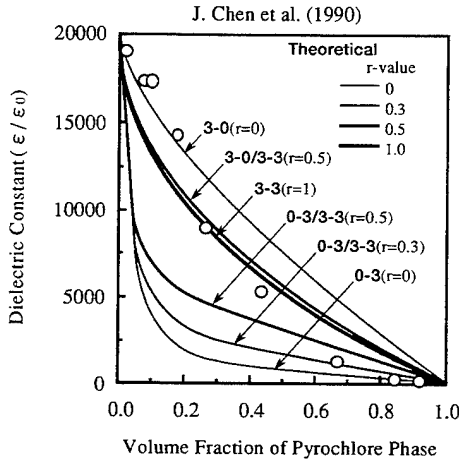


Fig.3. Comparison between the experimental[1] and theoretical values for PMN-pyrochlore phase mixture, assuming that  $\varepsilon(\text{pyrochlore phase})/\varepsilon_0 = 180$  and  $\varepsilon(\text{PMN})/\varepsilon_0 = 20,000$ .

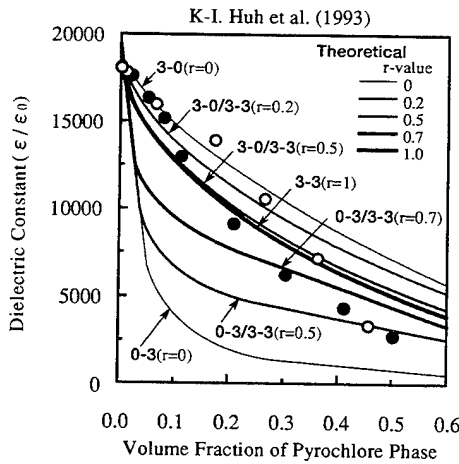


Fig.4. Comparison between the experimental[5] and theoretical values for PMN-pyrochlore phase mixture, assuming that  $\varepsilon(\text{pyrochlore phase})/\varepsilon_0 = 180$  and  $\varepsilon(\text{PMN})/\varepsilon_0 = 19,000$ . (○ : Agglomerated pyrochlore powder, ● : Dispersed pyrochlore powder [5])

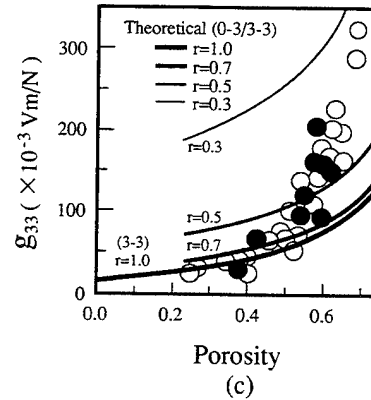
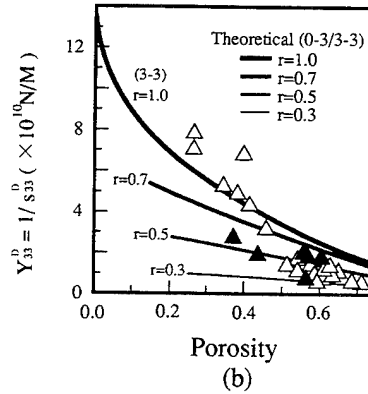
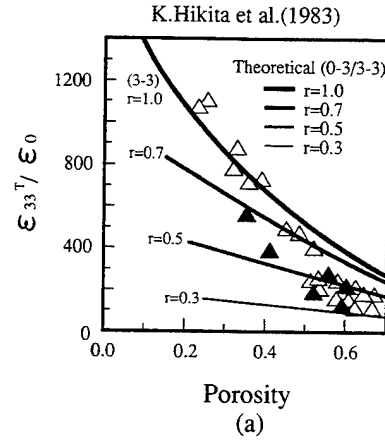


Fig.5. Comparison between the experimental values for the porous PZT ceramics prepared by Hikita et al.[12] and theoretical ones based on a model combining 0-3 and 3-3 models, assuming that  $\varepsilon_{33}(\text{pores})/\varepsilon_0 = 1$ ,  $\varepsilon_{33}(\text{PZT})/\varepsilon_0 = 2100$ ,  $g_{33}(\text{pores}) = 0$ ,  $g_{33}(\text{PZT}) = 14 \times 10^{-3} \text{ m/V}$ ,  $Y_{33}(\text{pores}) = 1/s_{33}(\text{pores}) = 0$  and  $Y_{33}(\text{PZT}) = 1/s_{33}(\text{PZT}) = 13.5 \times 10^{11} \text{ N/m}$ .

constant in PMN-pyrochlore diphasic mixture.

Figures 3 and 4 show comparisons between the experimental results [1][5] and theoretical ones calculated according to the equations (1)(7)(8) and (10) as functions of volume fraction of pyrochlore phase (phase 1) and r-value ( $0 \leq r \leq 1$ ).

Assuming that the PMN-pyrochlore diphasic mixture changes its connectivity from 3-0 to 3-3 and then 3-3 to 0-3 with the increase of volume fraction of pyrochlore phase as suggested by K-I.Huh et al.[4], good agreements between theoretical and experimental results were observed. Next, let us discuss porosity dependences of dielectric, elastic and piezoelectric constants of porous PZT ceramics prepared by Hikita et al.[12] at porosities of 0.5-0.7.

Calculated values based on 3-3 model fitted the experimental values well at porosities of 0.2-0.45, but not at porosities of 0.5-0.7.[7] The previous paper has reported that this discrepancy may be explained if porous 3-3 PZT ceramics with low connectivity were formed in high-porosity region (0.5-0.7) rather than in the low-porosity region (0.2-0.45).[7]

Figure 5 shows comparisons between the experimental values and calculated ones based on the modified 3-3 model, assuming that the porous ceramics with low connectivity correspond to diphasic (ceramic bulk-open pore) composite changing its connectivity from 3-3 to 0-3. A good agreement between theoretical and experimental results was observed.

#### Summary and Conclusions

- (1) Theoretical equations for dielectric, elastic and piezoelectric constants of diphasic composite changing its connectivity from 3-0 (or 0-3) to 3-3 were obtained based on a model combining cubes and 3-3 models.
- (2) This theory was applied to the experimental results for variations of dielectric constant in PMN-pyrochlore phase mixture and for the properties of highly porous PZT ceramics. Assuming that diphasic composite such as PMN-pyrochlore phase and PZT ceramic bulk-pores changed its connectivity from 3-0 to 3-3 and then 3-3 to 0-3 with the increase of a phase, good agreements between experimental and theoretical results were observed.

#### Appendix A. Theoretical Equations for Dielectric Loss Tangent ( $\tan \delta$ ) Based on Series and Parallel Models.

The theoretical equations for  $\tan \delta$  of series and parallel models are obtained as follows.

For  $\overline{\tan \delta}_{11}$  from series models and  $\tan \delta_{33}$  from parallel model,

$$\overline{\tan \delta} = ({}^1v \cdot {}^1\varepsilon \cdot {}^1\tan \delta + {}^2v \cdot {}^2\varepsilon \cdot {}^2\tan \delta) / ({}^1v \cdot {}^1\varepsilon + {}^2v \cdot {}^2\varepsilon) \quad (\text{A-1})$$

and for  $\tan \delta_{33}$  from series models and  $\overline{\tan \delta}_{11}$  from parallel model when  $({}^1\tan \delta)^2 \ll 1$  and  $({}^2\tan \delta)^2 \ll 1$

$$\overline{\tan \delta} = ({}^1v \cdot {}^2\varepsilon \cdot {}^1\tan \delta + {}^2v \cdot {}^1\varepsilon \cdot {}^2\tan \delta) / ({}^1v \cdot {}^2\varepsilon + {}^2v \cdot {}^1\varepsilon) \quad (\text{A-2})$$

#### Appendix B. Theoretical Equations for Dielectric Loss Tangent ( $\tan \delta$ ) Based on Modified Cubes Model.

$$\text{Dielectric loss tangent } \overline{\tan \delta}_{33}, \overline{\tan \delta}_{22}, \overline{\tan \delta}_{11};$$

$$\overline{\tan \delta}_{33} = (A_3 + B_3) / \overline{\varepsilon}_{33} \quad (\text{A-3})$$

where

$$A_3 = a^2 [a + (1-a)n]^2 [a \cdot {}^1\tan \delta_{33} / {}^1\varepsilon_{33} + (1-a)n \cdot {}^2\tan \delta_{33} / {}^2\varepsilon_{33}] [a / {}^1\varepsilon_{33} + (1-a)n / {}^2\varepsilon_{33}]^2 \quad (\text{A-4})$$

$$B_3 = \{1 - a^2 [a + (1-a)n]\} \cdot {}^2\varepsilon_{33} \cdot {}^2\tan \delta_{33} \quad (\text{A-5})$$

$$\overline{\varepsilon}_{33} = a^2 [a + (1-a)n]^2 / [a / {}^1\varepsilon_{33} + (1-a)n / {}^2\varepsilon_{33}] + \{1 - a^2 [a + (1-a)n]\} \cdot {}^2\varepsilon_{33} \quad (\text{A-6})$$

and volume fraction of phase 1  ${}^1v$ ;

$${}^1v = a^3. \quad (\text{A-7})$$

Equations for  $\overline{\tan \delta}_{11}$  and  $\overline{\tan \delta}_{22}$  can be obtained by substituting  $\tan \delta_{11}$  and  $\tan \delta_{22}$  for  $\tan \delta_{33}$ ,  $\varepsilon_{11}$  and  $\varepsilon_{22}$  for  $\varepsilon_{33}$ ,  $\ell$  and  $m$  for  $n$ , [10] respectively, in eqs. (A-3)(A-4) and (A-5).

(Equations for mechanical loss tangent  $\overline{\tan \delta}_m$  can be obtained by substituting  $1/s$  for  $\varepsilon$  and  $\tan \delta_m$  for  $\tan \delta$  in eqs.(A-3)(A-4) and (A-5).)

#### References

- [1] Jie Chen and Martin P.Harmer, "Microstructure and Dielectric Properties of Magnesium Niobate-Pyrochlore Diphasic Mixtures", *J.Amer.Ceram.Soc.* 73[1]68-73(1990).
- [2] O.Wiener, "Lamellare Doppelbrechung"(in Ger.), *Phys.Z.*, 5, 332-338(1904).
- [3] K.Lichtenecker, "Die Dielektrizitätskonstante natürlicher und künstlicher Mischkörper"(in Ger.), *Phys.Z.*, 27, 115-158(1926).
- [4] R.E.Newnham, D.P.Skinner and L.E.Cross, "Connectivity and Piezoelectric-Pyroelectric Composites", *Mater.Res.Bull.*, 13[5] 525-536(1978).
- [5] Kang-Il Huh, Jeong-Joo Kim and Sang-Hee Cho, "Variation of Dielectric Constant with Grain Size and Volume Fraction of Pyrochlore Phase in the PMN-Pyrochlore Diphasic Mixtures", *Proc. of Fulrath Memorial Int'l Symp. on Advanced Ceram.* (Aug.29-31,1993, Tokyo), ed. by N.Ichinose (CNT Inc. Tokyo, 1993)pp.61-68.
- [6] H.Banno, "Effects of Shape and Volume Fraction of Closed Pores on Dielectric, Elastic, and Electromechanical Properties of Dielectric and Piezoelectric Ceramics-A Theoretical Approach", *Amer.Ceram.Soc.Bull.* 66[9]1332-1337(1987).
- [7] H.Banno, "Effects of Porosity on Dielectric, Elastic, and Electromechanical Properties of Pb(Zr,Ti)O<sub>3</sub> Ceramics with Open Pores:A Theoretical Approach", *Jpn.J.Appl.Phys.*, 32[9]4212-4217(1993).
- [8] H.Banno, "Pore-structure versus Properties of PZT Ceramics", *Proc. of Fulrath Memorial Int'l Symp. on Advanced Ceram.* (Aug.29-31,1993, Tokyo), ed. by N.Ichinose (CNT Inc. Tokyo, 1993)pp.11-18.
- [9] A.Safari, *Ph.D.Thesis, The Penn. State Univ.* (1983) 34-48.
- [10] H.Banno, "Theoretical Equations for Dielectric, Piezoelectric and Elastic Properties of a 0-3 Composite Based on Modified Cubes Model - A General Solution -", *Jpn.J.Appl.Phys.* 28(1989), Suppl.28-2; *Proc. of the 7th Meeting on Ferroelectric Materials and Their Applications*, Kyoto 1989, pp.190-192.
- [11] H.Banno, "Recent Progress in Science and Technology of Flexible Piezoelectric Composite in Japan", *Proc. of 7th Int'l Symp. on Applications of Ferroelectrics (IEEE-ISAF'90)* pp.67-72.
- [12] K.Hikita, K.Yamada, M.Nishioka and M.Ono: *Proc.4th Meeting on Ferroelectric Materials and Their Applications*, *Jpn.J.Appl.Phys.* 22(1983)Suppl.22-2, pp64-66.



# Piezoelectric Composites : Thermal Stabilization and Improvement of Properties

L. N. SYRKIN, N. N. FEOKTISTOVA, and E. T. KANCHEROVA

RESEARCH and DEVELOPMENT INSTITUTE "MORFIZPRIBOR", ST. PETERSBURG, 197376, RUSSIA

**Abstract** - Piezoelectric composites containing modified crystals SbSJ as an active phase have very high volume ("hydrostatic") sensitivity and an acoustic impedance close to that of water. But the dependence of piezoelectric voltage coefficient  $g_h$  on temperature  $T$  is rather strong. Composites based on the PZT - ceramics, on the other hand, have high thermal stability but comparatively low values of  $g_h$ . The aim of this research is improvement of piezoelectric transducers made of both types of composites.

THE SHORTCOMING of SbSJ - base piezoelectric materials results from low Curie temperature of SbSJ [1,2]. A large body of research made possible to rise  $T_c$  of doped crystals SbSJ (e.g. CGS - 2 [1]) and of composites containing such crystals (e.g. CMB - 2 [3]) to values of 55 - 65°C but not higher. The upper limit  $T_{max}$  of operating temperature range  $\Delta T$  went up correspondingly to 35 - 40°C. The temperature range would be quite sufficient for some applications, such as certain of the medical apparatus and hydroacoustic transducers (hydrophones). But the strong reversible temperature dependence of  $g_h$  within this range (a twofold decrease of  $g_h$ ) hinders the use of these new piezoelectric materials. In the same way  $g_h$  drops while hydrostatic pressure increases up to 60 - 80 MPa.

The proposed method of thermal - and pressure - stabilization of CMB - type piezoelectric elements is based on the peculiarities of ferroelectrics nearby the Curie point.

Let us consider the influence of the input capacity  $C'$  on the real sensitivity of hydrophone  $\gamma'$

$$\gamma' = \frac{\gamma C}{C + C'} \quad (1)$$

where  $\gamma$  is idle sensitivity of transducer,  $C$  - its capacity;  $C'$  includes the input capacity of the head amplifier and, if necessary, capacity of the special connected capacitor. The active component of input impedance is disregarded here. Piezoelectric transducers made of SbSJ - base materials are characterized by an increasing  $C$  and decreasing  $\gamma$  within an operating range of  $T$  or  $p$ , i.e. near  $T_c$ . These changes are due to corresponding variations of the dielectric permeability and piezoelectric coefficient  $g_h = d_h / \epsilon \epsilon_0$ , where  $d_h$  is volume piezomodulus and  $\epsilon_0$  is free space permeability.

At the same time the product of  $\gamma$  and  $C$ , which is proportional to  $d_h$ , increases with  $T$  or  $p$  except very narrow ranges of  $T$  or  $p$  close to phase transition point. Therefore, as it is seen from (1),  $\gamma'$  approaches  $\gamma$  with  $C' \ll C$ , i.e.  $\gamma'$  increases with  $T$  or  $p$ . On the other hand,  $\gamma'$  approaches  $\gamma C / C'$  with  $C' \gg C$ , i.e. decreases with  $T$  or  $p$ . Thus, it is possible to chose a certain value of  $C' = C^*$  such that the variation of  $\gamma'$  in the operating ranges of  $T$  or  $p$  would be minimum. This value is deduced from the equations:

$$\gamma'(T_1) = \gamma'(T_2) \text{ or } \gamma'(p_1) = \gamma'(p_2).$$

Using (1) we have

$$\frac{\gamma_1 C_1}{C_1 + C^*} = \frac{\gamma_2 C_2}{C_2 + C^*} \quad (2)$$

where  $\gamma_1, \gamma_2, C_1, C_2$  are values of  $\gamma$  and  $C$  at the certain chosen  $T$  or  $p$  ( $T_1$  and  $T_2$  or  $p_1$  and  $p_2$ ) in the range that has to be stabilized, extreme values  $T$  or  $p$  in particular.

Further we shall consider only thermal stabilization, the conclusion for pressure stabilization being quite analogous.

From the solution of Eq. (2) one can find  $C^*$  in relative units.

$$\frac{C^*}{C_3} = \frac{C_1}{C_3} \cdot \frac{\frac{\gamma_1}{\gamma_2} - 1}{1 - \frac{\gamma_1 C_1}{\gamma_2 C_2}} = \frac{\frac{\epsilon_1}{\epsilon_3} \left( \frac{g_1}{g_2} - 1 \right)}{1 - \frac{d_1}{d_2}} \quad (3)$$

Here we have introduced  $C_3$  and  $\epsilon_3$  - the values of  $C$  and  $\epsilon$  with  $T = T_0$  where  $T_0$  is the certain temperature of support, for example  $T_0 = 20^\circ \text{C}$ . Substituting  $C' = C^*$  into (1) from (3), with regard to the experimental temperature dependencies of  $\epsilon$  and  $g_h$ , we obtain the sensitivity  $\gamma'$  of stabilized piezoelectric transducer as a function of  $T$ , in relative units

$$\frac{\gamma'(T)}{\gamma_3} = \frac{\frac{\epsilon(T)}{\epsilon_3} \cdot \frac{g(T)}{g_3} \left( 1 - \frac{\epsilon_1 g_1}{\epsilon_2 g_2} \right)}{\frac{\epsilon_1}{\epsilon_3} \left( \frac{g_1}{g_2} - 1 \right) + \frac{\epsilon(T)}{\epsilon_3} \left( 1 - \frac{\epsilon_1 g_1}{\epsilon_2 g_2} \right)} \quad (4)$$

where  $\gamma_3 = \gamma(T_0)$ ,  $\epsilon_1 = \epsilon(T_1)$ ,  $\epsilon_2 = \epsilon(T_2)$ ,  $g_1 = g_h(T_1)$ ,  $g_2 = g_h(T_2)$ .

Under these conditions the equivalent capacitance  $C_{eq}$  and the specific sensitivity (or efficiency) of hydrophone are given by

$$C_{eq} = C + C^*, \quad \gamma' \sqrt{C_{eq}} = \frac{(\gamma \sqrt{C})}{\sqrt{1 + \frac{C^*}{C}}} \quad (5)$$

It is easy to see that the qualitative characteristic of thermal stabilization is determined by the choice of  $T_1$  and  $T_2$  (i.e. by  $C^*$ )

and by the character of dependencies  $\varepsilon(T)$ ;  $g_h(T)$ . Particularly the positions ( $T_{min}$ ,  $T_{max}$ ) of lower and upper limits of operating temperature range  $\Delta T$ , the average value  $\bar{\gamma}'$  and temperature variation  $(\Delta \gamma')_{max}$  across this range are adjustable within the capability of the method. These positions ( $T_{min}$ ,  $T_{max}$ ) may be different from  $T_1$  and  $T_2$ . In this case, as a rule, the greater is  $\Delta T$  and the lower is  $(\Delta \gamma')_{max}$ , the less is  $\bar{\gamma}'$ . Thus the thermal stabilization is obtained at the cost of a certain decrease of transducer sensitivity.

The choice of  $\Delta T$ ,  $\bar{\gamma}'$ , and  $(\Delta \gamma')_{max}$  should be carried out from operational considerations, according to the general requirements for piezoelements or transducers. The next step is setting the values of  $T_1$ ,  $T_2$  and calculations  $C^*$ ,  $\gamma'(T)$ .

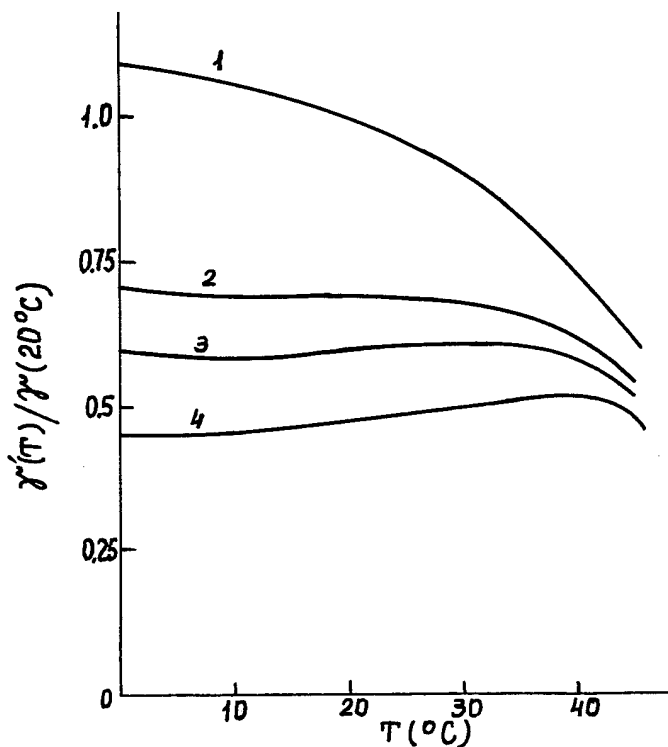


Fig. 1. Normalized voltage sensitivity versus temperature  $T$  for unstabilized (1) and stabilized (2-4) transducers, with  $T_1=20^\circ\text{C}$  and various  $T_2$  ( $^\circ\text{C}$ ): 2-25, 3-35, 4-45.

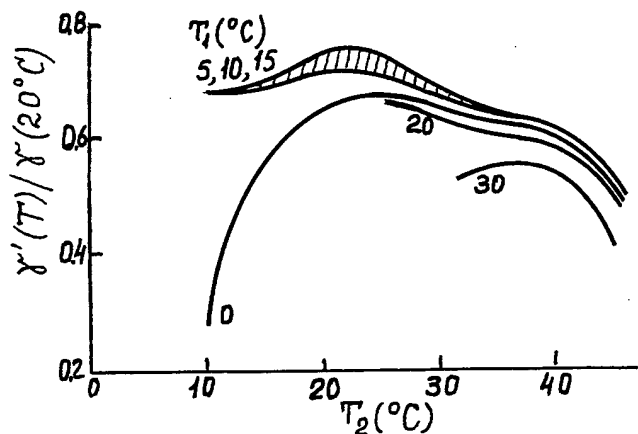


Fig. 2. Normalized voltage sensitivity  $\gamma$  of CMB-2 transducer versus  $T_2$  with  $T_1=20^\circ\text{C}$  and various  $T_1$  ( $^\circ\text{C}$ ) indicated by the curves. Operating temperature range: 0-35°C.

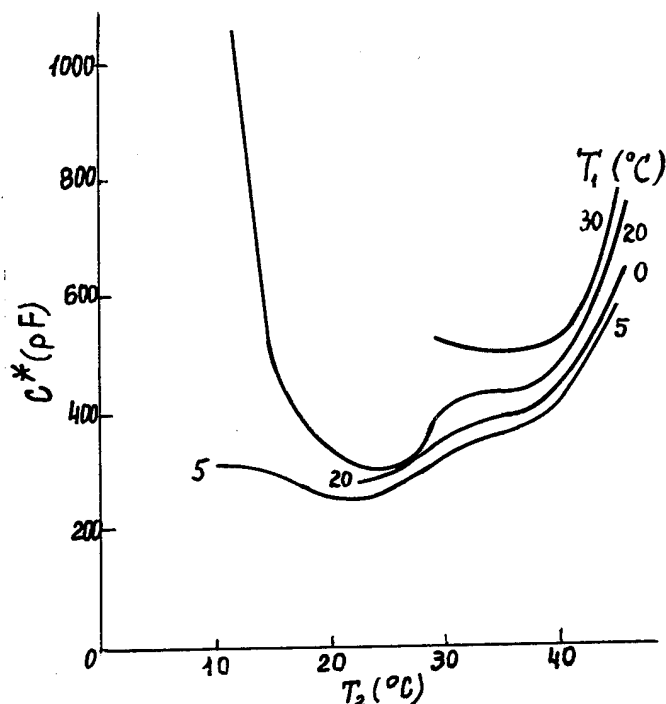


Fig. 3. Capacitance of the additional capacitor  $C^*$  versus temperature  $T_2$  with various values of  $T_1$  ( $^\circ\text{C}$ ) indicated by the curves. Capacitance  $C$  of the CMB-2 transducer at  $20^\circ\text{C}$  is 650pF;  $\gamma(20^\circ\text{C})=450\text{mkV/Pa}$ .

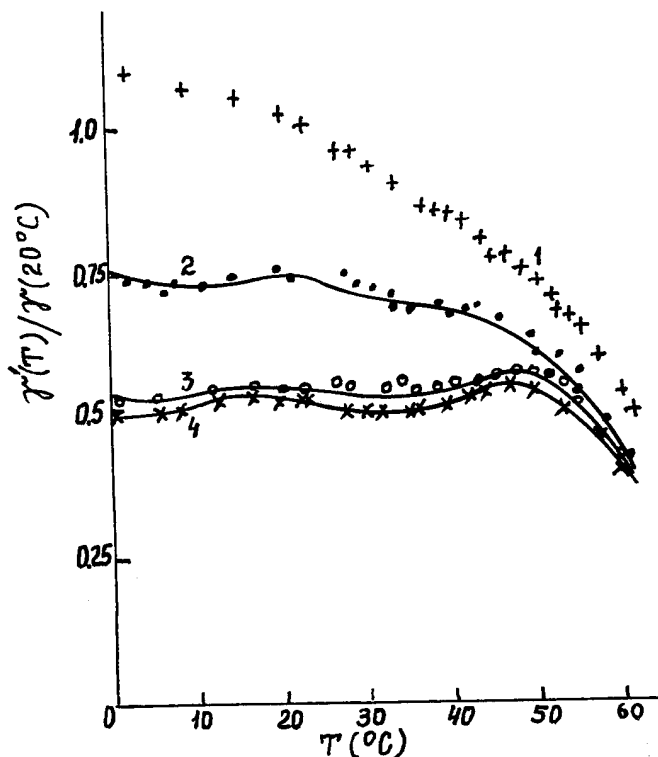


Fig. 4. Calculated (solid lines) and observed (dots) normalized temperature dependences of sensitivity for unstabilized (1) and stabilized (2-4) piezoelectric elements made of modified crystals SbSJ (CGS-2) with various  $T_1$ ,  $T_2$  and  $C^*$ .  
 $T_1$  ( $^\circ\text{C}$ ): 2-0, 3-10, 4-35;  
 $T_2$  ( $^\circ\text{C}$ ): 2-20, 3-50, 4-50;  
 $C^*$  (pF): 2-20, 3-45, 4-49.3.

As is evident from Figs 1 - 4, the chief disadvantage of piezocrystals CGS - 2 and of composite CMB - 2 (strong temperature dependence of  $g_h$  and  $\gamma$ ) may be eliminated by the developed method. An agreement between theory and experiment is quite satisfactory (Fig 4). It is significant that the sensitivity  $\gamma'$  remains very high if not identical to its initial value  $\gamma$  (less by 25 - 50 % than  $\gamma$  with  $T = 20^\circ\text{C}$ ). Temperature variation of  $\gamma'$  in the region up to  $45 - 50^\circ\text{C}$  may be reduced to a very small quantity - from  $\pm 1.5\%$  to  $\pm 3\%$ , i.e. no more than that with high stable piezoceramic transducers, the sensitivity  $\gamma'$  being considerably greater. Thereby the field of application of SbSJ - based piezoelectric materials is greatly increased.

Consider next the composites containing piezoceramics as an active phase. These materials are characterized by higher limiting values of an operating temperature ( $T_{max} \gg 50^\circ\text{C}$ ). But the main problem here is to increase the hydrostatic voltage coefficient  $g_h$  or sensitivity  $\gamma$ . In this connection we have investigated the influence of polymeric phase Poisson ratio  $\mu$  on the sensitivity  $\gamma$  for various composite elements and transducers. Samples of composite with 1 - 3 - 0 connectivity patterns for middle layer of sandwich - type transducer were formed using the "dice - and - fill" technique [4], two solid surface layers of transducer made from PZT - ceramics and titanium. The perforated PZT - polymer composite samples with 3 - 1 - 0 connectivity patterns were similar to that investigated in [5].

Mixtures of polyurethane and glass microballoons (MB) have been used as a polymeric phase in both types of composite elements. The Poisson ratio was regulated by varying the concentration of MB in polyurethane.

We have applied the finite element method to calculate  $g_h$  and  $\gamma$  of samples in an analogous way to [6]. It was found for 3 - 1 - 0 composite that the change in Young modulus of polymer by a factor of five holding  $\mu = \text{constant}$  has no effect on  $g_h$ . But the reduction of  $\mu$  from 0.48 to 0.3 causes the increase of  $g_h$  by the factor 3.5. For sandwich - type composite elements there is a double rise of  $\gamma$  with the decrease of  $\mu$  from 0.48 to 0.3 and a 10 % rise of  $\gamma$  with the decrease of  $\mu$  from 0.3 to 0.15.

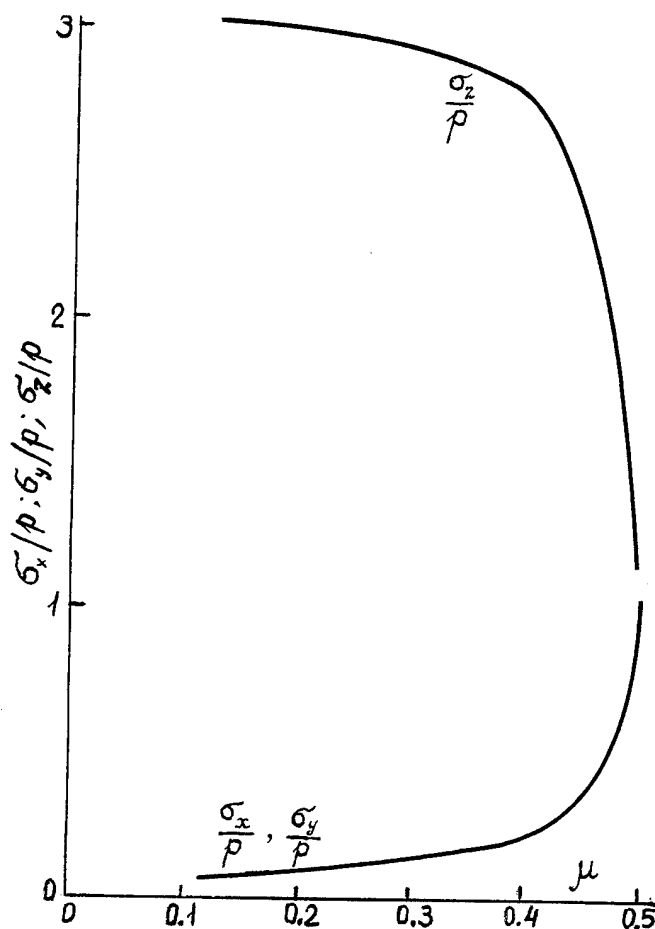


Fig.5. The normalized  $\mu$  -dependence of the longitudinal  $\sigma_x$  and transverse ( $\sigma_y, \sigma_z$ ) stress components in the central element of (1-3) piezoceramic-polymer composite structure. Here  $p$  is acoustic pressure.

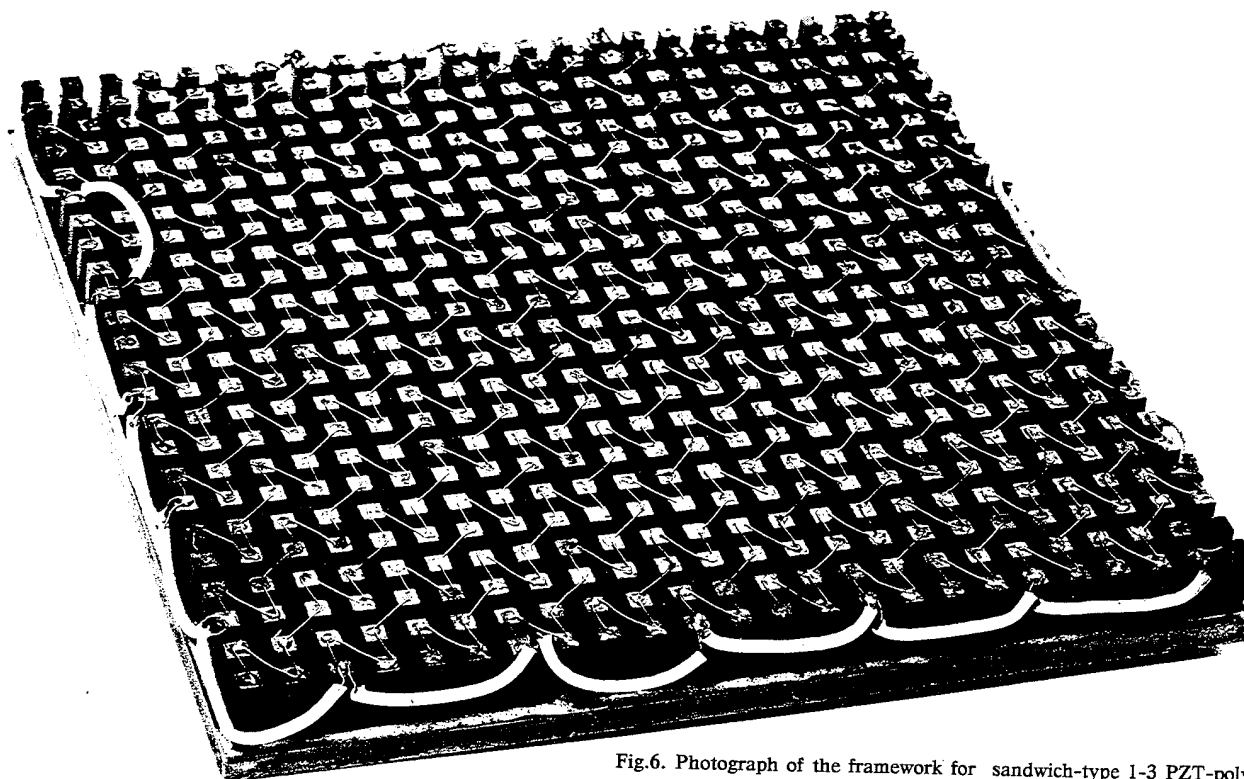


Fig.6. Photograph of the framework for sandwich-type 1-3 PZT-polymer macrocomposite.

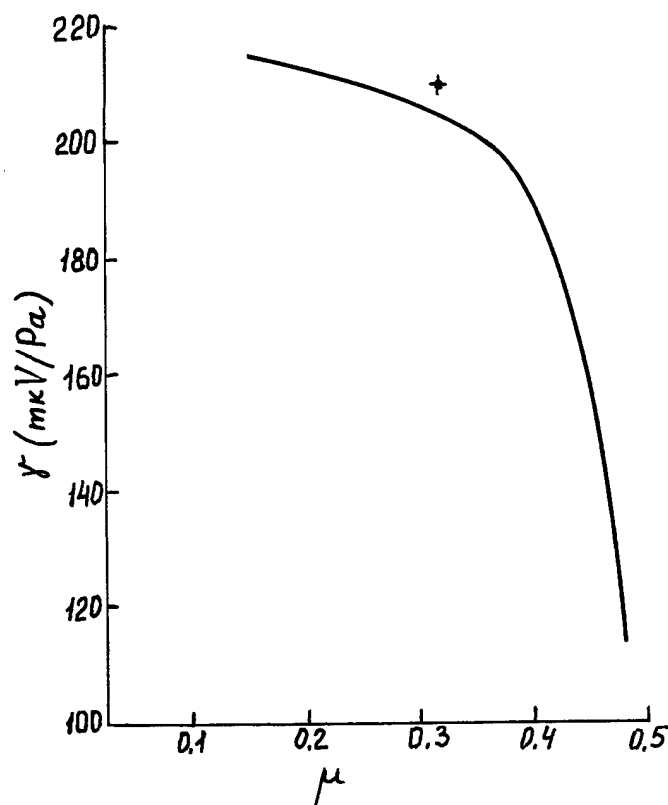


Fig.7. The calculated (solid lines) and experimental (dot) sensitivity  $\gamma$  versus  $\mu$  for PZT-polymer 1-3 composite transducer.

The results of calculations correlate with experimental data, the measurements being carried out on piezoelectric elements and hydrophones of both mentioned types made of PZT-polymer composites. Thus, it was shown that the optimal Poisson ratio of polymeric phase in these composites must be close to 0.3.

#### REFERENCES

- 1 L.M. Belyaev, A.A. Grekov, P.L. Zaks, V.A. Lakhovitskaya, B.A. Popovkin, N.P. Protsenko, V.D. Spitsyna, L.N. Syркин, L.N. Tatarenko and N.N. Feoktistova, "Antimony sulphoiodide piezoelectric materials for electroacoustic transducers", *Sov. Phys. Acoust.*, vol. 23, pp 463 - 464, Sept - Oct. 1977.
- 2 A.S. Bhalla, R.E. Newnham, T.R. Shrout and L.E. Cross, "Piezoelectric SbSJ : polymer composites", *Ferroelectrics*, vol. 41, pp. 207 - 211, 1982.
- 3 L.N. Syркин, E.T. Kancherova and N.N. Feoktistova, "Volume - sensitive piezoelectric composites for electroacoustic transducers", *Ferroelectrics*, vol. 143, pp. 287 - 298, 1993.
- 4 H.P. Savakus, K.A. Klicker and R.E. Newnham, "PZT - epoxy piezoelectric transducers : a simplified fabrication procedure", *Mat. Res. Bull.*, vol. 16, pp. 677 - 680, 1981.
- 5 A. Safari, R.E. Newnham, L.E. Cross and W.A. Schulze, "Perforated PZT - polymer composites for piezoelectric transducer applications", *Ferroelectrics*, vol. 41, pp. 197 - 205, 1982.
- 6 S. Davanzo, A. Safari and R.E. Newnham, "Finite element modeling of perforated PZT - polymer composites", *Ferroelectric Letters*, vol. 3, pp. 109 - 121, 1985.

# Piezoelectric Properties of 1-3 Composites of PZT in P(VDF-TrFE) Copolymer

K.W.Kwok, H.L.W.Chan and C.L.Choy

Department of Applied Physics and Materials Research Center,  
Hong Kong Polytechnic,  
Hung Hom, Kowloon, Hong Kong

## ABSTRACT

PZT/P(VDF-TrFE) 1-3 composites were fabricated by embedding pre-sintered PZT rods in a pre-poled copolymer matrix. The rods were then poled using an electric field much lower than the coercive field of the copolymer. The electromechanical coupling factor  $k_t$ , and the resonance characteristics of the composites were measured. The resonance characteristics of the composites were found to be dominated by the individual PZT rods. Poling of the copolymer matrix results in broadening of the main resonance peak. For transducer applications, it is advisable to pole the copolymer and the PZT rods in the same direction as this gives a higher  $k_t$  value.

## INTRODUCTION

1-3 composite piezoelectric materials have attracted considerable interest recently because of their relatively high electromechanical coupling factor and low impedance as compared with the constituent materials. However, most of the composites were made of piezoelectrically active ceramic and piezoelectrically passive polymer. Since piezoelectricity can be activated in bulk unstretched samples of P(VDF-TrFE), it is now feasible to prepare composites with both phases piezoelectrically active. Moreover, the piezoelectric constants of PZT and P(VDF-TrFE) have opposite sign, so it is of interest to investigate how the piezoelectricity as well as the direction of dipole alignment of each phase affect the resultant piezoelectric properties of the composites.

In this work, 1-3 composite samples were fabricated by embedding PZT ceramic rods in a pre-poled P(VDF-TrFE) copolymer matrix. Previous experimental results [1] showed that electrical breakdown occurred across the PZT phase when trying to pole the copolymer matrix insitu, thereby making it impossible to pole both phases simultaneously. The impedance characteristics of the composites were investigated by using an impedance analyzer

(HP4194A), and their  $k_t$  values were calculated by the method of Sherit et al [2]. Stopband structures of these composites were found and also discussed.

## SAMPLE PREPARATION

PZT powder of grain size between 1 and 3  $\mu$ m was used in this work to make rods of 1 mm diameter. The powder was supplied by the Shanghai Institute of Ceramics, and has properties similar to the Vernitron (Morgan Matroc Ltd) PZT-4 composition. The rods were extruded through a home-made die and sintered at 1300°C for about 6 hours. To measure the piezoelectric properties of the ceramic component, a rod sample of length 0.78 mm was cut from a long fired rod (sample A).

An extruded unpoled vinylidene fluoride-trifluoroethylene (80/20) copolymer sheet supplied by Atochem North America Inc. was used as the composite matrix. The sheet was 0.8 mm thick, and its Curie transition temperature for the first heating ( $T_c$ ) and melting temperature were 124.4°C and 149.0°C respectively, indicating a TrFE content of slightly higher than 20% [3]. In order to optimize the piezoelectric properties of the thick sheet samples, they were poled by using a two-step poling process at 115°C under an electric field of 30 MV/m [4]. A disk-shaped sample (Sample B) was then made from the poled copolymer.

A series of holes of 1 mm diameter were drilled in the pre-poled copolymer sheets, in a square pattern with 3 mm center-to-center periodicity, and the fired PZT rods were inserted into these holes. To glue the PZT rods to the copolymer, the composites were immersed into epoxy (Shell 815 + hardener C), and then degassed for 15 minutes. After curing of the epoxy, the composites were cut into disks about 0.7 mm thick and 12 mm in diameter. The ceramic volume percentage was about 8%. The composite was re-poled again at 85°C under an electric field of 3 MV/m for half an hour in order to align the PZT dipoles. Sample E was re-poled in a direction parallel

to the poling direction of the matrix, while sample F was re-poled in an anti-parallel direction. As the poling temperature was well below the matrix Curie temperature, and 3 MV/m was too low to disrupt the polarization in the copolymer, the pre-existed piezoelectric properties of the matrix was retained. Sample C was a composite sample without re-poling. Sample D was prepared by using a similar method, but the copolymer matrix was not pre-poled. All the samples used in this work are summarized in Table 1.

To confirm the assumption that repoling the composite at 85°C under an electric field of 3 MV/m for half an hour will not lead to any piezoelectric activity in the copolymer, a copolymer sample was poled using the above conditions and no resonance was observed.

TABLE 1  
Description of the samples.

Sample	Constitutes
A	poled PZT rod
B	poled copolymer
C	pre-poled copolymer, unpoled PZT
D	unpoled copolymer, poled PZT
E	copolymer and PZT poled in the same direction
F	copolymer and PZT poled in the opposite direction

## EXPERIMENTAL RESULTS

An impedance analyzer (HP4194A) was used to measure the impedance characteristics of the samples. The electromechanical coupling factor  $k_t$  was determined by the method of Sherrit et al [2] which took into account the mechanical and dielectric loss in the copolymer matrix. The  $k_t$  value was evaluated from the strongest resonance of each sample. Since the second harmonic for the radial mode resonance was very weak for most of the samples, the electromagnetic coupling factor  $k_p$  were not determined.

### 1. Thickness mode resonance

The impedance vs frequency plots of the samples are shown in Figs. 1 to 6, and the values of  $k_t$  are given in Table 2. The poled PZT rod (sample A, Fig.1) has a strong resonance at 2 MHz and two weak resonances at 2.7 MHz and 3.9 MHz. These three resonances, although weaker, can still be found in

sample D (Fig.2), i.e. after the ceramic rods have been inserted into the unpoled copolymer matrix, showing that the soft copolymer matrix does not greatly modify the resonances of the individual rods.

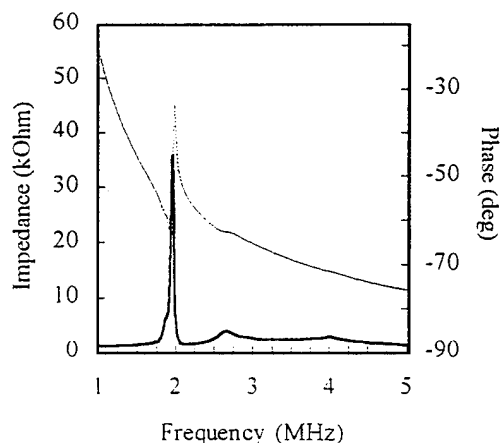


Fig.1 Impedance (--) and phase (—) plot for sample A.

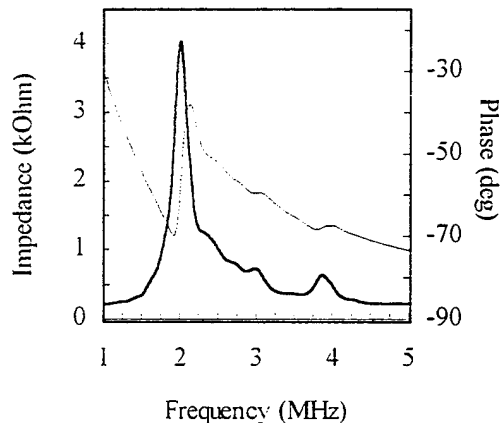


Fig.2 Impedance (--) and phase (—) plot for sample D.

The thickness resonance of the poled copolymer sample B (Fig.3) is observed at 1.4 MHz. After inserting the unpoled PZT rods (sample C), the thickness resonance of the matrix becomes weaker and occurs at a slightly higher frequency of 1.5 MHz (Fig.4). This is because sample C is thinner. The  $k_t$  value of sample C is lower than that of sample B (Table 2).

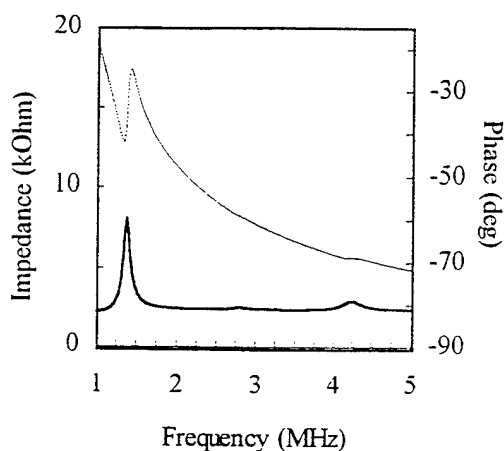


Fig.3 Impedance (--) and phase (—) plot for sample B.

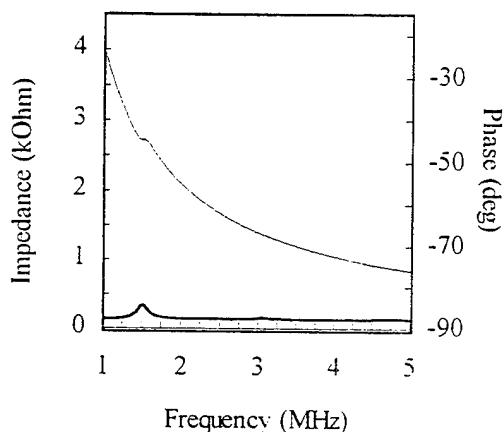


Fig.4 Impedance (--) and phase (—) plot for sample C.

Comparing samples E and F (Figs 5 & 6), the weak copolymer resonance is still observable in both samples. The PZT rod resonances can also be seen. Due to the fact that the diameter of the rod is very close to its thickness, the different resonance modes of the rods and the copolymer merge together to form a resonance with a broad shoulder. Whether this material is suitable for fabricating wide band transducer is worth pursuing and will be left for future study. It is important to note that poling of the matrix in a direction parallel or anti-parallel to the PZT rods does not give rise to distinct difference in the thickness resonance characteristics. This is because the PZT rod is much stiffer than the copolymer and thus dominates the composites resonances. However,  $k_t$  of sample E (PZT and copolymer poled in the same direction) is higher than that of sample F (with the two phases poled oppositely). Hence, in transducer applications,

it is advisable to pole the copolymer and PZT in the same direction to give a high  $k_t$ .

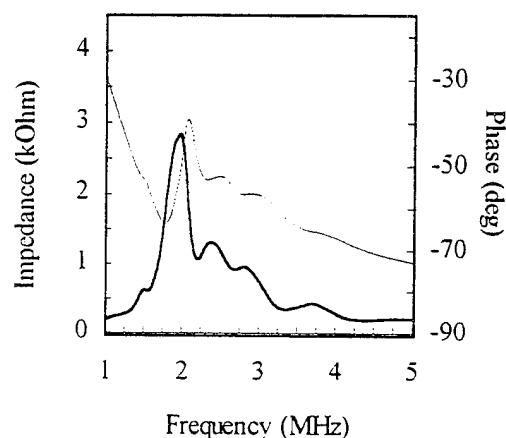


Fig.5 Impedance (--) and phase (—) plot for sample E.

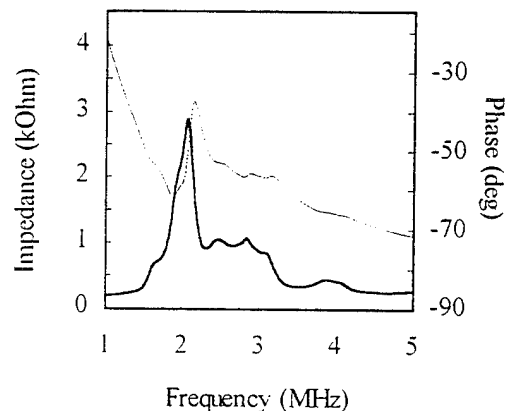


Fig.6 Impedance (--) and phase (—) plot for sample F.

TABLE 2

The thickness and electromechanical coupling factor for the samples.

Samples	Thickness (mm)	$k_t$
B	0.78	0.22
C	0.71	0.13
D	0.70	0.36
E	0.71	0.45
F	0.68	0.30

## 2. Planar mode resonance

The fundamental planar mode resonance was found at 85 kHz. The resonance frequency depends only on the diameter of the sample and is the same for samples B to F. The second harmonic of the radial mode is very weak and can hardly be observed.

## 3. Stopband resonance

In addition to the characteristic resonances of the PZT rods and the copolymer matrix, 1-3 composites also have stopband resonances due to Bragg reflection in the periodic array of PZT rods [5]. Two weak stopband resonances at frequencies about 490 kHz and 730 kHz were found in sample D (with unpoled copolymer matrix). When the rods and the copolymer were poled in the same direction (sample E), the stopband resonances were slightly enhanced and were found at 500 kHz and 780 kHz. However, in sample F where the rods and the copolymer were poled oppositely, the stopband resonances shifted to higher frequencies (660 kHz and 810 kHz).

## CONCLUSION AND DISCUSSION

The resonance characteristics of PZT/P(VDF-TrFE) 1-3 composites with two piezoelectric phases were studied. The followings were observed:

1. In all of the 1-3 composites studied, the characteristic resonances of the individual PZT rods are clearly observable. The copolymer matrix does not significantly modify the characteristic resonances of the individual PZT rods, because the soft copolymer matrix does not impose an appreciable clamping on the rods. Detailed calculations of the resonance frequencies of the individual rods will be reported later.

2. The thickness resonance of the poled copolymer matrix is very weak and, in the present sample geometry, merges with the PZT resonances to form a broad resonance peak. Whether this material can be used to make broadband transducer will need further investigation.

3. The resonance characteristics of the samples with PZT and copolymer poled in the same direction and poled oppositely are quite similar. The electromechanical coupling constant  $k_t$  is higher if the two phases are poled in the same direction.

4. The radial mode resonance of the 1-3 composites depends only on the diameter of the sample and is independent of sample poling history.

5. Stopband resonances are observed; and when the two piezoelectric phases are poled oppositely, they shifted to higher frequencies.

## ACKNOWLEDGMENTS

The authors would like to thank Prof. Q. Yin of the Shanghai Institute of Ceramics for supplying the ceramic powder. Financial support from the Hong Kong Research Grants Council (RGC) is also acknowledged.

## REFERENCES

- [1] H. Taunaumang, I.L. Guy and H.L. Chan, "Electromechanical Properties of 1-3 Piezoelectric Ceramic/Piezoelectric Polymer Composites", *J. Appl. Phys.*, Vol 76, part 1, p.484, 1994.
- [2] S. Sherit, H.D. Wiederick and B.K. Mukherjee, "Non-iterative Evaluation of the Real and Imaginary Material Constants of Piezoelectric Resonators", *Ferroelectrics*, Vol. 134, pp.111-119, 1992.
- [3] P.E. Bloomfield and S. Preis, "Piezoelectric and Dielectric Properties of Heat Treated and Polarized VF<sub>2</sub>/VF<sub>3</sub> Copolymers", *IEEE Trans. Electrical Insul.*, Vol. EI-21, pp.533-537, 1986.
- [4] H.L.W. Chan, Z. Zhao, K.W. Kwok and C.L. Choy, "Enhancement of Piezoelectric Activity in P(VDF-TrFE) Copolymer using Two-step Poling", *Proc. 8th Intl. Symp. on Electrets (ISE8)*, Paris, France, Sept. 1994.
- [5] B.A. Auld, "High Frequency Piezoelectric Resonators", *Proc. 1986 IEEE Intl. Symp. on Application of Ferroelectrics (ISAF)*, pp.288-295.



## Study on PZT4/VF<sub>2</sub>/VF<sub>3</sub> Piezoelectric 0-3 Composites

H.L.W. Chan, Y. Chen and C.L. Choy  
Dept. of Applied Physics and Materials Research Center,  
Hong Kong Polytechnic,  
Hung Hom, Kowloon, Hong Kong

### ABSTRACT

PZT4/VF<sub>2</sub>/VF<sub>3</sub> 0-3 composites with different volume percent of ceramic have been fabricated. The dielectric constants and electrical resistivities of the composites were measured as functions of temperature in order to find the optimum poling conditions. The electromechanical properties of the piezoelectric composites were also measured and compared to model calculations.

### INTRODUCTION

Piezoelectric ceramic/piezoelectric polymer 0-3 composites represent a class of piezoelectric materials having potential to replace conventional piezoceramics and piezopolymers. After combining the two phases in a 0-3 connectivity, the composite must be poled in a high electric field in order to elicit piezoelectric response. One important parameter we need to consider in the poling of a composite is the ratio of the resistivities  $\rho$  of the constituent phases since it governs the effective poling field across each phase. (Maxwell-Wagner effect [1]). Another parameter is the relaxation time  $\tau$  of the composite, which determines the poling time. Both  $\rho$  and  $\tau$  are functions of temperature. In order to find the optimum poling temperature and poling time, the dielectric constants and resistivities of the PZT-4 ceramic, VF<sub>2</sub>/VF<sub>3</sub> copolymer and 0-3 composites with different volume fraction of ceramic were measured as functions of temperature.

### COMPOSITE PREPARATION

The VF<sub>2</sub>/VF<sub>3</sub> copolymer supplied by Atochem North America Inc. has a nominal VF<sub>3</sub> content of 30%. The DSC (Differential Scanning Calorimetry) endotherms of the as-supplied pellets was measured at a heating rate of 10°C/min using a Perkin Elmer DSC7 Thermal Analyzer. The Curie transition temperature for the first heating ( $T_c$ ) of the copolymer was 105°C and the melting temperature  $T_m$  was 155°C. This indicated that the VF<sub>3</sub> content of the copolymer was several percent higher than 30. [2]

The PZT powder supplied by the Shanghai Institute of Ceramics has a grain size between 1 and 3  $\mu\text{m}$  and has properties similar to the Vernitron (Morgan Matroc Ltd.) PZT-4 composition. The copolymer pellets were first dissolved in Methyl-Ethyl-Ketone (MEK), and then a suitable amount of ceramic powder was blended into the solution. The mixture was then poured onto a petri-dish and after

evaporation of the solvent, the mixture was triturated. Then the composite was moulded into disc shape by hot pressing at 37.7 kg/mm<sup>2</sup> and 200°C in a compression machine. Composite discs with different volume percent of ceramic formed using the method described above have a diameter of 12.5 mm and thickness ranging from 0.5 to 0.9 mm.

### RESISTIVITY MEASUREMENTS

Polymers tend to have higher resistivities while ceramics have somewhat lower resistivities. The resistivities of both the ceramic and polymer decrease as the temperature increases but usually the gradient is higher for the polymer. Experimental measurements of the ceramic and the copolymer resistivities  $\rho_c$  and  $\rho_p$  were carried out in order to find a suitable poling temperature for the composite.

The constant voltage method [3] was used to measure the resistance of the unpoled samples, a 100V d.c voltage was applied to the sample using the built-in voltage source of Keithley 617 Electrometer, and the resistance of the sample was measured using the same electrometer. Resistivities of the samples are shown in Fig.1. A sharp decrease of the copolymer resistivity was observed at about the Curie temperature (105°C). This indicated that if the composites were poled above 100°C, the resistivity ratio  $\rho_p/\rho_c$  would be about 10, which is close to the ratio of the coercive field of the copolymer and ceramic at high temperature.

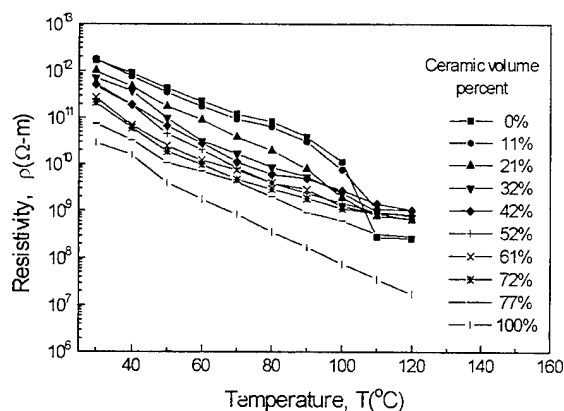


Fig.1 Resistivities of the 0-3 composites vs temperature.

## DIELECTRIC CONSTANT MEASUREMENTS

The capacitance of the unpoled disc samples at 1 kHz was measured using an HP4194A Impedance Analyzer and the resulting dielectric constants at different temperatures are shown in Fig. 2. A relaxation peak was observed near the Curie temperature of the copolymer [4]. This peak is prominent for the pure copolymer but becomes broader as the volume percent of ceramic increased.

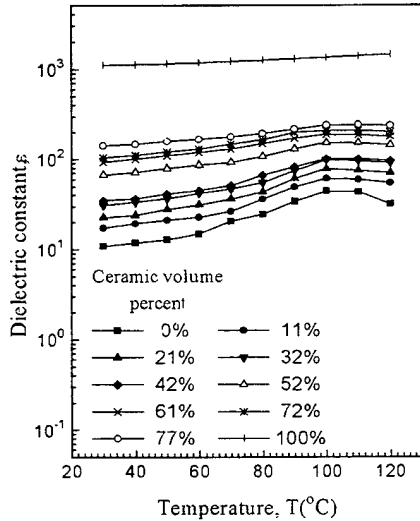


Fig.2 Dielectric constants of the composites vs temperature.

Values of the measured dielectric constants were compared to various models, namely, the Voigt (parallel) model, Reuss (series) model, Yamada model [eqn. (1)] and Furukawa model [eqn. (2)] for 0-3 composites [5-7]. In the Yamada model:

$$\epsilon = \epsilon_p \{ 1 + [n\phi(\epsilon_c - \epsilon_p)] / [n\epsilon_p + (\epsilon_c - \epsilon_p)(1 - \phi)] \} \quad (1)$$

where  $\epsilon$ ,  $\epsilon_c$  and  $\epsilon_p$  are the dielectric constants of the composite, ceramic and copolymer respectively,  $\phi$  is the volume fraction of the ceramic and  $n$  is a parameter describing the shape of the ellipsoidal particles [5]. In the Furukawa model for dispersed spherical particles, the dielectric constant of a composite was given as:

$$\epsilon = \epsilon_p [2\epsilon_p + \epsilon_c - 2\phi(\epsilon_p - \epsilon_c)] / [2\epsilon_p + \epsilon_c + \phi(\epsilon_p - \epsilon_c)] \quad (2)$$

It was noted that at a lower temperature (e.g. 30°C, as shown in Fig. 3a), the experimental results agreed very well with the Yamada model with a shape parameter  $n$  of 4.3,

which is different from the previously reported value of 8.5 for the PZT-PVDF 0-3 composites [5], the Furukawa model gave values slightly lower than the experimental measurements. However, as the temperature increased, for high volume percent of ceramic, the Furukawa model agreed better with the experimental results (Fig. 3b) than the Yamada model with  $n=4.3$ . If  $n=3$  was used in eqn. (1), the predicted values from the Yamada model and Furukawa model were identical.

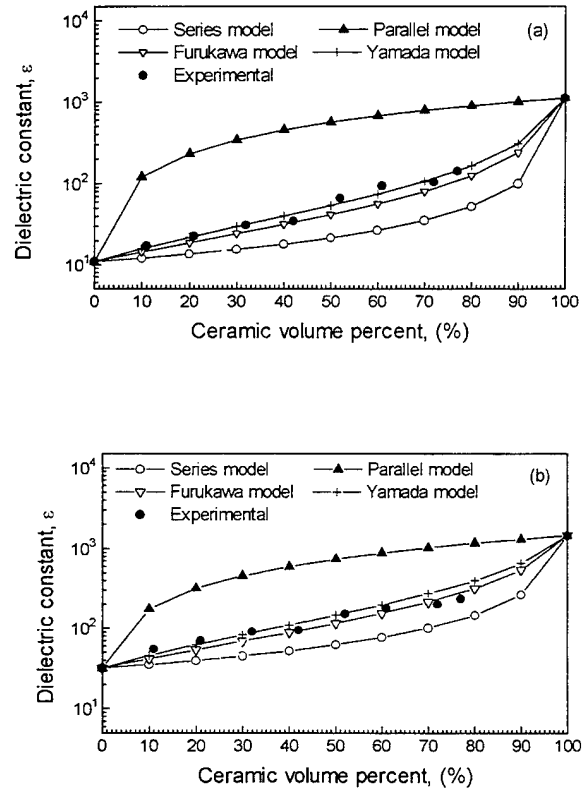


Fig.3 Dielectric constant of the composites as a function of volume percent of ceramics. (a) at 30°C, (b) at 120°C.

In previous reports [5-8], 0-3 composites were prepared by mixing the copolymer and ceramic powder in a hot rolling mill. As the copolymer was still highly viscous in its molten state, clustering of the ceramic powder might become a problem. In the present work, since the ceramic powder was dispersed in a very dilute copolymer solution, it is very likely that each ceramic particle would be coated with a layer of copolymer. This is consistent with the assumptions of the Yamada and Furukawa models [5,6] and hence a close agreement can be obtained even for high volume percent of ceramic.

# RELAXATION TIME OF THE 0-3 COMPOSITES

If the composite disc samples were modeled as a parallel plate capacitor having the measured values of resistivity  $\rho$  and dielectric constant  $\epsilon$ , the RC constant and hence the relaxation time  $\tau = 1/(RC) = \rho\epsilon$  can be evaluated. It is seen from Fig. 4 that the relaxation time  $\tau$  dropped from several hundred seconds to several seconds as the temperature increased from 30 to 120°C. However, during poling, a very high d.c. electric field was applied to the sample. Since the resistivity of a dielectric increases in an electric field [9], the value of  $\rho$  (and hence  $\tau$ ) during poling may be much higher than  $\rho$  (and  $\tau$ ) measured under normal condition. Hence much longer poling time  $t_p$  (typically two hours) was used to ensure that  $t_p \gg \tau$ .

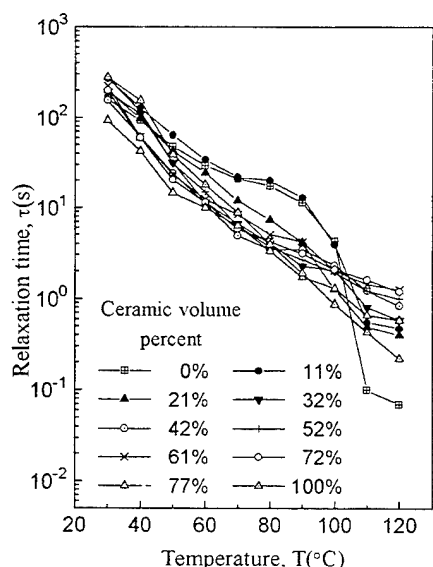


Fig. 4 Relaxation time of the composites vs temperature.

## POLING AND PIEZOELECTRIC PROPERTIES OF THE SAMPLES

DC thermal poling was used to pole the samples in an oil bath at 120°C, and the typical poling conditions were tabulated in Table 1. Values of the thickness electromechanical coupling coefficient  $k_t$  were evaluated using the method proposed by Sherrit et al [10] taking into account the high loss in the copolymer. The charge constants  $d_{33}$  was measured using a Pennebaker model 8000 piezo  $d_{33}$  tester from American Piezo-Ceramics, Inc.. The volume fraction of ceramic  $\phi$  was calculated using the measured density.

TABLE I  
THE PROPERTIES OF PZT-4/P(VDF/TrFE) 0-3 COMPOSITES.

Ceramic volume fraction $\phi$	$\rho$ (kg/m <sup>3</sup> )	Dielectric constant $\epsilon$	$k_t$	$d_{33}$ (pC/N)	Poling condition (120°C)
0	1878.5	9.81	0.27	-38.4	3h, 26kv/mm
0.11	2515.1	14.75	0.23	-30.9	2h, 24kv/mm
0.21	3033.8	22.57	0.21	-26.5	2h, 22kv/mm
0.32	3635.9	31.29	0.16	-23.2	2h, 19kv/mm
0.42	4237.4	35.21	0.19	-22.8	2h, 16kv/mm
0.52	4775.5	63.72	--	-14.9	2h, 14kv/mm
0.61	5273.9	94.11	--	13.2	2h, 12kv/mm
0.72	5907.6	101.5	0.13	26.2	2h, 11kv/mm
0.77	6193.6	134.12	0.19	33.4	2h, 12kv/mm
1.00	7452.0	910.05	0.47	177.3	1h, 1kv/mm

From Table 1, it can be seen that the  $d_{33}$  constants of the composites decreased from -30.9 pC/N at  $\phi = 0.11$  to a small value of -14.9 pC/N at  $\phi = 0.52$ , then changed sign to +13.2 pC/N at  $\phi = 0.61$ , and remain positive for higher value of  $\phi$ . This strongly suggested that the copolymer phase also contributed to the  $d_{33}$  value of the composite. As a first estimate of the contribution of both phases to the  $d_{33}$  constant, assume

$$d_{33} = \alpha\phi G d_{33c} + (1-\phi)d_{33p} \quad (3)$$

where  $\alpha$  is the ceramic poling ratio,  $d_{33c}$  and  $d_{33p}$  are the charge constants of the ceramic and copolymer respectively, and  $G$  represents the local field coefficient [5],

$$G = n\epsilon / [n\epsilon + (\epsilon_c - \epsilon)] \quad (4)$$

Using  $n = 4.3$  and  $\alpha = 0.6$ ,  $d_{33}$  of the composites were calculated and shown in Fig. 5 together with the measured values. It is clear that equations (3) and (4) give the right trend indicating that the  $d_{33}$  contribution of the copolymer tended to cancel the contribution of the ceramic.

The thickness electromechanical coupling coefficient  $k_t$  of the composites was smaller than that of the ceramic or the copolymer, especially around  $\phi = 0.5$  to 0.66. The

thickness mode resonance peaks, although visible, were very weak.

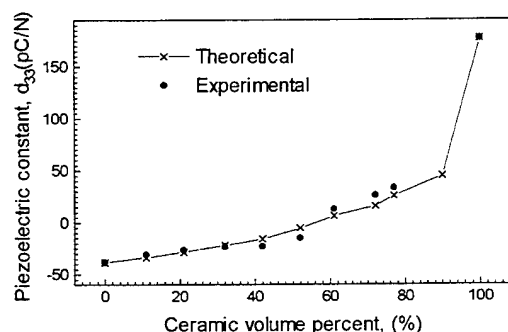


Fig. 5 Measured  $d_{33}$  values compared to the theoretical values calculated using eqn. (3).

#### CONCLUSION AND DISCUSSION

0-3 composites of PZT4/VF<sub>2</sub>/VF<sub>3</sub> copolymer with different volume percent of ceramic were fabricated using solution cast and hot-press method. The dielectric strength of these composites is lower than that prepared using hot two-roll mill and hence breaks down more easily under high poling field. However, using a dilute solution of the copolymer can help to circumvent powder clustering problem and the ceramic particles are likely to be surrounded by copolymer layers as modeled by previous workers, hence the dielectric constants of the composites agreed very well to the model predictions even for high volume percent of ceramic.

The poling temperature was chosen to be 120°C, at which the copolymer resistivity was rather low, hence the resistivity ratio of the two phases was about 10, which is close to the ratio of their coercive fields. However, since the Curie temperature of the copolymer used in this experiment was 105°C, in order to pole the copolymer, the electric field must be kept on when the composite was cooled through its Curie temperature  $T_c$  ( $T_c$  for the composites was also around 100°C).

The contribution to the piezoelectric activities by the two piezoelectric phases seemed to cancel each other resulting in a variation of  $d_{33}$  from negative to positive as the ceramic content increased.  $k_t$  was also fairly small. In transducer applications, it is not desirable to have a cancellation effect, hence, we are trying to pole the two phases oppositely so that reinforcement will occur. Details of this poling study will be reported later [11].

#### ACKNOWLEDGEMENTS

The authors would like to thank Prof. Q. Yin of the Shanghai Institute of Ceramics for supplying the ceramic powders. The first and the second author would also like to thank Dr. P.W. Chan for his encouragement and support. Financial support from the Research Grants Council (RGC) is also acknowledged.

#### REFERENCES

- [1] A.R. Von Hippel, "Dielectrics and Waves", John Wiley and Sons, 1954, pp.228.
- [2] P.E. Bloomfield and S. Preis, "Piezoelectric and Dielectric Properties of Heat Treated and Polarized VF<sub>2</sub>/VF<sub>3</sub> Copolymers", *IEEE Trans. Electrical Insul.*, Vol. EI-21, pp533-537, 1986.
- [3] User Manual, Keithley 617 Electrometer.
- [4] T. Furukawas, M. Ohuchi, A. Chiba and M. Date, "Dielectric Relaxation and Molecular Motions in Homopolymers and Copolymers of Vinylidene Fluoride and Trifluoroethylene", *Macromolecules*, Vol. 17, pp.1384-1390, 1984.
- [5] T. Yamada, T. Ueda and T. Kitayama, "Piezoelectricity of a hig-content lead ziconate titanate/polymer composite", *J. Appl. Phys.*, Vol. 53, pp. 4328-4332, June, 1982.
- [6] T. Furukawa, K. Ishida and E. Fukada, "Piezoelectric properties in the composite systems of polymers and PZT ceramics", *J. Appl. Phys.*, Vol. 50, pp.4904-4912, July, 1979.
- [7] C.J. Dias and D.K. Das-Gupta, "Piezo- and Pyroelectricity in Ferroelectric Ceramic-Polymer Composites", Chap. 8 in "Ferroelectric Polymers and Ceramic-Polymer Composites", ed. D.K. Das-Gupta, Trans Tech Pub., Switzerland, pp. 217-248, 1994.
- [8] H. Yamazaki and T. Kitayama, "Pyroelectric Properties of Polymer-Ferroelectric Composites", *Ferroelectrics*, Vol. 33, pp. 147-153, 1981.
- [9] J. Malecki and B. Hilczer, "Dielectric Behaviour of Polymers and Composites", Chap. 7 in "Ferroelectric Polymers and Ceramic-Polymer Composites", ed. D.K. Das-Gupta, Trans Tech Pub., Switzerland, pp. 181-216, 1994.
- [10] S. Sherit, H.D. Wiederick and B.K. Mukherjee, "Non-iterative Evaluation of the Real and Imaginary Material Constants of Piezoelectric Resonantors", *Ferroelectrics*, Vol.134, pp. 111-119, 1992.
- [11] H.L.W. Chan, Y. Chen and C.L. Choy, "A poling study of PZT/P(VDF-TrFE) copolymer 0-3 composites", in proceeding of the 2nd Pacific-Rim Conference on Ferroelectric Applications Melbourne, Australia, Nov., 1994.

## CHARACTERIZATION OF PZT HOLLOW-SPHERE TRANSDUCERS

J. T. Fielding, Jr., D. Smith, R. Meyer, Jr., S. Trolier-McKinstry, and R. E. Newnham  
Materials Research Laboratory

The Pennsylvania State University, University Park, PA 16802

**Abstract**—Millimeter size, hollow spheres of lead zirconate titanate have been fabricated by blowing gas through a fine-grained slurry of PZT-5. Techniques were developed for the classification of defects in green and sintered spheres. The spheres were poled radially between inner and outer electrodes. The dielectric and piezoelectric properties were characterized for poled spheres. The two principal resonances were a breathing mode near 700 KHz and a wall thickness mode near 10 MHz. Hydrostatic  $d_h$  coefficients  $\sim 1,000$  pC/N were measured. Pulse-echo measurements were also performed to characterize transducer performance. Potential applications for these miniature omnidirectional transducers include biomedical imaging, flow noise sensors and hydrophones.

### INTRODUCTION

Piezoceramics based on the lead-zirconate lead-titanate (PZT) solid solution system have been widely employed for transducer and actuators since their discovery in the 1950's.[1] PZT-based materials offer several advantages including large piezoelectric coefficients, moderate operating temperature range, and resistance to mechanical and electrical stress-induced depolarization. Development programs have been initiated in areas such as ceramic-polymer composites, multilayer and flextensional transducer/actuators to address the electrical/mechanical impedance matching and strain limitations inherent in bulk materials.

Another area which has received significant interest recently is the miniaturization of piezoelectric sensors and actuators. Improved resolution and smaller size are required for potential applications such as probes for *in vivo* biomedical imaging, flow noise sensors and as embedded sensors for nondestructive evaluation. Transducers produced from hollow spheres may satisfy size and performance requirements.

The spheres utilized in this study were fabricated using a process developed at the Georgia Institute of Technology based on the Torobin patent. [2,3] The process is discussed in detail elsewhere. The process has been utilized to produce large quantities of monosized spheres from many ceramic compositions with relatively uniform wall thicknesses. A variety of diameters, and wall thicknesses, ranging from 1 to 6 mm and 30 to 100  $\mu\text{m}$ , respectively, have been produced with alumina and mullite powders by modifying the slurry properties and processing conditions.[4,5]

In general, a slurry containing PZT powder (UPI 501A, Ultrasonic Powders, Inc.) is injected through a coaxial nozzle with air passing through the center, exiting in a hollow cylindrical form. Upon exiting, surface tension and hydrostatic forces close the end of the cylinder. The internal gas pressure inflates the bubble until the pressure equalizes to that of the cylinder. At this pressure, the bubble breaks free, forming a sphere. The binder is then removed from the spheres in a burn-out step and sintering at elevated temperatures is performed to achieve densification.

Preliminary studies have been performed on hollow sphere transducers developed by Meyer et al. at the Materials Research Laboratory of the Pennsylvania State University.[6]

The dielectric properties and resonance behavior of  $\sim 2.5$  mm diameter PZT spheres was characterized. The two principal resonances observed were a breathing mode near 700 KHz and a wall thickness mode near 12 MHz. The electrode configuration for the radially poled mode is shown in Fig. 1

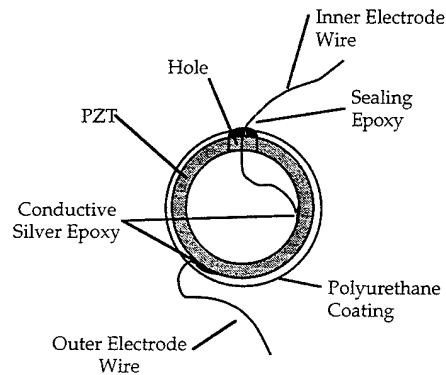


Figure 1. Electrode configuration of radially poled PZT hollow sphere transducer.

In this paper, the physical characteristics of and sources of mechanical defects in PZT hollow spheres are investigated. The measured dielectric and electromechanical behavior is presented. Discrepancies between measured and theoretical capacitance are discussed with relation to defects and nonuniformities in the wall thickness and internal electrode. Results of hydrostatic piezoelectric  $d$ -coefficient measurements are presented. As a possible explanation, the calculated stress distribution within the hollow sphere is discussed.

### PHYSICAL CHARACTERIZATION OF PZT HOLLOW SPHERES

A main objective of the study was to evaluate the feasibility of economically fabricating transducers from PZT hollow spheres produced using the Torobin process. Important mechanical criteria, measured in both green and sintered spheres, are uniformity and lack of defects in the diameter and wall thickness. With respect to electrical properties, important criteria are the capacitance, center frequency and bandwidth for the two resonance modes. A limiting factor to the maximum yield achievable was determined to be the quality of as-received green PZT hollow spheres.

The green PZT spheres were evaluated using a visual inspection along with a 'sink-float' test to identify major defects. In the sink-float test, spheres were placed in a beaker of deionized  $\text{H}_2\text{O}$ , set in a vacuum chamber, and a vacuum was drawn. Air is drawn from the interiors of spheres with small cracks, which fill with  $\text{H}_2\text{O}$  and settle after the vacuum is removed. From visual examinations,  $\sim 50\%$  of the as-received spheres exhibited visual flaws such as holes,

dimples and cracks. Approximately 20% of the as-received spheres passed the sink-float test, indicating a significant fraction of the spheres had latent defects not observable using visual inspection techniques.[7]

Physical properties were measured for 100 green spheres that passed the sink-float test. The measured green sphere diameter was  $3.31 \text{ mm} \pm 2\%$ . The average asphericity was calculated to be 1.88%, with a maximum of 6%.

To evaluate defects in sintered spheres, material lots that passed the sink-float test were processed. A binder burn-out step of  $550^\circ\text{C}$  for 30 minutes was followed by a sintering step at  $1285^\circ\text{C}$  for 90 minutes. Sintering was performed on Pt foil in  $\text{Al}_2\text{O}_3$  crucibles using  $\text{PbO}+\text{ZrO}_2$  source powder to minimize lead volatilization from the spheres.

To characterize the PZT microstructure and uniformity of the wall thickness, cross-sections of spheres were examined using environmental scanning electron microscopy (ESEM). The average grain size was  $\sim 2.5 \mu\text{m}$ , but as shown in Figs. 2a and 2b, there was significant porosity along with microcracking observed in all spheres evaluated.[7] The wall thickness variation was larger than expected, varying from  $\sim 80 \mu\text{m}$  in thick areas to  $25\text{--}30 \mu\text{m}$  in thinner wall sections. Improvements in the fabrication procedure have been proposed to minimize this variation. These defects coupled with the wall thickness variation may partially explain the lower than expected dielectric properties.

## FABRICATION OF PZT HOLLOW SPHERE TRANSDUCERS

The first step in transducer fabrication was the drilling of a small hole through the thin wall to allow for electroding and electrically contacting the inside wall. Several ( $\sim 30$ ) spheres were mounted in a thermoplastic embedding compound to minimize chip out and cracking during drilling. A  $1.02 \text{ mm}$  diameter (#60) bit was used with a small drill press to create the holes. After drilling the thermoplastic/ceramic mount was reheated above  $T_m$ , the spheres were removed and any residue was cleaned off using acetone.

The internal electrode was generated by injecting an air dry Ag paint solution (#200, Demetron, Inc.). The interior surface of the sphere was completely coated and dried for several hours. Incomplete coverage resulted when air was trapped in some of the spheres during electrode injection, resulting in degraded dielectric properties. Prior to depositing the outer electrode, a masking ring was created around the hole using a thin layer of rubber cement. The outer electrode was applied by sputtering Au for 1 minute, resulting in a thickness  $\sim 1500 \text{ \AA}$ . The mask layer was then removed leaving an insulation band to prevent shorting between the internal and external electrodes.

Electrical lead wires, consisting of  $0.76 \text{ mm}$  Ag, were attached to the inner and outer electrodes using a conductive Ag epoxy (#, Epoxy Technology, Inc.) and cured at  $250^\circ\text{C}$  for 1 hour. The hole was then sealed using Ecobond 45 epoxy (Emerson and Cuming). The entire sphere was dip-coated with polyurethane (Dexter Hysol us-0089) to permit submerged hydrostatic and near-field sensitivity measurements. Finally, the hollow spheres were polarized in a dielectric fluid (Fluorinert FC40, 3M Co.) at room temperature using a field of  $30 \text{ KV/cm}$  for 1 minute.

## ELECTRICAL CHARACTERIZATION OF SPHERES

The dielectric and electromechanical properties of PZT hollow spheres were measured and compared to calculated values for the capacitance and resonance frequency. Additionally, hydrostatic and pulse-echo measurements were performed to further characterize the response of the hollow sphere transducers.

Capacitance values and admittance spectra were measured using an HP 4194 impedance / gain-phase analyzer. The average  $1 \text{ KHz}$  capacitance and dielectric loss of the PZT spheres were  $1,440 \text{ pF}$  and  $0.037$ , respectively. The average dielectric constant was  $675$ , significantly lower than the typical value of  $1,850$  reported for UPI-501A ceramics. Again, the deviation in calculated  $K$  is due to wall thickness variation, electrode issues, microcracks and porosity observed in the sphere walls.

Polarization versus electric field behavior was evaluated. Using a calculated equivalent electrode area, the remanent polarization  $P_r$  and coercive field  $E_c$  at room temperature were found to be  $32 \mu\text{C/cm}^2$  and  $21 \text{ KV/cm}$ , respectively.[7]

Admittance spectra were utilized to observe the resonance behavior of the hollow spheres. The fundamental vibration mode is the breathing mode, consisting of a volumetric expansion and contraction. Typical admittance and phase spectra from  $200 \text{ KHz}$  to  $2 \text{ MHz}$  for the breathing mode in hollow spheres are shown in Fig. 3a. The planar coupling coefficient  $k_p$  was calculated using the following equation: [8]

$$k_p^2 = 1 - \frac{f_r^2}{f_a^2} \quad (\text{Eqn. 1})$$

The average  $k_p$  value for the spheres was  $0.35$ , lower than  $0.60$  for the bulk material due to asphericity, electrode imperfections, and clamping due to the polyurethane coating.

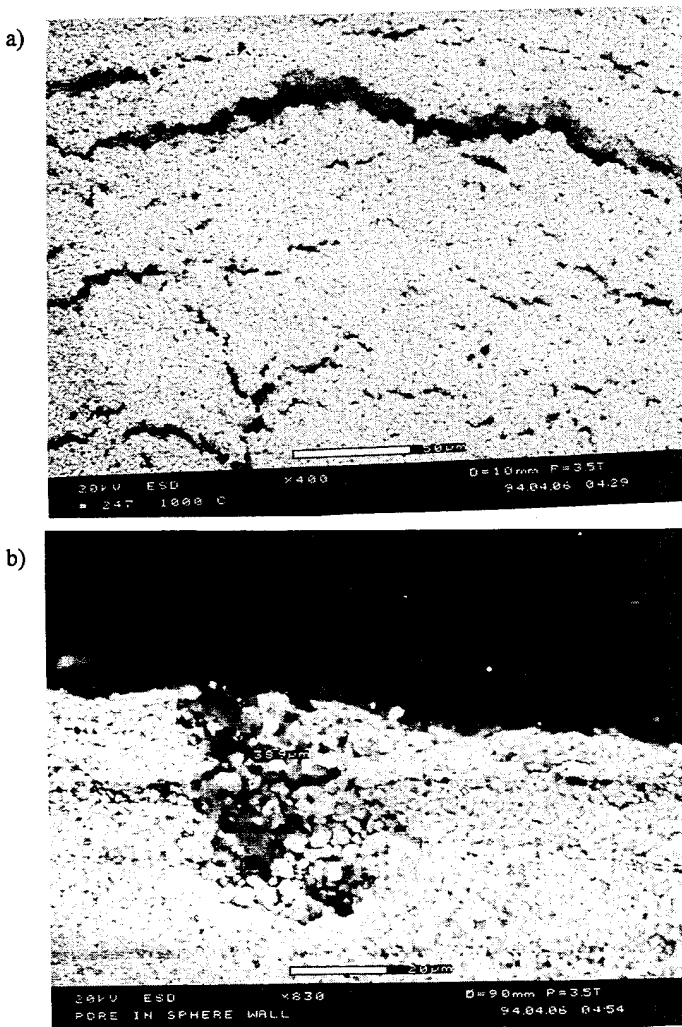


Figure 2. ESEM photomicrographs of the wall cross-section in sintered PZT hollow spheres, illustrating a) microcracking and b) porosity.

Admittance spectra were also used to observe the thickness mode resonance. In Fig. 3b, a resonance is observed ~12.1 MHz. Thickness mode resonances were not observed in all spheres evaluated and the weak response may be due to large variations in wall thickness, higher order harmonics of the breathing mode and impedance matching issues.

Hydrostatic measurements were made on spherical transducers for comparison with other current and potential hydrophone materials. Measurements were made in an oil bath at pressures from 100 to 1000 pounds with a 40 Hz stimulus. Values of  $d_h$  for several spheres, both sealed and unsealed, are shown in Fig. 4. For the sealed spheres,  $d_h$  values ranging from 600 to 1,000 pC/N were measured. This can be compared to the theoretical value of 2,910 pC/N, calculated assuming a uniform stress distribution of a perfect PZT hollow sphere.[7] Variation in  $d_h$  values may be attributed to the quality of the seal combined with the previously identified issues and indicates additional development is required.

Preliminary pulse-echo measurements were performed to determine the sensitivity of the hollow sphere transducers. A typical time and frequency response for a hollow sphere transducer for the breathing mode is shown in Fig. 5a,b. The center frequency and bandwidth were 710 KHz and 79%, respectively. A large bandwidth is desirable in commercial transducer applications. Spurious modes observed in the response result from imperfections in the sphericity and lack of 1/4 wavelength matching layers in the transducer. Further development of a matching layer material is required.

It was not possible to resolve the thickness mode frequency response. This is due to nonuniform wall thickness and higher order harmonics from the breathing mode. A significant improvement in wall thickness uniformity will be required to produce a sharp thickness mode response.

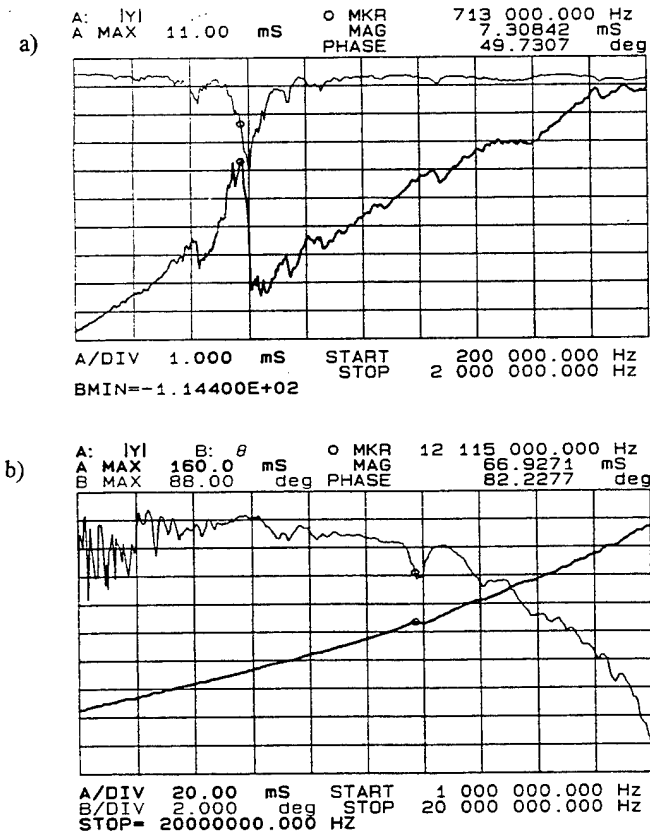


Figure 3. Admittance spectra for a PZT hollow sphere transducer for the a) breathing and b) thickness resonance modes.

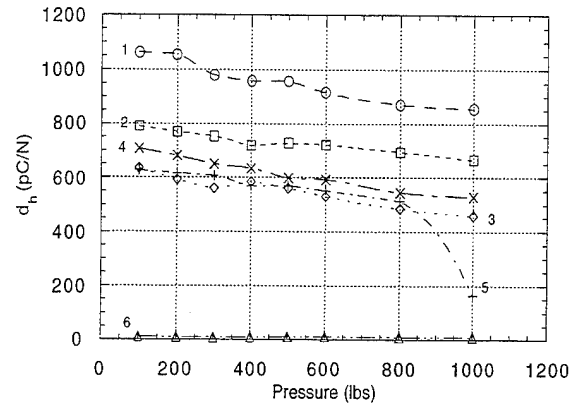


Figure 4. Hydrostatic  $d_h$  coefficient as function of applied load for sealed spheres (1-5) and an unsealed sphere (6).

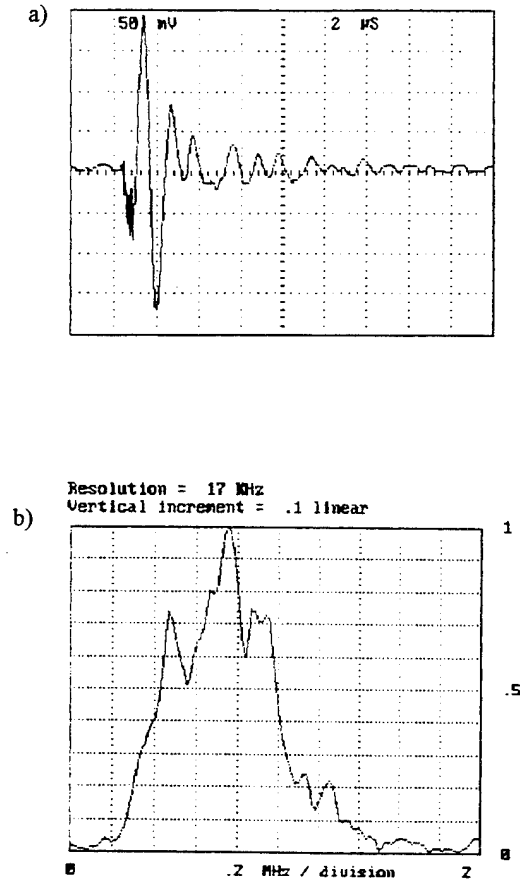


Figure 5. A) Time-domain and b) frequency domain of PZT hollow sphere transducers measured using pulse-echo method.

## SUMMARY

Analyses of defects and physical characteristics in PZT hollow spheres, in the as-received materials and introduced during processing, was performed. Several areas of opportunity were identified. Significant visual and latent defects were found in the green spheres along with wall thickness variations within a sphere between 50 and 150  $\mu\text{m}$ . The dielectric and electromechanical properties were characterized for hollow spheres with a radially poled electrode configuration. Capacitance values were lower than expected due to electrode issues, nonuniform wall thickness, and microcracking observed in the walls. Large hydrostatic piezoelectric coefficients, with  $d_h$ 's  $\sim 1,100$  pC/N were measured. With improvements to the fabrication procedure, this processing technique may be able to yield large quantities of inexpensive piezoelectric hollow spheres. The piezoelectric properties may be utilized in several biomedical, flow noise and non-destructive evaluation applications.

## ACKNOWLEDGMENTS

The authors would like to thank Dr. Hal Kunkel at Echo Ultrasound, Reedsville, PA for his assistance in performing pulse-echo field sensitivity measurements.

- [1] B. Jaffe, W. R. Cooke, Jr. and H. Jaffe, *Piezoelectric Ceramics*, Academic Press (1971).
- [2] A. T. Chapman, J. K. Cochran, J. M. Britt, and T. J. Hwang, "Thin-Wall Hollow Spheres," DOE-ECUT Program, ORNL Subcontent 86X-22043C, Annual Reports, 1987, 1988, 1989, Department of Energy, Washington, DC.
- [3] L. B. Torobin, "Methods of Making Hollow, Porous Microspheres," U.S. Patent No. 4,671,909 (1987).
- [4] A. T. Chapman, J. K. Cochran, M. K. Adicks, G. E. Carlson, P. R. Chu, J. H. Chung, R. B. Clancy, T. R. Ford, S. D. Furlong, T. J. Hwang, C. M. Moore, and M. J. Shapiro, "Thin-Wall Hollow Spheres from Slurries," Materials Engineering Department, Georgia Institute of Technology, Poster Presentation for Advanced Industrial Concepts Materials Program, Department of Energy, Albuquerque, NM (1991).
- [5] J. K. Cochran, G. E. Carlson, P. R. Chu, J. H. Chung, R. P. Gonzales, T. J. Hwang, A. S. Jensen, and L. A. Touryan, "Thin-Wall Hollow Spheres from Slurries," Materials Engineering Department, Georgia Institute of Technology, Poster Presentation for Advanced Industrial Concepts Materials Program, Department of Energy, Pleasanton, CA (1992).
- [6] R. Meyer, Jr., H. Weitzing, Q. Xu, Q. Zhang, and R. E. Newnham, "Lead Zirconate Titanate Hollow-Sphere Transducers," *J. Am. Cer. Soc.*, **77** [6], 1669-72 (1994).
- [7] D. R. Smith, "Lead Zirconate Titanate Microspheres for Ultrasonic Applications," M.S. Thesis, The Pennsylvania State University, (1994, to be published).
- [8] D. A. Berlincourt, D. R. Curan, and H. Jaffe, "Piezoelectric and Piezomagnetic Materials and Their Function in Transducers," pp. 169-257 in *Physical Acoustics*, Vol. 1, Part A, Edited by W. P. Mason, Academic Press, NY (1964).



# Fabrication of 2-2 Connectivity PZT / Thermoplastic Composites for High Frequency Linear Arrays

W. Huebner, M. R. Reidmeyer, and J. W. Stevenson

Department of Ceramic Engineering  
University of Missouri-Rolla  
Rolla, Missouri 65401

L. Busse

Tetrad Corporation  
Englewood, CO 80112

## ABSTRACT

An alternate approach for fabricating PZT/polymer composites with 2-2 connectivity with fine scales is described. Thin ( $\leq 20\mu\text{m}$ ) sintered PZT plates and sheets of a thermoplastic polymer film ( $\leq 10\mu\text{m}$ ) were bonded together via thermal processing. Stack sintering of tape cast PZT generated the necessary PZT plates, while tape cast polymers were used to control the thermoplastic thickness. Composite blocks were cut to required dimensions for linear arrays, electroded, and poled. Electromechanical properties were measured to evaluate the composites. The significance of this fabrication technique is that it is able to generate 2-2 structures at a scale level unachievable by conventional dice-and-fill fabrication methods.

## INTRODUCTION

Piezoelectric composites are now widely used for many ultrasonic transducer applications. Reviews by Gururaja et. al [1], Smith [2-5] and Oakley [6] clearly illustrate the influence of scale, connectivity and symmetry on the properties of composite piezoelectrics, and lend guidance to the transducer engineer for their application. In essence, the biggest advantage of using a piezoelectric composite compared to its monolithic counterpart is its higher electromechanical coupling coefficient, which in turn leads to higher sensitivities and broader bandwidths.

An ongoing trend in medical ultrasonics is to increase the frequency of imaging systems ( $\geq 10\text{ MHz}$ ), for applications such as phased linear array transducers used for laparoscopy and, in the future, intravascular imaging. However, these transducers must have a very fine spacing of the piezoelectric elements ( $\leq 50\mu\text{m}$ ) in order to minimize acoustic clutter associated with grating lobes. In addition, subdivision of the piezoelectric into smaller elements would minimize coupling to unwanted lateral vibrational modes, with concurrent improvements in the thickness coupling coefficient. Currently, the synthesis techniques needed to achieve the requisite scale and periodicity of the composite have become the effective limitation for their exploitation at higher frequencies.

For instance, Figure 1 shows a typical process for fabricating a phased linear array, a modified "dice-and-fill technique" [7]. The finest interelement spacing is controlled by the kerf width of the saw blade, which is currently  $\approx 25\text{-}40\mu\text{m}$ . The  $\text{Pb}(\text{Zr,Ti})\text{O}_3$  (PZT) can be reliably diced into structures  $\approx 50\mu\text{m}$  in size. This scale is sufficient for 10 MHz transducers, but higher frequencies will dictate a further reduction. Considerations of dicing technologies coupled with grain size and strength limitations of the ceramic dictate that new fabrication technologies be developed, which is the subject of this paper.

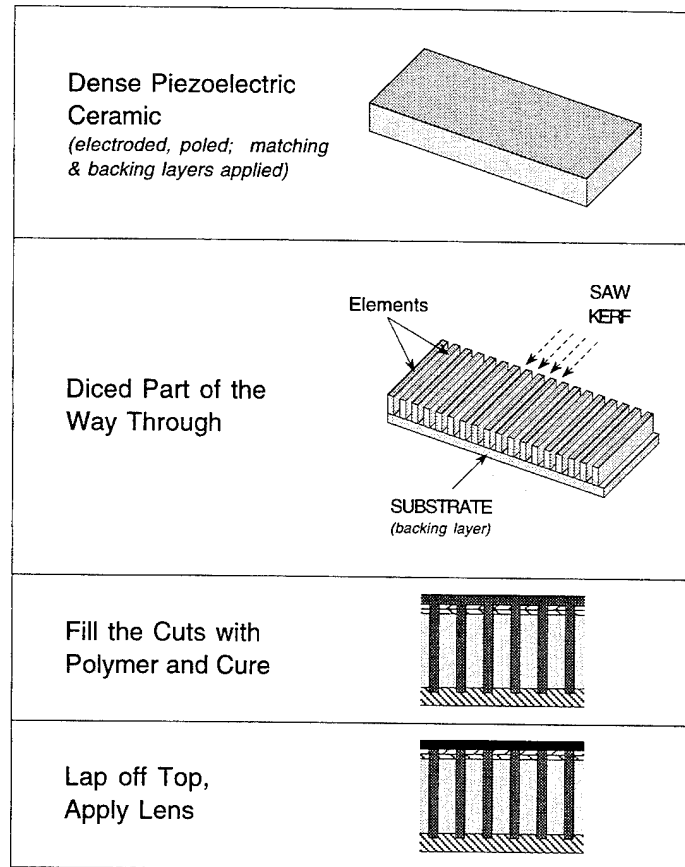
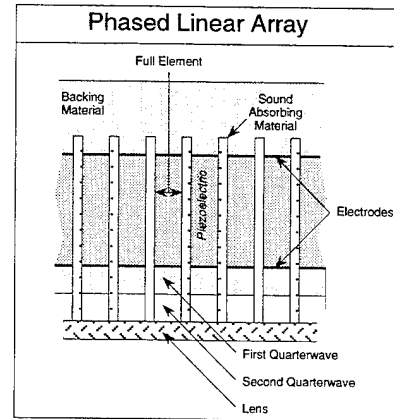


Figure 1. Schematic illustration of the dice and fill technique used to fabricate phased linear arrays.

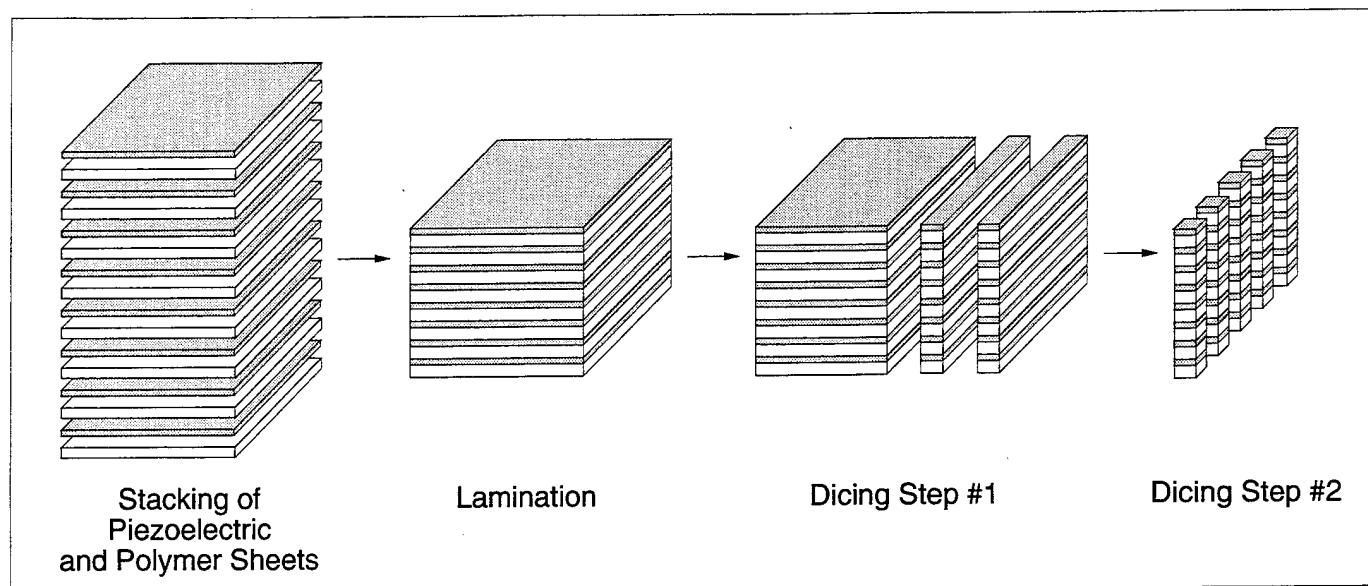


Figure 2. Overview of the process used to synthesize the 2-2 composites.

The process is simple; pre-sintered PZT plates are joined together using a thermoplastic adhesive polymer film to yield a composite with 2-2 connectivity. Dicing is only used to achieve the final transducer geometry. This technique allows for the fabrication of finer scale composites, and is described below.

### EXPERIMENTAL PROCEDURE

Sintering of tape cast PZT was used to produce the piezoelectric elements. Slurries were prepared by dispersing a pre-calcined soft PZT powder in a solution containing 17 ml ethanol, 8 ml toluene, 0.5 g Menhaden fish oil, and 3 g polyvinyl butyral. The slurries were de-aired, cast on glass substrates with a single knife doctor blade, and dried at room temperature in air. The PZT tapes were cast at various thicknesses ranging from 30 to 250  $\mu\text{m}$  to obtain sintered thicknesses ranging from 10 to 55  $\mu\text{m}$ . Square sections (2 cm x 2 cm) of the tapes were stack-sintered using polished PZT setters (85  $\mu\text{m}$  thickness),  $\text{PbZrO}_3$  powder as the lead source, and covered with an  $\text{Al}_2\text{O}_3$  crucible. Binders were burned out in air at 450°C, followed by sintering at 1250°C for 30 minutes. The PZT setters maintain a high  $\text{PbO}$  activity around the tapes and result in flat elements.

Polyvinyl formal (PVF) was chosen as the thermoplastic due to its excellent adhesive strength to PZT. A PVF solution was prepared for tape casting by dissolving it in ethanol and toluene. After being cast on glass substrates with the doctor blade at varying thicknesses, PVF films were dried at room temperature in air. The thickness of the films was adjusted between 9 and 20  $\mu\text{m}$  by varying the casting thickness.

Figure 2 exhibits the procedure for preparing the composites. Sintered PZT plates and PVF films were alternately stacked and then laminated by heating (210°C) the stacks in a vacuum oven under uniaxial compression (0.1MPa). Transducers were sliced out of the composite block using a dicing saw (Kulicke & Soffa Industries, Model 775 Wafer Saw), electroded with sputtered gold, then poled at room temperature at 25 kV/cm for 30 minutes. Resonance and dielectric measurements were performed with an impedance analyzer (Hewlett-Packard 4194A Impedance Analyzer with a 41941A Impedance Probe and 16092A Test Fixture).

### RESULTS AND DISCUSSION

This fabrication technique dictates that the sintered PZT plates are thin and flat, and that the thermoplastic polymer has good adhesion to the PZT. Using stack sintering, PZT plates with thicknesses between 10 and 55  $\mu\text{m}$  were easily achieved, in all instances for substrates 1.5 x 1.5 cm. Larger area plates were difficult to handle, but considerations of the final transducer size make it unnecessary to make larger composite blocks. Densities were  $\geq 98\%$  theoretical, and grain sizes were  $\approx 3\text{--}5\text{ }\mu\text{m}$ . During initial studies the piezoelectric properties of individual plates were evaluated to make sure the sintering process did not result in inactive surfaces. Poling was easily achieved without breakdown, with  $d_{33}$  coefficients  $\geq 500\text{ pC/N}$ , and a  $k_p \approx 60\%$  (thickness mode resonance too high to measure). Hence this process allows for the synthesis of thin PZT elements as well as independent control over the grain size. Other strategies for fabricating structures at this scale level also result in smaller grain sizes, which is detrimental to the piezoelectric properties of PZT ceramics [8].

Figure 3 shows a series of SEM micrographs of lapped composites with differing PZT and PVF thicknesses. Clearly the PVF provided excellent adhesion to the PZT plates; bonding at the PZT/polymer interfaces was uniform with only a few noticeable voids or delaminations. The PZT elements were not fractured. Note the smallest thickness of the PVF is  $\approx 9\text{ }\mu\text{m}$ ; this results in an interelement spacing that is three times closer than can be achieved using dicing.

The electrical performance of the composites of Figure 3 are contained in Table I. Values of the thickness electromechanical coupling coefficients of the composites,  $\bar{k}_t$ , were calculated from the impedance measurements using [9]:

$$\bar{k}_t^2 = \frac{\pi}{2} \frac{f_{\min}}{f_{\max}} \tan\left(\frac{\pi}{2} \frac{f_{\max} - f_{\min}}{f_{\max}}\right) \quad (1)$$

where  $f_{\min}$  and  $f_{\max}$  are the frequencies of minimum and maximum impedance corresponding to the thickness resonant mode. The mechanical quality factor,  $Q_m$ , was calculated using [9]:

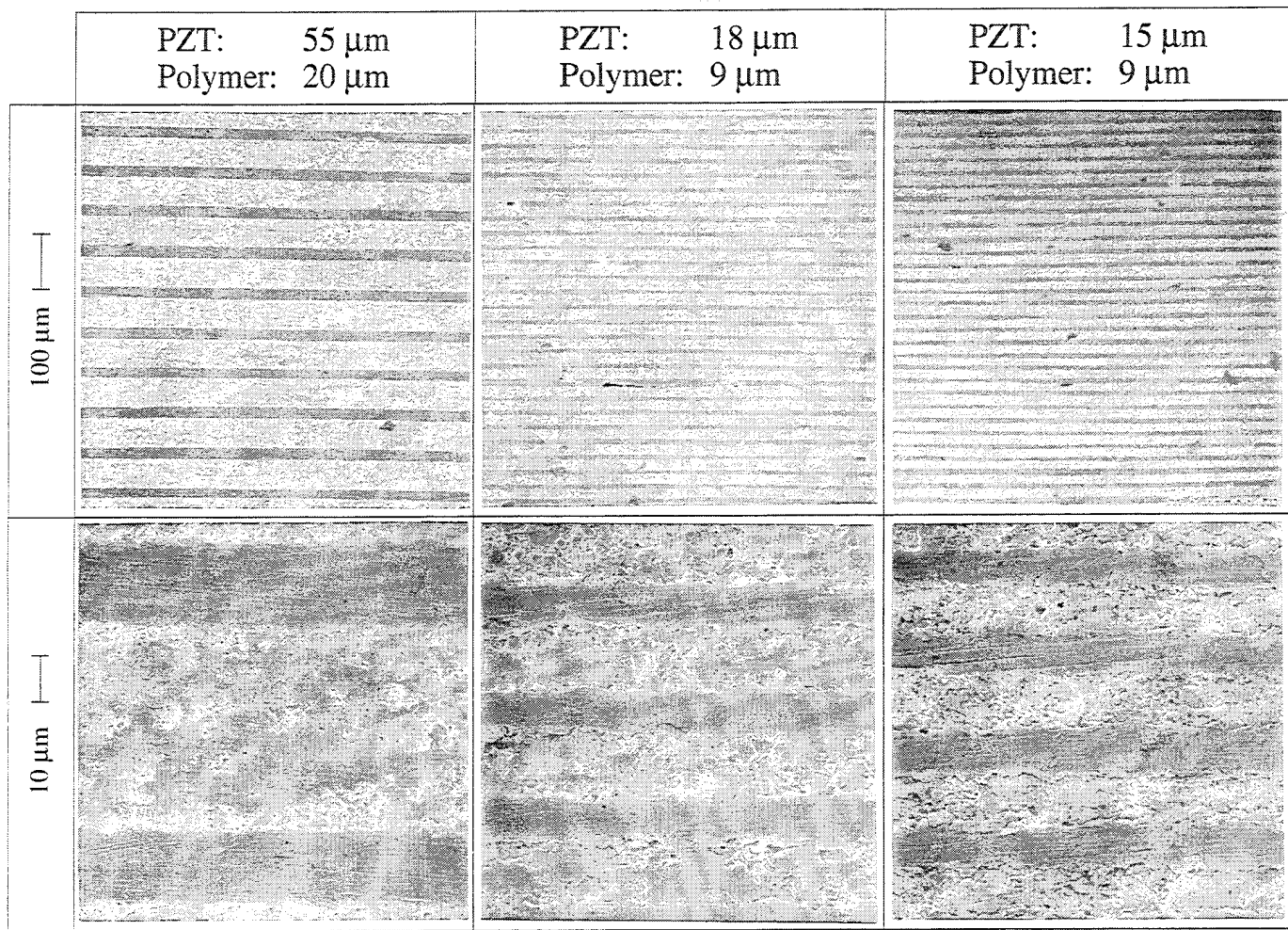


Figure 3. SEM micrographs of several PZT/PVF composites with varying PZT and PVF thicknesses.

$$Q_m = [4\pi \Delta f |Z_m| C]^{-1} \quad (2)$$

where  $\Delta f = f_{\max} - f_{\min}$ ,  $|Z_m|$  is the magnitude of the electrical impedance at  $f_{\min}$ , and  $C$  is the capacitance measured at 1 kHz.

Figure 4 exhibits the thickness mode impedance and phase angle plot, for the third composite shown in Figure 3. This composite was 250  $\mu\text{m}$  thick, with 105 elements composed of 15  $\mu\text{m}$  thick PZT elements separated by 9  $\mu\text{m}$  thick layers of PVF. The thickness mode resonance is sharp, with  $k_t=0.68$ . The lower frequency harmonics are due to the planar mode resonance of the PZT bars ( $\approx 400$  kHz). For an actual transducer the overall dimensions would move the planar resonance closer to the thickness mode, and hence could be a problem. Materials with a high  $k_t/k_p$  ratio such as a modified lead titanate compositions would minimize this problem, albeit at the expense of sensitivity.

As shown in Table I, values of  $k_t$  for the composites ranged between 0.63-0.68. These high values of  $k_t$ , are similar to values of  $k_t$  reported for PZT/epoxy composites prepared by the dice-and-fill technique [10] and approach the  $k_{33}$  value for soft PZT compositions. The high electromechanical coupling shown by these composites make them excellent candidates for linear array transducer applications operating at frequencies  $\geq 10$  MHz.

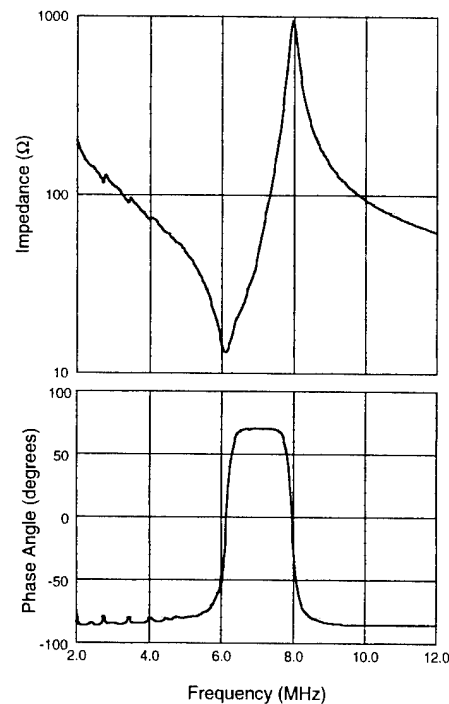


Figure 4. Thickness mode resonance results for a 250  $\mu\text{m}$  thick, composite with 105 elements composed of 15  $\mu\text{m}$  thick PZT elements separated by 9  $\mu\text{m}$  thick layers of PVF.

TABLE I

## ELECTROMECHANICAL PROPERTIES OF PZT/PVF COMPOSITES

# of PZT Elements	PZT thickness ( $\mu\text{m}$ )	PVF thickness ( $\mu\text{m}$ )	$k_t$	$Q_m$
60	55	20	0.63	5.5
105	15	9	0.64	5.1
105	18	9	0.68	5.1

## CONCLUSIONS

A simple technique for fabricating PZT/polymer composites was developed which allows for the fabrication of 2-2 composites on a finer scale than allowed by dice-and-fill techniques. PZT plates with sintered thicknesses as low as 10  $\mu\text{m}$  were produced. The thickness of the polymer could be reduced down to 9  $\mu\text{m}$ , which yields an interelement spacing three times smaller than that attainable with the dice-and-fill technique. This technique offers the additional advantage of being able to build aperiodic structures by simply changing the thickness of the polymer film. By adding filler materials to the polymer, one would also expect the attenuation of the intervening polymer could be increased, which would decrease crosstalk between elements.

Acknowledgments

Financial support was provided by Tetrad Corporation and N.I.H. Grant HL 44230.

## REFERENCES

- [1] T.R. Gururaja, A. Safari, R.E. Newnham and L.E. Cross, "Piezoelectric Ceramic-Polymer Composites for Transducer Applications," pp. 93-128 in *Electronic Ceramics*, ed. L.M. Levinson, Marcel Dekker, New York, New York (1987).
- [2] W.A. Smith and A.A. Shaulov, "Composite Piezoelectrics: Basic Research to a Practical Device," *Ferroelectrics*, **87**, 309-320 (1988).
- [3] W.A. Smith, "The Role of Piezocomposites in Ultrasonic Transducers," p. 755-766, *Proceedings of the 1989 IEEE Ultrasonics Symposium* (1989).
- [4] W.A. Smith, "The Application of 1-3 Piezocomposites in Acoustic Transducers," pp. 145-152, *Proceedings of the 1990 IEEE Symp. on the Applications of Ferroelectrics*, (1991).
- [5] W.A. Smith, "The Key Design Principle for Piezoelectric Ceramic / Polymer Composites," pp. 825-838, *Recent Advances in Adaptive and Sensory Materials and Their Applications*, ed. by C.A. Rogers and R.C. Rogers, Technomic Publishing, Lancaster, PA (1992).
- [6] C.G. Oakley, "Analysis and Development of Piezoelectric Composites for Medical Ultrasound Transducer Applications," Ph.D dissertation, Penn State University (1991).
- [7] H.P. Savakus, K.A. Klicker, and R.E. Newnham, "PZT-Epoxy Piezoelectric Transducers: A Simplified Fabrication Procedure," *Mat. Res. Bull.*, **16**, 677-680, 1981.
- [8] A.H. Webster and T.B. Weston, "The Grain-Size Dependence of the Electromechanical Properties in Lead Zirconate-Titanate Ceramics," *J. Can. Cer. Soc.*, **37**, 41-44, 1968.
- [9] IRE Standards on Piezoelectric Crystals: Measurements of Piezoelectric Ceramics, 1961.
- [10] H. Takeuchi and C. Nakaya, "PZT/Polymer Composites for Medical Ultrasonic Probes," *Ferroelectrics*, **68**, 53-61, 1986.

**Abstract** — Rochelle salt nanocrystals are grown in the small pores of a porous glass (Corning porous VYCOR glass, average pore diameter 6 nm) and silica-gels with two different pore sizes, 20 nm and 100 nm. Crystallization characteristics of Rochelle salt nanocrystals are studied by X-ray diffraction method. We also measure dielectric property,  $^1\text{H}$  NMR relaxation, and IR reflectance of the nanometer sized Rochelle salt crystals embedded in porous glass. Results of nanocrystals are compared with bulk Rochelle salt and differences in the observed properties are explained in the light of size effects of the ferroelectric material. A possible application of the new material form is found.

## INTRODUCTION

Physical properties of materials sometimes depend on the size of sample. Typical examples can be found in critical phenomena and phase transition properties such as lowering of melting temperature of small particles [1], disappearance of magnetism in ultrafine particles of magnetic materials [2], and increase in the critical field of "zero-dimensional" superconductors which are again ultrafine particles of superconducting materials [3]. However, for the finite size effect to be manifested one need to constrain the particle size smaller than the correlation length of the interacting species relevant to the transitions.

For ferroelectricity which is due to the coupling of electric dipole moments formed by ionic displacements the critical size is not well known and may depend on materials and specific measurement conditions. Nevertheless, it is on the order of a few tens nm [4]. For smaller samples than the critical size one cannot expect the bulk ferroelectricity anymore, however, properties of the small size particles can be interesting and may be useful in applications due to the residual interactions between the dipoles [5]. Properties of small sized ferroelectric material have been studied experimentally and theoretically [6].

There have been appeared different approaches to the generation of small size ferroelectric particles to facilitate the study of size dependent properties. Examples are coprecipitation technique, noble gas condensation or coevaporation methods [7], and alkoxide process [8]. Each method has its own advantages and drawbacks. We develop a new method by which one can control the size of nanocrystalline particles easily, and furthermore, without introducing strain to the crystals. The method has been applied already [6] to fabricate  $\text{KH}_2\text{PO}_4$  (KDP),  $\text{NH}_4\text{H}_2\text{PO}_4$  (ADP) and  $\text{NH}_4\text{H}_2\text{AsO}_4$  (ADA) nanocrystals and we present here some of our results on the  $\text{NaKC}_4\text{H}_4\text{O}_6 \cdot 4\text{H}_2\text{O}$  (Rochelle salt) nanocrystals.

Rochelle salt (RS) is the first ferroelectric crystal discovered [9], however, it is unusual that the ferroelectric phase appears between two nonferroelectric phases separated by the two Curie points  $T_{c1} = 24^\circ\text{C}$  and  $T_{c2} = -18^\circ\text{C}$ . Even though there have been a number of studies on the structures of the two nonferroelectric phases, identification of the structures is still an intriguing problem [10]. Antipolar ordering of dipoles into two sublattices was claimed for the low temperature nonferroelectric phase [11]. Particle size dependent dielectric constant was studied down to 20 ~ 50  $\mu\text{m}$  sizes as a function of temperature and showed smearing of the prominent peak structures at the two Curie temperatures as the particle size was decreased [12]. We believe further study on the smaller size RS will shed some light on the nature of ferroelectric phase transition and the nonferroelectric phases. This report is an initial step of our efforts in that direction.

## EXPERIMENTAL PROCEDURES AND RESULTS

We first examine the pore size distribution of the porous glass and then describe the fabrication method of nanocrystalline Rochelle salt embedded in the porous glass together with experimental results.

## Pore Size Distribution

Porous materials possess many small pores. Sizes of the pores are frequently broadly distributed. There are a number of methods to examine the pore size distribution including the gas adsorption/desorption technique, mercury intrusion method and nuclear magnetic resonance relaxation analysis (NMRA) methods [13]. Recently an interesting method was developed [14] to facilitate the pore size distribution measurements. It utilizes the size dependent reduction in melting temperatures of liquids confined in the pores.

The difference in melting temperatures of bulk,  $T_{m,bulk}$ , and small size particles with size  $x$ ,  $T_m(x)$ , is given by the Gibbs-Thompson relation [1],

$$T_{m,bulk} - T_m(x) = k/x. \quad (1)$$

In the above the proportionality constant  $k$  is a characteristic of the liquid material and is given by

$$k = 4 \sigma T_{m,bulk} / (x \Delta H_f \rho_s), \quad (2)$$

where  $\sigma$  is the surface energy of the solid-liquid interface,  $\Delta H_f$  is the bulk enthalpy of fusion, and  $\rho_s$  is the density of the solid.

By choosing the proper liquid material (cyclohexane was used in Ref. [14]) to be filled in the pores, one can get the pore size distribution  $f(x)$  from the temperature variation of NMR signal intensity  $I(T)$ , which is a measure of the volume fraction of material in liquid phase at temperature  $T$ , by

$$f(x) = k/x^2 (dI/dT). \quad (3)$$

We use the method to investigate the size distribution of Corning porous VYCOR glass 7930 and the result in Fig. 1 is confirming both the mean size and relatively narrow size distribution of pores as inferred by the manufacturer.

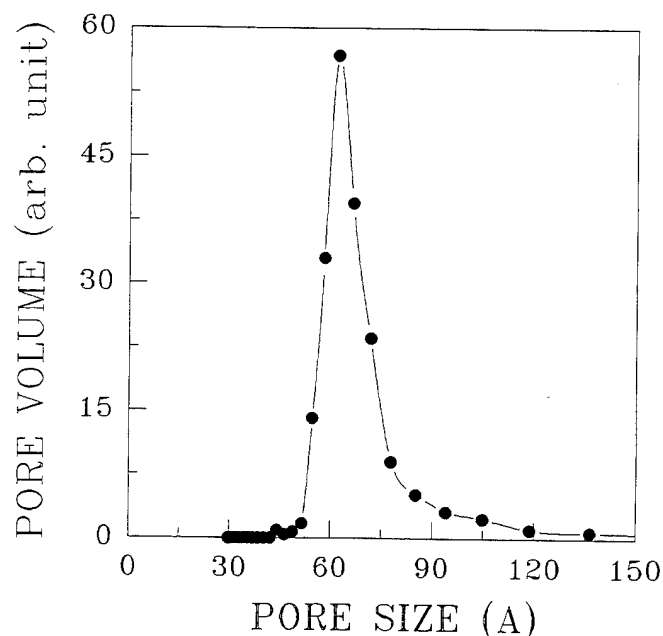


Fig. 1: Pore size distribution of Corning VYCOR glass. It is obtained from the  $^1\text{H}$  NMR spin-echo intensity measurement as a function of temperature after the pores are filled with cyclohexane following the method of Ref. [14].

The nanocrystals of RS are grown in the pores of porous glass by following two steps. First, aqueous solution of RS is impregnated into the glass plate upto an incipient wetting condition where all the pores of the glass are filled. Then, the impregnated glass is dried in an oven to allow crystallization of RS inside the pores.

The idea of this impregnation technique of ferroelectric nanocrystals is borrowed from the well known preparation method of supported platinum catalysts. We intend to take advantage of the method, i.e. relatively uniform size and shape of the crystals formed with minimal strain introduced. Furthermore, the crystal sizes can be controlled very easily by changing the concentration of the solution but are remained below a limit naturally given by the pore size. The average size of crystals,  $d_{av} = 4.8$  nm, is estimated from the amount of material impregnated and using the known pore size and porosity (relative pore volume  $\approx 28\%$ ) of the glass.

The same sample preparation method is also applied to two different silica-gels with pore sizes 20 nm and 100 nm to obtain larger RS nanocrystals,  $d_{av} = 15$  nm and 75 nm, respectively, for the purpose of comparison.

#### X-ray Diffraction Study

X-ray diffraction peaks can be used to verify the crystallization into minute RS crystals as well as to confirm the size of crystals from the extra broadening due to small size of particles using the Scherrer method.

For X-ray diffraction measurements a powder diffractometer (Rigaku Model D/Max-3C) is used. The X-ray diffraction patterns shown in Fig. 2 are measured by Cu K $\alpha$  line using Ni filter at room temperature and indicate the impregnated samples in the largest pores (Fig. 2b) are RS crystals with the same lattice parameters as bulk (Fig. 2a). One can notice the broad background of the gel matrix together with a broadening of diffraction peaks which is a characteristic of small-sized samples. The estimated particle size from the peak broadening is 40 nm, however, due to the large instrumental linewidth the difference is not considered seriously.

For smaller size RS particles embedded in smaller pores of silica-gel (Fig. 2c) and Corning glass (Fig. 2d) the peaks are not seen possibly due to extensive line broadening.

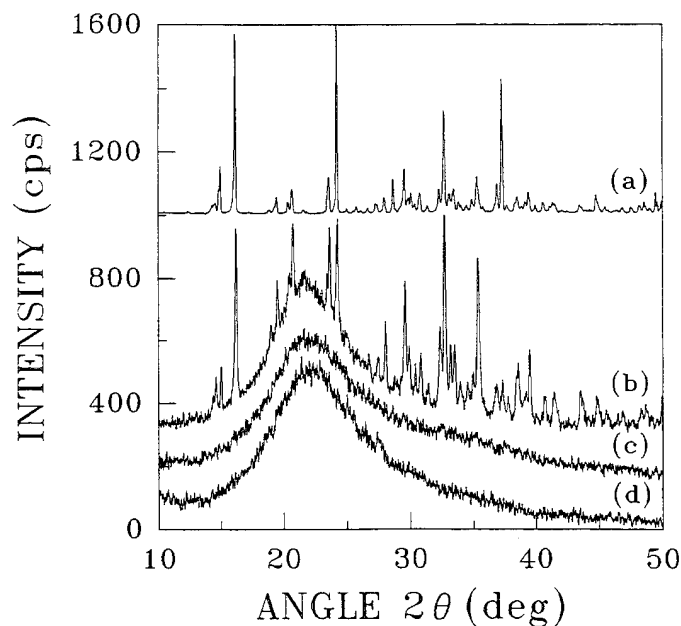


Fig. 2: X-ray diffraction pattern of RS samples. Data are for (a) 10  $\mu$ m powder representing bulk RS, (b) 75 nm particles embedded in 100 nm pores of silica-gel, (c) 15 nm particles in 20 nm pores of silica-gel, and (d) 4.8 nm particles in 6 nm pores of Corning VYCOR glass. The intensity of sample (a) is divided by 100 and spectra are shifted vertically to be more discernible.

#### Dielectric Measurements

Dielectric properties of RS nanocrystals embedded in Corning porous VYCOR glass are studied and compared with single crystalline and powder pellet form RS samples. For dielectric measurements the RS powders of 10  $\mu$ m particle size are pelletized in a compression unit with pressure up to 30 MPa.

All the samples are of thickness 1.2 ~ 1.5 mm. Both faces of each sample are coated with silver paint (Western Gold & Platinum, Type 1570 Screen Silver Paint) to form electrodes with 8 mm diameters. The real and imaginary parts of electrical impedance of the samples are measured by using a LCR meter (HP 4275A) at ten different frequencies ranging from 10 kHz to 10 MHz.

Data shown in Fig. 3 are examples of temperature dependent dielectric constants measured at 1 MHz. As the particle size is decreased the well known peaks in dielectric constant of RS at two Curie temperatures (Fig. 3a) are decreased (Fig. 3b) and then disappeared (Fig. 3c). The decrease in peak heights of the powder pellet sample is due to inhomogeneous nature of the sample [12]. Characteristic features of the three different samples are the same when these are measured at different frequencies, but the magnitudes of the dielectric constant depend on the measurement frequency. Particularly, the rise of dielectric constant with increasing temperature for the RS nanocrystal sample embedded in the porous glass becomes steeper when it is measured at lower frequencies. It even exceeds 1000 when measured at 10 kHz and temperatures above room temperature.

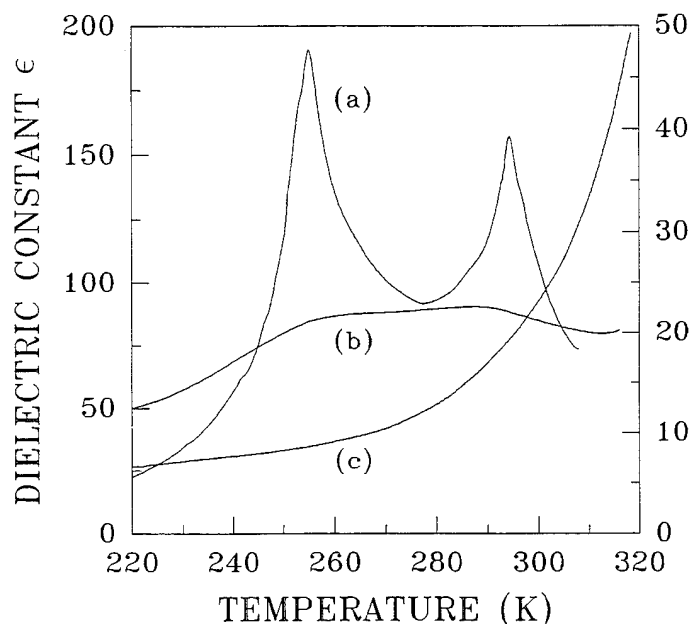


Fig. 3: Temperature dependent dielectric constant of (a) the RS single crystal with electric field in the direction of a-axis, (b) powder pellet, and (c) nanocrystals embedded in porous glass measured at 1 MHz. Scales on the left vertical axis are for curve (a) and the ones on the right axis are for curves (b) and (c).

Measurements of imaginary part, i.e. the dielectric loss, show the similar behavior. The ratio between the imaginary and real parts of complex dielectric constants is loss  $\tan\delta$  and that of the porous glass sample embedded with RS nanocrystals increases with rising temperature as shown in Fig. 4. The loss  $\tan\delta$  measured at 10 kHz shows a broad peak at around 295 K. The warming and cooling experiments show no significant difference.

To convert the measured apparent dielectric constants of the glass plate embedded with RS nanocrystals into those of RS nanocrystals one need to use a form of approximations, i.e. the Bottcher's effective medium formula for an example [12].

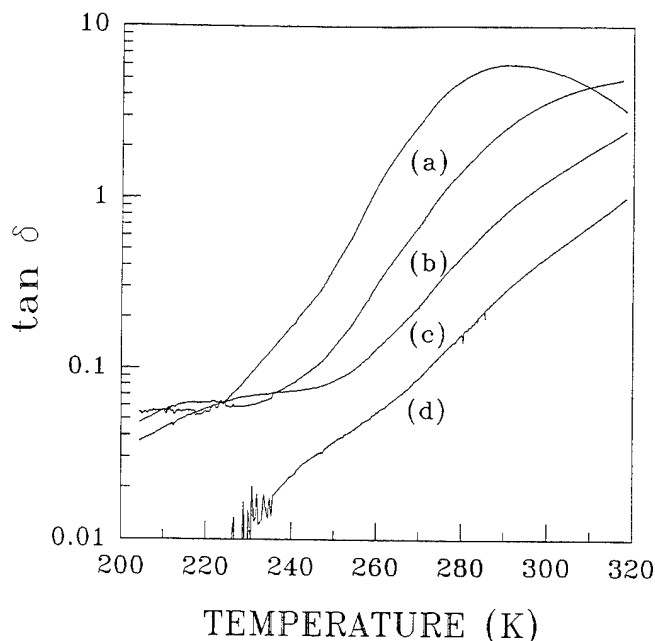


Fig. 4:  $\tan \delta$  of porous glass sample embedded with RS nanocrystals measured at frequencies (a) 10 kHz, (b) 100 kHz, (c) 1 MHz, and (d) 10 MHz.

#### $^1\text{H}$ Nuclear Magnetic Resonance (NMR) Relaxation

$^1\text{H}$  NMR studies are made with a homebuilt pulse NMR spectrometer operating at 15 MHz and an electromagnet with magnetic field  $B = 3.5$  kOe. Typical characteristics of the spectrometer are  $2.5 \mu\text{s}$   $90^\circ$  pulsewidth,  $10 \mu\text{s}$  receiver deadtime, and rf phase coherent. Add-and-subtract phase alternating signal average technique is used to be able to discern the echo signal from ringdown noise formed after strong rf pulses. Usual Hahn-echo sequence is used to measure the spin-spin relaxation time. For convenience a simple repetitive saturation method is used for the spin-lattice relaxation measurements. In the method the spin-echo signal intensity after repetition of a  $90^\circ$ - $\tau$ - $90^\circ$  pulse sequence is measured with a fixed pulse separation time  $\tau$  and repetition time  $t$ . The spin-lattice relaxation time  $T_1$  is found from the intensity by

$$E(t) = E_0(T) \{1 - \exp(-t/T_1)\}. \quad (4)$$

In the above  $E_0(T)$  is the equilibrium echo signal height of a sample at an absolute temperature  $T$  and can be obtained by choosing a long enough repetition time, i.e.  $t \gg T_1$ .

The spin-lattice relaxation time measurements shown in Fig. 5 indicate difference of  $T_1$  at low temperatures between the bulk RS and nanocrystals embedded in porous glass. The  $T_1$  of bulk sample shows an increase as temperature is lowered. A slight dip in  $T_1$  below the monotonic temperature dependence at the two Curie temperatures is due to slowing down of spin dynamics near the phase transitions. Only a part of protons in the molecules are involved in the ferroelectric transitions and the effect on  $T_1$  is not large.

The spin-lattice relaxation time of RS nanocrystals embedded in porous glass, on the other hand, shows very different behavior than the bulk sample. The temperature dependence becomes greatly reduced and only a slight increase in  $T_1$  is noticed when it is cooled down to 200 K.

The spin-spin relaxation times  $T_2$  of the both samples are less temperature dependent. The  $T_2$  of RS embedded in porous glass drops from  $500 \mu\text{s}$  at 310 K to about  $70 \mu\text{s}$  at 190 K. In contrast, the  $T_2$  of bulk RS is about  $40 \mu\text{s}$  and, furthermore, independent of temperature.

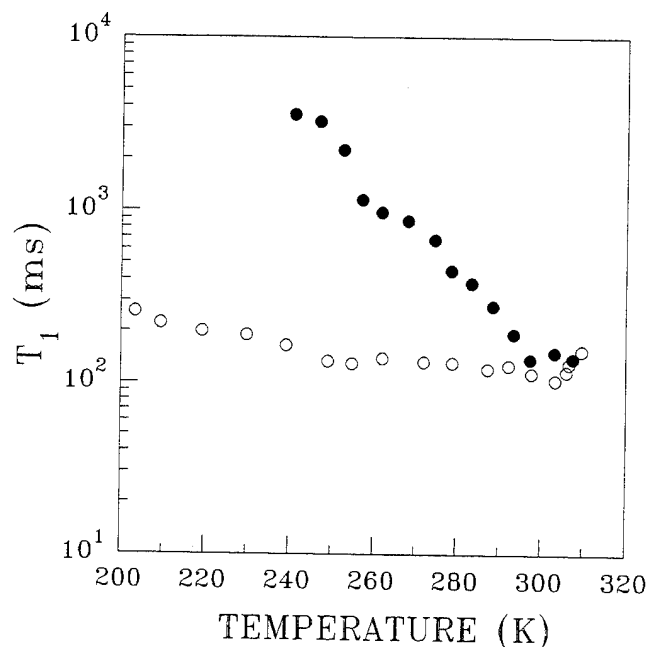


Fig. 5: Temperature dependence of spin-lattice relaxation time of (a) bulk RS sample (powders of  $10 \mu\text{m}$  size particles) and (b) the RS nanocrystals embedded in porous glass.

#### IR Reflectance

Infrared reflectivity is measured for the RS nanocrystals embedded in porous glass. The reflectivity shown in Fig. 6 is measured by using a Fourier transform spectrometer (BOMEM Inc.) with Globar source and MCT detector at room temperature. The spectrum from the sample (Fig. 6a) shows the characteristic peak structures of bulk RS (Fig. 6b), in particular at  $700 \text{ cm}^{-1}$ ,  $1300 \text{ cm}^{-1}$ ,  $1600 \text{ cm}^{-1}$ , and  $3300 \text{ cm}^{-1}$ , in addition to the two prominent peaks from the porous glass matrix (Fig. 6c). We need more work to analyze the spectra due to inhomogeneous nature of the sample.

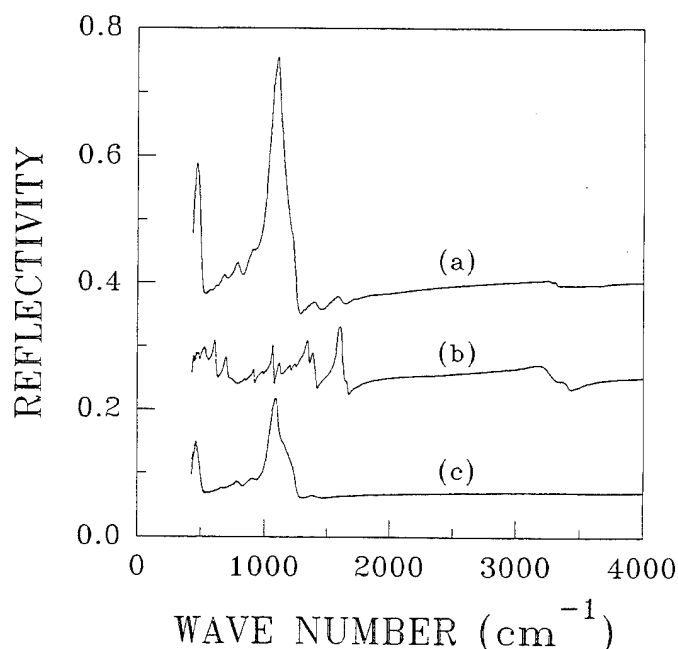


Fig. 6: IR reflectance of (a) RS nanocrystals embedded in porous glass, (b) bulk RS crystal, and (c) porous glass without RS nanocrystals. Spectra are shifted vertically to be more discernible.



## DISCUSSIONS

The Corning's porous VYCOR glass 7930 is shown to have a narrow pore size distribution peaked at 6 nm by using a new NMR method of pore size determination [14]. The porous glass has advantages over the other forms of porous matrix, such as silica-gels, in that it is readily available in a plate form and transparent. The porous glass is used to prepare the nanometer sized RS particles by confining the aqueous solution of RS to its small pores before crystallization is proceeded by drying the solution.

X-ray diffraction measurements confirm the crystallization into RS particles of 75 nm size in the 100 nm pores of silica-gel. However, no diffraction peak can be identified for samples prepared in smaller pores of silica-gel or the porous glass. This can be due to either extensive broadening related to the smaller size of particles or the formation of glass phase instead of single crystallites. The expected X-ray line breadth from the small size effect is about 5 and 16 times larger for the spectra (c) and (d) of Fig. 2, respectively, than that of (b).

Dielectric properties of the small sized samples of RS are interesting not only to figure out the critical size for phase transitions but also to find out a new possibility in applications. The dielectric measurements shown in Fig. 3 indicate the critical size for RS is larger than 4.8 nm. We need to increase the pore size to locate the critical size and this is our next plan.

On the other hand the high dielectric constant of the porous glass sample embedded with nanometer sized RS can be of some use. However, the high loss  $\tan\delta$  and its large temperature and frequency dependences must be improved to be useful in application. The frequency and temperature dependences of real and imaginary parts of dielectric constant of the sample may due to ionic motions, possibly near the surface of nanometer sized particles or in glass phase. In any case, as temperature is lowered slowing down of the motion is evident from the frequency dependent shift of the peak temperature of  $\tan\delta$  as in Fig. 4.

In contrast to the difficulties in analyzing dielectric data of an inhomogeneous system, such as the porous glass embedded with RS particles, NMR is a valuable tool of studying the inhomogeneous system since it probes nuclear spins with a simple weighting factor,

the spin density.  $^1\text{H}$  NMR can be considered as an important tool for RS since some of the protons of RS are involved in the ferroelectric phase transition. However, the spin-spin or spin-lattice relaxation time of RS does not reflect the transition largely and this is due to the irrelevance of the majority protons to the transition dynamics [16]. The exponential increase in Fig. 5 of the spin-lattice relaxation time of bulk RS when temperature is lowered reflects freezing of lattice vibrations. The much less temperature dependence of  $T_1$  in RS embedded in porous glass is an indication

that the protons in the sample are as mobile (or rotatory), irrespective of temperature, as in the paraelectric phase of bulk. This is another evidence for the absence of phase transition in the 4.8 nm sized RS.

The IR data in Fig. 6 can also be used to envisage the nature of nanometer sized RS in porous glass, however, we need further study due to the complexity in analyzing the reflectivity data of the inhomogeneous system.

## SUMMARY

A new fabrication method of nanometer sized RS crystals utilizing porous materials, such as porous glass and silica-gel, is developed. Three different sizes, 4.8 nm, 15 nm and 75 nm, of particles are made and X-ray diffraction peaks, at least of the largest particles, confirm the formation of RS crystals in the pores. Dielectric and

$^1\text{H}$  NMR spin relaxation measurements on the smallest particle samples indicate big difference from the bulk RS. We interpret the difference as due to absence of phase transitions in the nanometer sized RS. Hence the critical size for the ferroelectric phase transition of RS should be larger than 4.8 nm. We also find the nanometer sized RS particles possess interesting dielectric and NMR properties which can be considered as due to the presence of highly mobile protons down to low temperatures. The high dielectric constant of the sample can be useful in applications after the temperature and frequency dependent characteristic is improved.

## ACKNOWLEDGMENTS

The authors acknowledge contributions from K. S. Hong in  $^1\text{H}$  NMR experiments. The X-ray and IR measurements were made in the Inter-University Center for Natural Science Research Facilities. This work was supported by the Korea Science and Engineering Foundation through the Research Center for Dielectric and Advanced Matter Physics.

## REFERENCES

- [1] C. L. Jackson and G. B. McKenna, "The melting behavior of organic materials confined in porous solids," *J. Chem. Phys.*, vol. 93, pp. 9002-9011, December 1990.
- [2] P. W. Selwood, *Adsorption and Collective Paramagnetism*. New York: Academic, 1962, ch. 3.
- [3] R. A. Buhrman and W. P. Halperin, "Fluctuation diamagnetism in a 'zero-dimensional' superconductor," *Phys. Rev. Lett.*, vol. 30, pp. 692-695, April 1973.
- [4] M. H. Frey and D. A. Payne, "Nanocrystalline barium titanate: Evidence for the absence of ferroelectricity in sol-gel derived thin-layer capacitors," *Appl. Phys. Lett.*, vol. 63, pp. 2753-2755, November 1993.
- [5] R. Bachmann and K. Barner, "Stable suspensions of ferroelectric  $\text{BaTiO}_3$  particles," *Solid State Commun.*, vol. 68, pp. 865-869, 1988.
- [6] For example see E. K. Jang and I. Yu, "Properties of nanocrystalline ferroelectrics," (and references therein) presented at the third Dielectric and Advanced Matter Physics Symposium and the first Korea-Japan Binational Conference on Ferroelectrics, Pusan, Korea, January 20-22, 1994 and in press as a supplementary issue of *J. Korean Phys. Soc.*
- [7] P. Marquardt and H. Gleiter, "Ferroelectric phase transition in microcrystals," *Phys. Rev. Lett.*, vol. 48, pp. 1423-1425, May 1982.
- [8] K. Ishikawa, K. Yoshikawa and N. Okada, "Size effect on the ferroelectric phase transition in  $\text{PbTiO}_3$  ultrafine particles," *Phys. Rev. B.*, vol. 37, pp. 5852-5855, April 1988.
- [9] J. Valasek, "Piezoelectricity and allied phenomena in Rochelle salt," *Phys. Rev.*, vol. 17, pp. 475-481, 1921.
- [10] J. Kobayashi, K. Uchino, and T. Asahi, "Optical properties of Rochelle salt," *Phys. Rev. B.*, vol. 43, pp. 5706-5712, March 1991.
- [11] B. Zeks, J. C. Shukla, and R. Blinc, "Dynamics of ferroelectric Rochelle salt," *Phys. Rev. B.*, vol. 3, pp. 2306-2309, April 1971.
- [12] A. Mansingh and S. S. Bawa, "Dielectric properties of compressed Rochelle-salt powders," *phys. stat. sol. (a)*, vol. 21, pp. 725-731, 1974.
- [13] F. D'Orazio, J. C. Tarczon, W. P. Halperin, K. Eguchi, and T. Mizusaki, "Application of nuclear magnetic resonance pore structure analysis to porous silica glass," *J. Appl. Phys.*, vol. 65, pp. 742-751, January 1989.
- [14] J. H. Strange and M. Rahman, and E. G. Smith, "Characterization of porous solids by NMR," *Phys. Rev. Lett.*, vol. 71, pp. 3589-3591, November 1993.
- [15] T. Mitsui, "Theory of the ferroelectric effect in Rochelle salt," *Phys. Rev.*, vol. 111, pp. 1259-1267, September 1958.
- [16] R. Blinc, E. M. Peterson, and D. E. O'Reilly, "NMR study of water molecule dynamics in ferroelectric Rochelle salt," *Phys. Lett.*, vol. 28A, pp. 624-625, February 1969.



# LEAD ZIRCONATE TITANATE-LEAD SILICATE PIEZOELECTRIC GLASS-CERAMICS

B. Houng and M. J. Haun  
Colorado Center for Advanced Ceramics  
Colorado School of Mines  
Golden, CO 80401

**Abstract** - Piezoelectric glass-ceramics consisting of lead zirconate titanate in a lead silicate matrix have been developed. A small region of compositions in this system yield the desired combination of glass formability, densification and crystallization behavior, and piezoelectric properties.  $\text{SiO}_2$  is required for glass formability, while excess  $\text{PbO}$  allows low temperature processing. The amounts of these constituents are limited by the optimization of piezoelectric properties. Selected compositions were melted and roller quenched to form amorphous ribbon. The glass ribbon was processed using two methods, either by directly heat treating to crystallize the PZT phase, or by ball milling into a glass powder. Pressed glass powders of selected compositions in this system densify to closed porosity at  $850^\circ\text{C}$  with piezoelectric  $d_{33}$  and  $g_{33}$  coefficients of 38 pC/N and  $33 \times 10^{-3}$  Vm/N. This research demonstrates the feasibility of developing piezoelectric glass-ceramics with low processing temperatures that utilize powder processing techniques, such as pressing, screen printing, or tape casting, and indicates the potential incorporation of these materials into low-fire multilayer packages as sensors or actuators.

## INTRODUCTION

Glass-ceramics are utilized in a wide variety of applications, and many useful techniques are established to control the crystallization behavior, microstructural development, and resulting properties[1]. The development of ferroelectric glass-ceramic compositions with useful piezoelectric properties will allow the advantages of glass-ceramic processing, such as forming methods and lower heat treatment temperatures, to be utilized. Glass powders of these compositions can be prepared into pastes for screen printing onto thick-film circuits or into slurries for tape casting and integration into multilayer packages. The low firing temperatures inherent in glass-ceramic materials allow for potential compatibility with existing thick film conductors, dielectrics, and resistors.

Ferroelectric phases, such as  $\text{PbTiO}_3$ ,  $\text{BaTiO}_3$  and  $\text{NaNbO}_3$ [2-4], have been crystallized from glass since the 1960's for dielectric and electrooptic applications, but useful piezoelectric properties were achieved only recently by Wu and Zhu[5,6]. These lead titanate based glass-ceramics were found to not densify well in powder form at low temperatures ( $< 1000^\circ\text{C}$ ) [7]. However, with addition of excess  $\text{PbO}$  compositions in this system will densify to closed porosity at  $850^\circ\text{C}$ , and can be electrically poled to produce piezoelectric and pyroelectric activity[7]. Very little research has investigated the crystallization of PZT from a glass[7-11]. Brandmayr and DiVita[8] mentioned the processing of PZT glass-ceramics, but very little details and no electrical properties were provided. Park and Yamane[9] studied the crystallization behavior and dielectric properties of PZT glass-ceramics in the  $\text{PbO-TiO}_2\text{-ZrO}_2\text{-GeO}_2$  system. But no piezoelectric or

pyroelectric properties were reported. Cornejo and Haun[10,11] investigated the crystallization and densification behavior and resulting ferroelectric properties in the  $\text{Pb}_5\text{Ge}_3\text{O}_{11}\text{-PbTiO}_3\text{-PbZrO}_3$  glass-ceramic system. Multiple ferroelectric phases of  $\text{Pb}_5\text{Ge}_3\text{O}_{11}$  and PZT crystallized in these compositions, and the pyroelectric properties were investigated[11]. The first piezoelectric properties of PZT glass-ceramics were reported by Houng and Haun[7]. This research is continuing, and additional results on PZT based glass-ceramics are presented in this paper.

## EXPERIMENTAL PROCEDURE

A wide range of compositions were studied in the  $x\text{Pb}(\text{Zr}_y\text{Ti}_{1-y})\text{O}_3 \cdot z\text{PbO} \cdot w\text{SiO}_2 \cdot u\text{B}_2\text{O}_3$  system, where  $x=0.33\text{-}0.74$ ,  $y=0\text{-}0.52$ ,  $z=0\text{-}0.44$ ,  $w=0\text{-}0.57$ , and  $u=0\text{-}0.57$ . This paper focuses on two glass compositions:  $59.95(\text{PbZr}_{0.52}\text{Ti}_{0.48})\text{O}_3 \cdot 13.35\text{PbO} \cdot 26.7\text{SiO}_2$  and  $60(\text{Pb}_{0.85}\text{Sr}_{0.15})(\text{Zr}_{0.49}\text{Ti}_{0.45}\text{Nb}_{0.04}\text{Mn}_{0.02})\text{O}_3 \cdot 6.4\text{PbO} \cdot 25.6\text{SiO}_2 \cdot 8\text{Al}_2\text{O}_3$ . The second composition illustrates the effect of various additives ( $\text{SrO}$ ,  $\text{MnO}_2$ ,  $\text{Nb}_2\text{O}_5$ , and  $\text{Al}_2\text{O}_3$ ), which were previously investigated by Wu and Zhu[5,6] in lead titanate based glass ceramics to improve the electrical properties. These compositions have a higher PZT content than the compositions reported by the authors in reference 7. A mistake was made in the formula of the compositions previously reported. In reference 7 compositions  $60(\text{PbZr}_{0.52}\text{Ti}_{0.48})\text{O}_3 \cdot 20\text{PbO} \cdot 20\text{SiO}_2$  and  $85(\text{Pb}_{0.85}\text{Sr}_{0.15})(\text{Ti}_{0.94}\text{Nb}_{0.04}\text{Mn}_{0.02})\text{O}_3 \cdot 10\text{SiO}_2 \cdot 5\text{Al}_2\text{O}_3$  were actually  $42.8(\text{PbZr}_{0.52}\text{Ti}_{0.48})\text{O}_3 \cdot 28.6\text{PbO} \cdot 28.6\text{SiO}_2$  and  $73.9(\text{Pb}_{0.85}\text{Sr}_{0.15})(\text{Ti}_{0.94}\text{Nb}_{0.04}\text{Mn}_{0.02})\text{O}_3 \cdot 17.4\text{SiO}_2 \cdot 8.7\text{Al}_2\text{O}_3$  respectively.

The starting materials were reagent grade  $\text{Pb}_3\text{O}_4$ ,  $\text{TiO}_2$ ,  $\text{ZrO}_2$ ,  $\text{SrCO}_3$ ,  $\text{MnO}_2$ ,  $\text{Nb}_2\text{O}_5$ ,  $\text{Al}_2\text{O}_3$  and  $\text{SiO}_2$ .  $\text{Pb}_3\text{O}_4$  was chosen as a starting material instead of  $\text{PbO}$  to reduce the possibility of reduction to metallic lead and subsequent reaction with the platinum crucible. The batches were mixed by ball milling with zirconia media in methanol for 12 hours, dried at  $50^\circ\text{C}$ , and transferred to a platinum crucible for melting. The batches were placed into a furnace and melted for 15 minutes at  $1100\text{-}1300^\circ\text{C}$  depending on the composition. The molten liquid was then quenched by pouring into a twin-roller quencher to form glass ribbon. Glass powder was prepared from the ribbon by ball milling in methanol with zirconia media for twenty-four hours. The glass powder was pressed into pellets without binder at a pressure of 10,000 psi. The pressed pellets (10 mm in diameter and 1-2 mm thick) were heated on a platinum sheet to various temperatures ranging from  $450$  to  $1200^\circ\text{C}$  at a rate of  $10^\circ\text{C}/\text{min}$  and held for 1 hour.

The resulting glass-ceramic samples were ground into powder for x-ray diffraction, and polished and electroded with sputtered gold followed by a layer of air-dried silver paint for electrical property measurements. The dielectric constant was measured at 10 KHz on a Hewlett Packard HP4284A LCR meter. Ferroelectric hysteresis loops were measured with a Radiant Technologies RT66A Test System. The samples were then poled for 30 minutes to 1 hour at 180°C. The microstructures were also analyzed with SEM.

## RESULTS AND DISCUSSIONS

### X-ray Diffraction

The  $59.95(\text{PbZr}_{0.52}\text{Ti}_{0.48})\text{O}_3 \cdot 13.35\text{PbO} \cdot 26.7\text{SiO}_2$  and  $60(\text{Pb}_{0.85}\text{Sr}_{0.15})(\text{Zr}_{0.49}\text{Ti}_{0.45}\text{Nb}_{0.04}\text{Mn}_{0.02})\text{O}_3 \cdot 6.4\text{PbO} \cdot 25.6\text{SiO}_2 \cdot 8\text{Al}_2\text{O}_3$  compositions are referred to as compositions 1 and 2, respectively, in the following discussion. X-ray diffraction patterns of compositions 1 and 2 as-quenched and after firing at various temperatures for one hour are shown in Figure 1. After firing at 450°C, pyrochlore and perovskite PZT crystallized. The intensity ratio of the pyrochlore to perovskite decreased as  $\text{Al}_2\text{O}_3$  was added. Metastable pyrochlore lead titanate was observed by Martin[12] in the  $\text{PbO-TiO}_2\text{-SiO}_2\text{-B}_2\text{O}_3$  glass-ceramic system. Kokubo et al.[13] also found that metastable pyrochlore lead titanate occurred in  $\text{PbO-TiO}_2\text{-SiO}_2\text{-Al}_2\text{O}_3$  system. Their research also found that the addition of  $\text{Al}_2\text{O}_3$  promoted the formation of perovskite.

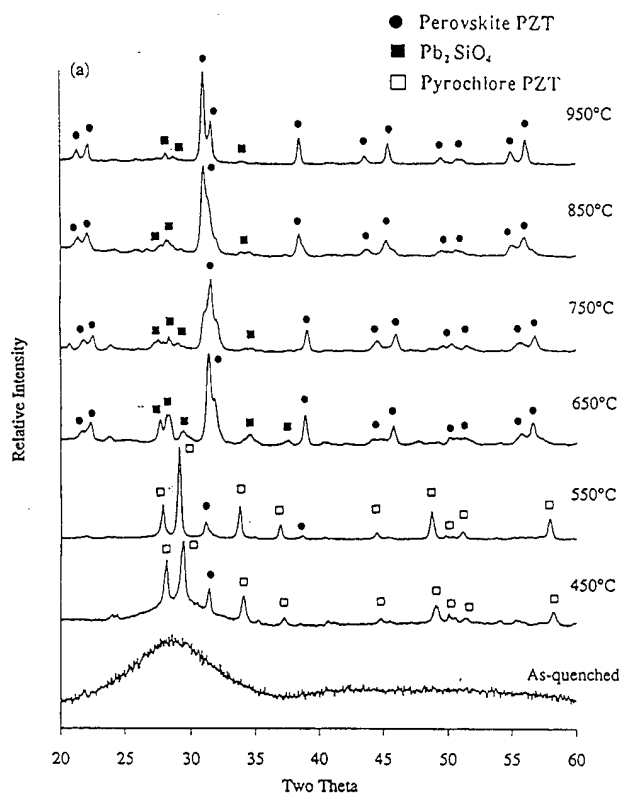


Figure 1 X-ray diffraction patterns for (a)  $59.95(\text{PbZr}_{0.52}\text{Ti}_{0.48})\text{O}_3 \cdot 13.35\text{PbO} \cdot 26.7\text{SiO}_2$  and (b)  $60(\text{Pb}_{0.85}\text{Sr}_{0.15})(\text{Zr}_{0.49}\text{Ti}_{0.45}\text{Nb}_{0.04}\text{Mn}_{0.02})\text{O}_3 \cdot 6.4\text{PbO} \cdot 25.6\text{SiO}_2 \cdot 8\text{Al}_2\text{O}_3$  heat treated at various temperatures.

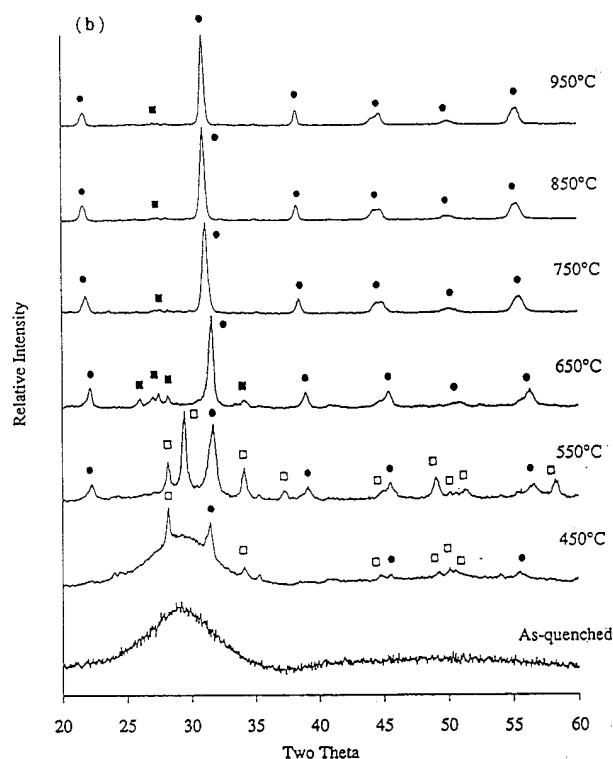


Figure 1 shows that as the heat treatment temperature was increased to 650°C, the metastable pyrochlore PZT phase disappeared in both compositions and perovskite PZT became the dominant phase with a minor amount of  $\text{Pb}_2\text{SiO}_4$ . The tetragonal splitting of the perovskite peaks for composition 1 were not observed in composition 2, indicating that the additives in composition 2 decreased the c/a ratio of the tetragonal phase, and/or promoted more rhombohedral phase. The effect of these additives and the Zr/Ti ratio on the crystallization behavior and properties is currently being further investigated.

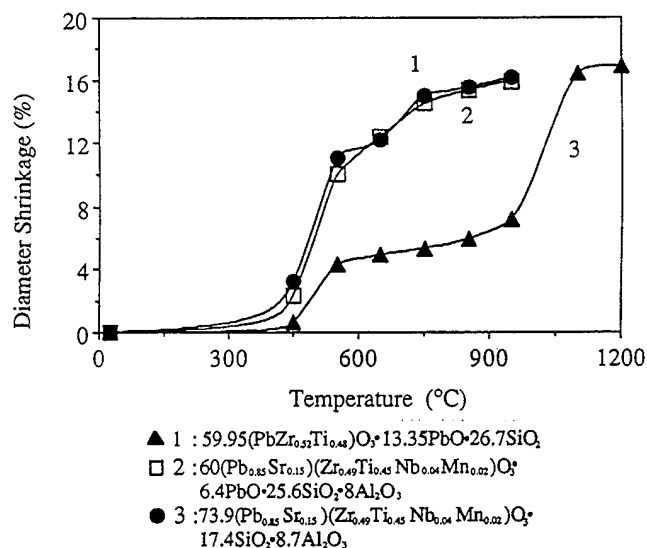


Figure 2 Densification behavior of compositions with (1 and 2) and without (3) excess PbO addition.

## Densification Behavior

Figure 2 shows the densification behavior of compositions 1 and 2 compared to that of a composition without excess PbO. In the figure the diameter shrinkage of pellet samples is plotted versus temperature. Closed porosity corresponds to about 15% shrinkage. At a temperature of 450°C the samples start to soften and densify due to presence of the glass phase. At higher temperatures the  $\text{Pb}_2\text{SiO}_4$  phase (see Figure 1) which has melting temperature of about 747°C[14], may also contribute to densification of the samples. The  $73.9(\text{Pb}_{0.85}\text{Sr}_{0.15})(\text{Zr}_{0.49}\text{Ti}_{0.45}\text{Nb}_{0.04}\text{Mn}_{0.02})\text{O}_3 \cdot 17.4\text{SiO}_2 \cdot 8.7\text{Al}_2\text{O}_3$  composition without excess PbO did not densify until significantly higher temperatures at  $\approx 1100^\circ\text{C}$ .

Figure 3 shows SEM photographs of fractured surfaces of pellets of composition 1 fired at 850 and 950°C for 1 hour. These photos indicate that the samples densified to closed porosity. Figure 4 shows SEM photographs of polished and etched (in 50% HF solution for 30 seconds) surfaces of pellets of composition 1. This etching procedure removed the residual glass phase leaving the crystalline PZT and  $\text{Pb}_2\text{SiO}_4$  phases. Figure 4 shows that by firing at 850°C the sample densified with 2-3  $\mu\text{m}$  sized grains. Increasing the firing temperature to 950°C resulted in grain sizes increasing to around 5-10  $\mu\text{m}$ . The microstructures of composition 2 have very similar to those shown in Figures 3 and 4 for composition 1.

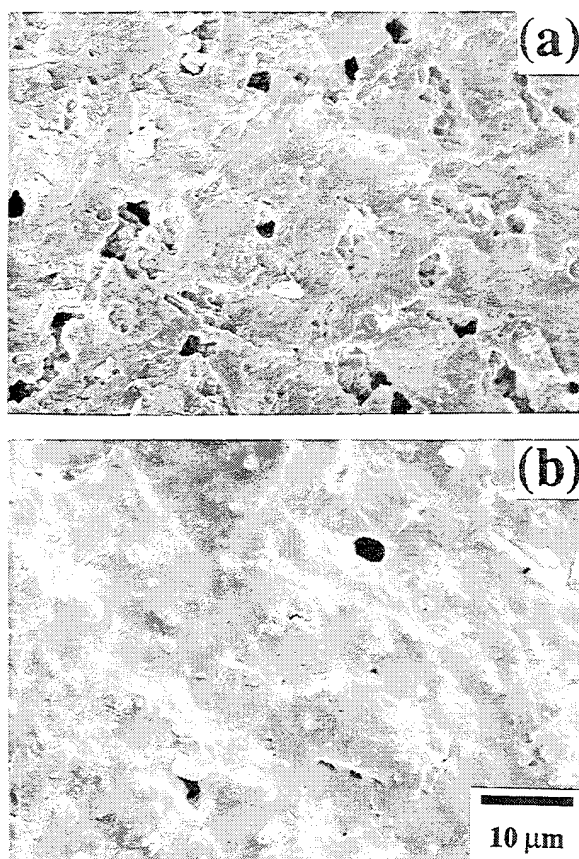


Figure 3 SEM photographs of the fractured surface of the  $59.95(\text{PbZr}_{0.52}\text{Ti}_{0.48})\text{O}_3 \cdot 13.35\text{PbO} \cdot 26.7\text{SiO}_2$  composition heat treated at (a) 850 and (b) 950°C.

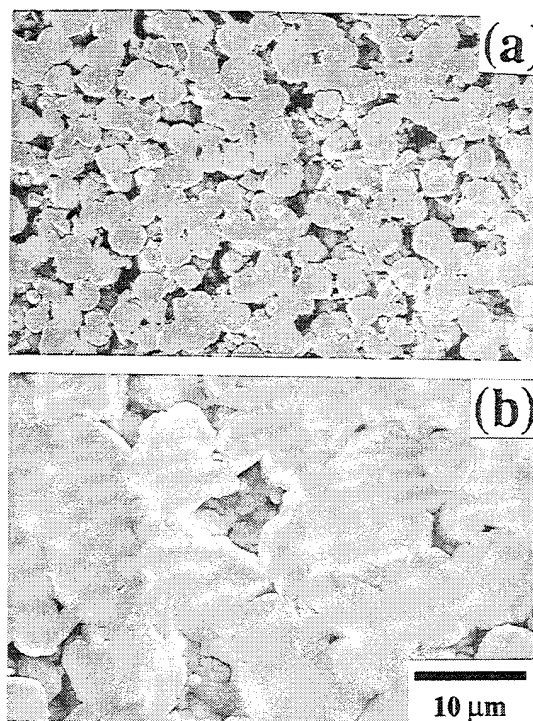


Figure 4 SEM photographs of the polished and etched surface of the  $59.95(\text{PbZr}_{0.52}\text{Ti}_{0.48})\text{O}_3 \cdot 13.35\text{PbO} \cdot 26.7\text{SiO}_2$  composition heat treated at (a) 850 and (b) 950°C.

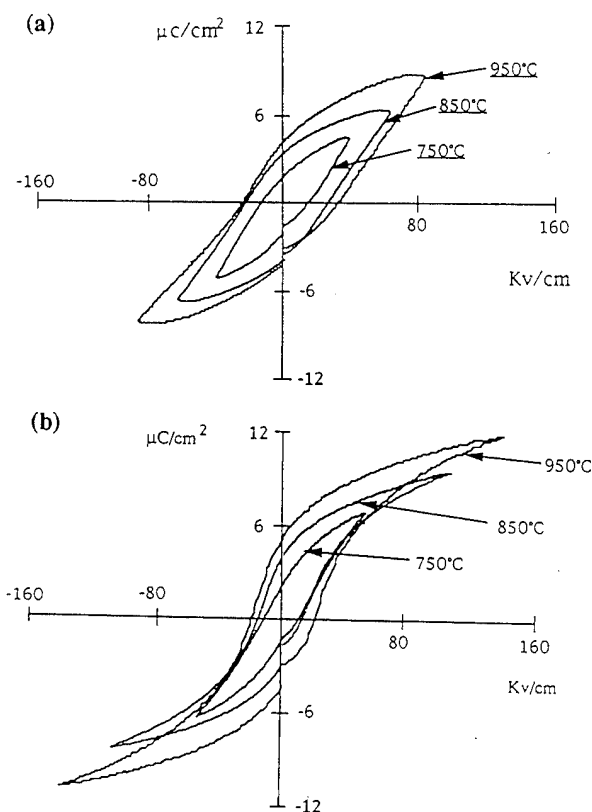


Figure 5 Ferroelectric hysteresis loops for (a)  $59.95(\text{PbZr}_{0.52}\text{Ti}_{0.48})\text{O}_3 \cdot 13.35\text{PbO} \cdot 26.7\text{SiO}_2$  and (b)  $60(\text{Pb}_{0.85}\text{Sr}_{0.15})(\text{Zr}_{0.49}\text{Ti}_{0.45}\text{Nb}_{0.04}\text{Mn}_{0.02})\text{O}_3 \cdot 6.4\text{PbO} \cdot 25.6\text{SiO}_2 \cdot 8\text{Al}_2\text{O}_3$  heat treated at various temperatures with one hour hold times.

The addition of strontium and niobium oxides in PT or PZT lowers the curie temperature and improves the ability to electrically pole the samples[15]. The addition of manganese dioxide increases the electrical resistivity, and lowers the dissipation factor[16]. The hysteresis loops of compositions 1 and 2 fired at various temperatures are shown in Figure 5. The applied AC electric fields were increased on both compositions until breakdown occurred. Composition 1 without any additives showed more rounded and unsaturated loops with higher coercive fields, and electrical breakdown at relatively low electric fields ( $\approx 45$ -80 KV/cm depending on the sample firing temperature). Composition 2 with niobium and manganese oxides additions resulted in more square hysteresis loops, higher spontaneous polarization, lower coercive fields, and higher breakdown fields ( $\approx 70$ -140 KV/cm).

The electrical properties of these two compositions are summarized in Table 1. The dielectric constant of both compositions were similar. The addition of strontium and niobium oxides will normally increase the dielectric constant, but alumina addition from the glass phase may also diffuse into PZT, which will reduce the dielectric constant. The  $d_{33}$  coefficients of the glass-ceramic samples fired at 850 and 950°C are significantly less than that of pure PZT, but the  $g_{33}$  coefficients are similar in value.

Table 1 Electrical Properties of Compositions 1, 2 and pure PZT.

Composition	59.95(PbZr <sub>0.45</sub> Ti <sub>0.48</sub> )O <sub>3</sub> ·13.35PbO·26.7SiO <sub>2</sub>		60(Pb <sub>0.45</sub> Sr <sub>0.35</sub> )(Zr <sub>0.49</sub> Ti <sub>0.45</sub> Mn <sub>0.02</sub> Nb <sub>0.06</sub> )O <sub>3</sub> ·6.4PbO·25.6SiO <sub>2</sub> ·8Al <sub>2</sub> O <sub>3</sub>		* Pure Pb(Zr <sub>0.52</sub> Ti <sub>0.48</sub> )O <sub>3</sub>
	850°C, 1hr	950°C, 1hr	850°C, 1hr	950°C, 1hr	$\approx 1285^\circ\text{C}$
K'(at 10 KHz)	124	127	129	131	730
D.F. (%)	1.4	1.5	0.7	0.8	0.4
$\rho$ ( $\times 10^{10} \Omega\text{cm}$ )	3.2	4.3	46.8	60.4	—
Ps ( $\mu\text{C}/\text{cm}^2$ ) <sup>#</sup>	5.6	6.4	6.8	7.8	—
Pr ( $\mu\text{C}/\text{cm}^2$ )	2.6	3.0	3.3	3.7	$\approx 35$
Ec (KV/cm)	25	38	19	25	$\approx 10$
$d_{33}$ (pC/N)	26	28	38	44	223
$g_{33}$ ( $10^{-3} \text{Vm/N}$ )	23	25	33	38	34.5

\* From reference 16

# Ps is the maximum polarization value from the hysteresis loops.

## SUMMARY

The crystallization behavior and electrical properties of PZT glass-ceramics with lead silicate matrices have been investigated. Results of compositions with and without additions of strontium, niobium, manganese, and aluminum oxides was presented. The compositions with excess PbO densified to closed porosity at 850°C, while compositions without excess PbO did not densify until  $\approx 1100^\circ\text{C}$ . Samples processed at 850°C resulted in piezoelectric  $d_{33}$  and  $g_{33}$  coefficients of 38 pC/N and  $33 \times 10^{-3} \text{Vm/N}$ . This research demonstrates the feasibility of developing piezoelectric glass-ceramics with low processing temperatures that utilize powder processing techniques, such as pressing, screen printing, or tape casting.

This research was supported by Office of Naval Research (Contract # N00014-92-5-1390) and National Science Foundation (Contract # DMR 9158312).

## REFERENCES

- [1] P. W. McMillan, *Glass-Ceramics*, Academic Press, NY, 1979.
- [2] C. G. Bergeron and C. K. Russell, "Nucleation and Growth of Lead Titanate from a glass," J. Am. Ceram. Soc., Vol. 48, No. 3, pp. 115-118, 1965.
- [3] A. Herczog, "Microcrystalline BaTiO<sub>3</sub> by Crystallization from Glass," J. Am. Ceram. Soc., Vol. 47, No. 3, pp. 107-115, 1964.
- [4] M. M. Layton and A. Herczog, "Nucleation and Crystallization of NaNbO<sub>3</sub> from Glasses in the Na<sub>2</sub>O-Nb<sub>2</sub>O<sub>5</sub>-SiO<sub>2</sub> System," J. Am. Ceram. Soc., Vol. 50, No. 7, pp. 369-375, 1967.
- [5] M. Wu and P. Zhu, "Piezoelectric and Pyroelectric Properties of Ferroelectric Glass-Ceramics," Chinese Phys. Lett., Vol. 2, No. 5, pp. 235-238, 1985.
- [6] M. Wu and P. Zhu, "Piezoelectricity, Pyroelectricity and Ferroelectricity in Glass Ceramics Based on PbTiO<sub>3</sub>," J. Non-Cryst. Solids., Vol. 84, pp. 344-351, 1986.
- [7] B. Hounig and M. J. Haun, "Lead Titanate and Lead Zirconate Titanate Piezoelectric Glass-Ceramics," Proceedings of the 8th International Meeting on Ferroelectricity, Gaithersburg, MD, Aug. 8-13, 1993.
- [8] R. J. Brandmayr and S. DiVita, "Method of Processing Ferroelectric Devitrifiable Glass Ceramics," US Patent 3,862,829, Jan. 28, 1975.
- [9] W. K. Park and M. Yamane, "Glass-Ceramics of System Pb(Zr<sub>0.5</sub>Ti<sub>0.5</sub>)O<sub>3</sub>-GeO<sub>2</sub>," Glastechn. Ber., Vol. 62, No. 5, pp. 187-189, 1989.
- [10] I. A. Comejo, J. Collier and M. J. Haun, "Ferroelectric and Crystallization Behavior in the Pb<sub>3</sub>Ge<sub>3</sub>O<sub>11</sub>-PbTiO<sub>3</sub>-PbZrO<sub>3</sub> Glass-Ceramic System," Proceedings of the 8th International Meeting on Ferroelectricity, Gaithersburg, MD, Aug. 8-13, 1993. (accepted for publication in Ferroelectrics).
- [11] I. A. Comejo, "Low Temperature crystallization of Pb<sub>3</sub>Ge<sub>3</sub>O<sub>11</sub>-PbTiO<sub>3</sub> and Pb<sub>3</sub>Ge<sub>3</sub>O<sub>11</sub>-Pb(Zr<sub>0.5</sub>Ti<sub>0.5</sub>)O<sub>3</sub> Glass-Ceramic Systems with Multiple Ferroelectric Phases for Pyroelectric Applications," Ph.D. Thesis, No. T-4631, Colorado School of Mines, Golden, Colorado, Aug. 1994.
- [12] F. W. Martin, "A Metastable Cubic Form of Lead Titanate Observed in Titania Nucleated Glass Ceramics," Phys. and Chem. of Glass., Vol. 6, No. 4, pp. 143-146, 1965.
- [13] T. Kokubo, H. Nagao, and M. Tashiro, "Crystallization of PbO-TiO<sub>2</sub>-Al<sub>2</sub>O<sub>3</sub>-SiO<sub>2</sub> Glasses and Dielectric Properties of Their Crystallized Products," Yogyo-Ktokai-Shi, Vol. 77 No. 9, pp. 293-300, 1969.
- [14] R. M. Smart and F. P. Glasser, "Compound Formation and Phase Equilibria in the System PbO-SiO<sub>2</sub>," J. Am. Ceram. Soc., Vol. 57, No. 9, pp. 378-382, 1974.
- [15] A. J. Moulson and J. M. Herbert, *Electroceraamics*, Chapman and Hall, NY, 1990.
- [16] Y. Matsuo, M. Fujimura and H. Sasaki, "Lead Titanate Ceramics Doped with Manganese Oxide," J. Am. Ceram. Soc., Vol. 48, No. 2, pp. 111-112, 1965.
- [17] B. Jaffe, W. R. Cook Jr. and H. Jaffe, *Piezoelectric Ceramics*, Academic Press, NY, 1971.

# Electric Properties and Domain Structures in $\text{Ba}(\text{Ti},\text{Sn})\text{O}_3$ Ceramics

Ki-Young Oh, Kenji Uchino and L. Eric Cross

International Center for Actuators and Transducers, Materials Research Laboratory,  
The Pennsylvania University, University Park, PA 16802

**Abstract-** The  $\text{Ba}(\text{Ti},\text{Sn})\text{O}_3$  ceramics are known as relaxor materials and they show very small hysteresis of field induced strains and field induced polarizations. Optical study was attempted to explain these dielectric properties. Domain structures and motions in  $\text{Ba}(\text{Ti}_{1-x}\text{Sn}_x)\text{O}_3$  ( $x=0, 0.05, 0.1, 0.13$ ) ceramics were observed under an electric field at various temperatures using a high resolution CCD microscope system. Electrical properties such as field induced strains, dielectric properties and field induced polarization characteristics were also measured. The  $\text{Ba}(\text{Ti}_{1-x}\text{Sn}_x)\text{O}_3$  ceramics showed a significant difference in domain structures and motions with changing in the composition. The domain structure became tiny and complex with increasing  $x$ . Changes of domain structures due to the phase transitions were also observed with varying temperature. The domain reorientation was easily induced with rising and falling an electric field. The results of domain observations can explain the electrical properties well.

## 1. Introduction

Observation of domain structures and domain motion is very useful for understanding the physical properties of ferroelectric materials because domains are fundamentally associated with ferroelectricity. For the past few years we have been reporting on the dynamic domain motion in single crystals such as barium titanate and lead zinc niobate based compositions<sup>1,2</sup>.

This paper concerns the domains in  $\text{Ba}(\text{Ti}, \text{Sn})\text{O}_3$  ceramics.  $\text{Ba}(\text{Ti}, \text{Sn})\text{O}_3$  solid solutions are known as typical relaxor ferroelectric materials, and they exhibit dielectric and electromechanical characteristics associated with relaxor ferroelectrics such as very small hysteresis in the field induced polarization and strain<sup>3,4</sup>. These materials may provide a new category of useful actuator ceramics. Our investigation is focused on the domain motion in these materials as a means of analyzing the electrical characteristics.

## 2. Experimental Procedure

Samples of  $\text{BaTiO}_3$ (BT),  $\text{Ba}(\text{Ti}_{0.95}\text{Sn}_{0.05})\text{O}_3$ (BTS-5),  $\text{Ba}(\text{Ti}_{0.9}\text{Sn}_{0.1})\text{O}_3$ (BTS-10) and  $\text{Ba}(\text{Ti}_{0.87}\text{Sn}_{0.13})\text{O}_3$ (BTS-13) were prepared by a conventional mixed oxide method. Mixed powders were calcined at 1100 °C for 2 hours. Disks 13 mm in diameter were pressed and sintered at 1350 °C for 10-50 hours in air. Sintered disks were sliced and polished 100  $\mu\text{m}$  in thickness. One side of each sample was finished with 0.25  $\mu\text{m}$  diamond paste and attached on to a glass plate using resin; then the other side was polished and finished with 0.25  $\mu\text{m}$  diamond paste so that the sample thickness was less than 30  $\mu\text{m}$ . Gold electrodes were sputtered on the sample surface with a gap of 800  $\mu\text{m}$ , and then silver wires were attached to the electrode as shown in Figure 1.

Domain motions of samples were observed with a high-resolution (480,000 pixels) CCD microscope (Japan Hightech Co.) at various temperatures with an electric field applied parallel to the surface. Figure 2 shows the CCD microscope system. The reasons of using this CCD microscope are; 1) a SEM or TEM has higher magnification but it is difficult to apply electric field to sample and 2) an ordinary optical microscope can not record the quick domain motion.

The dielectric constant versus temperature curve was measured

in the temperature range from -100 to 200 °C using an automated Hewlett Packard system. Polarization versus electric field (P-E) curves were measured with a Sawyer-Tower circuit. Strain-field characteristics were measured using a linear differential transformer.

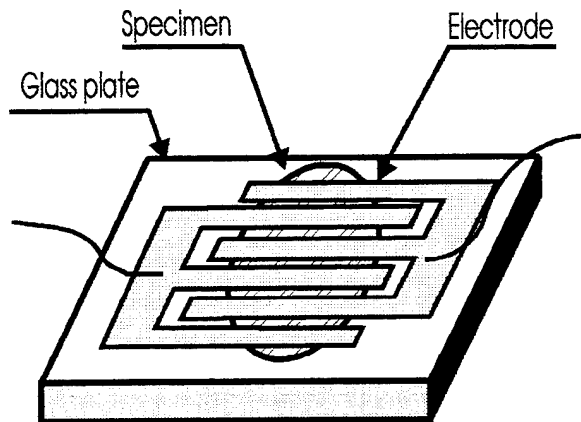


Fig. 1 Configuration of Sample.

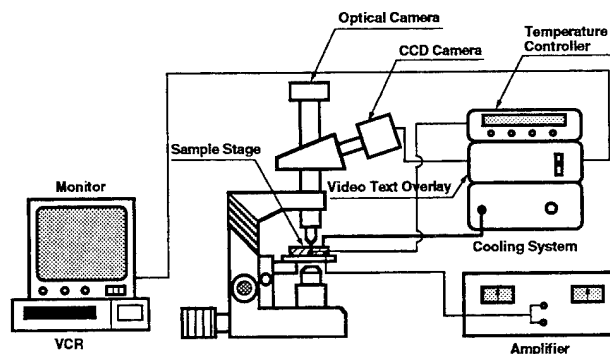


Fig. 2 Configuration of CCD Microscope system.

## 3. Results and Discussions

Figure 3 shows the temperature dependence of permittivity for BT, BTS-5, BTS-10 and BTS-13. The Curie temperature shifts to the lower side, and the shape of the peak becomes remarkably broader with increasing Sn content. The Curie temperatures of BT, BTS-5, BTS-10 and BTS-13 are 121.4, 85.7, 46.1 and 25.3 °C, respectively.

Electrical and electromechanical properties such as the P-E and field-induced strain characteristics were measured at room temperature, and the results are shown in Figs. 4 and 5. Compared with the BT sample, the BTS samples show smaller remanent polarization and less hysteresis. This is due to the Curie temperature shift to lower temperatures and the change of the phase transition characteristic from sharp to diffuse with increasing Sn content. The crystal structure of both BTS-10 and BTS-13 at room temperature was found to be pseudo-cubic. The field induced strain curves show a trend similar to the P-E curves (Fig. 5). With increasing Sn content, the hysteresis becomes smaller.

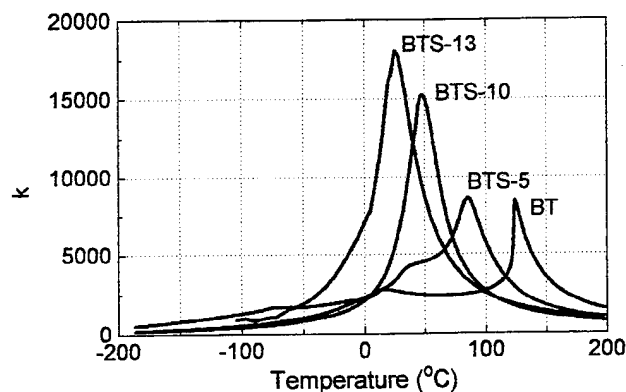


Fig. 3 Permittivity vs. temperature characteristics of BTS samples.

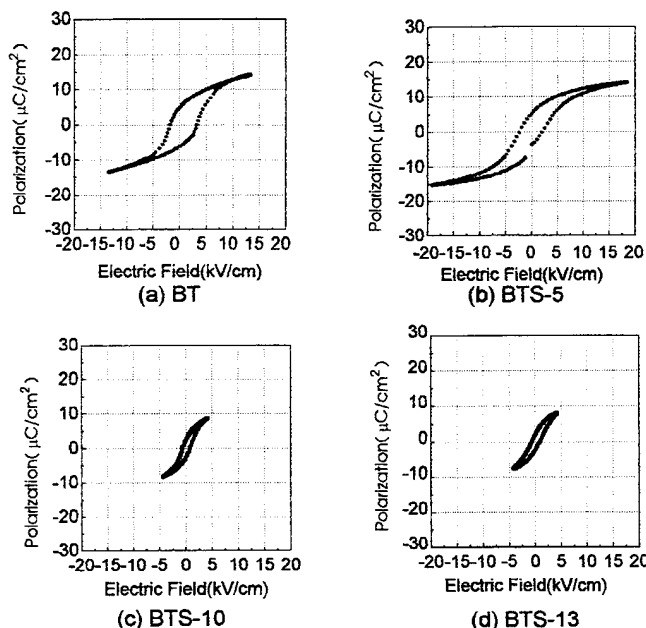


Fig. 4 Field induced polarization characteristics of BTS samples.

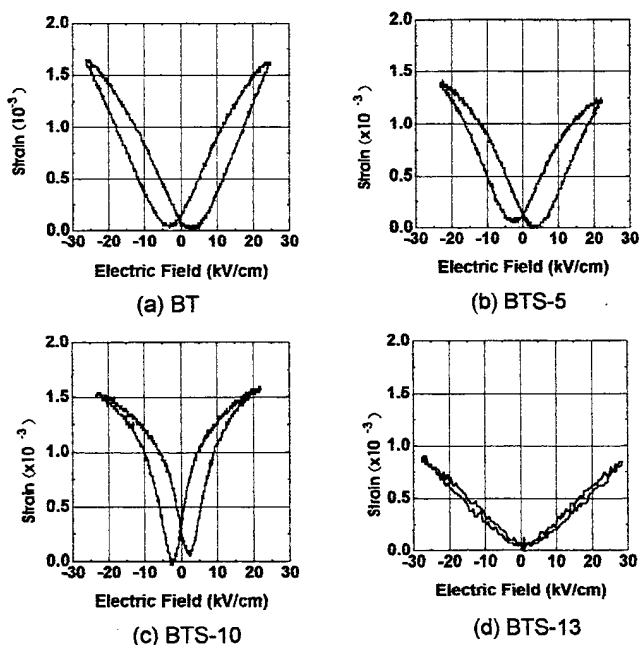


Fig. 5 Field induced strain characteristics of BTS samples.

Figure 6 shows the typical domain structures of BT, BTS-5, BTS-10 and BTS-13 samples at room temperature. The domain walls of BT are very clear straight lines, and the width of domain is rather thick. On the contrary, the domains of BTS-5 are tiny and less well defined. With increasing Sn content, these domain walls became more tiny and less well defined and finally, could not even be found in large grains (BTS-13). Variation of the domain structure with

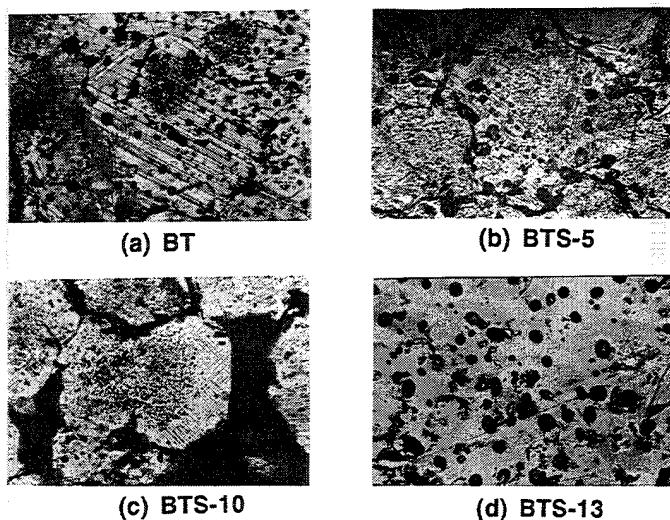


Fig. 6 Domain structures of BTS samples at room temperature.

temperature was also observed, and the results are shown in Figs. 7 and 8. With increasing temperature, the domain walls became unclear and disappeared completely above the Curie temperature. BTS-5 showed clear and simple domain structure at 55 °C because it shows tetragonal phase at this temperature. When the temperature

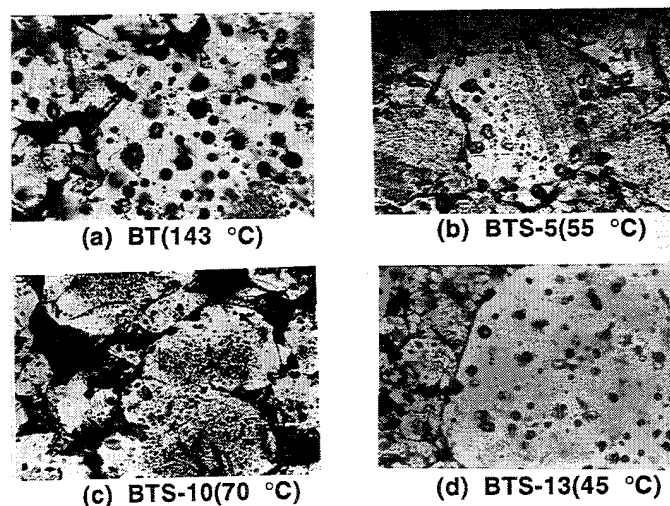


Fig. 7 Domain structures of BTS samples at high temperature.

was decreased, the BT and BTS samples showed different results. For the BT samples, the domain structures became difficult to define and some part of the large domains were divided into small spindle shape domains suddenly at 0 °C. We attribute this to the phase transition from tetragonal to orthorhombic at this temperature. The difference between the domain shapes in the tetragonal and orthorhombic phases is very clear, however the difference between domain shapes in the orthorhombic and rhombohedral phases is not significant. BTS-5 sample showed clear phase transitions from tetragonal to orthorhombic as shown in Fig.3 but it didn't show any sudden change of domain shape due to the phase transition like BT samples. The BTS-10, BTS-13 samples showed a gradual change



of domain structures with decreasing temperature. The domain walls became clear, in general, at a lower temperatures. It is noteworthy that the BTS-13, which does not show any domain walls at room temperature, shows obvious domain walls at low temperature (Fig.8). The domain size at this temperature is tiny and the domain walls are rather difficult to distinguish.

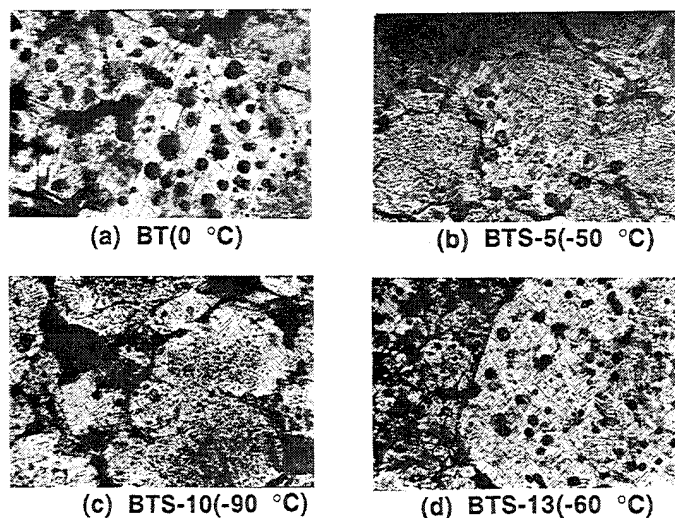


Fig. 8 Domain structures of BTS samples at low temperature.

Figures 9 and 10 show domain motion of the BT and BTS samples as a function of electric field at room temperature. A field of  $\pm 10$  kV/cm was applied to the samples. The BT samples showed  $90^\circ$  and  $180^\circ$  domain switching with application of the electric field. When  $+10$  kV/cm was applied to the BT sample, the domain walls were reoriented by  $90^\circ$  (Fig.9(b)). The reoriented domain walls remained even after removing the electric field (Fig.9(c)). The reoriented domain walls returned to their initial orientation when a small negative bias was applied (Fig.9(d)). The hysteresis of the domain motion is associated with the hysteresis in the P-E and field induced strain characteristics. BTS-5 sample also showed small hysteresis of domain motion. Poled domain shape is different from both of initial state and with field state. On the contrary, the BTS-

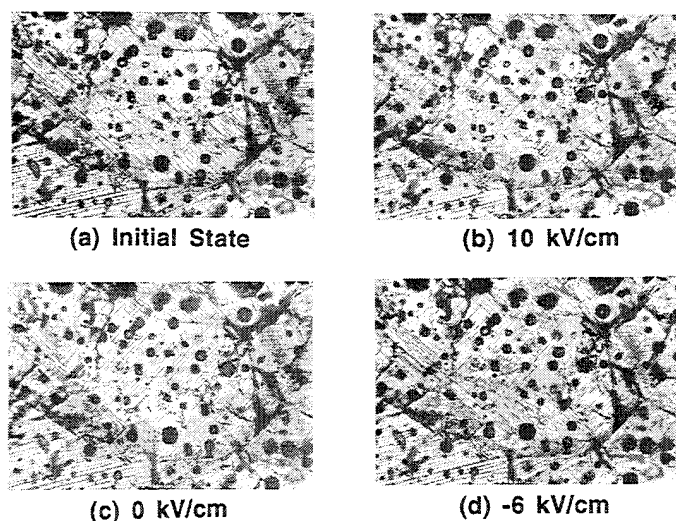


Fig. 9 Variation of domain structures of BT sample under an electric field.

10,13 samples did not show any hysteresis of domain motion as shown in Fig. 10,11. Applying an electric field up to  $+10$  kV/cm to the BTS-10 sample induces domain growth from tiny and complex domains to large and simple domains, and the domain structure returns to its initial state as the electric field is removed. In the case of the BTS-13 sample, the domain walls were observed only when an electric field of  $\pm 5$  kV/cm was applied, and these domain walls disappeared above  $\pm 5$  kV/cm as well as zero field. The domain dynamics of the BTS-13 sample is associated with the small hysteresis of P-E and field induced strain characteristics.

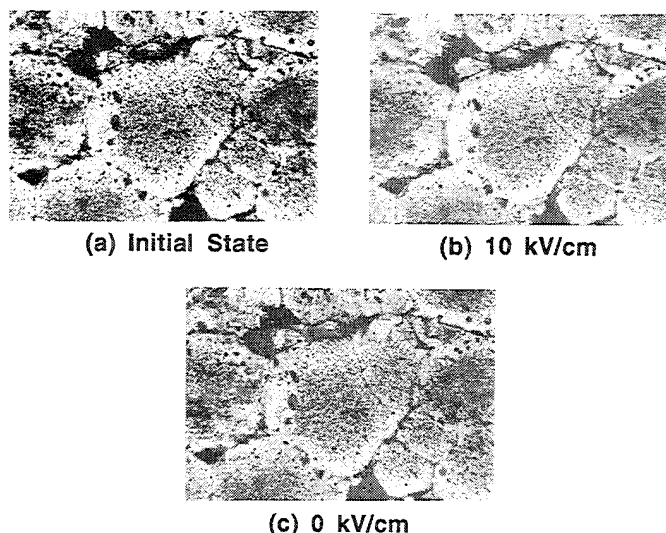


Fig.10 Variation of domain structures of BTS-10 sample under an electric field.

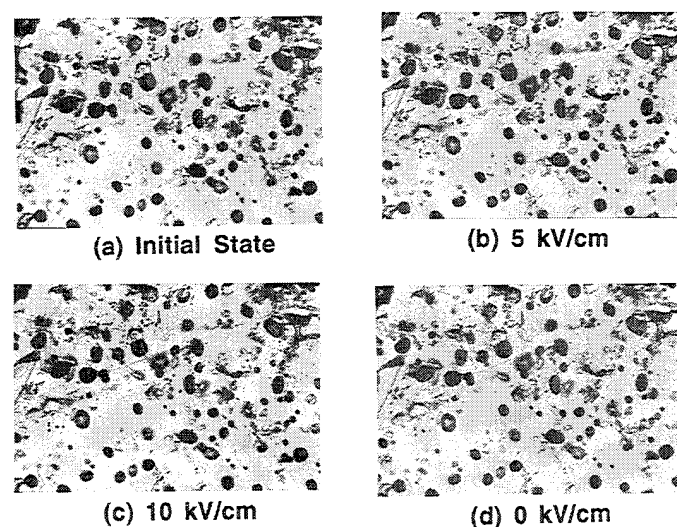


Fig.11 Variation of domain structures of BTS-13 sample under an electric field.

#### 4. Conclusions

Domain structures of  $\text{Ba}(\text{Sn,Ti})\text{O}_3$  become drastically smaller, less well-defined and more complex with increasing Sn content. These micro domain configurations are rather similar to those of the relaxor ferroelectric  $\text{Pb}(\text{Zn}_{1/3}\text{Nb}_{2/3})\text{O}_3$ <sup>1)</sup>.

The domain motion of the  $\text{BaTiO}_3$  and  $\text{Ba}(\text{Ti}_{0.95}\text{Sn}_{0.05})\text{O}_3$  ceramic show hysteresis under an electric field, while the  $\text{Ba}(\text{Ti}_{0.9}\text{Sn}_{0.1})\text{O}_3$  and  $\text{Ba}(\text{Ti}_{0.87}\text{Sn}_{0.13})\text{O}_3$  samples do not exhibit hysteresis; this explains reasonably the superior nonhysteretic characteristic in the induced strain curve of  $\text{Ba}(\text{Ti,Sn})\text{O}_3$ .

## REFERENCES

1. K. Kato, K. Suzuki and K. Uchino, "Observation of Domain Motion in Ferroelectric Single Crystals with a Diffuse Phase Transition" *J. Ceram. Soc. Jpn.*, **98** [5] 840-45 (1990)
2. K. Uchino, "Relaxor Ferroelectrics" *J. Ceram. Soc. Jpn.*, **99** [10] 829-35(1991)
3. J. Von Cieminski, H. Th. Langhammer, and H.P. abicht, "Peculiar Electromechanical Properties of Some Ba(Ti,Sn)O<sub>3</sub> Ceramics" *Phys. Stat. Sol. (a)* **120**, 285-93 (1990)
4. J. Von Cieminski and H. Beige, "High-signal electrostriction in ferroelectric materials" *J. Phys. D: Appl. Phys.* **24** 1182-86 (1991)



# Influence of Proton-Exchange Conditions on Ferroelectric Domain Inversion Caused in $\text{LiTaO}_3$ Crystals

Ailie Tourlog and Kiyoshi Nakamura  
Faculty of Engineering, Tohoku University  
Sendai 980, Japan

**Abstract** — Proton exchange followed by heat treatment of  $\text{LiTaO}_3$  crystals causes domain inversion at the negative surface. The dependence of the ferroelectric inversion layer thickness on the proton-exchange time and temperature is experimentally investigated. The results show that there exists a threshold in proton-exchange time and temperature for forming the inversion layer, and that the inversion layer thickness can be approximately expressed by a unique function of the proton-exchanged layer thickness.

## INTRODUCTION

The domain inversion phenomenon [1]-[4] caused in  $\text{LiTaO}_3$  crystals by proton exchange[5] and heat treatment has received much attention. In the inverted domains, the odd rank tensors, such as piezoelectric, pyroelectric and nonlinear optic constants are opposite in sign to the original ones. This character of the inverted domains of  $\text{LiTaO}_3$  is useful for surface acoustic wave devices [6],[7], quasi-phase-matched second-harmonic generation (QPM SHG) devices [8],[9], and pyroelectric IR detectors [10]. It is important both for understanding of the domain inversion mechanism and for practical use of inverted domains to examine the dependence of the thickness of the inverted domains on the proton-exchange and heat treatment processes. So far, the dependence has been partly investigated[1]-[4],[11]. It has been shown that the inversion layer thickens with increasing the heat treatment time to a certain extent, but it remains almost constant for a long heat treatment, and that the inversion layer could hardly be formed for the case of very slow temperature elevation. For precise control of the inversion layer thickness, the proton-exchange temperature and time are more convenient parameters. However, the data published so far on the dependence of the inversion layer thickness on the proton-exchange conditions are insufficient. Although the relationship between the inversion layer and the proton-exchanged layer is very basic and important for better understanding of the phenomenon, it has not been

clarified yet.

In this paper, the dependence of the inversion layer thickness upon the proton-exchange time and temperature are reported, and the relation between the thicknesses of the inversion layer and the proton-exchanged layer is discussed.

## EXPERIMENTAL

The samples used in the experiments for investigating the influence of the proton-exchange conditions on the domain inversion were 0.5-mm-thick single-domain Z-cut  $\text{LiTaO}_3$  plates. The plates were proton exchanged in a melt of benzoic acid for 10 min to 20 h at temperatures ranging from 160°C to 250°C. After cleaning in methanol, samples were cut along the crystallographic  $X$  axis. To measure the thickness of the proton-exchanged layer, the cross section of the samples was polished and etched in a mixture of HF and  $\text{HNO}_3$ , and then observed with a polarizing microscope. Figure 1 is a photomicrograph of the cross section of a sample proton-exchanged for 20 h at 243°C. The proton-exchanged layer about 3.2  $\mu\text{m}$ -thick can be seen. Then, the samples were heat

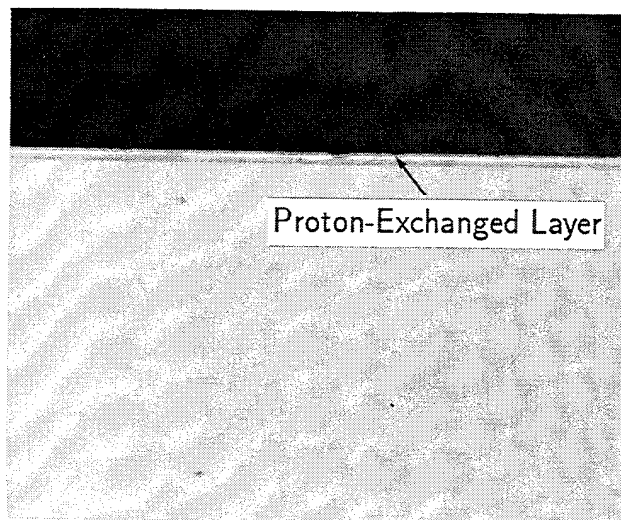


Fig.1 Photomicrograph of cross section of a sample proton-exchanged for 20 h at 243°C. The proton-exchanged layer about 3.2  $\mu\text{m}$ -thick can be seen.

treated for 1 h at 590°C which is a little below the Curie temperature, and the period of temperature elevation was kept constant (1 h) for all samples. After heat treatment, the sample was cut again, polished, and etched for measuring the inversion-layer thickness with an optical microscope.

The measured thicknesses of the proton-exchanged layer and inversion layer of the plates proton exchanged at 243°C are shown in Fig.2 as functions of the proton-exchange time  $t_{PE}$ . A threshold of the proton-exchange time to cause a domain inversion exists at about 20 min. Figure 3 shows the dependence of the proton-exchanged layer and inversion layer thicknesses upon the proton-exchange temperature  $T_{PE}$  under constant proton-exchange time. The proton-exchange was car-

ried out at several temperatures ranging from 180°C to 250°C for 6 and 20 h. A threshold of the proton-exchange temperature also exists, as no inversion layer was formed at about 190°C for proton exchange time of 6 h.

## DISCUSSION

To explain the mechanism of the domain inversion phenomenon the following model has been proposed by the authors[3],[4]: During proton exchange process, excess protons may be diffused into  $\text{LiTaO}_3$  plate, thereby yielding positive space charges; Consequently, an internal electric field directed outward from the plate builds up by the space charges near the surface;

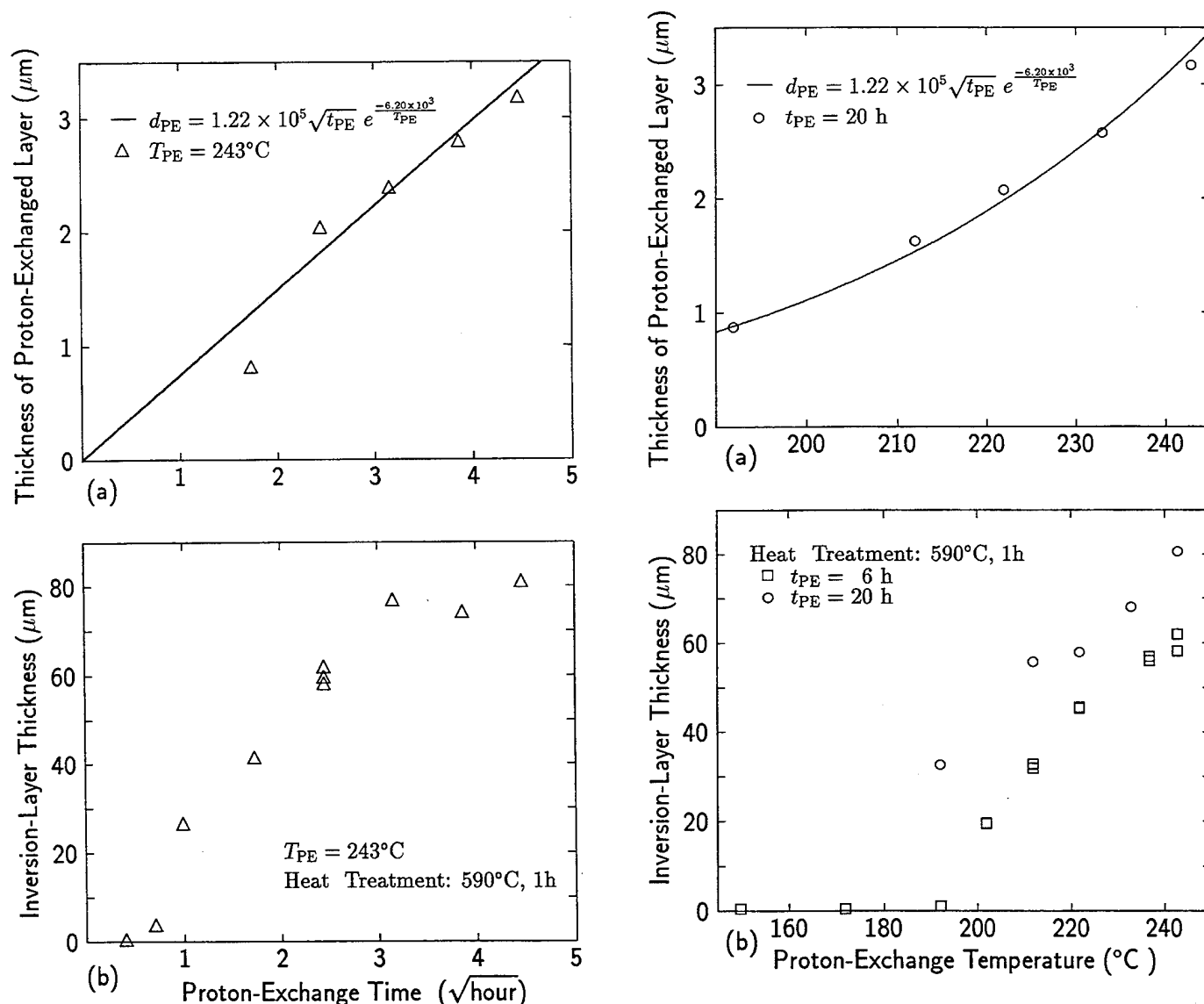


Fig.2 Dependence of (a)proton-exchanged layer thickness and (b)inversion layer thickness on proton-exchange time. Samples were proton-exchanged at 243°C and heat treated for 1 h at 590°C.

Fig.3 Dependence of (a)proton-exchanged layer thickness and (b)inversion layer thickness on proton-exchange temperature. Samples were proton-exchanged for 6 h or 20 h and heat treated for 1 h at 590°C.

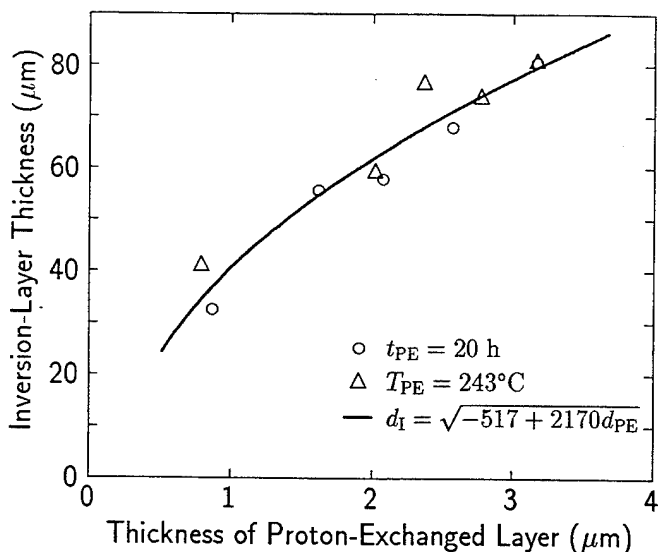


Fig.4 Relation between inversion layer thickness and proton-exchanged layer thickness.

The electric field in the proton-exchanged layer may caused a local domain reversal only at the negative surface when the plate is heated to a high temperature where the coercive field of  $LiTaO_3$  is sufficiently low. Some experimental results have been shown to support the space-charge field model[12],[13]. A similar model for explaining the mechanism has been presented by Mizuuchi et al[14].

According to the model, the existence of the thresholds in proton exchange time and temperature to cause a domain inversion may be explained as follows: Below the threshold, the internal electric field built up by space charges may not reach the coercive field at the heat treatment temperature, and therefore the spontaneous polarization may not be inverted.

From Figs.2 and 3, the relations between the thickness of the proton-exchanged layer and that of the inversion layer can be obtained. Figure 4 represents the relations both for constant proton-exchange temperature of  $234^\circ C$  and for constant proton-exchange time of 20 h. As seen from this figure, the inversion layer thickness  $d_I$  has a strong correlation with the thickness of the proton-exchanged layer  $d_{PE}$ . The inversion layer thickness  $d_I$  can be approximately expressed by a unique function of  $d_{PE}$ .

$$d_I = \sqrt{-517 + 2170 d_{PE}} \quad [\mu m] \quad (1)$$

This function is shown in Fig.4 with a solid curve.

The inversion-layer thickness is much thicker than that of the proton-exchanged layer. Based on the space-charge field model, this may be explained as follows: The protons in the proton-exchanged layer diffuse deep into the substrate during the heat treatment

process, and therefore the proton-exchanged layer thickens.

## CONCLUSIONS

The dependence of the inversion-layer thickness on the proton-exchange conditions has been experimentally investigated. It has been shown that there exists a threshold in proton-exchange time and temperature to cause a domain inversion, and that the inversion layer thickness can be approximately expressed by a unique function of the thickness of the proton-exchanged layer. These experimental results are useful for precise control of the inversion layer thickness for practical use.

## ACKNOWLEDGEMENT

This work was supported in part by the Asahi Glass Foundation.

## REFERENCES

- [1] K. Nakamura, H. Ando, M. Hosoya and H. Shimizu, "Formation of ferroelectric inversion layers in  $LiTaO_3$  plates by utilizing proton exchange," *Tech. Rep. IEICE Jpn.*, US87-37, pp. 17-22, 1987 [in Japanese].
- [2] K. Nakamura and H. Shimizu, "Ferroelectric inversion layer formed by heat treatment of proton-exchanged  $LiTaO_3$ ," *Appl. Phys. Lett.*, vol. 56, pp. 1535-1536, 1990.
- [3] A. Tourlog and K. Nakamura, "Single-domain surface layers formed by heat treatment of multi-domain  $LiTaO_3$ ," *Tech. Rep. IEICE Jpn.*, US91-49, pp. 15-20, 1991.
- [4] K. Nakamura, M. Hosoya and A. Tourlog, "Antipolarity domain nucleation and growth during heat treatment of proton-exchanged  $LiTaO_3$ ," *J. Appl. Phys.*, vol. 73, pp. 1390-1394, 1993.
- [5] J.L.Jackel, C.E.Rice, and J.J.Veselka, "Proton exchange for High index waveguides in  $LiNb_3$ ," *Appl. Phys. Lett.*, vol. 41, pp. 607-608, 1982.
- [6] A. Tourlog, K. Nakamura and H. Shimizu, "Leaky surface acoustic wave on  $LiTaO_3$  substrates with a ferroelectric inversion layer," in *Proc. of Inter. Congress on Acoustics*, vol. 2, C7-6, Sep. 1992.
- [7] K. Nakamura and A. Tourlog, "Effect of a ferroelectric inversion layer on the temperature characteristics of SH-type surface acoustic waves

on 36° Y-X LiTaO<sub>3</sub> substrates," *IEEE Trans. UFFC*, (to be published).

- [8] J. Webjörn, F. Laurell and G. Arvidsson, "Fabrication of periodically domain-inverted channel waveguides in lithium niobate for second harmonic generation," *J. Lightwave Tech.*, vol. 7, pp. 1597-1600, 1989.
- [9] K. Mizuuchi, K. Yamamoto and T. Taniuchi, "Second-harmonic generation of blue light in a LiTaO<sub>3</sub> waveguide," *Appl. Phys. Lett.*, vol. 58, pp. 2732-2734, 1991.
- [10] K. Nakamura and M. Itagaki, "Pyroelectric IR detectors using periodic inverted domains of LiTaO<sub>3</sub>," *Jpn. J. Appl. Phys.*, vol. 33, No.9B, 1994, (in press).
- [11] K. Mizuuchi and K. Yamamoto, "Fabrication of periodic domain inversion in an *x*-cut LiTaO<sub>3</sub>," *Appl. Phys. Lett.*, vol. 62, pp. 1860-1862, 1993.
- [12] A. Tourlog and K. Nakamura, "Low-frequency dielectric responses of proton-exchanged LiTaO<sub>3</sub>," *Jpn. J. Appl. Phys.*, vol. 32, pp. 4370-4372, 1993.
- [13] K. Nakamura and A. Tourlog, "Single-domain surface layers formed by heat treatment of proton-exchanged multidomain LiTaO<sub>3</sub> crystals," *Appl. Phys. Lett.*, vol. 63, 1993.
- [14] K. Mizuuchi and K. Yamamoto, "Domain inversion in LiTaO<sub>3</sub> using proton exchange followed by heat treatment," *J. Appl. Phys.*, vol. 75, pp. 1311-1318, 1993.

# HREM Studies of Ordered Superstructure in PMN and PLMN Ceramics

Liu Yinmei, Song Chengyu, Wen Baosong  
Shanghai Institute of Ceramics, Chinese Academy of Sciences  
1295 Dingxi Road, Shanghai 200050, China

**Abstract** — Pure and La-doped lead magnesium niobate have been studied by high resolution electron microscopy combining with computer simulation. There show nanosize superstructural microdomains in the [110] HREM image of  $\text{Pb}(\text{Mg}_{1/3}\text{Nb}_{2/3})\text{O}_3$ , and the domains grow up to an extent of about 40nm~over 150nm by 10~20% La-doping. Through the computer simulation and processing, the superstructure is confirmed relating to the ordering on the B-sites, and explicit description and explanation of the ordered structure, the microdomains' form and growth are given.

## INTRODUCTION

Structural order-disorder on the B-sites of a large group complex perovskite oxides  $\text{A}(\text{B}'\text{B}'')\text{O}_3$  has been widely considered responsible for the diffuse phase transition and dielectric relaxation, and has more or less influences on many other properties as well[1-2]. There is discovered and demonstrated existing some nonstoichiometric 1:1 ordering on the B-sites of the perovskite lead magnesium niobate  $\text{Pb}(\text{Mg}_{1/3}\text{Nb}_{2/3})\text{O}_3$ [3-4]. Because of the short-range character of the ordering, the selected area electron diffraction (SAED) pattern and centered-dark-field (CDF) image just show weak superlattice spots  $\{h+1/2, k+1/2, l+1/2\}$  and a nanosize of ordered microdomains. By the method of  $\text{La}^{3+}$  cations substitution on the A-sites which can effectively promote the B-sites' ordering and enlarge the microdomains[5-7], the TEM observations still reveal not much of the superstructural characters and details as a result of the instrumental detective limitation. In this paper, we use high resolution electron microscopy (HREM), under the help of computer simulation and processing, to study three kinds of ceramics  $\text{Pb}(\text{Mg}_{1/3}\text{Nb}_{2/3})\text{O}_3$  (PMN),  $\text{Pb}_{0.9}\text{La}_{0.1}(\text{Mg}_{1.1/3}\text{Nb}_{1.9/3})\text{O}_3$  (PLMN10) and  $\text{Pb}_{0.8}\text{La}_{0.2}(\text{Mg}_{0.4}\text{Nb}_{0.6})\text{O}_3$  (PLMN20), and realize the ordered superstructure and its microdomains directly and comprehensively.

## EXPERIMENTAL

PMN and PLMN are prepared according to the fabrication process developed by Swarts and Shrout[8], first the columbite phase  $\text{MgNb}_2\text{O}_6$  is calcined at 1000°C for 6 hours, then the powders of  $\text{Pb}_3\text{O}_4$ ,  $\text{La}_2\text{O}_3$  and  $\text{MgNb}_2\text{O}_6$  are mixed for the second calcination at 850°C for 2 hours. The sintering temperatures of the pressed pellet samples are between 1200°C ~ 1300°C inside a covered alumina crucible. Analyzed by X-ray diffraction, only PLMN contain a little pyrochlore phase, and SEM certifies the grain growth of all are quite well.

Samples for electron microscope observation are made by both ion-beam thinning and crushing, the high resolution images in addition to the electron diffraction patterns are obtained with a JEM-200CX high resolution electron microscope at room temperature. In the computer simulation and processing, AST386 microcomputer, HP Laserjet printer and Scanjet scanner with a resolution of 300DPI are involved.

## RESULTS AND DISCUSSION

### Computer Simulation of HREM Image

As the contrast of a HREM image is a function of specimen thickness, objective lens defocus and many other factors, computer simulation is usually employed to aid interpreting the HREM image and identifying the crystal structure. By calculating through the computer program the datum of supposed crystal structure with varied experimental conditions of image-forming such as different specimen thickness and defocus values, a series of simulated images will be given out, and later be compared with the HREM images so as to confirm the supposed crystal structure if they match well.

Fig.1 is the typical perovskite structure of PMN, in (a) fully disordered B-site cations form a simple cubic structure and in (b) fully 1:1 ordered B-site cations form a face-centred cubic structure. The unit cell parameter of the later is twice that of the former.

Fig.2 are twelve computer simulated images of different specimen thickness and defocus values for PMN disordered structure and ordered structure respectively. The [110] zone are selected common for both simulated images and HREM images because only along that direction can the 1:1 ordering on the B-sites be clearly observed. From Fig.2, it is obvious that the contrasts of the simulated images for the ordered structure are dissimilar to those for the disordered structure, which implies a twice long periodicity in the former.

### Ordered Structure and Microdomains in HREM Images

The HREM images with corresponding SAED patterns attached of PMN and PLMN along the [110] direction are shown in Fig.3-5. From the patterns, all have the expected cubic symmetry with additional  $(1/2, 1/2, 1/2)$  superlattice spots, which indicate that twice periodic superlattice appears along the  $\langle 111 \rangle$  directions, i.e. there yields a superstructure of face-centered cell with parameter  $a=2a_0$ . As the analysis conditions are kept same, the brightness of PLMN superlattice spots being stronger than that of PMN's gives the evidence that La-doping in PMN facilitates the formation of superstructure.

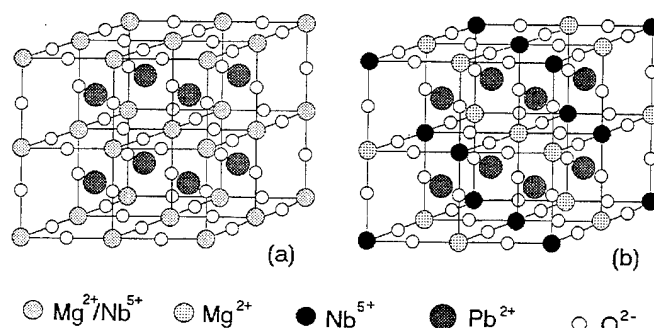


Fig.1 Structure models of perovskite PMN for (a) disordering on B-sites and (b) 1:1 ordering on B-sites.

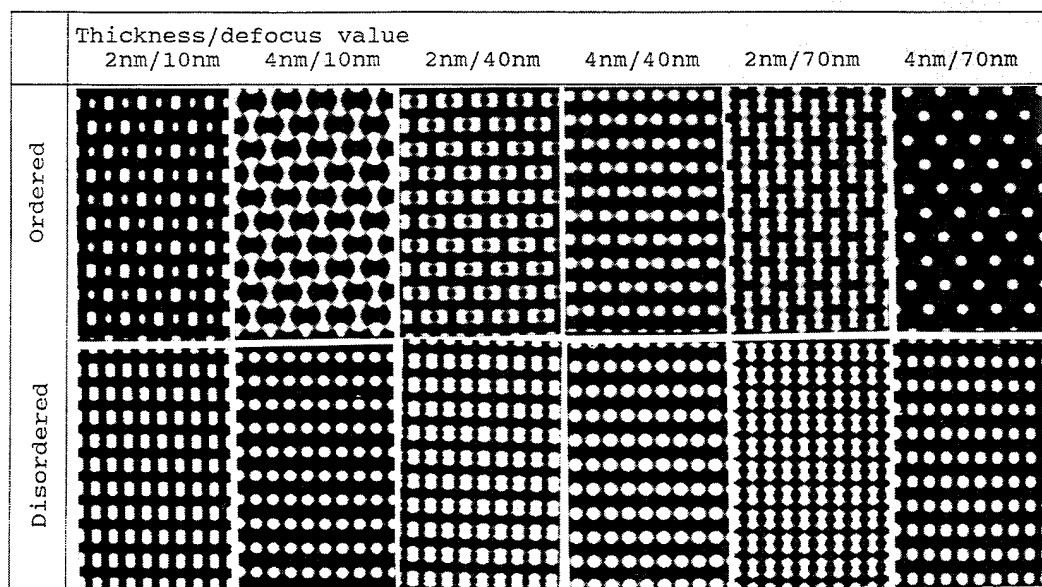


Fig.2 Through-focal/through-thickness series of simulated images for ordered and disordered structures.

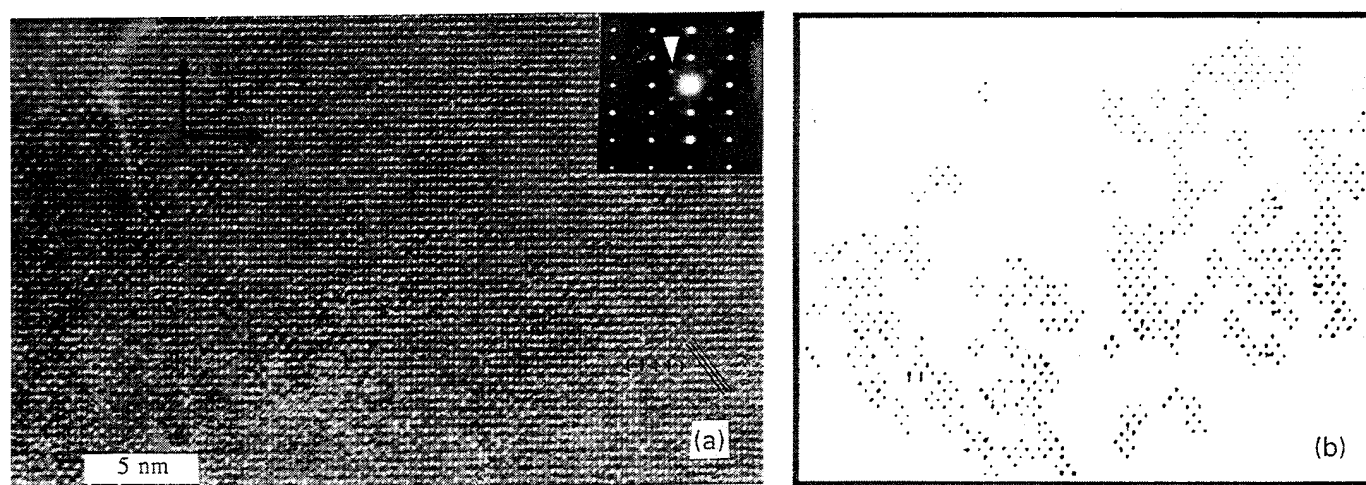


Fig.3 (a) HREM image and corresponding SAED pattern of PMN.  
(b) Computer processed image of (a), showing the nano-sized domains with a network form.

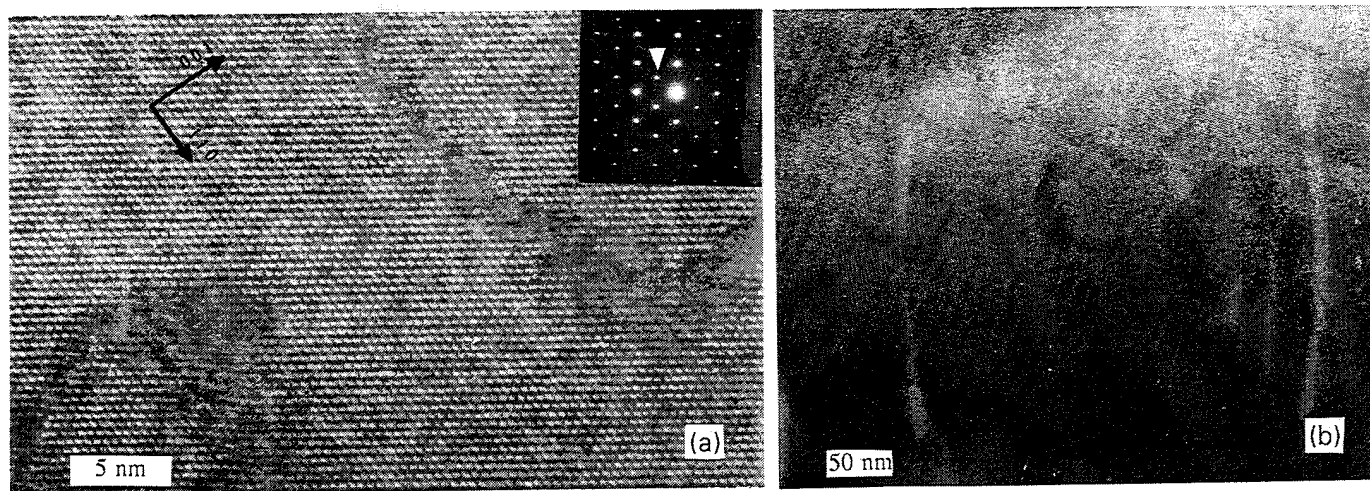


Fig.4 (a) HREM image and corresponding SAED pattern of PLMN10.  
(b) A low magnified image of (a), showing curved domain boundaries.

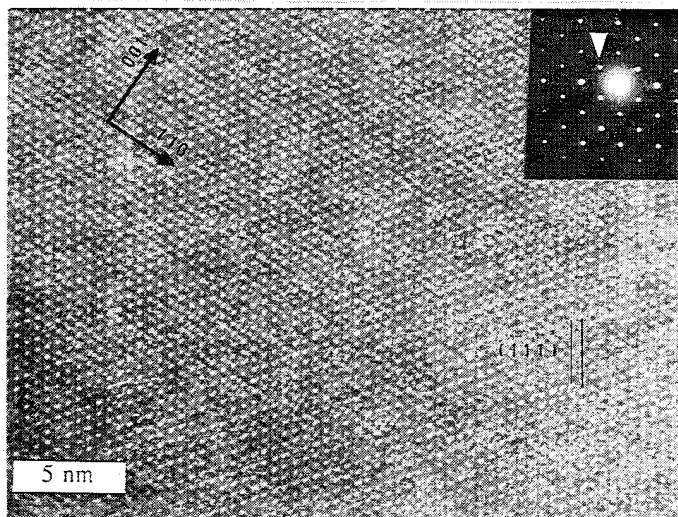


Fig.5 HREM image and corresponding SAED pattern of PLMN20.

In the HREM image of PMN(Fig.3a), there show regular-distributed bright dots spaced by about  $4\text{\AA}$  ( $a_c$ ) on the [001] direction and  $2.83\text{\AA}$  ( $a_c/\sqrt{2}$ ) on the [110] direction, forming a rectangle lattice. Most of the dots are as bright as each other and give out an even contrast. Comparing the HREM image with the simulated(Fig.2), disordered structure of B-site cations' arrangement is confirmed to be the main feature of the pure PMN. Nevertheless, in a few areas about nanosize, some dots become less bright or almost fade one over two along the [001] and [110] directions. And such phenomenon could be more clearly observed in the images of PLMN, that is, bright dots alternate with weak dots spreading over the great part of the HREM image of PLMN10(Fig.4a) and the whole of the HREM image of PLMN20(Fig.5), forming a rhombic lattice. This result like what the patterns have shown, just illustrates the presence of a superstructure with double unit cell parameter. After the comparison between the HREM images and the simulated(Fig.2), the superstructure could be found in good agreement with the ordered structure of 1:1 arrangement on the B-sites, which means  $\text{Mg}^{2+}$  cations and  $\text{Nb}^{5+}$  cations occupy the B-sites of the perovskite alternatively, exhibiting a face-centered structure with double period as Fig.1b shows. So it is concluded that an ordered superstructure of  $\text{Mg}^{2+}:\text{Nb}^{5+}=1:1$  emerges in PMN, and the ordered regions (named microdomains formally) would grow up to much larger size in the La-doped specimens and become their important microstructural features.

#### *The Effect of La-doping and the Form of Ordered Microdomains*

The 1:1 ordering on the B-sites in PMN is nonstoichiometric which deviates from the proportion of 1:2 of the overall chemical composition. This will certainly cause the compositional fluctuation of rich niobium outside the domains and rich magnesium inside the domains, and further lead to the generation of space charges at the domain boundaries, which will reversely inhibit the domains' growth and make them just about nanosize. By introducing high valence dopants such as  $\text{La}^{3+}$  to replace some  $\text{Pb}^{2+}$  cations and adjusting the  $\text{Mg}^{2+}:\text{Nb}^{5+}$  ratio closer to 1:1 for charge balance, it would counteract the effect of the space charges, reduce the compositional fluctuation and benefit long range ordering on the B-sites, so the ordering is promoted and the domains are enlarged[5-7]. The HREM analysis results of the pure and La-doped PMN specimens precisely speak for the fact.

In the pure PMN, there are ordered microdomains about 1~5nm well-distributed in the disordered matrix in a form of imperfect network, rather than a form of isolated islets as they seem to be according to the CDF image[9], and Fig.3b shows the network form more clearly through the computer processing of the HREM image. In the 10% La-doped PMN, the microdomains grow up to 20~40nm and are separated by long narrow wavy disordered areas as Fig.4b shows, which are called antiphase domain boundaries in some papers[5,6]. The ordered regions in the 20% La-doped PMN are much larger, which is hard to estimated from the HREM image.

## CONCLUSION

- (1) By HREM, 1:1 ordering on the B-sites of PMN is discovered, and its ordered microdomains are recognized.
- (2) La-doping on the A-sites could promote the ordering degree and enlarge the microdomains.
- (3) Relevant computer simulation and processing greatly help to confirm the ordered or disordered structure and reveal the forms of ordered microdomains.

## REFERENCES

- [1] N.Setter and L.E.Cross, "The Role of B-site Cation Disorder in Diffuse Phase Transition Behavior of Perovskite Ferroelectrics," *J.Appl.Phys.*, vol.51(8), pp.4356-60, 1980.
- [2] K.Uchino, S.Nomura, L.E.Cross, R.Newnham and S.J.Jang, "Review: Electrostrictive Effect in Perovskites and Its Transducer Applications," *J.Mater.Sci.*, vol.16, pp.569-78, 1981.
- [3] H.B.Krause, J.M.Cowley and J.Wheatley, "Short-range Ordering in  $\text{Pb}(\text{Mg}_{1/3}\text{Nb}_{2/3})\text{O}_3$ ," *Acta Cryst.*, vol.A35, pp.1015-17, 1979.
- [4] E.Husson, M.Chubb and A.Morell, "Superstructure in  $\text{Pb}(\text{Mg}_{1/3}\text{Nb}_{2/3})\text{O}_3$  Ceramics Revealed by High Resolution Electron Microscopy," *Mater.Res.Bull.*, vol.23, pp.357-61, 1988.
- [5] J.Chen, H.M.Chan and M.P.Harmer, "Ordering Structure and Dielectric Properties of Undoped and La/Na-Doped  $\text{Pb}(\text{Mg}_{1/3}\text{Nb}_{2/3})\text{O}_3$ ," *J.Am.Ceram.Soc.*, vol.72(4), pp.593-98, 1989.
- [6] M.P.Harmer, J.Chen, P.Peng, H.M.Chan and D.M.Smyth, "Control of Microchemical Ordering in Relaxor Ferroelectrics and Related Compounds," *Ferroelectrics*, vol.97, pp.263-74, 1989.
- [7] N.de Mathan, E.Husson, P. Gaucher and A.Morell, "Modification of the B-site Order of  $\text{Pb}(\text{Mg}_{1/3}\text{Nb}_{2/3})\text{O}_3$  Ceramics By Thermal Annealing or By La-doping," *Mater.Res.Bull.*, vol.25, pp.427-34, 1990.
- [8] S.L.Swatz and T.R.ShROUT, "Fabrication of Perovskite Lead Magnesium Niobate," *Mater.Res.Bull.*, vol.17, pp.1245-50, 1982.
- [9] T.R.ShROUT, W.Huebner, C.A.Randall and A.D.Hilton, "Aging Mechanisms in  $\text{Pb}(\text{Mg}_{1/3}\text{Nb}_{2/3})\text{O}_3$ -based Relaxor Ferroelectrics," *Ferroelectrics*, vol.93, pp.361-372, 1989.



# Controlled chaos in ferroelectric systems

R. Habel, S. Blochwitz and H. Beige  
 Fachbereich Physik, Martin-Luther-Universität Halle-Wittenberg,  
 D-06108 Halle/Saale, Germany

The value of nonlinear coefficients in ferroelectric crystals grows near the phase transition. Therefore a series resonance circuit consisting of a linear coil and a nonlinear capacitor that is made of ferroelectric material can show all features of nonlinear dynamical systems: period-doubling, hysteresis and chaotic behavior. In periodic windows we can fit experimental data-sets to a model equation. In the chaotic region it is necessary to use a method of controlling chaotic systems to switch into periodic behavior. This method perturbs the system only in a very small range. The advantage of the control method introduced by Ott, Grebogy and Yorke is that one can get all needed parameters of control only by system measurements without using any kind of model. In a real physical system it is very difficult to determine these perturbations as fast as needed. That's why we achieve control of chaos using an universal electronic unit.

## INTRODUCTION

In many fields of nature, science and engineering we can find nonlinear phenomena. Most of them are very complex and difficult to understand like processes in the atmosphere, some of them seem simple like a nonlinear resonance circuit, the system of our investigation.

In periodic states we use a model which describes the system and fit the data to this model. In the chaotic regions it's impossible to fit the data. So we stabilize the system with very small perturbations to a period one without changing the system characteristics. We developed an electronic unit with special features to do this.

The nonlinearity of the resonance circuit is given by a capacitor with a nonlinear dielectric material. The capacitor is a thin crystal (0.1-1.0 mm) of the investigated material with thin metallic surface films. We use crystals of triglycine sulfate (TGS) and betaine arsenate (BA) at a temperature below the phase transition.

This capacitor is connected in a series resonance circuit, which is shown in fig. 1.

There is  $L$  the linear inductance,  $C_{nl}$  the nonlinear capacitor,  $C_{lin}$  and  $R$  a linear capacitor and a linear resistor for measure the dielectric displacement  $D$  and their derivation  $j$  (current density) in the system. The series resonance circuit is driven by a sinusoidal voltage.

The model we use to describe the dynamics of the nonlinear series resonance circuit is based on a substitution of the ferroelectric capacitor with a parallel-circuit that consists of an ideal nonlinear capacitance and a linear resistor. The former one models the nonlinear ferroelectric properties, whereas the latter one stands for the dielectric losses.

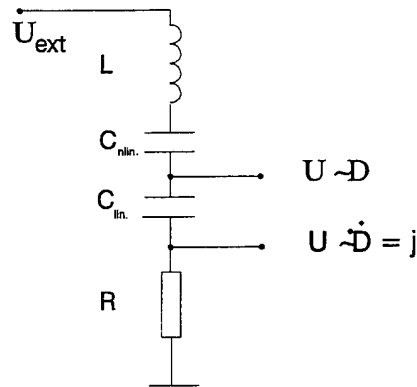


Fig. 1: Nonlinear series resonance circuit

Analyzing the new circuit with Kirchhoff's laws yields

$$U_{ext} = L F \frac{d^2 D}{dt^2} + \left[ \frac{Lh}{R_{C_{nl}}} (\alpha_2 + 3\alpha_4 D^2 + \dots) * FR_{L_0} \right] \frac{dD}{dt} + h(\alpha_2 D + \alpha_4 D^3 + \dots)$$

where  $\alpha_2$  and  $\alpha_4$  are the coefficients of a generalized Landau-Potential

$$V_{nl} = \frac{\alpha_2}{2} D^2 + \frac{\alpha_4}{4} D^4$$

This model equation can be fitted to periodical experimental data sets by a numerical method [14].

## METHODS OF NONLINEAR DYNAMICS

A system can be characterized by the motion in the phase space, but if the system is chaotic, then the quantity of data is very large. To reduce this quantity without loss of interesting information we use a method introduced by Poincaré. Fig. 2 shows this method in the case of a 2-dimensional phase space. In consideration of time we have a 3-dimensional space. If the system is driven periodically, these 3 coordinates can be transformed into cylindrical coordinates. The angle is represented by time. Let  $P$  be an 2-dimensional hyperplane transversal to the trajectory at a point  $x_0$ . Then this hyperplane is crossed by the trajectory every  $T$  seconds, where  $T$  is the period length. So a sequence of points on the so called Poincaré section can be described.



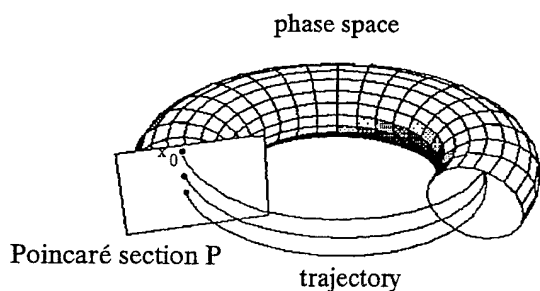


Fig. 2: Construction of an poincaré section

If the system is periodic with period  $p$ , then  $p$  Points  $x(t)$  exist on the hyperplane and these points satisfy the condition  $x(t_i) = x(t_i + p \cdot T)$ . On chaotic motion an infinit number of different points exist on the poincaré section and a strange attractor can be obtained. The fig. 3 shows a strange attractor of the nonlinear series resonance circuit with betaine arsenate.

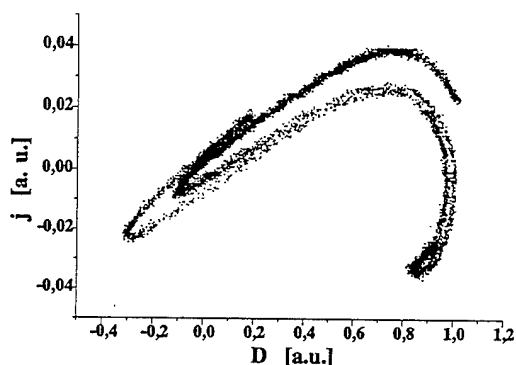


Fig. 3: Attractor of betaine arsenate

Using the poincaré section the local dynamics of the system at a given point can be determined by a linearization in a small neighborhood of this point. It isn't necessary to know the dynamical equations describing the system.

A typical route to chaos of a dynamical system is the well-known Feigenbaum scenario. This scenario starts from a stable state of the system. This state is  $1T$  periodic and corresponds with one point in the poincaré-section that is observed at a certain value of an external parameter (e. g. frequency). If this external parameter is increased (or decreased) the system switches suddenly at a so called bifurcation point to a  $2T$  periodic state that corresponds to two points in the poincaré section. Further increasing or decreasing respectively of the external control parameter yields more bifurcation points, each doubling the periodicity of the system. Finally, when the number of points in the poincaré section goes to infinity, the system has reached a chaotic region.

For the dielectric nonlinear circuit this situation is illustrated in fig. 4. In this figure the D-coordinate of the poincaré section is recorded experimentally versus the value of the external parameter. Note that there is no higher periodicity than  $4T$  due to the limited resolution of the A/D-converter.

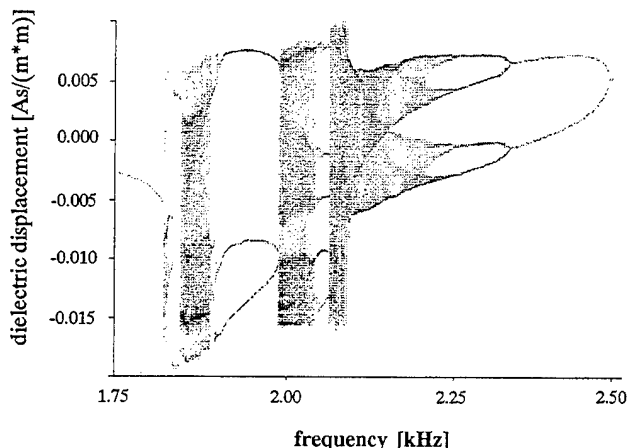


Fig. 4: Bifurcations of betaine arsenate

#### CONTROLLING METHOD

We want to use the method proposed by Ott, Grebogy and Yorke (OGY) [1]. This method is using the specific properties of the unstable periodic saddle orbits embedded in the chaotic attractor. These saddle points have stable and unstable directions of motion. The basic idea of the control method is to change a parameter (which can vary from outside of the system) in a small range and to force the system to the stable direction. We achieved control of the chaos-region only with very small perturbations of the system. The value of this perturbation should be selected in such way, that the system approaches that orbit in the next time if it is found next of this unstable periodic orbit. The system meets the requirements, if it depends on a parameter, which is variable in a small interval and we have an iterative map (poincaré section) with unstable periodic orbits. The formula introduced by OGY is the following equation

$$\partial a = -\frac{\lambda_u}{f_u^* w} f_u^* \partial \xi_n.$$

There the vector  $f_u$  is the unstable contravariant basis vector. This vector gives the direction of the unstable manifold of the fixed point. The parameter  $\lambda_u$  is the corresponding eigenvalue, the vector  $w$  comes from the linearisation and  $\delta \xi_n$  is the difference between the fixed point  $\xi_F$  and the momentary system state  $\xi_n$ .

In our case we have an 2-dimensional poincaré section of the nonlinear series resonance circuit, so one can write down the perturbation after some equivalent transformations

$$da = a - (b \cdot D + c \cdot j).$$

There are  $D$  and  $j$  the system state and  $a, b$  and  $c$  are parameters which are constant.

The parameter  $da$  is multiplied by us with a factor  $v$  ( $v$  is approximately 1.0). In practice we have found, that the perturbation can be decreased without losing control for a smaller influence of the system. We had also found, that in case of noisy systems it's possible to reach control by increasing the perturbation, the used formula looks like

$$da = v \cdot [a - (b \cdot D + c \cdot j)].$$

This equation shows, that the formula confines to two multiplications and two additions/subtractions, if the parameters are adequate summarized.

We chose the driving amplitude of the series resonance circuit as an external parameter of perturbation.

The advantages of this method are listed as follows:

- \* One can get all needed parameters of control only by measuring of the system without using any kind of model.
- \* It needs only very small perturbations.

These features are the main reasons for universal usability of this method.

The sum of calculating and IEEE-bus transfer time effects an nonelectable phase shift in the used frequency range of the series resonance circuit. We investigate a quick system for controlling chaos, the frequency is 1-5 kHz. For this reason we chose a technique with an electronic unit. This control system calculates the perturbation with the formula given by Ott, Grebogy and Yorke on a hardware based way like an analog-computer and has some additional features for system requirements.

The electronic unit calculates the perturbation parameter continuously, but we need only the value in the very moment of getting a point in the poincaré section (until we get the next point). That's why we need a Sample&Hold circuit triggered by the driving generator.

We demand a very small value for perturbation, but it may be that this parameter is not small. That happens every time the state of the system is far from the fixed point. In this case, the system can't be perturbed. So we need a window-discriminator to prevent the unit from perturbing. The output of this discriminator modulates the driving voltage, that comes from the generator.

No modulation takes place, if the calculated perturbation is zero or too high.

## EXPERIMENTAL SETUP

Figure 5 shows our experimental setup.

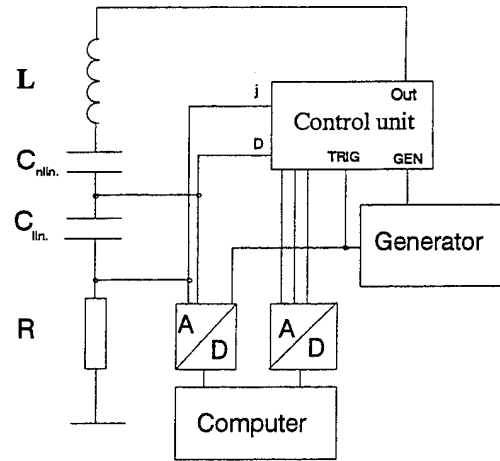


Fig. 5: Experimental setup

On the left-hand side one can see the nonlinear series resonance circuit with the linear inductance  $L$ , the nonlinear capacitor  $C_{nlin}$ , the linear driving capacitor  $C_{lin}$  and the resistor  $R$ , which are used to get the signals of the system. These signals are digitized by the digitizer and transmitted via IEEE-bus to the controlling computer. We can watch the phase space by an analog device, too. The time of measurement is locked to the driving frequency by the trigger signal of the generator. So we get a poincaré section of the phase space. All parameters are calculated by the controlling computer from this map. This computer adjusts the electronic unit, too.

The parameters  $a, b$  and  $c$  are generated by a D/A-converter and are brought into the electronic unit. They are constantly, if the environment of the system (temperature, driving frequency, etc.) is not changed. The controlling computer can calculate other problems like determining other unstable orbits of the chaotic attractor after adjusting the controlling unit. The electronic unit realize the real control process on a hardware based system by perturbing the nonlinear series resonance circuit with small modulation of the driving voltage.

## RESULTS

The results of the control are shown in fig. 6. There are shown the control perturbation in percent of driving amplitude and the dielectric displacement vs. the control step.

In the left hand side the control is switched off and then is switched on. One can see, that the perturbation is smaller than 1% for success of chaos control.

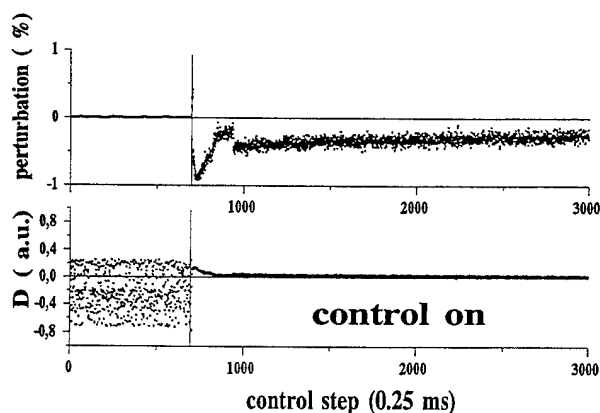


Fig. 6: Results of control process

In first time after the control is switched on, the perturbation is large - the system is forced to a stable orbit. A smaller perturbation is needed to hold the system in a periodic window, if this orbit is reached.

#### SUMMARY

Ferroelectric materials within a series resonance circuit show interesting effects like period doubling and chaos (e.g. fig. 4). To fit the data obtained from a measurement to our model a periodic non-chaotic state is needed for success. In chaotic regions we control the resonance circuit with very small perturbations of driving amplitude by a method introduced by Ott, Grebogy and Yorke. The formula is modified for a 2-dimensional system. To do the control as fast as needed at higher frequencies we use a universal electronic unit to reduce the phase shift. The control-parameter needed for this unit are obtained only from a measurement using a time series at the poincaré section without any kind of model. In the next time we will control higher periodic orbits in order to improve our model and to use the infinite collection of unstable periodic orbits in the nonlinear dynamical system.

#### ACKNOWLEDGEMENT

This work has been supported by the Sonderforschungsbereich 185 der Deutschen Forschungsgemeinschaft and the Ministerium für Wissenschaft und Forschung des Landes Sachsen-Anhalt. One of us (S. B.) is supported by the Studienstiftung des Deutschen Volkes.

- [1] E. Ott, C. Grebogy, J.A. Yorke, *Phys. Rev. Lett.*, p. 1196, 1990.
- [2] H. Beige, M. Diestelhorst, R. Forster, T. Krietsch, "Chaos near structural Phase Transitions", *Phase Transitions*, 37 (1992), pp. 213-238
- [3] E. Brauer, H. Beige, L. Flepp, M. Klee, "Series Resonance Circuit with ferroelectric Capacitor", *Phase Transitions*, 42 (1993), pp. 169-187
- [4] E. Brauer, S. Blochwitz, H. Beige, "Chaos and Regularity in a Ferroelectric Duffing-like Oscillator", in *Proceedings of the Conference Nonlinear Dynamics of electronic Systems NDES '93*, Dresden (Germany), 1993
- [5] A. Hübler: *Helvetica Physica Acta*, 62, 343, 1989
- [6] B. Hübinger, R. Doerner, W. Martienssen, *Zeitschrift für Physik B [Condensed Matter]*, 90, 103, 1993
- [7] U. Dressler, G. Nitsche, *Phys. Rev. Lett.*, 68, 1, 1992
- [8] W. L. Ditto, S. N. Rauseo, M.L. Spano, "Experimental control of chaos", *Phys. Rev. Lett.*, 65 (1990), pp. 3211-3214
- [9] E. R. Hunt, "Stabilizing high-period orbits in a chaotic system - The diode resonator", *Phys. Rev. Lett.*, 67, 15, 1991, pp. 1953-1955
- [10] K. Pyragas, A. Tamasevicius, "Experimental control of chaos by delayed self-controlling feedback", *Phys. Lett. A*, 180, 1993, pp. 99-102
- [11] M. Diestelhorst, R. Hoffmann, H. Beige, "Nonlinear Properties of TGS- and BaTiO<sub>3</sub>-Crystals with Defects", *Jpn. J. Appl. Phys.*, 24 (1985), Supl. 24-2, p. 1019
- [12] E. Brauer, S. Blochwitz, H. Beige, *Bifurcation and Chaos*, vol. 4, no. 2, 1994
- [13] H. Beige, M. Diestelhorst, R. Forster, J. Albers, J. Petersson, *Z. Naturf.* 45a, 958 (1990)
- [14] S. Blochwitz, *PhD Thesis*, Martin-Luther-University Halle-Wittenberg, (in German)

**Abstract** — In interpreting the properties of thin film ferroelectrics, it is useful to have baseline electrical property data on thinned single crystals and ceramics over the same thickness range. In this study, the properties of thinned BaTiO<sub>3</sub> have been investigated. To examine the quality of the surfaces produced, spectroscopic ellipsometry (SE) was used. This technique is capable of depth profiling the optical properties of dielectric materials with a resolution in the Angstrom range. It was found that both polishing and chemical etching lead to disturbed regions on the sample surface due to mechanical damage, residual roughness, and chemically inhomogeneous layers. As expected in the case of mechanical polishing, the depth of the damaged layer increased with grit size. For both polishing and etching it is possible to prepare surfaces with less than ~200 Å of optically detectable damage. It was shown that for unelectroded c-domain BaTiO<sub>3</sub>, irreversible changes in the SE spectra as a function of temperature occur if measurements are made immediately after polishing. It was also shown that if a gradient in the polarization exists at the surface of the sample, it appears to be confined to a layer on the order of 100 Å thick.

## INTRODUCTION

Many techniques have been utilized over the years to investigate the properties of ferroelectric surfaces. As most of these were indirect, however, information on the thickness and electrical properties of the anomalous region near the surface is limited. SE, while still indirect, permits depth profiling of the optical properties of a sample in the near surface region, and so should be useful in re-examining the question of surface layers on ferroelectrics.

## EXPERIMENTAL PROCEDURE

Depth profiling of the ferroelectric surfaces was performed using a rotating analyzer spectroscopic ellipsometer adapted for measurements of transparent materials. Details on the configuration and calibration of the instrument and the achromatic compensator have been given elsewhere [1]. In most cases, data were acquired and modeled over the wavelength range of 400 - 800 nm.

A top-seeded melt-grown BaTiO<sub>3</sub> crystal was polished to a final grit size of 0.05 µm γ-Al<sub>2</sub>O<sub>3</sub> using kerosene as a solvent. The crystal was then poled to eliminate 90° twins. To check for contamination of the surface with organic phases, the sample was exposed to a 60 eV Ar ion beam. The same crystal was also etched in a 1:1:3 mixture of H<sub>2</sub>O<sub>2</sub>, HCl, and deionized H<sub>2</sub>O to remove the polishing damage.

SE measurements were made at room temperature with and without an achromatic compensator. Measurements on single crystal BaTiO<sub>3</sub> were collected at incidence angles of 56°, 60°, 75°, and 80° at each temperature. The chamber was then heated to the next temperature and the cycle was repeated. To prevent cracking the crystal, the ramp rates on both heating and cooling were maintained at ≤ 0.1°C/min. All four data sets at each temperature were modeled simultaneously using computer code which accounted for the optical anisotropy of the sample. Since the design of the heating chamber did not permit measurements to be made in the straight-through position with the sample in place, all data at elevated temperatures were collected without the compensator. Data taken without a compensator were modeled using the Ψ data only, whereas data taken with the compensator were modeled using tanΨ and cosΔ spectra.

A mechanically polished 9.5/65/35 PLZT ceramic sample was examined. One face was polished with 1 µm

diamond paste, cleaned in acetone, and measured at an angle of incidence of 80° with the compensator. The process was then repeated after repolishing with 0.25 µm diamond and 0.05 µm γ-Al<sub>2</sub>O<sub>3</sub>.

## MECHANICALLY POLISHED SINGLE CRYSTAL BaTiO<sub>3</sub>

The SE data for mechanically polished BaTiO<sub>3</sub> at all temperatures were shifted in a manner consistent with the formation of a low dielectric constant layer on the crystal surface. On "cleaning" the surface with the low voltage bombardment, the SE spectra shifted slightly towards calculated values for an "ideal" BaTiO<sub>3</sub> surface. As the sputtering voltage used is below the threshold at which any of the cations should be dislodged, these changes are probably associated with the removal of embedded organic species. Although the SE results can be modeled well with the addition of a layer of either surface roughness or an oscillator with unknown properties at the crystal surface, it is unlikely that the low energy bombardment utilized could significantly alter the degree of surface roughness. Consequently, the oscillator model is probably more realistic. Under this assumption, the defective layer was found to be ~165 Å thick (140 - 180 Å in different spots on the crystal), and the refractive index was depressed considerably below either value for bulk BaTiO<sub>3</sub> (see Fig. 1). These results are consistent with Jyomura et al.'s conclusion that mechanically polished ceramic ferroelectric specimens possessed a non-ferroelectric, non-crystalline surface layer which leads to lowered measured remanent polarization and dielectric constant values, and a decrease in the squareness of the hysteresis loops in thin samples [2].

It is probable that the interface between the surface layer and the unperturbed BaTiO<sub>3</sub> is not atomically abrupt. Attempts were made to model the SE data for mechanically polished BaTiO<sub>3</sub> with two or more surface layers, but this was found to produce unacceptable correlation between parameters, and large 90% confidence limits.

Using the single oscillator model, data for high temperatures were also fitted, allowing the strength, position, and damping of the oscillator as well as the layer thickness to vary in each case. Results for the surface layer thickness and dispersion curves as a function of temperature are shown in Fig. 1. Following sputter cleaning of the surface with 60 eV Ar ions in an oxygen ambient, the refractive index increased by 0.04 while the layer thickness remained approximately constant. At the same time, the imaginary component of the refractive index of the surface layer decreased, suggesting that the surface cations were not reduced during the sputtering.

In Fig. 1 it is clear that both the surface layer thickness of mechanically polished BaTiO<sub>3</sub> and its refractive index are nearly temperature independent between 20 and 100°C, confirming that the surface layer is not dependent entirely on the bulk polarization. Moreover, the significant depression of the surface layer refractive index below either  $n_a$  or  $n_c$  for bulk BaTiO<sub>3</sub> suggests that the surface is not a dense perovskite. This was supported by ion surface scattering measurements, where contamination from carbon (probably as an organic compound) and Al (probably as residue from the polishing) was detected in the top few Angstroms of the sample. However, no evidence for long range changes in the cation stoichiometry or organic content was determined by SIMS for mechanically polished crystals.

These results suggest that the observed depression in the refractive index of the surface is not due to an intrinsic change in the ferroelectric properties at the surface. It is likely that the low refractive index for the observed surface layer of a mechanically polished (001) BaTiO<sub>3</sub> crystal is due to a combination of damage to the crystal (i.e. amorphization), contamination from second phases embedded during polishing, and residual roughness. While the depth of this layer will vary with the quality of the polished surface, it is

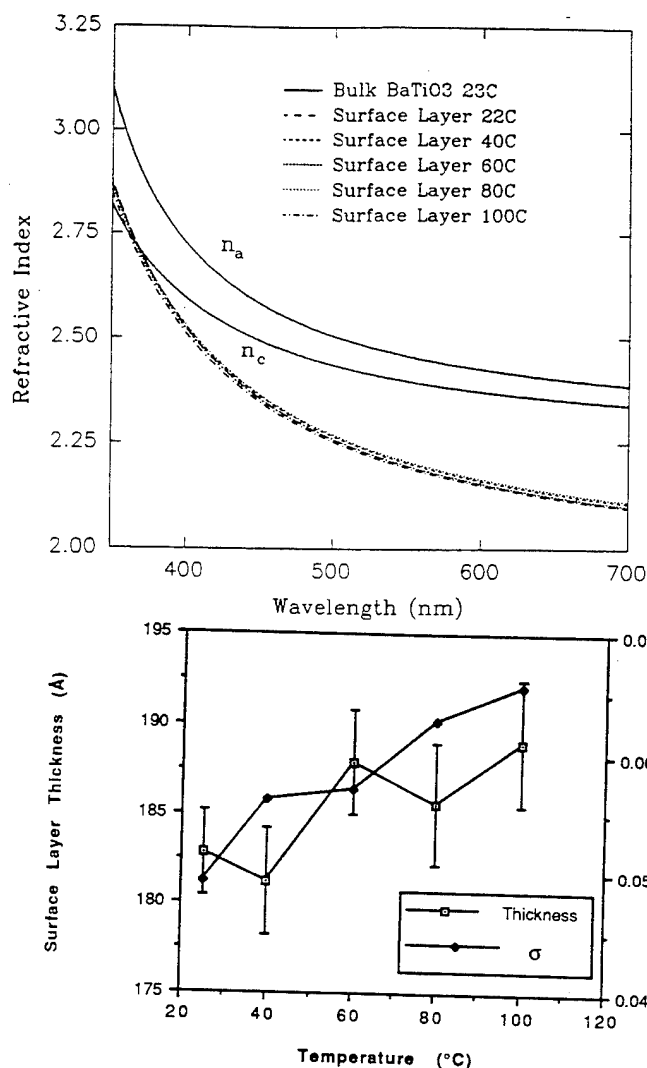


Fig. 1: Refractive index and thickness of the surface layer on a mechanically polished BaTiO<sub>3</sub> crystal as a function of temperature.

possible to produce damaged layers which are optically less than a couple hundred Ångströms thick.

#### CHEMICALLY ETCHED SINGLE CRYSTAL BaTiO<sub>3</sub>

Following etching, the increased roughness led to further deviation of the SE data from the values expected for perfectly terminated BaTiO<sub>3</sub>.

Three classes of behavior were observed on heating an etched crystal depending on how the crystal had been poled. Following mechanical poling to eliminate 90° twins the  $\Delta$  and  $\Psi$  spectra showed modest variations with temperature up to 115°C. Similarly, the effective refractive index determined by direct inversion is only slightly temperature dependent. In contrast, after electrical poling, the  $\Delta$  and  $\Psi$  spectra and the effective  $n$  changed considerably on heating (Fig. 2). On cooling, the spectra usually remained near the highest temperature values. When hysteretic behavior was observed, the high temperature values were then stable with time.

If a sample which demonstrated hysteretic behavior as a function of temperature was reheated without re-poling, the initial large changes in  $\Delta$  and  $\Psi$  on heating were not repeated. The hysteresis could be restored by re-poling the sample. The magnitude of the shift in the curves with temperature was considerably larger than that the known temperature dependence of the refractive indices of (001) BaTiO<sub>3</sub>. It was also independent of whether the polarization was directed towards or away from the measured surface. No evidence was

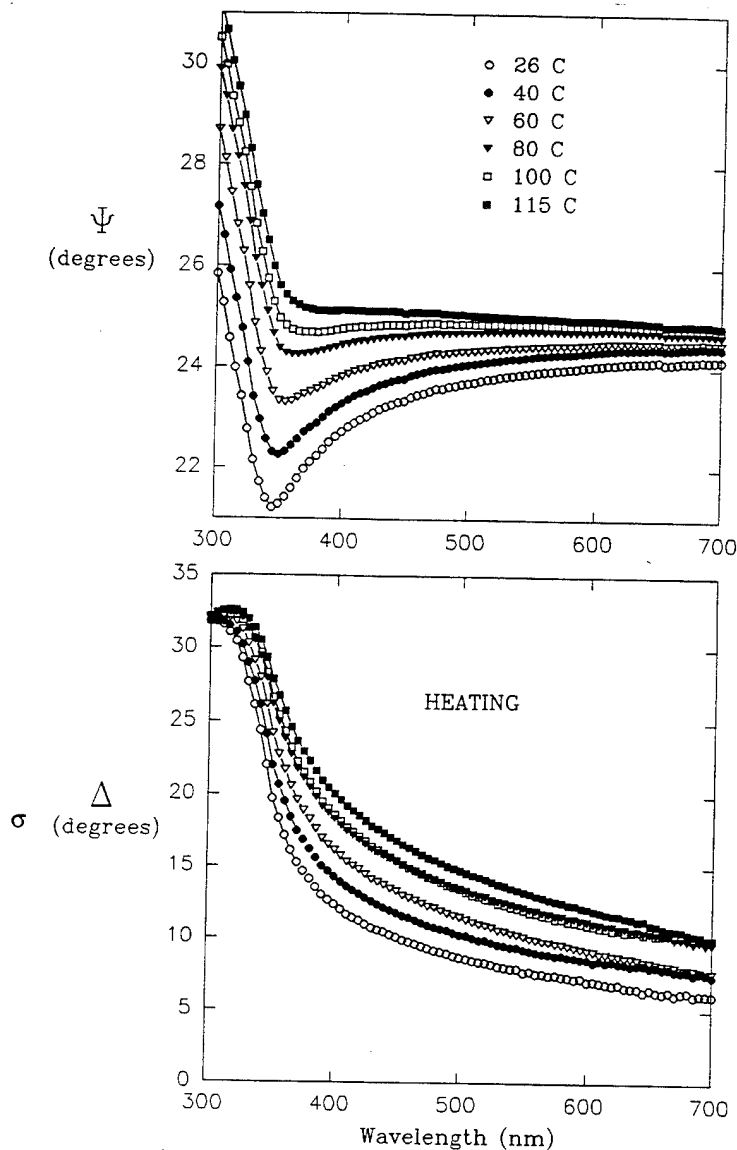


Fig. 2:  $\Delta$  and  $\Psi$  as a function of temperature for a chemically etched poled BaTiO<sub>3</sub> crystal

found for the generation of macroscopic 90° twins during heating runs, although some 180° domain reversal occurred (as determined in d<sub>33</sub> measurements before and after heating).

If the data were modeled as a layer of roughened BaTiO<sub>3</sub> on (001) BaTiO<sub>3</sub>, these changes were accommodated by allowing the thickness and the volume fraction of air in the roughened layer to increase with temperature and (most often) saturate near the highest temperature values. This is clearly unphysical. Attempts were made to eliminate the temperature dependence of the physical parameters defining the roughness by incorporating additional phenomena into the modeling. Among the possibilities considered were the presence of space charge or high electric fields in the sample and a-domains at the sample surface. It was found that first two possibilities did not eliminate the temperature dependence of the apparent roughness. Thus, while the poled BaTiO<sub>3</sub> surface may be influenced by the presence of a space charge or an internal electric fields, these factors do not control the hysteresis in the SE data. Due to the larger changes in the extraordinary index with temperature, however, allowing a-domains to form on the surface mitigated the temperature dependence of the roughness layer somewhat.

It is believed that the substantial temperature dependence of  $\Delta$  and  $\Psi$  spectra for the poled BaTiO<sub>3</sub> single

crystal was associated with either the presence of bulk defect dipoles or the existence of  $90^\circ$  domains near the sample surface. Defect dipoles would tend to align under the influence of a strong electric field, but would not be expected to disorder thermally in exactly the same way as the spontaneous polarization. Consequently, on heating the sample, a progressive disordering of the dipoles could lead to the substantial temperature dependence of  $\Delta$  and  $\Psi$ . Once thermal randomization occurred, the defect dipoles would not reorder unless re-exposed to a high electric field. This would account for the observed hysteresis in the SE data on temperature cycling of the sample.

As suggested previously, the presence of a-domains also partially eliminates the temperature dependence of the apparent roughness. It is not clear, however, why poling would result in a layer of reversed domains at the surface.

To avoid complications due to the large temperature dependence of  $\Delta$  and  $\Psi$  of well-poled samples, more extensive modeling was performed primarily on samples which did not show anomalously large variations in the spectra with temperature. Among the possibilities considered in these models were the presence of a-domains in the surface region, the existence of a gradient in the spontaneous polarization, and the existence of space charge at the sample surface.

#### Modeling with a-Domains at the Surface

Several investigators [3,4] have suggested that the domain structure of BaTiO<sub>3</sub> crystals and ceramics can differ in the surface and the bulk of the material. To account for the possibility of partial switching to a-domains at the surface, additional modeling was performed by superimposing a layer of "polycrystalline" material over the layer of surface roughness for the etched BaTiO<sub>3</sub> crystal.

An example of the best fit model of this type is shown in Fig. 3 alongside the one and two-layer roughness model without a-domains. While modeling the data with a-domains resulted in approximately the same  $\sigma$  value as the two-layer roughness model, the volume fraction of air in the layer of surface roughness is strongly temperature dependent. This is not physically reasonable. Consequently, the presence of a-domains at the surface of etched, un-electroded top-seeded melt-grown BaTiO<sub>3</sub> was not confirmed by the optical data.

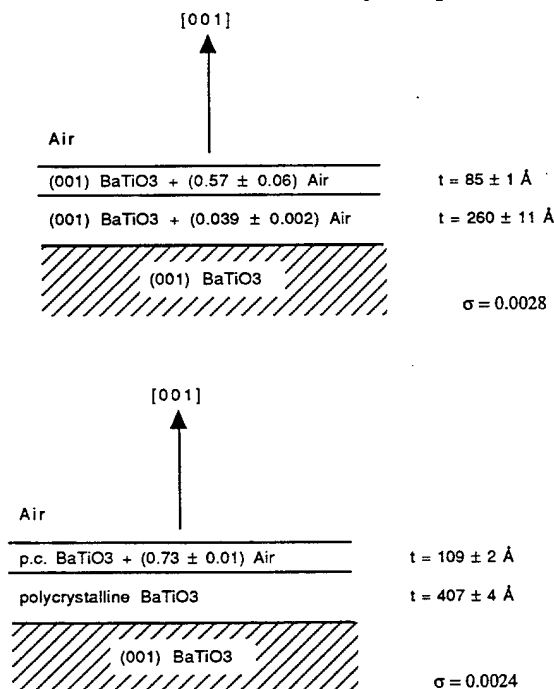


Fig. 3: Modeling of chemically etched BaTiO<sub>3</sub> with and without a-domains at the surface

#### Polarization Gradient Modeling

In order to investigate the possibility of a decay in the spontaneous polarization at the surface of an etched crystal, the near surface region was modeled with an exponentially decaying polarization superimposed over the surface roughness. For the models tried, the best fit parameters yielded decay lengths on the order of  $150 \pm 90 \text{ \AA}$ . This is close to the dimension at which SE becomes insensitive to the presence of a polarization gradient in (001) BaTiO<sub>3</sub>. The calculated values for the surface polarization were typically negative, again implying that if a polarization gradient exists in the crystal, either the assumptions utilized in the modeling are a poor description, or the scale is sufficiently small that SE cannot properly characterize it. In any event, there is no proof on the basis of the current modeling for supposing a polarization gradient within an unelectroded crystal exists with a scale extending beyond  $\sim 100 \text{ \AA}$ .

The SE-obtained value for the polarization decay length is on the same order as other estimates of the correlation length for ferroelectricity in the paraelectric phase of BaTiO<sub>3</sub>. Yamada et al. [5] and Comes et al. [6,7] for example, have estimated the correlation length at  $\sim 20$  and  $40 - 100 \text{ \AA}$ , on the basis of inelastic neutron scattering and X-ray data. As discussed by Kretschmer and Binder [8], the decay in the polarization at a ferroelectric surface should be on the order of the correlation length for ferroelectricity in insulating materials in which space charge effects can be neglected.

#### Space Charge Modeling

The data was also modeled by adding a layer of space charge to the rough BaTiO<sub>3</sub> surface. It was found that when this was done,  $\sigma$  dropped by approximately one half from the value modeled with one layer of roughness alone. Moreover, the parameters describing the surface roughness became roughly temperature independent (see Fig. 4). It can also be seen in that figure that as the temperature is increased,  $E_p$ , which is related to the concentration of charge carriers, decreases. This is a realistic possibility if the charge is, in fact, localized near the surface to compensate the spontaneous polarization.

In light of this modeling, it is believed that the surface of chemically etched BaTiO<sub>3</sub> which did not show large hysteresis in the SE data with temperature is best described as a roughened material which may have an accumulation of free carriers concentrated at the surface. There is no definitive

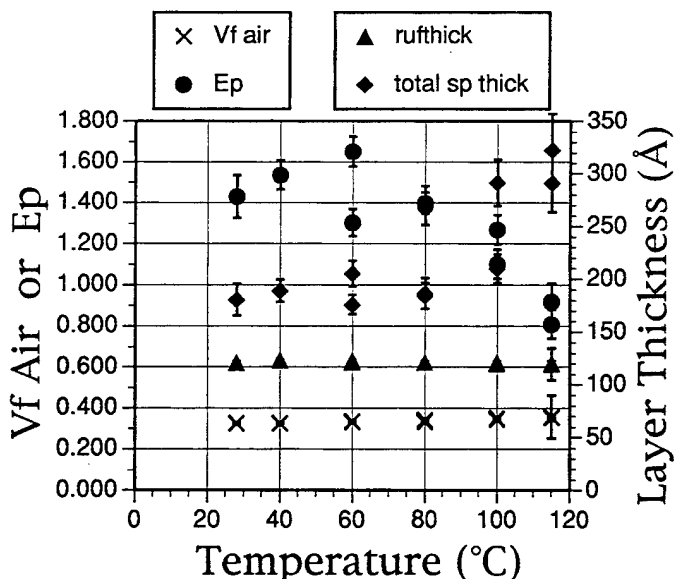


Fig. 4: Space charge modeling of chemically etched BaTiO<sub>3</sub>

optical evidence for the presence of a gradient in the polarization as the surface is approached. Consequently, if there is a polarization gradient, it is probably contained within a very thin surface layer.

#### POLISHED 9.5/65/35 PRISM

Fig. 5 shows both the experimental data for the prism and reference spectra. It is clear from the figure that as the surface finish is improved, deviation of the measured SE data from the bulk data decreases. Thacher has reported that direct inversion of SE data for PLZT prisms yields poor agreement with minimum deviation data [9]. This depends strongly on the quality of the surface finish. Thus, the effective refractive index following the 1 $\mu$ m polish is, in agreement with Thacher's conclusions, both low and too dispersive relative to the transmission data. In contrast, the dispersion curves for the sample following the 0.25 $\mu$ m and especially the 0.05 $\mu$ m polishing steps match the bulk data reasonably well.

The finite values for  $\Delta$  in each case, however, confirm the existence of a surface layer for all of the surface treatments examined. Modeling the system with a layer of roughness over the reference data for the bulk of the prism resulted in negative thicknesses for the surface roughness when the sample was polished with 0.25 $\mu$ m or 0.05 $\mu$ m grit. Consequently, this type of model was abandoned. Reasonable fits could be obtained in all cases, however, by describing the optical properties of the surface layer with an oscillator and permitting the layer thickness to vary. It was found that for grit sizes of 1 $\mu$ m, 0.25 $\mu$ m and 0.05 $\mu$ m, the surface layer thickness decreased from  $397 \pm 27 \text{ \AA}$  to  $115 \pm 40 \text{ \AA}$  to  $33 \pm 8 \text{ \AA}$ . This agrees with Jyomura et al. [2] conclusion that the depth of the damaged layer scales with the polishing powder grit size. At the same time, the refractive index of the surface layer progressively decreased. The strong link between the surface layer properties and the polishing procedure suggests that mechanical damage is dominant in lapped or polished materials.

#### CONCLUSION

In conclusion, it was shown that mechanically polished and chemically etched ferroelectrics show the presence of an optically detectable surface layer with properties considerably different from the bulk material. With careful surface preparation, the thickness of these layers can be reduced to a couple of hundred Angstroms in thickness. The major contributor to the defective surface layers is damage introduced during the processing rather than fundamental changes in the ferroelectric properties at the surface. The existence of a surface layer of some type can often be confirmed immediately by the presence of substantial  $\Delta$  values.

#### REFERENCES

- [1] P. Chindaudom and K. Vedom, "Determination of the optical function  $n(\lambda)$  of vitreous silica by spectroscopic ellipsometry with an achromatic compensator," *Appl. Opt.*, vol. 32, pp. 6391-6397, 1993.
- [2] S. Jyomura, I. Matsuyama, and G. Toda, "Effects of the lapped surface layers on the dielectric properties of ferroelectric ceramics," *J. Appl. Phys.* vol. 51, pp. 5838-5844, 1980.
- [3] E. C. Subbarao, M. C. McQuarrie, and W. R. Buessem, "Domain effects in polycrystalline barium titanate," *J. Appl. Phys.* vol. 28, pp. 1194-1200, 1957.
- [4] T. N. Lezgintseva, "Concerning the structure of surface layers in BaTiO<sub>3</sub> crystals," *Sov. Phys. - Sol. State*, vol. 7, 785-788, 1965.
- [5] K. Binder, "Surface effects on phase transitions in ferroelectrics and antiferroelectrics," *Ferroelectrics* vol. 35, pp. 99-104, 1981.

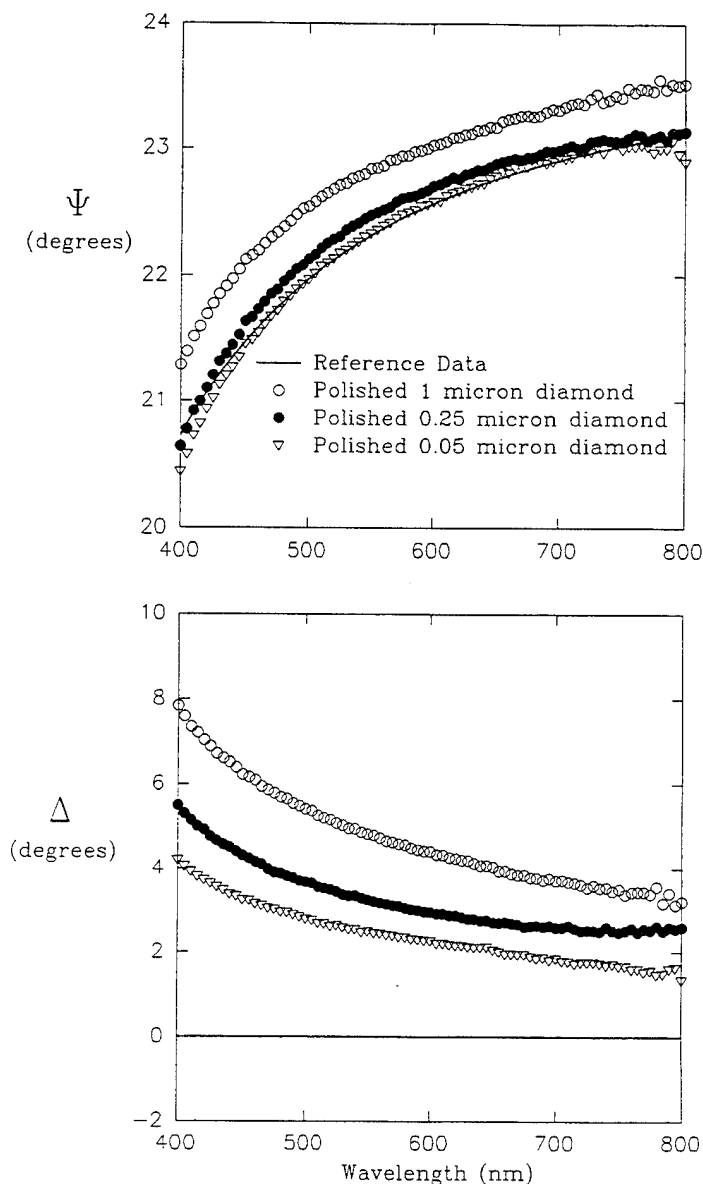


Fig. 5: Experimental and reference spectra for a 9.5/65/35 PLZT prism

- [6] Y. Yamada, G. Shirane, and A. Linz, "Study of critical fluctuations in BaTiO<sub>3</sub> by neutron scattering," *Phys. Rev.*, vol. 177, pp. 848-857, 1969.
- [7] M. Lambert and R. Comes, "The chain structure and phase transition of BaTiO<sub>3</sub> and KNbO<sub>3</sub>," *Sol. State Commun.*, vol. 7, pp. 305-308, 1969.
- [8] R. Comes, M. Lambert, and A. Guinier, "The chain structure of BaTiO<sub>3</sub> and KNbO<sub>3</sub>," *Sol. State Comm.*, vol. 6, pp. 715-719, 1968.
- [9] R. Kretschmer and K. Binder, "Surface effects on phase transitions in ferroelectrics and dipolar magnets," *Phys. Rev.*, vol. B20, pp. 1065-1076, 1979.
- [10] P. D. Thacher, "Refractive index and surface layers of ceramic (Pb,Ln)(Zr,Ti)O<sub>3</sub> compounds," *Appl. Opt.*, vol. 16, pp. 3210-3213, 1977.

# Brillouin scattering in single crystals of $\text{Rb}_{1-x}(\text{ND}_4)_x\text{D}_2\text{AsO}_4$

Chi-Shun Tu and V. Hugo Schmidt

Department of Physics, Montana State University  
Bozeman, Montana 59717

**Abstract**—The LA[100] (a-axis) Brillouin backscattering phonon spectra have been measured as a function of temperature (20–370 K) in the mixed deuterated ferroelectric (FE)–antiferroelectric (AFE) system  $\text{Rb}_{1-x}(\text{ND}_4)_x\text{D}_2\text{AsO}_4$  (DRADA- $x$ ) for ammonium concentrations  $x=0$ , 0.10 and 0.28. The Brillouin frequency shift with decreasing temperature shows hardening (positive coupling) whose steepness decreases with higher  $\text{ND}_4$  content. For  $\text{RbD}_2\text{AsO}_4$  (DRDA), a Landau-Khalatnikov-like maximum (which persists in weaker form for  $x=0.10$ ) was observed and the polarization relaxation time is estimated to be  $\tau=3.8\times 10^{-12}/(T_c-T)$  sec, where  $T_c$  is the ferroelectric transition temperature. For both  $x=0.10$  and 0.28, a broad damping peak anomaly which is stronger in  $x=0.28$  was observed and can be connected with the dynamic order parameter fluctuations. Taking into account earlier NMR and dielectric results, we conclude that the local structure competition between FE ordering and AFE ordering is the origin of these broad damping anomalies.

## I. INTRODUCTION

Since the discovery that the deuterated[1] family with the formula  $\text{A}_{1-x}(\text{ND}_4)_x\text{D}_2\text{BO}_4$  [ $\text{A}=\text{Rb}$  (or  $\text{K}$ ) and  $\text{B}=\text{P}$  (or  $\text{As}$ )] exhibits a deuteron glass state for certain values of  $x$ , similar to the proton glass state observed in the undeuterated family,[2-5] many experimental techniques have been used in order to understand the nature of this deuterated family. In these systems, there is competition between the ferroelectric (FE) ordering and the antiferroelectric (AFE) ordering, each characterized by specific configurations of the acid protons or deuterons. The random distribution of the  $\text{Rb}$  and  $\text{NH}_4$  (or  $\text{ND}_4$ ) ions produces frustration which suppresses the long-range electric order. Spontaneous polarization revealed that  $\text{RbD}_2\text{AsO}_4$  (DRDA) has a first-order FE transition at  $T_c=165$  K.[6] Dielectric results indicated that at  $T_m=146$  K DRADA-0.10 goes from the PE (paraelectric) to a PE/FE phase coexistence region, and then to another frequency dependent coexistence (FE/deuteron glass) region at  $T_g=60$  K ( $f=0.05$  MHz). Here  $T_m$  is the temperature which corresponds to the dielectric maximum. DRADA-0.28 has no FE phase but has a frequency-dependent transition from the PE to the deuteron glass phase at  $T_g=65$  K ( $f=0.1$  MHz).[6] Field-heated, field-cooled and zero-field-heated static permittivity also revealed that below  $T_c=38$  K (nonergodic temperature) the system enters a nonergodic state in which on practical time scales the acid deuterons of the O-D...O bonds cannot rearrange sufficiently to reach all energetically allowed configurations.[7]

Earlier results of Brillouin transverse phonon spectra on mixed proton glass crystals,  $\text{Rb}_{0.65}(\text{NH}_4)_{0.35}\text{H}_2\text{PO}_4$  (RADP-35),[8,9] showed that the polarization couples linearly to the strain. In addition, Courtens *et al.* investigated the longitudinal sound waves with  $q//[100]$  for RADP-35 and found that the phonon modes were coupled quadratically (electrostrictively) with the linear coupling forbidden by symmetry.[10]

The temperature dependence of the half-width in RADP-35 exhibited a strong broad peak near 50 K that is much higher than the Vogel-Fulcher temperature  $T_{VF}=9$  K. These experimental data[8-10] were analyzed assuming two contributions to the sound velocity, namely dynamic and static (space-dependent only) polarization fluctuation. This analysis led to the conclusion that a static Edward-Anderson-like order parameter[10] must already exist in RADP-35 far above  $T_{VF}$ . Such a parameter is used as an indication of a system forming slow, long-range polarization fluctuations while it progresses to a glass-like state.

In principle, the acoustic coupling contributions include both static and dynamic effects.[11] Although the dynamic coupling always produces a negative contribution (softening) to the real part of the complex elastic stiffness change  $\Delta c^*$ , [11] the static effect can have either sign contribution, depending on whether the phase transition is of first or second order.[9,11,12] According to the Landau free energy expansion with a single order parameter, the second-order transition gives a negative contribution in elastic stiffness change but the first-order can give either positive (hardening) or negative contribution for both linear and quadratic couplings.[11,12] Several first-order examples that showed different elastic coupling behaviors can be found in Refs. 11-13.

We report here the temperature and concentration dependences of frequency shift and half-width (damping) for LA[100] phonons in mixed crystals  $\text{Rb}_{1-x}(\text{ND}_4)_x\text{D}_2\text{AsO}_4$ , with  $x=0$ , 0.10, and 0.28 from 370 to 20 K upon cooling. In particular, these results will be compared with the earlier NMR and dielectric measurements.

## II. EXPERIMENTAL PROCEDURE

Single crystals of  $\text{Rb}_{1-x}(\text{ND}_4)_x\text{D}_2\text{AsO}_4$ , ( $x=0$ , 0.10, and 0.28) were grown from aqueous solutions with certain ratios of  $\text{RbD}_2\text{AsO}_4$  (DRDA) and  $\text{ND}_4\text{D}_2\text{AsO}_4$  (DADA). These crystals were carefully polished to be rectangular with average size of  $1.2\times 0.4\times 0.2$  cm<sup>3</sup>. In our experiments the Brillouin spectra were obtained from back-scattering geometry with scattering geometry  $x(z,u)x$ . Here, "u" means that the collection was not polarization discriminated. In order to reduce the low-lying frequency mode of the Raman spectra, we used a narrow-band (1 Å) interference filter. All samples were illuminated along the [100] phonon direction (a-axis), by a Lexel Model 95-2 argon laser with  $\lambda=514.5$  nm, so the longitudinal phonons with wave vector along [100] were studied. Scattered light was analyzed by a Burleigh five-pass Fabry-Perot interferometer. To acquire more accurate data of frequency shift and half-width, the Brillouin doublets were adjusted to appear in the third order with respect to the Rayleigh line. The laser line broadening due to the jittering was claimed by the manufacturer to be about 10 MHz (half-width).[12] The laser power was kept below 100 mW. A Leybold RGD-210 closed-cycle refrigerator was used with a LakeShore DRC-91C temperature controller. The error of temperature



reading was controlled to better than  $\pm 0.1$  K and measured to  $\pm 0.01$  K by a calibrated silicon diode thermal sensor placed on the optical sample holder. The sample was cooled from 370 down to 20 K by steps and the data were collected automatically through an analog-digital converter. Results were found to be reproducible for all three compounds.

For determination of natural-phonon half-width, the natural-phonon spectrum and the instrumental function were assumed to have Lorentz distribution, and the broadening due to collection optics was assumed to have rectangular distribution. In this case, the natural-phonon half-width  $W_{ph}$  is given by [14]

$$W_{ph} = \left( W_{obs}^2 - W_{ang}^2 \right)^{\frac{1}{2}} - W_{inst} \quad (1)$$

where  $W_{obs}$ ,  $W_{inst}$ , and  $W_{ang}$  represent the observed, instrumental, and collection optical half-widths, respectively. For back-scattering ( $\theta = 180^\circ$ ), the  $W_{ang}$  is negligible. [15] In our experiments,  $W_{inst} \sim 0.02$  FSR where FSR is the free spectrum range obtained by measuring fused quartz.

### III. RESULTS AND DISCUSSION

Actual LA[100] phonon spectra of the anti-Stokes Brillouin component are shown in Figs. 1a-1c for  $x=0$ , 0.10 and 0.28, respectively. The data shown here are for several temperatures near the maximum value of half-width. The solid lines are fits of the Lorentz profile, from which the half-width  $W_{obs}$  and frequency shift can be obtained. The frequency shift temperature dependence indicates a positive coupling contribution with decreasing temperature for each compound. Comparing the half-width for different  $x$  values, we notice that the average damping value increases as ammonium concentration increases. This dependence may result from the stronger local structural FE/AFE competition that can induce larger fluctuations, especially for intermediate  $x$  values such as  $0.3 \leq x \leq 0.7$  in RADP. [1-5]

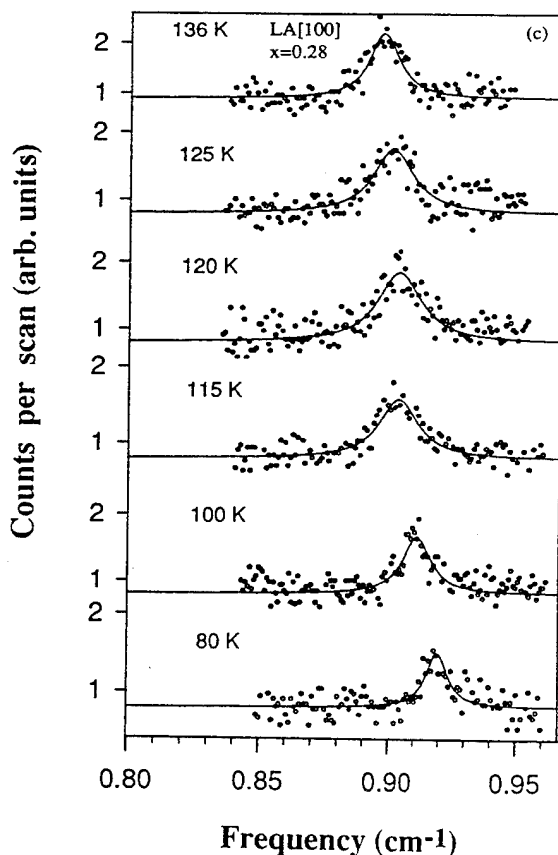
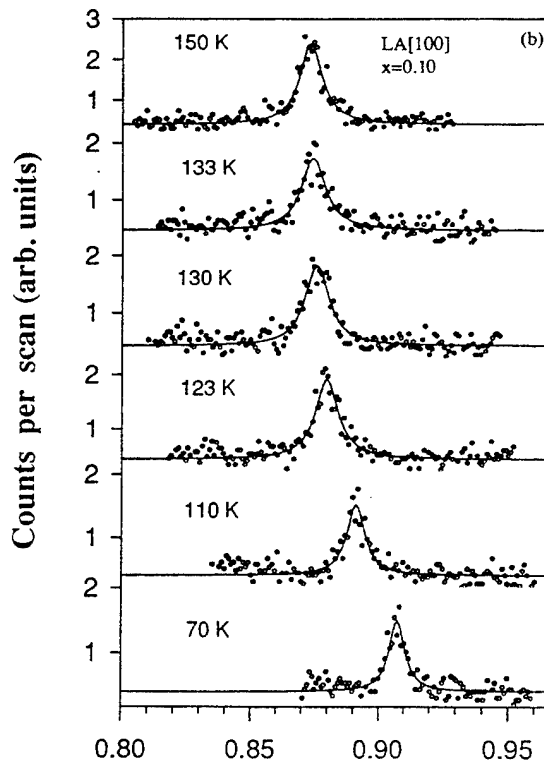
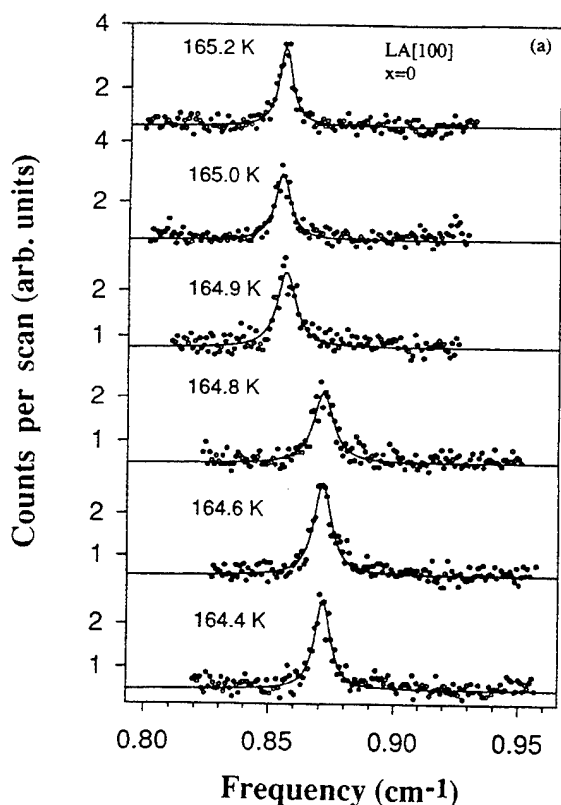


Figure 1. Anti-Stokes components of the LA[100] Brillouin frequency shift for temperatures around the maximum value of half-width for (a)  $x=0$  (DRDA), (b)  $x=0.10$  and (c)  $x=0.28$ . The open circles are the measured data and solid lines are the Lorentz fits.

In order to estimate the coupling effect, we calculate the bare (uncoupled) phonon frequency  $\omega_a$ , by fitting the frequency shift at high temperature where coupling is assumed to be negligible. The bare phonon frequency is defined as the phonon frequency in the absence of FE or AFE transition effects. The temperature dependence of  $\omega_a$  can be described by a Debye anharmonic approximation as follows:[8-10]

$$\omega_a(\tau, x) = \omega_a(\tau = 0, x) \left[ 1 - A(x) \Theta(x) F\left(\frac{\Theta(x)}{\tau}\right) \right] \quad (2)$$

where  $\Theta(x)$  is the Debye temperature,  $x$  is the ammonium concentration,  $A(x)$  presents the amount of anharmonicity,  $\omega_a(0, x)$  is the zero-temperature bare phonon frequency and  $F$  is the Debye function for internal energy,[16]

$$F\left(\frac{\Theta}{\tau}\right) = \frac{3}{\left(\frac{\Theta}{\tau}\right)^4} \int_0^{\frac{\Theta}{\tau}} \frac{u^3}{e^u - 1} du \quad (3)$$

as tabulated, for example, by Abramowitz and Stegun.[17]

The temperature dependences of the Brillouin shift and half-width for  $x=0, 0.10$  and  $0.28$  are shown in Figs. 2-4, respectively. The solid lines in frequency shift are the calculations of Eq. (2) with parameters of Table I. Those parameters  $A$ ,  $\omega_a(T=0)$  and  $\Theta$  of Table I are from the fits of Eq. (2) to the high temperature ( $\geq 270$  K) measured values of the Brillouin shift. Here we assume that temperatures above 270 K are far above the coupled region since all phase transitions occur below 200 K. One finds that  $\Theta$  and  $\omega_a(0, x)$  tend to increase from the DRDA side to the DADA side, as expected in view of the higher frequency of the modes on the DADA-rich side.[16] Also, the anharmonic factor  $A$  increases with considerably higher  $\text{ND}_4$  content.

Fig. 2 for  $x=0$  (pure DRDA) shows a sharp damping peak at 164.8 K associated with an upward step in frequency which is expected, since the  $\text{KH}_2\text{PO}_4$  (KDP) family has linear  $\eta\mu$ -type piezoelectric coupling.[11,14] Here  $\eta$  is the order parameter and  $\mu$  is the strain. Such a sharp damping maximum for longitudinal acoustic phonons can be connected with the Landau-Khalatnikov relaxation-type mechanism.[11,14] The dashed line in half-width of Fig. 2 is a

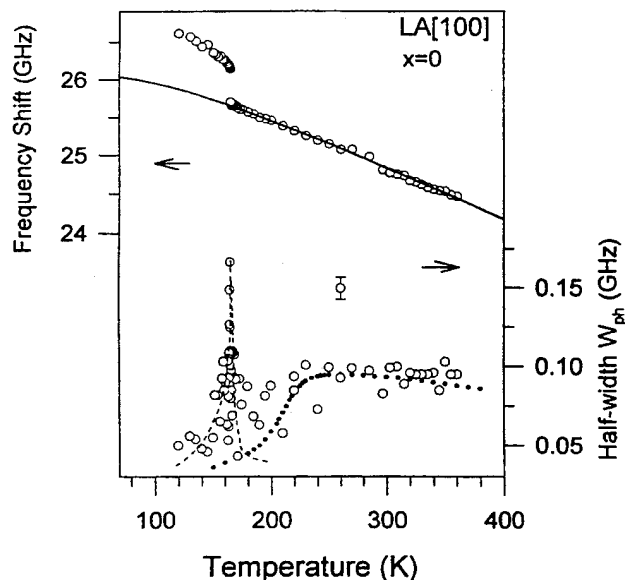


Figure 2. Frequency shift and half-width vs. temperature of the LA[100] phonons for  $x=0$  (DRDA). The solid line for frequency shift is the Debye anharmonic calculation with parameters from Table I. The dashed line and solid circles for half-width are the qualitative estimates for the Landau-Khalatnikov and pure lattice anharmonic contributions, respectively. The error bar indicates the error range for the half-width experimental points.

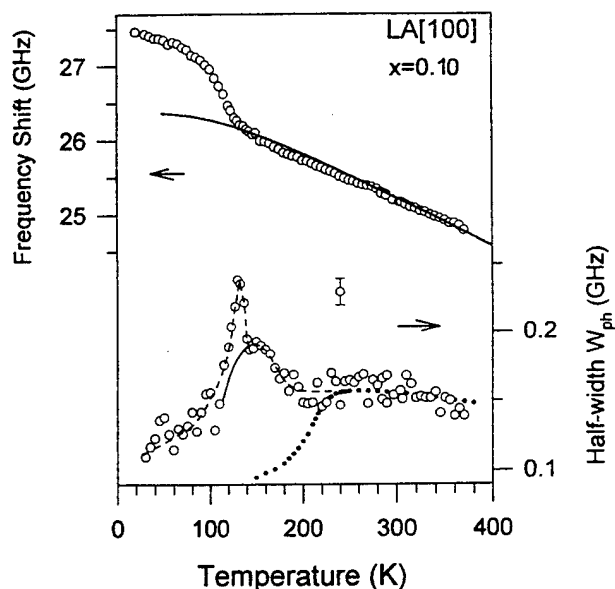


Figure 3. Frequency shift and half-width vs. temperature of the LA[100] phonons for  $x=0.10$ . The solid line for frequency shift is the Debye anharmonic calculation with parameters from Table I. The solid line and solid circles for half-width are the estimates of fluctuations and pure lattice anharmonic contributions, respectively. The dashed line is guide to the eye. The error bar indicates the error range for the half-width experimental points.

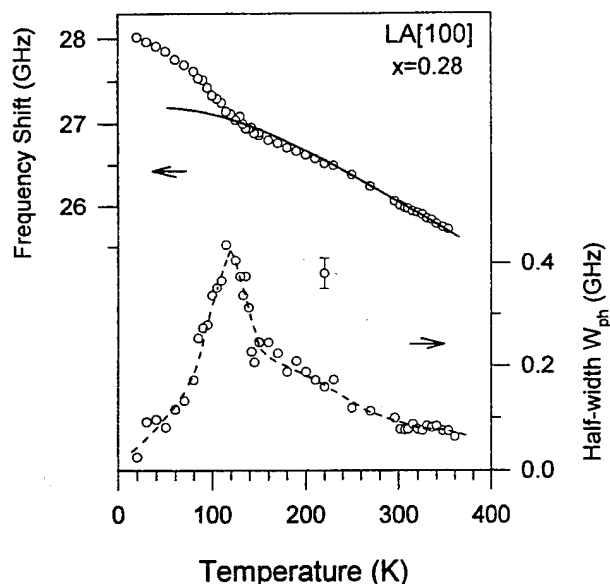


Figure 4. Frequency shift and half-width vs. temperature of the LA[100] phonons for  $x=0.28$ . The solid line for frequency shift is the Debye anharmonic calculation with parameters from Table I. The dashed line is guide to the eye. The error bar indicates the error range for the half-width experimental points.

qualitative estimate for this relaxation portion. We also try to estimate the pure lattice-anharmonic contribution by solid circles, which is the typical anharmonic half-width observed in Brillouin scattering for dielectrics.[10,18] For linear coupling with the assumption of a single relaxation time, the sound velocity and the attenuation  $\alpha$  in the FE phase can be given by[14]

TABLE I: Parameters from the fits of Eq. (2) to high temperature measured values of frequency shift:

	$\omega_a(T=0)$ (GHz)	$A$ (K <sup>-1</sup> )	$\Theta$ (K)
DRDA	26.08	$2.70 \times 10^{-4}$	400
DRADA-0.10	26.37	$2.76 \times 10^{-4}$	480
DRADA-0.28	27.20	$2.84 \times 10^{-4}$	520

$$V^2 = V_\infty^2 - \frac{V_\infty^2 - V_0^2}{1 + \omega^2 \tau_0^2 t^{-2}} \quad (4)$$

$$\alpha = \frac{\omega^2 \tau_0 t^{-1}}{2V^3} \frac{V_\infty^2 - V_0^2}{1 + \omega^2 \tau_0^2 t^{-2}} \quad (5)$$

where  $t$  is the reduced temperature  $(T_c - T)/T_c$ , and  $\tau_0$  is the elementary individual-dipole relaxation time in the expression  $\tau = \tau_0 t^{-1}$  for the relaxation time  $\tau$ . The velocities  $V_\infty$  and  $V_0$  designate the high- and low-frequency limit velocities, respectively. From Eqs. (4) and (5) we can obtain the relation[14]

$$\omega \tau_0 = \frac{T - T_m}{T_c} \quad (6)$$

By this relation we can calculate the elementary relaxation time  $\tau_0$ . Here,  $T_m = 164.8$  K is the temperature at which the half-width is maximum and the FE transition temperature  $T_c$  is defined as the point at which the frequency shift curve is steepest. For the LA[100] phonons of DRDA, we obtain the following result:

$$T_c - T_m \sim 0.1 \text{ K}; \quad \tau_0 \sim 2.3 \times 10^{-14} \text{ sec}; \quad \tau \sim 3.8 \times 10^{-12} / (T_c - T) \text{ sec}$$

The elementary dipole relaxation time  $\tau_0$  obtained from the LA[100] phonons of DRDA is short compared to that of other order-disorder ferroelectrics. For instance,  $\tau_0$  is  $1.2 \times 10^{-13}$  sec for potassium dihydrogen phosphate (KDP) and  $1.3 \times 10^{-12}$  sec for deuterated potassium dihydrogen phosphate (DKDP).[14]

Instead of a sharp peak, the damping data of Fig. 3 for  $x=0.10$  exhibits a smooth growth from  $\sim 200$  down to  $\sim 130$  K, associated with a slowly rising anomaly in frequency shift above the Debye curve of Eq. (2). Such an increasing of damping which begins far above  $T_m = 146$  K must be associated with the order parameter fluctuations.[11] A qualitative estimate of this fluctuation contribution is given by the solid curve in Fig. 3 with maximum near 146 K. Beside this broad damping background, one can note that there is an additional peak appearing near 130 K and can be connected with the Landau-Khalatnikov maximum.

What are the origins of these two damping maximums in DRADA-0.10? The  $\text{ND}_4^+$  deuteron NMR spectra[19] of DRADA-0.10 showed a gradual disappearance of the doublet near 131 K where the single broad linewidth grows to its full size, from which it was concluded that below 131 K the FE phase portion is greater than PE in the crystal and becomes the dominant ordering. This result is consistent with the presence of PE/FE phase coexistence as evidenced by dielectric results which show that an gradual ferroelectric transition begins at  $T_m = 146$  K and is mostly completed at  $\sim 120$  K.[6] Furthermore, the real part of dielectric permittivity  $\epsilon_{11}(T)$  shows deviation from the Curie-Weiss law below 160 K.[6] This high-temperature dielectric anomaly below 160 K can be associated with the onset of short-range antiferroelectric order due to the freezing-in of the  $\text{ND}_4$  reorientations and implies a growth of local structural competition (between FE and AFE ordering). On the whole, one can expect that such FE/AFE ordering competition, which can suppress a long-range-order ferroelectric transition and generate the order parameter fluctuations, is responsible for both FE/PE phase coexistence and development of the

broad damping peak centered at  $\sim 146$  K. Also, the rapid growth of FE ordering near 130 K is the origin of the Landau-Khalatnikov-like maximum in DRADA-0.10.

A even stronger damping temperature dependence which shows a growth from  $\sim 300$  down to  $\sim 120$  K (see Fig. 4) is observed for  $x=0.28$ , associated with a smoothly rising frequency shift. This strong broad damping reveals that fluctuations are the dominant dynamic mechanism. As one knows,[11] the dynamic fluctuation contribution for longitudinal acoustic phonons is a characteristic of a  $\eta^2\mu$ -type coupling, squared in order parameter and linear in strain.[11,14] However, it is difficult to see a Landau-Khalatnikov maximum (associated with the Edwards-Anderson order parameter in this case)[10] above such a strong fluctuation background. Taking into account earlier dielectric permittivity  $\epsilon_{11}(T)$  results which showed a deviation from the Curie-Weiss law below 140 K,[6] we conclude that neither FE nor AFE ordering but rather the local structural competition mechanism (between FE and AFE orderings) is the origin of this strong broad damping anomaly centered near 120 K. Since the fluctuations usually indicate a random force resulting from the substitutional disorder,[11] the difference of damping behavior between DRADA-0.28 and DRADA-0.10 also implies that this random force is stronger in the  $x=0.28$  crystal.

In summary, a main feature of the acoustic phonon spectra in DRADA ( $x=0, 0.10$ , and  $0.28$ ) for LA[100] phonons is that the frequency shift shows a positive (hardening) instead of a negative coupling contribution (softening) at the phase transition. The sign of the coupling contribution may be related to the temperature responses of lattice parameters  $a(T)$  and  $c(T)$ . However, the measurements we performed on pure DRDA for LA[001] ( $c$ -axis) phonons, not reported here, revealed a negative contribution at the FE transition temperature. This work was supported in part by NSF Grant DMR-9017429 and DOE Equipment Grant FG05-91ER79046.

- [1] V.H. Schmidt, S. Waplak, S. Hutton and P. Schnackenberg, Phys. Rev. B **30**, 2795 (1984).
- [2] E. Courtens, J. Phys. Lett. (Paris) **43**, L199 (1982).
- [3] Z. Trybula, V.H. Schmidt, J.E. Drumheller, D. He and Z. Li, Phys. Rev. B **40**, 5289 (1989).
- [4] C.-S. Tu, V.H. Schmidt and A.A. Saleh, Phys. Rev. B **48**, 12483 (1993).
- [5] F.L. Howell, N.J. Pinto and V.H. Schmidt, Phys. Rev. B **46**, 13762 (1992).
- [6] N.J. Pinto, Ph. D. Thesis, Montana State University, 1992.
- [7] N.J. Pinto, K. Ravindran and V.H. Schmidt, Phys. Rev. B **48**, 3090 (1993).
- [8] E. Courtens, R. Vacher and Y. Dagorn, Phys. Rev. B **33**, 7625 (1986).
- [9] E. Courtens, R. Vacher and Y. Dagorn, Phys. Rev. B **36**, 318 (1987).
- [10] E. Courtens, F. Huard and R. Vacher, Phys. Rev. Lett. **55**, 722 (1985).
- [11] W. Rehwald, Adv. Phys. **22**, 721 (1973).
- [12] Z.M. Liu, Ph. D. Thesis, Montana State University, 1990.
- [13] Landolt-Bornstein, New Series, Vol. III/16b, edited by K.-H. Hellwege (Springer, Berlin, 1982).
- [14] T. Hikita, P. Schnackenberg and V.H. Schmidt, Phys. Rev. B **31**, 299 (1985).
- [15] H.G. Danielmeyer, J. Acoust. Soc. Am. **47**, 151 (1970).
- [16] C. Kittel, *Introduction to Solid State Physics*, 5th Ed. (Wiley, New York, 1976), pp. 137.
- [17] *Handbook of Mathematical Functions*, 7th printing, edited by M. Abramowitz and I.A. Stegun (Dover, New York, 1970), pp. 998.
- [18] P. Bonnet, M. Boissier, C. Vedel, and R. Vacher, J. Phys. Chem. Solids **44**, 515 (1983).
- [19] N.J. Pinto, F.L. Howell and V.H. Schmidt, Phys. Rev. B **48**, 5983 (1993).

# Ferroelectric Transition in the Ternary System of $\text{Pb}(\text{Mg}_{1/3}\text{Nb}_{2/3})\text{O}_3$ - $\text{La}(\text{Mg}_{2/3}\text{Nb}_{1/3})\text{O}_3$ - $\text{PbTiO}_3$

T.B. Wu, K.S. Liu and J.L. Chen

Department of Materials Science and Engineering, National Tsing Hua University  
Hsinchu, Taiwan, R.O.C.

**Abstract**--Ferroelectric transition of ceramics in the ternary system of  $(1-x-y)\text{Pb}(\text{Mg}_{1/3}\text{Nb}_{2/3})\text{O}_3 - x\text{La}(\text{Mg}_{2/3}\text{Nb}_{1/3})\text{O}_3 - y\text{PbTiO}_3$  with  $x=0.05 \sim 0.13$  and  $y=0.275 \sim 0.575$  were investigated by the measurements of X-ray diffraction, dielectric properties and P-E hysteresis. Three morphotropic phases of perovskite structure, i.e. cubic, tetragonal and rhombohedral, were involved in the study. An increase of  $\text{PbTiO}_3$  content would cause the structure evolve to the tetragonal phase;  $\text{Pb}(\text{Mg}_{1/3}\text{Nb}_{2/3})\text{O}_3$ , the rhombohedral phase; and,  $\text{La}(\text{Mg}_{2/3}\text{Nb}_{1/3})\text{O}_3$ , the cubic phase. A triple point was found at the composition of  $x=0.11$  and  $y=0.425$ . For the composition in the tetragonal phase field, a normal ferroelectric transition and hysteresis characteristic of high coercive field,  $E_c$ , over remanent polarization,  $P_r$ , were observed. However, for that in the rhombohedral or cubic phase field, a diffuse phase transition and hysteresis characteristic of low  $E_c$  over  $P_r$  were found. Moreover, the composition at triple point has shown the most significant diffuseness of phase transition, and excellent dielectric properties of  $k \approx 16000$  with high frequency and temperature stability result.

## INTRODUCTION

Perovskite lead magnesium niobate,  $\text{Pb}(\text{Mg}_{1/3}\text{Nb}_{2/3})\text{O}_3$  (abbreviated PMN), is a well-known ferroelectric relaxor for its broad dielectric maximum at the transition temperature ( $T_c \sim -15^\circ\text{C}$ ). [1-3] The magnitude of this maximum decreases and the transition temperature increases with increasing frequency. [4-6] Such a dielectric behavior characterizes the diffuse phase transition from a cubic paraelectric to a rhombohedral ferroelectric phase for the PMN. [7] Although the  $T_c$  is below room temperature, it can be easily shifted upward by adding the  $\text{PbTiO}_3$  (abbreviated PT) in PMN, which (PT) is a normal ferroelectric material having a transition from cubic to tetragonal near  $490^\circ\text{C}$ . Compositions in the PMN-PT solid solution exhibit a morphotropic phase boundary (MPB) separating the rhombohedral and tetragonal phases at about 32.5 mol% PT, and anomalous ferroelectric properties were observed for compositions lying near the MPB. [8] Another MPB separating the cubic and rhombohedral phases at about 10 mol% PT in the PMN-PT solid solution also attracts attention for its superior dielectric and electrostrictive properties. [3,9]

The lanthanum magnesium niobate,  $\text{La}(\text{Mg}_{2/3}\text{Nb}_{1/3})\text{O}_3$  (abbreviated LMN), is also a rhombohedral perovskite. [10] It forms solid solution with PMN and PT. [11] The addition of LMN was found to enhance an ordering of  $\text{Mg}^{2+}$  and  $\text{Nb}^{5+}$  cations,

[12,13] but the ordering would be repressed by the incorporation of  $\text{Ti}^{4+}$  ions. [11] In the ternary system of PMN-LMN-PT (abbreviated PLMNT), both of the tetragonal/rhombohedral (T/R) and rhombohedral/cubic (R/C) phase boundaries has an intersection at a triple point separating the three phase fields. [11] In this work, the ferroelectric transition of the compositions around the triple point was investigated.

## EXPERIMENTALS

Five PLMNT series having the composition  $(1-x-y)\text{PMN} + x\text{LMN} + y\text{PT}$  with  $x=0.05, 0.07, 0.09, 0.11$  and  $0.13$ , respectively, and different  $y$  values,  $(0.275 \sim 0.575)$  were selected in this study. Reagent grade powders of  $\text{PbO}$ ,  $\text{MgO}$ ,  $\text{Nb}_2\text{O}_5$  and  $\text{TiO}_2$  were used for the preparation of all compositions with a method proposed by Swartz and Shrout. [14] The  $\text{MgO}$  and  $\text{Nb}_2\text{O}_5$  powders were first mixed in a proper ratio, calcined at  $1000^\circ\text{C}$  for 6 hours, then mixed with suitable amount of  $\text{PbO}$ ,  $\text{TiO}_2$  and  $\text{La}_2\text{O}_3$  powders and calcined again at  $800^\circ\text{C}$  for 4 hours. The final powders were pressed into pellets of 13mm in diameter and 2.5mm in thickness. Following binder burn-out at  $500^\circ\text{C}$ , the pellets were sintered at  $1250^\circ\text{C}$  for 2 hours.

The crystalline structure of sintered pellets was investigated by X-ray powder diffractometry (XRD) with  $\text{Cu K}\alpha$  radiation. The microstructure was observed by scanning electron microscopy (SEM). The polarization vs. electric field (P-E) characteristics was measured with a modified Sawyer-Tower circuit. The dielectric properties were also measured in a temperature range from  $-20^\circ$  to  $140^\circ\text{C}$  with an impedance analyzer.

## RESULTS AND DISCUSSION

All sintered specimens had a density larger than 95% theoretical value and a uniform microstructure with grain size gradually increased from 2 to  $8\ \mu\text{m}$  with increasing the LMN content from 5 to 13 mol%. The specimens were found to be pure perovskite by XRD. Figure 1 shows the  $\text{K}\alpha_2$ -separated profiles of 200 and 222 peaks, of the 5 mol% LMN series of specimens. In accordance with the structural evolution from rhombohedral (pseudo-cubic) to tetragonal, the 200 peak gradually broadened with a shoulder appearing at low  $2\theta$  angle side of the peak, and finally splitted into two separate peaks, with increasing the PT content of the specimens. However, a single 222 peak was always observed irrespective of the PT content. The inability to resolve the rhombohedral phase

from cubic by XRD indicated the low rhombohedrality of the structure. Similar results were also found for other series of PLMNT. As the appearance of a shouldered or doublet 200 peak denotes a coexistence of both rhombohedral (or cubic) and tetragonal phases in the specimen, the exact composition of phase boundary is difficult to determine. For convenience, the last composition having a shouldered or doublet 200 peak was considered as the location of MPB, and the compositions above the boundary would be purely tetragonal, for which two clearly separative peaks of 200 diffraction were observed. The result was shown in Fig.2.

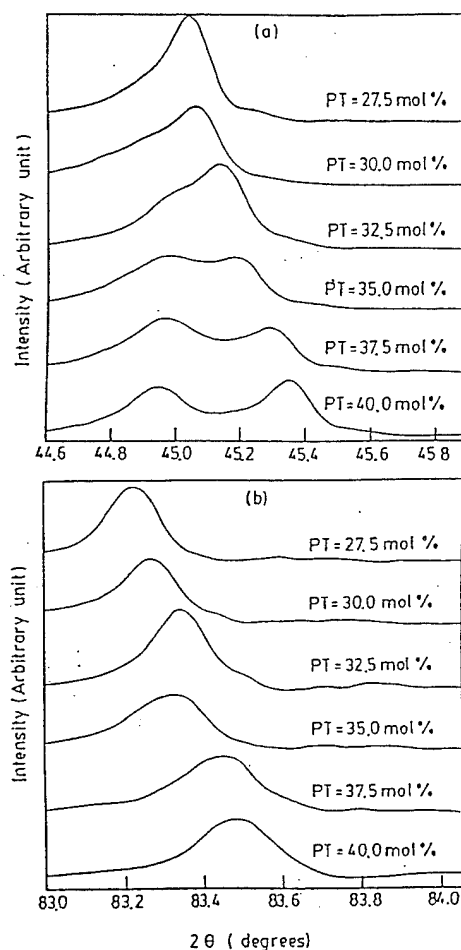


Fig.1 Peak profiles ( $K\alpha_2$ -separated) of (a) 200 and (b) 222 diffractions of 5 mol% LMN series.

Although it was unable to distinguish the rhombohedral from the cubic by XRD, the phase boundary separating these two phases could be defined at the compositions having the  $T_c$  near room temperature through the measurement of dielectric constant ( $k$ ) against temperature ( $T$ ). The  $k$ - $T$  relationships of the five PLMNT series are shown in Fig.3, and the R/C phase boundary determined by this method was also indicated in Fig.2. This phase boundary intersected with the T/R phase boundary at a composition around PT=42.5 mol% and LMN=11 mol%, at which a triple point separating the three phase fields was defined.

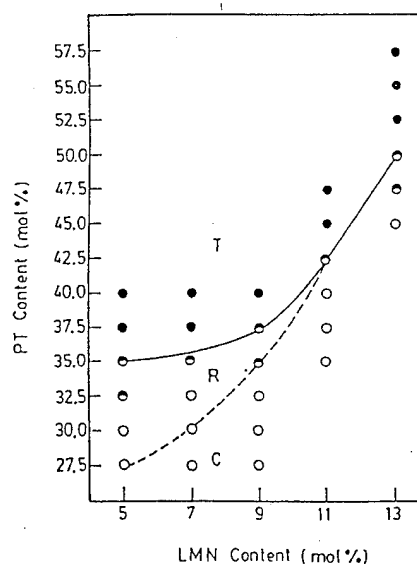


Fig.2 The tetragonal/rhombohedral (solid line) and rhombohedral/cubic (broken line) phase boundaries of PLMNT system; compositions having tetragonal structure are marked by the solid circles, rhombohedral or cubic structure the open circles, and mixed phases the half-solid circles.

It was noticed from Fig.3 that higher dielectric maxima appeared at compositions around the T/R or the T/C phase boundary in each PLMNT series, but the magnitude was gradually decreased with increasing the LMN content. Moreover, a diffuse phase transition (characterized by a broad dielectric peak) was found for the compositions lying below the T/R phase boundary, but a relatively normal phase transition (i.e. a relatively sharper dielectric peak) occurred for above the boundary. It denoted that the diffuse phase transition preferred to occur in the structural transition from cubic to rhombohedral rather than from cubic to tetragonal. The diffuse phase transition implies an equilibrium of at least two coexisted phases within a certain temperature range.[15] As the rhombohedral phase had a structure very close to the cubic one, the two would have a much better crystallographic compatibility than that between the tetragonal and cubic. Therefore, the coexistence of rhombohedral and cubic phases would be favorable during the transition.

Figure 4 shows the remanent polarization ( $P_r$ ) and coercive field ( $E_c$ ), of the five series of specimens measured from the P-E hysteresis loop. The  $P_r$  and  $E_c$  values gradually increased with increasing the PT content in each PLMNT series. In general, a relatively "hard" ferroelectric characteristic, i.e. a high  $E_c$  over  $P_r$  ratio, was observed for compositions having a pure tetragonal phase, but a relatively "soft" characteristic, i.e. a low  $E_c/P_r$ , for compositions having the rhombohedral structure.

Five compositions having the  $T_c$  near room temperature had attracted special attention for their

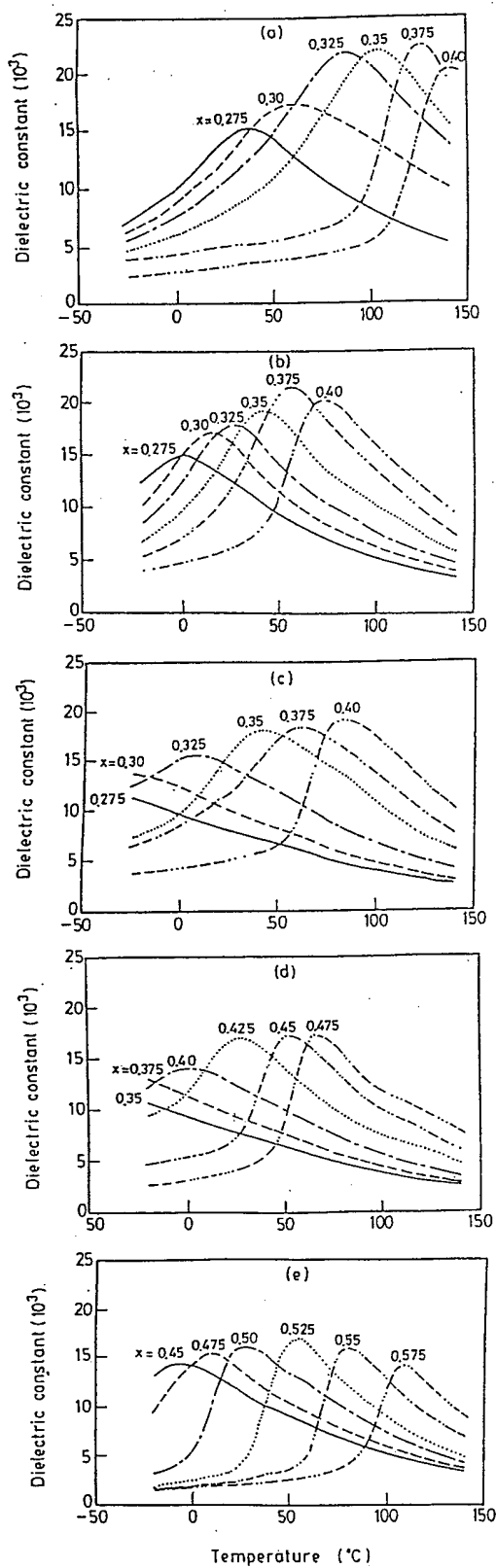


Fig.3 Temperature dependence of dielectric constant for  $(1-x-y)$ PMN- $y$ LMN- $x$ PT with  $y =$  (a) 0.05, (b) 0.07, (c) 0.09, (d) 0.11, and (e) 0.13, measured at 1KHz.

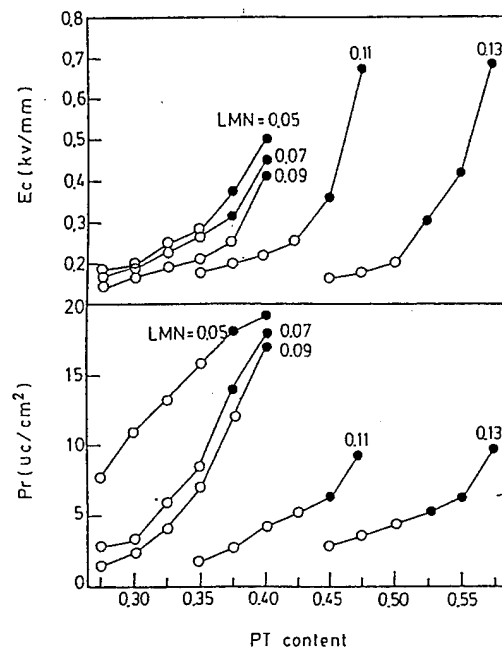


Fig.4 Change of coercive field ( $E_c$ ) and remanent polarization ( $P_r$ ) against the PT content.

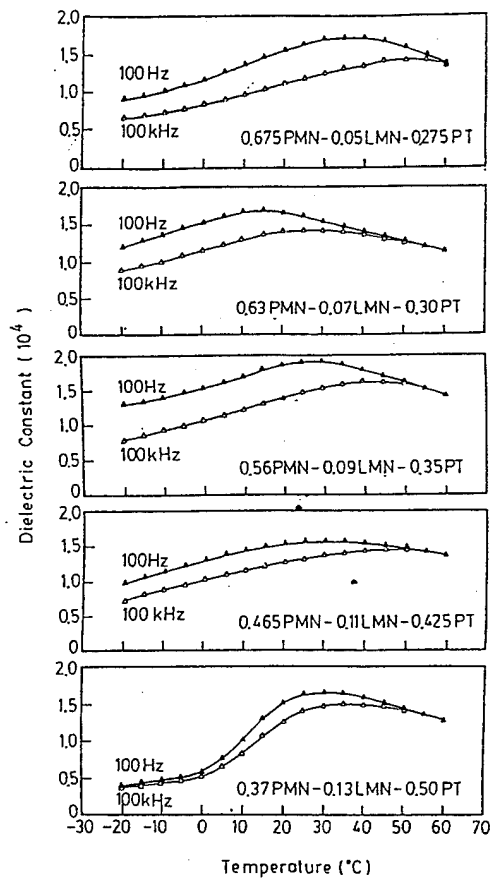


Fig.5 Temperature dependence of dielectric constant at 100 and 100K Hz for five PLMNT specimens having  $T_c$  near room temperature.

potential applications in capacitors and electrostrictive actuators. The frequency dispersion (from 100 to 100K Hz) of dielectric constant of these five compositions was shown in Fig.5. Among them, the three lying near the R/C phase boundary were found to have similar relaxor characteristic, i.e. a broad dielectric peak with the maximum decreased for a value of  $\Delta K_{\max} \sim -3000$  and the temperature of this maximum increased of  $\Delta T_c \sim 15^\circ\text{C}$ . Contrarily, the one near the T/C phase boundary had shown a relatively normal ferroelectric characteristic, i.e. a sharper dielectric peak with  $\Delta K_{\max} \sim -1500$  and  $\Delta T_c \sim 5^\circ\text{C}$ . However, the composition at the triple point revealed a quite abnormal characteristic; there were a lowest reduction of dielectric maximum,  $\Delta K_{\max} \sim -1000$ , and a largest shift of  $T_c$ ,  $\Delta T_c \sim 20^\circ\text{C}$ , in the frequency dispersion of the broad dielectric peak. Such an abnormal characteristic is probably due to the coexistence of all of the three phases, i.e. cubic, rhombohedrol and tetragonal, at the transition temperature for this composition. As a consequence, it possessed an optimum combination of high dielectric constant ( $K_{\max} \sim 16000$  at 1KHz) and superior stability against the change of temperature and frequency, as compared to the other four compositions.

## CONCLUSIONS

The ferroelectric phase transition of five series of PLMNT ceramics containing LMN from 5 to 13 mol%, respectively, was investigated. A T/R phase boundary was determined from the change of 200 peak profile of XRD and a R/C phase boundary was also determined at compositions having the Curie temperature near room temperature. The two phase boundaries intersected at a composition around PT=42.5 mol% and LMN=11 mol%, at which a triple point separating the three phase fields was defined. A diffuse phase transition occurred for the compositions located below the T/R phase boundary, but a relatively normal ferroelectric transition appeared for those above the boundary. The former also showed a "soft" ferroelectric characteristic, i.e. a low  $E_c/P_r$ , and the latter a relatively "hard" characteristic, i.e. a high  $E_c/P_r$ . Moreover, the composition at the triple point had a dielectric characteristic showing an optimum combination of high dielectric constant and superior stability against the change of temperature and frequency.

## ACKNOWLEDGEMENT

This work was supported by the National Science Council of R.O.C. under contract NSC-81-0404-E007-608.

## REFERENCES

- [1] G.A. Smolenski and A.I. Agranovskaya, "Dielectric polarization and losses of some complex compounds," *Sov. Phys.-Tech. Phys. (Engl. Transl.)*, vol. 3, pp. 1380-82, July 1961.
- [2] V.A. Bokov and I.E. Myl'nikova, "Ferroelectric properties of monocrystals of new perovskite compounds," *Sov. Phys.-Solid State (Engl. Transl.)*, vol. 2, pp. 2428-32, Nov. 1961.
- [3] S.L. Swartz, T.R. Shrout, W.A. Schulze, and L. E. Cross, "Dielectric properties of lead-magnesium niobate ceramics," *J. Am. Ceram. Soc.*, vol. 67, pp. 311-15, May 1984.
- [4] V.A. Bokov and I.E. Myl'nikova, "Electrical and optical properties of single crystals of ferroelectrics with diffuse phase transition," *Sov. Phys. - Solid State (Engl. Transl.)*, vol. 3, pp. 613-23, Mar. 1961.
- [5] K. Uchino and S. Nomura, "Critical exponents of the dielectric constants in diffused-phase-transition crystals," *Ferroelectrics*, vol. 44, pp. 55-61, 1982.
- [6] L.E. Cross, "Relaxor ferroelectrics," *Ferroelectrics*, vol. 76, pp. 241-67, 1987.
- [7] C.A. Randall, A.S. Bhalla, T.R. Shrout, and L. E. Cross, "Classification and consequences of complex lead perovskite ferroelectrics with regard to B-site cation order," *J. Mater. Res.*, vol. 5, pp.829-34, Apr. 1990.
- [8] S.W. Choi, T.R. Shrout, S.J. Jang and A.S. Bhalla, "Dielectric and pyroelectric properties in the  $\text{Pb}(\text{Mg}_{1/3}\text{Nb}_{2/3})\text{O}_3$ - $\text{PbTiO}_3$  system," *Ferroelectrics*, vol. 100, pp. 29-38, 1989.
- [9] K. Uchino and S. Nomura, "Electrostrictive effect in perovskites and its transducer applications," *J. Mater. Sci.*, vol. 16, pp. 569-78, 1981.
- [10] L.J. Lin and T.B. Wu, "Structure evolution from  $\text{Pb}(\text{Mg}_{1/3}\text{Nb}_{2/3})\text{O}_3$  to  $\text{La}(\text{Mg}_{2/3}\text{Nb}_{1/3})\text{O}_3$ ," *J. Am. Ceram. Soc.*, vol. 76, pp. 1360-63, June 1991.
- [11] L.J. Lin and T.B. Wu, "Morphotropic phase boundaries in the ternary system of  $\text{Pb}(\text{Mg}_{1/3}\text{Nb}_{2/3})\text{O}_3$ - $\text{La}(\text{Mg}_{2/3}\text{Nb}_{1/3})\text{O}_3$ - $\text{PbTiO}_3$ ," *Mater. Lett.*, vol. 11, pp. 222-25, June 1991.
- [12] J. Chen, H.M. Chan, and M.P. Harmer, "Ordering structure and dielectric properties of undoped and La/Na-doped  $\text{Pb}(\text{Mg}_{1/3}\text{Nb}_{2/3})\text{O}_3$ ," *J. Am. Ceram. Soc.*, vol. 72, pp. 593-98, Apr. 1989.
- [13] L.J. Lin and T.B. Wu, "Ordering behavior of lead magnesium niobate ceramics with A-site substitution," *J. Am. Ceram. Soc.*, vol. 73, pp. 1253-56, May 1990.
- [14] S.L. Swartz and T.B. Shout, "Fabrication of perovskite lead magnesium niobate," *Mat. Res. Bull.*, vol. 17, pp. 1245-50, 1982.
- [15] D. Barb, E. Barbulescu, and A. Barbulescu, "On the ferroelectric structural phase transition in solid solutions," *Phys. Stat. Sol.(a)*, vol. 73, pp. 603-10, 1982.

# Dielectric and Piezoelectric Properties of Ceramics in The Lead Indium Niobate - Lead Scandium Tantalate Solid Solution.

E.F. Alberta and A.S. Bhalla

Materials Research Laboratory, The Pennsylvania State University, University Park, PA 16802, U.S.A.

## ABSTRACT

The dielectric and piezoelectric properties of the solid solution:  $(x) \cdot \text{Pb}(\text{In}_{1/2}\text{Nb}_{1/2})\text{O}_3 - (1-x) \cdot \text{Pb}(\text{Sc}_{1/2}\text{Ta}_{1/2})\text{O}_3$  [PIN/PST(x)] have been investigated. The two compositions that have been studied are  $x=0.025$  and  $0.975$ . The degree of long range ordering in PIN/PST(0.975) was found to be  $0.73$  (i.e., 73% ordered.) Dielectric maximum was found to be at  $10^\circ\text{C}$  and the pyroelectric maximum was found to be at  $0^\circ\text{C}$ . The average dielectric constant from heating and cooling cycles was found to have a maximum of  $1470$ , and corresponds to a dielectric loss of  $3\%$ . The maximum pyroelectric response was found to be  $0.002 \text{ C}^\circ\text{K}^{-1}\text{m}^{-2}$ . At room temperature  $d_{33}$  and  $d_{31}$  were found to be  $0 \text{ pC/N}$  with poling fields of up to  $45 \text{ kV/cm}$ . Upon cooling to  $-30^\circ\text{C}$  a ferroelectric hysteresis loop appears with  $E_c = 9.86 \text{ kV/cm}$  and  $P_r = 4.5 \text{ mC/cm}^2$ .

## INTRODUCTION

Earlier studies have shown that both  $\text{Pb}(\text{In}_{1/2}\text{Nb}_{1/2})\text{O}_3$  [PIN] and  $\text{Pb}(\text{Sc}_{1/2}\text{Ta}_{1/2})\text{O}_3$  [PST] are relaxor ferroics in which the degree of B-site cation ordering can be thermally controlled. Previous studies have mainly focused on solid solutions involving the normal ferroelectric  $\text{PbTiO}_3$  [PT] with either PIN or PST. Recently, however, the system PIN-PST [PIN/PST(x)] has begun to be studied due to the unique combination both order-disorder behavior and antiferroelectric-ferroelectric phase transformations.

PIN has been found to have the rhombohedrally distorted perovskite structure (that is, either the space group  $R3m$  or  $R3$ ). Disordered PIN crystals are relaxor ferroelectrics and undergo a cell doubling phase transformation into an ordered antiferroelectric phase. PST has also been shown to be rhombohedral. However, Disordered PST crystals are relaxor ferroelectrics and undergo a cell doubling phase transformation into an

ordered ferroelectric phase. This combination of first-order (anti)ferroelectric behavior, relaxor behavior and the presents of variable order-disorder regions may prove to be interesting on both a theoretical and practical levels.

In this paper we will focus on the composition PIN/PST(0.025) and PIN/PST (0.975). The dielectric and piezoelectric properties of this as-fired PIN/PST ceramics will be described.

## RESULTS

The degree of ordering in the as-fired ceramics has been determined by superstructure reflections in x-ray diffraction patterns. The long-range order parameter,  $S$ , has been determined by referring the intensity ratios of the superstructure/fundamental reflection pairs (111 and 200 in this case) and comparing them to those determined for an ordered structure. This relation is given as follows:

$$S^2 = \left[ \frac{I_{\text{Superlattice}}}{I_{\text{Baselattice}}} \right]_{\text{Obs}} \times \left[ \frac{I_{\text{Superlattice}}}{I_{\text{Baselattice}}} \right]_{S=1} \quad [1]$$

Stenger and Burggraaf have determined the ratio  $[I_{111}/I_{200}]$  under perfect order ( $S=1$ ) to be  $1.33$ . Before any electrical measurements were made the degree of ordering for as-fired PIN/PST(0.025) was determined to be  $73\%$ .

The temperature dependence of the dielectric constant was determined in the temperature range  $-100^\circ\text{C}$  to  $100^\circ\text{C}$ .  $K$  was found to reach a maximum at  $10^\circ\text{C}$  of  $1500$  during heating of  $4^\circ\text{C/min}$  and  $1440$  during cooling at  $4^\circ\text{C/min}$ . The dielectric loss at temperatures less than  $10^\circ\text{C}$  was found to be approximately  $4\%$ . The inverse dielectric constant follows the "Curie-Weiss Squared" law for both heating and cooling.



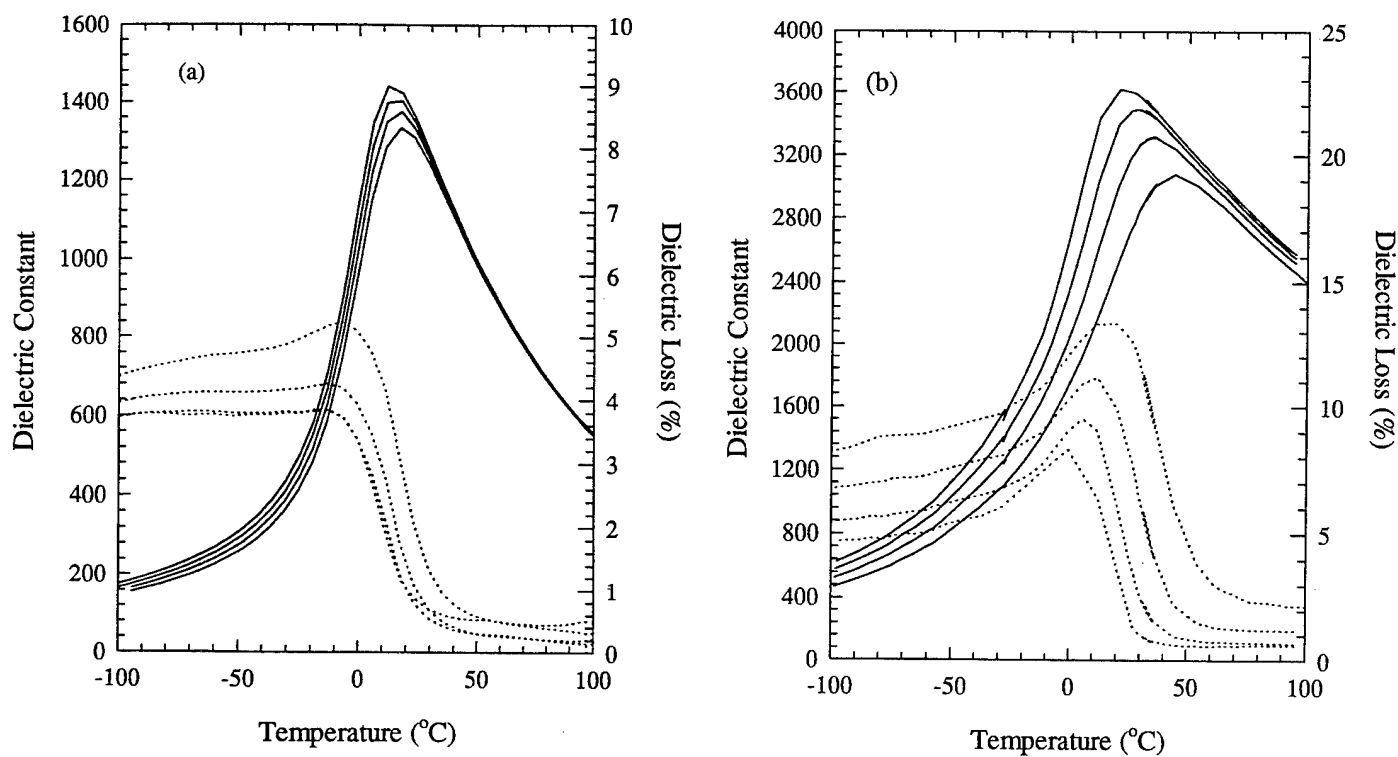


**Figure 1.** Dielectric Constant and Loss at 100 Hz, 1 kHz, 10 kHz, and 100 kHz for: (a) PIN/PST(0.025) and (b) PIN/PST (0.975).

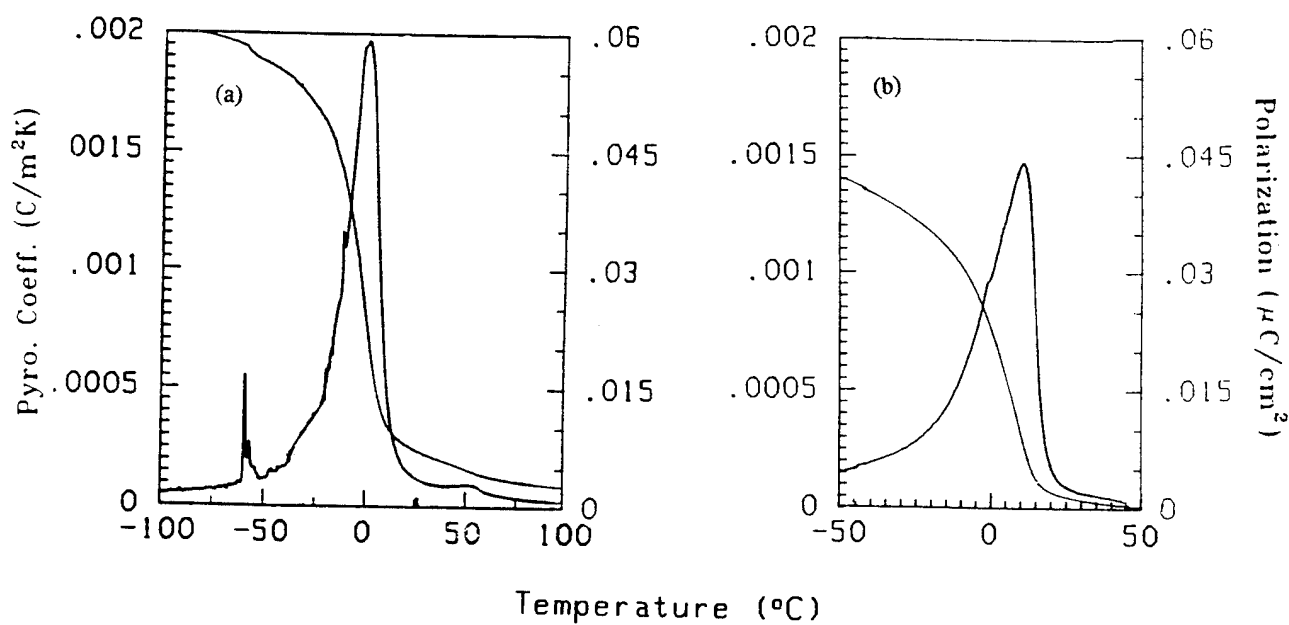


**Figure 2.** Pyroelectric coefficient and Polarization behavior of: (a) PIN/PST(0.025) and (b) PIN/PST(0.975).

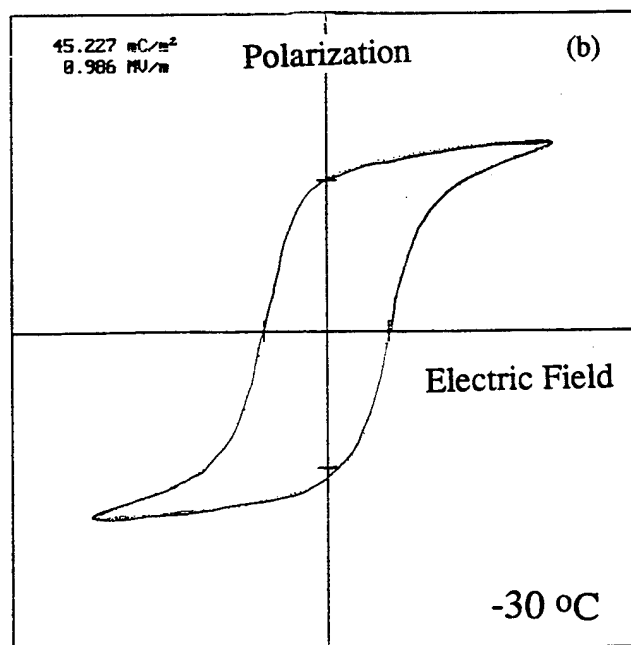
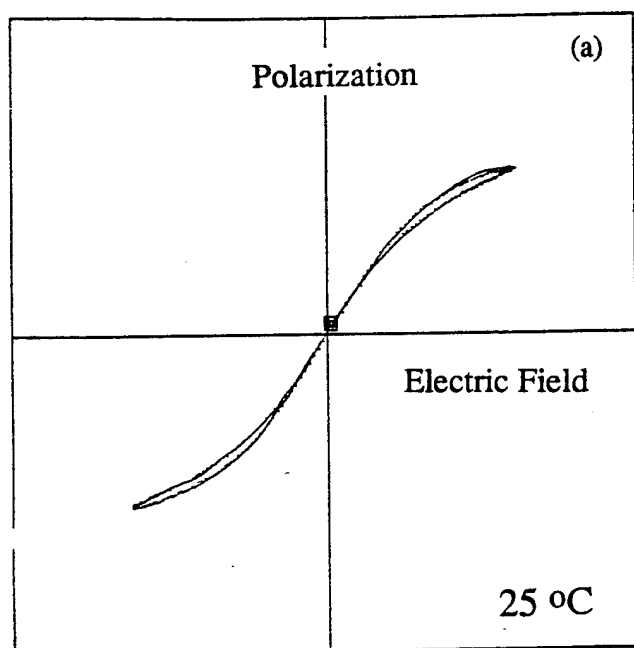


Figure 3. Dielectric hysteresis loops for PIN/PST(0.025) at: (a) 25°C and (b) -30°C ( $P_r=4.52 \mu\text{C}/\text{cm}^2$  and  $E_c=9.86 \text{ kV}/\text{cm}$ ).

Using the Byer-Roundy technique the pyroelectric coefficient,  $p_3$ , was determined for the temperature range of -100°C to 100°C. The polarization was then calculated from the pyroelectric coefficient. The polarization behavior showed a relatively long tail between 10°C and 150°C. At room temperature the polarization was found to be  $7 \mu\text{C}/\text{cm}^2$ . The polarization continues to increase with decreasing temperature to a saturated maximum value of  $64 \mu\text{C}/\text{cm}^2$  at 100°C. The pyroelectric response was found to reach a maximum value of  $0.002 \text{ C}/^\circ\text{K}\cdot\text{m}^2$  at 0°C.

Hysteresis measurements were also conducted in the temperature range -100°C to 100°C using a modified Sawyer-Tower circuit. Initially, at room temperature, the unpoled ceramics displayed "antiferroelectric" hysteresis loop. After cooling to -100°C and slowly heating to -30°C the samples showed typical ferroelectric behavior with  $P_r=4.52 \mu\text{C}/\text{cm}^2$  and  $E_c=9.86 \text{ kV}/\text{cm}$ . Further heating to room temperature causes the loop to shrink. At room temperature the remnant polarization had decreased to  $1.13 \mu\text{C}/\text{cm}^2$  and the coercive field had decreased to  $5.03 \text{ kV}/\text{cm}$ . Upon further heating (to 45°C for example) the hysteresis loop slims dramatically and the remnant polarization slowly disappears. In addition, as illustrated in the pyroelectric measurement, the polarization curve has a tail extending to slightly over 150°C.

Following these experiments  $d_{33}$  was found to be  $0 \text{ pC}/\text{N}$  as determined by a Berlincourt  $d_{33}$  meter. Poling at or above room temperature with fields up to  $45 \text{ kV}/\text{cm}$  was found to have no effect on  $d_{33}$ . In addition, no  $d_{31}$  was detected even with applied electrical biases of up to  $\pm 23 \text{ kV}/\text{cm}$ . No attempt has yet been made to pole and/or measure the piezoelectric coefficients at lower temperatures.

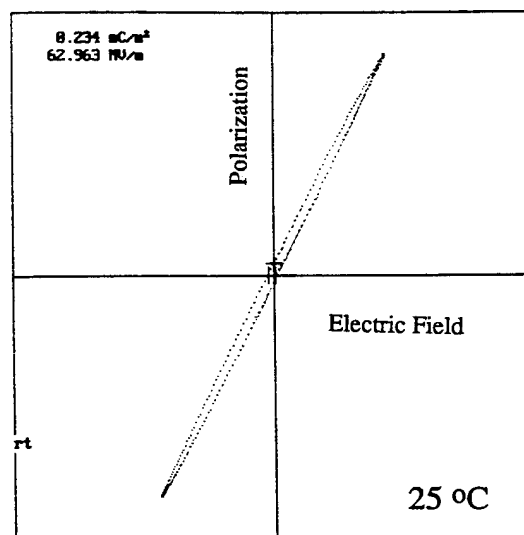


Figure 4. Dielectric hysteresis loop for PIN/PST(0.975) at room temperature.

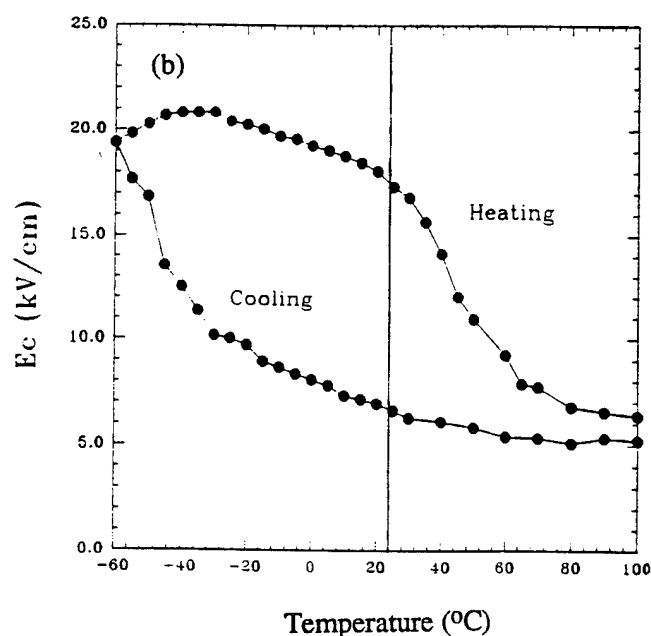
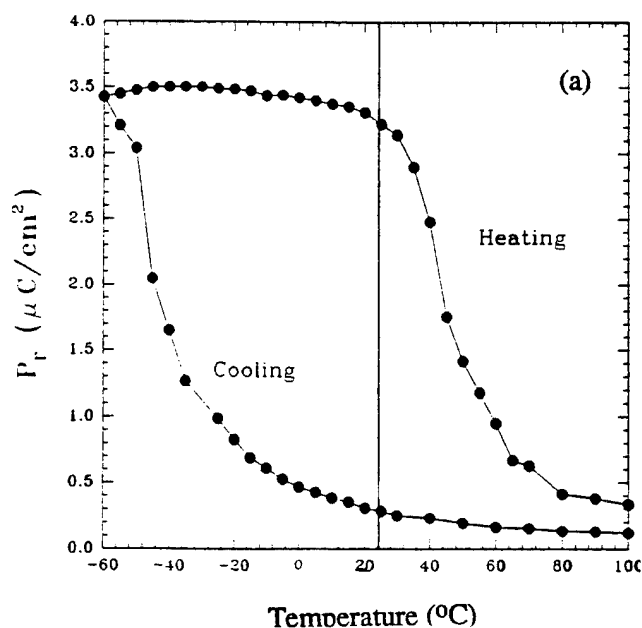


Figure 5.  $P_r$  and  $E_c$  as a function of temperature for PIN/PST(0.025).  
Determined from dielectric hysteresis loops.

## CONCLUSIONS

To summarize the dielectric properties of PIN/PST(0.025) have been determined. The degree of long range ordering in these samples was found to be 0.73 (i.e., 73% ordered.) Dielectric maximum was found to be at 10°C and the pyroelectric maximum was found to be at 0°C. At their maximum temperatures, the average dielectric constant, loss, and pyroelectric coefficient were determined to be 1470, 3%, and 0.002 C°K·m<sup>2</sup>, respectively. Finally, at or above room temperature  $d_{33}$  and  $d_{31}$  was found to be 0 pC/N with poling fields of up to 45 kV/cm.

## REFERENCES

[1] Giniewicz, J.R., A.S. Bhalla, and L.E. Cross, "Pyroelectric Response and Depolarization behavior of  $(1-x)\text{Pb}(\text{Sc}_{1/2}\text{Ta}_{1/2})\text{O}_3$  -  $(x)\text{Pb}(\text{Sc}_{1/2}\text{Ta}_{1/2})\text{O}_3$  Materials", *Ferroelectrics*, **118** 157-164 (1991).

[2] Giniewicz, J.R., Ph.D. Thesis, The Pennsylvania State University, 1991.

[3] Groves, P., "Fabrication and Characterisation of Ferroelectric Perovskite Lead Indium Niobate," *Ferroelectrics*, **65** 67-77 (1985).

[4] Park, S.S., and W.K. Choo, "Pyroelectric and Dielectric Properties of Lead Indium Niobate Ceramics," *Ferroelectrics*, **118** 117-122 (1989).

[5] Setter, N., Ph.D. Thesis, The Pennsylvania State University, 1980.

[6] Setter, N., and L.E. Cross, "Flux Growth of Lead Scandium Tantalate and Lead magnesium Niobate Single Crystals," *J. Cryst. Growth*, **50** 555-556 (1980).

[7] Zhili, C., Y. Xi, and L.E. Cross, "Reversible Pyroelectric effect in  $\text{Pb}(\text{Sc}_{1/2}\text{Ta}_{1/2})\text{O}_3$  Ceramics Under DC Bias," *Ferroelectrics*, **44** 271-276 (1989).

# AN EVALUATION OF LEAD-ZIRCONATE BASED CERAMICS FOR USE IN NON-VOLATILE FERROELECTRIC MEMORY DEVICES.

E.F. Alberta and A.S. Bhalla

Materials Research Laboratory, The Pennsylvania State University, University Park, PA 16802, U.S.A.

## ABSTRACT

This paper will present an initial evaluation of the lead zirconate - lead zinc niobate solid solution for use in non-volatile ferroelectric memory devices. Previous work has shown that the  $(x)\text{PbZrO}_3 - (1-x)\text{Pb}(\text{Zn}_{1/3}\text{Nb}_{2/3})\text{O}_3$  [PZZN] system has "square" hysteresis loops accompanied by large remnant polarizations. In particular, compositions near the room temperature antiferroelectric to ferroelectric phase boundary will be investigated.

## INTRODUCTION

Previous work within the PZZN system has shown that a pseudomorphotropic phase boundary exists at  $x=93.0$  mol%PZ. This boundary separates the rhombohedral ferroelectric phase from the antiferroelectric orthorhombic phase at room temperature. Based on these works an investigation into the hysteresis behavior of PZZN has been undertaken. For the initial work hot pressed ceramic samples have been used. It is generally known that bulk and thin film properties can vary; however, this work is an indication that the thin film form of this material may be interesting from an applications point of view.

## RESULTS

Compositions with less than 93.0 mol% PZ are found to be ferroelectric with bias independent piezoelectric coefficients. As an example of the ferroelectric phase, PZZN(92.5) will be used. The antiferroelectric phase will be represented by the composition PZZN(93.5). From dielectric data one can find two phase transformations in PZZN(92.5), one near  $-50^\circ\text{C}$  (from cooling runs) and the second at  $218^\circ\text{C}$ . These anomalies correspond to the low- to high-temperature rhombohedral phase change and the high-temperature rhombohedral to cubic phase change, respectively. In PZZN(93.5), however, the phase transformations are from orthorhombic to high-temperature rhombohedral to cubic. At room temperature the dielectric constant is between 150 to 450 with losses of about 4% at 1kHz. Other work has also

shown that the dielectric constant of the ferroelectric phases are decreased with increasing bias fields and are decreased in the antiferroelectric phases. The typical effect of bias applied to a poled ferroelectric is shown in figure 1.

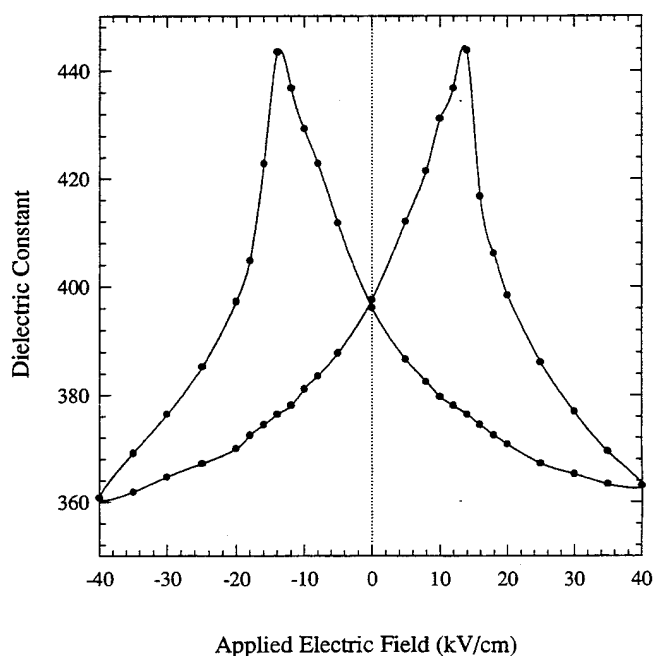
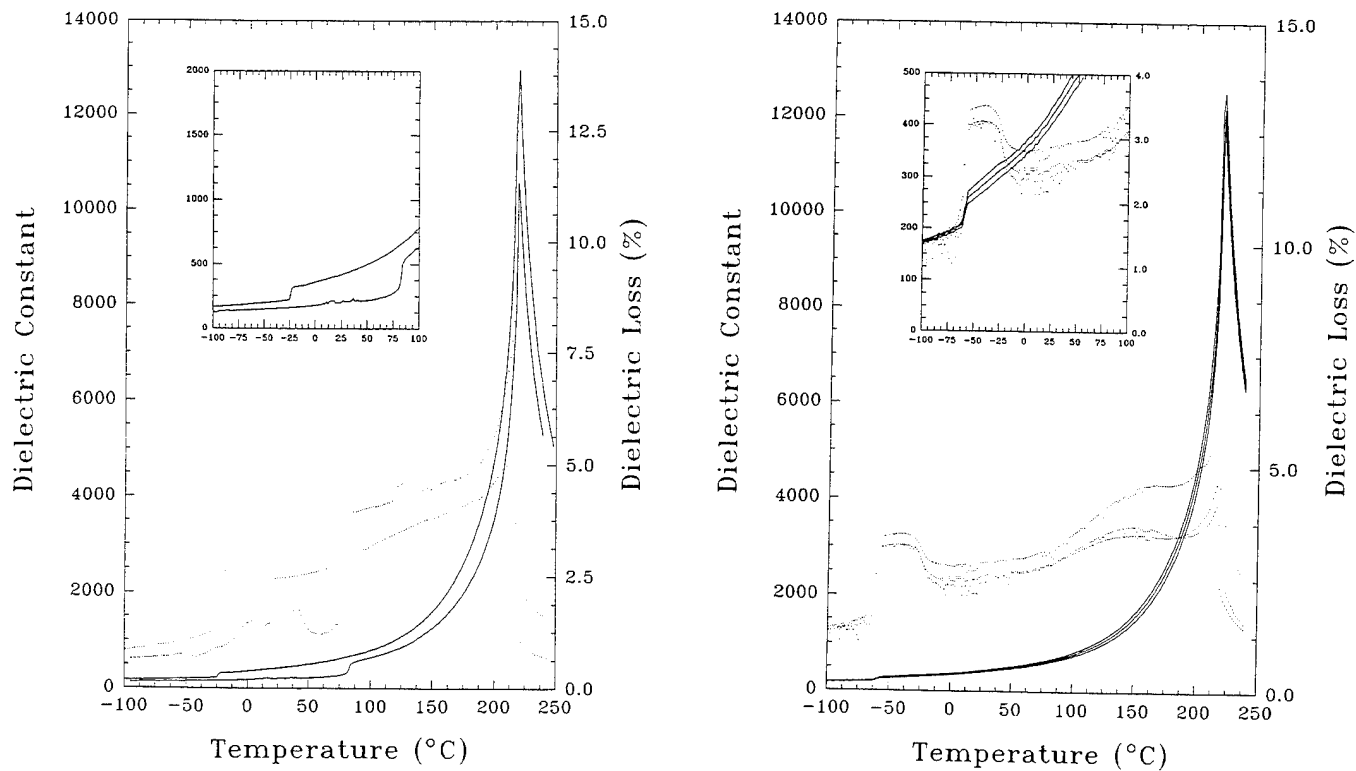
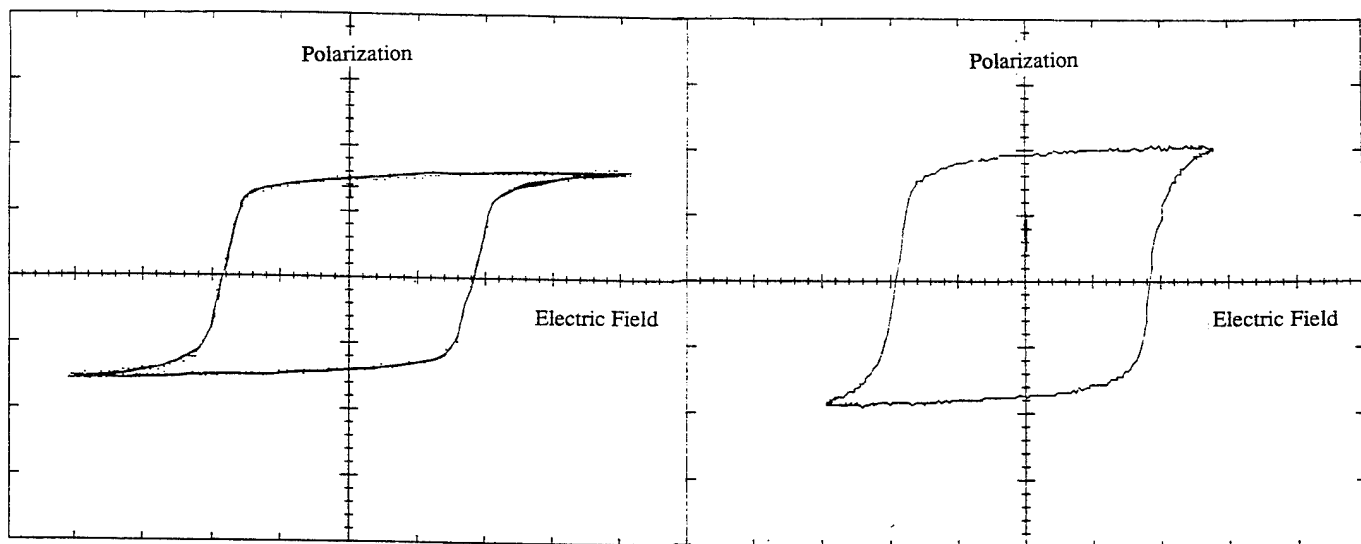


Figure 1. The effect of electrical bias on the dielectric constant of PZZN(92.5) at room temperature.

Hysteresis behavior can be found in the next few figures. Typical room temperature hysteresis curves can be found in Figure 3. PZZN(93.5) displays an interesting behavior. The antiferroelectric phase cannot be field-forced with field up to 70 kV/cm; however, the composition is easily poled near the antiferroelectric-ferroelectric phase transformation. Saturated values of  $d_{33}$  and  $P_s$  can be obtained after poling at  $100^\circ\text{C}$  with 8 kV/cm for 1 to 2 minutes. The effect of temperature on this field-and-temperature forced ferroelectric phase can be found in figure 4. This plot indicates the antiferroelectric phase becomes



**Figure 2.** The dielectric constant and loss as a function of temperature for: (a) PZZN(92.5) heating and cooling and (b) PZZN(93.5) at 1 kHz, 10 kHz and 100 kHz.



**Figure 3.** Typical hysteresis loops at room temperature for: (a) PZZN(92.5),  $E_c=15.25$  kV/cm and  $P_r=32.2$   $\mu\text{C}/\text{cm}^2$  and (b) PZZN(93.5) (poled at 100°C),  $E_c=16.36$  kV/cm and  $P_r=29.1$   $\mu\text{C}/\text{cm}^2$ .

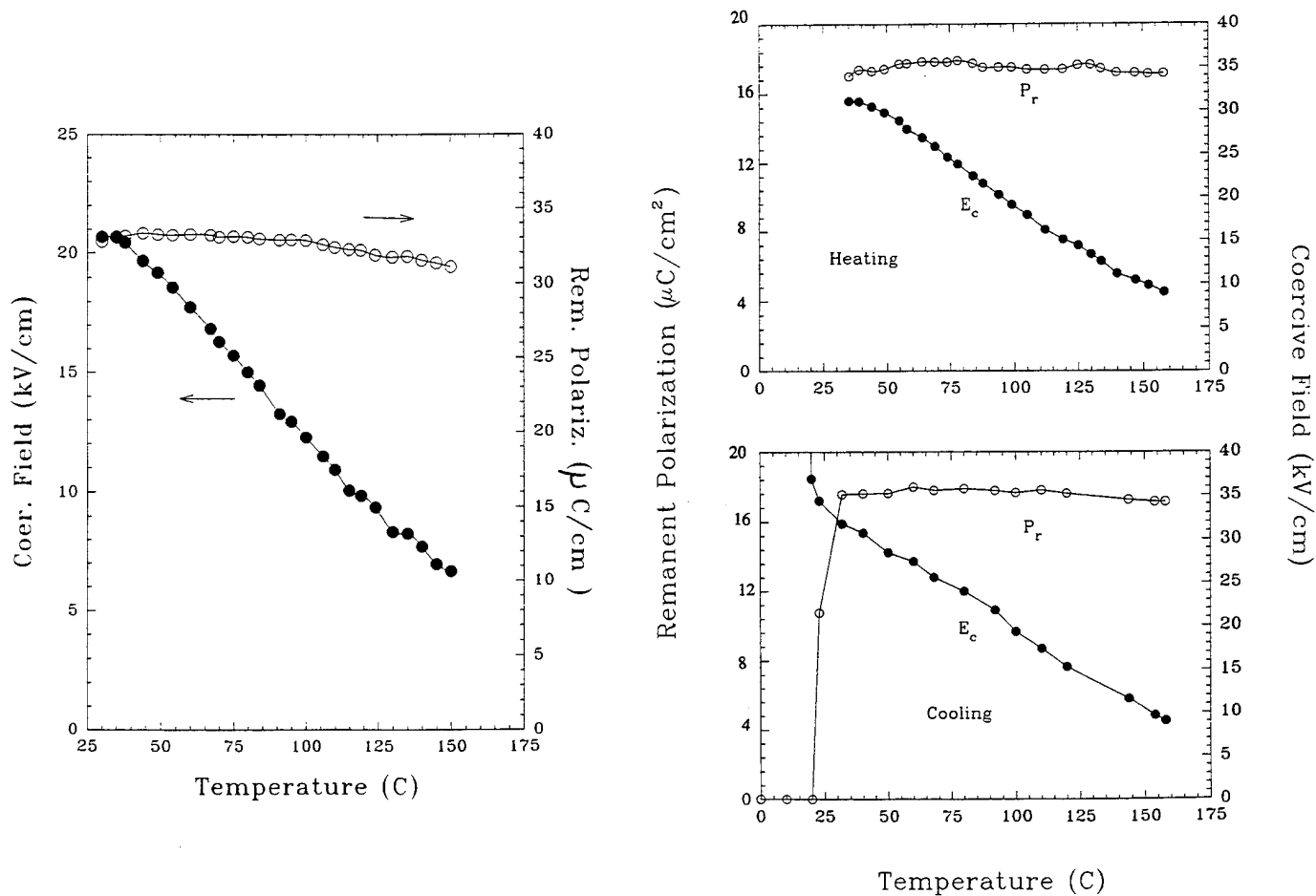


Figure 4. Polarization as a function of temperature (from hysteresis measurements) for: (a) PZZN(92.5) and (b) PZZN(93.5).

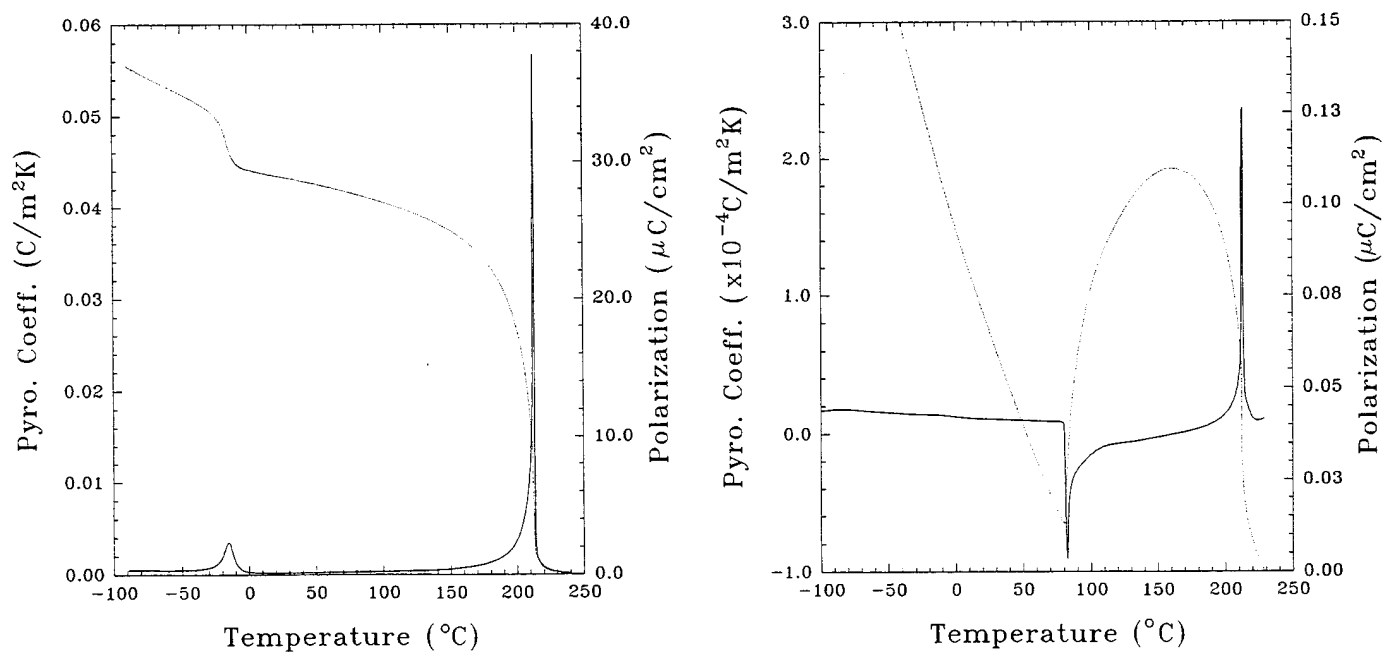


Figure 5. Pyroelectric response of PZZN ceramics (data taken during heating) for: (a) PZZN(92.5) and (b) PZZN(93.5).

stable at slightly less than room temperature which is approximately 50°C higher than indicated by the dielectric constant data. The ferroelectric composition, PZZN(92.5), displays a remnant polarization of 32.2  $\mu\text{C}/\text{cm}^2$  which is approximately equal to that for PZZN(93.5). However, this composition does not depole below room temperature and is easily poled at room temperature with 20 kV/cm for 1 to 2 minutes.

Typical pyroelectric responses of these materials are shown in figure 5. One can easily see the ferroelectric to ferroelectric phase change at -5°C for PZZN(92.5) and the resulting change in the polarization. For PZZN(93.5) the situation is slightly more complicated. Even when poled at 100°C the sample depoled in the process of cooling to the start temperature. Even with this loss of polarization, the plot is useful in determining the location of the antiferroelectric to ferroelectric phase transition which is at 83°C.

## CONCLUSIONS

Using ceramic specimens, some important information has been obtained towards the use of PZZN in non-volatile memory applications. Most notable are the ease of poling, the large remnant polarizations, and the existence of square hysteresis loops. Clearly more work needs to be done with this material, especially in the area of thin films.

## REFERENCES

- [1] Alberta, E.F., "The Dielectric, Piezoelectric, and Pyroelectric Properties of Lead Zirconate - Lead Zinc Niobate - Lead Titanate Ceramics," M.S. Thesis, The Pennsylvania State University, University Park PA (1994).
- [2] Lian, J., M. Adachi, E. Shiosake, and A. Kawabata, "Phase Transitions in the  $\text{PbZr}_3$  -  $\text{PbTiO}_3$  -  $\text{Pb}(\text{Zn}_{1/3}\text{Nb}_{2/3})\text{O}_3$  System," Ferroelectrics, **96** 127 (1989).
- [3] Lian, J., and T. Shiosake, "Phase Transitions Characteristics in  $\text{PbZrO}_3$  Based PZT-PZN Solid Solution Ceramics," IEEE Trans. on Ultrasonics and Frequency Control, **38** [6] (1991).
- [4] Takenaka, T., A.S. Bhalla, and L.E. Cross, "Dielectric, Piezoelectric and Pyroelectric Properties of Lead Zirconate-Lead Zinc Niobate Ceramics," J. Am. Ceram. Soc., **72** [6] 1016-23 (1989).
- [5] Takenaka, T., K. Komiya, and K. Sakata, "PbZrO<sub>3</sub>-Based Composite Pyroelectric Ceramics," IEEE Proc. International Symposium on the Applications of Ferroelectrics, IEEE, Piscataway (1991).

# Ferroelectric Ceramics in the $\text{Na}_{0.5}\text{Bi}_{0.5}\text{TiO}_3$ - $\text{K}_{0.5}\text{Bi}_{0.5}\text{TiO}_3$ , $\text{Na}_{0.5}\text{Bi}_{0.5}\text{TiO}_3$ - $\text{PbTiO}_3$ and $\text{K}_{0.5}\text{Bi}_{0.5}\text{TiO}_3$ - $\text{PbTiO}_3$ Systems

O. Elkechai and J.P. Mercurio  
Laboratoire de Matériaux Céramiques et Traitements de Surface  
URA CNRS n° 320, Faculté des Sciences  
123, Avenue Albert-Thomas  
87060 LIMOGES CEDEX, FRANCE

**Abstract** -The study of the  $\text{Na}_{0.5}\text{Bi}_{0.5}\text{TiO}_3$  -  $\text{K}_{0.5}\text{Bi}_{0.5}\text{TiO}_3$ ,  $\text{Na}_{0.5}\text{Bi}_{0.5}\text{TiO}_3$  -  $\text{PbTiO}_3$  and  $\text{K}_{0.5}\text{Bi}_{0.5}\text{TiO}_3$  -  $\text{PbTiO}_3$  systems was carried out using X-ray diffraction, DSC and dielectric measurements. The limits of the rhombohedral ( $\text{Na}_{0.5}\text{Bi}_{0.5}\text{TiO}_3$ -rich side) and orthorhombic ( $\text{K}_{0.5}\text{Bi}_{0.5}\text{TiO}_3$ , and  $\text{PbTiO}_3$ -rich side) solid solutions were determined, as well as the evolutions of their lattice parameters as a function of composition. Ceramic materials have been prepared by natural sintering (1090-1220°C / 0.5 h) of powders obtained by solid state reaction (900-1000°C / 20 h) of the corresponding oxides and carbonates. The dielectric permittivities of these materials have been measured in a wide frequency range between 20 and 800°C. The results showed that they all are ferroelectric at room temperature and some of them exhibit a relaxor-type behaviour. Several peculiar compositions showed the best piezoelectric characteristics for this type of ceramic materials.

## INTRODUCTION

Lead titanazirconate ceramics (PZT) are the most currently used ferroelectric materials in the field of piezoelectric applications. A noticeable feature of these materials is the occurrence in the phase diagram of morphotropic phase boundary (MPB) which separate tetragonal and rhombohedral ferroelectric regions. Solid solutions with compositions close to the MPB present the best electromechanical properties.

In the research of new complex systems able to show interesting piezoelectric characteristics, care should be taken that thermal and time stability of the properties is connected with the value of the Curie temperature of the components. Moreover, previous works had shown that the more favourable situation corresponds to the case where the MPB is located between tetragonal and rhombohedral phases[1].

With this point of view, a study was started on the following systems  $\text{Na}_{0.5}\text{Bi}_{0.5}\text{TiO}_3$  -  $\text{K}_{0.5}\text{Bi}_{0.5}\text{TiO}_3$  (NBT-KBT),  $\text{Na}_{0.5}\text{Bi}_{0.5}\text{TiO}_3$  -  $\text{PbTiO}_3$  (NBT-PT) and  $\text{K}_{0.5}\text{Bi}_{0.5}\text{TiO}_3$  -  $\text{PbTiO}_3$  (KBT-PT) which fulfil the above mentioned criteria. Actually NBT is rhombohedral with a Curie temperature close to 320°C, and KBT and PT are tetragonal with Curie temperatures of 380 and 490°C respectively[2]. This paper presents the results of crystal chemistry, dielectric and piezoelectric properties of some materials belonging to this family.

## EXPERIMENTAL

Polycrystalline compounds were prepared by solid state reaction of the corresponding oxides or carbonates. Stoichiometric mixtures of reagent grade  $\text{TiO}_2$ ,  $\text{Bi}_2\text{O}_3$ ,  $\text{Na}_2\text{CO}_3$ ,  $\text{K}_2\text{CO}_3$  and  $\text{PbO}$  (or  $\text{PbCO}_3$ ) were thoroughly mixed and calcined in alumina crucibles between 900 and 1000°C for 20 hours. Further calcinations were necessary to achieve complete reaction.

Phase characterization and morphotropic phase boundary limits were determined by X-ray diffraction with a Siemens D5000 diffractometer (graphite monochromator,  $\text{CuK}\alpha$  radiation). The lattice parameters were refined by a least-squares method. The structural evolution of the compounds with temperature was observed using a high temperature X-ray attachment (Anton Parr HTK) working between room temperature and 1000°C. Differential scanning calorimetry analyses were performed in air atmosphere using a Netzsch STA 409 DSC device.

Disk-shaped ceramics with 10 mm diameter and 1 mm thick were sintered in air at 1090-1220°C according to the composition. The thermal cycle consisted of heating at 5°Cmin<sup>-1</sup> up to the highest temperature (dwelling time 30 min) followed by natural cooling to room temperature in the oven. Samples with 90-95% of the theoretical density were obtained. After polishing, they were coated with a low temperature silver or gold paste fired at 600°C for 10 min, aged overnight at 100°C and left for 24 hours at room temperature before measurements.

Low frequency dielectric measurements were carried out between room temperature and 1000°C (at increasing and decreasing temperature) at chosen frequencies in the range 10 kHz - 5 MHz using a HP 4194A impedance analyser. Piezoelectric characteristics of poled ceramics (3 kVmm<sup>-1</sup>, 2h, 140°C, silicone oil) were obtained either using a Berlincourt-type piezometer or by calculation from the resonance-antiresonance spectra according to IRE standards[3].

## RESULTS AND DISCUSSION

### Structural and dielectric properties

At room temperature, NBT is rhombohedral ( $a = 0.3891$  nm,  $a = 89.6^\circ$ ) whereas KBT and PT are tetragonal with the following lattice parameters, KBT :  $a = 0.3918$  nm,  $c = 0.3996$  nm and PT :  $a = 0.3900$  nm,  $c = 0.4154$  nm.



**NBT-KBT system** :X-ray diffraction data showed two  $\text{Na}_{0.5-x}\text{K}_x\text{Bi}_{0.5}\text{TiO}_3$  solid solution ranges, rhombohedral on the sodium-rich side and tetragonal on the potassium- rich side, separated by a biphasic region for  $0.08 < x < 0.3$ . Figure 1 gives the evolutions of the lattice parameters as a function of the system composition. They logically increase with  $x$  according to the increase of the mean ionic radius which change from 0.134 nm (Na,Bi) to 0.147 nm (K,Bi).

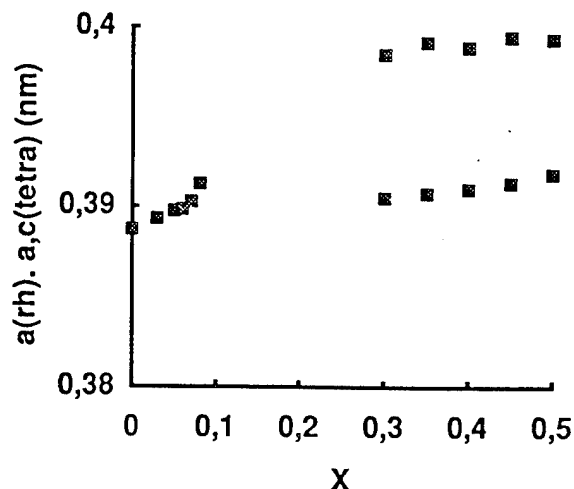


Fig. 1.  $\text{Na}_{0.5-x}\text{K}_x\text{Bi}_{0.5}\text{TiO}_3$  : Lattice parameters vs  $x$

Nevertheless the tetragonality of the K-rich solid solutions does not change with composition ( $c/a = 1.02$ ).

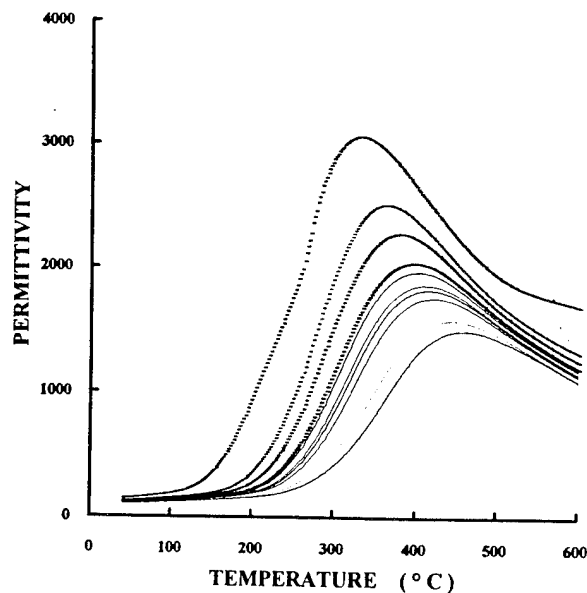


Fig. 2.  $\text{Na}_{0.5}\text{Bi}_{0.5}\text{TiO}_3$  : Permittivity vs temperature

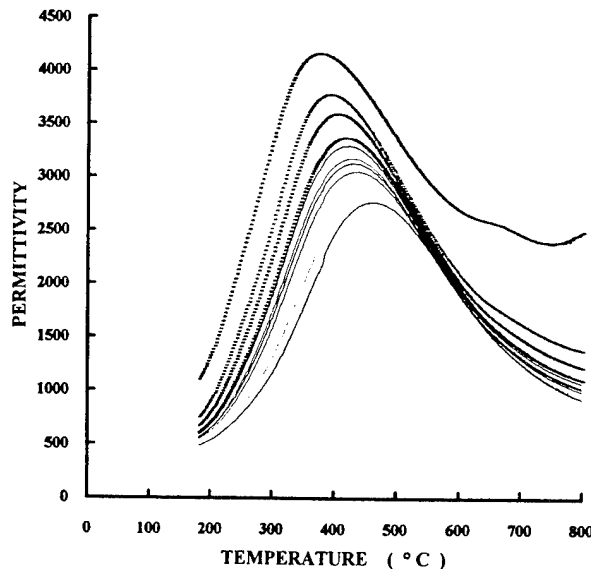


Fig. 3.  $\text{K}_{0.5}\text{Bi}_{0.5}\text{TiO}_3$  : Permittivity vs temperature

The variations of the dielectric permittivity of NBT and KBT with temperature at several frequencies (from 10 kHz to 3 MHz) are shown in Fig. 2 and 3. The curves clearly show a relaxor-type behaviour : the maximum of the permittivity decreases and is strongly shifted towards high temperatures when the measuring frequency increases. A very slight endothermal signal in the DSC curve of NBT ( $\Delta H = -0.3 \text{ Jg}^{-1}$ ) at about  $308^\circ\text{C}$  seems to correspond to this diffuse phase transition ( $T_m = 320^\circ\text{C}$  at 10 kHz). The thermal variations of the permittivities have been measured only for compositions belonging to single phase regions. In both rhombohedral ( $0 < x < 0.08$ ) and tetragonal ( $0.30 < x < 1$ ) ranges, the relaxor behaviour is still present without any significant change of  $T_m$  with composition and frequency (Fig. 4).

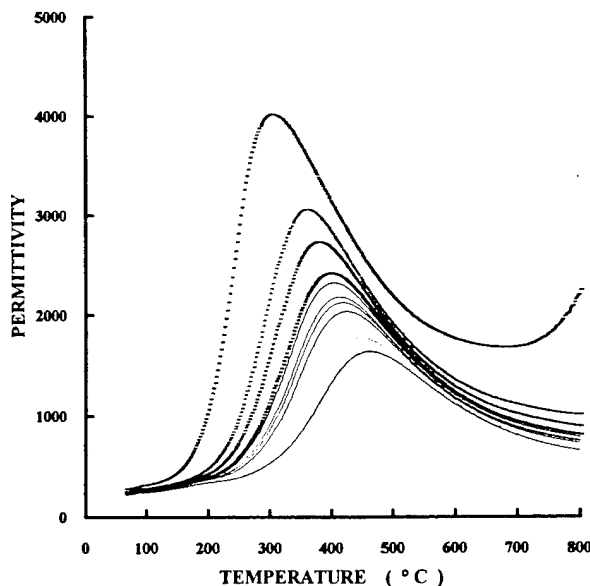


Fig. 4.  $\text{Na}_{0.45}\text{K}_{0.05}\text{Bi}_{0.5}\text{TiO}_3$  : Permittivity vs temperature

**NBT-PT system :** In the  $(\text{Na}_{0.5})_{1-x}(\text{Bi}_{0.5})_{1-x}\text{Pb}_x\text{TiO}_3$  system a narrower biphasic range has been found for  $0.09 < x < 0.20$  (Fig. 5). The lattice parameter of the rhombohedral solid solution increases very slightly with increasing  $x$ . In the tetragonal domain, the lattice parameters  $a$  and  $c$  increase almost linearly as  $x$  increases from 0.20 to 1, and the  $c/a$  ratio changes from 1.02 to 1.06 ( $\text{PbTiO}_3$ ).

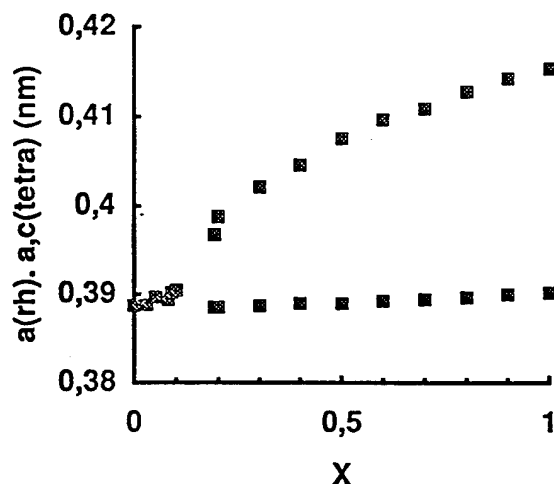


Fig. 5.  $(\text{Na}_{0.5}\text{Bi}_{0.5})_{1-x}\text{Pb}_x\text{TiO}_3$  : Lattice parameters vs  $x$

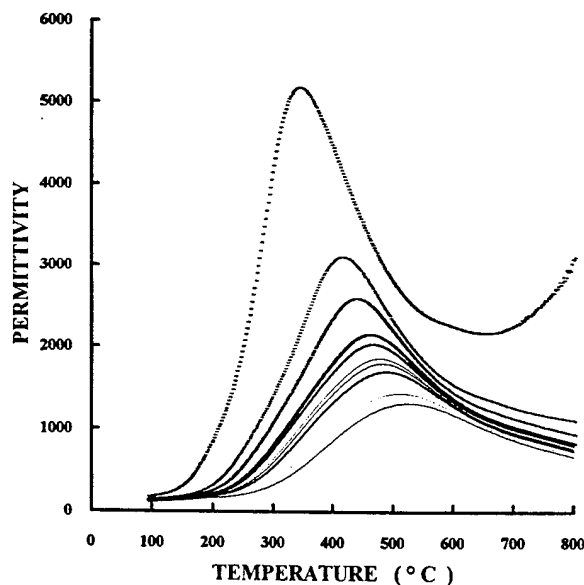


Fig. 6.  $(\text{Na}_{0.5}\text{Bi}_{0.5})_{0.92}\text{Pb}_{0.08}\text{TiO}_3$  : Permittivity vs temperature

The thermal and frequency evolutions of the dielectric permittivities are strongly dependent on the nature of the solid solutions. For the rhombohedral compositions, a frequency dispersion was observed related to a relaxor-type behaviour as shown in Fig. 6 for  $x = 0.08$ . The associated  $T_m$  decreases as  $x$  increases in agreement with previous data and confirmed by DSC measurements. For tetragonal compositions, the behaviour was rather different. The dielectric anomaly presents a very steep increase on the low temperature side and the permittivity peak becomes narrower as the lead content increases. For low lead rate, there is a little frequency dispersion which vanishes as  $x$  increases from 0.2 to 1 as shown in Fig. 7 for  $x = 0.4$ . The Curie temperatures - determined by both permittivity and DSC - present a maximum ( $500^\circ\text{C}$ ) around  $x = 0.8$  with a thermal hysteresis between heating and cooling estimated to  $15\text{--}20^\circ\text{C}$ .

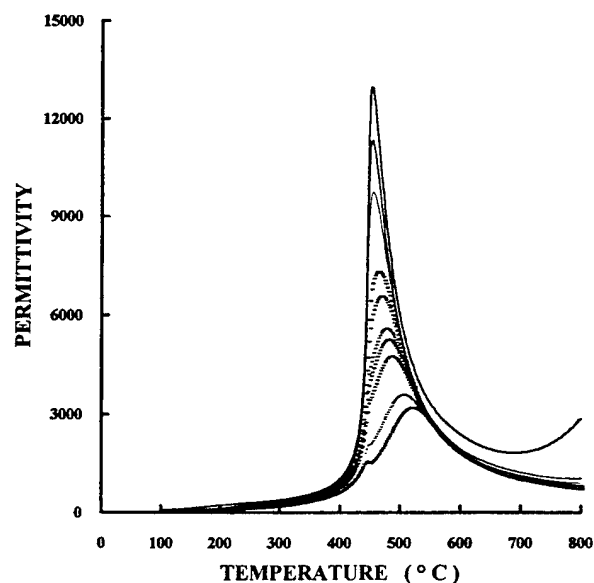


Fig. 7.  $(\text{Na}_{0.5}\text{Bi}_{0.5})_{0.6}\text{Pb}_{0.4}\text{TiO}_3$  : Permittivity vs temperature

**KBT-PT system:**  $\text{K}_{0.5}\text{Bi}_{0.5}\text{TiO}_3$  and  $\text{PbTiO}_3$  can form a complete series of tetragonal solid solutions. The lattice parameters vary almost linearly with  $x$  : as  $x$  increases,  $a$  slightly decreases and  $c$  increases so as the tetragonality  $c/a$  change from 1.02 to 1.06 (Fig. 8). Preliminary dielectric experiments have shown that the overall behaviour of the KBT-PT system is similar to NBT-PT. As an example, the thermal variation of the dielectric permittivity of a low lead content ceramics ( $x = 0.03$ ) is almost the same as that observed for pure KBT (Fig. 9).

#### Piezoelectric properties

The piezoelectric properties were carried out only on NBT-KBT and NBT-PT ceramics with compositions corresponding to the rhombohedral range, i.e. ceramics with low lead content. Some electromechanical characteristics are given in Tables 1 and 2. As for PZT ceramics, the piezoelectric constant  $d_{33}$  and the electromechanical coupling factors are enhanced for compositions close to the highest limit of the rhombohedral range.

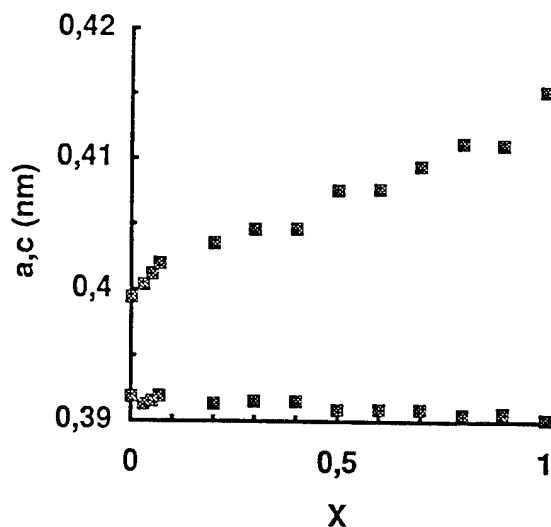


Fig.8.  $(K_{0.5}Bi_{0.5})_{1-x}Pb_xTiO_3$  : Lattice parameters vs x

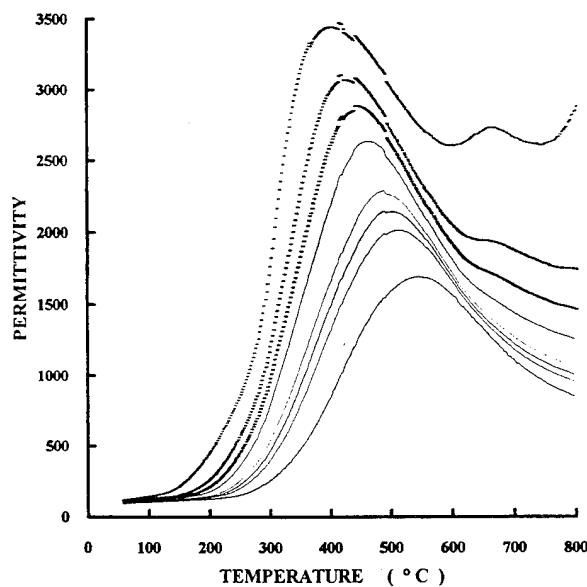


Fig.9.  $(K_{0.5}Bi_{0.5})_{0.97}Pb_{0.03}TiO_3$  : Permittivity vs temperature

x	$d_{33}$ (pC N <sup>-1</sup> )	$k_p$ (%)	$N_p$ (Hz m)
0	70	12	3220
0.03	45	11	2900
0.05	73	14	2780
0.06	31	10	2680
0.07	59	16	2750
0.08	96	21	2800

TABLE 1  $Na_{0.5-x}K_xBi_{0.5}TiO_3$  : Piezoelectric data

x	$d_{33}$ (pC N <sup>-1</sup> )	$k_p$ (%)	$N_p$ (Hz m)
0	70	12	3220
0.05	51	11	2900
0.08	52	21	2660
0.10	110	27	2980

TABLE 2.  $(Na_{0.5})_{1-x}(Bi_{0.5})_{1-x}Pb_xTiO_3$   
Piezoelectric data

## CONCLUSION

This study has shown that piezoelectric ceramics with improved characteristics can be obtained within the NBT-KBT, NBT-PT and KBT-PT systems. Further experiments are in progress in order to investigate more deeply the nature of the phase transitions in these systems.

## REFERENCES

- [1] B. Jaffe, W.R. Cook and H. Jaffe, Piezoelectric ceramics, Academic Press, London 1971
- [2] G.A. Smolenskii, V.A. Isupov, A.I. Agranovskaia and N.N. Krainik, *Fiz. Tverdogo Tela*, 2, 2982 (1960)
- [3] I.R.E. Standards on Piezoelectric Crystals, Proc. I.R.E., 49, 1161 (1961)
- [4] T. Takenaka, K. Sakata and K. Toda, *Ferroelectrics*, 106, 375 (1990)

Ceramics with compositions  $Na_{0.42}K_{0.08}Bi_{0.5}TiO_3$  and  $Na_{0.45}Bi_{0.45}Pb_{0.1}O_3$  show the best piezoelectric characteristics ( $d_{33}$  and  $k_p$ ) for materials without lead or with very low lead content.

# Ferroelectric Properties of the Mixed Aurivillius Phase $\text{Bi}_7\text{Ti}_4\text{NbO}_{21}$

R. Maalal, M. Manier, J.P. Mercurio and B. Frit  
Laboratoire de Matériaux Céramiques et Traitements de Surface  
URA CNRS n° 320, Faculté des Sciences  
123, Avenue Albert-Thomas  
87060 LIMOGES CEDEX, FRANCE

**Abstract** - Room and high temperature X-ray diffraction, DSC, dilatometric and dielectric measurements have shown that the mixed Aurivillius phase  $\text{Bi}_7\text{Ti}_4\text{NbO}_{21}$  presents two characteristic temperatures. The first one - close to  $675^\circ\text{C}$  - seems to be attributed to a ferroelectric - paraelectric transition connected with a structural change from orthorhombic to tetragonal. The second one, strongly observed by dielectric measurements would concern a possible ferroelastic - paraelastic phase transition.

## INTRODUCTION

Bismuth titanate niobate  $\text{Bi}_7\text{Ti}_4\text{NbO}_{21}$ , a mixed layer bismuth oxide compound of the "Aurivillius phases" family, is known to present two dielectric anomalies at about  $675$  and  $830^\circ\text{C}$  [1,2]. In a previous work, strongly oriented dense ceramics obtained by hot forging showed a large anisotropy of the dielectric constants with respect to the forging direction [3]. A thorough study of this particular behaviour cannot be undertaken on ceramics only. So, this paper deals with a comparison of some dielectric characteristics obtained on both sintered ceramics and flux-grown single crystals.

## EXPERIMENTAL

$\text{Bi}_7\text{Ti}_4\text{NbO}_{21}$  powders were prepared by solid state reaction of the corresponding oxides. Stoichiometric mixtures of reagent grade  $\text{Bi}_2\text{O}_3$ ,  $\text{TiO}_2$  and  $\text{Nb}_2\text{O}_5$  were thoroughly mixed and calcined at  $850^\circ\text{C}$  for 15 hours in alumina or platinum crucibles. After crushing, the powders were heated at higher temperatures in order to assure complete reaction. Dense ceramics were obtained by natural sintering of uniaxially pressed pellets at  $1100$ - $1150^\circ\text{C}$  for 4h in flowing oxygen. Oriented ceramics were elaborated by a hot-forging technique described elsewhere [3].

Single crystals were grown using a flux technique : a mixture of  $\text{Bi}_7\text{Ti}_4\text{NbO}_{21}$  powder with excess  $\text{Bi}_2\text{O}_3$  (1:4 mole ratio) was heated in closed platinum crucibles at  $5^\circ\text{Cmin}^{-1}$  up to  $1200^\circ\text{C}$ , kept at this temperature for 5h and cooled down to  $700^\circ\text{C}$  at  $5^\circ\text{Ch}^{-1}$ . After some dwell at  $700^\circ\text{C}$ , the crucibles were allowed to cooled down to room temperature. Translucent greyish plate-like single crystals 20 to 100 mm thick and up to  $4\text{ mm}^2$  area were extracted from the solidified batch by lapping with HCl 1M.

X-ray diffraction patterns and their evolution with temperature were performed using a Siemens D5000 powder diffractometer fitted with a Anton Parr high temperature attachment. DSC experiments were carried out on a Netzsch STA 409 device. Piezoelectric coupling factors were determined from resonance-antiresonance measurements with a HP 4194A impedance analyser.

## RESULTS AND DISCUSSION

### Ceramic materials

In order to get more information on the dielectric behaviour of this phase, X-ray powder diffraction patterns were performed between room temperature and  $1000^\circ\text{C}$ . The thermal variations of the lattice parameters with temperature are given in Fig. 1. Assuming an orthorhombic symmetry at

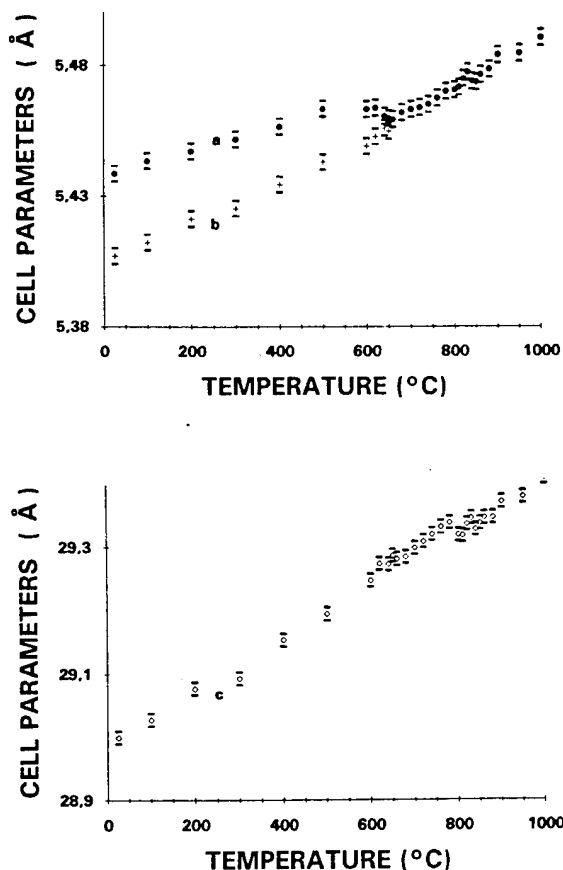


Fig. 1. Lattice parameters vs temperature

room temperature, the observed evolution of both *a* and *b* lattice parameters would correspond to a change towards a tetragonal symmetry at about 670°C. This result was confirmed by comparison of the calculated volume variation and the thermal expansion - determined by dilatometry - which showed the same changes at the same temperatures (Fig. 2 and 3).

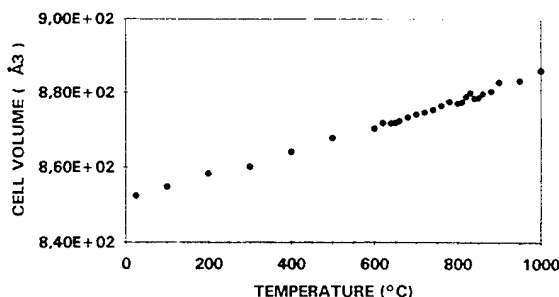


Fig. 2. Cell volume vs temperature

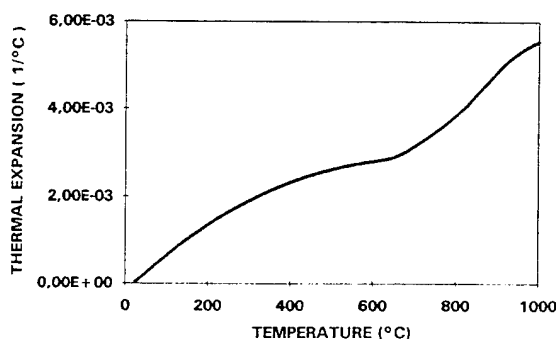


Fig. 3. Thermal expansion vs temperature

As mostly Aurivillius phases,  $\text{Bi}_7\text{Ti}_4\text{NbO}_{21}$  is ferroelectric at room temperature. Actually, it can be poled in the same way as  $\text{Bi}_4\text{Ti}_3\text{O}_{12}$ , thus giving a piezoelectric effect.

Should this phase transition at 630°C correspond to a ferroelectric to paraelectric transition? A first answer to this question should be given by studying the electromechanical coupling factor of a poled ceramic as a function of temperature. Fig. 4 shows a typical resonance signal obtained for the planar vibration mode. Within the accuracy of the experiment, the resonance-antiresonance signal, which is almost constant as the temperature rises, can no longer be measured above 500°C (Fig. 5).

This set of results is consistent with a structural change at about 630°C. So, the first characteristic temperature would be attributed to a ferroelectric-paraelectric transition. This assumption was supported by the observation of an endothermal anomaly ( $\Delta H = -5.4 \text{ Jg}^{-1}$ ) at 636 °C in the DSC scans performed on sintered samples (Fig. 6a). This value is similar to that found for  $\text{Bi}_4\text{Ti}_3\text{O}_{12}$ , but the transition occurs within a much larger temperature range (Fig. 6b) which could explain the temperature scattering observed according to the different techniques used in this study.

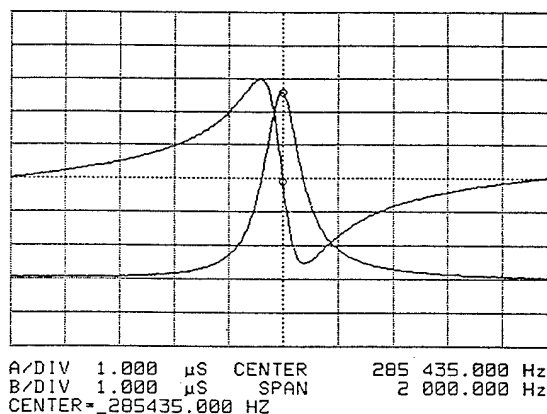


Fig. 4. Resonance signal in the planar mode

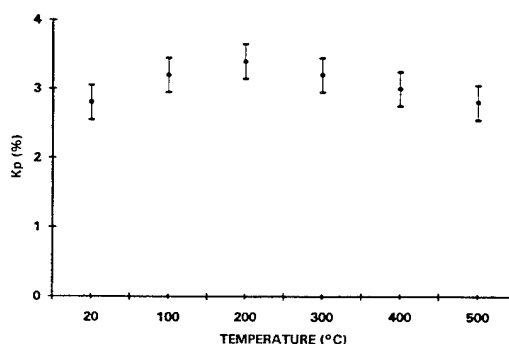


Fig. 5. Electromechanical coupling factor vs temperature

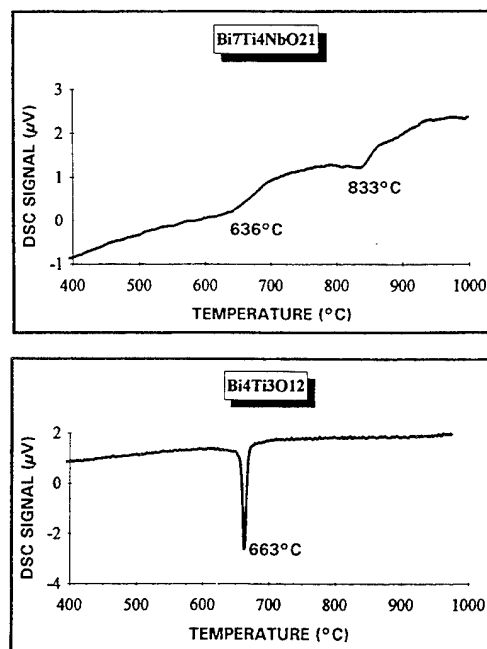


Fig. 6. Differential scanning calorimetry of  $\text{Bi}_7\text{Ti}_4\text{NbO}_{21}$  and  $\text{Bi}_4\text{Ti}_3\text{O}_{12}$

### Single crystals

After separation from the solidified flux, the single crystals were individually checked by X-ray diffraction. A typical diffraction pattern obtained from the major crystal face, is shown in Fig. 7 : as only reflections from (00l) planes were observed, the crystal face was defined as normal to the c axis.

The c parameter computed from the above reflections is 2,900 nm, in close agreement with the powder results. These observations are coherent with similar studies carried out on  $\text{Bi}_4\text{Ti}_3\text{O}_{12}$ [4].

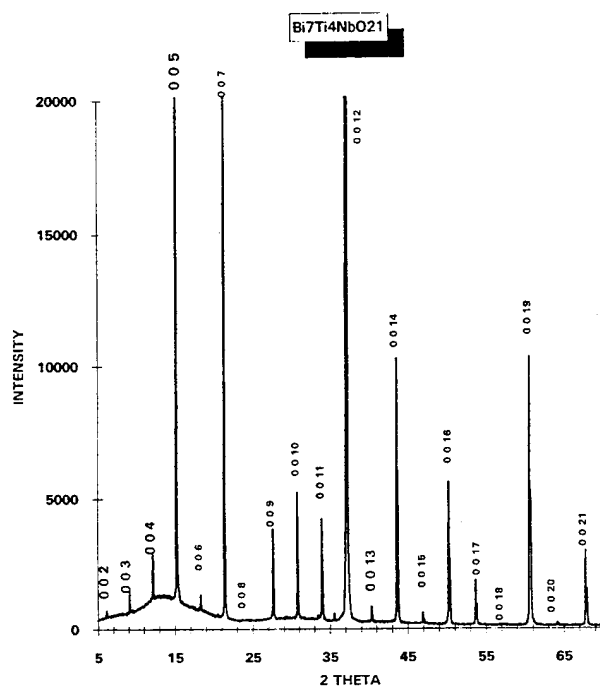


Fig.7. Single crystal diffraction pattern (major face)

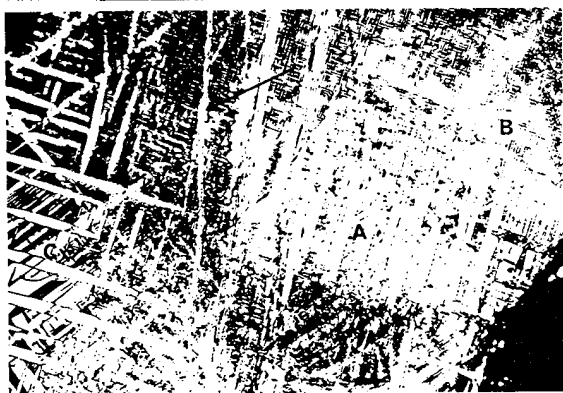


Fig.8. Single crystal observed in polarized light

When observed through a polarized light microscope, the crystal surface reveals a texture made of mainly 180 and 90° domains with 1-3 mm width (Fig. 8). Such a texture has already been observed in ferroelectric  $\text{Bi}_4\text{Ti}_3\text{O}_{12}$  and  $\text{NaBi}_4\text{Ti}_3\text{FeO}_{15}$  single crystals [5].

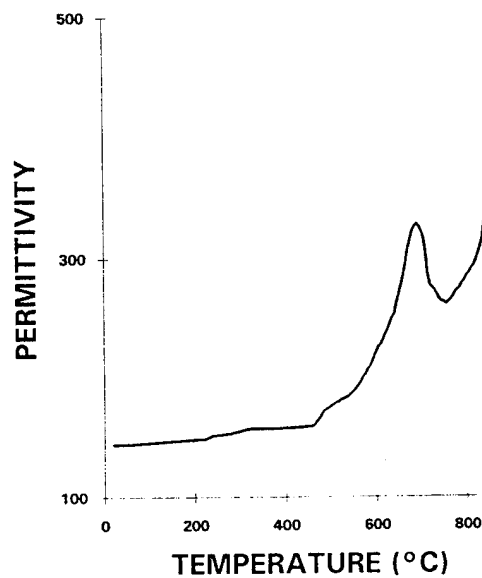


Fig.9a. Dielectric permittivity  $\epsilon_{ab}$  (see text)

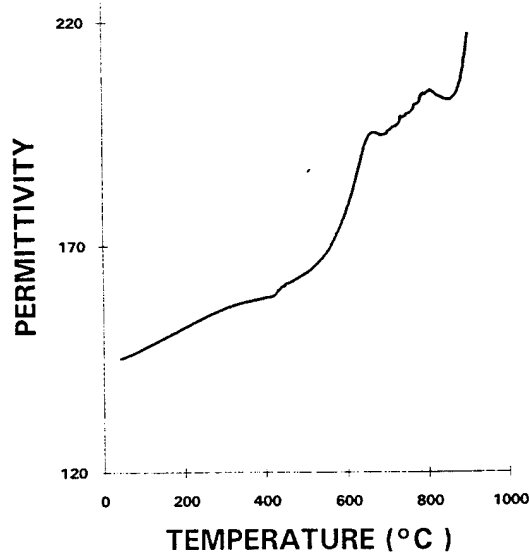


Fig.9b. Dielectric permittivity  $\epsilon_c$  (see text)

For dielectric measurements, gold electrodes were painted on major faces or on the edges of single crystals in order to separate the different contributions to the permittivity (respectively  $\epsilon_c$  and  $\epsilon_{ab}$ ). The dielectric constant in the c-direction is about 145 at room temperature (the value obtained for  $\epsilon_{ab}$  is not accurate because of the difficulty of measuring the actual dimensions of the electrode areas). The temperature dependence of the dielectric constants are given in Fig. 9. As expected from measurements on sintered ceramics,  $\epsilon_{ab}$  presents two anomalies at about 680 and 850°C, the first one surely connected with the ferroelectric-paraelectric transition. A reasonable assumption would be that the highest one correspond to a ferroelastic-paraelastic phase transition [6]. The  $\epsilon_c$  behaviour is striking. The presence of shoulders at temperature close to the characteristic temperatures found for  $\epsilon_c$  would mean that, at least for the first one, there would be a component of the polarization along the c-axis (as in  $\text{Bi}_4\text{Ti}_3\text{O}_{12}$ ). Further experiments are currently in progress in order to support such a hypothesis.

#### CONCLUSION

This study has shown that the mixed Aurivillius phase  $\text{Bi}_7\text{Ti}_4\text{NbO}_{21}$  seems to present independant ferroelectric and ferroelastic behaviours. The strong anisotropy of the dielectric constants has been establish on single crystals. A more thorough study by high temperature optical microscopy and transmission electron microscopy is now in progress.

#### REFERENCES

- [1] T. Kikuchi, *J. Less-Common Metals*, **52**, 163 (1977)
- [2] T. Kikuchi, A. Watanabe and K. Uchida, *Mat. Res. Bull.*, **12**, 229 (1977)
- [3] R. Maalal, M. Manier, J.P. Mercurio and B. Frit, *Proc. 3rd Int. Conf. Electroceramics, Maubeuge (F)*, 62 (1992)
- [4] Y. Masuda, H. Masumoto, A. Baba, T. Goto and T. Hirai, *Jpn. J. Appl. Phys.*, **31**(1), 3108 (1992)
- [5] F. Kubel and H. Schmid, *Ferroelectrics*, **129**, 101 (1992).
- [6] R. Von der Mühl, Private communication.

# Enhanced Densification of SrTiO<sub>3</sub> Perovskite Ceramics

Kuo-Shung Liu, and I-Nan Lin<sup>+</sup>

Department of Materials Science and Engineering

<sup>+</sup>Materials Science Center

National Tsing-Hua University, Hsinchu 30043, Taiwan, R.O.C.

## Abstract

The densification of SrTiO<sub>3</sub> materials has been enhanced by using the novel sintering techniques. The hiping and microwave sintering, on the other hand, can enhance the diffusion of the ions markedly such that the undesired feature of the mixed oxide powders is easily overcome and the materials are well sintered. The densification of the materials has already started when microwave sintered at 1220°C, but the growth of the grains can occur only when microwave sintered at 1250°C. The migration of grain boundaries can be effectively triggered by applying a short temperature pulse at the onset of densification process.

## I. Introduction

SrTiO<sub>3</sub> (STO) materials are one of the family of the ferroelectric perovskites, which possess paraelectric characteristics with dielectric constant around  $\epsilon_r = 285 \sim 320$  at room temperature, since the tetragonal to cubic phase transformation of these materials occurs at  $T_c = -168^\circ\text{C}$  (1,2). They are widely used as materials for high voltage capacitors (3), grain boundary barrier capacitors (GBBL) (4,5), low voltage non-ohmic thermistors (varistor) (6,7) and voltage controlled microwave dielectrics (8,9).

Preparation of STO ceramics via conventional mixed oxide (MO) route is difficult due to high sintering temperature ( $>1400^\circ\text{C}$ ) needed to densify the materials. The low sinterability of the powders can be ascribed to (i) the large and non-uniform particle size resulted from mechanical pulverization process and (ii) low activity caused by the high calcination temperature adopted to convert the raw materials into perovskite phase. Synthesis of STO powders via chemical routes, such as sol-gel (10,11), hydrothermal (12), coprecipitation (13) and spray pyrolysis (14), have been widely utilized for improving the activity and purity of the STO powders. The sinterability of the powders has been improved significantly, but the control of microstructure is not completely successful. The purpose of this research is to investigate the possibility of enhancing the densification rate of the STO materials using non-conventional densification technique, such as microwave sintering (MS), so as to circumvent the difficulty encountered in chemical route of preparing STO powders.

## II. Experiments

In the mixed oxide (MO) process, the reagent grade SrCO<sub>3</sub> and TiO<sub>2</sub> powders<sup>+</sup>, of 1:1 molar ratio, were mixed

with deionized water and using zirconia grinding media in a plastic jar. The mixture, after drying, was calcined in air at 1100°C for 4 hrs, followed by pulverization using ball milling process.

Two non-conventional densification processes were used to investigate the sintering behavior of the samples made of MO powders. They were hot isostatic processing (HIP) and microwave sintering (MS) processes. In hiping process, the pellets were hermetically sealed in a stainless steel capsule, slowly heated to 1200°C, pressurized to 1800 Kg/cm<sup>2</sup> and soaking at the hiping conditions for 1 hr. In the microwave sintering process, a 2.45 GHz microwave from a commercial generator (Gerling GL107 magnetron) was introduced into an applicator. The temperature was measured using a thermocouple placed near the surface of the samples. The sintering temperature was increased fastly to around 1200°C, 1220°C or 1250°C as soon as the microwave power was fed into the applicator. The samples were soaked at that temperature for 10~30 minutes and then rapidly cooled by shutting off the microwave power. The crystal structure and microstructure of the powders and ceramic samples were examined using Rigaku D/max-IIIB X-ray diffractometer (XRD) and Joel 840A scanning electron microscope (SEM), respectively.

<sup>+</sup> SrCO<sub>3</sub>, Merck Co., 99.5%; TiO<sub>2</sub>, Merck Co., 99%

\* Ti(OEt)<sub>4</sub>, Merck Co., 95%; Sr(CH<sub>3</sub>COO)<sub>2</sub>•1/2H<sub>2</sub>O, Strem Chemicals, 98%

## III. Results and Discussions

The microstructures of these samples sintered by conventional process are shown in Fig. 1. The sintering of MO powders is very difficult. Figure 1a reveals that large proportion of voids still remained even when the samples were sintered at 1400°C (2 hrs). The grain size distribution is very non-uniform. Grains of submicron size are observed distributing among the abnormally big grains all over the samples.

It has been demonstrated that using the high activity powders prepared via chemical routes can effectively circumvent the undesired feature of the mixed oxide (MO) powders, such as low activity and non-uniformity in particle size distribution. However, the chemical processes are cumbersome and the control of cationic segregation is very difficult. The other alternatives to promote the densification process of the materials is to enhance the diffusion of species so as to overcome the above mentioned shortcomings of the MO powders. A non-conventional sintering process, viz. the microwave sintering (MS)



technique, is, thereafter, employed for this purpose.

Before discussing the effect of parameters in microwave sintering process on the microstructural evolution of the STO materials, the characteristics of the materials densified by the hot isostatic pressing (HIP) technique is firstly examined. This process is chosen to facilitate the comparison of the densification techniques, since the hipping process is the most effective process available for densifying the ceramic materials. Figure 7a shows that the materials have developed dense and uniform microstructure, with the grains of 5  $\mu\text{m}$  in size, when hipped directly from the green compact of powders at only 1200°C for 1 hr, under 1800 Kg/cm<sup>2</sup>. The beneficial effect of high pressure on promoting diffusion process is clearly demonstrated.

Figures 2b~2d, on the other hand, indicate that the microwave sintering process can densify the MO materials as effective as the hipping process. The necking between the adjacent grains is clearly observed in Fig.2b, suggesting that the sintering process has already started at 1200°C. But large number of voids shown in the figure indicates that higher sintering temperature is apparently needed to densify the materials. Figure 2c shows that the materials are effectively sintered at 1220°C for 10 minutes ( $\approx 94.3\%$  true density). This sintering temperature is more than 200°C lower than that needed to densify STO materials by conventional process. The grain size is around 1~2  $\mu\text{m}$ .

Increasing the microwave sintering temperature to 1250°C (Fig.2d) results in the samples of nearly the same density ( $\approx 94\%$  true density) but with the grains grown to larger than 10  $\mu\text{m}$ . Figures 3a~3c indicate that the grains grow only moderately, from 1  $\mu\text{m}$  to 4  $\mu\text{m}$  and the density increases from 94.3 % to 95 % true density, when the soaking period at 1220°C extends from 10 minutes to 30 minutes. These figures reveal that although the densification process already starts at 1200°C, the growth of grains occurs only at higher temperature. The activation energy for grain boundary migration is, therefore, concluded to be higher than that for the diffusion of cations and anions required for densification. To further examine such phenomena, the microstructural evolution of the samples densified by the microwave sintering process with slightly different temperature profile was studied.

As shown in Fig.4, the temperature profile A is to slowly increase the temperature to 1220°C, maintaining at that temperature for 10 minutes and then fastly cooled ( $> 170^\circ\text{C}/\text{min}$ ). The temperature profile B, on the other hand, is very similar to the temperature profile A except that a short pulse of microwave power was fed into the sample as the temperature reach 1220°C such that the temperature ramps up from 1220°C to around 1260°C for very short period ( $\sim 2$  min.). The corresponding micrographs are shown in Figs.4a and 4b, respectively, which demonstrate that the granular structure of the samples microwave sintered via the two temperature profiles are tremendously different from each other. Huge grains of the size around tens of microns are obtained for samples sintered via profile B, compared to the 1  $\mu\text{m}$  grain size for samples sintered via

profile A. The short temperature pulse has effectively trigger the growth of the grains.

The mechanism which markedly enhance the densification of the materials in the microwave sintering process is, however, not really understood. It has been explained either by the lowering of activation energy (Q) for diffusion <sup>(15)</sup> or the promotion of the pre-exponential factor ( $D_0$ ) of interdiffusivity <sup>(16)</sup> through the altering of correlation factor in the relationship

$$D = D_0 \exp(-Q/kT)$$

The electric field effect on crystal lattice has also been proposed to enhance the flux of ionic diffusivity <sup>(17)</sup>, that is,

$$\bar{J} = -Bn\left(\frac{\partial G}{\partial x} + NZeE\right)$$

where B is the mobility, n is ion concentration, G and N are free energy and Avogadro constant, Ze is effective charge and E is the applied electric field. The Lorentz force exerted onto the species (of charge q) by the electric (E) and magnetic (B) field of the microwave.

$$\bar{F} = q\left(\bar{E} + \frac{1}{c}\bar{V} \times \bar{B}\right)e^{j\omega t}$$

is yet another factor need to be considered, since it will force the charged species to vibrate with the same frequency as microwave ( $\omega$ ). Such kind of forced vibration may increase the jump frequency and provide the charged species an additional energy to overcome the diffusion barrier. In other words, both the pre-exponential factor and the effective activation energy will be altered due to the interaction of charged species with the field in microwave. Besides the above mentioned mechanisms, the special feature of the microwave sintering process, which is the uniform and rapid heating, may also result in the enhancement of densification. Since the heating of materials in this process is caused by the absorption of the microwave energy (through dissipation factor), the materials in the core region of the samples can be heated up as efficient as the materials surrounding the core region. There is no need for heat to transport. The temperature of the samples is, thereby, increasing homogeneously and rapidly such that the densification process (e.g. necking) proceeds simultaneously all over the samples. The sintering rate is thus increased. Moreover, rapid heating, which can be as fast as  $\sim 150^\circ\text{C}/\text{min}$ , has also been observed to markedly enhance the sintering of materials. All these characteristics can account for the increase of the densification kinetics in the microwave sintering process.

#### IV. Conclusions

(1) In the mixed oxide process, high density and uniform grain size distribution materials have been obtained when hipped or microwave sintered at 200°C lower than that needed to densify the samples via conventional sintering process.

(2) The densification of the samples has already started when microwave sintered at 1220°C, but the growth of the grains can occur only when microwave sintered at 1250°C.

(3) The migration of grain boundaries can also be effectively triggered by applying a short temperature pulse at the onset of densification process.

## References

- [1]. Atsushi Okazaki, Yuji Soejima, Nobuhiko Ohama and K. Alex Muller, "High-Resolution X-ray Diffraction Study Structural Phase Transition in  $\text{SrTiO}_3$ ", *Jpn. J. Appl. Phys., Suppl.* 24-2, p.257 ~ 59(1985).
- [2]. Manfred Kahn, Darnall P. Burks, Ian Burn and Walter A. Schulze, "Ceramic Capacitor Technology", p.191~274 in *Electronic Ceramics - Properties, Devices and Applications*, Ed. by Lionel M. Levinson, Marcell Dekker, Inc., New York, 1988.
- [3]. Hiroataka Yamamoto and Shinobu Fujiwara, "Material Development on High Reliability  $\text{SrTiO}_3$  Series Ceramics Having Dielectric Constant, Low Dissipation Factor and Voltage Independing Characteristics", *Ceramics*, V.20[6], p.488~95(1985).
- [4]. Masayuki Fujimoto and W. David Kingery, "Microstructures of  $\text{SrTiO}_3$  Internal Boundary Layer Capacitors During and After Processing and Resultant Electrical Properties", *J. Am. Ceram. Soc.*, V.68[4], p.169~73(1985).
- [5]. Wernicke, R., "Grain Boundary Phenomenon in Electronic Ceramics", Ed. by L. M. Levinson, *Adv. in Ceram.*, V.1, p.261, Am. Ceram. Soc., Columbus, Ohio, (1981).
- [6]. A.M.S. Correia and J. L. Baptista, "Electrical Properties of Bismuth-doped Non-stoichiometric Strontium Titanate Ceramics", *Mater. Sci. Eng.*, V.A109, p.183~87(1989).
- [7]. Daisuke Kaino, Junichi Funayama and Nobutatu Yamaoka, "Electrical Properties of A  $(\text{Sr,Ca})\text{TiO}_3$  base Ceramic Varistor", *Jpn. J. Appl. Phys., Suppl.* 24-3, p.120~22(1985).
- [8]. H.K. Varma, P. Krishma Pillai, M.M. Sreekumax, K.G.K. Warriar and A.D. Damodaran, "Strontium Titanate Prepared by Spray Drying of Redispersed Metal Alkoxide Gel", *Br. Ceram. Trans. J.*, V.90, p.189~91(1991).
- [9]. Masahira Yahagi, Tadashi Hashimoto, "Microwave Dielectric Resonators and Applications", *Electron. Ceram.*, V.19, p.39~43(1988).
- [10]. J.S. Smith II, R.T. Dolloff and K.S. Mazdiasni, "Preparation and Characterization of Alkoxy-Derived  $\text{SrZrO}_3$  and  $\text{SrTiO}_3$ ", *J. Am. Ceram. Soc.*, V.53[2], p.91~95(1970).
- [11]. Toshihiro Kasai, Yoshiharu Ozaki and Syouzou Yamamoto, "Preparation of  $\text{BaTiO}_3$  and  $\text{SrTiO}_3$  from Metal Alkoxides", *Yogyo-Kyokai-Shi*, V.95[10], p.68~74(1987).
- [12]. M.I. Diaz-Guemes, T. Gonzalez Carreno, C.J. Serna and J.M. Palacios, "Mechanism of Formation of  $\text{MTiO}_3$  (M=Sr or Ba) by the Gel Method", *J. Mater. Sci.*, V.24, p.1011~1014(1989).
- [13]. H.S. Potdar, S.B. Deshpande, P.D. Godbole, V.G. Gunjikar and S.K. Date, "Low Temperature Synthesis of Ultrafine Strontium Titanate ( $\text{SrTiO}_3$ ) Powders", *J. Mater. Res.*, V.7[2], p.429~34(1992).
- [14]. Osamu Sakurai, Nobuyasu Mizutani and Masanori Kato, "Microstructure of  $\text{SrTiO}_3$  Spherical Fine Particles Prepared by Ultrasonic Spray Pyrolysis of Metal Alkoxide", *Yogyo-Kyokai-Shi*, V.94[8], p.117~21(1986).
- [15]. Mark A. Janney and Hal D. Kimrey, *Mater. Res. Soc. Symp. Proc.*, 189, p.215(1991).
- [16]. J.D. Katz and R.D. Blake, V.M. Kenkre, *Ceram. Trans.*, 21, p.95(1991).
- [17]. Robert E. Reed-Hill, *Physical Metallurgy Principles*, 2nd ed., Chap.10, p.378(1973).

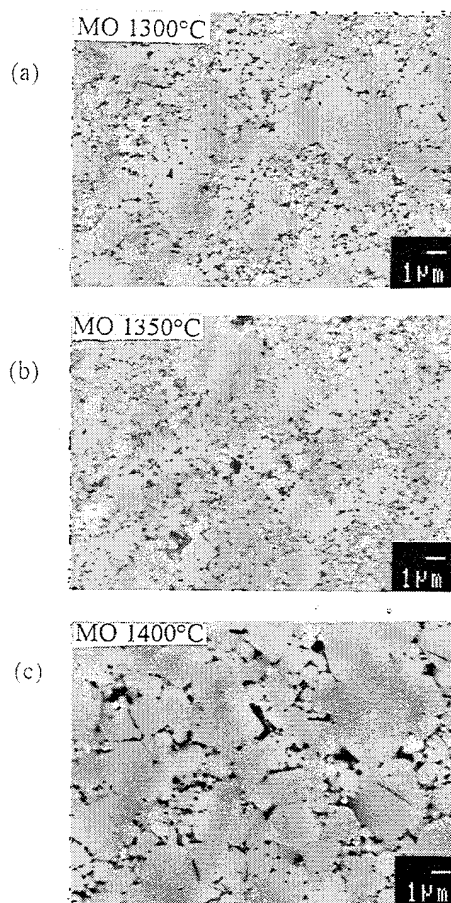


Fig.1. The microstructure of  $\text{SrTiO}_3$  samples made of the powders prepared by mixed oxide (MO) method and sintered at (a)1300°C, (b)1350°C and (c)1400°C for 2 hrs, respectively.

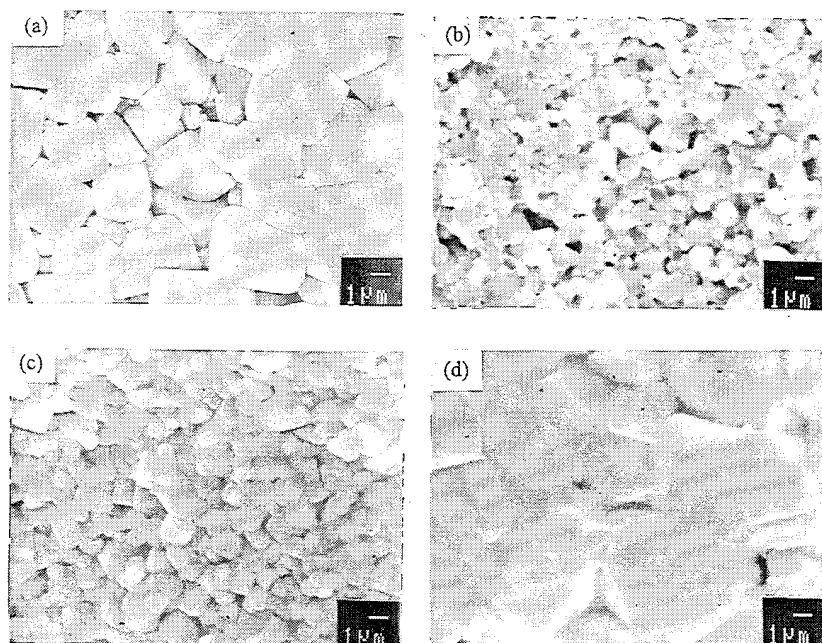


Fig.2. The microstructure of  $\text{SrTiO}_3$  samples densified by (a) hipping at  $1200^\circ\text{C}$  for 1 hr ( $1800 \text{ Kg/cm}^2$ ) and microwave sintering at (b)  $1200^\circ\text{C}$  (10 min.), (c)  $1220^\circ\text{C}$  (10 min.), and (d)  $1250^\circ\text{C}$  (10 min.).

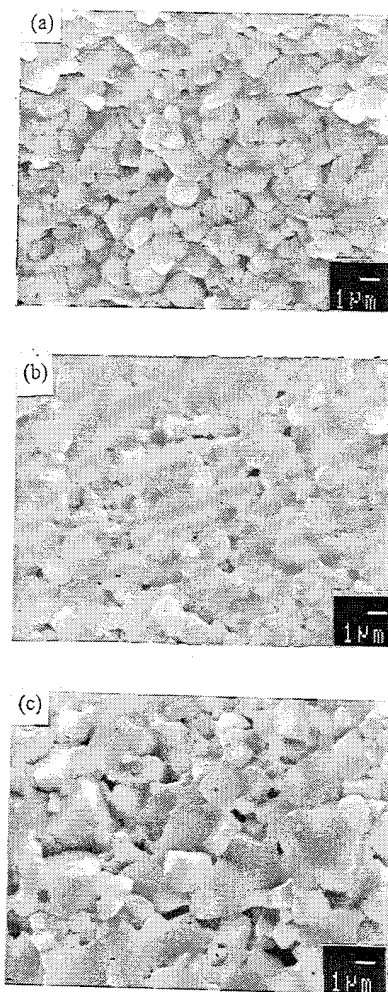


Fig.3. The microstructure of  $\text{SrTiO}_3$  samples microwave sintered at  $1220^\circ\text{C}$  for (a) 10 min. (b) 20 min. and (c) 30 min..

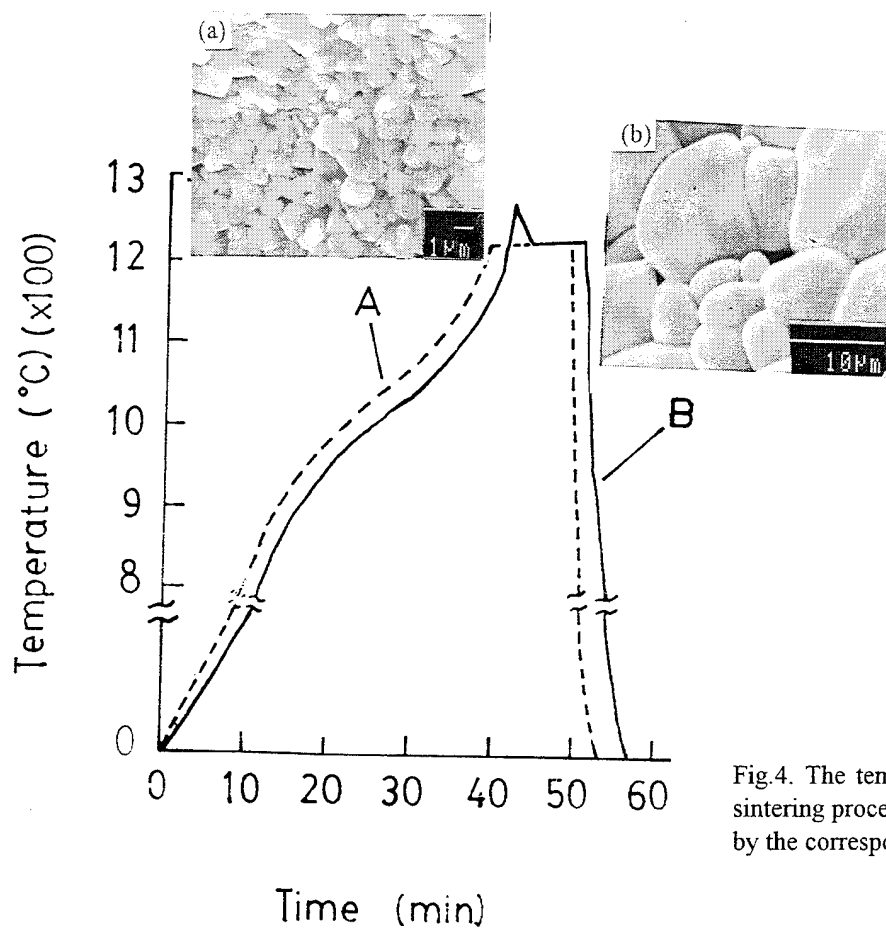


Fig.4. The temperature profile (A & B) in the microwave sintering process and microstructure of the samples sintered by the corresponding profiles.

# Phase Transition of Ferroelectric ( $\text{Na}_{1/2}\text{Bi}_{1/2}$ ) $\text{TiO}_3$

Seung-Eek Park and Su-Jin Chung

Dept. of Inorganic Materials Engineering, College of Engineering,  
Seoul National University, Kwanak-gu, Seoul, Korea

**Abstract** - Crystals of ( $\text{Na}_{1/2}\text{Bi}_{1/2}$ ) $\text{TiO}_3$  were grown by flux technique as well as Czochralski method. It has been found that non-stoichiometry which was induced during the crystal growing by the Czochralski method owing to the volatilization of Bi-rich phase resulted in a less lattice distortion from cubic symmetry. A long-range cationic ordering was also found in both crystals but the degree of ordering was very low. It could be confirmed that the tetragonal phase should be nonpolar. On the base of these results, the phase transition behaviors of two NBT crystals have been investigated with the observation of twin configuration.

## INTRODUCTION

After Smolenskii et al. [1] found ferroelectric ( $\text{Na}_{1/2}\text{Bi}_{1/2}$ ) $\text{TiO}_3$  (abbreviated to NBT) many investigations on the phase transitions of NBT have been followed. It has been generally accepted that NBT has two phase transitions with decreasing temperature, i.e., one from cubic to tetragonal at about 540°C and another from tetragonal to rhombohedral at 270°C [2,3]. But there has been almost no effort to investigate the phase transition of NBT from the crystallographic point of view. Because NBT is of simple structure of perovskite it would be possible to suggest the space group of each phases if the ordering configuration of A-site cations and the dielectric properties were confirmed. However, only short-range ordering has been observed by neutron diffraction [4] or Raman study [5] and the dielectric property of intermediate tetragonal phase is not clear yet.

Besides, although the control of stoichiometry of NBT is much easier than that of lead containing piezoelectric materials, it is expected that the volatilization of Na and Bi during heat treatments will bring unwanted effects on the properties and the phase transition behaviors. In this study crystals of NBT have been prepared by the flux technique and the Czochralski method. The purposes of the crystal growing are not only to investigate the long-range cation ordering of NBT but also to find out the effects of volatilization of Na and Bi on the stoichiometry for a guideline of future works. Phase transition behaviors for the two crystals have been investigated and the transition sequence of NBT has been discussed based on the super-subgroup relationship.

## EXPERIMENTAL PROCEDURE

Crystals grown by flux technique (abbreviated to fx crystal) were obtained by slow cooling technique with 20 wt.% excess of  $\text{Bi}_2\text{O}_3$  and of  $\text{Na}_2\text{CO}_3$  as self flux. Yellowish brown NBT crystals (abbreviated to Cz crystal) of 1.5 cm diameter weighing 70g were also grown by the Czochralski method from the melt whose starting composition was stoichiometric. The crystal was pulled and rotated at the rate of 6 mm/h and 20 rpm, respectively.

XRD patterns, single crystal rotating and Weissenberg photographs, and powder diffraction using high temperature Guinier-Lenne camera were employed to observe the structure and its change for the two crystals. The differential scanning calorimetry (DSC) analysis was also carried out on heating. Twin configurations were observed under cross-nicol condition at the temperature range of 25°C to 400°C.

Dielectric constant variations on temperature of 25°C to 500°C and on measuring frequencies of 1 kHz to 100 kHz for both crystals were measured on heating and cooling using HP4194A. Pt paste for ion blocking as well as Ag pastes were used as electrode.

## RESULTS and DISCUSSION

### *Crystal Growing and Nonstoichiometry*

We found that the melting temperature of NBT would be about 1290°C from the DTA/TG curve but the volatilization was increased sharply at the melting point. As crystal growing generally needs a very slow cooling rate (1 ~ 5°C/hr) at high temperature flux growing was employed using 20 wt.% of excess  $\text{Na}_2\text{O}$  and  $\text{Bi}_2\text{O}_3$  as a self-flux for compensating the composition change. The crystals with dark brown color and cuboidal shape were obtained by flux growing. In crystal growing by Czochralski method, however, it could be easily expected that the growing should not be straight forward because of the volatile constituents. Owing to the lack of preceding works about crystal growing of NBT, the melt of the stoichiometric composition was prepared. It took 16 hr to grow Cz crystal and the volatilization of Bi-rich phase resulted in the deposition of yellowish powders inside the furnace. The XRD patterns of fx crystal and Cz crystal of NBT is shown in Fig. 1. The pattern of fx crystal in Fig. 1 clearly shows rhombohedral splits. This confirms the previous report [6] on NBT, i.e., NBT have a rhombohedral symmetry at room temperature with  $a = 3.886\text{\AA}$  and  $\alpha = 89.6^\circ$ . However, the pattern of Cz crystal in Fig. 1 does not show any split. The difference in the XRD patterns of two crystals can be ascribed to the volatilization of Bi-rich phase during the growing of Cz crystal. In order to investigate the composition of Cz crystal more precisely, quantitative EPMA analysis was employed using the fx crystal as the standard. As shown in table 1, it is obvious that Cz crystal is Bi-deficient. Therefore it can be concluded that the non-stoichiometry has been induced in Cz crystal due to the volatilization thus resulted in the difference in the XRD patterns.

The ferroelectricity of two crystals has been checked by the Sawyer-Tower circuit. Both crystals show a similar hysteresis loop in the  $p = f(E)$  curve with a saturation at about 70 kV/cm. From the precise X-ray diffraction patterns with an enhanced resolution, it could be found that Cz crystal is

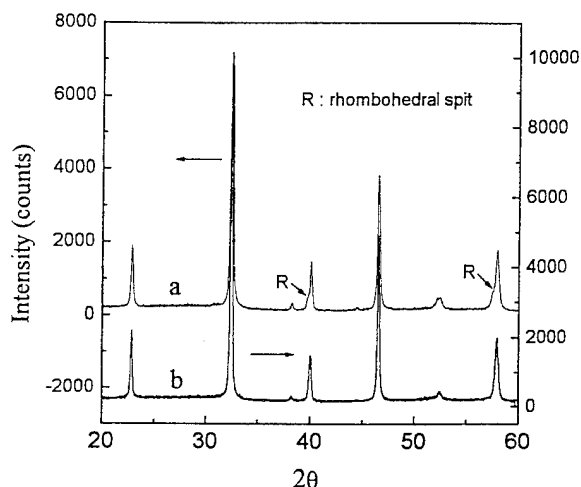


Fig. 1 X-ray diffraction patterns of  $(\text{Na}_{1/2}\text{Bi}_{1/2})\text{TiO}_3$  crystals grown by (a) flux technique and (b) Czochralski method.

pseudo-cubic with slight lattice distortion from ideal cubic. Thus it can be concluded that non-stoichiometry in Cz crystal decreases the lattice distortion.

#### Long-range Ordering of A-site Cations

The NBT crystals in this study have a long-range ordering but the degree of ordering identified with the intensities of superlattice reflections were very low. Very faint superlattice spots with  $(h+1/2, k+1/2, l+1/2)$  type can be observed in rotating photograph. Therefore, it can be safely assumed that the intermediate tetragonal and high temperature cubic phase of NBT is not a primitive one but body-centered and face-centered, respectively, and that the space group of rhombohedral phase is  $R3c$  [4] rather than  $R3m$  [6].

#### Ferroelectric Phase Transition of NBT Crystal

The point group of ferroelectric crystal is usually a subgroup of that of the high-temperature paraelectric crystal because the former crystal includes all the symmetry operations the latter crystal has [7]. Referring to Aizu [8], this rule can be applied to the ferroelastic phase transition. From the view point of ferroelasticity the sequence of phase transition of NBT is normal because the point group of paraelastic phase, i.e.,  $m3m$ , is the supergroup of all point groups of subsequent tetragonal and rhombohedral ferroelastic phases.

From the view point of ferroelectricity the sequence of phase transition of NBT is abnormal because the tetragonal phase is known to be paraelectric [2,9]. If the tetragonal phase of NBT were polar, the sequence of phase transition might be normal as in the case of ferroelasticity. Zvirgzds et al. [3] suggested on the base of the observation of a second maximum in  $\epsilon_r$  vs. temperature curve near  $450^\circ\text{C}$  that the tetragonal phase of NBT be antiferroelectric at least. Fig. 2 and Fig. 3 show  $\epsilon(T)$  curves of fx and Cz crystals. Here a diffuse second maximum near  $450^\circ\text{C}$  is obvious at low frequency, too. This observation implies that the tetragonal phase may be polar. Therefore the phase transition of both crystals was investigated using a higher temperature Guinier-

Table 1 Composition analyses of Cz crystal by EPMA using the Fx crystal as Standard (at.%)

	Fx Crystals as standard	Cz Crystal
Na	(25)	26.41
Ti	(50)	51.96
Bi	(25)	21.63

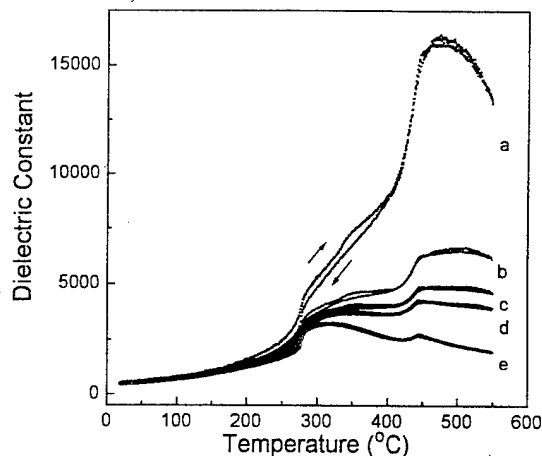


Fig. 2 Temperature dependence of dielectric constant in fx crystal for various measuring frequencies of (a) 1 kHz, (b) 4 kHz, (c) 7 kHz, (d) 10 kHz, (e) 100 kHz (using Ag electrode).

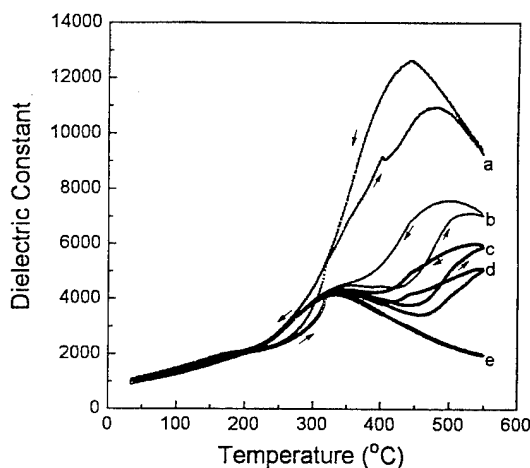


Fig. 3 Temperature dependence of dielectric constant in Cz crystal for various measuring frequencies of (a) 1 kHz, (b) 4 kHz, (c) 7 kHz, (d) 10 kHz, (e) 100 kHz (using Ag electrode).

Lenne camera and DSC. From the abrupt decrease in line width of  $(110)$  reflection and bending of reflections on Guinier film for fx crystal show the rhombohedral  $\leftrightarrow$  tetragonal phase transition at about  $250^\circ\text{C}$ . Owing to the smaller rhombohedral distortion the main reflection of Cz crystal does not show any remarkable change. Unfortunately the tetragonal  $\leftrightarrow$  cubic transition can not be detected in X-ray diffraction film due to the small tetragonality of NBT ( $c/a < 1.003$  [3]).

Fig. 4 shows the result of DSC work. Here both crystals have two endothermic peaks at about same temperature. The first anomaly at  $230^\circ\text{C}$  coincides well with the temperature showing a hump in  $\epsilon(T)$  curve and the rhombohedral  $\leftrightarrow$

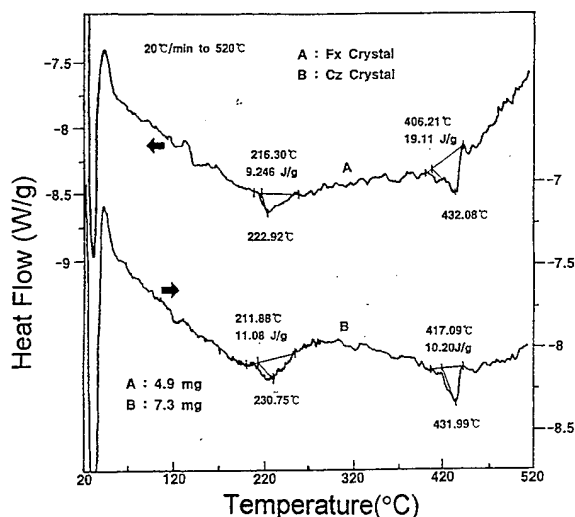


Fig. 4 DSC curves for  $(\text{Na}_{1/2}\text{Bi}_{1/2})\text{TiO}_3$  crystals

tetragonal transition in the X-ray diffraction work. Other investigator [2] reported the anomaly at 300°C on heating. The second anomaly at 430°C, however, has not been reported yet. This temperature seemed to be very close to that of the second maximums in  $\epsilon(T)$  curve shown in Fig. 2 and Fig. 3. However this temperature is quite different from tetragonal  $\leftrightarrow$  cubic transition temperature [3]. Therefore it was necessary to investigate the origin of maximum at about 450°C. In the case of ceramics with high ionic conductivity, the interaction between electrode and ions sometimes results in an unexpected variation in the conductivity. Therefore, instead of Ag-electrode, a platinum electrode has been applied on the two crystals and it can be found that the second maxima at about 450°C would disappear. These mean that the second maxima in  $\epsilon(T)$  curves shown in Fig. 2 and 3 do not originate from the ferroelectric phase transition thus it can be concluded that the tetragonal phase of NBT is non-polar. From this result, it can be suggested that the space group of tetragonal crystal be  $I4/mmm$ .

The super and subgroup relations in ferroelectric phase transition of NBT are very peculiar. As previously mentioned, the paraelectric tetragonal is neither ferroelectric nor supergroup of ferroelectric phase but subgroup of high temperature cubic. Therefore it can be concluded that NBT is the example of exception among the perovskite materials, which does not obey the rule of the normal ferroelectric phase transition sequence.

#### Hysteresis during the ferroelectric phase transition

The differences between phase transition behaviors of the two crystals can be found in Fig. 5(a) that shows the  $\epsilon(T)$  curves at 100 kHz. Cz crystal shows large temperature hysteresis during diffuse phase transition (abbreviated to DPT) as reported (see Fig. 5(b) [2]). But the fx crystal does not show as much hysteresis as Cz crystal does. It is very interesting that  $\epsilon(T)$  curve in Fig. 5(b) was also taken with crystal grown by Czochralski method [2]. Therefore it can be said that the nonstoichiometry and/or structure variation can make an effect on ferroelectric phase transition behavior.

#### Twin configurations of NBT crystals

Fx crystal has a lamellar twinning structure whereas Cz crystal has a herring-bone type banded structure. This herring-bone type twinning could be explained by the larger dimension of Cz crystal since it is frequently observed under a 3-dimensional clamped condition. In addition, the twin configurations of both crystals did not show any changes irrespective of tetragonal to rhombohedral (abbreviated to T  $\leftrightarrow$  R) phase transition except the isotropization. As previously reported [2,9] the isotropization and the freezing of twin configuration is hardly understood. The isotropization has been observed in the temperature range of 240°C to 270°C on heating and 230°C to 200°C on cooling. This isotropization of NBT is very peculiar because it is in the middle of the phase transition from rhombohedral to tetragonal, and vice versa. The isotropization means that there is no contribution of optically anisotropic constituents thus the crystal must be cubic within the resolution limit of an optical microscope. How a crystal can be cubic in the middle of a phase transition from rhombohedral to tetragonal? Therefore the only possible

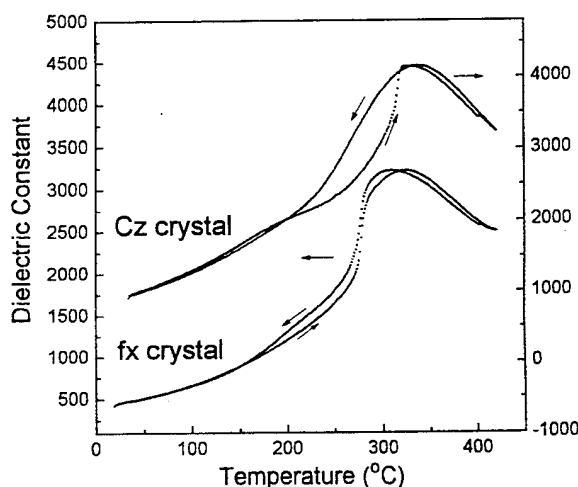


Fig. 5(a) Temperature dependence of dielectric constant of NBT crystals for measuring frequency of 100 kHz.

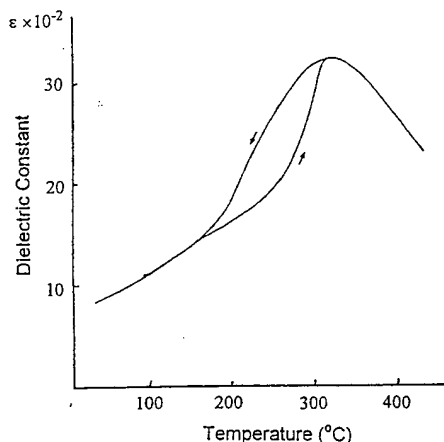


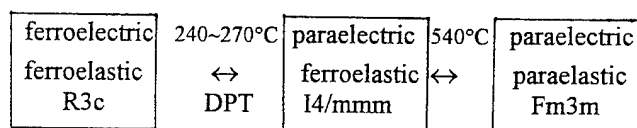
Fig. 5(b) Temperature dependence of dielectric constant in crystal grown by Czochralski method [2].

explanation is that the global symmetry (global means within the resolution limit of optical microscope) of NBT in the isotropization range should be cubic. This deduction implies that the crystal may be a mixture of very small rhombohedral and tetragonal regions (probably less than few hundred nm) in the temperature range of isotropization during DPT.

## CONCLUSION

In the Cz crystal, the volatilization resulted in a non-stoichiometry and the symmetry of Cz crystal was found to be pseudo-cubic with a very small distortion from the ideal cubic whereas fx crystal had a rhombohedral symmetry. A long-range ordering of Na and Bi cations has been observed on crystal rotating photograph. However the degree of ordering was very low.

Though the  $\epsilon(T)$  curve can show another maximum, the tetragonal phase is nonpolar because  $\epsilon(T)$  maximum at high temperature should be originated from the combination effect of space charge polarization and electrode reaction. Therefore the ferroelectric phase transition sequence of NBT is an example of abnormal transition which does not obey crystallographic super-subgroup relationship as follows.



Cz crystal also showed more temperature hysteresis in  $\epsilon(T)$  curve during DPT. The symmetry of NBT in the temperature range of isotropization should be cubic within the resolution limit of optical microscope.

## REFERENCES

- [1] G. A. Smolenskii, V. A. Isupov, A. I. Agranovskaya, and N. N. Kainik, "New Ferroelectrics of Complex Composition. IV," *Soviet Physics - Solid State*, vol. 2, no. 11, pp2651-2654, 1961.
- [2] I. P. Pronin, P. P. Symikov, V. A. Isupov, V. M. Egorov, and N. V. Zaitseva, "Peculiarities of Phase Transitions in sodium-Bismuth Titanate," *Ferroelectrics*, vol. 25, pp395-397, 1980.
- [3] J. A. Zvirgzds, P. P. Kapostins, and J. V. Zvirgzde, "X-ray Study of Phase Transitions in Ferroelectric  $\text{Na}_{0.5}\text{Bi}_{0.5}\text{TiO}_3$ ," *Ferroelectrics*, vol. 40, pp75-77, 1982.
- [4] S. B. Vakhrushev, B. G. Ivanitskii, B. E. Kvyatkovskii, and A. N. Maistrenko, "Neutron Scattering Studies of the Structure of Sodium Bismuth Titanate," *Soviet Physics - Solid State*, vol. 25, no. 9, pp1504-1506, 1983.
- [5] I. G. Siny, T. A. Smirnova, and T. V. Kruzina, "The Phase Transition Dynamics in  $\text{Na}_{1/2}\text{Bi}_{1/2}\text{TiO}_3$ ," *Ferroelectrics*, vol. 124, pp207-212, 1991.
- [6] Chang-lin G., *Acta Physics Sinica*, Wu Li Husuen Pao, vol. 31, p1119, 1982.
- [7] K. Aizu, "Possible Species of Ferroelectrics," *Physical Review*, vol. 146, no. 2, pp423-429, 1966.
- [8] K. Aizu, "Possible Species of "Ferroelectric" Crystals and of Simultaneously Ferroelectric and Ferroelastic

Crystals," *Journal of the Physical society of Japan*, vol. 27, no. 2, pp387-396, 1969.

[9] S. B. Vakhrushev, V. A. Isupov, B. E. Kvyatkovsky, N. M. Okuneva, and I. P. Pronin, "Phase Transitions and Soft Modes in Sodium Bismuth titanate," *Ferroelectrics*, vol. 63, pp153-60, 1985.

# Microstructural Studies of Modified SBN Ceramics

S. Narayana Murty, S. Bangar Raju, A. Bhanumathi

Solid State Physics Labs., Dept. of Physics, Andhra University, Visakhapatnam 530 003 INDIA

G. Padmavathi

Dept. of Engineering Physics, AU College of Engineering, Andhra University, Visakhapatnam 530 003 INDIA

K. Linga Murty

Depts. of Nuclear Engineering and Materials Science Engineering, North Carolina State University, Raleigh NC 27695 U.S.A

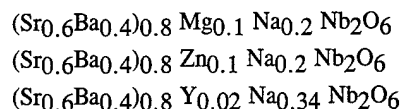
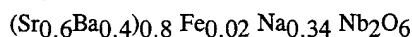
**Abstract** Strontium Barium Niobate ( SBN ) is a ferroelectric solid solution with tetragonal tungsten bronze structure. SBN exhibits excellent pyroelectric and electro-optic properties. Solid solutions of  $(\text{Sr}_x \text{Ba}_{1-x})_{0.8} \text{Na}_{0.4} \text{R}_y \text{Nb}_2\text{O}_6$  where  $\text{R}_y = \text{Y, Zn, Mg, Fe}$ , have been prepared by the conventional ceramic technique. The microstructures were studied with the aid of Scanning Electron Microscope on fractured surfaces of the ceramic compositions and the average grain diameter was measured by linear intercept method. The results are discussed in relation to the grain sizes.

## INTRODUCTION

The tungsten bronze structure ferroelectrics are a large class of technically important materials. The properties of these materials are very sensitive to the amount of substitution, preparation and sintering conditions. The system Strontium Barium Niobate with tetragonal tungsten bronze structure has been extensively studied by various researchers [1-5]. SBN has the highest electro-optic coefficient and high pyroelectric coefficient [2,6,7]. The structure consists of a framework of  $(\text{BO}_6)$  oxygen octahedra sharing corners in such a way that there are three different types of interstitial sites A, B and C. These three sites can accommodate different metal atoms. The general formula is  $\text{AB}_2\text{O}_6$  where, A is a divalent metal atom and B is either niobium or tantalum. Generally, additives are used for the aid of densification or control of grain growth so as to improve the useful properties of these ceramics. When the interstitial vacancies are filled partially or fully with alkali elements, Curie temperature is raised. The purpose in introducing Na is to increase the density and raise  $T_c$ . With the introduction of Na, A position vacancies result from volatility of Na and these vacancies aid sintering process. The effect of different cations on the structural properties and ferroelectric properties of SBN ceramics are reported in this communication.

## EXPERIMENTAL

Solid solutions of the following compositions were prepared by the conventional ceramic technique.



Suitable proportions of analytical reagent grade with a purity of 99.99% starting materials in accordance with the solid state reaction were dry ground into fine powder and calcined in platinum crucibles. The mixture is pressed into disks and sintered in air on platinum foil. The firing conditions are the same as reported earlier [8-10]. The materials were characterized by X-ray diffraction. The dielectric dispersion was measured on H.P. LF Impedance Analyzer model 4192 A with 16095 A as probe fixture in the temperature range 30 - 400°C. The microstructures of sintered disks were examined by JEOL JSM-35 CF Scanning Electron Microscope.

## RESULTS AND DISCUSSION

The measurements were made by fracturing the sample, evaporating a thin layer ( $\sim 400\text{\AA}$ ) of gold on to it and observing under high magnifications at 10KV. The sample surfaces were sputtered with gold employing a sputter coater so as to eliminate or reduce the electronic charge which builds up rapidly in a non-conducting specimen when scanned by a beam of high energy electrons. The microstructural studies were carried out with the aid of Scanning Electron Microscope on fractured surfaces of the ceramic compositions. Scanning Electron Micrographs of different compositions are shown in Figures 1-4. The grain sizes were measured using STOE, Germany film measuring device. The average grain diameters were calculated by linear intercept method [11].

Room temperature dielectric constant values and Curie temperatures are shown in Table I. In all the compositions, a broad transition is observed which is a characteristic of diffuse phase transition. Both the room temperature dielectric constant and peak dielectric constant decreases gradually with the increase of ionic radius of the additive cations. The Curie temperature was observed around 200°C for all compositions. The substituted ionic sizes and their site occupancy play an important role in determining the dielectric constant. It was also observed that the dielectric constant peak shifts to higher





Figure 1. SEM micrograph of Fe doped SBN



Figure 2. Microstructure of Mg doped SBN



Figure 3. Micrograph of Zn doped SBN

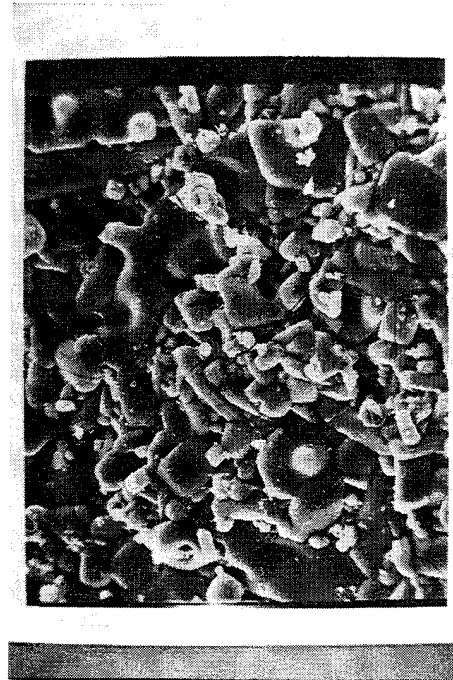


Figure 4. SEM micrograph of Y doped SBN

Table I

## Dielectric Data of Modified SBN Ceramics

Sample	$\epsilon_{RT}$				$\epsilon_{Tc}$				$T_c$			
	1KHz	100KHz	500KHz	1MHz	1KHz	100KHz	500KHz	1MHz	1KHz	100KHz	500KHz	1MHz
Fe(SBN)	998	302	293	289	3440	1403	1368	1353	205	200	200	205
Mg(SBN)	645	255	253	251	3787	1282	1217	1199	202	195	195	195
Zn(SBN)	111	201	194	190	627	1202	1110	986	205	200	205	207
Y(SBN)	98	92	85	82	1330	283	273	261	235	205	210	215

Table II

Sample	Ionic Radius ( $\text{\AA}$ )	$T_c$ ( $^{\circ}\text{C}$ )	Grain size ( $\mu\text{m}$ )
Fe <sub>0.02</sub> (SBN)	0.64	205	2.8
Mg <sub>0.1</sub> (SBN)	0.66	202	4.4
Zn <sub>0.1</sub> (SBN)	0.74	205	6.5
Y <sub>0.02</sub> (SBN)	0.89	235	3.5

temperatures slightly and the dielectric constant values decrease with increasing frequency.

The broadening of the transition has been attributed to disorder in the arrangement of the cations on one or more crystallographic sites in the structure leading to microscopic heterogeneity in the composition and thus a distribution of different local Curie points. And also the dielectric loss peak shifts to a higher temperature upon increasing the frequency.

The average grain diameters are presented in Table II. The Scanning Electron Micrographs of Fe Mg, Zn and Y addition reveal a slightly melted appearance which may be due to liquid phase sintering. The liquid phase probably results from the reaction of cations and Na with SBN [10]. The addition of cations promoted grain growth. The average grain sizes are about 2.8, 3.5, 4.4 and 6.5  $\mu\text{m}$  for Fe, Y, Mg and Zn. The addition of Y assisted the grain growth. This may be the reason for the part of the decrease in dielectric constant values.

#### ACKNOWLEDGEMENTS

Thanks are due to DST, New Delhi, India for the award of research grants. One of the authors (SNM) wishes to acknowledge CSIR, New Delhi for Research Associateship.

#### REFERENCES

[1] M.H. Framcombe and B. Lewis, *Acta Cryst.*, **11**, (1958) 696.

[2] P.V. Lenzo, E.G. Spences and A.A. Ballman, *Appl. Phys. Lett.*, **11**, (1967) 23.  
 [3] A.M. Glass, *J. Appl. Phys.*, **40**, (1969) 4699.  
 [4] R.R. Neurgaonkar, *Ferroelectrics*, **91**, (1989) 209.  
 [5] T.R. Shrout and S.L. Swartz, *Proce. 8th. IEEE International Symposium on Applications of Ferroelectrics, Greenville, SC, September, (1992)* pp 80.  
 [6] R.R. Neurgaonkar and L.E. Cross, *Mat. Res. Bull.*, **21**, (1986) 893.  
 [7] R. Clarke and J.C. Burfoot, *Ferroelectrics*, **8**, (1974) 505.  
 [8] S. Narayana Murty, K. Umakantham, K.V. Ramana Murthy, K.C. Mouli, G. Padmavathi, A. Bhanumathi and K. Linga Murty, *J. Mater. Sci. Lett.*, **11**, (1992) 607.  
 [9] S. Narayana Murty, K.V. Ramana Murthy, K.C. Mouli, A. Bhanumathi, S. Bangar Raju, G. Padmavathi, and K. Linga Murty, *Ferroelectrics*, (1994) In Press.  
 [10] S. Narayana Murty, K.V. Ramana Murthy, G. Padmavathi, A. Bhanumathi and K. Linga Murty *Proce. 8th. IEEE International Symposium on Applications of Ferroelectrics, Greenville, SC, September, (1992)* pp 209.  
 [11] E.D. Case, J.R. Smyth and V. Monthel, *J. Amer. Cer. Soc.*, **64C**, (1981) 24.

# Frequency Response of MgO:LiNbO<sub>3</sub> Crystals

B.M.Jin, A.S.Bhalla

Materials Research Laboratory, The Pennsylvania State University,  
University Park, PA 16802, U.S.A.

I.W.Kim, B.C.Park

Dept. of Physics, University of Ulsan, Ulsan, Korea

*Abstract* - MgO-doped congruent LiNbO<sub>3</sub> were grown by the Czochralski method. All MgO-doped LiNbO<sub>3</sub> have higher growing temperature than that of pure one. Frequency dependence dielectric spectra was performed to study the relaxational and conduction mechanism. Strong low frequency dispersion indicated that main conduction of MgO-doped LiNbO<sub>3</sub> is the hopping charge carrier which may be caused by defect or Mg-ion. Impedance spectra measurement shows that this system satisfies not a Debye but a Jonscher's "Universal law".

## INTRODUCTION

Pure LiNbO<sub>3</sub>(LN) was a good candidate for optical devices, but because of optical damage (photorefractive effect), so many researchers have tried to solve this disadvantage. MgO-doped LN (congruent compositions) is one of possible solutions. As mentioned in previous reports [1-3], MgO doping has played a great role in pure LN and increased the laser strength by 100 times. An interesting point is that every physical property of MgO-doped LN (ex.: transition temperature, activation energy, optical band gap, optical absorption spectra, shift of OH- vibration frequency, density and electric activation energy based on the our previous measurements [4]) has threshold composition at just above 5mole% of MgO concentration. In this study, we are trying to

test the conduction mechanism of Mg-ion inside the LN crystal by impedance spectroscopy.

## EXPERIMENT

A series of MgO-doped LiNbO<sub>3</sub> single crystals were grown by the Czochralski method from melt. Each composition of MgO from pure to 10 mole% were added to pure LiNbO<sub>3</sub>. All doping has higher melting point than pure ones. There were no shape changes in grown crystals but there were slight color changes and we believed that they were originated by intrinsic point defects resulting from Mg incorporation. Grown crystals were cut from the original bowl and polished by alumina powder. All measurements were done only on c-plate samples. Pt-paste was used as electrodes on polished sample surfaces. Impedance spectroscopy was performed by using the Impedance Analyzer (HP 4192A) from 5Hz to 13 Mhz. Careful calibration was done to reduce the stray impedance before measurements.

## RESULTS AND DISCUSSION

Fig.1 shows the real and imaginary impedance spectra in frequency domain at several MgO contents. Spectra of selected MgO composition are plotted in order to avoid confusion. As the MgO contents increased, the relaxational

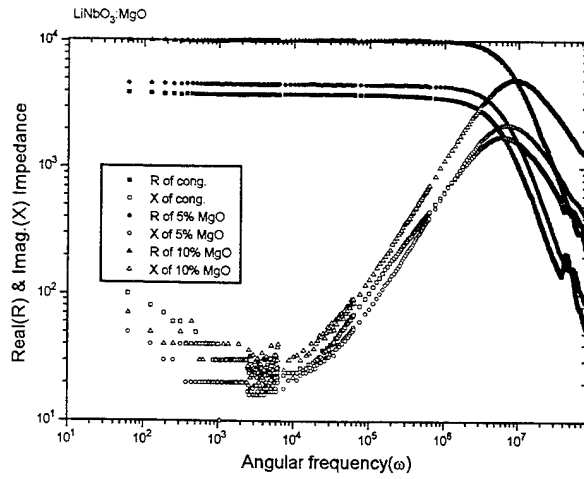


FIGURE 1. Real and imaginary impedance vs. frequency at several selected MgO compositions.

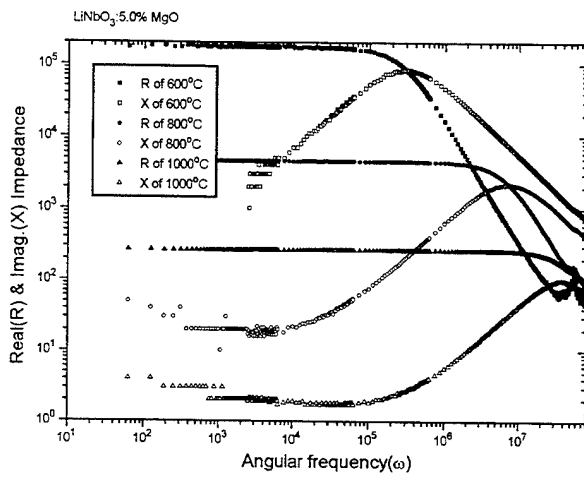


FIGURE 2. Real and imaginary impedance vs. frequency at several selected temperatures.

frequencies (peak frequency of imaginary impedance) move toward the higher frequency region and magnitudes of real impedance are reduced. A small kink at the high end frequency is due to the piezoelectric resonance. Temperature dependent impedance spectra were shown in Fig.2. As temperature increased, the relaxational frequency also increased a result similar to adding more MgO. There is the possibility of another relaxational mechanism at very low frequency region in both figures. It is unclear what kind of mechanism caused this without measuring the very low frequency dispersion in detail. This relaxation is now being studied by using a mHz frequency analyzer. Whenever imaginary impedance spectra have a peak in measured

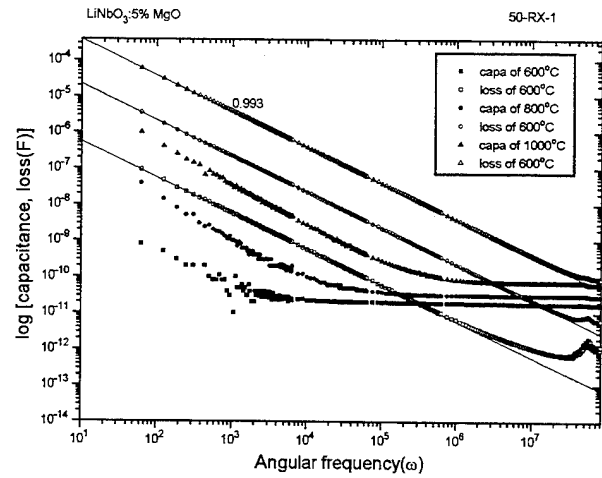


FIGURE 3. Capacitance & loss vs. frequency at several temperatures. Curve fitting the loss below the  $\omega_c$  was done using the equation mentioned in the text.

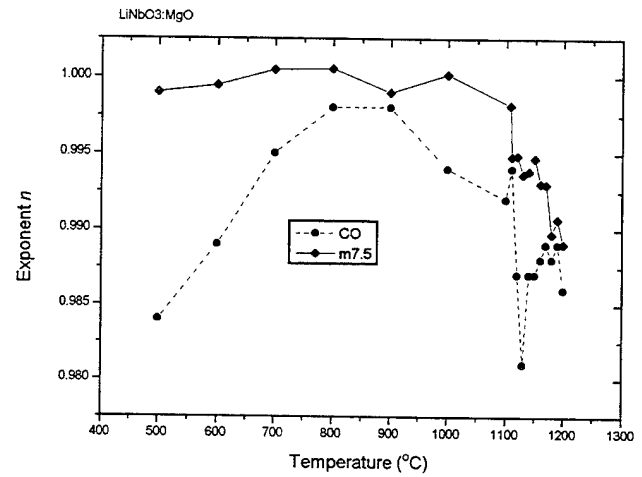


FIGURE 4. Temperature variation of critical exponent which is determined from the slope of below the critical frequency.

frequency range, it is hard to possess a same peak frequency in dielectric constant spectra - namely, in dielectric spectra it should have a linear relationship with frequency, although low frequency has a rapid down slope. The result is shown in Fig.3 at several different temperatures. This type of response has been discussed in detail by Hill and Pickup[5], and Jonscher [6]. Real and imaginary components are given by

$$C(\omega) \propto G(\omega)/\omega \propto \omega^{-n_1} \quad 0 < n_1 < 1$$

at frequencies below  $\omega_c$  and

$$C(\omega) \propto G(\omega)/\omega \propto \omega^{-n_2} \quad 0 < n_2 < 1$$

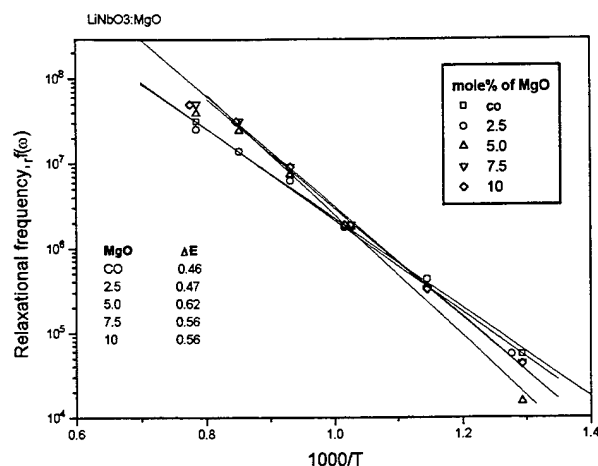


FIGURE 5. Relaxational frequency determined from the peak frequency of capacitive loss vs. inverse temperature to show the satisfaction of ionic conductivity in ferroelectric region. Activation energy has a maximum at 6mole% of MgO concentration.

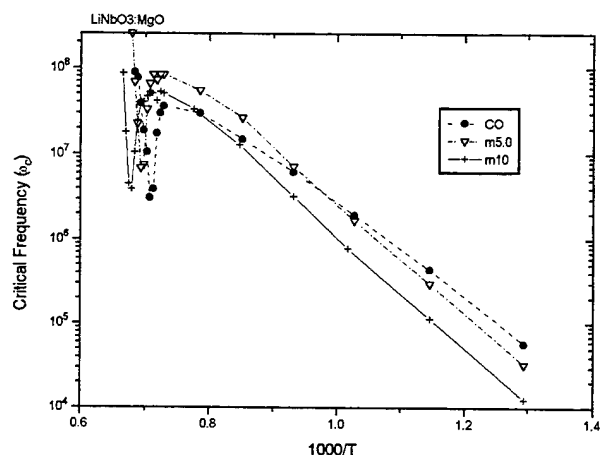


FIGURE 6. Critical frequency variation depending on the temperature which is determined from the result of extrapolating the slope of real and imaginary capacitances.

The spectra shown in Fig.3 differs from the ideal response in a number of ways. First, below 700°C, the slopes of real and imaginary capacitance at low frequency do not have the same tendencies. As going up above 900°C, both slopes have same tendencies and the tendency to “almost dc”, i.e. nearly frequency-independent conductivity evident with rising temperature. This will be clear when it is drawn on conductivity vs. temperature. This means that at low temperatures, the interface effect between electrodes and the surface of the sample still remains. Beyond 900°C, both

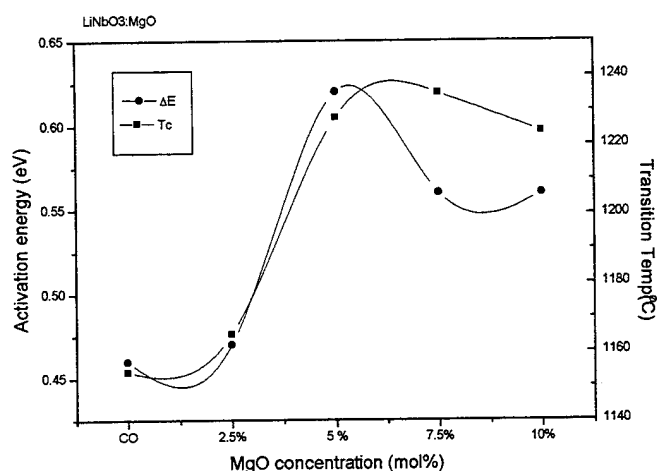


FIGURE 7. Activation energy( $\Delta E$ ) and transition temperature ( $T_c$ ) vs. mole% of MgO incorporation. Both properties have a maximum - threshold composition and in this composition laser damage threshold increases 100 times.

slopes satisfy the above relation. Second, above  $\omega_c$ , loss still deviates from the slope of the capacitance. This can be explained that further polarization process still remains in this high frequency region or because of the thermal conduction at high temperatures. This is evident from their different physical characteristics, the strong dispersive region being closely akin to dc conduction, with substantial charge movements in the material, or the high frequency regime being due to more “dipole-like” localized hopping of charges, if not to molecular dipoles as such. Temperature dependency of critical exponent,  $n$  which is determined from  $n_1$ , is drawn in Fig.4 for selected temperatures. All critical exponents has a minimum value at transition temperature in every MgO content indicating the restoring force should be a minimum of around the transition temperature[7]. All the compositions except pure LiNbO<sub>3</sub> has a critical exponent value around unity through all temperatures indicating that it is often identified with the presence of hopping conduction by electrons. Relaxational frequency can be determined by selecting the peak frequency from either dielectric loss or imaginary loss of impedance. Temperature dependency of this relaxational frequency was plotted in Fig.5. Because of limiting frequency sweep range, relaxational frequencies were determined only below 1000°C. The activation energy calculated from this frequency was presented as an inset of

this figure. A 5mole% of MgO incorporation has a maximum activation energy value. By consideration of below and above slope of this activation energy, it is concluded that real MgO composition of maximum activation energy is just above 5mole% (see fig.7). More detailed investigation was done by evaluating the critical frequency far beyond the measured frequency range. In other words, using the tendency of the slope, the spectra were extrapolated far above the limited range of the frequency. Determined values of using this methods are plotted in Fig.6 and it indicates the pure ionic conductivity behavior below the transition temperature - in ferroelectric region. The activation energy obtained from this method is a little bit different from previous ones in magnitudes, but has a same tendency within experimental and calculating error ranges. Final results were shown in Fig.7. Activation energy and transition temperature ( $T_C$ ) have a peak around 6mole% of MgO concentration. These results were consistent with the results of density and absorption measurements done by our laboratory previously [7]. The detailed defect mechanism will be analyzed in another article by explaining the variation of density and optical band gap depending on the compositions.

#### CONCLUSION

Impedance spectroscopy was investigated to study the relaxational mechanism of impurity doping into a pure congruent  $\text{LiNbO}_3$ . Large dispersion in low frequency (below 1 MHz) and low temperature (below 900°C) was originated from the hopping electron caused by the intrinsic defect of Mg ion incorporation. Not a dielectric Cole-Cole plot but a Impedance Cole-Cole plot means that this system has a pure hopping conduction by defects in low frequency regime, especially. Small deviation of parallelism below critical frequency indicates that there should be another mechanism at a very low frequency region. Big deviation of conductive loss above the critical frequency indicates that further polarization process is going on far beyond the measured frequency range or thermal conduction at high temperatures. There is good consistency of threshold composition of MgO measured separately by the activation energy and transition temperature.

#### REFERENCES

- [1] W.Rossner, B.C.Grabmaier and W.Wersing, *Ferroelectrics*, vol.93, pp.57-65, 1989
- [2] J.Koppitz, O.F.Schirmer, M.Wohlecke, A.I.Kuznetsov and B.C.Grabmaier, *Ferroelectrics*, vol.92, pp.233-241, 1989
- [3] K.L.Sweeney, L.E.Halliburton, D.A.Bryan, R.R.Rice, R.Gerson and H.E.Tomaschke, *J.Appl.Phys.*, vol.57, pp1036, 1985
- [4] I.W.Kim, B.M.Jin and A.S.Bhalla, "Growth and Characterization of  $\text{MgO}:\text{LiNbO}_3$  Crystals" in *Proceeding on the ISAF-9*, 1994
- [5] R.M.Hill and C.Pickup, *J. Mater.Sci.*, vol.20, pp.4431, 1985
- [6] A.K.Jonscher, *Dielectric Relaxation in Solids*, London: Chelsea Dielectrics Press, 1983, ch.5, pp161-253
- [7] B.M.Jin, A.S.Bhalla, J.B.Kim and J.N.Kim, *J.Mater.Sci.:Mater.Electronics*, vol.4, pp.225-228, 1993

# Lithium Niobate Single Crystals with Improved Sound Speed Resistance to the Light Influence

N.I. Deriugina, M.K. Sheinkman

Ukrainian Academy of Science, Semiconductors Physics Institute, Prospekt Nauki, 45, Kiev, 252028, Ukraine

**Abstract** -- We have learned the possibilities of decreasing of photoinduced lithium niobate acoustic characteristics changes. We have shown that the doping of lithium niobate crystals with Mg impurity and special ultrasonic treatment significantly decrease the sound speed and electro mechanical parameter changes in lithium niobate, which were caused by visible light influence.

## OBJECT OF THE WORK

The efficiency of lithium niobate acousto-optic devices for laser radiation control is limited by sound speed changes in lithium niobate single crystals upon the visible range radiation influence. The purpose of our investigation is to increase the sound speed resistance of lithium niobate single crystals to the visible range light influence by means of Mg-doping and ultrasonic treatment of lithium niobate crystals.

## RESULTS AND DISCUSSIONS

### Doping

It is known that the presence of the Mg impurity significantly effects on the optical damage processes in lithium niobate [1]. The light refract index changes ( $\Delta n$ ) upon the influence of light efficiently decrease by means of doping the lithium niobate crystals by Mg impurity. It is naturally to suppose that Mg ions effect on photoinduced sound speed changes ( $\Delta v$ ), as well as this impurity effects on photoinduced changes  $\Delta n$ . We have made the comparative measurements of photoinduced acoustic parameter changes in pure and doped  $\text{LiNbO}_3$  in the order to investigate the influence of doping on the increasing of acoustic characteristics resistance to the light influence.

We have measured the photoinduced  $\Delta v$  in the pure lithium niobate and in the  $\text{LiNbO}_3:\text{Mg}$  with different concentration of Mg impurity (0,86; 3,0; 5,0 %). The measurements had been made by means of resonance-antiresonance methods on the samples with following dimensions  $X*Y*Z=4*10*2 \text{ mm}^3$  [2,3]. Lithium niobate single crystals have been grown by Dr. K. Polgar in the Research Laboratory for Crystal Physics of the Hungarian academy of science in Budapest. The gold electrodes were deposited on the ends of samples by evaporation in the vacuum. The measurements were made in the dark and at irradiating by white light from lamp with power of 500 Wt. The installation time of stationary measured parameter value achieved 2 minutes. The longitudinal waves where

excited in the samples on the 300kHz frequency. The acoustic parameter changes, created by light, were stable during several days after switching the light off. Crystal can be returned to the initial condition by heating it up to 100 C and following cooling it in the dark up to the room temperature.

The relative changes of the lithium niobate acoustic characteristics in depending on the percentage of Mg are represented on fig.1 (curves. 1,2). The curve 1 shows changes of sound speed  $\Delta v/v^d = (v^l - v^d)/v^d$  where  $v^l$  and  $v^d$  are sound speed values in the light and in the dark correspondingly. The changes of parameter  $\alpha = \Delta K_{22}/K_{22}^d$  in depending on the Mg concentration are shown on the curve 2. Here  $\Delta K_{22}/K_{22}^d = (K_{22}^l - K_{22}^d)/K_{22}^d$  is relative change of electro-mechanical coupling coefficient. The  $\Delta v/v^d$  and  $\alpha$  in depending on the concentration of Mg are correlate. As it can be seen on the fig.1, Mg impurity doping causes considerable decreasing of the photoinduced changes of lithium niobate acoustic characteristics.

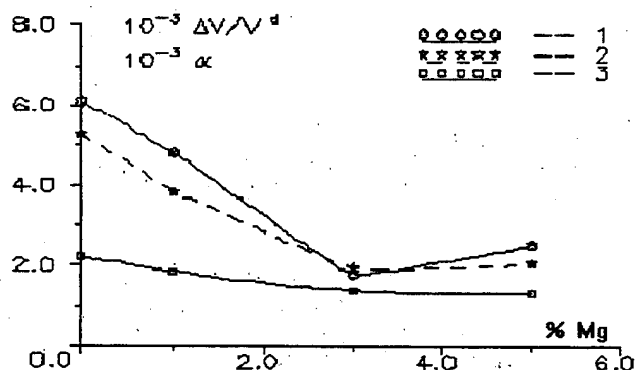


Fig.1. The depending of sound speed and electro-mechanical coupling parameter changes on Mg impurity content.

We shall mark that the values of photoinduced sound speed changes and photorefractive effect in the lithium niobate are connected ( $\Delta v/v^d \sim \Delta n/n$ ). It is well known that the injection of Mg impurity in the  $\text{LiNbO}_3$  with Mg concentration equal to 4,5% causes threshold (up to 100 times) decreasing of photorefractive effect value. At the same time we haven't observed the threshold decreasing of  $\Delta v/v^d$  in the single crystals  $\text{LiNbO}_3:\text{Mg}$  with Mg concentration equal to 5%. It may be explained by values of threshold concentration of Mg depends on condition of given crystal



grows, its composition and can be above 4,5% up to (6 -- 8)% [4].

Photoinduced changes of sound speed in lithium niobate are caused by changes of spontaneous polarization value, which results from appearing of depolarizing electric field during the lighting in the mediums with selected direction. The mechanism of Mg impurity influence on the lithium niobate acoustic characteristics changes are on the stage of establish.

#### Ultrasonic Treatment

The value of  $\Delta V$  depends significantly on the crystal defect structure. Effective method of the structure defect density reducing in lithium niobate is the special ultrasonic treatment of crystals. The ultrasonic treatment wave intensity must be lower then that one that can cause the generation of point defects and crystal dislocation [5].

We have investigated the influence of ultrasonic treatment on pure and Mg-doped lithium niobate single crystals in the order to decrease the unwanted effect of acoustic parameter changes as result of light action. The significantly (in several times) decreasing of photoinduced sound speed changes can be achieved after ultrasonic treatment of lithium niobate samples at room temperature during 1--3 hours. The amplitude of relative acoustic deformation was equal  $(6--9)10^{-4}$  at the frequencies, which were equal to (0.1--10) MHz. Results of ultrasonic treatment application are demonstrated on fig.1 (curve 3).

The dependings of photoinduced  $\Delta V/V^d$  on the time and amplitude of ultrasonic treatment and on the Mg concentration as well, are shown on the fig.2 and fig.3.

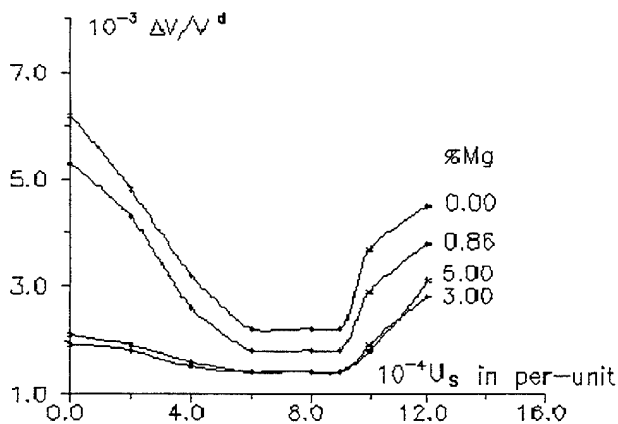


Fig.2. The depending of the photoinduced sound speed changes on relative amplitude of ultrasonic treatment and Mg impurity concentration.

It is reasonable to suppose that ultrasonic treatment as Mg impurity doping of lithium niobate causes the oriented defect ordering and as result of this the decreasing of photoinduced sound speed changes. This agrees with conclusions [5] about results of ultrasonic influence on semiconductor crystals and also with the data about creating defect processes in  $\text{LiNbO}_3:\text{Mg}$  [4].

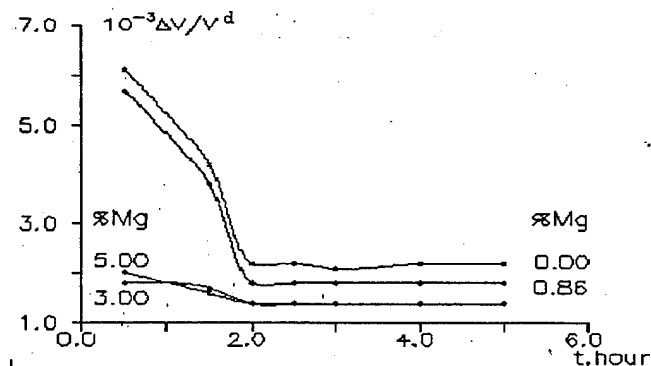


Fig.3. The depending of the photoinduced sound speed changes on the time of ultrasonic treatment and Mg impurity concentration.

The resistance of pure lithium niobate acoustic parameters to the light influence at the optimal regimes of ultrasonic treatment is comparable to that one in the Mg-doped lithium niobate. The exiting from the optimal regimes decreases the positive ultrasonic treatment influence.

#### CONCLUSIONS

We shall like to note that doping by Mg impurities during crystal growth and ultrasonic treatment are the effective methods of producing the  $\text{LiNbO}_3$  single crystals with improved resistance of acoustic characteristics to the visible light influence. We consider that ultrasonic treatment may be applied for optical strength increasing as well as Mg-doping. The ultrasonic treatment has the advantage of cheapness and simplicity. It is important for the practical application of ultrasonic treatment that such procedure of improving  $\text{LiNbO}_3$  characteristics may be used for ready made crystals and for lithium niobate working elements of acousto-optics devices as well.

#### REFERENCES

- [1] K.L. Sweeney, L.E. Halliburton, D.A. Bryan, R.R. Rice, R. Gerson, H.E. Tomaschke, "Threshold effect in Mg-doped lithium niobate," *Appl. Phys. Lett.*, **47**, pp. 805-807, N7, 1984.
- [2] A.A. Demidenko, V.N. Piskovoj, "At the theory of resonance investigation methods of electromechanical crystall properties," *Ukrainian Journal of Physics*, **20**, pp. 221-228, N2, 1975.
- [3] A.P. Zdebsky, N.I. Deriugina, A.N. Annaniazov, G. Garyagdiev, G. Corradi, K. Polgar, "Photo- and acousto stimulated elcetromechanical parameter changes of  $\text{LiNbO}_3:\text{Mg}$ ," *Letters to the Journal of Technical Physics*, **14**, pp.21-74 N23, 1988.
- [4] I.M. Zaritski, L.G. Rakitina, G. Corradi, K. Polgar and A.A. Bugay, "A new trapped-hole radiation defect in heavily Mg doped  $\text{LiNbO}_3$ ," *J. Phys. Condens. Mater*, **3**, pp. 8457-8465, June, 1991.
- [5] A.P. Zdebsky, M.K. Sheinkman, A.N. Annaniazov, G. Garyagdiev, "The influence of ultrasonic load on the acousto- and electric characteristics of CdS", *Solid State Physics*, **29**, pp. 1135-1139, N4, 1987.

# Growth and Characterization of $\text{MgO}:\text{LiNbO}_3$ Crystals

I.W.Kim

Dept. of Physics, University of Ulsan, Ulsan, Korea

B.M.Jin, A.S.Bhalla

Materials Research Laboratory, The Pennsylvania State University,  
University Park, PA 16802, U.S.A.

J.W.Kim

Dept. of Physics, DongEui University, Pusan, Korea

**Abstract** - Congruent  $\text{MgO}:\text{LiNbO}_3$  (MLN) single crystals doped with 0, 2.5, 5.0, 7.5 and 10.0 mole% of MgO contents were grown by the Czochralski method. The grown crystals were water clear without any precipitation. The density and Curie temperature ( $T_c$ ) for MLN crystals were measured. It was found that the density curve has a one minimum and maximum at 2.5 mole% and 5.0 mole%, respectively. The Curie temperature increases first with the MgO concentration and decreases again when the concentration of MgO goes beyond the threshold limit ( $[\text{Mg}]_c$ , 5.0~7.5 mole%). We also measured optical absorption edges and I.R. absorption spectra at room temperature for MLN crystals. There existed a threshold concentration of nearly 6.0 mole%. The I.R. absorption peak appeared at  $3470\text{ cm}^{-1}$  in 0~5.0 mole% and  $3534\text{ cm}^{-1}$  in 7.5~10.0 mole% and peak shifts at about  $60\text{ cm}^{-1}$  toward the shorter wavelength side. We carefully assumed that the substitution of  $\text{Mg}^{2+}$  for  $\text{Nb}^{5+}$  would weaken the cation-oxygen bond with its neighbouring  $\text{O}^{2-}$  ion, and the distortion of oxygen octahedron of MLN crystals would change in some degrees with the increasing MgO ratio. This distortion of oxygen would affect many physical properties of the MLN crystals.

## INTRODUCTION

Since 1965 Ballman[1] has reported the successful growth of  $\text{LiNbO}_3$  single crystals by the Czochralski method.  $\text{LiNbO}_3$

has been studied extensively because of its high device potentials[2-5]. However, short wavelength laser radiation induced refractive index inhomogeneities, which has been named "optical damage", impose limits on optical device performance. Ashkin et al.[6] first discovered the optical damage in  $\text{LiNbO}_3$  and  $\text{LiTaO}_3$  in a study of the photorefractive effect. In 1980 Zhong et al.[7] reported that  $\text{LiNbO}_3$  with a 4.6 or higher mole% of MgO added to the melt had a resistance to the optical damage of about 100 times as great as that of the pure ones. Several optical and physical properties of MLN crystals exhibit abrupt changes when Mg is raised above the critical Mg concentration,  $[\text{Mg}]_c$ .

During recent years, the questions as to the origin of the Mg-doping concentration threshold and impurity mechanism of  $[\text{Mg}]_c$  in congruent crystals have been a matter of controversy. Many papers have reported these phenomena. Grabmaier and Otto[8] reported that MLN crystals should maintain the same crystal structure as pure  $\text{LiNbO}_3$  for MgO contents up to 25 mole%. Therefore, the role of the position of  $\text{Mg}^{2+}$  cation in the MLN crystal in relation to the threshold effect is of interest and importance. Sweeney et al.[9] considered that two types of Mg existed, i.e. the simple  $\text{Mg}^+$  ion ( $\text{MgLi}$ )<sup>+</sup> and the  $\text{Mg}^+$  complex. Polgar et al.[10] observed that  $\text{Mg}^{2+}$  cations above the threshold may produce the same kind of aggregates. Feng et al.[11] suggested by defect chemistry that there are different types of Mg contained defect lattices in the crystals at different Mg doping levels. At the  $\text{Mg} > [\text{Mg}]_c$ , there will be a main source causing a sharp

change of the ionic environments by Nb-site  $\text{Mg}^{2+}$  ( $\text{Mg}_{\text{Nb}}^{2+}$ ). In this work, we have grown a high-concentration of MLN crystals with a MgO concentration of up to 10 mole%. Based on the data which are obtained from the density,  $T_C$ , optical absorption edge and I.R. absorption spectra of the MLN crystals, we discussed the MgO doping level threshold effect and carefully proposed a mechanism of MgO doped defect lattice.

## EXPERIMENT

The  $\text{LiNbO}_3$  crystals were grown by the Czochralski technique using a computer control. The purity of the starting materials, MgO,  $\text{Nb}_2\text{O}_5$  and  $\text{Li}_2\text{CO}_3$ , was all 99.9%. Crystals were grown along the c-axis to a size of about 20 mm in diameter and 25 mm in length. Transparent and crack free crystals were obtained. Before being cut, the crystals were annealed for two weeks at a temperature of 1090°C. The density was measured with the Archimedes method on a chemical balance of 0.1 mg sensitivity. The recording of the dielectric properties was performed by computer controlled measuring equipment with an HP 4192A Impedance Analyzer (5Hz-13MHz). The measured values were recorded while slowly heating the samples at 1°C /min from room temperature to about 1240 °C in an air atmosphere. The optical absorption edge and IR absorption spectra were measured by a CARY 5(Varian) UV-VIS-Near IR spectrophotometer in a wavelength range of 180 nm-3300 nm.

## RESULTS AND DISCUSSION

Fig. 1 shows the density and the Curie temperature as a function of the MgO content of crystals grown from a congruent melt composition. At 2.5 mole% Mg content, the density dropped slightly and at 5.0 mole% Mg content, the density increased again and obviously exceeded 7.5 mole% it decreased again. There are therefore two threshold concentrations in this measurement. Our result agree with Feng et al. that the density tends to vary with different MgO ratio. The Curie temperature was determined from the

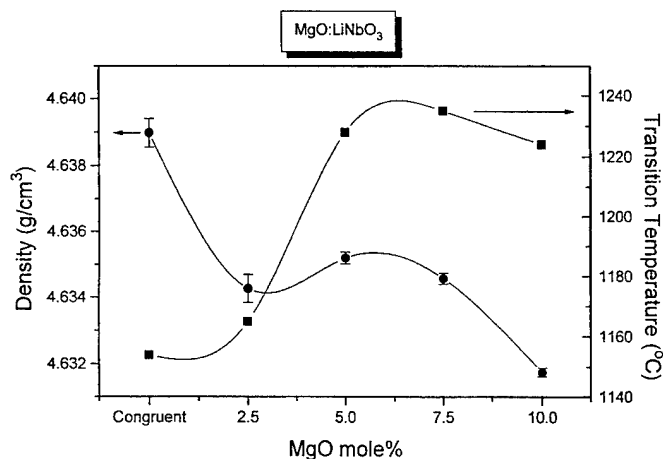


FIGURE 1. The density and the Curie temperature of the MLN crystals as a function of the MgO content.

dielectric peak (fig 2), indicating the ferroelectric phase transition. The Curie temperature increased with increase of the MgO content and reached a maximum of 1235°C at 7.5 mole% MgO, then decreased again. The Curie temperature is strongly dependent on MgO ratio. Its value increased about 80 °C by changing from congruent to 7.5 mole%. Many researchers have explained the experimental results of a defect lattice of MLN crystals with Mg doping. Lerner et al.[12] reported that the density of  $\text{LiNbO}_3$  crystals increases

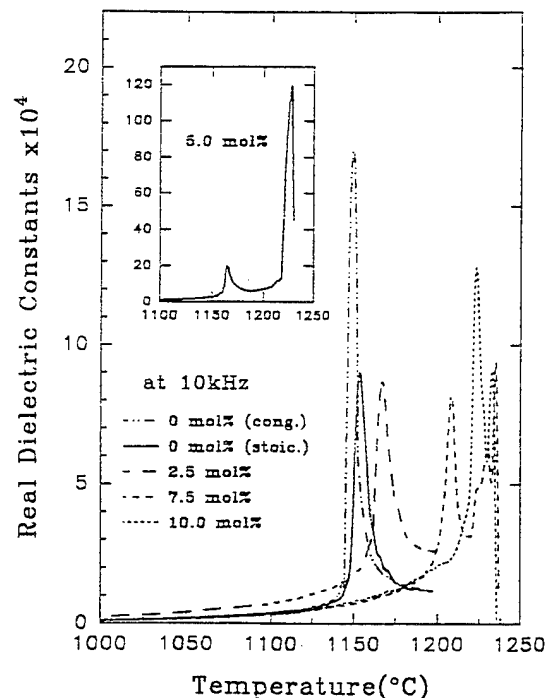


FIGURE 2. The phase transition behavior of the MLN crystals.

when the ratio of Li/Nb decreases. They explained that it will also be caused by vacancies or substitution of  $\text{Li}^{1+}$  ions by  $\text{Nb}^{5+}$  ions. Qiren Zang et al.[13] measured densities of MLN and proposed different defect models for MLN crystals with MgO ratios. They reported that MgO may be incorporated in excessive Nb and that this additional Mg substitution can cause lattice defect when the Mg doping ratio is less than 2.7 mole%. When the MgO doping level exceeds  $[\text{Mg}]_c$  - around 5.3%, the density decreases gradually, and there would be some abrupt changes on the defect lattice structure. O'Bryan and Gallagher [14] reported that the  $T_c$  variation relationship to the Mg concentration can be explained by the cation vacancy content regardless of whether these are formed by Li deficiency or by the addition of impurity ions. The addition of MgO changes the vacancy content properties such as  $T_c$ . It should show a strong dependence on the defect structure. Grabmaier et al.[15] proposed that every Mg ion incorporated on an Li site also generates an Li vacancy. An increase of Mg content will be accompanied by a decrease of Nb vacancies, and thus the increase in the Curie temperature can be explained. Above  $[\text{Mg}]_c$  contents, Nb vacancies are no longer present and Mg is also incorporated into Nb sites.

The results of our experiment indicate that the abrupt changes in the physical properties of the MLN crystals occur in the range of 5.0~7.5 mole% of MgO. In this crystal structure, the Nb-O bond is stronger than that of Mg-O. When an  $\text{Mg}^{2+}$  ion was substituted for an  $\text{Nb}^{5+}$  ion, bonding between the  $\text{O}^{2-}$  ions and  $\text{Mg}^{2+}$  will be elongated, and bonding between  $\text{O}^{2-}$  ions and  $\text{Nb}^{5+}$  will be shortened. The volume of oxygen octahedron that surrounds  $\text{Mg}^{2+}$  ions, therefore, becomes greater than that of  $\text{Nb}^{5+}$ .

Experimentally, we found that the change rate of  $T_c$  with MgO in a 0~5 mole% region was steeper than that of a 7.5~10.0 mole% region. This result indicates that the influences of Mg on the  $T_c$  in an MLN crystal is different depending on the kinds of vacancy sites created by Mg. It is difficult to determine experimentally the exact positions of the absorption edges of MLN crystals. In the present work, we measured the relative shift of the absorption edge. Fig. 3 shows the optical absorption edge as a function of the MgO contents. The

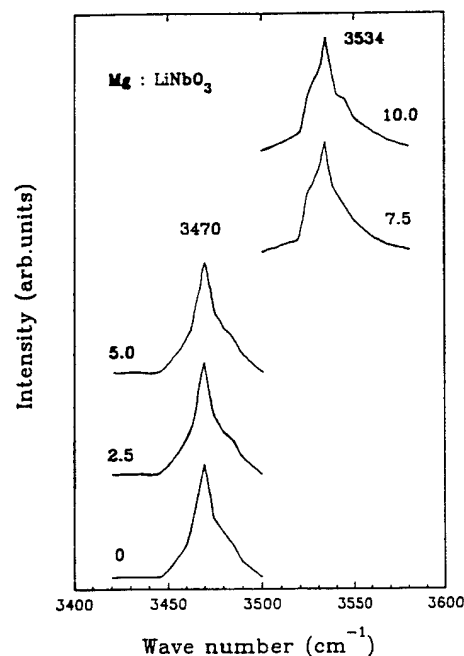


FIGURE 3. The optical absorption edge of the MLN crystals as a function of the MgO content.

absorption edge shifts toward the shorter wavelength region by increasing the MgO. The maximum optical absorption edge occurs in the region between 5.0~7.5 mole% of MgO. When the MgO ratio exceeds the  $[\text{Mg}]_c$ ,  $\text{Mg}^{2+}$  may occupy the  $\text{Nb}^{5+}$  site, and this substitution makes another lattice defect. This effect changes the gap of the forbidden band, and the optical absorption edge shifts toward the longer wavelength side after  $[\text{Mg}]_c$ . Absorption energy is maximum at around 6 mole% (Fig.3). According to the Polgar model [10], below the  $[\text{Mg}]_c$ , the  $\text{Mg}^{2+}$  hinders the  $\text{Nb}^{5+}$  substitution into the  $\text{Li}^{1+}$  site, and  $\text{Mg}^{2+}$  occupy the normal  $\text{Li}^{1+}$  sites gradually. Above the  $[\text{Mg}]_c$ , some new types of Mg incorporation (namely, Mg aggregation with Nb) are produced. The movement of the absorption edge may be attributable to the distortion of electronic energy band structures resulting from the Mg ions replacement in Nb-site. Fig.4 shows the I.R. absorption spectra of MLN crystals. It was found that the I.R. absorption spectra of MLN was broadened. When the MgO doping ratios are less than 5.0 mole%, the peak position is  $3470\text{ cm}^{-1}$  and unchanged. When the MgO doping ratio is 7.5 and 10.0 mole%, the I.R. absorption peak position is  $3534\text{ cm}^{-1}$  and shifts  $64\text{ cm}^{-1}$  toward the ultraviolet side. When the MgO doping ratio

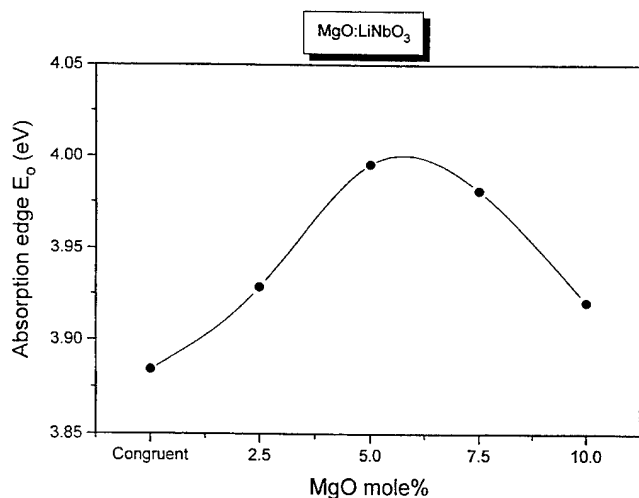


FIGURE 4. I.R. absorption spectra of the MLN crystals as a function of the MgO content.

exceeds the threshold concentration,  $Mg^{2+}$  may occupy the  $Nb^{5+}$  site, form a strongly negative charge center  $(Mg_{Nb})^{-3}$  and the  $H^+$  ion in an  $LiNbO_3$  crystal tends to gather in the  $(Mg_{Nb})^{-3}$  vicinity. The substitution of  $Mg^{2+}$  for  $Nb^{5+}$  will weaken the cation-oxygen bond with its neighbouring  $O^{2-}$  ion and strengthen the  $OH^-$  bonding. This result shifts the I.R. absorption peak into violet region. We assume that the distortion of oxygen octahedron of MLN crystals will change by some degrees by increasing the MgO ratio. This distortion of oxygen will affect the intensity of the Nb-O bond vibration, resulting in the change in the energy band structure of the MLN crystals.

#### CONCLUSIONS

$LiNbO_3$  single crystals doped with up to 10.0 mole% of MgO were grown without any precipitation. At 2.5 mole% Mg content, the density slightly drops and at 5.0 mole%, density increases again and at above 7.5 mole% it decreases gradually. The Curie temperature increased with the increase of the MgO content and reached a maximum of 1235 °C at 7.5 mole%. The optical absorption edge shifts toward the shorter wavelength region by increasing the MgO. The maximum optical absorption edge occurs at about 6 mole% of MgO. When MgO doping ratios are less than 5.0 mole%, the I.R. absorption peak position is 3470  $cm^{-1}$ . Above 7.5 mole%, the I.R. absorption peak position is 3534  $cm^{-1}$  and shifts 64

$cm^{-1}$  toward the ultraviolet side. We implied that the substitution of  $Mg^{2+}$  for  $Nb^{5+}$  will weaken the cation-oxygen bond with its neighboring  $O^{2-}$  ion. The distortion of oxygen octahedron of MLN crystals changed with increasing the MgO ratio, and this distortion affected many physical properties of the MLN crystals.

#### REFERENCE

- [1] A.A. Ballman, *J.Am.Ceram.Soc.* vol. 48, pp.112, 1965.
- [2] K. Nassau, H.J. Levinstein and G.M. Loiacono, et al., *J.Phys.Chem. Solids*, vol. 27, pp.983, 1966.
- [3] M.E. Lines and A.M. Glass, *Principles and Applications of Ferroelectrics and Related Materials*, Oxford, Clarendon Press, 1977.
- [4] A.M. Prokhorov and Yu S Kuzminov, *Physics and Chemistry of Crystalline Lithium Niobate*, Adam Hilger, 1990.
- [5] Yuhuan Xu, *Ferroelectric Materials and Their Applications*, New York: Elsevier Science Pub., ch.6, pp.247-, 1991.
- [6] A. Ashkin, G.D. Boyd, J.M. Dziedzic, R.G. Smith, A.A. Ballman, J.J. Levinstein and K. Nassu, *Appl. Phys. Lett.*, vol. 9, pp.72, 1966.
- [7] Gi-guo Zhong et al., *Proc.11th Inter. Quantum Electronic Con., IEEE Con., No. 80 CH 15610-0*, June, pp.631, 1980.
- [8] B.C. Grabmaier and F. Otto, vol. 79, pp.682, 1986.
- [9] K.L. Sweeny, L.E. Halliburton, D.A. Bryan, R.R. Rico, R. Gerson and H.E. Tomaschke, *J.Appl.Phys.*, vol. 57, pp.1036, 1985.
- [10] K. Polgar, L. Kovacs, I. Foldvari and I. Gravers, *Solid State Comm.* vol. 59, pp.325, 1986.
- [11] Feng Xi-Qi, Zhang Qi-ren, Ying Ji-Feng et al., *Science in China*, vol. A 33(1), pp.108, 1990.
- [12] P.Lerner, C.Legras and J.P.Dumas, *J.Cryst.Growth*, Vol.3, pp.231, 1968
- [13] Qiren Zang and Xiqi Feng, *Phys.Stal.Sol.* (a) vol.121, pp.429, 1990.
- [14] H.M. O'Byran, P.K. Gallagher and C.D. Brandle, *J.Am.Ceram. Soc.*, vol. 68, pp. 493, 1985.
- [15] B.C. Grabmaier, W. Wersing and W. Koestler, *J.Crystal Growth*, vol. 110, pp.339, 1991.

# Studies on Ag and Pb Doped Bi-Sr-Ca-Cu-O Superconductors

V. Syamalamba<sup>1</sup>, S. Narayana Murthy<sup>2</sup>, G. Padmavathi<sup>1</sup>, K. V. Ramana Murthy<sup>3</sup>, Ch. V. V. Satyanarayana<sup>1</sup>

<sup>1</sup>Dept. of Engineering Physics, AU College of Engineering, Andhra University, Visakhapatnam 530 003 INDIA

<sup>2</sup>Solid State Physics Laboratories, Dept. of Physics, Andhra University, Visakhapatnam 530 003 INDIA

<sup>3</sup>Dept. of Engineering Physics, S. R. K. R. Engineering College, Bhimavaram 534 202 AP INDIA

**Abstract** - Superconducting oxide materials with nominal composition Bi-Sr-Ca-Cu<sub>2</sub>O<sub>6.8</sub> modified with Ag and Pb were synthesized by the solid-state reaction method. The materials were characterized by powder X-ray diffraction. The transition temperatures are dependent on the heat treatment. The superconducting transition temperatures were observed at 93.4 K and 69 K.  $T_c^{\text{onset}}$  was decreased to 91 K for silver and lead substituted compound.

## INTRODUCTION

Since the discovery of superconductivity by Bednorz and Muller [1] in La-Ba-CuO system with K<sub>2</sub>NiF<sub>4</sub> structure [2] oxide superconductors [3] have been the subject of tremendous research and developmental interest throughout the world. Following the heels of LaBaCuO discovery, superconductivity above liquid nitrogen temperature was reported by Wu *et al* [4] in Y-Ba-CuO and Maeda *et al* [5] found onset of superconductivity ~ 105 K in Bi-Sr-Ca-CuO. Most recently, even higher- $T_c$  (~ 120 K) phases were discovered in Tl-Ba-Ca-CuO system [6,7].

Bismuth based superconducting copper oxides have two superconducting phases with  $T_c$ 's higher than the boiling point of liquid nitrogen, the highest  $T_c$  phase (~ 105 K) and a lower  $T_c$  phase (~75 K). It is well known that the properties of oxide superconductors depend strongly on the synthesis technique and processing conditions. In order to increase the high- $T_c$  phase, an addition of excess Ca and Cu and prolonged sintering [8-10] have been attempted. The introduction of Pb in Bi-Sr-Ca-CuO system helps the formation of Bi<sub>2</sub> Sr<sub>2</sub> Ca<sub>2</sub> Cu<sub>3</sub> O<sub>10+ $\beta$</sub>  (2223) phase. Among these efforts, the partial substitution of Pb for Bi has been effective in increasing the ratio of the high- $T_c$  phase.

Silver mechanically supports the brittle ceramic superconductors and can be easily worked into different geometry. Silver is the most suitable metal for fabrication of wires because it is chemically inert. In this communication we report the effect of partial substitution of bismuth by silver and lead in polycrystalline Bi-Sr-Ca-CuO samples on the superconducting properties.

## EXPERIMENTAL

### Material preparation

The following compositions have been prepared by standard powder-metallurgical technique.

(1). Bi<sub>1</sub> Sr<sub>1</sub> Ca<sub>1</sub> Cu<sub>2</sub> O<sub>6.8</sub>

(2). Bi<sub>0.5</sub> Ag<sub>0.5</sub> Pb<sub>0.5</sub> Sr<sub>1</sub> Ca<sub>1</sub> Cu<sub>2</sub> O<sub>6.8</sub>

Stoichiometric amounts of high purity (99.99%) reagent grade Bi<sub>2</sub>O<sub>3</sub>, SrCO<sub>3</sub>, CaCO<sub>3</sub>, PbO, Ag<sub>2</sub>O and CuO commensurate with the chosen nominal compositions were dry ground and ball-milled in alcohol. The mixtures were calcined in platinum crucibles at 800°C and 850°C for 24 hrs. This procedure was repeated three times to ensure good homogeneity. The substance was pressed into small discs and sintered on platinum foil at 880°C for 18 hrs and allowed to cool very slowly along with the furnace. Again the samples were heat treated at 850°C and 875°C for 15 hrs to achieve good results.

### Measurements

X-ray diffraction patterns were taken for all the synthesized compounds on a Philips X-ray diffractometer operating at 40 KV and 20 mA current using CuK $\alpha$  radiation with Ni filter. An inductance bridge with Carrier frequency amplifier test set up consisting of two coils each containing 4000 turns of 50  $\mu$ m diameter copper wire mounted suitably on a perspex base dipped in liquid nitrogen was used to quickly check the samples for superconductivity. The test sample is pre-cooled and introduced into one coil. This gave an indication whether they are superconducting at 77K or not. A positive deflection is indicative of Meissner effect (Flux expulsion).

The four probe resistivity measurements were carried out in a simple liquid nitrogen dewar following the Van der Pauw's [11] method modified by Montgomery [12] and the voltage drop across the sample was measured with Keithley Nanovoltmeter. Ultrasonically diffused indium metal contacts were made on the pellets. Temperatures were measured with a calibrated Chromel - Alumel thermocouple.

## RESULTS AND DISCUSSION

The powder synthesis techniques are likely to play a crucial role in the preparation of bulk materials. The solid state reaction is the most common process and usually requires several heating and grinding cycles. The X-ray diffraction pattern of Ag and Pb doped BiSrCaCu<sub>2</sub>O<sub>6.8</sub> is shown in Figure 1. A small

amount of unreacted CuO was exhibited in the form of impurity peaks. Successive grinding and refining eliminated the impurity peaks. The series of dominant diffraction peaks of the high-  $T_c$  phase are seen with the characteristic peaks of  $2\theta = 23.9^\circ$ ,  $28.8^\circ$ ,  $33.8^\circ$  and  $80^\circ$  K phase whose characteristic peaks are  $2\theta = 5.7^\circ$ ,  $23.2^\circ$ ,  $27.5^\circ$  are observed. The patterns were indexed and the accurate lattice parameters were obtained by least square fitting (LSQ) procedure of the high angle X-ray diffraction lines using a computer program. All the peaks are indexed [13] assuming that the high-  $T_c$  phase has a tetragonal unit cell belonging to the  $P4/mmm$  space group. The refined lattice parameters are  $a = b = 0.5354$  nm and  $c = 3.7250$  nm. The results are shown in Table 1 and Table 2.

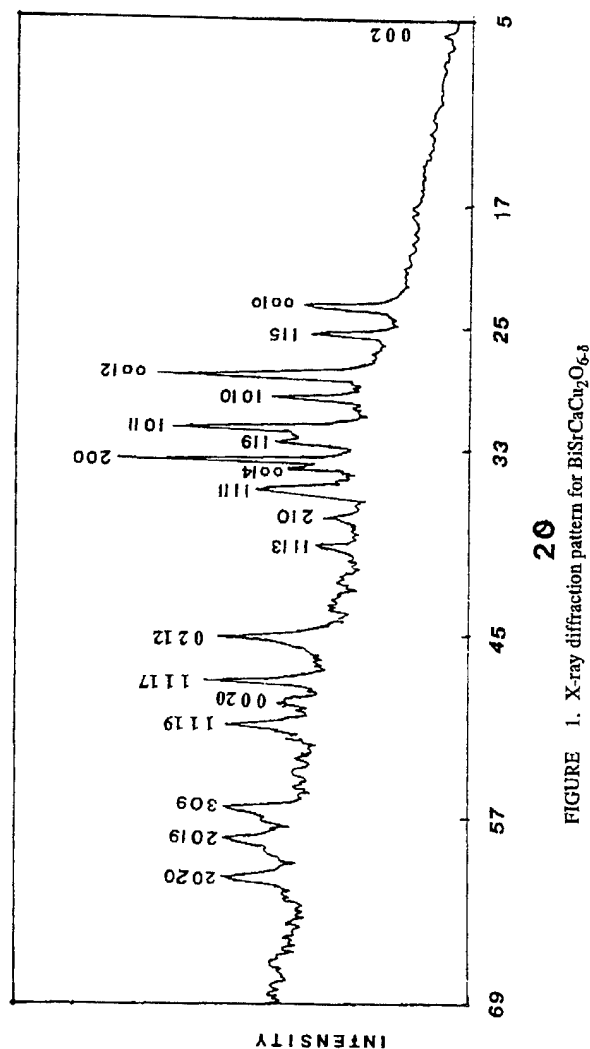


FIGURE 1. X-ray diffraction pattern for  $\text{BiSrCaCu}_2\text{O}_{6.3}$

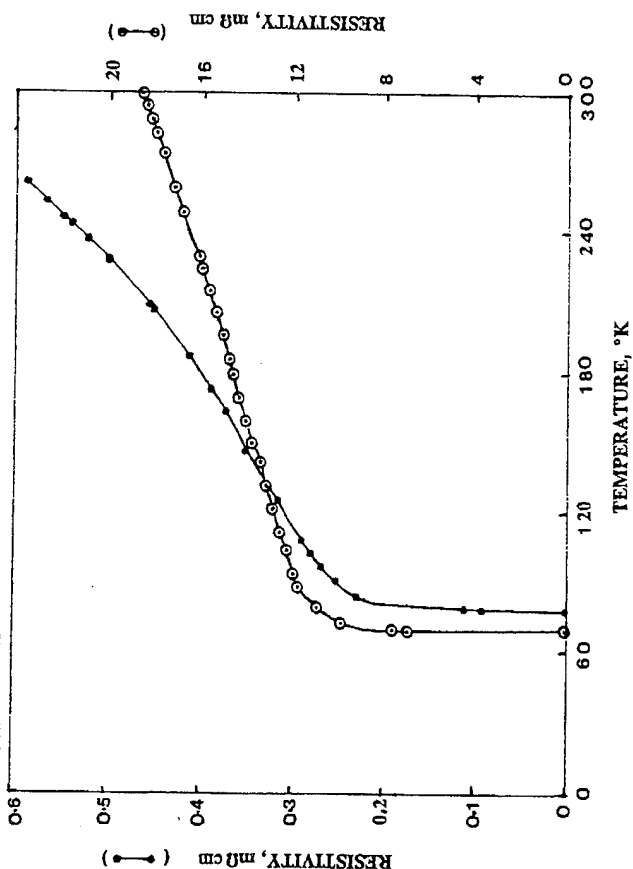


FIGURE 2. Variation of resistivity with temperature.

The results of electrical resistivity showed typical metallic behaviour at room temperature and a sharp transition to superconducting state starting around 94 K. The temperature dependance of the resistivity of the samples are shown in Figure 2. The room temperature resistivities are in the order of m ohm cm which shows the good quality of the samples. Zero resistance  $T_c$  was observed at 69 K for Bi-Sr-Ca-CuO and 77 K for silver and lead substituted compound. The superconducting transition ( $T_c^{\text{onset}}$ ) was observed at 93.4 K for BiSrCaCuO and it decreased to 91 K for Ag and Pb doped composition. It is evident from the figure that the addition of Ag and Pb decreases the  $T_c^{\text{onset}}$  and enhances the  $T_c^{\text{zero}}$  slightly to 77 K. The values are in good agreement with the literature values [14-16]. In 2nd composition, the resistivity shows a sharp drop by reducing the transition width  $\Delta T_c$  to 14 K. The presence of silver and lead might be the reason for the decrease of  $T_c^{\text{onset}}$  value in 2nd composition. Further, the material undergoes liquid phase sintering due to PbO which aids densification. In our earlier [17-19] work on Y-Ba-CuO system, we have observed that the superconducting transitions were decreased with lead substitution.

Motoi *et al* [20] have found that prolonged annealing for 20 hrs at 800°C under various oxygen partial pressures enhanced the onset transition temperatures to 94 K. The triple Cu-O layered structure of high  $T_c$  phase is stabilized by the addition of Pb. The role and importance of  $\text{CuO}_2$  layers in the enhancement of superconducting properties of oxide superconductors has been a point of uncertainties. Theoretical results suggest that increase in  $\text{CuO}_2$  layers might result in the enhancement of  $T_c$  but the experimental results has shown that the enhancement of  $T_c$  up to three  $\text{CuO}_2$  layers only *ie*;  $n = 3$  in  $\text{Bi}_2\text{Sr}_2\text{Ca}_{n-1}\text{Cu}_n\text{O}_x$ . Additional firing of the sample changes the semiconducting behaviour to metallic. The additional heat treatment promoted the superconducting properties by rendering the transition much sharper. The simultaneous substitution of Ag and Pb reduced the superconducting transitions remarkably. Similarly, Nishi *et al* [21] studied the effect of titanium in  $\text{BiSrCaCuO}$  and found that  $T_c^{\text{off}}$  was not much effected.

TABLE 1 X-ray diffraction data

Constrained refinement with A/B = 1.000000

	A	B	C	$\alpha$	$\beta$	$\Gamma$
INITIAL	5.353	5.353	37.160	90	90	90
Refined	5.354	5.354	37.250	90	90	90
Std dev	0.043	0.043	0.230	0	0	0

$$\text{SIGMA}(W*D^{**2}) = 0.84e-03$$

$$\text{WEIGHTED R} = 1.49 \text{ percent}$$

$$\text{No. of CYCLES} = 3$$

-h----k----l----rho.o----rho.c----diff-----wt-

0	0	2	0.0668	0.0537	0.0131	1.00
0	0	10	0.2651	0.2685	-0.0034	1.00
1	1	5	0.2851	0.2963	-0.0112	1.00
0	0	12	0.3158	0.3222	-0.0064	1.00
1	0	10	0.3351	0.3270	0.0081	1.00
1	0	11	0.3554	0.3494	0.0060	1.00
1	1	9	0.3641	0.3580	0.0061	1.00
2	0	0	0.3771	0.3735	0.0036	1.00
0	0	14	0.3814	0.3758	0.0056	1.00
1	1	11	0.3965	0.3962	0.0003	1.00
2	1	0	0.4159	0.4176	-0.0017	1.00
1	1	13	0.4352	0.4377	-0.0025	1.00
0	2	12	0.4964	0.4933	0.0031	1.00
1	1	17	0.5286	0.5273	0.0013	1.00
0	0	20	0.5421	0.5369	0.0052	1.00
1	1	19	0.5584	0.5744	-0.0160	1.00
3	0	9	0.6110	0.6102	0.0008	1.00
2	0	19	0.6308	0.6322	-0.0014	1.00
2	0	20	0.6563	0.6541	0.0022	1.00

TABLE 2 Resistivity data of Bi-Sr-Ca-CuO system

Composition	$T_c^{\text{onset}}$ K	$T_c^{\text{zero}}$ K	Meissner effect at 77 K	$\Delta T_c$ K
1.	93.42	69	YES	24.4
2.	91	77	YES	14

- 1 --  $\text{Bi}_1\text{Sr}_1\text{Ca}_1\text{Cu}_2\text{O}_{6-\delta}$   
2 --  $\text{Bi}_{0.5}\text{Ag}_{0.5}\text{Pb}_{0.5}\text{Sr}_1\text{Ca}_1\text{Cu}_2\text{O}_{6-\delta}$

## ACKNOWLEDGEMENTS

Thanks are due to the University Grants Commission, New Delhi for the award of research grant. One of the authors (SNM) is thankful to Council of Scientific and Industrial Research, New Delhi for Research Associateship.

## REFERENCES

- [1] J. G. Bednorz and K. Alex Muller, *Z. Phys.*, **B 64**, (1986) 189.
- [2] J. M. Tarascon, L. H. Greene, W.R. McKinnon, G.W. Hall and T. H. Geballe, *Science*, **235**, (1987) 1373.
- [3] K. Alex Muller, *Phase Transitions* (preprint).
- [4] M. K. Wu, J. R. Ashburn, C. J. Torng, P. H. Hor, R. L. Meng, L. Gao, Z. H. Huang, Y. Q. Wang and C. W. Chu, *Phys. Rev. Lett.*, **58**, (1987) 908.
- [5] H. Maeda, Y. Tanaka, M. Fukutomi and T. Asano, *Jpn. J. Appl. Phys.*, **27**, (1988) L209.
- [6] Z. Z. Sheng and Allen M. Hermann, *Nature*, **332**, (1988) 138.
- [7] L. Gao, Z. J. Huang, R. L. Meng, P. H. Hor, J. Bechtold, Y. Y. Sun, C. W. Chu, Z. Z. Sheng and Allen M. Hermann, *Nature*, **332**, (1988) 623.
- [8] A. Sumiyama, T. Yoshitosh, H. Endo, J. Tsuchiya, N. Kijima, M. Mizuno and Y. Oguri, *Jpn. J. Appl. Phys.*, **27**, (1988) L542.
- [9] B. W. Statt, Z. Wang, M. J. Lee, J. V. Yakhmi, P. C. De Camargo, J. F. Major and J. W. Rutter, *Physica C*, **156**, (1988) 251.
- [10] D. Kovacheva, K. Petrov, V. Lovchinov, E. Nazarova, P. Docheva, G. Melnikiev and V. Kovachev, *Physica C*, **162-164**, (1989) 1227.
- [11] L. J. Van der Pauw, *Philips Res. Rep.*, **13**, (1958) 1; *Philips Res. Rev.*, **20**, (1958) 220.
- [12] H. C. Montgomery, *J. Appl. Phys.*, **42**, (1971) 2971.
- [13] U. Endo, S. Koyama and T. Kawai, *Jpn. J. Appl. Phys.*, **27**, (1988) L1476.



- [14] K. Konstantinov, D. Kovacheva, N. Balcev, V. Kovachev, **J. Mater. Sci. : Materials in Electronics**, **3**, (1992) 127.
- [15] K. Mori, Y. Isikawa, T. Ban, K. Sato and K. Rokudo, **Physica C**, **162-164**, (1989) 923.
- [16] T. Fujii, Y. Nagano and J. Shirafuji, **J. Crystal Growth**, **110**, (1991) 994.
- [17] A. Bhanumathi and S. Narayana Murty, **Ferroelectrics**, **102**, (1990) 351.
- [18] S. Narayana Murty, K. Umakantham, A . Bhanumathi and K. Linga Murty, **Jpn. J. Appl. Phys.**, **30**, (1991) 472.
- [19] S. Narayana Murty, K. Umakantham, S. Bangar Raju, K. Linga Murty, **Ferroelectrics**, (1994) In Press.
- [20] Y. Motoi, Y. Ikeda, H. Uwe and T. Sakudo, **Physica C**, **162-164**, (1989) 929.
- [21] Y. Nishi, K. Nozaki, T. Kurotaki, Y. Kita and K. Oguri, **J. Mater. Sci. Lett.**, **11**, (1992) 1211.

# DIELECTRIC AND PIEZOELECTRIC PROPERTIES OF STACKED AND PLATED PVDF, P(VDF/TeFE), P(VDF/TrFE) AND CERAMIC/RUBBER COMPOSITE THICK FILMS

Philip E. Bloomfield

Drexel University, Biomedical Engineering and Science Institute, Philadelphia, PA 19104

**Abstract** -- We measured the properties of nine different piezoelectric materials, as supplied, and as further processed to increase their hydrostatic sensitivity. We studied the effect of electrode material, stiffening plates, and multiple layering on the piezoelectric and dielectric properties of the thick piezopolymer films. Dielectric measurements and thickness mode  $d_{3t}$ , lateral mode  $d_{31}(d_{32})$ , and hydrostatic mode  $d_h$  piezoelectric coefficients were measured at different stages of the films' processing into layered stacks. The polymer films were bonded together to produce two-layer and three-layer thick films. Metal stiffening plates bonded to the films' outside surfaces inhibit lateral response and hence improve hydrostatic voltage response. The highest sensitivities result from the thickest P(VDF/TrFE) samples with the lowest dielectric constants and stiffest clamping plates.

## INTRODUCTION

We discuss and present the results of our investigation of the thickness and hydrostatic voltage sensitivity dependence of piezoelectric polymers on VDF-comonomer composition (homopolymer PVDF or copolymerized with TeFE (tetrafluoroethylene) or TrFE (trifluoroethylene), sample thickness, and clamping of the sample's lateral response.

As is well understood, a sample's voltage response is directly proportional to the product of the piezoelectric voltage coefficient and the sample thickness. Also, the hydrostatic piezoelectric voltage coefficient  $g_{3h}$  equals the  $g_{33}$  response diminished by the sum of the lateral responses:

$$g_{3h} = g_{33} + g_{31} + g_{32}, \quad |g_{31} + g_{32}| < |g_{33}|$$

$$|g_{3h}| = |g_{33} + g_{31} + g_{32}| < |g_{33}|, \quad g_{33} < 0, \quad g_{31}, g_{32} > 0 \quad (1)$$

With  $\epsilon$  the sample's dielectric constant in the polar direction and  $v = 1, 2, 3, h$ , or  $t$  we note that the piezoelectric voltage coefficients are related to the piezoelectric strain coefficients by

$$g_{3v} = d_{3v} / \epsilon \quad (\text{V/m})/\text{Pa} \quad (2)$$

The first index, 3, stands for the polar (thickness) direction while the second index stands for the mechanical direction. The (closed circuit,  $E_3=0$ ) thickness mode charge response to stress in the thickness direction  $d_{3t}$  is measured while the sample is laterally clamped ( $S_1=S_2=0$ ).

We first adhered a steel plate to one surface of a piezoelectric film sample. This reduces  $d_{3t}$  and increased  $d_{3h}$  somewhat. Then we adhered steel plates to both outside surfaces of the piezoelectric film sample. This approximately doubled the hydrostatic piezoelectric response- As noted the

voltage response equals the charge response divided by the dielectric constant. Here the major differences between the four polymer compositions are exhibited. For the NTK ceramic/rubber composite  $\epsilon/\epsilon_0=39$ ; for the PVDF samples  $\epsilon/\epsilon_0=12-14$ ; for the P(VDF/TeFE) samples  $\epsilon/\epsilon_0=10.5-11.5$ ; and for the P(VDF/TrFE) samples  $\epsilon/\epsilon_0=6.8-8.5$ .

In sections below we discuss the measurements carried out and the mechanical properties of the metal stiffening plates utilized, and derive formulae for clamped  $d_{3t}$  and  $d_{3h}$ .

## ORIGINATION AND PREPARATION OF SAMPLES

Commercial samples of polarized and metallized piezoelectric sheets were obtained. They are listed here with [(i) Source; and (ii) Origin]. Dimensions specify thickness. All P(VDF/TrFE) films were 75/25 molar composition.

(A) 530 $\mu\text{m}$  uniaxially oriented (simultaneously rolled and poled) PVDF films with vacuum deposited aluminum electrodes [(i) Solvay Tech. Inc; (ii) Thompson CSF, France].

(B) 775 $\mu\text{m}$  uniaxially oriented P(VDF/TeFE:81/19 molar composition) films with silver elastomeric electrodes [(i) NUSC 1991, New London, CN; (ii) Pennwalt Corp.].

(C) 500 $\mu\text{m}$  unoriented P(VDF/TrFE) films with Ni/Al vacuum deposited electrodes [(i) Atochem, Valley Forge, PA]

(D) 110 $\mu\text{m}$  uniaxially oriented PVDF films with silver elastomeric electrodes [(i) DTRC, Washington, DC; (ii) Atochem, USA].

(E) 900 $\mu\text{m}$  unoriented P(VDF/TrFE) film with 187 $\mu\text{m}$  brass plate electrodes [(i) 1990 DTRC].

(F) 500 $\mu\text{m}$  unoriented P(VDF/TrFE) film with silver elastomeric electrodes [(i) DTRC 1991; (ii) Atochem, USA].

(G) 2.3mm ceramic composite with 500 $\mu\text{m}$  conducting rubber electrodes [(i) NTK Rubber Co., Japan].

(H) 468 $\mu\text{m}$  unoriented P(VDF/TrFE) film with 225 $\mu\text{m}$  aluminum plate electrodes [(i) Atochem, USA].

(I) 781 $\mu\text{m}$  unoriented P(VDF/TrFE) film with 125 $\mu\text{m}$  aluminum plate electrodes [(i) NUSC 1991].

Samples (A)-(D) were measured individually and at two and three times thickness by bonding several films in series with thin non-conducting epoxy. Also 310 $\mu\text{m}$  steel plates were bonded on one side and both sides of the samples to provide them with stiff plate electrodes. Measurements were made on samples (E)-(I) as received.

## PROPERTIES MEASURED

We measured the dielectric properties, capacitance and loss-

tangent at 0.020, 0.046, 0.100, 1, 5, 10, and 20 kHz. For samples (A)-(D) we measured  $d_{31}$  and  $d_{32}$ . The piezoelectric charge coefficients,  $d_{31}$  and  $d_{32}$ , were measured for all samples. We calculated the hydrostatic voltage sensitivity:  $S = 20 \log [t \cdot g_{3h} (V/Pa) / (1V/\mu Pa)] = 20 \log (10^{-6} \cdot t^p \cdot g_{3h})$  dB (3)

## THEORY OF PIEZOELECTRIC STRAIN AND CHARGE COEFFICIENTS FOR A CLAMPED SAMPLE

Here we derive the piezoelectric coefficients which are effective when a sample is laterally clamped by thick metal plates. This consideration is important for the two cases: (1) When measuring the charge response  $d_{33}$  to a stress  $T_3$  by imposing a tensile or compressive stress on a sample whose lateral dimensions are large compared to thickness, the sample is both self-clamped and clamped by the measuring apparatus. (2) When measuring the charge response  $d_{ch}$  to hydrostatic stress of a sample which is constrained by bonded stiffening plates, the sample is clamped by the thick metal electrodes.

**Calculation of  $d_{3T}$ :** Consider first the measurement of the charge response to a stress  $T_3$  imposed in the thickness direction by clamping plates (by glass plates driven by a shaker apparatus or by thick platens of a hydraulic press). The clamping plates impose lateral stresses  $T_1^p$  and  $T_2^p$  on the piezofilm which in turn by Newton's third law reacts back on each plate with opposing stresses  $T_1^b$  and  $T_2^b$ ,

$T_3 = T_3^p = T_3^b$ ,  $T_k^b = -\gamma T_k^p$ , ( $k=1,2$ ),  $\gamma = t^p/(2t^b)$ . (4) Here the superscripts b and p refer to the metal (brass) and piezopolymer materials, respectively and  $\gamma$  is the polymer to metal thickness ratio. For closed circuit ( $E_3=0$ ) conditions:

$$D_3 = d_{33}T_3 + d_{31}T_1^p + d_{32}T_2^p \equiv d_{3T}T_3 \quad (5)$$

$$S_k^b = S_{k1}^b T_1^b + S_{k2}^b T_2^b + S_{k3}^b T_3 = S_k^p = S_{k1}^p T_1^p + S_{k2}^p T_2^p + S_{k3}^p T_3. \quad (6)$$

In these equations  $k=1$  or 2 and we assume equilateral strains in the two adhered materials. For piezofilm stretched uniaxially along the 1-axis  $s_{11}=s_{22}$  and  $s_{12}=s_{13}=s_{23}$ . We consider here only the isotropic case where  $s_{11}=s_{22}$  and  $s_{13}=s_{23}$ . Inserting (4) into (6) yields:

$$T_1^p = T_2^p = c_{112}(s_{13}^p - s_{13}^b)T_3 \quad (7)$$

$$\text{where } c_{112} \equiv [s_{11}^p + s_{12}^p + \gamma(s_{11}^b + s_{12}^b)]^{-1}. \quad (8)$$

Then substituting (7) into (5) yields:

$$d_{3T} = d_{33} - c_{112}(s_{13}^p - s_{13}^b)(d_{31} + d_{32}). \quad (9)$$

Note that  $d_{3T}$  is smaller in magnitude than  $d_{33}$  since  $s_{11}^p > |s_{12}^p|$ ,  $|s_{13}^p| > |s_{13}^b|$ , and  $s_{12}^p, s_{13}^p, d_{33} < 0$  while  $d_{31} > 0$ .

**Calculation of  $d_{ch}$ :** Next consider the closed circuit charge response to applied hydrostatic stress. Here, the lateral pinning stresses of eq. (4) are also present.

$$T_{1h} = T_{2h} = T_{3h} = T_h \quad (10)$$

$$D_3 = d_{33}T_h + d_{31}(T_h + T_1^p) + d_{32}(T_h + T_2^p) = d_{3h}T_h + d_{31}T_1^p + d_{32}T_2^p \equiv d_{ch}T_h \quad (11)$$

$$S_k^b = S_{k3}^b T_h + S_{k1}^b (T_h + T_1^p) + S_{k2}^b (T_h + T_2^p) = S_k^p \quad (12a)$$

$$S_k^p = S_{k3}^p T_h + S_{k1}^p (T_h + T_1^p) + S_{k2}^p (T_h + T_2^p)$$

$$S_k^p = (S_{k1}^p + S_{k2}^p + S_{k3}^p)T_h + S_{k1}^p T_1^p + S_{k2}^p T_2^p. \quad (12b)$$

Here  $S_{k1}^p + S_{k2}^p + S_{k3}^p = s_{11}^p + 2s_{12}^p = (1/3) \cdot \text{compressibility}$ , (13) is the linear hydrostatic compliance,  $s_{1h}$ . Then insert (4) in eqs. (12) to obtain (14) which with (11) yields (15):

$$T_1^p = T_2^p = c_{112}(s_{1h}^p + s_{1h}^b)T_h \quad (14)$$

$$\begin{aligned} d_{ch} &= d_{33} - c_{112}[s_{13}^p - s_{13}^b - (1+\gamma)(s_{11}^b + s_{12}^b)](d_{31} + d_{32}) \\ &= d_{3h} - c_{112}(s_{1h}^p - s_{1h}^b)(d_{31} + d_{32}) \\ &= d_{3h} + c_{112}[(1+\gamma)(s_{11}^b + s_{12}^b)](d_{31} + d_{32}). \end{aligned} \quad (15)$$

In the last line of equation (15) we see how the clamped thickness mode piezoelectric coefficient is diminished to yield the clamped hydrostatic piezoelectric constant [3].

## DISPOSITION OF SAMPLES AND THEIR ELECTRODES

In Tables 1 and 2 and the Figure we present mechanical properties of PVDF and metal plate electrodes and stacks.

### 1. PLATE AND PVDF MECHANICAL PROPERTIES [1,2]

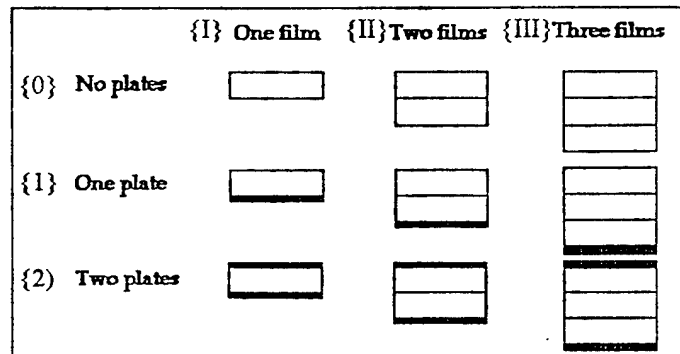
	$\rho(\text{g/cm}^3)$	$E(\text{GPa})$	$v(\text{km/s})$	$Z(\text{MRayl})$
Al	2.7	70	5.09	13.7
Steel	7.9	205	5.09	40.2
Brass	8.5	110	3.6	30.6
PVDF	1.8	9*	2.24	4.0

Data are mass density [ $\rho$ ], average modulus of elasticity [ $E=(s_{11})^{-1}$  for the metals; and elastic stiffness\*  $c_{33}$  for PVDF], longitudinal sound velocity [ $v$ ], and acoustic impedance [ $Z$ ].

### 2. COMPLIANCES [1-3] AND THICKNESS RATIOS

	$s_{11}(\text{GPa})^{-1}$	$s_{12}(\text{GPa})^{-1}$	$\gamma$
Al	0.014	-0.005	1.04(H), 3.12(I)
Steel	0.0049	-0.002	$[(t^p)/620\mu\text{m}](\text{A-D})$
Brass	0.0091	-0.003	2.41(E)
P(VDF/TrFE)	0.33	-0.14	

Samples (A)-(D) are pictured schematically in the Figure. As indicated one thickness ( $t^p$ ) of samples (A), (B), (C), (D), two of (A), (B), (C), and three of (C) were used to make the steel plate clamped stacks.



### Piezopolymer Film and 310 $\mu\text{m}$ Steel Plate Configurations

Films (A), (B), (C), (D) used in Configuration {I.0}, {I.2}.

Films (A), (B), (C) in Config. {II.1}, {II.0}, {II.1}, {II.2}

Films (C) used in Configuration {III.0}, {III.1}, {III.2}.

# PIEZOELECTRIC CHARGE COEFFICIENTS, HYDROSTATIC VOLTAGE SENSITIVITIES AND DIELECTRIC CONSTANTS OF SINGLY, DOUBLY, AND TRIPLY STACKED, PLATED SAMPLES

Note: Measurements were carried out at room temperature.

**Thickness Mode,  $d_{3t}$ :** The perfect clamping described above is modified for longitudinal stress imparted by a Berlincourt-Type- $d_{33}$ -Meter. Films thicker than a few hundred  $\mu\text{m}$  are not thin compared to the clamping plate radius (0.5-3mm). One observes effective " $d_{33}$ "s increasing from  $d_{3t}$  toward  $d_{33}$  as the sample thickness increases.

## 3. Measurement of $-d_{3t}(\text{pC/N})$ -Berlincourt-Type: 20-100Hz Films A-D according to pictured scheme with steel plates:

A:	<u>{I.0}</u>	<u>{I.1}</u>	<u>{I.2}</u>	<u>{II.0}</u>	<u>{II.1}</u>	<u>{II.2}</u>		
	34	23	16	34	28	20		
B:	<u>{I.0}</u>		<u>{I.2}</u>	<u>{II.0}</u>	<u>{II.1}</u>	<u>{II.2}</u>		
	29		14	29	26	16		
C:	<u>{I.0}</u>	<u>{I.1}</u>	<u>{I.2}</u>	<u>{II.0}</u>	<u>{II.1}</u>	<u>{II.2}</u>	<u>{III.1}</u>	<u>{III.2}</u>
	33	24	18	31	27	18	30	18
D:	<u>{I.0}</u>		<u>{I.2}</u>					
	29		15					

Samples F and G: F: 28, G: 44

Films A and C (vacuum deposited electrodes) have the highest  $d_{3t}$  coefficients. Films B, D, and F (Ag elastomeric electrodes) have their  $d_{3t}$ 's reduced by 15% compared to films A and C. One plate reduces  $d_{3t}$  by 10-30% while  $d_{3t}$  is reduced by ~50% for plates on both sides of the sample.

**Transverse Mode,  $d_{31}$  and  $d_{32}$ :** During measurement stress was imposed at 20-100 Hz on clamped single film samples cut 5/1 in the stressed/unstressed transverse directions. For films A, B, and D  $d_{31} > d_{32}$  since they had been uniaxially stretched in the 1-direction during production. Films C and F, being unoriented, have  $d_{31} \approx d_{32}$ .

## 4. Measurement of $d_{31}$ and $d_{32}(\text{pC/N})$ -20-100Hz

	A:	B:	C:	D:	F:
$d_{31}$ :	24	18	14	24	13
$d_{32}$ :	7	8	14	5	13

Uniaxially oriented PVDF films (A and D) have highest  $d_{31}$  and lowest  $d_{32}$ ; uniaxially oriented VDF/TeFE copolymer film B has lower anisotropy; and unoriented P(VDF/TrFE) films (C and F) have  $d_{31}$  and  $d_{32}$  balanced. Note that film A has the largest value of ( $d_{31} + d_{32}$ ).

**Hydrostatic Mode,  $d_{3h}$ , Dielectric Constant,  $\epsilon/\epsilon_0$ , Loss Tangent,  $\tan\delta$ , and Hydrostatic Voltage Sensitivity, S** The hydrostatic charge response is measured at 20-200Hz in a calibrated loudspeaker-driven air chamber. Consistent results are obtained for films thicker than 100 $\mu\text{m}$ . The capacitance

and  $\tan\delta$  were measured on an automated self-averaging audio frequency bridge. From the sample dimensions  $\epsilon/\epsilon_0$  was calculated and then from eqs. (2) and (3)  $g_{3h}$  and S were found.

## 5. Dielectric and Hydrostatic Response: Samples (D)-(I)

	20-100Hz			1kHz		10kHz
	$-d_{3h}$	$-g_{3h}$	S	$\epsilon/\epsilon_0, \tan\delta$		
D:	8	0.08	-221	11.7, 0.01	11.5, 0.01	11.2, 0.03
D{I,2}:	20	0.19	-213	11.7, 0.06	11.5, 0.02	11.2, 0.03
E:	19	0.32	-191	6.8, 0.01	6.7, 0.01	6.5, 0.02
F:	13	0.20	-200	7.5, 0.02	7.3, 0.01	7.0, 0.03
G:	34	0.10	-193	38.9, 0.08	34.7, 0.26	15.9, 1.08
H:	17	0.28	-198	6.8, 0.01	6.7, 0.01	6.5, 0.02
I:	14	0.21	-195	7.4, 0.02	7.2, 0.01	7.1, 0.02

## 6. Dielectric and Hydrostatic Response for Sample (A)

Note:  $t^P\{I\}=530\mu\text{m}$ ,  $t^P\{II\}=1060\mu\text{m}$

	20-100Hz			1kHz		10kHz
	$-d_{3h}$	$-g_{3h}$	S	$\epsilon/\epsilon_0, \tan\delta$		
{I.0}	11	0.10	-205	12.2, 0.013	11.8, 0.017	11.5, 0.04
{I.2}	17.5	0.16	-201	12.5, 0.02	12.1, 0.02	11.7, 0.04
{II.0}	9.3	0.08	-201	12.6, 0.014	12.3, 0.018	11.9, 0.04
{II.1}	10.5	0.10	-200	12.5, 0.03	11.9, 0.02	11.5, 0.04
{II.2}	17	0.15	-196	12.5, 0.03	12.1, 0.02	11.7, 0.04

## 7. Dielectric and Hydrostatic Response for Sample (B)

Note:  $t^P\{I\}=770\mu\text{m}$ ,  $t^P\{II\}=1530\mu\text{m}$

	20-100Hz			1kHz		10kHz
	$-d_{3h}$	$-g_{3h}$	S	$\epsilon/\epsilon_0, \tan\delta$		
{I.0}	13	0.14	-199	10.6, 0.009	10.4, 0.01	10.2, 0.02
{I.2}	16.4	0.16	-198	10.8, 0.015	10.5, 0.01	10.3, 0.02
{II.0}	12	0.12	-194	10.9, 0.016	10.6, 0.017	10.4, 0.02
{II.1}	12	0.13	-194	11.0, 0.03	10.6, 0.015	10.3, 0.02
{II.2}	17	0.15	-192	10.9, 0.04	10.6, 0.017	10.3, 0.02

## 8. Dielectric and Hydrostatic Response for Sample (C)

Note:  $t^P\{I\}=500\mu\text{m}$ ,  $t^P\{II\}=1010\mu\text{m}$ ,  $t^P\{III\}=1510\mu\text{m}$

	20-100Hz			1kHz		10kHz
	$-d_{3h}$	$-g_{3h}$	S	$\epsilon/\epsilon_0, \tan\delta$		
{I.0}	12.2	0.17	-201	8.2, 0.02	7.9, 0.016	7.7, 0.03
{I.1}	14.3	0.21	-200	7.8, 0.02	7.6, 0.02	7.4, 0.03
{I.2}	21	0.29	-197	8.0, 0.02	7.8, 0.016	7.6, 0.03
{II.0}	10.5	0.15	-197	8.0, 0.02	7.7, 0.02	7.5, 0.03
{II.2}	19.1	0.27	-191	8.1, 0.03	7.7, 0.02	7.5, 0.03
{III.0}	10.7	0.15	-193	8.1, 0.02	7.9, 0.02	7.6, 0.03
{III.1}	13.3	0.19	-191	7.8, 0.04	7.3, 0.03	7.1, 0.04
{III.2}	19.6	0.26	-188	8.3, 0.05	8.0, 0.02	7.8, 0.03

From eq.(15) we see that smaller  $\gamma$  implies greater enhancement of  $d_{3h}$ . This is illustrated in Table 5. With steel clamping plates on both sides of film D and  $\gamma=0.18$  sensor D{I,2} has 2½ times the hydrostatic activity of film D.

Sensors (H) and (I) are constructed similarly of Al plate clamping electrodes and P(VDF/TrFE) piezofilm; however  $\gamma(H)=1.04$  and  $\gamma(I)=3.12$ ; so, as expected,  $d_{3h}(H) > d_{3h}(I)$ . From Table 8 similar piezofilm (C) has  $d_{3h}=-12.2\text{pC/N}$  enhanced for C{I.2} to  $-21\text{pC/N}$  by  $\gamma=0.81$  stiffer steel plates. Also sensor (E) with  $\gamma=2.41$  intermediate stiffness brass plates has its  $d_{3h}$  enhanced to a value intermediate to that of sensors (H) and C{I.2}. Of all the piezofilms sample D shows the most enhancement (smallest  $\gamma$  with stiffest metal). Sample C shows the next highest fractional increase of activity for a single film. Samples A and C show the same fractional increases for multiply layered films; sample B shows the least fractional increase with addition of two steel stiffening plates. Note that sensor B{II.2} and C{III.2} have similar thicknesses; however the TrFE copolymer sensor has higher activity than the TeFE copolymer.

## DISCUSSION AND CONCLUSIONS

In this paper the formulae for the clamped thickness mode and hydraulic pressure mode piezoelectric constants are given [in eqs (9) and (15)]. For complete clamping (cc) which can be achieved in a hydraulic press with thick steel platens or in a Berlincourt meter utilizing thick large diameter flat steel probes or in a hydraulic pressure cell when the sample is clamped with thick stiff plates ( $\gamma \approx 0$ ;  $s_{13}^P \approx s_{12}^P$ ;  $s_{12}^b$ ;  $s_{11}^b \ll s_{12}^P$ ,  $s_{11}^P$  and film diameter = clamping diameter  $\gg t^P$ ) eq. (9) or eq. (15) yields:

$$d_{3\text{cc}} \approx d_{3\text{hcc}} \approx d_{33} - (s_{11}^P + s_{12}^P)^{-1} s_{12}^P (d_{31} + d_{32}). \quad (16)$$

Thus for complete clamping the thickness and hydraulic pressure modes are equal.

We note that in the limit of no clamping  $\gamma \rightarrow \infty$  and we obtain from formulae (9) and (15) that  $d_{3t} \rightarrow d_{33}$  and  $d_{ch} \rightarrow d_{3h}$ .

From Tables 5-8 we construct Tables 9 and 10 to compare the hydrostatic figure of merit for the various samples.

### 9. No clamping plates: $d_h(\text{pC/N})$ , $g_h(\text{V/m/Pa})$ , $d_h g_h(1/\text{TPa})$

	A	IIA	D	B	IIB	C	IIC	IIIC	F	G
$-d_{3h}$	11	9.3	8	13	12	12.2	10.5	10.7	13	34
$-g_{3h}$	0.10	0.08	0.08	0.14	0.12	0.17	0.15	0.15	0.20	0.10
$d_h g_h$	1.1	0.74	0.64	1.82	1.44	2.07	1.58	1.58	2.6	3.4

### 10. Films with 2 clamping plates

	A	IIA	D	B	IIB	C	IIC	IIIC	E	H	I
$-d_{3h}$	17.5	17	20	16.4	17	21	19.1	19.6	19	17	14
$-g_{3h}$	0.16	0.15	0.19	0.16	0.15	0.29	0.27	0.26	0.32	0.28	0.21
$d_h g_h$	2.8	2.55	3.8	2.62	2.55	6.09	5.16	5.10	6.08	4.76	2.94
$\gamma$	0.85	1.71	0.18	1.24	2.47	0.81	1.63	2.44	2.41	1.04	3.12

Tables 9 and 10 are summary tables presenting the room temperature hydrostatic figure of merit for free and clamped

piezopolymer films, respectively. We see that among the free films the ceramic rubber composite material G has the highest  $d_h g_h$  product. The P(VDF/TrFE) films F and C have the next highest values. All of the clamped piezofilm  $d_h g_h$  products exceed the unclamped values. Here the highest values are associated with the P(VDF/TrFE) films C and E.

We note that the brass clad sample E (as well as the steel clad sample C) has slightly higher  $d_h g_h$  value than in [3] where the smallest  $\gamma$  obtained was 1.5 and yielded  $d_h g_h = 5.36$ . Sample E's lower  $\epsilon$  value is responsible for its higher figure of merit. On the other hand Sample C has higher  $d_{33}$  and  $(d_{31} + d_{32})$  values than in [3]  $\{d_{33} = d_{3h} - (d_{31} + d_{32}) = -40$  versus 33.5 and 21.4, respectively}.

The  $d_{3t}$  measurements reported in Table 3 were not taken under completely clamped conditions so that only the values measured with the sample sandwiched between metal plates corresponds to eqs. (9) and (16). For example using the approximate values from Table 2 eq. (16) yields

$$d_{3\text{cc}} \approx -40 + 0.737 \cdot 28 = -19.4 \quad (17)$$

which compares with measured value -18 in Table 3.

The factor  $\gamma$  has been dropped from eq. (16). If included, the second term in eq. (16) would be enhanced by 0.5% for Sample II.2C and by 15% for Sample E (thus reducing the value of  $d_{3\text{cc}}$ ) for example.

We have studied the piezoelectric properties of unclamped and plate-clamped oriented and unoriented thick piezofilms of three copolymerized VDF compositions. The metal plates were aluminum, brass, and steel. Formulae for the clamped  $d_{33}$  and  $d_{3h}$  were derived and discussed. Reasonable agreement between measurement and theory was obtained. Smaller  $\gamma$  is desired to enhance  $d_{ch}$ ; however the voltage sensitivity  $S$  depends directly on the sample thickness (See eq.(3) and Tables 5-8). Reasonable and practical design parameters can be chosen to achieve useful devices. [4]

## ACKNOWLEDGEMENTS

We wish to thank Tim Diep and Francisco Castro of the ECE Dept. for help with the  $d_{3h}$  and dielectric measurements which were funded by the Carderock Division of Naval Surface Warfare Center.

## REFERENCES

- [1] Charles Kittel, *Introduction to Solid State Physics*, 3rd ed., 1968, John Wiley & Sons, Inc., N.Y.
- [2] Lawrence H. Van Vlack, *Elements of Materials Science and Engineering*, 6th ed., 1989, Addison-Wesley, N.Y.
- [3] The first form of eq. (15) was given without derivation by H. Wang, Q.M. Zhang, L.E. Cross, and A.O. Sykea, *Ferroelectrics*, **150**, 255-266 (1993). Note that these authors'  $\gamma$  is twice that used here.
- [4] DTRC, NUSC, Jim Powers, private conversation.

# Concurrent Session - 1C: Piezoelectrics

# DEVELOPMENT OF 1-3 PZT-POLYMER COMPOSITE FOR LOW FREQUENCY ACOUSTICAL APPLICATIONS

C. RICHARD, R.Y. TING<sup>1</sup>, C. AUDOLY<sup>2</sup>

INSA - Laboratoire de Génie Electrique et Ferroélectricité  
69621 VILLEURBANNE Cedex - France

<sup>1</sup>U.S. Naval Research Laboratory-USRD, Orlando, FL 32856-8337

<sup>2</sup>DCN Ingénierie Sud - BP.30 - 83800 Toulon Naval - France

**Abstract** - Piezoelectric 1.3 composites of PZT-epoxy and PZT-polyurethane compositions were developed for investigations in low-frequency acoustical applications. Samples with different PZT volume fractions and varying PZT rod aspect ratios (from 4x4x9 to 1x1x9 mm<sup>3</sup>) were fabricated by using the "dice and fill" method. Experimental measurement in the 3.3 mode in air was carried out by using a Laser-Doppler Vibrometry (LDV) technique. Strain profiles of the composite sample driven by a low-frequency ac electric field excitation was obtained. The result showed that PZT rod aspect ratio has a drastic effect on composite performance. A quasi-static model based on an isolated 1.3 composite unit-cell was developed to account for the stress transfer at the PZT-polymer interface. Analysis result showed that an aspect ratio of 20 or higher is necessary for low frequency sensing or projecting application of 1.3 piezocomposites. For use in the 3.3 mode, a soft polymer was shown to be preferred, since the longitudinal clamping of the PZT rod is greater for hard resins.

## INTRODUCTION

Piezoelectric composites made of PZT rods aligned in parallel and embedded in a polymer matrix are interesting materials. They exhibit piezoelectric properties comparable and even better than the bulk PZT material ones. It is then possible to develop a material presenting simultaneously the active properties of the PZT and a very low weight since the density of a 10% PZT volume fraction composite is only 1700 Kg/m<sup>3</sup>. Many studies have been carried out in order to predict the performances of a 1.3 PZT-Polymer composite. Most of these studies [1][2] are derived from the parallel model assuming equal strain of both components. Those results are effective in the case of a composite with an ideally fine structure or with a high PZT volume fraction. Recently, more comprehensive studies of the mechanisms of stress-transfer in the composite and its consequences on the composite performances have been proposed [3][4] showing and quantifying the great importance of the composite structure scale factor or of the PZT rod aspect ratio (ratio of the length to the rod radius or rod half width).

It is also the purpose of this study to quantify the error due to the equal strain assumption and to propose a simple alternative model taking into account the size of the rod and allowing to give the general trends related to the rod aspect ratio.

The experimental and theoretical results given are concerned essentially with the 1.3 composite used in the 3.3 quasi-static mode. The composite sample preparation is first presented, then the measurement procedure is described. A theoretical model, derived from structural composite studies is proposed, which is based upon a simplified expression of the shear stresses appearing at the PZT-polymer interface. Finally, the results are compared and discussed.

## EXPERIMENTAL

### Sample Fabrication and Material Data

Because the main advantage of a 1.3 composite is its low density, the present study is principally focused on samples in the low PZT volume fraction range. Two sets of five 1.3 composites samples with square rods have been made using a single PZT material and two polymer resins. In each set, 3 PZT volume fractions were investigated (10, 20, 40 %) with a rod aspect ratio equal to 18. The aspect ratios were then compared (4.5, 9 and 18) for a 10 % PZT volume fraction (see Table 3). The samples were 49 mm in diameter and 9mm thick.

The PZT material, P188 (Quartz & Silice, St Gobain Nemours - France) is a Navy type II PZT. Its physical properties are given on Table 1. Note that the characteristics obtained in this study are slightly different to the nominal constants of P188, perhaps due to imperfect poling conditions. The actual values are measured by a resonance method on test samples poled in the same conditions as the composites.

Two polymer resins were used: a rather hard epoxy resin: EPON 828 (Schell Chemical Company, Oak Brook, IL), and a polyurethane: PR1538 (Products Research & Chemical Corp., Glendale, CA). The physical properties of these materials are given in Table 2.

The 1.3 composite samples were made with the "dice and fill" method [5]. The unpoled ceramic block was 48 mm in diameter and 12 mm thick. In order to achieve the necessary PZT rod aspect ratios and volume fractions, 3 diamond blades have been used (for a 20 mils, 40 mils and 80 mils kerf) and a 9 mm slot depth has been maintained for the whole cutting operation. A complete description of the samples is given in Table 3. The embedding was carried out in one stage for the epoxy samples and in 3 stages for the polyurethane ones in order to facilitate the degassing of the resin after pouring. The polyurethane resin was cured overnight at 80°C. Two types of curing processes were used with the epoxy resin : an overnight curing at 125°C with a 2,5 %

**TABLE 1** : Physical properties of PZT P188 measured with a resonance method.

data	nominal poling	This study poling
$\rho$ (Kg/m <sup>3</sup> )	7800	7800
$\epsilon_{33}^E$ ( $10^{-12}$ .Pa <sup>-1</sup> )	20.3	19.5
$\epsilon_{33}^D$ ( $10^{-12}$ .Pa <sup>-1</sup> )	9.60	9.30
$d_{33}$ (pC/N)	427	380
$d_{31}$ (pC/N)	-202	-180
$\epsilon_r$	1930	1600

**TABLE 2** : Physical properties of the polymer resins  
(at 1KHz and 25°C )

data	EPON 828	PRC PR1538
$\rho$ (Kg/m <sup>3</sup> )	1190	1097
E ( Gpa )	2.65	0.08
$\sigma$ ( Poisson's ratio )	0.36	0.49

BCI<sub>3</sub> amine cure agent (samples 6,9 and 10) or an over-night curing at room temperature with an EPON cure agent U (samples 7-8). The room temperature curing process was finally selected over a high temperature one in order to avoid cracks observed in the resin and on the rods due to volumic expansion of the resin. The composite samples were electroded with a silver paint and poled in an oil bath at 80°C for 15 minutes under a 1KV/mm electric field.

#### Measurements

This study essentially deals with  $d_{33}$  measurements. They were made using a Laser Doppler Vibrometry (LDV) technique. The measurements were carried out with a DANTEC DISA 55X laser doppler vibrometer measuring locally (the laser spot diameter is 1/4 mm) the vibration speed of the aimed surface. This compact measurement device includes the He-Ne laser, the Bragg cell, the optical path and the photodetectors. The small vibration speed obtained with 1.3 composites driven in the quasi static mode (sinusoidal 1 KHz - 50 to 70 V<sub>RMS</sub> signal) imposed the use of a lock-in-amplifier (EGG Model 5204) synchronized to the driving signal applied to the sample.

The sample was set up vertically in the center of a ring shaped holder and mounted with 3 small rubber pads at 120° each. The holder was also mounted on a sliding table allowing the scanning of the composite surface in order to measure the strain profile of the sample. As a consequence of the imprecision of the position of the rubber pads on the lateral surface of the composite and of resonances of the holder, a parasitic rigid body and flexural motion of the sample is added to the piezo electric strain. In order to correct these superimposed motions, two scanings were necessary exactly at the same location and on each side of the sample (Fig.1). To make this correction properly, the sample holder was made to be able to rotate, and its rotation axis has to correspond exactly to the scanning path on the composite which has also to be a symmetry axis of the composite sample: the diameter. Then the total piezoelectric strain is obtained by summing up the displacements measured (amplitude and phase) on both faces of the sample.

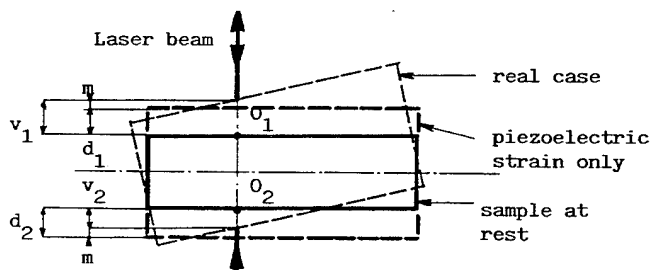


**FIGURE 1:** Dual measurement principle: m is the rigid body or flexural motion.  $d_1$  and  $d_2$  are the dilatational motions.  $v_1$  and  $v_2$  are the total measured motions. Then the total piezoelectric strain is :  $d_1 + d_2 = v_1 + v_2$

Figure 2 shows the strain profiles obtained with this method accross a portion of the diameter of the P188/PR1538 1.3 composite samples. The total axial strain is represented normalized to a 1V electric excitation. Also plotted on this figure are average profiles obtained by a superposition and an averaging of the elementary strain pattern obtained along the scanning. This final average strain profile is used to compute a resulting  $d_{33}$  of the composite. This computation is done assuming that the contour lines on the composite follow the square pattern of the rods. Those results are given on Table 3. Also noted on Table 3 are the dielectric and density measurements. Dielectric measurements were made on an HP 4192 A LCR-meter.

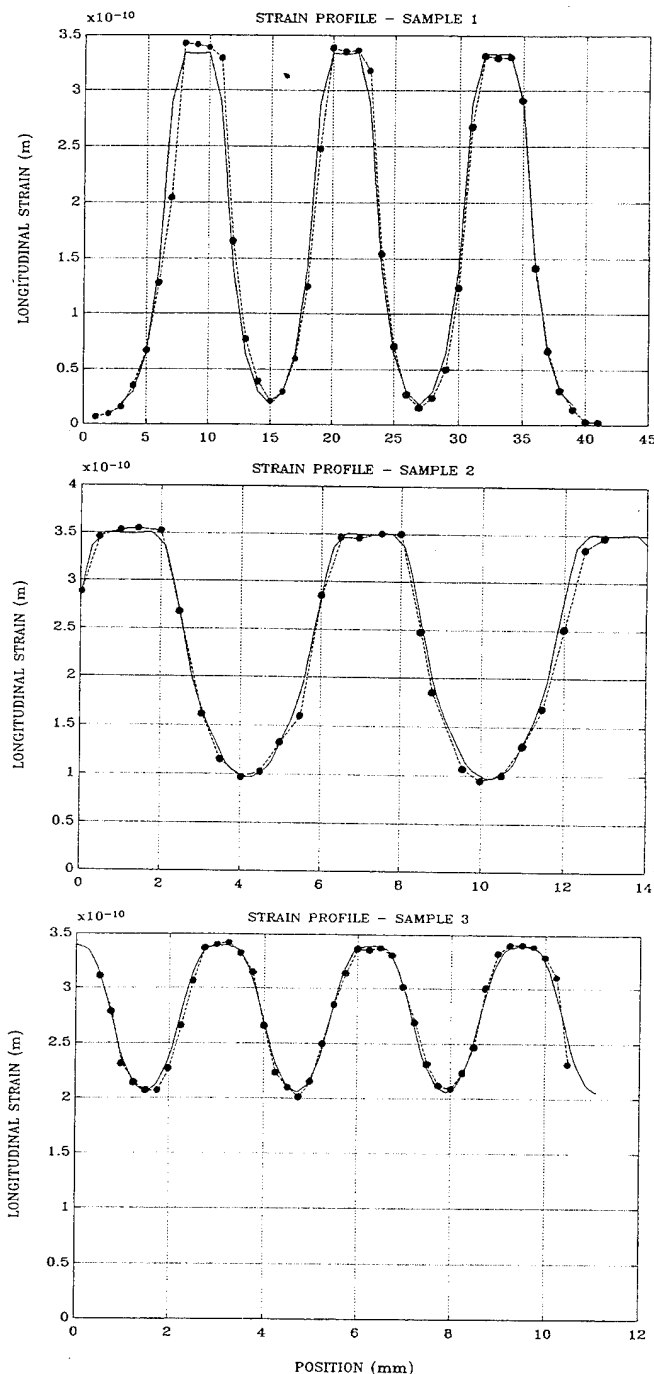


**FIGURE 2:** Total strain profiles obtained on P188/PR1538 1.3 composites with a 10% PZT volume fraction. The rod widths are 4mm (top), 2mm (middle) and 1mm (bottom). The measurements (dotted curves) are normalized to a 1V excitation. The continuous lines are average profiles.



**TABLE 3:** 1.3 composite sample description, fabrication and measurement data.  
The sample diameter is 49mm .

Sample number	1	2	3	4	5	6	7	8	9	10
Polymer	PR1538	PR1538	PR1538	PR1538	PR1538	EPON	EPON	EPON	EPON	EPON
PZT vol. (%)	11	11	10	21	42	11	11	10	21	42
Thickness (mm)	10	9.1	9.1	9.1	9.1	9.5	8.9	8.1	8.8	8.6
rod width (mm)	4	2	1	1	1	4	2	1	1	1
$\rho$ (Kg/m <sup>3</sup> )	1602	1737	1755	2399	3647	1686	1826	1823	2510	3748
$\epsilon_r$	129	160	159.5	305	607	136	177	171	352	669
$d_{33}$ (pC/N)	103	172	250	324	345	106	107	112	247	310

### THEORETICAL APPROACH

In order to derive  $d_{33}$  theoretical values taking intoaccount the PZT rod aspect ratio, a simple one-dimensional model was derived from a modelling basis developed earlier for structural composite materials [6][7]. If the PZT volume fraction is small enough [3], it can be assumed that the composite has the same properties as a unit cell consisting of a cylindrical PZT rod in a resin tube.

The problem then considered is a PZT rod (radius  $r_f$  length =  $\ell$ ) embedded in a polymer tube (outer radius  $R$ ). ( $x'Ox$ ) is the axis of the rod, and a slice  $dx$  thick is considered at the abscissa  $x$  of this assembly (Figure 3). Otherwise noted, the following notations are in agreement with ANSI Std.176-1987. The lateral stresses  $P_{T1}$  and  $z_{T1}$  respectively in the polymer and in the PZT are supposed to be zero. The longitudinal stresses  $P_{T3}$  and  $z_{T3}$  are functions of  $x$ . An electrical potential  $\phi(x)$  is also considered. The constitutive equations for both components are :

$$\text{for the polymer : } P_{S3} = \frac{dw}{dx} = P_{S33} \cdot P_{T3} \quad (1)$$

$$\text{for the PZT : } z_{S3} = \frac{du}{dx} = z_{S33} \cdot z_{T3} - d_{33} \cdot \frac{d\phi}{dx} \quad (2)$$

As there are no electrical space charges in the PZT :

$$\text{div } D = 0 \quad \text{then} \quad \frac{d^2\phi}{dx^2} = g_{33} \cdot \frac{dz_{T3}}{dx} \quad (3)$$

The expressions of the stress-transfer are derived from [6] and [7]. This transfer results from shear stresses at the PZT-polymer interface due to the mismatch of the local axial displacements  $w(x)$  and  $u(x)$ , of the polymer and the PZT, respectively. The shear is assumed to take place in the resin, because of its lower shear modulus, and in a region  $b_i$  wide.  $b_i$  is called the effective thickness of the interface

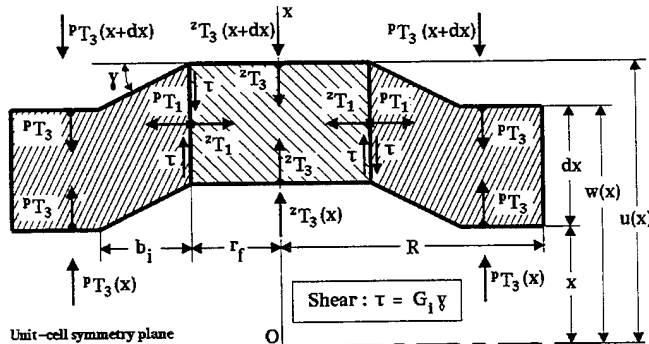


**FIGURE 3:** Elementary slice of the theoretical unit-cell

and in the dilute limit is defined as :

$$b_i = r_f \cdot \ln(R / r_f) \quad (4)$$

By considering the equilibrium of both parts of the composite slice described in Figure 3, the variation of stress in the PZT is then the opposite of the variation of stress in the polymer and is due to the shear, hence

$$\pi \cdot r_f^2 \cdot \frac{dz_{T3}}{dx} = - 2 \cdot \pi \cdot r_f \cdot G_i \cdot \frac{w(x) - u(x)}{b_i} \quad (5)$$

$$\pi \cdot (R^2 - r_f^2) \cdot \frac{dP_{T3}}{dx} = - \pi \cdot r_f^2 \cdot \frac{dz_{T3}}{dx} \quad (6)$$

where  $G_i$  is the shear modulus of the polymer resin. Equations (1) to (6) simultaneously lead to :

$$\frac{d^3 z_{T3}}{dx^3} = \alpha^2 \cdot \frac{dz_{T3}}{dx} \quad (7)$$

$$\text{with : } \alpha^2 = \frac{2 G_i v}{r_f \cdot b_i} \cdot \left( \frac{P_{S33}}{1-v} + \frac{z_{S33}^D}{v} \right) \quad (8)$$

$v$  is the PZT volume fraction also equal to  $(r_f/R)^2$ .

Due to considering symmetry, the solution of (7) is :

$$z_{T3} = I_2 \cdot \text{ch}(\alpha x) + I_3 \quad (9)$$

The boundary conditions can finally be applied, essentially the voltage  $U$  and the external pressure (zero in air) applied at both ends. The displacements  $u(x)$  and  $w(x)$  are then :

$$u(x) = a \cdot \text{sh}(\alpha x) + b \cdot x \quad \text{and} \quad w(x) = c \cdot \text{sh}(\alpha x) + b \cdot x$$

with:

$$a = I_2 \cdot \frac{z_{S33}^D}{\alpha} ; \quad b = I_2 \cdot \text{ch}\left(\frac{\alpha \ell}{2}\right) \cdot \frac{v}{1-v} \cdot P_{S33}$$

$$c = - I_2 \cdot \frac{v}{1-v} \cdot \frac{P_{S33}}{\alpha} ; \quad A = \frac{v}{1-v} \cdot P_{S33} + z_{S33}^E$$

$$I_2 = \frac{U}{\ell} \cdot \left( \frac{g_{33} \cdot \text{sh}\left(\frac{\alpha \ell}{2}\right)}{\frac{\alpha \ell}{2}} - \frac{A}{d_{33}} \cdot \text{ch}\left(\frac{\alpha \ell}{2}\right) \right)^{-1}$$

At  $x = \pm \ell/2$  the strain profile of the composite cell can be represented as shown in Figure 4. Averaging the axial strain, it is then possible to derive a resulting  $d_{33}$  value for the composite.

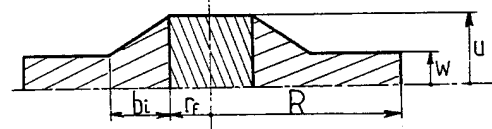


**FIGURE 4:** Schematic strain profile given by the model.

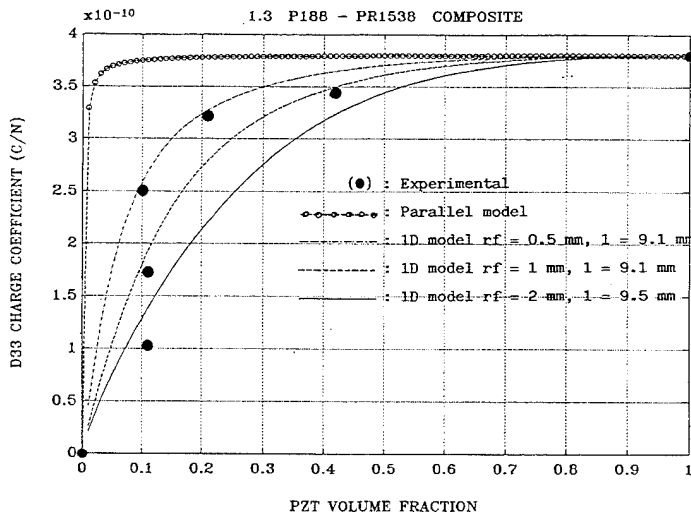


FIGURE 5:  $d_{33}$  versus the PZT volume fraction for a P188/PR1538 1.3 composite.

#### RESULTS AND DISCUSSION

The great influence of the PZT rod aspect ratio on the efficiency of the composite is clearly visible on the profile measurements given on Figure 2. The undulation on the surface decreases greatly as the rod aspect ratio or the PZT volume fraction increases. For low PZT volume fraction and small aspect ratio (coarse rods), the PZT rods are nearly free to move alone, resulting in a small motion of the polymer, even in air. The same kind of undulations are observed with the P188/EPON 828 composite samples. The main difference in this case is a smaller axial displacement. These results can also be observed in Figures 5 and 6. They show, respectively for P188/PR1538 and P188/EPON828,  $d_{33}$  versus the PZT volume fraction. A comparison is proposed between the results of a simple parallel model (equal strain assumption) represented by the upper curve, the results of the proposed model for different aspect ratios and the experimental results (dots). The simulations have been performed with the data given in Tables 1 and 2. A good agreement is observed in the case of the polyurethane type samples. The rod shape does not seem to be critical. The experimental study has been made with square rods and the theoretical approach with cylinders. The error on the lateral surface ( $\pi/4$  factor) does not induce an important mismatch. A slightly less ideal agreement is observed in the case of the epoxy type samples, especially for samples 7 and 8. Note that there is an uncertainty concerning the epoxy type sample fabrication due to difficulties in the curing of the epoxy, leading to cracks which certainly modify the physical properties of the material. Another unknown is also the polarization of the PZT. The strong polymer resistance to the high strain imposed by the poling field can either result in an incomplete poling, or in an alteration of the mechanical properties of the interface. For this reason, it would be better to pole the PZT prior the embedding or to machine a prepoled ceramic.

Nevertheless, it is shown that as the aspect ratio increases, the proposed model converges toward the parallel model representing the ideal homogenized composite.  $d_{33}$  figures representing nearly 75% of the ideal value can be obtained with a rod aspect ratio equal to 20 in the case of a 10% PZT volume fraction. Finally it is also observed that for operation in the 3.3 mode, a soft polymer, offering less resistance to the piezoelectric rod strain results in higher piezoelectric properties.

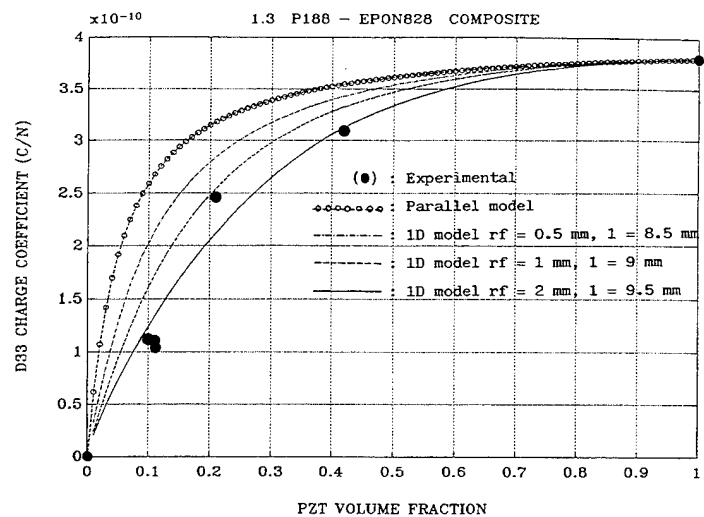


FIGURE 6:  $d_{33}$  versus the PZT volume fraction for a P188/EPON828 1.3 composite.

#### CONCLUSION

This study pointed out the strong relationship of a 1.3 composite performance with the PZT rod size and especially for low PZT contents. It accentuated the importance of the interface region where the stress and strain transfer occurs between the active and passive parts. This contact surface has to be as large as possible to ensure a good coupling. For a given volume fraction and thickness, this surface increases with the number of rods and for a given total volume, with the rod aspect ratio. It is shown that in the 3.3 quasi-static mode and for a 10% PZT volume fraction composite, performances nearly as high as for an ideally fine structured composite are obtained with PZT rods with a length at least equal to 20 times the radius.

#### ACKNOWLEDGEMENTS

This work was jointly supported by the U.S. Naval Research Laboratory, Orlando, Florida and the DCN-Ingénierie Sud, Toulon, France.

#### REFERENCES

- [1] W. A. Smith, "Modeling 1-3 Composite Piezoelectrics: Hydrostatic Response", *IEEE Trans. on UFFC*, Vol.40, No.1, pp. 41-49, 1993.
- [2] H. Jensen, "Determination of Macroscopic Electro-Mechanical Charact. of a 13 Piezoceramic/Polymer Composite by a Concentric Tube Model", *IEEE Trans. on UFFC*, Vol.38, No.6, pp. 591-594, 1991.
- [3] Q.M. Zhang, W. Cao, H. Wang, L.E. Cross, "Characterization of the performance of 1-3 type piezocomposite for low-frequency applications", *J. Appl. Phys* Vol.73, No.3, pp. 1403-1410, 1993.
- [4] C. Richard, "Etude expérimentale et théorique de composites piézoélectriques de connectivité 1.3.1 pour hydrophone", These INSA Lyon 1992.
- [5] H.P. Savakus, K.A. Klicker, R.E. Newnham, "PZT-Epoxy Piezoelectric Transducers: A Simplified Fabrication Procedure", *Material Research Bulletin*, Vol.16, pp. 677-680, 1981.
- [6] H.L. Cox, "The elasticity and strength of paper and other fibrous materials", *Brit. J. Appl. Phys.*, Vol.3, pp. 72-79, 1952.
- [7] M.F. Marmonier and al., "Etude par éléments finis de l'essai de déchaussement d'une fibre enchâssée dans une matrice", *J. Meca. Théor. et Appl.*, Vol.7, No.6, pp. 741-765, 1988.

# Fine-Scale, Large Area Piezoelectric Fiber/Polymer Composites for Transducer Applications

V. F. Janas, S. M. Ting, S. S. Livneh, F. R. Walker  
R. Schaeffer, T. F. McNulty, and A. Safari  
Department of Ceramic Engineering  
Rutgers, The State University of New Jersey  
Piscataway, NJ 08855-0909

## ABSTRACT

Several methods of forming piezoelectric ceramic/polymer composites for possible transducer applications were demonstrated. These methods include the replication technique, tape casting, honeycomb dicing, and ceramic fiber weaving. In the replication technique, activated carbon fibers or fabrics are soaked in a PZT precursor solution and then arranged into desired structures. The soaked structures are dried and fired, yielding a ceramic relic with the same structure. Three types of structures were developed: Shells, Combs, and Weaves. The highest  $d_{33}$  of 290 pC/N was found in the shell structure, and the  $d_{hgh}$  of both the shell and weave designs were about  $5,000 \times 10^{-15} \text{ m}^2/\text{N}$ . The results of scaling-up the weave structure from  $2.5 \times 2.5 \text{ cm}^2$  to  $10 \times 10 \text{ cm}^2$  are reported. The feasibility of producing larger area samples using relic tile arrays is also discussed. In the tape casting technique, 2-2 and 1-3 structures were formed using thin PZT tapes. The tapes are stacked, with spacers separating the layers, and the stack is embedded in polymer. Dicing the stack results in a composite with 1-3 connectivity. The thin tape technique can be used to develop composites with ceramic or polymer volume gradients and multifunctional ceramics. Dicing of PZT honeycombs yields 1-3 composites with uniquely shaped rods. Shapes included "I"s, "T"s, and "L"s. In the ceramic fiber weaving technique, green PZT fibers are woven through a PZT honeycomb support structure. The structure is fired to sinter the PZT fibers, and embedded with polymer to yield 1-3 composites. All 1-3 composites showed high and uniform piezoelectric coefficients across the electroded area.

## 1. INTRODUCTION

Many ceramics exhibit piezoelectric behavior, with lead zirconate titanate (PZT) being the most extensively used piezoelectric transducer material. Though cheap and easy to fabricate, the hydrostatic "Figure of Merit" ( $d_{hgh}$ ) is low, so PZT has limited use as a hydrophone. Also, there is a poor acoustic match between ceramics and the transmitting media, and stiff ceramics can not be formed onto curved surfaces [1]. Piezoelectric polymers [2] solve the problems of acoustic match and transducer formability. The most common piezoelectric polymers, polyvinylidene fluoride (PVDF) and poly(vinylidene fluoride-trifluoroethylene), or P(VDF-TrFE) copolymer, demonstrate piezoelectric properties when the polymer chains are oriented. The limitation with polymers is they have low electromechanical coupling, low dielectric constant, and high cost of fabrication [1].

Composites [3] of piezoelectric ceramics and inactive polymers have become the material of choice for transducers. Their electromechanical properties are close to those of monolithic ceramics, while their acoustic impedances close to those of polymers [1]. The connectivity [4], or arrangement of component phases in the composite, is a critical parameter for the electromechanical performance of the composite. The common connectivities are 0-3, and 1-3, where the first digit refers to the dimensionality of the active (piezoelectric ceramic) phase, while the second digit refers to that of the polymer phase.

The applications of piezoelectric composites are distinguished by the frequency of the acoustic waves involved. In medical imaging systems, where the drive is towards fine resolution, there is a desire to increase the frequency of the generated sound wave. For low frequency hydrophone applications, large area piezoelectric materials are desired. A large array will capture more acoustic energy than a small array [5], and acts as a filter to flow induced noise, the noise produced as a ship moves through water.

Numerous processing techniques have been developed for forming fine scale ( $<50 \mu\text{m}$ ) 1-3 piezoelectric composites. The most promising are the lost mold technique [6], injection molding [7], and the relic process [8,9]. In the relic process, activated carbon fibers or fabrics are soaked in a ceramic precursor solution either before or after arrangement into desired structures. The fibers are fired, yielding a ceramic relic with the same structure. Relics are embedded in an epoxy matrix and polished to yield a composite.

In this paper, several methods for the preparation of piezoelectric ceramic/polymer composites are discussed with interest in forming fine scale/large area composites. The methods include: the relic process, tape casting, honeycomb dicing, and ceramic fiber weaving. Results from the following structures are reported: Relic Weave, Relic Shell, Relic Comb, Tape Cast Stacked, Tape Cast Diced, Honeycomb Diced, and Ceramic Fiber Woven. Optimization of properties for all composites are sought. Composites with the Relic Weave structure were scaled-up, with a goal of large area properties equivalent to their smaller scale counterparts.

## 2. EXPERIMENTAL

### 2.1 Relic Process

The relic process [8,9] starts with commercially available activated novoloid- (phenol-aldehyde-) derived woven carbon fabric obtained from American Kynol, Inc. (ACC-507-15 Kynol Carbon™). The fabrics consisted of plain weave yarns (37 picks per inch by 36 ends per inch. Each yarn contained between 360 and 375 individual  $10\text{-}20 \mu\text{m}$  diameter carbon fibers. The fabrics were soaked in PZT precursor solution before arrangement into desired structures. They were dried at  $60^\circ\text{C}$ , and heat treated in air ( $550^\circ\text{C}$  for 10 hrs., followed by  $700^\circ\text{C}$  for 4 hrs.) to burn out the carbon. The resulting relic had the same structure as the original carbon template. To sinter the relic, it was fired at  $1285^\circ\text{C}$  for 1 to 2 hours in a sealed crucible containing a lead zirconate source powder.

The PZT relics were vacuum infiltrated with an epoxy matrix (Eccogel™ epoxy resin grades 1365-45 or 1365-80, Emerson and Cumming, Dewey and Almy Chemical Division, Canton, MA) to form a piezoelectric ceramic/polymer composite. After curing, samples were polished and electroded with sputtered gold or air dried silver paint. Composites were poled using either conventional or corona poling [8], after which the electromechanical properties were evaluated.

The weave structure is schematically shown in Figure 1. The goal of this work was to enlarge the sample area by over an order of magnitude from  $2.5 \times 2.5 \text{ cm}^2$  to  $10 \times 10 \text{ cm}^2$ . Woven structures were prepared by soaking 15-20 sheets of activated carbon fabric. The soaked sheets were dried, stacked, and weighed down with fired zirconia blocks prior to firing. The weights prevented curling up of the top sheets, yielding uniformly thick samples. In addition,  $5.0 \times 5.0 \text{ cm}^2$  samples were prepared by using fired  $2.5 \times 2.5 \text{ cm}^2$  structured in an array. The fired samples were placed 2 by 2 square prior to epoxy infiltration. The object was to determine if arraying of smaller pieces could be used as an alternative for scale-up.

The shell structure is shown in Figure 2. A strip of activated carbon fabric, 3.5-cm wide by 75-cm long was soaked in PZT precursor solution. While still wet, the fabric was rolled in a helical fashion around a center point. Composite processing was completed as described above. Polishing, electroding, and poling were done perpendicular to the fabric rolling direction.

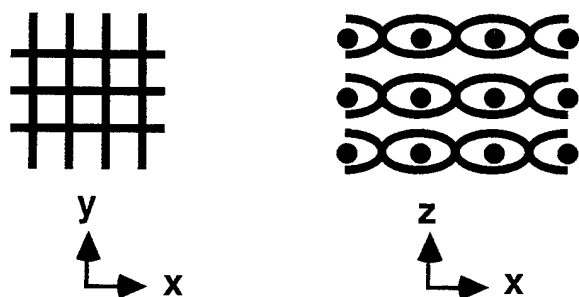
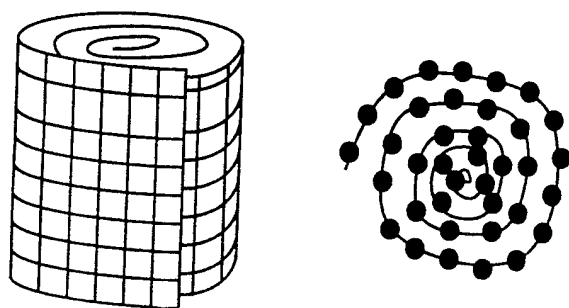
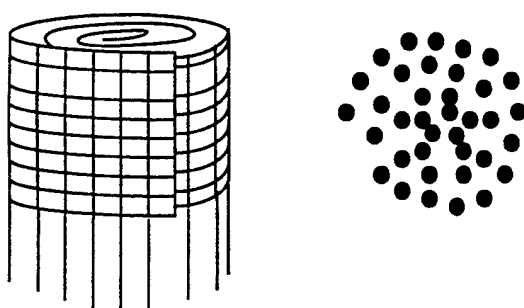


FIGURE 1: Weave Structure.



Side View Top View  
FIGURE 2: Shell Structure.

The comb structure is shown in Figure 3. Like the shell structure, the starting point for the comb is a strip of activated carbon fabric, 3.5-cm wide by 75-cm long. From this fabric, one-half of the long yarns were removed. The modified fabric was soaked in PZT precursor solution. While still wet, the fabric was rolled in a helical fashion around a center point. The resulting structure had two sections: one, reminiscent of the shell structure, the other, unidirectional fibers. Processing was completed as described above.



Side View Top View  
FIGURE 3: Comb Structure.

## 2.2 Tape Cast Composites

PZT tape was obtained by tape casting fine PZT powder as described elsewhere [10]. The tapes were fired to sinter the PZT. The tapes used in this study were  $240\mu\text{m}$  thick, though intentions are to use tapes as thin as  $50\text{--}100\mu\text{m}$ . Tapes were stacked, as shown in Figure 4, with a spacer support placed between each layer. The stack was vacuum infiltrated with Spurr's Epoxy (E.F. Fullum, Inc., Schenectady, NY) to form a piezoelectric ceramic/polymer composite with a connectivity of 2-2.

To create a 1-3 composite, the 2-2 structure was diced perpendicular to the tapes as shown on Figure 4, prior to electroding and poling. The diced stack was vacuum reinfiltred with Spurr's Epoxy matrix to complete composite formation. Polishing, electroding, and poling were done perpendicular to the stacking direction.

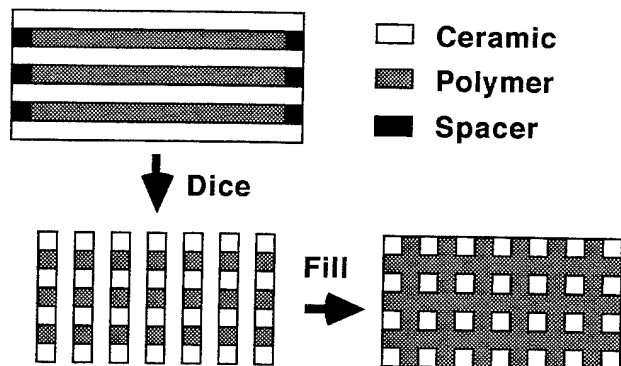


FIGURE 4: Schematic of Forming Tape Cast Composite Structures.

## 2.3 Diced Honeycomb Composites

PZT ceramic honeycombs were extruded and fired following a previously developed technique [11]. The honeycombs were diced and filled with Spurr's Epoxy as schematically shown in Figure 5. The dicing step broke the 3-dimensional connectivity of the ceramic phase, yielding a composite with 1-3 connectivity when refilled with epoxy. The cross-sectional shape of the ceramic rods was varied by changing the location of the cuts through the ceramic. The various rod shapes are shown in Figure 6. The volume fraction of the ceramic phase was varied between 15 and 30 percent by changing the thickness of the resinoid blade used in cutting the honeycomb.

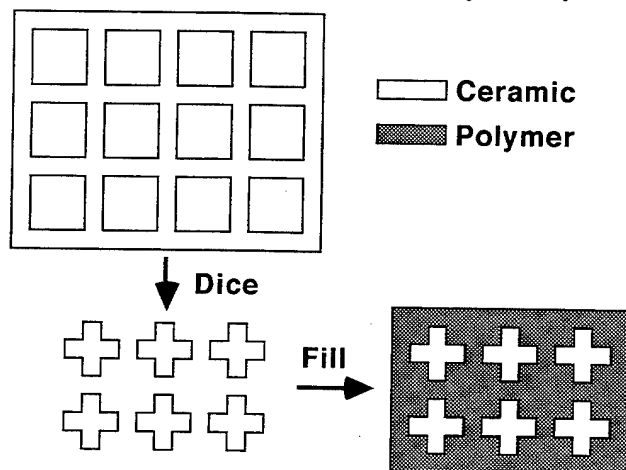


FIGURE 5: Schematic of Diced Honeycomb Composites.



FIGURE 6: Rod Shapes in Diced Honeycomb Composites.

## 2.4 Woven PZT Composites

Green PZT fiber yarns (200 filament,  $10\mu\text{m}$  diameter) were prepared via the Viscous Suspension Spinning Process (VSSP) [12] at Advanced Cerametrics, Inc., Lambertville, NJ. The yarn was sized using a polyvinyl alcohol solution, and woven through a supported PZT honeycomb as schematically shown in Figure 7. The structure was heat treated in air ( $550^\circ\text{C}$  for 10 hrs., followed by  $700^\circ\text{C}$  for 4 hrs.) to burn out the binder, and fired at  $1285^\circ\text{C}$  for 1 to 2 hours in a sealed crucible containing a lead zirconate source powder. The fired structure was embedded in Spurr's Epoxy, and the honeycomb supports were ground off to yield a 1-3 composite.

## 2.5 Electromechanical Properties

After poling, composites were aged for 24 hours prior to measurement of electromechanical properties. Capacitance and dielectric loss factors were measured at 1 kHz with a Hewlett-Packard Model 4194A impedance/gain phase analyzer. A Channel

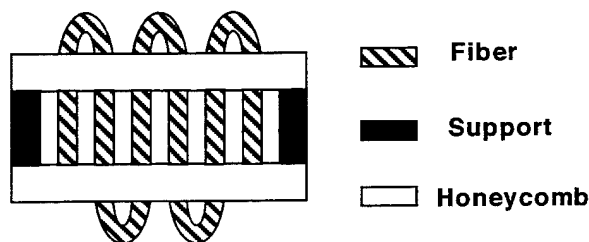


FIGURE 7: Schematic of Woven PZT Composites.

Products Model CPDT-3300 piezo  $d_{33}$  meter was used to directly measure the  $d_{33}$  coefficient of the composites at 100 Hz. The  $d_h$  of the composites was measured dynamically by comparing the hydrostatic response of the specimens to that of a standard. Values of  $g_{33}$  and  $g_h$  were calculated using the measured values of  $d_{33}$ ,  $d_h$  and  $K$ . To assess the variability of properties across samples larger than  $2.5 \times 2.5 \text{ cm}^2$ , these samples were cut into  $2.5 \times 2.5 \text{ cm}^2$  specimens.

### 3. RESULTS AND DISCUSSION

#### 3.1 Relic Composites

Typical properties of the fine scale structures are found in Table I. The shell and weave structures, with connectivities of 2-3, yielded electromechanical properties intermediate between 1-3 and 3-3 composites [3]. The value of  $d_h$  for both structures were higher than that of a 1-3 composite. The values of  $d_{hgh}$  (about 5,000) are exceptional, which translates to excellent potential for hydrophone applications for these composites.

TABLE I: Properties of Relic Composites.

Structure	Shell	Comb	Weave
PZT Volume %	33	29	37
$d_{33}$ (pC/N)	290	230	180
$K$	150	85	140
$\tan \delta$ (%)	4.3	5.8	3.2
$g_{33}$ (mVm/N)	220	300	150
$d_h$ (pC/N)	80	20	80
$g_h$ (mVm/N)	60	25	65
$d_{hgh}$	4,800	500	5,200
(X10 <sup>-15</sup> m <sup>2</sup> /N)			

The comb structure (1-3 connectivity) showed promising results. The  $d_{33}$  and  $K$  values fall near those reported for composites with 1-3 connectivity [3]. The values of  $d_h$ ,  $g_h$ , and  $d_{hgh}$  are lower than those reported in earlier work. Further work is needed to optimize these properties.

Typical woven composite properties as a function of sample size are shown in Table II. The table shows good agreement in electromechanical properties between all composite sizes. Scale-up issues, such as differential ceramic sintering, are possible explanations of the slight decrease in properties. However, the results show the feasibility of processing larger woven composites.

The tile array technique for scaling-up the size of woven composites also showed good results. The perceived disadvantage of this technique was the small discontinuities (< 0.1-cm) of the piezoelectric ceramic at the tile to tile contact points. The discontinuities were polymer rich regions that may have localized effects on the electromechanical properties of the composite. To examine this possibility, the  $5.0 \times 5.0 \text{ cm}^2$  arrays were cut into nine smaller specimens, and the properties of the specimens, some with no discontinuities and some with multiple discontinuities, were measured. Typical properties of a  $5.0 \times 5.0 \text{ cm}^2$  array composite are shown on Table II. The table shows that the array has properties that match those of the smaller, one-piece composites. So, arraying is a feasible method for forming composites of limitless area.

TABLE II: Properties of Woven Composite Versus Size.

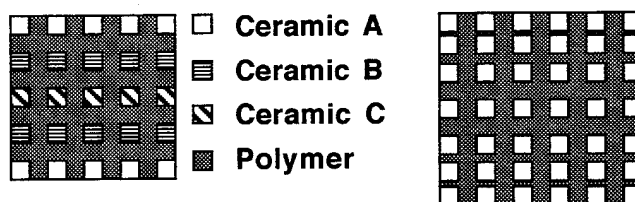
Size (cmXcm)	2.5X2.5	5.0X5.0 Array	10.0X10.0
PZT Volume %	37	37	37
$d_{33}$ (pC/N)	180	170	150
$K$	140	130	125
$\tan \delta$	3.2	3.5	3.7
$g_{33}$ (mVm/N)	150	160	135
$d_h$ (pC/N)	80	60	65
$g_h$ (mVm/N)	65	55	60
$d_{hgh}$	5,200	3,300	3,900
(X 10 <sup>-15</sup> m <sup>2</sup> /N)			

#### 3.2 Tape Cast Composites

The electromechanical properties of the composites are shown on Table III. For the 1-3 composite, the values of  $d_{33}$ ,  $K$ ,  $d_h$  and  $g_h$  all fall near those reported for composites with 1-3 connectivity which were formed by the dice and fill technique [3]. Further work is needed in tape cast composites to decrease the size of the PZT pillars. In addition, by varying the composition or spacing of the tapes in stack, composites with multiple active phase and/or volume fraction gradients could be formed. These concepts are schematically shown in Figure 8. This may open the possibility of using the same composite for several applications simultaneously.

TABLE III: Properties of Tape Cast Composites.

Structure	2-2	1-3
PZT Volume %	50	25
$d_{33}$ (pC/N)	370	300
$K$	300	230
$\tan \delta$	1.7	2.1
$g_{33}$ (mVm/N)	140	150
$d_h$ (pC/N)	25	40
$g_h$ (mVm/N)	10	20
$d_{hgh}$	250	800
(X10 <sup>-15</sup> m <sup>2</sup> /N)		



• Multiple Materials • Volume Fraction Gradient  
FIGURE 8: Novel Tape Cast Composite Designs.

#### 3.3 Diced Honeycomb Composites

The electromechanical properties of the diced honeycomb composites as a function of rod cross-sectional shape are shown on Table IV. All composites contain ceramic at the same loading. The table shows that properties are independent of rod shape. The effect of rod shape on composite resonance behavior is currently being investigated.

There are several limitations in the diced honeycomb technique for forming fine scale/large area 1-3 composites. The technique is dependent on extruded ceramic honeycombs. The current size limit on these structures is approximately 20 cm, with wall thicknesses of > 150  $\mu\text{m}$ .

#### 3.4 Woven PZT Composites

The electromechanical properties of the woven PZT fiber composites are shown on Table III. The values of  $d_{33}$ ,  $K$ ,  $d_h$  and

TABLE IV: Properties of Diced Honeycomb and Woven PZT Fiber Composites.

Property	"+"	"L"	"T"	Woven
PZT Volume %	25	25	25	10
$d_{33}$ (pC/N)	440	500	480	230
$K$	650	630	660	110
$\tan \delta$	2.5	2.6	2.3	2.0
$g_{33}$ (mVm/N)	75	90	80	240
$d_h$ (pC/N)	65	65	75	30
$g_h$ (mVm/N)	10	10	15	30
$d_{hgh}$	650	650	1125	900
(X10 <sup>-15</sup> m <sup>2</sup> /N)				

$g_h$  all fall near those reported for composites with 1-3 connectivity which were formed by the above techniques. Further work is needed in these composites to increase the volume fraction of PZT in the composite, and to decrease the spacing between the ceramic pillars.

Woven PZT fiber composites show great promise for forming fine scale and large area piezoelectric ceramic/polymer composites with various connectivities. The individual PZT fibers are as fine as 10- $\mu$ m diameter, and there is almost an infinite number of fiber architectures which can be achieved by textile operations such as braiding, weaving, and knitting [13]. The PZT fibers may also be interwoven with other fibers, yielding composites with multiple active phases.

#### 4. SUMMARY

Several methods of forming piezoelectric ceramic/polymer composites for possible transducer applications were demonstrated. These methods include the replication technique, tape casting, honeycomb dicing, and ceramic fiber weaving. The relic process formed fine scale and large area piezoelectric ceramic/polymer composites with various connectivities. The fine scale shell and the comb structures, displayed excellent electromechanical properties. Both will be investigated as alternative composites for transducer applications. The relic weave structure was scaled-up from 2.5X2.5 cm<sup>2</sup> to 10X10 cm<sup>2</sup> with no loss in electromechanical properties. By arraying the smaller scale counterparts, composites of limitless area may be formed. Tape cast composites formed also displayed excellent electromechanical properties. In addition, these composites show promise in future novel composite microstructures. Honeycomb composites may be diced to form 1-3 composites with a variety of rod shapes, while woven PZT fiber composites show promise for forming fine scale and large area piezoelectric ceramic/polymer composites with various connectivities.

#### ACKNOWLEDGMENTS

The authors would like to acknowledge the financial support of the Office of Naval Research, URI program, which made this work possible.

#### REFERENCES

- [1] T.R. Gururaja, "Piezoelectric Transducers for Medical Ultrasonic Imaging", *American Ceramic Society Bulletin*, vol. 73, No. 5, pp. 50-55, 1994.
- [2] L.F. Brown, "Ferroelectric Polymers: Current and Future Ultrasonic Applications", in *Proceedings 1992 IEEE Ultrasonics Symposium*, 1992, pp. 539-550.
- [3] T.R. Gururaja, A. Safari, R.E. Newnham and L.E. Cross, "Piezoelectric Ceramic-Polymer Composites for Transducer Applications", in *Electronic Ceramics*, ed. L.M. Levinson, New York: Marcell-Deckker, Inc., 1987, pp. 92-145.

- [4] R.E. Newnham, D.P. Skinner and L.E. Cross, "Connectivity and Piezoelectric-Pyroelectric Composites", *Material Research Bulletin*, vol. 13, pp. 525-536, 1978.
- [5] R.H. Tancrrell, D.T. Wilson and D. Ricketts, "Properties of PVDF Polymer for Sonar", in *Proceedings 1985 IEEE Ultrasonics Symposium*, 1985, pp. 624-629.
- [6] K. Lubitz, A. Wolff and G. Preu, "New Piezoelectric Composites for Ultrasonic Transducers." *Ferroelectrics*, vol. 133, pp. 21-26, 1992.
- [7] L.J. Bowen and K.W. French, "Fabrication of Piezoelectric Ceramic/Polymer Composites by Injection Molding", in *Proceedings 1992 IEEE 8th International Symposium on the Applications of Ferroelectrics*, 1992, pp. 160-163.
- [8] D.J. Waller and A. Safari, "Piezoelectric Lead Zirconate Titanate Ceramic Fiber/Polymer Composites", *Journal of the American Ceramic Society*, vol. 75, pp. 1648-1655, 1992.
- [9] S.M.Ting, S.S. Livneh, V.F. Janas and A. Safari, "Processing Fine Structure Piezoelectric Ceramic/Polymer Composites for Transducer Applications", in *Proceedings of the 7th International SAMPE Electronics Conference*, 1994, pp. 680-691.
- [10] R.E. Mistler, D.J. Shanefield, and R.B. Runk, "Tape Casting of Ceramics", in *Ceramic Processing Before Firing*, eds. G.Y. Onoda, and L.L. Hench, New York: John Wiley and Sons, 1978, ch. 30, pp. 411-447.
- [11] A. Safari, A. Halliyal, R.E. Newnham, and I.M. Lachman, "Transverse Honeycomb Composite Transducers", *Material Research Bulletin*, vol. 17, pp. 301-308, 1982.
- [12] R.B. Cass, "Fabrication of Continuous Ceramic Fiber by the Viscous Suspension Spinning Process", *Ceramic Bulletin*, vol. 70, no. 3, pp. 424-429, 1991.
- [13] F.K. Ko, "Preform Fiber Architecture for Ceramic Matrix Composites." *Ceramic Bulletin*, vol. 68, no. 2, pp. 401-414, 1989.

# 3-3 Composite Hydrophones from Distorted Reticulated Ceramics

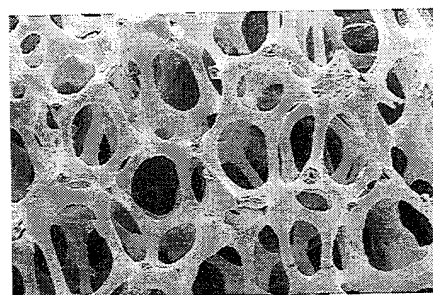
M. J. Creedon, S. Gopalakrishnan, W.A Schulze  
New York State College of Ceramics,  
Alfred University  
Alfred, NY 14802

**Abstract:** Application of reticulated ceramic technology to the fabrication of 3-3 lead zirconate-titanate (PZT)/epoxy composite hydrophones has been investigated. Directional distortion of the ceramic structure to enhance the composite hydrostatic response has also been studied. Composite fabrication is described and the effects of polymer type, distortion, volume percent PZT and poling field on the hydrophone properties are presented. In general, the results indicate that reticulated ceramic composites (RCC's) have properties which are comparable to other 3-3 PZT/epoxy composites. Composites which contained the stiffer Spurr epoxy significantly out performed those containing a softer Eccogel epoxy. In addition, a distorted structure and higher density improved hydrophone response. The novel use of reticulated ceramic technology provides substantial improvement in manufacturability over other methods and allows fabrication of sensitive, low density hydrophones.

## INTRODUCTION

The use of composites of lead zirconate-titanate (PZT) and various polymers for hydrophone applications has been studied extensively over the years [1, 2]. The lower dielectric constants of composites provide immediate benefits in the hydrostatic voltage coefficient because of the relationship,  $g_h = d_h / \epsilon_0 K_{33}^T$ . The hydrostatic charge coefficient,  $d_h (= d_{33} + 2d_{31})$ , is enhanced by reducing the contributions of the lateral components of the coefficient. Stress transfer from a compliant matrix material to the ceramic phase is another mechanism for improving performance. Composites which incorporate rods of PZT embedded in an epoxy matrix (1-3 connectivity) take advantage of these mechanisms and have proven to be quite effective hydrophone materials [3]. Composites with 3-3 connectivity have reinforcement in the lateral directions to further decouple negative contributions from lateral stresses. Methods which have been developed for making 3-3 composites include lost wax replication of a coral skeleton [4] and mixing of burnable plastic spheres with the PZT before forming (BURPS) [5]. These processes have limitations which make them undesirable for large scale applications such as large passive sensor arrays.

The present study addresses the issues of fabricating a low density composite using a technique which lends itself to large scale production of 3-3 PZT /polymer composites. The macro-structure of reticulated ceramics, usually used in applications such as molten metal filters and low mass kiln furniture, closely resembles the coral structure used by Skinner et al. [4]. Reticulated ceramics are created by coating an organic foam substrate (i.e., polyurethane) with a ceramic slurry, pyrolyzing the foam, and then sintering



1 mm

**Figure 1.** Scanning electron micrograph of the structure of reticulated PZT ceramic.

the ceramic [6]. The resulting structure is made up of hollow ligaments of ceramic which form the edges of close packed cells, primarily pentagonal dodecahedra. One of the main advantages this process offers for the fabrication of piezoelectric composites, especially in terms of large scale hydrophone production, is its proven fabrication versatility. Another advantage, and the focus of this study, is that the relatively spherical isotropic cell structure of the foam can be elongated, approximating laterally reinforced rods. Consequently, distortion toward an interconnected 1-3 configuration should enhance the hydrostatic response by decoupling the  $d_{33}$  and  $d_{31}$  responses. The voltage coefficient will increase as a result of lowering the overall dielectric constant of the material.

The primary goal of this study is to evaluate the use of reticulated ceramic technology in the fabrication of composite hydrophones. In an effort to determine the optimum configuration for the RCC hydrophone, the effects of distortion, density, and matrix polymer are being investigated. To insure attainment of the maximum response from the PZT, the effects of poling field were also investigated and provided some unexpected results and insight. The results of this on going work are presented below.

## EXPERIMENTAL PROCEDURE

### Foam Distortion

The foam substrate used in the fabrication of these reticulated ceramics was a standard polyurethane polymer foam. The foam was supplied by Hi-Tech Ceramics, Inc. of Alfred, NY in pore sizes of 15, 30, 45, and 65 pores per inch (ppi). It should be pointed out that the "ppi" designations used in the industry do not reflect the actual number of pores per linear inch in the foam. Table I indicates the approximate actual pore dimensions for the



materials used. To achieve the distorted structure, blocks of "as received" foam were placed in a fixture which holds

Table 1. Actual Pore Sizes of Starting Foams

PPI Designation	Actual Pore Dim. (mm)
15 PPI	4 x 3.5
30 PPI	3 x 2
45 PPI	2 x 1.5
65 PPI	1 x 1

the piece at both ends and allows elongation to any desired length up to 50% of the original length. For this work, the full 50% length increase was used. The entire fixture was then placed in an oven preheated to 180°C and held there for approximately 30 minutes.

### PZT Processing

Unfired samples of undistorted and distorted reticulated PZT were prepared in densities of 10 and 15 volume percent PZT by Hi-Tech Ceramics, Inc. The two different densities were attained by applying different amounts of slurry to the substrate. A commercially available PZT-5H was used.\* The unfired samples provided by Hi-Tech, Inc. were burned out and sintered on PZT-5H setter blocks in closed alumina crucibles. During burnout, an oxidizing atmosphere was maintained by propping the crucible lid open. Below 800°C, the lid was closed and the samples sintered at 1300°C for 1 hour. A PbO rich atmosphere within the crucible was provided by surrounding the setters with a commercial lead zirconate source powder\*. The densities of the sintered materials were determined by the displacement method using isopropyl alcohol as the immersion liquid.

### Composite Fabrication

Composites were prepared by vacuum infiltrating the fired ceramics with a "soft" mixture of Spurr epoxy† and a much more compliant Eccogel 1365-65 epoxy.§ Both materials were cured at 60°C for ≈12 hours. The composite blocks were then sliced into smaller blocks approximately 1 cm square by 0.4 cm thick. Their surfaces were ground flat and parallel and electroded with an air dry silver paint.†† The electroded composites were poled in a 70°C stirred oil bath at 20-25 kV/cm for 20 minutes.

To determine the effects of poling field, two sets of samples (10 vol% and 15 vol% PZT) were made with distorted ceramics infiltrated with Spurr epoxy. Each sample was successively poled under the conditions above, from 5 to 30 kV/cm in 5 kV/cm increments. Values of  $d_{33}$ ,  $d_h$ ,  $K_{33}^T$  were obtained after each poling cycle.

\* Morgan Matroc, Inc., Electro Ceramics Div., Bedford, OH

† No. 51350, Spurr Epoxy, Ernest F. Fullam, Inc., Latham, NY

§ Emerson and Cumming, Canton, MA

†† Cat. No. 22-246, GC Electronics, Rockford IL

### Electromechanical Testing

The composite  $d_{33}$  was determined using a Berlincourt  $d_{33}$  Piezo Meter (hemispherical contacts).‡ Sixteen measurements were averaged to get the reported value. Capacitance, measured at 1 kHz with an HP4192A impedance analyzer, was used to calculate dielectric constant,  $K_{33}^T$ . Measurements of  $d_h$  were made in an oil filled chamber over the pressure range from 1.7 MPa (250 psi) to 6.9 MPa (1000 psi.) An oscillating (400 Hz) hydrostatic pressure wave was produced by a piston mounted on a stack of piezoelectric washers inside the tank. The sample and standard voltage signals were amplified and measured using a lock-in amplifier to filter unwanted noise. The value of  $d_h$  was determined by comparing the response of the sample to that of a standard of known  $d_h$  using the following formula:

$$d_{h(\text{composite})} = V_c A_{std} d_{h(std)} / V_{std} A_c \quad (1)$$

where  $V_c$ ,  $V_{std}$ ,  $A_c$ , and  $A_{std}$  are the voltage signals of the composite and standard, and the electrode areas of composite and standard, respectively. The values of  $d_h$  reported are an average of  $d_h$  over the entire pressure range.

## RESULTS AND DISCUSSION

### Composite Macro-structure

An analysis of the reticulated structure shows the complex nature of these materials. The cell sizes are reduced during firing due to a linear shrinkage of about 16%. Upon close examination of the fired material, the tubular nature of the reticulated ligaments is revealed (Figures 1 and 2). Comparing these two figures, the difference between the undistorted and distorted structures can easily be seen. The distorted material resembles an interconnected rod structure, with somewhat irregular spacing of the rods and lateral supports. The Spurr epoxy readily infiltrates and fills the ceramic ligaments. The Eccogel epoxy, being much more viscous than the Spurr, did not fill the structure as completely, leaving some regions of the hollow ligaments unfilled.

The average composite densities were 1.63 g/cm<sup>3</sup> and 1.90 g/cm<sup>3</sup> for the 10 and 15 vol.% materials, respectively. The densities of the undistorted composites were quite uniform from one polymer to another but varied slightly in the distorted materials, most likely due to differences in the structure caused by the stretching process. The ceramic density was approximately 95% of the powder pycnometer density of 7.864 g/cm<sup>3</sup>.

### Electromechanical Characterization

**Isotropic vs. Distorted Structure:** In Figures 3 and 4, it can be seen that the composites with a distorted ceramic

‡ Channel Products, Inc., Chesterland, OH



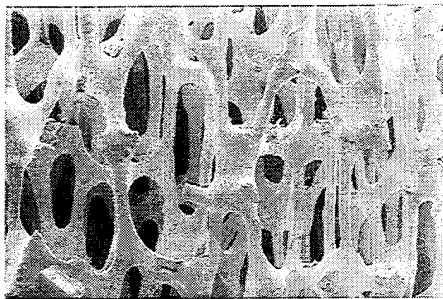


Figure 2. Scanning electron micrograph of a distorted reticulated PZT ceramic.

structure, in general, had superior hydrostatic charge coefficients and figures of merit. The distortion tends to straighten the ceramic path between electrodes allowing for an increased level of poling of the ceramic. In addition, as described earlier, the lateral reinforcement of the near vertical rods helps to decouple the longitudinal and lateral responses. The improvement over the undistorted composites, however, was not as large as expected. The Spurr epoxy may simply be too stiff to allow effective transfer of stress to the ceramic.

**Polymer Matrix Effects:** It was found that the Eccogel epoxy was completely inadequate as a matrix material for these composites. This can be seen in a comparison of Figures 3 and 5. The problem can be blamed directly on the flexibility of the Eccogel polymer, which allows delicate reticulated ceramics to be damaged during cutting and grinding. Evidently, a stiffer polymer is needed which can provide the needed support for the reticulated structure during processing but not so stiff as to diminish the response of the composite.

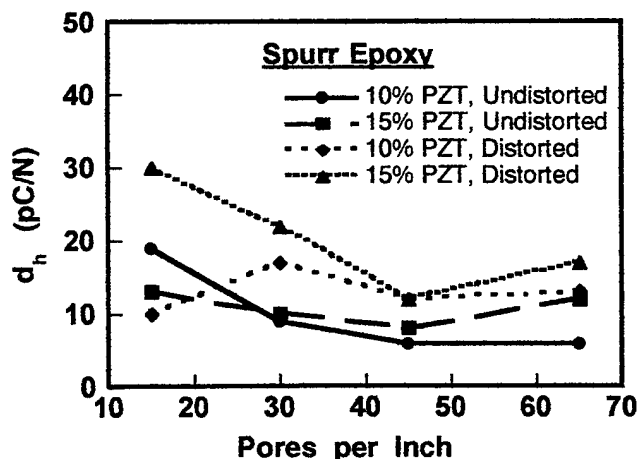


Figure 3. Hydrostatic charge coefficient,  $d_h$ , as a function of pore size for the undistorted and distorted Spurr epoxy/PZT composites of 10 and 15 vol.% ceramic.

**Effects of Volume Percent PZT:** The 15 volume percent composites were found to have higher charge coefficients (in general) for both the undistorted and distorted composites (Figure 3). This is to be expected since a greater amount of active material produces a greater response. Because the figure of merit,  $d_{gh}$ ,

(Figure 4) is inversely proportional to dielectric constant, somewhat different behavior is seen. Since higher vol.% PZT results in higher  $K_{33}^T$ ,  $d_{gh}$  is constrained by a lower

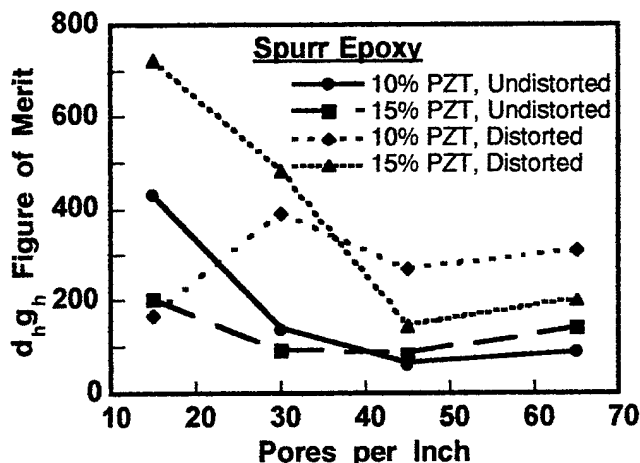


Figure 4. Hydrostatic figure of merit,  $d_{gh}$ , as a function of pore size for the undistorted and distorted Spurr epoxy/PZT composites of 10 and 15 vol. % ceramic.

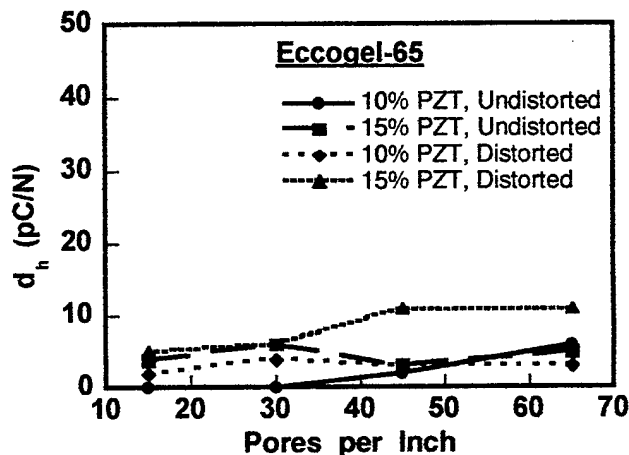


Figure 5. Hydrostatic charge coefficient,  $d_h$ , as a function of pore size for undistorted and distorted Eccogel epoxy/PZT composites of 10 and 15 vol.% ceramic.

$d_{gh}$ . This becomes evident at the finer pore sizes. However, the 15 ppi, 15 vol.% composite still had a higher figure of merit than any of the others. The fact that the  $d_{gh}$  for the 10 vol.% composites with finer pore sizes was comparable or superior to that of the 15 vol.% composites emphasizes the importance of structural distortion.

**Poling Field Effects:** It was found that poling of individual samples with successively higher fields initially improves electromechanical properties but causes a significant decrease after about 10 kV/cm (Figure 6). This behavior was seen for the solid material as well as the composites. An "over-poling" effect is intrinsic to the "soft" PZT-5H material and is due primarily to an increase in domain wall motions in the over-poled ceramic. Notice, however, that the drop in the  $d_h$  of the 15 vol.% composites is slightly steeper than that for the solid PZT-

5H indicating that the decrease may not be due solely to material effects. Figure 7, which plots the ratio of  $d_h$  to  $d_{33}$ , provides more insight. If the decrease were strictly a material effect, the ratio would remain constant over the full range of poling fields (as was observed for solid material). The decrease in the ratio indicates a more rapid decrease in  $d_h$  than  $d_{33}$  which points toward a structural effect. One possibility is that at higher poling fields, the structural features perpendicular to the field are being poled more and are then able to contribute negatively to the hydrostatic response. When poled at lower fields, these elements remain relatively inactive and act as lateral reinforcement for the rod-like structure.

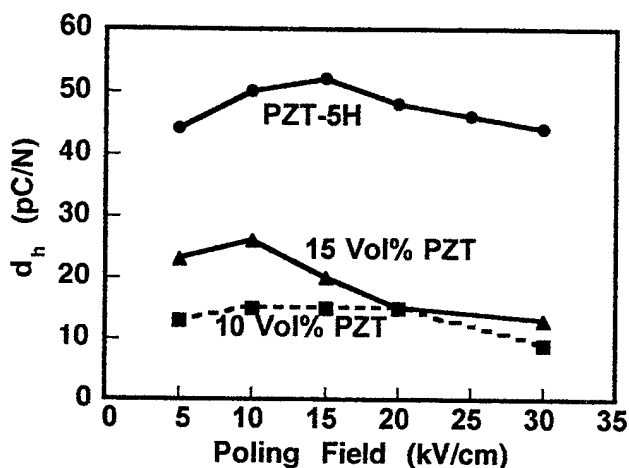


Figure 6. Hydrostatic charge coefficient,  $d_h$ , vs. poling field. This behavior was typical of all the samples tested.

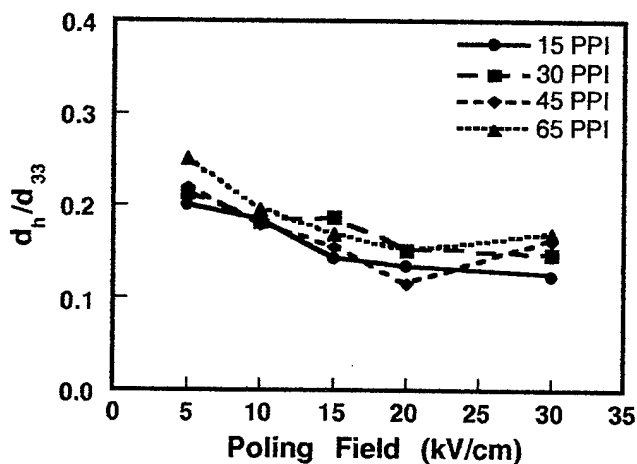


Figure 7. Ratio of  $d_h/d_{33}$  as a function of poling field indicating a faster increase in  $d_h$  than  $d_{33}$ .

## CONCLUSIONS

The use of reticulated ceramic technology in 3-3 piezoelectric composites has been shown to be a viable fabrication method. It was shown that distortion of the ceramic structure significantly improves the hydrophone response. Reticulated ceramics of higher density and larger pore sizes were also more effective for use in these

composite hydrophones. In order to support the ceramic, a relatively stiff polymer matrix is required so that damage during processing is avoided. The poling field was also found to be important. Not only can the material be over-poled, so can the reticulated structure.

Finally, the hydrostatic properties of these materials compare favorably with other types of 3-3 PZT/epoxy composites when normalized for density [2]. A unique advantage that reticulated ceramic technology offers is that improvements of the structure are possible without sacrificing manufacturability. Changes which could improve performance are the use of a different polymer matrix material, the incorporation of a rigid electrode, or further elongation of the structure. Planned work includes these and other possibilities.

## ACKNOWLEDGMENTS

The authors wish to thank the technical specialists at the College of Ceramics and the personnel at Hi-Tech Ceramics, Inc. for their support in this effort. The authors are also grateful for the funding provided by the Office of Naval Research through Grant No. N00014-92-J-4025.

## REFERENCES

- [1] R. E. Newnham, D. P. Skinner and L. E. Cross, "Connectivity and Piezoelectric-Pyroelectric Composites," *Mat. Res. Bull.*, vol. 13, pp. 525-536, 1978.
- [2] T. R. Gururaja, A. Safari, R. E. Newnham and L. E. Cross, *Piezoelectric Ceramic-Polymer Composites for Transducer Applications*. L. M. Levinson, Ed., Electronic Ceramics, New York, NY:Marcel Dekker, Inc., 1987. pp. 92-128
- [3] K. A. Klicker, J. V. Biggers and R. E. Newnham, "Composites of PZT and Epoxy for Hydrostatic Transducer Applications," *J. Am. Ceram. Soc.*, vol. 64[1], pp. 5-9, 1981.
- [4] D. P. Skinner, R. E. Newnham and L. E. Cross, "Flexible Composite Transducers," *Mat. Res. Bull.*, vol. 13, pp. 599-607, 1978.
- [5] K. Rittenmyer, T. Shrout, W. A. Schulze and R. E. Newnham, "Piezoelectric 3-3 Composites," *Ferroelectrics*, vol. 41, pp. 189-195, 1982.
- [6] F. F. Lange and K. T. Miller, "Open-Cell, Low-Density Ceramics Fabricated from Reticulated Polymer Substrates," *Adv. Cer. Mat.*, vol. 2[4], pp. 827-831, 1987.

# Concurrent Session - 2C: Thin Films

# Comparison of the Properties of Pb(Zr,Ti)O<sub>3</sub> Thin Films Obtained by MOCVD Using Different Source Materials

Tadashi Shiosaki and Masaru Shimizu

Department of Electronics, Faculty of Engineering, Kyoto University  
Yoshida Honmachi, Sakyo-ku, Kyoto 606, Japan

**Abstract:** The properties of Pb(Zr,Ti)O<sub>3</sub> (PZT) thin films grown by MOCVD using a variety of source materials were compared and discussed. In the growth of the PZT thin films, three different Pb precursors were used - Pb(C<sub>2</sub>H<sub>5</sub>)<sub>4</sub>, Pb(DPM)<sub>2</sub> and (C<sub>2</sub>H<sub>5</sub>)<sub>3</sub>PbOCH<sub>2</sub>C(CH<sub>3</sub>)<sub>3</sub>. Ti(O-i-C<sub>3</sub>H<sub>7</sub>)<sub>4</sub> and Zr(O-t-C<sub>4</sub>H<sub>9</sub>)<sub>4</sub> were also used as the Ti and Zr precursors. The oxidizing gases used were O<sub>2</sub>, NO<sub>2</sub>, and O<sub>2</sub> containing O<sub>3</sub>. When using three different Pb precursors, it was found that there was a difference in the growth temperature required to obtain perovskite PZT films. It seemed that differences in the electrical properties observed may be due to differences in the orientation, crystallinity, film composition and film thickness. When O<sub>2</sub> containing O<sub>3</sub> was used, an improvement in breakdown voltage was observed.

## 1. Introduction

In the past several years, a variety of ferroelectric and high dielectric constant thin films, including Pb(Zr,Ti)O<sub>3</sub> (PZT), (Pb,Lu)(Zr,Ti)O<sub>3</sub> (PLZT), BaTiO<sub>3</sub>, SrTiO<sub>3</sub>, (Ba,Sr)TiO<sub>3</sub> (BST) and Bi<sub>4</sub>Ti<sub>3</sub>O<sub>12</sub>, have been studied for their potential application to dynamic random access memories and ferroelectric non-volatile memories. Before the practical fabrication of these memory devices can be achieved, several issues still remain to be solved. These include the standardization of the thin film process, the mechanism of the leakage current and fatigue phenomenon, and the interface conditions between the electrode metal and ferroelectric thin film.

In order to produce high quality and reliable ferroelectric thin films, many techniques, such as sputtering, laser ablation, sol-gel processing, metallorganic decomposition (MOD), metalorganic chemical vapor deposition (MOCVD) and liquid source chemical vapor deposition (LSCVD), have been utilized. We think that among these techniques, MOCVD is the most promising method for a number of reasons. These include the high controllability of the film composition and crystallinity, high growth rate and good step coverage characteristics. The deposited films displayed a high degree of crystallization even without post annealing. MOCVD is also a process compatible with the Si LSI process and offers the possibility of scaling up the process to commercial-based production.

However the MOCVD technique has also disadvantages. It requires a complicated and large-scaled system, and the search for appropriate precursors has proven to be difficult.

In order to confirm the advantages of the MOCVD method for utilization in commercial based production, we have performed a number of tests on the MOCVD growth of PZT films. In the MOCVD method, precursors displaying a high vapor pressure, low decomposition temperature, low human toxicity, high stability and a low tendency toward homogeneous nucleation in the vapor phase are required. In the early stage of our experiments, Pb(C<sub>2</sub>H<sub>5</sub>)<sub>4</sub> (tetraethyl lead) was used as a Pb precursor because it is a liquid with a high vapor pressure and therefore is easy to use by utilizing the conventional bubbling method. However this

precursor has not been used legally in commercial-based production systems in Japan due to a high human toxicity. Pb(DPM)<sub>2</sub> (DPM: Dipivaloylmetane), Pb(AcAc)<sub>4</sub> (AcAc: Acetylacetone), Pb(HFA)<sub>4</sub> (HFA: Hexafluoroacetylacetone) and Pb(FOD)<sub>2</sub> (FOD: Heptafluorobutanoylpivaloylmetane), on the other hand, are solid precursors with a low vapor pressure and therefore are considered safe.

In the next stage of experiments, Pb(DPM)<sub>2</sub> as a Pb precursor was used to obtain large area PZT thin films on a 6 inch Si wafer. A new Pb precursor, (C<sub>2</sub>H<sub>5</sub>)<sub>3</sub>PbOCH<sub>2</sub>C(CH<sub>3</sub>)<sub>3</sub> (triethyl n-pentoxyl lead: TEPOL), which was developed to overcome the disadvantages of the above-mentioned Pb precursors, was also used. Three kinds of oxidants, O<sub>2</sub>, NO<sub>2</sub> and O<sub>3</sub>, were also used. From our detailed investigations, we have found that the growth behavior and electrical properties of PZT thin films are different when different kinds of precursors and oxidants are used.

In this paper, we compare the growth behavior and electrical properties of films obtained by MOCVD using different kinds of source materials.

## 2. Experimental Procedure

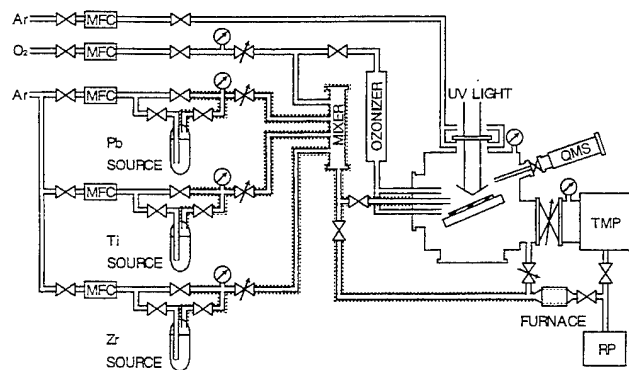
In our experiments, two kinds of MOCVD system were used. One is a homemade system and other is a commercial-based one for the growth of ferroelectric thin films on a 6-8 inch Si wafer. Schematic diagrams of MOCVD systems used are shown in Fig.1. Both systems consisted of a gas supplying system, reaction chamber and evacuation system. In the gas supplying system, there were temperature controlled baths and ovens for keeping the precursor vessels at a constant temperature. Stainless-steel pipes connecting the gas supplying system to the reaction chamber were heated to prevent solidification of the precursors inside the pipes. When the precursor was a liquid, it was transferred by the conventional bubbling method. When the precursor was a solid at room temperature, it was heated and introduced into the reaction chamber by the sublimation method. The carrier gas flow rates were controlled precisely using mass flow controllers. The reactor chambers were of a vertical type. The exhaust was released to the air through a thermal decomposition furnace.

In the growth of PZT thin films, Pb(C<sub>2</sub>H<sub>5</sub>)<sub>4</sub> (purity: 99.9999%), Pb(DPM)<sub>2</sub> (purity: 99.9%), (C<sub>2</sub>H<sub>5</sub>)<sub>3</sub>PbOCH<sub>2</sub>C(CH<sub>3</sub>)<sub>3</sub> (purity: 99.99%), Zr(O-t-C<sub>4</sub>H<sub>9</sub>)<sub>4</sub> (purity: 99.9999%) and Ti(O-i-C<sub>3</sub>H<sub>7</sub>)<sub>4</sub> (purity: 99.9999%) were used as precursors. The oxidizing gases used were O<sub>2</sub> (purity: 99.995%), NO<sub>2</sub> (1% diluted with Ar, purity: 99.9%) and O<sub>2</sub> containing O<sub>3</sub> (0-12 wt%). The substrate used was (111)/Pt/SiO<sub>2</sub>/(100)Si.

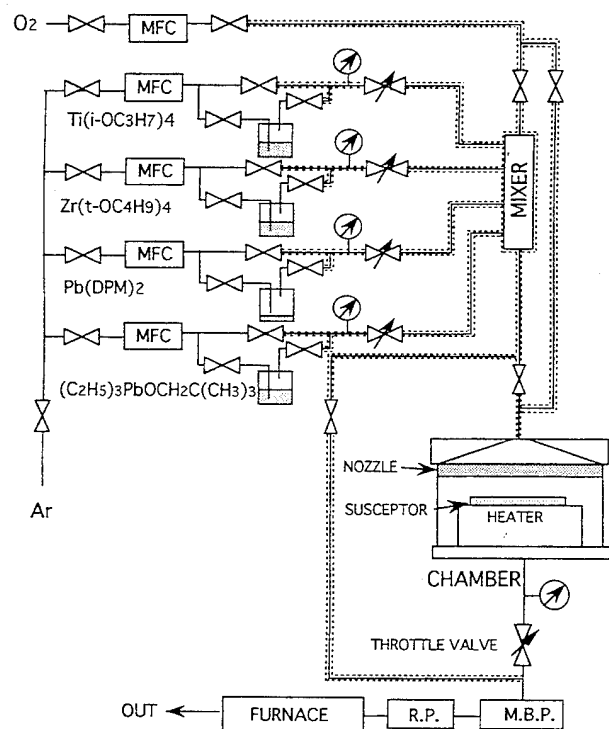
## 3. Results and Discussion

### 3.1 Crystalline structure of PZT films obtained using three different Pb precursors

The crystalline phase and orientation of PZT films on Pt/SiO<sub>2</sub>/Si were investigated. Tetragonal and rhombohedral



(a)



(b)

Fig.1 Schematic diagrams of MOCVD system used (a) home-made system, (b) system for large area growth.

perovskite PZT films were successfully obtained when three kinds of Pb precursors and  $O_2$  as an oxidant were used. The crystalline structure of the PZT films obtained was affected by the substrate temperature and gas supply ratio of  $[Zr]/([Zr]+[Ti])$ , where  $[Zr]$  and  $[Ti]$  were the amounts of Zr and Ti gases supplied. Figure 2 shows the change in the crystalline phase of the films grown at different substrate temperatures and gas supply ratios of  $[Zr]/([Zr]+[Ti])$  when  $Pb(C_2H_5)_4$  and  $O_2$  were used. Tetragonal PZT films were grown at  $[Zr]/([Zr]+[Ti])$  ratios lower than 0.65 and at substrate temperatures higher than  $550^\circ C$ . At high gas supply ratios of  $[Zr]/([Zr]+[Ti])$ , pyrochlore films and  $ZrO_2$  films were formed, substrate temperatures higher than  $630^\circ C$  being required to obtain rhombohedral PZT thin films. In Fig.2, the other phases denote the pyrochlore phase and  $ZrO_2$ .

When  $Pb(DPM)_2$  was used as a Pb precursor, tetragonal PZT films were also grown at  $[Zr]/([Zr]+[Ti])$  ratios lower than 0.6 and at substrate temperatures higher than  $550^\circ C$ , as shown in Fig.3 [1]. In this case, growth temperatures higher than  $600^\circ C$  were also

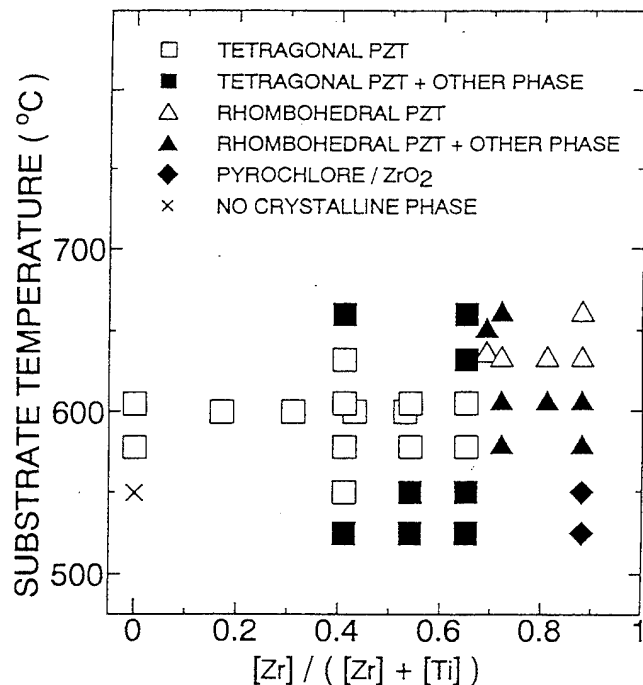


Fig.2 Crystalline phase diagram of PZT films grown using  $Pb(C_2H_5)_4$  and  $O_2$ .

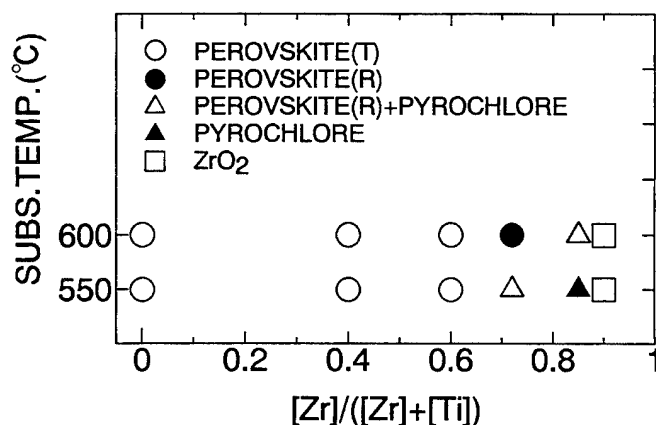


Fig.3 Crystalline phase diagram of PZT films grown using  $Pb(DPM)_2$  and  $O_2$ .

required to obtain rhombohedral PZT thin films. The formation of  $ZrO_2$  at higher Zr content region was also observed. Funakubo et al. reported that PZT films were grown epitaxially on (100)MgO at  $700^\circ C$  using  $Pb(DPM)_2$  precursor [2].

When the new Pb precursor  $(C_2H_5)_3PbOCH_2C(CH_3)_3$  (TEPOL) was used to grow PZT films, a decrease in the growth temperature was observed [3]. Figure 4 shows a crystalline phase diagram of PZT thin films grown using TEPOL. In these experiments, the oxidizing gas used was  $O_2$ . From a series of experiments, it was found that tetragonal and rhombohedral perovskite PZT thin films were grown at substrate temperatures higher than  $460^\circ C$  and  $500^\circ C$  respectively – substrate temperatures which were  $90^\circ C$  and  $130^\circ C$  lower than when  $Pb(C_2H_5)_4$  as a Pb precursor and  $O_2$  as an oxidant were used. Dormans et al. also reported growth of PZT films with good crystallinity and high polarization values at  $700^\circ C$  using  $Pb(C_2H_5)_3(O-t-C_4H_9)$  as a new Pb precursor [4]. These experimental facts indicate that TEPOL is a promising Pb precursor for MOCVD of Pb-based ferroelectric thin films.

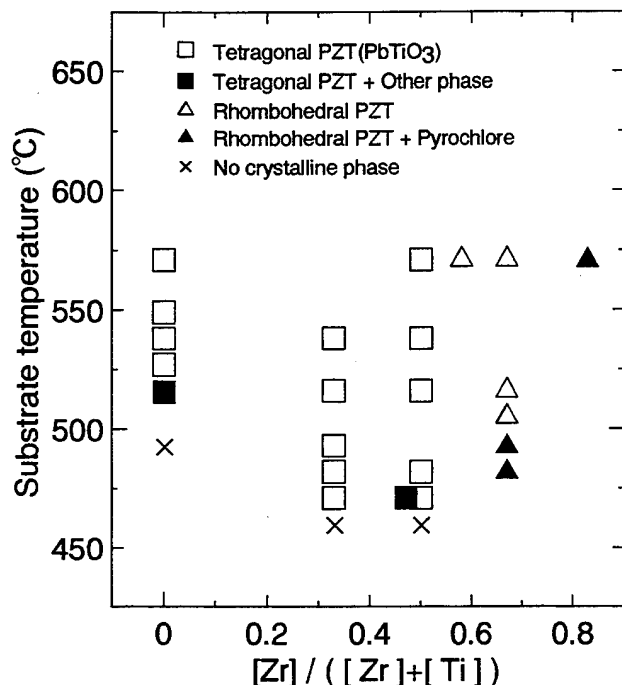


Fig.4 Crystalline phase diagram of PZT films grown using  $(C_2H_5)_3PbOCH_2C(CH_3)_3$  and  $O_2$ .

In MOCVD, film composition could be easily controlled by changing the carrier gas flow rate [5]. The relative Pb content of the films increased as the substrate temperature increased in the range from 550°C to 600°C, a range where the oxidation process of the tetraethyl seemed to be rate-determining. The Pb/(Zr+Ti) composition ratio of the films were not changed by changing the gas supply ratio of  $[Zr]/([Zr]+[Ti])$ .

### 3.2 Electrical properties of PZT films obtained using three different Pb precursors

Various electrical properties, such as the relative dielectric constant ( $\epsilon_r$ ), remanent polarization ( $P_r$ ), coercive field ( $E_c$ ) and leakage current, of the PZT films obtained using the three kinds of Pb precursors were investigated.

The dependence of the relative dielectric constant on the gas supply ratio of  $[Zr]/([Zr]+[Ti])$  when  $Pb(C_2H_5)_4$  and  $O_2$  were used is shown in Fig.5. PZT films (film thickness: 260–320 nm) grown at 605°C showed  $\epsilon_r$  values ranging from 110 to 470 and a maximum  $\epsilon_r$  value of 470 at a  $[Zr]/([Zr]+[Ti])$  of 0.65. Keijser et al. reported  $\epsilon_r$  values of about 450–1050 [6].  $\epsilon_r$  values of 200–350 in c-axis oriented PZT films grown using  $Zr(DPM)_4$  was also reported by Sakashita et al. [7]. The ferroelectric properties were evaluated by D-E hysteresis loops.  $P_r$  and  $E_c$  were also affected by the substrate temperature and film composition. Figure 6 represents the dependence of  $P_r$  and  $E_c$  on the substrate temperature. Most of the PZT films showed an asymmetric hysteresis loop and therefore the values of the sum of the positive and negative remanent polarizations  $(+P_r) + (-P_r)$  and average coercive field were estimated to characterize the ferroelectricity of the films in Fig.6.  $P_r$  and  $E_c$  were influenced by gas supply ratio of  $[Zr]/([Zr]+[Ti])$ . They decreased as the  $[Zr]/([Zr]+[Ti])$  ratio increased. This behavior of  $P_r$  and  $E_c$  was similar to that of other reported literature [6,7]. The leakage current characteristics of the films obtained were also affected by the substrate temperature and gas supply ratio of  $[Zr]/([Zr]+[Ti])$ . Among the PZT films

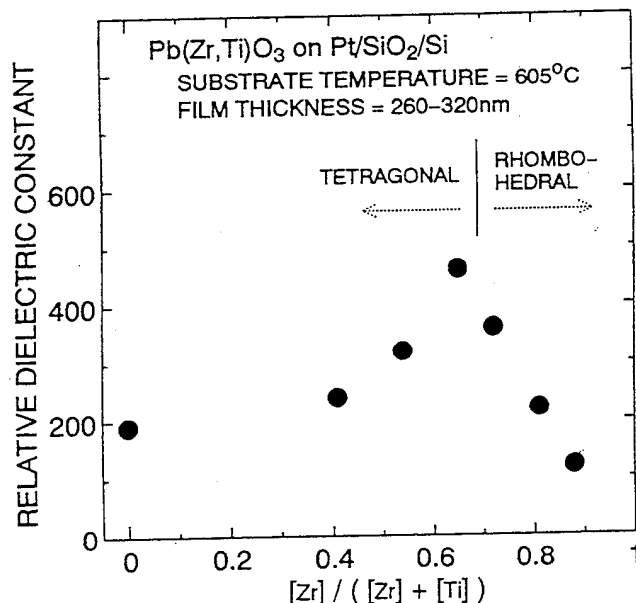


Fig.5 Dependence of the  $\epsilon_r$  on the gas supply ratio of  $[Zr]/([Zr]+[Ti])$ .

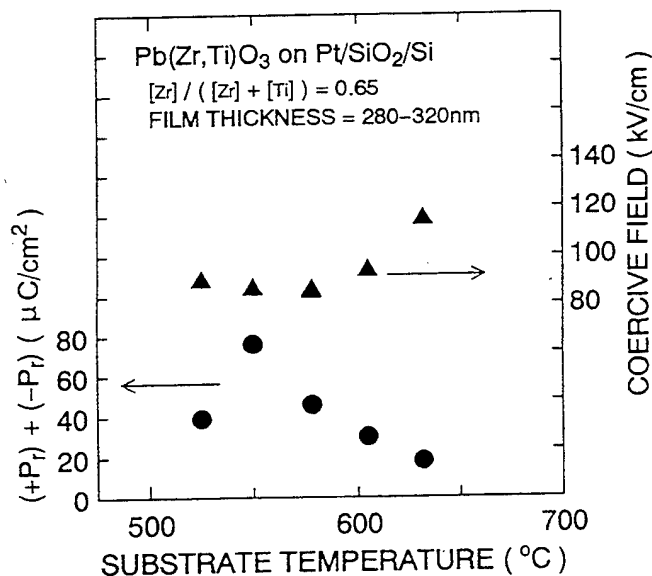


Fig.6 Dependence of  $P_r$  and  $E_c$  on the substrate temperature.

obtained at substrate temperatures ranging from 520°C to 660°C, PZT films grown at 550°C showed a minimum leakage current density of  $10^{-7}$  A/cm<sup>2</sup>. The leakage current also decreased as  $[Zr]/([Zr]+[Ti])$  ratio increased as shown in Fig.7. One of reasons for this decrease in the leakage current density may be due to microstructural change in the film structure.

When  $Pb(DPM)_2$  was used as a Pb precursor, PZT films (film thickness: 100–160 nm) grown at 600°C under various  $[Zr]/([Zr]+[Ti])$  ratios using a commercial-based MOCVD system showed  $\epsilon_r$  values of 50–600, and  $P_r$  and  $E_c$  were 9–38  $\mu$ C/cm<sup>2</sup> and 70–220 kV/cm, respectively [1]. The minimum leakage current was  $10^{-6}$  A/cm<sup>2</sup>. Kashiwara and Itoh et al. reported that  $\epsilon_r$  of PZT films grown at 700°C under various carrier gas flow rates were 500–1700 and typical  $P_r$  and  $E_c$  were 18  $\mu$ C/cm<sup>2</sup> and 55 kV/cm, respectively [8,9].

PZT thin films (film thickness: 230–400 nm) grown at 580°C

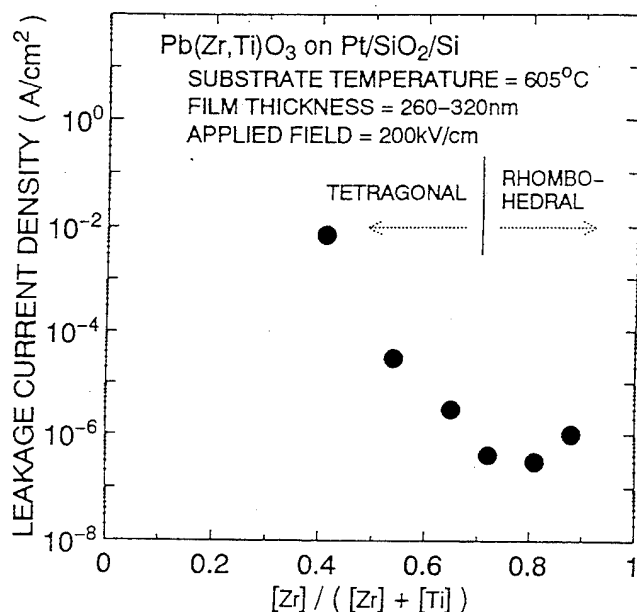


Fig. 7 Leakage current densities of PZT films.

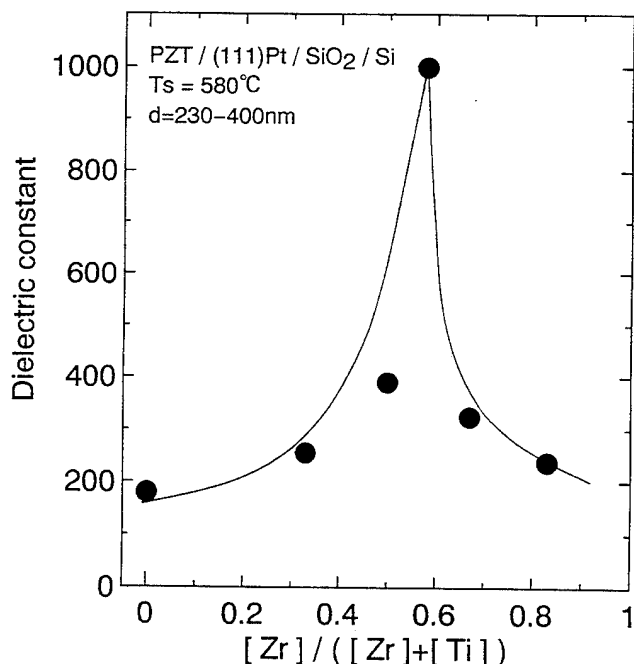


Fig. 8 Dependence of the  $\epsilon_r$  on the gas supply ratio  $[Zr]/([Zr]+[Ti])$  ratio when TEPOL and  $O_2$  were used.

using TEPOL as a new Pb precursor showed a maximum  $\epsilon_r$  value of 1000 as shown in Fig. 8 [3]. The  $P_r$  and  $E_c$  of the PZT films obtained were 15–20  $\mu C/cm^2$  and 70–90 kV/cm, respectively. These  $\epsilon_r$ ,  $P_r$  and  $E_c$  values were nearly same as those of PZT films grown using  $Pb(C_2H_5)_4$  and  $Pb(DPM)_2$  as a Pb precursor.

At this stage, a difference in the fatigue characteristics of the films grown using the three different kinds of Pb precursors was not observed.

The electrical properties ( $\epsilon_r$ ,  $P_r$  and  $E_c$ ) are usually dependent on the film thickness and growth temperature, and therefore the differences in the electrical properties of PZT films grown using these three kinds of Pb precursors can not be analyzed definitively. At this stage, from our experimental results, we think that in the use of the three kinds of Pb precursors mentioned above, there is a

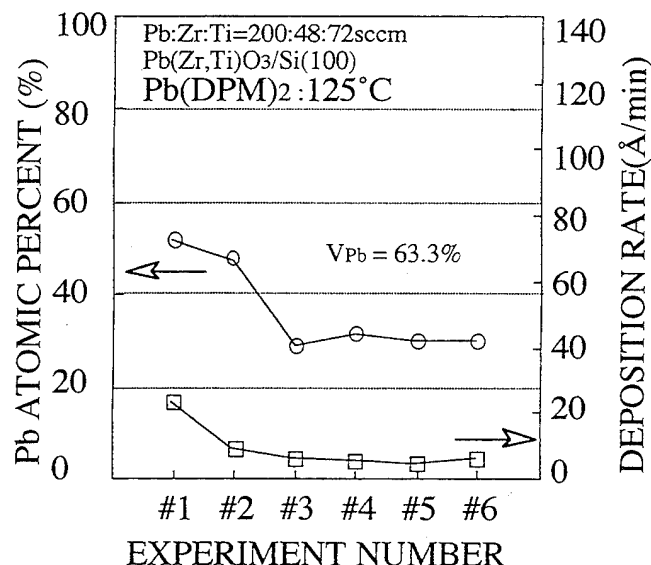


Fig. 9 Variation of the Pb content in the films and deposition rate with each performance of the experiment when a solid Pb precursor ( $Pb(DPM)_2$ ) was used.

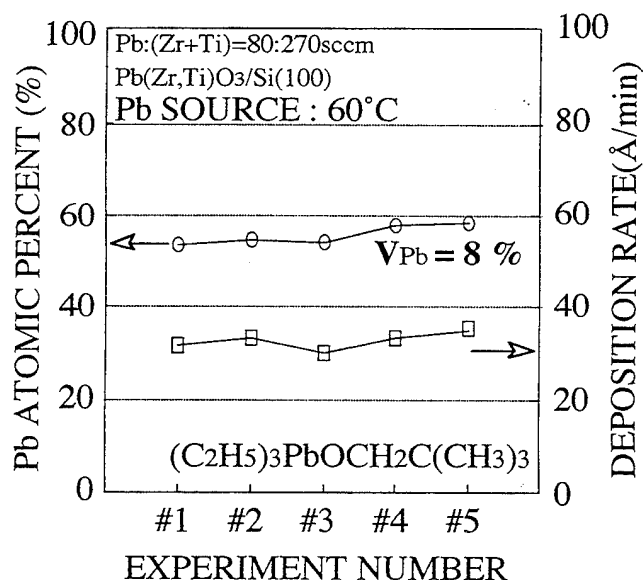


Fig. 10 Variation of the Pb content in the films and deposition rate with each performance of the experiment when a liquid Pb precursor (TEPOL) was used.

difference in the growth temperature required to obtain perovskite PZT films. However it seems that distinct differences in the electrical properties of the PZT films could not be attributable to the differing Pb precursors. Differences in the electrical properties may be due to the differences in the orientation and crystallinity of the PZT films obtained under the various growth conditions.

### 3.3 Reproducibility of the film composition using a solid and a liquid precursor

The reproducibility of the PZT film composition and deposition rate with each performance of the experiment was investigated, both when a solid ( $Pb(DPM)_2$ ) and a liquid (TEPOL) as Pb precursor was used [10,11].

When a solid  $Pb(DPM)_2$  precursor was used at a source temperature of 125°C, the Pb component in the PZT films and the

deposition temperature decreased each time the experiment was performed, as shown in Fig 9. The change in the Pb content,  $V_{pb}$ , which was defined as (maximum Pb content - minimum Pb content)/(average Pb content), was 63.6%. When the Pb precursor temperature was set at 140°C - which was higher than its melting point of around 130°C -  $V_{pb}$  was improved and was 11.8%. These changes in the Pb content and deposition rate were due to an instability in the supplying Pb source. Because the Pb source used was a solid which had a low vapor pressure, stabilization of the Pb supply over a long period was difficult compared with using a liquid source. Figure 10 shows the variation of the Pb content in the PZT films and deposition rate with each performance of the experiment when a liquid precursor, TEPOL, was used. A dramatic improvement,  $V_{pb}=8\%$ , was observed in the variation of the Pb content and in the deposition rate, compared with when a solid  $Pb(DPM)_2$  precursor was used. When TEPOL was used as a Pb precursor, uniform PZT films with a variation in the Pb, Zr and Ti components of less than 1.5% were successfully obtained on a 6 inch Si wafer [10,11].

### 3.4 Crystalline structure of PZT films using three different oxidizing gases

The growth of PZT films using  $O_2$  as an oxidizing gas is mentioned above. In this section, film growth using  $NO_2$  and  $O_2$  containing  $O_3$  as oxidizing gases is mainly described. One of main reasons for the use of  $NO_2$  and  $O_3$  as oxidizing gases is that they have longer optical absorption wavelengths and therefore an improvement of film properties is expected in photo-MOCVD of PZT thin films [12]. The details are referred to previous papers [12,13].

When  $NO_2$  was used as an oxidizing gas, tetragonal PZT films were obtained at substrate temperatures as low as 535°C - a substrate temperature which was 15°C lower than when tetragonal films were grown using  $O_2$  instead of  $NO_2$  (Fig.2), as shown in Fig.11. Rhombohedral PZT films were also obtained as low as 540°C, as was the case when rhombohedral films were grown using  $O_2$ . Growth temperatures higher than 600°C were required to obtain rhombohedral PZT films at high Zr content regions.

By using  $O_2$  containing  $O_3$  (5 wt%), perovskite PZT films were obtained at substrate temperatures ranging from 560°C to 625°C. However no dramatic change in the crystalline orientation or decrease in the growth temperature was observed.

### 3.5 Electrical properties of PZT films using three different oxidizing gases

When  $NO_2$  was used, PZT films (film thickness: 95-110 nm) grown under various  $[Zr]/([Zr]+[Ti])$  ratios showed  $\epsilon_r$  values ranging from 150 to 350.  $P_r$  and  $E_c$  were 6-34  $\mu C/cm^2$  and 100-163 kV/cm, respectively. The leakage current density also decreased as the  $[Zr]/([Zr]+[Ti])$  ratio increased, and the minimum leakage current density was  $10^{-8} A/cm^2$ , as was the case when  $O_2$  was used.

When  $O_2$  containing  $O_3$  (5 wt%) was used, a very interesting phenomena was observed. We found an improvement in the leakage current characteristics, in particular an improvement in the breakdown voltage, as shown in Fig.12. PZT films grown using pure  $O_2$  as an oxidizing gas showed lower breakdown voltages than those of films grown using  $O_2$  containing  $O_3$ . In this experiment, PZT films grown by photoenhanced MOCVD showed the highest breakdown voltages. At this stage, taking the results of the cross-sectional observations of the films into consideration, we

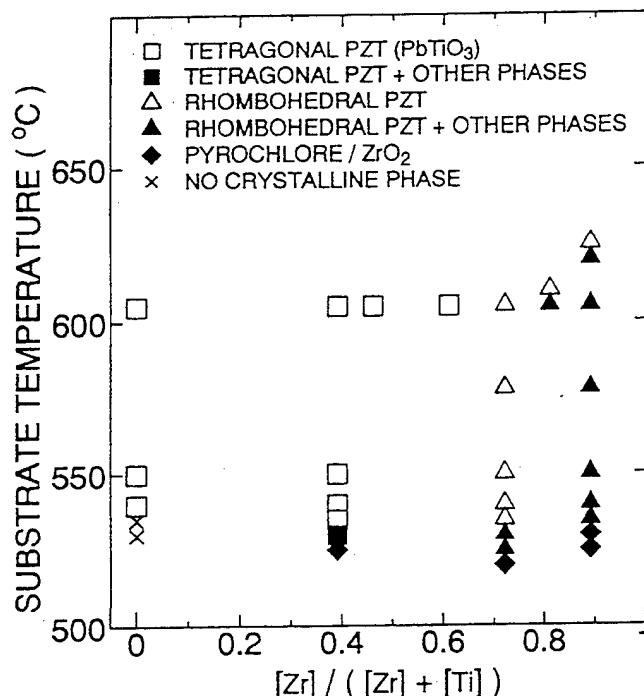


Fig.11 Crystalline phase diagram of PZT films grown using  $Pb(C_2H_5)_4$  and  $NO_2$ .

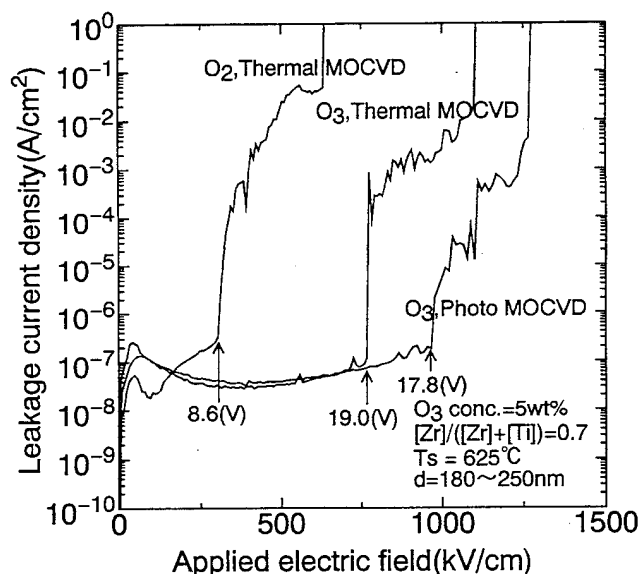


Fig.12 Leakage current characteristics of PZT films grown using  $O_2$  and  $O_2$  containing  $O_3$  (5 wt%).

think that one of the main causes of the improvement in the breakdown voltages may be due to the microscopic change in the film structure [14]. Other reasons may be due to an improvement in the interface flatness between the upper electrode and the surface of the PZT film, a decrease in the oxygen vacancies, or a change in the film composition. An improvement in the breakdown voltage was also observed when TEPOL was used instead of  $Pb(C_2H_5)_4$  as a Pb precursor.

No significant change in the fatigue characteristics was observed regardless of whether  $O_2$  or  $O_3$  was used.



#### 4. Conclusions

The crystalline and electrical properties of PZT thin films grown by MOCVD using different source materials were investigated. When three different Pb precursors –  $\text{Pb}(\text{C}_2\text{H}_5)_4$ ,  $\text{Pb}(\text{DPM})_2$  and  $(\text{C}_2\text{H}_5)_3\text{PbOCH}_2\text{C}(\text{CH}_3)_3$  – were used, it was found that there was a difference in the growth temperature required to obtain perovskite PZT thin films. However it seems that distinct differences in the electrical properties could not be attributable to the use of differing Pb precursors.

The effects of the use of three different oxidizing gases –  $\text{O}_2$ ,  $\text{NO}_2$  and  $\text{O}_2$  containing  $\text{O}_3$  – on the properties of PZT films were also investigated. No dramatic decrease in the growth temperature was observed. However, in particular, a dramatic improvement in the breakdown voltage was observed, when  $\text{O}_2$  containing  $\text{O}_3$  was used.

#### Acknowledgements

The authors would like to thank Messrs. T.Katayama, M.Sugiyama and H.Fujisawa for their technical assistance and discussions. This work was partly supported by a Grant-in-Aid for Scientific Research (B)(No.04452176), (C)(No.05650302), and a Grant-in Aid for Scientific Research on Priority Areas (2)(No.04205075) from the Ministry of Education, Science and Culture, and by a Mazda Foundation's Research Grant and a research grant from the Foundation for the Promotion of Material Science and Technology of Japan

#### References

- [1] M.Shimizu, M.Fujimoto, T.Katayama, T.Shiosaki, K.Nakaya, M.Fukagawa and E.Tanikawa, "Growth and Characterization of Ferroelectric  $\text{Pb}(\text{Zr,Ti})\text{O}_3$  Thin Films by MOCVD Using a 6 Inch Single Wafer CVD System", *Mat. Res. Soc. Symp. Proc.* Vol.310, pp.255–260, 1993.
- [2] H.Funakubo, K.Imashita, N.Kieda and N.Mizutani, "Formation of Epitaxial  $\text{Pb}(\text{Zr,Ti})\text{O}_3$  Film by CVD", *Nippon Seramikkusu Kyokai Gakujutu Ronbunshi*, Vol.99, pp.248–250, 1991.
- [3] M.Shimizu, M.Sugiyama, H.Fujisawa and T.Shiosaki, "Preparation of PZT Thin Films by MOCVD Using a New Pb Precursor", in *Proceedings of the 6th International Symposium on Integrated Ferroelectrics*, 1994.
- [4] G.J.M.Dormans, M.de Keijser, P.J.van Veldhoven, D.M.Frigo, J.E.Holewijn, G.P.M.van Mier and C.J.Smit, "Triethyllead ter-Butoxide, a New Precursor for Organometallic Chemical Vapor Deposition of Lead Zirconate Titanate Thin Films", *Chem. Mater.*, Vol.5, pp.448–451, 1993.
- [5] M.Shimizu, K.Hayashi, T.Katayama and T.Shiosaki, "Compositional Control of Ferroelectric  $\text{Pb}(\text{Zr,Ti})\text{O}_3$  Thin Films by Reactive Sputtering and MOCVD", in *Proceedings of the 8th IEEE International Symposium on Application of Ferroelectrics*, 1992, pp.428–431.
- [6] M.de Keijser, P.J.van Veldhoven and G.J.M.Dormans, "Organometallic Chemical Vapor Deposition of Lead Zirconate-Titanate Thin Films", *Mat. Res. Soc. Symp. Proc.*, Vol.310, pp.223–234, 1993.

- [7] Y.Sakashita, T.Ono, H.Segawa, K.Tominaga and M.Okada, "Preparation and Electrical Properties of MOCVD-deposited PZT Thin Films", *J. Appl. Phys.*, Vol.69, pp.8352–8357, 1991.
- [8] K.Kashihara, H.Itoh, K.Tsukamoto and Y.Akasaka, "Formation of PZT Films by MOCVD", in *Ext.Abs. of the 1991 International Conference on Solid State Device and Materials*, 1991, pp.192–194.
- [9] H.Itoh, K.Kashihara, T.Okudaira, K.Tsukamoto and Y.Akasaka, "MOCVD for PZT Thin Films by Using Novel Metalorganic Sources", in *Technical Digest of International Electron Device Meeting*, 1991, pp.831–834.
- [10] T.Shiosaki, C.S.Kang, M.Shimizu, M.Fukagawa, K.Nakaya and E.Tanikawa, "Growth and Properties of PZT Thin Films on a 6–8 Inch Wafer by MOCVD", in *Proceedings of 1993 PAC RIM Meeting*, 1993.
- [11] T.Shiosaki, M.Shimizu and M.Kinoshita, "Characterization of PZT Films Grown by MOCVD on 6–8 Inch Si Wafers", in *Proceedings of the 6th International Symposium on Integrated Ferroelectrics*, 1994.
- [12] M.Shimizu, T.Katayama, M.Sugiyama and T.Shiosaki, "Thin Film Growth of  $\text{Pb}(\text{Zr,Ti})\text{O}_3$  by Photoenhanced Metalorganic Chemical Vapor Deposition Using  $\text{NO}_2$ ", *Jpn. J. Appl. Phys.*, Vol.32, pp.4074–4077, 1993.
- [13] M.Shimizu, M.Sugiyama, T.Katayama and T.Shiosaki, "Photoenhanced MOCVD of  $\text{PbZr}_x\text{Ti}_{1-x}\text{O}_3$  Thin Films", *Appl. Sur. Sci.*, Vol.79/80, pp.293–298, 1994.
- [14] M.Shimizu, H.Fujisawa, M.Sugiyama and T.Shiosaki, "Effects of  $\text{O}_3$  on Growth and Electrical Properties of  $\text{Pb}(\text{Zr,Ti})\text{O}_3$  Thin Films by Photoenhanced Metalorganic Chemical Vapor Deposition", to be published in *Jpn. J. Appl. Phys.*, 1994.

# Physical Vapor Deposition of Antimony Sulpho-Iodide (SbSI) Thin Films and Their Properties

Narayanan S. and R. K. Pandey  
Center for Electronic Materials, Electrical Engg. Dept.  
Texas A & M University, College Station, TX 77843-3128.

**Abstract** – The objective of this work is to fabricate thin films of Antimony Sulfo-Iodide (SbSI) semiconductor ferroelectric and to evaluate its properties. SbSI films (2–4  $\mu\text{m}$  thick) have been fabricated on Pt/Ta/SiO<sub>2</sub>/Si structures by physical vapor transport in evacuated sealed ampoules. The preferred orientation of these films was (311) as indicated by powder XRD patterns and the films were close to stoichiometric as revealed by EDS analysis. SEM micrograph reveals random orientation of needle like crystallites throughout the surface of the film. A maximum dielectric constant of 500 was measured at a Curie temperature of 21 °C.

## INTRODUCTION

SbSI, the material with the highest Curie temperature in the class of V-VI-VII compounds, also has the highest dielectric constant. The crystal structure of this compound was determined by Donges et al. [1] in 1950. Later, photoconductivity in this compound was discovered by Nitsche et al. [2] in 1960 and ferroelectricity by Fatuzzo et al. [3] in 1962.

The growth and properties of single crystals of SbSI has been extensively studied since its discovery by vapor and melt growth. Calculation of the growth parameters was not difficult because of the well established physico-chemical properties. Crystals as large as  $5 \times 7 \times 10 \text{ mm}^3$  have been grown [4] by modified vapor growth technique. Growing larger crystals of this material is still proven to be difficult because of i) the large difference in vapor pressure of Sb, S and I and ii) large anisotropy in growth rate along c-axis.

In the paraelectric phase, SbSI is described by the  $D_{2h}^{16}$  (Pnam) space group. In the low temperature ferroelectric phase, the structure is defined as  $C_{2v}^o$  (Pna2). It crystallizes in orthorhombic structure ( $D_{2h}^{16}$  symmetry) with the following lattice constants:  $a = 8.49 \text{ \AA}$ ;  $b = 10.1 \text{ \AA}$ ; and  $c = 4.16 \text{ \AA}$ . The crystal structure of SbSI is shown in Fig. 1. It has a structure composed of  $(\text{Sb}_2\text{S}_2\text{I}_2)_n$  double chains. The binding in the chain is of the covalent type and weak Van der Waals bonds are formed between the neighboring chains.

Regarding the properties of SbSI, the high interest is probably due to the fact that it is a semiconductor ferroelectric, i.e., it is a ferroelectric which also possesses semiconducting properties. The Curie temperature of this material is 22 °C and the peak dielectric constant is 50,000 [4]. The absorption edge lies in the red or near infra-red and its ferroelectric properties change when

optically excited and for this reason it is also called a photoferroelectric. The spontaneous polarization in the range of  $30 \mu\text{C}/\text{cm}^2$  and pyroelectric current of the order of 1.3 nA at Curie temperature [5] has been measured. SbSI has the highest

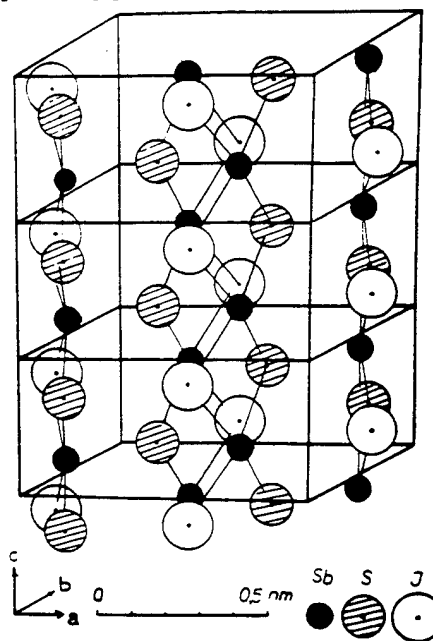


Fig. 1. Crystal Structure of SbSI

value of refractive index ( $\sim 4.5$  along c-axis) of any known material. This adds to its importance for development of electro-optic devices provided defect-free large crystals become readily available. It was also found by Li et al [6] that temperature changes of the order of  $10^{-3} \text{ }^\circ\text{C}$  was detectable by monitoring the reflectance coefficient of SbSI using null ellipsometry.

On the contrary to the study of single crystals, there have been only few studies on thin film fabrication of SbSI. Films have been fabricated by e-beam evaporation [7], flash evaporation [8], thermal evaporation [9] on various substrates. All these films resulted in amorphous structure and post deposition annealing was carried to gain some order of crystallinity. Moreover the properties measured were much less than that of single crystals.

This paper deals with the fabrication of thin films of SbSI on Pt/Ta/SiO<sub>2</sub>/Si structures by physical vapor transport in closed ampoules and evaluation of their properties.

## EXPERIMENTAL DETAILS

SbSI thin films were grown in a two-zone Trans-Temp transparent gold coated furnace using evacuated quartz ampoules. Films were grown using different evaporation and substrate temperatures, evaporation rate and source to substrate distance. The volume of the ampoule was  $\sim 20 \text{ cm}^3$ . The Pt/Ta/SiO<sub>2</sub>/Si substrates were mounted on a quartz rod at a distance of about 3 inches from the source material. Various charge compositions ranging from stoichiometric SbSI to 90% Sb<sub>2</sub>S<sub>3</sub> and 10% SbI<sub>3</sub> were tried. Once the charge and the substrate are loaded, the ampoule was evacuated to a vacuum of about  $10^{-5}$  Torr and sealed off. The handling of the charge material and the ampoules were carried in Argon atmosphere in a glove box.

The ampoule is then loaded in the two-zone furnace where the temperatures are programmed to give a desired gradient within the ampoule. It was found that the gradient (dependent on source to substrate distance) and the substrate temperature were very critical in film deposition. The evaporation temperature was  $\sim 300^\circ\text{C}$  and the substrate temperature was  $150\text{--}200^\circ\text{C}$ . Higher supersaturations were possible because of steeper temperature gradients within the ampoule. Control of the evaporation rate of antimony iodide was possible by controlling the temperature in the low temperature zone. Once the experiment is over the substrates were removed by snap cutting the ampoules.

Compositional analysis of the films was made by Energy Dispersive Spectroscopy (EDS). The structure of the films were studied using X-ray powder diffraction (XRD) patterns and the surface morphology was examined by scanning electron microscopy (SEM).

## RESULTS AND DISCUSSIONS

Films with thickness in the range of  $2 - 4 \mu\text{m}$  were grown on Pt/Ta/SiO<sub>2</sub>/Si structures. The film formation of SbSI is accompanied by liquid condensation of Antimony Iodide (SbI<sub>3</sub>) on Pt prior to nucleation. The liquid condensed either forms a continuous film or separates into tiny droplets depending on the surface roughness of the substrate. As the substrate temperature increases, needle crystallites nucleate in the liquid. As substrate temperature increases further, the liquid SbI<sub>3</sub> partially evaporates and partially gets incorporated into SbSI. This suggests that the mechanism of nucleation is through a Vapor-Liquid-Solid (VLS) mechanism rather than a direct VS mechanism. This mechanism is also observed by Pankrashov et al. [10].

Powder XRD pattern of a  $4 \mu\text{m}$  thick film is shown in Fig. 2. An asterisk in this figure stands for the substrate. A double asterisk indicates an unidentified peak. From this figure it can be seen that the preferred orientation of the films is (311). The peak corresponding to this plane is in proximity to the Pt(111) peak. This preferred orientation is also observed for flash evaporated

films by Mansingh et al. [8]. The lattice constants calculated by least square fit method from the powder diffraction pattern is shown in Table 1. The calculated values match very well with that of the single crystal values reported in the literature.

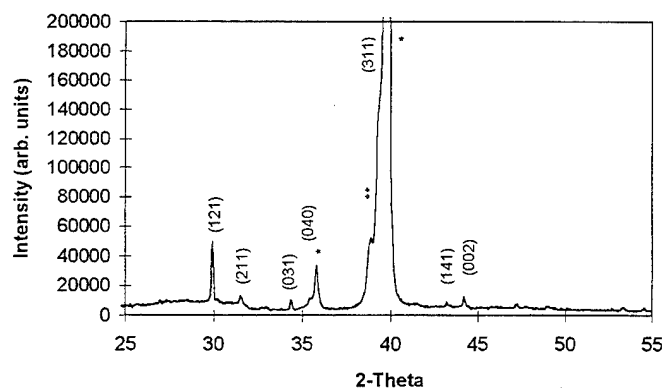


Fig. 2. Powder diffraction pattern of a SbSI film.

Table 1. Lattice parameters calculated from XRD pattern.

	a Å	b Å	c Å
SbSI crystal (reported)	8.527	10.14	4.089
Thin film	8.563	10.15	4.097

SEM micrograph reveals randomly oriented crystallites as is also evident from the XRD patterns. The grain size of the crystallites was of the order of  $0.5\text{--}1 \mu\text{m}$ . The results of EDS

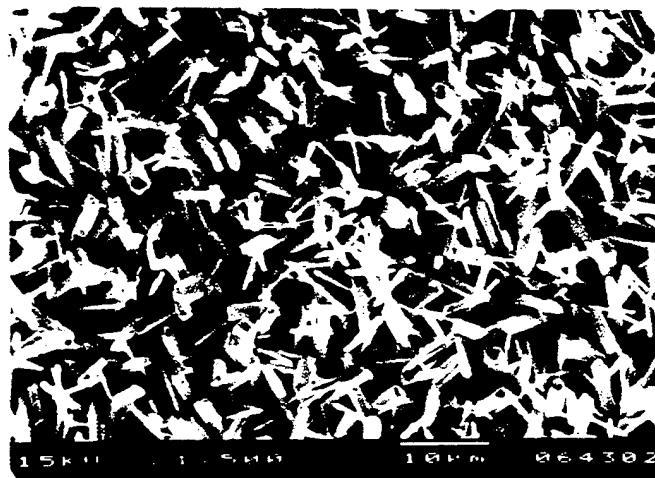


Fig. 3. SEM micrograph of an as grown film of SbSI

analysis is shown in Table 2. These numbers indicate the atomic percentage of Sb, S and I (accuracy  $\pm 3\%$ ). Theoretical values should then be 33.33% for each of the three elements in the compound. Measurements were made on the same sample at three different points. Considering an accuracy of 3%, one can say that the films were close to stoichiometric.

The dielectric constant versus the temperature relation is shown in Fig. 4. The transition was rather broad with a peak dielectric constant of 500 at a Curie temperature of 21 °C. The broad transition can be attributed to the random orientation of the crystallites in the film. The peak pyroelectric coefficient of the film as measured by the Byre-Roundy technique with a heating rate of 1 °C/min was 0.18  $\mu\text{C}/\text{cm}^2/\text{K}$ .

Table 2. EDS analysis of a SbSI film

Sb %	S %	I %
35.84	33.30	30.86
36.09	31.95	31.96
35.87	32.92	31.21

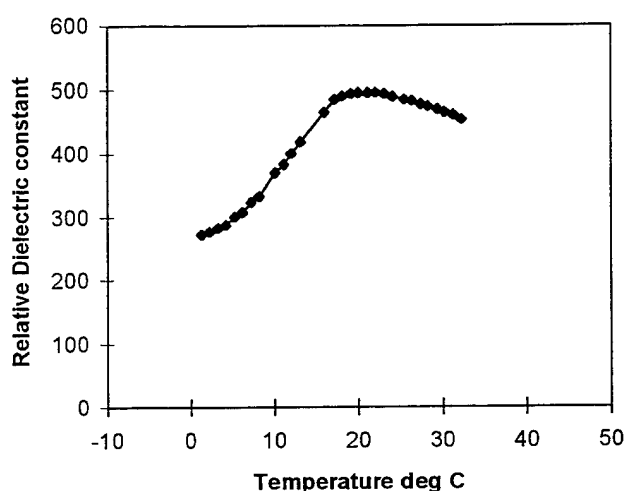


Fig. 4. Dielectric constant vs. temperature for a SbSI film.

### CONCLUSION

SbSI films with thickness in the range of 2-4  $\mu\text{m}$  have been grown on Pt/Ta/SiO<sub>2</sub>/Si structures by physical vapor transport in sealed evacuated ampoules. The substrate temperature during deposition was in the range of 150-200 °C. The preferred orientation of these films was (311) as indicated by powder XRD patterns and the films were close to stoichiometric as revealed by EDS analysis. SEM micrograph reveals random orientation of needle like crystallites throughout the surface of the film. A maximum dielectric constant of 500 was measured at a Curie temperature of 21 °C. The transition was broad due to random orientation of the crystallites.

Further studies are in progress to improve the orientation of the films and to deposit the films on optically transparent substrates to study the optical properties. Also, the effect on addition of transport agents like sulfur and iodine on film properties will be seen.

The authors would like to thank Dr. Hung-Dah Shih and Mr. Dave Witter of Texas Instruments, Dallas, for helpful discussions and Mr. Mike White of CEM for technical help. The authors also gratefully acknowledge the sponsors Texas Instruments, Dallas, TX and NASA Center for Space Power for this work.

### REFERENCES

- [1] E. Donges, "Über selenohalogenide des dreiwertigen antmons und Wismuts Über antimon (III)-selenid", *Z. Anorg. Chem.*, vol. 263, pp. 280-287, December 1950.
- [2] R. Nitsche and W. J. Merz, "Photoconduction in ternary V-VI-VII compounds", *J. Phys. Chem. Solids*, vol. 13, pp. 154-155, May 1960.
- [3] E. Fatuzzo, G. Harbeke, W. J. Merz, R. Nitsche, H. Roetschi and W. Ruppel, "Ferroelectricity in SbSI", *Phys. Rev.*, vol. 127, pp. 127-128, September 1962.
- [4] L. A. Zadorozhnaya, V. A. Lyachovitskaya, E. I. Givargizov and L. M. Belyaev, "Vapor growth of SbSI on a seed", *J. Cryst. Growth*, vol. 41, pp. 61-66, November 1977.
- [5] K. Toyoda, "Electrical properties of SbSI crystals in the vicinity of the ferroelectric Curie point", *Ferroelectrics*, vol. 69, pp. 201-215, August 1986.
- [6] J. Li, D. Viehland, A. S. Bhalla and L. E. Cross, "Pyro-optic studies for infra-red imaging", *J. Appl. Phys.*, vol. 71, pp. 2106-2112, March 1992.
- [7] M. Yoshida, K. Yamanaka and Y. Hamakawa, "Semiconducting and dielectric properties of c-axis oriented SbSI thin film", *Jap. J. Appl. Phys.*, vol. 12, pp. 1699-1705, November 1973.
- [8] A. Mansingh and T. Sudarsena Rao, "Growth and characterization of flash-evaporated ferroelectric antimony sulphoiodide thin films", *J. Appl. Phys.*, vol. 58, pp. 3530-3535, November 1985.
- [9] P. K. Ghosh, A. S. Bhalla and L. E. Cross, "Preparation and electrical properties of thin films of antimony sulphur iodide (SbSI)", in *Proceedings of IEEE-ISAF '83*, 1983, pp. 29-33.
- [10] A. I. Pankrashov, L. A. Zadorozhnaya and E. I. Givargizov, "Oriented Crystallization of SbSI on amorphous substrates by artificial epitaxy", *Sov. Phys. Crystallogr.*, vol. 32, pp. 429-431, May-June 1987.



# Concurrent Session - 4A: Actuators and Electrostrictions

Gene H. Haertling  
Gilbert C. Robinson Department of Ceramic Engineering  
Clemson University, Clemson, SC 29634-0907

**Abstract** -- On-going studies have shown that the PLZT compositional system is one which yields materials possessing some of the highest coefficients for piezoelectric and electrostrictive actuators. It has also been found that PLZT ceramics are near ideal for achieving the ultra-high displacements recently reported for the Rainbow (Reduced and Internally Biased Oxide Wafer) actuators. In order to determine the optimum composition or compositions for these Rainbow actuators, a study was conducted by preparing and processing selected formulations throughout the PLZT system. Results from this study indicate that, like the conventional direct extensional-mode materials, the maximum Rainbow bending displacements occur in materials located compositionally at the morphotropic ( $FE_{rhomb} - FE_{tet}$ ) and Curie point ( $FE - PE$ ,  $PE - AFE$ ) phase boundaries. Examples of specific compositions for each of these regions are 2/53/47, 9/65/35 and 8.5/70/30 (La/Zr/Ti), respectively. Microstructural (grain size), electrical (dielectric constant, dissipation factor) and electromechanical (axial displacement) data are presented for selected compositions in the system.

## INTRODUCTION

It has long been known that the PLZT compositional system is a very versatile one which yields materials possessing maximum dielectric properties and some of the highest known electromechanical coefficients for piezoelectric devices such as speakers, hydrophones, ignitors, accelerometers, motors, sensors and actuators [1-2]. In general, these optimum properties are found in materials located compositionally along the morphotropic (MPB) phase boundary ( $FE_{rh} - FE_{tet}$ ) separating the rhombohedral and tetragonal ferroelectric phases, as shown in Figure 1 by the double cross-hatched region. Other properties of interest (e.g., pyroelectric and electrooptic) are optimized in compositions located along the boundaries separating the FE polar phases from the antiferroelectric (AFE) and paraelectric (PE) non-polar phases. Compositions which typify these materials are more popularly known as electrostrictive relaxors and are indicated in Figure 1 by the single cross-hatched region identified as the SFE (slim FE hysteresis loop) region [3].

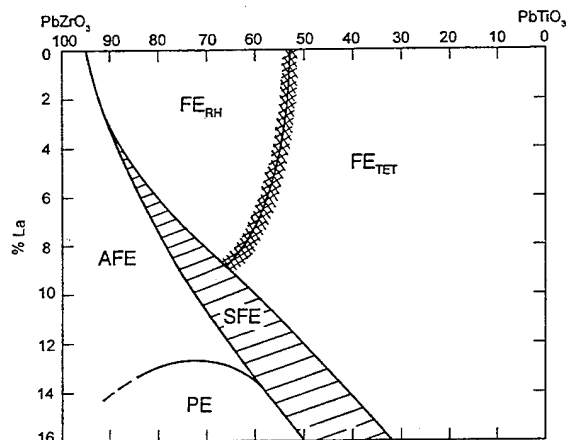


Figure 1. Room temperature phase diagram of the PLZT system showing phase stability regions and phase boundaries of interest.

Although the PLZT relaxor materials were developed over two decades ago for electrooptic applications such as shutters, displays and modulators, they have now been found to be quite suitable for electrostrictive actuator devices where non-memory, lower hysteresis properties are required.

Also, it has recently been reported that PLZT ceramics are excellent materials for achieving ultra-high displacements when they are processed into Rainbow actuator benders which are similar in operation to the unimorph benders with the exception that the Rainbows are a monolithic structure [4-5]. As single-element Rainbows, the PLZT materials are able to achieve very high displacements (up to 3mm) at moderate loading or lesser displacements at loads of up to 10 kg. A variety of applications are foreseen for these devices, however, before they can be developed it is necessary that the phenomena producing the high displacement in these materials be understood more thoroughly and that the composition of the material selected for a given application be the optimum one.

Therefore, it is the purpose of this investigation to (1) study the characteristics of a broad range of compositions in the PLZT solid solution system as Rainbow benders, (2) identify specific compositions with maximum displacement properties and (3) gain more insight into the strain amplification mechanisms involved in the Rainbow ceramics.

## EXPERIMENTAL PROCEDURE

Several series of compositions in the PLZT system were prepared from the raw material oxides via a conventional mixed oxide process as outlined in the flowsheet of Figure 2. These

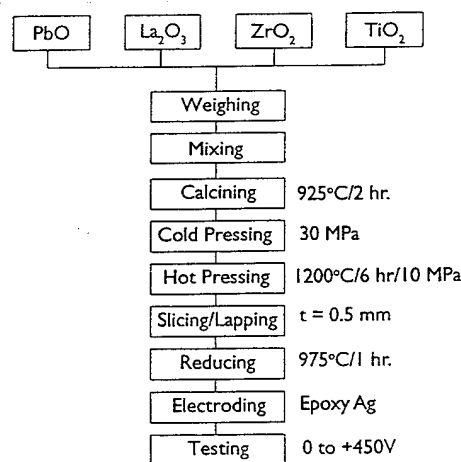


Figure 2. Flowsheet for Rainbow process.

compositions, compounded according to a B-site formula[3], ranged in Zr/Ti ratio from 90/10 to 30/70 and La content from 1 to 15 atom percent. A total of sixty individual compositions were formulated, weighed, wet mixed with distilled water, dried and calcined at 925°C for 2 hours in closed alumina crucibles. The milled and dried powders were first cold pressed as pre-form slugs and then hot pressed at 1200°C for 6 hours at 10 MPa. This procedure yielded a fully dense material with grain sizes

varying from 1.5 to 6 microns. Subsequent steps in the fabrication of the wafers included slicing and lapping them to a thickness of 0.5 mm.

A Rainbow was produced from a lapped part by placing the wafer on a flat graphite block which was supported on a zirconia carrier plate. A second zirconia plate of the same size as the wafer was placed on top of the wafer in order to shield the top side of the wafer from chemical reduction and to minimize thermal shock to the part during processing. The assembly was placed into a furnace preheated to 975°C and held there for one hour, removed from the furnace while hot and cooled naturally to room temperature in about 45 minutes. When cool, the dome shaped wafer was lifted from the graphite block, sanded lightly on the reduced (concave) side to remove any metallic lead particles and to expose the reduced layer, and then electroded with DuPont 5504N epoxy silver paint cured at 200°C for 30 minutes. Although a silver electrode was applied to the reduced side of the wafer, it was used primarily to insure good electrical contact to the conductive reduced PLZT which actually was the bottom electrode. Since the reduced PLZT layer was measured to be 0.15mm thick for the selected reducing conditions, the net thickness of the PLZT piezoelectric was 0.35mm.

Standard electrical measurements of capacitance (1 kHz), dissipation factor and dc hysteresis loops were run on all of the samples after electroding. Displacement measurements were usually made using a positive pulse voltage source and a mechanical dial indicator [8], however, selected tests were also run using a LVDT in order to compare results and to obtain the full displacement loop with + and - voltages.

Grain size measurements were determined from optical micrographs of polished and etched parts at a magnification of x1250 using the linear intercept method.

## RESULTS AND DISCUSSION

### Grain Size

Grain sizes of the hot pressed PLZT parts ranged from 1.5 microns (um) average diameter to 6.0 um. In general, the larger grain size materials were found to be located along each of the phase boundaries mentioned previously; i.e., between the AFE, PE and FE phases, while compositions in the interior of the phase stability regions possessed minimal grain sizes with the 4% La series having the smallest. Examples of this behavior are illustrated in Figures 3 and 4 as functions of Zr/Ti ratio and La content, respectively. The reason for this behavior is not

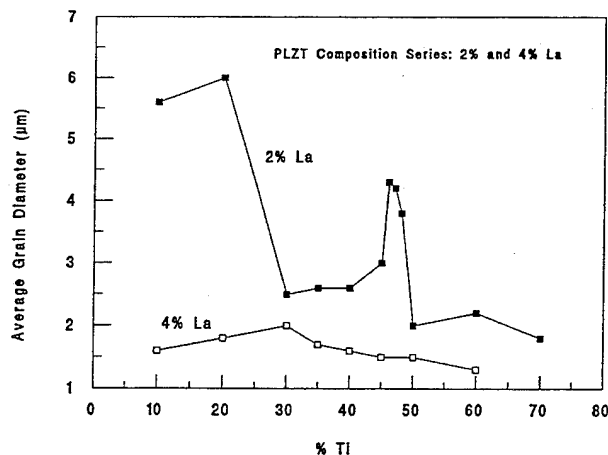


Figure 3. Grain size as a function of composition for materials in the PLZT system at 2 and 4 atom % La.

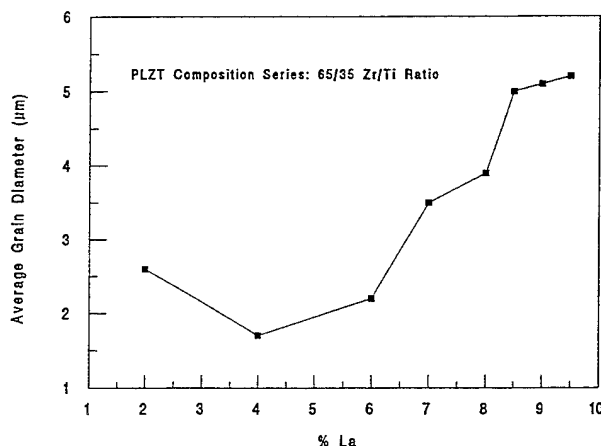


Figure 4. Grain size as a function of composition for materials in the PLZT system at a Zr/Ti ratio of 65/35.

understood at this time; however, previous experience with PLZT materials for electrooptics confirms the existence of large grain sizes (up to 15 um) for 9/65/35. Obviously, this present set of grain sizes exists for the materials hot pressed at the selected conditions, and this would change as the as the temperature or time was varied; but when comparing all compositions at the same conditions, one can only speculate at this stage that chemical and structural factors such as excess lead oxide in the B-site formula, vacancies in the lattice or mixed phases in the phase boundary compositions are instrumental in producing these results.

Grain size is an important factor in the displacement characteristics of Rainbows just as it is already known to be a significant factor in other properties of piezoelectrics such as dielectric constant, coupling and d constant. Figure 5 shows the effect of grain size on axial displacement for composition 1/53/47.

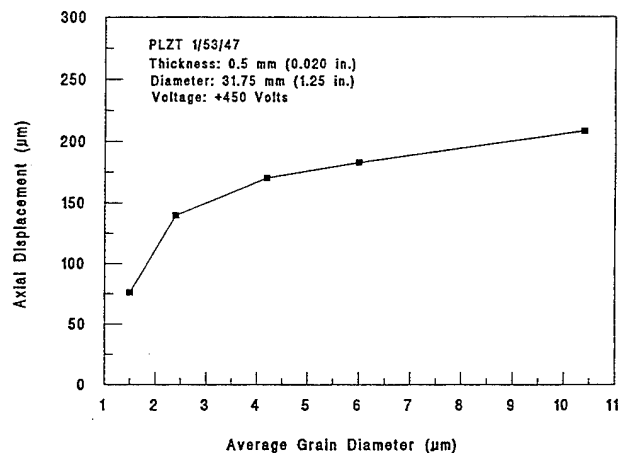


Figure 5. Grain size dependence of axial displacement for PLZT 1/53/47 Rainbow.

The grain sizes for this composition were obtained by hot pressing at temperatures from 1000 to 1200°C. As can be seen, grain sizes less than approximately 2 um lessen the displacement characteristics and those greater than about 8 microns are of little additional benefit. An optimum grain size range is estimated to be from 6 to 7 microns.

### Electrical Properties

#### Dielectric Properties - Small-signal dielectric properties of



several compositions of varying Zr/Ti ratio at 2% and 6% La concentration are given in Figures 6 and 7, respectively. Values

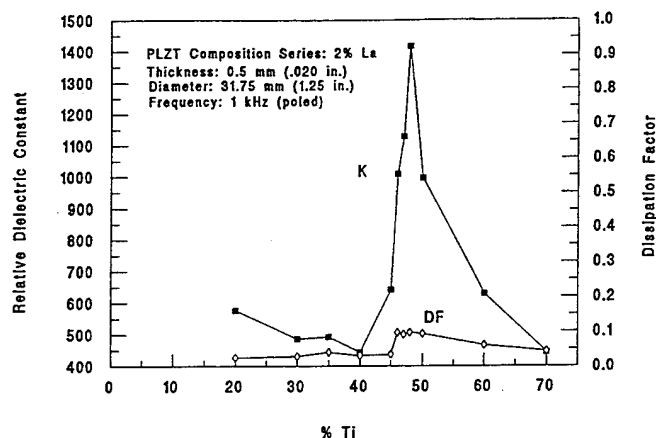


Figure 6. Small signal dielectric properties of composition series at 2% La.

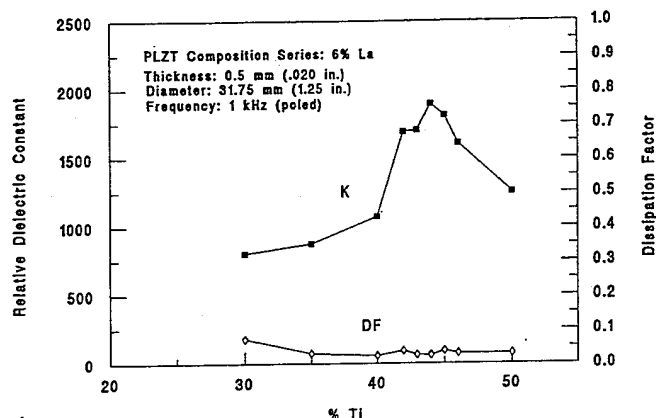


Figure 7. Small signal dielectric properties of composition series at 6% La.

ranged from a low of 444 for 2/60/40 to a high of 1896 for 6/56/44. As expected, dielectric constant peaked at the MPB for both series of compositions, however, the anomaly was especially pronounced for the 2% La series. The maximum value of 1416 was possessed by composition 2/52/48. Dissipation factors ranged from 2.4% to 9.7% with the higher values occurring in the MPB compositions.

A second series of compositions with varying La contents at Zr/Ti ratios of 65/35 and 70/30 are shown in Figures 8 and 9, respectively. In this series, dielectric constants were observed to increase in a regular manner from low values at 2% La to maximum values at 8.5 - 9% La. Actual values ranged from 486 to 3264 for the 70/30 group, and the 65/35 values also fell within this range. Dissipation factors as high as 9.8% and as low as 2.8% were measured, again with the higher values occurring at the FE - AFE and FE - PE phase boundaries. These values are typical of those obtained in previous work on PLZT materials.

**Hysteresis Loops** - Typical examples of dc hysteresis loops for compositions 1/53/47 and 9/65/35 are given in Figure 10. The loop in Figure 10 (A) was taken on the ferroelectric Rainbow element (1/53/47) in its virgin condition before any other measurements were made. It should be noted that on the initial application of positive voltage to +450V there was approximately 60% of the total remanent polarization switched rather than the usual 50% one ordinarily observes in a virgin,

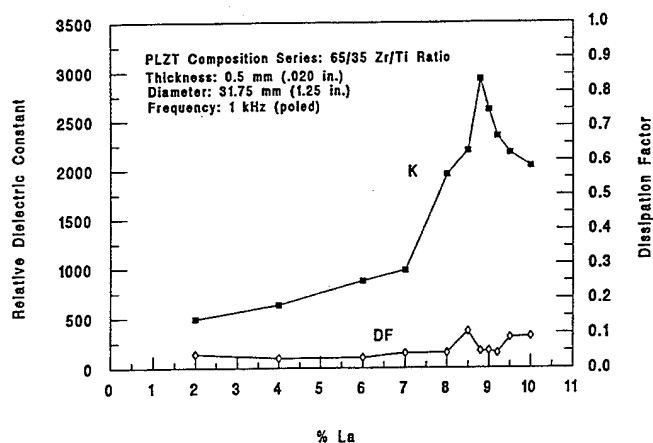


Figure 8. Small signal dielectric properties of composition series at 65/35 Zr/Ti ratio.

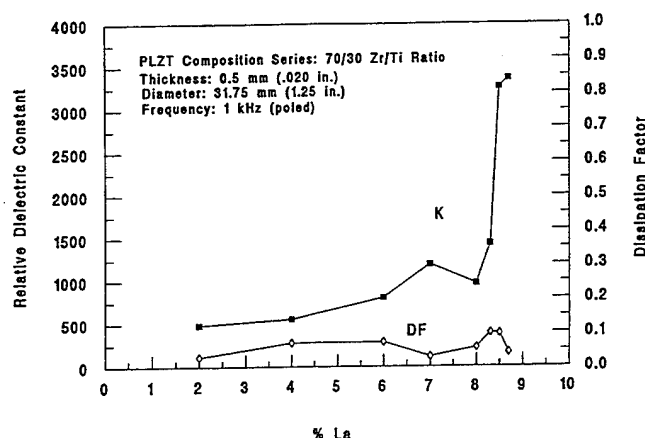


Figure 9. Small signal dielectric properties of composition series at 70/30 Zr/Ti ratio.

randomly oriented ceramic.. This behavior is highly unusual and indicates that the Rainbow ceramic was partially poled before testing. Additional audio and piezoelectric tests of other virgin parts also indicated that the elements were partially poled to varying degrees; i.e., some very little and others as high as 75%.

One explanation for this condition occurring in the electrically virgin state is that the mechanical compressive and tensile stresses produced in the Rainbow wafer during processing are acting together to switch some of the domains in this soft ferroelectric/ferroelastic material. Since uniform stress is a

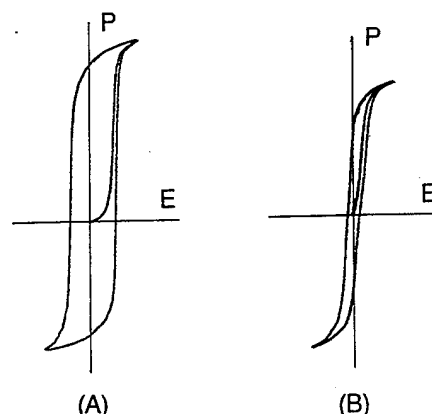


Figure 10. Typical hysteresis loops for Rainbow PLZT compositions (A) 1/53/47 and (B) 9/65/35.

symmetrical quantity, it is recognized that it alone is insufficient to produce a net polarization in a given direction even though it may be of sufficient magnitude to switch domains; however, a stress gradient such as produced by the Rainbow bending process is a vector quantity and can, indeed, produce the observed effect. This non-uniform stress is believed to be responsible for the partial poling of the Rainbow wafers.

Measured properties on the above wafer were:  $P_R = 44.8 \text{ uC/cm}^2$ ,  $E_C = 7.5 \text{ kV/cm}$ , dielectric constant = 1210 and dissipation factor = 0.047.

The virgin loop of Figure 10(B) is a typical one for the electrostrictive (9/65/35) type of Rainbow materials and is very similar to that obtained on bulk electrooptic material. Measured properties on this wafer were:  $P_{10\text{KV/CM}} = 28.3 \text{ uC/cm}^2$ , dielectric constant = 3142 and dissipation factor = 0.085. As a matter of course, no unsymmetrical hysteresis loops were observed in the electrostrictive materials, and none was expected, since there are no stable domains in these materials at zero electric field. Conceivably, a high enough stress could precipitate stable domains in a very near-ferroelectric material, however, a study of this effect is beyond the scope of this investigation.

**Displacement Loops** - Displacement vs. electric field (butterfly) loops for the Rainbow wafers described above are shown in Figure 11. As before, Figure 11(A) illustrates the Rainbow axial motion as the sample is electrically switched from zero to +450V, to -450V and back to zero, however, in this case this loop was not taken on the virgin wafer. It may be noted that this loop is remarkably similar to that observed when measuring the direct extensional (longitudinal, lateral) displacements via the piezoelectric  $d_{33}$  or  $d_{31}$  coefficients. The value of displacement in the + voltage direction was measured at 190.5  $\mu\text{m}$ , and the total amount of displacement (+/-) was 432  $\mu\text{m}$ .

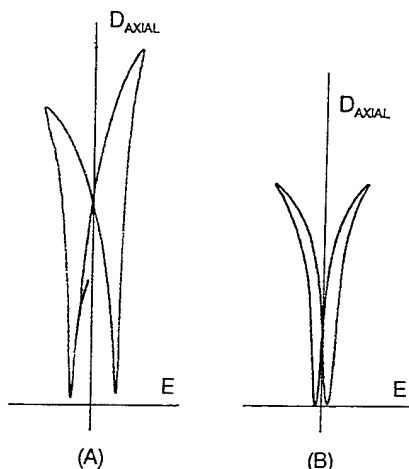


Figure 11. Axial displacement loops of samples in Figure 10.

Figure 11(B) shows the displacement loop of the electrostrictive Rainbow material (9/65/35) mentioned above. Since 9/65/35 is a relaxor material there should be little or no memory, and the same value and sign of displacement should be obtained whether a + or a - voltage is applied. One can see by switching this sample through a full voltage loop that a small amount of remanent displacement (strain) is present which is probably due to the close proximity of this composition to a FE phase. A further indication of this incipient FE phase is the higher than normal value of  $P_{10}$  ( $P_{10} = 28.4$  vs.  $18.0 \text{ uC/cm}^2$ ) as given above. Measured value of total displacement for this wafer was 178  $\mu\text{m}$ .

**Displacement vs. Composition** - Displacement data as a function of composition in the PLZT phase diagram is shown in Figure 12. In this figure, the stars indicate the location of most

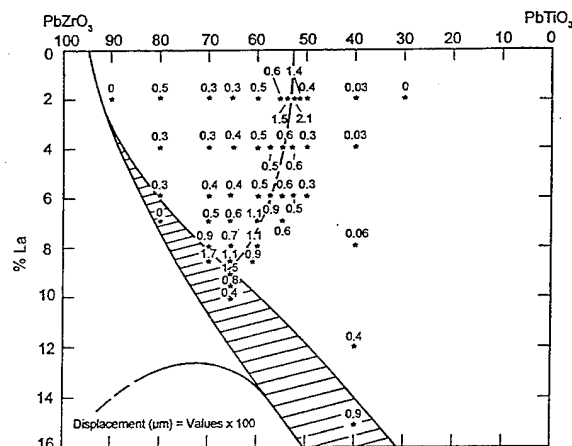


Figure 12. Rainbow displacement data for the PLZT system overlaid with the phase diagram of Figure 1 (values in microns are to be multiplied by 100).

of the compositions prepared, and the values given are those obtained from the dial micrometer measurements at zero to +450 volts. As such, they represent approximately one-half of the total switching displacement available from the FE materials but all of the displacement available from the SFE relaxor materials. It may be noted in this diagram that the maximum displacements were found to occur along the same phase boundaries mentioned previously; i.e., the  $FE_R - FE_T$ ,  $FE - PE$  and  $FE - AFE$  boundaries, where other properties also are maximized. It should also be mentioned that the phase boundaries shown in Figure 12 are the same as those of Figure 1 because Figure 1 was simply overlaid on the displacement data and drawn in. The location of these boundaries were determined to be nearly identical to those which could be located by the displacement data. A comparison of these boundary locations at various levels of La are given in Table 1.

Table 1. Morphotropic phase boundary compositions determined from displacement data compared with ref. 3.

% La	PLZT (Ref. 3)	PLZT Rainbow (This Work)
2	2/53/47	2/53/47
4	4/55/45	4/55/45
6	6/58/42	6/57/43
7	7/60/40	7/61/39
8	8/62/38	8/60/40
Boundary	8.6/65/35	8.5/70/30

The values of displacement varied from essentially zero (equivalent to the direct extensional modes) to a high of 210  $\mu\text{m}$  for composition 2/52/48, which would indicate that maximum displacement occurs just on the tetragonal side of the MPB boundary. Other maxima occur at 9/65/35 (152  $\mu\text{m}$ ) and 8.5/70/30 (168  $\mu\text{m}$ ) for the electrostrictive materials at their respective boundaries. It is interesting to note that no significant anomaly or trend occurred near the AFE - FE boundary where one would expect a large electric field induced volume change in

going from a small AFE unit cell to a larger FE unit cell. For compositions 2/90/10 and 4/90/10 which are near this boundary, it was observed that the Rainbow curvature was reversed from convex up (reduced side concave) to near flat or convex down (reduced side convex). In some cases, an electroded part of this type exhibited an axial displacement which could be tested simply by turning the wafer upside down and then operating as normal. Obviously, this region of the phase diagram should be studied further, but such depth was beyond the scope of this investigation.

Some of the possible reasons for maximum Rainbow displacements to occur at phase boundaries are (1) maximum piezoelectric constants ( $d_{33}$  and  $d_{31}$ ) occur at the boundary, (2) mixed or metastable phases exist, (3) maximum domain reorientation is possible, (4) higher mechanical compliance of the structure exists, (5) electric field enforced phases are possible and even probable in some cases and (6) larger grain sizes may occur in the mixed phase region at the boundary. To some degree, all of these effects are probably operative in the Rainbow devices, however, a more in-depth study is required to identify the dominant mechanisms.

Figures 13 through 17 deal with a closer look at the compositional variation of displacement as a function of Zr/Ti

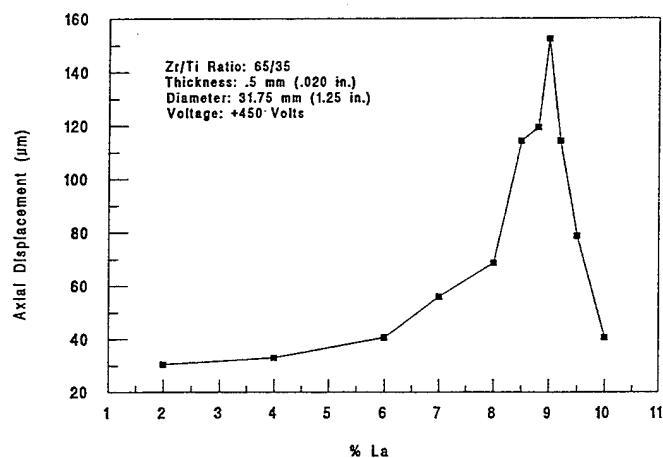


Figure 15. Displacement characteristics of PLZT Rainbow ceramics as a function of La content at a 65/35 Zr/Ti ratio.

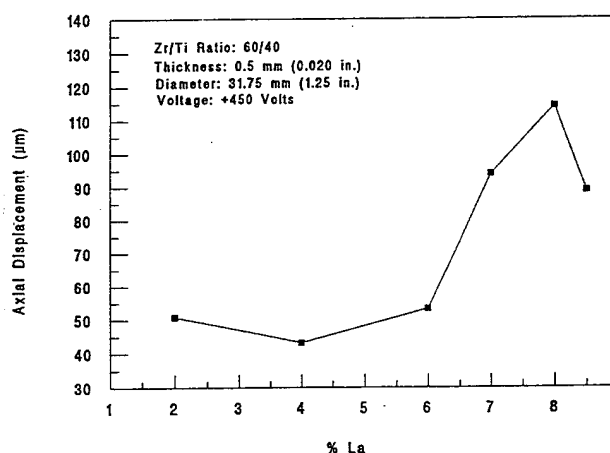


Figure 16. Displacement characteristics of PLZT Rainbow ceramics as a function of La content at a 60/40 Zr/Ti ratio.

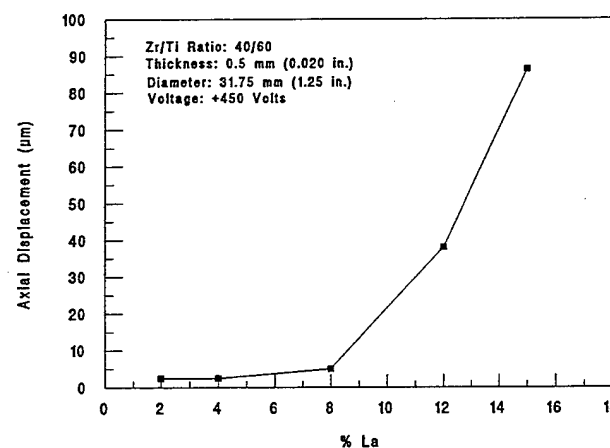


Figure 17. Displacement characteristics of PLZT Rainbow ceramics as a function of La content at a 40/60 Zr/Ti ratio.

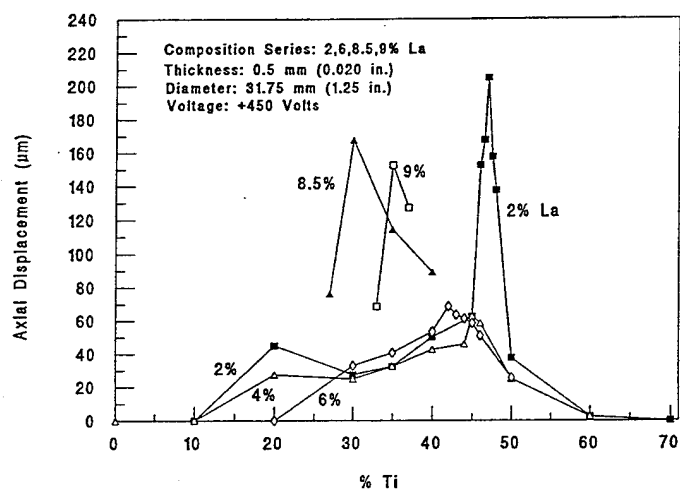


Figure 13. Displacement characteristics of PLZT Rainbow ceramics as a function of Zr/Ti ratio at selected levels of %La.

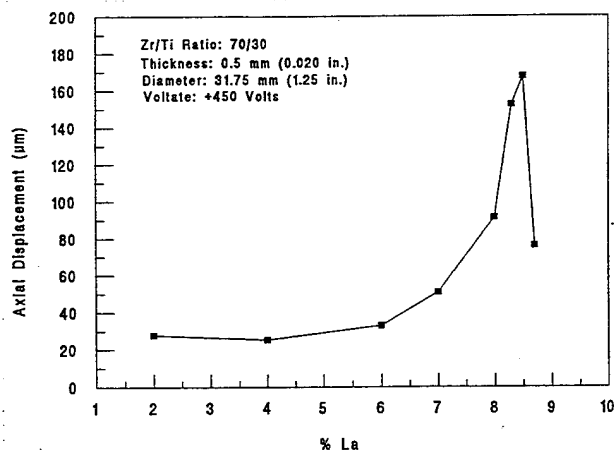


Figure 14. Displacement characteristics of PLZT Rainbow ceramics as a function of La content at a 70/30 Zr/Ti ratio.

ratio (% Ti) at several levels of La concentration or of % La at several different Zr/Ti ratios. Each of these figures again emphasizes the significantly larger displacements existing in the phase boundary compositions.

## CONCLUSIONS

This investigation indicates that the PLZT compositional system is a very fruitful area for producing and studying the unique characteristics of the Rainbow ceramics. No difficulty was experienced in fabricating any of the compositions into Rainbow wafers with the exception of four compositions near the AFE - FE phase boundary. The results of this investigation clearly show that (1) maximum axial displacement is obtained in compositions in or near the morphotropic phase boundary or the phase boundary separating the FE phases from the non-polar (AFE, PE) phases, (2) grain size is a factor in achieving high displacement, i.e., larger grain size is desirable, (3) the compressive and tensile stresses produced in the Rainbow process are instrumental in partially pre-poling the Rainbow ceramic and (4) other mechanisms, in addition to the piezoelectric  $d_{31}$  coefficient, are very likely responsible for the unusually large displacements observed. A maximum displacement of 210 microns for a single, dome-mode Rainbow ceramic was found to occur in PLZT 2/52/48 when activated from zero to +450 volts. Since all of the displacements in this investigation were obtained on Rainbow ceramics with a diameter-to-thickness ratio (31.75 mm x 0.5 mm or 63.5 to 1) conducive to producing a dome-type displacement rather than a saddle type, significantly higher displacement values are to be expected for larger diameter and thinner parts with a higher ratio [4].

## ACKNOWLEDGEMENT

This work was supported by NASA under grant No. NAG-1-1301 and ONR under grant No. N0014-94-1-0563.

## REFERENCES

1. D. Berlincourt, "Current Developments in Piezoelectric Applications of Ferroelectrics," *Ferroelectrics*, 10, 111-119, 1976.
2. G.H. Haertling, "Piezoelectric and Electrooptic Ceramics," in *Ceramic Materials for Electronics*, Relva Buchanan, ed., 139-225, Marcel Dekker, Inc., New York, 1986.
3. G.H. Haertling and C.E. Land, "Hot Pressed (Pb,Lu)(Zr,Ti)O<sub>3</sub> Ferroelectric Ceramics for Electrooptic Applications," *J. Am. Ceram. Soc.*, 54, 1-11, 1971.
4. Gene H. Haertling, "Rainbow Ceramics - A New Type of Ultra-High-Displacement Actuator," *Bull. Am. Ceram. Soc.*, 73, 93-96, 1994.
5. Gene H. Haertling, "Chemically Reduced PLZT Ceramics for Ultra-High Displacement Actuators," *Ferroelectrics*, 154, 101-106, 1994.

# PIEZOELECTRIC ACTUATORS/ ULTRASONIC MOTORS -- Their Developments and Markets --

Kenji Uchino  
International Center for Actuators and Transducers  
Intercollege Materials Research Laboratory  
The Pennsylvania State University, University Park, PA 16802

**Abstract** -- Recent development trend of piezoelectric actuators/ ultrasonic motors is reviewed from the Japanese patent disclosure, and their future market is predicted, which may reach up to \$ 10 billion in the year of 2000.

## INTRODUCTION

Eighteen years have passed since the intensive development of piezoelectric/ electrostrictive actuators started, and the focus has been shifted to practical device applications presently. Piezoelectric shutters (Minolta Camera) and automatic focusing mechanisms (Canon) in cameras, dot-matrix printers (NEC) and part-feeders (Sanki) have been commercialized and mass-produced already by several tens thousand pieces per month. During these commercialization, new designs and drive/control techniques of the ceramic actuators have been mainly developed in these a couple of years [1 - 3]. A number of patent disclosures have been found particularly in Japanese industries such as NEC, TOTO Corporation, Matsushita Electric, Brother Industry, Toyota Motors, Tokin, Hitachi Metal, Toshiba.

The piezoelectric actuators and ultrasonic motors have been developed by private industries in Japan, aiming at the applications to precision positioners and compact motors, and are too practical to be supported by the Japanese government. Only a big national project relating to this area is currently on "Micromechanisms", which mostly covers the silicon micro-machining-related micromotors. On the contrary, the developments in the USA are mainly supported by the military-related government institutions, are mainly focused on active vibration control.

This paper reviews recent development trend of the piezoelectric actuators/ ultrasonic motors viewed from the Japanese patent disclosure, and predicts their future market.

## DEVELOPMENT TREND VIEWED FROM THE PATENT DISCLOSURE

Table 1 summarizes 550 patents concerning piezoelectric actuators and ultrasonic motors disclosed during January 1988 - July 1990 in Japan, which is classified with respect to the patent submitter and the technical content. Tabulation was made using 4 large categories; material, design, drive/control and application, each of which is further classified into composition, fabrication process; multilayer, displacement magnification mechanism, bimorph, others; drive technique, control technique; servo displacement transducer, pulse-drive motor and ultrasonic motor.

Most of the top-ten companies (NEC, TOTO Corporation, Matsushita Electric, Brother Industry, Toyota Motors, Tokin, Hitachi Metal, Toshiba, Nippon Denso, Fuji Electric) have already started to supply the products of piezoelectric actuators/ultrasonic motors or their application devices. Only TOTO Corporation and Fuji Electric have not disclosed their target explicitly.

### Development Trend in the Technical Content

The patent disclosure was graphed with respect to the technical content for 508 patents during 1972 - 84 in Fig.1 and for 550 patents during 1988 - 90 in Fig.2, respectively. It is noticeable that the device application shares most of the patents in Fig. 1, while it shares only 1/4 in Fig.2. The actuator design is significant in the recent years and shares more than half of the patents. Regarding the application, servo displacement transducers and pulse drive motors share 40 % and 43 %, respectively, in Fig.1, and the ultrasonic motors share only 5 %. On the contrary, in Fig.2 the servo displacement transducer and the pulse motor share only 8 % each, and the ultrasonic motor's ratio is increased up to 11 %.

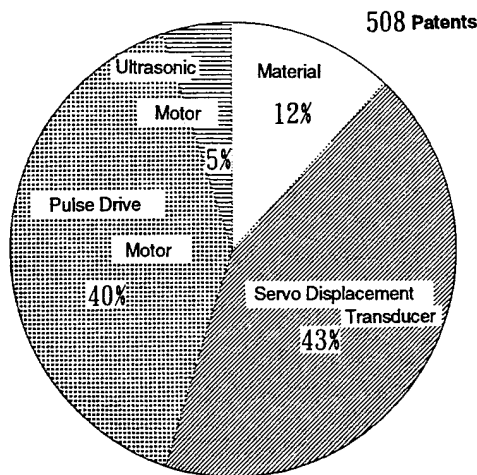


Fig.1 The ratio of 508 piezo-actuator related patents with respect to the technical content disclosed during 1972 - 84.

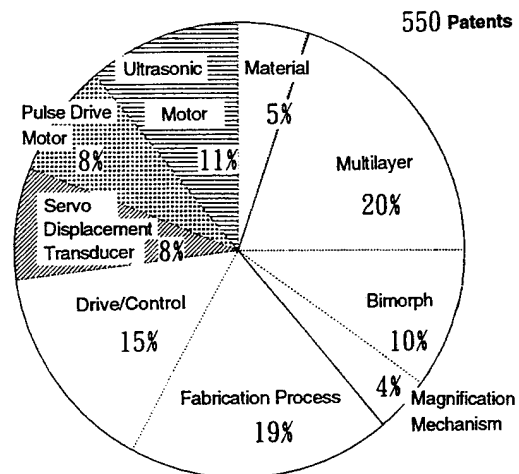


Fig.2 The ratio of 550 piezo-actuator related patents with respect to the technical content disclosed during 1988 - 90.

Table 1 Summary of the patent disclosure relating to piezoelectric actuators and ultrasonic motors disclosed during January 1988 - July 1990 in Japan. Classification is made with respect to the patent submitter and the technical content.

Technical Content Patent Submitter	Total	Material		Design			Drive/Control			Application						
		Composition	Fabrication Process	Multilayer	Magnification Mechanism	Bimorph	Others	Drive Technique	Control Technique (Sensor System included)	Servo Displacement Transducer		Pulse Drive Motor		Ultrasonic Motor		
										Optical Usage	Mechanical Usage	Optical Usage	Mechanical Usage	Propagating Wave	Standing Wave	Vibratory Piece
NEC	69			35	6		16	2	1	3	1		2		3	
TOTO Corp.	40						16	6	2				16			
Matsushita Electric	30	11				8	2	1			3			3		2
Brother Industry	27				2		15	8	2							
Toyota Motors	25			7			6	4	5		3					
Tokin	23			7		3	9	1					1	1	1	
Hitachi Metal	20			12							1		7			
Toshiba	19				1	1	6	1		2	5		1			2
Nippon Denso	16			10	1			3	1		1					
Fuji Electric	16			8		1	3	1	1		1					1
Hitachi	15					1	3	3	3		3				1	1
Murata Mfg.	12			3	1	2	3	3								
Minolta Camera	11					5	1						5			
Ube Industry	10					9			1							
Tosoh	10	7	1			2										
Malcon Electronic	10														10	
NTK	9			2	1		5								1	
Olympus	9			3		3	1								1	1
Canon	8				1		2	1	1				1		1	1
MITI-Ind.Lab.	8										8					
JUKI	8							8								
Yokokawa Electric	8		1	1		2	2		1	1						
Mitsubishi Electric	7		3			2							2			
Matsushita Denko	6			1											4	1
Mitsubishi Kasei	6			3		2	1									
Sumitomo Spec. Metal	5			2			2	1								
Toshiba Ceramics	4		1			3										
Japan Auto-Parts R&D Lab.	4			2			2									
NEC Home Elec.	4										1			2		1
Fujitsu	4		2	1		1										
Miki Pulley	4														4	
Rion	4														3	1
ALPS Electric	3			1											2	
Kansai NEC	3							2	1							
COPAL	3			1				1				1				
Shimadzu	3				1			1		1						
OMRON	3					1	1	1								
Others	84	3	1	9	7	8	14	7	6	1	10		6	2	2	8
Total	550	21	9	108	21	54	110	55	25	8	37	1	41	8	33	19

The development of the piezoelectric actuators on the first stage was focused on inexpensive mass-production devices such as computer-related apparatus, displays, sensors by electronic manufacturing companies. Typical examples are found in dot-matrix printers by NEC, swing CCD image devices by Toshiba, VCR tracking heads by Sony and Matsushita Electric and piezoelectric relays by Omron. Recently, however, on the second stage chemical companies including organic/petro-chemical industries have started to be involved in these electro-ceramic areas (TOTO Corporation, Tokin, Hitachi Metal, Murata Manufacturing Co., Ube Industry, Tosoh, NTK, Mitsubishi Kasei, Sumitomo Special Metal, Toshiba Ceramics). Using the fine manufacturing technology of raw ceramic powders, they are trying to expand their territory to the device application in collaboration with optic or mechanical industries. When used in precision cutting machines, the quality and reliability of the actuator are essential rather than its price.

### Recent Developments in the Leading Companies

In the following the recent development contents of the leading companies are described in detail.

**NEC** -- Their patents cover all the areas; design, drive/control and application. As the manufacturing pioneer of the multilayer piezoelectric actuators which were initially proposed by K. Uchino of The Pennsylvania State University (formerly Sophia University), NEC is still keeping the leading position in the piezoelectric actuator area. The development is focused on the design of the multilayer devices and their fabrication process, as well as the displacement magnification mechanism. A dot matrix printer was the first piezo-actuator product. A sketch of the printer head appears in Fig.3(a) [4]. The printing element is composed of a multilayer piezoelectric device, in which 100 thin ceramic sheets 100 $\mu$ m in thickness are stacked, together with a sophisticated magnification mechanism (Fig.3(b)). The magnification unit is based on a monolithic hinged lever with a magnification of 30, resulting in an amplified displacement of 0.5 mm and an energy transfer efficiency greater than 50%. The drive/control technique relating to the printer application is also remarked.

**TOTO Corporation** -- Most of the patents are related to the short stroke continuous drive type plungers, which will be suitable to their toilet chambers. Cylinder type ceramic actuators and a pulse voltage control are focused to be used.

**Matsushita Electric** -- Different from the recent research trend, they submitted 11 patents relating to the piezoelectric materials. Their materials slightly doped with magnetic ions have been remarkably improved in aging of actuator characteristics. The principle is the usage of the spin-orbit interaction of the magnetic ions under an external magnetic field. The bimorph design has mainly been developed aiming to the applications to VCR head control and ultrasonic motors.

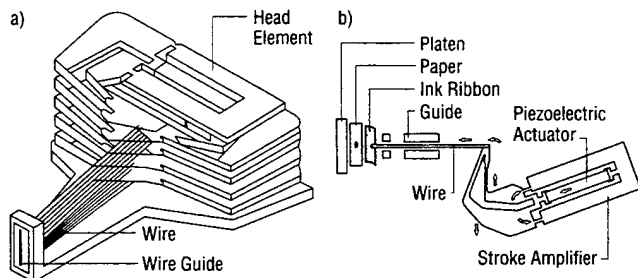


Fig.3 Structure of a printer head (a), and a differential-type piezoelectric printer-head element (b) (NEC).

**Brother Industry** -- Their patents are on the basic mechanisms combining parallel springs with piezoelectric actuators and their driving techniques. Practical applications have not been disclosed yet.

**Toyota Motors** -- The designs and fabrication processes of multilayer actuators have been intensively investigated, and using these actuators new fuel jet valves are now on development as well as their control techniques. A smart electronic shock absorber of automobile suspension (Fig.4) was commercialized by Toyota Motors[5]. The roughness of the road is detected as a vibration acceleration with a 5-layered piezosensor, and the signal is fed-back to a 88-layered piezoactuator through a power amplifier, in order to change the shock-absorption control valve. This feedback system can provide the controllability and the comfortability of a car simultaneously.

**Tokin** -- As one of the main suppliers of piezoelectric actuators, they submitted the patents mainly on the device designs such as bimorphs and multilayers, and their fabrication processes. Particular attention is paid on a fabrication process of cylinder type actuators and the application to card punchers. Figure 5 shows a Tokin's cylinder type piezoelectric gyroscope, which can be used to detect the noise motion of a handy video camera[6]. Among the 6 electrode strips, two of them are used to excite total vibration and the other two pairs of electrode are used to detect the Coriolis force or the rotational acceleration cause by the hand motion. By using the gyro signal, the image vibration can be compensated electrically on a monitor display.

**Hitachi Metal** -- Their research has been concentrated on the multilayer actuator design and its application to fluid jet devices.

**Toshiba** -- Various patents can be found covering fabrication technique of ceramic devices, piezoelectric fans, ring laser gyros, 2-dimensional piezo-drive devices etc.

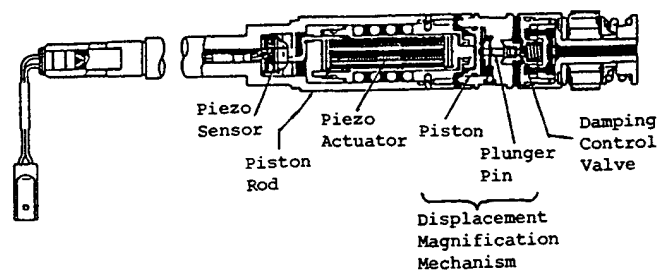


Fig.4 Smart electronic shock absorber of automobile suspension with a piezoelectric sensor/actuator system (Toyota).

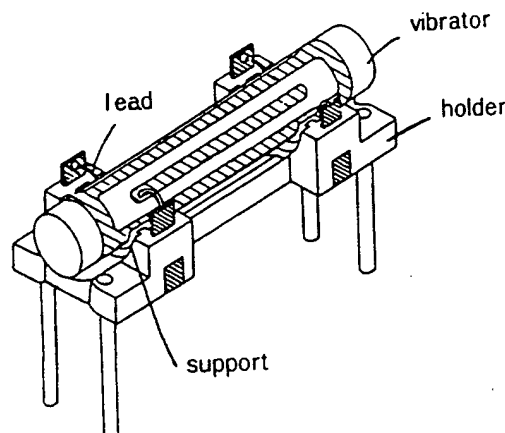


Fig.5 Piezoelectric ceramic cylinder vibratory gyroscope (Tokin).

**Nippon Denso** -- Most of their patents concern the designs and fabrication processes of multilayer piezo-actuators. Multi-valve mechanisms for fluid control are their original application area. The above-mentioned Toyota adaptive automobile suspension was developed in collaboration with Nippon Denso.

**Fuji Electric** -- Designs and fabrication processes of multilayer piezoelectric actuators are being developed. Various applications can be found in their patents including piezoelectric pumps, mechanical claspers, piezoelectric relays, micro-manipulators etc.

**Hitachi** -- Their research is to manufacture precision positioners with the development of the piezo-actuator designs and the control technique.

**Murata Manufacturing** -- Patents on the actuator designs such as multilayers and bimorphs.

**Minolta Camera** -- All patents relate to the camera shutters using a piezo-bimorph. Figure 6 shows the structure of the new shutter, which possesses advantages in simplicity and compactness in comparison with the conventional mechanical spring type [7].

**Ube Industry** -- A unique company who is developing intensively bimorph type piezoelectric actuators.

**Tosoh** -- Bimorph fabrication is remarked firstly. Original monomorph actuators have also been developed using semiconductive piezoelectric ceramics in collaboration with K. Uchino. A monomorph device has been developed to replace the conventional bimorphs, with simpler structure and manufacturing process. The principle is a superposed effect of piezoelectricity and semi-conductivity (Fig.7(a)) [8]. The contact between a semiconductor

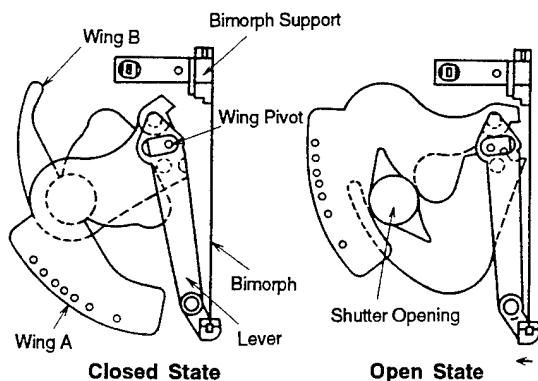


Fig.6 Compact camera shutter using a piezoelectric bimorph (Minolta Camera).

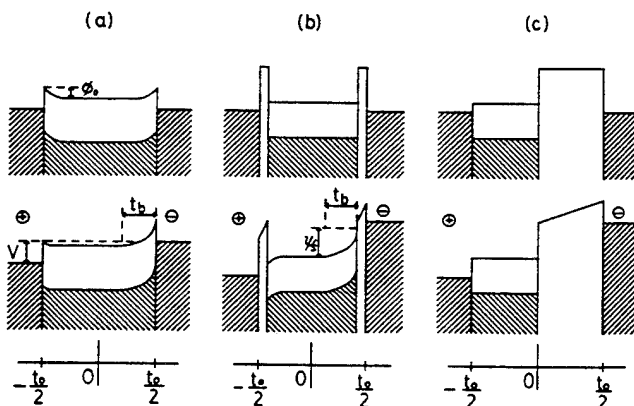


Fig.7 Electron energy band (Schottky barrier) models in monomorph devices (n-type semiconductor). (a) Schottky type, (b) Metal-Insulator-Semiconductor structure with very thin insulative layers, and (c) MIS structure with a thick insulative layer (K.Uchino & Tosoh).

and a metal (Schottky barrier) causes non-uniform distribution of the electric field, even in a compositionally uniform ceramic. Suppose that the ceramic possesses also piezoelectricity, only one side of a ceramic plate tends to contract, leading to a bending deformation in total. A monomorph plate with 30mm in length and 0.5 mm in thickness can generate 200 $\mu$ m tip displacement, in equal magnitude of that of the conventional bimorphs [9]. The recent "rainbow" actuators originally proposed by G. Haertling and manufactured by Aura Ceramics [10] are a modification of the semiconductive piezoelectric monomorphs, where half of the piezoelectric plate is reduced so as to make a thick semiconductive electrode to cause a bend (Fig.7(c)) [11].

## Ultrasonic Motor Developments

**Shinsei Kogyo** -- The pioneering company of the ultrasonic motors is not fabricating them, but marketing them, obtaining the royalty of the basic patents from Canon, Fukoku, and Nasca. Their product, the propagating-wave type (surface-wave or "surfing" type) combines two standing waves with a 90 degree phase difference both in time and in space, and is controllable in both rotational directions (Fig.8) [12]. By means of the traveling elastic wave induced by the thin piezoelectric ring, a ring-type slider in contact with the "rippled" surface of the elastic body bonded onto the piezoelectric is driven in both directions by exchanging the sine and cosine voltage inputs. Another advantage is its thin design, which makes it suitable for installation in cameras as an automatic focusing device.

**Fukoku** -- Manufacturer of the Shinsei's ultrasonic motors (\$ 500) by a production rate of 20,000 pieces /year. No particular research is held in this company.

**Canon** -- They are utilizing the Shinsei's ultrasonic motors for automatic camera focusing systems. Various investigations about the camera mounting are being done, especially on reducing the rotation sounds in any cases. About 80 % of the exchange lenses in "EOS" series installed the ultrasonic motors already in 1992. The production amount 300 K pieces/year and the average lens cost \$700 can provide the total sales at the moment as \$ 210 million.

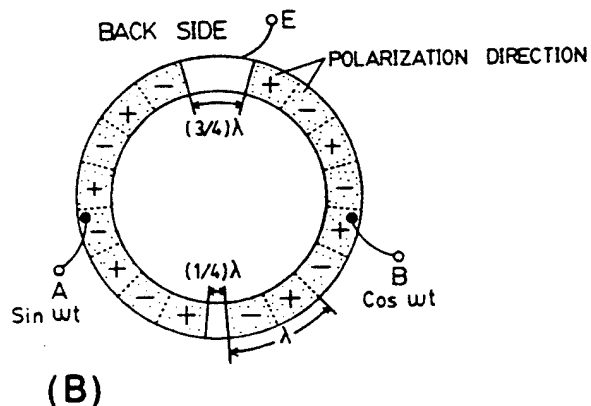
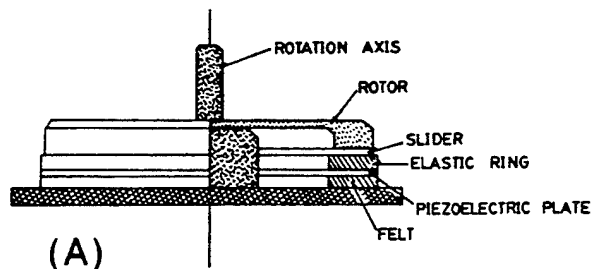


Fig.8 Design of the surface wave type motor (a), and its electrode configuration (b) (Shinsei Kogyo).



**Seiko Instruments** -- They have trially commercialized miniature ultrasonic motors (10 mm in diameter) at relatively expensive prices (\$1500) and at the production amount of just several hundred pieces/year. If the installation into watches is realized, the market size will be incredibly large.

**Nasca** -- They are manufacturing the Matsushita's motors trially (\$ 500 - \$1500, several 100 pieces/year). The research has been done by Matsushita Electric.

**THK** -- Axial ultrasonic motors have been commercialized by combining the screw systems with Shinsei's ultrasonic motors (currently several 100 pieces scale).

**SUN-SYN** -- They developed precision x-y stages using linear type ultrasonic motors, which were originally proposed by K. Uchino, ALPS Electric and Nissan Motors. An ultrasonic linear motor is equipped with a multilayer piezoelectric actuator and fork-shaped metallic legs as shown in Fig.9 [13]. Since there is a slight difference in the mechanical resonance frequency between the two legs, the phase difference between the bending vibrations of both legs can be controlled by changing the drive frequency. The walking slider moves in a way similar to a horse using its fore and hind legs when trotting. A trial motor 20 x 20 x 5 mm<sup>3</sup> in dimension exhibited a maximum speed of 30 cm/s and a maximum thrust of 0.9 kgf with a maximum efficiency of 20%, when driven at 98kHz of 6V (actual power = 0.7 W).

**Malcon Electronics** -- Standing wave type ultrasonic motors are their target, and now under development.

**AlliedSignal** -- The only company in the USA who is manufacturing the ultrasonic motors.

**Rion and Piezotech** were reported to have developed various different ultrasonic motors, but are not commercializing them yet.

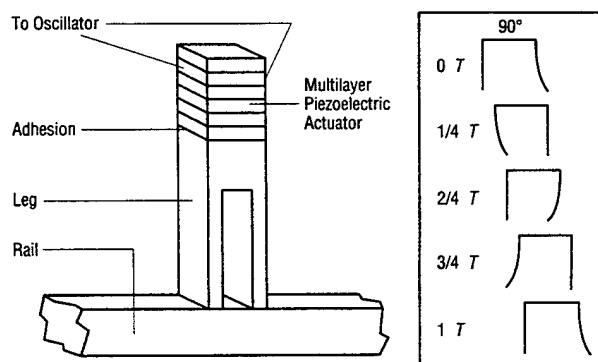


Fig.9 Ultrasonic linear motor of a vibratory coupler type (K.Uchino & Nissan Motors).

## MARKET OF PIEZOELECTRIC ACTUATORS/ULTRASONIC MOTORS

A couple of years ago Mr. Sekimoto, President of NEC, expressed his desire to the piezoelectric actuators in his New Year's speech that the market-share of piezoelectric actuators and their employed devices would reach up to \$ 10 billion (\$ 10<sup>10</sup>) in the near future.

### Ceramic Actuator Elements

Presently NEC and Tokin are producing multilayer actuators roughly at 1 million pieces/year rate in each company. They are sold averagely by \$ 100 per piece. Consequently, the total market value reaches \$ 200 million. In 5 years the production rate will be expected to increase by 10 times, instead of the cost decrease by 1/4, leading to the total market growth up to \$ 500 million.

Using these multilayer actuators, various electronic devices will be manufactured with the additional value by presumably 10 times. For example, the dot-matrix printer by NEC costs averagely \$ 3,000 using the multilayer actuators of \$ 100. The production amount was about 100 K pieces/year in 1986, leading the total sales of \$ 300 million. Therefore, the sales of the final products using the piezoelectric actuators will be expected to reach \$ 5 billion in total in 2000.

### Camera-Related Applications

Piezo-bimorph type camera shutters have been widely commercialized by Minolta Camera. The production amount of "Mac Dual" series is about 300 K pieces/year. Although the actuator itself costs inexpensive ( \$ 1/ piece), the camera costs about \$ 350, then consequently total sales exceed \$100 million.

Canon's automatic focusing systems utilizing an ultrasonic motor are very famous. About 80 % of the exchange lenses in "EOS" series installed the ultrasonic motors already in 1992, and all the camera motors will be replaced by the ultrasonic motors by 2000. The production amount 300 K pieces/year and the average lens cost \$700 can provide the total sales at the moment as \$210 million.

### Ultrasonic Motors

The actual market of ultrasonic motors opened in June 1986 when Shinsei Industry started to supply the trially manufactured ultrasonic motors using a propagation wave type. After that, Shinsei Industry has developed various applications including a remarkable success in Nuclear Magnetic Resonance medical instruments. Mass-produced samples (1500 pieces) were firstly employed for automatic curtain drawers in the New Tokyo Municipal Building in 1990; this accelerated the wide commercialization.

In 1991, an automobile application, which must be one of the key usages of the ultrasonic motors, was realized for head-rest control in Toyota New Crown. Canon succeeded in EOS exchange lens applications, and are presently developing much smaller inexpensive motors which will be applicable to automatic winding of the film. Applications of the ultrasonic motors to cameras will be undoubtedly successful in these three years. Seiko Instrument has started to distribute their miniaturized 10 mm motors, especially suitable for watch applications. Sanki's part-feeders are now sold at a rate of 20 K pieces/year averagely by \$ 500/piece, resulting in the total sales of about \$10 million. One of the future largest markets of the ultrasonic motors will be the automatic window shutter system. The system unit price of \$2,000 multiplied by 100 K sets/year can provide the sales amount of \$ 200 million. Future big market includes the applications to floppy drive, CD/laser disk drive etc.

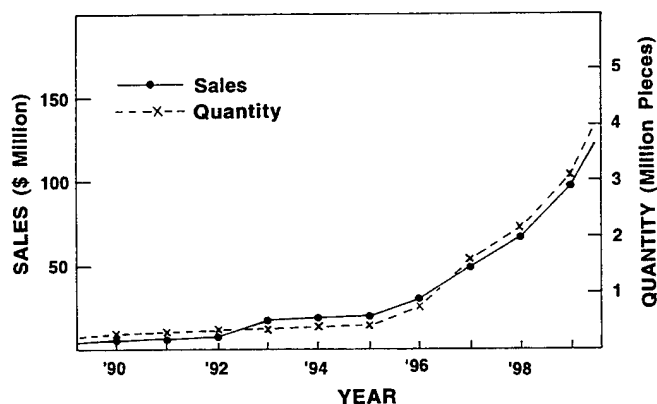


Fig.10 Market-share prediction of ultrasonic motors (motor part only).

Matsushita Electric proposed a big dream to replace all the conventional miniaturized electromagnetic motors, most of which are now produced by Mabuchi at a production rate of 1 billion pieces/ year. Even if the each motor cost is very low (\$ 3/each), the total sales are remarkably large (\$ 3 billion/year). Just 10 % replacement of the conventional electromagnetic motors with the new ultrasonics motors can provide \$ 300 million sales per year; this will again provide \$ 3 billion sales as final device products.

Figure 10 shows the expected market size of the ultrasonic motor itself. The amount in 2000 will reach up to \$150 million, suggesting the total sales of the final products will exceed \$ 2 billion.

### SUMMARY

Taking account of the estimated annual sales of \$500 million for ceramic actuator elements, \$300 million for camera-related devices and \$150 million for ultrasonic motors, piezoelectric/electrostrictive actuators and ultrasonic motors are expected to increase in market share to more than \$ 1 billion in 2000. Regarding the final actuator-related products, \$10 billion by Mr. Sekimoto will not be very different from the realistic amount, and a bright future is anticipated in many application fields.

Finally, the author would like to appreciate all the companies who supplied the data listed in this paper.

### REFERENCES

- [1] K.Uchino, Piezoelectric/Electrostrictive Actuators, Morikita Publishing, Tokyo (1986)
- [2] K.Uchino, Bull.Am.Ceram.Soc., **65**(4), 647 (1986)
- [3] K.Uchino, MRS Bull., **18**(4), 42 (1993)
- [4] T.Yano, I.Fukui, E.Sato, O.Inui and Y.Miyazaki, Proc. Electr. & Commun.Soc., p.1-156 (Spring,1984)
- [5] Y.Yokoya, Electronic Ceramics, **22**, No.111, 55 (1991)
- [6] Tokin Corporation, Catalogue "Ceramic Gyro"
- [7] Minolta Camera, Catalogue "Mac Dual I, II"
- [8] K.Uchino, M.Yoshizaki, K.Kasai, H.Yamamura, N.Sakai and H.Asakura, Jpn.J.Appl.Phys., **26**(7), 1046 (1987)
- [9] K.Uchino, M.Yoshizaki and A.Nagao, Ferroelectrics, **95**, 161 (1989)
- [10] Aura Ceramics, Inc., Catalogue "Rainbow"
- [11] K.Uchino, M.Yoshizaki and A.Nagao, Jpn.J.Appl.Phys., **26**, Suppl.26-2, 201 (1987)
- [12] Y.Akiyama (Editor), Ultrasonic Motors/Actuators, Triceps, Tokyo 1986
- [13] M.Tohda, S.Ichikawa, K.Uchino and K.Kato, Ferroelectrics, **93**, 287 (1989)

# Fatigue Behaviour of Multilayer Piezoelectric Actuators

B. Zickgraf, G.A. Schneider, F. Aldinger  
Max-Planck-Institut für Metallforschung  
Pulvermetallurgisches Laboratorium  
Heisenbergstraße 5, 70569-Stuttgart, Germany

**Abstract** — Fatigue experiments of multilayer PZT actuators are presented, carried out under various electrical and mechanical loading conditions. Impedance measurements of cycled actuators are made to determine nondestructively their actual state of degradation. Some fracture surface examinations are described and occurring crack patterns are shown. For a detailed investigation of crack initiation and crack growth at electrode tips and interface layers model experiments with 2-layer samples are performed with in situ crack growth observations. Different crack types are found and possible crack growth mechanisms are suggested.

## Introduction

Multilayer actuators based on piezoelectric ceramics are found more and more in applications combining precise micromovement with high mechanical forces and high electrical loading. Furthermore piezoelectric devices such as shock absorbers or injection systems are driven in frequency ranges of up to some thousand hertz resulting in actuator fatigue and mechanical degradation. The driving mechanisms of crack growth or layer delamination under high mechanical and electrical loading are only little understood. To increase actuator reliability detailed investigations of the influence of various loading parameters on actuator fatigue are necessary. In this paper long time testing experiments of square type actuators under different loading conditions are described. Furthermore the tool of impedance spectroscopy was used as a characterization measurement of the cycled samples and changes in impedance curves with increasing loading time were related to progressive actuator degradation.

In order to distinguish more clearly between electrically and mechanically induced crack growth in piezoelectric materials a second experiment with simpler sample geometry and reduced loading parameters compared to the multilayer components was performed to investigate crack initiation and crack growth at critical points inside the model actuators such as inner electrode tips or ceramic-electrode interface layers.

## Experiment

### Multilayer Actuators

The geometry of the square-type actuators is shown schematically in figure 1. Tape cast PZT-layers with

thicknesses of 35 to 65  $\mu\text{m}$  were provided with AgPd-electrodes and stacks were produced with 20 to 30 layers. After the normal manufacturing procedure of cofiring, sintering and poling some initial electrical characterization measurements followed.

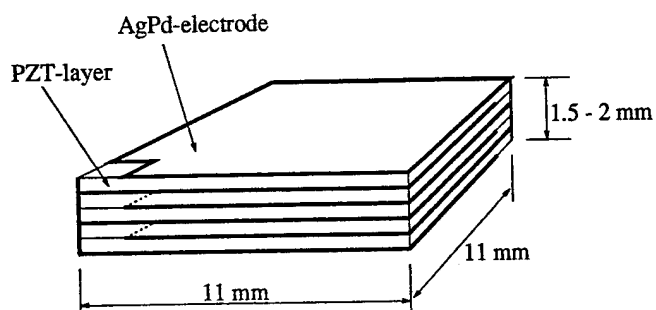


Figure 1: Multilayer actuator geometry

During cyclic loading different mechanical and electrical test parameters were varied. On the mechanical side clamping forces of 500 to 3000 N were applied and the stiffness of the clamping mechanism could be modified by using various belleville-springs with different spring rates. As electrical boundary conditions different driving signals with sinusoidal, triangular and trapezoidal shape were applied, cycling at frequencies between 200 and 1000 Hz. Depending on the respective ceramic layer thickness the maximum driving voltage was adjusted to result in an electric field strength of 1 to 2 kV/mm. Figure 2 shows a scheme of the test facility with function generator and power amplifier on the sample input side.

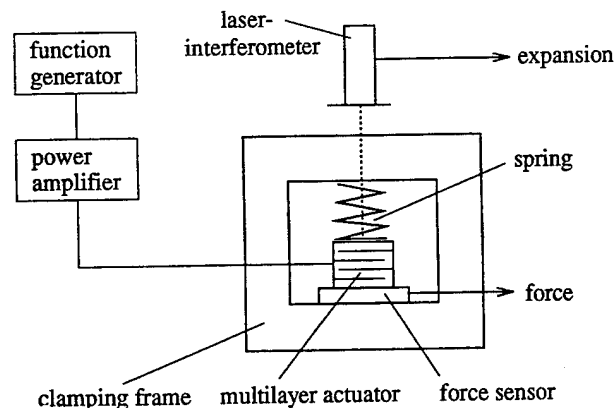


Figure 2: Scheme of test facility

Actuator response such as thickness expansion and produced forces were measured with a laser interferometer (Hommel) and a quartz force sensor (Kistler), respectively. Testing, monitoring and data acquisition was carried out computer controlled.

Actuator degradation was determined using impedance measurements as a nondestructive characterization method [1]. At definite frequencies piezoelectrically induced length vibrations were excited and the two characteristic impedance curve peaks belonging to the serial resonance frequency  $f_s$  (impedance minimum) and the parallel resonance frequency  $f_p$  (impedance maximum) were examined for changes with increasing number of loading cycles. These changes were directly correlated to internal degradation effects such as crack growth or layer delamination.

### Model Samples

For the second type of experiments bar shaped samples were used with two PZT-layers of 200  $\mu\text{m}$  thickness each subjected to the electric field and three AgPd-electrode layers with three internal electrode tips. Figure 3 shows the chosen sample geometry. In analogy to some paper published by Furuta et al. [2] a side face of the sample was polished and during cycling in situ observations of crack initiation and crack growth were performed using a long distance microscope and video system (Questar/Panasonic).

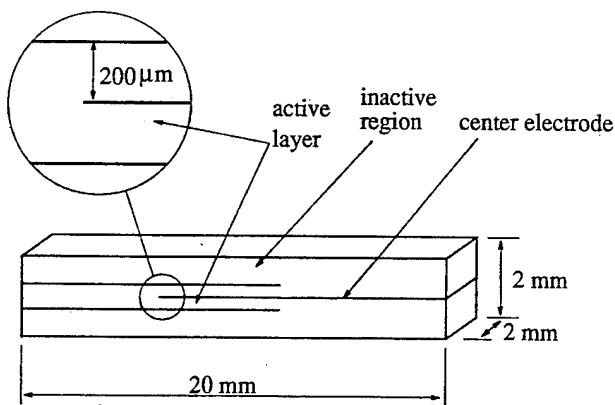


Figure 3: Geometry of model sample

The samples were driven bipolar with a trapezoidal voltage signal of 0.1 Hz frequency. Applied field strength was from 0.5 to 2.5 kV/mm. No external mechanical forces were applied to the samples to reduce loading complexity and to simplify the crack growth studies.

## Results

### Multilayer Actuators

Depending on the applied driving voltage and the number of belleville-springs used for clamping maximum actuator

forces in the range of 2 to 20 N were measured remaining almost constant during the cycling procedure. No slow decrease in force peak value with increasing cycling time could be detected. The actuators expanded in thickness direction from 200 to 800 nm depending on the driving voltage. Stiffness calculations of the clamping mechanism showed, that the stiffness of the actuators was more than 1000 times higher than the clamping stiffness. Therefore the actuators always reached nearly their no-load expansion regardless of the clamping stiffness.

The comparison of impedance measurements carried out with increasing numbers of loading cycles revealed a marked decrease in  $f_p$ -impedance peak (figure 4) together with the occurrence of a more and more distorted impedance curve with multiple-peak-shape.

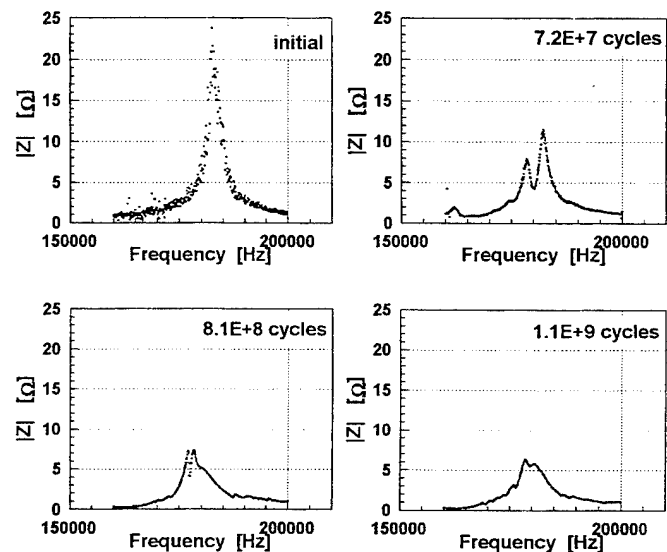


Figure 4: Decrease of impedance during cycling

Examinations of the fracture surfaces of failed samples showed numerous intergranular cracks perpendicular to the electrode structure (figure 5). Crossing of cracks and delaminations of the ceramic-electrode-interface also were found (figure 6).

At the end of actuator lifetime most of the samples failed by sudden dielectric breakdown resulting in thermal damage with different fracture modes compared to the fatigue damage. Figure 7 shows a breakdown region with large pores of evaporated ceramic material and transgranular cracks and a clearly different microstructure compared to the fatigue crack regions.



Figure 5: Fracture surface of failed multilayer actuator

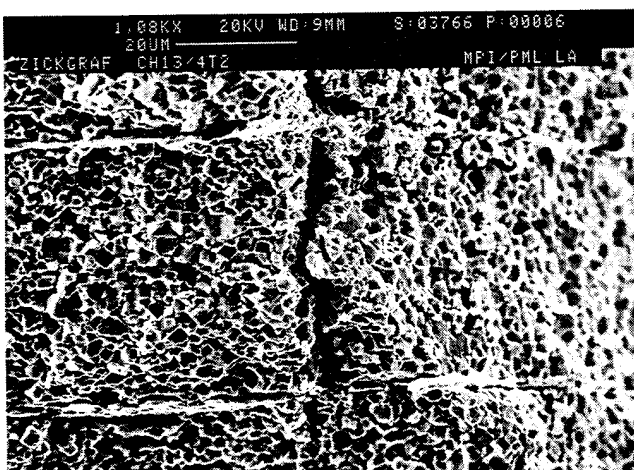


Figure 6: Crossing cracks with interface delaminations

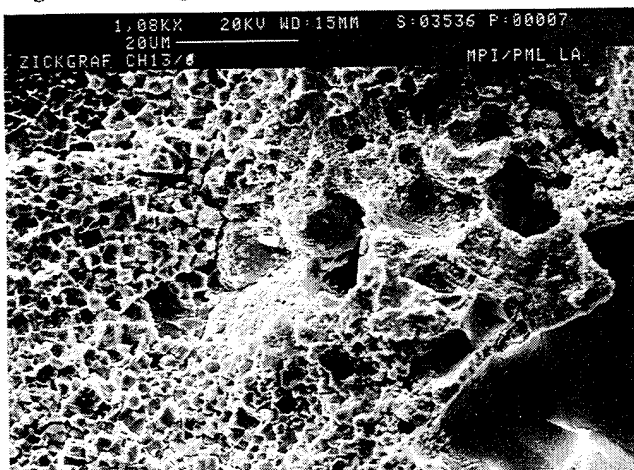


Figure 7: Region with dielectric breakdown damage

During long time testing the actuators were cycled up to  $2.5 \cdot 10^9$  cycles and in figure 8 a lifetime map of failed actuators is displayed. Cycling at lower field strength resulted in a higher number of reached loading cycles and a Wöhler-type correlation between field strength and cycles was found. Samples cycled with 500 Hz showed a stronger fatigue effect than those cycled with 1000 Hz.

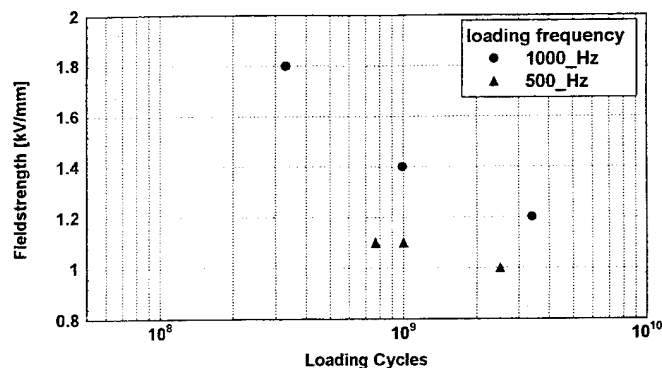


Figure 8: Lifetime map

### Model Samples

After only a few bipolar loading cycles 8 to 10 nearly equidistant cracks occurred perpendicular to the electrode layers leaving the electrodes intact so the inner sectors of the broken ceramic layers could still be cycled ((1) in figure 9). Additionally slow growing cracks starting at the electrode tips were detected ((2) in figure 9).

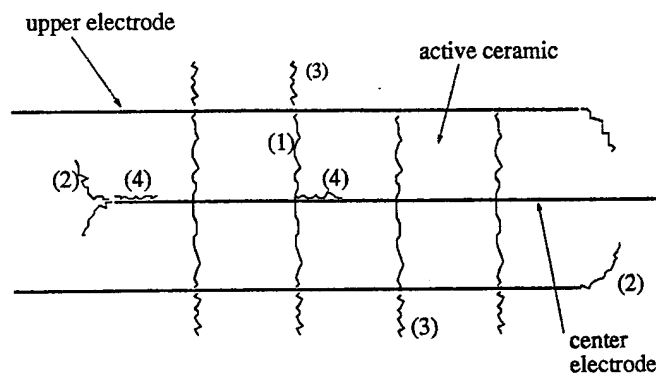


Figure 9: Crack pattern at model actuator

After approximately 500 cycles subcritically growing cracks were found in the upper and lower ceramic regions not subjected to an electric field that originated from the early found perpendicular cracks ((3) in figure 9).

Finally interface delaminations were observed starting at the center electrode tip as well as at the crossing of center electrode and the segmentation cracks ((4) in figure 9 and figure 10). Cycling with 2 kV/mm field strength instead of 2.5 kV/mm resulted in a reduced number of segmentation cracks and a total number of reached cycles until breakdown from 5500 compared to 2200 cycles at 2.5 kV/mm field strength. Model actuators cycled with 0.5 kV/mm field strength showed no crack formation even after 50.000 loading cycles.

The final failure mode of the model actuators was dielectric breakdown with molten electrode material and thermal destruction of electrode layers and adjacent ceramic regions (figure 11).

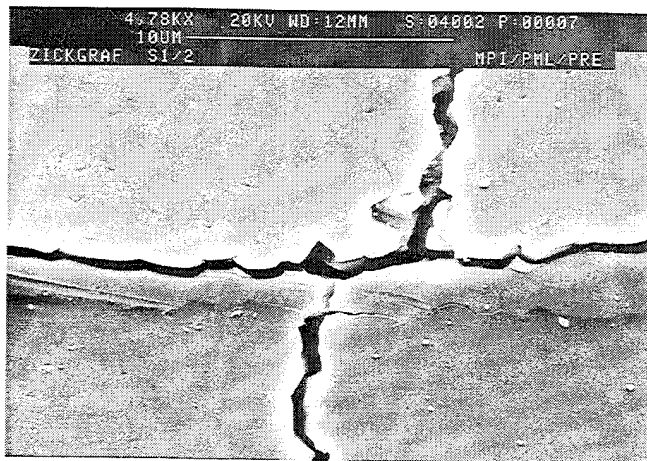


Figure 10: Interface delaminations at segmentation-cracks

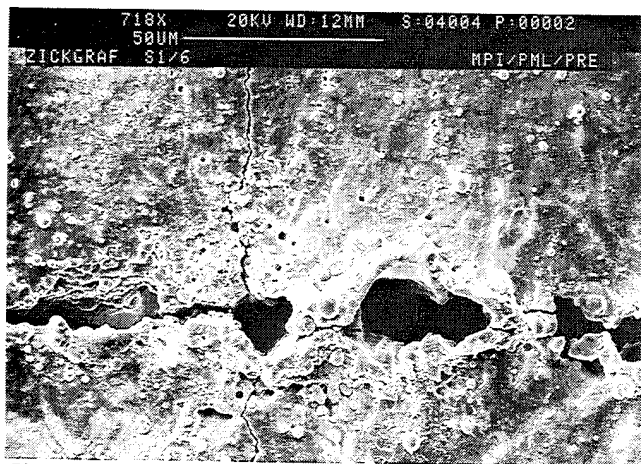


Figure 11: Model actuator after dielectric breakdown

## Discussion

### Multilayer Actuators

Although tested actuators reach their lifetime and fail by dielectric breakdown without showing clear changes in force signal or thickness expansion the mechanical degradation can be detected using impedance spectroscopy. The mechanical quality factor of the vibrating actuators is lowered by energy dissipation due to friction at the crack faces of internal fatigue cracks. The found crack direction mainly oriented perpendicular to the electrode structure is caused by compressive stresses in thickness direction resulting in tensile stresses in xy-direction. Fracture of the ceramic layers is always guided by interface delaminations. To discuss the question whether they are a result or the origin of cracks in the ceramic one has to consider that electrode delaminations act as internal electrode tips with an electric field singularity and increased mechanical strains and stresses. This singularities are regarded to create driving forces for further interface crack growth as also observed in the model actuator experiments.

The mechanisms of dielectric breakdown at the end of actuator lifetime are not fully understood yet, but melting

and solidification of some electrode material together with silver migration along cracks through the ceramic layers are thought to be a reason for an electrical short circuit. The final failure mechanism of the multilayer actuators appears to be always a combination of mainly mechanically induced fatigue cracks serving as conducting path for an electrical breakdown in the last loading cycle.

### Model samples

Most of the observed cracks are induced through mechanical constraints. The early separation cracks are the result of high tensile stresses parallel to the layer structure because of the clamping effect of the upper and lower inactive ceramic parts. These regions not subjected to an electrical field do not follow the contraction of the active layers perpendicular to the electric field direction and therefore high tensile stresses in the active layers arise. This is no degradation effect and occurs during the first cycles.

The small cracks growing into the inactive regions also have a mechanical driving force. The contraction of the independent sectors of the active ceramic produces shear stresses in the upper and lower electrode that act as tensile stresses in the inactive ceramic and cause subcritical crack growth.

Delaminations and cracks starting at the electrode tips are more likely to be either electrically initiated and mechanically driven or completely electromechanically driven. In this case the electric field directly applies an additional driving force on the crack together with the mechanical driving forces from the piezoelectrically induced strains and stresses. Distinguishing between these to different driving mechanisms shows to be difficult in the ferroelectric state of the ceramic and experiments above its Curie-temperature could be a possibility to determine the influence of the electric field alone.

## Acknowledgements

The authors gratefully acknowledge the support of this work by Dr. Kempter and Dr. Lubitz from Siemens.

## References

- [1] O. Boser, P. Kellawon, R. Geyer, „Electromechanical Resonances in Ceramic Capacitors and Their Use for Rapid Nondestructive Testing“, *J.Am.Ceram.Soc.*, **72** [12] 2282-86 (1989)
- [2] A. Furuta, K. Uchino, „Dynamic Observation of Crack Propagation in Piezoelectric Multilayer Actuators“, *J.Am.Ceram.Soc.*, **76** [6] 1615-17 (1993)

# Concurrent Session - 1C: Piezoelectrics

Q. M. Zhang, X. Geng, Y. Shui, Wenwu Cao, and L. E. Cross  
Materials Research Laboratory, The Penn State University  
University Park, PA 16802

**Abstract:** A dynamic theory is developed for piezocomposites with 2-2 connectivity. By solving the coupled dynamic equations in the piezoceramic plate and polymer region subjected to the boundary conditions at the ceramic-polymer interface, the distributions of the elastic and electric variables in a composite are obtained. The electromechanical coupling factor, the acoustic impedance, the resonant frequency, and the elastic coupling between the polymer and ceramic at the thickness resonance can be determined. The effects of modes coupling on the thickness resonance and lateral resonance are elucidated and the dependence of the frequency of these resonant modes on the composite thickness can be estimated. Theoretical results are compared with experimental observations.

## I. Introduction

The heart of an ultrasonic transducer is the piezoelectric element which performs the energy conversion between the electric form and mechanical form. To meet the broadened applicational needs and increase the signal sensitivity and resolution of an ultrasonic transducer, there is a constant effort on improving the piezoelectric transducer materials. The introduction of the piezoceramic polymer composites in the late seventies opened a new avenue of high quality ultrasonic transducer materials. The low insertion loss, short ringing time, adjustable acoustic impedance, as well as agility in the material properties are some of the advantages that a piezocomposite possesses.<sup>1-4</sup>

The typical configurations of the currently commercially available piezocomposites are either in 2-2 connectivity form or 1-3 connectivity form, as schematically drawn in figure 1. The important parameters for an ultrasonic transducer material are the electromechanical coupling factor, acoustic impedance, electric impedance, and mechanical quality factor, etc. In addition, unlike a monolithic piezoelectric material, the polymer phase in a composite is often piezoelectric inactive while it provides a low acoustic impedance path for the mechanical energy flow with the medium. Therefore, it is critical to have an effective elastic coupling between the polymer matrix and the piezoceramic elements so that the advantages of the low acoustic impedance of the polymer matrix and high electromechanical coupling factor of the ceramic elements can be fully made use of.

Being a diphasic material, the composite properties can vary over a wide range and most notably, as have been observed by many experiments, the properties of a piezocomposite will vary as the sample thickness is changed.<sup>3</sup> The periodic structure in a composite will also introduce resonant modes which may interfere with the thickness resonance and degrade the performance of the transducer.<sup>5</sup> To design an ultrasonic composite transducer properly and make best use of a composite material for a specific application require a quantitative understanding of how each design parameter affect the effective properties of a composite. It is the purpose of this paper to present the results of a recent theoretical modeling on establishing a quantitative structure-property relationship for the ultrasonic piezoceramic polymer composite as well as related experimental work. Due to the space limitation, only the results for the 2-2 composite will be presented.

## II. Theory

For a typical 2-2 composite as shown in figure 1, the dimensions in the  $x_1$ - and  $x_2$ -directions can be taken as infinite; therefore, the problem is two-dimensional with no dependence on the  $x_2$ -component. For the results discussed here, the dimension in the  $x_3$ -direction (thickness  $t = 2L$ ) is also assumed to be much larger than the lateral period  $d$  and the effect of the two end faces is neglected. The effect of the finite thickness and hence, the two end surfaces on the properties of a composite can be treated based on the results here with a proper summation of partial waves. They will be discussed

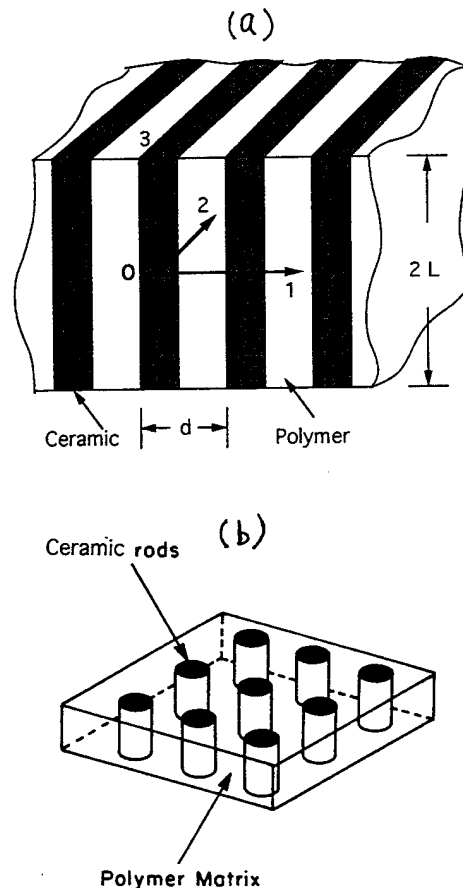


Figure 1. Schematic drawing of piezoceramic polymer composites with (a) 2-2 connectivity; (b) 1-3 connectivity.

in the future. The approach adopted here is similar to that used in treating the static properties of a piezo-composite.<sup>6</sup> That is, the elastic and electric equations for both the piezoceramic plate and polymer matrix are solved first, and the coupling between the two phases is established through the boundary conditions. Using the coordinate system in figure 1, the governing equations for the problem are

$$\frac{\partial T_3}{\partial x_3} + \frac{\partial T_5}{\partial x_1} = \rho \frac{\partial^2 u_3}{\partial t^2}, \quad \frac{\partial T_1}{\partial x_1} + \frac{\partial T_5}{\partial x_3} = \rho \frac{\partial^2 u_1}{\partial t^2}, \quad \text{and } \text{div } \vec{D} = 0 \quad (1)$$

where  $T_i$  are the stress tensors,  $\vec{D}$  is the electric displacement,  $u_i$  are the elastic displacements and in eq. (1) and in the following the contracted notations for the stress and strain tensors are used. The constitutive equations for the piezoceramic phase are

$$\begin{aligned} T_1 &= c_{11}^c u_{1,1} + c_{13}^c u_{3,3} - e_{13}^c E_3 \\ T_3 &= c_{33}^c u_{3,3} + c_{13}^c u_{1,1} - e_{33}^c E_3 \\ D_1 &= \epsilon_{11}^c E_1 + e_{15}^c (u_{3,1} + u_{1,3}) \\ D_3 &= \epsilon_{33}^c E_3 + e_{33}^c u_{3,3} + e_{11}^c u_{1,1} \end{aligned} \quad (2)$$

where  $u_{i,j}$  denote the derivative of  $u_i$  with respect to the  $j$ th-coordinate and  $E_i$  are the electric fields,  $c_{ij}^c$  are the elastic stiffness coefficients at constant  $E$  field,  $e_{ij}$  are the piezoelectric coefficients,  $\epsilon_{ij}$  are the dielectric constants at constant strain, and  $D_i$  are the electric displacement vector. Similar equations can be written for the polymer phase with  $e_{ij} = 0$  and all the other parameters replaced by



those of the polymer. In the normal ultrasonic transducer operation frequency range, the quasi-electrostatic approximation can be used for the electric field,<sup>7</sup> i.e.

$$\vec{E} = -\nabla\Phi \quad (3)$$

where  $\Phi$  is the electric potential. Combining eqs (1), (2) and (3) yields the equation of motion for  $u_1$ ,  $u_3$ , and  $\Phi$ . For a harmonic motion, the general solution to the equation is of the form

$$\begin{aligned} u_3 &= A \exp(i(hx_1 + \beta x_3 - \omega t)) \\ u_1 &= B \exp(i(hx_1 + \beta x_3 - \omega t)) \\ \Phi &= C \exp(i(hx_1 + \beta x_3 - \omega t)) \end{aligned} \quad (4)$$

where  $A$ ,  $B$ , and  $C$  are three constants,  $\omega$  is the angular velocity. Substituting equation (4) into eq. (1) through the constitutive relations, we obtain three homogeneous equations with three undetermined constants,  $A$ ,  $B$ , and  $C$ . The condition for a non-trivial solution is that the determinant of the coefficients vanishes. For the ceramic plate, this implies

$$\begin{vmatrix} c_{33}^c \beta^2 + c_{44}^c h^2 - \rho \omega^2 & (c_{13}^c + c_{44}^c) \beta h & e_{33} \beta^2 + e_{15} h^2 \\ (c_{13}^c + c_{44}^c) \beta h & c_{11}^c h^2 + c_{44}^c \beta^2 - \rho \omega^2 & (e_{15} + e_{31}) \beta h \\ e_{33} \beta^2 + e_{15} h^2 & (e_{15} + e_{31}) \beta h & -(\epsilon_{11} h^2 + \epsilon_{33} \beta^2) \end{vmatrix} = 0 \quad (5)$$

Equation (5) yields three roots of  $h$ , denoted as  $h_1^c$ ,  $h_2^c$ , and  $h_3^c$ , for each pair of  $\omega$  and  $\beta$ , corresponding to the quasi-longitudinal, quasi-shear, and quasi-electromechanical waves, respectively.

For each  $h_i^c$ , the ratio among  $A$ ,  $B$ , and  $C$  can be determined and the general solutions have the form

$$\begin{aligned} u_3^c &= \sum_i R_i^c f_i \cos(h_i^c x_1) \sin(\beta x_3) \\ u_1^c &= \sum_i R_i^c g_i \cos(h_i^c x_1) \sin(\beta x_3) \\ \Phi^c &= \sum_i R_i^c t_i \cos(h_i^c x_1) \sin(\beta x_3) \end{aligned} \quad (6)$$

where  $i$  in the summation runs from 1 to 3.  $f_i$ ,  $g_i$  and  $t_i$  are the cofactors  $A_{k1}(i)$ ,  $A_{k2}(i)$ , and  $A_{k3}(i)$  of the determinant (5) (where  $h$  is replaced by  $h_1$ ,  $h_2$ , and  $h_3$  for  $i = 1, 2$ , and  $3$ , respectively). In deriving equation (6), the symmetry conditions in both the  $x_1$ - and  $x_3$ -directions for a piezo-active mode have been used. Similar equations can be written for the polymer region except  $x_1$  in equation (6) should be replaced by  $(x_1 - d/2)$  and all the parameters used should be those of the polymer phase.

Eq. (6) and the corresponding equation for the polymer phase contain six constants,  $R_i^c$  and  $R_i^p$  ( $i = 1, 2, \text{ and } 3$ ). They can be determined from the boundary conditions at the ceramic-polymer interface ( $x_1 = v d/2$ , where  $v$  is the volume content of the ceramic in a composite), which are:

$$u_1^c = u_1^p, u_3^c = u_3^p, T_1^c = T_1^p, \text{ and } T_5^c = T_5^p \quad (7)$$

$$\text{and } \Phi^c = \Phi^p \text{ and } D_1^c = D_1^p \quad (8)$$

For six homogeneous equations with six undetermined constants ( $R_i^c$  and  $R_i^p$ ), the condition for a non-trivial solution is that the determinant of the coefficients vanishes, i.e.,

$$R = |\text{coefficients of } R_i| = 0 \quad (9)$$

Eq. (9) is a transcendental equation which yields the relations between  $\omega$  and  $\beta$ , the dispersion curves for the composite. From that, one can find  $R_i^c$  and  $R_i^p$ , and hence the various stress, strain, and electric field distributions in a composite at the resonant mode.

### III. Results and Discussions

Shown in figure 2(a) is the dispersion curves for the two lowest branches of the dispersion curves calculated from eq. (9) for a 2-2 composite made of PZT-5H and Spurr's epoxy. The ratio  $\omega/\beta$  at small  $\beta d$  from the branch 1 yields the effective velocity of the composite at constant  $D$ ,  $v^D$ , in the  $x_3$ -direction. In figure 2(b),  $v^D$  as a function of the ceramic volume content is presented. For comparison, the experimental data measured from the corresponding composites as well as the result from an earlier quasi-static model (modified for 2-2 piezocomposites), which has been widely used,<sup>4</sup>

are also shown. The agreement between the current theory and experiment is excellent. From the relations  $\bar{\rho} = v \rho^c + (1-v) \rho^p$  and  $\bar{Z} = \bar{\rho} v^D$ , where  $\rho$  is the density, the acoustic impedance can be evaluated and the result for a 2-2 composite with PZT 5H ceramic plate and Spurr's epoxy is shown in figure 2(c).

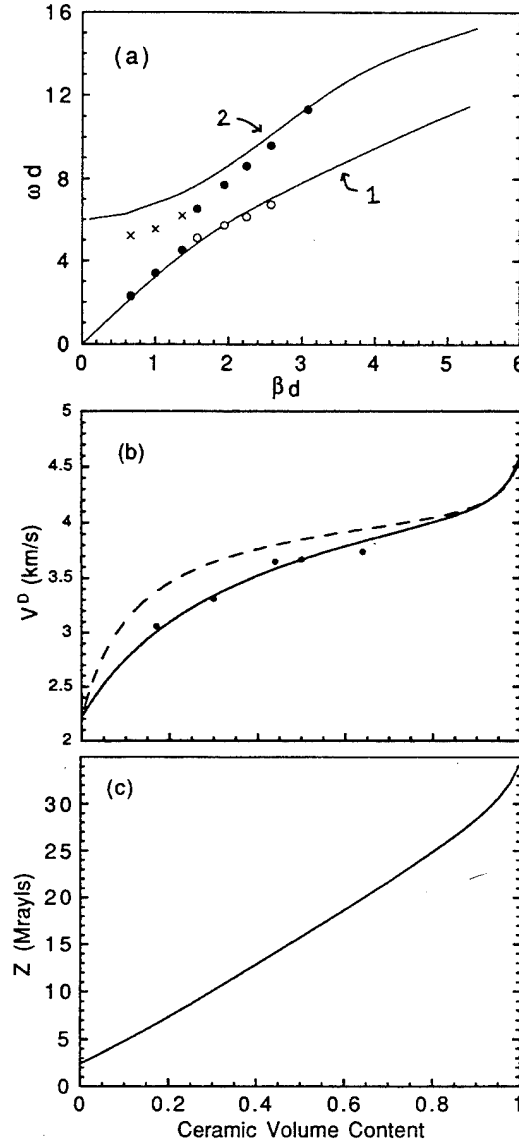


Figure 2. (a) The dispersion curves for a 2-2 composite made of PZT 5H plates and Spurr's epoxy. Under the approximation that  $\lambda = 2t$ , where  $t$  is the thickness of the composite, the experimentally observed resonant modes can be compared with the theoretical prediction.

(b)  $v^D$  as a function of the ceramic volume content for a composite made of PZT 5H and Spurr's epoxy.

(c) The acoustic impedance  $Z$  as a function of the ceramic volume content for a 2-2 composite with PZT 5H and Spurr's epoxy.

The information on the strain, stress, and electric field distributions in a composite at a resonant mode derived enables us to evaluate the electromechanical coupling factor for that resonance from the relation

$$k^2 = U_{int} / (U_E U_M) \quad (10)$$

where  $U_{int}$ ,  $U_E$ , and  $U_M$  are the exchange energy, electric energy, and mechanical energy terms in the total energy of a piezo-material, respectively,

$$U_{int} = \frac{1}{2} \epsilon_{ki} \epsilon_{kj} S_i S_j, \quad U_M = \frac{1}{2} s_{ij}^E S_i S_j, \quad U_E = \frac{1}{2} \epsilon_{ij}^E E_i E_j \quad (11)$$

For a composite material, the quantities in eq. (11) should be integrated on one repeating unit of the composite.

On the other hand, making use of the IEEE definition,<sup>8</sup>

$$\left(\frac{v^E}{v^D}\right)^2 = (1 - k_t^2) \quad (12)$$

where  $v^E$  is the velocity at the constant E field,  $k_t$  can be calculated in a much simpler manner.

For a single phase material,  $v^E (= \sqrt{c_{33}^E/\rho})$  can be found from the dispersion curve by setting  $E = \text{constant}$  in the wave equations. For a composite material discussed here, we assume that a similar approach can also be used in the limit of  $\beta \rightarrow 0$  where the electric fields in the polymer and ceramic regions are nearly equal. Therefore, similar to the procedure of deriving  $v^D$  but utilizing only the elastic equations and boundary conditions,  $v^E$  for a composite can be obtained. The coupling factor  $k_t$  thus determined is plotted in figure 3, along with the experimental data from the corresponding composites and the result from the earlier quasi-static model (for 2-2 composites made of PZT 5H and Spurr's Epoxy). Good agreement is obtained between the theoretical prediction and the experimental data.

From the theoretical model developed, the dependence of  $k_t$  on the elastic properties of the polymer phase and the piezoelectric properties of the ceramic phase can be evaluated.

At the thickness resonance, the thickness  $t$  of a sample is equal to half of the resonant wavelength  $\lambda$ . Making use of this relation, the variation of the material properties of a composite with thickness ( $\beta = 2\pi/\lambda = \pi/t$ ) can be extrapolated from the dispersion curves. With this spirit, the experimental results of the change of the resonant frequency for the thickness mode and the first lateral mode with the sample thickness are plotted in figure 2(a). The experimental data points can be described by the theoretical dispersion curves reasonably well even though the model here is initially intended to treat a composite of small  $\beta d$ .

Several observations can be made from figure 2(a). As a composite becomes thinner ( $\beta d$  increases), the thickness resonant mode approaches the lateral resonant mode, and as a result of modes coupling, the resonant frequencies for the two modes are affected. For a composite transducer, the thickness resonance is always marked in the impedance curve by the strongest resonant peak and having the largest ratio of  $(f_p - f_s)/f_p$  where  $f_s$  and  $f_p$  are the series and parallel resonant frequencies. On the other hand, by nature, the lateral resonance, originated from the periodic structure of a composite, is weak and can be identified by the fact that  $u_3$  at the center ( $u_3(\text{cent})$ ) of polymer region is  $180^\circ$  out of phase with that at the center of the ceramic plate. Based on these, on figure 2(a), the data points are marked by black dots for the thickness resonance and crosses for the lateral resonant modes. Above the modes coupling region, the resonant mode on the branch 1 gradually disappears. However, even though the frequency of the resonance in this region is close to or even higher than those marked by the crosses,  $u_3$  in the polymer region and ceramic region are still in phase with a larger difference in the vibration amplitude between the two regions. The mode here is a result of the modes coupling and when the thickness

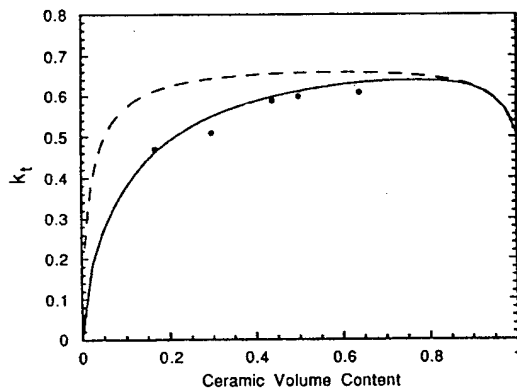


Figure 3. The thickness coupling factor as a function of the ceramic volume content for a 2-2 composite of PZT 5H piezoceramic and Spurr's epoxy.

mode moves away, the mode in this region disappears. Therefore, we do not mark them as either lateral or thickness resonance.

For all these resonant modes, the vibration amplitude of  $u_3$  in the polymer region is always larger than that in the ceramic plate. It is also observed both experimentally and theoretically that for the thickness resonance on the branch 2 (above the modes coupling region),  $u_3$  in the center of the polymer region is  $180^\circ$  out of phase with that in the center of the ceramic plate. In another words,  $u_3$  in the polymer region and in the ceramic plate are in phase for the resonant modes on the branch 1 and out of phase for the resonant modes on the branch 2. Due to the fact that  $u_3$  of the ceramic and polymer in the branch 2 is out of phase, the influence of the two end faces of a composite (traction free boundary condition when there is no acoustic load on a composite) will be more important. The model presented does not take this into account and hence, it is expected that the discrepancy between the theory and experiment will become severe in the branch 2, as shown in figure 2(a).

An effective stress transfer between the polymer and ceramic plate requires  $u_3$  in the two regions in phase and having nearly the same amplitude. Shown in figure 4 is the ratio of  $u_3(\text{cent})$  of the polymer to  $u_3(\text{cent})$  of the ceramic plate measured on the surface of a 2-2 composite with 44% ceramic content and  $d/\lambda = 0.13$ , where the thickness resonant frequency  $f_t$  (at 770 kHz) is about half of the lateral resonant frequency  $f_l$ . The amplitude ratio between the two regions is equal to one up to a frequency of about 800 kHz, beyond that frequency, the vibration amplitude in the polymer phase increases rapidly. The phase between the vibrations in the two regions also exhibits the similar trend. The two vibrations are in phase up to about 950 kHz and above that, the two vibrations show large phase difference. This clearly sets a limit on the ratio of  $d/\lambda$ , beyond which the stress transfer between the two regions in a composite will be reduced significantly and the performance of a composite, hence, will be affected.

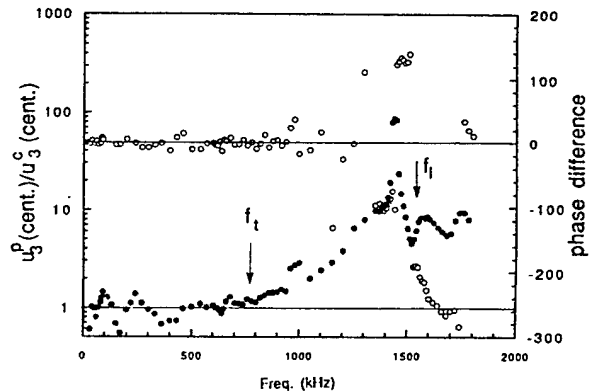


Figure 4. The ratio of the vibration amplitude of  $u_3$  at the center of polymer gap ( $u_3^p$ ) to that at the center of ceramic plate (solid circles) and phase difference between the two (open circles) measured at the surface of a 2-2 composite with ceramic volume content 44 %. The data was acquired using a laser dilatometer while the composite was driven by an electric field.

#### IV. Summary and Acknowledgement

In summary, a dynamic model on piezoceramic polymer composites is developed which provides near exact solution for a 2-2 piezocomposite at small  $d/\lambda$  ratio. Based on this model, a quantitative relationship between the composite effective properties and the design parameters of constituents is established, and the effect of the modes coupling between the thickness and lateral resonances on their resonant behavior (i.e. resonance frequency, strain and stress distributions, etc.) is elucidated. Extension of this model to 1-3 composite and to include the boundary conditions at the two end faces is currently underway.

The authors wish to thank Dr. J. Yuan and Dr. H. Kunkel for many stimulating discussions and for measuring the elastic properties of Spurr's epoxy. This work was supported by the Office of Navy Research under Grant No: N00014-93-1-0340.

References:

1. W. A. Smith and A. A. Shaulov, *Ferro.* 87, 309 (1988).
2. R. E. Newnham, et. al. *Mater. in Engin.* 2, 93 (1980).
3. T. R. Gururaja, et. al. *IEEE Trans. on Sonics and Ultrasonics*, *SU* 32, 499 (1985).
4. W. A. Smith and B. Auld, *IEEE Trans. UFFC* 38, 40 (1988).
5. B. A. Auld, et al., *Proc. Ultrasonic Symp. (IEEE, 1983)*, p. 554.
6. Q. M. Zhang, et al., *IEEE Trans. UFFC* 41, (1994).
7. B. A. Auld, "Acoustic Fields and Waves in Solid" (John Wiley & Sons, New York, 1973).
8. IEEE Standard on piezoelectricity (ANSI/IEEE Standard 176-1987, 1988).

Institut Franco-Allemand de Recherches,  
5, rue du Général Cassagnou,  
68301 Saint-Louis, France

**Abstract** - Ferroelectric polymers are the most recent class piezoelectric and pyroelectric materials developed. The most common piezoelectric polymers are PVDF, based on the monomer  $\text{CH}_2\text{-CF}_2$  and copolymers PVDF with  $\text{C}_2\text{F}_3\text{H}$ . Under high hydrostatic pressure, piezoelectric polymers exhibit well defined piezoelectric response. Piezoelectric response of shock compressed PVDF film prepared with attention to mechanical and electrical processing exhibits precise, well defined reproducible behavior to 35 GPa. P(VDF-TrFE) copolymers exhibit unique piezoelectric properties over a wide range of temperature depending on the compositions. Under high shock pressure loading, unique piezoelectric response is also observed. In particular, first record of detonation profile is presented. These polymers have the potential for new shock wave sensors with unique characteristics.

## INTRODUCTION

The polar polymer polyvinylidene fluoride (PVDF) and its copolymers with 20 mol % - 50 mol % trifluoroethylene (TrFE) possess a variety of scientifically interesting and technologically important properties which have made them among the most widely investigated polymers [1,2]. They exhibit large dielectric, piezoelectric and pyroelectric constants and were the first known ferroelectric polymers. Nylon polymers (Nylon 11, 7 etc...) has been reported to exhibit relatively large piezoelectric and pyroelectric activities. [4]

PVDF is a partially crystalline linear polymer with a carbon backbone in which each monomer  $[-\text{CH}_2\text{-CF}_2-]$  unit has two dipole moments, one associated with  $\text{CF}_2$  and the other with  $\text{CH}_2$ . In the crystalline phase, PVDF exhibits a variety of molecular conformations and crystal structures depending on the method of preparation [1]. Melt cast films have the helical  $\alpha$  form in which the molecular conformation is transgauche (TGTG), and the chains are packed in an antipolar unit cell. By stretching, the  $\alpha$  phase in the film transforms to the  $\beta$  phase in which the molecular conformation in the all-trans (TT) planar zigzag with the dipole moments

perpendicular to the chain axis. This  $\beta$  form exhibits reversible spontaneous polarization and is therefore the most useful ferroelectric and strongly piezoelectric phase.

An unusual property of PVDF is that the forces responsible for ordering the dipoles in the ferroelectric phase are sufficiently strong that the polymer melts before it undergoes a ferroelectric paraelectric transition. It is known, however, that copolymers of VDF and TrFE,  $[\text{CHF-CF}_2]$ , with 20-50 mol % TrFE favour the  $\beta$  phase, and these copolymers exhibit ferroelectric transitions below the melting point ( $T_m$ ). Poling of PVDF and the copolymers in the ferroelectric (FE) phase results in well ordered molecular conformation of the crystalline phase with a well defined remanent polarization [5].

Previously conducted studies have shown that adequately polyvinylidene fluoride films can serve as the active material in a piezoelectric shock wave stress gauge [5]. Today there are reproducible materials which make it possible to study the material's piezoelectric properties and to evaluate the potential application for these ferroelectric polymers under high pressure and shock wave action.

In the present paper, informations about well precised poled PVDF, P(VDF-TrFE) are pointed out. The piezoelectric response of PVDF and copolymers under high hydrostatic pressure, is reported. Piezoelectric behavior of PVDF as well as of P(VDF-TrFE) copolymers under shock wave action will be outlined. First detonation profile with a PVDF shock gauge record is presented.

## FERROELECTRIC POLYMERS

**PVDF** : An orientation of the film is activated by stretching it just below the polymer's softening point with subsequent stretching and annealing. This process changes the crystalline structure of the film to the desired  $\beta$  polar phase. The PVDF material of the present work was biaxially stretched by Rhône Poulenc Films. Biaxially orientation leads to a more uniform thickness distribution (25  $\mu\text{m}$ ) and no wrinkling effect. Such prepared films are isotropic in

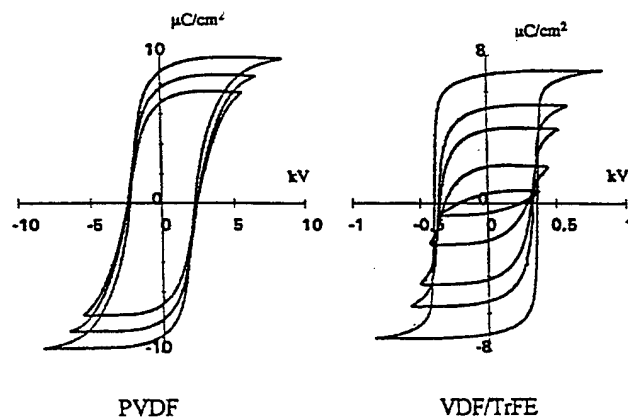


Figure 1. Hysteresis curves versus voltage : PVDF 25  $\mu\text{m}$  thick, 9mm<sup>2</sup> area, P(VDF-TrFE) 70/30 8 $\mu\text{m}$  thick, 4 mm<sup>2</sup> area.

mechanical properties as well as in piezoelectric properties.

**VDF/TrFE copolymers :** The structure, ferroelectric properties and melting temperature of VDF/TrFE copolymers are known to depend on composition. We have chosen for the present work the P(VDF<sub>0.7</sub>-TrFE<sub>0.3</sub>) composition because (i) it has the same crystalline  $\beta$  phase as PVDF at room temperature, (ii) it exhibits well defined and widely separated  $T_c$  and  $T_m$  and (iii) it has potential for applications. The samples, 1 to 25  $\mu\text{m}$  thick, were deposited by spin coating of the VDF/TrFE copolymers under a liquid form on a glass substrate. Then the film was removed from the substrate and annealed, in order to eliminate the solvent and to enhance crystallisation of the copolymer. The resin was available from Solvay. The samples 25 $\mu\text{m}$  to 1mm thick, were prepared by compression molding of the melt followed by quench into either water or air. The samples were annealed at 413 K.

## POLING PROCESS OF FERROELECTRIC POLYMERS

In the preparation of piezoelectric polymers and copolymers it is in general necessary to apply a high poling electric field to an essentially insulating material. The poling process is the same as that established for PVDF [5,6], and provides a means for achieving a homogeneous polarization at a predetermined level. Examples of hysteresis loops histories on 23  $\mu\text{m}$  thick biaxially stretched PVDF films as well as on 8  $\mu\text{m}$  spin coated P(VDF-TrFE) (70/30) film are given Figure 1. Active area, displacement current and remanent polarization are precisely determined for each PVDF ( $9 \mu\text{C}/\text{cm}^2$ ) or P(VDF-TrFE) ( $7.5 \mu\text{C}/\text{cm}^2$ ) film prepared.

## PIEZOELECTRIC HYDROSTATIC PRESSURE RESPONSE OF PVDF AND P(VDF-TRFE) COPOLYMERS.

Prior works have shown that the piezoelectric response of ferroelectric polymers under hydrostatic compression was reversible at low pressure level. In a most cases, experimentations were conducted in a quasi isothermal regime. Study of the adiabatic piezoelectric response has been investigated by inducing hydrostatic compression pressure. In order to have an adiabatic phenomenon, the compression pulses must be generated rapidly [8]. Toward this end, a high pressure chamber has been designed and built in which hydrostatic compression pulses above 1,5 GPa can be generated on the polymer sample and with a total pulse-length of 10 ms. It is possible to plot the "electrical charge released" diagram in a quasi adiabatic regime (figure 2). This diagram shows that the response of both PVDF and P(VDF-TrFE) copolymers is reversible until and above 0,7 GPa. Higher activity is observed with P(VDF-TrFE) copolymers.

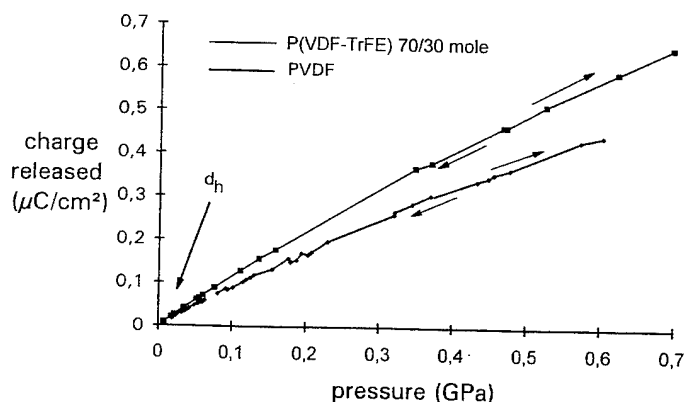


Figure 2. Electrical charge released versus hydrostatic pressure

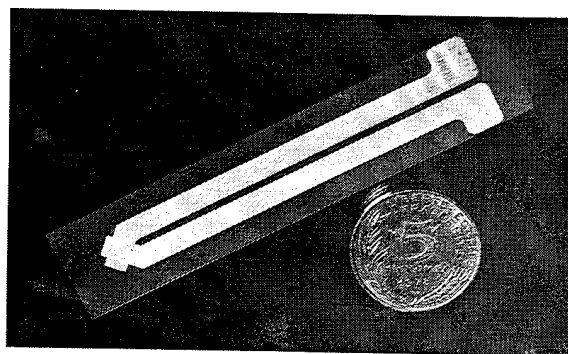
## HIGH PRESSURE PIEZOELECTRIC RESPONSE OF PVDF AND P(VDF-TRFE) UNDER SHOCK LOADING

**Background** Studies of shock compression response of PVDF [3] and P(VDF-TrFE) copolymer [9] in a "standard" configuration have been especially a continuing effort of ISL, Sandia National Laboratories to develop high quality, reproducible sensors material and to determine their physical characteristics under high pressure shock compression. In fact, shock-compression gauges cannot be "calibrated". Even in the direct shock experiment, the controlled shock-compression experiment serves as a shock-calibration only if the reproducibility of the piezoelectric polymer is evaluated quantitatively and a persistent reproducible material is available. Previous observations [10] of the PVDF piezoelectric charge response data to 50 GPa show significant deviations from idealised, continuous behavior between about 12 and 20 GPa.

## EXPERIMENTATION

Considerations [6] of the effects of shock properties of standard materials, electronic circuit, the PVDF material and the gauge package have lead to PVDF polymer gauges as well as low inductance gauges with a new poling procedure, in order to identify the origin of the deviations observed.

**Low inductance gauges precisely poled :** Figure 3 shows the PVDF gauge and his electrical configuration and "How PVDF is working". Low inductance PVDF gauges will be minimized for gauges having electrical leads with separation equal to zero. Figure 3, shows that low inductance and high precision gauge requires a low RC time, (R : resistance of the leads and the current viewing resistor, C : capacitance value of the gauge), control of the maximum displacement current and remanent polarization value.



## HOW PVDF IS WORKING

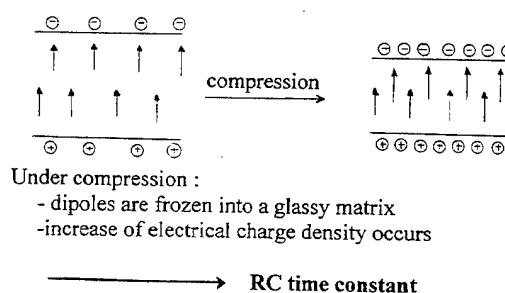
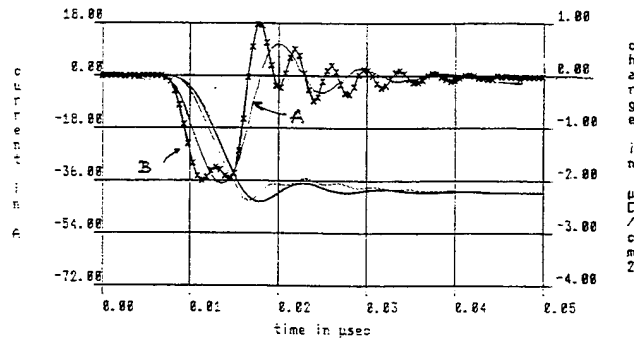


Figure 3. PVDF gauge : electrical configuration and "How PVDF is working".

*Tools* Impact loading is produced by controlled impact in a powder gun. The symmetrical impact of an impactor and target copper provides the loading [6]. The PVDF gauge is insulated on both sides with a Kel-F film of 110  $\mu\text{m}$  in thickness and is placed on the impact surface. Kel-F matches the shock impedance of the PVDF. The initial stress wave produced is that typical of the impact of the copper impactor on the PVDF gauge. (Figure 4) This wave then, reverberates between the impactor and target until stress equilibration is reached [2,6].



( Shock pressure: 3.5 GPa )  
A: standard gauge  
B: low inductance gauge

Figure 4. Initial stress (Current and charge)

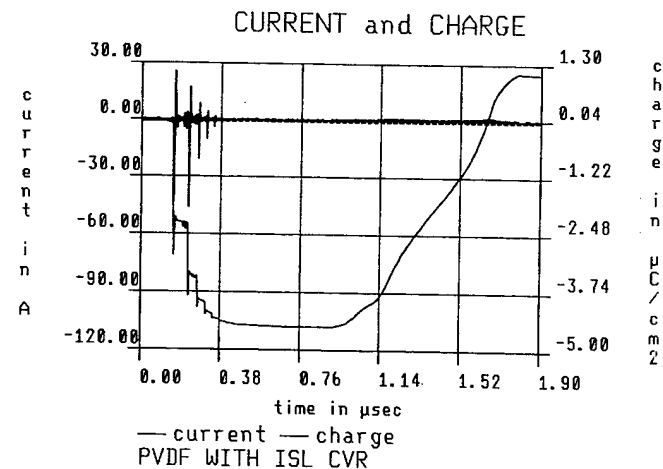


Figure 5. Experimental record ( Shock pressure: 12.95 GPa )

The responses are measured in the "current mode" [6] to provide both a simple circuit and the most revealing electrical behavior. The current response provides a direct measure of stress rate. Upon integration of the current pulse, the electrical charge-versus -time is obtained (figure 4 and figure 5).

## RESULTS

As we can see on figure 4, the ring up records observed indicate rise time of 3.5 ns for a standard gauge [2] and of 2 ns for a low inductance and low RC time gauge. The electrical charge is a continuous function of the shock pressure until 35 GPa, figure 6.

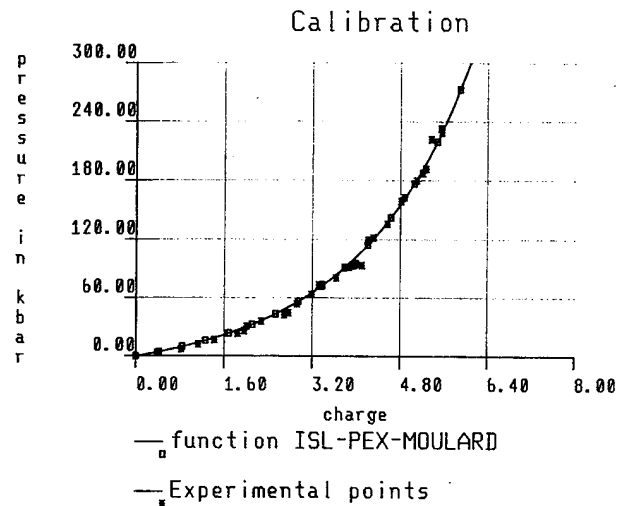


Figure 6 : Pressure versus charge [ $\mu\text{C}/\text{cm}^2$ ].

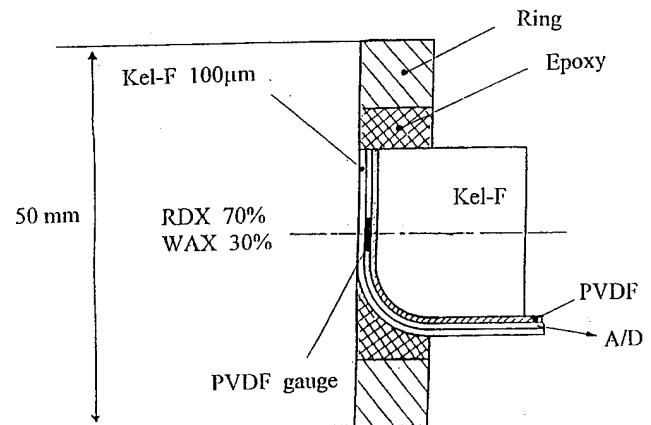


Figure 7 : Experimental set-up for detonation for shock-compressed PVDF measurement.

## DETONATION PROFILE MEASUREMENT

It should be recalled that PVDF works differently in a powder gun experiment where it rings up to the final pressure, as compared to an explosive single-shock experiment.

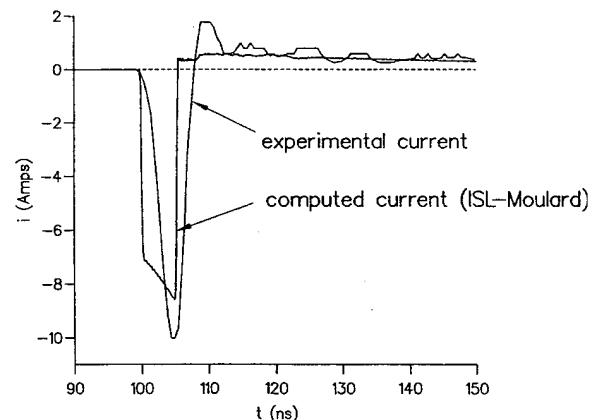


Figure 8 : Detonation pressure profile (current).

# Detonation pressure: computed and measured

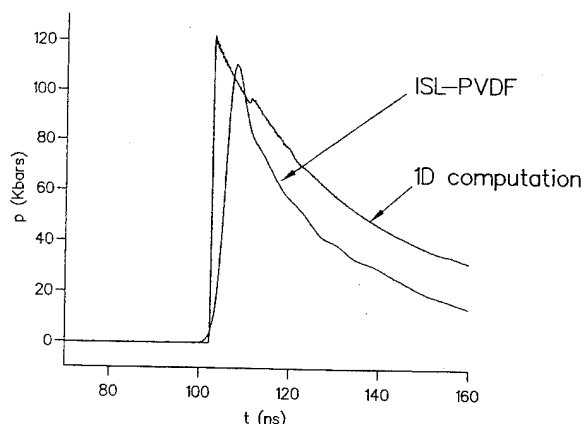


Figure 9 : Detonation pressure profile (stress)

We have tried to use these "ad hoc shielded" new gauges in an explosive single shock experiment. The figure 7 gives the scheme of the experimentation. The explosive is a mixture of hexogen and wax 70/30 in weight percent. The figure 8 and 9, give the experimental and theoretical current as well as the theoretical and experimental pressure in the vicinity of the explosive. It should be pointed out that the rise time of the current is equal to 2 ns. The pressure attains 10.5 GPa and indicates a detonation pressure greater than 20 GPa inside the explosive.

## P(VDF-TrFE) BEHAVIOR

*Piezoelectric response under shock compression* The piezoelectric response of P(VDF-TrFE) copolymers under shock loading has been reported in a previous paper [9]. All these results show that in first approximation, the response of the P(VDF-TrFE) gauge is a continuous function of the shock pressure until 28 GPa. The piezoelectric response is observed to be higher than that of PVDF.

## CONCLUSION

Some high pressure applications of ferroelectric polymers has been presented. PVDF stress rate gauges show continuous response with high reproducibility to pressure approaching 35 GPa. It appears that low inductance electrode lead designs and reproducible remanent polarization are (significantly) improving the precision of the piezoelectric response of the PVDF gauges under shock loading. After ten years studies of PVDF gauge shock response we were able to record the detonation pressure profile of a specific explosive.

## REFERENCES

- [1] A.J. Lovinger, *Jap J. Appl. Phys.* 24, Supplement 24-2, 18 (1985)
- [2] *Ferroelectrics* 32 Nos 1-4 (1981) and 115 N°4 (1991).
- [3] R.A. Graham, *Solids under High Pressure Shock Compression*, New York: Springer Verlag, 1993, ch 5.2, pp 103-113.
- [4] J. Scheinbeim, "New Ferroelectric and Piezoelectric Polymers" in *Proceedings ISAF '92*, 1992, pp. 248-249.
- [5] F. Bauer, *Ferroelectrics*, 49, 231 (1983), 115, (1991).
- [6] F. Bauer, R.A. Graham, M.U. Anderson, H. Lefebvre, L.M. Lee and R.P. Reed, "Piezoelectric Response of Precisely Poled PVDF to Shock Compression greater than 10 GPa", in *Proceedings of the ISAF 92*, 1992, pp. 273-276.
- [7] R. Heintz, *Thesis*, University Paris VII, 1990.

- [8] H. Lefebvre, *Thesis*, University Lyon N°93-0048, 1993.
- [9] F. Bauer, R.A. Graham, L.M. Lee, "Properties of VF<sub>2</sub>/ VF<sub>3</sub> Ferroelectric Copolymers; Electrical Response under High Pressure Shock Loading", in *Proceedings of the ISAF'90*, 1990, pp.288-291.
- [10] R.A. Graham, M.U. Anderson, F. Bauer, R.E. Setchell, "Piezoelectric Polarization of the Ferroelectric Polymer PVDF from 10 MPa to 10 GPa: Studies of Loading - Path Dependence," in *Shock Waves in Condensed Matter-1991*, 1992, pp. 883-886.

# High Frequency Dielectric and Electromechanical Properties of Ferroelectric Nylons

L.F. Brown, J.I. Scheinbeim\*, and B.A. Newman\*

Department of Electrical Engineering

South Dakota State University

201 Harding Hall, P.O. Box 2220

Brookings, SD 57007

\*Polymer Electroprocessing Laboratory

Department of Materials Science and Engineering

Rutgers University

P.O. Box 909

Piscataway, NJ 08855-0909

**Abstract**--The first measurements of high frequency dielectric and thickness-mode electromechanical properties of ferroelectric nylons are reported. Two sets of nylon 11 film samples were produced. The first set was melt-quenched and poled, while the second set was melt-quenched and then cold-drawn at room temperature before poling, resulting in a three-dimensionally ordered sample. Gold electrodes, 10 mm by 10 mm, were evaporated on opposing sample surfaces. The remanent polarization of the unoriented sample was  $27 \text{ mC/m}^2$  while that of the oriented sample was  $52 \text{ mC/m}^2$ . Samples of each film were placed in a programmable environmental chamber and connected to a Hewlett Packard 4195A Network/Impedance Analyzer via a custom remote fixture. Broadband measurements were made of the clamped capacitance and dissipation factor, thickness-mode electromechanical coupling coefficient  $k_t$ , mechanical quality factor  $Q_m$ , and longitudinal sound velocity  $v_l$  for each sample over a temperature range of  $20^\circ\text{--}160^\circ\text{C}$ . Comparisons of the properties were made between oriented and unoriented film samples. The results showed  $k_t$  values in the 0.03-0.11 range, and  $Q_m$  values of 8-10 above the glass transition temperatures of the samples (approximately  $60\text{--}70^\circ\text{C}$ ). The results show promise for high temperature ferroelectric nylon sensing applications.

## INTRODUCTION

The ferroelectric (odd-numbered) nylons have generated recent interest for high temperature transducer applications which cannot be addressed with other piezo/pyro/ferroelectric materials. With bulk material properties similar to PVDF and other polymers, the nylons may offer superior performance for high temperature applications which are beyond the safe operating temperature of PVDF and the copolymers. The purpose of this work was to study the basic dielectric and electromechanical properties of the nylons to assess their potential for high frequency transducer applications. Of particular interest was their high frequency thickness-mode properties which are important to the operation of resonance-mode ultrasonic transducers. This work was carried out on ferroelectric nylon 11 materials.

The odd-numbered nylons are known to possess a polar crystalline form which can be rendered ferroelectric

through electroprocessing [1-2]. Extensive studies have been conducted on the low frequency dielectric and piezo/ferroelectric properties of nylon 11 and nylon 7, including the temperature dependence of their lateral mode properties (i.e.,  $d_{31}$ ), and the effects of annealing [3]. The higher dipole density of the lower ordered nylons, such as nylon 5, and nylon 7, results in predictably higher remanent polarization which may even be competitive with PVDF-based copolymers [4, 5].

The high internal dielectric and mechanical losses of the nylon 11 materials used in this study presented a challenge in accurately determining their electromechanical properties. This paper describes the preparation and electroprocessing of the nylon 11 samples, the method of characterization used to determine their high frequency dielectric and electromechanical properties, and summarizes the results for both oriented and unoriented samples. A comparison of these results is made with typical properties of PVDF and PVDF-based copolymer materials.

## SAMPLE PREPARATION

Two sets of nylon 11 film samples were produced. The samples were prepared by quenching melt-pressed films in ice water. Thin gold electrodes, with 10 mm by 10 mm overlap, were evaporated onto opposing surfaces of the films to facilitate electroprocessing and characterization. An unoriented set was melt-quenched and poled, while an oriented set was produced by melt-quenching films and then uniaxially cold-drawing (2.8:1) at room temperature before poling, resulting in three-dimensionally ordered samples. The typical remanent polarization of the unoriented samples was  $27 \text{ mC/m}^2$  while that of the oriented samples was  $52 \text{ mC/m}^2$ . Polarization was carried out using a maximum electric field of  $250 \text{ MV/m}$  as described in [4].

Following polarization, the thickness of each sample was mapped and test specimens of smaller size were selected for maximum thickness uniformity and highest surface quality. The area of each test specimen was selected such that the magnitude of its impedance was in the range of  $50\text{--}250 \Omega$  at the fundamental half-wave thickness mode resonance frequency of the sample. This assured accurate measurement of the broadband dielectric properties near resonance.



## BROADBAND DIELECTRIC MEASUREMENTS

Test specimens were connected to a test fixture and remotely located in a Thermotron environmental chamber. The free-air capacitance and dielectric loss tangent ( $\tan\delta_e$ ) were measured with a Hewlett-Packard 4195A Impedance Analyzer over a broad range of frequencies including the fundamental thickness mode resonance of the specimen. Resonance was easily detected by the sharp changes in dielectric properties and occurs when the sample thickness is  $1/2$  wavelength. The measurements were then analyzed using a resonance technique method similar to [6-8] whereby the parameters of a one-dimensional thickness-mode Mason's model were varied until the features of the model's input dielectric properties matched those of the sample within a specified tolerance. The parameters of the Mason's model are the dielectric and electromechanical properties of interest:

- $C_0$  clamped capacitance, (F)
- $\tan\delta_e$  clamped dielectric loss tangent
- $k_t$  thickness electromechanical coupling coefficient
- $Q_m$  mechanical quality factor ( $Q_m = 1/\tan\delta_m$ )
- $v_l$  longitudinal sound velocity, (m/s)

Figure 1 shows the actual broadband dielectric measurements made at 100°C for a 21.2- $\mu\text{m}$  thick unoriented sample of 0.310" x 0.152" size. The clamped dielectric properties, derived from the resonance technique, are also shown in the figure. The thickness mode resonance for this sample was determined to be 43.1 MHz, giving a longitudinal sound velocity of 1828 m/s. A similar set of measurements is shown in Figure 2 for a 12.8  $\mu\text{m}$ -thick 0.194" x 0.159" oriented sample.

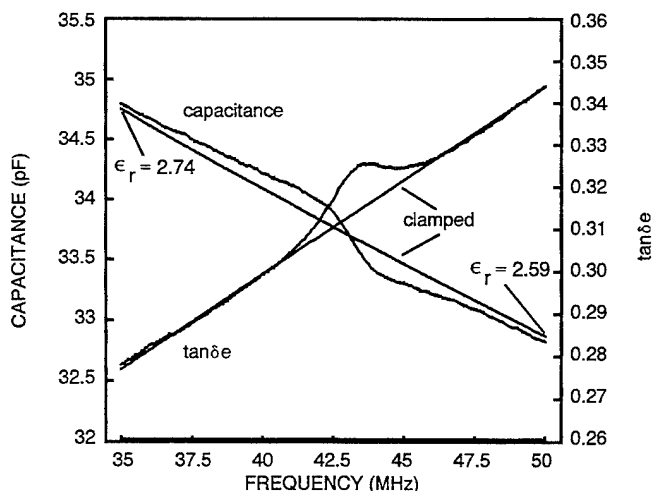


Fig. 1. Broadband dielectric measurements, and derived clamped dielectric properties, of 21.2  $\mu\text{m}$ -thick unoriented nylon 11 sample taken at 100°C.

## ANALYSIS RESULTS

Similar measurements were made on both samples at 20°C temperature increments in the range of 20-160°C. A comparison between the properties of the oriented and unoriented materials is shown in Table 1. Although the

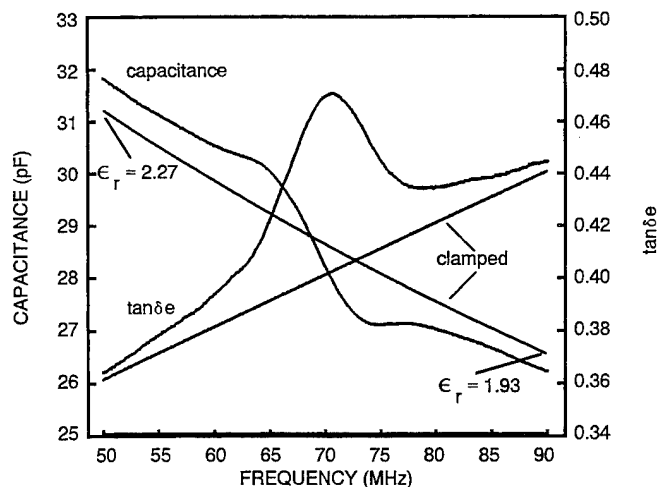


Fig. 2. Broadband dielectric measurements, and derived clamped dielectric properties, of 12.8  $\mu\text{m}$ -thick oriented nylon 11 sample taken at 100°C.

dielectric properties are similar, the oriented sample exhibited much higher electromechanical coupling as expected from its higher remanent polarization (i.e., crystallinity). Of particular note is the low acoustic impedance of the materials. The 2.1-2.4 MRayl value for the nylons is significantly lower than even PVDF and suggests efficient broadband operation of a nylon 11 based ultrasonic transducer operating in tissue, water, or other low impedance material.

Table 1. Comparison of measured oriented and unoriented nylon 11 properties.

Type	$\epsilon_r$	$\tan\delta_e$	$k_t$	$Q_m$	$v$ (m/s)	$Z$ (MRayl)
Oriented (20°C)	2.2	0.12	10.5	8.5	2100	2.42
Oriented (100°C)	2.2	0.38	10.5	7.5	1800	2.10
Unoriented (20°C)	2.4	0.12	3.3	8	2100	2.42
Unoriented (100°C)	2.6	0.40	3.3	8	1800	2.10

A comparison of the oriented nylon 11 properties with typical values for PVDF and P(VDF-TrFE) [9, 10], which has the highest remanent polarization of current known polymers, is summarized in Table 2. Of greatest concern for low frequency medical applications (i.e., 1-10 MHz) is the low dielectric constant and high dielectric loss tangent of the nylon 11. The low mechanical Q and very low acoustic impedance of the nylons should offer greater bandwidth than PVDF and P(VDF-TrFE) for an ultrasonic transducer operating in water or tissue. However, the advantage is likely overcome by the nylon 11's lower electromechanical coupling and higher internal dielectric and mechanical losses. Whether or not nylon-11 offers definite advantages over PVDF or P(VDF-TrFE) as an ultrasonic transducer will likely depend on the physical

requirements of the transducer and operating temperature. For instance, the nylon 11 materials can safely operate at temperatures much higher than PVDF without depolarizing.

Table 2. Comparison of oriented nylon 11 with typical properties of PVDF and P(VDF-TrFE) at 20-100°C (10-50 MHz).

Parameter	PVDF	P(VDF-TrFE)	Oriented Nylon-11
$\epsilon_r$	5.0	4.0	2.2
$\tan\delta_e$	0.25	0.12	0.25
$k_t$	.15	0.30	0.11
$Q_m$	13	25	8
$v$ (m/s)	2200	2400	2000
$Z$ (MRayl)	3.96	4.27	2.30

Figure 3 illustrates the measurements of electromechanical coupling ( $k_t$ ) and mechanical quality factor ( $Q_m$ ) for the oriented nylon 11 material over the temperature range of 20-160°C. The results show good thermal stability over the broad temperature range. The electromechanical coupling coefficient for the oriented nylon 11 is much lower than that of PVDF as expected from its lower dipole density. However, these results confirm the potential for the lower numbered odd nylons (i.e., nylon 7, nylon 5) to possess higher electromechanical coupling than PVDF and possibly P(VDF-TrFE) since theory predicts much higher remanent polarization in nylon 5 and nylon 7 than for nylon 11 [4, 5].

Similarly, Figure 4 illustrates the temperature dependence of the 60 MHz clamped dielectric properties and longitudinal sound velocity over the same 20-160°C temperature range. The dielectric constant can be seen to become approximately constant below the glass transition temperature of approximately 70°C. The longitudinal sound velocity shows the linear temperature characteristics indicative of polymers and typical of PVDF [11].

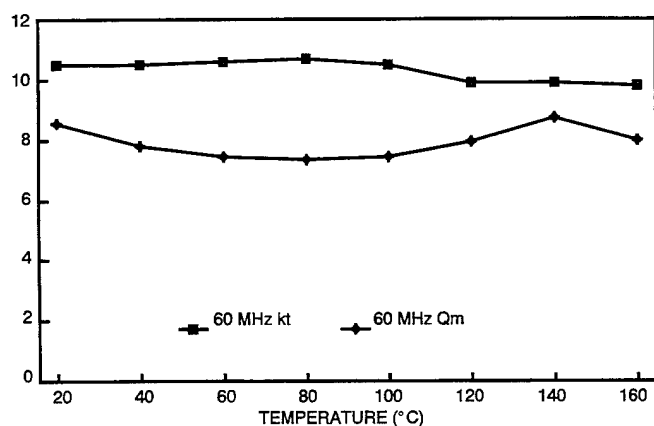


Fig. 3. Measured properties of oriented nylon sample.

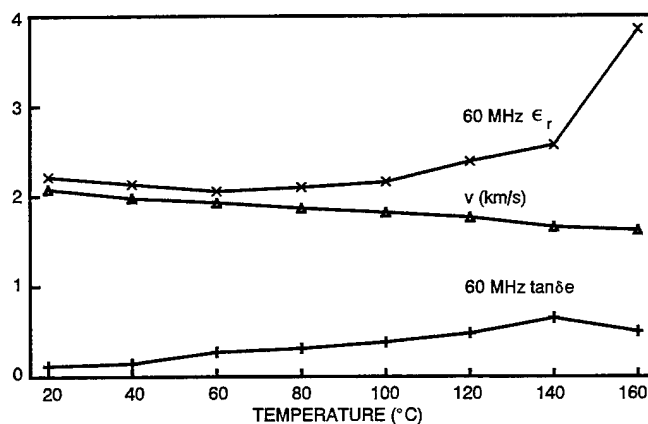


Fig. 4. Dielectric properties of oriented nylon 11 sample at 60 MHz.

## CONCLUSIONS

The high frequency dielectric and electromechanical properties of both oriented and unoriented ferroelectric nylon 11 were analyzed over a temperature range of 20-160°C. The nylons exhibited dielectric and mechanical losses similar to PVDF, but significantly higher than that of P(VDF-TrFE). The electromechanical coupling coefficient of the oriented nylon 11 was lower than oriented PVDF as expected from its lower dipole density. The low dielectric constant of these nylon materials may be the biggest drawback for ultrasonic transducer applications in the 1-10 MHz range of frequencies for medical applications. The acoustic impedance of nylon 11 is significantly lower than PVDF and PVDF-based copolymers and should offer superior bandwidth performance for ultrasonic transducers operating into low impedance media such as water, tissue, and other polymers. Future studies will focus on the properties of nylon 9, 7, and 5 which still show the greatest promise for high temperature ferroelectric nylon sensor applications.

## REFERENCES

- [1] J. Scheinbeim, J. Lee, and B. Newman, "Ferroelectric Polarization Mechanisms in Nylon-11", *Macromolecules*, Vol. 25, 1992, pp. 3729-33.
- [2] J. Lee, Y. Takase, B. Newman, and J. Scheinbeim, "Ferroelectric Polarization Switching in Nylon-11", *Journal of Polymer Science: Part B: Polymer Phys.*, Vol. 29, 1991, pp. 273-277.
- [3] J. Lee, Y. Takase, B. Newman, and J. Scheinbeim, "Effect of Annealing on the Ferroelectric Behavior of Nylon-11 and Nylon-7", *Journal of Polymer Science: Part B: Polymer Physics*, Vol. 29, 1991, pp. 279-286.
- [4] J.I. Scheinbeim and B.A. Newman, "Electric Field-Induced Changes in Odd-Numbered Nylons", *Transient Polymer Science*, Vol. 1, No. 12, Dec., 1993, pp. 394-400.
- [5] J. Scheinbeim and B. Newman, "New Ferroelectric and Piezoelectric Polymers", In *Proc. 1992 IEEE International Symposium Applications of Ferroelectrics*, No. 92CH3080-9, 1993, pp. 248-249.

- [6] H. Ohigashi, "Electromechanical Properties of Polarized Polyvinylidene Fluoride Films as Studied by the Piezoelectric Resonance Method", *Journal of Applied Physics*, Vol. 47, No. 3, March 1976, pp. 949-955.
- [7] L. Brown and D. Carlson, "Ultrasound Transducer Models for Piezoelectric Polymer Films", *IEEE Transactions on Ultrasonics, Ferroelectrics, and Frequency Control*, Vol. 36, No. 3, 1989, pp. 313-318.
- [8] D. Turnbull, M. Sherar, and F. Foster, "Determination of Electromechanical Coupling Coefficients in Transducer Materials with High Mechanical Losses", *Proc. 1988 IEEE Ultrasonics Symposium*, No. 88CH2578-3, pp. 631-634.
- [9] *The Applications of Ferroelectric Polymers*. Ed. by T.T. Wang, J.M. Herbert, and A.M. Glass, New York: Chapman and Hall, 1988, Chap. 11, pp. 237-273.
- [10] *Medical Applications of Piezoelectric Polymers*. Ed. by P.M. Galetti, D. De Rossi, and A.S. De Reggi, New York: Gordon and Breach, 1988, pp. 189-202.
- [11] L.F. Brown, "A Study of Commercial Disposable Ultrasonic Transducers for Quantitative Nondestructive Evaluation", in *Review of Progress in Quantitative NDE*, Vol. 13, Ed: D.O. Thompson and D.E. Chementi, Plenum Press, New York (1994), pp. 693-700.

# Dependence on Supramolecular Structure and on Charge Injection Conditions of Ferroelectric Switching of PVDF and its Blends with PMMA

A. Becker, M. Stein, and B.-J. Jungnickel  
Deutsches Kunststoff-Institut (German Plastics Institute)  
D-64289 Darmstadt (Germany)

**Abstract** — PVDF is a semicrystalline polymer with very interesting ferroelectric, pyroelectric and piezoelectric properties. It is the aim of the present paper to prove the importance of the amorphous phase for the strength of the respective activity coefficients. To this end, the structure and the dynamics of this particular phase is varied by blending with PMMA and by suitable annealing. It will be shown that the electric efficiency is governed to a large extent by the type, the number, the mobility, and the properties of trapping sites of injected charges which migrate through, and reside in, the amorphous phase.

## INTRODUCTION

The polarization of PVDF is usually attributed to the crystalline phase in this semicrystalline material. It should be therefore proportional to the degree of crystallinity which can be varied to a sufficiently large extent only by blending with an amorphous non-crystallizing second polymer like PMMA. Respective investigations reveal however that the polarisation drops with increasing PMMA content much faster than the degree of crystallinity (Fig. 1). This reveals that the amorphous phase plays an important rôle for ferroelectricity. In principle, several ways of action are possible. At first, an immediate polarization contribution of the amorphous phase should be taken into consideration. Since, however, the material is far above the glass transition temperature of PVDF of about  $-40^{\circ}\text{C}$ , a stable polarization is possible only in the crystal/amorphous interphase. Corresponding calculations show that the respective amount is rather small. It can and will play a deciding rôle only for piezoelectricity and pyroelectricity [1]. Next, the dielectricity of the amorphous phase can change with crystallinity and PMMA content. This variation, again, is too small according to  $\epsilon$ -measurements. Depolarization effects by virtue of the shape of the crystalline entities are also too small according to structure measurements in order to account for the measured relations. Finally, conductivity and charge injection effects are possible. In fact, it had been found that the amount and the temporal stability of remanent polarization depends to a large extent on the possibility of charge injection during action of the electric field when poling the sample or performing hysteresis measurements [2]. The action of the injected charges during poling can be understood formally as a displacement of the electrodes into the sample material with corresponding increase of the efficient electric field. On the other hand, after removal of the external field, these charges stabilize the polarization orientation of the individual entities by the electric fields which they create. The injected charges are characterized by their

- type,
- injection rate,
- migration rate,

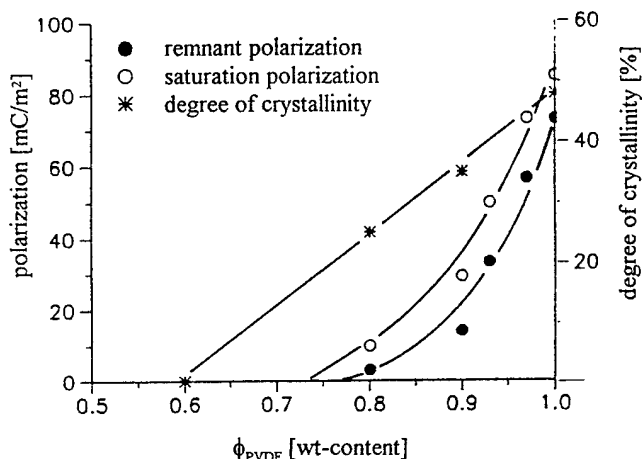


Fig. 1: Saturation and remanent polarizations, respectively, and degree of crystallinity in dependence on composition  $\phi_{\text{PVDF}}$  of PVDF/PMMA blends.

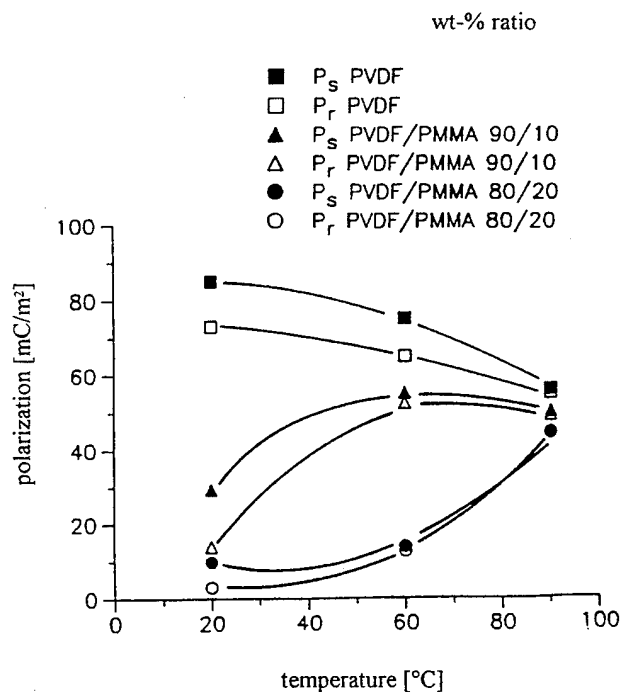


Fig. 2: Saturation ( $P_s$ ) and remanent ( $P_r$ ) polarizations, respectively, of several PVDF/PMMA blends in dependence on temperature during hysteresis measurements.

- trapping site location, and
  - trapping site potential depth.
- These characteristics can be modified by
- variation of measuring temperature,
  - sample annealing,
  - change of electrode material,
  - structure change by blending,
  - electric field application and reversal, i.e. multiple hysteresis loops, and
  - suitable poling technique and poling conditions.
- Some of these features and their consequences will now be proved and discussed in more detail.

## EXPERIMENTAL RESULTS

In Fig. 2, the saturation and remanent polarizations, respectively, of several PVDF/PMMA blends are shown in dependence on the temperature during hysteresis measurements. At sufficiently elevated temperature, the polarizations assume those values which are to expect according to the proportionality to the degree of crystallinity (cf. Fig. 1). This can be understood if it is assumed that the thermally induced increase of injection and migration rates, respectively, causes higher local electric fields and stabilize the resulting polarization. The conductivity of PVDF/PMMA blends (Tab. 1) which drops with increasing PMMA content to the same degree as the polarization (cf. Fig. 1) rises with temperature accordingly. This underlines moreover the importance of chain mobility in the amorphous phase for the amount and the stability of polarization and the necessity to surpass sufficiently the glass transition temperature.

The injection rate dependence and the dependence on the type of injected charges can be demonstrated by the electrode material dependence of the nonlinearity of dielectricity of PVDF. It is defined in complex notation and in the frequency domain:

$$D = P_r + \varepsilon_0[(1 + \chi_1)E + \chi_2 E^2 + \dots] \quad (1)$$

( $D$ : dielectric displacement,  $P_r$ : remanent polarization,  $\chi_i$ : dielectric susceptibility of the  $i$ -th order,  $E$ : electric field,  $\varepsilon_0$ : permittivity of the vacuum;  $D$ ,  $\chi_i$  and  $E$  are complex and frequency dependent). We have in real notation

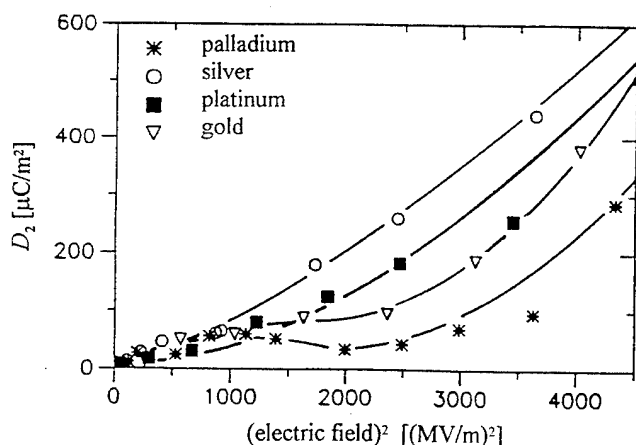


Fig. 3: Dependence of the amplitude  $D_2$  of the second harmonic dielectric response of poled PVDF on the used electrode material ( $\omega = 150\text{s}^{-1}$ ,  $T = 20^\circ\text{C}$ ).

$\phi_{\text{PVDF}}$ [wt-%]	$\sigma [10^{-15}(\Omega\text{cm})^{-1}]$ 23°C	$\sigma [10^{-15}(\Omega\text{cm})^{-1}]$ 90°C
100	5	700
90	0.8	200
80	0.04	40

Tab. 1: Conductivity  $\sigma$  of PVDF/PMMA blends at different temperatures.

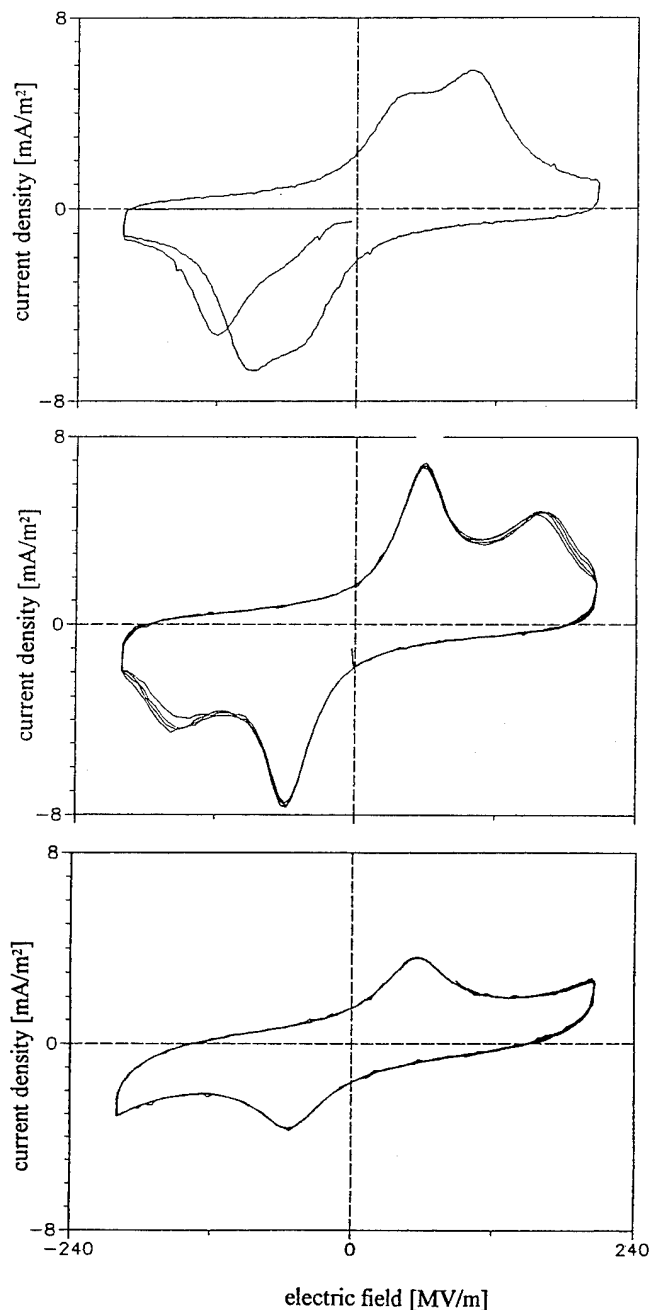


Fig. 4: Polarization current hysteresis loops of PVDF after different numbers of hysteresis cycles (annealed at  $160^\circ\text{C}$  for 17h,  $\omega = 0.003\text{s}^{-1}$ , curves corrected for Ohm conductivity and for capacity currents).

above: cycle 1,  
center: cycles 23 through 26,  
bottom: cycles 39 through 43.

$$E = E_0 \cos \omega t \rightarrow D = \sum_n [D_n \cos(n\omega t - \delta_n)] \quad (2)$$

where the  $D_n$  are the amplitudes of the  $n$ -th harmonic response. It is found by comparison of Eqs. 1 and 2 that

$$D_n = \varepsilon_0 [c_n \chi_n E_0^n + c_{n+2} \chi_{n+2} E_0^{n+2} + \dots] \quad (3)$$

where the  $c_n$  are certain constants. In Fig. 3, the amplitudes  $D_2$  of the second harmonic response are given for several electrode materials as used during permittivity measurement. It is obvious that a second harmonic exists in poled PVDF, that it depends remarkably on the actual electrode material, and that its strength increases with increasing ionization energy of the latter. The bended courses of all the functions  $D_2(E_0^2)$  indicate the existence of still higher harmonics.

Annealing of the PVDF films at a temperature above 160°C causes some interesting changes in the course of the hysteresis loops. They are visualized best by the polarization current hystereses which in fact are the initially measured functions. Whereas not annealed material exhibits the familiar smooth loops, annealed samples exhibit two distinct maxima (Fig. 4). In principal, this is a well known phenomenon but the curves of Fig. 4 exhibit some unusual features. At first, the relative strengths of the two maxima vary independently with the hysteresis cycle number. Moreover, both the remnant and the saturation polarizations of the annealed samples as considered here assume their maximal values immediately in the first hysteresis cycle, and decrease gradually with increasing cycle number. In contrast, remnant and saturation polarizations, respectively,

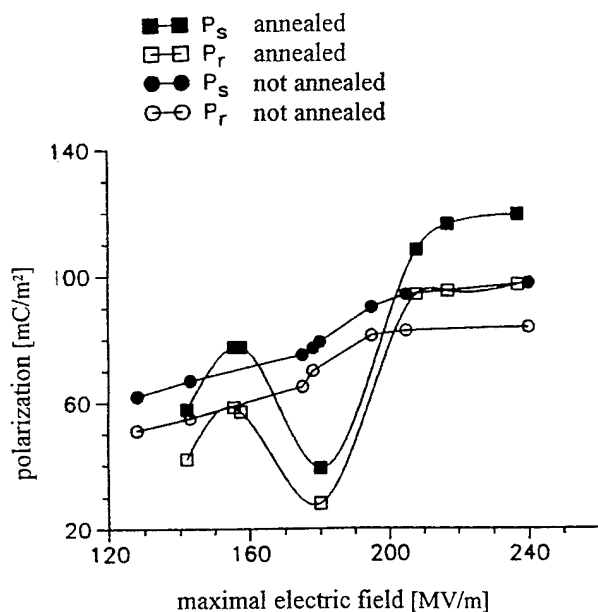


Fig. 5: Saturation ( $P_s$ ) and remanent ( $P_r$ ) polarizations, respectively, of not annealed and annealed at 160°C for 17h PVDF films in dependence on the maximal electric field strength, after 20 poling cycles.

increase usually with increasing cycle number until approaching a certain equilibrium value.

From Fig. 5 it is moreover evident that the described drop in polarization is not only linked with the annealing treatment but occurs just in a limited range of hysteresis field strengths. The corresponding hysteresis loops themselves at high cycle numbers are displayed in Fig. 6.

X-ray diffraction measurements proved that the annealing did not cause drastic changes of the supermolecular structure. In particular, the crystal transformation into the so-called  $\gamma$ -modification which basically can occur upon annealing at high temperature is negligible. The crystallinity increased only slightly.

We believe that the observed features, in particular the complicated dependence of the hysteresis contours on cycle number, annealing conditions, and electric field, can be explained and understood by the competing actions and influences of

- dipole reorientation in the polarized regions, i.e., the crystallites,
- the migration of existing charges within the material under the influence of the external electric field with steadily reversing direction, and
- the steady injection of new charges when applying and reversing the electric field.

In fact, the importance of the very first poling - irrespective whether it is performed separately in order to create a polarization or during starting an hysteresis experiment - for the polarization changes during all later hysteresis cycles is evident from our experiments and is in accordance with the proposed processes on a molecular level. It becomes more clear when looking at the polarization decrease with rising hysteresis cycle number in more detail. In Fig. 7, the distribution of the polarization across the film thickness in an annealed sample after different hysteresis cycle numbers is displayed. Obviously, the polarization distribution does not change its sign with every cycle as a whole. In contrast, the initial distribution - that after the first removal of the electric field (Fig. 7 above left) - is very stable and changes its course and sign only gradually. Finally a almost perfect bimodal polarization distribution is reached. The polarization decrease with increasing poling cycle number is therefore only feigned by an asymmetrical distribution of polarization across the film thickness which in turn is caused by the complicated migration conditions of injected charges.

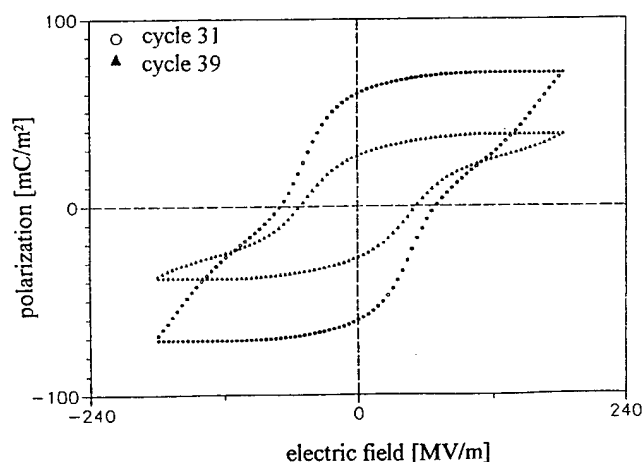


Fig. 6: Hysteresis loops of PVDF after different numbers of poling cycles (annealed at 160°C for 17h,  $\omega = 0.003\text{s}^{-1}$ , curves corrected for Ohm conductivity and for capacity currents).

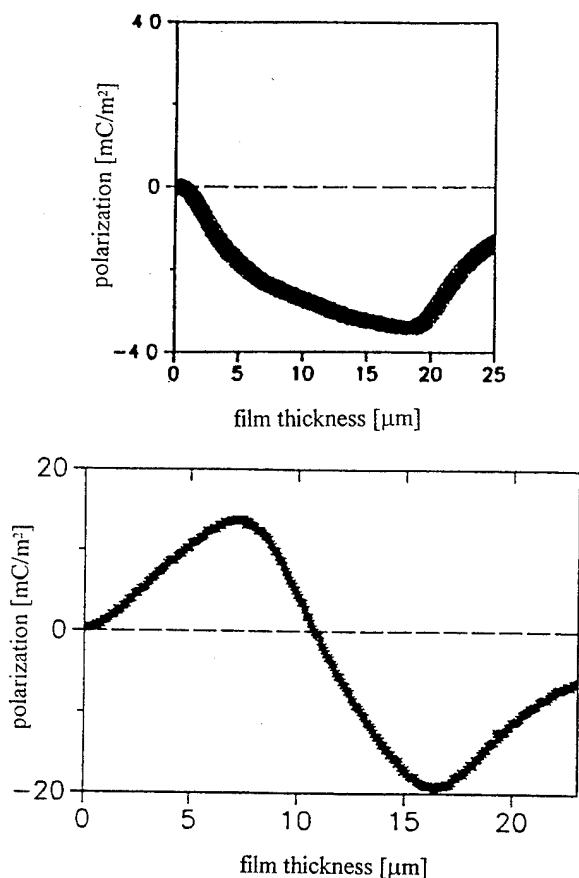


Fig. 7: Polarization distribution across film thickness in a PVDF film annealed at 160°C for 17h (Maximal electric field: 180MV/m;  $\omega = 0.003\text{s}^{-1}$ ).

above left: after (first) poling,  
 above right: after 18 hysteresis cycles,  
 left: after 50 hysteresis cycles.

## SUMMARY AND CONCLUSIONS

The present investigations and the conclusions which must be drawn from them can be summarized as follows:

- The amount and the stability of remnant polarization are decisively determined by the structure and the dynamics of the amorphous phase. The latter can be changed by, e.g., blending, annealing or variation of measuring temperature.
- The action of the amorphous phase reflects the action of injected charges, i.e., in fact, the amount and the stability of remnant polarization are decisively determined by the location, the type, and the number of injected charges, and by the trapping site potential depth.
- The injection conditions during the first poling (irrespective whether this poling has been performed separately or by starting an hysteresis experiment) determine the material behavior during all later switching and poling cycles. The already residing charges compete then with those newly injected, and the migration of both competes with the reorientation dynamics of the polarization.
- In certain well ordered samples, the hysteresis current exhibits two maxima. The strengths of both are not related but depend on the hysteresis cycle number. They can be attributed to the contributions of domains, the polarization orientation of which is fixed to a large extent by space charges, and others, the polarization of which reorients under the influence of the applied field.
- The dependences of polarization parameters on the experimental conditions can be understood only when the spatial distribution of polarization across the sample thickness is also known.

- At suitable conditions, the overall polarization is near zero whereas the local polarization can assume considerably high values of both signs, such forming a bimorphous material. More details about the investigations as reported here are published elsewhere [3,4].

## ACKNOWLEDGEMENT

Financial support from the Bundesminister für Wirtschaft through the Arbeitsgemeinschaft industrieller Forschungsvereinigungen e.V. (AiF), grant no 8053, is gratefully acknowledged.

## REFERENCES

- [1] P. Harnischfeger and B.-J. Jungnickel, *Features and Origin of the Dynamic and the Nonlinear Piezoelectricity in Poly (Vinylidene Fluoride)*, Polym. Adv. Techn., vol. 1, pp. 171-179, 1990.
- [2] E. Bihler, G. Neumann, G. Eberle, and W. Eisenmenger, *Influence of Charge Injection on the Formation of Remanent Polarization in P(VDF-TrFE) Copolymers*, IEEE Ann. Rep. CEIDP, 1990.
- [3] A. Becker, *Untersuchungen zur Ferroelektrizität von Polyvinylidenfluorid*, Master Thesis, Technische Hochschule Darmstadt, 1993.
- [4] M. Stein, *Untersuchungen zur Polarisationsdynamik in Mischungen aus Polyvinylidenfluorid und Polymethylmethacrylat*, PhD Thesis, Technische Hochschule Darmstadt, 1993.

# Concurrent Session - 2C: Thin Films



# Characteristics of NDRO Ferroelectric FETs With a Poly-Si Floating Gate

Takashi Nakamura, Yuichi Nakao, Akira Kamisawa and Hidemi Takasu  
ROHM CO.,LTD. 21, Saiin Mizosaki-cho, Ukyo-ku, Kyoto 615, Japan

## Abstract

Non-destructive read out memory FET using ferroelectric gate insulator has been developing remarkably and device such as to use buffer layer has been requiring for high process technology. But it is very difficult to deposit on buffer layer the same as deposition directly on Si. After making FET by deposition of ferroelectric on prepared floating gate, our evaluation carried out. This FET is MFMIS structure which consists of Si-sub, gate SiO<sub>2</sub>, floating gate, PZT and control gate electrode in order from the bottom. PZT was deposited at the Zr/Ti (=52/48) ratio by sol-gel method. Polycrystalline silicon (poly-Si) was used as floating gate which was ferroelectric bottom electrode. IrO<sub>2</sub> and Ir and other materials coated on the poly-Si for ferroelectric deposition. We succeeded in deposition of PZT with good ferroelectricity, because IrO<sub>2</sub> and Ir can prevent Pb and other elements from diffusing into poly-Si and gate SiO<sub>2</sub>. Memory effect of this FET was confirmed.

## 1. Introduction

Ferroelectric memory FETs such as a metal-ferroelectric-semiconductor (MFS) structure have been studied.<sup>1-4)</sup> But, conventional MFS structure has many problem such as difficulty of deposition of ferroelectric thin films directly on Si, diffusion of Pb, Ti and other elements into SiO<sub>2</sub>/Si interface and increase of trap density. In order to solve these problem, we proposed a metal-ferroelectric-metal-insulator-semiconductor (MFMIS) structure having a floating gate as a bottom electrode between a ferroelectric thin film and the gate SiO<sub>2</sub>. Conventional gate SiO<sub>2</sub> can be used and ferroelectric thin films can be grown on bottom electrodes which have a good matching with the ferroelectric materials due to adopt the MFMIS structure.

## 2. Experimental

Pb(Zr<sub>0.52</sub>Ti<sub>0.48</sub>)O<sub>3</sub>(PZT(52/48)) thin films were used as ferroelectric materials. PZT films were grown by conventional sol-gel method. The process flow chart of sol-gel method for PZT growth is shown in Fig. 1. Ir, IrO<sub>2</sub> and Pt were used as control

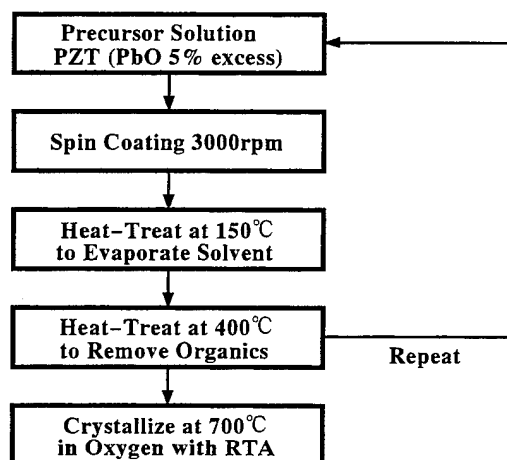


Fig. 1. Process flow chart of sol-gel method for PZT growth.

and floating gate (top and bottom electrodes). The electrode materials were deposited by RF magnetron sputtering without substrate heating and annealed at 400°C after deposition.

Thickness of the thin films was measured by scanning electron microscopy (SEM) images of the cross section. The depth profiles of PZT capacitors were analyzed by secondary ion mass spectrometry (SIMS). The electric properties were measured by semiconductor parameter analyzer (HP4145B).

## 3. Results and Discussion

### 3.1. MFMIS FET

MFMIS FET has a floating gate between a control gate (top electrode) and a gate SiO<sub>2</sub>. The operation of MFMIS FET is shown in Fig. 2. Bias of a top electrode controlled of charge in floating gate. This charge is occurred by ferroelectric polarization. A surface inversion layer is formed by this charge in floating gate. Threshold voltage ( $V_{TH}$ ) is shifted according to direction of ferroelectric polarization.

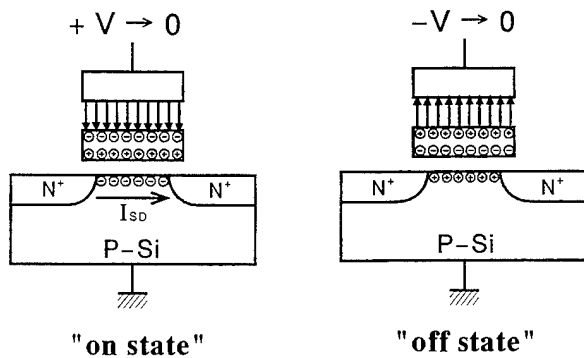


Fig. 2. The operation of MFMIS FET.

### 3.2. MFMIS FET with Pt Floating Gate

As the basic research for this study, we fabricated simple MFMIS FET with Pt as control gate and floating gate. The FET which was composed of Pt(200 nm) / PZT(240 nm) / Pt(200 nm) / SiO<sub>2</sub>(25 nm) / Si-sub showed memory effect. However, the FET did not exhibit enough stable properties.

The cause of such unstableness was diffusion of ferroelectric component elements into gate SiO<sub>2</sub> through the Pt bottom electrode. Due to the diffusion, gate SiO<sub>2</sub> and Pt/SiO<sub>2</sub>/Si interfaces were inferior in quality.

### 3.3. PZT films on Ir/IrO<sub>2</sub>

We tried to fabricate MFMIS FET with poly-Si floating gate in order to obtain high-quality gate SiO<sub>2</sub>. But, perovskite PZT films were not obtained directly on poly-Si and on Pt/poly-Si layered films due to diffusion and silicide formation. So, IrO<sub>2</sub> films were used as barrier layers to block the diffusion and silicide formation.

Figure 3 shows SIMS depth profiles Pt/PZT/Pt/SiO<sub>2</sub>/Si and Pt/IrO<sub>2</sub>/PZT/Ir/IrO<sub>2</sub>/poly-Si/SiO<sub>2</sub>/Si structures. In the case of the Pt/PZT/Pt/SiO<sub>2</sub>/Si structure, Pb, Zr and Ti were diffused into gate SiO<sub>2</sub> through Pt. On the other hand, when an Ir/IrO<sub>2</sub>/poly-Si layered structure was used as floating gate, ferroelectric component elements were never diffused into gate SiO<sub>2</sub> and floating gate. As the result, high-quality gate SiO<sub>2</sub> and good poly-Si/SiO<sub>2</sub>/Si interfaces could be obtained. In addition, PZT films have much improved in fatigue properties, when Ir/IrO<sub>2</sub> layered films were used as bottom electrodes.<sup>5)</sup>

### 3.4. Electrical Properties

The model of typical MFMIS FET in this study is shown in Fig. 4. The MFMIS FET consists of a conventional MOS FET and a PZT capacitor. There were 1.0–80 μm P-ch and N-ch FET in the test chip. The coupling ratio of PZT to SiO<sub>2</sub> was controlled thickness and area of PZT capacitors.

Figure 5 shows a I<sub>D</sub>-V<sub>G</sub> characteristic of 1.2 μm P-ch MFMIS FET. The shift in V<sub>TH</sub> or the memory window for a bias sweep of ±15V was about 3.3V. The value of this memory window depended on thickness, area and growth condition of PZT thin film capacitors.

Figure 6 shows I<sub>D</sub>-V<sub>D</sub> characteristics of this MFMIS FET with +15V and -15V applied to the control gate with respect to substrate. The difference of I<sub>D</sub>-V<sub>D</sub> curves were found between after +15V applied and -15V applied. There was correspondence between the difference and shift in V<sub>TH</sub> of the I<sub>D</sub>-V<sub>G</sub> characteristic in Fig 5. In order to confirm influences to gate SiO<sub>2</sub> or poly-Si/SiO<sub>2</sub>/Si interfaces, FET characteristics before and after PZT process. The characteristics after PZT process were measured after PZT thin films were etched out. As the result, there was little difference in MOS FET characteristics between before and after PZT process.

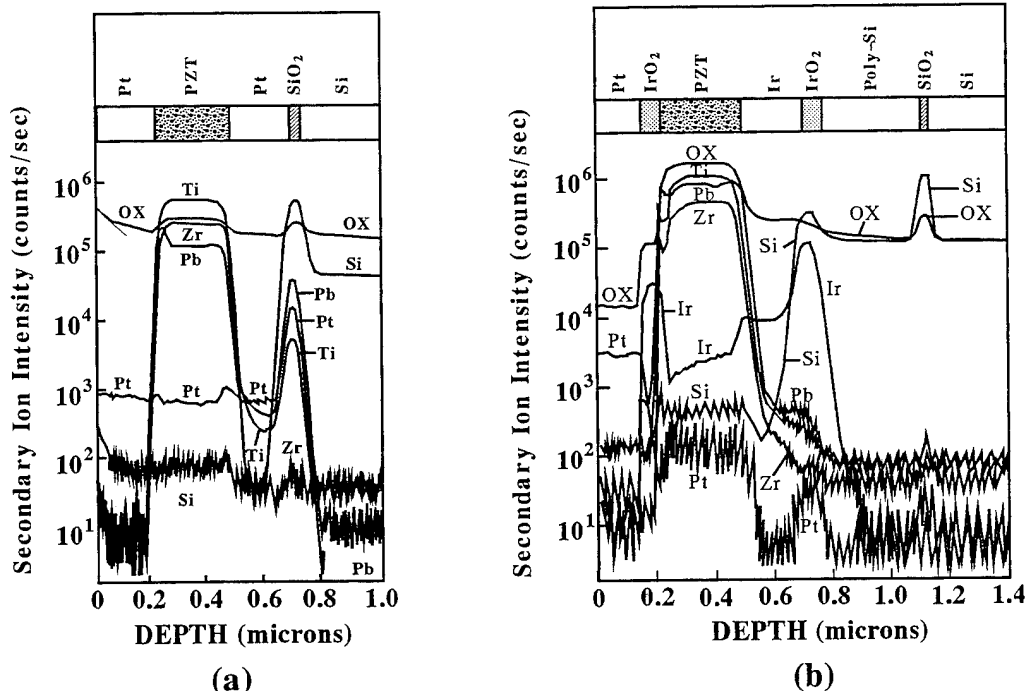


Fig. 3. SIMS depth profiles of (a) Pt/PZT/Pt/SiO<sub>2</sub>/Si and (b) Pt/IrO<sub>2</sub>/PZT/Ir/IrO<sub>2</sub>/poly-Si/SiO<sub>2</sub>/Si structures.

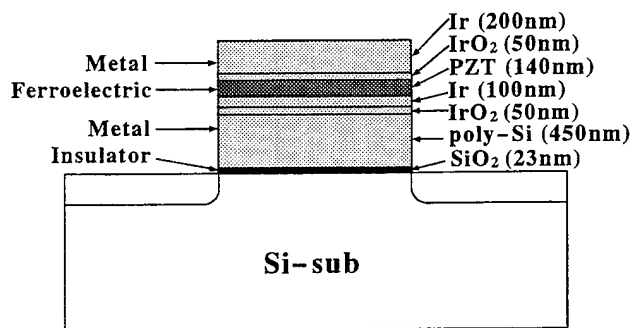


Fig. 4. The model of typical MFMIS FET in this study.

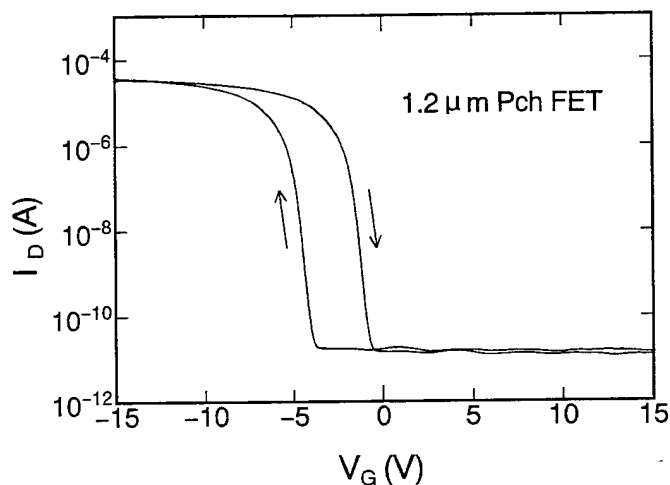


Fig. 5.  $I_D$ - $V_G$  characteristics of 1.2  $\mu$ m P-ch MFMIS FET.

#### 4. Conclusions

We prepared MFMIS FETs as non-volatile ferroelectric memory devices. MFMIS FET has a floating gate between a ferroelectric thin film and a gate insulator. Memory effects were obtained on simple MFMIS FET with Pt floating gate. But, this FET characteristics were not stable. So, Ir/IrO<sub>2</sub>/poly-Si layered structures were used as new floating gate materials. As the result, very stable FET characteristics were obtained due to high-quality gate SiO<sub>2</sub> and good poly-Si/SiO<sub>2</sub>/Si interfaces. The memory windows by  $I_D$ - $V_G$  measurement were about 3.3V for a bias sweep of  $\pm 15$ V.

#### Acknowledgement

The authors would like to thank Mr. Katsumi Ogi and the other staff of Mitsubishi Materials Corporation for the supply of ferroelectric source materials. They would like also to thank Professor Tadashi Shiosaki and Dr. Masaru Shimizu (Kyoto University) for valuable discussions.

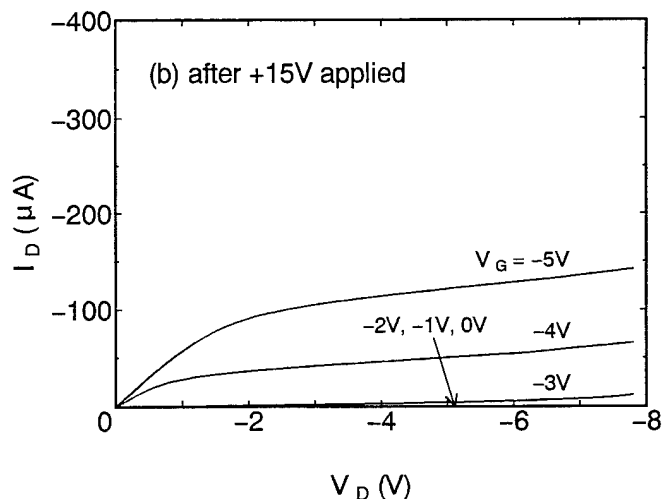
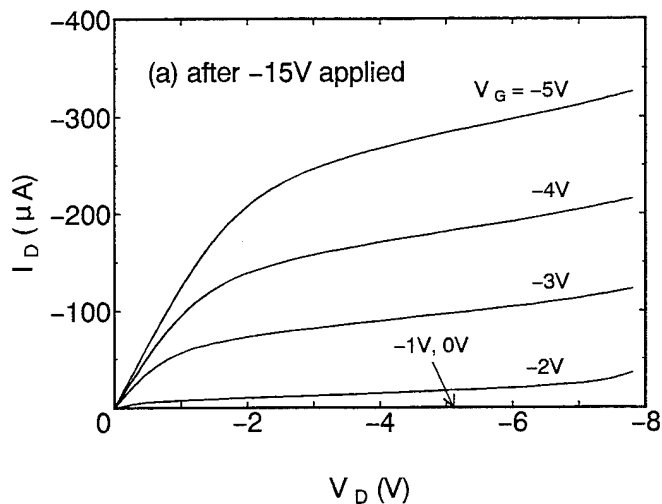


Fig. 6.  $I_D$ - $V_D$  characteristics of 1.2  $\mu$ m P-ch MFMIS FET.

#### References

- 1) S. Y. Wu, "Memory Retention and Switching Behavior of Metal-Ferroelectric-Semiconductor Transistor," *Ferroelectrics*, vol.11, pp.379-383, 1976
- 2) Y. Matsui, Y. Higuma, M. Okuyama, T. Nakagawa and Y. Hamakawa, "PLZT Thin Film Gate Nonvolatile Memory FET," *Proc. 1st Meet. Ferroelectric Materials and Their Applications*, vol.1977, pp.37-42, 1977
- 3) C. H.-J. Huang, H. Lin and T. A. Rabson, "LiNbO<sub>3</sub> Thin Film Capacitor and Transistor Processed by a Novel Method of Photo Induced Metallo-Organic," *Proc. Int. Symp. Appl. Ferroelectrics*, pp.332-335, 1992
- 4) D. R. Lampe, D. A. Adams, S. Siuharoy and H. Buhay, "NDRO FERRAM : Design and Integration," *Proc. 4th Int. Symp. Integrated Ferroelectrics 1992*, pp.99-108.
- 5) Y. Nakao, T. Nakamura, A. Kamisawa and H. Takasu, "Study on Ferroelectric Thin Films for Application to NDRO Non-volatile Memories," *Proc. 6th Int. Symp. Integrated Ferroelectrics 1994* in press

# Ferroelectric Thin film Bismuth Titanate Prepared from Acetate Precursor

Yanxia Lu, David T. Hoelzer, and Walter A. Schulze  
Alfred University, Alfred, NY 14802

Bruce Tuttle, and B. G. Potter  
Sandia National Lab, Albuquerque, NM 87185

## ABSTRACT

Bismuth Titanate ( $\text{Bi}_4\text{Ti}_3\text{O}_{12}$ ) thin films were fabricated by spin coat deposition - rapid thermal processing (RTP) technique. Acetate derived solution for deposition was synthesized by blending dissolved bismuth acetate in aqueous acetic acid, and then adding with titanium acetate. A series of electrically insulating, semiconducting and conducting substrates were evaluated for  $\text{Bi}_4\text{Ti}_3\text{O}_{12}$  films deposition. While X-ray diffraction and TEM analyses indicated that the initial perovskite crystallization temperature was  $500^\circ\text{C}$  or less for these  $\text{Bi}_4\text{Ti}_3\text{O}_{12}$  films, a  $700^\circ\text{C}$  crystallization treatment was used to obtain single phase perovskite films.  $\text{Bi}_4\text{Ti}_3\text{O}_{12}$  film crystallographic orientation was shown to depend on three factors: substrate, the number of coating layers and thermal processing. While preferred c-direction orientation was observed for films deposited on silver foil substrates, preferred a-direction orientation was obtained for films deposited on both Si and Pt coated Si wafers. The films were dense, smooth, crack-free and had grain sizes ranging from 20 nm to 400 nm. Film thickness and refractive index were determined using a combination of ellipsometry, waveguide refractometry and TEM measurements. Both low field dielectric and ferroelectric properties were measured for an 800 nm thick film deposited on a Pt coated MgO substrate. A remanent polarization of  $38 \mu\text{C}/\text{cm}^2$  and a coercive field of  $98 \text{ kV}/\text{cm}$  was measured for this film that was crystallized at  $700^\circ\text{C}$ .

## I. INTRODUCTION

Bismuth titanate ( $\text{Bi}_4\text{Ti}_3\text{O}_{12}$ , abbreviated BIT) is an important ferroelectric (FE) material. Single crystal BIT is a layer-structure compound and has a very high Curie temperature ( $675^\circ\text{C}$ ). Above the Curie temperature, it possesses a pseudo-tetragonal structure proposed by Aurivillius<sup>1</sup>. As temperature decreases below  $T_c$ , spontaneous polarization in the b-direction results in increasing the lattice distortion<sup>2</sup> of (a/b), the structure becomes monoclinic at room temperature as reported by Cummins and Cross<sup>3</sup>. However, x-ray and neutron diffraction data are consistent with a polar orthorhombic structure<sup>4</sup> with  $a=5.411\text{\AA}$ ,  $b=5.448\text{\AA}$ ,  $c=32.83\text{\AA}$ . We will use the orthorhombic symmetry and notation for the rest of this paper. The interest in BIT for practical applications has focused on its ferroelectricity and its electro-optical switching behavior. Single crystal BIT has two spontaneous polarizations with magnitude of  $50\pm5 \mu\text{C}/\text{cm}^2$  in the b-direction and  $4.0\pm0.1 \mu\text{C}/\text{cm}^2$  in the c-direction, they can be reversed independently. Switching of  $P_s$  in the c-direction changes the birefringence and tilt the optical indicatrix of BIT in the b-c plane by approximately  $10^\circ$  which is attractive for electro-optic devices. In addition, the large spontaneous polarization in the b-direction makes BIT potentially useful for applications requiring large values of switching charge.

Polycrystalline BIT has been readily fabricated by various processes. Preferentially oriented bulk BIT ceramics and thin films have received a great deal of attention for the development for both high temperature piezoelectric and integrated semiconductive devices. In the past few years, a lot of effort has been devoted towards for making highly grain-oriented bismuth titanate bulk ceramics<sup>5,6</sup>. There are a few reports on BIT thin film fabrication; for example, by pulsed laser deposition<sup>7,8</sup>, solution chemistry<sup>9</sup>, and rf and reactive diode sputtering<sup>10</sup>.

However, there has been no report of highly oriented thin films produced by wet chemical techniques. The purpose of this study is to investigate the evolution of perovskite BIT thin film from acetate precursors. Further, substrate technologies and associated film processing techniques which lead to preferential grain orientation in BIT thin films are discussed. The ferroelectric properties of BIT film is also presented

## II. EXPERIMENTAL PROCEDURE

Bismuth titanate thin films were deposited using spin coating and then crystallized using rapid thermal processing (RTP) on a variety of substrates: single crystal silicon, silver foil, glass, alumina, and Pt coated single MgO substrates.

The acetate-derived precursor solutions were prepared by dissolving bismuth acetate [ $\text{Bi}(\text{COCCH}_3)_3$ , solid form] in aqueous glacial acetic acid containing 20 vol% of water at room temperature. A colorless solution was obtained, and titanium acetate [75% Titanium bis(acetylacetonate) diisopropoxide in isopropanol  $\text{Ti}(\text{CH}_3\text{COCHCOCH}_3)_2\cdot(\text{OC}_3\text{H}_7)_2$ , liquid form] was then added to the solution. The ratio of bismuth to titanium used in these solutions was slightly higher than the stoichiometric value of 4:3 in order to promote perovskite phase formation. A ratio of BiAca to TiAca of 1.492 was obtained by carefully weighing the initial precursors, which is approximately 12mol% excess Bi compared to the stoichiometric value. The final precursor solution was a clear yellowish solution. A series of solutions were synthesized with concentrations ranging from 0.05M to 0.3M to determine the effort of solution concentration on film quality. The solutions were stable over a period of several months.

Films were fabricated by depositing multiple spin coat layers and then crystallized by rapidly thermal processing. Before coating, the substrates were cleaned by alcohol or acetone and some of them were annealed at  $400^\circ\text{C}$  for 10 minutes. The precursor solution was deposited on a given substrate using a filtered syringe, and then spun the substrate for 30 seconds at 3000 rpm. The film dried quickly at room temperature and was then crystallized at a fixed temperature in the range of  $400^\circ\text{C}$  to  $800^\circ\text{C}$  for 2 minutes. After the layer cooled, it was cleaned using an EFFA duster and the next layer was then deposited. The film was crystallized for 15 minutes after the last layer was deposited. Films ranging in thickness from 100 nm to 1000 nm were fabricated by this multilayer deposition process. Among the techniques used to characterize the BIT thin films were x-ray diffraction, differential thermal analysis (DTA), thermalgravimetric analysis (TGA), atomic force microscopy (AFM), scanning electron microscopy (SEM), transmission electron microscopy (TEM), and ellipsometry.

Resistivity, low field dielectric constant, remanent polarization and coercive field were among the properties measured for the BIT film deposited on a Pt coated MgO substrate. The 100 nm thick Pt layer was rf magnetron sputter deposited at ambient. While an HP 4192 impedance analyzer was used for the low field dielectric measurements, a Radiant Technologies TR66A ferroelectric tester was used to obtain ferroelectric hysteresis loops. Typically, low voltages (0.1 Vrms) were used to minimize ferroelectric domain contributions to the low field dielectric constants measured. Resistivity measurements (dc) were made by applying 20 volts and measuring the current two seconds after the voltage was applied. The details of the electrical fatigue measurements on this BIT film will be presented in the discussion section of this paper.

### III. RESULTS AND DISCUSSION

#### 1. The BIT Phase Formation

X-ray diffraction was used to monitor  $\text{Bi}_4\text{Ti}_3\text{O}_{12}$  phase evolution as a function of crystallization temperature, as shown in Figure 1. All BIT films in Figure 1 were deposited on

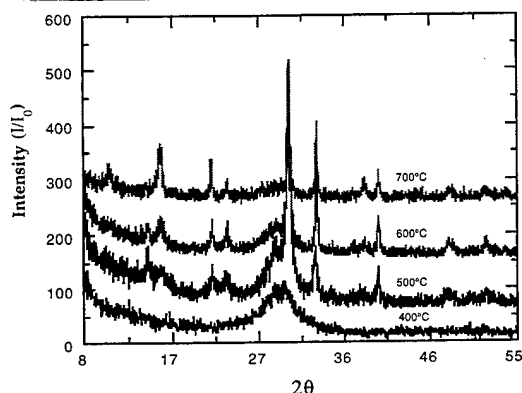


Figure 1. The BIT phase evolution versus temperature. Each film was made by four-layer coatings from 0.09 acetate precursor.

silicon(100) single crystal wafers. A native oxide ( $\text{SiO}_2$ ) layer approximately 5 nm thick is estimated to be on the Si wafer surfaces. The results indicate that the structure of the film which was crystallized at 400°C was essentially amorphous by X-ray diffraction analysis and pattern contained a broad maxima around the highest intensity peak (117) of BIT. As temperature increases, the amorphous phase partially transforms into a highly crystalline perovskite phase, as evidenced by the sharp, high intensity diffraction peaks for the film crystallized at 500°C. The intensity of the major diffraction peaks of the BIT thin films further increase with increasing crystallization temperature, while the broad maxima decreased and eventually disappeared for the 700°C crystallization temperature. Since the perovskite diffraction peaks are so sharp, we attribute the broad maxima to a nanocrystalline pyrochlore phase. The sharp diffraction peaks for the film crystallized at 700°C indicated that the perovskite crystallinity was well defined at this temperature.

The X-ray diffraction patterns of Figure 1 demonstrate that the acetate-derived solution process results in substantial crystallization at 500°C. The crystallization temperature is less than previous reports of BIT materials fabricated by solid state reaction or molten salt synthesis. From X-ray diffraction and TEM measurements, no second phase was detected between the BIT film and the  $\text{SiO}_2/\text{Si}$  substrate. The  $\text{SiO}_2$  layer was approximately 5 nm thick, which is below the detection limit for our instruments. Obviously, if BIT films can be deposited directly on Si with no oxide formation, this would be a great step forward for integrated ferroelectric applications. Whether these acetate-derived BIT films can be fabricated directly on Si with absolutely no interface oxide formation has yet to be determined. Our results indicated that little or no reaction occurred between BIT films and the following substrate:  $\text{MgO}$ , sapphire or Pt-coated  $\text{MgO}$ .

#### 2. Crystallographic Orientation of BIT Thin Films

The crystallographic orientation of BIT thin films fabricated in this study was characterized by X-ray diffraction and TEM analysis. A highly c-oriented BIT film was obtained after deposition on a Ag foil substrate as shown by the X-ray diffraction pattern in Figure 2. No evidence of crystallite orientations other than (001) was observed. BIT films with multiple crystallite orientations are obtained after one layer deposition on single crystal silicon substrates, as shown in Figure 3. Once again, the  $\text{SiO}_2$  thickness is estimated to be approximately 5 nm. Similar crystallite orientation was found for the films deposited on either Si(100) or Si(111) substrates, as expected, if a thin native oxide layer is present on these substrates.

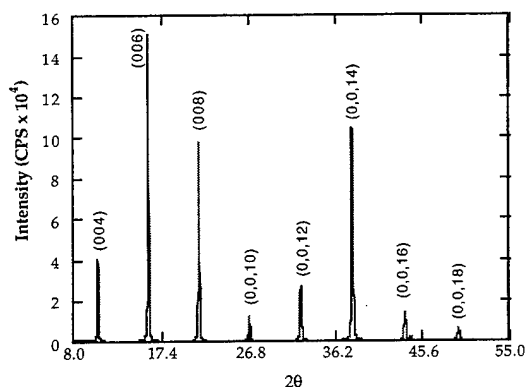


Figure 2. XRD of BIT thin film deposited on silver foil. The film is 5 layers coating and fired at 700°C.

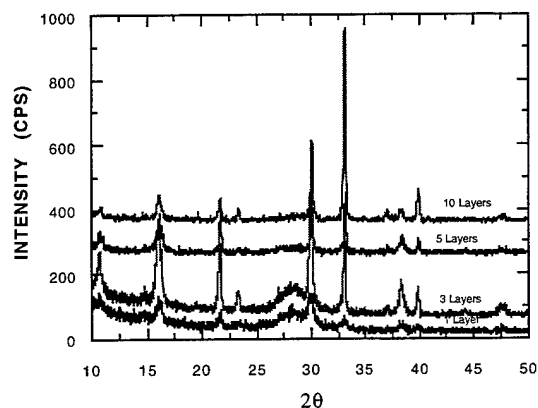


Figure 3. Grain orientation versus the number of coating layer. The films were deposited at 750°C for 2 minutes from 0.0 9M precursor.

The degree of crystallographic orientation in a thin film is not always determined solely by the substrate lattice parameter. The surface nanotopography and cleanliness of the substrate are other factors that may affect BIT film structure. Silicon wafers have an almost atomistically smooth surface, whereas, the silver foil substrates have a rolled surface. The surface characterizations of BIT thin films deposited on these substrates were given in Figure 4 and Figure 5 respectively. The grain growth in the direction normal to the silicon wafer was shown in Figure 4, and the film on silver substrate is far different morphologically than the BIT film deposited on Si. The grains

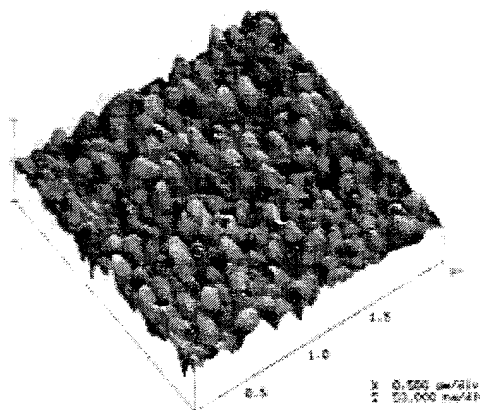


Figure 4. The AFM micrograph of BIT thin film deposited on Si<100> substrate.

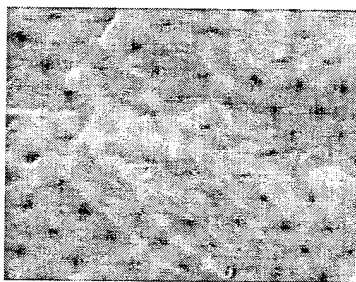


Figure 5. The SEM micrograph of BIT thin film deposited on silver foil.

are platelike, with the a-b plane of the BIT film being oriented parallel to the silver foil surface resulting in a high degree of c-orientation perpendicular to this surface. These results suggest that the nanotopography of the underlying substrate strongly effects the crystalline morphology and orientation of BIT films. Our postulation is similar to that reported by Shu-Yau Wu and coworkers<sup>11</sup>.

We have also determined the variation of grain orientation with the number of coating layer as determined by XRD (as shown in Figure 3) and TEM analysis. There is no significant preferential orientation for the films deposited on silicon for the first layer. As the number of coating layer increases, up to 5 layers, the diffraction intensities in the (001), (200) and (111) directions increased. With further increase in the number of deposition layers, the orientation in (200) direction increased, while the volume fraction of crystallites with (001) type orientation decreased. The variation in crystallite orientation with the number of deposition layers is shown in Figure 6, for which, plots of Lotgering orientation factors in

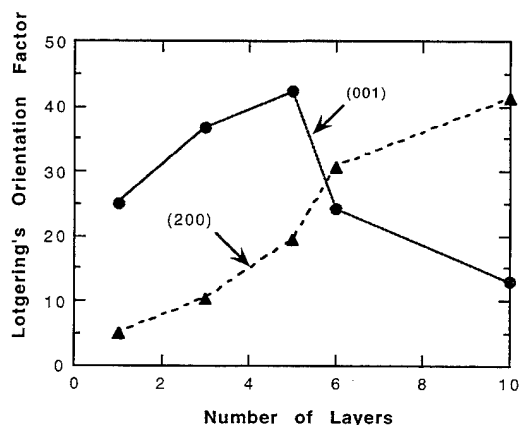


Figure 6. The Lotgering's orientation factors in (001) and (200) directions versus the number of coating layers for BIT film deposited on silicon wafer substrate.

(001) and (200) directions as a function of number of coating layers are presented. The maximum c-direction orientation occurs for the 5 layer film. When the number of coating layers were greater than 10, the (200) orientation was dominant. The Lotgering orientation factor for the (200) direction was 42.0%, which indicates that almost half the BIT grains in this film had this orientation.

The preferential orientation in (200) direction (corresponding to the b-axis in the monoclinic) of BIT thin film is very attractive because the largest value of spontaneous polarization lies in the monoclinic a-c plane and in the a-direction,  $P_{sa}=50 \mu\text{C}/\text{cm}^2$ . For the oriented polycrystal, if a-c or b-c (the a and the b can be switched under electrical field) plane is parallel to the substrate, the a and b directions can be reversed by an applied electrical field<sup>12</sup>, and a large change in dynamic polarization will be measured. As the degree of (200) orientation increases, a higher remanent polarization should be achieved in BIT films. This phenomena may be attractive for next generation, high density memories or optical display

applications. The basic principle of operation for the metal ferroelectric semiconductor (MFST) device is to control the surface conductance of a bulk semiconductor (silicon) and to perform the memory function<sup>13</sup>. Therefore, a high remanent polarization is desired to obtain a sufficient modulation.

### 3. Characterization of BIT Thin Films

#### 3.1 Morphology

The BIT thin films fabricated in this study were for the most part transparent. A systematic change in interference color was observed for BIT films deposited on Si wafers as a function of thickness. The films appeared shiny when deposited to various substrates, such as: silicon, glass, MgO, Ag, and sapphire. Large uniform areas and crack-free thin films were observed using optical microscopy, SEM and AFM. The films were very dense with no apparent porosity by these techniques. The average particle size increased for 20 nm to 400 nm as the coating layer increased from 1 to 10, for BIT film deposited using 0.09 M solutions. Figure 7 shows the AFM images which clearly illustrate particle size variation. The surface roughness

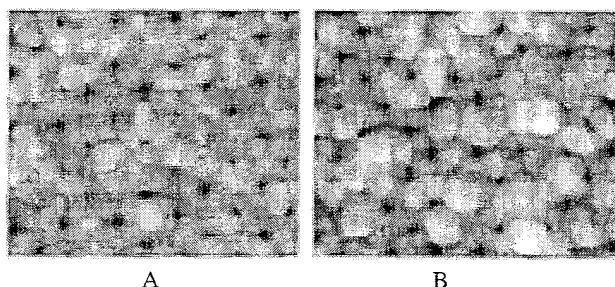


Figure 7. The AFM micrographs show the particle size versus the number of coating layer. (A) Three layer, (B) Five layers.

increased as the number of coating layers increased. This was attributed to the increase in grain size of the BIT films with increasing layer thickness. Microscopic analysis indicates that high quality films were produced by the acetate process.

It must be emphasized that the surface condition of substrate affects the nanomorphology of the film. Since the Si wafer is extremely smooth, the particle size of the BIT film was very small (less than 100 nm) and the surface of the film was also very smooth. However, the BIT film deposited on the Ag foil exhibited a distinctly different surface morphology. The particle size was extremely large compared to the size of the BIT grains for the films deposited on Si substrate. Pores were also observed in films with a reduced number of coating layers. These observations suggest that an epitaxial type finish for the underlying substrate is most appropriate for production of high quality ferroelectric thin films.

#### 3.2 Thickness

The thickness of the various BIT thin films was indicated by the interference colors, as previously noted. Film thickness were measured by both a Manual Ellipsometry and by TEM analysis. Figure 8 shows the film thickness as a function of both

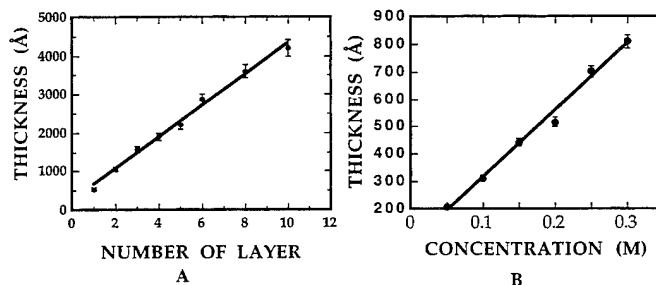


Figure 8. The thickness variation versus the number of coating layers (8A) and concentration of precursors (8B).

the number of deposition layers and the concentration of solution. Linear relationships were observed in both cases, within the accuracies indicated on the plots. These thickness measurements were further confirmed by TEM analysis for a select group of these films. While a thickness of approximately 270 nm was measured from TEM analysis for a 10 layer film deposited from 0.1M solution on Si substrate and crystallized at 700°C, a thickness of 255 nm obtained by ellipsometer measurements. The accuracy of the ellipsometer measurements is approximately  $\pm 40$  nm. The variation of thickness as function of crystallization temperature did not significantly change. Thus, ultimate BIT film thickness can be controlled by either the number of coating layers or the concentration of the precursor solution.

#### 4. Property Evaluation of BIT Thin Films

#### 4.1 Refractive Index

The refractive indices of the films were measured using both a Gaertner model L1117 manual ellipsometer and a waveguide refractometry technique<sup>14</sup> technique. The average refractive index for the BIT films was determined to be  $2.60 \pm 0.05$  using ellipsometry. Iterative fits to the raw data obtained using waveguide refractometry failed to completely describe the angular positions of reflectivity minima corresponding to waveguide modes within the BIT film/MgO system. Approximate limits on the probable refractive index, however, do suggest an average refractive index in the 2.6 range for this sample. It is important to note that the inability to obtain a fit to the raw data indicates that the film may not possess macroscopically uniform optical properties defined by a single refractive index. Although a change in refractive index with film thickness may be used to describe the observed behavior, a unique fit to the raw data can not be obtained in this case due to the corresponding increase in adjustable parameters describing the unknown films. Within the assumptions used to model the thin film/substrate system, both techniques give results which are in fair agreement with the single crystal value of refractive index that are on the order of 2.68.

## 4.2 Dielectric Properties

A reasonably saturated, dielectric hysteresis loop was obtained for a 760 nm thick BIT film deposited on a Pt coated MgO substrate, as shown in Figure 9. While a 20 volt peak signal was used to electrically switch the ferroelectric film, 11.5 ms was required to obtain the hysteresis loop. The bottom electrode was fabricated by RF magnetron sputtering a 100 nm thick Pt film on a MgO substrate (Atomergic corporation) with an epitaxial finish. The top Pt electrodes were also deposited by RF magnetron sputter deposition and had an area of  $1.55 \times 10^{-3} \text{ cm}^2$ . A remanent polarization of  $38 \text{ } \mu\text{C}/\text{cm}^2$  and relative lower coercive field of  $98 \text{ kV}/\text{cm}$  were measured. These properties compare favorably to the previous works<sup>15,16</sup>. Measured dc resistivities were essentially polarity independent and were on the order of  $4 \times 10^8 \text{ ohm-cm}$ . The percentage of electrode dots tested that gave good electrical properties was not large, as only 15% of the dots tested were not electrical shorts. For the highly c-oriented BIT film deposited on silver foil a low voltage (0.1 Vrms), 10 kHz dielectric constant of 108 was obtained. This value is approximately that measured for BIT single crystals in the c-direction. A higher dielectric constant of approximately 550 and a dissipation factor of 0.037 was measured for the BIT film of Figure 9 that contained multiple crystallite orientations.

### 4.3 Fatigue measurements

The electrical fatigue performance of the BIT film deposited on a Pt/MgO substrate was considerably better than that obtained for a PZT 40/60 film with Pt electrodes. For both films, a 250 kv/cm, sinusoidal field was used to fatigue the specimens. After  $1.2 \times 10^8$  cycles, the polarization of the PZT 40/60 film decreased from 24.5 to 10  $\mu\text{C}/\text{cm}^2$ ; The difference in remanent polarization compared to the BIT film electrode dot tested in Figure 9 indicates that there is presently some variability in our processing.

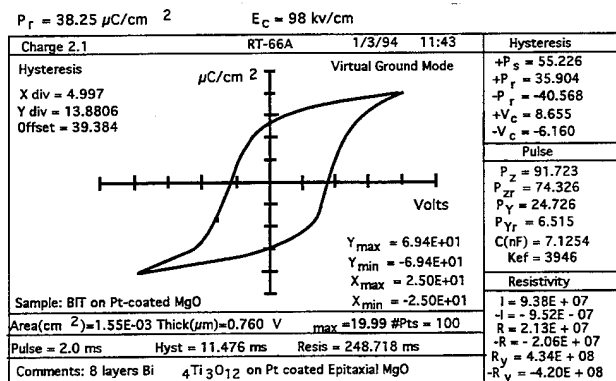


Figure 9. The hysteresis loop of BIT thin film deposited on Pt-coated MgO single crystal

#### IV CONCLUSIONS

Single phase  $\text{Bi}_4\text{Ti}_3\text{O}_{12}$  thin films were fabricated from acetate-derived solutions. Substantial perovskite crystallization occurred for temperature as low as  $500^\circ\text{C}$ . From precursors that were clear and relatively stable with time, BIT films that were dense, homogeneous and crack-free were fabricated. The crystallographic orientation of BIT thin film were shown to depend on the type of substrates used and the condition of the surface of the substrates. Preferential (200) oriented films were obtained by multiple layer deposition on single crystal silicon wafers. BIT films that were highly (002) oriented were fabricated on silver foil substrates. The refractive index measured for the BIT thin film in this study is approximately  $2.6 \pm 0.1$ , which is close to the value of single phase polycrystal BIT. The thickness of the films varied linearly both with the concentration of the precursor solution and the number of coating layers. A remanent polarization of  $38 \mu\text{C}/\text{cm}^2$  and coercive field of  $98 \text{ kv}/\text{cm}$  was measured for a BIT film deposited on Pt/MgO substrate and crystallized at  $700^\circ\text{C}$ .

## References

- 1 B. Aurivillius, *Arkiv. Kemi*, **1**, [54], 463(1949); **1**, [58], 499(1949)
- 2 S. E. Cummins and L. E. Cross, "Electrical and Optical Properties of  
Ferroelectric  $\text{Bi}_4\text{Ti}_3\text{O}_{12}$  Single Crystals," *J. Appl. Phys.*, **39**[5], 2268(1968)
- 3 E. C. Subbarao, "Ferroelectricity in  $\text{Bi}_4\text{Ti}_3\text{O}_{12}$  and its Solid Solution,"  
*Phys. Rev.*, **122**[3], 804-807(1961)
- 4 J. F. Dorrian, R. E. Newnham and D. K. Smith, "Crystal Structure of  
 $\text{Bi}_4\text{Ti}_3\text{O}_{12}$ ," *Ferroelectrics*, **3**, 17-27(1971)
- 5 Tadashi Takenaka and Koichiro Sakata, "Grain Orientation and  
Electrical Properties of Hot-Gorged  $\text{Bi}_4\text{Ti}_3\text{O}_{12}$  Ceramics," *J. J. of App.*  
*Phys.*, **19**, No. 1, 31-39(1980).
- 6 V. K. Seth, MS Thesis, "Fabrication and Electrical Properties of Grain-  
oriented Bismuth Titanate Ceramics," Alfred University, 1986.
- 7 H. Buhay, et. al. "Pulsed Laser Deposition (PLD) of Oriented Bismuth  
Titanate Films for Integrated Electronic Applications," PP. 62-71, *Proc.*  
*Inter. Symp. on Integr. Ferro*, 3<sup>rd</sup>, 1991.
- 8 R. Ramesh, et. al., "Epitaxial Growth of Ferroelectric Bismuth Titanate Thin  
Films by Pulsed Laser Deposition," *Appl. Phys. Lett.*, **57**[15], 1505(1990)
- 9 H. Wang, et.al. "Ferroelectric Thin Films of Bismuth Titanate Prepared by  
MOCVD," *Ferroelectrics thin films II*, **243**, 213-216(1992)
- 10 W. J. Takei, N. P. Formigoni, et.al, "Preparation and Epitaxy of Sputtered  
Films of Ferroelectric  $\text{Bi}_4\text{Ti}_3\text{O}_{12}$ ," *J. Vac. Sci. Technol.*, **7**[3], 442(1970)
- 11 Shu-Yau Wu, "Polarization Reversal and Film Structure in Ferroelectric  
 $\text{Bi}_4\text{Ti}_3\text{O}_{12}$  Films Deposited on Silicon," *J. Appl. Phys.*, **50**[6], 4314(1979)
- 12 S. E. Cummins and L. E. Cross, "Electrical and Optical Properties of  
Ferroelectric  $\text{Bi}_4\text{Ti}_3\text{O}_{12}$  Single Crystals," *J. App. Phys.*, **39**[5], 2268(1968).
- 13 Shu-Yau Yu, "A New Ferroelectric Memory Device, Metal-Ferroelectric-  
Semiconductor Transistor," *IEEE Trans. on Elec. Dev.*, **ED-21**[8], 499(1974)
- 14 B. G. Potter, Jr., M. B. Sinclair, et.al, *Appl. Phys. Lett.* **63**(16) 2180(1993)
- 15 Shu-Yau Wu, "Polarization Reversal and Film Structure in Ferroelectric  
 $\text{Bi}_4\text{Ti}_3\text{O}_{12}$  Films Deposited on Silicon," *J. Appl. Phys.*, **50**[6], 4314(1979)
- 16 K. Sugibuchi, Y. Kurogi and N. Endo, "Ferroelectric Field-effect Memory  
Device Using  $\text{Bi}_4\text{Ti}_3\text{O}_{12}$  Film," *J. Appl. Phys.*, **46**[7], 2877(1975).





# Concurrent Session - 4A: Actuators and Electrostriction

# Electrostriction Measurements in Diffuse Phase Transition Materials and Perovskite Glass Ceramics

V. Sundar, K. Wa Gachigi, D. McCauley, K.A. Markowski, and R.E. Newnham  
Intercollege Materials Research Lab., The Pennsylvania State University,  
University Park, PA 16802

**Abstract** - Materials with diffuse phase transitions are of much interest for applications in very smart systems. The main advantage they have over conventional materials is the tunable nature of their nonlinear properties such as electrostriction [1]. Electrostriction is the fundamental mechanism of electromechanical coupling in these and all insulating materials, and is of interest for sensor, actuator, and tunable transducer applications. Electrostriction measurements are also of interest in trying to better understand the nature of the diffuse transition.

In this study, a group of ferroics (Ca/PMN-PT, La/PMN-PT, PLZT, BTS, and BST) with diffuse transitions were tested using the first converse effect. This technique involves measuring the stress dependence of the dielectric stiffness  $\beta_{ij}$  to obtain electrostrictive tensor coefficients. This method has been previously verified by measuring separated  $Q_{ijkl}$  coefficients for low-K dielectrics.  $Q_{33}$  coefficients of the order of  $10^{-3} \text{ m}^4/\text{C}^2$  were obtained for the ferroics. A figure of merit is proposed for evaluating these ferroics in sensor applications, based on their fractional change in capacitance under applied stress. A preliminary correlation of the electrostriction effects with the diffuseness of the phase transition (DPT) is also done.

A family of perovskite glass ceramics with different modifiers that had been subjected to different ceramming temperatures was also investigated and found to have promising sensor applications. The electrostrictive and dielectric properties were found to vary with the heat treatment.

## INTRODUCTION

### Phenomenology of Electrostriction

From the Devonshire formalism of the thermodynamic phenomenology, two equivalent forms of the electrostrictive effect, the 'direct' and the 'converse' effect may be derived. If the strain  $x_{ij}$  in a material is expressed as :

$$\begin{aligned} x_{ij} &= S_{ijkl}^E X_{kl} + M_{mnij} E_m E_n \quad \text{and} \\ x_{ij} &= S_{ijkl}^P X_{kl} + Q_{mnij} P_m P_n. \end{aligned}$$

where  $S_{ijkl}$  is the elastic compliance tensor under appropriate boundary conditions and  $X_{kl}$  the components of elastic stress, the 'direct' effect  $Q$  and  $M$  coefficients are defined as :

$$\begin{aligned} M_{mnij} &= 1/2 (\delta^2 x_{ij} / \delta E_m \delta E_n)_X \quad \text{and} \\ Q_{mnij} &= 1/2 (\delta^2 x_{ij} / \delta P_m \delta P_n)_X \end{aligned}$$

Alternatively, the 'converse' effect  $Q$  and  $M$  coefficients may be expressed in terms of the dielectric permittivity  $\epsilon_{kl}$  as :

$$\begin{aligned} M_{mnij} &= (\epsilon_0/2) (\delta \epsilon_{ij} / dX_{mn})_P \quad \text{and} \\ Q_{mnij} &= [1/2\epsilon_0 (\epsilon - 1)^2] (\delta \epsilon_{ij} / dX_{mn})_P \end{aligned}$$

The magnitude of the  $Q$  coefficients vary from the order of  $10^0$  in low-K dielectrics to  $10^{-3} \text{ m}^4/\text{C}^2$  for relaxor ferroelectrics. The effects are comparatively large in oxide perovskite structures, due to their inherently large spontaneous polarizations and dielectric permittivities. Strains of the order of  $10^{-6}$  are easily attained. In contrast, simple oxides develop strains of the order of  $10^{-11}$ , a very small value [2].

This study was undertaken with the primary purpose of establishing a reliable and accurate electrostriction measurement system that could measure coefficients over a wide range of electrostrictive and dielectric properties. This system, calibrated by checking with direct method measurements, is then used to measure both low-K dielectrics and ferroic materials with much larger electrostriction effects.

## CONVERSE METHOD MEASUREMENTS

### The Basis of Compressometry

The equation for the capacitance  $C$  of a parallel plate insulator, may be separated, and differentiated with respect to stress  $X$  applied to give :

$$\begin{aligned} \frac{\delta \ln K}{\delta X} &= \left[ \frac{(\Delta C/C)}{\Delta x} - \frac{\delta \ln(A/d)}{\delta X} \right] \\ &= [B_i (\text{measured}) - S_i (\text{from literature})] \end{aligned}$$

where  $K$  is the permittivity,  $A$  the area of the sample,  $d$  its thickness,  $S_i$  are linear combinations of elastic compliances, and  $B_i$  pressure dependences of the capacitance for the given cut. For a given cut of a crystal,  $M'$  and  $Q'$ , the coefficients for the cut, for the first converse effect, are given by :

$$\begin{aligned} M' &= (\epsilon_0 K/2) [B_i - S_i] \\ Q' &= [K/2\epsilon_0(K-1)^2] [B_i - S_i] \end{aligned}$$

$M'$  and  $Q'$  are related to crystal  $M$  and  $Q$  coefficients by using the equations for rotated cuts. We may use these equations to solve for  $Q_{11}$ ,  $Q_{12}$ ,  $Q_{44}$  (cubic crystals) by a least squares method, or use  $Q_h$  as additional input for an extra equation. In this work, the least squares method is used.

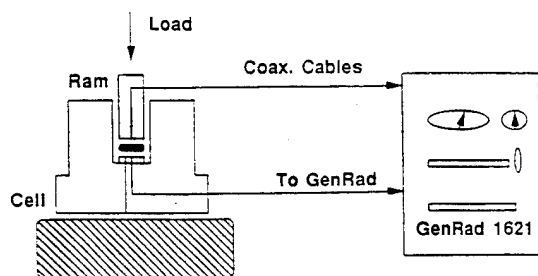
### The Compressometric System

Techniques for measuring the converse effect call for precision evaluation of dielectric properties. Other requirements are stable temperature control and the establishment of 'true' stress systems - completely hydrostatic if the hydrostatic  $Q_h$  coefficients are being measured and truly uniaxial stresses in compressometry. The system developed here is based on that of Sun. et. al. [3].

The compressometer system is designed for the application of a truly uniaxial and homogeneous pressure on the sample surface. Dead weights are used for this, in a direct loading scheme. This feature is related to one of the advantages of this technique. The dielectric susceptibility changes linearly with applied stress, and inhomogeneities in applied stress, averaged out by a comparatively large sample diameter (2 cm approx., as contrasted to beam diameters of fractions of an mm in the interferometer) are further diluted by the linear relationship. In the laser interferometric method, inhomogeneities in the applied field are magnified by the fact that it appears as a squared term in the displacement-field relation [4]. A schematic of the compressometer system is shown in Fig.1.

The thermal mass of the compression jig is large enough to smooth out minor drifts in ambient temperature. The drift in the fractional change in capacitance is less than 7 ppm/min under quiet conditions.

**Fig. 1 : Schematic of the Compressometer**



The electrical stability of the system is also of a high order. The capacitance of the sample holder itself is less than 20 aF. The intrinsic conductance is less than  $1 \times 10^{-7}$  nS. Care is taken to ensure that the only capacitance path is through the sample itself, and all signal leads are coaxial and electrically guarded. The capacitance measurement is done in a three-terminal mode using a General Radio 1621 Capacitance Measurement System capable of measuring down to 0.1 aF.

The capacitance resolution is on the whole better than 1 ppm, and the resolution in change in capacitance is less than 8 aF, even as estimated in a worst case analysis. This system is a powerful technique to establish the signs and magnitudes of the electrostriction constants of even low permittivity, low  $M$  value materials.

## EXPERIMENTAL PROCEDURES

### Materials for Investigation

The samples used were well characterized single crystals for the low-K dielectrics, and ceramic samples characterized by X-ray and DTA measurements for the ferroics and the perovskite glass ceramics.

The fluoride perovskite  $\text{KMnF}_3$  tested was obtained in three orientations,  $\langle 100 \rangle$ ,  $\langle 110 \rangle$  and  $\langle 111 \rangle$  [5,6].

Ferroic materials were chosen keeping in mind the four proposed mechanisms for the source of diffuse phase transitions. PMN-PT (type 1, order-disorder effects), PLZT (type 2, defect clusters),  $\text{BaTi}_x\text{Sn}_{1-x}\text{O}_3$  (type 3, graded chemical composition), and  $\text{BaSr}_x\text{Ti}_{1-x}\text{O}_3$  (type 4, pinched phase transitions) were the families of ferroics tested [7].

The perovskite glass ceramics were a series of Corning glasses, variations on a base composition. These were composed of 86 wt% ferroic phases, 14 wt% zinc aluminosilicate. The ferroic phases consisted of 50% PMN, 50-x%  $\text{BaTiO}_3$ , and x% modifier. The magnesium aluminosilicate analogs of the glasses were also tested.

The samples were obtained in the form of thin discs 2.3mm in diameter, thicknesses varying between 0.78 and 1.1 mm, with plane parallel faces. After being polished to optical finishes, the crystals were electroded with sputtered gold. Since the capacitance changes being measured range from very small to fairly large, guard electrodes were inscribed on the sample faces.

### Dielectric Testing and Characterization.

All samples were characterized dielectrically before compressometry tests were performed on them. The dielectric constants of the samples were measured at room temperature using an HP 4270 LCR meter sensitive to 0.1 pF.

The HP 4270 LCR meter slaved to a microcomputer with a furnace attached was then used to measure the temperature and frequency characteristics of the capacitance for the perovskite glass ceramics. Some typical results are shown in fig. 2. The ferroic materials are comparatively well documented, and the low-K dielectrics show little variation in the range of measurement.

Differential thermal analysis tests were performed on the perovskite glass ceramics to observe the evolution of phases. The prominent peaks were an endothermic around 637°C, indicating softening in the matrix. An exotherm at 769°C corresponds to the crystallization of the PMN-BT ferroic phase. This was verified by X-ray diffraction. The next exotherm at 911°C corresponds to the crystallization of various silicate phases. endotherms at 1082°C and 1165°C are thought to correspond to melting reactions. The DTA plot for 888VH glass ceramic is shown in fig.3.

### Capacitance Measurements Under Stress

As a check of the compressometry system, the samples were then placed in the compressometer stressing cell without any load applied, and their capacitances measured using a GenRad 1621 bridge, which is sensitive to 0.1 aF. The capacitances were found to be in good agreement with the HP system measurements, within the limits of error for the less sensitive HP system.

A possible source of error was felt to be the effect of sample surface roughness or unevenness under stress. Different axial orientations of an uneven sample could produce changes in capacitance at the aF measurement level unrelated to the electrostriction effect. The diametrical deformation of disk shaped samples under stress, in interaction with the friction between the sample and the ram extender faces is another source for concern, as it might destroy the axial symmetry of loading.

To check for surface roughness effects, measurements of capacitance changes with different axial orientations for the same sample at low loads (0 and 1 kg) were made, and found to be consistent to within 2%, which is acceptable in this range.

**Table 1 : Electrostriction results for ferroics**

Composition (with $T_{\text{max}}$ , °C)	K (RT, 1kHz) )	$Q_{33} \times 10^{-3}$ $\text{m}^4/\text{C}^2$	FOM $\times 10^{-10}$ $\text{Pa}^{-1}$
3%Ca/PMN-PT (Type 1, -38)	3943.5	3.33	1.39
5%Ca/PMN-PT (Type 1, -52)	3562.6	5.21	2.26
La/PMN-PT (1/93/7) (Type 1, -7)	12862.6	6.41	13.76
PLZT (11/65/35) (Type 2, 39)	5876.3	7.04	6.80
BTS (x=0.87) (Type 3, 8)	10253.4	9.92	17.51
BST (x=0.35) (Type 4, 25)	25435.3	6.86	33.12

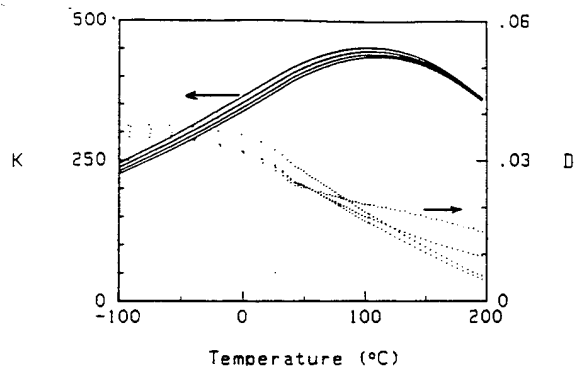


Fig. 2 : Dielectric constant and loss vs. Temperature plotted for the base composition perovskite glass ceramic 888VE.

Diametrical deformation effects were checked by using a thin mylar film placed between the sample and the plexiglass ram extenders to take up any surface unevenness.

To measure the separated electrostriction of cubic samples,  $\text{KMnF}_3$  for example,  $\langle 100 \rangle$ ,  $\langle 110 \rangle$ , and  $\langle 111 \rangle$  oriented crystals of 2.3 cm diameter and 0.8 mm thickness were used. After dielectric characterization, they were placed in the compressometer cell, and small static loads of up to 4kg mass were applied in steps of 0.5 kg on the samples. For the ceramic samples, Q33 is measured directly.

The change in capacitance for each step in load is measured during loading and unloading. Since the GenRad 1621 is an analog capacitance bridge, capacitance measurement is done by iterative balancing of capacitive and loss components of the impedance under test, a time-consuming and involved process. However, the excellent sensitivity, resolution, and robustness of the system compensate for this.

The two changes are now averaged to give a nett change in capacitance. This change  $\Delta C$  is now used along with the measured baseline capacitance before each loading step to calculate  $\Delta C/C$ . A plot of this fractional change in capacitance versus stress now gives us the factor  $B_i$  in the compressometry equations, for each orientation. This was used as input in calculating the separated electrostriction coefficients of the materials.

## RESULTS AND DISCUSSIONS

An analysis of the results for all the samples exhibits a good linearity for the  $\Delta C/C$  vs.  $X$  plots. The sensitivity of the system is illustrated in fig.4, showing the low levels of capacitance measured for the fluoride perovskite  $\text{KMnF}_3$ . The results for the ferroics are shown in fig.5, for comparison. The linearity of the capacitance changes on stressing is an important verification of the method used, since the premise is that the first converse effect is a linear variation. A direct loading scheme at low loading (up to 4kg masses) is thus shown to be acceptable. The results for low-K dielectrics have been confirmed by interferometric measurements [7].

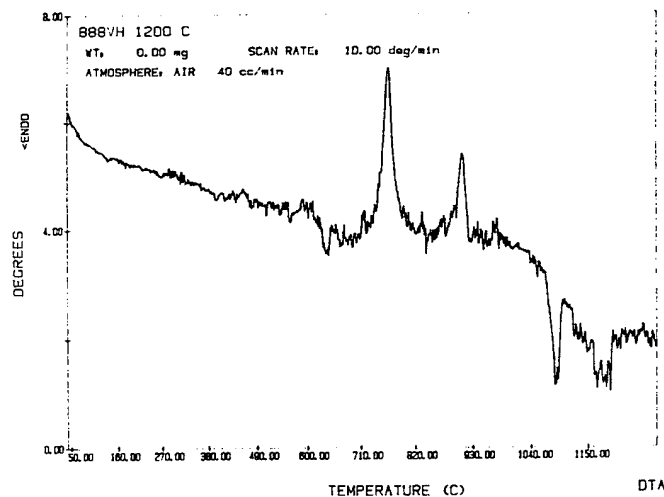


Fig. 3 : DTA results for a typical perovskite glass ceramic.

The results for the ferroics are summarized in table 1. A figure of merit corresponding to the fractional change of capacitance on stressing,  $dC/CX$ , is used to evaluate the materials for potential stress sensor applications. While the type 3 and type 4 materials show highest values, it is felt that the phase transition may not be diffuse enough, considering the fact that these materials dielectrically almost metastable in the room temperature region.

The diffuseness of phase transition DPT, here defined as the difference in temperatures corresponding to the dielectric constant maximum at 1MHz and 1 kHz, ( $DPT = \Delta(T_{max}) = T_{max}(1\text{MHz}) - T_{max}(1\text{kHz})$ ) was evaluated for PMN based relaxors [8]. It is seen that this factor appears to be affected by the degree of B-site cation order, and increases with long range order in the B-site.

The temperature coefficient of electrostriction TCE is defined as  $TCE = d(\ln x)/dT$ . This may be approximated as  $(\Delta x/\Delta T \times)$  over a small range of 25°C. This decreases with increasing cation order in PMN based relaxors. Relaxor materials operating in a range around RT would benefit from a low TCE and a large DPT. An interesting correlation between these two factors is:  $DPT \times TCE \approx 0.22 \pm 0.03$ . This correlation helps in directing the search for better relaxor materials. Fig. 6 shows the DPT vs. TCE relation form PMN solid solutions. Values used in plotting this graph are taken from the literature [8,9].

For the perovskite glass ceramics, the results are summarized in table 2. The electrostriction constants are of the order of  $10^{-2}$  as expected, intermediate between those of the low-K dielectrics and the relaxor ferroelectrics with large electrostriction effects.

Of interest was the fact that a small change in the ceramming temperature for Sr-doped glass from 850-900°C produced a significant difference in the figure of merit defined before. This

Table 2 : Perovskite Glass Ceramics -Electrostriction Results

Glass designation, modifier, Ceramming Temp. in °C	Dielectric Constant, ( RT, 1 kHz)	Q <sub>33</sub> ( m <sup>4</sup> /C <sup>2</sup> )	dC/CX (x10 <sup>-15</sup> Pa <sup>-1</sup> )
888VE,(Base) 900	296.8	0.079	0.96
888YT, Ta,900	369.34	0.055	4.13
888ZG, Cd, 900	287.7	0.042	3.25
888ZF, Sr, 850	273.2	0.083	3.85
888ZF, Sr, 900	438.41	0.064	6.16

led us to investigate the effect of increasing Sr substitution on a series of glasses, from 1% to 5%. However, the maximum electrostrictive effect was seen around 1.25%, and dielectric properties decreased with further substitution. It would thus appear that only small amounts of SrTiO<sub>3</sub> are beneficial.

The large number of phases present in these materials make an exact separation of electrostrictive contributions complex. An effort is under way to track both batch compositions and the volume fraction composition to better correlate the effect with different crystallite sizes nucleated in these samples.

## CONCLUSIONS

The above initial investigations have shown that the technique of compressometry is a reliable and accurate procedure to investigate electrostrictive properties over a wide range of materials and magnitudes. The electrostriction phenomenon assumes further importance when we realize that commercially popular piezoelectric materials are in effect polarization biased electrostrictive systems. A system capable of investigating this effect is of value in both theoretical and application-oriented investigations. Future efforts are towards tracking this phenomenon through the phase transition to improve our understanding of both electrostriction and the nature of the transition.

## ACKNOWLEDGEMENTS

The authors wish to thank Dr. Thomas Shrout of the IMRL for providing the ferroic samples and Dr. Bruce Aitken of Corning, Inc. for providing the perovskite glass ceramic samples.

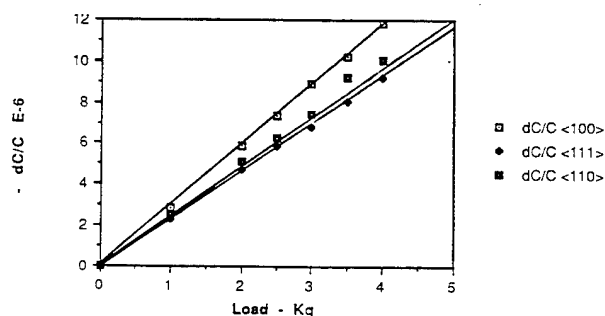


Fig. 4 : dC/C vs. X - Compressometry results for KMnF<sub>3</sub>.

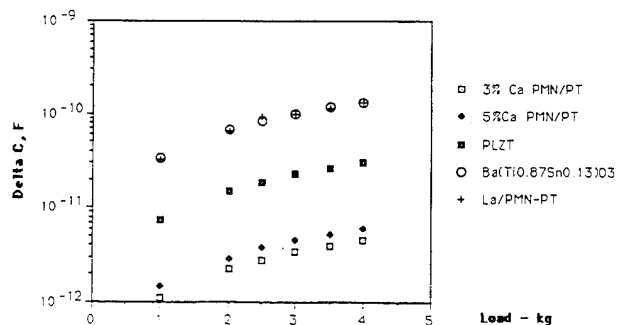


Fig. 5 : Summary of dC vs. X results for ferroics.

## REFERENCES

- [1] R.E. Newnham, "Tunable Transducers : Nonlinear Phenomena In Electroceramics", presented at the Conference on the Chemistry of Electronic ceramic materials, Jackson, WY, Aug. 17-22, 1990.
- [2] V. Sundar and R. E. Newnham, "Electrostriction And Polarization", *Ferroelectrics*, vol. 135, pp431-446, 1992.
- [3] Y.M. Sun, Z.P.Chang, W.Y. Pan, W.W. Cao, L.E. Cross, "Complete Determination Of Electrostriction Tensor Components Of KMnF<sub>3</sub> Single Crystals At Room Temperature", *J. Mat. Sci. Lett.*, vol. 7, pp327-330, 1988.
- [4] Z.Y. Meng, Th. Kwaaitaal, W.M.M. van den Eijnden, "Quadratic Electrostriction Effect In CaF<sub>2</sub>, SrF<sub>2</sub>, And BaF<sub>2</sub> Single Crystals", *J. Appl. Phys.*, vol. 21, pp175-180, 1988.
- [5] V. Sundar and R. E. Newnham, "Anisotropy In Electrostriction And Elasticity", *J. Mat. Sci. Lett.*, vol. 13, pp799-801, 1994.
- [6] K. Rittenmyer, *Electrostriction in Cubic Halide Compounds*, Ph.D. Dissertation, The Pennsylvania State University, (1984).
- [7] V. Sundar, J.F. Li, D. Viehland and R.E.Newnham, "Measurements Of Electrostriction Coefficients In Low-K Dielectrics", (to be published).
- [8] S. Nomura and K. Uchino, "Electrostrictive Effect In PMN-Type Materials", *Ferroelectrics*, vol. 50, pp197-213, 1983.
- [9] D. J. Voss, S. L. Swartz, and T. R. Shrout, "The Effects Of Various B-Site Modifications On The Dielectric And Electrostrictive Properties Of Lead Magnesium Niobate", *Ferroelectrics*, vol 50, pp203-208, 1983.

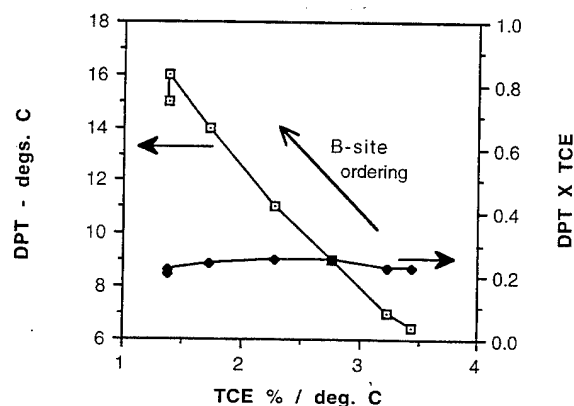


Fig. 6 : DPT vs. TCE plots for doped PMN with increasing B-site modification ( Refs. 8,9)

# Electro-Mechanical Coupling in 8/65/35 PLZT

Christopher S. Lynch

Mechanical and Environmental  
Engineering Department  
University of California  
Santa Barbara, California 93106

**Abstract** - This work presents the experimental characterization of 8/65/35 PLZT subjected to stress and electric field loading above the coercive field. Strain vs. electric field and electric displacement vs. electric field hysteresis loops as well as stress vs. strain and stress vs. electric displacement are measured. The limitations of linear constitutive modeling and the limitations of large strain ferroelectrics as actuator materials are examined. The results indicate a stress vs. strain curve that clearly shows the "yield" or ferroelastic switching stress is an important criteria for assessing the capability of actuator ceramics. A low threshold of ferroelastic switching means the piezoelectric effect is easily clamped.

## I. INTRODUCTION

This work presents the results of an experimental investigation of the electro-mechanical behavior of 8/65/35 PLZT (8at% La, 65 lead zirconate, 35 lead titanate). Jaffe, Cook, and Jaffe<sup>1</sup> provide a review of ferroelectric ceramic materials. Ceramic PZT is produced by high temperature sintering an agglomerate of ferroelectric crystallites. Diffusion of material at the boundaries of the crystallites results in densification followed by grain growth. When densification is complete, and grain growth has progressed sufficiently to give the desired microstructure, the ceramic is cooled. As the temperature cools through the Curie temperature, the single crystal grains undergo a diffusionless structural transition from a paraelectric (cubic) to a ferroelectric (tetragonal, orthorhombic, or rhombohedral depending on material and composition) state.

Figure 1a shows the high temperature cubic and the room temperature tetragonal forms of lead titanate. This  $ABO_3$  perovskite contains an  $A^{+2}$  ion at each corner of the unit cell, a  $B^{+4}$  ion at the center of the unit cell, and an  $O^{-2}$  ion at the center of each face. The tetragonal unit cell has an ionic dipole moment due to displacement of the central  $Ti^{+4}$  ion relative to the surrounding  $O^{-2}$  ions. The polarization is, by definition, the dipole moment per unit volume. The coupling between strain and electric field is a consequence of this polar structure.

Under small loads the polarization of the unit cell can undergo a reversible change in one of two ways: 1. An applied stress deforms the crystal structure. This changes the  $a/c$  ratio, resulting in a relative displacement of the positive and negative ions. and 2. An applied electric field changes the relative displacement of the positive and negative ions. This also changes the  $a/c$  ratio, inducing deformation of the crystal structure. These linear effects are the direct and converse piezoelectric effects<sup>2</sup>. In addition to this coupling between strain and polarization, there is an elastic and a dielectric effect. These effects are linear at small loads.

Energy considerations lead to coupled linear constitutive laws<sup>3</sup> written, with stress and electric field as independent variables, as

$$e_{ij} = s_{ijkl}\sigma_{kl} + d_{ijn}E_n \quad (1)$$

$$D_m = d_{klm}\sigma_{kl} + \epsilon_{mn}E_n \quad (2)$$

where  $e_{ij}$ =strain,  $s_{ijkl}$ =elastic compliance,  $\sigma_{ij}$ =stress,  $d_{ijk}$ =piezoelectric coefficient,  $E_n$ =electric field,  $D_m$ =electric displacement,  $\epsilon_{mn}$ =dielectric permittivity, indices vary from 1 to 3, and summation on repeated indices is implied.

Ferroelectric switching occurs when an applied electric field exceeds the coercive field and thus moves the central ion to another of the six off center tetragonal sites. This changes the direction of polarization to that most closely aligned with the electric field (see Figure 1b). Similarly, ferroelastic switching occurs when a sufficiently large compressive stress squeezes the unit cell towards a cubic state. This causes the central ion to move to one of the side sites at  $90^\circ$  (see Figure 1c), changing the direction of polarization to that most closely aligned perpendicular to the stress. The switching process is not homogeneous. It occurs by twin boundaries (domain walls) sweeping through the crystal. The switching process is also non-linear and is not described by the linear approximation of the constitutive laws stated as equations 1 and 2.

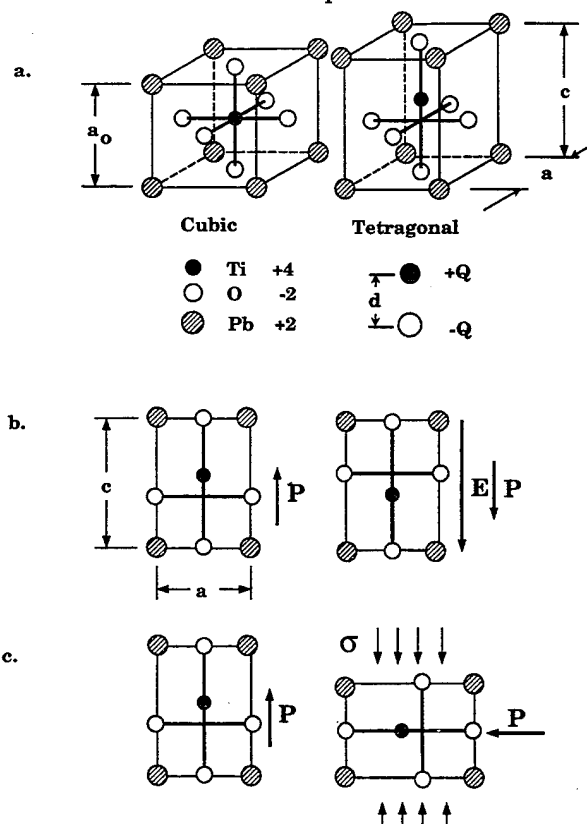


Figure 1. a. The high temperature cubic and low temperature tetragonal forms of lead titanate, an  $ABO_3$  perovskite type oxide. The low temperature tetragonal structure has a spontaneous polarization given by the dipole moment per unit volume. b. A  $180^\circ$  switch in the direction of polarization is induced by an electric field above the coercive field. c. A  $90^\circ$  switch in the direction of polarization is induced by a compressive stress above the coercive stress.

In this work, PLZT is first polarized by application of an electric field in excess of the coercive field, thus aligning the polarization of each of the grains. The field is cycled positive and negative and the strain and electric displacement are recorded. The electric displacement is measured as the charge per unit area on the electrodes. The PLZT is next subjected to compressive stress parallel to the polarization. The high magnitude uniaxial stress changes the polarization of the ceramic by 90° switching<sup>4,5,6,7,8</sup> resulting in a non-linear stress vs. strain curve. The switching behavior and the resulting non-linearities have been modeled using a Preisach criterion<sup>9,10</sup>. This model reproduces the shape of the observed hysteresis curves under both electrical and mechanical loading.

## II. EXPERIMENTAL PROCEDURES

### A. Materials and Specimen Preparation

The material chosen for this study is a hot pressed lanthanum doped lead zirconate titanate (Aura Ceramics). This material comprises an 8 at% lanthanum substitution in a 65 at% lead zirconate 35% lead titanate solid solution, denoted 8/65/35 PLZT, with a 5  $\mu\text{m}$  grain diameter. This composition is very near a rhombohedral-tetragonal morphotropic boundary<sup>13</sup>. Table 1 lists the material properties. This material is ferroelectric at room temperature, displays a symmetric electric displacement vs. electric field hysteresis loop, and a corresponding symmetric butterfly shaped strain vs. electric field hysteresis loop.

Samples are cut to 10 mm cubes, polished, and electroded with sputtered Au/Pd.

### B. Testing and Measurements

#### 1. Stress and Electric Field Loading

Figure 2 shows the loading arrangement. The sample is first subjected to electric field and then to uniaxial stress loading. The silicone oil bath prevents high voltage arcing. The sample is isolated from the test frame by two alumina blocks, one on top and one on bottom. A servo-

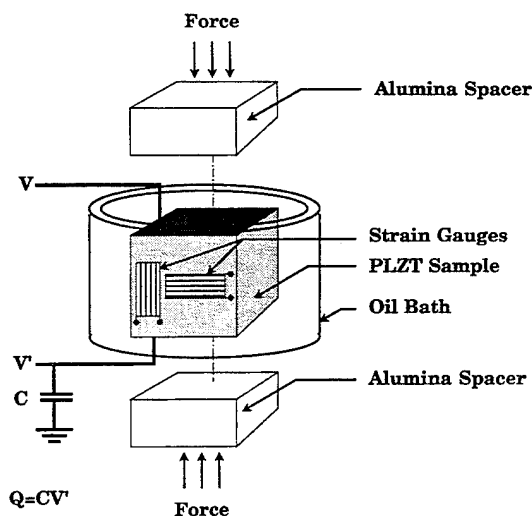


Figure 2. Schematic of the electro-mechanical loading system. The sample is immersed in an oil bath. A servohydraulic test frame applies a force that is monitored by a load cell. A high voltage amplifier applies an electric field. Strain and electric displacement are monitored during the test.

hydraulic test frame (Material Test Systems) applies the compressive stress and a high voltage amplifier (Trek Inc.) applies the electric field.

### 2. Instrumentation

**a. strain** Longitudinal and transverse strain gauges are bonded to the center of one face to measure the strain parallel (longitudinal) and perpendicular (transverse) to the polarization direction. The strain gauges are connected to a wheatstone bridge that is balanced with the material in the as cooled, not polarized, state. This gives a natural reference state for the strain measurements.

**b. stress** A 100 kN load cell mounted on the test frame monitors the force applied to the sample.

**c. electric displacement** The charge that flows to and from the sample's electrodes is measured by monitoring the voltage on an 8  $\mu\text{F}$  capacitor connected from the bottom of the sample to ground. The charge per unit area on the electrodes is equal to the normal component of the electric displacement. The capacitor is temporarily short circuited in the as cooled, non polarized, state. This gives a natural reference for the electric displacement measurements.

**d. electric field** A high voltage triangle wave ( $\pm 8 \text{ kV}$  at 0.02 Hz) is applied to the upper sample electrode.

## III. EXPERIMENTAL RESULTS AND DISCUSSION

The experimental results are presented in Figure 3 A through F. The linear effects are shown on these plots, making the limitations of linear analysis graphically clear. These plots are discussed in sequence in this section.

### A. Electric Displacement- $D_3$ vs. Electric Field- $E_3$

The electric displacement vs. electric field is shown in Figure 3A. The amplitude of the cyclic electric field is slowly increased until the full hysteresis loop shown in Figure 3A develops. At point A the electric field is zero and the sample has remanent polarization of  $+0.25 \text{ C/m}^2$ . A negative electric field (opposite the direction of polarization) is applied. At point B, the electric field has reached the coercive field, 0.36 MV/m. Here the direction of polarization of the sample begins to switch. At point C the polarization has reversed and is now aligned with the negative electric field. The electric field is reduced to zero at point D. The remanent polarization is now  $-0.25 \text{ C/m}^2$ . A positive electric field (opposite the present direction of polarization) is now applied. When the electric field level reaches the coercive field at point E, the polarization again begins to switch. At F, the polarization is in the original direction and is aligned with the present positive electric field. The electric field is reduced to zero and the material returns to point A.

When the sample is in the polarized state at either point A or D, the electric displacement is linearly proportional to small changes of electric field. This linear dielectric effect is described by equation 2 which, at zero stress, gives

$$D_3 = \epsilon_{33} E_3 \quad (3)$$

Equation 3 is fairly accurate in the range of  $-0.1 \text{ MV/m} \leq E_3 \leq +0.2 \text{ MV/m}$ . Outside of this range, non-linear effects must be considered. The slope in Figure 3A gives a relative permittivity of  $\epsilon_{33}/\epsilon_0 = 6356$ , where the permittivity of free space is  $\epsilon_0 = 8.85 \times 10^{-12} \text{ farad/m}$

### B. Strain- $e_{33}$ vs. Electric Field $E_3$

The strain is monitored simultaneously with the electric displacement and is plotted in Figure 3B. The

strain and electric field are initially at the point (0,0) toward the bottom center of Figure 3B. As the amplitude of the cyclic electric field is increased, the hysteresis loop shown in Figure 3B eventually develops. At point A the material has remanent polarization and remanent strain, both positive. The lettered points in Figure 3B correspond to the same letters in Figure 3A. When a negative electric field is applied, the ions in the crystal structure experience a force that moves them toward a cubic state. This distorts the structure toward that of the unpoled ceramic. When the coercive field is reached at point B, the direction of polarization begins to switch. The negative strain is due to 90° switching as shown in Figure 1C. (Remember the zero strain state is the unpoled state, a quasi-cubic state. When 90° switching has collapsed the structure, the strain is negative.) After the polarization has switched to the direction of the applied electric field, the electric field acts to stretch the unit cell, giving a positive strain at point C. When the electric field is then

reduced to zero, the remanent strain at point D coincides with that at point A but the remanent polarization is negative. Now, as a positive electric field is applied to the negatively polarized material, the ions in the crystal structure again experience a force that move them toward a cubic state. The coercive field is reached at point E, and the polarization has completely switched direction again at point F. The electric field is reduced to zero and the material returns to point A with positive remanent polarization and remanent strain.

When the material is in the polarized state, the strain is linearly proportional to small changes in electric field at zero stress. In this case, equation 1 reduces to

$$e_{33} = d_{333}E_3 \quad (4)$$

The slope of the strain vs. electric field curve in Figure 3B is the linear piezoelectric coefficient  $d_{333}$ . The slope in gives  $d_{333}=1188 \times 10^{-12} \text{ m/V}$

#### C. Strain- $e_{11}$ vs. Electric Field- $E_3$

The transverse strain vs. electric field is shown in Figure 3C. This strain vs. electric field hysteresis loop is approximately -1/2 of the loop shown in Figure 3B. Again, at small electric field the strain is linearly proportional to the applied electric field at zero stress. In this case equation 1 reduces to

$$e_{11} = d_{113}E_3 \quad (5)$$

The slope of the strain vs. electric field curve in Figure 3C is the linear piezoelectric coefficient  $d_{113}$ . Figure 3C gives  $d_{113}=-590 \text{ m/V}$ . Note  $d_{311}=-0.5d_{333}$ .

#### D. Strain Ratio $-e_{11}/e_{33}$ vs. Electric Field $E_3$

The negative ratio of transverse to longitudinal strain is plotted in Figure 3D as a function of applied electric field. This ratio is approximately 0.5, indicating the switching process conserves volume. The large excursions away from 0.5 occur when the transverse strain passes through zero. It is interesting to note that the volume of the material appears to increase slightly as the electric field drives the material toward a cubic state. This is indicated by a strain ratio greater than 0.5 on the linear portion of the curve in figure 3D.

#### E. Stress- $\sigma_{33}$ vs. Longitudinal Strain- $e_{33}$

The polarized ceramic is next subjected to compressive stress. The resulting stress vs. longitudinal strain plot is shown in Figure 3E. The material starts at zero stress with remanent strain of the fully polarized ceramic. See Figure 3B. As the stress magnitude is increased, there is initially a substantial reduction in the tangent modulus. This is caused by stress induced 90° switching. At -80 MPa the switching is nearly complete and the modulus appears linear elastic. The stress is unloaded to zero and the final strain is negative relative to the unpoled state. Linear elastic effects are described by equation 1 at zero electric field which, under uniaxial stress loading reduces to

$$e_{33} = s_{3333}\sigma_{33} \quad (6)$$

The slope in Figure 3E is the Young's modulus, the inverse of the compliance. For this material, equation 6 is only valid to compressive stress levels of about 7 MPa. Compressive stress higher than this results in depolarization, placing a severe limitation on this PLZT as an actuator material. The slope of the curve in Figure 3F gives a compliance of  $s_{3333}=14.7 \times 10^{-12} \text{ m}^2/\text{Nt}$ . This corresponds to a Young's modulus of  $Y_3=68 \text{ GPa}$ .

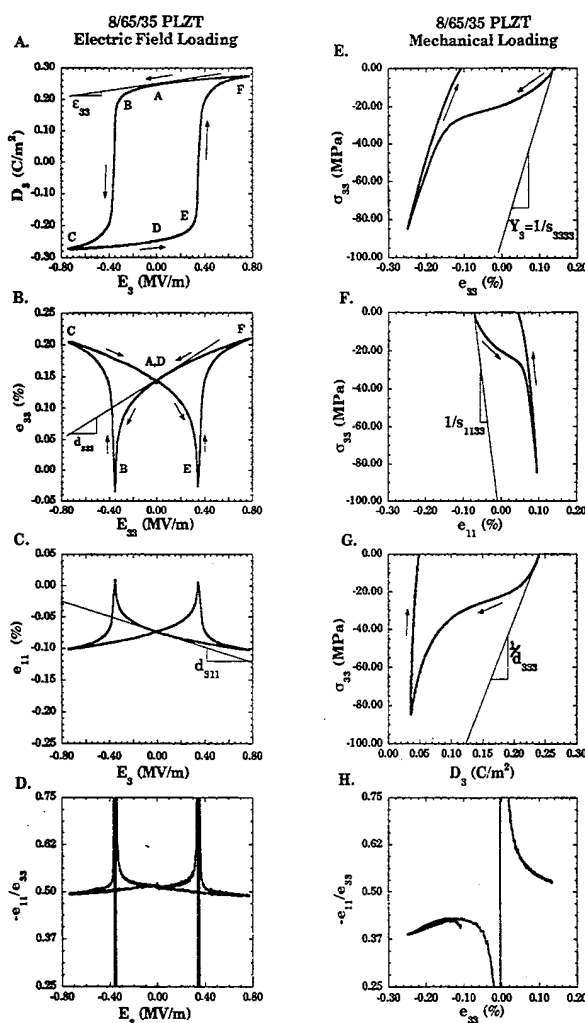


Figure 3. Experimental results for 8/65/35 PLZT: A. Electric displacement vs. electric field hysteresis loop. B. Longitudinal strain vs. electric field butterfly hysteresis loop. C. Transverse strain vs. electric field butterfly hysteresis loop. D. Point by point calculated strain ratio plotted as a function of electric field. E. Stress vs. longitudinal strain for the poled sample. F. Stress vs. transverse strain for the poled sample. G. Stress vs. electric displacement during the stress cycle. H. Point by point strain ratio during the stress cycle.



The stress vs. strain curve shown in Figure 3E is a classical shape memory effect. Stress induces a permanent change of strain via 90° switching. A subsequent application of electric field re-polarizes the material, returning the strain to its initial value (with the caveat that repeated switching results in fatigue crack growth).

#### F. Stress- $\sigma_{33}$ vs. Transverse Strain- $e_{11}$

The stress vs. transverse strain curve in Figure 3F is similar to the stress vs. longitudinal strain curve in Figure 3E. The initial slope relating the stress to the transverse strain is the inverse of the compliance  $s_{1133}$ . For this case of uniaxial stress loading at zero electric field, equation 1 reduces to

$$e_{11} = s_{1133}\sigma_{33} \quad (7)$$

The slope of the curve in Figure 3F gives a compliance of  $s_{1133} = 7 \times 10^{-12} \text{ m}^2/\text{Nt}$ .

#### G. Stress- $\sigma_{33}$ vs. Electric Displacement- $D_3$

The Stress as a function of electric displacement is shown in Figure 3G. The initial electric displacement is equal to the remanent polarization. See Figure 3A. The slight reduction in polarization from the remanent polarization seen in Figure 3A is due to the aging effect. The shape of this curve is similar to the stress vs. strain curve. The non-linear portions of each curve are the result of 90° switching. As the material switches, there is a large strain change and a large electric displacement (polarization) change.

The initial slope of the stress vs. electric displacement curve corresponds to the converse piezoelectric effect. Thermodynamics tells us the inverse of this slope should be the same as the slope of the strain vs. electric field curve in Figure 3B. For small magnitude uniaxial stress loading at zero electric field, equation 2 reduces to

$$D_3 = d_{333}\sigma_{33} \quad (8)$$

The slope of the curve in Figure 3G gives  $d_{333} = 1180 \times 10^{-12} \text{ C/Nt}$  (or  $\text{m/V}$ ). It is apparent from the curve that this linear approximation is only valid to stress levels of about 7 to 10 MPa.

#### H. Negative Strain Ratio $-e_{11}/e_{33}$ vs. Strain $e_{33}$

The strain ratio is calculated point by point from the data of Figures 3E and F and plotted against the longitudinal strain  $e_{33}$ . This allows a direct comparison with the stress cycle shown in Figure 3E. As stress is initially applied, the strain ratio is almost 0.5, indicating a constant volume switching process. The upward and downward excursions are the result of the transverse strain passing through zero. At high stress most of the switching has stopped. At this point the strain ratio is about 0.38. The material has undergone a transition from switching induced strain to elastic strain.

**Table 1. Properties of 8/65/35 PLZT**

Material Properties	Measured	Published
Piezo coeff., $d_{333}$ ( $\times 10^{-12} \text{ m/V}$ )	1188	682
Remanent pol., $P^R$ ( $\text{C/m}^2$ )	0.25	0.30
Coercive field, $E_c$ ( $\text{MV/m}$ )	0.36	0.36
Curie temperature, $T_c$ ( $^\circ\text{C}$ )		110
Relative permitt., $\epsilon_r = \epsilon/\epsilon_0$	6356	3350
Elastic modulus, $Y_3$ (GPa)	68	80

## VI. CONCLUDING REMARKS

This paper presented an experimental study of the non-linear response of 8/65/35 PLZT at room temperature. The non-linear behavior was compared with the linear approximations to demonstrate the range of validity of linear assumptions. The linear equations are only valid through a narrow range of the material response.

Stress vs. strain curves should be considered when assessing candidate materials for actuator applications. 8/65/35 PLZT has an extraordinarily large piezoelectric coefficient, yet is a very poor candidate for actuator applications. The material just can't push very hard and thus will not operate under high load. There is an additional problem with this material as an actuator. It is a relaxor, and thus its response is temperature and frequency dependent. Raise the temperature 10°C and it will depole at 2 MPa. Raise the temperature 50°C and it will spontaneously depole. Measure  $d_{333}$  quasi-statically and it is 1188, but measure it at 10 KHz and it is only 640.

## VII. ACKNOWLEDGMENTS

This work was supported by ONR through contract N0014-931-0200.

## VIII. REFERENCES

1. Jaffe B., W.R. Cook, and H. Jaffe, "Piezoelectric Ceramics", p 162, Academic Press London and New York, 1971.
2. Cady W.G., "Piezoelectricity", Vols. 1 and 2, Dover 1964.
3. Lines and Glass, "Principles and Applications of Ferroelectrics and Related Materials", Oxford 1977
4. Cao, H. and A.G. Evans, "Non-linear Deformation of Ferroelectric Ceramics", J. Am. Ceram. Soc. 76 [4] 890-96 (1993).
5. Berlincourt D, H.H.A. Krueger, "Domain Processes in Lead Titanate Zirconate and Barium Titanate Ceramics", J. Appl. Phys., 30 (11), 1804-1810, 1959.
6. Krueger H.H.A., D. Berlincourt, "Effect of High Static Stress on the Piezoelectric Properties of Transducer Materials", J. Acoust. Soc. Am., 33 (10), 1339-1344, 1961.
7. Krueger H.H.A., "Stress Sensitivity of Piezoelectric Ceramics: Part 1. Sensitivity to Compressive Stress Parallel to the Polar Axis", J. Acoust. Soc. Am., 42 (3), 636-645, 1967.
8. Krueger H.H.A., "Stress Sensitivity of Piezoelectric Ceramics: Part 2. Sensitivity to Compressive Stress Perpendicular to the Polar Axis", J. Acoust. Soc. Am., 43 (3), 583-591, 1968.
9. Chan K. H., N. W. Hagood, "Modeling of Nonlinear Piezoceramics for Structural Actuation", Proceedings SPIE, Smart Structures and Materials, Ed. N.W. Hagood, Vol 2190, pp 194, 1994.
10. Hwang S.C., C.S. Lynch, and R.M. McMeeking, "Ferroelectric/Ferroelastic Interactions and a Polarization Switching Model", Submitted to Acta Met. June 1994
11. Haertling G.H., "PLZT Electrooptic Materials and Applications- a Review" Ferroelectrics, 75, 22-25, 1987.

Z. Xu, Xunhu Dai, and Dwight Viehland, Department of Materials Science and Engineering, University of Illinois, Urbana, Illinois 61801

Antiferroelectric lanthanum-modified lead zirconate titanate (PLZT) specimens with a La-content of 2 at.% and a Zr/Ti ratio of 95/5 (PLZT 2/95/5) have been investigated by dielectric spectroscopy, Sawyer-Tower polarization (P-E) measurements, and hot-stage transmission electron microscopy (TEM). La "impurities" have been found to induce a  $1/x[110]$  incommensurate structure from the commensurate antiferroelectric orthorhombic (AFE<sub>0</sub>) PbZrO<sub>3</sub> (PZ) structure. The incommensurate structure was found to be stable below the temperature of the dielectric maximum, evolving slowly with decreasing temperature towards the commensurate AFE<sub>0</sub> PZ structure. The incommensuration is believed to arise due to a competition between "broken" dipolar (ferroelectric) and sublattice (antiferroelectric) interactions.

### I. Introduction

The antiferroelectric phase region of the PLZT crystalline solution series has previously not been investigated, except for the early studies by Haertling [1]. In fact, the effect of "impurities" on antiferroelectricity has not yet been studied. Recently, incommensuration has been observed in Sn-modified lead zirconate titanate ceramics,  $\text{Pb}_{0.98}\text{Nb}_{0.02}(\text{Zr}_{1-x}\text{Sn}_x)_{1-y}\text{Ti}_y\text{O}_3$  (PZST  $x/y/2$ ).  $1/x[110]$  incommensurate reflections were observed in selected area electron diffraction (SAED) patterns on cooling below the temperature of the dielectric maximum ( $T_{\text{max}}$ ) for PZST 43/8/2 and 42/4/2 specimens. The modulation wavelength of the incommensurate structure ( $\lambda$ ) was found to become temperature independent on cooling below  $\sim 100^\circ\text{C}$ , indicating a pinning into long-lived metastable states [2]. At significantly lower temperatures, an incommensurate-commensurate transformation was observed [3]. The low temperature commensurate state was isomorphous with antiferroelectric orthorhombic (AFE<sub>0</sub>) PbZrO<sub>3</sub> (PZ). Compositional heterogeneity ("impurities") was suggested to be responsible for the incommensuration.

In this paper, we report the effect of "impurities" on antiferroelectricity. La "impurities" have been found to induce incommensuration in  $(\text{Pb}_{1-x}\text{La}_x)(\text{Zr}_{0.95}\text{Ti}_{0.05})\text{O}_3$  for  $x=0.02$  (PLZT 2/95/5).

### II. Experimental Procedure

Studies were performed by hot-stage transmission electron microscopy (TEM), dielectric spectroscopy, and Sawyer-Tower (P-E) polarization techniques. Polycrystalline specimens were prepared by a mixed-oxide method from high purity (>99.9%) PbO and ZrO<sub>2</sub> powders. Discs were prepared by hot pressing at  $1150^\circ\text{C}$  for 2 hours and a subsequent post-annealing at  $1300^\circ\text{C}$  for 2 hours in a PbO-rich environment. Dense specimens were obtained, which were second phase free to x-ray diffraction. The TEM studies were done on a Phillips EM-420 microscope operating at an accelerating voltage of 120 kV, using a double tilt hot-stage. Electron diffraction patterns were obtained along the  $\langle 001 \rangle$  as a function of temperature. Temperature dependent complex dielectric permittivity measurements were made by a Hewlett-Packard 4284A inductance-capacitance-resistance (LCR) meter in conjunction with a Delta Design 9023 test chamber at a heating rate of  $4^\circ\text{C}/\text{min}$ .

### III. Results and Discussion

The complex dielectric response for PLZT 2/95/5 is shown in Figure 1. A maximum dielectric constant of 4500 is evident near  $220^\circ\text{C}$ . A secondary anomaly was observed near  $120^\circ\text{C}$  on heating and near  $90^\circ\text{C}$  on cooling. Temperature dependent P-E investigations, illustrated in Figures 2(a)-(f), indicate that both the lower and intermediate temperature states are antiferroelectric. At  $25^\circ\text{C}$  (Figure 2(a)), a spontaneous polarization could not be induced for field strengths in excess of 3 kV/mm. Nonlinearities in the P-E behavior did not become evident on heating until near  $175^\circ\text{C}$  (Figure 2(b)), however saturation was not achieved until temperatures above  $190^\circ\text{C}$  (Figure 2(c)). In this temperature range ( $175\text{--}190^\circ\text{C}$ ), phase switching from antiferroelectric to ferroelectric states can clearly be seen. The P-E behavior in this temperature range (25– $190^\circ\text{C}$ ) clearly shows that the secondary dielectric anomaly reflects an antiferroelectric-antiferroelectric transformation. On further increment of the temperature for 2/95/5 (Figures 2(d)-(f)), the double hysteresis loop characteristics of the P-E curves became less pronounced. At  $215^\circ\text{C}$ , no evidence of antiferroelectricity was observed.

$\langle 001 \rangle$  SAED patterns for 2/95/5 at various temperatures are illustrated in Figures 3(a)-(f).  $1/4\langle 110 \rangle$  superlattice reflections are evident at room temperature (Figure 3(a)) which possess strong streaking along the  $\langle 110 \rangle$ . On increasing the temperature to  $90^\circ\text{C}$  (Figure 3(b)), the  $1/4\langle 110 \rangle$  reflections became split along the  $\langle 110 \rangle$

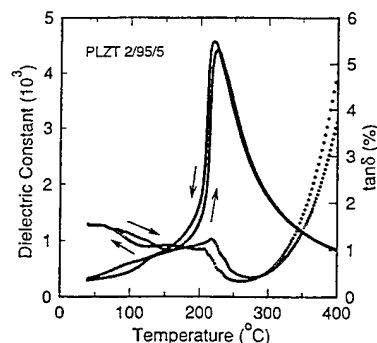


Figure 1. Dielectric Constant and loss factor of PLZT 2/95/5.

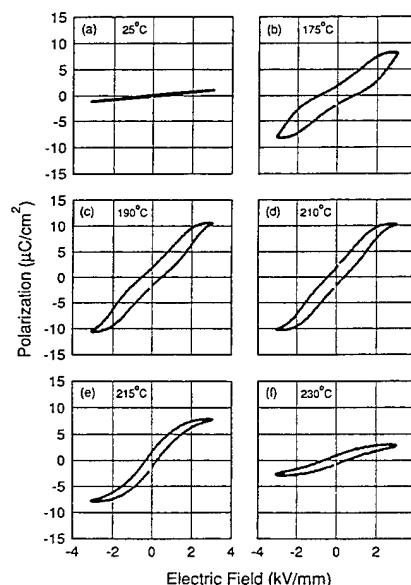


Figure 2. Dielectric hysteresis measurements of PLZT 2/95/5 at various temperatures. (a)  $25^\circ\text{C}$ , (b)  $175^\circ\text{C}$ , (c)  $190^\circ\text{C}$ , (d)  $210^\circ\text{C}$ , (e)  $215^\circ\text{C}$ , and (f)  $230^\circ\text{C}$ .

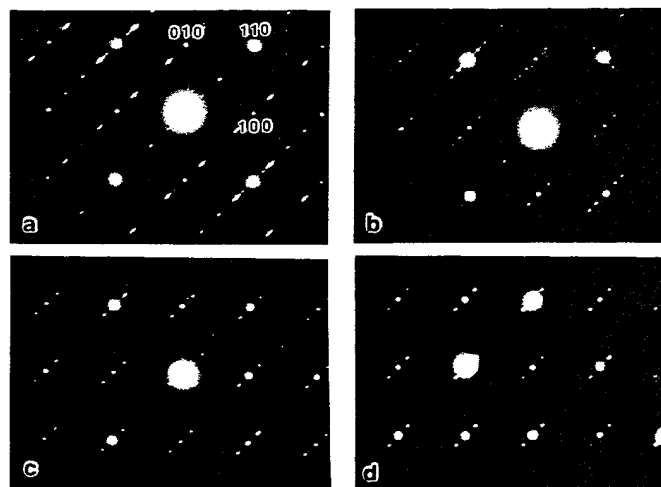


Figure 3.  $\langle 001 \rangle$  SAED patterns for PLZT 2/95/5 at various temperatures. (a)  $25^\circ\text{C}$ , (b)  $90^\circ\text{C}$ , (c)  $115^\circ\text{C}$ , (d)  $175^\circ\text{C}$ , (e)  $225^\circ\text{C}$ , and (f)  $325^\circ\text{C}$ .

into multiple incommensurate reflections, indicating an intermediate state which is characterized by an intergrowth of structural modulations as will be shown later by high resolution lattice images. In addition, the degree of  $\langle 110 \rangle$  streaking was decreased relative to room temperature. At 115°C (Figure 3(c)), no evidence of  $1/4\langle 110 \rangle$  reflections was observed. Rather,  $1/x\langle 110 \rangle$  incommensurate reflections were apparent. These results clearly reveal that an incommensurate-commensurate transformation occurred between 90 and 115°C. Dielectric spectroscopy revealed an anomaly in this temperature range, which most probably reflects the transformation. However, local regions of incommensuration were even found at room temperature, indicating that the transformation is diffuse. With increase of temperature to 175°C (Figures 3(d)), the position of the incommensurate reflection can be seen to become closer to the main reflection, indicating  $\lambda$  increases with increasing temperature. In this temperature range, the stability of the antiferroelectric state is decreasing, as evidence by the decrease in the coercive field in the P-E investigations. Upon heating to 225°C, no incommensurate reflections were evident, as shown in Figure 3(e). Rather, diffuse  $1/2\langle 110 \rangle$  superlattice reflections were present in the SAED patterns. Diffuse  $1/2\langle 110 \rangle$  reflections remained visible in the SAED patterns above 325°C (Figure 3(f)). The  $1/2\langle 110 \rangle$  superlattice reflections may reflect ferroelectric tendencies. Metastable orthorhombic ferroelectric tendencies have previously been suggested by Fesenko et al. [4] by phenomenological predictions and by Tanaka and Saito [5] from symmetry considerations of convergent beam electron diffraction patterns.

Lattice imaging of commensurate and incommensurate reflections revealed the existence of domain-like striations. Figures 4(a) and (b) illustrate  $\langle 001 \rangle$  lattice images taken from a commensurate reflection at low and high magnifications, respectively. Bright and dark fringes of various widths can be seen in Figure 4(a), indicating an intergrowth of structural modulations of different periodicities along the  $\langle 110 \rangle$ . The periodicity corresponded to the modulation wavelength calculated from the  $\langle 001 \rangle$  SAED pattern. An intergrowth of structural modulations with different periodicities can be more clearly seen in the high resolution lattice image given in Figure 4(b). Structural modulations of various periodicities are indicated by arrows. This intergrowth of structural modulations is responsible for the  $\langle 110 \rangle$  streaking observed in the SAED patterns. The  $\langle 001 \rangle$  SAED patterns always exhibited streaking along the  $\langle 110 \rangle$ , whenever intergrowth of structural modulations along the  $\langle 110 \rangle$  were observed in the lattice images. This indicates that the intergrowth results in internal strain along the  $\langle 110 \rangle$ . Similar  $\langle 001 \rangle$  SAED patterns and intergrowth phenomena have been observed in antiferroelectric PZST [3]. The lattice image corresponding to the incommensurate reflections, shown in Figure 4(c), revealed no intergrowths of periodicities between fringes, but rather the spacing between fringes was uniform and incommensurate with the lattice. Correspondingly, only very weak streaking (if any) was observed in the SAED patterns.

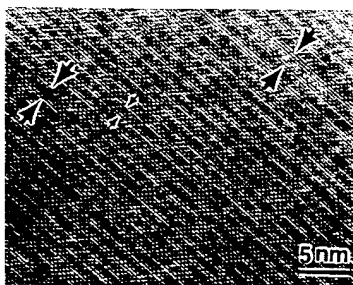


Figure 4. Lattice images of PLZT 2/95/5 at (a) low magnification and (b) high magnification.

The results presented in this paper near conclusively demonstrates that incommensuration is induced in Pb-based perovskites by impurities. Incommensuration is not observed in AFE<sub>0</sub> PbZrO<sub>3</sub> or any undoped Pb-based antiferroelectric. In consideration that identical  $1/x\langle 110 \rangle$  incommensurate reflections and  $\langle 110 \rangle$ -orientated domain-like striations have previously been reported by several of the authors in PZST 42/4/2 and 43/8/2, we believe that incommensuration may be a common feature of impure and/or compositionally inhomogeneous antiferroelectrics which has previously eluded investigators. One question which must be answered is what drives the formation of an incommensurate region between the paraelectric and the commensurate antiferroelectric orthorhombic states.

Incommensuration is generally believed to arise due to competing interactions which favor different structures. On the antiferroelectric side of the Pb(Zr<sub>1-y</sub>Ti<sub>y</sub>)O<sub>3</sub> (PZT) phase diagram ( $y < 0.05$ ), antiferroelectric and ferroelectric phases are known to be very close in free energy. Consequently if impurities interrupt the translational invariance of the long-range ordered state, a competition between "broken" dipolar interactions (associated with ferroelectric tendencies) and the sublattice interactions (associated with antiferroelectric tendencies) may develop. This competition could, then, result in incommensuration of the polar order in "dirty" antiferroelectric materials. Some similarities between incommensurate antiferroelectrics and relaxor ferroelectrics should be evident, i.e., "impurities" interrupt long-range order. However, "impurity"-driven incommensuration does not result from a complete disruption of the antiferroelectric order as La-contents as low as 2 at.% were found to result in incommensuration, whereas a complete disruption of the ferroelectric order is required to establish the nanopolar domain state of relaxors.

#### IV. Conclusions

Two important conclusions can be drawn from this work. (1) Impurity-induced incommensuration has been observed for the first time in antiferroelectric orthorhombic PZT. Incommensuration was found to appear near the temperature of the dielectric maximum on cooling. Near room temperature, an incommensurate-commensurate transformation was observed. (2) Incommensuration is believed to result from a competition between "broken" dipolar interactions (favoring ferroelectric ordering) and sublattice interactions (favoring antiferroelectric ordering). This indicates that the coupling between the polar order parameter and incommensuration is proper.

#### Acknowledgements

This work was supported by the Office of Naval Research (ONR) under contract No. N00014-92-J-1522.

#### References

- [1] G. Haertling and C. Land, J. Am. Cer. Soc. 54, 1 (1971).
- [2] Z. Xu, D. Viehland, and D. Payne, J. Appl. Phys. 74, 3406 (1993).
- [3] Z. Xu, D. Viehland, and D. Payne, Proceedings ISAF 94.
- [4] O. Fesenko, R. Kolesova, and Y. G. Sindeyev, Ferroelectrics 20, 1777 (1978).
- [5] M. Tanaka and R. Saito, Proc. 7th European Congress on Electron Microscopy 1, 402 (CECEM Leiden, 1980).

# Field-Induced Piezoelectric Materials For 100 kHz-10 MHz Transducer Applications

J. T. Fielding, Jr., S. J. Jang, and T. R. Shrout  
Materials Research Laboratory

The Pennsylvania State University, University Park, PA 16802

**Abstract-** Several electrostrictive materials were investigated as candidates for high frequency transducer applications. Families investigated included  $(1-x)\text{Pb}(\text{Mg}_{1/3}\text{Nb}_{2/3})\text{O}_3$ - $(x)\text{PbTiO}_3$  and PLZT relaxors, and Sr- and Sn- substituted  $\text{BaTiO}_3$  normal ferroelectrics. The field dependent dielectric, piezoelectric and elastic properties were characterized at frequencies between 100 kHz and 5 MHz. The large magnitude and E-field tunability of the electromechanical and elastic properties observed in several of the materials may present opportunities for several new transducer applications, such as biomedical imaging and non-destructive evaluation.

## INTRODUCTION

The usage of piezoelectric ceramics for transducer and actuator applications has increased rapidly in the past decade. Currently, conventional piezoceramics are employed in many mature applications, such as sonar, welding and buzzers. Several families of electrostrictive materials have been investigated for emerging actuator and transducer applications such as micro-positioning and biomedical imaging.[1,2] Desirable performance criteria for selecting materials for transducer applications include large and reproducible induced piezoelectric coefficients, low losses, rapid response time and a wide operating temperature range

The primary criteria, to induce a large piezoelectric effect, can be achieved by selecting materials in which a large polarization can be produced by the application of an external electric field. The piezoelectric charge coefficient  $d_{ijk}$  is defined as follows:

$$d_{ijk} = 2 \chi_{mk} \epsilon_0 Q_{ijmn} P_n \quad (\text{Eqn. 1})$$

where  $\chi_{mk}$ ,  $Q_{ijmn}$ , and  $P_n$  are the dielectric susceptibility, electrostrictive coefficient and total polarization, respectively.

Electrostrictive materials offer several other advantages over piezoceramics for transducer applications. These are compared in Table I.[3,4] The field dependence of the dielectric, piezoelectric and elastic properties allows the tuning of the electromechanical coupling  $k_{ij}$  and mechanical Q. Also, the induced electromechanical coupling vanishes upon removal of the electric field, reducing spurious noise, which is important in several transducer applications.

Several material families, solid-solution forming systems having prototype perovskite structures in the paraelectric phase, have been selected as potential candidates for electrostrictive transducer applications. The polarization change mechanisms and general electric field-polarization relations have been classified elsewhere by Cross.[5] Sr substituted barium titanate  $(\text{Ba}_{1-x}\text{Sr}_x)\text{TiO}_3$  normal ferroelectrics were selected for several reasons: the sharp phase transition; larger values of  $K_{\max}$  compared to  $\text{BaTiO}_3$ ; the ability to controllably shift the Curie temperature  $T_C$  downwards; and the extensive investigation of the piezoelectric and electrostrictive effects in  $\text{BaTiO}_3$ . [6] Values for the field-induced coupling factors  $k_{33}$  and  $k_p$  were  $\sim 0.5$  and  $0.3$ , respectively, at temperatures near  $T_C$ .

Sn-substituted barium titanate  $\text{Ba}(\text{Sn}_x\text{Ti}_{1-x})\text{O}_3$  ferroelectrics exhibit "pinching" of the phase stability regions of the rhombohedral, orthorhombic, tetragonal and cubic phases, produced by compositional heterogeneity.[7] Large permittivities ( $K_{\max} > 25,000$  at 1 kHz) have been reported along with a linear strain-electric field response and large induced piezoelectric coefficient ( $d_{33} \sim 650$ -750 pC/N) at lower E-field levels ( $< 5$  kV/cm).[8]

Table I. Comparison of selected properties between piezoelectric and electrostrictive materials [3]

Parameter	Piezoelectric	Electrostrictive (Relaxor-based)
Strain/Field dependence	Linear	Non-linear
Field-induced strains	$> 0.1\%$	$> 0.1\%$
Hysteresis	Larger (5-30%)	Minimal ( $< 5\%$ )
Switching speed ( $\mu\text{s}$ )	Slower ( $1 > 10$ )	Faster ( $0.1 - 10$ )
Transition temperature (i.e., operating range)	Higher $T_{\max}$	Lower $T_{\max}$
Frequency dependence	Small	Larger
Dielectric Properties	$K_{\max}$ 1,000-4,000	$K_{\max}$ 15,000-30,000
Electromech. props.	Large, rel. E-field independent	Large, Adjustable $P_{\text{ind}}, d_{ij}, k_{ij} \Rightarrow f(E, \omega)$
Aging (%/time decade)	Large (0.5-2.5)	Smaller (0-0.5)

Two relaxor ferroelectric families, lead magnesium niobate-lead titanate  $(1-x)\text{Pb}(\text{Mg}_{1/3}\text{Nb}_{2/3})\text{O}_3$ - $(x)\text{PbTiO}_3$  (PMN-PT) and La-doped lead zirconate-titanate  $\text{Pb}_{1-x}\text{La}_x(\text{Zr}_{1-y}\text{Ti}_y)_{1-x/4}\text{O}_3$  (hereafter referred to as PLZT) were selected due to the large polarizations and maximum permittivities, broad anomaly in the dielectric response, and anhysteretic strain-electric field behavior available over a broad range of temperatures reported.[9] The breadth of the micro- to macro-polar transition region, described by  $\Delta T = T_{\max} - T_d$ , gives an indication of the operating temperature range for potential devices.

In PMN, the transition temperature  $T_{\max}$  and depolarization temperature  $T_d$  increase with increasing PT content.[10] The maximum dielectric permittivity  $K_{\max}$  was observed to increase with increasing PT content up to values of  $x \sim 0.30$ -0.33, achieving levels  $> 30,000$  (@ 1 kHz).[10] The maximum dielectric loss is  $\sim 0.10$  at 1 kHz and decreases rapidly to values  $\leq 0.01$  at temperatures  $> T_{\max}$ . The diffuseness of the transition and  $\Delta T$  were observed to decrease with increasing PT content, exhibiting a sharp dielectric transition for values of  $x > 0.33$ . These observed effects indicate a change in the relaxor nature with increasing additions of a normal ferroelectric.

Large and adjustable E-field induced piezoelectric coefficients in PMN-PT ceramics at lower frequencies (i.e.,  $< 200$  kHz) have been previously reported.[11] At the higher frequencies of interest in this study, Takeuchi reported field-induced thickness coupling factor  $k_t$  values of 0.45 for 0.91PMN-0.09PT ceramic specimens, measured at 7.5 MHz.[2]

PLZT compositions near the MPB have been extensively studied for electrooptic applications.[12] The broad dielectric transition, large permittivities ( $K_{\max}$ 's  $\sim 4,000$ -11,000), and large polarizations ( $> 30 \mu\text{C}/\text{cm}^2$ ) indicate the potential for a large field-induced piezoelectric effect over a broad temperature range. With increasing La content,  $K_{\max}$  decreases, the transition broadens, and  $T_{\max}$  and  $T_d$  are shifted to lower temperatures. Of interest for actuator and transducer applications, anhysteretic field-induced strains  $\sim 2.5 \times 10^{-3}$  have been reported by several investigators for  $x/65/35$  compositions with  $x=0.07$ -0.11.[12]

In this study, several compositions in each of the families were processed. The field dependent dielectric, piezoelectric and elastic properties were evaluated at frequencies between 100 kHz and 5 MHz and at temperatures in the various polarization regimes of interest.

## EXPERIMENTAL

Powders were prepared using reagent grade oxides and processed using conventional mixed oxide techniques described elsewhere.[3] Batches with the following compositions were processed:  $(\text{Ba}_{1-x}\text{Sr}_x)\text{TiO}_3$  with  $x=0.175, 0.20, 0.25, 0.30$ ;  $\text{Ba}(\text{Ti}_{1-x}\text{Sn}_x)\text{O}_3$  with  $x=0.10, 0.13$ ;  $(1-x)\text{PMN}-(x)\text{PT}$  with  $x=0.07, 0.10, 0.125, 0.15$ ; PLZT x/65/35 with  $x=8, 9, 9.5, 10$  and 11%. For PMN-PT powders, the columbite precursor method was utilized to maximize perovskite formation.[13] PMN-PT and PLZT compositions were calcined for 4 hours at 700°C and 875°C, respectively. BST and BTSn compositions were calcined at 1225-1275°C for 4 hours. X-ray diffraction analysis was used to ensure proper phase formation. For PMN-PT specimens, pyrochlore content measured using XRD was less than 3%. Disks with 1.27 and 2.54 cm diameters were pressed at 150 MPa.

PMN-PT and PLZT disks were sintered for 2 hours at 1150-1200 °C and 1275 °C, respectively. BST and BTSn discs were sintered on  $\text{ZrO}_2$  setters at 1350-1375 °C for 2-4 hours. Weight loss and geometric densities were calculated. Specimens were precision lapped to 0.5 mm thickness to produce a dilatational thickness mode resonance ~4.5-5 MHz. Au was sputtered, thickness ~1500Å, on the major faces for electrodes.

Dielectric property measurements included characterization of the field and temperature dependence of the relative dielectric permittivity and dielectric loss, performed over the frequency range from 0.1 kHz to 100 kHz using capacitance bridges (HP 4274 and 4275) and from 1 to >5 MHz using complex impedance data obtained from an impedance analyzer (HP3577A). In addition, the polarization versus electric field and pyroelectric behavior were examined and compared between families, using a Sawyer-Tower circuit, and the static Byer-Roundy technique, respectively.

High frequency field-induced electromechanical coupling factor were obtained from measurements of the series ( $f_s$ ) and parallel ( $f_p$ ) resonances, performed using a HP3577A network analyzer with HP35677A S-parameter test set configured for a one-port input reflection technique. Typical applied d.c. bias levels used for the measurements were between 1 and 15 kV/cm. The radial coupling factor  $k_p$  was calculated using a polynomial curve fitting equation.[14]. The dilatational thickness mode coupling factor  $k_t$  was calculated using the following equation: [14]

$$k_t^2 = \frac{\pi}{2} \frac{f_s}{f_p} \cdot \text{TAN} \frac{\pi}{2} \frac{(f_s - f_p)}{f_p} \quad (\text{Eqn. 2})$$

The effect of applied electric field on the elastic properties of representative specimens from the various material families were examined at several temperatures. Using information obtained from the resonance measurements combined with physical measurements, the frequency constant, elastic compliance  $s_{11}^E$  and stiffness  $c_{33}^D$  coefficients, and mechanical quality factor  $Q_m$  were calculated.

Several temperature regions were selected for measurement, depending on the material family. For the normal and "pinched" ferroelectric compositions, temperatures were selected in the span  $T_c \pm 30^\circ\text{C}$ . For relaxor ferroelectrics, resonance measurements were made over a range from the micro-polar region ( $T > T_{\text{max}}$ ) to well below the depolarization temperature  $T_d$ .

## RESULTS AND DISCUSSION

### Dielectric Properties

A summary of the dielectric properties for the various families investigated is presented in Table II. Larger polarizations were measured for the Pb-based relaxor families. Values of  $P_{\text{ind}}$  decreased rapidly for temperature  $> T_c$  in the  $\text{BaTiO}_3$  based families.

The highest small signal permittivities were observed in PMN and BTSn compositions. The low frequency dielectric constant and polarization behavior is shown for a 0.90PMN-0.10PT composition in Figure 1a. The micro-macro transition region,  $\Delta T$ , was 25-45 and 100-140 °C for the PMN-PT and PLZT relaxor families, respectively. Values for  $K_{\text{max}}$  (@ 1 kHz) were 27-36,000 for the PMN and 5,300-11,000 for the PLZT compositions investigated. The low frequency dielectric constant and polarization behavior for a  $\text{Ba}_{0.70}\text{Sr}_{0.30}\text{TiO}_3$  composition is shown in Figure 1b. For the BST and BTSn compositions, maximum values of  $K$  were 18-20,000 and 26-32,000, respectively. At temperatures above  $T_{\text{max}}$ , all the families exhibited low losses at 1 kHz. However, at 1 MHz, the dielectric loss increased to ~0.01 for the PLZT relaxor compositions. Minimal frequency dispersion was observed in the  $\text{BaTiO}_3$ -based families as compared to the PMN and PLZT relaxors.

A large field dependence of the permittivity was exhibited by all but the PLZT families. Values of  $K_{\text{max}}$  at 1 MHz and 10 kV/cm applied field for the BST/BTSn and PMN-PT families were ~4,000-5,500 and 8,500-10,500 respectively.

### Electromechanical Properties

Large field-induced coupling factors were obtained for the material families investigated. A summary of the electromechanical properties is shown in Table III. Maximum  $k_t$  values for the PMN-PT and PLZT families were 0.48 and 0.50, respectively. The field dependence of the coupling factor and polarization for a 0.90PMN-0.10PT specimen at two temperatures, 50°C ( $T \sim T_{\text{max}}$ ), and 75°C ( $T > T_{\text{max}}$ ), is shown in Figure 2. There was no remanent  $k_t$  observed after field removal for temperatures  $> T_d$ . The E-field dependence of  $k_t$  correlates fairly well with  $P_{\text{ind}}$  behavior at the measurement temperatures.

Table II. Summary of dielectric properties for compositions evaluated

Material Type	$P_{\text{max}}$ ( $\mu\text{C}/\text{cm}^2$ )	$K_{\text{max}}$	$K_{\text{max}}$ @1 MHz	$K_{\text{max}}$ @1 MHz E=10kV/cm	D. F. max.	$\Delta T$ (°C)	Transition Behavior	K Field Depend.
Relaxor I (1-x)PMN-(x)PT	28-35	Large (28-36,000)	24,000	8,800	0.08	20-30	Broad (dispersive)	Moderate
Relaxor II PLZT	30-40	Moderate (6-10,000)	9,000	8,500	0.10	100-140	Very broad (dispersive)	Minimal
Normal ( $\text{Ba}_{1-x}\text{Sr}_x$ ) $\text{TiO}_3$	16-19	Moderate (15-20,000)	16,400	5,400	0.05	0	Very narrow	Strong
"Pinched" $\text{Ba}(\text{Ti}_{1-x}\text{Sn}_x)\text{O}_3$	18-21	Large (28-35,000)	29,000	(7,000)	0.1	0	Very narrow	Strong

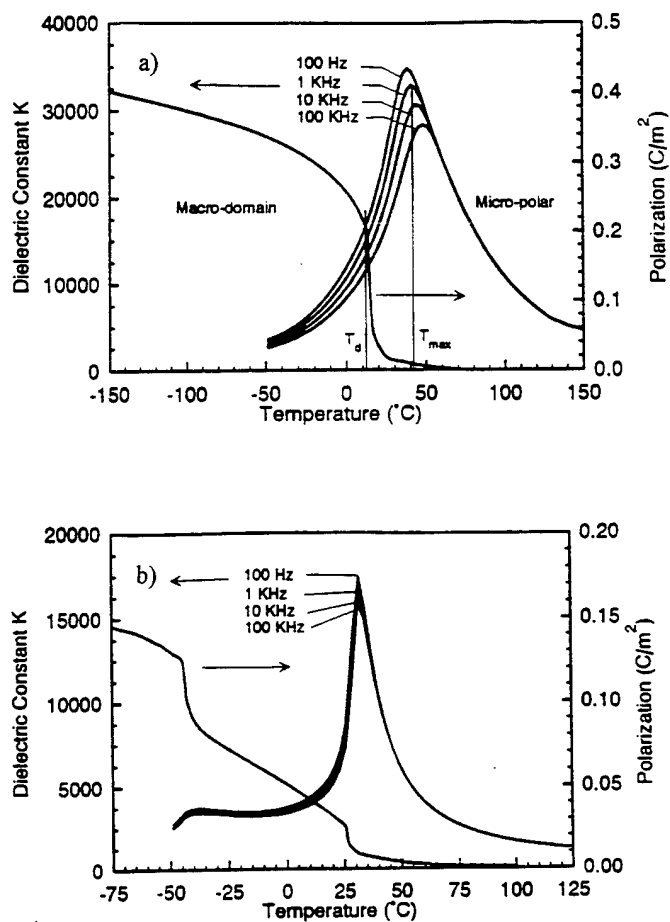


Figure 1. Polarization and dielectric constant as function of temperature for a) 0.90PMN-0.10PT relaxor and b)  $\text{Ba}_{0.70}\text{Sr}_{0.30}\text{TiO}_3$  normal ferroelectrics.

Large values of  $k_t$  (~0.50) were obtained for several of the BST compositions. However, as shown in Figure 3, values for the  $k_t$  decrease rapidly for temperatures greater than a few degrees above  $T_c$ . At temperatures below  $T_c$ , significant remanent  $k_t$  values were measured due to macro-domain switching. The relaxor compositions, with a broad micro-macro transition region, exhibited significantly wider temperature region for obtaining large induced  $k_t$ 's without hysteresis.

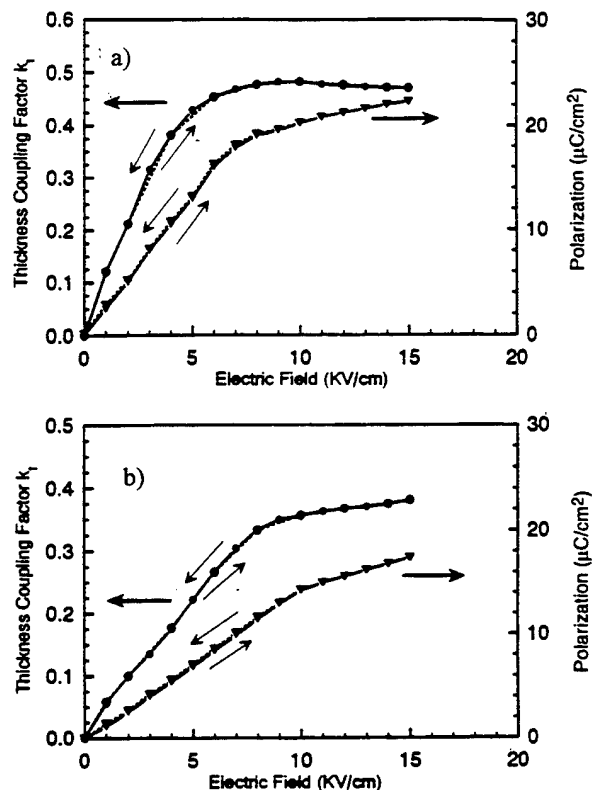


Figure 2. Field-induced thickness coupling factor  $k_t$  for a composition at a)  $50^\circ\text{C}$  ( $T \sim T_{\text{max}}$ ) and b)  $75^\circ\text{C}$  ( $T > T_{\text{max}}$ ).

Table III. Summary of field-induced electromechanical properties for material families investigated

Material Type	Example	$k_t$ max.	$k_p$ max.	$E_{\text{sat}}$ (kV/cm)	Temp. Range	$Q_m$	$N_t$ (Hz-m)	$C_{33}^D$ ( $\times 10^{10}$ N/m <sup>2</sup> )
Relaxor I	(1-x)PMN-(x)PT	0.48	0.40	3-5	Broad	80	2,000	17-18
Relaxor II	PLZT	0.50	0.35	>5	Broad	50	2,100	16-19
Normal	$(\text{Ba}_{1-x}\text{Sr}_x)\text{TiO}_3$	0.50	0.30	4-6	Narrow	250	2,300	20-21
"Pinched"	$\text{Ba}(\text{Ti}_{1-x}\text{Sn}_x)\text{O}_3$	0.43	0.27	4-6	Narrow	280	2,500	21-23
Piezoceramic	PZT-5H	0.5	0.67	—	Narrow	65	1,950	15

The elastic coefficients exhibited a softening around  $T_{\max}$  and subsequent stiffening with increasing temperatures. A stiffening of the elastic coefficients was observed with increasing field at all measurement temperatures, with a reduced field dependence corresponding to the switching and saturation of the polarization at temperatures  $\leq T_{\max}$ . Values for  $c_{33}^D$  and  $s_{11}^E$  were comparable to those of the respective piezoceramics in the BaTiO<sub>3</sub>, PMN-PT and PLZT families.

Several observed characteristics are of interest in transducer applications. Due to the external electric field, the  $k_t/k_p$  anisotropy is significantly larger than observed in conventional BaTiO<sub>3</sub>- and PZT-based piezoceramics. The mechanical quality factor,  $Q_m$ , also was field-dependent. In PMN-PT compositions,  $Q_m$  was adjustable in the range 80-220. This would be of interest as a dynamic/internal mechanism for adjusting damping/bandwidth in transducers.

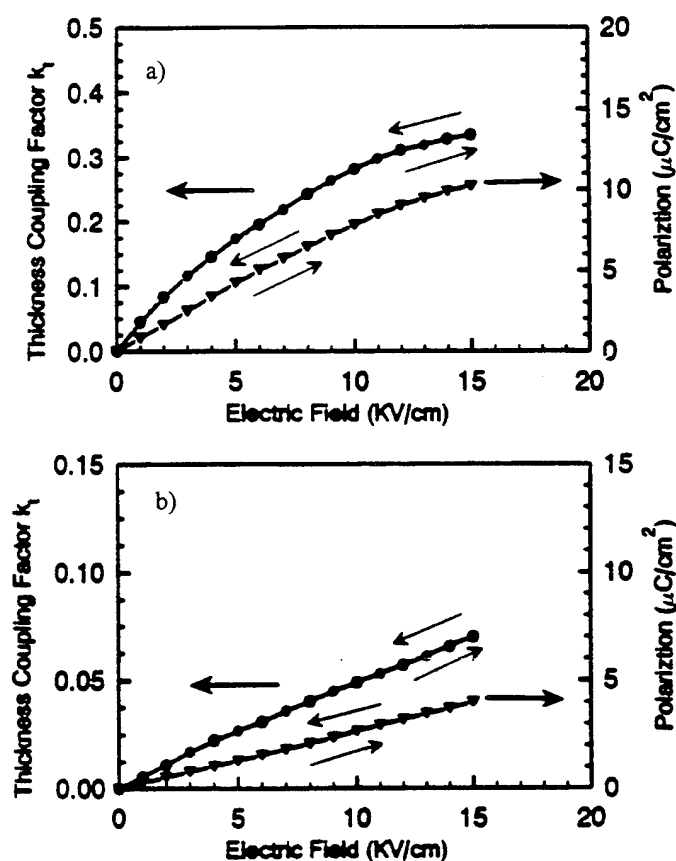


Figure 3. Field-induced thickness coupling factor  $k_t$  for a Ba<sub>0.70</sub>Sr<sub>0.30</sub>TiO<sub>3</sub> composition at a) 40°C ( $T > T_c$ ) and b) 60°C ( $T > T_c$ ).

## CONCLUSIONS

A large field-induced piezoelectric effect was measured in several of the families evaluated, with values of  $k_t \sim 0.50$ . The temperature range for obtaining large electromechanical properties without hysteresis can be related to the underlying polarization mechanism. The relaxors exhibit a much broader temperature region than the BaTiO<sub>3</sub>-based normal ferroelectrics, where significant  $P_{\text{ind}}$  can be achieved only a few degrees above  $T_c$ . PMN-PT relaxors offer large  $K$ 's, low losses, and adjustable induced piezoelectric and elastic properties. However, the strong frequency dependence of the dielectric properties of relaxors may reduce the other advantages in some fixed frequency, tunable transducer applications.

## REFERENCES

- [1] K. Uchino, "Electrostrictive Actuators: Materials and Applications," *Am. Ceram. Bull.*, **65** [4], pp. 647-652 (1986).
- [2] H. Takeuchi, H. Masuzawa, and C. Nakaya, "Relaxor Ferroelectric Transducers," *Proceedings of 1990 Ultrasonics Symposium*, 697 (1990).
- [3] J. T. Fielding, Jr., "Field-Induced Piezoelectric Materials for High Frequency Transducer Applications," Ph.D. Thesis, The Pennsylvania State University, (1993).
- [4] W. Y. Pan, "Ferroelectric Type Materials for Actuator Applications," Ph.D. Thesis, The Pennsylvania State University (1988).
- [5] L. E. Cross, "Piezoelectric and Electrostrictive Sensors and Actuators for Adaptive Structures and Smart Materials," *Proc. AME 110th Annual Mtg.*, San Francisco (1989).
- [6] E. Fatuzzo, and W. J. Merz, *Ferroelectricity*, 104-147, John Wiley and Sons, New York (1967).
- [7] K. Toyoda, T. Kato and Y. Sakabe, "Re-examination of the Phase Transitions in BaTiO<sub>3</sub>-based Solid Solutions," *Ferroelectrics*, **108**, 227-232 (1990).
- [8] J. von Cieminski, H. T. Langhammer and H. P. Abrecht, "Peculiar Electromechanical Properties of Some Ba(Ti, Sn)O<sub>3</sub> Ceramics," *phys. stat. sol.*, (a) **120**, 285-293 (1990).
- [9] S. J. Jang, K. Uchino, S. Nomura and L. E. Cross, "Electrostrictive Behavior of Lead Magnesium Niobate Based Ceramic Dielectrics," *Ferroelectrics*, **27**, 31-34 (1982).
- [10] S. W. Choi, T. R. Shrout, S. J. Jang and A. S. Bhalla, "Dielectric and Pyroelectric Properties in the PMN:PT System," *Ferroelectrics*, **100**, 29 (1989).
- [11] J. Kuwata, K. Uchino, and S. Nomura, "Electrostrictive Coefficients of Pb(Mg<sub>1/3</sub>Nb<sub>2/3</sub>)O<sub>3</sub> Ceramics," *Jap. Jnl. of App. Phys.*, **19** [11], 2099-2103 (1980).
- [12] G. H. Haertling and C. E. Land, "Hot-Pressed (Pb,La)(Zr,Ti)O<sub>3</sub> Ferroelectric Ceramics for Electrooptic Applications," *J. Am. Ceram. Soc.*, **54** [1], pp. 1-11 (1971).
- [13] S. L. Swartz and T. R. Shrout, "Fabrication of Perovskite Lead Magnesium Niobate," *Mat. Res. Bull.*, **17**, 1245-1250 (1982).
- [14] IEEE Standard on Piezoelectricity, ANSI/IEEE Std 176-1978, The Institute of Electrical and Electronic Engineers, Inc., New York (1978).

# Concurrent Session - 3C: Dielectrics



# The Application of Microwave Ceramics

Takashi Okawa\*, Hideki Utaki\*, Takahiro Takada<sup>1</sup>  
Sumitomo Metal Industries, Ltd.

\*Electronics Components Division.

<sup>1</sup> Higashi Mukojima Nishi, Amagasaki, Hyogo 660, Japan.

\*Research & Development Center.

1-8 Fuso, Amagasaki, Hyogo 660, Japan.

Sumitomo Metal Industries, Ltd. (SMI) has developed and commercialized the microwave dielectric ceramics with variable characteristics. These ceramics found in cellular phone technology, which has dramatically increased this year in Japan. We present and discuss the application of microwave ceramics as one of the ceramic components maker.

The microwave devices such as the co-axial dielectrics and the high frequency capacitor, which are applied by our original advanced ceramic properties, are introduced in present paper.

Further, a multi-layer dielectric resonator and a voltage control oscillator (VCO), which are used by our developed low firing materials, will also be discussed.

## 1. Introduction

Recently, microwave communication systems such as satellite broadcasting, mobile phone, and cordless telephone are making remarkable progress with an increase in communication systems.

The demand for the mobile phone in Japan has been dramatically increasing since this April. In April 1994, the purchase system of mobile phone has started in Japan.

As the multimedia technology is attracting great attention, personal handy phone system (PHS) and GPS navigation systems will become large market in Japan near future.

However many electronics company have started business in this market and hard competition is inevitable.

This will naturally bring about the requirements of more severe performance on important components which are made of microwave dielectric ceramics for the equipment.

This paper shows (1) a variety of microwave ceramic material and parts made of the materials which Sumitomo Metal Industries, Ltd. (SMI) produces, (2) application of those materials, and (3) a multi-layer type microwave ceramic device which is opening up a path to a new area of development in Japan.<sup>(1)</sup>

## 2. Microwave Dielectric Materials

### 2-1. Required properties for microwave dielectric materials

The important characteristics of microwave dielectric ceramics are the following;

- (1) A high dielectric constant ( $\epsilon_r$ )
- (2) High Q value
- (3) A low temperature coefficient ( $\tau_f$ )

the wavelength of the electromagnetic wave in a dielectric material is reduced by a factor of  $\epsilon_r^{-1/2}$ , as shown in the equation (1). For the size reduction of device, the dielectric constant must be high.<sup>(2)</sup>

$$\lambda_g = \lambda_0 \times \epsilon_r^{-1/2} \quad (1)$$

whereas

$\lambda_g$ : The wavelength in the dielectric material

$\lambda_0$ : The free space wavelength

$\epsilon_r$ : The relative permittivity

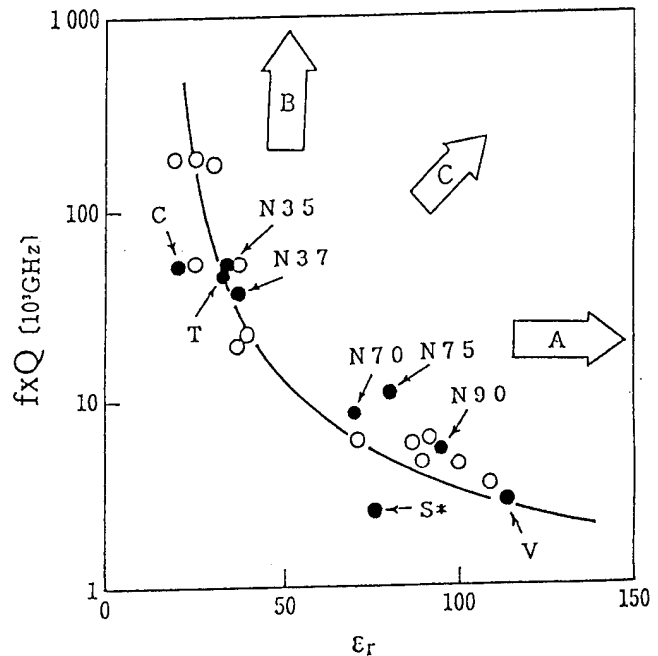


Fig. 1  $\epsilon_r$  and  $f \times Q$  for the materials with low temperature coefficient ( $\tau_f$ ).

In the case of microwave dielectric ceramics, the value of the  $f \times Q$  is an inherent property of each material.<sup>(3)</sup> The  $f \times Q$  can be considered as a reference for evaluation of the material.

The relationship between  $\epsilon_r$  and  $f \times Q$  are shown in Fig. 1. The black points indicate the material manufactured by SMI. The materials in a direction A have high  $\epsilon_r$ , but those  $f \times Q$  are low. The material in a direction B have high  $f \times Q$ , but those  $\epsilon_r$  are low. The material in a direction C is the perfect to satisfy the three important characteristics of microwave dielectric ceramics. However, this kind of material has not found out at this moment. In practice, variable materials are selected according to usage.

### 2-2. Microwave dielectric materials in SMI.

Properties of the materials manufactured by SMI are shown in Table 1. N35 and N37 are the materials in a direction B. Their advantageous points are high permittivity and low cost, because of the  $\text{BaO-TiO}_2\text{-WO}_3$  ceramics. These materials are suitable for usage in large device applications.

N70, N90 and V are the materials in a direction A. The advantageous points of N70 and N90 are very high Q in spite of high  $\epsilon_r$  which is 115.

S is the special material for multi-layer microwave devices explained in the later section. Its  $\epsilon_r$  value is 75 in spite of low sintering temperature of 900°C.

## 3. The application of microwave ceramics

The following introduces microwave components to which the microwave dielectric materials are applied.

### 3-1. Resonators

Fig. 2 shows the representative resonator types currently in use. The mode of electromagnetic field decides the type of resonator.<sup>(4)</sup>

Generally, the higher the Q value is, the larger the size of resonator is. The following is a detailed explanation of each resonator type.

#### (a) TEM mode resonators (coaxial type resonators):

$\lambda/4$  resonator is the most common type of coaxial type resonator, which is shown in Photo 1, because of its small size. It is widely used as filters in mobile phone and many other radio communications equipment. Photo 2 shows the dielectric filters using the coaxial type resonators. Several resonators are combined with capacitors or inductances to achieve required filter response.

Generally, the unloaded Q value affects the frequency characteristics of filter response.<sup>(5)</sup> To achieve a sharp shaped filter response, it is necessary to use resonators with a very high unloaded Q value. Fig. 4 shows the relationship between the resonator's external dimension(D) and the resonator's unloaded Q value. The unloaded Q value of resonator increases with increasing of D. In Fig. 4, the dotted line shows the calculated unloaded Q values of resonators. The practical resonators have only about 50% unloaded Q of the calculated value because of low conductive electrode.<sup>(5)</sup>

As research progress in the area of electrode, resonators with a higher unloaded Q value may become possible.

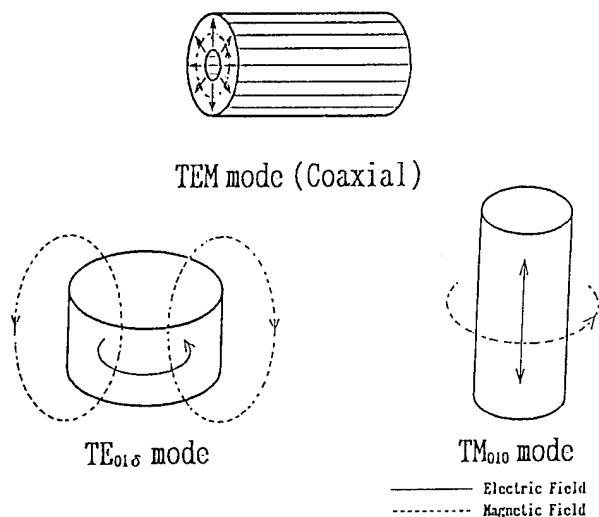


Fig. 2 Various type of dielectric resonators.

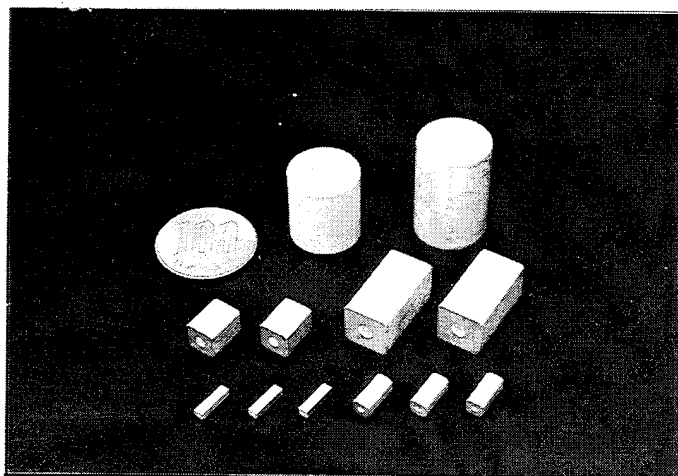


Photo 1 Coaxial type resonators.

Table 1 Microwave dielectric materials manufactured by Sumitomo Metal Industries, Ltd.

CODE	$\epsilon_r$	$f \cdot Q$ [GHz]	$\tau f$ [ppm/°C]	Material Systems
C	21	>50000	5	MgTiO <sub>3</sub> -CaTiO <sub>3</sub>
T	35	>45000	-2	(ZrSn)TiO <sub>4</sub>
N35	35	>48000	2	BaO-TiO <sub>2</sub> -WO <sub>3</sub>
N37	37	>38000	4	
N70	70	>9500	5	REO-BaO-TiO <sub>2</sub> RE: Rare Earth
N75	76	>10500	0	
S*	75	>2500	-8	
N90	91	>5500	7	
V	115	>3000	25	

\* Firing Temp. 900°C

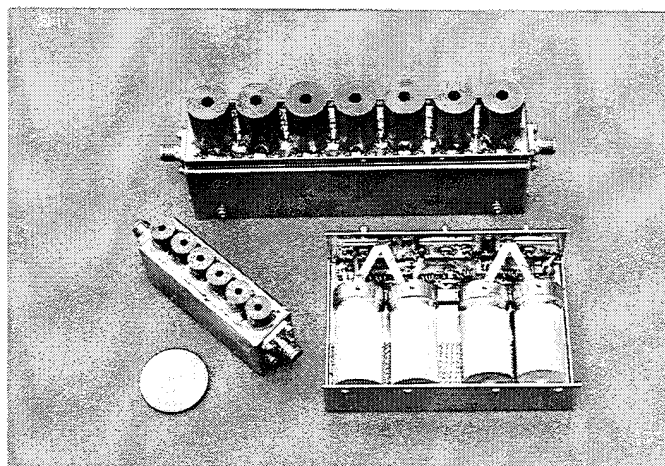


Photo 2 Dielectric filters made of coaxial resonators.

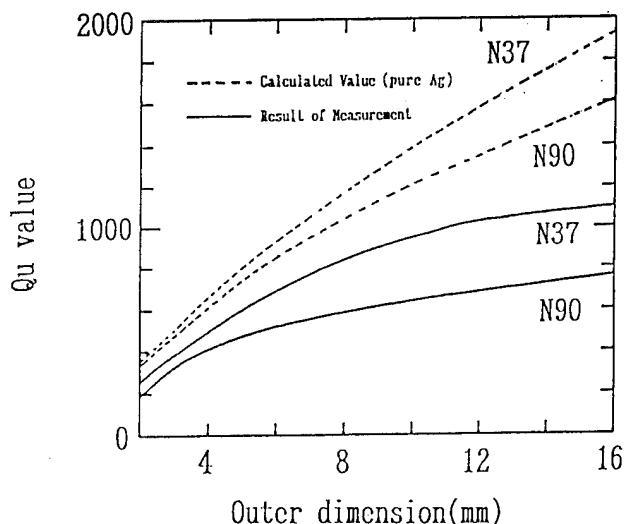


Fig. 3 Outer dimension and Qu for coaxial resonators.

### (b) $TE_{018}$ mode resonator and $TM_{010}$ mode resonator

$TE_{018}$  mode resonator is suitable for the resonator with high Q such as channel-filters for the base station.  $TE_{018}$  mode resonator has the highest Q value in the types of resonator, but the size is largest. However  $TM_{010}$  mode resonator has about 65% Q value of  $TE_{018}$  mode resonator, the size is about 15% of  $TE_{018}$  mode resonator.<sup>(5)</sup> Recently, to reduce the size of the channel-filter using  $TM_{010}$  mode resonator, the size is about 15% of  $TE_{018}$  mode resonator has been started in Japan. Photo 3 shows various type  $TE_{018}$  mode resonators and  $TM_{010}$  mode resonators for the base station.

### 3-2. Other applications

Introduce below are an example of microwave dielectric ceramic applications for others such as high frequency capacitors and RF matching circuit using microwave dielectric substrate.

#### (a) High frequency capacitors

Fig. 5 shows the equivalent circuit for two pole type dielectric filter. High frequency capacitors that use microwave dielectric ceramics are mainly used as capacitances such as  $C_1$  and  $C_2$  in this diagram. Because these capacitances such as  $C_1$  and  $C_2$  strongly affect the frequency characteristics of filter, these capacitances are required the very small tolerance, high temperature stability, and high Q in microwave frequency region. Photo 4 shows the SMD type and single layer type high frequency capacitors manufactured by SMI. Fig. 6 shows a comparison of the high frequency characteristics of this SMD type capacitor with other type capacitors. With the help of the simple structure using microwave dielectric ceramics, this SMD type capacitor has higher Q than conventional type resonators.

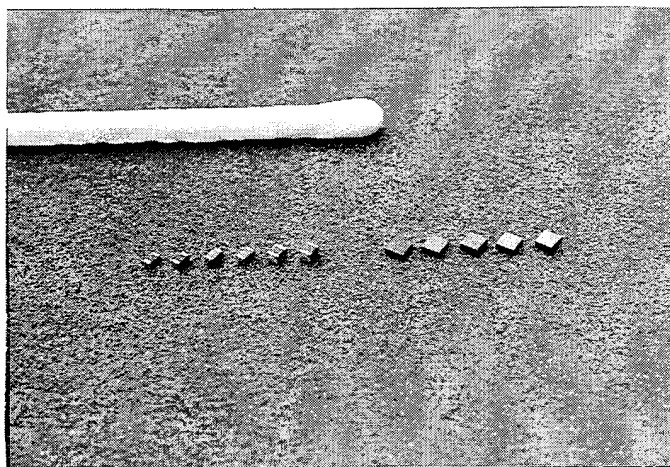


Photo 4 High frequency capacitors.

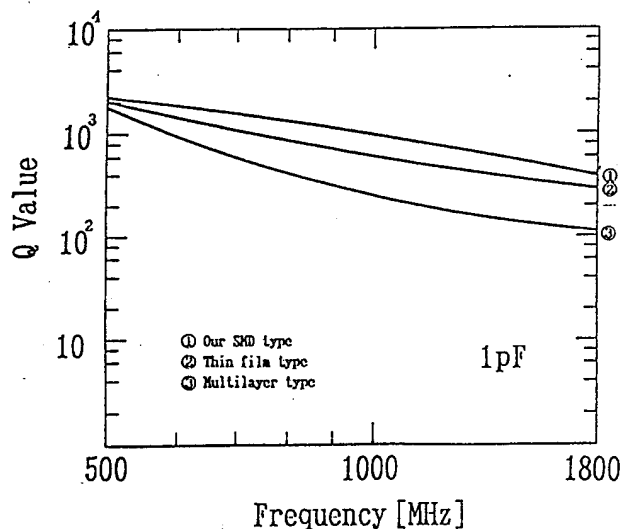


Fig. 5 Comparison of Q values for capacitors.

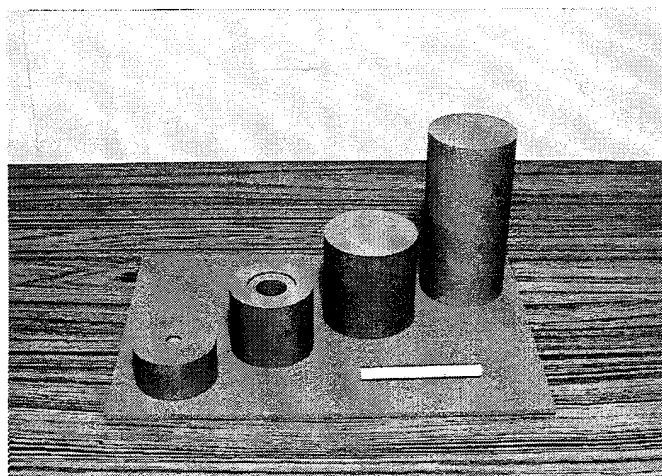


Photo 3 Resonators for the base station.

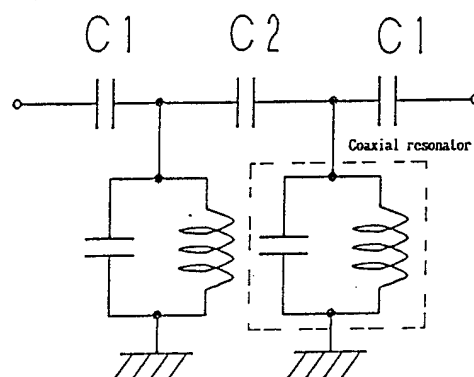


Fig. 4 Equivalent circuit for two pole filter.

#### (b) RF matching circuit using microwave dielectric substrate

Fig. 7 is an example of a matching circuit between the GaAs FET and outer circuit. Since the characteristic impedance of the GaAs FET is generally low (about  $11\Omega$ ), it is necessary to achieve the impedance matching with outer circuits (characteristics impedance of  $50\Omega$ ) in high frequency. Microwave dielectric ceramics are also used as a capacitance in matching circuit applications. An RF matching circuit using microwave dielectric substrate forms capacitances of the circuit with electrode patterns.

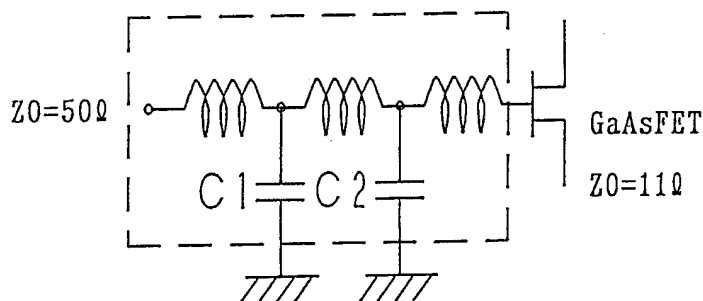


Fig. 6 Matching circuit for GaAsFET.

Photo 5 is an example of RF matching circuit using microwave dielectric substrate. However majority of RF matching circuit of this type conventionally used alumina, it is expected that microwave dielectric substrates will be commonly used for reducing the size of GaAs AMP in near future.

#### 4. The Multi-layer Type Resonators & VCO

The last group of product introduced in this paper are microwave devices of multi-layer structure.<sup>(1),(7)</sup>

##### 4-1. Superiority of multi-layer structure

If the permittivity of microwave dielectric ceramics were high, the size of devices could be reduced from that of conventional type device, as described above. However there is a certain limitation ( $\epsilon_r=115$ ) considering the balance of other microwave characteristics. Therefore, use of multi-layer structure is expected to serve as a mean of further down sizing device. Fig. 8 shows various types of multi-layer resonators and filters. The merits of using multi-layer structure are as follows.

##### (a) The shorter length of devices by curved electrode

The multi-layer structure enables production of curved internal electrode, which are impossible to produce with the press forming method. Length of the devices can be made shorter than resonant wave length as shown in Fig. 8.

##### (b) The thinner thickness

Conventional coaxial type structure, the internal electrodes are formed by print method. Many types of internal electrode can be produced in the same dielectric ceramics body. Multi-layer structure for device helps the integration of elements as shown in Fig. 8.

##### 4-2. Low firing materials

As described above, the multi-layer structure is highly effective in down sizing devices. However, in microwave frequency ranges, metals with low conductive losses must be used for the internal electrodes due to a shallower skin depth (depth of electromagnetic wave penetration into the conductor).

Representative metals with low conductive losses are Cu, Ag and Au. However, the melting points of those metals are below 1100°C, as shown in table 2. Because the firing temperatures of conventional microwave dielectric ceramics are high (about 1300°C), those metals cannot be used as internal electrodes in co-fire method. As a result, SMI has successfully developed a microwave dielectric materials with a dielectric constant of 75 and low sintering temperature of 900°C. Table 3 shows the characteristics of this materials.

Table 2 Properties of the metals with low resistivity.

Metal	Electric Resistivity [25°C, 10 <sup>-11</sup> Ω·cm]	Melting points [°C]
Cu	1.72	1083
Ag	1.67	960.5
Au	2.27	1063

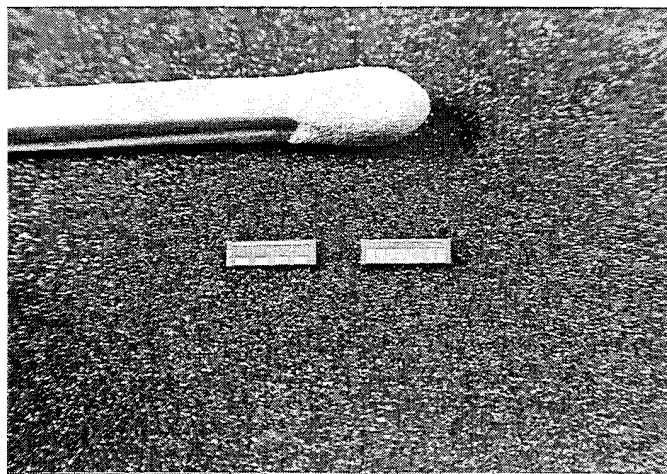


Photo 5 RF matching circuit using microwave dielectric substrate for GaAsFET.

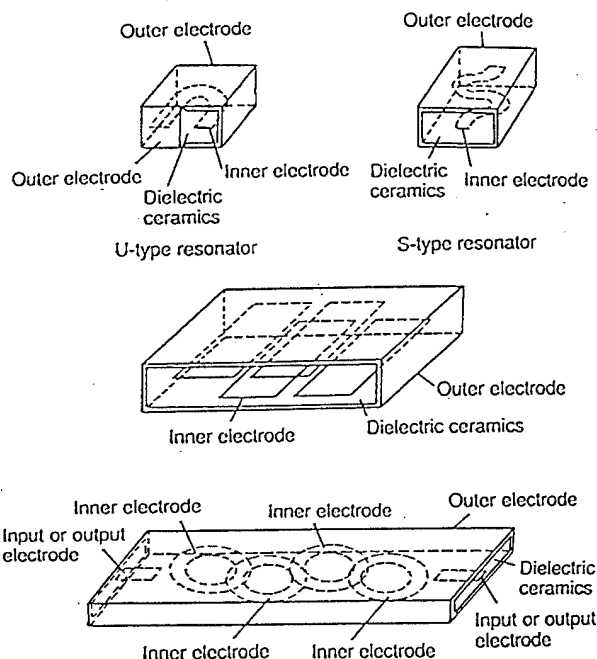


Fig. 7 Various type of multi-layer dielectric resonators and filters.

Table 3 Properties of the material for multi-layer dielectric devices.

Firing temperature	[°C]	900
Dielectric constant	$\epsilon_r$	75
$f \cdot Q$	[GHz]	>2500
Temperature coefficient of resonant frequency	[ppm/°C]	<±15

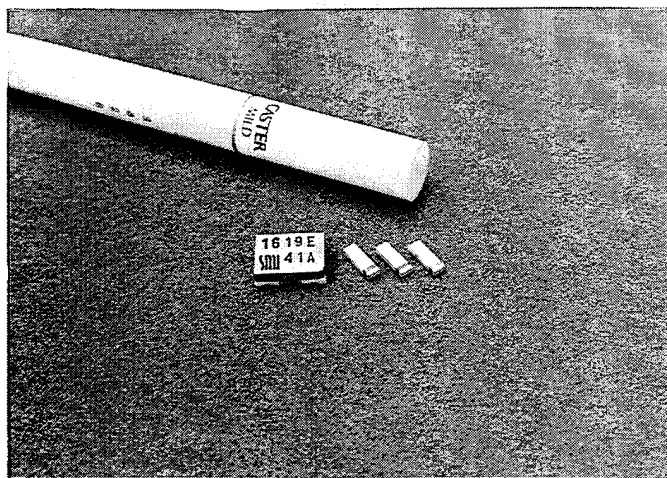


Photo 6 Multi-layer resonators and VCO manufactured by Sumitomo Metal Industries, Ltd.

#### 4-3. Applications of low firing material

Photo 6 shows the multi-layer type resonators and VCO manufactured by SMI. Fig. 9 shows the external dimensions of the multi-layer resonator. Thickness of the resonator is only 0.9 mm and this resonator has surface-mountable design. Table 4 shows the characteristics for multi-layer resonator and VCO loaded with this resonator, the size of VCO is the smallest in the industry, while maintaining high performance.

#### 5. Conclusion

In this paper, various microwave materials and components made from C, T, N35, N37, N70, N90 and V materials which are currently manufactured by SMI were introduced.

Five years ago, SMI introduced low temperature firing microwave materials with a high dielectric constant<sup>(7)</sup>. Ever since then, development of multi-layer microwave devices have been attracting the industry's attention.

The multi-layer dielectric resonators and the ultra-compact VCO introduced in this paper are the examples of the result of the development efforts.

SMI will continue to develop and commercialize microwave dielectric materials, components and devices that offer superior features to answer the needs of microwave communications equipment manufactures.

#### Acknowledgments

The author wish to thank Dr. A. S. Bhalla and Dr. Sei-Joo Jang for their sincere encouragement and their invitation to this meeting. The assistance of many colleagues with reviewing the manuscript is gratefully acknowledged.

#### References

- (1) T. Okawa and H. Utaki, "The Development of a Multi-layer Dielectric Filter Using Low Temperature Fired Microwave Ceramics", The Sumitomo Search, 47, pp.117-21 (1991).
- (2) J. K. Flourde, D. F. Linn, H. M. O'Bryan, Jr. and J. Thomson, "Ba<sub>2</sub>TiO<sub>20</sub> as a Microwave Dielectric Resonator", J. Am. Ceram. Soc., 58 [9]-[10], pp. 418-20 (1975).
- (3) Y. Konishi, "Novel Dielectric Waveguide Components Microwave Applications of New Ceramic Materials", Proceedings of The IEEE, 79 [6], pp. 726-40 (1991).
- (4) Y. Kobayashi "A Mode Chart for Cylindrical Dielectric Resonators", Rec. Professional Groups, Inst. Electron. Commun. Eng. Japan, MW 68-27, Aug. (1968).
- (5) G. L. Matthaei, L. Young and E. M. T. Jones, "Microwave Filters, Impedance-Matching Networks and Coupling Structures", McGraw-Hill, (1964).
- (6) Electronic Ceramics 19 92, Gakukensya Tokyo April (1988).
- (7) T. Okawa, "Multi-layer Dielectric Filter Using Low Temperature Fired Microwave Ceramics", Dai 10 kai Denshi Zairyo Touronkai Procceding, 25-26 (1990). (in Japanese)

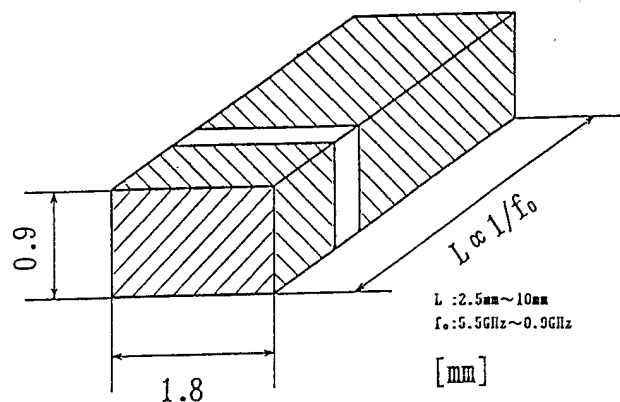


Fig. 8 External dimension of the multi-layer resonator.

Table 4 Properties of the multi-layer resonator and VCO.

Multi-layer resonator	
Resonant frequency [GHz]	2.1
Unloaded Q	>120

VCO	
Supply voltage [V]	3.0±0.15
Current consumption [mA]	≤5
Output power [dBm]	≥-5
Oscillator frequency [MHz]	1600
Tuning voltage [V]	0.5~2.5
Tuning sensitivity [MHz/V]	20
C/N ratio [dBc/Hz] 25KHz Offset	100

# INVESTIGATION OF AGING EFFECTS FROM HIGH VOLTAGE PROFILES IN CERAMIC PHASE SHIFTER MATERIALS

S. Stowell, L.C. Sengupta, E. Ngo, M.E. O'Day, and R. Lancto  
U.S. Army Research Laboratory, Materials Directorate, AMSRL-MA-CA,  
Watertown, MA 02172-0001

**Abstract-** Ceramic composite materials comprised of  $\text{Ba}_{0.60}\text{Sr}_{0.40}\text{TiO}_3$  and Alumina and other non-ferroelectric oxides have been fabricated for use in phased array antennas. These composites have shown superior electronic properties and have been incorporated into several antenna designs. However, minimal testing has been accomplished to determine the electrical aging and fatigue caused by the large electric fields required to operate these devices. In this paper, a systematic study of the effect of the application of large fields will be presented. The electronic properties of the BSTO-Oxide composites (pre-voltage application) will be presented and include the dielectric constant, loss tangent, and tunability (change in dielectric constant with applied field). The study of the change in the electronic properties after large voltages applications include results on the electronic aging and fatigue of the material and appropriate conditioning of the material for application in phased array antenna systems.

## INTRODUCTION

Phased array antennas can steer transmitted or received signals either linearly or in two dimensions without mechanically oscillating the antenna. These antennas are currently constructed using ferrite phase shifting elements. Due to the type of circuit requirements necessary to operate these antennas, they are costly, large and heavy. Therefore, the use of these antennas has been limited primarily to military applications which are strategically dependent on such capabilities. In order to make these devices available for many other commercial and military uses, the basic concept of the antenna must be improved. If ferroelectric materials could be used for the phase shifting element instead of ferrites, phased array antennas would be totally revolutionized.

A ceramic Barium Strontium Titanate,  $\text{Ba}_{1-x}\text{Sr}_x\text{TiO}_3$ , (BSTO), phase shifter using a planar microstrip construction has been demonstrated [1]. In order to meet the required performance specifications, maximum phase shifting ability, the electronic properties in the low frequency (KHz) and microwave regions (GHz) must be optimized. As part of this optimization process, various composites of BSTO and non-ferroelectric oxides have been formulated. The BSTO-Alumina composite has a patent on its formulations and the other composites which are designated herein as BSTO-Oxide II and BSTO-Oxide III currently have a patent undergoing the filing process. All of these composites possess improved electronic properties. The comparison of the compositions and phase formation of the various BSTO-oxide ceramic composites will be made and related to their electronic properties. This report will outline some of the initial findings and compare them to the results found for pure BSTO. Finally, the 20 wt% BSTO-Alumina, 20 wt% BSTO-Oxide II, and 20 wt% BSTO-Oxide III specimens have been electronically aged and fatigued at high applied voltages which imitate operational voltage profiles. The results have been analyzed and appropriate conditioning of the specimens has been suggested.

## EXPERIMENTAL

### *Ceramic Processing*

Powder forms of Barium Titanate and Strontium Titanate were obtained from Ferro Corporation, Transelco Division, Pen

Yan, N.Y. (product nos. 219-6 and 218 respectively), stoichiometrically mixed to achieve  $\text{Ba}_{0.6}\text{Sr}_{0.4}\text{TiO}_3$  and ball-milled in ethanol using 3/16" alumina media for 24 hrs. The resulting BSTO was then air-dried, calcined at  $1100^\circ\text{C}$  and mixed with either powder alumina (ALCOA Industrial Chemicals, Bauxite, AR, distributed by Whittaker, Clark, and Daniels, South Plainfield, N.J., product no. A16-SG) or a second oxide (oxide II) or a third oxide (oxide III) in the proper weight percent and ball-milled again in a slurry of ethanol using the alumina grinding media for an additional 24 hrs.

3 wt% of Rhoplex B-60A (Rohm and Haas Co., Philadelphia, PA) binder is added to the resulting BSTO-Oxide mixture. The mixture is then air-dried and dry-pressed uniaxially to a pressure of approximately 7000 p.s.i.. Sintering schedules were obtained by employing a deflectometer such as Mitutoyo digimatic indicator and miniprocessor (Mitutoyo Corp., Paramus N.J.). It should be noted that all of the examined samples have % liquid absorption of less than 2%.

Two metallization techniques were employed one involved painting on two circular, aligned electrodes, one on either side of the specimens, using high purity silver paint (SPI Supplies West Chester, PA) and attaching wires using high purity silver epoxy, Magnobond 8000, made by Magnolia Plastics, Inc., Chamblee, GA. The other technique utilized the screen printing of electrodes using silver conductive ink (FERRO #3350, Electronic Materials Division, Santa Barbara, CA) and wires were attached by dipping the specimens in a bath of 2% silver, 62% tin and 36% lead solder.

### *Electronic Measurements*

The dielectric constants,  $\epsilon'$ , loss,  $\tan \delta$ , % tunability were determined for all composites before application of high voltages. The % tunability of a material is determined using the following equation:

$$\% \text{ tunability} = \{ \epsilon'(0) - \epsilon'(V_{\text{app}}) \} / \{ \epsilon'(0) \} \quad (1)$$

The tunability measurements were taken with an applied electric field which ranged from 0 to 3.0 V/micron ( $\mu\text{m}$ ). The electronic properties given in the tables were measured at a frequency of 1 KHz. Capacitance measurements for all materials were taken using an HP4284A LCR meter. Further calculations were done to correct for the effect of fringe capacitance.

Further electronic data were acquired after applying large dc fields to the materials. Again, the capacitance measurements for all materials were taken using an HP4284A LCR meter. The temperature during acquisition of both the aging and fatigue data was held constant to within  $\pm 1/2^\circ\text{C}$ .

Electronic aging was accomplished by determining the drift in the dielectric constant of the specimen at zero and elevated voltages and the return of the specimen to the zero value dielectric constant was observed. The dielectric constants of the materials were measured at zero bias and then again when a field of  $+1.5 \text{ V}/\mu\text{m}$  was applied. The field was sustained for 30 minutes and a reading was taken at one minute intervals during this time period. The field was then decreased to zero and the dielectric constant was again recorded.



The fatigue data was accomplished by determining the dielectric constant of the part at zero bias, then again upon the application of +1.5 V/ $\mu\text{m}$  and when the field was decreased to zero again and then the dielectric was recorded at a bias of -1.5 V/ $\mu\text{m}$  and again as field was decreased to zero. The above consisted of one cycle and the specimens were subjected to at least two and a half to five cycles.

## RESULTS AND DISCUSSION

### SEM and X-ray Diffraction Analysis

SEM examination of the individual bulk ceramic layers of the BSTO-Alumina composite revealed that a second phase became apparent in alumina additions as low as 10 wt%. The phase became more dominant at 35 wt% alumina and then disappeared at the 60 wt% alumina content. Likewise, the x-ray results revealed that when alumina is added to BSTO in small amounts, < 20 wt%, a second phase of Barium Aluminum Titanate,  $\text{Ba}_3\text{Al}_{10}\text{TiO}_{20}$ , is formed. In compositions having between 20 and 40 wt% alumina another second phase of Barium Aluminum Titanate forms, ie.  $\text{BaAl}_6\text{TiO}_{12}$ . In this composition range we are also seeing traces of Barium Aluminum Oxide. At 60 wt% and 80 wt% alumina we were unable to discern which phase was most prevalent or even if all three phases were present and at 80 wt% alumina definite  $\text{Al}_2\text{O}_3$  peaks became apparent.

SEM examination of the individual BSTO-Oxide II and BSTO-Oxide III compositions showed very little microstructural difference with added percentages of oxide. The x-ray results for the BSTO-Oxide II composites reveal that initially oxide II appears to be absorbed into the BSTO lattice structure. At compositions from 5-50 wt% oxide II, BSTO is the more dominant pattern, but at 60 wt%, oxide II becomes predominant. It is also interesting to note that no second phase materials were detected at any of the compositions for this composite. Similar results were observed for the BSTO-Oxide III composites. The only variation for this composite is that traces of oxide III are apparent even with only a 1 wt% addition.

### Electronic Properties

The results for the electronic properties of the BSTO-Alumina composites are shown in Table 1. The dielectric constant of the specimens is quickly reduced for compositions up to 35 wt% alumina at which point the rate of reduction in the dielectric constant is diminished. The dielectric loss,  $\tan \delta$ , reported here for all specimens includes the loss caused by the metal contact, improved metallization for these materials will definitely result in  $\tan \delta < 0.01$ . The tunability of the composites is maintained at reasonable levels (>10%) up to 20 wt% alumina at which time the tunability decreases rapidly. Table 2 contains the electronic data for the BSTO-Oxide II ceramic composites. As shown in Table 2 the loss tangents of the materials are relatively low (<0.02). It appears that as the dielectric constant decreased the loss was lowered. The dielectric constant of the composites decreases with the addition of oxide II. The electronic data for the BSTO-Oxide III composites are shown in Table 3. The semi-log plot of the dielectric constants of the BSTO-Alumina composites, the BSTO-Oxide II composites and the BSTO-Oxide III composites is shown in Fig. 1. As shown in Fig. 1, the rate of reduction is similar for both composites for compositions < 20 wt%. However, between 20 wt% - 50 wt% the rate of reduction in the dielectric constant is less than that of the BSTO-Alumina composites. The decrease in the dielectric constant for the two sets of composites is again similar from 60 wt%-100 wt% additive content. However, the

**TABLE 1.** Electronic Properties of BSTO-Alumina Ceramic Composites.

Alumina Content (wt%)	Dielectric Constant	Loss Tangent	% Tunability	Electric Field (V/ $\mu\text{m}$ )
0.0	3299.08	0.0195	19.91	0.73
1.0	2606.97	0.0122	22.50	0.76
5.0	1260.53	0.0630*	13.88	0.67
10.0	426.74	0.0163	4.79	0.39
15.0	269.25	0.0145	5.72	0.87
20.0	186.01	0.0181	3.58	0.48
25.0	83.07	0.0120		
30.0	53.43	0.0135	5.13	2.21
35.0	27.74	0.0029	0.51	0.83
40.0	25.62	0.1616*		
60.0	16.58	0.0009	0.01	0.60
80.0	12.70	0.0016		
100.0	8.37	0.0036		

\* samples had poor contacts

**TABLE 2.** Electronic Properties of BSTO-Oxide II Ceramic Composites.

Oxide II Content (wt%)	Dielectric Constant	Loss Tangent	% Tunability	Electric Field (V/ $\mu\text{m}$ )
0.0	3299.08	0.0195	19.91	0.73
1.0	2696.77	0.0042	46.01	2.72
5.0	2047.00	0.0138	12.70	0.76
10.0	1166.93	0.0111	7.68	0.68
15.0	413.05	0.0159	5.07	1.11
20.0	399.39	0.0152	5.39	0.76
25.0	273.96	0.0240	6.02	1.02
30.0	233.47	0.0098	1.21	0.73
35.0	183.33	0.0091	5.87	0.95
40.0	162.26	0.0095	0.70	0.71
50.0	92.73	0.0071	1.67	1.12
60.0	69.80	0.0098		
80.0	17.31	0.0056		
100.0	15.98	0.0018	0.05	0.27

magnitude of the dielectric constant for all of the BSTO-Alumina composites is less than that of the BSTO-Oxide II and BSTO-Oxide III composites. This may be due to the formation of the second phases in the BSTO-Alumina composites. As shown in Fig. 2, the loss tangent of the BSTO-Oxide III composites are extremely low for most all compositions (decreases slightly with an increase in oxide III). These formulations could therefore be used at higher operating frequencies, i.e., at millimeter wave range, @ 77 GHz. As shown in Fig. 1, the other electronic properties are similar to BSTO-Oxide II, except for the fact that the dielectric constants are even higher for these composites in the range 15-60 wt%. The tunability decreases slowly with increase in oxide III content and the composites exhibit high tunabilities (>10%) up to 60 wt% oxide III which was not the case for the other oxides.

The results for the aging of the composites are shown in Fig. 3. The graph shows the normalized (change in the dielectric constant) versus time in minutes. As stated previously the specimens were held at zero bias and at 1.5 V/ $\mu\text{m}$  for thirty minutes. The percentage drift (or change) in the dielectric constants at these voltages has been determined. The data indicates that the BSTO-Alumina (20 wt%) had a 0.727% change in the dielectric constant before bias and showed a 1.102% drift at bias and a 0.267% drift when again returned to zero. Likewise, the BSTO-Oxide II (20 wt%) specimen showed 2.280% drift before biasing, at bias showed a 0.373 % drift, and when returned showed a 0.452% drift. The BSTO-Oxide III sample showed a 0.410% before biasing, a 1.304% drift at bias, and a 0.808 % drift when returned to zero. It is apparent none of the specimens showed significant

**TABLE 3.** Electronic Properties of BSTO-Oxide III Ceramic Composites.

Oxide III Content (wt %)	Dielectric Constant	Loss Tangent	% Tunability	Electric Field (V/ $\mu$ m)
0.0	3299.08	0.0195	19.91	0.73
1.0	1276.21	0.0015	16.07	2.32
5.0	1770.42	0.0014		
10.0	1509.19	0.0018		
15.0	1146.79	0.0011	7.270	1.91
20.0	1079.21	0.0009	15.95	2.33
25.0	783.17	0.0007	17.46	2.45
30.0	750.93	0.0008	9.353	1.62
35.0	532.49	0.0006	18.00	2.07
40.0	416.40	0.0009	19.81	2.53
50.0	280.75	0.0117*	9.550	2.14
60.0	117.67	0.0006	11.08	2.70
80.0	17.00	0.0008	0.61	1.72
100.0	13.96	0.0009		

\* samples had poor contacts

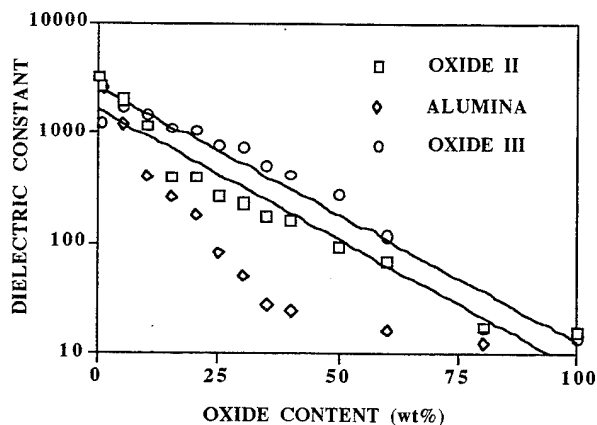


**Figure 1.** Semi-log plot of the Dielectric Constant versus Oxide Content (wt%) for BSTO-Alumina, BSTO-Oxide II, and BSTO-Oxide III composites.

drifting in their dielectric constants. However, it was noticed that the dielectric constant at zero bias was less when the specimens were returned to zero after biasing. The original value of the dielectric constant of the virgin material was however, regained after the specimen was left sitting for a period of time (the exact recovery time required has not yet been identified). This indicates no remnant polarization existed as expected for paraelectric materials of this type. However, the decreased value of the dielectric constant led us to examine the fatigue experienced by the specimens.

Fig. 4 shows the fatigue experienced by the composites. The tunability of all of the specimens, after the initial biasing cycle, is constant throughout application of the fields, even though the specimens experience typical capacitor-like logarithmic damping of their dielectric constants. For pre-conditioning of the materials, the BSTO-Alumina constants require 5 or more biasing cycles for stabilization of their dielectric constants, whereas the BSTO-Oxide II and BSTO-Oxide III require about 2 to 2 1/2 cycles. Since the dielectric constants of the materials were observed to return to their pre-bias values, the voltage conditioning should be done after each start-up period for the antenna or, if the antenna is left without application of electric field. The time after which the voltage application has to be done has not yet been determined.

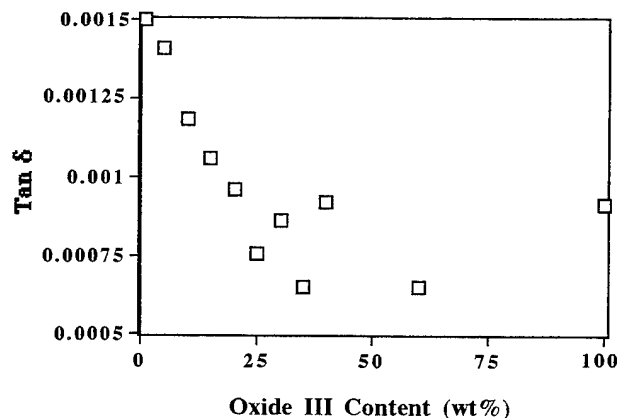


**Figure 2.** Loss Tangent versus Oxide III Content (wt %) for BSTO-Oxide III composites.

## CONCLUSIONS

Composites of BSTO and non-ferroelectric oxide ceramics have been fabricated and characterized. The composites have all demonstrated adjustable electronic properties. The dielectric constant of the BSTO-Alumina composites decreases faster than the BSTO-Oxide II and the BSTO-Oxide III composites from 20-50 wt% alumina content and is related to the formation of multiple second phases for the BSTO-Alumina composites. The BSTO-Oxide III composites exhibited the lowest loss tangents and the overall highest dielectric constants. The low loss tangents make higher operating frequencies possible. All composites showed very little drifting of the dielectric constants at zero fields or with an applied bias of 1.5 V/ $\mu$ m. The samples did exhibit typical capacitor-like damping of their dielectric constants but the before bias value of the dielectric constants of all specimens returned after a period of time (of which has presently not been exactly determined). The tunabilities of all of the specimens did not vary with voltage cycling.

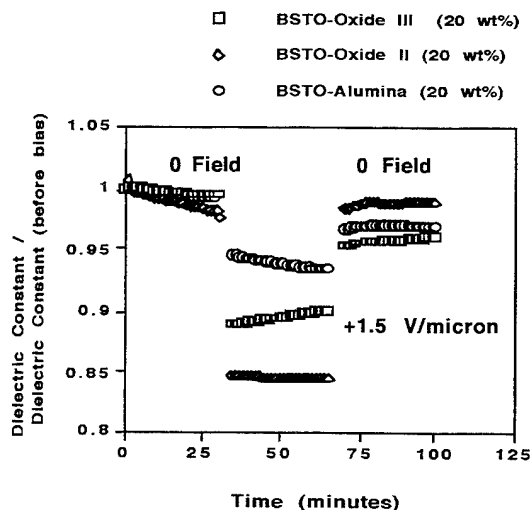


**Figure 3.** Fractional Dielectric Constant (Dielectric Constant / Dielectric Constant (before bias) vs. Time (minutes) for BSTO-Oxide Composites (20 wt%) measured at 1 KHz.



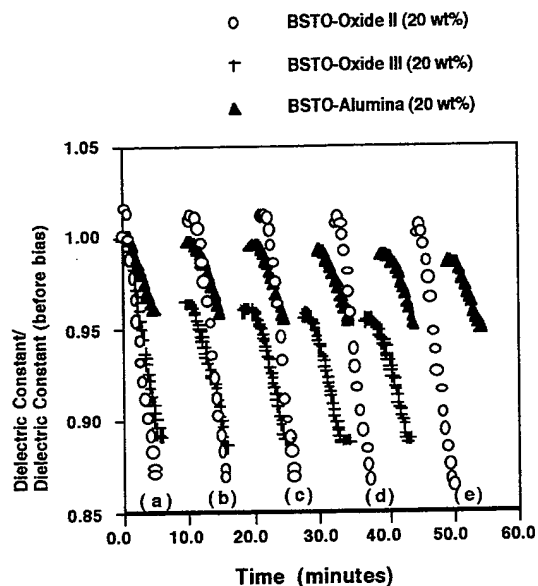


**Figure 4.** Normalized Dielectric Constants vs. Time for BSTO-Oxide Composites (20 wt%) (a = +1.5 V/ $\mu$ m, b = -1.5 V/ $\mu$ m, c = +1.5 V/ $\mu$ m, d = -1.5 V/ $\mu$ m, and e = +1.5 V/ $\mu$ m).

It was noticed that pre-conditioning of the specimens is necessary to achieve a steady-state value for the zero-bias dielectric constants. This was achieved with 2 to 2 1/2 voltage cycles for the BSTO-Oxide II and BSTO-Oxide III specimens and over 5 cycles for the BSTO-Alumina composites.

#### REFERENCES

- [1] R.W. Babbitt, T. E. Koscica, and W.E. Drach, "Planar Microwave Electro-optic Phase Shifters," *Microwave Journal*, vol. 35, pp. 63-79, June 1992.



# Concurrent Session - 1D: Piezoelectrics

# Electro-Mechanical Characteristics of Lead-Zirconate-Titanate Ceramics Under Vibration-Level Change

Sadayuki Takahashi\*

NEC Corporation, Miyazaki, Miyamae-Ku,  
Kawasaki-Shi 216, Japan  
and

Seiji Hirose\*

Yamagata University, Yonezawa-Shi, Yamagata 992, Japan  
and

Kenji Uchino and Ki-Young Oh  
The Pennsylvania State University, MRL,  
University Park, PA 16802

**Abstract** -- Electro-mechanical characteristics by changing the vibration-level were studied in lead-zirconate-titanate (PZT) based ceramics using the constant current/velocity driving method. The fractional changes of Young's modulus and mechanical dissipation factor are a function of the square of the effective vibration velocity. The increase of the dissipated-vibration-energy with the vibration-level change causes heat generation. Ferroelectric hysteresis loss is assumed to affect the dissipated-vibration-energy through the mechanical dissipation factor.

## I. INTRODUCTION

High-power piezoelectric devices, such as ultrasonic motors and piezoelectric actuators, have been vigorously studied in recent years [1]. A very high level or a great amplitude of piezoelectric vibration is required for these applications, and lead-zirconate-titanate (PZT) based piezoelectric ceramics are usually used for these devices. It has been shown, however, that a lot of heat generation as well as a drastic change in piezoelectric properties occurs in these ceramics under a high vibration-level [2]-[6]. The magnitude of the vibration-level in the high-power usage has been limited by these phenomena.

We have studied the electro-mechanical characteristics under a high vibration-level, aiming to develop the high-power usage piezoelectric materials [7]-[9]. The new measurement method of electro-mechanical characteristics under a high vibration-level was established. According to the method, the vibration-level dependence of electro-mechanical characteristics in PZT based ceramics was measured.

This paper deals with the stability of the electro-mechanical characteristics and the heat generation phenomena under the vibration level change in PZT based ceramic materials. The cause of the heat generation is discussed from the view point of a dissipated-vibration-energy due to internal friction.

## II. EXPERIMENTAL

The PZT ceramics with the basic composition of  $\text{Pb}(\text{Zr}_{0.54}\text{Ti}_{0.46})\text{O}_3$  and the ceramics doped with 0.5wt% of  $\text{Nb}_2\text{O}_5$  or  $\text{Fe}_2\text{O}_3$  were used here. The dopant Nb and Fe are known as a typical donor and an acceptor, respectively. Specimens of the ceramics were prepared by the conventional powder metallurgy technology.

Electro-mechanical characteristics were measured on the fundamental length expansion mode excited by the constant current/velocity driving circuit. Rectangular plate vibrators with 43mm long, 7mm wide and 2mm thick were used for all measurements.

The vibration-level was represented by the effective vibration velocity  $V_o$  which was an universal parameter of the vibration-level. The  $V_o$  value was determined by the following relation:

$$V_o = \sqrt{2} \pi f_o \xi_m, \quad (1)$$

where  $\xi_m$  and  $f_o$ , are the maximum vibration-amplitude and resonant frequency, respectively. The  $\xi_m$  was observed using an optical displacement sensor.

The temperature of the piezoelectric ceramic vibrators was measured by a thin thermocouple which was forced to contact the vibrational nodal line. The temperature initially increased with a time  $t$  while the vibrator was driven, but it converged on the constant value after heat generation and radiation reached their equilibrium state. This equilibrium temperature was defined as the temperature of vibrators here.

## III. RESULTS AND DISCUSSIONS

### A. Vibration-Level Dependence of Electro-Mechanical Characteristics

In Figs. 1(a) and (b), 2(a) and (b) Young's modulus  $Y_o^E$ , permittivity  $\epsilon_{33}^T$ , electro-mechanical coupling factor  $k_{31}$  and mechanical dissipation factor  $Q_m^{-1}$  in PZT ceramics with various dopants are shown as a function of  $V_o$ , respectively. The  $Y_o^E$  value decreases with increasing  $V_o$ , whereas  $\epsilon_{33}^T$ ,  $k_{31}$  and  $Q_m^{-1}$  increase. These behaviors are markedly affected by the dopant. All properties in the Nb-doped PZT begin to change from a relatively low vibration level in comparison with the case in the Fe-doped PZT. The undoped one is somewhere in between.

In Figs. 3 and 4 the fractional change of Young's modulus  $\Delta Y_o^E / (Y_o^E)_o$  and mechanical dissipation factor  $\Delta Q_m^{-1} / (Q_m^{-1})_o$  are plotted as a function of  $V_o$ . The relations can be expressed as the following empirical formulas:

$$\frac{\Delta Y_o^E}{(Y_o^E)_o} = \alpha_Y V_o^2, \quad (2)$$

$$\frac{\Delta Q_m^{-1}}{(Q_m^{-1})_o} = \alpha_{Q^{-1}} V_o^2, \quad (3)$$

where  $(Y_o^E)_o$  and  $(Q_m^{-1})_o$  are the values of  $Y_o^E$  and  $Q_m^{-1}$  in the case when  $V_o \rightarrow 0$ , respectively. The  $\alpha_Y$  and  $\alpha_{Q^{-1}}$  are the nonlinear constants of  $Y_o^E$  and  $Q_m^{-1}$ , respectively and the constants depend on the materials.

The nonlinear constants determined experimentally are summarized in Table I. The constant represents the stability of materials as the vibration-level changes, for instance, a lower constant means a more stable material. The constant for the Fe-doped PZT is smaller and the Nb-doped PZT is larger than the undoped one. In short, the Fe-doped PZT is the most stable material as the vibration-level changes among these three compositions.

\*Present address: The Pennsylvania State University, MRL, University Park, PA 16802, USA

The  $|\alpha_r|$  is plotted versus  $\alpha_{Q^{-1}}$  in Fig. 5, and the proportional relationship can be seen between them. The value of  $\alpha_{Q^{-1}}$  is larger than  $|\alpha_r|$  by approximately two orders of magnitude.

#### B. Heat Generation and Dissipated-Vibration-Energy

Temperature rise of the vibrator  $\Delta T$  is shown as a function of  $V_0$  in Fig. 6(a). The  $\Delta T$  increases with  $V_0$  and sharply goes up when  $V_0$  reaches a certain value. Presently, it is impossible to obtain a higher vibration-level, since the maximum vibration-level is limited by the heat generation phenomenon. The magnitude of the maximum vibration-level increases in the order of Nb-doped, undoped and Fe-doped PZT.

Figure 6(b) shows the dissipated-vibration-energy per one second  $\omega_0 W$  as a function of  $V_0$ . The  $\omega_0 W$  was calculated by the following equations [10]:

$$\omega_0 W = U \omega_0 Q_m^{-1}, \quad (4)$$

$$U = \bar{u} V = \frac{1}{2} \kappa Y_0^E S_m^2 V, \quad (5)$$

$$S_m = \frac{\pi \xi_m}{l}, \quad (6)$$

$$Y_0^E = \frac{l^2}{\pi^2} \rho \omega_0^2, \quad (7)$$

where  $U$ ,  $\bar{u}$ ,  $\omega_0$ ,  $S_m$ ,  $l$ ,  $V$ ,  $\rho$  and  $\kappa$  means stored mechanical energy, average energy density of  $U$ , resonant angular frequency, maximum strain, vibrator length, volume, density and shape factor, respectively. The shape factor depends on the vibrator shape and vibration mode. In this case  $\kappa = 1/2$ . The behavior of  $\omega_0 W$  versus  $V_0$  seems analogous to that of the temperature rise as shown in 6(a). In Fig. 7 the  $\Delta T$  is confirmed to be approximately proportional to the  $\omega_0 W$ . This fact suggests that the temperature rise is caused by the dissipated-vibration-energy.

In Fig. 8 the  $\Delta T$  determined both experimentally and theoretically are represented as a function of time  $t$  for Fe-doped PZT. The calculation was carried out according to the following equation:

$$\Delta T = \frac{\omega_0 W t}{Mc}, \quad (8)$$

where  $M$  ( $\sim 4.7g$ ) was the mass and  $c$  ( $\sim 0.42J / g \text{ } ^\circ C$ ) was the specific heat, respectively. The experimental value initially increases with  $t$  and then gradually converges on a constant value. Whereas the calculated one monotonously increases with  $t$ , since the effect of heat radiation is not taken into account. It is clear, however, that the experimental value initially increases along with the calculated one. This fact also suggests that the dissipated-vibration-energy causes the temperature rise as well as the results of Figs. 6 and 7.

#### C. Dissipated-Vibration-Energy and Mechanical Dissipation Factor

Equation (4) can be rewritten as follows using Eqs. (5), (6) and (7):

$$\omega_0 W = \frac{1}{2} M V_0^2 \omega_0 Q_m^{-1}, \quad (9)$$

where  $M$  is the mass. Thus the  $\omega_0 W$  is determined by  $V_0$  and  $\omega_0 Q_m^{-1}$  which means the dissipated ratio of the vibration energy per one second. The relation among the above three parameters of  $\omega_0 W$ ,  $V_0$  and  $\omega_0 Q_m^{-1}$  is shown in Fig. 9. The calculated value coincides with the experimental one. The lower the  $\omega_0 Q_m^{-1}$  is, the higher the practical upper limit of the vibration-level becomes. The  $\omega_0 Q_m^{-1}$  value depends on the materials.

In Fig. 10 the fractional change  $\Delta \omega_0 Q_m^{-1} / (\omega_0 Q_m^{-1})_0$  is plotted as a function of  $V_0$ , where  $(\omega_0 Q_m^{-1})_0$  is the  $\omega_0 Q_m^{-1}$  value for  $V_0 \rightarrow 0$ . The following same empirical formula as Eqs.(2) and (3) is derived:

$$\frac{\Delta(\omega_0 Q_m^{-1})}{\omega_0 Q_m^{-1}} = \alpha V_0^2, \quad (10.a)$$

or

$$\omega_0 Q_m^{-1} = (\omega_0 Q_m^{-1})_0 (1 + \alpha V_0^2). \quad (10.b)$$

The  $\alpha$  values are also listed in Table I. At a high vibration level ( $V_0 > 1 \text{ m/s}$ ),

$$\alpha V_0^2 \gg 1, \quad (11)$$

$$\omega_0 Q_m^{-1} \approx \alpha (\omega_0 Q_m^{-1})_0 V_0^2. \quad (12)$$

Thus the  $\omega_0 Q_m^{-1}$  can be represented approximately as an explicit function of  $V_0$ . In the case when  $V_0$  is constant, the dissipated-vibration-energy, in the other words the heat generation quantity is in proportion to  $\alpha (\omega_0 Q_m^{-1})_0$  which is the constant value depending on the vibration mode, shape and size of the vibrator and material. The smaller the  $\alpha (\omega_0 Q_m^{-1})_0$  is, the higher the practical upper limit of the vibration-level becomes after all.

#### D. Effects of Ferroelectric Hysteresis

The sharp increase of  $\omega_0 W$  in the case of  $V_0$  exceeding a certain value is resulted from the drastic increase of  $Q_m^{-1}$  since  $\alpha_{Q^{-1}} \gg |\alpha_r|$ .

The  $Q_m^{-1}$  is described as functions of elastically-originated dissipation factor  $\psi$ , dielectrically-originated dissipation factor  $\phi$  and  $k_{31}$  as follows [11]:

$$Q_m^{-1} = \frac{1}{1 - k_{31}^2} (\psi + k_{31}^2 \phi). \quad (13)$$

Considering that the change of  $Q_m^{-1}$  with changing the vibration-level is mainly caused by the change of  $\phi$  and the  $\phi$  is a sum of the intrinsic dielectric loss and the ferroelectric hysteresis loss due to domain wall motion [12],[13], it is reasonable to consider that the heat generation under the high vibration-level is basically caused by the ferroelectric hysteresis loss.

Ferroelectric hysteresis loop measured by applying the field with 0.1 Hz parallel to the polarization direction is shown in Fig. 11. The magnitude of the hysteresis loop increases in the order of Fe-doped, undoped and Nb-doped PZT. This order of the magnitude coincides with the results of Figs.6 (a) and (b).

The effective driving electric field  $E_{dc}$  is shown as a function of  $V_0$  in Fig. 12. The  $E_{dc}$  necessary to realize a certain  $V_0$  value increases in the order of Fe-doped, undoped and Nb-doped PZT. This enhances the difference between the magnitude of the hysteresis loss at the same  $V_0$  value in the three composition PZT ceramics.

#### IV. CONCLUSION

Electro-mechanical characteristics in various PZT ceramics were studied as the vibration-level was changed by using the constant current / velocity driving method. The changes in the Young's modulus and mechanical dissipation factor are a function of the square of effective vibration velocity. The drastic increase of temperature occurs above a certain vibration-level. This phenomenon gives the practical upper limit of the vibration-level.

The dissipated-vibration-energy due to internal friction was calculated. The result suggests that the abrupt temperature rise with the vibration-level increase is caused by the increase in the dissipated-vibration-energy. The energy is proportional to the mechanical dissipation factor which is very sensitive to the magnitude of ferroelectric hysteresis loop.

# REFERENCES

- [1] S. Takahashi, *Ferroelectric Ceramics*. (Eds. N. Setter and E. L. Colla), Basel: Birkhauser Verlag, 1993, pp. 349-362.
- [2] R. A. Gdula, "High-field losses of adulterated lead zirconate-titanate piezoelectric ceramics," *J. Am. Ceram. Soc.*, vol. 51, pp. 683-687, 1968.
- [3] J. H. Belding and M. G. McLaren, "Behavior of modified lead zirconate-titanate piezoelectric ceramics," *Ceram. Bull.*, vol. 49, pp. 1025-1029, 1970.
- [4] H. J. Hagemann, "Loss mechanisms and domain stabilization in doped BaTiO<sub>3</sub>," *J. Phys. C: Solid State Phys.*, vol. 11, pp. 3333-3344, 1978.
- [5] K. Lubitz and W. Wersing, "Automatic performance testing of piezoelectric ceramics for power transducers," *Ferroelectrics*, vol. 40, pp. 237-244, 1982.
- [6] K. Uchino, H. Negishi and T. Hirose, "Drive voltage dependence of electromechanical resonance in PLZT piezoelectric ceramics," *Jpn. J. Appl. Phys.*, vol. 28, Suppl. 28-2, pp. 47-49, 1989.
- [7] S. Takahashi and S. Hirose, "Vibration level characteristics of lead - zirconate - titanate piezoelectric ceramics," *Jpn. J. Appl. Phys.*, vol. 31, Pt. 1, No. 9B, pp. 3055-3057, 1992.
- [8] S. Takahashi and S. Hirose, "Vibration level characteristics for iron doped lead-zirconate-titanate piezoelectric ceramics," *Jpn. J. Appl. Phys.*, vol. 32, Pt. 1, No. 5B, pp. 2422-2425, 1993.
- [9] S. Takahashi, S. Hirose and K. Uchino, "Stability of PZT piezoelectric ceramics under vibration level change," *J. Am. Ceram. Soc.* [to be published]
- [10] K. Nagai and M. Konno, *Electro-Mechanical Vibrators and Their Applications*, Tokyo: Corona-Sha, 1974, pp. 41-44. [in Japanese]
- [11] T. Ikeda, *Fundamentals of Piezoelectric Materials Science*, Tokyo: Ohm-Sha, 1984, pp. 85-87. [in Japanese]
- [12] S. Hirose, Y. Yamayoshi, M. Taga and H. Shimizu, "A method of measuring the vibration level dependence of impedance-type equivalent circuit constant," *Jpn. J. Appl. Phys.*, vol. 30, Suppl. 30-1, pp. 117-119, 1991.
- [13] B. Lewis, "Energy loss processes in ferroelectric ceramics," *Proc. Phys. Soc.*, vol. 73, pp. 17-24, 1959.

Table I. Nonlinear constants of Young's modulus,  $\alpha_y$ , mechanical dissipation factor,  $\alpha_{Q^{-1}}$  and  $\omega_0 Q_m^{-1}$ ,  $\alpha$ .

PZT specimen	$\alpha_y$ (s <sup>2</sup> /m <sup>2</sup> )	$\alpha_{Q^{-1}}$ (s <sup>2</sup> /m <sup>2</sup> )	$\alpha$ (s <sup>2</sup> /m <sup>2</sup> )
Nb-doped	-7.7 x 10	4.6 x 10 <sup>3</sup>	4.5 x 10 <sup>3</sup>
undoped	-5.8	8.5 x 10 <sup>2</sup>	8.4 x 10 <sup>2</sup>
Fe-doped	-1.3 x 10 <sup>-1</sup>	1.7 x 10	1.7 x 10

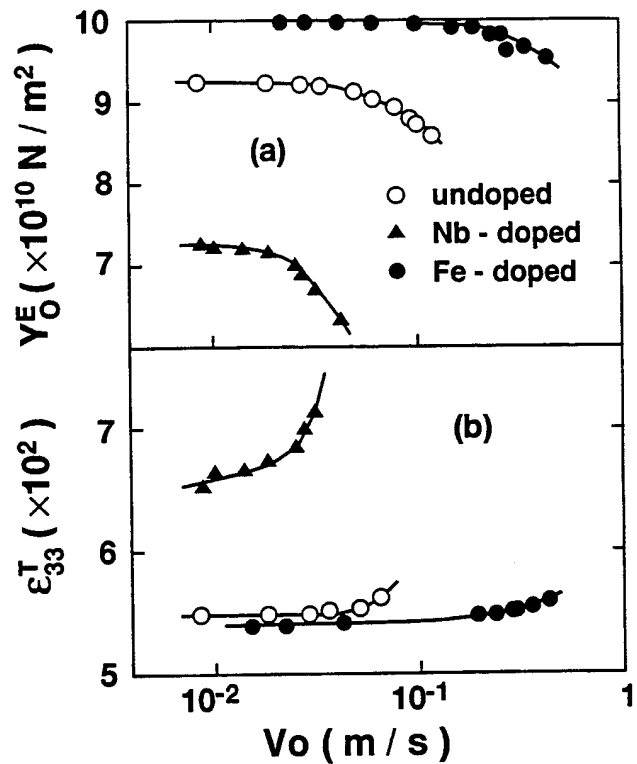


Fig. 1 Vibration-level characteristics of Young's modulus  $Y_0^E$  (a) and permittivity  $\epsilon_{33}^T$  (b).

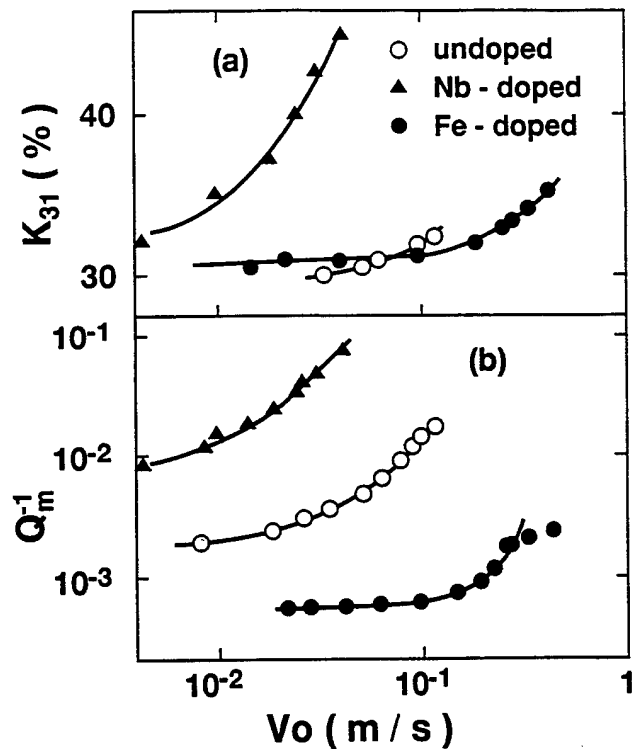


Fig. 2 Vibration-level characteristics of electro-mechanical coupling factor  $k_{31}$  (a) and mechanical dissipation factor  $Q_m^{-1}$  (b).

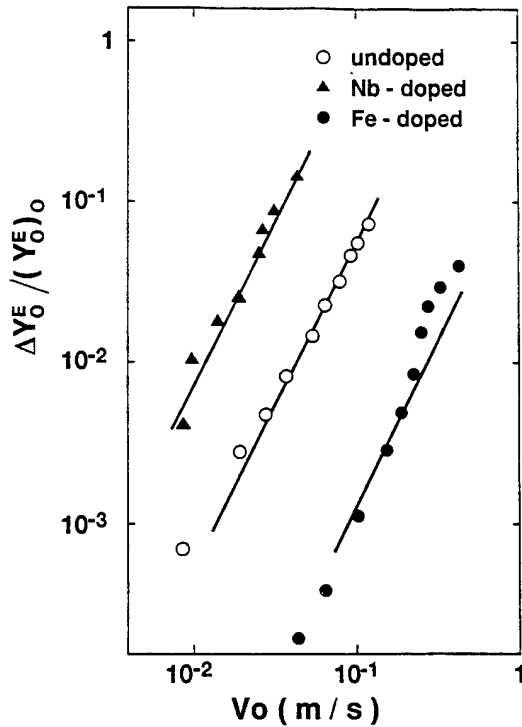


Fig. 3 Vibration-level characteristics of fractional change of Young's modulus  $\Delta Y_0^e / (Y_0^e)_0$ .

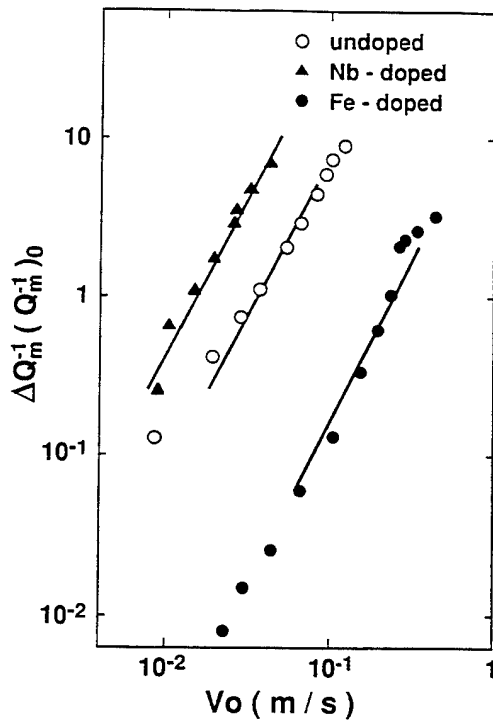


Fig. 4 Vibration-level characteristics of fractional change of mechanical dissipation factor  $\Delta Q_m^{-1} / (Q_m^{-1})_0$ .

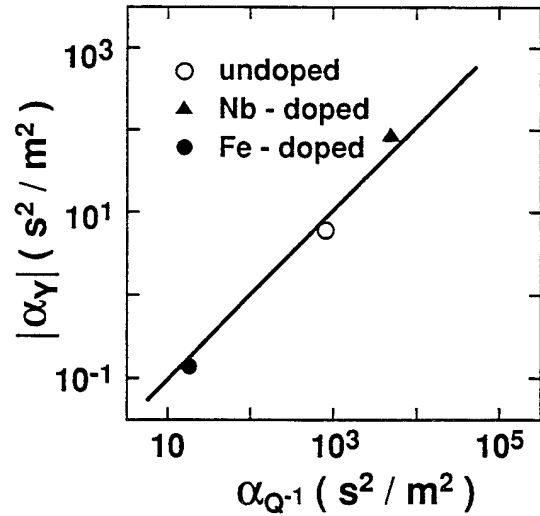


Fig. 5 Relation between the nonlinear constant of Young's modulus  $|\alpha_Y|$  and that of mechanical dissipation factor  $\alpha_{Q^{-1}}$ .

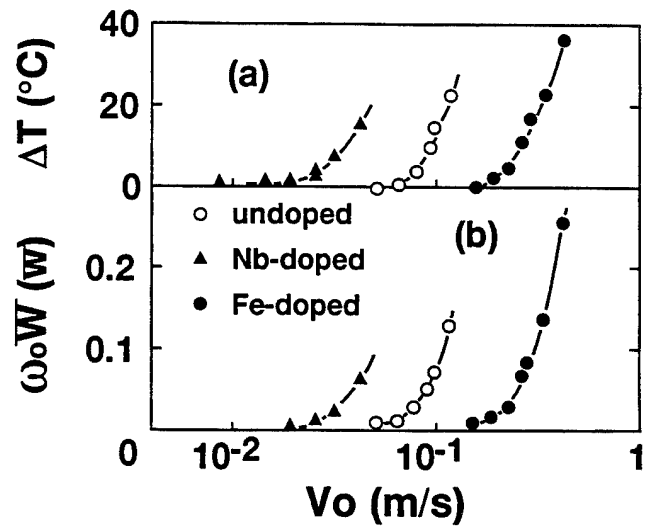


Fig. 6 Vibration-level characteristics of temperature rise  $\Delta T$  (a) and dissipated-vibration-energy per one second  $\omega_0 W$  (b).

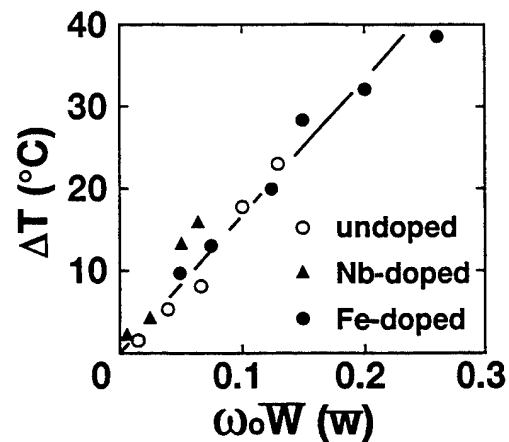


Fig. 7 Relation between temperature rise  $\Delta T$  and dissipated-vibration-energy per one second  $\omega_0 W$ .

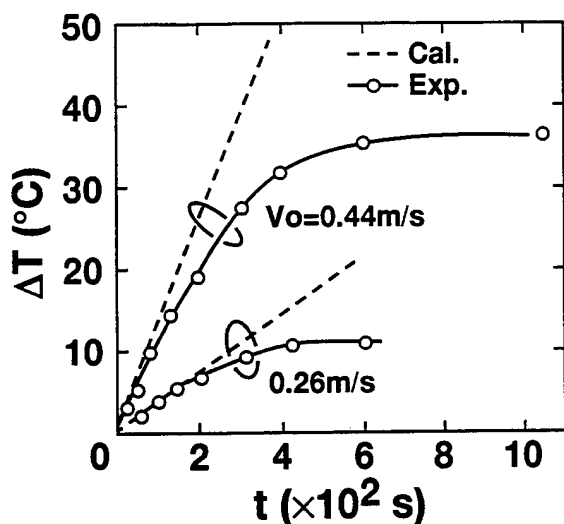


Fig. 8 Both experimental and calculated results for time dependence of temperature rise  $\Delta T$  in Fe-doped PZT ceramics.

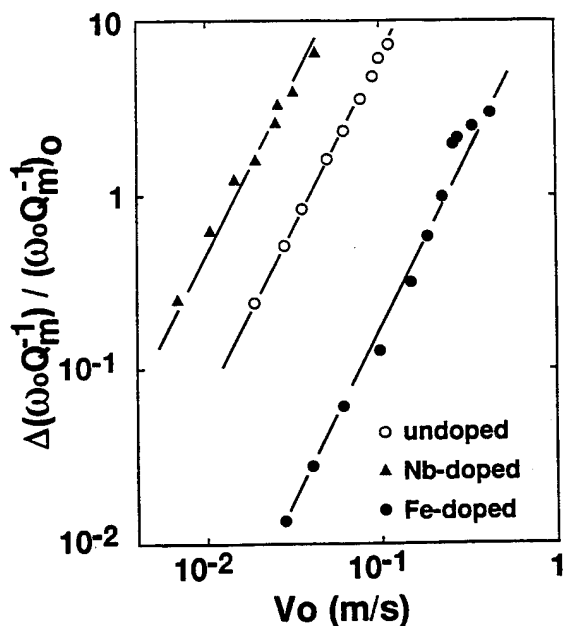


Fig. 10 Vibration-level characteristics of the fractional change  $\Delta(\omega_0 Q_m^{-1}) / (\omega_0 Q_m^{-1})_0$ .

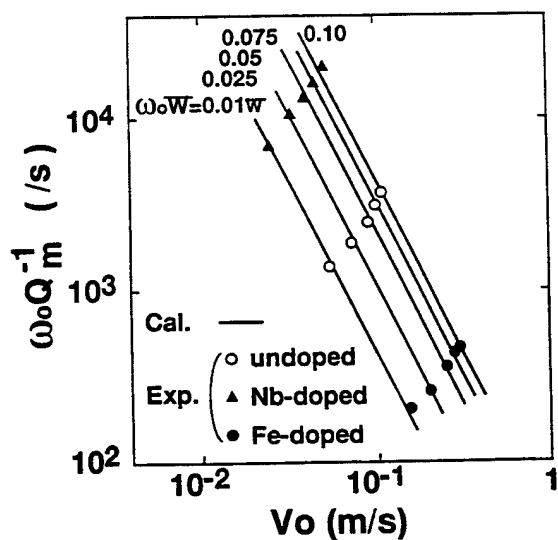


Fig. 9 Relation among three parameters of dissipated-vibration-energy per one second  $\omega_0 W$ , effective vibration velocity  $V_0$  and dissipated ratio of the vibration energy per one second  $\omega_0 Q_m^{-1}$ .

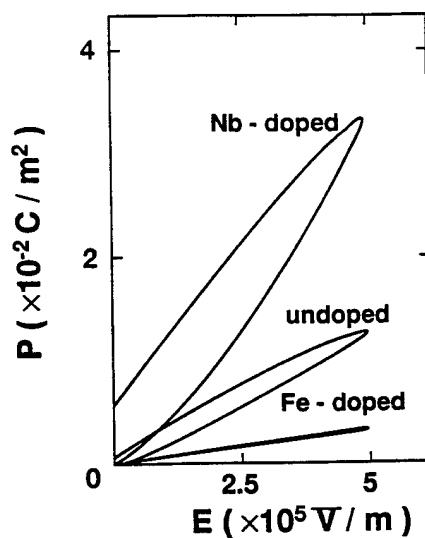


Fig. 11 Ferroelectric hysteresis loop measured by applying an electric field of 0.1Hz parallel to the polarization direction.



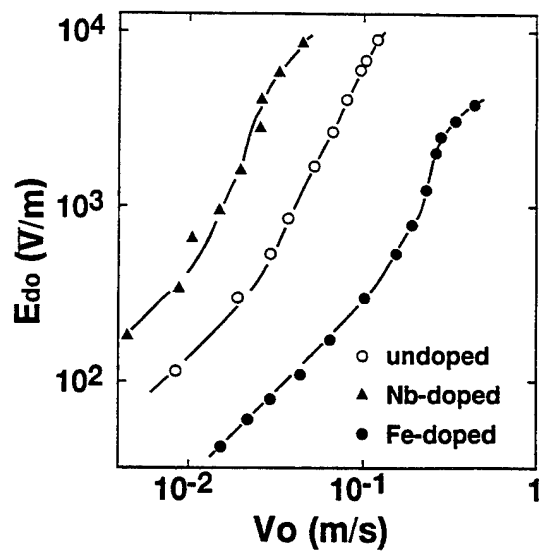


Fig. 12 Relation between effective driving electric field  $E_{do}$  and effective vibration velocity  $V_o$ .

# TYPICAL CHARACTERISTICS OF A PIEZOELECTRIC CERAMIC MATERIAL FOR SQUEEZE IGNITERS

D. Audigier, L. Eyraud, P. Eyraud, F. Eyraud, N. Glissa, P. Gonnard, M. Troccaz and M. Sprumont,\*

Laboratoire de Génie Electrique et Ferroélectricité, INSA, Bât. 504, 69621 Villeurbanne Cédex, France

\* Quartz et Silice, BP 102, 77793 Nemours Cédex, France

**Abstract** - A squeeze igniter is a mechanical-electrical reversible piezoelectric transducer working under a slow quasi isothermal stress and generating numerous sparks. The mechanism of the energy conversion under a constant stress in a spark igniter is analysed from the linear diagram strain-stress  $S_3$  ( $T_3$ ) of a piezoceramic. To withstand the highest stresses reversibly applied without depolarizing the sample, PZT type materials with suitable substitutions and oxygen vacancies are chosen. In order to improve the number of sparks and the energy of each spark the materials must offer both high  $g_{33}$  and  $\epsilon_{33}^T$  coefficients and a high static leakage resistance in the operating stresses range. These conditions are achieved for the best with the help of slightly hard PZT solid solutions doped with undervalenced ions on the Pb site and lying on the rhombohedral side of the MPB.

## INTRODUCTION

In piezoelectric sparks generators the mechano-electrical energy conversion under uniaxial stress is achieved following either a quasi-static compression (squeeze type igniters) or a dynamic compression (pulsed stress of a few microsecond duration). The impact striking igniters have been recently studied [1] [2] [3] ; it appears that very important non linearities of the electromechanical coefficients, owing to high stresses and electric fields, are observed and consequently the electromechanical conversion cannot be described any more using the classical low level piezoelectric coefficients. During the impact unusually high values of  $s_{33}^E$ ,  $d_{33}$  and  $\epsilon_{33}^T$  coefficients are shown off as well as an important increase of the loss tangent. The more suitable compositions are those offering the best compromise between the highest figure of merit  $d_{33}g_{33}$ , the lowest increase of the losses  $\tan\delta$  and a good reversibility under repetitive applied stresses.

The purpose of the present paper is to investigate the phenomena occurring during a quasi-static compression and to define the required characteristics of suitable PZT piezoceramics (perovskite structure  $ABO_3$ ).

## MODEL FORMULATION OF THE QUASI STATIC MECHANOELECTRICAL CONVERSION

### Theoretical basis of the quasi static mechano electrical conversion

"Strain-stress" and "Electric field-stress" diagrams are well suited to describe simply the mechano-electrical conversion (Figures 1 and 2). The interelectrode distance determines the disruptive electric voltage (about 3000 V for a 2 mm gap in air) and the electric field in the piezoceramic :  $Ed = \frac{3000}{\ell}$  ( $\ell$  = length of the rod).

The number  $n$  of sparks during a compression up to a maximum stress  $T_m$  is depending on the  $g_{33}$  coefficient :

$$n = \frac{T_m}{T_d} = \frac{T_m}{Ed} g_{33} \text{ with } Ed = g_{33} T_d. [4]$$

The electric discharge occurring at constant stress the electric energy of each spark is :  $W = \frac{1}{2} (s_{33}^E - s_{33}^D) T_d^2 \cdot v$  where  $v$  is the volume of piezoelectric material.

With  $k_{33}^2 = \frac{s_{33}^E - s_{33}^D}{s_{33}^E} = \frac{d_{33}g_{33}}{s_{33}^E}$  it is obtained :

$$\frac{W}{v} = \frac{1}{2} d_{33} g_{33} T_d^2 = \frac{1}{2} \epsilon_{33}^T E_d^2.$$

The energy of each spark is mainly depending on the permittivity  $\epsilon_{33}^T$ .

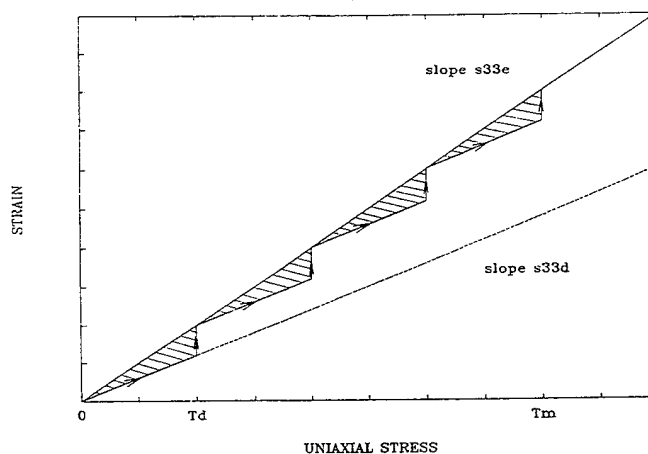


Figure 1 : Strain versus stress

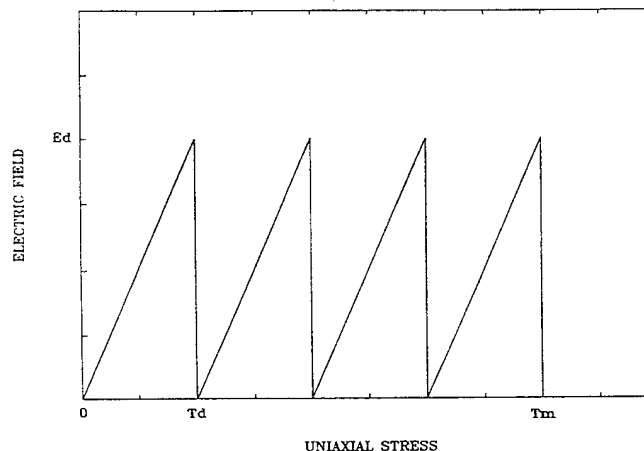


Figure 2 : Electric field versus stress

**Remark** : The preceding diagrams don't take into account the important residual electric field which subsists at the spark extinction [4].

### Non linearities of the electromechanical coefficients under a static stress

A special device leading to  $d_{33}$  and  $\varepsilon_{33}^T$  dynamic measurements under high static uniaxial stress has been built [5]. These measurements are compared with quasi static ones as a function of the uniaxial stress :  $d'_{33}$  is the slope of the "electric charges versus stress" curve in short circuit conditions,  $\varepsilon_{33}^T$  is measured by a Sawyer-Tower method performed at various static stresses (6000 V p.p,  $f = 0.2$  Hz, rod 15 mm length, 6.35 mm diameter).  $\varepsilon_{33}^T$  and  $tg \delta$  are also measured between 300 - 30 Hz with the help of a Schering bridge (1500 V rms) at various static stresses.

Figure 3 shows the variations of both static and dynamic coefficients as a function of uniaxial stress for a hard PZT composition (P190). The increase in  $d'_{33}$  is more important than the  $d_{33}$  one whereas the  $\varepsilon_{33}^T$  value remains quite close to the  $\varepsilon_{33}^T$  one. As a consequence the static voltage coefficient  $g'_{33}$  presents a strong increase versus stress.

The reversibility is good up to 120 MPa but a complete reversibility is obtained by limiting the stress at a value nearly corresponding to the maximum of the figure of merit  $d_{33}g_{33}$ .

In squeeze igniters the frequency of the sparks is depending on both the stress ramp rate and the interelectrode distance. A typical value is about 20 Hz and the corresponding piezoelectric coefficients would be near the dynamic ones.

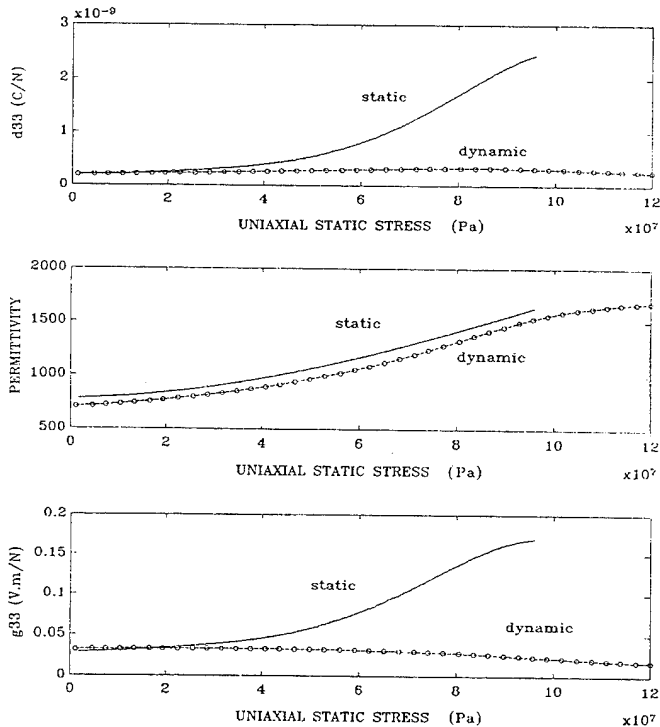


Figure 3 : Static and dynamic (120 Hz) piezoelectric coefficients versus uniaxial stress

### Theoretical basis taking into account non linearities

In order to correctly describe the quasi static conversion two important effects have to be introduced :

- Non linearities of  $s_{33}^E$  and  $d_{33}$  coefficients during the compression
- Effect of an unnegligible leakage resistance.

Assuming a linear stress-time dependence ( $T = at$ ) the equivalent electrical model is composed of a current generator

$\left( I_o = d_{33} \frac{dT}{dt} A = ad_{33}A, A : \text{sample area} \right)$  supplying a capacitance  $C_o$  in parallel with a leakage resistance  $R_o$  (Figure 4).

A variation of the  $d_{33}$  value increases the voltage rise whereas the leakage resistance drastically limits the open circuit voltage. A compensation of these two effects is possible for a critical value of the time constant  $\tau_c = R_o C_o = (2ab)^{-1}$  where  $b = \frac{1}{d_{330}} \frac{d(d_{33})}{dT}$

For P190 material with  $b \approx 2.8 \cdot 10^{-8} \text{ m}^2 \text{ N}^{-1}$  and at a stress rising rate  $a = 100 \text{ MPa s}^{-1}$  a typical value is  $\tau_c = 180 \text{ ms}$ .

The open circuit voltage versus time is represented in Figure 5 for five typical conditions.

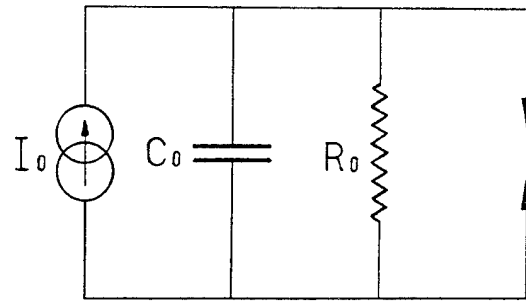


Figure 4 : Equivalent circuit of a piezoceramic under linear compression

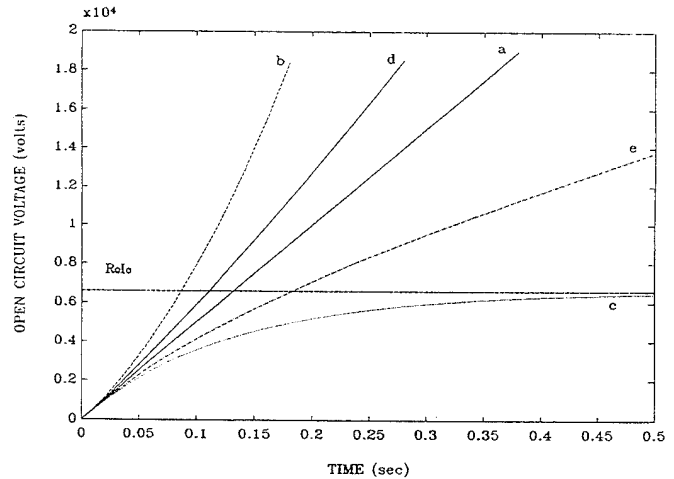


Figure 5 : Open circuit voltage versus time during a compression

- a : constant  $d_{33}$ ,  $\tau \infty$
  - b :  $d_{33} = d_{330} (1 + bT)$ ,  $\tau \infty$
  - c : constant  $d_{33}$ ,  $\tau$  unnegligible,  $V_M = R_o I_o$
  - d :  $d_{33} = d_{330} (1 + bT)$ ,  $\tau > \tau_c$
  - e :  $d_{33} = d_{330} (1 + bT)$ ,  $\tau < \tau_c$
- for  $\tau \rightarrow \tau_c$ , d and e  $\rightarrow$  a

## RESULTS AND DISCUSSION

### Test methodology

Two piezoceramics rods are inserted in a special test device. A high insulation ensures both negligible external losses and capacitance. A static prestressing (10 MPa) is applied and then stress cycles, with a 70 MPa amplitude, are generated with the help of a motorized cam. The duration of an "up and down" cycle is adjustable but the results given in this paper relate to 1.4s.

The number of sparks per cycle  $n_c$  is measured with a 2 mm interelectrode distance between metallic points. The sparks are counted up by detecting the short range electromagnetic field with an antenna followed by a comparator (Figure 6)

In the case of a material delivering 20 sparks per cycle the equivalent frequency of the sparks is 14 Hz.

Short circuit charges  $Q_{sc}$  delivered during an "up and down" cycle are also measured through a rectifier and a high value capacitance (Figure 6).

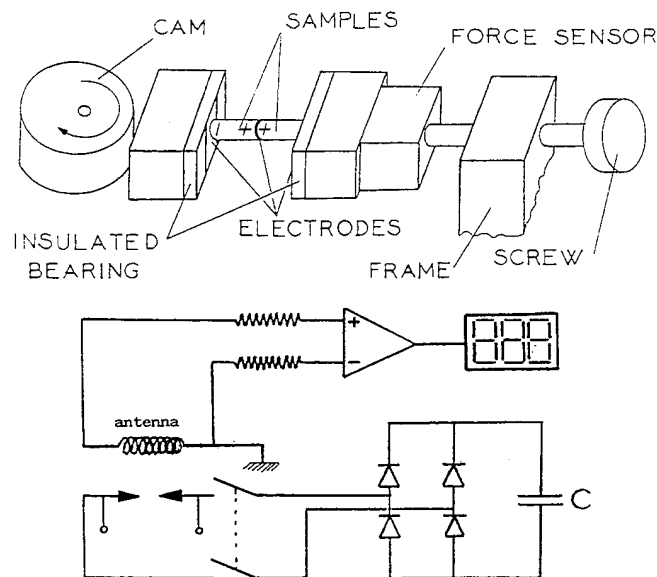


Figure 6 : Experimental set up for squeeze testing of piezoceramics

Five compositions are tested :

- A : PZT + 2 % Fe + 1,25 % Mn on B site
- B : PZT + 0,5 % Fe + 0,6 % Mn on B site
- C : PZT + 1 % (Na, K) on A site
- D : Industrial material P190 (Quartz et Silice, France)
- E : Industrial material SONOX (Hoechst, Germany)

### Effects of the Zr /Ti ratio

It is well known that in PZT materials an uniaxial stress favors the tetragonal phase [6] [7]. Consequently a composition (as for example A composition, Zr = 56 % in Figure 7) situated on the rhombohedral side of the phase transition, with a low initial  $d_{33}$  value will present under a high uniaxial stress a maximum value of this coefficient, due to the stress induced shift of the morphotropic phase boundary (MPB). In the same way Figure 7 shows the corresponding variations of the  $\epsilon_{33}^T$  and  $g_{33}$  coefficients.

As a result compositions situated on the rhombohedral side of the MPB present the following advantages :

- The combined effects of both the classical increase of  $d_{33}$  versus stress and the change of phase induced by stress lead to a strong increase of  $d_{33}$ , from which it results important electric charges released in short circuit.
- The  $g_{33}$  voltage coefficient keeps a high value despite the increase of the permittivity  $\epsilon_{33}^T$ , from which it should result an important number of sparks.

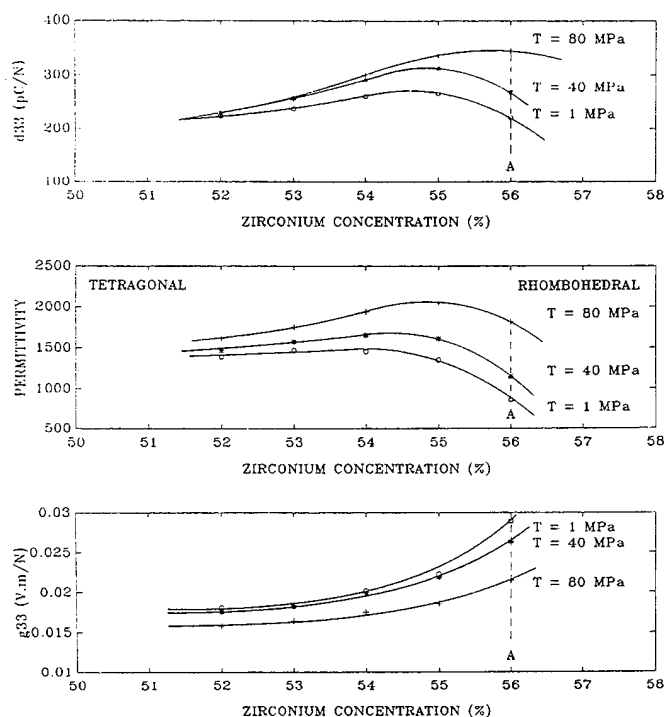
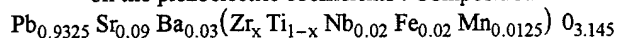


Figure 7 : Influence of the MPB shift induced by an uniaxial stress on the piezoelectric coefficients : Composition



### Influence of the very low frequency losses

Despite a high  $g_{33}$  value up to 80 MPa some compositions don't deliver a sufficient number of sparks during compression. Measurements of the loss tangent at high electric field and various stresses as a function of frequency indicate two kinds of behaviour :

- for suitable materials the loss tangent slightly decreases at low frequencies but increases with the uniaxial stress (composition D, figure 8). In every case the time constant remains above the critical value ( $\text{tg}\delta = 1/\omega\tau$ ).
- for other compositions such as B (Figure 8) an anomalous increase of the loss tangent is observed at low frequencies and consequently the time constant falls under 100 ms.

The origin of this important quasi static conduction is not clear. It is probably due to a segregation of some additives ions (such as Mn, Ni...) at the grain boundary when they are added in too large concentrations (Figure 9)[8].

That is the reason why many hard compositions are not suitable for squeeze igniters.

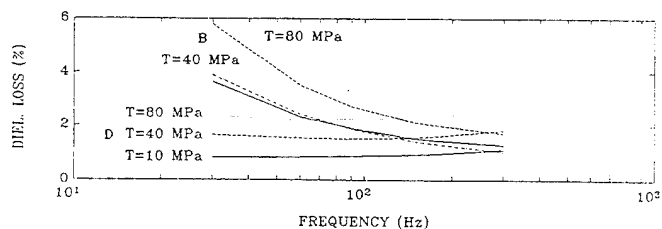


Figure 8 : Loss tangent as a function of frequency at various stresses (at 1500 V on 15 mm length samples)

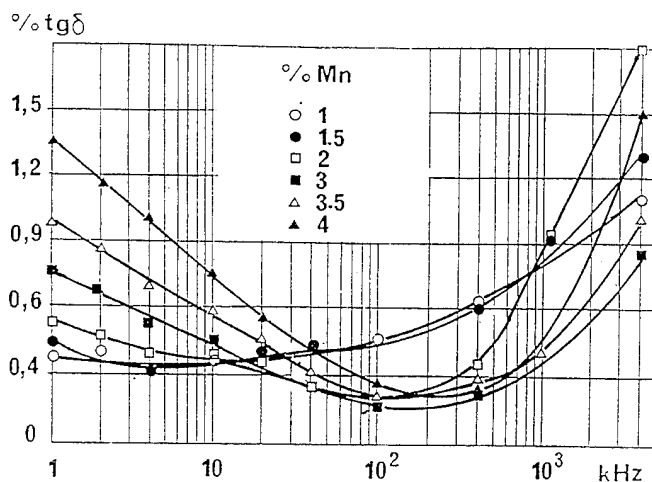


Figure 9 : Loss tangent of PZT ceramics doped with Mn as a function of frequency [9]

It is not possible to keep a good reversibility under repetitive compressions with soft compositions. So it is necessary to harden these compositions without increasing the static conductivity. This may be achieved by substituting undervalenced ions on the A site, but not on the B site which is the usual way.

In impact igniters a good stabilization had been obtained by substituting a small amount of Na or K ions on the Pb site [10]. By using these ions at higher concentrations in materials for squeeze igniters it is possible to keep both a high time constant at low frequency and a good stability under repetitive so licitations.

#### Ageing under repetitive compression

Figure 10 shows different behaviours of ageing according to the composition of the piezoceramics. In an industrial point of view, the most interesting materials must generate the greatest number of sparks during the first up and down cycles and present the lowest ageing.

These conditions are not respected with materials doped with undervalenced ions, such as Mn, Fe (A, B, D types) on the B site, whereas materials doped with Na or K on the A site present a smaller ageing rate (C type).

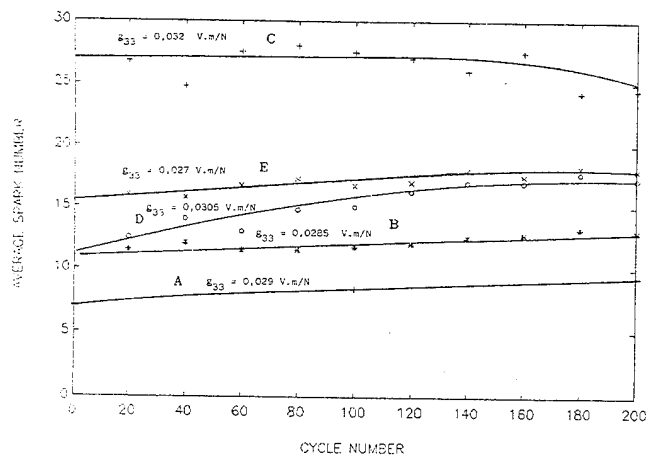


Figure 10 : Ageing as a function of the number of compressive cycles  $n_c$

#### CONCLUSION

The quasi static energy conversion with piezoelectric materials is an involved problem taking into account non linearities and conduction effects.

In typical squeeze igniters the characteristics between 10 - 80 MPa of a suitable piezoceramic should be :

- High voltage coefficient  $g_{33}$  and high permittivity  $\epsilon_{33}^T$
- High time constant at low frequency
- Zero ageing

It results from this study that PZT compositions which lie on the rhombohedral side of the MPB are the most favorable.

For stability requirements a slightly hard composition is necessary. However by using dopants on the B site the quasi static conductivity is often reinforced whereas it is lowered by using monovalent doping ions on the A site, with a very small ageing rate.

#### REFERENCES

- [1] P. Gonnard, C. Garabédian, H. Ohanessian, L. Eyraud, *Ferroelectrics*, vol. 134, pp. 93-98 (1992)
- [2] P. Gonnard, C. Garabédian, H. Ohanessian, L. Eyraud, *Proc. 8th IEEE, Int. Symp. on the Appl. of Ferroelectrics* (1992)
- [3] P. Gonnard, C. Garabédian, C. Richard, D. Audigier, L. Eyraud, *Silicates Industriels*, pp. 209-212 (1992)
- [4] C. Garabédian, P. Gonnard, H. Ohanessian, *J. Phys. III, France*, 3, pp. 1603-15 (1993)
- [5] D. Audigier, C. Richard, C. Descamps, M. Troccaz, L. Eyraud, *Proc. IMF 8*, (1993)
- [6] B. Jaffe, W.R. Cook, H. Jaffe, *Piezoelectric ceramics*, Acad. Press, London (1971)
- [7] S. Stotz, *Ferroelectrics*, vol. 76, pp. 123-32 (1987)
- [8] M.D. Glinchuk, I.P. Bikov, V.M. Kurliand, M. Bondys, T. Kala, K. Nejezhleb, *Phys. Stat. Sol.* 122, pp. 341-46, (1990)
- [9] L. Eyraud, P. Gonnard, M. Troccaz, *Ferroelectrics*, pp. 127-31 (1989)
- [10] H. Ohanessian, P. Gonnard, *Rev. Phys. Appl.* 22, pp. 47-53 (1987)

# Investigation on Piezoelectric Ceramics with High $d_{33}$ , $d_{31}$ for a New Type of Rotational Stepper Motor<sup>①</sup>

Zhilun Gui, Wei Zhong, Shuxiang Dong, Longtu Li and Xiaowen Zhang  
Department of Materials Science & Engineering  
Tsinghua University, Beijing 100084, China

**Abstract**—A quaternary system ceramics with high piezoelectric constants particularly in high  $d_{31}$ , high  $d_{33}$  was studied. The composition of materials is PMN-PNN-PZT doping with oxides of Sr, Bi, Sn and La etc. The properties of the materials are as follow:  $d_{33} = (600-750)10^{-12} \text{C/N}$ ,  $d_{31} = (-300--398) \times 10^{-12} \text{C/N}$ ,  $K_p = 0.68-0.75$ . By using this materials, a new type of rotational stepper motor, piezoelectric electro-rheological motor had been made. This kind of motor has unique advantages: no vibration noise, zero wear, low consumed power, large travel range and high resolution etc.

## INTRODUCTION

Piezoelectric ceramics was developed rapidly in the past few decades. It had been used widely for various kinds of vibrators such as filters, buzzers and transducers in electronic industries. Recently the development of ultrasonic motor and actuator is remarkable. It is necessary to meet the requirement of optical and precise machinery and automatic controlling technique. Compared with electromagnetic motors the characteristics of piezoelectric motors are listed below: They can control the displacement with high accuracy range up to several tens of micrometers; possessing high response speed; large generative force; small size and low consuming power.

Therefore, the piezoelectric ceramics is suitable for the application on low driving power and miniturization of devices.

Only the high performance piezoelectric ceramics can satisfy the need of ultrasonic motor. The properties must be satisfied both the requirements of conventional hard-type and soft-type piezoelectric ceramics. This paper aimed at researching on the high  $d_{31}$ , high  $d_{33}$  piezoelectric ceramics. The compositions of PMN-PNN-PZT doped with Sr, Sn, Bi, La are reported

and the behaviours of ER fluid-rotational stepper motor made from this cermaics were also introduced.

## EXPERIMENTAL PROCEDURE

The compositions of the sample are as follow:  
 $\text{Pb}_{1-a}\text{Sr}_a(\text{Mg}_{1/3}\text{Nb}_{2/3})_x(\text{Ni}_{1/3}\text{Nb}_{2/3})_y\text{Ti}_z\text{Zr}_w\text{O}_3$   
 $+a_1\text{mol}\%\text{SnO}_2+a_2\text{mol}\%\text{La}_2\text{O}_3+a_3\text{mol}\%\text{Bi}_2\text{O}_3$   
where  $x+y+z=1$ ,  $0 < x < 0.35$ ,  
 $0 < y < 0.30$ ,  $0.10 < z < 0.50$ ,  
 $0.10 < w < 0.50$ ,  $a = 0-10$ ,  $0 < a_1 < 10$ ,  
 $0 < a_2 < 10$ ,  $0 < a_3 < 10$

The chemical grade and analytical grade raw materials  $\text{Pb}_3\text{O}_4$ ,  $\text{TiO}_2$ ,  $\text{ZrO}_2$ ,  $\text{Nb}_2\text{O}_5$ ,  $\text{Mg}(\text{OH})_2$ ,  $4\text{MgCO}_3 \cdot 6\text{H}_2\text{O}$ ,  $\text{Ni}(\text{AC})_2$ ,  $\text{SnO}_2$ ,  $\text{La}_2\text{O}_3$ ,  $\text{SrCO}_3$ ,  $\text{Bi}_2\text{O}_3$  were used. Powders were prepared by oxide synthesis processing. Samples were formed into disc with diameter of 15mm and thickness of 1mm under the pressure of about 100MPa. The samples were sintered at  $1200^\circ\text{C}-1300^\circ\text{C}$  for 1-4hrs. The electrodes of samples were coated with silver paste and fired. The samples were polarized by a DC electric field at 3-4KV/mm in  $120^\circ\text{C}$  silicon oil. Dielectric properties of samples were measured by automatic bridge. Piezoelectric properties were measured by resonance-antiresonance method. The microstructure and mechanism of doping and modifying of the materials were analyzed by means of XRD. SEM and Laser Raman Scattering Spectrum.

## RESULTS AND DISCUSSION

### 1. The influence of doping $\text{Sr}^{2+}$

Figure 1 shows the effect of doping  $\text{Sr}^{2+}$  on properties of PMN-PNN-PZT ceramics. It reveals that the dielectric constant  $\epsilon_{33}^T / \epsilon_0$ , piezoelectric constant  $d_{33}$  and electromechanical coupling factor  $K_p$  increase obviously with  $\text{Sr}^{2+}$  content increasing. Until  $\text{Sr}^{2+}$  contents up to 6mol%,  $d_{33}$  and  $K_p$  decline. This fact is related to the crystal structure of the ceramics. The ionic radius of  $\text{Sr}^{2+}$  (1.44 Å) approaches to that of  $\text{Pb}^{2+}$  (1.49 Å), it is pre-

<sup>①</sup>This research is supported by National Science and Technology Committee of China

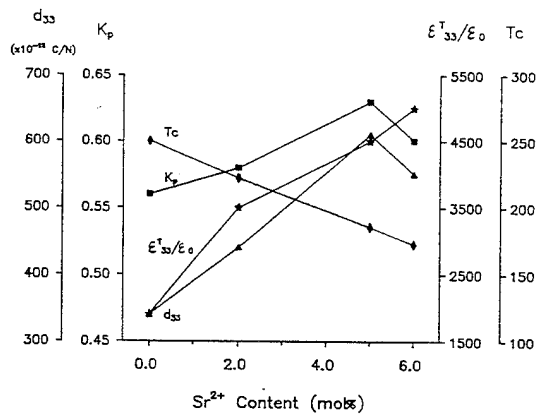


Fig.1 Piezoelectric properties as a function of Sr<sup>2+</sup> content for PMN-PNN-PZT ceramics S.T = 1270°C

Table 1 c / a of unit cell at different Sr<sup>2+</sup> contents of PMN-PNN-PZT

Sr <sup>2+</sup> contents mol%	a(Å)	C(Å)	c / a
0	4.060	4.084	1.0059
2	4.050	4.070	1.0049
5	4.053	4.064	1.0027
6	4.050	4.054	1.0012

ferred to enter A site of ABO<sub>3</sub> structure. Table 1 shows the parameters of unit cell at different Sr<sup>2+</sup> contents. It can be seen from Table 1 that c / a decrease with Sr<sup>2+</sup> content increasing. It is beneficial to polarizing. Thus d<sub>33</sub> and K<sub>p</sub> increase with Sr<sup>2+</sup> content increasing. However, our experimental results showed that c / a reached to

a critical value. After then the unit cell changed gradually from tetragonal to cubic, which resulted in decreasing the piezoelectricity. So we can see from Figure 1 that 5 mol% Sr<sup>2+</sup> dopant may be the optimum value for the system. The results also showed that the Curie peaks shift leftward and upward after doping with Sr<sup>2+</sup>. This may be one of the main reasons for the fact that doping Sr<sup>2+</sup> can increase the dielectric constant.

The ceramics doped with Sn<sup>4+</sup> showed the similar rule as doping with Sr<sup>2+</sup>.

## 2. The effect of doping with La<sup>3+</sup>

Table 2 shows the effect of doping La on properties. The result show that the d<sub>31</sub>, d<sub>33</sub> and K<sub>p</sub> increased remarkably after doping with La 1 mol% and also show that the Curie peaks shift leftward and upward. The properties showed in Table 2 are satisfactory enough for making ultrasonic motor.

## 3. Application

The piezoelectric ceramics has been applied to piezoelectric electrorheological rotational stepper motors.

Figure 2 shows the construction of the piezoelectric electrorheological rotational stepper motor. In the construction of the motor, ER fluid performs clamping function for output axis in place and clutch on-off function for transmitting torque produced by torsional piezoelectric transducer of the motor. This motor has the characteristic of eliminating vibration, zero wear, and low consuming power as a piezoelectric-electrorheological linear stepper motor.

The operational method of piezoelectric electrorheological rotary motor is in rotating "inchworm" type shown in figure 3. In the first step, the ER clutch 1 is

Table 2 Additives of PMN-PNN-PZT Ceramics on Properties

No	additives (mol%)	ε <sub>33</sub> <sup>T</sup> / ε <sub>0</sub>	K <sub>p</sub>	d <sub>33</sub> (10 <sup>-12</sup> C / N)	d <sub>31</sub> (10 <sup>-12</sup> C / N)
1	0	2100	0.58	350	-187
2	Sr = 5 Sn = 0	4400	0.63	595	-284
3	Sr = 5 Sn = 3	5700	0.65	700	-334
4	Sr = 5 Sn = 2 La = 1	5989	0.70	740	-398

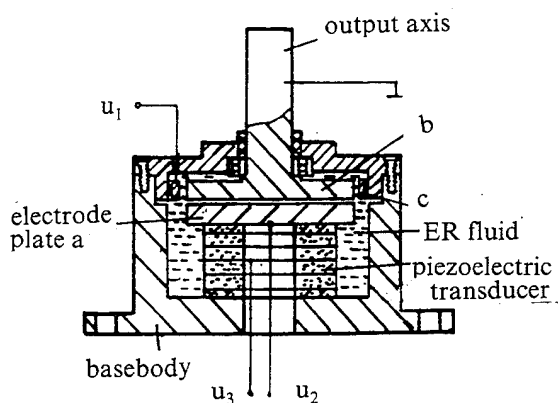


Fig.2 The construction of the piezoelectric electrorheological rotational stepper motor.  $u_1$ ,  $u_2$ ,  $u_3$  are voltage applied to ER clamp, ER clutch and piezoelectric transducer respectively.

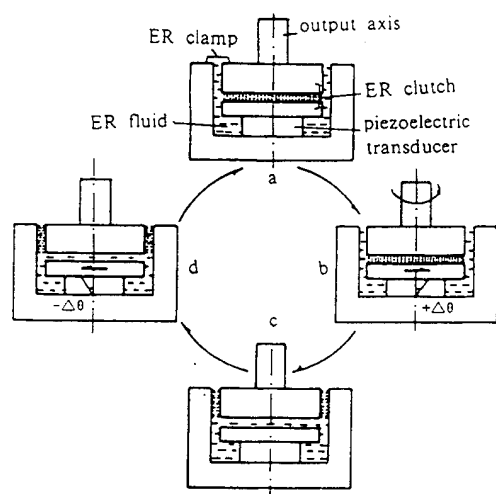


Fig.3 The operation principle of the piezoelectric electrorheological rotary stepper motor.

activated with a high voltage  $u_1$  to make ER fluid between electrode plate a and b change to a solid state and hold the plate b with a (Figure 3(a)). This is shown as follow, in step two, by a torsion of the torsional piezoelectric

transducer 3 with a variable voltage  $u_3$  to drive the electrode plate b rotating towards positive direction as shown in figure 3(b). During the third step the ER clutch 1 is released and can move freely after removing the voltage. At the same time, the ER clamp 2 is activated to hold in place with a high voltage  $u_2$  between electrode b and c, and the voltage across the piezoelectric transducer is held constant and keeps it torquing (Figure 3(c)). In the fourth step, the voltage applied to the piezoelectric transducer 3 is brought to negative which cause the transducer rotating towards negative. Thus the output axis has rotated towards positive direction at a small angular  $\Delta\theta$  (Figure 3(d)). The cycle of operation as mentioned above is repeated, the output axis will rotate forward to the positive direction continuously. If the operational sequence is reversed, the output axis will rotate toward reversed direction.

The voltage applied to ER clamp and clutch is 1000V, and to piezoelectric transducer is 0~300v. When operation frequency is 100 Hz, the rotary stepper speed of  $0 \sim 10^{-1}$  rad/min can be acquired.

This kind of the piezo-ER rotary stepper motor, due to its eliminated vibration, zero wear and low consumed power, will be applied to robots, high precise machinery and automatic controlling techniques etc.

## CONCLUSIONS

1. PMN-PNN-PZT ceramics by doping with Sr, Bi, Sn and La could be obtained with high  $d_{31}$ ,  $d_{33}$  and high  $\varepsilon_{33}^T/\varepsilon_0$ .

2. A new type of ER-piezoelectric rotational stepper motor has been made by this ceramics. This kind of motor has promising prospect in robots, high precise machinery and automatic controlling techniques.

## REFERENCES

- [1] Z.L.Gui, L.T.Li, S.H.Gao and X.W.Zhang, "Low Temperature Sintering of Lead-Based Piezoelectric Ceramics" J.Am. Ceram. Soc., 72[3]91989)486-491.
- [2] US patent 4, 882, 078 (89)



# The Dielectric, Piezoelectric and Hydrostatic Properties of PLZT Based Rainbow Ceramics

S. Sherit, H.D. Wiederick and B.K. Mukherjee  
Royal Military College of Canada, Kingston, Ontario K7K 5L0, Canada

and

G.H. Haertling  
Clemson University, Clemson, South Carolina 29634-0907, USA.

## ABSTRACT

It has recently been shown that the selective reduction of one surface of a high-lead-containing piezoelectric or electrostrictive ceramic wafer results in a stress-biased wafer with a unique domed structure that leads to high electromechanical displacement and enhanced load-bearing capability. These ceramics have been called rainbow ceramics and their very high displacements make them very promising materials for transducers and actuators. The dielectric, piezoelectric and hydrostatic properties of a variety of PLZT based rainbow ceramics have been measured and analysed. The samples exhibited a strong piezoelectric effect in the poling direction (effective  $d_{33}$  of the order of  $10^{-8}$  C/N) under low planar and hydrostatic pressures but as the pressure was increased there was a marked decrease in the strength of the piezoelectric response which passed through a minimum and then increased to the level of typical values for PZT ceramic. Some samples were plated and these had a low pressure hydrostatic voltage coefficient that was considerably greater than that of PZT along with a reasonable level of thickness mode electro-mechanical coupling. However, as the hydrostatic pressure was increased, the hydrostatic voltage coefficient decreased towards typical values for PZT. The rainbow ceramics show considerable promise as material for actuators and, possibly, for shallow water sonar transducers.

## INTRODUCTION

A new type of ceramic bender has recently been produced by the high temperature chemical reduction of one surface of a high-lead-containing piezoelectric or electrostrictive ceramic wafer which results in a stress-biased dome like structure that is capable of achieving very high axial displacements [1]. The reduced (concave) side of the wafer can serve as one of the electrodes. This type of ceramic has been called a "rainbow" (reduced and internally biased oxide wafer) ceramic. When a voltage is applied to a rainbow ceramic, the dome height varies as a function of the magnitude and polarity of the voltage and this motion is largely a consequence of the lateral contraction produced in the material due to the lateral piezoelectric coefficient  $d_{31}$ . Rainbow ceramics have been produced using ceramics such as lead zirconate titanate (PZT), lead lanthanum zirconate titanate (PLZT) and lead magnesium niobate (PMN). Single elements of rainbow ceramics, 0.2 mm thick, have produced displacements of 1 mm which represents a very high strain of 500%. Since rainbow ceramics are also easy and cheap to produce, they show considerable promise as materials for actuators and sonar activators. This paper reports on the measurement and analysis of the dielectric, piezoelectric

and hydrostatic properties of a range of PLZT based rainbow ceramic specimens which are described in Table 1. The specimens had a lanthanum content of 1.0 % and a lead zirconate content of 53 %. The samples were 0.5 mm thick discs which were electroded with Dupont 5504N silver epoxy and they all had a dome like appearance. Samples 4 and 5 had their rims glued to 1 mm thick brass plates whose diameters are given in Table 1. A specimen without electrodes was used to determine the density which was found to be  $7575 \pm 100 \text{ kgm}^{-3}$ .

Table 1: The Specimens

Sample Number	Diameter/ Plate Diameter (cm)	Plate
1	1.31	none
2	3.15	none
3	3.14	none
4	3.16 plate - 3.4	brass
5	1.31 plate - 1.32	brass

## RESONANCE MEASUREMENTS

A Hewlett Packard Model 4192 Impedance Analyser was used to measure the impedance of the samples as a function of frequency. In addition to radial and thickness mode resonances, the samples showed bending mode resonances; in the case of sample 1 the bending mode resonance occurred at about 30 kHz. The impedance spectra of the samples have been analysed using Smits' method [2] and our own techniques [3] although it should be stressed that the geometry of these dome shaped samples does not correspond strictly to the geometry assumed in deriving the resonance equations. An analysis of the thickness and radial mode resonances of samples 1, 2 and 3 gave the material constants shown in Tables 2 and 3 in which the symbols used have the usual definitions as given in the IEEE Standard on Piezoelectricity [4]. These tables show that there are large differences in the material constants measured for the various samples and this is likely to be due to small differences in the curvatures and aspect ratios of the dome shaped samples. The curvature is a result of the reduction process and small variations in composition and processing conditions would produce differences in

**Table 2: Thickness mode material constants measured at 4 MHz and 20°C**

	Sample 1	Sample 2	Sample 3
$k_t$	0.359(1 - 0.12i)	0.355(1 - 0.31i)	0.327(1 + 0.12i)
$c_{33}^D$ ( $10^{11}$ N/m <sup>2</sup> )	1.35(1 + 0.020i)	1.06(1 + 0.069i)	1.19(1 + 0.068i)
$\epsilon_{33}^S$ ( $10^{-9}$ F/m)	6.39(1 - 0.33i)	6.87(1 - 1.1i)	11.3(1 - 0.35i)
$h_{33}$ ( $10^9$ V/m)	1.62(1 + 0.049i)	1.23(1 + 0.15i)	0.99(1 + 0.33i)

**Table 3: Radial mode material constants measured at 20°C**

	Sample 1	Sample 2	Sample 3
$s_{11}^E$ ( $10^{-11}$ m <sup>2</sup> /N)	1.55(1 - 0.023i)	1.81(1 - 0.023i)	2.15(1 - 0.038i)
$s_{12}^E$ ( $10^{-11}$ m <sup>2</sup> /N)	-0.517(1 - 0.023i)	-0.742(1 - 0.023i)	-1.22(1 - 0.038i)
$d_{31}$ ( $10^{-12}$ C/N)	-140(1 - 0.088i)	-123(1 - 0.085i)	-83(1 - 0.22i)
$\epsilon_{33}^T$ ( $10^{-9}$ F/m)	13.3(1 - 0.0915i)	11.6(1 - 0.077i)	7.8(1 - 0.21i)
$\sigma^p$	0.334	0.410	0.566
$k_p$	0.52(1 - 0.043i)	0.48(1 - 0.047i)	0.43(1 - 0.11i)

the curvatures of the samples which would significantly affect the material constants.

In Figure 1, which shows the thickness resonance of sample 1, the experimental points are compared to the fit obtained by using the material constants found for this sample. It can be seen that the fit is acceptable around the fundamental mode but there is significant dispersion at higher frequencies. Besides, the first thickness resonance occurs close to 4 MHz and it follows that a non-dispersive material would have a second resonance at around 12 MHz whereas this occurs at about

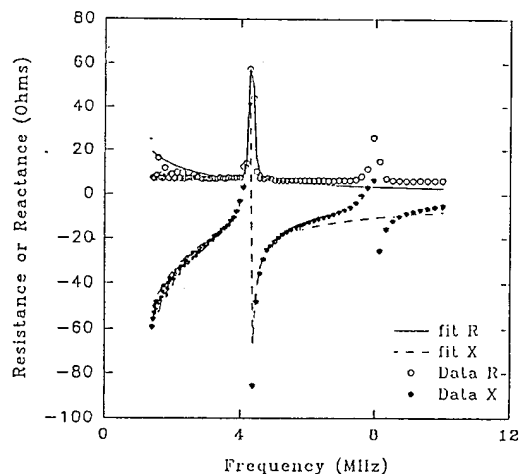


Figure 1. The resistance and reactance versus frequency for sample 1. The experimental points are compared with the lines which represent fits obtained by using the derived material constants.

7.5 MHz in the figure. Finally the figure shows that the base-lines for the data and the fit differ substantially at frequencies higher than the first resonance frequency. All of this evidence points to a significant dispersion in the dielectric, elastic and piezoelectric constants of the material.

Another interesting feature is that the second thickness mode resonances of the larger samples are inductive and yield negative values of permittivity; this is due to the high conductivities of these samples at high frequencies.

Samples that were bonded to plate electrodes had thickness resonances that saturated the measuring circuit while their radial modes were smaller than those for the unbonded samples. This suggests that the electrode plate acts to clamp  $d_{31}$  more than  $d_{33}$  with a resulting enhancement in  $k_t$ .

#### DIELECTRIC MEASUREMENTS

The capacitances of the specimens were measured at a frequency of 1000 Hz at room temperature. The average values for the permittivity, the dielectric constant and the loss tangent for samples 1, 2 and 3 are given in Table 4.

**Table 4: Dielectric Constants (averaged over samples 1, 2 and 3)**

Property	Units	Value
Permittivity $\epsilon_{33}^T$	$10^{-9}$ F/m	$14 \pm 1$
Dielectric Constant $K_{33}^T$		$1540 \pm 110$
Loss Tangent $\tan \delta$		$0.086 \pm 0.012$

#### THE PIEZOELECTRIC CHARGE CONSTANT

The value of the piezoelectric charge constant,  $d_{33}$ , for the material was obtained by using a point force head on a Berlincourt type  $d_{33}$  meter which was operated at a frequency of 200 Hz. The value of  $d_{33}$  was found to vary over the surface of the samples; to find if this was due to coupling to the bending mode of the sample, measurements were made at 12 points spaced 1 mm apart along a diameter of the slightly domed samples. Our results for sample 1 are shown in Figure 2 where the three curves represent the values obtained (a) when the measurements were made with the curvature of the dome shaped sample facing downwards so that the sample formed a cavity with the base plate of the meter with the positive terminal at the point head (indicated as "+ up" data in the figure), (b) when the measurements were made with the sample curvature facing upwards ("down" data in the figure) and (c) the average of the two measurements made in (a) and (b). Figure 4 shows that the apparent  $d_{33}$  values are quite large and can reach up to 12,000 pC/N at the centre of the specimen. It is likely that this large value is due to the addition of the normal uniaxial compression of the ceramic material and the bending modes of the dome shaped sample. In order to elucidate this better the  $d_{33}$  was measured as a function of uniaxial compression.

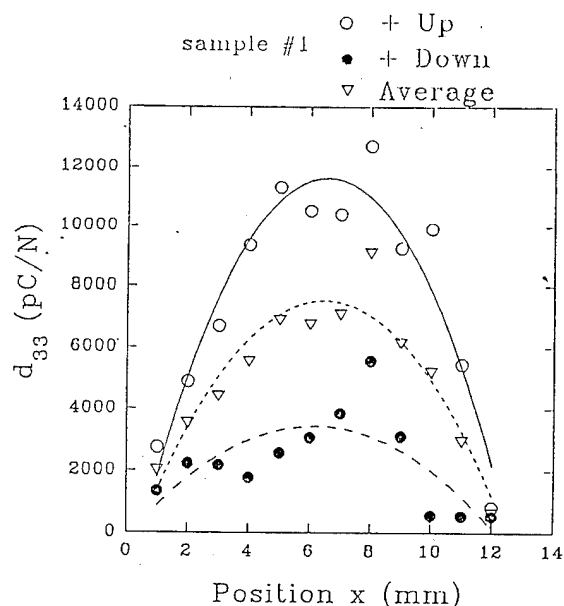


Figure 2. The effective  $d_{33}$  value as a function of distance along a diameter of sample 1. The significance of the three curves has been explained in the text.

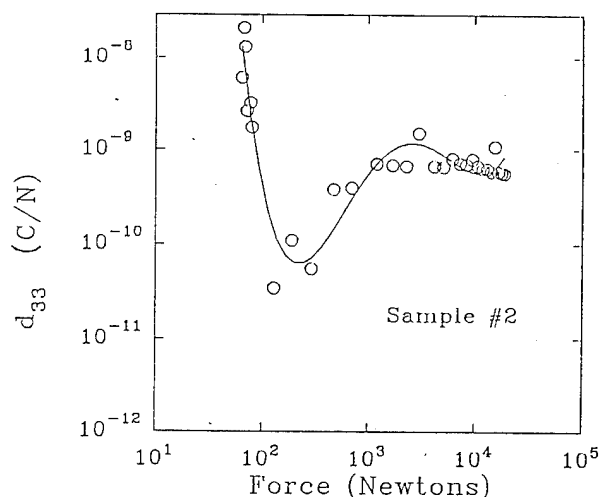


Figure 3. The effective  $d_{33}$  as a function of the compressional force applied to sample 2.

sion using a method which has been reported earlier [5]. Our results for sample 2 are shown in Figure 3 and it can be seen that  $d_{33}$  has a value of about 10,000 pC/N at low applied force but it then decreases rapidly as the dome shaped sample is flattened out as a result of increasing force and it passes through a minimum at a force of about 200N from which point it rises up to typical ceramic values as the ceramic undergoes compression. It can therefore be concluded that the large  $d_{33}$  values are indeed caused by the bending of the dome shaped sample when a stress is applied; after the rainbow material has become flat, it begins to act like a plain bulk ceramic disc.

It should be noted that the voltage - force curves of the specimens show hysteresis and this behaviour is very similar to that shown by bulk PZT discs [5]. The hysteresis is due to the time-dependence of the piezoelectric response of the rainbow ceramic.

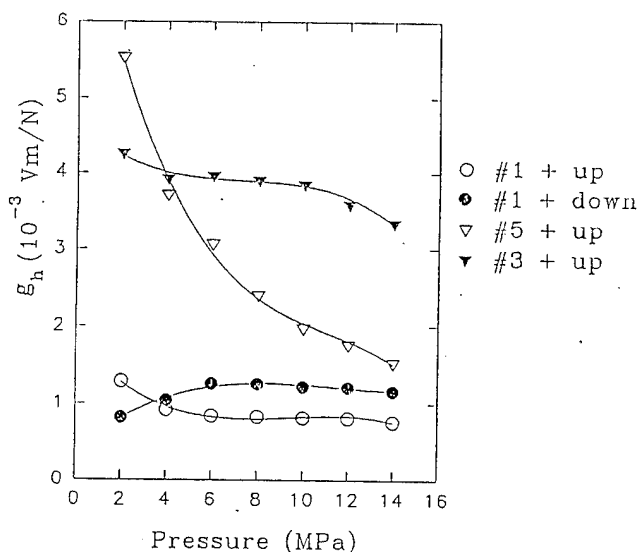


Figure 4. The hydrostatic voltage coefficient,  $g_h$ , as a function of the hydrostatic pressure for different samples and orientations.

#### HYDROSTATIC PROPERTIES

The hydrostatic voltage constants,  $g_h$ , of the rainbow specimens have been measured at a frequency of 400 Hz and as a function of pressure using a SENSOR  $g_h$  apparatus. Our results for samples 1, 3 and 5 are shown in Figure 4. Two series of measurements were carried out on sample 1: the results indicated by "+ up" correspond to the dome shaped sample being placed with its curvature facing down and forming a small cavity with the base plate of the apparatus while the results indicated by "+ down" correspond to the rainbow ceramic sitting on the base plate with its curvature facing up. The hydrostatic voltage response is the sum of the contributions arising from the bending of the dome shaped rainbow and the compression of the ceramic itself. In the case of sample 1, the bending effects are small since the edge of the rainbow ceramic can move laterally on the base plate and so the  $g_h$  value is close to that of standard bulk PZT ceramic. The small difference between the two series of measurements on sample 1 is probably due to the different contributions from the bending of the specimens. Samples 1 and 3 are similar in that both were not bonded to a base plate so that the hydrostatic pressures are identical on both faces and the dome does not undergo any flattening due to the hydrostatic pressures. Sample 3, which has the bigger radius, has a larger value of  $g_h$  and this is perhaps due to the larger bending deflections which are possible in this case. Sample 5 is a rainbow ceramic of the same radius as sample 1 but it is bonded to a brass plate about 1 mm thick so that the hydrostatic pressure is not now transmitted to the inner surface of the rainbow and the dome gradually flattens as the external static pressure is increased. At low pressures the flattening is negligible, but since the rim of the rainbow is bonded, the bending response to the signal is considerably greater than in the case where the rainbow is not bonded (as in sample 1) and hence the much larger value of  $g_h$ . As the pressure increases, the rainbow gradually flattens, the bending contributions decrease and the  $g_h$  value approaches that of a normal bulk PZT ceramic.

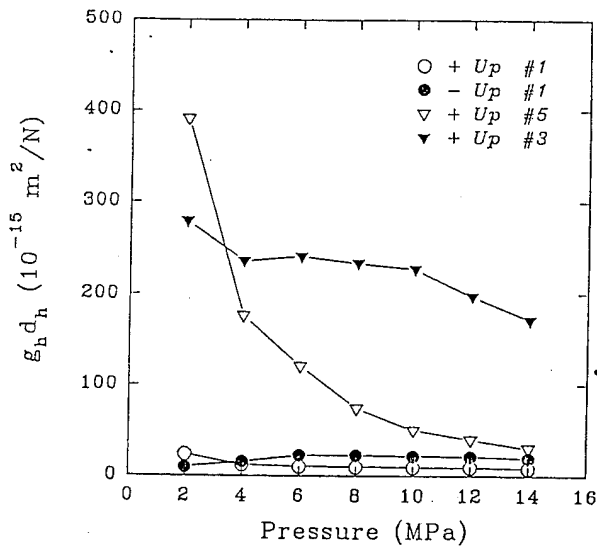


Figure 5. The hydrostatic figure of merit for samples 1, 3 and 5.

Figure 5 shows the hydrostatic figure of merit,  $g_h d_h$ , of samples 1, 3 and 5. The small rainbow (sample 1) has a figure of merit that is substantially lower than that of PZT while the larger rainbow ceramic (sample 3) has a figure of merit which is comparable to that of PZT.

The  $g_h d_h$  values for sample 4 are shown as a function of pressure in Figure 6. This sample is a large rainbow ceramic, 3.16 cm in diameter, bonded to a 1 mm thick brass plate and its behaviour is qualitatively similar to that of sample 5 which is smaller. At high pressures the values are slightly lower than the nominal values for normal bulk PZT but they rise dramatically at low pressures. At low pressure this sample has a very high  $g_h$  value of about 0.8 Vm/N

Finally it may be noted that both Figures 3 and 6 show minima. This is explained by the fact that there are two contributions to charge generation: bending of the dome shaped samples and compression of the ceramic. These two contributions are not independent but are coupled with the strain being relieved by the bending action of the monomorph.

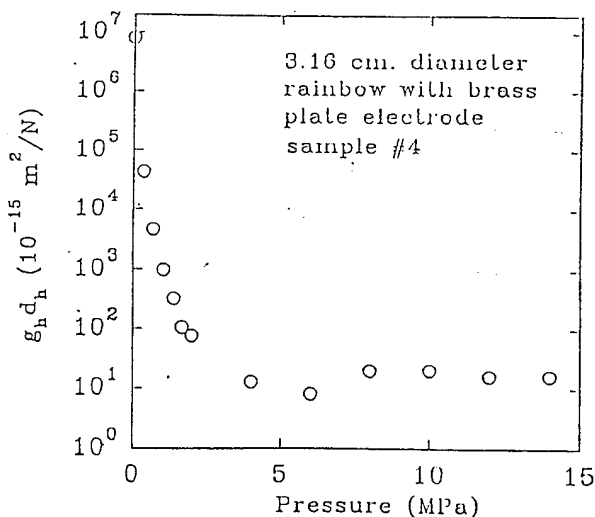


Figure 6. The hydrostatic figure of merit as a function of pressure for sample 4.

The set of PLZT based rainbow specimens analysed by us have shown a strong piezoelectric response under low planar and hydrostatic pressures but there is a marked decrease in the strength of the response as the pressure is increased. The larger response at low pressures is thought to be due to the bending of the samples and the consequent release of charge.

The resonance curves of the specimens were somewhat distorted by the presence of the bending modes. The material constants were determined for the radial and thickness modes of operation and these were found to exhibit geometric effects and dispersion.

The rainbow samples that were not bonded to a base plate had hydrostatic properties in the same range as ordinary bulk PLZT with some variation depending on the orientation of the sample in the measurement apparatus. However the rainbow samples that were bonded to electrode plates showed substantially better hydrostatic properties but, as the static pressure increased, these decreased to values similar to those of bulk PLZT.

The dielectric properties of the rainbow samples were similar to those of PLZT.

In conclusion, the rainbow ceramic material shows considerable promise as an actuator material where large displacements are required (solid state speakers, pumps, switches, positioners etc.) and, possibly, for shallow water sonar projectors. The large pressure dependences exhibited by the material reduce its applicability in deep water applications, although, with proper design, it may be possible to maintain a pressure-independent sensitivity that will be somewhat greater than that of PZT, the current standard in sonar transducer materials.

## REFERENCES

- [1] G.H. Haertling, "Rainbow Ceramics - A new Type of Ultra-High-Displacement Actuator", *American Ceramic Society Bulletin*, vol.73, pp.93-96, January 1994.
- [2] J.G. Smits, "Iterative Method for Accurate Determination of the Real and Imaginary Parts of the Material Coefficients of Piezoelectric Ceramics", *IEEE Trans. Sonics and Ultrasonics*, vol.SU-23, pp.393-402, June 1976.
- [3] S. Sherit, N. Gauthier, H.D. Wiederick and B.K. Mukherjee, "Accurate Evaluation of the Real and Imaginary Material Constants for a Piezoelectric Resonator in the Radial Mode", *Ferroelectrics*, vol.119, pp.17-32, 1991.
- [4] *IEEE Standards on Piezoelectricity*, ANSI/IEEE Std.176-1987.
- [5] S. Sherit, D.B. Van Nice, J.T. Graham, B.K. Mukherjee and H.D. Wiederick, "Domain Wall Motion in Piezoelectric Materials under High Stress", *Proceedings of the Eighth IEEE International Symposium on Applications of Ferroelectrics - ISAF '92*, 1992, pp.167-170.

# Nonlinear Stress-Strain Behavior of Piezoelectric Ceramics under Tensile Loading

Toshio Tanimoto, Kohji Yamamoto and Tohru Morii  
Department of Materials Science and Ceramic Technology  
Shonan Institute of Technology  
Fujisawa, Kanagawa 251 JAPAN

**Abstract** – Fracture strength and stress-strain behavior under tensile stress in piezoelectric ceramics have been investigated with special emphasis on the effect of environmental temperature. The materials used in this work are the commercial piezoelectric ceramics,  $\text{PbZrO}_3\text{-PbTiO}_3$  (PZT) and PLZT. An attempt was first made to evaluate the tensile strength properties at the room temperature of PZT samples having a specially designed specimen geometry. Not only fracture strength, but also elastic properties, tensile modulus and Poisson's ratio, were evaluated and then the stress-strain behavior under tension for piezoelectric ceramics, PZT and PLZT, was confirmed to be nonlinear. The nonlinearity in the stress-strain relationship under compression loading has already been reported by some investigators. However, very little work has been done on the tensile stress-strain relationship, as studied in this paper. The results of tensile test for PZT samples at the various environmental temperatures indicated that the stress-strain response of poled and nonpoled samples was nonlinear independent of test temperature. The strength of both the poled samples and the nonpoled samples increased linearly against test temperature. Moreover, acoustic emission monitoring was performed simultaneously during tensile tests, and thus the tensile failure process in piezoelectric ceramics was discussed. It was also pointed out that the tensile strength of PLZT increased monotonically against the amount of La.

## SPECIMEN PREPARATION AND EXPERIMENTAL METHOD

The materials used in the present study are the commercially available piezoelectric ceramics,  $\text{PbZrO}_3\text{-PbTiO}_3$  (PZT) and PLZT with various compositions. PLZT (Hayashi Kagaku Co., Ltd.) employed here had four kinds of composition,  $(\text{Pb}_{0.920}, \text{La}_{0.080})(\text{Zr}_{0.65}, \text{Ti}_{0.35})\text{O}_3$ ,  $(\text{Pb}_{0.910}, \text{La}_{0.090})(\text{Zr}_{0.65}, \text{Ti}_{0.35})\text{O}_3$ ,  $(\text{Pb}_{0.905}, \text{La}_{0.095})(\text{Zr}_{0.65}, \text{Ti}_{0.35})\text{O}_3$  and  $(\text{Pb}_{0.880}, \text{La}_{0.120})(\text{Zr}_{0.40}, \text{Ti}_{0.60})\text{O}_3$  (hereinafter referred to as 8/65/35, 9/65/35, 9.5/65/35 and 12/40/60, respectively). In general, it is considered that the tensile test for ceramic specimens is quite difficult to perform because fracture during a tensile test occurs easily at the gripping area. This is due to the inherent low fracture toughness of most ceramic specimens. In the present work, an attempt was made to evaluate the tensile strength properties of samples having a specially designed specimen geometry, as shown in Fig.1. In this method, tabs were bonded to both sides of the plate to prevent fracture at the gripping area. The tabs are tapered in order to reduce the stress concentration effect at the gripping area. The material selected for end tabs was chopped-glass-mat reinforced polyester. It is ductile and soft as compared to ceramic specimens, which is a requirement in this tensile test. The stress distribution in the vicinity of the tab was calculated by a finite-element method (MARC) to determine the validity of the adopted specimen geometry [1].

The tensile test was performed for both the nonpoled and the poled samples. In the poled sample, DC current was applied to the thickness direction of the plate. In the present tensile test, the stress was applied to the specimen perpendicular to the poling direction, as shown in Fig.1. Strain gauges were mounted on all tested specimens in two directions, parallel and transverse to the loading direction, in order to measure the longitudinal and the transverse strain, respectively. The specimen was led to failure at a constant cross-head speed of 0.5mm/min using the Instron universal testing machine (type 4206). The tensile tests were conducted under various temperatures (-30, -10, 23, 80 and 150°C) in the environmental chamber.

Acoustic emission (AE) monitoring was performed during tensile loading to investigate the fracture process of the specimen. AE signals were measured using the Physical Acoustic Corporation 3000 acoustic emission instrument. The transducer had a resonant frequency of 500kHz and the AE system threshold level was set at 40dB.

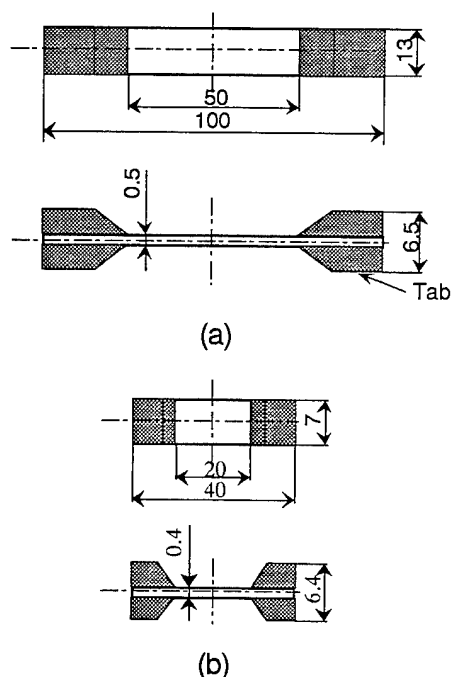


Fig.1 Geometry of (a) PZT and (b) PLZT samples.

## EXPERIMENTAL RESULTS AND DISCUSSION

Our previous work [2] indicated that the compressive strength properties of PZT and  $\text{BaTiO}_3$  samples in the direction parallel to poling were considerably improved by poling. In this case, residual tensile stress induced by poling, which occurred in parallel and reversed directions to external load, was thought to increase the fracture strength. Aging and repoling are believed to stabilize the polarization.

Table I Comparison of tensile strength between nonpoled and poled PZT samples.

Specimen		Tensile strength (MPa)
Type 31	nonpoled	49.4
	poled	51.3
Type 33	nonpoled	43.5
	poled	38.8

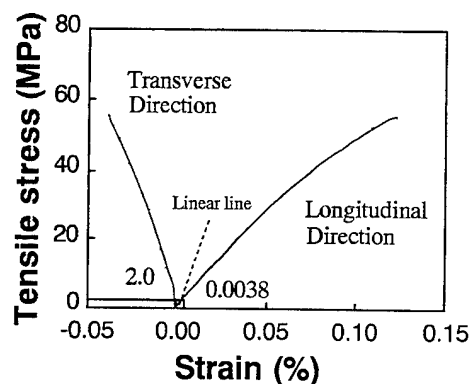


Fig.2 Tensile stress-strain curves in longitudinal and transverse directions for PZT sample.

As shown in Table I, tensile fracture strength of PZT in the poling direction (TYPE 33 in which the poling was applied to the longitudinal direction of the PZT plate) decreased in comparison with that for the nonpoled sample. In this case, residual tensile stress induced by poling, in which the internal stress direction is in the same direction as applied external stress, probably decreases tensile fracture strength. On the other hand, tensile fracture strength in TYPE 31 in which the poling was applied to the thickness direction of the PZT plate was slightly increased by poling. It is extremely important to note that the deformation behavior observed for PZT is nonlinear (Fig.2). In Fig.2 the strain was measured in both longitudinal and transverse direction to the loading direction. Such behavior was observed in both TYPE 31 and TYPE 33, regardless of poling. These nonlinearities begin at lower stress levels. For example, in the case shown in Fig.2, the fracture strength for poled PZT was 57.6MPa, while nonlinearity occurred when the stress exceeded 2.0MPa.

For a more detailed consideration of these effects, the correlation between tensile fracture strength and normalized stress at a proportional limit in the stress-strain relationship was investigated for TYPE 31 of PZT (Fig.3). In the abscissa, stress value at the beginning of nonlinearity is divided by its tensile fracture strength. A negative correlation was observed. As a result, tensile fracture strength is said to increase with decrease in the normalized stress at the proportional limit. In other words, the stronger the nonlinear behavior is, the higher the fracture strength is. Next, the correlation between the fracture strength and ultimate strain at failure was examined, as shown in Fig.4. The positive correlation observed suggests that fracture strength can be enhanced by increasing ultimate fracture strain. Fig.5 shows the tensile stress-strain curves of the poled samples at test temperature of -30, 23 and 150°C. The strain was measured in both longitudinal and transverse direction to the loading direction. Therefore the tensile stress-longitudinal strain curve and the tensile stress-transverse strain curve are shown in Fig.5. The nonlinearity of stress-strain curve became remarkable as the test temperature became higher. In particular, the stress-longitudinal strain curve at 150°C indicated the significant nonlinear behavior. Nonlinearity in stress-transverse strain curve is much smaller than that in stress-longitudinal strain curve. The stress-strain curve at -30°C was almost linear up to relatively high stress. Therefore it is considered that the stress-strain behavior turns from ductile to brittle nature at about -30°C. The tensile fracture strength was higher at higher test temperature. It is considered that the tensile fracture strength is closely related to the nonlinear stress-strain behavior. Fig.6 shows the relation between the normalized strain at proportional limit and the test temperature. The proportional limit is the point where the stress-strain curve begins to indicate the nonlinearity. The normalized strain is defined as the ratio of the strain at proportional limit to the strain at failure. The normalized strain at proportional limit decreased monotonically against the test temperature. This result means that the PZT sample behaves as if it were a viscoelastic material with increase of test temperature. The temperature dependence of the tensile strength is shown in Fig.7. The strength of both the poled samples and the nonpoled samples increased linearly against test temperature. The tensile strength of PZT samples with tetragonal structure and spontaneous strain below the Curie point, becomes higher, as the test temperature is raised and the crystalline structure approaches cubic. According to the present test result, the fracture strain increased with increase of test temperature. This tendency is more remarkable in the poled samples than in the nonpoled samples. As mentioned above, the nonlinear stress-strain behavior is remarkable at higher test temperature. Therefore the nonlinear stress-strain behavior may lead to the increase of strain at failure. In addition, positive correlation was observed between the strength and the strain at failure independent of environmental temperature, and the strength is higher with increase of strain at failure. The effect of poling never appeared in this relation. The tensile fracture strength may be enhanced as a result of increased ultimate fracture strain at higher test temperature, as shown in Fig.7.

In order to further investigate nonlinear response in this material, a cyclic loading and unloading test was performed. In this test, cyclic stress was gradually increased in a stepwise fashion. The test result for nonpoled PZT (Fig.8(a)) indicates that there exists plastic deformation even at low stress levels. Hysteresis in loading/unloading is apparently irreversible. On the other hand, plastic deformation for poled PZT is reduced, as can be seen in Fig.8(b). Mechanical nonlinearity and the nonrecoverable nature is

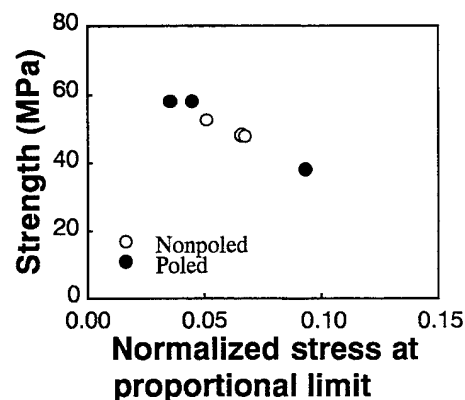


Fig.3 Correlation between tensile strength and normalized stress at proportional limit for PZT sample.

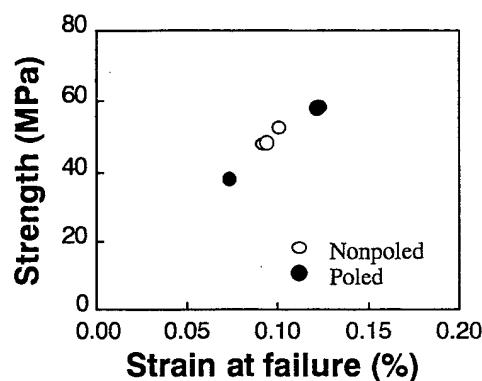


Fig.4 Correlation between tensile strength and strain at failure for PZT sample.

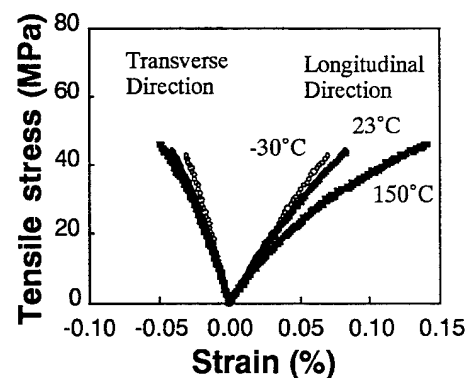


Fig.5 Tensile stress-strain curves in longitudinal and transverse directions at various test temperature.

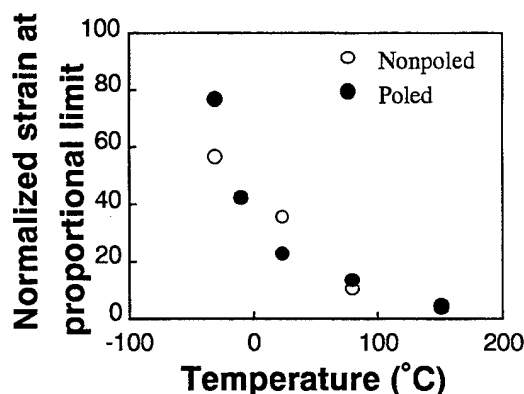


Fig.6 Correlation between normalized strain at proportional limit and test temperature.

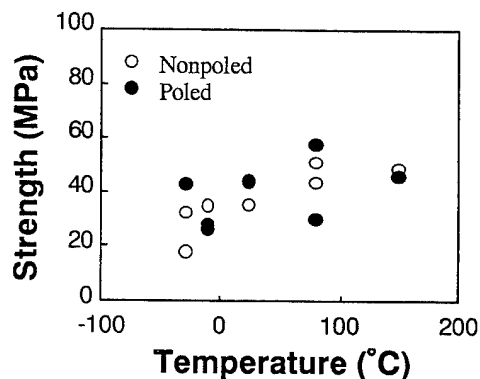


Fig.7 Correlation between tensile strength and test temperature.

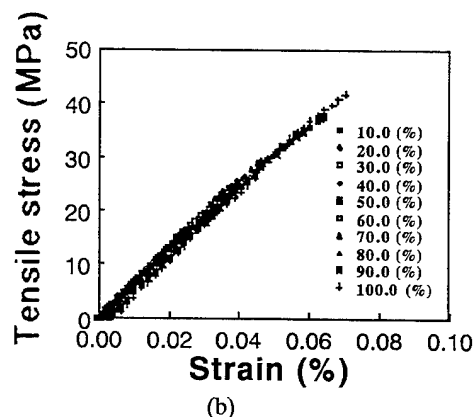
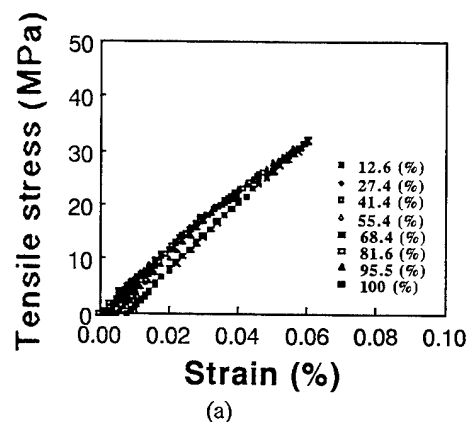


Fig.8 Stress-strain histories during cyclic loading and unloading test for (a) nonpoled and (b) poled PZT.

Table II Comparison of tensile modulus between nonpoled and poled PZT.

Specimen		Tensile modulus (GPa)	
		Tangent	Secant
PZT	nonpoled	65.3	52.5
	poled	62.3	50.0

Table III Comparison of Poisson's ratio between nonpoled and poled PZT.

Specimen		Poisson's ratio	
		Corresponding to tangent modulus	Corresponding to secant modulus
Type 31	nonpoled	0.30	0.35
	poled	0.33	0.35

attributable to ferroelastic domain movement. The mechanism responsible for the nonlinear deformation in the piezoelectric materials involves  $90^\circ$  domain movement. Cao and Evans [3] have already reported a similar nonlinearity in the stress-strain response

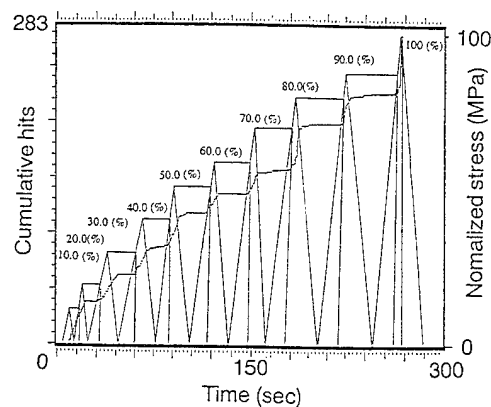


Fig.9 Acoustic emission during loading-unloading test of PZT.

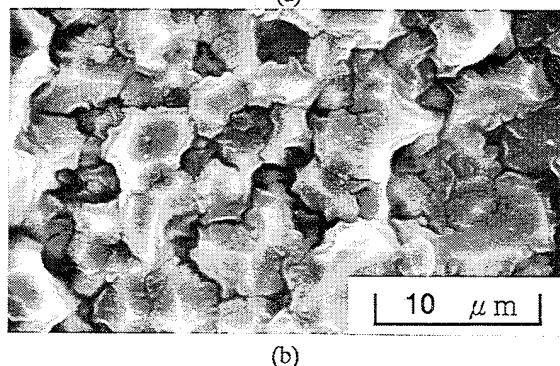
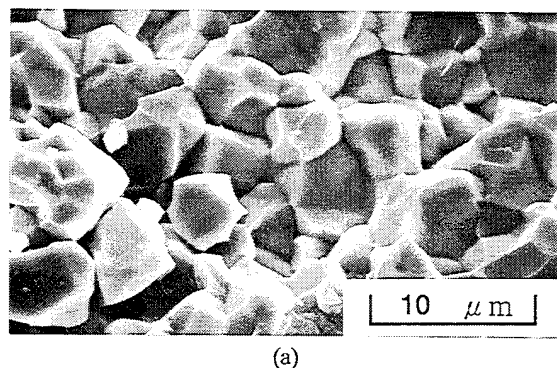


Fig.10 SEM micrographs of the fractured surfaces in tensile test for (a) nonpoled and (b) poled PZT samples.

under compressive stress for piezoelectric and antiferroelectric materials. They explained these effects from the viewpoint of ferroelastic domain switching, with a yield criterion controlled by a deviatoric effective stress. A further detailed study of such nonlinear behavior in the mechanical stress-strain response may lead to development of advanced piezoelectric ceramics which can withstand large displacements and/or large forces.

It is of little value to evaluate Young's modulus of this material because of the severe nonlinearity in stress-strain behavior. Thus, two kinds of elastic moduli, tangent modulus and secant modulus, were evaluated. The former is a tangent modulus at the proportional limit, and the latter modulus was obtained from the slope of the line connecting the original point and the ultimate stress at fracture. As shown in Table II, which shows results for TYPE 31, both tangent modulus and secant modulus were significantly decreased by polarization in PZT. In addition, the values of Poisson's ratio obtained for the definition of the respective moduli indicate that Poisson's ratio is also markedly affected by polarization (Table III). It is reasonable to assume that the presence of internal stress induced by poling will probably increase the transverse contraction when subjected to tensile loading. As pointed out in our previous work [2], mechanical properties of piezoelectric ceramics are considerably



affected by differences in poling conditions, such as applied voltage values in poling, aging treatment after poling, and repoling. For example, compressive strength and fatigue resistance are enhanced with an increase of applied DC voltage. These findings may lead to the possibility of designing piezoelectric ceramics having desired modulus and Poisson's ratio by choosing optimum poling conditions.

During the loading-unloading test, acoustic emission monitoring was performed simultaneously in order to obtain information on the fracture process. As can be seen in Fig.9, no AE signal occurred before exceeding previously experienced stress levels in loading/unloading histories. The so-called Kaiser effect [4] holds for this material. This suggests that the fracture process of this material under tensile loading corresponds to indominant crack propagation in conventional metallic materials.

The SEM micrographs of the fractured surfaces in tensile tests for nonpoled PZT and poled PZT are shown in Fig.10. In the nonpoled sample, the fracture was found to be intergranular with rather brittle appearance. In the poled sample, on the other hand, the appearance of fracture in the vicinity of the grain boundary appears ductile, and wrinklelike deformation may be observed. Further investigation on this difference in the fracture pattern is necessary to explore the reason for nonlinearity and irreversibility of the stress-strain response of piezoelectric ceramics. This may enable us to develop piezoelectric ceramics possessing high deformability and high strength, which is required, for instance, in application to high deformation and large force actuators.

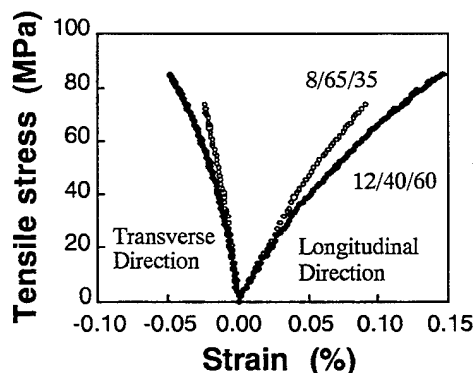


Fig.11 Tensile stress-strain curves in longitudinal and transverse directions of PLZT samples.

Table IV Tensile test results of PLZT samples.

Specimen	Strength (MPa)	Tangent modulus (GPa)	Secant modulus (GPa)	Poisson's ratio (tangent modulus)	Poisson's ratio (secant modulus)
8/65/35	67.3	91.5	75.4	0.255	0.294
9/65/35	69.2	92.2	84.8	0.277	0.290
9.5/65/35	73.2	112.9	94.0	0.280	0.305
12/40/60	76.6	84.3	63.3	0.330	0.317

The tensile stress-longitudinal strain curve and the tensile stress-transverse strain curve for PLZT samples are shown in Fig.11. The nonlinearity of stress-strain curve became marked as the amount of La is increased. Particularly, the stress-longitudinal strain curve for PLZT of 12/40/60 composition indicated significant nonlinear behavior. It is extremely important to notice from Table IV that the tensile strength of PLZT increased monotonically against the amount of La. As the PLZT samples with tetragonal structure approaches cubic structure, with increasing the amount of La, tensile fracture strength increases. This is similar to the above-mentioned temperature dependence of fracture strength in PZT samples. It is also observed that the Poisson's ratio increases with increase in the amount of La. Young's modulus increased with increase in the amount of La with respect to PLZT samples of 8/65/35, 9/65/35 and 9.5/65/35. On the other hand, the Young's modulus for PLZT of 12/40/60 is lower when compared with above-mentioned PLZT samples (8/65/35, 9/65/35 and 9.5/65/35). As a result, the amount of La was found to significantly affect the mechanical properties of piezoelectric ceramics. Fig.12 shows the SEM micrographs of fractured surface in tensile test for the PLZT samples of 8/65/35 and

12/40/60. The PLZT of 12/40/60 showed transgranular appearance and it is quite different when compared with PLZT of 8/65/35.

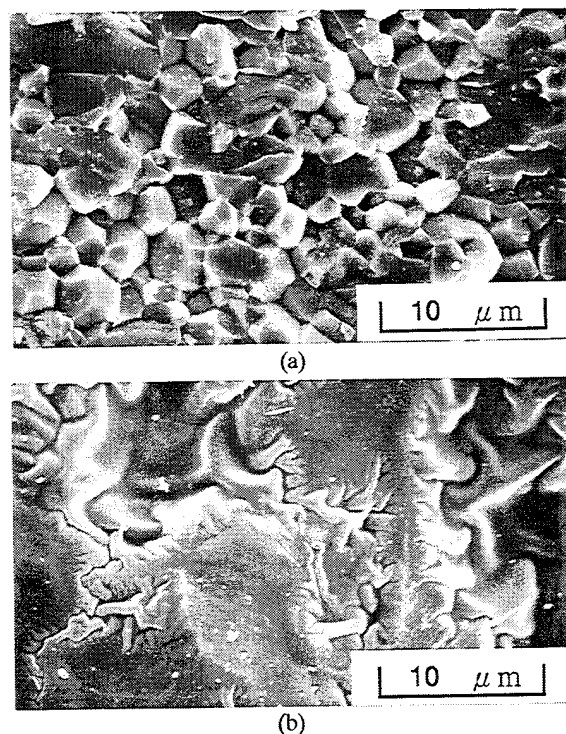


Fig.12 SEM micrographs of the fractured surfaces in tensile test for PLZT samples of (a) 8/65/35 and (b) 12/40/60.

## CONCLUSIONS

The present investigation on tensile stress-strain behavior of piezoelectric ceramics under various temperatures led to the following conclusions.

1. The stress-strain response in  $\text{PbZrO}_3\text{-PbTiO}_3$  (PZT) under tensile loading is confirmed to be nonlinear. The nonlinearity of stress-strain response is stronger with higher test temperature. As a result, it was clarified that the stronger nonlinearity is, the higher the fracture strength is.
2. Test results also suggest that the tensile fracture strength can be enhanced by increasing the ultimate strain at failure. The enhancement of ultimate fracture strain may be a key in developing advanced piezoelectric ceramics possessing high deformability and high strength, which we required, for instance, in application to high-deformation and large-force actuators.
3. The fracture of the nonpoled samples was found to be intergranular with rather brittle appearance. On the other hand, the appearance of fracture in the vicinity of the grain boundary appeared ductile in the poled samples.
4. The nonlinearity of stress-strain curve became marked as the amount of La is increased in PLZT samples. It is very interesting to note that the tensile strength of PLZT increased monotonically against the amount of La. As a result, the amount of La was found to significantly affect the mechanical properties of piezoelectric ceramics.

## REFERENCES

- [1] T. Tanimoto and K. Okazaki, "Mechanical and electrical properties of electronic ceramics under high stress condition and microstructures", 1990 IEEE 7th Int. Symp. Applications of Ferroelectrics, IEEE No.90CH2800-1, pp.40-43, 1990.
- [2] T. Tanimoto and K. Okazaki, "Electrical degradation process and mechanical performance of piezoelectric ceramics for different poling conditions", 1992 IEEE 8th Int. Symp. Applications of Ferroelectrics, IEEE No.92CH3080-9, pp.504-507, 1992.
- [3] H. Cao and G. Evans, "Nonlinear deformation of ferroelectric ceramics", *J. Am. Ceram. Soc.*, vol.76, pp.890-896, 1993.
- [4] J. Kaiser, Dr. Thesis, Technische Hochschule, Munich, Germany, 1950.





# Concurrent Session - 2D: Thin Films

# Sol-Gel Barium Titanate Thin Films on Nickel Alloy Electrodes

T. Ogawa, S. Saitoh<sup>1</sup>, O. Sugiyama<sup>1</sup>, A. Kondoh<sup>1</sup>, T. Mochizuka<sup>2</sup> and H. Masuda<sup>2</sup>

Shizuoka Institute of Science and Technology, Fukuroi, Japan

<sup>1</sup> Shizuoka Industrial Research Institute of Shizuoka Prefecture, Shizuoka, Japan

<sup>2</sup> Murakami Corporation, Shizuoka, Japan

**Abstract :** A nickel(Ni) alloy has been applied to bottom electrodes of BaTiO<sub>3</sub> thin films and 2–6 mole % La modified BaTiO<sub>3</sub> thin films prepared by sol-gel processing. The gel films on a substrate of soda-lime glass with Ni alloy bottom electrodes were crystallized at a temperature of 600 °C. The grains with the size of 1–2  $\mu$ m consisted of subgrains(20 nm) and the grain size was decreased with increasing La substitution. The remanent polarization of the films decreased with the increase of La substitution and with the decrease of the grain size.

## INTRODUCTION

A special Ni alloy has been utilized for electrodes in conjunction with (Pb,La)TiO<sub>3</sub> thin films prepared by rf magnetron sputtering [1–4] and PZT thin films by excimer laser ablation [4–8]. The principal reason for use of the Ni alloy include the following: Electrode materials formed on substrates resist oxidation up to 600 °C in the oxygen gas atmosphere during preparation of the ferroelectric thin films. Furthermore, electrode materials which don't react with PbO are required. This alloy possesses excellent thermal stability and oxidation-resisting properties compared to inconel 601 [9]. These properties were obtained for the alloy film as well as the alloy bulk [1,2]. The superior characteristics were due to a thin layer of alumina(Al<sub>2</sub>O<sub>3</sub>) precipitated on the surface of the alloy electrode. This layer prevented oxidation and PbO from diffusing into the alloy electrode. It has been confirmed that the Ni alloy was suitable for the bottom electrodes of the ferroelectric thin films prepared by PVD such as sputtering and laser ablation [1–8].

In this pursuit, therefore, the Ni alloy electrodes were applied to bottom electrodes of BaTiO<sub>3</sub> thin films prepared by sol-gel processing which is one of chemical processings.

## EXPERIMENTAL

Most of the difference to prepare the alloy bottom electrodes between PVD and sol-gel processing was

as follows. In PVD, after sputtering the Ni alloy target on the substrate in the presence of pure Ar gas at a substrate temperature(Ts) of 400 °C, (Pb,La)TiO<sub>3</sub> films were fabricated in an atmosphere with 10 % O<sub>2</sub> gas by volume [1] (100 vol % O<sub>2</sub> gas in case of PZT films by ablation [6]) at a Ts of 600 °C. In the beginning of this process, while the substrate temperature was being raised to 600 °C, the surface of the alloy film was oxidized, and as a result, a dense oxide film composed primarily of Al<sub>2</sub>O<sub>3</sub> was produced on the surface of the alloy electrode. In sol-gel processing, soda-lime glass plates were used as substrates, of which dimensions were 40 mm in length, 10 mm in width and 1 mm in thickness. Ni alloy films were deposited on the substrates in pure Ar gas by sputtering to form bottom electrodes at a Ts of 400 °C, and then they were heated in air at 400 °C for 1 hour in order to form the Al<sub>2</sub>O<sub>3</sub> thin layer on the surface of the alloy electrodes. After the glass substrates with the Ni alloy bottom electrodes were dipped into Ba, Ti and La alkoxide as precursor solutions, the substrates were dried up to 500 °C. Their mixing ratios of the alkoxide were set to be the compositions as shown in Table I. The processes from dip-coating to drying were repeated 5 times, finally the glass substrates were fired at a temperature of 600 °C for 2 hours. Figure 1 shows the sample preparations of BaTiO<sub>3</sub> (BT) and (Ba,La)TiO<sub>3</sub>(BLT) thin films.

Table I The compositions of sol solutions for dipping.

No.	Composition
(a)	BaTiO <sub>3</sub>
(b)	Ba <sub>0.98</sub> La <sub>0.02</sub> TiO <sub>3</sub>
(c)	Ba <sub>0.96</sub> La <sub>0.04</sub> TiO <sub>3</sub>
(d)	Ba <sub>0.94</sub> La <sub>0.06</sub> TiO <sub>3</sub>

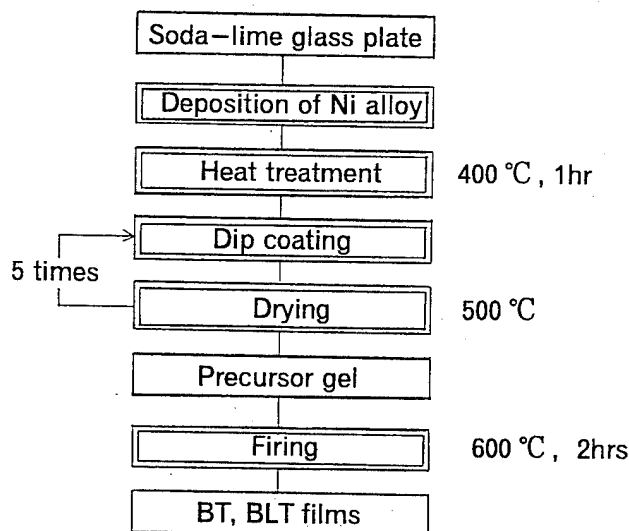


Fig. 1 Sample preparation of BaTiO<sub>3</sub> and (Ba,La)TiO<sub>3</sub> thin Films.

The precursor gel films were investigated by thermal analysis and the films annealed at various temperatures were studied by X-ray diffraction (Cu K $\alpha$ ). The film surfaces and the depth analysis at the interface between the Ni alloy bottom electrodes and BT films were investigated by FE-SEM (JEOL JSM-6300F) and XPS (Shimadzu ESCA K-1) respectively. Measurements of electrical properties were carried out using the sandwich-type capacitor with  $5 \times 5 \text{ mm}^2$  area. The relative dielectric constant ( $\epsilon_r$ ) and  $\tan \delta$  were measured at 1 kHz by Impedance/Gain-Phase Analyzer (HP4194A). The D-E hysteresis loops were observed using a Sawyer-Tower circuit at 60 Hz.

## RESULTS AND DISCUSSION

### Drying and annealing gel films

The thermal analysis of the precursor gels of Ba<sub>0.98</sub>La<sub>0.02</sub>TiO<sub>3</sub>, Ba<sub>0.96</sub>La<sub>0.04</sub>TiO<sub>3</sub> and Ba<sub>0.94</sub>La<sub>0.06</sub>TiO<sub>3</sub> were shown in Fig. 2. The weight of the gels decreased monotonously at a temperature of 200 °C to 500 °C and reach a constant over 500 °C. The two exothermic peaks were observed at 280 °C and around 550–600 °C. We believe that the peak at 280 °C was due to burn out alcohol and the peak around 550–600 °C corresponded to crystallization of the films. The two endothermic peaks came from vaporization of organic compounds. Therefore, the drying condition was decided from above results of the thermal analysis of the gels.

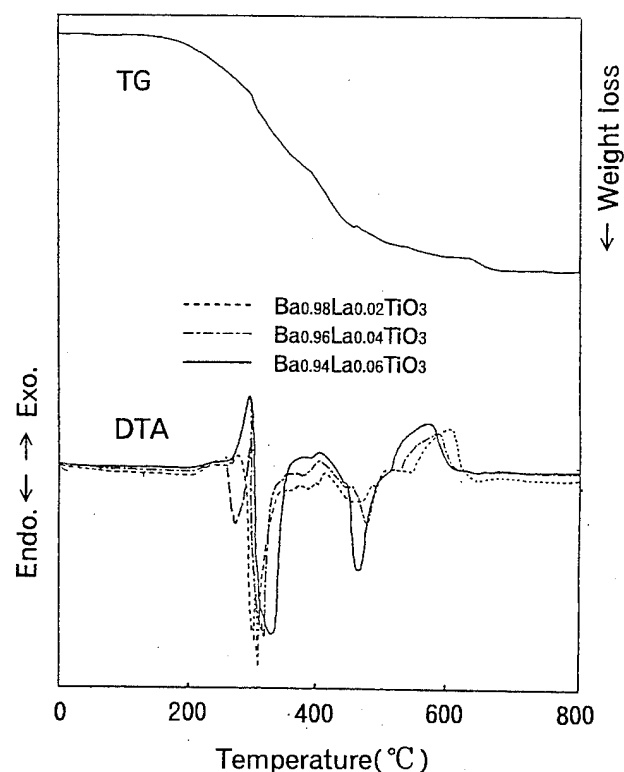


Fig. 2 Thermal analysis (TG, DTA) of precursor gels; TG sample, Ba<sub>0.94</sub>La<sub>0.06</sub>TiO<sub>3</sub>.

Figure 3 shows the X-ray diffraction patterns of thin films on the glass plates with the alloy electrodes after annealing at 500 °C and 600 °C. The films annealed below 500 °C were amorphous and the films annealed at 600 °C became polycrystal. It was clarified that the exothermic peaks around 550–600 °C were the crystallization temperature of the amorphous gels, which decreased with the increase of La substitution as shown in Fig. 2.

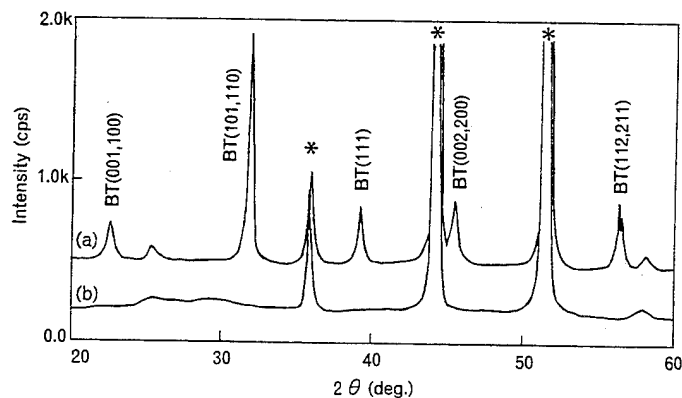


Fig. 3 X-ray diffraction patterns of gel films on glass substrates after annealing at 600 °C (a) and 500 °C (b). Diffraction lines from Ni alloy electrodes are shown by \* marks.

### Interface between Ni alloy electrode and BT film

Figure 4 showed a depth profile of a structure of Au top electrode/ BLT film/ Ni alloy bottom electrode/ glass substrate investigated by XPS. An Ar<sup>+</sup> ion etching was used on the condition of 2 kV– 20 mA. As the depth was

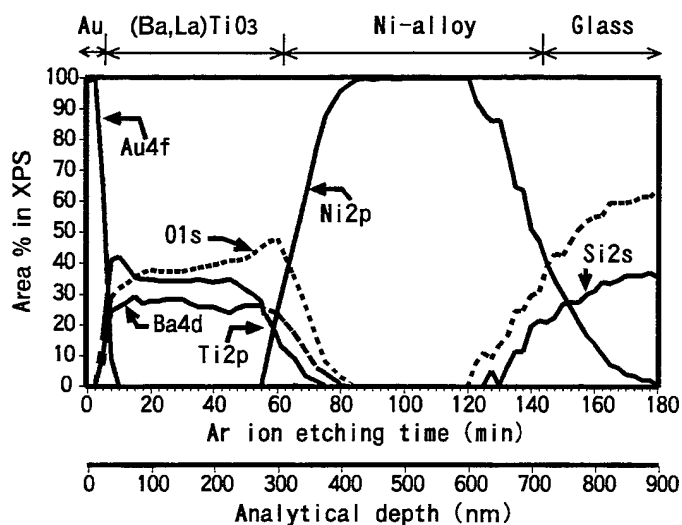


Fig. 4 Depth profile of Au/Ba<sub>0.94</sub>La<sub>0.06</sub>TiO<sub>3</sub>/Ni alloy/glass.

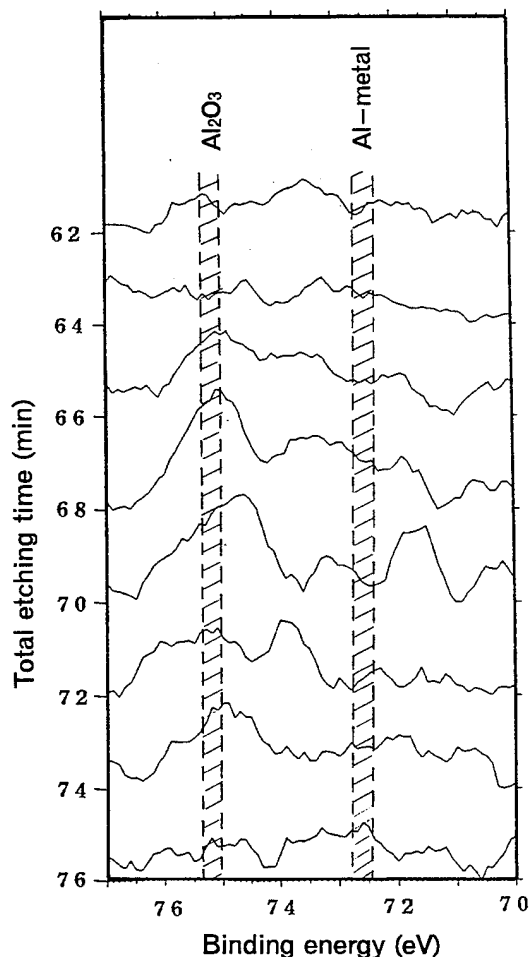


Fig. 5 Al<sub>2</sub>p peak profiles at the interface between the alloy electrode and BT film.

estimated by the etching ratio of SiO<sub>2</sub>, the thicknesses of the BLT film and alloy film were 300 nm and 400 nm respectively. These thicknesses well fitted the ones by evaluating SEM observation of the fracture surface of the films. The depth analysis at the interface between the alloy electrode and BT film was shown in Fig. 5. The small peaks at 75.2 eV which would belong to Al<sub>2</sub>O<sub>3</sub> were observed in the total etching time between 68 and 70 min, therefore, the thickness of the Al<sub>2</sub>O<sub>3</sub> layer was estimated to be 10–20 nm.

### Surface of BT and BLT films

The surface morphology of BT and BLT films on the Ni alloy electrodes was shown in Fig. 6. The grains with the size of 1–2  $\mu$ m consisted of subgrains with 20 nm in diameter, as it were cauliflower-like morphology. It was thought that the grain growth was promoted by the Al<sub>2</sub>O<sub>3</sub> thin layer on the Ni alloy electrode. In addition, the grain size was decreased with increasing La substitution from 0 to 4 mole%, and the cauliflower-like morphology was not clear in case of 6 mole% La. We believe that these microstructures of the films were assumed to have a close relation with the electrical properties.

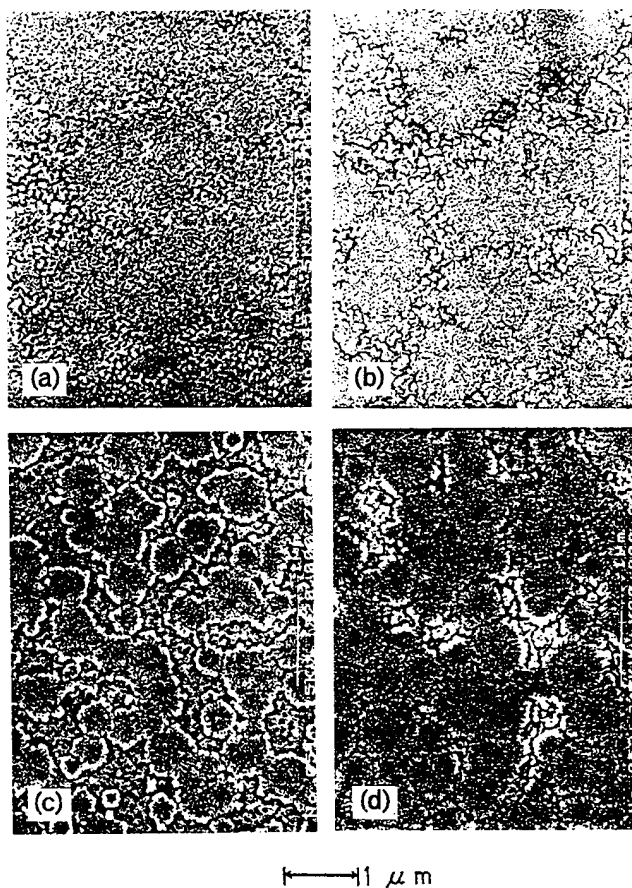


Fig. 6 FE-SEM images of BT and BLT film surfaces; (a)BaTiO<sub>3</sub>, (b)Ba<sub>0.98</sub>La<sub>0.02</sub>TiO<sub>3</sub>, (c)Ba<sub>0.96</sub>La<sub>0.04</sub>TiO<sub>3</sub>, (d)Ba<sub>0.94</sub>La<sub>0.06</sub>TiO<sub>3</sub>.

### Dielectric and ferroelectric properties of BT and BLT films

Dielectric and ferroelectric properties were measured for the structure of Au top electrode/ BT and BLT films/ Ni alloy bottom electrode/ glass substrate. Table II summarized the results of dielectric measurements and D-E hysteresis loops of the BT and BLT films at room temperature. The  $\epsilon_r$  and  $\tan \delta$  of the  $0.4 \mu\text{m}$ -thick BT films were 100 and 4.0 % respectively. The  $\epsilon_r$  slightly decreased and the  $\tan \delta$  increased with La substitution. Further, the remanent polarization( $P_r$ ) and coercive field( $E_c$ ) of the BT film were  $3.6 \mu\text{C}/\text{cm}^2$  and  $150 \text{ kV}/\text{cm}$  under an applied field of  $500 \text{ kV}/\text{cm}$ . A typical D-E hysteresis loop of the BT film was shown in Fig. 7.

Table II Dielectric and ferroelectric properties of  $\text{Ba}_{1-x}\text{La}_x\text{TiO}_3$  Thin Films.

x	$\tan \delta$ (%)	$\epsilon_r$	E (kV/cm)	$P_r$ ( $\mu\text{C}/\text{cm}^2$ )	$E_c$ (kV/cm)
0.00	4.0	100	500	3.6	150
0.02	2.9	73	500	1.3	300
0.04	4.1	90	1000	0.9	600
0.06	10.3	98	---	---	---

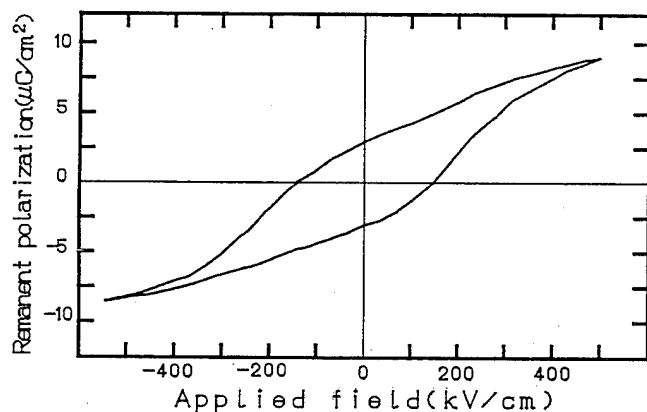


Fig. 7 D-E hysteresis loop of the BT film.

The clear hysteresis loop, however, could not be observed for the film with 6 mole % La substitution, because of a relatively large  $\tan \delta$ . The  $E_c$  increased with increasing the amount of La substitution. In case of the films with higher La substitution, it was necessary for high applied fields( $E$ ) to obtain saturated hysteresis loops. The  $P_r$  decreased with increasing La substitution, even if high  $E$  was applied to the films. Figure 8 showed the La substitution dependence of the grain size of the films and  $P_r$ . Since the grain size decreased with increasing La substitution, it was concluded that the  $P_r$  decreased with decreasing the grain size of the films as shown in Fig. 9.

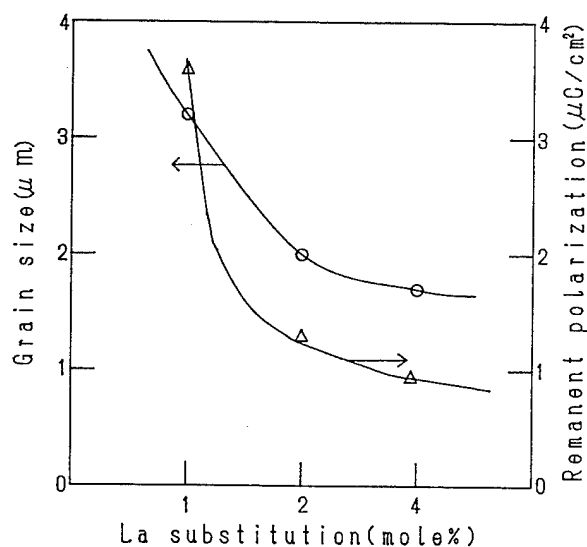


Fig. 8 La substitution dependence of the grain size of films and  $P_r$ .

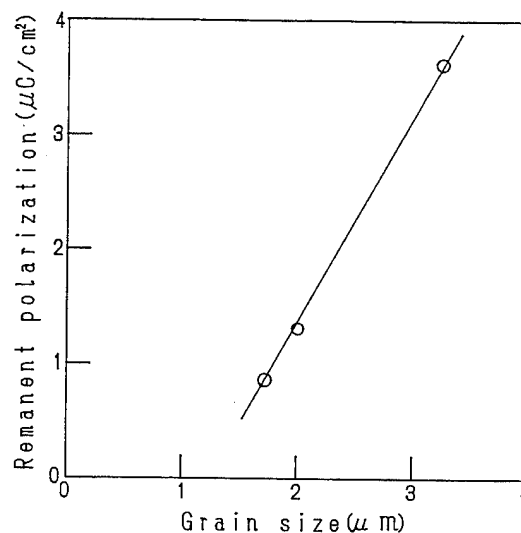


Fig. 9 Grain size dependence of  $P_r$ .

The  $P_r$  in this study was considerably higher than ones of the BT films in other reports [10–11] but smaller than those of bulk ceramics by a conventional powder processing [12]. It was thought that the difference in  $P_r$  was due to the bottom electrode materials. Basically platinum(Pt) has been utilized for bottom electrodes in conjunction with BT,  $\text{PbTiO}_3$  and PZT because Pt possesses low chemical activities at a high temperature. Pt electrodes, however, are likely to promote resolving the BT and BLT compositions into its elements and to produce the second phases.

We believe that the decomposition on Pt electrodes came from a small sticking coefficient of BaO, TiO<sub>2</sub> and La<sub>2</sub>O<sub>3</sub> on Pt electrode; that is, oxide-metal contact. In this study, the surface of the Ni alloy electrode is coated with Al<sub>2</sub>O<sub>3</sub> layer. Since this layer promoted to produce the perovskite oxide phase because of oxide-oxide contact, relatively high Pr were obtained at the films on the alloy electrodes in comparison with the one of the films on Pt electrodes. Figure 10 shows the temperature dependence of  $\epsilon_r$  of BT and Ba<sub>0.94</sub>La<sub>0.06</sub>TiO<sub>3</sub> films. The peaks were observed around 180 °C. Since the  $\epsilon_r$ 's of the films were almost same at room temperature, the peak  $\epsilon_r$  of the Ba<sub>0.94</sub>La<sub>0.06</sub>TiO<sub>3</sub> film was higher than the one of the BT film. It was thought that this phenomenon was due to the film with small grains by La substitution.

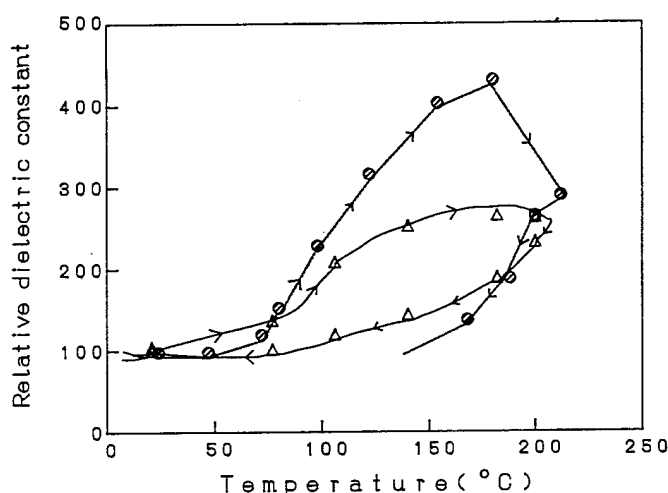


Fig. 10 Temperature dependence of  $\epsilon_r$   
( $\Delta$ : BaTiO<sub>3</sub> film,  $\bigcirc$ : Ba<sub>0.94</sub>La<sub>0.06</sub>TiO<sub>3</sub> film).

## SUMMARY

A Ni alloy electrodes were applied to bottom electrodes of BaTiO<sub>3</sub> thin films prepared by sol-gel processing. The alloy electrodes possessed low reactivity with BaO, in addition to excellent thermal stability and resistance to oxidation. Since the dielectric and ferroelectric properties were evaluated with the alloy electrodes, it has been confirmed that the alloy was suitable for the bottom electrodes of BaTiO<sub>3</sub> thin films prepared by chemical processings such as sol-gel processing.

## ACKNOWLEDGMENTS

This work was partly supported by the fund of Fukuroi-shi.

## REFERENCES

- [1] T.Ogawa, "Application of Nickel Alloy Electrode to Characterization of Crystal Oriented PbTiO<sub>3</sub> Thin Films," *Integrated Ferroelectrics*, vol. 1, pp.99-110, 1992.
- [2] T.Ogawa, "Ceramic Electronic Component and Method of Fabricating the Same," United States Patent No. 5088002, Feb. 11, 1992.
- [3] T.Ogawa, S.Shindou, A.Senda and T.Kasamami, "Ferroelectricity of Lanthanum-Modified Lead-titanate Thin Films Deposited on Nickel Alloy Electrodes," in *Mat. Res. Soc. Symp. Proc.*, vol. 243, 1992, pp.93-99.
- [4] T.Ogawa, "Preparation and Evaluation of Ferroelectric Thin Films," presented at the 1993 PAC RIM Meeting on International Symposium on Ferroelectric Thin Films, Honolulu, Hawaii, Nov. 7-10, 1993.
- [5] H.Kidoh, T.Ogawa, H.Yashima, A.Morimoto and T.Shimizu, "Influence of Laser Fluence on Structural and Ferroelectric Properties of Lead-Zirconate-Titanate Thin Films Prepared by Laser Ablation," *Jpn. J. Appl. Phys.*, vol. 30, pp.2167-2169, Sep. 1991.
- [6] H.Kidoh, T.Ogawa, H.Yashima, A.Morimoto and T.Shimizu, "Preparation of Pb(Zr,Ti)O<sub>3</sub> Films on Si Substrate by Laser Ablation," *Jpn. J. Appl. Phys.*, vol. 31, pp.2965-2967, Sep. 1992.
- [7] T.Ogawa, H.Kidoh, H.Yashima, A.Morimoto and T.Shimizu, "Ferroelectricity of Lead-Zirconate-Titanate Thin Films Prepared by Laser Ablation," in *Mat. Res. Soc. Symp. Proc.*, vol. 243, 1992, pp.501-506.
- [8] T.Ogawa, H.Kidoh, H.Yashima, A.Morimoto and T.Shimizu, "Ferroelectric Properties of PZT Thin Films Deposited by Laser Ablation on Nickel Alloy Electrode for Use with Silicon Substrate," presented at the 8th International Meeting on Ferroelectricity, Gaithersburg, Maryland, Aug. 8-13, 1993.
- [9] R.B.H.Herchenroeder, "Method of Heat Treating Nickel-Base Alloys for Use as Ceramic Kiln Hardware and Product," United States Patent No.4312682, Jan. 26, 1982.
- [10] C.H.Lee and S.J.Park, "Preparation of Ferroelectric BaTiO<sub>3</sub> Thin Films by Metal Organic Chemical Vapour Deposition," *J. Mater. Sci., Mater. in Electronics* vol. 1, pp.219-224, 1990.
- [11] T.Tuchiya, T.Kawano, T.Sei and J.Hatano, "Preparation of Ferroelectric BaTiO<sub>3</sub> Films by Sol-Gel Process and Dielectric Properties," *J. Cerm. Soc. Japan*, vol. 98, pp.743-748, Aug. 1990 (in Jpn).
- [12] B.Jaffe, W.R.Cook, Jr. and H.Jaffe, *Piezoelectric Ceramics*. New York: Academic Press, 1971, ch. 5, pp.53-114.

# Rapid Thermal Processing of Sol-Gel Derived PZT 53/47 Thin Layers

Charles D.E. Lakeman, Zhengkui Xu and David A. Payne

Department of Materials Science and Engineering, Materials Research Laboratory, and Beckman Institute,  
University of Illinois at Urbana-Champaign, Urbana, IL 61801

**Abstract:** The method of rapid thermal processing (RTP) has been suggested to be a means by which the formation of intermediary phases in sol-gel derived  $\text{Pb}(\text{Zr,Ti})\text{O}_3$  (PZT) thin layers can be suppressed before the crystallization of the desired perovskite phase. However, the dependence of densification and crystallization processes in sol-gel derived materials on thermal processing conditions such as heating rate,  $\alpha$ , and firing temperature,  $T_f$ , can lead to differences in the properties of otherwise identical materials prepared by different thermal profiles. In this paper, the effects of thermal processing conditions on the properties of PZT 53/47 (i.e.,  $\text{Zr:Ti} = 53:47$ ) thin layers are reported. The evolution of structure after RTP was examined by diffuse reflectance FTIR spectroscopy, and electron microscopy. It was found that crystallization of the perovskite phase shifted to higher temperatures, and the shrinkage normal to the plane of the substrate decreased, with increasing heating rate.

## INTRODUCTION

Despite the widespread interest in integrated ferroelectrics, the lack of control over a large number of process variables has been reflected in the scatter of property values reported in the literature [1]. Factors which can influence the measured properties include microstructure and compositional heterogeneities [2, 3, 4], variations in the degree of structural perfection of the crystallites [5, 6], space charge effects, and intrinsic size effects [1], among others. Of these, microstructure and compositional heterogeneities, and crystallite perfection can be related to the processing conditions.

The formation of non-ferroelectric intermediary phases prior to crystallization of the desired perovskite phase during the sol-gel processing of PZT thin layers is commonly recognized [2, 3, 4, 7, 8]. Diffraction patterns obtained from these intermediary phases have generally been attributed to a pyrochlore structure [7], however, there has recently been some speculation that the structure is fluorite rather than pyrochlore [8]. Nevertheless, the consequences of the coexistence of secondary phases with perovskite are that values of measured properties are somewhat deteriorated compared with those of phase-pure materials.

One of the methods that has been proposed to avoid the formation of undesirable additional phases is rapid thermal processing (RTP). By kinetically limiting the nucleation of second phases, improvements in properties have been reported for thin layer PZT [9]. However, few details have been reported on the relationships between the heating rate and the densification and crystallization behavior of sol-gel derived PZT. Densification of sol-gel derived materials is frequently described in terms of viscous flow, in which the energy dissipated by the reduction of surface area of a porous body is expended at a rate proportional to the square of the strain rate [10]. However, such models assume either isothermal sintering, or, in a few constant heating rate experiments, a simple dependence of material viscosity on temperature. Since the viscosity of gels evolves constantly during heating, and is complicated by pyrolysis, these models have had limited success in predicting densification behavior. In this paper, we describe various processes which occur during heat-

treatment of sol-gel derived  $\text{Pb}(\text{Zr}_{0.53}\text{Ti}_{0.47})\text{O}_3$  (PZT 53/47) thin layers which have been deposited on platinized silicon substrates, and address the effects of different heating rates on shrinkage and perovskite phase formation.

## EXPERIMENTAL

The preparation of precursor solutions was carried out by a method similar to that of Budd *et al.* [11], and is described in detail elsewhere [12]. Amorphous PZT 53/47 thin layers were deposited onto platinized silicon substrates by spin-coating pre-hydrolyzed alkoxide precursors. Each layer was heat-treated at 300°C on a hot-plate before the subsequent deposition and heat-treatment of sequential layers to build up the desired thickness. Specimens were heated at 50°C/min, 500°C/min, and 5000°C/min to temperatures between 350°C and 700°C in 50°C intervals in a Research Inc. Micristar 828D/E RTP system. Immediately upon reaching the desired temperature, specimens were quenched in order to obtain a snapshot of the structure which had evolved to that temperature. In other words, the specimens were at the peak temperature for less than 1 second (Figure 1). The thickness of each coating was measured before and after heat-treatment on a Dektak 3030 profilometer. Plan-view specimens were prepared for TEM analysis from as-deposited coatings, and from those fired at selected temperatures. The microstructure and microchemistry of the thin layers were examined on Phillips CM 12 and 420 transmission electron microscopes, equipped with Kevex energy dispersive X-ray analysis (EDXA) systems. The evolution of structure during higher temperature treatment was also monitored by diffuse reflectance fourier transform infrared (FTIR) spectroscopy (IBM model IR-32 fitted with a Spectrattech diffuse reflectance assembly). An uncoated substrate was used to obtain the background spectrum.

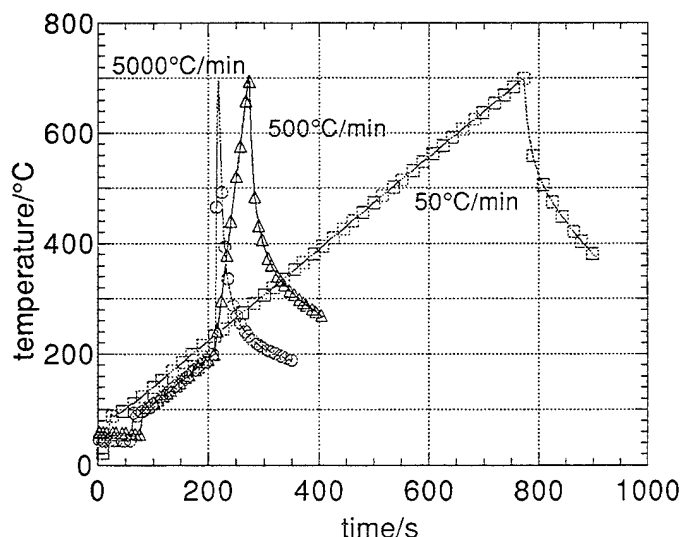


Figure 1 Rapid thermal processing



## RESULTS AND DISCUSSION

We have previously reported the general features of the evolution of structure and composition in sol-gel derived PZT thin layers which were heated at 50°C/minute [13]. It was determined that medium-range order develops during low-temperature (300°C) heat treatment. Microstructural and microchemical data indicate the existence of compositional heterogeneity at the nano-scale level in low-temperature heat-treated thin layers. This is in agreement with EXAFS data for heat-treated gels of the same composition [14], and follows from chemical models of similar precursors [15], [16]. After higher temperature heat treatment, structural rearrangement occurred, and the composition became more uniform. An intermediate phase crystallized before the perovskite phase, at temperatures between 500°C and 550°C. The perovskite phase was observed to nucleate from the intermediate phase which was in agreement with previous studies [7], [8].

Figure 2 compares the shrinkage of PZT thin layers as a function of temperature for different heating rates up to ~700°C. Until 450°C, there was little difference in the shrinkage of specimens fired at the three different rates, however, at higher temperatures, it became apparent that for faster heating rates, the onset of the major portion of the shrinkage was shifted to higher temperatures. In addition, for very fast heating rates (5000°C/min), the overall shrinkage was significantly less than for slower heating rates. As discussed earlier, it is difficult to model the densification behaviour of sol-gel derived materials due to the complexity of the temperature-dependent viscosity and pyrolysis behavior, however, from these results, it is apparent that the conditions under which sol-gel PZT thin layers are fired significantly influence their final properties due to induced structural variations. Thus, in order to evaluate the differences induced by different heating rates, a study of the evolving structure by TEM and FTIR methods was undertaken.

XRD data reported elsewhere indicate that crystallization was shifted to higher temperatures as the heating rate increased [17]. TEM indicated that coatings which had been heated at 500°C/minute to 650°C showed evidence of initial crystallization (Figure 3 a)). A few isolated perovskite grains were found in a matrix of an intermediary phase. There was also some evidence of a second non-perovskite phase (Figure 3 b)) which had a

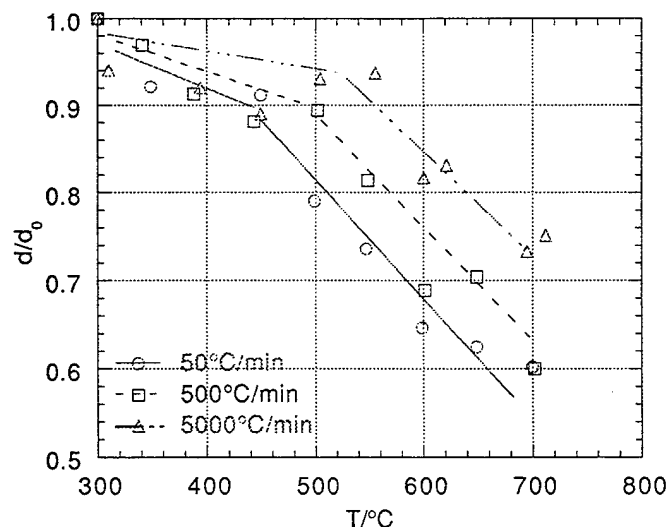


Figure 2 Shrinkage of sol-gel derived PZT 53/47 thin layers on platinized silicon substrates as a function of rapid thermal processing conditions

similar structure to the bulk of the matrix, but which was less well crystallized, as determined by electron diffraction. EDXA was used to determine that there was compositional heterogeneity in the microstructure. The major phase was found to be of a similar composition to the desired PZT 53/47 perovskite phase, however, the other non-perovskite phase was found to be lead-deficient and zirconium-rich. Nevertheless, by heating to 700°C a fully perovskite coating was formed (Figure 4). Interestingly, a few strain contours were observed in the perovskite grains formed

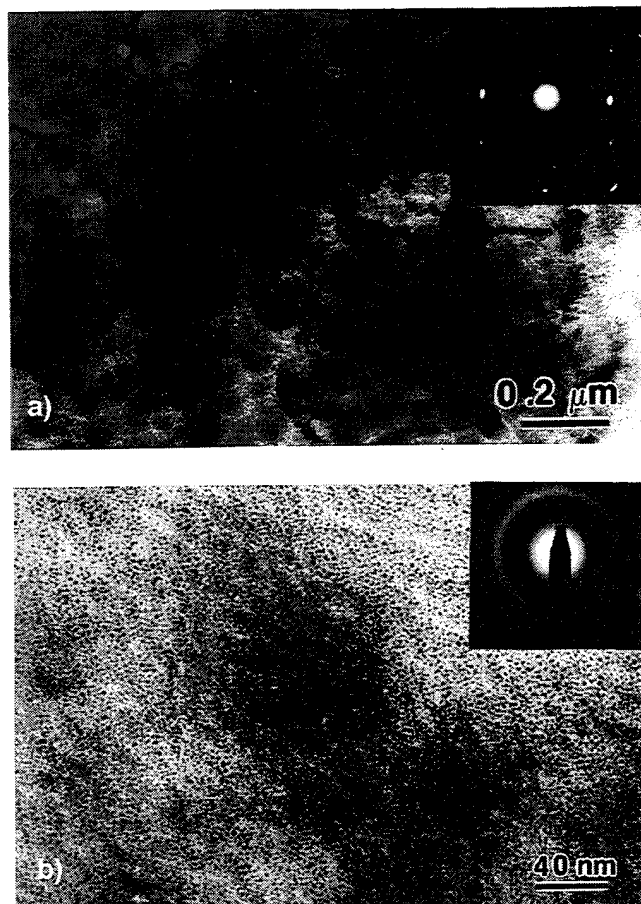


Figure 3 Transmission electron photo-micrographs of PZT 53/47 thin layers heated at 500°C/minute to 650°C. a) Structure typical of most of the coating; b) pocket of poorly crystallized Zr-rich pyrochlore-type phase.

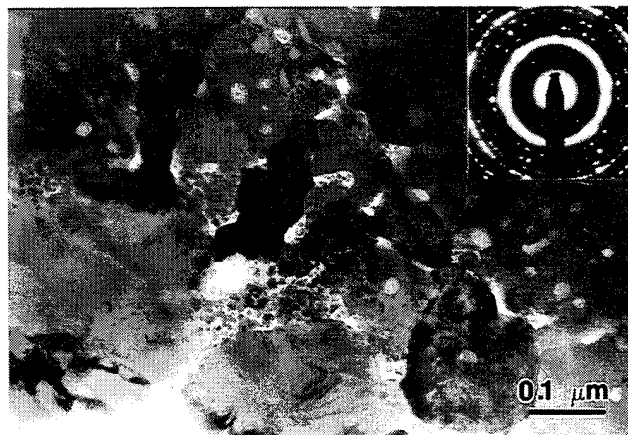


Figure 4 Transmission electron photo-micrograph of PZT 53/47 thin layer heated at 500°C/minute to 700°C.

under these conditions. Similar features were previously reported by Kwok and Desu, and were attributed to the strain which would arise due to a volume decrease (~5.7%) at the "pyrochlore to perovskite" transformation [7]. It is believed that the strain contours were not observed in coatings heated more slowly [13], since a longer time at temperatures above the crystallization temperature allowed for some thermal strain relief.

On very rapid heating (5000°C/min) a different crystallization pathway was observed. Under these conditions, coatings heated to 695°C were amorphous as determined by electron diffraction. Figure 5 a) indicates the coatings showed non-uniform contrast similar to that observed in low-temperature (i.e., 300°C, 450°C) treated coatings which was previously attributed to compositional heterogeneity [13]. On heating to 712°C, a high perovskite phase content resulted (Figure 5 b)). However, there were more strain contours observed for these coatings than in those heated at 500°C/min, supporting the argument that slower heating rates allow for strain to be relieved thermally. In addition, significant compositional heterogeneity was observed by EDXA, even in perovskite coatings (Figure 6). The dominant perovskite phase was found to be slightly titanium-rich when compared with the bulk stoichiometry (Figure 6 i)), however a few grains with high contrast were observed which were determined to be zirconium-rich, with almost no titanium (Figure 6 ii)). Also, a nanocrystalline minor phase was also observed, which was found to be lead-deficient, and zirconium-rich when compared with perovskite (Figure 6 iii)).

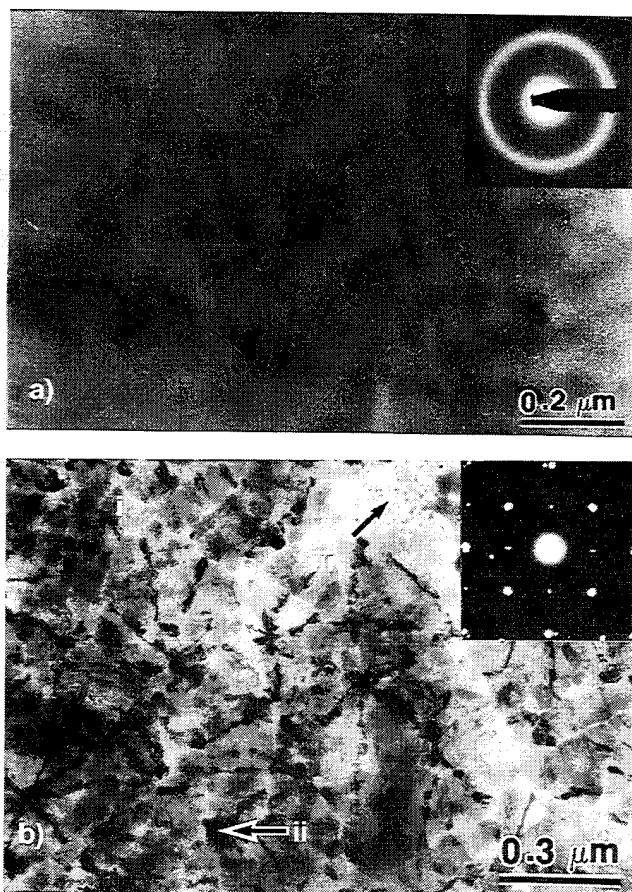


Figure 5 Transmission electron photomicrographs of PZT 53/47 thin layers heated at 5000°C/min to a) 695°C, and b) 712°C. Note i) bright grains, ii) dark grains, and iii) pockets of nanocrystalline phase.

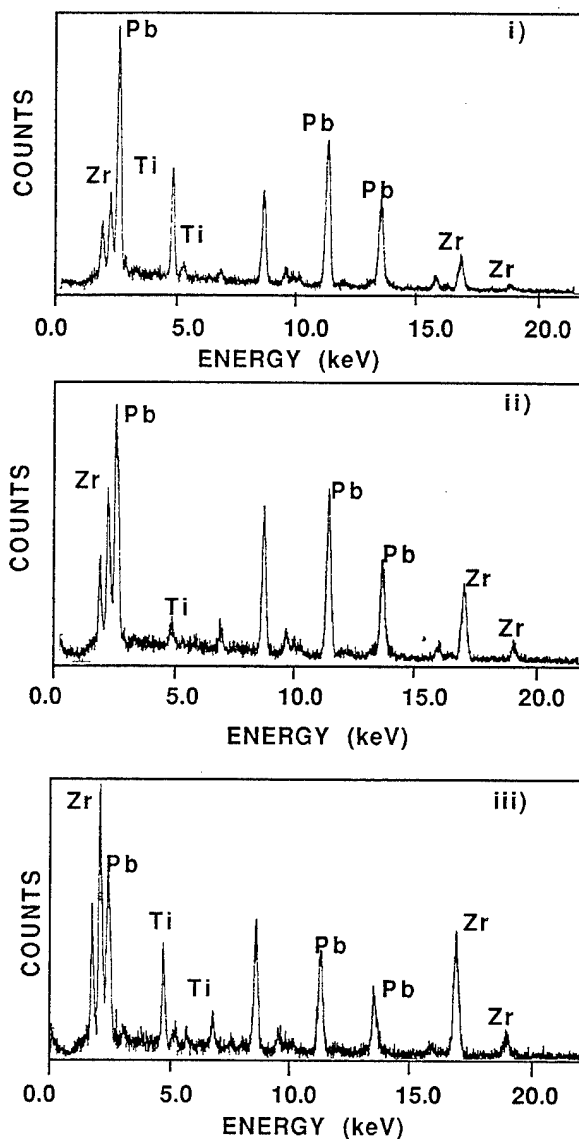


Figure 6 EDXA spectra from PZT 53/47 thin layer heated at 5000°C/min to 712°C; i) major perovskite phase, ii) dark perovskite grains, iii) nanocrystalline phase (see figure 5 b).

Some of these differences can be addressed after comparing the FTIR spectra taken from thin layers as a function of heat treatment conditions. Figure 7 compares the room temperature FTIR spectra taken from coatings heated under the different heating rates just before crystallization. There are 3 features to note in these spectra. First, the position of the  $\text{BO}_6$  stretching mode absorption ( $\sim 680\text{cm}^{-1}$  [18]) shifts to higher frequencies with increasing heating rate. Second, the band remains comparatively broad at a high temperature, and third, there is evidence in the spectra from coatings heated at 5000°C/min of peak splitting. These features may be attributed to structural rearrangements which could occur at higher temperatures. A shift of the absorption to higher frequencies may suggest a stiffening network, whereas a broad absorption indicates a poorly defined environment around the  $\text{BO}_6$  octahedra. The splitting of the absorption may be attributed to separate  $\text{TiO}_6$  and  $\text{ZrO}_6$  environments in the gel structure. These features were all observed in spectra taken from coatings which were processed at lower temperatures [13]. In another paper, we proposed that structural rearrangements would occur during heating which would lead to densification and compositional

homogeneity prior to crystallization of the perovskite phase [13]. These data suggest that rearrangement processes are limited under more rapid heating rates, and that compositional variations may persist in rapidly heated coatings.

Extremely rapid heating ("up-quenching") of aqueous precursors of doped (e.g., MgO) zirconia has been reported to result in crystallization of metastable solid solutions rather than the expected mixtures of phases [19]. For high temperature annealing ( $T \geq 900^\circ\text{C}$ ), the thermodynamically predicted phases evolved [19]. Balmer and co-workers described this phenomenon in terms of kinetically limited crystallization. In the precursors, it was assumed that there was a uniform distribution of the components. With very rapid heating, there was insufficient time for material transport to take place, with the result that normally segregated components (i.e., MgO) were held in solid solution to much higher concentrations than predicted from the phase diagram. Since the precursor solutions were aqueous solutions of acetates and nitrates, the assumption of uniform distribution is reasonable, since they had not undergone any significant polymerization or precipitation reactions.

The argument can now be reversed and applied to sol-gel derived PZT thin layers in which compositional heterogeneity is found in the precursors. In this case, rapid crystallization results in the formation of a mixture of phases as the thermodynamically metastable state, and subsequent high temperature annealing results in compositional uniformity. However, extended time at elevated temperatures would be deleterious to the dielectric and ferroelectric properties of the coating due to

interfacial reactions and electrode boundary conditions.

#### SUMMARY

The evolution of structure in sol-gel derived PZT 53/47 thin layers which were deposited on platinized silicon was monitored by analytical electron microscopy, and diffuse reflectance FTIR spectroscopy. During high-temperature heat-treatment, structural rearrangement reduced the compositional heterogeneity which was inherent in the as-deposited coatings [13]. However, if the heating rate was too rapid, compositional fluctuations remained in the dense crystalline microstructure which resulted in lower values of the measured dielectric and ferroelectric properties. For slower heating rates, an intermediary phase crystallized first, from which the perovskite phase eventually nucleated and grew. For the most rapid heating rate, the formation of the intermediary phase was circumvented, but at the cost of residual compositional heterogeneity.

#### ACKNOWLEDGEMENTS

The research was supported by the Basic Energy Sciences Division, U.S. Department of Energy, under Grant No. DEFG02-91ER45439. The use of facilities in the Center for Microanalysis of Materials at the University of Illinois is acknowledged. We thank Dr. L. Ma and Mr. S. Sengupta for useful discussions during the course of this work.

#### REFERENCES

- 1 R.E. Newnham, K.R. Udayakumar, and S. Troler-McKinstry, in *Chemical Processing of Advanced Materials*, eds L.L. Hench, J.K. West, New York: J. Wiley & Sons, 1992, p. 379.
- 2 L.N. Chapin and S.A. Myers, *Mat. Res. Soc. Symp. Proc.*, 1990, vol. 200, p. 153.
- 3 C.C. Hsueh and M.L. McCartney, *Mat. Res. Soc. Symp. Proc.*, 1990, vol. 200, p. 219.
- 4 B.A. Tuttle, R.W. Schwartz, D.H. Doughty and J.A. Voigt, *Mat. Res. Soc. Symp. Proc.*, 1990, vol. 200, p. 159.
- 5 Z. Surowiak, E. Nogas, A.M. Margolin, S.V. Biryukov, and I.N. Zakharchenko, *Ferroelectrics*, vol. 115, p. 21, 1991.
- 6 S.V. Biryukov, V.M. Mukortov, A.M. Margolin, Yu.I. Golovko, I.N. Zakharchenko, V.P. Dudkevich, and E.G. Fesenko, *Ferroelectrics*, vol. 56, p. 115, 1984.
- 7 C.K. Kwok and S.B. Desu, *Appl. Phys. Lett.*, vol. 60, p. 1430, 1992.
- 8 A.P. Wilkinson, J.S. Speck, A.K. Cheetham, S. Natarajan and J.M. Thomas, *Chem. Mater.*, vol. 6, p. 750, 1994.
- 9 J. Chen, K.R. Udayakumar, K.G. Brooks and L.E. Cross, *J. Appl. Phys.*, vol. 71, p. 4465, 1992.
- 10 C.J. Brinker and G.W. Scherer, *Sol-Gel Science: The Physics and Chemistry of Sol-Gel Processing*. San Diego: Academic Press, 1990.
- 11 K.D. Budd, S.K. Dey and D.A. Payne, *Br. Cer. Proc.*, 1985, vol. 36, p. 107.
- 12 C.D.E. Lakeman, and D.A. Payne, *J. Am. Ceram. Soc.*, vol. 74, p. 3091, 1992.
- 13 C.D.E. Lakeman, Z. Xu and D.A. Payne, Submitted to *J. Mater. Res.*, July, 1994.
- 14 S.S. Sengupta, L. Ma, D. L. Adler, and D.A. Payne, Submitted as a Communication to *J. Mater. Res.*, May, 1994.
- 15 L. Ma, and D.A. Payne, *Chem. Mater.*, vol. 6, p. 875, 1994.
- 16 H.K. Chae, D.A. Payne, Z. Xu, and L. Ma, In press, *Chem. Mater.*, August, 1994.
- 17 C.D.E. Lakeman, PhD Thesis, University of Illinois at Urbana-Champaign, 1994.
- 18 J.T. Last, *Phys. Rev.*, vol. 105, p. 1740, 1957.
- 19 M.L. Balmer, F.F. Lange and C.G. Levi, *J. Am. Ceram. Soc.*, vol. 74, p. 946, 1992.

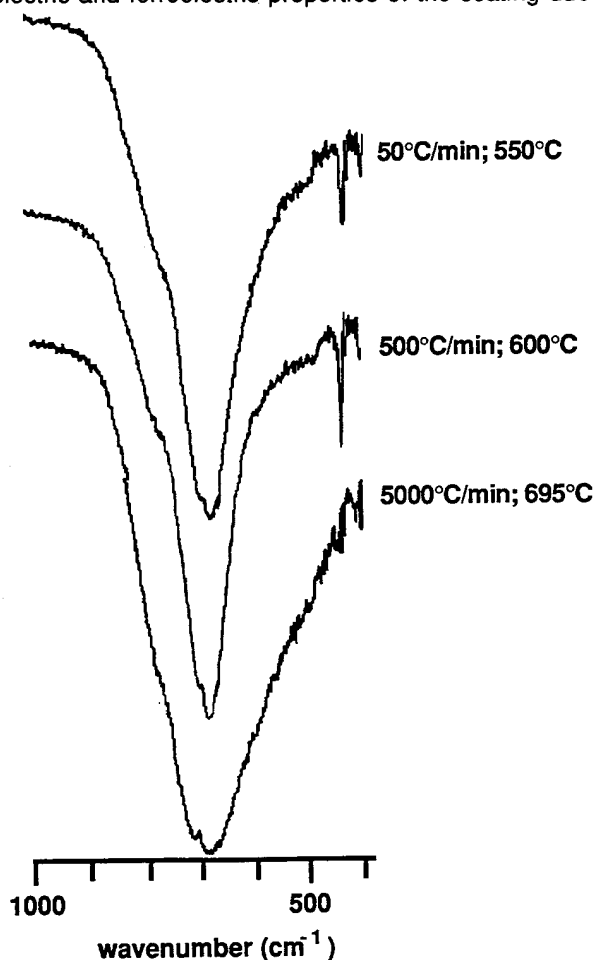


Figure 7 Room temperature diffuse reflectance FTIR spectra from gel-derived PZT thin layers heated at different rates, just before crystallization.

# The Formation of a Fine-Patterned Ferroelectric Thin Film from a Sol-Gel Solution Containing a Photo-Sensitive Water-Generator

Nobuyuki Soyama, Go Sasaki, Tsutomu Atsuki,  
Tadashi Yonezawa and Katsumi Ogi  
Central Research Institute, Mitsubishi Materials Corporation  
1-297 Kitabukuro-cho, Omiya, Saitama 330, Japan

**Abstract** - A fine-patterned PZT film was successfully formed from a photo-sensitive sol-gel solution by means of UV-irradiation. This solution was prepared from lead acetate, zirconium n-butoxide, titanium i-propoxide, 2-methoxyethanol. O-nitrobenzyl alcohol (NBA) was used as a water-generator. Spin-coated PZT gel films on various substrates were irradiated with UV rays through a photo-mask pattern to facilitate hydrolysis reaction and developed with developer. The obtained pattern was a negative of the mask. The films were finally annealed for crystallization. The obtained films had perovskite structures and good electrical properties.

## Introduction

Ferroelectric thin films, such as PZT, PLZT and  $\text{Bi}_4\text{Ti}_3\text{O}_{12}$ , have been recently drawing attention as attractive materials for application to electronic devices such as dynamic random access memory [1] and nonvolatile random access memory [2] and are being actively studied. There are many formation techniques of ferroelectric thin films such as sputtering, metalorganic chemical vapor deposition and sol-gel method. Among them, the sol-gel method is the best method in precise control of composition and cost performance.

On the other hand, in order to apply these materials to devices, the development of a fine-patterning technique is essential. There are many reports on fine-patterning techniques of the thin films by dry-etching processes [3]. But such techniques have many problems such as too many steps in the processes and high cost.

We have studied the photo-sensitivity of sol-gel solutions and developed simple fine-patterning techniques by the wet-etching process. We reported that 1) fine patterns of PZT thin film were fabricated using a photo sensitive sol-gel solution by UV-irradiation whose energy was estimated to be  $9 \text{ J/cm}^2$  [4], and 2) by using a more photo-sensitive sol-gel solution with an photo-reacted acid-generator, patterns were fabricated using less UV-irradiation than the first samples, and its estimated energy was  $1 \text{ J/cm}^2$  [5]. However both solutions also had problems. Though the PZT film fabricated from the former solution had good crystallinity and good electrical properties, the solution's photo-sensitivity was too low photo-sensitive, and the required energy to obtain patterns was too high. On the other hand, the latter solution was ten times more photo-sensitive than the former, but the PZT film fabricated from the latter solution had bad crystallinity and bad electrical properties due to sulfur left over from the decomposition of the acid-generator.

In this study, we prepared a new photo-sensitive sol-gel solution containing o-nitrobenzyl alcohol (NBA) as a water-generator, which generated water through a photo-reaction. By using this solution, we fabricated fine-patterns of PZT thin films by UV-irradiation and evaluated their properties.

## Experimental procedure

Lead acetate  $[\text{Pb}(\text{CH}_3\text{COO})_2 \cdot 3\text{H}_2\text{O}]$ , zirconium n-butoxide  $[\text{Zr}(\text{OC}_4\text{H}_9)_4]$  and titanium i-propoxide  $[\text{Ti}(\text{OCH}(\text{CH}_3)_2)_4]$  were used as starting materials. 2-methoxyethanol was used as solvent. Lead acetate was dissolved by heating in 2-methoxyethanol, and the solution was boiled in order to remove water. After the dehydrated solution was cooled to below  $50^\circ\text{C}$ , zirconium n-butoxide and titanium i-propoxide were added to the solution. Next, the solution was diluted with 2-methoxyethanol. The concentration of the obtained solution was 10wt%  $\text{PbZr}_{0.52}\text{Ti}_{0.48}\text{O}_3$ . Finally, an amount of NBA equal to 5wt% of the total solution was added to this solution. UV absorption spectra of this solution was measured using an UV-Vis spectrometer.

PZT thin films were fabricated following the method outlined in fig.1 and table 1. The used substrate were silicon for patterning and Pt/Ti/SiO<sub>2</sub>/Si for electrical measurement.

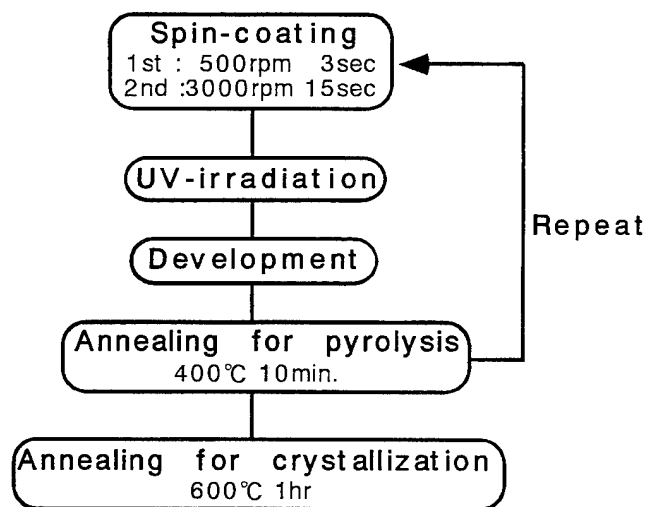


Fig.1 Flow diagram for fabrication of fine patterned PZT thin film

Table 1 UV irradiation and development condition

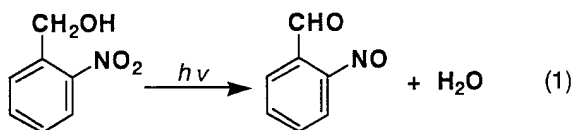
Light source: generic UV lamp
Irradiation energy: $0 \sim 1800 \text{ mJ/cm}^2$
Developer: 1:1 mixture of 2-methoxyethanol and 2-propanol
Development time: $0 \sim 120 \text{ sec}$

The film thickness was measured by ellipsometer. The composition of the film was analyzed by electron probe microanalysis (EPMA). The crystalline phase was identified by a X-ray diffractometer. The shape and surface morphology of the patterned film was observed by optical microscopy. The electrical properties such as dielectric constant, polarization-electric field (P-E) characteristics and current-voltage (I-V) characteristics were measured using a LCR meter, RT-66A(Radiant technology) and Keithley 236 respectively. To study the effect of NBA, the film fabricated from a PZT solution without NBA was also measured electrical properties (conventional process).

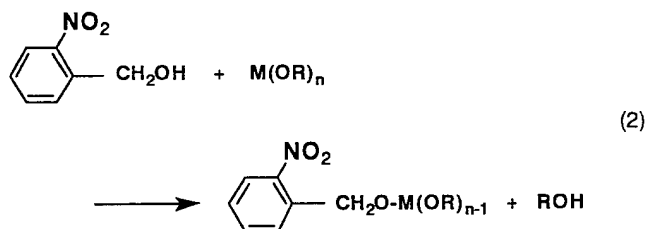
### Result and Discussion

#### Properties of a photo-sensitive solution

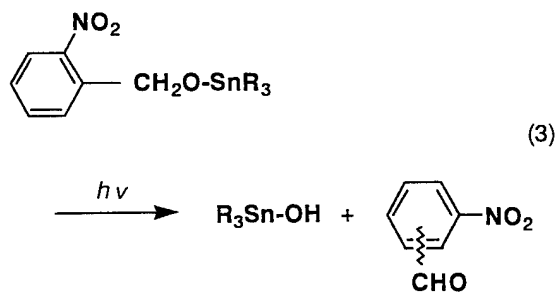
It has been known that NBA generates water through photoreaction as shown in eq. 1 [6].



But it is difficult to think of NBA existing in the PZT sol-gel solution alone. It is thought that NBA is bound to zirconium or titanium atom through a alcohol exchange reaction in the solution as shown in eq. 2.



Moreover, recently an interesting photo-reaction of Sn NBA alkoxide as shown in eq. 3 has been reported by a University of New Mexico research group [7].



It is thought that 1) the same photo-reaction is taking a place in the UV-irradiated gel film fabricated from the photo-sensitive PZT solution and 2) the generated titanium and zirconium hydroxides in the film are polymerized to form long chains and 3) the polymerized area in the film becomes insoluble.

Fig. 2 shows UV absorption spectra of NBA and PZT solution with and without NBA. The absorption peak of NBA can be seen at about 260nm and the absorption peak of PZT solution with and without NBA can be seen at about 240nm. It is presumed that the

above-mentioned reactions were caused by light of this wavelength area.

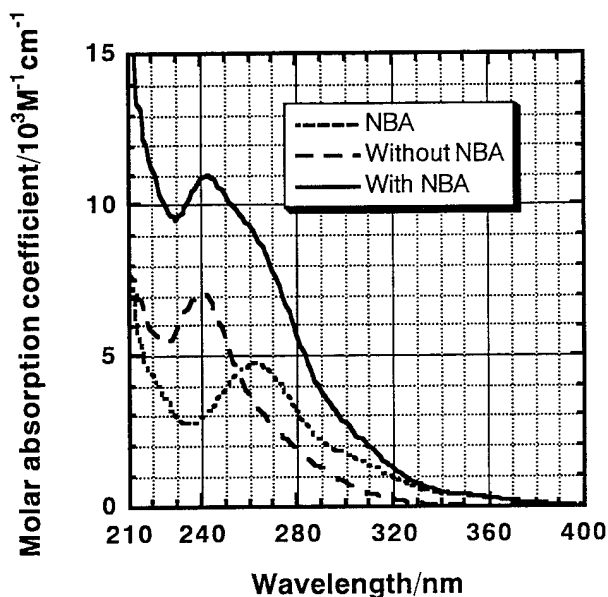


Fig.2 UV absorption spectra of NBA and PZT solution with and without NBA

#### Patterning of PZT film

The films fabricated on Si substrates from the photo-sensitive PZT solution with NBA were irradiated by UV rays at various energy levels and then each sample was developed varying the development time. After annealing at 400°C for 10min, film thickness of the samples were measured. The relationship between development time and remaining film thickness on the substrate is shown in fig.3. From these results, one can see that while the non UV irradiated film dissolved completely, the film became increasingly insoluble as the irradiation level was increased.

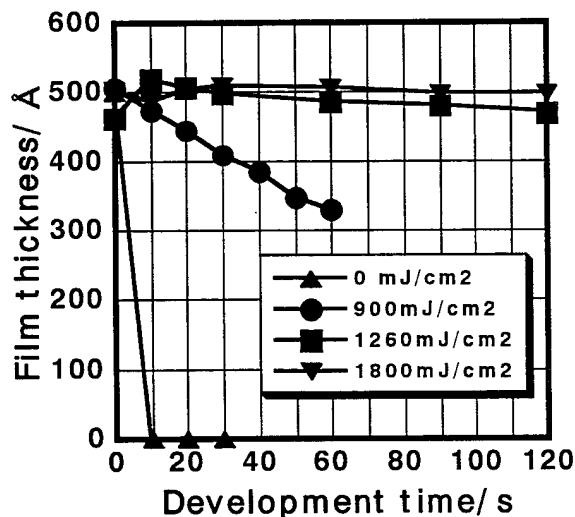


Fig.3 The relationship between development time and remaining film thickness

Fig.4 shows the relationship between irradiation energy and etching time. From this result, one can see that the film became insoluble when the irradiation energy was above 1260mJ/cm<sup>2</sup>.

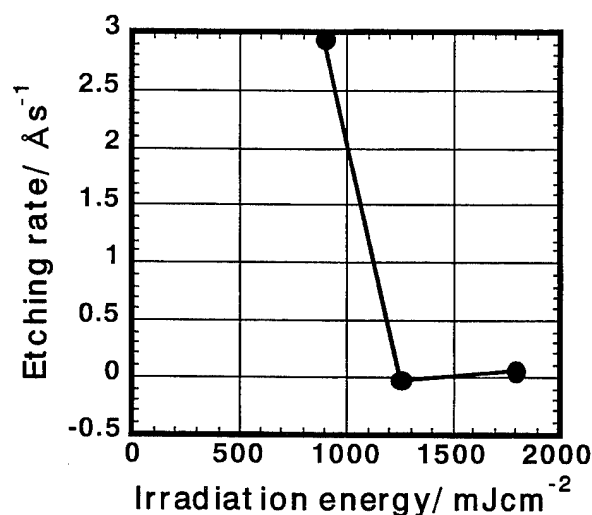


Fig.4 The relationship between irradiation energy and etching time

Fig.5 shows the optical micrograph image of patterned PZT film, which was fabricated under the following conditions: the light source was a KrF laser; the irradiation energy was 2000mJ/cm<sup>2</sup>; the developer was 1:1 mixture of 2-methoxyethanol and 2-propanol; the development time was 30sec. One can see lines running parallel to one another about 10 to 20 microns apart from one another. From this result, one can see this method's potential versatility in making PZT films.

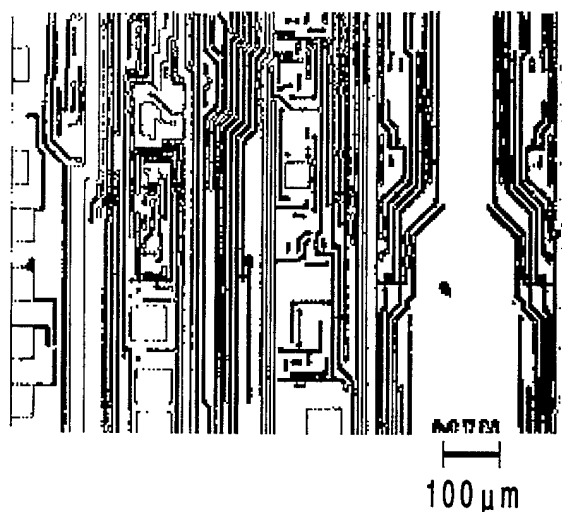


Fig.5 Optical micrograph image of patterned PZT film

The composition of PZT films were analyzed by EPMA. A pre-developed PZT film was compared with a developed film

fabricated by this new process. The results are shown in table 2. From these results, it is clear that no particular elements in the film dissolved preferentially in developer during the development process.

Table 2 Composition of PZT films

	wt%			
	Pb	Zr	Ti	O
Pre-developed	70.33	16.05	5.96	7.70
developed	70.17	15.96	6.12	7.76

#### Properties of the obtained PZT films

Fig.6 shows X-ray diffraction pattern of the obtained PZT film. The film fabricated by this new process had only the perovskite structure.

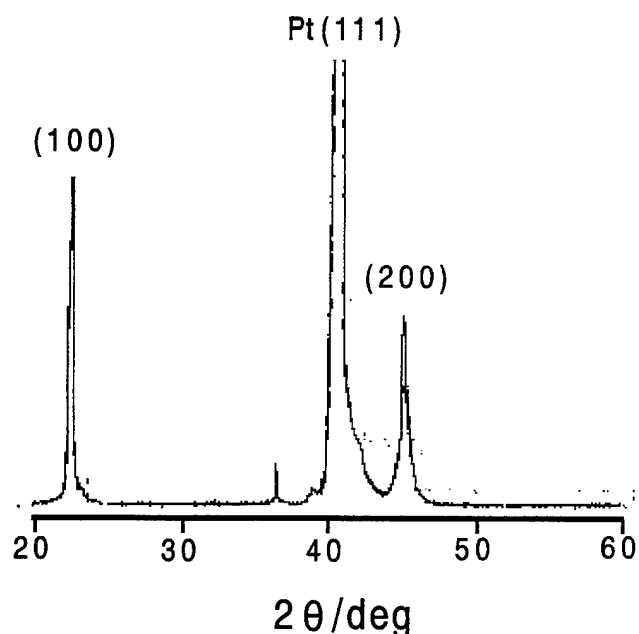


Fig.6 X-ray diffraction pattern of the obtained PZT film

Electrical properties of PZT films such as dielectric constant and dielectric loss were measured and are shown in table 3. A film fabricated by conventional process was compared with a film fabricated by this new process. The properties of both films showed almost the same values as well.

Table 3 Electrical properties of PZT films

	dielectric constant dielectric loss	
Conventional process	1032	0.13
New process	897	0.14

Fig.7 shows P-E characteristics of PZT films. Both showed

similar hysteresis loop and similar ferroelectric properties. Remanent polarization of the film fabricated by conventional and new processes were  $17.3 \mu\text{C}/\text{cm}^2$  and  $15.8 \mu\text{C}/\text{cm}^2$  and coercive field of the both were  $62.6$  and  $72.0 \text{ kV}/\text{cm}$ , respectively.

### Summary

A new highly photo-sensitive PZT sol-gel solution was prepared by adding NBA as a water-generator. A fine-patterned PZT film was successfully formed from this solution by UV irradiation. The minimum irradiation energy of UV rays to obtain the pattern was estimated to be about  $1.2 \text{ J}/\text{cm}^2$ . The properties of a film fabricated by this new process was the similar as those of a film fabricated by the conventional process. The obtained film had perovskite structure. The leakage current density at 3 volts was  $1.3 \times 10^{-7} \text{ A}/\text{cm}^2$ , the remanent polarization was  $15.8 \mu\text{C}/\text{cm}^2$  and the coercive field of the film was  $72.0 \text{ kV}/\text{cm}$ , respectively.

### Acknowledgements

The authors would like to thank Mr. A. Kamisawa, Mr. T. Nakamura and Mr. Y. Nakao of Rohm Corp. Ltd., for providing the substrate used in this study.

### References

- [1] T. Okudaira, A. Hachisuka, N. Soyama, K. Ogi, H. Arima, T. Matsukawa and K. Horie: Ext. Abstr.Int. Conf. Solid State Devices and Materials, Yokohama 1991 (Business Center for Academic Societies Japan, Tokyo, 1991) 204.
- [2] J.F.Scott and C.A.Araujo: Science 246 (1989) 973.
- [3] H. Aoki, T. Hashimoto, E. Ikawa, T. Kikkawa, S. Yamamichi, T. Sakuma and Y. Miyasaka: Ext. Abstr.Int. Conf. Solid State Devices and Materials, Tsukuba 1992 (Business Center for Academic Societies Japan, Tokyo, 1992) 554.
- [4] Y. Nakao, T. Nakamura, K. Hoshiba, K. Sameshima, A. Kamisawa, N. Soyama, K. Abe and K. Ogi: Jpn. J. Appl. Phys. 32 (1993) 4141.
- [5] G. Sasaki, N. Soyama, T. Atsuki, T. Yonezawa and K. Ogi: Ext. Abstr. 41st Spring Meeting of the Japan Society of Applied Physics and Related Societies, Kanagawa, March, 30p-ME6.
- [6] B. Amit and A. Patchornik: Tetrahedron lett., p.2205 (1973)
- [7] C. Roger, M. J. Hampden-Smith and C. J. Brinker: American Chemical Society Meeting, San Francisco, California, Spring 1992

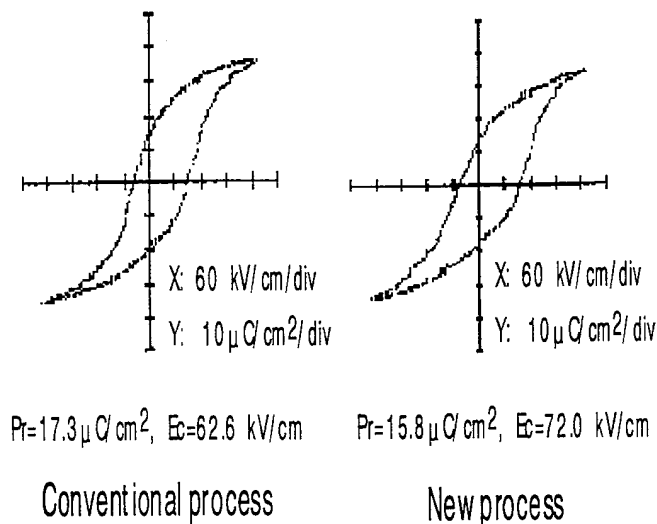


Fig.7 P-E characteristics of PZT films

Fig.8 shows current I-V characteristics of PZT films. Both had good and similar I-V characteristics. The leakage current density at 3 volts for both samples was about  $1.3 \times 10^{-7} \text{ A}/\text{cm}^2$ .

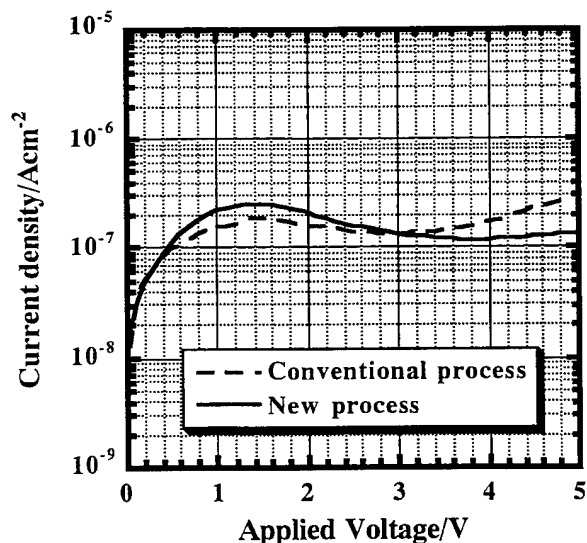


Fig.8 I-V characteristics of PZT films

# PZT-Film Compositional Development and Physical Properties

A. Schönecker, H.-J. Gesemann, S. Merklein \*, W. Grond \*, K. Franke #, M. Weihnacht #  
 Fraunhofer-Inst. Cer.Tech.&Sint.Mat., Winterbergstr. 28, D-01177 Dresden, \*Fraunhofer-Inst. of Silicat Research,  
 Neunerplatz 2, D-97082, Würzburg,  
 #Institute of Solid State Mat. Res., post-box D-01171,  
 Germany

**Abstract** - The preparation - structure - property relationships on relatively thick (0.5 ... 1.5  $\mu\text{m}$ ) polycrystalline PZT-films have been studied. The PZT-films were prepared by sol-gel processing from high molarity precursor sols (>2M) on Pt-metallized polycrystalline  $\text{Al}_2\text{O}_3$ -substrates. Special emphasis was given to the dependence of film properties on Zr/Ti-ratio, Pb-concentration, and thickness. Particularly, new approaches are necessary to deduce the familiar material data of compact PZT on films. Laser induced surface acoustic waves proved to be useful to deduce mechanical and geometrical parameters. Electrical scanning force microscopy made nanoscaled poling experiments possible in areas less than 300 nm  $\times$  300 nm. In order to qualify the material system for application in the printing process the investigations were directed to higher thickness of films, enlarged coating area and improvement of material properties.

## INTRODUCTION

The background of the here discussed development concerns the use of ferroelectric films as image memory in the printing process [1]. Therein, local poling of the ferroelectric films regulates the lateral surface charge pattern and thus the distribution of deposited toner particles. Technical systems are based on ferroelectric film coatings on metallized  $\text{Al}_2\text{O}_3$  rollers. The application implies two significant differences to the so far known approaches of ferroelectric film processing: need of relatively thick films > 5  $\mu\text{m}$  and large coating areas of about 10  $\text{dm}^2$ . We are investigating two different approaches, at the moment. One uses thick film technology based on a slurry containing low sintering PZT-powders [2]. The second one uses thin film technology based on sol-gel process with high molarity sols and is discussed in the present paper.

The functional properties of the obtained films must be valued with respect to the application needs. Serious problems are the simultaneous control of mechanical and electrical properties as well as their homogeneity over large areas.

## PREPARATION

### Film processing

The PZT-films were deposited on polycrystalline  $\text{Al}_2\text{O}_3$ -substrates (99.6 %, grain size 2  $\mu\text{m}$ ). Pt was used as an intermediate electrode.

The applied sol precursor is characterized by high solid phase concentration (about 40 mass%) and excellent long term stability under atmosphere [3]. The flow-chart of Figure 1 illustrates the procedure of PZT-film preparation. Excess lead in the sol promotes the crystallization of PZT in the film. Concentrations of Pb in the sol and films within the range between 1 ... 1.2 mol have been studied.

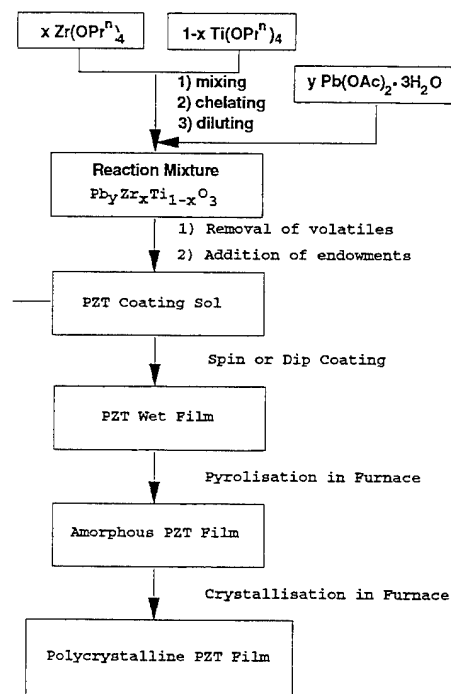


Figure 1 : General procedure of PZT-film preparation used in this work



Further, the Zr/Ti-ratio was varied in the a wide range (0.50/0.50, 0.53/0.47, 0.56/0.44, 0.63/0.34 and 0.69/0.31) in order to tailor the electrical material properties.

Inspection of pyrolysis, cristallization and sintering by means of IR-spectroscopy and TGA/DTA measurements as well as X-ray diffraction showed crystalline films to be well formed at 700 °C.

A final film thickness of 0.5 - 0.7  $\mu\text{m}$  was usually reached with one coating step, but the formation of crackfree up to 2  $\mu\text{m}$  thick films could also be demonstrated .

## RESULTS AND DISCUSSION

### Quality of the PZT-films

The SEM micrograph in Figure 2, showing the fracture edge of a dip coated PZT-film, demonstrates the state of the art. The film has been prepared in one coating step. The film thickness is 2  $\mu\text{m}$  and the PZT grain size is 100 nm.

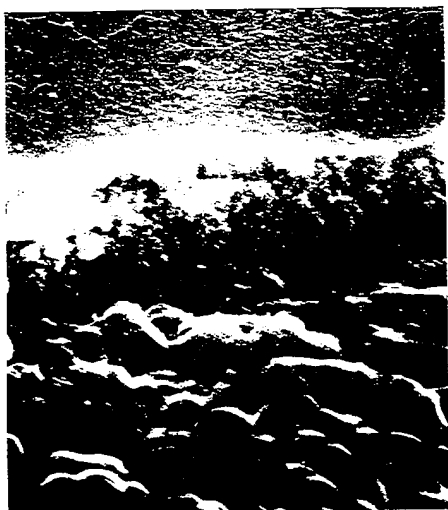


Figure 2 : Fracture edge of a 2  $\mu\text{m}$  thick PZT-film; grain size is about 100 nm.

### Dielectric and ferroelectric properties : mm scaled electrodes

Circular gold electrodes 1 mm in diameter were sputtered on the surface to form capacitorlike structures. Then dielectric and ferroelectric properties were measured at contacted areas with isolation resistance of  $> 10 \text{ MOhm}$ , which can be regarded to be close to the material defined value. Areas with defects were thus excluded. The electrical properties were measured at room temperature using standard equipment and methods: impedance bridge for permittivity and loss factor measurement and integrating series capacitor

circuit for recording the ferroelectric hysteresis loop with typical 5 Hz. Results of electrical material data are given in Figures 3 to 5.

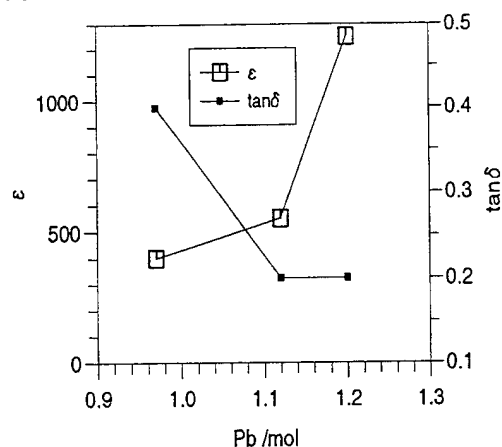


Figure 3: Permittivity and dielectric loss factor vs. Pb-concentration at Zr/Ti-ratio of 0.53/0.47.

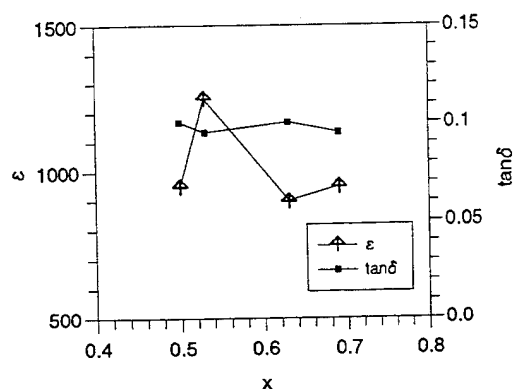


Figure 4: Permittivity and dielectric loss factor vs. Zr-concentration ( $\text{Pb}(\text{Zr}_x \text{Ti}_{1-x})\text{O}_3$ ).

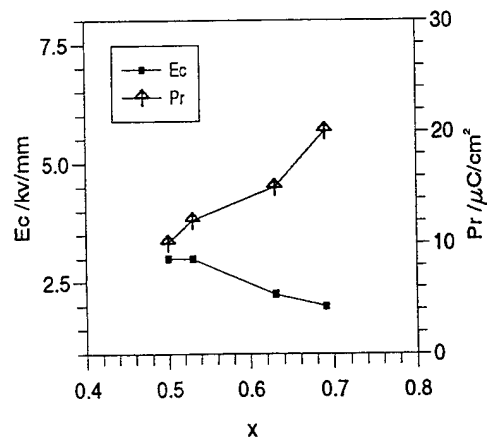


Figure 5: Coercivity and remanent polarisation vs. Zr-concentration ( $\text{Pb}(\text{Zr}_x \text{Ti}_{1-x})\text{O}_3$ ).

The electrical properties of the films revealed the following trends: excess lead improves the dielectric (Figure 3) as well as the ferroelectric properties markedly. An excess concentration of 0.2 mol was chosen in the series with variation of Zr/Ti-ratio.  $P_r$  increases and  $E_c$  decreases with growing Zr content, e.g. the PZT becomes soft. At Zr/Ti-ratio of 0.53/0.47  $\epsilon_r$  shows it's highest value due to morphotropic phase composition. These results correspond to the literature [4].

### SAW-analysis

A method to characterize PZT-films in a non-destructive manner is the analysis by laser induced surface acoustic waves (SAW). The method was developed to determine mainly mechanical (density, elastic moduli) and geometrical (thickness) parameters from SAW dispersion curves in the frequency region 30 - 500 MHz [5], [6].

These frequencies allow to evaluate films with thicknesses in the nanometer range. The measuring area is about  $3 \times 3 \text{ mm}^2$  and can be placed at any point of the surface. If the experimental conditions are chosen very carefully, the method delivers also piezoelectric data. In this case the dispersion curves of free and metallized surfaces of PZT-films have to be compared.

High performance of this method has been achieved due to accuracy of velocity measurement  $< 10^{-4}$  and using a computer program on nonlinear regression of SAW propagation in layered structures [7].

Figure 6 shows measured (dotted) and calculated (solid) dispersion curves obtained from the fitting procedure, for the cases: a) Pt ground electrode on  $\text{Al}_2\text{O}_3$ -ceramic substrate, b) with additional PZT-layer, and c) with silver top electrode.

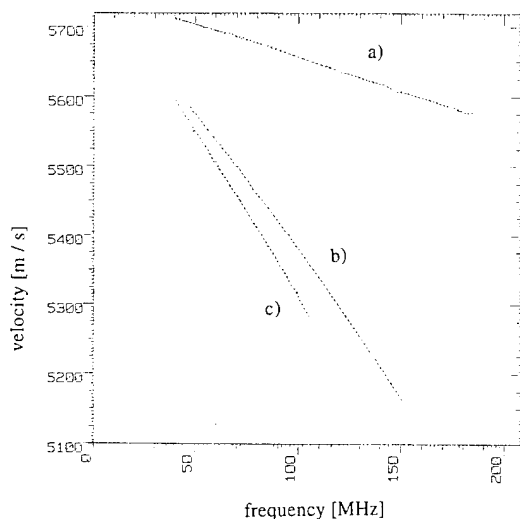


Figure 6 : Dispersion curves of surface acoustic waves of a) Pt ground electrode on  $\text{Al}_2\text{O}_3$ -substrat, b) additionally, with PZT-film and c) silver top electrode on PZT.

The curve a) was used to determine Pt layer thickness (126 nm) and ceramic substrate elastic modulus (388 GPa). From this, case b) can be treated to derive PZT layer data: mass per area (thickness times density)  $6.9 \times 10^{-4} \text{ g/cm}^2$ , and E-modulus 41 GPa. Curve c) delivers top metallization data: thickness 149 nm of Ag-layer.

The mechanical influence of metal layer should be eliminated by two step metallization if the piezoelectric efficiency is deduced by electric shorting of the surface.

### Electrical SFM

A scanning force microscope with light fiber sensor has been used [8] to detect the in-plane spatial distribution of remanent polarization state of ferroelectric layers depending on applied poling fields. Figure 7 shows both the topography and polarization distribution of the same area of a PZT-layer on  $\text{Al}_2\text{O}_3$  substrate. The groove in the upper left part of topographic picture comes from the ceramic substrate. The size of PZT-crystallites is in the order of 100 ... 200 nm. The polarization pattern was obtained after application of 30 V by a scanning poling procedure using the microscope tip (one second at each point) in order to create the same initial state for the whole investigated area. After this, in a second step -7 V were applied only within the marked square. One can see a more or less elevated polarization level within the square due to the -7 V poling process (that comes true also for the upper part of the figure if the perspective view is taken into account).

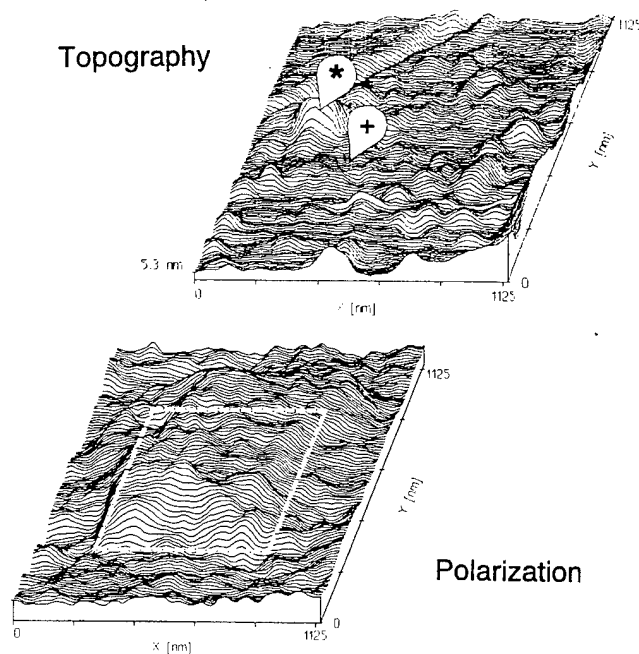


Figure 7 : Topography and polarization distribution after local poling.

Figure 8 shows local poling characteristics. In our case, a local poling characteristic is the result of successive applying of voltages to the SFM tip in steps of 1 V, interchanged with measurement of the actual remanent polarization value after each poling process. In this way, local differences of ferroelectric switching behaviour can be made visible as shown for the points (+) and (\*) in Figure 7. Note asymmetric hysteretic behaviour also in the case of only one electrode (ground).

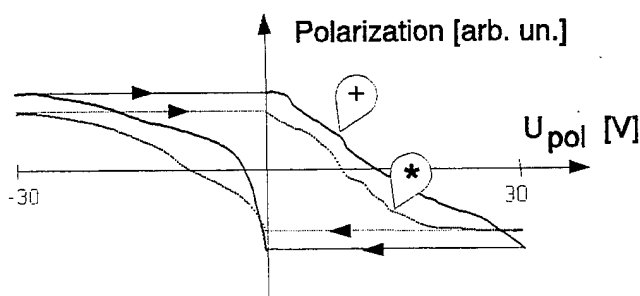


Figure 8: Local poling characteristics (remanent polarization after successive raised poling voltage) at different points obtained from electrical SFM measurements.

#### CONCLUSION

Sol-gel processing was qualified to give PZT-films with thicknesses of about 1  $\mu\text{m}$  per coating step. This opens the possibility of an effective fabrication of PZT-coatings

> 5  $\mu\text{m}$  on Pt-metallized  $\text{Al}_2\text{O}_3$ -substrates.

Remanent polarization can be tailored to meet the demands of application in the printing process, which is > 10  $\mu\text{C}/\text{cm}^2$ .

SAW-analysis proved to be useful to deduce mechanical and geometrical parameters. Determination of piezoelectric efficiency is expected by further improvement of the method.

Electrical SFM opens the possibility of inspection of nanoscaled poling behaviour and is seen as the key for improving the functional properties for printing application.

#### ACKNOWLEDGEMENTS

The authors wish to thank D.Schneider, FhI Mat.Phys.& Thin Film Engin., for measuring the dispersion curves by laser induced SAW.

#### REFERENCES

- [1] A.Hirth, R.Weis, „Printing with Ferroelectric Material“ in *Proceedings of the Conference Soc. Imaging Science and Technology* 9, pp. 181-184, 1993.
- [2] H.-J. Gesemann, L.Seffner,L. Preparation and Application of PZT Thick Films, to be presented at Electroceramics IV, Aachen, Sept. 1994.
- [3] S.Merklein,D.Sporn,and A.Schönecker: “Preparation of Ferroelectric Lead Zirconate Titanate Thin Films Using High Molarity Precursor Sols“, in *Proceedings of Ferroelectric Thin Films III*, Mat.Res.Soc.Symp. 310 , 1993, 263-268.
- [4] K. Iijima, I. Ueda and K. Kugimiya, „Ferroelectric Films“ ed. by A. S. Bhalla and K. M. Nair, The American Ceramic Society, 1992, pp. 33 - 40.
- [5] D. Schneider, T. Schwarz, and B. Schultrich, "Determination of elastic modulus and thickness of surface layers by ultrasonic surface waves", *Thin Solid Films*, vol.219, 1992, pp. 92-102.
- [6] D. Schneider, T. Schwarz, H. Ollendorf, and M. Weihnacht, "Nondestructive evaluation of coated materials by laser induced surface waves", *ASNT Fall Conference Paper Summaries Book*, 1994.
- [7] R. Wobst, "The generalized eigenvalue problem and acoustic surface wave computations", *Computing*, vol.39, pp.57-69, 1987.
- [8] K. Franke, J. Besold, W. Haessler, C. Seegebarth, "Modification and detection on ferroelectric PZT films by scanning force microscopy", *Surface Science Letters*, vol.302, pp.L283-L288, 1994.

# Antiferroelectric To Ferroelectric Phase Switching Thin Films In The Lead Zirconate Stannate Titanate Solid Solution System

C.J. Gaskey, K.R. Udayakumar, H.D. Chen, L.E. Cross, Materials Research Laboratory, The Pennsylvania State University, University Park, PA, 16802

## **Abstract**

Thin films of lead zirconate stannate titanate (PSZT) with slight additions of niobium and lanthanum have been prepared by the sol-gel, spin coat process. Antiferroelectric tetragonal and orthorhombic compositions have been evaluated on the criteria of P-E loop squareness, maximum polarization and field induced strain for the applications of energy storage and conversion in integrated devices. The orthorhombic compositions in both the niobium and lanthanum doped systems have shown square loop hysteretic behavior with large switchable polarizations ( $30\text{--}40\mu\text{C}/\text{cm}^2$ ), and field-induced strains of 0.33% have been measured in the niobium doped system, thus both systems provide attractive possibilities for practical use.

## **Introduction**

Amidst the recent explosion of ferroelectric and dielectric thin film research, brought about by the utility of such films in both computer memory and microelectromechanical system applications, antiferroelectric phase switching systems have been relatively overlooked; a surprising fact considering that as early as 1961 lead zirconate ceramics, modified with tin and titanium, were hailed by Jaffe<sup>1</sup> as a "new circuit element" with applications in electromechanical and electrothermal energy conversions, as well as energy storage. Due to the small difference in free energy between the ferroelectric and antiferroelectric states in these systems, switching between the two states can be easily occasioned by temperature, pressure and electric field. The actual usefulness of these ceramic antiferroelectrics was limited due to the fact that the AFE-FE switching fields are on the same order as the breakdown fields, a problem which is inherently overcome in thin films, due to their much larger breakdown fields, on the order of 1MV/cm.

Brooks<sup>2</sup> et al has conducted an investigation of the switching behavior of sol-gel prepared thin films in the La-doped PSZT system, focusing on compositions previously studied by Pan<sup>3</sup> et al in the bulk ceramic form. Switching was observed in the P-E loops and confirmed by the double butterfly appearance of the C-V plots, and strains of 0.16% were measured in an AFE tetragonal composition; however the nature of the switching as seen in the P-E loop seems to quite different in the films when compared to the bulk, with the switching arms of the loop showing less verticality and more polarization remaining at the zero field position in the films. Stresses induced by the substrate and a possible metastable coexistence of FE and AFE phases were named as possible culprits for the degradation of properties.

In this study greater attention has been devoted to the Nb-doped PSZT system in the hope of developing compositions that show the square type of hysteresis, as delineated by Berlincourt in the bulk ceramic, and higher strains, characteristics necessary to meet modern device requirements. In addition it has been noted by Taylor<sup>4</sup> that the Nb-doped PSZT ceramics are characterized by higher resistivities, greater resistance to aging, and lower free energy and coercive fields in the ferroelectric phase than their La-doped counterparts. Compositions in both the AFE tetragonal and orthorhombic phase fields have been investigated, and through suitable tailoring of the compositional and precursor chemistry, square loop compositions have been developed in both the Nb and La-doped PSZT that would appear to be highly useful as decoupling capacitors in multi-chip modules and as an electromechanical energy conversion medium in microsystems.

## **Experimental Procedure**

Films in this study were prepared by a modified sol-gel technique, the details of which are described elsewhere.<sup>5</sup> Lead acetylacetonate was used as an alternative lead precursor due to its superior chelating properties, which impart to the solution an extended lifetime before hydrolysis and increased hydrolysis resistance upon spinning. Crystallization was achieved by furnace annealing at 700°C for 15 minutes, after

which sputtered platinum top electrodes with diameters ranging from 0.8-6.35 mm were applied and annealed at 550°C for 60 minutes to improve electrical contact.

Polarization-electric field loops were recorded by a modified Sawyer-Tower circuit, with samples driven by 5-20 V, 30 Hz signals; small signal dielectric permittivities and loss tangents were measured using an HP impedance analyzer both with and without bias, at room temperature and as a function of increasing temperature. Film thicknesses were determined from a profilometer trace, crystal phases were characterized by a grazing incidence x-ray diffractometer, and field induced strains were measured using a double beam laser interferometer, capable of resolving surface displacements down to  $10^{-2}\text{\AA}$ .

### Results and Discussion

Film thicknesses ranged from 0.15-0.7 $\mu\text{m}$ , with distinct switching observed down to approximately 0.2 $\mu\text{m}$ . The films had no problem crystallizing into a pure perovskite phase as seen in Fig. 1, the diffraction pattern for the tetragonal composition #1 (see Table 1 for compositional information).

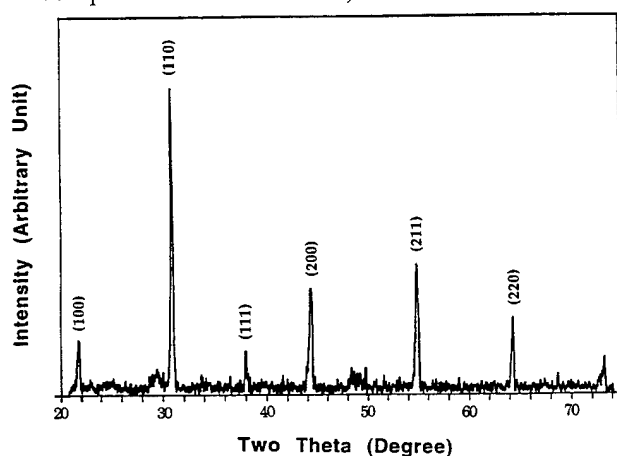


Fig. 1 X-ray diffraction pattern of composition #1, showing crystallization into the perovskite phase.

Fig. 2 shows the dependence of dielectric constant on temperature for Nb-doped orthorhombic composition #3; two phase transitions can be seen corresponding to AFE-FE and FE-PE, although the former is very slight.

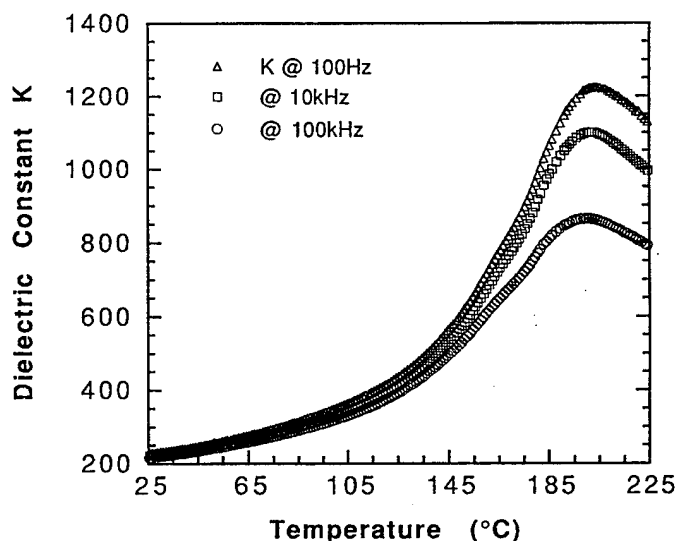


Fig. 2 Dielectric constant as function of temperature for composition #3. Applied voltage = 5 mV.

The difference in switching behavior between tetragonal and orthorhombic compositions is illustrated by figures 3 and 4. A slanted type loop is exhibited by tetragonal composition #2, while a square loop is seen for composition #3.

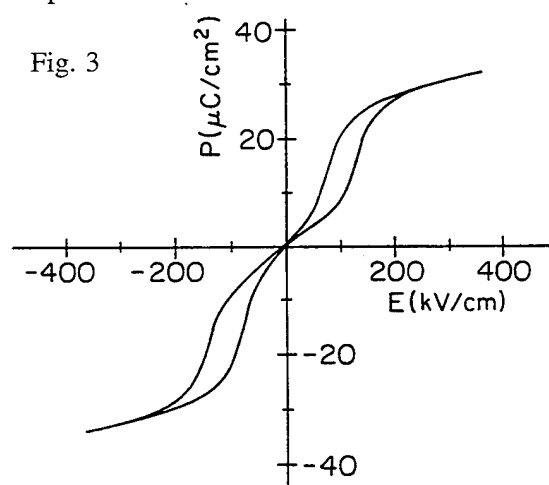


Table 1: Summary of phase switching characteristics of Nb-doped lead zirconate stannate titanate thin films

Film Composition	Thick- ness ( $\mu\text{m}$ )	$\epsilon_r$ at 1kHz	$\tan \delta$	$E_{\text{AFE} \rightarrow \text{FE}}$ (kV/cm)	$E_{\text{FE} \rightarrow \text{AFE}}$ (kV/cm)	$P_{\text{max}}$ ( $\mu\text{C}/\text{cm}^2$ )
1) $\text{Pb}_{0.99}\text{Nb}_{0.02}(\text{Zr}_{0.57}\text{Sn}_{0.38}\text{Ti}_{0.05})_{0.98}\text{O}_3$	0.56	530	0.015	60	30	26
2) $\text{Pb}_{0.99}\text{Nb}_{0.02}(\text{Zr}_{0.65}\text{Sn}_{0.31}\text{Ti}_{0.04})_{0.98}\text{O}_3$	0.44	530	0.016	85	45	35
3) $\text{Pb}_{0.99}\text{Nb}_{0.02}(\text{Zr}_{0.85}\text{Sn}_{0.13}\text{Ti}_{0.02})_{0.98}\text{O}_3$	0.45	240	0.005	175	75	40

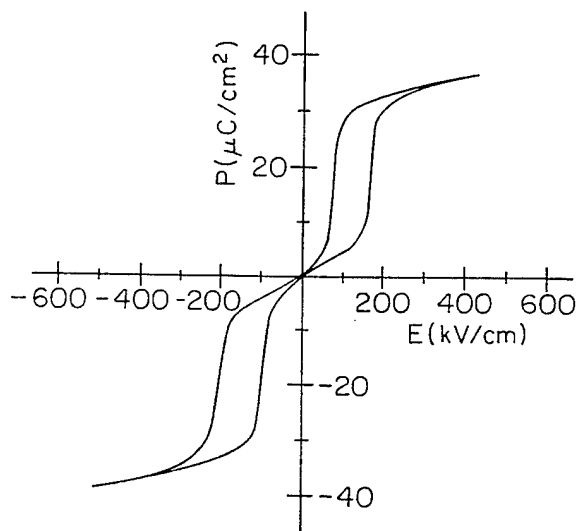


Fig. 4 Square P-E behavior as seen in composition #3.

Switching and dielectric properties for the Nb-doped PSZT compositions studied are summarized in Table 1. All compositions were characterized by very low losses, and properties were stable over the entire range of electrode sizes, up to 6.35 mm in diameter.

Square hysteresis is also shown in figure 5 for a La-doped composition otherwise equivalent to composition #3; the switching fields for this composition are much higher.

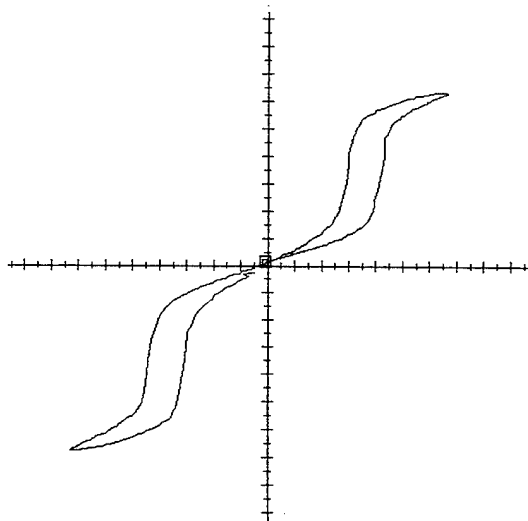


Fig. 5 P-E response of La-doped composition equivalent to composition #3.  $P_{\max} = 33 \mu\text{C}/\text{cm}^2$ ,  $E_F = 350 \text{ kV}/\text{cm}$ ,  $E_A = 250 \text{ kV}/\text{cm}$ .

The field induced longitudinal strain for a film of composition #3 is shown in Fig. 6. The values increased as a function of ac driving field up to 0.33% at 100 kV/cm with an applied dc bias of 100 kV/cm.

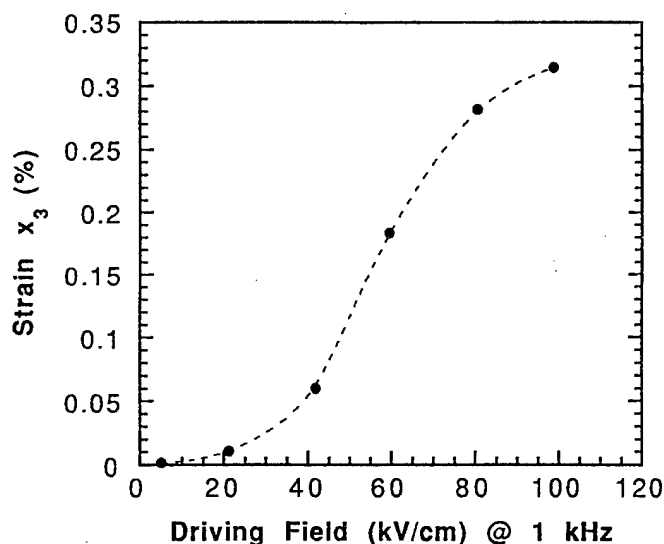


Fig. 6 Field induced strain as a function of ac driving field at 1 kHz for composition #3. The film was maintained at a dc bias of 100 kV/cm.

### Conclusions

Thin films of AFE Nb-doped PSZT have been prepared by a modified sol-gel method and phase-switched with the application of appropriate electric fields. "Square" switching behavior, with maximum polarizations of  $40 \mu\text{C}/\text{cm}^2$  have been shown in an orthorhombic composition; in addition, strains of 0.33% have been measured. These properties make the composition a viable choice for applications in decoupling capacitors for multichip modules and in micromechanical actuation.

### References

- [1] B. Jaffe, "Antiferroelectric Ceramics with Field-Enforced Transitions: A New Nonlinear Circuit Element," *Proc. IRE*, vol. 49, pp. 1264-1267, August 1961.
- [2] K.G. Brooks, J. Chen, K.R. Udayakumar, and L.E. Cross, "Electric field forced phase switching in La-modified lead zirconate titanate stannate thin films," *J. Appl. Phys.*, vol. 75, pp. 1699-1704, 1 February 1994.
- [3] W.Y. Pan, Q.M. Zhang, A.S. Bhalla, and L.E. Cross, "Field-Forced Antiferroelectric-to-Ferroelectric Switching in Modified Lead Zirconate Titanate Stannate Ceramics," *J. Amer. Cer. Soc.*, vol. 72 [4], pp. 571-78, 1989.
- [4] G.W. Taylor, "Electrical Properties of Niobium-Doped Ferroelectric  $\text{Pb}(\text{Zr}, \text{Sn}, \text{Ti})\text{O}_3$  Ceramics," *J. Appl. Phys.*, vol. 38 (12), pp. 4697-4706, November 1967.
- [5] C.J. Gaskey, K.R. Udayakumar, H.D. Chen, and L.E. Cross, "Square hysteresis loops in large area phase switching Nb-doped lead zirconate stannate titanate thin films," *J. Appl. Phys.*, (Submitted 1994).

# Poster Session - P2: Thin Films

# STRUCTURE AND OPTICAL PROPERTIES OF PbTiO<sub>3</sub>-SiO<sub>2</sub> NANO-COMPOSITES THROUGH SOL-GEL TECHNIQUE

Qifa Zhou<sup>1</sup> Jinxiu Zhang<sup>1</sup> Liangying Zhang<sup>2</sup> and Xi Yao<sup>2</sup>

<sup>1</sup>Department of Physics, Zhongshan University, Guangzhou 510275

<sup>2</sup>Electronic Materials Research Laboratory, Xi'an Jiaotong University, Xi'an 710049, P. R. China

## ABSTRACT

Transparent glass with a composition of PbO-TiO<sub>2</sub>-SiO<sub>2</sub> have been prepared by hydrolysis and polycondensation of mixed metal alkoxides in solutions containing Pb(Ac)<sub>2</sub>·3H<sub>2</sub>O, Ti(OC<sub>2</sub>H<sub>5</sub>)<sub>4</sub>, Si(OC<sub>2</sub>H<sub>5</sub>)<sub>4</sub>, C<sub>4</sub>H<sub>10</sub>O<sub>2</sub> and C<sub>5</sub>H<sub>8</sub>O<sub>2</sub>. The crystallization behaviour in the gels were analyzed by differential thermal and thermogravimetric analyses(DTA-TG), X-ray diffraction(XRD) and infrared spectroscopy(IR) in detail, the linear refractive index was measured by ellipsometer, the refractive index at 632.8 nm was as high as 1.885, the optical energy band gap was estimated as 2.35eV from the UV-optical absorption spectrum. The third-order nonlinear optical susceptibility ( $\chi^{(3)}$ ) was determined by the degenerate four-wave mixing(DFWM) method, the  $\chi^{(3)}$  value was as high as  $6.63 \times 10^{-11}$  esu. It was shown that the materials exhibit large third-order susceptibility.

## INTRODUCTION

Nonlinear optical properties have recently stimulated great interest because of their high potential for optical functional devices, such as optical modulators, optical switches, or optical memories which were demonstrated using optical nonlinearity. So far, there have been reports of many organic and inorganic compounds having large optical nonlinear susceptibility, among them, inorganic glasses possess a great potential for practical uses from the viewpoint of transparency, ease of fabricating planar waveguide, thermal stability, and high durability under laser irradiation. To obtain effective functions, large third-order nonlinear susceptibility is naturally preferable. The studies of developing materials with large  $\chi^{(3)}$  can be divided into two categories[1], one is the study of large homogeneous  $\chi^{(3)}$  glasses, such as high index glasses. Vogel et al[2] examined the optical nonlinearity of silicate glasses containing Ti<sup>4+</sup> and Nb<sup>5+</sup> ions in order to design compositions for nonlinear optics. Nasu et al[3] found that chalcogenide glasses with refractive indices from 2.0 to 2.5 have  $\chi^{(3)}$  as high as  $10^{-11}$  esu. The other is kind of the glasses containing oxide semiconductor microcrystals, for example, Jain and Lind first reported high nonlinear susceptibility ( $\chi^{(3)}$ ) is high  $10^{-9}$  esu in CdS<sub>x</sub>Se<sub>(1-x)</sub> microcrystals doped glasses[4], in which the electron and hole are quantum confined by a deep potential well, the large, resonant third-order nonlinearity of these small particles expands their application to new optical devices.

Recently, a lot of work has been done on the preparation of microcrystalline semiconductor doped glasses such as CdS, PbS, CuCl[5-7]. However, almost no work has been reported on optical properties of lead titanate microcrystal doped silica glasses derived from the sol-gel process. this new process is attractive for

glass preparation because it provides glasses of unusual composition, high purity, and good homogeneity at temperatures significantly lower than those required by the conventional melting technique. In this study, PbO-TiO<sub>2</sub>-SiO<sub>2</sub>(PTS) gels under different composition were prepared by the sol-gel method using metal alkoxides, and structure changes of gels with different heat treatments were carefully analyzed by means of DTA-TG, XRD and IR, and optical absorption spectra and refractive index were studied. Experimental results indicated that the optical absorption edge of samples was blue-shifted about 0.2eV, and the materials exhibit large third-order nonlinear susceptibility.

## EXPERIMENT PROCEDURE

### 1. Preparation of the starting solution and gelation

Gels with the composition of PTS by weight ratio have been prepared by hydrolysis and polycondensation of metal alkoxide using lead acetate trihydrate[Pb(Ac)<sub>2</sub>·3H<sub>2</sub>O], tetrabutyl titanate[Ti(OC<sub>4</sub>H<sub>9</sub>)<sub>4</sub>] and silicon tetraethoxide(TEOS)[Si(OC<sub>2</sub>H<sub>5</sub>)<sub>4</sub>]. Firstly, the lead-titanium(Pb-Ti) complex alkoxide as a starting materials were mixed in solution in the same molar ratio to form directly Patio<sub>3</sub> microcrystal in SiO<sub>2</sub> matrix.

The prescribed amount of lead acetate trihydrate first dissolved in 2-methoxyethanol in a molar ratio of 1:3 at 70 °C in a vessel, followed by heating to 120 °C so as to remove water. After cooling to 70 °C, tetrabutyl titanate was added under stirring, and the mixed solution was heated again to about 120 °C under refluxing for 1h, the formation of Pb-Ti complex alkoxide was demonstrated by using IR spectroscopy of the CH<sub>3</sub>COOC<sub>4</sub>H<sub>9</sub> solution[8]. Because the speed of TEOS hydrolysis-polymerization is much slower than the reaction of titanium butoxide, in our experiment, acetylacetone(C<sub>5</sub>H<sub>8</sub>O<sub>2</sub>) was first added to the solution of Pb-Ti complex solution to slow the reactivity, then TEOS was added to the solution under stirring. No base and acid, or DCCA such as N-dimethyl formate catalyst was used in this system.

The homogeneous and transparent solution prepared above was poured into a polypropylene beaker, and kept temperature at 25 °C with a loose cover. The solution increased in viscosity as the hydrolysis-condensation reaction proceeded, then the container was again tightly sealed and the wet gel was aged at 60 °C for one week. After shrinkage due to syneresis, the gel was open to air and kept temperature at 80 °C in an oven for about one week.



## 2. Drying of gels

The drying rate of gels is very important for obtaining a big gel glass. The monolithic dried gel thus obtained was heated to 150 °C at a rate of 0.5 °C/min and there for 2h, and then heated to 300 °C at the same rate and held there for 2h, to remove residual organic matter, then heated up to the desired temperature and holding for 2h. In this paper, properties of the samples(#4) was mainly investigated except note composition.

## RESULTS AND DISCUSSION

### 1. Crystallization behaviour of gels

On heating both residual organic matter and water incorporated during the synthesis of the gels were removed by heating to temperature above 400 °C, DTA and TG curves are shown in Fig.2. The gels show two endothermic peaks at temperature between 90 and 200 °C, accompanied by a large weight loss, primarily due to the removal of water and alcohol trapped in micropores. The exothermic peaks accompanying the weight loss at temperatures between 300 and 400 °C are probably attributable to oxidation of acetate groups, or to the decomposition of unhydrolyzed alkoxy groups. Another two exothermic peaks are observed in DTA curves between 550 and 680 °C, with no corresponding decrease in TG curve, which may correspond to crystallization of PTS gels.

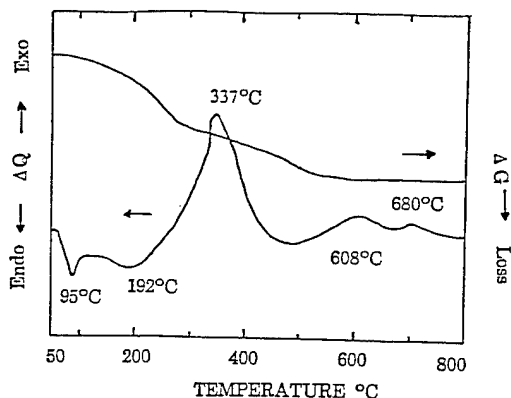


Fig.1 DTA and TG curves of the PTS gel

Fig.2 shows XRD patterns of PTS glasses heated at various temperature. Because of the small fraction of microcrystals precipitated in the glass, a slowly speed in XRD experiment is required. Heating at a temperature lower than 500 °C, only shows the typical amorphous halo pattern, several broad peaks on the background are observed with increasing temperature above 500 °C. From Fig.3(a),(b) as shown, the size of the microcrystalline precipitated in the matrix is very small by Scherer equation, and they consist mainly of  $\text{PbTi}_3\text{O}_7$  below 650 °C. On heating at higher temperature (e.g. 680 °C) from Fig.2(c), the XRD peaks height of sample increase rapidly and the structure of sample changes from  $\text{PbTi}_3\text{O}_7$  to perovskite phase ( $\text{PbTiO}_3$ ) mainly, a new phase is formed around 680 °C, the samples appear translucent due to the larger crystallines with the higher temperature. this is in agreement with DTA curves that there are two exothermic peaks appeared.

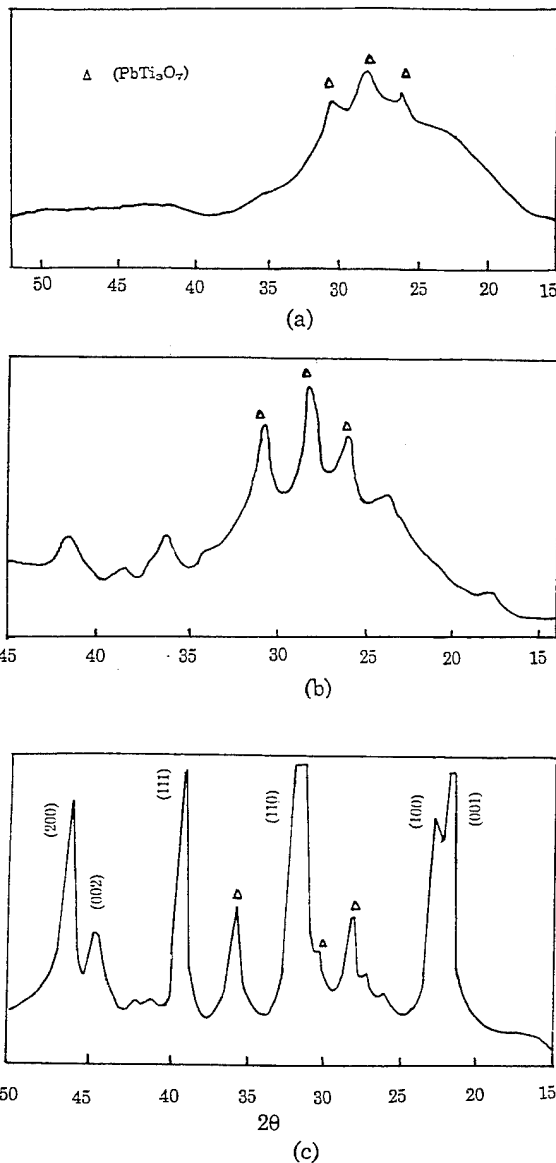


Fig.2 XRD patterns of PTS gels heated at various temperature for 2h: (a) 550 °C, (b) 600 °C and (c) 680 °C

Some clues to the bonding in complex glass systems may be obtained by making infrared absorption measurements under various conditions which are known to provide an important tool in studying the structural changes of materials. Samples were ground in a clean mortar into a fine powder, and mixed with KBr to make the thin pellets by pressing. The IR absorption spectra of the series of PTS gels with different heating temperature are shown in Fig.3, the numerical values of the detectable absorption band maxima in the infrared spectra of samples are compiled in table I. It is observed from Fig.3 and Tab.I that the positions of the absorption bands are in very close agreement with those reported by earlier workers about silicate-titanium glass system[9-10]. The absorption peaks in the range 1200-1600 $\text{cm}^{-1}$  are assigned to unhydrolyzed acetate groups, peaks of acetate groups decrease in intensity with an increase of heat-treatment temperature and almost disappear around 350 °C. The nonheated gels show a relatively intense absorption band around 3400 $\text{cm}^{-1}$ ,

which is attributed to water and OH groups. However, the intensity of the band decreases with increasing temperature of heat-treatment, and reaches a very small level corresponding to that of water merely absorbed by the KBr pellets above 500 °C, this indicates that the compositions scarcely contain water or OH groups after acetate groups are removed. The absorption peaks over 400-1080cm<sup>-1</sup> in all of the examined gel heated to 600 °C are assignable to Si-O-Ti bond and Si-O-Si bond, another, two new absorption peaks appears around 570 and 620 cm<sup>-1</sup> when temperature is over 600 °C, it is suggested that vibration peaks of lead titanate microcrystalline precipitated in glasses.

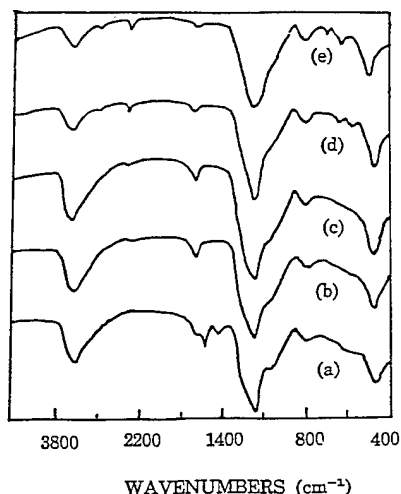


Fig.3 Change of IR spectrum of PTS gels with different temperature: (a) gel, (b) 350 °C, (c) 500 °C, (d) 600 °C and (e) 680 °C

Table I Analysis of the IR absorption spectra from Fig.3

Absorption peak position(cm <sup>-1</sup> )	corresponding vibration	variation tendency with increasing Tem.
3400	Si-OH, H-OH	Abating
1600	C=O	Abating
1400	CH <sub>2</sub> , CH <sub>3</sub>	Vanishing at 350 °C
1080	Si-O-Si	No significant change
950	Si-O-Ti	Abating
800	Si-O-Si	No significant change
620	C*	Strengthening
570	C*	Strengthening
450	Si-O-Si, O-Si-O	Strengthening

C\* Microcrystal vibration peaks

## 2. Optical absorption spectra

The measurement of optical absorption and particularly the absorption edge is important especially in connection with the theory of the electronic structure of materials. According to Davis-Mott theory[11], the absorption coefficient  $\alpha(\omega)$  is given by

$$\alpha(\omega) = A (\hbar\omega - E_{\text{gap}})^2 / \hbar\omega \quad (1)$$

where  $\alpha(\omega)$  is the absorption coefficient,  $A$  is a constant,  $E_{\text{gap}}$  is the optical gap energy and  $\hbar\omega$  is the photon energy of the incident radiation. Fig.4 shows the absorption spectra of PTS glasses under different temperature for two hours. It is observed that the absorption edges of samples show a long tail, suggesting

a broad distribution of microcrystal size precipitated in glasses. It is also cleared that the position of the fundamental absorption edge shifts to longer wavelengths with an increase of heating temperatures.

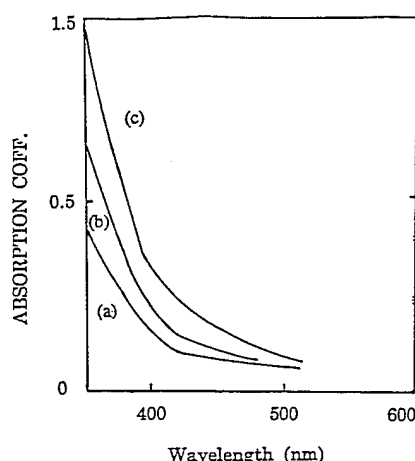


Fig.4 Optical absorption spectra of PTS glasses: (a) 500 °C, (b) 550 °C and (c) 600 °C for 2h

The absorption coefficient  $\alpha(\omega)$  can be determined near the absorption edge from the relation by [12]

$$\alpha(\omega) = 1/d \ln(I_0/I) \quad (2)$$

where  $d$  is the thickness of the sample,  $I_0$  and  $I$  are the intensities of the incident and transmitted beams, in our work, the thickness of the sample is 1.1mm, so  $\alpha(\omega)$  is calculated from Fig.4 and formula (2). According to formula (1), it is given below

$$(\alpha\hbar\omega)^{1/2} = A^{1/2} (\hbar\omega - E_{\text{gap}}) \quad (3)$$

Fig.5 represent  $(\alpha\hbar\omega)^{1/2}$  as a function of photon energy  $\hbar\omega$  for PTS glasses. The values of the optical energy gap are obtained by extrapolating from the linear region of the plots of  $(\alpha\hbar\omega)^{1/2}$  against  $\hbar\omega$  to  $(\alpha\hbar\omega)^{1/2} = 0$ , it can be seen that the values of optical gap  $E_{\text{gap}}$  decrease from 2.35eV to 2.15eV, the shifts exhibit a microcrystal size in matrix dependence mainly upward in energy as the microcrystal size decrease.

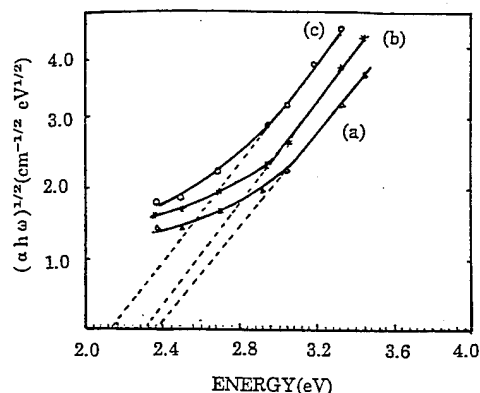


Fig.5  $(\alpha\hbar\omega)^{1/2}$  as a function of photon energy  $\hbar\omega$  for PTS glasses : (a) 500 ° C, (b) 550 ° C and (c) 600 ° C for 2h

### 3. Refractive index and nonlinear optical properties

The refractive indices of the glasses with four composition are measured by elimpsometer at 632.8nm, and calculated using theoretical glass compositions. Experiment and theory results of samples are shown in table II

Table II Glass composition and refractive indices

Sample number	Composition(Wt%)			Refractive index	
	PbO	TiO <sub>2</sub>	SiO <sub>2</sub>	n <sub>meas</sub>	n <sub>cal</sub>
#1	22.08	7.92	70.0	1.885	1.837
#2	25.75	9.25	65.0	1.898	1.889
#3	29.45	10.55	60.0	1.909	1.937
#4	33.13	11.87	55.0	1.915	1.989

It is seen from table II that the refractive indices of glasses increase with increasing in PbO-TiO<sub>2</sub> content of samples, when lead titanate content is 45%(#4 sample) refractive index of the sample is much higher(1.9) than that of pure silica(1.5). Experimental results indicate refractive index of the samples can be enhanced due to the greater concentration of atoms with high atomic number doped glasses.

Degenerate four-wave mixing was tested at wavelength of 1.06  $\mu$ m using a Nb:YAG pulse laser at a repetition rate of 2Hz and plus width of 10ns, a standard DFWM setup with an angle of 2 degrees between the forward pump beam and the probe beam, the sample thickness is about 2mm, variation of beam diameter over the sample thickness is low, third-order optical nonlinear susceptibilities of PTS glasses are obtained, the highest  $\chi^{(3)}$  of PTS glass(#4) is  $6.63 \times 10^{-11}$  esu, while  $\chi^{(3)}$  of the silicon oxide glass is about on the order of  $10^{-13}$  esu[13]. The third-order susceptibility of the PTS glasses is largely enhanced due to exist of microcrystalline and high refractive index of the samples possessed. Therefore, it is believed that the higher  $\chi^{(3)}$  would be obtainable if high content PbO-TiO<sub>2</sub> microcrystal doped silicate glasses were prepared, which is a future objective of our research work.

### ACKNOWLEDGEMENTS

The project were financially supported by Chinese National Advanced Material Research Project.

### REFERENCE

1. H.Nasu, Y.Ibara and K.Kubodera, J.Non-Cryst. Solids, 110(1989), 229.
2. E.M.Vogel, S.G.Kosinski, D.M.Krol, J.L. Jackel, S.R.Fribery, M.K.Oliver and J.D.Powers, J.Non-Cryst.Solids, 107(1989), 244.
3. H.Nasu, M.Nakamura, K.Kamiya, M.Kobayashi and K.Kubodera, J. Am.Ceram.Soc., 73(1990), 1794.
4. R.K.Jain and R.C.Land, J. Opt. Soc. Am., 73(1983), 647.
5. M.Nogami, K.Nagasaka and M.Takata, J.Non-Cryst. Solids, 122(1990), 101.
6. M.Nogami, Y.Q.Zhu, Y.Tohyama and K.Nagasaka J. Am. Ceram. Soc., 74(1991), 238.
7. B.G.Potter Jr. and J.H.Simmons, Phys. Rev., 37(1988), 10838.
8. J.B.Blum and S.R.Gurkovich, J. Mater. Sci., 20(1985), 4479.
9. E.M.Ernsberger, J.Amer. Ceram. Soc., 60(1977), 91.
10. M.Yamane, J.Non-Cryst. Solids, 144(1981), 181.
11. E.A.Davis and N.F.Mott, Phil.Mag., 22(1970), 903.
12. R.H.Sunds, Phys. Rev., 99(1955), 1222.
13. S.H.Kim, T.Toko and S.Sakka, J. Amer. Ceram. Soc., 76(1993), 865.

# Precursor Dependent Properties of $\text{Ba}_{1-x}\text{Sr}_x\text{TiO}_3$ Thin Films Fabricated by Sol-Gel Method

J. Kim, S.-I. Kwun and J.-G. Yoon\*

Department of Physics, Seoul National University, Seoul 151-742, Korea

\*Department of Physics, University of Suwon, Kyunggi-do 445-743, Korea

**Abstract:** Thin films of barium strontium titanate,  $\text{Ba}_{1-x}\text{Sr}_x\text{TiO}_3$ , were deposited on Si and ITO/glass substrates with 200 ~ 300 nm thickness by sol-gel method. The precursor solution of BST was prepared by mixing the 0.2 M precursor solutions of  $\text{BaTiO}_3$  and  $\text{SrTiO}_3$  with proper molar ratio. The x-ray diffraction (XRD) patterns show characteristic peaks with weak and broad features indicating that the polycrystalline BST film has poor crystallinity. The grain size and the surface morphology of the films were investigated by atomic force microscope (AFM). Especially, dependence of the film structures on the treatments of precursor solution such as hydrolysis and modification with acetic acid was investigated. The I-V (current-voltage) characteristics of the films was also dependent on the precursor structure. The C-V (capacitance-voltage) behavior of the films with MIS (metal - insulator - semiconductor) and MIM (metal - insulator - metal) structures were studied. Also, dielectric permittivity which was very strongly dependent on the crystallinity of the films was discussed in conjunction with precursor structures.

## INTRODUCTION

Ferroelectric thin films have been promising candidates for applications such as high dielectric capacitor of DRAM(dynamic random access memory), non-volatile memories, electro-optic devices and IR detectors because of their ferroelectric and pyroelectric properties. Among the various ferroelectric materials, Sr-doped  $\text{BaTiO}_3$  (BST) has outstanding properties since its ferroelectric transition temperature is shifted from 120 °C to -200 °C according to the doping rate of Sr. The dielectric constant of  $\text{Ba}_{0.65}\text{Sr}_{0.35}\text{TiO}_3$  ceramic at room temperature can be raised up to 1000 on paraelectric phase.

BST thin films usually have been deposited by sputtering[1,2] or laser ablation[3] while much works have not been reported with sol-gel method. The main advantage of the sol-gel processing in depositing ferroelectric thin film is that some materials can easily and accurately be doped to change the composition of the films because the precursors are mixed at molecular level. Also, large area of homogeneous film can be obtainable with relatively low temperature heat treatment. In this study,  $\text{Ba}_{0.5}\text{Sr}_{0.5}\text{TiO}_3$  and  $\text{Ba}_{0.65}\text{Sr}_{0.35}\text{TiO}_3$  thin films have been deposited on a Si wafer and ITO (indium tin oxide) coated glass by sol-gel method and dependence of film quality on the precursor structure has been investigated.

The precursor structures have been modified by pre-hydrolysis and acetic acid additive. Hydrolysis plays an important role in the sol-gel processing. Metal alkoxide solution reacts readily with water to form hydrolyzed molecules and these molecules can link together in a condensation reaction. If enough water is supplied to the solution, large molecules containing metals can be formed and these become ferroelectric ceramic through the heat treatment. Thus, pre-hydrolyzed precursor solution

is ready to condensate during the coating process. Acetic acid additive was used for controlling the condensation reaction. The condensation rate can be controlled by varying pH of the precursor solution since reduction of the pH is known to reduce the condensation rate during deposition and drying stage[4].

The thin films were investigated by x-ray diffractometer to observe the microstructure of the films. AFM was used to investigate the dependence of grain size and surface morphology of the films on the precursor solution. Also, electrical properties of the films have been investigated by I-V and C-V measurements.

## EXPERIMENTALS

The choice of starting materials and solvent is very important for a good quality of thin film in sol-gel processing.  $\text{BaTiO}_3$  precursor was prepared by using barium di-isopropoxide [ $\text{Ba}(\text{i-C}_3\text{H}_7)_2$ ] and titanium tetra-isopropoxide [ $\text{Ti}(\text{i-C}_3\text{H}_7)_4$ ] as starting materials. 2-methoxyethanol (ethylen glycol) was used as the solvent. Since 2-methoxyethanol acts as a chelating agent to form a chelated derivative with metal complexes[5], precursor solution becomes more stable and it reduces cracking of the film during drying and annealing processes.  $\text{Ba}(\text{i-C}_3\text{H}_7)_2$  was added dropwisely to the diluted  $\text{Ti}(\text{i-C}_3\text{H}_7)_4$  solution in excessive isopropanol for a molar ratio  $\text{Ba}:\text{Ti} = 1:1$  with stirring. By refluxing and distilling the solution in 2-methoxyethanol at 124 °C for 24 hours, 2-methoxyethanol based 0.2 M  $\text{BaTiO}_3$  precursor solution was obtained. On the other hand, strontium hydroxide [ $\text{Sr}(\text{OH})_2 \cdot 8\text{H}_2\text{O}$ ] and  $\text{Ti}(\text{i-C}_3\text{H}_7)_4$  were used for the  $\text{SrTiO}_3$  precursor.  $\text{Sr}(\text{OH})_2 \cdot 8\text{H}_2\text{O}$  was dissolved under  $\text{N}_2$  atmosphere in 2-methoxyethanol and dehydrated by refluxing and distilling in the solution for 12 hours to make metal organic solution.  $\text{Ti}(\text{i-C}_3\text{H}_7)_4$  was added to that solution dropwisely, and refluxed and distilled at 124 °C for 24 hours in 2-methoxyethanol. The 0.2 M  $\text{SrTiO}_3$  precursor solution was resulted from the reaction process. Powders obtained from these solutions were confirmed to be  $\text{BaTiO}_3$  and  $\text{SrTiO}_3$  by x-ray powder diffraction experiment. The final precursor solutions of  $\text{Ba}_{0.5}\text{Sr}_{0.5}\text{TiO}_3$  and  $\text{Ba}_{0.65}\text{Sr}_{0.35}\text{TiO}_3$  were prepared by mixing the  $\text{BaTiO}_3$  and  $\text{SrTiO}_3$  precursor solutions for a molar ratio of 50:50 and 65:35 respectively. In addition to an untreated precursor solution, the other two types of precursor solutions were prepared by adding water with a molar ratio of  $\text{Ti}:\text{H}_2\text{O} = 1:3$  or acetic acid. These solutions gave somewhat different film structures from that of the untreated precursor which will be discussed in the following section.

For the substrates, (100) Si (p type) wafers with the size of about  $1 \times 1 \text{ cm}^2$  without etching silicon oxide layer and ITO coated glasses were used. Small particulates in the precursor solution were removed using 0.2  $\mu\text{m}$  microfiber syringe filter, and then spin-coated on

the substrates at about 3500 rpm. Since the wet film contained much solvent and water, it was necessary to heat the film on a hot plate maintained at 150 °C for 15 min. Thicker films can be made by using concentrated precursor solution but the film is apt to be cracked during the heat treatment. Therefore thickness of the film was controlled by repeating coating process for several times. Because the films obtained in this way were amorphous, heat treatment of the films at 500 ~ 700 °C was necessary for crystallized film.

## RESULTS AND DISCUSSIONS

### *Microstructure and surface morphology*

Fig. 1 shows the XRD patterns of the  $\text{Ba}_{0.5}\text{Sr}_{0.5}\text{TiO}_3$  films of about 0.3  $\mu\text{m}$  thickness deposited on (100) Si substrate with heat treatment at 700 °C. Thickness of the films was measured by  $\alpha$ -step profilometer. Weak and broad characteristic peaks may result from poor crystallinity of the films. Samples of heat treated at lower temperature, which are not shown in the figure, have much poor crystallinity. As to the precursor dependence of the XRD patterns, the film deduced from acetic acid modified precursor shows weaker features of the peaks while there are no clear differences in the crystallinity for the other films deduced from untreated and pre-hydrolyzed precursors. It is considered that the restricted condensation of the precursor with acetic acid additive may result in the insufficient crystallization of the film. In the drying stage, the competition between evaporation (which compacts the film) and condensation (which stiffens the film increasing its resistance to compaction) is known to affect the film structures[4].

Observation of the surface morphology of the films shows clear dependence of grain growth on the precursors. AFM images of the surface morphology of the  $\text{Ba}_{0.5}\text{Sr}_{0.5}\text{TiO}_3$  films are shown in Fig. 2. Surface roughness is smooth within 200 Å. Grain size of the films is about 1000 ~ 2000 Å, which is much larger than other previous reports[1,6]. Films deduced from the untreated precursor and the pre-hydrolyzed one show

uniform distribution of grains of size about 1000 Å. On the other hand, the film deposited using acetic acid modified precursor shows unique feature of grains. Rod-like grains of about 2000 Å long are aligned in the same direction. It is thought that a directional grain growth may also be due to the restricted condensation of the precursor. However, it is not clear yet whether this directional morphology is related to the oriented grain growth because of its poor crystallinity.

The XRD patterns and the surface morphology of  $\text{Ba}_{0.65}\text{Sr}_{0.35}\text{TiO}_3$  thin films show similar features. The difference in XRD shown in Fig. 3 is a shift of the (110) peak position to the left, which is due to the change of the lattice constant along the Sr doping rate. The change of the lattice constant calculated from the data is about 0.02 Å increase compared to  $\text{Ba}_{0.5}\text{Sr}_{0.5}\text{TiO}_3$  film. Surface morphology of the film of this composition shows another feature for untreated precursor. Smaller grains attached to the larger grains could be observable. The size of smaller grains is estimated to be 500 Å while that of larger ones is about 1500 Å. This result would be due to slow grain growth process of this film. Increasing

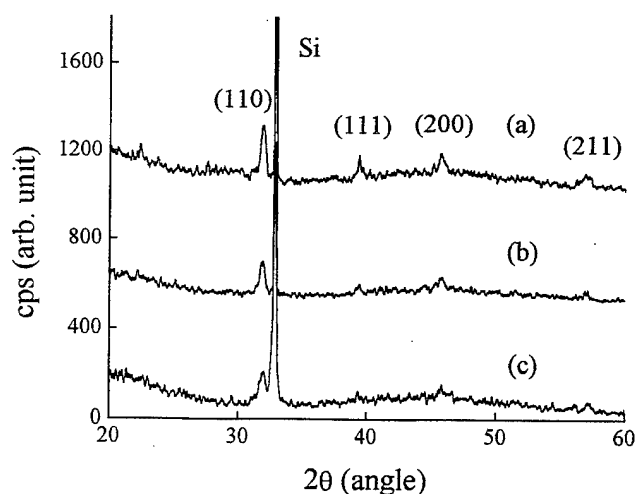


Fig. 1 XRD patterns of the  $\text{Ba}_{0.5}\text{Sr}_{0.5}\text{TiO}_3$  films grown by using (a) untreated, (b) pre-hydrolyzed and (c) acetic acid modified precursor solution on (100) p-type Si.

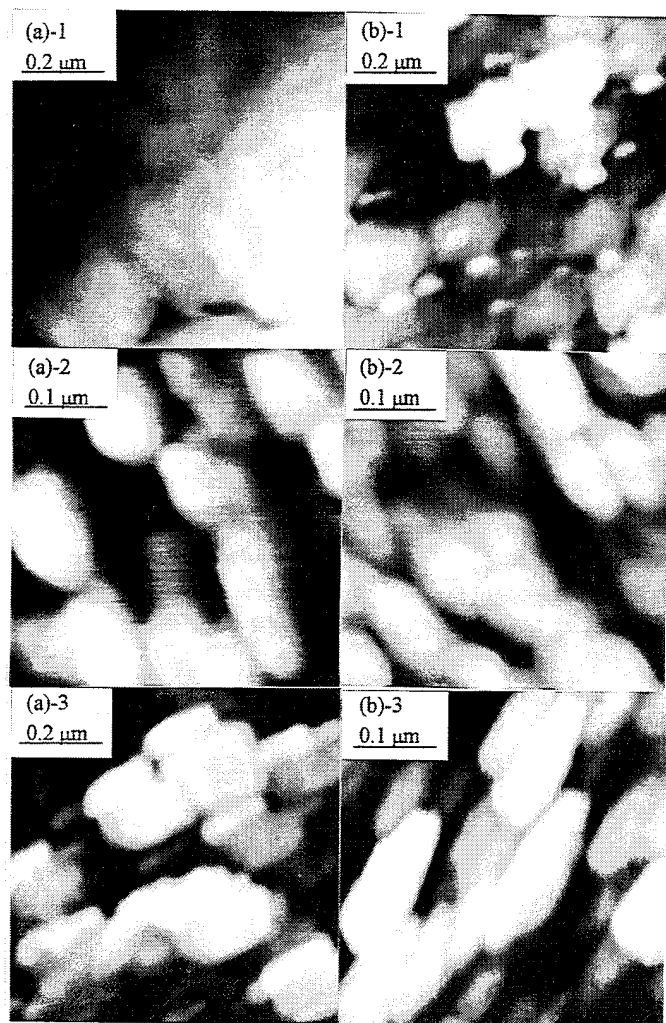


Fig.2 AFM images of (a)  $\text{Ba}_{0.5}\text{Sr}_{0.5}\text{TiO}_3$  and (b)  $\text{Ba}_{0.65}\text{Sr}_{0.35}\text{TiO}_3$  films. 1, 2 and 3 come under the films grown by using untreated, pre-hydrolyzed and acetic acid modified precursor solution, respectively.

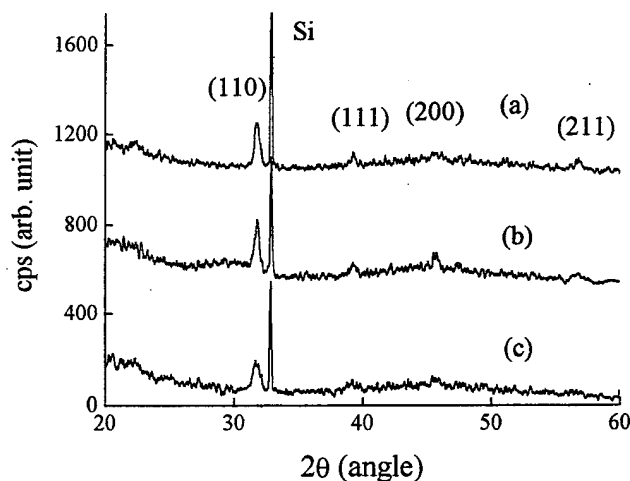


Fig. 3 XRD patterns of the  $\text{Ba}_{0.65}\text{Sr}_{0.35}\text{TiO}_3$  films grown by using (a) untreated, (b) pre-hydrolyzed and (c) acetic acid modified precursor solution on (100) p-type Si.

tendency of the grain size with increasing Sr contents has been reported[1]. Smaller grains in the film of Ba rich composition may grow much slowly during heat treatment. All the samples of our observation were heat treated in air at 700 °C for 1 hr. The possibility of slow grain growth process will be tested in future investigations.

#### Current-voltage characteristics

The I-V characteristics of the  $\text{Ba}_{0.65}\text{Sr}_{0.35}\text{TiO}_3$  thin films grown by using three different types of the precursor solution in log-log plot are shown in Fig. 4. The leakage current was measured in MIS structure using the Keithley 617 programmable electrometer with negatively biased Au top electrode. Current density of the

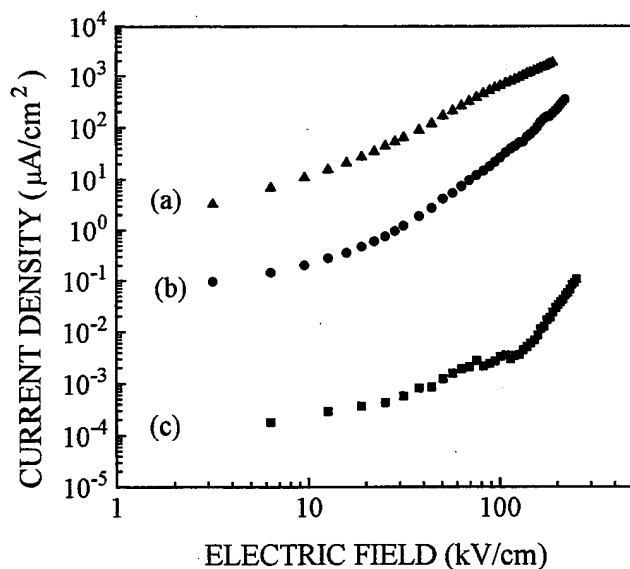


Fig. 4  $\log(J)$ - $\log(E)$  plot of the leakage current of the  $\text{Ba}_{0.65}\text{Sr}_{0.35}\text{TiO}_3$  films grown by using (a) pre-hydrolyzed, (b) untreated and (c) acetic acid modified precursor solution in MIS structure. Top electrode is negatively biased.

film prepared from the pre-hydrolyzed precursor solution shows very leaky behavior, which is larger than the film deduced from the untreated precursor solution to an order of magnitude. In conjunction with the film structure, amounts of void distribution along intergranular boundaries may cause larger leakage current. In contrast, acetic acid additive would make the film more compact, and this results in much lower leakage current of the film as shown in the Fig. 4. In addition, though not shown in the figure, heterojunction effects have been observed, which means that the polarity of the bias voltage affects the leakage current of the film. This effect was most pronounced for the film deduced from acetic acid modified precursor. Oxygen deficiency in the films resulted from annealing process[7] may be the origin of this effect. From our observations, it is conjectured that the control of hydrolysis and condensation rate may affect on the formation of oxygen deficiency during heat treatment.

At low electric field less than 50 kV/cm, ohmic conduction behavior is observed suggesting that the leakage current is dominated by the thermally activated free carriers caused by impurities or vacancies. In the high field region, the leakage current depends on  $E^n$  with  $n = 2 \sim 5$ . For the film deduced from acetic acid modified precursor,  $n$  has a value of 4.8. This result may be originated from the injection of trapped charges by the bias field.

#### Capacitance-voltage characteristics

C-V characteristics of the  $\text{Ba}_{0.5}\text{Sr}_{0.5}\text{TiO}_3$  thin film grown by the untreated precursor solution in MIS configuration are shown in Fig. 5. A 10 mV ac signal with frequency of 100 kHz was applied to the film. The MIS structure can be considered as a series connection of capacitors originated from BST layer,  $\text{SiO}_2$  and the transition region of the inversion layer. However, since transition-region capacitance goes to large value at low frequency ( $\leq 100$  kHz)[8], only the capacitances of BST and  $\text{SiO}_2$  contribute to the total capacitance. The dielectric constant calculated from the data, when transition-region capacitance is supposed to be infinite, is about 50 which is relatively small. This result may be due to the poor crystallinity and void distributions in the

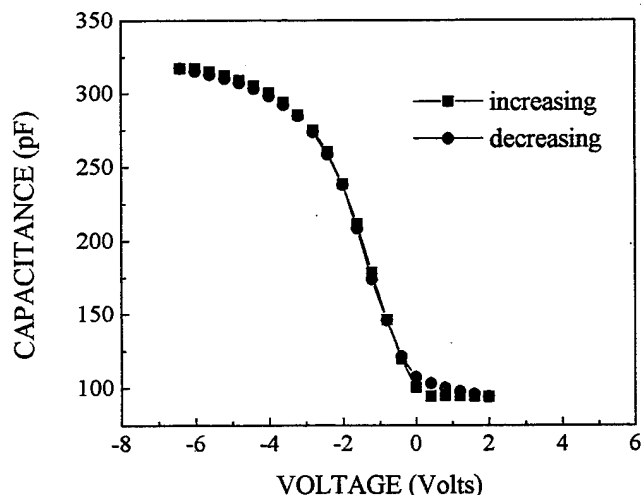


Fig. 5 C-V characteristics of the  $\text{Ba}_{0.5}\text{Sr}_{0.5}\text{TiO}_3$  films in MIS structure.

film, or perhaps the approximation of infinite value of the transition-region capacitance is not appropriate to this case.

C-V characteristics of the  $\text{Ba}_{0.5}\text{Sr}_{0.5}\text{TiO}_3$  thin film grown on the ITO coated glass were also measured in MIM configuration (Fig. 6). All the films were annealed at 600 °C to avoid melting of glass. Amorphous film deduced from acetic acid modified precursor did not show the voltage dependence of the capacitance. For the crystallized film deduced from untreated precursor, asymmetric C-V characteristics with bias field was observed. This result may be caused by Schottky emission over the two dissimilar metal-insulator interface barriers with top (Au) and bottom (ITO) electrodes.

## CONCLUSIONS

$\text{Ba}_{0.5}\text{Sr}_{0.5}\text{TiO}_3$  and  $\text{Ba}_{0.65}\text{Sr}_{0.35}\text{TiO}_3$  thin films were deposited on the silicon and ITO coated glass substrates with  $\sim 0.3 \mu\text{m}$  thickness by sol-gel method using three different types of precursor solution. Film structures and the surface morphology were found to be dependent on the precursor structures. The films grown by using acetic acid modified precursor have relatively poor crystallinity compared with other films from XRD patterns, but leakage current of these films is about three order of magnitude lower than the film deduced from untreated precursor. The dielectric constant of  $\text{Ba}_{0.65}\text{Sr}_{0.35}\text{TiO}_3$  thin film calculated from the C-V data is greater than 50. Relatively higher leakage current and lower dielectric constant may be due to voids distributed along grain boundaries.

## REFERENCES

- [1] H. Kawano, K. Morii and Y. Nakayama, "Effects of crystallization on structural and dielectric properties of thin amorphous films of  $(1-x)\text{BaTiO}_3-x\text{SrTiO}_3$  ( $x=0-0.5, 1.0$ )", *J. Appl. Phys.*, vol. 73, pp. 5141-5146, May 1993.
- [2] T. Horikawa, N. Mikami, T. Makita, J. Tanimura, M. Kataoka, K. Sato and M. Nunoshita, "Dielectric properties of  $(\text{Ba},\text{Sr})\text{TiO}_3$  thin films deposited by RF sputtering", *Jpn. J. Appl. Phys.*, vol. 32, pp. 4126-4130, September 1993.
- [3] P. Bhattacharya, T. Komeda, K. H. Park and Y. Nishioka, "Comparative study of Amorphous and crystalline  $(\text{Ba}, \text{Sr})\text{TiO}_3$  thin films deposited by laser ablation", *Jpn. J. Appl. Phys.*, vol. 32, pp. 4103-4106, September 1993.
- [4] C. J. Brinker and G. W. Scherer, *Sol-Gel Science*, Academic Press, 1990, ch. 13, pp. 797-826
- [5] G. Yi and M. Sayer, "Sol gel processing of thick PZT films", in Proceedings of the 8th ISAF, 1992, pp. 289-292.
- [6] K. A. Vorotilov, E. V. Orlova, V. I. Petrovsky, M. I. Yanovskaja, S. A. Ivanov, E. P. Turevskaya and N. Ya. Turova, " $\text{BaTiO}_3$  films on silicon wafers from metal alkoxides", *Ferroelectrics*, vol. 123, pp. 261-271, 1991.
- [7] Eugene Loh, "A model of dc leakage in ceramic capacitors", *J. Appl. Phys.*, vol. 53, pp. 6229-6235, September 1982.
- [8] S. Wang, *Fundamentals of Semiconductor Theory and Device Physics*, Prentice-Hall, Inc., 1989, ch. 9, pp. 428-432.

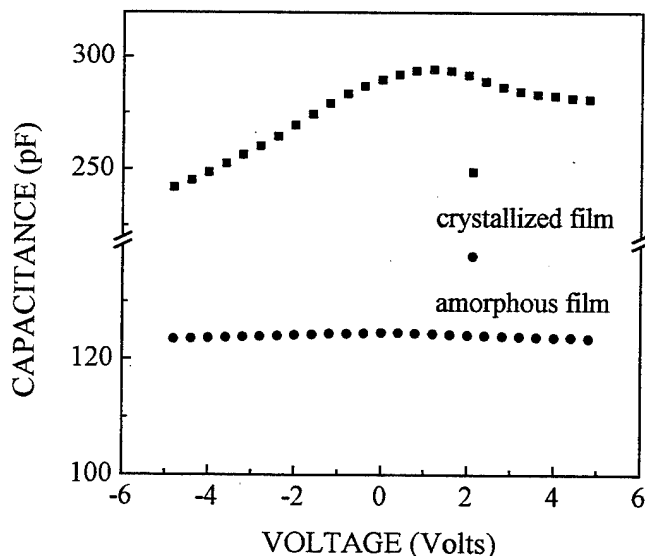


Fig. 6 C-V characteristics of the  $\text{Ba}_{0.65}\text{Sr}_{0.35}\text{TiO}_3$  films in MIM structure.

# SOL-GEL PREPARATION OF BARIUM STRONTIUM TITANATE THIN FILMS

D. Tahan, A. Safari, and L. C. Klein  
Center For Ceramic Research  
Rutgers University  
Piscataway, NJ 08855-0909

## ABSTRACT

Barium strontium titanate,  $(\text{Ba}_x\text{Sr}_{1-x})\text{TiO}_3$ , thin films of various compositions were prepared by a spin coating technique. Processing parameters were optimized to develop stable solutions which yielded crack-free films with relatively low crystallization temperatures. XRD and thermal analysis techniques were used to characterize the films and gels. The dielectric constant and dissipation factor of the films were measured as a function of temperature and frequency. Leakage current was measured as a function of voltage and time. It was determined that ethylene glycol was a necessary component of the solution to increase stability and to decrease the crystallization temperature of the films. A dielectric constant of 400 and a dissipation factor of 0.04 was measured at 1 kHz for films of the approximate composition  $(\text{Ba}_{0.8}\text{Sr}_{0.2})\text{TiO}_3$  with a thickness of 400 nm. Films of this composition maintained low leakage current densities for extended time periods when measured at an applied field of 0.08 MV/cm. The BST thin films therefore exhibited properties sufficient for application as DRAM capacitors.

## INTRODUCTION

Barium titanate is well known for its application as a capacitor material. It exhibits a narrow dielectric peak with a high dielectric constant at a Curie temperature of 120°C. This dielectric peak can be broadened and shifted to lower temperatures with the incorporation of strontium into the lattice[1]. The properties of barium strontium titanate (BST) can therefore be tailored for specific applications including capacitors, piezoelectric transducers, and optical signal processing[2,3]. Increasing the strontium content in BST allows the Curie temperature to be shifted below room temperature. In this way, BST can be made paraelectric at room temperature, exhibiting a high dielectric constant, low leakage current and a large dielectric breakdown strength[3]. These characteristics make BST thin films particularly useful for applications as DRAM capacitors[3,4].

Although some reports exist on the fabrication of BST thin films by sputtering and laser ablation, little information has been published on the production of these films by sol-gel techniques. Sol-gel offers significant advantages over alternative film fabrication methods such as purity, homogeneity, stoichiometry control, the ability to coat large and complex area substrates, ease of processing, and the possibility of lower processing temperatures[5,6]. It was therefore the objectives of this research to optimize a sol-gel process to obtain  $(\text{Ba}_x\text{Sr}_{1-x})\text{TiO}_3$  thin films with properties suitable for DRAM capacitors through analysis of the solution and film characteristics such as crystallization temperature as well as dielectric properties. The effects of composition and processing parameters on the final film properties were studied.

## EXPERIMENTAL PROCEDURE

$(\text{Ba}_x\text{Sr}_{1-x})\text{TiO}_3$  solutions with a concentration of 0.75 M and compositions of  $x=1.0$ , 0.8 and 0.6 were prepared by dissolving the appropriate ratio of barium and strontium acetates in acetic acid under a nitrogen atmosphere. This was followed by the addition of a stoichiometric amount of titanium IV isopropoxide. Ethylene glycol was then added to a portion of this solution, in an acetic acid to ethylene glycol ratio of 3 to 1. This ratio allowed the acetates to dissolve easily, along with increased solution stability. This solution was then heated at 90°C for approximately 1 hour to permit reaction between the acetic acid and the ethylene glycol. Both the acetic acid and the acetic acid/ethylene glycol solutions were studied in terms of solution stability, crystallization temperature and film quality. DTA was performed with a rate of 20°C/min in air on solution samples which were dried at 100°C for a period of 24 hours.

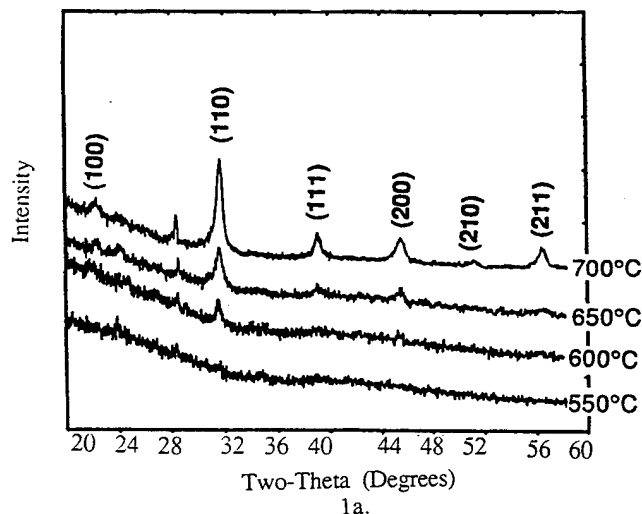
Films were prepared by spin coating the solutions at 7500 RPM for 90 seconds onto (100) Si and (100) Pt/Ti/SiO<sub>2</sub>/Si substrates. The films were heated on a hot plate at 300°C to dry and pyrolyze the organics, followed by a heat treatment in air or oxygen at elevated temperatures. This process was repeated to produce multilayer films.

The crystallinity of the films was characterized by XRD. A Pt top electrode was sputtered on the films to characterize the electrical properties. Properties such as the capacitance and dissipation factor of films coated on the Pt sputtered Si substrates were measured as a function of frequency, temperature and composition using a HP4194A Impedance/Gain-Phase Analyzer. Leakage currents were measured as a function of voltage and time using a programmable electrometer (Keithley 617).

## RESULTS AND DISCUSSION

Upon comparing the acetic acid solution to the acetic acid/ethylene glycol solution, it was noticed that the former solution yielded a white precipitate after only a couple of days, while the latter remained stable to precipitation. The crystallization temperatures of the gels and films were determined by XRD and DTA. Figures 1a and b show XRD patterns of BST (80/20) films which were heated at various temperatures. Perovskite BST began to crystallize at 600°C and 500°C for films made from the acetic acid and the acetic acid/ethylene glycol solution, respectively. DTA patterns for the dried solutions can be seen in Figures 2a and b. These patterns support the XRD data in that the exothermic crystallization peak was shifted from 600-670°C for the acetic acid solution to 510-580°C for the acetic acid/ethylene glycol solution. These results support the conclusion that ethylene glycol is a necessary component of the solution to increase stability and also to decrease crystallization temperatures.

The dielectric constant and dissipation factor of films approximately 400 nm thick as a function of strontium content at different frequencies is illustrated in Figures 3a and b, respectively.





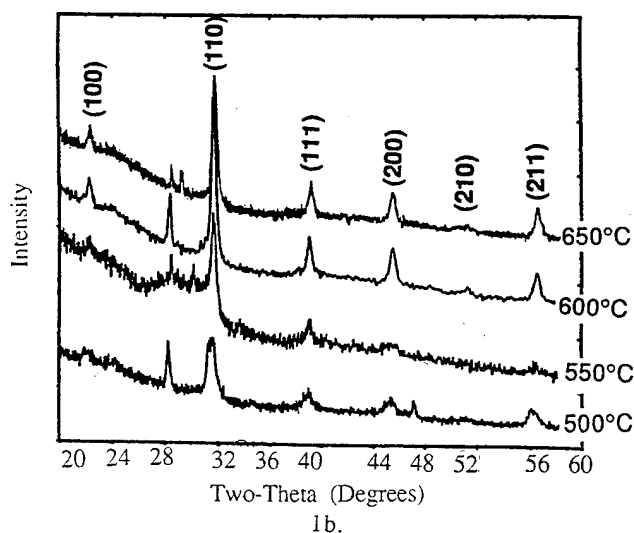


Figure 1. XRD of films heated at various temperatures made from the a.) acetic acid solution, and b.) acetic acid/ethylene glycol solution.

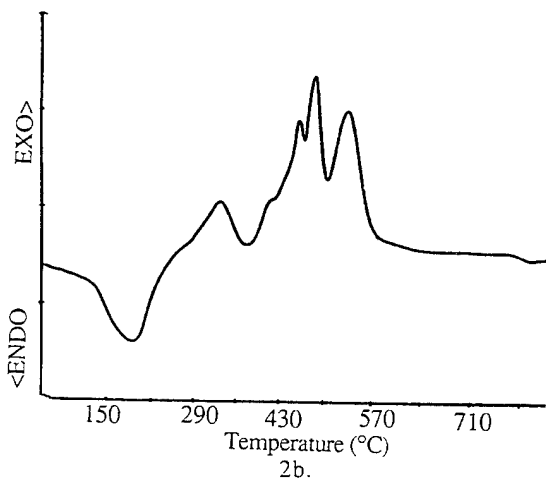
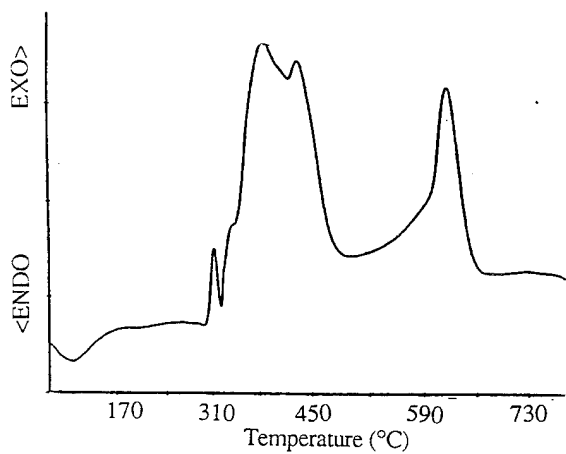


Figure 2. DTA of dried a.) acetic acid solution and b.) acetic acid/ethylene glycol solution.

The room temperature dielectric constant was approximately 350, 400, and 425 for films of the compositions  $x=1.0$ , 0.8, 0.6, respectively. The dielectric constant was not seen to vary significantly with frequency for a fixed composition. The dissipation factor remained constant over all compositions tested, with a value of approximately 0.04. The minimum dissipation factor for each composition, approximately 0.03, was measured at a frequency of 10 kHz.

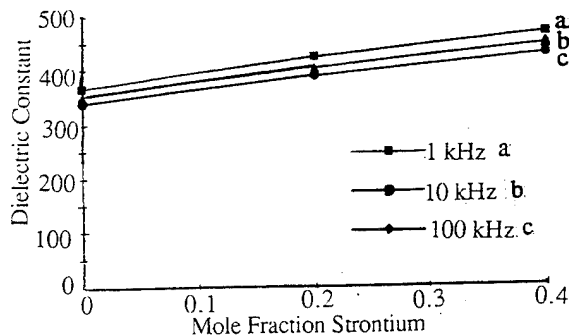


Figure 3a.) Dielectric constant versus composition.

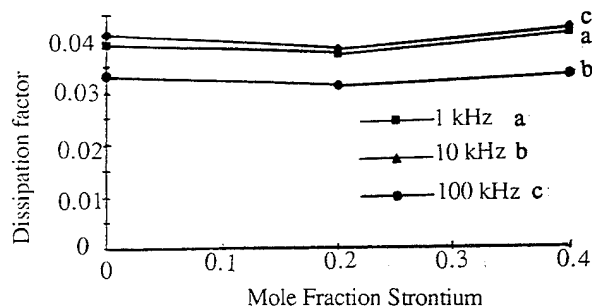
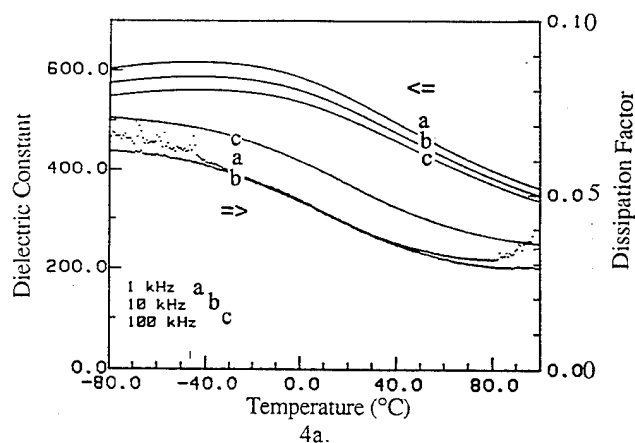


Figure 3b.) Dissipation factor versus composition.

Figures 4a and b plot the dielectric constant and dissipation factor versus temperature for the compositions of  $x=0.6$  and 1.0 (pure  $\text{BaTiO}_3$ ), respectively. The dielectric peak for the composition  $x=0.6$  was very broad, with a maximum dielectric constant of approximately 600 at a temperature of  $-40^\circ\text{C}$ . The dissipation factor ranged from 0.03 to 0.05 over the temperature range of  $-80$  to  $100^\circ\text{C}$ . The plot for the composition  $x=1.0$  does not show a peak at  $0^\circ\text{C}$  as is expected for pure barium titanate. The dielectric constant remained relatively constant at approximately 400 over the entire temperature range with a dissipation factor not exceeding 0.05. Similar results were explained by the effects of a submicron grain size [7].



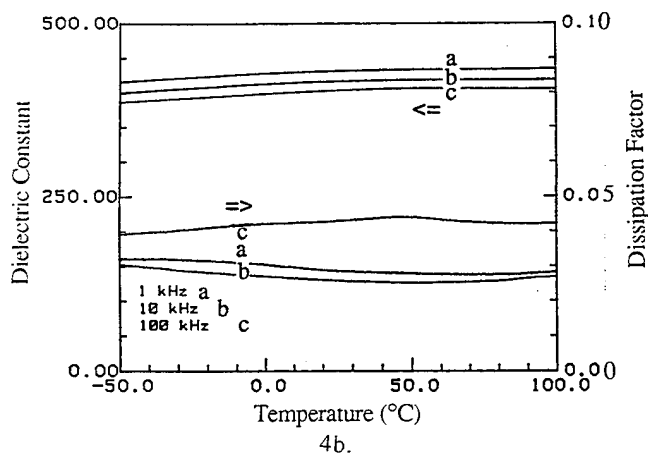


Figure 4. Dielectric constant and dissipation factor versus temperature for films of the compositions a.)  $x=0.6$  and b.)  $x=1.0$  (pure barium titanate).

Leakage current is a limiting factor of DRAM capacitors. High leakage currents are undesirable because they require more frequent refreshing, use more power, and limit the maximum field that may be applied across the device[8]. Figure 5 is a typical graph of leakage current density as a function of applied voltage for a film of the composition  $x=0.8$ . The current density increased gradually up to a voltage of approximately 6 volts. An applied voltage greater than this was seen to increase the current density dramatically. It has been reported that the current density for a practical 256 Mb DRAM capacitor must not exceed  $3 \mu\text{A}/\text{cm}^2$ [3]. Analysis of the leakage current data shows that these films fit this criterion.

Figures 6a and b are typical plots of leakage current density versus time for an  $x=0.8$  film measured at 3 and 5 volts (fields of 0.080 and 0.133 MV/cm), respectively. The leakage current remained low over the time span of 10,000 s for an applied voltage of 3 V, while an applied voltage of 5 V caused the leakage current to exceed the  $3 \mu\text{A}/\text{cm}^2$  criterion after only several seconds.

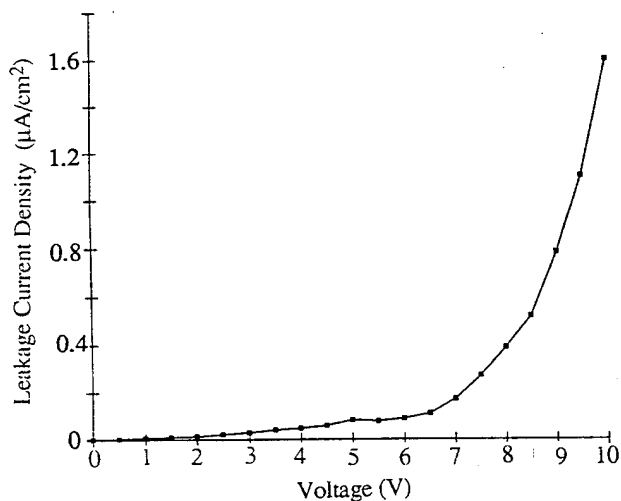


Figure 5. Leakage current density versus applied voltage for films with  $x=0.8$ .

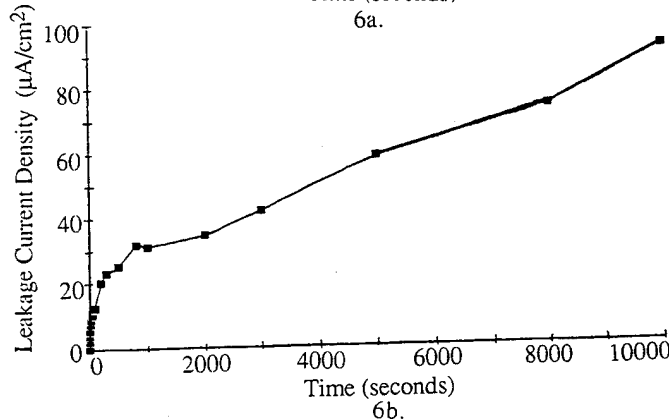
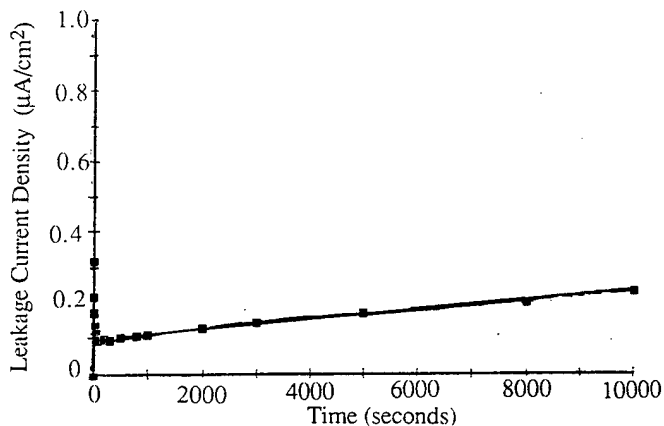


Figure 6. Leakage current density versus time at an applied voltage of a.) 3 V and b.) 5 V.

A typical plot of the capacitance as a function of applied electric field for films of the composition  $x=0.8$  is illustrated in Figure 7a. The capacitance had a maximum value of 1.7 nF with a slight applied field, and did not change drastically with voltage over the range of -10 to 10 V (electric fields of -0.26 to 0.26 MV/cm). This data was used to calculate the charge storage density using the equation  $Q=\epsilon\epsilon_0E$ , where  $\epsilon$  is the permittivity,  $\epsilon_0$  is the permittivity of free space, and  $E$  is the applied field[3]. The charge storage density is plotted against the applied field in figure 7b. A practical 256 Mb DRAM capacitor requires a charge storage density of approximately  $40 \text{ fC}/\mu\text{m}^2$ [3], which is obtained by the  $x=0.8$  films as seen in the diagram.

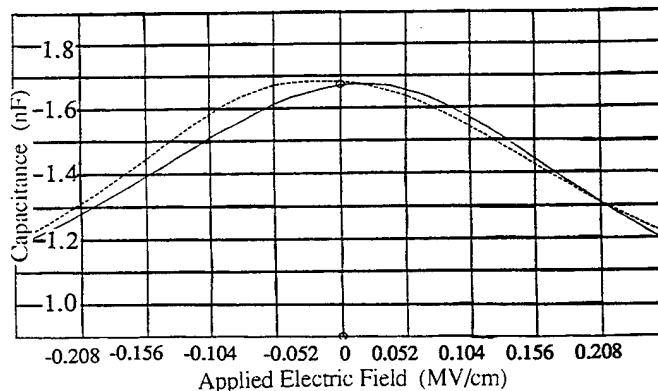


Figure 7a.) Capacitance versus applied electric field for films with  $x=0.8$ .

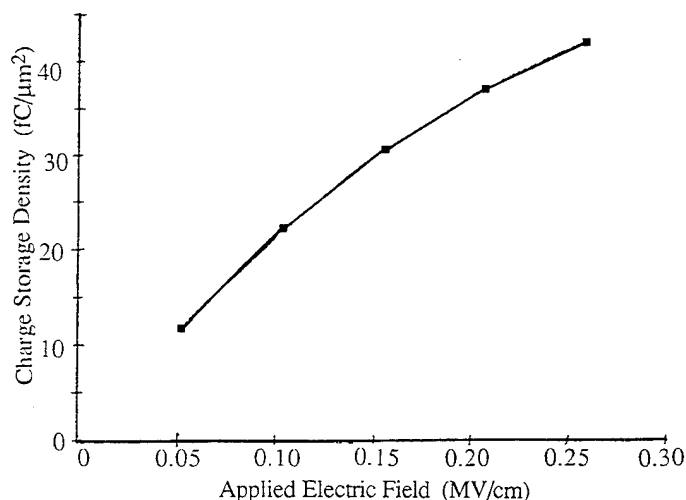


Figure 7b.) Charge storage density versus applied electric field.

### CONCLUSIONS

$(\text{Ba}_x\text{Sr}_{1-x})\text{TiO}_3$  thin films of various compositions were prepared by a sol-gel technique. Ethylene glycol proved to be a necessary component of the solution, increasing stability and decreasing the film crystallization temperature. A dielectric constant of approximately 400 was obtained for  $x=0.8$  films (thickness = 400 nm), with a  $\tan \delta$  less than 0.05. The films were presumed to have a submicron grain size, explaining the dielectric behavior as a function of temperature. The electrical properties of the films, such as charge storage density and leakage current as a function of applied voltage and time, proved to be sufficient for application of the films as DRAM capacitors.

### ACKNOWLEDGMENT

The authors would like to thank the NJ Commission on Science and Technology for the financial support of this research.

### REFERENCES

- [1] M. Klee, "Low-Temperature Processing of  $\text{BaTiO}_3$ ,  $\text{BaTi}_{1-x}\text{Zr}_x\text{O}_3$  and  $\text{Ba}_{1-x}\text{Sr}_x\text{TiO}_3$  Powder", *Journal of Materials Science Letters*, **8**(8), 1989, pp. 985-988.
- [2] H.-W. Wang and D. A. Hall, "The Effect of Dysprosium on the Microstructure and Dielectric Properties of  $(\text{Ba}_{1-x}\text{Sr}_x)\text{TiO}_3$  Ceramics", *IEEE, International Symposium on Applications of Ferroelectrics*, 1992, pp. 1-10.
- [3] D. Roy and S. B. Krupanidhi, "Excimer Laser Ablated Barium Strontium Titanate Thin Films for Dynamic Random Access Memory Applications", *Applied Physics Letters*, **62**(10), 1993, pp. 1056-1058.
- [4] K. Koyama, T. Sakuma, S. Yamamichi, H. Watanabe, H. Aoki, S. Ohya, Y. Miyasaka and T. Kikkawa, "A Stacked Capacitor With  $(\text{Ba}_x\text{Sr}_{1-x})\text{TiO}_3$  for 256M DRAM", *IEEE, International Electron Devices Meeting Technical Digest*, 1991, pp. 823-826.
- [5] S. L. Swartz and V. E. Wood, "Ferroelectric Thin Films", *Condensed Matter News*, **1**(5), 1992, pp. 4-13.
- [6] G. Yi and M. Sayer, "Sol-Gel Processing of Complex Oxide Films", *Ceramic Bulletin*, **70**(7), 1991, pp. 1173-1179.
- [7] M. H. Frey and D. A. Payne, "Nanocrystalline Barium Titanate: Evidence for the Absence of Ferroelectricity in Sol-Gel Derived Thin-Layer Capacitors", *Applied Physics Letters*, **63**(20), 1993, pp. 2753-2755.
- [8] J. Carrano, C. Sudhama, V. Chikarmane, J. Lee, A. Tasch, W. Shepherd and N. Abt, "Electrical and Reliability Properties of PZT Thin Films for ULSI DRAM Applications", *IEEE Transactions on Ultrasonics, Ferroelectrics and Frequency Control*, **38**(6), 1991, pp. 690-702.

# PULSED LASER DEPOSITION (PLD) OF FERROELECTRIC THIN FILMS IN CONJUNCTION WITH SUPERCONDUCTING OXIDES

S. Sengupta, L.C. Sengupta, and W. E. Kosik  
U.S. Army Research Laboratory, Materials Directorate, Metals/Ceramics Division  
Watertown, MA 02172

**Abstract:** The possibility of combining ferroelectrics and superconductors has been of interest for use in memory storage devices. Additionally, superconductors offer crystal structures compatible to the epitaxial growth of the ferroelectric,  $\text{Ba}_{0.6}\text{Sr}_{0.4}\text{TiO}_3$  (BSTO), which is cubic at this stoichiometry. BSTO has a lattice constant of 3.94 Å as compared to the superconducting  $\text{Pr}_{2-x}\text{Ce}_x\text{CuO}_4$  tetragonal single crystal which also has a lattice constant of  $a=3.94$  Å.

In this study, ferroelectric thin films of BSTO were deposited on single crystals of  $\text{Pr}_2\text{CuO}_4$  and  $\text{Pr}_{2-x}\text{Ce}_x\text{CuO}_4$ . The optical constants of the substrates, single crystals of  $\text{Pr}_2\text{CuO}_4$  and  $\text{Pr}_{2-x}\text{Ce}_x\text{CuO}_4$ , were determined using Variable Angle Spectroscopic Ellipsometry (VASE) and the composition and crystal structure were examined using Rutherford Backscattering Spectrometry (RBS) with ion beam channeling. The substrate/film interfaces and the compositional variation in the films were also studied with RBS and with SEM / EDS. Glancing angle x-ray diffraction was used to verify the epitaxial nature of the films. The effect of the deposition parameters (laser repetition rate, oxygen backfill pressure, and deposition geometry) on the quality of the films was experimented with and the optimized parameters were used.

## INTRODUCTION

There has been a significant interest in the possibility of combining superconductors with ferroelectrics for application in memory storage devices by using the superconductors for electrodes [1]. The idea of using single crystal superconductors for substrates however, has not been rigorously investigated. There are advantages to using these oxides as substrates. One of which is the excellent lattice match between the Barium Strontium Titanate,  $\text{Ba}_{0.6}\text{Sr}_{0.4}\text{TiO}_3$ , BSTO, and the crystal. Also the possibility of using the substrate itself as the bottom electrode is an attractive alternative to a metallic bottom electrode which can cause shorting [2].

In this study, the Top Seeded Solution Growth technique has been used to obtain single crystals of  $\text{Pr}_{2-x}\text{Ce}_x\text{CuO}_4$  ( $x=0$  and  $x=0.17$ ). This technique, unlike other growth procedures, can produce large specimens that contain fairly uniform dopant distributions [3]. The  $\text{Pr}_2\text{CuO}_4$  substrate has been annealed in an attempt to decrease its resistivity. The effect of the Ce doping and annealing on the optical constants has been monitored using VASE and the effect of both the Ce doping and annealing on the crystal structure of the substrates has been examined using RBS with ion beam channeling.

Films of  $\text{Ba}_{0.6}\text{Sr}_{0.4}\text{TiO}_3$  have been deposited onto the crystals using Pulsed Laser Deposition (PLD); the films were then examined using RBS, SEM / EDS, and glancing angle x-ray diffraction. The effect of the deposition parameters on the quality of the films as measured by the above named analytical techniques will be discussed.

## EXPERIMENTAL

The single crystal specimens were c-axis oriented such that the c-axis is perpendicular to the crystal surface. The as-grown crystals were analyzed using the techniques mentioned above. The details of the RBS and VASE experiments will be given

below. The  $\text{Pr}_2\text{CuO}_4$  crystal was annealed at 950°C for about 15 hours in flowing argon. The crystal was then re-examined [4].

The PLD was accomplished using a krypton-fluoride excimer laser with a wavelength of 248 nm and a repetition rate of 10 Hz. The average pulse energy was 300 mJ. The oxygen partial pressure in the chamber was 200 mT and the substrate temperature was 520°C. The substrate temperature was monitored by clamping the thermocouple in-between the heater and the substrate. The ceramic targets were prepared according to a description published previously [5]. The ablation target chosen for this work was  $\text{Ba}_{0.6}\text{Sr}_{0.4}\text{TiO}_3$ .

The RBS technique involves the acceleration of  $\text{He}^+$  ions to 2 MeV by a National Electrostatics Corporation (NEC) tandem pelletron accelerator. This  $\text{He}^+$  ion beam is collimated to a 1 mm diameter beam which is incident upon the crystal / film. The scattered helium ions were detected at a backscattering angle of 170° with a surface barrier detector. The energy resolution of the detection system is 20 KeV to 25 KeV. The (001) channeled spectra were obtained by rotating the samples about the beam axis ( $\phi$ ) and perpendicular to it ( $\theta$ ), until a minimum yield was located. The minima in the backscattering yield occurs when the incident beam is aligned with certain planar and/or axial symmetry directions in the crystal, i.e., channeling. When the beam is not aligned in either direction, no channeling is present and the *random* spectrum is obtained. The energy detection system is calibrated with a standard prior to data acquisition. The elements in the crystal are determined from the detected energies of the backscattered ions which are related to the mass of the atoms. The composition of the crystals / films were obtained by utilizing the software program RUMP to fit the data [6].

The ellipsometry data was obtained using a J.A. Woollam VASE. In this system, the elliptically-polarized light produced by reflecting plane-polarized light from the surface under study is modulated by a rotating analyzer. Both the wavelength of the monochromatic incident light and the angle of incidence can be varied. At each wavelength, after 150 revolutions of the analyzer, a data acquisition program subtracts a reading obtained with the shutter closed from a reading obtained with the shutter open. During a measurement, the wavelength is scanned from 4000 Å to 8000 Å at steps of 100 Å. Two angles of incidence were examined at each spot.

## RESULTS AND DISCUSSION

### *Analysis of the Single Crystal Substrates*

**RBS Results:** Figures 1 and 2 show the random and channeled RBS spectra of  $\text{Pr}_2\text{CuO}_4$  and  $\text{Pr}_{2-x}\text{Ce}_x\text{CuO}_4$  single crystals. The insets show an expanded energy scale (x-axis) of the channeled spectra. The horizontal axis is proportional to the energy at which the backscattered ion was detected. The vertical axis is the normalized yield. The ratio of the elements (in atomic %) were determined by the best fit of the RUMP simulation. The ratio of the elements and the minimum yield obtained for each element are given in Table 1.

**Table 1.** Elemental Proportions (Atomic%) and Minimum Yields (%) Obtained from the Best RUMP Fit to the RBS Data for  $\text{Pr}_2\text{CuO}_4$  and  $\text{Pr}_{2-x}\text{Ce}_x\text{CuO}_4$ .

Sample	Pr (%), Min. Yield (%)	Ce(%), Min. Yield (%)	Cu(%), Min. Yield (%)	O(%), Min. Yield (%)	Pt(%), Min. Yield (%)
$\text{Pr}_2\text{CuO}_4$	29.0, 5	N/A N/A	12.0, 5	58.0 N/A	1.0 5
$\text{Pr}_{2-x}\text{Ce}_x\text{CuO}_4$	22.1, 4	4.5, 4	14.4, 40	58.4 N/A	0.6, 40

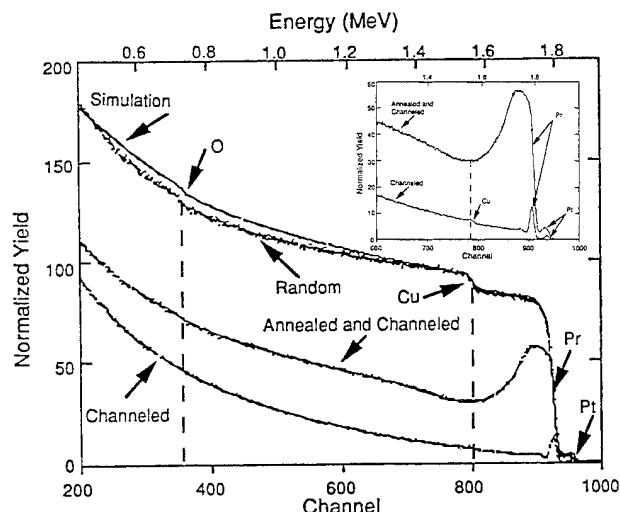


**Figure 1.** Random and channeled RBS spectra and simulation obtained from a fit to data for  $\text{Pr}_2\text{CuO}_4$ . Inset shows expanded energy scale (x-axis) for the channeled spectra.

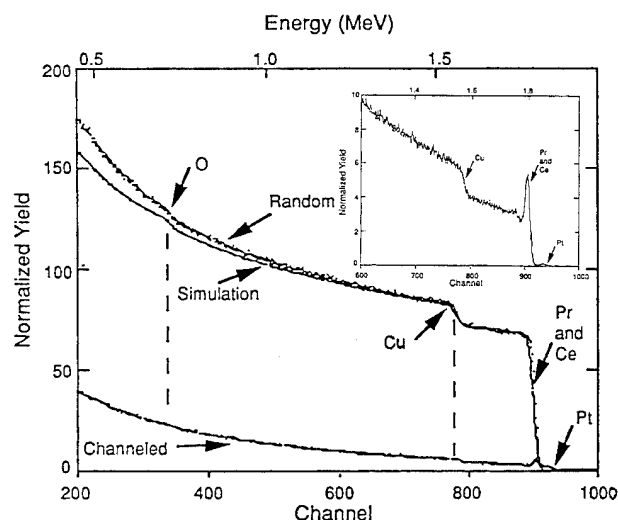


**Figure 2.** Random and channeled RBS spectra and simulation obtained from a fit to data for  $\text{Pr}_{2-x}\text{Ce}_x\text{CuO}_4$ . Inset shows expanded energy scale (x-axis) for the channeled spectra.

As indicated in Fig. 2, Pr and Ce atoms cannot be resolved in the RBS spectra due to similar mass; so in the simulation  $x = 0.17$  for Ce is used in place of Pr in the doped specimen. This value for  $x$  was determined from the x-ray diffraction data. As seen in the figures, Pt (up to 1%) is incorporated into the crystal through contamination by the crucible. It should be noted that Pt is seen to exhibit channeling behavior which can be observed by the definite appearance of a sharp peak and a low minimum yield in the channeled spectra. This indicates that Pt is in the substitutional sites. It is assumed that Pt substitutes for Cu in the specimen, as was seen in a previous report [7]; where substitution causes the critical temperature,  $T_c$ , to decrease.

In general, the minimum yield obtained for the elements, as seen in Table 1, is very low indicating the crystal is well-oriented and the crystalline structure is very well-ordered. As shown in the figures, most elements appear predominantly substitutional since channeling occurs for all elements in both crystals. However, as shown in Figure 2 (inset), for the  $\text{Pr}_{2-x}\text{Ce}_x\text{CuO}_4$  sample, Cu/Pt do not channel as well as indicated by the higher yield. Since both Cu and Pt appear to channel relatively poorly in this specimen, it is consistent with Pt substituting for Cu in the material. Also, the poor channeling may indicate that Cu/Pt are slightly displaced from their lattice sites. Previous workers have noticed a bending of Cu-O chains upon doping in the material [8]. The Ce doping may also cause this distortion in the crystal. The channeled spectrum for the annealed  $\text{Pr}_2\text{CuO}_4$  sample is shown in Figure 1. As shown in the figure, the minimum yield for the Pr has increased to  $\sim 30\%$ . However, the yield is not as high as for a random spectrum. This implies some disorder, from the creation of oxygen vacancies and/or surface realignment. Also, the back ledge of the spectrum does not have as low a yield as the unannealed sample. This could be due to the presence of oxygen vacancies throughout the sample or from dechanneling from the disordered surface.

**VASE Results:** In Figs. 3 and 4, the VASE spectra of the imaginary part of the dielectric function for both  $\text{Pr}_2\text{CuO}_4$  and the  $\text{Pr}_{2-x}\text{Ce}_x\text{CuO}_4$  are shown. As shown in Fig. 3, an absorption peak appears at 1.5 eV (at 8000 Å). This absorption peak has been assigned to a bound charge transfer excitation from the Cu(3d) to O(2p) in the Cu oxygen plane [9,10]. The sharpness of the transition may be due to the lack of a decay channel for the excited carrier [7]. In Figure 4, which shows the VASE spectrum of the  $\text{Pr}_{2-x}\text{Ce}_x\text{CuO}_4$  specimen, the material becomes conducting upon doping with Ce, the 1.5 eV transition is suppressed from the introduction of free-carriers which act to produce screening of the Cu oxygen planes. In Fig. 5, the VASE spectrum of the imaginary part of the dielectric function of the annealed  $\text{Pr}_2\text{CuO}_4$  sample is shown. The oscillator strength for the transition is decreased (transition is weakened) and it is shifted downward in energy. The weakening and downward shift of the peak may be caused by the opening of a decay channel for the carrier. The decay channel may be viewed as disorder in the material as also observed in the RBS data.

#### *Analysis of the Films and Film / Substrate Interfaces*

**SEM / EDS Results:** The SEM micrograph of the surface of the BSTO film on the  $\text{Pr}_2\text{CuO}_4$  substrate is shown in Fig. 6. As shown in the figure, the film surface is fairly uniform. However, particulates are evident on the surface. EDS was performed on the particulates, and results show that the particulates consist of Ba, Sr, Ti, and O. Pr and Cu are also present. It is apparent from the compositional analysis, that the particulates have been expelled from the target. Also as noted above, the compositional analysis of the film reveals the elements from the target and from the substrate.

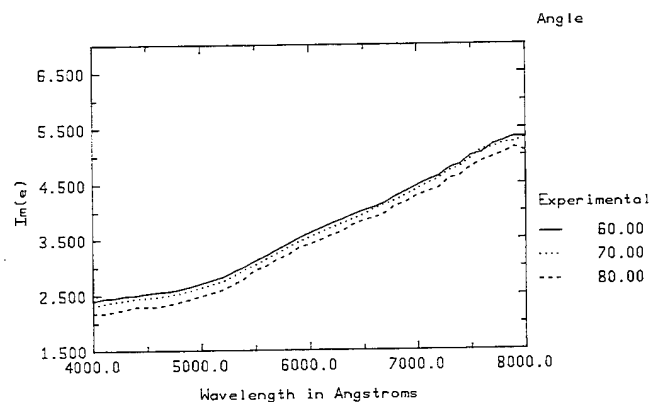


**Figure 3.** VASE spectrum of the imaginary part of the dielectric function versus wavelength for the  $\text{Pr}_2\text{CuO}_4$  sample,  $\theta = 60^\circ$ ,  $70^\circ$  and  $80^\circ$ .

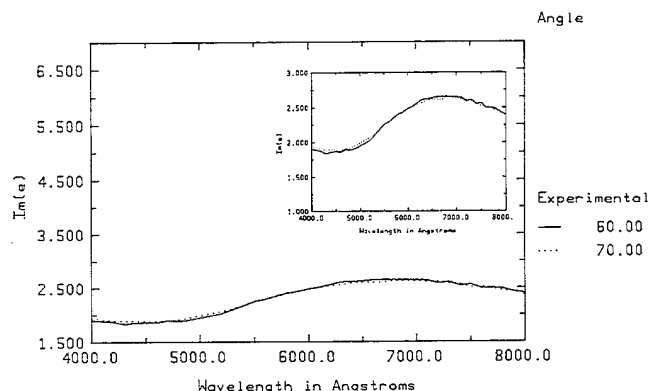


**Figure 4.** VASE spectrum of the imaginary part of the dielectric function versus wavelength for the  $\text{Pr}_{2-x}\text{Ce}_x\text{CuO}_4$  sample,  $\theta = 60^\circ$  and  $70^\circ$ , (inset shows an expanded y-scale of the sample).

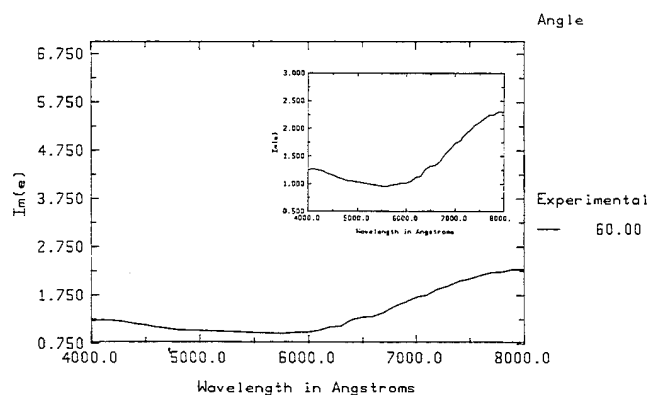


**Figure 5.** VASE spectrum of the imaginary part of the dielectric function versus wavelength for the annealed  $\text{Pr}_{2-x}\text{Ce}_x\text{CuO}_4$  sample, (inset shows an expanded y-scale of the sample),  $\theta = 60^\circ$ .

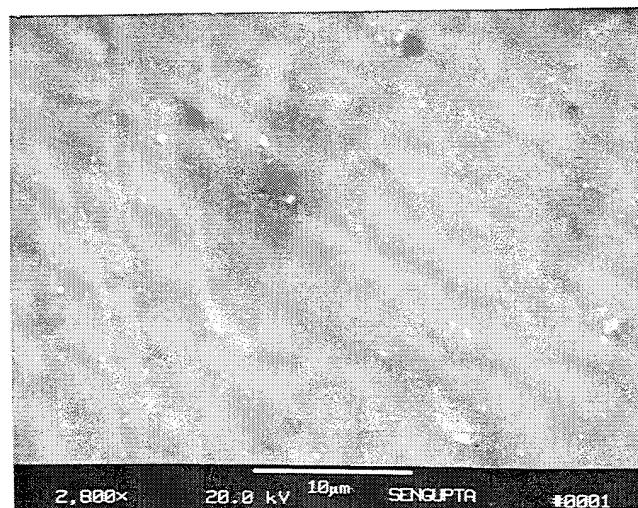


**Figure 6.** SEM micrograph of the  $\text{Ba}_{0.6}\text{Sr}_{0.4}\text{TiO}_3$  film deposited on  $\text{Pr}_2\text{CuO}_4$  single crystal substrate.

The nominal thickness of the film was measured by a Dektak profilometer to be 3000 Å which made it transparent to the electron beam. The EDS analysis of the BSTO film deposited on  $\text{Pr}_{2-x}\text{Ce}_x\text{CuO}_4$  specimen also revealed Ba, Sr, Ti and O as well as Pr, Ce, and Cu.

**RBS Results:** The RBS spectrum for the BSTO film on the  $\text{Pr}_2\text{CuO}_4$  substrate is shown in Fig. 7. The dotted line is the measured data for the RBS spectra and the solid line is the RUMP fit to the data. As shown in the Fig. 8, this fit was done by subtracting the measured RBS spectra for the  $\text{Pr}_2\text{CuO}_4$  single crystal and by adding the stoichiometrically correct peaks for Ba, Sr, and Ti. Therefore it is evident from the fit to the data, that the film that was deposited was stoichiometrically identical to the target, which is Ba = 0.60, Sr = 0.40, and Ti = 1.03, and O = 3.0.

However, as shown in Fig. 9, the simulated spectrum does not show a good fit to the RBS spectrum of the BSTO film (inset shows the expected positions for Ba, Sr, and Ti) on Ce doped  $\text{Pr}_2\text{CuO}_4$ . This may be attributed to the poor surface quality of the substrate. As observed for the substrate, from the RBS data, it is apparent that the crystal has a oxygen rich and disordered surface as indicated by the poor channeling for Cu/Pt sites. Therefore the front part of the spectrum is seen to slope downward or "roll-off". Therefore, the RBS data cannot make any conclusive analysis of the film deposited on this substrate.

**Glancing Angle X-ray Diffraction:** The glancing angle x-ray diffraction data for the BSTO film deposited on  $\text{Pr}_2\text{CuO}_4$  is shown in Fig. 10 (inset shows the x-ray diffraction pattern for the  $\text{Ba}_{0.6}\text{Sr}_{0.4}\text{TiO}_3$  target material). A rotating anode x-ray unit emitting  $\text{Cu-K}\alpha$  (1.5415 Å) emission was used as the source. The x-ray beam was incident on the sample at an angle of 1 degree to the surface of the film. The x-ray pattern matches closely to that for  $\text{Ba}_{0.6}\text{Sr}_{0.4}\text{TiO}_3$ . The  $hkl$  values for these peaks are indicated on the figure. However, another phase is also present in the film. This phase corresponds to  $\text{Ba}_{0.91}\text{Sr}_{0.09}\text{TiO}_4$  and the x-ray peaks for this phase are indicated on the figure by an asterisk. As shown in the inset the target material does not contain this secondary phase and it is not observed when the films are deposited on other

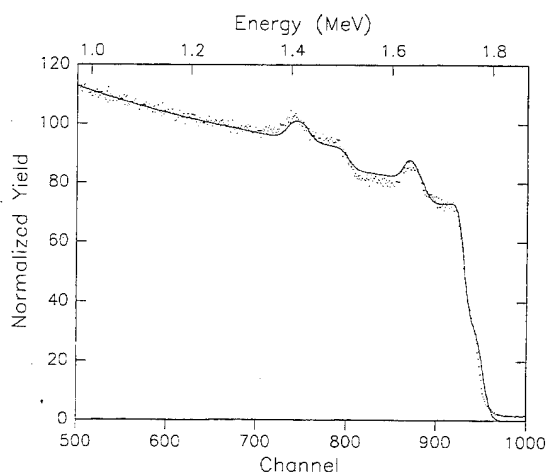


**Figure 7.** RBS spectrum for the BSTO /  $\text{Pr}_2\text{CuO}_4$  sample (dotted line) and a fit to the data (solid line) obtained from the measured data for the  $\text{Pr}_2\text{CuO}_4$  substrate and the film containing  $\text{Ba}_{0.6}\text{Sr}_{0.4}\text{TiO}_3$ .

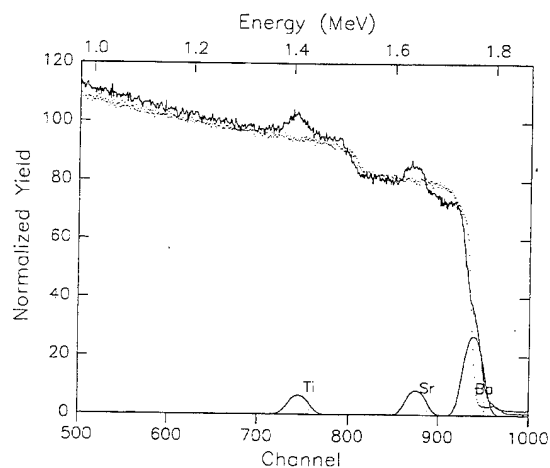


**Figure 8.** RBS spectrum for the BSTO /  $\text{Pr}_2\text{CuO}_4$  sample (solid line) and the RBS spectrum for the  $\text{Pr}_2\text{CuO}_4$  crystal (dotted line) and the corresponding peaks for Ba, Sr, and Ti.

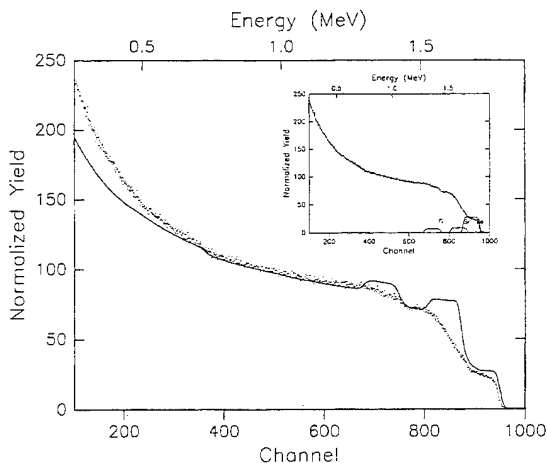


**Figure 9.** RBS spectrum for the BSTO /  $\text{Pr}_{2-x}\text{Ce}_x\text{CuO}_4$  sample (dotted line) and a fit to the data (solid line), (inset shows the expected position of the Ba, Sr, and Ti peaks).

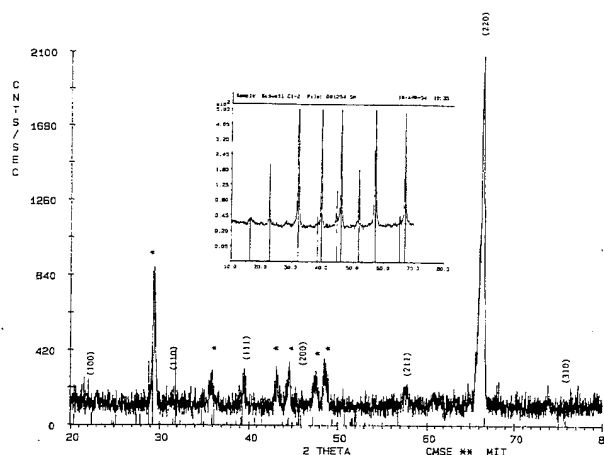


**Figure 10.** Glancing Angle X-ray Diffraction pattern for BSTO deposited on  $\text{Pr}_2\text{CuO}_4$  (inset shows the x-ray diffraction pattern for the  $\text{Ba}_{0.6}\text{Sr}_{0.4}\text{TiO}_3$  target material).

substrates. The presence of this phase may be attributed to the film-substrate interaction, possibly due to the presence of surface disorder (oxygen vacancies) as indicated by the RBS and VASE data of the substrate. Further investigations on the specimen are currently being done.

## CONCLUSION

The crystal structures and composition of the cuprate crystals were investigated using RBS with ion beam channeling. The minimum yields obtained for the elements in the crystals indicate that the crystals are well-oriented and very ordered. The addition of Cerium to the material causes a slight displacement of Cu from its normal lattice site. Also, Pt was included in the crystals due to the contamination from the crucible. The spectrum of the annealed crystal shows disorder which was confirmed by RBS and VASE data.

The RBS spectrum of the laser ablated BSTO /  $\text{Pr}_2\text{CuO}_4$  film indicated similar film and target compositions. However, the presence of a barium rich secondary phase ( $\text{Ba}_{0.91}\text{Sr}_{0.09}\text{TiO}_4$ ) was evident from x-ray studies. This phase may have been created due to the presence of the oxygen vacancies present in the substrate due to annealing. The RBS data of the BSTO /  $\text{Pr}_{2-x}\text{Ce}_x\text{CuO}_4$  sample is inconclusive due to the poor surface quality of the substrate. The incorporation of superconducting electrodes with ferroelectric materials is presently under investigation.

## ACKNOWLEDGMENTS

The authors wish to thank Dr. Arlete Cassanho for the cuprate crystals and Dr. Allen Kirkpatrick of Epion Corporation, Bedford, MA for his help.

## REFERENCES

- [1] O. Vendik, I. Mironenko, and L. Ter-Martirosyan, *Microwaves and RF*, pp. 67-70, July 1994.
- [2] S.B. Desu, *J. of Integrated Ferroelectrics*, in press (1994).
- [3] A. Cassanho et al., *J. Crystal Growth*, vol. 96, pp. 999 (1988).
- [4] L.C. Sengupta, S. Sengupta, W.E. Kosik, and J.D. Demaree, *J. Cryst. Growth*, vol. 128, pp. 817-823 (1993).
- [5] L.C. Sengupta, S. Stowell, E. Ngo, M.E. O'Day and R. Lancto, *J. of Integrated Ferroelectrics*, in press (1994).
- [6] L.R. Doolittle, *Nuclear Instru. Meth.*, vol B9, p. 334 (1985).
- [7] Y. Hidaka, *Proc. of 2nd ISS '89*, T. Ishoguro and K. Kajimura, eds., Springer-Verlag, p. 229 (1990).
- [8] J.M. Tarascon, et al., *Phys. Rev. B*, vol. 40, p. 4494 (1989).
- [9] S. Tajima, et al., *J. Opt. Soc. Am.*, vol. B6, p. 475 (1989).
- [10] M.K. Kelly, P. Barboux, J.M. Tarascon, and D.E. Aspnes, *Phys. Rev. B*, vol. 40, p. 6747 (1989).

Donhang Liu and David A. Payne

Department of Materials Science and Engineering, Materials Research Laboratory, and Beckman Institute,  
University of Illinois at Urbana-Champaign, Urbana, IL 61801

**Abstract** — Lead scandium tantalate (PST) was prepared by sol-gel processing, and the crystallization into the perovskite phase was determined at reduced temperatures (600–700°C). The extent of B-site cation ordering was also determined as a function of cooling conditions. Results are reported for the integration of capacitors on silicon with a capacitance density greater than 200 fF/ $\mu\text{m}^2$ . A preferred (111) orientation was obtained, with  $(\frac{1}{2}\frac{1}{2}\frac{1}{2})$  B-site cation partial ordering. No evidence was obtained for A-site Pb vacancy ordering. Results are reported for X-ray diffraction and selected-area electron diffraction investigations.

## INTRODUCTION

Lead scandium tantalate ( $\text{Pb}(\text{Sc}_{0.5}\text{Ta}_{0.5})\text{O}_3$ ) in the perovskite structure ( $\text{ABO}_3$ ) is an important candidate material for pyroelectric imaging and other advanced dielectric applications [1]. In addition,  $\text{Pb}(\text{Sc}_{0.5}\text{Ta}_{0.5})\text{O}_3$  (i.e., PST) is a complex perovskite ( $\text{A}(\text{B}'\text{B}'')\text{O}_3$ ) in which cation ordering on the B-site (i.e., Sc and Ta) can be manipulated by thermal processing conditions. This makes modifications to the dielectric response characteristics possible by appropriate heat-treatment procedures.

Despite the attractive potential for PST in various dielectric applications, a major practical problem has been the high firing temperatures (>1500°C) required for the densification of insulating ceramics [2]. In addition, temperatures greater than 1200°C are usually required for the development of the perovskite structure, and the elimination of a lower temperature intermediary phase, which has deleterious properties.

In the past few years, the chemical sol-gel route has gained increasing attention as a practical alternative to conventional mixed-oxide processing for the deposition of electrical ceramics in thin-layer form. Several advantages of the sol-gel method include, lower densification and crystallization temperatures, and the ability to coat complex shapes. A wide variety of perovskite materials have been processed at reduced temperatures [3–7]. In our previous work on the preparation of perovskite PST thin-layer ferroelectrics [8,9], we reported an improved one-step method for the sol-gel processing of dense insulating thin layers at 750°C. In this paper, we report further on reduced temperature crystallization (650°C), with preferred orientation, and B-site cation ordering.

B-site cation ordering was suggested by Smolenskii as a mechanism for relaxor behavior [10]. The dispersion in weak-field dielectric properties with temperature was attributed to a distribution of B-site cations between two equivalent crystallographic sites. This was confirmed by Setter and Cross for the diffuse phase transition behavior for PST [2,11,12]. The degree of order for B-site cations can be enhanced by annealing at temperatures below the sintering temperature and with slow cooling. Ordered structures exhibit normal ferroelectric behavior with a sharp phase transformation temperature ( $T_c$ ), whereas disordered materials exhibit a diffuse phase transformation behavior. Ordered microregions were

observed by Harmer *et al.* in PST single crystals by transmission electron microscopy (TEM) [13,14].

High sintering temperatures (>1500°C) are often required for the densification of perovskite PST ceramics [2, 11, 18], which leads to the possible creation of A-site vacancies by Pb loss. A crystallographic model for the ordering of A-site lead vacancies has been proposed [15], with a doubling of the unit cell, similar to the case for B-site ordering. However, ordered A-site vacancies would give  $\{h + \frac{1}{2}, k + \frac{1}{2}, 0\}$  superlattice spots whereas ordered B-site cations would give  $\{h + \frac{1}{2}, k + \frac{1}{2}, l + \frac{1}{2}\}$  reflections in selected-area electron diffraction patterns (SAED). This would lead to two types of ordering in PST, if A-site vacancies were formed.

In this paper, we report recent results for the reduced temperature crystallization and ordering in sol-gel derived PST thin layers. B-site cation ordering was determined, but A-site Pb vacancy ordering was not observed.

## EXPERIMENTAL PROCEDURE

We follow a procedure previously reported for the synthesis and processing of PST by a sol-gel method [9]. Briefly, scandium acetate ( $\text{Sc}(\text{CH}_3\text{COO})_3 \cdot x\text{H}_2\text{O}$ ) was dehydrated in vacuum at 60°C for 2 h and dissolved in 2-methoxyethanol ( $\text{CH}_3\text{OCH}_2\text{CH}_2\text{OH}$ ). An appropriate amount of tantalum ethoxide ( $\text{Ta}(\text{OCH}_2\text{CH}_3)_5$ ) was introduced and the mixed-solution was heated to reflux for the formation of a scandium tantalate (ST) precursor solution. The ST solution was hydrolyzed by addition of 1 equivalent of  $\text{H}_2\text{O}$  for each mole of total B-site cation and refluxed for 24 h, and aged for 48 h to promote oligomer complexation in the Sc-Ta precursor solution. Similarly, anhydrous lead acetate ( $\text{Pb}(\text{CH}_3\text{COO})_2$ ) was mixed with 2-methoxyethanol and heated under reflux for 4 h, followed by vacuum distillation. The procedure was repeated twice to obtain a clear viscous solution, which was diluted with 2-methoxyethanol. The as-prepared ST and Pb precursor solutions were combined at room temperature with vigorous stirring. An excess amount (18 mole%) of the Pb precursor solution was used to compensate for any possible Pb loss during subsequent heat-treatment.

Bulk translucent PST gels were formed on addition of excess  $\text{H}_2\text{O}$  (mole of  $\text{H}_2\text{O}$ :mole of  $\text{Sc} \approx 560:1$ ); and thin layers were deposited on platinized  $\text{Si}(100)/\text{SiO}_2/\text{Ti}/\text{Pt}$  substrates by spin-casting partially hydrolyzed PST precursor solutions ( $\text{H}_2\text{O}:\text{Sc}=2:1$ ). After each deposition, the specimens were heated on a hot plate at 300°C, followed by heat treatment in a box furnace at 600°C. Thicker coatings were formed by sequential deposition and heat treatment of spin-cast layers (4–5 times). Different annealing conditions were investigated for the development of ordered structures.

Phase development and B-site cation ordering was monitored by X-ray diffraction (XRD) and transmission electron microscopy (TEM). Gold electrodes ( $\sim 4.5 \times 10^{-4} \text{ cm}^2$ ) were sputter-deposited through a mask for electrical contacts. The bottom and top electrodes were probed by micropositioners and contacted to an impedance analyzer. A



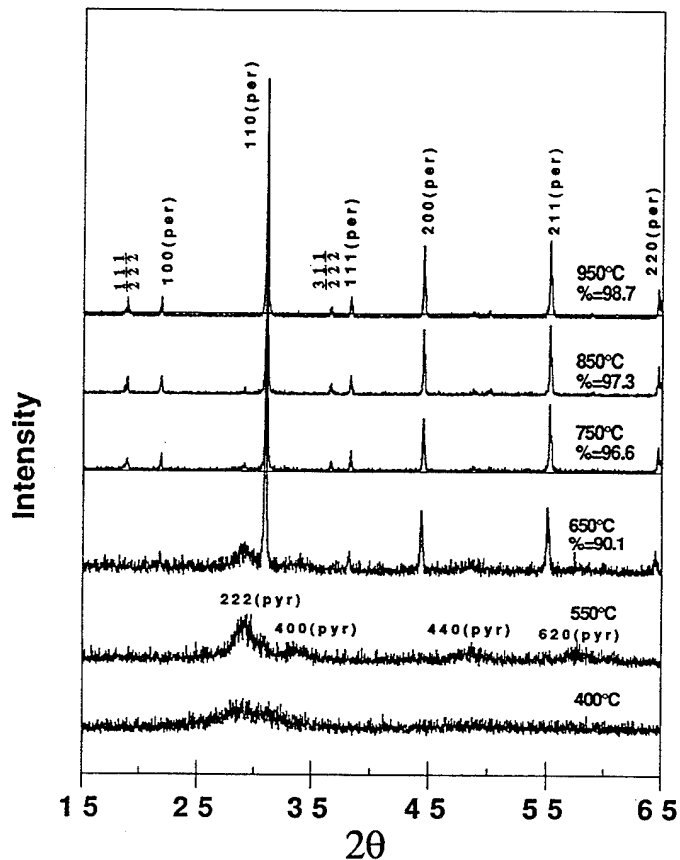


Fig. 1 Crystallization of the perovskite phase and the development of structural ordering. (The perovskite phase content (%) is defined by eq. (1) in the text)

weak a.c. signal (0.25 V/cm) was used. P-E hysteresis loops were recorded on a Sawyer-Tower circuit at 50 Hz.

## RESULTS AND DISCUSSION

### 3.1 Crystallization and B-site cation ordering in PST powders

Figure 1 gives XRD data ( $2\theta=15-65^\circ$ ) for PST powders which were heat treated at a particular temperature for 1h before quenching to room temperature. The amorphous gel

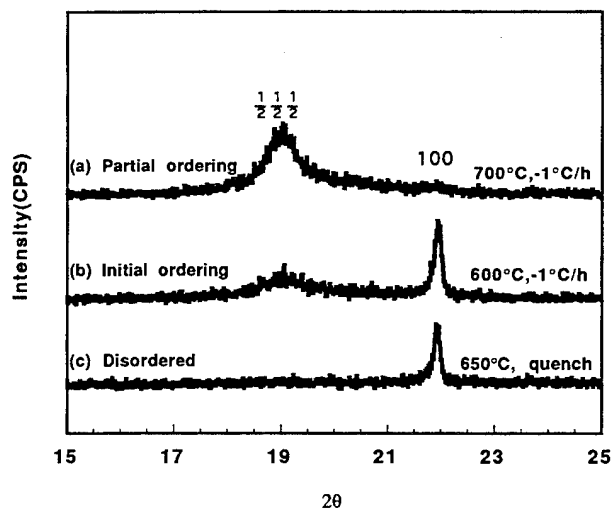


Fig. 3 XRD data for three PST thin layers with different degrees of structural ordering after different heat treatment conditions.

crystallized initially into an intermediary phase (designated by pyr) at 550°C before transforming into the desired perovskite structure (per) at higher temperatures. The extent of phase conversion was estimated from peak intensity data, by

$$\% \text{ perovskite} = \frac{I(110)_{\text{per}}}{I(222)_{\text{pyr}} + I(110)_{\text{per}}} \times 100. \quad (1)$$

The perovskite phase content was estimated at 90.1% after heat treatment at 650°C, 96.6% at 750°C, 97.3% at 850°C, and 98.7% at 950°C. This was a substantial reduction in crystallization temperature compared with conventional mixed-oxide processing.

In addition to the primary perovskite reflections, Fig. 1 indicates superlattice reflections attributed to B-site cation ordering, and indexed by  $(\frac{1}{2}\frac{1}{2}\frac{1}{2})$  and  $(\frac{3}{2}\frac{1}{2}\frac{1}{2})$ . From the  $(\frac{1}{2}\frac{1}{2}\frac{1}{2})$  superlattice reflections, a long-range order parameter ( $S$ ) can be calculated according to [11]

$$S_{\frac{111}{222}}^2 = \frac{\left( \frac{I_{\frac{111}{222}}}{I_{100}} \right)_{\text{observed}}}{\left( \frac{I_{\frac{111}{222}}}{I_{100}} \right)_{\text{calculated, for } S=1}} \quad (2)$$

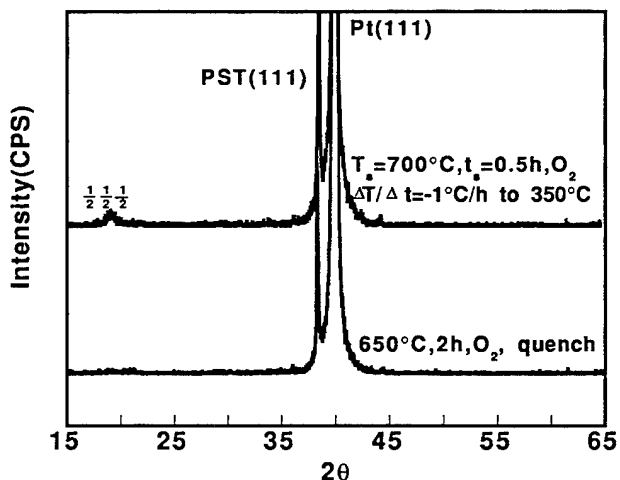


Fig. 2 Preferred (111) orientation and the development of B-site cation ordering in PST thin layers crystallized on platinized Si(100).

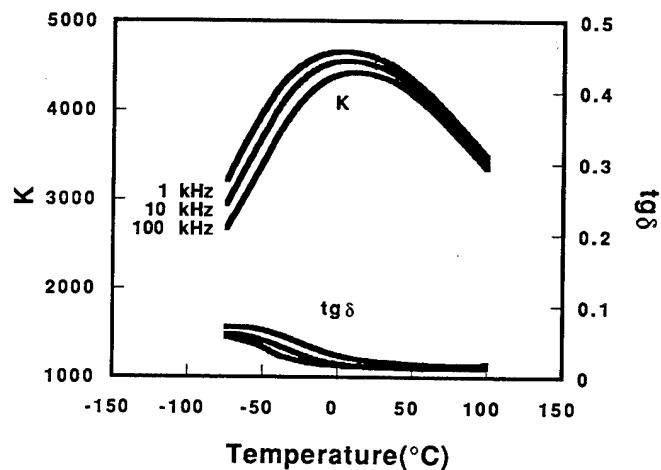


Fig. 4 Dielectric properties as a function of temperature and the diffuse phase transformation behavior observed for an integrated PST capacitor on silicon.

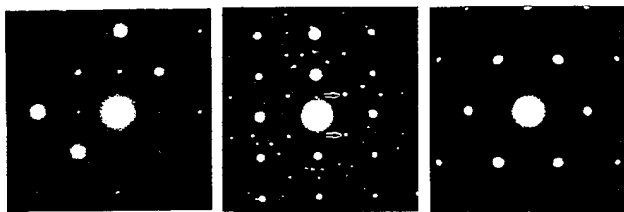


Fig. 5 SAED patterns along the three zone axes (from left:  $\langle 00\bar{1} \rangle$ ,  $\langle 10\bar{1} \rangle$ ,  $\langle 11\bar{1} \rangle$ ), after slow cooling from elevated temperature. Arrows indicate the superlattice spots attributed to B-site ordering.

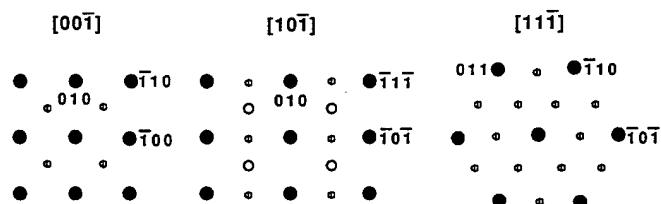


Fig. 6 Projection of calculated SAED patterns for the three primary zone axes of cubic perovskite, where the open circles represent superlattice reflections for B-site cation ordering, the shadowed spots indicate superlattice reflections for A-site Pb vacancy ordering.

Values of  $S$  were estimated at 0.76 for 750°C, 0.83 for 850°C, and 0.88 for 950°C.

### 3.2 Crystallization and B-site cation ordering in PST thin layers

XRD data for a crystallized PST thin layer are given in Fig. 2. Preferred orientation (111) was detected between  $2\theta=15-65^\circ$  for material heat treated at 650°C. After heat treatment at 700°C, and with slow cooling ( $-1^\circ\text{C/hr}$ ) to 350°C,  $(\frac{1}{2}\frac{1}{2}\frac{1}{2})$  superlattice reflections were detected. That is, (111) preferred orientation with  $(\frac{1}{2}\frac{1}{2}\frac{1}{2})$  partial ordering. There was a systematic absence of other reflections. Figure 3 indicates that the partial ordering could only be detected after slow cooling from elevated temperature. A high degree of (111) preferred orientation was obtained with only a minor (100) reflection, from which the long-range order parameter ( $S$ ) could not be estimated (Eq. (1)) unlike the previous discussion for random powders (3.1).

After heat treatment and various annealing conditions, the PST thin layers were found to be dense and insulating, and exhibited a diffuse phase transformation with a peak value of dielectric constant between 3000 and 5000 at  $T_c$  (Fig. 4). This was for a  $0.3\mu\text{m}$  thin-layer, with a capacitance density of  $100-200\text{fF}/\mu\text{m}^2$ .

### 3.3 TEM of ordering in PST thin layers

Figure 5 gives selected-area electron diffraction (SAED) patterns for the  $\langle 00\bar{1} \rangle$ ,  $\langle 10\bar{1} \rangle$ , and  $\langle 11\bar{1} \rangle$  zone axes observed from grain-oriented (111) and partially-ordered PST thin-layers deposited on Pt/Si(100). Some superlattice spots can be seen along the  $\langle 10\bar{1} \rangle$  projection. Figure 6 indicates the possible SAED patterns which can be calculated for a cubic perovskite structure. The open spots are possible  $\{h+\frac{1}{2}, k+\frac{1}{2}, l+\frac{1}{2}\}$ -type reflections for B-site cation ordering; the shadowed spots are  $\{h+\frac{1}{2}, k+\frac{1}{2}, 0\}$ -type reflections which are structurally forbidden for B-site cation ordering. The latter are possible for A-site vacancy ordering in Pb-based perovskites [15].



Fig. 7 Central dark-field image of an ordered PST layer illustrating APBs between ordered domains.

Evaluation of Figs. 5 and 6 indicates the observed superlattice reflections are in accordance with B-site cation ordering. Apparently, A-site vacancy ordering (which has been reported for PST single crystals with B-site ordering [13,14]) was not detected in this case. This could be due to the greatly reduced temperatures (600-700°C) developed for the crystallization of sol-gel PST and the excess PbO used in the present study. Figure 7 illustrates the anti-phase boundaries (APBs) which were detected between ordered regions, in accordance with B-site ordering. The APBs were obtained for the  $\langle 10\bar{1} \rangle$  projection.

### 3.4 Reduced-temperature crystallization and ordering

A significant reduction in crystallization temperature was determined for perovskite phase development in sol-gel derived powders and thin layers (600-700°C) compared with conventional mixed-oxide processing (1560°C) [2, 11]. B-site cation ordering was also detected in this temperature region (600-700°C) for slowly cooled specimens. The ordering occurred at temperatures which were 200-300°C less than for conventional powder processing [2, 18]. The ordering appears to be associated with the reduced-temperature crystallization behavior for sol-gel derived PST. No association with A-site Pb vacancies was detected, unlike previous reports for B-site cation ordering in PST [17,18]. In the present study, the lower temperatures obtained for the crystallization and ordering in perovskite are attributed to the molecular mixing of Sc and Ta in the precursor prior to sol-gel processing [9].

## SUMMARY

Sol-gel processing was used to prepare dense insulating thin layers of perovskite PST with (111) orientation on platinized Si(100). B-site cation ordering was obtained under slow cooling conditions and appeared to be associated with material which contained a high perovskite phase content. The reduction in crystallization temperature for sol-gel derived PST resulted in ordered structures at lower temperatures. SAED results were consistent with B-site cation ordering, and no evidence was obtained for A-site vacancy ordering. The results should contribute to the fabrication of PST devices at reduced temperatures. Integrated capacitors were formed with dielectric constants of 4500 at 25°C and with capacitance densities of approximately  $200\text{fF}/\mu\text{m}^2$ .

## ACKNOWLEDGMENTS

The research was supported by the US DOE under contract number DE-DMR-FG02-91ER45439. The use of facilities in

the Center for Microanalysis of Materials at the University of Illinois is greatly appreciated. We acknowledge the assistance of our colleagues in the Materials Chemistry Group in the Beckman Institute, especially Dr. L. Ma, Dr. T. Tani, Mr. M.H. Frey, and Mr. C.D.E. Lakeman.

# REFERENCES

- [1] R. W. Whatmore, N. M. Shorrocks, P. C. Osbond, S. B. Stringfellow, C. E. Carter, and R. Watton, "Modified Lead Scandium Tantalate for Uncooled LWLR Detection and Thermal Imaging," in *Proceeding of the Eighth IEEE ISAF Meeting*, 1992, pp202-05.
- [2] N. Setter and L. E. Cross, "The Role of B-Site Cation Disorder in Diffuse Phase Transition Behavior of Perovskite Ferroelectrics," *J. Appl. Phys.*, vol. 51, pp4356-60, 1980.
- [3] K. D. Budd, S. K. Dey and D. A. Payne, "Sol-Gel Processing of  $\text{PbTiO}_3$ - $\text{PbZrO}_3$  and PLZT Thin Films," *Br. Ceram. Proc.*, vol 36, pp107-21, 1985.
- [4] K. D. Budd and D. A. Payne, "Ceramic Processing of Thin-Layer Capacitors by Sol-Gel Methods," in *Ceramic Powder Processing Science*, H. Hausner, G. R. Messing and S. Hirano, Editors, Deutsche Keramische Gesellschaft, 1989, pp513-20
- [5] K. D. Budd and D. A. Payne, "Sol-Gel Processing of Thin-Layer Dielectrics in Lead Titanate-Based Systems," *Inst. of Phys. Conf. Ser. (UK)* vol. 10, pp13-22, 1989.
- [6] L. F. Francis, Y.-J. Oh, and D. A. Payne, Sol-Gel Processing and Properties of Lead Magnesium Niobate Powders and Thin Layers," *J. Mat. Sci.*, vol. 25, pp5007-13, 1990.
- [7] L. F. Francis and D. A. Payne, "Thin-Layer Dielectrics in the  $\text{Pb}[(\text{Mg}_{1/2}\text{Nb}_{1/2})_{1-x}\text{Ti}_x]\text{O}_3$  System," *J. Am. Ceram. Soc.*, vol. 74, pp3000-10, 1991.
- [8] D. Liu, L. Ma, D. A. Payne, and D. D. Viehland, "Sol-Gel Synthesis of  $\text{Pb}(\text{Sc}_{0.5}\text{Ta}_{0.5})\text{O}_3$  Powders and Thin Layers," *Mater. Lett.*, vol. 17, pp319-22, 1993.
- [9] D. Liu, L. Ma, and D. A. Payne, Sol-Gel Derived  $\text{Pb}(\text{Sc}_{0.5}\text{Ta}_{0.5})\text{O}_3$  Thin Layers with Higher Dielectric Permittivity and Reduced Processing Temperatures," *Br. Ceram. Proc.* (to be published, 1994)
- [10] G.A. Smolenskii, V.A. Isupov, A.I. Agranovskaya, and S.N. Popov, "Ferroelectrics with Diffuse Phase Transitions," *Sov. Phys. Solid State-Engl. Transl.*, vol. 2, pp2584-94, 1961.
- [11] N. Setter and L.E. Cross, "The Contribution of Structural Disorder to Diffuse Phase Transition in Ferroelectrics," *J. Mater. Sci.*, vol. 15, pp2478-82, 1980.
- [12] L.E. Cross, "Relaxor Ferroelectrics," *Ferroelectrics*, vol. 76, pp241-67, 1987.
- [13] M.P. Harmer, A. Bhalla, B. Fox, and L.E. Cross, "Electron Microscopy of Ordered Domains in Lead Scandium Tantalate  $\text{Pb}(\text{Sc}_{0.5}\text{Ta}_{0.5})\text{O}_3$ ," *Mater. Lett.*, vol. 2, pp278-79, 1984.
- [14] H.M. Chan, M.P. Harmer, A. Bhalla, and L.E. Cross, "TEM of the Relaxor Material  $\text{Pb}(\text{Sc}_{0.5}\text{Ta}_{0.5})\text{O}_3$ ," *Jpn. J. Appl. Phys.*, vol. 24[suppl. 2], pp550-52, 1985.
- [15] C. Randall, D. Barber, R. Whatmore, and P. Groves, "Short-Range Order Phenomena in Lead-Based Perovskites," *Ferroelectrics*, vol. 76, pp277-82, 1987.
- [16] E. Salje and U. Bismayer, "Order Parameter Behavior in the Relaxor Ferroelastic Lead Scandium Tantalate", *J. Phys: Condens. Matter*, vol. 1, pp6967-76, 1989.
- [17] C. Feng and W.A. Schulze, "Characterization of Lead Scandium Tantalate Ceramics Prepared by Precipitation Method," *J. Am. Ceram. Soc.*, vol. 72, pp2008-10, 1989.
- [18] H.-C. Wang and W.A. Schulze, "Order-Disorder Phenomenon in Lead Scandium Tantalate," *J. Am. Ceram. Soc.*, vol. 73, pp1228-34, 1990.

# Preparation of Epitaxial LiNbO<sub>3</sub> Films by the Sol-gel Method.

K. Terabe, N. Iyi, H. Suematsu, I. Sakaguchi, Y. Matsui,  
K. Kitamura and S. Kimura

National Institute for Research in Inorganic Material  
Namiki 1-1, Tsukuba-shi, Ibaraki 305, JAPAN

**Abstract** -- The effect of substrates on the crystallinity and interdiffusion behaviors in sol-gel derived LiNbO<sub>3</sub> films were investigated using X-ray diffraction, transmission electron microscopy and secondary ion mass spectroscopy. The epitaxial films were obtained on (0001)-sapphire, (0001)-LiTaO<sub>3</sub> and (0001)-5%MgO doped LiNbO<sub>3</sub> substrates with similar crystal structures, but with a variety of lattice constants. When sapphire, which has the largest lattice mismatch with the film, was used, the resulting films heat-treated at 500 °C showed a low degree of crystallinity. On the other hand, the films on LiTaO<sub>3</sub> and 5% MgO doped LiNbO<sub>3</sub>, which have smaller lattice mismatches, showed better degrees of crystallinity. Furthermore, these epitaxial films were formed without serious interdiffusion. Our study shows LiNbO<sub>3</sub> films, for the practical application such as optical waveguides, can be prepared by the sol-gel method using a substrate with a small lattice mismatch.

## I. INTRODUCTION

Lithium niobate (LiNbO<sub>3</sub>) is one of the promising ferroelectric materials for optical waveguides and surface acoustic wave (SAW) devices etc.. Films of single crystalline LiNbO<sub>3</sub> are required for practical applications as integrated electro-optical devices. For the preparation of the hetero-epitaxial films, physical vapor deposition and liquid phase epitaxy processes have been widely used [1-4]. However, chemical processes, such as a sol-gel method, have become of major interest lately. There are many advantages to the sol-gel method such as a low process temperature, better control of the composition and high productivity.

Partlow et al. reported that homoepitaxial LiNbO<sub>3</sub> films were obtained by the sol-gel method using metal alkoxides [5]. Afterwards, hetero-epitaxial LiNbO<sub>3</sub> films, with preferred orientation on sapphire substrates, were prepared using double metal alkoxide (LiNb(OC<sub>2</sub>H<sub>5</sub>)<sub>6</sub>) [6]. Then films, without any misoriented planes on sapphire, were synthesized using non-hydrolyzed metal double alkoxide [7]. However, grain growth and a large amount of faults, such as dislocations and twins, were observed for the hetero-epitaxial LiNbO<sub>3</sub> films [8-9]. This shows that the crystallinity of the resulting films on sapphire substrates was low, and therefore improving the quality of the films appears to be still important.

So far only sapphire has been reported as the substrate

for making hetero-epitaxial LiNbO<sub>3</sub> films by the sol-gel method [6-7,9-10]. For preparation of epitaxial films by physical vapor deposition methods, it is well known that the lattice mismatch between the films and the substrate considerably influences the crystallinity of the resulting film. In our study, three kinds of substrate ((0001)-sapphire, (0001)-LiTaO<sub>3</sub> and (0001)-5%MgO doped LiNbO<sub>3</sub>) with crystal structures similar to that of LiNbO<sub>3</sub>, but with a variety of lattice constants, were used for the preparation of hetero-epitaxial LiNbO<sub>3</sub> films. The mismatch of the lattice parameters between the LiNbO<sub>3</sub> films and the sapphire, LiTaO<sub>3</sub> and 5%MgO doped LiNbO<sub>3</sub> substrates is 8.18%, 0.13% and 0.06% for a axis, respectively. For the lattice parameter of c axis, the sapphire substrate has the largest lattice mismatch, the same as that for a axis [11]. The formed films on these substrates were characterized in an attempt to clarify the conditions for making better quality films by the sol-gel method.

## II. EXPERIMENTAL PROCEDURE

Figure 1 shows the flow chart for the synthesis of LiNbO<sub>3</sub> films. The preparation procedure is based on the synthetic method reported by Hirano et al. [6]. Lithium ethoxide (LiOC<sub>2</sub>H<sub>5</sub>) and niobium pentaethoxide (Nb(OC<sub>2</sub>H<sub>5</sub>)<sub>5</sub>) were used as raw materials. Equal molar amounts of these alkoxides were dissolved in absolute ethanol to give the mixed alkoxide solution (0.3 M%). The mixed solution was refluxed for 24 hrs. to synthesize a double metal alkoxide (LiNb(OC<sub>2</sub>H<sub>5</sub>)<sub>6</sub>).

The prepared solution of double metal alkoxide, without the addition of water, were spin coated on substrates at 2000 rpm, because it is known that films with better quality are obtained using the non-hydrolyzed alkoxides [7,12]. Optically polished single crystalline (0001)-sapphire, -LiTaO<sub>3</sub> and -5%MgO doped LiNbO<sub>3</sub> were used as substrates. Prior to coating, these substrates were cleaned in a mixed solution of acetone and benzene, an aqueous hydrochloric acid solution and deionized water using an ultrasonic bath, then dried in a oven at ~200 °C. The coating step were repeated to achieve a desired thickness (150~200 nm). As-coated precursor films were heated to 500 °C for 30 min. at the heating rate of 5 °C/min. in an atmosphere of oxygen and water vapor, and then the furnace was cooled to room temperature.

Structural characterization was performed by X-ray powder diffraction (XRD: Philips PW-1800), X-ray rocking

curve measurements (Rigaku RAD-C model) and transmission electron microscopy (TEM: JEOL 2000EX). The specimens for TEM observation were prepared by polishing and ion-milling. Interdiffusion behaviors between the films and the substrates were investigated by secondary ion mass spectroscopy (SIMS: CAMECA IMS-4F).

### III. RESULT AND DISCUSSION

The smooth and dense textures of the resulting films, after heat-treatment at 500 °C, were observed on the substrates (sapphire, LiTaO<sub>3</sub> and 5% MgO doped LiNbO<sub>3</sub>) by scanning electron microscopy and atomic force microscopy [11]. The value of the average roughness was 4.45 nm for the film on 5% MgO doped LiNbO<sub>3</sub>. Figure 2 shows a High resolution electron microscopy (HREM) image of cross-sectional films on (0001)-sapphire substrate. The fringes corresponding to lattice plane (01 $\bar{1}$ 2) run continuously across the interface as observed in the HREM image of the film and substrate. Because of the difference between the spacing of the lattice planes for LiNbO<sub>3</sub> (3.75 Å) and sapphire (3.48 Å), misfit dislocations (indicated by arrows in the figure) were observed at about every fourteenth of the fringes. The HREM image confirms that the film grows epitaxially on sapphire substrate. The selected area diffraction pattern, including both the LiNbO<sub>3</sub> film and the sapphire substrate, is shown in Figure 3. The diffraction pattern further demonstrates the epitaxial growth. The film grew with the same orientation as that of the sapphire substrate. The shift of



Figure 2. High resolution electron microscopy image of cross-sectional films on (0001)-sapphire substrate. Arrows indicates misfit dislocations.

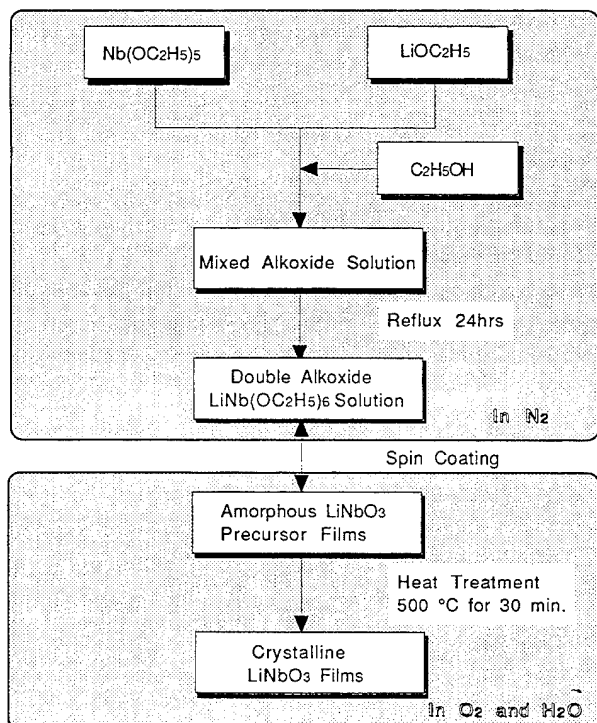


Figure 1. Flow chart for preparing LiNbO<sub>3</sub> films.

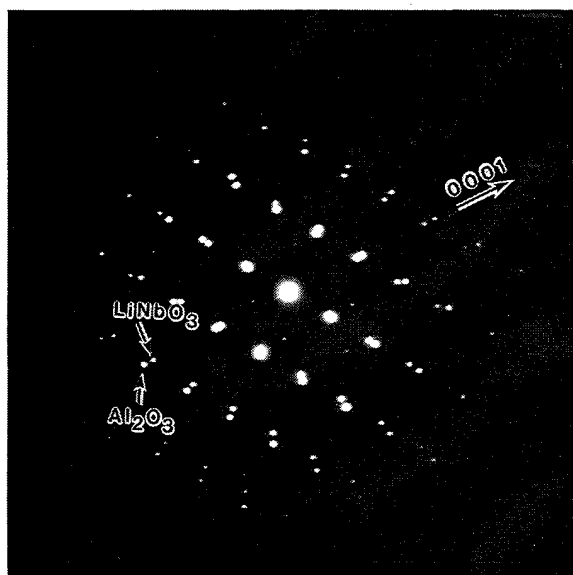


Figure 3. Selected area diffraction pattern for the interface between the LiNbO<sub>3</sub> film and the sapphire substrate.

reflection position between the film and the substrate is caused by the difference in lattice parameters. The epitaxial growth behavior of  $\text{LiNbO}_3$  films on sapphire was also suggested by Hirano et al. and Nashimoto et al. using reflection high energy electron diffraction and TEM [8, 13].

The XRD patterns of the films on sapphire,  $\text{LiTaO}_3$  and 5%  $\text{MgO}$  doped  $\text{LiNbO}_3$  substrates, after heat-treatment at  $500^\circ\text{C}$ , are shown in Figure 4. All resulting films showed the highly preferred orientation along the substrates orientation (0001). The prepared films on the sapphire, with the large lattice mismatch, showed a small XRD peak of the (10 $\bar{1}$ 4) reflection, indicating a different orientation. On the other hand, no peaks of other reflections were observed for the films on  $\text{LiTaO}_3$  and 5%  $\text{MgO}$  doped  $\text{LiNbO}_3$  with small lattice mismatch. The XRD result suggests that the films on these substrates grow epitaxially, but a small amount of different orientation grain was easily formed on the sapphire substrate which has a larger lattice mismatch.

Table I shows the results of X-ray rocking curves for the films which are the same as those shown in Figure 4. The values in the table are in full-width at half maximum (FWHM) of the diffraction peak for the films and the substrates [11]. The FWHM value for the film on sapphire was very large compared to that of the single crystal substrate. On the other hand, the FWHM values for the films on the  $\text{LiTaO}_3$  and 5%  $\text{MgO}$  doped  $\text{LiNbO}_3$  substrates were small, and approached the values of the single crystal substrates. The results of the rocking curves show that the crystallinity of the epitaxial films improves with decreasing lattice mismatch.

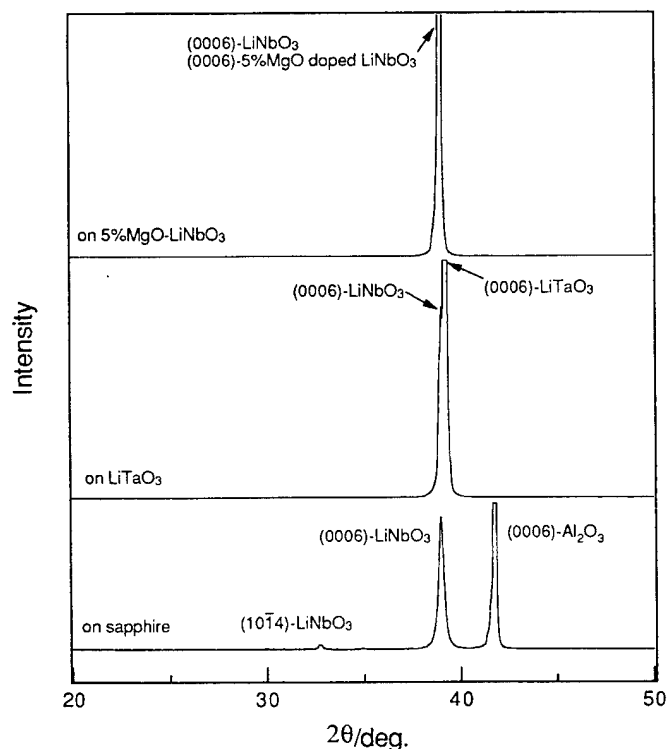


Figure 4. X-ray diffraction patterns of the prepared  $\text{LiNbO}_3$  films after heat-treatment at  $500^\circ\text{C}$  on the substrates.

Table I  
Data of X-ray rocking curve measurements for the epitaxial films and substrates.

Substrates	Values of FWHM (w/sec.)	
	$\text{LiNbO}_3$ films	Substrates
sapphire	1458.0	25.2
$\text{LiTaO}_3$	150.0	26.0
5% $\text{MgO}$ doped $\text{LiNbO}_3$	118.8	26.9

The interdiffusion behaviors of the films on  $\text{LiTaO}_3$  and 5%  $\text{MgO}$   $\text{LiNbO}_3$ , after heat-treatment at  $500^\circ\text{C}$ , are shown in Figures 5 and 6, respectively. The interdiffusion behaviors of  $\text{Mg}$ ,  $\text{Nb}$  and  $\text{Ta}$  ions were observed. Among these ions, the small divalent  $\text{Mg}$  ion interdiffused relatively fast, but the diffusion distance in the films was only  $\sim 50$  nm. It is reported that the interdiffusion between  $\text{LiNbO}_3$  films and sapphire substrate is scarcely observed by Rutherford back scattering measurements [13]. These results mean that epitaxial films on these substrates can be prepared without serious interdiffusion.

In conclusion, we investigated the effect of the substrate on the quality of  $\text{LiNbO}_3$  films prepared by the sol-gel method. Epitaxial films were obtained on all substrates (sapphire,  $\text{LiTaO}_3$  and 5%  $\text{MgO}$  doped  $\text{LiNbO}_3$ ) with similar crystal structure, but with a variety of lattice parameters. The crystallinity of the resulting films, after heat-treatment at  $500^\circ\text{C}$ , improved with decreasing lattice

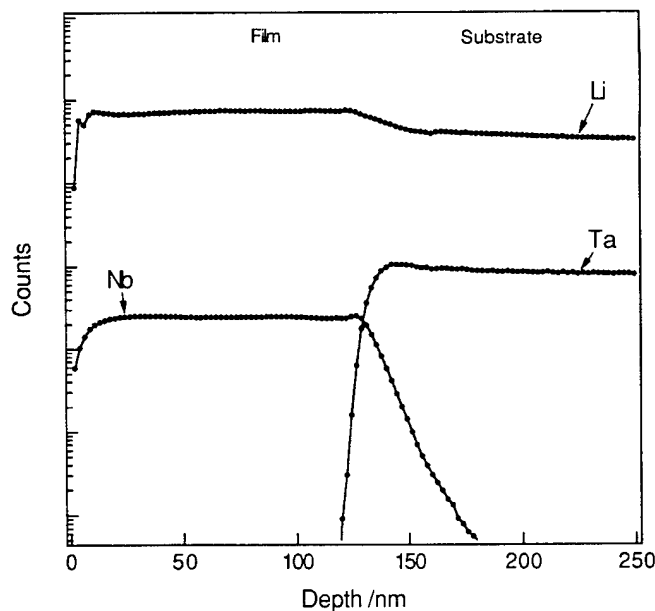


Figure 5. SIMS profile of the epitaxial films on  $\text{LiTaO}_3$  substrate.

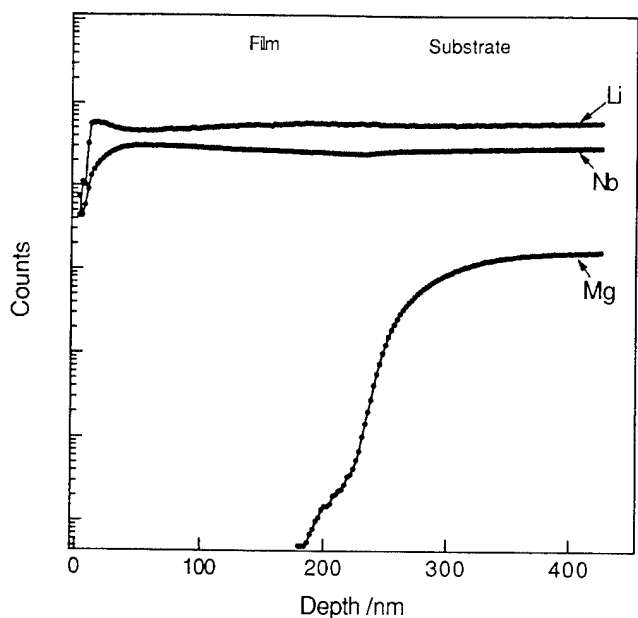


Figure 6. SIMS profile of the epitaxial films on 5% MgO doped LiNbO<sub>3</sub> substrate.

mismatch. When using the LiTaO<sub>3</sub> and 5% MgO doped LiNbO<sub>3</sub> substrates, with smaller lattice mismatch, the crystallinity of the resulting films approached that of a single crystal. Furthermore, the films were obtained without serious interdiffusions. Our results suggest LiNbO<sub>3</sub> films, for practical applications such as optical waveguides, can be prepared by the sol-gel method using a substrate with a smaller lattice mismatch than sapphire.

#### ACKNOWLEDGMENT

We would like to thank Mr. Y. Kitami and Mr. K. Kurashima for TEM observation and also Dr. D. Frankel for valuable discussion at National Institute for Research in Inorganic Materials.

#### REFERENCE

- [1] S. Takada, M. Ohnishi, H. Hayakawa and N. Mikoshiba, "Optical waveguides of single-crystal LiNbO<sub>3</sub> film deposited by rf-sputtering," *Appl. Phys. Lett.*, vol. 24, p. 490, 1974
- [2] Y. Shibata, K. Kaya, K. Akashi, K. Kanai, T. Kawai and S. Kawai, "Epitaxial growth of LiNbO<sub>3</sub> thin films by excimer laser ablation method and their surface acoustic wave properties," *Appl. Phys. Lett.* vol. 61, p.1000, 1992
- [3] S. Miyazawa, "Growth of LiNbO<sub>3</sub> single-crystal film for optical waveguides," *Appl. Phys. Lett.*, vol. 23, p.198, 1973
- [4] A. Yamada, H. Tamada and M. Saitoh, "J. Crystal Growth, vol. 132, p. 48, 1993
- [5] D. P. Partlow and G. Gregg, "Properties and microstructure of thin LiNbO<sub>3</sub> film prepared by a sol-gel method," *J. Mater. Res.*, vol. 2, p. 595, 1987.

- [6] S. Hirano and K. Kato, "Preparation of crystalline LiNbO<sub>3</sub> films with preferred orientation by hydrolysis of metal alkoxides," *Adv. Ceram. Mater.*, vol. 3, p. 503, 1988
- [7] K. Nashimoto and M. J. Cima, "Epitaxial LiNbO<sub>3</sub> thin films prepared by a sol-gel process," *Mater. Lett.*, vol. 10, p. 348, 1991
- [8] K. Nashimoto, M. J. Cima and W. E. Rhine, "Structure and optical properties of polycrystalline and epitaxial LiNbO<sub>3</sub> thin films derived by a sol-gel method," *Ceramic Transactions*, vol. 25, p. 371, 1992
- [9] V. Joshi and M. L. Mecartney, "The influence of water of hydrolysis on microstructural development in sol-gel derived LiNbO<sub>3</sub> thin films," *J. Mater. Res.*, vol. 8, p. 2668, 1993
- [10] N. H. Hur, Y. K. Park, D. H. Won and K. No, "Effect of substrates on the growth and properties of LiNbO<sub>3</sub> films by the sol-gel method," *J. Mater. Res.*, vol. 9, p. 980, 1994
- [11] K. Terabe, N. Iyi, K. Kitamura and S. Kimura, "Effect of substrates on the crystallinity and morphology of sol-gel derived epitaxial LiNbO<sub>3</sub> films," *J. Mater. Res.*, *submitted*
- [12] K. Terabe, N. Iyi and S. Kimura, *J. Mater. Res.*, "Structural developments during heating in LiNbO<sub>3</sub> precursors synthesized by the sol-gel method," *J. Mater. Sci.*, *submitted*
- [13] S. Hirano, K. Kikuta and K. Kato, "Processing of stoichiometric and Ti doped LiNbO<sub>3</sub> films with preferred orientation from metal alkoxides," *Mater. Res. Soc. Symp. Proc.*, vol. 200, p. 3, 1990

# Preparation and Characterization of Manganese Doped Lead Titanate Films By SOL-GEL Techniques

R.P. Tandon, V. Raman, Ramadhar Singh and Amarjeet K. Narula  
National Physical Laboratory, New Delhi - 110 012, India.

**Abstract** - In the present investigation, sol-gel method has been adopted to make manganese doped lead titanate (PT) films with perovskite structure by reacting liquid precursors to form a sol. The films were deposited on stainless steel substrate by using multilayer spin coating technique. The films were then annealed at temperatures close to 550°C. The films were crack free and the ferroelectric behavior was established by studying their hysteresis loop measurements. Dielectric constant was found to be around 300 and coercive field was greater than 60 kV/cm for films with finer grain sizes. The films fired at 550°C exhibited remanent polarization values close to 25 micro-coulomb/cm<sup>2</sup>.

## INTRODUCTION

Numerous attempts [1-4] have been made in the past to investigate thin films of ferroelectric materials such as  $PZT[Pb, Zr(TiO_3)]$ ,  $PT(PbTiO_3)$  and more recently  $(Ba_{1-x}Sr_x)TiO_3$ . In spite of the processing difficulties, these films are receiving lot of attention due to their possible applications for non-volatile memories, infrared sensors, display devices and several other allied applications. Of these, lead titanate has been particularly fascinating for many years from both fundamental and applied point of view. This material has very high Curie temperature ( $\sim 490^\circ\text{C}$ ) and large lattice anisotropy ( $c/a \sim 1.064$ ) in the tetragonal phase.

The main emphasis of the present day research on these materials is to integrate them with micro-electronics at affordable production costs. Unfortunately, even at the present level of understanding and experience, the sol-gel derived films of lead titanate have found limited utility as it is extremely difficult to get crack free film and they often develop cracks on drying due to shrinkage and stresses taking place during gel to oxide conversion. To overcome this problem, a number of different approaches [5,6] have been adopted to get superior films and the future prospects of these devices rest on the success of making crack free ferroelectric films.

In the present paper we report the results of our investigations in which an attempt has been made to obtain good quality films of lead titanate having composition  $Pb_{1-x}Mn_xTiO_3$  ( $x = 0.01$ ) by sol-gel route. The films were characterized by Fourier transformed infrared spectroscopy and X-ray diffraction investigations. Their dielectric constant and hysteresis loop behaviour are also presented.

## EXPERIMENTAL

Lead acetate trihydrate (3.75 gm) and manganese acetate (0.025 gm) were dissolved in 5 ml of methoxy ethanol at  $70^\circ\text{C}$  to get a clear solution. The solution was allowed to cool to room temperature ( $\sim 25^\circ\text{C}$ ) and was mixed with 4 ml of acetyl acetone and 3 ml of titanium isopropoxide with constant stirring. The solution was heated to  $100^\circ\text{C}$  with constant stirring and then it was allowed to cool down to room temperature before it was coated on a stainless steel substrate by spin coating technique. The films so obtained were  $\sim 8 - 10 \mu\text{m}$  thick.

The sol obtained above was hydrolyzed by adding mixture of methoxy ethanol and distilled water (1:1) and kept for gelling, ageing and drying at  $60^\circ\text{C}$  in an oven. The gel was sintered at different temperatures ranging from  $400 - 650^\circ\text{C}$ . It was noticed that while sintering at  $650^\circ\text{C}$  the gel lost around 25% wt which can be attributed to the loss of water molecules, alcohols and organic molecules present in the gel.

The FTIR spectra of the Mn doped lead titanate films was obtained by KBr method using a Fourier transformed infrared spectrometer (Nicolet). The X-ray diffraction pattern of the films was taken by X-ray diffractometer (Siemens, D-500).

A parallel plate capacitance was formed by using gold electrodes (area  $\sim 0.8 \text{ mm}^2$ ) patterned by vacuum evaporation through the masks. The dielectric parameters were evaluated by a HP-4192A LF Impedance Analyser at 10 kHz. Modified Sawyer Tower Circuit was used to carry out hysteresis loop measurements at 50 Hz.

## RESULTS AND DISCUSSION

It is well-known that titanium alkoxides are very susceptible to the presence of moisture and therefore, it was complexed with chelating agent (acetyl acetone) to inhibit the precipitation of titanium oxide. In the present case, we added acetyl acetone to titanium isopropoxide which yielded clear solution stable in nature. Pure lead titanate films usually develop cracks which render them unsuitable for any meaningful device application. Addition of manganese certainly helped in yielding crack free, dense and superior lead titanate films.

The films were subjected to IR examination and the results are shown in Fig. 1. The IR spectrum of this material shows a broad absorption band around  $600 \text{ cm}^{-1}$  which is attributed to the metal-oxygen bonding. This lattice mode is due to a stretching vibration of  $TiO_6$  octahedra in which the Ti atom moves opposite to the  $O_6$  octahedra.



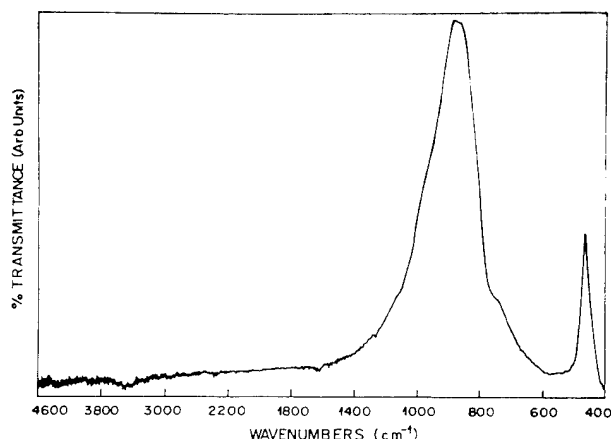


Fig. 1 FTIR spectra of Mn-doped  $\text{PbTiO}_3$  film.

The formation of the tetragonal phase in lead titanate was ascertained by X-ray diffraction pattern shown in Fig. 2. The calculated  $d$  values were found to be in agreement with the values reported earlier. It was also evident that Mn addition did not cause any changes in the perovskite type tetragonal lattice of the lead titanate. The average grain size ( $t$ ) of the films was calculated from Scherrer's equation [7] given as

$$t = \frac{0.9}{B \cos \theta} \quad (1)$$

where  $B$  is the broadening of the diffraction line at  $\theta$  measured at half its maximum intensity. The average grain size was found to be about 500 Å and remained unaffected by manganese addition.

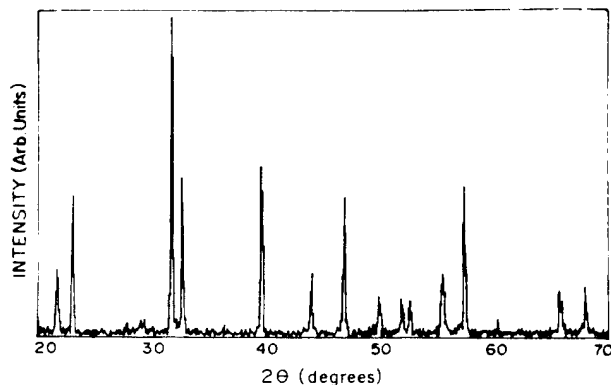


Fig. 2 X-ray diffraction pattern of Mn-doped  $\text{PbTiO}_3$ .

The strain along 'a' and 'c' axes can be evaluated from the lattice constants using the relation

$$X_1 = (a - a_c)/a_c \text{ and } X_3 = (c - a_c)/a_c \quad (2)$$

where 'a' and 'c' are the tetragonal lattice constants and  $a_c$  is the equivalent cubic cell constant given by  $(a^2 c)^{1/3}$ . From this, the room temperature value of tetragonality ( $c/a$ ) was estimated to be 1.071 which nearly half a percent greater than the value obtained for bulk  $\text{PbTiO}_3$  indicating thereby that the films were elongated along c-axis. This difference in the lattice constants of bulk  $\text{PbTiO}_3$  and films clearly suggests that the films were under strain.

There were significant changes in the dielectric constant values (measured at 10 kHz) of the film with the sintering temperature as is evident from Fig. 3. A large increase in the dielectric constant was observed at 525°C which marked the onset of the crystallization after they assumed near constant values. The highest values achieved for dielectric constant was  $\sim 300$  (at 10 kHz) and the dissipation factor was found to be  $\sim 0.009$ .

The existence of the ferroelectricity was confirmed by studying the hysteresis loop of the films. One such typical hysteresis loop is shown in Fig. 4 which gave a coercive field values close to 65 kv/cm and remanent polarization around 25 micro-coulomb/cm<sup>2</sup>. It appears that this lower value of remanent polarization may be due to the smaller grain size and the strains present in the films. These values are not the ideal ones yet sufficiently high for a possible device application. The addition of manganese has clearly helped in yielding a crack free, dense and relatively superior quality films of lead titanate.

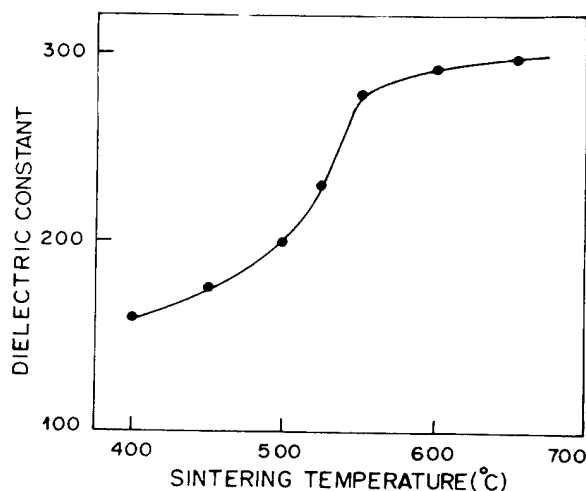
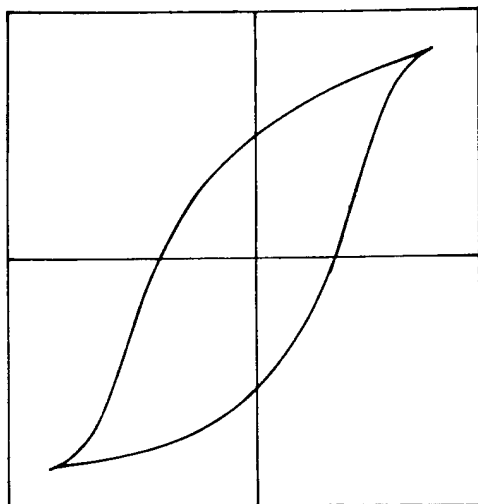


Fig. 3 Effect of sintering temperature on the dielectric constant of Mn-doped  $\text{PbTiO}_3$  film.



**Fig. 4** Typical hysteresis loop of Mn-doped  $\text{PbTiO}_3$  film.

#### ACKNOWLEDGEMENTS

The authors are grateful to Professor E.S.R. Gopal, Director, National Physical Laboratory for his keen interest in this work. One of the authors (A.K.N.) is thankful to the Council of Scientific and Industrial Research, New Delhi, India for the award of Junior Research Fellowship.

#### REFERENCES

- [1] K.D. Budd, S.K. Dey and D.A. Payne, "Sol-Gel Processing of  $\text{PbTiO}_3$ ,  $\text{PbZrO}_3$ , PZT and PLZT Thin Films", Proc. Br. Ceram. Soc., vol. 36, pp. 107-121, 1985.
- [2] K.D. Budd, S.K. Dey and D.A. Payne, Better Ceramics Through Chemistry II, eds. C.J. Brinker et. al. (MRS, Pittsburgh), 1986, pp. 711.
- [3] R. Takayama, Y. Tomita, K. Iijima and I. Ueda, "Preparation and Characteristics of Pyroelectric Infrared Sensors Made of C-axis Oriented La-Modified  $\text{PbTiO}_3$  Thin Films", J. Appl. Phys. vol. 61, pp. 411-415, 1987.
- [4] A. Tsuzuki, A. Murakani, I.K. Kani, K. Watari and Y. Torii, "Preparation and Ferroelectric Properties of Sol-Gel Derived  $(\text{Pb,Ca})\text{TiO}_3$  Thin Films", J. Mater. Sci. Letts., vol. 10, pp. 125-128, 1991.
- [5] S.J. Milne and S.H. Pyke, "Modified Sol-Gel Process for the Production of Lead Titanate Films", J. Amer. Cer. Soc., vol. 74, pp. 1407-1410, 1991.
- [6] N.J. Phillips and S.J. Milne, "Diol-based Sol-Gel System for the Production of Thin Films of  $\text{PbTiO}_3$ ", J. Mater. Chem., vol. 1, pp. 893-894, 1991.
- [7] B.D. Cullity, Elements of X-ray Diffraction, (Addison-Wellsely Publishing Company, Inc.), 1978, pp. 284.

# Effects of Sol-Gel PZT Film Thickness and Electrode Structure on the Electrical Behavior of Pt/PZT/Pt Capacitors

E.A. Kneer, D.P. Birnie III, U. of AZ., Dept. of Mat. Science and Engr, Tucson, AZ 85721  
G. Teowee, Donnelly Corporation, 4545 Fort Lowell Road, Tucson, AZ 85712  
J.C. Podlesny, WYKO Corporation, Tucson, AZ 85706

**Abstract** - Sol-gel derived lead zirconate titanate (PZT) films were deposited and crystallized on platinized Si/SiO<sub>2</sub> and Al<sub>2</sub>O<sub>3</sub> wafer substrates in the film thickness range of 500 - 7000 Å. Electrical testing was conducted to evaluate the effect of PZT film thickness on capacitor performance. Optical microscopy and AFM data were used to identify factors which might cause shorting in crystallized PZT films. Thin films of Ti or TiO<sub>x</sub> were used for Pt bottom and top electrode adhesion in the substrate/Pt/PZT/Pt structured device. The effect of these adhesion layers has been investigated for several electrode composites. The fatigue behavior of these devices has been analyzed and compared.

## INTRODUCTION

Sol-gel derived PZT thin films have been used extensively in the development of MFM structured capacitors for non-volatile memory applications. One of the major problems in this area has been the limited choice of bottom electrode materials for which the sol-gel derived PZT is nucleated. Among the most popular electrode materials at present are RuO<sub>2</sub> and Pt. The RuO<sub>2</sub> and Pt systems have been compared in several studies<sup>1,2</sup>. Although the RuO<sub>2</sub>/PZT/RuO<sub>2</sub> electrode system has exhibited better fatigue performance than Pt/PZT/Pt structured capacitors, the use of Pt as a bottom electrode material continues to attract attention in research and industry<sup>3,4</sup>.

The focus of this study is to evaluate the range of sol-gel PZT film thicknesses which can be nucleated to produce reliable MFM structured capacitors on platinized Si/SiO<sub>2</sub> and Al<sub>2</sub>O<sub>3</sub> substrates. The composite electrodes fabricated for this study are listed as follows:

- a) Al<sub>2</sub>O<sub>3</sub>/Ti/Pt/PZT/TiO<sub>x</sub>/Pt or "Al<sub>2</sub>O<sub>3</sub>/Ti(TiO<sub>x</sub>)"
- b) Si/SiO<sub>2</sub>/Ti/Pt/PZT/TiO<sub>x</sub>/Pt or "SiO<sub>2</sub>/Ti(TiO<sub>x</sub>)"
- c) Si/SiO<sub>2</sub>/Ti/Pt/PZT/Ti/Pt or "SiO<sub>2</sub>/Ti(Ti)"
- d) Si/SiO<sub>2</sub>/TiO<sub>x</sub>/Pt/PZT/Ti/Pt or "SiO<sub>2</sub>/TiO<sub>x</sub>(Ti)"

## EXPERIMENTAL PROCEDURE

All test devices were fabricated using polished 2" (111) Si, or basal Al<sub>2</sub>O<sub>3</sub> wafer substrates. Initially, a 2400 Å SiO<sub>2</sub> layer was grown on the Si substrates by dry thermal oxidation. The Al<sub>2</sub>O<sub>3</sub> and Si/SiO<sub>2</sub> substrates were then sputter coated with films of either 500 Å Ti, or 100 - 150 Å TiO<sub>x</sub> for Pt adhesion. A film of Pt approximately 3000 Å thick was then sputter coated over the adhesion layer, and the bottom electrodes were annealed at 500°C for 15 minutes in N<sub>2</sub>. Layers of 53/47 sol-gel PZT were deposited over the platinized substrates by spin coating. The sol-gel films were deposited in the 500 - 7000 Å thickness range by using multiple densified coatings of 1M or 0.5M sol-gel, and different spin RPMs to vary the PZT film thickness. The sol-gel films were densified at 500°C for 30 minutes per spin-on coat. The densified coatings were then crystallized in one step at 700°C for 30 minutes (0.1 l/min O<sub>2</sub>). Following PZT crystallization, films of either 200 - 300 Å Ti, or 40 - 60 Å TiO<sub>x</sub> were deposited for Pt top electrode adhesion. A 1500 Å Pt top electrode was then patterned over the PZT/adhesion layer using a lift-off technique. The MFM structured devices were then post-metallization annealed at 700°C for 30 minutes to equilibrate device capacitor response.

Hysteresis, pulse response, retention, and fatigue behavior were measured using the Radiant Technologies RT-66A test system. All data were collected using two probe, top to bottom testing of individual 130 x 130 μm<sup>2</sup> Pt top electrodes, and monolithic Pt bottom electrode. Sample fatiguing was performed using an external function generator. All sample capacitors were fatigued using an alternating square wave (10 ns rise time). Remanent polarization refers to the value of switched minus unswitched charge (P\* - P<sup>^</sup>) from RT-66A data. Peak voltages used for fatigue, charge, and hysteresis testing were normalized with respect to PZT film thickness, i.e. 2000Å PZT = 5 volts, 3000 Å PZT = 7.5 volts, etc..

## RESULTS AND DISCUSSION

### Bottom Electrode Effects on PZT Film

One of the main goals of this study was to determine the minimum sol-gel PZT film thickness which could be crystallized to produce reliable Pt/PZT/Pt structured capacitors. Major factors that limit the minimum thickness of sol-gel films include: 1) Formation of hillocks during Pt bottom electrode annealing<sup>5</sup>, 2) excessive diffusion of Ti in Ti/Pt bottom electrodes causing a high level of Pt surface roughness<sup>6</sup>, 3) pinholes in fired PZT films, 4) incomplete nucleation of very thin PZT films, and 5) reaction of the Pt bottom electrode during PZT nucleation, i.e. the Pt surface roughness increases below the PZT during firing<sup>7</sup>.

Three types of bottom electrodes were evaluated for this study. Al<sub>2</sub>O<sub>3</sub>/Ti/Pt, Si/SiO<sub>2</sub>/Ti/Pt, and Si/SiO<sub>2</sub>/TiO<sub>x</sub>/Pt. Prior to sol-gel deposition, the annealed Al<sub>2</sub>O<sub>3</sub>/Ti/Pt and SiO<sub>2</sub>/Ti/Pt electrodes had a peak to valley Pt surface roughness of 400 - 500 Å. The SiO<sub>2</sub>/TiO<sub>x</sub>/Pt electrodes had a surface roughness of 200 - 300 Å, but hillocks were also present on the Pt surface. These hillocks had a density of about 1 hillock/25 μm<sup>2</sup>, and had a height of 2000 - 3000 Å as measured by AFM. After sol-gel crystallization, it was found that Si/SiO<sub>2</sub>/TiO<sub>x</sub>/Pt electrodes produced a high level of capacitor shorting with PZT films below 2300 Å. This result suggests that shorting due to hillocks may place a limit on the minimum PZT film thickness which can be used with Si/SiO<sub>2</sub>/TiO<sub>x</sub>/Pt electrodes.

The Al<sub>2</sub>O<sub>3</sub>/Ti/Pt and Si/SiO<sub>2</sub>/Ti/Pt devices also exhibited significant capacitor shorting below a PZT film thickness of about 2000 Å. One of the probable causes of this shorting are pinholes in the fired PZT film. Figure 1 shows that pinholes are visible on the top surface of a 1700 Å Pt top electrode covering a 2000 Å PZT film (a). Pinholes were not observed in thicker PZT films which did not short (b). Pinholes were present despite using multiple PZT coatings. This may be due to the fact that the 1M PZT solution was diluted to 0.5M in order to deposit thinner PZT films. PZT films from 1M solutions did not typically display pinholes. Only the SiO<sub>2</sub>/TiO<sub>x</sub>/Pt/PZT/Ti/Pt structured capacitors were fabricated using 1M sol-gel PZT. In this case, the 1M sol-gel was spun at higher RPMs to achieve thinner coatings.

Another issue is the reconfiguration of the Pt surface during sol-gel nucleation. Figure 2 is the top surface of a 4000 Å PZT film nucleated on Si/SiO<sub>2</sub>/Ti/Pt (left) and Si/SiO<sub>2</sub>/Pt (right), where half of the Si/SiO<sub>2</sub> substrate was coated with 500 Å Ti prior to Pt deposition. Figure 3 is the etched-back Pt surface of the same Pt electrode in Figure 2. The Pt surface appears

to have acquired a surface roughness consistent with the general shape of the crystallizing perovskite rosettes. In prior work<sup>7</sup>, AFM showed that the annealed Pt surface of a Si/SiO<sub>2</sub>/500 Å Ti/Pt bottom electrode increased from around 200 Å to over 500 Å following PZT crystallization and etch-back. In Figure 3, the Si/SiO<sub>2</sub>/Ti/Pt side appears to have reacted much more significantly than the Si/SiO<sub>2</sub>/Pt side. This is probably due to Ti diffusion up through the Pt film during PZT crystallization.

#### Microstructure

Figure 2 clearly shows the difference in PZT film microstructure for SiO<sub>2</sub>/Ti/Pt (left) or SiO<sub>2</sub>/Pt (right) bottom electrode composites. The PZT grain size is much smaller and more homogeneous on the SiO<sub>2</sub>/Ti/Pt electrode side compared to the SiO<sub>2</sub>/Pt electrode side. SiO<sub>2</sub>/TiO<sub>x</sub>/Pt electrodes produced the same PZT microstructure as SiO<sub>2</sub>/Pt electrodes. Pinholes, hillocks, or excessive surface roughness are thought to typically cause immediate capacitor failure due to shorting. In contrast, the difference in PZT microstructure is thought to have an impact on capacitor electrical performance. If Figures 4 and 5 are examined closely, it is apparent that electrodes using Ti for Pt bottom electrode adhesion display a significant drop in initial remanent polarization upon fatiguing. In contrast, capacitors using the SiO<sub>2</sub>/TiO<sub>x</sub>/Pt bottom electrode do not exhibit as significant a loss, but fatigue more quickly (Figure 6). This difference in behavior is thought to be a PZT microstructure related phenomenon. XRD studies need to be conducted to determine the degree of orientation in the two distinctly different films. By reducing the electric field strength, it is possible to eliminate the initial remanent polarization loss observed for SiO<sub>2</sub>/Ti/Pt bottom electrode capacitors. Figure 7 shows that as the peak voltage was decreased for fatigue cycle testing, the initial remanent polarization loss for the three composite bottom electrodes decreased. Figure 8 is a graph of fatigue behavior for the 2600 Å PZT test capacitors fatigued at peak voltages where initial remanent polarization loss is minimized, and polarization response is maximized. In Figure 8, the fatigue behavior is nearly identical for the three different bottom electrode based capacitors when the peak voltage is reduced to avoid the initial remanent polarization drop. Additionally, the fatigue performance of the devices improves dramatically. Most notably, the SiO<sub>2</sub>/TiO<sub>x</sub>/Pt electrode capacitor displayed a loss of only 28% of initial remanent polarization after  $5.0 \times 10^{10}$  fatigue cycles. This is a significant improvement over fatigue behavior observed in Figure 6. Figure 9 is the RT-66A charge printout for the SiO<sub>2</sub>/TiO<sub>x</sub>/Pt/2600 Å PZT/Ti/Pt capacitor after it was fatigued to  $5.0 \times 10^{10}$  cycles at 2.5 volts peak. Despite extensive fatiguing, the capacitor exhibits excellent symmetry, and a remanent polarization of  $7.8 \mu\text{C}/\text{cm}^2$ . Coercive voltages are below 0.5 volts.

#### Electrical Testing of PZT Films

Electrical testing was conducted to evaluate the behavior of PZT films of different thickness. Figure 10 is a graph of the initial remanent polarization of PZT films of different thickness on various composite electrodes. The standard deviation is shown for five test capacitors per data point. These statistics were used to select representative capacitors for fatigue testing.

From Figures 4 - 6, the remanent polarization values increased with increasing PZT film thickness, but did not sustain the values when tested at normalized voltage conditions beyond about  $10^8$  fatigue cycles. In general, the spontaneous polarization values increased marginally with increasing PZT film thickness. The dielectric constants were in the 1700 - 2000 range for PZT films of 2000 - 2600 Å. The dielectric constant seemed to level off at about 2300 - 2400 with thicker PZT films

at normalized voltage conditions. The values for coercive voltage increased with increasing PZT film thickness. Electrical shorting was observed for nearly all PZT films below 2000 Å thickness. This is thought to be caused by either pinholes in the PZT film, bottom electrode Pt hillocks, excessive surface roughness due to excessive Ti diffusion, incomplete PZT nucleation, or a combination of these factors. Thicker PZT films above 3000 Å shorted an extremely low percentage of the time. The retention of PZT films was also evaluated. All the test capacitors tested displayed nearly flat line retention out to 18 hours. The maximum loss in initial remanent polarization was at most 1 - 2 %. Further retention tests was not conducted.

#### Effect of Top Electrode Adhesion Layer

The effect of using 200 - 300 Å Ti vs. 40 - 60 Å TiO<sub>x</sub> can be seen by comparing Figures 4 and 5. The difference in fatigue behavior for the SiO<sub>2</sub>/Ti(TiO<sub>x</sub>) and SiO<sub>2</sub>/Ti(Ti) composites were minor. The most significant difference was that the coercive voltages for SiO<sub>2</sub>/Ti(TiO<sub>x</sub>) composites were considerably higher than for SiO<sub>2</sub>/Ti(Ti) composites by 0.5 - 1.0 volts. Spontaneous polarization and pulse response values were also somewhat higher for SiO<sub>2</sub>/Ti(Ti) composites. The specific reason for this behavior is a topic for future research.

#### Performance of Sapphire Substrates

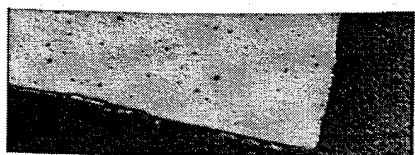
The only major difference observed using sapphire vs. silicon substrates is that the initial remanent polarization values for sapphire were much higher than for identically prepared silicon based devices. See Figures 5 and 10. Above  $10^9$  fatigue cycles, the sapphire and silicon based capacitors had nearly identical behavior when tested at normalized voltage. At very low voltages (1.5 V), the sapphire and silicon substrate devices also had similar fatigue behavior.

### CONCLUSIONS

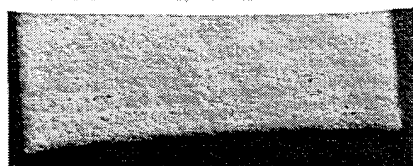
For this study, the reliability of nucleated PZT films on platinized silicon and sapphire substrates was evaluated. It was found that pinholes in the PZT film, bottom electrode surface roughness, or hillocks may limit the useful PZT film thickness to above 2000 Å due to capacitor shorting. PZT films above 3000 Å were extremely reliable. The general electrical behavior of PZT films was evaluated with respect to PZT film thickness. An extensive evaluation of the fatigue behavior of PZT films on various electrode composites was conducted. It was found that lowering the peak fatigue testing voltage could significantly improve capacitor fatigue performance, while still maintaining high capacitor pulse response values. Figure 9 shows the hysteresis and pulse response measured for a 2600 Å PZT film which operated at 2.5 volts peak out to  $5 \times 10^{10}$  cycles with only a 28% drop in initial remanent polarization ( $9.7 \mu\text{C}/\text{cm}^2$ ). The device coercive voltages were below 0.5 volts. This is excellent performance for a Pt/PZT/Pt structured capacitor. Additionally, the effect of using sapphire vs. silicon substrates, and the use of Ti vs. TiO<sub>x</sub> for Pt top electrode adhesion were discussed.

### ACKNOWLEDGEMENTS

We are grateful for the ability to use sol-gel solutions which were developed by G. Teowee, J.M. Boulton, and D.R. Uhlmann under the support of the Air Force Office of Scientific Research. This work was supported by the United States Navy, contract #N00014-90-C-2130.



a) Pt on PZT film. PZT: 2000 Å. 500x mag.



b) Pt on PZT film. PZT: 5600 Å. 500x mag.

Figure 1: View of  $130 \times 130 \mu\text{m}^2$  Pt top electrodes. Pin holes appear in the Pt film when PZT films 2000 Å thick and below are used. These pin holes may contribute to device failure.

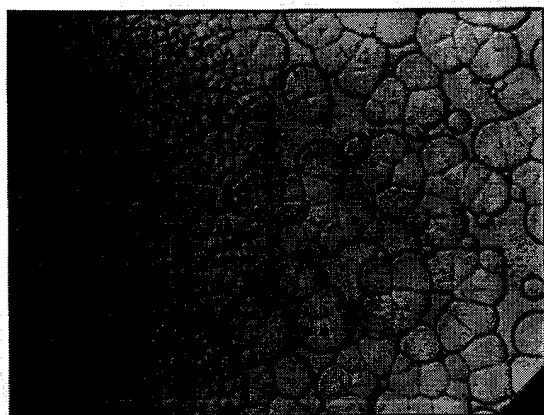


Figure 2: Top surface of nucleated PZT film. Left side of micrograph is PZT nucleated on a Si/SiO<sub>2</sub>/500 Å Ti/Pt bottom electrode. Right side of micrograph is PZT nucleated on a Si/SiO<sub>2</sub>/Pt bottom electrode. 500x mag.

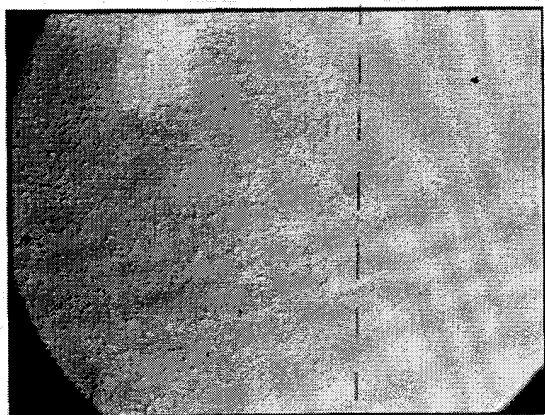


Figure 3: Etched back Pt bottom electrode from Figure 2. The Pt surface shows visible surface roughness consistent with PZT grain size. 500x mag.

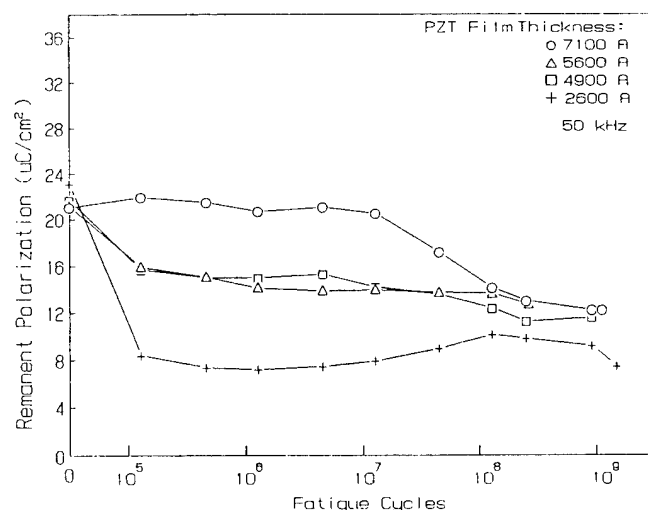


Figure 4: Fatigue behavior for Si/SiO<sub>2</sub> substrate MFM capacitors using 500 Å Ti for Pt bottom electrode adhesion and 200 - 300 Å Ti for Pt top electrode adhesion.

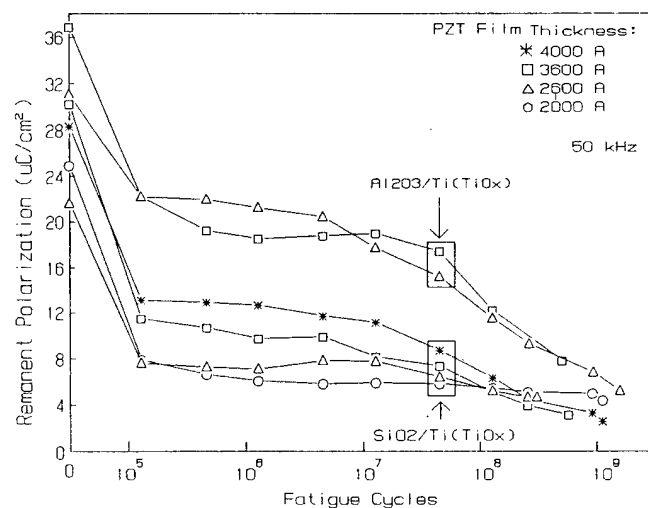


Figure 5: Fatigue behavior for Si/SiO<sub>2</sub> and Al<sub>2</sub>O<sub>3</sub> substrate MFM capacitors using 500 Å Ti for Pt bottom electrode adhesion and 60 - 100 Å TiO<sub>x</sub> for Pt top electrode adhesion.

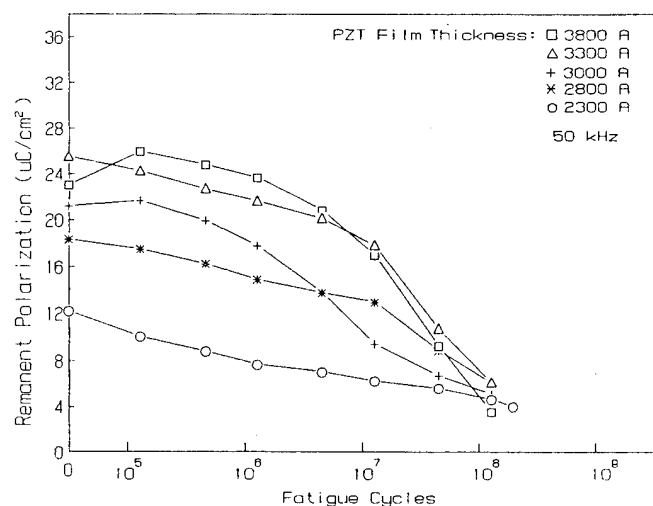


Figure 6: Fatigue behavior for Si/SiO<sub>2</sub> substrate MFM capacitors using 60 - 100 Å TiO<sub>x</sub> for Pt bottom electrode adhesion and 200 - 300 Å Ti for Pt top electrode adhesion.

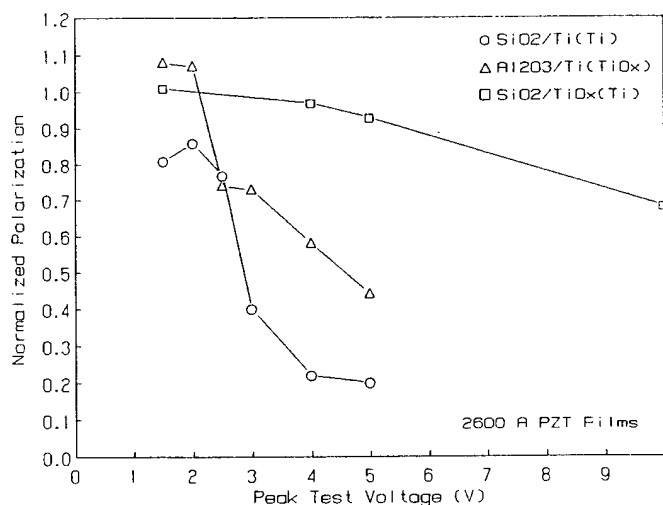


Figure 7: Graph showing initial loss in remanent polarization (normalized) as a function of peak test voltage for 2600 Å PZT capacitors fatigued at 10 kHz to  $10^6$  cycles.

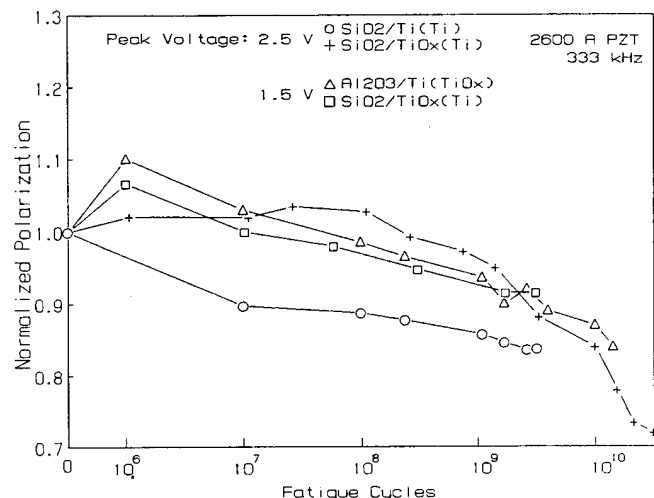


Figure 8: Graph showing normalized remanent polarization as a function of fatigue cycling for electrode composites tested at 1.5 and 2.5 volts peak.

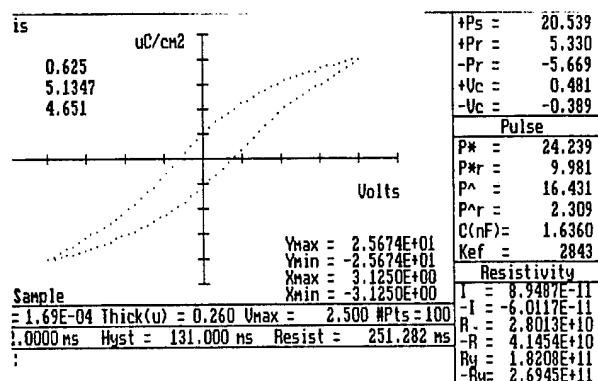


Figure 9: Hysteresis and pulse response measured at 2.5 volts peak for  $\text{SiO}_2/\text{TiO}_x(\text{Ti})$  composite MFM capacitor. 2600 Å PZT film. Capacitor was fatigued to  $5 \times 10^{10}$  cycles prior to testing.

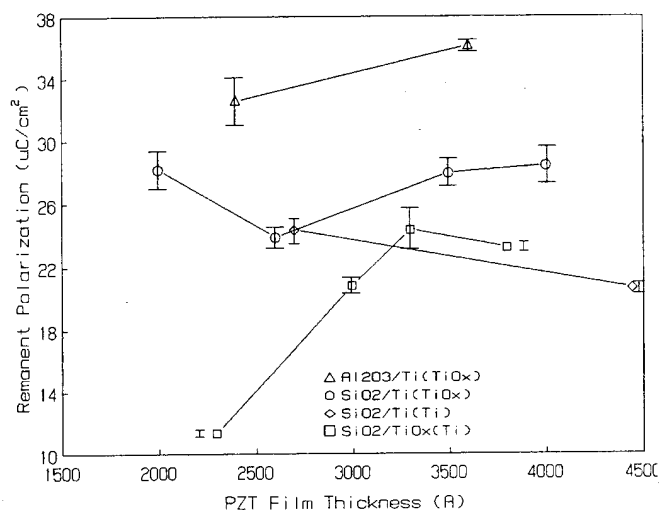


Figure 10: Graph of initial remanent polarization for MFM structured devices. Standard deviation shown for 5 test pads per point. Normalized voltage (5 volts = 2000 Å).

## REFERENCES

1. D.P. Vijay and S.B. Desu, "Electrodes for  $\text{PbZr}_{1-x}\text{Ti}_x\text{O}_3$  Ferroelectric Thin Films," *J. Electrochem. Soc.*, Vol. 140, No. 9, Sep. 1993, p. 2640.
2. K.R. Bellur et al., "Electrical Characterization of Sol-Gel Derived PZT Thin Films," *1992 IEEE Int. Symp. on Appl. of Ferroelectrics*, p. 448.
3. Radiant Technologies, Inc., *FE Quarterly*, Summer 1994, 1009 Bradbury S.E., Albuquerque, NM 87106.
4. K. Sameshima et al., "Preparation of  $\text{Pb}(\text{Zr},\text{Ti})\text{O}_3$  Films on Pt/Ti/Ta Electrodes by Sol-Gel Process," *Jpn. J. Appl. Phys.*, Vol. 32, (1993) p. 4144.
5. E.A. Kneer, D.P. Birnie III, G. Teowee, and J.C. Podlesny, "Investigation of Surface Roughness and Hillock Formation on Platinized Substrates used for Pt/PZT/Pt Capacitor Fabrication," *ISIF 1994 6th Int. Symp. on Int. Ferroelectrics*, to be published.
6. E.A. Kneer, D.P. Birnie III, G. Teowee, and J.C. Podlesny, "Evolution of Surface Relief during Firing of PZT Thin Films," *Ferroelectrics*, Vol. 152, (1994) pp. 67-72.
7. E.A. Kneer, "Ferroelectric Memory Device Fabrication using Sol-Gel Derived PZT Thin Films," Masters Thesis (1994), University of Arizona, Tucson, AZ 85721.

# Electrical Properties of PZT Thin Films Derived From Sol-Gel solution Containing Photo-Sensitive Water-Generater

Yuichi NAKAO, Takashi NAKAMURA, Akira KAMISAWA, Hidemi TAKASU,  
Nobuyuki SOYAMA<sup>1</sup>, Go SASAKI<sup>1</sup>, Tsutomu ATSUKI<sup>1</sup>, Tadashi YONEZAWA<sup>1</sup>, and Katsumi OGI<sup>1</sup>

Rohm Co.,Ltd., 21 Saiin, Mizosaki-cho, Ukyo-ku, Kyoto 615, Japan

<sup>1</sup>Mitsubishi Materials Corporation, Central Research Institute,  
1-297 Kitabukuro-cho, Omiya, Saitama 330, Japan

## Abstract

The photo sensitivity of sol-gel solution of  $\text{PbZr}_x\text{Ti}_{1-x}\text{O}_3$  (PZT) was confirmed. A coated film of the sol-gel solution on Si and Ir/IrO<sub>2</sub>/SiO<sub>2</sub>/Si substrates was exposed to an excimer laser and developed with 2-methoxyethanol diluted with isopropyl alcohol. More than 900 mJ/cm<sup>2</sup> of exposure was required to obtain the micro patterns. The film was finally annealed at 700°C for 60 s by rapid thermal annealing (RTA). From this process, half-micron patterns of PZT films were obtained. The 200-nm-thick film showed  $P_r$  of 16.6  $\mu\text{C}/\text{cm}^2$  and  $E_c$  of 38.8 kV/cm. After  $1 \times 10^{12}$  cycles of switching pulses, the films showed no degradation of remanent polarization. Studying for 1-transistor-type ferroelectric memory, metal-ferroelectric-metal-insulator-semiconductor (MFMS) structure was prepared with this process.

## 1. Introduction

$\text{PbZr}_x\text{Ti}_{1-x}\text{O}_3$  (PZT) thin films are being investigated as highly potential materials for micro-device applications, such as capacitors for dynamic random access memory (DRAM),<sup>1)</sup> nonvolatile random access memory,<sup>2)</sup> self-learning metal ferroelectric semiconductor (MFS)<sup>3)</sup> and many kinds of sensors. It is important and essential to develop a fine patterning technique for device application of PZT thin films. However, there are few reports on fine patterning techniques of ferroelectric thin films. Dry-etching processes for the submicron patterning have been reported.<sup>4)</sup>

We have studied micro patterning technique using photo-sensitive sol-gel solution.<sup>5)</sup> However, shapes of micro patterns and the electrical properties of the film were not satisfactory. Moreover, higher energy was needed to obtain patternings than the ordinary photo-resist. In order to achieve higher sensitivity, the photo-sensitive water-generater was added to PZT sol-gel solution. In this paper, we reported a micro-patterning technique of PZT thin films using a photo sensitive sol-gel solution containing water generater.

## 2. Experimental

### 2.1. Sample preparation

The process flow diagram for sample preparation is shown in Fig. 1. Substrates used were p-type (100) silicon wafers and iridium wafers (Ir(200nm) / IrO<sub>2</sub>(50nm) / SiO<sub>2</sub>(600 nm) / Si(100)). Ir and IrO<sub>2</sub> were deposited by RF magnetron sputtering system. PZT sol-gel solution prepared was spin-coated on the wafers. There were two types of sol-gel solution which were different in concentration: 10 wt% and 20 wt%. After spin coating, the wafers were exposed to UV light (248 nm) using Nikon KrF excimer laser stepper (NSR-2005 EX8A). Step-and-repeat exposure was done with the resolution chart reticle at the intensity ranging from 0.1 to 2.5 J/cm<sup>2</sup>. The exposed area of the sol-gel thin film became insoluble in 2-methoxyethanol (which is the solvent of sol-gel solution) and negative patterns were obtained by development with 2-methoxyethanol diluted with isopropyl alco-

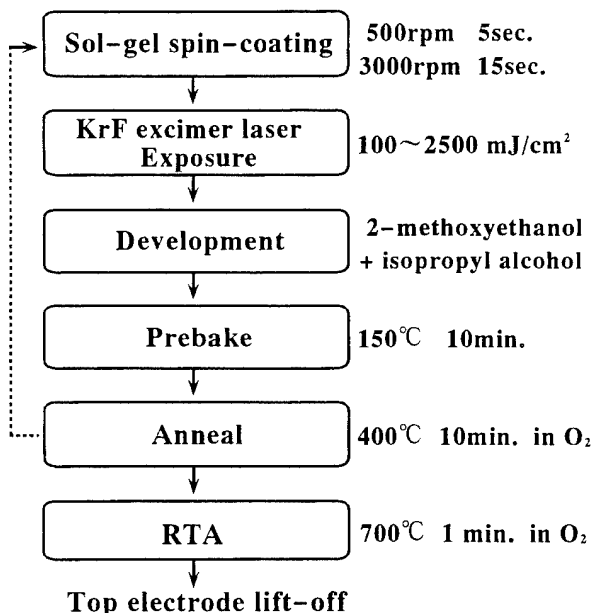


Fig. 1 Process flow diagram for micro patterns of PZT.

hol. In the case of using only 2-methoxyethanol for developer, it was too fast to stop the development just the proper time. From the exposure energy, the minimum irradiation energy required to obtain fine patterns was estimated to be  $900 \text{ mJ/cm}^2$ . (Fig. 2) The sensitivity became about 10 times higher compared with last experiment.<sup>5)</sup>

After development, samples were baked at  $90^\circ\text{C}$  for 10 min. In the next step, developed patterns were heated at  $400^\circ\text{C}$  for 30 min in  $\text{O}_2$  in order to eliminate organic components. Finally the patterned films were annealed at  $700^\circ\text{C}$  for 60 s in  $\text{O}_2$  by RTA. After heat treatments, 10 wt% sol-gel solution formed 50 nm thick PZT film. 20 wt% solution formed 100 nm thick film.

## 2.2. Micro patternings with the excimer laser stepper

Figures 3 and 4 are scanning electron microscope (SEM) photographs of the developed pattern. We were able to obtain micro patternings of PZT thin films. The minimum size of the patterns was  $0.3 \mu\text{m}$ . Final annealing reduced the film thickness by 35%. However, this photo lithography technique we developed is not satisfactory in that there is a residue of PZT around the patterns after development.

The film thickness was 50 nm which was measured from SEM photograph. The film consisted of a perovskite phase of (111) orientation and other peaks were also observed.

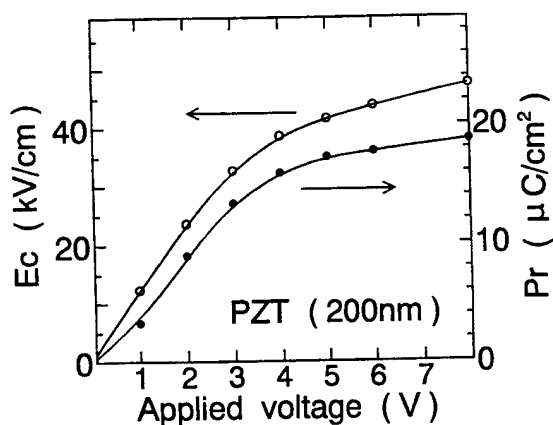
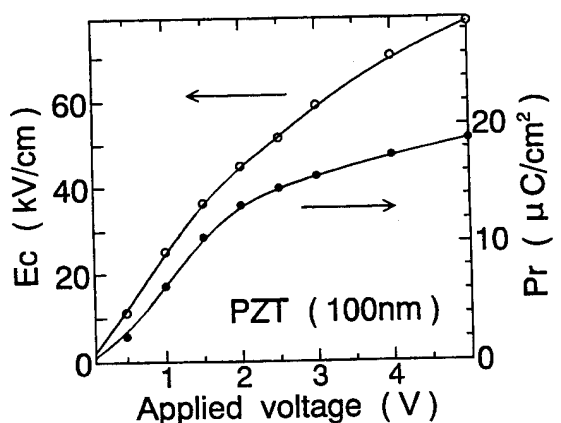


Fig. 5  $P_r$  and  $E_c$  vs. applied voltage for 100 nm and 200 nm thick PZT.

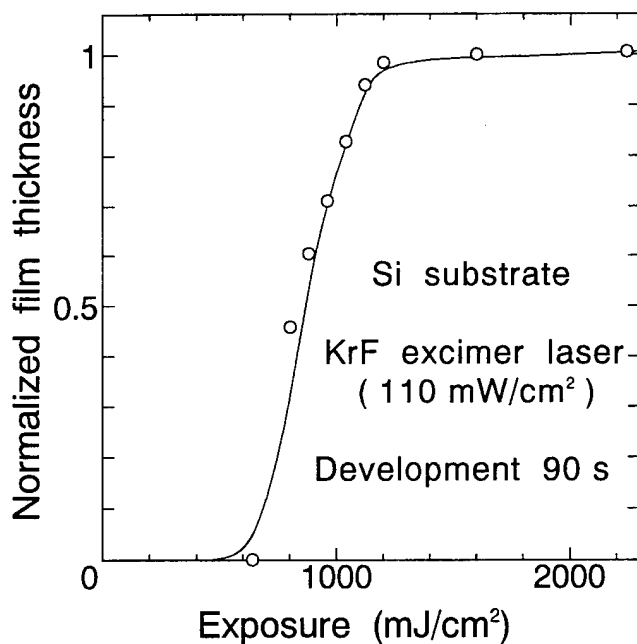


Fig. 2 Photo-sensitive sol-gel solution characteristic curve.

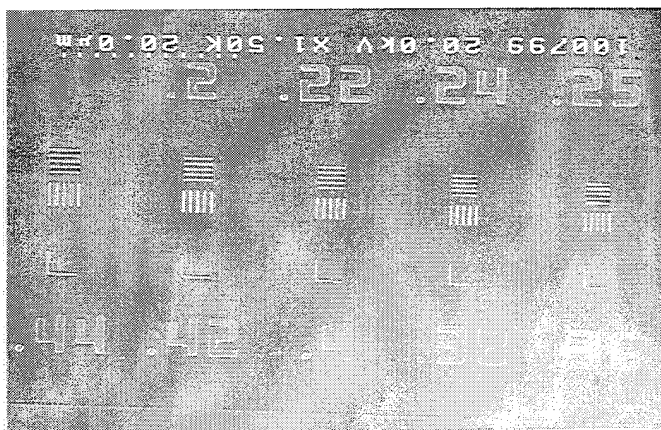


Fig. 3 SEM photograph ( $0.36\text{--}0.44 \mu\text{m}$  L/S). After development, on Si. Exposure energy:  $9 \text{ J/cm}^2$ .

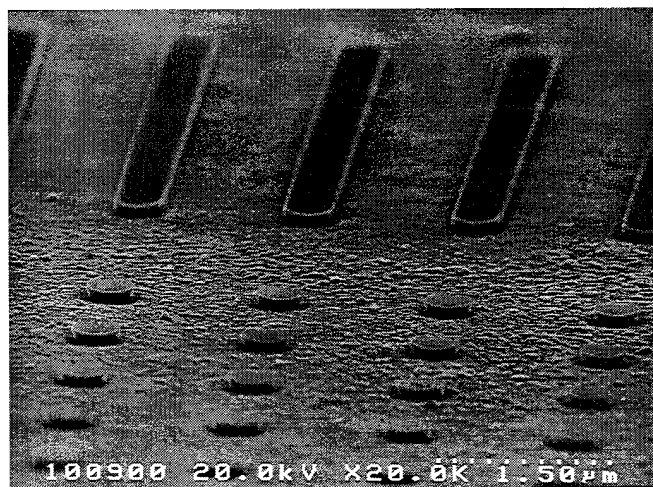


Fig. 4 SEM photograph ( $0.8 \mu\text{m}$  lines and dots). After RTA, on Ir/IrO<sub>2</sub>. Exposure energy:  $25 \text{ J/cm}^2$ .



### 2.3. Electrical properties

Special samples were prepared for electrical measurements. Electrical properties of the samples fabricated with excimer laser stepper were not measured because of large leakage current caused by very thin PZT film thickness. So, we tried to get thicker PZT film. Spin-coated films without patterns were irradiated with UV light. After heat treatment and annealing, platinum top electrodes with thickness of 200 nm were deposited on the film by RF magnetron sputtering through a mask.

A hysteresis loop was measured by a digital oscilloscope using a Sawyer-Tower circuit with 100 kHz sinusoidal waves and voltage of 1–6 V applied. Remanent polarization ( $P_r$ ) and coercive field ( $E_c$ ) were plotted in Fig. 5.  $P_r$  and  $E_c$  of 200 nm-thick-PZT were  $16.7 \mu\text{C}/\text{cm}^2$  and  $40.0 \text{ kV}/\text{cm}$ , respectively (Fig. 6). Dielectric constant and loss tangent were 1100 and 0.05, respectively, measured with a LCR meter at 1 MHz, 30 mV rms. Capacitance of 200 nm thick PZT film was plotted along the applied voltage in Fig. 7. Fatigue properties of 200 nm-thick-film were shown in Fig. 8. After  $10^{12}$  of switching pulses applied, no change of remanent polarization was observed.

Leakage current density were  $8.65 \times 10^{-5} \text{ A}/\text{cm}^2$  at 2.0 V ( $100 \text{ kV}/\text{cm}$ ). Electrical properties were almost same as those of the PZT films fabricated by the ordinary sol-gel process except for leakage current.

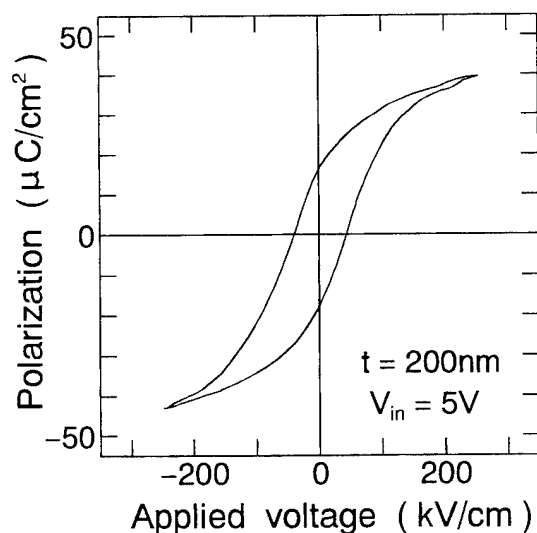


Fig. 6 Hysteresis loop of PZT thin film (200 nm).

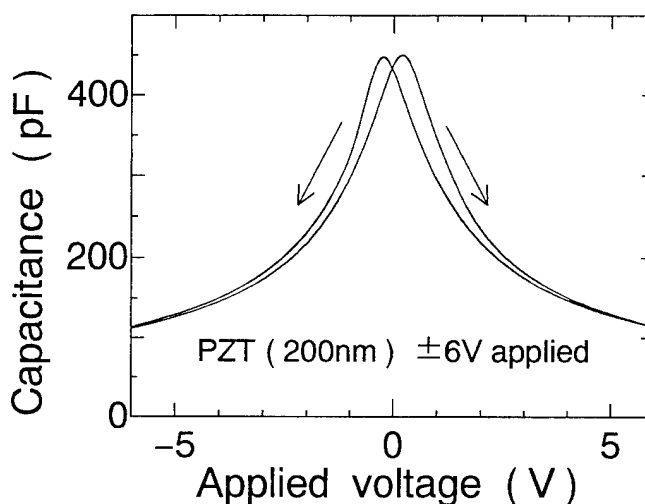


Fig. 7 C-V curve of PZT thin film (200 nm).

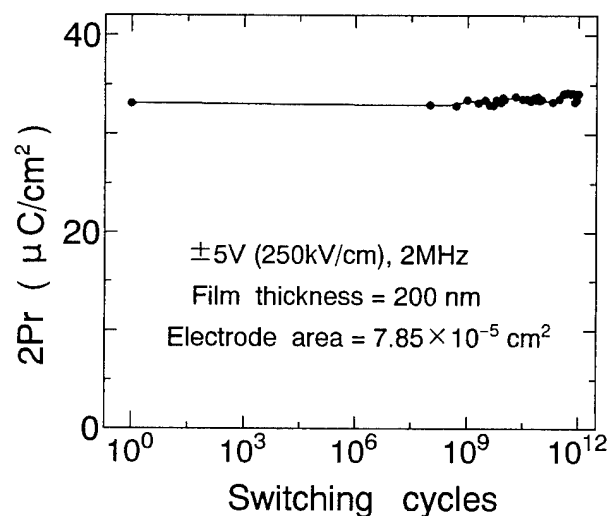


Fig. 8 Fatigue characteristic of PZT thin film (200 nm).  
Ir/IrO<sub>2</sub>/PZT/Ir/IrO<sub>2</sub>/SiO<sub>2</sub>/Si.

### 2.3. MFMIS Capacitor

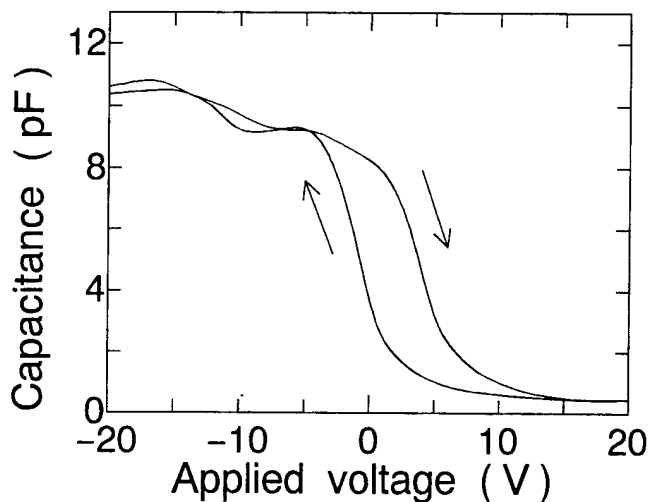
Metal - ferroelectric - metal - insulator - semiconductor (MFMIS) capacitors were prepared (Ir / IrO<sub>2</sub> / PZT / Ir / IrO<sub>2</sub> / SiO<sub>2</sub> / p-Si). Ir(200 nm) and IrO<sub>2</sub>(50 nm) were deposited as electrodes by lift-off process with sputter. PZT patterns were formed on bottom electrodes by 20 wt% photo-sensitive sol-gel solution. The areas of top and bottom electrodes were  $5.03 \times 10^{-5}$  and  $7.85 \times 10^{-5}$  A/cm<sup>2</sup>, respectively. Capacitance-voltage characteristic curve was shown in Fig. 9. Hysteresis caused by ferroelectric polarization was observed.

### 4. Conclusions

It was confirmed that PbZr<sub>x</sub>Ti<sub>1-x</sub>O<sub>3</sub> ( $x=0.52$ ) thin films prepared using the sol-gel solution could be patterned up to the minimum size of 0.4–0.6  $\mu$ m by excimer laser (KrF: 248 nm) exposure and 2-methoxyethanol development. The minimum exposure energy to obtain patterns was estimated to be 900 mJ/cm<sup>2</sup>. The typical remanent polarization and coercive field are 16.7  $\mu$ C/cm<sup>2</sup> and 40.0 kV/cm, respectively. The obtained PZT thin films between Ir/IrO<sub>2</sub> electrodes which were annealed at 700°C in oxygen showed no fatigue after  $1 \times 10^{12}$  switching cycles. It is certain that this technique is one of the promising candidates for high-density integration of ferroelectric capacitors.

### Acknowledgement

The authors would like to thank Mr. T. Hayashi (Nikon Corporation) for offering the excimer laser stepper for the present study.



MFMIS capacitor  $\pm 20$ V applied

Fig. 9 C-V curve of MFMIS capacitor.

Ir/IrO<sub>2</sub>/PZT(200nm)/Ir/IrO<sub>2</sub>/SiO<sub>2</sub>(25nm)/Si.

### References

- (1) R. Moazzami, P. D. Maniar, R. E. Jones, Jr., A. C. Campbell and C. J. Mogab: IEDM Tech. Dig. (1992) p.973.
- (2) J. F. Scott and C. A. Araujo: Science **246** (1989) 1400.
- (3) T. Inoue, T. Ohsuna, L. Luo, X. D. Wu, C. J. Maggiore, Y. Yamamoto, Y. Sakurai and J. H. Chang: Gekkan Semiconductor World **1** (1992) 99 [in Japanese].
- (4) M. R. Poor, A. M. Hurd, C. B. Fleddermann and A. Y. Wu: Mater. Res. Soc. Symp. Proc. **200** (1990) 211.
- (5) Y. Nakao, T. Nakamura, K. Hoshiba, K. Sameshima, A. Kamisawa, K. Abe, N. Soyama and K. Ogi: Jpn. J. Appl. Phys. **32** (1993) 4141.

## MECHANISMS CONTROLLING PHASE FORMATION IN PZT THIN FILMS

S.B. Majumder, D.C. Agrawal and Y.N. Mohapatra  
Materials Science Programme  
and  
V.N. Kulkarni  
Department of Physics  
Indian Institute of Technology  
Kanpur - 208016, India

**Abstract** - Factors controlling the formation of the perovskite phase in sol-gel prepared PZT film were studied. Perovskite was found to form quite easily, even in very thin films on sapphire, polycrystalline  $\text{Al}_2\text{O}_3$  and NaCl but only in relatively thick films on quartz, glass and Si. Formation of the perovskite phase is also favoured in (a) films with low Zr/Ti ratio and high Pb content (b) films heated rapidly to annealing temperature and (c) films annealed in  $\text{N}_2$  ambient. RBS studies show that large deficiency of Pb develops in films which remain in the pyrochlore structure due to reaction at the interface or due to diffusion into the interface. The initial transformation from amorphous to pyrochlore is believed to be due to enhanced strain energy barrier for the amorphous  $\rightarrow$  perovskite transformation.

### I. INTRODUCTION

Thin films of PZT with composition near the morphotropic boundary are often found to have a paraelectric pyrochlore structure unlike the powder and the bulk forms which almost invariably exist in the ferroelectric perovskite phase. Formation of this phase has been reported to depend on parameters such as film thickness, nature of the substrate, chemical composition of the film etc. However, this dependence has not been systematically studied and the underlying mechanisms are still poorly understood. We have carried out a systematic study of the effect of these parameters on the structures of the film. Concentration profiles across the substrate - film interface have also been measured with a view to understand the role of the diffusion across the interface on the stability of the phase.

### II. EXPERIMENTAL PROCEDURES

A sol-gel method, shown schematically in Fig 1, was used to deposit film of desired thickness on various substrates.

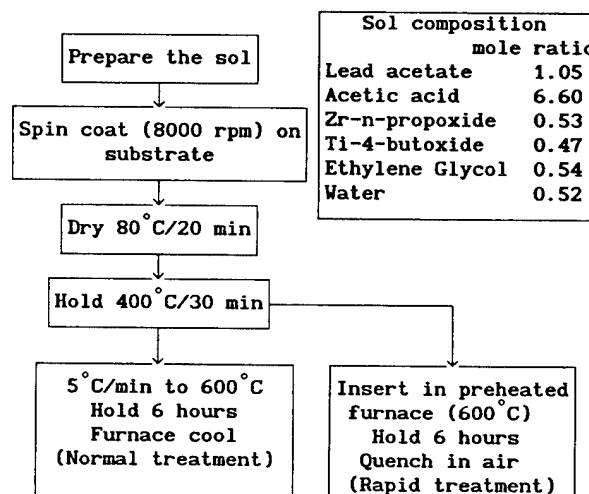


Fig 1. Schematic of the sol-gel method for PZT film preparation.

The thickness of the film was measured using a surface profilometer. Phases in the film were determined by X-Ray diffraction. RBS spectra were obtained using 1.7 MeV  $\text{He}^+$  ion and analysed using the RUMP software package [1].

### III. RESULTS AND DISCUSSION

From amongst the substrates used, the perovskite phase forms quite easily, even when the film thickness is small ( $< 0.6 \mu\text{m}$ ), on Sapphire, polycrystalline  $\text{Al}_2\text{O}_3$  and  $\text{NaCl}$  but not on quartz, glass, Si, and stainless steel (Fig 2). However, when the film thickness is increased substantially ( $> 1.5 \mu\text{m}$ ), perovskite phase forms on all the substrates. Formation of the perovskite phase is also favoured in (a) film with low Zr / Ti ratio and high Pb content, (b) films heated rapidly to annealing temperature and (c) films annealed in a  $\text{N}_2$  ambient.

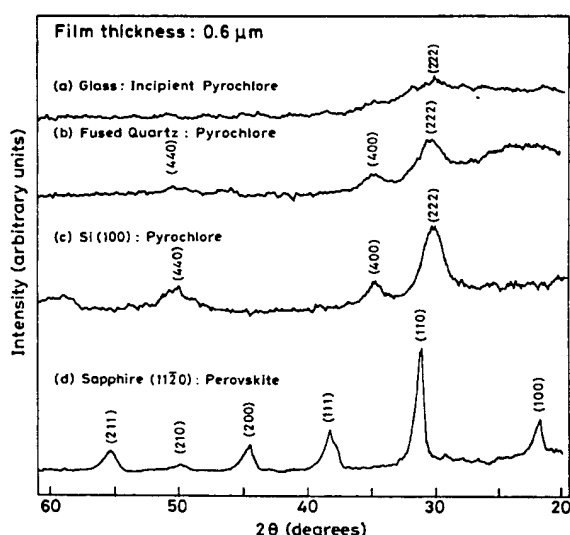
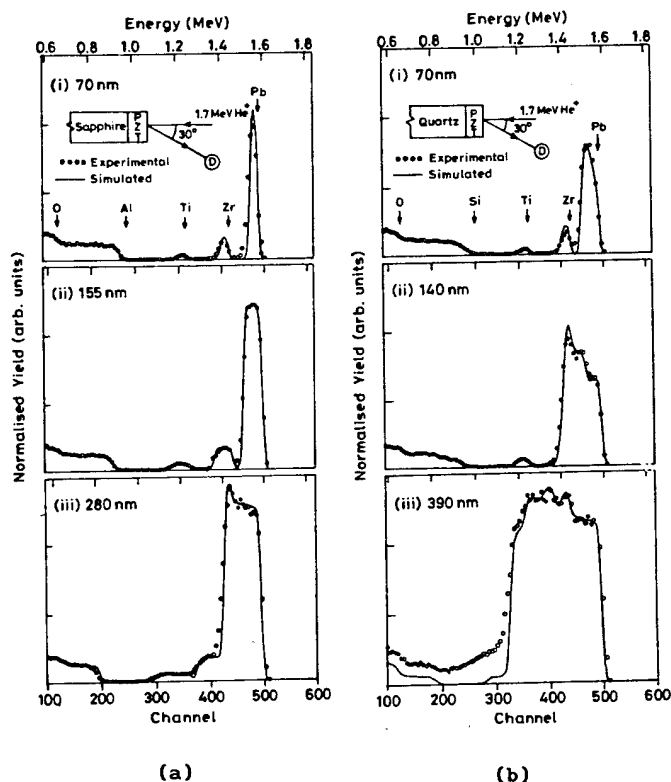


Fig 2. X-ray diffractograms of  $0.6 \mu\text{m}$  PZT film on different substrates.

Similar effects of film thickness, substrate, rate of heating and excess  $\text{PbO}$  have also been reported in a scattered manner in the literature [2-8]. Conflicting results have been reported on the effect of Zr / Ti ratio [9-10].

To explain these results, we have looked at the deficiency of Pb that may arise in the film due to a reaction at the interface or diffusion of Pb from the film into the substrate. As reported [6-8] and as observed in this work also, a crucial factor favouring the formation of the pyrochlore structure is the presence of a large Pb deficiency in the film. This may be because of the difference in the pyrochlore and perovskite structures. The deficient pyrochlore structure ( $\text{A}_2\text{B}_2\text{O}_{7-x}$  with  $0 < x < 1$ ) consists of a network of corner shared octahedra with  $\text{O}^{2-}$  - A -  $\text{O}^{2-}$  chains going through them [11]. The latter do not contribute significantly to the stability of the structure so that the pyrochlore structure can tolerate large deficiency of A(Pb) and O, unlike the perovskite structure.

The RBS data indeed shows striking difference in the concentration profiles of Pb in the films on sapphire and quartz. Fig 3 shows the RBS spectra and the analysis. It can be seen that on sapphire there is only a slight loss of Pb, due to volatilisation and there is no reaction or diffusion of Pb across the interface. On quartz, however there is substantial migration of Pb - concentration in the surface layer is drastically reduced from the initial  $\text{Pb}_{1.05}$  to  $\text{Pb}_{0.32}$ . Similar deficiencies in Pb are also expected to be produced in case of Si, glass and stainless steel substrates, all of which are known to react with PZT [4].



Substrate	RBS Simulation Structure	Layer No	Layer Thickness Å
Sapphire (1120)	$\text{Pb}_{.92}\text{Zr}_{.53}\text{Ti}_{.47}\text{O}_3$	1	700
	$\text{Al}_2\text{O}_3$	2	15000
Quartz	$\text{Pb}_{.32}\text{Zr}_{.53}\text{Ti}_{.47}\text{O}_3$	1	400
	$\text{Pb}_{.40}\text{Zr}_{.53}\text{Ti}_{.47}\text{O}_{2.5}\text{Si}_{.5}$	2	400
	$\text{Pb}_{.36}\text{Si}_{1.0}\text{O}_{2.25}$	3	800
	$\text{SiO}_2$	4	20000

Fig 3. RBS spectra of of PZT films of different thicknesses on (a) sapphire (b) quartz (c) results of analysis of RBS data for the 70nm films.

Although it has been known that Pb deficiency inhibits the formation of the perovskite structure, the above results clearly show that a deficiency in Pb caused by a reaction of the film with the substrate or diffusion of Pb into substrate is almost the sole reason for not attaining the perovskite structure in thin films on substrates like Si, quartz, glass, stainless steel etc. Other factors which have been proposed from time to time such as strain energy or size effect, lattice mismatch between the substrate and the film etc, do not seem to be important.

When the film thickness is increased, the concentration of Pb does not fall significantly in the top layers so that perovskite phase is able to form near the top surface. Films with higher Ti content also form perovskite more easily because Ti binds Pb more strongly than does Zr.

The role of strain energy, in fact, appears to be in making it easier for the amorphous  $\rightarrow$  pyrochlore transformation to be favored over the amorphous perovskite transformation as the latter involves a larger reduction (6.62% more) in volume. The sol-gel prepared films undergo considerable shrinkage on annealing and get stressed in tension. It is therefore energetically favourable for the amorphous film to first transform to pyrochlore rather than perovskite (Fig 4). The pyrochlore can then subsequently, at higher temperatures transform to perovskite if excessive Pb deficiency has not already developed.

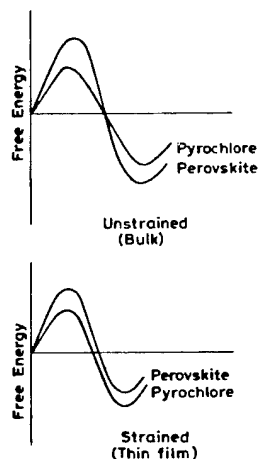


Fig 4. Schematic comparison of the free energy changes involved in the amorphous  $\rightarrow$  pyrochlore and amorphous  $\rightarrow$  perovskite transformation. A larger shrinkage in the latter makes the transformation to perovskite more difficult.

#### IV. SUMMARY

Thin films of PZT form a pyrochlore phase on some substrates like Si, quartz, glass etc essentially because of depletion of Pb from the film due to reaction and diffusion into the substrate. If the film is thick ( $\geq 1.5 \mu\text{m}$ ) then Pb depletion near the top of the film is not so severe in the times used for heat treatment, and the top layer can exist in perovskite structure. In substrates which do not react with PZT (eg. sapphire, platinum) the perovskite phase forms even in very thin films. In the films, such as sol-gel prepared films, which initially have an amorphous structure, the pyrochlore phase forms first due to lower strain energy and subsequently transforms to perovskite at higher temperature if no significant Pb deficiency develops.

#### REFERENCES

- [1] L.R.Doolittle, *Nucl. Inst. Method*, vol.B9, pp. 334, 1985.
- [2] Y.Takahashi, Y.Matsuoka, K.Yamaguchi, M.Matsuki and K.Kobayashi, "Dip coating of PT, PZ and PZT films using alkoxide - diethanolamine method," *J. Mater. Sci.* vol.25, pp. 3960-3964, 1990.
- [3] C.K.Kwok, S.B.Desu and L.Kammerdiner, "Effect of the thermal processing conditions on ferroelectric PZT thin films," in *Mat. Res. Soc. Symp. Proc.* vol.200, pp. 83-89, 1990.
- [4] V.K.Seth and W.A.Schulze, "Fabrication and characterization of ferroelectric PLZT 7/65/35 ceramic thin films and fibers," *Ferroelectrics*. vol.112 pp. 283-307, 1990.
- [5] Z.Surowiak, M.Loposzko, I.N. Zakharchenko, A.A.Bakirov, E.A.Marchenko, E.V.Sviridov, V.M.Mukhortov and V.P.Dudkevich, "Thin ferroelectric films of the lead zirconate titanate type obtained by r-f sputtering," *Thin Solid Films*. vol.205, pp. 76-84, 1991.
- [6] S.B.Krupanidhi, H.Hu and V.Kumar, "Multi-ion beam reactive sputter deposition of ferroelectric  $\text{Pb}(\text{Zr,Ti})\text{O}_3$  thin films," *J. Appl. Phys.* vol.71, pp. 376-388, 1992.
- [7] B.A.Tuttle, R.W.Schwartz, D.H.Doughty and J.A.Voigt, "Characterization of chemically prepared PZT thin films," in *Mater. Res. Soc. Symp. Proc.* vol.200, pp. 159-165, 1990.
- [8] A.H.Carim, "Microstructure of solution processed lead zirconate titanate (PZT) thin films," *J. Am. Ceram. Soc.* vol.74, pp. 1455-1458, 1991.
- [9] M.Klee, R.Eusemann, R.Waser, W.Brand and H.van Hal, "Processing and electrical properties of  $\text{Pb}(\text{Zr}_{1-x}\text{Ti}_x)\text{O}_3$  ( $x = 0.2 - 0.75$ ) films: Comparison of metallorganic decomposition and sol-gel process," *J. Appl. Phys.* vol.72, pp. 1566-1576, 1992.
- [10] C.V.R.Vasant Kumar, R.Pascual and M.Sayer, "Crystallisation of sputtered lead zirconate titanate films by rapid thermal processing," *J. Appl. Phys.* vol.71, pp. 864-874, 1992.
- [11] M.A.Subramanian, G.Aravamudan and G.V.Subba Rao, "Oxide pyrochlores - A Review," *Prog. Solid State Chem.* vol.15, pp. 55-143, 1983.

# "SOL-GEL PROCESSED FERROELECTRIC BARIUM TITANATE THIN FILMS AND CERAMICS"

By

H. Basantakumar Sharma and Abhai Mansingh  
Department of Physics & Astrophysics  
University of Delhi, Delhi(INDIA) 110 007

**Abstract**— Ferroelectric barium titanate  $\text{BaTiO}_3$ , thin films and ceramics were prepared by polymeric Sol-Gel processing technique from barium acetate,  $\text{Ba}(\text{CH}_3\text{COO})_2$ , and titanium isopropoxide,  $\text{Ti}(\text{OC}_3\text{H}_7)_4$ , precursors. It is shown that the ceramic prepared from the sol-gel derived powder give higher packing density and piezoelectric coupling constant,  $d_{33}$ , as compare to conventional ceramics prepared by solid state reaction. By properly adjusting the viscosity of the stock solution and using spin coating technique, it has been possible to fabricate homogeneous and uniform films of  $\text{BaTiO}_3$  on different substrates. The as grown films are amorphous, which can be crystallized into ferroelectric tetragonal phase by a post deposition annealing at  $700^\circ\text{C}$ . The lattice constants of the films are close to the bulk values. The polarization hysteresis, C-V and G-V measurements as well as the dielectric anomaly at about  $125^\circ\text{C}$  clearly establish the ferroelectricity in the films. The dielectric and ferroelectric properties of bulk ceramics and thin films are compared and discussed.

## INTRODUCTION

$\text{BaTiO}_3$  ceramics have been prepared mainly by conventional thermochemical reactions [1], which relies at high temperatures. Recently sol-gel technique have utilized for the fabrication of  $\text{BaTiO}_3$  ceramics [2].  $\text{BaTiO}_3$  thin films have been prepared using rf sputtering technique [3], activated reactive evaporation [4], hydrothermal [5], pulsed laser deposition [6] and sol-gel technique [7]. Sol-gel technique has the advantages of low cost, high purity, fine grain size, easier compositional control and short fabrication cycle. In this paper we report the structural, dielectric, and ferroelectric properties of  $\text{BaTiO}_3$  bulk ceramics and thin films prepared by sol-gel technique.

## EXPERIMENTAL

Barium acetate [ $\text{Ba}(\text{CH}_3\text{COO})_2$ ] and titanium isopropoxide [ $\text{Ti}(\text{OC}_3\text{H}_7)_4$ ] was first dissolved in acetic acid [ $\text{CH}_3\text{COOH}$ ] and an equimolar amount of  $\text{Ti}(\text{OC}_3\text{H}_7)_4$  was then added to the above solution. The stock solution was prepared by diluting the above mixture with methoxyethanol [ $\text{CH}_3\text{OCH}_2\text{CH}_2\text{OH}$ ] and filtration. Thin films were deposited by spin coating of the above solution at 2000 rpm for 20 seconds on glass, quartz, silicon and stainless steel substrates. Thicker films were prepared by multiple depositions accompanied by pre-firing at  $350^\circ\text{C}$  between layers for fifteen minutes. These films were finally annealed at  $700^\circ\text{C}$  for one hour in air for crystallization. For the preparation of bulk ceramics, the stock solution was set aside (for about 24 hours)

till a white opaque gel was obtained.  $\text{BaTiO}_3$  powder was prepared from the gel by drying at  $350^\circ\text{C}$  for 1 hour and the powder was again fired at  $700^\circ\text{C}$  for two hours in air for crystallization. The bulk ceramic in the form of circular disc (1 cm diameter, 0.01 cm thick) was prepared by pressing the powder and then sintering at  $1300^\circ\text{C}$  for two hour in air. The discs were electroded with silver paste and poled. Thin films for electrical measurements were fabricated on stainless steel substrates, silver electrodes,  $1.96 \times 10^{-3} \text{ cm}^2$  in area, were deposited on the films by vacuum evaporation to serve as top electrodes.

The microstructure of the thin films and ceramics were characterized by a JEOL JSM-840 scanning electron microscope (SEM). X-ray diffractometer was used for structural characterization of the  $\text{BaTiO}_3$  thin films and bulk ceramics.

The polarization hysteresis in  $\text{BaTiO}_3$  bulk ceramics and thin films were obtained using a modified Swayser-Tower bridge in metal-ferroelectric-metal (MFM) configuration. The capacitance voltage (C-V) and conductance-voltage (G-V) hysteresis in thin films was measured at 1 MHz using PAR410 C-V plotter. The dielectric constant and dielectric loss of the thin films and ceramics were measured by using GR 1616 capacitance bridge.

## RESULTS AND DISCUSSIONS

The compressed powder pallet gave a dielectric constant ( $\epsilon'$ ) of only 180. This lower value may be attributed to the lower density ( $3.59 \text{ g-cm}^{-3}$ ) of the pallet. The dielectric constant was increase from 698 to 800 for ceramics sintered at  $1100^\circ\text{C}$  and  $1300^\circ\text{C}$  respectively. The thin films showed a thickness dependent dielectric constant, however, for films of thickness above  $1 \mu\text{m}$  there was hardly any change in the dielectric constant. So the results of the film of thickness  $1.2 \mu\text{m}$  are presented. The dielectric constant of the ceramics and thin films as a function of frequency and temperature are reported shown in figs. 1(a) and 1(b) respectively. It may be noted that the sintered ceramic hardly showed any dispersion while a large dispersion was observed. The dispersion may be due to space charge dispersion. [8]. The lower frequency limiting value represents the dielectric constant of the film and high frequency limiting value that of the space charge. This is confirmed from the fact that the peak in  $\epsilon'$  is well defined at 0.1 KHz and decreases with frequency and finally disappears at 100 KHz. It may be pointed out that the in thin film the dielectric constant is substantially lower than that of the sintered ceramics, even if contribution for space

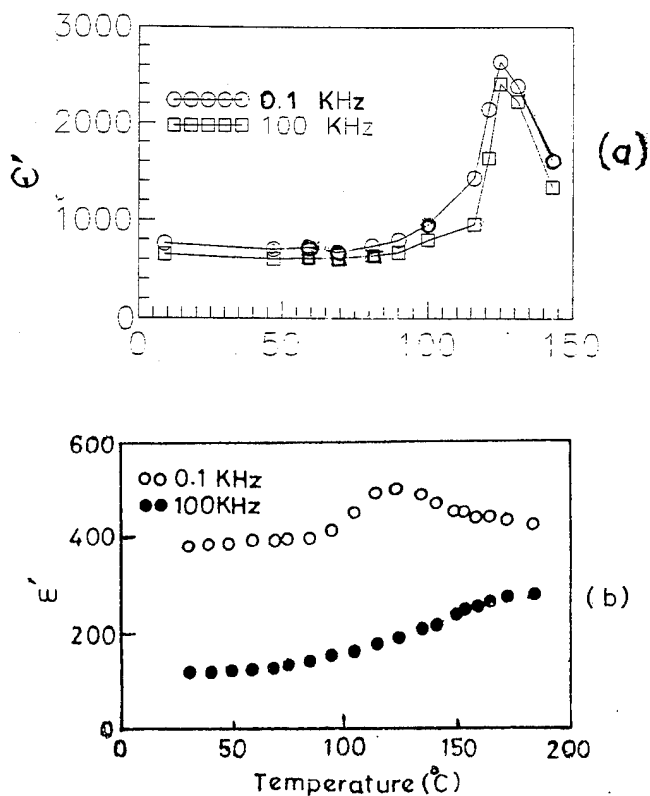


Fig.1 Dielectric constant as a function of temperature of sol-gel derived  $\text{BaTiO}_3$  (a) ceramic and (b) thin film on stainless steel substrate

charge dispersion are taken into account. The peak value is lower and the peak is broader in films.

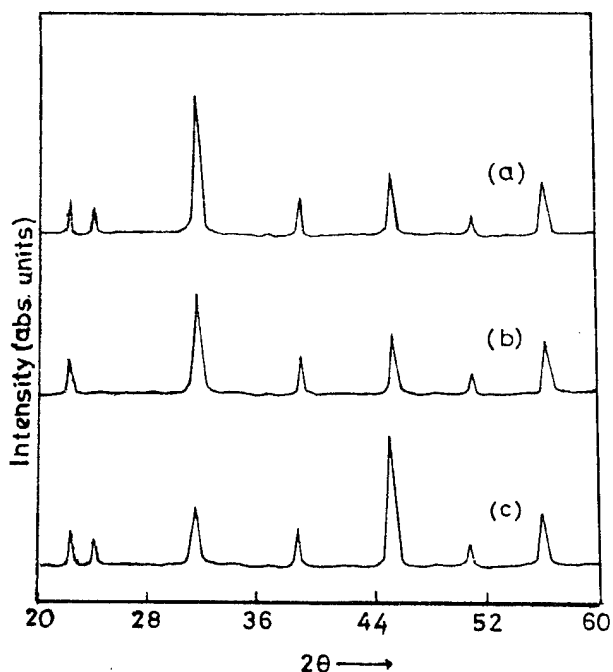


Fig.2. X-ray diffraction pattern of Sol-gel derived  $\text{BaTiO}_3$  (a) powder (b) thin film on quartz substrate and (c) ceramic.

The as grown films and powder was found to be amorphous. The x-ray diffraction pattern of powder, thin film on quartz substrate annealed at  $700^\circ\text{C}$  and sintered ceramic at  $1300^\circ\text{C}$  are shown in figures 2(a), 2(b) and 2(c) respectively. The annealed film and powder have tetragonal structure with preferred orientation along (101 and 110) directions. But sintered ceramics have preferred orientation along (002) direction and the splitting of the peaks at (002 & 200) was apparently observed (fig.3). The c/a of the film and powder is 1.020 and that of the sintered ceramic is 1.013 respectively. Figures 3(a) and 3(b) show the SEM micrographs of the thin film on silicone annealed at  $700^\circ\text{C}$  substrate and sintered ceramic respectively. The thin film has average grain size of  $\approx 0.02 \mu\text{m}$  and that of the sintered ceramic  $\approx 4.00 \mu\text{m}$ .

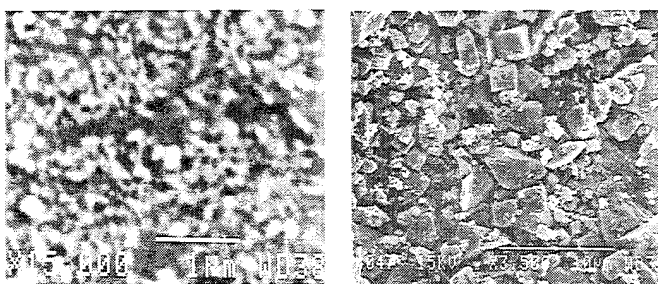


Fig.3. Scanning electron micrograph of  $\text{BaTiO}_3$  (a) thin film annealed at  $700^\circ\text{C}$  and (b) ceramic sintered at  $1300^\circ\text{C}$ .

The room temperature polarization-field (P-E) hysteresis of  $\text{BaTiO}_3$  thin film on stainless steel substrate at an applied frequency 50 Hz is shown in Fig.4. Figure 5 shows the capacitance-voltage (C-V) and conductance-field (G-V) characteristics. The

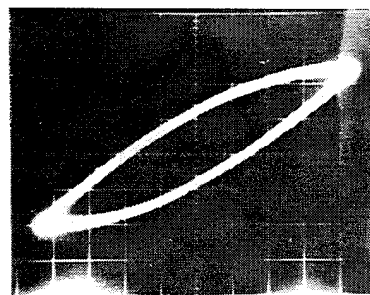


Fig.4. P-E hysteresis loop of sol-gel derived  $\text{BaTiO}_3$  thin film of thickness  $1.2 \mu\text{m}$  on stainless steel substrate

appearance of the butterfly loop in the C-V and G-V characteristics together with P-E hysteresis loop (Fig.5) confirms the ferroelectric nature of our films. Similarly, a perfect hysteresis loop was obtained for ceramic samples. The values of ceramic were found to be  $P_r$ ,  $P_s$  and  $E_c$   $11.1 \mu\text{C}\cdot\text{cm}^{-2}$ ,

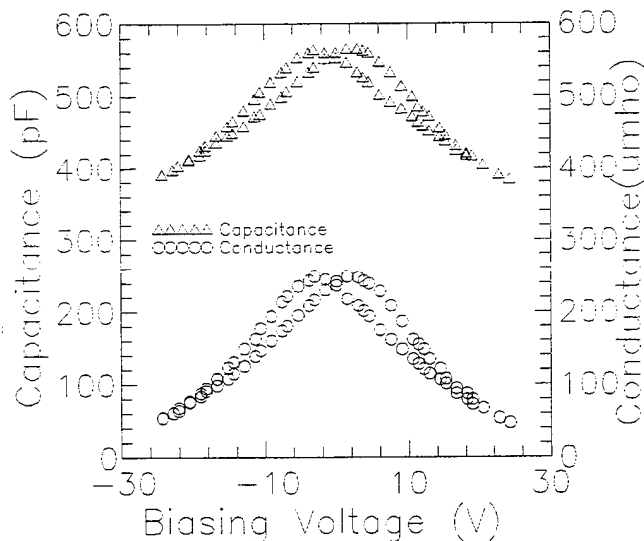


Fig.5. C-V and G-V characteristics of sol-gel derived BaTiO<sub>3</sub> thin film on stainless steel substrate

19.2  $\mu\text{C-cm}^{-2}$  and 8 KV-cm, whereas that of the films were 5.4  $\mu\text{C-cm}^{-2}$ , 12.8  $\mu\text{C-cm}^{-2}$  and 79 KV-cm respectively. The value of  $p_r$  and  $p_s$  of the films is much lower than that of the film, whereas  $E_c$  of the films is higher than that of the ceramics. The difference in the values of  $p_r$ ,  $p_s$  and  $E_c$  of the thin films and ceramics may due to the difference in the grain size and existence of the spaces charge region at the film-substrate interface. The value of piezoelectric coefficient,  $d_{33}$ , of the poled ceramic samples increases with the increase of sintering temperature. Ceramic sintered at 1100°C gave a  $d_{33}$  of 110 C/N and saturated to a value of 187 C/N after sintering temperature 1200°C onwards which is closed to the highest reported values.

#### CONCLUSIONS

The precursors and the procedure used for the preparation of BaTiO<sub>3</sub> thin films and ceramics by sol-gel technique can give high quality thin films and ceramics of BaTiO<sub>3</sub>. The dielectric constant and spontaneous polarization of thin films are lower than the ceramics, while coercive field of thin films is higher. These may be due to the smaller grain size of the films and the existence of space charge and film substrate interface.

#### ACKNOWLEDGEMENT

One of the authors (HBS) is thakful to University Grant Commision (INDIA) for financial support during the present work.

#### REFERENCES

1. B. Jaffe, W.R. Cook and H. Jaffe, Piezoel-ectric Ceramics, Academic Press, London, 1971, 69
2. H. Basantakumar Sharma, R.P. Tandon, Abhai Mansingh, R. Rup, Dielectric and piezoelectric properties of sol-gel

- derived barium titanate ceramics, J. Mater. Science Lett. Vol.12, 1795-1796, 1993.
3. K. Sreenivas, Abhai Mansingh and M. Sayer, Amorphous barium titanate thin films, J. Appl. Phys. Vol.62, 4476-4473.
4. K. Ijima, T. Terashima, K. Yamamoto, K. Hirata and Y. Bando, Preparation of ferroelectric BaTiO<sub>3</sub> thin films by activated evaporation, Appl. Phys. Lett., Vol.56, pp.527-529, 1990.
5. R.R. Bacsá, J.P. Daugherty and L.J. Piliore, Low temperature synthesis of BaTiO<sub>3</sub> thin films on Si substrates by hydrothermal reaction, Appl. Phys. Lett., Vol.63, pp.1053-1055, 1993.
6. H.F. Cheng, M.H. Yeh, K. Sunh and I.N. Lin, Characteristics of BaTiO<sub>3</sub> films prepared by pulsed laser ablation, Jpn. J. Appl. Phys. vol.32, pp.5656-5660, 1993
7. T. Hayashi, N. Ohji, K. Hirihara, T. Fukunaga and H. Maiwa, Preparation and properties of BaTiO<sub>3</sub> thin films by sol-gel, Jpn. J. Appl. Phys. vol.32, pp.4092-4094, 1993
8. Abhai Mansingh and M. Sayer, To be published



# PROCESS/STRUCTURE/PROPERTY RELATIONS OF BARIUM STRONTIUM TITANATE THIN FILMS DEPOSITED BY MULTI-ION-BEAM SPUTTERING TECHNIQUE

C.-J. Peng\*, and S.B. Krupanidhi#

Intercollege Material Research Laboratory

Pennsylvania State University, University Park, PA 16802

\* Present address: Material Research Laboratories, Industrial Technology Research Institute, Hsinchu, Taiwan, R.O.C.

# Also with Department of Engineering Science & Mechanics

## ABSTRACT

(Ba<sub>1-x</sub>Sr<sub>x</sub>)TiO<sub>3</sub> (BST) thin films with various x were deposited at various substrate temperatures by multi-ion-beam sputtering (MIBERS) technique. A strong correlation was found among processes, structures and properties of the films. For thin films grown at substrate temperature of room temperature and subsequently annealed at 700°C, the microstructure is polycrystalline through the film thickness with a presence of void layer which results in low dielectric constant (K) and continuous decrease of current in current-time (I-t) behavior. For films deposited at high substrate temperature and annealed at 700°C, the columnar structures are remained without void layer, and the dielectric constant become much higher. The I-t behavior resembles that of ceramics and single crystals. Nb-dopant in BST thin films lowered the dielectric constant, dissipation factor and leakage current, and improve the time-dependent dielectric breakdown (TDDB). Current-voltage (I-V) characteristics can be related to the process and microstructure as well.

## I. Introduction

Ferroelectric materials in paraelectric phase, due to much higher dielectric constant over conventional nitride-oxide materials, are currently receiving much attention to be used as the capacitor materials in replace of traditional silicon oxide/nitride for ultra large scale integration (ULSI) dynamic random access memory (DRAM) applications, especially for memory densities higher than 64 Mb<sup>1</sup>. The higher dielectric constant of ferroelectric materials allows the capacitor remaining to be planar and still maintain high enough charge storage. Thus the manufacturing processes can be dramatically simplified.

BST is the most promising candidate dielectric material to be used in ULSI DRAMs due to its paraelectric phase (for x>0.3) at room temperature and thus no aging and fatigue effects. Besides, BST solid solution ceramics has high dielectric constant at room temperature, low temperature coefficient of capacitance and is a thermally stable compound (compared with lead-based ferroelectrics). BST solid solution ceramics also have very low dissipation factors (~0.0015 for x=0.5).<sup>2</sup>

In this paper, results on structures and electrical properties of BST films prepared by MIBERS techniques are reported. Close relationships between structures and electrical properties are constructed. MIBERS has been successfully applied to the growth of other ferroelectric materials, such as PZT films<sup>3</sup>. Details of the MIBERS technique have been described elsewhere<sup>4</sup>. The effects of doping on dielectric constant, leakage current and TDDB behavior are also presented.

## II. Experimentals

Three focused Ar<sup>+</sup> beams were used to sputter a SrO, BaO and a Ti-metal target respectively. The deposition chamber was first pumped down to a base pressure of ~2x10<sup>-6</sup> torr by cryopump. Then the argon (as the precursor of Ar<sup>+</sup>) was bled through the ion guns and oxygen was bled into the chamber directly (molecular ratio of Ar/O<sub>2</sub> was 1), give rise to a total pressure about 4x10<sup>-4</sup> torr. The

BST films were deposited onto unheated or heated Pt-coated Si substrates. The growth rates of near stoichiometric BST films were estimated to be ~1.3 nm/min. All as-grown films were annealed in oxygen atmosphere at 700°C for 2~8 hrs. Nb-doping was performed by attaching a thin sheet of Nb metal onto the Ti-target surface during sputtering. The amount of doping concentration were determined by the area of Nb-sheet by trial and error. Crystal structures were examined by Scintag PAD V diffractometer. 0.3 mm diameter gold dots were deposited onto film surface as top electrodes. Low signal dielectric properties were measured with HP 4194A impedance analyzer. I-V characteristics, time-domain dielectric response and TDDB were measured using HP 4140B pA-meter and computer.

## III. Results and Discussions

### A. Processes and Structures

The structures determined by x-ray diffraction (XRD) for BST films grown *ex-situ* or *in-situ* (at substrate temperature (T<sub>s</sub>) of 400°C) and subsequently annealed at 700°C for 2 hrs were near random polycrystalline structure for various Sr content. However, the microstructure of *ex-situ* and *in-situ* crystallized films showed distinct differences. For *ex-situ* deposited films, which were grown under low adatom mobility conditions by physical vapor deposition, the microstructure is generally porous columnar structure, which is the Zone I of the well-known structure zone model (SZM).<sup>4</sup> Post-deposition annealing may change the microstructure of as-deposited films due to thermally induced diffusion, nucleation and growth depending on the original structure. For amorphous as-grown films, the inhomogeneous nucleation and subsequent grain growth may lead to the breakdown of columnar structure, resulting in random polycrystalline grains through the film thickness. For well-crystallized films, however, notable *recrystallization* may not take place and grain growth may lead to the decrease of the number of columnar boundaries. In fact, we found that there are two types of microstructure of BST films grown by MIBERS technique after annealed at 700°C: *ex-situ* grown films showed multi-grains structures through the film thickness (Type I), and *in-situ* crystallized films showed columnar structure even after annealed at 700°C for 8 hrs (Type II).<sup>5</sup>

### B. Electrical Properties

All *ex-situ* deposited films, regardless of the compositions (Sr content), show relative low K (<200) even after annealed at 700°C. The reason is related to the void layer near film-substrate interface for films deposited under low adatom mobility. Figure 1 shows the K and dissipation factors (tanδ) of *in-situ* deposited films (T<sub>s</sub>=400°C) and post-deposition annealed at 700°C for 2 or 8 hrs as a function of Sr content. As shown in the figure, only annealing for long times could tanδ be reduced and thus exhibit the real K of films without the contributions from dc conduction. To insure near complete oxidation for *in-situ* deposited films, we annealed the *in-situ* deposited MIBERS films at 700°C for 8 hrs by conventional oven annealing. The K increased from 237 for BaTiO<sub>3</sub> to a maximum of 563 for (Ba<sub>0.5</sub>Sr<sub>0.5</sub>)TiO<sub>3</sub> and decreases again for higher Sr content. Note that the value ~350 of K for SrTiO<sub>3</sub> is higher than the single crystal value ~300. The higher value may be due to the

incomplete oxidation of  $\text{SrTiO}_3$  grains and become the so called "grain boundary barrier layer capacitors" so that the effective dielectric constant is higher than the single crystal value. The higher K values of *in-situ* deposited films than that of *ex-situ* films is due to the elimination of void layer resulted from high adatom mobility during deposition.

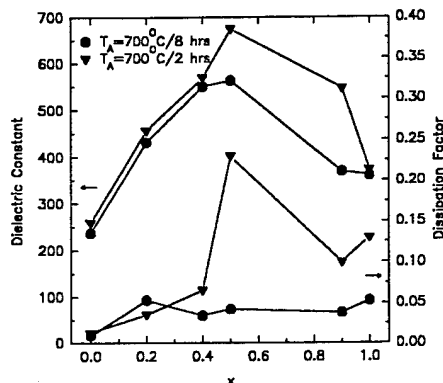


Fig. 1: Dielectric constant and dissipation factor of  $0.4 \mu\text{m}$   $(\text{Ba}_{1-x}\text{Sr}_x)\text{TiO}_3$  films deposited at  $T_s=400^\circ\text{C}$ .

Recently, impedance analysis in the time domain have been used to investigate the different microstructure effects on the mechanism of the dc electrical conduction and breakdown of perovskite-type titanate.<sup>6</sup> It was found that, the current after applying dc voltage step is due to conduction through the bulk Ni-doped  $\text{SrTiO}_3$  ceramics (grain size  $\sim 2 \mu\text{m}$ ) at very short time ( $\sim 0.03$  sec) at  $483^\circ\text{K}$  and an electric field of  $100 \text{ V/cm}$ , and then, pronounced Maxwell-Wagner polarization of the grain boundaries take place at  $t \sim 0.03$  sec. In the single crystal of the same composition, only a slightly polarization contribution of the electrodes at  $t \sim 2$  sec was observed.<sup>7</sup> In thin films, the transition time between the polarization and the conduction regime is  $\sim 0.3$  sec at  $483^\circ\text{K}$ , and an extrapolation to  $298^\circ\text{K}$  reveals the transition time of  $\sim 10^5$  sec.<sup>18</sup> The transition time also depends on electric field, with the transition time decreases as electrical field increases. There is a significant difference between the space charge polarization behavior of the ceramics/single crystals and thin films, with the former show a Debye relaxation:  $I \propto \exp(-t/\tau)$ , where  $\tau$  is Debye relaxation time of Maxwell-Wagner polarization of the grain boundaries and electrode, while the latter shows a Curie-von Schweidler law (or universal law):  $I \propto t^n$ , where  $n$  is constant and less than 1. For our films, we found that there are two types of time-domain response corresponding to the two types of microstructures. Type I is shown in Fig. 2, with the polarization behavior follow Curie-von Schweidler law for Type I films. The  $n$  values shown are between 0.32 and 0.56 for  $\text{BaTiO}_3$  films deposited at R.T. and annealed at  $700^\circ\text{C}$  for 8 hrs. Type II of time-domain response is Debye-type relaxation, as shown in Fig. 3, for Type II films grown at high substrate temperature ( $\geq 400^\circ\text{C}$ , i.e. as-grown films are crystallized) and subsequently annealed at higher temperatures. The relaxation times are shown in the figure and are larger for lower voltages. The main difference between these two types should be related to the corresponding microstructures. The Type II is also consistent to the results of Waser for ceramics, i.e. the grain size is large compared to the space-charge layer thickness ( $\sim 0.1 \mu\text{m}$ ). For our case, the grain size of Type II should be referred to the length of the columns which are about the same size as of film thickness  $\sim 0.4 \mu\text{m}$ , but not the width of columns which are shown on the surface morphology with the size of  $\sim 0.03 \mu\text{m}$ .

The Curie-von Schweidler behavior is a relatively slow relaxation process and is intimately related to the inevitable presence of a finite amount of disorder in all orientally polarization media. The behavior is based on the fact that individual polarization or depolarization events do not take place independently of each other

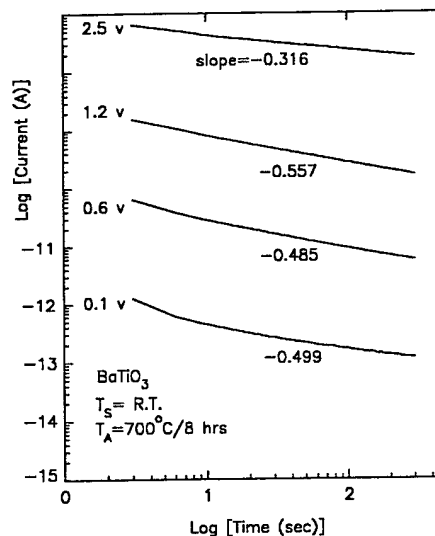


Fig. 2: Type I dielectric response. Each curve is displaced w.r.t. the previous one by one decade for clarity.

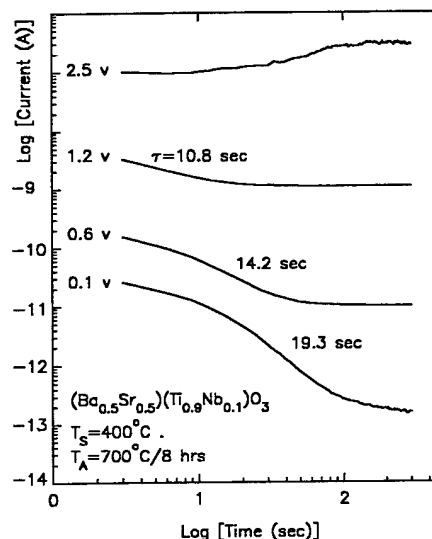


Fig. 3: Type II dielectric response. Each curve is displaced to the previous one by one decade for clarity.

but, rather interact cooperatively<sup>8</sup>. It is well known that the various order or disorder regions may have different physical properties, e.g. electrical conductivity and permittivity. It would be evident therefore that the presence of such non-uniformity might reflect itself on the dielectric relaxation of solids. For our case, the possible differences in the two types of films due to different processing may be that: i) More ordered structure in films deposited at high substrate temperature than that deposited at room temperature, ii) More numbers of grain boundaries through the film thickness for Type I films. Type I films may be regarded to be more disorder, and non-uniformity. Therefore, Type I films continuously response to the electric field for a longer time.

The I-V characteristics of our films shows two types of I-V dependence, as shown in Fig. 4. Curve (a) type is common in undoped MIBERS films, regardless they were deposited at R.T. or high temperature and the Sr content in BST films. Curve (b) type occurred in *in-situ* donor-doped films (deposited at high  $T_s$ ). The conduction mechanism of our films is most likely been SCLC<sup>5</sup>. Curve (b) type behavior in Fig. 4 suggests that heavily donor-doped films deposited at higher substrate temperatures have discrete shallow traps, possibly donor state of  $\text{Nb}_{\text{Ti}}$ . The near vertical regime (iii) which has a slope of 16 corresponding to trap-filled limit (TFL) law is preceded by trap-distributed region (ii) (slope=2.6-3) and followed by a discrete trap-free but trap-distributed regime (iv)

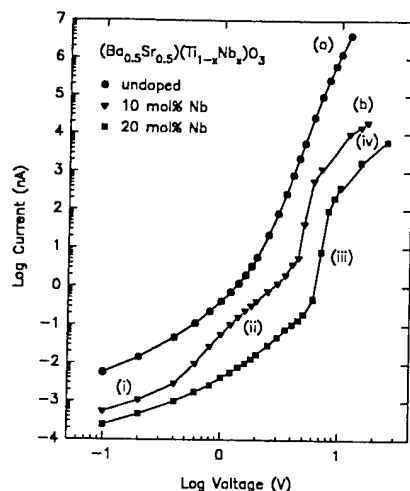


Fig. 4: Two types of I-V characteristics of BST films. (0.4  $\mu$ m).

(slope  $\sim 3$ ). Such a discrete trap embedded in a background of distributed traps was also seen in organic molecular crystals of anthracene by Helfrich and Mark<sup>9</sup> and by Adolph et. al.<sup>10</sup> The trapped electron density ( $n_t$ ) present in the films can be calculated from the trap-filled limit voltage ( $V_{TFL}$ ) and the equation:<sup>11</sup>

$$V_{TFL} = \frac{e n_t d^2}{K \epsilon_0} \quad (1)$$

where  $e$  is electronic charge,  $d$  is film thickness,  $K$  is dielectric constant of the films and  $\epsilon_0$  is the permittivity of free space, to be  $\sim 10^{18} \text{ cm}^{-3}$ . From the ratio of current jump ( $\theta$ ), i.e. regime (iii), one can readily calculate the energy level of the discrete traps by the equation:<sup>11</sup>

$$\theta = \frac{n}{n_t} = \frac{N_c}{g N_t} \exp\left(\frac{E_t - E_c}{k T}\right) \quad (2)$$

where  $n$  is the free electron concentration under injection,  $n_t$  is the trapped electron concentration,  $N_c$  is the effective density of states in the conduction band,  $g$  is degeneracy factor ( $\sim 2$ ),  $N_t$  is concentration of traps,  $E_t$  the energy level of the traps in energy band,  $E_c$  is the energy level of the bottom of the conduction band,  $k$  the Boltzman constant, and  $T$  the absolute temperature ( $^{\circ}\text{K}$ ). For our case, e.g. 20 mol% Nb films in Fig. 8,  $\theta = 5.7 \times 10^{-3}$ ,  $N_c = 1.4 \times 10^{21} \text{ cm}^{-3}$  at  $298^{\circ}\text{K}$ ,<sup>12</sup>  $N_t = 4.29 \times 10^{20} \text{ cm}^{-3}$  assuming the effective concentration of  $\text{Nb}_{Ti}$ . Due to the difficulty of incorporation of donor dopant in thin films, the fraction of incorporation was estimated to be  $\sim 0.15$  at an annealing temperature of  $700^{\circ}\text{C}$  for 2 eV heat of solution. One then can obtain the energy level of the discrete traps by equation (5) to be  $\sim 0.144 \text{ eV}$ , which is in a good agreement with  $0.12 \text{ eV}$  of  $\text{Nb}_{Ti}$  from literature.<sup>12</sup>

For undoped films deposited at  $T_s = 400^{\circ}\text{C}$ , there was no such near vertical regime, indicating the absence of discrete-traps (either shallow or deep traps). The non-linearity at high electric fields was believed to be due to the distributed-traps induced by the unavoidable acceptor impurities in titanate perovskite systems.<sup>13</sup> These acceptor impurities may come from the target or the sputtering chamber. As described in Sec. A, the microstructures of films are the same (Type II) for both undoped and Nb-doped films. The difference between undoped and Nb-doped films thus must attribute to the differences in chemistry, i.e. doping effect.

Another source resulting in curve (a) type I-V behavior is due to microstructure variations. Structural disorder or defect is well-known to be one kind of electron traps. This kind of disorder can occur even in materials with high chemical purity. These structure

disorders may not have a uniquely defined environment. There will be differences from one trap site to another, from nearest neighbor to next nearest neighbor.<sup>8</sup> The net result will be a broad smearing out of the level. For our curve (a) type films deposited at low substrate temperature, we believe that the grain boundaries are the dominant structure disorder, and are the trap centers. This can be realized from the Nb-doped films with the same composition as curve (b) type but deposited at lower substrate temperatures ( $T_s \leq 300^{\circ}\text{C}$ ). The effects of discrete-traps are overshadowed by distributed traps, so that curve (a) type looks like been stretched out from curve (b) type. The difference between these films is that the films deposited at low substrate temperature and annealed at  $700^{\circ}\text{C}$  contain more number of grain boundaries through the film thickness. This argument can be supported by our MOD films doped with high donor concentration, which only show curve (a) type behavior, and the slopes at high field regime are in the same range ( $7.5 \sim 10$ ).<sup>14</sup> Waser<sup>6</sup> also observed the same I-V characteristics in doped  $\text{BaTiO}_3$  and  $\text{SrTiO}_3$  thin films with no vertical regime.

TDDB is also referred as resistance degradation of dielectrics which shows a slow increase of the leakage currents under dc field stress at room temperature or elevated temperatures. Degradation may take place at much lower electric field than the field for dielectric breakdown or thermal breakdown. This type of failure is a reliability issue and is the limiting factor for the lifetime of capacitors, including thin film capacitors. TDDB is characteristic of the intrinsic materials, the processing and electrode materials. Our results show that Nb doping in BST thin films can significantly improve the endurance of TDDB. The undoped films last only  $\sim 90$  min. long at electric field of  $0.25 \text{ MV/cm}$  and the current increased up to the instrument limit ( $10^{-2} \text{ A}$ ), while the endurances are much longer for Nb-doped films (517 and  $>1298$  min. for 10 mol% and 20 mol% doped films respectively). The donor-doped materials apparently can reduce the concentration of oxygen vancancy and thus increase the time to breakdown. The TDDB behavior of Type I films is also better than that of Type II films, due to the oxygen vacancies have to electromigrate longer paths for films with multi-grains through the film thickness.

#### IV. Conclusions

Close relationships among processing, structures and properties have been established for BST thin films deposited by MIBERS. The relationships can be schematically shown as Fig. 5. Some major conclusions may be summarized as followings:

1. Microstructure of BST thin films could be classified into two types: (a) Type I structures with multi-grains through the film thickness for amorphous as-grown films after high temperature annealing, and (b) columnar structure (Type II) which remained even after high temperature annealing for well-crystallized films deposited at high substrate temperatures.

2. Dielectric constant as high as 563 was observed for  $0.4 \mu\text{m}$   $(\text{Ba}_{0.5}\text{Sr}_{0.5})\text{TiO}_3$  films deposited at  $T_s = 400^{\circ}\text{C}$  and annealed at  $700^{\circ}\text{C}$  for 8 hrs.

3. Two types of time-domain response corresponding to the two types of microstructure have been observed, with Type I response (Curie-von Schweidler law) for Type I films and Type II response (Debye relaxation) for Type II films. Type I behavior may be attributed to the presence of high density of disordered grain boundaries.

4. Two types of I-V characteristics could be seen depending on the chemistry of the films (doped or undoped) and substrate temperature during deposition. Only the films doped with high donor concentration and deposited at high substrate temperature showed space-charge-limited conduction with discrete shallow traps embedded in trap-distributed background at high electric field. The

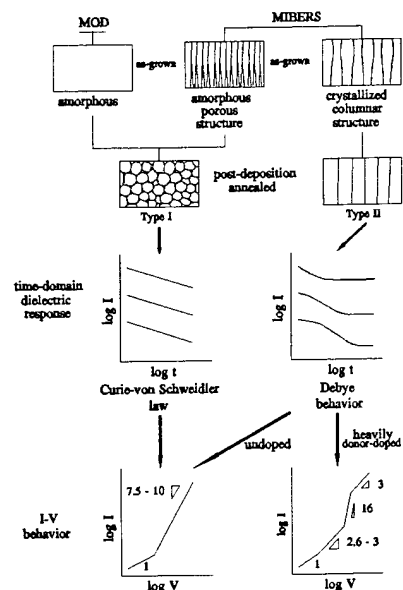


Fig. 11: Relationships between structures and electrical properties in BST films.

trapped electron density was determined to be  $\sim 10^{18} \text{ cm}^{-3}$  and the energy level of the shallow discrete traps was calculated to be  $\sim 0.144 \text{ eV}$  below the conduction band. All other non-bombarded films showed trap-distributed SCLC behavior with slope of  $\sim 7.5-10$  due to the presence of grain boundaries through the film thickness or traps induced by unavoidable acceptor impurities in the films.

5. Donor-doping could significantly improve the TDDB behavior of BST thin films, most likely due to the lower oxygen vacancy concentration resulted from donor-doping.

### References

1. L.H. Parker and A.F. Tasch, IEEE Circuits and Devices Magazine, p.17-26, Jan. (1990).
2. U. Syamaprasad, R.K. Galgali and B.C. Mohanty, Mater. Lett., 7 [5/6] 197 (1988).
3. S.B. Krupanidhi, H. Hu and V. Kumar, J. Appl. Phys., 71 [1] 376-88 (1992).
4. J.A. Thornton, J. Vac. Sci. Technol., 12 [4] 830 (1975).
5. C.-J. Peng and S.B. Krupanidhi, to be published in J. Mater. Res.
6. R. Waser and M. Klee, Proc. of 3rd International Symposium on Integrated Ferroelectrics, Colorado Springs, CO, 1991, pp.288-305.
7. R. Waser, J. Am. Ceram. Soc., 74 [8] 1934-40 (1991).
8. A.K. Jonscher, Dielectric Relaxation in Solids, Chelsea Dielectrics Press, London, UK, (1983), pp.161-253.
9. W. Helfrich and P. Mark, Z. Phys., 171, 527 (1963).
10. J. Adolph, E. Baldinger, W. Czaja and I. Granacher, Phys. Lett., 6, 137 (1963).
11. L.A. Lampert and P. Mark, Current Injection in Solids, Academic Press, p. 23, (1970).
12. A.M.J.H. Seuter, Philips Res. Repts., Suppl. [3] 50 (1974).
13. D.M. Smyth, Prog. Solid State Chem., 15, 145 (1984).
14. C.-J. Peng and S.B. Krupanidhi, to be published in J. Appl. Physics.

# STUDY OF $\text{Ba}_{1-x}\text{Sr}_x\text{TiO}_3(100)$ EPITAXIAL THIN FILMS PREPARED BY LASER DEPOSITION

N. J. Wu, H. Lin, K. Xie, X. Y. Li, Jia Li and A. Ignatiev  
Texas Center for Superconductivity and Space Vacuum Epitaxy Center  
University of Houston, Houston, Texas 77204-5507

## Abstract

Heteroepitaxial  $\text{Ba}_{1-x}\text{Sr}_x\text{TiO}_3$  ( $x = 0.4$  and  $x = 0.5$ ) thin films of thickness from 20 nm to 500 nm were grown on high  $T_c$  superconducting  $\text{YBa}_2\text{Cu}_3\text{O}_{7-x}$  (YBCO) thin film substrates by laser ablation. Perovskite-type BST(100) on c-oriented YBCO/ $\text{LaAlO}_3(100)$  started to form at 500 °C and exhibited good crystallinity at 550°C - 620°C. The films were characterized in the temperature range of 20 K to 300 K by polarization-versus-electric field (P-E), capacitance-versus-voltage (C-V) and current-versus-voltage (I-V) measurements. Both BST(100) thin films with  $x = 0.4$  and  $x = 0.5$  showed ferroelectric behavior below room temperature with maximum polarization of 3  $\mu\text{C}/\text{cm}^2$  and 1.4  $\mu\text{C}/\text{cm}^2$ , respectively. Resistivity above  $10^{11}$  Ohm-cm were obtained in the temperature range from 30K to 300K. The properties of interface and phase transitions will be discussed.

## Introduction

The interest in  $\text{Ba}_{1-x}\text{Sr}_x\text{TiO}_3$  (BST) thin films has been motivated by potential applications in memory devices, dielectric capacitors and electro-optic devices. When  $\text{Ba}^{2+}$  ions in  $\text{BaTiO}_3$  are partially replaced by  $\text{Sr}^{2+}$ , the electronic and optical properties of solid solution  $\text{Ba}_{1-x}\text{Sr}_x\text{TiO}_3$  can be tailored over a broad range with a molar ratio  $x$  from 0 to 1. The Curie point of  $\text{BaTiO}_3$  decreases linearly with increasing concentration of Sr.<sup>(1)</sup> Our recent interest is to develop single crystal BST ferroelectric films with Curie temperature near and below room temperature, and to integrate the ferroelectrics with high temperature superconductors. These efforts have driven this work in the integration of BST ( $x = 0.4$  and  $x = 0.5$ ) with  $\text{YBa}_2\text{Cu}_3\text{O}_{7-x}$  (YBCO) substrates.

The lattice and chemical match between perovskite-type YBCO and ferroelectrics has allowed for the growth of epitaxial multilayers for fundamental and application studies.<sup>(2,3)</sup> Oxide electrodes, such as YBCO and LSCO (La-Sr-Co-O) have been recently shown to reduce fatigue in ferroelectric materials, which could enhance the commercial value of the technology.<sup>(2,4)</sup> The combining of both superconducting and ferroelectric properties of the heterostructures can open new opportunities for novel opto-electronic devices and high-speed digital electronics.<sup>(5)</sup>

Although there have been several investigations<sup>(2,3)</sup> on the development of  $\text{ABO}_3$  oxide films on cuprate high  $T_c$  superconducting substrates, there have been few description of the ferroelectric properties for these heterostructure in the low temperature regime. In this paper, we report on the synthesis of BST (100) thin films ( $x = 0.4$  and 0.5) deposited by pulsed laser deposition on c-oriented YBCO. The growth conditions, the crystalline structures and the interface properties of the BST(100)/c-oriented-YBCO heterostructures, as well as the ferroelectric and dielectric properties

of BST thin films on YBCO in the temperature range of 20 K to 300 K will be discussed.

## Fabrication of BST/YBCO Heterostructures

Thin film laser deposition was performed in a vacuum chamber with controlled oxygen pressure. Bulk superconducting YBCO and dielectric BST targets were irradiated at an incident angle of 45° with a KrF excimer laser (248 nm wavelength). C-oriented YBCO thin films were first deposited on  $\text{LaAlO}_3(100)$  at substrate temperature of 745 °C in  $\text{O}_2$  pressure of 200 mTorr. The detailed deposition conditions and the target requirements for making high quality YBCO films have been described elsewhere.<sup>(6)</sup> The lattice structures and superconducting transition temperatures  $T_c$  of YBCO thin films were measured before and after BST thin film growth and were found not to vary. The transition temperatures for the c-oriented YBCO films were nominally 83-89 K in our Au/BST/YBCO heterostructures.

BST thin films were deposited on top of the YBCO films which were partially covered by a contact mask during the deposition for the generation of a micro-capacitor. Optimization of the deposition conditions for BST thin films was undertaken by varying the deposition temperature from 400 °C to 650 °C and the ambient  $\text{O}_2$  pressure from 50 mTorr to 300 mTorr.

## Composition and Interface

The chemical composition of the deposited BST films was determined by electron probe microanalysis (EPMA) and Auger electron spectroscopy (AES). The content of Ba, Sr, Ti and O in the BST films could be determined by EPMA only for the thick BST films since barium existed in both the BST film and the bottom YBCO layer. This was done for 1  $\mu\text{m}$  thick BST films on YBCO substrates. Fig.1 shows the composition of  $\text{Ba}_{0.6}\text{Sr}_{0.4}\text{TiO}_3$  films deposited in the temperature range of 480°C to 600°C. The ratio of Ba to Sr did not show obvious change within the  $\Delta x = \pm 0.01$ . However, the Ti concentration in BST ( $x = 0.4$ ) was diminished at deposition temperatures above 540°C and was reduced ~ 2% in the films deposited at 600°C as compared to the films grown at 500°C. Such variation in Ti content with substrate temperature may be attributed to the high vapour pressure and poor sticking coefficients of Ti in comparison with Sr and Ba during laser ablation. Similar results of composition vs. deposition temperature have been obtained for  $\text{Ba}_{0.5}\text{Sr}_{0.5}\text{TiO}_3$  thin films deposited on c-oriented YBCO. Thus, a narrow temperature window exists for BST film synthesis on c-axis oriented YBCO at elevated temperatures.

BST/YBCO interface abruptness was investigate by AES and XPS measurements on the BST/YBCO samples. For

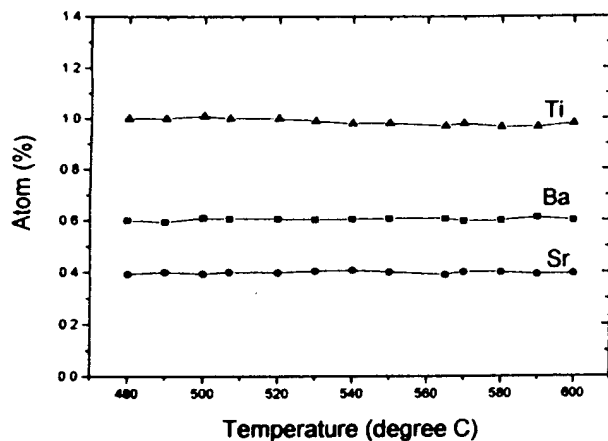


Figure 1. The temperature dependence of the composition of a  $\text{Ba}_{0.6}\text{Sr}_{0.4}\text{TiO}_3(100)$  on c-oriented YBCO/LaAlO<sub>3</sub>(100).

comparison, very thin BST films (~ 10-20 nm) were also deposited on YBCO/LaAlO<sub>3</sub>(100) under the same conditions as the thick BST films (~ 300 nm). Fig. 2 represents a depth profile of  $\text{Ba}_{0.5}\text{Sr}_{0.5}\text{TiO}_3$  with thickness of 20 nm deposited at 540 °C on c-oriented YBCO film. The depth profile shows the composition of the BST film is near stoichiometric and constant from the surface. The BST/YBCO interface where a BST/YBCO transition or mixing region of about 20 nm wide was observed. We believe that the initial YBCO surface roughness may contribute to the measurement of an apparently wide BST/YBCO interface.

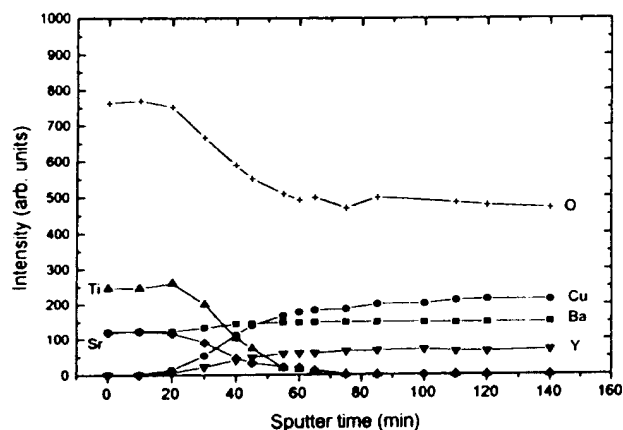


Figure 2. AES-XPS depth profile for the  $\text{Ba}_{0.5}\text{Sr}_{0.5}\text{TiO}_3(100)/\text{c-YBCO}$  heterostructure (one minute sputter time = 0.65 nm).

### Crystal Structure of BST Thin Films

Both types of BST thin films ( $x = 0.4$  and  $0.5$ ) deposited on c-oriented YBCO at substrate temperatures below 480°C did not show any crystallinity as determined by x-ray diffraction. Perovskite-type  $\text{Ba}_{0.5}\text{Sr}_{0.5}\text{TiO}_3(100)$  films started to form at 500°C - 550°C growth temperatures, and exhibited good crystallinity in the temperature range of 550°C - 620°C, as shown in Fig. 3. The (100) direction of the  $\text{Ba}_{0.5}\text{Sr}_{0.5}\text{TiO}_3$  film is parallel to the c-axis of YBCO film. The  $d_{(100)}$  spacing obtained from the (100) peak of the BST film is 0.397 nm in the deposition temperature range of 500°C to 640 °C, which is close to that of bulk BST ( $a = 0.3947$  nm).

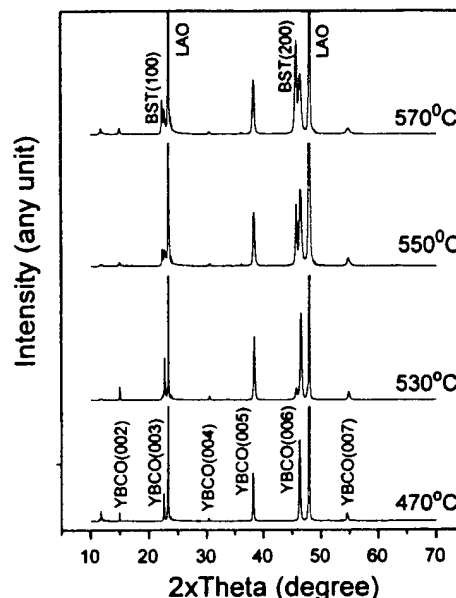


Figure 3. XRD patterns for  $\text{Ba}_{0.5}\text{Sr}_{0.5}\text{TiO}_3(100)$  films on c-oriented YBCO/LaAlO<sub>3</sub>(100) at different deposition temperatures.

The optimized growth condition for  $\text{Ba}_{0.6}\text{Sr}_{0.4}\text{TiO}_3$  has found to be similar to that for  $\text{Ba}_{0.5}\text{Sr}_{0.5}\text{TiO}_3$ . The  $d_{(100)}$  of the  $\text{Ba}_{0.6}\text{Sr}_{0.4}\text{TiO}_3$  thin film on YBCO is 0.399 nm which is also close to that of bulk BST ( $a = 0.3966$  nm).

It is well known that the volume of the unit cell exhibits a linear decrease with increasing Sr concentration in the  $\text{BaSrTiO}_3$  solid solution.<sup>(1)</sup> It has also been reported that lattice compression in the (100) plane was observed in BST thin films grown on MgO with no preferential orientation.<sup>(7)</sup> Lattice compression would require Ba deficiency which would be consistent with the high vapor pressure of Ba. The ratio of Ba to Sr in the BST films has been determined by EPMA for 1  $\mu\text{m}$  thick BST films as described above, as well as for similar films directly deposited on LaAlO<sub>3</sub> under equivalent conditions. EPMA analyses showed no obvious evidence of Ba deficiency or additional Ba in our BST ( $x = 0.4$  and  $x = 0.5$ ) thin films. In fact, the measured  $a = 0.397$  nm for  $\text{Ba}_{0.5}\text{Sr}_{0.5}\text{TiO}_3$  and  $a = 0.399$  nm for  $\text{Ba}_{0.6}\text{Sr}_{0.4}\text{TiO}_3$  are ~ 0.58% and 0.61% larger than the lattice constant in standard cubic bulk BST respectively.

Expansion along the growth direction of thin films has been seen for the high  $T_c$  superconducting films and ferroelectric films.<sup>(8)</sup> Its effects on ferroelectric properties would be of interest for future studies. Since there is an in-plane lattice mismatch of 2% ~ 3.9% between YBCO and BST, XRD pole figure analyses and Raman scattering measurements are currently underway to further understand the lattice structure, particularly in-plane structure changes and in-plane alignment in BST/YBCO heterostructures.

BST thin films deposited on Pt coated-Si or Pd coated-Si are nominally polycrystalline because of both lattice mismatch and interface chemistry.<sup>(9)</sup> In contrast, the oriented YBCO oxide substrate offers a much better chemical and structural base for perovskite BST film epitaxy with resultant crystalline BST film growth on YBCO.

In addition, the surface morphologies of BST (100) are significantly smoother than that of  $\text{Pb}(\text{Zr}_{0.52}\text{Ti}_{0.48})\text{O}_3$  (PZT) thin films deposited on c-oriented YBCO. This is probably due to both a better lattice constant match for BST than PZT on YBCO, and/or stronger interatomic affinity between BST and YBCO.

### Ferroelectric Properties of BST Films

The ferroelectric properties of the oriented BST films were studied in the temperature range of 20 K to 290 K, which is relevant to the ferroelectric phase transitions of BST, the superconducting transition of YBCO, and to the potential applications of integrated ferroelectric/superconducting devices.

A metal-ferroelectric-metal (MFM) device configuration was used for capacitance measurements. Top gold electrodes with contact areas of  $2 \times 10^{-3} \text{ cm}^2$  were deposited by sputtering Au onto the BST film surface, and the YBCO films were used for the bottom electrodes.

The ferroelectric properties of the system were defined by hysteresis loop measurements using a Sawyer-Tower bridge circuit with a 1 kHz sine wave.  $\text{Ba}_{0.5}\text{Sr}_{0.5}\text{TiO}_3(100)$  thin films showed ferroelectric behaviour below  $\sim 250\text{K}$  by the hysteresis loop measurements. For a 100 nm thick  $\text{Ba}_{0.5}\text{Sr}_{0.5}\text{TiO}_3(100)$  film the remnant polarization and coercive field are nominally  $1.4 \mu\text{C}/\text{cm}^2$  and  $4.1 \times 10^4 \text{ V}/\text{cm}$  respectively at  $T = 66 \text{ K}$ , and  $0.8 \mu\text{C}/\text{cm}^2$  and  $3.3 \times 10^4 \text{ V}/\text{cm}$  at  $201\text{K}$ . Similar results were obtained for  $\text{Ba}_{0.6}\text{Sr}_{0.4}\text{TiO}_3(100)$  films. For a 500 nm thick  $\text{Ba}_{0.6}\text{Sr}_{0.4}\text{TiO}_3(100)$  film the remnant polarization and coercive field are  $3 \mu\text{C}/\text{cm}^2$  and  $3.4 \times 10^4 \text{ V}/\text{cm}$  respectively at  $41\text{K}$ . The polarization of the film decreased with increasing temperature, as shown in Fig. 4. At  $\sim 250\text{K}$  the  $\text{Ba}_{0.6}\text{Sr}_{0.4}\text{TiO}_3(100)$  film became paraelectric, which is consistent with the Curie temperature of the bulk material<sup>(1,10)</sup>.

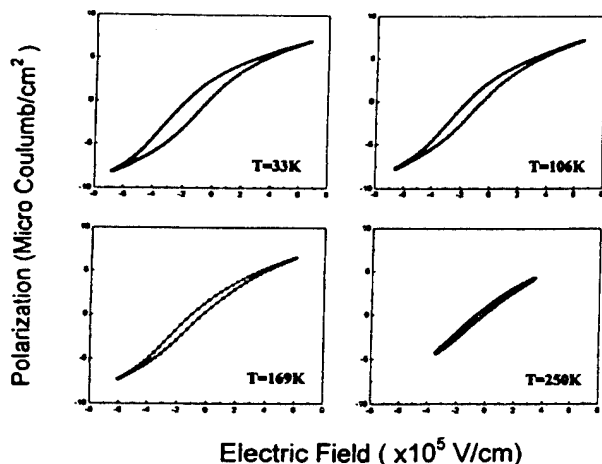


Figure 4. Polarization versus electric field for a  $\text{Au}/\text{Ba}_{0.6}\text{Sr}_{0.4}\text{TiO}_3(100)/\text{YBCO}$  capacitors under different temperature (BST film thickness  $d=200 \text{ nm}$ ).

### Dielectric Properties of BST Films

Capacitance measurements were performed using a Keithly 590 capacitance-voltage meter with a small ac signal (30 mV-100 mV) at 1 MHz while the dc bias voltage was swept back and forth between -15 and +15 volts at a sweep rate of 0.5 V/sec. The capacitance versus temperature plot for epitaxial  $\text{BST}(100)/\text{c-YBCO}$  shows one broad peak, as seen in Fig. 5. The maximum capacitance for the  $\text{Ba}_{0.5}\text{Sr}_{0.5}\text{TiO}_3(100)$  film,  $C_{\text{max}}(100)$  ( $x = 0.5$ ) appeared at  $\sim 100 \text{ K}$  (Fig. 5a) whereas for  $\text{Ba}_{0.6}\text{Sr}_{0.4}\text{TiO}_3$  thin films  $C_{\text{max}}(100)$  ( $x = 0.4$ ) is at  $\sim 170\text{K}$  (Fig. 5b). This was only slightly influenced by the BST film thickness in the range of 70 nm to 600 nm, by the BST film deposition temperature in the range of  $550^\circ\text{C}$  to  $620^\circ\text{C}$ , and by the measurement temperature from room temperature down to 20 K. It is interesting to note that the behavior of capacitance versus temperature shows slight thickness dependence for  $\text{BST}(110)$  films. The peak in capacitance increases from 110 K to 156 K with increasing  $\text{BST}(110)$  thin film thickness.<sup>(11)</sup> This may be due to the fact that  $\text{BST}(110)$  films are not as high of crystalline quality in the thickness range of 100-500 nm as are the  $\text{BST}(100)$  films.

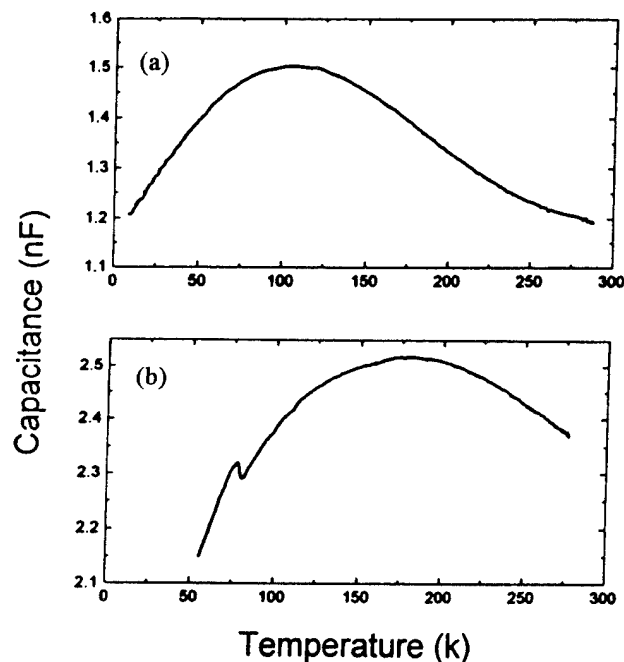


Figure 5. Capacitance as a function of temperature for  $\text{Au}/\text{Ba}_{1-x}\text{Sr}_x\text{TiO}_3(100)/\text{YBCO}$  heterostructures: (a)  $x=0.5$ , BST film thickness  $d = 320 \text{ nm}$ , (b)  $x=0.4$   $d=200 \text{ nm}$ .

The different structural phases of bulk BST have the same structures as  $\text{BaTiO}_3$ , e.g. cubic, tetragonal, orthorhombic and rhombohedral. The Curie temperature, at which the ferroelectric-paraelectric transition occurs for bulk  $\text{Ba}_{0.5}\text{Sr}_{0.5}\text{TiO}_3$  is at  $\sim 230 \text{ K}$  and for bulk  $\text{Ba}_{0.6}\text{Sr}_{0.4}\text{TiO}_3$  at  $\sim 250 \text{ K}$ .<sup>(1,10)</sup> This is evidenced in the bulk by a peak in the capacitance vs. temperature curve (C-T). However, there is no equivalent peak in the capacitance-temperature curves for either the  $\text{Ba}_{0.5}\text{Sr}_{0.5}\text{TiO}_3(100)$  or the  $\text{Ba}_{0.6}\text{Sr}_{0.4}\text{TiO}_3(100)$  thin films. It is not clear why the paraelectric-ferroelectric transition could be seen by hysteresis loop measurements, but not by C-T measurements, though it is usually difficult to

measure the phase transitions in ferroelectric thin films because of undefined contact effects, films being under tension or compression, or the lack of epitaxial completeness with different sizes of grains.<sup>(7, 12)</sup> A very broad peak identified down is, however, seen in the  $\text{Ba}_{0.5}\text{Sr}_{0.5}\text{TiO}_3(100)/\text{c-YBCO}$  and the  $\text{Ba}_{0.6}\text{Sr}_{0.4}\text{TiO}_3(100)/\text{c-YBCO}(100)$  system. It is not clear if these broad maxima correspond to structural phase transitions in the BST films. Again note that even in bulk BST single crystals the tetragonal-orthorhombic ( $T_1$ ) and the orthorhombic-rhombohedral transitions ( $T_2$ ) produce only weak peaks in C-T curves at  $T_1 = \sim 190\text{K}-220\text{K}$  and  $T_2 = \sim 150\text{K}-165\text{K}$ , respectively.<sup>(1,10)</sup> In addition, it is also not clear if the peak for the  $\text{Ba}_{0.6}\text{Sr}_{0.4}\text{TiO}_3(100)$  films at  $\sim 170\text{K}$  is at a higher temperature than for the  $\text{Ba}_{0.5}\text{Sr}_{0.5}\text{TiO}_3(100)$  film at  $\sim 100\text{K}$  due to an intrinsic behavior. It is obvious that for the complex BST/YBCO system additional studies of structure and electronic properties at low temperatures need to be done before determining the complete phase transition properties. A critical point to be made, however, is that both the BST(100) films with  $x = 0.4$  and  $0.5$  are ferroelectric below  $250\text{K}$ .

A second peak in C-T curves (Fig. 5) often occurred at  $78\text{K} - 85\text{K}$  due to the normal-superconducting transition of YBCO layer. This second peak in C-T may be caused by the proximity effect of superconducting YBCO layer. The proximity effect of superconducting YBCO could improve the properties of the interface between BST and YBCO layers. But this capacitance peak is too large to be due only to the proximity effect. The non-linear normal-superconducting transition behavior and non-linear ferroelectric properties could form a complex LCR system and would induce a big signal at the normal-superconducting transition temperature  $T_c$  in ac-measurement. A theoretical model simulation is in progress to better understand this point.

The dielectric constant measured for the BST films in this study ranges from  $100 - 450$ , which is lower than that of single crystal bulk BST ( $> 2000$ ). This difference may be due to the oriented grain crystalline nature of the BST films, and is supported by reports that the dielectric constant increases with increasing grain size.<sup>(12)</sup>

The resistivity for the BST/YBCO ( $x=0.4$  and  $x=0.5$  in BST films) structure was found only slightly change with temperature in the temperature range of  $20\text{K}$  to  $300\text{K}$ . The resistivity for a  $320\text{nm}$  thick  $\text{Ba}_{0.5}\text{Sr}_{0.5}\text{TiO}_3(100)$  films is about  $2 \times 10^{11}\text{Ohm-cm}$ , as shown in Fig. 6.

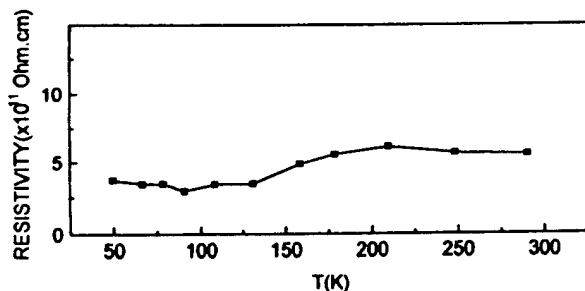


Figure 6. Resistivity as a function of temperature for a  $\text{Au/Ba}_{0.5}\text{Sr}_{0.5}\text{TiO}_3(100)/\text{YBCO}$  substrate.

## Summary

Both  $\text{Ba}_{1-x}\text{Sr}_x\text{TiO}_3(100)$  ( $x = 0.4$  and  $0.5$ ) thin films showed ferroelectric behavior below room temperature. Maximum polarization of  $1.4\text{ }\mu\text{C/cm}^2$  for  $\text{Ba}_{0.5}\text{Sr}_{0.5}\text{TiO}_3(100)$  and  $3.0\text{ }\mu\text{C/cm}^2$  for  $\text{Ba}_{0.6}\text{Sr}_{0.4}\text{TiO}_3$  on c-oriented YBCO were obtained. The paraelectric-ferroelectric transition occurred at  $\sim 250\text{K}$  for both BST(100) ( $x=0.4$  and  $x=0.5$ ) thin films. The capacitance versus temperature curves indicate principally one ferroelectric maximum in addition to a peak due to the YBCO normal-superconducting transition. The maximum capacitance  $C_{\text{max}}(100)$  of  $\text{Ba}_{0.5}\text{Sr}_{0.5}\text{TiO}_3(100)$  was at about  $100\text{K}$  and  $C_{\text{max}}(100)$  of  $\text{Ba}_{0.6}\text{Sr}_{0.4}\text{TiO}_3(100)$  appeared at  $\sim 170\text{K}$ . The dielectric constant of BST films ranged between  $100 - 450$  which is smaller than that of bulk BST, and maybe due to incomplete crystallinity in the thin films. The resistivity of  $\sim 10^{11}\text{ Ohm-cm}$  was attained in the temperature range of  $30\text{K}-300\text{K}$ .

## Acknowledgments

The authors wish to thank T. Q. Huang and Q. Yu for the assistant in this study. This work was supported in part by Texas Center for Superconductivity, NASA and the R. A. Welch Foundation.

## References

- [1] F. Jona and G. Shirane, *Ferroelectric Crystals*, Dover Publications, Inc., New York, 1993, P.248.
- [2] R. Ramesh, A. Inam, W. K. Chan, B. Wilkens, K. Myers, K. Remsch, D. L. Hart and J. M. Tarascon, *Science*, 252 (1991) 944.
- [3] N. J. Wu, A. Ignatiev, A. Mesarwi, H. Lin, K. Xie and H. D. Shih, *Jpn. J. Appl. Phys.* 32 (1993) 5019.
- [4] R. Dat, D. J. Lichtenwalner, O. Auciello and A. I. Kingon, *Appl. Phys. Lett.* 64 (1994) 2673.
- [5] H. Lin, N. J. Wu, K. Xie, X. Y. Li and A. Ignatiev, *Appl. Phys. Lett.* Aug. 1994.
- [6] X. Y. Li, Master thesis, University of Houston, 1994.
- [7] V. Mehrotra, S. Kaplan, A. J. Sievers, E. P. Giannelis, *J. Mater. Res.*, 8 (1993) 1209.
- [8] K. Fujimoto, Y. Kobayashi and K. Kubota, *Thin Solid Film*, 196 (1989), 249.
- [9] D. Roy and B. Krupanidhi, *Appl. Phys. Lett.* 62 (1993) 1056.
- [10] L. Benguigui, *Phys. Stat. Sol. (a)* 46 (1978) 337.
- [11] N. J. Wu, H. Lin, K. Xie, X. Y. Li and A. Ignatiev, (to be published).
- [12] T. Horikawa, N. Mikami, T. Makita, J. Tanimura and M. Kataoka, *Jpn. J. Phys.*, 32 (1993) 4126.



S.M. Landin and M.J. Haun  
Colorado Center for Advanced Ceramics  
Colorado School of Mines  
Golden, Colorado 80401

**Abstract-** This work investigates the crystallization of pure  $\text{Pb}_5\text{Ge}_3\text{O}_{11}$  (PG) and compositions in the  $\text{Pb}_5\text{Ge}_3\text{O}_{11}$ - $\text{PbZr}_{0.5}\text{Ti}_{0.5}\text{O}_3$  (PG-PZT) system. PG is of interest due to its low processing temperatures and possible application as pyroelectric sensors and nonvolatile ferroelectric memories. Compositions in the PG-PZT system crystallize to form multiple ferroelectric phases at relatively low temperatures, potentially offering a unique combination of ferroelectric properties and processing conditions. Ferroelectric thin films in the PG-PZT system were fabricated on (111) Pt-coated silicon substrates using sol gel processing techniques. Rapid thermal processing was utilized to investigate the time/temperature dependencies of crystallization, phase transformations and orientation of both  $\text{Pb}_5\text{Ge}_3\text{O}_{11}$  and  $\text{PbZr}_{0.5}\text{Ti}_{0.5}\text{O}_3$ .  $\text{Pb}_5\text{Ge}_3\text{O}_{11}$  films with a thickness of 2000Å crystallized with a c-axis orientation of greater than 90% when heat treated at 700°C for 30 seconds.

## INTRODUCTION

Lead germanate,  $\text{Pb}_5\text{Ge}_3\text{O}_{11}$  (PG), is a uniaxial ferroelectric with a spontaneous polarization aligned with the c-axis. PG has a second order phase transition [1] from a ferroelectric trigonal phase to a paraelectric hexagonal phase at approximately 177°C [2]. Lead germanate has attracted interest for several possible applications in the microelectronics industry. Due to its uniaxial nature, lead germanate has only 180° domains, therefore internal strains should not cause any relaxation of the polarization [3]. This is a favorable characteristic for memory storage applications. Single crystal PG is reported to have a dielectric constant of 50 and a pyroelectric coefficient of  $12 \times 10^{-6} \text{C/cm}^2\text{C}$  [4] along the c-axis. The combination of these two properties makes PG an attractive candidate for pyroelectric elements.

Polycrystalline PG has reduced ferroelectric properties, however orientation of the c-axis can increase the properties closer to those of single crystals [4]. The rapid orientation of the PG (001) has been observed in both thick and thin films [5-10]. Thin films of PG have been fabricated through a variety of methods including; vacuum condensation [11], sputtering [7,12-16], thermal evaporation [17], flash evaporation [18,19], laser ablation [8,20] and sol gel [8,10]. Lee and Dey [9] have reported excellent results for the sol gel processing of lead germanate thin films. Their results show the possibility of producing crack free, c-axis oriented, 1600Å films on platinized silicon substrates with a processing temperature of 450°C. For these films they report well saturated P-E hysteresis loops with  $P_r = 3.3 \mu\text{C/cm}^2$ .

The possibility of combining PZT with PG has been investigated to a limited extent [6,21-23]. The idea is to combine the excellent electrical properties of PZT with the low processing temperatures of PG. Cornejo [6] has found an enhancement of the pyroelectric coefficient for thick film compositions in the PG-PZT system when compared to pure PG.

## PROCEDURE

Precursors for the sol gel processing consisted of lead(II) acetate  $[\text{Pb}(\text{C}_2\text{H}_3\text{O}_2)_2 \cdot 3\text{H}_2\text{O}]$ ,<sup>a</sup> germanium ethoxide  $[\text{Ge}(\text{OC}_2\text{H}_5)_4]$ ,<sup>b</sup> titanium isopropoxide  $[\text{Ti}(\text{OC}_3\text{H}_7)_4]$ ,<sup>c</sup> and zirconium n-propoxide  $[\text{Zr}(\text{OC}_3\text{H}_7)_4]$ ,<sup>d</sup> with a solvent of 2-methoxyethanol  $[\text{C}_3\text{H}_8\text{O}_2]$ .<sup>a</sup> The processing followed

successive stages of reflux/distillation as outlined in Figure 1. Compositions studied include  $\text{Pb}_5\text{Ge}_3\text{O}_{11}$  (PG),  $\text{PbZr}_{0.5}\text{Ti}_{0.5}\text{O}_3$  (PZT),  $4\text{Pb}_5\text{Ge}_3\text{O}_{11}$ - $\text{PbZr}_{0.5}\text{Ti}_{0.5}\text{O}_3$  (4PG-PZT), and  $\text{Pb}_5\text{Ge}_3\text{O}_{11}$ - $4\text{PbZr}_{0.5}\text{Ti}_{0.5}\text{O}_3$  (PG-4PZT). Because of the large difference between the formula weights of PG and PZT, the molar ratios are very different from the weight or volume ratios. The 4PG-PZT composition corresponds to volume percents of 95% PG and 5% PZT, while the PG-4PZT corresponds to 56% PG and 44% PZT.

Spin coating<sup>e</sup> was utilized for the formation of the thin films on (111)Pt-coated silicon substrates.<sup>d</sup> The precursor solutions were filtered to 0.2μm immediately prior to spinning. Individual layers of 1500Å were formed by spinning at 4000 RPM for 30 seconds. Final thicknesses were obtained by applying successive layers with a one minute annealing between each layer to remove residual organics. Rapid thermal processing was used to thermally process the thin films. Heating and cooling rates were adjusted to 33°C/sec (2000°C/min).

The degree of c-axis orientation attributed to the films was calculated using the technique described by Lotgerling [24]. Basically, this compares the (001) intensities in the oriented film with those of a non-oriented sample and can be thought of as a "quality factor" for the degree of orientation.

## RESULTS AND DISCUSSION

### Phase Development

**$\text{Pb}_5\text{Ge}_3\text{O}_{11}$ :** Single layer, 1500Å films of PG were deposited and heated at a rate of 33°C/sec (2000°C/min) to a soak temperature without any prior annealing. The x-ray diffraction data (Fig.2) shows that by 60 seconds at 600°C or 30 seconds at 700°C, the PG films have achieved a

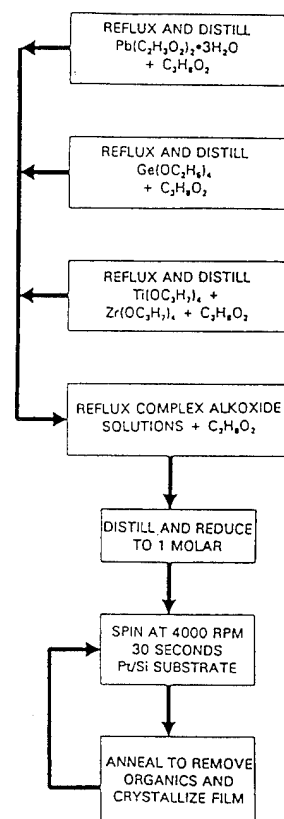


Figure 1. Flowchart of overall processing steps.

<sup>a</sup> Aldrich, Milwaukee, WI

<sup>b</sup> Gelest, Inc., Tullytown, PA

<sup>c</sup> Specialty Coating Systems, Inc., Indianapolis, IN, Model P6204

<sup>d</sup> Ramtron Corp., Colorado Springs, CO

degree of c-axis orientation greater than 90%. Films fired at 500°C did not reach this degree of orientation even after 10 minutes. Firing for 30 seconds at 600°C or 10 seconds at 700°C crystallized an additional phase which appears to correspond to  $\text{Pb}_3\text{GeO}_5$  [25]. This 3-1 phase was metastable and disappeared at longer firing times indicating that the stoichiometry of the composition was not the cause of the 3-1 formation. The 3-1 phase did not appear in any samples fired at 500°C.

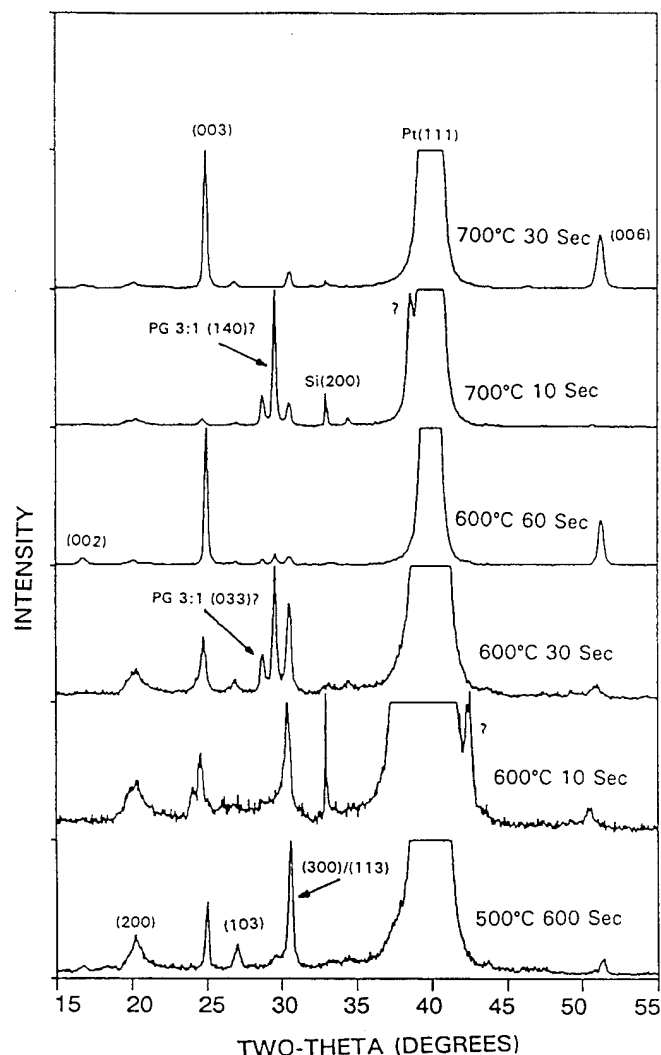


Figure 2. X-ray diffraction data for single layer PG films (1500Å). Heating and cooling rates  $\approx 33^\circ\text{C}/\text{sec}$ .

The crystallization of films with multiple layers was also investigated. The application of successive layers increased the degree of orientation. Four-layer films with a one minute, 500°C annealing after each of the first three layers and 10 minutes at 500°C after the fourth layer show c-axis orientations in excess of 60%. Films annealed at 700°C for one minute after the first three layers and 700°C for ten minutes after the final layer show orientations greater than 98% (Fig. 3).

$4\text{Pb}_3\text{Ge}_3\text{O}_{11}-\text{PbZr}_{0.5}\text{Ti}_{0.5}\text{O}_3$  and  $\text{Pb}_3\text{Ge}_3\text{O}_{11}-4\text{PbZr}_{0.5}\text{Ti}_{0.5}\text{O}_3$ : The influence of PZT on the crystallization behavior of PG in thin films is illustrated by the x-ray diffraction data in Figure 4. These films were all annealed at 500°C for one minute after each of the first three layers and 10 minutes at 700°C after the fourth layer. The PZT shifted the PG (001) peaks to a lower d-spacing (higher  $2\theta$ ). The 4PG-PZT composition shows a splitting of the (003) and (006) peaks. The PG(003) peak was located at  $d=3.54\text{\AA}$ , and shifts to  $d=3.44\text{\AA}$  in the PG-4PZT films. This

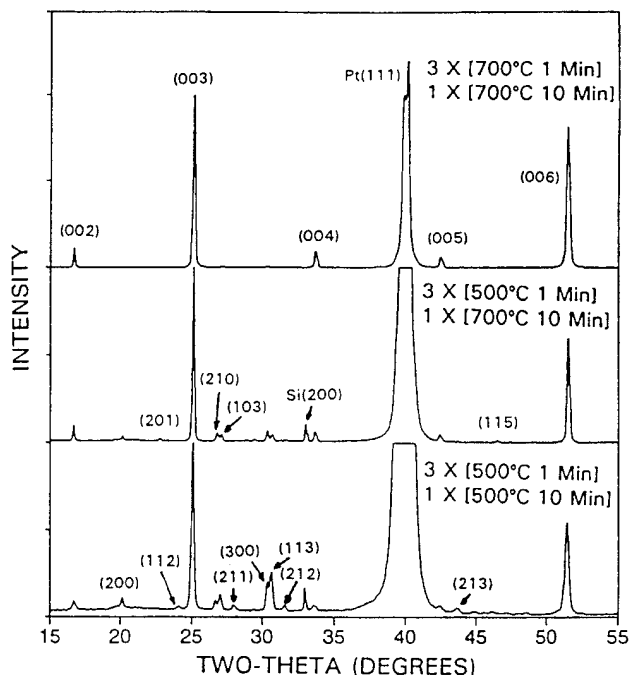


Figure 3. X-ray diffraction data for 4-layer PG films (6000Å). Heating and cooling rates  $\approx 33^\circ\text{C}/\text{sec}$ .

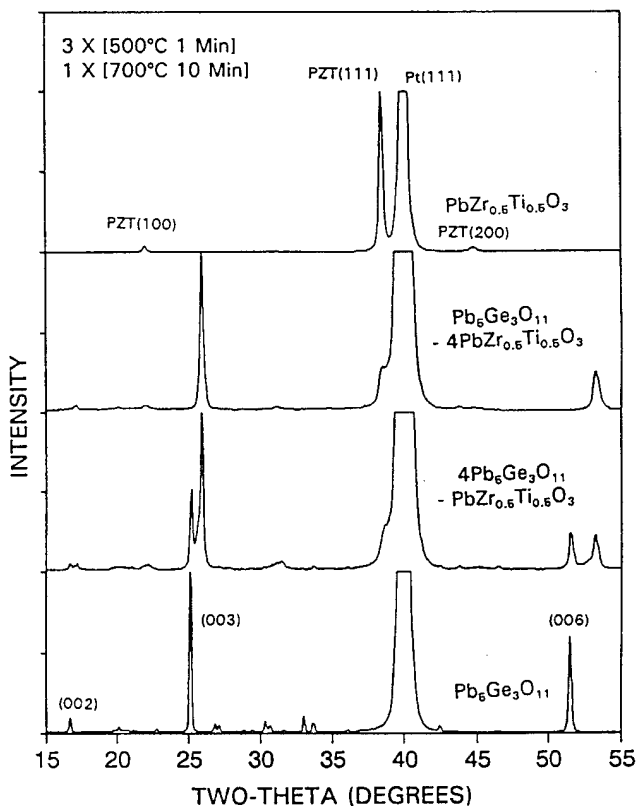


Figure 4. X-ray diffraction data for 4-layer films (6000Å) of PZT, PG-4PZT, 4PG-PZT and PG. Annealing conditions of 1 min at 500°C after each of the first 3 layers and 10 min at 700°C after the final layer.

progression of peak shifting can be seen in Figure 5 which shows x-ray diffraction data for single layer films of PG-4PZT and 4PG-PZT heated at a rate of 33°C/sec to 700°C. This structural change may be due to a partial solubility/substitution of either  $\text{Ti}^{4+}$  or  $\text{Zr}^{4+}$  into the PG, or from a combined stress effect of a high thermal expansion PG phase combined with an intermediate expansion PZT phase on a low expansion silicon substrate. Previous research [10] did not indicate any shift of the PG (001) lines in PG-PZT sol-gel compositions dried to form powders. Attempts were also made to anneal at lower temperatures after heat treatments to crystallize the films, however these heat treatments did not affect the position of the diffraction lines. Additional research is needed to further understand this behavior.

Figures 4 and 5 show that the PZT phase in pure PZT, 4PG-PZT and PG-4PZT compositions crystallized with a strong (111) orientation, epitaxially with the (111) platinum surface of the substrates. This orientation occurred after 60 seconds at 700°C in the pure PZT and PG-4PZT compositions. The PZT and PG-4PZT compositions initially crystallized a randomly oriented pyrochlore phase which is completely converted to the perovskite phase by 60 seconds at 700°C (Fig.5). The pyrochlore to perovskite conversion was delayed until 120 seconds in the 4PG-PZT films. In addition, the pyrochlore phase in this composition showed a cubic orientation, which was not observed in the PZT or PG-4PZT films.

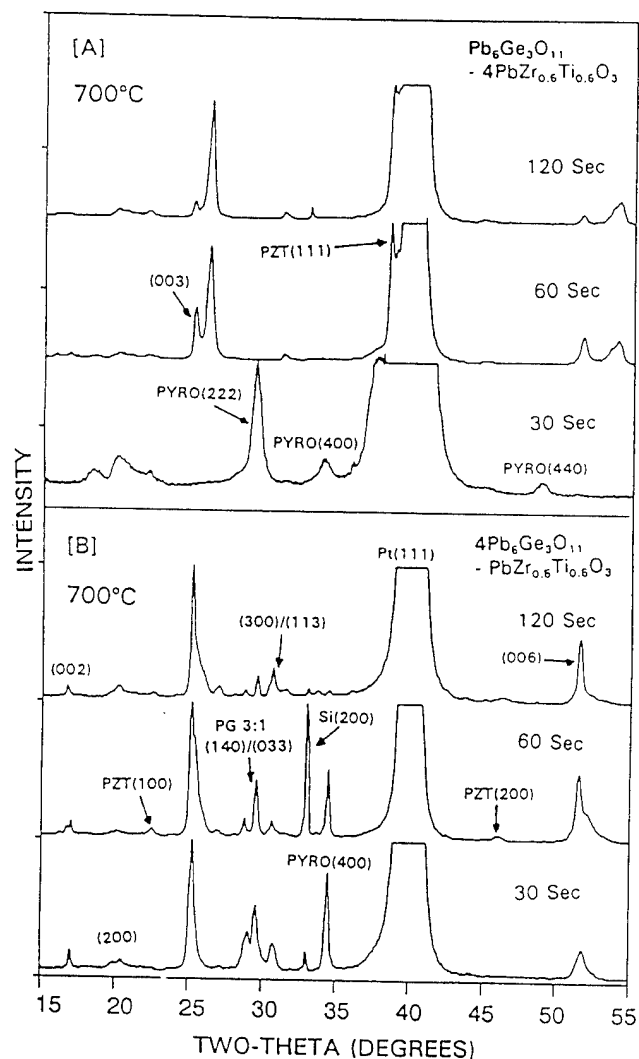


Figure 5. X-ray diffraction data for single layer PG-4PZT [A] and 4PG-PZT [B] films (1500Å). Heating and cooling rates  $\approx 33^\circ\text{C}/\text{sec}$ .

### Electrical Properties

Figure 6 shows the dielectric constant and loss of a 1.2 $\mu\text{m}$  PG film fired at 700°C for 10 minutes. The very broad peak in the dielectric constant shows a room temperature value of approximately 25 with the peak located at approximately 170°C. These results are similar to other work reported on PG thin films [14,17,19]. Schmitt et al.[14] observed that a decrease in grain size dramatically increased the breadth of the transition, while reducing the maximum peak in the dielectric constant. They reported that a 170°C transition temperature corresponded to a grain size of approximately 500nm. Thin films formed by flash - evaporation [19] showed a room temperature dielectric constant of approximately 20 for a 1.6 $\mu\text{m}$  thickness. These films showed a very broad transition with a maximum dielectric constant of only a factor of 1.6 above the room temperature value. PG films formed by thermal evaporation [17] showed a room temperature dielectric constant of approximately 12 with peak ratios of only 1.5-3 for 2 $\mu\text{m}$  thicknesses. Glass et al.[3] also investigated grain size effects in PG crystallized from glass. They reported an unstable polarization in PG with grain sizes less than 1 $\mu\text{m}$ .

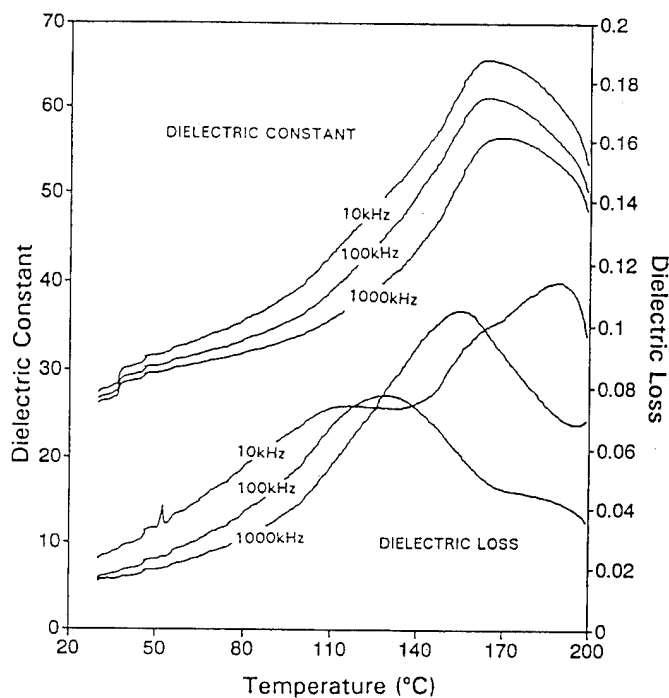


Figure 6. Dielectric data for an 8-layer PG film (1.2 $\mu\text{m}$ ). Annealing conditions of 1 min at 700°C after each of the first 7 layers and 10 min at 700°C after the final layer.

Attempts at measuring the electrical properties of PG thin films were met with a variety of difficulties. The large difference in the thermal expansion of PG and silicon (and PZT) appears to be a source for the development of large stresses contributing to film cracking. The PG films also crystallize to a very porous structure. Both of these factors contributed to difficulties in electrically contacting the samples and obtaining realistic properties. The processing temperatures appear to play a critical role in the final integrity of the film. These problems and questions are being addressed by ongoing research, and data are being collected on dielectric, ferroelectric, and pyroelectric properties of the thin films.

## SUMMARY

PG thin films show a rapid crystallization to c-axis orientation. 1500Å films showed orientations of greater than 90% after 60 seconds at 600°C or 30 seconds at 700°C. The deposition of successive layers with a one minute annealing between layers significantly increased the film orientations, especially at low temperatures.

The addition of PZT to PG has the effect of shifting the PG(001) peaks to a lower d-spacing in thin films. The degree and rate of shifting is related to the amount of PZT present. A PG-4PZT (44% PZT by volume) composition appears to bring this shifting to completion with the magnitude being equivalent to a reduction of the PG c-axis cell parameter by approximately 0.3Å. PZT, either in pure form or in a PG-PZT composition, shows strong (111) orientation epitaxially with the (111) platinum on the silicon substrates.

Many difficulties were encountered in the processing of lead germanate thin films suitable for the testing of electrical properties. These problems include porous structures and film cracking and are being addressed through continuing research. Initial results on dielectric properties of PG films show a low, broad peak in the dielectric constant that is shifted to approximately 170°C. These results are similar to those reported by other investigators [14,17,19].

## ACKNOWLEDGEMENT

This research was supported by the Office of Naval Research, Contract #N00014-92-J-1390, and the National Science Foundation, Contract #DMR-9158312. The authors would also like to thank Ramtron Corp. for their donation of silicon substrates.

## REFERENCES

- [1] K. Hisano and J.F. Ryan, "Raman Scattering from the ferroelectric Mode in  $5\text{PbO} \cdot 3\text{GeO}_2$ ," *Solid State Comm.*, Vol.11, No.1, pp.119-121, (1972).
- [2] H. Iwasaki, K. Sugii, T. Yamada and N. Niizeki, "5PbO · 3GeO<sub>2</sub> Crystal; A New Ferroelectric," *App. Phys. Lett.*, Vol.18, No.10, pp.444-445, (1971).
- [3] A. Glass, K. Nassau and J. Shiever, "Evolution of Ferroelectricity in Ultrafine-Grained  $\text{Pb}_3\text{Ge}_3\text{O}_{11}$  Crystallized from the Glass," *J. Appl. Phys.*, Vol.48, No.12, pp.5213-5216, (1977).
- [4] K. Takahashi, "Pyroelectric Sensors of Lead Germanate Thick Films," in *Advanced Ceramics*, edited by S. Saito (Oxford University Press, 1988), Ch.14, pp.240-253.
- [5] K. Takahashi, S. Shirasaki, K. Takamatsu, N. Kobayashi, Y. Mitarai and K. Kakegawa, "Pyroelectricity of Preferably - Oriented  $\text{Pb}_3\text{Ge}_3\text{Si}_x\text{O}_{11}$  Thick Films Prepared by the Printing Technique," *Jpn. J. Appl. Phys.*, Vol.22, pp.73-76 (1983).
- [6] I.A. Cornejo, "Low Temperature Crystallization of  $\text{Pb}_3\text{Ge}_3\text{O}_{11}$ - $\text{PbTiO}_3$  and  $\text{Pb}_3\text{Ge}_3\text{O}_{11}$ - $\text{Pb}(\text{Zr}_{1/2}\text{Ti}_{1/2})\text{O}_3$  Glass-Ceramic Systems with Multiple Ferroelectric Phases for Pyroelectric Applications," Ph.D. Thesis, T-4631, Colorado School of Mines, Golden, CO, July, 1994.
- [7] G. Kleer, H. Schmitt, H. Müser and K. Ehse, "Sputtered Ferroelectric Thin Films of Lead Germanate," *Ferroelectrics*, Vol.26, pp.757-760, (1980).
- [8] S. Krupanidhi, D. Roy, N. Maffei and C. Peng, "Pulsed Excimer Laser Deposition of Ferroelectric Thin Films," in *Proceedings of the 3rd International Symposium on Integrated Ferroelectrics*, Colorado Springs, CO, April 3-5, 1991, pp.100-115.
- [9] J.J. Lee and S.K. Dey, "Processing of a Uniaxial Ferroelectric  $\text{Pb}_3\text{Ge}_3\text{O}_{11}$  Thin Film at 450°C with C-Axis Orientation," *Appl. Phys. Lett.*, Vol.60, No.20, pp.2487-2488, (1992).
- [10] S.M. Landin and M.J. Haun, "Solution-Derived Ferroelectrics in the  $\text{Pb}_3\text{Ge}_3\text{O}_{11}$ - $\text{PbTiO}_3$ - $\text{PbZrO}_3$  System," *Ferroelectrics*, Vol.152, pp.91-96, (1994).
- [11] Y. Tomashpol'skii and M. Pentcheva, "Ferroelectric Behavior of Vacuum Condensates of Lead Germanate," *Sov. Phys. Solid State*, Vol.15, No.6, pp.1304, (1973).
- [12] H. Schmitt and G. Kleer, "Reactive Sputtering of Ferroelectric Lead Germanate  $\text{Pb}_3\text{Ge}_3\text{O}_{11}$ ," *Proc. 4th Coll. Internat. S.I. Plasmas e.l., Pulverisation Cath.*, Nice, 1982, pp.137-141.
- [13] H. Schmitt, R. Kartheim and G. Kleer, "Production and Properties of Undoped and Doped Lead Germanate Thin Films," *Ferroelectrics*, Vol.51, pp.35-39, (1983).
- [14] H. Schmitt, H.E. Müser, R. Kartheim and G. Kleer, "Properties of Undoped and Doped Ferroelectric Lead Germanate Thin Films," *Ferroelectrics*, Vol.56, pp.141-144, (1984).
- [15] H. Schmitt and G. Kleer, "Transformation from the Glassy State in Sputtered Amorphous Films of the Ferroelectric Lead Germanate  $\text{Pb}_3\text{Ge}_3\text{O}_{11}$ ," *Mat. Res. Bull.*, Vol.20, pp.829-833, (1985).
- [16] H. Maiwa, N. Ichinose and K. Okazaki, "Preparation of  $\text{Pb}_3\text{Ge}_3\text{O}_{11}$  Thin Films by Multiple Cathode Sputtering," *Proceedings of the 8th International Meeting on Ferroelectricity*, Gaithersburg, MD, August 8-13, 1993.
- [17] A. Mansingh and S. Krupanidhi, "Preparation and Properties of Thermally Evaporated Lead Germanate Films," *J. Appl. Phys.*, Vol.51, No.10, pp.5408-5412, (1980).
- [18] S. Krupanidhi, A. Mansingh and M. Sayer, "I-V & C-V Characteristics of Ferroelectric Lead Germanate on Silicon," *Ferroelectrics*, Vol.50, pp.117-122, (1983).
- [19] A. Mansingh and S. Krupanidhi, "Electrical and Structural Properties of Flash - Evaporated Ferroelectric Lead Germanate Films on Silicon," *Thin Solid Films*, Vol.80, pp.359-371, (1981).
- [20] C. Peng, D. Roy and S. Krupanidhi, "Oriented Lead Germanate Thin Films by Excimer Laser Ablation," *App. Phys. Lett.*, Vol.60, No.7, pp.827-829, (1992).
- [21] W. Schulze and J. Biggers, "Piezoelectric Properties of  $\text{Pb}_3\text{Ge}_3\text{O}_{11}$  Bonded PZT Composites," *Mat. Res. Bull.*, Vol.14, pp.721-730, (1979).
- [22] J. Collier, I. Cornejo and M. Haun, "Ferroelectric Thick-Films for Piezoelectric Applications," *Proceedings of the 8th International Meeting on Ferroelectricity*, Gaithersburg, MD, August 8-13, 1993, Accepted for publication in *Ferroelectrics* (1993).
- [23] I. Cornejo, J. Collier and M. Haun, "Ferroelectric and Crystallization Behavior in the  $\text{Pb}_3\text{Ge}_3\text{O}_{11}$ - $\text{PbTiO}_3$ - $\text{PbZrO}_3$  Glass-Ceramic System," *Proceedings of the 8th International Meeting on Ferroelectricity*, Gaithersburg, MD, August 8-13, 1993, Accepted for publication in *Ferroelectrics* (1993).
- [24] F.K. Lotgerling, "Topotactical Reactions with Ferrimagnetic Oxides Having Hexagonal Crystal Structures - I," *J. Inorg. Nucl. Chem.*, Vol.9, pp.113-123, (1959).
- [25] H. Hasegawa, M. Shimada and M. Koizumi, "Phase Relations and Crystallization of Glass in the System  $\text{PbO-GeO}_2$ ," *J. Mat. Sci.*, Vol.8, No.12, pp.1725-1730, (1973).

# PARAELECTRIC PROPERTIES OF PLT(28) REACTIVELY SPUTTERED BY MULTI-ELEMENT METAL TARGET

H. H. Kim and K. S. Sohn

Department of Electrical and Computer Engineering  
New Jersey Institute of Technology  
Newark, NJ 07102

L. M. Casas, R. L. Pfeffer, and R. T. Lareau  
Army Research Laboratory-EPSC, AMSRL-EP-EC-M  
Fort Monmouth, NJ 07703

## ABSTRACT

Lead lanthanum titanate (PLT, La=28 mol %) thin films were prepared by a multi-element metal target using reactive dc magnetron sputtering system. A post-deposition annealing treatment was applied to all as-deposited PLT thin films at the temperature ranges of 450–750 °C. Metal(Pt)–PLT–metal(Pt) (MDM) configuration as a planar capacitor of ULSI DRAM application is fabricated on Pt/Ti/SiO<sub>2</sub>/Si multi-layer substrate. The best results of dielectric constant and dissipation factor, using the paraelectric PLT thin film of 200 nm thick, were 1216 and 0.018, respectively. The highest charge storage density was 12.5  $\mu\text{C}/\text{cm}^2$  and the lowest leakage current density was 0.1  $\mu\text{A}/\text{cm}^2$ .

## INTRODUCTION

With the successful development of dynamic random access memory (DRAM) technology, the reduction of memory cell is subsequently required, reducing the area of the storage capacitor. It is, therefore, necessary to increase the charge storage density of the capacitor to maintain adequate operation. The requirement for high charge storage density has been achieved through improvements in the processing technology, reduction of the dielectric thickness, and innovations in the cell design [1]. The film thickness of the dielectric has been reduced to less than 10 nm in order to retain a sufficient charge storage in current DRAM technologies. A further reduction in thickness may have a deleterious impact such as a direct tunneling through thin dielectric films and has reached the fundamental limit in device processing technology. Hence, the thin dielectric materials such as conventional dielectrics do not appear to be sufficient for ultra large scale integration (ULSI) DRAMs. As a result, a new dielectric material that permits a capacitor with higher charge storage per unit area and is compatible with semiconductor processing is required for use in ULSI DRAMs.

Ferroelectric materials as an alternative dielectric with a higher dielectric constant have been widely considered by a number of researchers [1,2]. Lead lanthanum titanate ( $\text{Pb}_{1-x}\text{La}_x\text{Ti}_{1-x/4}\text{O}_3$ ; PLT) of the various ferroelectrics has excellent dielectric, electro-optic and piezoelectric properties with the control of composition in this system [3]. For DRAM application, the hysteresis property of ferroelectrics is not actually desirable, and the capacitor operates only as a linear capacitor. Therefore, paraelectric PLT (28) films with extremely high dielectric constant and normal dielectric characteristics offer significant advantages for next generation of DRAM capacitor.

The most important requirements in recent ULSI DRAM technologies with planar capacitor are high charge storage density, low leakage current density, and extremely high dielectric constant. In this paper, the dielectric and paraelectric properties of MDM capacitor using the PLT (28) thin films were investigated.

## EXPERIMENTAL PROCEDURE

Paraelectric (non-ferroelectric) PLT (La=28 mol %) thin films were prepared by a multi-element metal target using reactive dc magnetron sputtering system. The ratio of each component area on the multi-element metal target was set by the modified Sigmund's method, suggesting sputtering yields for Pb, La, and Ti metals. A post-annealing treatment to all as-deposited PLT thin films was applied at temperatures ranging from 450 to 750 °C for crystallization into the cubic perovskite structure. The composition of paraelectric PLT thin (200 nm) films by Auger electron spectroscopy (AES) showed 28 mol % of La content and the crystalline structure by X-ray diffraction (XRD) measurements allowed obviously the paraelectric perovskite phases at the annealing temperature above 550 °C.

All electrical measurements for DRAM application are performed utilizing a MDM configuration capacitor using the paraelectric PLT (28) thin films of 200 nm thick as a dielectric layer. Dielectric measurements are carried out on a Boonton 7200 capacitance meter with a peak voltage of 10 mV (i.e. 500 V/cm) and a frequency of 1 KHz. The most frequently used test to characterize ferroelectric or paraelectric PLT thin films is a typical Sawyer-Tower circuit [4]. This is an excellent measurement technique for establishing the relationship of polarization to electric field. Polarization-electric field (P-E) characteristics for charge storage density ( $Q_c$ ) is investigated by an HP54501A digitizing Oscilloscope and Wavetek (Model 270) Function Generator. Additional electrical characteristics such as, current-voltage (I-V)

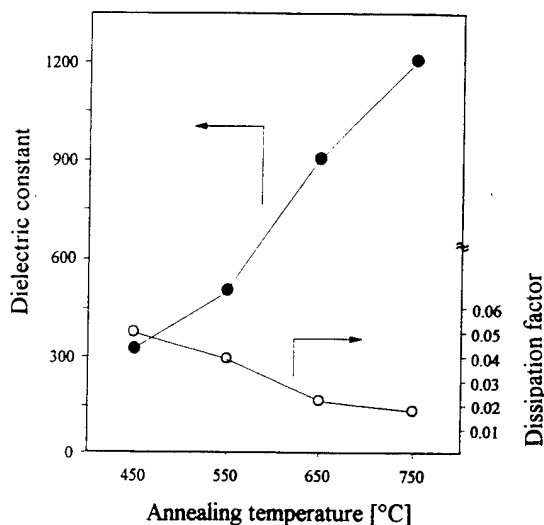


Fig. 1. Dielectric constant and dissipation factor of PLT (28) thin films as a function of post-annealing temperature.

plot for leakage current density and voltage-time (V-t) measurements for charging transient, are of interest for a capacitor dielectric of the 1-T DRAM cell. These topics are the subject of reliable characteristics and the transient behavior of paraelectric PLT (28) thin films. The current-voltage characteristics for leakage current density are measured by an HP4145B Semiconductor Parameter Analyzer.

### RESULTS AND DISCUSSION

#### Dielectric properties

The dielectric constant and dissipation factor (loss tangent) as a function of post-annealing temperature are presented in Figure 1. The dielectric constant increases significantly and the dissipation factor decreases slightly, as the annealing temperature is increased. The dielectric properties are dependent on the changes in the stoichiometric composition as well as in relative quantities of amorphous and crystalline structures with variation of annealing heat treatment. Thus, with a rise in annealing temperature, the amorphous phase and the excess PbO structure with poor dielectric properties disappear. It is transformed into the crystalline structure, i.e., the paraelectric perovskite PLT phase. Conversely, the dissipation factor is reduced from 0.051 to 0.018 with the increasing annealing temperature. It also depends on the existence of the amorphous and excess PbO phases.

The dielectric constant of the PLT thin films was sometimes difficult to measure, because of the low resistance of the films and the presence of microcracks and porosity caused by high temperature treatment. Fox et al [5] have commented that the dielectric properties can be expressed by morphological conditions of the thin films with coexistence of the three phases such as perovskite PLT phase, excess PbO and air. The excellent dielectric properties of PLT thin films are achieved by the continuity of the perovskite PLT phase. The PbO phase and porosity resulting from Pb evaporation give rise to the discontinuity of the perovskite PLT phase in the thin films. The PbO phase has a higher conductivity than the perovskite PLT phase. The dielectric constant decreases and the dissipation factor increases due to the presence of excess PbO phases in the films annealed at lower annealing temperature. The best results of dielectric constant and dissipation factor at low field measurement (500 V/cm), as shown in Figure 1, are approximately 1216 and 0.018, respectively.

#### Charge storage density

The polarization-electric field (P-E) characteristics of the

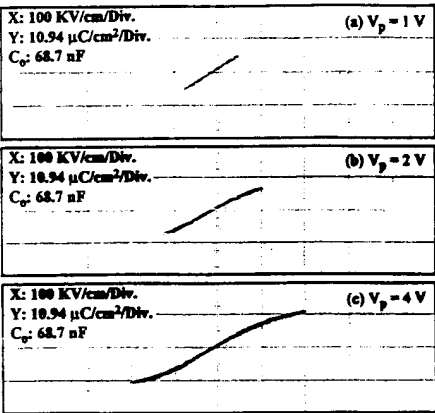


Fig. 2. P-E characteristics with different peak voltages for 200 nm PLT (28) thin film at 750 °C for 5 min.

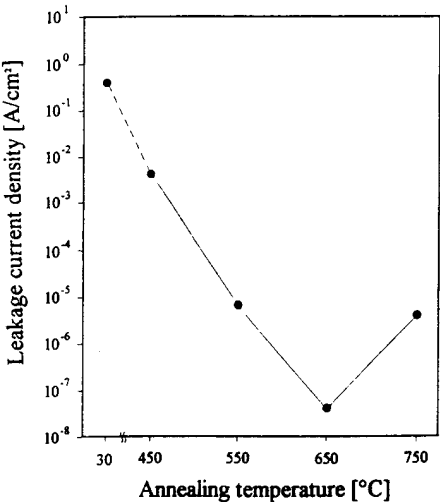


Fig. 3. Leakage current density as a function of annealing temperature for PLT films at 150 KV/cm (3 V).

paraelectric PLT (28) thin films are measured using a typical Sawyer-Tower circuit with a 500 Hz sine wave. The P-E measurements of the films under different peak voltages are presented in Figure 2. The paraelectric PLT (28) thin film is annealed at 750 °C for 5 min. The P-E curve at low peak voltage of 1 V (50 KV/cm) is similar with the linear behavior of a normal dielectric material as shown in Figure 2 (a). The P-E characteristics are gradually developed to the paraelectric state of nonlinear behavior, as the peak voltage increases enough. The P-E curve at a peak voltage of 2 V presents the prominent paraelectric nonlinear behavior. The charge storage density at the peak voltage of 4 V (200 KV/cm) is around 12.5 μC/cm² as shown in Figure 2 (c), and the effective dielectric constant is about 706.

#### Leakage current density

The leakage current density is one of important limiting factors for the DRAM capacitor dielectric. High leakage current places important limitation in the operation of a unit memory cell. It is necessary therefore to reduce the leakage current per unit area in order to prevent the capacitor from discharging between refreshing cycles. The leakage current density as a function of post-annealing temperature is shown in Figure 3. The lowering trend of leakage current with different annealing temperature at the electric field of 150 KV/cm (3 V) is presented. The leakage current density

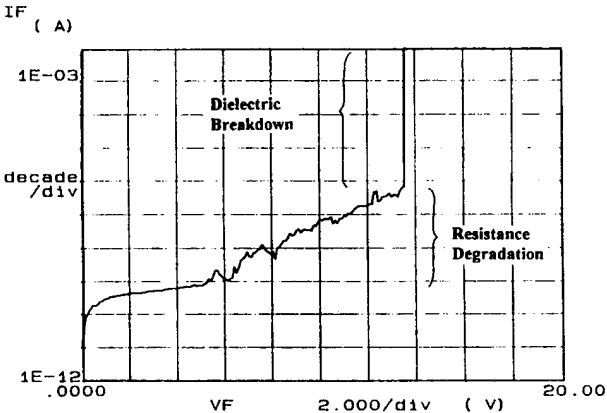


Fig. 4. The phenomena of dc voltage-induced resistance degradation suddenly rising in the leakage current level prior to dielectric breakdown.

diminishes slightly except at 750 °C, as the post-annealing temperature increases. It is noted that the leakage current density with the increasing annealing temperature is closely related to the degree of crystallinity. Since the intensity of each diffraction peak is proportional to the effect of a rise in post-annealing temperature, the paraelectric PLT (28) thin films are further crystallized into the cubic perovskite phase. The PLT thin film annealed at 750 °C exhibits larger leakage current density than that at 650 °C. This elevation in leakage current observed at high heat treatment shows a similar tendency with the results from Chikarmane et al [6], suggesting that the vaporization of Pb at high annealing temperature leads to the augmentation of oxygen vacancies.

Figure 4 shows the dc voltage-induced resistance degradation and the dielectric breakdown in the paraelectric PLT thin film (200 nm) annealed at 650 °C. The leakage current is 85 nA (2.5  $\mu$  A/cm<sup>2</sup>) at a reference voltage of 5 V. The resistance degradation starts slowly at 5 V (250 KV/cm) prior to the dielectric breakdown at 13.5 V (675 KV/cm). Waser et al [7] and Baiatu et al [8] discussed in detail the phenomena of resistance degradation in the perovskite-type titanates, SrTiO<sub>3</sub> films. The resistance degradation under dc voltage stress is closely related to the ionic current in the interior of the dielectrics caused by the electromigration of oxygen vacancies across grain boundaries and the specific defect structure in the films. The electromigration of oxygen vacancies, which are positively charged, tend to segregate toward the cathode under the applied dc voltage. The oxygen vacancies are depleted in the anode side and concentrated into the cathod side. The oxygen vacancy concentration is increased in the cathod region between both electrodes with a rise of the dc voltage. Therefore, such a field-induced segregation results in the increase of the electrical conductivity in the dielectric titanate, and then leads to the phenomena of dc voltage-induced resistance degradation. It is supposed that the dc voltage-induced resistance degradation is observed at a somewhat low electric field because the top electrode is biased positively.

#### Voltage time measurements

Voltage-time (V-t) characteristics are another method used to estimate the charge storage density which is calculated from the transient response of a MDM capacitor using the unipolar pulse measurement technique. The switching voltage is monitored with an oscilloscope by measuring the voltage drop across a grounded resistor in series with the film capacitor. Figure 5 (a) shows the schematic test circuit with a peak voltage of the unipolar pulse and a 1 K $\Omega$  load resistor as a series resistance to simulate the transistor of the DRAM unit cell. The charge storage density is gained by the estimation of the triangular area as shown in Figure 5 (b). The switching time ( $t_s$ ) is defined as the time that decays to a point 90 % down from the maximum current transient value. The simple approximation for the charge storage density is estimated as the following [9]:

$$Q_c = \frac{1}{A} \int i dt = \frac{1}{A} \int_0^{\infty} \frac{V_{max}}{R_L} e^{-\frac{t}{\tau}} dt$$

$$\cong \frac{V_{max} t_s}{2 R_L A}$$

where,  $V_{max}$  is the maximum response voltage,

$R_L$  is the load resistance, and

$A$  is the area of the paraelectric MDM capacitor.

The transient response is nearly exponential as shown in Figure 5 (b).

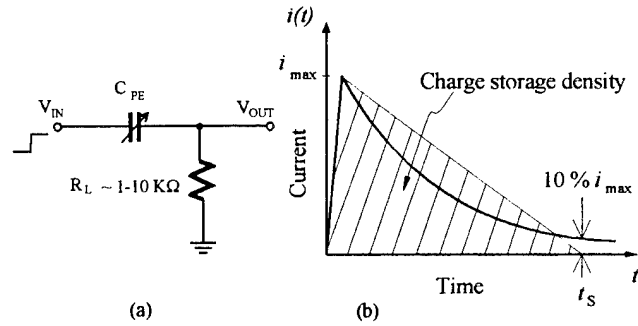


Fig. 5. (a) Schematic test circuit with a peak voltages of unipolar pulse and a load resistor, (b) the estimation of triangular area from transient response of I-t curve shows charge storage density.

Figure 6 presents the voltage-time curves with the different peak voltage of the unipolar pulse experiments for the estimation of charge storage density and charging time. The triangular area (i.e., charge storage density) is also increased, as the peak voltage of unipolar pulse increases. The detailed results, compared with the data of P-E measurements, are summarized in Table 1. It is noted that the charge storage density is 11.3  $\mu\text{C}/\text{cm}^2$  at 4 V (200KV/cm) peak voltages. The charge storage density estimated by the above equation produces an inaccuracy of about 9.7 % by comparison with the P-E characteristics.

#### CONCLUSION

The reactively sputtered PLT (28) thin films by multi-component metal target appeared to have the paraelectric properties with high charge storage density, low leakage current density, and extremely high dielectric constant. The dielectric constant and dissipation factor in the paraelectric PLT thin film, annealed at 750 °C, are

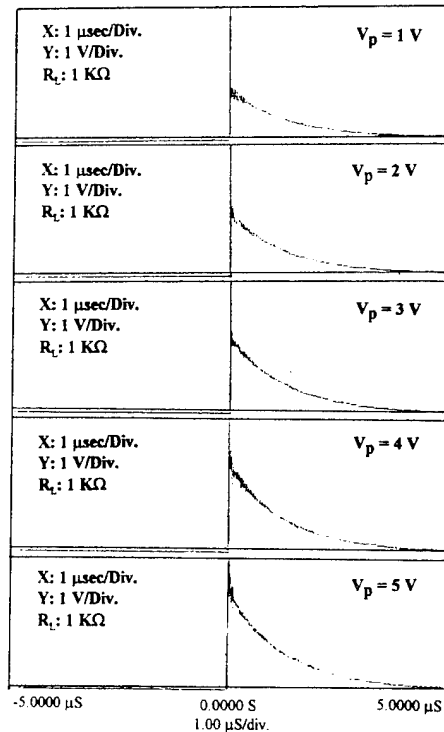


Fig. 6. Voltage-time characteristics of PLT (28) MDM capacitors with different peak voltage of unipolar pulse.

**Table 1.** Charge storage density calculated by V-t measurements in comparison with the results of P-E measurement.

Peak Voltage (V)	Electric Field (KV/cm)	V-t plot		P-E plot	
		Charge Density ( $\mu\text{C}/\text{cm}^2$ )	Effective Dielectric Constant	Charge Density ( $\mu\text{C}/\text{cm}^2$ )	Effective Dielectric Constant
1	50	5.22	1179	3.2	723
2	100	6.80	768	6.0	678
3	150	8.59	647	—	—
4	200	11.30	638	10.3	580
5	250	13.26	599	—	—

1216 and 0.018, respectively. The charge storage density of PLT thin film annealed at 750 °C is around 12.5  $\mu\text{C}/\text{cm}^2$ . The leakage current density of film treated at 650 °C was 0.1  $\mu\text{A}/\text{cm}^2$  at the electric field of 0.25 MV/cm<sup>2</sup>. It is clear from the results mentioned above that the optimization between minimum leakage current density and maximum charge storage density is essentially adjusted by the conditions of the post-deposition annealing process.

Paraelectric PLT thin films are a potentially attractive candidate for the storage dielectric capacitor in future DRAMs. PLT thin films with a linear dielectric characteristic offer significant advantages over conventional dielectrics and are also preferable to nonlinear ferroelectric thin films for the operation of ULSI DRAMs.

#### REFERENCES

- [1] L. Parker, and A. Tasch. "Ferroelectric Materials for 64 and 256 Mb DRAMs." IEEE Circuit Dev. Mag. pp. 17, Jan. 1990.
- [2] A. Tasch. "Storage Capacitor Dielectric Issues and Requirements in Gigabit One-Transistor Cell MOS RAMs." 184th Electrochem. Soc. Meeting, New Orleans, pp. 238, 1993.
- [3] H. Adachi and K. Wasa. "Sputtering Preparation of Ferroelectric PLZT Thin Films and Their Optical Application." IEEE Trans. Ultra. Ferro. Freq. Control, vol. 38, no. 6, pp. 645, 1991.
- [4] C. Sawyer, and C. Tower. "Rochelle Salt as a Piezoelectric." Phys. Rev. 35, 269, 1930 or Diamant, H., K. Drenck, and R. Pepinsky. "Bridge for Accurate Measurement of Ferroelectric Hysteresis." Rev. Sci. Instru. vol. 28, no. 1, pp. 30, 1957.
- [5] G. Fox, and S. Krupanidhi. "Composition/Structure/Property Relations of Multi-Ion-Beam Reactive Sputtered Lead Lanthanum Titanate Thin Films: Part III. Electrical Properties." J. Mater. Res. vol. 8, no. 9, pp. 2203, 1993.
- [6] V. Chikarmane, C. Sudhama, J. Kim, J. Lee, A. Tasch, and S. Novak. "Effects of Post-Deposition Annealing Ambient on the Electrical Characteristics and Phase Transformation Kinetics of Sputtering Lead Zirconate Titanate (65/35) Thin Film Capacitors." J. Vac. Sci. Technol. vol. 10, no. 4A, pp. 1562, 1992.
- [7] R. Waser, T. Baiatu, and K. Härdtl. "dc Electrical Degradation of Perovskite-Type Titanate: I. Ceramics." J. Amer. Ceram. Soc. vol. 73, no. 6, pp. 1645, 1990.
- [8] T. Baiatu, R. Waser, and K. Härdtl. "dc Electrical Degradation of Perovskite-Type Titanate: III. A Model of the Mechanism." J. Amer. Ceram. Soc. vol. 73, no. 6, pp. 1663, 1990.
- [9] J. Carrano, C. Sudhama, V. Chikarmane, J. Lee, A. Tasch, W. Shepherd, and N. Abt. "Electrical and Reliability Properties of PZT Thin Films for ULSI DRAM Applications." IEEE Ultra. Ferro. Freq. Control, vol. 38, no. 6, pp. 690, 1991.



# Ferroelectric Properties of (Pb,La)TiO<sub>3</sub> Thin Films by Multiple Cathode Sputtering

Hiroshi Maiwa, Noboru Ichinose<sup>1</sup> and Kiyoshi Okazaki

Shonan Institute of Technology, 1-1-25 Tsujidou-Nishikaigan,  
Fujisawa, Kanagawa 251, Japan

<sup>1</sup>Waseda University, 3-4-1 Okubo, Shinjuku-ku, Tokyo 169, Japan

**Abstract** (Pb,La)TiO<sub>3</sub> (PLT, La/Ti=0.17, 0.20 and 0.24) thin films were prepared by multiple cathode rf-magnetron sputtering. Perovskite PLT could be obtained on various substrates at 460 ~ 540 °C. The electrical properties of these films were investigated. The PLT thin films deposited on Pt/MgO substrate exhibited higher crystallinity, squarer hysteresis loops and higher remanent polarization (Pr) values compared to the films on the Pt/SiO<sub>2</sub>/Si substrate. By lowering substrate temperature, ferroelectric properties were improved. By controlling the Pb/Ti incident ratio, thin films with different Pb contents were formed at 460 °C. The Pb-deficient PLT film showed weak ferroelectric behaviour. While, the Pb-rich PLT film showed a saturated hysteresis loop. The fatigue resistance was increased with the Pb content. The relation between ferroelectric properties and the Pb content are discussed in terms of the build-up of space charge.

## INTRODUCTION

In recent years, ferroelectric thin films such as lead zirconate titanate (PZT) have been attracting great attention because of their potential applications in nonvolatile random access memory (NVRAM) [1], dynamic random access memory (DRAM) and pyroelectric sensors [2][3].

NVRAM devices will require stable long-term performance to be successful [1]. However, ferroelectrics lose their remanent polarization (P<sub>r</sub>) as the number of switching cycles increase. This phenomenon is generally called ferroelectric fatigue, and is one of the major concern in terms of the reliability of NVRAM devices. Though acceptable fatigue performance has been achieved by several groups [4][5][6][7], the exact reason for the improvement of the fatigue resistance is unknown. Several groups have suggested different fatigue mechanisms which include the growth of conducting dendrite [8], build-up of space charge due to mobile oxygen vacancies [9], defect entrapment at electrode-ferroelectric film interface [10] and physical device degradation [11]. However, none have been fully understood yet.

In this study, multiple cathode rf-magnetron sputtering was used to deposit (Pb,La)TiO<sub>3</sub> (PLT) thin films on various substrates. This method offers a highly controllable deposition process because the sputtering rate of each target can be changed individually [12]. Compared to a compound target, larger rf power can be input to the metal target. PLT was chosen because it can be grown at lower substrate temperatures compared to PZT, and because its properties can be controlled with lanthanum content. An attempt has been made to understand the role of substrate temperature, La and Pb content on ferroelectric properties.

## EXPERIMENTAL

The apparatus employed in this experiment is shown in Fig.1. The sputtering targets used were 3-inch disks of PbO (99.99%), La (99.9%) and Ti (99.99%) metal, and each target was individually controlled by rf power supply. The substrates were Pt/SiO<sub>2</sub>(1000nm)/Si, RuO<sub>2</sub>/Ru/SiO<sub>2</sub>(1000nm)/Si, Pt/MgO and RuO<sub>2</sub>/Ru/MgO. A ruthenium oxide (RuO<sub>2</sub>) film was formed by reactive sputtering in an atmosphere of argon/oxygen gas mixture [13]. The substrates were fixed to the rotary-type substrate holder through a load-lock chamber. The substrate holder was rotated at a speed of 11.25rpm. Input RF power for Ti was kept at 450W, and that for PbO was at 55W ~ 75W. Reactive sputtering was carried out in a mixed gas of argon and oxygen [14].

The chemical composition of the films was determined by inductively coupled plasma spectroscopy (ICP) and electron probe microanalysis (EPMA). Thin film crystallography was performed by X-ray diffraction (monochromated CuK $\alpha$  radiation). The surface morphology was observed by a field-emission scanning electron microscope (FE-SEM). A typical deposition rate was 0.8 ~ 0.9nm/min.

270nm-thick film was used for electrical measurements. Au thin films were evaporated at room temperature as the top electrode with a diameter of 0.2mm. Ferroelectric properties were measured using the Radiant Technology RT66A tester operating in the virtual ground mode. Fatigue measurement was also conducted with the RT66A tester.

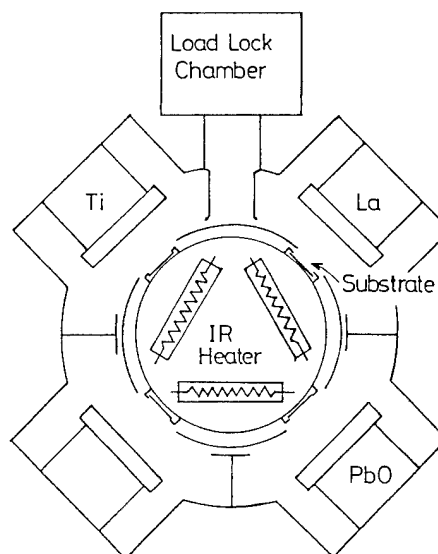


Fig.1 Schematic of a cross section of multiple cathode sputtering.

## RESULTS AND DISCUSSION

### Film preparation

Figure 2 shows X-ray diffraction patterns of the PLT(La/Ti=0.17) thin films deposited on various substrates at 460 °C. Films having a perovskite structure could be obtained. This result suggests that multiple cathode sputtering using metal target was effective in lowering the substrate temperature compared to the sputtering using compound target [3].

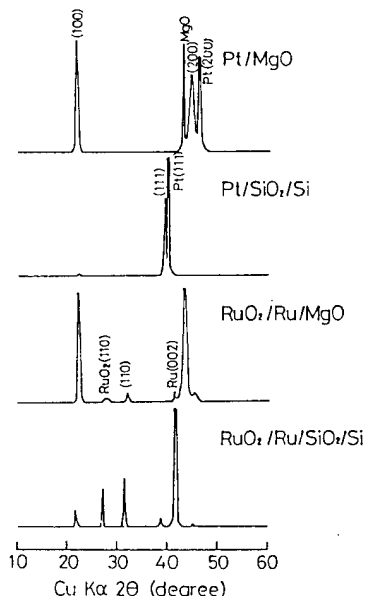


Fig.2 X-ray diffraction patterns of PLT thin films deposited on various substrates at 460 °C.

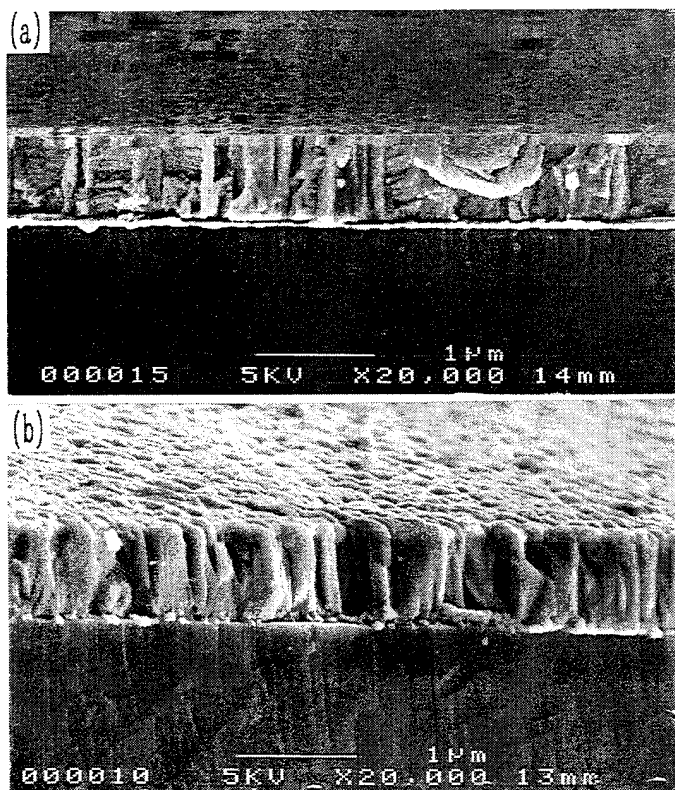


Fig.3 FE-SEM photograph of the surface of PLT thin films deposited on (a)Pt/MgO and (b)RuO<sub>2</sub>/Ru/MgO at 460 °C.

PLT films with preferred c-axis orientation were formed on Pt/MgO and RuO<sub>2</sub>/Ru/MgO substrates. On the other hand, films deposited on Pt/SiO<sub>2</sub>/Si showed preferred orientation in the (111) plane. In the case of RuO<sub>2</sub>/Ru/SiO<sub>2</sub>/Si, perovskite PLT films formed did not show any preferred orientation.

Figure 3 shows FE-SEM micrographs of the PLT thin films deposited on (a)Pt/MgO and (b) RuO<sub>2</sub>/Ru/MgO at 460 °C. The PLT thin film on Pt/MgO consists of fine grains. While the one on RuO<sub>2</sub>/Ru/MgO consist of larger grains of about 300nm. The difference in grain size may be attributed to the difference of the electrode. In the case of the platinum electrode, the Pt grains were not observed by FE-SEM. On the other hand, the grain size of ruthenium oxide was 300 ~ 400nm [13].

### Lanthanum content dependence

Figure 4 shows that hysteresis loops of the PLT (La/Ti=0.17, 0.20, 0.24) thin films deposited on Pt/SiO<sub>2</sub>/Si substrates at 460 °C. With increasing lanthanum content, coercive field ( $E_c$ ) and  $P_r$  decreased. In PLT (La/Ti=0.17, 0.20) films, their polarization decreased after  $\pm 5V \cdot 10^7$  cycle switching. On the other hand, PLT (La/Ti=0.24) film exhibited slim loop, nearly paraelectric behavior, because its Curie temperature is near room temperature. Its hysteresis loop almost unchanged after  $\pm 5V \cdot 10^7$  cycle switching. This film is considered to be suitable for DRAM application.

### Substrate and substrate temperature dependence

Figure 5 shows that hysteresis loops of the PLT (La/Ti=0.17) thin films deposited on (a) Pt/SiO<sub>2</sub>/Si and (b) Pt/MgO at 460 °C and 540 °C. The PLT films deposited on Pt/MgO substrate exhibited squarer hysteresis loops and higher  $P_r$  values, compared to the films on the Pt/SiO<sub>2</sub>/Si substrate. In the film on Pt/MgO, remarkable hysteresis shift on E-axis was observed.

Compared to the film deposited at 540 °C, the film deposited at 460 °C showed lower  $E_c$ , suggesting the film deposited at lower temperature contained less strain derived from substrate and/or defects. Their fatigue characteristics were shown in Fig.6. It is noted the film deposited at 540°C exhibited worse fatigue resistance. We reported previously that, from XPS analysis, Pb-deficient layer were formed at film/substrate interface probably due to the Pb re-evaporation from substrate [14]. Therefore, it is presumed that the defect at film/substrate interface decreased by lowering substrate temperature, then ferroelectric properties and fatigue resistance were improved.

The fatigue resistance on ruthenium oxide was improved by using RuO<sub>2</sub> as both the top and bottom electrode. These results will be reported in another paper [13].

### Lead content dependence

In order to clarify the Pb content dependence, PLT (La/Ti=0.20) films with various Pb content were deposited on Pt/SiO<sub>2</sub>/Si substrates at 460 °C. The hysteresis loops and the fatigue characteristics of these samples are shown in Fig.7 and Fig.8, respectively. Pb-deficient, Pb<sub>0.75</sub>La<sub>0.20</sub>TiO<sub>3</sub> film exhibited a slim loop, which suggests this film showed weak ferroelectric behavior. With increasing lead content, hysteresis loop became saturated and their  $P_r$  increased compared to the Pb-deficient film. Fatigue resistance increased with increasing Pb content. It

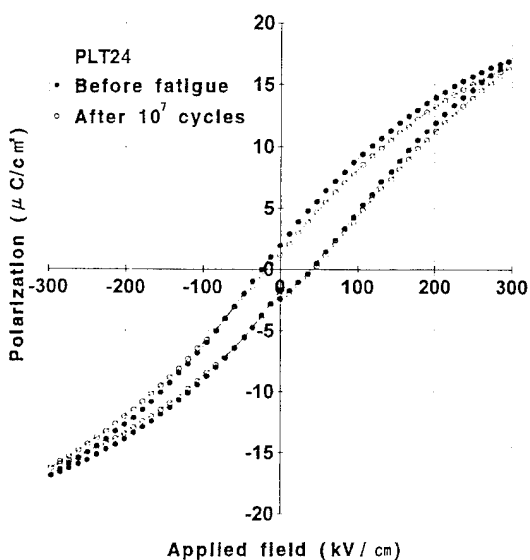
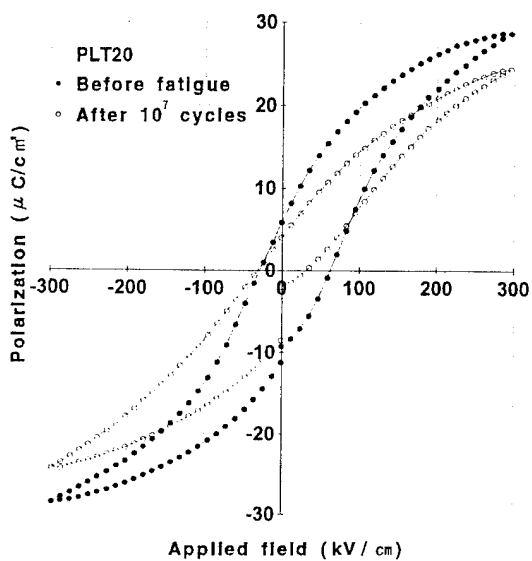
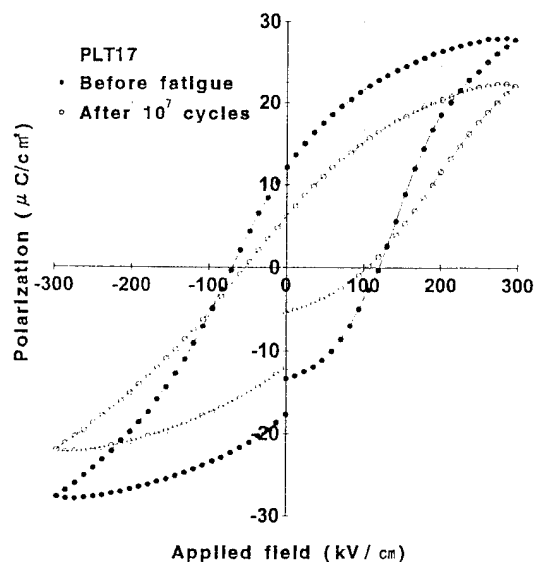


Fig.4 Hysteresis loops of PLT (La/Ti=0.17, 0.20, 0.24) thin films deposited on the Pt/SiO<sub>2</sub>/Si substrate at 460 °C before and after 10<sup>7</sup> switching cycles.

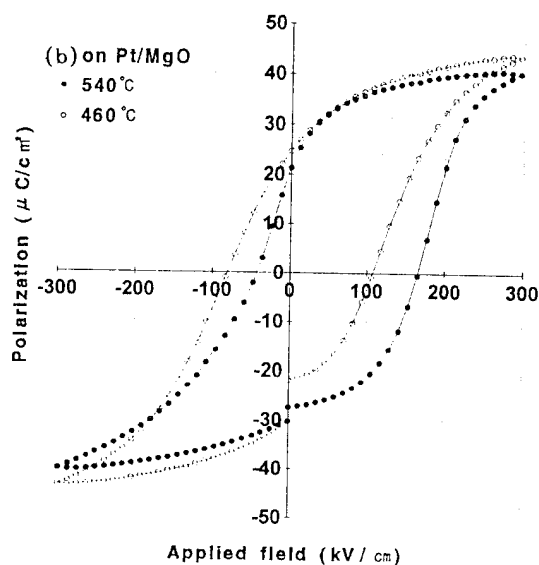
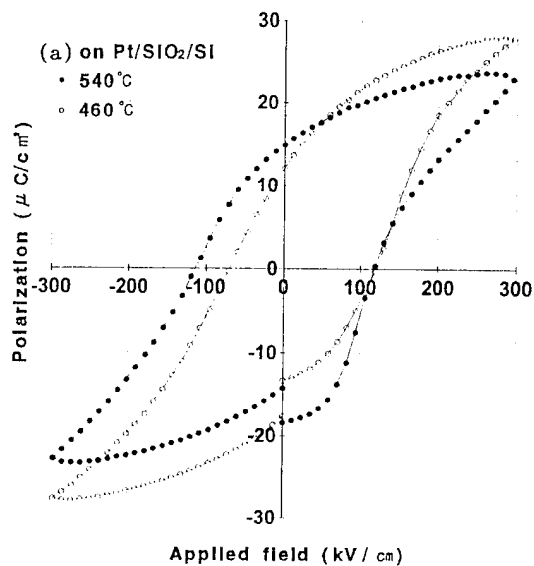


Fig.5 Hysteresis loops of PLT thin films deposited on (a) Pt/SiO<sub>2</sub>/Si and (b) Pt/MgO at 540 °C and 460 °C.

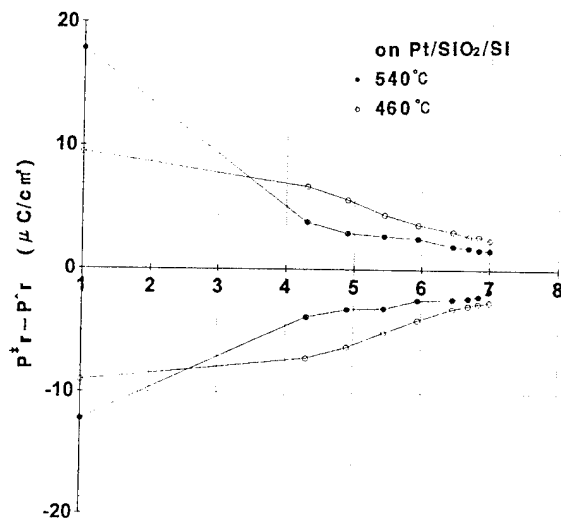


Fig.6 Fatigue characteristics of PLT thin film deposited on Pt/SiO<sub>2</sub>/Si 540 °C and 460 °C. P\*ṛ: switched remanent polarization, P̂ṛ: Non-switched remanent polarization.

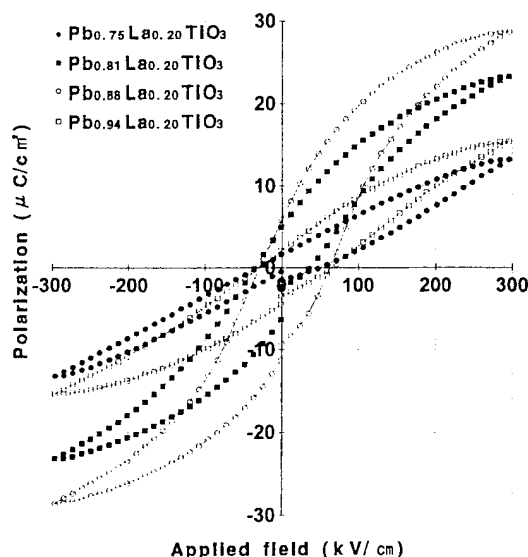


Fig.7 Hysteresis loops of PLT thin films deposited on the Pt/SiO<sub>2</sub>/Si substrate at 460 °C.

Pb<sub>0.75</sub>La<sub>0.20</sub>TiO<sub>3</sub>, Pb<sub>0.81</sub>La<sub>0.20</sub>TiO<sub>3</sub>,  
Pb<sub>0.88</sub>La<sub>0.20</sub>TiO<sub>3</sub> and Pb<sub>0.94</sub>La<sub>0.20</sub>TiO<sub>3</sub>.

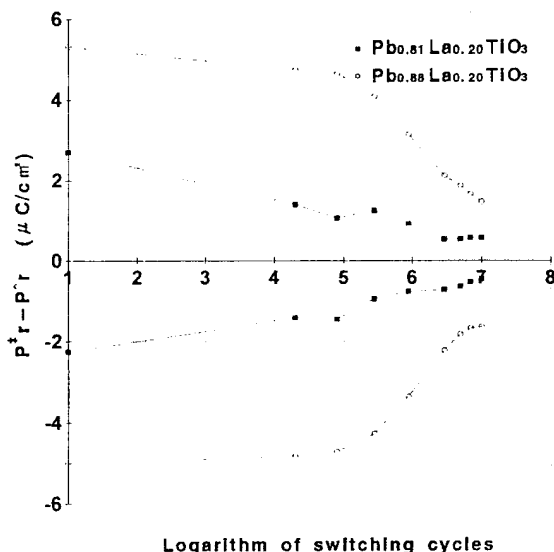


Fig.8 Fatigue characteristics of PLT thin films deposited on the Pt/SiO<sub>2</sub>/Si substrate at 460 °C.  
Pb<sub>0.81</sub>La<sub>0.20</sub>TiO<sub>3</sub> and Pb<sub>0.88</sub>La<sub>0.20</sub>TiO<sub>3</sub>.

is considered that excess Pb content compared to the stoichiometric composition inhibited the build-up of space charge at film-substrate interface [14]. On the other hand, in the film with too excessive Pb content, Pb<sub>0.94</sub>La<sub>0.20</sub>TiO<sub>3</sub>, degraded film quality. This is probably due to the appearance of PbO as second phase in the films.

#### CONCLUSIONS

This paper has shown that perovskite PLT thin films could be obtained at 460 °C by multiple cathode rf-magnetron sputtering. And the substrate temperature and Pb content of the PLT thin films affected the ferroelectric properties. The PLT thin films deposited on Pt/MgO substrate exhibited squarer hysteresis loops and higher Pr values compared to the

films on the Pt/SiO<sub>2</sub>/Si substrate. By lowering substrate temperature, fatigue resistance increased. In Pb-rich film exhibited better ferroelectric properties and fatigue resistance, compared to the film close to the stoichiometric composition. From the results presented in this paper, it is presumed that the Pb-deficiency at the film/substrate promoted the build-up of the space charge, thus accelerating fatigue.

#### ACKNOWLEDGEMENT

The authors would like to thank to Miss Makiko Miyaji and Mr. Tomoyuki Ibaraki for FE-SEM observations. This work was supported in part by a Grant-in-Aid for Scientific Research from the Ministry of Education, Science and Culture of Japan.

#### REFERENCES

- [1] J.F.Scott and C.A.Paz de Araujo, "Ferroelectric memories," *Science* vol.246 pp.1400-1405, 1989.
- [2] K.Iijima *et al.*, "Epitaxial growth and the crystallographic, dielectric and pyroelectric properties of lanthanum-modified lead titanate thin films," *J.Appl.Phys.* vol.60 pp.2914-2919, 1986.
- [3] N.Nagao *et al.*, "Preparation and properties of (Pb,La)TiO<sub>3</sub> pyroelectric thin films by RF-magnetron sputtering," *Jpn.J.Appl.Phys.* vol.32 pp.4065-4068, 1993.
- [4] K.R.Bellur *et al.*, "Electrical characterization of sol-gel derived PZT thin films" in *Proceedings of 8th IEEE International Symposium on the Application of Ferroelectrics*, Greenville, SC, 1992, pp.448-451.
- [5] R.Ramesh *et al.*, "Fatigue and retention in ferroelectric Y-Ba-Cu-O/Pb-Zr-Ti-O/Y-Ba-Cu-O heterostructures," *Appl.Phys.Lett.*, vol.61 pp.1537-1539 1992.
- [6] R.Dat *et al.*, "Polycrystalline La<sub>0.5</sub>Sr<sub>0.5</sub>CoO<sub>3</sub>/PbZr<sub>0.53</sub>Ti<sub>0.47</sub>O<sub>3</sub>/La<sub>0.5</sub>Sr<sub>0.5</sub>CoO<sub>3</sub> ferroelectric capacitors on platinized silicon with no polarization fatigue," *Appl.Phys.Lett.*, in press.
- [7] K.Tominaga *et al.*, "Switching and fatigue characterization of (Pb,La)(Zr,Ti)O<sub>3</sub> thin films by metalorganic chemical vapor deposition," *Jpn.J.Appl.Phys.*, vol.32 pp.4082-4085 1993.
- [8] H.M.Duiker *et al.*, "Fatigue and switching in ferroelectric memories: Theory and experiment," *J.Appl.Phys.* vol.68 pp.5783-5791 1990.
- [9] J.F.Scott *et al.*, "Quantitative measurement of space-charge effects in lead zirconate-titanate memories," *J.Appl.Phys.*, vol.70(1)pp.382-388, 1991.
- [10] I.K.Yoo and S.B.Desu, "Fatigue modeling of lead zirconate titanate thin films," *Mater.Sci.Eng.*, vol.B13, pp.319-322 1992.
- [11] D.J.Johnson *et al.*, "Measuring fatigue in PZT thin films," *Mater.Res.Soc.Symp.Proc.* vol.200 pp.289-295, 1990.
- [12] H.Maiwa, N.Ichinose and K.Okazaki, "Crystalline structure of PbTiO<sub>3</sub> thin films by multiple cathode sputtering," *Jpn.J.Appl.Phys.*, vol.31 pp.2163-2166, 1992.
- [13] H.Maiwa, N.Ichinose and K.Okazaki, "Preparation and properties of Ru and RuO<sub>2</sub> thin film electrodes for ferroelectric thin films," *Jpn.J.Appl.Phys.*, in press.
- [14] H.Maiwa, N.Ichinose and K.Okazaki, "Electrical properties of (Pb,La)TiO<sub>3</sub> thin films by multiple cathode sputtering," submitted to *Jpn.J.Appl.Phys.*

# Properties of $\text{PbTiO}_3$ Grown by the Multiple Magnetron Sputtering Method

R. C. Hoffman, K. K. Deb and D. A. Jackson  
Army Research Laboratory, Infrared/Optics Technology Office,  
Ft. Belvoir VA 22060

**Abstract**—Deposition behavior of lead titanate as grown on silicon substrates by the multiple magnetron sputtering method from metallic titanium and lead targets has been investigated. The films have been analyzed by RBS, SEM and x-ray diffraction to determine film composition, structure, and morphology. The perovskite phase of  $\text{PbTiO}_3$  has been observed. Preliminary dielectric measurements indicate an  $\epsilon_r$  of about 75 with a high loss tangent. The films will be used to fabricate a dynamic test device with the ultimate goal of fabricating a high performance uncooled infrared sensor array.

## Introduction

Recently, ferroelectric thin films have found application in uncooled infrared sensors having low power consumption and light weight coupled with relatively high sensitivity.  $\text{PbTiO}_3$  has a high spontaneous polarization and a high pyroelectric coefficient, giving  $\text{PbTiO}_3$  a relatively high figure-of-merit for pyroelectric detectors [1-5]. Deposition of  $\text{PbTiO}_3$  on Si substrates is crucial to integration of the sensor material with the thermal isolation structure and the readout circuitry. Sputtering has long been used as a method for depositing  $\text{PbTiO}_3$ , but conventional sputtering from a  $\text{PbTiO}_3$  ceramic target suffers from a variety of deficiencies. These include shifting target composition during deposition and negative-ion effects which etch the film during deposition. Off-axis sputtering alleviates the negative-ion effect to a large extent, but suffers the disadvantage of low deposition rate. Multisector metallic targets composed of lead and titanium wedges allow for sputtering in oxygen at high deposition rates with reduced negative-ion effect [6]. The disadvantage of this method is the tedious adjustment of the surface area of the lead or titanium wedges to achieve stoichiometry. This adjustment process necessitates opening the system to perform adjustments. By sputtering from two or more metallic targets independently, one simply needs to adjust only the relative power delivered to the lead and titanium targets to achieve stoichiometry.

In this paper we present experimental data on the preparation of  $\text{PbTiO}_3$  thin films by the multiple magnetron method [7], as well as results of the compositional, dielectric and structural analyses.

## Experimental

### Description of Apparatus

The apparatus for thin film  $\text{PbTiO}_3$  deposition by the multiple magnetron method consisted of a vacuum chamber containing a rotating heater/substrate holder, gas feedthroughs and a three-gun magnetron sputtering head. The entire

chamber was pumped to a  $10^{-5}$  Pa background pressure by a turbopump. Samples were placed and removed by a movable sample arm. A load-lock chamber eliminated having to vent the sputtering chamber to air to remove or place samples. Argon was supplied to the Ti gun and oxygen was supplied to the substrate via a gas ring surrounding the substrate. This reduced the oxygen concentration near the Ti gun, increasing the sputtering rate of Ti. Because of the disparity in sputtering rates between Ti and Pb, two Ti targets were used.

### Deposition Conditions

Typical sputtering conditions showed 600W of RF (Radio Frequency) power delivered to the two Ti targets and 20-25W delivered to the Pb target. Ar pressure was typically  $5.3 \times 10^{-1}$  Pa, and  $\text{O}_2$  pressure was typically  $6.0 \times 10^{-1}$  Pa. The targets were presputtered for one hour prior to deposition. A typical deposition was 3 hr, giving a deposition rate of about  $100 \text{ nm/hr}$ . The thin films were deposited on a variety of substrates. Si was used as a substrate to grow films needed for Rutherford backscattering (RBS) compositional analysis or x-ray diffraction. Si substrates coated with 200 nm of  $\text{ZrO}_2$  as a passivation layer and 200 nm of Pt as a bottom electrode were used to conduct electrical measurements as were Si/RuO<sub>x</sub> substrates, which are known to exhibit superior electrical properties [8].

### Properties of Deposited Films

The as-deposited films were yellowish in color and adhere well to the substrate. The films were annealed at 650C for one hour to form the perovskite phase. The x-ray diffraction data for a typical film are shown in Figure 1. The

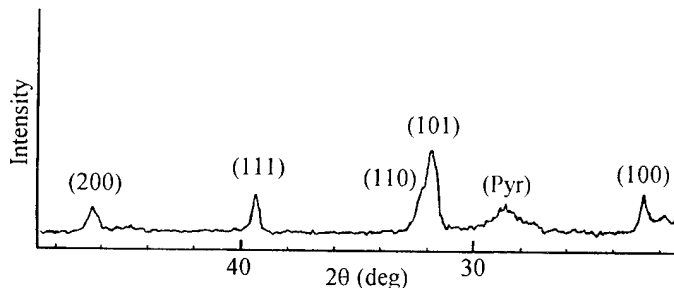


Figure 1. X-Ray diffraction pattern of  $\text{PbTiO}_3$  annealed thin film.

(101) reflection is the strongest, but the (201), (111), (110) and (100) perovskite reflections are also present. There is also a residual pyrochlore peak.

An SEM micrograph of two annealed films are shown in Figure 2. The split view shows a film as grown and annealed on a Si substrate (upper left), and a film as grown

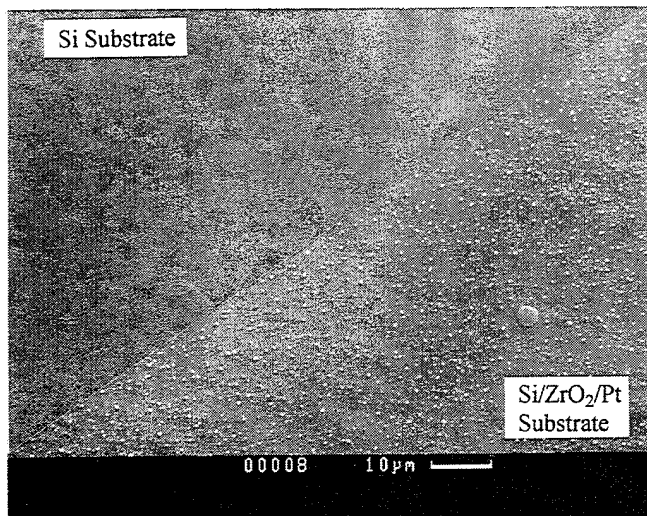


Figure 2. SEM micrograph of annealed PbTiO<sub>3</sub> thin film.

and annealed on a Si/ZrO<sub>2</sub>/Pt substrate (lower right). The morphology of the film as grown on Si is essentially smooth, with some texture visible on the order of 1-3 micrometers. Micrographs of films grown on Si/ZrO<sub>2</sub>/Pt substrates revealed the deleterious effect of bottom Pt electrode hillock formation on the subsequent growth of PbTiO<sub>3</sub>. These films showed raised features on the order of 0.5 to 1 micrometer on the surrounding smooth area. It is suspected that these areas may

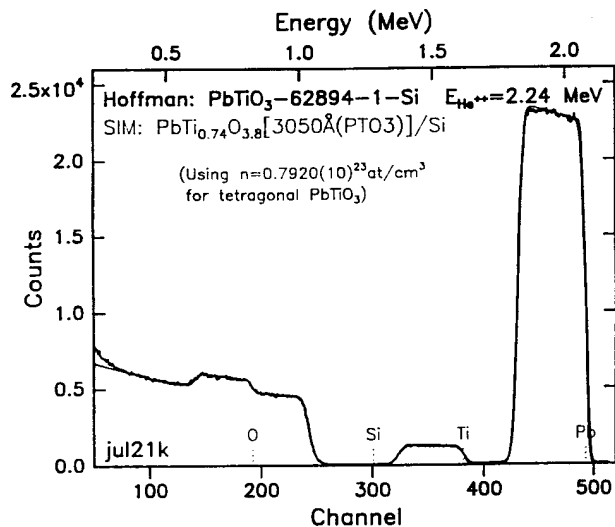


Figure 3. RBS compositional analysis of unannealed PbTiO<sub>3</sub> thin film.

also be PbO rich. These raised areas apparently caused shorting of the bottom and top contacts in completed devices using Pt electrodes.

RBS analysis of the unannealed as-deposited film showed a composition of PbTi<sub>0.74</sub>O<sub>3.8</sub> (Figure 3). The film showed a significant surplus of Pb which was probably largely lost on crystallization. The excess Pb was not necessarily detrimental as it has been shown to aid film crystallization [6].

Preliminary Dielectric measurements using a Si/RuO<sub>x</sub>/PbTiO<sub>3</sub>/RuO<sub>x</sub> capacitor configuration showed a dielectric constant  $\epsilon_r$  of about 75, with a high loss tangent of

about 10 at 30 Hz. In this test device the RuO<sub>x</sub> layers were approximately 200 nm thick and the PbTiO<sub>3</sub> layer about 300 nm thick.

#### Future work

The film growth techniques described will be used to integrate PbTiO<sub>3</sub> into a Si-based monolithic test device containing Pt resistance thermometers and internal heating devices to measure the dynamic properties of PbTiO<sub>3</sub> thin films as a detector material. Additional dielectric measurements will undertaken to determine and optimize the pyroelectric coefficient, dielectric constant, loss tangent and figure-of-merit of the PbTiO<sub>3</sub> devices.

#### Acknowledgments

The authors would like to gratefully acknowledge Dr. R. Pfeffer of ARL Ft. Monmouth for performing the RBS analysis of the thin films and to Dr. W. Wilber, also of ARL Ft. Monmouth, for the x-ray diffraction data. The author would also like to acknowledge Mr. F. Wolfgram for the SEM micrograph, Mr. S. Tomarchio for his general assistance.

#### References

- [1] K. Iijima, Y. Tomita, R. Takayama, I. Ueda, "Preparation of C-Axis Oriented PbTiO<sub>3</sub> Thin Films and Their Crystallographic, Dielectric, and Pyroelectric Properties," *J. Appl. Phys.*, vol. 60, pp. 361-367 July 1986.
- [2] Y. Matsui, M. Okayuma, N. Fujita, Y. Hamakawa, "Laser Annealing to Produce Ferroelectric-Phase PbTiO<sub>3</sub> Thin Films," *J. Appl. Phys.*, vol. 52 no. 8, pp. 5107-5111, August 1981.
- [3] R. Takayama, Y. Tomita, K. Iijima, I. Ueda, "Preparation and Characteristics of Pyroelectric Infrared Sensors made of C-Axis Oriented La-Modified PbTiO<sub>3</sub> Thin Films," *J. Appl. Phys.*, vol. 61 no. 1, pp. 411-415, January 1987.
- [4] M. Okayuma, Y. Hamakawa, "Preparation and Basic Properties of PbTiO<sub>3</sub> Ferroelectric Thin Films and Their Device Applications," *Ferroelectrics*, vol. 63, pp. 243-252, 1985.
- [5] M. Okayuma, K. Ohtani, T. Ueda, Y. Hamakawa, "Si-Monolithic Integrated Pyroelectric Infrared Sensor Made of PbTiO<sub>3</sub> Thin Film," *J. of Infrared and Millimeter Waves*, vol. 6 no. 1, pp. 71-78, 1985.
- [6] R. Watton, "Ferroelectric Materials and IR Bolometer Arrays: From Hybrid Arrays Towards Integration," *Integrated Ferroelectrics*, vol. 4 no. 3, pp. 175-186, 1994.
- [7] S. Krupanidhi, "Thin Film Ferroelectrics Tutorial," Presented at Army Research Laboratory, Electronics and Power Sources Directorate, Ft. Monmouth NJ, May 27-28, 1993.
- [8] A. Grill, W. Kane, J. Viggiano, M. Brady, R. Laibowitz, "Base Electrodes for High Dielectric Constant Oxide Materials in Silicon Technology," *J. Mater. Res.*, vol. 7 no. 12, pp. 3260-3265, 1992.

# Annealing Effects on the Polarity of Stored Charge of BaTiO<sub>3</sub> Films on Si

L. H. Chang and W. A. Anderson  
State University of New York at Buffalo  
Center for the Electronic and Electro-Optic Materials  
Department of Electrical and Computer Engineering  
Buffalo, NY 14260

**Abstract** – A high quality BaTiO<sub>3</sub>/p-Si interface was achieved at substrate temperature of 500°C by using RF magnetron sputtering. In-situ annealing at the same temperature was carried out to study the charge behavior of BaTiO<sub>3</sub> films on Si substrate. Depending on the annealing oxygen pressure and annealing condition, both polarities of effective oxide charge in the metal-ferroelectric-semiconductor, Au/BaTiO<sub>3</sub>/p-Si, structure was observed. It is believed that the density of electronic states, generated at the interface due to the asymmetry of the structure between BaTiO<sub>3</sub> and Si substrate, and the positive oxide charges, depending on the degree of the metal-oxygen reaction for different annealing oxygen pressures and annealing durations, determine the behavior of oxide charge.

## INTRODUCTION

Barium titanate (BaTiO<sub>3</sub>) is a ferroelectric material possessing a very high dielectric constant which shows promise in future micro-electronic and photonic applications [1-3]. The electrical and structural properties of the BaTiO<sub>3</sub> films are well characterized from different aspects based on a capacitor configuration of metal/ferroelectric/metal (MFM) [4]. However, depositing BaTiO<sub>3</sub> films on Si substrates is inevitable since the operation of many proposed devices relies on the field effect in silicon [5]. Characterization of the charge behavior and interface properties of BaTiO<sub>3</sub> films on Si have been studied through various deposition techniques with different deposition conditions [6-9]. However, the study of the annealing effect, which is an important technique to improve the interface quality and control the charge polarity of the metal/ferroelectric/semiconductor (MFS) structure, on BaTiO<sub>3</sub> films, has been very few [10].

The charge behavior and interface characteristics of the capacitor with a configuration of Au/BaTiO<sub>3</sub>/p-Si was studied in this experiment by using RF magnetron sputtering. The best performance of as-deposited BaTiO<sub>3</sub> films in terms of electrical and interface properties was carried out at a substrate temperature in the range of 470°C to 550°C. By controlling different annealing oxygen pressures and annealing durations, both polarities of oxide charges were observed.

## EXPERIMENTAL DETAILS

In this study, BaTiO<sub>3</sub> thin films were deposited on p-type (100) Silicon with resistivity of 1-4 Ω-cm by using RF (13.56 MHz) magnetron sputtering. The silicon wafers were ultrasonically cleaned in trichloroethylene, acetone, and methanol, followed by rinsing in deionized water several times. Buffer HF was used to remove the native oxide on the Si surface before Al was thermally evaporated on the back surface as a back ohmic contact.

The total pressure, Ar + O<sub>2</sub>, of the sputtering chamber was maintained at 10 mTorr with O<sub>2</sub> partial pressure of 0.5 mTorr. A power density of about 4.9 W/cm<sup>2</sup> was applied on one inch BaTiO<sub>3</sub> target with purity of 99.98%. The substrate temperature during sputtering was kept at 500°C. In-situ annealing durations, from 10 to 60 min, and annealing oxygen pressures, from vacuum to 1 mTorr, were con-

ducted to study the charge behaviors and the interface properties of BaTiO<sub>3</sub> films on Si substrates. The thickness of the BaTiO<sub>3</sub> films was measured by an ellipsometry with a wavelength of 632.8 nm. The thickness of the BaTiO<sub>3</sub> films studied in this experiment was around 240-320 nm. To complete the MFS capacitors, Au dots, with a diameter of 0.66 mm, were thermally evaporated onto the BaTiO<sub>3</sub> films.

The charge state densities of the MFS capacitors were determined by high frequency (1 MHz) C-V measurements from a HP 4280A 1 MHz C meter/plotter. Quasistatic C-V measurements were carried out to evaluate the interface state densities by a Keithley model 595 Quasistatic CV meter.

## RESULTS AND DISCUSSION

High frequency (1 MHz) room temperature C-V measurements were carried out on the MFS, Au/BaTiO<sub>3</sub>/p-Si capacitors. By comparing with the ideal MFS C-V curves, the flat band voltage will be obtained for the ferroelectric films with a certain amount of trapped charges. A negative flat band shift implies effective positive charges residing at the BaTiO<sub>3</sub>/Si interface. On the other hand, effective negative charges cause the C-V curve to shift to more positive of gate bias with respect to the ideal C-V curve. Experimentally, it was found that the total charges in the ferroelectric BaTiO<sub>3</sub> film could be positive or negative. The polarity of the oxide charges of the sputtered BaTiO<sub>3</sub> films depends on annealing oxygen pressure and annealing duration under which the BaTiO<sub>3</sub> films were deposited.

It has been found that MFS capacitors with a deposition temperature in the range of 470°C to 550°C gave the best performance in terms of the electrical and interface properties. Fig. 1 shows the typical high frequency C-V curve for BaTiO<sub>3</sub> films deposited at 500°C. Negative charges with a density in the range of  $4.46 \times 10^{11}/\text{cm}^2$  was found in Fig. 1. It was reported that by using the partially ionized beam deposition technique, the charge density at the BaTiO<sub>3</sub>/Si inter-

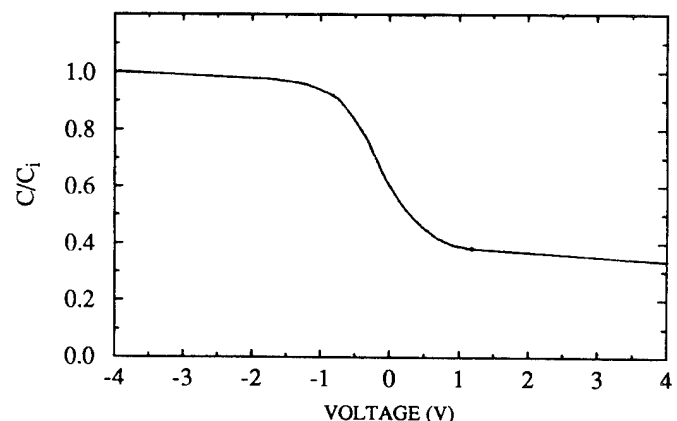


Fig. 1 Typical high frequency (1 MHz) C-V characteristics for BaTiO<sub>3</sub> films deposited at 500°C.

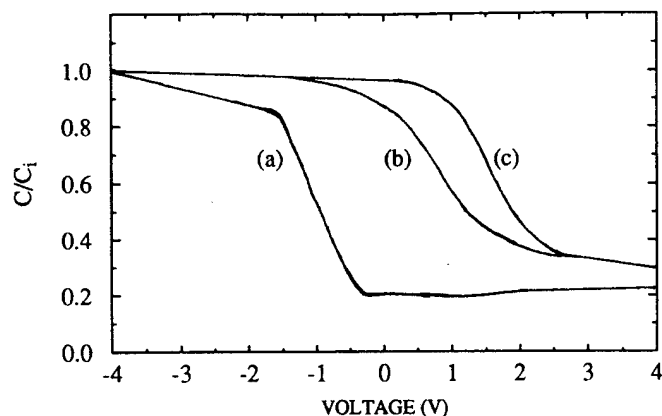


Fig. 2 High frequency C-V characteristics for BaTiO<sub>3</sub> films deposited on Si at 500°C followed by in-situ annealing at the same temperature for 30 min in (a) vacuum, (b) oxygen pressure of  $1 \times 10^{-5}$  Torr, and (c) oxygen pressure of  $5 \times 10^{-4}$  Torr.

face can be dramatically controlled [7]. The positive oxide charges were believed to generated in the BaTiO<sub>3</sub> films due to the incomplete reaction between the oxygen and the metal atoms during BaTiO<sub>3</sub> film deposition. However, certain amount of the electronic states will reside at the interface due to the asymmetry of the structure between BaTiO<sub>3</sub> and Si substrate. If the oxygen ions have sufficient surface mobility, a more complete reaction between the oxygen and the metal atoms will be achieved. Different annealing oxygen pressures and annealing durations will determine the amount of positive oxide trapped charges in the BaTiO<sub>3</sub> film due to the degree of metal-oxygen reaction. Depending on the annealing conditions, insulator charge of both polarities in the Al/YSZ/Si<sub>3</sub>N<sub>4</sub>/SiO<sub>2</sub>/Si structure was reported [5].

Fig. 2 shows the high frequency C-V curves for BaTiO<sub>3</sub> films deposited at 500°C followed by in-situ annealing at the same temperature for 30 min in (a) vacuum, (b) O<sub>2</sub> pressure of  $1 \times 10^{-5}$  Torr, and (c) O<sub>2</sub> pressure of  $5 \times 10^{-4}$  Torr. The charge densities of the corresponding films are in the range of positive  $2.17 \times 10^{12} / \text{cm}^2$ , negative

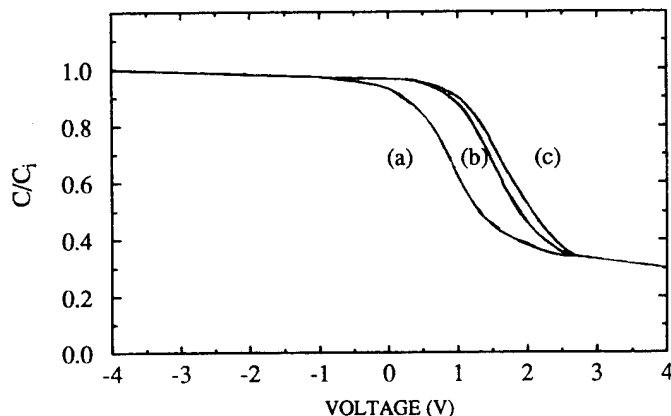


Fig. 3 High frequency C-V characteristics for BaTiO<sub>3</sub> films deposited on Si at 500°C followed by in-situ annealing at the same temperature in oxygen pressure of  $5 \times 10^{-4}$  Torr for (a) 10 min, (b) 30 min, and (c) 60 min.

$1.01 \times 10^{12} / \text{cm}^2$ , and negative  $2.04 \times 10^{12} / \text{cm}^2$ , respectively.

It is believed that in-situ annealing in proper oxygen ambient will provide more completion of the Ba-Ti-O reaction for the as-deposited film and consequently further reduce the amount of positive oxide trapped charges in the bulk BaTiO<sub>3</sub>. However, in-situ annealing in vacuum for as-deposited BaTiO<sub>3</sub> films resulted in oxygen deficiency in the bulk BaTiO<sub>3</sub> film which may introduce trapped holes into the oxide. The trapped holes which have been generated by impact ionization located at the Si/SiO<sub>2</sub> interface was also reported [11]. The shift of flat band voltage to more negative values and a little distortion of C-V curve were observed in Fig. 2(a) to support the deduction. If as-deposited BaTiO<sub>3</sub> films were in-situ annealed in a sufficient oxygen pressure, a more complete Ba-Ti-O reaction can be obtained resulting in the reduction in the number of sputtering positive oxygen ions which remain unreacted in films during deposition. The results were confirmed by Fig. 2(b) and Fig. 2(c). For in-situ annealing in oxygen pressure greater than  $5 \times 10^{-4}$  Torr, the C-V measurements showed no significant difference from Fig. 2(c) with the same annealing duration.

**Table 1:** Summary of the flat band voltage shift and the total oxide charge density for BaTiO<sub>3</sub> films deposited on Si at 500°C with different in-situ annealing oxygen pressures and annealing durations.

Annealing oxygen pressure (Torr)	Annealing duration (min)	Film thickness (nm)	C <sub>i</sub> (pF)	ε <sub>i</sub>	V <sub>FB</sub> (V)	N <sub>ox</sub> (/cm <sup>2</sup> )
(as-deposited)	(as-deposited)	300	788	78.1	-0.31	$4.46 \times 10^{11}$
Vacuum	30	268	1152	102	-1.03	$2.17 \times 10^{12}$
$1 \times 10^{-5}$	30	286	1038	98	0.53	$1.01 \times 10^{12}$
$5 \times 10^{-4}$	30	303	1041	104.2	1.07	$2.04 \times 10^{12}$
$1 \times 10^{-3}$	30	305	1042	105	1.11	$2.11 \times 10^{12}$
$5 \times 10^{-4}$	10	302	941	93.8	0.6	$1.03 \times 10^{12}$
$5 \times 10^{-4}$	60	305	1092	110	1.09	$2.17 \times 10^{12}$



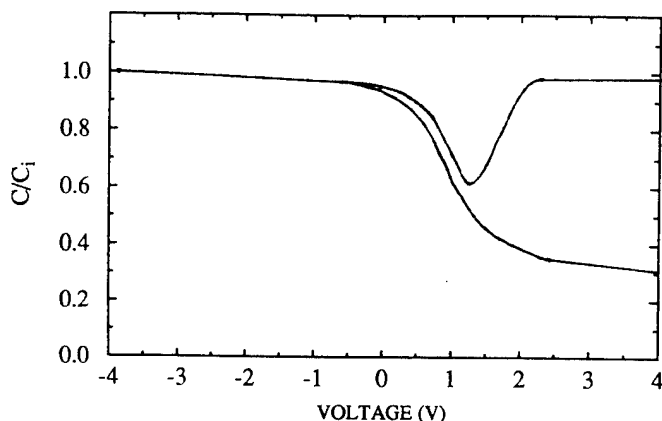


Fig. 4 High frequency and Quasistatic C-V characteristics of the MFS capacitors with BaTiO<sub>3</sub> films deposited on Si at 500°C followed by in-situ annealing in O<sub>2</sub> pressure of 5x10<sup>-4</sup> Torr for 10 min.

Fig. 3 shows the high frequency C-V curves for BaTiO<sub>3</sub> films deposited at 500°C followed by in-situ annealing at the same temperature in O<sub>2</sub> pressure of 5x10<sup>-4</sup> Torr for (a) 10min, (b) 30 min, and (c) 60 min. The negative charge densities of the corresponding films are in the range of 1.03x10<sup>12</sup>/cm<sup>2</sup>, 2.04x10<sup>12</sup>/cm<sup>2</sup>, and 2.17x10<sup>12</sup>/cm<sup>2</sup>, respectively. Different annealing durations also determined the amount of positive oxide trapped charges in the bulk BaTiO<sub>3</sub> due to the degree of complete metal-oxygen reaction. This resulted in the electronic states at the interface making enough compensation for or exceeding the remanent positive oxide charges in bulk BaTiO<sub>3</sub> depending on the annealing durations. However, for films annealed in O<sub>2</sub> ambient for more than 30 min, no further flat band voltage shift was observed. This is attributed to the saturation of metal-oxygen reaction under such annealing temperature.

The flat band voltage shift and the effective oxide charge density for BaTiO<sub>3</sub> films deposited on Si at 500°C with different in-situ annealing oxygen pressures and annealing durations are summarized in Table I.

Fig. 4 shows the typical high frequency and quasistatic C-V curves for BaTiO<sub>3</sub> films deposited on Si at 500°C followed by in-situ annealing in O<sub>2</sub> pressure of 5x10<sup>-4</sup> Torr for 10 min. The interface-trap density, located over the onset of inversion but not strong inversion evaluated based on a simplified approach [12], was in the range of 9x10<sup>11</sup>/eV-cm<sup>2</sup>.

## CONCLUSION

BaTiO<sub>3</sub> thin films have been successfully deposited on Si substrate with high quality BaTiO<sub>3</sub>/Si interfaces at 500°C by using RF magnetron sputtering.

Both polarities of effective oxide charge, depending on the annealing oxygen pressure and annealing duration, in the metal-ferroelectric-semiconductor, Au/BaTiO<sub>3</sub>/p-Si, was observed. The density of electronic states, generated at the interface due to the asymmetry of the structure between BaTiO<sub>3</sub> and Si substrate, and the positive oxide charges, depending on the degree of the metal-oxygen reaction for different annealing oxygen pressures and annealing durations, determined the polarity of oxide charge. For the as-deposited film at 500°C, a positive charge density in the range of 4.3x10<sup>11</sup>/cm<sup>2</sup> was detected. The negative charge density in the range of 1x10<sup>12</sup>/cm<sup>2</sup>, however, was observed after in-situ annealing of the as-deposited BaTiO<sub>3</sub> film in an O<sub>2</sub> pressure of 5x10<sup>-4</sup> Torr for 10 min.

Controllable polarity of oxide charge was achieved for the BaTiO<sub>3</sub> films deposited at 500°C through different annealing oxygen pressures and annealing durations.

## ACKNOWLEDGEMENT

This work was supported by the New York State Science and Technology Foundation, Center for Electronic and Electro-Optic Materials and Ohmtek, Inc.

## REFERENCES

- [1] P.Li and T.-M.Lu, Appl. Phys. Lett. 57, 2336, 1990.
- [2] Q.X.Jia, L.H.Chang, and W.A.Anderson, J. Electronic Mater. 23, 551, 1994.
- [3] V.S.Dharmadhikari and W.W.Grannemann, J. Appl. Phys. 53, 8988, 1982.
- [4] Q.X.Jia, J.Yi, Z.Q.Shi, L.H.Chang, K.K.Ho, and W.A.Anderson, Proc. MRS Meeting 284,523, 1992.
- [5] Y.Miyahara, J. Appl. Phys. 71, 2309, 1992.
- [6] C.A.T.Salama and E.Siciunas, J. Vac. Sci. Tech. 9, 91, 1971.
- [7] P.Li and T.-M.Lu, Phys. Rev. B43, 14261, 1991.
- [8] J.K.G.Panitz and C.C.Hu, Vac. Sci. Technol. 16, 315, 1979.
- [9] V.S.Dharmadhikari and W.W.Grannemann, J. Vac. Sci. Technol. A1, 483, 1983.
- [10] L.H.Chang and W.A.Anderson, presented at the 36th Electronic Materials Conf. (EMC), Boulder, Colorado, June 22-24, 1994
- [11] J.C.Hsieh, Y.K.Fong, and C.W.Chen, J. Appl. Phys. 73, 5038, 1993.
- [12] R.Castagne and A.Vapaille, Surf. Sci. 28, 157, 1971.

# PREPARATION OF $\text{Bi}_4\text{Ti}_3\text{O}_{12}$ THIN FILMS BY REACTIVE MAGNETRON SPUTTERING USING METAL TARGET AND THEIR EVALUATIONS

Takashi Yamamoto and Hiroyuki Matsuoka  
Department of Electrical Engineering  
The National Defense Academy, Yokosuka, 239 Japan

## Abstract

As sputtered ferroelectric and (001) oriented  $\text{Bi}_4\text{Ti}_3\text{O}_{12}$  thin films were prepared on a Pt/Ti/SiO<sub>2</sub>/Si substrate at a comparatively low temperature around 330 °C, by a reactive magnetron sputtering using Bi and Ti metal target. The chemical composition of deposited film is determined by the multi-element structure of target designed by a sputtering yield of Bi and Ti, which was changed by the gas ratio of the Ar<sup>+</sup> and O<sub>2</sub> and the value of input rf-power. Dielectric constant was 100 at 1kHz. The remanent polarization and the coercive field were 7uC/cm<sup>2</sup> and 51.2 kV/cm, respectively.

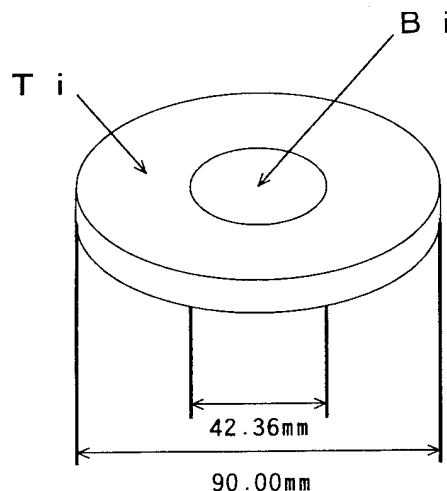


Fig. 1 Schematic figure of metal target for  $\text{Bi}_4\text{Ti}_3\text{O}_{12}$  film.

## 1.Introduction

Recently, with the progress of thin film technology, ferroelectric random-access memory (FRAM) have attracted much attention from the viewpoints of high density, nonvolatility and high access speed. As a candidate in FRAM material, PT, PZT, PLZT,  $\text{BaTiO}_3$  and bismuth titanate( $\text{Bi}_4\text{Ti}_3\text{O}_{12}$ ), were studied mainly.

$\text{Bi}_4\text{Ti}_3\text{O}_{12}$  (BIT) is a typical ferroelectric material with a high Curie point around 675°C and a strong anisotropy of crystal structure and resulting electrical properties. However, only several papers have reported on BIT for FRAM application, compared with above-mentioned other materials.

Toyoda et al. reported the synthesis and properties of BIT thin films by sol-gel processing. A pyrochlore-free and (001) perovskite phase was formed only above 670°C. The remanent polarization and coercive field were 4  $\mu\text{C}/\text{cm}^2$  and 1.8 kV/cm, respectively and dielectric constant was 120.<sup>1)</sup> Nakamura et al. reported the preparation of oriented BIT thin films by MOCVD. The c-axis-oriented BIT films were grown on  $\text{Bi}_2\text{Ti}_2\text{O}_7$  buffer layer/Pt/SiO<sub>2</sub>/Si substrate above 550°C. The remanent polarization and coercive field were 0.6  $\mu\text{C}/\text{cm}^2$  and 13 kV/cm, respectively and dielectric constant was 180.<sup>2)</sup>

In this paper, stoichiometric BIT thin films were prepared on Pt/Ti/SiO<sub>2</sub>/Si substrate by a reactive rf-magnetron sputtering in Ar and O<sub>2</sub> pre-mixed gas using Bi and Ti metal targets with a multi-element structure. Ferroelectric properties were measured for FRAM application.

Materials		Ti	Pt
RF power	( W )	100	100
Substrate temperature	( °C )	220	400
Gas pressure	( Pa )	1.0	1.0
Sputtering time	( min. )	15	2
Target-substrate distance	( mm )	35	35
Sputtering gas		Ar	Ar
Thickness	( Å )	3500	8000

Table I Sputtering conditions for Ti and Pt films as lower electrodes

RF power	( W )	100
Substrate Temperature	( °C )	250-400
Gas pressure	( Pa )	0.7-5
Sputtering time	( min. )	30-90
Target-substrate distance	( mm )	35
Sputtering gas		Ar:O <sub>2</sub> =50:50

Table II Sputtering conditions for  $\text{Bi}_4\text{Ti}_3\text{O}_{12}$  films

## 2. Experimental procedure

Schematic figure of multi-element target is given in Fig. 1. The inner and outer diameters of metal Bi and Ti were determined by some considerations of sputtering yield of Bi and Ti metal; ion energy = 380eV (input rf-power of 100W), used gas; Ar:O<sub>2</sub> = 50:50, chemical composition; Bi:Ti = 4 :3. Table I shows the fabrication conditions of Ti and Pt lower electrode on SiO<sub>2</sub>/Si substrate. The orientation of Ti and Pt films were (010) and (111), respectively. Table II shows the fabrication conditions of BIT film.

## 3. Results and discussions

Figure 2 show the X-ray diffraction patterns (XRD) of as-sputtered BIT films on Pt/Ti/SiO<sub>2</sub>/Si substrate. As can be seen, any as sputtered BIT films showed a perovskite single

phase,(see  $2\theta = (0010)$  and  $(0012)$  peaks), although a pyrochlore phase ( $\text{Bi}_2\text{Ti}_2\text{O}_7$ ) ( $2\theta = 30$  deg.) was reported on the low substrate temperature below 630°C by sol-gel and 560°C by MOCVD.<sup>1,2)</sup> With changing the sputtering conditions, such as sputtering gas pressure and substrate temperature, grown BIT

thin films could be divided into four kinds of perovskite phases as shown in Fig. 2(a), 2(b), 2(c) and 2(d). The (0010) XRD peak in Fig. 2(a) is weak, while that in Fig. 2(b) is strong and can be observed the c-axis orientation of BIT.

The non-perovskite phases showed by black circles coexisted in Fig. 2(d). With increasing the substrate temperature, the (0010) XRD peak decreased and the back ground at the low  $2\theta$  angles region in XRD pattern increased. By such four kinds of XRD patterns, the sputtering conditions can be classified.

Figure 3 shows the BIT crystallinity by various sputtering gas pressure (Pa) and substrate temperature ( $^{\circ}\text{C}$ ). Open triangles, squares, circles correspond to the crystallinity shown by the XRD patterns in Fig. 2(a), 2(c), 2(b). Moreover, with increasing the substrate temperature above  $380^{\circ}\text{C}$ , the crystallinity decreased as shown in Fig. 2(d) independent on sputtering gas pressure. In previous paper, we reported the fabrication of  $\text{Pb}(\text{Zr}_{0.53}\text{Ti}_{0.47})\text{O}_3$  (PZT) thin films on the same substrate,

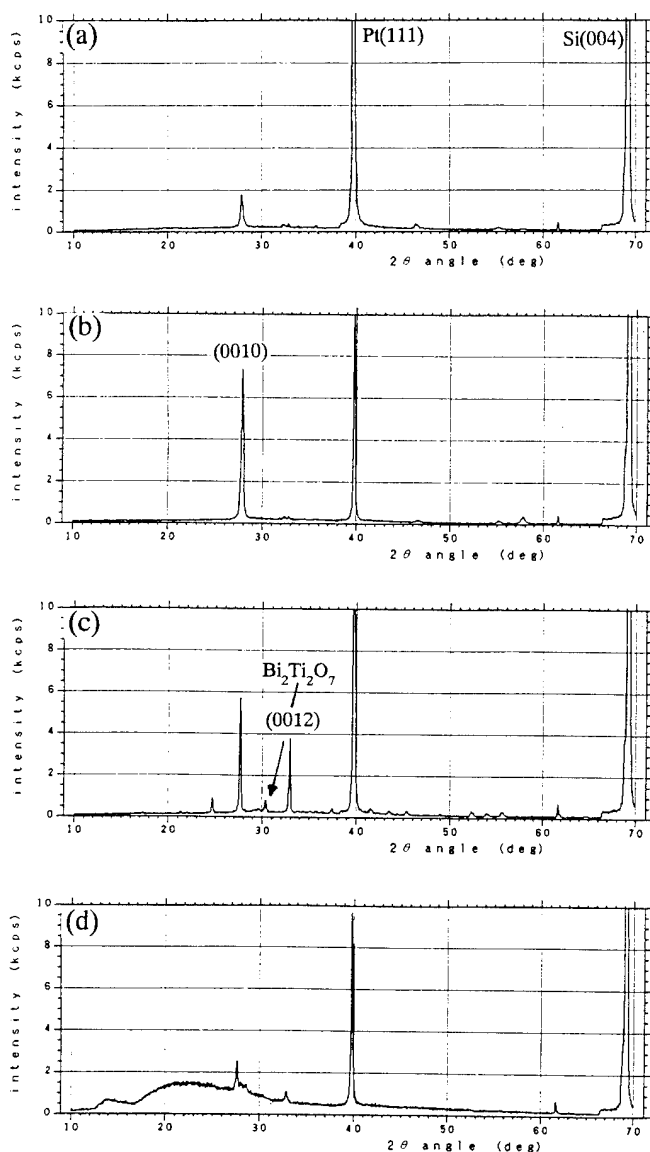


Fig. 2 X-ray diffraction patterns of  $\text{Bi}_4\text{Ti}_3\text{O}_{12}$  film prepared by various sputtering gas pressure (Pa) and substrate temperature ( $^{\circ}\text{C}$ ). (a); 5Pa,  $330^{\circ}\text{C}$ , (b); 3Pa,  $330^{\circ}\text{C}$ , (c); 3Pa,  $300^{\circ}\text{C}$  and (d);  $2\text{Pa}$ ,  $380^{\circ}\text{C}$ .

such as  $\text{Pt/Ti/SiO}_2/\text{Si}$  substrate by the same reactive magnetron sputtering using the Pb, Zr and Ti metal.<sup>3)</sup> The fabrication temperature of PZT perovskite phase was above  $500^{\circ}\text{C}$  and is comparatively low, compared with those using the ceramic target ( $700^{\circ}\text{C}$ ). In those fabrication process, first of all, a pyrochlore phase was fabricated and with increasing the substrate temperature, a single perovskite phase was fabricated. The pyrochlore phase of BIT was  $\text{Bi}_2\text{Ti}_2\text{O}_7$ . As can be seen in Fig. 2, it was found that the pyrochlore phase was not easy to fabricate in the reactive magnetron sputtering. Figure 4 shows the typical cross section of BIT film on  $\text{Pt/Ti/SiO}_2/\text{Si}$  substrate by SEM. The surface of

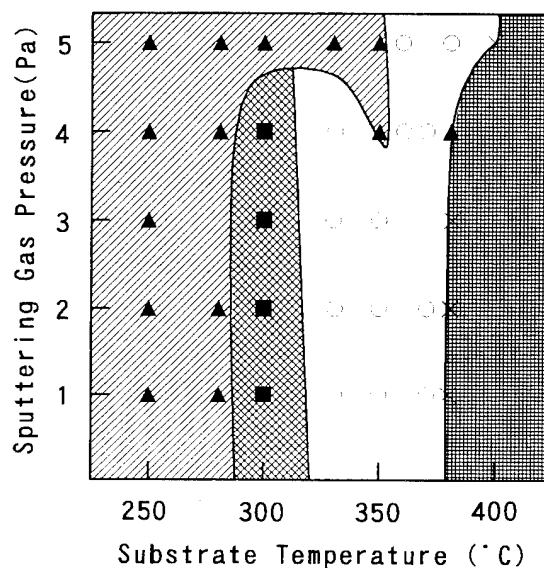


Fig. 3 BIT crystallinity at various sputtering gas pressure (Pa) and substrate temperature ( $^{\circ}\text{C}$ ).

film was smooth and the same layer structure as that of the ceramics was not found. From the cross section, it was estimated that the deposition rate was  $1.7\text{ }\mu\text{m/h}$  under the sputtering conditions of 100 W, 1Pa,  $330^{\circ}\text{C}$ . That of PZT film

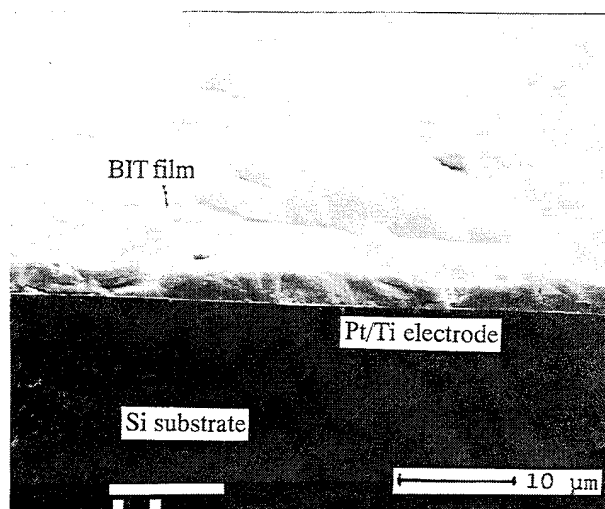


Fig. 4 Cross section of BIT film on  $\text{Pt/Ti/SiO}_2/\text{Si}$ . Sputtering conditions; 100W, 1Pa,  $330^{\circ}\text{C}$

was  $0.18 \mu\text{m/h}$  under the sputtering conditions of 100 W, 5 Pa,  $550^\circ\text{C}$ . As the deposition rate was independent on the sputtering conditions in the reactive sputtering, the difference of deposition rates of BIT and PZT films was dependent on the chemical composition. Figure 5 shows the typical top surface morphology of BIT thin film. The piled up area with a diameter of 0.3 to  $3 \mu\text{m}$  can be seen in every places and the hollow areas were divided into the smooth areas with a diameter of  $5 \mu\text{m}$ . Figure 6 shows the typical micrograph of D-E hysteresis curve of c-axis oriented

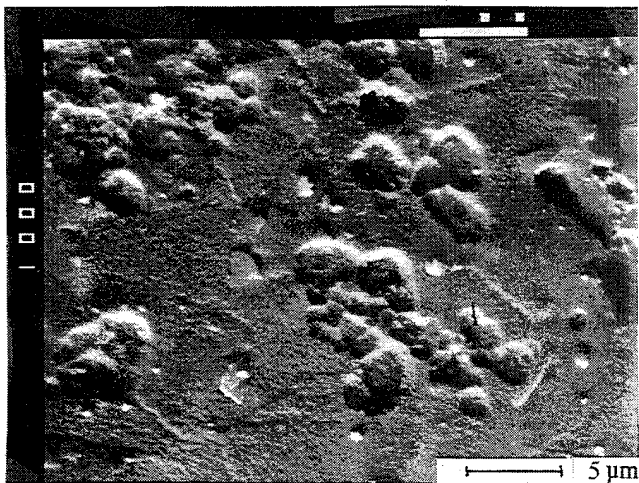


Fig. 5 Top surface of BIT thin film on Pt/Ti/SiO<sub>2</sub>/Si Sputtering conditions; 100W, 1Pa and  $330^\circ\text{C}$

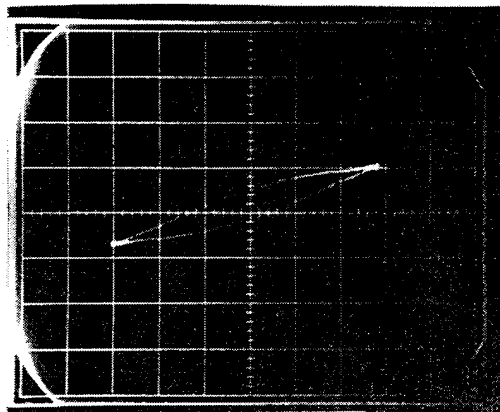


Fig. 6 D-E hysteresis curve of BIT thin film on Pt/Ti/SiO<sub>2</sub>/Si. Film thickness is  $1.7 \mu\text{m}$ .

BIT film on Pt/Ti/SiO<sub>2</sub>/Si. The remanent polarization ( $P_r$ ) and coercive field ( $E_c$ ) were  $7 \mu\text{C/cm}^2$  and  $51.2 \text{ kV/cm}$ , respectively, where the film thickness was  $1.7 \mu\text{m}$ . The value of  $P_r$  was comparatively large in reported BIT thin films. It was reported that the values of  $P_r$  in single crystal BIT were  $50 \mu\text{C/cm}^2$  and  $4 \mu\text{C/cm}^2$ , respectively along the am- and cm-axis with  $5^\circ$  with respect to a- and c-axis in monoclinic crystal structure and the value of  $P_r$  in ordinary BIT ceramics was  $18 \mu\text{C/cm}^2$ . When compared those values with our data, it might be certainly considered that the value of  $P_r$  was increased by the slight decline of crystal axis.

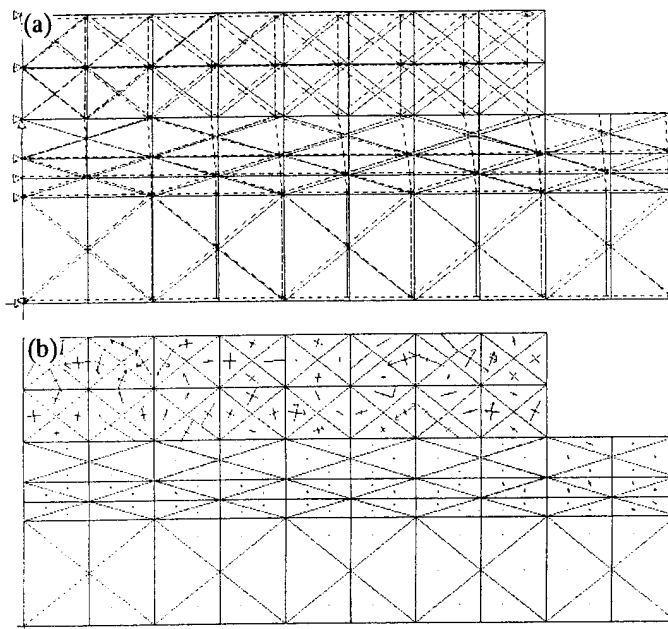


Fig. 7 Displacement and stress distribution in BIT( $1 \mu\text{m}$ ) thin film on Pt( $0.1 \mu\text{m}$ )/Ti( $0.1 \mu\text{m}$ )/SiO<sub>2</sub>( $0.1 \mu\text{m}$ )/Si( $1 \text{mm}$ )

Figure 7(a) and 7(b) show the displacement and stress distribution in BIT thin film on Pt/Ti/SiO<sub>2</sub>/Si substrate, when cooled to  $25^\circ\text{C}$  from  $500^\circ\text{C}$  by a finite element method. The large displacements in x and y directions, i.e. into the plane were calculated, compared with those in z direction. As shown in Fig. 7(b), the compressive and tensile stress maintained the balance, because the BIT film was uniformly shrunk. Therefore, the dielectric properties were not so affected by the stress. The dielectric constant was 100 at 1 kHz.

#### 4. Conclusions

Oriented Bi<sub>4</sub>Ti<sub>3</sub>O<sub>12</sub> thin films were prepared by a reactive magnetron sputtering using a Bi and Ti metal. Some of the conclusions that have been made are:

- C-axis oriented perovskite phase was prepared by a comparatively low substrate temperature around  $350^\circ\text{C}$  independent on the sputtering gas pressure.
- BIT thin films were strongly oriented on Pt/Ti/SiO<sub>2</sub>/Si substrate.
- Deposition rate was  $1.7 \mu\text{m/h}$ .
- The remanent polarization and coercive field were  $7 \mu\text{C/cm}^2$  and  $51.2 \text{ kV/cm}$ , respectively and the dielectric constant was 100 at 1 kHz.

#### Acknowledgements

This work was supported by Foundation for Promotion of The Murata Science Foundation.

#### References

- (1) M. Toyoda, Y. Hamaji, K. Tomono and D.A. Payne: Jpn. J. Appl. Phys. 32 4158 (1993).
- (2) T. Nakamura, R. Muhammet, M. Shimizu and T. Shiosaki: Jpn. J. Appl. Phys. 32 4086 (1993)
- (3) T. Yamamoto, T. Imai and T. Shiosaki: Proc. of Int'l Sympo. on Applications of Ferroelectrics 317 (1992)

# RF-SPUTTERED $\text{LiNbO}_3$ FILMS FOR PIEZOELECTRIC APPLICATIONS

Azamat Bakirov, Aron Margolin, Larisa Resnichenko, Evgeny Sviridov and Vladimir Dudkevich

Institute of Physics, Rostov State University,  
194, Stachki Ave, Rostov-on-Don, 344104, Russia

**Abstract.** Polycrystalline  $\text{LiNbO}_3$  films on the stainless steel substrates fabricated by rf cathode sputtering with no preliminary polarisation had the effective longitudinal piezoelectric modulus  $d_{33} = (6.0 \div 8.5) \cdot 10^{-12} \text{ C/N}$ . This value is 60 - 80 percent of  $d_{33}$  for the poled ceramics of the same composition [9] and 30 - 40 percent of  $d_{33}$  for the ceramics determined from the  $d_{ij}$  values for a single crystal (a superficial estimation). The high "self-polarisation" of  $\text{LiNbO}_3$  films first observed by N. Foster [2] may be a result of their growth in a ferroelectric phase.

Some characteristics of models of the dynamic strain sensors based on  $\text{LiNbO}_3$  films are described.

## INTRODUCTION

One of the fields of application of ferroelectric films is connected with the use of the piezoelectric effect (devices on surface acoustic waves, dynamic strain sensors, accelerometer etc.) [1].

The piezoelectric effect in ferroelectric films was observed for the first time for  $\text{LiNbO}_3$  films on the fused quartz substrates fabricated by three-electrode cathode sputtering at the deposition temperature ranging from 330-390°C [2]. The electromechanical coupling factor  $K_t$  for longitudinal thickness modes was found to be  $\sim 0.08$  for the unpoled polycrystalline films obtained by this technique (for  $\text{LiNbO}_3$  crystals in the z-direction  $K_t = 0.07$ ).

The "self-polarization" of this kind during film growth was observed for heteroepitaxial rf-sputtered  $\text{PbTiO}_3$ /(001) $\text{MgO}$  films [3-5]. It was established from domain etch patterns that the value of "self polarisation" was about 0.7 of  $P_s$  of the single-domain  $\text{PbTiO}_3$  crystal that is in good agreement with the pyroelectric coefficient value of  $2.5 \cdot 10^{-4} \text{ C} \cdot \text{m}^{-2} \cdot \text{K}^{-1}$  at room temperature reported in rf [4] for the same films (for single-domain  $\text{PbTiO}_3$  crystals the pyroelectric coefficient is  $(4 \pm 0.5) \cdot 10^{-4} \text{ C} \cdot \text{m}^{-2} \cdot \text{K}^{-1}$  [6]).

It should be noted that, as far as we know, such a "self-polarisation" in the films of other ferroelectrics was not observed. The negligible "self-polarisation" seems to be characteristic of all the ferroelectric films fabricated by cathode sputtering ( $\text{BaTiO}_3$  films on Pt substrates [7],  $\text{Pb}(\text{Zr},\text{Ti})\text{O}_3$  films on the substrates of platinised  $\text{Al}_2\text{O}_3$  ceramics [8] etc.).

At the same time, the high "self-polarization" of

polycrystalline  $\text{LiNbO}_3$  and heteroepitaxial  $\text{PbTiO}_3$ /(001) $\text{MgO}$  films the origin of which is not yet elucidated is a fairly "convenient" phenomenon for applications. In this connection, the present paper deals with a study of rf-sputtering  $\text{LiNbO}_3$  films.

## EXPERIMENTAL PROCEDURE

The 2  $\mu\text{m}$  to 4  $\mu\text{m}$  thick films were deposited on alumina, stainless steel and Pt substrates by rf cathode sputtering from the  $\text{LiNbO}_3$  powder target in an  $\text{O}_2$ -atmosphere. The sputtering conditions were as follows: for the specific high-frequency power of 15  $\text{W}/\text{cm}^2$  the substrate temperature varied from 360 to 500 °C, the oxygen pressure from 30 to 60 Pa and the target-to-substrate distance from 9 to 12 mm. The film growth rate was 0.4-0.7  $\mu\text{m}/\text{h}$ .

From the data of X-ray studies (x-ray diffractometer DRON-3,  $\text{CoK}\alpha$ ,  $\beta$ -filter) it follows that the films obtained at any combinations of parameters are the polycrystalline  $\text{LiNbO}_3$  with no marked preferred orientation of crystallites. X-ray diffraction showed no reflections of impurity phases.

The crystallites of  $\text{LiNbO}_3$  films (electron microscope Tesla-613, the Pt-C replica technique) had no clear faces. Their mean sizes increased from 0.01-0.02  $\mu\text{m}$  to 0.2 - 0.3  $\mu\text{m}$  with the increase of substrate temperature and gas pressure within above limits.

The unit cell parameters of the films having the crystallite sizes of 0.1 - 0.3  $\mu\text{m}$  in the hexagonal state were as follows:  $a = (5.146 \pm 0.003) \text{ \AA}$ ,  $c = (13.818 \pm 0.005) \text{ \AA}$  and  $c/a = 2.69$  (for bulk polycrystalline samples [9] and the target powder  $a = (5.150 \pm 0.001) \text{ \AA}$ ,  $c = (13.816 \pm 0.001) \text{ \AA}$  and  $c/a = 2.69$ ). Some properties of the films such crystallite sizes are described below.

At room temperature the dielectric permittivity  $\epsilon = 35 - 50$  and the dielectric loss angle tangent  $\text{tg}\delta = 0.05 - 0.07$  at the frequency  $f = 1.6 \text{ kHz}$  and the measuring electric field strength  $E_m = 10^4 \text{ V/m}$  (for bulk polycrystalline samples  $\epsilon = 42-48$  and  $\text{tg}\delta = 0.010 - 0.013$  [9]). At  $T > 300^\circ\text{C}$ ,  $\text{tg}\delta$  rapidly increased that made measurements difficult. It should be noted that for the  $\text{LiNbO}_3$  ceramics the increase of  $\text{tg}\delta$  took place at higher temperatures ( $T > 450^\circ\text{C}$ ) [9].

The dielectric hysteresis loops at the 50 Hz frequency were not recorded at the electric field strength up to  $5 \cdot 10^7$

V/m.

The effective longitudinal piezoelectric modulus  $d_{33}$  of the films (the  $x_3$  axis is a normal to the substrate surface) measured by the quasistatic method [7] was in the range of  $(6,0 - 8,5) \cdot 10^{-12}$  C/N (for the modified poled  $\text{LiNbO}_3$  ceramics  $d_{33} = (10 \pm 0,5) \cdot 10^{-12}$  C/N [9]). The application of the external d.c. "depoling"  $5 \cdot 10^7$  V/m electric field and the repeated heating to 500 °C did not result in the change of the  $d_{33}$  value of the films.

The models of dynamic strain sensors having a mass less than 0,05 g were based on the  $\text{LiNbO}_3$  films deposited on stainless steel substrates. They were flat chips with dimensions of  $3 \times 3 \times 0,1$  mm. The tests of these sensors were conducted using a standart fish-bellied beam which is usually used in calibrating such sensors made of the bulk material at low frequencies. The sensors were pasted or welded (point electric welding) to the flat beam surface the strain of which was determinated by independent methods. It is clear that the piezoelectric signal of the sensor having no directivity diagram (complete rotational symmetry with respect to  $x_3$ ) must be proportional to the sum of main components of the strain tensor in the plane of conjugation with the surface of the object under test. In the case of the fish-bellied beam this sum is  $\epsilon(1-\nu)$ , where  $\epsilon$  is the strain in direction of its axis and  $\nu$  is the Poisson's coefficient of the metal of which it is made.

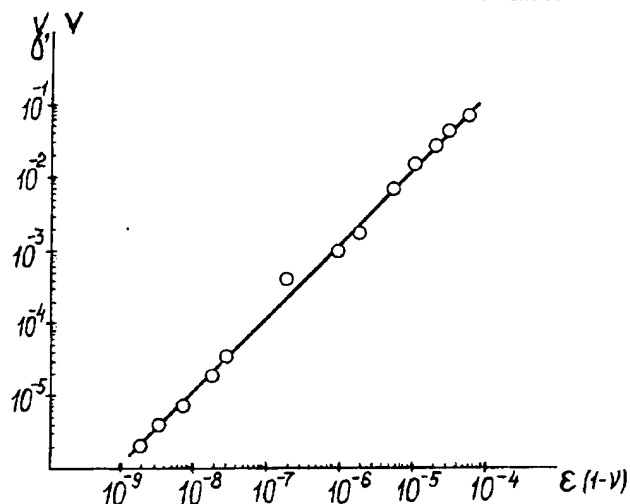


Fig.1 The piezoelectric signal of the isotropic sensor with the unpoled  $\text{LiNbO}_3$  film as a function of the sum of main components of the strain tensor of the fish-bellied beam surface.

Fig. 1 shows the piezoelectric signal of one of such isotropic sensor as a function of the sum  $\epsilon(1-\nu)$ . It can be seen from this figure that this dependence is linear in a wide range of measurements of this sum (from  $10^{-9}$  to  $10^{-4}$ ) and the sensor response is great.

### DISCUSSION

The polycrystalline  $\text{LiNbO}_3$  films very close in structure and properties to the bulk polycrystalline samples of the same composition were fabricated by rf cathode sputtering from stoichiometric targets.

The lowering of the temperature at the beginning of the increase of  $\text{tg} \delta$  in the films is attributed to a small Li deficiency

which, as shown in rf [2], may be eliminated by introducing the Li excess into the target.

A direct support to the conclusions made in rf [2] that the substratal "self-polarisation" arises in rf-sputtered  $\text{LiNbO}_3$  films was given by the present study. Indeed, in a simple geometric model of noninteracting crystallites for the completely poled ceramics (all possible 180° domain reorientations) it is easily to obtain the following relation:

$$d_{33} = \frac{3}{2\pi} \sum_{\theta=0}^{\pi/2} \sum_{\beta=0}^{2\pi/3} d_{33}(\theta, \beta) \sin \theta d\theta d\beta \quad (1)$$

where

$$d_{33}(\theta, \beta) = (d_{15} + d_{31}) \cos \theta \sin^2 \theta + d_{22} \sin^3 \theta (4 \cos^3 \beta - 3 \cos \beta) + d_{33} \cos^3 \theta, \quad (2)$$

where  $d_{ij}$  is the piezoelectric modulus of the  $\text{LiNbO}_3$  crystal and  $d_{33}$  is the effective longitudinal piezoelectric modulus of the ceramics. Using the  $d_{ij}$  values of given in rf [10]  $d_{33}$  was calculated ( $d_{33} = 18 \cdot 10^{-12}$  C/N). Hence, the effective longitudinal piezoelectric modulus of the films ranges from 30 to 40 percent of the maximum one for, the ceramics the relations (1) and (2) give virtually only the superficial estimation).

It should be noted in conclusion that the high "self-polarization" of  $\text{LiNbO}_3$  films seems to be a result of their growth in a ferroelectric phase.

### REFERENCES

- [1] S.T. Swartz, V.E. Wood, "Ferroelectric thin films" *Condensed Matter News*, vol. 1, N 5, pp. 4-13, 1992.
- [2] N.F. Foster, "The deposition and piezoelectric characteristics of sputtered lithium niobate", *J. Appl. Phys.*, vol. 40, N 1, pp. 420-429, 1969.
- [3] E.V. Sviridov, V.A. Alyoshin, Yu.I. Golovko, I.N. Zakharchenko, V.M. Mukhortov, V.P. Dudkevich, "Rentgenografic and electron-microscopic data on heteroepitaxial  $\text{PbTiO}_3/(001)\text{MgO}$  films", *Phys. Stat. Sol. (a)*, vol. 121, pp. 157-162, 1990.
- [4] K. Iijima, S. Kawashima, I. Ueda, "Dielectric and pyroelectric properties of  $\text{PbTiO}_3$  thin films", *Jap. J. Appl. Phys.*, vol. 24, suppl., pp. 482-484, 1985.
- [5] Z. Surowiak, V.M. Mukhortov, V.P. Dudkevich, "Phase transition and domain structure in  $(\text{Ba}_{1-x}\text{Sr}_x)\text{TiO}_3/(100)\text{MgO}$  and  $\text{PbTiO}_3/(100)\text{MgO}$  thin films", *Ferroelectrics*, vol. 133, pp. 1-16, 1993.
- [6] E.G. Fesenko, V.G. Gavrilachenko, A.F. Schetchev, "Domain structure of many-axis ferroelectric crystals", Rostov-on-Don: Izd. Rostov State University, 185 p., 1990.
- [7] S.V. Biryukov, I.N. Zakharchenko, A.A. Bakirov, A.M. Margolin and V.P. Dudkevich, "Piezoelectric properties of rf-sputtering  $\text{BaTiO}_3$  films", In: "Problems of automatisatation in strength experiment", Moscow: Izd. Center of Scientific-technical information "Volna", pp. 189-198, 1986.

- [8] T. Fukami, S. Fujii, "Asymmetric hysteresis loops of ferroelectric PZT films", Jap. J. Appl. Phys. vol. 24, N 5, pp. 632-633, 1985.
- [9] E.G. Fesenko, L.A. Reznichenko, V.A. Chernyshkov, O. N. Razumovskaya, V.G. Smotrakov, E.S. Tsukhotskii and L.A. Shilkina, "Preparation and study of highly dence lithium metaniobate ceramics", Izv. AN SSSR, vol.21, N 2, pp. 317-319, 1985.
- [10] Yu. S. Kuzminov, "Li niobate and tantalate", Materials for nonlinear optics, Moscow: Izd. "Nauka", 223 p, 1975.

# The growth behavior of Pb-Containing perovskite thin films using pulsed laser deposition technique

I-Nan Lin, Kuo-Shung Liu, Shun-Lih Tu, Sheng-Jenn Yang  
Materials Science Center, Dep. Mater. Sci. & Eng., National  
Tsing-Hua University, Hsinchu, Materials R&D  
Center, CSIST, Lung-Tan, Taiwan, R.O.C

## Abstract

The PLZT films highly textured in (110) orientation have been successfully grown on SrTiO<sub>3</sub>-buffered silicon substrates. The films deposited by pulsed laser deposition process are assumed to be formed via a two-step process, i.e., cluster adherence and phase transformation. The beneficial effect of using STO as buffer layers involves enhancing the kinetics of phase transformation from amorphous to perovskites. Thereby, the loss of Pb-species in the films is thus suppressed. The optimum dielectric constants obtained are around  $\epsilon_r=490$  for PLZT/STO/Si films deposited at 550°C (1 mbar Po<sub>2</sub>) and post-annealed at 550°C (1 atm Po<sub>2</sub>). Furthermore, the corresponding charge storage density is around  $Q_c \approx 1.5 \mu\text{C}/\text{cm}^2$  at 50 KV/cm, applied field strength.

## I. INTRODUCTION

Lead base ferroelectric thin films, e.g. PbTiO<sub>3</sub> (PT), Pb(Zr<sub>1-x</sub>Ti<sub>x</sub>)O<sub>3</sub> (PZT) and Pb<sub>1-x</sub>La<sub>x</sub>(Zr<sub>y</sub>Ti<sub>1-y</sub>)<sub>1-x/4</sub>O<sub>3</sub> (PLZT), have attracted a substantial amount of attention<sup>1-3</sup> due to their great potential for applications as pyroelectric detectors, piezoelectric vibrators, electro-optic devices and nonvolatile random access memories. The pulsed laser deposition (PLD) technique, which has been successfully used for depositing high-T<sub>c</sub> YBa<sub>2</sub>Cu<sub>3</sub>O<sub>7-x</sub> (YBCO) superconductor films<sup>4-5</sup>, possesses several advantages in synthesizing oxide films and has, therefore, found extensive usage in synthesizing PZT-series thin films.

Synthesis of PZT series thin films on Si-substrate, which is important for practical application, is even more difficult to obtain. Therefore, the primary purpose of this paper involves systematically examining the effects of processing parameters on the characteristics of the deposited PLZT films. The sources which cause the formation of pyrochlore phase and the factors which result in Pb<sup>2+</sup>-ions deficit in the films are also discussed.

## II. EXPERIMENTAL

The laser beam from XeCl laser (308 nm, Lambda Physik 205i) of an energy density of 3 J/cm<sup>2</sup> was used for growing PLZT films via a pulsed laser deposition technique. In the single-step process, the films were deposited at 350°C~750°C in 1 mbar oxygen pressure (Po<sub>2</sub>), which was followed by 10 minutes of annealing at depositing temperature (1 atm Po<sub>2</sub>). In the two-step process, the films were deposited at room temperature (0.01 mbar Po<sub>2</sub>), which was followed by post-annealing at 350°C~550°C for 10 minutes in 1 atm Po<sub>2</sub>. The substrates used for growing PLZT via the above mentioned process were Pt-coated silicon (Pt/Ti/SiO<sub>2</sub>/Si). Various kinds of materials were

also used as substrates. Synthesizing the (110) textured PLZT films necessitated using the (110) SrTiO<sub>3</sub> (STO) films as a buffer layer. The textured buffer layer was obtained by growing the STO films onto P-type (100) silicon substrate at 650°C and 1 mbar oxygen pressure. The PLZT (5/70/30) films were then deposited on top of STO films, in situ, at 350°C to 650°C substrate temperature and 1 mbar, 0.1 mbar or 0.01 mbar oxygen pressure for 10 minutes. The crystal structure of the PLZT films was examined via the X-ray diffraction technique (Rigaku, D/max-IIIB). The capacitance-voltage properties of the films were measured using an H.P.4194A impedance analyzer; in addition, the charge storage density of the films was evaluated from charge-discharge signals in response to a square shaped pulse.

## III. RESULTS

The effect of substrate temperature on the crystallinity of the PLZT films is shown in Fig. 1. This figure reveals that the phases which dominate the structure of the films change with the depositing temperature. Crystalline films can be obtained when the substrate temperature is higher than 350°C. However, those films deposited at either 350°C, 400°C or 450°C are predominated with pyrochlore ( $\pi$ ) phases. Only when the substrate temperature has been increased to 550°C can the formation of the undesired pyrochlore phase be suppressed, which subsequently results in perovskite (P) phase. But the secondary phases (Z), which are zirconium containing oxides (Zr<sub>1-x</sub>Ti<sub>x</sub>O<sub>2</sub>), start to appear and its proportion increases with depositing temperature. Only the diffraction peaks corresponding to the secondary phase are observable for the films deposited with the substrate temperature higher than 650°C. These results indicate that the temperature range at which the perovskite phase can be formed is very narrow when the oxygen pressure is controlled at 1 mbar for deposition and at 1 atm for annealing.

Another set of experiments, which are to deposit the films at room temperature (0.01 mbar) and then post-anneal them at 550°C in a high oxygen pressure environment (1 atm), are designed for the purpose of suppressing the vaporization of Pb<sup>2+</sup>-ions. Figures 2a~2d reveal that the crystal structure of the films changes with the annealing temperature. The as-deposited films are amorphous with very diffuse peaks, which is of a relatively small intensity. Those appear at around  $2\theta=31^\circ$ . The films annealed at 350°C still contain a significant amount of pyrochlore phase. The diffraction peaks which correspond to pyrochlore phase completely disappear when the films were annealed at 450°C or even at a higher temperature. The success in obtaining perovskite phase free of pyrochlore phase in



these cases implies that the cationic concentration supplied by the laser induced plume is of proper composition for forming the perovskite phase. No deficit in  $\text{Pb}^{2+}$ -ions occurs in the as deposited amorphous films; in addition, the post-annealing proceeded under 1 atm oxygen pressure at 550°C does not cause any  $\text{Pb}^{2+}$ -ions loss. Therefore, the occurrence of pyrochlore phase shown in 350°C-annealed films (Fig. 2b) must arise from mechanisms other than the  $\text{Pb}^{2+}$ -ions deficiency in the films.

The sequence of phase transformation of the room temperature deposited films closely resembles that of the sol-gel derived PLZT powders<sup>20</sup>. From this, it has been proposed that lead titanates compound (e.g.  $\text{PbTiO}_3$ ,  $\text{Pb}_2\text{Ti}_2\text{O}_6$  etc.) were formed preferentially at an early stage of phase transformation; in addition, these compounds converted into the perovskite structure later through means of reacting with the residual  $\text{ZrO}_2$  and  $\text{La}_2\text{O}_3$  particles. The same reacting sequence might also occur for the crystallization process of the PLZT films during annealing. Furthermore, a significant proportion of pyrochlore phase would be expected to coexist with the perovskite phase when the annealing temperature is not high enough. The transformation of pyrochlore phase into perovskite phase by combining with the unreacted  $\text{ZrO}_2$  (or  $\text{La}_2\text{O}_3$ ) clusters can be completed only when annealed at a sufficiently high enough temperature. This is in accordance with the phenomenon observed in Figs. 2a-2d. Therefore, this phenomena implies that the PLZT perovskite phase synthesized by pulsed laser deposition process is possibly formed via a two-step process, i.e., (i) the adhere the species contained in the laser induced plume onto the substrate as clusters and then followed by (ii) transform those phase into a crystalline structure.

Examining the mechanisms which influence the formation of the phases other than the perovskite was next undertaken by precoating a thin layer of Pb or PbO on the substrate for the purpose of compensating for the loss of  $\text{Pb}^{2+}$ -ions. The PLZT films were then deposited at 550°C (1 mbar  $\text{Po}_2$ ) for 10 minutes and annealed at 550°C (1 atm  $\text{Po}_2$ ) for 10 minutes. Precoating a thin layer of Pb or PbO underneath the PLZT films is shown in Figure 3a to have enhanced the formation of perovskite phase; in addition, the formation of pyrochlore phase has also been completely suppressed. However, a significant amount of PbO and Z phases appears. The presence of PbO peaks, which are indicated by the triangular symbols, suggests that the amount of PbO is abundant enough to compensate for the possible Pb-loss which might potentially occur during depositing process. The appearance of Z phase, which is similar to the one observed in the films in-situ deposited at a high substrate temperature (c.f. Fig. 1), can apparently be ascribed to the loss of  $\text{Pb}^{2+}$ -ions. These phenomena therefore imply that the underlying PbO layer, which can effectively suppress the formation of pyrochlore phase in the initially grown PLZT films, is incapable of diffusing through the films to the surface so as to compensate for the  $\text{Pb}^{2+}$ -ions loss. The deficiency in  $\text{Pb}^{2+}$ -ions always occur for the thin film surface whenever they are synthesized at 550°C in low oxygen pressure.

The above results indicate that the substrate temperature should be limited when the films were deposited under 1 mbar  $\text{Po}_2$ , i.e. less than 550°C, in order

to avoid the formation of Z phase in the in-situ deposition process. However, formation of perovskite phase has to be enhanced such that the presence of preferentially formed pyrochlore phase can be reduced. For this purpose, various kinds of substrates were tested. The PLZT films were in-situ deposited at 450°C/1 mbar and followed by 450°C/1 atm post-annealing. Figure 3b shows that among the substrate materials examined only the  $\text{SrTiO}_3$  surface can actually enhance the formation of the perovskite structure. The silicon surface can trigger the growth of the perovskite phase as effective as the Pt surface does; however, a significant amount of pyrochlore phase still persists (labelled as Si and Pt). The  $\text{SiO}_2$  surface of the fused quartz substrates completely fails in nucleating the perovskite phase such that only the pyrochlore phase is observable (labelled as Qz). The  $\text{SrTiO}_3$  (STO) surface, no matter whether deposited on the bare silicon or the platinum coated silicon substrate, can completely suppress the formation of pyrochlore phase (labelled as STO(Si) and STO(Pt)). The success in synthesizing the perovskite phase on  $\text{SrTiO}_3$  coated materials implies, again, that the species provided by the laser ablated plume are actually of proper proportion to grow PLZT films.

The phenomenon that the  $\text{SrTiO}_3$  buffer layer can markedly enhance the nucleation of perovskite structure has also been observed in the synthesis of  $\text{YBa}_2\text{Cu}_3\text{O}_7$  (YBCO) superconducting films, in which the preferred orientation of YBCO films completely imitate the orientation of the  $\text{SrTiO}_3$  single crystal substrate.<sup>21</sup> This phenomenon has been ascribed to the close match in the crystal structures and the lattice parameters between STO and YBCO phases. This same mechanism may also be applied towards PLZT/STO thin film system. Thereafter, the arrangement of cations and anions of STO layer would affect the atomic arrangement of PLZT films. Restated, the textured characteristics of the PLZT films might thus be modified by controlling the preferred orientation of the STO buffer layers. Examining such an effect was performed by depositing the PLZT films on (110) preferred-oriented STO buffer layer. This layer was synthesized by pulsed laser deposition on (100) Si-substrate, at 650°C and 1 mbar  $\text{Po}_2$ .

Figures 4 shows that the atomic arrangement of the PLZT films thus obtained are actually related to that of STO buffer layer. Those films are highly textured in (110) orientations. It demonstrates, again, that a sufficiently high enough substrate temperature (>450°C) is still required for triggering the growth of perovskite phase. The pyrochlore phase would be preferentially formed whenever there is no high enough driving force to overcome the energy barrier for nucleating the perovskite phase. This behavior is similar to that of the films deposited on Pt-coated silicon in the annealing experiments (c.f. Figs. 2a-2d). The lowest substrate temperature required for completely converting the adhered species into perovskite phase is 550°C. Too high of a substrate temperature (650°C) would, again,

induces the loss of  $\text{Pb}^{2+}$ -ions and subsequently result in second (Z) phases. However, the conditions required for growing the perovskite phase on  $\text{SrTiO}_3$  buffer layer are not as stringent as those placed on Pt-coated silicon.

#### IV. CONCLUSIONS

The PLZT films highly textured in (110) orientation have been successfully grown on  $\text{SrTiO}_3$ -buffered silicon substrates. The films deposited by pulsed laser deposition process are assumed to be formed via a two-step process, i.e., cluster adherence and phase transformation. The beneficial effect of using STO as buffer layers involves enhancing the kinetics of phase transformation from amorphous to perovskites. The loss of  $\text{Pb}^{2+}$ -ions in the films is thus suppressed and is ascribed to the higher sticking coefficient of  $\text{Pb}^{2+}$ -ions onto the  $\text{SrTiO}_3$  surface than that onto Pt surface. The optimum dielectric constants obtained are around  $\epsilon_r=490$  for PLZT/STO/Si films deposited at  $550^\circ\text{C}$  (1 mbar  $\text{Po}_2$ ) and post-annealed at  $550^\circ\text{C}$  (1 atm  $\text{Po}_2$ ). Furthermore, the corresponding charge storage density is around  $Q_c \approx 1.5 \mu\text{C}/\text{cm}^2$ , at 50 KV/cm, deposited at  $550^\circ\text{C}$  (1 mbar  $\text{Po}_2$ ) and post-annealed at  $550^\circ\text{C}$  (1 atm  $\text{Po}_2$ ). Furthermore, the corresponding charge storage density is around  $Q_c \approx 1.5 \mu\text{C}/\text{cm}^2$ , at 50 KV/cm, applied field strength.

#### ACKNOWLEDGMENT

The authors gratefully appreciate the support of National Science Council, Taiwan, Republic of China under the contract No. NSC 82-0404-E-007-127, 82-0208-M-003-009, 83-0404-E-003-001, 83-0404-E-007-050.

#### REFERENCES

- 1L. M. Sheppard, *Ceram. Bull.*, **71**, 85 (1992).
- 2J. F. Scott, and C. A. P. de Araujo, *Science*, **246**, 1400 (1989).
- 3F. P. Gnadinger, and D. W. Bondurant, *IEEE Spectrum*, **7**, 30 (1989).
- 4X. D. Wu, S. A. Shaheen, N. Jisrawi, Y. H. Min-Lee, W. L. McLean, and M. Croft, *Appl. Phys. Lett.*, **51**, 619 (1987).
- 5X. D. Wu, D. Dijkkamp, S. B. Ogale, A. Inam, E. W. Chase, P.F. Miceli, C. C. Changm, J. M. Tarascon, and T. Venkatesan, *Appl. Phys. Lett.*, **51**, 861 (1987).
- 6H. Adachi, and K. Wasa, *Mat. Res. Soc. Symp. Proc.*, **200**, 103 (1990).
- 7K. S. Grabowski, J. S. Horwitz, and D. B. Chrisey, *Ferroelectrics*, **116**, 19 (1991).
- 8J. S. Horwitz, K. S. Grabowski, D. B. Chrisey, and R. E. Leuchtner, *Appl. Phys. Lett.*, **59**, 1565 (1991).
- 9H. Kidoh, T. Ogawa, A. Morimoto, and T. Shimizu, *Appl. Phys. Lett.*, **58**, 2910 (1991).

Phys. Lett., **58**, 2910 (1991).

10H. Tabata, T. Kawai, S. Kawai, O. Murata, I. Fujioka, and S. I.

Minakata, *Appl. Phys. Lett.*, **59**, 2354 (1991).

11H. Kidoh, T. Ogawa, H. Yashima, A. Morimoto, and T. Shimizu, *Jpn. J. Appl. Phys.*, **30**, 2167 (1991).

12R. E. Leuchtner, K. S. Grabowski, D. B. Chrisey, and J. S. Horwitz, *Appl. Phys. Lett.*, **60**, 1193 (1992)

13S. Otsubo, T. Maeda, T. Minamikawa, Y. Yonezawa, A. Morimoto, and T. Shimizu, *Jpn. J. Appl. Phys.*, **29**, L133 (1990).

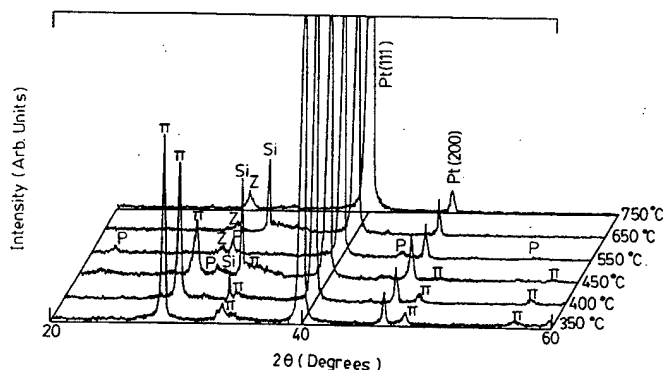


Fig. 1 The x-ray diffraction patterns of PLZT films in-situ deposited on Pt-coated silicon ( $\text{Pt/Ti/SiO}_2/\text{Si}$ ) with substrate temperature varying from  $350^\circ\text{C}$  to  $750^\circ\text{C}$  under 1 mbar oxygen pressure.

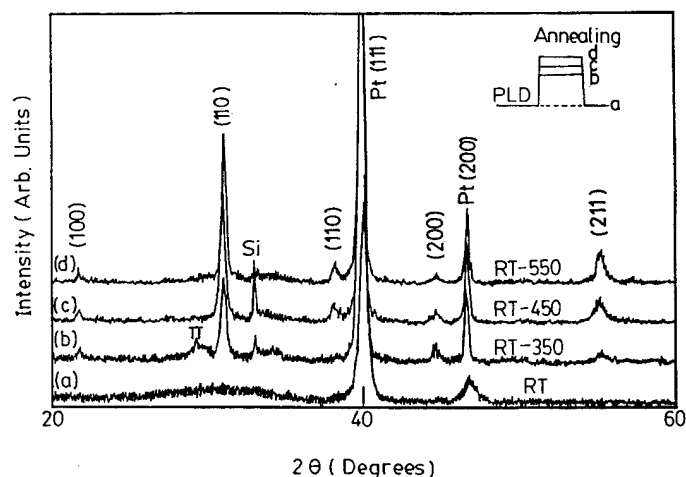


Fig. 2 The x-ray diffraction patterns of PLZT films deposited at room temperature ( $\text{Po}_2=0.01$  mbar), followed by (a) no annealing and (b)  $350^\circ\text{C}$ , (c)  $450^\circ\text{C}$  and (d)  $550^\circ\text{C}$  annealing (1 atm  $\text{Po}_2$ ).

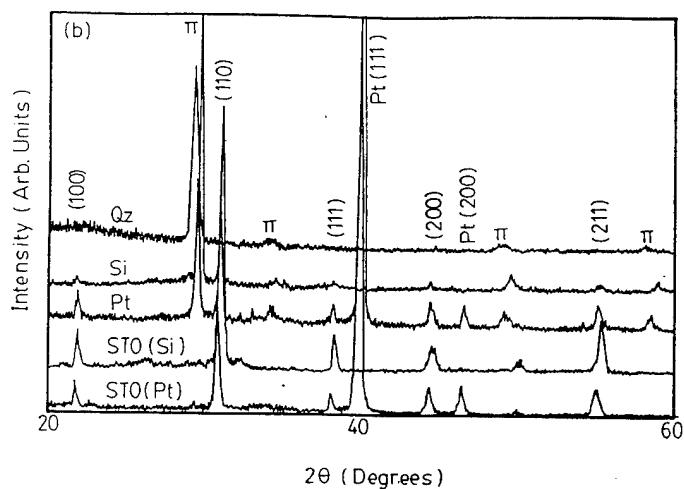


Fig. 3 The x-ray diffraction patterns of PLZT films deposited on Quartz (Qz), Si, Pt/Ti/SiO<sub>2</sub>/Si (Pt), STO/Si (STO(Si)), STO/Pt/Ti/SiO<sub>2</sub>/Si (STO(Pt)) at 450°C/1 mbar, followed by 450°C (Po<sub>2</sub>=1 atm) annealing.

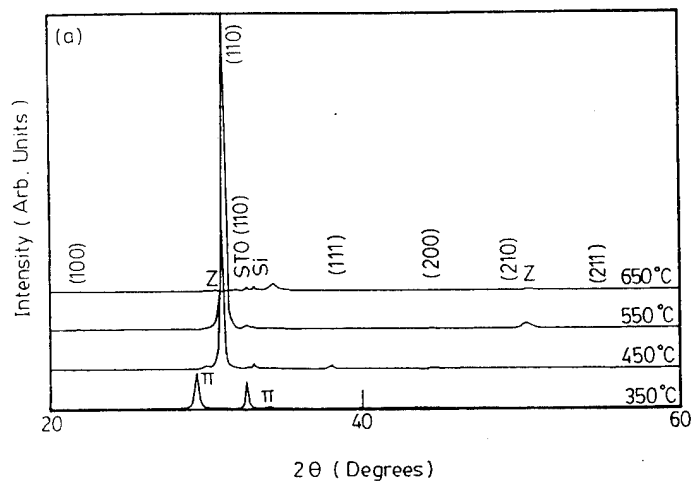


Fig. 4 The x-ray diffraction patterns of PLZT films deposited on (110) textured SrTiO<sub>3</sub> buffer layer with (a) deposition temperature varying from 350°C to 650°C under 1 mbar oxygen pressure.

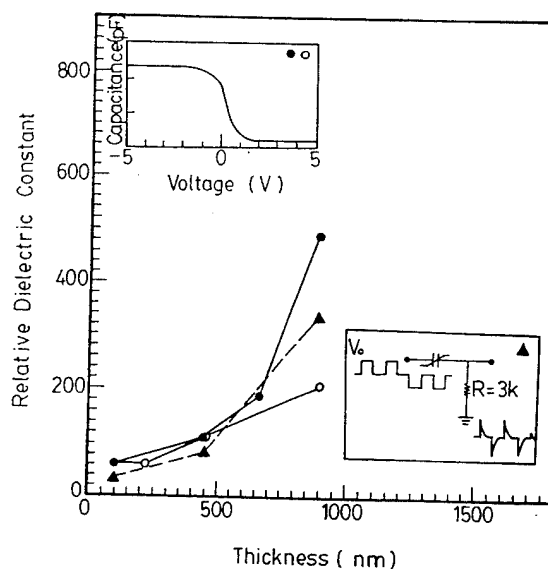


Fig. 5 The variation of effective dielectric constant of the (110) PLZT/STO/Si films with the thickness of the films.

# Development and Electrical Characterization of Lead Zirconate Titanate Thick Films on Silicon Substrates

H. D. Chen, K. R. Udayakumar, and L. E. Cross  
Materials Research Laboratory  
The Pennsylvania State University  
University Park, PA 16802

J. J. Bernstein, and L. C. Niles  
The C. S. Draper Laboratory  
Cambridge, MA 02139

## ABSTRACT

Fabrication of thick films of lead zirconate titanate (PZT) on buffered silicon substrates, and evaluation of its dielectric, ferroelectric, and electromechanical properties constitute the subject matter of this study. It has been demonstrated, for the first time, that crack free thick films of PZT can be fabricated on silicon. Films 12  $\mu\text{m}$ -thick obtained by screen printing on a single pass show dielectric permittivity of 200, tangent losses of 0.05, remanent polarization of 2.5  $\mu\text{C}/\text{cm}^2$ , and coercive field of 40 kV/cm. The field induced longitudinal piezoelectric coefficient recorded 50 pC/N at appropriate drive and dc bias conditions. The piezoelectric voltage coefficient was calculated to be  $36 \times 10^{-3}$  V-m/N, larger than that of a poled bulk ceramic. These results are promising for the utility of PZT thick films in micromachined acoustic sensor arrays, vibration sensors and other applications.

## INTRODUCTION

In the area of microelectronics, "thick film" has traditionally meant the application of specially formulated pastes onto an insulating substrate in a certain processing sequence to produce passive components; this, when connected to active devices and other discrete components results in the hybrid integrated circuit. Major applications for dielectric inks in a hybrid circuit include insulating layers in MLCs, crossovers, capacitors, encapsulation, and hermetic seals. Thick film circuits are printed on 99+% alumina, 96% alumina, beryllia and aluminum nitride, as conductors and dielectrics. With the enormous strides made in silicon micromachining, fabricating sensors and actuators on silicon, instead of ceramic substrates, in conjunction with on-chip

electronics, provides the possibility of creating true micromechanical systems, a precursor to the integrated machines of the future. Ferroelectric films such as lead zirconate titanate (PZT) useful for sensing and actuation have, for the most part, been investigated for its utility in semiconductor memories where the thickness range of interest has been 100-350 nm, primarily from considerations of polarization reversal voltage to be held lower than the operating voltage of 5 Volts. For the thicker films required for elasto-dielectric devices, in this study, the screen printing technology has been adopted from the now-mature hybrid microelectronics field to engineer "thin" thick films on silicon substrates; the films have been evaluated for its dielectric, ferroelectric and electromechanical properties to assess its utility in advanced micromechanical sensors.

## FILM PROCESSING

The following ingredients constituted the thick film dielectric ink: sub-micron sized undoped lead zirconate titanate powders, obtained commercially, as the primary functional component; lithium carbonate and bismuth oxide as the bonding agent; a DuPont proprietary organic thixotropic printing vehicle; and  $\alpha$ -terpineol as the solvent. PZT powders and the additives were dispersed in alcohol, mixed in a vibratory mill for 24 hours, dried at 400°C, and screened through a 200 mesh sieve. The powders were then mixed with the organic portion of the constituents which defines the rheological characteristics, and determines the printability of the ink; a three-roll mill aided in the final blending of the mix. The thixotropic paste is allowed to flow through the pattern on the screen by a rubber squeegee blade that traverses the surface of the screen at

a controlled speed, and deposits on to the substrate. After printing, the substrate is allowed to stand to remove the mesh marks, dried at 110°C for an hour to remove the solvents, and then fired in air. The maximum temperature at which the films could be fired was 850°C for 15 minutes; higher temperatures led to the blistering of the Ti/Pt underlayer. Densification studies by other researchers [1] of PZT thick films 10  $\mu\text{m}$ -thick on alumina substrates indicate that the films have to be sintered to 1150°C to reduce the number of pores. The solid loading of the inks was such as to yield a film thickness of 12  $\mu\text{m}$  in a single pass, the thickness profiles being recorded by an Alpha-Step 100 profilometer. The X-ray diffraction pattern of the films fired at 850°C indicated the formation of single phase perovskite structure.

## ELECTRICAL CHARACTERISTICS

The dielectric permittivity and dissipation losses were measured on an HP 4274A multi-frequency LCR meter at frequencies ranging from 100 Hz to 100 kHz, with top platinum electrode diameters varying from 0.8 mm to 6.35 mm; this is recorded in Table I. The lower permittivity of the PZT films, compared to the

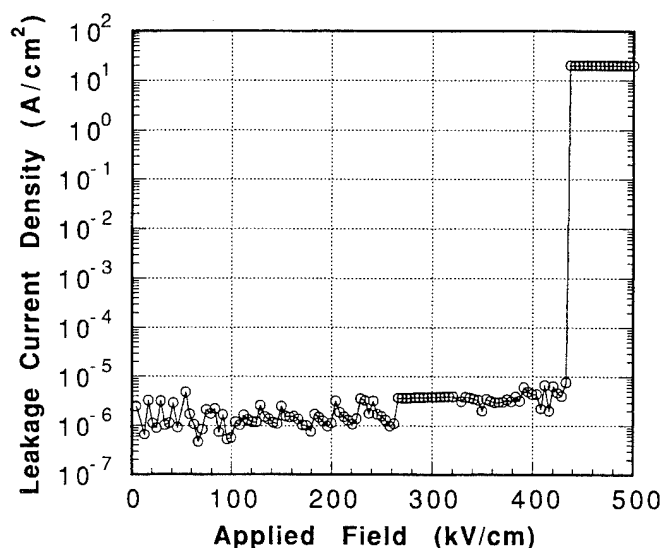


Fig. 1 Leakage current density plotted as function of applied electric field, to determine the breakdown field. In this figure, the breakdown field is at around 440 kV/cm.

bulk, may be attributed to the less than completely densified films. The dielectric breakdown strength of the films were obtained by measuring the leakage current as a function of applied field (Fig. 1) at 5 kV/cm intervals; the leakage current density at fields lower than the breakdown voltage was in the  $\mu\text{A}/\text{cm}^2$  range.

Table 1 Frequency and electrode size dependent dielectric properties of 12  $\mu\text{m}$ -thick screen printed PZT films

Electrode diameter	Relative Permittivity, $\epsilon_r$				$\tan \delta$			
	100 Hz	1 kHz	10 kHz	100 kHz	100 Hz	1 kHz	10 kHz	100 kHz
0.8 mm	320	220	270	250	0.06	0.06	0.06	0.09
1.6 mm	240	220	200	180	0.05	0.05	0.06	0.08
2.77 mm	210	190	160	130	0.06	0.08	0.12	0.33
3.175 mm	190	170	150	120	0.06	0.08	0.12	0.35
3.56 mm	200	180	150	100	0.095	0.09	0.15	0.59
5.94 mm	230	200	170	110	0.099	0.105	0.16	0.65
6.35 mm	230	200	170	90	0.08	0.095	0.17	0.86

The breakdown strength of the films is approximately 450 kV/cm. The high temperature capacitance measurement showed that the Curie point of the films was at about 360°C, slightly lower than the bulk ceramic value.

The polarization hysteresis plot of the films is shown in Fig. 2; the remanent polarization and coercive field are 2.5  $\mu\text{C}/\text{cm}^2$  and 40 kV/cm, respectively. The hysteresis traces in the figure has been taken at applied fields of 100 kV/cm to 175 kV/cm, at 25 kV/cm intervals. The remanent polarization is higher than that reported on PZT films with PbO additive [2], and comparable to that of PZT films with lead germanium silicate additive [3].

The field-induced displacements of the films were measured with a double beam laser interferometer that has the capability to measure strains of the order of  $10^{-2}$  Å with a lock-in amplifier [4]. Plotted in Fig. 3 are the film surface displacements as a function of ac exciting electric field at two different dc bias fields. The linear plot shows that the films confirm to the converse piezoelectric effect. The longitudinal piezoelectric strain coefficient  $d_{33}$  calculated from the strain and the probing field is plotted in Fig. 4 as a function of dc bias. The maxima is at 50 pC/N, beyond which  $d_{33}$  drops; this is predominantly a reflection of the weak field dielectric response under cyclic bias,

what with the polarization charge saturating at high applied fields. The piezoelectric voltage coefficient  $g_{33}$  derived from  $d_{33}$  and the low signal relative permittivity  $\epsilon_{33}$  under the same conditions is shown in Fig. 5. At 40 kV/cm dc bias and 4 kV/cm driving field, at which  $d_{33}$  is maximum (Fig. 4), the piezoelectric voltage coefficient is  $36 \times 10^{-3}$  V-m/N; the poled PZT bulk ceramic of equivalent composition shows a magnitude of  $20 \times 10^{-3}$  V-m/N [5].

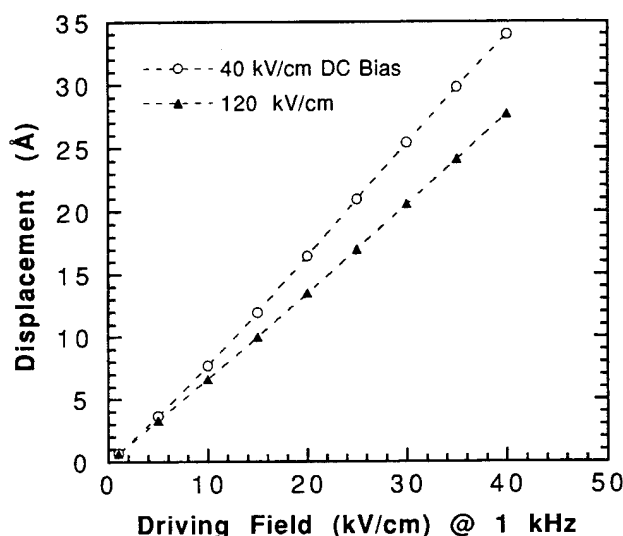


Fig. 3 Displacement of the film surface as a function of ac field at constantly held dc bias of 40 and 120 kV/cm.

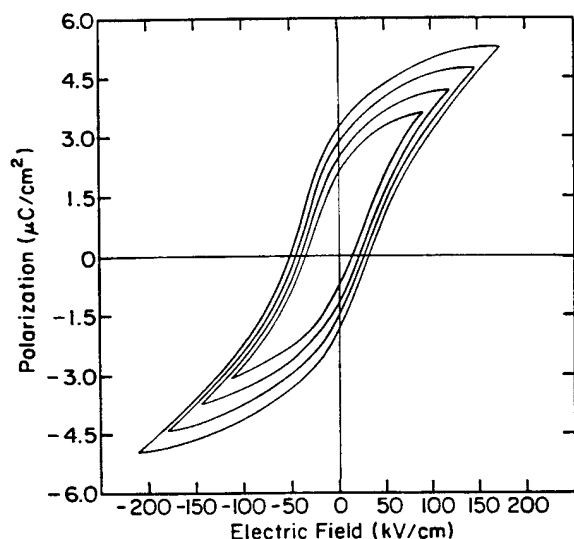


Fig. 2 Polarization-electric field hysteresis traces of the 12  $\mu\text{m}$ -thick PZT film at applied fields varying from 100 (inner loop) to 175 kV/cm (outer loop), at 25 kV/cm intervals.

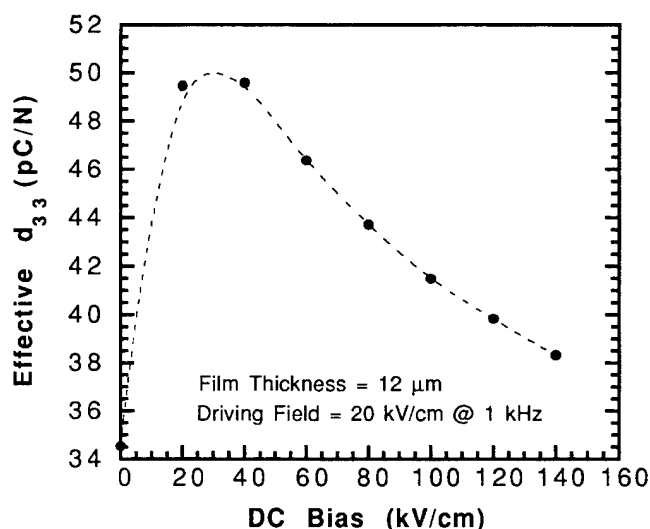


Fig. 4 Effective longitudinal piezoelectric strain coefficient  $d_{33}$  variation with dc bias; the slope of displacement-voltage curve yields the effective  $d_{33}$

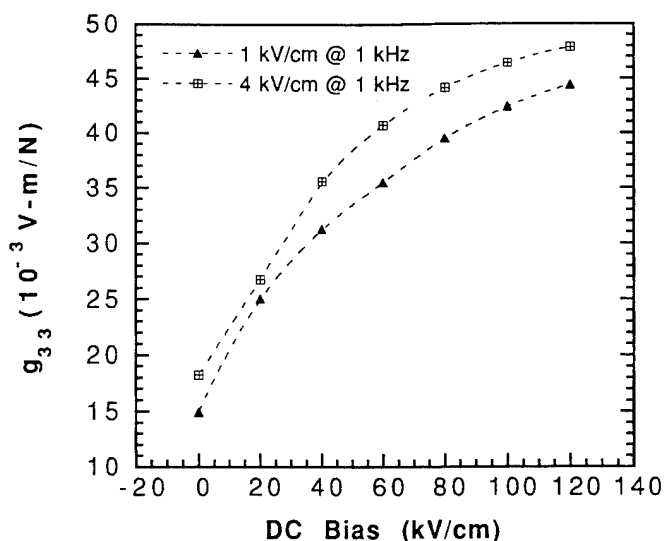


Fig. 5 Piezoelectric voltage coefficient  $g_{33}$  which is the ratio of open circuit field to mechanical stress plotted at varying dc bias. The data has been culled from the dielectric response and  $d_{33}$  response to dc bias.

### SUMMARY

This is the first study to demonstrate that crack-free thick films of PZT can be fabricated on silicon substrates; earlier studies have used alumina or stainless steel substrates. The motive has been to combine silicon

micromachining with screen printing with the expectation of realizing a broad range of sensors including vibration sensors and arrays of ultrasound detectors. To assess its utility in these devices, the dielectric, ferroelectric and piezoelectric properties were evaluated. The magnitude of the longitudinal piezoelectric voltage coefficient is indicative of its feasibility in the thickness and hydrostatic mode for sensing.

### REFERENCES

- [1] H.-X. Zhang, S. Leppavuori, A. Uusimaki, P. Karjalainen, and R. Rautioaho, in *Proceedings of the 8th International Meeting on Ferroelectricity*, (in Press)
- [2] B. Morten, G. De Cicco, A. Gandolfi, and C. Tonelli, *Hybrid Circuits*, **28**, 25 (1992)
- [3] J. Collier, I. A. Cornejo, and M. J. Haun, in *Proceedings of the 8th International Meeting on Ferroelectricity*, (in Press)
- [4] Q. M. Zhang, W. Y. Pan, and L. E. Cross, *Jl. Appl. Phys.*, **63**, 2492 (1988)
- [5] D. P. Skinner, R. E. Newnham, and L. E. Cross, *Mat. Res. Bull.*, **13**, 599 (1978)

# The Structural Phase Transition in PZT Ferroelectric Films

Lev Sapozhnikov, Irina Sem, Irina Zakharchenko,  
Evgeny Sviridov, Vladimir A. Alyoshin,  
and Vladimir Dudkevich.

Rostov State University, Institute of Physics,  
Rostov-on-Don 344104, Russia.

**Abstract.** The  $\text{Pb}(\text{Zr,Ti,W,Cd})\text{O}_3$  (PZT) films were deposited by rf-sputtering of stoichiometric targets in an oxygen atmosphere. Epitaxial films had a tetragonal unit cell at room temperature. The unit cell parameter vs temperature curve showed a kink at phase transition temperature characteristic of the bulk material. Polycrystalline films had a pseudocubic unit cell. In spite of the presence of a full set of ferroelectric properties no anomalies in the temperature dependence of the unit cell parameter at phase transition were observed. The only evidence of the presence of the structural phase transition to a cubic phase was the essential decrease of intensity of X-ray reflections with an odd sum of indices as in the epitaxial films. Just these reflection intensities are most sensitive to the displacement of Zr and Ti cations with respect to Pb on approaching the Curie point temperature.

## Introduction

A study of the properties of thin ferroelectric films is of great interest because of the possibility of their microelectronic applications. A study of characteristics of polarization switching (switching time, polarization value, ageing, fatigue etc.) is now the focus of attention that is due to the possibilities of using films as nonvolatile memory devices. All available data on the film crystal structure of the film (type of distortion of the unit cell, special features of manifestation of structural phase transitions, domain structure type etc.) determining to a large extent their physical properties are insufficient and, sometimes, contradictory. There are many published works on distinction of the film structure from the structure of the bulk material of the same composition [1-6]. For instance, the possibility for the boundary between the tetragonal and rhombohedral phase in PZT films to be displaced either to the  $\text{PbTiO}_3$  side [1] or to the  $\text{PbZrO}_3$  side [2] was reported. The essential distinction of the unit cell parameters of the films from those of the ceramics [1,3,4-6] and the rise [2,3,5,7] or the lowering [2] of the structural phase transition temperature in the films was found to be also possible.

The distinction between crystal structures of the film and the bulk material discussed in rare cases is expected to be due to the difference in the film and substrate unit cell parameters and their thermal expansion coefficients [4,7-9]. However, in the limits of only these assumptions we shall be hardly able to explain the observed considerable increase (to  $4.22 \text{ \AA}$  [6]) or decrease (to  $4.08 \text{ \AA}$  [3]) of the unit cell parameter  $c$  of

the  $\text{PbTiO}_3$  film in comparison with the normal one ( $c = 4.15 \text{ \AA}$ ). Furthermore, it is impossible to explain in terms of film-substrate interaction the additional increase of the Curie point temperature  $T_c$  in  $\text{PbTiO}_3$  films from  $550$  to  $600^\circ\text{C}$  after removal of the substrate [5] ( $T_c$  of the bulk material is  $490^\circ\text{C}$ ). The present paper reports new results on a study of peculiarities of structure and phase transitions of epitaxial and polycrystalline PZT films which give rise to some other questions.

## Experimental Procedure

PZT films were rf-sputtered in the pure oxygen atmosphere. The hot-pressed ceramics of the composition  $\text{Pb}(\text{Zr,Ti,W,Cd})\text{O}_3$  corresponding to the region of co-existence of the tetragonal (T) and rhombohedral (R) phases with the unit cell parameters  $a_T = 4.06$ ,  $c_T = 4.12 \text{ \AA}$ , and  $a_R = 4.075 \text{ \AA}$ ,  $\alpha = 89.76^\circ$ , respectively, were used as targets. The films were deposited on (001)MgO crystal cuts and polycrystalline Pt and alumina under the oxygen pressure  $P = 0.8\text{-}1.4$  torr and at the substrate temperature  $T = 500\text{-}600^\circ\text{C}$ . The thickness of epitaxial and polycrystalline films ranged from  $0.3$  to  $0.5 \mu\text{m}$  and from  $1$  to  $2 \mu\text{m}$ , respectively. X-raying was performed on diffractometer DRON-3 (Cu  $K\alpha$ , Co  $K\alpha$ ) in the attachment GP-13 for polycrystalline samples supplied with a furnace.

## Results and Discussion

**Epitaxial films** At room temperature, only different orders of the same reflection corresponding to the parameter  $c^* = 4.100 + 0.002 \text{ \AA}$  close to the  $c$  parameter of the initial target were recorded from the surface of the films deposited on single-crystal substrates. The data on reflections recorded from the crystallographic planes of the films not parallel to the surface ( $hkl, h\bar{k}l, hkl$ ) indicated that the films were epitaxial with  $[100], (001) // \text{PZT}$   $[100], (001)$  MgO orientation. Interplanar spacings from the  $(224)$ ,  $(\bar{2}24)$  and  $(2\bar{2}4)$  - planes were found to be the same within the experimental error ( $\Delta d = 6 \cdot 10^{-4} \text{ \AA}$ ) that allowed one to regard the unit cell distortion as tetragonal. The parameter  $c^*$  vs temperature curve having the drop characteristic of the parameter  $c_T$  of the tetragonal unit cell of the bulk material on approaching  $T_c$  and the kink in the vicinity of  $T_c$  (the Curie temperature of the bulk material is  $365^\circ\text{C}$ ) is an evidence in favour of this assumption (see Fig.1). The unit cell parameter  $a^*$  along the substrate surface calculated under this assumption was found to be  $4.074 \pm 0.01 \text{ \AA}$  that is



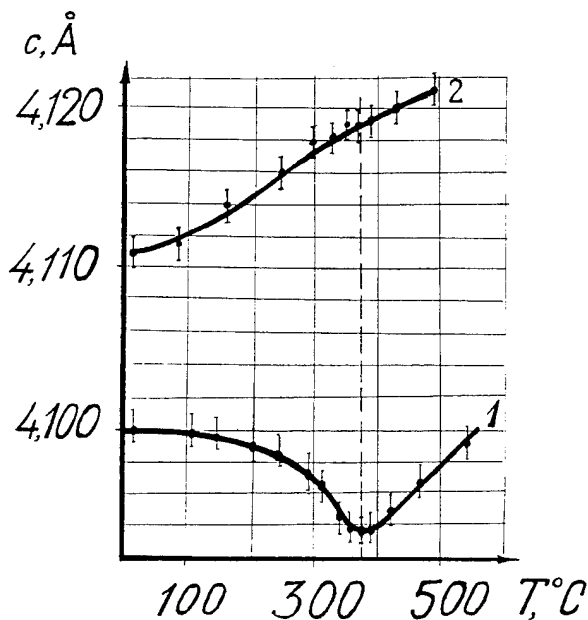


Figure 1. The temperature dependence of unit cell parameters of the epitaxial (1) and polycrystalline (2) PZT film.

slightly larger than  $a_r$  for the bulk material. The unit cell parameters calculated on the assumption of rhombohedral distortion  $a = 4.100 \text{ Å}$ ,  $90^\circ - \angle < 0.04^\circ$  were in much worse agreement with those of the initial target.

The observed absence of the tetragonal splitting in XRD patterns and the preferred c-orientation in epitaxial PZT/(001)MgO films were not surprising. Previously, we have proposed a model which allowed the prediction of the domain structure type of epitaxial films (the preferred a- or c-orientation) under the assumption of a rigid adherence of the film with the substrate [10]. This assumption implied the equality of the tangential geometrical sizes of the film to those of the substrate both at the deposition temperature and at room temperature. This model took account of the values of thermal expansion coefficients of the film and the substrate and the value of spontaneous deformation of the film unit cell. The model was expected to be valid for relatively thick ( $0.2 \mu\text{m}$ ) films and it correctly predicted the absence of a-domains in epitaxial (Ba,Sr)TiO<sub>3</sub>/(001)MgO films and the presence of approximately 30 per cent of a-domains in the case of PbTiO<sub>3</sub>/(001)MgO ones. These predictions were confirmed by X-ray studies and the observation of domain structure (electron microscopy) [10]. In the limits of this model, on cooling the epitaxial PZT/(001)MgO films the phase transition is expected to take place under the conditions of strong planar compression which can be only partially decreased at the expense of the formation of the completely c-domain structure. However, the dependence of the diffraction reflection half-width on temperature induced us to doubt the complete c-orientation of the films. Figure 2 represents these dependences for PZT/(001)MgO (curve 1) and BST/(001)MgO (curve 2) films. It can be seen from this Figure that unlike the completely c-domain BST films where one can observe the increase of the reflection half-width on approaching the Curie temperature, the reflection half-width markedly decreased in PZT films upon heating. A possible explanation of the different behaviour of

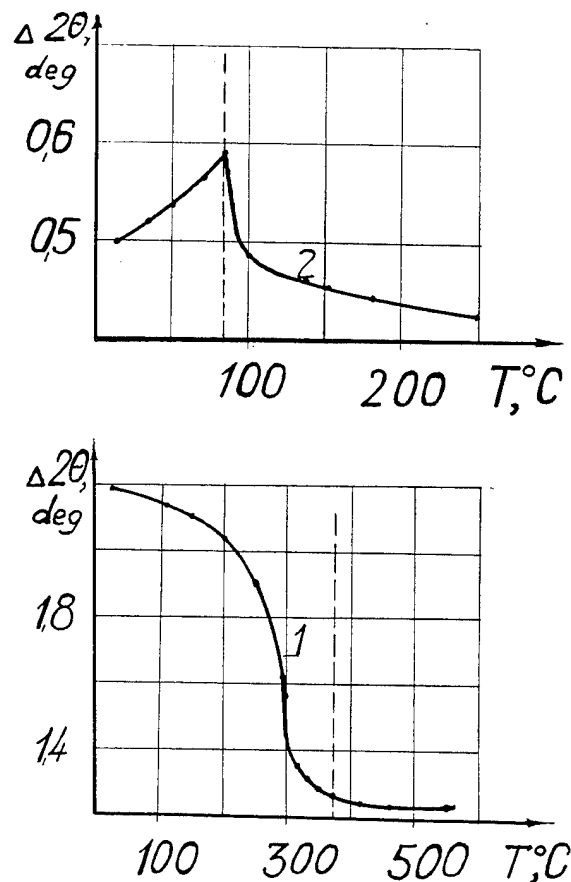


Figure 2. The temperature dependence of the diffraction reflection width of epitaxial PZT/(001)MgO (curve 1) and c-domain (Ba,Sr)TiO<sub>3</sub>/(001)MgO [7] (curve 2) films.

temperature dependences of the reflection half-width in BST and PZT films is in the assumption of the polydomain state of the PZT film. In this case, the reflections observed in XRD patterns must consist of the h00- and 00l- type components which are not splitted because of the increased half-width of individual reflections. The artificial separation of the observed lines into two reflections showed the possibility of existence of 25 per cent of a-domains in the epitaxial PZT films. The tetragonal unit cell parameters ( $c = 4.108$  and  $a = 4.075 \text{ Å}$ ) defined after the separation were found to be closer to the starting material than those determined initially.

The appearance of a-domains in epitaxial PZT/(001)MgO films in spite of their predicted absence in accordance with the above mentioned model of rigid adherence of the films with the substrate may be due to the existence of the transition layer of the impurity phase. The presence of this layer was established by electron microscopy studies of the side cuts of the films and confirmed by X-ray studies after chemical removal of the perovskite film. This layer may play a role of a damping one partially releasing the film from the mechanical influence of the substrate.

Figure 3 represents the variation in integral intensity of the 003 reflection as a function of temperature. The considerable drop accompanying the phase transition is observed in the region corresponding to the kink in the

$I_{003}$ , arb units

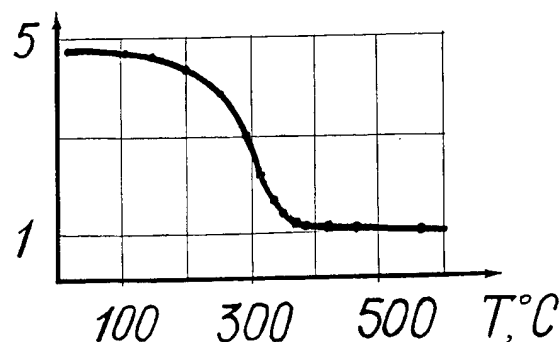


Figure 3. The temperature dependence of integral intensity of the 003 reflection of the epitaxial PZT/(001)MgO film.

c(t) curve (Fig.1, curve 1). The estimations of the possible variation in intensities corresponding to the  $P4mm \rightarrow Pm3m$  phase transition were made by calculating the structural factors for both space groups. In the tetragonal phase the coordinates of Pb, Ti, and O atoms in  $PbTiO_3$  were used as coordinates of Pb, Ti(Zr), and O atoms in the PZT film. In the cubic phase the coordinates of Pb, Ti, and O atoms were supposed to be 000,  $1/2 \ 1/2 \ 1/2$ , and  $1/2 \ 1/2 \ 0$ , respectively. The ratio of thus calculated intensities before and after phase transition was expected to be  $\sim 2$ . The probable presence of a 300 component in the reflection would decrease this ratio. However, the observed ratio was about 5. The difference of the observed and calculated data may be due to the structure imperfection of the material in both film phases which does not allow the use of the formulae of structural factors valid for the ideal perovskite structure. The second possible reason of the difference is the presence of accidental point defects.

**Polycrystalline films** The films on polycrystalline substrates were polycrystalline with no preferred crystallite orientation. The unit cell could be determined only to a pseudocubic approximation with the parameter  $a = 4.110 \text{ \AA}$  that is close to the parameter  $c$  of the tetragonal unit cell of the starting ceramics. As can be seen from Figure 1 (curve 2), however, no anomalies in the temperature dependence of the unit cell parameter in polycrystalline films were observed. In contrast to epitaxial films, the diffraction reflection widths remained practically constant over a whole temperature range (20-550°C). At the same time, the films possessed a set of ferroelectric properties such as the presence of switchable polarization, piezoactivity, and the maximum on the dielectric permittivity vs temperature curve. The only "structural" evidence of the transition of the film to a cubic phase was, as in the case of epitaxial films, the drop in integral intensity of reflections with an odd sum of indices.

## References

- [1] H. Watanabe, T. Mihara, and C.A. Paz de Araujo, "Device effects of various Zr/Ti ratios of PZT thin

films prepared by sol-gel method", *Integrated Ferroelectrics*, vol.1, pp. 293-304, 1992.

- [2] J. F. Scott, "Phase transitions in ferroelectric thin films", *Phase Transitions*, vol.30, pp. 107-110, 1991.
- [3] B.S. Kwak, E.P. Boyd, and A. Erbill, "Metalorganic chemical vapor deposition of  $PbTiO_3$  thin films", *Appl. Phys. Lett.*, vol.53, pp. 1702-1704, 31 October 1988.
- [4] N. Tohge, S. Takahashi, and T. Minami, "Preparation of  $PbZrO_3$ - $PbTiO_3$  ferroelectric thin films by sol-gel process", *J. Am. Ceram. Soc.*, vol.74, pp. 67-71, 1991.
- [5] K. Iijima, S. Kawashima, I. Ueda, "Dielectric and pyroelectric properties of  $PbTiO_3$  thin films", *Japan J. Appl. Phys.*, vol.24-2, pp. 482-484., 1985.
- [6] E. Yamaka, H. Watanaba, H. Kimura, H. Kanaya, and H. Ohkuma, "Structural, ferroelectric and pyroelectric properties of highly c-axis oriented  $Pb1-x \text{ Cax TiO}_3$  thin film grown by radio-frequency magnetron sputtering," *J. Vac. Sci. Technol.*, A6 (5), pp. 2921-2928, Sep/Oct 1988.
- [7] V.M. Mukhortov, Yu.I. Golovko, V.A. Aleshin, E.V. Sviridov, V.I.M. Mukhortov, V.P. Dudkevich, and E.G. Fesenko, "Ferroelectric phase transition in heteroepitaxial films of  $(BaSr)TiO_3$ ," *phys. stat. sol.(a)*, vol.77, pp. k37-40, 1983.
- [8] Z. Surowiak, Ya.S. Nikitin, E.V. Sviridov, V.M. Mukhortov, and V. P. Dudkevich, "The influence of thermoelastic stresses on phase transitions in thin ferroelectric films", *Izv. AN SSSR, ser. Fiz.*, vol.55, pp. 500-505, 1991 (Russian).
- [9] Ya.S. Nikitin, S.V. Biryukov, E.V. Sviridov, Yu.I. Golovko, I.N. Zakharchenko, V. M. Mukhortov, and V.P. Dudkevich, "Polarization switching processes in heteroepitaxial  $(BaSr)TiO_3/(001)MgO$  films", *Ferroelectrics*, vol.120, pp. 197-200, 1991.
- [10] E.V. Sviridov, V.A. Alyoshin, Yu.I. Golovko, I. N. Zakharchenko, V. M. Mukhortov, and V. P. Dudkevich, "Rontgenographic and electron-microscopy data on heteroepitaxial  $PbTiO_3/(001)MgO$  films," *phys. stat. sol.(a)*, vol.121, pp. 157-162, 1990.

# The Control of Ferroelectric Film Texture upon RF Sputtering

Azamat Bakirov, Evgeny Sviridov and Vladimir Dudkevich

Institute of Physics, Rostov State University,

194, Stachki Ave, Rostov-on-Don, 344104, Russia

**Abstract.** Polycrystalline  $\text{Pb}(\text{Zr}_{0.53}\text{Ti}_{0.45}\text{W}_{0.01}\text{Cd}_{0.01})\text{O}_3$  films on the stainless steel substrates were fabricated by rf sputtering the stoichiometric ceramic targets in an  $\text{O}_2$ -atmosphere. The effect of potential  $U_b$  biasing the substrate with respect to the high-frequency discharge plasma on film microstructure was studied. It was established that the main effect is the formation of the (001) texture at  $U_b < -20\text{V}$  on nonorienting substrates. The origin of this effect is discussed.

## Introduction

The appearance of the preferred crystallite orientation (texture) in the ferro-electric and superconducting films of complex oxides fabricated by vacuum evaporation [1] and cathode sputtering [2-4] was observed by many investigators. It is common knowledge [2-4] that in the sputtering technique the texture character depends on the substrate temperature, the gas pressure and, to a lesser degree, on the substrate material. The effect of the potential shifting the substrate with respect to the high-frequency discharge plasma on the texture of  $\text{PbTiO}_3$  films was reported in RF [3]. However, the complex studies the results of which could be a foundation for understanding the mechanism of the texture formation in the future were not carried out. In this connection, the present paper deals with a study of the effect of the bias potential on the texture of  $\text{Pb}(\text{Zr}_{0.53}\text{Ti}_{0.45}\text{W}_{0.01}\text{Cd}_{0.01})\text{O}_3$  films.

## Sputtering Condition and the Film Composition

Raw polycrystalline  $\text{Pb}(\text{Zr}_{0.53}\text{Ti}_{0.45}\text{W}_{0.01}\text{Cd}_{0.01})\text{O}_3$  films of about  $3\text{ }\mu\text{m}$  thickness were deposited on stainless steel substrates ( $40 \times 30 \times 0,1\text{ mm}^3$ ) by pulse rf sputtering from stoichiometric ceramic targets in the pure  $\text{O}_2$ -atmosphere. The gas pressure was  $90\text{ Pa}$ , the target-to-substrate distance was  $7\text{ mm}$ , the substrate temperature was  $600\text{ }^\circ\text{C}$ , the mean high-frequency power was  $18\text{ W/cm}^2$ , the pulse duration was  $200\text{ }\mu\text{s}$ , the pulse pause was  $300\text{ }\mu\text{s}$  and the potential biasing the substrate with respect to the earth setup base plate and the earth high-frequency oscillator pole ( $13,6\text{ MHz}$ ) varied from  $-80$  to  $+80\text{ V}$ .

The electron microscope Tesla-613 (the direct Pt-C replica technique) and the X-ray diffractometer Dron-3 ( $\text{CuK}\alpha$ ,  $\text{FeK}\alpha$ ,  $\beta$ -filter) with the Bragg-Brentano focusing were used to control microstructure and the texture character. The Bragg-Brentano focusing is useful in studying the textures because only the crystallites the corresponding crystallographic planes (hkl) of which are parallel to the sample surface contribute to the

formation of the HKL reflection.

## Results and Discussion

The film composition in its main metallic components ( $\text{Zr/Ti}$  and  $\text{Pb}/(\text{Zr}+\text{Ti})$ ) was the same as the target one. The error of determination of the above ratios was  $\pm 0,03$  due to the averaging over twenty "points" for every sample. The oxygen, W and Cd contents were not determined.

The effect of the bias potential  $U_b$  on the film composition was negligible; however, the mean crystallite size slightly increased (from  $0,4$  to  $0,6\text{ }\mu\text{m}$ ) on varying  $U_b$  from  $+80$  to  $-80\text{ V}$ .

No splitting of reflections into multiplets connected with the existence of spontaneous deformation and  $90^\circ$  twinning was observed in X-ray diffraction patterns and only the component of each multiplet corresponding to the largest interplanar spacing was recorded. This effect seems to be a result of two-dimensional compression of the film by the substrate because the splitting of reflections was observed after the separation of the films from the substrates for polycrystalline  $(\text{K},\text{Na})\text{NbO}_3$  films obtained by rf cathode sputtering [5].

It was established from X-ray diffraction patterns (that the bias potential  $U_b$  had no marked effect on the angular position of reflections but caused the relation of their intensities to be changed. Fig. 1 represents the results of measurements of integral intensities. Here, the relations of intensities of the three brightest reflections (002, 011 and 112) to their total intensity, that is, the values of  $I_{002}/\Sigma$ ,  $I_{011}/\Sigma$  and  $I_{112}/\Sigma$ , where  $\Sigma = I_{002} + I_{011} + I_{112}$ , were plotted as ordinate to characterize the texture. Horizontal lines show the corresponding relations for the powder of the same composition, that is, for the nontextured sample. It can be seen from this Figure that the formation of nontextured polycrystalline films took place at  $U_b > +20\text{ V}$ , and at  $U_b < +20\text{ V}$  the (001) texture was formed, that is, the unnormally large number of crystallites occupied the (001) plane parallel to the substrate. The degree of the texture increased with the decrease of  $U_b$  and at  $U_b < -60\text{ V}$  the formation of the 100 per cent (001) texture took place. This result agrees well with the data on the formation of the (001) texture in  $\text{PbTiO}_3$  films on Si substrates biased negatively with respect to the high-frequency discharge plasma.

We have carried the test which was a direct evidence of the important role of selective sputtering of nuclei of different orientation on the negatively biased substrate. The target being a dielectric substrate was sputtered. One part of the substrate was covered with a film having the strong (001)

texture and other part with a nontextured film. It was found that the rate of ionic etching of the second part is four times as high as that of the first part. Moreover, X-ray diffraction patterns of the second part showed the drastic increase of the relative intensity of 001 and 002 reflections after etching. Further work is needed to discuss the origin of texture in more detail.

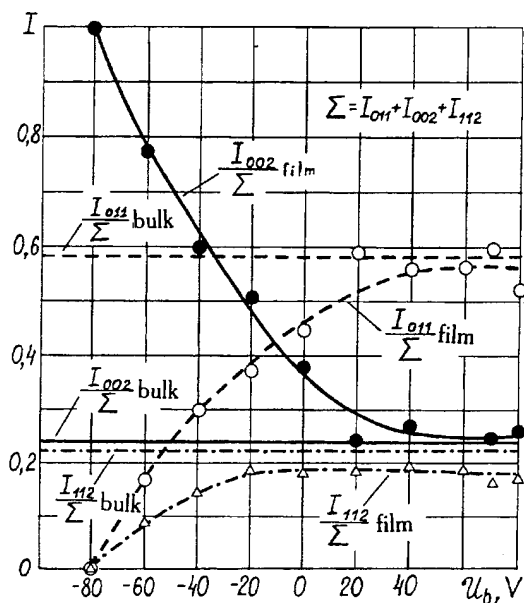


Fig. 1. The change of the crystallite orientation in the  $\text{Pb}(\text{Zr}_{0.53}\text{Ti}_{0.45}\text{W}_{0.01}\text{Cd}_{0.01})\text{O}_3$  film depending on the potential  $U_b$  biasing the substrate with respect to the high-frequency discharge plasma.

### References

- [1] Y. Iijima, "Dielectric constant of deposited  $\text{BaTiO}_3$  thin films", Jap. J. Appl. Phys., vol. 24, suppl. 24-2, pp. 401-403, 1985.
- [2] T. Nagatomo, T. Kasaka, S. Omori, O. Omoto, "Fabrication of  $\text{BaTiO}_3$  films by RF planar-magnetron sputtering", Ferroelectrics, vol. 37, N 1/2, pp. 681-684, 1981.
- [3] M. Okuyama, T. Ueda, Y. Hamakawa, "Preparation of oriented  $\text{PbTiO}_3$  ferroelectric thin films on silicon", Jap. J. Appl. Phys., vol. 24, suppl. 24-2, pp. 619-621, 1985.
- [4] O. Michikami, H. Asano, Y. Katoh, S. Kubo, "Synthesis of Y-Ba-Cu-O thin films on sapphire substrates by RF magnetron sputtering", Jap. J. Appl. Phys. vol. 26, N 7, pp. L1199-L1201, 1987.
- [5] A.M. Margolin, Z. S. Surowjiak, I.N. Zakharchenko, V.A. Aleshin, Z. K. Chernyshova, M.G. Radchenko and V.P. Dudkevich, "RF-sputtering of ferroelectric  $(\text{K},\text{Na})\text{NbO}_3$  films", Zh. techn. fiz., vol. 58, N 12, pp. 1127-1132, 1988.

Ramadhar Singh, R.P. Tandon, R.D.P. Sinha<sup>1</sup> and Subhas Chandra  
National Physical Laboratory, Dr. K.S. Krishnan Road, New Delhi - 110 012, India

<sup>1</sup>Department of Physics, S.R.K. Goenka College, Sitamarhi - 843 301.

**Abstract** - The ac conductivity and dielectric relaxation behavior of uniaxially stretched polyvinylidene fluoride (PVDF) films (~25  $\mu\text{m}$  thick) has been measured in the temperature range 77-400K and in the frequency range 100 Hz - 10 MHz. In the low temperature region up to 100K, the measured ac conductivity is nearly independent of temperature and shows strong frequency dependence which could be well described by the relation,  $\sigma(\omega) = A\omega^s$ , where the exponent 's' has been found close to unity. At temperatures above 200K, the ac conductivity shows a strong temperature dependence. The measured dielectric constant in this temperature region shows a frequency dispersion. The activation energy of the relaxation calculated by Fuoss approach is ~0.18 eV confirms the existence of dipolar relaxation around 260K and is identified as the  $\beta$ -relaxation.

year the PVDF film poled at 378K, retain about half of their initial properties [3]. A review of physics and chemistry of PVDF reveals that it is a unique polymer and its ferroelectric behavior combined with its superb mechanical properties and ease of fabrication makes it more useful for piezoelectric and pyroelectric applications. PVDF is a serious contender with its more conventional ceramic counter part and exhibits advantages over it for use as hydrophones and also in the design of new transducers especially a needle type hydrophone [4]. Very little data on dielectric relaxation behavior of PVDF have been reported in literature [5,6], however, the detailed studies of mechanism of low frequency ac conduction and dielectric relaxation behavior are lacking. The present investigation is an attempt to provide data for low frequency ac conduction and dielectric relaxation of solution grown and uniaxially stretched PVDF films.

## INTRODUCTION

The practical applications of polymeric materials have given a great stimulus to the studies of their dielectric and electrical properties [1]. There have been a large number of studies [1,2] of long chain linear polymers but the interpretation of their relaxational behavior remains uncertain. The study of dielectric constant ( $\epsilon'$ ) and loss ( $\epsilon''$ ) as a function of frequency and temperature is very useful in understanding the relaxation phenomena in polymeric materials [1,2]. These studies have revealed two or three types of relaxation processes namely;  $\alpha$ ,  $\beta$ ,  $\gamma$  respectively which in their turn appears from high temperature side to low temperature side or low frequency side to high frequency side [2]. The  $\alpha$ -relaxation or the primary relaxation process is attributed to the rotation of dipoles from one quasi-stable state to another in which the diffusional motion of the segment occurs whereas the  $\beta$ -relaxation is associated with the partial orientation of dipoles in the range of local environments where the large scale rearrangement of the main chain is frozen.

After the discovery of piezoelectricity in PVDF [3], the interest has been generated for its piezoelectric and pyroelectric applications during the last two decades. PVDF is polymerized from its monomer VDF which has a large dipole moment ( $\mu$ ) of  $7.56 \times 10^{-13} \text{ cm}$  and then this polymer (PVDF) may also exhibit a large net dipole moment if it crystallizes into a suitable phase [3]. At present four crystalline phases  $\alpha$ ,  $\beta$ ,  $\gamma$  and  $\delta$  of PVDF are known. The crystallization from melt at atmospheric pressure produces  $\alpha$ -phase which is nonpolar, nonpyroelectric and nonpiezoelectric in nature. However, the  $\beta$ -phase of PVDF has made it most important because it is intrinsically piezoelectric. The  $\beta$ -phase is achieved by uniaxial or biaxial stretching of the melt crystallized PVDF. Investigations have revealed that PVDF has a long term temperature stability which even after one

## EXPERIMENTAL

PVDF in white powder form was obtained from M/s. Polysciences, USA. Films of PVDF (~100  $\mu\text{m}$  - 300  $\mu\text{m}$  thick) were prepared by solution evaporation technique described elsewhere [7]. The films were very smooth and translucent in appearance. Small pieces were cut from the films and were uniaxially stretched at an elevated temperature 433K by using a especially designed stretching device. A stretching ratio of 1:5 was achieved. Aluminium films were vacuum deposited on both sides of the stretched film thus making a metal - polymer-metal structure. The ac conductivity [ $\sigma_m(\omega)$ ] and dielectric constant ( $\epsilon'$ ) were measured by using a GR1615A capacitance bridge in the frequency range 100 Hz - 100 kHz and by HP4192A-LF Impedance Analyser in the frequency range 100 kHz - 10 MHz in a especially designed three terminal cell. The dc conductivity was measured by a Keithley 617 electrometer.

## RESULTS AND DISCUSSION

The measured ac conductivity [ $\sigma_m(\omega)$ ] as a function of reciprocal temperature in the range 77-400K and in the frequency range 100Hz - 100kHz of uniaxially stretched PVDF film is shown in Fig.1. At low temperatures a frequency dependent conductivity described [8] by  $\sigma(\omega) = A\omega^s$  is observed where the exponent 's' is observed to be less than unity. The activation energy of the carriers calculated at 77K is ~0.012 eV gives the evidence of electronic hopping conduction [9] at low temperatures. An estimate of the density of states near the Fermi level  $N(E_F)$  can be possible in this low temperature region by using the expression derived by Austin and Mott [10]. According to Austin and Mott [10]

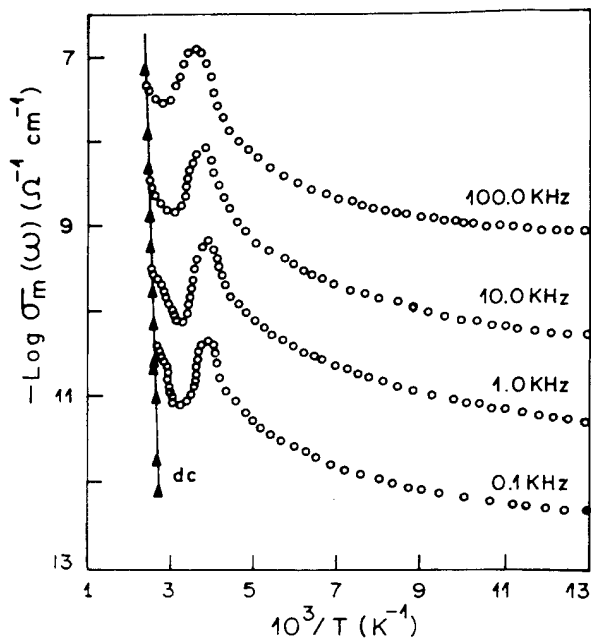


Fig. 1 Variation of measured conductivity  $\sigma_m(\omega)$  as a function of reciprocal temperature at four fixed frequencies.

$$\sigma(\omega) = \frac{1}{3} \pi e^2 k_B T [N(E_F)]^2 \alpha^{-5} \omega [\ln(v_{ph}/\omega)]^4 \quad (1)$$

where  $e$  is the electronic charge,  $k_B$  is the Boltzmann's constant,  $\omega = 2\pi f$ ,  $v_{ph}$  is a frequency factor and  $\alpha$  is the radius of the carrier wave function. Assuming  $v_{ph} = 10^{13}$  Hz and  $\alpha = 0.4 \text{ \AA}$  (which roughly corresponds to the nearest neighbor hopping), the values of  $N(E_F)$  have been calculated after taking the value of measured ac conductivity at 77K and is of the order of  $10^{20} \text{ cm}^{-3} \text{ eV}^{-1}$ . The reasonable estimate of  $N(E_F)$  from Eq. (1) suggests that the hopping near the Fermi level is between the nearest-neighbor sites. In spite of the fact that Eq. (1) gives reasonable estimate of  $N(E_F)$ , it fails to explain the temperature dependence of  $\sigma(\omega)$ . Equation (1) predicts a linear temperature dependence of  $\sigma(\omega)$ , however, the measured values show very weak temperature dependence of  $\sigma(\omega)$  in the low temperature region. Pollak [11] has argued that the temperature dependence of ac conductivity is due to multiple hops but it has been shown [12] that multiple hops cannot give strong temperature dependence of  $\sigma(\omega)$  in amorphous semiconducting glasses.

In the high temperature region the measured ac conductivity  $\sigma_m(\omega)$  is observed to be both temperature and frequency dependent and ultimately it approaches the dc conductivity  $\sigma_{dc}$ . It is observed that a peak in  $\epsilon''$  or  $\sigma(\omega)$  defined by [8]

$$\omega \epsilon_0 \epsilon'' = \sigma_m(\omega) - \sigma_{dc} = \sigma(\omega) \quad (2)$$

is really observed for each frequency just below the temperature at which  $\sigma_m(\omega)$  becomes equal to  $\sigma_{dc}$ . These loss peaks shifts towards higher temperature for higher frequencies. However, these loss peaks cannot be taken as a conclusive evidence of the existence of dielectric loss peaks because the temperature dependence of  $\sigma_{dc}$  is much larger than  $\sigma(\omega)$  and so at some temperatures  $\sigma_{dc}$  may become larger than  $\sigma(\omega)$  and therefore  $\sigma_m(\omega)$  would appear equal to  $\sigma_{dc}$  within the accuracy of measurement. In the low temperature region carrier hopping occurs within the system in which a characteristic relaxation frequency  $f_0$  is difficult to define, however, in the high temperature region, where  $\sigma_m(\omega)$  approaches  $\sigma_{dc}$ , the ac component of conductivity  $\sigma(\omega)$  may give clear evidence for  $f_0$ . In particular  $\epsilon''$  derived from Eq. (2) may show a Debye type peak at  $f = f_0$ . A difficulty in this approach is that both  $\sigma_m(\omega)$  and  $\sigma_{dc}$  are comparable and the error in  $\sigma(\omega)$  is large [12]. So it is necessary to examine both  $\epsilon'$  and  $\epsilon''$  to justify an analysis in terms of Debye-type dispersion.

The dielectric constant  $\epsilon'$  according to Debye relation is given by

$$\epsilon' - \epsilon_\infty = \frac{\epsilon_0 - \epsilon_\infty}{1 + (f/f_0)^2} \quad (3)$$

where  $\epsilon_0$  and  $\epsilon_\infty$  are the static and infinite frequency dielectric constants,  $f$  and  $f_0$  are the measuring and relaxation frequencies. The plot of  $\epsilon'$  as a function of temperature (Fig. 2) shows that there is a little change in  $\epsilon'$  with temperature in the low temperature region, however, it has a sharp rise at temperature at which the measuring frequency becomes equal to the relaxation frequency.

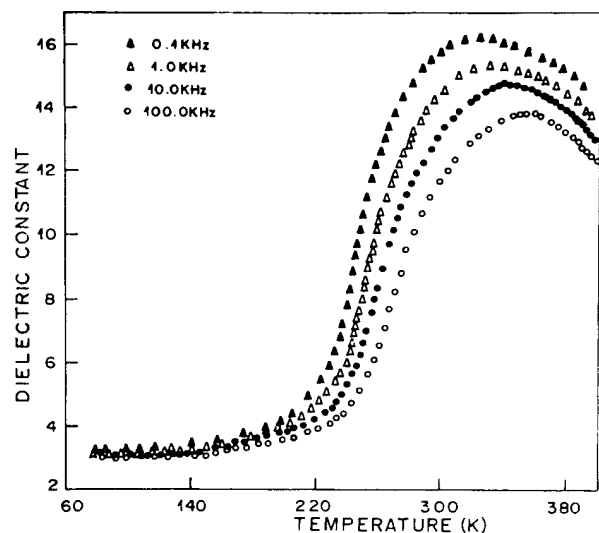


Fig. 2 Variation of measured dielectric constant ( $\epsilon'$ ) as a function of temperature at four fixed frequencies.

It is evident that the region where there is a strong temperature dependence of  $\epsilon'$  at a given frequency (Fig. 2) is the same at which  $\sigma_m(\omega)$  approaches  $\sigma_{dc}$  (Fig. 1). Thus the variation of  $\epsilon'$  with temperature confirms the existence of Debye type loss peaks indicated in Fig. 1. The measured values of  $\epsilon'$  at a given frequency will give an estimate of  $\epsilon_0$  at temperatures higher than the temperature region where  $\epsilon'$  shows a strong temperature dependence. The measured values at 0.1, 1, 10 and 100 kHz clearly show a saturation region at the high temperature end and this may be taken as an estimate of  $\epsilon_0$ . The estimated value of  $\epsilon_0$  as a function of reciprocal temperature is shown in Fig. 3. The dielectric constant as a function of frequency in the range 100Hz-10MHz is

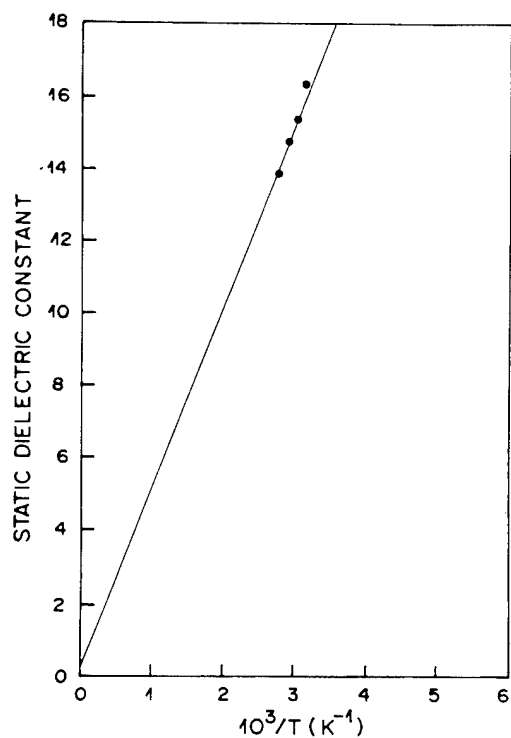


Fig. 3 Plot of  $\epsilon_0$  versus  $10^3/T$ .

shown in Fig. 4. It is evident from Fig. 4 that a near static region is seen at temperature 321K. The variation of dielectric loss as a function of temperature at fixed frequency of 1 kHz is shown in Fig. 5. A hump is seen in the low temperature region, however, in the high temperature region a loss peak around 260K is observed. The activation energy of this relaxation is calculated by the Fuoss approach [1] and is  $\sim 0.18$  eV which gives the evidence of dipolar relaxation and is identified as the  $\beta$ -relaxation [2,9]. A clear and comprehensive role of dipolar rearrangement on the generation of piezoelectricity can only emerge after investigations on a large number of stretched - unstretched samples. A model is being considered to explain the observed behavior of ac conductivity of PVDF films as a function of frequency and temperature in terms of  $\sigma_1(\omega)$  and  $\sigma_2(\omega)$  which will appear elsewhere.

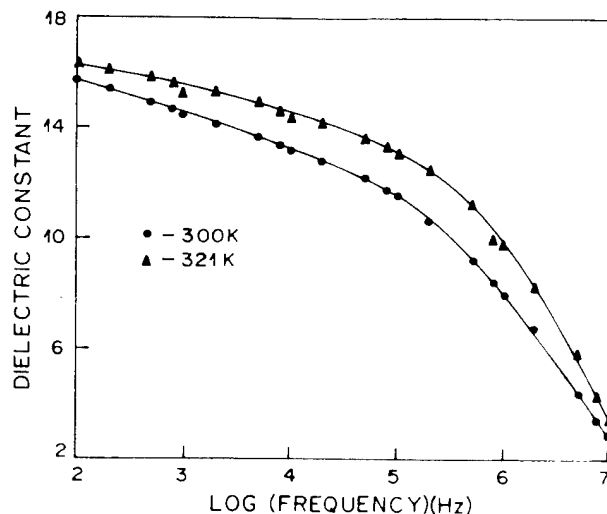


Fig. 4 Variation of  $\epsilon'$  as a function of frequency at two fixed temperatures.

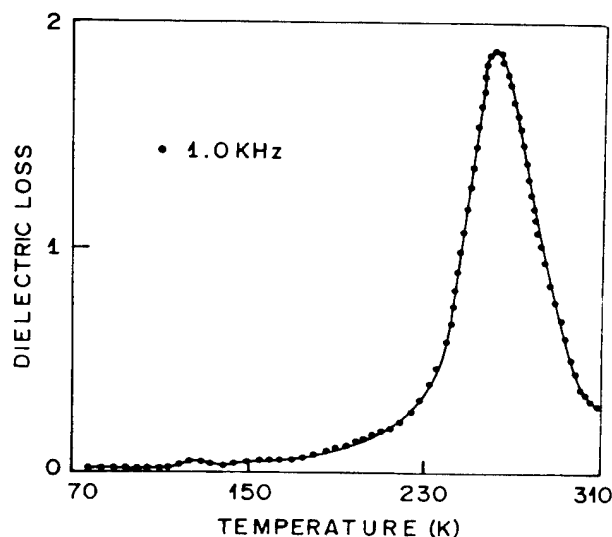


Fig. 5 Plot of dielectric loss as a function of temperature at 1 kHz.

#### ACKNOWLEDGEMENT

The authors are grateful to Professor E.S.R. Gopal, Director, National Physical Laboratory, New Delhi, India for his keen interest and permission to publish this work.

# REFERENCES

- [1] R. Singh, V.S. Panwar, R.P. Tandon, N.P. Gupta and S. Chandra, "Low frequency ac Conduction and Dielectric Relaxation in Vinylchloride: Vinylacetate Copolymers", J. Appl. Phys., vol. 72, pp. 3410-3416, 1992.
- [2] N.G. McCrum, B.E. Read and G. Williams, "An Elastic and Dielectric Effects in Polymeric Solids", John Wiley & Sons, London, 1967.
- [3] A.J. Lovinger, "Ferroelectric Polymers", Science, vol. 220, pp. 115-1121, 1983.
- [4] M. Platte, "PVDF Ultrasonic Transducers", Ferroelectrics, vol. 75, pp. 327-337, 1987.
- [5] Y. Miyamoto, H. Miyaji and K. Asai, "An Isotropy of Dielectric Relaxation in Crystal Form II of Poly(vinylidene Fluoride)", J. Polym. Sci: Polym Phys. Ed., vol. 18, pp. 597-606, 1980.
- [6] N. Koizumi, N. Haikawa and H. Habuka, "Dielectric Behavior and Ferroelectric Transition of Copolymers of Vinylidene Fluoride and Trifluoroethylene", Ferroelectrics, vol. 57, pp. 99-119, 1984.
- [7] R. Singh, V.S. Panwar, P.C. Mehendru and N.P. Gupta, "Thermal Degradation in Vinylchloride: Vinylacetate Copolymers", vol. 9, pp. 932-934, 1990.
- [8] N.F. Mott and E.A. Davis, "Electronic Processes in Non-Crystalline Materials", Oxford Univ. Press, London, 1979.
- [9] A.K. Jonscher, "Electronic Properties of Amorphous Dielectric Films", Thin Solid Films, vol. 1, pp. 213-234, 1967.
- [10] I.G. Austin and N.F. Mott, "Polarons in Crystalline and Non-Crystalline Materials", Adv. inn Phys., vol. 18, pp. 41-102, 1969.
- [11] M. Pollak, "On the Frequency Dependence of Conductivity in Amorphous Solids", Philos. Mag., vol. 23, pp. 519-542, 1971.
- [12] A. Mansingh, R.P. Tandon and J.K. Vaid, "Dielectric Relaxation in Vanadium Phosphate Glasses", J. Phys. Chem. Solids, vol. 36, pp. 1267-1271, 1975.



Vinay Gupta and Abhai Mansingh  
Department of Physics & Astrophysics  
University of Delhi, Delhi 110 007, India.

**Abstract**— High quality crystalline c-axis oriented Zinc Oxide (ZnO) film has been deposited on various substrates by rf sputtering in pure argon ambient. The effect of post deposition annealing (300K to 1073K) on the structural and optical properties of sputtered ZnO thin film have been investigated. It is found from the XRD pattern that the intensity and the grain size increases with annealing temperature and becomes maximum for 1063K. Also the asymmetric factor approaches to the value of one. The lattice constant and stress as a function of annealing temperature shows that upto 673K, there is a state of stress relief and above 673K, it goes in a state of compression. The SEM photograph also demonstrate that the grain size increases with annealing temperature, however, cracks are observed on the surface of the films annealing temperature 873K. The optical band gap of the film is found to be minimum (3.23eV) for the films annealed at 673K, whereas refractive index and packing density is maximum.

#### INTRODUCTION

In thin film form, excellent piezoelectric and optical properties of ZnO make it useful for surface acoustic wave and integrated acousto-optic devices [1]. Many reports exist in the literature on the influence on the oxygen partial pressure and substrate temperature on the structural properties and optical properties of rf sputtered ZnO thin films [2-4]. Few reports are also available on the influence of the post deposition annealing on the structural property of the thin films of this material [5-7]. However, not much attention have been paid towards the study of the influence of the post deposition annealing on the optical properties and correlation with the structural properties. In the present paper we report the influence of the post deposition annealing on the structural and optical properties and try to correlate them.

#### EXPERIMENTAL PROCEDURE

Sputtering of ZnO film at room temperature on the quartz and 7059 Corning glass substrates was performed in pure argon ambient from a hot pressed 99.999% pure ZnO ceramic target using a Nordiko NM 2000 system. The detail of the sputtering are reported else where [8]. The structural properties of the films were investigated by a Philips PW 1130 X-ray diffractometer. The surface morphology of the films was investigated with the help of Jeol JSM-840 scanning electron microscope. The optical transmittance measurements were carried out using Shimadzu UV-260 spectrometer. The films were annealed in a quartz tube furnace at different temperatures and were held at temperature for one hour in an air atmosphere and then cooled to room temperature. The as

deposited ZnO films annealed at 473 K, 673 K, 873 K and 1073 K are labeled as Z1, Z2, Z3, Z4 and Z5 respectively.

#### RESULT AND DISCUSSION

Figure.1 shows the  $\text{Zn}(\text{L}_{3/2}\text{M}_{4/5})$  Auger transition for as grown and sputter etched ZnO film. Only one peak at 265 eV was observed. Since the binding energy of metallic zinc is  $\approx 260.2$  eV, therefore, we can conclude that zinc in our sputtered film exists only in the oxidized state. Zinc signal was found to be practically unchanged due to sputter etch.

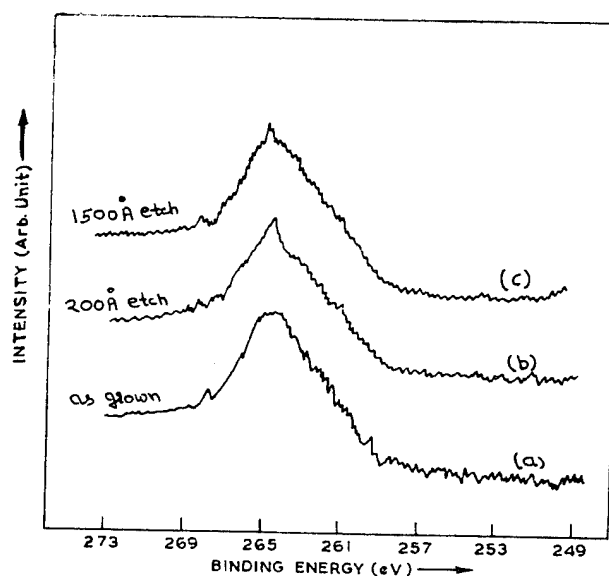


Fig.1  $\text{Zn}(\text{L}_{3/2}\text{M}_{4/5})$  XPS spectra of ZnO film.

Figure.2 shows the O(1s) XPS spectrum. One peak corresponding to binding energy 531.2 eV was observed in the as deposited film (fig.2a) showing the presence of oxygen contamination which are located at the interstitial sites or grain boundaries. After short etching (fig.2b), a peak at lower binding energy  $\approx 530.4$  eV was also observed which corresponds to lattice oxygen in ZnO. As the film etch time increases, the O(1s) level shows up and after a long time etching, during which bulk of the film was etched

( $\approx 1500\text{\AA}$ ), the higher binding energy peak was absent. Due to air exposure a contamination of oxygen on the film surface makes a layer rich in oxygen. This layer was of small thickness and can be easily eliminated after few minutes of sputter etching. The estimated value of atomic concentrations from the composition analysis was found to be 49.8 % and 50.2 % for oxygen and zinc elements respectively. It is interesting to note that the films sputtered in pure Argon ambient from oxide target are almost stoichiometric.

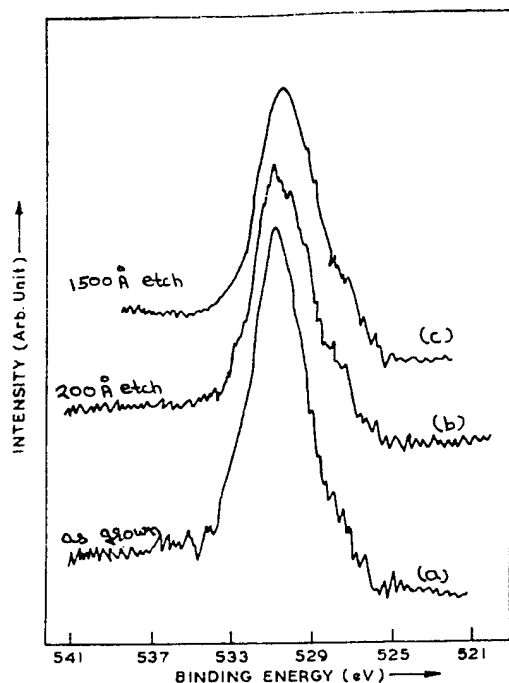


Fig.2 O(1s) XPS spectra of ZnO film.

Figure 3 shows the X-ray line profiles of the sputtered ZnO thin film deposited on quartz substrate as a function of annealing temperature. Only one peak corresponding to (002) plane was observed in the X-ray spectra for all the samples, indicating that all films are highly c-axis oriented with (002) plane parallel to the substrate. The peak intensity shows a slow increase with annealing temperature up to 673 K, while at higher annealing temperature the peak intensity and sharpness of the peak shows a rapid increase. The angular peak position of the ZnO powder [ASTM;36-1451] is shown by a dotted line at  $2\theta = 34.43^\circ$  in fig.3. The angular peak position of as grown film is less than the powder value indicating that film are in a uniform state of stress with tensile components parallel to c-axis. It is also observed that with increase in annealing temperature, the peak position of (002) plane shift towards the powder value and coincide with it at 673 K. Whereas after annealing at higher temperature ( $>673$  K), the (002) peak position again start to deviate from the powder value but in the opposite direction.

The lattice constant 'c' of as grown film is large as compare to unstressed powder value indicating that the unit cell is elongated along the c-axis, and compressive forces act in the plane of the film. These compressive forces becomes weaker as the annealing temperature increases, resulting in the decrease in 'c' value. The stress in the film can be estimated using [9]

$$\sigma = 5 \times 10^{11} (c_0 - c) / c_0 \text{ dyne/cm}^2 \quad (1)$$

where ' $c_0$ ' is the lattice constant of the bulk. The estimated values of stress produced in the film are plotted as a function of annealing temperature in fig.4. The as grown film has a stress of about  $-1.66 \times 10^{10}$  dyne/cm<sup>2</sup>, which is comparable to the reported

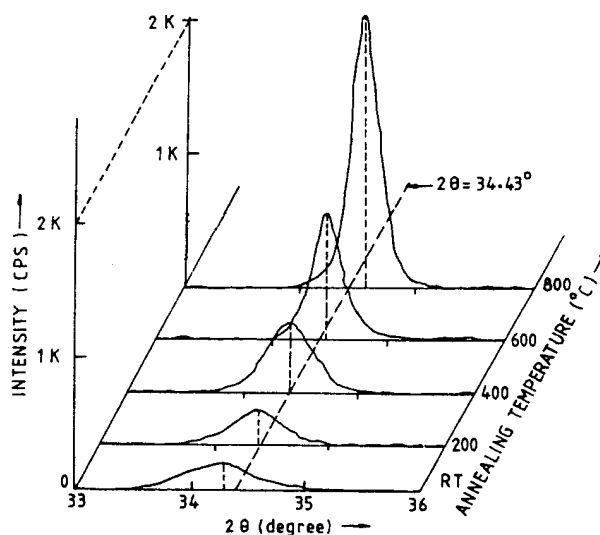


Fig.3 Influence of post deposition annealing on the XRD line profile.

values  $(-1.8 \text{ to } -8.0) \times 10^{10}$  dyne/cm<sup>2</sup> for the sputtered as grown ZnO film [9,10]. The negative sign indicate the presence of compressive forces in the film. The as grown film becomes completely stress free at 673 K. The difference in sputtering parameters and the substrate used may be responsible for the wide scatter 573 K to 973 K in the reported values of stress relieve temperature (SRT) for sputtered films [5-7] and our values are well within this range. After further annealing ( $>673$  K) film goes into a state of compression. The origin of stress in sputtered films may be associated with interstitial oxygen and/or defects in lattice. After annealing, the interstitial oxygen is probably removed and the defects in lattice annealed out. This continues up to 673K and film becomes almost stress free. The X-ray line profile of as grown film is asymmetric and the asymmetric factor is about 0.75. The asymmetric factor was found to increase with annealing temperature and seems to approaches the value of one at 1073K.

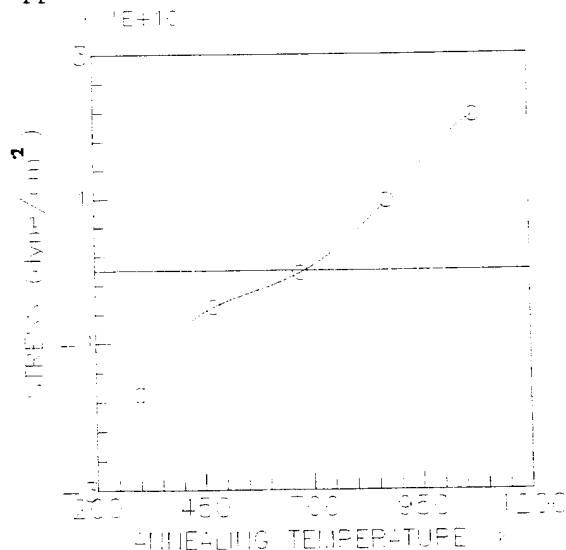


Fig.4 Stress in the film as function of annealing temperature.

Figure.5 shows the variation of grain size with annealing temperature. The grain size increases drastically with the increase in annealing temperature above 673 K. At 673 K, it appears that small crystallites coalesce to make large crystallites. This process has also been suggested by Hickernell [7] at the same annealing temperature in the form of recrystallization for sputtered ZnO film. The process of coalesce causes major grain growth resulting into microcrack and roughness on the surface of film which is also confirmed by our scanning electron microscope and surface profiler analysis.

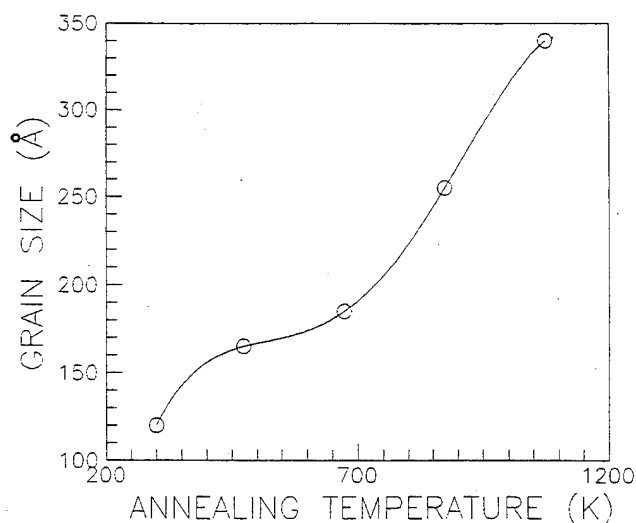


Fig.5 Variation of grain size with annealing temperature.

The influence of post deposition annealing on the average roughness is found to be very small up to SRT (Table-1), whereas it increases rapidly above SRT. The rapid increase in the surface roughness may be due to the major grain growth.

Table-1 Influence of post deposition annealing on band gap, refractive index, surface roughness and packing density.

Sample	Band gap (eV)	Refractive index at $\lambda=700\text{nm}$	Average roughness (Å)	Packing density
Z1	3.31	1.909	41	0.95
Z2	3.27	1.955	46	0.98
Z3	3.23	1.988	47	0.99
Z4	3.26	1.949	61	0.97
Z5	3.28	1.912	99	0.89
single crystal	3.20-3.43	2.004	—	1.00

The scanning electron micrographs of the as grown film and films annealed at 673 K and 1073 K are shown in fig.6. The small crystallites of ZnO in the as grown film are apparent (fig.6a). With increase in annealing temperature up to 673 K (fig.6b), the voids in the films decreases continuously with not much changes in the surface roughness and the

grain size. As evident from fig.6c, microcracks were developed in the films annealed above 673K with considerable increase in the surface roughness. A process of coalesce resulting into occurrence of major grain growth is clearly observed at temperatures above 673K (fig.6c).

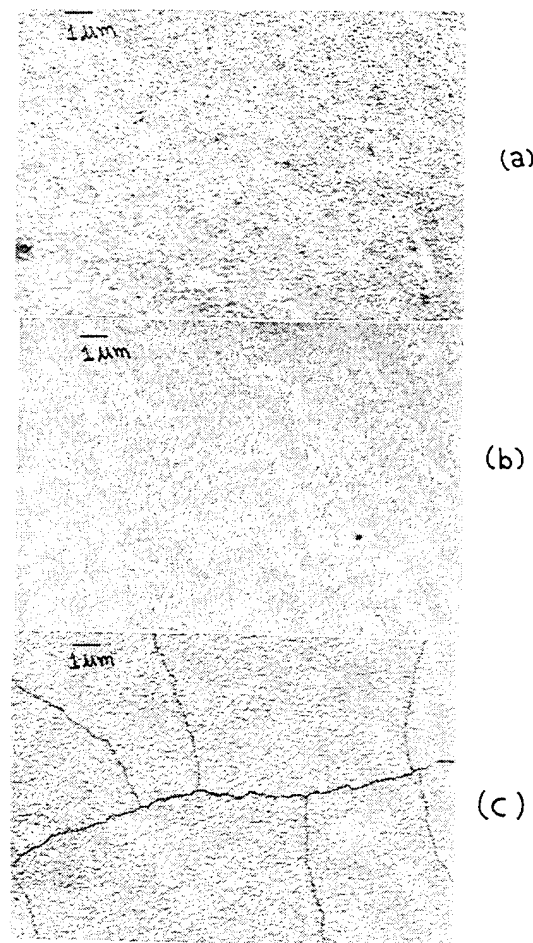


Fig.6 Influence of post deposition annealing on microstructure (a) Z1, (b) Z3 and (c) Z4.

Transmission spectra of the ZnO films annealed at different temperature are shown in fig.7. The transmission is minimum for the film annealed at 673 K and is maximum for the as grown film. For all the films, the variation of transmission with wavelength are principally due to interference phenomenon and the envelop of fringes start to shrink dramatically after annealing above 673 K (fig.7). The increase in surface roughness may be responsible for such type of shrinks in the fringes [11].

The estimated values of the optical band gap at different annealing temperatures are reported in Table-1. The change in the optical band gap with annealing temperature is comparatively small but a minimum is shown at 673 K (Table-1). The estimated values of refractive index at  $\lambda=0.70\mu\text{m}$  by following the method given by Swanepol [12] for the films annealed at different annealing temperature are also reported in Table-1 along with that of single crystal [13]. The refractive index increases with increase in annealing temperature up to SRT. At 673 K, the value of refractive index is maximum and close to that of single crystal. Above 673 K annealing

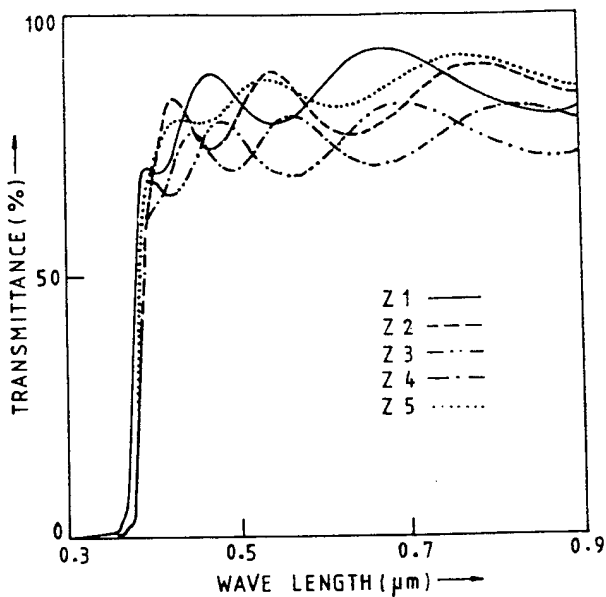


Fig.7 Influence of post deposition annealing on optical transmission.

temperature, the refractive index again starts decreasing. The increase in refractive index is associated with the decrease in the band gap [13]. A similar behaviors is observed in the present work.

Hickernell [7] observed a peak in the refractive index for annealing temperature of 873 K. The peak in the refractive index in the present work occurs at 673 K annealing temperature. This difference in the temperature may attributed to the different fabrication parameters between the present work and that reported by Hickernell [7]. In the present work the structural studies shows the appearance of microcracks above 673 K and the refractive index starts to decrease. Hence, the variation of refractive index may be attributed to the change in the packing density with annealing temperature. Many attempts have been made to correlate the packing density with refractive index of the material and after assuming cylindrical crystallites the values of packing density was evaluated using the expression given by Macleod [14] and are reported in Table-1. The value of packing density is found to be maximum at SRT and nearly equal to one i.e. film annealed at 673K is bulk like.

#### CONCLUSION

Zinc oxide films sputtered from oxide target at room temperature substrate in argon ambient are nearly stoichiometric and are in a state of compressive stress. Post deposition annealing treatment at 673 K relieves the stress completely (SRT). SEM analysis shows that as grown films are columnar in nature with fine crystallites. The area of voids decreases with increasing temperature up to SRT (673 K) and packing density is maximum. Above SRT there is a process of recrystallization and cracks develop in the films. The present work shows that 673 K is the best post deposition annealing temperature for films grown at unheated substrate to get high quality ZnO films.

#### ACKNOWLEDGEMENT

One of the authors (VG) is grateful to the Council of Scientific and Industrial research (INDIA) for financial support in the present work.

#### REFERENCES

- [1] T.Shiosaki, N.Kitamura and A.Kawabata, "Integrated SAW-AO-deflector and photo-detector on Si", in proceedings of the 7<sup>th</sup> international symposium on applications of ferroelectrics, held at the University of Illinois, Urbana (USA), on June 6-8, 1990, pp. 296-301.
- [2] L.Meng, M.Andritschky and M.P.D.Santos, "Optical properties of ZnO thin films deposited by dc reactive sputtering, Vacuum, Vol. 44 (2), pp. 105-109, 1993.
- [3] A.Valentini, A.Quirini and L.Vasanelli, "Optical properties of ZnO films deposited by r.f. sputtering on sapphire substrate", Thin Solid Films, Vol.176, pp. L167-71, 1989.
- [4] S.Takada, "Relation between optical properties and crystallinity of ZnO thin films prepared by rf magnetron sputtering", J.Appl.Phys., Vol. 73 (10), pp. 4739-42, 1993.
- [5] R.J.Lad, P.D.Funkenbusch and C.R.Aita, "Post deposition annealing behaviour of rf sputtered ZnO film", J.Vac.Sci.Tec., Vol. 17 (4), pp. 808-11, 1980.
- [6] H.K.Kim and M.Mathur, "ZnO films deposited on GaAs substrates with a SiO<sub>2</sub> thin buffer layer", J.Electron.Mater., Vol. 22 (3), pp. 267-73, 1993.
- [7] F.S.Hickernell, "Post-deposition annealing of Zinc oxide films", in proceeding of the 1981 IEEE Ultrasonics symposium, 1981, pp. 489.
- [8] V.Gupta and A.Mansigh, "Hopping conduction in insulating rf-sputtered Zinc Oxide films", Phys. Rev.B, Vol. 49 (3), pp. 1989-95, 1994.
- [9] S.Maniv, W.D.Westwood and E.Colombini, "Pressure and angle of incidence effects in reactive planar magnetron sputtered ZnO layers", J.Vac.Sci.Tech. Vol.20 (2), pp. 162-70, 1982.
- [10] M.S.Raven and B.Belmekki, "Growth and orientation of r.f.-sputtered polar compounds", Thin Solid Films, Vol. 80, pp. 85-91, 1981.
- [11] R.Swanepoel, "Determination of surface roughness and optical constants of inhomogeneous amorphous Si films", J.Phys.E : Sci.Instrum., Vol.17, pp.896-903, 1984.
- [12] R. Swanepoel, "Determination of the thickness and optical constants of amorphous silicon" J.Phys.E : Sci. Instrum., Vol. 16, pp. 1214-22, 1983.
- [13] A.N.Pikhtin and A.L.Yas'kov, "Refractive index and birefringence of semiconductors with the wurtzite structure", Sov.Phys. Semicond., Vol. 15 (1), pp. 8-12, 1981.
- [14] H.A.Macleod, "Structure-related optical properties of thin films", J.Vac.Sci. Tech. A, Vol. 4 (3), pp. 418-22, 1986.

# PROCESSING AND CHARACTERIZATION OF SAMARIUM AND MANGANESE MODIFIED LEAD TITANATE THIN FILM

Chen-Lung Fan and Wayne Huebner  
University of Missouri-Rolla, Rolla, MO 65401

## ABSTRACT

Samarium and manganese modified lead titanate thin films were fabricated by spin-coating an amorphous citrate precursor. These films transformed into an oxide film upon heat treatment at 400°C or above. Relatively large area and crack-free thin films could be obtained by this process both easily and inexpensively. The rheological behavior of the precursor solution, as well as its thermal decomposition and phase development were studied by means of DSC/TGA and XRD. The thickness and grain size of the oxide film were examined by TEM and SEM.

## INTRODUCTION

Lead titanate  $\text{PbTiO}_3$  (PT) exhibits many intriguing features such as a high Curie Temperature ( $T_c \approx 490^\circ\text{C}$ ), large  $k_t$  to  $k_p$  ratio, and a large pyroelectric coefficient, which qualifies it to be one of the candidates suitable for making acoustic transducers or pyroelectric detector [1]. Due to its large  $c/a$  ratio, however, it cannot be sintered to high density without falling apart when it cools through  $T_c$ . To overcome this drawback and still maintain its interesting properties, it has to be doped to lower the  $c/a$  ratio [2]. Among these effective dopants,  $\text{Sm}^{3+}$  and  $\text{Ca}^{2+}$ -doped PT are two major systems which demonstrate superior properties [3, 4]. In this study PT doped with 10 mol%  $\text{Sm}^{3+}$  and 2 mol%  $\text{Mn}^{2+}$  was chosen as the compositional system to work with.

The purpose of this study was to synthesize  $\text{Sm}^{3+}$  and  $\text{Mn}^{2+}$  modified PT thin films by spin coating of amorphous citrate precursor on various substrates. Compared with chemical vapor deposition (CVD) [5, 6], physical vapor deposition (PVD), and relatively inexpensive sol-gel process [7, 8], the process used in this study is even more inexpensive. It also offers the advantage of easier control of the chemical stoichiometry and of having a variety of selections of starting materials. Generally all water soluble metal salts can be the starting materials provided that the metal salts are compatible with one another, unlike CVD and sol-gel processes which require few available and expensive precursors. The problems associated with the amorphous citrate process lie on the requirement of heat treatment at 400°C or above in order to convert the precursor resin into oxide thin film. Therefore care has to be taken on controlling the precursor film thickness to ensure a crack-free thin oxide film is to be obtained after heat treatment. In addition, selection of a substrate material with a compatible thermal expansion coefficient is also very important to the perfection of the thin film. Those problems and concerns will be discussed in the following sections.

## EXPERIMENTAL PROCEDURE

Titanium isopropoxide, lead carbonate, samarium carbonate, manganese acetate, and citric acid were used as the starting materials. The process, as shown in the flow chart of Fig. 1, starts with a titanium citrate complex solution, since titanium isopropoxide is not water soluble and is subject to hydrolysis. Citric acid was first dissolved in distilled water with a pH value of  $\approx$  one, followed by the addition of ammonium hydroxide until the pH value reaches six (solution A). On the other hand, titanium isopropoxide was diluted with isopropyl alcohol to 50 vol.% (solution B). Solutions A and B were mixed and heated on a hot plate. Upon mixing, titanium isopropoxide underwent a fast hydrolysis reaction, forming titanium hydroxide which was then gradually dissolved into the solution. The solution thus made can be concentrated by boiling off more water in the solution, and can be stored indefinitely in a liquid form without forming precipitates. It can also be further concentrated and vacuum dried into a crystallized form, as confirmed by XRD. In this study, it was kept in the solution form and standardized gravimetrically to determine the specific amount of titanium ions in the solution. Lead carbonate, samarium carbonate, and manganese

acetate were also standardized to achieve better control over the stoichiometry of the final thin oxide film.

The desired amount of titanium solution was heated on a hot plate until the temperature reached 100°C, then a suitable amount of lead carbonate, samarium carbonate, and manganese acetate were added into the solution to prepare the precursor for the oxide composition of  $(\text{Pb}_{0.9}\text{Sm}_{0.1})(\text{Ti}_{0.98}\text{Mn}_{0.02})\text{O}_3$ . Carbon dioxide was released when the carbonates reacted with titanium citrate solution, and all the cations were chelated with citric acid forming a citrate complex. The complex solution was then oven-dried at 100°C until all the water was driven off leaving a pile of cracked-up resin powders which can be redissolved into water to make up solutions with different concentrations. Especially for the preparation of spin-coating precursor solution, it is necessary to know the concentration of the solution so that the process can be easily controlled. Otherwise, the concentration of the solution will depend on how much water remains in the solution, which is very difficult to control and to reproduce since water is vaporizing all the time during the preparation of the citrate complex solution at temperature as high as 100°C. The resin powders were then collected for DSC/TGA studies and for the preparation of the precursor solution for spin coating.

The rheological behavior of the precursor solutions with different concentrations was characterized by a HAAKE viscometer.

Spin coating was carried out by a computerized spin coater which has the ability to controlling acceleration and soak time. Generally speaking, higher solution concentration gives rise to thicker coating layer and higher spin speed favors lower coating thickness. Therefore it is really a matter of compromising the solution concentration and the spin speed in order to obtain an optimum coating thickness, which allows the formation of a uniform and crack-free thin oxide film after heat treatment. In this study, 20wt.% as the solution concentration and 0 rpm up to 2000 rpm in 30 seconds as the acceleration schedule was chosen to prepare the thin films for all the studies.

After the precursor solution was coated on to a silicon wafer or polished kovar substrate, it was heat treated at 400°C for 10 minutes in a Linberg box furnace for all the organic species to be oxidized, leaving behind a uniform thin oxide film. Multiple coatings could be done by repeating the procedures to build up the thickness. The measurement of film thickness was performed by SEM and the grain size of the film was illustrated by TEM.

## RESULTS & DISCUSSION

The oven dried resin, unlike the room temperature vacuum-dried resin, appeared to be x-ray amorphous and exhibited a yellowish color. To characterize the rheological behavior of the precursor solution, shear stress as a function of shear rate was measured on the solutions with different concentrations. Fig. 2 shows this behavior for 20, 40, 50, and 60 wt.% of the precursor solutions. Although the sets of data are somewhat fluctuating, they still show a linear trend of the shear stress as a function of the shear rate and there is no yield stress associated with them. This qualifies the solution with concentration of 60 wt.% or below as a Newtonian solution. The corresponding average viscosities are 3, 5, 10, and 50 mPas for 20, 40, 50, and 60 wt.%, respectively. Compared with that of water, which is about 1 mPas, the viscosities are still on the low. As the concentration increases further, the viscosity increases drastically (Fig. 3). At 75wt.% the viscosity is 37,000 mPas, which is about 750 times that of the 60 wt.% solution.

Normally it is required to have medium viscosity (100-1000 mPas) for the spin coating process to be successful, provided that the viscosity does not change during the coating process. If the precursor solution has too low viscosity, there will no solution coated on the substrate after the spinning process since all the solution is spun away. However, if the solution viscosity is too high, the coating layer will not be very uniform and probably too thick to obtain a crack-free thin oxide film. Note that the coating thickness results from the combining result of the solution concentration and the spinning speed. Therefore, for low

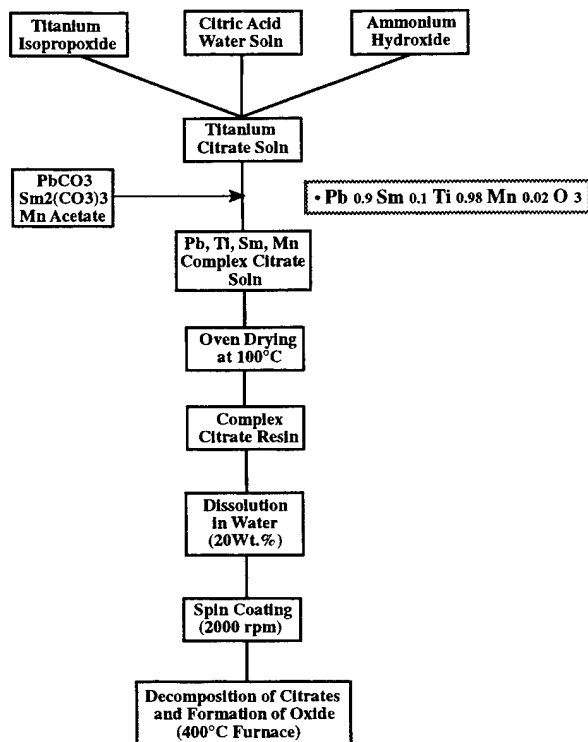


Figure 1. Flow chart of the experimental procedures.

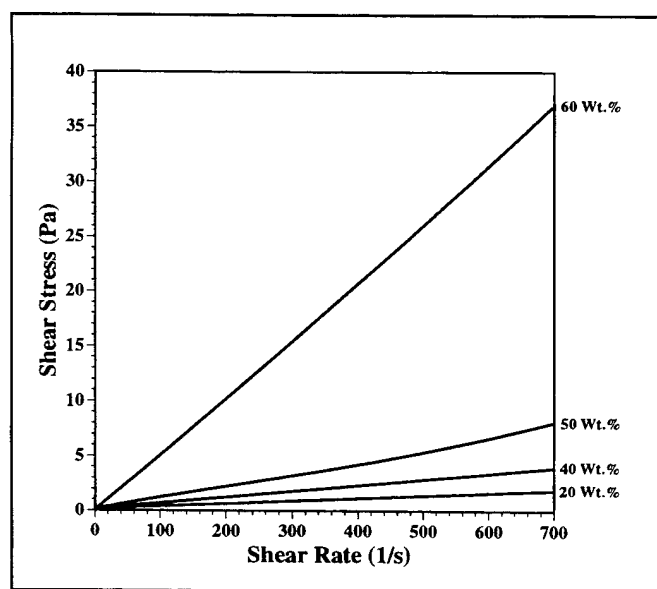


Figure 2. Shear stress as a function of shear rate for precursor solution with different concentrations.

concentration, say 20wt.%, low spin speed will be favorable, and for high concentration, say 70wt.%, high spin speed is favorable, assuming that the viscosity does not change as the process goes on. Unfortunately, the viscosity of the solution increases as the spinning process goes mainly due to the loss of water content, which results in increase of solution concentration and in turn increase of the viscosity. As can be seen in Fig. 3, when the solution concentration increases to above 70 wt.% the viscosity increases hundreds of times of that of the 20 wt.% solution. Therefore it is not difficult to understand that 20 wt.% solution can be spin-coated on a substrate, thereby forming a thin layer of precursor resin. The 20 wt.% solution keeps drying out as the process goes, while some of the excess solution is spun away when the viscosity of the solution is still low enough to allow that to happen.

After the precursor resin is spin-coated, heat treatment converts the resin film to an oxide film. Soon after a substrate is inserted into a Linberg box furnace, the resin film starts turning brown and black due to the charring of the resin and then the color goes away about five to ten minutes after the substrates being inserted into the furnace. These colorless thin films are transparent to visible light, which indicates the good uniformity of the thin films. Basically this process can be applied to any substrate which is thermally durable such as glass, silicon wafer, and stainless steel. To meet the requirements of different purposes, substrates have to be selected properly. For example, glass substrates can be selected for optical application, silicon wafer for TEM study, and stainless steel for electroceramic application since the substrate is not only a substrate but also a conductive electrode. In this study, silicon wafer was used as the substrate to prepare TEM specimen and kovar, a low thermal expansion alloy, was used as the substrate for grain growth studies mainly because of its low thermal expansion coefficient. This allows the thin film to adhere to the substrate tightly without being debonded due to thermal expansion mismatch at temperatures higher than 400°C.

Fig. 4 shows the DSC/TGA study on the oven-dried resin. (5°C/min. up to 1000°C). It can be seen that the resin starts decomposing at  $\approx 200^\circ\text{C}$  judging from the exotherm and accompanying weight loss, and it finishes decomposing before 500°C. At temperature higher than 500°C there is no exotherm or weight loss. The final product of the experiment was determined as perovskite PT powders by XRD.

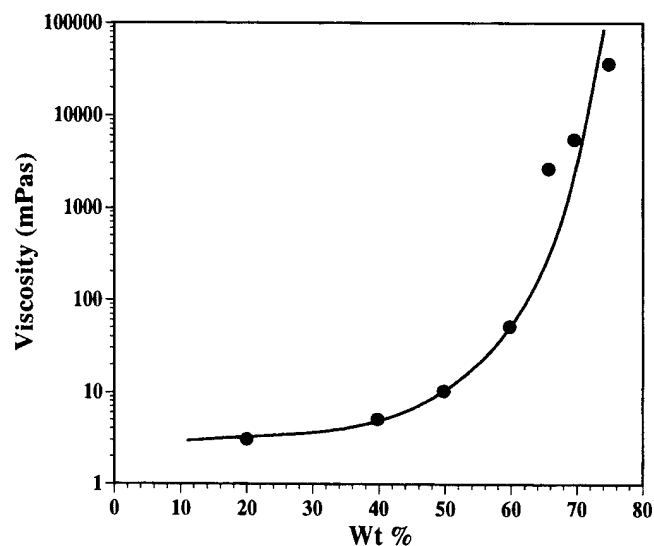


Figure 3. Viscosity as a function of solution concentration.

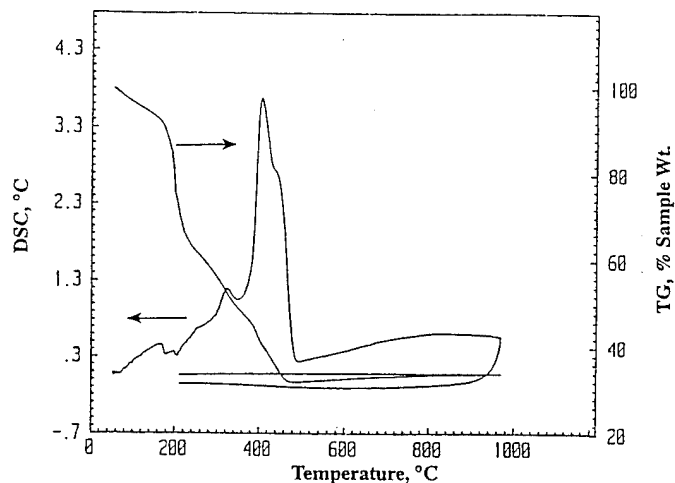
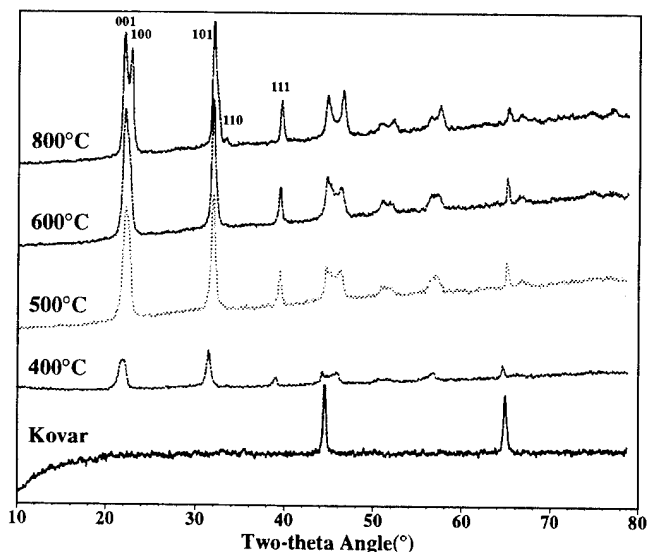


Figure 4. DSC/TGA versus temperature for the oven dried precursor resin.

Presumably the decomposition temperature of the bulk resin should be the same as the thin resin film on the substrates, however, there are some slight differences between them. In the case of the DSC/TGA study, the resin powders were put in an  $\text{Al}_2\text{O}_3$  crucible. And it is foreseeable that those powders near the surface will experience thermal radiation from the furnace more directly than those near the bottom of the crucible. Perhaps even more importantly those powders on the surface are experiencing higher oxygen partial pressure than those in the interior. Therefore the decomposition behavior of the resin is indeed an overall result of a kinetic process, and it may not reflect the real decomposition temperature. But it is still safe to say that the resin decomposes in the temperature range from 200°C to about 500°C. On the other hand, thermal decomposition of the resin films on substrates would be more uniform since the film is so thin that the temperature or  $\text{pO}_2$  gradient between the top and bottom surface is negligibly small.

Fig. 5 shows the x-ray diffraction patterns for the kovar substrate and for the modified lead titanate thin films on kovar which has been heat treated at 400, 500, 600, and 800°C for 30 minutes. As can be seen from the figure, the thin films have crystallized at temperature as low as 400°C. And there is no black carbon residue found visually on the film treated at 400°C, which confirms that the resin films can be fully converted to crystallized oxide films at this temperature. Compared with the DSC/TGA data, which shows a wide temperature range from 200 to 500°C, it clearly shows that the decomposition temperature suggested by the DSC/TGA study is a result of an overall kinetic process. As the films were treated at higher temperatures, the diffraction peaks became sharper and narrower, which indicates the crystal size is increasing. When the temperature gets up to 800°C, the tetragonal splitting of the peaks corresponding to (001) and (100) planes can be clearly seen. This confirms that the crystal structure of the film is tetragonal phase and the reason that the diffraction patterns for below 800°C show cubic like structure is due to line broadening caused by the small crystal size of the film.

Another interesting observation regarding the diffraction patterns in Fig. 5 is that the crystals in the film exhibit a preferred orientation. According to the standard powder diffraction file for tetragonal PT (JCPDS file # 6-0452), the relative peak heights correspond to (001), (100), (101), (110), and (111) planes are 25, 50, 100, 55, and 40, respectively. However, the peak heights for the thin film show different relative intensities, namely 100, 87, 100, 6 and 32, respectively, as compared in Table I. Clearly the peak intensities of (001) and (100) planes for the thin film are significantly higher than that for the powder diffraction file. Also the (001) peak intensity is higher than the (100) peak intensity unlike the powder diffraction file of which the (001) peak intensity is only half the (100) peak intensity. Another feature regarding the change in peak intensity is that (110) peak intensity for the thin film almost diminishes, relative peak intensity of 6, as compared with that of 55 for the powder diffraction file. All these observations indicate that the film is somewhat preferred oriented along [001] direction.



PbTiO<sub>3</sub>, tetragonal, JCPDS # 6-0452

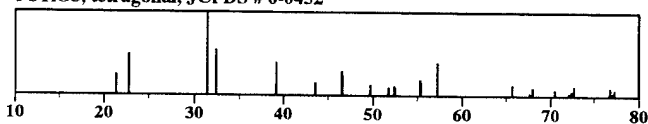


Figure 5. X-ray diffraction patterns at different temperatures of the PT thin films on kovar substrates.

It is known that pure PT has a  $T_c \approx 490^\circ\text{C}$ . For the  $\text{Sm}^{3+}$  and  $\text{Mn}^{2+}$  doped PT composition used in this study, the  $T_c \approx 350^\circ\text{C}$  due to the lower c/a ratio. There are two possibilities for the preferred orientation: one is that the atoms in the film aligned themselves along the crystal direction of the substrate thus forming preferred oriented crystals, provided that the lattice mismatch between the film and the substrate is not too much; the other one is that the crystals align themselves along c direction during phase transformation from cubic to tetragonal phase. Since the kovar substrate used in this study is not even a single crystal material, it is unlikely for the crystals in the film to grow on the substrate along a specific direction. Therefore the preferred orientation of the crystals in the thin film on kovar is believed to form during phase transformation. For thin films on substrates, there is only one free direction for the crystals in the film to either expand or to shrink because the dimensions of the substrate is constant which gives rise to a constraint stress along the substrate plane. In other words, the films on the substrates are two-dimensionally constrained, and if there will be any dimension change, while still remain the integrity of the films, it has to be happening along the normal direction of the substrate.

For PT to transform from the cubic to the tetragonal phase, it does not require atomic rearrangement and can be done simply by expanding in c direction and shrinking in a direction. Considering the peak intensity data shown in Table I, there are indeed more crystals whose c axes are perpendicular to the substrate since the peak intensity of (001) plane is much higher than what would be expected if all the crystals are randomly oriented. In mind with all the aforementioned arguments, it confirms that the preferred orientation of the crystals in the thin film is a result of reorientation of the crystals which happens during phase transformation from cubic to tetragonal phase.

Table I. Comparison of peak heights of x-ray diffraction patterns of PT thin film and that of JCPDS file # 6-0452.

(h, k, l)	001	100	101	110	111
Intensity JCPDS # 6-0452	25	50	100	55	40
Intensity PT film	100	87	100	6	32



Fig. 6 shows the TEM micrograph of the lead titanate thin film after being stripped off the silicon wafer. The coating process was exactly the same as that used for coating on kovar. After the silicon wafer was coated with a layer of precursor resin, it was first treated at 400°C to convert the resin into oxide thin film, and then it was immersed into a 10wt.% sodium hydroxide water solution preheated at 80°C. Soon after the immersion, sodium hydroxide started reacting with the silicon wafer, and the thin film was stripped off the substrate as soon as the bonding between the film and the substrate was destroyed. The stripped film was then transported into a 250 ml beaker which contains 200 ml of water solution, 98 vol.% of water and 2 vol.% of methanol, to wash away the residual sodium hydroxide on the film. Then the film was lifted and supported on a copper grid for TEM study. According to Fig. 5, the grain size was estimated ranging from less than 10 nm to a few tens nm, though the film contains a few layer of grains which makes the measurement of grain size more difficult.

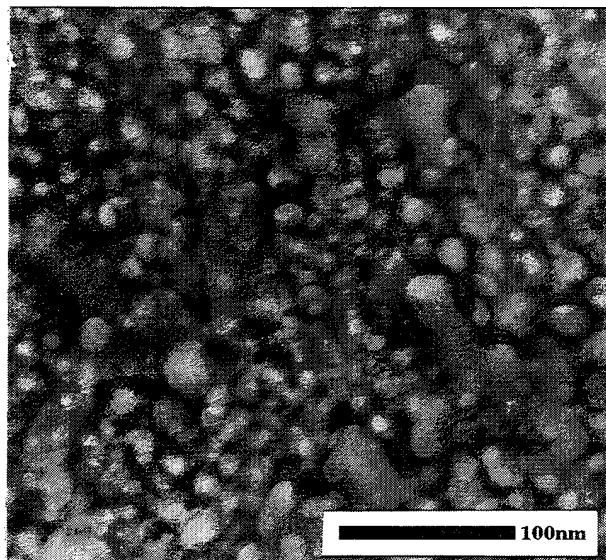


Figure 6. TEM micrograph of the PT thin film stripped off the silicon wafer.

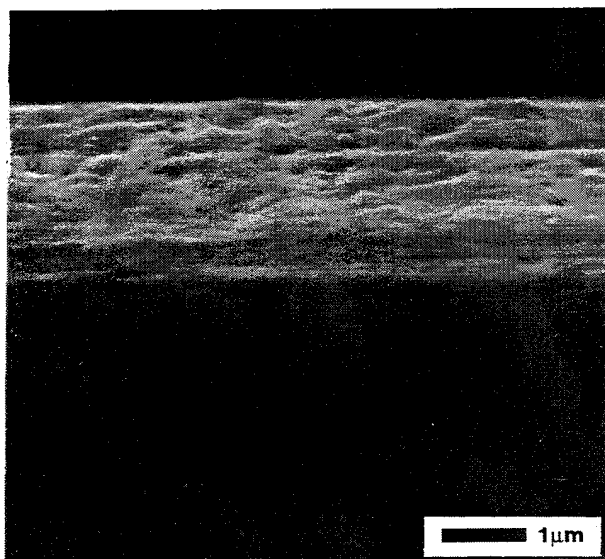


Figure 7. SEM micrograph of the PT thin film on kovar substrate.

Fig. 7 shows the SEM micrograph of the cross section of lead titanate thin film coated on kovar and heated at 800°C. The sample was first mounted with epoxy and then ground with a 600 grit paper followed by polishing with 0.3 μm alumina polishing media. The film thickness is about 2.3 μm after 40 coatings. Therefore the average thickness of a single coat is about 0.06 μm. Although it is a little troublesome to coat forty times in order to build up 2.3 μm layer of film, it was demonstrated useful in coating on glass substrates for optical application, which does not necessarily require film thickness of more than 1 μm.

## CONCLUSIONS

Samarium and manganese modified lead titanate thin films were successfully fabricated by first spin coating a layer of amorphous citrate precursor resin on glass, silicon wafer, and kovar substrates, followed by heat treatment at 400°C to convert the resin film to oxide film. X-ray result shows that perovskite phase was obtained after the heat treatment and also the crystals in the film were preferred oriented mainly along [001]. The grain size of the film treated at 400°C ranges from less than 10 nm to a few tens nm as indicated by the TEM micrograph. The average film thickness for a single coat is about 0.06 μm, which is very suitable for optical applications rather than dielectric or piezoelectric applications. Therefore more work will be concentrated on optical application of films made by this process. In addition, grain growth of a free standing film, also made by this process, is currently undergoing in the authors' group and will be published soon.

## REFERENCES

- [1] Laurel M. Sheppard, Advances in Processing of Ferroelectric Thin Films, *Am. Cer. Soc. Bull.*, Vol. 71, No. 1, 1992.
- [2] A. Ahmad et al, Processing and Characterization of Ca, Ce, and Na Ion Doped Lead Titanates, *Proc. of the Eighth International Symposium on Application of Ferroelectrics*, IEEE, New York (1992).
- [3] Takashi Takahashi, Lead Titanate Ceramics with Large Piezoelectric Anisotropy and Their Applications, *Am. Cer. Soc. Bull.*, Vol. 69, No. 4, 1990.
- [4] Thitima Suwannasiri and Ahmad Safari, Effect of Rare-Earth Additives on Electromechanical Properties of Modified Lead Titanate Ceramics, *J. Am. Cer. Soc.*, **76** [12] 3155-58 (1993).
- [5] Kwang Ho Kim et al, Effect of Antimony Addition on Electrical and Optical Properties of Tin Oxide Film, *J. Am. Cer. Soc.*, **77** [4] 915-21 (1994).
- [6] Toshiro Maruyama and Susumu Arai, Electrochromic Properties of Tungsten Trioxide Thin Films Prepared by Chemical Vapor Deposition, *J. Electrochem. Soc.*, Vol. 141, No. 4, April 1994.
- [7] Charles D.E. Lakeman and David Payne, Processing Effects in the Sol-Gel Preparation of PZT Dried Gels, Powders, and Ferroelectric Thin Layers, *J. Am. Cer. Soc.*, **75** [11] 3091-96 (1992).
- [8] Debtosh Kundu et al, Preparation and Optical Property of Sol-Gel-Derived Cu-SiO<sub>2</sub> Thin Films, *J. Am. Cer. Soc.*, **77** [4] 1110-12 (1994).



## RELATIONSHIPS BETWEEN THERMAL TREATMENT AND PROPERTIES OF PLT THIN FILMS

YUN LIU, LIANGYING ZHANG AND XI YAO  
Electronic Materials Research Laboratory(EMRL)  
Xi'an Jiaotong University, Xi'an, 710049, China

### Abstract

The effect of thermal treatment conditions on the structures and properties of PLT10 thin films are presented in this paper. Better ferroelectric properties could be obtained when the film is heated up to 600°C with 3°C/min and holded for one hour. Better dielectric properties were observed when the film is heated up to 550°C with 3°C/min and holded for one hour.

### Introduction

How to prepare ferroelectric thin films with good properties has become extremely important for their applications. The key factor of preparing thin film is thermal treatment in MOD method. Various properties of thin films would be seriously affected by conditions of thermal treatment. Thermal treatment conditions of PLT10 thin film deposited on the silicon substrate were discussed in this paper. Good ferroelectric properties of PLT films prepared with MOD method could be obtained when films are heated up to 600°C with 3°C/min and holded for one hour. Better dielectric properties were observed when the films are heated up to 550°C with 3°C/min and holded at for one hour.

### Experimental

The PLT thin films on the single crystal silicon substrates with SiO<sub>2</sub> layer were prepared by repeating the spinning-coating and pyrolysis processes. Singular layers were treated at 180°C for 30 minutes to remove the solvent and even layers were treated at 400°C (3°C/min) for 30 minutes to complete the pyrolysis of organic species. After multiple coatings, the deposited films were annealed in air to form perovskite structure. In order to obtain good dielectric and ferroelectric properties, Therefore, the conditions of thermal treatment of the last layer are studied as below:

- (1) Different holding temperature (°C): 550, 600, 650, 700, (1h, 3°C/min).
- (2) Different holding time (hours): 0.5, 1, 5, 20 (500°C, 3°C/min).
- (3) Different rate of temperature-rising(°C/min): 1, 3, 8 (550°C, 1h).

For measurement of various electric properties, bottom electrode of platinum with the thickness of 100nm was deposited by DC sputtering method, and top electrode of gold dot with 1mm in diameter was also made.

### Measurement and Discussion

#### 1. Micro structure

Figure 1 a-c shows the SEM photographics with different holding time in thermal treatment process. Grain size gradually increased with the time, but if the time was continuously increased, the change of grain size was not obvious. The reason is that relatively dense structure with larger grains has been formed, and there is not enough space for grains to grow up.

Figure 1 d-f obviously presented different grain sizes: grain size in the film at the rate of 1°C/min is the largest. The smallest one is obtained at the rate of 8°C/min.

Figure 1g-j shows that grain size gradually grew up the temperature with increasing the temperature. If temperature continued to rise, very typical grain of ceramic materials would be observed<sup>[1]</sup>.

#### 2. XRD analysis

Films with pure perovskite phase were prepared in each case for various thermal treatment conditions and orientation of ferroelectric thin film will be obviously affected by these conditions (as shown in figure 2). If the

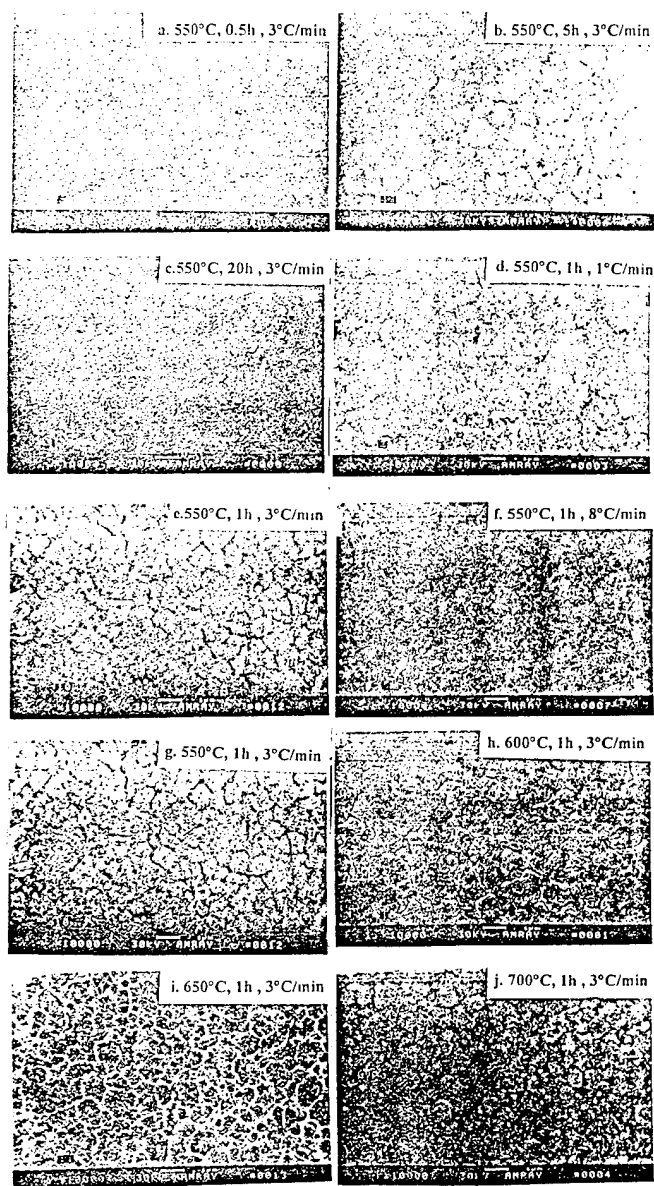


Fig.1 SEM photographs of thin films  
 $I(100)/[I(100)+I(101)]$  was defined as orientation, a-axis preferential orientation was observed in PLT thin films[2]. A-axis orientation increases from 27% with 0.5h to 74% with 20h as shown in figure 2. Therefore orientation was enhanced with increasing holding time. The orientation of films also changed with temperature and rate of temperature-rising.

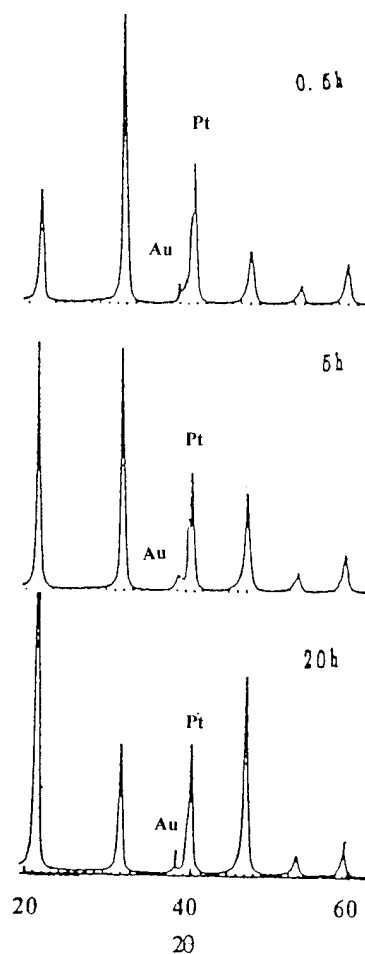


Fig.2 XRD patterns of thin films

### 3. Ferroelectric properties

P-E hysteresis loops were measured with a modified Sawyer-Tower circuits. Figure 3a shows that above one hour or holding time  $P_r$  remained invariant with increasing holding time. This is because that reversion of electro-domain is almost the same for the same grain sizes. Therefore, only one hour of holding time is needed to obtain larger remanent polarization. Coercive field ( $E_c$ ) slightly increased with increasing the time. If  $E_c$  need to be decreased, holding time would be decrease correspondingly. For shorter time, lower  $P_r$  could be obtained due to crystallization. The best holding time is one hour. For too long time, vacancy and pin hole would make the properties drop down. Improvement on ferroelectric property is not obvious with increasing the rate of temperature-rising (shown in figure 3b).  $P_r$  and  $E_c$

have a little increasing with increasing the rate of temperature-rising because reversion of domain was restrained for small grain size. At higher temperature, larger remanent polarization (Pr) was obtained as shown in figure 3c because electro-domain was easily reversed with the growth of grain.

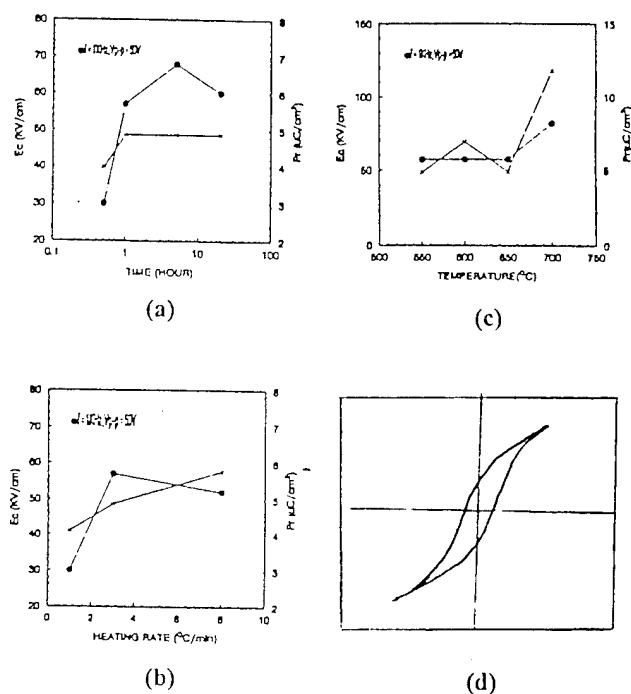


Fig.3 Ferroelectric properties (a-c.  $E_c$  and  $P_r$  vs conditions of thermal treatment; d. P-E hysteresis loops at 600°C with 3°C/min for 1h.)

Thus, Better ferroelectric properties could be obtained when the film is heated up to 600°C with 3°C/min and holded for one hour. Figure 3d shown the P-E hysteresis loop at 1KHz,  $V_p-p=80V$ , and calculated  $P_r$  and  $E_c$  are  $9.15\mu C/cm^2$  and 70KV/cm respectively .

#### 4. Dielectric properties

Dielectric constants and loss angle tangents of PLT film were measured by HP 4274A LCR and 4275A LCR meter with frequency of 1KHz under AC 0.05V. Figure 4a-c presented the relationships between dielectric properties and conditions of thermal treatment. For shorter time, higher  $\tan\delta$  will be obtained due to poor crystallization. The best holding time is one hour. Under this condition dielectric constant and loss of the film are lower. Better dielectric properties would be obtained

when rate of temperature-rising is 3°C/min. Lower dielectric constants and loss were obtained at 550°C.

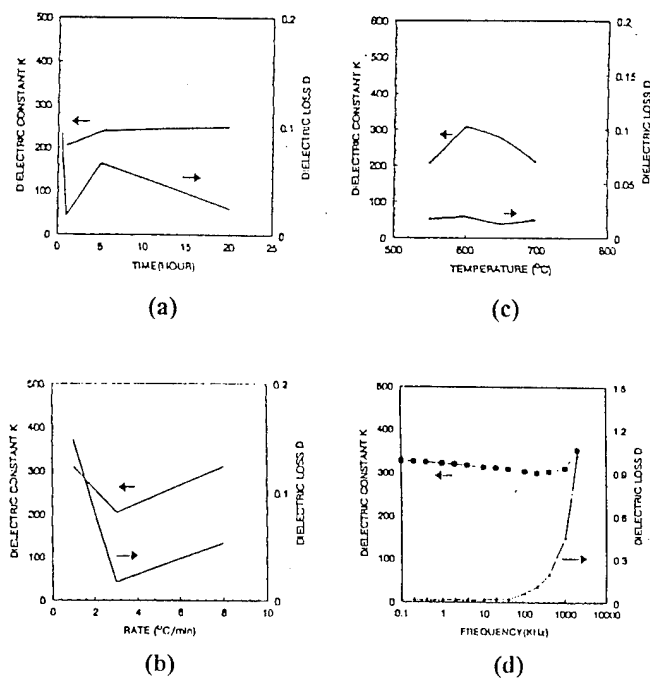


Fig.4 Dielectric properties (a-c. dielectric constant and loss vs conditions of thermal treatment; d. dielectric constant and loss vs frequency at 550°C with 3°C/min for 1h.)

Therefore, better dielectric property of PLT film prepared by MOD method was observed at 550°C with 3°C/min for one hour of holding time (as shown in figure 4d).

#### Conclusions

- 1, Micro structure of PLT film will be seriously affected by conditions of thermal treatment.
- 2, Thermal treatment temperature, holding time and rate of temperature-rising only affected dielectric properties.
- 3, Better ferroelectric properties could be obtained when the film is heated up to 600°C with 3°C/min and holded for one hour. Better dielectric properties were observed when the film is heated up to 550°C with 3°C/min and holded for one hour.

#### Acknowledgment

Financial support for this work was provided by the National Advanced Materials Research Program in China.

## References

1. Ping Sun, PH D Dissertation, Preparation and properties of PLZT thin films derived from metallo-organic precursors, 1993.
2. Yun Liu, Wei Ren, Jihui Qiu, Liangying Zhang and Xi Yao, Preparation of PLT thin films by thermal decomposition of metallo-organic compounds, IMF8, 1993.

# Piezoelectric Response of PZT Thin Film Actuated Micromachined Silicon Cantilever Beams

K. G. Brooks, D. Damjanovic, and N. Setter  
Laboratoire de Céramique, EPFL  
Lausanne, Switzerland

Ph. Luginbuhl, G.A.-Racine, and N.F. de Rooij,  
IMT, Uni. Neuchâtel  
Neuchâtel, Switzerland

**Abstract** - Micromachined cantilever beams actuated by sol-gel derived lead zirconium titanate (PZT) thin films are reported. Rectangular cantilevers of sub millimeter dimensions and several different aspect ratios were fabricated. The PZT films utilized for these structures were 0.44  $\mu\text{m}$  thick. The natural resonance frequencies of the beams were determined from impedance measurements. The resonance frequency was found to follow a  $L^{-2}$  dependence, where  $L$  is the cantilever length. An effective elastic constant,  $s_{11}$ , for the beam structures of  $15.7 \times 10^{-12} \text{ m}^2\text{N}^{-1}$  was thus calculated. The effect of bias fields on the effective electromechanical coupling factor,  $k_{31}$ , was also determined from the resonance data. Maximum  $k_{31}$  values measured were approximately 0.15, or about half of those reported for PZT bulk ceramics.

## INTRODUCTION

Piezoelectric thin films are currently being investigated for use in micro-sensors and actuators. The basic possible geometries include membranes, bridges and cantilever beams. Of these, cantilever beams are a convenient object for the study of the effective piezoelectric properties of the thin film structures. An understanding of which is essential for the design and modeling of more complex devices such as micropumps and micromotors. Due to the small scale of such cantilevers (with thickness on the order of 1 to 20  $\mu\text{m}$ , and lengths less than 1 mm) and the strong effect of the PZT/electrode interfaces which has been reported by many researchers in the area of PZT films for ferroelectric memories, it is not clear how the performance will scale down, when compared to monomorph and bimorph structures prepared from bulk ceramics. Data in the literature is quite sparse, with a few groups reporting on the measurement of the piezoelectric properties of PZT films as prepared on Si bulk substrates. Polla has reported on the preparation of PZT thin film based cantilevers prepared by a surface micromachining technique, although no detailed measurements of the piezoelectric response are described.<sup>1</sup>

In this paper, we report on the measurement of the piezoelectric response of PZT thin film actuated micromachined cantilever beams using resonance methods. The technique is analogous to that reported by Deschanvres et al. who have investigated the piezoelectric response of ZnO actuated micro-beams.<sup>2</sup> Such a technique can be used to obtain the effective elastic constant of the beams and the electromechanical coupling coefficient. This information can then be used to aid in the design of piezoelectric thin film based micro-sensors and actuators.

## EXPERIMENTAL

### PZT Film Preparation

The PZT films investigated in this study were prepared by a sol-gel processing technique, the details of which have been previously reported<sup>3</sup>. The process is based on the early work of Budd et al.<sup>4</sup> whereby a precursor solution is prepared from Pb acetate, Zr n propoxide and Ti isopropoxide in 2 methoxyethanol solvent. The substrates used consisted of 3 inch silicon wafers with 0.6  $\mu\text{m}$  of  $\text{Si}_3\text{N}_4$ , 10 nm of Ta (adhesion layer) and 70 nm of Pt (bottom electrode). PZT films were prepared by spin coating a 0.2 M precursor solution at 1900 rpm for 40 s, followed by drying at 150°C, and pyrolysis at 350°C for 15 s. Six layers are deposited, and the film rapidly thermally annealed at 600°C for 60 s. A second set of layers is then deposited and the film annealed a second time at 600°C for 5 min. The final PZT film thickness, (for all structures reported herein) as measured by profilometry was 0.44  $\mu\text{m}$ .

### Cantilever Structuring

The process sequence used to prepare the top electrodes (Ta bonded Pt), passivation ( $\text{SiO}_2$ ) and contact metallization (Pt) has been previously reported<sup>5</sup>. After the KOH bulk micromachining step, in which a 14  $\mu\text{m}$  thick Si membrane is retained, the cantilever beams were freed from the membrane by plasma etching. Individual dies (4 x 6 mm) were then cut from the wafer and packaged by mounting in plastic with epoxy and wire bonding to contact pads. A scale drawing of the cantilever structures measured is shown in Fig. 1. An optical micrograph of one of these structures is shown in Fig. 2.

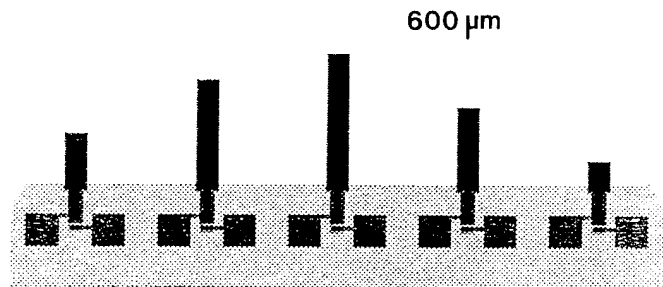


Fig. 1 Scale drawing showing the five different cantilever structures investigated. All are 200  $\mu\text{m}$  in width and have aspect ratios ( $L \times W$ ) of 2, 4, 5, 3 and 1 respectively, from left to right.

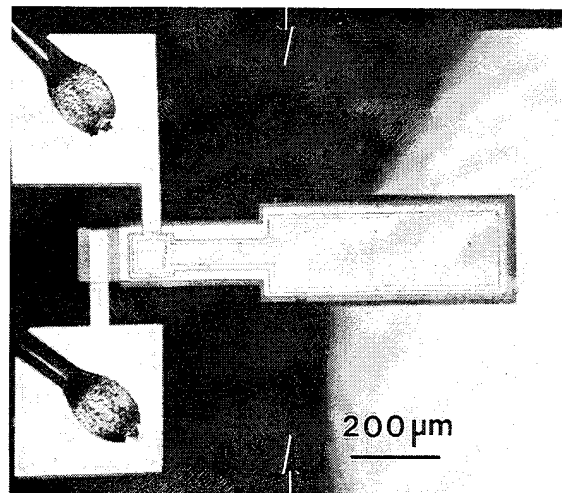


Fig. 2 Optical micrograph of cantilever beam of aspect ratio 2.

### Resonance Measurements

Resonance measurements were done using an HP 4194A Impedance/Gain Phase Analyzer. AC voltages between 10 mV and 1 V (equipment limited) and bias fields of between -20 and +20V (-450 and +450 kV/cm) were investigated.

## RESULTS AND DISCUSSION

The electromechanical resonance of the various cantilever structures was investigated by measuring the impedance as a function of frequency. The fundamental resonance frequency is given by:

$$f_0 = \frac{\lambda^2 t}{4\pi L^2} \sqrt{\frac{1}{3s_{11}^E \rho}} \quad (1)$$

where  $\lambda$ ,  $t$ ,  $L$ ,  $s$  and  $\rho$  are the eigen value for the fundamental mode, the thickness and length of the cantilever, the elastic compliance constant, and the density.<sup>6</sup> For Si cantilever beams of different lengths and nominally the same thickness and width, the resonance frequencies were measured with an AC field of 10 mV and no applied bias. The results are shown in Fig. 3, where the measured fundamental resonance frequencies are plotted as a function of  $1/L^2$ . By fitting a straight line to the data which passes through the origin, an  $R$  value of 0.9994 was obtained. The resulting linear equation was then used to calculate the effective  $s_{11}$  coefficient for a beam. An average density of  $2.75 \times 10^6 \text{ gm}^{-3}$  was calculated using experimentally determined thicknesses and handbook densities for the Si,  $\text{Si}_3\text{N}_4$ , Pt, and  $\text{SiO}_2$  layers. The effective  $s_{11}$  constant was determined to be  $14.1 \times 10^{-12} \text{ m}^2\text{N}^{-1}$ . This value is close to the value for bulk PZT of the morphotropic boundary composition, being  $13.8 \times 10^{-12} \text{ m}^2\text{N}^{-1}$ .<sup>6</sup> The value for silicon is  $9.34 \times 10^{-12} \text{ m}^2\text{N}^{-1}$ .<sup>7</sup> One might expect the calculated value to be nearer to that of silicon, however due to difficulties in accurately determining the average density and the role of residual internal stresses (the cantilevers have a slight upward curvature due to stress) the calculated value is reasonable.

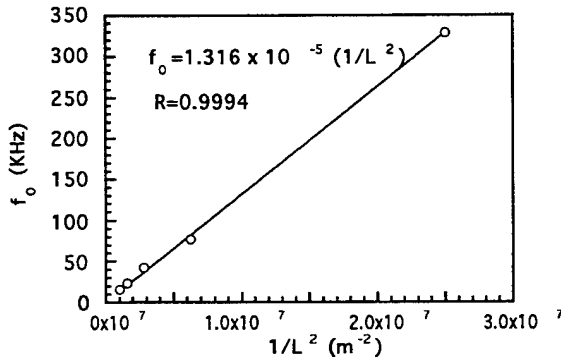


Fig. 3 Fundamental resonance frequency of cantilevers of different aspect ratios plotted as a function of  $1/L^2$ , with equation for best fit line through the origin. See text for details.

The effective electromechanical coupling coefficient  $k_{31}$  can also be determined from resonance data. The coupling factor,  $k_s$  of the test structures is given by (2).<sup>2</sup>

$$k_s = \sqrt{\frac{\pi^2 \Delta f \Delta |Z|}{8 f_0 |Z_0|}} \quad (2)$$

with the different values as indicated in Fig. 4.

The effective coupling factor  $k_{31}$  of the piezoelectric film is then given by:

$$k_{31} = \sqrt{\frac{t}{3d}} k_s \quad (3)$$

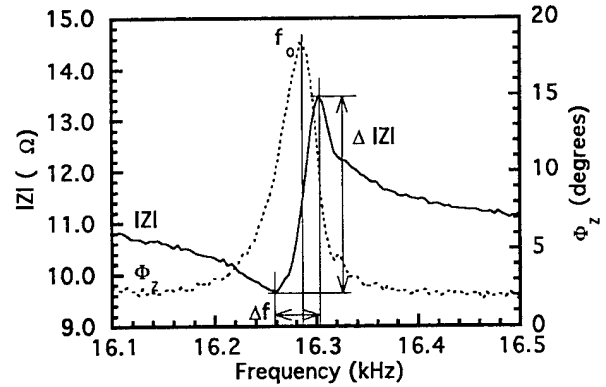


Fig. 4 Typical experimental resonance curve for PZT thin film actuated cantilever beam. The parameters indicated are used to calculate the coupling factor,  $k_s$ , as given by equation (2). This data was obtained from a cantilever of aspect ratio 5, driven with a 10 mV signal, with 10 V bias.

where  $t$  is the beam thickness and  $d$  the thickness of the PZT thin film. The effect of bias voltage on  $k_{31}$  for a beam of aspect ratio 5, measured with a 10 mV signal is shown in Fig. 5. The data is symmetric, although centered about a negative bias of 2 to 3 V. This shift is believed to result from some poling of the PZT film which occurs during the final plasma etching of the cantilever beams. We also note that with decreases of the bias voltage, some hysteresis is present, and the value returns to essentially the non-biased or virgin state. This can be seen clearly in Fig. 6, in which the resonance peaks for increasing bias field and after removal of the bias are superimposed. As shown in Fig. 5, and Fig. 7, the maximum values of  $k_{31}$  obtained were about 0.15. This is about 1/2 of that reported for bulk PZT samples of the same composition.

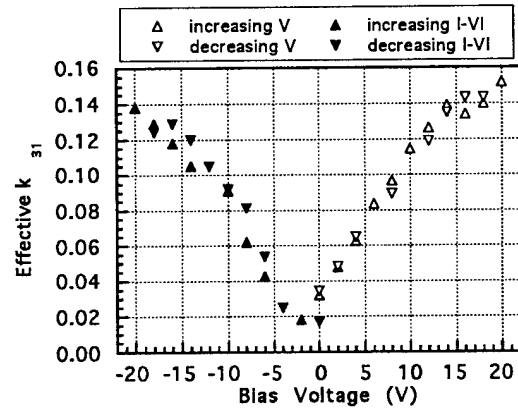


Fig. 5 Effective  $k_{31}$  as a function of bias voltage for cantilever of aspect ratio 5 (see text for details).

The effect of cantilever aspect ratio on  $k_{31}$  as a function of positive bias voltage is shown in Fig. 7. For beams with aspect ratios of 1, 3 and 5, almost identical trends and values were observed.

It was further observed that electrical breakdown occurred for bias fields in excess of approximately 750 kV/cm. The dielectric constant of the PZT films was found to be approximately 540, measured at 10 kHz and 10 mV signal.

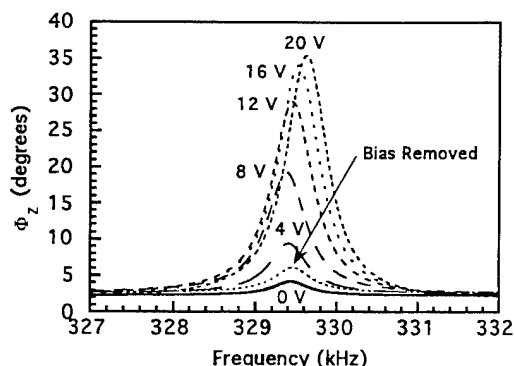


Fig. 6 Resonance peaks for increasing bias, and after removal of bias voltage showing the slight poling effect of the bias. Cantilever of 1:1 aspect ratio, with 500mV measuring signal.

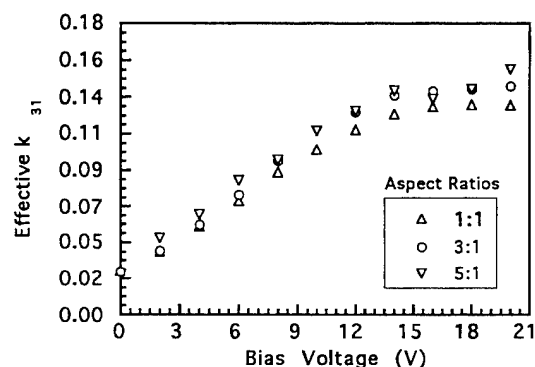


Fig. 7 Effective  $k_{31}$  as a function of positive bias voltage for cantilevers of aspect ratios 1, 3 and 5.

## CONCLUSIONS

In this paper we have reported on initial resonance experiments to determine the piezoelectric properties of PZT actuated micromachined cantilever beams. The resonance frequency was found to fit well to the expected  $1/L^2$  dependence for the measured beams of aspect ratios between 1 and 5. The effective  $k_{31}$  coefficient was determined using the resonance technique. A maximum  $k_{31}$  of 0.15 was measured, which is about 1/2 of the value reported for bulk ceramics. The functional dependence of  $k_{31}$  on bias voltage and the absolute values obtained were found to be independent of cantilever aspect ratio over the range investigated. This relatively simple method is a powerful tool for investigating the piezoelectric response of PZT thin film actuated microdevices.

## ACKNOWLEDGMENTS

Funding for this project was by the Swiss government through the M2S2 (groupement de laboratoires pour la micromécanique sur silicium en Suisse) program and by CEPF (Program Prioritaire Matériaux).

## REFERENCES

- [1] P. Schiller and D.L. Polla, "Integrated Piezoelectric Microactuators Based on PZT Thin Films," in *Proceedings of the 7th International Conference on Solid State Sensors and Actuators*, 1993, pp.154-157.
- [2] J. L. Deschanvres, P. Rey, G. Delabouglise, M. Labeau, J. C. Joubert, and J. C. Peuzin, "Characterization of Piezoelectric Properties of Zinc Oxide Thin Films Deposited on silicon for Sensors Applications," *Sensors and Actuators A*, vol. 33, pp.43-45, May, 1992.
- [3] K. Brooks, D. Damjanovic, A. Kholkin, I. Reaney, N. Setter, P. Luginbuhl, G.-A. Racine, N. F. de Rooij, and A. Saaman, "PZT Films for Micropumps," in *Proceedings of the 6th International Symposium on Integrated Ferroelectrics*, 1994, in press.
- [4] K.D. Budd, S.K. Dey and D. A. Payne, "Sol-Gel Processing of  $\text{PbTiO}_3$ ,  $\text{PbZrO}_3$ , PZT, and PLZT Thin Films," *Brit. Ceram. Proc.*, vol. 36, pp.107-121, October 1985.
- [5] G.-A. Racine, R. Luthier, P. Luginbuhl, K. Brooks, N. Setter and N.F. de Rooij, "Hybrid Ultrasonic Elastic Force Motors Micromachined in Silicon," in *Proceedings of the 6th International Symposium on Integrated Ferroelectrics*, 1994, in press.
- [6] L. Kiesewetter and J.-M. Zhang, D. Houdeau and A. Steckenborn, "Determination of Young's Moduli of Micromechanical Thin Films Using the Resonance Method," *Sensors and Actuators A*, vol. 35, pp.153-159, December 1992.
- [7] J. M. Herbert, *Ferroelectric Transducers and Sensors*, New York: Gordon and Breach, 1982, appendix B, p.395.
- [8] S. P. Murarka and M. C. Peckerar, *Electronic Materials, Science and Technology*. New York: Academic Press, 1989, appendix 4, p. 595.

# Fatigue and Retention Behaviors of Pt-PZT-Metal Capacitors with Various Top Metallizations

G. TEOWEE, E.L. QUACKENBUSH, C.D. BAERTLEIN  
Donnelly Corp., 4545 E. Fort Lowell Rd., Tucson, AZ 85712

J.M. BOULTON and D.R. UHLMANN,  
Arizona Materials Laboratories, Department of Materials Science and Engineering, Tucson, AZ 85712

**Abstract** - The PZT-substrate or PZT-electrode interface can affect the FE properties and specifically the fatigue behaviour. Typical Pt-PZT-Pt capacitors exhibited fatigue resistance up to  $10^8$  -  $10^9$  cycles, while  $\text{RuO}_2$ ,  $\text{La}_{0.5}\text{Sr}_{0.5}\text{CoO}_3$  and  $\text{YBa}_2\text{Cu}_3\text{O}_7$  electrodes have been reported in literature to yield fatigue-free devices up to  $10^{11}$  -  $10^{12}$  cycles. In an early study which compared the fatigue behaviour of bulk PLZT ceramics with various metal electrodes, it was found that In offered the best fatigue performance (up to  $10^9$  cycles). A series of sol-gel derived PZT 53/47 films were fired to 700C to achieve single-phase FE perovskite films. Bottom electrode (or the substrate) consisted of sputtered Pt on oxidized Si wafers. Monolithic capacitors were obtained by depositing top electrodes of Ag, Au, Au-Pd, Pd and Pt. All the capacitors exhibited fatigue, manifested by lower values of  $P_r$ ,  $E_c$  and  $\epsilon_r$ , but higher leakage currents after cycling.

## INTRODUCTION

Lead zirconate titanate (PZT) is an extensively explored ferroelectric (FE) material in thin film and bulk forms, utilized in a wide range of applications [1]. It is a solid solution containing lead titanate (PT) and lead zirconate (PZ) in various stoichiometric ratios. PZT x/y refers to  $\text{Pb}(\text{Zr}_{x/100}\text{Ti}_{y/100})\text{O}_3$  where  $x, y \leq 100$  and  $x + y = 100$ . In the PZ-PT phase diagram, the rhombohedral-tetragonal boundary is the most important feature, termed the morphotropic phase boundary (MPB). It is located at about 53 atom % Zr, 47 atom % Ti (PZT 53/47). The dielectric constant, electromechanical coupling factor and piezoelectric coefficients achieve their maximum values here [1]. Lately, PZT thin films have been investigated for applications in non-volatile FE memory and ultra high density DRAM's.

Fatigue and retention problems in PZT films remain formidable obstacles towards the full implementation of integrated FE technology. Fatigue refers to the dynamic degradation of FE and dielectric properties (especially polarization values) with cycling or switching while retention pertains to the static loss of polarization with standing time. Both of these phenomena affects the sensing capabilities of circuitries involved in FE memory. There have been many models postulated for the origin of fatigue which include PZT - electrode interface [2], impurity vacancy pairs [3], space charge effects [4], metallic diffusion from electrodes [5] and microcracking at interface [5,6]. Defects in the films such as oxygen and lead vacancies, play an important role in fatigue since they are mobile under electrical stress and can migrate (and further trapped) at PZT-electrode interfaces or grain/domain boundaries [e.g. 7]. A model of the formation of oxygen-deficient  $\text{Ti}^{3+}$  dendrites due to impact ionization has also been proposed [8]. While each of the model fits one particular set of experimental data, there exists **no universally-accepted model or explanation** for the general phenomenon of fatigue behaviour. One complication which arises is the dependence of fatigue on several intrinsic and extrinsic factors namely the crystal structure (i.e. tetragonal or rhombohedral lattices dictated by the Zr/Ti stoichiometry), grain size, film thickness, porosity (intra and intergranular) and phase assembly. For examples, thicker PZT films (up to 8000Å) seemed to exhibit

no fatigue until  $10^{12}$  cycles [9] and (111)-oriented films [10] exhibited better fatigue resistance than c-axis or (001)-oriented PZT films [11]. The fatigue rate also depends on the composition of PZT films - MPB films exhibited the lowest rate and tetragonal PZT showed the highest rate while rhombohedral PZT offered intermediate rate [12]. However, on the contrary, it was also reported that the MPB films exhibited the worst fatigue and retention behaviours [13]; apparently processing conditions, especially post-metallization annealing affected the fatigue resistance.

The fatigue behaviour in PZT films indicates that it is an interfacial phenomenon rather than a bulk one. The PZT-substrate interface has been reported to affect significantly the FE properties and specifically the fatigue behavior. The bottom electrode (or the substrate) is typically a noble metal, namely Pt and/or Au which is inert towards oxidation. Oxide electrodes, namely  $\text{RuO}_2$  and  $\text{YBa}_2\text{Cu}_3\text{O}_7$ , have attracted considerable recent attention [e.g., 14 and 15 respectively]. Such electrodes were reported to yield excellent fatigue-free PZT films up to  $10^{10}$  -  $10^{11}$  cycles. In an earlier study, Fraser and Maldonado [5] compared the fatigue behavior of bulk PLZT ceramics with various metal electrodes namely Al, Cr-Au, Pb, PbO-Ag, Sn-Ag, Ag, Ga and In and found that In provided the best fatigue performance (up to  $10^9$  cycles).

There is presently a lack of studies directed to exploring systematically the effect of different metallization on thin film FE capacitors. The present authors have studied the effect of top electrodes on the dielectric and FE properties of solgel derived PZT capacitors in a previous paper [16]. In contrast, there have been numerous studies forming low resistance ohmic contacts to bulk FE or titanate ceramics using e.g., Ni, Ag/Au, Cu and Co/Ag [e.g., 17 and 18] for bulk capacitor applications. By varying the top metallization while maintaining the lower substrate constant (namely Pt), the nature of the top metal-PZT interface can be determined especially by changing the polarity of the applied field. The present paper presents the results of using various top noble metal electrodes on the fatigue and retention properties of sol-gel derived PZT thin films.

## EXPERIMENTAL

The precursor solutions based on the MPB composition (namely PZT 53/47) were prepared using Pb acetate and Ti/Zr alkoxides. Fifteen mole % excess PbO was incorporated in the precursor to compensate for PbO loss during post-deposition annealing. The substrates were Si(100) wafers which had been thermally oxidized before being sputtered with Pt to yield Pt (1500Å) /  $\text{SiO}_2$  (1500Å) / Si. Spincoating was performed using a Headway Spinner at 2000 rpm for 30s. The precursor solution was filtered using a syringe filter (0.2µm) to minimize particle contamination. The green films were fired at 400C to burn off the organics, yielding films  $\approx$  2000Å thick per coating. To obtain thicker films, multiple coatings were performed. Typically, three coatings were used to obtain films about 0.6µm thick. Finally, the



films were fired at 700C to crystallize them to single-phase perovskite.

Top electrodes of Ag, Au and Pd with thicknesses of 1500Å and diameters of 0.5 mm were evaporated through a shadow mask using a Varian Vacuum Evaporator VE 10. The top Pt and Au-Pd electrodes were sputtered. The monolithic PZT capacitors were completed by obtaining back-contact by acid-etching exposed portions of the films which had been coated with an acid resist. The acid resist was removed by rinsing with toluene. These capacitors were not subjected to any post-metallization annealing prior to testing. The final device configuration for the capacitor arrays is shown in Figure 1.

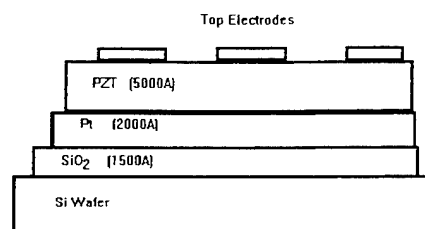


FIGURE 1 Device configuration for the Pt-PZT-top metal electrodes

The phase assembly in the films was monitored by x-ray diffraction (XRD) using a Scintag Diffractometer. The area of most of the capacitors used for electrical characterization was  $1.96 \times 10^{-3} \text{ cm}^2$ ; the dielectric properties were obtained using an HP 4192A LF Impedance Analyzer; and the FE properties, including the fatigue and retention behaviors, were measured using the programs FATIGUE and RETAIN in a Radiant Technologies RT-66A Ferroelectric Test System. Some of the ageing behaviours of the capacitors were observed using the program AGEING. An external SRI 30MHz function generator was used to cycle the capacitors up to  $4 \times 10^9$  cycles with 10V peak-to-peak 100KHz sine waves. For retention measurements, -5V, +5V and -5V pulses were used for first read, write and second read.

## RESULTS AND DISCUSSION

A typical microstructure of these films showed that the films were very dense with grain size of around 1 - 2  $\mu\text{m}$ . XRD results indicate that the PZT 53/47 films fired to 700C were confirmed to be single-phase perovskite and are ferroelectric as evident by the hysteresis loops obtained in the capacitors. However, the hysteresis loop characteristics were different for each top metal as indicated in Tables 1a and b which shows the values of the remanent polarization ( $P_r$ ), coercive field ( $E_c$ ) and dielectric constant ( $\epsilon_r$ ) before and after fatigue for  $4 \times 10^9$  cycles

respectively measured using the RT 66A Ferroelectric Test System. The FE values represent the average values of the positive and negative values in the hysteresis loops. Not only did firing temperature, firing time and composition (i.e. Zr/Ti stoichiometry) affect the film properties but the choice of top electrode used also impacted on the ferroelectric properties [13,16]. The effects of fatigue can be clearly observed namely the decreases of the values of  $P_r$ ,  $E_c$  and  $\epsilon_r$ . Pd and Au/Pd top electrodes yielded PZT capacitors with the highest values of  $P_r$  but they tended to deteriorated quite dramatically with cycling. There also was a general shift in the hysteresis loop to the left along the field axis after cycling indicative of built-in field arising from probably space-charge build-up during fatiguing. Pt-PZT-Au capacitors seemed to fatigue the least as indicated by the relatively small decline of  $P_r$ ,  $E_c$  and  $\epsilon_r$  compared to when other top electrodes are used. The dependence of fatigue behavior on the top electrode used can be attributed to the PZT-top metal interface[ see e.g. 16].

Table 1a. Ferroelectric Properties of PZT Capacitors with various top electrodes before fatigue.

Top Metal	$P_r$ ( $\mu\text{C}/\text{cm}^2$ )	$E_c$ (kV/cm)	$\epsilon_r$
Ag	12.39	26.28	3591
Au	9.04	24.59	2579
Au-Pd	39.98	18.74	7678
Pd	34.72	39.33	5879
Pt	11.57	22.21	3205

Table 1b. Ferroelectric Properties of PZT Capacitors with various top electrodes after fatigue

Top Metal	$P_r$ ( $\mu\text{C}/\text{cm}^2$ )	$E_c$ (kV/cm)	$\epsilon_r$
Ag	6.06	16.78	1678
Au	7.64	22.78	2279
Au-Pd	8.43	17.06	2746
Pd	5.65	20.82	4146
Pt	4.33	16.4	1670

The fatigue behaviours of the capacitors with different top metallizations are shown in Fig. 2. The criterion chosen to illustrate the effect of fatigue on polarization was the quantity  $\Delta P$  ( $= P^* - P^\wedge$  according to the RT 66a terminology) which reflected the difference in switched and unswitched charges [19] which is a better parameter to quantify fatigue behaviour rather than  $P_r$  since  $\Delta P$  is involved in differential sensing to detect charges during memory operation. All the capacitors exhibited a decrease in  $\Delta P$ 's with cycling after about  $10^7$  cycles; capacitors with Pd top electrodes seemed to degrade the most while capacitors with Au top electrodes were the least affected.

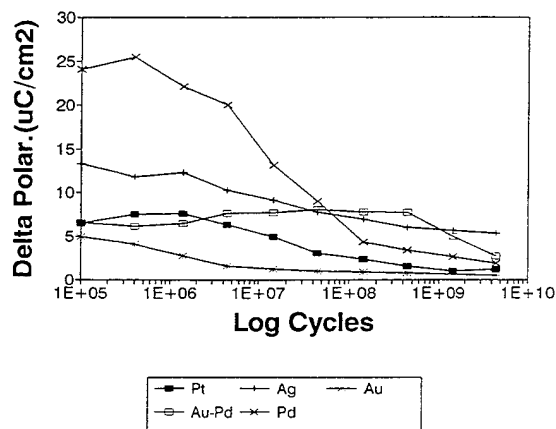


Figure 2. Effect of cycling on  $\Delta P$ 's of PZT capacitors with various top metallizations.

The retention profile of the capacitors were fairly independent with time up to  $10^4$  secs as shown in Fig. 3. PZT capacitors with Pd and Pt top electrodes exhibited a slight decrease of  $P^*$  with time while  $P^*$  in capacitors with Au top metallizations was very stable with time. Ageing of a Pt-PZT-Pt capacitor was investigated using the AGEING program with RT 66A and the results are shown in Figure 4. Quite similar to the retention profile, the ageing profile remained constant with time (measured up to  $10^4$  secs).

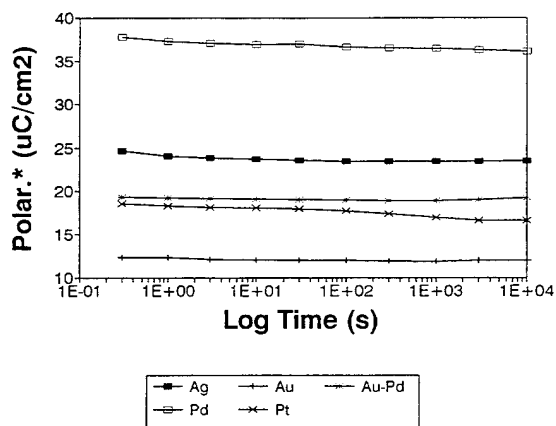


Figure 3. Retention profiles of PZT capacitors with various top electrodes as a function of time.

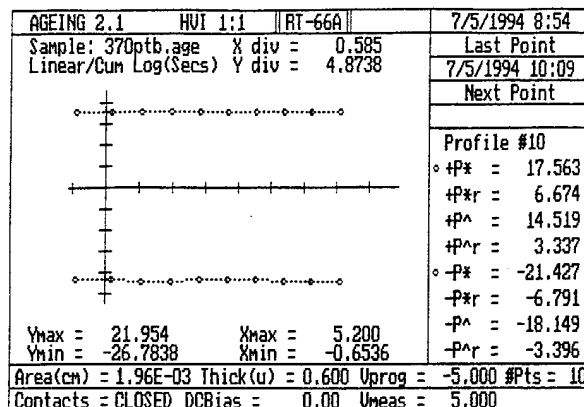


Figure 4. Ageing profile of a Pt-PZT-Pt capacitor up to  $10^4$  secs.

The leakage currents of the capacitors tended to increase after fatigue as shown in Fig. 5 for the case of a Pt-PZT-Pd capacitor; the increase of about 1 order of magnitude after cycling for  $4 \times 10^9$  cycles can impact deleteriously on overall microcircuitry performance in real devices employing such integrated FE capacitors.

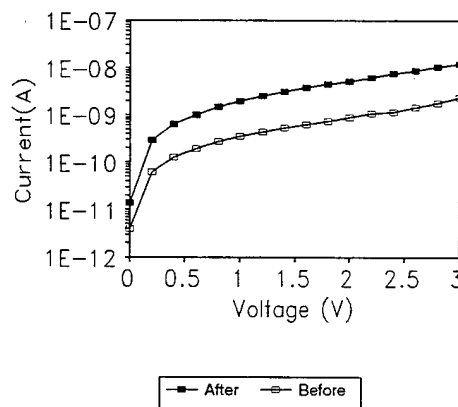


Figure 5. The I-V characteristics of a Pt-PZT-Pd capacitor before and after fatiguing for  $4 \times 10^9$  cycles.

## CONCLUSIONS

Pt-PZT-top metal capacitors were prepared using top electrodes of Ag, Au, Au-Pd, Pd and Pt based on PZT 53/47 films which were fired to 700C to convert them into single-phase perovskite films. There exists a strong dependence of ferroelectric

and dielectric properties of these capacitors on the top metal used indicating the significance of the PZT - top electrode interface in affecting device behaviours. All the capacitors investigated in the present study fatigued; the values of  $P_r$ ,  $E_c$  and  $E_r$  decreasing while the leakage currents tended to increase after  $4 \times 10^9$  cycles with the capacitors containing Au top electrodes having the most fatigue resistance. The retention and ageing profiles of the capacitors, on the other hand, were quite stable with time.

### ACKNOWLEDGEMENTS

The financial support of both Donnelly Corporation and the Air Force Office of Scientific Research is gratefully acknowledged.

### REFERENCES

1. B.Jaffe, W.R.Cook and M.Jaffe, Piezoelectric Ceramics, Academic Press, 1971.
2. I.P.Batra, P.Wurfel and B.D.Silverman, *Phy. Rev. Lett.*, 30, 384(1971).
3. G.H.Jonker, *J. Amer. Ceram. Soc.*, 55, 57(1972).
4. R.H.Plumlee, Sandia Labs Rep. SC-RR-67-730(1967).
5. D.B.Fraser and J.R.Maldonado, *J.Appl. Phys.*, 41, 2172(1970).
6. Q.Jiang, W.Cao and L.E.Cross, *J.Amer. Cer. Soc.*, 77, 211(1994).
7. I.K.Yoo and S.B.Desu, *Mater. Sci. & Eng. B13*, 319(1992).
8. H.M.Duiker, P.D.Beale, J.F.Scott, C.A.Paz de Araujo, B.M.Melnick, J.D.Cuchiaro and L.D.MacMillan, *J.Appl. Phys.*, 30, 2149 (1990).
9. K.Iijima, I.Ueda and K.Kagimaya, *Jpn. J. Appl. Phys.*, 30, 2149(1991).
10. S.A.Mansour and R.W.Vest, *Integ. Ferroelectrics*, 1, 57(1992).
11. H.N.Al-Shareef, K.D.Gifford, M.S.Ameen, S.H.Ron, P.D.Hren, O.Auciello and A.I.Kingon, *Ceram. Trans.*, 25, 97(1990).
12. A.R.Modak and S.K.Dey, *Proc. 1st Cer. Sci & Tech. Congress*, 1989.
13. G.Teowee, J.M.Boulton, M.N.Orr, C.D.Baertlein, R.K.Wade, D.P.Birnie III and D.R.Uhlmann, *MRS Symp. Proc.*, 310, 423(1993).
14. S.D.Bernstein, T.Y.Wong, Y.Kisler and R.W.Tustison, *J.Mater. Res.*, 8, 12(1993).
15. R.Ramesh, W.K.Chan, B.Wilkens, T.Sands, J.M.Tarascon and V.G.Keramidas, *Integ. Ferroelectrics*, 1,
16. G.Teowee, C.D.Baertlein, E.A.Kneer, J.M.Boulton and D.R.Uhlmann, to be published in *Cer.Trans.*, 1994.
17. S.Wada and F.Ishiguro, *Jpn. Kokai* 75 84 896, July 1975.
18. R.Ashida, R.Urahara and N.Mori, *Jpn. Kokai* 75 38 095, April 1975.
19. Operating manual for RT66A Ferroelectric Test System, Radiant Technologies.

# ELECTRODE STRESS EFFECTS ON ELECTRICAL PROPERTIES OF PZT THIN FILM CAPACITORS

Ilsub Chung, I.K. Yoo, W. Lee, C.W. Chung, and J.K Lee

*Samsung Advanced Institute of Technology, Kyeheung, Kyungki, Korea*

Seshu B. Desu

*Department of Materials Science and Engineering, VA Tech., Blacksburg, VA 24061*

## Abstract

It is well known that electrode/ PZT interface affects the electrical properties of PZT thin film capacitors. Electrode stress is one of the key parameters which determine the interface characteristics. Here we report the effects of bottom electrode stress on the properties of Pt/PZT/Pt capacitors. PZT films were deposited by MOD method on Pt/Ti/SiO<sub>2</sub>/Si substrates with various bottom electrode stresses. Structural and compositional analyses were made by TEM/TED, XTEM, XRD. Stress variations due to subsequent processing steps were measured by using laser deflection method. Finally, electrical properties were evaluated by testing hysteretic properties, fatigue, and leakage current. Guidelines for reliability improvement of PZT thin film capacitors can be made by correlating the above results.

## Introduction

Extensive studies are being carried out on ferroelectric thin films for the applications in DRAMs as well as non-volatile memory[1,3]. Among the various ferroelectric materials, much attention has been paid to PZT family films due to their promising properties[4]. However, there are several problems that should be overcome to realize the integration of these into semiconductor devices. One of the associated problems is to establish a suitable metallization scheme for the ferroelectric capacitor. The choice of the electrode material is restricted by the interaction between the ferroelectric material and electrode at the processing temperatures involved even though a principle requirement is a high electrical conductivity. So far, platinum is widely used as the electrode due to its processing simplicity. Yet, there are some important issues in connection with the use of platinum as an electrode for PZT families. One of those is a fatigue phenomenon which is a progressive decrease in the remanent polarization as signal cycles. It is believed that intrinsic defects such as oxygen vacancies are likely to determine the fatigue rates of ferroelectric capacitors in conjunction with ferroelectric-electrode interface as well as domain mobility[5]. Thus, many effort to control vacancy concentrations as well as interface states have been made to improve the fatigue characteristic. Other issues such as orientation, morphology, and stress are also attracting many attention related with the device performance[6,7]. Among them, stress is considered as one of the most important parameters that affects the properties of ferroelectric thin films. It is well known that high

tensile stresses cause either cracks or peelings of thin films, whereas compressive stresses above a certain limit result in hillock formations. Thus, the film thickness is limited by the stress of film, in particular, which is very critical in spin coating. In addition to the effects aforementioned, stresses also modify domain structure, Curie point, and switching properties. Such effects of the stress in ferroelectric films are further complicated by the electrostriction which is originated from piezoelectric effects. In spite of the importance of film stresses, only limited studies were available up to now. Desu investigated stresses of BaTiO<sub>3</sub> thin films which were sputter-deposited on both Si and Sapphire substrates[9]. He found that Curie point and coercive fields increase while remanent polarization decrease with increasing compressive stresses. On the other hand, Garino obtained higher residual stresses at pyrochlore formation temperature regions that was 500 °C to 570 °C [10]. They suggested that the films containing pyrochlore phase give higher residual stresses because a thermal expansion coefficient of the pyrochlore phase is larger than that of the perovskite phase. In this paper, we investigated the effect of an initial stress of the bottom electrode (Pt/Ti) on PZT fatigue behavior. We created various values of stresses in bottom electrode by changing the deposition conditions such as deposition temperature(T<sub>d</sub>) and annealing temperature(T<sub>a</sub>).

## Experimental Procedure

20 nm Ti and 200 nm Pt were sequentially sputter-deposited onto (111) oriented Si substrates, passivated with a thermally grown silicon dioxide (SiO<sub>2</sub>) layer. Films were made at different substrate temperatures ranging from 25 °C to 400 °C. Then, they were annealed at various temperatures ranging from 100 °C to 400 °C for 30 minutes in vacuum. Sol-gel derived PZT films were prepared from a metalorganic solutions of lead acetate, zirconium n-propoxide and titanium iso-propoxide dissolved in acetic acid and n-propanol. The solutions were hydrolyzed to form the precursor. About 10% excess lead was added to the precursor to compensate for the loss of lead during a high temperature processing. Films were spin coated at 2000 rpm for 40 sec. and subsequently dried at 150 °C for 5 minutes. The same cycle was repeated to obtain desired thickness of 200 nm. The coated films were annealed at 650 °C for 30 minutes in a quartz tube furnace under an oxygen atmosphere. Microstructure and interdiffusion were examined by transmission

electron microscopy. X-ray diffraction was used to identify phase and to determine a preferred growth orientation. Thin film stress was calculated from wafer curvature measurements using FLEXUS. The electrical measurements such as hysteresis loop, fatigue were done by utilizing RT66A and HP8116A pulse generator. A 30  $\mu\text{m}$  X 30  $\mu\text{m}$  size of capacitor patterns were obtained by dry etching using ion-milling machine. The fatigue measurements were done by applying square waves at 5V and 1 MHz.

### Results and Discussion

The evolution of stresses of Pt/Ti films are shown in Fig 1.(a) and Fig 2.(b) as a function of either the deposition temperature ( $T_d$ ) or the annealing temperature ( $T_a$ ). Most sputter-deposited Pt/Ti films were in a state of compressive stress. In addition, the stress tended to decrease as the deposition temperature increased at a constant annealing temperature. We attempted to interpret our results based on a simple stress equation. The total stress is given by the sum of the intrinsic stress( $\sigma_i$ ), thermal stress( $\sigma_t$ ), and external stress ( $\sigma_e$ ). If we assume that the contribution from the external stress term is negligible, stress variations come from the first two terms, namely, the intrinsic stress( $\sigma_i$ ) and the thermal stress( $\sigma_t$ ). Since the thermal expansion coefficient of Pt is much larger than that of Si, most sputter-deposited Pt films are in a state of compressive stresses due to the dominant effect of the thermal stress term. However, above the substrate temperature of 300  $^{\circ}\text{C}$ , we found our assumption is not valid because the external stress term is necessary to compensate for the large value of the thermal stress in order to be the tensile stress. The existence of the external stress indicates that a certain reaction takes place at the interface between Pt and Ti layer, which was indicated earlier in literature[11].

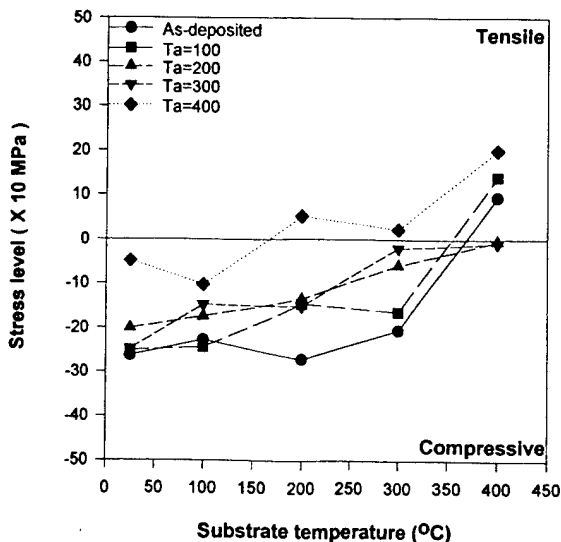


Figure 1.(a) Stress variations with respect to deposition temperatures

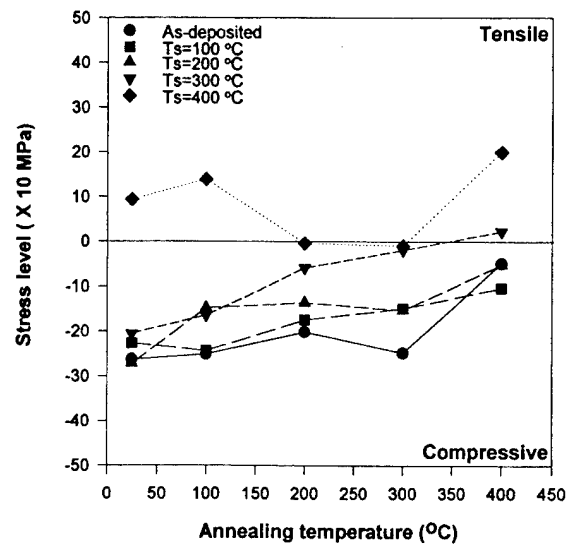


Figure 1.(b) Stress variations with respect to annealing temperatures

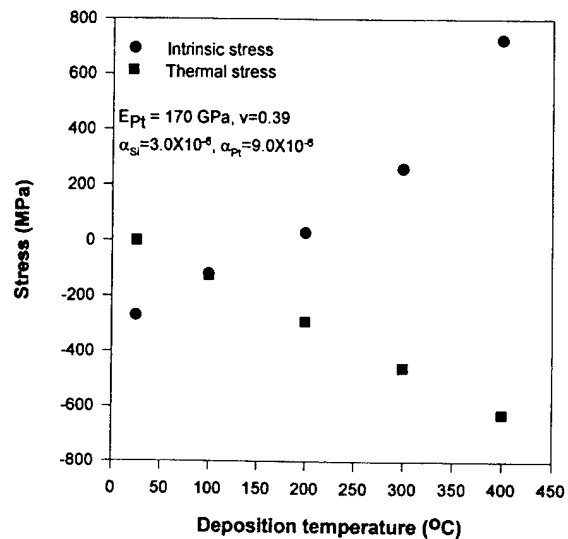


Figure 2. Thermal stress and intrinsic stress variations based on calculation

The tendency stress reduction with the increasing the deposition temperature can be explained by the role of intrinsic stress. The variation of intrinsic stress as the function of the deposition temperature is given in Fig. 2. Since the mobility at the surface during the deposition is determined by the deposition temperature, the mobility increases as the deposition temperature increases. The enhanced mobility shifts the intrinsic stress from compressive to tensile. This tensile stress compensates the compressive thermal stress as the deposition temperature increases thereby decreasing total stress as the deposition temperature increases. On the other hand, for a given deposition temperature, the stress decreases as the annealing temperature increases due to the stress relaxation.

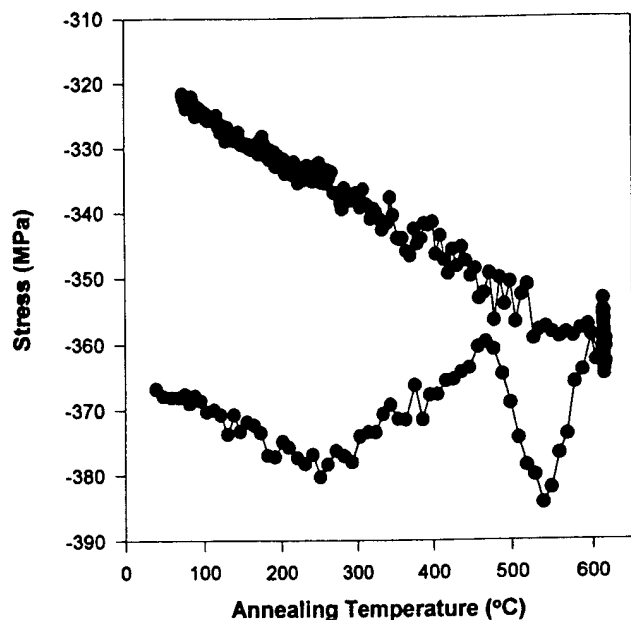


Figure 3. In-situ measured Pt/Ti stress variations due to annealing

The stress variation during heating and cooling cycle is given in Fig. 3, which was measured from as-deposited sample. Pt/Ti film responds elastically until the annealing temperature reaches to 250 °C. A sudden change in the stress appeared near 250 °C, which resulted from a deformation associated with a constrained volume shrinkage. This trend continued from 250 °C to 500 °C. Another abrupt change in Pt film stress happened near 500 °C due to the reaction at the interface between Pt and Ti layer. There was a relaxation in stress, as the annealing temperature is increased further. Finally, Pt/Ti film followed the elastic respond during the cooling cycle. The fatigue behaviors with respect to different electrode stresses are given in Fig. 4. The average fatigue cycle was around  $10^6$  -  $10^7$  depending on the deposition conditions of Pt films. That is in agreement with most of the reported data obtained from ion-milled samples. Interestingly, we found that the better fatigue behaviors were obtained at a certain region of compressive stresses. Higher compressive samples yielded worse fatigue properties than that of lower compressive stress. It is not clear yet how the stress of the electrode affects the fatigue characteristics. As shown in Fig. 5, we did not observe any structural differences in X-ray diffraction patterns even though the deposition temperature was changed from 25 °C to 400 °C. Furthermore, the X-ray data obtained from PZT films also showed no differences (see Fig. 6). Thus, we suggest that the interface modification resulted from the electrode stress that affects either PZT nucleation process or PZT domain formations. In other words, the surface roughness of the bottom electrode which might have been modified by the stress is likely to relate to the grain size of PZT film. In Fig. 7. a high resolution cross-section image

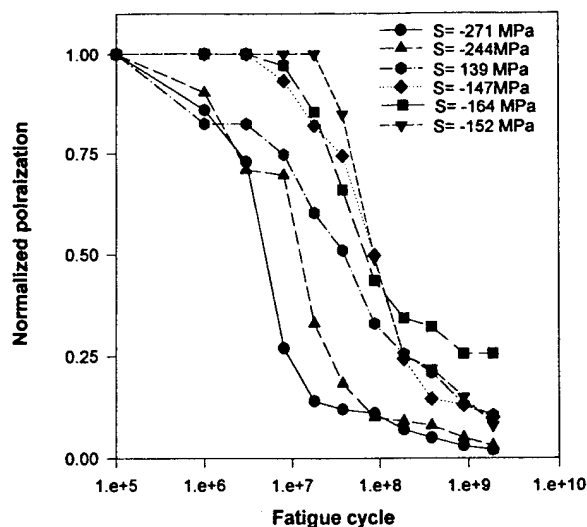


Figure 4. Fatigue behaviors with different values of stresses

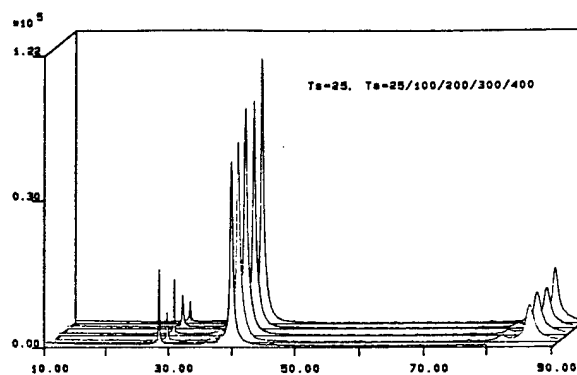


Figure 5. X-ray diffraction patterns obtained samples annealed at different temperatures

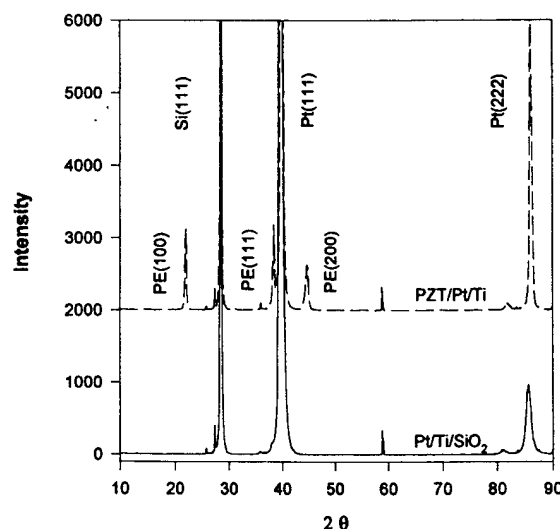


Figure 6. X-ray diffraction patterns for Pt/Ti and PZT/Pt/Ti film

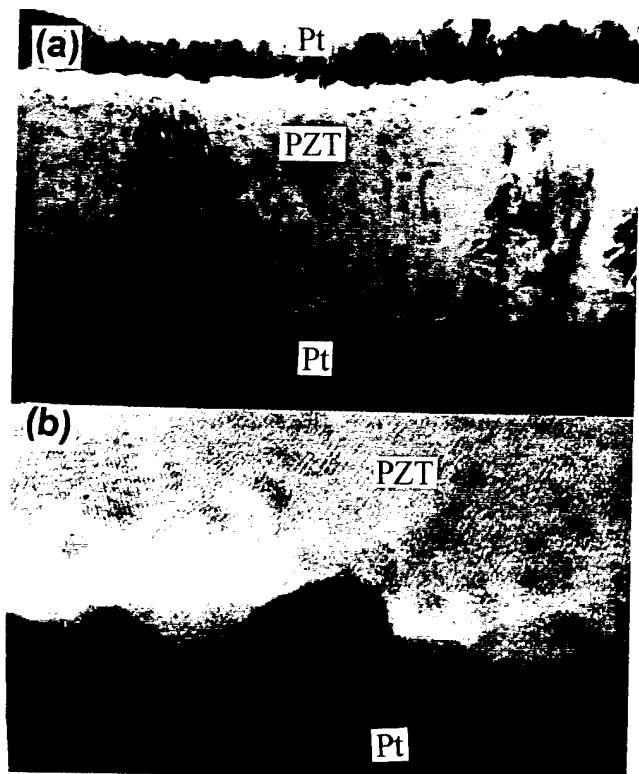


Figure 7. TEM cross-sectional images  
(a) bright field image  
(b) high resolution lattice image

showed a rough interface which was probably created by the stress. Another observation which would support our approach is that the Pt peak shift after the formation of PZT film. Pt(111) and Pt(222) peaks obtained before and after PZT deposition are given in Fig. 8. In this figure, both Pt(111) and Pt(222) are shifted to the higher  $2\theta$  values. Since the d-spacing is inversely proportional to  $2\theta$ , the decrease in d-spacing means a compressive stress in 111 direction. Such a vertical stress suggests a shrinkage in the film thickness thereby causing the roughness in the bottom electrode surface.

#### Summary and conclusion

We investigated the effects of the initial stress of the bottom electrode (Pt/Ti) on PZT fatigue behavior. Higher compressive stresses yield worse fatigue properties than those of lower compressive stresses. Similarly, the films which are in a tensile stress also showed an early degradation in spite of a slight improvement in fatigue property compared to highly compressed samples. It is not clear yet how the stress of bottom electrode influenced the fatigue behavior. However, we suggest that it is related with the PZT film nucleation process. Further detailed studies are being undertaken to study the interface modification due to the bottom electrode stress.

#### References

- [1] J. Carrano, C. Sadhama, J. Lee, A. Tasch and W. Miller, IEDM-89 p.255,1989
- [2] J. Scott and C. Paz de Arauzo, Science, 246, pp.1400, 1989
- [3] Gen H. Haertling, J. Vac. Sci. Technol. A, vol.9, no.3, pp.414-420
- [4] B. A. Tuttle, D. C. McIntyre, C. H. Seeger, T. J. Garino, W. L. Warren, J. T. Evans, and R. W. Waldman, Mater. Res. Soc. Symp. Proc. Vol. 310, pp.71, 1993
- [5] I. K. Yoo and S. B. Desu, Phys. Stat. Sol. A, Vol.133, PP.565-573, 1992
- [6] R. Ramesh, J. Lee, T. Sands, V. G. Keramidas and O. Auciello, App. Phys. Lett. Vol.64, no.19, pp.2511-2513, 1994
- [7] G. Spierings, M. Ulenaers, G. Kampschoer, H. A. M. van Hal, and P. K. Larsen, J. App. Phys. Vol.70, no.4, pp.2290-2298,1991
- [8] G. A. Rossetti, jr., L. Eric Cross, and K. Kushida, Appl. Phys. Lett. Vol. 59, no.20, pp.2524-2526, 1991
- [9] S. B. Desu, Phys. Stat. Sol. A, Vol.141, pp.119, 1994
- [10] T. J. Garino and Mark Marrington, Mat. Res. Soc. Proc. Vol. 243, pp.341-347, 1992
- [11] K. Sreenivas, Ian Reaney, T. Maeder, N. Setter, C. Jagadisch, and R.G. Elliman, J. Appl. Phys. Vol.75, no.1, PP.232-239, 1994

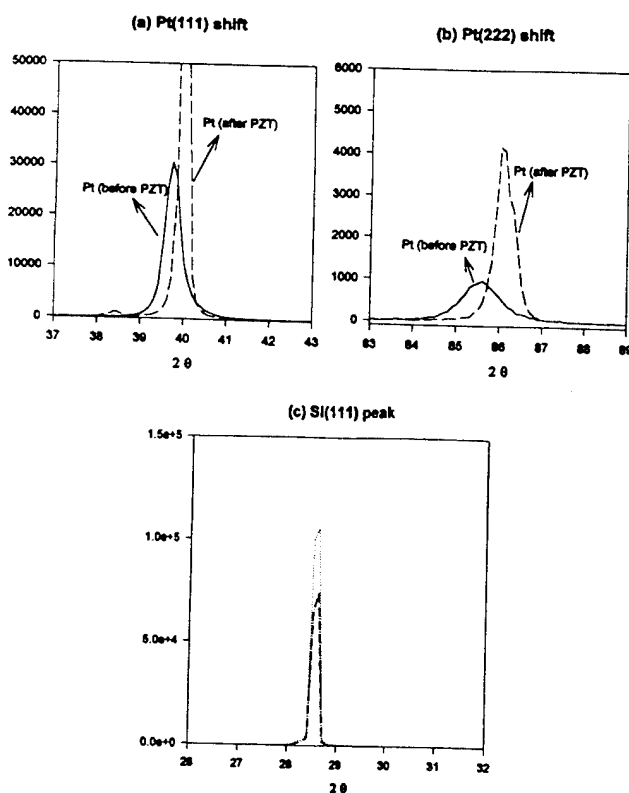


Figure 8. Pt X-ray peak shift after PZT deposition  
(a) Pt(111) peak shift  
(b) Pt(222) peak shift  
(c) Si peak before and after PZT deposition

# Breakdown in Lead Zirconate Titanate (PZT) Thin Film Capacitors

In Kyeong Yoo

Samsung Advanced Institute of Technology,  
San 14-1, Nongseo-ri, Kiheung-eup, Yongin-kun, Kyungki-do, 449-900, Korea

Seshu Babu Desu

Department of Materials Science and Engineering  
College of Engineering, VA Tech,  
Blacksburg, VA 24061, U.S.A.

## ABSTRACT

Lifetime of PZT capacitors was defined and evaluated by measuring critical number of cycles where electrical degradation (increase of leakage current) begins to dominate polarization during fatigue tests. It was observed that external failure (electrode burst) occurs during fatigue before electrical degradation at high voltage and/or temperature. The normal internal failure (electrical degradation and breakdown) is predominant at relatively lower voltage and/or temperature. PZT capacitors with smaller electrode size shows shorter lifetime, and gentler input cycles (triangular wave rather than square wave, for example) reduces external failure, which implies breakdown under AC input voltage is related to thermal process. It was noticed that fatigue mechanism is not directly related to thermal breakdown.

## INTRODUCTION

Since 64K PZT FRAM and 256K Y1 FRAM were developed, it has been realized that devices using FRAM are on the verge of commercialization. Radio frequency identification devices (RF ID), for example, are under development for the remote monitoring application. These devices require relatively low density in comparison with other memories such as DRAM and it is feasible to create niche market in a short period of time. However, reliability improvement of PZT and processing technologies of Y1 are still on issue for stable FRAM market, even for the low density devices. These issues will get more serious as density increases. As for PZT, fatigue, ageing, imprint, and leakage current have been studied extensively in order to understand their mechanisms for simultaneous improvement of each degradation. Breakdown, however, has been studied based on DRAM concept even though FRAM's operational condition is different from that of DRAM. For example, Time Dependent Dielectric Breakdown (TDDB) test is one of typical DRAM tests. In case of FRAM, alternating pulses or unipolar pulses are applied for both "write" and "read". Therefore, it is plausible to test breakdown under alternating and unipolar pulse stress. An accelerated fatigue/breakdown test (unified test) was proposed based on this concept[1,2]. In this test, asymmetric polarization and electrical degradation were observed simultaneously. But breakdown mechanism under this condition has not been fully understood. As set forth, many authors reported breakdown in PZT under DC conditions[3-8]. J.F. Scott et al provided an extensive discussion on PZT breakdown mechanisms[9], avalanche breakdown was invoked by B.M. Melnick et al[10,11], thermal breakdown mechanism in

strontium titanate film was extended to PZT by Waser and Klee[12]. As long as breakdown in PZT is evaluated using AC signals and/or unipolar pulses, these mechanisms should be also discussed in conjunction with such conditions. In this paper, breakdown evaluation technique was proposed by defining lifetime of ferroelectric capacitors. Breakdown mechanisms under AC voltage stress were also discussed.

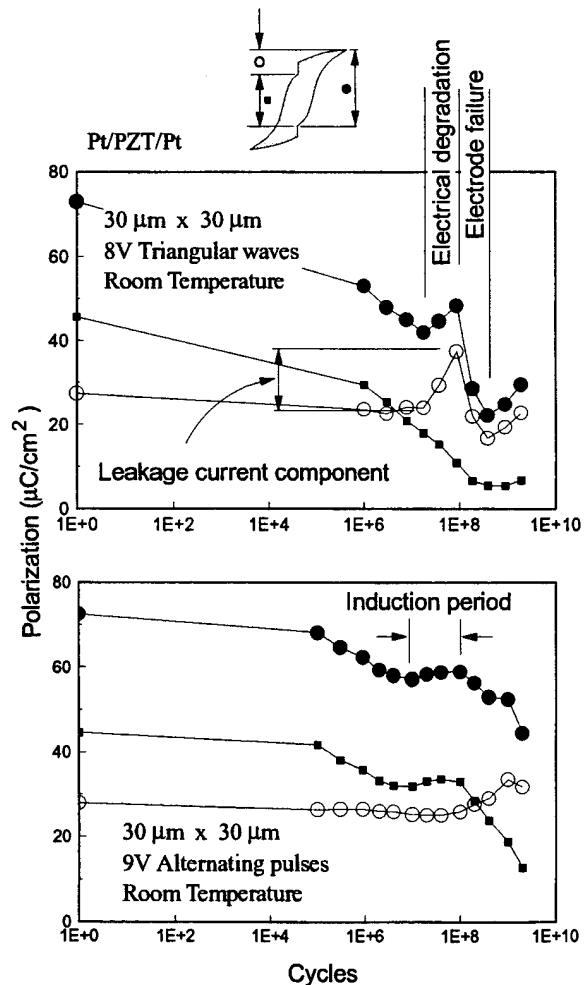


Figure 1

Effects of electrical degradation and external electrode failure on polarization measurements. Induction period is distinguished from electrical degradation by checking nonswitching polarization or net remanent polarization



## TESTS AND RESULTS

Sputtered PZT with three sizes ( $100\text{ }\mu\text{m} \times 100\text{ }\mu\text{m}$ ,  $50\text{ }\mu\text{m} \times 50\text{ }\mu\text{m}$ , and  $30\text{ }\mu\text{m} \times 30\text{ }\mu\text{m}$ ) of top electrode was tested by utilizing RT66A version 2.1 and HP8116A pulse generator. Polarization response at various test voltages, temperatures, and signal types were measured. An example of fatigue curve is shown in Figure 1, where switching ( $P^*$ ) and non-switching ( $P^A$ ) polarization and true remanent polarization ( $dP$ ) were plotted. In case of test using triangular wave, switching polarization decreases initially during fatigue, increases when leakage current begins to dominate polarization, and suddenly decreases again followed by second increase. It was observed that the top electrode bursts during such abrupt polarization loss. Figure 2 shows a typical burst on the electrode, which is a sort of burning and peeling. When this external failure occurs, effective contact area decreases and so does polarization, as a result. During electrical degradation, however, leakage current component may contribute to both switching and non-switching polarization but it does not affect true remanent polarization because this is measured at zero voltage, where leakage current cannot be involved. The electrical degradation can proceed even after electrode burst as long as input signals are applied, so that polarization curve increases again after sufficient electrode burst. Sometimes, polarization variation due to such electrical degradation and electrode burst is confused with polarization induction, because polarization in this period also appears to increase initially and decrease after a while. But, fortunately, since polarization induction occurs only in remanent polarization, the induction can be distinguished from electrical degradation/external failure by comparing true remanent polarization and/or non-switching polarization for each case. In summary, switching polarization is detected in parallel with non-switching polarization for the external failure, and with true remanent polarization for the polarization induction. The source of the induction is not so clear yet, but based on the fact that depolarization (transient polarization, rapid depolarization, or fast decay;  $P^A$  in RT66A parameters [13]) decreases during the induction period, it is thought that retentivity was improved by alternating signals in such a manner that linearly capacitive interlayer such as semiconductive vacancy layer [14] has become conductive during consecutive fatigue.

When test condition varies, the period when external failure occurs also changes. For example, as shown in Fig. 3, external failure appears before electrical degradation appears when square wave with higher voltage is applied, on the contrary, even at higher temperature, the external failure occurs after electrical degradation when triangular wave with lower voltage is applied. It is proposed, therefore, that accelerated unified test should be carried out on condition that external failures do not occur, because systematic evaluation can be interrupted by such an extreme failure.

## BREAKDOWN MECHANISM

Breakdown should be evaluated with no external failure in order to avoid false evaluation, as mentioned above. When the ferroelectric lifetime is defined as fatigue test

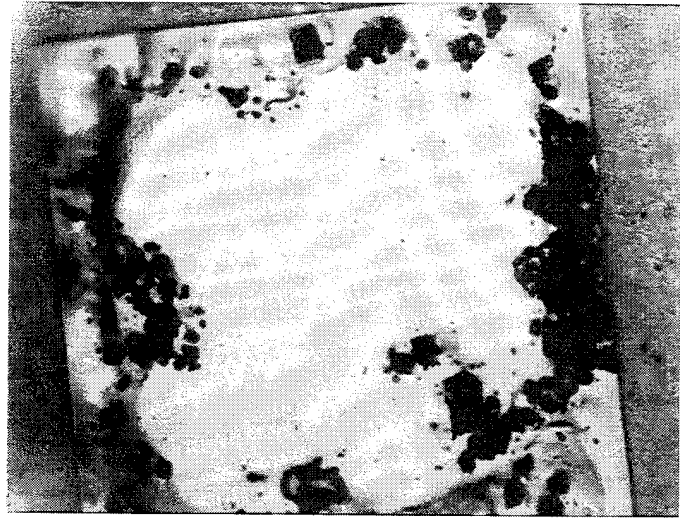


Figure 2  
Burst on top electrode during fatigue tests, which may be due to local heating by continuous voltage cycling.

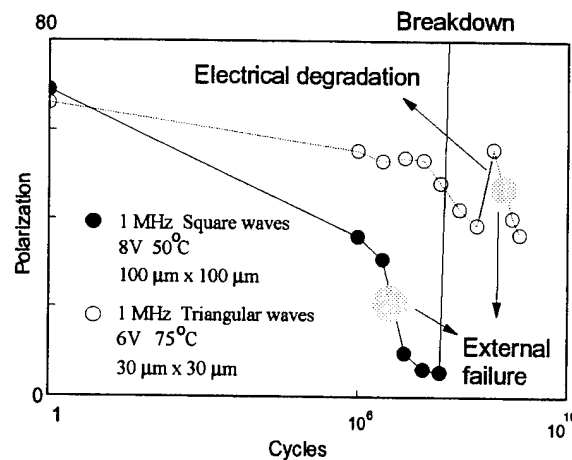


Figure 3  
Examples of external failure (electrode burst) which occurs before or after electrical degradation depending on test condition.

cycle where electrical degradation component becomes dominant and polarization curve begins to increase. This definition with generic polarization curve during fatigue test is illustrated in Fig. 4. Pure polarization component and leakage current component were separated each other and detected polarization is marked as an effective polarization. The generalized polarization curve in Fig. 4 can change depending on test conditions. However, for the lifetime evaluation, the electrode burst should appear after electrical degradation, at least.

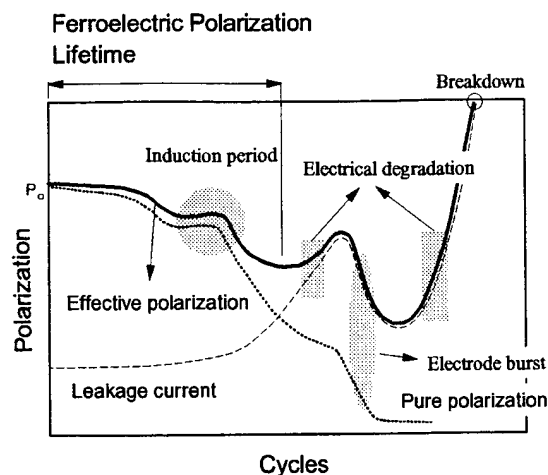


Figure 4  
Generic polarization curve for ferroelectric capacitors from a fatigue test's viewpoint

In Fig. 5, ferroelectric lifetime was measured for capacitors with various electrode sizes. Switching polarization plot provides information that electrical degradation is involved during test. It is clear, from true remanent polarization plot, that there is no induction period during this test and the lifetime can be determined from Fig. 5. As seen in Fig. 5, lifetime is almost independent of electrode size, but it is noted that smaller electrode gives higher electrical degradation. When the fact that breakdown mechanism is related to electrical degradation is considered, it can be said that breakdown mechanism during fatigue test is a thermal process, as discussed by J.F. Scott[9]. Based on the thermal processing theory, smaller electrode has lower chance to dissipate the heat and gives faster electrical degradation and thermal breakdown.

Voltage and temperature dependences are also presented in Fig. 6. The data is more or less scattered. This may be because polarization level and leakage current level are not symmetrically dependent on such conditions. In addition, avalanche (electronic breakdown mechanism) may be involved at certain voltages or temperatures.

It is well known that fatigue rate decreases as temperature increases. In Fig. 7, fatigue curves at room temperature and 100°C are shown using two parameters; switching polarization and true remanent polarization. The switching polarization curve at 100°C appears to have similar fatigue rate to that at room temperature and electrical degradation begins to appear after a while. But true remanent polarization curve clearly shows that fatigue rate is slower at 100°C than that at room temperature.

As far as fatigue mechanism is concerned, chemical potential barrier lowering at the interface can improve endurance[3]. The potential barrier can be reduced by applying heat. In this case fatigue may reduce but breakdown will occur earlier.

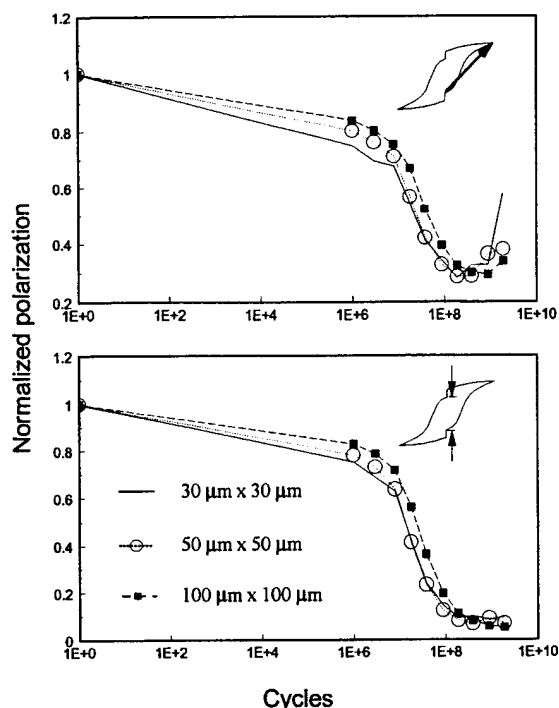


Figure 5  
Electrode size effect on lifetime. Even though lifetime is almost independent of electrode area, electrical degradation is strongly dependent on the electrode size.

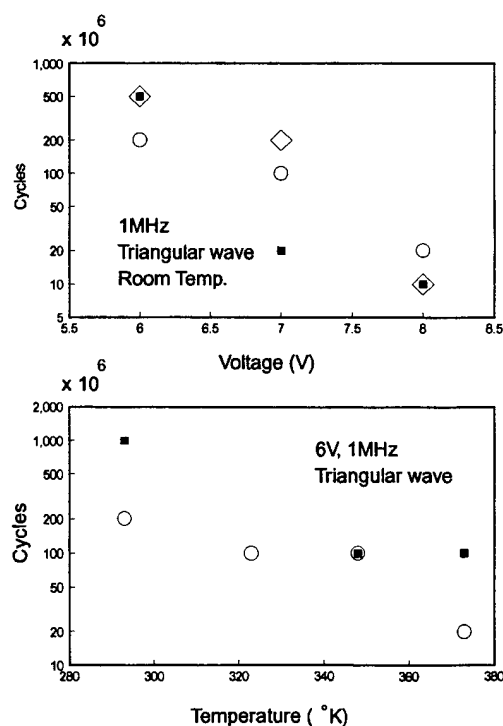


Figure 6  
Voltage and temperature effects on lifetime. Scattered data may stems from avalanche (impact ionization) during electrical degradation.

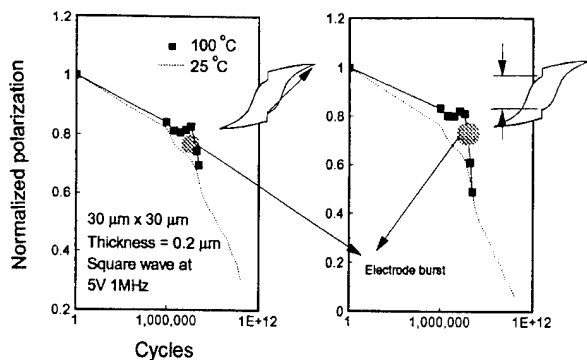


Figure 7

Fatigue versus temperature. Decrease of fatigue rate at higher temperature may be related to lowering of potential barrier at the interface. It is seen that electrode burst is related to thermal process.

## CONCLUSION

By defining lifetime of ferroelectric capacitors and evaluating them at various test conditions, following conclusions were obtained.

- 1) Electrical degradation and breakdown mechanisms are related to thermal process. In this case, avalanche may be involved in electrical degradation.
- 2) Accelerated unified test should be developed on condition that external failure (electrode burst) is not involved because it hinders normal lifetime evaluation.
- 3) Electrode with high thermal conductivity is recommended in order to delay breakdown. In this case the electrode should form lower chemical potential of vacancies at the interface to minimize fatigue.

## References

- [1] In K. Yoo and Seshu B. Desu, ISAF Proceedings of 8th IEEE, 1992, pp.225-228.
- [2] D.P. Vijay, C.K. Kwok, W. Pan, In K. Yoo, and S.B. Desu, ISAF Proceedings of 8th IEEE, 1992, pp.408-411.
- [3] S.B. Desu and In K. Yoo, Integrated Ferroelectrics, vol.3, 1993, pp. 365-376.
- [4] J. Carrano, C. Sadhama, J. Lee, A. Tasch and W. Miller, IEDM Conf. 1989, p.255.
- [5] G.M. Choi, H.L. Tuller and D. Goldschmidt, Phys. Rev., B34, 1986, pp. 6972.
- [6] H.P. Frederikse, W.R. Thurber and W.R. Hosler, Phys. Rev., 134, 1964, p.A442.
- [7] L.H. Parker and A.F. Tasch, IEEE Circ. Dev. Mag. Jan 1990, p.17.
- [8] D. Sudhama, J.C. Carrano, L.H. Parker, V. Chikarmane, J.C. Lee, A.F. Tasch, W. Miller, N. Abt and W.H. Shepherd, Mat. Res. Soc. Symp. Proc. 200, 1990, p.331.

- [9] J.F. Scott, B.M. Melnick, L.D. McMillan, and C.A. Paz de Araujo, Integrated Ferroelectrics, vol.3, 1993, pp.225-243.
- [10] B.M. Melnick, J.F. Scott, C.A. Araujo and L.D. McMillan, Ferroelectrics, Special Von Hippel Issue, 1992.
- [11] J.F. Scott, C.A. Araujo, B.M. Melnick, L.D. McMillan and R. Zuleeg, J. Appl. Phys. 70, 1991, p.382.
- [12] R. Waser and M. Klee, Integrated Ferroelectrics, 2, 1992, pp.23-40.
- [13] In K. Yoo and S.B. Desu, 6th ISIF, 1994, in press.
- [14] T. Mihara, H. Yoshimori, S. Takahashi, H. Nakano, C.A. Paz de Araujo, and L.D. Mcmillan, 5th ISIF presentation, 1993.

# HEAT FLOW AND $D^*$ OF MULTILAYER THIN FILM PYROELECTRIC DETECTOR

Q. Kang, W.G. Liu, L.Y. Zhang, and X. Yao

Electronic Materials Research Laboratory,  
Xi'an Jiaotong University, Xi'an 710049, CHINA

## ABSTRACT

The pyroelectric responses of multilayer, thin film pyroelectric detector under both isolated and heat sink boundary conditions are completely analyzed. The multilayer detector is composed of pyroelectric layer/thermal isolation layer/silicon substrate. The analytical result shows that when the thickness of the isolation layer is increased, the detectivity,  $D^*$  at low frequencies will be improved, and as the thickness of pyroelectric layer is decreased, the high frequency response becomes better.  $D^*$  of a detector with 1  $\mu\text{m}$  PLZT/ 10  $\mu\text{m}$  porous silica /0.5 mm silicon is higher than that of the detector with 10  $\mu\text{m}$  PLZT/ 1  $\mu\text{m}$  porous silica /0.5 mm silicon in a wide frequency range. In order to get a better performance of a multilayer thin film detector, the thicknesses of the two layers should be chosen very carefully. This analysis provides a guide for the preparation of the multilayer thin film pyroelectric detectors.

## INTRODUCTION

It is well known that thin film pyroelectric detectors have a wide band response, and are able to work at room temperature without cooling. In order to prepare integrated pyroelectric detector array, it is advantageous to deposit the pyroelectric thin film onto a silicon wafer. Since the silica substrate has a high thermal conductivity, which may be detrimental to the operation of the device<sup>1-4</sup>. To overcome this problem, an thermal isolation layer is introduced. So the multilayer detector is composed of pyroelectric layer/thermal isolation layer/silicon substrate. Porous silica thin film, which has a very low thermal conductivity<sup>5</sup>, is considered to be a very promising isolation material. One aim of this study is to find out the effectiveness of each thin film.

Heat flow of a two-layer structure has been partially solved by B. R. Holeman<sup>2</sup>, and A. van der

Ziel<sup>3</sup>. This paper will present the solution of a three-layer structure and its application to the detectivity  $D^*$  of the thin film composite.

## THEORY

Heat flow in multilayer is sinusoidally modulated by a radiation source. Steady state conditions are assumed, and the transient effects are ignored. The temperature variation of the pyroelectric thin film

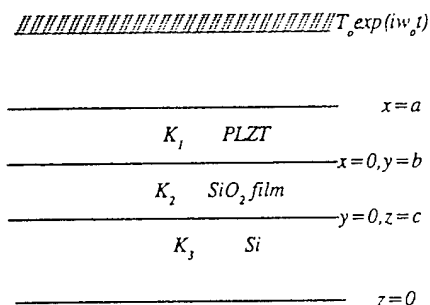


FIG. 1 Cross section of the pyroelectric multilayer thin film composite.

can be separated into time varying and time independent parts. The later part has no effect to the pyroelectric response, will not be considered. B. R. Holeman reported various treatments of one layer as well as heat sink model of two layers in his paper. In 1973, A. van der Ziel presented a solution of a two-layer structure with an isolated boundary, and gave a discussion to  $D^*$ . On the bases of their works, solutions of three layer model under different boundary conditions are expressed here. The schematic of the pyroelectric thin film composite is shown in FIG. 1

The one dimensional form of the heat flow equation is

$$\frac{\partial \theta}{\partial t} = k \frac{\partial^2 \theta}{\partial x^2} \quad (1)$$

$$k = \frac{K}{\rho C} \quad (2)$$

where  $\theta$  is temperature,  $t$  is time,  $x$  is distance,  $k$  is thermal diffusivity,  $K$  is thermal conductivity,  $\rho$  is density,  $c$  is specific heat.

The modulated radiation falls on the front surface of the detector (An absorbing layer is deposited on top of the detector). Where  $H$  is radiation conductance. It assumes that the radiation is completely absorbed<sup>2</sup>. The temperature and the heat flow at the interface are continuous. At the back surface of the substrate, there are two kinds of boundary conditions. One boundary condition is that the rear surface is linked to a heat sink, and the other boundary condition assumes that the surface keeps isolated. In most case, the average temperature variation of the pyroelectric thin film can be expressed in the following form:

For heat sink model:

$$\begin{aligned} T_m = T_0 & \left\{ \cosh(w_2 b) \sinh(w_3 c) + \frac{K_3 w_3}{K_2 w_2} \sinh(w_2 b) \cosh(w_3 c) \right\} \frac{\sinh(w_1 a)}{w_1 a} \\ & + \left[ \frac{K_2 w_2}{K_1 w_1} \sinh(w_3 c) \sinh(w_2 b) + \frac{K_3 w_3}{K_1 w_1} \cosh(w_3 c) \cosh(w_2 b) \right] \frac{\cosh(w_1 a) - 1}{w_1 a} \frac{1}{\Phi} \\ \Phi = & \left[ \frac{K_1 w_1}{H} \sinh(w_1 a) + \cosh(w_1 a) \right] \left\{ \cosh(w_2 b) \sinh(w_3 c) + \frac{K_3 w_3}{K_2 w_2} \sinh(w_2 b) \cosh(w_3 c) \right\} \\ & + \left[ \frac{K_2 w_2}{K_1 w_1} \cosh(w_3 c) + \frac{K_3 w_3}{K_1 w_1} \sinh(w_3 c) \right] \left\{ \frac{K_1 w_1}{H} \cosh(w_1 a) + \sinh(w_1 a) \right\} \\ & + \left[ \frac{K_2 w_2}{K_1 w_1} \sinh(w_3 c) \sinh(w_2 b) + \frac{K_3 w_3}{K_1 w_1} \cosh(w_3 c) \cosh(w_2 b) \right] \end{aligned} \quad (3)$$

For isolation model:

$$\begin{aligned} T_m = T_0 & \left\{ \cosh(w_3 c) \cosh(w_2 b) + \frac{K_3 w_3}{K_2 w_2} \sinh(w_2 b) \sinh(w_3 c) \right\} \frac{\sinh(w_1 a)}{w_1 a} \\ & + \left[ \frac{K_2 w_2}{K_1 w_1} \cosh(w_3 c) \sinh(w_2 b) + \frac{K_3 w_3}{K_1 w_1} \sinh(w_3 c) \cosh(w_2 b) \right] \frac{\cosh(w_1 a) - 1}{w_1 a} \frac{1}{\Psi} \end{aligned}$$

$$\Psi = \left[ \cosh(w_1 a) + \frac{K_1 w_1}{H} \sinh(w_1 a) \right] \left\{ \cosh(w_3 c) \cosh(w_2 b) + \frac{K_3 w_3}{K_2 w_2} \sinh(w_2 b) \cosh(w_3 c) \right\}$$

$$\sinh(w_3 c) + \left[ \frac{K_1 w_1}{H} \cosh(w_1 a) + \sinh(w_1 a) \right] \left\{ \frac{K_2 w_2}{K_1 w_1} \cosh(w_3 c) \sinh(w_2 b) \right.$$

$$\left. + \frac{K_3 w_3}{K_1 w_1} \cosh(w_2 b) \sinh(w_3 c) \right\} \quad (4)$$

$D^*$  of the pyroelectric thin film composite is

$$D^* = \frac{(A \Delta f)^{\frac{1}{2}}}{NEP} \propto \frac{p T_m}{H T_0} \left( \frac{w_0 a}{\epsilon \epsilon_0 4 K T \tan \delta} \right)^{\frac{1}{2}} \quad (5)$$

where, only the noise due to dielectric losses of the detector is considered.

Of course, if the thermal isolation layer or substrate is set to be zero, or the materials of such two layers are the same, the above solutions reduce to previous forms<sup>2,3</sup>.

## RESULTS AND DISCUSSIONS

According to the formula (5), the detectivity of thin film detectors can be estimated numerically. The physical parameters used in this paper are listed in table I.

Table I Physical parameters used in calculations

	PLZT	SiO <sub>2</sub>	Si
thickness(μm)	1	1	500
K (W/mK)	0.8	0.14	170
C <sub>p</sub> (W/m <sup>3</sup> )	2.5×10 <sup>6</sup>	1.39×10 <sup>6</sup>	1.75×10 <sup>6</sup>
p (C/m <sup>2</sup> K)	1.0×10 <sup>-3</sup>	-	-
ε <sub>r</sub>	1400	-	-
tanδ	0.005	-	-

The thickness of the thermal isolation layer used in calculation is 0μm, 1μm, 10μm, from FIG. 2, the  $D^*$  in low frequency can be improved when the

thickness of thermal isolation layer is high; but the high frequency response keeps the same. Corresponding to a fix frequency, the thermal isolation layer has a

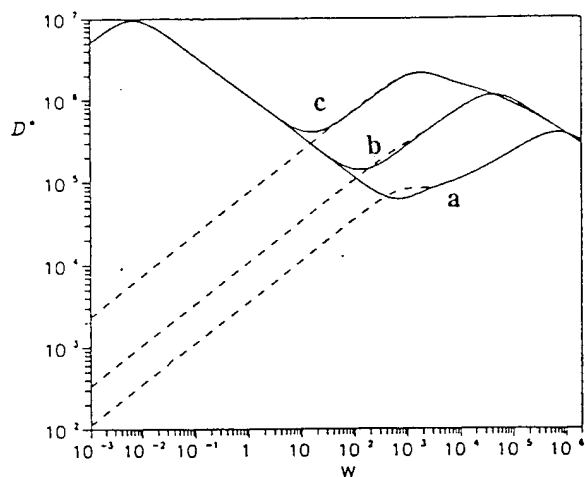


FIG. 2  $D^*$  vs  $w$  for three thicknesses of thermal isolation layer (a:  $0\mu\text{m}$ ; b:  $1\mu\text{m}$ ; c:  $10\mu\text{m}$ ). Solid: isolation model, dashed: heat sink.

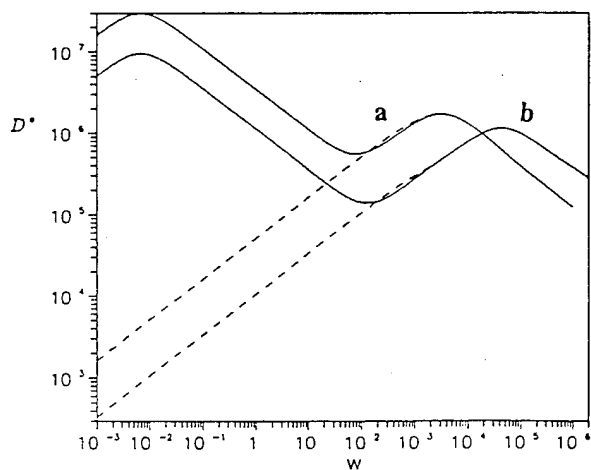


FIG. 3  $D^*$  vs  $w$  for different thicknesses of pyroelectric thin film (a:  $10\mu\text{m}$ , b:  $1\mu\text{m}$ ). Solid: isolation model, dashed: heat sink.

maximum thickness, above this limit, its effect is the same. From FIG. 3, it is quite evident that as the pyroelectric film becomes thinner (From  $10\mu\text{m}$  to  $1\mu\text{m}$ ), the high frequency detectivity  $D^*$  becomes better, but  $D^*$  at low frequencies is spoiled, in other words, the peak of  $D^*$  moves toward high frequencies.

Both conditions agree at high frequencies (See FIG. 2-4), as all other practical models are just between them, the boundary conditions of the back surface of the substrate have no evident effect.

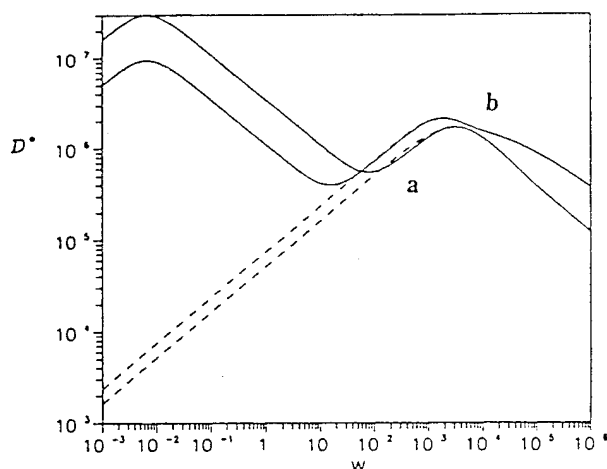


FIG. 4  $D^*$  vs  $w$  for two different cases (a:  $10\mu\text{m}$  PLZT/ $1\mu\text{m}$   $\text{SiO}_2$ / $0.5\text{mm}$  Si; b:  $1\mu\text{m}$  PLZT/ $10\mu\text{m}$   $\text{SiO}_2$ / $0.5\text{mm}$  Si). Solid: isolation model, dashed: heat sink.

How to compose a multilayer pyroelectric thin film detector is a very practical problem. From the above analysis, it's clear that both the pyroelectric film and the thermal isolation film affect the performance of the device greatly. Two different kinds of multilayer thin films have been computed here. The detectivity of them is shown in FIG. 4. In a wide frequency range, the  $D^*$  of a detector with  $1\mu\text{m}$  PLZT/ $10\mu\text{m}$   $\text{SiO}_2$ / $0.5\text{mm}$  Si is higher than that of the detector with  $10\mu\text{m}$  PLZT/ $1\mu\text{m}$   $\text{SiO}_2$ / $0.5\text{mm}$  Si. Therefore, during the preparation of the three layer thin film detector, the two layers should be chosen very carefully so as to gain a better

performance of the detector.

## CONCLUSIONS

1. The temperature distributions of a three-layer thin film detector have been solved, which can degenerate the previous works using simple models.
2. The thermal isolation layer performs a great role in the multilayer thin film composite, for a better operation at low frequencies, it should be as thick as possible. If the detector works at a given frequency, there exists a maximum thickness of the isolation layer. The pyroelectric layer becomes thinner, the peak of  $D^*$  moves to higher frequencies.
3. If one wants a satisfactory operation in a wide frequency range, the pyroelectric multilayer thin film composite should be chosen carefully. This analysis provides a guide for the preparation of the multilayer thin film pyroelectric detectors.

## ACKNOWLEDGMENTS

Thanks should be given to Miss J.P. Ren for her encouragement and assistance in the first author's work. This work is supported by the Chinese National Advanced Materials Research Project.

## REFERENCES

1. H. Blackburn and H. C. Wright, *Thermal analysis of pyroelectric detectors*, Infrared Phys. 10, 191(1970).
2. B. R. Holeman, *Sinusoidally modulated heat flow and the pyroelectric effect*, Infrared Phys. 12, 25(1972).
3. A. van der Ziel, *Pyroelectric response and  $D^*$  of thin pyroelectric films on a substrate*, J. Appl. Phys. 44, 546(1973).
4. W. Liu, Q. Kang, L. Zhang and X. Yao, *Dynamic pyroelectric response of PLT thin film*, IMF8, USA,(1993).
5. J. C. Lampropoulos, M. R. Joily, C. A. Amsden, S. E. Gilman, M. J. Sinicropi, D. Diakomohalis and S. D. Jacobs, *Thermal conductivity of dielectric thin films*, J. Appl. Phys. 66, 4230(1989).

## NUCLEATION AND CRYSTALLIZATION BEHAVIOR OF MOD DERIVED PZT THIN FILM

S.B. Xiong, X.Q. Wu, L.Y. Zhang and X. Yao  
Electronic Materials Research Laboratory  
Xi'an Jiaotong University, Xi'an 710049, CHINA

**Abstract** --- Nucleation and crystallization behavior of PZT thin films are studied by XRD, SEM and isothermal DTA techniques. It is found experimentally that the perovskite crystal nucleation rate is much higher than the perovskite crystallites' growth rate at the temperature of 460°C. The crystallization centers grow into grains through swallowing the surrounding amorphous substrate. Too large grains appear in thin films due to the number of perovskite nucleus with crystallites' size greater than critical size is not enough. Dense, crack-free and perovskite PZT thin films with grain size of 0.3-0.6  $\mu\text{m}$  were obtained by optimizing the heat treatment.

### Introduction

PZT thin films are of considerable interest for the applications of electronics and opto-electronics such as FRAM[1], sensors, waveguide modulator [2]. MOD technique is one of the major preparation techniques of PZT thin films [3]. The formation of the thin films includes several transformation steps, precursors - Sol - amorphous films - polycrystalline films. The transformation from amorphous to polycrystalline films includes two changes: nucleation and growth. The temperature of maximum crystal nucleation rate doesn't coincide with that of maximum crystal growth rate. It is necessary to study the temperature dependence of nucleation rate and growth rate to obtain dense, fine

grained, crack-free and pure perovskite thin film by optimizing the heat treatment.

In this paper, we report the results of studies on the nucleation and crystallization behavior of MOD derived PZT thin films.

### Experimental

#### *Preparation of PZT Thin Film*

PZT films were prepared by MOD using multilayer spinning onto Pt/SiO<sub>2</sub>/Si substrates. The initial metallo-organic compound as precursors for PZT films are lead acetate, tetra-n-butyl titanate and zirconyl heptanoate. Zirconyl heptanoate compound and PZT precursor solution were synthesized in this lab [4]. The precursor solution was deposited on Pt/SiO<sub>2</sub>/Si substrates at 3000 RPM using a photo-resist spinner. The film was given a 30 minutes heat treatment, at the temperature of 400°C, to decompose residual organics. The additional coating could be deposited repeatedly after the thermal decomposition. Usually the sample films consisted of six layers and were 520nm thick after heat treatment. A final heat treatment at temperatures ranging from 460°C to 600°C was used to nucleate and crystallize the thin films.

#### *Characterization*

Relations of time, temperature and transformation



of the crystallization of PZT precursor solution were studied by isothermal DTA techniques. XRD patterns of PZT thin films were obtained on Regaku D/Max 2000 diffracto-meter using monochromatic Cu K $\alpha$  radiation at room temperature. SEM was used to examine the surface micro graph and estimate grain sizes of PZT ferroelectric thin films. The composition of the thin films was analyzed by EDXS (Energy Dispersal X-ray Spectrum) techniques.

### Results and Discussion

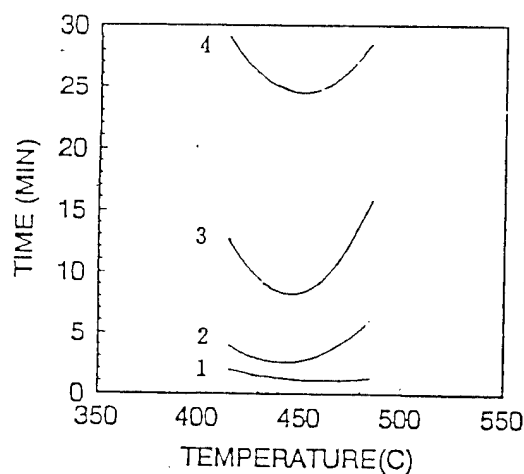


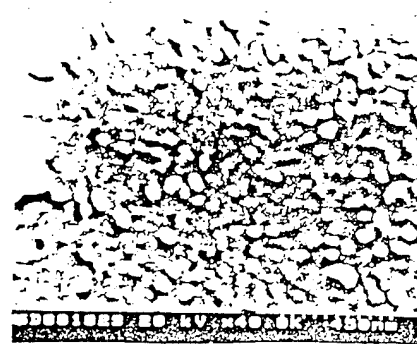
Fig.1 Relation of T-T-T of PZT solution

Relation of time , temperature and transformation (T-T-T) of the crystallization of PZT solution is shown in Fig.1. The decomposition rate is same at different nucleation temperature ( 440°C - 460°C ) as the curve in Fig.1 shows, but the maximum reaction rate is at about 460°C as the other curves in Fig.1 show.

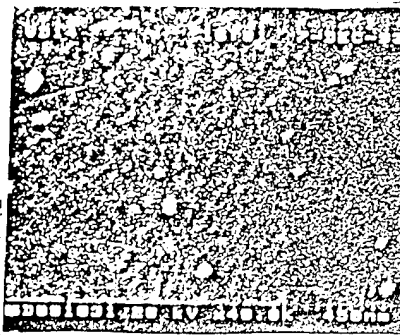
Surface micrographs of PZT thin films annealed at 460°C for various time is shown in Fig.2. For 10 min. heat treatment, many spindle-like particles with diameter of 300 nm in thin film can be seen. For 20 min., spindle-



(a) 10 min



(b) 20 min.



(c) 30 min.

Fig.2 SEM micrographs of thin films for various heat treatment time at 460°C

like particles disappear and many ball-like particles with diameter of 50 nm appear.

For 30 min., ball-like particles in thin film almostly vanish and a smooth surface is obtained. The composition of the micro region containing spindle-like or ball-like particle was measured by EDXS. The micro region is rich in lead. The experimental results indicates that the lead diffuses in thin film and finally maintains equilibrium.

XRD patterns of thin film treated for various time at 460°C are shown in Fig.3. The structure of PZT thin film is not perovskite until heat treatment time is longer than 12 hours. This indicates that the grain growth can be very slow at 460°C. The diffraction peak at 33° (2θ) is not

stemmed from perovskite, and needs to be identified. The XRD spectrum of PZT thin film with treatment time of 30 min. shows that the structure of thin film is still amorphous, but SEM and DTA techniques show that the crystallization reaction has started. This fact can be easily understood, if we think that the nucleation rate is much higher than the growth rate and that the crystalline grains are nano-sized micro crystals which can not be detected by XRD. The PZT thin films are composed of nano crystallites, amorphous background and interfaces. So XRD patterns of the thin films are certainly amorphous. As the treatment time is long enough, nanocrystallites can grow into crystal grains; XRD pattern of thin film will show distinct perovskite structure. This has been confirmed in Fig.3(d).

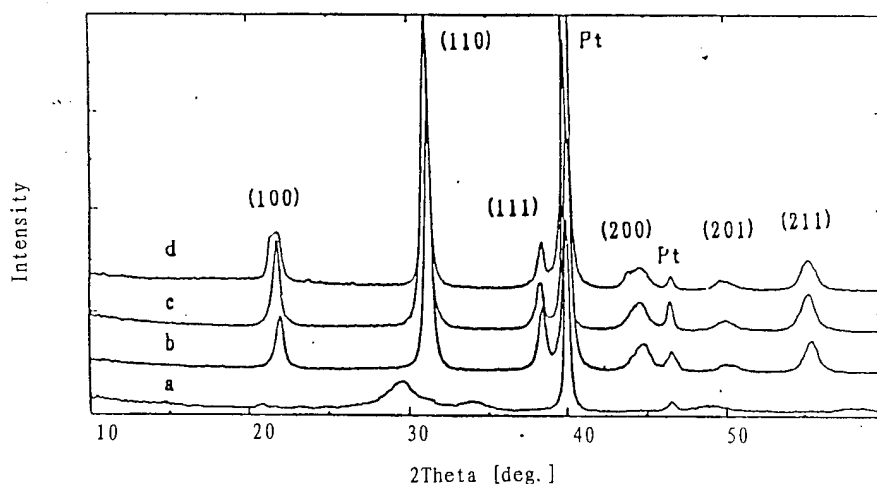
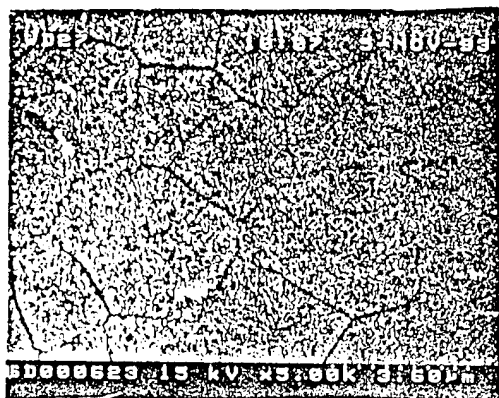


Fig.3 XRD patterns of thin films for various heat treatment time at 460°C  
(a) 10min (b) 20min (c) 30min (d) 720min

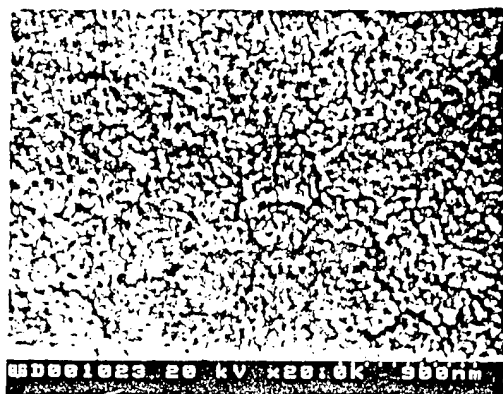
Fig.4 is the SEM micro graphs of PZT thin films for various nucleation and crystallization time temperature combinations. As Fig.4(a) shows, the grain size is about 3μm for nucleation time of 120 seconds at 460°C and growth time of 1800 seconds at 550°C, the grain size of Fig.4(b) is about 0.5μm for nucleation time of 1800 seconds at 460°C and growth time of 1800 seconds. The last can obtain submicrometer grain size thin film. It is well known that the more the number of crystallization nucleus with size greater than critical size is, the smaller

the grain size of the thin film is. Crystallization centers grew into large grains through swallowing the amorphous, pyrochlore background and micro crystallites with size smaller than critical size [5]. At 460°C, the grain size for nucleation time of 20 seconds is almostly 6 times larger than that for nucleation time of 1800 seconds, but both thin films are dense, pure perovskite. This indicates that the nucleation rate can be much higher than the growth rate at 460°C and dense, crack-free and pure perovskite thin films can be prepared by adjusting

the heat treatment process to produce enough number of nuclei with size greater than critical size.



(a) common process



(b) optimized process

## Conclusion

Nucleation and crystallization of PZT thin films are studied by XRD, SEM and isothermal DTA techniques. It is found experimentally that the nucleation rate of perovskite crystallites is much higher than the growth rate at 460°C. Crystallization centers grow into large grains through swallowing the amorphous, pyrochlore background and micro crystallites with size smaller than critical size. Too large grains appear due to the number of perovskite nucleus with grain size greater than critical size is not enough. PZT thin films with grain size of 0.3-0.6  $\mu\text{m}$  can be obtained by optimizing the heat treatment process.

## Acknowledgment

This work was supported by the National Advanced Materials Research Project of China

## Reference

- [1] J. Evans, R. Womack, An Experimental 512 bit Nonvolatile Memory with Ferroelectric Storage Cell, *IEEE J.S.S.Circuits*, 23(5):1171-1175 (1988)
- [2] A.B. Wenger, S.R.J. Brueck and A.Y. Wu, Integrated PLZT Thin Film Wave guide Modulators, *Ferroelectrics*, 116: 195-204(1991)
- [3] R.A. Roy, K.F. Etzold and J.J. Cuime, Ferroelectric Thin film Synthesis, Past and Present: A Select Review, *Mat.Res.Soc. Symp.Proc.*, 200:141-152
- [4] P. Sun, Preparation and Characterization of PLZT Thin film, *Ph.D. Dissertation*, Xi'an Jiao-tong University, Dec. 1992(in Chinese)
- [5] I. Heckelmann et al., *Textures and Microstructures*, 14-19:769-774(1991)

Fig.4 SEM micrographs of thin films treated by different heat treatment processes

# The Structural and Acoustic Properties of Sputtered Aluminum Nitride on Silicon

F. S. Hickernell  
Motorola GSTG  
8201 E. McDowell  
Scottsdale, AZ 85252

H. M. Liaw  
Motorola SPS  
2100 E. Elliott Rd.  
Tempe, AZ 85284

**Abstract** - The structural and acoustic properties of reactively sputtered aluminum nitride (AlN) on silicon have been characterized. The AlN films were grown on (100) silicon wafers, having a 200nm thick layer of PECVD silicon nitride, at substrate temperatures in the 300°C to 500°C range, with a low background sputter pressure, and a high deposition rate. X-ray, atomic force microscopy and transmission electron microscopy measurements defined the structural properties. Surface acoustic wave (SAW) propagation measurements in the frequency range from 50 MHz to 1.5 GHz defined the acoustic properties. A strong correlation was found between the structural properties and the measured SAW velocity and propagation loss characteristics. One micrometer thick films with high intensity (002) plane x-ray diffraction intensities, closely packed uniform grains, approximately 30nm in diameter, and a surface roughness less than 10nm, had SAW velocity dispersion characteristics, coupling factors and propagation losses close to those of epitaxial AlN. Electron diffraction characteristics taken over several grains perpendicular to the columnar structure resembled a single crystal diffraction pattern. Deviation of the films structural properties from these epitaxial-like conditions was observed when more than one-half percent of oxygen was incorporated in the films.

## INTRODUCTION

Aluminum nitride has been considered as an attractive thin film piezoelectric material for high frequency bulk acoustic wave (BAW) and surface acoustic wave (SAW) devices. Early work on AlN film growth used metal-organic chemical vapor deposition (MO-CVD) and rf sputtering for the epitaxial growth of AlN on sapphire at temperatures exceeding 1000°C [1-3]. These epitaxial AlN films showed very promising SAW device properties. This included high surface acoustic wave velocity, low propagation loss, moderate coupling factors, and near zero SAW temperature coefficient of delay. Electromechanical coupling coefficients ( $K^2$ ) of 0.3% to 0.8% were achieved when the AlN was deposited on the R-plane of sapphire and from 0.04% to 0.3% when it was deposited on the sapphire basal plane [4]. However, this high growth temperature and the use of sapphire as the substrate are not compatible with on-chip acoustic wave devices fabricated by current semiconductor IC processes. An alternative technique for the preparation of AlN thin films is by reactive sputtering at a lower temperature, typically below 500°C [5]. Well oriented polycrystalline films have been demonstrated to be feasible for fabrication of bulk acoustic wave (BAW) resonators [6] as well as surface acoustic wave (SAW) devices [7]. The AlN films produced by this method are polycrystalline and are expected to give lower electromechanical coupling constants and higher propagation losses than the epitaxial films. The work reported in this paper shows that polycrystalline AlN films with particular structural properties do in fact perform like epitaxial films.

The AlN films investigated in this study were deposited on thinly nitrided silicon substrates by dc magnetron sputtering using a commercially available ultra-high vacuum system. The highest quality films had very dense, uniform, small-diameter, columnar grain growth and a smooth upper growth surface. The grains were singular in crystallinity, c-axis normal oriented, with a very high lattice continuity between grains exhibiting epitaxial-like electron diffraction patterns. Deviations from this high quality condition was found when oxygen was present in the films.

Surface acoustic wave (SAW) measurements were carried out by fabricating interdigital electrode transducers of thin-film aluminum directly on the top AlN surface. Because AlN is piezoelectric, surface waves could be launched and detected between pairs of transducers. Insertion loss versus frequency measurements were used to determine SAW velocities and propagation loss and to estimate the piezoelectric quality of the film. The measurements were made over the frequency region from 50 MHz to above 1.5 GHz using a network analyzer. The acoustic properties measured were correlated with the structural property measurements and with theoretical performance based on the properties of the crystalline material.

## FILM AND TRANSDUCER PROCESSING

Four inch, (100) oriented silicon wafers, boron doped with resistivities in the range of 7 to 14 ohm-cm were used as substrates. A 200 nm thick layer of amorphous PECVD silicon nitride was deposited on the silicon which promoted film adhesion and provided nominal electrical insulation. The AlN was deposited in a commercially available sputtering system with ultra-high vacuum capabilities. Films were sputtered in the temperature range from 300 to 500 degrees centigrade at low background sputter pressure, high nitrogen gas content, and high deposition rates. Such conditions produced high quality films and minimized oxygen incorporation. The film thicknesses were from 500 nm to 3000 nm.

The SAW transducers were fabricated on the AlN forming a matrix array of Al interdigitated electrodes on the top surface. The aluminum layer, 100 to 200 nm thick, was deposited, patterned and etched by conventional semiconductor processes. Each transducer had 10.5 split finger electrode pairs with individual finger widths of 15 microns and spacings of 10 microns to facilitate harmonic generation. The wavelength of the fundamental SAW mode was 100 micrometers. The electrode fingers had an overlap of 2.54 mm and two adjacent transducers were spaced 3.8 mm apart. The pattern was repeated with an equal spacing throughout the whole 100 mm diameter on the (100) Si wafer. The transducer strings were aligned parallel to the Si wafer major flat with the SAW propagation direction along the (110) axis of the silicon substrate.

## STRUCTURAL AND COMPOSITION MEASUREMENTS

Three basic instruments were used to characterize the structural properties of the polycrystalline AlN films: x-ray, atomic force microscopy (AFM), and transmission electron microscopy (TEM). In addition composition measurements were made using Auger spectroscopy. The composition measurements were made to determine the presence of oxygen in the films which is known to disrupt the structural properties and affect acoustic performance.

The x-ray measurements probe within the film to determine if there is a preferred orientation of crystallites, and the density of such crystallites. The x-ray diffraction patterns of the samples used in this study showed the appearance of a strong (002) peak near  $2\text{-}\theta = 36.2^\circ$ . Other major crystallographic planes were either not observed or insignificant in intensity as compared to that of (002). Thus, as expected, the preferred orientation of the polycrystalline film was with the c-axis of the hexagonal AlN perpendicular to the substrate surface. As the x-ray count intensity increased the  $2\text{-}\theta$  peak position moved closer to  $36.2^\circ$ . This was also accompanied by a decrease in the full-width-half-maximum (FWHM) which would be indicative of increasing polycrystalline grain size. The grain size calculated was between 30 nm and 50 nm. From the Auger analysis the films with low XRD patterns contained oxygen content up to 6%, whereas the samples with counts greater than 100 cps/nm had an oxygen content less than 0.5%, the limit for the Auger analysis.

The AFM measurement of surface morphology shed additional light on the grain structure. The surface showed a columnar grain growth with varying degrees of grain size and surface roughness. The low x-ray count, high oxygen content films had a very irregular grain pattern and a rough surface. For a 3% oxygen content columnar grain size averaged near 100 nm and surface peak to valley roughness was in the range of 14 to 32 nm. The films with oxygen content less than 0.5% and high x-ray count had a very smooth surface with closely packed uniform size grain columns of 30 to 35 nm and a peak to valley surface roughness of 3 to 9 nm. This indicated a very uniform growth condition. An AFM photo looking down on the top surface of such an AlN film is shown in Figure 1. The apparent increase in grain size from the increasing x-ray FWHM values was not borne out by the AFM measurements.

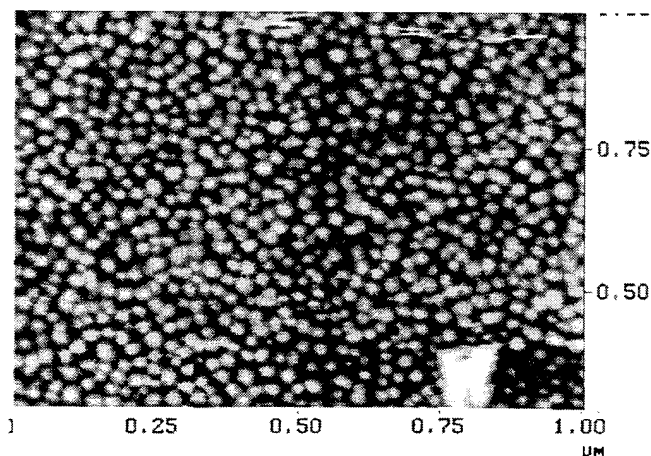


Fig. 1. AFM view of the top surface of a 1.0 sputtered AlN film with average columnar grain diameters of 30 to 35 nm and a 6 nm average peak to valley surface roughness.

The transmission electron microscopy (TEM) measurements of the cross-section of the AlN films revealed even more information about the growth conditions, particularly for those with high x-ray count and smooth surface. The optical image verified that the grain columns were uniform in growth from the surface with a diameter in the 30 to 35 nm range. The images indicated a singular crystallite orientation within a grain. Electron diffraction patterns over several grains taken perpendicular to the columnar structure of high x-ray diffraction intensity films of 1.0 micrometer thickness did not show any trace of a ring-pattern (see Figure 2). The discrete spot-pattern indicated that the c-axes of the sputtered polycrystalline films were highly aligned, and there was a strong lattice continuity between grains. This indicated that the structural properties of the fine grain sputtered polycrystalline AlN film closely approximated the structure of single crystal epitaxial grown films. The light and dark field optical images from poorer films indicated that early growth was well c-axis aligned but degraded as the growth continued. For such films the electron diffraction pattern at the film/substrate boundary showed a combination of spot and ring patterns which evolved into ring patterns at the top of the film. For high quality films with thicknesses approaching 3000 nm, the combination of spot and ring patterns were also seen.

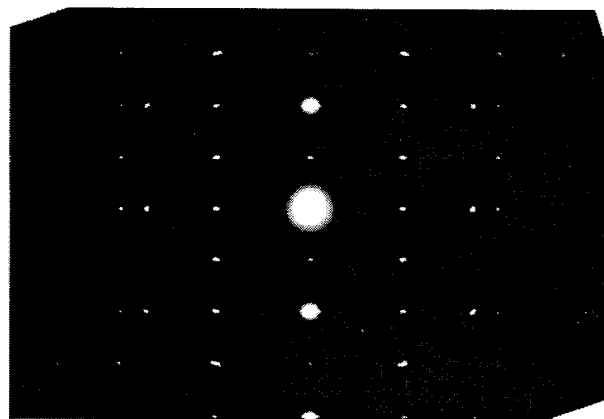


Fig. 2. Transmission electron diffraction pattern over several grains of the cross-section of a 1.0 micron sputtered AlN film on silicon.

## ELECTRICAL MEASUREMENTS OF ACOUSTIC PROPERTIES

Transmission measurements between pairs of transducers were made with a 50 ohm network analyzer test set. The basic measurement was the insertion loss between pairs of transducers with different spacings as a function of frequency. Fundamental and harmonic SAW responses were measured from 50 MHz to over 1.5 GHz in some cases. SAW velocities were calculated from an accurate measurement of the frequency multiplied by the corresponding fixed wavelength value. This generated a SAW velocity dispersion characteristic which allowed comparison between films and to the theoretical characteristic based upon the elastic constants developed from epitaxial film growth [4].

By measuring the insertion loss between transducers with different separations a linear change in loss was observed representing the SAW propagation loss of the film/substrate at a particular frequency. A graphical representation of propagation loss versus frequency could then be developed for comparison between the sputtered films and epitaxial films. By subtracting out the propagation loss a single transducer conversion loss value was obtained from which a coupling factor could be estimated indicating the piezoelectric quality of the film.

The SAW properties arising from Rayleigh wave propagation is a sensitive function of film structure. The Rayleigh wave has much stronger shear motions along the c-axis than compressional motions normal to the c-axis in the film. The wave motion is very sensitive to the lateral film structure interconnecting the film grains. At low frequencies the velocity is representative of the substrate. As the frequency increases, wave motion is influenced more by the film's properties. The SAW phase velocity is plotted as a function of film-thickness to acoustic-wavelength ratio. For ratios near 1, the propagation properties are representative of the film.

Figure 3 is a plot of SAW phase velocity versus film-thickness to acoustic-wavelength ratio for four films representative of the types analyzed in this investigation. Also shown as a continuous line is the theoretical velocity dispersion characteristic using the accepted elastic constant values for AlN (Tsubouchi et al [4]), the measure constants for PECVD silicon nitride (Hickernell et al [8]), and the constants for silicon (Slobodnik [9]). The two films represented by the darkened triangle and square are fine grain samples with very high x-ray counts and thicknesses of 2800 nm and 1000 nm respectively. The dispersion characteristics are very close to theoretical values differing by only about 1 - 2% at the higher thickness to wavelength ratios. This velocity difference of 1 - 2% for the best films implies an average elastic constant decrease of only 2 - 4% of the film's constants from that of single crystal material. The other two films, each 1000 nm thick, had lower x-ray counts and oxygen in the 0.6 - 2% region. The difference in velocity characteristic is very obvious with the velocity minimum being shifted to higher thickness to wavelength ratios as film quality degraded.

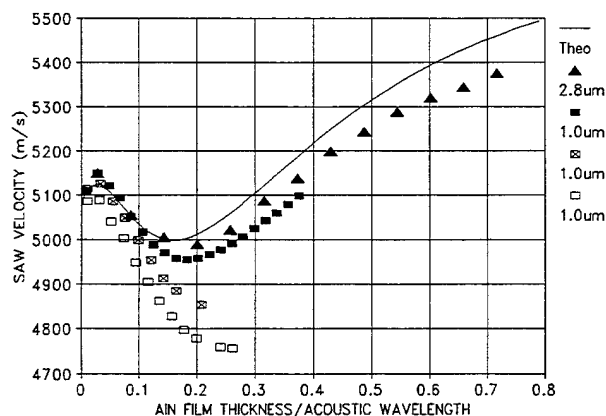


Fig. 3. SAW velocity dispersion as a function of film-thickness to acoustic-wavelength ratio for sputtered AlN on nitrided silicon. Filled triangle and square data points are representative of high quality films. Solid line represents SAW velocity dispersion characteristic using theoretical crystalline AlN elastic constants.

The SAW propagation loss is an even more sensitive function of film structure, particularly at the higher propagation frequencies. Figure 4 shows the SAW propagation loss as a function of frequency for four films of two different thicknesses. The loss characteristic is close to a frequency squared relationship as shown by the solid line. This indicates intrinsic phonon loss mechanisms are dominant. The loss is approximately 10 dB/cm at 1 GHz for the 1000 nm thick films. For comparison, the three filled triangle data points are representative of the loss for epitaxial AlN films on sapphire.

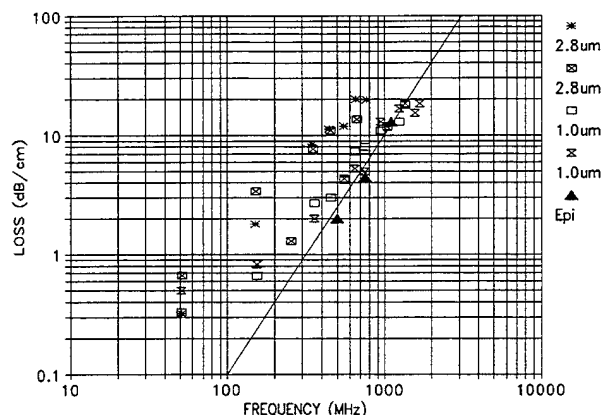


Fig. 4. SAW propagation loss as a function of frequency for four films of two thicknesses for sputtered AlN on silicon. The solid line represents a frequency squared relationship characteristic of intrinsic phonon loss mechanisms. The three filled triangle data points are representative of AlN epitaxial film losses on sapphire.

Very low SAW propagation losses close to those measured for epitaxial films on sapphire were obtained with the high quality polycrystalline films 1000 nm thick. The 2800 nm thick films have propagation losses 2 to 3 times larger. These higher SAW propagation losses in the thicker films at equivalent frequencies are another indication that there is some degradation of film quality as the growth continues beyond 1000 nm. This was apparent in the electron diffraction measurements but did not appear as a deviation in the velocity characteristics. If the propagation loss is plotted as a function of film-thickness to acoustic-wavelength ratio, all the data points lie close to a straight line irrespective of film thickness.

The coupling factors for high quality films were estimated from the transducer insertion losses. The coupling factors for the best sputtered films were 0.35% corresponding to film thicknesses of 1000 nm and thickness to wavelength ratios between 0.2 and 0.4.

## CONCLUSIONS

Based upon the results of the structural analysis and the SAW measurements it is apparent that high quality AlN films with properties similar to epitaxial films can be deposited by sputtering techniques on silicon having an amorphous silicon nitride on its surface. The x-ray characteristics show a high intensity for (002) orientation with other crystallite orientations essentially absent. A reduced x-ray intensity was associated with the presence of oxygen in the films. The structural characteristics of the high XRD films are small uniform c-axis oriented columnar grains with a diameter of 30 - 35 nm, a smooth surface boundary with less than 10 nm peak to valley roughness, and single crystal like lattice continuity between individual grains. The SAW properties of velocity and loss for 1000 nm films are very close to those predicted for a single crystal material using constants developed from high temperature epitaxial film growth on sapphire. Because of the small grains (30 nm) these films should be useful for producing SAW and BAW integrated acoustic devices to 10 GHz and possibly higher.

There are two film process problems which if successfully addressed would enhance the use of sputtered aluminum nitride for acoustic wave device development. It has been the experience in this investigation that the small uniform grain growth can only be maintained for film thicknesses up to about 2000 nm. For some low frequency acoustic wave devices operating near 1.0 Ghz it would be advantageous to be able to grow film thicknesses up to 6000 nm and maintain the small columnar grain structure. This will require additional process modifications and possibly the use of intermediate films for stress control. The second is controlling the angle of inclination of the c-axis of the AlN film to achieve higher coupling factors. This has been done with epitaxial films on sapphire by use of different substrate cuts. Possible ways this might be accomplished are by texturing an amorphous surface, using a special silicon cut, or by modifying the deposition conditions.

#### ACKNOWLEDGMENTS

The authors thank Wayne Cronin for the deposition of AlN films, Marc Chason for the x-ray diffraction measurements, Harland Tompkins for x-ray and Auger evaluations, Theresa Hopson for the atomic force microscopic evaluations, Peter Fejes for the TEM examinations, Claudia Jensen for SAW transducer fabrications, and Virginia Hernandez for SAW transducer testing. This has been a cooperative effort between the Government Systems and Technology Group and the Semiconductor Products Sector of Motorola. The authors thank their respective managements for the support given this program.

#### REFERENCES

- [1] P. J. Hagon, L. Dyal and K. M. Lakin, "Wide band UHF compression filters using aluminum nitride on sapphire," *Proc. IEEE Ultrason. Symp.*, pp. 274-275, 1972.
- [2] M. T. Duffy, C. C. Wang, G. D. O'Clock Jr., S. H. McFarlane III, and P. J. Zanzucchi, "Epitaxial growth and piezoelectric properties of AlN, GaN, and GaAs on sapphire or spinel," *J. Electronics Materials*, vol. 2, no. 2, pp. 359-372, 1973.
- [3] A. J. Shuskus, T. M. Reeder, and E. L. Paradis, "Rf-sputtered aluminum nitride films on sapphire," *Appl. Phys. Lett.*, vol. 24, pp. 155-156, 1974.
- [4] K. Tsubouchi and N. Mikoshiba, "Zero temperature-coefficient SAW devices on AlN epitaxial films," *IEEE Trans. Sonics and Ultrason.*, vol. SU-32, no. 5, pp. 634-644, 1985.
- [5] T. Shiosaki, T. Yamamoto, T. Oda, K. Harada, and A. Kawabata, "Low temperature growth of piezoelectric AlN film for surface and bulk wave transducers by rf reactive plasma magnetron sputtering," *Proc. IEEE Ultrason. Symp.*, pp. 451-454, 1980.
- [6] K. M. Lakin, J. S. Wang, G. R. Kline, A. R. Landin, Y. Y. Chen, and J. D. Hunt, "Thin film resonators and filters," *Proc. IEEE Ultrason. Symp.*, pp. 466-475, 1982.
- [7] L. C. Pearce, R. L. Gunshor, and R. F. Pierret, "Sputtered aluminum nitride on silicon for SAW device applications," *Proc. 1981 IEEE Ultrason. Symp.*, pp. 381-383, 1981.
- [8] T. S. Hickernell, F. M. Fleigel, and F. S. Hickernell, "The elastic properties of thin-film silicon nitride," *Proc. IEEE Ultrason. Symp.*, pp. 445-448, 1990.
- [9] A. J. Slobodnik, E. D. Conway, and R. T. Delmonico, *Microwave Acoustics Handbook - Air Force Cambridge Research Laboratories*, 1973.

# Electrical Properties of PZT Thin Films with Ir and IrO<sub>2</sub> Electrodes

Takashi Nakamura, Yuichi Nakao, Akira Kamisawa and Hidemi Takasu  
ROHM CO.,LTD. 21, Saiin Mizosaki-cho, Ukyo-ku, Kyoto 615, Japan

## Abstract

The development of ferroelectric memory device requires a though understanding of the fatigue properties of ferroelectric thin films. PZT thin films by sol-gel method on Pt/Ti were reduced residual polarization by continuous polarization reverses about 10<sup>8</sup> cycles. In this paper, we regard Ir, IrO<sub>2</sub> and these layer films as electrode materials and have evaluated electric characteristic of PZT thin film capacitors. Regarding a ferroelectric material, we used PZT(Zr/Ti=52/48) by sol-gel method.

By using Ir and IrO<sub>2</sub> electrodes, diffusion barrier effect becomes very good, therefore they can prevent Pb and other elements from diffusing into electrode and polycrystalline silicon (poly-Si). PZT thin films using Ir/IrO<sub>2</sub> layer electrodes show no fatigue up to 10<sup>12</sup> cycles of  $\pm 5V$  switching pulse.

## 1. Introduction

Ferroelectric thin film capacitors using PZT as ferroelectric materials have been investigated for memory applications. <sup>1)</sup> Pt or Pt/Ti electrodes are widely used in these capacitors, because Pt has a small lattice mismatch for PZT and good heat-resistance. However, PZT thin film capacitors using Pt or Pt/Ti electrodes have an important problem of fatigue. For example, our capacitors using Pt/Ti electrodes were reduced to half remanent polarization by continuous polarization reverses of about 10<sup>8</sup> cycles. In order to solve such a problem new ferroelectric materials <sup>2)</sup> and new electrode materials <sup>3,4)</sup> are studied.

In addition, the development of ferroelectric memory devices require an improvement in matching to conventional silicon process. When Pt or Pt/Ti was used as electrodes of PZT capacitors directly on Si and poly-Si, perovskite PZT was not obtained due to annealing at high temperature. Ir and IrO<sub>2</sub> films were used as new electrode materials in order to solve these problems, in this study.

## 2. Experimental

Pb(Zr<sub>0.52</sub>Ti<sub>0.48</sub>)O<sub>3</sub> (PZT(52/48)) films grown by conventional sol-gel method were used as ferroelectric materials. <sup>5)</sup> The films were finally annealed at 700°C for 1 min in pure oxygen by rapid thermal annealing (RTA).

Pt, Ir, IrO<sub>2</sub> and other metals were used as the electrode materials of the PZT capacitors. The electrode materials were deposited by RF magnetron sputtering system. As the substrate to fabricate the capacitors, oxidized Si wafers (SiO<sub>2</sub>(600 nm) / Si(100)) and poly-Si coated oxidized Si wafers (poly-Si(450 nm) / SiO<sub>2</sub>(25 nm) / Si(100)) were used.

X-ray diffraction (XRD) was used to investigate the crystallographic properties. Thickness of the thin films was measured by scanning electron microscopy (SEM) images of the cross section. Microstructures of the PZT and electrode films were observed using a transmission electron microscope (TEM). The depth profiles of these capacitors were analyzed by secondary ion mass spectrometry (SIMS). The *D-E* hysteresis loops were measured by conventional Sawyer-Tower circuit at 1kHz.

## 3. Results and Discussion

### 3.1. The PZT thin films on IrO<sub>2</sub> electrodes

IrO<sub>2</sub> single layer films were used as electrodes of PZT capacitors. Oxidized Si wafers (SiO<sub>2</sub>(600nm) / Si(100)) were used as substrates. The electrodes were formed by reactive RF magnetron sputtering using a Ir target without substrate heating. (Substrate temperature was about 150°C during sputtering.) These films were annealed at various temperature by RTA after deposition. Annealing temperature of bottom and top IrO<sub>2</sub> electrodes were (a) no annealing, (b) 400°C, (c) 500°C, (d) 600°C and (e) 700°C, respectively. Figure 1 shows a SEM photograph of a IrO<sub>2</sub> film annealed at 600°C by RTA. When IrO<sub>2</sub> films were annealed at other temperature, similar surface morphologies to that in Fig. 1 were exhibited. PZT thin films were grown by sol-gel method with preannealing at 400°C and final annealing at 700°C. Figure 2 shows a process flow chart of IrO<sub>2</sub> / PZT / IrO<sub>2</sub> capacitors.

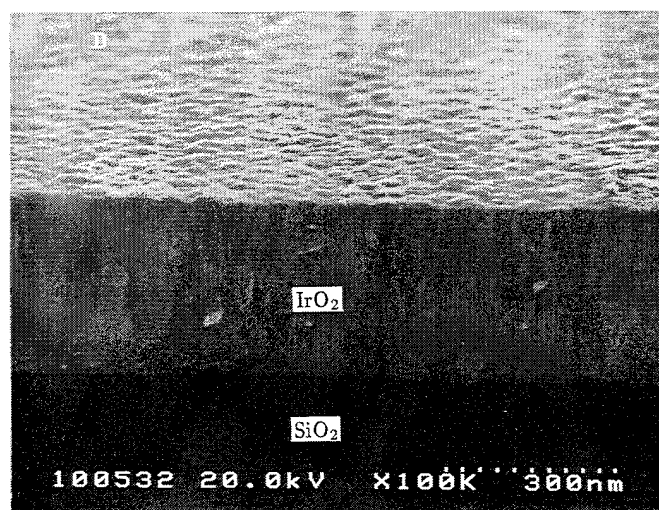


Fig. 1. A SEM photograph of IrO<sub>2</sub> thin films. (annealed by RTA at 600°C after deposition)



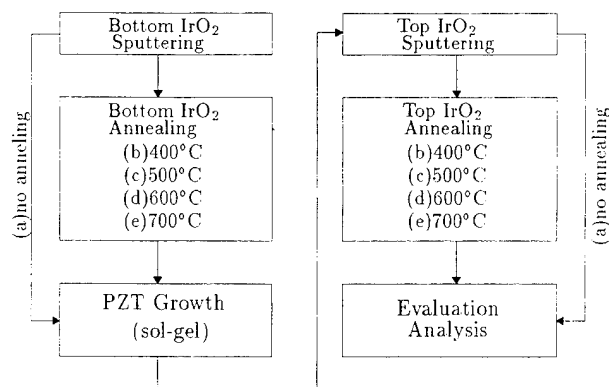


Fig. 2. A process flow chart of IrO<sub>2</sub>/PZT/IrO<sub>2</sub> capacitors.

PZT single phase films were obtained all of the capacitors. IrO<sub>2</sub> and PZT films had crystal grains of which the axis was randomly oriented. One of their XRD charts is shown in Fig. 3. There was very little difference between their crystallinity.

On the other hand, these capacitors had some different electric properties. Every capacitors showed the value of remanent polarization ( $P_r$ ) and coercive field ( $E_c$ ) were about 12  $\mu\text{C}/\text{cm}^2$  and 40 kV/cm, respectively. However, there was the dependence of fatigue properties and leakage current on electrode annealing temperature. The fatigue properties of PZT thin films with electrodes annealing at various temperature are shown in Fig. 4. Switching cycles mean the number of  $\pm 5$  V switching pulses applied to PZT thin films. The frequency of the pulses is 2MHz. When bottom and top IrO<sub>2</sub> electrodes were annealed at 400°C,  $P_r$  of PZT thin films decreased by only 5% below initial remanent polarization ( $P_0$ ) after  $10^{10}$  switching cycles. An improvement in a fatigue property was obtained by electrode annealing, but on the contrary as annealing temperature went up too high, a fatigue property was degraded. We considered that the cause of such a degradation of a fatigue property was interaction or interdiffusion at the PZT/IrO<sub>2</sub> interface during annealing of PZT films and electrodes.

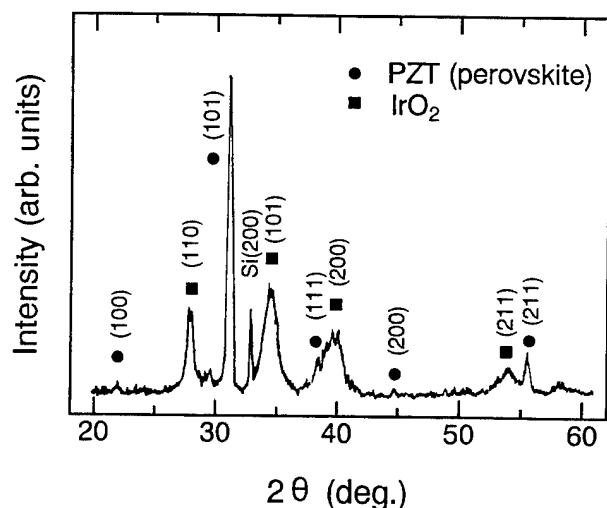


Fig. 3. A X-ray diffraction pattern of a PZT/IrO<sub>2</sub> structure. (annealed by RTA at 600°C after deposition)

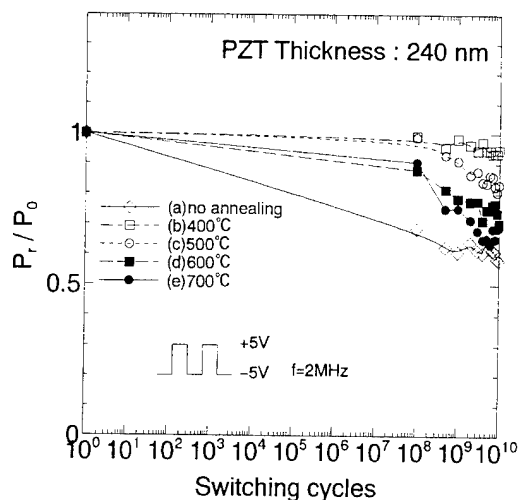


Fig. 4. Fatigue properties of PZT thin films using IrO<sub>2</sub> bottom and top electrode with electrode annealing at various temperature.

In order to compare properties of PZT capacitors between using IrO<sub>2</sub> and Pt electrodes, PZT capacitors using Pt top electrodes were fabricated. Bottom electrodes, PZT growth condition, electrodes annealing and other conditions of these capacitors were same as those using IrO<sub>2</sub> top electrodes. Fatigue properties of capacitors using Pt top electrodes were inferior to those using IrO<sub>2</sub> electrodes. However, there was little dependence of characteristics of these capacitors on annealing temperature at high temperature. Figure 5 shows leakage current of PZT capacitors using Pt and IrO<sub>2</sub> top electrodes. In the case of PZT capacitors using IrO<sub>2</sub> electrodes, leakage current increased by electrode annealing at more than 500°C. The increase may be also caused by interaction or interdiffusion at the PZT/IrO<sub>2</sub> interface.

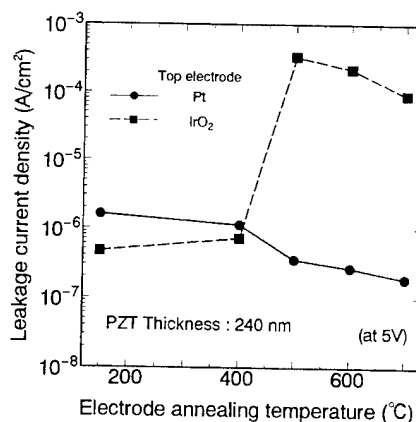


Fig. 5. Leakage current characteristics of PZT capacitors using IrO<sub>2</sub> and Pt top electrodes with electrode annealing at various temperature.

### 3.2. $\text{IrO}_2$ films using as barrier layer

When  $\text{IrO}_2$  films used as electrodes of PZT capacitors, fatigue properties were improved, but there was dependence of fatigue properties and leakage current. Leakage current and fatigue properties were degraded after high temperature annealing. So,  $\text{IrO}_2$  films used as barrier layer under Pt and Ir electrodes. Pt and Ir films deposited on 50–70 nm thick  $\text{IrO}_2$  films by RF magnetron sputtering system without substrate heating and annealed at  $400^\circ\text{C}$  after deposition. The thickness of both Pt and Ir was about 200 nm. PZT thin films grown by sol-gel method on Pt and Ir.  $\text{IrO}_2$  films deposited on PZT thin films as top electrodes and annealed at  $400^\circ\text{C}$ .

Microstructures of electrodes and PZT films were observed by TEM. In Fig. 6 and Fig 7, a TEM photograph of a conventional PZT/Pt/Ti structure and a PZT/Pt/ $\text{IrO}_2$  structure were shown, respectively. Using a Pt/Ti bottom electrode caused interdiffusion and interaction of Ti and made a Pt/Ti interface obscure. Pt on the Ti layer exhibited very poor crystalline and a PZT/Pt interface was very rough. There were a few voids at Pt/PZT interface. On the other hand, when a Pt/ $\text{IrO}_2$  electrode was used, Pt/ $\text{IrO}_2$  and PZT/Pt interfaces were very clear and smooth, and good crystalline Pt was obtained. In the case of using a Ir/ $\text{IrO}_2$  electrode, similar observational result to using Pt/ $\text{IrO}_2$  was obtained.

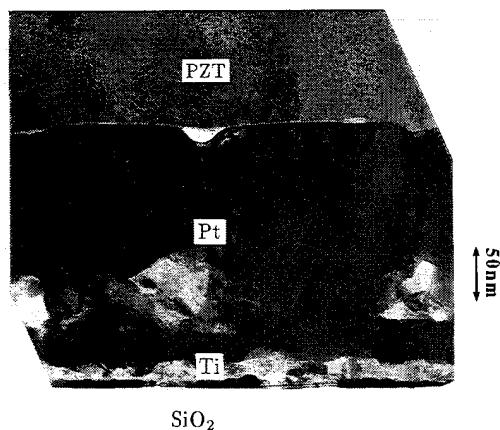


Fig. 6. A TEM image of a PZT/Pt/Ti structure.

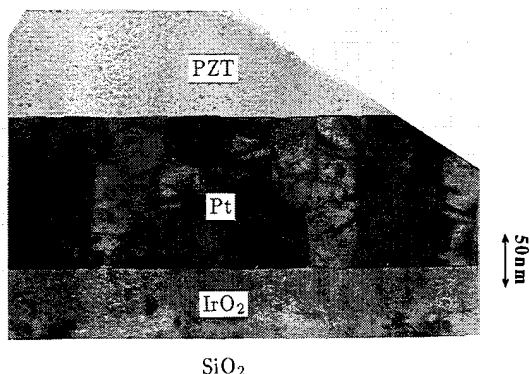


Fig. 7. A TEM image of a PZT/Pt/ $\text{IrO}_2$  structure.

### 3.3. PZT capacitors on poly-Si

PZT capacitors with good properties could be obtained on polycrystalline silicon (poly-Si) by using  $\text{IrO}_2$ . X-ray diffraction (XRD) patterns of PZT thin films using (a) Pt, (b) Pt/Ti and (c) Pt/ $\text{IrO}_2$  electrodes on poly-Si are shown in Fig. 8. The perovskite phase is not found and very strong PtSi peaks and a small pyrochlore peak are shown in films on Pt/poly-Si. This film has no ferroelectric properties. In Fig. 8-(B), many PtSi and TiSi peaks are found. The film on Pt/Ti/poly-Si has perovskite phases, but the ferroelectric properties of this film are very poor. From other analyses, we know that Ti under Pt was oxidized by oxygen though the Pt during final annealing. When a Pt/ $\text{IrO}_2$  layer was used as a bottom electrode, a very strong Pt (111) peak and perovskite PZT phase were obtained, and no PtSi peak could be found (Fig 8-(c)). Pt was connected electrically with poly-Si completely. The electric properties of the PZT film capacitors on poly-Si with  $\text{IrO}_2$  layer were as good as those of the PZT thin film capacitors using  $\text{IrO}_2$  on  $\text{SiO}_2$ . It seemed that the advantage was brought by the diffusion barrier effect and the lack of reactivity of  $\text{IrO}_2$  with Si at high temperature.

In order to confirm the barrier effect of  $\text{IrO}_2$ , depth profiles for elements of PZT and electrodes were measured by SIMS method. Figure 9 shows SIMS depth profiles of PZT capacitors using Pt/ $\text{IrO}_2$  and Ir/ $\text{IrO}_2$  as bottom electrodes on MOS structure. It was confirmed from the profiles of the capacitors using a Pt/ $\text{IrO}_2$  electrode that Pb diffused into the Pt layer, but the diffusion was stopped at the surface of  $\text{IrO}_2$ . In the case of the capacitor using an Ir/ $\text{IrO}_2$  bottom electrode, Pb never diffused into electrodes, because Ir was oxidized at the surface and grain boundaries of Ir films during thermal processing and such  $\text{IrO}_2$  probably had a good barrier effect. The result could be considered as showing the barrier effect of  $\text{IrO}_2$ .

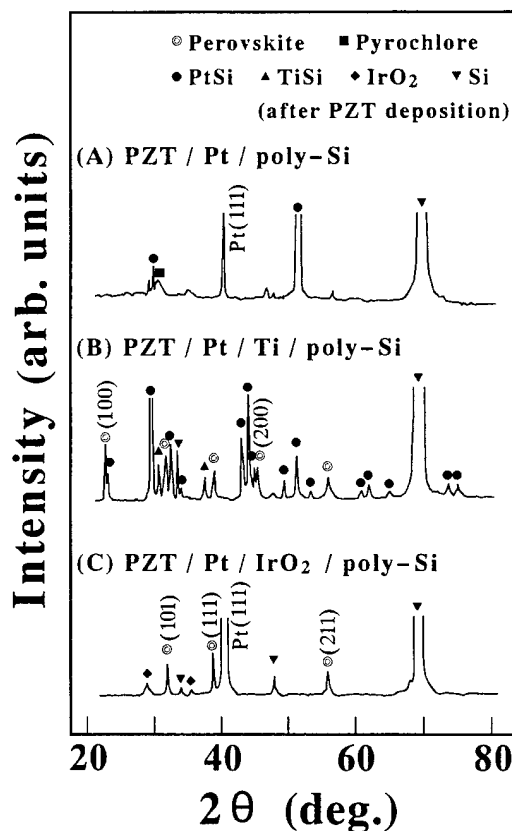


Fig. 8. X-ray diffraction patterns of PZT capacitors using various electrodes.

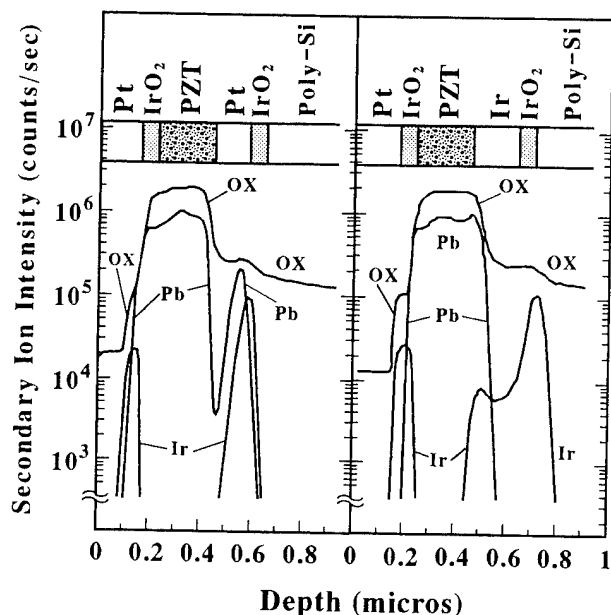


Fig. 9. SIMS depth profiles of PZT capacitors using Ir/IrO<sub>2</sub> and Pt/IrO<sub>2</sub> bottom electrodes. (only about Pb, Ir, Pt and O)

### 3.4. Fatigue properties

The fatigue properties of PZT thin films using Pt/Ti and Ir/IrO<sub>2</sub> electrodes are shown in Fig. 10.  $P_r$  of the PZT film on a Pt/Ti electrode was reduced to half by about  $10^8$  cycles of switching pulses. When a Ir/IrO<sub>2</sub> bottom electrode used,  $P_r$  of the PZT film showed no degradation up to  $10^{12}$  cycles. There were little difference of the fatigue properties between on Ir/IrO<sub>2</sub> and on Pt/IrO<sub>2</sub>. It is considered that the improvement in fatigue properties could be obtained by the diffusion barrier effect of Ir and IrO<sub>2</sub>.

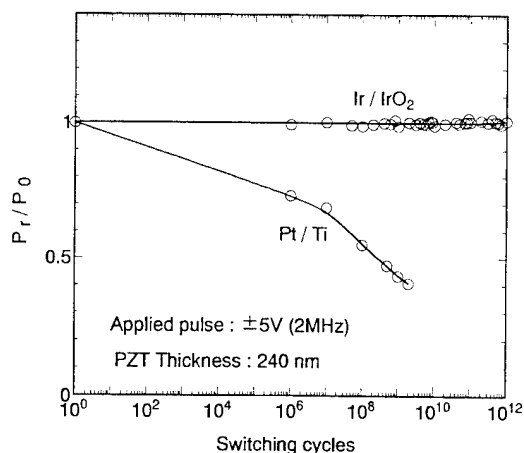


Fig. 10. Fatigue properties of PZT thin films on Ir/IrO<sub>2</sub> and Pt/Ti.

PZT thin film capacitors were prepared using Ir and IrO<sub>2</sub> films as new electrodes. When IrO<sub>2</sub> films used as bottom and top electrodes of PZT capacitors, an improvement of a fatigue property was obtained, but on the contrary as electrode annealing temperature went up too high, leakage current and fatigue properties were degraded. The PZT capacitors on Ir/IrO<sub>2</sub> and Pt/IrO<sub>2</sub> had good properties not only on SiO<sub>2</sub> but also on poly-Si and showed no fatigue up to  $10^{12}$  cycles of  $\pm 5$  V switching pulses. The advantages of IrO<sub>2</sub> films were probably caused by their diffusion barrier effect and the lack of reactivity with Si at high temperature.

### Acknowledgement

The authors would like to thank Mr. Katsumi Ogi and the other staff of Mitsubishi Materials Corporation for the supply of ferroelectric source materials. They would like also to thank Professor Tadashi Shiosaki and Dr. Masaru Shimizu (Kyoto University) for valuable discussions.

### References

- 1) C. K. Kwok, D. P. Vijay, S. B. Desu, N. R. Parikh and E. A. Hill, "Conductive Oxide Electrodes for Ferroelectric Films," Proc. 4th Int. Symp. Integrated Ferroelectrics, Colorado Springs, 1992, pp.412.
- 2) K. R. Bellur, H. N. Al-Shareef, S. H. Rou, K. D. Gifford, O. Auciello and A. I. Kingon, "Electrical Characterization of Sol-Gel Derived PZT Thin Films," Proc. 8th IEEE Int. Symp. Applications of Ferroelectrics, Greenville, 1992 (IEEE, Piscataway, 1992), pp.448.
- 3) R. Ramesh, W. K. Chan, H. Gilchrist, B. Wilkens, T. Sands, J. M. Tarascon, V. G. Keramidas, J. T. Evans, Jr, F. D. Gealy and D. K. Fork, "Oxide Ferroelectric/Cuprate Superconductor Heterostructures: Growth and Properties," Mat. Res. Soc. Symp. Proc. (1992), vol.243 pp.477.
- 4) J. T. Cheung, P. E. D. Morgan and R. Neurgaonkar, "Pulsed Laser Deposition of Epitaxial and Conductive La<sub>0.5</sub>Sr<sub>0.5</sub>CoO<sub>3</sub> Films for Ferroelectric Device Applications," Proc. 4th Int. Symp. Integrated Ferroelectrics, Colorado Springs, 1992, pp.158.
- 5) K. Sameshima, T. Nakamura, K. Hoshiba, Y. Nakao, A. Kamisawa, T. Atsuki, N. Soyama and K. Ogi, "Preparation of Pb(Zr,Ti)O<sub>3</sub> Films on Pt/Ti/Ta Electrodes by Sol-Gel Process," Jpn. J. Appl. Phys., vol.32 pp.4144-4146, 1993.

# Electrical Conduction and Dielectric Behaviour of $\text{Ge}^{4+}$ -Substituted Magnesium Ferrites

D.R. Sagar, S.N. Chatterjee, Chandra Prakash\* and Pran Kishan

Microwave Division, Solidstate Physics Laboratory,

Lucknow Road, Delhi - 110 054, India

**Abstract:** Series of magnesium ferrites with generic formula  $\text{Mg}_{1-x}\text{Ge}_x\text{Fe}_{2-2x}\text{O}_4$  were prepared by ceramic method. From XRD studies it is seen that a limited range of  $x$  values yields single phase spinel material and only such samples were investigated further. The lattice parameter data was found to be consistent with the ionic size and concentration of the substituent employed. The dc resistivity ( $\rho$ ) in general was found to increase with  $x$  and can be understood on the basis of cation content redistribution on the two sublattices in accordance with the site occupancy preference of the substituent and the magnetic moment data. The activation energies obtained from temperature variation studies in the ferrimagnetic region (below Curie temperature) show a trend similar to that of  $\rho$ . The results of dielectric measurements with frequency and substitutional level are also discussed.

## INTRODUCTION

Simultaneous presence of magnetic and dielectric nature of ferrites is vastly exploited in a variety of applications at different frequencies. The special feature of these materials is that the properties can be tailored over wide ranges by appropriate substitution of various ions in the chemical formula unit and control of processing procedures. Magnesium ferrites have been found suitable for use in memory cores and in latching microwave devices due to their inherent rectangular hysteresis loop behaviour and low loss characteristics. Achieving desired properties for specific purposes, studies have been carried out by incorporating several cations of different valence states in the crystal structure [1-3]. The content and occupancy at either octahedral and/or tetrahedral sites is of prime importance in deciding the properties of the resulting material. In an earlier publication [4] we reported cation distribution for tetravalent germanium substituted magnesium ferrites. The present paper reports the electrical properties for this series of materials.

## EXPERIMENTAL DETAILS

The chemical formula unit of  $\text{Mg}_{1-x}\text{Ge}_x\text{Fe}_{2-2x}\text{O}_4$  with varying  $x$  values has been used for preparing the samples. Normal ceramic methods consisting of mixing the raw

materials ( $\text{MgCO}_3$ ,  $\text{GeO}_2$  and  $\text{Fe}_2\text{O}_3$  of AR grade here), preforming the powder at 1000 °C for 4 hours, second mixing/grinding stage, compacting the powder in disc and toroidal shapes and finally sintering at 1300 °C for 4 hrs were employed. The details are given in an earlier publication [4]. The amount of substituent i.e.  $\text{Ge}^{4+}$  was increased in small steps. The structural studies were carried out by powder X-ray diffraction technique for ascertaining the formation of spinel structure and presence, if any, of any unwanted or unreacted phases. From the XRD patterns it was seen that only a limited range of  $x$  values yielded single phase spinel formation. For the samples with  $x > 0.4$ , the presence of unreacted chemicals was noticed. Adjustments of processing parameters, particularly sintering temperatures and duration did not result in formation of single phase samples for the said higher  $x$  values. The studies carried out were confined to only these particular samples.

The magnetisation measurements were carried out using a vibrating sample magnetometer model PAR 155 coupled with a closed cycle refrigeration system and a high temperature oven in the range of 80K to the Curie temperature of the respective sample.

The electrical conductivity measurements were made in the temperature range 300 K to the Curie temperature of the specimen. The two probe method was employed for measurements. Air dry silver epoxy was used for making electrical contacts on the flat surfaces of the specimens. From the plots of  $\log \rho$  vs inverse of temperature, activation energies were determined. The same specimens were used for dielectric measurements in the frequency range upto 10 MHz.

## RESULTS AND DISCUSSION

The lattice constant values ' $a$ ' obtained from XRD patterns for the series of materials prepared are given in Fig.1. It is seen that ' $a$ ' decreases with increase in substitutional level  $x$ . In the present case the tetravalent  $\text{Ge}^{4+}$  ion is being substituted in the form of a composite ion ( $\text{Mg}_{0.5}^{2+}\text{Ge}_{0.5}^{4+}$ ) for  $\text{Fe}^{3+}$  ion. The ionic radius of composite ion is smaller than that of  $\text{Fe}^{3+}$  ion (ionic radii of  $\text{Ge}^{4+}$ ,  $\text{Mg}^{2+}$  and  $\text{Fe}^{3+}$  are 0.44, 0.78 and 0.67 Å respectively [5]). Replacement of bigger ion by smaller ion results in

\* Presently with: Materials Research Laboratory, Pennsylvania State University, University Park, PA 16802, USA.

shrinkage of the lattice and hence a decrease in lattice constant in this case with increasing  $x$ .

Variation of magnetic moment ( $M_0$ ) and Curie temperature ( $T_c$ ) with germanium content  $x$  is depicted in Fig. 1. 0°K magnetic moment values were obtained by extrapolating the variations observed in magnetisation over the range 80K to Curie temperature. The behaviour has been explained by the authors [4] on the basis of cationic distribution on the two sites in the spinel structure.

Fig. 2 shows the variation of dc resistivity ( $\rho$ ) at room temperature and activation energy ( $E_p$ ) with  $x$ .  $\rho$  is

observed to increase with  $x$  and can be understood on the basis of site occupancy of different valence ions in the crystal structure. It is well established that  $\text{Ge}^{4+}$  ions have preference for tetrahedral (A) site [6,7]. The dominant mode of conduction in these ferrites is the charge transport between  $\text{Fe}^{2+}$  and  $\text{Fe}^{3+}$  ions, by hopping mechanism, present on the equivalent crystallographic sites. A small amount of  $\text{Fe}^{2+}$  ions is formed during preparation of ferrite samples depending on sintering conditions. It is known that partial reduction of  $\text{Fe}^{3+}$  to  $\text{Fe}^{2+}$  can take place at elevated firing temperatures. A complete reoxidation of  $\text{Fe}^{2+}$  does not, however, take place in dense samples. This conversion is proportional to the total iron ion content present at each site.

Substitution of tetravalent ion as well as additional divalent magnesium ion in the formula unit reduces the overall iron content in the composition. A corresponding decrease in its conversion to divalent ions is expected alongwith. On this basis the observed increase in resistivity with  $x$  is understood. With the temperature the  $\rho$  shows the expected semiconducting behaviour of linear variation of  $\log \rho$  with inverse of temperature. The measurements were taken upto temperatures not exceeding the Curie temperatures of the corresponding samples. The activation

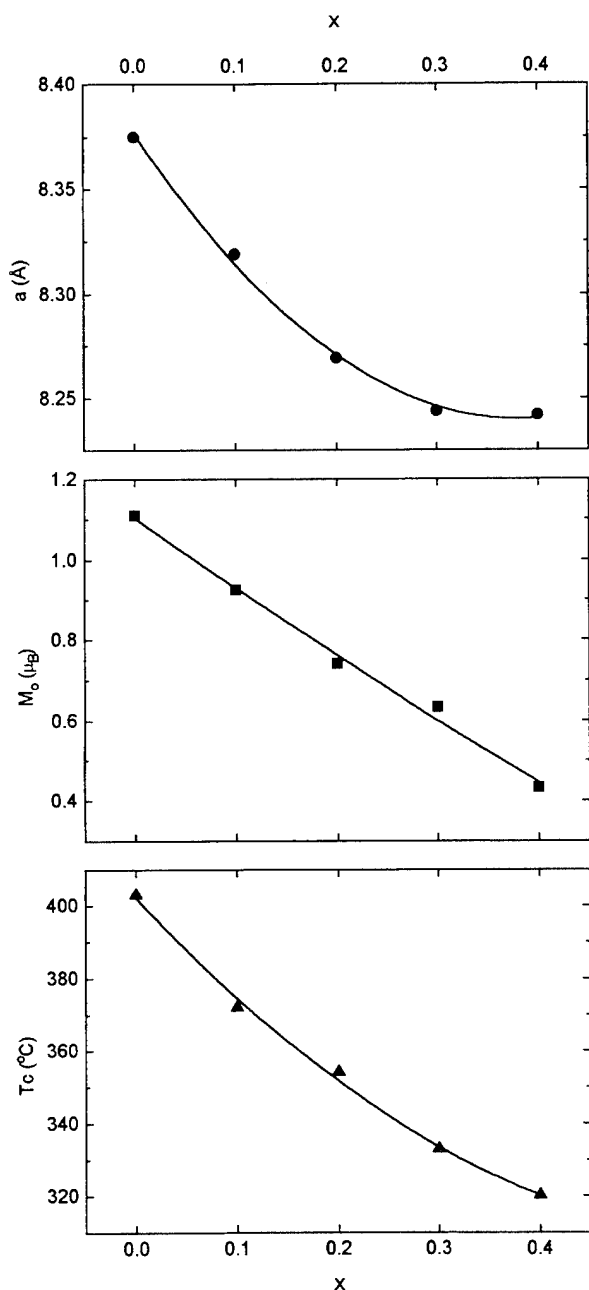


Fig. 1. Variation of lattice constant ( $a$ ), 0K magnetic moment ( $M_0$ ) and Curie temperature ( $T_c$ ) with  $x$  for  $\text{Mg}_{1+x}\text{Ge}_x\text{Fe}_{2-2x}\text{O}_4$ .

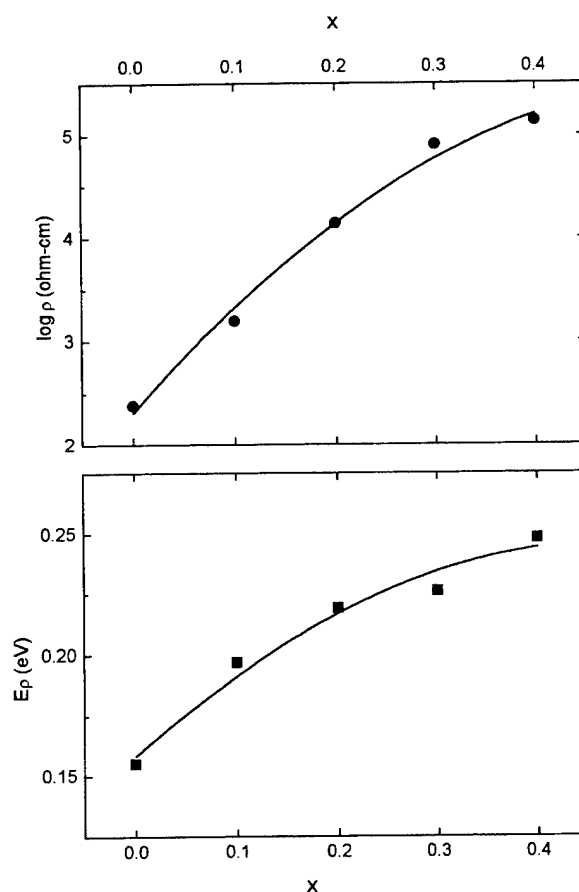


Fig. 2. Variation of resistivity ( $\log \rho$ ) and activation energy ( $E_p$ ) with  $x$  for  $\text{Mg}_{1+x}\text{Ge}_x\text{Fe}_{2-2x}\text{O}_4$ .

energy ( $E_p$ ) values calculated from the above said data are shown in Fig.2. The trend of  $E_p$  with the substitution level is similar to the one shown by  $\rho$  thus indicating that higher values of activation energy corresponds to higher values of the resistivity.

The dielectric constant ( $\epsilon'$ ) measurements were carried out on these samples over the frequency range upto 10MHz. The results are given in Fig.3. The  $\epsilon'$  value shows a decrease with increasing  $x$  at all frequencies. The decrease being large at low frequencies. Earlier studies [8-10] on dielectric behaviour of ferrites showed that the mechanism of dielectric polarisation is similar to that of conduction i.e. the electron exchange interaction between  $Fe^{2+}$  and  $Fe^{3+}$  results in a local displacement of the electrons in the direction of an electric field which determines the polarisation of the ferrites. In the present case as explained above, the effective number of divalent iron ions, which take part in electron exchange i.e. polarisation, decreases with increasing substitutional level  $x$ . This results in a decrease in dielectric constant with  $x$ . The variation of dielectric constant for all the samples

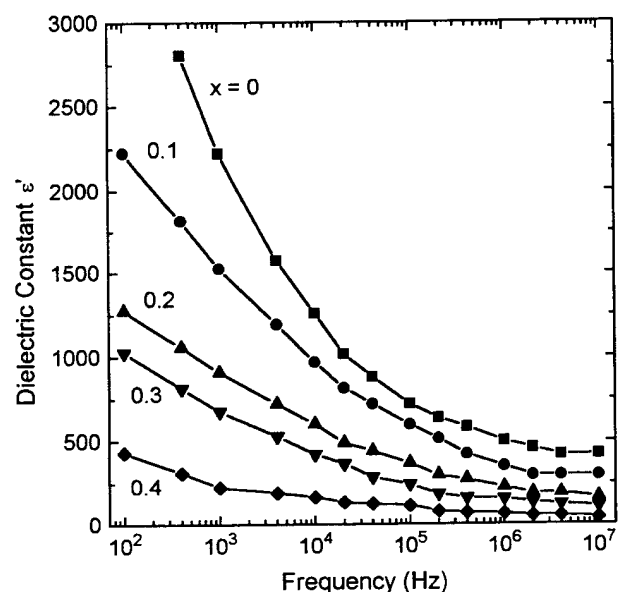


Fig. 3. Variation of dielectric constant with frequency for  $Mg_{1+x}Ge_xFe_{2-2x}O_4$ .

shows dispersion with frequency which is due to Maxwell-Wagner interfacial polarisation [11,12]. It is in agreement with Koops' phenomenological theory [13].

## REFERENCES

- [1] G. Blasse, *Philips Res. Reports Suppl.* 3, 91 (1964).
- [2] H.N. Pandya and R.G. Kulkarni, "Magnetic Behaviour of  $Ni_{1-x}Ge_xFe_2O_4$ ", *Solid State Commun.*, Vol. 61, pp. 645-7, 1987.
- [3] G.J. Baldha and R.G. Kulkarni, "Mössbauer Studies of Spinel System  $Ge_xCu_{1-x}Fe_2O_4$ ", *Solid State Commun.*, Vol. 49, pp. 169-72, 1984.
- [4] D.R. Sagar, Chandra Prakash and Pran Kishan, "Cation Distribution in Germanium-Substituted Magnesium Ferrites", *Solid State Commun.*, Vol. 68, pp. 193-5, 1988.
- [5] J. Smit and H.P.J. Wijn, *Ferrites*, Philips Tech. Library 1959, p.143.
- [6] R.G. Kulkarni and G.J. Baldha, "Spin Glass Behaviour of the Spinel  $Ge_xCu_{1-x}Fe_2O_4$ ", *Solid State Commun.*, Vol. 53, pp. 1001-3, 1987.
- [7] Rustum Roy and Della M. Roy, "An Experimental Study of the Formation and Properties of Synthetic Serpentine and Related Layer Silicate Minerals", *Amer. Min.*, Vol. 39, pp. 957-75, 1954.
- [8] Chandra Prakash and J.S. Baijal, "Dielectric Behaviour of Tetravalent Titanium-Substituted Ni-Zn Ferrites", *J. Less-Common Met.*, Vol. 107, pp. 51-7, 1985.
- [9] N. Rezlescu and E. Rezlescu, "Dielectric Properties of Copper Containing Ferrites", *Phys. Stat. Solidi A*, Vol. 23, pp. 575-82, 1974.
- [10] P.V. Reddy and T.S. Rao, "Dielectric Behaviour of Mixed Lithium-Nickel Ferrites at Low Frequencies", *J. Less-Common Met.*, Vol. 86, pp. 255-61, 1982.
- [11] J.C. Maxwell, *Electricity and Magnetism*, Oxford University Press, Oxford, 1929, Section 328.
- [12] K.W. Wagner, *Ann. Phys.*, Vol. 40, pp. 817, 1913.
- [13] C.G. Koops, "On the Dispersion of Resistivity and Dielectric Constant of Some Semiconductors at Audiofrequencies (Ni-Zn Ferrites)", *Phys. Rev.*, Vol. 83, pp. 121-4, 1951.

# Dielectric Properties and D.C. Resistivity of Magnesium-Substituted Lithium Ferrites

Sumitra Phanjoubam<sup>1</sup>, Deepika Kothari<sup>2</sup>, Chandra Prakash<sup>3\*</sup> and Pran Kishan<sup>3</sup>

<sup>1</sup>Deptt of Physics, Manipur University, Canchipur, Imphal-795003, INDIA.

<sup>2</sup>Centre for Dev. of Physics Education, Rajasthan Univ., Jaipur-302004, INDIA.

<sup>3</sup>Microwave Division, Solidstate Physics Laboratory, Lucknow Road, Delhi - 110054, INDIA.

**Abstract:** The paper reports the influence of magnesium substitution on structural and electrical properties of lithium ferrites. The samples with compositional formula  $\text{Li}_{(1-x)/2}\text{Mg}_x\text{Fe}_{(5-x)/2}\text{O}_4$  with  $x$  ranging from 0.1 to 0.9 were prepared by standard dry ceramic method. XRD shows all the samples to be single phase spinel and the value of lattice constant was found to increase with increasing substitution level  $x$ . The room temperature d.c. resistivity increases with  $x$ . The variation has been explained in terms of hopping mechanism and the cation distribution. The resistivity with temperature shows a change in slope which does not corresponds to Curie temperature. The activation energy determined from the slopes in two temperature regions shows a large difference. It has been interpreted in terms of two conduction mechanisms i.e. ionic and electronic. The dielectric measurements were carried out at room temperature in the frequency range 10 kHz to 10 MHz. Dielectric constant shows a dispersion with frequency for all the samples. The dielectric loss decreases with frequency and does not show any peak with frequency for any of the samples.

## INTRODUCTION

The lithium ferrite which is an inverse spinel has excellent rectangular hysteresis loop properties which can be suitably tailored by appropriate substitution of cations to use the material for some specific application. The properties are predominantly governed by the distribution of cations on tetrahedral and octahedral sites and the type and amount of substitution. A number of investigators [1-4] have studied the influence of various substituents on its different properties. Recently [5] we reported the effect of magnesium substitution on Mössbauer and magnetic properties of lithium ferrites. On the basis of these studies a cation distribution was established. The aim of the present paper is to report d.c. resistivity and dielectric properties for these materials with compositional formula  $\text{Li}_{(1-x)/2}\text{Mg}_x\text{Fe}_{(5-x)/2}\text{O}_4$ .

## EXPERIMENTAL DETAILS

The ferrite samples with compositional formula  $\text{Li}_{(1-x)/2}\text{Mg}_x\text{Fe}_{(5-x)/2}\text{O}_4$ ,  $x = 0.1, 0.3, 0.5, 0.7$  and  $0.9$  were prepared by conventional double sintering ceramic method.

Appropriate quantities of AR grade of  $\text{Li}_2\text{CO}_3$ ,  $\text{MgO}$  and  $\text{Fe}_2\text{O}_3$  were taken and thoroughly mixed in an agate jar mill in presence of distilled water. The dried mixture was pre-fired at  $800^\circ\text{C}$  for 5 hrs. The reacted powder was ball milled again and granulated using a small amount of PVA as binder. The discs were pressed and finally sintered at  $1200^\circ\text{C}$  for 4 hrs followed by slow cooling.

X-ray diffraction patterns were recorded for all the samples. The d.c. resistivity measurements were carried out by two probe method. Electrical contacts were made by applying air dried silver epoxy on flat surfaces of the discs of uniform thickness. The measurements were made using a Keithley digital electrometer model 614 from room temperature to 425K. Dielectric measurements were made on the same specimens using a HP4275 multifrequency LCR meter at room temperature. The capacitance,  $C$ , and loss tangent,  $\tan\delta$ , were measured in the frequency range 10 kHz to 10 MHz. The dielectric constant,  $\epsilon'$ , was calculated using the formula  $\epsilon' = C.t/\epsilon_0 A$ , where  $t$  is the thickness of the specimen,  $A$  is the area of the cross-section and  $\epsilon_0$  the permittivity of the free space.

## RESULTS AND DISCUSSION

X-ray powder diffraction analysis shows all the samples to be single phase spinel structure. From the observed  $d$  values, the lattice constant ' $a$ ' was calculated. Its variation with magnesium content  $x$  is shown in figure 1. The lattice constant increases with increasing  $x$  in the system  $\text{Li}_{(1-x)/2}\text{Mg}_x\text{Fe}_{(5-x)/2}\text{O}_4$ . The variation can be explained in terms of different ionic radii of the cations involved. In the system under investigation, a composite ion  $\text{Li}_{0.5}^{1+}\text{Fe}_{0.5}^{3+}$  is being replaced by  $\text{Mg}^{2+}$  ion. The ionic radii of  $\text{Li}^{1+}$ ,  $\text{Fe}^{3+}$  and  $\text{Mg}^{2+}$  are 0.68, 0.67 and 0.78 Å, respectively.  $\text{Mg}^{2+}$  ion, being larger in size than composite ion, causes the unit cell to expand which results in an increase in the value of lattice constant with increasing magnesium concentration. This explains the observed variation.

The d.c. resistivity  $\rho$  was observed to increase with  $x$  in the compositional formula  $\text{Li}_{(1-x)/2}\text{Mg}_x\text{Fe}_{(5-x)/2}\text{O}_4$ . The variation is shown in figure 2. The electrical conduction in ferrites can be explained by hopping mechanism involving electron exchange between ions of the same element

\* Presently with: Materials Research Laboratory, Pennsylvania State University, University Park, PA 16802, USA.

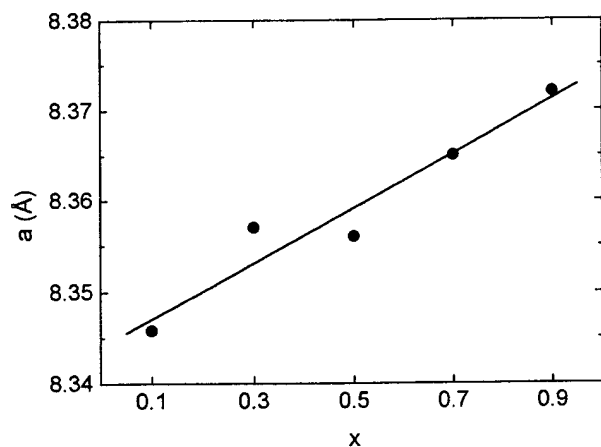


Fig. 1. Variation of lattice constant (a) with x for  $\text{Li}_{(1-x)/2}\text{Mg}_x\text{Fe}_{(5-x)/2}\text{O}_4$ .

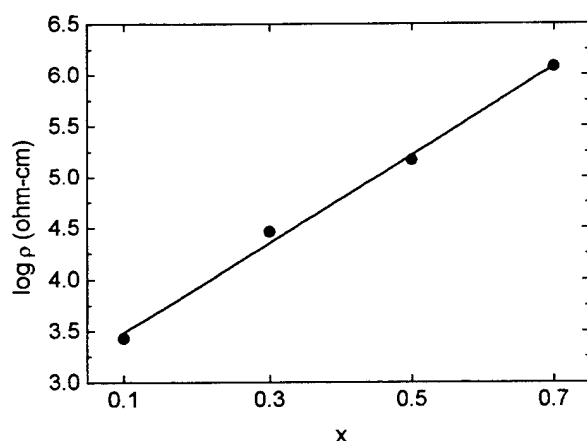
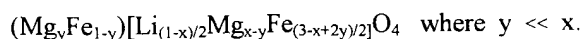


Fig. 2. Variation of d.c. resistivity ( $\log \rho$ ) with x for  $\text{Li}_{(1-x)/2}\text{Mg}_x\text{Fe}_{(5-x)/2}\text{O}_4$ .

present in more than one valence state and distributed randomly over crystallographically equivalent lattice sites. In the present case electronic conduction takes place by hopping between  $\text{Fe}^{2+}$  and  $\text{Fe}^{3+}$  ions present at octahedral (B) sites [6]. In addition to this, the lithium ferrite spinels may exhibit ionic conductivity also as it contains reducible iron ions and lithium ions [7,8].  $\text{Fe}^{2+}$  ions may be formed due to the partial evaporation of lithium during sintering process [9]. These  $\text{Fe}^{2+}$  ions preferentially occupy the B sites and B-B hopping between  $\text{Fe}^{2+}$  and  $\text{Fe}^{3+}$  is the dominant mode of conduction.

For the present series of materials, the general cation distribution had been inferred from Mössbauer studies [5] to be:



Here cations enclosed by parentheses occupy tetrahedral (A) sites and those enclosed by square brackets

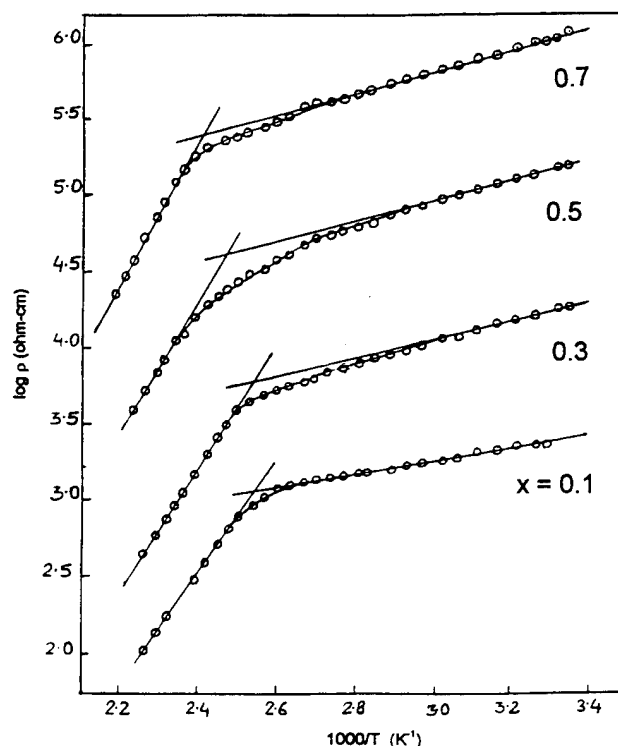


Fig. 3. Variation of  $\log \rho$  with inverse of temperature ( $1/T$ ) for  $\text{Li}_{(1-x)/2}\text{Mg}_x\text{Fe}_{(5-x)/2}\text{O}_4$ .

occupy octahedral (B) sites. It is seen that an increase in Mg content x leads to a reduction in  $\text{Li}^{1+}$  and iron ions at B sites. A corresponding decrease in conversion of  $\text{Fe}^{3+}$  to  $\text{Fe}^{2+}$  is expected resulting in a decrease in conduction electrons thereby increasing the resistivity with increasing x. This explains the observed behaviour.

The plots of  $\log \rho$  vs  $1/T$  for all the specimens are given in figure 3. A change in slope was observed for all the samples which is in agreement with the earlier observations on similar materials [10-12]. Two ranges of activation energies were obtained corresponding to the two slopes. Fig. 4 shows the plot of activation energy ( $E_p$ ) versus composition. The temperature at which change in the slope is observed does not correspond to the measured Curie temperature [5] of the respective sample. The existence of two parallel conduction mechanisms with different activation energies may therefore be responsible for this change in slope [13]. The observed curves of Fig. 4 could be divided into two regions with different activation energies: region I or low temperature region with  $E_p$  between 0.08 eV and 0.15 eV and region II or high temperature region with  $E_p$  between 0.72 eV and 0.93 eV for samples with different x values. As mentioned above lithium ferrites may exhibit ionic conductivity too in addition to electronic conductivity. The ionic conduction has high activation energy [10], the conduction in region II may therefore be due to this mechanism. However, in region I with low activation energy the dominant mode of conduction may be electronic conduction. It is observed



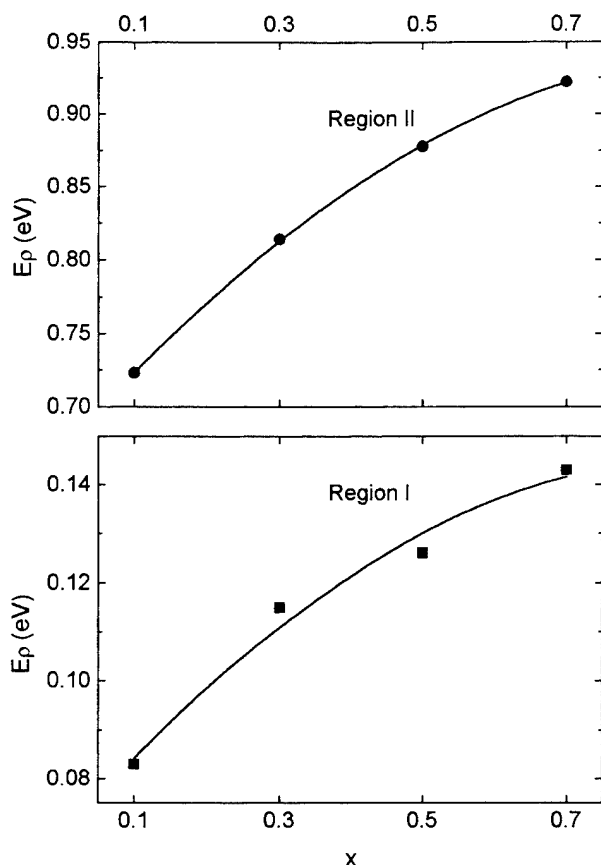


Fig. 4. Variation of activation energy ( $E_p$ ) for region I and region II with  $x$  for  $\text{Li}_{(1-x)/2}\text{Mg}_x\text{Fe}_{(5-x)/2}\text{O}_4$ .

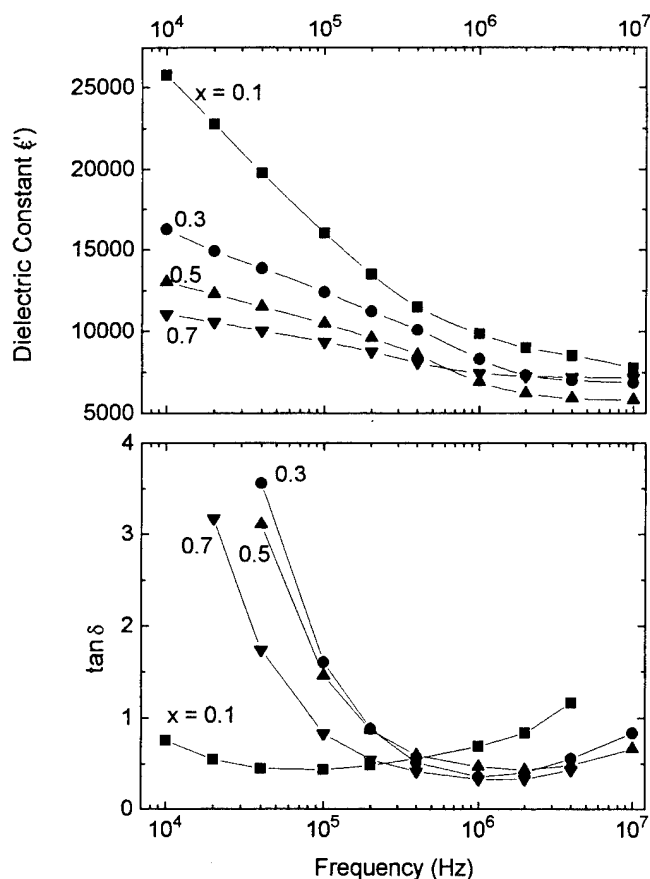


Fig. 5. Variation of dielectric constant and  $\tan\delta$  with frequency for  $\text{Li}_{(1-x)/2}\text{Mg}_x\text{Fe}_{(5-x)/2}\text{O}_4$ .

that the activation energy for both the regions increases with increasing magnesium content  $x$  which, as expected, is in accordance with the variation of resistivity with  $x$ .

Fig. 5 depicts the variation of dielectric constant ( $\epsilon'$ ) and loss tangent ( $\tan\delta$ ) with frequency at room temperature in the frequency range 10 kHz to 10 MHz. A dispersion in relative permittivity ( $\epsilon'$ ) with frequency can be seen for all the samples. It is observed that  $\epsilon'$  is very high in the low frequency range and it decreases with frequency. At high frequencies the value of  $\epsilon'$  is low and becomes less dependent on frequency. This has also been observed previously by other workers for similar materials [14-16].

The observed variation of dielectric constant with frequency can be attributed to the space charge polarisation, which is due to an inhomogeneous dielectric structure as discussed by Maxwell [17] and Wagner [18] and is in agreement with Koops phenomenological theory [19]. In the low frequency range,  $\epsilon'$  decreases with increasing substitutional level  $x$ . As mentioned above, at room temperature the dominant mode of conduction is electron hopping between  $\text{Fe}^{2+}$  and  $\text{Fe}^{3+}$  and the number of  $\text{Fe}^{2+}$  ions decreases with increasing  $x$ . With decreasing ferrous ions which are responsible for polarisation, a decrease in dielectric constant is expected with  $x$ . It can be seen from

Fig. 5 that  $\tan\delta$  does not show any peak with frequency in the frequency range under study, for any of the samples. The absence of the peak is perhaps due to small contribution of dielectric permittivity to show any observable variation of loss factor with frequency.

## REFERENCES

- [1] G. Blasse, *Philips Res. Reports Suppl.* Vol. 3, p. 91, 1964.
- [2] J.W. Young and J. Smit, "Mössbauer Effect Studies for Lithium Zinc Ferrites", *J. Appl. Phys.* Vol. 42, pp. 2344-8, 1971.
- [3] J.L. Dorman, "Mössbauer Studies of Substituted Lithium Ferrites: Influence of Supertransferred Hyperfine Fields and Relaxation", *Rev. Phys. Appl.*, Vol. 15, pp. 1113-21, 1980.
- [4] Pran Kishan, "Synthesis and Studies on Substituted Lithium Ferrites", Ph.D. Thesis, Delhi Univ., 1987.
- [5] J.S. Baijal, Sumitra Phanjoubam, Deepika Kothari, Chandra Prakash and Pran Kishan, "Hyperfine Interaction and Magnetic Studies of Li-Mg Ferrites", *Solid State Commun.*, Vol. 83, pp. 679-682, 1992.

- [6] E.J. Verwey, P.W. Haayman and F.C. Romeijn, "Physical Properties and Cation Arrangement of Oxides with Spinel Structures: II Electronic Conductivity", *J. Chem. Phys.*, Vol. 15, pp. 181-7, 1947.
- [7] Tsuneo Matsui and J. Bruce Wagner, Jr, "Electronic Properties of  $\text{LiFe}_5\text{O}_8$ ", *J. Electrochem. Soc.*, Vol. 124, pp. 1141-3, 1977.
- [8] F.F.Y. Wang, "Electron Conduction in Single Crystal Lithium Ferrite", *Amer. Ceram. Soc. Bull.*, Vol. 49, p. 499, 1970.
- [9] N. Rezlescu, D. Condurache, C. Naum and E. Luca, "On the Physical Properties of Lithium-Zinc Ferrites", *Rev. Roum. Phys.* Vol. 18, pp. 727-34, 1973.
- [10] R. Manjula, V.R.K. Murthy and J. Sobhanadri, "Electrical Conductivity and Thermoelectric Power Measurements of Some Li-Ti Ferrites", *J. Appl. Phys.*, Vol. 59, pp. 2929-32, 1986.
- [11] W. Kirsten, "Polaronic DC Conduction in Titanium Substituted Ni-Fe Ferrites", *Phys. Stat. Solidi A*, Vol. 28, pp. 447-53, 1975.
- [12] Clinton F. Jefferson and C. Kenneth Baker, "Mechanism of Electronic Conduction in Ni-Fe Ferrites", *IEEE Trans. Magnetics*, Vol. MAG-4, pp. 460-4, 1968.
- [13] J. Smit and H.P.J. Wijn, *Ferrites*, Philips Tech. Library 1959.
- [14] O.S. Josyulu and J. Sobhanadri, "DC Conductivity and Dielectric Behaviour of Cobalt-Zinc Ferrites", *Phys. Stat. Solidi A*, Vol. 59, pp. 323-9, 1980.
- [15] Pran Kishan, D.R. Sagar and Prem Swarup, "Electrical Conductivity and Dielectric Behaviour in Zinc Substituted Lithium Ferrites", *J. Less-Common Met.*, Vol. 108, pp. 345-51, 1985.
- [16] Chandra Prakash and J.S. Baijal, "Dielectric Behaviour of Tetravalent Titanium-Substituted Ni-Zn Ferrites", *J. Less-Common Met.*, Vol. 107, pp. 51-57, 1985.
- [17] J.C. Maxwell, *Electricity and Magnetism*, Oxford University Press, Oxford, 1929, Section 328.
- [18] K.W. Wagner, *Ann. Phys.*, Vol. 40, pp. 817, 1913.
- [19] C.G. Koops, "On the Dispersion of Resistivity and Dielectric Constant of Some Semiconductors at Audiofrequencies (Ni-Zn Ferrites)", *Phys. Rev.*, Vol. 83, pp. 121, 1951.



# Poster Session - P3: Dielectrics

# Investigation of $\text{Bi}_{0.5}\text{Na}_{0.5}\text{TiO}_3\text{-PbTiO}_3$ System for High Temperature Dielectrics

S. Kuharungrong and W.A. Schulze  
NYS College of Ceramics at Alfred University  
Alfred, NY 14802

**Abstract** -- Bismuth Sodium Titanate (BNT) has been investigated widely in terms of phase transitions, dielectric, piezoelectric and pyroelectric properties. The first transition temperature of this material is about 220 °C. However, doped with Pb this material gives a higher dielectric constant and a lower phase transition temperature. The dielectric properties and structure of  $x\text{PbTiO}_3 - (1-x)\text{Bi}_{0.5}\text{Na}_{0.5}\text{TiO}_3$  solid solution are investigated. The phase boundary of this system is between 15-17%Pb. Pb also decreases the broadness of BNT dielectric response. Modifications with cations such as  $\text{K}^+$  and  $\text{La}^{3+}$  in 10%Pb doped BNT were studied in terms of dielectric properties and broadened phase transitions.

## I. INTRODUCTION

$\text{Bi}_{0.5}\text{Na}_{0.5}\text{TiO}_3$  (BNT) has multiple and broad phase transitions. It has a rhombohedral [1] ferroelectric phase [2] at room temperature and transforms to an antiferroelectric [3] and paraelectric phase [4] above 220 °C and 320 °C, respectively. Many studies have been performed on BNT and BNT-based solid solution with lead free or low lead content as a candidate for piezoelectric [5]-[7] or pyroelectric [5],[8] devices. Only a few [9],[10] studied the dielectric properties of Pb doped BNT. These results showed a phase boundary in  $\text{Bi}_{0.5}\text{Na}_{0.5}\text{TiO}_3\text{-PbTiO}_3$  (BNT-PT) solid solution in different regions, 0-10% Pb from ref [9] and 13% Pb from ref [10]. In this paper the phase boundary of this system was studied from dielectric measurements and x-ray diffraction as a function of %Pb. The broadness of the Curie peak was investigated as a function of %Pb. In addition, modifications with K and La on 0.9BNT-0.1PT were also studied.

## II. EXPERIMENTAL TECHNIQUES

All compositions were prepared by reacting reagent grade oxides or carbonates. After ball-milling with ethanol and zirconia media, the dried mixture was calcined at 750 °C in air for two hours. The calcined material was milled with polyvinyl alcohol binder. The dried powder was pressed into disks. After binder burn-out, the disks were sintered at 1200 °C with an hour soaking period in a closed crucible.

Temperature dependence of the dielectric constant and loss tangent were measured by a HP4192A Impedance Analyzer. The disks were electroded with fired-on gold paste. All data were collected every 2 °C with increasing temperature at 2 °C/min. The broadness parameter above the Curie point was calculated as a function of %Pb following Isupov's model [11].

The structures at room temperature for BNT-PT system were determined by x-ray powder diffraction.

## III. RESULTS AND DISCUSSION

Figure 1 shows the change of the dielectric constant ( $K'$ ) as a function of temperature for the BNT-PT system at a frequency of 10 kHz. This result indicates that the maximum  $K'$  ( $K'_{\text{max}}$ ) increases as the %Pb increases. In addition, the first transition temperature decreases as %Pb increases and abruptly disappears at 17% Pb.

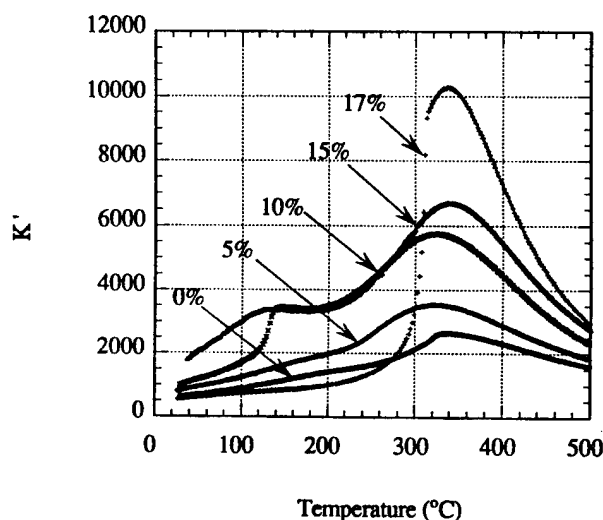


Fig. 1 Change in dielectric constant with temperature for BNT-PT solid solution at a frequency of 10 kHz.

Figure 2 shows the results of the reciprocal dielectric constant as a function of  $T - T_m$  ( $T_m$  is the temperature at  $K'_{\text{max}}$ ) and %Pb. This indicates that the experimental results fit quite well with the Isupov's model [11]. His model showed that above the Curie point there was predominately parallel mixing of the polar phase and nonpolar phase in the relaxor material. As the temperature increases, the polar

phase decreases. The parabolic temperature dependence of  $1/K'$  changes to linear at higher temperature. The broadness parameter,  $\sigma$ , and the Curie constant,  $C$ , of this system at a frequency of 10 kHz is given in Table 1.

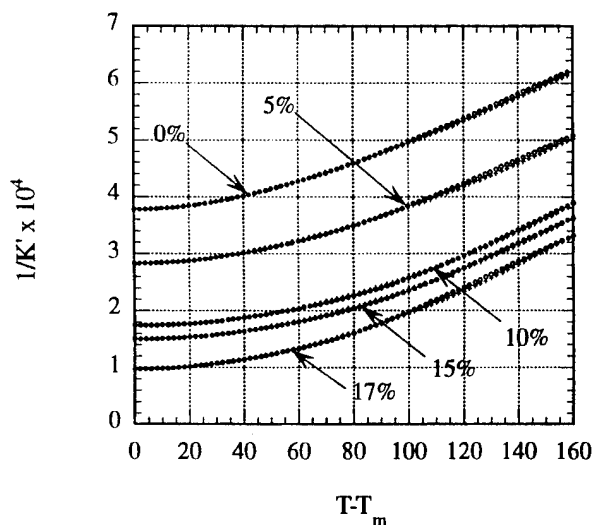


Fig. 2 Dependency of the reciprocal dielectric constant on the temperature above the Curie point of BNT-PT by following Isupov's model at 10 kHz (+ = from experiment, o = from calculation)

Table 1. Parameters governing temperature dependence of the  $K'$  above the Curie point for  $(100-x)\text{BNT} - x\text{PT}$  solid solution

x	$10^4/K'_{\text{max}}$	$\sigma$ (°C)	$C \times 10^5$ (°C)
0	3.78	108.9	4.42
5	2.83	107.6	4.59
10	1.74	99.3	4.19
15	1.50	91.9	4.56
17	0.97	64.6	4.33

The broadness parameter,  $\sigma$ , decreases with increasing Pb content and anomalously decreases as the structure becomes more ordered at 17%Pb. As Pb is added to BNT, three types of ions (Bi, Na and Pb) are believed to be in the A lattice sites with a coordination number of 12. This should increase the heterogeneity of the composition. However, the size and polarizability of  $\text{Bi}^{3+}$  is close to that of  $\text{Pb}^{2+}$ . This actually decreases the compositional fluctuations due to the decrease of  $\text{Na}^+$ . In other words, above the Curie temperature the broadness of  $K'$  decreases as the concentration of Pb increases.

Figure 3 shows the x-ray diffraction patterns of BNT-PT solid solution at room temperature. These results indicate that BNT, 10%Pb and 15%Pb doped BNT have the same structure. However, the structure changes to tetragonal at 17%Pb. Therefore, the phase boundary at

room temperature of this solid solution is at 15-17%Pb. This also is in agreement with the dielectric data of this system.

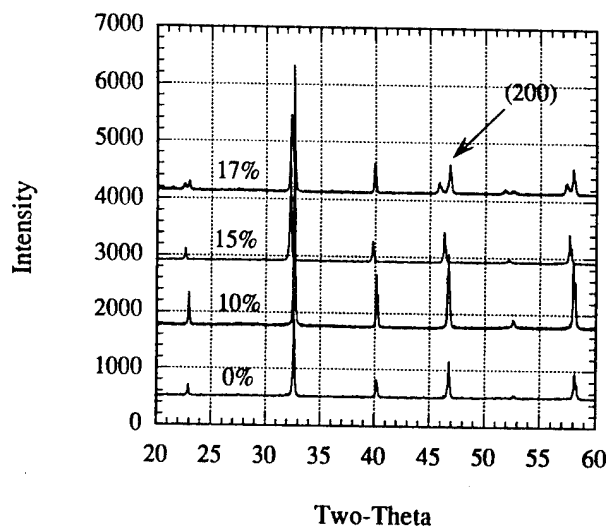


Fig. 3 XRD patterns of BNT, 10%, 15% and 17%Pb doped BNT at room temperature.

Figures 4 and 5 show the  $K'$  and loss tangent as a function of temperature and frequency of 10%Pb doped BNT (BN10PT) with K partially replacing Na. Doped with K this material gives a broader  $K'$  than that of BN10PT and the first phase transition shifts towards a lower temperature.

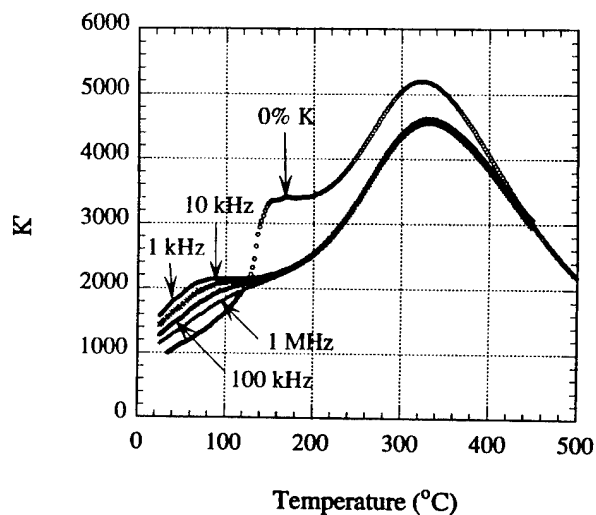


Fig. 4 Change in dielectric constant with temperature for  $0.9\text{Bi}_{0.5}\text{Na}_{0.4}\text{K}_{0.1}\text{TiO}_3-0.1\text{PbTiO}_3$  sintered at 1160 °C

Figures 6 and 7 show the  $K'$  and loss tangent of La doped BN10PT. Partial substitutions of La for Bi in this material yield a broad and stable  $K'$  over a few hundred degree Celsius. The  $K'$  and loss tangent of La doped BN10PT are lower than those of BN10PT.

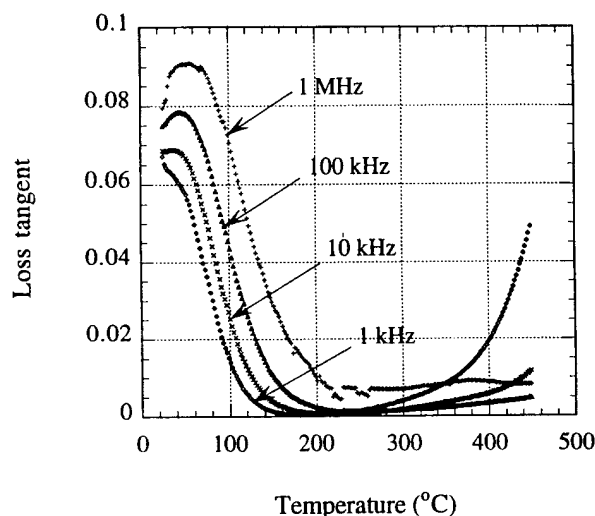


Fig. 5 Change in loss tangent as a function of temperature for  $0.9\text{Bi}_{0.5}\text{Na}_{0.4}\text{K}_{0.1}\text{TiO}_3\text{-}0.1\text{PbTiO}_3$  sintered at  $1160^\circ\text{C}$

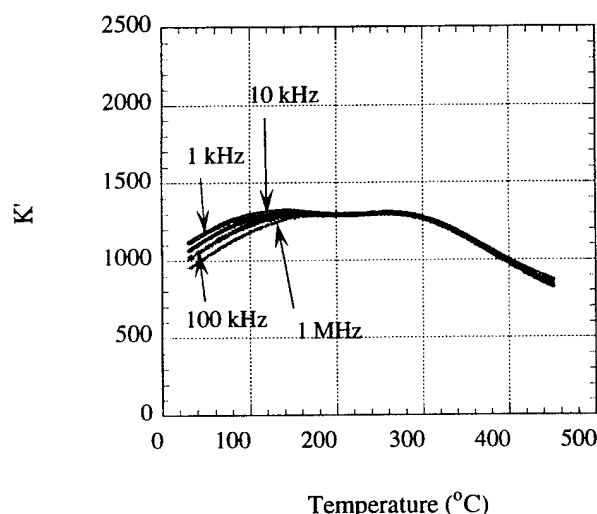


Fig. 6 Change in dielectric constant with temperature for  $0.9\text{Bi}_{0.4}\text{La}_{0.1}\text{Na}_{0.1}\text{TiO}_3\text{-}0.1\text{PbTiO}_3$  sintered at  $1200^\circ\text{C}$

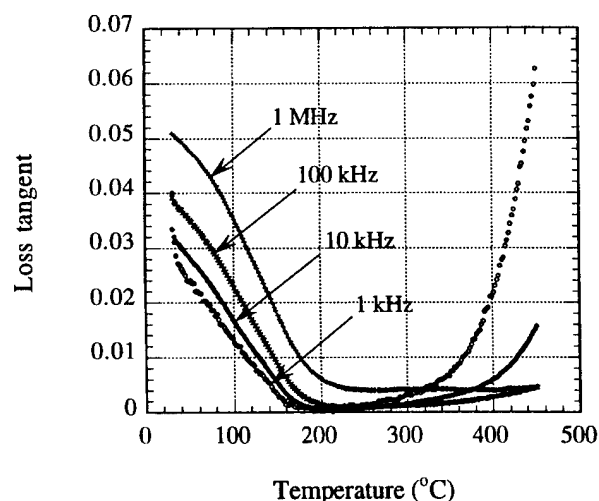


Fig. 7 Change in loss tangent as a function of temperature for  $0.9\text{Bi}_{0.4}\text{La}_{0.1}\text{Na}_{0.1}\text{TiO}_3\text{-}0.1\text{PbTiO}_3$  sintered at  $1200^\circ\text{C}$

## IV. CONCLUSIONS

Pb substitution increases  $K'$ , lowers the first transition temperature and decreases the broadness above the Curie temperature. The phase boundary of the BNT-PT system is between 15%Pb and 17%Pb in BNT. Doped with K or La the stability of  $K'$  improves. Thus, these compositions are attractive materials for a stable high temperature capacitor.

## REFERENCES

- [1] V.V. Ivanova, A.G. Kapyshev, Y.N. Venevtsev and G.S. Zhdanov, "X-ray determination of the symmetry of the ferroelectric compounds  $(\text{K}_{0.5}\text{Bi}_{0.5})\text{TiO}_3$  and  $(\text{Na}_{0.5}\text{Bi}_{0.5})\text{TiO}_3$  and the high temperature phase transitions in  $(\text{K}_{0.5}\text{Bi}_{0.5})\text{TiO}_3$ ," Academy of Sciences USSR Bulletin, Phys. Series vol. 26 pp. 358-360, 1962.
- [2] G.A. Smolenskii, V.A. Isupov, A.I. Agranovskaya and N.N. Krainik, "New Ferroelectrics of Complex Composition IV," Soviet Physics - Solid State vol. 2 pp.2651-2654, May 1961.
- [3] Koichiro Sakata and Yoichiro Masuda, "Ferroelectric and Antiferroelectric Properties of  $\text{Na}_{0.5}\text{Bi}_{0.5}\text{TiO}_3\text{-SrTiO}_3$  Solid Solution Ceramics," Ferroelectrics vol. 7 pp.347-349, 1974.
- [4] I.P. Pronin, P.P. Syrnikov, V.A. Isupov, V.M. Egorov and N.V. Zaitseva, "Peculiarities of Phase Transitions in Sodium-Bismuth Titanate," Ferroelectrics vol. 25 pp.395-397, 1980.
- [5] T. Takenaka and K. Sakata, "Dielectric, Piezoelectric and Pyroelectric Properties of  $(\text{BiNa})_{0.5}\text{TiO}_3$  - Based Ceramics," Ferroelectrics vol. 95 pp.153-156, 1989.
- [6] T. Takenaka, K. Sakata and K. Toda, "Acoustic Wave Characteristics of Lead-Free  $(\text{Bi}_{0.5}\text{Na}_{0.5})_{0.99}\text{Ca}_{0.01}\text{TiO}_3$  Piezoelectric Ceramic," Jpn. J. Appl. Phys. Supplement vol. 28-2 pp. 59-62, 1989.
- [7] T. Takenaka, K. Maruyama and K. Sakata, " $(\text{Bi}_{0.5}\text{Na}_{0.5})\text{TiO}_3$  -  $\text{BaTiO}_3$  System for Lead-Free Piezoelectric Ceramics," Jpn. J. Appl. Phys. vol. 30 pp. 2236-2239, 1991.
- [8] M.S. Gadzhiev, A.K. Abiev, V.A. Isupov and I.G. Ismailzade, "Pyroelectric Properties of  $(\text{Na}_{0.5}\text{Bi}_{0.5})\text{TiO}_3$  and  $(\text{K}_{0.5}\text{Bi}_{0.5})\text{TiO}_3$  solid solutions," Sov. Phys. Solid State vol. 27 pp. 1502, August 1985.
- [9] V.A. Isupov, P.L. Strelets, I.A. Serova, N.D. Yataenko and T.M. Shirobokikh, "Peculiarities of Ferroelectric Phase Transitions in Solid Solutions of the  $\text{Na}_{0.5}\text{Bi}_{0.5}\text{TiO}_3$  -  $\text{PbTiO}_3$  System," Soviet Physics - Solid State vol. 6 pp.615-619, September 1964.
- [10] K. Sakata, T. Takenaka and Y. Naitou, "Phase Relations in the  $\text{Bi}_{0.5}\text{Na}_{0.5}\text{TiO}_3$  -  $\text{PbTiO}_3$  solid solution ceramics and its piezoelectric properties," The Fifth U.S-Japan Seminar on Dielectric and Piezoelectric Ceramics pp.239-242, December 1990.
- [11] V.A. Isupov, "Ferroelectrics having a weakly broadened phase transition," Sov. Phys. - Solid State vol. 28 pp.1253-1254, July 1986.

# ABSTRACT

Aerogels are nanostructured materials containing a large volume of interconnected porosity, which are generated by the supercritical drying of sol-gel systems. Barium metal and titanium butoxide derived sol has been used to generate transparent alcogels. Supercritical drying using liquid carbon dioxide generates an aerogel structure, which on firing crystallises to barium titanate. The chemical evolution has been followed from the sol to the final fired product using FTIR, whilst the fired microstructure has been studied using transmission electron microscopy. The work is being carried out with the aim of utilising the large amount of interconnected porosity to create 3-3 functional ceramic-polymer composites.

# INTRODUCTION

Nanostructure materials have become the focus in many cases either for the improvement of existing properties or the development of new systems. Examples of these are the current interest in developing nanocomposite ceramics for enhanced fracture toughness [1] and the pursuit of quantum wires and dots for their optoelectronic characteristics [2]. One category of materials which meets the criteria on nanostructure is that of porous media, such as zeolites aerogels and porous silicon. These offer the potential for use as membranes, catalytic supports, sensors, optical devices and composite structures. This paper concentrates on extending aerogel technology to ferroelectric systems with the intention of creating a porous crystalline product to act as the skeleton for 3-3 ceramic-polymer composites. Currently aerogels have been made from materials such as silica, [3] and titania [4]. Applications of aerogels have exploited the extremely high specific surface area and volume of interconnected porosity and also the low refractive index ( $\approx 1$ ) and thermal conductivity [5].

# EXPERIMENTAL

Aerogels are derivatives of sol-gel processing which have been supercritically dried to avoid shrinkage during the removal of solvent from the alcogel, thus effectively retaining the gel structure intact. The barium titanate sol was produced using a similar route to Vorotilov *et al.* [6], involving the refluxing of Ba metal with a 10% solution of Ti-butoxide in butan-1-ol for  $\approx 8$  hours at  $\approx 120^\circ\text{C}$ . After stabilising the sol with acetic acid, hydrolysis lead to the formation of an alcogel which was then aged to increase its strength and to allow some shrinkage so that the gels could be removed from the moulds.

Various solvents may be used to generate the supercritical fluid but liquid  $\text{CO}_2$  was used due to its inert nature, room temperature operation ( $T_{\text{critical}} \approx 31^\circ\text{C}$ ,  $P_{\text{critical}} \approx 70$  bar) and the commercial availability of the apparatus. Liquid  $\text{CO}_2$ , however, is immiscible with alcohols under normal conditions and an intermediary solvent, acetone, is required to ensure the complete replacement of butanol by liquid  $\text{CO}_2$ .

Firing of aerogels was carried out at temperatures in the range  $500$ – $1300^\circ\text{C}$ , using a  $\text{N}_2$  atmosphere up to  $350^\circ\text{C}$ , followed by an  $\text{O}_2$  atmosphere. Some samples were also fired using a wet  $\text{O}_2$  atmosphere to promote grain growth.

The chemical reactions occurring throughout the processing were investigated by FTIR, using a liquid cell with KBr windows or by diffuse reflectance from powders, with a ratio of  $0.5$  g to  $0.01$  g of KBr powder to sample. The microstructures were characterised using XRD, TEM and UV-spectrophotometry.

# RESULTS AND DISCUSSION

## (a) FTIR

Fig. 1a shows the IR-spectra of the BaTi-butoxide sol before any additional processing. The peaks in the range  $1465$ – $1380\text{ cm}^{-1}$  correspond to the stretching and bending vibrations of the  $\text{CH}_3$  groups, while a series of peaks below  $1115\text{ cm}^{-1}$  relate to M-O-C vibrations of butoxy groups directly bonded to a metal. Peaks below  $\approx 850\text{ cm}^{-1}$  are probably due to the presence of some M-O-M linkages. The addition of acetic acid is accompanied by an exothermic reaction and the formation of a white gelatinous precipitate for acid concentrations of  $R_a \leq 3$  (where  $R_a = [\text{CH}_3\text{COOH}]/[\text{Ti}]$ ). The IR-spectra of the resulting stabilised sol

A  
b  
s  
o  
r  
b  
a  
n  
c  
e

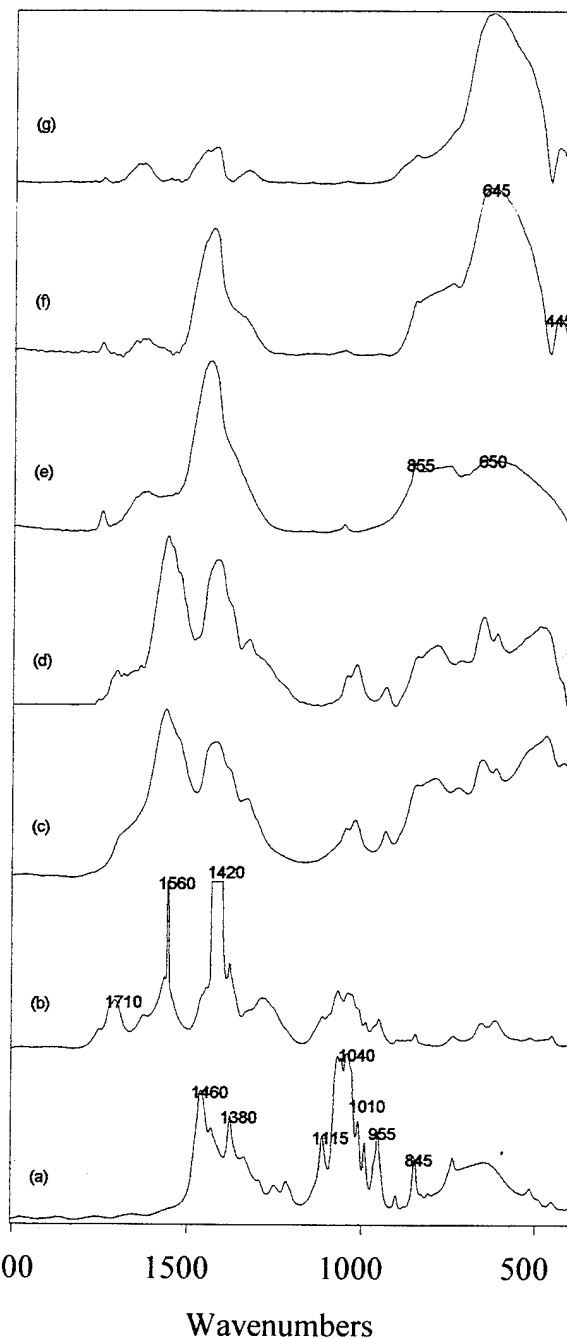


Fig. 1 FTIR spectra for (a) BaTi-butoxide sol, (b) stabilised sol, (c) alcogel  $R_w = 16$ , (d) aerogel  $R_w = 16$  (e-g) aerogels fired at  $500^\circ\text{C}$ ,  $600^\circ\text{C}$  and  $800^\circ\text{C}$  respectively.

is shown in Fig. 1b. The peaks at  $1710\text{ cm}^{-1}$  ( $\text{C}=\text{O}$  stretch, dimer) and  $1285\text{ cm}^{-1}$  ( $\nu_{\text{sym}} \text{CH}_3$  deformation,  $\text{COH}$  bending) are associated with free acetic acid or some monodentate acetate ligands. The peaks at  $1565\text{ cm}^{-1}$  ( $\nu_{\text{asym}} \text{COO}$ ) and  $1420\text{ cm}^{-1}$  ( $\nu_{\text{sym}} \text{COO}$ ) are related to bidentate acetate ligands, probably bridging as  $\Delta\nu \approx 140\text{ cm}^{-1}$  [7]. Addition of water to the stabilised sol leads to the formation of a gel, the spectrum of which is shown in Fig. 1c. The peaks at  $1560\text{ cm}^{-1}$  and  $1420\text{ cm}^{-1}$  remain unaffected whilst the intensity of peaks below  $860\text{ cm}^{-1}$  increases. This would suggest that the bidentate ligands remain



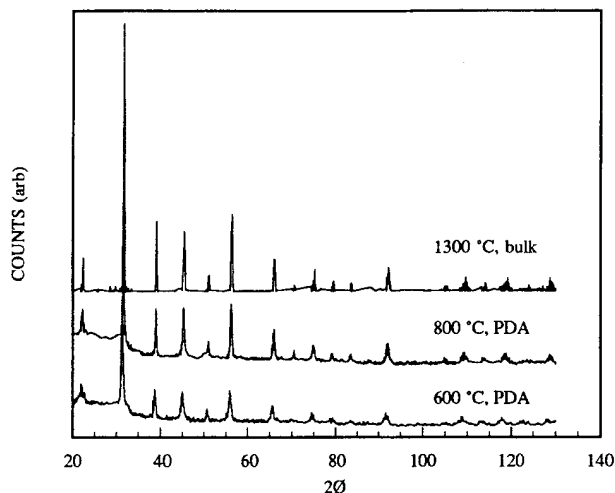


Fig. 3 XRD plots for fired aerogels. (PDA = partially densified aerogels, bulk = aerogel powder calcined at 600 °C, pressed and fired at 1300 °C) unchanged by the polycondensation process while the concentration of M-O-M bonds increases. The spectrum of the aerogel, Fig. 1d, is very similar. This would seem to imply that no further change occurs during the supercritical drying stage and that the peak at 1710  $\text{cm}^{-1}$  is partly due to the presence of some monodentate acetate ligands. The spectra of aerogels fired at 500 °C, 600 °C and 800 °C are shown in Fig. 1e-g [8]. At 500 °C the particles are crystalline, as indicated by the broad band 860-450  $\text{cm}^{-1}$ , while the peak at 1420  $\text{cm}^{-1}$  shows that they still contain acetate impurities, which are only removed by firing at a temperature  $\geq 800$  °C. We suspect that these correspond to barium acetate as this would correlate with the identification of large crystals, which formed during the ageing process, made by XRD at Reading University. Perovskite is only formed at temperatures  $\geq 600$  °C and is accompanied by the development of distinct peaks at  $\approx 640$   $\text{cm}^{-1}$  and 445  $\text{cm}^{-1}$ .

One of the most striking features of the FTIR results is the development of the broad lattice vibrational features for the sintered gels, Fig. 1 c-g, from the molecular vibrational features, Fig. 2a-b. The relatively large width of FTIR features for the sintered gels is due to the coupling of the infra-red photons to several lattice vibrational modes, i.e.: the formation of polaritons [9]. This particular material system provides an ideal medium for the study of the change from molecular vibration to lattice vibration behaviour. We also suggest that FTIR spectra will be useful to quantify the sol to gel formation stages.

#### (b) XRD

Fig. 2 shows the spectra for aerogel samples fired at 600 °C, 800 °C and 1300 °C. All samples are crystalline but the perovskite phase is only formed at  $T \geq 600$  °C. The peaks are broad at the lower firing temperatures with lower intensities.

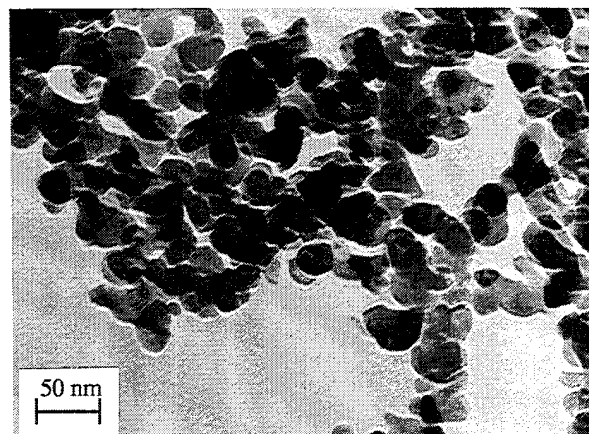
#### c) Particle Size Analysis

A preliminary investigation measuring the diffuse reflectance from an as-produced aerogel using UV spectrophotometry indicates a blue shift of  $\approx 40$  nm in the absorption edge with respect to that of the bulk ceramic. Assuming a simple infinite potential well model and electron and hole mass equal to that for a free electron, this corresponds to a particle size of 1.4 nm.

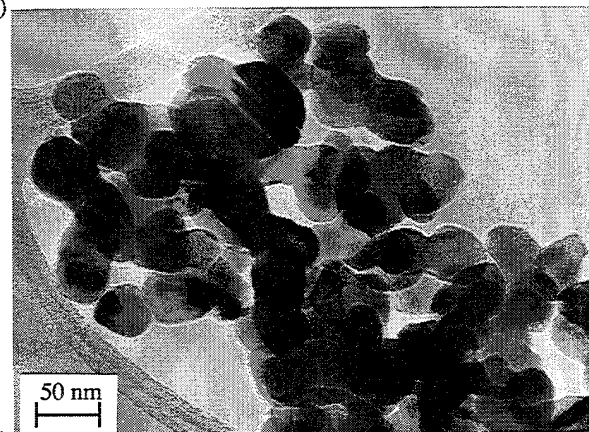
Aerogels fired at 600 °C and 800 °C show no shift in the absorption edge and have a particulate microstructure as shown in the TEM micrographs in Fig. 3a-b. All particles are faceted, with a median particle size of  $\approx 10$  nm and  $\approx 35$  nm respectively, and form an interlinking network of chains. As can also be seen there is some evidence of internal structure, which will be the subject of future HREM work.

#### (d) Dielectric Properties

Samples fired at 700 °C for 1 hour and 900 °C for 5 hours in a wet  $\text{O}_2$  atmosphere have similar permittivities of  $\approx 40$  and  $\approx 30$  respectively at room temperature and 1 kHz. No ferroelectric transition was apparent on heating the 700 °C sample to 150 °C.



(a)



(b)

Fig. 3 Nanoparticulate fired aerogels, (a) 600 °C, 1 hr (b) 800 °C, 1 hr.

### CONCLUSION

We have successfully made barium titanate aerogels and are the first to report on high optical quality aerogel in this material. We have recorded the grain growth following heat treatment of the aerogel and have followed the development of an interconnected porous structure using XRD, TEM and FTIR. We have also observed for the first time in such materials a quantum size effect absorption edge shift for the as-produced aerogels. These materials can now be exploited as a matrix to make a 3-3 ceramic-polymer composite.

### REFERENCES

- [1] K. Niihara, "New design concept of structural ceramics - ceramic nanocomposites" *The Centennial Issue of the Ceramic Society of Japan, J.Ceram.Soc.Jpn.*, **99** [10] 974-82 (1991)
- [2] A. D. Yoffe, "Low-dimensional systems, quantum size effects and electronic properties of semiconductor microcrystallites (zero-dimensional systems) and some quasi-2-dimensional systems" *Advances in Physics* **42**, 173, (1993)
- [3] T. Woignier, J. Phalippou, and M. Prassas, "Glasses from aerogels. 1. The synthesis of monolithic silica aerogels. 2. The aerogel glass transformation" *J.Mater.Sci.* **25** (1991) 3111-3126
- [4] L. K. Campbell, B. K. Na, and E. I. Ko, "Synthesis and characterisation of titania aerogels" *Chem.Mater.* 1992, Vol.4, No.6, pp.1329-1333
- [5] H. D. Gesser, and P. C. Goswami, "Aerogels and related porous materials" *Chem.Rev.* 1989, Vol.89, No.4, pp.765-788
- [6] Vorotilov, Orlova, Petrovsky, Yanoskaja, and Ivanov "BaTiO<sub>3</sub> films on silicon wafers from metal alkoxides" *Ferroelectrics*, 1991, vol.123, pp.261-271
- [7] S. Doeuff, M. Henry, C. Sanchez, J. Livage "Hydrolysis of titanium alkoxides: modification of the molecular precursor by acetic acid" *J. Non. Cryst. Solids* **89** (1987) 206-216
- [8] J. T. Last "Infrared-absorption studies on barium titanate and related materials" *Phys Rev.* Vol. 105, No. 6 pp. 1740-50 (1957)
- [10] M. E. Lines and A. M. Glass "Principles and applications of ferroelectric materials and related materials" Oxford University Press, (1979), Ch. 7, pp.216

# Parametric Small Signal Amplification near Bifurcations

M. Diestelhorst, H. Beige and R.-P. Kapsch  
Martin-Luther-Universität  
Fachbereich Physik / Experimentelle Physik II  
Friedemann-Bach-Platz 6  
D-06108 Halle, Germany

**Abstract:** The nonlinear dielectric properties of ferroelectrics during polarization reversal are used to amplify small periodic perturbations. The ferroelectric serves as a nonlinear capacitor in a series-resonance circuit. The inductance is a linear one. Such a series-resonance circuit is a system which offers many features of nonlinear dynamical systems. It is possible to observe different types of bifurcations (pitchfork bifurcations, period-doubling cascades and chaotic behaviour) well known from the theory of nonlinear dynamical systems. Near such bifurcations the system can amplify suitable chosen periodic perturbations. These perturbations are coupled into the system by amplitude modulation of the driving voltage. Different types of bifurcations have been investigated concerning their ability of amplifying small signals.

## INTRODUCTION

One characteristic feature of ferroelectric materials is their nonlinear dielectric behaviour. The greatest effect of dielectric nonlinearities is observed during polarization reversal. These properties may be used to introduce nonlinearities into an ordinary series-resonance circuit. The ferroelectric serves as a nonlinear capacitor, which is connected to a linear inductance. In this paper we used ferroelectric TGS as the nonlinear dielectric.

The driven nonlinear series-resonance circuit is an interesting dynamical system. It has been shown, that this system exhibits both pitchfork (symmetry-breaking) and period-doubling bifurcations [1, 2]. The onset of these dynamical instabilities may be controlled by external parameters, e.g. the amplitude of the driving voltage or the frequency of the driving voltage.

Near the onset of dynamical instabilities the system is very sensitive to external perturbations. It has been proven theoretically that nonlinear dynamical systems can act to amplify small periodic perturbations [3]. Experimental results of small signal amplification near period-doubling bifurcations of the nonlinear series circuit with ferroelectric TGS-capacitor have been published earlier [4-6]. Here we present results of small signal amplification in the same system near symmetry-breaking bifurcations.

## SMALL SIGNAL AMPLIFICATION NEAR A PITCHFORK BIFURCATION

The behaviour of the nonlinear series-resonance circuit with ferroelectric TGS-capacitor may be described by the following equation:

$$\frac{d^2 D_2}{dt^2} + \frac{R}{L} \frac{dD_2}{dt} + \frac{d}{AL} (\alpha D_2 + \gamma D_2^3) = \frac{1}{AL} U_0 \cos \omega t, \quad (1)$$

where  $D_2$  is the dielectric displacement along the ferroelectric axis,  $R$  and  $L$  represent the losses and the inductance of the circuit respectively. The TGS-sample is bar-shaped with the thickness  $d$  along the ferroelectric axis and the electroded surfaces  $A$  normal to this axis.

The coefficients  $\alpha$  and  $\gamma$  describe the effective potential of the TGS-crystal in the ferroelectric state. As could be shown earlier, they are mainly determined by properties of domain switching of the ferroelectric capacitor [1,2]. The coefficient  $\alpha$  is negative,  $\gamma$  is positive, therefore the nonlinear series circuit is a forced oscillator in a double

minimum potential.

If the amplitude of the driving voltage  $U_0$  is chosen, that the field strength across the ferroelectric sample is in the order of magnitude of the coercive field, pitchfork bifurcations may be observed. In this case of bifurcations the phase portrait loses its symmetry and becomes asymmetric (Figure 1). For the observation of phase portraits of the series-resonance circuit we used the method of direct registration of voltages proportional to the dielectric displacement  $D_2(t)$  and the current density  $dD_2(t)/dt$  by an oscilloscope [2].

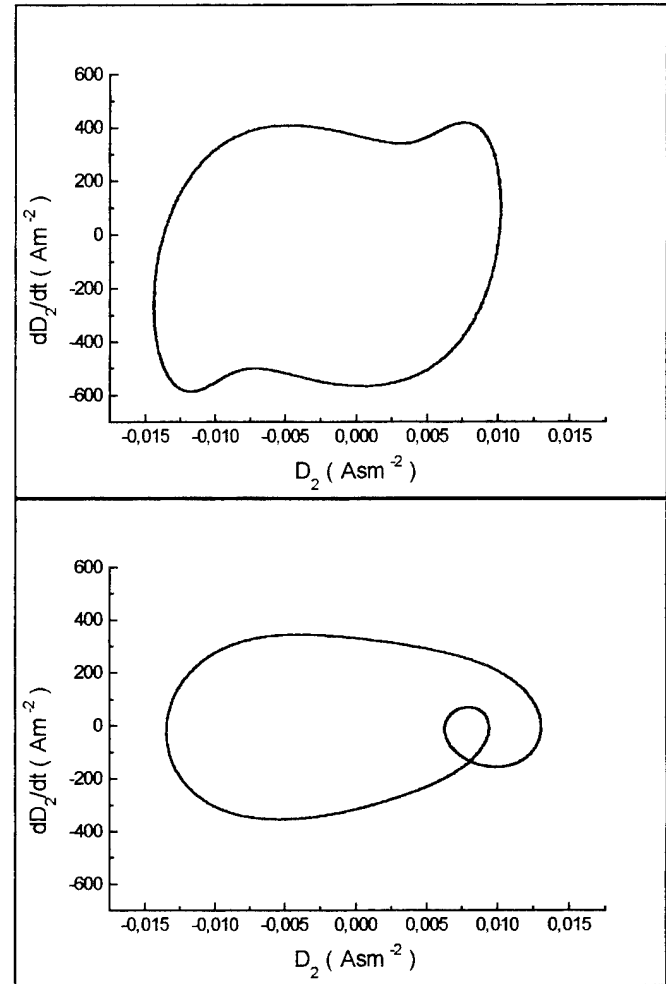


Figure 1: Symmetric (at the top) and asymmetric (at the bottom) phase portrait of the series circuit.

The pitchfork bifurcation shown in Figure 1 occurred during the variation of the driving frequency  $f_0$  from 3870 Hz to 3800 Hz at constant amplitude of the driving voltage  $U_0 = 17.3$  V. So it has been shown, that the distance  $\epsilon$  of the series-resonance circuit from the pitchfork bifurcation may be controlled by means of variation of the frequency of the driving voltage. At the bifurcation the parameter  $\epsilon$  becomes zero. Another possibility of controlling the distance  $\epsilon$  is the variation of the amplitude of the driving voltage.

The idea behind the effect of small signal amplification is the following: If a dynamical system (e.g. the resonance circuit) approaches a bifurcation it becomes more and more instable against periodic perturbations. So it may happen, that suitable chosen perturbations are amplified, if the system is near the bifurcation. In our experiments the perturbation was introduced into the circuit by a modulation of the amplitude  $U_0$ . It has been predicted [3], that in the case of pitchfork bifurcations with a modulation of one parameter - as in the case of the

series-resonance circuit driven with amplitude-modulated voltage - the system should amplify signals with frequencies that are near odd multiples of the frequency of the driving voltage. If the amplitude is modulated with a frequency  $f_{\text{mod}} = f_0 + \Delta$ , additional peaks should arise in the spectrum of  $D_2(t)$ . They are expected to be centered around even multiples of the driving voltage at frequencies  $f_- = 2k f_0 - \Delta$  and  $f_+ = 2k f_0 + \Delta$ . The height of these additional peaks depends on the distance  $\epsilon$  as well as on the difference  $\Delta$  between the driving and the modulation frequencies in the following manner [3]:

$$S(f) \sim \frac{1}{\epsilon^2 + (2\pi \Delta)^2} \quad (2)$$

As shown in Figure 1 it is possible to reduce the parameter  $\epsilon$  by a decrease of the frequency  $f_0$  from 3870 Hz to 3800 Hz. According to relation (2) this should lead to an increase of the peaks  $f_-$  and  $f_+$ , if the frequency  $f_0$  is tuned towards the pitchfork bifurcation at about 3805 Hz and the difference  $\Delta = f_{\text{mod}} - f_0$  is kept constant. In Figure 2 there is presented the qualitative confirmation of the influence of decreasing distance  $\epsilon$  on the height of the peaks  $f_-$  and  $f_+$  around the second harmonic of the frequency  $f_0$  of the driving voltage.

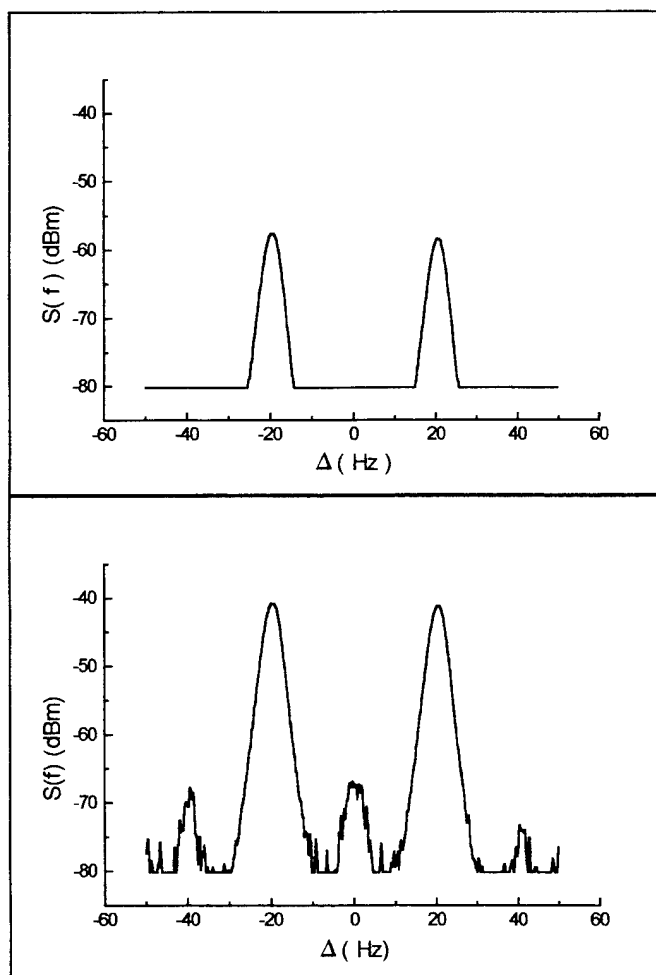


Figure 2: Small signal amplification at greater distance from the bifurcation (at the top,  $f_0 = 3870$  Hz) and at very small distance (at the bottom,  $f_0 = 3815$  Hz). The difference  $\Delta$  had been adjusted to  $\Delta = 20$  Hz.

The two peaks at  $\Delta = \pm 20$  Hz are strongly dependent on the distance of the series-resonance circuit from the bifurcation. This dependence is shown in detail in Figure 3. A decrease of the parameter  $\epsilon$  leads to an increase of the height of the peaks around the second harmonic. Analogous behaviour may be observed around the higher even harmonics of  $f_0$ .

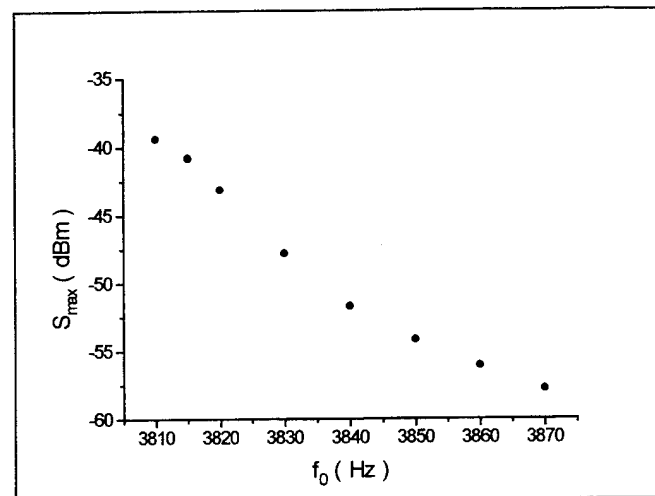


Figure 3: Dependence of the height of peaks at  $f_-$  and  $f_+$  around  $2 f_0$ . The decrease of  $f_0$  corresponds to a decrease of  $\epsilon$ .

## CONCLUSION

Pitchfork bifurcations in the nonlinear series-resonance circuit may be used to amplify small signals of frequencies near odd multiples of the frequency of the driving voltage. There arise pairs of peaks around even multiples of the driving frequency in the signal of the circuit. The difference to small signal amplification in the case of period-doubling [4-6] consists in the conditions of signals to be amplified. Near period-doubling bifurcations signals of frequencies near half the driving frequency are amplified. This leads to additional peaks around odd multiples of half the driving frequency in the signal of the circuit.

## REFERENCES

- [1] M. Diestelhorst, "Nichtlineares Verhalten im ferroelektrischen TGS", in *Proceedings of the 15. Frühjahrsschule Ferroelektrizität in Fincken*, 1987, MLU WB 1987/67 (O 24), pp. 68-77.
- [2] H. Beige, M. Diestelhorst, R. Forster, T. Krietsch, "Chaos near Structural Phase Transitions", *Phase Transitions*, vol. 37, pp. 213-238, 1992.
- [3] K. Wiesenfeld and B. McNamara, "Small-Signal Amplification in Bifurcating Dynamical Systems", *Phys. Rev.*, vol. A33, pp. 629-642, 1986.
- [4] M. Diestelhorst, "Nonlinear Behaviour of Ferroelectrics", in *Proceedings of the 19th Spring Conference on Ferroelectricity in Burscheidungen*, 1991, pp. 98-104.
- [5] M. Diestelhorst and H. Beige, "Small signal amplification in a nonlinear series circuit with TGS-capacitor", *Ferroelectrics*, vol. 141, 153-158, 1993.
- [6] M. Diestelhorst, H. Beige and R.-P. Kapsch, "A parametric ferroelectric amplifier", presented at the IMF-8, Gaithersburg, USA, August, 1993.

# Pore-Dependent Dielectric and Electrical Properties of Barium Titanate Ceramic

Kyeong Ho Cho and Hee Young Lee\*

Departments of Electronic Engineering and Materials Science and Engineering\*

Yeungnam University

Kyongsan, 712-749, KOREA

**Abstract** – Dielectric and electrical properties of pore-containing barium titanate ceramic were studied. Porosity was controlled in the 5 - 37% range, and two different sizes of spherical pores were successfully incorporated into the ceramic using 25  $\mu\text{m}$  and 80  $\mu\text{m}$  polymer microspheres. The transition from closed porosity to open porosity was found to be pore size dependent and occurred at lower porosity value as pore size decreased. In addition, the gradual decrease of both dielectric constant and Curie temperature was noticed as porosity increased. The amount of pores greatly affected the resistance of barium titanate ceramic. A qualitative model, which is based on lumped parameters, is proposed in an attempt to rationalize experimental results.

## INTRODUCTION

Recently, it was reported that the shape and volume fraction of closed pores severely influenced the dielectric, elastic and electromechanical properties of piezoelectric ceramics such as lead zirconate titanate [1]. As the amount of pores, i.e. porosity, increases, dielectric properties such as dielectric constant is expected to be reduced according to the rule of mixture or the property averaging principle.

Although many papers on the porosity effect in dielectric ceramics have been published [1-6], relatively little is understood about the effect of pore size and porosity on the dielectric and electrical properties of barium titanate ceramic.

In an effort to better understand how porosity and pore size affect the dielectric constant and the electrical resistivity of barium titanate ceramic, narrow size-distributed polymer microspheres were used in order to include pores of different sizes in

the ceramic on purpose. However, due to the rather large size of available microspheres, coarse-grained microstructure was attempted in this study. In the following, up-to-date results and discussions on the above issues are presented in some detail.

## EXPERIMENTAL PROCEDURE

Oxalate-derived barium titanate powder with the cation sub-lattice ratio of  $A/B = 0.995$  and the mean particle size of 1.3  $\mu\text{m}$  was used in this study. In order to prepare sintered ceramics with varying porosities and pore sizes, two different grades of commercial microspheres were mixed with granulated barium titanate powder up to 20% in weight. The mean sizes of two different polymer microspheres used in this study were 25  $\mu\text{m}$  and 80  $\mu\text{m}$ , respectively. In order to maintain uniform grain sizes after sintering, powder compacts in disc shape were fired at 1400°C for 60 minutes.

Complex impedance measurements were made for sintered and electroded samples using a Hewlett-Packard 4192A impedance analyzer. Typically resistance and reactance values were measured across a frequency range usually up to 1 MHz, in order to minimize an error from lead inductance. Two probe dc resistance was determined using a Keithley 617 electrometer during impedance measurement, while four - probe dc resistivity was estimated for bar - shaped samples cut from discs of the same lot.

Sample temperatures were maintained at values in the 470 - 550°C range during the impedance measurement. This was necessary because the resistance limit of the bridge was only about 1.3 M $\Omega$ , and elevated temperatures were required to bring sample resistance below this value.

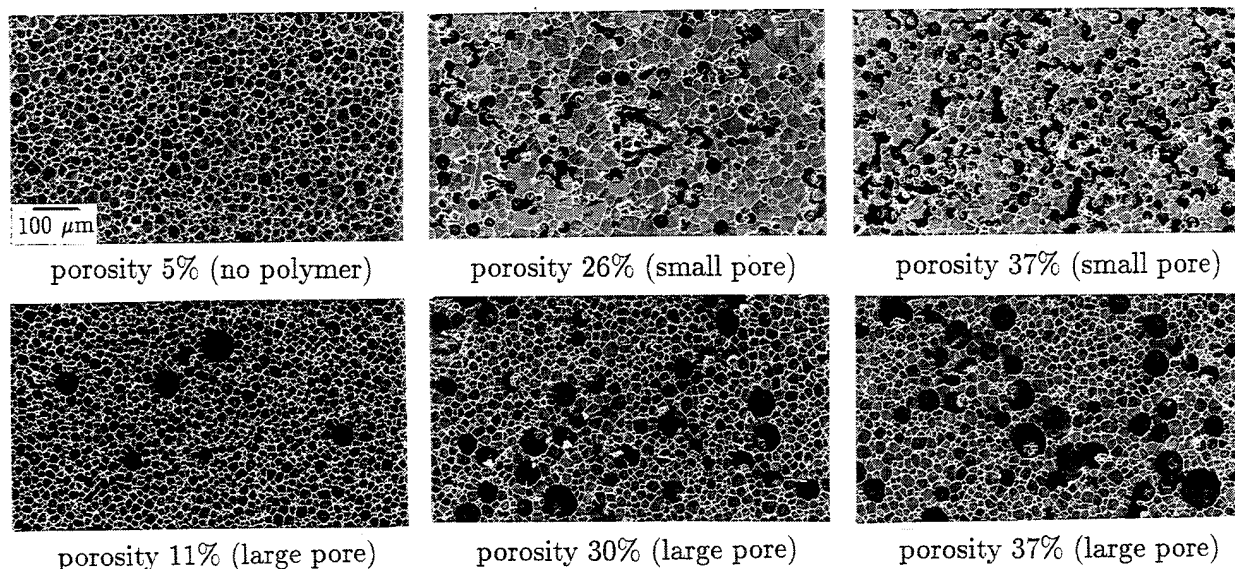


Fig.1 Scanning electron micrographs of sintered surface of undoped barium titanate ceramics with different porosities.

## RESULTS AND DISCUSSION

### Microstructure

As seen in Fig. 1, microstructures of sintered disks are almost independent of polymer loading and uniform with average grain size of about  $35 \mu\text{m}$ . Measured porosity values of sintered pellets range from 5% to 37%. When microspheres were added in the same amount, the grade with the smaller microspheres yielded larger porosity value than the one with the larger microspheres. This result is in good agreement with previously reported data by Arai et al. [3].

From the figure, it is noted that the isolated pores start to be connected as porosity increases beyond about 26% for the small pore samples, whereas the onset of pore connection seems to be more than 30% for the large pore samples.

Therefore, it is concluded that the transition from closed porosity to open porosity is pore size dependent and occurs at lower porosity value as pore size decreases. The published results by Fang et al. [4], in which the transition occurred at about 10% porosity for fine-grained barium titanate ceramic, may be regarded as a demonstration of pore size dependence. Similar pore size dependence of dielectric properties is observed and discussed in the next section in some detail.

### Dielectric Property

In Fig. 2, dielectric constant values measured for

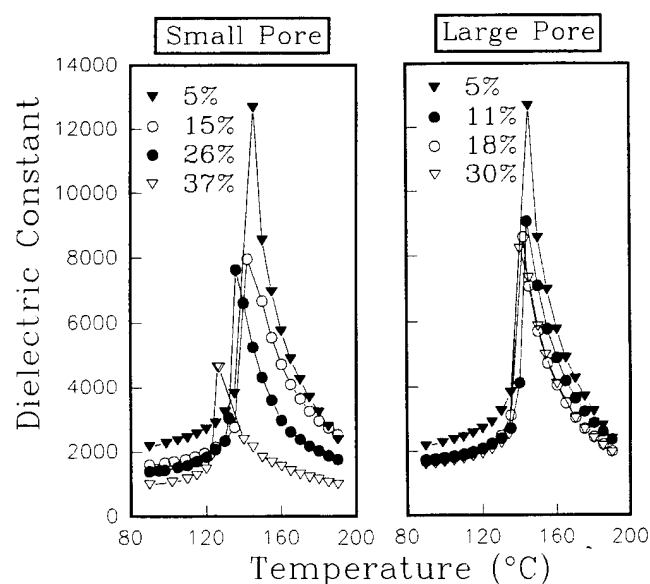


Fig.2 Apparent dielectric constant as a function of temperature for barium titanate ceramics with different porosities and pore sizes.

samples having different porosities were plotted as a function of temperature. Porosity dependences of Curie temperature and dielectric constant at its maximum were illustrated in Fig. 3. It is seen that both Curie temperature and dielectric constant at Curie point decrease as porosity increases. Small pores seem to be more effective in reducing Curie point than large pores, which is in good agreement with the published data [4].

In Fig. 4, room temperature dielectric constant values were plotted as a function of porosity. There are two experimental findings worth some attention in this figure. First, it was found that barium

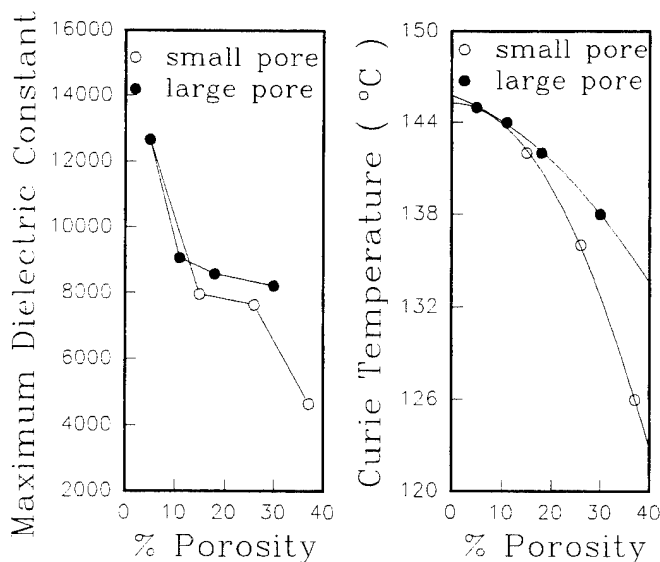


Fig.3 Curie temperature and maximum dielectric constant as a function of porosity for barium titanate ceramics with different pore sizes.

titanate ceramic samples with small pores showed lower dielectric constant than those with large pores, when the porosity values were equal to each other. Secondly, the decrease of dielectric constant with porosity could not be represented by single mixing rule curve. It looks like there exist two linear regions and the transition from one region to the other is pore size dependent. These results are in agreement with the ones obtained from the sintered microstructure in Fig. 1, and also with the published results [5]. Two linear regions are attributable to closed pore and open pore regions. When the amount of pores is little, they can be

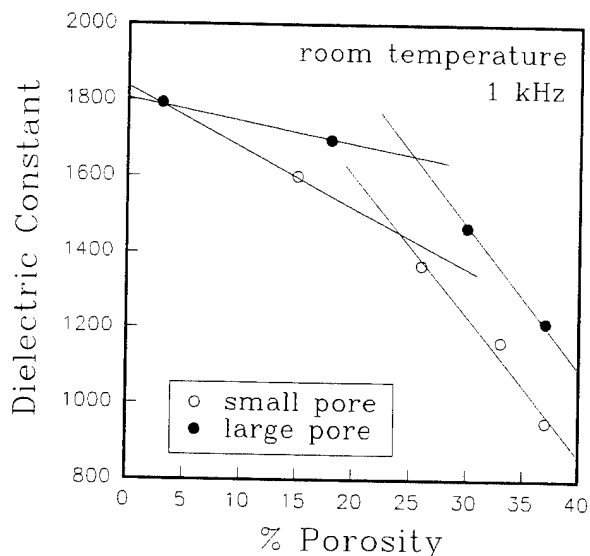


Fig.4 Room temperature dielectric constant as a function of porosity for barium titanate ceramics with different pore sizes.

regarded as isolated closed pores distributed in ceramic bulk. In this case, the Wiener's mixing rule can be applied [6].

$$K = \frac{2K_m(1 - v_p)}{2 + v_p} \quad (1)$$

where  $v_p$  is the porosity,  $K$  and  $K_m$  are apparent dielectric constant and dielectric constant of matrix phase, respectively.

The foregoing equation seems to be applicable below 26% or 30% porosities depending on the size of microspheres used. Above the critical porosity values, pores start to be connected to one another so that they form continuous paths and become open pores. At the transition, it is noted that the dielectric constant value starts to drop rapidly as porosity increases further. In the open pore region, the modified Niesel's equation was supposed by Fang et al. [4], which may be rearranged as

$$K = \frac{K_m(9 - 14v_p)}{9 + v_p} \quad (2)$$

Dielectric constant values calculated by these equations match well with experimental data as indicated in the figure. In summary, the abrupt decrease of both dielectric constant and Curie temperature was noticed as porosity increased. The transition was attributable to the onset of open porosity. In addition, it was observed that both porosity and pore size had effects on determining dielectric properties of barium titanate ceramic.

### Electrical Resistivity

Complex impedance plots for barium titanate ceramics with the same pore size but the different porosities at 520°C were illustrated in Fig. 5. It is apparent that two clearly discernible impedance semicircles or arcs are observed. This result is in accord with the published results by Lee et al. [7,8], where threshold grain diameter for partial depletion responsible for two semicircles is on the order of 1  $\mu\text{m}$ .

According to the grain boundary model proposed by Lee et al. [7,8], two impedance semicircles observed in this case may be ascribed to grain boundary and grain contributions with increasing frequency. Contact impedance semicircle is not observed because it vanishes at high temperatures [9].

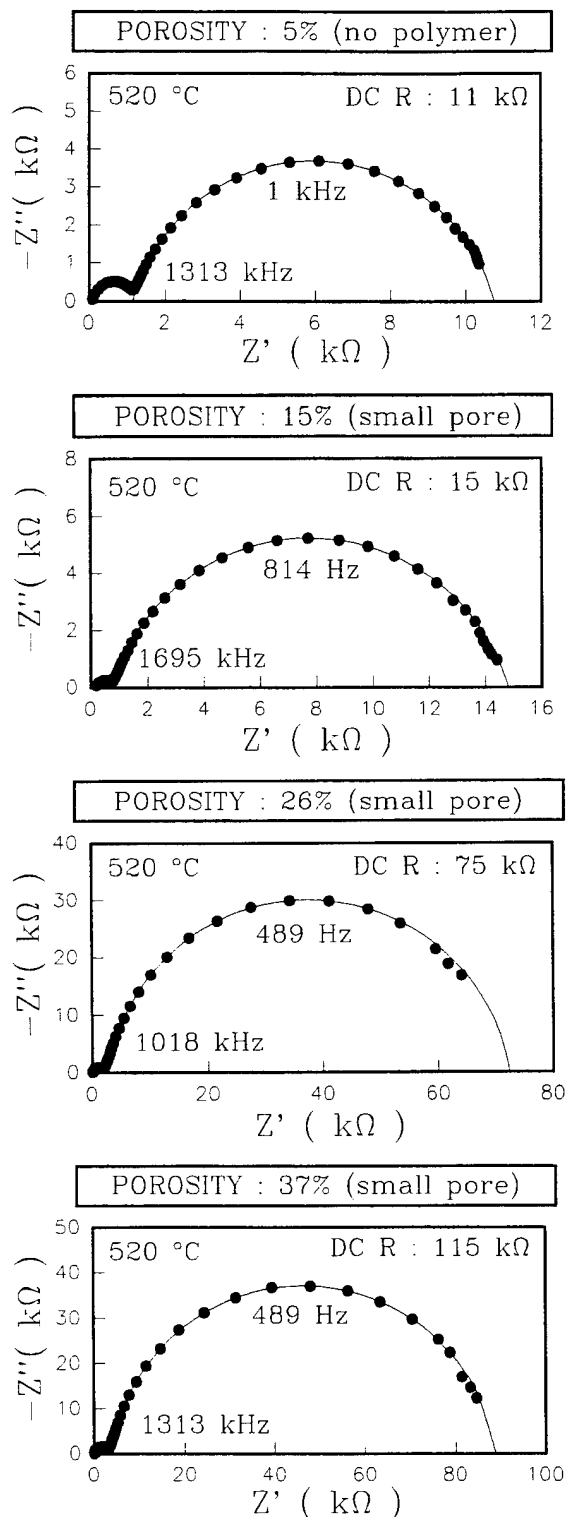


Fig.5 Complex impedance patterns of barium titanate ceramics with different porosity values at 520°C  
(Measured two-probe dc resistance value is included.)

It seems that the apparent resistance value of barium titanate increases as porosity increases. Especially as it crosses the closed-to-open pore transition around 26% porosity, steep increase of resistance is observed. According to the analysis of impedance plots, this increment is reflected as the

sum of both grain and grain boundary resistivity increases.

Grain and grain boundary resistivity values calculated on the assumption of the cube model are tabulated in Table 1 for barium titanate ceramics with different porosities. The reason why grain and grain boundary resistivities are changing with porosities of the approximately same pore size has not been investigated or discussed by the other researchers yet. Based on the lumped parameter model we proposed previously [7,8,9], we can postulate a possible answer to the above question in a qualitative way as the following.

Table.1 Calculated resistivity of grain and grain boundary for barium titanate ceramic with different porosities at 520°C.

% porosity	$\rho_g$ ( $\Omega$ cm )	$\rho_{gb}$ ( $\Omega$ cm <sup>2</sup> )
5%	1954	95
15%	1912	140
26%	6081	691
37%	8837	844

The increase of grain resistivity above the closed-to-open pore transition seems to be related to the decreasing amount of grain-to-grain junction. As long as all the grains are connected in three dimensions, grain resistivity is hardly affected. Thus, below transition or in the closed pore region, grain resistivity remains approximately constant. However, as some of the grains are isolated due to porosity increase, grain resistivity may now contain surface resistance component connected in series to true grain resistivity. As porosity further increases, the equivalent surface length is expected to rise so that grain resistivity increases. Whereas grain resistivity is only affected beyond the transition, i.e. in the open pore region, grain boundary resistivity is raised from the beginning as porosity increases. This may be because the grain boundary contact area is gradually reduced with porosity increase.

In Fig. 6, relaxational time constants which were obtained from the peaks of corresponding impedance plots in Fig. 5 were depicted as a function of inverse temperature. The temperature dependence of relaxational time constant is written as

$$\tau = \tau_0 \exp(E/kT) \quad (3)$$

where  $E$  is an activation energy for relaxation.

From the figure, it is interesting to notice that the activation energy for grain relaxation increases with porosity and approaches to the value corresponding to grain boundary relaxation, whereas that for grain boundary is almost unchanged. From the viewpoint of the model we have just postulated, this may be explained in terms of grain percolation. As the fraction of isolated grains increases, series resistance due to pore surface which may be trapped in the grain starts to dominate grain or bulk relaxation.

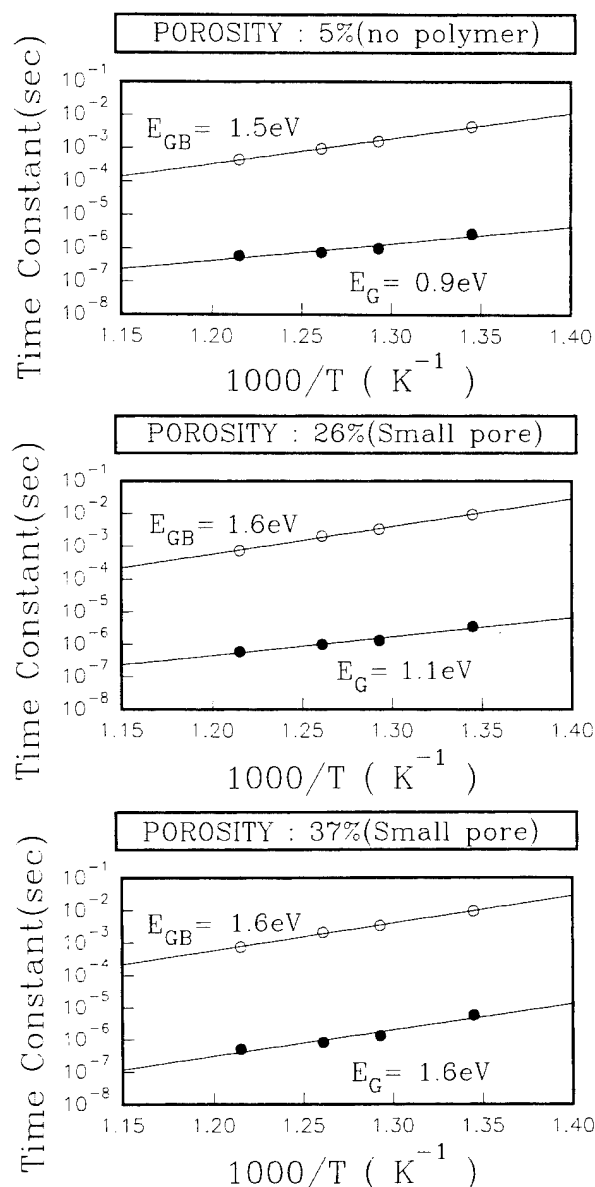


Fig.6 Arrhenius plot of relaxational time constant for barium titanate ceramics with different porosities.

The another experimental evidence in support of the foregoing argument is shown in Fig. 7, where four-point dc resistivity is plotted as a function of inverse temperature. Resistivity activation energies, which is expected to be similar to relaxation activation energy [8,9], exhibit the analogous trend

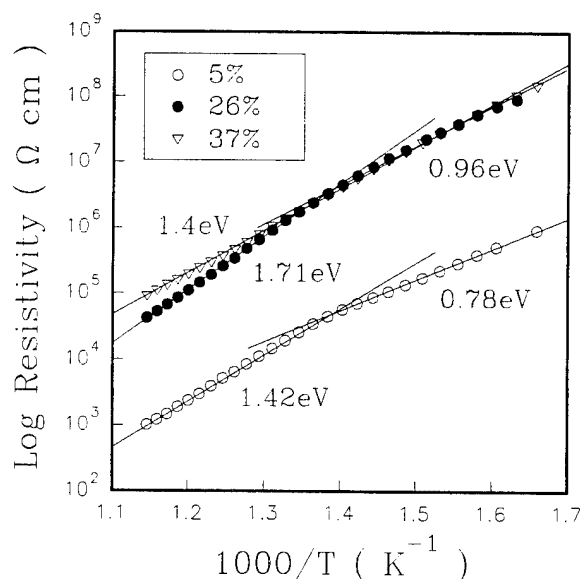


Fig.7 Arrhenius plot of dc resistivity for barium titanate ceramics with different porosities.

(Resistivity activation energy is included in the figure.)

with porosity. Barium titanate ceramic with 37% porosity displays single activation energy from 300 to 600°C range. The same activation energy often means the same mechanism, which is in this case the conduction mechanism. We therefore propose the conduction in this material is governed by interface mechanism such as hopping between impurity states along or across pore surface or grain boundary.

## SUMMARY AND CONCLUSIONS

The transition from closed porosity to open porosity was pore size dependent and occurred at lower porosity value as pore size decreased.

The abrupt decrease of both dielectric constant and Curie temperature was noticed as porosity increased. The transition was attributable to the onset of open porosity. In addition, it was observed that both porosity and pore size had effects on determining dielectric properties of barium titanate ceramic.

The amount of pore greatly affected the resistance of barium titanate ceramics. In the closed-pore region, only grain boundary resistivity was increased with porosity increase, whereas in the open-pore region, both grain and grain boundary resistivities were raised with porosity increase. A qualitative model which could explain this observation was proposed, based on the lumped parameter model. The approach of the activation energy of grain relaxation to that of grain boundary



with porosity increase was referred to the single conduction mechanism such as hopping along or across interfaces.

## ACKNOWLEDGEMENT

We would like to thank Transelco Division of Ferro Corporation, Sakai Kagaku Kogyo Limited, and Cabot Corporation for providing various titanate powders. This work was supported by the Ministry of Educational Research Fund for Advanced Materials in 1993.

## REFERENCES

- [1] H. Banno, *Ceram. Bull.*, 66[9], pp. 1332-1337, 1987.
- [2] D. S. McLachlan et al., *J. Am. Ceram. Soc.*, 73[8], pp. 2187-2203, 1990.
- [3] T. Arai et al., *Proc. Ceram. Soc. Japan*, Fall Meeting, 1990, p. 126.
- [4] T.-T. Fang et al., *J. Am. Ceram. Soc.*, 76[5], pp. 1205-1211, 1993.
- [5] T. Ota et al., in *Electronic Ceramic Materials*, J. Nowotny (ed.), Trans Tech Pub., 1992, pp. 185-246.
- [6] D. A. Payne et al., in *Ceramic Microstructures '76*, R. M. Fulrath and J. A. Pask (eds.), Westview Press, 1976, pp. 584-597.
- [7] H. Y. Lee and L. C. Burton, in *Proc. Eighth IEEE International Symposium on Applications of Ferroelectrics*, Greenville, SC, Aug. 1992, pp. 98-102.
- [8] K. H. Cho and H. Y. Lee, *J. Kor. Phys. Soc.*, to be published 1994.
- [9] H. Y. Lee, K. H. Cho and H.-D. Nam, *Ferroelectrics*, vol. 154, pp. 143-148 1994.

# Degradation Behavior of Ca-Doped Barium Titanate Ceramic Capacitors

Min Huh, Kyeong Ho Cho, Hyo-Duk Nam and Hee Young Lee\*

Departments of Electronic Engineering and Materials Science and Engineering\*,  
Yeungnam University,  
Kyongsan, 712-749, KOREA

**Abstract**—Electrical degradation of calcium-containing MLCCs having nickel internal electrode was studied using a highly accelerated life test set-up. Both extrinsic and intrinsic failures were identified in commercial MLCCs. From the estimated values of degradation parameters such as voltage exponent factor and pseudo-activation energy, it was found that the intrinsic failure took place by thermal runaway. Although, the degradation pattern for nickel electrode MLCCs was similar to that for common palladium electrode MLCCs, the maximum rated lifetime of the former was in the range of 5 to 30 years and was, in general, shorter than that of the latter. This difference was ascribed to the difference in oxygen vacancy concentrations. Thus, possible degradation mechanisms should be related to oxygen vacancy movement. Among them are reduction model, grain boundary barrier model and de-mixing model.

## INTRODUCTION

Over the last two decades, multilayer ceramic capacitor (MLCC) industries have grown continuously thanks to the rapid development of electronics industries. In particular, the never-ending miniaturization of integrated circuits has accelerated the development of miniaturized capacitors, which has been attempted by the use of high permittivity dielectric and the reduction of single dielectric layer thickness. Comparing to the disc-type ceramic and other classes of capacitors, MLCCs profit from higher volumetric efficiency, high reliability, low cost and readiness for miniaturization.

At present, the most MLCCs are based on barium titanate [1]. This is due to the establishment of appropriate manufacturing processes and the sufficient knowledge of dielectric properties of modified barium titanate ceramics. However, there has been constant search for improvement in miniaturization, volumetric efficiency,

manufacturing cost, *etc.* One of the several ways for cost reduction is the use of inexpensive metals as internal electrode.

Base metals such as nickel and copper have long been studied as possible substitutes for costly metals such as platinum or palladium as internal electrode in barium titanate-based MLCCs. Although nickel electrode MLCCs are commercially available to some extent, the reliability of the devices has not been fully established. It is commonly believed that nickel electrode MLCCs are prone to faster degradation than precious metal electrode MLCCs. Possible causes for faster degradation has been attributed to the presence of low resistance grain boundary phase [2] and increased oxygen vacancies [3,4]. In general, calcium impurity is added to the dielectric composition in order to prevent the reduction of dielectric during co-firing in reducing atmosphere, when nickel is used as internal electrode. Since calcium impurity is not usually required for precious metal electrode MLCCs, any difference in degradation behavior may be related to the presence of calcium.

With this background in mind, we have studied the degradation behavior of calcium-doped commercial MLCCs by monitoring leakage current for a period of time. An accelerated lifetime under very high voltage and temperature stresses has been determined, and the result is used to evaluate degradation parameters. A possible mechanism of degradation is also presented.

## DEGRADATION MECHANISMS

MLCC failure modes may be divided into extrinsic and intrinsic breakdown mechanisms. Extrinsic mechanisms are due, for the most part, to defective or non-optimized processing, to damage by user, to environmental reactions, *etc.* and responsible for most of the infant mortalities.

MLCCs which might show this type of failure can almost be screened out by a burn-in or highly accelerated life test (HALT).

Intrinsic mechanisms are due to the inherent chemistry and physics of the device, and not to faulty manufacture. A lifetime determined by intrinsic failure mechanisms is thus an important criterion which may be used to compare reliability of devices for similar applications. It is often considered as the utmost limit of device performance. To date, several models have been proposed as an intrinsic degradation mechanism. They include grain boundary deterioration model [5,6], de-mixing model [7], reduction model [4], and grain boundary potential barrier model [8]. Except for the grain boundary deterioration model, the other three models are related to oxygen vacancy movement and can explain the exponential increase of leakage current with time in region 2 of Fig. 1 [4,7-9].

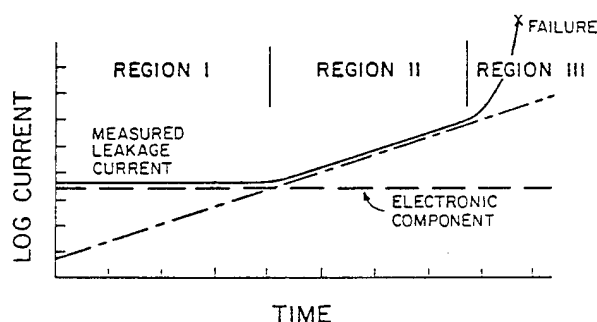


Fig. 1 Generic plot of leakage current versus time for intrinsic mechanisms [9].

### Accelerated Lifetime

There are many ways of defining accelerated lifetime for MLCCs. It may be the duration of degradation experiment when the resistance of the sample is reduced by three to four orders of magnitude from initial equilibrium value [10], when leakage current reaches 100  $\mu A$  regardless of initial leakage current [11], or when the resistance of sample is reduced to 70% of the initial value [12]. In this study, the lifetime was defined as the time when the leakage current was raised by two orders of magnitude from initial equilibrium value. Empirical equation proposed by Minford was utilized in order to estimate degradation parameters [10].

$$\frac{t_1}{t_2} = \left[ \frac{V_2}{V_1} \right]^n \exp \left\{ \frac{E_s}{k} \left[ \frac{1}{T_1} - \frac{1}{T_2} \right] \right\} \quad (1)$$

where  $t_1$  and  $t_2$  are lifetimes under conditions 1 and 2,  $V_1$  and  $V_2$  are constant dc voltages applied to the samples,  $E_s$  is the pseudo-activation energy for degradation,  $T_1$  and  $T_2$  are sample temperatures,  $k$  is the Boltzmann constant, and  $n$  is the voltage exponent parameter.

### EXPERIMENTAL PROCEDURE

Commercially available nickel internal electrode MLCCs with Y5V temperature specification from two different vendors were used as samples in this study. Degradation behavior was studied utilizing a HALT technique [11,12], widely accepted as industrial standard among electronics industries. HALT is different from MIL standard accelerated life test (ALT), in that the former is 48 hour life test under 140°C and eight-times the rated voltage stress, whereas the latter is 1000 hour life test under 125°C and twice the rated voltage stress [10-12,14]. Since equation (1) is applicable to the two to eight times rated voltage and 85 to 170°C temperature stresses, HALT and ALT data can equally be used to estimate the mean-time-to-failure (MTTF) at the rated voltage and 85°C, which is known as the maximum rated lifetime.

In Fig. 2, an experimental HALT set-up we had used was schematically illustrated. It consisted of a high voltage source, an electrometer (Keithley 617), a scanner with current switching card (Keithley 705/7158), and a personal computer (HP Vectra).

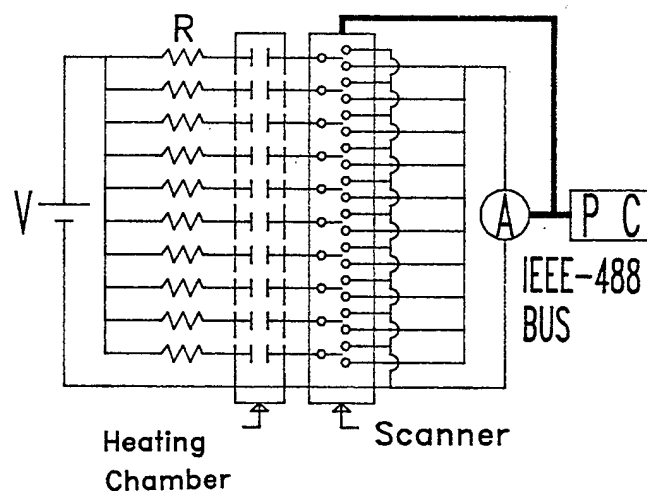


Fig. 2 A schematic for the HALT set-up.

During degradation experiments, sample temperatures were maintained at constant temperature of either 150 or 170°C. In order to apply the same voltage stress to MLCCs from

different lots, the thickness of dielectric layer was determined from scanning electron micrographs. Typically two to five times the rated voltage was used. The qualitative analyses of composition for dielectrics and electrodes were made by the energy dispersive analysis of X-ray (EDAX).

## RESULTS AND DISCUSSION

### *Microstructure and Composition*

Scanning electron micrographs of polished surfaces of MLCC samples from two commercial suppliers (denoted as Sample A and Sample B) were shown in Fig. 3. Thicknesses of dielectric layers determined from the figure were  $17\text{ }\mu\text{m}$  for sample A and  $13\text{ }\mu\text{m}$  for sample B. Energy dispersive spectra

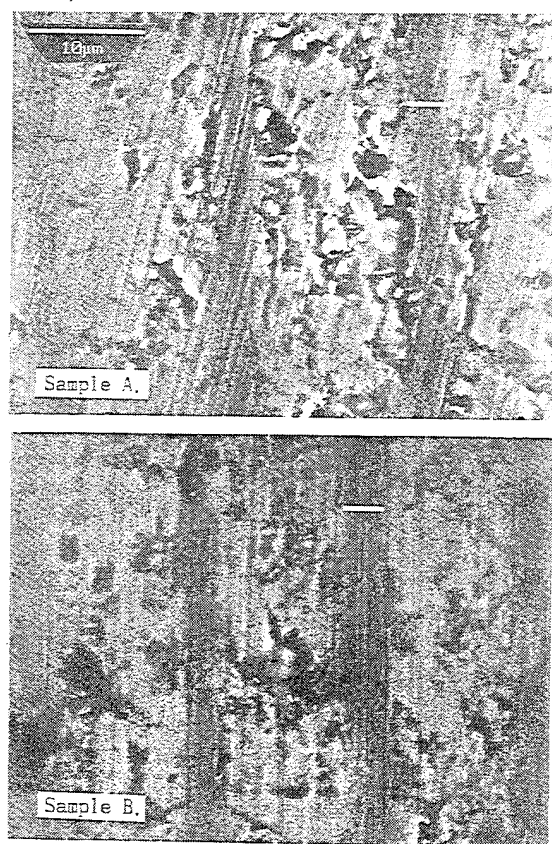


Fig. 3 Scanning electron micrographs of polished samples of commercial nickel electrode MLCCs.

of X-rays for dielectric and electrode regions were exhibited in Fig. 4. It is clearly seen that both samples include calcium in dielectric composition and nickel in electrode composition.

### *Degradation Behavior*

The results of degradation experiments using the

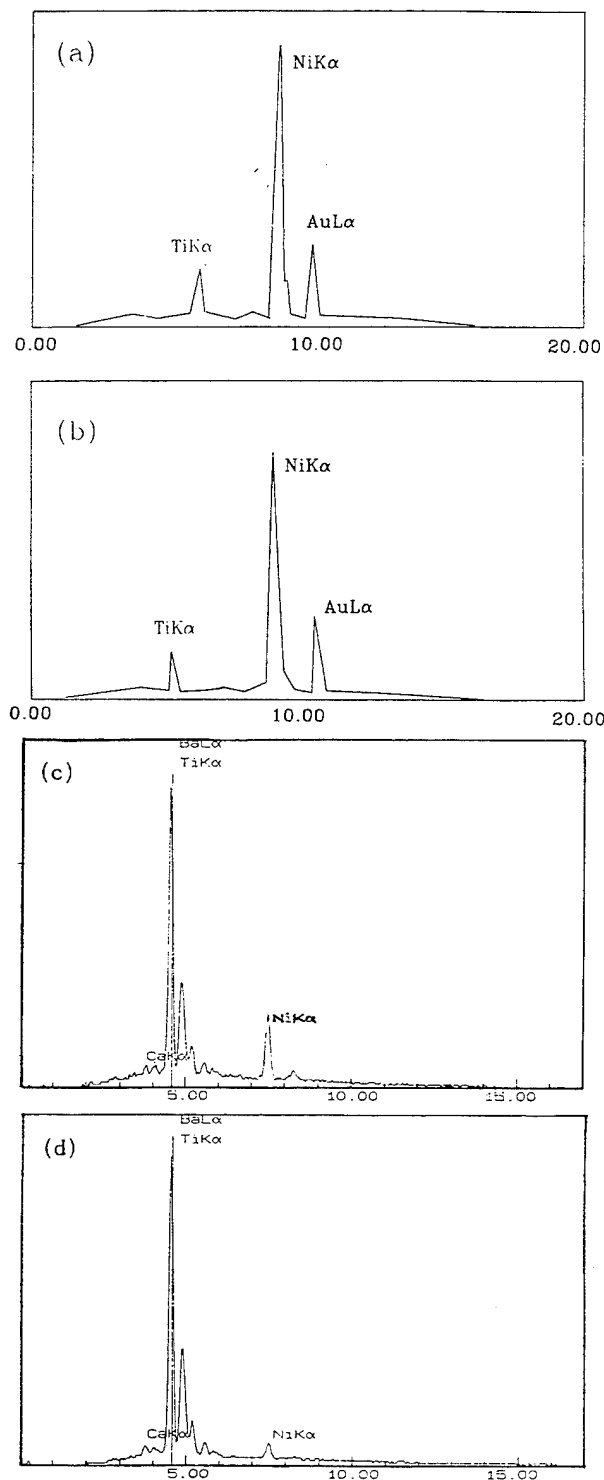
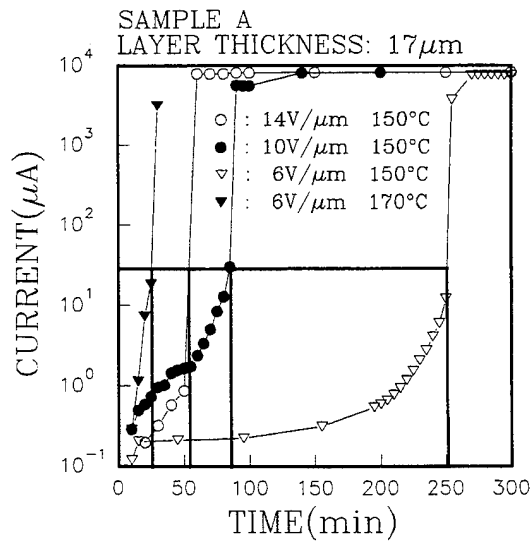


Fig. 4 EDAX spectra of dielectric and electrode area in Fig. 3.

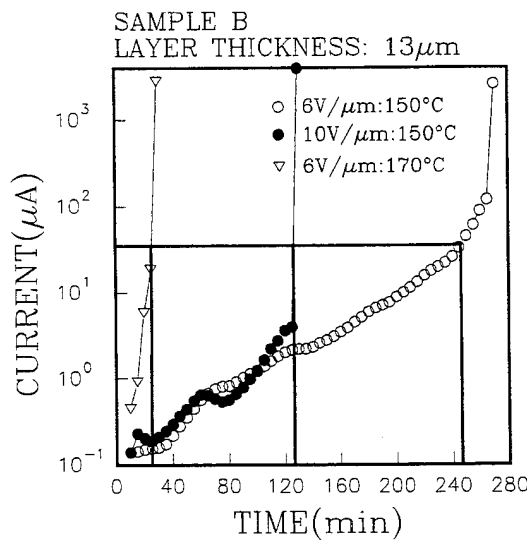
(a) Sample A, electrode (b) Sample B, electrode  
(c) Sample A, dielectric (d) Sample B, dielectric

HALT set-up were exhibited in Fig. 5. The observed current saturation at about  $9\text{ mA}$  in Sample A is caused by a resistor connected in series to the electrometer. It is apparent that the degradation behavior follows the generic intrinsic degradation curve shown in Fig. 1, so that the

degradation mode for both samples is intrinsic. Due to relatively harsh stress conditions we have used,



(a)



(b)

Fig. 5 Leakage current versus time for  
(a) Sample A and (b) Sample B.

the region 2 in Fig. 1, where degradation proceeds at constant rate, often appeared from the beginning of test. Substituting the data taken from Fig. 5 into equation (1), we have determined the degradation parameters, *i.e.* the voltage exponent factor, *n*, and the pseudo-activation energy, *E<sub>s</sub>*. The results were tabulated in Table 1. The voltage exponent factors of nickel electrode MLCC samples are approximately 2.89 and 1.9, for Sample A and Sample B, respectively. The value for Sample A is close to 3, which is an industrial standard [14,15]. However, *n* value for Sample B is somewhat lower than the values reported for normal MLCCs with Z5U or Y5V specifications in the literature [14]. Using the data

in the table, the lifetimes at the maximum rated condition, *i.e.* 85°C and 50 V for Sample A and 85°C and 35 V for Sample B, were estimated and approximately equal to 30 and 5 years, respectively.

Table 1. Degradation parameters for nickel electrode MLCCs.

	Sample A	Sample B	Reference[13,14]	
<i>n</i>	2.86	1.90	2 ~ 4	
<i>E<sub>s</sub></i> (eV)	1.84	1.82	1.87~1.96 (TRA)	1.49 (ARD)

When these values are compared to those of normal palladium electrode MLCCs, it is apparent that the nickel electrode MLCCs shows roughly an order-of-magnitude shorter lifetimes [10-15]. Since oxygen vacancy concentration for nickel electrode MLCCs is much higher than that for normal MLCCs [3], the observed shorter lifetime for the former should have something to do with increased vacancies. On the other hand, the calculated pseudo-activation energy is in close agreement with that for thermal runaway failure mode [13], so that the degradation seems to proceed by intrinsic thermal mechanism. It is to be noted that statistical analysis [2,10-12,14,15] has not been attempted, since we have only measured 5 samples for each test condition. Occasionally, some of these samples showed almost instantaneous failure, which was attributable to extrinsic breakdown, or avalanche breakdown. This case was not included in Fig. 5. Possible models which can explain the observed degradation curve include reduction model, grain boundary barrier reduction model, or de-mixing model out of the four models mentioned above. These models are based on the assumption of oxygen vacancy movement. Grain boundary deterioration model is excluded here since it can not explain the constant increase of leakage current in Fig. 1 and Fig. 5.

## SUMMARY AND CONCLUSIONS

It was found that the voltage exponent factor for Sample A was typical of MLCCs, whereas that for Sample B was approximately 1.9 and somewhat low. This result is reflected as the shorter lifetime of Sample B under the maximum rated condition.

The calculated pseudo-activation energy was in close agreement with that for thermal runaway failure mode, so that the intrinsic degradation was considered to take place by thermal runaway.

Possible models which can explain the observed degradation curve include reduction model, grain boundary barrier reduction model, or de-mixing model. These models are based on the assumption of oxygen vacancy movement. Further study is in progress in an effort to correlate oxygen vacancy concentration with lifetime of MLCCs.

## ACKNOWLEDGEMENT

We would like to thank Prof. G. M. Choi of Pohang University of Science and Technology for his kind support in this work. Experimental assistance from Mr. S. T. Jeon is also greatly acknowledged. This work was supported by the Ministry of Education Research Fund for Advanced Materials in 1992.

## REFERENCES

- [1] J.M. Herbert, *Ceramic Dielectrics and Capacitors*, Gordon and Breach, 1985, pp. 128-187.
- [2] S. Sumita *et al.*, *J. Am. Ceram. Soc.*, vol. 74, pp. 2739-2746, 1991.
- [3] Y. H. Han, in *Proc. 5th Symp. Electronic Ceramics*, Seoul, Korea, Nov. 1991, pp. 114-119.
- [4] H. Y. Lee and L. C. Burton, *IEEE Trans. Components, Hybrids, Manuf. Technol.*, vol. CHMT-9, pp. 469-474, 1986.
- [5] E. Loh, *J. Appl. Phys.*, vol. 53, pp. 6229-6235, 1982.
- [6] H. Neumann and G. Arlt, *Ferroelectrics*, vol. 69, p. 179, 1986.
- [7] R. Waser *et al.*, *J. Am. Ceram. Soc.*, vol. 73, pp. 1645-1653, 1990.
- [8] I. K. Yoo, F. W. Stephenson and L. C. Burton, *IEEE Trans. Components, Hybrids, Manuf. Technol.*, vol. CHMT-10, pp. 274-282, 1987.
- [9] L. C. Burton *et al.*, *Intrinsic Mechanisms of Multilayer Ceramic Capacitor Failure*, Annual Report, ONR Contract No. N00014-83-K-0168, 1986.
- [10] W. J. Minford, *IEEE Trans. Components, Hybrids, Manuf. Technol.*, vol. CHMT-5, pp. 297-300, 1982.
- [11] R. Munikoti and P. Dhar, *IEEE Trans. Components, Hybrids, Manuf. Technol.*, vol. CHMT-11, pp. 342-345, 1988.
- [12] R. Munikoti and P. Dhar, *IEEE Trans. Components, Hybrids, Manuf. Technol.*, vol. CHMT-11, pp. 346-350, 1988.
- [13] B. S. Rawal and N. H. Chan, in *Proc. 34th Electronic Components Conf.*, New Orleans, LA, May 1984, pp. 184-188.
- [14] R. Confer *et al.*, in *Proc. 41st Electronic Components Technol. Conf.*, Atlanta, GA, May 1991, pp. 320-322.
- [15] S. K. Kurtz *et al.*, *J. Am. Ceram. Soc.*, vol. 72, pp. 2223-2233, 1989.

# Dielectric Breakdown in PLZT 9.5/65/35 Ceramics

E. Furman<sup>+</sup> and L. E. Cross<sup>\*</sup>

<sup>+</sup> The Gilbert C. Robinson Department of Ceramic Engineering,  
Clemson University, Clemson, SC 29634-0907

<sup>\*</sup> Materials Research Laboratory  
The Pennsylvania State University, University Park, PA 16802

**Abstract** — There is currently a trend to reduce the thickness of the dielectrics and to operate them at higher field levels. Understanding and controlling the breakdown strength will permit higher operating fields. The main goal of this work was to establish the breakdown mechanism in PLZT ceramics. The breakdown experiments were conducted with both hot-pressed and conventional ceramics. The breakdown strength was studied as a function of electrode material, voltage polarity, ramp rate, and temperature. All of the results were consistent with electromechanical breakdown being the dominant mechanism.

## INTRODUCTION

With the renewed interest in ferroelectric thin film devices, properties of the ferroelectric materials at high field receive greater attention. To operate devices at higher fields requires an increased understanding of their breakdown mechanism. Dielectric breakdown sets the upper limit on the useful operating electric field.

The purpose of this work was to identify breakdown mechanism in PLZT 9.5/65/35 ceramics. Three possible mechanisms of electrical breakdown were considered: electrical, thermal, and electromechanical. Electrical breakdown involves one of several possible mechanisms leading to electrons gaining more energy from the field than they lose to the lattice. Possible origins of instability are discussed by O'Dwyer [1]. Unlike the electrical breakdown, thermal breakdown does not invoke a new mechanism that is not present at lower fields. Instead, breakdown is assumed to occur when Joule's heat causes thermal runaway. Electromechanical breakdown refers to cases where the breakdown occurs as a result of electromechanical interactions within the material.

The various breakdown mechanisms have distinguishing characteristics. Electrical breakdown requires less time to develop than the other two mechanisms, and it usually has a weaker temperature dependence. The thermal breakdown strength is inversely proportional to the ambient temperature and electrical conductivity, and directly proportional to the thermal conductivity of the electrode and dielectric material. Electromechanical breakdown is relatively slow, and for the case of subcritical crack growth, depends on environmental conditions [2].

Hot-pressed and sintered samples of PLZT 9.5/65/35 ceramics with different electrodes and varying thicknesses were used. Breakdown was also studied as a function of temperature and ramp rate.

## EXPERIMENTAL PROCEDURE

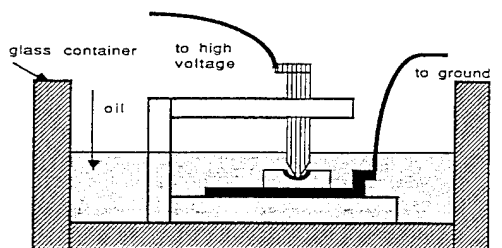
Mixed oxide ceramics were produced in batches of 200 grams. The mixtures were milled for 8 hours using zirconia balls in ethanol. The dried powders were calcined for 7 hours at 750 °C. The calcined powders were ground in a mortar to pass an 80 mesh sieve and then recalcined. The samples were then sintered in a controlled lead atmosphere at 1280 °C in a closed alumina crucible. The hot-pressed samples were supplied by Motorola Corporation. Densities of the samples were determined by utilizing Archimedes' principle. Samples and powders were characterized by XRD, qualitative spectrographic analyses, and SEM. For the breakdown experiments, semispherical indentations were drilled in the hot-pressed and some of the conventional samples, and then polished. The final polishing step was accomplished using an aqueous slurry of 3  $\mu\text{m}$  alumina powder. For other conventionally sintered samples, a custom-made die was used to produce semispherical indentations in the sample pressing step. The purpose of using samples with indentations is to avoid edge breakdown. The apparatus was configured to study breakdown strength as a function of voltage ramp rate. Each breakdown event was recorded with a digital oscilloscope. Three types of electrodes were used: gold, aluminum, and a saturated aqueous NaCl solution.

Gold electrodes were sputtered on the faces of the polished samples using a DC Magnetron Sputtering unit (SCD 040 Sputtering System, Balzers Corp.) and aluminum electrodes were deposited in the evaporation unit (VE10, Varian Corp.). The arrangements for measuring electrical breakdown for metallic and aqueous electrodes are shown in Figure 1. Unless stated otherwise, all experimental data presented is for gold electroded samples with the ramp rate of 1000 V/sec.

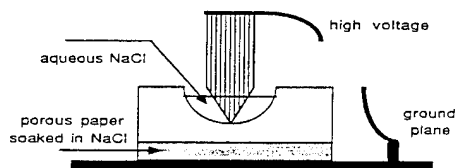
## RESULTS AND DISCUSSION

### *Sample Characteristics*

The sintered ceramics were 92.5% to 96% dense, and the hot-pressed samples were more than 99% dense. The location and strength of the diffraction peaks were in good agreement, as is shown in Figure 2. Quantitative spectrographic analyses of the calcined powder is shown in Table 1. The impurities detected had concentrations below 200 ppm. Impurities in such small amounts are likely to be soluble in the perovskite structure, and should act as acceptors in PLZT. The average grain size was approximately 3.5  $\mu\text{m}$  in the conventional ceramics and 7.5  $\mu\text{m}$  in the hot-pressed samples, as



(a)



(b)

Figure 1. Sample holders used in the breakdown experiments for (a) solid and (b) liquid electrodes.

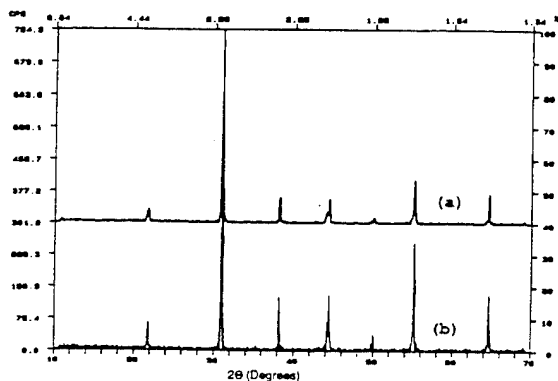


Figure 2. X-ray diffraction pattern for (a) hot-pressed and (b) conventional ceramics.

Table 1. Qualitative spectrographic analysis of PLZT powder.

Level	Element
Major Elements (>2%)	Pb, Ti, Zr, La
Minor Elements (0.02 - 2%)	—
Trace Elements (<0.02%)	Al, Mg, Si, Fe, Ca
Not Detected	Nb, Mo, B, Cr, Ni, Co, V, Be, Ba, Sr, Cu, Y

determined from the SEM micrographs using the linear intercept method.

#### Breakdown Properties

The dependence of the dielectric breakdown on temperature for the conventional samples is shown in Figure 3. It can be seen that there is no strong temperature dependence of the breakdown strength on temperature in PLZT. In comparison, in ferroelectric substances such as  $\text{NaNO}_2$  and  $\text{BaTiO}_3$  there is a significant reduction in strength, associated with thermal breakdown, as temperature is increased. PLZT has very high resistivity which makes thermal breakdown less likely.

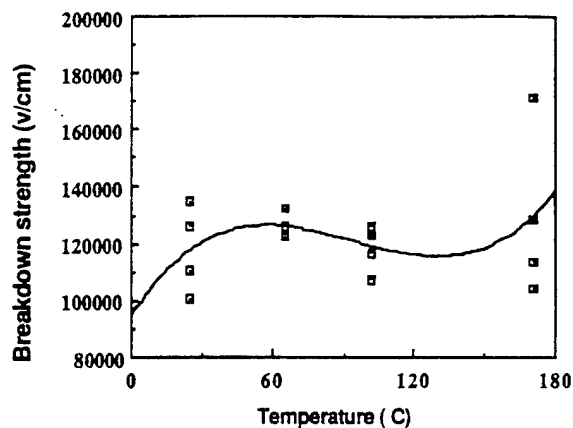


Figure 3. Dielectric breakdown strength of conventional ceramics as a function of temperature. Solid line represents polynomial fit.

The ramp rate dependence of the breakdown strength at room temperature is shown in Figure 4 for the gold-electroded samples. An unpaired t-Test was used to compare the mean values of breakdown for various ramp rates. It was determined with a 90% degree of confidence that the mean breakdown strength for the  $10^5$  and  $10^6$  V/sec. ramp rate was greater than the breakdown strength of samples tested with  $10^3$  V/sec. ramp rate. The ramp rate dependence of the breakdown strength, with the relatively low ramp rates used, suggests that the breakdown mechanism is probably not electric.

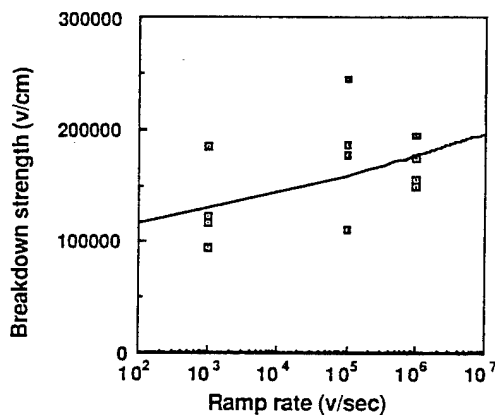


Figure 4. Ramp rate dependence of the breakdown strength for conventional ceramics. Sample thickness range:  $0.02 \pm 0.005$  cm.

The comparison of the breakdown strength of samples with gold and aluminum electrodes is shown in Table 2. The use of different metal electrodes may have an effect in case of electric breakdown and thermal breakdown, and much less so for the electromechanical breakdown. Since the work functions of aluminum (4.4 eV) and gold (5.2 eV) [3] are significantly different, the charge injection at high field voltage via the Schottky mechanism operating in PLZT [4] could be different for the two electrodes. The null hypotheses, that the mean breakdown strengths for the two types of the electrodes are the same, could not be rejected (with a 90% degree of certainty). It is possible that the Fermi level is pinned by the defect states at the surface, in which case the current injection will not be influenced by the electrode.



**Table 2.** Comparison of the breakdown strength of conventional PLZT ceramics with gold and aluminum electrodes at room temperature.

Electrode Material	Sample Thickness (cm)	Breakdown Strength (V/cm)	Average Strength (V/cm)
Gold	0.140	48103	44112
	0.147	44626	
	0.142	45070	
	0.147	44626	
	0.145	47448	
	0.145	39724	
	0.150	38703	
	0.144	44596	
Aluminum	0.145	37256	42977
	0.146	47123	
	0.145	45241	
	0.142	40563	
	0.141	41986	
	0.145	36414	
	0.145	52966	
	0.144	46667	
	0.141	38582	

The thickness dependence of the breakdown strength for hot-pressed and conventional ceramics is shown in Figure 5. Significantly more scatter was observed in values of the breakdown strength for the conventional samples, especially at smaller thicknesses, compared to the hot-pressed samples. Though the average strength of the conventional samples is considerably smaller than that of the hot-pressed samples,

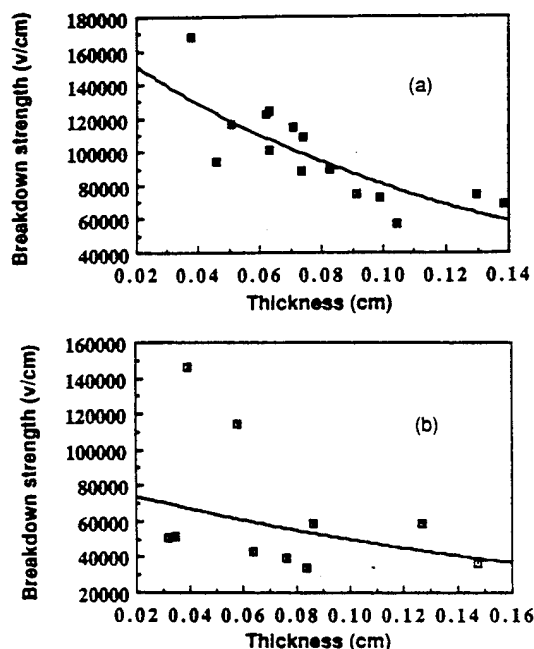


**Figure 5.** Room Temperature breakdown strength as a function of thickness for (a) hot-pressed and (b) conventional ceramics. Solid line represents exponential fit.

their maximum strengths are comparable and have similar temperature dependence. The best fit of the data resulted in the following expressions:

$$E_{br}(\text{hot-pressed}) = 17.8 * t^{-0.64} \quad (1)$$

$$E_{br}(\text{conventional}) = 21.4 * t^{-0.36} \quad (2)$$

Equations (1) and (2) relate the breakdown strength  $E_{br}$  (in units of kV/cm) to the sample thickness  $t$  (in units of cm). The hot-pressed samples have greater sensitivity to the thickness in comparison to the conventional samples. Gerson and Marshall [5] have studied the thickness dependence of breakdown strength of PZT ceramics. The samples studied were 95% dense, and had thicknesses in the range 0.1 – 0.6 cm. The thickness dependence of the breakdown strength in PZT fits the expression:

$$E_{br}(\text{PZT}) = 27.2 * t^{-0.39} \quad (3)$$

Comparing equations (2) and (3), it can be seen that, though the magnitudes of the breakdown strength are somewhat higher in PZT, the slopes of the thickness dependencies of breakdown are almost identical.

Results for the aqueous-NaCl-electroded PLZT samples tested at a 1000 V/sec. ramp rate are shown in Figure 6. The breakdown strength values have a wide scatter, but little dependence on how the indentations were made. The breakdown strength for the samples with the aqueous electrodes was well below that for the samples with gold electrodes, as is shown in Figure 7. The best fit to all the samples tested for the gold- and aqueous-electroded samples are compared. For liquid electrodes, both the absolute magnitude and the thickness dependence of the breakdown strength of PLZT are lower compared to the conventionally electroded samples.

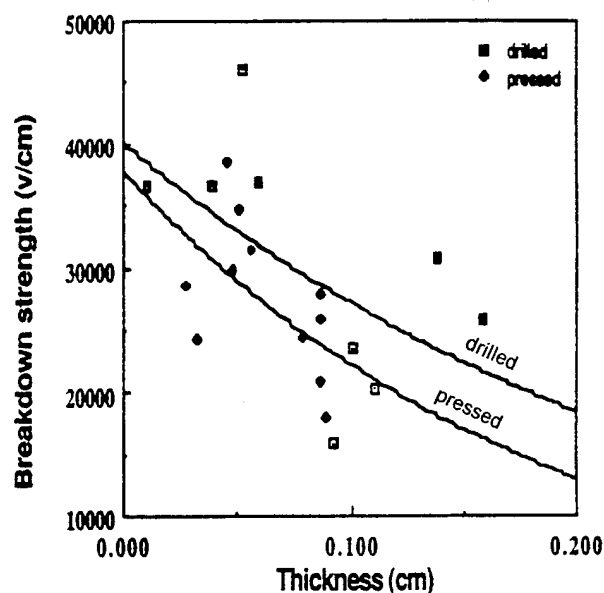


**Figure 6.** Comparison of the breakdown strength for liquid-electroded conventional ceramics for drilled versus pressed indentations. Solid line represents exponential fit.

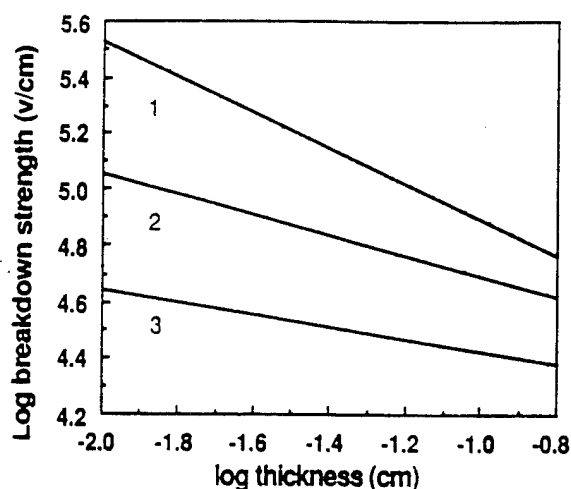


Figure 7. Power law fit of the dielectric breakdown strength as a function of thickness for:  
 (1) gold-electroded hot-pressed samples  
 (2) gold-electroded conventional samples  
 (3) liquid-electroded conventional samples

The use of liquid electrodes, with their greater thermal mass compared to the thin metal electrodes, should enhance the heat dissipating ability of a sample. In the case of thermal breakdown, an increase in the breakdown strength would be expected. On the other hand, the electromechanical breakdown strength should be reduced, since the corrosive liquid, such as water, is known to enhance the speed of the subcritical crack growth [2]. Thus, experimentally observed lowering of the breakdown strength of PLZT samples in the presence of liquid electrodes supports the possibility of electromechanical breakdown.

The experimental results strongly support the hypothesis of an electromechanical breakdown mechanism in PLZT 9.5/65/35 bulk ceramics. The weak temperature dependence of the breakdown strength and the reduction of the breakdown strength with the use of aqueous electrodes are in contradiction with the expected behavior of samples characterized by thermal breakdown. The pulse rate dependence of the breakdown strength at relatively low pulse rates used in this study is the strongest evidence against the electrical breakdown. The strong thickness dependence of experimentally observed breakdown strength does not favor either the intrinsic electrical breakdown mechanism, which should be independent of thickness, or the Seitz's avalanche breakdown theory, which has a logarithmic thickness dependence [1]. The observation that gold and aluminum electrodes give the same breakdown strength does not support field-emission initiation of the breakdown at the cathode.

The most likely mechanism is electromechanical breakdown. It is supported by an increasing breakdown strength for steeper ramp rates, and, in particular, by a reduction of the breakdown rate in the presence of corrosive electrodes. Large scatter in the breakdown strength for the conventional samples points to the importance of strength-limiting flaws. Observations of micro- and macro-cracks prior to the breakdown in this and previous studies [6], support electro-mechanical breakdown. PLZT ceramics are capable of large field-induced strain and have relatively low mechanical

fracture toughness, making them susceptible to the field-initiated cracking.

The electromechanical breakdown mechanism may occur as a sequence of steps. Applying electric field to the PLZT ceramic samples induces nonuniform strain in adjacent grains which happen to have different crystallographic axis with respect to the electric field. Because of the partial clamping exerted at the grain boundaries, stresses develop. The presence of defects, such as preexisting pores and micro-cracks, further enhances local stresses, and cracks begin to propagate at a sufficiently high electric field level. The presence of a corrosive substance further enhances the crack propagation rate. As the crack continues to grow, it further distorts the electric field, until the local field exceeds the critical level needed to cause sample destruction, and thermal or electrical breakdown occurs. Even though thermal or electrical breakdown may cause ultimate damage, it is electro-mechanical damage to the sample, occurring prior to the final destruction, which is likely to be the rate-limiting step.

#### SUMMARY

The goal of this work was to establish the breakdown mechanism in PLZT ceramics. Three possible mechanisms were considered as candidates to cause the breakdown: electric, thermal, and electromechanical. The breakdown experiments were conducted with both hot-pressed and conventional ceramics. The breakdown strength was studied as a function of electrode material, voltage polarity, ramp rate, and temperature. All of the results were consistent with electromechanical breakdown being the dominant mechanism.

#### ACKNOWLEDGMENT

The authors are grateful to Professor W. Schulze of Alfred University for useful discussions. This work was supported by the Center for Dielectric Studies at The Pennsylvania State University.

#### REFERENCES

- [1] J. J. O'Dwyer, *The Theory of Electrical Conduction and Breakdown in Solid Dielectrics*. Oxford: Clarendon Press, 1973.
- [2] B. G. Koepke and K. D. McHenry "Fracture and Deformation of PZT," *Ferroelectrics*, vol. 28, pp. 343-346, 1980.
- [3] S. M. Sze, *Physics of Semiconductor Devices*. New York: John Wiley & Sons, 1981, ch. 5, pp. 246-312.
- [4] E. Furman, W. Gu, and L. E. Cross, "Electrical Properties of PLZT 9.5/65/35 Ceramics," in *Proc. of 7th Int. Symp. on Applications of Ferroelectrics*, 1990, pp. 588-590.
- [5] R. Gerson and T. Marshall, "Dielectric Breakdown of Porous Ceramics," *J. Appl. Phys.*, vol. 30, number 11, pp. 1650-1653, 1959.
- [6] W. R. Salaneck, "Some Fatiguing Effects in 8/65/35 PLZT Fine Grained Ferroelectric Ceramic," *Ferroelectrics*, vol. 4, pp. 97-101, 1972.

Sea-Fue Wang, Wayne Huebner, and Joseph P. Dougherty  
Center for Dielectric Studies  
Materials Research Laboratory  
The Pennsylvania State University  
University Park, PA 16802

**Abstract**—Reducing the sintering temperature of BaTiO<sub>3</sub> has typically been achieved through the use of a fluxing agent to promote densification by liquid phase sintering. Liquid phase formation in these systems is due either to the melting of the flux or to the formation of a eutectic liquid between the flux and BaTiO<sub>3</sub>. In this paper, the correlation between the wettability and interfacial reactions between fluxes and BaTiO<sub>3</sub> with respect to the densification behavior associated with liquid phase sintering, and the resulting dielectric properties is presented. Fluxes used in this study include 5ZnO·2B<sub>2</sub>O<sub>3</sub>, 5CdO·2SiO<sub>2</sub>, Pb<sub>5</sub>Ge<sub>3</sub>O<sub>11</sub>, CuO·TiO<sub>2</sub>, 3Bi<sub>2</sub>O<sub>3</sub>·B<sub>2</sub>O<sub>3</sub>, and LiF.

## INTRODUCTION

The wettability of fluxes on a ceramic is very important for densification during sintering. A non-wetting liquid,  $\theta > 90^\circ$ , may lead to swelling of the compact during sintering, segregation, and possible melt extrusion through open porosity. A wetting liquid,  $\theta < 90^\circ$ , will attempt to occupy the lowest free energy positions and hence will preferentially flow into fine scale porosity due to capillary forces.<sup>1,2</sup> When there is insufficient liquid to fill all of the porosity, these capillary forces will pull the particles together to minimize the free energy. This effect gives rise to the rearrangement stage and rapid initial densification during liquid phase sintering. Usually wetting is aided by solubility of the solid in the liquid or the formation of intermediate compounds.

In addition to serving as a liquid phase to promote densification, the fluxes may act as a second phase layer to dilute the dielectric properties, or serve as a Curie point shifter for BaTiO<sub>3</sub> when they are incorporated into the BaTiO<sub>3</sub> lattice. The characteristics of grain boundary phases in ceramics, such as composition, connectivity, volume fraction, and defect chemistry, can have a significant impact on their dielectric properties. If the liquid phase has a low solubility in BaTiO<sub>3</sub> and is persistent throughout liquid phase sintering, then the solidified, interconnected liquid phase surrounding the BaTiO<sub>3</sub> will result in an intergranular boundary layer. The dielectric properties will be diluted, and can be modeled by the brick wall model. On the other hand, if the liquid phase has a high solubility in BaTiO<sub>3</sub> and acts as a transient phase during liquid phase sintering, then the dilution of the dielectric properties is reduced.<sup>3</sup>

In this study, the correlation between the wettability and interfacial reactions with respect to the densification behavior associated with liquid phase sintering, and the resulting dielectric properties is characterized. Although the formation of low melting temperature fluxes described in the literature have been complex, several simple flux systems, including 5ZnO·2B<sub>2</sub>O<sub>3</sub>, 5CdO·2SiO<sub>2</sub>, Pb<sub>5</sub>Ge<sub>3</sub>O<sub>11</sub>, CuO·TiO<sub>2</sub>, 3Bi<sub>2</sub>O<sub>3</sub>·B<sub>2</sub>O<sub>3</sub>, and LiF, which have been shown to be effective sintering additives,<sup>3-8</sup> were selected for use in this work.

## EXPERIMENTAL PROCEDURE

Commercial TAM-HPB BaTiO<sub>3</sub> and Pb<sub>5</sub>Ge<sub>3</sub>O<sub>11</sub>, 3Bi<sub>2</sub>O<sub>3</sub>·B<sub>2</sub>O<sub>3</sub>, 5CdO·2SiO<sub>2</sub>, CuO·TiO<sub>2</sub>, 5ZnO·2B<sub>2</sub>O<sub>3</sub>, and LiF fluxes were used in this study. Except for the LiF and CuO·TiO<sub>2</sub> systems, the raw materials for each flux were mixed/milled in methyl alcohol in a polyethylene jar with ZrO<sub>2</sub> media using a ball mill. After drying, these powders were transferred to a platinum crucible and heated at a temperature elucidated from DTA/TGA analyses. Following melting, they were quenched and then milled to pass through a 320 mesh screen. For the microstructural development and dielectric properties studies, these fluxes were also mixed/milled with the BaTiO<sub>3</sub> to achieve submicron particles. For the contact angle determinations, the fluxes were pressed into 0.254 cm (0.1-in) diameter pellets.

Wetting experiments were carried out in a tube furnace in air

using the Sessile-drop method. Contact angles were double-checked through optical observations of cross-sections. Temperatures of liquid phase formation at each flux system were also determined using DTA with a heating rate of 10°C/min on BaTiO<sub>3</sub> powders mixed with excess flux (20wt%). Pellets of mixtures also were heated up to 1100°C and quenched, followed by XRD analysis on the polished surface to obtain the phases that were solidified or decomposed from the liquid phase during cooling.

HPB BaTiO<sub>3</sub> was mixed/milled for 24 h with specific volume fractions of fluxes in methyl alcohol using a Sweco mill (polyethylene jar, ZrO<sub>2</sub> media). Dried powders were characterized (particle size  $\approx 0.7 \mu\text{m}$ ) and mixed with DuPont 5200 binder and then pelletized. Pellets were sintered at 900–1150°C for 2 h (heating rate: 6°C/min, cooling rate: 3°C/min).

Dilatometric analyses were performed to characterize the shrinkage of the flux-sintered BaTiO<sub>3</sub> with temperature at a heating rate of 3°C/min. The dilatometric curves were compared with the temperature of liquid formation, which was obtained using DTA, although the heating rates of the DTA and dilatometric analyses were slightly different.

## RESULTS AND DISCUSSION

### 1. Wettability and Reaction of Fluxes on BaTiO<sub>3</sub>

Results of Sessile drop experiments for various fluxes on BaTiO<sub>3</sub> substrates are given in Table 1. Four types of Sessile drop configurations were observed in this study. The first type has no compositional changes in the flux, and only trace amount of fluxes

Table 1 Wetting Angles of Various oxides on the BaTiO<sub>3</sub> substrate

Compounds	Temperature (°C)	Contact Angle (°)
LiF	875	0
BaLiF <sub>3</sub>	850	12
PbO	900	0
Pb <sub>5</sub> Ge <sub>3</sub> O <sub>11</sub>	750	8
Bi <sub>2</sub> O <sub>3</sub>	800	0
B <sub>2</sub> O <sub>3</sub>	460	73
	600	36
	800	11
3Bi <sub>2</sub> O <sub>3</sub> ·B <sub>2</sub> O <sub>3</sub>	750	19
5CdO·2SiO <sub>2</sub>	1200	14
5ZnO·2B <sub>2</sub> O <sub>3</sub>	1050 (before rxn)	32
	(after rxn)	24
CuO·TiO <sub>2</sub>	1050 (before rxn)	61
	(after rxn)	22

diffuse into BaTiO<sub>3</sub>; 3Bi<sub>2</sub>O<sub>3</sub>·B<sub>2</sub>O<sub>3</sub> is an example from this study. The second type exhibits a chemical reaction between the BaTiO<sub>3</sub> and flux, which results in spreading ( $\theta = 0$ ); LiF and Bi<sub>2</sub>O<sub>3</sub> are examples from this study. The third type exhibits complete solubility of the flux in the BaTiO<sub>3</sub>, which results in spreading; PbO is an example from this study. The fourth type has an acute contact angle owing to a high solubility of BaTiO<sub>3</sub> in the flux, and a limited solubility of the flux in the BaTiO<sub>3</sub>; BaLiF<sub>3</sub>, Pb<sub>5</sub>Ge<sub>3</sub>O<sub>11</sub>, 5CdO·2SiO<sub>2</sub>, CuO·TiO<sub>2</sub>, and 5ZnO·2B<sub>2</sub>O<sub>3</sub> are examples from this study.

The melting temperatures of flux components and those of possible eutectic liquids between fluxes and BaTiO<sub>3</sub> were measured by DTA on mixtures of BaTiO<sub>3</sub> and 20 wt% fluxes with a heating rate of 10°C/min. The results are summarized in Table 2. Details of these results are discussed below:

### (i) LiF System

LiF has been shown to be an effective sintering aid for BaTiO<sub>3</sub> by several investigators.<sup>4</sup> During Sessile drop measurements, rapid spreading ( $\theta = 0^\circ$ ) was observed at the melting temperature of LiF. XRD analyses on the surface of the LiF-wetted specimen of BaTiO<sub>3</sub> indicated that BaLiF<sub>3</sub> and LiTiO<sub>2</sub> formed. Formation of these compounds was also reported by Lin, while Bonnet et al. and Anderson et al. showed the presence of Li<sub>2</sub>TiO<sub>3</sub> in their study.

As shown by the DTA results (Table 2), a eutectic melt is formed at 750°C from mixtures of BaTiO<sub>3</sub> and LiF. Comparing this result with the phase diagram of BaLiF<sub>3</sub>-LiF, it seems that the melt that forms at 750°C is due to the eutectic reaction between BaLiF<sub>3</sub> and excess LiF. During cooling, the eutectic liquid recrystallized into LiTiO<sub>2</sub> and BaLiF<sub>3</sub>. Results from DTA studies on mixtures of BaTiO<sub>3</sub> and LiF with addition of BaCO<sub>3</sub> show endothermic peaks at 632 and 720°C, which correspond to eutectic liquid formation. This correlates well with studies that have shown LiF additions to Ba-excess BaTiO<sub>3</sub> (adjusted by BaCO<sub>3</sub>) lower the sintering temperature.

BaLiF<sub>3</sub>, an intermediate product in the LiF-wetted specimen of BaTiO<sub>3</sub>, has also been shown to be an effective sintering aid. The wetting angle was found to be 12°. DTA results show that mixtures of BaTiO<sub>3</sub> and BaLiF<sub>3</sub> did not exhibit any liquid formation other than the incongruent melting of BaLiF<sub>3</sub> at 845°C.

### (ii) Bi<sub>2</sub>O<sub>3</sub>-B<sub>2</sub>O<sub>3</sub> System

DTA results on a mixture of BaTiO<sub>3</sub> and Bi<sub>2</sub>O<sub>3</sub> showed the presence of three endothermic peaks at 575, 719, and 789°C, and the  $\alpha$ -Bi<sub>2</sub>O<sub>3</sub> to  $\delta$ -Bi<sub>2</sub>O<sub>3</sub> at 728°C. These three peaks are most likely due to eutectic liquid formation, although further studies would be needed to confirm this hypothesis. The first two endothermic peaks are very small. During the wettability study, no visible reaction was observed at temperatures below the melting point of Bi<sub>2</sub>O<sub>3</sub>, which is 807°C. Above the melting temperature, a rapid spreading of Bi<sub>2</sub>O<sub>3</sub> on BaTiO<sub>3</sub> was obtained. XRD analyses on the surface of Bi<sub>2</sub>O<sub>3</sub>-wetted

Table 2 DTA results of oxides and mixtures, which shown the endothermic peaks corresponding to the temperature at which liquid formed

Compounds	Melting Point(°C)
LiF	865
BaLiF <sub>3</sub>	845
BaTiO <sub>3</sub> -LiF	750
BaTiO <sub>3</sub> -BaLiF <sub>3</sub>	845
BaTiO <sub>3</sub> -LiF-BaCO <sub>3</sub>	632
	720
PbO	886
GeO <sub>2</sub>	1115
BaTiO <sub>3</sub> -GeO <sub>2</sub>	1083
Pb <sub>2</sub> GeO <sub>7</sub>	742
BaTiO <sub>3</sub> -Pb <sub>2</sub> GeO <sub>7</sub>	736
	781
Bi <sub>2</sub> O <sub>3</sub>	807
B <sub>2</sub> O <sub>3</sub>	450
3Bi <sub>2</sub> O <sub>3</sub> -B <sub>2</sub> O <sub>3</sub>	625
BaTiO <sub>3</sub> -Bi <sub>2</sub> O <sub>3</sub>	575
	719
	789
BaTiO <sub>3</sub> -3Bi <sub>2</sub> O <sub>3</sub> -B <sub>2</sub> O <sub>3</sub>	542
	655
	768
SiO <sub>2</sub>	1723
5CdO-2SiO <sub>2</sub>	1191
BaTiO <sub>3</sub> -5CdO-2SiO <sub>2</sub>	1046
5ZnO-2B <sub>2</sub> O <sub>3</sub>	1043
BaTiO <sub>3</sub> -5ZnO-2B <sub>2</sub> O <sub>3</sub>	834
CuO-TiO <sub>2</sub>	1034
BaTiO <sub>3</sub> -CuO	1030
BaTiO <sub>3</sub> -CuO-TiO <sub>2</sub>	1024

specimen of BaTiO<sub>3</sub> show the presence of Bi<sub>2</sub>O<sub>3</sub> and a small amount of BaBi<sub>4</sub>Ti<sub>4</sub>O<sub>15</sub>.<sup>5</sup>

A glass former, B<sub>2</sub>O<sub>3</sub>, was added to the Bi<sub>2</sub>O<sub>3</sub> (3Bi<sub>2</sub>O<sub>3</sub>-B<sub>2</sub>O<sub>3</sub>) to determine its affect on the wettability and sintering behavior. DTA results showed the temperature of the three endothermic peaks associated with liquid phase formation were lowered by the B<sub>2</sub>O<sub>3</sub> additions to 542, 655, and 768°C. The wetting angle of 3Bi<sub>2</sub>O<sub>3</sub>-B<sub>2</sub>O<sub>3</sub> was 19° at 750°C. XRD analysis on a mixture of BaTiO<sub>3</sub> and 20wt% 3Bi<sub>2</sub>O<sub>3</sub>-B<sub>2</sub>O<sub>3</sub> cooling from 1100°C show that a glass phase, Bi<sub>2</sub>O<sub>3</sub>,

and small amounts of BaBi<sub>4</sub>Ti<sub>4</sub>O<sub>15</sub> phases exist. Subbarao et al have suggested that BaBi<sub>4</sub>Ti<sub>4</sub>O<sub>15</sub> forms at  $\approx 800^\circ\text{C}$ , and redissolves at higher temperatures.

### (iii) 5PbO-3GeO<sub>2</sub> System

Wetting studies showed that PbO readily spread on BaTiO<sub>3</sub> at temperatures greater than its melting temperature of 886°C. Pb<sub>5</sub>Ge<sub>3</sub>O<sub>11</sub> was first reported by Payne as a flux for BaTiO<sub>3</sub>, providing a high dielectric constant and breakdown strength and a low dissipation factor.<sup>6</sup> As shown by the DTA results, Pb<sub>5</sub>Ge<sub>3</sub>O<sub>11</sub> is another flux that exhibits a eutectic melting point lower than 800°C. The two temperatures associated with liquid phase formation are the melting of Pb<sub>5</sub>Ge<sub>3</sub>O<sub>11</sub> at 736°C and a eutectic liquid between Pb<sub>5</sub>Ge<sub>3</sub>O<sub>11</sub> and BaTiO<sub>3</sub> at 781°C. The wetting angle of this flux on BaTiO<sub>3</sub> is 8°.

### (iv) 5CdO-2SiO<sub>2</sub> System

Cadmium silicates, such as 2CdO-SiO<sub>2</sub>, 5CdO-2SiO<sub>2</sub>, and 3CdO-SiO<sub>2</sub> have been used as fluxes for BaTiO<sub>3</sub>, as first reported by Maher. Among these compounds, 5CdO-2SiO<sub>2</sub> was found to be the most effective sintering aid. 5CdO-SiO<sub>2</sub> has a melting temperature at 1191°C (Table 2). Mixtures of 5CdO-SiO<sub>2</sub> and BaTiO<sub>3</sub> exhibit a eutectic temperature at 1046°C. The wetting angle of 5CdO-SiO<sub>2</sub> on BaTiO<sub>3</sub> was found to be 14° at 1200°C. XRD analysis on a mixture of BaTiO<sub>3</sub> and 20wt% 5CdO-2SiO<sub>2</sub> quenched from 1100°C shows the existence of CdO and BaCdSi<sub>2</sub>O<sub>7</sub>. The formation of BaCdSi<sub>2</sub>O<sub>7</sub> may explain the precipitation of CdO, which was observed in Maher's study.<sup>7</sup>

### (v) 5ZnO-2B<sub>2</sub>O<sub>3</sub> System

Similar to the CdO-2SiO<sub>2</sub> system, mixtures of 5ZnO-2B<sub>2</sub>O<sub>3</sub> and BaTiO<sub>3</sub> exhibited eutectic liquid phase formation at 834°C, which is much lower than the melting point of the flux itself (1043°C). The wetting angle before visible reaction occurs is 32°, and after reaction is 24°. XRD analysis on a mixture of BaTiO<sub>3</sub> and 5wt% 5ZnO-2B<sub>2</sub>O<sub>3</sub> quenched to 1100°C revealed the presence of ZnO and an unknown phase.

### (vi) CuO-TiO<sub>2</sub> System

The addition of CuO to BaTiO<sub>3</sub> results in eutectic liquid formation when CuO partially decomposes at 1070°C according to the reaction:  $4\text{CuO} \leftrightarrow 2\text{Cu}_2\text{O} + \text{O}_2$  (equilibrium  $\text{PO}_2 \approx 0.4 \times 10^{-5}$  Pa at 1070°C<sup>15</sup>). With the addition of TiO<sub>2</sub>, the eutectic temperature is reduced to 1024°C (Table 2). Hennings showed that on cooling, a Cu<sub>3</sub>TiO<sub>4</sub> phase recrystallized, although the results from this study could not confirm the identification of the recrystallized phase.<sup>8</sup> There exist over 20 compounds in the CuO-TiO<sub>2</sub> system. The wetting angle of CuO-Cu<sub>2</sub>O-TiO<sub>2</sub> on BaTiO<sub>3</sub> is initially 61° at 1050°C, which is very high for liquid phase sintering. However, with time the CuO-Cu<sub>2</sub>O-TiO<sub>2</sub> eutectic liquid reacts with the BaTiO<sub>3</sub> and reduces the contact angle to 22°. There must be a limited solubility of BaTiO<sub>3</sub> in the flux, since Hagemann's studies showed that excessive additions of CuO-TiO<sub>2</sub> reduced the densification.

## 2. Relationship of the Wettability and Solubility to the Densification Behavior of Fluxed-BaTiO<sub>3</sub>

The temperature at which liquid phase formation occurs directly impacts dimensional changes during densification of a ceramic. This is especially significant for some flux systems that exhibit more than one liquid phase formation temperature. Liquid formation may affect the densification process through changing the volume of the liquid phase, the wettability of the liquid, the solubility of the solid in the melt, and the formation of recrystallized solid compounds.

Figure 1 shows the dilatometric results and corresponding DTA curves, which exhibit two types of sintering behavior. The first type contains one sintering step that occurs at the temperature of liquid phase formation. In this case this corresponded to the 5.0 wt% (4.0 v%) 5CdO-2SiO<sub>2</sub> (Figure 1a) and 5.0 wt% (7.0 v%) 5ZnO-2B<sub>2</sub>O<sub>3</sub> (Figure 1b) fluxes. Sintering proceeded with increasing temperature

until the samples were densified. The second type of sintering behavior exhibits more than one shrinkage step, such as for the 10 wt% (8.1 v%)  $3\text{Bi}_2\text{O}_3\cdot\text{B}_2\text{O}_3$  and 2 wt% (4.5 v%) LiF (Ba/Ti=1.02), as shown in Figures 1c and 1d. The changes in shrinkage rate correspond to the temperatures at which different liquid phases form associated with solid particle formation. In the case of  $\text{BaTiO}_3$  with  $3\text{Bi}_2\text{O}_3\cdot\text{B}_2\text{O}_3$ , the contraction below  $650^\circ\text{C}$  is negligible, even though there is a small endothermic peak at  $542^\circ\text{C}$ , as indicated in the DTA curve. This is due to a trace amount of liquid phase generation. Eutectic liquid phase formation at the interface between solid  $\text{BaTiO}_3$  and solid  $3\text{Bi}_2\text{O}_3\cdot\text{B}_2\text{O}_3$  at temperatures  $<700^\circ\text{C}$  was kinetically limited. The change in shrinkage rate at  $\approx 800^\circ\text{C}$  corresponds to the melting point of  $\text{Bi}_2\text{O}_3$ .  $\text{BaBi}_4\text{Ti}_4\text{O}_{15}$  was observed after quenching, but it is unknown whether it is present at high temperatures, as suggested by Subbaro.

For the  $\text{BaTiO}_3$  with LiF additions (Ba/Ti=1.02, adjusted by  $\text{BaCO}_3$ ), the onset of densification at  $\approx 600^\circ\text{C}$  corresponds to the

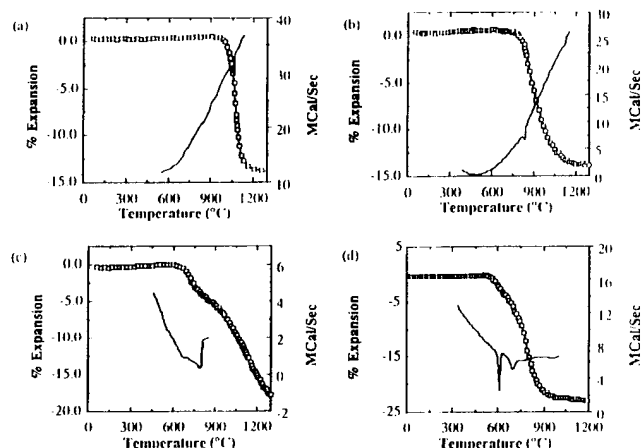


Figure 1 Dilatometric results and DTA curves of  $\text{BaTiO}_3$  with (a) 5wt% of  $5\text{CdO}\cdot 2\text{SiO}_2$ , (b) 5wt%  $5\text{ZnO}\cdot 2\text{B}_2\text{O}_3$ , (c) 10wt% of  $3\text{Bi}_2\text{O}_3\cdot\text{B}_2\text{O}_3$ , and (d) 2wt% LiF (2m%  $\text{BaCO}_3$  addition).

inflection point at  $123^\circ\text{C}$ , suggesting that a grain core-shell structure is formed.

For the  $5\text{ZnO}\cdot 2\text{B}_2\text{O}_3$ ,  $5\text{CdO}\cdot 2\text{SiO}_2$ ,  $\text{CuO}\cdot\text{TiO}_2$ , and  $3\text{Bi}_2\text{O}_3\cdot\text{B}_2\text{O}_3$  systems, there was no apparent grain growth and no shift in the Curie point. However, the magnitudes of the dielectric constant are tremendously different. The dielectric constant of  $\text{BaTiO}_3$  with 10wt% of  $3\text{Bi}_2\text{O}_3\cdot\text{B}_2\text{O}_3$  is only 1300 at room temperature, and that of  $\text{BaTiO}_3$  with 5wt% of  $5\text{CdO}\cdot 2\text{SiO}_2$  is 3400. The density, volume, and connectivity of the flux are the factors that contribute to

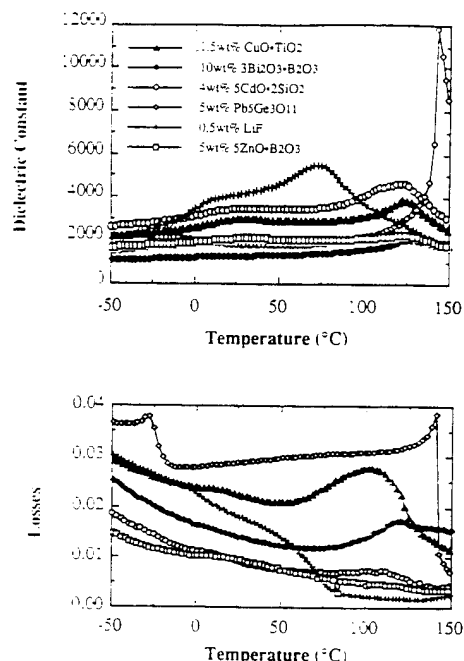


Figure 2 Dielectric constant and losses of  $\text{BaTiO}_3$  sintered with various fluxes at  $1000^\circ\text{C}$  for 2 hours.

Table 3 Characteristics of dielectric properties of  $\text{BaTiO}_3$  sintered with various oxides

Flux Composition	Wt% Added	Density (g/cm <sup>3</sup> )	Grain Size ( $\mu\text{m}$ )	$K_{\text{max}}$	$K_{\text{RT}}$	$(\tan\delta)_{\text{RT}}$	$T_c$ (°C)
$5\text{ZnO}\cdot 2\text{B}_2\text{O}_3$	5	5.71	0.7	2300	2100	0.01	124
$\text{Pb}_5\text{Ge}_3\text{O}_{11}$	5	5.99	6	12000	1800	0.03	143
$0.74\text{Bi}_2\text{O}_3\cdot 0.26\text{B}_2\text{O}_3$	10	5.64	0.7	2100	1300	0.01	126
LiF (Ba/Ti=1.02)	0.5	5.89	1.5	5500	4100	0.02	70
$5\text{CdO}\cdot 2\text{SiO}_2$	4	5.91	0.7	4600	3400	0.01	122
$\text{CuO}\cdot\text{TiO}_2$	1.5	5.54	0.7	3900	3000	0.02	123

eutectic liquid between LiF- $\text{BaCO}_3$ . The change in shrinkage at  $\approx 720^\circ\text{C}$  is due to the formation of another eutectic liquid formation.

### 3. Dielectric Properties

The dielectric constant and losses of  $\text{BaTiO}_3$  sintered with various fluxes measured at 1000 Hz are shown in Figure 2 and summarized in Table 3. The losses of these systems are all less than 3%. For  $\text{BaTiO}_3$  sintered with  $\text{Pb}_5\text{Ge}_3\text{O}_{11}$  and LiF, the Curie points were shifted, while  $5\text{CdO}\cdot 2\text{SiO}_2$  additions broadened the transition.  $\text{BaTiO}_3$ -5wt%  $\text{Pb}_5\text{Ge}_3\text{O}_{11}$  exhibits a sharp transition at  $143^\circ\text{C}$ , and confirms the formation of a  $\text{Ba}(\text{Pb})\text{TiO}_3$  solid solution.  $\text{BaTiO}_3$ -0.5wt% LiF exhibits a diffuse phase transition located at  $73^\circ\text{C}$  with an

these changes in the dielectric constant. Comparing the dielectric constant with the amount of flux added one concludes that residual grain boundary phases must be strongly affecting the dielectric constant.

### SUMMARY

Eutectic melts form during sintering of fluxed- $\text{BaTiO}_3$ . Observed wetting angles of the fluxes on  $\text{BaTiO}_3$  were distributed between  $65^\circ$  and  $0^\circ$  (spreading). The wettability of a flux on  $\text{BaTiO}_3$  substrate was enhanced if a eutectic reaction or significant interdiffusion occurred. The appearance of the liquid phase correlated directly with a sharp change in the sintering rate. The wettability and

intersolubility of flux on BaTiO<sub>3</sub> significantly altered the dielectric properties due to porosity formation and the characteristics of the grain boundary. Lower contact angles and interdiffusion of fluxes resulted in lower residual porosity and lower volume fractions of an interconnected second phase.

#### REFERENCES

- [1] W.D. Kingery, "Densification during Sintering in the Presence of a Liquid Phase. I. Theory," J. Appl. Phys., 30[3], 301-310 (1959).
- [2] N.M.Parikh and M. Humenik, "Cermets: II, Wettability and Microstructure Studies in Liquid Phase Sintering," J. Am Ceram. Soc., 40[ 9], 315-20 (1957).
- [3] I. Burn, "Flux-Sintered BaTiO<sub>3</sub> Dielectrics," J. Matr. Sci., 17[5], 1398-1408 (1982).
- [4] D.A. Tolino and J.B. Blum, "Effect of Ba:Ti ratio on Densification of LiF-Fluxed BaTiO<sub>3</sub>," J. Am. Ceram. Soc., 68,[11], C292-94 (1985).
- [5] K.R. Chowdary and E.C. Subbarao, "Liquid Phase Sintering," Ferroelectrics, 37, 689-92 (1981).
- [6] D.A. Payne and S.M. Park, "Heterophasic Ceramic Capacitor," U.S. Patent 4,218,723 (1980).
- [7] G.H. Maher, "Ceramic Capacitor and Method for Making the Same," U.S. Patent 4,266265 (1981).
- [8] D. Hennings, "Liquid Phase Sintering," Ber. Dt. Keram. Ges., Vol. 55, No. 7, 359-60 (1978).

# Low-Firing $\text{Pb}(\text{Mg}_{1/3}\text{Nb}_{2/3})\text{O}_3$ - $\text{PbTiO}_3$ - $\text{Pb}_3\text{Ge}_2\text{SiO}_{11}$ Compositions for Thick Film Capacitor Applications

Y. D. Kim, S. M. Landin, I. A. Cornejo, and M. J. Haun

Colorado Center for Advanced Ceramics  
Department of Metallurgical and Materials Engineering  
Colorado School of Mines, Golden, CO 80401

**Abstract** - Commercial ferroelectric thick films have been developed with high dielectric constants for capacitor applications. However, these compositions typically do not densify well in thick film form at characteristic firing temperatures (850 - 900°C), and thus require encapsulants to provide environmental stability. In this paper, ferroelectric compositions that can be fired at low temperatures with useful dielectric properties for thick film application are presented based on the combination of  $\text{Pb}(\text{Mg}_{1/3}\text{Nb}_{2/3})\text{O}_3$  (PMN) -  $\text{PbTiO}_3$  (PT) with  $\text{Pb}_3\text{Ge}_2\text{SiO}_{11}$  (PGS). The PGS melts at  $\approx 724^\circ\text{C}$ , and causes liquid phase sintering of the PMN - PT at low temperatures. Thick film samples of PMN - PT with 30 weight percent PGS and 5 weight percent PbO additions densify to closed porosity fired at  $850^\circ\text{C}$  for 10 minutes with a room temperature 1 KHz dielectric constant greater than 1500 and a dissipation factor less than 6%. Preliminary results indicate that these compositions are compatible with a commercial silver thick film conductor paste (DuPont 6160).

## Introduction

Lead-based relaxor ferroelectric compositions have been developed for multilayer capacitor applications with high dielectric constants and low firing temperatures [1-7]. These relaxor ferroelectric compositions have limited use in thick film form because of poor densification which results in the need for encapsulants to provide environmental stability. Recently, low firing thick film dielectrics based on lead iron niobate and lead iron tungstate with high dielectric constants have been developed [8-11]; however, these compositions do not densify to closed porosity. The main purpose of this research was to establish the potential of developing low fire ferroelectric compositions with useful dielectric properties by liquid phase sintering of the 0.93PMN - 0.07PT composition with PGS additions for thick film capacitor applications.

The PMN - PT solid solution and PGS were selected for this work based on their unique properties. The 0.93PMN - 0.07PT solid solution has a very high dielectric constant ( $\geq 20,000$ ) at room temperature [12]. PGS is an unusual ferroelectric crystal which can be formed into glass relatively easily because of the presence of the glass formers  $\text{GeO}_2$  and  $\text{SiO}_2$ . This composition has a high dielectric constant, even in glass form compared to most other glass compositions.

$\text{Pb}_3\text{Ge}_2\text{SiO}_{11}$  and/or  $\text{Pb}_3\text{Ge}_{3-x}\text{Si}_x\text{O}_{11}$  compositions have been investigated as sintering aids for  $\text{Pb}(\text{Fe}_{2/3}\text{W}_{1/3})\text{O}_3$  -  $\text{Pb}(\text{Fe}_{1/2}\text{Nb}_{1/2})\text{O}_3$  [1], PLZT [13], PZT [14-16], and  $\text{BaTiO}_3$  [17] to permit liquid phase sintering at low temperatures.

## Experimental Procedure

The 0.93PMN - 0.07PT solid solution composition was prepared by the columbite method [18]. In the first step of this method,  $\text{MgO}$  and  $\text{Nb}_2\text{O}_5$  were wet mixed, and then calcined in a covered alumina crucible at  $1200^\circ\text{C}$  for 48 hours to form  $\text{MgNb}_2\text{O}_6$ . The  $\text{MgNb}_2\text{O}_6$  was mixed with  $\text{PbO}$  and  $\text{TiO}_2$ , and calcined at  $800^\circ\text{C}$  for 4 hours to form the perovskite phase. To prepare the PGS powder,  $\text{Pb}_3\text{O}_4$ ,  $\text{SiO}_2$ , and  $\text{GeO}_2$  were mixed, and then calcined at  $700^\circ\text{C}$  for 6 hours in a covered platinum crucible. The 0.93PMN - 0.07PT and PGS powders were ball milled with zirconia media in distilled water for 24 hours. XRD was used to confirm the formation of the perovskite and  $\text{Pb}_3\text{Ge}_2\text{SiO}_{11}$  phases.

The 0.93PMN - 0.07PT solid solution powder was mixed with 5, 20, 30, and 40 weight percent PGS additions. These powders were mixed with zirconia media and distilled water for 12 hours, and then dried in an oven at  $100^\circ\text{C}$ . These compositions were mixed with an organic vehicle in a seven to three (inorganic to organic) weight ratio. The organic vehicle consisted of a nine to one weight ratio of pine oil to ethyl cellulose. The pastes were screen printed on polycrystalline 96% alumina thick film substrates (Donated by Coors Ceramic Company). Before screen printing the dielectric paste, an electrode consisting of pure platinum thick film paste (DuPont 9894) was screen printed and fired at  $1300^\circ\text{C}$  for 1 hour. This provided the bottom electrode for dielectric measurements. A DEK Model 250 screen printer and a 200 mesh screen were used.

One layer of dielectric paste was screen printed, and then dried at  $150^\circ\text{C}$  for 10 minutes. A second dielectric layer was printed on top of the first layer and dried. These two layers were then cofired on the alumina substrate in either a box or rapid thermal annealing furnace. This procedure was repeated four additional times to produce a total of 10 dielectric layers to reduce defects such as pin-holes. The samples were fired at 800 to  $1200^\circ\text{C}$  with a hold time from 10 minutes to 6 hours. Top electrodes were deposited by sputtering gold. Silver (DuPont 6160) and silver/palladium (DuPont 6134) thick film pastes fired at  $850^\circ\text{C}$  for 10 minutes were also evaluated as top and bottom electrodes.

A JOEL JAX-840 SEM equipped with an energy dispersive x-ray spectroscopy detector (EDS) was used to investigate the microstructural development. The capacitance and dissipation factor were measured from  $-55$  to  $125^\circ\text{C}$  at five frequencies, 0.1, 1, 10, 100, and 1000 KHz, with a Hewlett-Packard Precision LCR meter (HP 4284A) and a Delta Design temperature control box. The resistivity was measured by applying 100V DC at room temperature with a Radiant Technologies RT66A Test System.

## Results

Figure 1 shows the x-ray diffraction patterns of PMN - PT thick film samples with and without PGS additions, fired at  $900^\circ\text{C}$  for 10 minutes with a heating rate of  $580^\circ\text{C}/\text{min}$ . All of the x-ray diffraction peaks in the pattern for the PMN-PT without PGS addition (bottom pattern in Figure 1) correspond to the perovskite structure. The pyrochlore phase was not observed. With PGS additions to PMN - PT, the perovskite phase was partially converted to the pyrochlore phase. This is possibly due to the removal of lead from the PMN - PT by the PGS, which would cause the lead deficient pyrochlore phase to form. The amount of pyrochlore phase increased with increasing PGS addition, firing temperature, and time, but decreased with increasing heating rate.

Figure 2 shows the x-ray diffraction patterns at the surface of thick film PMN - PT with 30 weight percent PGS and 5 weight percent PbO. These films were fired at  $850^\circ\text{C}$  for 10 and 30 minutes with a heating rate of  $580^\circ\text{C}/\text{min}$ . The excess PbO addition significantly reduced the formation of the pyrochlore phase. No pyrochlore peaks were observed after firing at  $850^\circ\text{C}$  for 10 minutes, however, increasing the sintering time caused the pyrochlore phase to form.

Bulk samples of PMN - PT with 5 weight percent PGS additions densified to 93 percent of the theoretical density at  $850^\circ\text{C}$  for one hour.

However, the PMN - PT samples in thick film form did not densify at 850°C, even with 20 weight percent PGS and 5 weight percent PbO additions as shown in Figure 3. This illustrated the difficulty in densifying thick films because of the constrained sintering by the substrate in the parallel directions to the film. Figure 4 shows the fractured cross section of a thick film PMN - PT sample with 30 weight percent PGS and 5 weight percent PbO additions. This composition densified to closed porosity at 850°C, even with a short sintering time and very a fast heating rate (10 minutes, 580°C/min).

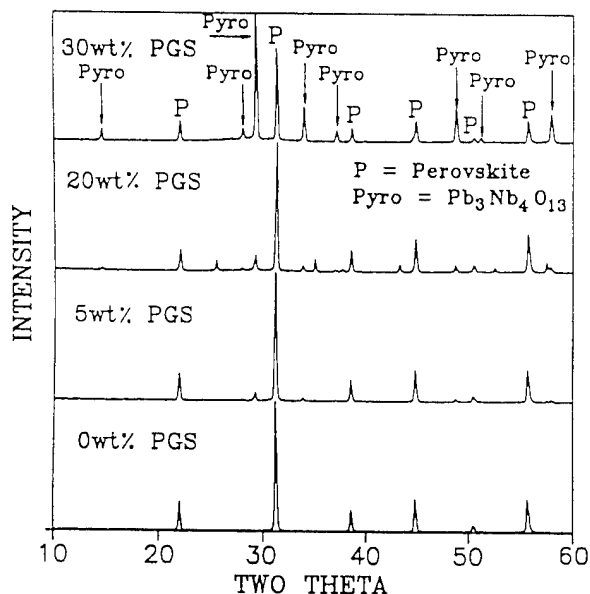


Figure 1 X-ray diffraction patterns of the surface of PMN - PT with 0, 5, 20, and 30 weight percent PGS addition thick film samples.

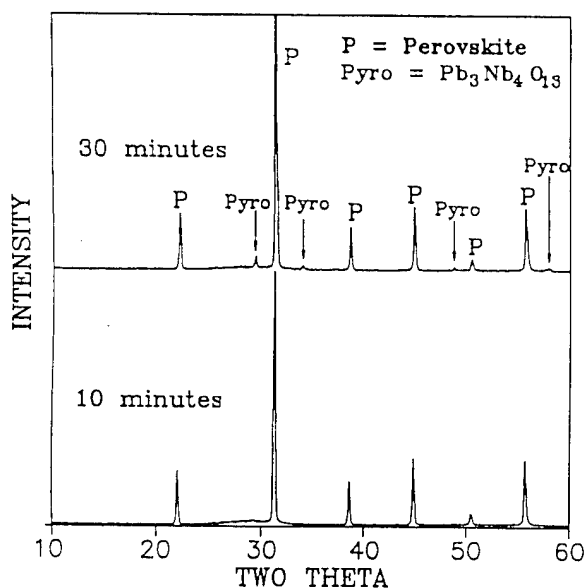


Figure 2 X-ray diffraction patterns of the surface of PMN - PT + 30 weight percent PGS + 5 weight percent PbO thick film samples.

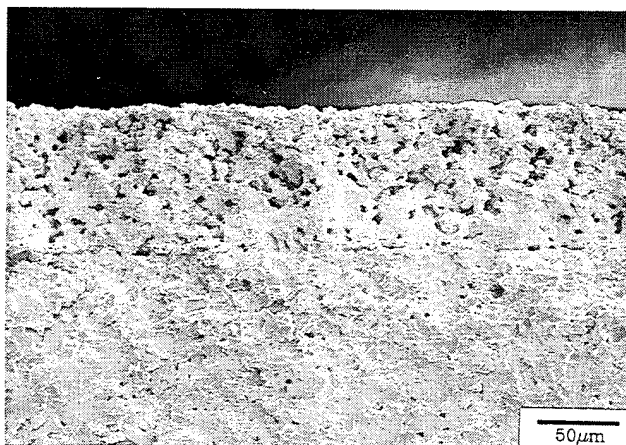


Figure 3 SEM micrograph of the fractured cross section of a PMN - PT + 20 weight percent PGS + 5 weight percent PbO thick film sample fired at 850°C for 10 minutes with a heating rate of 580°C/min.

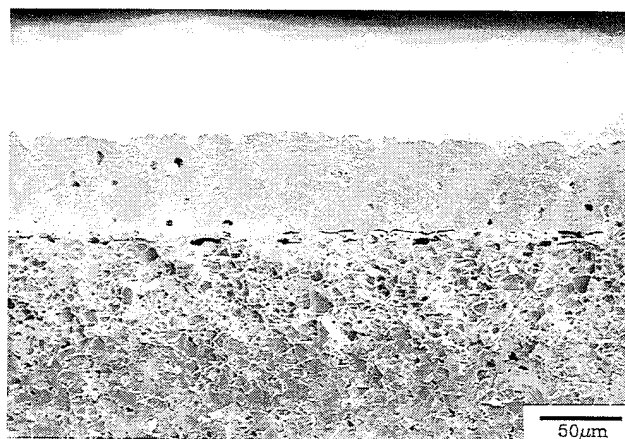


Figure 4 SEM micrograph of the fractured cross section of a PMN - PT + 30 weight percent PGS + 5 weight percent PbO thick film sample fired at 850°C for 10 minutes with a heating rate of 580°C/min.

The dielectric constant and dissipation factor of the thick film sample shown in Figure 4 is plotted versus temperature in Figure 5. Pure platinum thick film paste (DuPont 9894) was used as the bottom electrode and sputtered gold as the top electrode. Figures 4 and 5 show that PMN - PT with 30 weight percent PGS and 5 weight percent PbO densified to closed porosity in thick film form with a 1 KHz room temperature dielectric constant of about 1500 and a dissipation factor less than 6%. These results indicate the potential of achieving high dielectric constant thick film capacitor compositions that densify to closed porosity in typical thick film firing profiles without the need of an encapsulant.

The densification behavior and electrical properties for four different compositions in thick film form are summarized in the Table 1. All of these samples were fired at 850°C for 10 minutes with a heating rate of 580°C/min. The dielectric constant decreased with increasing PGS additions, however, 30 weight percent PGS is required to produce closed porosity. The dissipation factor and electrical conductivity of the composition with 20 weight percent PGS and 10 weight percent PbO are significantly higher than the other compositions, apparently because of the large additions of PbO and PGS. The temperature coefficient of capacitance (TCC) decreased significantly with increasing PGS additions. The PMN - PT with 30 weight percent PGS and 5 weight percent PbO had a TCC in the Y5S category.



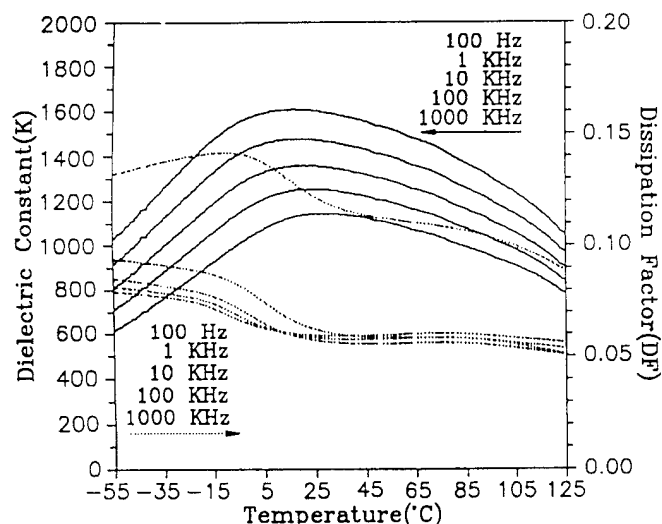


Figure 5 The dielectric constant and dissipation factor of a PMN - PT + 30 weight percent PGS + 5 weight percent PbO thick film sample fired at 850°C for 10 minutes with a heating rate of 580°C/min. Pure platinum thick film conductor paste (DuPont 9894) was used as the bottom electrode and sputtered gold as the top electrode.

Table 1 Summary of the densification behavior and electrical properties of four different thick film compositions.\*

	PMN-PT + 30wt% PGS + 5wt% PbO	PMN-PT + 20wt% PGS + 5wt% PbO	PMN-PT + 20wt% PGS + 10wt% PbO	PMN-PT + 5wt% PGS + 10wt% PbO
Densification	Closed porosity	Open/Closed porosity(?)	Open/Closed porosity(?)	Open porosity
Dielectric Constant ( $K_{max}$ at 1 KHz)	≈1500	≈1700	≈2200	≈2600
Capacitance change* (-30 ~ 85°C)	< -20%	< -30%	< -20%	< -36%
EIA Characteristic	Y5S	Y5T	Y5S	Y5U
Dissipation Factor (1 KHz, 25°C)	< 6%	< 5%	< 12%	< 6%
Resistivity (100V, 25°C)	> 10 <sup>10</sup> Ohm-cm	> 10 <sup>10</sup> Ohm-cm	> 10 <sup>8</sup> Ohm-cm	> 10 <sup>10</sup> Ohm-cm

\* Pure platinum thick film paste (DuPont 9894) was used as the bottom electrode and sputtered gold as the top electrode.

• Capacitance change (%) =  $\{ (C - C_{R.T.}) / C_{R.T.} \} \times 100$

Figure 6 shows the dielectric constant and dissipation factor plotted as a function of temperature for a PMN - PT with 30 weight percent PGS and 5 weight percent PbO thick film sample. These sample was fired with commercial silver electrodes (Dupont 6160). Figure 7 shows the fractured cross section of this sample. The maximum dielectric constant was greater than 800 with a dissipation factor less than 3% at 1 KHz. The dielectric constant and dissipation factor were lower than those of films with the same composition but with a platinum bottom electrode

and a sputtered gold top electrode (see Figure 5). This appears to be related to the inorganic additives in the commercial silver paste which can interact with the film, affecting the dielectric properties. Additional research is needed to further investigate this behavior, however these dielectric properties and densification behavior appear promising for thick film capacitor applications without the need for an encapsulant.

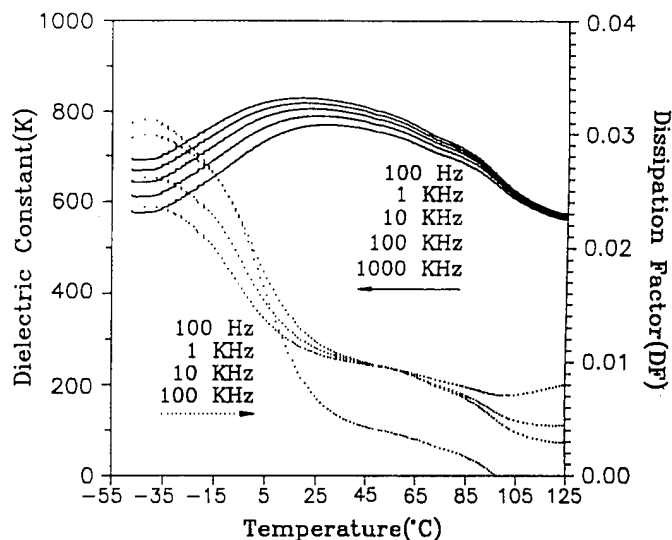


Figure 6 The dielectric constant and dissipation factor of a PMN - PT + 30 weight percent PGS + 5 weight percent PbO thick film sample fired at 850°C for 10 minutes with a heating rate of 580°C/min. Silver thick film conductor paste (DuPont 6160) was used as the top and bottom electrodes.

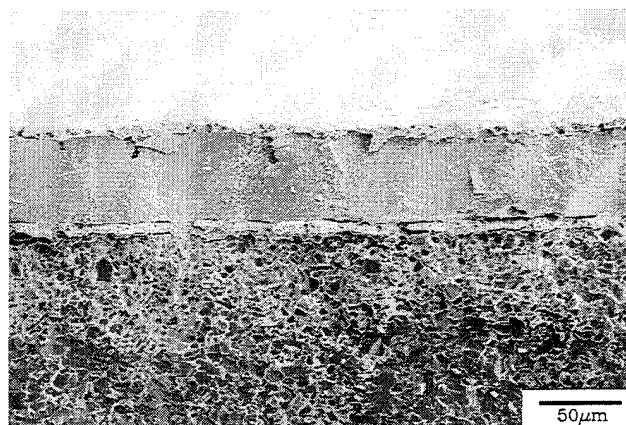


Figure 7 SEM micrograph of the fractured cross section of PMN - PT + 30 weight percent PGS + 5 weight percent PbO thick film sample fired with silver electrode (DuPont 6160) at 850°C for 10 minutes with a heating rate of 580°C/min.

## Summary

Crystalline PMN - PT and PGS were combined and prepared into thick film samples. Liquid phase sintering with PGS additions allows PMN - PT to densify at 850°C in thick film form. The PGS addition to PMN - PT caused the perovskite phase to convert to pyrochlore. Excess PbO additions to PMN - PT with PGS prevented the formation of the pyrochlore phase. Thick film PMN - PT densified to closed porosity with

30wt% PGS and 5wt% PbO additions in 10 minutes at 850°C with a heating rate of 580°C/min. This sample has a room temperature dielectric constant greater than 1500 and a dissipation factor less than 6% at 1 KHz. This combination of good densification behavior and high dielectric constant is very promising for thick film capacitor applications. In addition, preliminary results indicate that this composition is compatible with a commercial silver thick film conductor paste (Dupont 6160)

#### Acknowledgement

This research was supported by the Office of Naval Research under contract # N00014-92-5-1390 and by the National Science Foundation under contract # DMR-9158312.

#### References

- [1] S. J. Jang, W. A. Schulze and J. V. Biggers, "Low-Firing Capacitor Dielectrics in the System  $\text{Pb}(\text{Fe}_{2/3}\text{W}_{1/3})\text{O}_3$ - $\text{Pb}(\text{Fe}_{1/2}\text{Nb}_{1/2})\text{O}_3$ - $\text{Pb}_3\text{Ge}_3\text{O}_{11}$ ", *Ceram. Bull.*, Vol. 62 (2), pp. 216-218, 1983.
- [2] T. R. Shrout and A. Halliyal, "Preparation of Lead-Based Ferroelectric Relaxors for Capacitors", *Am. Ceram. Soc. Bull.*, Vol. 66 (4), pp. 704-711, 1987.
- [3] M. Yonezawa, "Low-Firing Multilayer Capacitor Materials", *Ceram. Bull.*, Vol. 62 (12), pp. 1375-1383, 1983.
- [4] M. Yonezawa and T. Ohno, "Ceramic Compositions Having High Dielectric Constant", U. S. Patent No. 4,078,938, Mar. 1978.
- [5] M. Yonezawa, K. Utsumi, and T. Ohno, "Ceramic Compositions", U. S. Patent No. 4,236,928, Dec. 1980.
- [6] D. A. Payne and S. M. Park, "Heterophasic Ceramic Composition", U. S. Patent No. 4,218,723, Aug. 1980.
- [7] H. D. Park and A. E. brown, "Ceramic Composition for Dielectric in Multilayer Capacitors", U. S. Patent No. 4,550,088, Oct. 1985.
- [8] S. L. Fu and G. F. Chen, "Low Firing Thick Film Dielectrics in the System  $\text{Pb}(\text{Fe}_{2/3}\text{W}_{1/3})_x(\text{Fe}_{1/2}\text{Nb}_{1/2})_{0.86-x}\text{Ti}_{0.14}\text{O}_3$ - $\text{Bi}_2\text{O}_3$ - $\text{Li}_2\text{O}$ ", *Am. Ceram. Soc. Bull.*, Vol. 66 (9), pp. 1397-1400, 1987.
- [9] T. Yasumoto, N. Iwase and M. Harata, "High Dielectric Constant Thick Film Capacitors Fireable in Air and Nitrogen Atmosphere", *The Int. J. for Hybrid Microelectronics*, Vol. 12 (3), pp.156-161, 1989.
- [10] T. C. Reiley, J. V. Badding, D. A. Payne and D. A. Chance, "A Low-Temperature Firing Thick Film Capacitor Material Based on Lead Iron Niobate/Tungstate", *Mat. Res. Bull.*, Vol. 19, pp. 1543-1549, 1984.
- [11] Z. Burn and L. Drozdyk, "Reliability of Thick-Film Capacitors", *Proceedings of the International Symposium on Microelectronics*, San Francisco, CA, October 19-21, 1992.
- [12] C. A. Randall, A. D. Hilton, D. J. Barber and T. R. Shrout, "Extrinsic Contributions to the Grain Size Dependence of Relaxor Ferroelectric  $\text{Pb}(\text{Mg}_{1/3}\text{Nb}_{2/3})\text{O}_3$  :  $\text{PbTiO}_3$  Ceramics", *J. Mater. Res.*, Vol. 8 (4), pp. 880-884, 1993.
- [13] M. Rusinko, "Dielectric Mixing in the  $\text{PLZT-Pb}_3\text{Ge}_3\text{O}_{11}$  System", B. Sc. Thesis, Penn. State University, University PARK, Pa., May 1975.
- [14] W. A. Schulze and J. V. Biggers, "Piezoelectric Properties of  $\text{Pb}_3\text{Ge}_3\text{O}_{11}$  Bonded PZT Compositions", *Mat. Res. Bull.*, Vol. 14, pp. 721-730, 1979.
- [15] J. Collier, "Ferroelectric Thick-Films for Piezoelectric Applications produced from Amorphous  $\text{Pb}_3\text{Ge}_3\text{SiO}_{11}$  and Crystalline  $\text{Pb}(\text{Zr,Ti})\text{O}_3$ ", M. Sc. Thesis, Colorado School of Mines, 1994.
- [16] J. Collier, I. A. Cornejo, and M. J. Haun, "Ferroelectric Thick-Films for Piezoelectric Applications", *Proceedings of the 8th International Meeting on Ferroelectricity*, Gaithersburg, MD, August 8-13, 1993, Accepted for Publication in *Ferroelectrics* (1993).
- [17] D. A. Payne and S. M. Park, "Heterophasic Ceramic Capacitor", U. S. Patent No. 4,158,219 June 1979.
- [18] S. L. Swartz and T. R. Shrout, "Fabrication of Perovskite Lead Magnesium Niobate", *Mat. Res. Bull.*, Vol. 17, pp. 1245-1250, 1982.

Z. Xu, Dwight Viehland, and D.A. Payne

Department of Materials Science and Engineering and Materials  
Research Laboratory, University of Illinois at Urbana-Champaign,  
Urbana, Illinois 61801

Antiferroelectric tin-modified lead zirconate titanate ceramics (PZST), with 42 at% Sn and 4 at% Ti, were studied by hot- and cold-stage transmission electron microscopy and selected area electron diffraction techniques. The previously reported tetragonal antiferroelectric state is shown to be an incommensurate orthorhombic state. Observations revealed the existence of incommensurate  $1/x<110>$  superlattice reflections below the temperature of the dielectric maximum. The modulation wavelength for this incommensurate structure was found to be metastably locked-in near and below room temperature. An incommensurate-commensurate orthorhombic antiferroelectric transformation was then observed at lower temperatures.

### I. Introduction

Tin-modified lead zirconate titanate ceramics,  $\text{Pb}_{(0.98)}\text{Nb}_{0.02}(\text{Zr}_{1-x}\text{Sn}_x)_{1-y}\text{Ti}_y)_{1-z}\text{O}_3$  (designated as PZST  $x/y/2$ ) are of interest as potential actuator and transducer materials. In this crystalline solution series, a field-induced antiferroelectric to ferroelectric phase transformation occurs. Associated with this transformation are large nonlinearities in the dielectric, electromechanical, and thermal mechanical response characteristics [1].

Recently, hot-stage transmission electron microscopy (TEM) and selected area electron diffraction (SAED) investigations were reported for PZST 42/4/2 and 43/8/2 [2].  $1/x<110>$  superlattice spots (s.s.) were found in the SAED patterns which were incommensurate (IC) with the fundamental periodicity of the lattice. Incommensurate modulations were reported in the tetragonal antiferroelectric phase region. The modulation wavelength varied between 20 and 30 Å, depending on composition and temperature. Corresponding lattice imaging revealed  $<110>$  orientated anti-phase domains (or domain-like striations). The periodicity between fringes was incommensurate with the lattice and correlated with the modulation wavelength determined from SAED patterns. The modulation wavelength for the incommensurate structure was found to decrease with decreasing temperature for PZST 42/4/2 and 43/8/2. For 43/8/2, the incommensurate antiferroelectric orthorhombic phase (previously called tetragonal antiferroelectric) transformed to a commensurate (C) rhombohedral ferroelectric phase near 95°C. However for 42/4/2, the incommensurate antiferroelectric state persisted below room temperature.

Currently, it is not known whether the low temperature orthorhombic antiferroelectric phase is commensurate or incommensurate. In addition, the mechanism by which the incommensurate antiferroelectric structure evolves to the commensurate orthorhombic antiferroelectric is unknown. The purpose of this investigation was to study the temperature dependence of the incommensurate structure of antiferroelectric PZST. Particular attention was paid to changes in the incommensurate structure on transformation to the orthorhombic antiferroelectric state from the tetragonal antiferroelectric.

### II. Experimental Procedure

The particular composition chosen for study was PZST 42/4/2, and ceramic specimens were prepared by a hybrid coprecipitation-mixed oxide method [3]. TEM specimens were formed by ultrasonically drilling 3-mm discs which were mechanically polished to ~100µm. The center portions of these discs were then further thinned by a dimpler to ~10 µm, and argon ion-milled to perforation. Specimens were coated with carbon before examination. The TEM studies were carried out on a Phillips EM-420 microscope operating at an accelerating voltage of 120 kV, with double tilt hot- and cold-stages.

The dielectric response of electroded ceramic specimens was measured as a function of frequency and temperature. Measurements were made in the temperature range of 230 to -150°C on cooling (unless otherwise stated) at a rate of 4°C/min in a Delta Design oven. Measurements were made on a HP 4284 LCR meter.

### III. Results

The temperature dependence of the  $<112>$  SAED pattern for PZST 42/4/2 between room temperature and 250°C is given in Figure 1.  $1/x<110>$  superlattice spots are clearly evident. The modulation wavelength ( $\lambda$ ) was found to be incommensurate with the lattice and

was approximately 20 Å at room temperature. The intensity of the  $1/x<110>$  superlattice spots decreased with increasing temperature, and the distance between the superlattice spots and the main reflection also decreased, indicating that  $\lambda$  increased with increasing temperature. The  $1/x<110>$  superlattice spots disappeared around 160°C (Figure 1(e)), which coincided with the temperature at which the antiferroelectric domains disappeared. In addition, diffuse  $1/2<110>$  and  $1/2<111>$  superlattice reflections were observed. A  $1/2<110>$  spot is indicated by an arrow. This new superlattice reflection first appeared on heating near 100°C (Figure 1(c)) and disappeared above 200°C, and was visible in the temperature range of the multicell cubic state.

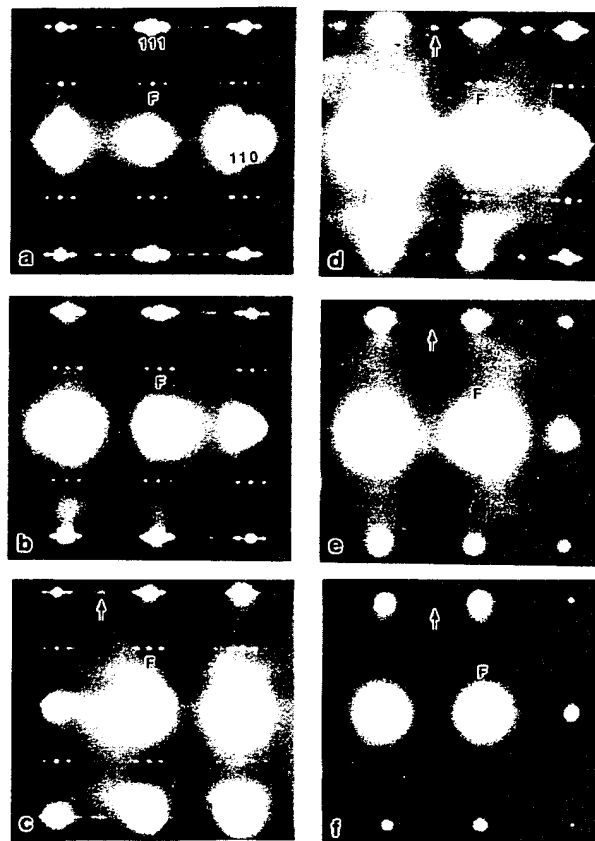


Figure 1.  $<112>$  SAED patterns as a function of temperature for PZST 42/4/2 on heating. (a) 25°C, (b) 70°C, (c) 100°C, (d) 130°C, (e) 160°C, and (f) 250°C.

SAED patterns were taken on cooling to elucidate the nature of the structural changes. The temperature dependence of the  $<001>$  SAED patterns for PZST 42/4/2 between room temperature and -180°C is given in Figures 2(a)-(f). In the temperature interval between 25°C and -36°C, typical  $1/x<110>$  superlattice reflections are evident (Figures 2(a) and (b)). The modulation wavelength associated with these reflections was relatively temperature independent in this temperature range and was found to be incommensurate with the lattice, indicating the incommensurate structure was metastably locked-in. No evidence of an incommensurate-commensurate transformation was found in this temperature range. On further cooling to -68°C (Figure 2(c)), sharp  $1/x<110>$  superlattice reflections were no longer visible, but rather streaking along the  $<110>$  began to be apparent. This streaking reflects the formation of a set of  $1/x<110>$  superlattice reflections. Stronger streaking was observed near -100°C (Figure 2(d)). On further cooling to -168°C, the  $1/x<110>$  superlattice reflections disappeared and  $1/4<110>$  reflections became apparent (Figure 2(e)). However, some diffuseness was evident around these reflections. Diffuseness of the  $1/4<110>$  reflections disappeared around -183°C. These results indicate that the incommensurate-commensurate phase transformation occurs gradually, via an intermediate condition, in the temperature range between -60 and -150°C. The low temperature commensurate phase was found to be isomorphous with antiferroelectric orthorhombic  $\text{PbZrO}_3$ .

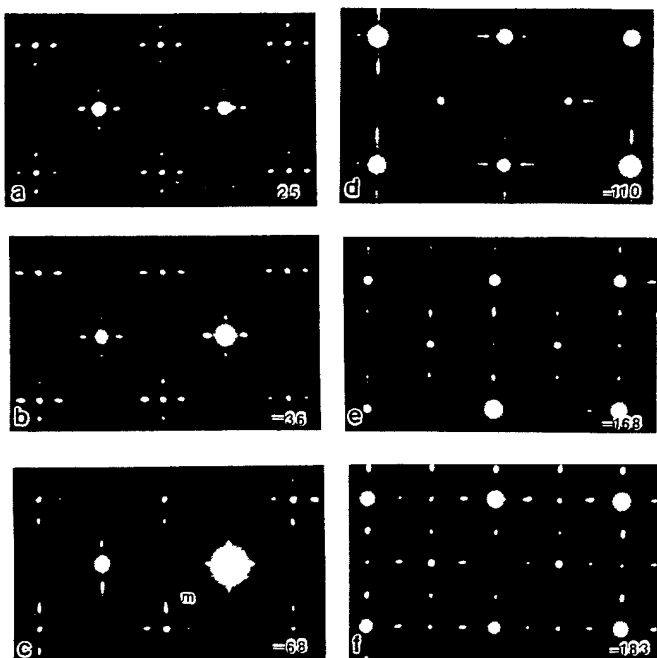


Figure 2.  $\langle 001 \rangle$  SAED patterns as a function of temperature for PZST 42/4/2 on cooling. (a) 25°C, (b) -36°C, (c) -68°C, (d) -110°C, (e) -168°C, and (f) -183°C.

#### IV. Discussion

Figure 3 gives the temperature dependence of  $\lambda$ , as calculated from the  $1/x\langle 110 \rangle$  superlattice spot (s.s.).  $\lambda$  was found to increase with increasing temperature, only for temperatures greater than  $\sim 100^\circ\text{C}$ . However, at temperatures between  $-50$  and  $50^\circ\text{C}$ ,  $\lambda$  was found to be relatively independent of temperature. In this temperature range the modulation remained incommensurate with the lattice. The results indicate that the phase of the incommensurate structure became metastably locked-in with decreasing temperature, rather than transforming to a normal commensurate state. Metastability in incommensurate structures can be attributed to defects [5], which may act to pin the phase of the incommensurate structure. Compositional heterogeneity in PZST, associated with an inhomogeneous Sn-distribution, may lead to analogous effects.

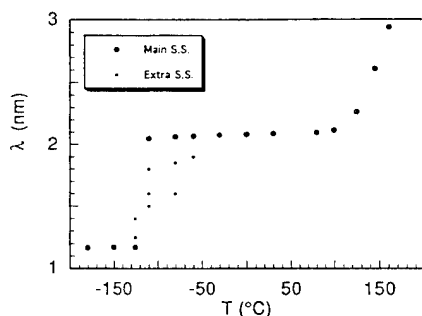


Figure 3. Modulation wavelength ( $\lambda$ ) as a function of temperature calculated from the  $1/x\langle 110 \rangle$  superlattice spots (s.s.).

At low temperatures, the value of  $\lambda$  can be seen to decrease in the temperature range  $-50$  to  $-100^\circ\text{C}$ , transforming to a commensurate relationship with the lattice periodicity. Two types of data points are shown in Figure 3 in this temperature range. The large points represent the wavelength associated with the main  $1/x\langle 110 \rangle$  superlattice reflection, and the smaller points represent the wavelength of extra  $\langle 110 \rangle$  superlattice reflections associated with the intergrowth of the  $\langle 110 \rangle$  structural modulations. This behavior is rather unusual, in that the incommensurate-commensurate transformational sequence would appear to proceed through an intermediate metastable range. The local polar symmetry in the previously designated tetragonal antiferroelectric state would appear to be orthorhombic, as indicated by the symmetry of the  $1/x\langle 110 \rangle$  superlattice reflections. A "true" tetragonal antiferroelectric state was not observed in this study, contrary to previous claims [6].

The observed transformation between incommensurate and commensurate states occurred gradually on cooling. The transformational region was  $\sim 50$ - $75^\circ\text{C}$  wide, as indicated in Figures 2(c)-(e). The results indicate unusual metastability of the incommensurate phase. Evidence of metastability in the incommensurate-commensurate transitional region can also be seen in the dielectric response characteristics, given in Figures 4(a) and (b). A minor anomaly in the dielectric constant ( $K$ ) with temperature ( $T$ ) was found near  $-25^\circ\text{C}$  (Figure 4(a)), associated with the transformation from the incommensurate to commensurate orthorhombic antiferroelectric states. An enhancement of these characteristics is given in Figure 4(b). Dielectric dispersion can be seen near the maximum, the degree of dispersion can also be seen to decrease on either side of the anomaly. The dispersive behavior gives possible evidence of fluctuation effects.

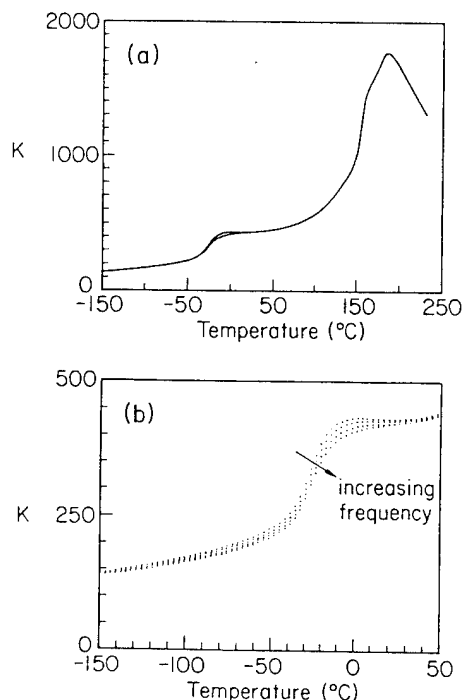


Figure 4. Dielectric response of PZST 42/4/2 as a function of temperature. The frequency used were  $10^2$ ,  $10^3$ ,  $10^4$ , and  $10^5$  Hz.

#### V. Conclusion

An incommensurate orthorhombic antiferroelectric state has been observed for the first time for PZST electroceramics by transmission electron microscopy and selected area electron diffraction. This phase was previously reported to be a tetragonal antiferroelectric. In addition, an incommensurate-commensurate orthorhombic antiferroelectric transformation was also observed at lower temperatures, again for the first time.

#### Acknowledgments

The research was supported by the DOE under DMR-DE-AC02-76ER01198 and by the ONR under N00014-92-J-1522. The use of facilities in the Center for Microanalysis of Materials in the Materials Research Laboratory at the University of Illinois at Urbana-Champaign is also acknowledged.

#### References

- [1] W. Pan, PhD Dissertation, Pennsylvania State University (1988).
- [2] Z. Xu, D. Viehland, and D.A. Payne, J. Appl. Phys. 74, 3406 (1993).
- [3] P. Yang, Ph. D Thesis, University of Illinois at Urbana-Champaign (1992).
- [4] M. Tanaka, R. Saito, and K. Tsuzuki, Jap. J. Appl. Phys. 21, 291 (1982).
- [5] P. Prelovsek, and R. Blinc, J. Phys. C 17, 577 (1984).
- [6] D. Berlincourt and H. Krueger, "Research on Piezoelectric Materials and Phenomena," Cleavite Report to Sandia National Laboratory, Project No. 323110, (1963).

# REACTION SEQUENCE OF PEROVSKITE FORMATION PROCESS IN PFW-PFN SYSTEM BY B-SITE PRECURSOR METHOD

Kyung Ki MIN and Nam Kyoung KIM  
Department of Inorganic Materials Engineering  
Kyungpook National University  
Taegu KOREA 702-701

## ABSTRACT

Reaction sequence of perovskite-phase formation and crystallographic properties in the PFW-PFN system are reported. Investigation is focused on the formation of perovskite phase by a "B-site precursor method." B-site precursors were formed directly from the constituent oxides or through a competition with a pyrochlore-related phase, while perovskite phases were developed through a competition with pyrochlores. Lattice parameters of PFW and PFN were 3.985 and 4.016 Å, respectively.

## INTRODUCTION

With the increasing demand for electronic equipment of reduced size and high integration density, circuit devices and components are required to have a compact design. Multilayer ceramic capacitors (MLCC's) have a high volumetric efficiency and meet the current trend of component miniaturization. In commercial MLCC fabrication, however, the expensive internal electrodes (palladium, platinum, or alloys thereof) must withstand the high firing temperatures of BaTiO<sub>3</sub>-based dielectric layers during cofiring.

As one possible solution, low-temperature-firable materials with high dielectric constants have been intensively searched for and several of the lead-based complex perovskites [e.g., Pb(Fe<sub>2</sub>W<sub>1/3</sub>)O<sub>3</sub>, Pb(Fe<sub>1/2</sub>Nb<sub>1/2</sub>)O<sub>3</sub>, Pb(Mg<sub>1/3</sub>Nb<sub>2/3</sub>)O<sub>3</sub> (hereafter designated as PFW, PFN, PMN), etc.] satisfy the requirements. Since these ceramics are sinterable at lower temperatures, the less-expensive silver-rich alloy can be used as electrodes for price reduction.

Numerous results have been reported on the application of the PFW-PFN system as potential candidate materials for high-K, low-temperature-firable capacitors.<sup>1-4</sup> For the synthesis of perovskite phase, a direct mixing of constituent oxides or carbonates has generally been used in earlier times. By this method, however, parasitic pyrochlore phase(s), formed between PbO and Nb<sub>2</sub>O<sub>5</sub>, usually remained in the structure and pyrochlore-free perovskite structure could not easily be attained. Presence of pyrochlores in the perovskite structure is reported detrimental to dielectric properties by greatly reducing the dielectric constants.

In an attempt to suppress the formation of pyrochlore phase(s), a novel method, called "columbite process," has been introduced to the PMN synthesis.<sup>5</sup> In this process, B-site components of Mg and Nb are reacted first into a columbite structure of MgNb<sub>2</sub>O<sub>6</sub>, which is then reacted with PbO to form the perovskite phase, with (almost) complete elimination of the harmful pyrochlore phase(s). Another alternative to the direct mixing of oxides, in the formation of the perovskite phase, incorporates a pre-reaction of PbO and Nb<sub>2</sub>O<sub>5</sub> to form Pb<sub>3</sub>Nb<sub>2</sub>O<sub>8</sub> followed by reaction with MgO,<sup>6</sup> effectiveness of which will be discussed later.

Regarding the formation mechanism of perovskite phases of PFW and PFN, several reaction sequences have been proposed,<sup>7-13</sup> overall conclusion of which is that development

of the perovskite structure does not occur directly from the constituent oxides, but rather involves a long and complex sequence of intermediate reactions. So far, however, they are all restricted to the reaction directly from raw chemicals, even though the "columbite process" has been resorted widely due to higher yield of perovskite phase.

In this work, the reaction mechanism of perovskite-phase formation by the "B-site precursor method (explained later)" in PFW-PFN system is investigated. In order to understand the sequence of reactions, phase formation during heat treatments was studied by x-ray diffraction (XRD). Crystallographic properties of the system are also reported.

## EXPERIMENTAL

The system studied is (1-x)Pb(Fe<sub>2</sub>W<sub>1/3</sub>)O<sub>3</sub> - xPb(Fe<sub>1/2</sub>Nb<sub>1/2</sub>)O<sub>3</sub> [(1-x)PFW-xPFN], with x ranging from 0 to 1 at an interval of 0.2. Raw chemicals used were PbO, Fe<sub>2</sub>O<sub>3</sub>, and Nb<sub>2</sub>O<sub>5</sub> of >99.9% purity and 99.8%-pure WO<sub>3</sub>. Wet-milled and dried powders forming B-site precursors of (1-x)(Fe<sub>2</sub>W<sub>1/3</sub>)O<sub>2</sub>-x(Fe<sub>1/2</sub>Nb<sub>1/2</sub>)O<sub>2</sub> in stoichiometric proportions were placed in a crucible and heat treatments were carried out at temperatures, usually from 500°C to temperatures of interest with 50°C intervals. The resulting major phases were then identified by powder XRD (CuKα, Ni filter). Based on the results, the B-site precursors were synthesized at appropriate temperatures and then reacted with PbO, also in stoichiometric proportions without any addition of excess amount. The following processes of heat treatment and phase identification were similar.

All of the resulting XRD patterns were semiquantitatively analyzed and probable reaction sequences are proposed. The relative amount of each phase was determined by comparing the intensity of major peaks. Lattice parameters of the compositions in the system were also determined.

## RESULTS AND DISCUSSION

In the synthesis of PMN, the "columbite process"<sup>5</sup> and "PbO-Nb<sub>2</sub>O<sub>5</sub> precursor method"<sup>6</sup> can be considered similar in that both methods incorporate a pre-reaction between two components followed by a reaction of the product with the third component. Pre-reaction of PbO and MgO, however, is meaningless since no binary compound exists between PbO and MgO.<sup>14</sup> Hence, two remaining possibilities are the two methods (pre-reaction of MgO-Nb<sub>2</sub>O<sub>5</sub> and PbO-Nb<sub>2</sub>O<sub>5</sub>), between which the former "columbite process" seems more effective since the inevitable formation of pyrochlore structures during direct mixing of oxides can be bypassed.

Meanwhile, the "PbO-Nb<sub>2</sub>O<sub>5</sub> precursor method" has not been adopted widely after introduction, since this technique involves with the formation of Pb<sub>3</sub>Nb<sub>2</sub>O<sub>8</sub> pyrochlore phase first and then reaction with MgO. Due to the refractoriness of MgO, there still remained unreacted pyrochlore phase(s), even when an excess amount of MgO was added, whose role was claimed to be effective in suppression of the pyrochlore phase(s).<sup>6</sup>

When the "columbite process" is applied to different

relaxors, e.g., PFN, pre-reaction between B-site precursors of  $\text{Fe}_2\text{O}_3$  and  $\text{Nb}_2\text{O}_5$  (by 1:1 mole ratio) produces  $\text{FeNbO}_4$  of a wolframite (and not columbite) structure, thus may be called a "wolframite process." The methods of "columbite process" and "wolframite process" may better be referred together as a more inclusive term of "B-site precursor method," which is used in this report.

Figures 1 and 2 show the XRD pattern developments of the B-site precursor forming processes for  $(1-x)(\text{Fe}_{2/3}\text{W}_{1/3})\text{O}_2-x(\text{Fe}_{1/2}\text{Nb}_{1/2})\text{O}_2$  (i.e.,  $(\text{Fe}_{(4-x)/6}\text{W}_{(1-x)/3}\text{Nb}_{x/2})\text{O}_2$ ):  $\text{Fe}_2\text{O}_3 + \text{WO}_3 \rightarrow \text{Fe}_2\text{WO}_6$  for  $x=0$  and  $\text{Fe}_2\text{O}_3 + \text{Nb}_2\text{O}_5 \rightarrow 2\text{FeNbO}_4$  for  $x=1$ . Phase analysis results corresponding to previous reactions are plotted in Figures 3 and 4, respectively.  $\text{Fe}_2\text{WO}_6$  was seen to be developed directly from the constituent oxides without any intermediate phases, while  $\text{FeNbO}_4$  was formed with a competition with a pyrochlore-related phase, composition of which may be presumed to be  $\text{FeNb}_2\text{O}_{6.5}$ , considering the disappearance of  $\text{Nb}_2\text{O}_5$  prior to  $\text{Fe}_2\text{O}_3$  (resulting in  $\text{Nb}_2\text{O}_5$ -rich composition) and considering the possibility of indexing assuming  $\text{Pb}_5\text{Nb}_4\text{O}_{15}$  pyrochlore structure (JCPDS 40-831). A non-negligible peak is observed and denoted by x in  $1100^\circ\text{C}$  of Figure 2. Though unindexable with the  $\text{Pb}_5\text{Nb}_4\text{O}_{15}$  pattern, the peak seems to belong to the pyrochlore phase, considering the concurrent emergence and disappearance with the pyrochlore-related phase. Pre-reaction temperatures of the B-site precursors ranged from  $1000^\circ\text{C}$  ( $x=0$ ) to  $1250^\circ\text{C}$  ( $x=1$ ) by referring to corresponding phase developments. The system  $(\text{Fe}_{(4-x)/6}\text{W}_{(1-x)/3}\text{Nb}_{x/2})\text{O}_2$  did not form a solid solution but a mixture of  $\text{Fe}_2\text{WO}_6$  and  $\text{FeNbO}_4$ , due probably to dissimilar structure.

Figures 5 and 6 show the XRD patterns of the perovskite-phase forming processes of  $3\text{PbO} + \text{Fe}_2\text{WO}_6 \rightarrow 3\text{Pb}(\text{Fe}_{2/3}\text{W}_{1/3})\text{O}_3$  and  $2\text{PbO} + \text{FeNbO}_4 \rightarrow 2\text{Pb}(\text{Fe}_{1/2}\text{Nb}_{1/2})\text{O}_3$ , respectively. In Figures 7 and 8 are shown the phase analysis results corresponding to previous reactions. The perovskite structures of PFW and PFN did not form directly from the constituent materials, but rather through a competition with pyrochlores at intermediate temperatures. Eventually, the perovskite phase became dominant at higher temperatures, but decomposition of the perovskites into recurrent pyrochlore (and other) phases occurred for PFN at still higher temperatures while melting preceded decomposition in PFW. Accordingly, syntheses of the perovskite phases were carried out at  $850^\circ\text{C}$  over the whole composition range and nearly phase-pure powders were obtained (Figure 9).

The sol-gel derived stoichiometric mixture ( $\text{PbO}:\text{Fe}_2\text{O}_3:\text{WO}_3=3:1:1$ ) involves four intermediate phases of  $\text{PbWO}_4$ ,  $\text{Pb}_2\text{WO}_5$ ,  $\text{Pb}_2\text{Fe}_2\text{O}_5$ , and pyrochlore during PFW formation.<sup>12)</sup> The directly mixed and coprecipitated mixture ( $\text{PbO}:\text{Fe}_2\text{O}_3:\text{WO}_3=4:1:2$  for  $\text{Pb}_2\text{FeWO}_{6.5}$  formation) also produces  $\text{PbWO}_4$ ,  $\text{Pb}_2\text{WO}_5$ , and pyrochlore ( $\text{Pb}_2\text{FeWO}_{6.5}$ ) phases as well as perovskite PFW during heating.<sup>13)</sup> In contrast, the current "B-site precursor method" involved direct formation or one intermediate pyrochlore-related phase during B-site formation and only one intermediate pyrochlore phase of  $\text{Pb}_2\text{FeWO}_{6.5}$  in PFW and  $\text{Pb}_3\text{Nb}_4\text{O}_{13}$  in PFN formation. This relatively simple (though two-step) process with higher perovskite yield supports the effectiveness of the "B-site precursor method."

Lattice parameters of the system were determined from Figure 9 with an introduction of a Nelson-Riley parameter.<sup>15)</sup> The results are plotted in Figure 10, where fairly good linearity demonstrates the complete solid solubility in the system PFW-PFN and satisfies the Vegard's law. Lattice parameters of 3.985 and 4.016 Å for PFW and PFN are also in good agreement with the reported data.<sup>7,8,16-20)</sup>

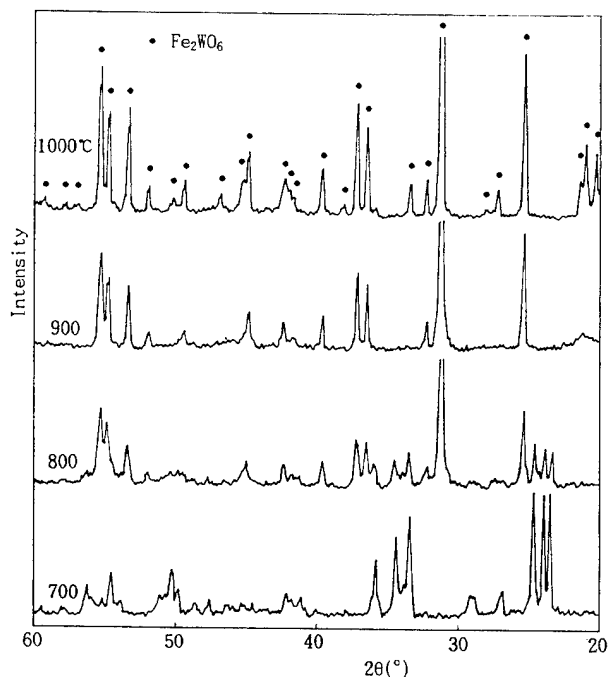


Figure 1. Powder x-ray diffractograms, showing reaction sequence of  $\text{Fe}_2\text{O}_3 + \text{WO}_3 \rightarrow \text{Fe}_2\text{WO}_6$ .

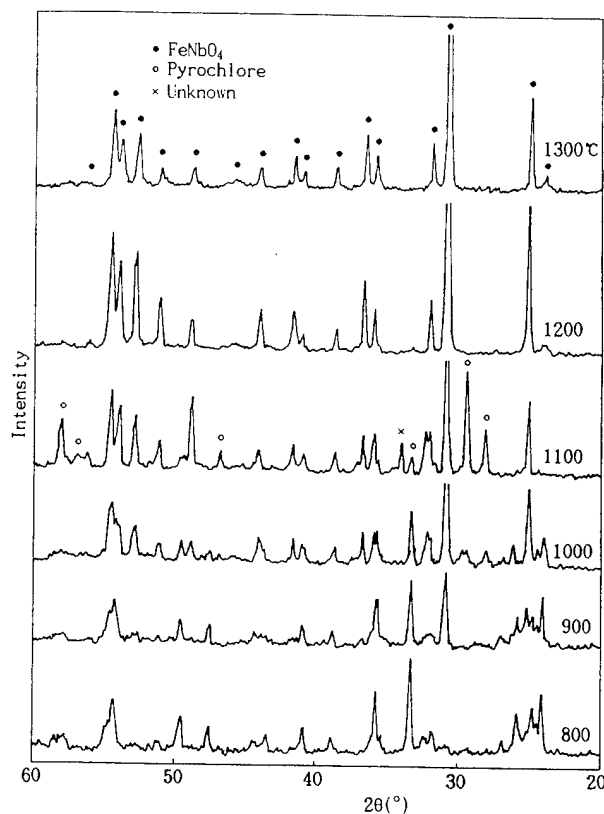


Figure 2. Powder x-ray diffractograms, showing reaction sequence of  $\text{Fe}_2\text{O}_3 + \text{Nb}_2\text{O}_5 \rightarrow 2\text{FeNbO}_4$ .

## SUMMARY

B-site precursors of  $\text{Fe}_2\text{WO}_6$  was formed directly from the constituent oxides while  $\text{FeNbO}_4$  was developed through a competition with a pyrochlore-related phase. The perovskite

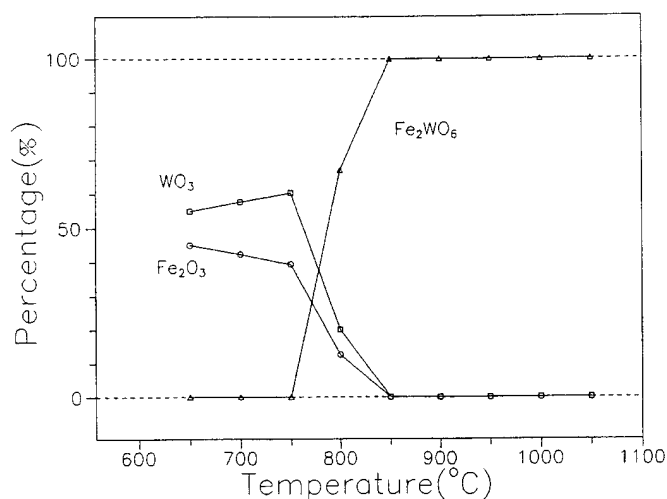


Figure 3. Relative amount of phases present during the reaction of  $\text{Fe}_2\text{O}_3 + \text{WO}_3 \rightarrow \text{Fe}_2\text{WO}_6$ .

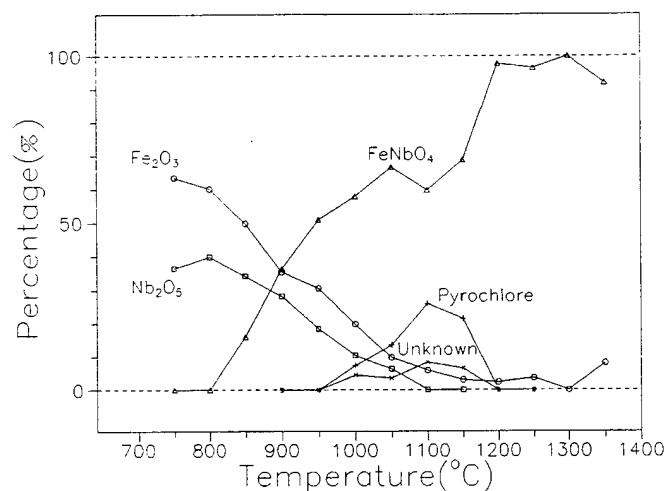


Figure 4. Relative amount of phases present during the reaction of  $\text{Fe}_2\text{O}_3 + \text{Nb}_2\text{O}_5 \rightarrow 2\text{FeNbO}_4$ .

structures were developed through a competition and displacement with pyrochlores. By the "B-site precursor method," almost phase-pure perovskite powders in the PFW-PFN system were obtained. Lattice parameters of PFW and PFN were determined to be 3.985 and 4.016 Å, respectively.

#### ACKNOWLEDGEMENTS

This work was supported in part by the Korea Ministry of Education and in part by the Korea Science and Engineering Foundation (KOSEF) through the Engineering Research Center (ERC) program of Center for Interface Science and Engineering of Materials (CISEM).

#### REFERENCES

1. H. Takamizawa, K. Utsumi, M. Yonezawa, and T. Ohno, *IEEE Trans. CHMT*, CHMT-4, 345 (1981).
2. M. Yonezawa, *Am. Ceram. Soc. Bull.*, 62, 1375 (1983).
3. Y. Shimada, K. Utsumi, T. Ikeda, and S. Nagasako, *Int. J. Hybrid Microelectronics*, 7, 29 (1984).

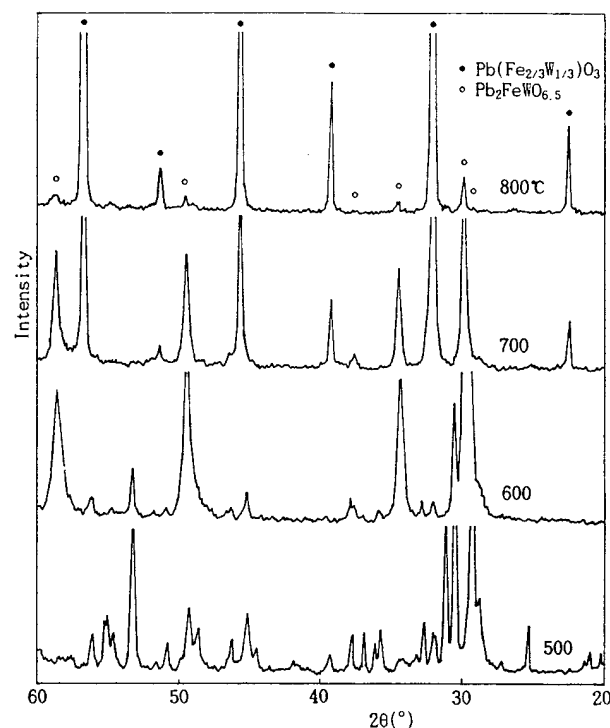


Figure 5. Powder x-ray diffractograms, showing reaction sequence of  $3\text{PbO} + \text{Fe}_2\text{WO}_6 \rightarrow 3\text{Pb}(\text{Fe}_{2/3}\text{W}_{1/3})\text{O}_3$ .

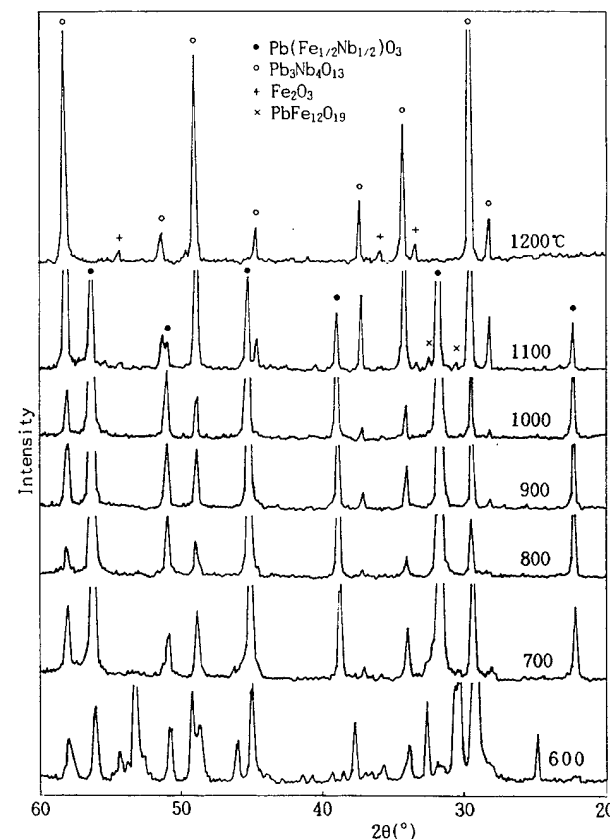


Figure 6. Powder x-ray diffractograms, showing reaction sequence of  $2\text{PbO} + \text{FeNbO}_4 \rightarrow 2\text{Pb}(\text{Fe}_{1/2}\text{Nb}_{1/2})\text{O}_3$ .

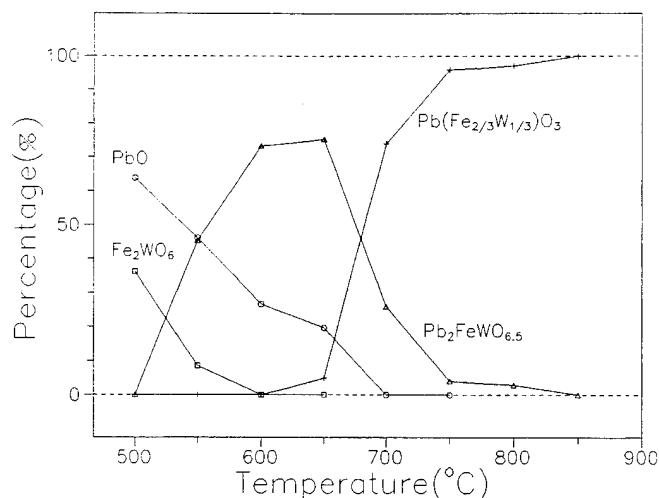


Figure 7. Relative amount of phases present during the reaction of  $3\text{PbO} + \text{Fe}_2\text{WO}_6 \rightarrow 3\text{Pb}(\text{Fe}_{2/3}\text{W}_{1/3})\text{O}_3$ .

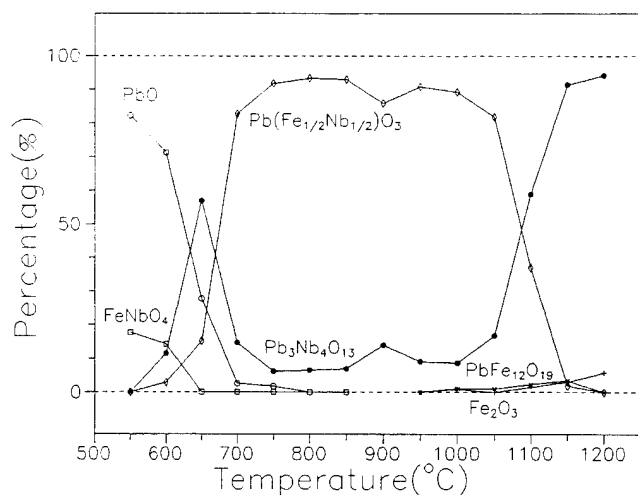


Figure 8. Relative amount of phases present during the reaction of  $2\text{PbO} + \text{FeNbO}_4 \rightarrow 2\text{Pb}(\text{Fe}_{1/2}\text{Nb}_{1/2})\text{O}_3$ .

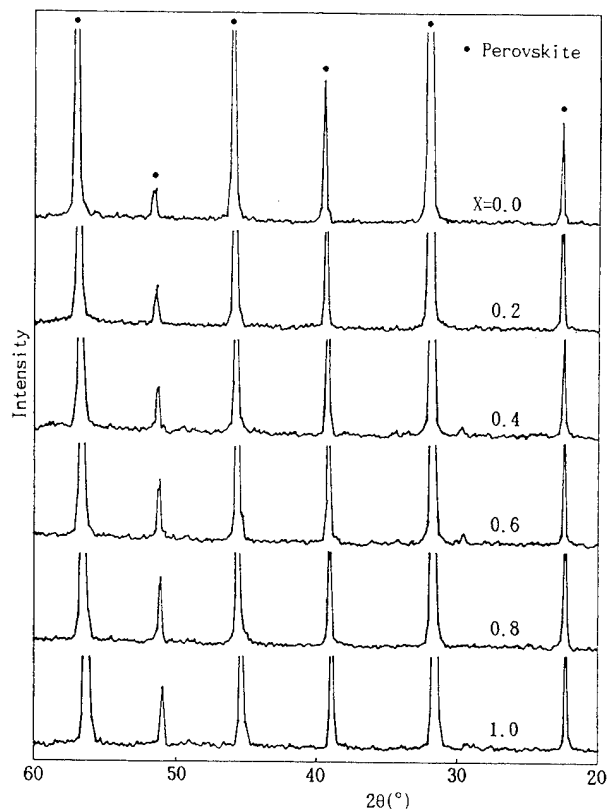


Figure 9. Powder x-ray diffractograms of  $(1-x)\text{PFW}-x\text{PFN}$  system, showing phase-pure perovskite structure.

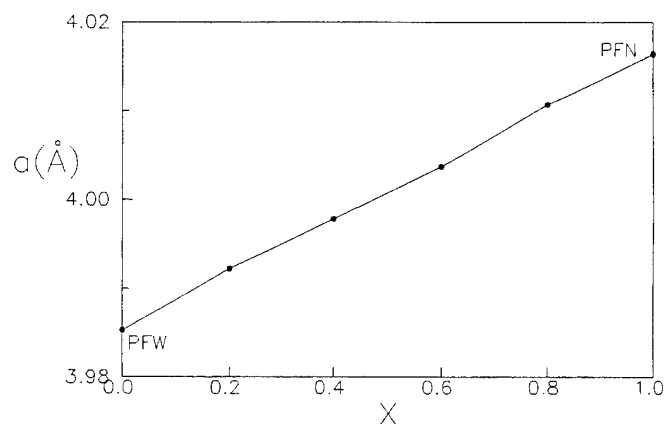


Figure 10. Variation of lattice parameter in the system  $(1-x)\text{PFW}-x\text{PFN}$ .

4. H. Takahara and K. Kiuchi, *Adv. Ceram. Mater.*, **1**, 346 (1986).
5. S. L. Swartz and T. R. Shrout, *Mater. Res. Bull.*, **17**, 1245 (1982).
6. J. P. Guha and H. U. Anderson, *J. Am. Ceram. Soc.*, **69**, C287 (1986).
7. A. I. Agranovskaya, *Bull. Acad. Sci. USSR, Phys. Ser.*, **24**, 1271 (1960).
8. M. Yonezawa, K. Utsumi, and T. Ohno, *Proc. 1st FMA*, F-7, 297 (1977).
9. M. Yonezawa and T. Ohno, *Jpn-US Study Sem. Diel. Piezoel. Ceram.*, T-8, 1 (1982).
10. M. Lejeune and J. P. Boilot, *Ceram. Int.*, **8**, 99 (1982).
11. M. P. Kassarian, R. E. Newnham, and J. V. Biggers, *Am. Ceram. Soc. Bull.*, **64**, 1108 (1985).
12. C.-H. Lu, K. Shinozaki, M. Kato, and N. Mizutani, *J. Mater. Sci.*, **26**, 1009 (1991).
13. C.-H. Lu, K. Shinozaki, and N. Mizutani, *J. Am. Ceram. Soc.*, **75**, 1303 (1992).
14. E. M. Levin, C. R. Robbins, and H. F. McMurdie, *Phase Diagrams for Ceramists*, 1969 Supplement, Fig. 2513, The American Ceramic Society, 1969.

15. B. D. Cullity, *Elements of X-Ray Diffraction* (2nd ed.), p. 356, Addison-Wesley, 1978.
16. C.-H. Lu, N. Ishizawa, K. Shinozaki, N. Mizutani, and M. Kato, *J. Mater. Sci. Lett.*, **7**, 1078 (1988).
17. V. A. Isupov, A. I. Agranovskaya, and N. P. Khuchua, *Bull. Acad. Sci. USSR, Phys. Ser.*, **24**, 1268 (1960).
18. C. F. Buhrer, *J. Chem. Phys.*, **36**, 798 (1962).
19. F. Galasso and W. Darby, *Inorg. Chem.*, **4**, 71 (1965).
20. A. V. Titov, O. I. Chechernikova, and Yu. N. Venevtsev, *Inorg. Mater.*, **14**, 891 (1978).



Z. Xu, Weng-Hsing Huang, and Dwight Viehland, Department of  
Materials Science and Engineering, Univ. of IL, Urbana, IL 61801  
and

R. R. Neurgaonkar, Rockwell International Science Center,  
Thousand Oaks, California 91358

Transmission electron microscopy (TEM) investigations have been performed on  $\text{Sr}_x\text{Ba}_{1-x}\text{Nb}_2\text{O}_6$  (SBN  $x/1-x$ ). Bright-field imaging of  $\langle 100 \rangle$ -orientated SBN 60/40 and 75/25 crystals revealed nanopolar domains with a strong shape anisotropy. The morphology of the nanopolar domains was needle-like. Selected area electron diffraction (SAED) patterns revealed the existence of  $1/x[110]$  incommensurate modulations. Dark-field imaging of the incommensurate reflections found the existence of nanometer-sized ferroelastic domains. Diffuse scattering was observed in the SAED patterns along the  $\langle 100 \rangle$ . This diffuse scattering is believed to arise due to strain gradient interactions between the A-site cation distribution and the incommensuration.

### I. Introduction

Numerous TEM investigations have been performed on tungsten bronze ferroelectrics [1-4]. These studies have revealed the existence of an incommensurate superlattice reflections along the  $\langle 110 \rangle$ . TEM has revealed superlattice reflections characterized by the modulation vector  $(h+[1+\delta/4], k+[1+\delta/4], 1/2)$ , where  $\delta$  is the incommensurability and is a noninteger. The incommensuration resides in the  $ab$  plane due to a shearing of the oxygen octahedra. The basis of each octahedron remains fixed in the  $ab$  plane, however the upper and lower vertices move parallel to this plane in opposite directions, resulting in a doubling of the unit cell along the  $c$ -direction. Dark-field imaging of the  $\frac{1}{x}[110]$  reflection has previously revealed ferroelastic domains. Most tungsten bronze ferroelectrics have a hierarchy of domain structures, possessing both ferroelectric and ferroelastic domains.

The purpose of this investigation was to study the compositional dependence of the microstructural property relationships in SBN as a function of Sr-content. A wide enough compositional range was chosen to ensure that the relaxor-like characteristics varied from weak to strong.

### II. Experimental Procedure.

The  $\text{Sr}_x\text{Ba}_{1-x}\text{Nb}_2\text{O}_6$  compositions chosen for study included  $x=0.50, 0.60$ , and  $0.75$  (designated as SBN 50/50, 60/40 and SBN 75/25, respectively). Both  $\langle 001 \rangle$  and  $\langle 100 \rangle$  orientated crystals were studied for each composition.

TEM specimens were formed by ultrasonically drilling 3-mm discs which were mechanically polished to  $\sim 100 \mu\text{m}$ . The center portions of these discs were then further thinned by a dimpler to  $\sim 10 \mu\text{m}$ , and argon ion-milled to perforation. Specimens were coated with carbon before examination. The TEM studies were carried out on a Phillips EM-420 microscope operating at an accelerating voltage of 120 kV. The dielectric response of electroded specimens was measured as a function of frequency and temperature. Measurements were made in the temperature range of 230 to  $-150^\circ\text{C}$  on cooling at a rate of  $4^\circ\text{C}/\text{min}$  in a Delta Design oven. Measurements were made by a HP 4284 LCR meter.

### III. Results and Discussion

Room temperature bright-field TEM micrographs are shown in Figures 1(a)-(c) for  $\langle 100 \rangle$ -orientated SBN 50/50, 60/40 and 75/25 crystals, respectively. Typical  $180^\circ$  ferroelectric domains can clearly be seen for SBN 50/50 (Figure 1(a)). The width of the domains in the  $bc$  plane was  $\sim 0.3 \mu\text{m}$ , and the length along the  $c$ -direction was  $>1 \mu\text{m}$ . On increasing the Sr-content, normal micron-sized domains were no longer evident. Rather, nanopolar domains were observed (Figure 1(b) and (c)). These nanopolar domains can be seen to possess a strong shape anisotropy. The morphology of these nanopolar domains was needle-like. No previous TEM investigations of SBN relaxor compositions have reported needle-like nanopolar domains. For SBN 60/40, the width of the nanopolar domains was  $\sim 200 \text{ \AA}$ . With increasing Sr-content, the size of the needle-like nanopolar domains decreased. For SBN 75/25, the width was  $\sim 100 \text{ \AA}$ .

The existence of nanopolar domains is known to be one of the characteristics of relaxor ferroelectrics [5-7]. The needle-like morphology of these domains for SBN 60/40 and 75/25 is in clear distinction to the near isotropic morphologies observed for the mixed B-site cation (PMN) [5,6] and PLZT [7] relaxor families. This distinction reflects an important difference between the tungsten bronze and perovskite families of relaxors. The macrosymmetry of SBN is tetragonal to x-ray diffraction, which is in agreement with the

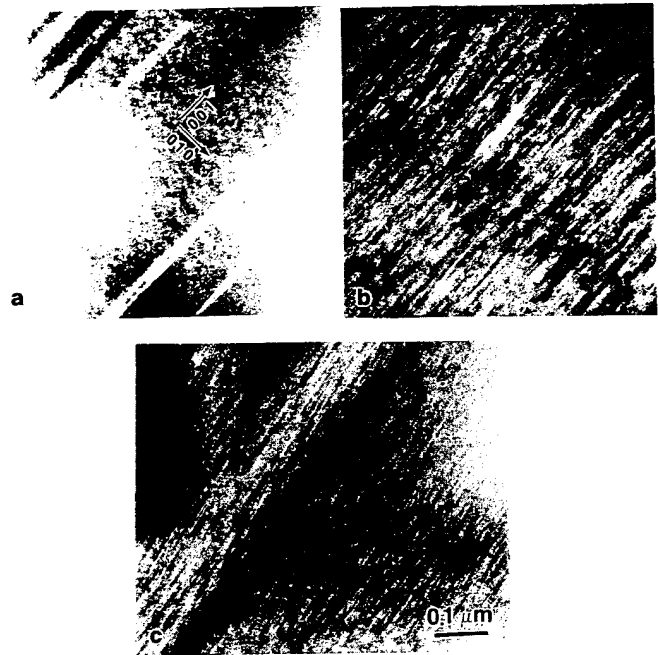


Figure 1. Room-temperature bright-field image for various SBN compositions. (a) SBN 50/50, (b) 60/40, and (c) 75/25.

local polar symmetry. However, the macrosymmetry of PMN is cubic by x-ray diffraction, which is in disagreement with the local rhombohedral polar symmetry. This difference in the morphologies of the nanopolar domains and resultant average macrosymmetries is also reflected in the dielectric response ( $\chi'$ ) characteristics. Strong orientational dependencies of  $\chi'$  have previously been reported for SBN relaxors [8,9]. The orientational dependence of  $\chi'$  as a function of temperature is illustrated in Figures 2(a) and (b) for  $\langle 001 \rangle$  and  $\langle 100 \rangle$  aligned SBN 75/25 crystals, respectively. The maximum  $\chi'$  along the  $\langle 001 \rangle$  was  $\sim 100$  times that along the  $\langle 100 \rangle$ . In contrast, the dielectric response of single crystals of mixed B-site cation relaxors has previously been reported to be nearly independent of crystallographic orientation [10]. These results clearly illustrate that the macroscopic properties of SBN reflect the shape anisotropy of the needle-like nanopolar domains and resultant macrosymmetry.

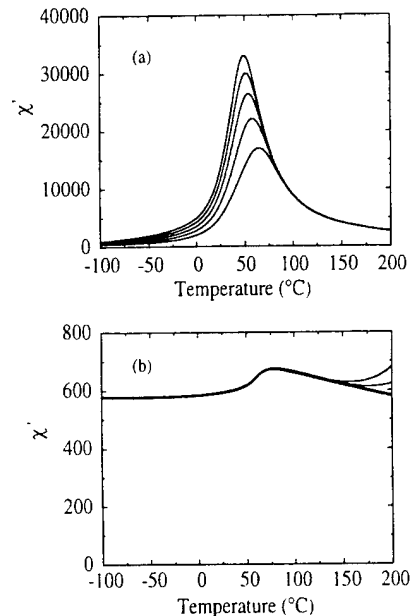


Figure 2. Dielectric constant for SBN 75/25 as a function of temperature for various crystallographic orientations. (a)  $\langle 001 \rangle$  and (b)  $\langle 100 \rangle$ .

The needle-like morphology of the nanopolar domains in SBN suggests that the translational invariance of the polarization is only broken in the *ab* plane and not along the *c*-direction. This indicates that there may be a strong crystallographic dependence of the symmetry breaking elements. Incommensuration has previously been reported in the *ab* plane of SBN 50/50. It might appear that incommensuration is, in part, responsible for the interruption of the normal ferroelectric domain structure. However, the ferroelectric domain structure has previously been reported to be independent of discommensurations in  $\text{Ba}_2\text{NaNb}_5\text{O}_{15}$  [1].

Room temperature  $\langle 110 \rangle$  SAED patterns are shown in Figures 3(a)-(c) for SBN 50/50, 60/40 and 75/25, respectively.  $1/x[110]$  superlattice reflections are clearly evident in all three figures, which were incommensurate with the fundamental periodicity of the lattice. The value of  $\delta$  was relatively independent of Sr-content and equal to  $\sim 0.19$ . Identical  $1/x[110]$  superlattice reflections have previously been reported for SBN 50/50 ( $\delta=0.195$ ), in addition similar reflections are known for BNN ( $\delta=0.01$ ). The  $1/x[110]$  incommensuration in tungsten bronzes is generally believed to be due to a shearing of the oxygen octahedra in the *ab* plane.

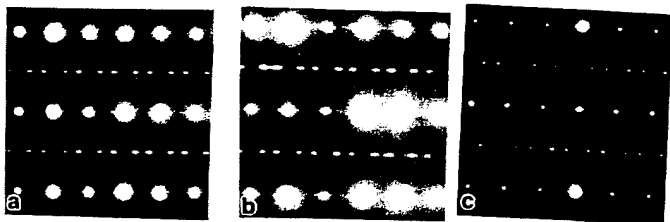


Figure 3. Room-temperature  $\langle 110 \rangle$  SAED patterns for various (100)-orientated SBN compositions. (a) SBN 50/50, (b) SBN 60/40, and (c) SBN 75/25.

Figures 4(a)-(c) show dark-field images for SBN 50/50, 60/40 and 75/25, respectively. Ferroelastic domains can be seen to be relatively small (on the nanometer scale), and consequently will be referred to as nanoelastic domains. The size of the nanoelastic domains increased with increasing Sr-content. For SBN 50/50, 60/40, and 75/25 the nanoelastic domains were  $\sim 100$ , 200, and 500 Å in diameter, respectively. Previous dark lattice imaging [3,4] of the  $1/x[110]$  reflections for SBN 50/50 have shown that the incommensurate modulation is one-dimensional, and indicates that the symmetry of the structure is orthorhombic. The periodicity of the lattice fringes was  $\sim 18$  Å along the  $\langle 110 \rangle$ .

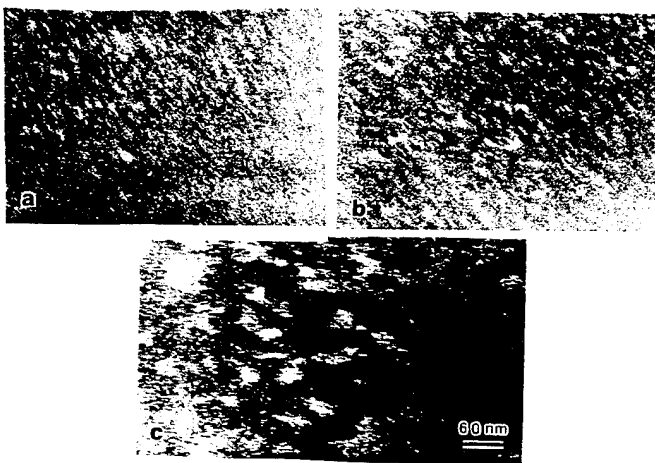


Figure 4. Room-temperature  $\langle 310 \rangle$  dark-field images for various (100)-orientated SBN compositions. (a) SBN 50/50, (b) SBN 60/40, and (c) SBN 75/25.

Previous dark-field imaging studies of incommensurate  $\langle 110 \rangle$  reflections for  $\text{Ba}_2\text{NaNb}_5\text{O}_{15}$  have revealed micron-sized ferroelastic domains [1]. The size of these ferroelastic domains is known to be dependent on thermal history, however the size of the nanoelastic domains for SBN was relatively independent of thermal annealing. It would appear that the nanoelastic domains in SBN do not possess the ability to coarsen to macroscopic scales. The residual incommensuration in BNN ( $\delta=0.01$ ) is believed to arise due to a pinning of the discommensurations by defects [1], as a consequence long-lived metastable states develop and the commensurate state is never reached. In BNN, the A-site cation occupancy is 6/6, i.e., a filled bronze structure. However, the A-site occupancy is only 5/6 for SBN,

i.e., an empty bronze. Consequently, significantly higher intrinsic channel defect concentrations exist in SBN. The inability of the nanoclastic domains to coarsen to the micron-scale may, then, reflect the unfilled nature of the 4-fold and 5-fold channels. The long-range driving force of the coarsening process (and reduction of  $\delta$ ) is the minimization of the strain energy density associated with the incommensuration. The channel defects in SBN are electrical neutral, however short-range strain interactions may exist due to nonuniform distributions of Ba and Sr in the 4- and 5-fold channels, respectively. A coupling between long-range and short-range strain interactions may, then, result in the stabilization (pinning) of the discommensurations. Consequently, quadrupolar fields which are random in the *ab* plane may be frozen-in from high temperatures.

Figures 5(a)-(c) show the  $\langle 101 \rangle$  SAED pattern for SBN 50/50, 60/40 and 75/25, respectively. Distinct diffuse scattering along the  $\langle 100 \rangle$  is evident. This diffuse scattering proves the presence of a planar disorder, which we believe may relate to the distribution of cations and vacancies on the 4-fold and 5-fold A-sites. In BNN, the ferroelectric and ferroelastic domain structures have been shown to be relatively independent. A possible influence of planar disorder in SBN might be to couple the incommensuration to the spontaneous polarization through gradient interactions. This might provide an explanation for the existence of relaxor behavior in the SBN crystalline solution series. One could conjecture that random frozen-in quadrupolar fields may break the translational invariance of the polarization in the *ab* plane. However, long-range translational invariance might remain in the *c*-direction. As a consequence, nanopolar domains with a needle-like morphology might form, rather than a normal ferroelectric domain structure.

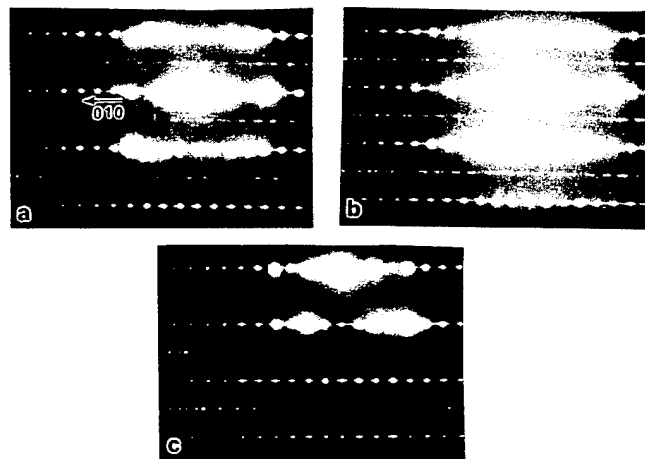


Figure 5. Room-temperature  $\langle 101 \rangle$  SAED patterns for various (100)-orientated SBN compositions. (a) SBN 50/50, (b) SBN 60/40, and (c) SBN 75/25.

#### IV. Conclusion

TEM and SAED studies have been performed on strontium barium niobate. These studies have revealed the existence of needle-like nanopolar domains in SBN 60/40 and 75/25. Dark-field imaging of the  $1/x\langle 110 \rangle$  incommensurate reflections revealed nano-sized ferroelastic domains. In addition, diffuse scattering was also observed along the  $\langle 110 \rangle$ , demonstrating the existence of a planar disorder which is believed to reflect the distribution of A-site cations. The incommensuration is believed to be coupled to the spontaneous polarization, via the distribution of A-site cations.

#### Acknowledgements

The research was supported by the Office of Naval Research under contract number N00014-92J-1522.

#### References

- [1] van Tendeloo, G., Amelinckx, S., Manolikas, C., and Shulin, W., 1985, *Phys. Stat. Sol. (a)* **91**, 483.
- [2] Manolikas, C., Schneck, J., Toledano, J., Kiat, J., and Calvarin, G., 1987, *Phys. Rev. B* **35**, 8884.
- [3] Bursill, L., and Lin, P., 1986, *Phil Mag.* **B 54**, 157.
- [4] Bursill, L., and Lin, P., 1987, *Acta Cryst. B* **43**, 49.
- [5] Chen, J., and Hamner, M., 1989, *J. Am. Cer. Soc.* **72**, 593.
- [6] Randall, C., and Bhalla, A., 1990, *J. Mat. Sci.* **29**, 5.
- [7] Randall, C., 1987, PhD Dissertation, University of Essex.
- [8] Glass, A., 1968, *J. Appl. Phys.* **40**, 4699.
- [9] Neurgaonkar, R., Hall, W., Oliver, J., Ho, W., and Cory, W., 1988, *Ferroelectrics* **87**, 167.
- [10] Huang, W., Neurgaonkar, R., and Viehland, D., 1994, *J. Appl. Phys.* (1 July 1994).

# The Effect Of High Temperature HIPing And Annealing On The Dielectric Properties Of Modified Lead Titanate Ceramics

M. R. Cockburn, D. A. Hall and C. E. Millar\*

Materials Science Centre, University of Manchester/UMIST, Manchester, M1 7HS, U.K.

\*Ferroperm A/S, Hejreskovvej 6, 3490 Kvistgård, Denmark.

## ABSTRACT

Studies on the hot isostatic pressing (HIPing) of Sm, Mn-doped lead titanate ceramics in an argon/oxygen atmosphere have shown that the HIPed materials exhibit a substantially lower dielectric loss than conventionally sintered materials ( $\tan \delta$  being reduced from approximately 0.02 to 0.01 at 1 kHz). The present work was carried out in order to identify the processing variables which are most important in effecting this reduction in loss. The materials were prepared by conventional solid state reaction and subjected to a variety of HIPing and annealing conditions. A mechanism involving the re-distribution of Mn ions among the Pb and Ti sites during HIPing is proposed to account for the observed changes in dielectric loss, which show a strong correlation with changes in the electrical conductivity.

## INTRODUCTION

Reports on HIPing (Hot Isostatic Pressing) as a post-sintering process for ceramics such as PZT and PLZT have shown a general improvement in dielectric, piezoelectric and mechanical properties due to a reduction in the residual porosity<sup>(1)</sup>. This technique is considered to be particularly relevant to piezoelectric ceramics used in high-frequency applications, for example thickness mode bulk resonators and SAW devices. In the former case, the reduction in porosity facilitates the machining and poling of thin (<500 $\mu$ m) sections, while in the latter a reduction in the attenuation of the surface wave is achieved<sup>(2)</sup>.

In previous work on the HIPing of modified lead titanate ceramics it was reported that HIPing in an Ar/O<sub>2</sub> atmosphere led to an unexpected reduction in dielectric loss, from 0.021 for the as-sintered to 0.007 for the HIPed material<sup>(1)</sup>. The present study was carried out in order to evaluate the effect of the processing variables (time, temperature and HIPing pressure) on the dielectric properties of Sm, Mn -doped lead titanate ceramics, and to elucidate the mechanism responsible for the observed reduction in loss.

## EXPERIMENTAL PROCEDURES

The materials used in the present study were Sm, Mn doped lead titanate ceramics, of composition  $\text{Pb}_{0.88}\text{Sm}_{0.08}\text{Ti}_{0.98}\text{Mn}_{0.02}\text{O}_3$ , prepared by conventional solid state reaction from the constituent oxides. The composition incorporated 2% Mn as a substitution on the Ti site in order to reduce the dielectric loss to an acceptable level<sup>(3)</sup>. The materials were sintered in air at 1230°C for 2 hours and then HIPed

in an 80% Ar/20% O<sub>2</sub> atmosphere under a variety of conditions. The processing conditions employed covered temperatures from 1000°C to 1200°C, HIPing pressures from 50 to 200 MPa, with processing times from 60 to 960 minutes. To complement these studies, a number of specimens HIPed under a given set of conditions (1100°C and 100 MPa for 60 min.) were re-annealed in air in order to establish the reversibility of the effects induced by the HIPing process. The resulting ceramic discs were then electroded using a fired on Ag/Pd paste (Du Pont 7474).

Dielectric measurements were carried out as a function of frequency (100 Hz to 300k Hz) at temperatures from 20 to 500°C using a Wayne Kerr 6425 LCR meter in combination with a wire-wound alumina tube furnace. Electrical contacts to the specimens were made via Pt foil electrodes. Two-probe resistivity measurements were carried out at room temperature under an electric field of 100 Vmm<sup>-1</sup> using a Chevin research HVA1B high-voltage amplifier together with a custom-built I-V converter.

## RESULTS

On comparing the room temperature dielectric properties of the as-sintered and HIPed materials it was evident that the HIPing treatment had a relatively minor effect on the permittivity but gave rise to a marked reduction in dielectric loss (table 1). The loss tangent exhibited a gradual reduction with increasing frequency, with the loss value of the HIPed ceramics being approximately half that of the as-sintered materials for these particular HIPing conditions. The HIPing process resulted in a substantial increase in density, from 7.60 to 7.74 gcm<sup>-3</sup> (i.e. from approximately 98% to >99.8% of the theoretical density).

*Table 1. Room temperature dielectric properties of as-sintered and HIPed Sm, Mn-doped lead titanate ceramics (HIPing conditions were 1100°C, 100 MPa and 60 mins).*

	1 kHz		10 kHz		100 kHz	
	$\epsilon_r$	$\tan\delta$	$\epsilon_r$	$\tan\delta$	$\epsilon_r$	$\tan\delta$
Sintered	212	0.0198	208	0.0096	205	0.006
HIPed	207	0.0104	205	0.0044	204	0.003

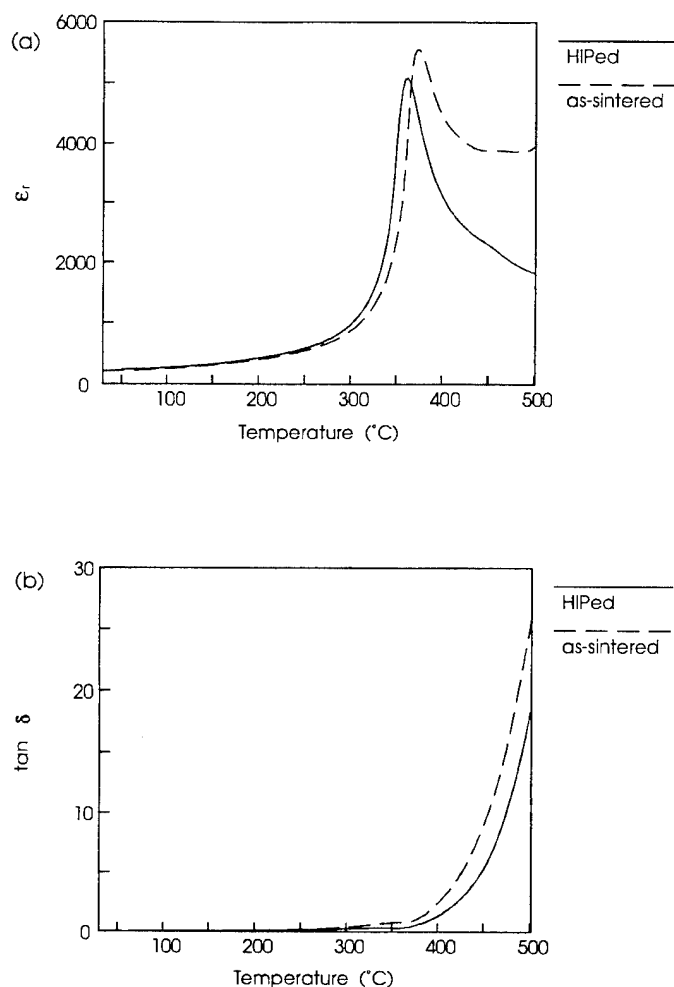


**Figure 1.** Temperature dependence of (a) relative permittivity and (b) loss tangent for as-sintered and HIPed materials (HIPing conditions : 100 MPa, 1100°C, 60 mins; 1 kHz data).

The dielectric losses for both the as-sintered and HIPed materials were found to rise sharply with increasing temperature (fig. 1), indicating an increasing contribution from electronic conductivity<sup>(4)</sup>. At room temperature the reduction in  $\tan \delta$  with increasing frequency is also characteristic of a loss mechanism related to electrical conductivity, although a simple inverse relationship between  $\tan \delta$  and frequency was not observed in this temperature range (table 1). Nevertheless, of the two major loss mechanisms in ferroelectrics (i.e. domain wall motion and electrical conductivity), it was considered that electronic conduction may play a more significant role in the observed behaviour.

With variations in the HIPing conditions employed, it was found that the measured dielectric loss exhibited a consistent reduction as the time, temperature or HIPing pressure were increased, as shown by the data presented in figs. 2 to 5. Furthermore, a strong correlation was established between the measured values of DC conductivity and dielectric loss. For ceramics HIPed at 1000°C under a pressure of 200 MPa, increases in the HIPing time gave rise to continuous reductions in the conductivity and loss (fig. 2). An increase in the HIPing pressure at a temperature of 1100°C yielded similar results (fig. 3). In contrast, at 1000°C and with a processing time of 60 min., there was apparently little change in the electrical properties as the HIPing pressure increased (fig. 4).

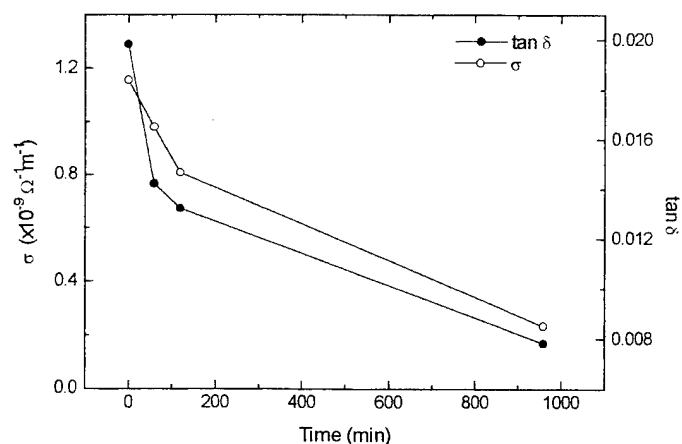


**Figure 2.** The effect of HIPing time on room temperature conductivity and loss tangent (200 MPa, 1000°C; 1 kHz data).

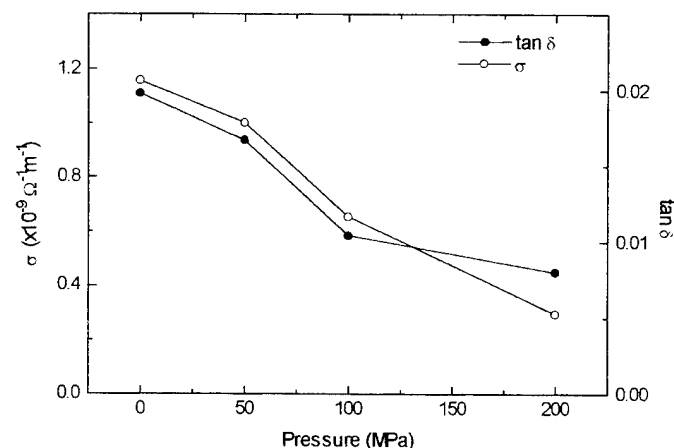


**Figure 3.** The effect of HIPing pressure on room temperature conductivity and loss tangent (60 mins, 1100°C; 1 kHz).

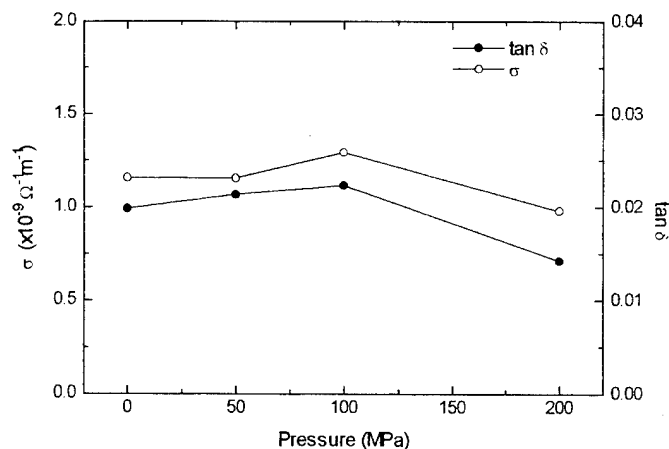


**Figure 4.** The effect of HIPing pressure on room temperature conductivity and loss tangent (60 mins, 1000°C; 1 kHz).

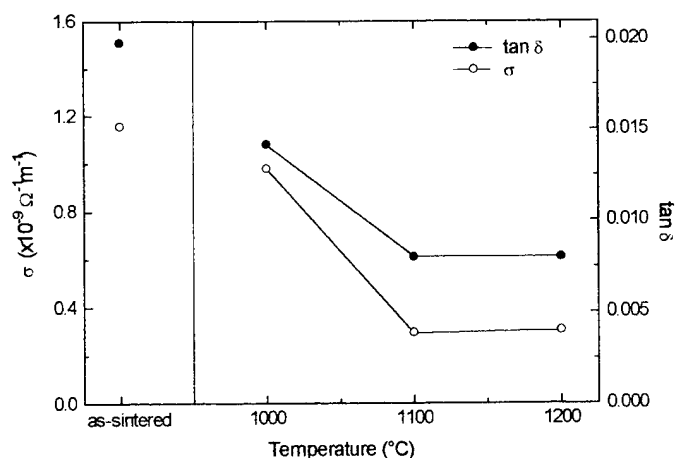


Figure 5. The effect of HIPing temperature on room temperature conductivity and loss tangent (60 mins, 200 MPa; 1 kHz data).

For materials HIPed at various temperatures it was found that an increase in temperature up to 1100°C gave substantial reductions in  $\tan \delta$  and  $\sigma$ . Beyond this level, a further increase in temperature yielded little change in properties (fig. 5). From the present results it appears that the maximum possible reduction in loss for a HIPing pressure of 200 MPa was from 0.0198 to approximately 0.0078. The corresponding reduction in DC conductivity was from  $1.16 \times 10^{-9}$  to  $2.32 \times 10^{-10} \Omega^{-1} \text{m}^{-1}$ .

Annealing experiments revealed that the reductions in dielectric loss and conductivity induced by the HIPing process were reversible to some extent, as shown by the data presented in table 2. However, values comparable to those of the as-sintered materials were not achieved after a long annealing time at 1000°C, perhaps due to the volatilisation of PbO from the specimen surfaces.

## DISCUSSION

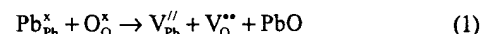
The data presented in the present work show a strong correlation between the DC conductivity and the AC dielectric loss of Sm, Mn-doped lead titanate ceramics, both of which exhibited substantial reductions as a result of the HIPing process. Therefore it can be suggested that the observed reduction in dielectric loss is associated with a reduction in conductivity. For the room temperature measurements which form the main part of the study, there is not an exact quantitative agreement between these two parameters. For example, a measured  $\tan \delta$  value of 0.0198 yields an apparent AC conductivity value of  $2.3 \times 10^{-7} \Omega^{-1} \text{m}^{-1}$  which is substantially higher than the measured DC conductivity of  $1.16 \times 10^{-9} \Omega^{-1} \text{m}^{-1}$ . Higher temperature measurements yielded a clear inverse relationship between  $\tan \delta$  and frequency and consequently a much better agreement between the measured AC and DC conductivity values.

It is likely that the observed changes in conductivity and dielectric loss are related to the tendency towards a new equilibrium state in which the oxygen content of the material is increased to some extent. For certain HIPing conditions (e.g. for temperatures above 1100°C), the relatively constant values of  $\tan \delta$  and  $\sigma$  may indicate that an equilibrium state has been achieved. In order to understand the observed changes in electrical properties as a result of the HIPing process, it will be necessary to consider the defect chemistry of the materials.

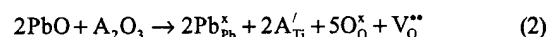
Table 2. Heat-treatment and subsequent dielectric loss values for HIPed Sm, Mn-doped lead titanate ceramics.

	1 kHz		10 kHz		100 kHz	
	$\epsilon_r$	$\tan \delta$	$\epsilon_r$	$\tan \delta$	$\epsilon_r$	$\tan \delta$
800°C, 3 hr	213	0.0108	210	0.0053	209	0.003
800°C, 12 hr	219	0.011	217	0.0052	216	0.003
1000 °C, 12 hr	200	0.0164	198	0.0074	197	0.0035

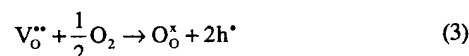
For lead titanate- and PZT-based ceramics, it is generally believed that the residual conductivity is p-type, either due to the volatilisation of PbO at elevated temperatures :



or to the presence of acceptor type impurities :



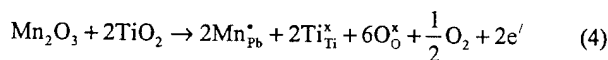
In either case, the presence of oxygen vacancies allows the incorporation of excess oxygen and, subsequently, the formation of electron holes :



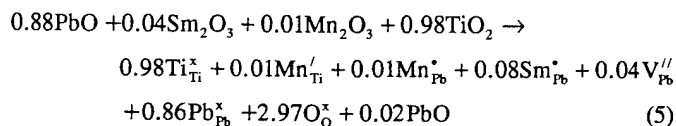
In such a case, an increase in the oxygen partial pressure during high-temperature equilibration would be expected to give rise to an increase in conductivity, which is contrary to the observations made in the present study. Therefore it may be concluded that the residual conductivity in the Sm, Mn-doped PbTiO<sub>3</sub> ceramics used in the present work is predominantly n-type.

The remaining difficulty is to provide a defect model for the predominant donor character of the as-sintered material which can then be used to describe the reduction in conductivity with increasing oxygen content. The key to such a model may lie in the role of manganese which is commonly incorporated in PbTiO<sub>3</sub>-based compositions to reduce the dielectric loss<sup>(3)</sup>. If Mn<sup>2+</sup> or Mn<sup>3+</sup> were incorporated solely on the Ti sites, this would result in an increase in the p-type conductivity according to equations 2 and 3. The well-established fact that the addition of Mn reduces the conductivity of PbTiO<sub>3</sub>-based ceramics indicates that a substantial proportion of Mn<sup>3+</sup> or Mn<sup>4+</sup> is incorporated as a donor on the Pb sites, as reported by Hennings and Pomplun<sup>(5)</sup>.

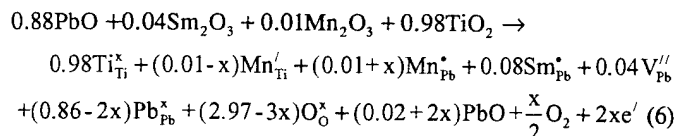
Their study showed that the proportion of Mn on the Pb site increased with reductions in the partial pressures of PbO and O<sub>2</sub>. If it is assumed that the Mn is present as Mn<sup>3+</sup> in order to simplify the argument, then the incorporation of Mn<sup>3+</sup> on the Pb sites can be represented by :



For the composition used in the present study,  $\text{Pb}_{0.88}\text{Sm}_{0.08}\text{Ti}_{0.98}\text{Mn}_{0.02}\text{O}_3$ , the following equation can be proposed to represent the formation of the perovskite phase, assuming that  $\text{Mn}^{3+}$  is incorporated in equal proportions on the Pb and Ti sites :

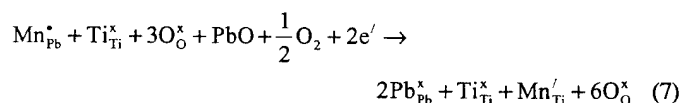


If an excess of Mn,  $x$ , is present on the Pb site, then equation (5) can be modified to represent the generation of free charge carriers :



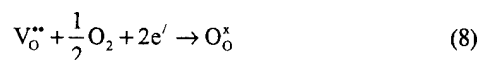
It is evident that a certain amount of excess PbO will always be present (for this composition) if any of the Mn is incorporated on the Pb site, and that an equal or greater proportion of Mn on the Pb site would suppress the formation of oxygen vacancies.

Following this argument, the observed reductions in conductivity and dielectric loss as a result of HIPing in  $\text{Ar}/\text{O}_2$  can be explained in terms of the re-distribution of Mn ions among the Pb and Ti sites :



Such a reaction would involve the creation of a new unit cell for each Mn ion changing site and the incorporation of part of the available excess PbO. The change in the Mn site distribution and the incorporation of excess PbO under high partial pressures of  $\text{O}_2$  and PbO was confirmed by Hennings and Pomplun for La, Mn -doped  $\text{PbTiO}_3$  using electron spin resonance and thermogravimetric techniques<sup>(5)</sup>.

Alternatively, if oxygen vacancies are present in substantial quantities in the as-sintered ceramics, then a more simple mechanism for incorporating excess oxygen would be as follows :



The apparent times required to reach an equilibrium state during HIPing and annealing are surprisingly long in comparison with  $\text{BaTiO}_3$  ceramics, where it has been found that equilibrium with respect to the oxygen content is established within 1 hr. for temperatures above  $1000^\circ\text{C}$ <sup>(6)</sup>. In the case of  $\text{BaTiO}_3$ , the changes in conductivity as a function of  $\text{Po}_2$  are thought to be due primarily to the diffusion of oxygen within the material. The reaction represented by equation (7) would involve the diffusion of both lead and oxygen species as well as the re-distribution of Mn ions, which may explain the requirement for extended equilibration times. Therefore, although further work will be required to establish the validity of the defect models presented above, an argument involving the incorporation of Mn ions on the Pb sites does provide a plausible explanation for the observed behaviour.

## CONCLUSIONS

It has been demonstrated that the dielectric loss of Sm, Mn -doped  $\text{PbTiO}_3$  ceramics can be reduced by a factor of 2 or more by HIPing in an  $\text{Ar}/\text{O}_2$  atmosphere. The variations in  $\tan \delta$  as a function of the HIPing conditions (time, temperature, pressure) showed a strong correlation with changes in electrical conductivity, indicating that electronic conduction may be the dominant loss mechanism in these materials. The apparent donor character of the materials is thought to be due to the incorporation of a significant proportion of Mn on the Pb sites. Similarly, the observed reductions in  $\tan \delta$  and  $\sigma$  as a result of HIPing can be explained in terms of a mechanism involving the re-distribution of Mn ions among the Pb and Ti sites.

## ACKNOWLEDGEMENTS

The authors would like to thank the EPSRC and Ferroperm Ltd for financial support.

## REFERENCES

1. C.E. Millar, W. Wolny, J. Ricote, C. Alemany and L. Pardo, "Electroceramics: Production, Properties and Microstructures", 185-193, Institute of Materials, London (1994).
2. C.E. Millar, L. Pederson, L. Pardo, J. Ricote, C. Alemany, B. Jimenez, and G. Feuillard, Proc ISAF '94 (1994).
3. S. Ikegami, I. Ueda and T. Nagata, J. Acoust. Soc. Amer. **50**, 1060-1066 (1971).
4. K.H. Hardtl, Ceramics Int. **8**, 121-127 (1982).
5. D. Hennings and H. Pomplun, J. Am. Ceram. Soc. **57**, 527-530 (1974).
6. H.J. Hagemann and D. Hennings, J. Am. Ceram. Soc. **64**, 590-594 (1981).

# LOOSELY ASSOCIATED ION INTERACTION IN THE OXIDE AND OXYFLUORIDE PYROCHLORES

Xiukai Cai, Liangying Zhang and Xi Yao  
Electronic Materials Research Laboratory  
Xi'an Jiaotong University, Xi'an, 710049, China

**Abstract** — A dielectric relaxation phenomenon was observed in the substituted pyrochlores. The dielectric behavior could be treated according to the Debye model. The activation energy derived from a coincidental determination of the temperature and frequency dependence of loss factors is approximately 0.23 eV, which can be related to a jump of a loosely associated ion pair formed by the replacement of a cation with different valence and the corresponding formation of a vacancy at normally occupied ion site. The period of atom vibration is of the order of  $10^{-12}$  sec or so. The influence of chemical compositions is discussed.

## INTRODUCTION

For practical applications in which it is desirable to obtain a high capacitance in the smallest physical space, the high dielectric constant materials must be used, and it is equally important to have a low dielectric loss, especially for the manufacturing Type I multilayer ceramic capacitors.

Energy losses in dielectrics result chiefly from the ion migration processes. Although the DC conduction migration losses are normally small, they may become important at low frequencies and high temperatures. Nevertheless, ion jump relaxation between two equivalent ion positions is responsible for the most part of the dielectric loss in ceramics in the medium frequencies for electrical applications.

For an ion jump, the jump frequency depends on the barrier separating the two ion positions. If we assume for simplicity that there is one relaxation time, the pure thermal stimulated process is given by [1]:

$$\tau(T) = \tau_0 \exp(U/kT)$$

Here  $\tau_0$  is the period of atom vibrations. For the pure theoretical Debye loss peak, the maximum energy loss occurs for a frequency equal to the jump

frequency,  $1/\tau$ , so the equation can be written as:

$$\omega_{\max}(T) = 1/\tau_0 \exp(-U/kT)$$

There is no difference between the frequency response at given temperatures and the temperature dependence at given frequencies. Once the coincidental measurements being carried out, by plotting the  $\log \omega_{\max}$  versus  $1000/T$ , it is possible to determine the activation energy for ion jump relaxation and the intrinsic jump frequency.

In this paper, the dielectric relaxation related to the loosely associated ion interaction in the  $\text{Bi}_2\text{O}_3$ - $\text{ZnO}$ - $\text{Nb}_2\text{O}_5$  based materials is reported.

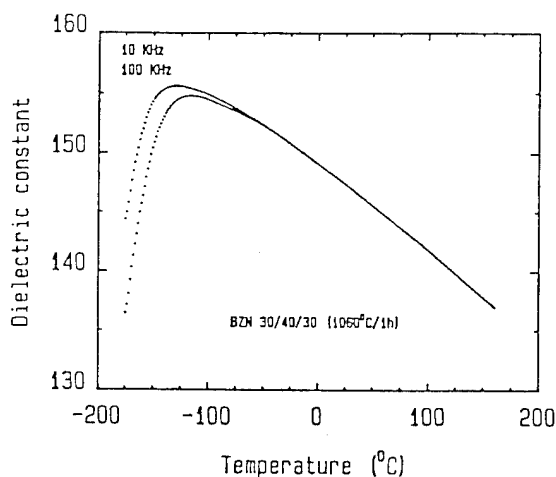
## EXPERIMENTAL

Dielectric measurements were conducted on sintered pellets with blocking silver electrodes. By using a computer controlled HP4274A automating LCR meter at given separate frequencies (1, 10, 100 KHz), the temperature dependences of dielectric constants and losses were obtained in the temperatures ranging from -190 to 250°C.

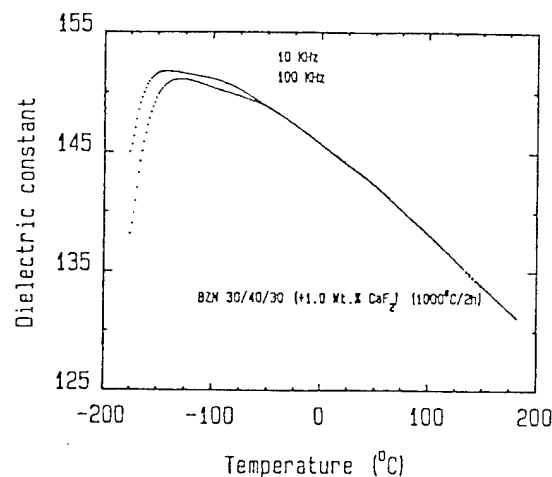
X-ray data on the powder of sintered ceramic body were recorded by Rigaku Dmax-2400 Diffractometer.

## EXPERIMENTAL RESULTS AND DISCUSSIONS

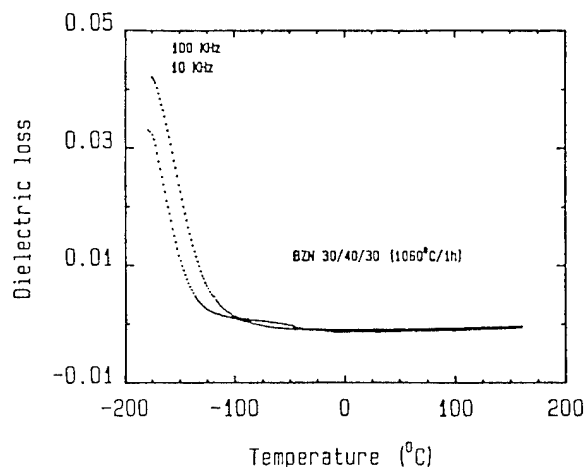
In the composition of  $(\text{Bi}_{1.5}\text{Zn}_{0.5})(\text{Zn}_{0.5}\text{Nb}_{1.5})\text{O}_7$ , the dielectric constant disperses with frequencies, and the maxima of dielectric constant occur at low temperatures as to below -100°C, the loss peak is beyond the measuring limit of liquid nitrogen temperatures, with only a sudden drop to a loss level close to zero being found, as shown in Figure 1. Although no full sketch of loss peak prevent the detailed analysis of dielectric behaviors, the only polarising mechanism characteristic of perfect cubic pyrochlore structure can be concluded.



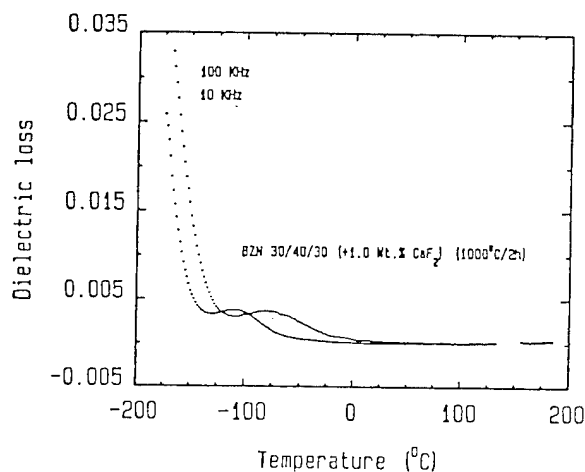
(a)



(a)



(b)



(b)

FIGURE 1 Temperature Dependences of Dielectric Constant and Dielectric losses for the composition  $(\text{Bi}_{1.5}\text{Zn}_{0.5})(\text{Zn}_{0.5}\text{Nb}_{1.5})\text{O}_7$

Once the  $\text{CaF}_2$  being added to the base composition of  $(\text{Bi}_{1.5}\text{Zn}_{0.5})(\text{Zn}_{0.5}\text{Nb}_{1.5})\text{O}_7$ , there occurs the second loss peak characteristic of dielectric relaxation, although the single cubic pyrochlore phase is maintained at low level (e.g. 1.0 wt.%, that is about 3.2 mol%) of  $\text{CaF}_2$  addition, as shown in Figure 2. The  $U$  and  $\tau_0$  was 0.211 eV and  $4.816 \times 10^{-12}$  respectively, which corresponds to the relaxation process of loosely associated ions.

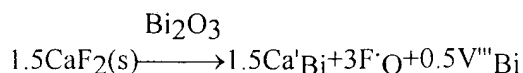
FIGURE 2 Temperature Dependencies of Dielectric Constants and Dielectric Losses for the Composition with 1.0 wt.%  $\text{CaF}_2$  added

Because of the larger  $\text{Ca}^{2+}$  with nearly equal size to that of  $\text{Bi}^{3+}$ , the possible process is the substituting of  $\text{CaF}_2$  for  $\text{Bi}_2\text{O}_3$ , and this can be ascertained by the same structure and dielectric properties between BZN 40/40/30 and BZN 30/40/40 formulations with 6.0 wt.%  $\text{CaF}_2$  doped.

Now the question is why the dielectric relaxation occurs in the cubic pyrochlore compositions with low dosage of  $\text{CaF}_2$  (0~6 mol%)



too. From the above results, it seems reasonable for  $\text{Ca}^{2+}$  to replace  $\text{Bi}^{3+}$ . Considering only ion substitutions, a possible process to form solid solutions is:



where all of the electrical neutrality, mass balance and lattice site relations are conserved [2].

It is the existence of bismuth cation vacancy that makes the movement of  $\text{Nb}^{5+}$  sited in the octahedra be relaxed, which is very similar to the situation in the rutile doped with alkaline earth metal oxides [3]. So the complex defects contribute to the dielectric relaxation.

Further consideration is the influence of cation substitutions based on  $\text{A}_2\text{B}_2\text{O}_6\text{O}'$  cubic pyrochlore structure whose main framework is a  $[\text{B}_2\text{O}_6]^{n-}$  network of vertex-shared octahedra. There is no doubt that whether the presence or absence of dielectric relaxation is closely related to the cation substitution in A or B site. Substitutions in A site will give a much more chances for generating dielectric relaxation because of the distortion of octahedra framework. For example, additions of slight larger amounts of  $\text{La}_2\text{O}_3$  to substitute for  $\text{Bi}_2\text{O}_3$  in the composition  $(\text{Bi}_{1.5}\text{Zn}_{0.5})(\text{Zn}_{0.5}\text{Nb}_{1.5})\text{O}_7$  leads to loss peak of dielectric relaxation, although there is no possible occurrence of defects such as vacancy, interstitial ions etc.. The  $U$  and  $\tau_0$  are 0.217 eV and  $5.183 \times 10^{-12}$ , being typical of the loosely associated ion interaction too.

When the relatively small amounts of substituting cations enter into the octahedra, the pyrochlore structure is basically untransformed, so the dielectric relaxation seldom occurs. In the substitutional solid solutions with  $\text{TiO}_2 + \text{WO}_3$  (1:1 mole ratio) added for replacing  $\text{Nb}_2\text{O}_5$ , there exists no relaxation peak even in the compositions with relative large amounts of substitutions (up to 20%).

### CONCLUSIONS

Different valent cation substitutions lead to dielectric relaxation resulting from the formation of possible defect state, although cubic pyrochlore structure is maintained.

There is much more chance for cation substitutions to generate defect structure in A site than in B site.

### ACKNOWLEDGEMENTS

The authors wish to thank H.F.Wang for helps in dielectric measurements and Z.Y.Cheng for helpful discussions.

### REFERENCES

- [1] L.Y.Zhang and X.Yao, *Physics of Dielectrics*. Xi'an: Xi'an Jiaotong University Press, 1992, ch.2, pp. 173-204.
- [2] W. D. Kingery, H. K. Bowen and D. R. Uhlmann, *Introduction to Ceramics*. New York-London-Sydney-Toronto: John Wiley and Sons Press, 1974, ch. 4, p. 130.
- [3] G. I. Skanavi, "Dielectric Constant and its Temperature Dependence for Crystals of the Type of Rutile and Perovskite", *Doklady Akad. Nauk. S. S. S. R.*, Vol. 59, pp. 231-234, 1948.

# THE STRUCTURE AND DIELECTRIC PROPERTIES OF NEW OXYFLUORIDES

Xiukai Cai, Liangying Zhang and Xi Yao  
Electronic Materials Research Laboratory  
Xi'an Jiaotong University, Xi'an, 710049, China

**Abstract** — The structure of solid solution  $\text{Bi}_{1.5}(\text{Zn}_{1-x}\text{Li}_x)\text{Nb}_{1.5}(\text{O}_{7-x}\text{F}_x)$  obtained by substitution of oxygen by fluorine in the oxide  $\text{Bi}_{1.5}\text{ZnNb}_{1.5}\text{O}_7$  is cubic pyrochlore for  $0 \leq x \leq 0.15$ . For  $0.80 \leq x \leq 1.00$ , a distorted modification with low symmetry results, while the mixed phases of the above two are formed for other values of  $x$  between 0.15 and 0.80. The temperature dependences of the dielectric constants have been studied, and a dielectric anomaly at low temperatures (less than  $-100^\circ\text{C}$ ) has been observed.

## INTRODUCTION

Substitution of a large amount of oxygen by fluorine in oxides may take place in such structures as rutile, perovskite, garnet and pyrochlore etc., owing to the similar size and chemical affinity between  $\text{O}^{2-}$  and  $\text{F}^-$  anions.

The structure of oxide pyrochlore  $\text{A}_2\text{B}_2\text{O}_6\text{O}'$  is composed of corner-shared  $(\text{B}_2\text{O}_6)^{n-}$  polyhedra, with the larger A cations filling the interstices and located within eight coordinated scalenohedra that contain six equally spaced O anions and two additional axial O' anions at a slightly shorter distance from the central cations. Thus the O' anions are bonded to cations of type A only and do not participate in the network forming of  $(\text{B}_2\text{O}_6)^{n-}$  polyhedra [1]. It is the unique seventh oxygen that can be replaced by several different atoms such as fluorine, sulfur, or chlorine, or even can be a vacancy in the structure, giving rise to the formula  $\text{A}_2\text{B}_2\text{O}_6$  or  $\text{ABO}_3$ —a defect pyrochlore. In certain cases even the oxygen atoms in the  $(\text{B}_2\text{O}_6)^{n-}$  polyhedra framework can also be replaced by fluorine atoms, generating a random arrangement in anion sites [2].

In the case of fluorine substitution for oxygen, in order to maintain the electrical neutrality, corresponding cation substitutions should be required. For example, fluorine substitution for oxygen and  $\text{Na}^+$  replacement of  $\text{Pb}^{2+}$  in  $\text{Pb}_2\text{Nb}_2\text{O}_7$  has been reported [3]. There is another way that the charge equilibrium can be satisfied, that is, the

corresponding reduction of the cationic charge (e.g., in  $\text{Fe}_3\text{O}_{4-x}\text{F}_x$ ).

In this paper, we report on the synthesis and dielectric properties of bismuth containing oxide and oxyfluorides of the type  $\text{Bi}_{1.5}(\text{Zn}_{1-x}\text{Li}_x)\text{Nb}_{1.5}(\text{O}_{7-x}\text{F}_x)$  ( $0 \leq x \leq 1$ ) with pyrochlore structure.

## EXPERIMENTAL PROCEDURES

The purities were at least 99.50 wt.% for all the reactants— $\text{Bi}_2\text{O}_3$ ,  $\text{ZnO}$ ,  $\text{LiF}$  and  $\text{Nb}_2\text{O}_5$ . Appropriate quantities of the starting materials were intimately mixed by grinding together in a nylon container with an agate motor filled. The samples in the form of pellets were prefired in air at  $800^\circ\text{C}$  for 2 hours and then sintered at  $900\sim 1080^\circ\text{C}$  for 3~5 hours.

X-ray diffraction data were obtained with a Rigaku Dmax-2400 diffractometer and Si ( $a=5.4305$  Å) as an external standard. Cell dimensions were refined by least squares method.

The dielectric measurements were conducted on sintered pellets,  $10 \pm 0.5$  mm diameter and  $1.5 \pm 0.5$  mm thick, deposited with Au electrodes by DC sputter. The temperature dependences of dielectric constants and  $\tan\delta$  were measured at the separate frequencies ranging from  $10^2$  to  $10^5$  Hz under weak ac fields using computer-controlled HP4274A automating LCR meter with temperatures ranging from  $-180$  to  $250^\circ\text{C}$ .

## RESULTS AND DISCUSSIONS

The ternary oxide  $\text{Bi}_{1.5}\text{ZnNb}_{1.5}\text{O}_7$  gives X-ray diffraction pattern which can be indexed as face centered cubic cell ( $\text{Fd}3\text{m}$ ) with a cell edge of  $10.5562 \pm 0.0002$  Å. The peak intensities and systematic absences are typical of the pyrochlore structure.

On the basis of above composition, substitution of fluorine for oxygen anions accompanied by lithium for zinc cations has been carried out. The formulations of substitutional solid solutions may be written as  $\text{Bi}_{1.5}\text{Zn}_{1-x}\text{Li}_x\text{Nb}_{1.5}\text{O}_{7-x}\text{F}_x$ .

At lower fluorine concentration ( $x \leq 0.15$ ), the solid solutions with cubic pyrochlore structure can be obtained, as illustrated in Figure 1.

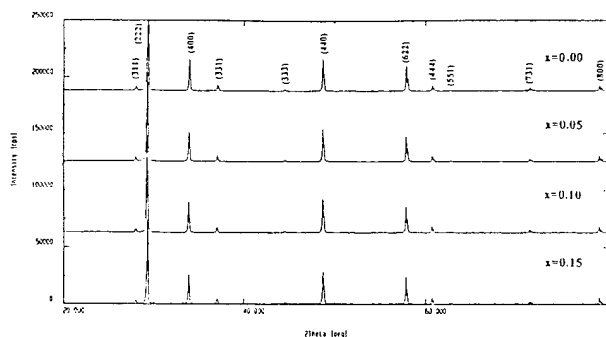
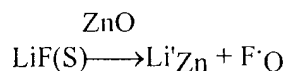


FIGURE 1 X-ray Diffraction Patterns for the Compositions  $\text{Bi}_{1.5}\text{Zn}_{1-x}\text{Li}_x\text{Nb}_{1.5}\text{O}_7$  with Cubic Pyrochlore Structure

Although there are several factors determining the extent of substitution in solid solutions, the major factor for oxides or oxyfluorides are the relative size and the valency. As for  $\text{Zn}^{2+}$  and  $\text{Li}^+$ , the ion radii from Shannon [4] are 0.74 Å(VI), 0.90 Å(VIII) and 0.76 Å(VI), 0.92 Å(VIII) respectively, apparently with the relative size less than 15%. In addition, the electrical neutrality can also be satisfied by the following process of substitution:



When the amount of substitution increases, the peaks corresponding to the second phase occur, the higher the dosage of fluoride addition, the stronger the line intensity of the impurified phase. Figure 2 gives the X-ray diffraction results of the compositions with mixed phases.

Perhaps the occurrence of the second phase is mainly due to the difference in behavior between oxygen and fluorine anions. From the standpoint of crystal chemistry, although the fluorides can be classified like the oxides in terms of the anionic packing and occupation of the interstitial positions, the coordination number in fluorides is higher than that in oxides as a result of the smaller covalence, thus the oxyfluorides sometimes have distorted surroundings when oxygen-fluorine substitution takes place.

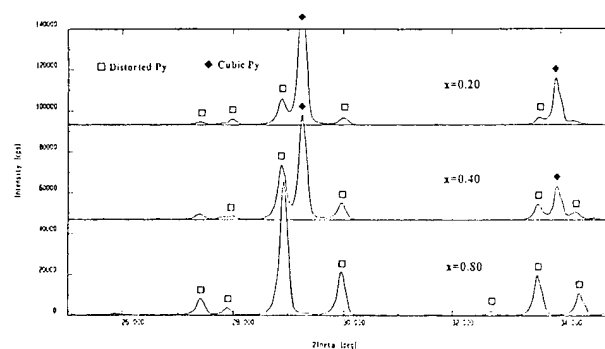


FIGURE 2 X-ray Diffraction Patterns for the Compositions with Second Phase Formed

For the samples of  $x=0.80$  and  $1.00$ , there exist equal numbers of X-ray diffraction lines, the only difference is the slightly shift of  $2\theta$  position. Referring to the X-ray diffraction results of  $3 \text{ PbO} \cdot \text{Nb}_2\text{O}_5$  with monoclinic pyrochlore structure, we index most of the intense lines for both compositions, as illustrated in Figure 4. The fact of partly nonindexed lines lead to the consideration of distorted pyrochlore with lower symmetry than the monoclinic.

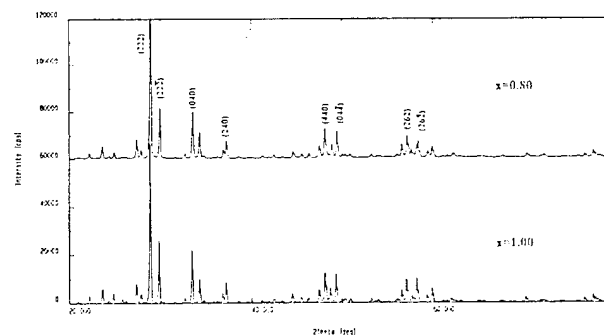


FIGURE 3 X-ray Diffraction Patterns for the Compositions  $\text{Bi}_{1.5}\text{Zn}_{1-x}\text{Li}_x\text{Nb}_{1.5}\text{O}_{7-x}\text{F}_x$  with Single Distorted Pyrochlore

Dielectric measurements show a dielectric anomaly at lower temperatures (less than  $-100^\circ\text{C}$ ), which is frequency dispersive and characteristic of the bismuth based cubic pyrochlore. The effect of the compositions of the oxyfluorides on the peak temperatures is demonstrated in Figure 4.

Apparently the peak is left shifted as a result of fluorine addition. This is very similar to the results found in ferroelectric or antiferroelectric oxides or oxyfluorides [5], where the less covalence of metal-fluorine leads to the small activation energy for ferroelectric-paraelectric phase transitions.

which is left shifted as a result of the fluorine-oxygen substitution.

#### ACKNOWLEDGEMENTS

The authors wish to thank Dr.X.L.Wang for X-ray diffraction analyses. This work was supported by National Advanced Materials Research Project of China.

#### REFERENCES

- [1] R. A. McCauley, "Structural Characteristics of Pyrochlore Formation", *J. Appl. Phys.*, Vol. 51, pp. 290-294, January 1980.
- [2] P.Hagenmuler, *Inorganic Solid Fluorides*. London: Academic Press, 1985, ch. 5, p. 245.
- [3] G. Campet, J. Claverie, M. Perigord, J. Ravez, J. Portier and P. Hagenmuller, "Sur de Nouvelles Phases Oxyfluorees Derives du Niobate de Plomb: Etudes Cristallographique et Dielectrique", *Mat. Res. Bull.*, Vol. 9, pp. 1589-1596, December 1974.
- [4] R. D. Shannon, "Revised Effective Ionic Radii in Halides and Chalcogenides", *Acta. Cryst.*, Vol. A32, pp. 751-768, May 1976.
- [5] J. Ravez, "Relationships between Curie Temperature and Chemical Bond in Octahedral Monodimensional Ferroelectrics", *Phase Tran.*, Vol. 33, pp. 53-64, January 1991.

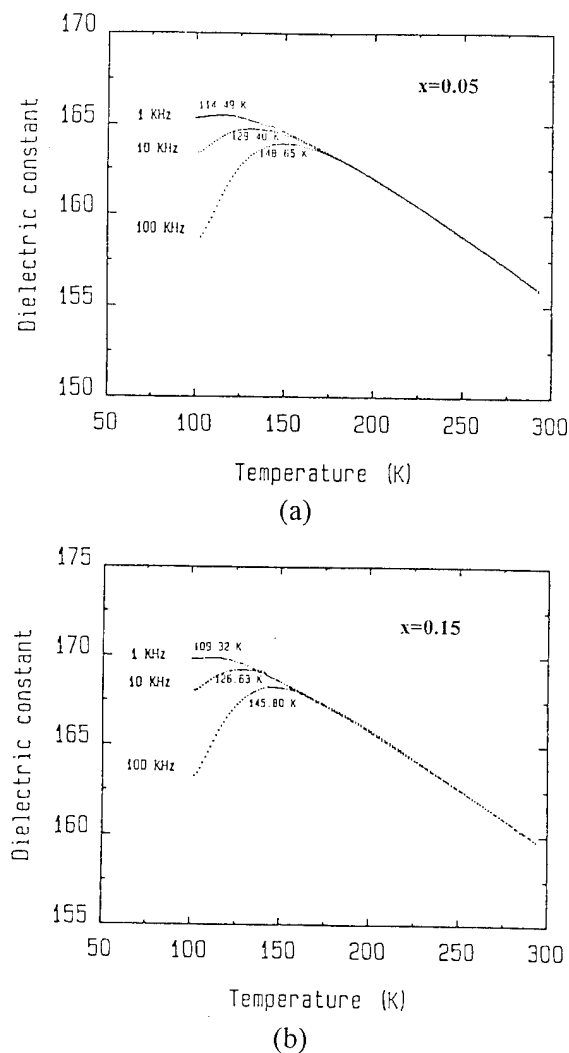


FIGURE 4 Temperature Dependences of Dielectric Constant for the Cubic Pyrochlore Solid Solutions:  $\text{Bi}_{1.5}\text{Zn}_{1-x}\text{Li}_x\text{Nb}_{1.5}\text{O}_{7-x}\text{F}_x$

#### CONCLUSIONS

For a series of fluoride additions, three distinct zones of phases can be divided into: single pyrochlore solid solutions, distorted pyrochlore with lower symmetry, and the mixes of the above two.

Low temperature dielectric anomaly is a common feature of cubic pyrochlores, the peak position of

# Dielectric Properties and Low Temperature Relaxation

## Studies of Doped TGS Single Crystals

B.M.Jin, S.Erdei and A.S.Bhalla

Materials Research Laboratory, The Pennsylvania State University,  
University Park, PA 16802, U.S.A.

**Abstract** - Several kinds of dopants (alanine,  $\text{LiVO}_3$  and valine) doped TGS were grown from solution by slow cooling method. Temperature dependence dielectric spectra were measured to study the variation of transition temperature,  $K_{\text{max}}$  and room temperature dielectric constant depending on the dopants. Furthermore, several pieces were selected to investigate the positional inhomogeneities of the same sample. D-E hysteresis loop measurements were done to check for the internal bias field ( $E_b$ ). We could not get a high figure of merit ( $p/K$ ) in valine doped TGS because of low temperature relaxation around  $-10^\circ\text{C}$ , although it has three times higher pyroelectric coefficient than that of alanine at transition temperature ( $T_C$ ).

### INTRODUCTION

Pure TGS was a good candidate for pyroelectric detector application. Nevertheless, this material has several disadvantages: First, because of low transition temperature ( $T_C = 49^\circ\text{C}$ ), there is a limitation in application temperature range. Second, aging effect after putting in room temperature for a long time or easy depolarization effect for heating it up to paraelectric phase, can hinder this material as a pyroelectric detector application, continuously. In order to overcome these disadvantages, many researchers have tried to maintain the irreversible polarization status inside the crystal - so called "internal bias field ( $E_b$ )". After discovering the fact that Glycine (I) is the main key of the ferroelectric transition, many researchers tried to maintain this site without altering external conditions like external electric field or thermal treatment below transition temperature[1-2]. One of the most

famous dopants to fulfill this requirement was alanine that has a chiral molecule which has an asymmetric structure. Alanine is a good material for preventing depolarization effect, but it is hard to grow a good optical quality crystal. Another trial was a doping of an inorganic material like Li, P or As etc [3-4]. They also get quite good results in improvement of high pyroelectric coefficient, low dielectric constant, high internal bias field and good quality crystal. There were very few reports that are related with the fact that all kinds of properties were improved by one kind of dopant.

In this paper, we are going to present a recent new trial for another kind of dopant -- valine: it has a same chiral molecule like a alanine but has a bigger molecule, so it is harder to incorporate into the glycine (I) site than alanine.

### EXPERIMENT

10 and 20 mole% alanine, 10% alanine + 10%  $\text{LiVO}_3$ , 10 and 20% valine doped TGS single crystals were grown by a slow cooling method in water solution. All these crystals were grown below transition temperature. 10% alanine doped and 10% alanine +  $\text{LiVO}_3$  doped crystal has a good quality without any kind of visible cracks. It is very difficult to grow the 20% alanine doped crystal bigger than 3 cm in diameter or without any defects, but it can get a high internal bias field. 10% and 20% valine doped TGS crystal was also grown. An interesting point is that in the case of valine doping in both percentages, we can grow a very high quality of single crystal without any kind of defect. Several sample plates were prepared from the same crystal but different parts along b-axis

in order to investigate the inhomogeneities of crystal. Before measurement, wet-cloth polishing was done to make a very smooth surface for electrodes. Relative dielectric constants were recorded during three continuous heating and cooling cycles to investigate the thermal hysteresis and thermal stability of the sample.

## RESULTS AND DISCUSSION

Fig.1 shows the relative real dielectric constant vs. temperature curves that indicates the variation of maximum dielectric constants depending on the kinds of impurities. 10% alanine doped crystal (marked as L10%) has a highest  $K_{\max}$ . By adding 10 mole% of  $\text{LiVO}_3$  to 10 mole% of alanine,  $K_{\max}$  can reduce 25% of previous  $K_{\max}$ . Quite a big decrease of  $K_{\max}$  was achieved by adding 20 mole% of alanine into pure TGS. 20% alanine doped crystal has a smaller dielectric constant at transition temperature and room temperature than any other impurity contents, but it is harder to grow optical quality and a large crystal without any kinds of defects. 10% alanine doped TGS does not have any kind of positional inhomogeneity throughout the whole crystal, but 20% alanine doped TGS has a positional inhomogeneity as shown in this figure (T1H, T2H and T3H data). Thermal hysteresis of 20% alanine doped TGS data were shown in Fig.2. T1 and T3 have

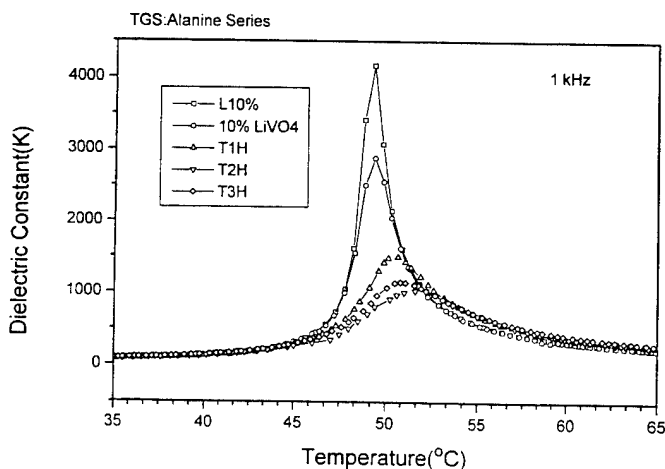


FIGURE 1. Relative dielectric constant vs. temperature of different amount of alanine contents. (L10%: alanine 10%, 10%  $\text{LiVO}_3$ : 10% alanine + 10%  $\text{LiVO}_3$  and T1H, T2H, T3H: 20% alanine doped but different positions in same crystal)

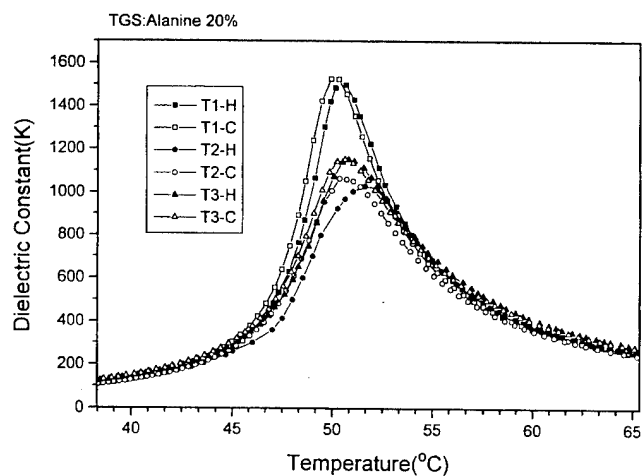


FIGURE 2. Thermal hysteresis of 20% alanine doped TGS crystals. T1, T2 and T3 indicate the distance from the seed position along b-axis in 1 cm apart, respectively (see text for more information).

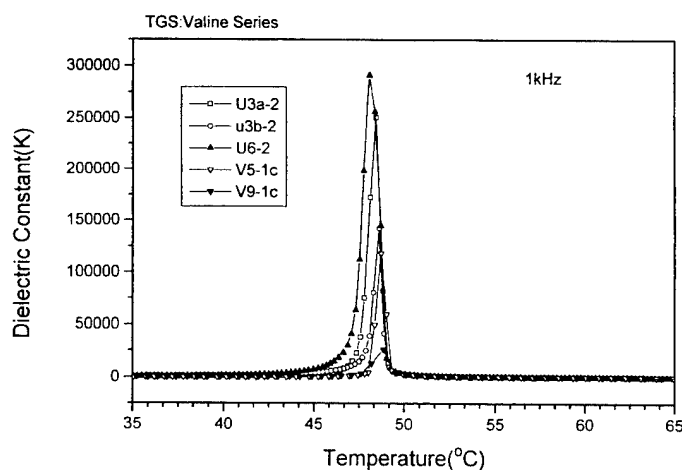


FIGURE 3. Thermal instabilities of valine doped TGS crystals. U's indicate 10% valine and V's for 20% valine doped TGS. 10% valine doped TGS has a larger dispersion than 20% valine.

negligible amount of hysteresis, but T2 has a bigger thermal hysteresis. T2 is in the nearest position from the seed, and T1 and T3 are in opposite positions from each other toward the outside from the seed. This hysteresis indicates not a first order phase transition characteristic but a thermal instability of that sample. Therefore, in TGS closer to the seed has a more unstable state than those of outside. 10% alanine doped shows no kind of that instability. This means that small amounts of impurity do not make any kind of inhomogeneity inside the crystal.

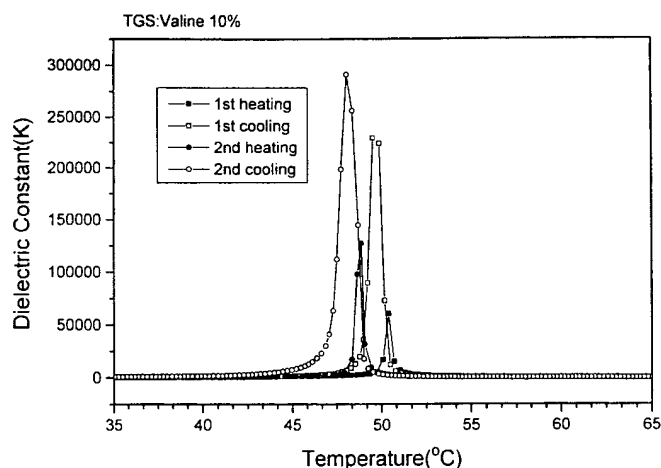


FIGURE 4. Thermal instabilities of successive heating and cooling runs for 10% valine doped TGS. This instability reduced in 20% valine doped TGS.

Fig.3 shows the dielectric constant vs. temperature of another kind of dopant - 10% and 20% valine doped TGS crystals. U's indicates 10% valine and V's for 20% valine at every different position. U3a and U3b are upper and lower sections of the same b-plate, and U6 is in the opposite side of U3's. V5 is the nearer position from seed than V9. 10% valine has too high  $K_{max}$  and a very sharp phase transition just vicinity of transition temperature. The  $K_{max}$  is significantly reduced at 20 mole% valine concentration. 10% valine doped TGS crystal was grown well without any kind of defect but has a very weak internal bias field (see Fig.5) and very big thermal instability (see Fig.4). During the three continuous heating and cooling cycles, magnitudes of  $K_{max}$  and  $T_C$  also changed, remarkably. The interesting thing is that 20% valine doped TGS has a smaller instability and larger internal bias field than 10% valine, although this is not shown in this paper. P-E hysteresis loop measurement, shown in Fig.5, indicated that alanine has the largest internal bias field ( $E_b=5\text{kV/cm}$ ) among the measured samples. Valine doped TGS has a very small  $E_b$  indicating that the ratio of doping is very small. One more interesting thing is that valine doped TGS has a big anomaly in dielectric constant around  $-10^\circ\text{C}$ , as shown in Fig.6. Because of this big anomaly, dielectric constant (K) at room temperature is too high and could not get a high figure of merit (p/K) when we measured it with the pyroelectric coefficient[5]. This anomaly decreases as the oscillating frequency increases and could not be observed at 100 kHz,

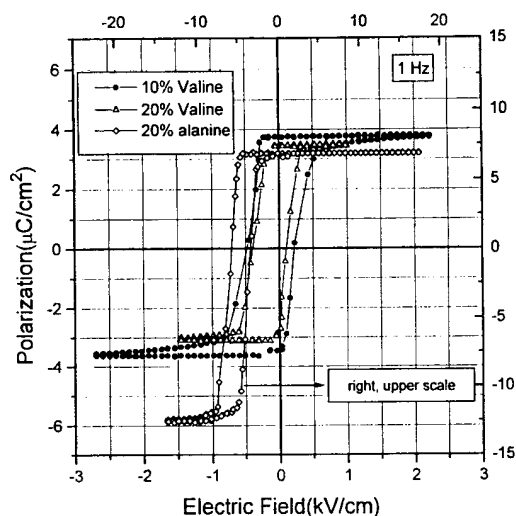


FIGURE 5. P-E hysteresis loop for alanine and valine doped TGS crystals. Alanine has a biggest internal bias field ( $E_b = 5\text{ kV/cm}$ ) among the measured samples. Alanine doped TGS has not only an internal bias field in field axis but also has a shift to lower polarization axis - it is not clear yet.

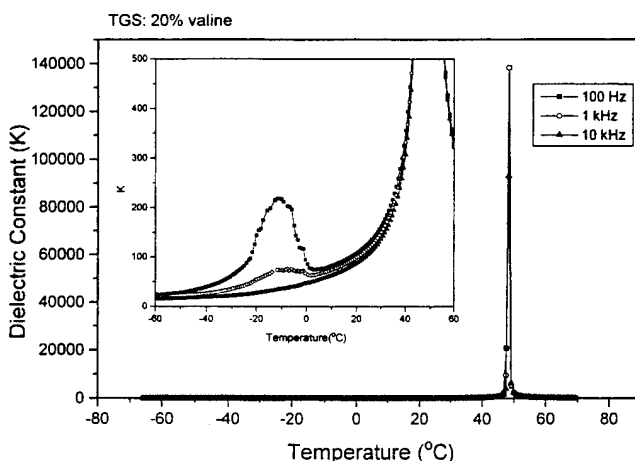


FIGURE 6. Low temperature dielectric constant measurement showing relaxational behavior at  $-10^\circ\text{C}$ . The effect of this relaxation goes up to room temperature causing a high dielectric constant at room temperature.

which means that it is not related to the phase transition but a relaxational mechanism. At this moment, it is not clear what kind of mechanism is included to generate this relaxation. After measuring the dielectric spectra in frequency domain, it will be more clearly understandable and this procedure is now in progress.

## CONCLUSION

Dielectric constant and P-E hysteresis measurements were done in several kinds of dopants doped TGS single crystals. Alanine can generate the largest internal bias field but it is hard to grow good quality and large size. Valine has been tried to test the effect of glycine (I) substitution effect instead of alanine. Valine has a bigger molecule than alanine, so it is hard to incorporate into crystal. The experimental results also show this expectation, but valine has two different and interesting properties. First, 10% valine has a very small internal bias field indicating small real substitution. 20% valine case,  $E_b$  is increased, but still retains a good quality of crystal without any defect. Second, there was big relaxation at  $-10^\circ\text{C}$ , which is causing the increase of room temperature dielectric constant. We could not observe this relaxation in alanine doped TGS, but every valine doped TGS has this relaxation and this study is in progress.

## REFERENCES

- [1] R.B.Lal and A.K.Batra, *Ferroelectrics*, vol.142, pp.51, 1993
- [2] E.T.Keve et al., *Ferroelectrics*, vol.3, pp.39, 1971
- [3] A.S.Bhalla, C.S.Fang, L.E.Cross and Y.Xi, *Ferroelectrics*, vol.54, pp.151, 1984
- [4] C.S.Fang, X. Yao, A.S.Bhalla and L.E.Cross, *Ferroelectrics*, vol.51, pp.9, 1983
- [5] B.M.Jin, S.Erdei, A.S.Bhalla, "Pyroelectric measurements on various kinds doped TGS Crystals" in Proceeding on the ISAF-9, 1994



# NON-LINEAR DIELECTRIC PROPERTIES OF $\text{KTa}_{1-x}\text{Nb}_x\text{O}_3$

R.K. PATTNAIK, and J. TOULOUSE  
Physics Department, Lehigh University  
16 Memorial Dr. East, Bethlehem, PA 18015,US

## ABSTRACT

We report measurements of the non-linear dielectric constant in the mixed crystal  $\text{KTa}_{1-x}\text{Nb}_x\text{O}_3$  with  $x = 15.7\%$  and  $1.2\%$ . For both concentrations the dielectric peak is observed to decrease with increasing field and to shift towards higher temperature. The dispersion  $\epsilon'(\omega)$ , is also suppressed by the field. On the framework of Landau theory, we fit  $\epsilon'(E)$  with an expansion in a power series of the applied dc field  $E$ .  $\epsilon^{(2)}$  is seen to exhibit two distinct temperature dependencies. At high temperatures, it scales as  $(T-T_c)^{-\gamma}$  where  $\gamma$  is found to be in fair agreement with Landau theory for low concentrations. At lower temperatures it then crosses over to a much weaker dependence. This crossover is interpreted as a transition from a weakly correlated (dynamic) regime to a strongly correlated (quasistatic) regime of polar clusters. The non-analyticity due to these polar clusters is discussed.

## INTRODUCTION

Mixed ferroelectrics have been a topic of interest for many groups because of their anomalous electrical<sup>1</sup> (dielectric, polarization) and mechanical<sup>2</sup> (elastic) properties and for its possible use in information storage, in non-linear optics etc. Non-linear characteristics of these materials are of importance and interest from both a theoretical and a practical point of view. We report here measurements of non-linear dielectric constant in the mixed crystal  $\text{KTa}_{1-x}\text{Nb}_x\text{O}_3$  with  $x = 15.7\%$  and  $1.2\%$ . The dc fields upto  $2.0 \text{ kV/cm}$  (for the  $15.7\%$ ) and  $400 \text{ V/cm}$  (for the  $1.2\%$ ) were applied. We summarize the results and discuss the

non-linearity on the framework of Landau theory. We show that the system has a cross over from dynamic to static regime of interaction. Finally we discuss the deviation of Curie-Weiss like response of  $\epsilon'(T)$  and the role of polar clusters in mixed ferroelectrics in the cross over and the non-analytic behavior pointed out earlier by Lyons<sup>3</sup>.

## SAMPLES, AND OUTLINE OF EXPERIMENT

Samples under study were  $15.178 \text{ mm}^2 \times .712 \text{ mm}$  KTN-15.7% and  $39.168 \text{ mm}^2 \times .88 \text{ mm}$  KTN-1.2%, with [100] direction being normal to the surface. Both samples were Aluminum coated (covering the entire face) by evaporation. Capacitance as a function of frequency (100 Hz to 2 MHz) was measured in the FC environment with HP-4194A Impedance/Gain phase Analyzer.

## RESULTS

- The dielectric constant (in the 15.7% sample) in the temperature region above  $162^\circ\text{K}$  exhibits Curie-Weiss like dependence. At lower temperatures it deviates (fig. 1).
- In KTN-15.7% upto  $170^\circ\text{K}$ , the dielectric constant is little influenced by the bias field (fig. 1).
- The transition (cubic to tetragonal) occurs at higher temperatures as the bias field is increased (fig. 1).
- The dc bias suppresses the dielectric constant and the peak broadens with increasing field (fig. 1).

- The other transitions (to lower symmetry) are smeared out as the field is increased (fig. 1).
- The frequency dependence of the dielectric constant is weakened (fig. 1).

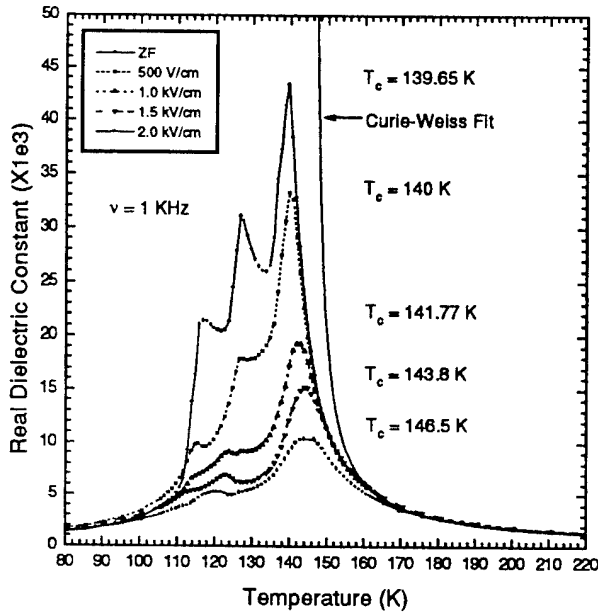


Fig.1: KTN15.7% sample  $\epsilon'(E)$  Vs. Temp. along with Curie-Weiss fit to the ZF measurement.  $T_c$  obtained from the fit is  $145.4^\circ\text{K}$ .

Similar results were obtained for the KTN-1.2% sample.

### ANALYSIS

Following the framework of Landau Model:

$$\epsilon(E) = \epsilon_0 + \epsilon_2 E^2 + \epsilon_4 E^4 + \dots$$

In order to determine the second order term,  $\epsilon_2$ , usually one:

- Fits the data with the above equation retaining only the first non-linear term,  $\epsilon_2$
- Obtains the temperature dependence,  $\epsilon \propto (T - T_c)^\gamma$

### RESULTS OF ANALYSIS:

- $\epsilon_2$  scales with temperature as  $(T - T_c)^\gamma$ ,  $T_c$  being the ZF transition temperature.

- For KTN-15.7% sample at high temperatures,  $\gamma \sim -5$  while near the transition, it slows down to  $\sim -2$  (fig. 2)
- For KTN-1.2% sample,  $\gamma \sim -4.4$  in the high temperature regime.

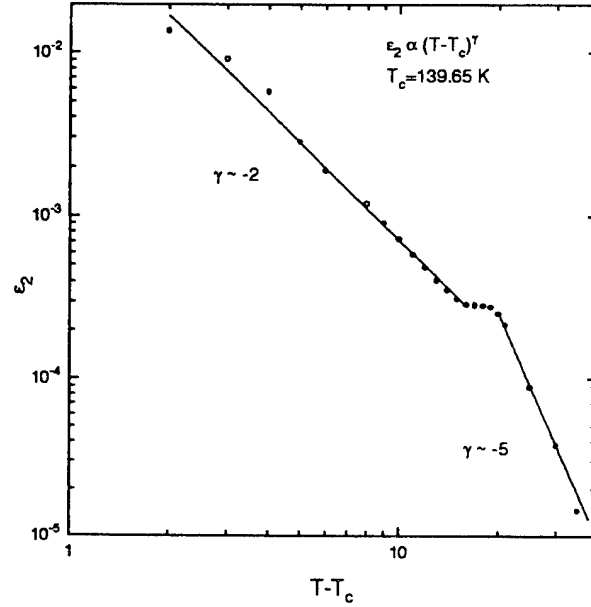


Fig.2:  $\epsilon_2$  Vs.  $(T - T_c)$  for the KTN-15.7% sample on a log-log plot

### DISCUSSION

Following Landau analysis we have obtained the second order non-linear dielectric constant  $\epsilon_2$ . It shows two regimes of temperature dependence. Starting from the high temperature regime with a stronger non-linearity it crosses over to a weaker non-linear state. To explain this we note that the *Nb* occupying an off center position, creates a dipole field around the defective unit cell. As a consequence a polar cluster is formed around each of these *Nb* sites with a correlation radius depending on the temperature. At high temperatures the *Nb* has sufficient thermal energy to hop between the 8 equivalent sites along the cube diagonals. In this temperature regime the dielectric response can be described adequately following Landau theory as evidenced by the later's Curie-Weiss like behavior. As the temperature is lowered the hopping slows down, and the correlation radius grows developing polar clusters. The polar clusters begin to respond as a single (giant) unit cell and the

dipole units inside the cluster are strongly correlated. As a result, the dielectric response slows down and crosses over to a static regime deviating from the Curie-Weiss like dependence. Although Landau theory predicts a weaker non-linearity in this temperature range, the explicit dependence of  $\epsilon'$  on temperature need to be analyzed with the polar clusters taken into account. In this regime the dielectric and polarization characteristics are influenced by the orientation of the polar clusters and the interaction between them. As a consequence the system can develop non-analytic nature as reported by Lyons<sup>3</sup>.

Our future work would involve efforts to understand the anomaly in more detail.

### REFERENCES

1. J. Toulouse, X. M. Wang, L.A. Knauss and L. A. Boatner, Phys. Rev. **B43**, 8297 (1991)
2. X. M. Wang, J. Toulouse and L. A. Boatner, Ferroelectrics **112**, 225 (1990)
3. K. B. Lyons, P. A. Fleury, T. J. Negran, and H. L. Crater, Phys. Rev. **B36**, 2465 (1987)

# Dielectric Permittivity in Paraelectric/Ferroelectric Coexistence Region in Several Proton Glasses

F. L. Howell, I. L. Fundaun, S. Stadler  
Dept. of Physics  
University of North Dakota, Grand Forks, ND 58202

S. C. Meschia, C. S. Tu, V. H. Schmidt  
Dept. of Physics  
Montana State University, Bozeman, MT 59717

**Abstract** We present results for the complex permittivities of several proton glasses of the form  $M_{1-x}(NZ_4)_xZ_2AO_4$ , where  $M=Rb$ ,  $Z=H$  or  $D$ , and  $A=As$  or  $P$ . All measurements were made perpendicular to the ferroelectric axis, so no effects of domain wall motion occurred. Phase coexistence was apparent in all species. The phosphate glasses exhibited a much narrower coexistence composition range than the arsenate glasses.

## I. INTRODUCTION

$RbH_2PO_4$  and corresponding potassium, cesium and arsenate compounds are ferroelectric, whereas  $NH_4H_2PO_4$  (ADP) and  $NH_4H_2AsO_4$  (ADA) are antiferroelectric. Mixed crystals of various concentrations of the ferroelectric and antiferroelectric components can be grown. Over a range of concentrations the response of these crystals is frustrated and no phase transition is exhibited. However, a range exists where either ferroelectric or antiferroelectric components can coexist with other dielectric phases. These crystals are, in many respects, the electrical analogs of magnetic "spin glasses," with pseudospin representing the two off-center hydrogen positions in the hydrogen bond. Unlike spin glasses and structural glasses, however, proton glasses possess random dc bias "fields" acting on these hydrogens. In proton glasses, there exists an ergodic limit below which the response to an external electric field exhibits thermal hysteresis [1].

Dielectric responses seen in these glasses are frequently modeled by lumped circuit elements or by multiple barriers. In any multiple barrier theory the height of at least some of the potential energy barriers must be posited to be as large as the thermal energy where the onset of nonlinearity occurs [2].

## II. EXPERIMENTAL PROCEDURE

Two types of capacitance measurement devices were used in the data collection process. The General Radio Precision Measurement Bridge is a manual bridge that was used for c-axis measurements and the low temperature b-axis measurements. A digital bridge, Model 6425 Wayne-Kerr Component Analyzer, was employed for confirmation of b-axis measurements and measurement of the deuterated crystals. The General Radio Model consisted of a GR 1616 Precision Capacitance Bridge and a GR 1621 Capacitance Measurement System, consisting of a GR 1316 Oscillator and a GR 1238 Detector. After warm-up the accuracy is within  $\pm 1$  percent. Measurements were taken by balancing the in-phase and quadrature readings on the detector.

The ratio arms of the capacitance bridge are transformer windings. Fixed-capacitance standards are used whose values range in decade steps from 1 aF to 100 nF. Loss in the measured capacitor is expressed as parallel conductance from the resolution limit of 0.1 f $\Omega$  to a maximum of 1 m $\Omega$ . The values of the set of five conductance standards are effectively extended by a series of resistance standards covering six decades. The Wayne-Kerr component analyzer has a direct readout of the sample capacitance and conductance and can be controlled by a computer via a general

purpose interface bus (GPIB/HPIB).

All samples were cooled slowly in liquid nitrogen to 77 K. They were then allowed to warm slowly to room temperature. Data were taken during the warming process. A thermocouple was embedded in teflon that fit tightly within a copper cylinder which was suspended less than 1 mm from the sample. The lower stem of the probe was wound with resistive wire and covered with a layer of plaster. A temperature controller regulated the amount of current flowing through the resistive wire. The sample probe was placed into a dewar and the lower portion covered with sand. Then the dewar was sealed with tape and styrofoam.

Measurements below 77 K were taken in a Princeton Applied Research Model 157 liquid helium cryostat. The rate of helium flow was controlled manually and temperature readings were taken with two LakeShore sensors: a CGR-2 carbon glass resistor and DT-500 diode. The CGR-2 was calibrated using superconducting transitions of various elements: lead, antimony, niobium and indium. The low-temperature probe held the sample by means of spring-loaded leads that "sandwiched" the sample into a position proximal to the heater and temperature measurement component.

## III. RESULTS AND DISCUSSION

Two crystals of  $Rb_{1-x}(NH_4)_xH_2PO_4$  (RADP) were grown in order to determine the shape of the phase diagram at low concentrations of ammonium. The concentrations of ammonium in the crystals,  $x=0.08$  and  $x=0.16$ , were assumed to resemble those of the solutions from which they were grown since (1) phase diagram results obtained using these concentrations agree qualitatively with previous results and (2) credible chemical analysis could not be obtained. The phase boundaries between ferroelectric (FE), paraelectric (PE), proton glass (PG) and the coexistent phases (F-P and F-G) are mapped in Fig. 1 as a function of temperature and concentration of ammonium  $x$  in the mixed crystals. This is the first report of coexistence of the ferroelectric phase with the paraelectric/proton glass phase in RADP. In an  $x=0.75$  crystal, a plateau preceded and followed by abrupt decreases in the derivative of the real part of the permittivity with decreasing temperature, together with the onset of dispersion in the imaginary part of the permittivity at the occurrence of the lower-temperature change in the derivative of the real part of the permittivity [4], indicate the existence of an antiferroelectric-proton glass coexistence region, although the authors at that time interpreted these phenomena as "reentrant behavior".

Dielectric measurements were made along the c (ferroelectric) and b axes of the undeuterated crystals. The real part of the dielectric permittivity very closely follows a Curie-Weiss behavior  $\epsilon' = C/(T - T_0) + \epsilon_1$  above the temperature  $T_C$  where ferroelectric behavior begins to occur, but differs substantially below  $T_C$ . Here  $\epsilon_1$  is the residual permittivity from the electronic and fast ionic response. The free parameters  $C$  and  $T_0$ , obtained for rubidium dihydrogen phosphate (RDP), were within one percent of the published values [5]. The mixed crystal

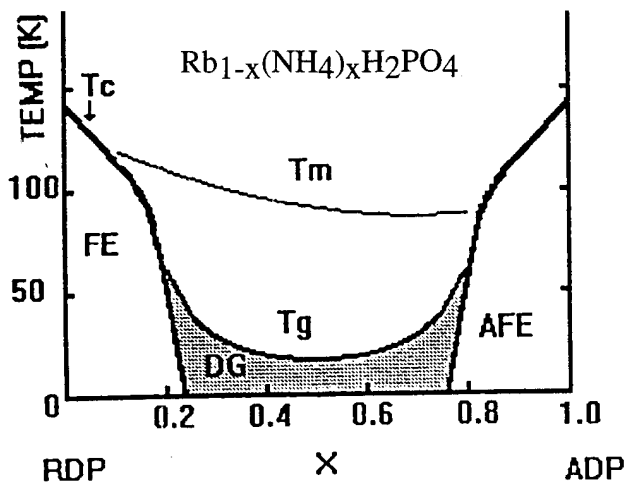


Fig. 1. Phase diagram for  $\text{Rb}_{1-x}(\text{NH}_4)_x\text{H}_2\text{PO}_4$  [3]. FE represents the ferroelectric phase, AFE represents the antiferroelectric phase and DG represents the proton/dipole glass phase. The mixed crystal exhibits complete Curie-Weiss behavior above  $T_m$ .

with sixteen percent ammonium substituted for rubidium (RADP  $x=0.16$ ) yielded a Curie-Weiss parameter  $T_0$  equal to 90.4 K and a Curie constant  $C$  of 5537 K. The RADP crystal having eight percent ammonium yielded a  $T_0$  of 117 K and a Curie constant of 3203 K. Knowing that the transitions in this region are ferroelectric, the results from the dielectric measurements could be added to those of previously published phase diagrams of concentration versus temperature [6]. The results so obtained agree qualitatively with the published phase diagrams.

Deuterated crystals were also grown from solutions with ammonium concentrations of 18 and 24 percent. As before, the concentration of ammonium in the crystal was assumed to be the same as that in the solution. The temperatures corresponding to the peaks in the imaginary part of the complex relative dielectric constant were assumed to follow a purely Arrhenius Law. By fitting to an Arrhenius behavior, an activation energy of 131 meV is obtained for deuterated RADP (d-RADP). By contrast the activation energy of the undeuterated crystal RADP ( $x=0.16$ ) is only 4.14 meV [7]. Phase data for d-RADP were obtained as before and added to previously published phase diagrams as shown in Fig. 2.

In addition, a crystal of RADA of 0.01 ammonium concentration was grown. The phase diagram containing this data point is shown in Fig. 3 for comparison with the phase diagrams of the related phosphate crystals. Note, however, that there is recent evidence from nuclear quadrupole resonance that the ferroelectric-paraelectric coexistence region extends as low as  $x=0.01$ , not 0.04 as shown in Fig. 3 [8].

#### IV. CONCLUSION

This study continues research into the disordered phase in  $\text{Rb}_{1-x}(\text{NH}_4)_x\text{H}_2\text{PO}_4$  (RADP). A ferroelectric transition and glassy freezing were observed in the RADP  $x=0.16$  crystal at 90.5 K and 20 K, respectively. A coexistence region occurs for RADP and from this it is suggested that the phase diagram for RADP should be modified to include a coexistence region from  $x=0.22$  to  $x=0.16$ . This modified phase diagram resembles the phase diagrams for deuterated RADP (d-RADP) and RADA.

The activation energy for RADP  $x=0.16$  was anomalously low compared to those of d-RADP  $x=0.18$  and RADA  $x=0.10$ . In addition, the real part of the residual dielectric permittivity of this sample is anomalously large at 2 K and continues to decrease with decreasing temperature [9]. Both of these anomalies may be associated with phonon-assisted tunneling [10].

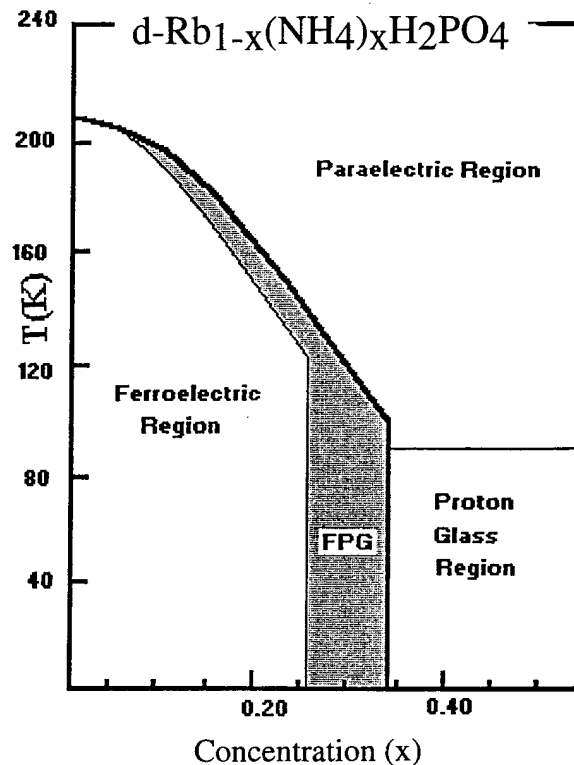


Fig. 2. Phase boundaries for  $\text{Rb}_{1-x}(\text{ND}_4)_x\text{D}_2\text{PO}_4$  ( $D=\text{deuterium}$ ) in the temperature-ammonium concentration plane. FPG represents a region of mixed ferroelectric and proton glass phases.

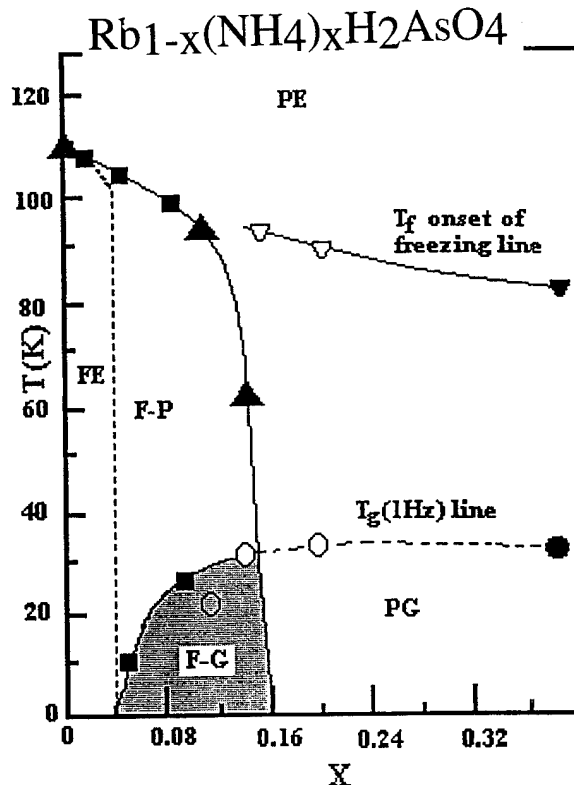


Fig. 3. Phase boundaries of  $\text{Rb}_{1-x}(\text{NH}_4)_x\text{H}_2\text{AsO}_4$  in the temperature-ammonium concentration plane. FE denotes the ferroelectric region, PE denotes the paraelectric region, F-P denotes the mixed ferroelectric and paraelectric region, F-G denotes the mixed ferroelectric and proton glass region and PG denotes the proton glass region.

# ACKNOWLEDGEMENTS

This work was support by National Science Foundation Grant DMR-9017429.

## REFERENCES

- [1] N. J. Pinto, K. Ravindran and V. H. Schmidt, "Field-heated, field-cooled, and zero-field-heated static permittivity of the deuteron glass  $\text{Rb}_{1-x}(\text{ND}_4)_x\text{D}_2\text{AsO}_4$ ," *Phys. Rev. B*, vol. 48, pp. 3090-3094, August 1993.
- [2] A. K. Jonscher, *Dielectric Relaxation in Solids*. London: Chelsea Dielectrics Press, 1983, ch. 5, p. 234.
- [3] Shane Stadler, *The Dielectric Properties of the Proton Glass  $\text{Rb}_{1-x}(\text{NH}_4)_x\text{H}_2\text{PO}_4$* . M. S. Thesis, University of North Dakota, 1992, p. 46.
- [4] M. Takashige, H. Teruchi, Y. Miura and S. Hoshino, "A Re-Entrant Glasslike Phase in  $\text{Rb}_{1-x}(\text{NH}_4)_x\text{H}_2\text{PO}_4$ ," *Jour. Phys. Soc. Japan*, vol. 54, pp. 3250-3253, 1985.
- [5] A.A. Volkov, G. V. Kozlov, S.P. Lebedev, A.V. Sinitski, S. Kamba, and J. Petzelt, "Soft Modes in RADP Glass," *Soviet Phys. JETP*, vol. 74, pp. 133-136, 1992.
- [6] Ref. [3], p. 36.
- [7] Ref. [3], pp. 47-49.
- [8] G. Papantopoulos, G. Papavassiliou, F. Milia, V. H. Schmidt, J. E. Drumheller, N. J. Pinto, R. Blinc and B. Zalar, " $^{75}\text{As}$  Nuclear Quadrupole Resonance in Weakly Substitutionally Disordered  $\text{Rb}_{1-x}(\text{NH}_4)_x\text{H}_2\text{AsO}_4$ ," *Phys. Rev. Lett.*, vol. 73, pp. 276-279, July 1994.
- [9] Ref. [3], p. 52.
- [10] A. Heuer and R. J. Silbey, "Tunneling in real structural glasses: a universal theory," *Phys. Rev. B*, vol. 49, pp. 1441-1444, January 1994.

Poster Session -  
P3MD/S: Microwave  
Dielectrics

# Effect of Perovskite Impurity Addition on Microwave Dielectric Properties of $Ba(Mg_{1/3}Ta_{2/3})O_3$ - $Ba(Ni_{1/3}Ta_{2/3})O_3$ Ceramics

Shin-Young Kim, Hee Young Lee, Cheul-Kee Yang, Jeong-Joo Kim\*,  
Tae Hong Kim\*\*, Tae Goo Choy\*\*

Department of Materials Science and Engineering ,  
Yeungnam University, Kyongsan, 712-749, Korea

\*Department of Inorganic Materials Engineering, Kyungpook  
National University, Taegu, 702-701, Korea

\*\* Electronics and Telecommunication Research Institute,  
Daejeon, 302-350, Korea

**Abstract** – Microwave dielectric properties in the system  $Ba(Mg_{1-x/3}Ni_{x/3}Ta_{2/3})O_3 - yBaZrO_3$  or  $Ba(Mg_{1-x/3}Ni_{x/3}Ta_{2/3})O_3 - zBaSnO_3$  were investigated with an emphasis on the sintering behavior, phase relations and microstructure-property relationships. The increase of  $Q$  value of 13000 at 6 GHz while achieving zero  $\tau_f$  occurred when  $y = 0.05$ . The addition of excess  $MgO$  had a detrimental effect on  $Q$  value improvement, which is attributable to the segregation of excess  $MgO$  along grain boundaries. The appearance of  $Ba_{1/2}TaO_3$  second phase would have negative effect on the improvement of  $Q$  value. Therefore, the fabrication of ceramics without any second phase should be crucial in obtaining improved microwave performance.

## INTRODUCTION

Single phase  $Ba(Mg_{1/3}Ta_{2/3})O_3$  (BMT) ceramic is known to have the highest quality factor ( $Q$ ) value among the microwave dielectric ceramics studied to date [1-4]. The material in this system is thus an excellent candidate for microwave communication system such as satellite communication. It is known that the phase transformation from disordered cubic to ordered hexagonal structure by means of proper heat treatment is essential to achieve high  $Q$  values. In addition, the precise control of defects such as grain boundary, pore, precipitate is considered to be important.

Recently, we have studied  $Ba(Mg_{1/3}Ta_{2/3})O_3 - Ba(Ni_{1/3}Ta_{2/3})O_3$  (BMT-BNT) system and found out that zero temperature coefficient of resonance frequency ( $\tau_f$ ) could be realized without impairing  $Q$  value much [5]. Since  $BaZrO_3$  (BZ) and  $BaSnO_3$  (BS) have the same perovskite structure with BMT - BNT and B-site ordering may be an important factor in achieving high  $Q$  values, we have performed research on the effect of the perovskite impurity

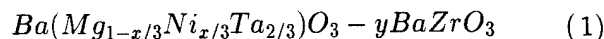
addition in BMT - BNT system.

In this paper, the effect of BZ or BS addition on phase relation, relative permittivity,  $Q$  and  $\tau_f$  is presented. Effect of second phase formation or stoichiometry on microwave dielectric properties will also be discussed.

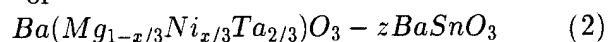
## EXPERIMENTAL PROCEDURE

Disk or cylinder-type samples were prepared by conventional mixed oxide process using  $BaCO_3$ ,  $MgO$ ,  $NiO$ ,  $Ta_2O_5$ ,  $ZrO_2$ ,  $SnO_2$  powders of high purity (better than 99.9%).

The general formula investigated in this study is written as



or



where  $x = 0.3$  and  $y, z = 0 - 0.15$ . From the result of the previous investigation on  $Ba(Mg_{1-x/3}Ni_{x/3}Ta_{2/3})O_3$  binary system [5],  $x$  value was fixed to 0.3 since  $\tau_f$  became approximately equal to zero when  $x = 0.25 - 0.30$  without impairing  $Q$  much.

Powder mixture, weighed according to the above formula, was mixed and calcined at 1350°C for four hours. Sintering of isostatically pressed pellets was carried out in air at 1600°C for 10 hours. Relative density of sintered samples was measured by immersion technique. Structural and compositional analyses were made by X-ray diffraction (XRD) technique. Lattice constant and the degree of ordering were determined from XRD patterns of specimen powders obtained from sintered samples. Microstructure of sintered samples was examined using a scanning electron microscope. The degree of ordering was calculated by comparing the relative intensity of (100) superlattice reflection peak



to that of (110, 102) peak. Microwave dielectric properties of cylinder-type samples were determined by measuring resonance frequency of  $TE_{011}$  mode using both post-resonator method and open cavity resonator method. The former was used for relative permittivity ( $K'$ ) measurement, while the latter was used for  $Q$  and  $\tau_f$  measurements. The temperature range of 25 - 100°C was used for  $\tau_f$  measurement. HP8510C network analyzer was utilized for the measurements of microwave properties in the range of 5 to 10 GHz.

## RESULTS AND DISCUSSION

### Sintering Characteristics

Scanning electron micrograph of sintered surface of  $Ba(Mg_{1/3}Ta_{2/3})O_3$  (BMT) ceramic with nominal stoichiometric composition was shown in Fig. 1. It is seen that there existed discrete second phase particles distinguishable from continuous matrix phase. According to the XRD pattern of the same sample shown in Fig. 2, the compositions of matrix and discrete phases were determined as BMT and  $Ba_{1/2}TaO_3$  (BT), respectively. The latter is

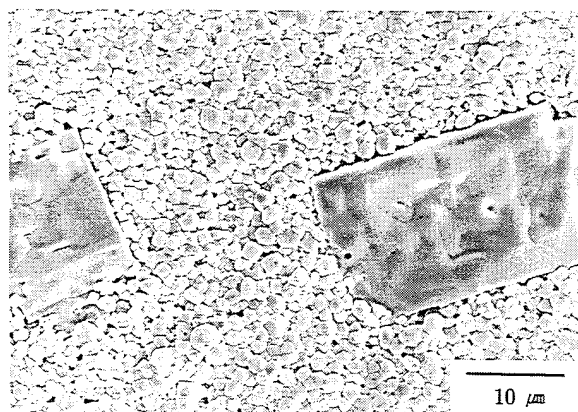


Fig. 1 Scanning electron micrograph of sintered surface of nominally stoichiometric BMT ceramic.

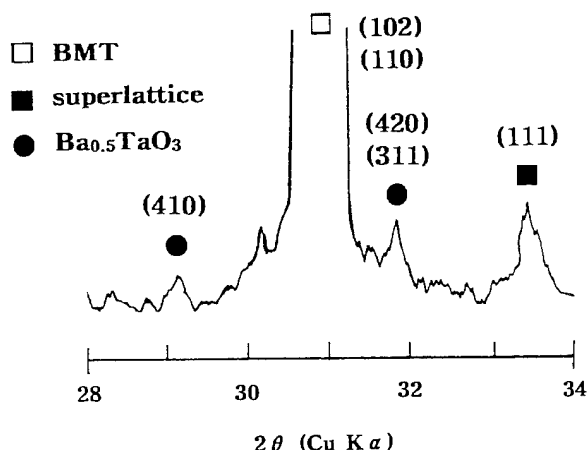


Fig. 2 XRD pattern of BMT ceramic sintered at 1600°C.

expected to degrade microwave dielectric properties, which will be discussed in detail. The same interpretation of microstructure was obtained by EDAX analysis [6]. In addition, similar phenomenon was reported by Kawashima in  $Ba(Zn_{1/3}Ta_{2/3})O_3$  (BZT) [7], where the evaporation of ZnO during sintering caused Zn deficiency and hence the second phase formation. Therefore, the unexpected appearance of second phase particles in BMT could also be attributed to the volatility of MgO at high temperatures, although it would be much less than that of ZnO. The very same event also occurred in  $Ba(Ni_{1/3}Ta_{2/3})O_3$  (BNT) ceramic. Since NiO has a lower melting temperature than MgO, NiO evaporation is expected to be more active. However, if excess MgO is added into the BMT powder mixture ( $BM + T$ ), the harmful BT phase can be eliminated. This is evident in Table 1 where the relative intensity of (420) reflection of BT phase is compared among the ceramics mentioned above.

Table 1. Relative intensity of (420) reflection of BT phase to (102) reflection of perovskite phase of perovskites.

Nominal composition	$Ba(Mg_{1/3}Ta_{2/3})O_3$	$Ba(Mg_{1/3}Ta_{2/3})O_3 + 6\% \text{ MgO}$	$Ba(Ni_{1/3}Ta_{2/3})O_3$
$I(420)/I(102) \times 100(\%)$	1.3	0	4.1

Sintered density of  $0.7Ba(Mg_{1/3}Ta_{2/3})O_3 - 0.3Ba(Ni_{1/3}Ta_{2/3})O_3$  (BMNT) ceramic as a function of the amount of  $BaZrO_3$  (BZ) or  $BaSnO_3$  (BS) impurity was illustrated in Fig. 3. It was found that the density usually decreased with impurity addition, except for the case when BZ was added to  $BM + T$ .

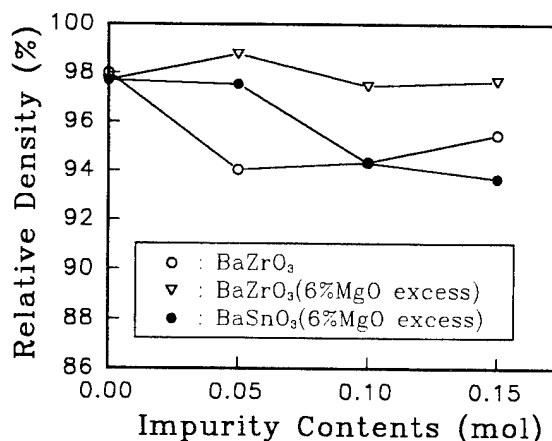


Fig. 3 Sintered density versus impurity content in BMNT.

Scanning electron micrographs of BMNT ceramics were shown in Fig. 4. It is seen that samples with excess MgO in starting powder

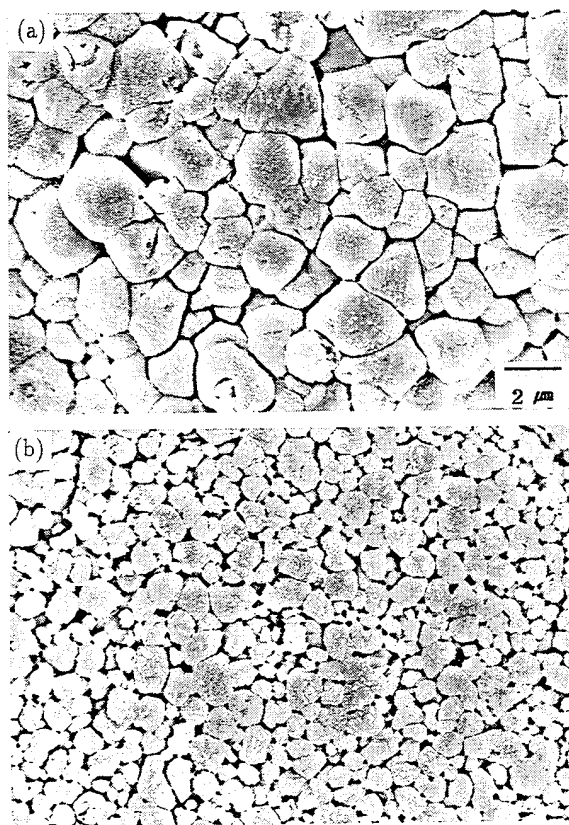


Fig. 4 Scanning electron micrographs of polished and etched surfaces of *BMNT* ceramic.  
(a) nominally stoichiometric (b) 6% *MgO* excess

resulted in the finer microstructure. This could be due to the segregation of *MgO* along grain boundaries [8]. Since the lattice constants of pseudocubic *BMNT*, *BS* and *BZ* ceramics are 0.4076, 0.4116, and 0.4180 nm, respectively, and since they crystallize in the same perovskite structure, it is expected that both *BMNT-BZ* and *BMNT-BS* system crystallize in perovskite. When the ionic radii of *B*-site ions were compared, *Zr* ion has the highest value, so that when it substitutes some of host *Mg*, *Ni* or *Ta* ions, the lattice would expand accordingly. The ionic radii of *Mg*, *Ni*, *Ta*, *Sn*, and *Zr* ions are 0.071, 0.070, 0.065, 0.070, and 0.073 nm, respectively. In addition, when *Zr* ion was substituted, due to relatively large difference in ionic sizes, the reduction of *B*-site ordering would be smaller than the case of *Sn* ion substitution.

Experimental results in support of this interpretation were exhibited in Fig. 5, where the lattice constant and degree of ordering for *BMNT-BZ* and *BMNT-BS* ceramics were plotted. It is apparent that the lattice constant linearly increased with *BZ* addition whereas it hardly changed with *BS* addition. The degree of ordering decreased in both cases, but some ordering remained in case of

*BZ* addition as explained above.

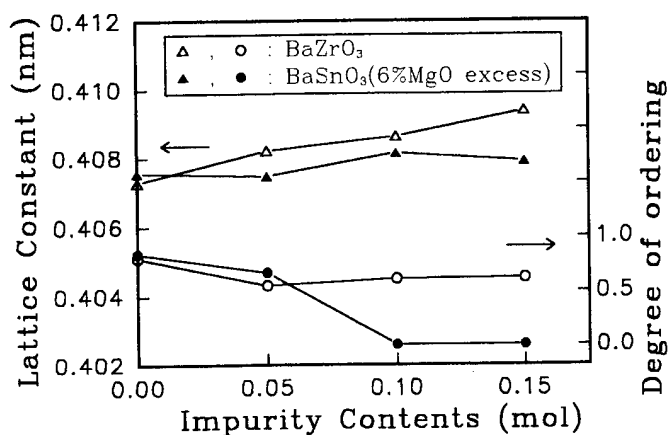


Fig. 5 Lattice constant and ordering parameter versus impurity content in *BMNT*.

### Microwave Dielectric Properties

Dielectric constant as a function of impurity addition in *BMNT-BZ* and *BMNT-BS* systems was plotted in Fig. 6. It was found that the dielectric constant linearly increased with *BZ* addition, whereas it decreased with *BS* addition. The former observation may be understood since the dielectric constant of *BZ* is equal to 40. However, the latter seems to be caused by the decrease of density with *BS* (Fig. 3).

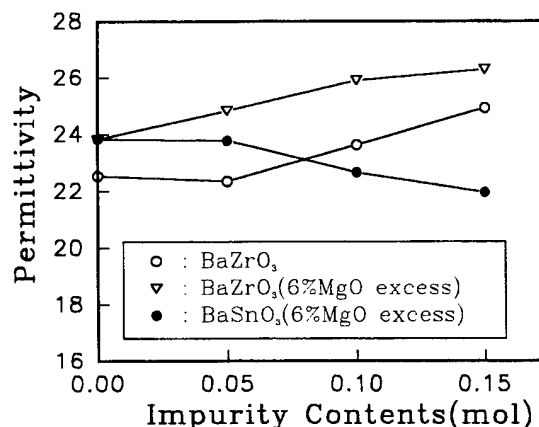


Fig. 6 Dielectric constant measured at 5 to 6 GHz versus impurity content in *BMNT*.

The variation of  $Q$  and  $\tau_f$  values with impurities was illustrated in Fig. 7. It was found that the  $Qf$  product increased at the beginning as the amount of *BZ* increased and then decreased beyond 10 mol% addition. Moreover, it was found that  $\tau_f$  value increased with *BZ* addition. These results are in good agreement with published results in a similar *BZT-BZ* system [9]. It is also seen

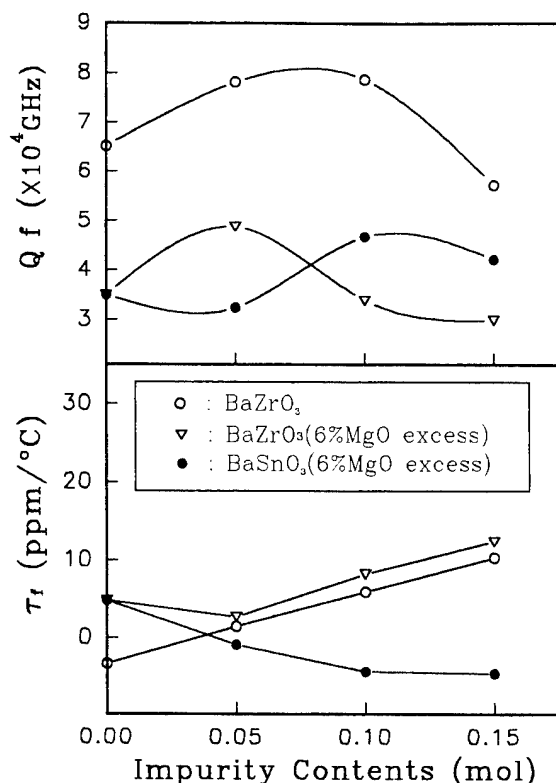


Fig. 7  $Qf$  product and  $\tau_f$  values versus impurity content in *BMNT*.

that the measured  $\tau_f$  value of *BMNT* was - 3.39 ppm/°C, so that zero  $\tau_f$  value was obtained when the amount of *BZ* was about 5 mol%. Therefore, it was possible to increase  $Q$  value and to achieve zero  $\tau_f$  at the same time. The addition of excess *MgO* proved to have detrimental effect on  $Q$  value improvement. This result is attributable to the segregation of excess *MgO* along grain boundaries.

It seems that *BS* addition resulted in a slight increase of  $Q$  value and a gradual decrease of  $\tau_f$  value. The latter is in accord with *BMT* - *BS* system reported previously [10]. From Fig. 5 and Fig. 7, it was also found that the correlation between the ordering parameter and  $Q$  value seemed to be absent.

Besides, it was found that the presence of *BT* second phase would have negative effect on the improvement of  $Q$  value. Typical data in support of this argument are listed in Table 2 below. It looks like that the addition of *BZ* into *BMNT* was effective in preventing the evaporation of *NiO* or *MgO*. Therefore, it is concluded that the achievement of ceramics without any second phase is crucial in obtaining improved microwave performance.

Table 2. Relative intensity of (420) reflection of *BT* phase to (102) reflection of perovskite phase and  $Qf$  product in *BMNT* ceramics.

Material	$\frac{I(420)}{I(102)} \times 100(\%)$	$Q \cdot f$
$Ba(Mg_{0.75}Ni_{0.25}Ta_{2/3})O_3 + 6\% MgO$	2.7	34900
$Ba(Mg_{0.75}Ni_{0.25}Ta_{2/3})O_3$	1.4	65100
$Ba(Mg_{0.75}Ni_{0.25}Ta_{2/3})O_3$ $0.05BaZrO_3$	0	78200

## SUMMARY AND CONCLUSIONS

The unexpected appearance of second *BT* phase in *BMT* could be attributed to the volatility of *MgO* at high temperatures, and could be avoided by excess *MgO* addition into the *BMT* powder mixture.

It was found that both *BMNT*-*BZ* and *BMNT*-*BS* system crystallize in perovskite within the experimental limit of present study. When *Zr* ion was substituted, due to relatively large difference in ionic sizes, the reduction of *B*-site ordering would be smaller than the case of *Sn* ion substitution.

It was found that the dielectric constant of *BMNT* ceramics linearly increased with *BZ* addition, but decreased with *BS* addition.

It was found that the increase of  $Q$  value while achieving zero  $\tau_f$  at the same time was realized in *BMNT* - 0.05*BZ* ceramic. The  $Q$  value at 6 GHz was higher than 13000.

It seems that *BS* addition resulted in a slight increase of  $Q$  value and a gradual decrease of  $\tau_f$  value.

It was concluded that the correlation between the ordering parameter and  $Q$  value seemed to be absent in the *BMNT* system.

The addition of excess *MgO* proved to have detrimental effect on  $Q$  value improvement. This result is attributable to the segregation of excess *MgO* along grain boundaries. It was also found that the presence of *BT* second phase would have negative effect on the improvement of  $Q$  value. Therefore, it was concluded that the achievement of ceramics without any second phase would be crucial in obtaining improved microwave performance.

## ACKNOWLEDGEMENT

We would like to extend our deep appreciation

of friendly help of Dr. Hee-Kyung Sung and Mr. Suk-Jin Lee of Electronics and Telecommunications Research Institute, Daejeon, Korea. This work was supported in part by the Yeungnam University Research Grants in 1994, and in part by the Korea Science and Engineering Foundation (KOSEF) through the Science Research Center (SRC) of Excellence Program.

## REFERENCES

- [1] S. Nomura *et al.*, *Japan. J. Appl. Phys.*, vol. 21, pp. L624-L626, 1982.
- [2] K. Matsumoto *et al.*, in *Proc. 6th Int. Symp. Appl. Ferroelectr.*, Bethlehem, PA, Jun. 1986, pp. 118-121.
- [3] K. Wakino *et al.*, *Microwave J.*, Jun. 1987, pp. 133-147.
- [4] K. Wakino and H. Tamura, in *Ceram. Trans.*, vol. 8, pp. 305-314, 1990.
- [5] S. Y. Kim *et al.*, *to be published in J. Kor. Ceram. Soc.*, 1994.
- [6] J.-A Lee, *M.S. Thesis*, Kyungpook National University, Korea, 1994.
- [7] S. Kawashima, *Cer. Bull.*, vol. 72, no. 5, pp. 120-126, 1993.
- [8] S. Y. Kim *et al.*, in *Proc. 10th Japan-Korea Seminar on New Ceramics*, Sasebo, Japan, Oct. 1993, pp. 313-316.
- [9] H. Tamura *et al.*, *J. Am. Ceram. Soc.*, vol. 67, pp. C59-C61, 1984.
- [10] H. Matsumoto *et al.*, *Japan. J. Appl. Phys.*, vol. 30, 2347-2349, 1991.

# FABRICATION AND CHARACTERIZATION OF BARIUM STRONTIUM TITANATE AND NON-FERROELECTRIC OXIDE COMPOSITES FOR USE IN PHASED ARRAY ANTENNAS AND OTHER ELECTRONIC DEVICES

L.C. Sengupta, E. Ngo, M.E. O'Day, S. Stowell, and R. Lancto  
U.S. Army Research Laboratory, Materials Directorate, AMSRL-MA-CA  
Watertown, MA 02172

**Abstract** - A ceramic ferroelectric phase shifting device has been demonstrated using  $\text{Ba}_{1-x}\text{Sr}_x\text{TiO}_3$  (BSTO) ceramics. As a part of an effort to optimize the electronic device performance in the phase shifter, various composites of BSTO combined with other nonelectrically active oxide ceramics have been formulated. In general, the composites have reduced dielectric constants,  $\epsilon'$ , where  $\epsilon = \epsilon' - i\epsilon''$ , and loss tangents,  $\tan \delta$ . The low dielectric constant and low loss tangent reduce the overall impedance mismatch and the insertion loss of the device. In addition, the overall tunability, change in the dielectric constant with applied voltage, is maintained at a relatively high level. The combination of electronic properties of these materials offer substantially higher operating frequencies, 10 GHz and above. Another application for one of the composites is for use as a capacitor-varistor surge protector. The microstructures including grain size and phase analysis have been examined using SEM and X-ray diffraction. The analysis of the phase formation, compositional variations, and grain size will be related to the electronic properties of the materials.

## INTRODUCTION

Phased array antennas can steer transmitted or received signals either linearly or in two dimensions without mechanically oscillating the antenna. These antennas are currently constructed using ferrite phase shifting elements. Due to the type of circuit requirements necessary to operate these antennas, they are costly, large and heavy. Therefore, the use of these antennas has been limited primarily to military applications which are strategically dependent on such capabilities. In order to make these devices available for many other commercial and military uses, the basic concept of the antenna must be improved. If ferroelectric materials could be used for the phase shifting element instead of ferrites, phased array antennas would be totally revolutionized.

A ceramic Barium Strontium Titanate,  $\text{Ba}_{1-x}\text{Sr}_x\text{TiO}_3$ , (BSTO), phase shifter using a planar microstrip construction has been demonstrated [1]. In order to meet the required performance specifications, maximum phase shifting ability, the electronic properties in the low frequency (KHz) and microwave regions (GHz) must be optimized. As part of this optimization process, various composites of BSTO and non-ferroelectric oxides have been formulated.

Another application for one of these materials is a combined capacitor-varistor device. In general, this would be used as a protective device in parallel with electronic information processing circuits to protect against spurious voltage surges and voltage transients. The capacitive aspect of the device would guard against low-amplitude and high frequency transients which cause errors in signal processing or in stored signals. The varistor function of the device protects against high-amplitude voltage surges. The device combination is a replacement for a capacitor Zener diode combination which is often bulkier than the circuit it is protecting.

The capacitor-varistor device has been attempted previously by appropriately doping  $\text{SrTiO}_3$  to form grain boundary phases or layers which exhibit the desirable characteristics [2]. Also discrete layers of  $\text{ZnO}$  and  $\text{Pb}(\text{Fe}_{1/2}\text{Nb}_{1/2})\text{O}_3$ - $\text{Pb}(\text{Fe}_{2/3}\text{W}_{1/3})\text{O}_3$  (dielectric constant of 27000 to 32000) have been fabricated [3]. The problem with the former

scheme has been with the high loss tangents and high threshold voltages derived from the metallic additives and the semiconducting capacitor. The problem associated with the latter scheme is with the processing of the lead based capacitor compounds and the deleterious diffusion between the  $\text{ZnO}$  varistor layers and lead-based capacitor layers.

The composites will be designated as BSTO-Oxide II, BSTO-Oxide III, BSTO-Oxide II / BSTO-Oxide III, BSTO-Oxide III Compound, and BSTO-IV since they all have patents pending on their formulations. All of these composites possess improved electronic properties. The comparison of the compositions and phase formation of the various BSTO-oxide ceramic composites will be made and related to their electronic properties. This report will outline some of the initial findings for these new ceramic composites.

## EXPERIMENTAL

### Ceramic Processing

Powder forms of Barium Titanate and Strontium Titanate were obtained from Ferro Corporation, Transelco Division, Pen Yan, N.Y. (product nos. 219-6 and 218 respectively), stoichiometrically mixed to achieve  $\text{Ba}_{0.6}\text{Sr}_{0.4}\text{TiO}_3$  and ball-milled in ethanol using 3/16" alumina media for 24 hrs. The resulting BSTO was then air-dried, calcined at  $1100^\circ\text{C}$  and mixed with an oxide (oxide II, oxide III, oxide II / oxide III, oxide III compound or oxide IV) in the proper weight percent and ball-milled again in a slurry of ethanol using the alumina grinding media for an additional 24 hrs.

Rholplex B-60A (Rohm and Haas Co., Philadelphia, PA) binder (3 wt%) is added to the resulting BSTO/oxide mixture. The mixture is then air-dried and uniaxially dry-pressed to a pressure of approximately 7000 p.s.i.. Sintering schedules were obtained by employing a deflectometer such as Mitutoyo digimatic indicator and miniprocessor (Mitutoyo Corp., Paramus N.J.). Porosity and liquid absorption was obtained by performing an immersion density in ethanol using a modified ASTM standard. It should be noted that all of the examined samples have liquid absorption of less than 2%.

Two metallization techniques were employed. One involved painting on two circular, aligned electrodes, one on either side of the specimens, using high purity silver paint (SPI Supplies West Chester, PA) and attaching wires using high purity silver epoxy, Magnobond 8000, made by Magnolia Plastics, Inc., Chamblee, GA. The other technique utilized the screen printing of electrodes using silver conductive ink (FERRO #3350, Electronic Materials Division, Santa Barbara, CA) and wires were attached by dipping the specimens in a bath of 2% silver, 62% tin and 36% lead solder.

### Electronic Measurements

The dielectric constants,  $\epsilon'$ , loss,  $\tan \delta$ , and % tunability were determined for all composites. The % tunability of a material is determined using the following equation:

$$\% \text{ tunability} = \{ \epsilon'(0) - \epsilon'(V_{\text{app}}) \} / \{ \epsilon'(0) \} \quad (1)$$

The tunability measurements were taken with an applied electric field which ranged from 0 to 3.0 V/micron ( $\mu\text{m}$ ). The electronic properties given in the forthcoming tables were measured at a frequency of 1 KHz. Capacitance measurements for all materials were taken using an HP4284A LCR meter. Further calculations were done to correct for the effect of fringe capacitance.

## RESULTS AND DISCUSSION

### BSTO-Oxide III, BSTO-Oxide II / Oxide III, BSTO-Oxide III Compound Composites

**SEM and X-ray Diffraction:** No secondary phases (other than BSTO and Oxide III) were identified by X-ray diffraction for the BSTO-Oxide III composites. Also the SEM photographs did not reveal any evidence of secondary phase formation. However, the BSTO-Oxide II / Oxide III composites revealed the existence of secondary phases at oxide additions of 10 wt%. Three distinct secondary phases were identified for these composites. The BSTO-Oxide III compound composites also revealed at least two secondary phases for oxide content above 30 wt%. These phases were evident as discolorations in the SEM photographs for both the BSTO-Oxide II / Oxide III and BSTO-Oxide III compound composites.

**Electronic Properties:** The electronic data for the BSTO-Oxide III, BSTO-Oxide II / Oxide III and BSTO-Oxide III compound composites are shown in Table 1. As shown in the table, the dielectric constants decrease with increase in oxide content and the tunability decreases slowly with increase in oxide content. In fact, the BSTO-Oxide III composites exhibit high tunabilities (>10%) up to 60 wt% oxide III which is not the case for the two other oxide additives. This difference could be due to the fact that the BSTO-Oxide III compounds do not exhibit secondary phases whereas the other two composites form multiple secondary phases as discussed previously. These non-ferroelectric phases will tend to inhibit tunability at high additive contents.

**TABLE 1.** Electronic Properties of BSTO-Oxide III, BSTO-Oxide II / Oxide III and BSTO-Oxide III Compound Ceramic Composites Measured at 1 KHz.

BSTO-Oxide III		* samples have poor contacts		
Oxide III Content (wt %)	Dielectric Constant	Loss Tangent	% Tunability	Electric Field (1"/Micron)
0.0	3299.08	0.0195	19.91	0.73
1.0	1276.21	0.0015	16.07	2.32
5.0	1770.42	0.0014		
10.0	1509.19	0.0018		
15.0	1146.79	0.0011	7.270	1.91
20.0	1079.21	0.0009	15.95	2.33
25.0	783.17	0.0007	17.46	2.45
30.0	750.93	0.0008	9.350	1.62
35.0	532.49	0.0006	18.00	2.07
40.0	416.40	0.0009	19.81	2.53
50.0	280.75	0.0117*	9.550	2.14
60.0	117.67	0.0006	11.08	2.70
80.0	17.00	0.0008	0.61	1.72
100.0	13.96	0.0009		

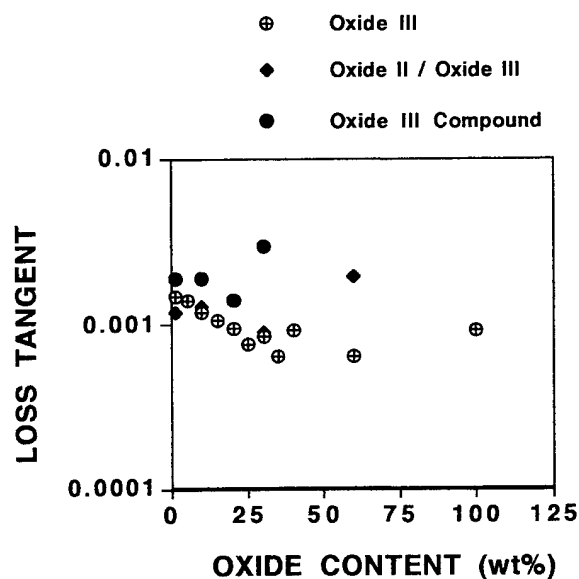
  

BSTO-Oxide II / Oxide III				
Oxide II / Oxide III Content (wt%)	Dielectric Constant	Loss Tangent	% Tunability	Electric Field (1"/Micron)
0.0	3299.1	0.0195	19.91	0.73
1.0	2515.3	0.0011	12.24	1.14
10.0	1868.9	0.0013	11.63	1.56
20.0	1016.0	0.0327*	10.89	1.33
30.0	389.06	0.0009	1.607	1.34
60.0	93.591	0.0022	0.450	0.99

### BSTO-Oxide III Compound

Oxide III Compound Content (wt%)	Dielectric Constant	Loss Tangent	% Tunability	Electric Field (1"/Micron)
0.0	3299.1	0.0195	19.91	0.73
1.0	2531.4	0.0019	18.58	1.66
10.0	1801.5	0.0019	13.29	1.34
20.0	959.27	0.0014	6.910	0.91
30.0	432.40	0.0030	7.347	0.51
60.0	63.192	0.0176	1.054	1.00

As shown in Fig. 1, the loss tangent of these composites are extremely low for most all compositions (decreasing slightly with an increase in oxide content).



**Figure 1.** Loss tangent vs. Oxide Content for BSTO-Oxide III, BSTO-Oxide II / Oxide III and BSTO-Oxide III Compound Composites measured at 1 KHz.

### BSTO-Oxide IV Composites

As mentioned previously, another application for one these composites, denoted as, BSTO-Oxide IV, is for use as a capacitor-varistor protection device. At high voltages, the varistor conducts current given by the power-law relation [4].

$$I = AV^\alpha \quad (2)$$

where V is the applied voltage, I is the current, A is the proportionality constant, and  $\alpha$  is the index of nonlinearity. Current conduction through the varistor prevents the voltage from exceeding a critical value in the electronic circuitry that is being protected. The nonlinear electrical conduction in the ceramic composite is due to the addition of oxide IV (no secondary phases were observed from X-ray diffraction and SEM analysis) in which electron tunneling through the grain boundaries occurs.

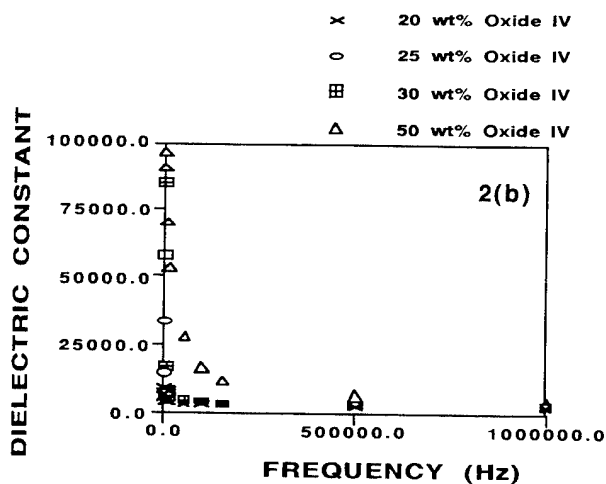
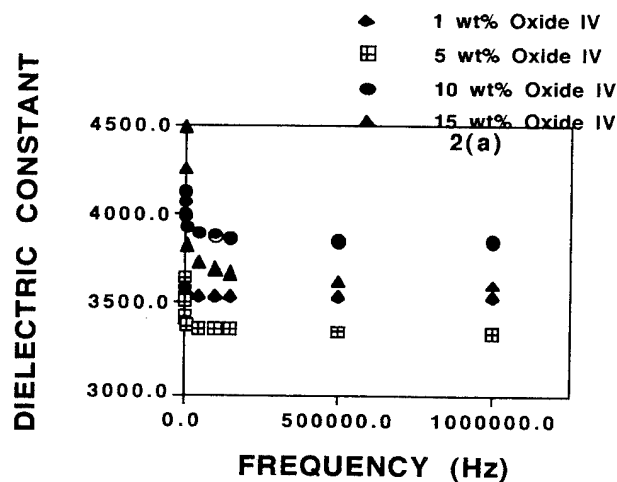
**Electronic Properties:** The electronic properties and the average grain size of the BSTO-Oxide IV composites are shown in Table 2. As shown in Fig. 2(a) and 2(b), the dielectric constant decreases with an increase in frequency. Also the loss tangent shows a decrease with increasing frequency as shown in Fig. 3(a) and 3(b). At low doping levels (1-15 wt%) the composites have

**TABLE 2.** Electronic Properties and Grain Size of BSTO-Oxide IV Composites Measured at 1 KHz.

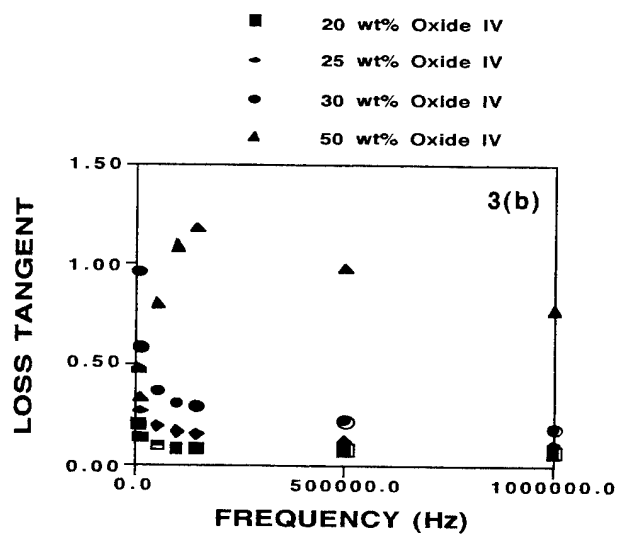
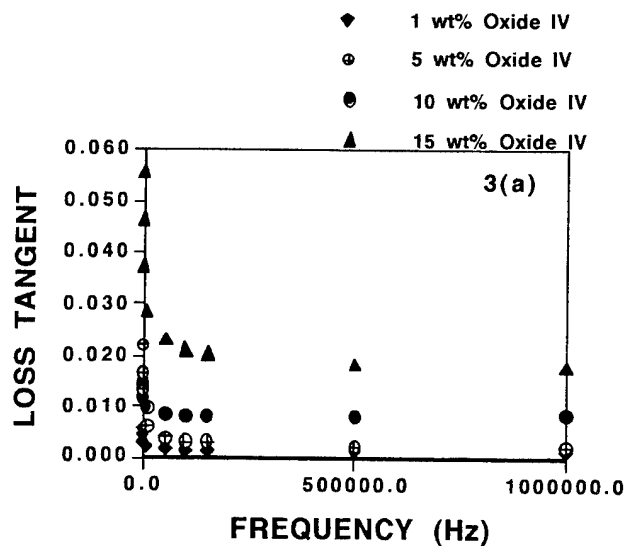
Oxide IV Content wt. %	Dielectric Constant	Loss Tangent	Tunability (Percent)	Electric Field (V/ $\mu$ m)
1.0	3756	0.00236	7.334	1.0
5.0	3416	0.01276	8.957	0.8
10.0	3908	0.01320	13.11	0.7
15.0	3942	0.03708	27.97	0.6
20.0	4685	0.19113	—	—
25.0	7520	0.46976	—	—
30.0	7859	0.46927	—	—
50.0	71922	0.46891	—	—

Oxide IV Content wt. %	Threshold Voltage	Nonlinearity Exponent	Grain Size ( $\mu$ m)
1.0	—	—	—
5.0	—	—	10.24
10.0	—	—	9.774
15.0	—	—	8.610
20.0	100	6.510	8.387
25.0	25	5.390	7.514
30.0	20	10.290	6.806
50.0	5	8.349	5.909



**Figure 2.** (a) Dielectric Constant vs. Frequency for BSTO-Oxide IV Composites (1, 5, 10, 15 wt%) (b) for BSTO-Oxide IV Composites (20, 25, 30, 50 wt%).



**Figure 3.** (a) Loss Tangent vs. Frequency for BSTO-Oxide IV Composites (1, 5, 10, 15 wt%) (b) for BSTO-Oxide IV Composites (20, 25, 30, 50 wt%).

large dielectric constants and possess low loss tangents and reasonably high tunabilities. These properties meet the requirements for various antenna applications (especially low frequency applications). At higher levels (20 - 50 wt%), the addition of oxide IV content continues to increase the dielectric constant drastically especially at low frequencies, and the composites begin to conduct current and exhibit non-ohmic behavior and the threshold voltage is seen to increase with an increase in oxide IV content.

Fig.4 (a) and (b) show the current versus voltage for several BSTO-Oxide IV (20, 25, 30 and 50 wt%) composites. It should be noted that as the oxide IV content is increased, the dielectric constant increases, and the non-linearity exponent increases. This increase in the non-linearity is definitely related to the decrease in the grain size as indicated in Table 2. However, contrary to the predicated behavior for pure oxide IV varistor

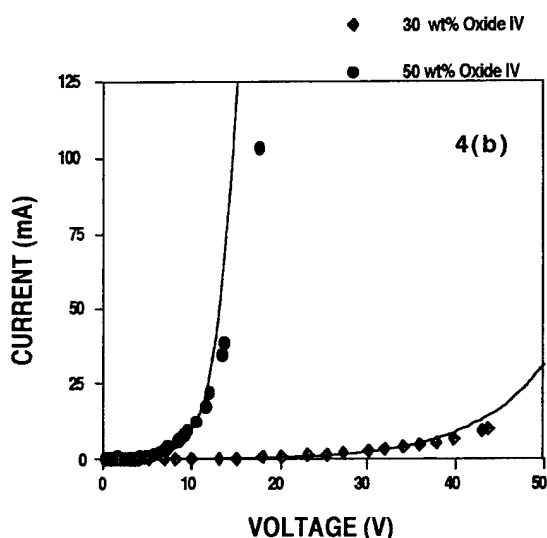
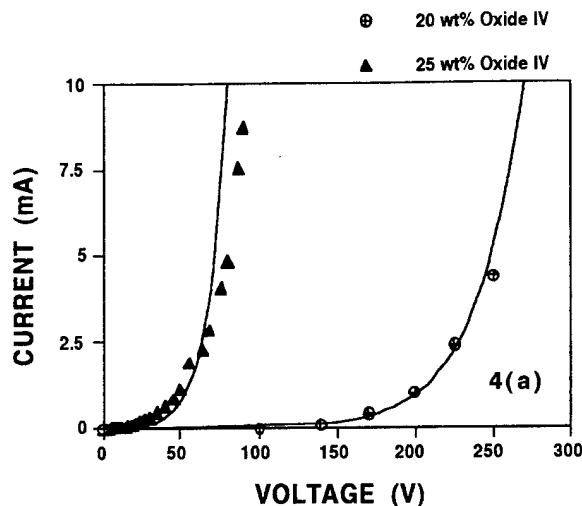


Figure 4. (a) Current vs. Voltage for BSTO-Oxide IV Composites (20 and 25 wt% oxide IV). (b) Current vs. Voltage for BSTO-Oxide IV Composites (30 and 50 wt% oxide IV).

compositions, the threshold voltage decreases with decrease in average grain size. Since the material formed is a composite it is difficult to determine if the grains of oxide IV are decreasing or if the BSTO grains are decreasing. The threshold voltage for the BSTO-Oxide IV (50 wt%) specimen is lower than reported for any bulk capacitor-varistor device (which was reported to be around 100 V) [2] and the capacitance is as high as that obtained for multilayered structures (nearly twice than that reported) [3]. Fig. 5 shows the dielectric constant versus temperature for the BSTO-Oxide IV (50 wt%). The figure shows that the dielectric is reasonably temperature stable at room temperature and above which is an important operating parameter for microelectronic circuits.

#### CONCLUSIONS

The BSTO-Oxide III, BSTO-Oxide II / Oxide III and BSTO-Oxide III compound ceramic composites possess extremely low loss tangents and high tunabilities. The data

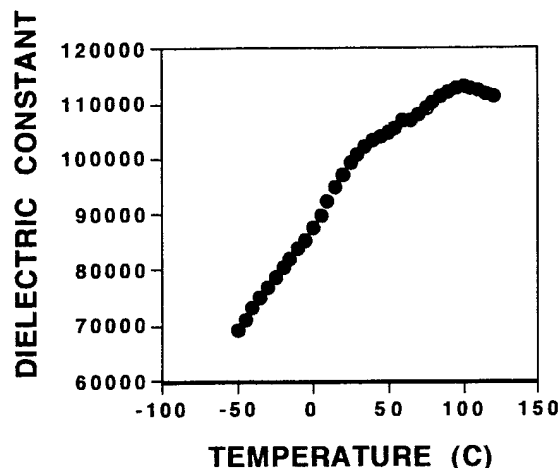


Figure 5. Dielectric Constant vs. Temperature for a BSTO-Oxide IV (50 wt%) composite measured at 1 KHz.

suggest that any composites containing oxide III or an oxide III compound will display similar electronic behavior. This is significant in that a family of composites has been identified which can potentially facilitate the operation of these ferroelectric phased array antennas at millimeter wave range frequencies due to much improved electronic properties.

The BSTO-Oxide IV materials exhibit behavior which renders them suitable for use both (at low oxide IV content < 15 wt%) in phased array antenna systems and (at high oxide IV content > 15 wt%) as a capacitor-varistor protection device for microelectronic circuits. The improved properties of these composites includes very low threshold voltages (@5 V), reasonable nonlinear coefficients, moderate to low loss tangents, tunable and extremely high dielectric constants, and temperature stability. It should be noted that the low threshold voltage accompanied by an extremely high dielectric constant was accomplished in a bulk ceramic (1mm thickness) and is less than that reported for thin film laminates [3].

#### REFERENCES

- [1] R.W. Babbitt, T. E. Koscica, and W.E. Drach, "Planar Microwave Electro-optic Phase Shifters," *Microwave Journal*, vol. 35, pp. 63-79, June 1992.
- [2] N. Yamaoka, M. Masuyama and M. Fukui, "SrTiO<sub>3</sub>-Based Boundary Layers Capacitor Having Varistor Characteristics," *Ceramic Bulletin*, vol. 62, pp. 698-703, 1983.
- [3] H.C. Ling, M.F. Yan, and W. W. Rhodes, "A Monolithic Device with Dual Capacitor and Varistor Functions," *J. Am. Ceram. Soc.*, vol. 72, pp. 1274-1276, 1989.
- [4] M. Matsuoka, "Nonohmic Properties of Zinc Oxide Ceramics," *Japanese Journal of Applied Physics*, vol. 10, pp. 736-746, 1970.



Takahiro Takada\* Sea Fue Wang, Shoko Yoshikawa, Sei-Joo Jang, and Robert E. Newnham  
Materials Research Laboratory, The Pennsylvania State University,  
University Park, PA 16802, U. S. A.

\*Current address: Research & Development Center, Sumitomo Metal Industries, Ltd.,  
1-8 Fuso, Amagasaki, Hyogo 660, Japan

The microwave dielectric properties and the sintering behavior of commercial BaO-TiO<sub>2</sub>-WO<sub>3</sub> dielectrics, N-35, with addition of various glasses; (1) simple glass formers, (2) ZnO-B<sub>2</sub>O<sub>3</sub> based, (3) B<sub>2</sub>O<sub>3</sub>-SiO<sub>2</sub> based and (4) Al<sub>2</sub>O<sub>3</sub>-SiO<sub>2</sub> based glasses were studied. The Q of N-35 sintered with a ZnO-B<sub>2</sub>O<sub>3</sub> glass system showed a sudden drop in the sintering temperature to around 1000°C. Results of XRD, thermal analysis and scanning electron microscopy suggest that the chemical reaction between N-35 and the glass had a larger effect on Q than density. A 5wt% addition of B<sub>2</sub>O<sub>3</sub> to N-35, when sintered at 1200°C, had the best dielectric properties, Q=8300 and K=34.1 at 8.5GHz, among the glasses. Q, K and density increased with sintering temperature from 1000 to 1200°C. The effects of the amount of glass added and the mixing method on the density and the dielectric properties will be discussed.

### Introduction

Mobilephone and satellite broadcasting in the microwave frequency have been widely commercialized during these past few years. In order to reduce the size of microwave devices in communication systems, the dielectric components must also be smaller. Multilayer devices have been developed to increase the volume efficiency.<sup>1</sup> In multilayer structures, it is imperative to lower the sintering temperature of the dielectric in order to cofire with low loss conductors such as silver and gold.

Liquid phase sintering using glass additives is the most effective and least expensive method. However, the microwave properties of dielectrics with glass-additions have not been investigated. This led us the study of the effects of glass flux on the sintering behavior and properties of commercial microwave dielectrics. In this paper, we discuss the sintering behavior and microwave dielectric properties of commercial BaO-TiO<sub>2</sub>-WO<sub>3</sub> dielectrics with addition of various glasses. Relationships among the sintering temperature, microstructural evolution, phase formation, and microwave dielectric properties of the B<sub>2</sub>O<sub>3</sub> and ZnO-B<sub>2</sub>O<sub>3</sub> glass commercial flux-sintered dielectric are presented.

BaTi<sub>4</sub>O<sub>9</sub> and Ba<sub>2</sub>Ti<sub>9</sub>O<sub>20</sub> are the two most common high Q dielectric materials used in the microwave frequency range. BaTi<sub>4</sub>O<sub>9</sub> was first reported by Roy,<sup>2</sup> and Ba<sub>2</sub>Ti<sub>9</sub>O<sub>20</sub> by Jonker,<sup>3</sup> in their study of BaO-TiO<sub>2</sub> system. Ba<sub>2</sub>Ti<sub>9</sub>O<sub>20</sub> decomposes into BaTi<sub>4</sub>O<sub>9</sub> and TiO<sub>2</sub> at temperatures higher than 1300°C during a peritectic reaction. Similarly, BaTi<sub>4</sub>O<sub>9</sub> decomposes into TiO<sub>2</sub> and a melt at 1428°C.<sup>4,5</sup> Both BaTi<sub>4</sub>O<sub>9</sub> and Ba<sub>2</sub>Ti<sub>9</sub>O<sub>20</sub> were studied as microwave dielectrics by O'Bryan and Plourde et al.<sup>6-9</sup> The dielectric properties of BaTi<sub>4</sub>O<sub>9</sub> and Ba<sub>2</sub>Ti<sub>9</sub>O<sub>20</sub> with several different additives have also been investigated in the microwave region.<sup>10-14</sup> The addition of WO<sub>3</sub> to the system BaO-TiO<sub>2</sub> results in multiple phases including BaTi<sub>4</sub>O<sub>9</sub>, Ba<sub>2</sub>Ti<sub>9</sub>O<sub>20</sub>, BaWO<sub>4</sub> and TiO<sub>2</sub>.<sup>10</sup> The solubility of WO<sub>3</sub> in BaTiO<sub>3</sub> is small (< 0.1 %) and the addition of WO<sub>3</sub> to BaTiO<sub>3</sub> increases the loss tangent of the ceramics.<sup>11</sup> However this BaO-4TiO<sub>2</sub>-0.1WO<sub>3</sub> ceramic was found to possess excellent microwave properties: K=35, Q=8400 at 6GHz and a  $\tau_f$  (temperature coefficient of resonant frequency) of nearly 0 ppm/°C. The additions of Al<sub>2</sub>O<sub>3</sub>, MnO, ZnO and Ta<sub>2</sub>O<sub>5</sub> to BaTi<sub>4</sub>O<sub>9</sub> were also examined.<sup>12-14</sup> The Q and  $\tau_f$  values were partially controlled by the firing atmosphere.<sup>13</sup>

### Experimental Procedure

N-35 powder supplied by Sumitomo Metal Ceramics Inc. was used as host material. This host material, sintered at 1360°C, was reported to consist of 9.9 vol% BaTi<sub>4</sub>O<sub>9</sub>, 84.4 vol% Ba<sub>2</sub>Ti<sub>9</sub>O<sub>20</sub> and 5.7 vol% BaWO<sub>4</sub> and possess the following properties: Q ≈ 8400, K = 36 at 6 GHz and  $\tau_f$  ≈ 0.<sup>10</sup> Ten glasses

were used in this study are shown in Table 1. We focused on the study for B<sub>2</sub>O<sub>3</sub> and ZnO-B<sub>2</sub>O<sub>3</sub>(ASF1495) because of the interesting sintering behavior and dielectric properties with firing temperature. The softening point of the ZnO-B<sub>2</sub>O<sub>3</sub>(ASF1495) is 595°C and the average powder size is 1.8μm.

The N-35 ceramic powders were mixed with 5-30 wt% glasses by agate mortar and pestle with ethanol for ≈ 1hr. Wet ball milling with ZrO<sub>2</sub> media was also used in order to understand the effect of mixing on densification and properties. The mixtures of N-35 and glass were granulated by adding polyvinyl alcohol (PVA) solution. After that, the dried powder was pelletized into a cylindrical disk for microwave dielectric measurement. The disks were first heat treated at 550°C for binder burn-out and then fired in air at temperatures between 800 and 1250°C for 4hrs (for pure N-35 dielectric, the sintering temperatures range was from 1000 to 1360°C) in air.

The sample densities were measured using the Archimedes method.

Dielectric characteristics at microwave frequencies (5.7-9.4 GHz) were measured by the Hakki-Coleman dielectric resonator method,<sup>15</sup> as modified and improved by Courtney.<sup>16</sup> An HP8510A network analyzer and an HP8340A sweeper were used for the microwave measurements. The permittivity was calculated from the resonant frequency of the TE<sub>011</sub> resonant mode. The error of Q and K were within 5 %.

XRD analysis was undertaken for phase identification of the sintered samples, using a SCINTAG VAX3100 system. The microstructure of the sample's fracture surface was observed by SEM (ISI-DS130). Differential thermal analysis was carried out using a Perkin Elmer-DTA1700. Identification of the N-35 and glass phases was carried out by EPMA image (Shimadzu-8705 WDX).

### Results and Discussion

#### Microwave dielectric properties of the host material (N-35)

The density, Q and K of the sintered BaO-TiO<sub>2</sub>-WO<sub>3</sub> host material (N-35) samples increased with sintering temperature as shown in Fig. 1. Even though the permittivity of the sintered N-35 ceramics was similar to the commercial sample value, the Q of the samples were less than the commercial sample value. The Q for sample sintered at 1360°C was 5900 at 7.2GHz (fxQ = 42000), somewhat lower than the N-35 commercial sample value 7200 at 6.1GHz (fxQ = 44000). The  $\tau_f$  was -6.7 ppm/°C and also less than the value of the N-35 commercial sample.

The discrepancy of fxQ and negative  $\tau_f$  may have resulted from the different phase contents caused by the difference in sintering atmosphere (samples were sintered in air in this study, whereas the commercial sample was sintered in an oxygen atmosphere).

According to the XRD results, N-35 powders before sintering consisted of BaTi<sub>4</sub>O<sub>9</sub>, BaWO<sub>4</sub> and TiO<sub>2</sub> phases, as shown in Fig. 2 (a). The TiO<sub>2</sub> content decreased and that of Ba<sub>2</sub>Ti<sub>9</sub>O<sub>20</sub> increased in the samples as the sintering temperature increased (Fig. 2 (b)-(d)). It is reported that the ratio of the various phases is important for  $\tau_f$ .<sup>6</sup> The total  $\tau_f$  of the dielectric can be calculated by a logarithmic mixture rule,<sup>17</sup> if the  $\tau_f$  of each of the phases in the dielectric is known.

#### Microwave dielectric properties and microstructures of glass-sintered N-35 ceramics

Sintering studies of the N-35 dielectrics with B<sub>2</sub>O<sub>3</sub>-SiO<sub>2</sub> and Al<sub>2</sub>O<sub>3</sub>-B<sub>2</sub>O<sub>3</sub> based commercial glasses were performed. The density and dielectric properties are shown in Table 1. The Q and K of the samples in these glass systems were 25-32 and 970-1900 respectively, which are smaller than those of the pure N-35

sample. The K and Q of  $\text{Al}_2\text{O}_3\text{-SiO}_2$  glass system were generally higher than those of the  $\text{B}_2\text{O}_3\text{-SiO}_2$  glass system. Therefore, the  $\text{Al}_2\text{O}_3\text{-SiO}_2$  glass system proved to be one of the most effective sintering aids without lowering K and Q.

The addition of lead ions to ceramics is known to increase the loss factor in the microwave frequency range.<sup>18</sup> Alkali ions in ceramics are also known to increase the loss factor.<sup>19</sup> In this study, N-35 was sintered with two different kinds of  $\text{PbO}$ -containing commercial glasses,  $\text{PbO-B}_2\text{O}_3\text{-SiO}_2$  and  $\text{PbO-Al}_2\text{O}_3\text{-SiO}_2$ . However, in this study, the Q did not decrease in comparison with other glass systems. We used an alkali ion including glass,  $\text{R}_2\text{O-B}_2\text{O}_3\text{-SiO}_2$  system, as a sintering aid. The dielectric properties of this sample were a little lower than those of the  $\text{B}_2\text{O}_3\text{-SiO}_2$  containing glasses as indicated in Table 1.

### (1) $\text{B}_2\text{O}_3$

The density, Q and K of N-35, with addition of  $\text{B}_2\text{O}_3$ , increased steadily with firing temperature up to  $1250^\circ\text{C}$ , as shown in Fig. 3. The densification was enhanced by liquid phase sintering. An endothermic peak at  $840^\circ\text{C}$  which is higher than the melting temperature of  $\text{B}_2\text{O}_3$ ,  $580^\circ\text{C}$  was observed as shown in Fig. 4(b). This demonstrates that the eutectic liquid formation at this temperature assisted in the densification. The K of N-35 with 5 wt%  $\text{B}_2\text{O}_3$  addition increased as the sintering temperature increased from  $1000$  to  $1200^\circ\text{C}$ . This is caused by improved densification at higher temperatures. The Q of the  $\text{B}_2\text{O}_3$  mixture increased from 2300 to 8300 for sintering temperatures from  $1000$  to  $1200^\circ\text{C}$  and dropped to 1000 at  $1250^\circ\text{C}$ . The Q of the sample fired at  $1200^\circ\text{C}$  was 8300, which is higher than that of pure N-35 sintered at  $1360^\circ\text{C}$ .

The color of the samples sintered at more than  $1100^\circ\text{C}$  was not uniform. The inner core 8mm in diameter was a uniform brown, similar to the color of N-35 sintered at  $1360^\circ\text{C}$ . The outer 1mm skin was light tan with abrupt color changes. The presence of the color change, which becomes darker at higher firing temperature, and the inhomogeneous color of the sample, may relate with the densification and microstructure shown in Fig. 5.

Scanning electron micrographs are shown in Fig. 5 (a) and (b). Needle-like morphology was observed at  $1000$  and  $1200^\circ\text{C}$ , which may indicate the present of  $\text{TiO}_2$  in  $\text{BaTi}_4\text{O}_9$ .<sup>4,6,9</sup> The part of the outer skin contained less Ti and more Ba than the inner core area as shown in Fig. 6. The large increase in Q and higher K for N-35 dielectrics with  $\text{B}_2\text{O}_3$  may be due to secondary phases such as  $\text{TiO}_2$  which has higher K (104) and Q (14000 at  $3\text{GHz}$ ).<sup>20</sup> Improved densification and the existence of  $\text{TiO}_2$  may have resulted in the superior dielectric properties at  $1200^\circ\text{C}$  brought on by  $\text{B}_2\text{O}_3$  addition.

Table 1. Properties of N-35 sintered with glasses

Glass material*	Glass amount (wt%)	Firing Temp. ( $^\circ\text{C}$ )	Q	K	Frequency (GHz)	Density ( $\text{g/cm}^3$ )
+ $\text{B}_2\text{O}_3$	5.0	1200	8300	34	8.5	3.8
+ $\text{ZnO-B}_2\text{O}_3$ (ASF1495)	5.0	1100	1200	29	5.8	4.0
+ $\text{ZnO-B}_2\text{O}_3\text{-SiO}_2$ (Corning7574)	5.0	1000	1200	27	7.0	4.0
+ $\text{BaO-B}_2\text{O}_3\text{-SiO}_2$ (Corning1415)	5.0	1100	1100	26	6.1	3.8
+ $\text{PbO-B}_2\text{O}_3\text{-SiO}_2$ (ASF1381)	5.0	1100	1100	25	6.0	3.7
+ $\text{R}_2\text{O-B}_2\text{O}_3\text{-SiO}_2$ (Corning7046)	5.0	1100	1000	25	6.1	3.5
+ $\text{Al}_2\text{O}_3\text{-B}_2\text{O}_3\text{-SiO}_2$ (ASF1760)	5.0	1100	970	31	5.7	4.2
+ $\text{Al}_2\text{O}_3\text{-SiO}_2$ (Corning1724)	5.0	1100	1800	32	5.6	4.2
+ $\text{RO-Al}_2\text{O}_3\text{-SiO}_2$ (ASF174)	5.0	1100	1900	30	5.7	3.7
+ $\text{PbO-Al}_2\text{O}_3\text{-SiO}_2$ (ASF1730)	5.0	1100	1400	27	6.1	3.2

\* $\text{R}_2$  is alkali and R is alkaline earth.

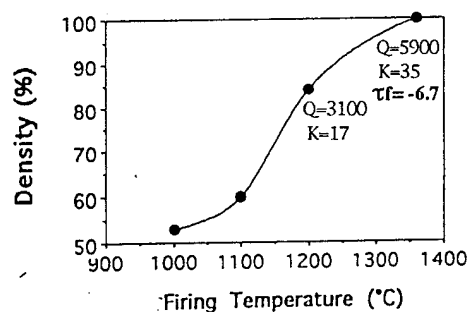


Fig. 1 Effect of firing temperature on density and microwave dielectric properties of N-35

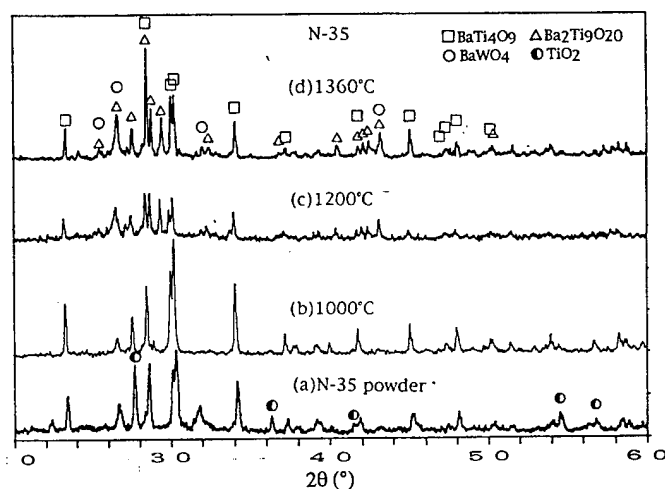


Fig. 2 XRD diagrams of N-35 (a) dielectric powder, and fired at (b)  $1000^\circ\text{C}$ , (c)  $1200^\circ\text{C}$  and (d)  $1360^\circ\text{C}$ .

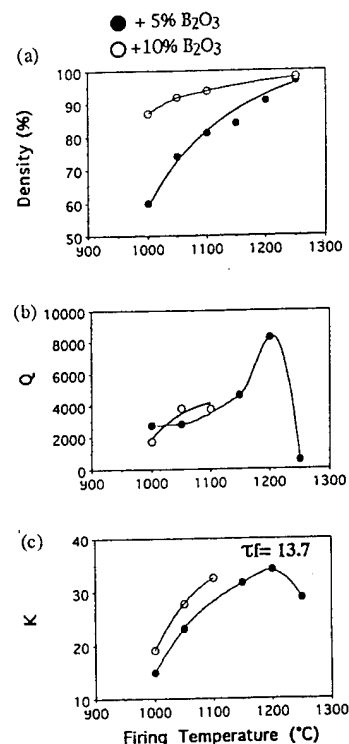


Fig. 3 Effect of  $\text{B}_2\text{O}_3$  addition to N-35 on (a) density and (b)(c) microwave dielectric properties with firing temperature.

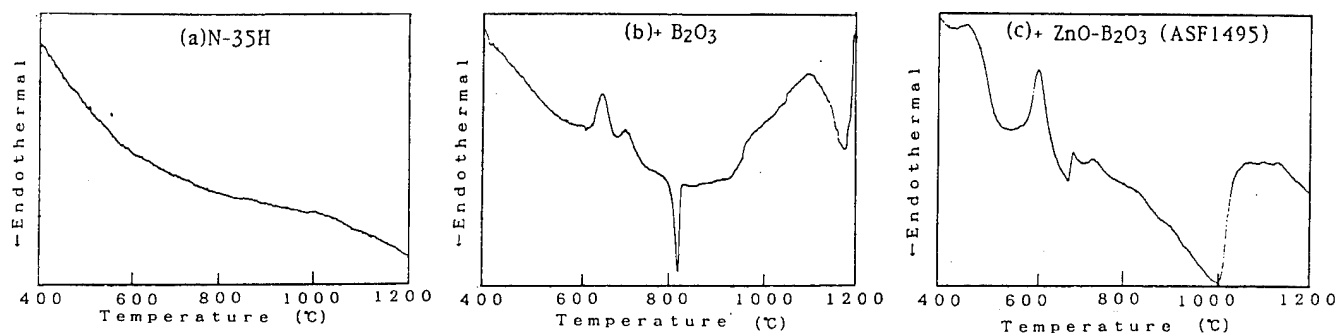


Fig. 4 Differential thermal analysis of (a) N-35, (b) N-35 with  $B_2O_3$ , (c) N-35 with  $ZnO-B_2O_3$ .

## (2) $ZnO-B_2O_3$ (ASF1495)

With 5 wt% addition of  $ZnO-B_2O_3$  (ASF1495), the densification continued to increase as the sintering temperature increased and reached a maximum at 1200°C with 94% of T.D. as shown in Fig. 7. Reactions between N-35 and glass can be recognized by a variation of the density with firing temperature. A maximum theoretical density of 94% was achieved at approximately 1200°C. As shown in Fig. 4 (c), a eutectic liquid was formed at a temperature of about 1010°C. This eutectic liquid phase significantly changed the Q value of the samples, as indicated in Fig. 7. The Q of the samples sintered at 1000°C were about 1800, and suddenly dropped to 970 when sintered at 1050°C. As sintering temperature increased further, the Q increased. The permittivities of the samples, however, did not follow the same trend. The permittivity remained almost constant with increasing sintering temperatures.

The color of the sample sintered at 900°C was a bright yellow-brown. With increasing firing temperature the sample appeared dark brown. The sides, top and bottom of the sample fired at 1200°C were darker color, similar to that of the N-35 sample fired at 1360°C. However, the inhomogeneous color change was not similar to the case of the  $B_2O_3$ .

The sample sintered at 1000°C had a higher Q than those sintered at higher temperatures although the density was lower. This indicates that the effect of the eutectic reaction on Q is more important than its effect on density. The glass in the sintered sample was retained during sintering, and may increase in volume when the eutectic liquid formation takes place. The segregation of the Zn and B in the Ba-Ti-W-O phases was observed by EPMA (Fig. 8).

The relationship between the microwave dielectric properties and density of the N-35 sample with  $ZnO-B_2O_3$  (ASF1495) additions are different than those for the samples of pure N-35 dielectric and those with  $B_2O_3$  additions, as indicated in Fig. 9. For N-35 sintered with  $ZnO-B_2O_3$ , the Q is almost constant despite the increase in density because of the glass remaining in the sintered ceramics. N-35 sintered with  $B_2O_3$  contained in homogeneous phases and  $TiO_2$  with needle-like morphology. Afterwards the  $B_2O_3$  either evaporates or is incorporated into the lattice, reducing the amount of second phase at the grain boundary. Furthermore, the acceptor dopant may reduce the oxygen vacancies and raise Q.

## (3) Different content of glass addition

The effect of glass addition on the microwave dielectric properties at different sintering temperatures was dependent on the chemistry of the glass, the chemical reactions, the phase changes during sintering, and the final density. For N-35 sintered with  $B_2O_3$  and commercial  $ZnO-B_2O_3$  (ASF1495) glass, the Q decreased with increasing glass content, despite the increase in density. The magnitude of K for N-35 fired with various amounts of glass was dependent on the sintered density. In general, the higher the sintered density, the higher the permittivity at the microwave frequencies.

## (4) Mixing effect

In this study, we used an agate mortar and pestle to mix the dielectrics and glasses in order to prevent any contamination during the milling process. As shown in Fig. 9, the densities of N-35 ceramics with 5 wt%  $ZnO-B_2O_3$  glass additions (ASF 1495) with ball milling have a 5% higher density than those mixed with mortar and pestle. This indicates that enhanced densification is

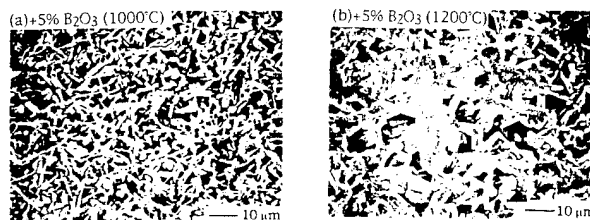


Fig. 5 Scanning electron micrographs of fracture surfaces of N-35 sintered with  $B_2O_3$  at (a) 1000°C and (b) 1200°C.

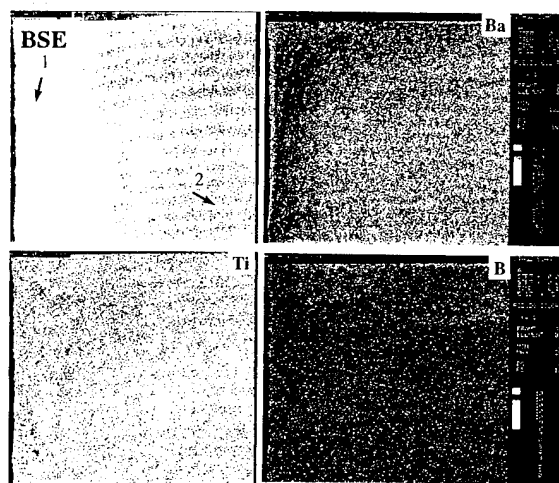


Fig. 6 EPMA images of N-35 sintered with  $B_2O_3$  at 1200°C.

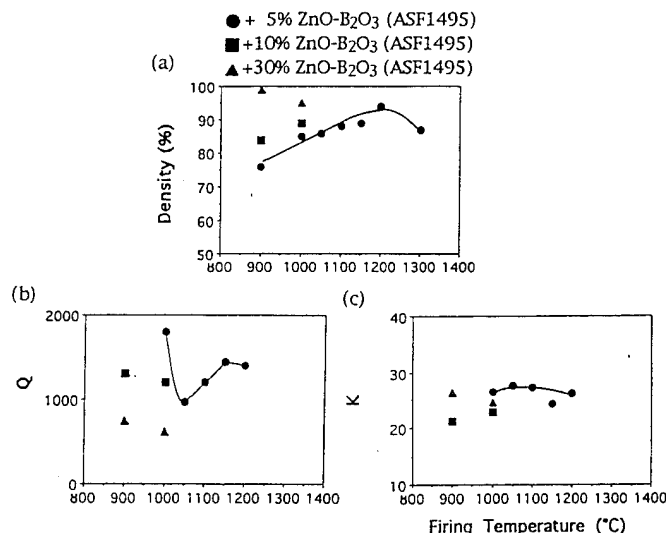


Fig. 7 Effect of  $ZnO-B_2O_3$  (ASF1495) addition to N-35 on (a) density and (b), (c) microwave dielectric properties with firing temperature.

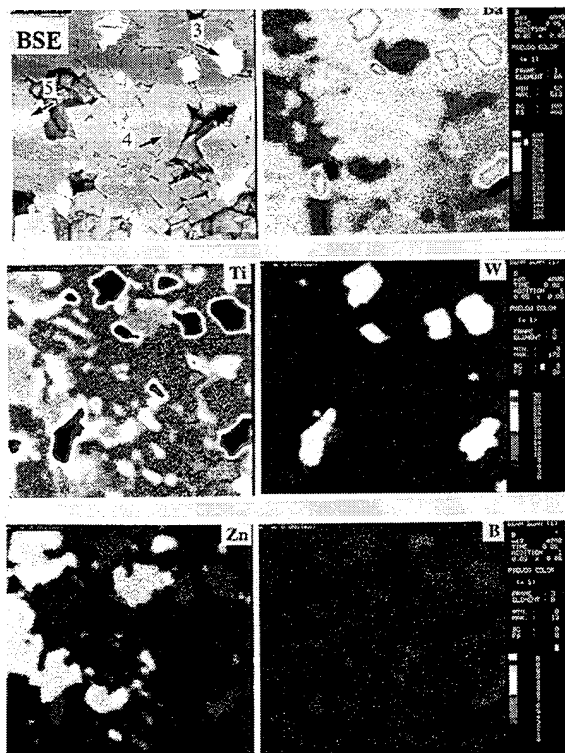


Fig. 8 EPMA images of N-35 sintered with ZnO-B<sub>2</sub>O<sub>3</sub>(ASF1495) at 1200°C.

achieved by better mixing. By further improving the mixing process, as in sol-gel coating or solution mixing, further improvements in density are expected.

### Conclusions

N-35 sintered with ZnO-B<sub>2</sub>O<sub>3</sub>, B<sub>2</sub>O<sub>3</sub>-SiO<sub>2</sub>, and Al<sub>2</sub>O<sub>3</sub>-SiO<sub>2</sub> glasses systems effectively lowered the sintering temperature.

For N-35 dielectrics sintered with 5 wt% B<sub>2</sub>O<sub>3</sub>, the Q was 8300 at 8.5 GHz, which is higher than that of pure N-35 sintered at 1360°C (Q=5900, at 7.2 GHz). The permittivity was 34 at 8.5GHz, which is higher than the value of log mixing rate. Generally the K and Q values increased with sample density. SEM showed a needle-like morphology, EPMA supported the existence of TiO<sub>2</sub>.

The Q of N-35, sintered with the ZnO-B<sub>2</sub>O<sub>3</sub> (ASF1495) glass system, showed a sudden drop at sintering temperatures near 1000°C, which was a result of the chemical reaction between the dielectric and glass. The glass was segregated in the sintered sample and the chemical reaction had a larger impact on the Q values than on density.

Density increased but the Q and K declined by increasing the glass content from 5 to 30 wt%. The process of mixing the host material with the glass had a significant effect on the densification as well as on the Q and K of the dielectrics.

### Acknowledgment:

The assistance of Mr. Ando and Ms. Oshida of Sumitomo Metal Technology Co. Ltd. with operating the EPMA and Dr. Morena of Corning Inc. with supplying the glass powders is gratefully acknowledged.

### References

- 1T. Okawa and H. Utaki, "The Development of a Multilayer Dielectric Filter Using Low Temperature Fired Microwave Ceramics," *The Sumitomo Search*, **47**, 117-21 (1991).
- 2D. E. Rase, and R. Roy, "Phase Equilibria in the System BaO-TiO<sub>2</sub>," *J. Am. Ceram. Soc.*, **38**, 102-13 (1955).

- N-35
- + 5% B<sub>2</sub>O<sub>3</sub>
- + 5% ZnO-B<sub>2</sub>O<sub>3</sub> (ASF1495)
- + 5% ZnO-B<sub>2</sub>O<sub>3</sub> (ASF1495) Ball milling

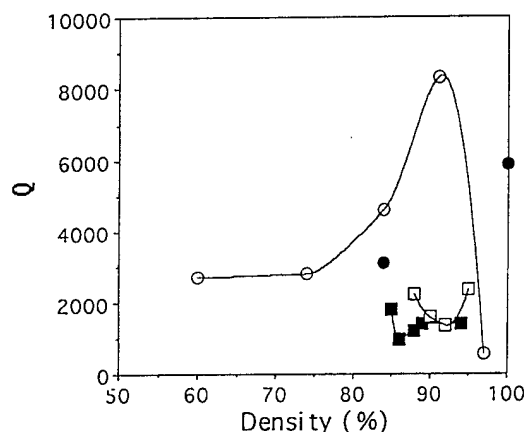


Fig. 9 Dependence of Q on density of N-35 sintered with B<sub>2</sub>O<sub>3</sub> and ZnO-B<sub>2</sub>O<sub>3</sub>(ASF1495).

3G. H. Jonker, and W. Kwestroo, "The Ternary Systems BaO-TiO<sub>2</sub>-SnO<sub>2</sub> and BaO-TiO<sub>2</sub>-ZrO<sub>2</sub>," *J. Am. Ceram. Soc.*, **41** [10] 390-94 (1958).

4H. M. O'Bryan, and J. Thomson, "Ba<sub>2</sub>Ti<sub>9</sub>O<sub>20</sub> Phase Equilibria" *J. Am. Ceram. Soc.*, **66** [1] 66-68 (1983).

5T. Negas, R. S. Roth, H. S. Parker, and D. Minor, "Subsolidus Phase relations in the BaTiO<sub>3</sub>-TiO<sub>2</sub> system," *J. Solid State Chem.*, **9**, 297-307 (1974).

6H. M. O'Bryan, Jr., J. Thomson, Jr., and J. K. Plourde, "A New BaO-TiO<sub>2</sub> Compound with Temperature-Stable High Permittivity and Low Microwave Loss," *J. Am. Ceram. Soc.*, **57** [10] 450-53 (1974).

7H. M. O'Bryan, Jr., and J. Thomson, Jr., "Phase Equilibria in the TiO<sub>2</sub>-Rich Region of the System BaO-TiO<sub>2</sub>," *J. Am. Ceram. Soc.*, **57** [12] 522-26 (1974).

8J. K. Plourde, D. F. Linn, H. M. O'Bryan, Jr., and J. Thomson, Jr., "Ba<sub>2</sub>Ti<sub>9</sub>O<sub>20</sub> as a Microwave dielectric Resonator," *J. Am. Ceram. Soc.*, **58** [9]-[10] 418-20 (1975).

9H. M. O'Bryan, Jr., and J. Thomson, "Temperature-Dependent Phase Boundaries for BaTi<sub>4</sub>O<sub>9</sub>, Ba<sub>4</sub>Ti<sub>13</sub>O<sub>30</sub>, and Ba<sub>6</sub>Ti<sub>17</sub>O<sub>40</sub>," *J. Am. Ceram. Soc.*, **68** [2] C70-C72 (1985).

10S. Nishigaki, S. Yano, H. Kato, T. Hirai, and T. Nomura, "BaO-TiO<sub>2</sub>-WO<sub>3</sub> Microwave Ceramics and Crystalline BaWO<sub>4</sub>," *J. Am. Ceram. Soc.*, **71** [1] C11-C17 (1988).

11V. Ern and R. E. Newnham, "Effect of WO<sub>3</sub> on Dielectric Properties of BaTiO<sub>3</sub> Ceramics," *J. Am. Ceram. Soc.*, **44** [4] 199 (1961).

12S. G. Mhasalkar, W. E. Lee, and D. W. Readey, "Processing and Characterization of BaTi<sub>4</sub>O<sub>9</sub>," *J. Am. Ceram. Soc.*, **72** [11] 2154-58 (1989).

13K. Mashima, M. Shinohara, S. Katsuyama, K. Kageyama, and H. Nagai, "Influence of Some Oxide Addition on Dielectric properties of BaTi<sub>4</sub>O<sub>9</sub>," *Huntai oyobi Hunmatsuyakin*, **38** [6] 735-39 (1991).

14S. Nomura, K. Tomaya, and K. Kaneta, "Effect of Mn Doping on the Dielectric Properties of Ba<sub>2</sub>Ti<sub>9</sub>O<sub>20</sub> Ceramics at Microwave Frequency," *Jpn. J. Appl. Phys.*, **22** [7] 1125-28 (1983).

15B. W. Hakki, and P. D. Coleman, "A Dielectric Resonator Method of Measuring Inductive Capacities in the Millimeter Range," *IRE Trans. Microwave Theory Tech.*, **MTT-8** 402-10, (1960).

16W. E. Courtney, "Analysis and evaluation of a method of measuring the complex permittivity and permeability of microwave insulators," *IEEE Trans. Microwave Theory Tech.*, **MTT18** 476-85, (1970).

17J. Wu, M. Chang, and P. Yao, "Reaction Sequence and Effects of Calcination and Sintering on Microwave Properties of (Ba,Sr)O-Sm<sub>2</sub>O<sub>3</sub>-TiO<sub>2</sub> Ceramics," *J. Am. Ceram. Soc.*, **73** [6] 1599-605 (1990).

18R. E. Newnham, S. J. Jang, Ming Xu, and Frederick Jones, "Fundamental Interaction Mechanisms between Microwaves and Matter," pp. 51-67 in *Ceramic Transactions*, Vol. 21, Edited by D. E. Clark, F. D. Gac, and W. H. Sutton, The American Ceramic Society, Columbus, Ohio, (19).

19J. O. Israd, "A Study of the Migration Loss in Glass and A Generalized method of Calculating the Rise of Dielectric Loss with Temperature," *IEE Paper 3636*, (1961) Int. Conf. Comp. Mats. Electron. Eng.

20H. Ouchi, "Trend of Microwave dielectric Ceramics," *Electronic Ceramics*, **19** [92] 9-19 (1988). in Japanese.

# DIELECTRIC PROPERTIES OF STRONTIUM AND LEAD BASED COMPLEX PEROVSKITE CERAMICS

S.A. GRIDNEV, N.G. PAVLOVA, S.P. ROGOVA, L.N. KOROTKOV and V.V. ZAENTSEV

Voronezh State Technical University,  
394711 Voronezh, Russia

**Abstract** -The dielectric properties and structure of the complex perovskite ceramics  $(0.7\text{PbZrO}_3 - 0.3\text{K}_{0.5}\text{Bi}_{0.5}\text{TiO}_3) + x\text{SrTiO}_3$  have been investigated in the temperature range from 283 K to 333 K with the intention of understanding a change of a sign which occurs in the temperature coefficient of the capacitance at  $x \approx 0.5$ .

## INTRODUCTION

The advancement of microwave circuits such as dielectric resonators in filters or oscillators in communications systems has required dielectric materials with a high quality factor ( $Q$ ), a high dielectric constant ( $\epsilon$ ) and a high temperature stability of resonant frequency without undesired effects on the other dielectric properties [1-3]. Their great advantage is to enable the reduction of size of the components. Therefore there has been an interest in new dielectric ceramics for microwave integrated circuits.

For this purpose, several studies of the perovskite compounds and their solid solutions have been made which make good dielectric materials [4-6]. On the other hand, there have been less works for dielectric properties on complex perovskite ceramics of ternary system [7].

The purpose of this paper is to show the experimental results of the dielectric properties of ternary  $0.7\text{PbZrO}_3 - 0.3\text{K}_{0.5}\text{Bi}_{0.5}\text{TiO}_3 + x\text{SrTiO}_3$  ceramic system and also to discuss the proper choice and optimization of compositions for high quality ceramic dielectric materials.

## EXPERIMENTAL

The specimens of the complex perovskite ceramics for  $0.1 \leq x \leq 0.9$  have been prepared by the conventional mixed oxide route. All the starting materials composed of  $\text{K}_2\text{CO}_3$ ,  $\text{Bi}_2\text{O}_3$ , and  $\text{TiO}_2$  as well as  $\text{PbO}$ ,  $\text{ZrO}_2$  and  $\text{SrO}$  powders with purity of 99.9 % were weighed out and ball milled for 16 hours in a polyethylene jar with agate balls and distilled water. The mixed raw materials were dried and pressed into pellets under pressure of 1000  $\text{Kg/cm}^2$ . Having been calcined at 1173 K for 2 hours in air the pellets were crushed in a mortar and remilled the same as the one for raw materials milling and finally screened through 80 mesh. The screened powder was dry-pressed into disks of 10 mm diameter and then fired at 1423 K for 3 hours in air. Particular attention was paid to avoid intermediate phases from the reaction products since the presence of second phases usually increases the dielectric losses of the materials, therefore it is important to prepare ceramics without any second phase.

The samples obtained were examined by X-ray diffraction analysis with  $\text{Cu K}\alpha$ -radiation and Ni-filter. A least mean square method of analysis was used to calculate lattice parameters.

Standard dielectric measurements were performed on thin ceramic discs within a temperature range of 283-

333 K and at frequencies varying from 100 Hz up to 1 MHz using a temperature controlled chamber. The temperature coefficient of capacitance ( $\alpha$ ) was calculated as  $1/c(\Delta c/\Delta T)$ . For details of experimental methods, see [8].

## RESULTS AND DISCUSSION

X-ray diffraction data for mixed oxide prepared ceramics revealed only single phase products. Dielectric measurements were made on dense (no water absorption) ceramic specimens. The complex perovskite compounds under study contain  $\text{SrTiO}_3$  as main dopant. The effect of this dopant on the temperature dependence of capacitance is shown in Figure 1. With an increase of  $\text{SrTiO}_3$ , capacitances within all temperature interval decrease and the curve becomes smoother. The temperature coefficient of capacitance  $\alpha_c$  for specimens is the slope of the line in Figure 1.

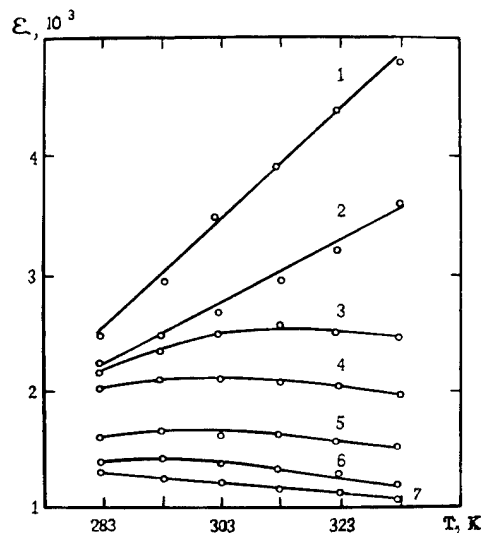


FIGURE 1 Temperature dependences of dielectric constant for various compositions: 1- $x=0.1$ , 2-0.2, 3-0.4, 4-0.5, 5-0.6, 6-0.7 and 7-0.9.

As is seen the specimens show the remarkable decreasing of  $\alpha$  and the dielectric constant with the  $\text{SrTiO}_3$  content increasing. But the dielectric constant remained rather high. The dielectric experiments revealed that  $\alpha$  experiences smooth variations with  $x$  and the change of sign occurs at  $x \approx 0.5$  (Figure 2). The most obvious behaviour within the common temperature interval is the existence of a negative  $\alpha$  in the Sr-rich compositions and the presence of a positive  $\alpha$  at  $x < 0.5$ . It must be stressed that  $\alpha_c$  tends to zero as the  $\text{SrTiO}_3$  dopant is close to  $x \approx 0.5$ .

## CONCLUSIONS

The investigation of dielectric properties and of the structure in the  $\text{PbZrO}_3\text{-K}_{0.5}\text{Bi}_{0.5}\text{TiO}_3\text{-SrTiO}_3$  system has shown a correlation between the magnitudes of  $\alpha$  and of dielectric constant and the composition, but the quality factor depends on process variables such as temperature, annealing time and atmosphere. The extensive study of the relation between the quality factor and the process variables is still needed to prepare good microwave dielectric ceramics and to fully explain the results.

## ACKNOWLEDGEMENTS

This work has been carried out with the support of the Russian Foundation for Fundamental Research, grant N 94-02-06591.

## REFERENCES

- [1] D.Kolar, S.Gaberscek, Z. Stadler and D. Suvorov "High stability, low loss dielectrics in the system  $\text{BaO} - \text{Nd}_2\text{O}_3 - \text{TiO}_2 - \text{Bi}_2\text{O}_3$ ", *Ferroelectrics*, vol.27, pp.269-272, 1980.
- [2] C.J. Rawn, D.P. Birnie and R.S. Roth "Stability of low temperature  $\text{BaZn}_2\text{TiO}_7$  in microwave dielectrics", in *Abstracts of the 8th Int.Meet.on Ferroelectricity*, Maryland, 1993, p.154.
- [3] J.Van Bladel, "Dielectric resonators", *Ferroelectrics*, vol.27, pp.285-288, 1980.
- [4] E.S. Kim and K.H. Yoon, "Microwave dielectric properties of complex perovskite  $\text{Ba}(\text{Mg}_{1/3}\text{Ta}_{2/3})\text{O}_3$ ", *Ferroelectrics*, vol.133, pp. 187-192, 1992.
- [5] E.L. Colla, I.M. Reaney and N. Setter, "The temperature coefficient of the relative permittivity of complex perovskites and its relation to structural transformations", *Ferroelectrics*, vol.133, pp.217-222, 1992.
- [6] N. Setter, E. Colla, D. Dube, J.Petzelt et al., "Structural aspects in ceramics for microwave resonators", in *Abstracts of the 8th Int. Meet. on Ferroelectricity*, Maryland, 1993, p.157.
- [7] T. Yamaguchi, Y.Komatsu, T. Otobe and Y. Murakami, "Newly developed ternary (Ca, Sr, Ba) zirconate ceramic system for microwave resonators", *Ferroelectrics*, vol.27, pp.273-276, 1980.
- [8] S.A. Gridnev, N.G. Pavlova, V.V. Gorbatenko and L.A. Shuvalov, "Newly developed multicomponent piezoceramic system for alternating pressure sensors", *Ferroelectrics*, vol.134, pp.53-57, 1992.

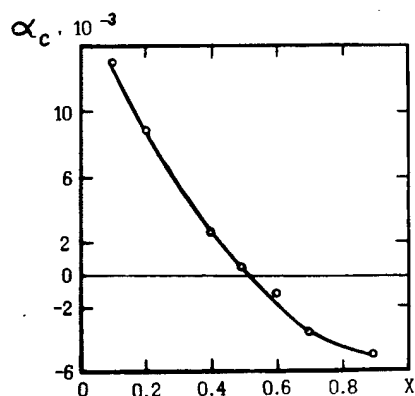


FIGURE 2  $\alpha_c$  as a function of  $\text{SrTiO}_3$ -concentration.

A comparison of data obtained with the  $\epsilon(T)$  curves in Figure 3 should give a reasonable explanation of the changes in  $\alpha$  in terms of the changes in the temperature position of the structural phase transition. In Figure 3 the plots for  $x=0.1$ , 0.4 and 0.7 show that the temperature interval, where we measure  $\alpha$  and the change in sign of  $\alpha$  is observed, belongs to the different sides of the diffused  $\epsilon(T)$  maximum near the phase transition. Sr-rich specimen ( $x=0.7$ ) shows the negative value of  $\alpha$ ; this result is in agreement with the work [4] in which  $\alpha_c$  of paraelectrics shows negative value.

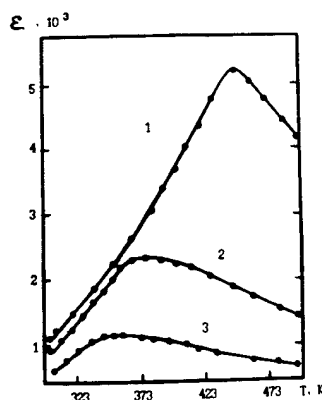


FIGURE 3. Temperature dependences of dielectric constant of various doped ceramics: 1- $x=0.1$ ; 2-0.4 and 3-0.7. ( $f=10$  kHz).



# Concurrent Session - 5A: Photorefractives



# The Use of Applied Electric Fields on the Photorefractive Tungsten Bronze Ferroelectrics

Nianyu Bei<sup>1</sup>, Galen C. Duree<sup>1</sup>, and Gregory J. Salamo<sup>1</sup>, Rakesh Kapoor<sup>2</sup>, Edward J. Sharp<sup>3</sup>, and Ratnaker R. Neurgaonkar<sup>4</sup>

<sup>1</sup>Physics Department of the University of Arkansas, Fayetteville, Arkansas 72701

<sup>2</sup>Physics Department of Alabama A&M, Normal, Alabama 35762

<sup>3</sup>Army Research Laboratory, Fort Belvoir, Virginia 20060

<sup>4</sup>Rockwell International Science Center, Thousand Oaks, California 91360

**Abstract**--The traditional method of determining the photorefractive effective charge density is to plot the photorefractive space charge field versus the crossing angle in a two-beam coupling experiment. The difficulty with this traditional measurement technique is that the apparatus must be moved several times in order to obtain data over the sufficient number of crossing angles needed for an accurate fit with theory. Moreover, with small crossing angles the overlap between the two crossing beams can easily extend over the entire crystal, while with larger crossing angles the overlap between the two beams becomes less certain.

In this paper we demonstrate an alternative method of determining the photorefractive charge density. In this approach we measure the phase shift between the optical intensity pattern in the crystal and the resulting index pattern, as a function of the magnitude of an applied d.c. field. By comparing the measured value of the d.c. field which produces a minimum phase shift with that predicted by theory the photorefractive effective charge density is found. In this case, only the magnitude of the applied field is varied and the apparatus remains fixed. The result is obtained quickly and with little error.

## INTRODUCTION

In this paper we discuss a technique to measure the trap density in photorefractive crystals. The technique is based on the use of interfering two laser beams in a crystal in the presence of an applied electric field. In the crystal the two light waves can be expressed as

$$E_T(x, z) = E_{T0} \exp[i(k_x x + k_z z)] \quad (1)$$

$$E_D(x, z) = E_{D0} \exp[i(-k_x x + k_z z)] \quad (2)$$

where  $k_x$  and  $k_z$  are components of the wavevector. The two light beams cross at an angle  $2\theta$  in the crystal with each beam making an angle  $\theta$  with the normal to the incident surface. If  $\phi$  is the phase shift between the grating and the interference pattern, the intensities of the output beams from the crystal can be written [Ref. 1] as

$$I_T(d) = I_T \cos^2(\kappa d) + I_D \sin^2(\kappa d) - (I_T I_D)^{1/2} \sin(2\kappa d) \sin\phi \quad (3)$$

$$I_D(d) = I_D \cos^2(\kappa d) + I_T \sin^2(\kappa d) + (I_T I_D)^{1/2} \sin(2\kappa d) \sin\phi \quad (4)$$

where  $I_T$  and  $I_D$  are the incident intensities and  $I_T(d)$  and  $I_D(d)$  are their intensities after passing through a crystal of thickness  $d$  with a coupling coefficient  $\kappa$ . In expressions (3) and (4), the first term corresponds to the transmitted component, the second term is the diffracted component, and the third term is the energy-exchange component between the two beams. From expressions (3) and (4) we can write the diffraction efficiency  $\eta$  as

$$\eta = \sin^2(\kappa d) \quad (5)$$

If the intensity of both beams is adjusted to be equal at the entrance of the crystal we can write the energy exchange efficiency in terms of the diffraction efficiency as

$$\epsilon = 2[\eta(1 - \eta)]^{1/2} \sin\phi \quad (6)$$

Therefore, expression (6) yields an expression for the phase shift between the intensity pattern and the index grating and is given by

$$\sin\phi = \epsilon / [2\eta(1 - \eta)]^{1/2} \quad (7)$$

$$\sin\phi = I_e / [2(I_d(I_0 - I_d))]^{1/2} \quad (8)$$

where  $I_e$ ,  $I_d$  and  $I_0$  are the magnitude of the energy exchange, the diffraction signal and the intensity of the transmitted beam. From these expressions we can see that by measuring  $I_d$ ,  $I_e$ , and  $I_0$ ,  $\phi$  can be determined [Ref 2,3,4].

## EXPERIMENTAL TECHNIQUE

The apparatus which we used to measure  $\phi$  as a function of applied d.c. electric field consisted of a HeNe laser oscillating at 6328Å with an output power of 5mw. We used ordinary polarized beams in order to minimize beam fanning and the corresponding intensity fluctuations which appear in energy exchange signals. After the polarizer, the laser beam was split into two beams  $I_D$  and  $I_T$  which intersected inside a thin sample of SBN 60 with 0.015% Cesium as a dopant (static dielectric constant  $\epsilon' = 950$ ) such that the grating vector is parallel to the c-axis. The beam splitter is 50% /50% to make the beam  $I_D$  have the same intensity as  $I_T$ . The angle  $2\theta$

between the two beams was  $22^\circ$ . The beam  $I_T(d)$  was detected with a photodiode. For all our observed intensity values the photodiode was linear. To avoid the observation of multi-exponential growth and decay times, the detected beam was expanded with a beam expander so that only the uniform portion of the beam was detected by the photodiode. The output of the diode was fed into a 602A Digitizing Signal Analyzer. After turning on both beams a growth curve was recorded and the energy exchange signal  $I_E$  was measured. When the grating reached its steady state we blocked the detected beam. The transmitted beam immediately went to zero, and the diffraction signal  $I_d$  was detected. Finally, the intensity of the transmitted beam  $I_0$  was measured. By substituting  $I_0$ ,  $I_E$ , and  $I_d$  into expression (8), we can calculate the phase shift between the grating and the interference pattern in the crystal.

After applying a d.c. field across a crystal we carried out the measurement described above yielding values for  $I_0$ ,  $I_E$ , and  $I_d$ . By substituting them into expression (8) we calculated both the  $\sin \phi$  and the  $\tan \phi$ . In order to get accurate results we varied the magnitude of the d.c. field and measured  $I_0$ ,  $I_E$ , and  $I_d$  for each d.c. field value  $E_0$ .

From the band transport theory we have

$$\tan \phi = \frac{E_D}{E_0} + \left( \frac{E_D^2}{E_0} + E_0 \right) \frac{1}{E_q} \quad (9)$$

$$\frac{1}{E_q} = \left( \tan \phi - \frac{E_D}{E_0} \right) / \left( \frac{E_D^2}{E_0} + E_0 \right) \quad (10)$$

Expression (9) gives a value of  $E_0$  for minimum  $\phi$  of  $E_0 = [E_D E_q + E_D^2]^{1/2}$ . Using expression (10) we are able to calculate a set of data for  $1/E_q$  vs  $E_0$ .  $E_q$  is defined as  $E_q = 4\pi e N_{eff} / \epsilon K_g$  where  $N_{eff}$  is approximately the trap density  $N_A$  for our crystal. Since we observe that  $E_q$  depends on  $E_0$  the dielectric constant  $\epsilon$  must depend on  $E_0$ . For the parameters used in our experiment we have

$$\begin{aligned} K_g &= \frac{2\pi}{\lambda} (2 \sin \theta) = 3.79 \times 10^4 \text{ cm}^{-1} \\ E_D &= \frac{K_B T K_g}{e} = 963.24 \text{ v/cm} \\ E_q &= \frac{4\pi e}{K_g} \left( \frac{N_{eff}}{\epsilon} \right) = (4.776 \times 10^{-11}) \left( \frac{N_{eff}}{\epsilon} \right) \end{aligned} \quad (11)$$

For our work we assume that the dependence of the dielectric constant  $\epsilon$  on the magnitude of the d.c. field  $E_0$  is

$$\begin{aligned} \epsilon(E_0) &= \epsilon' (1 + \alpha E_0 + \beta E_0^2) \\ &= \epsilon' [1 + f(E_0)] \end{aligned} \quad (12)$$

where  $\alpha$  and  $\beta$  are constants to be determined.

By combining expressions (10), (11) and (12) we can calculate  $1/E_q$  and  $N_{eff}/\epsilon'$  for each value of d.c. field  $E_0$ . Using these values we plotted  $\{(1+f(E_0)_i)/(1+f(E_0)_1)\}$  versus  $(E_0)_i$  as shown in Fig. 1. By fitting the data we found that  $\alpha = 0.0009515$  and  $\beta = -2.51 \times 10^{-7}$ . As a result we can write

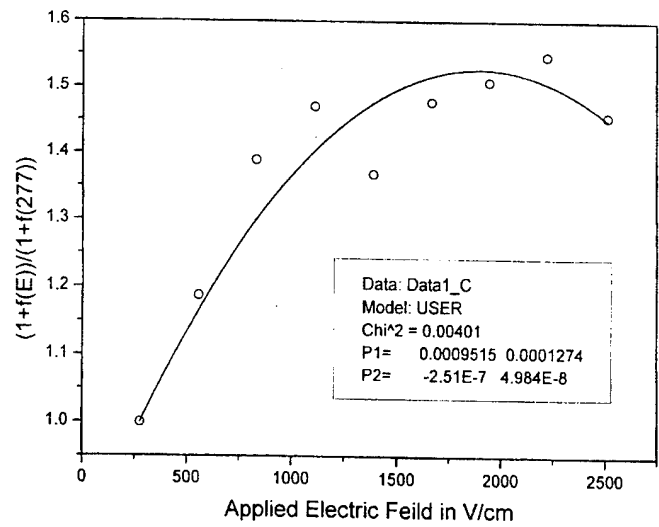


Fig 1. Determining the electric field dependence of the dielectric constant

$$E_q = \frac{4.776 \cdot 10^{-11}}{1 + 0.0009515 E_0 - (2.51 \cdot 10^{-7}) E_0^2} \left( \frac{N_{eff}}{\epsilon'} \right) \quad (13)$$

For each pair of  $E_0$  and  $E_q$  we can now calculate the value of  $N_{eff}/\epsilon'$ .

By taking the average, we obtained  $N_{eff}/\epsilon' = (4.54 \pm 0.38) \times 10^{13} (\text{cm}^{-3})$ . For our crystal the value of  $\epsilon'$  is 950. Therefore, we get  $N_{eff} = (4.31 \pm 0.36) \times 10^{16} (\text{cm}^{-3})$ . In [Ref. 2] an  $N_A$  value of  $(4.2 \pm 0.2) \times 10^{16} (\text{cm}^{-3})$  was reported for the crystal of SBN: 60 with 0.015% Rh. concentration. Our results are in good agreement with their reported value.

Also we plotted curves of  $\sin \phi$  vs  $E_0$ ,  $\tan \phi$  vs  $E_0$  and  $\epsilon$  vs  $E_0$ , respectively. They are shown in Fig. 2, 3, and 4.

In order to exam the accuracy of the  $N_A$  value which we obtained by using the phase-electric field method, we also did an experiment to measure  $N_A$  by using the traditional

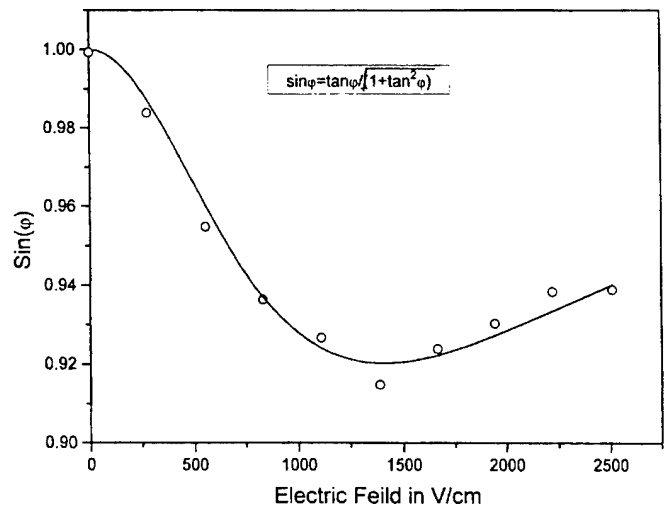


Fig 2. The  $\sin \phi$  as a function of applied field

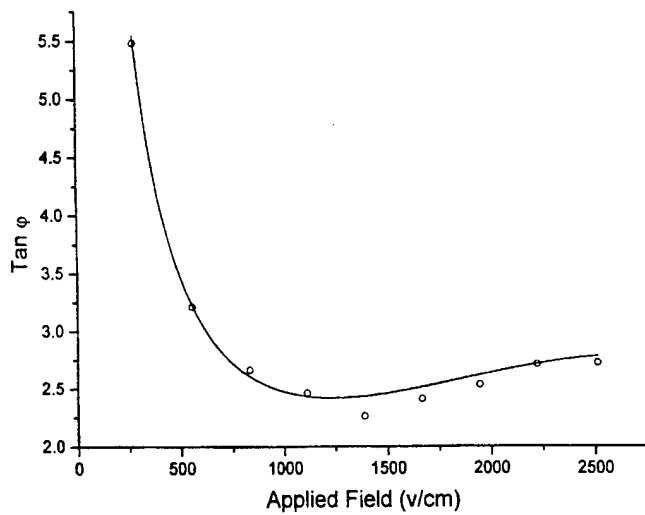


Fig 3. The  $\tan\phi$  as a function of applied field

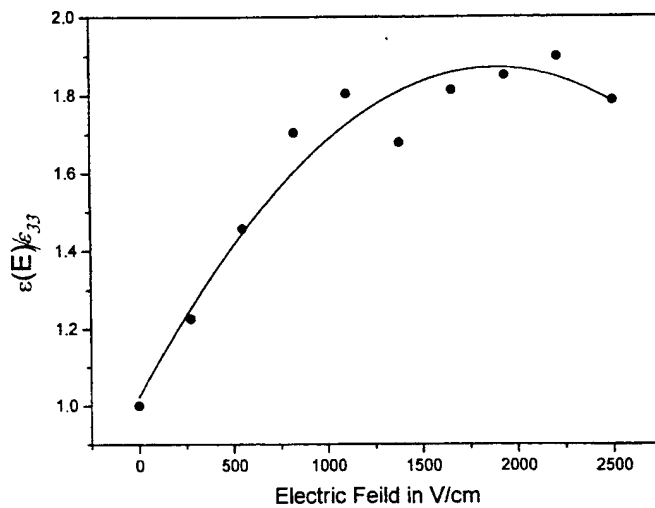


Fig 4. The dielectric constant as a function of applied field

method of changing the angle between the two crossing beams. The basic theory and measurement procedure are described in detail in [Ref. 5].

Due to two-beam coupling, the weak beam  $I_1$  experiences an increase in intensity along its propagation direction which is given by

$$\frac{I_{1c}}{I_1} = \frac{(1+m)e^{\gamma L_{\text{eff}}}}{1+me^{\gamma L_{\text{eff}}}} \quad (14)$$

where  $m = I_{01}/I_{02}$ , the ratio of the weak beam intensity to the strong beam intensity. Experimentally, we measured  $I_{1c}$ ,  $I_1$  and  $m$ , and then calculated  $\gamma L_{\text{eff}}$ . On the other hand

$$\gamma L_{\text{eff}} = A \frac{R_{\text{eff}}}{\cos\theta} \frac{K_g}{1+(K_g/K_0)^2} \quad (15)$$

where  $R_{\text{eff}} = n_e^4 r_{33} \cos^2\theta - n_o^4 r_{13} \sin^2\theta$  for an extraordinary ray,  $A$  is a constant,  $K_g$  is the grating constant and  $K_0^2 = \frac{4\pi e^2}{K_B T} \left( \frac{N_{\text{eff}}}{\epsilon} \right) = C \left( \frac{N_{\text{eff}}}{\epsilon} \right)$  provided  $C = 4\pi e^2 / K_B T$ . By

defining

$$f(\theta) = \frac{\cos\theta}{\cos^2\theta - \frac{n_o^4 r_{13}}{n_e^4 r_{33}} \sin^2\theta} \quad (16)$$

we will have

$$\gamma L_{\text{eff}} f(\theta) = B \frac{K_g}{1 + \frac{K_g^2}{C} \left( \frac{N_{\text{eff}}}{\epsilon} \right)} \quad (17)$$

where  $B$  is a constant. By plotting the data of  $\gamma L_{\text{eff}} f(\theta)$  vs  $K_g$  and fitting the data, we then obtained a value of  $N_{\text{eff}}/\epsilon$ . The fitting result (Fig. 5) gave us a value of  $N_{\text{eff}}/\epsilon = (4.59 \pm 0.31) \times 10^{13} (\text{cm}^{-3})$  which is in good agreement with our results using the phase measurement technique.

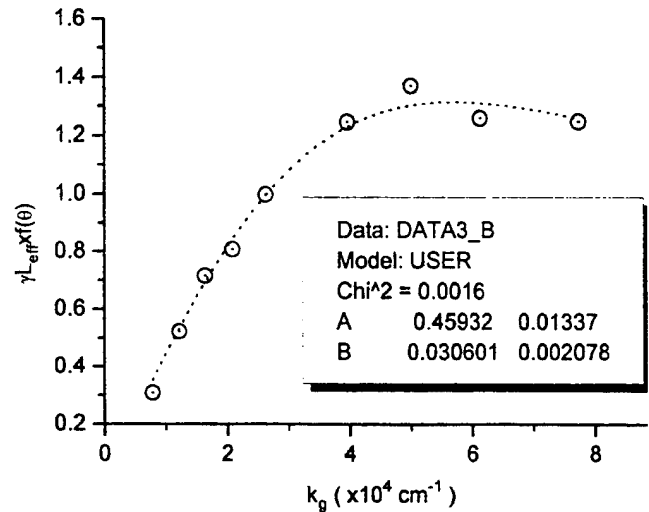


Fig 5. The photorefractive gain as a function of crossing angle

## CONCLUSION

We have demonstrated a technique for the measurement of the trap density in photorefractive materials. This technique has been shown to give the same result for the trap density as the conventional two-beam coupling technique but is more convenient to carry out in practice. The technique presented here also yields the electric field dependence of the dielectric constant.

## REFERENCES

1. H. Kogelnik, Bell Syst. Tech. J. Vol 48, 6929 (1969).
2. R.A. Vazquez et al, JOSA B, Vol 9, 1416 (1992).
3. R. Kapoor et al, Opt. Lett. Vol 8, No 9, May 1, (1993).
4. J.P. Wilde et al, Opt. Lett. Vol 17, 853 (1992).
5. G.L. Wood, G.J. Salamo et al, IEEE J. Quan. Electro. Vol QE-23, 2126 (1987).

# Ce:Fe:LiNbO<sub>3</sub> Photorefractive Crystal: Material Properties and Applications

(Invited)

F. T. S. Yu, A. S. Bhalla, S. Yin, F. Zhao, Z. Wu, and D. M. Salerno\*

Department of Electrical Engineering  
Pennsylvania State University  
University Park, Pennsylvania 16802

**Abstract** — A specially doped photorefractive (PR) crystal Ce:Fe:LiNbO<sub>3</sub>, and the effect due to Ce and Fe dopants are reported. We have found that the double-doped crystal exhibits higher PR sensitivity, larger dynamic range, broader spectral bandwidth, and lower scattering noise. It is about 10-times higher in PR sensitivity in the red light region (633nm), as compared with the reported data [1]. We have also discovered anomalous enhancement of PR effects which occur at 57°C, 70°C and 110°C. The anomalies are primarily due to possible structural phase-transitions of the crystal at these temperatures. Several applications of this specially doped PR (Ce:Fe:LiNbO<sub>3</sub>) crystal (both bulk and fiber) are also provided.

## I. INTRODUCTION

Photorefractive lithium niobate (LiNbO<sub>3</sub>) based materials have received broad promising applications in recent years, such as optical signal processing, random-access memories, large capacity interconnections, switching, etc. [2]. In these applications, high PR sensitivity and low scattering noise materials are needed. It is well known that these PR properties are influenced by doping, annealing, and other crystalline processes. For example, photo-induced charge transport process in LiNbO<sub>3</sub> can be greatly enhanced by transition-metal-dopants in different valence states. Fe, Cu, Cr, Mn, Ce, etc., dopants have been used to improve the PR properties of lithium niobate based materials [1, 3-5]. However, based on the approach by Yeh [6], the PR response time of a LiNbO<sub>3</sub> based material is in the order of a few seconds, which is much slower than the actual limit, which is in the order of milliseconds. On the other hand, light-induced scattering noise (e.g., initiated by crystalline imperfections and non-uniform doping) through high (PR) gain amplification would affect the signal-to-noise ratio (SNR) of the material. Therefore to broaden the application of the LiNbO<sub>3</sub> based materials, PR sensitivity should be improved and scattering noise has to be minimized.

## II. CRYSTAL PREPARATION

Both bulk and single crystal fiber LiNbO<sub>3</sub> based materials doped with Ce, Fe and Ce:Fe have been grown in the Material Research Laboratory (MRL) at the Pennsylvania State

University [7], in which the conventional Czochralski technique has been used to grow the bulk crystals, and the Laser Heated Pedestal Growth (LHPG) technique is used to fabricate the single crystal fibers.

By using the Czochralski process, a single crystal seed is dipped into a Platinum crucible containing the melt and then slowly withdrawn. The temperature of the crucible is heated by RF sources to about 1260°C. During the withdraw process, the melt solidifies onto the seed, for which the crystal is initiated by adjusting the input heat of the melt to control the crystal diameter. Crystals of 60mm in diameter and 50mm in thickness have been grown. The samples are poled to exhibit a single domain by heating the crystal to the Curie temperature (1220°C), where the crystals become paraelectric, in which a DC field (0.5~5V/cm) is applied for approximately 1 hour. To obtain a higher PR sensitivity, the crystals are annealed in vacuum chamber at ~800°C, for about 2-3 hours.

By using the laser-heated growth process, the tip of a small source crystal rod is uniformly heated with a high intensity CO<sub>2</sub> laser beam using a reflexicon with a parabolic mirror. By dipping the crystal seed into the molten zone the fiber growth can be initiated by pulling the fiber crystal (at rates of a few millimeters per minute) away from the melt, while feeding the source rod at a commensurate steady-state rate. Advantages of the LHPG technique include fast growth rate, no poling is needed, long crystalline fiber can be obtained, etc. Single crystal fibers of LiNbO<sub>3</sub> and SBN of diameters ranging from 100-1000μm have been successfully grown by using this technique.

## III. CHARACTERIZATION OF PHOTOREFRACTIVE PROPERTIES

Photorefractive sensitivity is one of the most important figures of merit of a PR material. For holographic applications, the PR sensitivity is defined as the energy density needed to give rise to a 1% diffraction efficiency for a 1mm thick storage material [1],

$$S = \frac{d(\eta^{1/2})}{dW} \frac{1}{L}, \quad (1)$$

where  $\eta$  is the diffraction efficiency,  $W$  is the total incident energy density, and  $L$  is the thickness of the crystal. Thus, once we know the dynamic diffraction efficiency  $\eta$  and the

corresponding input optical power  $W$ , we can proceed by Eq. (1) to obtain the PR sensitivity  $S$ .

The photorefractive recording time-constant determines the speed of a PR hologram formation, which is crucial to any real-time applications of the PR crystal. The build-up of the space-charge field can be shown, by using the Kukhtarev's model [5], to exhibit an exponential behavior. Hence the evolution of the diffraction efficiency can be expressed as [1]:

$$\eta(t) = \eta_{\max} \left(1 - e^{-t/\tau}\right), \quad (2)$$

where  $\eta_{\max}$  is the saturation value of the diffraction efficiency, and  $\tau$  is the response time-constant (or recording time constant). The time-constant can be measured from the evolution of the diffraction efficiency. For practical applications, a large diffraction efficiency and a fast time-constant are needed.

The maximum refractive index change  $\Delta n_{\max}$  of the PR crystal is referred to as the material dynamic range, which determines the maximum number of holograms that can be stored in the crystal.

It has been shown by Kogelnik [8] that the photo-induced refractive index change  $\Delta n$  is related to the diffraction efficiency  $\eta$  by

$$\eta = \exp\left(-\frac{\alpha L}{\cos \theta_i}\right) \sin^2\left(\frac{\pi L \Delta n}{\lambda \cos \theta_i}\right), \quad (3)$$

for transmission hologram, where  $\alpha$  is the optical absorption coefficient,  $L$  is the crystal thickness,  $\lambda$  is the wavelength of the incident light, and  $2\theta_i$  is the internal angle between the two incident beams. The dynamic range can be determined from Eq. (3) by measuring the saturation diffraction efficiency.

We have experimentally characterized the PR properties for three samples doped with Fe, Ce, and Ce:Fe, respectively, as tabulated in Table 1. Figure 1 shows the schematic of the experimental setup, in which a 10mW He-Ne laser is used to provide the writing beams. The power of the signal beam  $I_1$  and reference beam  $I_2$  are about the same, i.e.,  $I_1=I_2=2\text{mW}$ . The sizes of the two beams are about 1.5mm in diameter, and the external angle between them is about  $7^\circ$ . Extra-ordinary polarized lights are used, and the  $c$ -axis of the crystal is oriented at the incident plane. Note that this orientation allows the use of the largest electro-optic tensor element  $\gamma_{33}$ . An electronic shutter is placed in the reference arm, with a chopping rate of 1Hz and duty-cycle of 50%.

Figure 2 shows the evolution of the diffraction efficiency for the three samples, in which the lower envelop represents the diffraction efficiency evolution. It is therefore trivial that the recording time-constants  $\tau$ , the diffraction efficiencies  $\eta_{\max}$ , the PR sensitivities  $S$ , and the dynamic ranges  $\Delta n_{\max}$  can be measured, and the results are tabulated in Table 1. From these results we see that the sample with double-doping gives rise to the best overall PR properties. As compared with

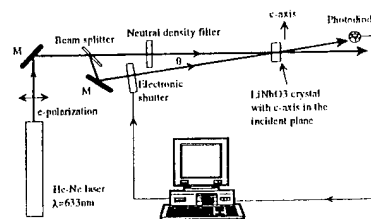


Fig. 1. Schematic of the experimental setup for photorefractive property characterization.

reported data by Günter and Huignard [1], our results show that there is about a 10-fold increase in the PR sensitivity. To our knowledge, this is the highest PR sensitivity that has been reported for LiNbO<sub>3</sub> based crystal in the red light region.

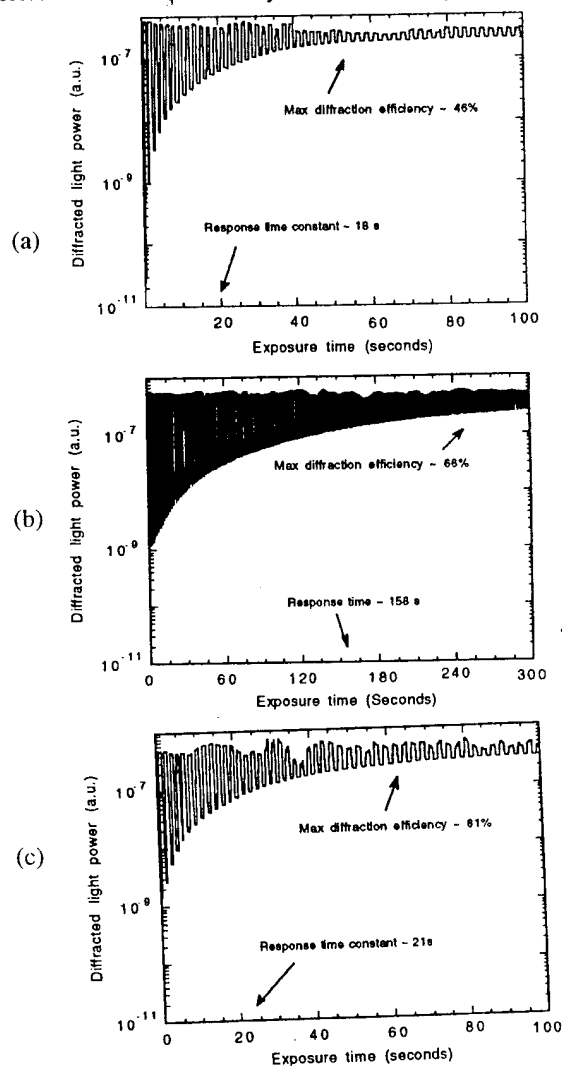


Fig. 2. Development of the photorefractive process. The lower envelop represents the diffraction evolution. (a) Fe:LiNbO<sub>3</sub>; (b) Ce:LiNbO<sub>3</sub>; and (c) Ce:Fe:LiNbO<sub>3</sub>.

Table 1. Photorefractive properties of LiNbO<sub>3</sub> with Fe, Ce, and Ce:Fe dopants

	Fe:LiNbO <sub>3</sub>	Ce:LiNbO <sub>3</sub>	Ce:Fe:LiNbO <sub>3</sub>
Doping concentration	Fe:0.08mol%	Ce:0.08mol%	Ce:0.08mol%, Fe:0.08mol%
Response time constant $\tau$ (seconds)	18	158	21
Dynamic range $\Delta n_{\max}$	$1.4 \times 10^{-4}$	$1.9 \times 10^{-4}$	$1.8 \times 10^{-4}$
Inverse of PR sensitivity $S^{-1}$ (mJ/cm)	17	97	14
Maximum diffraction efficiency $\eta_{\max}$	51%	66%	61%

#### IV. LOW TEMPERATURE PHASE-TRANSITIONS

One important advantage of LiNbO<sub>3</sub> is the high Curie point (~1220°C), which makes it very robust against temperature perturbations. In fact, all samples of LiNbO<sub>3</sub> show the high temperature phase-transition. Intrinsic LiNbO<sub>3</sub> samples show only one phase-transition, however doped LiNbO<sub>3</sub> based materials have been found to exhibit some low temperature transitions [9-10]. Notice that the doped LiNbO<sub>3</sub> crystals remain in the ferroelectric domain at low temperature phase-transitions, which have not been fully understood and no report has been given on the influence of the PR properties due to the low temperature phase-transitions

In this section, we will present our preliminary investigation on the PR effect (two-wave coupling constant, and phase-conjugate reflectivity) as affected by the low temperature phase-transitions of the Ce:Fe:LiNbO<sub>3</sub> crystal. Figure 3 shows the experimental setup, in which a Ce:Fe:LiNbO<sub>3</sub> crystal is mounted in a temperature (controlled) oven. The size of the sample is 10×10×1 (mm<sup>3</sup>), and the doping concentrations for both Ce and Fe are the same amount, 0.08mol%. The crystal c-axis is oriented at the incident plane, where the extra-ordinary polarized laser beam is used. A He-Ne laser provides the incident beams, with pump beam  $I_1$  and signal beam  $I_2$ . In our experiment, the intensities of the incident beam are  $I_1=4\text{mW}$ , and  $I_2=10\mu\text{W}$ , respectively. The strong pump beam is perpendicularly incident on the crystal, and the external angle between  $I_1$  and  $I_2$  is about 7°. An electronic shutter is placed in the pump arm, by which the pump beam can be modulated.

It has been shown by Yeh [6] that the two-beam coupling constant  $\Gamma$  can be approximated by

$$\Gamma \approx \frac{1}{L} \ln \left[ \frac{I_2'(L) \text{ with pump}}{I_2(L) \text{ without pump}} \right], \quad (4)$$

under the undepleted (pump) condition, where  $L$  is the crystal thickness,  $I_2(L)$  and  $I_2'(L)$  are the transmitted signal intensity with and without the pump beam.

Since the temperature range between 20°C and 120°C is important to the holographic thermal fixing process, we have measured the (saturation) coupling constant  $\Gamma$  as a function of

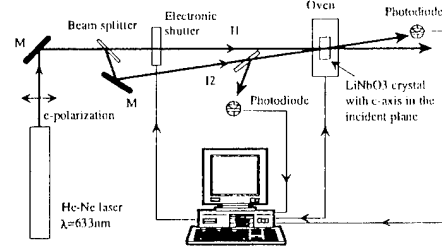


Fig. 3. Experimental setup for the measurement of low temperature phase transitions.

the crystal temperature and result is depicted in Figure 4(a). Thus we see that there are three peaks of coupling constant at 57°C, 70°C and 110°C that show possible structural phase-transitions at these temperatures. The largest  $\Gamma$  occurs at about 57°C and has about 45% increase in the coupling constant. We note that these phase-transition temperatures are similar to those reported by Ismailzade, *et al.* [9] and Engelmann, *et al.* [10].

We have also measured the phase-conjugate reflectivity  $R$  as a function of the crystal temperature between 20°C and 120°C and result is plotted in Figure 4(b).  $R$  is defined as the ratio of the phase-conjugate beam intensity to the signal beam intensity. This phase-conjugate beam is primarily due to the four-wave mixing process occurred among the pump, back reflection and signal beams. Again, we observe the peak reflectivities  $R$  at the same phase-transition temperatures as the coupling constants  $\Gamma$ , and the largest  $R$  is at about 70°C, which has about 300% increase in the reflectivity. We can also see that the peaks are about 3~4°C wide (full-width half maximum).

We would point out that, since the temperature gradient across the crystal section and the temperature fluctuations caused by the ambient air turbulence may be as large as several degrees Centigrade, the above mentioned peaks may in fact be much higher and narrower than what we have observed. We suggest further study of the phase-transitions and their impact on the PR properties of LiNbO<sub>3</sub> based materials, which include transmission electronic microscopy

(TEM), DTA, DSC, dielectric constant measurement, and others.

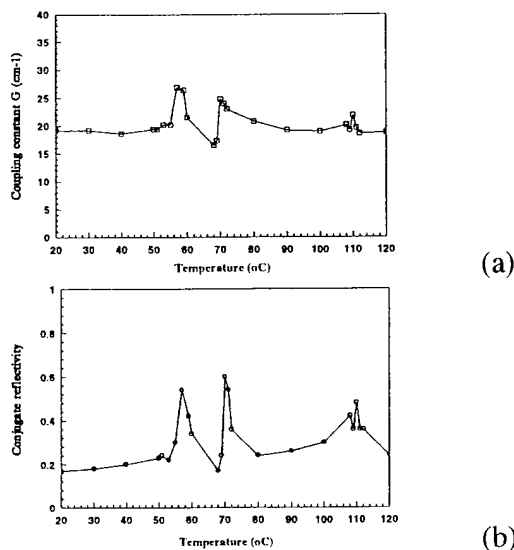


Fig. 4. Temperature dependency of the two-wave coupling constant  $\Gamma$  and phase-conjugate reflectivity  $R$ .

#### V. APPLICATIONS OF PR Ce:Fe:LiNbO<sub>3</sub> CRYSTAL (BULK AND FIBER)

##### A). High capacity wavelength-multiplexed image correlator

Optical pattern recognition is a viable field in optical signal processing, machine vision, target tracking, etc. As compared with the classic Vander Lugt filter, a PR crystal based image correlator has the advantages of real-time processing, large capacity and less stringent alignment requirement. We shall propose a reflection-type wavelength-multiplexed spatial filter, as applied to a high capacity correlator, as shown in Figure 5, in which a 1-cm cube z-cut Ce:Fe:LiNbO<sub>3</sub> crystal is used for the filter synthesis. A tunable diode laser (New Focus Model 6102 with a tuning range of 12nm at 670nm central wavelength) is used as the light source, for which reference targets can be sequentially recorded in the crystal. In read-out process, a target is displayed on the input spatial-light modulator (SLM), by which a correlation peak can be observed if the correct read-out wavelength is used.

Proof-of-concept experiments have been conducted as shown in Figure 6, in which a set of "P", "S", "U", "R", and "M" letters are used as the reference targets. In this experiment, we use a 0.1nm laser tuning step with a 10-second exposure for each hologram construction. The reconstructed holographic images and the corresponding correlation peaks are shown in Figure 6(b) and (c),

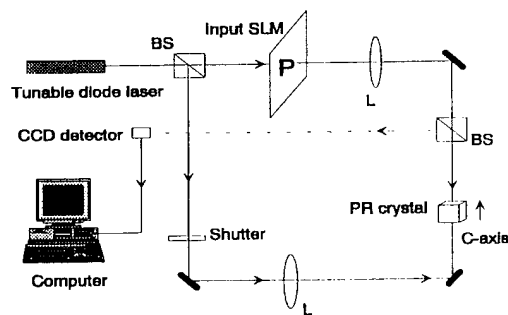


Fig. 5. Wavelength-multiplexed reflection correlator.

respectively. In view of these results, we see that the holographic images are faithfully reconstructed, by which a large-capacity optical correlator, in principle, can be developed using a reflection-type wavelength-multiplexed (PR) spatial filter.

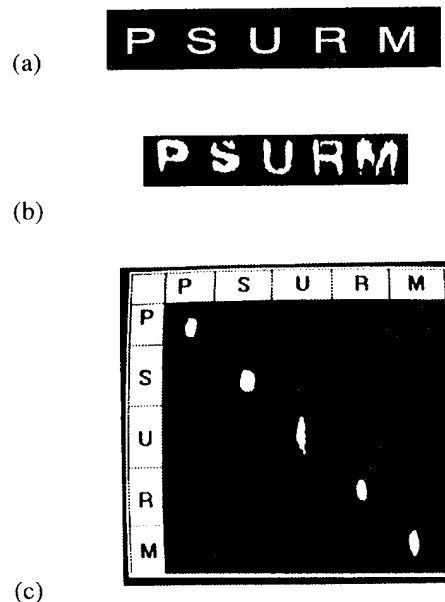


Fig. 6. Experimental results of the reflection wavelength-multiplexed correlator. (a) Input letter images; (b) Reconstructed images; (c) Auto-correlation peaks.

##### B). Tunable narrow-band in-fiber Bragg filter using PR crystal fiber

PR processes have been extensively studied in bulk materials for a variety of applications to optical signal processing and other photonic technologies. Unfortunately, the lack of availability of large single crystals severely limits the use of PR materials in practical applications.

On the other hand, PR fibers provide long length structure that can be utilized for some new applications, such

as high capacity fiber bundle memories, electro-optic fiber switches, fiber optic interconnections, and others [11-14].

Because of high electro-optic coefficient of the PR materials, it is possible to develop electrically tunable fiber optic switches. One of the major advantages of fiber switches must be its physical form, in which it can be easily coupled with fiber links in a fiber-optic network. Mention must be made that photonic switches have been used in fiber optic communication and reconfigurable networks. However, the integrated-optic photonic switches are difficult to fabricate and not convenient to interface with optical fibers. We shall now propose an electronic tunable (Bragg-diffraction) fiber switch using a Ce:Fe:LiNbO<sub>3</sub> fiber, as follows: Figure 7 shows a sketch of a fiber switch, in which an axial holographic grating is constructed by the counter-propagating beams (i.e., reflection-type fiber hologram) within the PR fiber [7, 12-14]. This axial grating can in fact be thermally fixed by heating the crystal fiber to about 150°C followed by a uniform illumination at room-temperature. Since the axial index grating acts as a notch filter, the wavelength that does not matched with the grating will be rejected (i.e., transmitted). It is apparent that by taking advantage of the high electro-optic constant (e.g., 30.8×10<sup>-12</sup>m/V for LiNbO<sub>3</sub>) of the PR fiber, the distribution of the index grating and the birefringence of the fiber can be varied by the applied electric field patterns within the fiber. In other words, the Bragg diffraction condition of the index grating can be manipulated by an external field patten, for which the matched wavelength of the grating can be shifted. Since the electro-optic effect takes place in a PR material almost instantaneously (e.g., <10<sup>-12</sup> s for LiNbO<sub>3</sub>), the tunable fiber switches would be very fast in the order of GHz to THz.

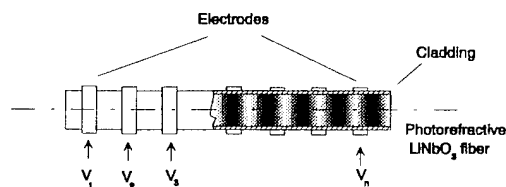


Fig. 7. A sketch of a tunable fiber switch.

The spectral bandwidth of the fiber switch can be shown to be inversely proportional to the length of the fiber [13],

$$\Delta\lambda = \frac{\lambda_0^2}{2nL}, \quad (5)$$

where  $\lambda_0$  is the wavelength in vacuum,  $n$  is the refractive index of the fiber, and  $L$  is the fiber length. To have a feeling of magnitude, we assume  $L=5\text{cm}$ ,  $\lambda_0=1.5\mu\text{m}$ , and  $n=2.28$ , for which we have  $\Delta\lambda=1.0\times 10^{-11}\text{m}$  (i.e., 1.3GHz), which is matched with the channel bandwidth of the fiber optic communication networks.

The wavelength shift  $\delta\lambda$  due to the external electric field induced index deviation  $\Delta n$  can be estimated by

$$\frac{\delta\lambda}{\lambda_0} = \frac{\Delta n}{n}, \quad (6)$$

where

$$\Delta n = -\frac{1}{2} n^3 \gamma_{\text{eff}} \Delta E.$$

Here  $\Delta E$  is the variation of the applied electric field, and  $\gamma_{\text{eff}}$  is the (effective) electro-optic coefficient of the fiber. In order to have a feeling of magnitude, we assume a PR (Ce:Fe:LiNbO<sub>3</sub>) fiber,  $n=2.28$ ,  $\gamma_{\text{eff}}=30.8\times 10^{-12}\text{m/V}$ ,  $\lambda_0=1.5\mu\text{m}$ , and  $\Delta E=100\text{V/mm}$ , for which we have  $\Delta n=1.8\times 10^{-5}$  and  $\delta\lambda=1.2\times 10^{-11}\text{m}$  (1.6GHz). Therefore we see that, by applying a specific electric field pattern along the fiber, a high speed fiber optic switch can be developed. The major merits of the proposed electro-optic fiber switch must be the high SNR, low loss and high extinction ratio, for which may warrant a wide variety of applications, particular to optical fiber networks.

## VI. CONCLUSION

We have presented a specially doped LiNbO<sub>3</sub> crystal (both bulk and fiber) and the PR effect due to dopants. We have found that double-doped Ce:Fe:LiNbO<sub>3</sub> crystal exhibits higher PR sensitivity, larger dynamic range, wider spectral bandwidth, and lower scattering noise, for which the crystal (bulk and fiber) would offer a variety of promising applications. In this study, we have found several anomalous PR sensitivities in the specially doped material, which occur at 57°C, 70°C and 110°C crystal temperatures. These anomalies are primarily due to the possible structural phase-transitions of the crystal. The application of this specially doped crystal to wavelength-multiplexed spatial filters is experimentally demonstrated, in which we have shown that a large capacity correlator using a tunable diode laser is feasible. We have also proposed an application of using this double-doped PR fiber to photonic switching. Owing to the high electro-optic coefficient of the material, a high speed electro-optic fiber switch in principle can be developed. In short, the specially doped (Ce:Fe:LiNbO<sub>3</sub>) material is at the threshold of practical reality, there is much that remains to be done before it becomes a wide spread of application.

\* D. M. Salerno is with the Photonics Group, U.S. Army Missile Command, Redstone Arsenal, AL 35898-5248.

## ACKNOWLEDGMENT

The support from Advanced Research Projects Agency through the U. S. Army Research Office under Contract No. DAAL 03-92-G-0328 and from Army Research Laboratory under Contract No. DAAL 01-93-K-0059 are acknowledged.



## REFERENCES

switching," *Appl. Opt.*, vol. 29, pp. 1059-1061, March 1990.

- [1] P. Günter, and J.-P. Huignard, ed., *Photorefractive Materials and Their Applications I*, Berlin: Springer-Verlag, 1989, ch. 3, pp.7-74.
- [2] for example, F. T. S. Yu, and S. Jutamulia, *Optical Signal Processing, Computing and Neural Networks*, New York: Wiley-Interscience, 1992, ch. 7, pp. 249-286.
- [3] E. Krätzig, and R. Sommerfeldt, "Influence of dopants on photorefractive properties of  $\text{LiNbO}_3$  crystals," in *SPIE Proceedings*, vol. 1273, pp. 2-11, 1990.
- [4] A. Ashkin, G. D. Boyd, J. M. Dziedzic, R. C. Smith, A. A. Ballman, J. J. Levinstein and K. Nassau, "Optically induced refractive index inhomogenities in  $\text{LiNbO}_3$  and  $\text{LiTaO}_3$ ," *Appl. Phys. Lett.*, vol. 9, pp. 72-74, 1966.
- [5] N. V. Kukhtarev, V. B. Markov, S. G. Odulov, M. S. Soskin and V. L. Vinetskii, "Holographic storage in electro-optic crystals, I. steady-state, and II. Beam coupling - light amplification," *Ferroelectrics*, vol. 22, pp. 949-964, 1979.
- [6] P. Yeh, "Two-wave mixing in nonlinear media," *IEEE J. Quantum Electron.*, vol. QE-25, pp. 484-519, 1989.
- [7] F. T. S. Yu, S. Yin, and A. S. Bhalla, "Wavelength-multiplexed holographic construction using a Ce:Fe: doped photorefractive fiber with a tunable visible-light laser diode," *IEEE Photon. Tech. Lett.*, vol. 5, pp. 1230-1233, October 1993.
- [8] H. Kogelnik, "Coupled wave theory for thick hologram gratings," *The Bell Sys. Tech. J.*, vol. 48, pp. 2909-2947, 1969.
- [9] I. G. Ismailzade, V. I. Nesterenko, F. A. Mirishi, "X-ray study of lithium niobate at high temperatures," *Sov. Phys.-Crystallogr.*, vol. 13, pp. 25-28, July 1968.
- [10] H. Engelmann, N. Krämer, H. Yuanfu, L. Rongchuan, and U. Gonser, "Investigation of anomalous transitions in  $\text{LiNbO}_3$  by Mössbauer spectroscopy," *Ferroelectrics*, vol. 69, pp.217-222, 1986.
- [11] S. Yin, H. Zhou, F. Zhao, M. Wen, Z. Yang, and F. T. S. Yu, "Wavelength-multiplexed holographic construction using a Ce:Fe:LiNbO<sub>3</sub> crystal with a tunable visible-light diode laser," *Opt. Comm.*, vol. 101, pp. 317-321, September 1993.
- [12] F. T. S. Yu, F. Zhao, H. Zhou, and S. Yin, "Cross-talk in a reflection-type wavelength-multiplexed photorefractive fiber hologram," *Opt. Lett.*, vol. 18, pp. 1849-1851, November 1993.
- [13] F. Zhao, H. Zhou, S. Yin, and F. T. S. Yu, "Wavelength-multiplexed holographic storage by using the minimum wavelength-channel separation," *Opt. Comm.*, vol. 103, pp. 159-162, November 1993.
- [14] S. Wu, A. Mayers, S. Rajan, and F. T. S. Yu, "Use of photorefractive fiber in optical interconnections and



# Concurrent Session - 6A: Pyroelectrics

# Uncooled Infrared Focal Plane Arrays

Paul W. Kruse  
Consultant, Infrared Technology  
6828 Oaklawn Avenue  
Edina, MN 55435

**Abstract** — Uncooled infrared focal plane arrays have been developed which employ four detection mechanisms: resistive bolometric, pyroelectric, ferroelectric bolometric and thermoelectric. They find application in thermal imaging systems for night vision. Each of the four mechanisms is described. Figures of merit are defined. The fundamental limits to the performance of thermal detectors are presented. The state-of-the-art of the four types of thermal detectors is described and the role of uncooled focal plane arrays in thermal imaging systems is discussed.

## INTRODUCTION

Thermal imaging systems are night vision systems which enable the user to view a scene by means of the infrared radiation emitted by everything within the field of view of the system. The focal plane array is that part of the system which transduces the image of the scene focused upon it by the infrared-transmitting lens into a signal, usually electronic, which, after amplification and signal conditioning, is then displayed as a visible image on the screen of a display device. Most scenes being viewed, e.g., the interior of a building or terrain of a battlefield, are at or near a temperature of 300°K. The wavelength distribution of 300°K radiation approximates that of a gray or blackbody whose peak spectral emission is at 10 $\mu$ m. Most thermal imaging systems therefore operate either in the 8-12 $\mu$ m atmospheric window or in the 3-5 $\mu$ m atmospheric window.

Thermal imaging systems in widespread use today employ photon detectors as the transducers. Here the absorption of infrared photons by the focal plane array causes the release of free electrons or holes within the semiconductor comprising the focal plane array. To suppress thermal excitation of free carriers due to the ambient temperature, focal plane arrays made of photon detectors are cooled to temperatures well below 300°K. For example, the most widely used photon detector, Hg<sub>0.8</sub>Cd<sub>0.2</sub>Te operating in the 8-12 $\mu$ m atmospheric window, must be cooled to the temperature of liquid nitrogen, 77°K. Others operating in the 3-5  $\mu$ m window, such as InSb, require less cooling, usually operating at or about 195°K. For field use mechanical refrigerators known as cryocoolers are employed.

The other major category of infrared detectors is that of thermal detectors. There are four principal categories: resistive bolometers, pyroelectric detectors, ferroelectric bolometers, which are also known as field-enhanced pyroelectric detectors, and thermoelectric detectors. Resistive bolometers are temperature sensitive resistors, made from metals, semiconductors, or superconductors, where they operate at the normal-to-superconducting transition edge. Pyroelectric detectors, made from ferroelectric materials, exhibit a polarization which depends upon the time rate of change of the detector temperature. Thus they are capacitors. Ferroelectric bolometers are similar to pyroelectric detectors, but an electric field is applied to enhance the output signal. Because pyroelectric detectors and ferroelectric bolometers respond to the time rate of change of their temperature, they require the incident radiation to be temporally modulated or "chopped." Thermoelectric detectors are junctions of dissimilar materials which exhibit the Seebeck effect. They are radiation-sensitive thermocouples. When several junctions are connected in series to enhance the signal voltage, the device is termed a "thermopile." Like pyroelectric detectors, thermoelectric detectors do not require an electrical bias.

In contrast to photon detectors, thermal detectors do not require cooling to exhibit adequate sensitivity. The tradeoff however, is that their photoresponse is relatively slow compared with that of most photon detectors. Whereas the response time of photon detectors is determined by the free carrier lifetime, which for most photon detectors at their operating temperature is microseconds or less, the response time of thermal detectors is the inverse of the rate at which they lose heat to their surrounding.

Thus the response time of thermal detectors is the ratio of their heat capacity to the thermal conductance of their principal heat loss mechanism. Typical response times of sensitive thermal detectors are milliseconds or more.

Thermal imaging systems are characterized by their frame rate, which is the number of frames of imagery displayed per second. Here a frame is the output of all the picture elements ("pixels") required to display a two-dimensional (2D) image. The 2D image can be produced by a 2D array of pixels such that there is a 1:1 correlation between the pixels in the focal plane array and on the screen. Alternatively, a linear array of pixels can be scanned across a scene by a moving mirror, each pixel generating a line of imagery whose point-to-point brightness variation corresponds to that of the scene being viewed.

In the U.S., most thermal imaging systems, including the common modular FLIR (Forward Looking Infrared) employed by the U.S. Armed Forces, operate at the standard TV frame rate of 30 frames per second. Thus the frame time is 33 msec. The pixel response time of a scanning thermal imaging system must be no greater than 33 msec divided by the number of resolution elements in a scanned line, which usually requires a response time much less than 1 msec. On the other hand, the pixel response time of a staring thermal imaging system must be no greater than 33 msec, which is compatible with the response time of thermal detectors. In practice, a response time of about 10 msec is employed.

Although thermal detection mechanisms have been known for many decades, it was the development of modern process technology which enabled their use in large pixel arrays. Today linear and 2D arrays of thermal detector (and photon detector also) are prepared by techniques similar to those used in the preparation of integrated circuits, although the material employed may or may not be silicon. It was this ability to make large arrays at relatively low cost which was the technical breakthrough enabling the development of uncooled infrared focal plane arrays based upon thermal detection mechanisms.

## THEORETICAL FOUNDATION

### Figures of Merit

Five figures of merit are employed to characterize the performance of infrared focal plane arrays, i.e., spectral response, responsivity, D\* (pronounced "dee-star"), response time and noise equivalent temperature difference (NETD). They are as follows:

- |                      |   |
|----------------------|---|
| Spectral response    | the dependence of the pixel output signal upon the wavelength of the incident radiation for a constant incident intensity per wavelength interval falling on the pixels. The units are dimensionless. |
| Responsivity         | the pixel output signal per Watt of incident radiant power falling on the pixel, expressed as Volts/Watt or Amps/Watt.  |
| D*                   | the pixel output signal-to-noise ratio per Watt of incident radiant power falling on the pixel, measured in a 1 Hz bandwidth. The units are cm Hz <sup>1/2</sup> /Watt.                               |
| Response Time $\tau$ | the time required for the pixel signal to decrease to 37% of its value after radiation is removed from the pixel.   |
| NETD                 | the change in temperature of a large blackbody in a scene being viewed by a thermal imaging system which will cause a   |

change in signal-to-noise ratio of unity in the output of a pixel upon which part of the blackbody is imaged.

#### Fundamental Limits [1]

All sensors are subject to upper bounds of performance arising from the nature of the phenomena being sensed. Photon detectors are subject to the BLIP (Background Limited Infrared Photodetector) limit arising from the statistical nature of the rate of arrival of photons from the background surrounding the scene being viewed. Thermal detectors are subject to two limits, the temperature fluctuation noise limit and the background fluctuation noise limit.

All thermal detectors warmed by absorption of incident infrared radiation return to their initial temperature when the radiation is removed. The manner by which they lose energy to their surroundings can in principle be by means of convection, conduction and radiation. Whatever the heat loss mechanism is, the ultimate sensitivity is set by temperature fluctuation noise. All infrared detectors, including thermal detectors, have internal noise. If these sources of internal noise are negligible by comparison, the ultimate performance of a pixel of a thermal detector arises from random fluctuations in the temperature of the pixel. These fluctuations are determined by the heat loss mechanism. It can be shown that the temperature fluctuation noise limit to  $D^*$  given by  $D_{TF}^*$  is

$$D_{TF}^* = \left( \frac{\eta^2 A_D}{4kT_D^2 G} \right)^{1/2} ; \quad (1)$$

where  $\eta$  is the absorptivity of radiant power by the pixel, the value of which lies between zero and unity,  $A_D$  is the area of the pixel,  $k$  is Boltzmann's constant,  $T_D$  is the temperature of the pixel, and  $G$  is the thermal conductance, expressed in Watts/degK, of the heat loss mechanism.

Equation (1) shows that the limit to the sensitivity of focal plane arrays based upon thermal detection mechanisms is determined by the thermal conductance  $G$ . The most important factor in array design is high thermal isolation, i.e., low thermal conduction. It is the design of the thermal isolation structure which controls the ultimate performance of focal plane arrays based on thermal detection mechanisms.

The response time  $\tau$  of all thermal detection mechanisms is given by

$$\tau = \frac{C}{G} ; \quad (2)$$

where  $C$  is the pixel heat capacity. Attaining high thermal isolation, i.e., a low  $G$  value, requires a low  $C$  value in order that  $\tau$  meet the system response time requirement. For example, if it is required that  $\tau$  be 10 msec, then, if  $G$  is  $10^{-7}$  Watts/degK,  $C$  must be  $10^{-9}$  Joules/degK. This requires very thin pixels of materials with low specific heats.

If the pixel is so well thermally isolated that the only heat loss mechanism is by radiation from the pixel to its surrounding, then the pixel is said to be background fluctuation noise limited. This is the ultimate manifestation of the temperature fluctuation noise limit. It can be shown that the background fluctuation noise limit  $D_{BF}^*$  of a pixel is given by

$$D_{BF}^* = \left[ \frac{\eta}{8k\sigma(T_D^5 + T_B^5)} \right]^{1/2} . \quad (3)$$

Here  $\sigma$  is the Stefan-Boltzmann constant and  $T_B$  is the background temperature.

The NETD is frequently employed to characterize the performance of a focal plane array. The expression for the NETD of a thermal imaging system is

$$NETD = \frac{(4F^2 + 1)V_N}{A_D \tau_0 R(\Delta P / \Delta T)_{\lambda_1 - \lambda_2}} . \quad (4)$$

Here  $F$  is the  $f$ /no. of the optics,  $V_N$  is the electrical noise within the system bandwidth,  $\tau_0$  is the transmittance of the atmospheric path between scene and system multiplied by the transmittance of the optics,  $R$  is the pixel responsivity and  $(\Delta P / \Delta T)_{\lambda_1 - \lambda_2}$  is a blackbody function. Assuming operation in the 8-12  $\mu$ m spectral interval and a 300°K scene temperature, the value of  $(\Delta P / \Delta T)_{\lambda_1 - \lambda_2}$  is  $2.62 \times 10^{-4}$  Watts/degK.

By definition, the relationship between  $R$  and  $D^*$  is

$$D^* = \frac{R(A_D B)^{1/2}}{V_N} ; \quad (5)$$

where  $B$  is the electrical bandwidth. Thus it is possible to express the temperature fluctuation noise limited NETD and the background fluctuation noise limited NETD by combining Eqs. (1), (3), (4) and (5).

$$NETD_{TF} = \frac{2T_D(4F^2 + 1)(kBG)^{1/2}}{\eta A_D \tau_0 (\Delta P / \Delta T_S)_{\lambda_1 - \lambda_2}} ; \quad (6)$$

and

$$NETD_{BF} = \frac{(4F^2 + 1)}{\tau_0 (\Delta P / \Delta T_S)_{\lambda_1 - \lambda_2}} \left[ \frac{8k\sigma B(T_D^5 + T_B^5)}{\eta A_D} \right]^{1/2} . \quad (7)$$

Here  $T_S$  is the scene temperature.

By assuming values of the parameters, the temperature fluctuation noise and background fluctuation noise limits to the NETD of thermal detectors can be determined. Figure 1 illustrates the limits for the values of the parameters shown. They are typical of the parameters of large uncooled staring focal plane arrays. Real arrays having excess internal noise will fall within the area bounded by the temperature fluctuation noise and background fluctuation noise limits.

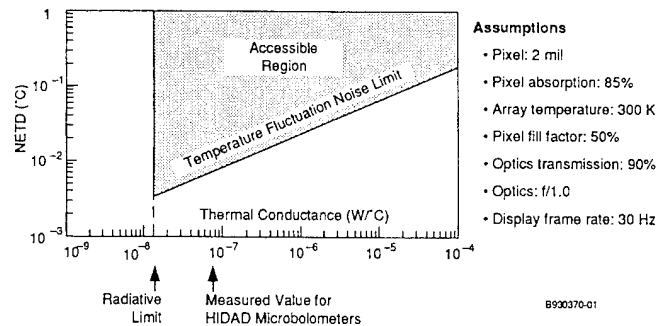


Figure 1: Noise Equivalent Temperature Difference of Uncooled Thermal Arrays as a Function of Thermal Conductance for the Assumed Values of the Parameters Listed. From R.A. Wood [3].

It is to be noted that the responsivity does not appear in Eqs. (1), (3), (6) and (7). High responsivity does not automatically give rise to either the temperature fluctuation noise limit or to the background fluctuation noise limit. It is possible in principle to attain these limits with a low responsivity. The value of having a high responsivity is to minimize the contribution to the total system noise from the electronics used to read out the signals from the focal plane array. Obviously, if the total noise is dominated by the electronics noise, the system cannot be temperature fluctuation noise or background fluctuation noise limited.

#### STATE-OF-THE-ART

##### Monolithic Thin Film 2D Resistive Bolometer Array

Wood and colleagues [2]-[4] have described the construction and performance of a 2D array of resistive bolometers developed under a Department of Defense program termed HIDAD (High Density Array Development). Organized into 240 rows and 336 columns, the array consists of 80,640 pixels, each  $50\text{ }\mu\text{m}$  square. Twelve arrays are processed on a 4 in. diameter silicon wafer. The pixel thermal isolation structure, see Figure 2, consists of a silicon nitride membrane upon which is deposited a sputtered thin film of vanadium oxide. The silicon nitride membrane is supported above the silicon substrate by two legs whose width, length and thickness have been adjusted to provide a thermal conductance of  $8 \times 10^{-8}$  Watts/degK. The heat capacity of each pixel is  $8 \times 10^{-10}$  Joules/degK; thus the thermal response time is 10 msec. Under each pixel in the substrate is a transistor employed as a self-closing matrix-addressable switch. Operating at 30 frames per second with  $f/1$  optics, the measured NETD is 0.040 degC. Thermal imagery which is equivalent to or better than that from scanned linear arrays of mercury cadmium telluride operating at 77°K is obtained at a far smaller system cost.

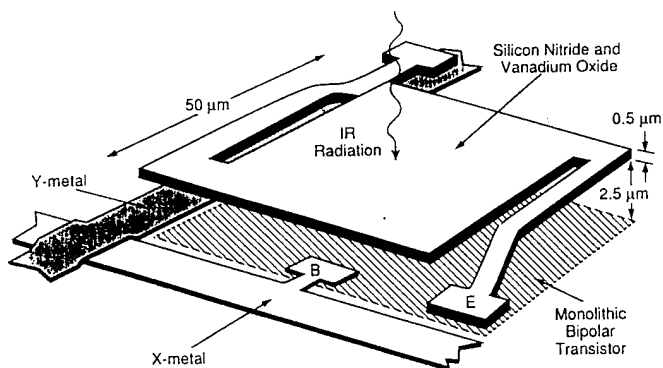


Figure 2: Thermal Isolation Structure Employed in Uncooled Monolithic Thin Film 2D Resistive Bolometer Array. From R.A. Wood, et al. [4].

##### Monolithic Thin Film 2D Pyroelectric Arrays

Polla and colleagues [5] have described the construction and predicted performance of a monolithic 2D array using the pyroelectric effect in thin film lead titanate. The lead titanate film is deposited upon a polysilicon thin film over an air gap, see Figure 3. The array consists of 4096 pixels each  $50\text{ }\mu\text{m}$  square organized in 64 columns and 64 rows. The pixel  $D^*$  value is  $2 \times 10^8\text{ cm Hz}^{1/2}/\text{Watt}$ . The NETD is unstated.

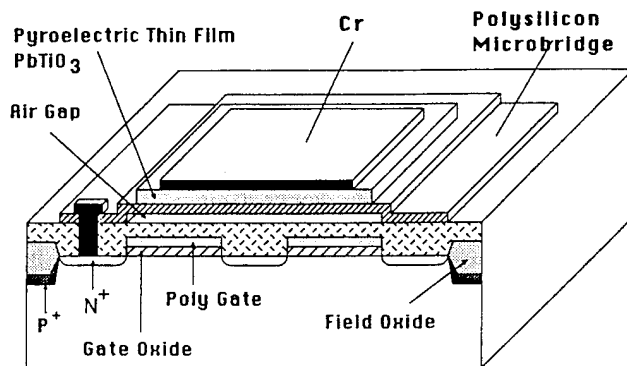


Figure 3: Thermal Isolation Structure Employed in Uncooled Monolithic Thin Film 2D Pyroelectric Array. From L. Pham, C. Ye and D.A. Polla [5].

Cole and colleagues [6] are developing a monolithic 2D thin film array also using the pyroelectric effect in lead titanate, but with a different thermal isolation structure from that of Polla. As Figure 4 show, the structure bears a marked resemblance to that employed by Wood and colleagues for their monolithic thin film arrays shown in Figure 2. This is not surprising since Cole is a collaborator with Wood on the latter. The predicted NETD of the monolithic thin film lead titanate pyroelectric array using  $f/1$  optics is 0.01 degC.

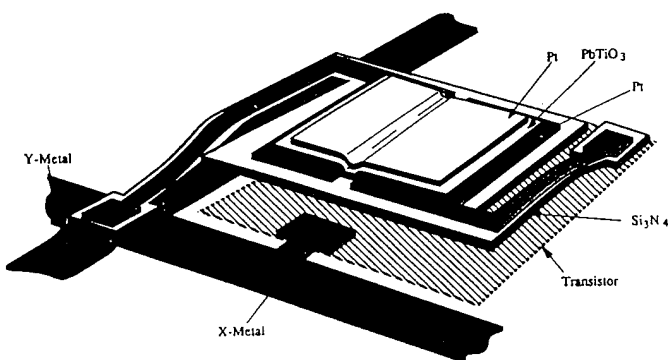


Figure 4: Thermal Isolation Structure Employed in Uncooled Monolithic Thin Film 2D Pyroelectric Array. Personal Communication from B.E. Cole and R.D. Horning, Honeywell Technology Center. See [6].

##### Hybrid 2D Pyroelectric Array

Butler and Iwasa [7] have described the construction and estimated performance of a 2D array of lithium tantalate pyroelectric pixels bump-bonded to a silicon array of multiplexers to read out the pyroelectric signals. Such construction which joins two arrays of differing materials is termed hybrid. Figure 5 illustrates the structure. The thermal conductance of the heat path from pixel to substrate is  $3.3 \times 10^{-6}$  Watts/degK. The prototype imaging system uses an array of  $192 \times 128$  pixels on  $50\text{ }\mu\text{m}$  centers. The predicted NETD is less than 0.1 degC with  $f/1$  optics when operating at 30 frames per second. A radiation chopper is required.

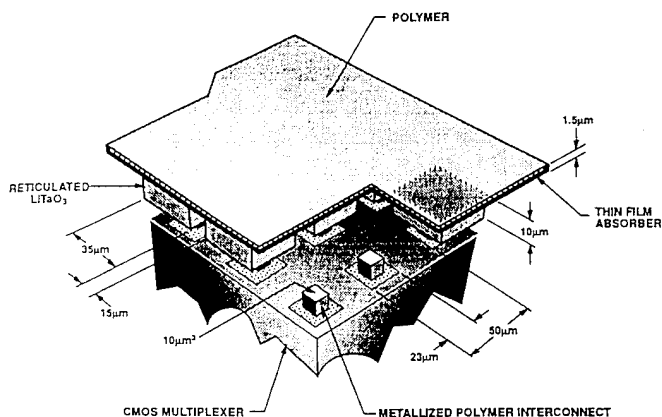


Figure 5: Thermal Isolation Structure of Uncooled Hybrid 2D Pyroelectric Array. From N. Butler and S. Iwasa [7].

#### Hybrid 2D Ferroelectric Bolometer Array

Hanson and colleagues [8, 9] have described the construction and measured performance of a ferroelectric bolometer hybrid 2D array, also known as a field enhanced pyroelectric hybrid array. Developed under a HIDAD contract having similar objectives to that of Wood and colleagues [2]-[4], Hanson and colleagues obtained equally impressive performance. They employed the ferroelectric ceramic barium strontium titanate (BST) whose ratio of barium to strontium was controlled so that the Curie point was at 22°C. Although the pyroelectric effect requires no electrical bias, Hanson and colleagues applied a bias which increased the responsivity over the unbiased value. The construction, see Figure 6, is hybrid wherein each BST pixel was bump bonded to a readout circuit in the underlying silicon substrate. With 245x328 pixels on 50 μm centers, the measured NETD with  $f/1$  optics at 30 frames per second was 0.07 degC. As with pyroelectric arrays, this array requires a radiation chopper.

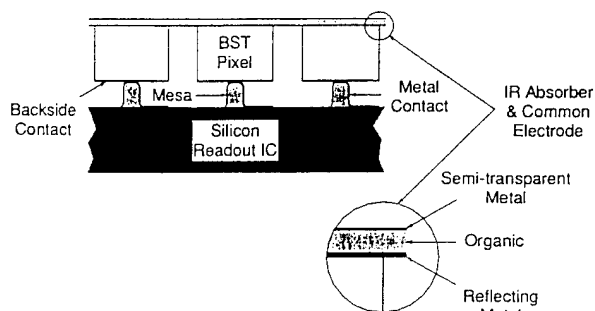


Figure 6: Thermal Isolation Structure of Uncooled Hybrid 2D Ferroelectric Bolometer Array. From Charles Hanson, et al. [8].

#### Monolithic Thin Film Thermopile Linear Array

Wilson and colleagues [10] have described the construction and performance of a 96 pixel linear array of thermopiles integrated on a silicon microstructure. Each pixel consists of several nickel iron/chromium thermocouples connected in series which have been deposited on a silicon nitride membrane over a silicon substrate. The measured NETD using  $f/0.73$  optics was 0.16 degC. The thermal response time was 5 msec. Neither radiation chopper nor electrical bias is required.

#### DISCUSSION

Uncooled infrared focal plane arrays based upon thermal detection mechanisms, including resistive bolometric, pyroelectric, ferroelectric bolometric and thermoelectric will have a major impact on thermal imaging systems. Although their response speed is much slower than that of photon detectors, it is sufficient for staring arrays operating at 30 frames per second. Performance equal to or superior to most cryogenic photon detector scanned arrays has been demonstrated. Array costs, especially for those employing monolithic construction, will be equal to or less than those for photon detector arrays. Systems cost will be substantially less because cryogenics are not required. Because of their low cost, thermal imaging systems employing uncooled thermal detectors will find widespread application not only in the military but also commercial fields. The largest application will probably be that of automobile night vision systems [11].

#### REFERENCES

- [1] P.W. Kruse, L.D. McGlauchlin and R.B. McQuistan, *Elements of Infrared Technology*, John Wiley and Sons, Inc., New York (1962), ch. 9.
- [2] R.A. Wood, C.J. Han and P.W. Kruse, *Integrated Uncooled Infrared Detector Imaging Arrays*, presented at IEEE Solid State Sensor and Actuator Workshop, Hilton Head Island, SC, June, 1992.
- [3] R.A. Wood, *Uncooled Thermal Imaging with Monolithic Silicon Focal Plane Arrays*, Proc. SPIE, vol. 2020, *Infrared Technology XIX*, pp. 34-41, July 1993.
- [4] R.W. Wood, et al., *Uncooled Monolithic Silicon Focal Plane Development*, Proc. IRIS Detector Specialty Group Meeting, Bedford, MA, August, 1992.
- [5] L. Pham, C. Ye and D.L. Polla, *Integrated Pyroelectric Detectors Based on Solid-State Micromachining and PbTiO<sub>3</sub> Thin Films*, Proc. IRIS Detector Specialty Group, Boston, MA, August, 1993.
- [6] B.E. Cole, R.D. Horning and P.W. Kruse, *PbTiO<sub>3</sub> Films Deposited by an Alternating Target Ion Beam Sputtering Technique*, Materials Research Society Fall Meeting, Boston, MA, December 2-6, 1991.
- [7] N. Butler and S. Iwasa, *Solid State Pyroelectric Imager*, Proc. SPIE, vol. 1685, *Infrared Detectors and Focal Plane Arrays II*, pp. 146-154 (1992).
- [8] C. Hanson, et al., *Uncooled Thermal Imaging at Texas Instruments*, Proc. SPIE, vol. 1735, *Infrared Detectors: State of the Art*, pp. 17-26, 1992.
- [9] C. Hanson, et al. *Low-cost Uncooled Focal Plane Array Technology*, presented at IRIS Detector Specialty Group Meeting, Bedford, MA, August 17, 1993.
- [10] M.L. Wilson, et al., *An Uncooled Thermo-Electric Microthermopile Camera Developed Using Silicon Microstructure Detectors*, presented at IRIS Detector Specialty Group Meeting, Boulder, CO, August 13-16, 1991.
- [11] *Defensive Driving*, Scientific American, September 1992, pp. 164B, 165B.

# Ferroelectric Ceramics and Thin Films for Uncooled Thermal Imaging Arrays

A. Patel\*, P.C. Osbond\*, N.M. Shorrocks\*, R.C. Twiney\*, R. Whatmore\*, and R. Watton\*\*.

\* GEC-Marconi Materials Technology, Caswell, Towcester, Northants NN12 8EQ, UK

\*\* DRA Malvern, St. Andrew's Road, Malvern, Worcs, UK

## Abstract

The pyroelectric effect in ferroelectric materials has long been used for the detection and imaging of long wavelength infra-red radiation. Lead scandium tantalate (PST) has been shown to have exceptionally good pyroelectric figures of merit, especially for small detectors of the type involved in the large arrays needed for uncooled solid state thermal imaging[1]. This paper will review the properties of PST in relation to those of other materials which have been considered for use in this role and discuss how the inclusion of dopants[2] can be used to modify the properties of the material in a way which would be beneficial to certain modes of detector operation, particularly with respect to the elimination of the requirement of cooling. Single element detectors and linear and two dimensional arrays have been made using PST. Their properties are compared with those of similar devices made using conventional pyroelectric ceramics. Ferroelectric thin films can now be made using sol-gel techniques whose figure-of-merit are comparable with those of bulk ceramic materials and the properties of these will be reviewed in relation to those of the ceramics discussed above and their potential for device applications discussed.

## Introduction

Infrared detection and thermal imaging are currently topics of strong interest for both military and commercial applications ranging from night vision, surveillance, driving aids, fire-fighting and security systems [3-5]. IR detectors of most interest operate in the 3-5 $\mu$ m and 8-14  $\mu$ m wavebands, corresponding to atmospheric "windows" of low absorption and also to thermal blackbody maxima at around room-temperature. At present commercially available high resolution systems utilise photoconductive or photovoltaic p-n junction detectors based on Cadmium Mercury Telluride (CMT), or Si-PtSi Schottky barriers [6-7]. However, the materials are difficult to grow and require cooling, usually to 77K for maximum ideal performance and therefore applications are limited to high value high power systems. Thermal detectors on the other hand do not require cooling and although the performance is lower, the technology is comparatively cheap and is thus able to provide low power compact IR cameras. The most successful uncooled arrays to date use a hybrid solder bumped technology and are based on ferroelectrics as the detector material, operating as pyroelectrics or (in a related mode) as dielectric bolometers[8-9]. Further improvement has continued with the development of phase transition materials such as Lead Scandium Tantalate(PST)[10]. The competition between detectors has become keener as the designs move towards integrated technologies involving direct deposition of the detector as a thin film onto the integrated circuit. This potentially would yield higher performance with reduced costs.

This paper will discuss the application of both hybrid and thin film PST for improved pyroelectric arrays, emphasising progress in the last few years. For a thorough discussion of the principles of pyroelectricity and ferroelectric material considerations, the reader is referred to Refs.[1 and 11-12].

### Ferroelectric Materials - PST

Ferroelectrics used as pyroelectric detectors, can loosely be divided into materials with high or low transition temperatures( $T_c$ ). The former, eg. LiTaO<sub>3</sub>, are characterised by low permittivity, high voltage response and good stability, and are useful for comparatively large area detectors. The development of an optimised pyroelectric ceramic based on modified lead zirconate has been extensively discussed elsewhere[2] and will not be reported here. The latter, such as PZT and PST based ceramics offer increased charge response and permittivity, providing a better impedance match to following electronics when used in applications requiring smaller detectors. They suffer from increased dielectric loss and from the risk of

progressive de-poling. Stable operation at  $T_c$  can be achieved by the application of a DC-bias field in the so called bolometer mode. An example of such a material is PST, (Pb(Sc<sub>0.5</sub>Ta<sub>0.5</sub>)O<sub>3</sub>) [13]. The material has a first order phase transition at 25-30°C, and when operated under bias has been reported[10] to yield very high reversible pyroelectric coefficients, which translate to material Figure-of Merit ( $F_D$ ) values defined as:

$$F_D = P / (C \sqrt{\epsilon \tan \delta})$$

where P = Pyroelectric coeff. (Cm<sup>-2</sup>K<sup>-1</sup>)

C = Volume heat capacity (2.7 x 10<sup>6</sup> Jm<sup>-3</sup>K<sup>-1</sup>)

$\epsilon$  = Absolute Permittivity

$\tan \delta$  = Dielectric loss (%)

of  $\sim 17 \times 10^{-5}$  Pa<sup>-1/2</sup>, more than double the values obtained for PZT ceramic. It should be noted that P and  $\epsilon$  (and thus  $F_D$ ) are strongly dependant upon applied field and temperature and must be measured over a range of conditions when dielectric bolometer operation is being considered.  $\epsilon$  and  $\tan \delta$  should also be measured at the frequency of interest (usually 50 to 200 Hz for thermal imaging applications).

PST has been shown to give excellent  $F_D$  when compared with other materials such as KTa<sub>x</sub>Nb<sub>1-x</sub>O<sub>3</sub>(KTN)[14], Ba<sub>0.65</sub>Sr<sub>0.35</sub>TiO<sub>3</sub>(BST 65/35)[15] and (Pb<sub>0.99</sub>La<sub>0.01</sub>)(Mg<sub>1/3</sub>Nb<sub>2/3</sub>)O<sub>3</sub>(PLa01MN)[16]. Figure 1 shows the temperature dependence of  $F_D$  under a field of 5V/ $\mu$ m when compared with BST65/35 and PLa01MN under similar field conditions and modified PZ at zero bias. It can be seen that the  $F_D$  for PST is 3.5 times the value for modified PZ at 25°C. The PST ceramic  $F_D$  peaks at a value 80% greater than its nearest dielectric bolometer rival BST65/35.

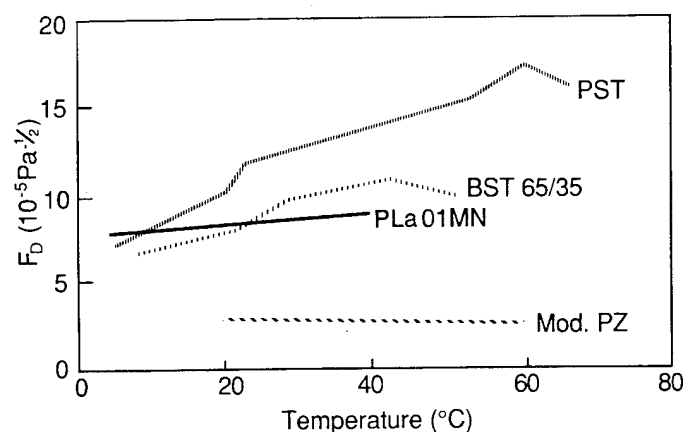


Fig. 1. Variation of  $F_D$  with temperature for several dielectric bolometer materials compared with Mod.PZ.

More recently, the properties of a solid solution (1-x)PST-(x)PbTiO<sub>3</sub> have been reported [17-18]; for an x value of 0.4, the Curie temperature was increased to 182°C and the maximum dielectric constant was >30,000. Some of our own results on this and a PbZrO<sub>3</sub> doped PST composition will be discussed here and compared with undoped-PST. Other studies[19] on doped PST have concentrated on K, Bi and PSN(lead scandium niobate) as the dopants, and will not be discussed here.



## Experimental Procedure

### Ceramic preparation

The detailed procedure for the preparation of PZ and PT modified PST ceramics is given in [20]. Briefly, three preparation routes were chosen. These were:

(A) Ball milling and a single calcination at 900°C of the starting oxides, followed by hot pressing the powder at 40MPa and 1200°C for 6hrs.

(B) ScTaO<sub>4</sub> was initially prepared via the high temperature wolframite prereaction stage, and then the separate preparation of PST and PZ/PT using standard milling and calcination techniques. Both powders were then milled together and calcined at 900°C. After hot pressing the ceramic was annealed at 1400°C for 4hrs, with PZ spacer powder to compensate for lead loss.

(C) ScTaO<sub>4</sub> and ZrO<sub>2</sub> were reacted and the calcined with PbO and hot-pressed at 1100-1200°C. The ceramic was not annealed in this case.

PST/PT ceramics were exclusively prepared using method B.

### Thin Film Preparation

The hybrid array designs involve a number of lengthy fabrication processes which ultimately determines the yield and costs as the size of the arrays increase, eg. ceramic slicing and polishing followed by laser reticulation and solder bump bonding. Integrated technologies on the other hand offer substantial reductions in terms of processing complexity and therefore a increased yield for very large array sizes, with reduced costs. For this approach, two key areas need to be addressed:

- Silicon micro machining, either bulk or surface - to fabricate thermally isolated structures on the IC.
- Deposition of the detector material on such structures, without any detrimental effects on the IC.

Reports on fabrication of such structures have been reported by Polla et al [21] using lead titanate as the detector material, to form a "sparse" array. Currently most effort is concentrated on the fabrication of dense 2D-array structures for thermal imaging applications for which materials with high F<sub>D</sub> values as thin films can be utilised.

Thin film PST was prepared as described in detail in Reference [22]. This route was chosen so as to avoid the formation of the pyrochlore phase, which severely degrades the dielectric properties and are the primary source cause of variations in dielectric properties. The composite film consisting of layers of ScTaO<sub>4</sub> interspersed with PbO layers was sintered in air at temperatures up to 900°C, in a lead rich environment. Films were typically prepared on sapphire(1102), gadolinium gallium garnet (GGG) and a MgO-coated sapphire. The MgO layer was incorporated as a release layer. We have also recently developed a method of depositing PST from a solution of all three precursors, onto metallised silicon substrates at a temperature of 600-650°C.

### Characterization

Phase analysis for both ceramic and thin film was achieved using an automated Philips PW1820 diffractometer system using Cu K<sub>α</sub> radiation. Microstructures were determined using scanning electron microscopy. Dielectric measurements were performed using a Wayne Kerr B6425 LCR meter, using IDE(interdigitated Cr/Au) electrodes for the films. Pyroelectric measurements were performed on a General Radio bridge type 1615-A.

## Results and Discussion

### Ceramic PST

PST-PZ samples prepared using Method A gave a appreciable amount of pyrochlore phase(20%). A very diffuse phase transition with a maximum dielectric constant,  $\epsilon_r$  of below 9000 occurring at about 70°C was observed. This poor value was attributed to the large concentration of low permittivity pyrochlore phase. Further, annealing at temperatures upto 1400°C resulted in only minor reduction in the pyrochlore phase with no change in the dielectric properties.

Ceramics prepared using Method B exhibited two peaks in dielectric constant and loss (D) over a temperature range of 0-120°C.

For all samples, the lower transition temperature  $T_{C1}$  occurred at ~35°C, whereas the higher  $T_{C2}$  was dependent on the ratio of PZ to PST. After annealing at 1400°C, the above ceramics were found to have single sharper peaks in  $\epsilon_r$  and D and the  $T_{C2}$  value was reduced. Tables I and II summarises the results of the dielectric properties pre- and post-annealing. It is also interesting to note that the X-ray data indicated distinct two phases from the PST-PZ powder and hot-pressed ceramic, the annealed ceramic has a single phase perovskite structure. These results indicate that a completely reacted solid solution between PST and PZ is not formed at 900°C, but that only after high temperature annealing is a single phase obtained.

TABLE I. Properties of PST-PZ ceramics after hot-pressing, prepared using Method B

x	Sample	$T_{C2}$ (°C)	$\epsilon_r$ (at $T_{C2}$ ) (1.5kHz)	D(at 120°C) (1.5kHz)	Density (g cm <sup>-3</sup> )
0.075	AL124	74	8000	0.00085	8.944
0.100	AL118	78	10200	0.00150	8.926
0.125	AL125	82	14200	0.00090	8.842
0.150	AL132	88	13000	0.00220	8.847
0.200	AL133	98	16000	0.00375	8.815

TABLE II. Properties of PST-PZ ceramics after annealing at 1400°C, prepared using Method B.

x	Sample	$T_{C2}$ (°C)	$\epsilon_r$ (at $T_{C2}$ ) (1.5kHz)	D(at 120°C) (1.5kHz)	Density (g cm <sup>-3</sup> )
0.075	AL124	48	26400	0.00030	8.939
0.100	AL118	58	24200	0.00410	8.794
0.125	AL125	60	30000	0.00080	8.887
0.150	AL132	68	25000	0.00240	8.847
0.200	AL133	87	26000	0.00310	8.803

Post-annealing also had a marked effect on the grain size with values of over 10µm being observed. This compares with a size of 1-2µm for samples as hot-pressed. Interestingly, the magnitude of the dielectric constant was strongly dependant on the annealing temperature and hence also the grain size[20].

Samples prepared using Method C indicate a very high and sharp  $\epsilon_r$  peak without high temperature annealing. Although the material microstructure was coarse grain with little or no ordering of the crystal lattice. The results also indicate that a solid solution had probably been formed during calcination. The results obtained after hot-pressing are summarised in Table III.

TABLE III. Properties of PST-PZ ceramics (for x = 0.125) prepared via Method C.

Hot-pressing temperature (°C)	Sample	$T_{C2}$ (°C)	$\epsilon_r$ (at $T_{C2}$ ) (1.5kHz)	D(at 120°C) (1.5kHz)	Density (gcm <sup>-3</sup> )	Grain size (µm)
1200	AL135	64	36000	0.00075	8.891	15
1150	AL143	70	27500	0.00085	8.898	4
1100	AL145	75	24000	0.00100	8.901	2

Unlike processing Method B, this Method gave fine grained samples exhibiting very high permittivities. Also, the  $T_{C2}$  value decreases with increase in hot-pressing temperature.

The PST-PT system exhibited similar properties to that shown by PST-PZ prepared via Method B. The dielectric results after annealing are summarised in Table IV. and the results broadly agree with those given by Giniewicz *et al.* [17], however, the  $T_{C2}$  values here are significantly higher, due probably to the inclusion of a hot-pressing stage.

TABLE IV. Properties of (1-x)PST-(x)PT ceramics after annealing at 1400°C

x	Sample	T <sub>C2</sub> (°C)	ε <sub>r</sub> (at T <sub>C2</sub> ) (1.5kHz)	D(at 120°C) (1.5kHz)	Density (g cm <sup>-3</sup> )
0.05	MB363	49	12000	0.00215	8.880
0.0625	AL114	57	12000	0.00215	8.875
0.0875	AL113	66	16900	0.00230	8.877
0.10	AL103	67	23400	0.00150	8.767
0.125	AL115	77	15300	0.00405	8.810

Figure 2 shows the variation of  $F_D$  for PST-PT(10%), PST-PZ(12.5%), in comparison with undoped PST. Significant increases in the optimum operating temperature have been obtained at modest doping levels. The peak value of  $F_D$  is comparable with that of undoped PST, while the PbZrO<sub>3</sub> doped material indicates significant improvements at high temperature  $>20 \times 10^{-5} \text{Pa}^{-1/2}$ .

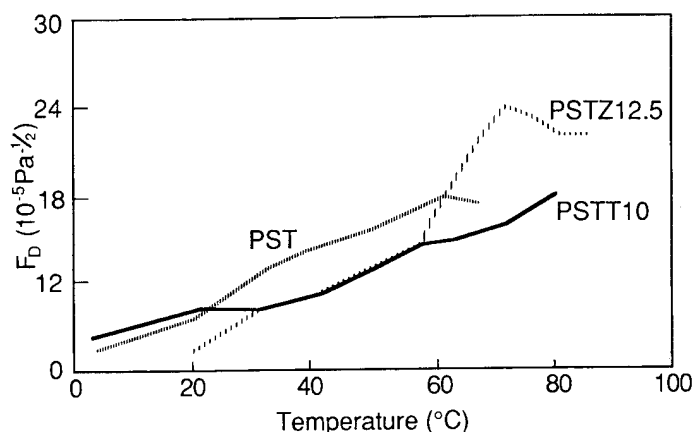


Fig. 2. Comparison of  $F_D$ /temperature for modified PST ceramics (a) PST; (b) (1-x)PST-(x)PT, x=0.1; (c) (1-x)PST-(x)PZ, x=0.125.

#### Thin Film PST

Deposition of PST onto unmetallised substrates has been demonstrated, with the maximum processing temperature of 900°C. This obviously is far too high for fully integrated structures, but it is still of merit for possible hybrid structures. We have shown recently that the growth of PST is viable from solution at temperatures of around 650°C. Indeed, sputtered PST is routinely deposited at temperatures of around 500°C[9].

Although, the low temperature films were highly crystalline (see Figure 3 they suffered from low values of  $\epsilon_r$  (typically  $1-2 \times 10^3$ , with D values of  $\sim 1\%$ ), mainly due to small grain size. For comparison, a X-ray diffractogram for a high temperature grown PST film on MgO/Sapphire is shown in Figure 4. Because the higher temperature fired films were routinely grown on insulating substrates, measurements were restricted to top IDE Cr/Au structures with a electrode gap of  $\sim 1 \mu\text{m}$ . As this was significantly greater than the film thickness, the measuring field was mostly parallel to the film surface.

The pyroelectric response, also with upto 50V bias, was derived from the ac current produced by modulating the substrate temperature, typically by 0.2Krms at 0.01Hz. Any stray capacitance from the substrate and spurious signals proportional to the temperature coefficient of resistivity were measured and calculated respectively, and the results corrected accordingly.

The dielectric data for a  $3 \mu\text{m}$  thick film with a grain size of  $\sim 0.6 \mu\text{m}$  is shown in Figure 5, with equivalent data for ceramic PST, produced as described above, to near full density with a grain size in the range  $1-2 \mu\text{m}$ . The  $T_C$  value estimated from the permittivity peak is low; typically the films have a value of 5-30K below the normal ceramic value ( $\sim 300\text{K}$ ). The zero bias curve for the thin film shows a diffuse curve compared to a relatively sharp curve for the ceramic. This is expected, because the degree of B-site ordering[13], is much less for the film, typically  $\sim 10\%$  compared to  $\sim 60\%$  for standard

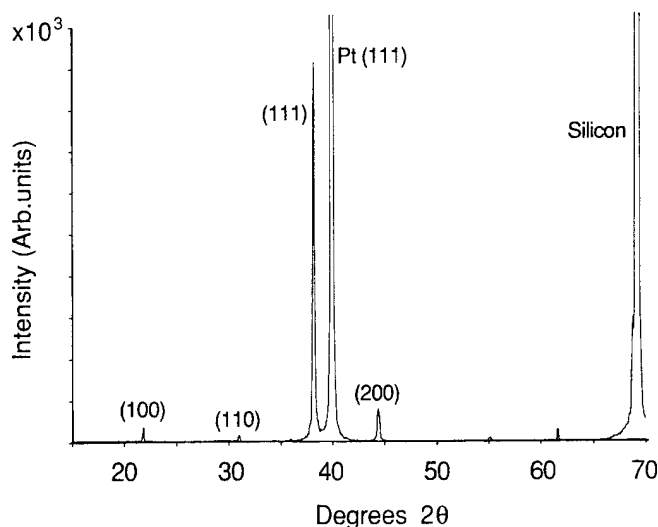


Fig. 3. X-ray diffraction trace of a typical PST film deposited on silicon at a temperature of 650°C.

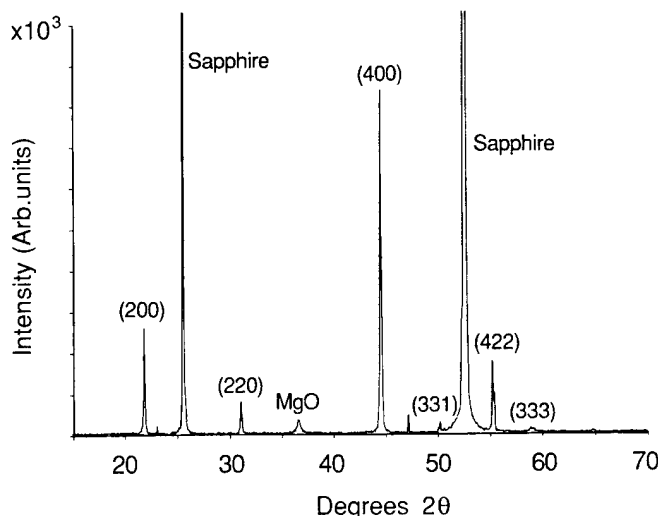


Fig. 4. X-ray diffraction trace of a high temperature PST film grown on MgO coated sapphire.

ceramic.

Both samples show a reduction in the dielectric peak, which is also shifted up by  $\sim 30\text{K}$ , as expected for a first order transition[10]. Also, both show similar dielectric loss behaviour; high ( $>10\%$ ) at transition and low ( $<1\%$ ) below. It was also lower under bias or in the paraelectric phase. The pyroelectric responses under bias, (Figure 5b), have similar magnitude, however, with the ceramic there is a detectable response associated with the biased permittivity peak, which is absent in the thin film due to the diffuse nature of the transition.

Thin films have shown a less consistent behaviour with, for example, the peak relative permittivities, which span over the range 1500-9000. The reason for this is not known, as there is no correlation between these values and either the film thickness, varied from  $0.3$  to  $5.8 \mu\text{m}$  or with the average grain size range of  $0.3-2 \mu\text{m}$ . This suggests that no significant degradation in the properties has been caused by either surface layer or inter-grain boundary effects.

A marked variation in the resistivity was observed with values ranging from  $0.3$  to  $3 \times 10^{10} \Omega\text{m}$  for most thin films, but is typically over  $10^{12} \Omega\text{m}$  for bulk ceramic.

#### PST Thin Film Release

As mentioned above, insulating substrates were normally used for films grown at high temperature. Therefore, to fabricate a hybrid pyroelectric device, the film has to be physically released from its substrate prior to further processing. We chose a thin layer of

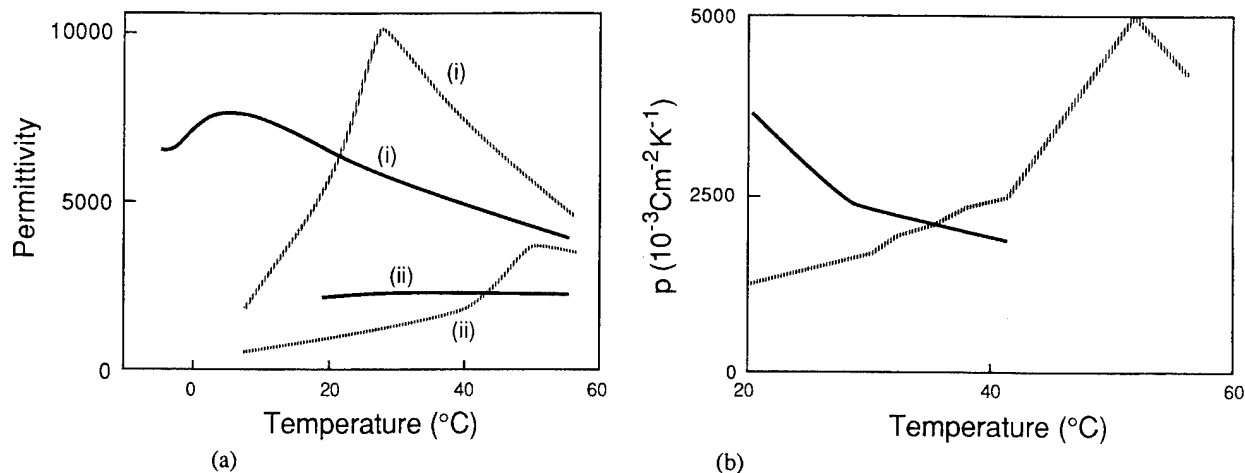


Fig.5. Thin Film (—) and bulk ceramic (----) PST dielectric properties. (i) at zero bias; (ii) at  $4.2 \times 10^6 \text{ Vm}^{-1}$ , (a) Relative permittivity and (b) pyroelectricity ( $p$ )

magnesium oxide as a release layer[23]; as PST films can be successfully grown on MgO single crystal, but is restricted to 1-2 $\mu\text{m}$  in thickness due to the thermal expansion mismatch (typically,  $11 \times 10^{-6} \text{K}^{-1}$  for MgO and  $6.5 \times 10^{-6} \text{K}^{-1}$  for PST). Sapphire which has a value of  $\sim 8 \times 10^{-6} \text{K}^{-1}$  is more closely matched; and films in excess of 5 $\mu\text{m}$  can be readily obtained, with good demonstrated film properties.

By using a thin deposited layer of MgO on sapphire, the thermal expansion characteristics of the composite substrate will be governed by sapphire. By using the same deposition scheme, PST films upto 4 $\mu\text{m}$  in thickness were obtained, showing high (100) orientation (Figure 4). Typical surface and cross-sectional SEM micrographs are shown in Figure 6.

Film release was facilitated by chemically etching away the MgO interlayer using phosphoric acid ( $\text{H}_3\text{PO}_4$ ). With both faces of the released film electroded, through film dielectric measurements were made possible. Dielectric measurements of a released 4 $\mu\text{m}$  film are shown in Figure 7. The peak permittivity was close to the value pre-release, but the peak was sharper, which may have resulted from the lifting of the clamping restrictions of the substrate, which would normally inhibit the dimensional changes associated with a phase transition. Also, the high (100) orientation would tend to favour the through film measurement, over the unreleased, made parallel to the surface, where a more random orientation of grains exists.

#### Film Pyroelectric Performance

The permittivity values obtained, would result in an element capacitance of a few pF, for high resolution 2d arrays. This would provide a good match for a MOSFET pre-amplifier, resulting in a detector noise dominated by the Johnson noise of the dielectric loss (D). The detector signal-to-noise would be proportional to the  $F_D$ [24]. The relevant properties of a range of pyroelectric materials has been compared previously[22]; The values of  $F_D$  for bulk and thin film PST are 15-17 and  $5-11 \times 10^{-5} \text{Pa}^{-1/2}$  respectively; although the values obtained for thin film PST are  $\sim 70\%$  of bulk values, it is still superior to most other bulk materials. Also, it is not known whether bulk materials would retain their properties as thin films.

Further development is required before these thin film properties can be utilised. As PST would normally be operated under bias, the finite resistivity results in a leakage current and hence a associated shot noise term. Also, the fully released films have been demonstrated over small areas, this needs to be extended to area's of the order of  $10^{-3} \text{m}^2$ , and to remove the PST intact onto a support layer suitable for 2d array processing technologies.

#### Integrated Arrays

There is currently a major effort world-wide to develop the next generation of linear and 2d fully integrated arrays, with a number of key technologies, such as thermally isolated micro bridges, insulating

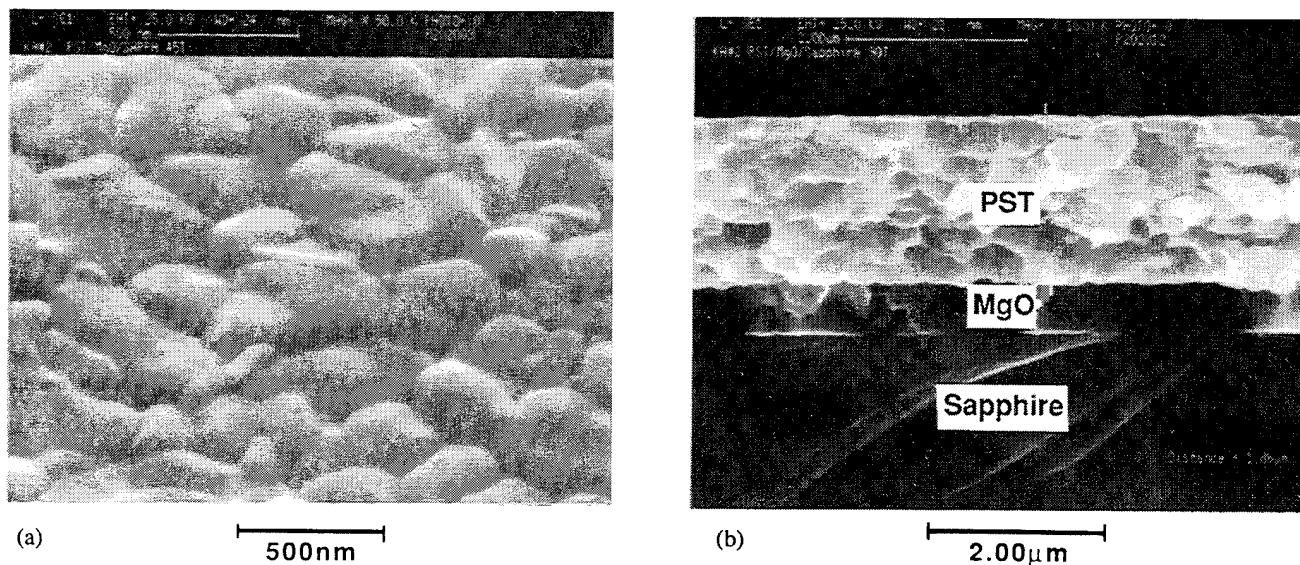


Fig.6. SEM micrographs of (a) surface and (b) cross-section of a PST film deposited on MgO/sapphire

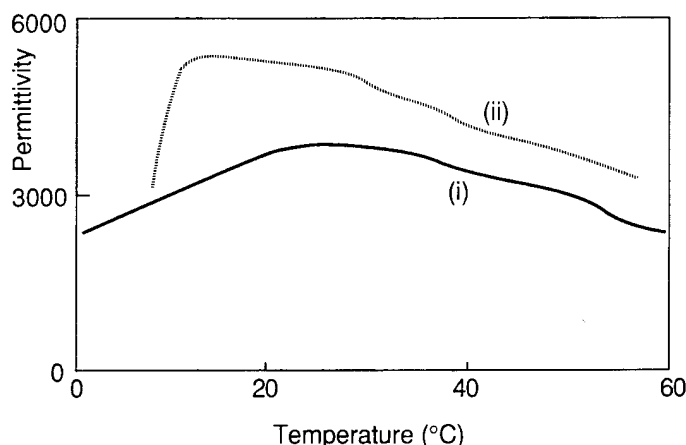


Fig. 7. Relative permittivity of thin film PST (i) before and (ii) after release from sapphire substrate

layers, IC compatibility which are under intense study. For example orientation effects are expected to change for deposition onto micro bridge structures, where the stress constraints may be different.

A possible schematic structure, suitable for an integrated array is shown below, Figure 8.

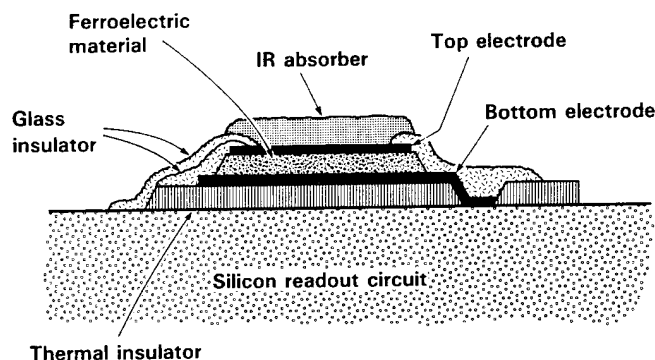


Fig. 8. A schematic cross-section of a thin film integrated thermal detector element

The potential rewards are high as demonstrated by the work of Ye. *et al* [21], where pyroelectric coefficients of the order of  $1 \times 10^{-3} \text{ Cm}^{-2}\text{K}^{-1}$  were obtained on a microbridge structure. It is speculated that when on a microbridge, temperature variations induced cause a bimaterial bending analogous to a bimetallic strip due to the thermal expansion mismatch, between the silicon bridge and the ferroelectric, which gives rise to a secondary piezoelectric signal which adds to the true pyroelectric component to give the observed high response. This type of structure is obviously not suited for PST applications due to deposition temperature restraints, however, a possible hybrid linear array thin film configuration has been described previously [25], utilising MgO release layers.

### Conclusions

The above results have shown that PZ- doped PST exhibits the highest dielectric constant at a  $x$  value of 0.125, using the optimum preparation route of Method C. Hot-pressed material from this route gave a dielectric constant and loss of 24000 and 0.1%, respectively when the average grain size was  $2\mu\text{m}$ . PST-PZ samples produced using Method B were found to be highly dependant on the annealing temperature and a true solid solution was only obtained for annealing temperatures of  $>1300^\circ\text{C}$ . PST-PT ceramics produced using method

B gave similar properties to PST-PZ from the same method. Pyroelectric measurements indicate useful performance for PST-PZ ceramic over undoped PST.

PST films derived from solution have been characterised electrically. Their pyroelectric values approach those measured on bulk ceramic. The combination of low thickness and high pyroelectric coefficients make them suitable for large 2d arrays. The properties also appear to be independent of grain size and thickness. A novel release layer technique has been demonstrated using MgO, which is a necessary step in the fabrication of a PST detector array.

A possible alternative array structure is also described, suitable for ferroelectric films grown at lower temperatures.

### Acknowledgement

This work has been carried out with the support of the Defence Research Agency (Malvern).

### References

- [1] R.W. Whatmore, "Pyroelectric Ceramics and Devices for Thermal Infra-red Detection and Imaging," *Ferroelectrics*, vol. 118, pp. 241-259 (1991).
- [2] R.W. Whatmore, "High Performance, Conducting Pyroelectric Ceramics" *Ferroelectrics*, vol. 49, pp. 201-210 (1983).
- [3] L.A. Berardinis, "Night Vision," *Mach.Des.*, pp. 57-61(1991).
- [4] J. Haystead, "Thermal Imaging," *Defence Electr.*, pp. 48-52(1991).
- [5] S. Borrello, "Focal Planes for Infrared Imaging," *Texas Instr. Tech.J.*, vol. 8, pp. 20-27 (1991).
- [6] W.F. Kosonocky, "Review of Infrared Image Sensors with Schottky-Barrier Detectors," *Optoelectronics*, Vol. 6(2), pp. 173-205 (1991).
- [7] C.H. Lucas, "Infrared Detection, Some Recent Developments and Future Trends," *Sens Actuators*, Vol. A25-A27, pp. 147-154(1991).
- [8] N.M. Shorrocks, S.G. Porter, R.W. Whatmore, A.D. Parsons, J.N. Gooding and D.J. Pedder, "Uncooled Infrared Thermal Detector Arrays," *Proc. SPIE -Int.Soc.Opt.Eng.*, Vol. 1320, pp. 88-94, (1990).
- [9] R. Watton, "Ferroelectric Materials and IR Bolometer Arrays: From Hybrids Towards Integration," *Integr.Ferroelectr.*, vol. 4(2), pp. 175-86 (1994).
- [10] N.M. Shorrocks, R.W. Whatmore, and P.C. Osbond, "Lead Scandium Tantalate for Thermal Detector Applications," *Ferroelectrics*, Vol. 106, pp. 387-392(1990).
- [11] B.M. Kulwicki, A. Amin, H.R. Beratan, and C.H. Hanson, "Pyroelectric Imaging," *Proc.of 8th IEEE ISAF'92*, pp. 1-11(1992).
- [12] S.B. Lang, "Guide to the Literature of Piezoelectricity and Pyroelectricity," *Ferroelectrics*, Vol. 146(1-4), pp. 153-369(1993).
- [13] C.G.F. Stenger, F.L. Scholten and A.J. Burggraaf., "Ordering and Diffuse Phase Transitions in  $\text{Pb}(\text{Sc}_{0.5}\text{Ta}_{0.5})\text{O}_3$  Ceramics," *Solid.State.Comm.*, Vol. 32, pp. 989-992(1979).
- [14] O.M. Stafsud and M.Y. Pines, "Characteristics of KTN Pyroelectric Detectors," *J. Opt.Soc. Am.*, Vol. 6, pp.1153-5(1971).
- [15] P.C.Osbond, N.I. Payne, N.M. Shorrocks, R.W. Whatmore and F.W. Ainger., "Dielectric and Microstructural Properties of BST Ceramics Prepared From Citrate Precursors," *Proc.6th. IEEE ISAF*, pp.348-51(1986)
- [16] R.W. Whatmore, P.C. Osbond and N.M. Shorrocks., "Ferroelectric Materials for Thermal IR Detectors," *Ferroelectrics*, Vol.76, pp.351-367(1986).
- [17] J.R. Giniewicz, A.S. Bhalla and L.E. Cross., "An Investigation of the Structural and Dielectric Properties of the Solid Solution System  $(1-x)\text{Pb}(\text{Sc}_{1/2}\text{Ta}_{1/2})\text{O}_3$ -(x)  $\text{PbTiO}_3$ ," *Ferroelectrics Lett.*, Vol. 12, pp.355(1990).
- [18] *Idem*, *Ferroelectrics*, Vol. 118, pp. 157(1991).
- [19] R.W. Whatmore, N.M. Shorrocks, P.C. Osbond, S.B. Stringfellow, C.F. Carter, and R. Watton., "Modified Lead Scandium Tantalate for Uncooled LWIR Detection and Thermal Imaging," *Proc.of 8th IEEE ISAF'92*, pp.202-205(1992).
- [20] P.C. Osbond and R.W. Whatmore., "High Dielectric constant ceramics in the  $\text{PbSc}_{0.5}\text{Ta}_{0.5}\text{O}_3$ - $\text{PbZrO}_3$  and  $\text{PbSc}_{0.5}\text{Ta}_{0.5}\text{O}_3$ - $\text{PbTiO}_3$  systems," *J. Mats. Sci.*, Vol. 28, pp. 1377-1384(1993).

- [21] C.Y. Ye, T. Tamagawa, Y.Y. Lin and D.L. Polla, " Pyroelectric Microsensors by Sol-Gel Derived  $\text{PbTiO}_3$  and  $\text{La-PbTiO}_3$  Thin Films," *Mats.Res.Soc.Symp.Proc.*, Vol. 243, pp. 61-66(1992).
- [22] A. Patel, N.M. Shorrocks, R.W. Whatmore., " Lead Scandium Tantalate Thin Films for Thermal Detectors," *Mats.Res.Soc.Symp.Proc.*, Vol. 243, pp. 67-72(1992).
- [23] A. Patel and R.W. Whatmore., " A method of Manufacturing Free Standing Perovskite Lead Scandium Tantalate Film," *Patent GB 9025547*, (1992).
- [24] R. Watton, M.V. Mansi., " Performance of a Thermal Imager Employing a Hybrid Pyroelectric Detector Array with MOSFET Readout," *SPIE*, Vol. 865, pp. 78-85(1988).
- [25] N.M. Shorrocks, A. Patel, R.W. Whatmore., " Pyroelectric Properties of Thin Film Lead Scandium Tantalate," *Ferroelectrics*, Vol. 133, pp. 35-40(1992).

B. Cole, R. Horning, B. Johnson, K. Nguyen, P.W. Kruse<sup>1</sup>, and M. C. Foote<sup>2</sup>  
Honeywell Technology Center  
<sup>1</sup>IR Technology  
<sup>2</sup>JPL

## Abstract

Honeywell has developed a unique uncooled thermal detector technology based on fabricating thin film structures with temperature sensitive detector materials. High TCR resistive materials such as VOx and YBaCuO, and pyroelectric PbTiO<sub>3</sub> have been used. Two dimensional imaging arrays of sizes up to 240x336 have been integrated with Si substrate electronics to achieve temperature sensitivities of less than .04 C operating at room temperature. The thin film detector materials are deposited on microstructure thin film pixels of 2 mil sizes which are subsequently thermally isolated from the substrate by etching away the underlying substrate. The thermal isolation of the microstructure pixel provides the temperature rise and the detector material provides the conversion to an electrical signal.

## Introduction

Infrared (IR) detectors fall into two main classes, thermal and photon detectors. Thermal detectors rely upon the detection of heat generated through the absorption of radiation. Photon detectors rely upon the direct photoexcitation of electrons to produce an electrical signal. Typically single element photon detectors are more sensitive to radiation because of their higher efficiency and higher speed. The main advantage of thermal detectors has been the ability to absorb radiation over a broad IR wavelength range. The main challenge for thermal detectors has been to make a structure which has measurable temperature rise for low radiation powers. Single element detectors have been used as calibration and radiometric standards.

Honeywell is currently developing a variety of thermal detector arrays which have the ability to detect radiation at high sensitivity, rivaling photon detectors. The two main reason for these dramatic improvements is that the detectors are highly efficient at converting radiative power into electrical signals and are integrated into an array to overcome the speed restrictions. Although each individual pixel is slow, designed with a time constant of 30 msec for video rates, the integration of these detectors into an array provides a low cost, high performance, large size, detector.

Thermal detectors under development consist of two types, bolometers and pyroelectric detectors. Both detector types rely upon the same basic thermal structure for the conversion of radiation to heat, the first step in the detection process. The bolometer and the pyro differ in the mechanism used to convert heat into an electrical signal. The thermal detector shown in Figures 1 and 2 is essentially common to all technologies. Each detector is typically of 2 mil size. All detector types require special films on the microbridge to enhance film growth. The amorphous VOx bolometer detector material can be grown directly on amorphous Si<sub>3</sub>N<sub>4</sub>. The superconductor requires a film of YSZ on the Si<sub>3</sub>N<sub>4</sub> to provide the crystal growth. The PbTiO<sub>3</sub> pyroelectric material requires a thin film of Pt for proper orientation and growth.

## Thermal Detector Pixel

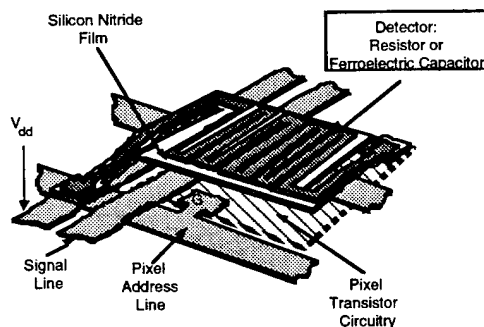


Figure 1: Schematic representation of two-level pixel structure

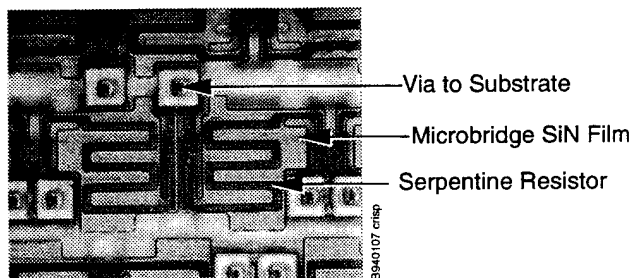


Figure 2: Photomicrograph of 50% fill factor 2 mil pixel with serpentine resistor.

The thermal properties of these detectors can be defined by the thermal mass,  $C_{th}$ , and thermal conductance,  $G_{th}$ . The dimensions of the leg structures are defined by photolithographic patterning and consist mostly of Si<sub>3</sub>N<sub>4</sub> films which have low thermal conductivity. The thermal conductivity of these films in vacuum is 10<sup>-7</sup> Watts/K. The pixel structure itself is supported over the underlying address electronics by the legs. In this two level design, the address real estate is located on the lower level. This enables the pixel fill factor to be very large, on the order of 50% or more, greatly enhancing IR absorption. The thermal mass of this 1μm thick suspended structure is 10<sup>-9</sup> Joules/K. The time constant defined by

$$\tau_{th} = C_{th} / G_{th}$$

is in the range of 10 msec.

## Bolometer Detector

The bolometer detector utilizes a film with a high temperature coefficient of resistance, TCR, defined as  $dR/(RdT)$ . The responsivity,  $R$ , which defines the signal produced by a radiation flux unit is given by

$$R = I_b R \frac{TCR \propto FF}{G_{th} (1 + \omega^2 \tau_{th}^2)^{1/2}}$$

where  $\alpha$  is the IR absorption coefficient for the band of interest, FF is the pixel fill factor,  $R$  is the pixel resistance,  $I_b$  is the bias current through the resistor, and  $\omega$  is the angular frequency if the radiation is chopped.

A figure of merit,  $F_{bol}$ , for bolometer detector material performance under fixed voltage bias conditions when Johnson noise in the resistor is the dominant noise source is

$$F_{bol} = TCR / (R)^{1/2}$$

For optimal performance, the array TCR needs to be as large as possible for a given pixel resistance. For the present 2D arrays, VOx is the detector material. This amorphous thin film is deposited by ion beam sputtering process where tight control of film oxygen content is maintained. This VOx thin film material with a resistivity of 0.1 Ohm-cm has a TCR of 2%. Although thermistor materials can provide higher TCRs, in the range of 5%, the significantly higher resistance negates any added benefit. Using this material we have fabricated arrays of size 240 x 336 pixels with a thermal sensitivity of better than .04 °C. The fabrication of arrays is totally compatible with Si processing technology. Unlike all long wavelength IR photon detectors which must operate at 77K temperatures to achieve high performance, these arrays operate at ambient temperatures. By changing the film oxygen stoichiometry and the resistivity we are able to change the TCR. Figure 4 is a plot of film TCR vs. film resistivity for 500 and 1000 Angstrom thick films. These individual films of different resistances can be described by different activation energies over a

100 C temperature range around room temperature. The activation energy, which can be derived, from the slope of  $\ln R$  vs  $1/T$  line is shown for one 13 Kohms/square VOx film deposited on Si<sub>3</sub>N<sub>4</sub> in Figure 4.

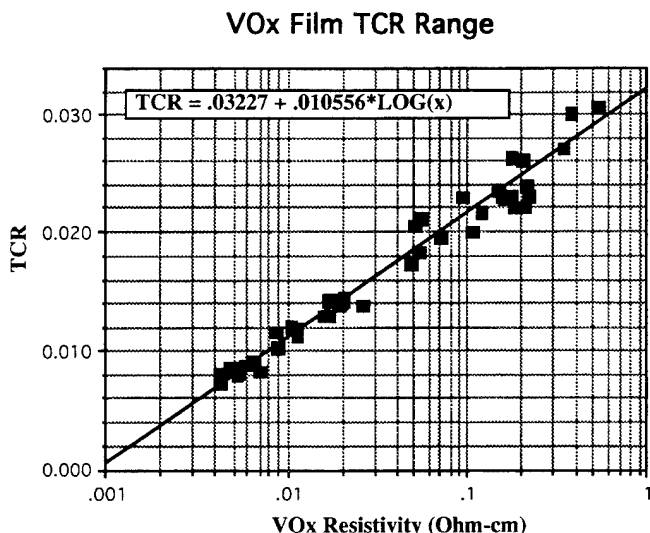


Figure 3: TCR vs VOx resistivity

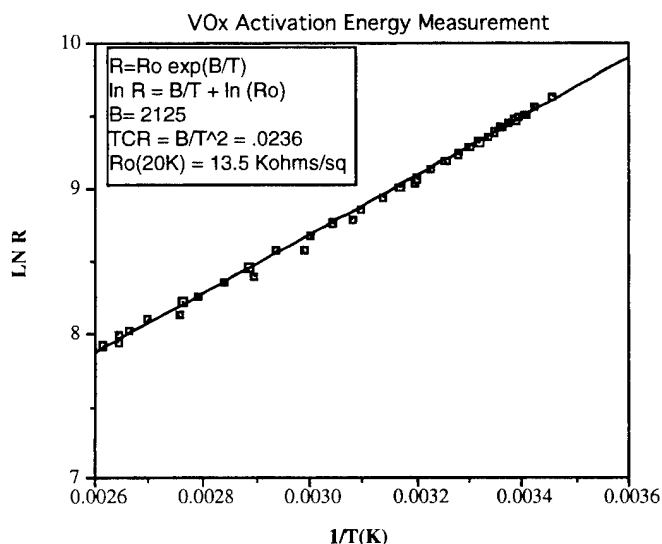


Figure 4: Activation energy analysis for one 500 Angstrom VOx film

#### High Temperature Superconducting Microbolometers

A superconductor at its transition edge is a very sensitive temperature sensing material for use on microbolometers. A temperature coefficient of resistance exceeding  $1.0 \text{ K}^{-1}$  at the transition midpoint of YBa<sub>2</sub>Cu<sub>3</sub>O<sub>7-x</sub> (YBCO) is not uncommon for good quality films with a transition temperature near 90 K.<sup>1</sup> Films such as these, combined with a thermal conductance of  $\sim 10^{-7}$  Watts/K achievable with silicon nitride microstructures fabricated by micromachining can theoretically give an infrared detectivity substantially higher than  $10^{10} \text{ cm Hz}^{1/2}/\text{Watt}$ .<sup>1</sup> The detectivity, a common figure of merit for infrared detectors which is normalized for the detector area, is defined as

$$D^* = \frac{(\text{detector area})^{1/2} (\text{Responsivity})}{(\text{noise voltage})}$$

A detectivity of  $10^{10} \text{ cm Hz}^{1/2}/\text{Watt}$  would be higher than that reported for any other type of thermal detector operating at a temperature greater than 70 K.<sup>2</sup>

To fabricate YBCO microbolometers with ideal sensitivity, the YBCO film must have a high temperature coefficient of resistance, a low level of electrical noise, and must be passivated from

damage caused by the etchant used to isolate the membrane from the substrate. To achieve a high temperature coefficient of resistance and low noise, the YBCO films must be epitaxial.<sup>1</sup> A thin film of epitaxial yttria-stabilized zirconia (YSZ) on silicon is known to provide a good buffer layer for growth of high quality epitaxial YBCO films on silicon wafers.<sup>3</sup> We have shown that YSZ also provides good passivation for the YBCO against attack by a solution of KOH in water, a common anisotropic etchant of silicon used in micromachining.<sup>1</sup> Thus, we have chosen to use YSZ as the epitaxial buffer layer underneath the YBCO.

Epitaxial films of YLa<sub>0.05</sub>Ba<sub>1.95</sub>Cu<sub>3</sub>O<sub>7-x</sub> superconductor were grown by pulsed laser deposition at the Jet Propulsion Laboratory on 3-inch silicon wafers. Following the procedure of Fork, et. al. for depositing epitaxial YBCO using epitaxial YSZ buffer layers on silicon,<sup>3</sup> the silicon wafers were pre-cleaned in an HF etchant solution to remove the native oxide.<sup>4</sup> Before depositing the superconductor, an epitaxial buffer layer of YSZ 1100 Å thick was deposited by pulsed laser deposition onto the bare silicon surface. The YBCO film, 680 Å thick, was then deposited epitaxially in-situ on top of the epitaxial YSZ. Finally, gold contact metal 800 Å thick was deposited in-situ directly on top of the superconductor.

At Honeywell, the films were patterned and processed into microbolometers. The details of this process have been described elsewhere.<sup>5</sup> After patterning and passivation, the devices were etched in ethylene diamine pyrocatechol (EDP), an anisotropic etchant of silicon, to etch the silicon from underneath the microbolometers and produce devices with low thermal conductance. The superconductor on the thermally isolated membranes was passivated against attack by the EDP from above by 1 μm of Si<sub>3</sub>N<sub>4</sub>, and from below by 1100 Å of epitaxial YSZ.

Fig. 5 shows the resistance and responsivity at 2 μA dc bias as functions of substrate temperature for a microbolometer fabricated from an epitaxial YBCO film on YSZ on silicon, and Fig. 6 shows an optical microscope picture of this device. The etch pit underneath the microbolometer is 105 μm x 140 μm. The responsivity was measured with a 449 K blackbody chopped at a frequency of 2.0 Hz and illuminating the microbolometer through an anti-reflection coated Ge window in the cryostat vacuum can. The measured thermal time constant of the device was 105 msec, resulting in a 3 dB rolloff of the responsivity at a frequency of 1.5 Hz. The temperature coefficient of resistance at the transition midpoint is  $0.64 \text{ K}^{-1}$  (measured at 0.5 μA bias, where self-heating is negligible). The thermal conductance was measured by resistive heating to be  $8.5 \times 10^{-8} \text{ W/K}$  at 95 K.

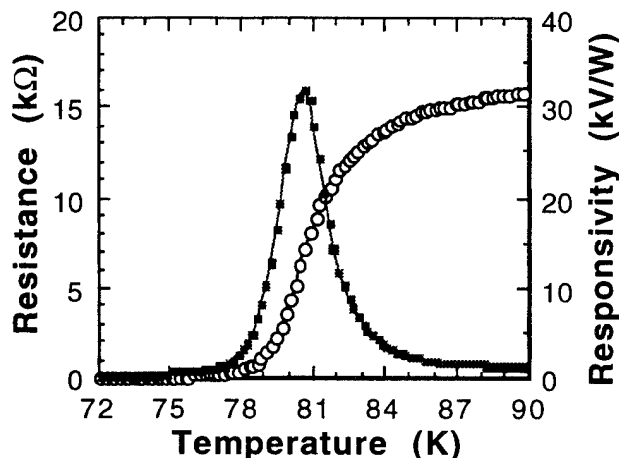


Figure 5: Resistance (open circles) and responsivity (closed squares) as functions of temperature for the superconductor microbolometer described in the text.

Noise measurements performed in a 2-probe configuration on the device of Fig.5 and Fig. 6 give a noise voltage at the microbolometer of  $50 \pm 10 \text{ nV/Hz}^{1/2}$  at 2.0 Hz with a dc bias current of 2.0 μA. This gives a  $D^*$  of  $8 \pm 2 \times 10^9 \text{ cm Hz}^{1/2}/\text{W}$ ,



and a noise equivalent power (NEP) of  $1.5 \times 10^{-12} \text{ W/Hz}^{1/2}$ . This value of  $D^*$  is higher than the highest value reported previously for a YBCO transition-edge microbolometer,<sup>2</sup> and is comparable to the highest reported  $D^*$  for a thermal detector operating at greater than about 70 K.

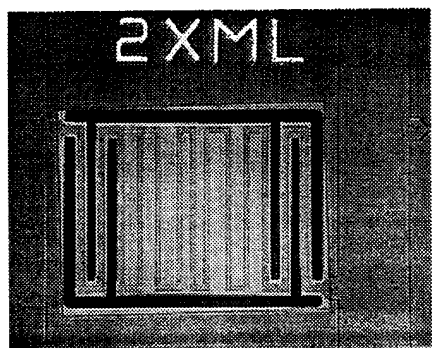


Figure 6: Optical microscope photograph of the superconductor microbolometer element of Figure 5 measurements.

### Pyroelectric Detectors

Pyroelectric detectors are being developed to use a similar thermal structure for IR detection. Rather than measuring a resistance change with temperature as in bolometers, pyroelectric detectors measure the change in polarization charge of a ferroelectric material. The responsivity,  $R$ , of a pyroelectric detector is given by

$$R = \frac{\omega p \alpha FF A}{G_{th} G_{el} (1 + \omega^2 \tau_{th}^2)^{1/2} (1 + \omega^2 \tau_{el}^2)^{1/2}}$$

where  $\alpha$  is the absorptance,  $FF$  is the fill factor,  $A$  is the detector area,  $p$  is the pyroelectric coefficient,  $\omega$  is the angular frequency of chopped radiation, and  $\epsilon$  is the dielectric constant, and  $G$  are the electrical and thermal conductances. When chopping the pyroelectric detector at frequencies which are high compared to the thermal and electrical time constant, the responsivity simplifies to

$$R = \frac{\epsilon p \alpha FF A}{C_{th} C_{el} \omega}$$

A figure of merit,  $F_{pyro}$ , for pyroelectric performance when dielectric loss tangent,  $\tan(\beta)$ , noise is dominant is

$$F_{pyro} = p / \epsilon d \tan(\beta)$$

where  $d$  is the film thickness. It can be seen from this formula that thin film detector material with the low dielectric constant,  $\epsilon$ , high pyroelectric coefficient,  $p$ , and low loss tangents are the best choices for detectors. Of the ferroelectrics, c-axis oriented  $\text{PbTiO}_3$  is one of the best materials. The present efforts are focused on growing oriented  $\text{PbTiO}_3$  films on the thermal structure of Figure 1 and 2. The  $\text{PbTiO}_3$  detector must be sandwiched between top and bottom electrodes to form a capacitor. At present Pt is the best material for growing substrate  $\text{PbTiO}_3$  detector material.

As described above, achieving a high fill factor requires that the IR sensing pixel be fabricated directly above the addressing electronics. This, in turn, requires that the substrate be a silicon wafer, typically having a dielectric film separating the electronics from the pixel. Excellent  $\text{PbTiO}_3$  and PZT films have been deposited on single crystal MgO substrates, but cofabrication of electronics is impossible in that case. Our goal has been to fabricate pyroelectric devices on silicon substrates, depositing  $\text{PbTiO}_3$  and related materials on  $\text{Si}_3\text{N}_4$  and Pt electrodes.

To achieve control of the film stoichiometry, a dual target ion beam sputtering system was built.<sup>6</sup> PbO and Ti sputtering targets are mounted on a movable stage in the chamber. The targets are alternately shuttled into the ion beam, depositing very thin layers of PbO and  $\text{TiO}_2$  on a heated silicon substrate. Film stoichiometry is controlled simply and accurately by varying the ratio of sputtering times from the PbO and Ti targets, eliminating a

common problem encountered in single target sputtering techniques. At the deposition temperature of 500-600°C, the thin layers quickly interdiffuse, producing a homogeneous layer of  $\text{PbTiO}_3$ . Additional targets, such as Zr, can be added to deposit PZT films, with the Zr:Ti ratio again controlled by the sputtering time from the respective targets. Stoichiometric  $\text{PbTiO}_3$  and PZT films are typically deposited at temperatures between 500°C and 600°C. An oxygen flow of 7-10 sccm is used during deposition. The deposition rate is 50 Å/min. and films are typically grown to ~0.5-1 µm thick.

Figure 7 shows x-ray diffraction results from three  $\text{PbTiO}_3$  films: one deposited directly on amorphous  $\text{Si}_3\text{N}_4$ , one on a Pt electrode layer (on top of  $\text{Si}_3\text{N}_4$ ) and the third on a (100) MgO single crystal substrate. The films deposited on  $\text{Si}_3\text{N}_4$  and on Pt both have the tetragonal perovskite phase. The (001)-(100) and (101)-(110) peaks show a strong tetragonal split. The (001) and (100) peaks are absent from the film deposited on the dielectric. In a randomly oriented film, the (001) peak would have half the intensity of the (100) peak. Thus the film on Pt shows some degree of preferred (001) orientation. This is the desired orientation for our pyroelectric structure. Given the choices of substrates we have restricted ourselves to, variation of other deposition conditions did not significantly increase the (001) orientation. The lower panel of Figure 7 shows  $\text{PbTiO}_3$  on a single crystal MgO substrate. On this substrate, both Pt and  $\text{PbTiO}_3$  can easily be grown epitaxially with the desired (001) orientation. PZT films were also deposited by adding Zr to the moveable target stage. These films again have a perovskite phase, as seen in Fig. 8; at times a peak from a  $\text{Pb}_3\text{O}_4$  phase was also observed. The Zr:Ti ratio was approximately 40:60.

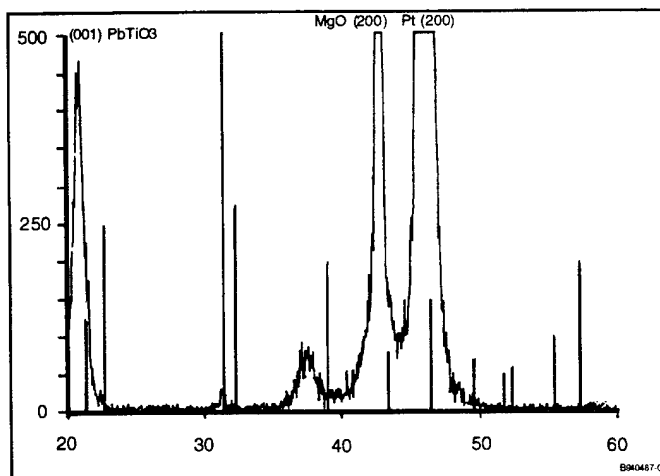
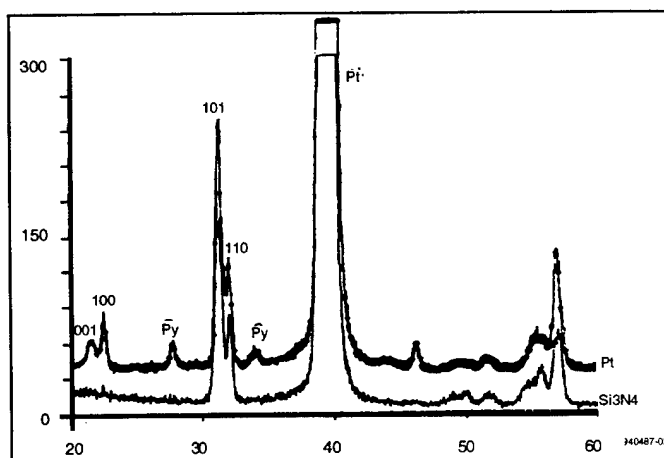


Figure 7: X-ray diffraction spectra of three  $\text{PbTiO}_3$  films deposited on  $\text{Si}_3\text{N}_4$ , Pt/ $\text{Si}_3\text{N}_4$ , and Pt on single crystal MgO.

$\text{PbTiO}_3$  films deposited on Pt are smooth, while  $\text{PbTiO}_3$  deposited directly on  $\text{Si}_3\text{N}_4$  tends to be rough. This is due both to the good lattice match between Pt and  $\text{PbTiO}_3$  and to the stress buffering effect of the metal film. Using a 500 Å Pt film, the  $\text{PbTiO}_3$  was



smooth, but contained small cracks. An intermediate 1000 Å film, seen in Fig. 9, had slight cracking. The cracks disappeared altogether for Pt thicker than about 1500 Å. Clearly, crack free films are required for capacitive devices. The roughness of the films on the dielectric present device fabrication issues. When using patterned Pt electrodes, the PbTiO<sub>3</sub> on the electrode is smooth but off the electrode is rough. Patterning, depositing and etching of the PbTiO<sub>3</sub> or other films that cross this boundary become difficult because of this difference.

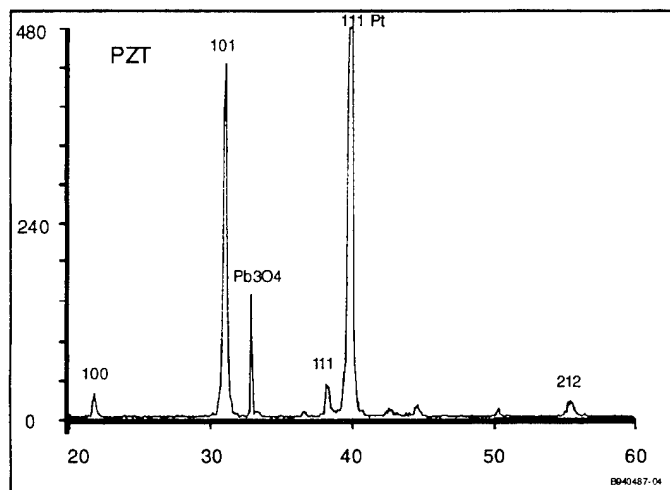


Figure 8: XRD spectra of PZT film deposited on Pt/Si<sub>3</sub>N<sub>4</sub>/Si substrate

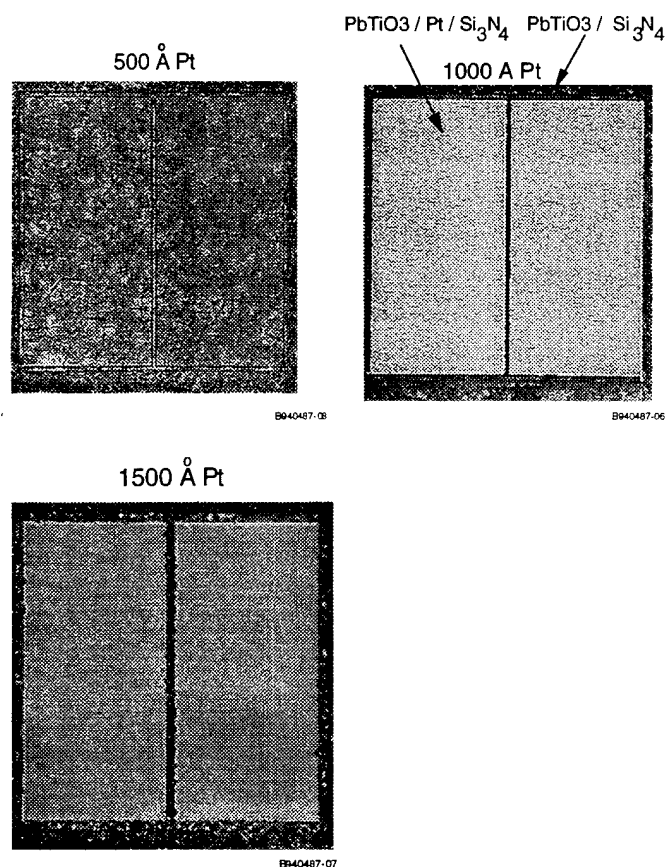


Figure 9: Photomicrograph of PbTiO<sub>3</sub> film morphology on Pt electrodes of three different thicknesses.

Dielectric properties have been measured on both PbTiO<sub>3</sub> and PZT films, and are summarized in Table 1. These values are in the vicinity of values for bulk materials of the same composition. PbTiO<sub>3</sub> and PZT films showed ferroelectric hysteresis, although the remanent polarization of the PbTiO<sub>3</sub> films tended to be low. The polarization of PZT was appropriate for the composition used.

Table 1. Dielectric properties of Ion Beam Sputtered Ferroelectric Films

Property	PbTiO <sub>3</sub>	PZT
Dielectric Constant	50-200	400-1000
loss tangent	0.002-0.04	0.04-0.05
Remanent polarization (μC/cm <sup>2</sup> )	3-4 (unpoled)	5-7 (unpoled)
Coercive field (kV/cm)		7
Pyroelectric coefficient (C/cm <sup>2</sup> K)	1 - 5 x 10 <sup>-8</sup>	

#### Summary

A two level thermal structure design with separated electronics and detector levels is well suited to IR detection. Microstructures have been integrated into addressable arrays to produce IR cameras with very high thermal resolution. The basic thermal detector pixel can be modified by combining a variety of temperature sensitive materials with thin film underlayers to form a range of thermal detector for different applications. The fabrication of these structures onto Si wafers can be made compatible with Si IC processes.

#### References

- [1] M.C. Foote, B.R. Johnson, and B.D. Hunt, "Transition edge YBa<sub>2</sub>Cu<sub>3</sub>O<sub>7</sub> microbolometers for infrared staring arrays", *proc. SPIE High-Temperature Superconducting Detectors: Bolometric and Nonbolometric*, January 1994 (in press).
- [2] J.C. Brasunas, B. Lakew, "High-T<sub>c</sub> superconductor bolometer with record performance", *Applied Physics Letters*, vol. 64, pp. 777-778, (1994).
- [3] D.K. Fork, D.B. Fenner, R.W. Barton, Julia M. Phillips, G.A.N. Connell, J.B. Boyce, and T.H. Geballe, "High critical currents in strained epitaxial YBa<sub>2</sub>Cu<sub>3</sub>O<sub>7-d</sub> on Si", *Applied Physics Letters*, vol. 57, pp. 1161-1163 (1990).
- [4] F.J. Grunthaner and P.J. Grunthaner, "Chemical and Electronic Structure of the SiO<sub>2</sub>/Si Interface", *Mater. Sci. Rep.* vol. 1, pp. 65-160 (1986).
- [5] B.R. Johnson, M.C. Foote, H.A. Marsh, and B.D. Hunt, "Epitaxial YBa<sub>2</sub>Cu<sub>3</sub>O<sub>7</sub> superconducting infrared microbolometers on silicon", *proc. SPIE Advanced Microdevices and Space Science Sensors*, July 1994 (to be published).
- [6] B.E.Cole, R.D.Horning and P.W.Kruse in *Ferroelectric Thin Films II*, A.I.Kington, E.R.Myers and B.Tuttle, eds., Materials Research Society Symposium Proceedings, Vol. 243, p185 (1992).

\* This work funded in part through contracts with ARO under contract #DAAL03-93-C-0020, and NASA/JPL.

# Uncooled Pyroelectric Thermal Imaging

Charles Hanson and Howard Beratan

Texas Instruments Incorporated  
Defense Systems and Electronics Group  
P.O. Box 655012, MS37  
Dallas, TX 75265

## ABSTRACT

Texas Instruments has been developing uncooled thermal imaging technology for the past 18 years with the promise that it would provide a low-cost solution to high-volume night vision applications. That promise is now being realized. Using technology developed for military applications with support from the U.S. Army Night Vision and Electronic Sensors Directorate (NVESD), the Advanced Research Projects Agency (ARPA), and the Balanced Technology Initiative (BTI), TI has teamed with Hughes Aircraft to provide a thermal imaging capability for police cruisers. The night vision kits include a thermal sensor, a pan and tilt head, mounting hardware, a display and a control center. The price of the introductory product is approximately \$6000.

## BACKGROUND

Uncooled thermal imaging at Texas Instruments began in the mid-1970's and has evolved into a major activity addressing multiple military and commercial applications. The present thrust began in late 1987 with demonstration of 2-mil pixels having an NETD of  $0.5^{\circ}\text{C}$  with  $f/1$  optics. This qualified Texas Instruments for the HIDAD program, a BTI program managed by NVESD and ARPA. The HIDAD program produced the technology that formed the basis for the developments discussed in this paper. It resulted in demonstration of an 80,000 ( $245 \times 328$ ) pixel array of detectors on  $48.5\mu\text{m}$  centers, having an array-average NETD of less than  $0.1^{\circ}\text{C}$  with  $f/1.0$  optics. The program further included demonstrating that array in a compact system.

Texas Instruments received one of two Low-Cost Uncooled Sensor Prototypes (LOCUSP) contract awards in 1990. Phase 1 of LOCUSP resulted in delivery of several units each of the Sight, Medium Range, Thermal Imaging (SMRTI), a sight for individual-served weapons, and the Sensor, Surveillance, Infrared (SSIR). Texas Instruments was the sole recipient of LOCUSP Phase 2 this year.

The technology is based upon the induced pyroelectric effect near the phase transition of the ferroelectric ceramic

barium-strontium titanate (BST). BST is a mixed-oxide perovskite ferroelectric with phase transition temperature determined by the barium-to-strontium ratio. The composition  $\text{Ba}_{0.64}\text{Sr}_{0.36}\text{TiO}_3$  has a transition near room temperature. Its low-field peak relative dielectric constant is high, typically 30,000, which significantly reduces the adverse effect of parasitic capacitance in the readout electronics. Operation near the transition gives the maximum voltage responsivity in spite of the high dielectric constant. Application of an electric field enhances material responsivity, but it reduces readout efficiency by reducing capacitance. Thus there is an optimum field that maximizes responsivity.

The detector array, shown in Figures 1 and 2, is reticulated to reduce thermal crosstalk between adjacent pixels. The backside of each pixel has a metal electrode that serves as one plate of a parallel-plate capacitor. The IR absorber is a three-layer resonant cavity. The bottom layer is an opaque metal film that also serves as the common electrode for the array of parallel-plate capacitors. On top of the metal film is a  $1.25\mu\text{m}$  thick layer of parylene that tunes the cavity for an absorption peak at approximately  $10\mu\text{m}$ . The top layer is a semi-transparent metal layer that matches the optical impedance of the cavity to that of free space. This structure can be optimized to obtain an absorptivity greater than 98 percent average over the  $7.5$  to  $13\mu\text{m}$  spectral region.

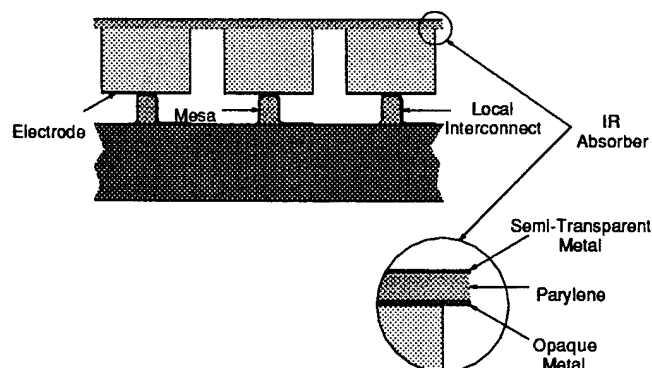
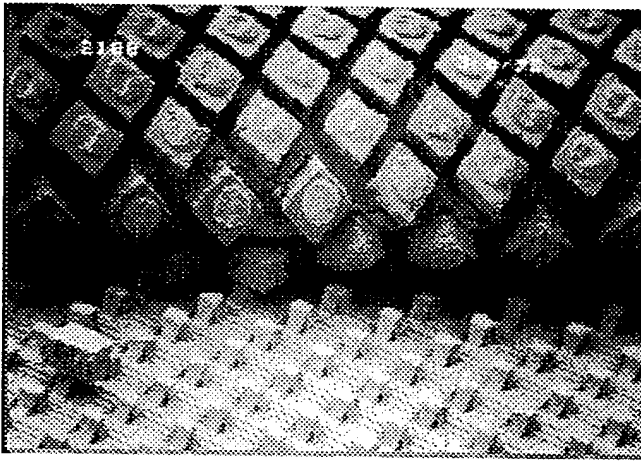
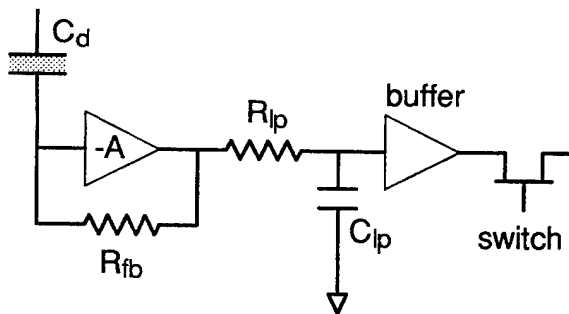


Figure 1 - Schematic view of detector pixel structure.



**Figure 2 - Uncooled focal plane array, showing the BST peeled back from the ROIC.**

The detector array interfaces with a readout IC (ROIC) that provides in the pixel unit cell a preamplifier, a low-pass noise filter, and a buffer. Figure 3 shows the unit cell schematic diagram. The ROIC is fabricated using a standard CMOS process with 1.0  $\mu\text{m}$  minimum geometry. The preamplifier is a simple CMOS inverter. The low-pass filter is a single-pole R-C circuit. The capacitor is the gate of an n-channel transistor biased to accumulation, and the resistor is actually a diode biased using a constant current source set with an off-chip voltage. In this way the characteristic frequency of the filter is externally adjustable. Outside the unit cell the ROIC provides further amplification and signal multiplexing to provide single-channel output suitable for video formatting.



**Figure 3 - Schematic diagram of the ROIC pixel unit cell.**

Thermal isolation between the detector array and the ROIC is provided by polyimide mesas, also shown in Figures 1 and 2. Each mesa has an over-the-edge metal run that contacts the ROIC unit cell input. The mesas and the detector pixels both have indium bumps which, when pressed together, form a permanent weld between the detector array and the ROIC.

The basic technology has remained constant throughout the development. The principal technical features are

- Ceramic BST mixed for a ferroelectric phase transition near room temperature
- Operation near the phase transition
- Applied electric field to boost responsivity and provide stability
- Reticulation for high MTF
- Bump bonding of the detector to an ROIC
- A mechanical chopper for field-difference processing and system simplification
- Long-wavelength IR (7.5 to 13  $\mu\text{m}$ ) sensitivity

## APPLICATIONS

Uncooled thermal imaging, in spite of its reduced performance in comparison to the cooled analog, offers numerous advantages for both military and commercial applications. First and foremost is its potential for low cost. This is important for any application in which the acquisition volume is high or in which the platform cost is low. The basic ferroelectric material technology itself is considerably less sensitive to fabrication processes than are most other materials used for IR detectors. This results in comparatively high yields and good uniformity of response, leading to lower production cost. The focal plane output is in a serial format that is readily processed using standard low-resolution digital devices and techniques. The resultant signal is NTSC/RS-170 compatible without reformatting. Because of this simplicity, the electronic system has a very low parts count, and it is compact, reliable and low cost. The absence of a cryogenic cooler or a multistage thermoelectric cooler is, of course, a significant cost-reducing feature. The absence of a scanner not only reduces cost directly, but also indirectly by simplification of the IR and visual optical systems. The only moving part in the system is a chopper, which is low-cost and reliable by virtue of its simplicity.

Other advantages of uncooled thermal imaging are its low weight and low power requirements. The electronic, mechanical and thermal simplicity described above leads to low weight and power as well as to low cost. A key feature that leads to this result is the use of a chopper with a detector that is inherently AC-coupled. This limits the dynamic range requirements for the electronic system and enables the use of a single-channel of low digital resolution components. This feature impacts weight, power and cost.

The general applicability of thermal imaging is limited at both the high cost, high performance end and the low cost, low performance end. The relevant question is generally,

"Can I get enough performance to do the job for a cost I can afford?" The answer, of course, depends upon the precise meaning of "enough performance" and "cost I can afford", and in various situations either of these can dominate. At the high end, platform cost is usually high and performance demands may border on the impossible, requiring a custom configuration. In these situations performance is the driving requirement. In the markets addressed by uncooled thermal imaging technology the reverse is true. Conventional thermal imaging systems have more than enough performance to meet the performance requirements of, for example, a rifle sight. However, the cost of such a system is many times that of the rifle itself, and it is therefore not readily justified. Uncooled thermal imaging technology fills the void between conventional thermal imagers that are too expensive and image intensification devices that have inadequate performance.

The rifle sight is an excellent example of an application of uncooled thermal imaging. The primary features required for such a sight are low acquisition cost, low life-cycle cost, light weight and simple logistical requirements. The necessity of low cost results from the low cost of the rifle and the desired widespread deployment. Aside from acquisition cost, life-cycle cost is dominated by the cost of batteries, and so low power dissipation and use of standard batteries are important design features. The present uncooled sight requires only six Watts of power from standard batteries, and the system weight is about 4.5 pounds.

Another application for which uncooled thermal imagers are well suited is perimeter surveillance. Range requirements for such applications are limited, and reliability and low maintenance are critical issues. The small size and low power of the uncooled thermal imagers make their presence unobtrusive. Low sensor cost and high reliability permit deployment for protection of relatively low-value sites.

An area of growing interest after the Gulf War is night vision driving aids for non-combat vehicles. Tanks, Bradley Fighting Vehicles, and armored personnel carriers are able to use modern thermal imaging equipment to advance in a battle zone, but logistic support vehicles generally do not have similar capabilities. This can leave forward positions without adequate support. Uncooled thermal imagers can be sufficiently low cost to be affordable in the large quantities required for support vehicles, and they can be small enough to be integrated effectively into thin-skinned vehicles. The Driver's Vision Enhancer (DVE) program, sponsored by PM Night Vision, is intended to provide this capability to three different military vehicles.

For non-military applications the considerations are similar, except that price is almost always an overriding factor. Texas Instruments and Hughes Aircraft have teamed to serve these markets. The principle applications that will drive development of the non-military market are cruiser-mounted sensors for police, surveillance sensors for buildings, parking lots and other sites, and driving aids for truckers. Of these, the police night vision aid will be the first application to see high-volume deployment. A product for this application is described in detail in the next section.

## THERMAL IMAGING FOR LAW ENFORCEMENT

For millennia, malicious violators of the public good have used the cover of darkness to conceal their deeds. So much so that in every language the terms "light" and "dark" have connotations of good and evil. Thermal imaging for common law enforcement officers effectively removes the cover, and without revealing that the cover has been removed. This provides an immense advantage to officers in many routine and emergency situations. Texas Instruments and Hughes Aircraft loaned several uncooled thermal imaging units to police departments across the US and in Canada in 1993. The officers were briefed on the use of the equipment and its potential for helping them do their jobs. As expected, the officers themselves discovered innovative ways to use this new capability. Some examples of real-life uses follow. Entering foliated areas such as city parks can be treacherous at night, and at best it is frustrating because there are so many places for a mugger to evade a search aided only by flashlights. With thermal imaging, however, finding people hiding in bushes is relatively easy. Often evidence such as narcotics thrown from a moving car becomes useless as evidence either because it cannot be found or because there is reasonable doubt that the object found was actually the object thrown. Use of thermal imaging permits ready location of such objects because of residual heat from the hand that threw them. This thermal signature clearly distinguishes these objects as the ones that were thrown, and video tapes of the IR imagery can be used as evidence in court. A fleeing car that swerves into a crowded parking lot is easily distinguished from similar cars by its thermal signature. Responses to an alarms for breaking and entering are simplified because broken windows and open doors are readily detected.

These uses of IR imaging technology are not new and unique to uncooled thermal imaging; however, their value has only become apparent after having placed uncooled IR imaging equipment in the hands of policemen in many locations. After using the equipment for several weeks, the officers found uses that were not anticipated, and market demand grew rapidly. Texas Instruments and Hughes Aircraft are responding to that demand by announcing

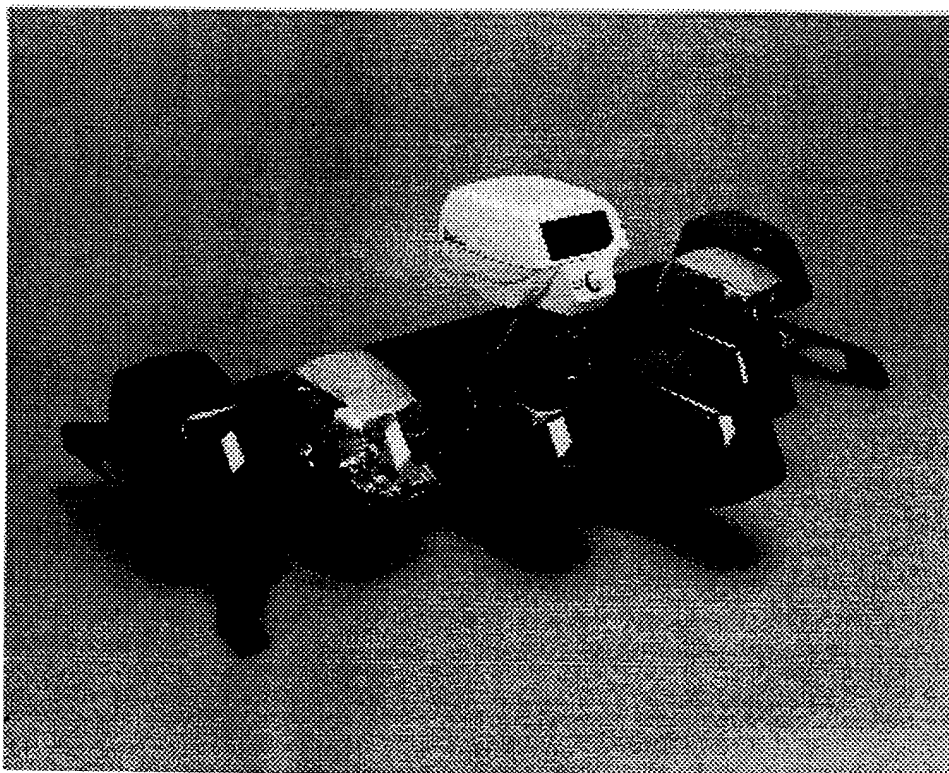


**Figure 4 - NIGHTSIGHT™ thermal imaging system mounted on a police cruiser light bar.**

NIGHTSIGHT™, an uncooled thermal imaging system provided as a kit for installation in police cruisers. The NIGHTSIGHT™ kit consists of an uncooled IR sensor, a pan and tilt head, a video display, a control console, and interface hardware. The sensor and pan and tilt head are shown mounted on a police light bar in Figure 3.1. The sensor is similar in concept to uncooled sensors developed for military applications<sup>1,2</sup>, although the design is different in many ways to reduce cost by taking advantage of less stringent requirements on weight and size. The sensor mounts on the top of the cruiser near the light bar. The front window has an automatic defroster and a wiper blade. A bracket is provided as an interface between the cruiser and the pan and tilt head. Two display options are available. One option provides a console display, and a second option provides a head-up display in front of the driver. A separate control console has a joy stick to control the pan and tilt head, and other controls for on/off, polarity, scan, pan reset

and wiper on/off. The scan control automates panning within limits set by the operator, and the pan reset control returns the pan head to its home position.

NIGHTSIGHT™ system performance is not very different from similar systems designed for military applications. The performance specifications are listed in Table 1. Only system prototypes have been built to date; systems in the standard configuration will be available to police departments by the end of this year at a price of approximately \$6,000.

#### FUTURE PLANS

The other commercial IR imaging markets to be developed in the near future are site surveillance and truckers' driving aids. However, there remains much to be done to prepare and execute near-term plans to develop the law enforcement IR imaging market. For the next year production preparations and market development will dominate activities. For the following year, emphasis will continue on cost reduction. During this time, development of the newer markets will not be neglected, and plans for new products will materialize.

<sup>1</sup> Hanson, Charles, *et.al.*, "Uncooled Thermal Imaging at Texas Instruments", *SPIE Vol. 1735 Infrared Detectors: State of the Art*, 1992, 17.

<sup>2</sup> Peranio, Leo, "Low-Cost Uncooled Sensor Prototypes (LOCUSP)", *IRIS Passive Sensors Proceedings*, February, 1993.

<b>Field of View</b>	28° by 18°
<b>Depth of Field</b>	20 feet to infinity (fixed focus)
<b>Standard Video Interface</b>	RS170/NTSC
<b>VCR Compatibility</b>	All standard formats
<b>Automatic Controls</b>	Contrast and Brightness
<b>Image Polarity</b>	Selectable
<b>Time to Operation</b>	< 30 seconds
<b>Operating Temperature</b>	-20°C to +50°C
<b>Max. Storage Temperature</b>	105°C
<b>Power Consumption</b>	6 Watts
<b>Operating Voltage</b>	12 VDC nom. / 24 VAC optional
<b>Package Integrity</b>	Waterproof
<b>Physical Size</b>	8"L x 6"W x 6"H
<b>Weight</b>	< 5 lbs.
<b>NETD</b>	< 0.12°C
<b>IFOV</b>	1.5 mrad

**Table 1 - NIGHTSIGHT™ Specifications**



# Concurrent Session - 2E: Thin Films



Abhai Mansingh,  
Department of Physics & Astrophysics,  
University of Delhi, Delhi-110007 India

M.Sayer  
Department of Physics, Queen's University,  
KINGSTON ON. K7L 3N6 Canada.

## ABSTRACT:

The parameters of the electrical equivalent circuit for crystalline ferroelectric films may be derived from measurements of the dielectric response as a function of frequency and of temperature. Careful corrections must be made to minimise complications due to electrode resistance and probe inductance. In general simple R-C circuit models representing features such as low permittivity surface layers are insufficient to describe the data, and a distribution of relaxation times must be introduced. A major contribution to dielectric loss at low temperatures results from electronic hopping conduction. This is evinced by a frequency dependent ac conductivity of the form  $\sigma(\omega) = A\omega^s$ .

## INTRODUCTION:

The properties of a ferroelectric capacitor reflect various features of the film and of its electrode structure. These include: 1) a dielectric constant and loss which depends on the composition and processing of the film and of its electrodes. The dielectric constant tends to be lower in the film than in the bulk material, and a wide range of values for a given material are often noted in the literature [1]. 2) In hysteresis experiments, the switched polarisation is similar to that of bulk materials and is similar for various methods of preparation. However, the coercive field is substantially higher. 3) Complex polarisation and time dependent breakdown phenomena are observed in dc leakage current and current-voltage studies [2]. Such phenomena are a function of the electrode material. 4) A frequency dependence can arise at high frequencies related to the electrode resistance, and to the methods used to connect the film to the measuring equipment.

## EXPERIMENTAL MEASUREMENTS OF FREQUENCY DISPERSION.

The dielectric response as a function of frequency is described by the dielectric constant  $\epsilon'$  and loss tangent  $\tan \delta$ . These quantities are evaluated from the parallel capacitance  $C_M$  and resistance  $R_M$  or  $\tan \delta_M$  measured by an ac bridge or network analyzer. Theoretical calculations are most often compared to the equivalent parallel capacitance  $C_p$  and resistance  $R_p$  of the sample with the implicit assumption of ideal conducting electrodes. However in a real system,  $C_M$  and  $R_M$  can have contributions from the lead inductance  $L$ , and due to the total contact, lead and electrode resistances between a measuring probe and the sample electrode.

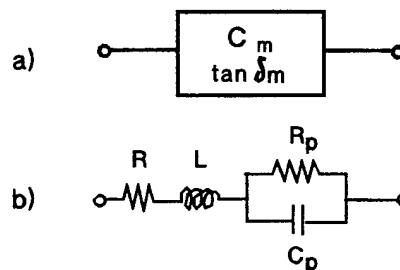


Figure 1 a) Measured film parameters. b) The circuit which is present. This includes lead inductance, series resistances and the equivalent parallel circuit  $C_p$  and  $R_p$  of the sample.

Analysis of this circuit is simplified if  $\tan \delta = 1/\omega R_p C_p$  for the sample is small ( $<0.1$ ). It can then be shown that:

$$\tan \delta_M = \frac{\omega C_p R + \tan \delta}{(1 - \omega^2 L C_p)} \quad (1)$$

$$C_M = \frac{C_p}{(1 + \tan^2 \delta_M)(1 - \omega^2 L C_p)} \quad (2)$$

$L$  and  $R$  both increase  $\tan \delta_M$ , while  $C_M$  is increased by  $L$  and is decreased by  $R$ . The effect is more pronounced at high frequencies, and the onset of frequency dependent effects shifts to lower frequencies if the capacitance (area) of the sample is larger. This is a quick check to distinguish between frequency dependent effects which are intrinsic to the sample and extrinsic ( $L, R$ ) effects.

A numerical computation may be used to determine the four unknowns  $C_p$ ,  $R$ ,  $L$  and  $\tan \delta$  from measurements at different frequencies. However,  $L$  and  $R$  also can be estimated by equating  $C_M$  and  $\tan \delta_M$  in the mid frequency range to  $C_p$  and  $\tan \delta$ . Assuming that these values are independent of frequency at high frequencies,  $L$  and  $R$  can be estimated from eqns. (1) and (2) by a single high frequency measurement of  $C_M$  and  $\tan \delta_M$ . Thus the results shown in Fig. 2 (a) for a 0.18  $\mu\text{m}$  thick sol gel PZT film on Pt/Al [3] are due to a series resistance of 8-10  $\Omega$  and a lead inductance of 3-4  $\mu\text{H}$ . For PZT on YCBO [4] (Figure 2(b)), the dispersion can be fully accounted for by the series resistance of the electrode - by neglecting  $L$  and calculating  $\epsilon'$  for the film from  $\epsilon'_M(1 + \tan^2 \delta_M)$ . Thus the drop in  $\epsilon'$  at high frequencies is due to extrinsic effects.

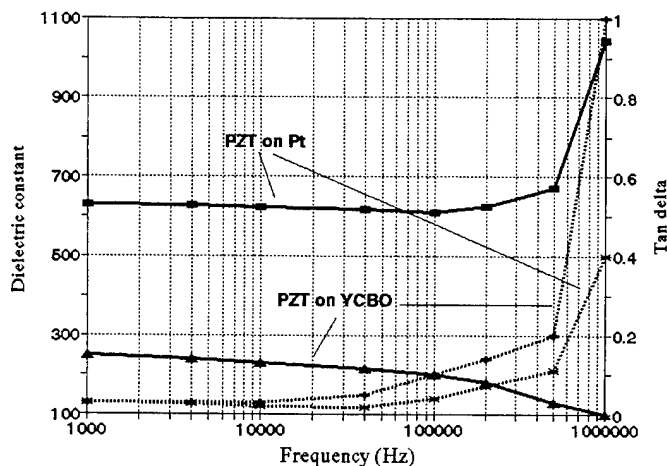


Figure 2: High frequency dielectric dispersion due to lead effects a) sol gel PZT on platinum [4], b) laser ablated PZT on YCBO [5]

### The Origin of Dielectric Dispersion

The low frequency dielectric dispersion in ferroelectric films can arise due to domain wall fluctuations, hopping conduction, or space charge dispersion. The dispersion is strongly linked to the microstructure of the film.

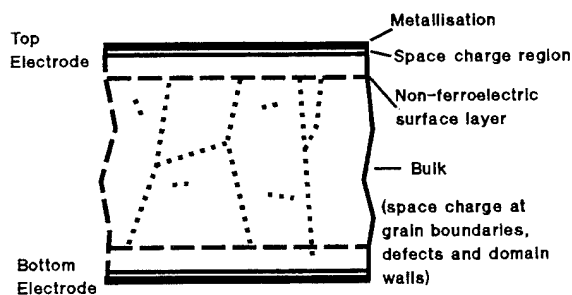


Figure 3: Structures within a ferroelectric capacitor

Figure 3 shows: 1) a space charge region between the metallisation and the insulator, 2) a non-ferroelectric layer at the surface of the film, 3) perpendicular and parallel grain boundaries, 4) defects distributed throughout the bulk. These structures may be created by chemical interactions, solid state diffusion or component loss during film and capacitor processing. They may result from nucleation and growth of crystallites within the film [5]. Such structures will be repeated for both top and bottom electrodes.

The field distribution between the elements, and the mechanism of charge transport and storage within each element will determine the measured properties of the capacitor. The conduction process in perovskite ferroelectric thin films has contributions from: 1) Free electrons (holes) in the conduction (valence) band. The number of these will depend on the temperature and the number of ionized defects. 2) Ionic conductivity due to transport through

vacancies and non-stoichiometry. 3) Hopping of electrons (holes) between reduced and unreduced states of transition metal ions. For example, charge compensation of oxygen vacancies may change the valence state of transition metal ions such as titanium from  $Ti^{4+}$  to  $Ti^{3+}$ . Localized hopping of electrons and ions will contribute only to dielectric loss. If hopping occurs in a system characterised by random jump distances and varying barriers heights, a frequency dependent conductivity of the form  $\sigma(\omega) = A\omega^s$  is expected. A and s are parameters and  $0.7 < s < 1$ . [6]. Dc conductivity and leakage current results from the long range hopping of localized electrons, free charge carriers and ions [7].

A generic equivalent circuit representing the above structure (Figure 3) is shown in Figure 4.

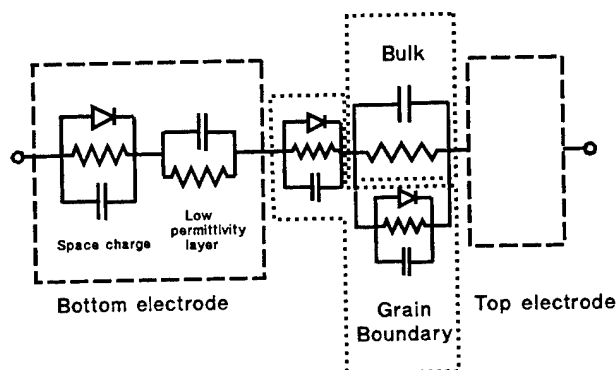


Figure 4 Electrical equivalent circuit representing all the features shown in Figure 3. The diode elements represent space charge effects. The components are duplicated at the bottom and top electrodes.

The space charge regions at the electrodes, grain boundaries and defect structures are shown by diode elements, Parallel R-C circuits represent the dielectric properties, and the conduction mechanism in the bulk and in the low permittivity surface layers respectively. Such a circuit will be repeated for the bottom and top electrodes. The extraction of values for the parameters of such a model can be a daunting task and the results must clearly reflect the realities of the physical structure.

Because of the high permittivity of a ferroelectric, even a very thin low permittivity surface or grain boundary layer can be significant at room temperature or slightly above. This is likely to be the major reason for the wide variation in the dielectric constant reported by different workers for films of the same composition. If no mobile charges (ions or electrons) are present, the measured capacitance is the series combination of the capacitance of the bulk and surface films. This is modified if conduction processes create a resistive path within either element. Since such processes are often both temperature and frequency dependent, apparent changes in dielectric

constant with temperature or frequency can actually be due to changes in charge transport. Thus the influence of a surface layer in single crystals such as TGS has been noted near the ferroelectric transition temperature when the capacitance of the bulk crystal becomes comparable to the interface capacitance [8]. In bulk ceramics, the surface layer capacitance is important in  $\text{PbTiO}_3$ , when the bulk conductivity of the samples becomes high [9]. In thin film PZT, surface layers are formed of non-ferroelectric pyrochlore films [10] and interfacial  $\text{TiO}_2$  layers resulting from the oxidation of Ti diffusing through platinum electrodes from an underlying glue layer [11].

#### A Simple Barrier Layer Capacitance Model

At high fields the change in space charge width denoted by the diodes in Figure 1 with electric field plays an important role in determining the shape of P-E hysteresis curve [12]. However, at low ac signals the diodes can be replaced by their equivalent resistances and capacitances. Incorporating all capacitances and resistances other than those of the bulk film into a single capacitance  $C_E$  and  $R_E$  leads to the simple equivalent barrier layer capacitance model shown in Figure 5.

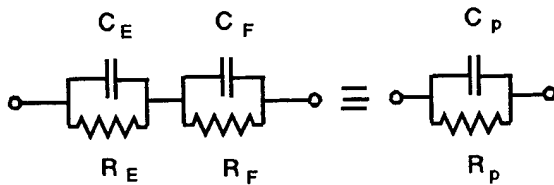


Figure 5: A simple circuit model representing the bulk material and the combined effects of electrodes at each surface.

The predictions of this model can be compared with experiment by calculating the equivalent capacitance  $C_p$  and conductance  $G_p = 1/R_p$  which would be measured by a dielectric bridge. Using the following equations.

$$C^* = \frac{(C'' - C')}{(1 + j\omega\tau)} \quad (3)$$

$$C_R = C_p - C' = \frac{(C'' - C')}{(1 + \omega^2 \tau^2)} \quad (4)$$

$$C_R = \frac{G_p}{\omega} - \frac{G''}{\omega} = \frac{\omega\tau(C'' - C')}{(1 + \omega^2 \tau^2)} \quad (5)$$

$$C' = \frac{C_F C_E}{C_F + C_E} \quad G'' = \frac{1}{R_F + R_E} \quad (6)$$

$$C'' = \frac{C_F + C_E \left(\frac{R_E}{R_F}\right)^2}{\left(1 + \frac{R_E}{R_F}\right)^2} \quad (7)$$

$$\tau = \frac{(C_F + C_E) R_E}{\left(1 + \frac{R_E}{R_F}\right)} \quad (8)$$

The capacitance predicted as a function of angular frequency  $\omega = 2\pi f$ , where  $f$  is the applied frequency, is shown in Figure 6. The parameters for the graph are given in the caption. The x-axis is expressed as a function of  $\omega\tau$ , where  $\tau$  is a time constant calculated from eqn. 8. This time constant contains the resistances  $R_E$  and  $R_F$  and hence the scaling of the x-axis is temperature dependent. The theoretical plot demonstrates that the magnitude of the measured capacitance and its frequency dependence is greatly influenced by the conductivity of the barrier region  $R_E$  and of the bulk film  $R_F$ . A low almost frequency independent value of  $C_p$  is predicted if  $R_F$  is less than  $R_E$  while the actual dielectric constant and width of barrier and film regions  $C_E$  and  $C_F$  remain unchanged. Useful information can be derived only if measurements are made over a wide temperature range.

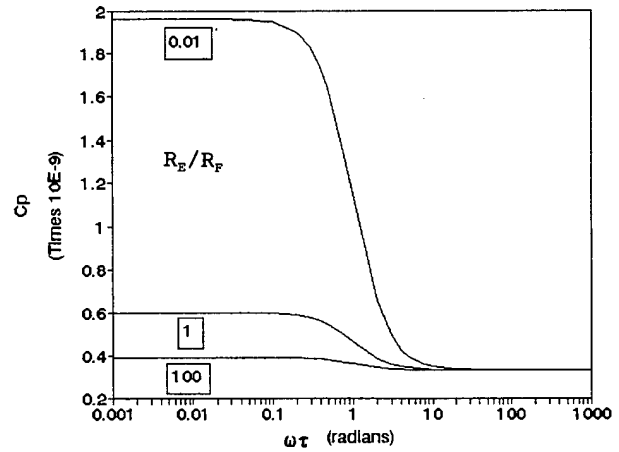


Figure 6: Measured capacitance versus  $2\pi f\tau$ , where  $\tau$  is given by eqn.6. The curves are calculated for ratios of  $R_E/R_F = 0.01, 1$  and  $100$  respectively.  $C_E = 4 \times 10^{-10}$  F,  $R_E = 1 \times 10^9 \Omega$ ,  $C_F = 2 \times 10^{-9}$  F, and  $R_F$  has appropriate values.

A low frequency-independent value of  $C_p$  or dielectric constant will be obtained even when  $R_E$  and  $R_F$  are much larger than the impedance of  $C_E$  and  $C_F$  respectively even at the lowest measuring frequency. This is evident from the experimental data of Figure (7). The dielectric constant of a sol gel derived barium titanate film deposited on a stainless steel substrate [13] shows a strong frequency dispersion at 300K while at 100K the dielectric constant is independent of frequency. An RF sputtered PZT film on a platinized alumina substrate [14] shows little dielectric dispersion at room temperature while a strong frequency dispersion is observed at higher temperatures.

The experimental dispersion data shown in Figure (7) could not be fitted over the entire frequency range using eqn.(4). In the dispersion region, the fall predicted by eqn.(4) with increasing frequency is much sharper than that experimentally observed.

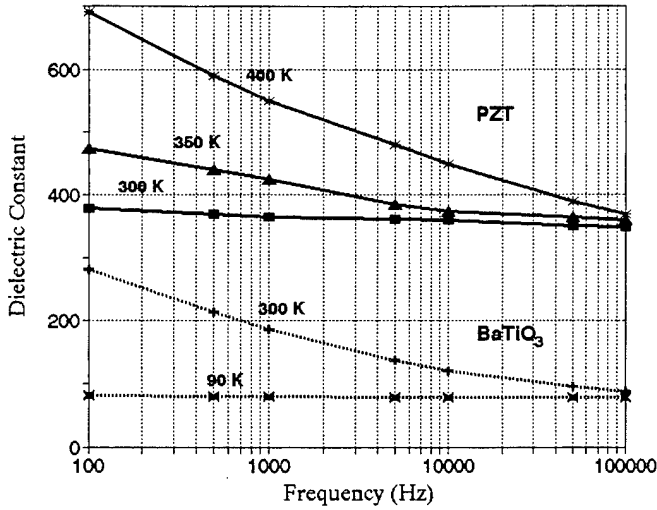


Figure 7: Dielectric dispersion of a sol gel film of BaTiO<sub>3</sub> on stainless steel at 300K and 90K [13], and an RF sputtered PZT on platinized alumina at 300K, 350K and 400K [14].

#### Capacitance Model Involving a Distribution of Relaxation Times

The deviation between the theoretical and experimental curves arises because all space charge regions, the metal-film interface and grain boundaries have been lumped into a single capacitance. A number of considerations suggest that this model is incorrect. The grains in a polycrystalline film are of random size and this size distribution will influence the dielectric constant of the film. Film growth on a substrate whose lattice constants do not match those of the film results in the growth of an initial layer whose properties will differ from those of the bulk. In PZT, lead loss at the surface during processing can lead to the crystallisation of a non-ferroelectric pyrochlore phase [10]. Thus, the local capacitance and resistance varies throughout a film, even within the specific elements incorporated into the equivalent circuit. The relaxation time calculated in eqn.(8) is therefore not a well defined quantity, and the variation of R and C will give rise to a distribution of relaxation times. Several distribution functions have been proposed to obtain the dielectric dispersion in polar liquids. The Cole-Cole distribution [7] has been the most successful in interpreting the data. The complex capacitance given in eqn.(3) is written as

$$C^* = \frac{(C'' - C')}{1 + (j\omega\tau)^{1-\alpha}} \quad (9)$$

where  $\alpha$  is an empirical parameter related to the width of the distribution which has a value between 0 and 1. The full expressions for  $C_p$  and  $G_p$  are,

$$C_p = C' + \frac{(C'' - C') (1 + (\omega\tau_{av})^{1-\alpha} \sin(\alpha\pi/2))}{1 + 2(\omega\tau_{av})^{1-\alpha} \sin(\alpha\pi/2) + (\omega\tau_{av})^{2(1-\alpha)}}$$

$$G_p = G'' + \frac{\omega(C'' - C')((\omega\tau_{av})^{1-\alpha} \cos(\alpha\pi/2))}{1 + 2(\omega\tau_{av})^{1-\alpha} \sin(\alpha\pi/2) + (\omega\tau_{av})^{2(1-\alpha)}}$$

Fits to the experimental data give the parameters  $\alpha$ ,  $\tau$ ,  $C''$ ,  $C'$  and  $G''$ . Assuming that  $R_F \gg R_E$  and  $C_F > C_E$ , the properties of the film and the barrier layer are computed from,

$$C_F = C'' \quad C_E = \frac{C'' - C'}{C''C'} \quad (12)$$

$$R_F = \frac{1}{G''} - R_E \quad R_E = \frac{\tau}{C''} \quad (13)$$

The implications of  $\alpha$  in changing the slope in the dispersion region is shown in Figure 8. All parameters  $C_F$ ,  $C_E$ ,  $R_E$  and  $R_F$  are kept fixed and only  $\alpha$  is changed.

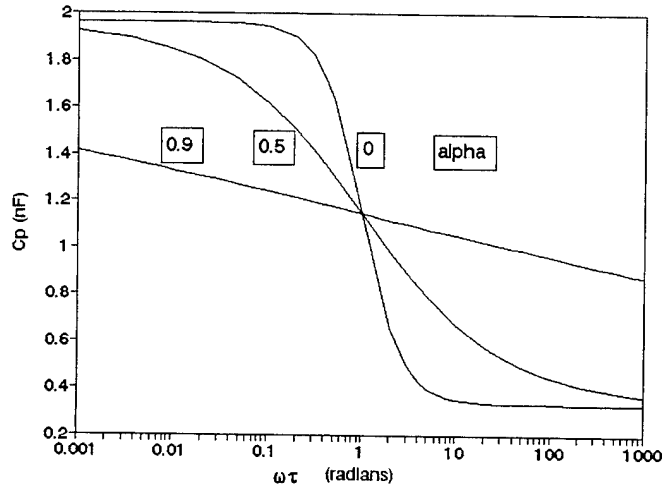


Figure 8: Theoretical plot of dielectric dispersion with  $C_E = 4 \times 10^{-10}$  F,  $C_F = 2 \times 10^{-9}$  F,  $R_E = 1 \times 10^8 \Omega$  and  $R_F = 1 \times 10^{10} \Omega$ . Values of  $\alpha$  are 0, 0.5 and 0.9.

Experimental data for  $C_p$  and  $G_p$  can be fitted to equations (10) and (11) by choosing  $C''$ ,  $C'$ ,  $\tau$ ,  $\alpha$  and  $G''$  by a procedure similar to that described elsewhere [15]. A typical fitting for a 1  $\mu$ m thick BaTiO<sub>3</sub> sol gel film on stainless steel is shown in Figure (9). Similar fittings were made for different thicknesses of BaTiO<sub>3</sub> films and for different temperatures in PZT films. The values of the fitting parameters for two thicknesses of BaTiO<sub>3</sub> films and for PZT films at different temperatures are reported in Table 1. The film and barrier parameters are estimated from eqns.(12) and (13).

The effective barrier capacitance is almost independent of film thickness and is weakly dependent on temperature. It is probable that the barrier parameters depend only on fabrication conditions and can be controlled by proper processing conditions to achieve near bulk values. However, it may not be possible to completely eliminate them and so the influence of the barrier parameters on the measured dielectric parameters of the film will be observed at higher temperatures.

	t (μm)	Temp K	C" (pf)	C' (pf)	α	τ (s)	G" (mho)
BaTiO <sub>3</sub>	0.65	300	3590	521	0.41	6.5 10 <sup>-4</sup>	6.5 10 <sup>-7</sup>
	1.0	300	2750	520	0.52	5.5 10 <sup>-4</sup>	1.5 10 <sup>-8</sup>
PZT	1.6	320	720	360	0.68	7.2 10 <sup>-5</sup>	1.3 10 <sup>-8</sup>
		400	2100	440	0.6	2 10 <sup>-4</sup>	7 10 <sup>-8</sup>

Table 1: Derived parameters of films and space charge regions

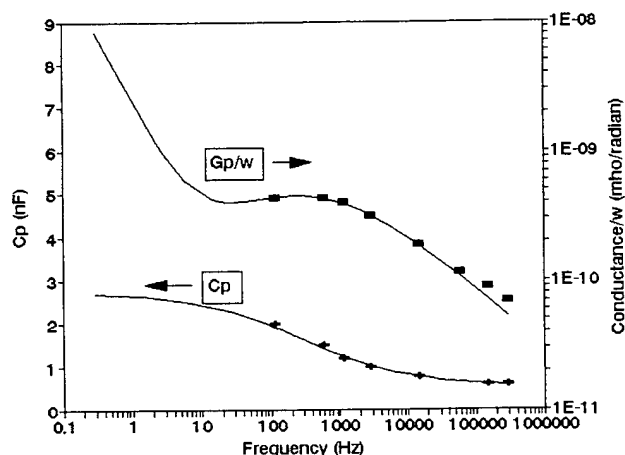


Figure 9: Comparison of experimental and theoretical data for a sol gel BaTiO<sub>3</sub> film. The theoretical curve is calculated with the following parameters:

$$\begin{aligned}
 C' &= 5.2 \times 10^{-10} \text{ F} & G'' &= 1.5 \times 10^{-8} \text{ mho} \\
 C'' &= 2.75 \times 10^{-9} \text{ F} & \tau &= 5.5 \times 10^{-4} \text{ s} \\
 \alpha &= 0.52
 \end{aligned}$$

If we assume that the dielectric constant of the barrier layer is 30, the effective thickness of the low permittivity region for an electrode area of  $2.25 \times 10^{-3} \text{ cm}^2$  is 500 Å. Such a large value indicates that  $C_x$  is mainly controlled by a low permittivity layer rather than by a space charge region associated with a conducting boundary. The layer thickness is only a very small fraction of the total volume and hence one would not expect it to greatly influence the spontaneous polarization. However the electric field will be divided across the two capacitors so that the coercive field will appear to be large as has been observed [1].

In contrast to crystalline films, amorphous films show a low value of dielectric constant and a small  $\tan \delta$ . The dielectric loss of crystalline films is greatly dependent on the crystallization process while for amorphous films it is invariably low for films prepared by different techniques. This is evident from Figure (10) in which data for

barium strontium titanate (BST) prepared by different rapid thermal annealing schedules and measured at room temperature is reported [16].

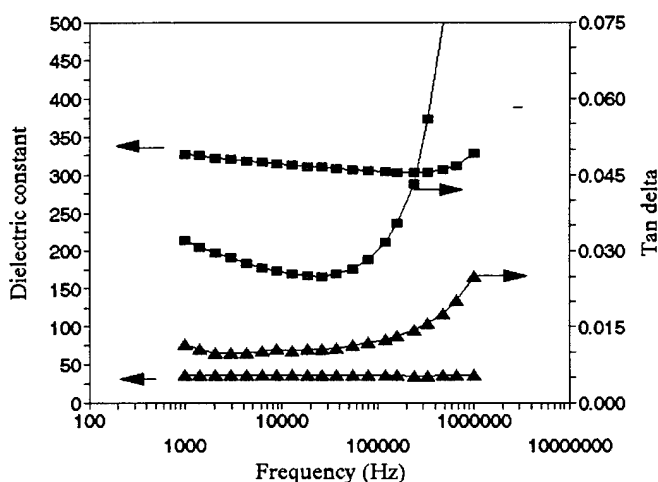


Figure 10: Dielectric constant and  $\tan \delta$  for amorphous  $\blacktriangle$  and crystalline  $\blacksquare$  barium strontium titanate films at 300K [16].

BST films prepared at a hold temperature of 700°C showed no evidence of crystallinity and  $\epsilon'$  and  $\tan \delta$  is low. The value of  $\epsilon'$  lies between 45 and 50 in common with amorphous films of PZT and BaTiO<sub>3</sub>. The loss tangent of BST which is crystallized by RTA at 750-800°C is substantially higher.

As shown in Figure 11, in BaTiO<sub>3</sub> crystallized by normal furnace annealing, the dielectric loss tangent dramatically falls on cooling to 90 K and becomes equal to that for amorphous films. Amorphous films show low loss both at 300K and 90K. The larger loss in the crystalline film is due to a larger concentration of oxygen vacancies after a longer time of annealing with a consequent increased contribution from ionic hopping. At low temperatures, ionic hopping makes little contribution and the dominant mechanism is electronic hopping. No evidence of a ferroelectric hysteresis loop was noted in any amorphous BST, BaTiO<sub>3</sub>, or PZT films.

At low temperatures the electronic hopping conduction dominates the conductivity.

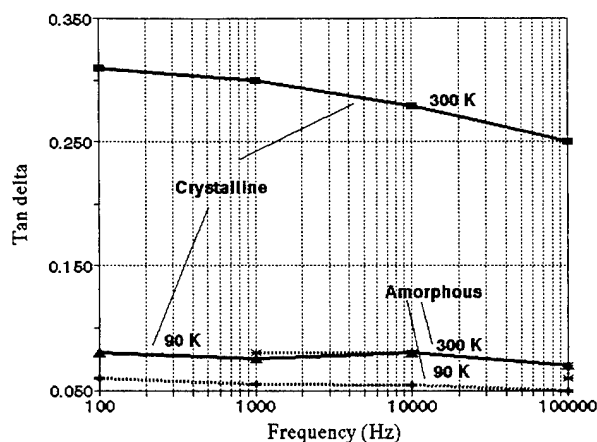


Figure 11: Dielectric loss tangent of amorphous and crystalline BaTiO<sub>3</sub> films at 300K and 90K.

This is shown in Figure (12) for a crystalline film of PZT. Similar results were obtained for amorphous films.

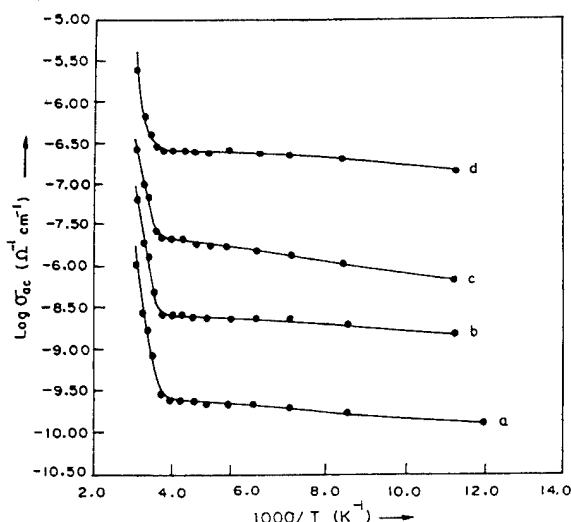


Figure 12: AC conductivity of crystalline PZT as a function of inverse temperature for four frequencies a) 100Hz, b) 1000Hz, c) 10,000Hz, d) 100 kHz.

A strong frequency dependence and a weak temperature dependence is observed, while at higher temperatures the conductivity starts to show a temperature dependence. The hopping conduction will give a frequency dependent polarization over and above the polarization of perovskite film. This will show a small frequency dispersion at low frequencies (around 1 to 10%) depending on the number of hopping carriers. Such a weak dispersion is commonly observed in all crystalline films.

The temperature at which the temperature dependence starts was found to be almost identical in both amorphous and crystalline films. This suggests that the conduction mechanism is same in both the films i.e. electronic hopping. It may be pointed out that even when ac conductivity appears with a relatively modest temperature dependence above 300K it is still substantially higher than the dc conductivity. This implies that leakage current and dielectric loss arise from

different mechanisms and that low leakage current does not mean a correspondingly low  $\tan \delta$ .

## Conclusions

Detailed dielectric response studies of both dielectric constant and loss over wide frequency and temperature regions are needed to achieve a proper understanding of the effects of microstructure, electrodes and film properties.

## Acknowledgements

This work was supported by the Natural Sciences and Engineering Research Council of Canada.

## References

- [1] M.Sayer, Z.Wu, C.V.R.Vasant Kumar, D.T.Amm and E.M.Griswold, "Ferroelectrics for Semiconductor Devices," *Can.J.Phys.* 70, 1159-1170, (1993)
- [2] S.B.Desu and I.K.Yoo, "Time Dependent Dielectric Breakdown in BaTiO<sub>3</sub> Thin Films," *J.Electrochem.Soc.*, 140, L133-L135 (1993).
- [3] E.M.Griswold - private communication
- [4] R.Ramesh, A.Inam, W.K.Chan, B.Wilkins, F.Tillerot, T.Sands and J.M.Tarascon, "Ferroelectric PbZr<sub>0.2</sub>-TiO<sub>0.8</sub>O<sub>3</sub> Thin Films on Epitaxial Y-Ba-Cu-O," *Integ. Ferroelect.*, 1, 205-212 (1992)
- [5] D.J.Eichorst and C.J. Baron, "Effect of Platinum Electrode Structures on Crystallinity and Electrical Properties of MOD-Prepared PZT Capacitors," *Mat.Res.Soc.Symp.Proc.* 30, 201-208 (1993).
- [6] N.F.Mott and E.A.Davis, *Electronic Processes in Non-Crystalline Solids*. 2nd Ed. Clarendon, Oxford 1979
- [7] M.Sayer and A.Mansingh, "Oxide Glasses" in *Amorphous Semiconductors III*, ed. M.Pollak, CRC Press, New York, 1-35 (1987)
- [8] A.Mansingh and S.R.J. Eswar Prasad, "Dielectric Behaviour of Ferroelectric Triglycine Sulphate near the Transition Temperature", *J.Appl.Phys.*, 48, 4307-4310 (1977)
- [9] P. Talwar - private communication
- [10] K.Sreenivas, I.Reaney, T.Maeder, N.Setter, C.Jagdish and R.G.Elliman, "Investigation of Pt/Ti bilayer Metallization on Silicon for Ferroelectric Thin Film Integration," *J.Appl. Phy.* 75, 232-239 (1994)
- [11] T.Mihara, H. Watanabe, H.Yoshimori, C.A.Paz de Araujo, B.Melnick, L.D.McMillan, "Process Dependent Electrical Characteristics and Equivalent Circuit Model of Sol-Gel Based PZT Capacitors," *Integ.Ferroelect.* 1, 269-291 (1992)
- [12] H.B.K. Sharma - private communication
- [13] S.Tandon - private communication
- [14] C.V.R.Vasant Kumar, R.Pascual and M.Sayer, "Crystallisation of Sputtered Lead Zirconate Titanate Films by Rapid Thermal Processing," *J.Appl.Phys.* 71, 864-874 (1992)
- [15] A.Mansingh, R.P.Tandon and J.K.Vaid, "AC Conductivity of Tungsten Phosphate Glasses," *Phys. Rev. B.*, 25, 4829 (1980)
- [16] M.Sedlar - private communication

# Switching in Ferroelectric Thin Films: How to Extract Information about Domain Kinetics from Traditional Current Data

V.Ya.Shur, E.L.Rumyantsev, S.D.Makarov and V.V.Volegov  
Institute of Physics and Applied Mathematics  
Ural State University,  
Lenin Ave.51,  
620083 Ekaterinburg, Russia

**Abstract** - In this paper we demonstrate the possibility of extracting original detail information about domain kinetics during polarization reversal in thin ferroelectric films from the switching current data. The developed method of mathematical treatment was verified by computer simulations and direct experiments in model ferroelectric single crystals.

## INTRODUCTION

Recently the interest in exploration of fast switching process has grown rapidly in view of some promising applications of integrated ferroelectrics in memory devices [1]. The measurement of transient current during application of square voltage pulses is practically the only method of experimental investigation of fast switching in thin ferroelectric films [2]. Up to now the extracted information is limited. The traditional mathematical treatment of experimental data commonly yield only field and temperature dependencies of switching time [3]. The polarization reversal is the result of arising and growing of great number of interacting domains accompanied by their coalescence. The process strongly depends upon the initial domain structure, the spatial distribution of nucleation sites and geometrical sizes of switched sample. It will be shown that this complicated behavior can be divided into several stages characterized by the definite sets of kinetic parameters. As a result, observed peculiarities of the shape of the transient current pulses are related to the changes of the type of the domain structure kinetics [4,5]. Therefore it is reasonable to propose that with adequate theoretical description the kinetic parameters of the main stages of domain evolution can be extracted even from the traditional integral measurements.

## CLASSICAL APPROACH

The theoretical description of the switching process [6,7] is usually based on Kolmogorov-Avrami (K-A) statistical theory [8,9]. Two limiting situations are considered usually [8,10]:  $\alpha$ -model - in which the number of domains is progressively increasing (the nucleation probability per volume  $\alpha$  usually is chosen to be constant during switching) and  $\beta$ -model - when all domains involved in switching are arising instantaneously at the very beginning of the process with the density  $\beta$  per volume (remnant domains). In both cases the domain wall velocity  $v$  is usually taken to be constant for switching under the action of rectangular pulses of electric field. The main equations used for the description of the time dependence of the fraction of the area occupied

by switched domains, which is proportional to the switching charge, runs as follows:

$$q(t) = 1 - \exp[-c\alpha v^n t^{n+1}/(n+1)] \text{ for } \alpha\text{-model} \quad (1)$$

$$q(t) = 1 - \exp(-c\beta v^n t^n) \text{ for } \beta\text{-model} \quad (2)$$

where:  $n$  - the dimensionality of the growth, depending upon the type of domain structure ( $n = 1$  or 1-D growth for lamellar domains,  $n = 2$  or 2-D growth for isolated cylindrical domains and  $n = 3$  or 3-D growth for bulk ones),

$c$  - the domains' shape constant.

The main problems arising while fitting of experimental data in ferroelectric films by Equations (1) and (2) are: firstly, obtained values of  $n$  are usually noninteger [11,12] and, secondly, it appears impossible to describe the decaying part of the experimental current pulses. So this theory can not adequately describe the observed phenomena in such objects in the whole time range. The reason is that K-A theory was formulated for infinite media only. But in thin films the edge effects are very important.

Recently Duiker and Beale [13], Ishibashi and Orihara [14] made an attempt to apply the modified K-A approach for the description of the behavior of real finite objects. It was pointed out that the effects due to the finite sizes are very important in polycrystal films and ceramics. In such objects the reconstruction of domain structure goes simultaneously and independently in individual grains of extremely small sizes.

K-A theory did not account for the fact that at the instant the growing domain touches the sample boundaries there occurs the local geometrical catastrophe. The domain ceases to grow in one of the directions - in other words the abrupt change of the shape constant occurs. This process statistically averaged over the switching volume significantly influences upon the shape of transient current pulse. Such effect is the most pronounced while observing the growth of wedge-like or lens-like domains (at the high anisotropy of domain wall velocity) which is rather typical for thin ferroelectric films.

## SWITCHING IN FINITE SAMPLES

We developed [15-17] the new description of the domain structure evolution in finite media in terms of the geometrical catastrophes. The proposed mathematical treatment based on simple model of domain kinetics during switching in finite samples allows us to overcome the above mentioned difficulties. Moreover the developed theory of geometrical

transformations predicts the drastic changes of growth geometry at the definite moments of the geometrical catastrophes. Such consideration appeared to be rather fruitful for obtaining the complete statistical information about the stages of domain kinetics concealed in integral data.

It was shown [15,17] that for  $\beta$ -model during switching in restricted sample with high anisotropy of sideways domain walls motion there are two important peculiarities: first, the averaged shape constant of the domains decreases during switching and, second, the dimensionality of domain growth drastically changes at the appropriate catastrophe moment  $t_{cat}$ . In other words  $\beta(2-D) \rightarrow \beta(1-D)$  geometrical transformation occurs. The influence of these peculiarities on the transient current diminishes with the increasing of effective sizes of the sample and in the limit the classical formula for  $\beta$ -model can be used.

The analogous descriptions of the transient current shape were used for any model situations: arbitrary value of sideways domain growth anisotropy (account for the size limits in both directions) and  $\alpha$ -model as well:

$$i(t) = (2 P_s l^2 n t^n / t_{0\alpha}^{n+1}) \{1 - [1 + 1/(n+1)] t/t_m\} \cdot \exp[-(t/t_{0\alpha})^{n+1} (1 - t/t_m)], \quad \text{for } \alpha\text{-model} \quad (3)$$

$$i(t) = (2 P_s l^2 n t^{n-1} / t_{0\beta}^n) [1 - (1 + 1/n) t/t_m] \cdot \exp[-(t/t_{0\beta})^n (1 - t/t_m)], \quad \text{for } \beta\text{-model} \quad (4)$$

where  $t_{0\alpha} = [c\alpha v^{n+1}/(n+1)]^{-1/(n+1)}$ ,  $t_{0\beta} = (c\beta v^n)^{-1/n}$ ,  $P_s$  - spontaneous polarization.

The decay time  $t_m$  (the characteristic time of the decreasing of the averaged shape constant) is the function of anisotropy, domains' shape and nucleation intensity. In any case the influence of the finiteness can lead only to decreasing of the growth dimensionality as a result of geometrical transformations/catastrophes.

Another kind of geometrical transformations take place due to spatial nonuniform distribution of nucleation sites. This situation is rather typical for real thin films. It must be stressed that in this case also the whole switching process can be divided into stages each characterized by integer value of growth dimensionality  $n$ . The peculiarity of this situation is that one can obtain even step increase of the growth dimensionality at the closing stage of the switching process. These effects are very pronounced, for example, when the most part of nucleation sites/remnant domains are situated at the edges of the sample/grain and also during «correlated» nucleation in «superstrong» field [5,18].

#### TESTING OF THE NEW APPROACH

The experimental examination of the model single crystals simultaneously by local and integral methods so as the computer simulation of domain evolution in two-dimensional case were used for testing of this new approach.

#### Computer simulation

In order to verify the validity of proposed description the computer simulations of the switching process by Monte

Carlo method were carried out on the 2-D matrix [15,17]. For every step the variation in the fraction of the area occupied by arising domains (the analog of transient current) was averaged over the great number (more than 1000) of independent realizations/computer experiments for obtaining statistically reliable results corresponding to the experimental conditions in polycrystal thin films. The computer experiments were done for  $\alpha$  - and  $\beta$  - models in the wide range of the model parameters for random and spatially nonuniform distribution of nucleation sites.

The results of computer experiments for  $\alpha$  - and  $\beta$  -models in all cases are fitted extremely good by the Equations (3) and (4) with integer values of growth dimensionalities (Figures 1 and 2).

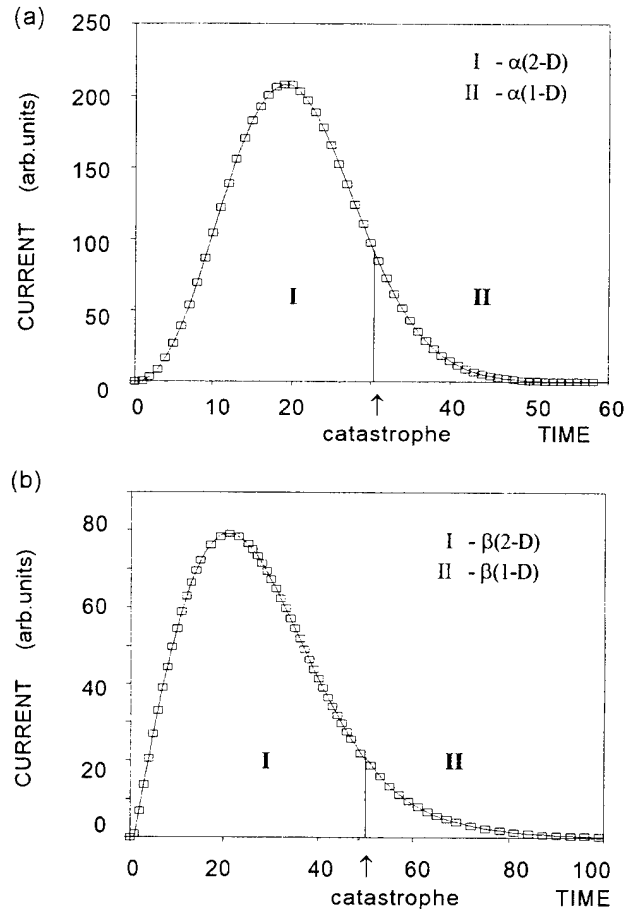


Figure 1. Computer simulation of switching process with random nucleation: a)  $\alpha$ -model, anisotropic domain growth; b)  $\beta$ -model, isotropic sideways domain growth. The points - results of computer experiments, the solid curves - fitting by Equations (3) and (4).

It is important to point out also that these formulas succeeded in describing the decaying part of the transient current which is impossible within the framework of the classical approach. The typical results of computer experiments for random (spatially uniform) nucleation for  $\beta$  - model with isotropic sideways domain growth and for  $\alpha$ -model with high anisotropic growth are shown on the Figures 1 and 2. The geometrical catastrophes accompanied by decreasing of growth dimensionality  $\beta(2-D) \rightarrow \beta(1-D)$  and  $\alpha(2-D) \rightarrow \alpha(1-D)$  are clearly seen in both cases.

The computer simulation of the switching process in the



case of spatially nonuniform nucleation rate had shown qualitatively different type of catastrophic changes of the growth dimensionality. The typical result for prevalent nucleation at the edges of the sample/grain and anisotropic sideways domain growth is shown on the Figure 2.

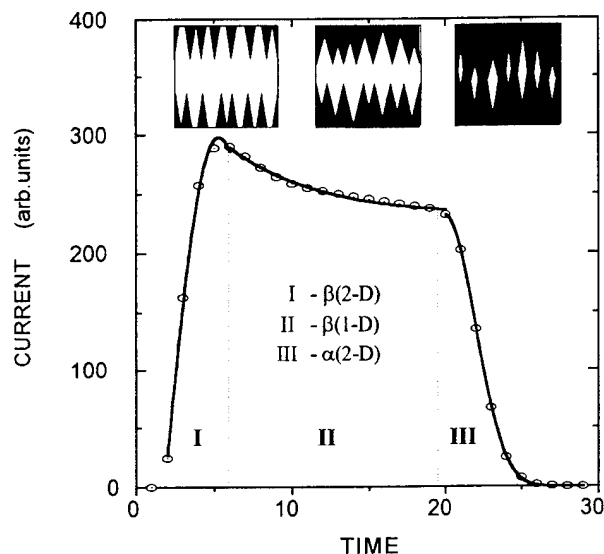


Figure 2. Computer simulation of switching process with spatially nonuniform nucleation:  $\alpha$ -model, nucleation near sample's edges only, anisotropic sideways domain growth. In insert - scheme of the domain structure at the different stages of switching. The points - results of computer experiments, the solid curves - fitting by Equations (3) and (4).

The unusual shape of transient current is successfully fitted taking into account the existence of two consecutive catastrophes. As a result of first catastrophe the shape of two saw-edged domains which are growing near the sample's edges became stable. Their zigzag walls are moving to meet each other during second stage. The step increase of the growth dimensionality at the second catastrophe is the result of their coalescence.

It was shown that fitting of the computer experiments data allowed to define the catastrophe moment and other model parameters with high precision. Furthermore the theoretical relations between model parameters and characteristics of domains' evolution are good enough for extracting the kinetic parameters from experimental integral data.

#### Switching of model single crystals

The complex experimental testing investigations of the switching process were done in thin plates (about 100  $\mu\text{m}$ ) of model single crystals with optically distinguished domains: lead germanate  $\text{Pb}_3\text{Ge}_3\text{O}_{11}$  (PGO) and bismute titanate  $\text{Bi}_4\text{Ti}_3\text{O}_{12}$  (BTO). Optical unit for real-time domains registration with the pulse dye laser as a light source was used to explore the domain kinetics with high spatial (about micron) and time (10 ns) resolution in wide range of switching times (up to microseconds). Transient current pulses and momentary domain patterns were simultaneously registered. All investigated samples had the controlled initial domain structure and only the  $180^\circ$  switching was observed. The BTO samples contains a very small concentration of twin

walls but they did not move during switching.

Two different types of initial domain structures were prepared in PGO: the single domain state (Figure 3a) and the controlled maze structure with high density of domain walls (Figure 3b) [19]. The mathematical treatment allows us to show the qualitative and quantitative difference in domain kinetics in these two cases.

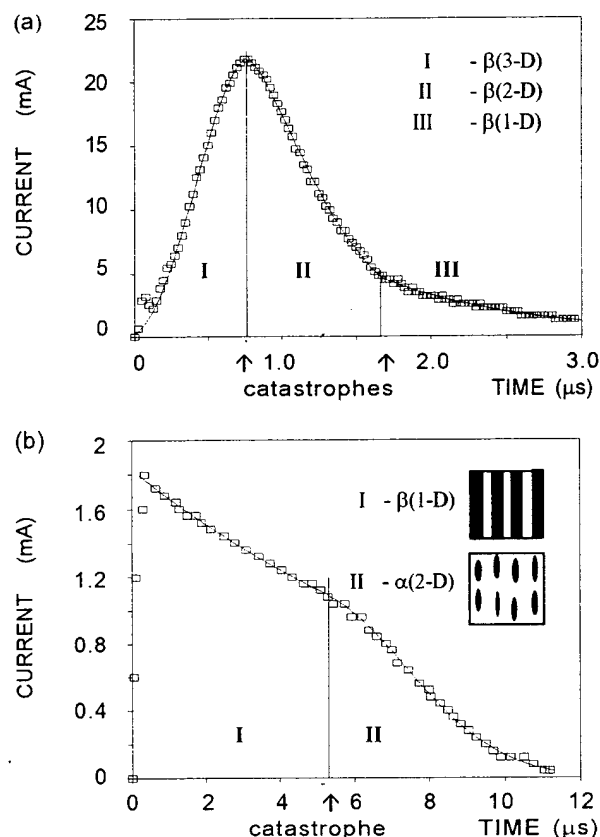


Figure 3. The transient current for PGO single crystal during switching from: a) single domain state and b) the meza domain structure. In insert - scheme of the domain structure at the different stages of switching. The points - experimental results, the solid curves - fitting by Equations (3) and (4).

Switching from single domain state demonstrate the  $\beta(2\text{-D}) \rightarrow \beta(1\text{-D})$  geometrical transformation in the decaying part of the current pulse. It is necessary to mention that the first catastrophe on Figure 3b is due to the relatively large dimension of the sample in polar direction ( $d = 130 \mu\text{m}$ ) and never can be realized in thin films. During switching from the maze domain structure we reveal another type of geometrical transformation  $\beta(1\text{-D}) \rightarrow \alpha(2\text{-D})$ . This fact enables us to state that the change from the maze to isolated cylindrical domains occurs. All predicted transformations of the types of domain structures are confirmed by direct real-time visualization of the domain kinetics.

It must be stressed that the width of domain maze elements in our experiments were about few microns and it was very difficult to observe the momentary domain patterns by optical methods. The proposed method was very effective even in this case for extracting the information about the «geometry» (type) of the initial domain structure and its changing during switching. In contrast to any method of the

visualization of momentary domain patterns the proposed method has practically no resolution limits.

#### DOMAIN KINETICS IN THIN FILMS

The method has been applied with much success for the studying of thin polycrystal films of lead titanate doped by lanthanum (PLT), prepared by magnetron sputtering (Figure 4) and lead zirconate titanate (PZT) films manufactured by sol-gel method (Figure 5a) and pulsed laser deposition (Figure 5b), so as epitaxial heterostructures  $\text{PbZr}_{0.48}\text{Ti}_{0.52}\text{O}_3/\text{YBa}_2\text{Cu}_3\text{O}_{7-x}$  deposited by laser ablation on single crystalline  $\text{SrTiO}_3$  substrates (Figure 6).

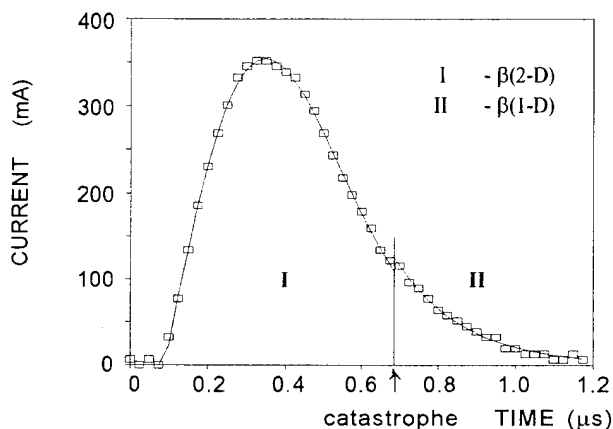


Figure 4. The transient current for PLT thin films produced by magnetron sputtering (points) fitted by Equation (4).

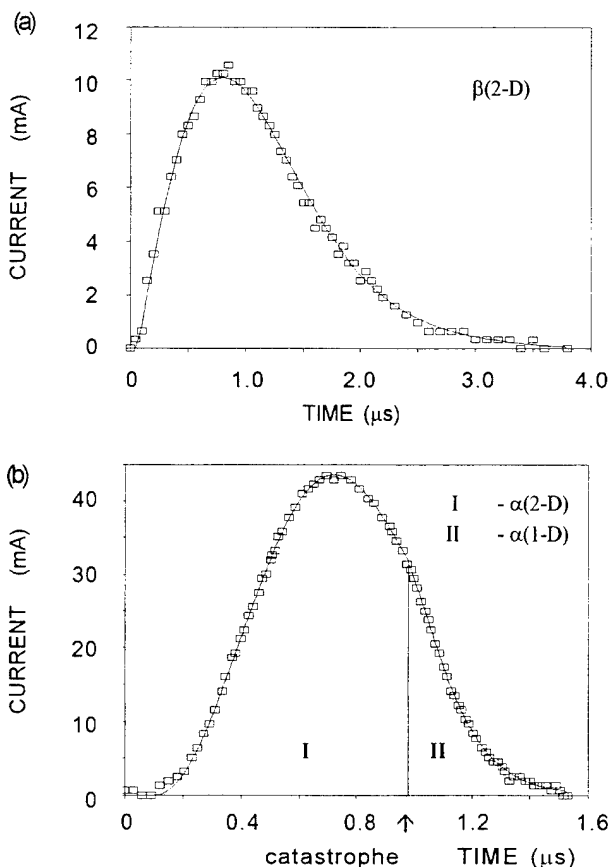


Figure 5. The transient currents for PZT thin films produced by: a) sol-gel method and b) laser ablation. Experimental points were fitted by Equations (3) and (4).

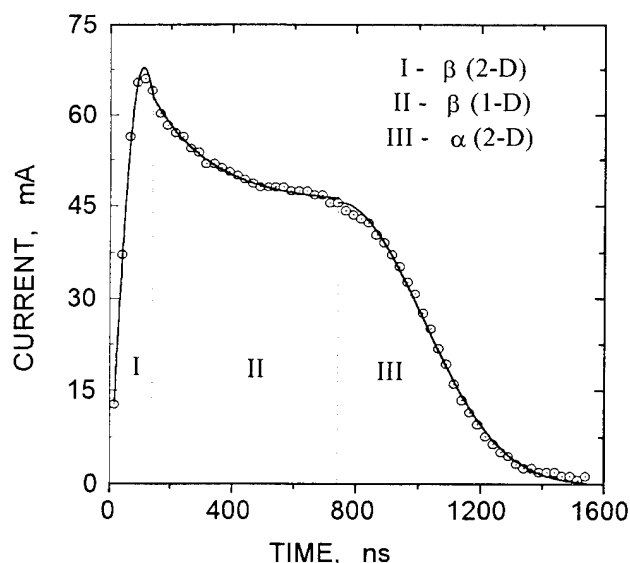


Figure 6. The transient current for epitaxial heterostructures PZT/ $\text{YBa}_2\text{Cu}_3\text{O}_{7-x}$ / $\text{SrTiO}_3$  produced by pulsed laser deposition. Experimental points were fitted by Equations (3) and (4).

It was demonstrated that the shape of transient pulses measured at the similar conditions are strongly depend not only upon the type of manufacturing method but also upon the technological parameters (film thickness, annealing temperature, material of substrate and electrodes and so on). All above mentioned types of the domain kinetics and geometrical transformations were realized in investigated films.

The  $\beta(2-D) \rightarrow \beta(1-D)$  and  $\alpha(2-D) \rightarrow \alpha(1-D)$  transformations during switching (Figure 4 and 5b) are rather typical. This kind of transformations was discussed above in details and confirmed by computer simulation. The considered transformations in first case can be interpreted as a result of growth of residual/remnant domains in the grains of small sizes. The second type can be realized during anisotropic growth of the increasing number of domains. The predicted domain evolution is in accordance with the results of the TEM observation of static domain patterns in thin films [20,21].

The absence of the transformations during whole switching pulse (Figure 5a) shows that the process finished before catastrophe moment. But even in this case the decreasing of the shape constant as a result of grain finiteness was taken into account during fitting.

Even the pulses with unusual shape similar to Figure 2 are registered under proper switching conditions in the epitaxial heterostructures (Figure 6). These peculiarities are due to the nonuniform spatial distribution of the nucleation sites. Probably they are located preferably near the edges of grains which are extremely large in epitaxial films.

The presented treatment of experimental results reveals the influence of initial domain structure upon the whole switching process. It is well-known that this initial structure strongly depends upon many technological factors. But practically always it is impossible to define the main characteristics of the domain structure. The proposed method allows to do this even in real devices. It opens the possibility

of the reproducible manufacturing of devices with controlled domain structure.

Within proposed mathematical treatment we can obtain such important parameters of domain structure evolution as: kinetic process dimensionality  $n$ , anisotropy of domain growth  $A$  and characteristic times  $t_o$ ,  $t_m$  and  $t_c$ . The knowledge of such parameters in turn makes it possible to describe the reconstruction of the domain structure in terms of the number of arising domains per volume ( $\alpha$  and  $\beta$ ) and their sideways velocities ( $v_x$  and  $v_y$ ). The obtain parameters are depended upon the voltage and temperature. They are changing significantly during aging and degradation.

#### CONCLUSION

It is important to understand that proposed method of mathematical treatment can be successfully used in traditional investigations of switching in any real integrated device for interpretation of various actual processes such as fatigue, degradation and so on in terms of domain kinetic parameters having clear physical meaning. Besides it allows to measure and control the geometry and spatial distribution of initial domains and to optimize the manufacturing of integrated devices by production of the desirable/optimal domain structures. The method has practically no resolution limits.

#### ACKNOWLEDGEMENTS

This work was supported in part by Russian Foundation of Fundamental Research under Grant No. 93-02-2451. It is a pleasure to acknowledge the many helpful stimulating discussions with P.K.Larsen and J.F. Scott. We are very grateful to V.I. Sarapulov for technical assistance and to L.A. Suslov, K.A. Vorotilov, V.V. Starostin and L.V. Gorodnic for providing some samples.

#### REFERENCES

- [1]. J.F.Scott and C.A.Paz de Araujo, "Ferroelectric Memories", *Science*, vol. 246, pp. 1400-1405, 1989; P.K.Larsen, R.Cuppens and G.A.C.M. Spierings, "Ferroelectric Memories", *Ferroelectrics*, vol. 128, pp.265-292, 1992.
- [2]. V. Ya. Shur and E. L. Rumyantsev, "Kinetics of Ferroelectric Domain Structure during Switching: Theory and Experiment", *Ferroelectrics*, (in press).
- [3]. E. Fatuzzo and W. J. Merz, *Ferroelectricity*. Amsterdam: North-Holland Publishing Company, 1967, p. 201.
- [4]. V. Ya. Shur, A. L. Gruverman, N. Yu. Ponomarev, E. L. Rumyantsev and N. A. Tonkachyova, "Domain Structure Kinetics in Ultrafast Polarization Switching in Lead Germanate", *JETP Lett*, vol. 53, pp. 615-619, 1991.
- [5]. V.Ya. Shur, A. L.Gruverman, N.Yu. Ponomarev, E.L. Rumyantsev and N. A. Tonkachyova, "Fast Reversal Process in Real Ferroelectrics", *Integrated Ferroelectrics*, vol. 2, pp. 51-62, 1992.
- [6]. E. Fatuzzo, "Theoretical Consideration on the Switching Transient in Ferroelectrics", *Phys. Rev.*, vol. 127, pp. 1999-2005, 1962.
- [7]. H. H.Wieder, "Model for Switching and Polarization Reversal in Colemanite", *J. Appl. Phys.*, vol. 31, pp. 180 -187, 1960.
- [8]. A. N. Kolmogorov, "A Statistical Theory of Metall Crystallization", *Izv. Acad. Nauk USSR, Ser. Math.*, vol. 3, pp. 355-359, 1937.
- [9]. M. Avrami, "Kinetics of Phase Change. I. General Theory", *J.Chem.Phys.*, vol. 7, pp.1103-1112, 1939.
- [10]. Y. Ishibashi and Y. Takagi, "Note of Ferroelectric Domain Switching", *J. Phys. Soc. Jap.*, vol.31, pp. 506-510, 1971.
- [11]. K. Dimmler, M. Parris, D. Butler, S. Eaton, B. Pouligny, J. F. Scott and Y. Ishibashi, " Switching Kinetics in Ferroelectric Thin-Film Memories", *J. Appl. Phys.*, vol. 61, pp. 5467-5470, 1985.
- [12]. J. F. Scott, L. Kammerdiner, M. Parris, S. Traynor, V. Ottenbacher, A. Shewabkeh and W. F. Oliver, "Switching Kinetics of Lead Zirconate Titanate Submicron Thin-Film Memories", *J. Appl. Phys*, vol. 64, pp. 787-792, 1988.
- [13]. H. M. Duiker and P. D. Beale, "Grain-Size-Effects in Ferroelectric Switching", *Phys. Rev. B*, vol. 41, pp. 490 -495, 1990.
- [14]. H. Orihara and Y. Ishibashi, "A Statistical Theory of Nucleation and Growth in Finite Systems", *J. Phys. Soc. Jap.*, vol. 61, pp. 1919-1925, 1992; Y. Ishibashi and H. Orihara, "Size Effect in Ferroelectrics Switching", *J. Phys. Soc. Jap.*, vol. 61, pp. 4650-4656, 1992.
- [15]. V. Ya. Shur, E. L. Rumyantsev, S. D. Makarov and V. V. Volegov, "How to Extract Information about Domain Kinetics in Thin Ferroelectric Films from Switching Transient Current Data", *Integrated Ferroelectrics*, 1994 (in press).
- [16]. V.Ya.Shur, E.L.Rumyantsev and S.D.Makarov, "On the Geometrical Phase Transformations in Finite Media: Computer Simulation and Experiment", presented at the MRS 1994 SM, San Francisco, CA, April 4-8, 1994.
- [17]. V.Ya. Shur, "Fast Polarization Reversal Process: Evolution of Ferroelectric Domain Structure in Thin Films", in *"Ferroelectric Thin Films: Synthesis and Basic Properties"*, Gordon and Breach Sci.Publishers, 1994, vol.1, Ch. A5, p.40 (in press).
- [18]. V.Ya. Shur and E.L.Rumyantsev, "Crystal Growth and Domain Structure Evolution", *Ferroelectrics*, vol.142, pp. 1-7, 1993.
- [19]. V.Ya. Shur, A.L. Gruverman, V.V. Letuchev, E.L. Rumyantsev and A. L. Subbotin, "Domain Structure of Lead Germanate", *Ferroelectrics*, vol. 98, pp.29-49, 1989.
- [20]. M. Huffman, J. Zhu and M. M. Al-Jassim, "Morphology and Domain Structure of Ferroelectric Lead Titanate and Lead Zirconate Titanate Thin Films, an Overview", *Ferroelectrics*, vol. 140, pp. 191-201, 1993.
- [21]. M. Klee, U. Mackens and A. De Veirman, "Pb(Zr<sub>x</sub>Ti<sub>1-x</sub>)O<sub>3</sub> Films Produced by a Modified Sol-Gel Technique: Thin Film Growth and Electrical Properties",

**Abstract** - Ferroelectrics are attractive as thin-film driver layers for high frequency resonators because of their piezoelectric nature. We consider various measures of performance usually applied to resonator materials, and list observed values for various ferroelectrics being developed for use in cellular radio and collision-avoidance radar. For these applications, our analysis shows that the material parameter of paramount importance is neither the electromechanical coupling nor the acoustic quality factor. We introduce a new metric for judging material suitability for high frequency resonator use. It is a combination of all of the physical quantities associated with acoustic wave propagation in piezoelectrics. Ranking ferroelectric thin-film materials by use of the new measure leads to a number of unconventional implications regarding the future technology of these devices.

## INTRODUCTION

Ferroelectric materials are used in a variety of electromechanical devices, such as resonators, filters, transducers, and delay lines, [1,2] as well as sensors and actuators [3-5]. The material properties of primary importance vary with the application. In wideband filters, for example, coupling coefficient considerations are paramount, whereas in narrowband designs, minimizing loss is paramount. Resonators have been gauged by a variety of material or circuit measures over the years. To an extent, the differing measures pertain to the intended uses, but none of the usual performance figures is entirely adequate for characterizing resonator materials for cellular radio, radar, and similar applications at the higher frequencies.

This paper considers some of the performance metrics traditionally applied to resonators and resonator materials. It then introduces a new metric for judging material suitability for high frequency resonator use, and tabulates its value for a number of materials. The new metric is a combination of all of the physical quantities associated with acoustic wave propagation in piezoelectric substances: mass density, dielectric permittivity, piezoelectric modulus, elastic stiffness and viscosity. Use of this characteristic number to rank resonator materials yields some nonobvious and somewhat counterintuitive conclusions that reflect on the directions the technology of these devices might take, and where the emphases for future progress might be placed.

## PIEZOELECTRIC RESONATORS

The earliest bulk wave piezoelectric resonators were bars [1]. To achieve the higher frequencies required by current applications, resonators now employ the thickness modes of plates, [1,2,6] and variants such as ring-supported [7-9] and thin-film [10,11] configurations. For the past half-century and more, the push to higher frequencies was driven by practical applications and miniaturization [12]; this trend continues today. During this time, a recurring question has been "What is the highest useful acoustic resonator frequency?" We shall find that there is substantial reason to believe that the material-limited upper frequency for many piezoelectrics is considerably higher than usually thought, and that in many cases the upper limit on frequency achieved is more a result of manufacturing limitations than of material deficiency.

### Acoustic Velocity

The acoustic velocity, given by

$$v = \sqrt{\frac{\bar{c}}{\rho}}, \quad (1)$$

is one of the important attributes characterizing an acoustic medium, as the resonance frequency of a plate of a given thickness is directly proportional to the velocity. The velocity depends primarily on the elastic stiffness  $\bar{c}^E$  and mass density  $\rho$  of the medium, and to a lesser extent on the piezoelectric properties of the medium through the piezoelectric contribution to the elastic stiffness:

$$\bar{c} = c^E + \frac{e^2}{\epsilon^S}. \quad (2)$$

The commonly used frequency constant,  $N_0$ , is equal to one-half of the wave velocity.

### Piezoelectric Coupling

The piezoelectric coupling factor  $k$  [6,9,17,18], is a dimensionless measure of electromechanical energy conversion efficiency in a piezoelectric resonator. It is determined by the piezoelectric, elastic, and dielectric constants as

$$k^2 = \frac{e^2}{\epsilon^S \bar{c}}, \quad (3)$$

and is bounded by ( $0 \leq k < 1$ ). The coupling factor is important in characterizing an acoustic medium, since it determines whether a resonator may be driven by an impressed voltage, and is a primary determinant of certain distinguishing frequencies of interest.

### Acoustic Loss

The material-limited losses in acoustic materials such as quartz are often discussed in terms of the product (Q-frequency) being a constant [13]. A related, and, for many purposes, a better measure is the motional time constant  $\tau_1$  [6,9,14,15], given by

$$\tau_1 = \frac{\eta}{\bar{c}}. \quad (4)$$

This quantity is dependent upon the acoustic viscosity and elastic stiffness of the medium [16].

### Equivalent Network

The Butterworth-Van Dyke (BVD) equivalent network of a piezoelectric resonator [1,2,6,15,18-20] is a simple, four-element circuit used to characterize the mechanical vibrations of the resonator in electrical terms. The network consists of a series  $R_1, L_1, C_1$  combination in parallel with a second capacitor,  $C_0$ . The nominal frequency of the resonator at harmonic  $M$  is given by

$$f^{(M)} = \frac{Mv}{2t} = \frac{MN_0}{t}. \quad (5)$$

This frequency is often called the series resonance frequency,  $f_s$ , and is used for normalizing the network functions. If present, dc conductivity is

modeled by the addition of a resistance  $R_0$  in parallel with  $C_0$  [3,15,21]. In deriving the new material metric, we assume small dc conductivity. However, the conclusions we arrive at regarding loss and the directions for future work are germane to the general case of arbitrary dc conductivity.

The BVD circuit element values [6,19,20] depend upon the physical parameters of the medium and the geometry of the structure. The relations between the circuit element values, material constants (physics factors), and associated geometric factors are shown in Table I for the case of a thin plate of thickness  $t$ , with coextensive electrodes of area  $A$  on the major surfaces. For simplicity, all material constants in Table I are taken to be scalars.

#### Figure of Merit Criterion

The immittance functions, e.g., reactance, of the BVD circuit may be obtained by network analysis. Despite the simplicity of the BVD circuit, there are quite a few distinguishing frequencies defined by the zeros and extrema of the various network functions [19]. For example, setting the reactance function to zero yields the quadratic equation

$$\left[ (1-x)^2 + \frac{x}{Q^2} \right] + \left( \frac{1}{r} \right) \cdot (1-x) = 0, \quad \sqrt{x} = \frac{f}{f_s}, \quad (6)$$

the roots of which define the resonance and antiresonance frequencies,  $f_R$  and  $f_A > f_R$ . Between  $f_R$  and  $f_A$  the reactance is positive, indicating that the crystal looks like an inductor; outside this range the reactance is negative and the crystal looks like a capacitor. For most oscillator applications, the crystal is operated in the region of positive reactance. It is found from (6) that the frequency separation  $\{f_A - f_R\}$  ("pole - zero" distance) depends jointly on  $Q$  and  $r$ .

The various measures used to describe the region and extent of resonance are detailed in reference [19]. For our purposes here it is enough to recognize that resonance as usually construed ceases to exist when the condition ( $f_R = f_A$ ) is satisfied. At this point the crystal just ceases to achieve a positive reactance, and its utility for frequency control and selection purposes is limited. The point at which ( $f_R = f_A$ ) is found by setting the discriminant of (6) equal to zero. This leads, in turn, to another quadratic on the square of the figure of merit,  $\mathcal{M} \equiv Q/r$ , as function of  $r$ :

$$r^2 \mathcal{M}^4 - 2r(2r+1)\mathcal{M}^2 + 1 = 0. \quad (7)$$

The roots of equation (7) can be factored to yield

$$\mathcal{M} = 1 + \sqrt{\left(1 + \frac{1}{r}\right)}. \quad (8)$$

Only the positive root applies, from which the criterion  $\mathcal{M} \equiv 2$  when ( $f_R = f_A$ ) is obtained for typical values of  $r$ . For values of  $\mathcal{M}$  of 2 or less, resonance ceases to exist [2]. Since  $Q$  decreases with absolute frequency and  $r$  increases with harmonic,  $\mathcal{M}$  is diminished both by increasing the harmonic as well as the frequency of operation. The limiting condition  $\mathcal{M} = 2$  thus imposes a constraint jointly upon frequency (or equivalently, the thickness) and harmonic. This is a very simple criterion, and we shall see that it leads to interesting conclusions. On the other hand, particular situations may require other criteria for  $\mathcal{M}$  or  $Q$ , etc., yet  $\mathcal{M}=2$  is a suitable condition for many purposes.

#### FREQUENCY LIMITS

We now invoke the  $\mathcal{M} \equiv Q/r = 2$  criterion to infer the frequency limits imposed on simple thickness mode resonators by the intrinsic phenomenological material constants of piezoelectric acoustic media. The quality factor  $Q$  is found from the motional time constant and the operating frequency  $f^{(M)}$  at the  $M^{\text{th}}$  harmonic as

$$Q = \frac{1}{2\pi f^{(M)} \tau_1} = \left( \frac{1}{2\pi \tau_1} \right) \cdot \left( \frac{1}{f^{(M)}} \right) \quad (9)$$

while the capacitance ratio  $r^{(M)}$  is found as

$$r^{(M)} = \frac{C_0}{C_1^{(M)}} = \left[ \frac{\pi^2}{8k^2} \right] \cdot M^2. \quad (10)$$

Therefore,

$$\mathcal{M} \equiv \frac{Q}{r} = \left[ \frac{4k^2}{\pi^3 \tau_1} \right] \cdot \left( \frac{1}{f^{(M)} \cdot M^2} \right). \quad (11)$$

which for  $\mathcal{M} = 2$  yields the condition

$$f^{(M)} \cdot M^2 = \left[ \frac{2k^2}{\pi^3 \tau_1} \right], \quad (12)$$

for which the product  $f^{(M)} \cdot M^2$  is equal to a constant. We now substitute (5) into (12) and solve for  $M$  to obtain

$$M^3 = \left[ \frac{2k^2}{\pi^3 \tau_1 N_0} \right] \cdot t; \quad (13)$$

hence

$$M^3 = \frac{t}{L_0}, \quad (14)$$

where  $L_0$  is the characteristic length of the piezoelectric medium:

$$L_0 \equiv \left( \frac{\pi^3}{2} \right) \cdot \left[ \frac{\tau_1 \cdot N_0}{k^2} \right] \quad (15)$$

The physical interpretation of  $L_0$  is that thickness for which  $\mathcal{M} = 2$  at the fundamental harmonic. By way of example, for AT-cut quartz,  $L_0 \approx 39.2$  nm, or roughly one hundred molecular spacings! The smallness of  $L_0$  compared to the usual resonator thicknesses encountered in practice leads one to conclude that substantially higher frequencies are available as far as the material constants are concerned; the difficulty in achieving such arises from an inability to fabricate resonators to the requisite thinness so that they can be used at the fundamental harmonic.

The characteristic length  $L_0$  can equivalently be expressed in terms of material (physics) constants by using

$$N_0 = \frac{v}{2} \quad (16)$$

along with (1), (3), and (4), such that (15) becomes

$$L_0 = \left( \frac{\pi^3}{4} \right) \cdot \left[ \frac{\bar{c}}{\rho} \cdot \frac{\eta \epsilon^S}{e^2} \right] \quad (17)$$

One sees that  $L_0$  contains every relevant acoustic parameter:  $\rho$ ,  $\epsilon^S$ ,  $e$ ,  $\bar{c}$ , and  $\eta$ . That is,  $L_0$  is a function of velocity, coupling, and loss.

For a given plate thickness  $t$ , the maximum usable harmonic is

$$M_{(\max)} = \left[ \frac{t}{L_0} \right]^{1/3}. \quad (18)$$

Of course,  $M_{(\max)}$  is to be rounded down to the nearest odd integer. At  $M_{(\max)}$ , the operating frequency is

$$f^{(M_{(\max)})} = \left[ \frac{N_0}{(L_0 \cdot t^2)^{1/3}} \right]. \quad (19)$$

The consequences of operating on a particular harmonic may be examined by considering plate resonators of differing thicknesses, such that  $M_{(\max)} = 1, 3, \text{ or } 5$ . The fundamental mode resonator has a thickness of  $L_0$ , while the harmonic resonator thicknesses are  $M^3 \cdot L_0$ . The frequencies at the intended harmonic are then

$$f^{(M)} = \left[ \frac{N_0}{L_0} \right] \cdot \left( \frac{1}{M^2} \right) = f_0 \cdot \left( \frac{1}{M^2} \right), \quad (20)$$

where the quantity

$$f_0 \equiv \frac{N_0}{L_0} \quad (21)$$

denotes the characteristic frequency of the acoustic medium; it is the limiting frequency for which  $\eta = 2$  at the fundamental harmonic. From (20), it is clear that, if one desires to attain high frequencies, one pays a severe penalty for using harmonics other than the fundamental. By way of illustration, data for AT-cut quartz and PZT-5A are given in Table II.

The issue then clearly focuses on the availability of technology for making thin films, membranes, and similar structures. Technology, not intrinsic material properties, is the real limitation. The use of sol-gel techniques [23-29] for processing ceramic thin films seems particularly promising for producing cost-effective ceramic resonators at UHF and higher frequencies. To be sure, there are certain material-related issues associated with growth, microstructure, surface finish, etc., but manufacturing problems, such as achieving films with adequate parallelism are, in reality, the main difficulty. With suitable attention focused less on material limitations and more on overcoming fabrication shortcomings, the way will be clear for achieving resonators at unprecedented frequencies.

#### PIEZOELECTRIC ACOUSTIC MATERIALS

The properties of piezoelectric materials for acoustic wave applications have been tabulated for a wide variety of substances [30,31]. However, even as measurement methods and apparatus have become increasingly more refined [17,18,32,33], there remains a lack of values for the elements of the viscosity tensor. As a consequence, values for  $L_0$  and  $f_0$  can be deduced only for those orientations and modes of vibration for which Q measurements have been reported.

Table III presents the fundamental piezoacoustic parameters for a number of ceramics [23-31, 34-37] and related ferroelectrics. Table IV similarly presents parameters of a representative semiconductor, gallium arsenide, [38-42] as well as zinc oxide and aluminum nitride, which are currently popular thin-film resonator materials. The notations "TE" and "LE" refer to thickness- and length-extension, respectively [18].

Figs. 1 and 2 show log-log plots of operating frequency versus plate thickness. Fig. 1 corresponds to the entries in the top portion of Table III, while Fig. 2 is plotted for the materials and cuts listed in Table IV. The lines for a given substance are drawn subject to the constraint  $\eta = 2$  and allowing the harmonic number M to be a continuous variable. Indicated on each line are the physically meaningful, odd-integer, values of M. Above each curve  $\eta < 2$ , while below each curve  $\eta > 2$ .

The ceramics in Fig. 1 exhibit characteristic frequencies that are in the range used for cellular radio. With advanced growth techniques, it is highly probable that inexpensive resonators capable of use in the GHz region can be fashioned of these materials. The entries in Fig. 2 are seen to be compatible with the frequencies of radar systems such as might be used for collision-avoidance in automobiles.

More generally, Fig. 3 shows the normally encountered ranges of motional time constant  $\tau_1$  and piezoelectric coupling factor k for poled ceramics, refractory crystals (such as lithium niobate and tantalate), quartz, and Si semiconductors. Also shown are values of the characteristic

frequency,  $f_0$ , found by rewriting (15) as

$$f_0 = \left( \frac{2}{\pi^3} \right) \cdot \left[ \frac{k^2}{\tau_1} \right]. \quad (22)$$

The characteristic frequency  $f_0$  thus appears in a natural fashion, benchmarking the different generic material classes. With proper attention, the region delimiting the piezoceramics can be extended downward to lower loss values, and consequently higher useful frequency domains.

#### CONCLUSIONS

We have introduced a new metric for gauging piezoelectric materials for high frequency resonator applications. It is a combination of velocity, coupling, and loss. Use of the measure leads one to conclude that piezoceramics and other ferroelectrics should be useful at frequencies into the GHz region. One concludes that much greater emphasis ought to be devoted in the future to devising advanced growth and fabrication methods for making such resonator structures commercially manufacturable.

#### REFERENCES

- [01] W. G. Cady, *Piezoelectricity*, New York: McGraw Hill, 1946; New York: Dover, 1964.
- [02] R. A. Heising, *Quartz Crystals for Electric Circuits*, New York: Van Nostrand, 1946, ch. 12, pp. 394-410.
- [03] J. van Randerdaat, ed., *Piezoelectric Ceramics*, Eindhoven, The Netherlands: N V Philips' Gloeilampenfabrieken, June 1968, 118 pp.
- [04] R. E. Newnham and G. R. Ruschau, "Smart electroceramics," *J. Am. Ceram. Soc.*, vol. 74, no. 3, pp. 463-480, March 1991.
- [05] G. H. Haertling, "Rainbow ceramics - a new type of ultra-high-displacement actuator," *Am. Ceramic Soc. Bulletin*, vol. 73, no. 1, pp. 93-96, January 1994.
- [06] A. Ballato, "Doubly rotated thickness mode plate vibrators," in *Physical Acoustics: Principles and Methods*, Vol. 13, (W P Mason and R N Thurston, eds.), New York: Academic Press, 1977, ch. 5, pp. 115-181.
- [07] G. K. Guttwein, A. Ballato, and T. J. Lukaszek, "VHF-UHF piezoelectric resonators," US Patent 3,394,677, issued September 1972.
- [08] M. Berté, "Acoustic-bulk-wave resonators and filters operating in the fundamental mode at frequencies greater than 100 MHz," *Electronics Lett.*, vol. 13, no. 9, 28 April 1977, pp. 248-250.
- [09] A. Ballato, T. J. Lukaszek, and G. J. Iafrate, "Subtle effects in high-stability quartz resonators," *Ferroelectrics*, vol. 43, nos. 1/2, pp. 25-41, 1982.
- [10] K. M. Lakin, G. R. Kline, R. S. Ketcham, A. R. Landin, W. A. Burkland, K. T. McCarron, S. D. Braymen, and S. G. Burns, "Thin film resonator technology," in *Proc. 41st Ann. Freq. Contr. Symp.*, May 1987, pp. 371-381.
- [11] K. M. Lakin, G. R. Kline, and K. T. McCarron, "High Q microwave acoustic resonators and filters," in *1993 IEEE MTT-S International Microwave Symp. Digest*, Vol. 3, June 1993, pp. 1517-1520.
- [12] US Congress, Office of Technology Assessment, *Miniaturization Technologies*, OTA-TCT-514, Washington, DC: US Government Printing Office, November 1991, 48pp.
- [13] H. E. Bömmel, W. P. Mason, and A. W. Warner, "Experimental

- evidence for dislocations in crystalline quartz," *Phys. Rev.*, vol. 99, pp. 1894-1896, 1955.
- [14] G. K. Guttwein, T. J. Lukaszek, and A. Ballato, "Practical consequences of modal parameter control in crystal resonators," in *Proc. 21st Ann. Freq. Contr. Symp.*, April 1967, pp. 115-137.
  - [15] B. Parzen, *Design of Crystal and Other Harmonic Oscillators*, New York: Wiley and Sons, 1985, ch. 3, "Piezoelectric Resonators," pp. 66-122 and 432-436.
  - [16] J. Lamb and J. Richter, "Anisotropic acoustic attenuation with new measurements for quartz at room temperature," *Proc. Roy. Soc. (London)*, vol. 293A, pp. 479-492, 1966.
  - [17] "IRE Standards on Piezoelectric Crystals: Determination of the Elastic, Piezoelectric, and Dielectric Constants - The Electromechanical Coupling Factor, 1958," IEEE Standard 178, *Proc. IRE*, vol. 46, no. 4, pp. 764-778, April 1958.
  - [18] "IEEE Standard on Piezoelectricity," IEEE Standard 176-1987, IEEE Press: New York, 54 pp.
  - [19] A. Ballato, "Resonance in piezoelectric vibrators," *Proc. IEEE*, vol. 58, no. 1, pp. 149-151, January 1970.
  - [20] A. Ballato, E. R. Hatch, M. Mizan, and T. J. Lukaszek, "Lateral field equivalent networks and piezocoupling factors of quartz plates driven in simple thickness modes," *IEEE Trans. Ultrason., Ferro., and Freq. Control*, vol. UFFC-33, no. 4, pp. 385-393, July 1986.
  - [21] A. Ballato and J. Ballato, "Measuring modern ferroelectrics accurately," *Am. Ceramic Soc. Bulletin*, vol. 73, no. 3, p. 224, March 1994. Also, *Am. Ceramic Soc. 96th Annual Meeting Abstracts Book*, April 1994, p. 77.
  - [22] R. Bechmann, "Elastic and piezoelectric constants of alpha-quartz," *Phys. Rev.*, vol. 110, no. 5, pp. 1060-1061, June 1958.
  - [23] L. L. Hench and J. K. West, *Principles of Electronic Ceramics*, New York: John Wiley & Sons, 1990.
  - [24] K. Han, A. Safari, and R. E. Riman, "Colloidal processing for improved piezoelectric properties of flexible 0 - 3 ceramic-polymer composites," *J. Am. Ceram. Soc.*, vol. 74, no. 7, pp. 1699-1702, July 1991.
  - [25] L. C. Klein, "Sol-gel processing," in *Engineered Materials Handbook, Vol. 4, Ceramics and Glasses*, ASM Intl., 1991, pp. 209-214.
  - [26] C. Livage, A. Safari, and L. C. Klein, "Sol-gel lead zirconate-titanate thin films: effect of solution concentration," in *Proc. Eighth IEEE Intl. Symp. on Appls. of Ferroelectrics (ISAF '92)*, Greenville, SC, August 1992, pp. 444-447. IEEE Catalog No. 92CH3080-9.
  - [27] J. B. Wachtman and R. A. Haber, eds., *Ceramic Films and Coatings*, Park Ridge, NJ: Noyes Publications, 1992.
  - [28] D. Tahan, A. Safari, and L. C. Klein, "The preparation of dielectric ( $\text{Ba}_{0.8}\text{Sr}_{0.2}\text{TiO}_3$ ) thin films by sol-gel method," in *Proc. Sixth US-Japan Seminar on Dielectric and Piezoelectric Ceramics*, 1993, pp. 47-50.
  - [29] H. Schmidt, "The sol-gel process for the synthesis and processing of ceramic powders," *Interceram*, vol. 43, no. 2, pp. 90, 93, March 1994.
  - [30] Landolt-Börnstein, *Numerical Data and Functional Relationships in Science and Technology, New Series, Group III: Crystal and Solid State Physics, Volumes III/1, 1966; III/2, 1969; III/3, 1969; III/9, 1974; III/11, 1979; III/16a, 1981; III/16b, 1982; and III/17a*, Berlin, New York: Springer-Verlag, 1982.
  - [31] J. G. Gualtieri, J. A. Kosinski, and A. Ballato, "Piezoelectric materials for acoustic wave applications," *IEEE Trans. Ultrason., Ferro., and Freq. Control*, vol. 41, no. 1, pp. 53-59, January 1994.
  - [32] *IEC Publication 483: Guide to Dynamic Measurements of Piezoelectric Ceramics (1976)*. New York: ANSI.
  - [33] "IEEE Standard Definitions of Primary Ferroelectric Terms," *ANSI/IEEE Standard 180-1986*, New York: IEEE Press, 21pp.
  - [34] I. Ueda and S. Ikegami, "Piezoelectric properties of modified  $\text{PbTiO}_3$  ceramics," *Jap. Jour. Appl. Phys.*, vol. 7, pp. 236-242, 1968. Reprinted in: *Piezoelectricity*, C. Z. Rosen, B. V. Hiresmath, and R. Newnham, eds., Key Papers in Physics series, New York: American Institute of Physics, 1992, pp. 175-181.
  - [35] B. Jaffe, W. R. Cook, Jr., and H. Jaffe, *Piezoelectric Ceramics*, New York: Academic Press, 1971.
  - [36] D. J. Waller and A. Safari, "Piezoelectric lead zirconate titanate ceramic fiber/polymer composites," *J. Am. Ceram. Soc.*, vol. 75, no. 6, pp. 1648-1655, June 1992.
  - [37] T. Suwannasiri and A. Safari, "Effect of rare-earth additives on electromechanical properties of modified lead titanate ceramics," *J. Am. Ceram. Soc.*, vol. 76, no. 12, pp. 3155-3158, December 1993.
  - [38] A. Ballato and C. D. Bosco, "Acoustic waves in cubic crystals: networks for semiconducting vibrators, and application to gallium arsenide," Technical Report DELET-TR-79-9, US Army Electronics R&D Command, Fort Monmouth, NJ, April 1979, 45pp.
  - [39] J. S. Blakemore, ed., *Gallium Arsenide*, Key papers in physics, No. 1, New York: American Institute of Physics, 1987, 401pp.
  - [40] S. Adachi, *Physical Properties of III - V Semiconductor Compounds*, New York: Wiley & Sons, 1992.
  - [41] R. Stokes and J. D. Crawford, "X-Band thin film acoustic filters on GaAs," *IEEE Trans. Microwave Theory Tech.*, vol. 41, no. 6/7, pp. 1075-1080, June/July 1993.
  - [42] J. Söderkvist and K. Hjort, "The piezoelectric effect of GaAs used for resonators and resonant sensors," *J. Micromech. Microeng.*, vol. 4, no. 1, pp. 28-34, March 1994.
  - [43] D. H. Turnbull, M. D. Sherar, and F. S. Foster, "Determination of electromechanical coupling coefficients in transducer materials with high mechanical losses," in *Proc. 1988 IEEE Ultrason. Symp.*, October 1988, pp. 631-634.
  - [44] H. Takeuchi, Y. Ito, S. Jyomura, K. Nagatsuma, and S. Ashida, "New piezoelectric ceramics with zero temperature coefficients for acoustic wave applications," in *Proc. 1980 IEEE Ultrason. Symp.*, November 1980, pp. 400-409.
  - [45] C. W. Lee, L. J. Bowen, J. M. Browne, A. Halliyal, A. S. Bhalla, and E. Ylo, "Acoustic wave properties of fiesnoite glass ceramics," in *Proc. 1984 IEEE Ultrason. Symp.*, November 1981, pp. 285-289.
  - [46] A. Halliyal, A. S. Bhalla, R. E. Newnham, and L. E. Cross, "Piezoelectric and elastic properties of barium germanium titanate and lithium borosilicate glass-ceramics," in *Proc. 1981 IEEE Ultrason. Symp.*, October 1981, pp. 315-318.

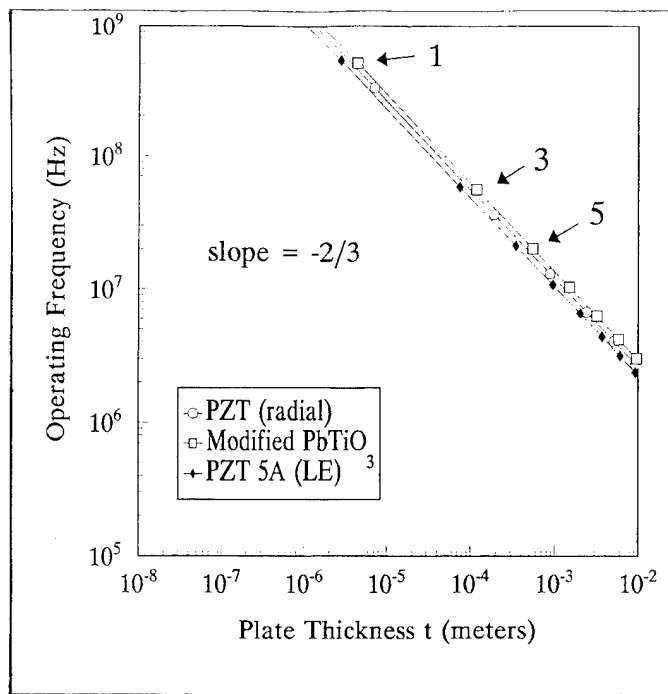


Fig. 1. Operating frequency versus plate thickness for ceramic materials, subject to the criterion  $\eta = 2$ . Harmonics of operation are indicated.

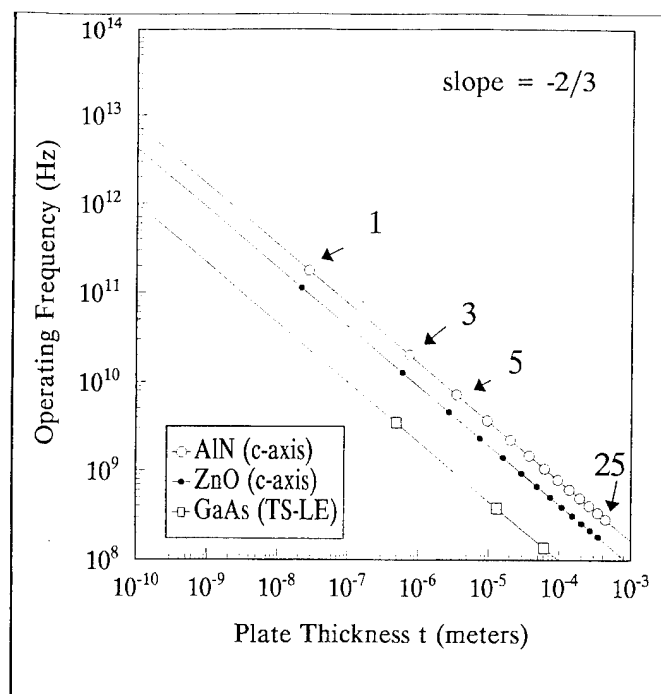


Fig. 2. Operating frequency versus plate thickness for aluminum nitride, zinc oxide, and semi-insulating gallium arsenide materials, subject to the criterion  $\eta = 2$ . Harmonics of operation are indicated.

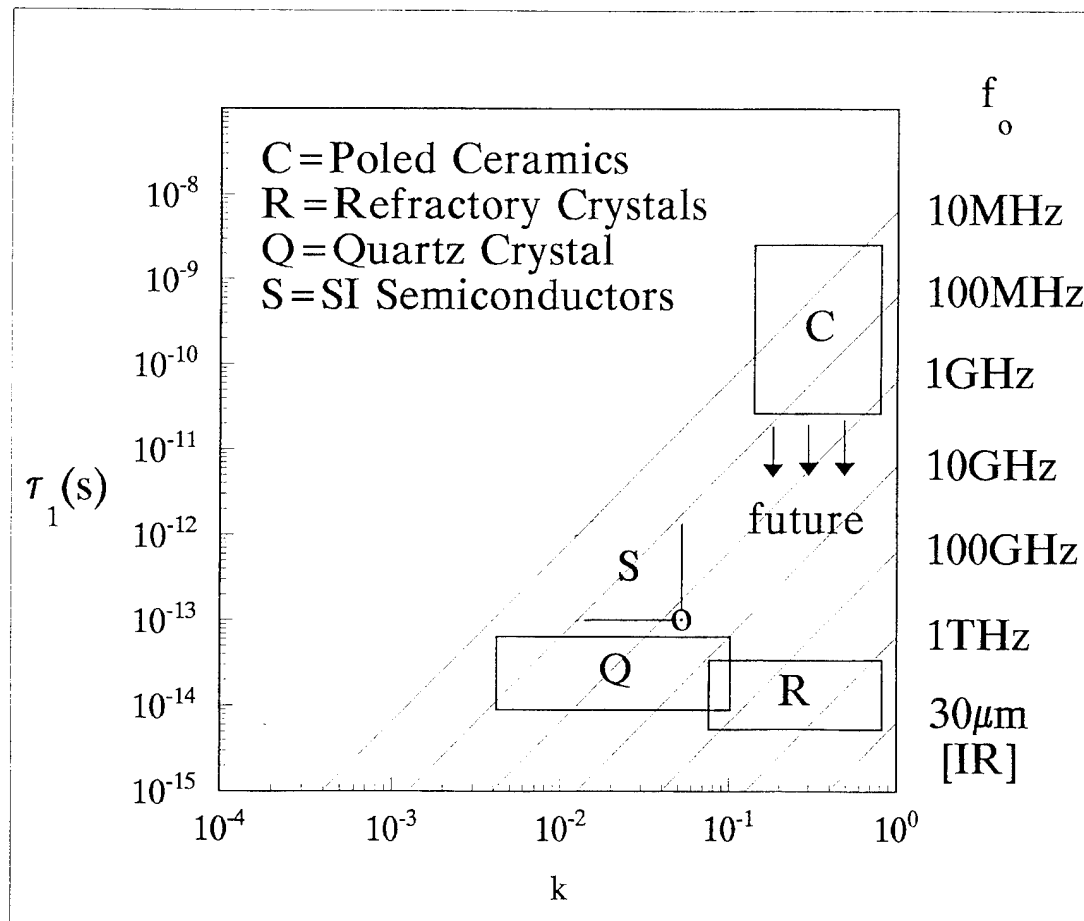


Fig. 3. Motional time constant ( $\tau_1$ ) and piezoelectric coupling coefficient ( $k$ ) ranges for ceramics, refractories, quartz, and semi-insulating (SI) gallium arsenide. Also shown are ranges of characteristic frequency,  $f_0$ .



TABLE I  
RELATIONS BETWEEN CIRCUIT PARAMETERS, PHYSICS FACTORS, AND GEOMETRIC FACTORS

	Circuit Parameter	Physics Factor	Geometric Factor
Effective Elastic Stiffness	-	$\bar{c} = c^E + \frac{e^2}{\epsilon^S}$	-
Wave Velocity	-	$v^2 = \frac{\bar{c}}{\rho}$	-
Piezoelectric Coupling	-	$k^2 = \frac{e^2}{\epsilon^S \bar{c}}$	-
Static Capacitance	$C_0$	$\epsilon^S$	$\frac{A}{t}$
Motional Resistance	$R_1^{(M)}$	$\frac{M^2 \pi^2 \eta}{8e^2}$	$\frac{t}{A}$
Motional Inductance	$L_1^{(M)} = L_1$	$\frac{\rho}{8e^2}$	$\frac{t^3}{A}$
Motional Capacitance	$C_1^{(M)}$	$\frac{8e^2}{M^2 \pi^2 \bar{c}}$	$\frac{A}{t}$
Capacitance Ratio	$r^{(M)} = \frac{C_0}{C_1^{(M)}}$	$\left[ \frac{\pi^2}{8k^2} \right] \cdot M^2$	-
Resonance Frequency	$f^{(M)} = \frac{\omega_M}{2\pi} = \frac{1}{2\pi} \sqrt{\frac{1}{L_1^{(M)} C_1^{(M)}}}$	$\frac{Mv}{2}$	$\frac{1}{t}$
Motional Time Constant	$\tau_1^{(M)} = R_1^{(M)} C_1^{(M)} = R_1 C_1 = \frac{1}{\omega_M Q_M}$	$\frac{\eta}{\bar{c}}$	-

TABLE II  
LIMITING OVERTONE FREQUENCIES OF QUARTZ AND CERAMIC PLATES  
SUCH THAT  $m = 2$  AT FIRST, THIRD, AND FIFTH HARMONICS

Plate	M	t	Quartz		PZT 5A	
			t ( $\mu\text{m}$ )	f (GHz)	t ( $\mu\text{m}$ )	f (MHz)
#1	1	$L_0$	0.0392	42.4	2.75	527
#2	3	$27 \cdot L_0$	1.06	4.71	74.3	58.6
#3	5	$125 \cdot L_0$	4.90	1.70	344	21.1

TABLE III  
FUNDAMENTAL CHARACTERISTICS OF SELECTED TYPES OF PIEZOELECTRIC RESONATOR

Type	$N_0$ (m/s)	$\tau_1$ (ps)	$k^2$ (%)	$L_0$ ( $\mu\text{m}$ )	$f_0$ (MHz)	Reference
PZT 5A (LE)	1450	11	9	2.75	527	[43]
Modified PbTiO <sub>3</sub>	2210	31.8	25	4.36	507	[44]
PZT/ radial	2300	53	27	7.00	328	[03]
Fresnoite (crystal)	2350	33.9	6.25	19.8	118	[45]
Fresnoite (glass)	2250	35.4	6.25	19.8	114	[45]
PZT 5A (TE)	2225	236	22.1	36.8	60.5	[43]
PZT/epoxy (LE)	1060	17	0.64	43.6	24.3	[43]
PZT/epoxy (TE)	1950	878	32.5	81.7	23.9	[43]
BGST	2600	102	2.25	183	14.2	[46]
BZT50	1870	575	10.24	163	11.5	[34]
BGT	2500	45.5	0.56	314	7.96	[46]
PVDF (TE)	1025	128	1.44	141	7.3	[43]

TABLE IV  
FUNDAMENTAL CHARACTERISTICS OF SELECTED TYPES OF THIN-FILM RESONATOR

Type	$N_0$ (m/s)	$\tau_1$ (ps)	$k^2$ (%)	$L_0$ ( $\mu\text{m}$ )	$f_0$ (GHz)	Reference
GaAs (TS/Lateral-Field)	1671	0.07	0.372	0.487	3.43	[42]
ZnO (c-axis oriented)	2500	0.045	8	0.022	115	[10]
AlN (c-axis oriented)	5000	0.032	9	0.028	181	[10]



# Concurrent Session - 5A: Photorefractives

# Mutually Pumped Phase Conjugation With High Spatial Resolution

Jan M. Yarrison-Rice, Edward J. Sharp<sup>1</sup>, Gary L. Wood<sup>1</sup>, Gregory J. Salamo<sup>2</sup>,  
Richard J. Anderson<sup>3</sup>, Robert Klanck<sup>4</sup>, and Ratnakar R. Neurgaonkar<sup>5</sup>

University of Miami, Department of Physics, Oxford, OH 45056

<sup>1</sup> U.S. Army Research Laboratory, Fort Belvoir, VA 22060-5838

<sup>2</sup> University of Arkansas, Department of Physics, Fayetteville AR 72701

<sup>3</sup> National Science Foundation, Arlington VA 22230

<sup>4</sup> University of Connecticut, Department of Physics, Storrs, CT 06268

<sup>5</sup> Rockwell Science Center, Thousand Oaks, CA 91360

**Abstract**--We present experimental results showing an improvement in the spatial resolution of phase conjugate images obtained from mutually pumped phase conjugators. Resolutions of  $>100$  lines/mm are presented and we demonstrate that this resolution can be achieved while performing image processing tasks such as the addition and subtraction of complex spatial distributions. These results represent greater than an order of magnitude improvement over previously reported resolutions obtained in photorefractive mutually pumped phase conjugators and approach the theoretical limit imposed by the grating spacing and crosstalk.

## INTRODUCTION

Photorefractive ferroelectric crystals have been the subject of numerous recent investigations owing to the particular ability of these materials to display high optical nonlinearities using only milliwatt input powers. One such nonlinear optical process involves the use of two mutually incoherent laser beams which pump each other simultaneously resulting in the formation of two phase conjugate wave fronts (double phase conjugation).<sup>1,2</sup> These devices, called mutually pumped phase conjugators (MPPCs) are unique to photorefraction, and have been demonstrated in a variety of geometries.<sup>3</sup>

MPPCs operating in the steady state exhibit stable conjugate output signals after some characteristic build-up time. The build-up time and the phase-conjugate reflectivities depend upon the particular crystal being used and also upon several other factors associated with the geometry and pumping conditions, such as beam intensities, angles of incidence, the relative coherence of the pumping beams, and the spot-size of the pumping beams. To date, the spatial resolution of images conjugated in MPPCs has been disappointing. In most cases the reported spatial resolution is only  $\sim 3$  to 5 cycles/mm.<sup>1,3,4,5,6,7</sup>

Recent work by Segev et. al.<sup>8</sup> indicates that high phase-conjugation fidelity can be obtained above a well defined gain threshold ( $\gamma_0 L \geq 2$ ). They used an input beam ratio of 0.87 and found that the fidelity threshold depends on the feature size of the spatial information carried on the beams, where the threshold decreases for input beams with increasing feature size. This suggests that high phase conjugation fidelity should be possible for beams carrying information with small feature size, if the crystal has a large  $\gamma_0 L$ , and should result in higher spatial resolution of the conjugated images. We demonstrate in this work that high resolution phase conjugate images are obtained for a wide range of input conditions using a "bridge" MPPC.<sup>2</sup>

## EXPERIMENT

The bridge MPPC was setup as shown in Fig.1. A large (6 mm x 13.4 mm x 12.2 mm) cerium doped SBN:60 crystal (0.01% cerium in the melt) was used as the MPPC. The output of a helium cadmium laser (14 mW) is collimated and divided into two beams by beam splitter #3. A delay line is used in beam #2 to insure that it is incoherent with beam #1. Both beams pass through positive masks (Air Force resolution targets) which are then imaged in a 2f-2f configuration into the photorefractive crystal. Imaging lenses #1 and #2 have focal lengths of 17.5 cm and 25 cm respectively. Each beam enters the crystal at an angle which was varied from  $5^\circ$  to  $70^\circ$  from the normal as discussed below. The beam diameters are  $\sim 2.5$  mm upon entering the sample. Neutral density filters, NDF's, were used to adjust the beam ratio,  $q = (\text{Beam \#1}/\text{Beam \#2})$ . The resulting phase conjugate replicas were imaged (with approximately 7X magnification) onto CCD cameras where they were photographed.

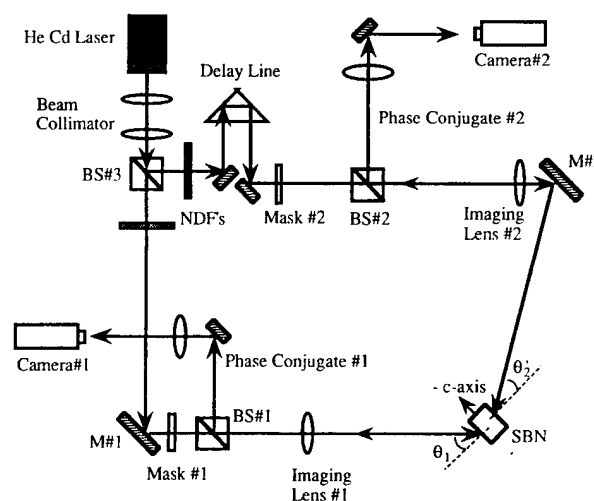


**Figure 1.** Experimental Apparatus for Double Pumped Phase Conjugator

## Beam Ratio

Several experiments were carried out with different spatial information impressed on the pair of input beams. The beams were each incident at about  $45^\circ$  to the normal and were adjusted to cross near the center of the crystal. The mask is placed in the beam at a

45° angle so that the horizontal and vertical features on the mask would be treated equally in the beam fanning and subsequent conjugation process. In the first experiment beam #1 carried spatial information and beam #2 had a near uniform spatial distribution. For this case, an example of the highest resolution obtained is shown in Fig. 2 (group 7, element 1 corresponds to 128 cycles/mm). In the second experiment, spatial information was imposed on both beams and similar high resolution was obtained.



Figure 2. Photograph of the phase conjugate image of the resolution chart displayed on CCD camera #1.

Additionally, as the beam ratio varied from  $\sim 0.02$  to 56, both the phase conjugate reflectivity and the resolution were monitored. In general, the spatial resolution obtained was observed to be high ( $\sim 100$  to 115 cycles/mm for beam #1 and  $\sim 85$  to 90 cycles/mm for beam #2) and independent of the beam ratio until the device would no longer support phase conjugation. There is however, a loss of contrast (or fidelity) at the extreme ratios as pointed out by Segev, et. al.<sup>8</sup> Figure 3 shows the effect of changing the beam ratio on both the phase conjugate reflectivity and the resolution. Similar reflectivity results were obtained by Bogodaev, et. al.<sup>9</sup>

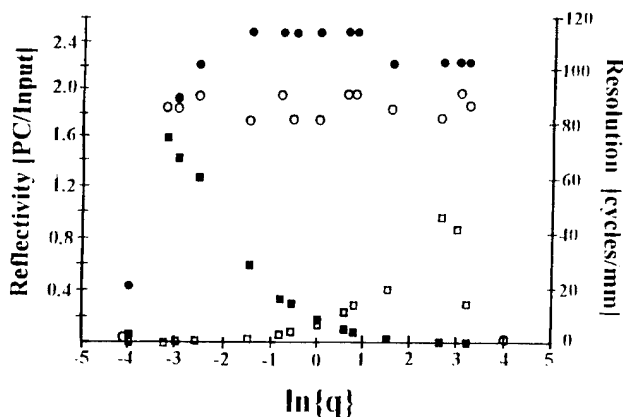


Figure 3. Phase conjugate reflectivity and corresponding resolution for the two input beams incident at 45° as a function of beam ratio. Circles indicate resolution and squares indicate reflectivity where solid are beam #1 and open are beam #2.

In other experiments, the resolution was determined as a function of the input angle from 4° to 65° and was found to be nearly independent of the input angle at  $\sim 125$  cycles/mm. At very small angles ( $\theta_1 \cong \theta_2 < 10^\circ$ ) the phase conjugate never forms, instead, the well-known ring pattern forms, but never collapses into a conjugate.<sup>2</sup> The resolution of the phase conjugate images was observed to improve from 30 cycles/mm at 1 mm beam diameters

to the maximum observed at  $\sim 125$  cycles/mm at  $\sim 4.5$  mm diameters. An input angle of  $\sim 45^\circ$  was used for both beams.

Using the technique described in Ref 10, we carried out the addition and subtraction of high resolution phase conjugate images. Two conjugate signals, one with a nearly uniform intensity profile and the other with a spatially modulated profile were interfered to obtain the contrast reversed phase conjugate image with a resolution of  $\sim 70$  cycles/mm.

#### Limits of Resolution

In the MPPC we study here, the transmission gratings are written by the input beams and their own scattered light. When a good imaging system ( $2f/2f$ , for example) is used to write the volume holograms two conditions must be met to optimize the resolution. One, the feature size of the object,  $d$ , must be much greater than the grating spacing,  $\Lambda_g$ , and two, the feature size must be much greater than the effective interaction length or  $d \gg L\Theta$ , where  $\Theta$  is the crossing angle of the scattered beam and the spatially modulated input beam. The resolution is optimized when  $\Lambda_g = L\Theta$ , or  $\Lambda_g^2 \sim L\lambda$ . For  $\lambda = 442$  nm and  $\Lambda_g = 1/125$  cycles/mm =  $8\mu\text{m}$ , we get an  $L_{\text{eff}} = 145\mu\text{m}$ . When the transmission loss of the input beam due to fanning reaches 0.65, and we express this as two-beam coupling loss,  $T_{\text{loss}} \sim 2/[1 + \exp(\Gamma L_{\text{eff}})]$  we can estimate the gain of our crystal as  $\Gamma \sim 50\text{ cm}^{-1}$ . This is a reasonable value suggesting that 125 cycles/mm is approaching the resolution limit for this device.

#### CONCLUSIONS

In conclusion, we have shown that high resolution phase conjugate imaging can be accomplished using MPPCs and we demonstrate that in the bridge MPPC this resolution approaches the theoretical limit imposed by the grating spacing and crosstalk. We show that the resolution is independent of the beam ratio for all values which can support phase conjugation. We estimate the gain of our crystal based on the observed resolution obtained and find it ( $50\text{ cm}^{-1}$ ) to be typical for moderately Ce-doped SBN:60 crystals. We also find that the resolution is independent of the incident angles of the beams provided the system will support phase conjugation.

#### REFERENCES

1. S. Weiss, S. Sternklar, and B. Fischer, "Double Phase-Conjugate Mirror: Analysis, Demonstration, and Applications," *Opt. Lett.* **12**:114-116 (1987).
2. E.J. Sharp, W.W. Clark, III, M.J. Miller, G.L. Wood, B.D. Monson, G.J. Salamo, and R.R. Neurgaonkar, "Double Phase Conjugation in Tungsten Bronze Crystals," *Appl. Opt.* **29**:743-749 (1990).
3. P. Yeh, T.Y. Chang, and M.D. Ewbank, "Model for Mutually Pumped Phase Conjugation," *J. Opt. Soc. Am. B* **5**:1743-1749 (1988).
4. M.D. Ewbank, "Mechanism for Photorefractive Phase Conjugation Using Incoherent Beams," *Opt. Lett.* **13**:47 (1988).
5. M.D. Ewbank, R.A. Vazquez, R.R. Neurgaonkar, and J. Feinberg, "Mutually Pumped Phase Conjugation in Photorefractive Strontium Barium Niobate: Theory and Experiment," *J. Opt. Soc. Am. B* **7**:2306-2316 (1990).
6. S. Sternklar, S. Weiss, and B. Fischer, "Optical Information Processing with the Double Phase Conjugate Mirror," *Opt. Eng.* **26**:423-427 (1987).
7. R.J. Anderson, E.J. Sharp, G.L. Wood, W.W. Clark, III, G.J. Salamo, and R.R. Neurgaonkar, "Mutually Pumped Phase Conjugator as a Moving-Object Correlator," *Opt. Lett.* **18**:986-988 (1993).
8. M. Segev, D. Engin, A. Yariv, and G.C. Valley, "Temporal Evolution of Photorefractive Double Phase-Conjugate Mirrors," *Opt. Lett.* **18**:1828-1830 (1993).
9. S. Orlov, M. Segev, A. Yariv, and G.C. Valley, "Conjugation Fidelity and Reflectivity in photorefractive Double Phase Conjugate Mirrors," *Opt. Lett.* **19**:578-580 (1994).
10. N.V. Bogodaev, V.V. Eliseev, L.I. Ivleva, A.S. Korshunov, S.S. Orlov, N.M. Polozokov, and A.A. Zozulya, "Double Phase-Conjugate Mirror: Experimental Investigation and Comparison with Theory," *J. Opt. Soc. Am. B* **9**:1493 (1992).
11. E.J. Sharp, G.L. Wood, G.J. Salamo, R.J. Anderson, J.M. Yarrison-Rice, and R.R. Neurgaonkar, "Photorefractive Image Processing Using Mutually-Pumped Phase Conjugators," *Proc. SPIE* **2234**:347 (1994).

# Large Electrooptic Modulation Using Ferroelectric Thin Films in a Fabry-Perot Cavity

Feiling Wang and Gene H. Haertling  
Gilbert C. Robinson Department of Ceramic Engineering  
Clemson University  
Clemson, South Carolina 29634-0907

**Abstract**— We report a reflective thin film ferroelectric light modulator which has exhibited optical phase modulation as large as fifty degrees and on/off signal ratio of twenty for intensity modulation. The large optical modulation was achieved by means of multiple reflection. A ferroelectric (FE) PLZT thin film material, deposited on Pt-coated silicon substrate, was used as the modulating medium. An indium-tin oxide (ITO) thin layer was deposited on the ferroelectric films as the top electrode. A He-Ne laser beam was obliquely incident on the ITO/FE/Pt structure. The light modulation was detected in the laser beam reflected from the thin film structure when a voltage signal was applied to the ITO and Pt electrodes. Unlike transmission-mode modulators, the sandwich of the ferroelectric films between the air-ITO and FE-Pt interfaces exhibited characteristics of a Fabry-Perot etalon. Near a Fabry-Perot peak, drastically enhanced light modulation than transmission devices was obtained. Design principles and the performance of the modulator are discussed.

## INTRODUCTION

A number of thin film ferroelectric materials, including lead lanthanum zirconate titanate (PLZT), barium titanate, lithium niobate, strontium barium niobate and lead magnesium niobate, have exhibited attractive birefringent electrooptic effect when deposited on suitable substrates [1]-[4]. Using these materials for optical modulation has been the focus of many studies. Integrated optical modulators using ferroelectric media may adopt three different designs, namely, transmission devices, waveguide devices and reflection devices. Transmission modulators are not compatible with opaque substrates; their usage are thus limited. They also suffer from shallow modulation depth because of the rather short optical path. Waveguide devices, such as total internal reflection (TIR) switch, using PLZT thin films grown on sapphire substrate have been successfully demonstrated [5].

With the advances in high-performance optoelectronic devices, it has become increasingly desirable to realize the integration of thin film optical modulators with semiconductor substrates to form hybrid devices [6]. Ferroelectric optical modulators in these devices may perform such functions as electrical-optical signal interface through spatial light modulation, intra- and inter-chip optical interconnections. The same ferroelectric media in these device may also perform all-optical operations, such as frequency doubling and optical logic, by using their outstanding optical nonlinearities. Combined with the more traditional task for ferroelectrics, namely, nonvolatile memory capability, ferroelectric thin films may become multifunctional media in various integrated optoelectronic devices. Using ferroelectric/electrooptic thin film for optical interconnection has been proposed by Lee and Ozguz [7],[8]. Enhanced phase re-

tardation by means of interference has been observed in PZT films by Dimos *et al* [9], however, incoherent light scattering has prevented a sufficient signal-to-noise ratio for intensity modulation.

In this paper we will report a reflection thin film ferroelectric spatial light modulator constructed on silicon substrates. By adopting a low finesse Fabry-Perot cavity, the modulator can achieve large phase modulation and high signal-to-noise ratio for intensity modulation. The device may be used as an implementation of free-space optical interconnections.

## DEVICE DESIGN AND THEORY OF MODULATION

The thin film light modulator was constructed on oxidized and Pt/Ti-metallized silicon wafers. Fine grain ferroelectric PLZT thin films were deposited on the metallized silicon substrates by using magnetron sputtering. An indium-tin oxide (ITO) layer was then sputter deposited on the ferroelectric thin films as top electrode. Figure 1 shows the schematic cross-section of the thin film modulator.

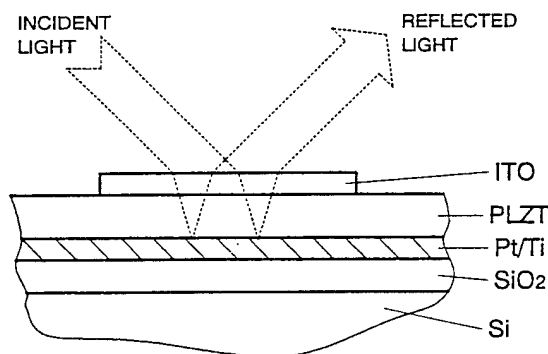


Figure 1. Schematic cross-section of the ferroelectric thin film reflection light modulator.

Linearly polarized light beam with equal amplitude for p-polarization (parallel to the incident plane) and s-polarization (perpendicular to the incident plane) was obliquely incident on the modulator as shown in Figure 1. Because of the polycrystalline nature of the ferroelectric thin films, the materials are optically uniaxial defined by the normal of the substrates. With an external electric field exerted through a voltage across the ITO and Pt layers, the extraordinary index  $n_e$  and ordinary index  $n_o$  experience field-induced changes,  $\Delta n_e$  and  $\Delta n_o$ , respectively. The corresponding changes in the indices for the p- and s-polarized light components are given by

$$\begin{aligned}\Delta n_p(\theta_2) &= \sin^2 \theta_2 \Delta n_e + \cos^2 \theta_2 \Delta n_o, \\ \Delta n_s &= \Delta n_o.\end{aligned}\quad (1)$$

where  $\theta_2$  is the refraction angle of the light beam inside the ferroelectric thin film material. As the ferroelectric films are bounded by the Pt and ITO layers, the light beam experiences multiple reflections. Although all three interfaces, namely, air-ITO, ITO-FE and FE-Pt interfaces, cause light reflection, the air-ITO and FE-Pt boundaries dominates the characteristics of the reflected light beam because of the moderate difference between ITO and FE in refractive index. The device therefore can be characterized as a low finesse Fabry-Perot reflector. Under an external electric field, the optical length of the Fabry-Perot etalon becomes different for p- and s-polarized light components because of the field-induced birefringence in the ferroelectric thin films according to Equation (1). The polarization state of the reflected light, therefore, can be modulated with an voltage signal. As expected from any Fabry-Perot etalon, the modulation of the light can be greatly enhanced when a critical optical length of the etalon is satisfied. In the present devices, the critical optical length is determined by the thickness of the films and the incident angle of the light. Theoretical modeling has resulted in an accurate prediction for the light modulation as a function of the thickness of the films and incident angle [10]. The following equation can be used to formally describe the phase difference  $\Delta\Gamma \equiv \Delta\Gamma_p - \Delta\Gamma_s$ , between the field induced phase change in p-polarized light  $\Delta\Gamma_p$  and s-polarization light  $\Delta\Gamma_s$ :

$$\Delta\Gamma = w_p \sin^2 \theta_2 \Delta n_e - (w_s - w_p \cos^2 \theta_2) \Delta n_o. \quad (2)$$

where  $w_p$  and  $w_s$  are complicated functions of indices and thickness of all the layers involved as well as the incident angle. Figure 2 shows the calculated  $w_p$  and  $w_s$  as functions of the thickness of the ferroelectric layer with other parameters given. The oscillation of  $w_p$  and  $w_s$  is caused by the alternating phase relation between the neighboring reflected partial light beams with the thickness change. Consequently the total phase retardation of the device,  $\Delta\Gamma$ , exhibits similar oscillation. A phase retardation maximum occurs as neighboring reflected partial beams differ in optical phase by 180 degrees. Under this condition, partial light is forced to remain in the ferroelectric films

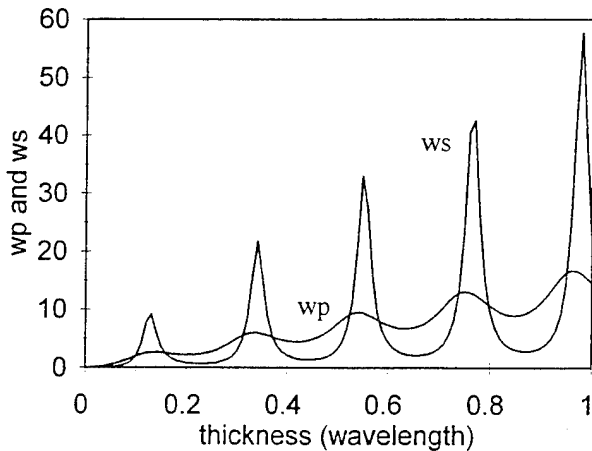


Figure 2. Calculated coefficients,  $w_p$  and  $w_s$ , as functions of the thickness of the electrooptic layer.

for a much longer average path, experiencing accumulated phase retardation.

In order to characterize the ferroelectric thin film modulator, a reflection differential ellipsometer [11] was employed to measure the field-induced phase retardation of the reflected light. The intensity modulation of the light beam was measured with the optical setup shown in Figure 3. Linearly polarized He-Ne laser beam of 632.8 nm wavelength was obliquely incident on the thin film modulator, upon which electric signals were applied. A light sensor is located after a polarizer to detect the light reflected from the modulator.

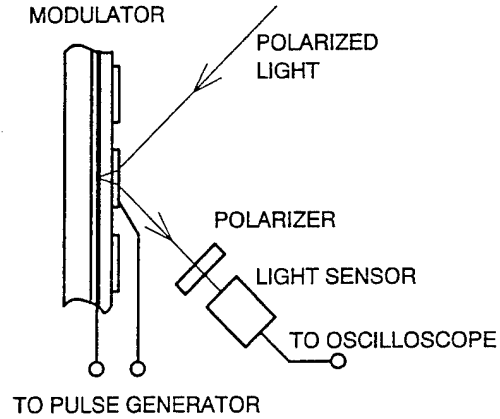


Figure 3. Light intensity modulation detecting system.

## EXPERIMENTAL RESULTS

Lead lanthanum zirconate titanate (PLZT) of composition 2/55/45 (La/Zr/Ti) was deposited on Pt/Ti-coated silicon substrate as the modulating medium. A post-deposition annealing process was employed to acquire the perovskite structure of the deposited thin films. Thickness of the PLZT films was approximately 480 nm. Indium-tin oxide layer of thickness approximately 350 nm was also sputter deposited on the PLZT films.

The phase shift of the reflected light beam as a function of the applied voltage, measured with the reflection differential ellipsometry, is shown in Figure 4. The measured phase shift roughly represented the birefringence,  $\Delta n = \Delta n_e - \Delta n_o$ , of the film when a proper incident angle was chosen for the measurement. As shown in the figure, the field-induced birefringence of the PLZT film exhibits a slightly asymmetric butterfly-shaped loop, typical for ferroelectric thin films. Field-induced phase shift loops were taken at various incident angles. A phase-shift peak was located at approximately 57 degrees, where phase shift reaches approximately 50 degrees. This peak is consistent with the model calculation, from which the thickness of the films was designed.

The performance of the device as a light intensity modulator was examined using the measuring system shown in Figure 3. Electric pulses were applied to the devices with 2 mm diameter ITO dots as top electrodes. Light intensity modulations, sensed by a photo-multiplier tube, were recorded by an oscilloscope. Figure 5 shows a light intensity modulation responding to electric pulses of 10 volts in peak height and 5 ms in pulse width. An on/off signal ratio of 12 was measured during this

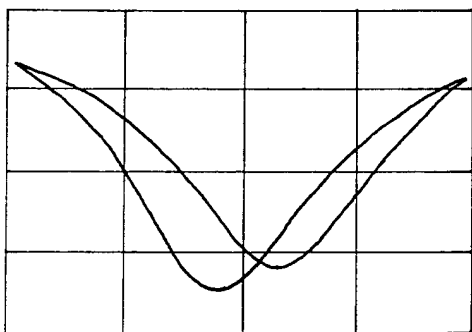


Figure 4. Field-induced relative phase shift (phase retardation) of the reflected light beam measured by using the reflection differential ellipsometer. The horizontal and vertical scales are 7.9 volts per division and 0.28 per division respectively.

operation. Higher on/off signal ratio may be acquired by further reducing the light in the off state. The on/off signal ratio as a function of the peak height of the pulses is shown by Figure 6. Light modulation remained substantial under pulses of peak height less than 5 volts, while modulation at 10 volts peak height was very visible.

Because of the large area of the top electrode for the convenience of the experiments, the rc constant limited the operation bandwidth of the devices. Under this limitation, intensity modulation at a frequency of 100 kHz was still detectable, although with much shallower modulation depth. The rc constant may be drastically reduced with reduced electrode area and wiring impedance, which will ultimately results in a material response limited operation bandwidth.

Because of the large field-induced birefringence in ferroelectric thin films,  $\Delta n_e - \Delta n_o \approx 0.02$  under a moderate external field, the modulator remained a substantial on/off signal ratio for intensity modulation even when the incident angle is a few degrees away from the Fabry-Perot peak. This property gives the ferroelectric modulator a great tolerance to the error of thickness control of the films, vital for practical fabrications.

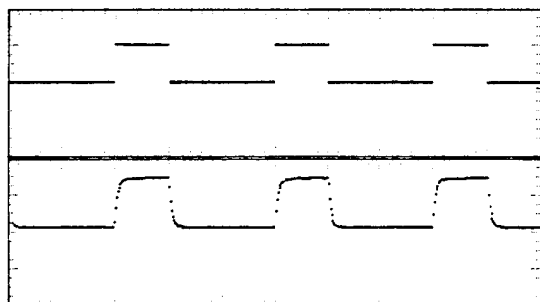


Figure 5. Light intensity modulation with electric pulses. The upper trace is the voltage signal applied to the modulator. The lower trace is the recorded light intensity reflected from the modulator. The horizontal scale is 5 ms per division. The vertical scale for the upper trace is 10 volts per division.

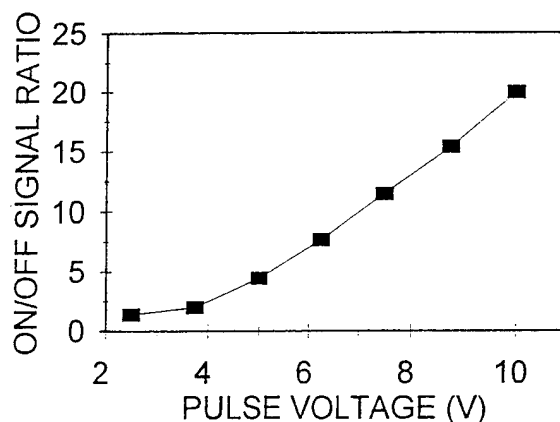


Figure 6. Light on/off ratio as a function of the pulse voltage.

## CONCLUSION

A thin film ferroelectric reflection spatial light modulator has been constructed on semiconductor substrates. The device consists of an ITO/PLZT/Pt thin film structure on oxidized silicon substrate. With the help of interference of multiple reflection, larger than 50 degrees phase shift in the reflected light from an obliquely incident light beam has been achieved. Using the device as an intensity light modulator, on/off signal ratio of twenty has been obtained with electric pulses of 10 peak voltage. This device may be used in various optoelectronic devices as an implementation of free-space optical interconnections.

## ACKNOWLEDGMENTS

The authors benefited greatly from numerous discussions with E. Furman concerning this subject. This work was sponsored by the Office of Naval Research under Contract No. N00014-91-J508.

## REFERENCES

- [1] K. D. Preston and G. H. Haertling, "Comparison of electro-optic lead-lanthanum zirconate titanate films on crystalline and glass substrates," *Appl. Phys. Lett.* vol. 60, pp.2831-33, June 1992.
- [2] A. Wegner *et al*, "Integrated PLZT thin film waveguide modulators" *Ferroelectrics*, vol. 116, pp. 195-204, 1991.
- [3] H. Adachi *et al*, "Electro-optic effects of (Pb,Lu)(Zr,Ti)O<sub>3</sub> thin films prepared by rf planar magnetron sputtering," *Appl. Phys. Lett.* vol. 42, pp. 867-68, May 1983.
- [4] F. Wang and G. H. Haertling, "Birefringent bistability in (Pb,Lu)(Zr,Ti)O<sub>3</sub> thin films with a ferroelectric-semiconductor interface," *Appl. Phys. Lett.* vol. 63, pp. 1730-32, Sep. 1993.
- [5] H. Higashino *et al*, "High speed optical TIR switched using PLZT thin-film waveguides on sapphire," *Japan. J. Appl. Phys.*, vol. 24, suppl. 24-2, pp. 284-86, 1985.
- [6] C. H.-J. Huang and T. A. Rost, presented at the 6th Interna-



- tional Symposium on Integrated Ferroelectrics, March 14-16, 1994, Monterey, California
- [7] S. H. Lee et al, "Two-dimensional silicon/PLZT spatial light modulator: design considerations and technology," *Optical Engineering*, vol. 25, pp. 250-60, Feb. 1986
  - [8] V. H. Ozguz, S. Krishnakumar and S. H. Lee, "Ferroelectric thin films for smart spatial light modulator applications," manuscript.
  - [9] D. Dimos, C. E. Land and R. W. Schwartz, "Electrooptic effects and photosensitivities of PZT thin films," *Ceramic Transactions*, vol. 25: Ferroelectric Film, (American Ceramic Society, Westerville, OH, 1992), pp. 323-39
  - [10] F. Wang *et al*, to be published.
  - [11] F. Wang *et al*, "Discrete electro-optic response in lead zirconate thin films from a field-induced phase transition," *Opt. Lett.*, vol.18, pp. 1615-17, Oct. 1993.

# Liquid Delivery CVD of PLZT Thick Films for Electro-Optic Applications

J.F. Roeder, S.M. Bilodeau, P.C. Van Buskirk, V.H. Ozguz<sup>1</sup>, J. Ma<sup>1</sup>, and S.H. Lee<sup>1</sup>

Advanced Technology Materials  
7 Commerce Drive  
Danbury, CT 06810

<sup>1</sup>Department of Electrical and Computer Engineering  
University of California at San Diego  
LaJolla, CA 92093

**Abstract** - PLZT films in the composition range 70/100 - 32/0/100 have been deposited by CVD from a single source reagent using a liquid delivery / flash vaporization approach. Single phase perovskite films ranging in thickness from 1 - 5  $\mu\text{m}$  were deposited on fused silica substrates at 535°C. The films had very strong crystallographic texture with [100] normal to the plane of the film. Optical loss per unit thickness was lower for thicker films suggesting that interfacial effects dominated losses. Very large electro-optic effects were observed in a number of the films. Birefringent shifts were measured by phase retardation in transmission mode with an electric field applied in the plane of the film using interdigitated electrodes. Birefringent shift varied quadratically with applied field and showed little hysteresis with R coefficients as high as  $5 \times 10^{-16} (\text{m/V})^2$ . The strength of the electro-optic effect is attributed to the high degree of crystallinity of the films and the a-axis orientation.

## INTRODUCTION

Ferroelectric materials have been the subject of numerous investigations for the past 50 years [1,2]. More recently, thin films have received attention for applications where bulk materials are difficult to integrate into microscopic structures [3]. Of the numerous ferroelectric materials,  $(\text{Pb},\text{La})(\text{Zr},\text{Ti})\text{O}_3$  or PLZT, is known to possess superior electro-optic effects. PLZT films have been deposited by a variety of methods, including RF sputtering [4-9], ion-beam sputtering [10,11], metal-organic decomposition [12-14], sol-gel processes [10,15], laser ablation [16] and metalorganic chemical vapor deposition (MOCVD) [17,18].

Of these thin film deposition process, MOCVD offers significant advantages in terms of high deposition rates, conformality, and scaling to large area deposition. Given the present state of the art in bulk and thin film materials, effective devices such as spatial light modulators (SLMs) will likely require an electro-optic film of approximately 10 microns in thickness [19,20]. Such thicknesses lie on the "thick" end of the thin film spectrum, beyond the practical limit for most thin film processes but within the capability of MOCVD. MOCVD is widely recognized as the process of choice for large area deposition and generally can be scaled to large areas. For the deposition of PLZT and other complex oxides, the liquid delivery technique used here allows excellent composition control [21,22] in an MOCVD process compared to traditional techniques involving the use of bubblers. In recent efforts to deposit  $\text{BaSrTiO}_3$  on 150 mm wafers, we have achieved run-to-run repeatability ( $1\sigma$ ) of 0.24 at% Ba, 0.18 at% Sr and 0.26 at% Ti. Target composition for the material was: 35 at% Ba, 15 at% Sr, 50 at% Ti.

The objective of the present work was to investigate electro-optic effects in thick x/0/100 type PLZT films (PLT) produced by MOCVD. (The notation x/y/1-y corresponds to the formula  $\text{Pb}_{1-x}\text{La}_x\text{Zr}_y\text{Ti}_{1-y}\text{O}_3$ . For example, a film with the composition 70/0/100 contains 3.5 at% La relative to the other metal elements.) PLT films typically crystallize into the perovskite phase more easily than Zr containing compositions, and have been used for this reason as seed layers below PLZT [9]. Inexpensive silica substrates were chosen for two reasons. First, they will be useful in several applications, such as hybrid transmissive or reflective SLMs, as well as optical waveguides. Second, the integration of electro-optic materials into devices with Si drive electronics will require barrier layers [23] to prevent diffusion of Pb into the active circuitry. In practice, such barriers will likely be amorphous oxides.

## EXPERIMENTAL PROCEDURE

Film deposition was performed in an inverted vertical reactor with the walls heated to approximately 200 °C to prevent condensation of the precursors. A two inch diameter SiC susceptor was heated by a high intensity lamp to 750°C. The surface temperature of the substrate was approximately 535°C as measured by a fine gauge thermocouple cemented to the surface of a calibration substrate. The liquid delivery technique was used to create the precursor gas stream. Solid precursors dissolved in a solvent were delivered into a vaporization zone by a liquid pump [24]. We have chosen bis- Pb ( $\text{Pb}(\text{thd})_2$ ), tris-tetramethylheptadionato La ( $\text{La}(\text{thd})_3$ ), and bis-isopropionate, bis-tetramethylheptadionato Ti ( $\text{Ti}(\text{OiPr})_2(\text{thd})_2$ ) as precursors for PLT deposition because they are stable with respect to ligand exchange in both the solution and the gas stream. Also,  $\text{Pb}(\text{thd})_2$  has the benefit of low room temperature volatility, in contrast to alkyl Pb ( $(\text{C}_2\text{H}_5)_4\text{Pb}$ ), which makes it comparatively safe to handle. Film growth was carried out in an oxidizing atmosphere of  $\text{O}_2/\text{N}_2\text{O}$  at reduced pressure of ~ 2 torr, controlled by a gate valve on the vacuum pump. Typical deposition parameters are listed in Table 1. Films of various compositions were produced by mixing precursor solutions of different compositions.

**Table 1.** MOCVD deposition parameters for PLT. Molar delivery rates are typical, but were varied from run-to-run to change the composition of the film.

Substrate temperature	535°C
Total reactor pressure	2.1 torr
Reactor wall temperature	>200°C
Reagent manifold temperature	220°C
Pb flow (typical)	28 $\mu\text{moles/min}$
La flow "	10 $\mu\text{moles/min}$
Ti flow "	59 $\mu\text{moles/min}$
Ar flow through precursor manifold	110 sccm
$\text{O}_2$ flow	450 sccm
$\text{N}_2\text{O}$ flow	450 sccm
Deposition rate	1.3 $\mu\text{m/hr}$

Films deposited by MOCVD were characterized for composition, crystallinity, optical transmission, and electro-optic response. Composition was measured with a Rigaku 3613 wavelength dispersive XRF wafer analyzer. Crystallinity was determined by x-ray diffraction using a Rigaku Dmax system in a Bragg-Brentano geometry ( $\Theta-2\Theta$ ) with  $\text{CuK}\alpha$  radiation and a monochromator. Optical properties were determined by UV-Vis spectrophotometry and FTIR. Electro-optic response was determined in selected films with the system shown in Figure 1, which uses crossed polarizers to convert polarization modulation into amplitude modulation. A transverse geometry was used, with Pt/Ti interdigitated electrodes (6  $\mu\text{m}$  in width separated by 6  $\mu\text{m}$ ) evaporated onto the films through a photolithographic mask. Intensity modulation of an incident He-Ne laser ( $\lambda = 632.8 \text{ nm}$ ) source as a function of square wave electric field step height was measured with the use of a lock-in amplifier. Prior to quantitative measurements, the system was calibrated with a well characterized bulk PLZT ceramic electro-optic element.

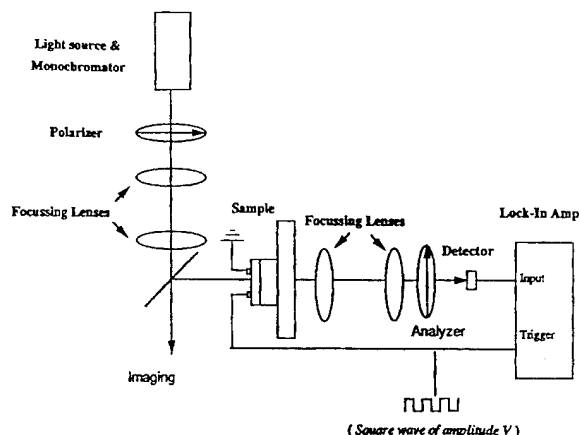


Figure 1. System used to measure electro-optic response in PLT films. The electric field was applied in the transverse geometry with interdigitated electrodes.  $\lambda = 633 \text{ nm}$ .

## RESULTS AND DISCUSSION

Desired film compositions were chosen according to the stoichiometric formula  $\text{Pb}_{1-x}\text{La}_x\text{Ti}_{1-x}/4\text{O}_3$ , which assumes B-site vacancy charge balance of  $\text{La}^{+3}$  substitution for  $\text{Pb}^{+2}$  [13]. The relationship of film composition to precursor solution composition is shown in Figure 2. Note that the relationship of film composition to precursor solution composition behaves similarly across the phase diagram in the vicinity of stoichiometric PLT and that a wide range of compositions from 7/0/100 to 32/0/100 was easily accessible in a series of deposition runs indicated by the numbers in the figure.

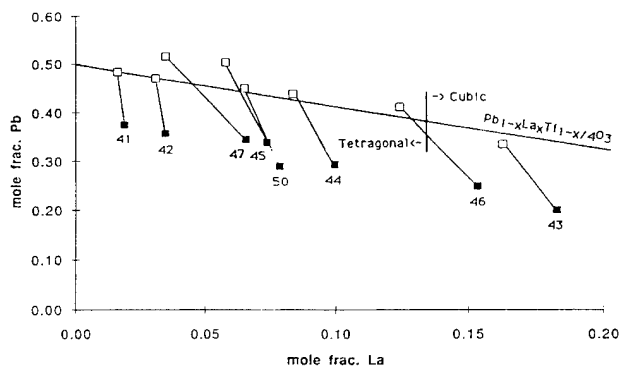


Figure 2. Relationship of film composition to precursor solution composition. Open symbols represent film composition, filled symbols represent solution composition. The inclined line represents stoichiometric PLT compositions. The sum of mole fractions of the Pb, La, and Ti = 1.0.

The deposition conditions resulted in dense, single phase perovskite films with grain sizes of approximately  $500\text{\AA}$  as calculated from the (200) peak width in x-ray diffraction patterns using the Scherrer formula. A typical diffraction pattern, shown in Figure 3, reveals a highly oriented film with the [100] direction perpendicular to the plane of the film. The [001] orientation was typically absent from the diffraction patterns. Given that the compositions of most films studied were below the tetragonal/cubic phase boundary (28/0/100), this means that the optic axis (c-axis) of the tetragonal crystallites lies within the plane of the film. Orientation within the plane of the film is likely random given the lack of a crystallographic template in the amorphous substrate. We suggest that the large mismatch in the coefficient of thermal expansion (CTE) for PLT ( $6.6 - 9.8 \text{ ppm}/^\circ\text{C}$ ) [10] and the silica substrate ( $\sim 2 \text{ ppm}/^\circ\text{C}$ ) is responsible for the high degree of out of plane orientation. Films with La contents greater than 26/0/100 (46 and 43 in Figure 2) showed cracking when deposited on silica. Cracking was exacerbated by the stress-thickness product in

the case of  $5 \mu\text{m}$  films deposited on silica. This effect was mitigated by deposition on the borosilicate glass, which had a better CTE match with the PLT.

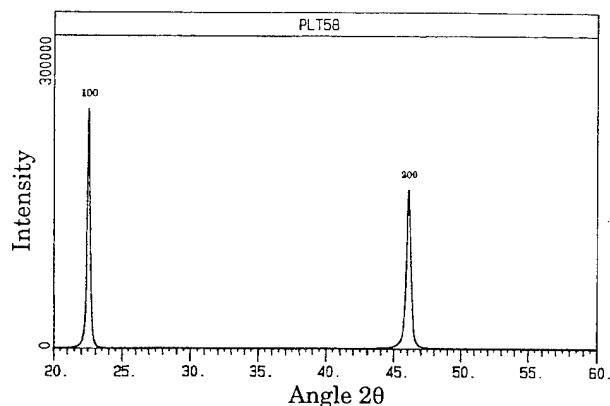


Figure 3. X-ray diffraction pattern from a  $5 \mu\text{m}$  thick 17/0/100 film deposited on fused silica. The absence of diffracted intensity from planes other than (100) and (200) indicates a highly [100] oriented film.

Representative UV-visible and IR spectra are shown in Figures 4 and 5 for a 17/0/100 film. Optical losses were low in the IR and were dominated by scatter losses in the visible regime. Scatter may be due to the PLT surface, which was somewhat rough as shown in the scanning electron micrograph in Figure 6. This is consistent with the fact that a  $5 \mu\text{m}$  film showed lower optical loss than a  $1 \mu\text{m}$  film than would be predicted by a linear dependence of loss on thickness. Another source of scatter may be at the PLT/ $\text{SiO}_2$  interface which underwent diffusion (see below). Further improvements are certainly possible in the area of transmission; MOCVD variables such as pressure and deposition rate could play a significant role in transparency and have yet to be investigated in detail.

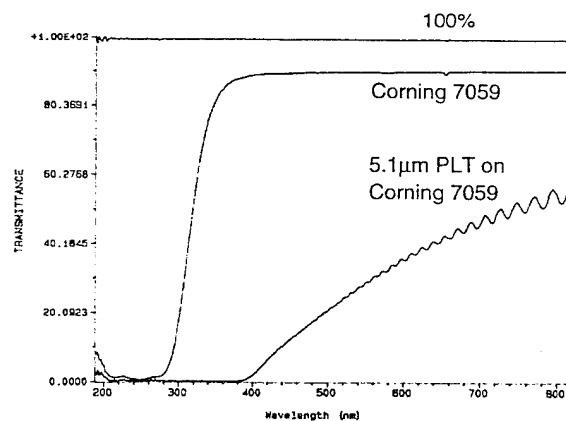


Figure 4. Spectral transmittance ( $\lambda = 180\text{--}820 \text{ nm}$ ) for a  $5.1 \mu\text{m}$  17/0/100 PLT film deposited by MOCVD on borosilicate glass in the UV-visible region.

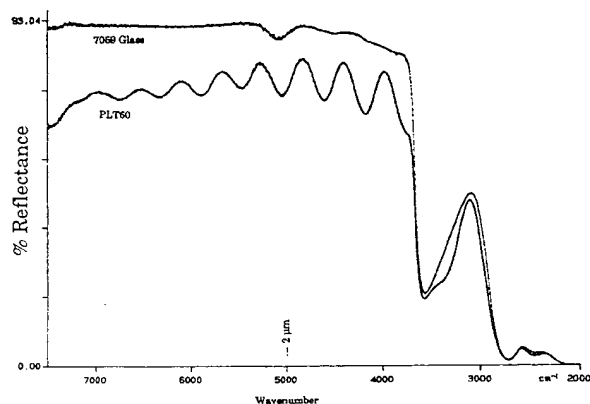


Figure 5. Spectral transmittance ( $\lambda = 1.3 - 20 \mu\text{m}$ ) for a  $5.1 \mu\text{m}$  17/0/100 PLT film deposited by MOCVD on borosilicate glass in the UV-visible region. Cut-off at approximately  $2.7 \mu\text{m}$  occurs due to the substrate.

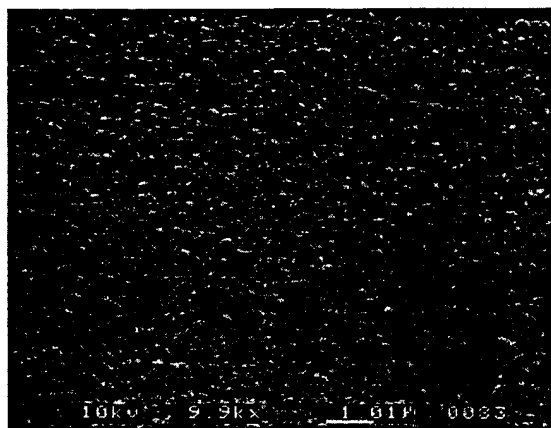


Figure 6. Scanning electron micrograph of a 17/0/100 film deposited by MOCVD at 2.1 torr total reactor pressure.

A large electro-optic response was found in a number of the films produced in this study. Quadratic electro-optic behavior with little hysteresis was observed in all cases. We found that poling the films using the same interdigitated electrodes had minimal effect on the response. This is in contrast to other reports [8] where films with La contents below 28/0/100 showed linear response after poling. At present, we do not have an explanation for the apparent disparity in results. The quadratic electro-optic coefficient ( $R$ ) was calculated from the observed change in transmitted intensity with applied field according to the following relationship:

$$R = C (\Delta I / t \Delta V^2) (d^2 \lambda / 2 \pi n^3)$$

where  $C$  = system constant,  $\Delta I$  = change in transmitted light intensity,  $t$  = film thickness,  $\Delta V$  = applied voltage (as squarewave),  $d$  = electrode spacing,  $\lambda$  = incident light wavelength,  $n$  = refractive index. Figure 7 shows the variation of birefringence with applied electric field for three different films of approximately  $1 \mu\text{m}$  thickness. These curves were calculated according to the relationship:

$$\Delta n = n^3 R E^2 / 2$$

where  $E$  = applied electric field. A refractive index of 2.5 was assumed in the calculations. One should note that small changes in  $n$  result in rather large changes in  $R$  due to the cubic dependence of  $R$  on  $n$ . Small errors in measured intensity are also possible. Therefore, these values should be considered accurate to approximately 25 %.

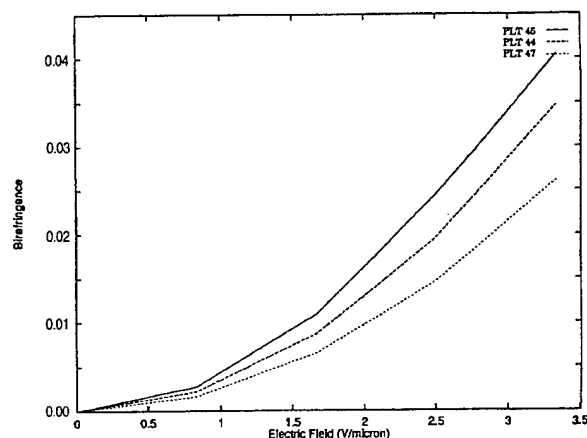


Figure 7. Birefringent shift versus applied electric field calculated from the experimentally measured  $R$  coefficients.

The variation of electro-optic coefficient with La content is shown in Figure 8. Here, we see a peak at approximately 12/0/100. All three films had rather large  $R$  coefficients for PLT [8,10] and similar values to those reported for 9/56/35 PLZT [9]. Large electro-optic response in PLT film is significant from the perspective that PLT is relatively easier to crystallize in the perovskite phase than PLZT and is a simpler system to control in a manufacturing environment. The strong electro-optic response of the films produced by MOCVD on silica is most likely related to a number of contributing factors. First, composition control is quite good. A SIMS depth profile taken through a 17/0/100 film is shown in Figure 9 which reveals that the film composition is unchanged throughout the thickness. This demonstrates the stability of the liquid delivery approach to MOCVD of complex oxides. Second, the films have high quality in terms of crystallographic orientation. Finally, and perhaps most importantly, the direction applied field was well aligned to the optic axis. While the in-plane orientation is likely random because of the amorphous substrate, the domain orientation is much more optimal than for a field applied through interdigitated electrodes on an [001] ( $c$ -axis) oriented film. The case of [111] oriented films, such as those produced on basal plane single crystal alumina represent an intermediate case.

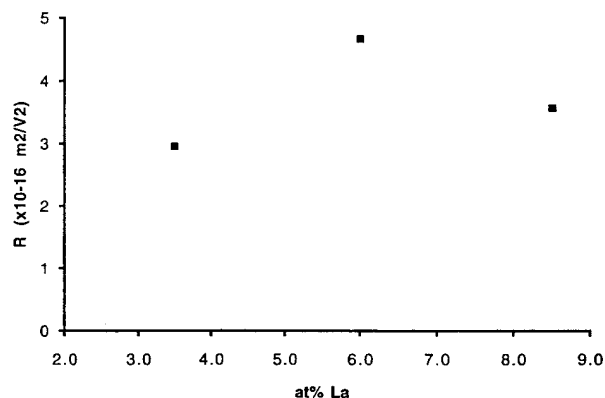


Figure 8. Variation of quadratic electro-optic coefficient with La content for films produced by MOCVD on fused silica substrates. Film thickness was approximately  $1 \mu\text{m}$ .

The SIMS analysis shows significant interdiffusion ( $\sim 1700 \text{\AA}$ ) at the PLT/SiO<sub>2</sub> interface. In addition, Si diffused throughout the bulk of the PLT film at approximately the 100 ppm level. This points out the need for diffusion barriers in this system as has been recently discussed by Brown, et.al. [23].

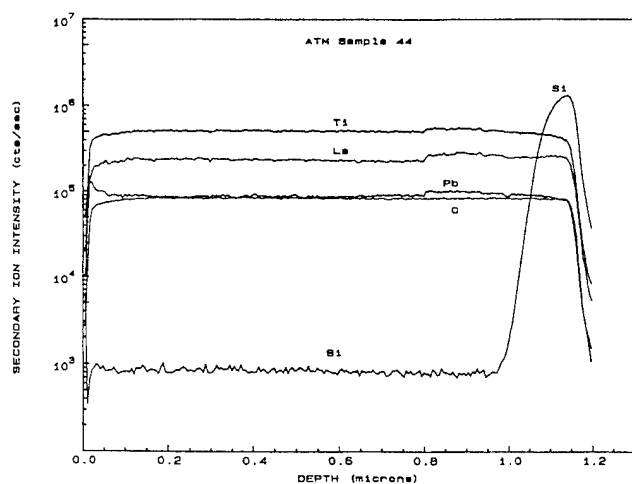


Figure 9. SIMS depth profile showing variation of composition as a function of depth in a 17/0/100 film. Uniform composition throughout the film results from a highly stable deposition process. (The small jump at  $\sim 0.8 \mu\text{m}$  occurred due to the start of a new SIMS acquisition.)

## CONCLUSIONS

High quality  $\text{PbLaTiO}_3$  films have been deposited by MOCVD using a liquid delivery approach. This approach affords a high degree of compositional control and flexibility. Highly oriented films were deposited on amorphous substrates with good optical transparency and strong quadratic electro-optic response. The quadratic electro-optic coefficient of the films in the range of 7/10/100 to 17/0/100 was found to reach a maximum value of  $R = 5 \text{ (m/V)}^2$  at 12/0/100.

## REFERENCES

- [1] Y. Xu, *Ferroelectric Materials and Their Applications*, New York: North-Holland, 1991.
- [2] B. Jaffe, W.R. Cook, Jr., and H. Jaffe, *Piezoelectric Ceramics*, New York: Academic Press, 1971.
- [3] G.H. Haertling, "Recent Developments in Bulk and Thin Film PLZT Materials and Devices," *Ferroelectrics*, vol. 131, 1992, pp. 1-12.
- [4] M. Ishida, H. Matsunami, and T. Tanaka, "Preparation and Properties of Ferroelectric PLZT Thin Films by RF Sputtering," *J. Appl. Phys.*, vol. 48, 1977, pp. 951.
- [5] M. Okuyama, T. Usuki, and Y. Hamakawa, "Epitaxial Growth of Ferroelectric PLZT Thin Film and their Optical Properties," *Appl. Phys.*, vol. 21, 1980, pp. 339-343.
- [6] T. Fukami, T. Sakuma, K. Tokunaga, H. Tsuchiya, "Ferroelectric Films Deposited by Reactive Sputtering and Their Properties," *Jap. J. Appl. Phys.*, vol. 22, Suppl. 22-2, 1983, pp. 18-21.
- [7] H. Adachi, T. Kawaguchi, M. Kitabatake, and K. Wasa, "Dielectric Properties of PLZT Epitaxial Thin Films," *Jap. J. Appl. Phys.*, vol. 22, Suppl. 22-2, 1983, pp. 11-13.
- [8] H. Adachi, T. Mitsuyu, O. Yamazaki, and K. Wasa, "Ferroelectric (Pb,La)(Zr, Ti) $\text{O}_3$  Epitaxial Thin Films on Sapphire Grown by rf-planar Magnetron Sputtering," *J. Appl. Phys.*, vol. 60, pp. 736-741, 1986.
- [9] H. Adachi and K. Wasa, "Basic Thin Film Process for Perovskite Ferroelectric Materials," *Mat. Res. Soc. Symp.*, vol. 200, pp. 103-114, 1990.
- [10] D.A. Tossell, J.S. Obhi, N.M. Shorrocks, A. Patel, and R.W. Whatmore, "Pyroelectric and Electro-optic Properties of Sol-gel and Dual Ion Beam Sputtered PLZT Thin Films," *Proceedings of the 8th ISAF*, 1992, pp. 11-18.
- [11] G.R. Fox and S.B. Krupanidhi, "Nonlinear Electrical Properties of Lead-Lanthanum-Titanate Thin Films Deposited by Multi-Ion-Beam Reactive Sputtering," *J. Appl. Phys.*, vol. 74, 1993, pp. 1949-1959.
- [12] K.D. Preston and G.H. Haertling, "Comparison of Electro-optic Lead-Lanthanum Zirconate Titanate Films on Crystalline and Glass Substrates," *Appl. Phys. Lett.*, vol. 60, 1992, pp. 2831-2833.
- [13] A.R. Khan, I.K. Yoo, and S.B. Desu, "Preparation and Characterization of Lead Lanthanum Titanate Thin Films by Metalorganic Decomposition," *Proceedings of the 8th Int. Symp. Applications of Ferroelectrics*, 1992, pp. 412-415.
- [14] R.W. Vest and J. Xu, "Preparation and Properties of PLZT Films from Metallo-organic Precursors," *Ferroelectrics*, vol. 93, 1989, pp. 21-29.
- [15] T. Tani and D.A. Payne, "Lead Oxide Coatings on Sol-Gel Derived Lead Lanthanum Zirconium Titanate Thin Layers for Enhanced Crystallization into the Perovskite Structure," *J. Am. Ceram. Soc.*, vol. 77, 1994, pp. 1242-1248.
- [16] D.H. Reitze, E. Haton, R. Ramesh, S. Etemad, D.E. Leaird, and T. Sands, "Electro-optic Properties of Single Crystalline Ferroelectric Thin Films," *Appl. Phys. Lett.*, vol. 63, 1993, pp. 596-598.
- [17] K. Tominaga, M. Miyajima, Y. Sakashita, H. Segawa, and M. Okada, "Preparation of c-axis Oriented PLT Thin Films by the Metalorganic Chemical Vapor Deposition Method," *Jap. J. Appl. Phys.*, vol. 29, 1990, pp. L1874-L1876.
- [18] P.C. Van Buskirk, J.F. Roeder, S. Bilodeau, S. Pombrik, and H. Beratan, "Chemical Vapor Deposition of  $\text{Pb}_{1-x}\text{La}_x\text{TiO}_3$ ," to be published in *Proceedings of ISIF'94*, 1994.
- [19] S. Krishnakumar, V.H. Ozguz, C. Fan, C. Cozzolino, S.C. Esener, and S.H. Lee, "Deposition and Characterization of Thin Ferroelectric Lead Lanthanum Zirconate Titanate (PLZT) Films on Sapphire for Spatial Light Modulator Applications," *IEEE Trans. Ultra., Ferro., and Freq. Control*, vol. 38, 1991, pp. 585-590.
- [20] A. Ersen, S. Krishnakumar, V. Ozguz, J. Wang, C. Fan, S. Esener, and S.H. Lee, "Design Issues and Development of Monolithic Silicon/Lead Lanthanum Zirconate titanate Integrated Technologies for Smart Spatial Light Modulators," *Appl. Optics*, vol. 31, 1992, pp. 3950-3965.
- [21] P.C. Van Buskirk, R. Gardiner, P.S. Kirlin, and S.B. Krupanidhi, "MOCVD growth of  $\text{BaTiO}_3$  in an 8" single wafer CVD system," *Proceedings of the 8th Int. Symp. Applications of Ferroelectrics*, 1992, pp. 340-343.
- [22] P. Kirlin, S. Bilodeau, and P. Van Buskirk, "MOCVD of  $\text{BaSrTiO}_3$  for ULSI DRAMs," to be published in *Proceedings of ISIF'94*, 1994.
- [23] R.E. Jones, P.D. Maniar, A.C. Campbell, R. Moazzami, J.L. Dupuie, R.B. Gregory, M.L. Kottke, M.L. Bozak, J.R. Williams and J.M. Ferrero, "Materials Interactions in the Integration of PZT Ferroelectric Capacitors," to be published in *Integrated Ferroelectrics*.
- [24] R.A. Gardiner, P.C. Van Buskirk, and P.S. Kirlin, "Liquid Delivery of Low Volatility MOCVD Precursors," to be published in *Proceedings of the Fall MRS Conference*, 1993.

## ACKNOWLEDGMENTS

The authors would like to thank Steven Novak of Evans East for the SIMS analysis. This work was sponsored by DOD through Wright Laboratories, Eglin AFB, under contract F08630-93-C-36.

# Concurrent Session - 6A: Pyroelectrics

# PbTiO<sub>3</sub> Thin Films For Pyroelectric Detection

A. Bell, Y. Huang, M. Kohli, O. Paul\* P. Ryser† and M. Forster†

Laboratoire de Céramique, EPFL, 1015 Lausanne, Switzerland

\*Physical Electronics Laboratory, ETH, Zürich, Switzerland

†Cerberus AG, Männedorf, Switzerland

**Abstract** — Due to its high pyroelectric coefficient, low permittivity and relatively low piezoelectric coefficients, lead titanate is an important candidate for use in pyroelectric detectors. Sol-gel processing of lead titanate thin films, in combination with micro-machining of silicon substrates, is being used for the development of low-cost infra-red detectors with properties equivalent to existing "bulk" or single crystal devices. Here we report on some aspects of the sol-gel chemistry, the optimisation of the pyroelectric figure of merit and the fabrication and characterisation of an infra-red detector, consisting of two pyroelectric elements on a micro-machined SiO<sub>2</sub>-Si<sub>3</sub>N<sub>4</sub> membrane.

## INTRODUCTION

The pyroelectric effect is well established for the detection of long wavelength infra-red radiation, as simple personnel and flame detectors, or in arrays for imaging applications [1]. Current fabrication technology for the majority of commercial devices employs ceramic plates (thickness  $\approx 50\mu\text{m}$ ), which are cut, lapped and polished from bulk ceramics. They are either diced to form discrete sensors, or reticulated to form imaging arrays. In either case, to maintain high responsivity and/or resolution, high thermal impedance mountings and interconnections are required. A number of advantages are foreseen in the use of ferroelectric thin films on semiconductor or ceramic substrates for pyroelectric detection. On the one hand, micro-machining of the substrate allows tailoring of thermal impedances to maintain high sensitivity [2 & 3] and on the other, the integration of read-out electronics may reduce noise and allow an increase in the complexity of the imaging systems.

In the "point" detector sector of the market, the currently dominant issue is that of cost. For these devices, although an increase in the voltage responsivity through the use of thin film technology may be attractive, for commercial viability it should be available at no extra, or preferably lower, cost. Moreover, the tendency of standardisation of device architectures, in keeping with second-sourcing policies, dictates that thin film-based detectors should have similar geometries to their "bulk" counterparts and be compatible with existing optics.

For point detection, the voltage per unit incident power or voltage responsivity ( $R_v$ ) is the most important device characteristic [1 & 4]. For a detector in series with a unity gain, high input impedance FET, of which the capacitance is negligible, it is given by:

$$R_v = \frac{pA\eta\omega R_g R_t}{\sqrt{(1 + \omega^2 \tau_c^2)(1 + \omega^2 \tau_t^2)}} \quad (1)$$

in which  $p$  is the pyroelectric coefficient,  $A$  is the area and  $\eta$  is the

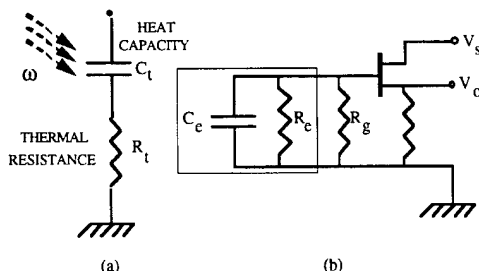


Figure 1. (a) Thermal and (b) electrical circuits of a pyroelectric detector.

emissivity of the active element;  $\omega$  is the angular modulation frequency of the input radiation. The electrical resistance of the detector is  $R_e$ , and is assumed to be much greater than that of a gate bias resistor,  $R_g$ , which, therefore, in combination with the electrical capacitance,  $C_e$ , defines the electrical time constant of the device,  $\tau_e (= R_g C_e)$ . Likewise, the thermal time constant,  $\tau_t$  is defined by the thermal capacitance of the sensor,  $C_t$ , and the thermal resistance to a constant temperature heat-sink,  $R_t$ . As can be seen from Figure 2, the maximum responsivity occurs at  $\omega_m = (\tau_t \tau_e)^{-0.5}$  with a value of

$$R_{vm} = \frac{pA\eta R_g R_t}{(\tau_e + \tau_t)} \quad (2)$$

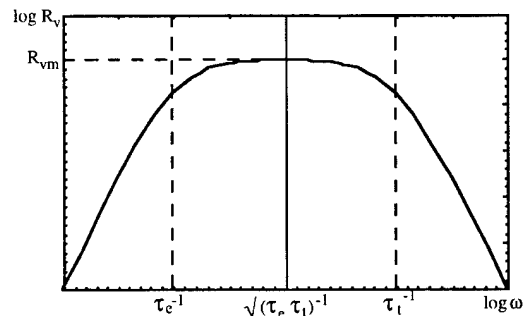


Figure 2. Theoretical voltage responsivity,  $R_v$ , of a pyroelectric detector as a function of radiation modulation frequency,  $\omega$ .

The modulation frequency of interest for the majority of point detectors is in the range 0.1 to 10 Hz. For most applications, the electrical and thermal time constants are adjusted to be approximately equal and at the lower limit of this range, giving  $R_v(\omega) \propto \omega^{-1}$ .

Thin film lead titanate (PbTiO<sub>3</sub>) has been reported by a number of authors to have suitable properties for pyroelectric detection due to its relatively high pyroelectric coefficient ( $p = 180 \mu\text{C m}^{-2} \text{K}^{-1}$ ) and low permittivity ( $\epsilon_r = 180$ ) [5], but is also favoured due to its comparative simplicity when employing relatively immature materials fabrication technologies. Highly c-axis oriented films for device applications have been deposited by r.f. sputtering with good epitaxy on single crystal MgO substrates with Pt electrodes [6]. A pyroelectric coefficient of over  $250 \mu\text{C m}^{-2} \text{K}^{-1}$  and a relative permittivity of 190 were obtained. Sol-gel techniques have also been used successfully to deposit PbTiO<sub>3</sub> films on silicon substrates with Pt electrodes [7 & 8], although with lesser degrees of preferred orientation than for sputtered films on MgO; values of the pyroelectric coefficient of  $140 \mu\text{C m}^{-2} \text{K}^{-1}$  and the relative permittivity of 150 are typical.

In view of the importance of keeping capital investment costs low when considering a replacement technology for low cost pyroelectric detection, the sol-gel approach is perhaps more promising than either sputtering or MOCVD. Hence, the motivation for the present study is to determine the feasibility of fabricating infra-red point detectors, from ferroelectric thin films on micro-machined substrates, by sol-gel deposition and simple back-side etching.

Here we report on some aspects of the sol-gel chemistry, the relationship between processing and pyroelectric properties, and the device design and characteristics.

The process chosen for the film deposition is similar to that reported by other authors [9], based upon the reaction of lead acetate and titanium isopropoxide as solutions in 2-methoxy ethanol (Figure 3). The exact process and assumed reaction sequence varies from author to author, particularly with respect to the species formed on refluxing lead acetate in 2-methoxy ethanol and the product of reaction between the titanium and lead precursors. The possible reactions in both cases have been modelled using the partial charge approach proposed by Livage [10] and the volatile products from each distillation step were analysed by gas chromatography; the results are summarised below.

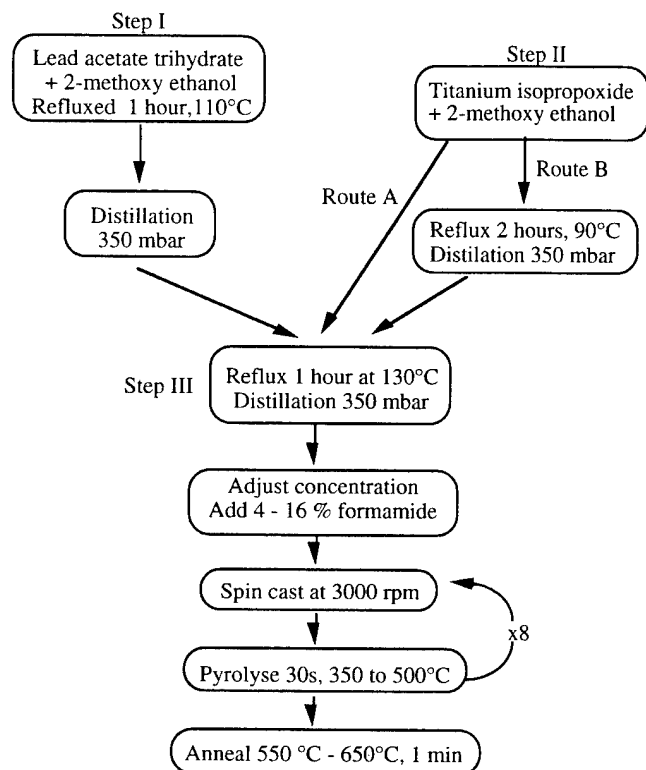
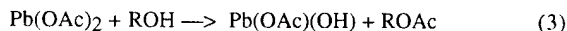


Figure 3. Sol-gel route for the preparation of lead titanate films.

The calculation of the partial charges assumed by particular chemical groups during reaction processes allows an assessment of the feasibility of each proposed reaction step, according to the sense of the partial charge of a departing group with respect to that of the remaining group. In the case of lead acetate  $[\text{Pb}(\text{CH}_3\text{COO})_2 \equiv \text{Pb}(\text{OAc})_2]$  in 2-methoxy ethanol, previous work had suggested the presence of a hydrated lead acetate methoxy ethoxide  $\text{Pb}(\text{OAc})_2 \cdot (\text{CH}_2\text{CH}_2\text{OCH}_3) \cdot x\text{H}_2\text{O}$  [11] or a basic lead acetate  $3\text{Pb}(\text{OAc})_2 \cdot \text{PbO} \cdot \text{H}_2\text{O}$  [12], after reflux. However, partial charge calculations suggest that the most likely reaction to occur is the formation of the 2-methoxy ethoxy acetate ester and a lead acetate hydroxide:



where  $\text{R} = \text{CH}_3\text{OCH}_2\text{CH}_2$ .

Analysis of the distillate from the reaction between lead acetate and 2-methoxy ethanol by gas chromatography has shown that between 0.1 and 0.2 moles of the ester per mole of lead acetate are produced, depending upon the concentration of lead acetate in the solvent. This is consistent with the partial charge calculations and suggests that the before the second step reaction, the lead precursor solution contains mainly lead acetate with 10 to 20 % lead acetate hydroxide.

The presence of this hydroxide may be of some importance to the next step in the process. Partial charge analysis of the subsequent reaction between lead and titanium solutions suggests that reaction between fully substituted titanium 2-methoxy ethoxide and lead acetate, to form a mixed metal species, is unlikely, however, reaction can occur

with the lead acetate hydroxide. Nevertheless, given the yields of the lead acetate hydrolysis, this process may be slow. On the other hand, the analysis reveals that reaction of lead acetate with partially substituted titanium alkoxides is far more probable, with a final product of  $(\text{RO})_3\text{TiOPb}(\text{OAc})$ .

Chromatography of the distillates from Step II/III indicate a greater quantity of ester is formed via Route A than via Route B, supporting the hypothesis that direct addition of the titanium isopropoxide, without any prior refluxing, to the lead precursor solution leads to a greater proportion of mixed metal species in the final solution. Consequently this route has been used for subsequent film preparation.

#### PROCESS - PROPERTY RELATIONSHIPS

A material figure of merit for voltage responsivity can be defined:  $p/(\epsilon_0 \epsilon_r)$ , where  $p$  is the pyroelectric coefficient,  $\epsilon_r$  is the relative permittivity and  $\epsilon_0$  the permittivity of free space. (Note the omission of the heat capacity of the pyroelectric material; its inclusion would be inappropriate for the case of thin films). It is expected that the pyroelectric coefficient should be highest and the relative permittivity should be lowest for films oriented with the [001] axis normal to the substrate. Hence the figure of merit should be related strongly to the preferred orientation exhibited by the films.

It has been reported that in order to obtain stoichiometric lead zirconate titanate (PZT) films, excess lead oxide is required to compensate for its evaporation during thermal treatment [13]. The work of Sato et al. [14], (Figure 4), in which final Pb/Ti ratios were measured by electron probe micro-analysis as a function of initial PbO excess and annealing temperature, imply that for lead titanate, the evaporation of PbO is not as great as in PZT. It appears that lead over-stoichiometry in lead titanate films tends towards self-correction, so that, independent of PbO excess up to 25%, annealing at 700°C for 1 minute results in stoichiometric films. Nevertheless, it is interesting to note the effects of PbO excess upon the film orientation and pyroelectric figure of merit.

For this study, the samples were those used as in the measurements of Figure 4 [14]. That is, films were prepared according to Figure 3, with appropriate amounts of excess lead acetate in Step I. A hot-plate was used for the pyrolysis steps between gel depositions and a rapid thermal processing furnace for the annealing step. X-ray diffraction analysis was carried out using a powder diffractometer. The preferred orientation was estimated using conventional symmetric  $\theta - 2\theta$  scans for the peaks  $h, k$  &  $l = 1$  or 0.

The function  $f_{hkl}$ ,

$$f_{hkl} = \frac{I_{hkl}}{I_{hkl}^s}, \quad (4)$$

$$f_{hkl} = \frac{1}{N} \sum_{hkl} \frac{I_{hkl}}{I_{hkl}^s}$$

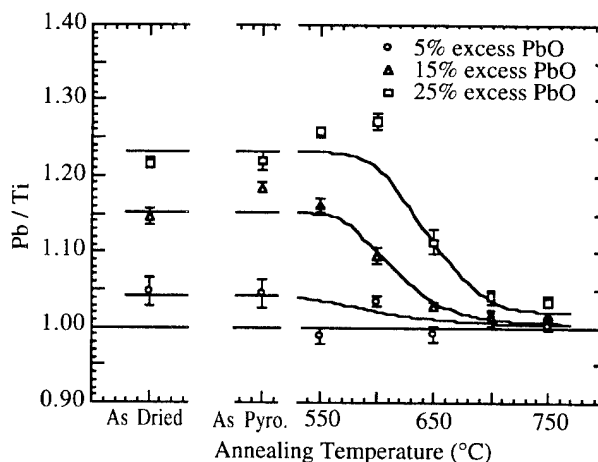


Figure 4. Pb/Ti ratio as measured by electron probe micro-analysis for as a function of annealing temperature.



Annealing temperature	600 °C				650 °C				700 °C		
Initial PbO excess	0	5	15	25	0	5	15	25	5	15	25
Final PbO excess		3.5 ±0.7	9.5±1.0	22±1.1		-1.0±1.1	2.9±0.6	11.3±1.6	1.3±1.1	1.5±0.7	4.2±0.9
$f_{001}$	0.93	1.88	1.53	2.95	0.21	0.65	1.70	2.52			
$f_{001} + f_{100}$	2.82	4.28	2.63	4.64	2.01	3.64	3.19	4.37			
$p / \mu\text{C m}^{-2} \text{ K}^{-1}$	73	68	63	49	45	131	96	60		105	
$\epsilon_r$ (1 kHz)	234	298	240	197	239	259	322	240		248	
$P/\epsilon_r / \text{kV m}^{-1} \text{ K}^{-1}$	35.0	26.0	29.4	28.2	21.5	57.6	33.9	28.2		47.4	

Table 1. Orientation and pyroelectric properties of PbTiO<sub>3</sub> films as a function of PbO excess and annealing temperature.

was used to express the relative importance of each of the orientations normal to the substrate, where the intensity of each  $[hkl]$  peak,  $I_{hkl}$ , is normalised, first by the equivalent relative intensity from the JCPDS standard for a random oriented polycrystalline sample,  $I_{hkl}^s$ , and then by the average of the normalised intensities,  $N$  being the number of peaks addressed. The maximum value of  $N$  for  $h, k$  &  $l = 1$  or  $0$ , is  $5$ , as is the maximum value for  $f_{hkl}$ . That is, a value of  $f_{001} = 5$  indicates a film in which all crystal planes oriented parallel to the substrate are associated with a normal  $[001]$  axis.

For the electrical measurements, a matrix of 0.5 mm diameter gold electrodes was deposited by sputtering. Measurements of capacitance and  $\tan \delta$  were carried out at 1 kHz. The pyroelectric coefficient was determined by applying a temperature modulation of amplitude 1°C and period 100 s to the sample whilst measuring the current with an electrometer. For a triangular wave temperature modulation, the pyroelectric coefficient can be calculated from the amplitude of the resulting current square wave. Films were measured both before and after poling by the application of 10 V for 10 minutes. The full characterisation of films annealed at 700°C was hindered by an increased incidence of short circuits.

The values of  $f_{hkl}$ , pyroelectric coefficient, relative permittivity and pyroelectric figure of merit are shown in Table 1 for 0 to 25% initial

PbO excess and annealing temperatures of 600 and 650°C for 1 minute. The pyrolysis temperature was 500°C. The final PbO excesses for the initially stoichiometric samples were not measured, but from the low values of pyroelectric coefficient and permittivity they are assumed to be slightly sub-stoichiometric. From the trends shown in Figure 4, the final PbO deficit is expected to be less than 5%; no free TiO<sub>2</sub> was observed in X-ray diffraction analyses of these samples.

In general, the  $[001]$  preferred orientation increases with increasing initial PbO excess, but decreases with increasing annealing temperature. However there is little correlation between the orientation and the electrical properties. Not surprisingly, the pyroelectric coefficient and the relative permittivity both increase as the final PbO excess approaches zero, as shown in Figures 5 and 6. However, the peak in permittivity occurs at around 2 to 3 % excess PbO, whilst that of the pyroelectric coefficient is nearer to the stoichiometric composition. The solid solubility of PbO in PbTiO<sub>3</sub> is practically zero, the excess PbO is thought to reside as discrete pockets or at grain boundaries. Thus, perhaps even at 1 kHz, there is a contribution to the permittivity from space charge effects associated with free PbO, which for small concentrations of excess PbO, offset the dilution of the permittivity.

The pyroelectric figure of merit is shown in Figure 7 and can be seen to peak close to the stoichiometric composition. The high permittivity

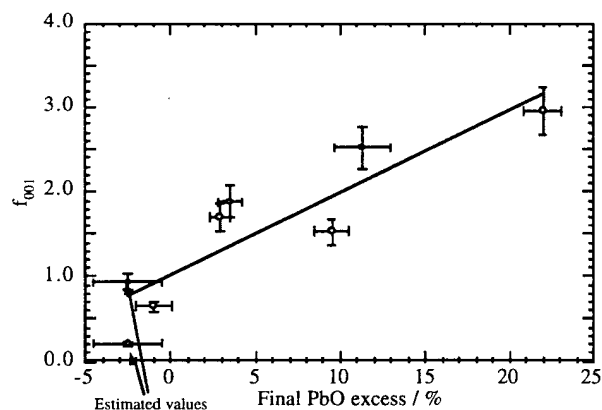


Figure 5. Preferred orientation as a function of final PbO excess.

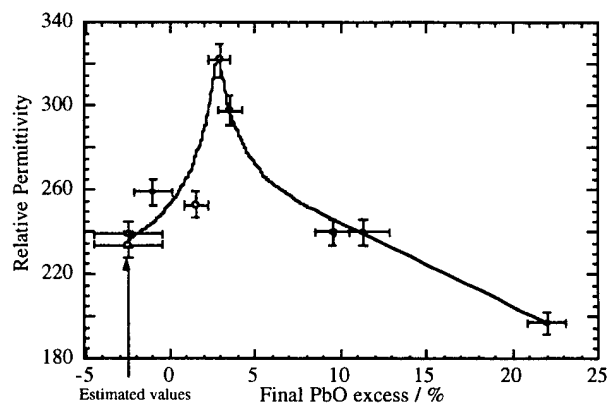


Figure 7. Relative permittivity as a function of final PbO excess.

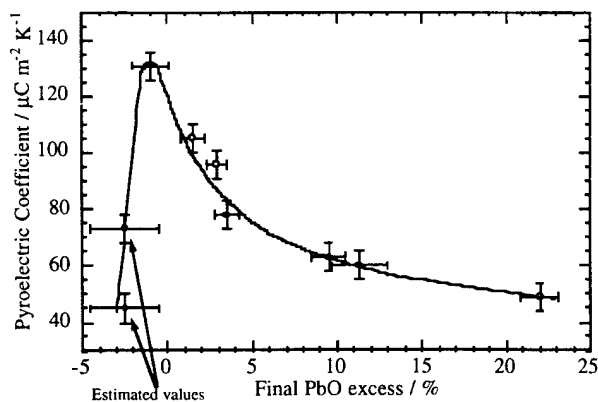


Figure 6. Pyroelectric coefficient as a function of final PbO excess.

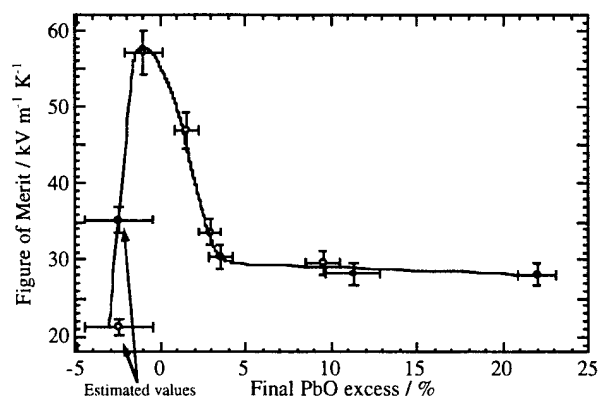


Figure 7. Figure of merit as a function of final PbO excess.

and low pyroelectric coefficient of the slightly over-stoichiometric samples combine to determine a rather narrow processing window in order to achieve the highest figure of merit. Optimisation within this window has produced figures of merit up to  $68 \text{ kV m}^{-1} \text{ K}^{-1}$ .

#### DEVICE FABRICATION

Device chips were designed to fit onto a standard TO5 header; this dictates the maximum chip size to be approximately  $5 \times 5 \text{ mm}$ . To form a dual element detector, compatible with standard I.R. detection optics, two active areas are defined, each with an aspect ratio of 2.6:1, as shown in Figure 8. The two elements have a common bottom electrode and are poled in the same sense with respect to the substrate. Within these constraints, devices of various membrane and element size have been fabricated.

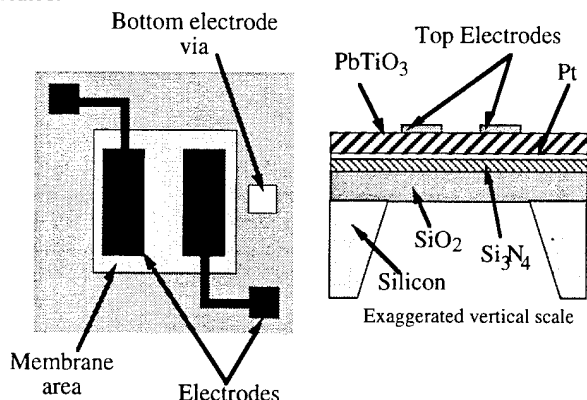


Figure 8. Dual element chip design; plan view and cross section.

The devices were prepared on standard, 4" diameter,  $300 \mu\text{m}$  thick, Si substrates as described previously [15]. To obtain mechanically stable membranes the difference in thermal expansion between the membrane and substrate must be minimised and adjusted to leave the membranes under a slight tensile stress at the completion of processing. This is achieved using composite membranes of  $6500 \text{ \AA}$   $\text{SiO}_2$  and  $2000 \text{ \AA}$   $\text{Si}_3\text{N}_4$ . On the front side of the wafers this bi-layer acts as the membrane, whilst at the backside it is patterned by standard photolithography and plasma etching to act as a mask during the subsequent silicon etching.

A continuous bottom electrode of  $1000 \text{ \AA}$  Pt on a  $100 \text{ \AA}$  Ta adhesion layer is deposited by sputter deposition. The  $\text{PbTiO}_3$  film is then deposited to a thickness of  $0.4 \mu\text{m}$ . Access to the bottom electrode, to facilitate poling, is made by etching vias using a 50% aqueous solution of HCl containing approximately 0.1 % HF. Infra-red absorbing top electrodes of nichrome are deposited by evaporation through a photo-resist mask. Finally, anisotropic etching of the backside of the devices is carried out in aqueous KOH solution (40 %) at  $60^\circ\text{C}$  for twenty hours, whilst protecting the front side. The resulting  $\text{SiO}_2/\text{Si}_3\text{N}_4$  membranes are  $0.7$  to  $0.8 \mu\text{m}$  thick, depending on etch time.

Devices were poled at room temperature for 10 minutes with  $-10 \text{ V}$  on the upper electrodes. The voltage response to a modulated heat source was measured as a function of modulation frequency. An example result is shown in Figure 9 for a  $1.56 \times 0.6 \text{ mm}$  active area on a  $3 \times 3 \text{ mm}$  membrane.

In comparison to conventional devices, the frequency response of the thin film-on-membrane device exhibits a plateau in responsivity around  $1 \text{ Hz}$ . This response is similar to that demonstrated for early prototypes of this structure [15] and can be explained in terms of a device with two thermal time constants. That is, at low frequencies there is sufficient time for the whole of the device, membrane and margin, to follow the heat flux modulation. The device therefore behaves like a conventional detector with a thermal time constant of  $> 10 \text{ s}$ . At higher frequencies, the membrane area can respond independent of the margin and the device behaves as though it has a much shorter time constant, which might be estimated from the result of Figure 9 to be in the range of  $0.3$  to  $1 \text{ second}$ . A more detailed model of the frequency response of as a function of device geometry is currently under development for comparison with experimental data.

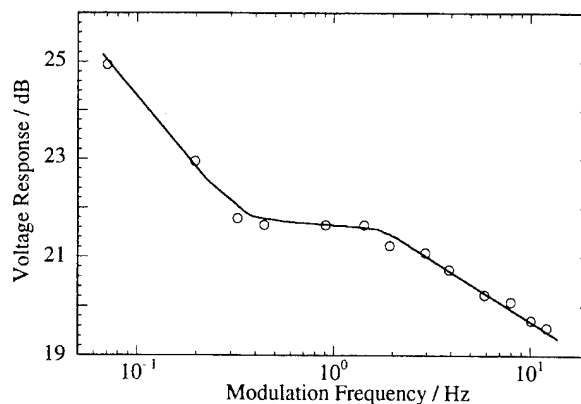


Figure 9. Voltage responsivity (arbitrary reference level) as a function of frequency for a single element.

#### CONCLUSIONS

The formation of the mixed metal species,  $(\text{RO})_3\text{TiOPb}(\text{OAc})$ , in the sol-gel preparation of  $\text{PbTiO}_3$ , is favoured by addition of unsubstituted titanium isopropoxide to the lead precursor and may be facilitated through the production of a lead acetate hydroxide in the reaction between lead acetate and 2-methoxy ethanol.

The pyroelectric figure of merit of  $\text{PbTiO}_3$  thin films is strongly dependent upon the Pb/Ti ratio of the films. It is suggested that a slight initial PbO excess is required to optimise the properties.

Thin film-on-membrane infra-red detectors, compatible with standard devices have been fabricated. Initial device geometries yield a frequency response which is thought to result from two thermal time constants, one for the chip as a whole and one for the membrane. The assumptions which lead to the derivation of Equation 1, are not valid for the device structures presently under study, and a new model for the responsivity is required.

**Acknowledgement.** This work was in part supported by the Swiss Priority Programme, LESIT.

#### REFERENCES

1. R.W. Whatmore, A. Patel, N.M. Shorrocks and F.W. Ainger, *Ferroelectrics* **104** 269 (1990)
2. S. Miyazaki, T. Kawai and M. Araragi, *Tech. Dig. 11th Sensor Symp.* p. 91 (1992)
3. C. Ye, T. Tamagawa and D. Polla, *J. Appl. Phys.* **70** 5538 (1991)
4. M.E. Lines and A. M. Glass, "Principles and Applications of Ferroelectrics and Related Materials" (Oxford Univ. Press, Oxford, 1977) p. 563
5. S. Ikegami, I. Ueda and T. Nagata *J. Acoust. Soc. Amer.* **50** 1060 (1971)
6. R. Takayama, Y. Tomita, K. Iijima and I. Ueda, *Ferroelectrics* **118** 325 (1991)
7. A. Patel, D.A. Tossel, N.M. Shorrocks, R.W. Whatmore and R. Watton, *Mat. Res. Soc. Symp. Proc.* **310** 53 (1993)
8. Y. Huang, M. Daglish, I. Reaney and A. Bell, *Third Euro-Ceramics* **2**, 699 (1993)
9. K.D. Budd, S.K. Dey and D.A. Payne, *Proc. Brit. Ceram. Soc.* **36** 107 (1985)
10. J. Livage and M. Henry, in *Ultrastructure Processing of Advanced Ceramics* p. 183, eds. J.D. Mackenzie and D.R. Ulrich, Wiley, New York (1988)
11. S. D. Ramamurthi, D.A. Payne, *J. Am. Ceram. Soc.* **73** 2547 (1990)
12. T.W. Dekleva, J.M. Hayes, L.E. Cross, *J. Am. Ceram. Soc.* **71** C280 (1988)
13. B.A. Tuttle, R.W. Schwartz, D.H. Doughty and J.A. Voigt, *Mat. Res. Soc. Symp. Proc.* **200**, 159 (1990).
14. E. Sato, Y. Huang, M. Kosec, A. Bell and N. Setter, submitted to *Appl. Phys. Lett.*
15. A. Bell, Y. Huang, O. Paul, Y. Nemirovsky and N. Setter, *Integ. Ferro.*, in press.

# Effect of Simultaneous Organic and Inorganic Dopants on the Characteristics of Triglycine Sulfate ( TGS ) Crystals

R. B. Lal, S. Etminan, and A. K. Batra  
Department of Physics  
Alabama A&M University  
Huntsville, AL 35762

**Abstract** - Effects of L-alanine + nickel and L-alanine + chromium are investigated on the dielectric and pyroelectric properties of TGS crystals. The crystals were grown by temperature lowering technique. Dielectric constant and pyroelectric coefficient measurements of these crystals are reported and compared with pure and L-alanine doped crystals. TGS crystals doped with chromium plus L-alanine and nickel plus L-alanine exhibit two to three times better materials figures of merit for pyroelectric infrared detectors over pure TGS crystals and L-alanine doped crystal. The Vicker's hardness of CrLATGS crystal was found to be two times of pure TGS crystals. Growth characteristics of these crystals are also presented.

## INTRODUCTION.

Triglycine sulfate (TGS) is one of the most studied ferroelectric materials. The interest in studying pure and doped TGS crystals has increased due to their promise in various devices for military system, astronomical telescopes, earth observation cameras, environmental analysis monitors, medical vidicons and Fourier Transform Infrared (FT-IR) instrumentation. These devices have many attributes such as low cost, low power requirements, a wide operating range of temperature and frequency, and room temperature operation compare to quantum detectors where low temperature cooling is required. Many efforts [1-2] have been made to improve the pyroelectric properties and growth of TGS crystals. It was found that substitution of small percentage of analine [3] introduced asymmetry in the hysteresis loop which gave the material a preferred poling direction, thus eliminating random poling of the material.

The objective of the present work is to investigate the effects of simultaneous doping of L-alanine and chromium and L-alanine and Nickel on the pyroelectric and dielectric properties and hardness of TGS crystals. Using these properties applicable figures of merit [1] are calculated for comparison over pure and L - alanine doped TGS crystals. Growth characteristics of these crystals are also presented in this paper.

## EXPERIMENTAL

Single crystal of pure and doped TGS crystals were grown from aqueous solution by temperature lowering technique using modified version of reciprocating crystallizer [4] . The amount of dopants were 15 mol % of L- alanine and 5000 ppm by weight of Nickel sulfate and Chromium sulfate respectively in the solution. The concentrate of Nickel and chromium ions was not quantitatively determined, however, incorporation of small amounts of impurities could be detected by indirect methods of dielectric and pyroelectric data. Saturated solution of TGS at 40°C were prepared using BDH Optran

grade crystalline powder. The growth solution containing required dopants was equilibrated in the crystallizer at 42°C for 48 hours. The temperature of the crystallizer was maintained at  $\pm 0.01^\circ\text{C}$ . The appropriate polyhedral TGS seed crystals were affixed to the seed holder with the Dow Corning silicone adhesive. The seed holder and seed crystals were preheated to 42°C before insertion into the growth cell. Seed crystals surface was allowed to dissolve slightly before the temperature was lowered to the correct saturation temperature and held there for 24 hours. Afterwards it was lowered at a programmed rate which increased from initial  $0.1^\circ\text{C}$  per day to  $0.3^\circ\text{C}$  per day. All the growth parameters were kept identical so as to balance out the effect of growth parameters on the properties of resulting crystals. After completion of the growth runs, the crystals were removed from solution and slowly cooled to room temperature to avoid any thermal shock. The growth data were then recorded. Transparent and high optical quality crystals were generally obtained. Thin slices of samples were cleaved perpendicular to b-axis of pure and doped crystals. These samples were lapped and polished using fine grit 5-3 micron alumina polishing paper and iso-propyl-alcohol as a lubricant. Silver electrodes were thermally evaporated onto major faces (010) of the crystal. A 1659 GenRad RLC bridge was used to measure the sample capacitance and dissipation factor during heating cycle. The pyroelectric current in these samples was measured by the direct method of Byer and Roundy [5]. The detailed calculation of electrical parameters are described elsewhere [6]. Vickers hardness was measured using a Leitz miniload machine with a load of 0.49N for a dwell time of 15s. Freshly cleaved and polished surfaces (010) were primarily tested.

## RESULTS

Table I describes the growth runs performed. The growth data of the crystals studied are given in Table II. It can be seen from Table II that growth yield is highest in the case of L-alanine doped crystal and lowest in case of chromium and L-alanine doped crystal. The axial velocity along [010] direction is twice as compared with [001] direction in all the crystals studied. The growth characteristics and habit of chromium doped crystals are quite different than pure TGS crystals [Fig.1]. Table III shows values obtained for dielectric constant and pyroelectric coefficients of these crystals. The calculated value of various figures of merit using above parameters are also presented in Table III. The values of dielectric constant and pyroelectric coefficient of pure TGS crystals are in good agreement with literature values. However, properties of TGS crystals vary widely in the literature because its physical properties depend on various factors,

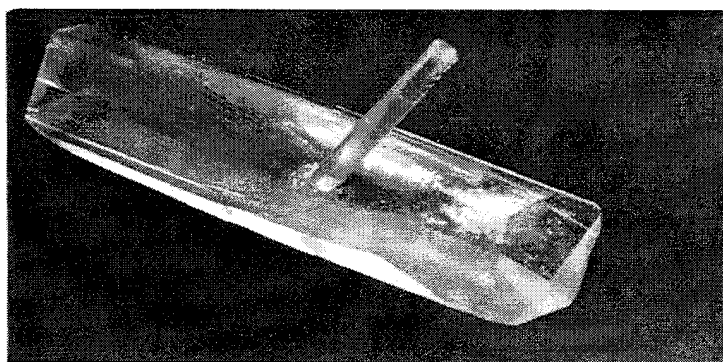


Fig.1. Habit of a CrLATGS crystal

Table I  
TGS Growth Runs Performed

Crystal	Concentration of L-alanine in the solution	Inorganic (I) dopant	Concentration of I-dopant in the solution (ppm)
TGS	-	-	-
LATGS	15 mol %	-	-
NiLATGS	15 mol %	NiSO <sub>4</sub>	5000
CrLATGS	15 mol %	Cr <sub>2</sub> (SO <sub>4</sub> ) <sub>3</sub>	5000

Table II  
Growth Data of TGS Crystals

Crystal	Yield (g/d/°C)	Growth (mm/°C/d)		Velocity V(010)/V(001)
		V(010)	V(001)	
TGS	0.170	0.88	0.340	2.58
LATGS	0.223	1.14	0.54	2.174
NiLATGS	0.0445	0.143	0.052	2.717
CrLATGS	0.042	1.0	0.50	2.0

Table III  
Materials Figures of Merit of Doped TGS crystals

Crystal	Temp (°C)	$F_i = P$ nC/cm <sup>2</sup> °C	$\epsilon'$	$F_v = p/\epsilon'$ nC/cm <sup>2</sup> °C	$F_{vid} = p/\sqrt{\epsilon'}$ nC/cm <sup>2</sup> °C	$F_D = p/\sqrt{\epsilon''}$ nC/cm <sup>2</sup> °C
TGS	35	45.0	70	0.64	5.4	52.3
	40	80.0	105	0.75	7.8	83.0
	45	160.0	250	0.64	10.0	152.6
LATGS	35	60.60	45	1.33	8.9	54.8
	40	94.40	60	1.57	12.2	99.5
	45	154.35	90	1.70	16.3	208.12
NiLATGS	35	82.50	51.6	1.60	11.46	213.0
	40	133.8	70.80	1.90	15.90	226.2
	45	186.2	104.10	1.80	18.30	240.4
CrLATGS	35	50.32	41.15	1.25	7.90	179.7
	40	86.90	54.9	1.60	11.74	299.6
	45	182.0	67.78	2.70	22.20	568.8

such as, growth conditions, history of the sample, method of measurement, and finally the growth pyramid from where the sample has been cut. It can be seen from Table III that pyroelectric coefficient of doped crystals is higher and dielectric constant is lower than pure TGS crystals which make them suitable for infrared devices. Furthermore, calculated figures of merit for doped crystals are higher than pure TGS crystals. NiLATGS and CrLATGS crystals have higher figure of merit than pure as well as LATGS crystals in the temperature range of 40°C-45°C. For high current responsivity ( $F_i$ ) NiLATGS based devices will be advantageous. For high voltage responsivity ( $F_v$ ) and detectivity ( $F_D$ ) NiLATGS and CrLATGS will be useful. However, actual use of the above crystals in infrared detectors or vidicons will determine if predicted improvement in signal to noise ratio is realized. LATGS crystals usually crack during polishing while CrLATGS and NiLATGS crystals do not. These crystals seem to be harder than pure TGS crystals. The Vicker's hardness number for CrLATGS crystal was  $188 \text{ gm } \mu\text{m}^{-2}$  where as pure TGS has a value of 89. The hardness of the other crystals will be reported later. This multiple doping technique seems to be useful for crack prevention and property enhancement in TGS crystals.

### CONCLUSION

It can be concluded that Chromium sulfate and Nickel sulfate plus L-alanine doped crystals are attractive for pyroelectric infrared detector applications because of high values of figures of merit and increased hardness as compared to pure and L-alanine doped crystals.

### ACKNOWLEDGEMENTS

The authors thank the National Aeronautics and Space Administration, Office of Commercial Programs, for the support of this work through grant no. 375-559-3 from the Consortium of Commercial Crystals Growth at Clarkson University, Potsdam, N.Y. We thank Jiann-Min Chang for hardness measurements.

### REFERENCES

- [1] R. B. Lal and A. K. Batra, "Growth and properties of triglycine sulfate(TGS) crystals:Review," *Ferroelectrics*, vol. 142, pp. 51-82 (1993).
- [2] Chang-Shui Fang and Ke-Cong Zhang, "Study of modified TGS crystals," *Ferroelectrics*, vol. 142, pp. 93-98 (1993).
- [3] P. J. Lock, "Doped triglycine sulfate for pyroelectric applications", *Appl. Phy. Letters*, vol 19, 390-1(1971).
- [4] M. D. Aggarwal and R. B. Lal, "A simple low cost reciprocating crystallizer for solution growth," *Rev. Sci. Instru.*, vol. 54(6), pp. 772-773 (1983).
- [5] R. L. Byer and C. B. Roundy, "Pyroelectric coefficient direct measurement technique and applications to a nanosecond response time detector", *Ferroelectrics*, vol.3, pp. 333-8 (1972).
- [6] Saeed Etminan, "Growth and characteristics of modified triglycine sulfate (TGS) crystals," *M.S. thesis*, Al. A&M University, Normal, Al. (1992).

# Pyrotransistor - GaAs FET With a "Pyroelectric Wafer" Gate

Y.M.Poplavko, V.A.Moskalyuk, A.I.Timofeyev and Y.V.Prokopenko

Kiev Polytechnic Institute, 37 Peremogi Ave, 252056 Kiev, Ukraine

**Abstract.** The multifunction properties of GaAs and other III-V semi-insulating crystals can be expanded by the artificial decreasing of their electric response symmetry that could be transformed from piezo- into a pyroelectric class. An artificial pyroelectricity of III-V type semiconductors can form a basis for one-crystal pyroelectric sensors. The voltage sensitivity of GaAs (111)-cut corresponds to one of PZT pyroelectric ceramics so the GaAs wafer could be used as thermal-to-electric transducer in a new microelectronic device named "pyrotransistor" that is uncooled far infrared detector based on MESFET technology.

## Introduction

The current tendency for modern night vision system's development is the increase of sensor elements number in the receiving matrix (focal plane array). This permits to get rid of optico-mechanical scanning unit and reduces the requirements to sensor element sensitivity because the response is accumulated at all frame duration. The essential feature of such elements is quite uniformity so the sensitivity of each separate elements should differ no more than 0.1%. Such uniformity is possible to realize with the application of the modern microelectronic processing. However, far infrared semiconductor sensors use photoconduction and need cooling.

Modern uncooled sensors are based on pyroelectric effect in some polar dielectrics. Pyroelectric ceramics is possible to integrate with semiconductor by microelectronic technology [1]. But the main problem of pyroelectric integrated sensor is to provide negligible thermal contact between pyroelectric transducer and high thermally conductive silicon wafer. So such arrays really need complicated system of packaging. Moreover, the rigid bound of several materials with sharp distinction between their chemical and thermal properties poses problems for technology. For example, as water-soluble pyroelectric-champion TGS so crystals of LiTaO<sub>3</sub>-type are difficult to integrate with semiconductor matrix processor. Moreover, all pyroelectric cells of such hybrid type "pyroprocessor" have different sensitivity so the effect from this matrix fall short of its ideal.

The possibility exists to use the artificial pyroelectricity in III-V polar semiconductors in order to apply the potentialities of microelectronics for one-crystal thermal imaging [2]. In the proposed case the GaAs-type wafer is a pyroelectric transducer itself while amplifiers and other microelectronics is no more than very thin epitaxial layers with an ultra low thermal mass.

## III-V Crystals Polar Properties

Gallium arsenide type crystals, in the first place, are semiconductors and, secondly, they are not pyro- but piezoelectrics. Nevertheless, it will be shown from here on how to get artificial pyroelectric response from piezoelectric of GaAs symmetry.

Piezoelectric and all the more pyroelectric properties of semiconductors have usually been out of consideration because of charge carriers screening effect. But in this work *charge generation process* is ignored so the term *charge separation* [3] has to be used. By this means semiconductor lattice is considered as dielectric and the only electric polarization should be taken into account. This is well represented by semi-insulating GaAs but largely for its solid solutions with AlP.

As a matter of fact, polar properties of GaAs type crystals was taken into account for charge carriers mobility and at the sacrifice of this polarity Gunn effect has been supposed. The goal to be sought is to transform the passive i-GaAs wafer into an active thermal-to-electric energy transducer. It is known that only the crystals of pyroelectric symmetry is operable as such transducers while GaAs type crystal are nothing more than piezoelectric.

Pyroelectricity is based on the spontaneous polarization  $P_s$  temperature dependence (the primary pyroeffect). The symmetry requires pyroelectric crystal to have unique polar axis which direction coincides with  $P_s$ . It is important that pyroelectric coefficient  $p_1$  includes also secondary coefficient from piezoelectrically transformed thermal strains. Only 10 from 20 piezoelectric classes of crystals allow pyroelectricity (primary and secondary). Others 10 piezoelectric classes show "latent" polar structure that is self-compensated if crystals are stress-free. But polarity manifests itself over a very wide limits: thermal conductivity of polar crystals is much less than non-polar ones and their thermal expansion coefficient passes through zero at low temperatures (at 60 K for GaAs) instead of showing  $T^3$ -dependence). Polar crystal microwave fundamental (lattice) absorption is vastly superior ones of central symmetric crystal and shows the low-temperature maximum of quasi-Debye type. Etching of (111)-GaAs plate depends crucially on "+" and "-" faces just as in pyroelectric crystals. At last, the growing GaAs crystal can swim in its melt just as the ice in the water because the arrangement of crystal polar bonds expands the material.

Recently it has been originally shown that uniform thermal influence induces pyroelectric response in all 20 piezoelectric classes of crystals if they are partially clamped [4]. In the case being considered the GaAs unit cell possesses an octupole-type latent polarity which has to be totally compensated because of its four 3-fold polar axes are crossing at angle of 109.5°. But the self-compensation could be artificially broken due to a partial limitation of strains under the special boundary conditions.

## Thermomechanically induced response

Thin GaAs crystal plate of (111)-cut shows a longitudinal piezoeffect  $P_3 = e_{33} x_3$  where "3" is [111]-axis and transverse piezoeffect  $P_3 = (e_{31} + e_{32}) x_3$ . The sum of piezoelectric coefficients  $e_{31} + e_{32} + e_{33} = 0$  so any scalar influence totally compensates each other if crystal is

free to expand. This compensation is shown on Fig.1b for GaAs crystal thermal treatment: piezoelectric contribution from the longitudinal strain component  $x_3 = a \Delta T$  is compensated by two transverse components  $x_1 = x_2 = -a \Delta T$ . If the last ones are forbidden by planar clamping the polarization  $P_3 = e_{33} \cdot a \cdot \Delta T$  will imitate "pyroelectricity" ( $a$  is thermal expansion coefficient). So the used effect is equivalent to the secondary pyroelectric effect that is inherent to pyroelectrics but previously unknown in piezoelectrics.

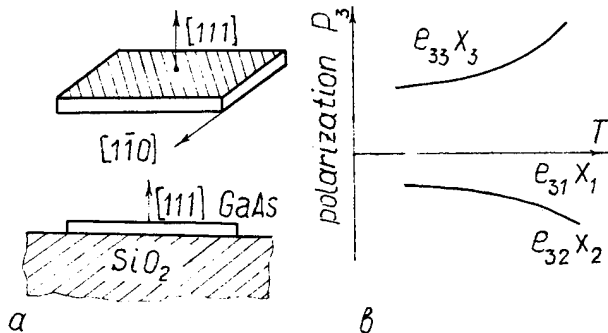


Fig.1. Thermal treatment of semi-insulating GaAs thin plate cemented on silica (a); thermal strains produce polarization (b).

Any variation of  $P_3$  with the temperature produces in GaAs artificial pyrocoefficient:

$$p_3 = dP/dt = 2\sqrt{3} d_{14} a / (4 S_{11} + 8 S_{12} + S_{44}),$$

where  $d_{14}$  is piezoelectric constant and  $S_{mn}$  is elastic compliance. It is evident that (111)-cut shows a maximum of effect. The angle dependence of  $p$  in the spherical coordinates is:

$$p(\theta, \varphi) = p_3 \sin 2\theta \sin \theta \sin 2\varphi$$

where  $\theta$  is the angle deflection from  $[111] = 3$  axis and  $\varphi$  is azimuth.

In our "static" experiments thin GaAs plate was cemented to hard substrate (fused silica in Fig.1a) with low thermal expansion coefficient. This is convenient for performing measurements but for device application the finned structure (produced by special etching) is sufficient to provide planar strains limitation. For the same purpose wafer-transducer could be compressed in its plane bounded by a rigid ring. In any case, only thermally induced thickness strain should be permitted and just in the direction of  $[111]$  type polar axis.

It was obtained that GaAs "pyrocoefficient" is  $1.5 \cdot 10^{-10} \text{ } \mu\text{C}/\text{m}^2\text{K}$  with the voltage sensitivity  $S_v = 0.02 \text{ m}^2\text{C}^{-1}$ . Our investigations show that some of III-V semiconductors that is capable to form solid solutions with GaAs have these parameters 10 times more. Above all, they are much closer to dielectrics than semi-insulating GaAs.

#### Construction of Pyrotransistor

GaAs type artificial "pyrotransducer" integrated with FET amplifier can be basis of a new microelectronic device named "pyrotransistor". The last one consists of MESFET with submicron channel that can be realized out of thin epitaxial layer deposited onto (111)-cut wafer operating as a "pyrogate".

Infrared radiation could be absorbed as by a special IR-absorbent covering the back side of wafer so due to internal IR absorption of wafer

(that could be explained by III-V crystal polar lattice and by its imperfections and doping).

The first method is usually used in the pyroelectric detectors based on the ferroelectric materials with the very high IR reflection and large near-surface IR absorption. Thermal diffusion from IR-absorbent to pyroelectric bounds operation speed. As applied to semi-insulating GaAs, the modulating frequency about 1 KHz is required at which the temperature wave length in GaAs wafer is about  $100 \mu\text{m}$ . The more thick wafer could not essentially increase the "pyroelectric" response.

The occasion of internal absorption seems to be more interesting because it is inherent to the III-V type crystals only that are semi-transparent for infrared radiation. Thermal-to-electric response could be got directly in the crystal lattice without any delay while MESFET is also capable to rapid operation with pulses rise about  $10^{-11}\text{s}$ . So the inertialess is one of the advantages of new device.

In GaAs and related crystals the absorption and transparency may be "resonant" in the range over 8-14 microns but an enlightenment layer is desirable in order to decrease IR reflection. Fig.2 shows the reflection coefficient for the  $100 \mu\text{m}$  wafer thickness near  $10 \mu\text{m}$  wavelengths as a function of GaAs dielectric absorption  $K''$ . The last depends on doping and can be controlled. At increased absorption the IR reflection is rather small but the only close-to-surface part of the wafer can work as transducer. In the opposite case IR radiation is absorbed in all bulk wafer while the reflection gains resonant character, Fig.2. The reflection coefficient passes through minimum and increases thereafter. The device with internal absorption could be applied for a very fast IR pulses measurements.

Modulation frequency of IR-radiation in the III-V crystal "pyrodetector" depends on the equilibrium concentration of charge carriers. In the standard ( $10^{-9} \text{ Ohm}^{-1}\text{m}^{-1}$  conductivity) semi-insulating GaAs the screening of pyroelectric field is overlooked at the modulation frequency 1 KHz. In some GaAs-III-V solid solutions this frequency would be reduced to 20 Hz.

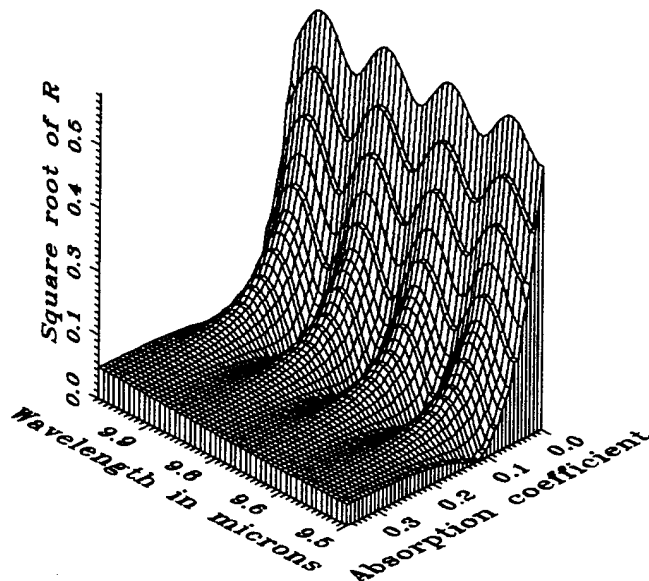


Fig.2 IR reflection coefficient modulus versus IR wavelength and GaAs crystal absorption coefficient ( $K''$  is the imaging part of complex dielectric permittivity).

The MESFET discussed below contains a high-level doped epitaxial layer deposited onto semi-insulated wafer-substrate, Fig.3. The submicron MESFET conducting channel is located near the boundary: epitaxial layer - substrate that is in the vicinity of potential energy minimum. The last is formed by the back-biased Schottky barrier and by the contact potential barrier from substrate. The response  $E_p$  is capable to change the potential barrier height and shape.

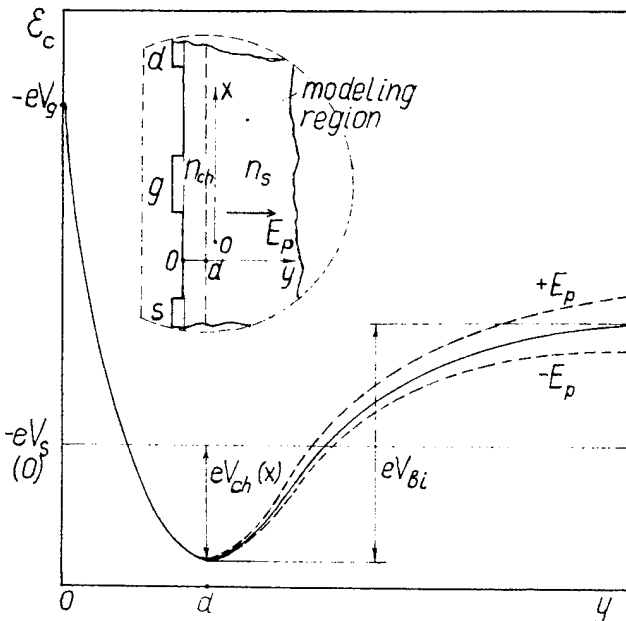


Fig.3. The shape of potential in the under-gate vicinity of channel: s - source, g - gate, d - epitaxial layer thickness,  $E_p$  - pyroelectric field.

Produced by the charge carriers diffusion into semi-insulating substrate from channel, the enrichment layer plays a crucial role in source-drain (S-D) conductivity if the channel length is less than  $1 \mu m$ . It is in short channel MESFET where S-D conductivity is strongly dependent on substrate potential due to the variations of the enrichment layer thickness. The last could be controlled by the wafer internal electric field  $E_p$ . Moreover, this field changes channel length that in its turn also controls a MESFET drain current.

Quasi two dimensional kinetic model [5] and the Monte-Carlo method [6] were used for MESFET pyrotransistor simulation. In the course of modelling of short-channel structure the main peculiarities of submicron device were accounted. Those are: drift speed overshoot, the substrate shunting influence and electrogradient effects. Some processes in the interface layer are also connected with the injection of charge carriers and their redistribution between channel and substrate. Simulation predicts that realization of submicron field structure pyrotransistor is possible with following main parameters:  $0.5 \mu m$  distance between drain and source electrodes;  $0.2 \times 500 \mu m$  gate size;  $0.06 \mu m$  thickness of epitaxial layer that has  $4 \cdot 10^{17} cm^{-3}$  doping level;  $100 \mu m$  thickness of substrate-wafer with a  $2 \cdot 10^{14} cm^{-3}$  doping level. This structure is possible to arrange over  $50 \times 50 \mu m^2$  crystal area in a meander type design. Simulations show the most profitable drain current control could be got near the threshold region of MESFET characteristics (if the gate potential is close to the pinch-off voltage). This mode of operation provides also the least noise factor of MESFET.

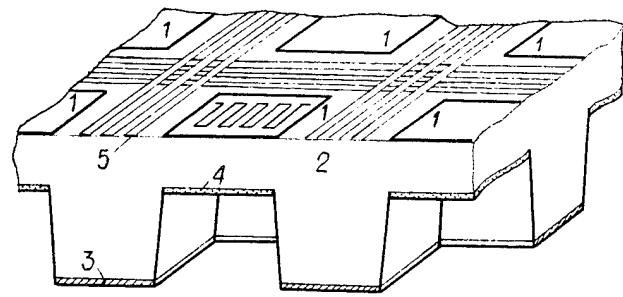


Fig.4. Detector cell in the crystal array:

1 - schematized MESFET, 2 - substrate (wafer), 3 - metallized ridges, 4 - absorbent layer in the valley, 5 - readout circuits.

As a result the wafer heating on  $0.1 K$  leads to drain current change in  $40 \mu A$  at gate potential  $V_g = 0 V$ . At the gate potential  $V_g = -1 V$  the change of drain current is  $50 \mu A$ .

Fig.4 shows the topology of "single cell-element" and its environment in form of valleys and ridges. Produced by the etching, a stepwise back-face of wafer is required to the partial clamping realization. The finned design provides IR reflection from metallized ridges and practically full absorption of valleys covered by IR-absorbent layer or by enlightenment layer if the wafer absorption is intrinsic. Each valley is an under-MESFET "pyroelectric" region.

#### Conclusion

Planar strain limitation in the [111]-cut of III-V type of semi-insulating crystals opens up possibilities for new type of microelectronic sensor that is uncooled and one-crystal array. The last has advantages as over semiconductor photonic arrays that need cooling so over pyroelectric ones produced by hybrid processing.

Hundreds of pyrotransistors on the same wafer would form matrix thermal image processor which sensitivity increases as square root from cells number. The current status of microelectronics can guarantee the identity of each cell in this one-crystal.

#### References

- [1] R. Watton, "Ferroelectric materials and IR bolometer arrays: from hybrid arrays towards integration", *Integrated Ferroelectrics*, vol.4, pp.175-186, 1994.
- [2] Y.M. Poplavko and L.P. Pereverzeva, "Artificial pyroelectricity in GaAs", *Journ. Tech. Fiziki (Russian)*, vol.62, pp.93-98, 1992.
- [3] L.B. Schein, P.J. Cressman and L.E. Cross, "Electrostatic measurements of tertiary pyroelectricity in partially clamped  $LiNbO_3$ ", *Ferroelectrics*, vol.22, pp.945-948, 1979.
- [4] Y.M. Poplavko and L.P. Pereverzeva, "Pyroelectricity of partially clamped piezoelectrics", *Ferroelectrics*, vol.130, pp. 361-366, 1992.
- [5] V.A. Moskalyuk and V.I. Timofeyev, "The simulation of electronic processes in channel and substrate of submicron field effect transistor", *Electronic technique, Microwave electronics*, No 2(426), pp.22-27, 1990.
- [6] V.V. Minakov, V.A. Moskalyuk and V. Timofeyev, "Submicron field effect analyses of some transistor models for adaptive designs", *Izvest. vuzov USSR, Radioelectronica*, vol.30, pp.64-72, 1988.



Concurrent Session -  
2E: Thin Films

# Antiferroelectric/Ferroelectric Composite Thin Films

D. E. Dausch, F. Wang and G. H. Haertling  
Gilbert C. Robinson Department of Ceramic Engineering  
Clemson University, Clemson, SC 29634-0907

**Abstract:** PLZT-based antiferroelectric (AFE) / ferroelectric (FE) composite thin films were fabricated by automatic spin coating and crystallized by rapid thermal processing. A computer-controlled automatic spin coat reactor was used to spin composite thin films from acetate precursors with successive layers of FE and AFE composition. Films were spun on platinum-coated silicon substrates and rapid thermal thermally processed at 700°C. Composite thin films exhibited improved AFE-type properties including increased dielectric constant (K) and saturation polarization ( $P_{\text{sat}}$ ) and decreased FE switching field ( $E_F$ ) compared to typical AFE compositions. X-ray diffraction results indicated that the composite thin films consisted of distinct AFE and FE phases. Modeling of the dielectric properties revealed linear series capacitor behavior within the composite thin films for low electric field conditions; however, nonlinear effects were apparent at high electric fields.

## INTRODUCTION

Because of their numerous unique properties and characteristics, PLZT ferroelectric materials have created new opportunities for the utilization of electronic ceramics. Few ferroelectric systems boast such wide ranging usefulness including electrooptic, piezoelectric, electrostrictive, pyroelectric and dielectric applications. In fact, the extent of their applicability is not completely known, as new compositions and modifications of the PLZT system are continually studied. The search for new materials with unique and improved properties will always persist.

One approach to the design of new electronic ceramics is to devise composite materials with alternate layers or mixing of different materials. Several investigations on bulk electronic ceramic composites have been reported. Shrout et al. [1] fabricated an antiferroelectric/ferroelectric composite by tape casting successive layers of soft ferroelectric PZT with antiferroelectric Sn-modified PSZT materials. This device yielded higher dielectric stability at high fields than conventional hard ferroelectrics. By stacking layers of compositions with positive and negative temperature coefficients, i.e. PMN and PMN-PT, respectively, composite resonators were fabricated with average values of temperature coefficients for more temperature stability [2]. PZT/PNZT multilayer composites fabricated by tape casting stabilized the temperature dependence of frequency constant and pyroelectric current [3]. Furukawa et al. [4] developed multilayer relaxor/BaTiO<sub>3</sub> capacitor composites with alternating layers of low- and high- Curie temperature dielectrics to meet X7R-type capacitor specifications.

It is clear that the production of composite bulk ceramics for electronic devices has been beneficial; however, this technique has yet to be applied to thin film devices. Similar advances in thin film technology could be attained by producing composite thin film materials. In this study, multilayer thin film structures consisting of antiferroelectric (AFE) PbZrO<sub>3</sub> and ferroelectric (FE) PLZT were fabricated by automatic spin coating and characterized. Dielectric properties and P-E hysteresis loops were examined along with the composite film structure from x-ray diffraction. Modeling of the dielectric properties according to a linear series capacitor model was also performed. These composite thin films could produce AFE-type materials with more desirable properties for thin film device applications.

## EXPERIMENTAL PROCEDURE

### Processing

Ferroelectric PLZT 2/55/45 (La/Zr/Ti), antiferroelectric PbZrO<sub>3</sub> (0/100/0) and composite AFE/FE thin films consisting of these compositions were spun on Pt-coated Si substrates using an automatic spin coat reactor [5]. In a single deposition chamber, this computer controlled spin coater contains an automatic fluid dispense system and rapid thermal processing unit with an in-situ laser ellipsometer for thickness measurement. Since the spin coater is capable of depositing one of three precursor stock solutions, composite thin films can be easily manufactured without reconfiguration of the spin coater or removal of the sample from the deposition chamber.

Deposited precursor solution was derived from liquid acetate precursors consisting of lead subacetate (mixed into liquid form with methanol and acetic acid), lanthanum acetate, zirconium acetate and titanium acetyl acetonate with methanol and water [6]. All of the thin films were spun at 2000 rpm for 30 seconds and rapid thermally processed at 700°C for 2 minutes per layer for 10 layers. A 5 minute rapid thermal post-anneal was also employed to ensure high quality films. For the 10 layer composite films, an initial deposition of  $x$  FE layers was followed by  $10-x$  AFE layers. Identification of these composites was denoted by  $F(x)A(10-x)$ . Pure AFE and FE thin films were also fabricated for modeling of the composite films.

The advantages of using RTP for the processing of FE thin films have previously been discussed [5,7]. Because of these benefits, rapid heating was chosen for the FE layers in composite thin films in order to optimize thin film properties; however, fast heating rates of at least 70°C per second for AFE layers caused thermal shocking during the AFE-to-FE phase transition in these layers resulting in rough film surfaces and poor electric properties. Hence, slower heating rates of approximately 25-30°C per second were necessary for AFE layer heat treatment and post-anneals. Variable heating rates were programmable in the rapid thermal processing unit of the automatic spin coater.

### Measurement

Evaporated Cu electrodes (1 mm diameter) were deposited for measurement of the dielectric and hysteresis loop properties of the thin films. Thin film capacitance was measured at 1 kHz using a Leader LCR meter with a 1 V ac signal and from 100 Hz to 40 MHz using a Hewlett-Packard 4194A impedance analyzer with a 100 mV ac signal. Capacitance was also measured as a function of dc bias at 1 kHz on the impedance analyzer. Hysteresis loops were measured using a Sawyer-Tower circuit with digital oscilloscope output at 1 kHz using an ac signal of  $\pm 40-45$  V. Total film thickness, measured before electrode deposition on the laser ellipsometer ( $\lambda=632.8$  nm) and a Tencor profilometer, was approximately 0.9 to 1.0  $\mu\text{m}$ . X-ray diffraction was performed on a Scintag XDS 2000 diffractometer using Cu-K $\alpha$  radiation.

### Composite Film Structure

X-ray diffraction was performed on the pure FE, AFE and composite thin films in order to reveal any macroscopic structural interaction between the FE and AFE layers of the composite materials. Figure 1 displays the x-ray diffraction pattern of an F5A5 composite film. As shown, distinct AFE and FE phases were the only phases evident in the diffraction pattern; furthermore, the d-spacings of the AFE and FE composite film peaks were equal to the d-spacings in the films of pure AFE and FE compositions, respectively. This result indicated that there was no large-scale interdiffusion between the AFE and FE layers since no intermediate phase or diffuse boundary with shifted d-spacings was detected. In addition, the residual strain caused by lattice mismatch between layers was negligible since the d-spacings in the composite films were unchanged from their pure component counterparts.

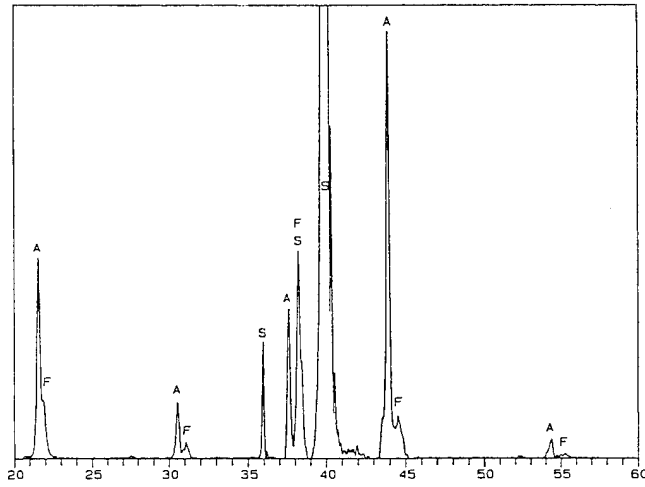


Figure 1. X-ray diffraction pattern of an F5A5 composite thin film. F = ferroelectric phase, A = antiferroelectric phase and S = substrate peak.

### Dielectric Properties and Modeling

The dielectric properties of the composite films were modeled according to an equivalent circuit of linear series capacitors based on the pure AFE and FE films. This type of analysis has been performed on bulk ceramic composites [1,2]. Experimental virgin and poled effective dielectric constants ( $K_{vir}$  and  $K_{pol}$ ) of the composite films measured at 1 kHz and 1 Vac are shown in Figure 2. The composite films which still maintained AFE-type double hysteresis loop behavior possessed poled dielectric constants ranging from 220 in the F2A8 film to as high as 376 for F7A3 compared to 174 in the pure AFE. As discussed in the next section, the F8A2 film possessed a FE-type single hysteresis loop. Effective dielectric constants were calculated based on pure AFE and FE film behavior from the expression

$$K_{eff} = \frac{K_A K_F t_{tot}}{K_F t_A + K_A t_F} \quad (1)$$

where the A and F subscripts denote AFE and FE layer dielectric constants and thicknesses and  $t_{tot}$  is the total thickness of the composite. Equation (1) was derived assuming constant electrode area. General agreement was found between the experimental and modeled results.

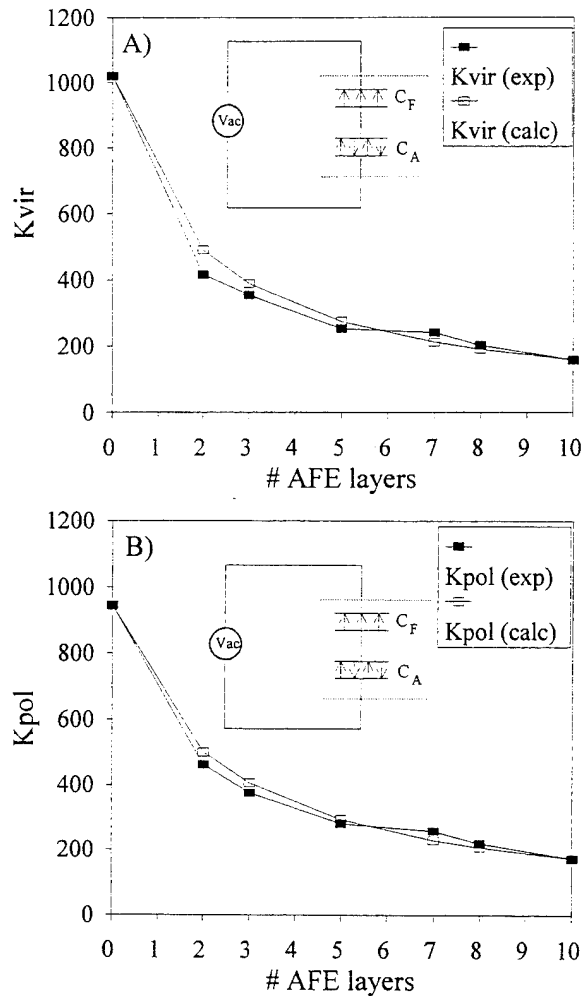


Figure 2. A) Virgin and B) poled effective dielectric constants of the composite thin films. Experimental (exp) results were measured at 1 kHz with a 1 V ac signal. The calculated (calc) results displayed were based on the linear series capacitor model shown.

Figure 3 displays the experimental  $K_{eff}$  of the F5A5 composite measured over a frequency range of 100 Hz to 40 MHz with a 100 mV ac signal. Typical ferroelectric thin film behavior was revealed with a dielectric relaxation at approximately 1 MHz [8]. Once again, agreement was exhibited between the experimental and modeled composite film results. The correspondence of the experimental results with these models suggested that at low ac voltage levels the composite films indeed behaved as series combinations of AFE and FE linear capacitors.

Disparity in this model did, however, occur when a dc bias was applied. Figure 4 shows  $K_{eff}$  for the pure AFE and FE films, the experimental composite films and the calculated composite film models as a function of increasing dc bias at 1 kHz using a 100 mV ac signal. In this case, the linear series capacitor model did not correspond with experimental results under high bias field conditions. Ferroelectrics are known to exhibit nonlinear domain switching at high electric fields [9]. Not only did the ferroelectric polarization behave nonlinearly within each composite layer as shown by the pure components, but the electric field distribution across the composite films varied nonlinearly as the total dc bias increased. Because of its lower dielectric constant, most of the total voltage was initially distributed across the AFE layer creating a higher internal electric field on the AFE layer than the average field applied on the total composite material. In this respect, the composite films could be considered voltage dividers with nonlinear

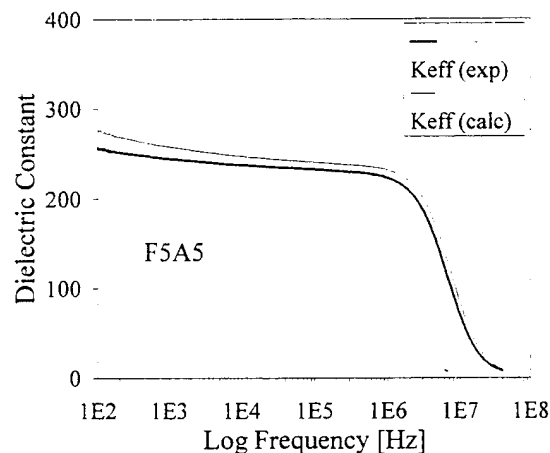


Figure 3. Effective experimental (exp) dielectric constant of the F5A5 composite measured with a 100 mV ac signal. Calculated (calc) results were based on the linear series capacitor model.

electric field distributions across the AFE and FE layers. As shown in Figure 4, the dielectric peaks at the AFE-to-FE phase transitions in the composite films were shifted to lower voltages compared to the series model predictions because of this nonlinear field distribution on the AFE layer. Modeling of these nonlinear effects is still in progress.

#### P-E Hysteresis Loop Data

As shown in Figure 4, the dielectric peaks became more intense in the composite films than the series capacitor model predicted. This was consistent with the hysteresis loops shown in Figure 5, where  $E_F$  continually decreased and the double hysteresis loops became more square with increasing number of ferroelectric layers in the composites. Figure 6 also displays this decrease in  $E_F$  and an increase in  $P_{sat}$ . Shrout et al. [1] suggested that in an AFE/FE composite, the voltage initially builds across the AFE layer and prevents switching of the FE layer. Once the AFE-to-FE phase transition field is reached, the domains in the FE layer are allowed to switch. This behavior was believed to occur in the composite thin films and, as discussed previously, caused a reduction in the average FE switching field  $E_F$  of the composite. Furthermore, the presence of the FE layer in the composite films increased the overall polarization of the material once  $E_F$  was reached, resulting in more square double hysteresis loops and increased  $P_{sat}$ .  $E_F$  ranging from 298 kV/cm (30 V/ $\mu$ m) for the F3A7 film to as low as 215 kV/cm (22 V/ $\mu$ m) for the F7A3 film were obtained with  $P_{sat}$  values between 35 and 38  $\mu$ C/cm<sup>2</sup>. Pure AFE properties were 330 kV/cm (33 V/ $\mu$ m) and 20  $\mu$ C/cm<sup>2</sup>, respectively.

As shown in Figure 6,  $P_{sat}$  values seemed to plateau between the F3A7 and F8A2 composites, and  $E_F$  continually decreased after the F2A8 composite in which  $E_F$  was 330 kV/cm, the same as for the pure AFE film. Widening of the center or low field portion of the double hysteresis loops was observed with increasing number of FE layers until the F8A2 composite revealed a single hysteresis loop similar to the pure FE film. This increased  $P_{sat}$  and decreased  $E_F$  should be beneficial for device application. Typically, pure AFE PbZrO<sub>3</sub> possesses a high AFE-to-FE transition field making it a less desirable composition for thin film device application; however, the use of composite films with improved AFE properties will make the application of AFE materials for electronic devices more feasible.

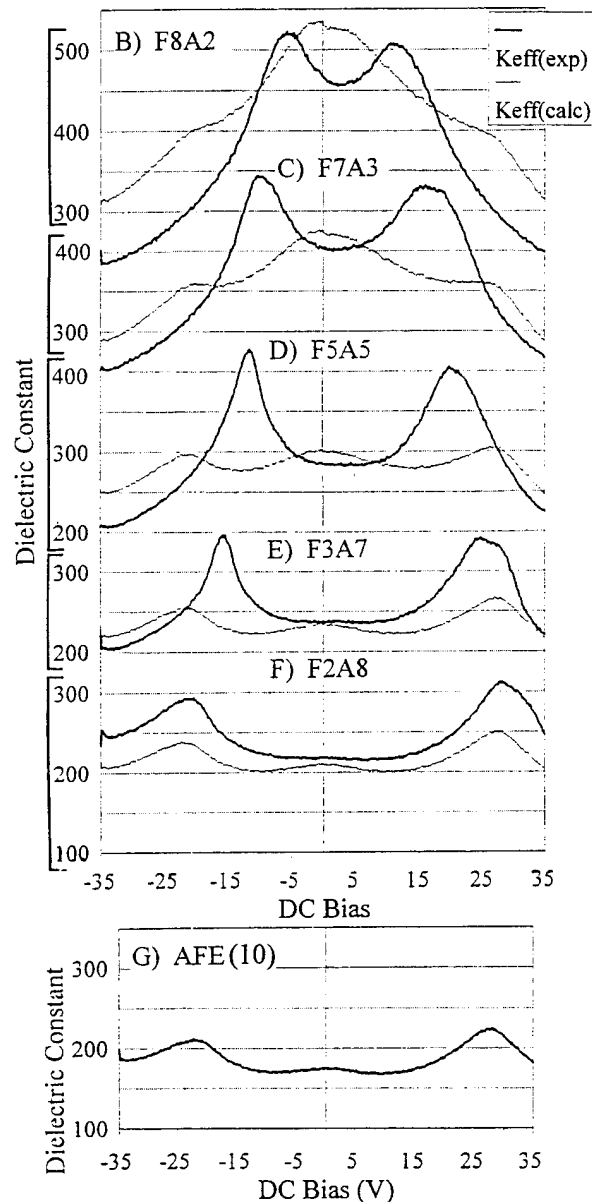
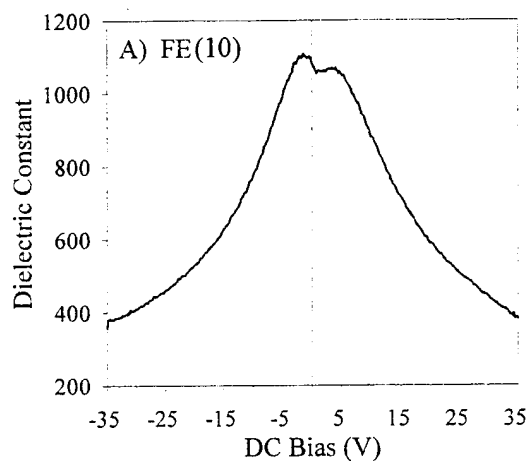


Figure 4. Effective experimental (exp) dielectric constant of A) pure FE, B) F8A2, C) F7A3, D) F5A5, E) F3A7, F) F2A8 and G) pure AFE thin films measured at 1 kHz with a 100 mV ac signal. Calculated (calc) results were based on the linear series capacitor model. The y-axis scale for B)-F) is 50 per division. The dc bias was cycled from negative to positive voltage.

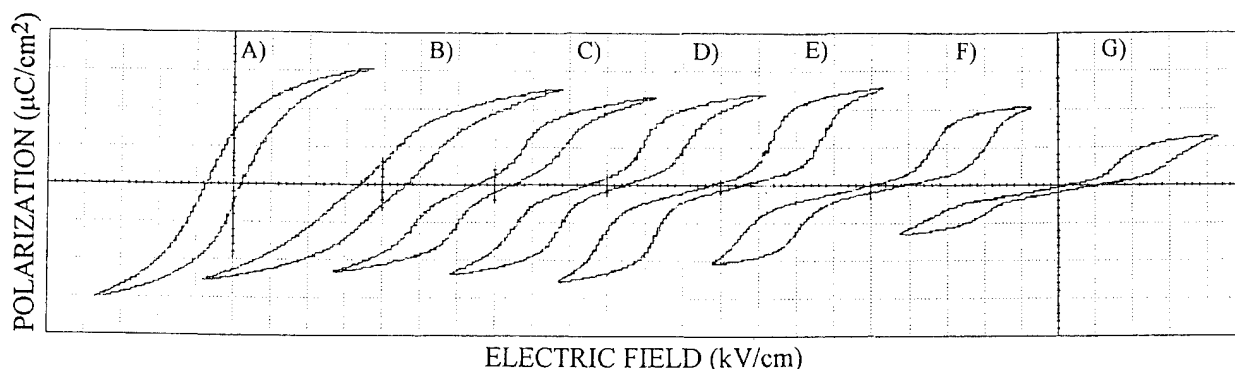


Figure 5. Hysteresis loops for A) pure FE, B) F8A2, C) F7A3, D) F5A5, E) F3A7, F) F2A8 and G) pure AFE thin films measured at 1 kHz with a  $\pm 40$ -45 V ac signal. The scale for the y-axis ( $P_{\text{sat}}$ ) is  $15 \mu\text{C}/\text{cm}^2$  per division, and the x-axis ( $E_F$ ) is  $100 \text{ kV}/\text{cm}$  per division.

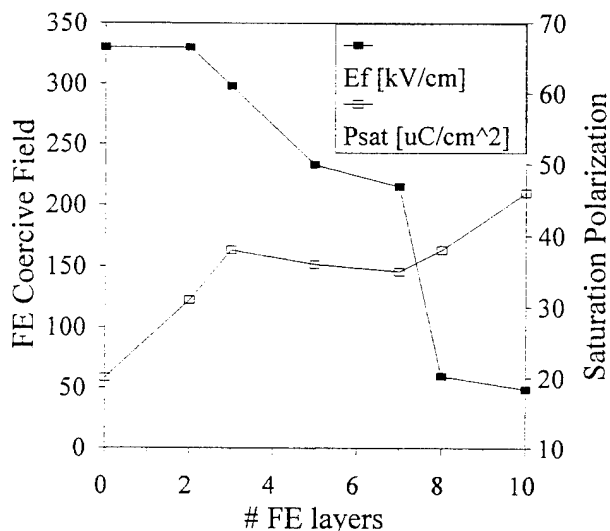


Figure 6.  $E_F$  and  $P_{\text{sat}}$  values for the AFE/FE composite films (#FE layers = 2 to 8) and for the pure AFE (#FE layers = 0) and FE (#FE layers = 10) films. Note that thin films with 8 or more FE layers possessed single hysteresis loops, while films with less than 8 FE layers exhibited double hysteresis loops.

#### SUMMARY

Composite AFE/FE thin films were spin coated from acetate precursors using an automatic spin coat reactor. PLZT 2/55/45 and  $\text{PbZrO}_3$  layers of variable thickness were deposited on Pt-coated Si substrates, and the electrical properties of these composites were observed. It was found that the dielectric constants of the composites were increased compared to pure AFE  $\text{PbZrO}_3$ , and the dielectric properties were modeled at low electric field according to a linear series capacitor model consisting of independent components of AFE and FE composition. While the model corresponded to experimental results for low field conditions, nonlinear behavior caused deviations in the predicted behavior with applied dc bias. It has been shown that the composite films behaved as voltage dividers because of the difference in dielectric constants between the AFE and FE layers in the composites causing a nonlinear distribution of internal electric field across the AFE and FE layers. This effect not only decreased the total electric field necessary to induce the AFE-to-FE phase transition, but it also prevented the FE layer from switching until  $E_F$  was reached. As a result, more square, better saturated double hysteresis loops were attainable with lower FE coercive fields. Dielectric constants as high as 300-400 were obtained in the composites compared to 150-175 for pure AFE composites. In addition,  $E_F$  was reduced from  $33 \text{ V}/\mu\text{m}$  to as low as  $21$ - $23 \text{ V}/\mu\text{m}$ , and  $P_{\text{sat}}$  was increased from 20 to  $35$ - $38 \mu\text{C}/\text{cm}^2$  in the composite films. It is believed that the development of composite thin film technology can lead to new

applications and improvements in existing thin film devices including improved and more applicable AFE-type materials.

#### ACKNOWLEDGMENT

The authors wish to thank Dr. Eugene Furman for his valuable assistance and advice. This work was supported by ONR under contract number N00014-94-1-0563.

#### REFERENCES

- [1] T. Shrout, W. A. Schulze and J. V. Biggers, "Electromechanical Behavior of Antiferroelectric-Ferroelectric Multilayer PZT Based Composites," *Ferroelectrics*, vol. 29, pp. 129-34, 1980.
- [2] T. R. Shrout, W. A. Schulze and J. V. Biggers, "Temperature Compensated Composite Resonator," *Ferroelectrics*, vol. 34, pp. 105-11, 1981.
- [3] H. Komiya, Y. Naito, T. Takenaka and K. Sakata, "Piezoelectric and Pyroelectric Composite Ceramics of the Multilayer Type by Tape Casting," *Jpn. J. Appl. Phys. Suppl.*, vol. 28-2, pp. 114-6, 1989.
- [4] O. Furukawa, M. Harata, M. Imai, Y. Yamashita and S. Mukaeda, "Low Firing and High Dielectric Constant X7R Ceramic Dielectric for Multilayer Capacitors Based on Relaxor and Barium Titanate Composite," *J. Mater. Sci.*, vol. 26, pp. 5838-42, 1991.
- [5] D. E. Dausch and G. H. Haertling, "Comparison of Properties Between Rapid Thermally Processed and Conventional Furnace Pyrolyzed PLZT Thin Films," to be published in *Integrated Ferroelectrics*, 1994.
- [6] G. H. Haertling, "PLZT Thin Films Prepared from Acetate Precursors," *Ferroelectrics*, vol. 116, pp. 51-63, 1991.
- [7] L. Shi, S. B. Krupanidhi and G. H. Haertling, "Development of Ferroelectric  $\text{Pb}(\text{Zr}_x\text{Ti}_{1-x})\text{O}_3$  Thin Films by Metallo-organic Decomposition Process and Rapid Thermal Annealing," *Integrated Ferroelectrics*, vol. 1, pp. 111-27, 1992.
- [8] M. Sayer, A. Mansingh, A. K. Arora and A. Lo, "Dielectric Response of Ferroelectric Thin Films on Non-Metallic Electrodes," *Integrated Ferroelectrics*, vol. 1, pp. 129-46, 1992.
- [9] S. Li, W. Cao, R. E. Newnham and L. E. Cross, "Electromechanical Nonlinearity of Ferroelectric Ceramics and Related Non-180° Domain Wall Motions," *Ferroelectrics*, vol. 139, pp. 25-49, 1993.

**Concurrent Session - 4B/1E:  
Electrostriction/Piezoelectrics**

# Composite Transducers and Actuators

Robert E. Newnham and Kelley A. Markowski  
Intercollege Materials Research Laboratory  
The Pennsylvania State University  
University Park, PA 16802 USA

**Abstract** – Composite materials have found a number of structural applications but their use in the electronics industry has been relatively limited. As the advantages and disadvantages of electroceramic composites are better understood, we can expect this picture to change.

In this paper we review some of the composite sensor and actuator studies carried out in our laboratory during the past decade. These functional composites make use of a number of underlying ideas including connectivity patterns leading to field and force concentration; the use of periodicity and scale in resonant structures; the symmetry of composite structures and its influence on physical properties; polychromatic percolation and coupled conduction paths; varistor action and other interfacial effects; sum, combination, and product properties; coupled phase transformation phenomena; and the important role that porosity and inner composites play in composite materials. These ideas provide a basic understanding of functional composites and have been discussed previously [1]. In this paper, we describe several composite piezoelectrics and thermistors which utilize some of these principles.

## COMPOSITE TRANSDUCERS

Early investigators concentrated on polymer-ceramic composites for use as hydrophones [2]. Several interesting connectivity patterns [3] were developed including 3-3 structures made by the replamine process [4] and by fugitive phase technique [5,6]. Then came the more useful 1-3 composites consisting of parallel PZT fibers embedded in a polymer matrix. These structures were made by extrusion [7], by dicing [8], and more recently by injection molding [9] and lithographic lost-wax techniques [10]. The coupling between the ceramic fibers and the polymer matrix is important [11]. In optimizing hydrophone performance, the  $d_{hg}h$  product was chosen as a figure of merit. The 1-3 composite increases  $d_h$  and  $g_h$  by reducing the  $d_{31}$  piezoelectric coefficient and the dielectric constant while maintaining the large  $d_{33}$  coefficient.

The usefulness of the 1-3 composite in high frequency applications for non-destructive testing and medical diagnostics was recognized later [12,13,14]. Biomedical transducers require resonant frequencies in the 1-10 MHz range, high electromechanical coupling coefficients, low acoustic impedance, and broad bandwidth. The 1-3 transducers manufactured by Siemens [10] have thickness resonances of 5-10 MHz, coupling coefficients  $k_t=0.67$ ,  $K=600$ ,  $\tan \delta < 0.025$ , and a mechanical  $Q$  about 10.

Poling is sometimes difficult for the long, slender PZT fibers used in 1-3 composites. Electric breakdown often occurs before poling is complete, and the transducer is ruined. Lower poling and driving fields are obtained when the spaghetti-like PZT fibers are replaced with macaroni-like PZT tubules. When electroded inside and out, the thin-walled tubes are poled and driven radially at relatively modest voltages. Radial motions are coupled to length-wise displacements through the  $d_{31}$  coefficient. Effective piezoelectric constants of about 8000 pC/N and large  $d_{hg}h$  products are achieved with these composites [15]. Other variants on the basic 1-3 structure include the 1-2-3 composite with transverse load bearing fibers [16], and the 1-3-0 composite with a foamed polymer matrix

[17], and the interesting woven fiber composites devised by Safari and co-workers [18].

Perhaps the simplest piezoelectric composite is the 0-3 transducer made by dispersing ceramic particles in a polymer matrix [19]. The NTK Piezo-Rubber films and cables are used as flexible hydrophones, keyboards, blood pressure cuffs, and musical instruments. They are made by hot-rolling  $PbTiO_3$  particles into a chloroprene rubber matrix [20].

As mentioned earlier PZT is widely used as a transducer material because of its high piezoelectric coefficients. However, for hydrophones applications, PZT is a poor material for several reasons. The hydrostatic piezoelectric coefficient,  $d_h (=d_{33} + 2d_{31})$ , is very low. The piezoelectric voltage coefficients,  $g_{33}$  and  $g_h$ , are low because of the high dielectric constant of PZT (1800). The acoustic matching of PZT with water is poor because of its high density ( $7.9 \text{ g/cm}^3$ ). Moreover, it is a brittle, non-flexible ceramic.

In the last decade, several investigators have tried to fabricate composites of PZT and polymers to overcome the above problems of PZT. It has been shown that it is possible to improve upon the piezoelectric properties of homogeneous PZT by the composite approach. The concept that the connectivity of the individual phases control the resulting properties has been demonstrated in a number of composites with different geometry and different connectivity of the individual phases. The hydrostatic piezoelectric properties of these composites are superior to single-phase PZT. However, some of the earlier composites suffer from disadvantages due to difficulty in preparation or reduction in hydrostatic sensitivity with increasing pressure. Thus, there still exists a need to further improve the piezoelectric properties of these composites. It is especially desirable to have the composites prepared without any problems in processing and fabrication and also show high figures of merit for hydrophone applications with little or no variation in static pressure sensitivity under hydrostatic loading.

It was demonstrated by Safari [18] that based on the theory of connectivity new composites with different connectivity patterns could be fabricated with enhanced performance. Most of the work involved composites with 1-3 and 2-3 connectivity, shown below in figure 1. These composites were prepared by drilling either circular or square holes in prepoled PZT blocks, in a direction perpendicular to the poled axis and by filling the drilled holes with epoxy. On the samples optimized for hydrophone performance, the  $g_h$  and  $d_{hg}h$  coefficients were about 4 and 40 times greater, respectively, for the 1-3 composites; and 25 and 150 times greater for the 2-3 composites compared to those of solid PZT. For 1-3 composites, there was practically no variation of  $g_h$  with pressure up to 8.4 MPa. In the case of 2-3 composites, there was a slight variation of  $g_h$  with pressure.

## BB Transducers

BB's are hollow spherical transducers a few millimeters in diameter, about the same size as the metallic pellets used in air rifles (BB guns). PZT BB's are mass produced, by a patented forming process in which air is blown through a PZT slurry of carefully controlled viscosity. The hollow spheres are 1-6 mm

in diameter with wall thickness of 0.1  $\mu\text{m}$ . Densities are about 1.3  $\text{g/cm}^3$  giving the BB a low acoustic impedance close to that of water and human tissue.

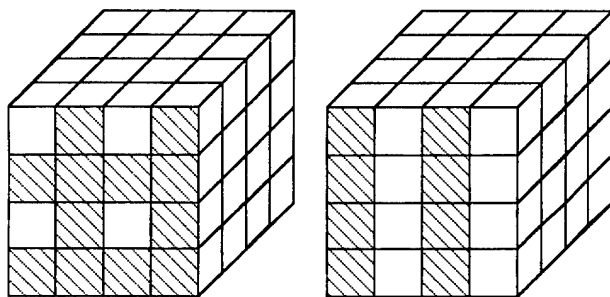
When embedded in a polymer matrix to form a 0-3 composite the BB spheres are surprisingly strong, and able to withstand large hydrostatic pressure without collapse. Close-packed transducer arrays are easily assembled.

When electroded inside and out, and poled radially the BB becomes an omnidirectional transducer [21] suitable for underwater or biomedical applications. For spheres with a 2.6 mm diameter and 90  $\mu\text{m}$  thick walls, the resonant frequencies are 700 kHz for the breathing mode ( $d_{31}$ ) and 10 MHz for the wall thickness mode ( $d_{33}$ ). BB's are small enough to be used in catheters for non-invasive surgery to act as beacons, sensors, and actuators. More than a million such procedures are now carried out annually.

### Zig-Zags and Smarties

Zig-zag actuators are split bimorphs in which two ceramic legs are driven independently to generate synchronized horizontal and vertical displacements. The legs are joined in a teepee-like configuration which imparts a rolling motion to the load. Typical motions are in the 1- 30  $\mu\text{m}$  range and look to be useful in piezomotor and conveyor belt applications [22].

Smarties are a family of composite transducers which combine two or more active elements to provide the sensing and actuating functions characteristic of a smart material. There are four solid-state actuator materials currently in use throughout the world [23]: Piezoelectric PZT, electrostrictive PMN, magnetostrictive  $\text{TbFe}_2$ , and NiTi shape memory alloy. We have begun to look at ways in which these materials can be joined to take advantage of the best features of each. Preliminary results on the first of these composite actuators - NiTi strips coated with sol-gel layers of PZT have been reported [24].



2-3 Connectivity

1-3 Connectivity

FIGURE 1

Two connectivity patterns utilized in composite transducers.

### FLEXTENSIONAL TRANSDUCERS "MOONIES"

In recent years, piezoelectric and electrostrictive ceramics have been used in many actuator applications. To meet these needs a new type of composite actuator based on a flextensional transducer has been developed [25-30]. This ceramic-metal composite actuator, or "moonie" consists of either a piezoelectric ceramic disc or a multilayer stack, sandwiched between two specially designed metal end caps. This design provides a sizable displacement, as well as a large generative force. In other words, it bridges the gap between the two most common types of actuators, the multilayer and the bimorph[31]. The shallow spaces under the end caps produce a

substantial increase in strain by combining the  $d_{33}$  and the  $d_{31}$  contributions to the ceramic. It is attractive for hydrophone, transceiver and actuator applications, and is especially advantageous for use as a non-resonant, low frequency projector in deep water.

The basic configuration of the moonie is shown in figure 2. The metal end caps serve as mechanical transformers for converting and amplifying the lateral motion of the ceramic into a large axial displacement normal to the end caps. Both the  $d_{31}$  ( $=d_{32}$ ) and  $d_{33}$  coefficients of the piezoelectric ceramic contribute to the axial displacement of the composite. Figure 3 below shows the enhanced displacement of the moonie actuator as a function of applied electric field compared to PZT ceramic.

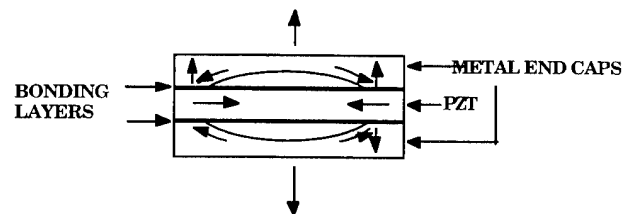


FIGURE 2

The geometry of the ceramic-metal composite actuator "Moonie". The arrows describe the direction of displacement.

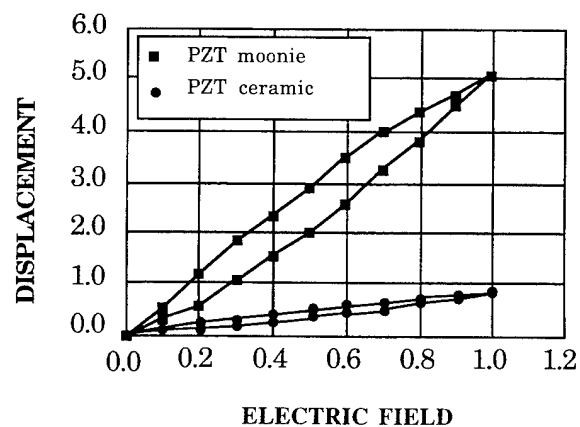


FIGURE 3

Typical static displacement of the moonie actuator as a function of the applied  $\vec{E}$  field.

### Applications of the Moonie

Three applications for this type of flextensional transducer, the moonie, have been explored [32]: they include hydrophone sensors, transceivers for fish finders, and positional actuators. Geometry and bonding effects on the resonance characteristics and displacement of the moonie transducer were investigated using finite element analysis (FEA).

### Hydrophone Applications of the Moonie

Hydrophone sensitivity depends on  $d_h$ , the hydrostatic piezoelectric charge coefficient, and  $g_h$ , the hydrostatic piezoelectric voltage coefficient. The moonie transducer was introduced as a hydrophone having the highest figure of merit,  $d_h \times g_h = 50,000 \times 10^{15} \text{ m}^2/\text{N}$ , which is about 500 times larger than the PZT ceramic, as well as maintaining high capacitance and pressure tolerance. The stress distribution of the moonie hydrophone under a hydrostatic pressure was



determined using FEA. FEA showed that extensional stresses along the radial and tangential directions were generated under a hydrostatic pressure, and contributed significantly to the very high figure of merit of the moonie.

In addition to this, the effect on prestresses caused by thermal treatment of the moonie were also estimated. The maximum stress concentration reached several hundred MPa. The maximum compressive stress concentration reaches about 300 MPa along the radial direction at the inner bonding edge, and 400 MPa extensive stress concentration occurs at the cavity located at the top of the cap.

The combined effect of high hydrostatic pressure (7 MPa corresponding to a 700 m water depth), and thermal processes were also estimated. Even 7 MPa hydrostatic pressure causes little deformation to the moonie hydrophone because the effect of relatively large prestress pressures exceed those of the hydrostatic environment. This is one of the reasons that the moonie hydrophone has high pressure tolerance.

### Transceiver for Fishfinder

Using FEA to design the moonie fish finder made it possible to predict the flexensional resonant frequency. The effect of the following five geometrical parameters: PZT diameter, PZT thickness, cap thickness, cavity size, and bonding layer thickness on the resonant frequency were carefully investigated. Among these parameters, the resonant frequency is sensitive to the diameter, cap thickness and cavity size. The bonding layer thickness, however, has little effect on the resonant frequency. It was found that the lowest flexensional frequencies are proportional to the square root of the cap thickness and inversely proportional to the square of the diameter. These results are demonstrated below in figures 4 and 5.

From the results obtained by Onitsuka [32] the moonie fish finders showed high response sensitivity but poor transmission. The high impedance of the moonie fish finder makes it difficult for practical for usage, but additional inductance will help to reduce the impedance.

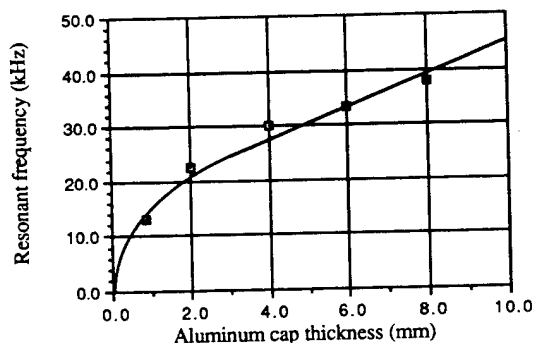


FIGURE 4

First resonant frequencies as a function of the aluminum cap thickness. Dimensions:  $dp=35$  mm,  $dm=35$  mm,  $dc=28$  mm,  $tp=2$  mm,  $h=0.2$  mm where  $dp$ =PZT diameter,  $dm$ =metal cap diameter,  $dc$ =cavity diameter,  $h$ =cavity depth,  $tp$ =PZT thickness, and  $tm$ =metal cap thickness.

### Actuator

Moonie actuators have very high effective  $d_{33}$  coefficients depending on the geometry. Effective  $d_{33}$  coefficients as large as 4,000 pC/N were obtained with brass caps 0.3 mm thick, but the value decreased rapidly toward the edge of the transducer. This is approximately ten times higher than the  $d_{33}$  of a PZT-5 ceramic. The characteristics of the moonie actuator depend markedly on the geometry and material combination. Among the geometric parameters, cavity diameter, cavity depth, and cap thickness are the main contributors to the displacement of a

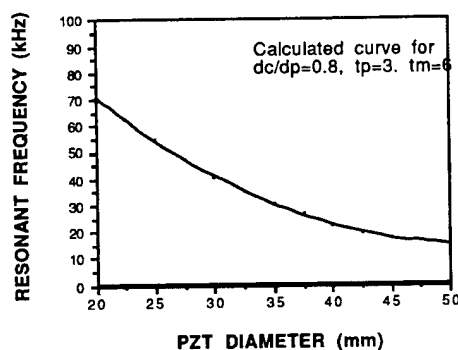


FIGURE 5

First resonant frequencies calculated by finite element analysis plotted as a function of the PZT diameter.

moonie actuator. An applied 1 kV/mm electric field produces a displacement of 22  $\mu$ m at the center of a carefully designed brass capped moonie actuator. By stacking two identical single moonies with these dimensions, the double stacked moonie actuator produced 40  $\mu$ m displacement. It was confirmed that the incorporation of a multilayer ceramic actuator as a moonie driver reduced the applied voltage to a practical range.

The load carrying capability of the moonie was measured experimentally and calculated by FEA. The calculated maximum load (300 gf.) at the effective working area of 3 mm<sup>2</sup> agrees with that obtained by the extrapolation of the experimental data.

By choosing the appropriate position on the caps, their desired displacement and generative force can be obtained. The moonie actuator has a great potential for many applications because of its unique characteristics.

### SMART MATERIALS

Smart materials[33] have the ability to perform both sensing and actuating functions. Passively smart materials respond to external change in a useful manner without assistance, whereas actively smart materials have a feedback loop which allows them to both recognize the change through an actuator circuit. Many smart materials are analogous to biological systems: piezoelectric hydrophones mentioned earlier are similar in mechanism to the "ears" by which a fish senses vibrations. Piezoelectrics with electromechanical coupling, shape memory materials that can "remember" their original shape, electrorheological fluids with adjustable viscosities, and chemical sensors which act as synthetic equivalents to the human nose are examples of smart electroceramics. "Very smart" materials, in addition to sensing and actuating, have the ability to "learn" by altering their property coefficients in response to the environment. Integration of these different technologies into compact, multifunction packages is the ultimate goal of research in the area of smart materials. We expect big changes to occur in this field during the coming decades.

### REFERENCES

- [1] R. E. Newnham, "Composite Electroceramics," *J. Mat. Education*, vol.7, p.605-651, 1985.
- [2] T.R. Gururaja, R.E. Newnham, K.A. Klicker, S.Y. Lynn, W.A. Schulze, T.R. Shrout and L.J. Bowen, "Composite Piezoelectric Transducers," in *Proceedings of the IEEE Ultrasonics Symposium*, vol. 2, 1980, pp.576-581.
- [3] R.E. Newnham, D.P. Skinner and L.E. Cross, "Connectivity and Piezoelectric-Pyroelectric Composites," *Mat. Res. Bull.*, vol 13, pp. 525-536, 1978.

- [4] D.P. Skinner, R.E. Newnham and L.E. Cross, "Flexible Composite Transducers," *Mat. Res. Bull.*, vol 13, pp. 599-607, 1978.
- [5] T.R. Shrout, W.A. Schulze, and J.V. Biggers, *Mat. Res. Bull.* vol. 14, pp. 1553, 1979.
- [6] K. Rittenmyer, T. Shrout, W.A. Schulze, and R.E. Newnham, "Piezoelectric 3-3 Composites," *Ferroelectrics*, vol. 41, pp. 189-195, 1982.
- [7] K.A. Klicker, J.V. Biggers and R.E. Newnham, "Composites of PZT and Epoxy for Hydrostatic Transducer Applications," *J. Am. Ceram. Soc.*, vol. 64, pp. 5-9, 1981.
- [8] H.P. Savakus, K.A. Klicker and R.E. Newnham, "PZT-Epoxy Piezoelectric Transducers: A Simplified Fabrication Procedure," *Mat. Res. Bull.*, vol. 16, no. 6, pp. 677-680, 1981.
- [9] L. Bowen, Proceedings IMF (1993 Gaithersburg, MD), *Ferroelectrics* (in press)
- [10] G. Preu, A. Wolff, D. Cames, U. Bast Euro-Ceramics II 3(1991) 2005
- [11] C. Richard, P. Eyraud, L. Eyraud, A. Pelourson, M. Richard Euro-Ceramics II 3 (1991)2001
- [12] T.R. Gururaja, W.A. Schulze, L.E. Cross, R.E. Newnham, B.A. Auld and Y.J. Wang, "Piezoelectric Composite Materials for Ultrasonic Transducer Applications. Part I: Resonant Modes of Vibration of PZT Rod-Polymer Composites," *IEEE Transactions on Sonics and Ultrasonics*, vol. 32, no. 4, pp. 481-498, 1985.
- [13] T.R. Gururaja, W.A. Schulze, L.E. Cross, R.E. Newnham, B.A. Auld and Y.J. Wang, "Piezoelectric Composite Materials for Ultrasonic Transducer Applications. Part II: Evaluation of Ultrasonic Medical Applications," *IEEE Transactions on Sonics and Ultrasonics*, vol. 32, no. 4, pp. 499-513, 1985.
- [14] W. Smith, IEEE Ultrasonics Symposium (1989) p. 755
- [15] W. Pan, Q.M. Zhang, A. Bhalla and L.E. Cross, "Field-Forced Antiferroelectric-to-Ferroelectric Switching in Modified Lead Zirconate Titanate Stannate Ceramics," *J. Am. Ceram. Soc.*, vol. 72, no. 4, pp. 571-578, April 1989.
- [16] M.J. Haun, R.E. Newnham and W.E. Schulze, "1-2-3 and 1-2-3-0 Piezoelectric Composites for Hydrophone Application," *Adv. Ceram. Mat.*, vol. 1, no. 4, pp. 361-365, 1986.
- [17] M.J. Haun and R.E. Newnham, "An Experimental and Theoretical Study of 1-3 and 1-3-0 Piezoelectric PZT-Polymer Composites for Hydrophone Applications," *Ferroelectrics*, vol. 68, pp. 123-129, 1986.
- [18] A. Safari, "Preforated PZT-Polymer Composites with 3-1 and 3-2 Connectivity for Hydrophone Applications," Ph.D. Thesis, The Pennsylvania State University, University Park, PA (1983)
- [19] J. Giniewicz, R.E. Newnham and A. Safari, "(Pb,Bi)(Ti,Fe,Mn)O<sub>3</sub>-Polymer 0-3 Composites for
- [20] H. Banno, "Recent Developments of Piezoelectric Ceramic Products and Composite of Synthetic Rubber and Piezoelectric Ceramic Particles," *Ferroelectrics*, vol. 50, no. 1-4, pp. 329-338, 1983.
- [21] S. Li, R.E. Newnham and L.E. Cross, "The Effective Masses in Domain Walls in Ferroelectric Polycrystalline Materials," (submitted 1993)
- [22] M.G. Matsko, Q.C. Xu and R. E. Newnham, "Zig-Zag Piezoelectric Actuators: Geometrical Control of Displacement and Resonance," *J. of Intelligent Mat. Systems and Structures*, (in press)
- [23] R.E. Newnham (Guest Editor), "Smart, Very Smart and Intelligent Materials," *Mat. Res. Bull.*, vol. 18, pp. 24-26, April 1993.
- [24] J. Chen, Q.C. Xu, M. Blaszkiewicz, R. Meyer and R.E. Newnham, "Lead Zirconate Titanate Films on Nickel-Titanium Shape Memory Alloys: SMARTIES," *J. Am. Ceram. Soc.*, vol. 75, no. 10, pp. 2891-2892, October 1992.
- [25] R.E. Newnham, Q.C. Xu and S. Yoshikawa, Transformed stress direction-acoustic transducer, U.S. Patent # 4,999,819, March 12, 1992
- [26] Q.C. Xu, S. Yoshikawa, J. Belsick, R.E. Newnham, "Piezoelectric Composites with High Sensitivity and High Capacitance for Use at High Pressures," *IEEE Transactions on Ultrasonics, Ferroelectrics and Frequency Control*, vol. 38, no. 6, November 1991.
- [27] Y. Sugawara, K. Onitsuka, S. Yoshikawa, Q. Xu, R.E. Newnham, and K. Uchino, Metal-Ceramic Composite Actuators," *J. Am. Ceram. Soc.*, vol. 75, no. 4, pp.996-998, April 1992.
- [28] Q.C. Xu, A. Dogan, J. Tressler, S. Yoshikawa and R.E. Newnham, "Ceramic-Metal Composite Actuator", in *Proceedings of the IEEE Ultrasonic Symposium*, Florida, 1991.
- [29] A. Dogan, Q.C. Xu, K. Onitsuka, S. Yoshikawa, K. Uchino and R.E. Newnham, "High Displacement Ceramic-Metal Composite Actuators (Moonie)," *Ferroelectric Special Issue for IMF8* (in press)
- [30] K. Onitsuka, A. Dogan, Q.C. Xu, J. Tressler, S. Yoshikawa, and R.E. Newnham, "Design Optimization for eramic-Metal Compostie Actuators (Moonie)", *Ferroelectric Special Issues for IMF8* ( in press)
- [31] K. Uchino, *Piezoelectric and Electrostrictive Actuators*. Tokyo: Morikita Publication, 1986.
- [32] K. Onitsuka, "Effects of Bonding and Geometry on the Flexensional Transducer, "Moonie",," Ph.D. Thesis, The Pennsylvania State University, University Park, PA (1993)
- [33] R.E. Newnham and G. Ruschau, "Smart Electroceramics," *J. Am. Ceram. Soc.*, vol. 74, no. 3, pp. 463-480, March 1991

# Nonlinear Dynamics and Ferroelectric Materials

S. Blochwitz, R. Habel, M. Diestelhorst and H. Beige

**Abstract**—The aim of the presented paper is to show that the application of analysis methods of dissipative chaotic systems is a useful tool for the study of structural phase transitions and the large signal behaviour of ferroelectric materials.

The series resonance circuit with a ferroelectric capacitor is a practical realization of a nonlinear dynamical system which exhibits period-doubling behaviour and chaos if the amplitude and the frequency of the driving voltage have suitable values. The response function of the nonlinear dynamical system is used for the determination of the nonlinear coefficients of the sample.

## I. INTRODUCTION

IT is well known that the structural phase transitions in ferroelectric materials are connected with strong nonlinear properties [1], [2]. So we should expect all features of nonlinear dynamical systems as period-doubling and deterministic chaos in these materials.

The aim of the presented paper is to show that the application of analysis methods of dissipative chaotic systems is a useful tool for the study of structural phase transitions and the large signal behaviour of ferroelectric materials. The investigation of the large signal behaviour is stimulated by the shift in the ferroelectrics research and development to thin films with the aim of miniaturization. The paper tries to connect the following topics as shown in figure 1.

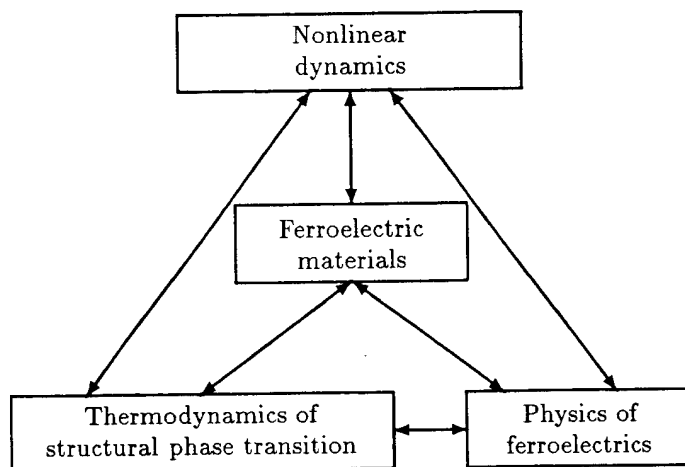


Fig. 1. Schematic illustration of the relation between the different topics in this paper

Martin-Luther-Universität  
Fachbereich Physik, Friedemann-Bach-Platz 6, 06108 Halle (Saale),  
Germany, email: e2ode@mmlucom.urz.uni-halle.de

Halle-Wittenberg,  
06108 Halle (Saale),

## II. DIELECTRIC NONLINEAR SERIES-RESONANCE CIRCUIT

THE investigated nonlinear dynamical system is a dielectric nonlinear series-resonance circuit, consisting of a linear inductance  $L_0$  and a dielectric nonlinear capacitance  $C_{nl}$ , e. g. a ferroelectric triglyzin sulfate crystal (see figure 2).  $R_S$  describes the loss of the resonance circuit.

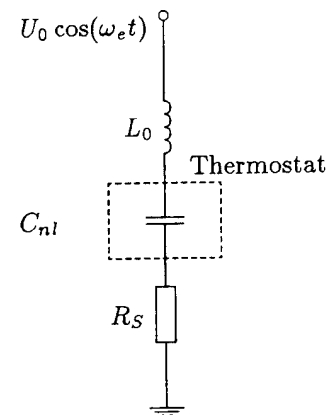


Fig. 2. Dielectric nonlinear series resonance circuit

The resonance circuit is driven by a sinusoidal voltage  $U_0 \cos(\omega_e t)$ . Then the differential equation (1) describes the behaviour of the circuit:

$$\ddot{D}_2 + \frac{\omega_{0e}}{Q} \dot{D}_2 + \frac{a}{L_0 b l} E_{nl} = \frac{U_0}{L_0 b l} \cos(\omega_e t). \quad (1)$$

Here  $D_2$  is the dielectric displacement,  $a$  the thickness,  $l$  the length and  $b$  the width of the sample. The electric field strength at the TGS-crystal along the ferroelectric axis is denoted by  $E_{nl}$ .  $Q$  stands for the quality of the resonance circuit and  $\omega_{0e}$  for its resonance frequency.

## III. NONLINEAR NATURE OF THE RESONANT SYSTEM

THE nonlinear properties of the series resonance circuit are determined by the nonlinear dielectric properties of the TGS-crystal.

The ferroelectric phase transition of second-order in TGS at  $\theta_c = 49^\circ\text{C}$  can be described by the thermodynamic potential [3]

$$G = G_0 + \frac{A}{2} D_2^2 + \frac{B}{4} D_2^4.$$

The basic assumption for the coefficients  $A$  and  $B$  are according to Landau's theory  $A = A_0(\theta - \theta_c)$  and  $B =$

const.  $> 0$ . The coefficient  $A_0$  is a positive constant. Note the following three cases are to be distinguished:

1. Paraelectric TGS ( $\theta > \theta_c$ ),
2. Ferroelectric TGS ( $\theta < \theta_c$ ) with small driving voltage,
3. Ferroelectric TGS ( $\theta < \theta_c$ ) with large driving voltage.

#### IV. PARAELECTRIC TGS ( $\theta > \theta_c$ )

At temperatures above the phase transition the coefficient  $A$  is positive. The potential has only one minimum and the electric field strength at the sample is calculated as

$$E_{nl} = \frac{\partial G}{\partial D_2} = AD_2 + BD_2^3 \quad \text{with } A > 0. \quad (2)$$

Inserting relation (2) into equation (1) yields

$$\ddot{D}_2 + \frac{\omega_{0e}}{Q} \dot{D}_2 + \omega_{0e}^2 D_2 + \frac{\omega_{0e}^2 B}{A} D_2^3 = \frac{\omega_{0e}^2 U_0}{aA} \cos(\omega_e t) \quad (3)$$

with  $\omega_{0e} = aA/L_0 bl$ . Expression (3) is the so-called Duffing equation [4].

#### V. FERROELECTRIC TGS ( $\theta < \theta_c$ ) WITH SMALL DRIVING VOLTAGE

At temperatures below the phase transition the coefficient  $A$  is negative. The thermodynamic potential becomes double-well. The equilibrium value of the dielectric displacement

$$D_{2sp} = \pm \sqrt{\frac{-A}{B}} \quad (4)$$

may be derived from the equilibrium condition of the potential. Exciting the series-resonance circuit with small amplitudes  $U_0$ , the dielectric displacement vibrates around the equilibrium values  $D_{2sp}$  of the crystal without an external field. There is no polarization reversal.

#### VI. FERROELECTRIC TGS ( $\theta < \theta_c$ ) WITH LARGE DRIVING VOLTAGE

If the amplitude of the driving voltage is increased, polarization reversal in the ferroelectric material may occur. This process is connected with the so-called dielectric hysteresis. The nonlinear relation between electric field strength  $E_{nl}$  and dielectric displacement  $D_2$  can be written as

$$E_{nl} = AD_2 + BD_2^3 \quad \text{with } A < 0. \quad (5)$$

At high amplitudes of the driving voltage the oscillator "feels" the whole potential and therefore the relevant differential equation is obtained with expression (5) in expression (1). The result is the Duffing equation in a double-well potential

$$\ddot{D}_2 + \frac{\omega_{0e}}{Q} \dot{D}_2 - \frac{\omega_{0e}^2}{2} D_2 + \frac{\omega_{0e}^2 B}{2A} D_2^3 = -\frac{\omega_{0e}^2 U_0}{2aA} \cos(\omega_e t) \quad (6)$$

with  $\omega_{0e} = -2aA/L_0 bl$ .

## VII. EXPERIMENTAL METHODS

NONLINEAR dynamical system may be conveniently analyzed by means of a multidimensional phase space, in which to any state of the system at any time corresponds a point. Therefore, to any motion of the system corresponds an orbit or trajectory. The trajectory represents the history of the dynamical system [5].

Figure 3 shows the block diagram of the measuring system for recording the phase portrait  $\dot{D}_2 = D_2(D_2)$  of the series-resonance circuit. For reasons of measurement two further components are attached to the resonance circuit introduced in figure 2. Using a linear capacitance  $C_{lin}$  and a linear resistor  $R_{lin}$  makes it possible to record time-dependent signals proportional to the dielectric displacement  $D_2$  on the specimen and the current density  $j_2 = \dot{D}_2$  through the specimen respectively. If these components satisfy the conditions  $C_{lin} \gg C_{nl}$  and  $R_{lin} \ll 1/(\omega C_{lin})$  the circuit is not influenced at all by these components. The measuring system is based on a fully programmable true dual-channel digitizer (Sony/Tektronix RTD-710).

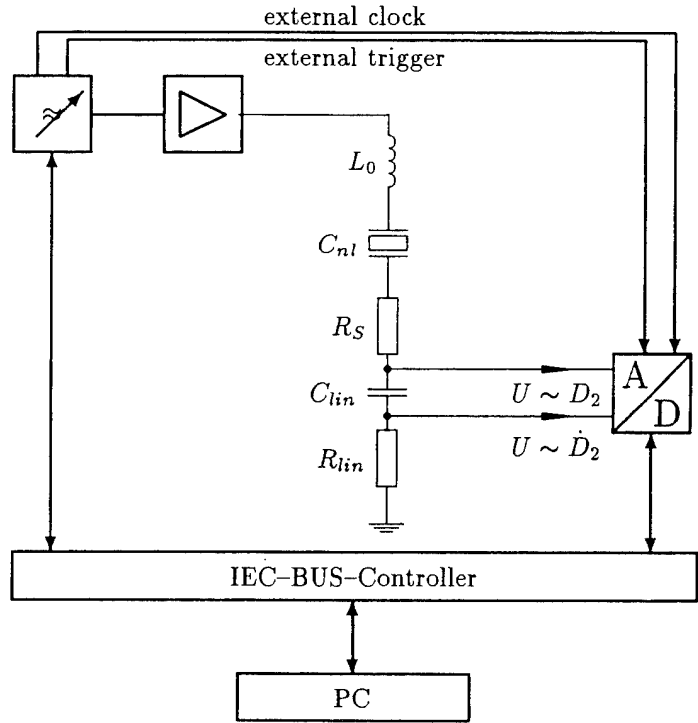


Fig. 3. Block diagram of the measuring system

With the measuring system the excitation, the hysteresis loop, the response function, the phase portrait, and the stroboscopic phase-portrait, i. e. the poincaré-section can be recorded.

## VIII. RESULTS AND DISCUSSION

### A. Study of structural phase transitions

We approached our goal to study the phase transition within two steps:

1. Periodic phase portraits of the series-resonance circuit have been recorded at different temperatures

above and below the phase transition.

2. The equations (3) and (6) are solved by numerical means. If for a certain set of values of the modelling parameters  $\{\omega_{0e}, A, B\}$  can be observed a simulated phase portrait that is very similar to the experimentally recorded one then these set of parameters will be accepted as valid for describing the system.

To make the term "very similar" more objective we applied two criteria that had to be fulfilled for stating the success of our visually controlled successive approximation:

- (i) The experimental phase portrait and the simulated one must be bounded by the same values for  $D_2$  and  $\dot{D}_2$ .
- (ii) Both curves must have the same internal structure.

In practice that simulating method is quite effective. It can be carried out at a personal computer. The figure 4 shows a successful simulation for a ferroelectric TGS-crystal ( $\theta = 39.1^\circ\text{C}$  in the 1T- and 2T-periodic case).

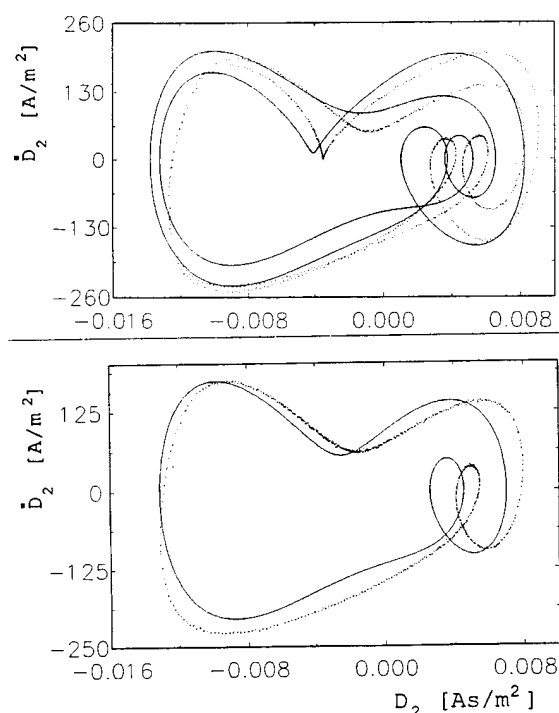


Fig. 4. Comparison of the experimentally recorded phase portrait (dotted line) and the computer simulation (solid line) of equation (6) in the 1T- and 2T-periodic case (upper and lower picture respectively).

It can be proved that there is a one to one mapping of phase portraits to the modelling parameters by Fourier-Transformation of equation (6) [9]. Also the power spectra of the experimentally recorded response function and the simulated one are in good agreement (see figure 5).

The comparison of experimentally recorded and numerical simulated signals provides the opportunity to determine the linear and nonlinear coefficients of the investigated system. The phase portrait gives information about the "effective thermodynamical potential". Figure 6 shows the

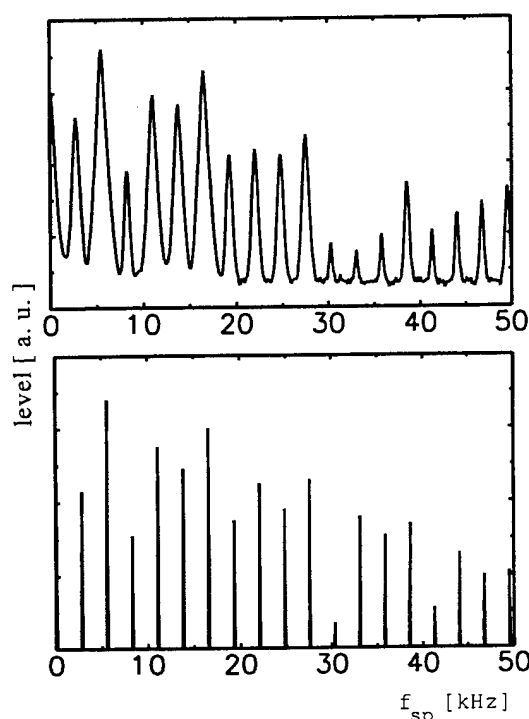


Fig. 5. Comparison of the power spectra of the experimentally recorded response function (upper picture) and the numerical calculated (lower picture) for the 2T-periodic case in figure 4.

effective thermodynamical potential of a TGS-crystal near the phase transition with the change from a one minimum potential to a double-well potential near the phase transition.

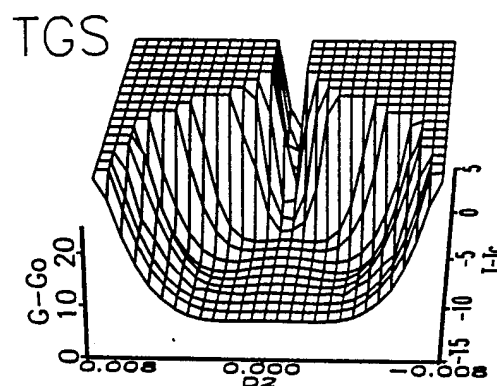


Fig. 6. Effective thermodynamical potential of a TGS-crystal near the phase transition

Figure 7 gives an example of the high sensitivity of the phase portrait against a bias field ( $E = 4\text{ kV/m}$ ) on the phase portrait in the ferroelectric phase.

So the recording and simulating of phase portraits is a new approach to the study of structural phase transitions. With the help of this method it can be studied especially the large signal behaviour and dynamical properties of various ferroelectric materials.

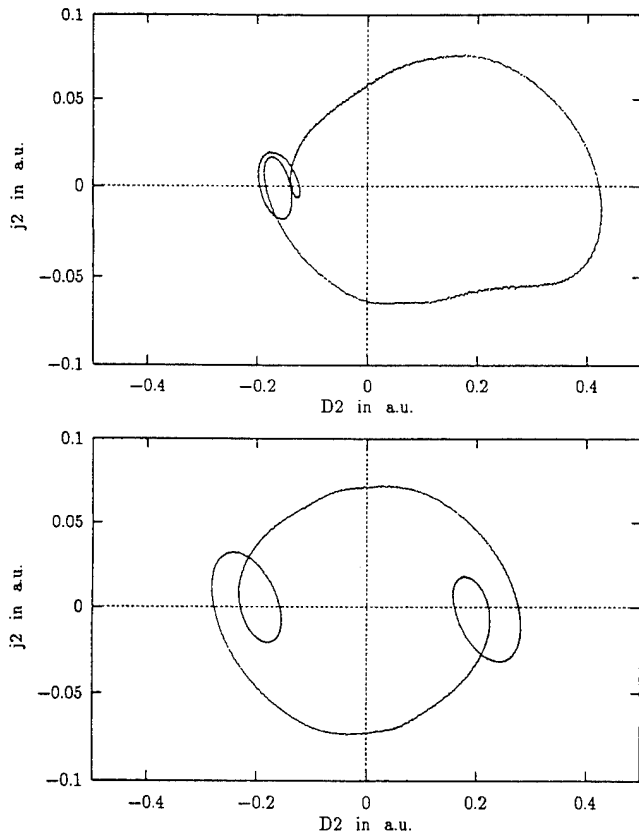


Fig. 7. Influence of a bias field on the phase portrait of a TGS-crystal in the ferroelectric phase (upper picture:  $E_{bias} = 4 \text{ kV/m}$  lower picture: no bias).

#### B. Characterization of thin ferroelectric films

A PZT-layer ( $\text{Zr/Ti} = 0.53/0.47$ ) with the thickness  $0.39 \mu\text{m}$  manufactured by Philips was investigated. The recorded phase portraits were used in order to determine the model coefficients of the thin ferroelectric film and aging process in the material [6], [7]. Figure 8 shows for two different temperatures the dielectric nonlinear coefficient  $B$  as a function of the excitation.

#### C. Characterization of a ferroelectric liquid crystal

Further we treated a thin ferroelectric liquid crystal with the thickness  $1.45 \mu\text{m}$  like the TGS crystal. This system has a ferroelectric phase between  $326 \text{ K}$  and  $332 \text{ K}$ . The result is shown in figure 9. The effective thermodynamical potential is — like that of TGS — changing from one minimum to double well at the phase transition, but note that the energy that is represented by that potential is about 10 times greater than the energy of the TGS-crystal.

### IX. SUMMARY

WE showed that the series resonance circuit with capacitors made from various ferroelectric materials can be well described by a Duffing-like differential equation. The dynamical properties of these materials can be determined by a visually controlled successive approximation of simulated phase portraits to experimentally record-

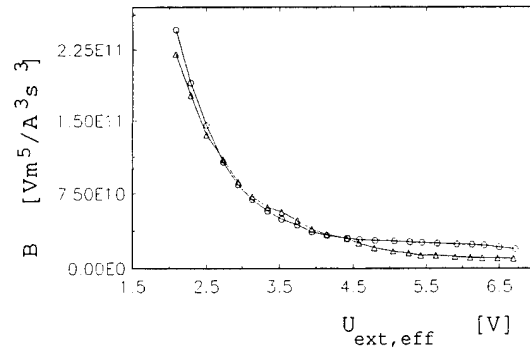


Fig. 8. Dielectric nonlinear coefficient  $B$  as a function of the excitation for two different temperatures ( $\diamond$ :  $\theta = 20^\circ\text{C}$ ,  $\triangle$ :  $\theta = 115^\circ\text{C}$ ).

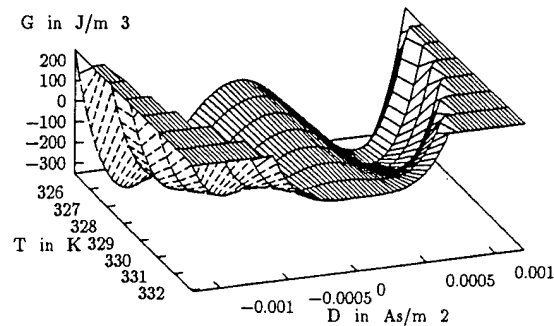


Fig. 9. Effective thermodynamical potential of a ferroelectric liquid crystal in its ferroelectric phase between  $326 \text{ K}$  and  $332 \text{ K}$ .

ed ones.

### X. ACKNOWLEDGEMENT

THIS work was supported by the Deutsche Forschungsgemeinschaft within the frame of the Sonderforschungsbereich "Nichtlineare Dynamik". One of us (S. B.) was supported by the "Studienstiftung des deutschen Volkes".

### REFERENCES

- [1] A. S. Sonin and B. A. Strukov: Einführung in die Ferroelektrizität, Akademie-Verlag 1974
- [2] M. Diestelhorst, R. Hofmann and H. Beige: Jpn. J. Appl. Phys, **24**, Suppl. 25-2, 1019 (1985)
- [3] M. E. Lines and A. M. Glass: Principles and Application of Ferroelectrics and Related Materials, Clarendon Press, Oxford, 1979
- [4] A. H. Nayfeh and D. T. Mook: Nonlinear Oscillations, Wiley Interscience Publications, New York 1979
- [5] H. G. Schuster: Deterministic Chaos, Physik Verlag Weinheim 1984
- [6] D. Hennings, M. Klee and R. Weyer: Acta. Mater., **3** (7/8), 334 (1991)
- [7] E. Brauer, H. Beige, L. Flepp and M. Klee: Phase Transitions **42**, 169 (1993)
- [8] E. Brauer, S. Blochwitz and H. Beige: International Journal of Chaos and Bifurcation **4**, vol. 4 (1994)
- [9] S. Blochwitz: PhD-Thesis (in German), Halle 1994

# Study on Characteristics of Standing Wave Motors

Longtu Li, Shuxiang Dong, Zhilun Gui, Wei pan and Xiaowen Zhang  
Department of Materials Science and Engineering  
Tsinghua University, Beijing 100084, P. R. China

**Abstract** -- A standing wave rotational motor was made by using PMS-PCS-PZT ceramics. The dynamic characteristics and equivalent circuit of motor were studied theoretically and experimentally. Using finite element method, the vibration modes of longitudinal-torsional coupler of standing wave motor were analyzed. With improvement of coupler construction, the rotational speed of motor is increased compared with the original one. The typical values of this motor are 270 r.p.m. with no load. The diameter of stator is 32 mm. Its resonance frequency, operation voltage and largest torque are 30 KHz, 24 V and 10 Kg-cm, respectively.

## INTRODUCTION

Compared with other kinds of piezoelectric motors, the standing wave motor possesses larger output torque and higher efficiency. But its rotational speed is lower than that of traveling wave motor. The typical values of standing wave motor reported by some researchers [1,2] are 120 r.p.m. with no load. The purpose of the present research is to increase rotational speed by improving the structure of standing wave motor.

In general, a Langevin-type ultrasonic motor is constructed by tightly contacting a rotor to a stator. The stator consists of a piezoelectric thickness vibrator, a longitudinal-torsional (L/T) coupler and a bending vibration plate [3]. The piezoelectric disks can generate a longitudinal ultrasonic vibration if an AC field is applied. This longitudinal ultrasonic vibration excites a flexural vibration in a thick disk of the torsion coupler. A square beam on the disk is torsioned by the flexural vibration of the disk. The elliptical vibration is excited on the top surface of stator by L/T coupler. When a rotor is contacted on the surface of the beam, it can be rotated by the friction force. Our experimental results show that the rotational speed can be increased by improving the structure of L/T coupler.

## EXPERIMENTAL PROCEDURE AND RESULTS

### 1. Piezoelectric ceramic composition

The composition of the piezoelectric vibrator is as follows:  $\text{Pb}[(\text{Mn}_{1/3}\text{Sb}_{2/3})_x(\text{Co}_{1/3}\text{Sb}_{2/3})_y\text{Ti}_z\text{Zr}_w]\text{O}_3$ ,  $x = 0 - 0.20$ ,  $y = 0 - 0.20$ ,  $z = 0.30 - 0.50$ ,  $w = 0.30 - 0.50$ ,  $x + y + z + w = 1$ .

The chemical grade  $\text{Pb}_3\text{O}_4$ ,  $\text{ZrO}_2$ ,  $\text{TiO}_2$ ,  $\text{Co}_2\text{O}_3$ ,  $\text{MnCO}_3$ , and  $\text{Sb}_2\text{O}_5$  powders were used as raw materials. Ceramic powder was prepared by mixing/solid-state reaction method, then pressed into disc samples with a

diameter of 15 mm and thickness of 1 mm under pressure of 100 MPa. The samples were sintered at 1200°C for 4 hours. After sintered, a silver paste was coated on the both side of the samples and fired to form electrodes. The electroded samples was then polarized by applying a DC field of 4 KV/mm at 120°C in silicon oil. Dielectric properties were measured by an automatic bridge. Piezoelectric properties were measured by resonance-antiresonance method. The measured results are  $K^p = 0.54$ ,  $d_{33} = 223 \times 10^{-12} \text{ C/N}$ ,  $\epsilon_{33}^T/\epsilon_0 = 1140$ ,  $Q_m = 1296$ ,  $T_c = 300^\circ\text{C}$ ,  $Y_{11}^E = 8.8 \times 10^{10} \text{ N/m}^2$ , and  $\tan\delta < 30 \times 10^{-4}$ , respectively.

Two piezoelectric ceramic disks with outer/inner diameters of 32 mm and 15 mm, and thickness of 2 mm, made from the above composition and processing, were contacted by facing each positive electrode surface to a thin copper plate. They were bolted tightly into a torsion coupler to form a stator. The piezoelectric disks generate a thickness vibration within a stator when an AC field is applied. This longitudinal vibration excites a bending vibration in a 5 mm thick disk of the torsion coupler. A square beam set diagonally on the disk is torsioned by the bending vibration of the disk. Therefore, the elliptical vibration required is created on the top surface of the torsion coupler.

A rotor was contacted tightly with a coil spring and a screw bolt to construct a piezoelectric ultrasonic motor. The rotor rotated depending on the contact pressure. Fig.1 shows the structure of a standing wave motor.

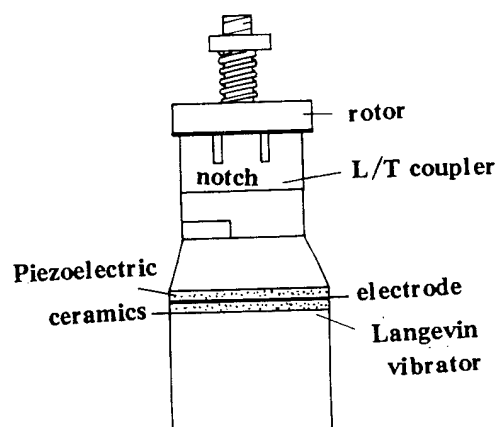


Fig. 1. Structure of Langevin-type standing wave motor.

## 2. Friction materials

A ceramic/metal composite was used as friction material, in which metal powders with  $\text{SiO}_2$ ,  $\text{Al}_2\text{O}_3$  and mullite additives were used as matrix, graphite and  $\text{MnS}_2$  were used as lubricants, and some metallic fibers were used as strengthen material. After formed, the composite was sintered in  $\text{N}_2$  and Ar atmosphere at  $1000^\circ\text{C}$  for 2 hours. The frictional coefficient, the density, bending strength and scuff rate of the frictional material are  $0.48 \sim 0.52$ ,  $4.98 \text{ g/cm}^3$ ,  $90 \text{ MPa}$  and  $4 \times 10^{-8} \text{ cm}^3/\text{kgf m}$ , respectively. In order to suppress noise during the friction processing, a suitable porosity level in the frictional material is necessary.

## 3. The improvement of L/T coupler

Based on the operation principle of standing wave motor, the elliptical vibration generator required in ultrasonic motor can be composed by coupling the longitudinal mode to the torsional mode at the same frequency. Thus, the L/T coupler play an important role in Langevintype ultrasonic motor. The improved L/T coupler is shown in Fig.2. It can be seen that two notches lie symmetrically to a square beam on the L/T coupler. According to the apparent elastic theory [4], the vibration of L/T coupler can be synthesized by a longitudinal vibration with longitudinal apparent elastic constant  $E_z$ , a flexural vibration with bending apparent elastic constant  $E_B$  and a torsional vibration with torsional apparent elastic constant  $E_T$ . The experimental results show that the rotational speed can be obviously increased in L/T coupler with notches. Fig.3 shows the relationship between rotational speed and frequency, indicating that the largest rotational speed occurs at about 30 KHz. Fig. 4 indicates that rotational speed increases with operation voltage. Fig.5 shows the relationship between rotational speed and torque. It can be seen that the rotational speed decrease with increasing of load

## FINITE ELEMENT ANALYSIS AND EQUIVALENT CIRCUIT

### 1. Finite element analysis of vibration mode for L/T coupler.

The finite element analysis of the first to the seventh order or even higher order vibration mode for L/T coupler was conducted. The results indicated that only the fourth or the fifth order vibration mode can be used for driving motor. Fig.6 and Fig.7 show the vibration mode and resonance frequency of both the fourth and fifth order for L/T coupler without and with notches. It is indicated that after notched, large torsional vibration can be obtained by a relatively smaller longitudinal exciting force. Therefore, L/T coupler with notches can increase the driving effect. It can be also seen that the resonance frequency of L/T coupler with notches is lower than that of without notches, due to the lower stiffness of the notched L/T coupler.

Fig. 8 shows a period dynamic processing of the fifth order vibration mode of L/T coupler with notches. In the above finite element analysis, the condition is that

the end of square beam of L/T coupler is free and the bottom of coupler is affected by a period longitudinal force.

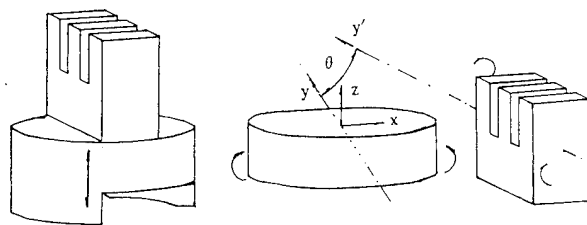


Fig. 2. Longitudinal - torsional coupler with notches.

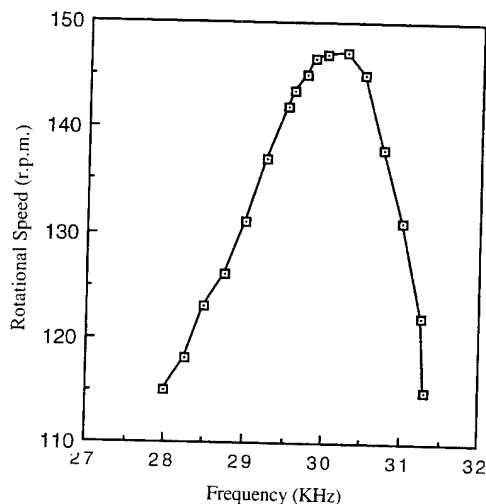


Fig. 3 The relationship between rotational speed and frequency.

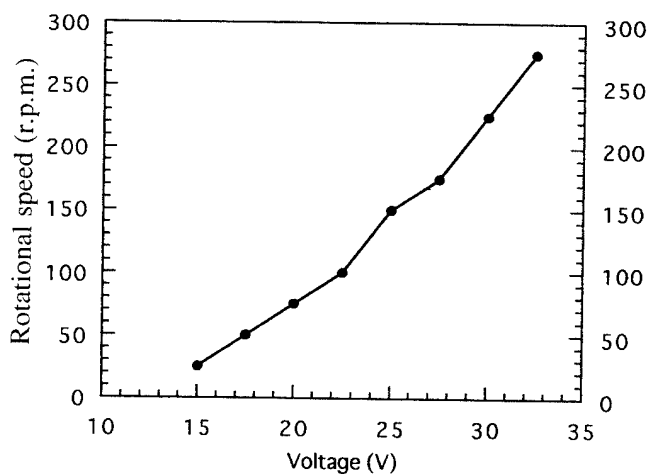


Fig. 4. The relationship between rotational speed and operation voltage.



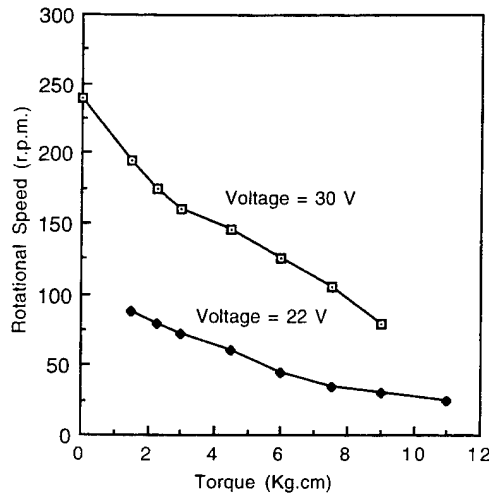


Fig. 5. The relationship between rotational speed and torque.

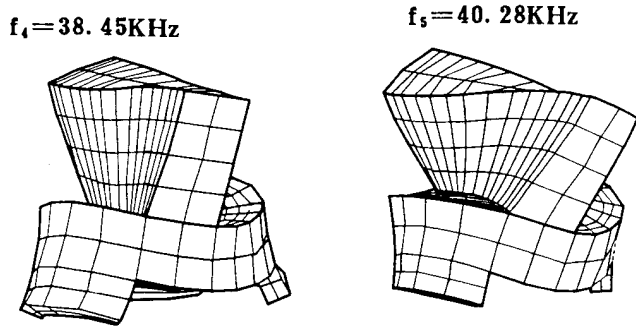


Fig. 6. The fourth and fifth order modes for longitudinal-torsional coupler without notches

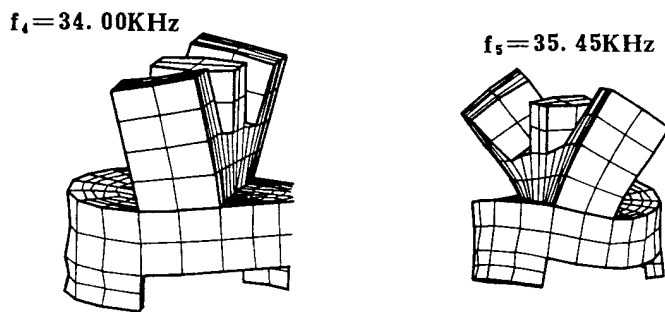


Fig. 7. The fourth and fifth order modes for L/T coupler with notches.

## 2. The equivalent circuit of L/T coupler for standing wave motor.

The stator of standing wave motor consists of a Langevin-type transducer and a L/T coupler. the electromechanical equivalent circuit of Langevin-type transducer can be deduced by normal electromechanical analogism. But the electromechanical network of L/T coupler can not be deduced directly by electro-

mechanical analogism, due to the presence of coupling vibration. According to apparent elastic theory, the equivalent circuit of L/T coupler can be shown in Fig.9, where  $Z_1 = \rho C_1 S_{1L}$ ,  $Z_2 = \rho C_2 S_{2L}$ ,  $C_z = \sqrt{Ez/\rho}$ ,  $S_{1L}$  and  $S_{2L}$  are the area of cylinder with length  $l_1$  and  $l_2$ ,  $\rho$  is the density of metallic match cylinder,  $Z_B$  and  $Z_T$  are the equivalent impedance of both bending vibration and torsional vibration,  $Z_1$  and  $Z_2$  are the equivalent impedance of longitudinal vibration,  $Z_{LL}$ ,  $Z_{LB}$  and  $Z_{LT}$  are the load impedance of longitudinal, flexural and torsional vibration, respectively.  $l_1$  and  $l_2$  are the length of underside and upside of metallic match body for longitudinal vibration,  $K = 2\pi f/v$ ,  $f$  is frequency and  $v$  is the wave velocity of longitudinal vibration.

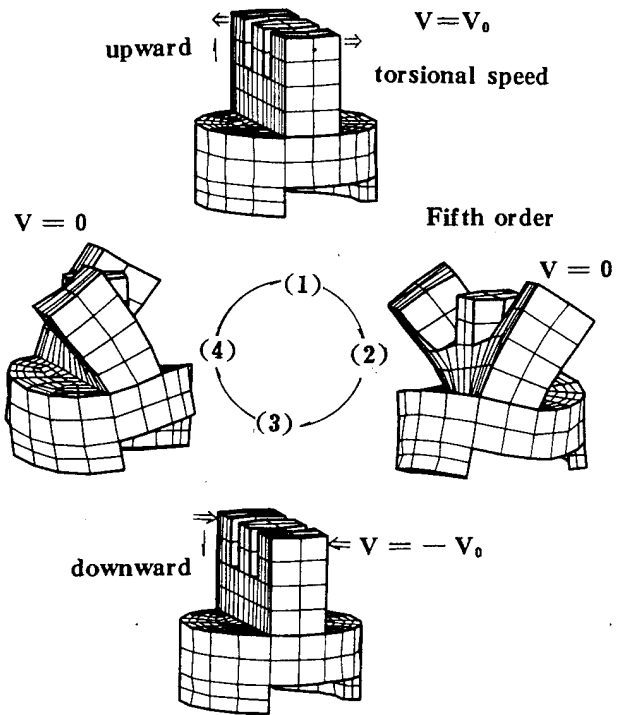


Fig. 8. Schematic of a period dynamic processing of fifth order vibration mode for L/T coupler.

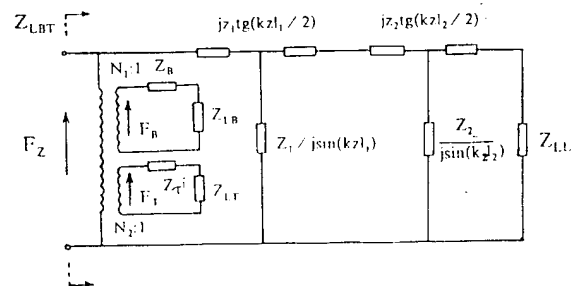


Fig. 9. Equivalent circuit of L/T coupler.

Fig. 10 shows the equivalent circuit of stator for standing wave motor.  $Z_b$ ,  $Z_b'$  are the equivalent impedances,

$$Z_b = j\rho_b V_b S_b \tan \frac{k_b l_b}{2}, \quad Z_b' = \frac{\rho_b V_b S_b}{j \sin(k_b l_b)},$$

where,  $\rho_b$ ,  $S_b$ ,  $E_b$  and  $V_b$  are the density, across-section area, elastic constant and acoustic velocity of underside match cylinder.  $V_b = \sqrt{\frac{E_b}{\rho_b}}$ ,  $k_b = \frac{2\pi f}{V_b}$ ,  $f$  is frequency.

$Z_e$ ,  $Z_e'$  and  $C_0$  are equivalent impedances and capacitance of piezoelectric ceramic vibrator.

$$Z_e = j\rho_e V_e S_e \tan(k_e l_e), \quad Z_e' = \frac{\rho_e V_e S_e}{j \sin(2k_e l_e)},$$

where  $\rho_e$ ,  $l_e$ ,  $S_e$  and  $V_e$  are the density, thickness, across-section area and acoustic velocity of piezoelectric ceramic vibrators.

$$V_e = \frac{1}{\sqrt{\rho_e S_{33}^E}}, \quad K_e = \frac{2\pi f}{V_e}, \quad n = \frac{S_e}{l_e} \frac{d_{31}}{S_{33}^E}.$$

$C_0 = S_e (1 - K_{33}^2) \epsilon_{33}^T / l_e$ ,  $n$  is electromechanical coupling coefficient.  $Z_{f1}$ ,  $Z_{f2}$  and  $Z_{f3}$  are the equivalent impedances of conical variable amplutuder.

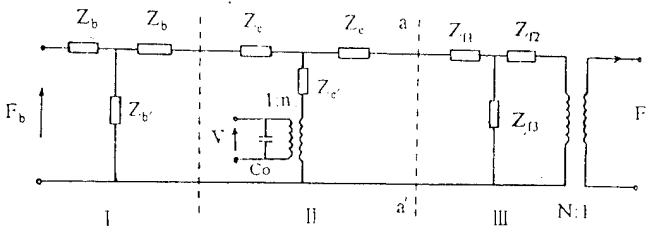


Fig. 10. Equivalent circuit of stator for standing wave motor.

Fig. 11 indicates the schematic of conical variable amplutuder, in which  $D_1$  and  $S_{f1}$  are the diameter and across-section area of under-section,  $D_2$  and  $S_{f2}$  are the diameter and across-section area of up-section for conical variable amplutuder, respectively.  $\rho_f$ ,  $V_f$  and  $l_f$  are the density, acoustic velocity and length of conical variable amplutuder.

$$Z_{f1} = jZ_{f0} \tan \frac{K_f l_f}{2} + j \frac{Z_{f0} \alpha}{K_f},$$

$$Z_{f2} = jZ_{f0} \tan \frac{K_f l_f}{2} - jZ_{f0} \frac{N\alpha}{K_f},$$

$$Z_{f3} = \frac{Z_{f0}}{j \sin(K_f l_f)},$$

where  $N = (S_1 / S_2)^{1/2} = \frac{D_{f1}}{D_{f2}}$ ,  $N$  is the ratio of under-

sectional diameter to up-sectional diameter of conical variable amplutuder.

$$\alpha = \frac{D_{f1} - D_{f2}}{D_{f1} l_f} = \frac{N - 1}{N l_f}, \quad \alpha \text{ is conicity}$$

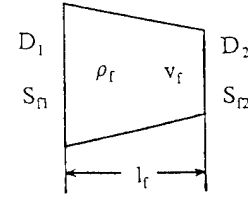


Fig. 11. Schematic of conical variable amplutuder.

$Z_{f0} = \rho_f V_f S_{f1}$ , it is the characteristic impedance,  $a - a'$  is the nodal face of equivalent circuit. Based on the imaginary impedance equals to zero at resonance situation, the frequency equations of leftside circuit of  $a - a'$  (I, II part) and rightside circuit of  $a - a'$  (III part) can be deduced:

$$\tan(K_e l_e) = \frac{\rho_e V_e}{\rho_b V_b} \cot(K_b l_b) \quad (1)$$

$$Z_{f1} + Z_{f3} + N^2 Z_{LBT} = 0 \quad (2)$$

where  $Z_{LBT}$  is the load impedance.

According to equation (1) and (2), the structure parameters of standing wave motor could be designed and calculated.

## CONCLUSION

1. The notched L/T coupler can increase the rotational speed of standing wave motor.
2. The  $\text{Pb}[(\text{Mn}_{1/3}\text{Sb}_{2/3})_x(\text{Co}_{1/3}\text{Sb}_{2/3})_y\text{Ti}_z\text{Zr}_w]\text{O}_3$  piezoelectric ceramics with excellent properties can be used for transducer in standing wave motors.
3. A metallic fiber reinforced metal/ceramic composite with metal matrix,  $\text{Al}_2\text{O}_3$ ,  $\text{SiO}_2$  and mullite additives, graphite and  $\text{MnS}_2$  lubricant is suitable friction material for standing wave motors.
4. The vibration mode and resonance frequency of L/T coupler has been analyzed using finite element method.
5. The finite element analysis is an effective method for studying the vibration modes of ultrasonic motors.

## REFERENCE

- [1] Akio Kumada, "A piezoelectric ultrasonic motor", *Jpn. J. of App. Phys.* Vol. 24, 739 - 741 (1985).
- [2] Jiromarn Tsujino et al., "Ultrasonic rotary motor using longitudinal - torsional vibration converter", Report of the Meetings, the Acoustical Society of Japan, Sep. 1990, pp.801.
- [3] Akio Kumada, "Ultrasonic motor using bending, longitudinal and torsional vibrations, *U.S. Patent*, Appl. No. 831578.
- [4] Mori. E. Itoh, K. Imamura, *Proc. Ultrasonic Intern.* 1977, 262 - 266.
- [5] J. Irjima, M. Wada, Y. Nakagawa and H. Itoh, "Ultrasonic motor using flexural standing wave", *Jpn. J. App. Phys.*, Vol. 26, Suppl. 26 - 1, pp.191 - 193 (1987)

# Mixing and Detection of Electrical Signals from 10 Hz to 20 GHz in a Electrostrictive Fiber Optic Sensor

S.T. Vohra and L. Fabiny  
Naval Research Laboratory  
Optical Science Division, Code 5670  
Washington, DC 20375

**Abstract** - The nonlinear strain-polarization relationship in electrostrictive ceramics is exploited to demonstrate for the first time, mixing and detection of electrical signals over 9 decades of frequency (10 Hz to 20 GHz) in a fiber optic electrostrictive sensor.

## INTRODUCTION

The nonlinear strain-polarization relationship in electrostrictive materials has previously been exploited to demonstrate novel fiber optic electric field sensors [1-3]. The nonlinear strain-polarization (electric field) relationship in electrostrictors can be written as  $e = ME^2$  where  $e$  is the induced strain in the material,  $E$  is the applied electric field and  $M$  is a frequency dependent effective electrostriction parameter [4]. In this work, the nonlinear strain-electric field relationship in a lead magnesium niobate (PMN) based electrostrictive transducer is exploited for the first time to demonstrate mixing and detection of electrical signals over 9 decades of frequency (10 Hz to 20 GHz).

Consider two AC electrical signals applied to the transducer,  $E_1 \cos \omega_1 t$  and  $E_2 \cos \omega_2 t$ . The fields will generate strain  $e = M(E_1 \cos \omega_1 t + E_2 \cos \omega_2 t)^2$  in the electrostrictor thus providing strain responses at  $\omega_1$ ,  $2\omega_1$ ,  $\omega_2$ ,  $2\omega_2$  and  $(\omega_1 \pm \omega_2)$ . Due to the mechanical nature of the effect, significant electrostriction is limited to frequencies below approximately 100 kHz. However, in order to obtain strain at  $(\omega_1 - \omega_2)$  we found that it is not necessary for the transducer to respond electrostrictively at  $\omega_1$  and  $\omega_2$ ; it is only necessary for the external fields  $E_1 \cos \omega_1 t$  and  $E_2 \cos \omega_2 t$  to induce electrical polarization at  $\omega_1$  and  $\omega_2$  for mixing to occur. We show that this effect can be successfully exploited to demonstrate a novel type of a heterodyne electrical mixer/detector using fiber optic interferometry. A similar technique has been used previously to demonstrate mixing and detection of RF magnetic signals ( $f < 10$  MHz) in a magnetostrictive transducer [5].

For an electrostrictive transducer driven by two ac electrical signals  $E_1 \cos \omega_1 t$  and  $E_2 \cos \omega_2 t$ , the strain response at the sum and difference frequencies  $(\omega_1 \pm \omega_2)$  can be written as

$$e_{(\omega_1 \pm \omega_2)} = M_{(\omega_1 \pm \omega_2)} (E_1 E_2 \cos(\omega_1 \pm \omega_2) t) \quad (1)$$

where  $M_{(\omega_1 \pm \omega_2)}$  is the value of  $M$  at frequency  $(\omega_1 \pm \omega_2)$ . One of the fields ( $E_1 \cos \omega_1 t$ ) can be regarded as the 'test' signal while the second field ( $E_2 \cos \omega_2 t$ ) can be regarded as a local oscillator (LO) whose frequency is tuned to maintain the desired intermediate frequency (IF).  $\omega_{IF} = (\omega_1 - \omega_2)$ . The sensor effectively acts as a heterodyne detection system where

the electrostrictive transducer functions as both the receiving element and the nonlinear mixing element. The resulting strain at IF is detected with a fiber optic interferometer. Considering only the difference term, the optical phase shift at the IF induced in the optical fiber attached to the electrostrictive transducer is given by

$$\phi_{\omega_{IF}} = (2\pi n \xi / \lambda) L M_{(\omega_1 - \omega_2)} E_1 E_2 [\cos(\omega_1 - \omega_2) t] \quad (2)$$

where  $L$  is the length of the fiber interacting with the transducer,  $n$  ( $= 1.5$ ) is the refractive index of the fiber core,  $\lambda$  is the free space wavelength of the light, and  $\xi$  ( $= 0.78$ ) is the strain-optic factor.

## EXPERIMENT

The experimental arrangement is shown in Figure 1. A lead titanate (PT) doped lead magnesium niobate (PMN) actuator stack,  $(PT)_{0.075}:(PMN)_{0.925}$ , placed inside an elliptically shaped aluminum shell forms the electrostrictive transducer. Single mode optical fiber is wrapped ( $L = 35$  meters) around the transducer and the assembly incorporated into a fiber Mach-Zehnder interferometer operating at  $\lambda = 1.3$   $\mu$ m. The sensor employed active homodyne demodulation with a PZT element in the reference arm. The electrostrictive coefficient at the IF, which was chosen to be 23.2 kHz due to a large mechanical resonance in the transducer at that frequency, was measured to be  $M_{(\omega_1 - \omega_2)} = 3.3 \times 10^{-15}$  ( $m^2/V^2$ ). The layer thickness ( $T$ ) of the electrostrictive actuator was 100  $\mu$ m. The test and the LO microwave signals from two synthesizers (HP 8341A) were combined with a conventional broadband electrical combiner and applied directly to the electrostrictive transducer. Although electrostrictive materials are capable of

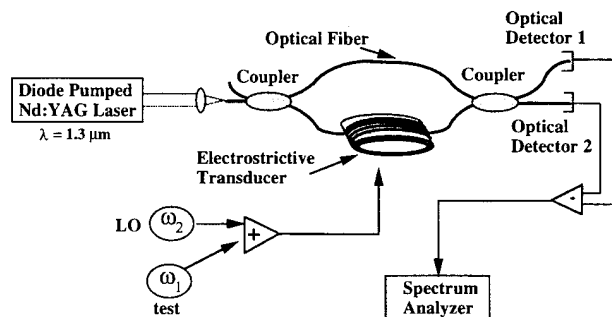


**Figure 1** Schematic of the fiber optic interferometer containing the PT:PMN electrostrictive transducer. The local oscillator (LO) and test signals were applied directly to the transducer. In more practical situations, the test signal will be the measurand signal from an antenna.

responding well above 20 GHz, we were limited in our experiments to less than 20 GHz due to equipment limitations. Short cable lengths were utilized for high frequency measurements and the electrical response at IF was continuously monitored to ensure no direct excitation of the transducer at IF by the input circuits.

## RESULTS AND DISCUSSION

Figure 2 is the interferometer response at the IF frequency, 23.2 kHz, as a function of test signal frequency  $\omega_1/2\pi$ . The LO frequency was automatically adjusted at each point to maintain  $\omega_{IF} = (\omega_1 - \omega_2)$ . The test signal frequency was varied from 10 Hz to 10 Giga-Hz. It is clear from Figure 2 that the electrostrictive fiber optic sensor responds at IF in the entire (9 decades in frequency) range. The interferometer noise floor was approximately  $0.5 \mu\text{rad}/\sqrt{\text{Hz}}$  at the intermediate frequency (IF) of 23.2 kHz.

From Figure 2 it is obvious that the response at IF is flat below 100 kHz. Between 100 kHz and 10 MHz the response of the sensor tends to roll-off at the rate of approximately 20 dB/decade. For signal frequencies above 10 MHz the response is more or less flat upto 10 GHz. The data shown in Figure 2 is not normalized to the excitation fields which tend to change as a function of frequency due to the capacitive effects in the transducer. The flat response at low frequencies ( $f < 100$  kHz) followed by a roll-off can be readily understood by a simple RC electrical model in which the electrostrictive transducer acts as the capacitor. However, the rate of the roll-off followed by another flat region above 10 MHz cannot be explained by the simple RC model. Furthermore, the dielectric coefficient of PMN:PT type electrostrictive materials, which tend to be strongly frequency dependent, is not well known for  $f > 100$  kHz, making it difficult to model the response in the entire frequency range with a simple RC type model. It is however clear from Figure 2 that nonlinear electrostrictive materials can be used as transducing elements in fiber optic interferometers to make high quality broadband electrical mixers and sensors.

We made more detailed measurements in the microwave regime since the device has potential to act as a high quality

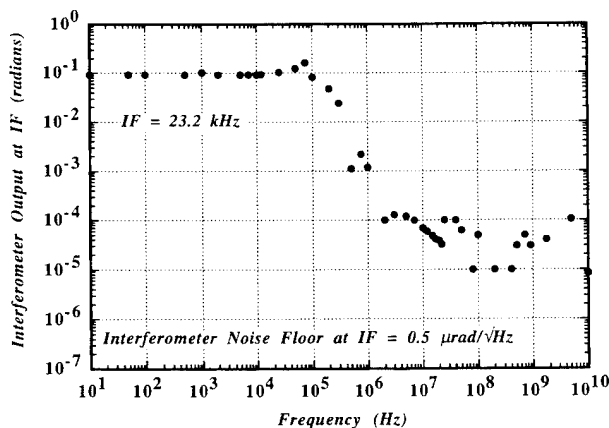


**Figure 2** Response of the electrostrictive fiber optic electric field mixer/sensor from 10 Hz to 10 GHz.

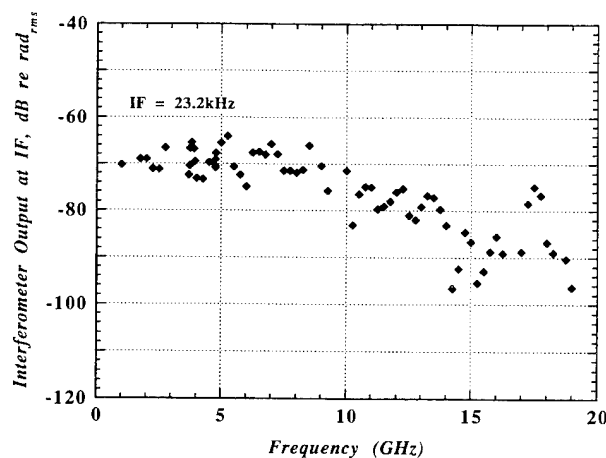


**Figure 3** Response of the electrostrictive fiber optic electric field mixer/detector in the microwave regime.

microwave mixer/detector. The results are described in Figure 3. The response at the IF is shown in terms of the optical phase shift and appears to be flat between 1 and 10 GHz. For  $(\omega_1/2\pi) \geq 10$  GHz the response tends to show a slight downward slope. This is most likely due to microwave losses in the material as well as sundry parasitic effects at high frequencies. With the LO amplitude of  $1.7 \times 10^{-3} \text{V}_{\text{rms}}$ , we detected signals below 10 GHz with a resolution of  $5 \times 10^{-6} \text{V}/\sqrt{\text{Hz}}$ , limited only by the  $0.5 \mu\text{rad}/\sqrt{\text{Hz}}$  interferometer noise level at the IF. Further improvements in the resolution can be achieved by improving the optical phase resolution at the IF and improving the electrical design of the transducer for carrying microwaves more efficiently. The device should be usable above 20 GHz since the polarization in the material is theoretically predicted to respond well above 40 GHz.

In summary, we have demonstrated for the first time, mixing and detection of electrical signals over 9 decades in frequency with a fiber-optic electrostrictive sensor. The technique utilized is a novel heterodyne detection scheme which relies on the nonlinear strain-polarization relationship in electrostrictive ceramics. We are currently investigating further improvements in signal-to-noise-ratio, increased frequency response and shifting the IF to higher frequencies.

We acknowledge many useful discussions with R.D. Esman, G. Gopalkrishnan and F. Bucholtz.

## REFERENCES

1. S.T. Vohra, F. Bucholtz and A.D. Kersey, Opt. Lett. 16, 1445 (1991).
2. S.T. Vohra and F. Bucholtz, Opt. Lett. 17, 372 (1992).
3. S.T. Vohra and L. Fabiny, Electron. Lett. 30, 444 (1994).
4. L.E. Cross, Ferroelectrics 76, 241 (1987).
5. F. Bucholtz, D.M. Dagenais and K.P. Koo, Electron. Lett. 25 (19), 1285 (1989).

**Concurrent Session - 5B/6B:  
Photorefractives/Pyroelectrics/  
Electrooptics**

# Optically Induced Ferroelectric Domain Gratings in SBN: Theory and Applications to Quasi-Phase Matching and Optical Data Storage

Anthony S. Kewitsch\*, Mordechai Segev\*, Akira Saito\*, Amnon Yariv\*, Gregory J. Salamo†, Terrence W. Towe†, Edward J. Sharp‡ and Ratnakar R. Neurgaonkar§

\*Department of Applied Physics, Caltech, Pasadena, California 91125

†Department of Physics, University of Arkansas, Fayetteville, Arkansas 72701

‡Army Research Laboratory, Fort Belvoir, Virginia 22060

§Rockwell International Science Center, Thousand Oaks, California 91360

**Abstract** -- Illuminating a photoconducting strontium barium niobate crystal with a low intensity optical standing wave generates dynamic as well as remnant polarization gratings. We study the kinetics of these gratings and present a thermodynamic model for the grating formation. Fundamentally, light induced space charge fields dynamically modify the positions of ions within the unit cell and tailor the electronic, optical, and acoustic properties of the material.

## INTRODUCTION

Light interference patterns can photoexcite mobile charge and generate periodic space charge fields with periods of typically 0.1 to 100 microns in photorefractive crystals. The space charge field amplitude is typically 0.1 to 1 kV cm<sup>-1</sup> in ferroelectrics such as Sr<sub>0.75</sub>Ba<sub>0.25</sub>Nb<sub>2</sub>O<sub>6</sub> (SBN:75). A fundamental question is whether these periodic space charge fields can spatially modulate the ferroelectric polarization in materials which possess a coercive field on the order of the space charge field. We present experimental evidence demonstrating that this is indeed the case in SBN:75. We observe dynamic domain gratings, which form simultaneously with the build-up of the space charge field, and remnant domain gratings, which persist long after the space charge field disappears.

These domain gratings are potentially useful in applications such as holographic data storage and second harmonic generation. For instance, one application is quasi-phase matching (QPM) of a second harmonic process, a technique to compensate for the phase mismatch of the fundamental and second harmonic beams. This is typically implemented by modulating the spontaneous polarization and as a consequence modulating the nonlinear coefficients. We experimentally demonstrate tunable QPM using dynamic as well as remnant domain gratings with periods equal to twice the coherence length of the second harmonic process. This all-optical technique achieves nearly instantaneously what would normally require complex and lengthy growth and materials processing and has the potential of achieving as large a second harmonic conversion efficiency as more mature technologies. We begin by describing a high intensity technique to optically record these domain gratings.

## HIGH INTENSITY DOMAIN FIXING

The standard models of steady state photorefractive space charge fields are intensity independent. However, when recording holograms with high intensities in the region of strong optical absorption, significant local heating occurs (2-5 °C for 10 W cm<sup>-2</sup>). As the crystal is heated closer to the Curie point, the polarization viscosity decreases and it is easier to modulate the ferroelectric polarization. In addition, intensity dependent photoferroelectric

phenomena may play an increasingly important role (e.g. electronic screening of ferroelectric dipole interaction). Thaxter and Kestigian [1] observed that the hologram lifetime during readout increased as the exposure level was increased beyond a threshold value, with enhanced hologram lifetimes of several minutes. Kewitsch et. al. [2] reported similar results displaying an exposure threshold for fixing of 100 J cm<sup>-2</sup>, with effectively infinite lifetimes. This exposure threshold is primarily attributed to local heating in the region of intense illumination.

Figure 1 is the experimental setup for writing transmission gratings with  $k_g$  parallel to the c axis. The time dynamics of the hologram recording and readout at different intensities are depicted in figures 2a and b. For gratings written with intensities of 1 W for more than 100 sec (figure 2a), a significant fixed grating persists upon readout (figure 2b). The chaotic nature of the diffraction efficiency at high intensities is a signature of thermally induced domain reversal and is called optical Barkhausen noise [3]. During the first several minutes of high intensity exposure, local heating and the periodic space charge fields partially depolarize the crystal. As domains reverse, they produce a depolarization current dP/dt. This time varying current noise introduces noise in the hologram diffraction efficiency. Indeed, the noise in diffraction efficiency is strongly correlated in time to the thermal noise in current across the crystal. The noise subsides as a steady state temperature is reached and as fringe stability is maintained. However, a weaker Barkhausen noise in both current and diffraction efficiency continues for the duration of the writing process.

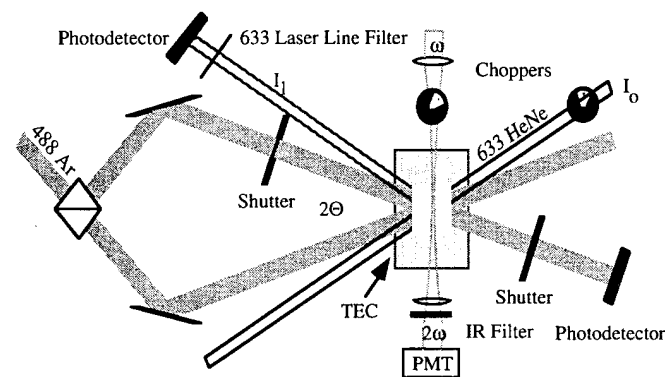


Fig. 1: Experimental setup for fixing and monitoring grating by optical diffraction and second harmonic generation. Source: Reference [4, 5].

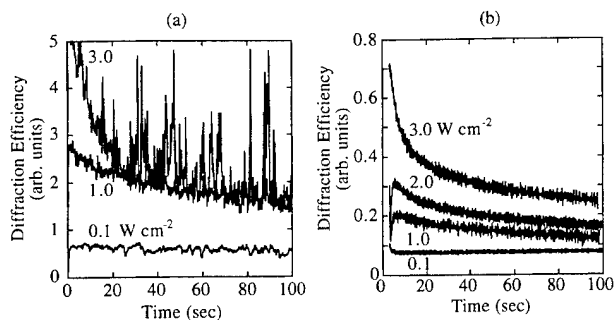


Fig. 2 (a) Diffraction efficiency during writing process for varying intensities. The noise at high intensities is due to optical Barkhausen pulses. (b) Diffraction efficiency during readout process with reference beam of same intensity. Note that magnitude of remnant polarization grating increases with exposure energy.

A domain grating written with high intensities is revealed microphotometrically [6]. Figure 3a illustrates the initial monodomain state following electrical poling. A polarization grating is then recorded with a period of 10 microns (figure 3b). This grating may be subsequently erased as in figure 3c by applying large poling electric fields, leaving a random multidomain crystal.

The experimental study of reference [2] indicates that the fixed diffraction efficiency during recording with high intensity beams ( $> 1 \text{ W cm}^{-2}$ ) increases for more than 8 hours upon continuous writing. Figure 4a depicts the first 2 hours of recording. Typical fixed diffraction efficiencies are 3%. Figure 4b illustrates the long term decay of a fixed hologram written at room temperature with a total intensity of  $4 \text{ W cm}^{-2}$  for 1 hour. Extrapolating this curve, the hologram is expected to survive at least several hundred days during continuous readout. The lifetime is further enhanced for readout with a weak plane wave, minimizing undesirable domain reversal due to the accumulation of space charge and pyroelectric fields on the periphery of a focused reference beam, in addition to local heating which reduces the polarization viscosity.

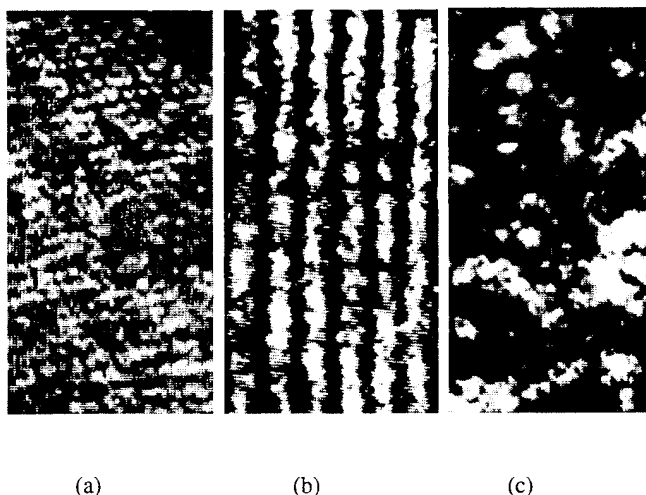


Fig. 3 Microphotometrically revealed domain grating with period of 10 microns. (a) poled crystal (b) domain grating (c) electrically erased grating.

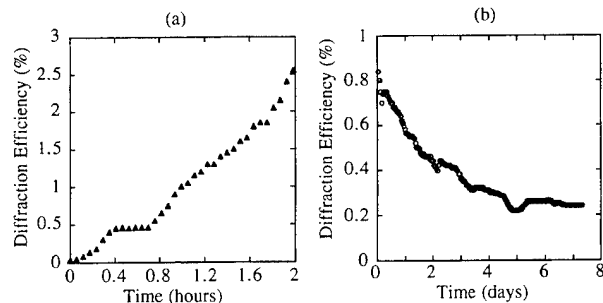


Fig. 4 (a) Long term hologram recording, illustrating monotonic increase of remnant diffraction efficiency. (b) Decay of remnant hologram diffraction efficiency at  $24^\circ\text{C}$  during continuous reconstruction with intense illumination (488 nm). Source: Reference [2].

These high intensity recordings are performed in initially poled crystals. Following a continuous recording process of two days, the macroscopic spontaneous polarization as measured from the electrooptic coefficient decreased by a factor of 10. This severe depolarization typically requires optical exposures on the order of  $10^5 \text{ J cm}^{-2}$ .

### SHORT EXPOSURE FIXING

High intensity fixing, using thermal effects and photorefractive space charge fields, leads to relatively strong fixed domain holograms. However, if a low intensity and short optical exposure is followed by a dark development stage, then space charge fields alone can produce fixed holograms. Note that the polarization change generally depends on the product of electric field and time in poling experiments, until saturation is reached. This is the motivation for using a dark development stage [4]. To make quantitative comparisons between the space charge and domain grating, the amplitude of the spatially periodic electric field is estimated from the measured diffraction efficiency during Bragg-matched reconstruction. In the symmetric transmission grating configuration with the grating vector  $\mathbf{k}_g$  parallel to the  $c$  axis, the amplitude of the net space charge field for an index grating produced through the linear electrooptic effect is, for small diffraction efficiencies and small half angle of the writing beams [7]:

$$E(\mathbf{k}_g = \mathbf{k}_1 - \mathbf{k}_2) = \frac{2\lambda e^{\alpha L/2} \sqrt{\eta(\mathbf{k}_g = \mathbf{k}_1 - \mathbf{k}_2)}}{\pi L n_0^3 r_{33}}, \quad (1)$$

where  $\mathbf{k}_g = \mathbf{k}_1 - \mathbf{k}_2$  expresses the Bragg condition for a diffraction maxima,  $\mathbf{k}_1$  and  $\mathbf{k}_2$  are the wave vectors of the signal and reference plane waves in the medium,  $\alpha$  is the absorption at the reconstruction wavelength  $\lambda$  in vacuum,  $L$  the interaction length of the readout beam and the volume grating,  $n_0$  the unperturbed index of refraction of the medium,  $r_{33}$  the dominant electrooptic coefficient for SBN:75 and  $\eta$  the diffraction efficiency defined as  $I_1/I_0$ , where  $I_1$  and  $I_0$  are the intensities of the diffracted and incident He-Ne beams, respectively (figure 1).

The remnant polarization modulation depends on the magnitude of the space charge field. To isolate the role of the space charge field, a short exposure technique is performed as follows: an arbitrary periodic space charge field is generated within the crystal by low intensity optical beams for typically a second. The exposure is followed by a dark development stage of typically minutes, during which time the domains stabilize in their reversed orientation. The dark development stage is effective because the space charge fields persist in the dark due to the low dark conductivity. Following a dark development stage of 10 minutes, the remnant polarization modulation exhibits a linear dependence on the initial field modulation (figure 5a). The efficiency of the fixing process, defined as the ratio of the bound charge field (corresponding to domain grating) to the initial space charge field, is 1%. These light induced domain patterns are produced in the absence of external electric fields or thermal effects.

$$\chi(T) = \frac{\beta}{(T_c - T)}, \quad T < T_c, \quad (3)$$

the decrease in the electrooptic coefficients, and the thermal scrambling of the domain grating all conspire to reduce the diffraction efficiency of the domain grating. Consequently, a two-stage fixing process, in which the domain grating generation is thermally assisted at elevated temperatures (30 to 37 °C) and then is frozen-in at slightly lower temperatures (25 to 20 °C) in the dark enhances both the grating modulation and lifetime.

The glassy ferroelectric properties of SBN reported in the literature [8] have several implications on the fixing method. We propose that the mechanism of optically induced domain reversal by space charge fields is a result of the macro-to-microdomain transformation under external electric fields [12]. External depoling fields in the presence of illumination have already been observed to produce a microdomain state in SBN [13]. In our experiments the periodic space charge is the source of the depoling field. To describe the kinetics of this process, we draw on the theory of spin glasses as applied to glassy ferroelectrics [12]. By cooling the crystal from above the Curie temperature to the freezing temperature  $T_f$  in the absence of an applied field, the ferroelectric is in a zero-field-cooled state in which long range ferroelectric order is absent. However, by cooling under an applied poling field, long range order can be frozen-in below  $T_f$ . This is conventionally called the field-cooled state. Depoling electric fields  $E$ , applied parallel to the  $c$  axis, lower the local freezing temperature through the deAlmeida-Thouless relationship [14]:

$$T_f(E) = T_f(0) \left[ 1 - \left( \frac{E}{A} \right)^{2/3} \right] \quad (4)$$

where  $A$  is a constant defined as  $A = k_B T / p_s$  and  $p_s$  is the freezing dipole moment. In our experiments the photogenerated space charge field is the source of this applied field. The periodic field spatially modulates the freezing temperature. In those regions where the freezing temperature is perturbed downward, the relaxation rate of the glassy polarization to the unpoled state increases dramatically. Therefore, in regions where the space charge field is parallel to the  $c$  axis, the long range order (or frozen-in polarization) will "thaw out" and reduce the polarization locally. In principle, large negative space charge fields ( $>1 \text{ kV cm}^{-1}$  for SBN:75) not only lower the freezing temperature as in equation 4, but also locally transform these microdomains into new inverted macrodomains (with dimensions typically greater than microns).

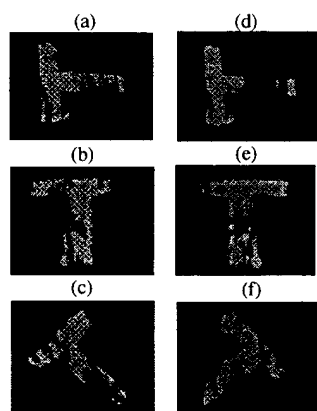


Fig. 8 Selective, page addressable fixing. Source: Reference [2].

## APPLICATIONS TO HOLOGRAPHIC DATA STORAGE

Holograms individually fixed in SBN (with a diffraction efficiency of 3%) do not require any post-writing processing, such as a heating cycle or an electrical fixing pulse [2, 4]. An increase in incident intensity, temperature (while below  $T_c$ ) or write time all tend to enhance the diffraction efficiency of the fixed hologram. A potential advantage of this technique is the ability to individually fix holograms (by increasing the exposure above a threshold of  $100 \text{ J cm}^{-2}$ ) that may be individually overwritten [2]. This rewrite property is important in applications such as holographic random access memories or reconfigurable optical interconnects and has not been demonstrated using conventional thermal fixing techniques in  $\text{LiNbO}_3$ . Figures 8(a-c) illustrate three angle multiplexed holograms stored in the image plane and individually fixed for 15 minutes with incident intensities of  $4 \text{ W cm}^{-2}$ . The poor image quality is due to index inhomogeneities caused by growth striations, typically the result of impurities in the crystal growth process. The images were captured on a CCD camera after all three pages were fixed. The third page (c) was then overwritten by a fourth for 20 minutes. The 3 original addresses were then readout. The original 2 pages (d,e) remained fixed, while the third page was replaced by a fourth (f) fixed image. Obviously, the fixing process of the latter holograms degrades all previously fixed gratings. Proper scheduling of exposures must be implemented to optimize the overwriting process.

## APPLICATIONS TO SECOND HARMONIC GENERATION

Polarization gratings spatially modulate the nonlinear susceptibility of the crystal and offer the potential of significantly increasing the conversion efficiency of nonlinear wave mixing processes for modulation periods equal to twice the coherence length. Nonlinear phenomena such as second harmonic generation (SHG) and sum and difference frequency mixing are essential to extending the range of wavelengths generated by lasers. Phase matching, which is usually a prerequisite for efficient conversion, can only be achieved in a small fraction of nonlinear materials. The obstacle is overcome by using quasi-phase matching (QPM) [15, 16] to periodically compensate for the phase mismatch between the fundamental and second harmonic waves due to the dispersion of the index of refraction. This technique relaxes the stringent phase matching requirements based on birefringence [17] or modal dispersion in waveguides [18]. QPM can be achieved by periodically poling a ferroelectric crystal so that the relevant nonlinear coefficients for SHG are spatially modulated with a period equal to twice the coherence length. For co-linear beams, the coherence length is  $L_c = \lambda/4 (n^{2\omega} - n^\omega)$ , where  $\lambda$  is wavelength in vacuum of the fundamental,  $n^\omega$  is the index of refraction at the fundamental wavelength and  $n^{2\omega}$  is the index at the second harmonic. In the absence of periodic domain inversion, the coherence length is the maximum effective crystal length that is useful in generating the second harmonic power. Coherence lengths exceeding a few mm are needed in practice for efficient conversion. In ferroelectric crystals such as  $\text{LiNbO}_3$  and SBN:75, the coherence length is on the order of a few microns for second harmonic generation in the visible; consequently, the non-phase matched conversion is negligibly small despite the relatively large nonlinear coefficients. For these and many other highly nonlinear materials, QPM is a means of increasing the effective crystal length.

By using the photorefractive space charge to modulate the local polarization, tunable QPM can be achieved using dynamic polarization gratings. These gratings respond nearly instantaneously to changes in the photogenerated space charge field. This technique has been demonstrated in SBN:75 for doubling fundamental wavelengths of 880 to 990 nm [4, 5]. Figure 1 illustrates the experimental setup for writing domain gratings and simultaneously generating the second harmonic.



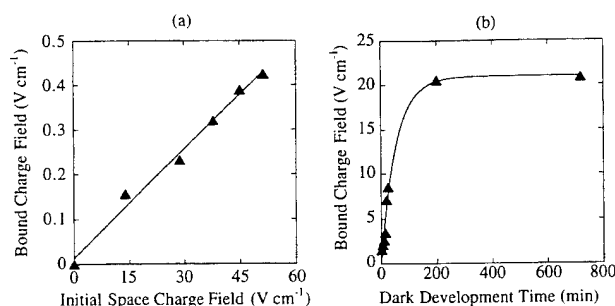


Fig. 5 (a) Dependence of remnant polarization grating on initial space charge field. (b) Dependence of remnant polarization grating on dark development time. Source: Reference [4].

The hysteresis is further enhanced by increasing the time duration of the dark development stage, or by applying an external depoling field during the development stage. For instance, a 1 second depoling field pulse of  $3 \text{ kV cm}^{-1}$  applied after the optical exposure increases the fixed diffraction efficiency of the domain grating by a factor of two. Also, longer dark development times increase the diffraction efficiency of fixed holograms by more than a factor of 100, as illustrated in figure 5b. For this set of experimental conditions (grating period =  $4 \text{ }\mu\text{m}$  and  $T = 25 \text{ }^\circ\text{C}$ ), the remnant polarization modulation saturates at approximately 0.02% of the spontaneous polarization, and the fixed grating buildup time is approximately 50 minutes.

#### GLASSY DOMAIN HOLOGRAMS

SBN possesses glassy ferroelectric properties that play a central role in the technique of optically induced domain gratings. SBN:75 is a relaxor [8] ferroelectric characterized by a diffuse phase transition and a low coercive field (of the order of  $1 \text{ kV cm}^{-1}$ ). In the ferroelectric phase, the  $\text{Nb}^{5+}$ ,  $\text{Sr}^{2+}$  and  $\text{Ba}^{2+}$  ions occupy one of two stable positions along the  $c$  axis. In the paraelectric phase, the ions are centrally located between the two stable positions [9]. The energy barrier separating the two equivalent polarization orientations scales with the volume of the microscopic domain, so a typical microdomain of characteristic length on the order of  $10 \text{ nm}$  may thermally fluctuate between the polarization states allowed by crystalline symmetry, analogous to a superparaelectric [10]. These thermal fluctuations are believed to freeze out as competing interactions (ferroelectric and antiferroelectric ordering) frustrate the fluctuations, leading to an enhanced remnant polarization grating lifetime.

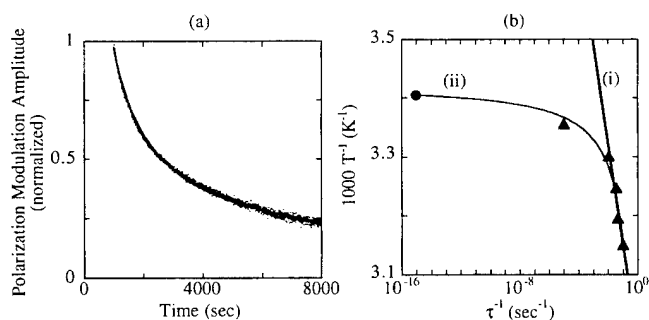


Fig. 6 (a) Power law decay of remnant polarization modulation amplitude at  $35 \text{ }^\circ\text{C}$ , typical of spin glasses. (b) Lifetime of remnant polarization modulation amplitude for different temperatures. (i) is Arrhenius activation process from a potential well, and (ii) is Vogel-Fulcher activation process for a system that exhibits freezing. Source: Reference [4].

The glassy nature of SBN has important implications on the lifetime of domain holograms. Although it is conventional to apply Gibb's free energy equilibrium arguments to evaluate the stability of domains, the stable glassy domain configuration may not necessarily be the equilibrium configuration. In fact, a non-equilibrium domain grating may be stable below a freezing temperature where the glassy polarization phase is inherently non-ergodic. At these temperatures the viscosity of the dipoles increases dramatically and freezes-in the polarization modulation. Figure 6a illustrates the thermally activated erasure of the domain grating at  $35 \text{ }^\circ\text{C}$ . The temporal response of the decay follows a  $t^{-\beta}$  law (as is common in spin glasses), where  $\beta$  is a measure of the polarization viscosity. The decay of the polarization grating was monitored continuously for  $10^4$  to as long as  $7 \times 10^5$  seconds. We verify that this decay indeed corresponds to a polarization grating by noting its insensitivity to optical intensity (as long as heating is avoided) and by erasing the grating electrically. We arbitrarily define the lifetime as the time in which the polarization modulation amplitude decays to 10% of its value at  $t = 1$  second, to avoid the unphysical singularity of the power law at  $t = 0$ . The lifetime of the grating at  $20 \text{ }^\circ\text{C}$  extends well beyond measurable times, yet the onset of freezing was readily apparent from the absence of grating decay after only 4000 seconds. By fitting a  $t^{-\beta}$  curve to the decay, we estimate that the lifetime is  $10^{15}$  seconds. The uncertainty of this value, while very large, does not influence the fit parameters significantly because of the divergence of the lifetime near the freezing temperature. The complete lifetime data is summarized in figure 6b. Data indicated by triangles correspond to measured lifetimes, the circle to an extrapolated lifetime. Each data point corresponds to two independent yet identical experiments. The functional fit (i) is the Arrhenius relation for the characteristic time  $\tau$  for thermal excitation out of a potential well of depth  $E_a$  for a system at temperature  $T$ . For a system that exhibits a polarization freezing temperature  $T_f$  (typical of glassy ferroelectrics), the Vogel-Fulcher law [11] is a more accurate empirical relationship between the decay time (i. e. the lifetime of the remnant domain hologram) and the temperature:

$$\frac{1}{\tau} = \frac{1}{\tau_0} \exp\left(\frac{-E_a}{k_B(T - T_f)}\right). \quad (2)$$

The freezing behavior is readily apparent for temperatures below  $30 \text{ }^\circ\text{C}$  in figure 6b, where the inverse lifetimes asymptotically approach zero. Fit (ii) illustrates the Vogel-Fulcher fit, with  $T_f = 19 \text{ }^\circ\text{C}$ ,  $E_a = 5 \text{ meV}$  and  $\tau_0 = 1 \text{ sec}$ , and displays excellent agreement with the data. This indicates that polarization gratings can be permanently frozen-in at sufficiently low temperatures.

The magnitude of the remnant polarization modulation shows a temperature resonance for experiments conducted at  $30$  to  $37 \text{ }^\circ\text{C}$  (figure 7). The dynamic grating response shows a similar temperature dependence. The weak response at low temperatures is due to the large viscosity of the glassy polarization. On the other hand, at temperatures above  $37 \text{ }^\circ\text{C}$ , the divergence of the static susceptibility according to the Curie-Weiss law:

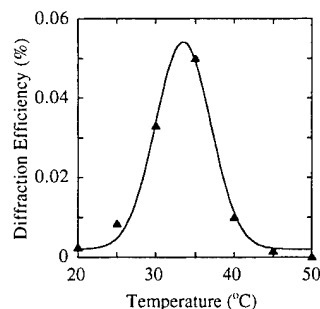


Fig. 7 Temperature resonance of magnitude of remnant polarization grating in SBN:75

The orientation of the crystalline axes of the SBN:75 crystal must be chosen so that both the grating vector and polarization of the fundamental beam have a significant projection along the *c* axis. The space charge field was used to invert domains, so a component of the grating vector along the poling axis is required. Similarly, the fundamental must have a significant projection of its electric field along the *c* axis to produce a large induced polarization at the second harmonic. The magnitude of the polarization at the second harmonic perpendicular to  $\mathbf{k}^{2\omega}$  (second harmonic wave vector) is:

$$P^{2\omega} = 2(d_{15}\sin^2\theta \cos\theta + d_{33}\cos^3\theta + d_{31}\sin^2\theta \cos\theta)E^\omega E^\omega, \quad (5)$$

where  $\theta$  is the angle of both  $P^{2\omega}$  and the polarization of  $E^\omega$  relative to the *c* axis. Although  $P^{2\omega}$  attains a maximum value at  $\theta = 0$  degrees, this orientation prevents the space charge field from having a significant component parallel to the *c* axis. However,  $P^{2\omega}$  remains significant for  $\theta$  as large as 45 degrees.  $\theta = 45$  degrees is a convenient tradeoff. By symmetry arguments, inverting the orientation of a ferroelectric domain changes the sign of all three nonlinear coefficients. Thus the effective nonlinear coefficient  $d_{\text{eff}} = (2d_{15} + d_{33} + d_{31})/2^{3/2}$  is modulated. The grating vector  $\mathbf{k}_g = \pi/\Lambda$  is oriented parallel to  $\mathbf{k}^\omega$  and  $\mathbf{k}^{2\omega}$  to maximize the overlap of the fundamental and second harmonic field profiles.

The QPM peak can be shifted in wavelength by writing polarization gratings with different periods. Figure 9a illustrates a typical QPM peak centered on 457.25 nm. The full width half maximum (FWHM) of the QPM peak was estimated using [19] in addition to the measured index dispersion data [20]. A FWHM of 0.2 nm for a crystal of thickness 4.25 mm is predicted, in close agreement with the measured FWHM of 0.175 nm from figure 9a. This observation confirms that the grating is uniform over the entire 4.25 mm propagation distance.

Several gratings with different periods can be written at the same or different locations within the volume of the crystal to tailor the spectral response of the SHG and can be rendered permanent by cooling and/or increasing the writing beam exposure. Figure 9b illustrates a series of QPM peaks written sequentially in the same volume, with the strongest enhancement peak corresponding to the last grating written. The spectral response can be designed by writing several gratings (either simultaneously or sequentially) with different periods. This figure also demonstrates that an enhancement of a factor of 17 above the background can be achieved by writing dynamic domain gratings. Typical single pass conversion efficiencies obtained experimentally are of the order of 0.01%. The SHG enhancement may be increased with higher intensity writing beams or with a lower intensity fundamental beam. While this second option decreases the conversion efficiency, both options increase the fringe visibility of the optical interference pattern and enhance the polarization modulation of the grating. This effect is explained by noting that the uniform fundamental beam is incoherent with the two writing beams and reduces the modulation index of the intensity grating. The degree of reduction depends on the absorption of the crystal at the fundamental wavelength. As a direct consequence the photoinduced space charge field and the polarization modulation are reduced by a factor of the modulation index.

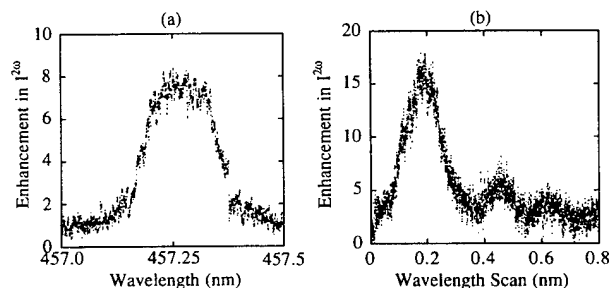


Fig. 9 (a) Typical QPM spectral response peak with a FWHM of 0.175 nm. (b) Multiple QPM peaks by writing several gratings sequentially. Source: Reference [5].

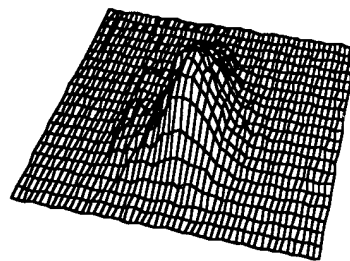


Fig. 10 Far field intensity profile of second harmonic (collimated TEM<sub>00</sub>). Source: Reference [5].

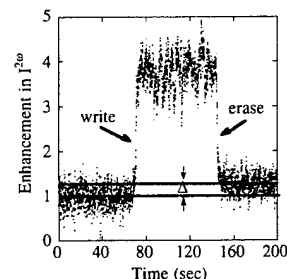


Fig. 11 Time evolution of second harmonic enhancement near center of QPM spectral response peak. Source: Reference [5].

The second harmonic beam exits the crystal in a well collimated, symmetric TEM<sub>00</sub> mode (figure 10). The polarization modulation extends well into the bulk since no degradation in second harmonic power is apparent while scanning the fundamental across the volume of the crystal. This demonstrates the uniformity of polarization gratings throughout the volume of the crystal.

The rapid enhancement of the second harmonic power during the writing of the volume hologram confirms the presence of dynamic domain gratings in addition to the more typical remnant domain grating. Figure 11 illustrates the time evolution of second harmonic power while writing a QPM grating with a total intensity of 1 W cm<sup>-2</sup>. The dynamic polarization grating tracks the free space charge grating in time. The transients in the peak enhancement are due to the decay and build-up of the grating as the optical fringes shift due to vibration, air currents and temperature changes. The buildup time constant of the QPM peak is approximately inversely proportional to intensity and is consistent with the photorefractive grating buildup times for SBN:75. At 1 W cm<sup>-2</sup> the build up time is 0.5 seconds, and at 0.33 W cm<sup>-2</sup> it is about 1.5 seconds.

## CONCLUSION

In summary, we have explored the fundamental phenomena associated with optically induced domain reversal, a physical effect in which light alone modulates the symmetry of a bulk crystal over distances on the order of optical wavelengths. We have isolated the role of the space charge field alone, by performing low intensity experiments in the absence of optical heating or external fields. We propose a thermodynamic description of the fixing process in the glassy ferroelectric phase of SBN which elucidates the kinetics of domain reversal. We believe this understanding also applies to reports of high intensity and electrical fixing of volume holograms in SBN [2, 21, 22, 23].

## ACKNOWLEDGEMENTS

The authors wish to thank Professor L. E. Cross for his extensive assistance regarding the ferroelectric properties of SBN. This work is supported by the ARPA and the Air Force Office of Scientific Research. A. Kewitsch would like to acknowledge the support of an ONR Fellowship.

## REFERENCES

- [1] J. B. Thaxter, M. Kestigian, *Appl. Opt.* **13**, 913-924 (1974).
- [2] A. S. Kewitsch, M. Segev, A. Yariv, R. R. Neurgaonkar, *Opt. Lett.* **18**, 1262-1264 (1993).
- [3] A. S. Kewitsch, A. Saito, M. Segev, A. Yariv, R. R. Neurgaonkar, *to be published*, (1994).
- [4] A. S. Kewitsch, M. Segev, A. Yariv, G. J. Salamo, T. W. Towe, E. J. Sharp, R. R. Neurgaonkar, *Phys. Rev. Lett.* **73**, August (1994).
- [5] A. S. Kewitsch, M. Segev, A. Yariv, G. J. Salamo, T. W. Towe, E. J. Sharp, R. R. Neurgaonkar, *Appl. Phys. Lett.* **64**, 1023-1025 (1994).
- [6] R. Matull, R. A. Rupp, *J. Phys. D: Appl. Phys.* **21**, 1556-1565 (1988).
- [7] P. Günter, J.-P. Huignard, Eds., *Photorefractive Materials and Their Applications I*, vol. 61 (Springer-Verlag, Berlin, 1989).
- [8] A. S. Bhalla, R. Guo, L. E. Cross, G. Burns, F. H. Dacol, R. R. Neurgaonkar, *J. Appl. Phys.* **71**, 5591 (1992).
- [9] P. B. Jamieson, S. C. Abrahams, J. L. Bernstein, *J. Chem. Phys.* **48**, 5048 (1968).
- [10] L. E. Cross, *Ferroelectrics* **76**, 241 (1987).
- [11] G. J. Fulcher, *J. Am. Cer. Soc.* **8**, 339 (1925).
- [12] D. D. Viehland, Dissertation, The Pennsylvania State University (1991).
- [13] M. Horowitz, A. Bekker, B. Fischer, *Appl. Phys. Lett.* **62**, 2619-2621 (1993).
- [14] J. R. de Almedia, D. J. Thouless, *J. Phys. A* **11**, 983 (1978).
- [15] J. A. Armstrong, N. Bloembergen, J. Ducuing, P. S. Pershan, *Phys. Rev.* **127**, 1918 (1962).
- [16] S. Somekh, A. Yariv, *Opt. Comm.* **6**, 301 (1972).
- [17] J. A. Giordmaine, *Phys. Rev. Lett.* **8**, 19 (1962).
- [18] P. K. Tien, *Appl. Opt.* **10**, 2395 (1971).
- [19] M. M. Fejer, G. A. Magel, D. H. Jundt, R. L. Byer, *J. Quant. Elect.* **28**, 2631 (1992).
- [20] E. L. Venturini, E. G. Spencer, P. V. Lenzo, A. A. Ballman, *J. Appl. Phys.* **39**, 343 (1968).
- [21] A. S. Kewitsch, M. Segev, A. Yariv, R. R. Neurgaonkar, *Jpn. J. Appl. Phys.* **32**, 5445-5446 (1993).
- [22] F. Micheron, G. Bismuth, *Appl. Phys. Lett.* **20**, 79-81 (1972).
- [23] Y. Qiao, S. Orlov, D. Psaltis, R. R. Neurgaonkar, *Opt. Lett.* **18**, 1004-1006 (1993).

# The Design, Processing, Evaluation and Characterization of Pyroelectric PVDF Copolymer/Silicon Mosfet Detector Arrays

Philip E. Bloomfield\*, Francisco Castro\*\*, and Roy M. Goeller\*\*\*

Drexel University, \*Biomedical Engineering & Science Institute, \*\*ECE Department, Philadelphia, PA 19104

\*\*\*Los Alamos National Laboratory, NIS-4, Los Alamos, NM 87545

**Abstract** -- We have developed a 64 element linear array of pyroelectric elements fully integrated on silicon wafers with MOS readout devices. The ferroelectric polymer film sensor deposited and polarized on the extended gate of the MOSFET results in a hybrid circuit, the pyroelectric-oxide-semiconductor field effect transistor (POSFET).

The fabrication of the wafers included the design of the various masks required to produce the layers which made up the transistor array: stopper layer, active layer, poly-silicon layer, contacts layer, and bottom electrode layer. A thin film of the ferroelectric copolymer P(VDF/TrFE) was spin coated onto the wafer. Patterned gold electrodes were sputtered as the top electrode layer. The ferroelectric copolymer was hysteresis poled in situ. Tests performed included the array's response to a CO<sub>2</sub> laser operating in the CW and single pulse modes at 10.6  $\mu\text{m}$ . We will present details of the design, processing, and testing of the fabricated devices.

## INTRODUCTION

Directly coupling the gate of an MOS transistor to a thin ferroelectric polymer transducer serves as the basis of a pyroelectric or piezoelectric imaging array [1,2]. PVDF and the VDF/TrFE copolymers are semicrystalline, the electric-field oriented crystalline component providing the macroscopic piezoelectric and pyroelectric activity. We utilized VDF/TrFE copolymers having molar ratios of VDF versus TrFE of 56/44, 61/39, and 70/30 since copolymers in this range of composition have the best pyroelectric response [3]. Rather than utilizing the epoxy-adhered PVDF film a la Swartz and Plummer, we have designed and fabricated a pyroelectric transducer array which utilizes a thin film of ferroelectric VDF/TrFE copolymer directly deposited from solution onto the extended gates of a silicon transistor array [1, 4]. We have designed and fabricated a small high density linear integrated array of pyroelectric elements fully integrated on silicon wafers with MOS readout. The pyroelectrically induced voltage biased enhanced current output of the MOS devices has been measured.

## DEVICE DESCRIPTION AND FABRICATION

The electronic interface to the pyroelectric transducer is an n-channel poly-silicon gate transistor with an extended aluminum gate. The source and drain regions, which are electron doped, are connected by a channel which is covered by a thin insulating film of silicon dioxide which itself is covered by the aluminum electrode gate. The combination of the channel, oxide layer, and gate acts as a capacitor. The VDF/TrFE copolymer film is sandwiched between a bottom aluminum electrode which is the extended gate of the MOS transistor and a top gold electrode which is the ground electrode during device operation. When the top electrode is exposed to radiation, the pyroelectric sensor modulates the electric field of the gate region. The greater the voltage produced on the gate due to the pyroelectric modulation, the lower the resistance between the source and drain and the greater the conduction.

Two arrays of transistors were designed to fit on each 50mm diameter  $\times$  0.33mm thick p-type silicon wafer. Each array had 32 pairs of transistors for a total of 64 transistors per array (Figure 1). The transistors in a pair are mirror images of each other. The fabrication of the wafers included the design of the different masks required to produce all the layers that make up the transistor array: stopper layer, active layer, poly-silicon layer, contacts layer, and bottom electrode layer. The masks were fabricated from computer generated mask designs [5]. In Figure 2 the transistor array layers are shown for a single transistor. The transistor region, consisting of the drain, source, and gate regions and contacts, is 0.3mm  $\times$  2.4mm. The gate area is  $14.5 \cdot 10^{-3} \text{mm}^2$  (10 $\mu\text{m} \times$  1.45mm). Each thin film sensor sits atop an extended gate of area 3.9mm<sup>2</sup> (0.39mm  $\times$  10mm).

The ratio between the gate voltage  $V_g$  and the transducer voltage  $V_T$  is the transfer ratio [1]:

$$V_g/V_T = \{1 + C_g/C_T\}^{-1}; \quad C_g = [C_{gs} + C_{sub} + C_{gd}(1 + A_v)] \quad (1)$$

Here  $A_v$  is the voltage amplification of the transistor amplifier circuit and  $C_{gs}$  and  $C_{gd}$  are the gate-to-source and gate-to-drain capacitances, respectively.  $C_{sub}$  is the extended gate to substrate (bulk) capacitance and  $C_T$  is the transducer (copolymer film) capacitance. In order to obtain a good transfer ratio one wants to

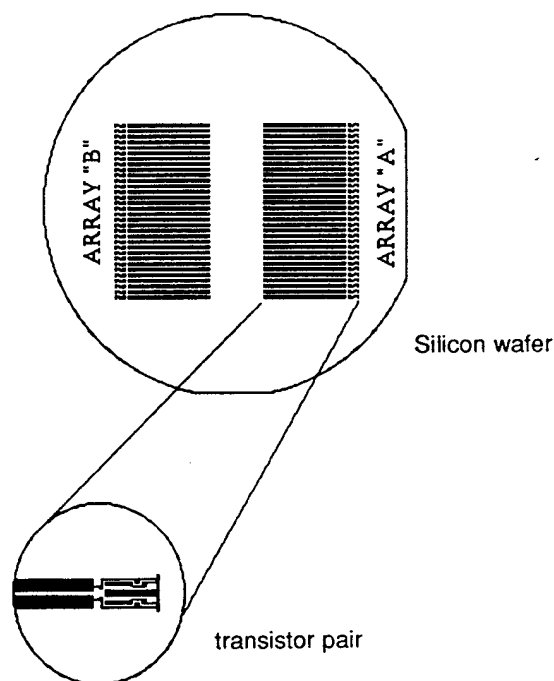


Figure 1. Silicon wafer transistor arrays and transistor pair.

minimize the  $C_g/C_T$  ratio. The use of a thick field oxide reduces  $C_{sub}$ . A voltage follower configuration can reduce the influence of  $C_{gs}$  and  $C_{gd}$ . The gate oxide, poly-silicon and bottom electrode aluminum thicknesses were the same as in [1]: 120nm, 500nm, and 200nm, respectively. However we increased the field oxide thickness from 0.6 $\mu$ m utilized in [1] to 1.2 $\mu$ m (by thermal deposition) for some of the wafers and to 3.0 $\mu$ m [1.2 $\mu$ m (thermally deposited) + 1.8 $\mu$ m (via CVD)]. From the above dimensions we can approximate (1) by  $V_g/V_T \approx \{1 + C_{sub}/C_T\}^{-1}$ . Utilizing the approximate values,  $\epsilon_{ox} \approx 4$  and  $\epsilon_T \approx 9$  we estimate for  $t_T = 7\mu$ m that  $C_g/C_T \approx 2.6$  or 1.0 for  $t_{ox} = 1.2\mu$ m or 3.0 $\mu$ m. Thus  $V_g/V_T \approx 0.28$  or 0.5, respectively.

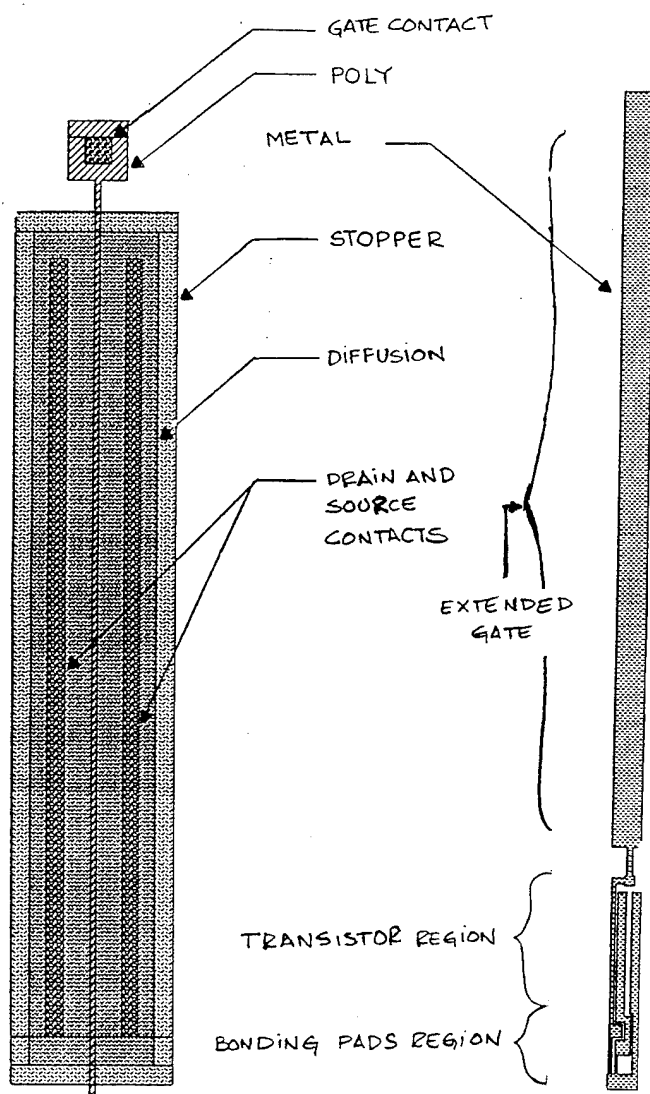


Figure 2. The design of individual transistor regions and layers.

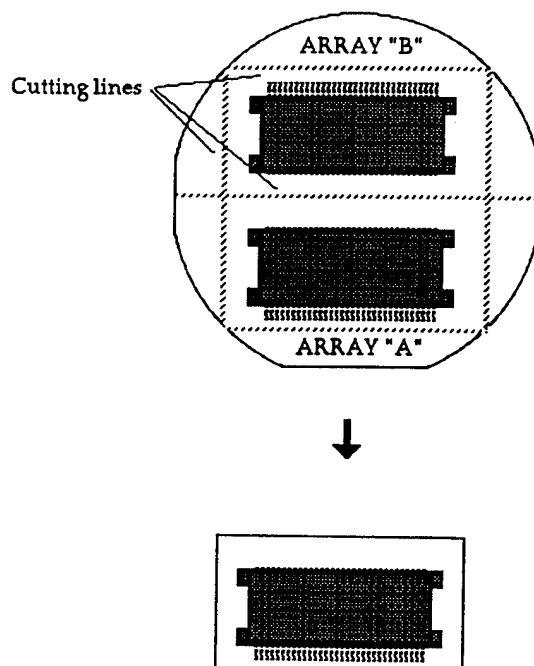


Figure 3. Wafer cutting to separate individual arrays.

#### FERROELECTRIC COPOLYMER PROCESSING

Six layers of copolymer were coated onto the wafer with a spin coating machine. When a twenty percent by weight solution of copolymer in methyl ethyl ketone was utilized, a copolymer thickness of  $\sim 7\mu$ m was achieved. A twenty-five percent solution produced  $\sim 15\mu$ m films. After each coating step, solvent evaporation from the wafer was accomplished by air drying for 25 minutes at R.T., followed by oven baking at 95°C for 45 minutes, followed by air cooling for 35 minutes. A thin gold electrode was sputtered through a mask onto the copolymer film (Figure 3).

To pole the film and to make contact to the device bonding pads part of the aluminum on the silicon wafer must be exposed. A thin coat of negative photoresist was spun on top of the thin copolymer film. After exposing the photoresist to UV light through a mask, the photoresist was removed from the gold metalization and the bonding pads area. The remaining photoresist protected the rest of the copolymer from being washed away by the acetone soaked cotton swabs used to remove the copolymer from the bonding pads. Note that we could not use positive photoresist because its developer would attack the copolymer.

The wafers were annealed for 1.5 hours at 135°C. The wafers were slowly cooled to prevent cracking of the copolymer film or electrode due to the different thermal expansion coefficients of the copolymer, electrode, and ceramic wafer. The annealing step enhances the copolymer's crystallinity and the subsequent achievable polarization.

We note from Figure 2 that all the source, drain, and gate electrodes in an array are connected together. During the poling step all are kept at common ground. The entire 64 element array was poled at once. After the poling step the source and gate electrodes are cut apart to isolate the individual transducers and to

make connections to the external circuitry. Hysteresis poling was carried out by applying a sinusoidal 0.01 Hz voltage signal:  $\pm 550\text{V}$  to the  $7\mu\text{m}$  films ( $\pm 80\text{V}/\mu\text{m}$ ) or  $\pm 1350\text{V}$  to the  $15\mu\text{m}$  films ( $\pm 90\text{V}/\mu\text{m}$ ). The polarization coercive field peaks occurred at ( $\sim \pm 50\text{V}/\mu\text{m}$ )  $\pm 350\text{V}$  or  $\pm 770\text{V}$  for the two film thicknesses, respectively. The peaks were very broad for the 56/55 composition and sharp for the 70/30 composition.

Each wafer had two arrays on it. The wafer was cut to separate the arrays so that they could be assembled and utilized separately (See Figure 3).

#### EXPERIMENTAL CHARACTERIZATION OF THE POSFET. PYROELECTRIC SENSOR'S RESPONSE TO CW AND SINGLE IR OPTICAL PULSES

Because of the silicon wafer design (FET exposed to the environment) all optical response measurements needed to be performed at an optical wavelength that could not generate charge carriers in the gate region of the FET. The POSFET was evaluated by measuring its response to a carbon dioxide laser operating at  $10.6\mu\text{m}$  in the CW mode and in the single pulse mode. At this infrared wavelength the measured electrical signals could only be produced by the pyroelectric effect.

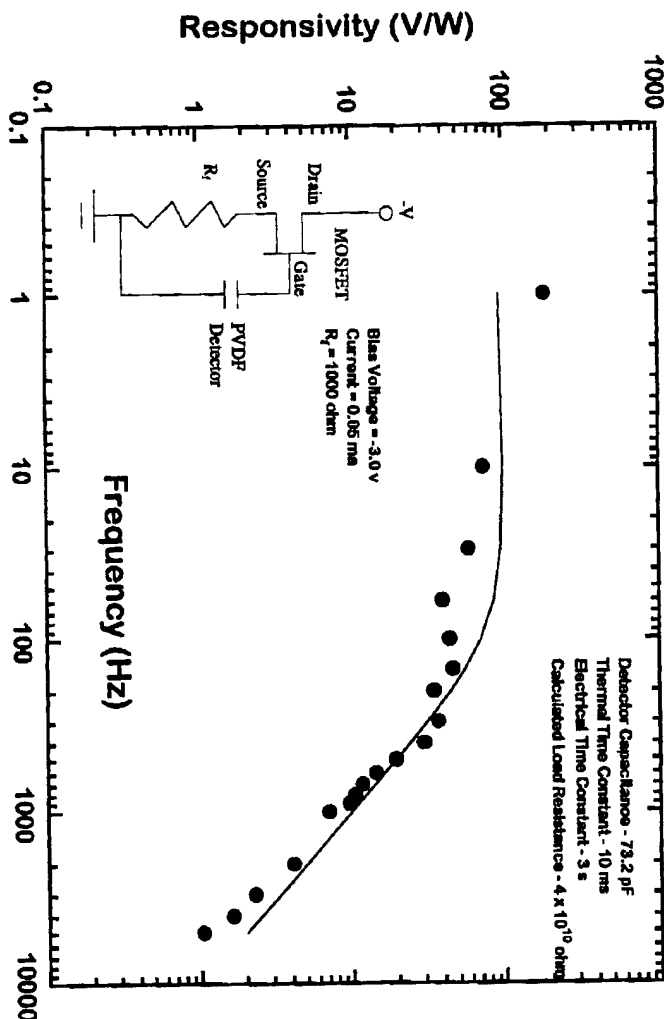


Figure 4. Frequency Response from single detector of the array.

The electrical circuit used to measure the charge induced field change in the MOSFET device is shown in Figures 4-6. The MOSFET can be used in either the common-source or source-follower configuration. The source-follower configuration was used in all evaluation measurements on the POSFET detectors. The MOSFET input stage will provide an impedance or load resistance of up to  $10^{11} \Omega$ . The output impedance is given by  $Z_{out} \approx R_L / (1 + g_m R_L)$ , where  $g_m$  is the low-frequency transconductance of the FET. The voltage gain of the source follower is approximately  $g_m Z_{out}$ . The values used for  $R_L$  were 100, 1000, and 10,000  $\Omega$  for the impulse response measurements and 1000  $\Omega$  for the frequency response measurement. Assuming  $g_m \approx 10^{-3} \text{ A/V}$  this corresponds to gains of 0.1, 0.5, and 0.9, respectively.

The thermal and electrical characteristics can be determined from the frequency response of the POSFET detector. An electrically controlled CW  $\text{CO}_2$  laser illuminated a portion of a single pixel on the array. The frequency response from a single pixel is given in Figure 4.

The thermal and electrical time constants can be determined from the measured data in Figure 4. The data is fitted to the formula,

$$V_T = (pWA\eta\omega\tau_{TH}\tau_e) / [I_T C_T c_p' (1 + \omega^2 \tau_{TH}^2)^{1/2} (1 + \omega^2 \tau_e^2)^{1/2}] \quad (2)$$

Here  $c_p'$  is the volumetric specific heat,  $p$  is the pyroelectric coefficient,  $W$  is the amplitude of the radiant power incident on the

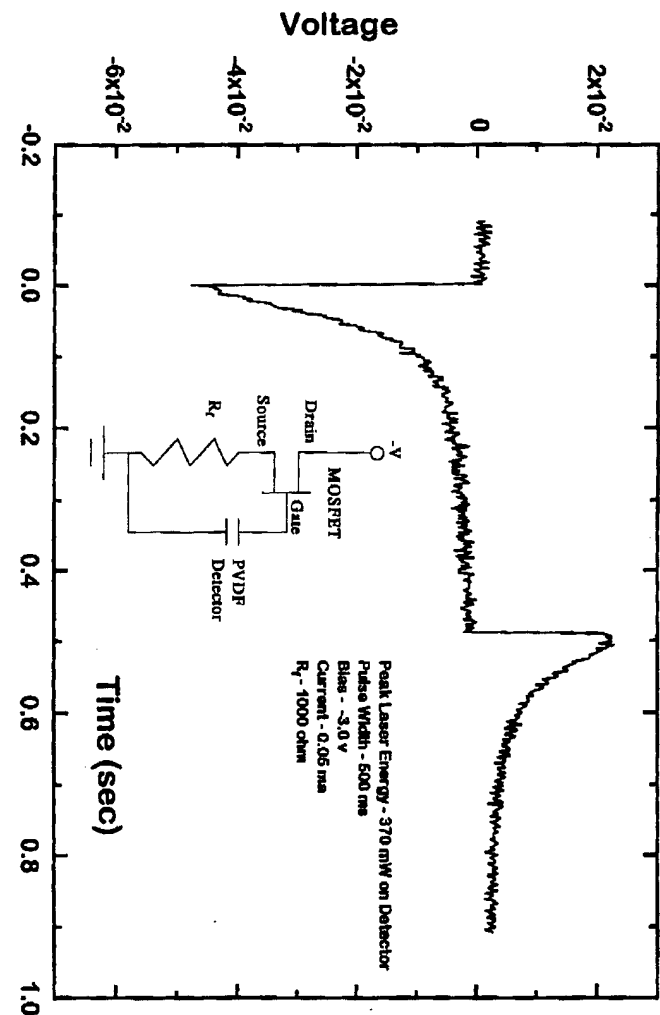


Figure 5. POSFET detector response to square wave illumination from a CW carbon dioxide laser ( $10.6\mu\text{m}$  IR, 500ms pulse width).

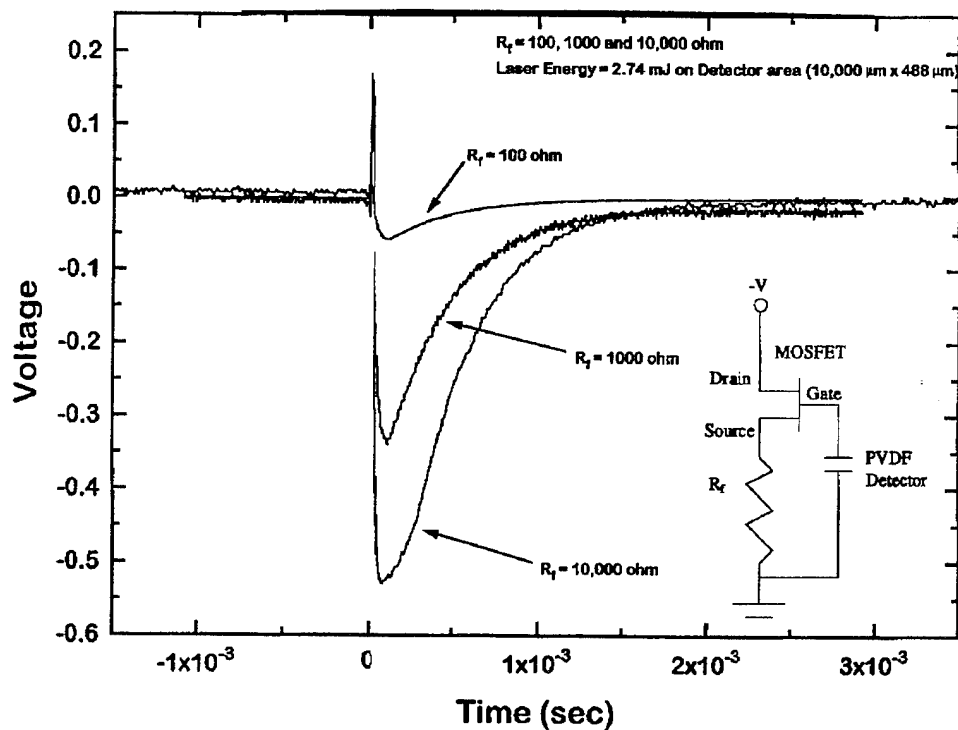


Figure 6. POSFET detector response to a pulsed CO<sub>2</sub> laser (10.6 μm IR, 50 μm width).

area  $A$  of the sensor, and  $\eta$  is the transducer emissivity [1]. The thermal time constant,  $\tau_{TH}$ , was found to be 0.01 sec. This time constant is typical for a pyroelectric material heat sunk to a thermal mass [1]. The electrical time constant was more difficult to determine to a high degree of accuracy because of the low frequencies involved;  $\tau_e$  was determined to be about 3 sec. The capacitance of a single pixel is estimated from the pixel area and copolymer thickness as 44 pF. The impedance or load resistance for this pyroelectric system was determined to be about 68 GΩ.

The peak responsivity occurred at low frequencies (< 50 Hz) and had a value of 100 V/watt. The characteristic voltage response between the thermal and electrical 3db roll-over points can be given by ( $\tau_{TH} < \tau_e$ )

$$R_V = R_i R_L (\tau_{TH} / \tau_e) \quad (3)$$

where  $R_i$  is the current responsivity and  $R_L$  is the load resistance. From (3) and a gain of 0.5 we calculated a current responsivity of 1.5 μA/watt.

The POSFET detector response to a  $t_0 = 500$  msec duration square wave illumination from a CO<sub>2</sub> laser is shown in Figure 5. The impulse response from the POSFET detector array was performed by illuminating a single pixel of the array with a  $t_0 = 50$  μsec (FWHM) CO<sub>2</sub> laser pulse. Figure 6 shows the impulse response for  $R_L$  values of 100, 1000, and 10,000 Ω which corresponds to amplifier gain values of 0.1, 0.5, and 0.9, respectively. The bias voltages were -3.5V, -3.0V, and -1.1V, the observed currents were 0.26mA, 0.05mA, and 0.028mA, and the responsivities were 20V/J, 92.7V/J, and 192V/J, respectively. At unity amplifier gain the energy response to the laser was measured at 200V/Joule.

We note that the data in Figures 5 and 6 can be understood as the pyroelectric response to pulsed radiation for the case  $\tau_{TH} < t_0 < \tau_e$  and  $t_0 < \tau_{TH} < \tau_e$ , respectively.

## REFERENCES

- [1] A. S. Fiorillo, J. Van der Spiegel, P. E. Bloomfield, and D. Esmail-Zandi, "A P(VDF/TrFE)-based Integrated Ultrasonic Transducer," *Sensors and Actuators*, **A21-A23** (1990), 719-725.
- [2] R. G. Swartz and J. D. Plummer, "Integrated Silicon-PVDF<sub>2</sub> acoustic Transducer Arrays," *IEEE Trans. Electron Devices*, **26** (1979), 1921-1931.
- [3] Y. Kubouchi, Y. Kumetani, T. Yagi, T. Masuda and A. Nakajima, "Structure and Dielectric Properties of Vinylidene fluoride Copolymers" *Pure Appl. Chem.*, **61** (1989), 83-90.
- [4] Copolymer powder obtained from Solvay Technologies, Inc., Brussels, Belgium.
- [5] The spin coating steps and the fabrication of the masks and MOSFET doped and electroded wafers were carried out at the University of Pennsylvania Moore School of Electrical Engineering Microfabrication Lab. with the technical support of Tom Carroll and the advice of Dr. Jan Van der Spiegel to whom we express our appreciation.

Poster Session - P4:  
Actuators and  
Electrostriction



M. Kuwabara, K. Morimo, S. Takahashi, H. Shimooka and T. Matsunaga  
 Department of Applied Chemistry, Faculty of Engineering, Kyushu Institute of Technology,  
 1-1 Sensui-cho, Tobata, Kitakyushu 804, Japan

**Abstract** — Positive temperature coefficient of resistivity (PTCR) characteristics of strictly single grain boundaries in barium titanate ceramics have been investigated. The results indicate that in the ceramic samples there existed grain boundaries exhibiting typically three different PTCR characteristics, which can be described as follows: 1) PTCR characteristics similar to those observed for usual ceramic samples, 2) an abrupt increase in resistivity by more than three orders at the Curie point, then, immediately followed by a monotonous decrease of it, and 3) substantially little or no resistivity jump. The second type of the PTCR characteristic cannot be interpreted at all by the Heywang model, which is based on the temperature dependence of the grain boundary barrier height determined by the dielectric constant in barium titanate which steeply decreases above the Curie point according to the Curie-Weiss law. A new possible mechanism of the PTCR effect is discussed.

### INTRODUCTION

It is well-known that doped semiconducting barium titanate ceramics exhibit an anomalous positive temperature coefficient of resistivity (PTCR) effect above the Curie point ( $\approx 120^\circ\text{C}$ ), and a grain boundary barrier layer model proposed by Heywang<sup>1</sup> has been accepted to interpret most adequately the PTCR effect. The Heywang model can be essentially described by the temperature dependence of the potential barrier height built at the grain boundaries, which is determined by the dielectric constant of the material, the amount of acceptor states formed at the grain boundaries and the donor concentration. This model was extended by Jonker<sup>2</sup> to interpret more appropriately the low resistance at room temperature by taking account of a compensation effect of surface states by spontaneous polarization below the Curie point.

To understand more directly the PTCR characteristics several investigations<sup>3,4</sup> have been made on single grain boundaries of barium titanate ceramics. Although grain boundaries examined in these studies were not strictly single boundaries, the results obtained clearly demonstrated the existence of grain boundaries exhibiting current-voltage characteristics which cannot be interpreted well by Heywang's barrier layer model. In this study, to obtain a much closer picture of the PTCR mechanism measurements of the PTCR characteristics of strictly single grain boundaries in barium titanate ceramics were carried out. For this purpose ceramic samples consisting of single grains sintered together in line were produced.

### EXPERIMENTAL

Ceramic samples consisting of single grains sintered together in line used for the present study were prepared as follows: Commercially obtained high-purity barium titanate (Fuji Titanium, HPBT-2; purity = 99.98%), 0.1mol%  $\text{La}_2\text{O}_3$  (semiconducting dopant) and 0.5mol%  $\text{TiO}_2$  (to enhance grain growth) were used as starting materials. A mixture of the starting powders was ball-milled with ethanol and nylon-coated iron balls as grinding media in a polyethylene container for 24h, into which adequate amounts of PVB (Polyvinyl butyral) and BPBG (Butyl phthalyl butyl glycolate) were then added to make a barium titanate slurry which was submitted to tape casting with a doctor blade. The obtained ceramic tape (thickness: 30-40  $\mu\text{m}$ ) was cut into string-like slabs (width:  $\approx 50 \mu\text{m}$ ), which were sintered at  $1370^\circ\text{C}$  for 2h in air to yield ceramic samples with desired grain structures.

Measurements of the PTCR characteristics of strictly single grain boundaries in the samples were carried out with In-Ga microelectrodes (two-probe method) put on the adjacent grains of their single boundaries to be examined. Such measurements were conducted on many single boundaries formed between grains with various types of growth pattern morphologies on their surfaces. Growth pattern morphologies of grains in the samples were observed by an optical microscope (OM).

### RESULTS AND DISCUSSION

Figure 1 shows a typical example of the grain morphologies of the ceramic samples produced in this study with growth patterns appearing on the grain surfaces. PTCR measurements were conducted for such single grain boundaries as this, adjacent grains of which had various types of growth patterns on them. Figures 2-4 show the PTCR characteristics and the current ( $I$ )-voltage ( $E$ ) characteristics at several temperatures obtained for single boundaries in the present ceramic samples. One may recognize that the PTCR characteristics shown in Figs. 2, 3 and 4 are essentially different from each other.

The PTCR characteristics of the single boundary of sample 1, shown in Fig. 2(A), are quite similar to those observed in usual ceramic samples except for the remarkable dependence of the characteristic upon applied bias above the Curie point. Figure 2(B), in which the  $\log I$  vs  $\log E$  plots of this sample are presented, demonstrate that the  $I$ - $E$  characteristic below the Curie point was nearly ohmic in the whole range of biases applied, while above the Curie point the  $I$ - $E$  characteristic showed a significant nonlinearity above around 0.1V. If a double Schottky-type potential barrier was formed at the grain boundary as assumed in the Heywang model, an exponential-type  $I$ - $E$  characteristics should be expected to appear. However, any exponential behavior can be seen in the  $I$ - $E$  characteristics shown in Fig. 2(B). The obtained  $I$ - $E$  characteristic above the Curie point seems to be rather much like space-charge-limited-current (SCLC).<sup>4</sup>

It is most interesting and important for better understanding of the PTCR mechanism that we could experimentally confirm the existence of grain boundaries which exhibit such PTCR characteristics as those shown in Figs. 3 and 4. Nemoto et al.<sup>4</sup> have found the existence of grain boundaries with no PTCR effect in ceramic samples, but they did make any interpretation at all about this phenomenon. Rather unfamiliar PTCR characteristics similar to those shown in Fig. 3 have also been reported several times in the literature,<sup>5,6</sup> but no careful attention has been paid for such behavior of the PTCR action whether this kind of PTCR characteristics can be interpreted by the Heywang model.

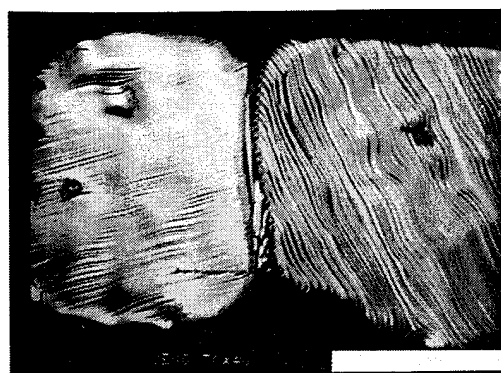


Fig. 1. A typical grain morphology of the samples used and growth patterns appearing on the grains. Bar indicates 50  $\mu\text{m}$ .

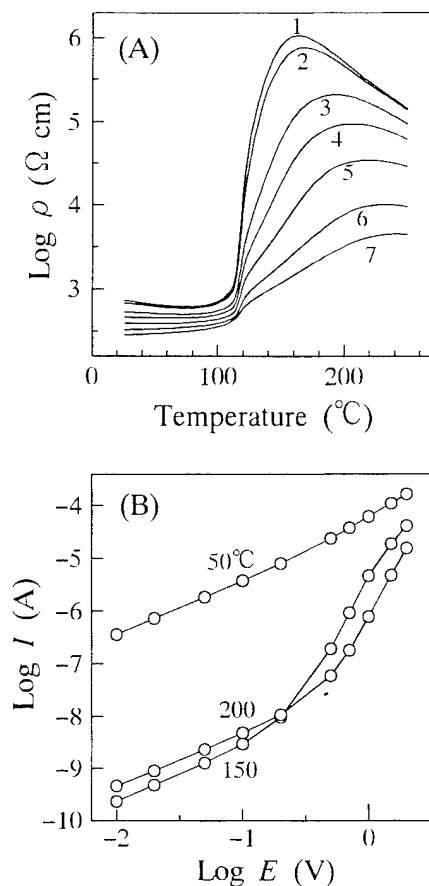


Fig. 2. (A) Resistivity-temperature characteristics at increased applied biases (curve 1; 0.1, 2; 0.2, 3; 0.5, 4; 0.7, 5; 1.0, 6; 1.5, 7; 2.0 V) and (B) current-voltage characteristics obtained at several temperatures for the single boundary of sample 1.

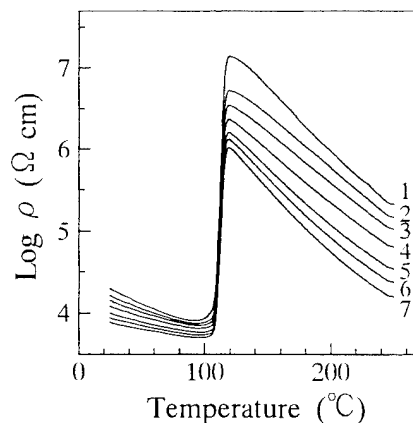


Fig. 3. Resistivity-temperature characteristics at increased applied biases (curve 1; 0.1, 2; 0.2, 3; 0.5, 4; 0.7, 5; 1.0, 6; 1.5, 7; 2.0 V) for the single boundary of sample 2.

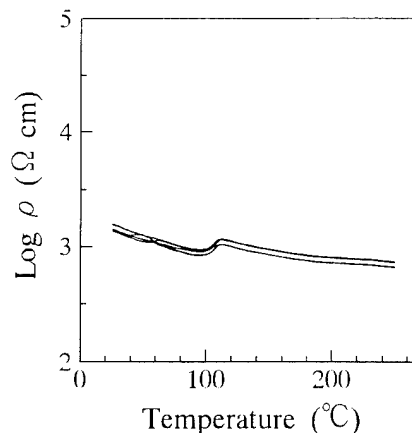


Fig. 4. Resistivity-temperature characteristics at various applied biases for the single boundary of sample 3.

To interpret consistently by the Heywang model these three types of PTCR characteristics observed in the present study, we can use only the difference in the amount of acceptor states at the grain boundaries in the respective samples: the grain boundary of sample 2 had the largest amount of acceptor states ( $>2 \times 10^{14} \text{ cm}^{-2}$ ), the smallest amount of acceptor states existed at the grain boundary of sample 3 ( $<1 \times 10^{13} \text{ cm}^{-2}$ ) and the boundary of sample 1 had acceptor states with a concentration between the two limiting cases.<sup>7</sup> However, this interpretation for these PTCR characteristics seem to be unlikely, because no such significant change in the room temperature resistivity as expected for the assumed differences in the amount of acceptor states can be seen. It may thus be concluded that the Heywang model cannot explain consistently all kinds of PTCR characteristics observed for single boundaries in the present samples; a new model is necessary to fully understand the PTCR effect.

One possible model to interpret well the PTCR characteristics observed in this study would be a modified Jonker's model; the essential of this model is that the compensation of surface acceptor states still occurs above the Curie point and determines the potential height of grain boundary barrier layers in the whole PTCR region. This model is based on the assumption that spontaneous polarization in the vicinity of grain boundaries remains up to a certain temperature over the Curie point. The temperature dependence behavior of spontaneous polarization is considered to vary in the grain boundaries with different spontaneous polarization domain structures and lattice mismatching; this gives rise to various types of PTCR characteristics and can explain well the bias dependence of the PTCR characteristics observed here. To confirm this point more decisively a further investigation is being performed.

#### REFERENCES

- [1] W. Heywang, "Resistivity anomaly in Doped Barium Titanate," *J. Am. Ceram. Soc.*, **47**, 484-490, 1964.
- [2] G.H. Jonker, "Some Aspects of Semiconducting Barium Titanate," *Solid State Electron.*, **7**, 895-903, 1964.
- [3] P. Gerthsen and B. Hoffman, "Current-Voltage Characteristics and Capacitance of Single Grain Boundaries in Semiconducting  $\text{BaTiO}_3$  Ceramics," *J. Am. Ceram. Soc.*, **16**, 617-622, 1973.
- [4] H. Nemoto and I. Oda, "Direct Examination of PTC Action of Single Grain Boundaries in Semiconducting  $\text{BaTiO}_3$  Ceramics," *J. Am. Ceram. Soc.*, **63**, 398-401, 1980.
- [5] I. Ueda and S. Ikegami, "Oxidation Phenomena in Semiconducting  $\text{BaTiO}_3$ ," *J. Phys. Soc. Jpn.*, **20**, 546-552, 1965.
- [6] V.J. Tennery and R.L. Cook, "Investigation of Rare-Earth Doped Barium Titanate," *J. Am. Ceram. Soc.*, **44**, 187-193, 1961.
- [7] A.M.J.H. Seuter, "Defect Chemistry and Electrical Transport Properties of Barium Titanate," *Philips Res. Repts. Suppl.* No. 3, 1-84, 1974.

# A STRESS-SENSING CERAMIC DEVICE BASED ON PTCR BARIUM TITANATE

Joseph S. Capurso and Walter A. Schulze  
New York State College of Ceramics at Alfred University  
Alfred, New York 14802

**Abstract** - Positive temperature coefficient of resistance (PTCR) barium titanate is used as the base material for a ceramic sensor which employs piezoresistivity to detect changes in applied stress. Tape-cast sheets of undoped (insulating) and PTCR (semiconducting) BaTiO<sub>3</sub> are laminated to produce a three-layer "trilaminate" - a sintered structure which has two PTCR layers separated by an insulating layer. The trilaminate is exposed to mechanical stress in a four-point bend configuration (placing one semiconducting layer completely in tension, the other in compression), and the resistivities for both stress states are measured concurrently as functions of the applied stress magnitude. The piezoresistivity coefficient ( $\pi$ ) is calculated from the slope of the linear resistivity-stress response. Piezoresistivity results are presented versus PTCR layer composition (counterdopant species) and furnace cooling conditions (grain boundary oxidation level). These results are interpreted with respect to Heywang's model of the grain boundary potential barrier.

## INTRODUCTION

Semiconducting barium titanate is a well-studied material which may exhibit a large increase in resistivity over a relatively small temperature range beginning near its Curie temperature ( $T_c$ ). It also exhibits *piezoresistivity* (stress-sensitive resistivity), making it a potential base material for stress-sensing applications.

The PTCR phenomenon was first observed in the mid-1950's [1], and was explained by Heywang in terms of a double Schottky potential barrier existing at the boundaries between semiconducting barium titanate grains [2]. He derived an expression for the height of the barrier ( $\phi_o$ ):

$$\phi_o = \frac{en_s^2}{8\epsilon_r\epsilon_o n_o} \quad (1)$$

where  $n_s$  is the number of electrons trapped at the grain boundary per unit area,  $n_o$  is the number of conducting electrons per unit volume in the bulk,  $\epsilon_r$  is the relative permittivity (dielectric constant), and  $\epsilon_o$  is the permittivity of free space. The resistivity of PTCR barium titanate ceramic with  $z$  grains per unit length is exponentially dependent on  $\phi_o$ :

$$\rho = \rho_b \left( 1 + \frac{zbkT}{e\phi_o} e^{\frac{e\phi_o}{kT}} \right) \quad (2)$$

where  $\rho_b$  is the resistivity of the bulk ( $\Omega\text{-cm}$ ) and  $b$  is the electron depletion region half-width.

Below  $T_c$ , these barriers are partially compensated by surface charge resulting from discontinuity of the normal polarization components of ferroelectric domains terminating at the grain boundary, according to Jonker [3]. This causes a suppressed resistivity in the ferroelectric state, resulting in an abrupt increase in resistivity once the domains vanish (barrier compensation disappears), above  $T_c$ .

The temperature dependence of  $\epsilon_r$  for paraelectric barium titanate (above  $T_c$ ) follows the Curie-Weiss law [4]:

$$\epsilon_r = \frac{C}{T - \Theta} \quad (3)$$

where  $C$  and  $\Theta$  are constants. So, as temperature increases,  $\epsilon_r$  decreases; causing an increase in barrier height and thus a dramatic rise in resistivity. Samara [5] showed that an analogous hydrostatic pressure dependence exists:

$$\epsilon_r = \frac{C'}{P - P_o} \quad (4)$$

raising the possibility that the grain boundary potential barrier may be adjustable through application of stress.

Relatively little attention has been focused on the piezoresistive effect in PTCR barium titanate. Early investigations of the stress sensitivity of semiconducting barium titanate disks [6,7] indicated that piezoresistivity is maximized at temperatures near  $T_c$  in the paraelectric state under uniaxial compressive stress, although discrepancies in the direction (sign) of resistance change were seen. Specifically, hydrostatic compression resulted in a positive change in resistance, while negative piezoresistivity was observed under uniaxial compression (indicating a non-uniform stress state). More recent work [8-11] further reinforces the concept of piezoresistivity being due to the temperature and stress sensitivity of  $\epsilon_r$  near the Curie temperature, through its effect on the magnitude of grain boundary potential barriers.

In this work, a four-point bending apparatus is used to apply stress to a *trilaminate* structure [12], which consists of two layers of PTCR barium titanate separated by a layer of insulating barium titanate. A photograph

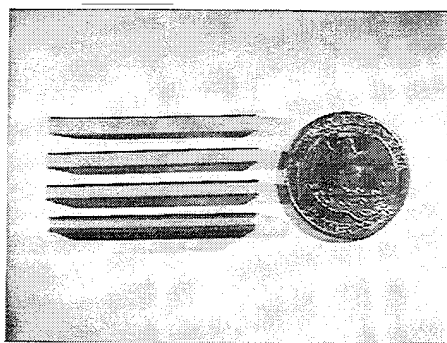


Fig. 1. Photograph of several trilaminates.

of several trilaminates is shown in figure 1. Using this configuration, the effect of stress on resistivity in both the compressive and tensile modes may be observed. This is an approach which minimizes shear stresses, and gives results which agree with the aforementioned model of the grain boundary potential barrier.

## EXPERIMENTAL

### Processing

Trilaminates are produced by laminating tape-cast sheets of barium titanate together and sintering at 1350°C to form a structure which can withstand a moderate mechanical stress. The composition of the trilaminate with respect to its thickness is determined by the stacking sequence of green tape layers, which are either insulating or semiconducting. Insulating tape is produced from as-received powder\*, while semiconducting tape consists of the same powder plus precipitated dopant(s): a 0.3 atom% lanthanum addition causes semiconductivity, and transition metal counterdopants (e.g. manganese, iron, cobalt) result in the formation of acceptor traps at the grain boundaries, enhancing the PTCR effect [13]. Details of dopant incorporation procedures, trilaminate formation, binder burnout, and sintering/cooling are described elsewhere [14].

### Testing

The four-point bend configuration is used to stress the trilaminate. This configuration provides a region of constant longitudinal stress between the two inner contact points (Fig. 2). Trilaminates are lightly ground on a 600M SiC pad to minimize surface flaws and to provide a clean, smooth surface for electroding. Electrical contact to the

trilaminate is made by evaporating aluminum metal onto either side, leaving a gap on each surface which is well within the region of constant longitudinal stress.

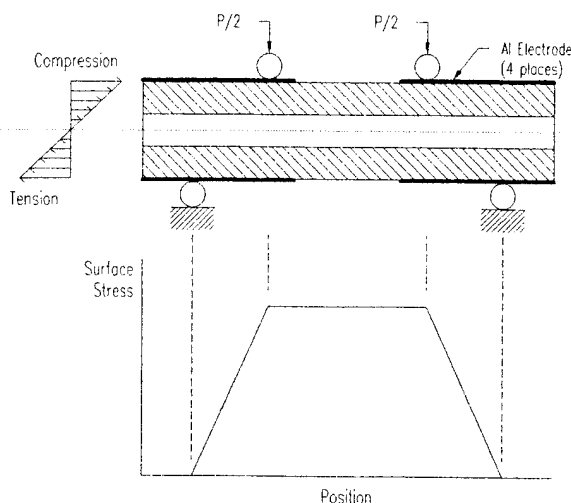


Fig. 2. Application of stress on a trilaminate in four-point bend.

Note that the upper semiconducting layer is in compression only, since it lies completely above the plane of zero stress. This layer undergoes a volumetric decrease, resulting in an overall constriction of unit cells and thus a decrease in relative permittivity ( $\epsilon_r$ ). Conversely, the lower semiconductor layer is strictly in tension, experiences a volumetric increase, an expansion of unit cells and therefore an increase in  $\epsilon_r$ . From Heywang's model (described earlier), one would therefore expect a resistivity increase in compression and a decrease in tension, due to the effect of  $\epsilon_r$  on the barrier height.

Piezoresistance testing is performed using a computer-controlled system which acquires resistance versus load data at 1°C intervals over a ten-hour ramp from 107°C to 143°C. Resistance is measured at 0.1 VDC†. The four loading points also act as electrical contacts to the aluminum electrodes on the trilaminate under test. Load is applied at 4.45 N intervals from 8.90 N to 26.7 N, then back down to 8.90 N; using a closed-loop load sensing/driving system which employs a stepper motor to drive the loading column. The slope and y-intercept of the least-squares regression line through these nine data points are calculated, and the isothermal piezoresistivity coefficient  $\pi$  is determined by dividing the slope by the intercept (resistance at zero stress,  $R_0$ ):

$$\pi = \frac{1}{R_0} \left( \frac{\partial R}{\partial \sigma} \right)_T \quad (5)$$

\* Code 219-9, Transelco Div., Ferro Corp., Penn Yan, NY.

† 4140B pA meter, Yokogawa-Hewlett-Packard, Ltd., Tokyo.

## RESULTS AND DISCUSSION

### Microstructure

A typical semiconductor-insulator interface microstructure is shown in figure 3. Note that the semiconducting material has a significantly larger grain size (40-60  $\mu\text{m}$ ) than the insulating material (10-30  $\mu\text{m}$ ),

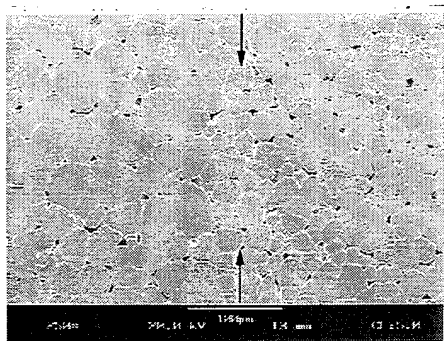


Fig. 3. SEM micrograph of a typical semiconductor/insulator interface (secondary electron image).

and that the interface is continuous and well-defined, with no lamination defects or abnormalities with respect to porosity. Grain boundary relief was obtained by thermal etching at 1325°C for 30 minutes in air.

### Piezoresistance

The piezoresistive response of a trilaminate is shown in figure 4, for several temperatures. Note that in all cases, the resistance ratio (resistance at some stress divided by unstressed resistance,  $R/R_0$ ) is greater than unity in compression and less than unity in tension, substantiating the arguments stated previously. Also note that the responses are linear, and are more pronounced in tension at these temperatures.

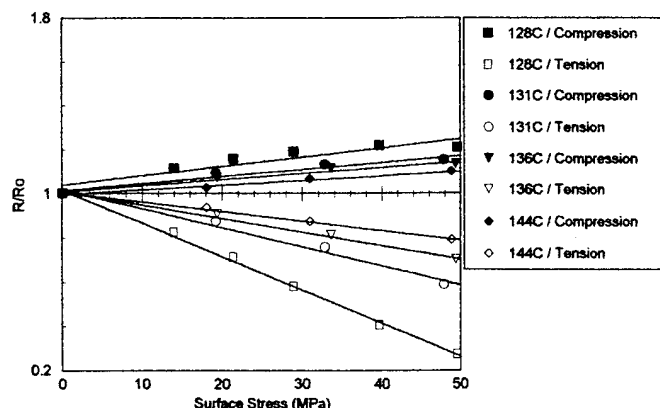


Fig. 4. Normalized resistance of a 9/18/9 layer trilaminate (0.30 at% La, 0.04 at% Mn) vs. surface stress at several temperatures above  $T_c$ .

It can be seen that the piezoresistive effect is reduced in magnitude as the temperature is increased above  $T_c$  ( $\approx 123^\circ\text{C}$ ). This is another confirmation that piezoresistivity is a result of changing relative permittivity, since  $\epsilon_r$  is most sensitive to pressure and temperature changes as  $T_c$  is approached from above, according to the Curie-Weiss dependencies (eq. 3,4).

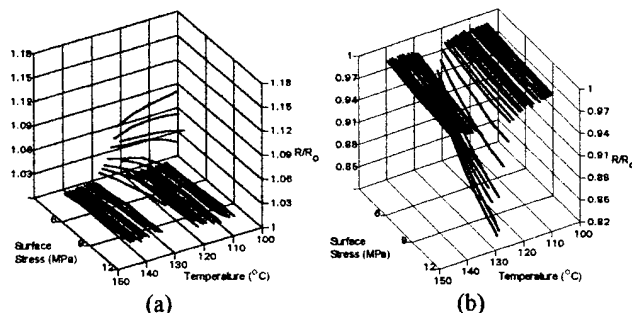


Fig. 5. Normalized resistance of a 3/30/3 layer trilaminate (0.30 at% La only) vs. surface stress and temperature, for regions under a) compression, b) tension.

Similar data were obtained for another trilaminate, over a wider temperature range extending both above and below  $T_c$ . These data are illustrated in figure 5 (a,b), where resistance ratio is plotted as a function of both temperature and applied stress: each line corresponds to a constant-temperature resistance-stress plot. Observe that the magnitude of piezoresistivity (slope) maximizes in the vicinity of  $T_c$ ; and that a smaller, yet non-zero slope is seen below  $T_c$ .

Trilaminates having differing counterdopants in the PTCR regions were produced to evaluate the effect of acceptor state level and density. Manganese is known to cause "deep" acceptor states [13], and was added at a 0.04 atom% level. Iron causes formation of shallow states, and was added at a 0.02 atom% level. Cobalt forms states between these two extremes, and was added at the 0.04 atom% level. Optimum counterdopant levels

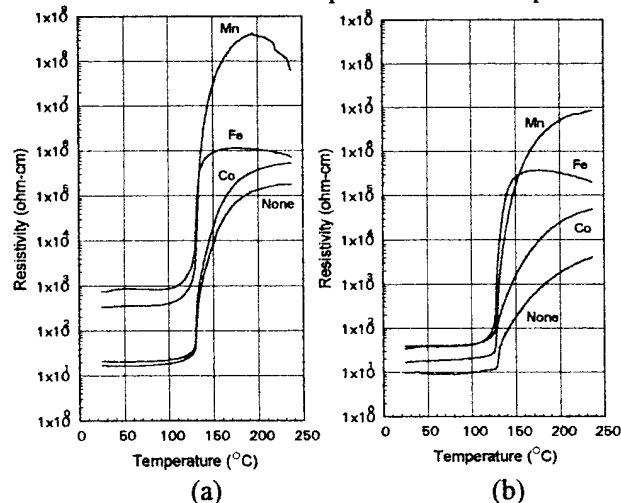


Fig. 6. PTCR response of pellets with different counterdopants, cooled from 1350°C to 500°C at (a) 1°C/min., (b) 10°C/min.

were obtained by increasing the addition until room temperature resistivity began to rise rapidly. The density of acceptor states can be adjusted by variation of the cooling rate from the 1350°C peak sintering temperature to 500°C, and is indicated by the steepness of the PTCR curve above  $T_C$ .

PTCR responses for these materials for two cooling rates are shown in figure 6, and figure 7 contains piezoresistivity plots for the same materials and conditions. Note that the piezoresistivity peak is basically equal and cooling-rate-independent for the Mn- and Fe-counterdoped trilaminates, but that cooling rate has a significant effect on the Co- and non-counterdoped samples. It is interesting to note that the Co- and non-counterdoped samples also show a change in initial PTCR slope with change in cooling rate, but the Mn and Fe

samples do not. These results indicate that piezoresistive response appears to be independent of acceptor level, but is somewhat sensitive to density of states.

## SUMMARY

A new type of stress-sensing device based on barium titanate - a *trilaminate* - has been described. The piezoresistive response of the trilaminate is in sign agreement with Heywang's model, and is more pronounced at temperatures near the Curie point, indicating that the basic mechanism responsible is a change in the relative permittivity of the material in the vicinity of grain boundaries. It was also seen that the piezoresistive response of PTCR barium titanate can be engineered to some degree through variation of counterdopant species and cooling conditions.

## REFERENCES

- [1] P.W. Haayman, R.W. Dam, and H.A. Klasens, "Method of Preparation of Semiconducting Materials," West German Patent 929,350, June 23, 1955.
- [2] W. Heywang, "Barium Titanate as a Semiconductor with Blocking Layers," *Solid State Elec.*, **3** [1] 51-8 (1961).
- [3] G.H. Jonker, "Some Aspects of Semiconducting Barium Titanate," *Solid State Elec.*, **7**, 895-903 (1964).
- [4] B. Jaffe, W.R. Cook, Jr., and H. Jaffe, *Piezoelectric Ceramics*, p. 77, Academic Press, New York, 1971.
- [5] G. Samara, "Pressure and Temperature Dependences of the Dielectric Properties of the Perovskites  $\text{BaTiO}_3$  and  $\text{SrTiO}_3$ ," *Phys. Rev.*, **171** [2] 378-86 (1966).
- [6] H.A. Sauer, S.S. Flaschen, and D.C. Hoesterey, "Piezoresistance and Piezocapacitance Effects in Barium Strontium Titanate Ceramics," *J. Am. Ceram. Soc.*, **42** [8] 363-6 (1959).
- [7] O. Saburi, "Piezoresistivity in Semiconductive Barium Titanates," *J. Phys. Soc. Japan*, **15** 733-4 (1960).
- [8] H. Igarashi, M. Michiue, and K. Okazaki, "Anisotropic Resistivity Under Uniaxial Pressure in PTC Ceramics," *Jpn. J. Appl. Phys.*, **24** [suppl. 24-2] 305-7 (1985).
- [9] A. Amin and M.B. Holmes, "Pressure and Temperature Dependencies of the Direct-Current Resistance of Semiconducting  $(\text{Ba},\text{Sr})\text{TiO}_3$  and  $(\text{Ba},\text{Pb})\text{TiO}_3$ ," *J. Am. Ceram. Soc.*, **71** [12] C482-3 (1988).
- [10] A. Amin, "Piezoresistivity in Semiconducting Positive Temperature Coefficient Ceramics," *J. Am. Ceram. Soc.*, **72** [3] 369-76 (1989).
- [11] A.B. Alles, M. Murphy, J.J. Symanski, C.L. Tremper, and W.A. Schulze, "Piezoresistivity Modeling of Grain Boundary Junctions in PTCR  $\text{BaTiO}_3$ ," submitted for publication.
- [12] A.B. Alles and W.A. Schulze, "Piezoresistive Sensor," United States Patent 5,225,126, July 6, 1993.
- [13] H. Ihrig, "PTC Effect in  $\text{BaTiO}_3$  as a Function of Doping with 3d Elements," *J. Am. Ceram. Soc.*, **64** [10] 617-20 (1981).
- [14] J.S. Capurso, A.B. Alles, and W.A. Schulze, "Processing of Laminated Barium Titanate Structures for Stress-Sensing Applications," accepted for publication in *J. Am. Ceram. Soc.*.

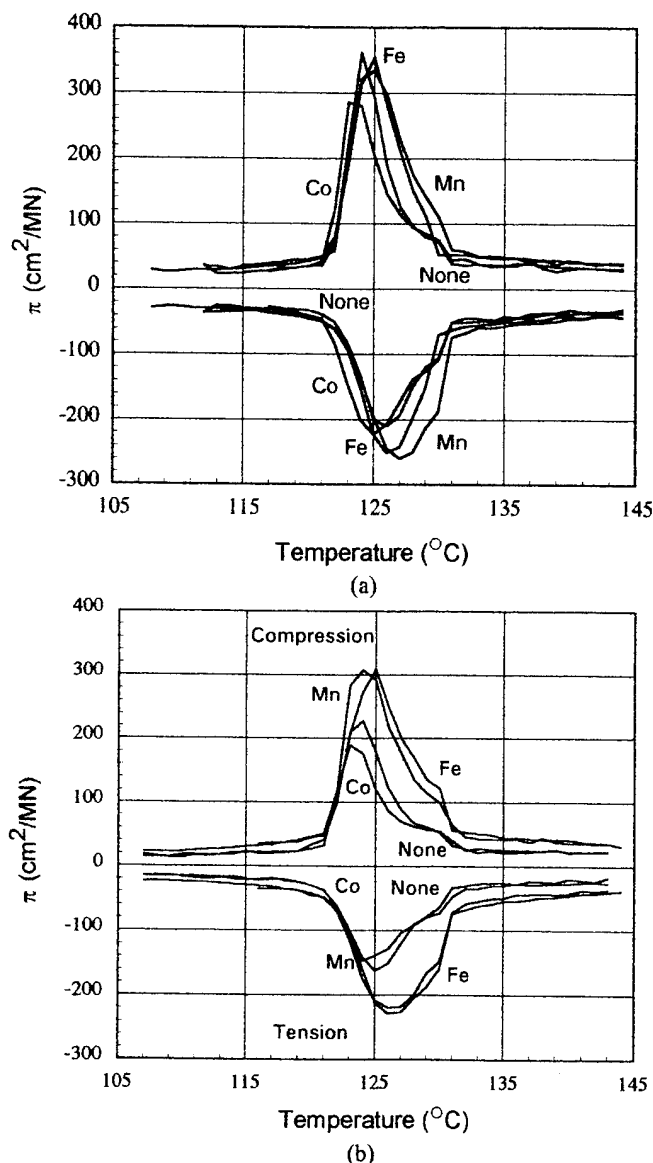


Fig. 7. Piezoresistive response of 4/28/4 layer trilaminates with different counterdopants, cooled from 1350°C to 500°C at (a) 1°C/min., (b) 10°C/min.

# THE DEVELOPMENT OF HIGH SENSITIVITY NTC THERMISTORS

Hiroshi Yamamoto\*, Akira Shibata, Keibunn Hajime, Fumio Takao, Katsuhiko Sugisawa, Yoshiyuki Niwatsukino, Hideki Shishiba and Shu-ichi Takeda

Komatsu Ltd., 1200 Manda, Hiratsuka-Shi, Kanagawa 254, Japan.

**Abstract** Several requirements for NTC thermistors used for office automation (OA) equipment and home electronics are small size, high sensitivity and high reliability.

Commonly used NTC thermistors do not have adequate reliability against thermal shock. Size reduction is difficult due to the multi-phase structure and porosity in ceramics. It is also difficult to realize the required properties because the resistivity-B value relationship control method has not been established.

So we have developed a method to control the properties of NTC thermistor by controlling the numbers and the valence of solid solution ions on A and B sites in the single phase spinel structure. Based on these methods, we have also established a method to make a more dense structure. A NTC thermistor series has been developed possessing small size, high sensitivity and high reliability.

## 1. INTRODUCTION

Recently, smaller and more reliable NTC thermistors have been required in office automation equipment (facsimile, copy machines etc.), home electronics (ovens, air-conditioners and refrigerators) and automobile. The required properties are (1) high reliability: especially thermal shock test, (2) wide series of electrical properties, (3) thermal time constant=1.7s-2.9s. At present, NTC thermistor compositions are spinel type transition metal oxide ceramics that are consist basically of Mn oxide and Co, Ni, Cu, Fe, Al oxides. Presently, NTC thermistor compositions research of spinel type transition metal oxide ceramics were began between 1950's and 1960's. Crystal structure of Mn-Ni oxides were researched by Larson et al. [1] and Hata et al. [2]. Crystal structure of Mn-Co oxides were researched by Aukrust et al. [3] and Aoki [4]. Crystal structure of Mn-Co-Ni oxides were researched by Yokoyama [5]. Relationships between various spinel oxides compositions and thermistor properties were researched by Futaki [6].

But when size reduction is proceeded on commonly used NTC thermistors, it is too difficult to have adequate reliability, especially, thermal shock due to the multi-phase structure, coarse grain size and porosity in the ceramics. It is also difficult to realize

the required properties because the resistivity-B value relationship control method has not established based on single phase cubic spinel. So we researched to establish NTC thermistor compositions that can get single phase cubic spinel in resistivity-B value range, commonly required in NTC thermistor. To develop NTC thermistor compositions, at first base composition that has single phase cubic spinel was determined, then substituted elements and those content amount were determined based on valence control and dilution principle which means other ions substitute into single phase spinel crystal. The manufacturing process conditions were determined based on a material design to get fine grains and dense sintering structure. Based on these material design concepts, we have developed compositions, designed manufacturing processes and succeeded to develop NTC thermistor sensors that satisfy required properties adequately. As an example of composition development and manufacturing process design, this paper mainly explains about R200=1k $\Omega$  sensor (Table-1).

## 2. EXPERIMENTAL PROCEDURE

Fig.1 shows a flow chart of high sensitivity NTC thermistors fabrication process. Regent grade materials of Mn<sub>3</sub>O<sub>4</sub>, NiO, Al<sub>2</sub>O<sub>3</sub>, that have over 99% purity were used as the starting materials. A fixed amount of powder was weighed within 0.1g accuracy. Those powders (1000g) and water (1500g) were mixed for 12hr by ball mill and dried.  $\phi$ 10 ZrO<sub>2</sub> balls were adopted as media because Zr<sup>4+</sup> ion does not substitute into spinel structure. A ball mill pot was a diameter of 100mm and a volume of 6 liters.

Table 1. The target properties of high sensitivity NTC thermistor (R200=1k $\Omega$ )

Zero-Power Resistance(at 200°C)	1k $\Omega$ ±5%
B Value (100~200°C)	4537K±3%
Thermal Time Constant	1.7~2.9s
Dissipation Factor	0.35~0.55mW
Maximum Operating Wattage	0.1mW
Operating Temperature Range	-50~250°C

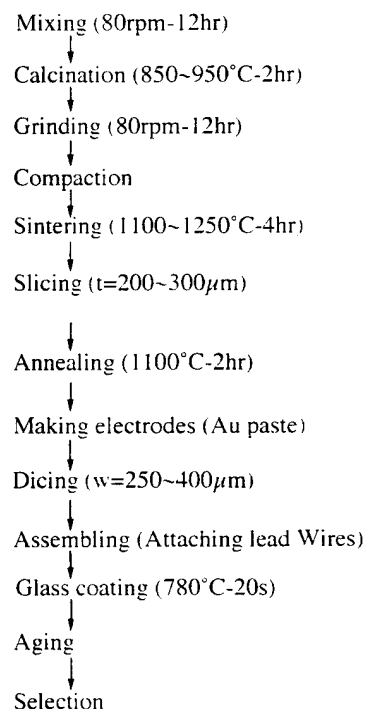


Fig.1 Flow chart of high sensitivity NTC thermistors fabrication process

\* Present Address : The Pennsylvania State University, MRL, University Park, PA 16802, USA

Dried powders were ground below 0.5mm granules. The granules were poured into ZrO<sub>2</sub> sheaths and calcinated at a range of temperatures from 800°C to 1200°C for 2hr. Increasing and decreasing temperature rate was 150°C/hr. Crystal structure of each calcinated condition was analyzed by powder X-ray diffraction analysis. The grain size of each calcinated condition was analyzed by SEM observation. Using same conditions as in the powder mixing, the calcined powder was ground and the particle size change was measured at each of the fixed sampling times by laser particle size distribution analyzer.

Considering to powder handling easiness, spray drying conditions were determined so as to get about 100μm size particles as possible. Granulated powder with the 40 to 60μm particle size distribution was obtained. PVA (poly vinyl alcohol) was used as a binder and poly ether conductor was used as a deflocculant chemical. Green compacts with a diameter of 30mm and thickness of 12mm were made by cold pressing. The compacting pressure was determined to saturate the green compact density. The compacting pressure was 2000Kg/cm<sup>2</sup>. The green compact density was 3.15 ~ 3.20 g/cm<sup>3</sup>. The green compacts were sintered at a range of temperatures from 1170 to 1350°C for 4hr. The increasing and decreasing temperature rate was 100°C/hr. The crystal structure of each sintering condition was analyzed by powder X-ray diffraction analysis and the grain size of each sintering condition was analyzed by SEM observation.

Ceramic wafers were cut from a sintered ingot using a diamond blade. The thickness ranged from 200μm to 300μm. The wafers were annealed at 1100°C for 2hr. Gold paste was printed on both side of wafer by a screen printer and baked at 850°C for 10min. The increasing and decreasing temperature rate was 35°C/min. Silver electrode was not selected since silver migrates into the glass during the glass sealing process. Fixed dimension chips (250 ~ 400 μm) were cut from the wafer by using a diamond blade. Dumet wire (Cu covered Fe-Ni wire) was attached on both side of the chip by using gold paste. After drying, a glass tube was inserted and sealed at 780°C for 20s. K<sub>2</sub>O-SiO<sub>2</sub>-PbO glass was selected because of its heat resistant property and thermal expansion coefficient which matches the ceramic and Dumet wire. The linear thermal expansion coefficient is 89 ~ 93x10<sup>-7</sup>/°C. Resistivity was measured at 25°C, 85°C, 100°C in a precise controlled water bath that was controlled within 0.04°C and 200°C in an alumina fluid isothermal bed that was controlled within 0.5°C. The B value was calculated from following equation.

$$B = (\ln R_{25} - \ln R_{85}) / (1/298.15K - 1/358.15K)$$

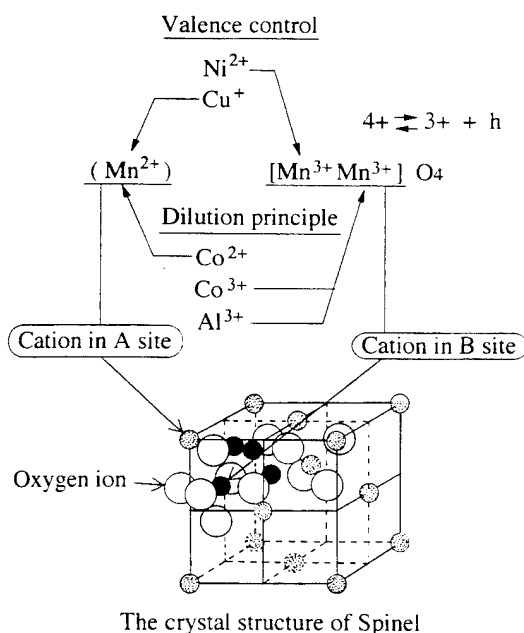


Fig. 2 The properties control principle of NTC thermistor

After the reliability tests, resistivity was measured at 25°C and 85°C. The conditions of thermal shock test were 10 cycles at 25°C for 15s in an oil bath to 200°C for 15s in the oil bath.

### 3. RESULTS AND DISCUSSIONS

#### 3-1 Composition System Investigation

Base compositions that show stable single phase cubic spinel were developed on low resistivity region and high resistivity region. The low resistivity base composition were determined Mn<sub>3</sub>O<sub>4</sub> : Co<sub>3</sub>O<sub>4</sub> = 42.7wt% : 57.3wt% based on researches about Mn-Co oxide system crystal structure. The high resistivity base composition was determined Mn<sub>3</sub>O<sub>4</sub> : NiO = 75.7wt% : 24.3wt% based on researches about Mn-Ni oxide system crystal structure.

Elements that control resistivity - B value relationship were determined by valence control and dilution principle that are mentioned next in detail. Conduction mechanism of NTC thermistor is below. In the case of Cu<sup>+</sup> ions substitution to A sites, the same number of Mn<sup>3+</sup> ions at B site of spinel structure change to Mn<sup>4+</sup> ions. Therefore, the number of holes increase and the resistivity decreases. This is valence control. Al, Fe, Co ions substitute on the B site, but that substitution does not change the valence of Mn<sup>3+</sup>, it only changes the distance between the Mn<sup>3+</sup> and Mn<sup>4+</sup>. As a result of the hole hopping probability change, B value (activation energy) and resistivity are changed [7]. This is dilution principle. (Fig. 2)

High resistivity compositions that show stable single phase cubic spinel structure were developed based on the Mn-Ni oxide system. The base composition is Mn<sub>3</sub>O<sub>4</sub> : NiO = 75.7wt% : 24.3wt%. In order to increase resistivity and not increase the B value, based on the dilution principle, Fe ions were substituted. High resistivity low B value compositions were developed by Cu<sup>+</sup> ions substitution to the Mn-Ni-Fe oxide system. Based on the dilution principle, high resistivity high B value compositions were developed by Al<sup>3+</sup> ions substitution to the Mn-Ni oxide system. Low resistivity compositions that show stable single phase cubic spinel were developed based on the Mn-Co oxide system. The base composition was Mn<sub>3</sub>O<sub>4</sub> : Co<sub>3</sub>O<sub>4</sub> = 42.7wt% : 57.3wt%. Based on valence control, low resistivity low B value compositions were developed by Cu<sup>+</sup> ions substitution to the base composition. Based on valence control, compositions between low resistivity low B value and high resistivity high B value composition were developed by Ti ions substitution to the Mn-Co-Cu oxide system. (Fig. 3)

Therefore, we have succeeded to develop NTC thermistor compositions that satisfy commonly required properties (resistivity range: 8 to 10000Ωcm at 25°C, B<sub>85/25</sub> value: 3100 to 4300K). All

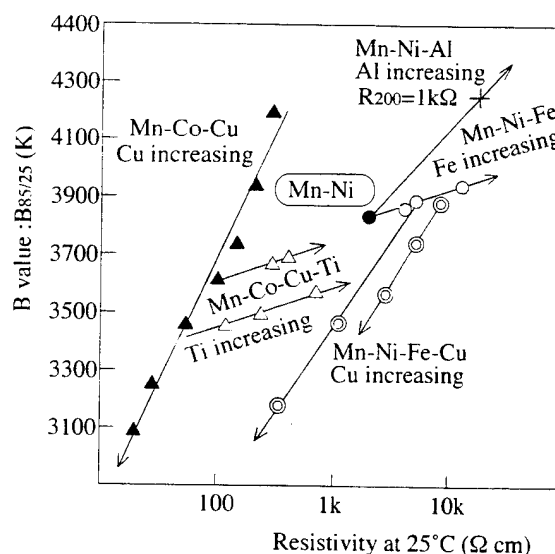


Fig. 3 High sensitivity NTC thermistor B value - resistivity map



compositions show single phase cubic spinel. As an example ( $R_{200}=1k\Omega$ ) of development in this paper, property matching was performed by  $Al^{3+}$  ions substitution to the high resistivity high B value composition. The composition was  $Mn_3O_4 : NiO : Al_2O_3 = 72.1wt\% : 23.1wt\% : 4.8wt\%$ .

### 3-2 High Reliability Realization

Property decay at thermal shock test is due to several reasons; ordinary NTC thermistors have the following ceramic structure (1) coarse grain size, (2) porosity, (3) two phase structure with rock-salt type oxide. These structures decrease the ceramic toughness. During a long time heat test, low reliability is due to the crystal structure and cation ions distribution change after sintering since it is not the equilibrium state under the high temperature. In order to achieve high reliability, the following must occur, (1) fine grain size, (2) sintered structure densification, (3) single phase cubic spinel structure, and (4) equilibrium treatment of cation ions distribution. It is a key point to realize a fixed property according to material design.

As an example of Mn-Ni-Al oxide system, how to determine manufacturing process conditions is described. Calcination condition was determined to generate single phase cubic

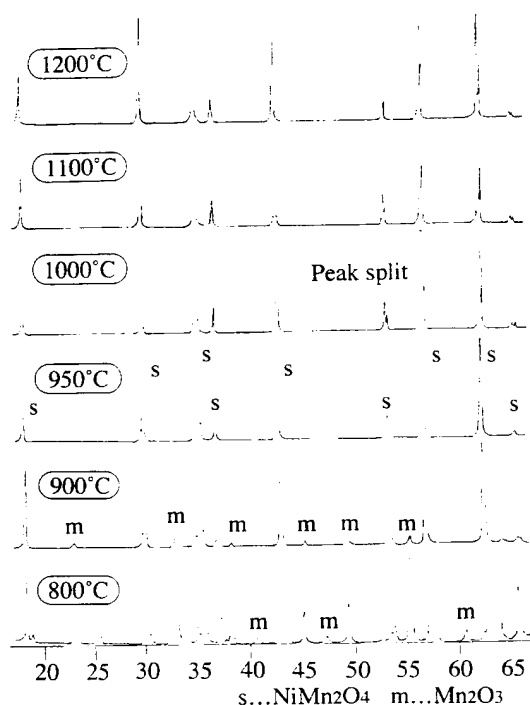


Fig.4 X-ray diffraction pattern as a function of calcination temperature

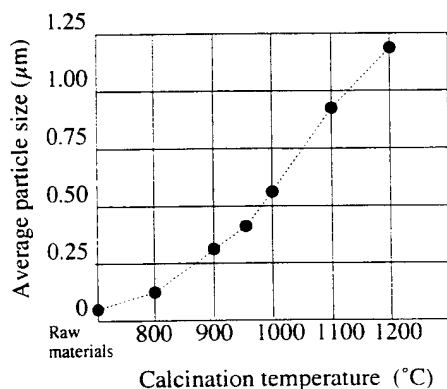


Fig.5 Particle size as a function of calcination temperature

spinel and get fine grain size. Fig.4 shows X-ray diffraction pattern as a function of calcination temperature.  $Mn_2O_3$  peaks exist below  $900^\circ C$ . Only cubic spinel peak pattern exists over  $950^\circ C$ . But above  $1000^\circ C$ , peaks in powder X-ray diffraction pattern split into 2 at high angle. As the defects in the crystal structure decrease, driving force and sinterability become weak. Fig.5 shows a average particle size change as a function of calcination temperature. The average particle size increases according to calcination temperature increasing. Low calcination temperature is suitable for getting fine grain size. So the calcination condition was determined at  $950^\circ C$  for 2hr. Fig.6 shows particle size change as a function of grinding time. After 10hr, average particle size change saturated around about  $1.5\mu m$ . Sub-micron powder has very good sinterability but it is too difficult to handle it. From manufacturing stand point, an average grain size of 1 to  $3\mu m$  can be achieved by grinding. So the grinding time was determined 12hr. Fig.7 shows X-ray diffraction pattern as a function of sintering temperature. Only cubic spinel peak pattern exists between  $1170$  and  $1350^\circ C$ . But  $NiO$  precipitation is observed at  $1350^\circ C$  by SEM observation. At high sintering temperature, rock salt type oxide is precipitated from single phase cubic spinel. On temperature decreasing after sintering, the rock salt type oxide shows solid-solution into single phase cubic spinel. This solid-solution needs oxygen diffusion which obeys Fick rule from outside, therefore, it is easy to show a composition change between inside and outside [8]. Fig.8 shows average grain size change as a function of sintering temperature. Fine grain size can be obtained at lower sintering temperature. So it is important to sinter at lower temperature for normalization of properties,

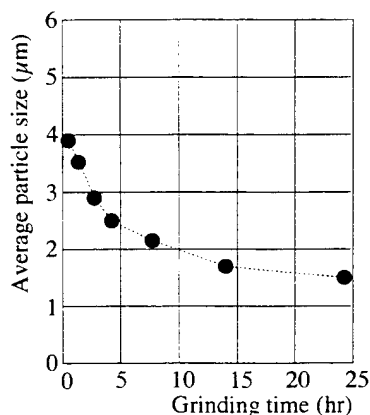
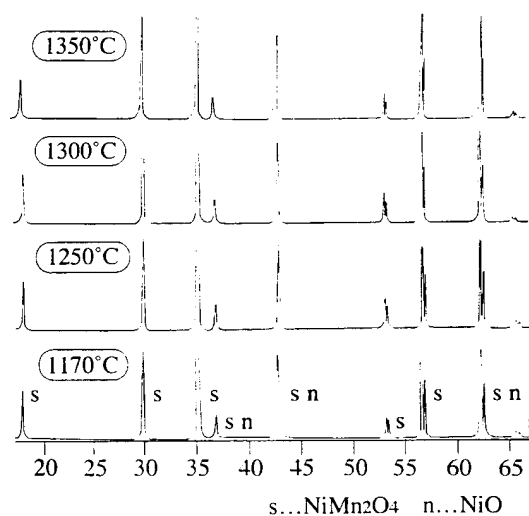


Fig.6 Particle size as a function of grinding time



Second phase (NiO) can be distinguished at  $1350^\circ C$  by SEM-photograph, but can't be distinguished by X-ray diffraction pattern.

Fig.7 X-ray diffraction pattern as a function of sintering temperature

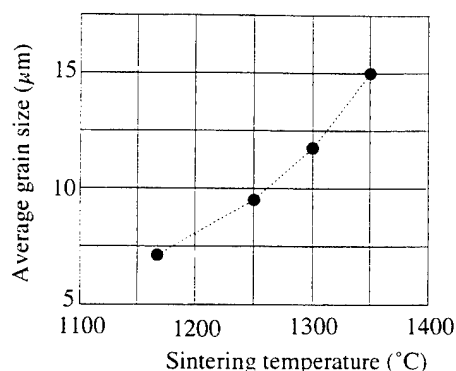


Fig.8 Influence of sintering temperature on average grain size

equilibration of cation ions distribution and obtention of fine grain size. The sintering condition was determined at 1250°C for 4hr. To get the equilibration of cation ions distribution, the annealing process was performed on the ceramic wafer at 1100°C for 2hr. Fig.9 shows a comparison between fine grain ( $\approx 8\mu\text{m}$ ) and coarse grain ( $\approx 23\mu\text{m}$ ) ceramic at thermal shock test. According to the thermal shock test, finer grain size improves reliability.

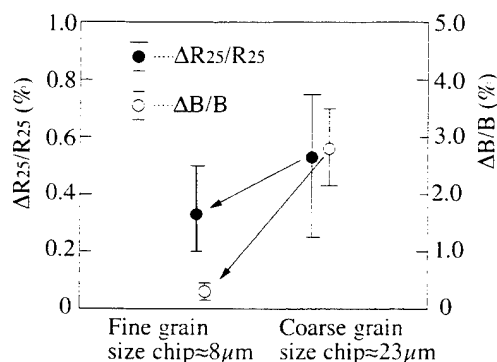


Fig.9 Influence of grain size on thermal shock reliability

### 3-3 Miniaturization

To achieve thermal time constant=1.7 to 2.9s, sensor miniaturization is necessary. In Fig.10, relationship between thermal time constant and sensor body volume is shown. To satisfy the required thermal time constant, it is necessary that the sensor body volume is under  $1.3\text{mm}^3$ . Then sensor dimension was determined to be a diameter of 0.9mm max. and a length of 2mm max. at the main body. The chip size is a thickness of 200~300 $\mu\text{m}$  and a length of 250~400 $\mu\text{m}$ . Before to start manufacturing, the dimension was certified to satisfy the required thermal time constant by FEM analysis. Fig.11 shows the structure of the high sensitivity NTC thermistor. Sensor shape is radial lead type. To endure miniaturization, it is so important to have fine grain size and a dense structure, and also not to have precipitation of another phase in the

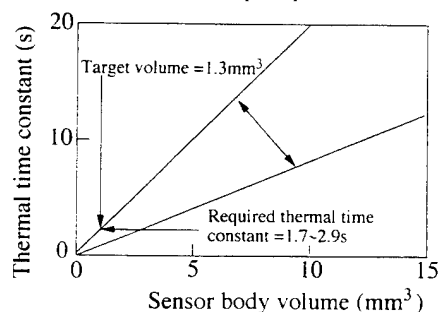


Fig.10 Relationship between thermal time constant and sensor body volume

ceramic. Developed ceramic chip is a key point to realize miniaturization. Taking into account the thermal expansion coefficient and sealing ability of the glass, Dumet wire (Cu coated Fe-Ni wire) was selected as the lead wire [9]. A linear thermal expansion coefficient of the Dumet wire is  $77 \sim 85 \times 10^{-7}/^\circ\text{C}$ . Considering the thermal expansion coefficient matching of the ceramic and glass,  $\text{K}_2\text{O-SiO}_2\text{-PbO}$  glass was adopted as sealing glass. A linear thermal expansion coefficient of the glass is  $89 \sim 93 \times 10^{-7}/^\circ\text{C}$  and that of ceramic is  $80 \times 10^{-7}/^\circ\text{C}$ . In response to requests, Ni plating is performed on lead wire to increase heat proof and anti-oxidation ability. The required thermal time constant (1.7 to 2.9s) was achieved by adopting this structure.

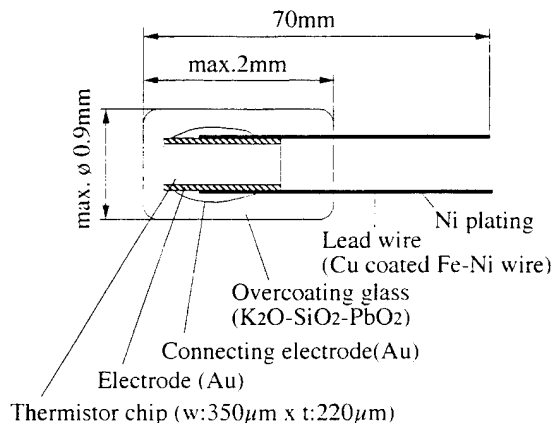


Fig.11 Structure of high sensitivity NTC thermistor

## 4. CONCLUSION

In this research, we have established the electrical properties control method of NTC thermistors using valence control and dilution principle on single phase cubic spinel. High reliability and miniaturization have been achieved by processing conditions optimization to get fine grains and dense structure. We have succeeded in developing high sensitivity NTC thermistors that have the three features below.

- (1) High reliability: especially thermal shock resistance
- (2) Compositions that can be tailored for a wide range electrical properties
- (3) Thermal time constant: 1.7s to 2.9s

## REFERENCES

- [1] E. G. Larson, et al., "Preparation, Semiconduction and Low-Temperature Magnetization of the System  $\text{Ni}_{1-x}\text{Mn}_{2+x}\text{O}_4$ ", *J. Phys. Chem. Solids*, vol.23, pp.1771-1781, 1962.
- [2] T. Hata, et al., "New Thermistor Materials", *National Technical Report*, vol.28 No.6, pp.131-142, December 1982.
- [3] E. Aukrust, et al., "Phase Relations in the System Cobalt Oxide-Manganese Oxide in Air", *J. Am. Ceram. Soc.*, vol.46, pp.511, 1963.
- [4] I. Aoki, "Tetragonal Distortion of the Oxide Spinel containing Cobalt and Manganese", *J. Phys. Soc. Jpn.*, vol.17 No.1, pp.53-61, 1962.
- [5] T. Yokoyama, et al., "Changes in Crystal Structure and Electrical Property of Mn-Co-Ni Oxides for Thermistor Material in Cooling Process after Firing", *J. Japan Ceramic Society*, vol.96 No.10, pp.985-989, 1988.
- [6] H. Futaki, "Study on Thermistor Materials", *Hitachi Research Center 20th Anniversary Paper Bundle*, pp.30-46, 1962.
- [7] M. Suzuki, "A.C. Hopping Conduction in Mn-Co-Ni-Cu Complex Oxide Semiconductors with Spinel Structure", *J. Phys. Chem. Solids*, vol.41, pp.1253-1260, 1980.
- [8] F. Golestani-Fard and S. Azimi, "Oxygen Evolution During the Formation and Sintering of Nickel-Manganese Oxide Spinel for Thermistor Applications", *J. Materials Science*, vol.22, pp.2847-2851, 1987.
- [9] K. Kudoh, et al., "Characteristics of the Oxidized Dumet Wire used as a Glass-Sealing Material", *Sumitomo Denki*, vol.116, pp.177-184, March 1980.

# Study on Piezoelectric Ceramic / Metal Composite thin Plate of Driving Stator for Travelling-wave Motor

Shuxiang Dong Longtu Li Xiaowen Zhang  
Department of Materials Science and Engineering  
Tsinghua University, Beijing, 100084, P.R. China

**Abstract**—In this paper the solution of general problems of bending vibration of the thin piezoelectric ceramic / metal composite plate of driving stator for travelling-wave motor was analysed. Considering the electromechanical coupling effect, the concepts of generalized stress and strain were introduced and generalized piezoelectric equations, the relation of generalized stress and strain, differential motion equation of thin composite plate satisfying were derived. Combining finite element method, the vibration mode of composite plate for travelling-wave motor was calculated considering the electromechanical coupling. Therefore, theoretical basis was provided for optimizing design of ultrasonic motor.

## I. INTRODUCTION

In typical bending travelling-wave rotatory motor, its driving stator is composed of thin piezoelectric ceramic / metal composite plate. Many theoretical analysis have been reported on bending vibration composite transducer made by piezoelectric ceramic / metal. In these cases axisymmetric supposition is usually introduced and the analysis is derived directly with analytic or semi-analytic methods.

In this paper, the solving method of general problems of bending vibration of the thin piezoelectric ceramic / metal composite plate of driving stator travelling-wave motor was analysed.

## II. GENERALIZED PIEZOELECTRIC EQUATIONS OF THE THIN PIEZOELECTRIC CERAMIC / METAL COMPOSITE PLATE

The driving stator of travelling-wave motor can be regarded as the problem of small deflection bending vibration of the thin plate. That is, the thickness  $h$  of the plate is far more less than the least dimension  $b$  of the middle face ( $h < \frac{b}{8} \sim \frac{b}{5}$ ).

Deflection  $w$  is far more less than the thickness of the plate ( $w < h$ ). For small bending deflection of thin

plate, strain relations expressed by deflection  $w$  can be achieved

$$\begin{aligned} S_x &= -z \frac{\partial^2 w}{\partial x^2} \\ S_y &= -z \frac{\partial^2 w}{\partial y^2} \\ S_{xy} &= -2z \frac{\partial^2 w}{\partial x \partial y} \end{aligned} \quad (1')$$

or  $[S] = z[\epsilon]$  (1)

$[S] = [S_x, S_y, S_{xy}]^T$  is the strain matrix of the thin plate,

$$[\epsilon] = -\left[\frac{\partial^2 w}{\partial x^2}, \frac{\partial^2 w}{\partial y^2}, 2\frac{\partial^2 w}{\partial x \partial y}\right]^T \text{ is curvature and torsion matrix.} \quad (2)$$

### 1. Governing equations of piezoelectric ceramic

The polarized direction of the thin piezoelectric ceramic plate is along the thickness direction ( $z$  direction), the electric field of piezoelectric ceramics can be considered as a homogeneous one and d-type piezoelectric equations<sup>[1]</sup> are applied, thus governing equations are given by

$$\begin{aligned} T_x &= Y_1(S_x + \nu_t S_y) - eE_z \\ T_y &= Y_1(\nu_t S_x + S_y) - eE_z \\ T_{xy} &= G_t S_{xy} \\ D_z &= e(S_x + S_y) + \epsilon E_z \end{aligned} \quad (3)$$

where

$$\begin{aligned} Y_t &= 1 / S_{11}^E, \nu_t = -S_{12}^E / S_{11}^E, \\ Y_1 &= Y_t / (1 - \nu_t^2), G_t = Y_t / 2(1 + \nu_t) \\ e &= d_{31} Y_t / (1 - \nu_t), \epsilon = \epsilon_{33}^T \left(1 - \frac{2K_{31}^2}{1 - \nu_t}\right). \end{aligned}$$

Express the first three equations of equations (3) with matrix.

$$[T]_t = z[D']_t[\epsilon] - [e]^T[E] \quad (4)$$

In equation (4), subscript "t" indicates the part of piezoelectric ceramics and

$$[D'_t] = \frac{Y_t}{1 - \nu_t^2} \begin{bmatrix} 1 & \nu_t & 0 \\ \nu_t & 1 & 0 \\ 0 & 0 & \frac{1 - \nu_t}{2} \end{bmatrix}$$

$$[e]^T = e \begin{bmatrix} 0 & 0 & 1 \\ 0 & 0 & 1 \\ 0 & 0 & 0 \end{bmatrix}, E = \begin{bmatrix} 0 \\ 0 \\ E_3 \end{bmatrix} \quad (5)$$

## 2. Governing equation of metal

For metal, let  $[e]=0$ , in equation (4) change  $Y_t, \nu_t, G_t$  into  $Y_m, \nu_m, G_m$  and governing equation of metal can be obtained.

$$[T]_m = \begin{bmatrix} T_x \\ T_y \\ T_{xy} \end{bmatrix}_m = z[D'_m][\varepsilon] \quad (6)$$

Subscript "m" in the equation indicates the part of metal, and

$$[D'_m] = \frac{Y_m}{1 - \nu_m^2} \begin{bmatrix} 1 & \nu_m & 0 \\ \nu_m & 1 & 0 \\ 0 & 0 & \frac{1 - \nu_m}{2} \end{bmatrix} \quad (7)$$

## 3. Generalized piezoelectric equations

According to equation (4) and (6), stress and strain compositions show linear variation along the thickness direction of the plate (z direction).

The first term of equation (4) and equation (6) are both odd functions of z. Furthermore, it is easy to prove that integral term of stress along the direction of the thickness of the plate is zero when poisson ratio of metal and piezoelectric ceramics  $\nu_m, \nu_t$  are almost identical. Under this condition, the position of the mid-face of thin piezoelectric ceramic / metal composite plate can be achieved: <sup>[2]</sup> (See figure 1)

$$t_{n2} = \frac{Y_2 h_m^2 + Y_1 h_t^2 + 2Y_1 h_t h_m}{2(Y_2 h_m + Y_1 h_t)}$$

$$t_{n1} = (h_m + h_t) - t_{n2} \quad (8)$$

The integral of the second term of equation (4) which is a vector related to applied voltage  $V_E$  is not

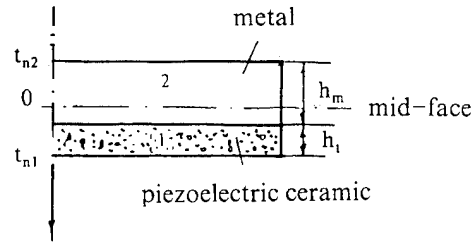


Fig.1 The position of the mid-face of thin Piezoelectric ceramic / metal composite plate.

zero. For thin piezoelectric plate, let:

$$[E] = [M_E]V_E, [M_E] = [0 \ 0 \ 1/h_t]^T \quad (9)$$

$$\text{Thus} \quad \int_{h_m - t_{n2}}^{(h_m - t_{n2}) + h_t} [e]^T [E] dz = V_E [H] \quad (10)$$

$$\text{in the above equation } [H] = h_t [e]^T [M_E] = e \begin{bmatrix} 1 \\ 1 \\ 0 \end{bmatrix} \quad (11)$$

Equation (10) shows that applied voltage can be transformed into an equivalent stress vector matrix, which makes thin piezoelectric composite plate bend.

According to equation (4), (6), the bending torque of the thin composite plate can be obtained by

$$[M] = \begin{bmatrix} M_x \\ M_y \\ M_{xy} \end{bmatrix} = \int_{-t_{n2}}^{h_m - t_{n2}} z \begin{bmatrix} T_x \\ T_y \\ T_{xy} \end{bmatrix}_m dz$$

$$+ \int_{h_m - t_{n2}}^{(h_m - t_{n2}) + h_t} z \begin{bmatrix} T_x \\ T_y \\ T_{xy} \end{bmatrix}_t dz$$

or

$$[M] = \{[D_m] + [D_t]\}[\varepsilon] - \alpha[e]^T [E]$$

$$= [D][\varepsilon] - \alpha[e]^T [E] \quad (12)$$

in equation (12),  $[D] = [D_m] + [D_t]$  is called generalized bending stiffness.  $[\varepsilon]$  is called generalized strain.  $[M]$  is called generalized stress or internal force,  $\alpha$  is a construction parameter. In a thin composite plate consisted of piezoelectric ceramics and metal, applied electric field  $[E]$  will produce an extra generalized internal force.

Write the fourth term in equation (3) in matrix form.

$$\begin{bmatrix} 0 \\ 0 \\ D_z \end{bmatrix} = ze \begin{bmatrix} 0 & 0 & 0 \\ 0 & 0 & 0 \\ 1 & 0 & 0 \end{bmatrix} \begin{bmatrix} -\frac{\partial^2 w}{\partial x^2} \\ -\frac{\partial^2 w}{\partial^2 y} \\ -2\frac{\partial^2 w}{\partial x \partial y} \end{bmatrix} + \epsilon \begin{bmatrix} 0 \\ 0 \\ E_z \end{bmatrix}$$

or  $[D_e] = z[e][\epsilon] + \epsilon[E]$  (13)

in the above equation,  $[D_e]$  indicates electric displacement vector matrix,  $[e]$  is piezoelectric stress constant matrix. Because electric displacement of piezoelectric ceramic keeps constant in cross section, that is  $\frac{\partial D_z}{\partial z} = 0$ , or  $\frac{\partial [D_e]}{\partial z} = 0$  in equation (13), integrate along  $z$  direction and obtain

$$[D_{eh}] = \alpha[e][\epsilon] + h_t \epsilon [I][E] \quad (14)$$

in equation (14),  $[I]$  is unit matrix,  $[D_{eh}] = h_t [D_e]$ . Because the problem has been changed into a plane one,  $[D_{eh}]$  is called the electric displacement vector of the plane problem.

(12), (14) are written again here:

$$\begin{aligned} [M] &= [D][\epsilon] - \alpha[e]^T [E] \\ [D_{eh}] &= \alpha[e][\epsilon] + h_t \epsilon [I][E] \end{aligned} \quad (15)$$

Equation (15) is the generalized piezoelectric equations under the condition of small bending deflection of the thin piezoelectric ceramic metal composite plate. However, they are correct only under the supposition of homogeneous electric field of piezoelectric ceramic. For a thin plate, the supposition is generally correct and they have been changed into planiform stress problem.

In the above two equations,  $[M]$ ,  $[\epsilon]$  are generalized stress and strain, correspondingly,  $[D_{eh}]$ ,  $[E]$  can be called generalized electric displacement and field.

Applied the same method, generalized piezoelectric equations with the independent variables of  $[\epsilon]$ ,  $[D_{eh}]$  can be achieved by

$$\begin{aligned} [M] &= \{[D_m] + [D_{t1}]\}[\epsilon] - \frac{\alpha}{h_t} [h][D_{eh}] \\ [E] &= -\frac{\alpha}{h_t} [h]^T [\epsilon] + \frac{1}{\epsilon h_t} [I][D_{eh}] \end{aligned} \quad (16)$$

in the above equations,

$$\begin{aligned} [h] &= \frac{e}{\epsilon} \begin{bmatrix} 0 & 0 & 1 \\ 0 & 0 & 1 \\ 0 & 0 & 0 \end{bmatrix} \\ [D_{t1}] &= \frac{1}{3} [(h_m - t_{n2} + h_t)^3 - (h_m - t_{n2})^3] [D'_{t1}] \end{aligned}$$

### III. THE RELATION OF GENERALIZED STRESS AND STRAIN OF THIN PIEZOELECTRIC CERAMIC / METAL COMPOSITE PLATE:

From the second equation of generalized piezoelectric equations (16),  $[D_{eh}]$  is solved and put into the first equation, the result is that

$$[M] = \{[D_m] + [D_{t1}] - [J]\}[\epsilon] - \frac{\alpha V_E}{h_t} [H]$$

that is

$$\begin{bmatrix} M_x + \frac{\alpha e}{h_t} V_E \\ M_y + \frac{\alpha e}{h_t} V_E \\ M_{xy} \end{bmatrix} = [D'] \begin{bmatrix} \epsilon_x \\ \epsilon_y \\ \epsilon_{xy} \end{bmatrix}$$

$$\text{or } [M'] = [D'][\epsilon] \quad (17)$$

in the above equation

$$[J] = \frac{\alpha^2 e^2}{h_t \epsilon} \begin{bmatrix} 1 & 1 & 0 \\ 1 & 1 & 0 \\ 0 & 0 & 0 \end{bmatrix}$$

Equation (17) shows that applied voltage adds equivalently internal force. Therefore, equation (17) is the relation of generalized stress and strain of the thin piezoelectric ceramic / metal composite plate.

### IV. DIFFERENTIAL MOTION EQUATION OF THE THIN PIEZOELECTRIC CERAMIC / METAL COMPOSITE PLATE

With equation (17) that expresses the relation of generalized stress and strain of the thin piezoelectric ceramic / metal composite plate derived above, the motion equation of the thin composite plate can be obtained directly.

Consider the equilibrium equations of generalized stress of a differential element, the motion equation of the differential element in z direction can be obtained by

$$\frac{\partial^2 M'_x}{\partial x^2} + 2 \frac{\partial^2 M'_{xy}}{\partial x \partial y} + \frac{\partial^2 M'_y}{\partial y^2} + q = (\rho_m h_m + \rho_t h_t) \frac{\partial^2 w}{\partial t^2} \quad (18)$$

in the equation,  $M'$  is generalized stress when considering electromechanical coupling effect,  $\rho_m, \rho_t$  are the density of metal and piezoelectric ceramic relatively.  $q$  is the applied force of unit area of differential element in z direction.

Put the relation (17) into equation (18) and notice

$\frac{\partial^2 V_E}{\partial x^2} = \frac{\partial^2 V_E}{\partial y^2} = \frac{\partial^2 V_E}{\partial x \partial y} = 0$ , thus equation (18) can be written as:

$$\begin{aligned} & - \left( \frac{\partial^2}{\partial x^2}, \frac{\partial^2}{\partial y^2}, 2 \frac{\partial^2}{\partial x \partial y} \right) \begin{bmatrix} \beta_1 & \beta_2 & 0 \\ \beta_2 & \beta_1 & 0 \\ 0 & 0 & \beta_3 \end{bmatrix} \begin{bmatrix} \frac{\partial^2}{\partial x^2} \\ \frac{\partial^2}{\partial y^2} \\ 2 \frac{\partial^2}{\partial x \partial y} \end{bmatrix} w + q \\ & = (\rho_m h_m + \rho_t h_t) \frac{\partial^2 w}{\partial t^2} \\ \text{or } & [\beta_1 \frac{\partial^4}{\partial x^4} + \beta_1 \frac{\partial^4}{\partial y^4} + 2(\beta_2 + 2\beta_3)] \frac{\partial^4 w}{\partial x^2 \partial y^2} + (\rho_m h_m + \rho_t h_t) \frac{\partial^2 w}{\partial t^2} = q \end{aligned} \quad (19)$$

where  $\beta_i$  ( $i=1,2,3$ ) is a parameter related with construction, mechanical characteristics of materials.

The above equation is the different motion equation of thin piezoelectric ceramic / metal composite plate.

## V. VIBRATION MODE OF THIN PIEZOELECTRIC CERAMIC / METAL COMPOSITE PLATE OF DRIVING STATOR FOR TRAVELLING-WAVE MOTOR

According to the generalized piezoelectric equations (15), vibration modes and resonance frequencies of thin piezoelectric ceramic / metal composite plate of driving

stator for travelling-wave motor can be calculated combining finite element method. Figure 2. shows a vibration mode for travelling-wave motor.

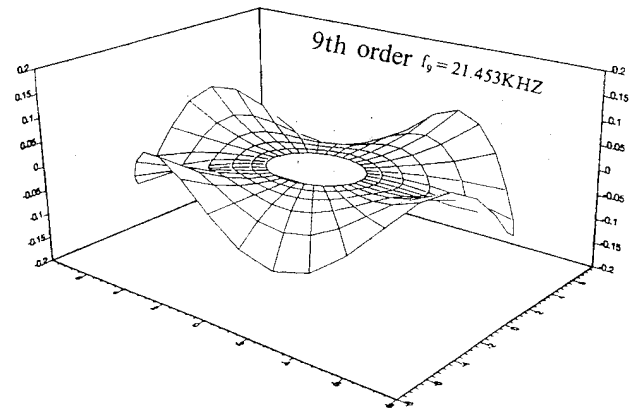


Fig.2 A vibration mode of piezoelectric ceramic / metal composite plate of driving stator for ultrasonic motor.

## VI. CONCLUSION

The governing equations and vibration modes of the thin piezoelectric ceramic / metal composite plate of the driving stator of bending travelling wave motor were studied theoretically. The concepts of generalized stress and strain were introduced and generalized piezoelectric equations, the relation of generalized stress and strain, differential motion equation of the thin piezoelectric ceramics / metal composite plate that small deflection bending vibration satisfied were derived.

The generalized piezoelectric equations can be applied not only in axisymmetric bending vibration, but also in anaxisymmetric. Combining finite element method, dynamic electromechanical coupling problems and vibration mode problems of thin piezoelectric ceramic / metal composite plate of any shape can be solved. It is very important for optimizing design of ultrasonic motor.

## REFERENCES

- [1] Mason, W.P, *Physical Acoustics*, Vol.1-Part A, Academic Press, New York and London, 1964
- [2] Takehiro Takano et al, "Non-axisymmetric contour vibration of clamped piezoelectric annular plates: analysis for the development of an ultrasonic motor", *J. Acoust. Soc. Jpn (E)* 11.3 (1990).

# PHOTO-ACOUSTIC DEVICES USING (Pb,La)(Zr,Ti)O<sub>3</sub> CERAMICS

Sheng-Yuan Chu and Kenji Uchino  
International Center for Actuators and Transducers  
Intercollege Materials Research Laboratory  
The Pennsylvania State University, University Park, PA 16802

**Abstract** -- Photostriction in ferroelectrics arises from a superposition of photovoltaic and inverse piezoelectric effects. This phenomenon provides promise for photo-acoustic devices, when the response has been sufficiently improved. In this paper, B-site donor doping was investigated in (Pb, La)(Zr, Ti)O<sub>3</sub> based ceramics with the aim of improving the response speed. Using a PLZT bimorph configuration, a photoacoustic device was trially fabricated, and the fundamental mechanical resonance was observed under intermittent illumination of purple-color light, having neither electric lead wires nor electric circuit.

## INTRODUCTION

Photostrictive effect is a phenomenon in which strain is induced in the sample when it is illuminated. This effect is focused especially in the field of optical communication, where the key components are solid state lasers as a light source, optical fibers as a transfer line, and displays/telephones as a visual/audible interface with the human. The former two components have been developed fairly successfully, and the photo-acoustic device (i. e. optical telephone or "photophone") will be eagerly anticipated in the next century. Photostrictive devices which function when they receive the energy of light will be particularly suitable for use in the above-mentioned fields.

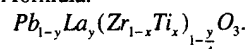
In principle, the photostrictive effect is the superimposing of a photovoltaic effect, where a large voltage is generated in ferroelectrics through the irradiation of light, and a piezoelectric effect, where the material expands or contracts from the voltage applied. The photovoltaic effect mentioned here generates a greater-than-band-gap voltage, and is quite different from that based on the p-n junction of semiconductors (i. e. solar battery).<sup>1-3</sup> It is generated when electrons excited by light move in a certain direction of the ferroelectric crystal due to the spontaneous polarization (i. e. crystallo-graphic anisotropy).

So far, most of the studies on the photovoltaic effect have been made on single crystals to clarify the origin of the effect.<sup>1-3</sup> However, our research group has been focusing on polycrystalline samples such as PbTiO<sub>3</sub>-based<sup>4,5</sup> and Pb(Zr, Ti)O<sub>3</sub>-based ceramics<sup>6,7</sup> from a practical application point of view. High photovoltage ( $\approx 1$  kV/cm) generators with relatively quick response ( $\approx 10$  sec) have been developed in the (Pb, La)(Zr, Ti)O<sub>3</sub> (PLZT) system. Moreover, bimorph-type photostrictive elements could exhibit large tip deflections under UV light illumination.<sup>6,7</sup>

In this paper, the photovoltaic effect in PLZT(3/52/48) based ceramics has been investigated as a function of B-site donor dopants. Then, using the PLZT bimorph, a photoacoustic device was trially fabricated, and the fundamental mechanical resonance was observed under intermittent illumination.

## SAMPLE PREPARATION

PLZT (x/y/z) samples were prepared in accordance with the following composition formula:



Since the photostriction figure of merit is defined as the product of the photovoltaic voltage and piezoelectric coefficient ( $x_{ph} = d_{33} \times E_{ph}$ ), PLZT(3/52/48) was selected due to its optimum photostrictive response within the PLZT system.<sup>6</sup> According to our preliminary study on impurity doping,<sup>7</sup> WO<sub>3</sub> doped PLZT ceramics were prepared.

Ceramic powders were prepared by a conventional mixed oxide technique. PbCO<sub>3</sub>, La<sub>2</sub>O<sub>3</sub>, ZrO<sub>2</sub>, TiO<sub>2</sub> and WO<sub>3</sub> were weighed in the appropriate proportions and mixed in a ball mill for 2 days using ethanol and zirconia grinding media. 0.5 wt% excess PbCO<sub>3</sub> was added to compensate for weight loss during calcination and sintering. The slurry was dried, then calcined in a closed alumina crucible at 950 °C for 10 hours. The calcined powder was ball-milled again for 48 hours. The samples were sintered in sealed alumina crucibles at 1270 °C for 2hrs. A PbO rich atmosphere was maintained with lead zirconate powder to minimize lead loss during sintering. Sintered samples were cut, polished and electroded with silver paste. Finally, each sample was poled at 15 kV/cm in silicone oil at 120°C.

The poled PLZT ceramics were used to make bimorph actuators. The elements were 20 x 4 x 0.15 mm<sup>3</sup>: the 4 x 0.15 mm<sup>2</sup> surface was electroded with silver paste and silver wires were attached. The bimorph actuator consisted of two bonded oppositely-poled ceramic plates (refer to Fig. 2).

## IMPURITY DOPING EFFECT

Impurity doping on PLZT affects the photovoltaic response significantly.<sup>7</sup> Regarding the photostriction effect, it is known that as the photovoltaic voltage increases, the strain value increases, and

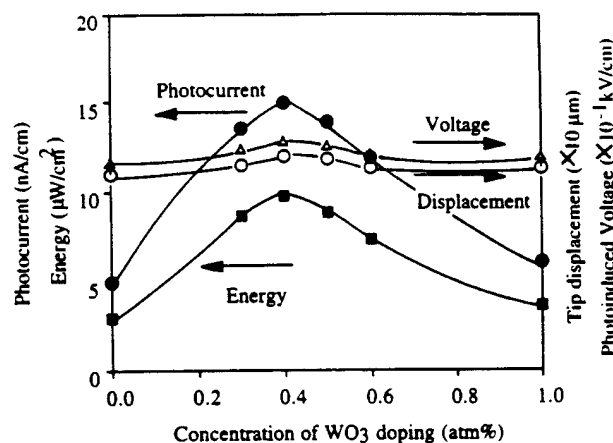


Fig. 1 Changes in photovoltaic current, voltage, power and tip displacement as a function of dopant WO<sub>3</sub> concentration in PLZT (3/52/48).

with increasing photo-current, there is an increase in the overall response. The photovoltaic response is enhanced by donor doping onto the B-site ( $\text{Nb}^{5+}$ ,  $\text{Ti}^{5+}$ ,  $\text{W}^{6+}$ ). On the other hand, impurity ions substituting at the A-site and/or acceptor ions substituting at the B-site, whose ionic valences are small (1 to 4), have no effect on the response.

Figure 1 shows the photovoltaic current, photovoltaic voltage, photo-induced tip displacement and stored energy ( $P=(1/2)I_{\text{max}} \times V_{\text{max}}$ ) in PLZT 3/52/48 samples plotted as a function of atm % of  $\text{WO}_3$  doping concentration. It was found that higher photovoltaic response can be obtained in  $\text{WO}_3$  doped samples. The photovoltaic voltage reaches 1 kV/mm, and the current is on the order of nA. The maximum of the saturated tip displacement was about 120  $\mu\text{m}$  for 0.4 atm%  $\text{WO}_3$  doped samples. The displacement of 30  $\mu\text{m}$  could be obtained in one second under a light intensity of 4  $\text{mW}/\text{cm}^2$  ( $\lambda = 370 \text{ nm}$ ).

### PHOTO-ACOUSTIC MEASUREMENT

The mechanical resonance frequency of this bimorph sample can be estimated according to the equation:

$$f_r = 0.158 \times \frac{t}{l^2} \sqrt{\frac{1}{\rho s_{11}^E}}, \quad (1)$$

where  $t$  and  $l$  are the thickness and length of the bimorph sample, respectively,  $\rho$  is the density and  $s_{11}^E$  is the elastic compliance of the ceramic. The calculated resonance frequency of the PLZT based bimorph, ( $\rho = 7.9 \text{ g}/\text{cm}^3$  and  $s_{11}^E = 16 \times 10^{-12} \text{ m}^2/\text{N}$ ), was about 3 kHz: too high for photo-induced resonance measurements. Therefore, a thin cover glass was attached to the bimorph sample to reduce the resonance frequency, as shown in Fig. 2. Initially, to determine the electromechanical resonance behavior, an ac. voltage was applied to the bimorph, and the tip displacement was monitored by changing the drive frequency, using the experimental setup shown in Fig. 3. Figure 4 shows the mechanical resonance characteristics obtained from this experiment. The resonance frequency was  $\sim 79 \text{ Hz}$  with a mechanical quality factor  $Q$  of  $\sim 30$ . The maximum displacement of this thin-plate attached sample was about 14  $\mu\text{m}$  at 80  $\text{V}_{\text{p-p}}$ .

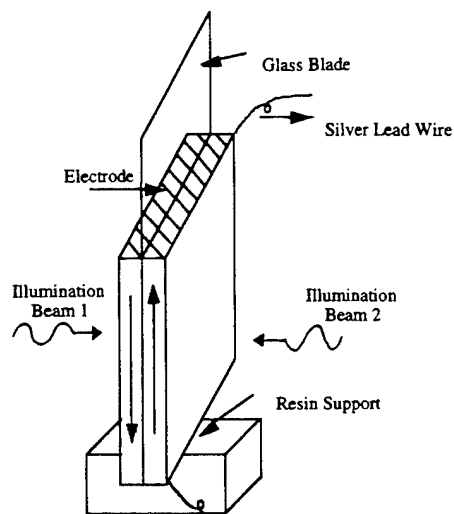


Fig.2 Configuration of a thin-plate attached photo-acoustic bimorph.

Then, the photo-induced mechanical resonance was measured using the system shown in Fig. 5. Radiation from a high-pressure mercury lamp (Ushio Electric USH-500D) was passed through a UV bandpass filter (Oriel Co., No.59811), an IR blocking filter (Oriel Co., No.59060), an optical focusing lens and an optical chopper to provide intermittent sample irradiation. A wavelength peak of 370 nm, where the maximum photovoltaic effect of PLZT is obtained, was used. A dual beam method was used to irradiate the two sides of the bimorph alternately.<sup>7)</sup> Two beams, A and B, were chopped so as to cause a 180 degree phase difference as illustrated

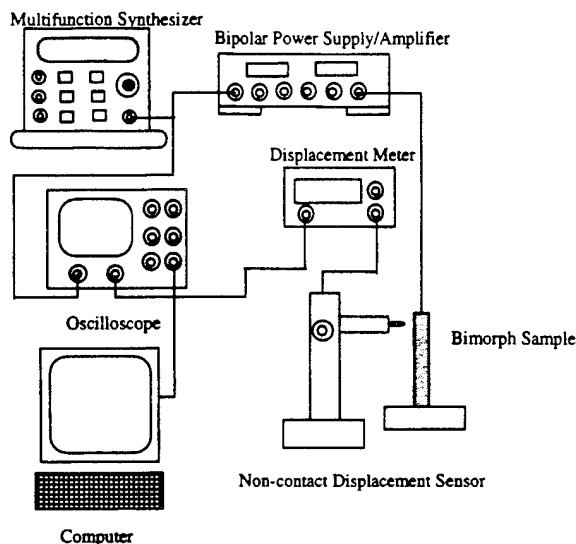


Fig.3 Experimental setup for the electro-mechanical resonance measurement.

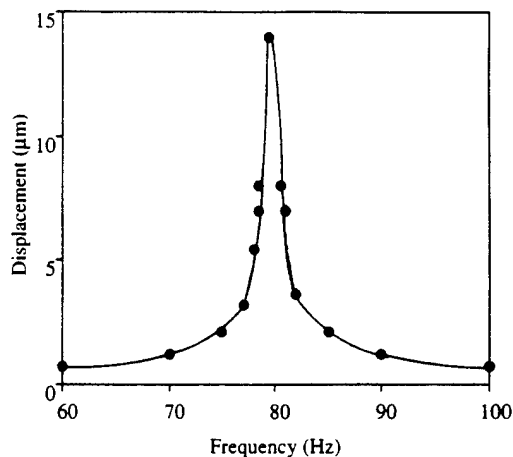


Fig.4 Electromechanical resonance behavior of the PLZT bimorph.



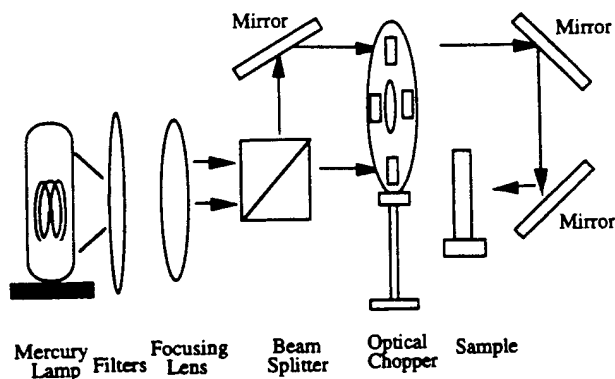


Fig.5 Experimental setup for the photo-induced mechanical resonance measurement.

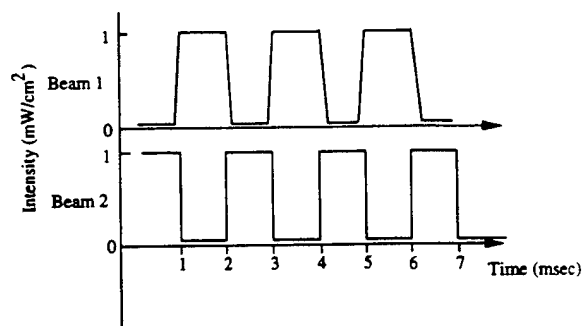


Fig.6 Wave forms for the two beams for illuminating the bimorph sample.

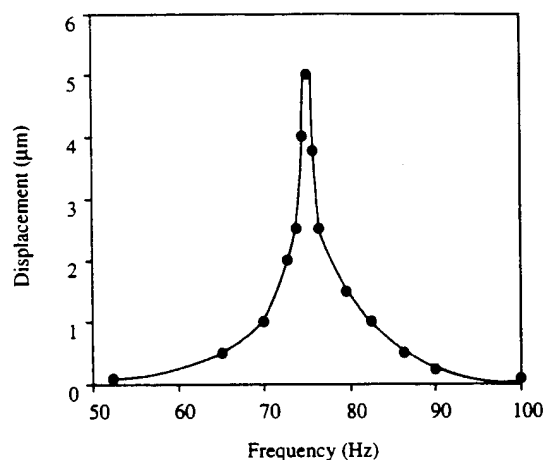


Fig.7 Photo-induced mechanical resonance behavior of the PLZT bimorph.

in Fig. 6. The slow recovery because of the low dark conductivity was overcome using this dual beam method. The mechanical resonance was then determined by changing the chopper frequency.

The tip displacement of the thin-plate-attached sample as a function of chopper frequency is presented in Fig. 7. Photo-induced mechanical resonance was successfully observed. The resonance frequency was about 75 Hz with the mechanical quality factor  $Q$  of about 30; in good agreement with the previous electromechanical data. The maximum tip displacement of this photostrictive sample was about 5  $\mu\text{m}$  of resonance.

## CONCLUSION

Photo-mechanical resonance of a PLZT ceramic bimorph actuator has been successfully induced using chopped UV irradiation, having neither electric lead wires nor electric circuit. A thin cover glass was attached on the bimorph structure to decrease the resonance frequency so as to easily observe the photo-induced resonance. The resonance frequency was 75 Hz with a mechanical quality factor  $Q$  of about 30 under dual beam operation. The maximum tip displacement of this sample was about 5  $\mu\text{m}$ , smaller than the level required for audible sound. However, the achievement of photo-induced mechanical resonance in the audible frequency range suggests the promise of photostrictive PLZT bimorph-type devices as photo-acoustic components, or "photophones", for the next optical communication age.

## ACKNOWLEDGEMENT

This work is supported by Army Research Laboratory (ARL), No. DAALO3-92-G-0244.

## REFERENCES

- [1] V. M. Fridkin, "Photoferroelectrics", Ed. by M. Cardona, P. Fulde, H. -J. Queisser, Solid State Sciences, New York, (1979), pp. 85.
- [2] A. M. Glass, D. von der Linde, D. H. Austin and T. J. Negran, *J. Elec. Mat.* **4** [5], 915-943 (1975).
- [3] V. M. Fridkin and B. N. Povov, *Sov. Phys. Usp.*, **21**(12), 981-991 (1978).
- [4] K. Uchino, Y. Miyazawa and S. Nomura, *Jpn. J. Appl. Phys.*, **21**, [12], 1671-1674 (1982).
- [5] K. Uchino, Y. Miyazawa and S. Nomura, *Jpn. J. Appl. Phys. Suppl.* **22-2**, 102-105 (1983).
- [6] T. Sada, M. Inoue and K. Uchino, *J. Ceram. Soc. Jpn.*, **5**, 545 (1987).
- [7] M. Tanimura and K. Uchino, *Sensors and Materials*, **1**, 47-56 (1988).

# Design Low Frequency Ultrasonic Transducers by 1-3 Tubular Piezocomposite

J. Chen, Q.M. Zhang and L.E. Cross

Materials Research Laboratory

The Pennsylvania State University, University Park, PA 16802.

Michael Trottier

FMI, Inc., Biddeford, Maine 04005

**ABSTRACT** Transverse piezoelectric (TP) mode 1-3 tubular piezocomposites have been developed recently for low frequency ultrasonic transducer applications. The new piezocomposites made of piezoceramic tubes embedded in a polymer matrix has many unique features, such as increasing the tunability on acoustic impedance, enhancing the effective piezoelectric responses and improving the electrical impedance matching with the driving circuit. This paper theoretically described the surface displacement profile of 1-3 tubular piezocomposites under an uniaxial stress. The effective piezoelectric coefficients of 1-3 tubular piezocomposites have been derived in terms of the tube volume fraction, tube size and the elastic constants of matrix polymer. The theoretical analysis and experimental results indicate that the elastic parameters of polymer matrix have significant effects on the performance of 1-3 tubular piezocomposites. By optimizing the structure of the composite and elastic properties of the polymer matrix, the 1-3 tubular piezocomposite has a exceptionally large effective piezoelectric coefficient,  $d_{33}$ , and less undesired resonance modes. A low electrical impedance and large effective piezoelectric coefficients suggest that the TP mode 1-3 tubular piezocomposites are superior to conventional 1-3 rod piezocomposites in low frequency ultrasonic transducer applications.

## INTRODUCTION

Piezoelectric ceramic-polymer composites have found numerous applications in the piezoelectric transducers. The most significant advantage of piezocomposites is the tunability of their physical properties, such as effective piezoelectric coefficients, acoustic impedance and effective elastic constants by changing the connectivity and matrix polymer properties of piezocomposites. As a example, because their high electromechanical coupling constant and relative low acoustic impedance, 1-3 rod piezocomposites have been successfully applied in advanced transducers, including medical imaging transducers in megahertz frequency regime and underwater acoustic transducers [1-4]. For high frequency applications 1-3 rod piezocomposite transducers have less problem in electrical impedance matching and output acoustic power. However, when frequencies fall in the kilohertz regime, namely, for those applications involving acoustic wave through air, water and concrete, such as autonomous vehicle guidance, manufacturing assembly, under water imaging, nondestructive test and noise control, the conventional 1-3 rod piezocomposite transducers suffer some difficulties due to their small effective strain coefficients, high electric impedance, hence, a small acoustic power output. To overcome those problems, a new type of 1-3 tubular piezocomposites have been recently proposed which shown several advantages over traditional 1-3 rod piezocomposites for hydrostatic transducer applications. The hydrostatic piezoelectric coefficient  $d_h$  and figure of merit  $d_h g_h$  are as high as 5,000 pC/N and  $6,000 \times 10^{-15} \text{ m}^2/\text{N}$  respectively [7-8]. In general, for an ideal piezo-acoustic transducer material, the basic parameters are large piezoelectric coefficients, good acoustic and electric impedance matching. The new 1-3 tubular piezocomposites have demonstrated those features by operating in the transverse piezoelectric (TP) mode. The effective longitudinal piezoelectric constant  $d_{33}$  of 1-3 tubular composites has a substantially large value by selecting a large tube wall thickness/length ratio, while the effective transverse piezoelectric constant  $d_{31}$  of 1-3 tubular composites can be tuned from negative to positive through optimizing the dimensions and piezoelectric constants the piezoceramic tubes. As a result, the hydrostatic coefficient,  $d_h = d_{33} + 2d_{31}$ , becomes exceptionally large. In addition, a low acoustic impedance can be achieved in 1-3 tubular piezocomposites by encasing an air phase inside the tubes which will significantly reduce the acoustic impedance of the composites.

Similar to other piezocomposites, the performance of TP mode 1-3 tubular piezocomposites depends on their structural design and the component selection. There are a number of parameters which are critical to the performance of TP mode 1-3 tubular piezocomposites, such as elastic constants of the matrix polymer and the dimension of piezoceramic tubes. Increasing the tunability of acoustic impedance, suppressing undesired resonant modes, and enhancing the sensitivity of the piezocomposites are the basic goals to design advanced piezocomposite transducers. In this paper, a static physical model will be addressed to analyze the effect of various designing parameters on the uniaxial piezoelectric response of TP mode 1-3 tubular piezocomposites based on the results of recent theoretical and experimental investigations.

## MODELING

One of the major concerns in the thickness resonant mode transducers is the effective longitudinal piezoelectric coefficient of materials. The performance of piezocomposite transducers is also determined by the surface displacement field. The basic idea of the model is to construct a static elastic equilibrium condition under an uniaxial loading pressure. The transferred stress on each single ceramic tube is not only from the surrounded polymer matrix, but also from the nearest piezoceramic tube neighbors. A cylindrical coordinate system  $(r, \theta, z)$  with the  $z$  and  $r$  directions along the axis of the piezoceramic tube and radial direction respectively, and  $\theta$  as the angular variable, has been chosen, see Fig. 1. Because it takes the contribution of neighbor tubes and periodic structure into consideration, this model is expected to be more closer to the practical case than pervious models in describing the static performance of 1-3 tubular piezocomposites. The piezoceramic tubes are poled and operated in radial direction, with a large aspect ratio. The stress transfer in 1-3 connectivity composites only enhance the piezoelectric response in the  $z$  direction near the surface region of the composite, therefore, a combination of rigid thin surface layers and soft polymer matrix is desirable to improve the stress transfer between polymer matrix and piezoceramic tubes without increasing the self-loading of the piezocomposite [6,8].

The effective longitudinal piezoelectric response of 1-3 tubular piezocomposites mainly controlled by both the effective piezoelectric coefficient  $d_{33}^{\text{eff}}$  of tubes and the elastic properties of the polymer matrix. Because the elastic stiffness of rigid surface layers is orders of magnitude higher than the soft polymer matrix, the surface displacement of the 1-3 tubular piezocomposite under an uniaxial stress is governed by the movement of rigid surface layers. Hence, a thin plate elastic equation can be used to describe the static displacement profile on the radiation surface of the composite. The basic elastic equation can be written in the following form [5]:

$$D \Delta^2 u - P = 0 \quad (1)$$

where  $D = \frac{h^3 Y}{12(1-\sigma^2)}$ ,  $h$  is the thickness of the rigid surface layer,

$Y$  and  $\sigma$  are the Young's modulus and Poisson's ratio of the rigid surface layers, respectively. The stress term  $P$  in the equation depends on external pressure and transferred stress from polymer matrix in the  $z$ -direction. By solving the above equation, we can obtain the surface displacement profile and then piezoelectric responses in the  $z$ -direction of the 1-3 tubular piezocomposite.

The displacement field on the composite surface can be divided into three regions (refer to Figure 1.):

Region i. inside the ceramic tube,  $r < r_1$

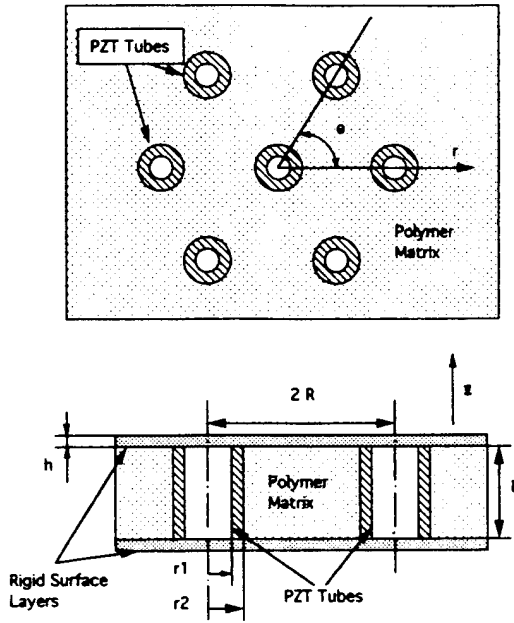


Figure 1. Schematic draw of 1-3 tubular composite. a). top view, b). cross section of the composite.

$$u = a_1 + \frac{P_1}{64D} r^4 + b_1 r^2 \quad (2)$$

Region ii. within the ceramic region,  $r_1 < r < r_2$

$$u = K \text{ (constant)} \quad (3)$$

Region iii. in the polymer matrix outside the ceramic tube,  $r_2 < r < R$

$$u_z = a_2 + \frac{P_1}{64D} \sum_{i=1} |\bar{r} - \bar{r}_i|^4 + b_2 \sum_{i=1} |\bar{r} - \bar{r}_i|^2 + c_2 \sum_{i=1} |\bar{r} - \bar{r}_i|^2 \ln |\bar{r} - \bar{r}_i| + d_2 \ln |\bar{r} - \bar{r}_i| \quad (4)$$

where  $a_1, a_2, b_1, b_2, c_2, d_2$  are the integration constants which can be determined from the boundary conditions: at polymer-ceramic interfaces, polymer phase has the same displacement as the ceramic phase; and  $\frac{\partial u}{\partial r} = 0$ .  $P_1$  is loading pressure in the  $z$ -direction.

Inside the tube region, at  $r=r_1$ ,  $u=k$  (constant) and  $\frac{\partial u}{\partial r} = 0$  then from equation (2),

$$a_1 = k + \frac{P_1}{64D} r_1^4 \text{ and } b_1 = -\frac{P_1}{32D} r_1^2 \quad (5)$$

substituting equation (5) into equation (2), the displacement on the radiation surface can be expressed as:

$$u_z = k + \frac{P_1}{64D} r^4 - \frac{P_1}{32D} r_1^2 r^2 + \frac{P_1}{64D} r_1^4 \quad (6)$$

In the polymer region ( $r_2 < r < 2R - r_2$ ), using boundary conditions: at  $r=r_2$  and  $r=2R-r_2$ ,  $u=k$  (constant); at  $r=r_2$  and  $r=R$ ,  $\frac{\partial u}{\partial r} = 0$ . The equation (4) can be written as

$$u_z = a_2 + \frac{P_2}{64D} f_1(r, \theta) + b_2 f_2(r, \theta) + c_2 f_3(r, \theta) + d_2 f_4(r, \theta) \quad (7)$$

where

$$\begin{aligned} f_1(r, \theta) &= \sum_i |\bar{r} - \bar{r}_i|^4; \\ f_2(r, \theta) &= \sum_i |\bar{r} - \bar{r}_i|^2; \\ f_3(r, \theta) &= \sum_i |\bar{r} - \bar{r}_i|^2 \ln |\bar{r} - \bar{r}_i|; \\ f_4(r, \theta) &= \sum_i \ln |\bar{r} - \bar{r}_i| \end{aligned}$$

With rigid surface layers, the iso-strain model is a good approximation to predict the stress transfer in the 1-3 tubular piezocomposite which means the decoupling of stress components in both  $z$  and  $r$  directions. The displacement inside the tube in radial direction can be expressed by the following elastic equation

$$u_r = a_3 r \quad (8)$$

and the strain within ceramic tubes is

$$u_{rr} = \frac{k}{t} = s_{33}^c (p + p_i) \quad (9)$$

at the polymer matrix  $r_2 < r < R$ , the radial displacement of the composite can be written as

$$u_r^p = a_4 r + \frac{b_4}{r} \quad (10)$$

where  $a_3, a_4, b_4$  and  $k$  are constants;  $t$  is the wall thickness of tubes;  $P$  and  $P_i$  are external pressure and transfer pressure, respectively.

By using these equations and boundary conditions, all integrated constants and then the displacement field of the composite will be obtained. Equations (3), (6) and (7) describe the surface displacement profile of 1-3 tubular piezocomposites. The effective piezoelectric coefficients of 1-3 tubular piezocomposites can be derived from the piezoelectric constitutive equations from the relationship of the uniaxial stress and the surface displacement. Figure 2-6 illustrated the predicted performance of 1-3 tubular composites with various polymer matrix and piezoceramic tube conditions.

In these calculations, the piezoelectric ceramic tubes are PZT 5H (trademark of Mogan Matroc, Inc., OH, for La doped PZT ceramics) with  $d_{33} = 593 \times 10^{-12}$  m/V,  $d_{31} = -274 \times 10^{-12}$  m/V,  $YE_{33} = 4.8 \times 10^{10}$  N/m<sup>2</sup> and  $sE_{33} = 21 \times 10^{-12}$  m<sup>2</sup>/N.

Figure 2 shows the piezoelectric performance of TP mode 1-3 tubular piezocomposite (25% ceramic tube volume fraction) as a function of the elastic constants of the polymer matrix under an uniaxial stress. The longitudinal piezoelectric response of 1-3 tubular piezocomposites has been normalized by the single piezoceramic tube. Unlike the hydrostatic piezoelectric coefficient of 1-3 tubular piezocomposites [7,8], the longitudinal piezoelectric response of the composite is less sensitive to Poisson's ratio of the matrix polymer within 0.15-0.364 range due to excluding the effect of Poisson's ratio on the effective  $d_{31}$  coefficient of the piezocomposite. However, the longitudinal piezoelectric coefficient of 1-3 tubular piezocomposites is rather sensitive to the stiffness of the matrix polymer. When the stiffness of the polymer is greater than  $1 \times 10^8$  N/m<sup>2</sup> the longitudinal piezoelectric response of 1-3 tubular piezocomposites decreases drastically as the stiffness of the polymer matrix increases. In the calculation, a spurs epoxy (Young's modulus  $4.8 \times 10^9$  N/m<sup>2</sup>) is used as the rigid face layers with the thickness of 1 mm. Figure 3 shows the relationship between the Young's modulus of the rigid surface layers and piezoelectric response of the 1-3 tubular piezocomposites. Obviously, in order to achieve a high longitudinal piezoelectric response, the rigid surface layer has to be 10 times stiffer than the rest of matrix polymer.

As an alternative to increase Young's modulus of the surface layers, increasing the thickness of the rigid surface layers also improves the stress transfer within 1-3 tubular piezocomposites. Figure 4 illustrates the longitudinal piezoelectric response as a function of the thickness of rigid surface layers and the outer diameters (OD) of tubes. Under the same tube volume fraction (25% in this case), the piezoelectric response increases as the thickness of rigid surface layers increases. There is a minimum thickness of rigid surface layers, below this thickness the longitudinal piezoelectric response of the composite will drop rapidly. The 1-3 tubular piezocomposite with a smaller tube OD is less sensitive to the thickness of rigid surface layers than the piezocomposite with a larger

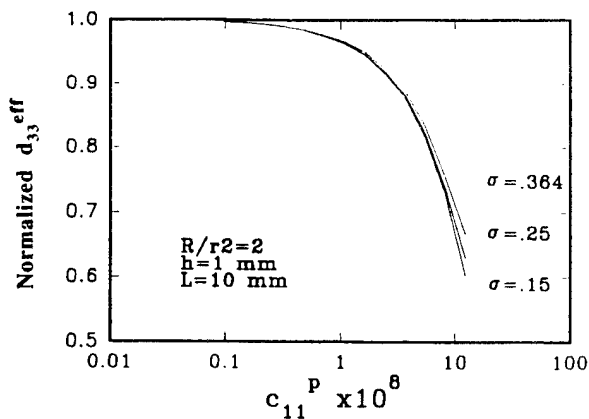


Figure 2. Longitudinal piezoelectric response of 1-3 tubular composites varies with the stiffness and Poisson's ratio of matrix polymer.  $h$  is the thickness of rigid face layers, the tube volume fraction is 25 %.

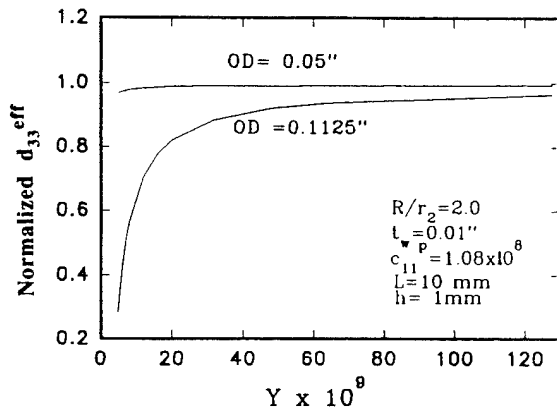


Figure 3. Longitudinal piezoelectric response of 1-3 tubular composites as a function of Young's modulus of rigid face layers. The tube volume fraction is 25 %, the diameter of tubes are 0.05" and 0.1125" respectively.

tube OD. Because, with a same tube volume fraction, the distance between two ceramic tubes is shorter in the composite of smaller OD tubes than that of larger size tubes. In other words, the 1-3 tubular piezocomposite with small OD tubes has a more uniform strain distribution.

As we have mentioned before, the piezoelectric response of 1-3 tubular piezocomposites is also closely related to the piezoceramic tube volume fraction. Figure 5 is the calculated results of the effective piezoelectric response as a function of the piezoceramic tube volume fraction for different Young's modulus of polymer matrix. As we expected, the effective piezoelectric response of 1-3 tubular piezocomposite declines with the decrease of the tube volume fraction. In the calculated region, the composite of a softer matrix polymer is less sensitive to the tube volume change than that of a harder matrix polymer. This may be attributed to the fact that the 1-3 tubular piezocomposite with a softer polymer matrix has a smaller self-loading effect than a hard polymer matrix. Therefore, in the design of a 1-3 tubular piezocomposite transducers, a soft polymer matrix is favorable to the longitudinal piezoelectric response, especially, in the region of low piezoceramic tube volume fractions.

## EXPERIMENTAL RESULTS

To verify the design concepts and the results of theoretical analysis, a number of 1-3 tubular piezocomposites were fabricated. The piezoceramic tubes were poled in the radial direction at 20 kV/cm electric field. The longitudinal piezoelectric coefficient of these

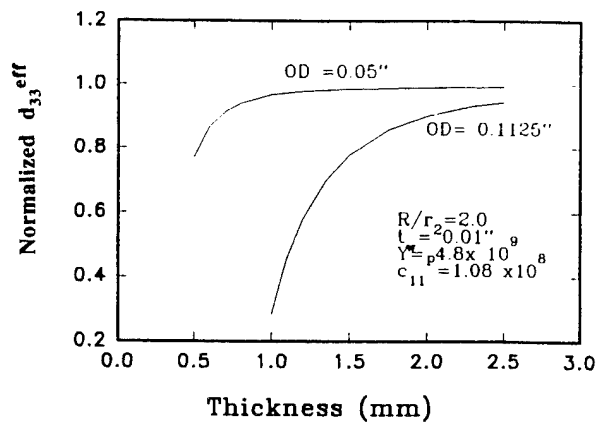


Figure 4. Thickness effect of rigid surface layers on the longitudinal piezoelectric response of 1-3 tubular composites.

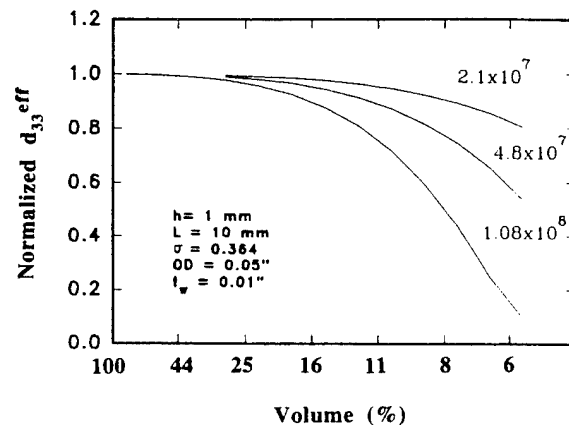


Figure 5. Effect of tube volume fraction on the piezoelectric response of 1-3 tubular composites

samples were measured by a laser dilatometer. The impedance spectra of the composites were measured by a HP 4192A impedance analyzer. The pulse-echo experiments were carried on the ultrasonic transducer analyzer (Panametrics, model 5052UA). The experimental results are described as follow.

1-3 tubular piezocomposites were made of the piezoceramic tube volume fraction from 5% to 20% and the dimensions of PZT 5H tubes were OD=0.635 mm, ID=0.381 mm and L=10 mm. As indicated by the theoretical calculation, rigid surface layers can offer an effective stress transfer between the polymer matrix and the piezoelectric tubes, the soft polymer matrix can reduce the self-loading effect of the piezocomposite. In this experiment, the initial combination of the samples used a hard spurrs epoxy (Polysciences Inc., Warrington, PA) as rigid surface layers and formed soft polyurethane (Miles Inc., Pittsburg, PA) as matrix polymer. The polyurethane was foamed by 50% volume fraction microballons (Expancel 551 DE 20, microspheres, Nobel Industries Sweden, Sundsvall, Sweden). The measurement of surface displacement shows that the 1-3 tubular piezocomposite with 5% volume piezoceramic tubes and 1 mm thick rigid surface layers has an effective  $d_{33}$  value of 3200 pC/N which is 6-7 times higher than the conventional piezoceramics (e.g. 593 pC/N for PZT 5H). Based on theoretical calculations, see Figure 2 and 3, it is clear that increasing the stiffness of the rigid surface layers and reducing the Poisson's ratio of the matrix polymer will further improve the piezoelectric performance of the composite. A 1-3 tubular piezocomposite with 20 % volume piezoceramic tubes and 1 mm rigid surface layers exhibited the effective  $d_{33}$  over 6000 pC/N which is close to the effective  $d_{33}$  of the single piezoceramic tube (6800 pC/N) and also has a good agreement with the calculated value by the model.

A 1-3 tubular piezocomposite transducer with 25% volume tubes and 20x20x9 mm in size was selected for the ultrasonic test. As a comparison, a 1-3 rod piezocomposite transducer with 40% volume ceramic rods and  $\phi$  30 mm in diameter was used in the experiment. Both transducers were air backed. Figure 6 plots the impedance spectra of 1-3 rod and tubular piezocomposite transducers. Clearly, the tubular transducer has much less undesired resonant modes than the rod transducer. This feature indicates the potential of 1-3 tubular piezocomposites for broadband resonant transducer applications. The drawback of 1-3 tubular piezocomposite transducers is their two structural resonant modes, namely, wall thickness mode and tube breathing mode always exist in 1-3 tubular piezocomposites. Those structural resonant modes may cause some troubles in their high frequency applications by the current technology.

The result of pulse-echo tests also shows the advantage of 1-3 tubular piezocomposites. Figure 7 exhibits the impulse responses of the low frequency (100 kHz) ultrasonic transducers made of 1-3 tubular piezocomposite and 1-3 rod piezocomposites. Obviously, the sensitivity of new tubular transducer is at least 10 dB higher than its counterpart. The high sensitivity is mainly attributed to the large effective longitudinal piezoelectric coefficient of 1-3 tubular piezocomposites.

### SUMMARY AND ACKNOWLEDGMENT

1. The combination of a soft polymer matrix and rigid face layers can improve the piezoelectric response and reduce the acoustic impedance of the composites. The requirement of the thickness and stiffness of rigid surface layers depends on the size of piezoceramic tubes.
2. The elastic stiffness of the matrix polymer should be at least about 10 times smaller than that of rigid surface layers to reduce the self load and increase the piezoelectric response of 1-3 tubular piezocomposites. However, a further reduction on the elastic stiffness of the matrix polymer has no advantage in the increase of the piezoelectric response, but detrimental the mechanical strength of 1-3 tubular piezocomposites. The optimum elastic stiffness of the soft polymer matrix is in the range of  $10^7$ - $10^8$  m<sup>2</sup>/N.
3. The low frequency ultrasonic transducers made of 1-3 tubular composites have high sensitivity and broadband which show the promising applications in nondestructive evaluation (NDE) of materials.

The authors appreciate Mr. X. Geng for useful discussions. This work was supported by ONR and FMI.

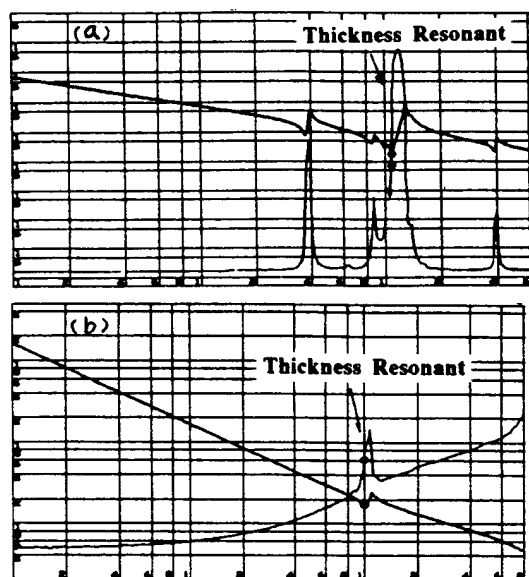


Figure 6. Impedance spectra for a) 1-3 rod piezocomposite transducer and b) 1-3 tubular piezocomposite transducer.

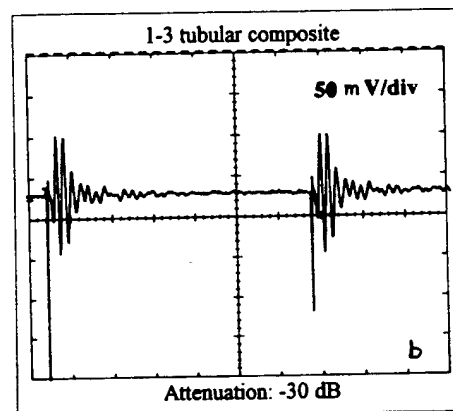
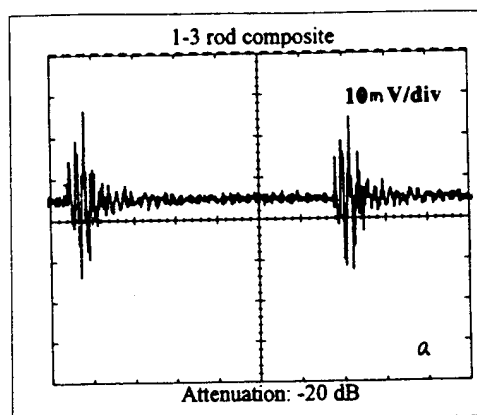


Figure 7. Impulse responses of a) 1-3 rod piezocomposite transducer and b) 1-3 tubular piezocomposite transducer.

### REFERENCES

- [1]. R. E. Newnham, D. P. Skinner, and L. E. Cross, "Connectivity and piezoelectric-polymer composites", *Mater., Res., Bull.*, Vol. 13, pp. 525-536, 1978.
- [2]. W. A. Smith, A. A. Shaolou, and B. A. Auld, "Design of piezocomposites for ultrasonic transducers", *Ferroelectrics*, Vol. 94, pp. 155-162, 1989.
- [3]. T. R. Gururaja, A. Safari, R. E. Newnham, and L. E. Cross, 1987, "Piezoelectric Ceramic-Polymer Composites for Transducer Applications" pp. 92-128 in *Electronic Ceramics*, edit by L.M. Levinson, Marcel Dekker, New York, New York.
- [4]. W. A. Smith, and B. A. Auld, "Modeling 1-3 composite piezoelectrics: thickness-mode oscillations" *IEEE Trans. Ultrason., Ferroelec., Freq. Contr.*, pp. 40-47, vol. 38, 1991.
- [5]. L.D. Landau, and Lifshitz, E.M., 1986, *Theory of Elasticity*, Pergamon.
- [6]. Q.M. Zhang, H. Wang and L. E. Cross, "Piezoelectric tubes and tubular composites for actuator and sensor applications", *J. Materials Science* (28), pp. 3962, 1993.
- [7]. Q.M. Zhang, et al., "Piezoelectric performance of piezoelectric-polymer composites with 2-2 connectivity-A combined theoretical and experimental study", *J. Applied Physics* (73), pp. 1403, 1993.
- [8]. J. Chen, Q. M. Zhang, L. E. Cross, and C. M. Trotter., "Modeling and design of 1-3 tubular composites for smart transducer applications", *Proceedings of ICIM'94*, pp. 316, 1994.

# Destruction Mechanism and Destruction Detection Technique for Multilayer Ceramic Actuators

Hideaki Aburatani and Kenji Uchino  
The Pennsylvania State University, IMRL  
University Park, PA 16802

Atushi Furuta and Yoshiaki Fuda  
Tokin Corporation, 6-7-1 Koriyama Taihakoku  
Sendai-city Miyagi-Pref. 982, Japan

**Abstract** -- The destruction process of piezoelectric actuators under bipolar driving was studied using Acoustic Emission (AE) monitoring and induced-displacement measurement. The effect of floating electrode over the internal electrode's end was also investigated. Floating electrodes can suppress the field concentration and cracking in the actuator.

## I. INTRODUCTION

Piezoelectric multilayer ceramic actuators have been widely used as key components of electromechanical devices, because of their large displacement, low driving voltage, quick response, large generative force and high electromechanical transduction capability[1],[2]. This type of actuator can be fabricated by a tape casting method with an interdigital electrode configuration that used in the conventional multilayer ceramic capacitor industry. The interdigital electrode (Fig. 1(a)) structure is appropriate for large-volume production, but the field concentration is an inevitable problem, which creates stress concentration and cracking in the actuators[3],[4]. Figure 1(b) and Fig. 1(c) show the plate-through and the interdigital with slits type electrode configurations which can provide uniform distribution of electric field and release the stress concentration respectively. The latter two designs, however, require much sophisticated technology, leading to high production cost. Note that in piezoelectric ceramic materials, the field concentration is equivalent to the stress concentration.

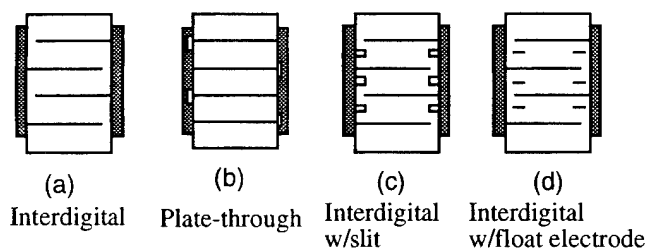


Figure 1 Various of internal electrode configuration.

This paper deals with the destruction mechanism the interdigital electrode type actuator first and a couple of detection techniques are introduced [5]. Finally, a new internal electrode design with float electrodes (Fig. 1 (d)), which can release the electric field concentration, will be proposed.

## II. EXPERIMENTAL

Piezoelectric  $\text{Pb}(\text{Ni}_{1/3}\text{Nb}_{2/3})\text{Zr,TiO}_3$  (PNN-PZT) ceramic was selected for this study, because this material is presently widely commercialized in co-fired multilayer actuators. The samples, prepared by a tape casting method, have two internal electrodes which is simulating the interdigital electrode configuration with an electrode gap of 200 $\mu\text{m}$ . Figure 2 shows the structure of samples. The floating electrodes were placed right over the end of internal electrodes and in the center of the layer.

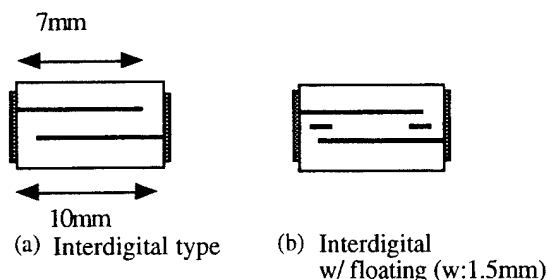


Figure 2 Structure of the samples. Layer thickness :200 $\mu\text{m}$ .

Figure 3 shows the measuring system consisting of a linear variable differential transducer (LVDT) (Millitron, Model 1301) and an acoustic emission sensor (NF Corporation, AE-905USF116). A large electric field was applied (KEPCO BOP 1000M) in order to accelerate the actuator collapse. The samples were bipolar-driven at 1 Hz by a triangular electric field of  $\pm 2.0\text{kV/mm}$ . To detect Acoustic Emission (AE), an AE sensor was placed under the actuator. The acoustic emission signal was amplified by 50dB, and a high pass filter (100kHz) was used to discriminate noise. Induced displacement were also monitored during the driving. Induced displacement measurement was held at the center of the samples.

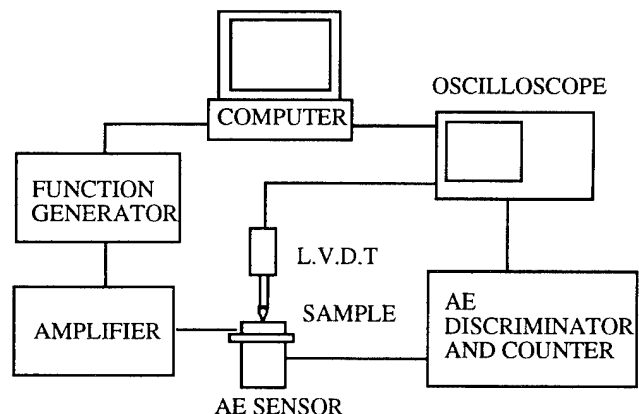


Figure 3 Measurement system.

## III. RESULTS AND DISCUSSIONS

### A. Crack and delamination

Figure 4 shows typical crack patterns in the samples. The crack is usually initiated at the edge of the internal electrode and propagates obliquely outward to another electrode (Fig. 4(a)). At the same time, delamination is generated between the electrode and ceramic interface (Fig. 4(b)). Occasionally, a crack which propagates vertically between a pair of internal electrodes is observed. This crack is probably due to an internal defect located near the electrode (Fig. 4 (b)) [6].

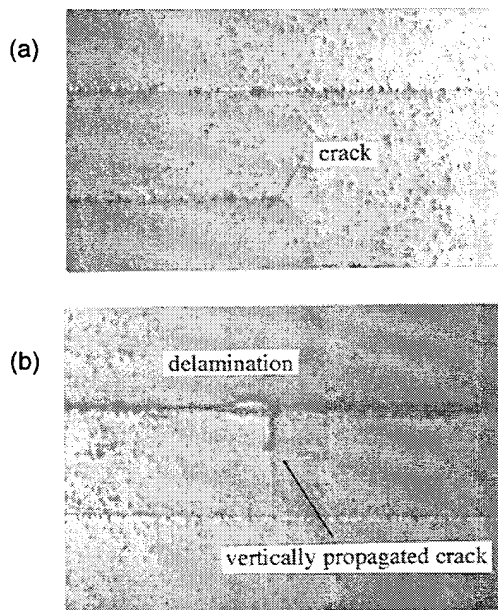


Figure 4 (a) Crack at the end of internal electrode.  
(b) Delamination and vertically-propagated crack.

#### B. Acoustic Emission

Figure 5 shows AE from the actuator plotted as a function of drive cycle. At the first stage, rather many AE were counted intermittently, which is caused by the poling process, and can be interpreted as the initiation of micro-crack. After this process, AE count is stabilized, owing to the alleviation of stress by micro-cracking. Continuous AE started after several thousands cycle, and the number of AE was remarkably increased. This AE indicates fast crack-growth and delamination in the actuator.

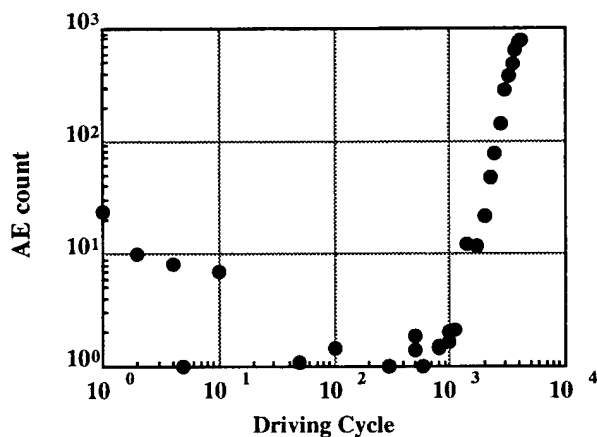


Figure 5 AE count as a function of drive cycle.

#### C. Change in induced displacement

Figure 6 shows the induced displacement change of the model actuator. Obvious change was observed after 7000-cycle. The magnitude of induced displacement hysteresis-loop increased, and sharpness at the coercive field was lost. These results indicate crack and delamination in an actuator, but it is difficult to distinguish these failure from thermal and aging effect.

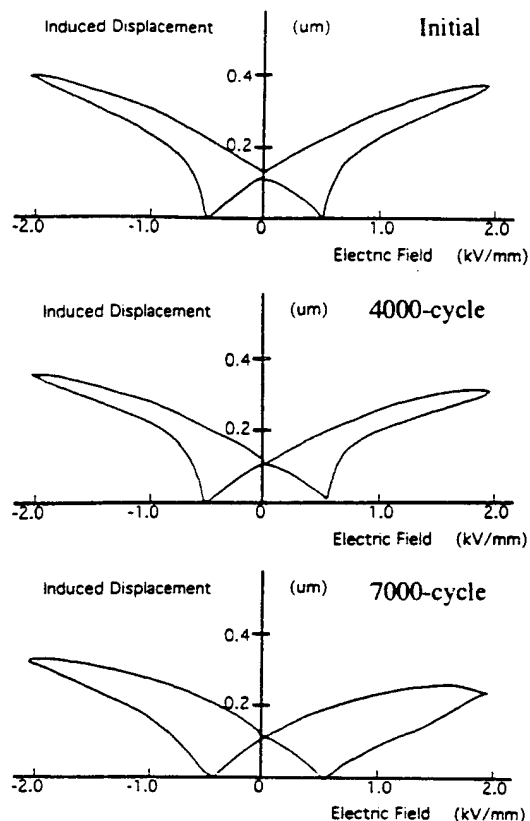


Figure 6 Induced displacement change in the interdigital type.

#### D. Effect of field suppression using float electrodes

Figure 7 shows comparison of AE generation among the Interdigital type and interdigital & floating electrode type actuators. It is clarified that the interdigital & float electrode type endure longer than the conventional interdigital type. This result implies that the floating electrode suppress the cracking at the end of internal electrode.

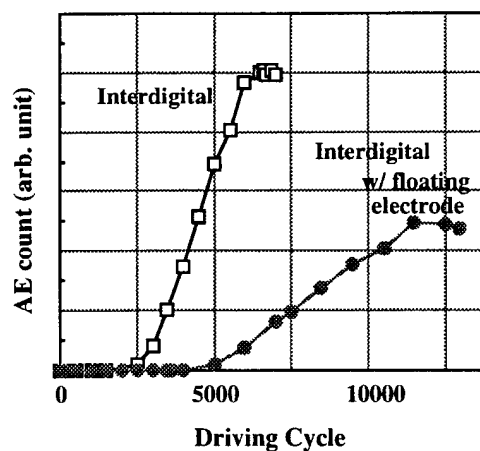


Figure 7 AE count in the interdigital and interdigital & floating electrode type actuators as a function of driving cycle.

#### IV. SUMMARY

The destruction process of the actuator was studied. Acoustic Emission related to the poling was observed. From induced-displacement measurement, indirect information about destruction was obtained. It is confirmed that AE monitoring can be an excellent actuator's failure predictor.

The effect of suppressing electrical field concentration was studied. It was clarified that suppressing electrical field by floating electrodes over the end of internal electrodes gives longer life time to the actuators.

#### V. ACKNOWLEDGMENT

This work was supported by the Office of Naval Research through Contract No. N00014-92-J-1510.

#### REFERENCES

- [1] K. Uchino, *Piezoelectric/Electrostrictive Actuators*. Tokyo, Morikita, Japan, 1986
- [2] K. Uchino, MRS bull. 18, 42 (1993)
- [3] S. Takahashi, A. Ochiai, M. Yonezawa, T. Yano, T. Hamatsuki and I. Fukui, "Internal Electrode Piezoelectric Ceramic Actuator," *Ferroelectrics*, vol.50, pp.181-190, (1983).
- [4] A. Furuta and K. Uchino, "Dynamic Observation of Crack Propagation in Piezoelectric Multilayer Actuators," *J. Am. Ceram. Soc.* vol.76 No. 6, pp.1615-1617 (1993).
- [5] Hideaki Aburatani Shuichi Harada, Kenji Uchino, Atushi Furuta and Yoshiaki. Fuda, "Destruction Mechanism in Ceramic Multilayer Actuators," *Jpn. J. Appl. Phys.*, vol 33, part 1, No. 5B, pp. 3091-3094 (1994)
- [6] Z. Suo, "Models for breakdown-resistance dielectric and Ferroelectric ceramics," *J. Mech. Phys. Solids.*, vol41, No. 7 pp1155-1176 (1993)



# ELECTROSTRICTIVE PROPERTIES OF $\text{PbZrO}_3\text{-K}_{0.5}\text{Bi}_{0.5}\text{TiO}_3$ CERAMICS

S.A. GRIDNEV, N.G. PAVLOVA and S.P. ROGOVA

Voronezh State Technical University,  
394711 Voronezh-26, Russia

**Abstract-** This paper reports a detailed study of the electrostrictive effect and related properties of unpoled ferroelectric ceramics  $(1-x)\text{PbZrO}_3 - x\text{K}_{0.5}\text{Bi}_{0.5}\text{TiO}_3$ , where  $x=0-1$ , using a sensitive capacitance dilatometer at room temperature. The material was found to exhibit a large electrostrictive coefficient  $Q_{11}$  of  $\approx 0.3 \text{ m}^4/\text{C}^2$  which is more than three times as large as that of single crystal  $\text{BaTiO}_3$ . Comparison with PZT ceramics indicates that new material is a potentially useful one for transducer application.

## INTRODUCTION

The electrostrictive actuators are widely used in various devices of adaptive optics and laser techniques, scanning microscopy and lithography, linear motors etc. The main advantages of the electrostrictive devices in comparison with the piezoelectric ones are smaller electromechanical hysteresis, higher temperature and time stabilities and absence of aging [1-3]. The most experiments on the electrostriction in ferroelectrics with diffuse phase transition were performed for lead magnesium niobate [1, 4] and its solid solutions [2, 5] or for the lead zirconate titanate [6, 7]. They are to day increasingly used as actuator materials. However, recent requirements for new displacive transducers with lower hysteresis and aging effects have promoted the development and study of a new family of electrostrictive ceramics.

The purpose of this paper is to show the experimental features of the electrostrictive properties of  $(1-x)\text{PbZrO}_3\text{-K}_{0.5}\text{Bi}_{0.5}\text{TiO}_3$  solid solutions near the morphotropic phase transitions and to try to understand an origin of a large electrostrictive effect of these materials.

## EXPERIMENTAL PROCEDURES

The complex perovskite  $\text{PbZrO}_3\text{-K}_{0.5}\text{Bi}_{0.5}\text{TiO}_3$  ceramics were prepared by the conventional mixed oxide route, described in detail in the literature [8]. All the starting oxide powders, in stoichiometric proportions, were mixed in a jar with agate balls in distilled water for 20 hours. The mixed reagents were dried and then calcined at  $850^\circ\text{C}$  for 3 hours in air. After remilling the screened powder was dry-pressed into discs of 10 mm diameter and 1 mm thick under a pressure of 1000 Kg/cm<sup>2</sup>. The samples were held for 1.5 hours at the sintering temperature of  $1050^\circ\text{C}$  and were cooled at the natural rate of the furnace. The high vapour pressure of PbO made it necessary to use 5 wt% excess PbO to keep a PbO atmospheres during the sintering process. Ceramic samples obtained were electroded with silver paint for the measurements of the dielectric and electrostrictive properties.

The characterization of the ceramic structure was carried out by X-ray powder diffraction method with Cu K $\alpha$ -radiation and Ni-filter.

Temperature dependences of dielectric constant ( $\epsilon$ )

and loss tangent ( $\text{tg}\delta$ ) of unpoled samples were measured at 10 KHz by a bridge LCR meter.

The electrostrictive coefficient  $Q_{11}$  was measured at room temperature using a sensitive capacitive dilatometer. DC electric field up to  $10^6 \text{ V/m}$  were applied perpendicular to the large plane of the samples. The length change  $\Delta L$ , or strain  $S=\Delta L/L$ , of the samples along the electric field direction, was measured by determining the capacitance change of air gap of the capacitive dilatometer with one capacitive plate driven by the sample.

## RESULTS AND DISCUSSION

X-ray diffraction investigation of prepared ceramics confirmed the presence of solid solution system which undergoes two morphotropic phase transitions from rhombic to rhombohedral phase at  $x=0.08$  and from rhombohedral to tetragonal phase near  $x\approx 0.5$ .

Typical longitudinal strain measurements taken at room temperature for composition with  $x=0.25$  are shown in Figure 1.

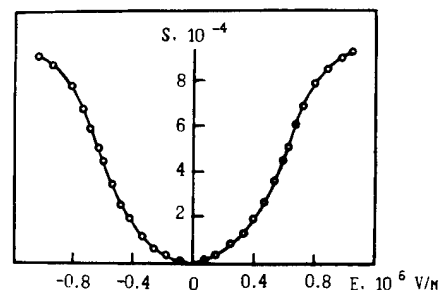


FIGURE 1. Strain-field dependence for the ceramics with  $x=0.25$ .

Clearly the low-field portion was quadratic in the strain-field relation. The electrostrictive coefficient  $Q_{11}$  was determined in that region by the expression

$$S = \Delta L/L = Q_{11} \cdot (\chi \cdot \epsilon_0)^2 \cdot E^2, \quad (1)$$

where  $\chi$  is the dielectric permittivity,  $\epsilon_0$  is the electrical constant. In the very high field<sup>0</sup> portion, the strain-field curve deviated from the quadratic behaviour to more linear behaviour due to saturation of the induced polarization.

It must be stressed that the slope of the  $Q_{11}(E)$  curve clearly decreased with decreasing of the grain size (Figure 2). This result is in accord with the strain-field behaviour of the materials with different

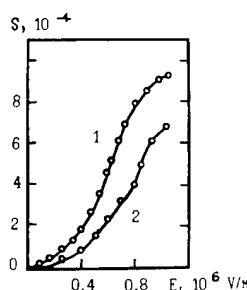


FIGURE 2. Strain-field dependence for  $x=0.31$  at mean grain size of  $\approx 7$  micron (1) and  $\approx 4$  micron (2).

granular structure [9].

Confirmation that the  $Q_{11}$  value is a function of composition is shown in Figure 3. The results are compared with dielectric constant data for the same compositions. As is seen, the anomalous concentration variation of the real component of dielectric permittivity is very similar to that of electrostrictive coefficient  $Q_{11}$  v.s. concentration  $x$ . It is evident that the induced polarization in the materials could be responsible for the  $Q_{11}(x)$  behaviour of this ceramic system.

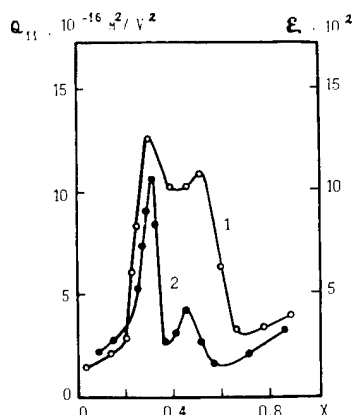


FIGURE 3. Dielectric constant (1) and electrostrictive coefficient (2) versus concentration  $x$  at 293 K.

Using the  $\chi$  value of 2000 measured at 50 kHz,  $Q_{11}$  was then determined to be  $0.32 \text{ m}^4/\text{C}^2$ . A comparison of  $Q_{11}$  measured with that of single-crystal  $\text{BaTiO}_3$  [10] shows that its value is at least three times as large as that of  $\text{BaTiO}_3$ .

If we apply a dc voltage 1000 V across a sample with  $10^{-3} \text{ m}$  thick of the compositions with  $x=0.25-0.3$ , about 1 micron expansion would be realized which is comparable with the piezoelectric strain observed in PZT at the same an electric field. Therefore, the high stable electrostrictive deformations appear to make the newly developed electrostriction ceramics suitable candidates for a number of specialized transducer applications.

This work was supported by Russian Foundation of Fundamental Research, grant N 94-02-06591.

## REFERENCES

- [1] V.V. Lemanov, N.K. Yushin, E.P. Smirnova et al., "Giant electrostriction of ferroelectrics with diffuse phase transition - Physics and applications", *Ferroelectrics*, vol.134, pp.139-144, 1992.
- [2] E.P. Smirnova, O.V. Rubinshtein and V.A. Isupov, "Dielectric and electrostrictive properties of PMN-based complex perovskites", *Ferroelectrics*, vol.143, pp.263-270, 1993.
- [3] L.E. Cross, "Ceramic sensors and actuators for smart materials and adaptive structures", *Ferroelectrics*, vol.133, p.11, 1992.
- [4] S.J. Lang, K. Uchino, S. Nomura and L.E. Cross, "Electrostrictive behaviour of lead magnesium niobate ceramic dielectrics", *Ferroelectrics*, vol.27, pp.31-34, 1980.
- [5] E.P. Smirnova, N.N. Parfenova and N.V. Zaitseva "Electrostriction of PMN-PSN solid solution", *Fiz. Tverd.Tela*, vol.25, pp.1830-1833, 1983.
- [6] K. Uchino and S. Nomura "Electrostriction in PZT-family antiferroelectrics", *Ferroelectrics*, vol. 50, pp.191-196, 1983.
- [7] K.M. Leung, S.T. Liu and J. Kyonka "Large electrostrictive effect in Ba:PZT and its application", *Ferroelectrics*, vol.27, pp.41-43, 1980.
- [8] S.A. Gridnev, N.G. Pavlova, V.V. Gorbatenko and L.A. Shuvalov, "Newly developed multicomponent piezoceramic system for alternating pressure sensors", *Ferroelectrics*, vol.134, pp.53-57, 1992.
- [9] W. Heywang, "Structural engineering of ferroelectrics", *Ferroelectrics*, vol.49, pp.3-14, 1983.
- [10] F. Jona and G. Shirane, *Ferroelectric Crystals*. New York: MacMillan, 1962, p.145.

# OPTICAL TWO CHANNEL ELONGATION MEASUREMENT OF PZT PIEZOELECTRIC MULTILAYER STACK ACTUATORS

A. Wolff, D. Cramer, H. Hellebrand, I. Probst and K. Lubitz  
Siemens AG, Corporate Research and Development, 81730 Munich, Germany

## Abstract

A fast optical deflection measurement of multilayer actuators is described. This two beam method eliminates the measuring problems arising from fixing one side of clamped actuators by detecting the movements of both sides of the actuator. The frequency range of this interferometric measurement reaches from static up to 200 kHz. In this way fast mechanical response can be detected even in the case of rectangular pulses. The accuracy of the deflection measurement is better than 1 %. The small and large signal effective  $d_{33}$  data of PZT multilayer actuators, consisting of up to 500 single layers, are determined using this method. The dependence of these data on clamping force and pulse duration is investigated. For characterization of reliability of multilayer actuators the maximum number of cycles under hard driving conditions of rectangular pulses with rise times of 10  $\mu$ s leading to maximum loading currents of 20 A is determined.

## 1. Introduction

Recently the interest in piezoelectric actuators has strongly increased worldwide [1,2]. These components are the fastest and most compact electro-mechanical actuators. The simultaneous characterization of the fast deflections and of the static and dynamic forces is presented using a contactless optical two channel elongation measurement, which also allows one to determine the spatially resolved deflection along the actuator cross section.

## 2. Experimental

### 2.1 Preparation of actuators

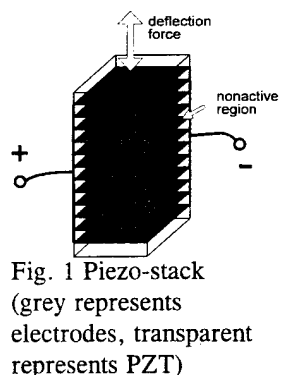


Fig. 1 Piezo-stack (grey represents electrodes, transparent represents PZT)

The actuators (Fig. 1, 2) were fabricated using a multilayer technique [3]. Starting with a 'green' organic binder-bound tape of PZT ceramic composition with suitable printed patterns of electrode paste, monolithic layered structures of various shapes and sizes are produced by laminating such green ceramic tapes using pressure and temperature to form a monolithic body. Subsequently, the organic binder is burned out and the composite of ceramic material and electrodes is sintered at 1130 °C.

After soldering, the actuators were poled with 2 kV/mm at room temperature. The dimensions and some typical data of the PZT type 5A multilayer actuators (see Fig. 2) are listed in Table 1:

total height	19 mm	39 mm
cross section	10x10 mm <sup>2</sup>	10x10 mm <sup>2</sup>
single layer thickness	80 $\mu$ m	80 $\mu$ m
capacity	4 $\mu$ F	8 $\mu$ F
electrical resistance	50 M $\Omega$	25 M $\Omega$
application temperature range	-40 °C to 150 °C	-40 °C to 150 °C

Table 1 Typical data of multilayer actuators of different heights

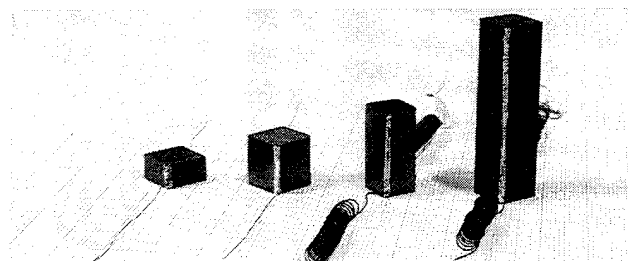


Fig. 2 Photograph of multilayer actuators (cross section 10x10 mm<sup>2</sup> and different heights)

### 2.2 Measurement setup

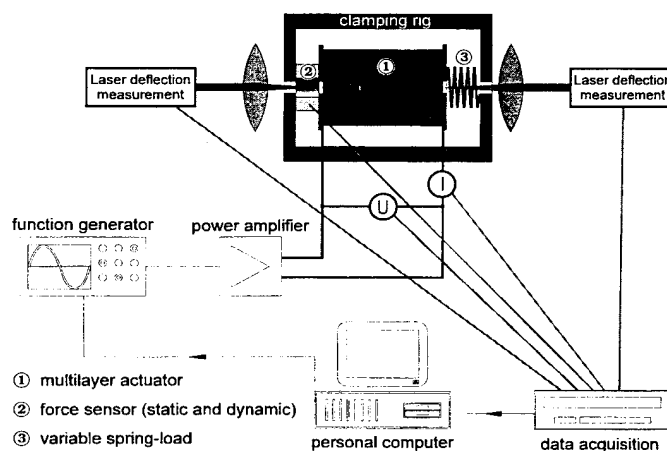


Fig. 3 Measurement setup

Fast deflection measurement is very important in characterization of actuators. The realization of an accurate dynamic deflection measurement requires optical methods. Two He-Ne laser beams focused on opposite actuator surfaces are reflected and subsequently detected with the respective laser Doppler deflection channel. The addition of both channels to the total deflection of the actuator eliminates vibrational disturbances. Bending of the clamping facility does not affect the accuracy. The overall accuracy is within 1 % using this two point deflection measurement with an upper limit of velocity of 2 m/s. Force measurement is achieved simultaneously by two different principles. Static and dynamic forces are determined using a strain gauge ring sensor (0 to 20 kN) and a quartz force ring sensor (0 to 1 kN), respectively. Both sensors are connected in series in opposition to the variable spring-load (see Fig. 3). The driving currents are measured by a hall-probe measurement. The actuators can be driven with a power amplifier (dc to 200 kHz, max. 3 A) or a pulse generator realizing rectangular voltage pulses with rise times of 10  $\mu$ s and peak currents of up to 50 A.

### 3. Results and discussion

#### 3.1 Static behavior

Static measurements (see Fig. 4) show the dependence of the static deflection on different load conditions.

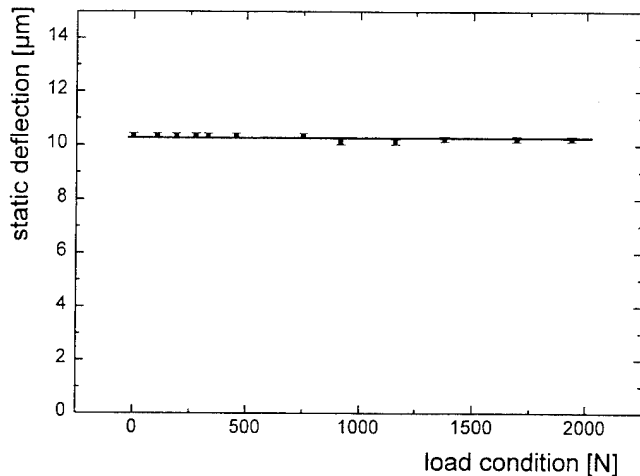


Fig. 4 Static deflection measurements vs. different load conditions (rectangular waveform, pulse duration 10 s, pulse amplitude 80 V, spring-loaded 1 N/μm)

At 1 kV/mm the measurement graph reflects an effective  $d_{33}$  value of about 550 pm/V independent of load conditions up to 2 kN, for the case of spring-loads with small stiffness of 1 N/μm in relation to the stiffness of the actuator (see next section).

#### 3.2 Evaluation of dynamic blocking force and stiffness of multilayer actuators

From Fig. 5 it can be seen that for different spring-loads the operating point values of maximum deflection show a linear working characteristic with a slope of -255 N/μm and -135 N/μm corresponding to actuator heights of 19 mm and 39 mm, respectively.

The common intersection at zero deflection results in a blocking force of  $2600 \pm 100$  N and an elastic modulus of  $(4.8 \pm 0.2) \cdot 10^{10}$  N/m<sup>2</sup> for both actuators of different heights. The maximum stiffness of the setup (spring removed) is limited by the superposition of the clamping rig and the static and dynamic force sensors (see slope of short dashed line of 90 N/μm in Fig. 5).

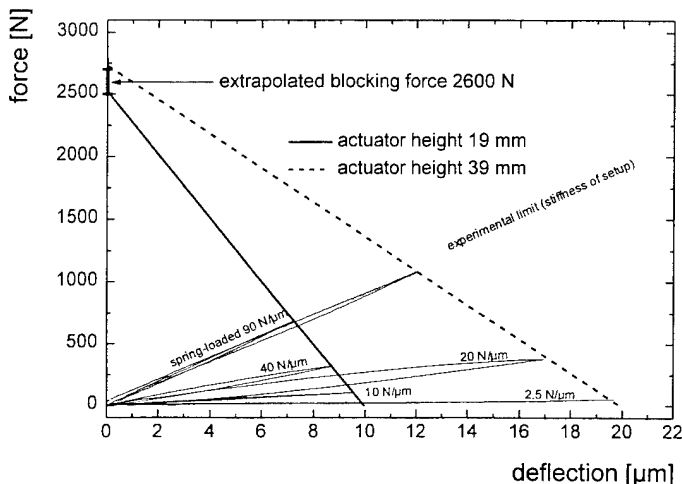


Fig. 5 Force vs. deflection measurement of different spring-loads (sinusoidal waveform, pulse duration 1 ms, pulse amplitude 80 V, load condition 1500 N)

#### 3.3 Measurement of hysteresis curves

Sinusoidal single pulses of different pulse durations in Fig. 6 show decreasing deflection of the actuator with decreasing pulse duration down to about 1 ms.

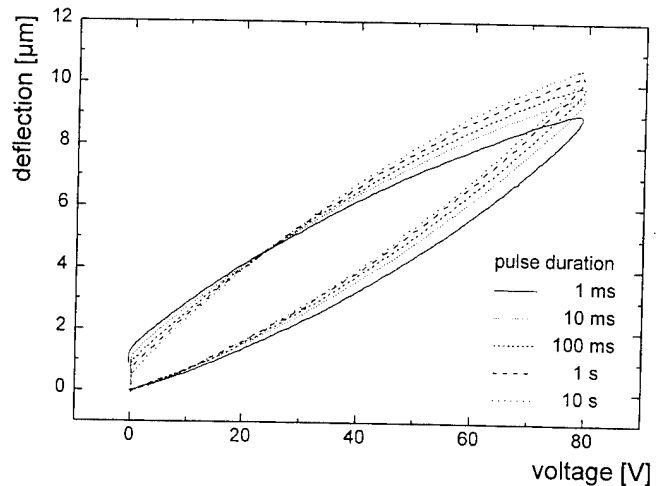


Fig. 6 Dynamic deflection vs. voltage for different pulse durations (sinusoidal waveform, pulse amplitude 80 V, load condition 900 N, spring-loaded 20 N/μm)

Additionally, the difference of zero voltage position before and after applying a single pulse to the actuator (hysteresis) increases with decreasing pulse duration down to about 1 ms. The nonlinearity between deflection and voltage for sinusoidal single pulses of different amplitudes is shown in Fig. 7. The effective  $d_{33}$  value has been measured to be 500 pm/V at 1 kV/mm with a sinusoidal pulse duration of 1 ms and 1500 N loading force.

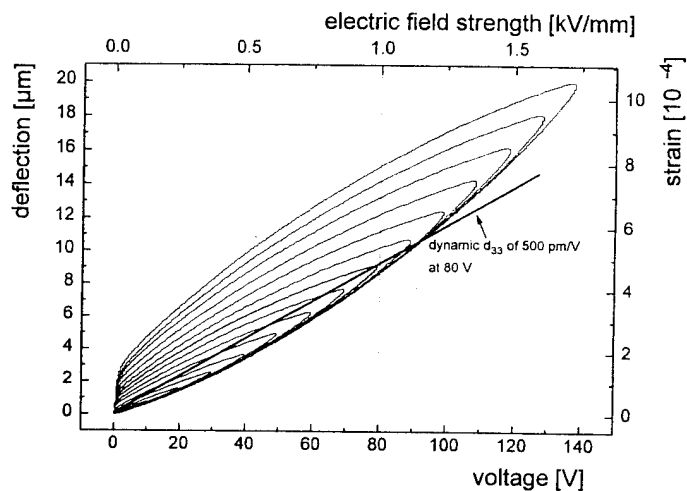


Fig. 7 Deflection vs. voltage measurement (sinusoidal waveform, pulse duration 1 ms, load condition 1500 N, spring-loaded 20 N/μm)

Similar to static measurements, the hysteresis effect increases with increased voltage amplitudes in the case of dynamic measurement.

#### 3.4 Transient behavior of actuators

In the case of rectangular pulses, the observed oscillations in Fig. 8a which did not occur at unclamped conditions reflect the vibration modes of the assembly of clamping rig, spring and static and dynamic force sensors. These vibrations cause oscillations of loading force and therefore oscillations in actuator deformation.

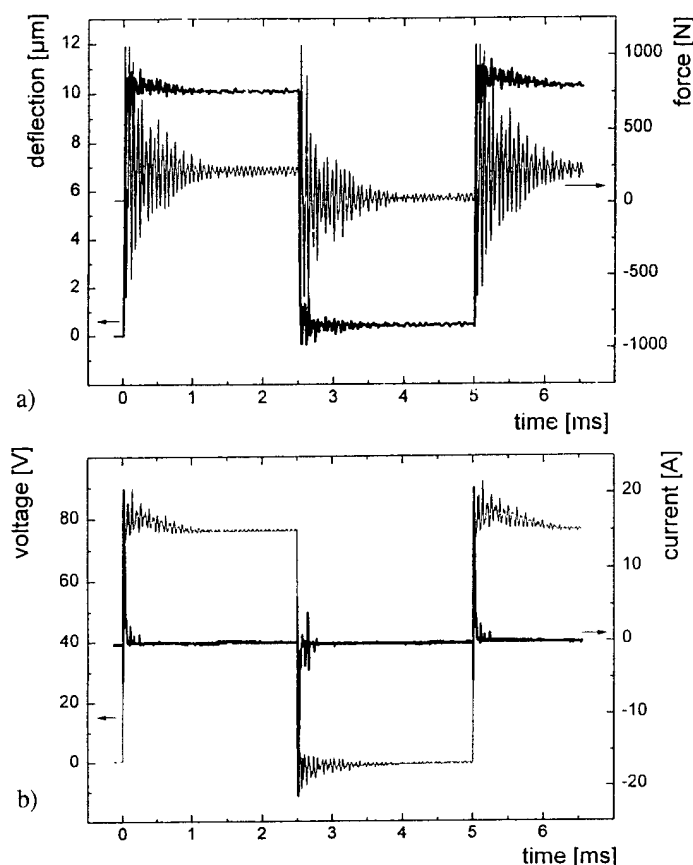


Fig. 8 a) Deflection and dynamic force vs. time measurement  
b) Voltage and current vs. time measurement  
(rectangular waveform, pulse duration 2.5 ms, pulse amplitude 80 V, load condition 1500 N, spring-loaded 20 N/ $\mu$ m)

The amplitude ratio of these dynamic force oscillations and deflection oscillations of about  $-300 \text{ N}/\mu\text{m}$  (negative because of different sign of force and deflection oscillations) is in a first approximation equal to the value of the slope of the working characteristic of  $-255 \text{ N}/\mu\text{m}$  discussed in section 3.2. The difference between these two values could be caused by the occurrence of additional inertial forces not considered here. The amplitude ratio of the values of force and deflection after decay of oscillations is  $20 \text{ N}/\mu\text{m}$  and reflects the stiffness of the spring-load.

The voltage and current oscillations in Fig. 8b are caused by transformation of the vibrations due to the direct piezoelectric effect.

Different types of delay between voltage and deflection have to be considered:

1. The delay between start of voltage pulse and start of actuator movement is about  $5 \mu\text{s}$ . This delay is independent of the maximum driving current.
2. The delay between start of movement and reaching 90 % of full deflection of the actuator depends strongly on the maximum of driving current. The higher this current, the faster the capacitance of the actuator is charged. With the present maximum of driving current of 20 A this delay time reaches  $50 \mu\text{s}$ .

### 3.5 Clamping effect of nonactive regions of actuator

The non electroded and unpoled regions (see Fig. 1) in combination with the solder on the electrodes are the causes for a reduced deflection at nonactive corners of about  $1.5 \mu\text{m}$  in the case of  $9.2 \mu\text{m}$  deflection at the centre of the actuator (see Fig. 9). Careful design of the shape and size of the non electroded area becomes very important for lifetime considerations discussed in the next chapter.

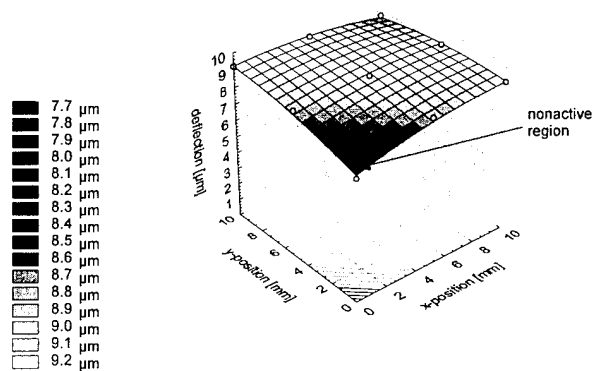


Fig. 9 Spatially resolved deflection measurement (sinusoidal waveform, pulse duration 1 ms, pulse amplitude 80 V, no load)

### 3.6 Durability and Long Term Performance

The long term performance of the described multilayer actuators has been observed up to  $10^9$  cycles (rectangular waveform with rise time of  $10 \mu\text{s}$ , frequency of 200 Hz with an amplitude of  $1 \text{ kV}/\text{mm}$ ). The endurance tests have been performed at room temperature under mechanical load conditions of 1000 N to reduce tensional stresses [4]. The maximum number of cycles achievable with actuators is strongly dependent on the driving conditions including applied electric field strength, driving frequency, maximum electric currents, mechanical bias load and temperature [5]. The influence of these driving conditions on the maximum number of cycles has to be investigated in detail because of its importance for future applications.

## 4. Conclusions and outlook

The effective  $d_{33}$  value has been measured as  $500 \text{ pm}/\text{V}$  at  $1 \text{ kV}/\text{mm}$  with a sinusoidal pulse duration of 1 ms and 1500 N loading force. The measured blocking force of 2600 N at  $1 \text{ kV}/\text{mm}$  and  $10 \times 10 \text{ mm}^2$  cross section is independent of actuator heights. The elastic modulus of the multilayer actuator of  $(4.8 \pm 0.2) \cdot 10^{10} \text{ N}/\text{m}^2$  is only slightly smaller than that of bulk PZT ( $5.3 \cdot 10^{10} \text{ N}/\text{m}^2$ ). At nonactive corners of the actuator a reduced deflection of  $1.5 \mu\text{m}$  is observed. A consistent characterization of the dynamic actuator behavior has been demonstrated using this new measurement setup. The described multilayer technique provides actuators with easy to handle low driving voltages ( $\leq 100 \text{ V}$  instead of some 10 kV) and high operating temperatures. In combination with the high speed of piezoelectric actuators in the  $50 \mu\text{s}$  range it offers a unique potential for fast actuator applications with excellent repeatability from cycle to cycle over the total life time of  $1 \cdot 10^9$  cycles.

## 5. References

- [1] H. Tsuka, J. Nakano and Y. Yokoya, IEEE Workshop on Electronic Application in Transportation, 1990.
- [2] R.E. Newnham and G.R. Ruschau, "Smart Electroceramics," J. Am. Ceram. Soc. 74[3], 1991, pp. 463-480.
- [3] H. Hellebrand, D. Cramer, I. Probst, A. Wolff and K. Lubitz, "Large piezoelectric monolithic multilayer actuators," in Proceedings of the 4th International Conference on New Actuators, Bremen, Germany, June 1994, pp. 119-122.
- [4] H. Cao, A.G. Evans, "Nonlinear Deformation of Ferroelectric Ceramics," J. Am. Ceram. Soc. 76(4), 1993, pp. 890-896.
- [5] T. Sakai, M. Ishikiriyama, R. Shimazaki, "Durability of Piezoelectric Ceramics for an Actuator," Jpn. J. Appl. Phys. 31(9B), 1992, pp. 3051-3054.

M. Kuwabara, E. Matsuyama, S. Takahashi, H. Shimooka, and Y. Urakawa  
 Department of Applied Chemistry, Kyushu Institute of Technology  
 1-1 Sensui-cho, Tobata, Kitakyushu 804, Japan

**Abstract** — Undoped barium titanate ceramics exhibiting a distinct positive temperature coefficient of resistivity (PTCR) effect have been produced by sintering high-purity barium titanate powder compacts in the temperature range 1300–1400°C in air. The formation of core-shell type duplex microstructures in the materials covered with a nearly full dense layer is responsible to this phenomenon that undoped barium titanate ceramics (which are normally insulating) were converted to semiconductors and, moreover, exhibited distinct PTCR effects. The core-shell grain structure is described as a duplex microstructure consisting of a large-grained ( $\approx 50\ \mu\text{m}$ ) semiconducting phase inside and a small-grained ( $< 10\ \mu\text{m}$ ) insulating phase outside.

## INTRODUCTION

Pure barium titanate (BTO) is insulating and ferroelectric at room temperature, and it is well-known that BTO can be easily converted to semiconductors either by doping with small amounts of donors (La, Sb, or Nb), or reducing at high temperatures in a reducing atmosphere. Doped semiconducting BTO ceramics exhibit an anomalous positive temperature coefficient of resistivity (PTCR) effect above the Curie point ( $\approx 120^\circ\text{C}$ ),<sup>1-3</sup> but no significant PTCR effects have been observed in reduced semiconducting barium titanate ceramics.<sup>4,5</sup> Sintering of undoped BTO powder compacts in air normally yields insulating BTO ceramics and does not produce semiconducting materials. It has really never been reported that sintering of undoped BTO powder compacts resulted in semiconducting BTO ceramics with as low a resistivity as  $100\ \Omega\text{-cm}$  at room temperature and moreover a distinct PTCR effect.

Contrary to this common knowledge about the semiconduction and PTCR effect in BTO ceramics produced in air, it has recently been reported<sup>6</sup> that a distinct PTCR effect was observed in undoped, high-purity BTO ceramics sintered in a specific temperature region around  $1350^\circ\text{C}$  in air. The materials were found to have a core-shell structure. This paper reports a quantitative examination of the change of the core-shell grain structures with sintering temperature and time and the influence of oxygen partial pressure of the sintering atmosphere used on the PTCR characteristics in the materials obtained.

## EXPERIMENTAL

Details of the procedure for preparation of samples were reported elsewhere.<sup>6</sup> A brief description of it is given here. High-purity commercial barium titanate was used (Fuji Titanium, Tokyo; Manufacture's analysis:  $\text{BaO}/\text{TiO}_2$  ratio = 1.001,  $\text{Fe} < 0.0007$ ,  $\text{Na} < 0.0007$ ,  $\text{Sr} < 0.0017$  (all in wt%),  $\text{Si}$  and  $\text{Al} < \text{detection limit}$ ). The barium titanate powder was ball-milled with ethanol and nylon-coated iron balls as grinding media in a polyethylene container for 24h. The powder was fired at  $600^\circ\text{C}$  for 2h in air to burn out completely organic compounds introduced by the ball-milling. The powder was then pressed into pellets (10 mm in diameter and  $\approx 1.5$  mm thick), followed by sintering at temperatures in the range of  $1250^\circ$  to  $1400^\circ\text{C}$  for 10–300 min in air with heating and cooling rates fixed at  $10^\circ\text{C}/\text{min}$  to yield the sintered bodies. Sintering of the powder compacts was also carried out under atmospheres with various oxygen partial pressures to investigate how oxygen partial pressure of sintering atmosphere influence the electrical properties of the ceramic materials obtained. Resistivity measurements were carried out in air on slabs cut from the ceramic bodies by the two-probe method using In-Ga alloy electrodes. Phase confirmation was made by x-ray diffractometry (XRD). This phase analysis demonstrated that no phases other than the perovskite one existed in all the present samples produced. Microstructures of the materials were examined by scanning electron microscopy (SEM).

## RESULTS AND DISCUSSION

Figure 1 shows an SEM fracture surface of a BTO ceramic with a duplex grain structure produced in this study and its schematic cross section. The duplex grain structure of the materials can well be described as being composed of a small-grained ( $< 10\ \mu\text{m}$ ) insulating phase outside and a large-grained ( $\approx 50\ \mu\text{m}$ ) semiconducting phase inside.

The thickness of the semiconducting phase formed inside the materials showed a significant dependence on the sintering condition used. The ratio of the thickness of the inner part of a semiconducting phase  $t$  to the sample thickness  $d$  increased with sintering temperature (hold time: 2h) and hold time (sintering temperature:  $1350^\circ\text{C}$ ), as shown in Figs. 2 and 3 respectively. From these figures it is obvious that the inner semiconducting part grows conspicuously with increasing sintering temperature and hold time at the sintering temperature. It is most interesting and important to recognize that the results shown in Figs. 2 and 3 indicate that the outer insulating layer in the materials become thinner with increased sintering temperatures and hold times and finally extinct; then it seems initially possible to produce an undoped BTO ceramic with its whole part semiconducting by firing in air. However, this can of course never happen.

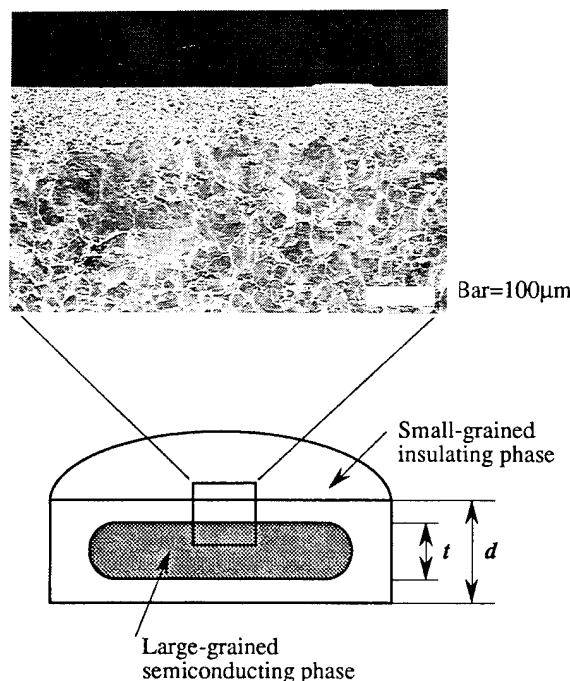


Fig. 1. SEM fracture surface of a ceramic produced with a duplex microstructure and a schematic of a cross section of the material.

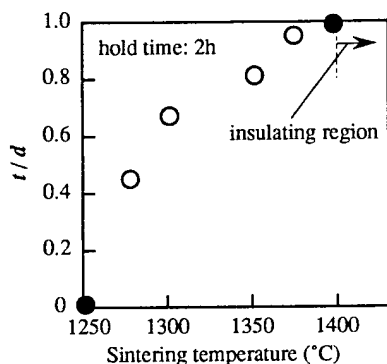


Fig. 2. Change of the ratio  $t/d$  with sintering temperature. Ceramics indicated by closed circles were totally insulating with a simple grain structure; a small-grained structure for the ceramic obtained at 1250°C and a large-grained one for the sample at 1400°C.

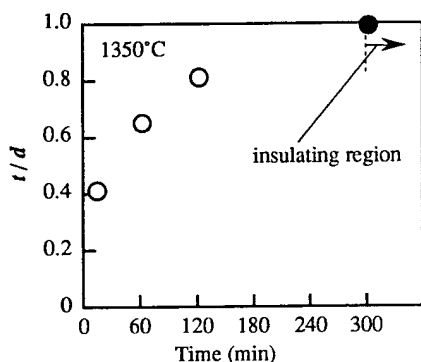


Fig. 3. Change of the ratio  $t/d$  with time for which sintering was carried out at 1350°C. The sample indicated by a closed circle was obtained to be totally insulating.

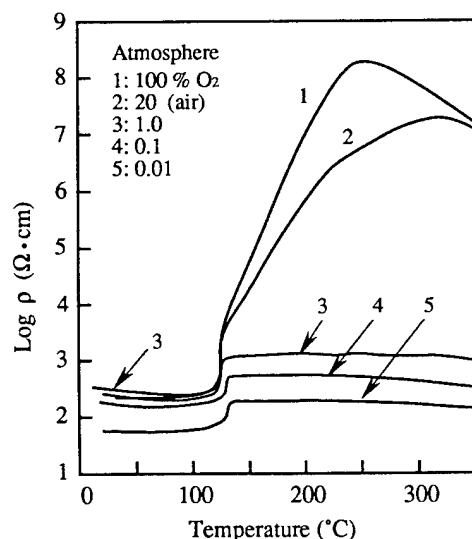


Fig. 4. Resistivity-temperature characteristics for undoped BTO ceramics sintered under atmospheres with various oxygen concentrations.

Ceramics indicated by closed circles in Figs. 2 and 3 were totally insulating with a large monosized grain structure. This means that the inner large-grained semiconducting part was converted into an insulator when the value of  $t/d$  reached unity. This phenomenon should be interpreted in connection with the formation mechanism of such a duplex microstructure as seen in the present samples. A discussion on this point has been done in terms of the oxygen partial pressure dependence of grain growth rate during sintering and the sinterability of the barium titanate powders used, where difference between the rates of out- and in-diffusion of oxygen in a ceramic at the sintering temperature played a key role to yield a relevant duplex microstructure.<sup>6</sup> This interpretation is supported by the fact that rapid grain growth of barium titanate in early-stage sintering is associated with the release of oxygen from the lattice.<sup>7</sup>

Figure 4 shows the resistivity-temperature characteristics for ceramics sintered at 1350°C for 2 h under atmospheres with various oxygen partial pressures. The data of Fig. 4 show the characteristics of only the inner semiconducting part of the respective materials. It is evident that undoped BTO ceramics sintered in air with such a duplex microstructure as is seen on the photograph of Fig. 1 exhibited a large PTCR effect of more than four orders of magnitude and its magnitude further increased by firing in a 100%  $O_2$  atmosphere. On the other hand, BTO ceramics sintered in a slightly reduced atmosphere in the oxygen partial pressure range  $10^{-1}$ – $10^{-3}$  Pa (corresponding to the oxygen concentration range 0.01–1.0 %  $O_2$ ) exhibited only small PTCR effects of less than one order of magnitude in spite of that the materials had the same duplex grain structures with an insulating layer outside.

In conclusion, undoped BTO ceramics with distinct PTCR effects were produced by sintering in air in the specific temperature region around 1350°C in this study. The materials had a duplex grain structure which was composed of a small-grained dense insulating layer outside and a large-grained semiconducting phase inside. The thickness of the outer insulating layer became thinner with either increasing sintering temperature and hold time at the sintering temperature. BTO ceramics produced under the conditions at which small-grained outer layers disappeared were converted into insulators; this is the normal state of undoped BTO ceramics produced in air. This clearly demonstrates that the duplex microstructure formed in the present materials played a key role in the production of undoped BTO ceramics sintered in air with low room temperature resistivity and a distinct PTCR effect.

#### REFERENCES

- [1] O. Saburi, "Properties of Semiconductive Barium Titanates," *J. Phys. Soc. Jpn.*, **14**, 1159–1174, 1959.
- [2] W. Heywang, "Resistivity anomaly in Doped Barium Titanate," *J. Am. Ceram. Soc.*, **47**, 484–490, 1964.
- [3] G.H. Jonker, "Some Aspects of Semiconducting Barium Titanate," *Solid State Electron.*, **7**, 895–903, 1964.
- [4] J. Daniels, K.H. Härdtl, and R. Wernicke, "The PTC effect of barium titanate," *Philips Tech. Rev.*, **38**, 73–82, 1978/79.
- [5] I. Ueda and S. Ikegami, "Oxidation Phenomena in Semiconducting  $BaTiO_3$ ," *J. Phys. Soc. Jpn.*, **20**, 546–552, 1965.
- [6] M. Kuwabara, "Positive temperature coefficient of resistivity effect in undoped barium titanate ceramics," *J. Appl. Phys.*, **76**, July 15, 1994.
- [7] M. Drofenik, A. Popovic, L. Irmančnik, D. Kolar, and V. Krasevec, "Release of Oxygen During the Sintering of Doped  $BaTiO_3$  Ceramics," *J. Am. Ceram. Soc.*, **65**, C-203–C-204, 1982.

## Electrically-induced Shape Changes in Cement-based Materials

Hua Ai, Jie-Fang Li, and Dwight Viehland, Department of Materials Science and Engineering and The Center for Advanced Cement Based Materials, University of Illinois, Urbana, IL 61801

The electromechanical behavior of hardened portland cement paste has been investigated as a function of measurement frequency and DC electrical bias using an interferometric technique. Large field-induced shape changes on the order of 100 Å have been found in millimeter thick specimens exposed to moisture. In addition, strong hysteresis effects were found on cycling a large AC field. Dry samples were found to exhibit no field-induced deformations. The mechanism underlying this anomalous behavior is believed to be an electro-osmotically induced swelling of the pore structures. Evidence in support of this hypothesis was found by corresponding investigations of porous silica gels.

### I. Introduction.

Nearly 20 years ago, Whittman observed an electromechanical effect in portland cement [1], which was strongly dependent on water content. He observed an electromechanical effect in centimeter-sized bars of hardened cement paste. A voltage ( $\sim 200$   $\mu$ V) was generated when an external load (2000 g) was applied to the specimen, and the converse effect of a bending displacement ( $\sim 20$   $\mu$ m) was detected upon the application of a voltage (200 V). No further experiments have been done to date to more thoroughly investigate this unexpected phenomena or to more clearly elucidate the nature of the underlying deformation mechanism. However, the influence of water diffusion under an electric field on the conduction properties in porous plugs is well-known [2,3], and is generally attributed to electro-osmotic forces. In electro-osmosis, an applied field acts upon ions in a liquid. The ions, then, move under the excitation, carrying along the liquid media. Consequently, it should be possible to establish nonuniform water distributions under AC or DC electrical fields in porous plugs, such as portland cement. This nonuniformity may provide a mechanism by which electrical energy can be converted to a mechanical deformation.

The purpose of this investigation was to study the electromechanical behavior of hardened cement paste. Attention was placed on developing an understanding of the mechanism by which electrical energy can be coupled to a mechanical deformation.

### II. Experimental Procedure

Ordinary portland cement (OPC) was hydrated at a water to cement ratio (w/c) of 0.40. Samples were made by casting into 1.25 cm x 2.5 cm cylinders, which were cured in a moist environment (100% relative humidity (r.h.)) for 8 weeks. Cylinders of hardened paste were then cut into samples of dimensions 4 mm x 4 mm x 4 mm. The cubes were polished to assure parallel faces and subsequently electroded with gold. A thin glass mirror was then epoxied on the top surface of each cubical sample to ensure an optical-quality reflective surface for interferometric measurements. The samples were mounted on copper discs, which were also used as a conductive base to make contact with the bottom electrode.

The samples were dried at 105°C for 48 hours before measurement, and subsequently placed in a desiccator to reabsorb water. After drying, all specimens were saturated in a moist atmosphere (100% r.h.) for 36.0 hours. Similar investigations were performed on porous silica samples which had been saturated in the humidity chamber for three days. These samples were obtained from Gel-Tech Incorporated and had average pore sizes of  $\sim 25$  Å.

A modified Michelson-Morley interferometer was used to measure field-induced shape changes. Details of the experimental procedure and technique can be found in previous publications [4,5].

### III. Results

#### III.1 Field-induced strain measurements for portland cement

The sample displacement as a function of AC electrical excitation is shown in Figure 1. The maximum sample displacement can be seen to be  $\sim 200$  Å. In consideration that the sample thickness was 4 mm, the maximum strain level can be estimated to be  $10^{-5}$  at 2 kV/cm. In consideration that the piezoelectric strain of PZT ( $d_{33} \sim 500$  pC/N) is  $\sim 5 \times 10^{-5}$  under AC driving fields of 2 kV/cm, the field-induced strain in the portland cement sample can be seen to be relatively large. However, larger displacements were not achievable, as the sample experienced dielectric breakdown at fields above 2.5 kV/cm.

Strong hysteresis in the  $\epsilon$ -E behavior is clearly evident in Figure 1. Arrows are shown in the figure to illustrate the direction of alternating field. On starting from a virgin state, a critical threshold is needed to be applied in order to observe induced displacements. Above this threshold a rapid increase in the displacement was found.

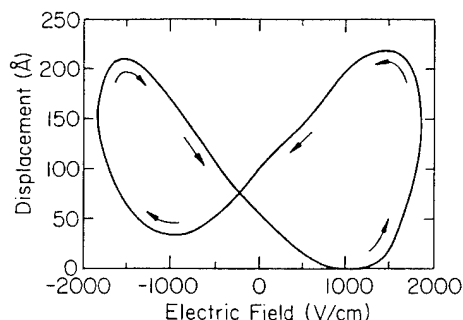


Figure 1. The displacement as a function of applied AC electrical field for portland cement. The measurement frequency was 1 Hz and the peak electrical field was 1.8 kV/cm.

No indications of saturation were observed in the response before breakdown was incurred. On decreasing the field, the value of the displacement was nonequivalent to that in the increasing direction, i.e., hysteresis. On reaching zero field, a small remanent displacement was retained. Upon reversing the AC driving field, the displacement was clearly switchable, as evidenced by the shape of the hysteresis loops.

#### III.2 Piezoelectric measurements of portland cement

Figure 2 shows a three dimensional plot of the effective  $d_{33}$  coefficient as a function of dc electrical bias and AC measurement frequency for a portland cement sample saturated in a humidity chamber for three days. At zero applied field, no piezoelectric response was observed. However as a superimposed DC electrical bias was applied, a piezoelectric response was induced. This induced response remained relatively small ( $< 2$  pC/N) until  $\sim 0.8$  kV/cm, at higher bias levels the effective  $d_{33}$  coefficient increased markedly approaching a value of  $\sim 14$  pC/N near 1.2 kV/cm using a measurement frequency of 15 Hz. Higher values of the piezoelectric coefficient were observed in some samples, approaching 50 pC/N in some cases. The magnitude of the piezoelectric activity was in general larger than that of quartz ( $d_{11} = 2.31$  pC/N) and significantly lower than that of PZT ( $d_{33} \sim 500$  pC/N).

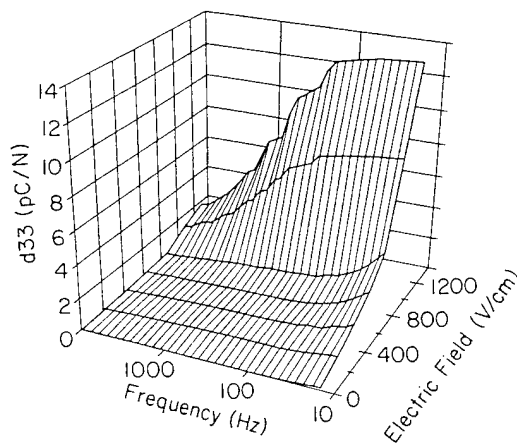


Figure 2. Effective  $d_{33}$  coefficient as a function of DC electrical bias and AC measurement frequency for portland cement.

One of the principle characteristics of the effective piezoelectric response was a strong relaxation with increasing frequency, as shown in Figure 2. Under a bias level of 1.2 kV/cm, the value of the effective  $d_{33}$  coefficient can be seen to decrease from  $\sim 14$  pC/N at a measurement frequency of 15 Hz to less than 2 pC/N at  $10^4$  Hz. The characteristics of this relaxation are qualitatively similar to that previously reported for the dielectric response by impedance spectroscopy [6]. The value of the effective  $d_{33}$  coefficient was  $\sim 14$  pC/N between  $10^2$  and 10 Hz, and was seemingly relatively frequency independent at lower frequencies.



#### IV. Discussion

The electromechanical effect was only found in samples which had been placed in a humidity chamber. Dry samples exhibited no field-induced shape changes or effective  $d_{33}$  coefficients. A possible explanation is that shape changes are incurred due to long-range water motion under electrical fields. To more thoroughly investigate this possibility, studies were performed in an optical microscope. Figures 3 illustrates a micrograph of the surface of a portland cement sample after cycling the field (2.5 kV/cm) several times around the hysteresis loop at a frequency of 1 Hz. This sample had been placed in a humidity chamber (100% rh) for three days. After cycling the field, water droplets can clearly be seen. This water did not condense from the atmosphere, as a glass microslide was placed on top of the sample surface. These results clearly show that long-range water motion occurs under electrical field and that in fact water can be forcibly driven out of the porous cement structure effectively drying the sample.

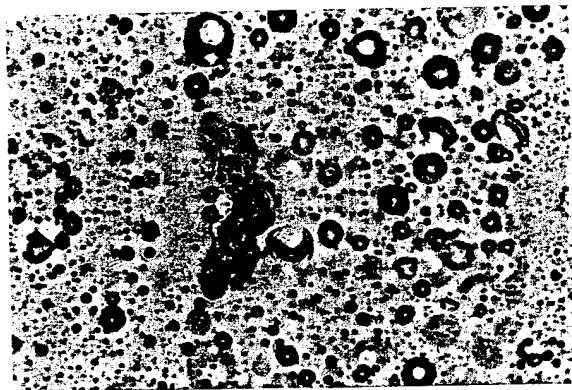


Figure 3. Optical micrograph of a portland cement sample surface after the strong-field measurement.

Water cannot by itself undergo long-range diffusion in response to a field, as it is not charged. The only intrinsic electrical response of water is to align its dipole moment with the field. However, if the internal surface of the cement is negatively charged, there will be an excess of positive ions in the surrounding double layer. An applied electrical field may, then, act upon ions in the diffuse part of the layer, leading to the development of a space charge (or double-layer) polarization. As a consequence of this ionic motion, water transport may be induced by an electrical field through the porous cement, i.e., electro-osmosis. Space charge polarization is characterized by a strongly dispersive dielectric response (known as the Maxwell-Wagner effect) in the frequency range between  $10^{-2}$  and  $10^5$  Hz. The relaxation effect arises due to the inability of the relatively slow ionic species to follow the electrical drive. In consideration that water transport is induced by the development of space charge (or double-layer) polarization associated with long-range ionic motion, the frequency dependence of the electromechanical properties should reflect that of a space charge mechanism. This is consistent with the results shown in Figure 2.

If the origin of the electromechanical behavior is due to electro-osmotic swelling, this effect should not be limited to portland cement samples, but rather may be a more general phenomena in any materials system which contains an interconnected network of gel-pore-like (or capillary-pore-like) structures. To more thoroughly investigate this possibility, studies were performed on porous silica glasses which contained an interpenetrating pore network with a mean pore size of 25 Å. These samples were commercial obtained from Gel-Tech Incorporated, were cut into similar sizes as the portland cement specimens, and were saturated in the humidity chamber for three days. Figure 4 shows the  $\epsilon$ -E behavior of a porous silica gel sample. Displacements of over 200 Å were achieved at field strengths below 300 V/cm. Assuming linearity, this corresponds to an effective  $d_{33}$  coefficient of nearly 400 pC/N. This value is approximately equal to that of the best PZT transducer materials ( $d_{33}$ ~500 pC/N). Again, strong hysteresis is clearly evident in this figure on cycling the field around the hysteresis loop. These results provide crucial evidence which strongly indicates that the origins of the electromechanical behavior in portland cement arise due to swelling effects in either the gel-pore or capillary-pore structure, but by no means gives conclusive proof of which pore structure is dominantly responsible for the effect.

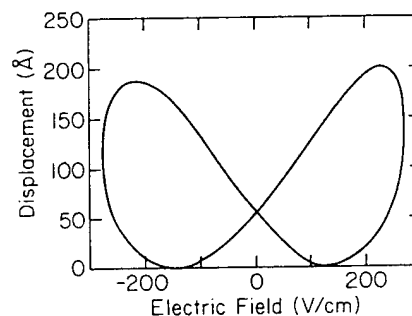


Figure 4. The displacement as a function of applied AC field for a porous silica gel sample. The measurement frequency was 1 Hz and the peak electrical field was 0.25 kV/cm.

#### V. Conclusion

Large field-induced shape changes have been observed in hardened cement pastes. This electromechanical response was found to be strongly dependent on measurement frequency, DC electrical bias, and exposure to moisture. In addition, strong hysteresis effects were found on cycling a large AC electrical field. The induced shape changes are believed to arise due to electro-osmotic-induced swelling of the pore structures under electrical bias. Similar results were then obtained on a porous silica gel containing an interpenetrating pore network with an average pore size of ~25 Å. The relevance of these results on cement-based structures is then discussed.

#### Acknowledgements

This research was supported by the NSF center for the Science and Technology of Advanced Cement Based Materials.

#### References

- [1] F.H. Wittmann, *Cement and Concrete Research*, Vol.3 (1973) 601-605.
- [2] R. Hunter, "Zeta Potential in Colloid Science: Principles and Applications", Academic Press, New York (1981).
- [3] R. Hunter, "Foundations of Colloid Science, Vol.I", Clarendon Press, Oxford (1989).
- [4] Q.M. Zhang, W.Y. Pan and L.E. Cross, *J. Appl. Phys.* 63 (8), 15 April 1988.
- [5] J. Li, P. Moses and D. Viehland, Submitted to *Rev. Sci. Inst.*
- [6] C.A. Scuderi, T.O. Mason and H.M. Jennings, *J. Mat. Sci.*, 26 (1991), 349-353.

# THE ROLE OF STATISTICAL DESIGN IN THE DEVELOPMENT OF ELECTROSTRICTIVE MATERIALS

S.E. Prasad, S. Varma and T. Hoang  
Sensor Technology Ltd. (B.M. Hi-Tech Division)  
P.O. Box 97  
Collingwood, Ontario, L9Y 3Z4, Canada

T.A. Wheat and A. Ahmad,  
Mineral Sciences Laboratories, CANMET  
Natural Resources Canada  
555 Booth Street  
Ottawa, Ontario, K1A 0G1, Canada

**Abstract** -- The role of statistical design in the development and optimization of ceramic products is examined with particular reference to lead magnesium niobate/lead titanate (PMN-PT) ceramic dielectrics. It is shown that considerable benefits can be derived by following an appropriate design in which a number of factors (processing parameters) are varied simultaneously while the system response such as density, dielectric constant, loss, etc. is monitored.

If it is assumed that complex factor interactions (e.g., having greater than three factors) can be ignored, only a fraction of the whole factorial matrix need be examined. Even in cases where only eight factors are involved each having only two levels, useful information can be obtained from only 16 trials drawn from the total of 256 trials ( $2^8$ ) required of a full factorial matrix. Such studies are valuable in screening and ranking the importance of the various factors on the system response. Examples of such screening designs and the subsequent modelling of the system response for the important process factors so identified are presented.

## INTRODUCTION

The properties of materials are strongly dependent on the processing steps required in transforming incoming raw materials to a final shipped product. Because of the overall complexity of materials processing, it can be a major challenge to produce optimized materials - particularly, when it is realized that a typical production flow sheet may have 30 or more process factors involved and each, ideally, should be set to a particular level. If each factor could be set to only two levels, then the full factorial matrix of possible combinations is  $2^{30}$  (over one billion) - in practice, many factors such as temperature, pressure, time, pH, etc. can be set to many levels, thereby making the matrix even more complex. Even at its simplest (two levels each), such a matrix is well beyond even the most generous budget.

With the increased pressure to maximize the return on all aspects of investment it is crucial to maximize the use of all resources, staff, facilities and equipment so that the developmental lead time and hence financial investment from R&D to production is minimized. This demands that any material development program be conducted in the most effective manner possible so that the maximum amount of information is obtained from the minimum amount of effort (resources, time, \$\$'s etc.). In turn, this requires consideration of the methodology by which any program is conducted.

In the past, R&D has been conducted using either a random "buck-shot" approach or, more commonly, a one-factor-at-a-time approach. Although both are easy to plan and conduct, they are not only very inefficient but also limiting in the amount of information that can be obtained. Some of the drawbacks include:

- an inability to identify any significant factor interactions and
  - an inability to determine the optimum operating conditions.
- Because of the complexity of the processes involved in making virtually all products, it is highly likely that one or more significant factor interactions occur: if they are not recognized, it is unlikely the process will be optimized - even if it is, the effort to determine the appropriate operating conditions was undoubtedly excessive.

In recent years, the increasing emphasis on improved quality in manufactured goods had led to a recognition that product variations arise from three basic sources: manufacturing variability, internal degradation of the product and the susceptibility of the process/product to uncontrollable external factors. Much of the quality assurance in the past has focused on inspection of the product and the use of Statistical Process Control (SPC) to minimize these variations. However, this is a reactive technique as it monitors the failure of a product to meet its specifications. It can not indicate what steps should be taken to bring the product back into specification, that is based on the experience of the production staff (additional invested effort), nor can it indicate what changes are required to improve the product. This is most easily understood by considering the following example of a two-factor problem that is examined one-factor-at-a-time.

## THE TRADITIONAL APPROACH

It is common to find that factors such as sintering temperature and time have an influence on the dielectric constant of ceramic materials. In the example below, it is assumed that a new material is under study in which the objective is to determine the optimum temperature-time conditions that yield a maximum value for K measured at 25°C within the temperature limits of 1100° to 1200°C and soak time of between 2 - 4h.

Two methodologies found in the literature for studying such systems are shown in Fig.1 (the random walk) and Fig.2 (one-factor-at-a-time). In both cases, nine experiments are shown. Of the two, the one-factor-at-a-time approach is the more commonly reported as it is easy to plan and conduct, however, the data can be misinterpreted.

Applying the conventional one-factor-at-a-time approach, it is assumed that a temperature of 1150°C (middle level of temperature) is acceptable to start the work, Fig. 2. Consequently, a series of experiments are performed at 1150°C and progressively increasing sintering times up to 4h. The results from this first set of experiments might indicate that K is maximized on firing at 1150°C for 3.5h. A further four experiments are then conducted for a sintering period of 3.5h at temperatures ranging from 1100° to 1200°C. The results from the second set of data might suggest that K is maximized on sintering at 1125°C (for 3.5h).

Given these data, it is tempting to assume that the optimum conditions have been found. However, when the temperature-time factor space was examined using statistically designed experiments

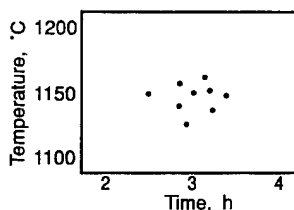


Fig.1 - Using a Random Walk Approach

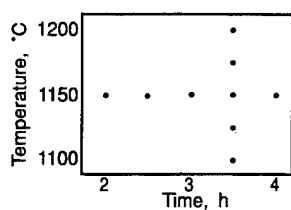


Fig.2 - The One-factor-at-a-time Approach

(SDE) and the contours of K determined over this space (by interpolation) using nine experiments in a full factorial design (two factors at three levels each) and verified (by check points) it was found that the initial conclusion was inaccurate as superior K values can be obtained using lower levels for both time ( $\approx 2.6h$ ) and temperature ( $\approx 1110^{\circ}C$ ), i.e., there is a strong two-factor interaction as indicated in the contour plot of Figure 3.

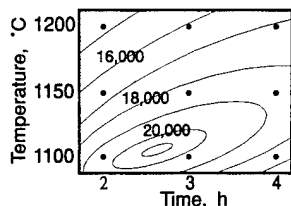


Fig.3 - Plot Obtained Using a Full Factorial Approach

It is this interaction of factors that is difficult to recognise when the work is conducted using either a random walk or one-factor-at-a-time methodology and, in turn, is probably the source of most of the difficulties in scaling up laboratory-developed processes through pilot to full production. Clearly, there is a need for a more rigorous approach in which the maximum amount of information is obtained from the minimum amount of effort. That need is met by the use of SDE which allows the user to distinguish the significant factors from the myriad factors initially considered in developing any process.

## STATISTICAL DESIGN OF EXPERIMENTS

The example of a contour plot of K vs sintering conditions shown in Fig. 3 is often the information required in establishing optimised conditions for a production process. Such information is obtained in two stages. Firstly, a series of screening experiments is conducted which results in a numerical ranking of the influence of each factor on the various responses studied (such as dielectric constant, loss factor, resistivity, Curie temperature, modulus of rupture, etc.). From such a complete ranking of all the factors studied, only those factors having an influence greater than experimental error (at a chosen confidence limit of typically 95%) are significant. Secondly, only the (usually few) significant factors are studied further to generate and verify a response surface map of the type shown in Fig. 3.

It is common to find that the independent factors involved in such designs are either "continuous" or "discrete": the former (quantitative) factors are those which can have any value within a given range, e.g., temperature, pressure, pH, time, etc., whereas the latter (qualitative) factors can only have single values, e.g., high or low, up or down, method A or B, etc. Within the continuous type of factors is a sub-set of particular interest to the materials scientist and these constitute the components of any mixture: they are continuous factors but with the additional constraint that their summation is 1 or 100%. The constraint differentiates them and their statistical designs from other process factors (continuous or discrete): they are often called mixture factors.

## What is the Basis for SDE?

The essence of SD to determine the influence of any set of factors on a process is based on the familiar full factorial matrix in which, for example, the influence of n factors at two levels (high and low, present and absent, etc.) on a product is determined using  $2^n$  trials. In such cases, the influence of each factor and factor interaction is readily determined.

### The Full Factorial Matrix

For simplicity, Fig. 4 shows the full matrix for a three factor (A, B and C), two-level (low[-], high [+]) design. Assuming a numerical value R ( $R_1, R_2, R_3, \dots R_8$ ) is obtained (such as density, bend strength, dielectric constant, etc.) as the response of the system or process to each trial condition (tc), then the numerical factor effect can be found by summing each column in the design [1]:

$$\text{Effect A} = 1/8[-R_1 + R_2 - R_3 + R_4 - R_5 + R_6 - R_7 + R_8]$$

$$\text{Effect B} = 1/8[- - + + - - + +]$$

$$\text{AB} = 1/8[+ - - + + - - +] \text{ etc.}$$

In this manner, all the factor and factor-interaction effects can not only be determined but also ranked in order of their importance on the selected response. However, it is frequently possible to study only a fraction of the full factorial matrix yet still obtain valuable information.

### The Fractional Factorial Matrix

It has long been recognized that all full factorial matrices are composed of statistically equivalent sub groups, each of which, in turn, can be further split into their own set of equivalent sub-sub groups and so on. In effect, each full factorial matrix can be divided into a succession of sub-sets giving rise to half, quarter, eighth, etc. fractional factorial matrices. This is illustrated in Fig.5 which shows the simple full factorial matrix of Fig.4 re-arranged in such a way

tc	Factors			Interactions				Res.
	A	B	C	AB	AC	BC	ABC	
	(D)	(E)	(F)	(G)				
1	-	-	-	+	+	+	-	R1
2	+	-	-	-	-	+	+	R2
3	-	+	-	-	+	-	+	R3
4	+	+	-	+	-	-	-	R4
5	-	-	+	+	-	-	+	R5
6	+	-	+	-	+	-	-	R6
7	-	+	+	-	-	+	-	R7
8	+	+	+	+	+	+	+	R8

Fig. 4 - Full Factorial Matrix.

that the matrix is presented in two parts (each a half factorial). The so-called "factor space" covered by three factors is represented in three dimensions by a cube, the corners of which represent the eight trial conditions. It can be seen that the two half fractions are mirror images of each other.

This existence of statistically equivalent fractional factorial sub-sets in a full factorial matrix has considerable importance to R&D, product development, process factor screening, etc., as it allows staff to decrease the number of experiments. However, a penalty is paid in this approach: as the full factorial matrix is reduced, so the degree of confounding (confusion) between factor effects and their multiple interactions increases. Figure 5 shows how this confusion arises. Assuming that only the experiments of a half factorial design are conducted,

tc	Factors			Interactions				Res.
	A	B	C	AB	AC	BC	ABC	
	(D)	(E)	(F)	(G)				
2	+	-	-	-	+	+	-	R2
3	-	+	-	-	-	+	+	R3
5	-	-	+	+	-	-	+	R5
8	+	+	+	+	+	+	+	R8
7	-	+	+	-	-	+	-	R7
6	+	-	+	-	+	-	-	R6
4	+	+	-	+	-	-	-	R4
1	-	-	-	+	+	+	-	R1

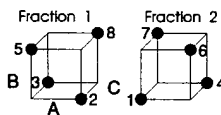


Fig. 5 - Fractional Factorial Matrices.

e.g., fraction 1, then it can be seen that the factor effect of A will be numerically equal to that of the interaction BC, i.e., in short

form  $A = BC$ , similarly,  $B = AC$  and  $C = AB$ . For fraction 2, the relationship is mirrored:  $A = -BC$ ,  $B = -AC$  etc.

This example is somewhat simplified and constrained - usually bigger matrices are employed in which all the main effects (primary factors) may not be confounded with two-factor (or three-factor) interactions. This reality has several practical consequences:

- Factors of particular interest may be assigned to those matrix columns that avoid confounding with two- or three-factor interactions - the confounding will occur with four- (or more) factor interactions. As four-factor (and higher) interaction effects are rare, it is a reasonable risk to assign factors of vital interest to those columns - any factor effect found being assumed to arise from the primary factor.
- If some (or all) factor interactions can be confidently ignored on the basis of prior knowledge, experiment, theory, etc. then additional factors may be added to the matrix. For example, column AB in Fig.4 could be assigned to a new factor D.

This opportunity to substitute additional factors for the original factor interactions can be continued progressively so that eventually up to seven factors (A - G, Fig.4) can be studied using only eight experiments. However, the trade-off is the loss of information on possible factor interactions that may occur - that is a decision for the researcher.

As it is impossible to discuss here the details of the derivation of various designs from the fundamental full factorial matrix and how such designs may be exploited in various situations, the reader is referred to various standard texts on the subject [1,2,3,4,5]. However, it is important to realize that the various designs (and the increasing number of commercially available software to create designs and analyze data so obtained) fall under the broad categories of:

- **Screening Designs** for process factors, mixture factors or both. This group includes full and partial factorials, Plackett-Burman and Taguchi designs;
- **Response Surface Designs** for process factors, mixture factors or both. These include Box-Behnken, Simplex, Extreme Vertices, Star and Central Composite designs.

## SD APPLIED TO MATERIALS DEVELOPMENT

The benefits of using SD throughout the spectrum from R&D to production are considerable. The methodology is rigorous and imposes organization and it also provides many options in planning any study. For SD methodology to have any validity, it is essential that only the design factors under study are varied - material substitution, etc. can not be accepted if there is no provision for such a variable in the original design and the methods and procedures used must be unchanged until the trials are completed. This raises a crucial point: it is essential before conducting even the first trial that detailed consideration has been given to the design - have all the factors been included, are they represented at sufficient levels? If these considerations are met, then it is highly probable that a design will be beneficial.

The appeal of SD in materials research is based on its universal application and the opportunities it affords to maximize the amount of information when operating under the constraints of limited time, budget, resources, etc. To illustrate these aspects, an example drawn from a program to develop PMN-PT ceramics is presented below. The first design deals with the challenge of screening factors to determine what are important while the second shows the benefits of using a response surface design to resolve the common conflict of producing a material for which the specific properties have to be compromised.

## The Processing of PMN-PT Dielectrics

The objective of the work was to develop a 0.9PMN:0.1PT-based sintered ceramic having a specified high density, high dielectric constant and low loss. A literature survey suggested that values of K have been reported between 14,000 and over 28,000 (over 37,000 with a modified composition) having D values ranging from 8% down to 3% for various compositions based on PT-doped PMN. As it was also intended to take the process into production, there was the additional constraint of developing an effective low-cost process suitable for a production environment.

Although there is considerable published material on the effect of various dopants added to the system, as yet, there is still dispute whether dopants (contaminants?) such as  $\text{SiO}_2$  or  $\text{ZrO}_2$  or excess PbO or MgO are beneficial in enhancing the properties.

Although it is possible to create experimental designs that combine both mixture factors and process factors in a single design, the analysis of the data is complex. Consequently, it was decided to approach the problem using two screening designs (Taguchi) to identify the significant processing factors and to then model the system further using a subsequent response surface design in which the compromise between low loss and high K can be determined.

The processing of a typical ceramic involves many factors.

Figure 6 shows a flow sheet that is typical for the batching, mixing, calcining, forming and firing of many ceramics. Some of the factors involved at each stage are shown and are assumed to have a choice of only two levels. If all factors were initially accorded equal importance then it can be appreciated that  $2^{27}$  possible factor combinations exist that would require examination in a full factorial study. However,

experience often allows one to reduce the number of factors by fixing a number such as choice of binder, forming pressure, mill type, milling media type, etc. In this way, the full matrix can be reduced to perhaps  $2^{14}$  - still too large for a complete study.

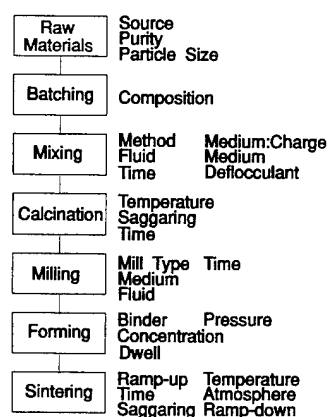


Fig 6 - Typical Flow sheet

The processing of PMN-PT followed a similar route to that shown in Fig. 6. Initially, a few "probing" experiments were conducted to establish reasonable values for the various factors and thereafter the work was conducted under design.

## Screening Designs

The initial screening design was based on a simple two-level partial factorial based on a Taguchi L8 design [6] which screened for the effects of two dopants, calcination temperature and time, and sintering temperature and time. From the data, it was concluded that changes in the calcination conditions had no effect on the dielectric constant and loss of sintered ceramic whereas the dopant levels and sintering conditions were important - the latter suggesting that the control of the lead atmosphere during sintering was important, typical of probably all the PbO-based materials.

After these initial eight experiments, a second set of eight tests was conducted using fixed calcination conditions and dopants and varying the sintering conditions further to examine other factors that could control the loss of PbO from system such as: the surface to volume ratio of the disc samples, the leakage from the saggars, the number of samples, the use of an "atmosphere" powder around

the samples and the free volume of the saggar cover. Again a Taguchi L8 design was used. The data of measured K at room temperature and 0.1 kHz ranged from 18,640 to 10,200. Manipulation of the data to determine the magnitude of the various factor effects resulted in the data shown in Fig. 7 which indicates that most factors have some effect but the dominant ones are the number of samples and the leakage from the saggar.

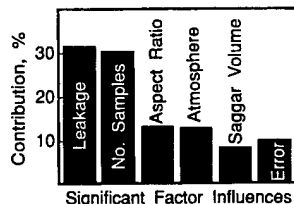


Fig. 7 - Factor Effects

Figure 8 presents the actual experimental K values with the values predicted by the model developed from the set of eight tc's studied. It can be seen that there is excellent agreement between the two. However, such agreement should not be regarded as conclusive evidence that the model developed represents the system well; that requires several "check" points. In this case, four other tc's were studied other than those used in the design. In all cases, the experimental data and the projected data were in excellent agreement suggesting the original model was adequate to project data to a confidence limit of 95%.

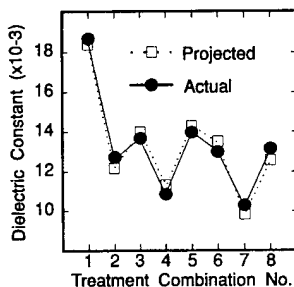


Fig. 8 - Comparison of actual and projected K values for each tc.

#### Response Surface Designs

Having established what factors influence the dielectric properties, it is necessary to optimize the factor levels so that ideally, high K and low loss materials are obtained. Unlike screening designs, which generally only use two levels for each factor, response surface designs require three or more levels so that an idea of the curvature of the response surface between levels can be obtained. There are several response surface designs such as the three-level Box-Behnken, face centred and star designs and the five-level central composite designs.

In the present case, a response surface design was used to model dielectric constant, (K), loss (D) and density to the factors: amount of "atmosphere" powder, saggar leakage, and sintering temperature. Given the choice between the lower sensitivity of a three-level Box-Behnken design (15 tc's) and a five-level Central Composite Design (21 tc's), the former was chosen to minimize experimental effort in the anticipation that the 6 tc's saving could be used as final check points to confirm the model developed from the initial 15 tc's.

One of the limitations in appreciating the data generated in this manner is that only two factors at a time can be presented on paper or screen (the third dimension is the response). Consequently, it is necessary to examine the various possible combinations of the factors studied to find conditions where, e.g., the maximum K and density, and minimum D values are realized. Figures 9-11 show the response surfaces generated for each response for samples sintered at 1200°C based on the 15 tc's. However, of real interest are those conditions where K and density exceed minimum values and D is less than a selected upper limit. This is determined by over-laying contour maps for each response and finding areas where the conditions are met, Fig. 12. In cases where there are several isolated areas that meet the criteria, it is common to choose those conditions that also meet other (secondary) criteria such as reduced firing temperature or time, use of the least amount of an expensive or toxic dopant, etc.

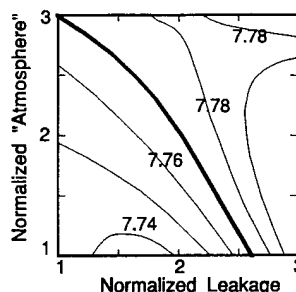


Fig. 9 - Contours for Density ( $\delta$ )

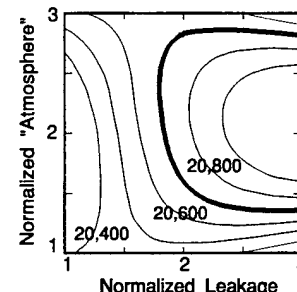


Fig. 10 - Contours for K

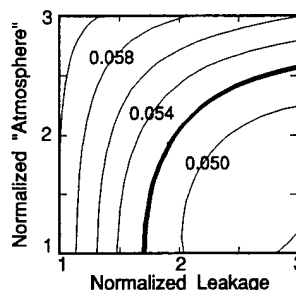


Fig. 11 - Dielectric Loss Contours

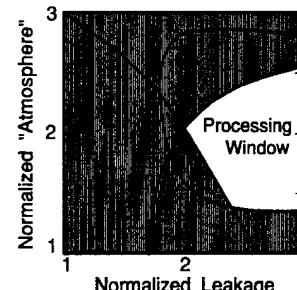


Fig. 12 - Overlays of K, D and  $\delta$

#### SUMMARY

The foregoing shows some of the benefits and considerations taken in applying SDE to the development of a ceramic dielectric. Although all ceramic systems are inherently complex, it is possible through a combination of experience, a few initial probing experiments and design to achieve a lot with the minimum effort. Although not obvious to first-time users of SDE, many of the benefits arise from the options that are presented when partial factorial matrices are used: there are many ways the factors can be assigned to the columns of the matrix and, hence, many factor confounding patterns can emerge. Equally important, SDE clarifies what can be learned of the influence of various factors and what can not - before the work has started.

#### REFERENCES

1. G.E.P. Box, W.G. Hunter and J.S. Hunter, *Statistics for Experimenters: An Introduction to Design, Data Analysis and Model Building*, J. Wiley & Sons, NY, 1978.
2. R.A. McLean and V.L. Anderson, *Applied Factorial and Fractional Designs*, M. Dekker Inc., NY, 1987.
3. J.A. Cornell, *Experiments with Mixtures: Designs, Models and the Analysis of Mixture Data*, J. Wiley & Sons, NY, 1990.
4. M.S. Phadke, *Quality Engineering Using Robust Design*, Prentice Hall, New Jersey, 1989.
5. A.I. Khuri and J.A. Cornell, *Response Surfaces, Designs and Analyses*, M. Dekker Inc., New York, 1984.
6. G. Taguchi, *System of Experimental Design*, Vols 1 and 2. Ed. D. Clausing, UNIPUB/Kraus Intl. Pubs., New York, 1987.

# High-Power Characteristics of Piezoelectric Materials

Seiji HIROSE, Sadayuki TAKAHASHI\*, Manabu AOYAGI  
and Yoshiro TOMIKAWA

Faculty of Engineering, Yamagata University, Yonezawa 992 Japan

\*R&D Group, NEC Corp., Miyazaki, Miyamae-ku, Kawasaki 216 Japan

**ABSTRACT** A measuring method of the high-power characteristics of the piezoelectric transducers and some experimental results are described. The vibrational velocity dependences of the equivalent circuit constants and the temperature rise were measured under the constant vibrational velocity control. In addition, when a high-power ultrasonic device such as an ultrasonic motor is practically used, the maximum efficiency is obtained at the antiresonance frequency, not at the resonance frequency. These phenomena are caused by the increase of the dielectric loss related to the vibrational velocity. In the paper, a measuring method and the experimental results of the dielectric loss under the high vibrational velocity are also described.

## 1. Introduction

In a piezoelectric ceramic transducer operating under high-power excitation, the quality factor  $Q$  of the transducer becomes lower, and therefore, heat generation at and around the maximum-stress position increases markedly. Even if the applied electric power is increased, almost only heat generation will increase, but the vibration energy will not. Under such a high-power operation, the equivalent electric circuit constants such as the mechanical quality factor  $Q$  cannot be measured by the ordinary admittance circle method, because the admittance circle becomes unstable.

In the paper, a measuring method of the equivalent electric constants from a lower vibrational velocity through a higher vibrational velocity is described. This is an improved measuring method modified from the perturbation method. During the measurement, the constant vibrational velocity control is performed for avoiding the jump phenomena in the resonance characteristics. The mechanical  $Q$  can be obtained easily by only three values of the driving voltage measured by the digital voltmeter in the vicinity of the resonance frequency and transferred to the micro-computer through GP-IB. By using this measuring method, measurements were performed on some piezoelectric transducer samples having various  $Q$  values.

In addition, a measuring method and the experimental results of the dielectric loss under the high vibrational velocity are also described.

## 2. Equivalent circuit and motional current

We employ the following fundamental equations for a piezoelectric transducer, which give the relation between the terminal current  $I$ , the terminal voltage  $V$ , the mechanical force  $F$  and the vibrational velocity  $v$ :

$$\begin{aligned} I &= j\omega C_d V + Av \\ F &= -AV + z_m v, \end{aligned} \quad (1)$$

where  $\omega$  is the angular-frequency,  $C_d$  is the damped capacitance,  $A$  is the force factor and  $z_m$  is the mechanical impedance under the electrically short-circuit condition. In the vicinity of a mechanical resonance,  $z_m$  is written as

$$z_m = r_m + j\omega m + s/j\omega, \quad (2)$$

where  $m$  is the equivalent mass,  $r_m = \omega_r m / Q_m$ ,  $s = m \omega_r^2$  and  $\omega_r$  is the resonance angular-frequency.

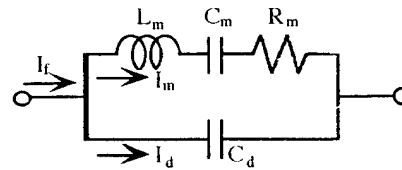


Fig.1 Admittance-type equivalent electric circuit

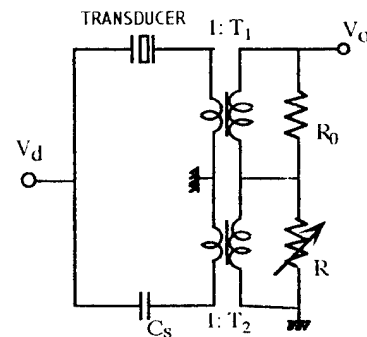


Fig.2 Differential circuit for detecting the motional current  $I_m$ .

The electric admittance  $Y_f$  of the mechanical force being free ( $F=0$ ) can be represented by the equivalent circuit shown in Fig.1. This is the admittance-type equivalent circuit. In Fig.1,  $L_m = m/A^2$ ,  $C_m = A^2/s$ ,  $R_m = r_m/A^2$ . The series resonance circuit represents the admittance given by  $Y_m = A^2/z_m$ .

The current  $I_m (= Y_m V_d)$  indicated in Fig.1 is called the motional current. From Eq.(1),

$$I_m = Av. \quad (3)$$

So,  $I_m$  is proportional to the velocity  $v$ .

### §3. Detection of motional current $I_m$

Figure 2 shows a differential circuit for detecting the motional current. Here,  $C_s$  and  $R$  are a capacitance and a resistance, respectively, for cancelling the damped capacitance  $C_d$ .

The output voltage  $V_o$  of the differential circuit in Fig.2 is given by,

$$V_o = -(R_d/T_1)Y_m V_d - j\omega[(R_d/T_1)C_d - (R/T_2)C_s]V_d \quad (4)$$

where  $T_1$  and  $T_2$  are the transformation ratio of current detection transformer. When  $R$  is adjusted for the resonance curve to be symmetric,  $V_o$  becomes equal to  $-(R_d/T_1)Y_m V_d$ , that is,  $-(R_d/T_1)I_m$ . Hence, the motional current  $I_m$  can be obtained from the output voltage  $V_o$ . When  $V_o$  is controlled to be constant, the motional current  $I_m$  and therefore, the vibration velocity  $v$  can be kept constant in the vicinity of  $\omega_r$ .

### §4. Method of Measuring equivalent circuit constants

Figure 3 shows the block diagram of the measuring apparatus. The frequency of the oscillator is controlled by the micro-computer through GP-IB. The signal of the oscillator is applied to the Auto Gain Controlled (AGC) amplifier and the power amplifier. The attenuators ATT1 and ATT2 are prepared for controlling the driving voltage applied to the transducer. When the attenuation of the ATT1 is decreased, the one of the ATT2 has to be increased. After this adjustment, the driving voltage can be enlarged in keeping the voltage  $V_c$  constant, where the voltage  $V_c$  is the feedback voltage applied to the control terminal of the AGC amplifier. Moreover,  $V_c$  is the value the value of which is decreased from the output voltage  $V_o$  of the differential circuit; that is, the value of  $V_o$  is decreased by the attenuator ATT2 and then becomes  $V_c$ . Differential

circuit including the test sample transducer has been already shown in Fig.2.

The digital voltmeters DVM1 and DVM2 are prepared for measuring the AC voltages; that is, the driving voltage  $V_d$  and the output voltage of the differential circuit  $V_o$ . The voltmeter DVM3 are for monitoring the AGC control voltage  $V_c$  (DC voltage). These voltages are transferred to the micro-computer through GP-IB, and then the equivalent circuit constants are obtained by using these experimental values as follows.

(1) Damped capacitance  $C_d$ : In Fig.2,  $R$  is adjusted so that the driving voltage  $V_d$  under constant velocity shows a symmetric resonance curve with respect to the resonance frequency on a logarithmic scale. After this adjustment, the damped capacitance is given by  $C_d = (T_1/T_2)(R/R_d)C_s$ .

(2) Resonance frequency  $f_r$ : When the constant vibration-velocity control (namely, constant  $I_m$  control) is employed,  $f_r$  is given by the frequency where the driving voltage  $V_d$  indicates minimum value. These frequencies can be obtained by automatic measurement system using micro-computer control<sup>(1)</sup>.

(3) Quality factor  $Q_m$ : Using the frequency perturbation method<sup>(2)</sup>, the quality factor  $Q_m$  can be obtained by

$$Q_m = \frac{2f_r}{f_2 - f_1} \sqrt{K_p(1 + K_p)} \quad (5)$$

where  $f_1$  and  $f_2$  are frequencies very close to the resonance frequency  $f_r$ , and are in the relation  $f_1 < f_r < f_2$ . In addition,  $K_p$  is the perturbation ratio, which is given by the following equation under the constant vibrational velocity control,

$$K_p = (V_d - V_{d0})/V_{d0} \quad (6)$$

where  $V_{d0}$  is the driving voltage at the resonance frequency  $f_r$ , and  $V_d$  is that at the frequency  $f_1$  or  $f_2$ . These values are measured by digital voltmeters and transferred to micro-computer through GP-IB. In this study, the value of  $K_p$  was selected below several percent.

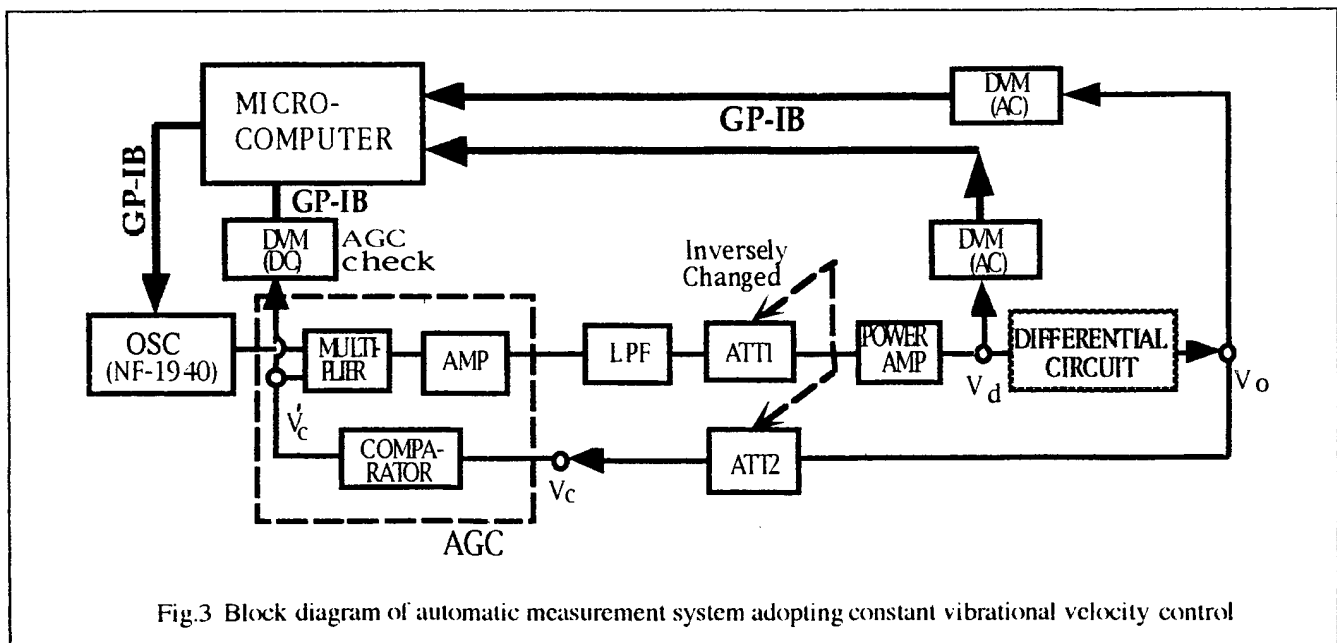


Fig.3 Block diagram of automatic measurement system adopting constant vibrational velocity control

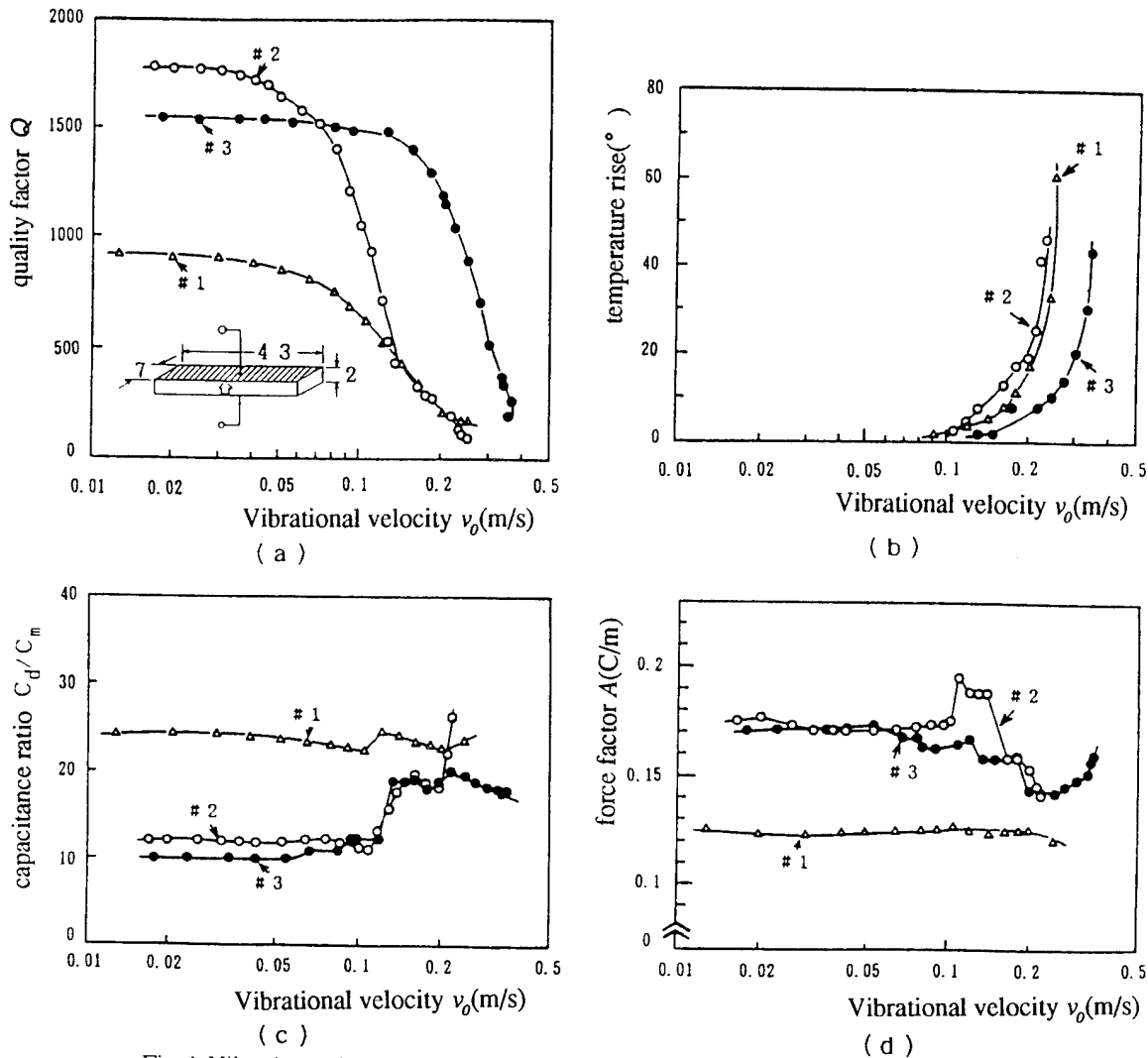


Fig.4 Vibration velocity dependence of the quality factor, temperature rise, capacitance ratio and force factor for three PZT family ceramic longitudinally vibrating transducers.

(4)Equivalent resistance  $R_m$ : Using the motional current  $I_m$  and the driving voltage  $V_{d0}$  obtained at  $f_r$ ,  $R_m$  is given by

$$R_m = \frac{V_{d0}}{I_m} (f=f_r) \quad (7)$$

(5)Equivalent inductance  $L_m$  and capacitance  $C_m$ : Since  $Q_m$ ,  $R_m$  and  $f_r$  were given, equivalent inductance  $L_m$  and capacitance  $C_m$  can be obtained by

$$L_m = \frac{Q_m R_m}{2\pi f_r}, \quad C_m = \frac{1}{(2\pi f_r)^2 L_m} \quad (8).$$

## 5. Experiments

Quality factor  $Q_m$ , temperature rise, capacitance ratio  $C_d/C_m$  and force factor  $A$  have been investigated on some PZT family ceramic rectangular bars. Vibration mode considered here is the fundamental longitudinal mode. Experimental results of  $Q_m$  and temperature rise are illustrated in Fig.4(a) and (b) as functions of the vibration velocity  $v_0$  which was measured at the end of the ceramic bar using the "Fotonic Sensor". Also, temperature rise was measured at the center of the ceramic

rectangular bar using a thermocouple. In Fig.4, the configuration and the dimensions of the test sample are illustrated.

## 6. Dielectric loss factor $\tan \delta$

As is well known, in the presence of finite dielectric loss-angle  $\delta$ , the mechanical  $Q$  of a piezoelectric transducer resonating under the open-circuit condition of the electric terminal is higher than that under the short-circuit condition. In relation to this effect of  $\delta$ , the maximum electroacoustic conversion efficiency is obtained at the mechanical resonance under the electrically open-circuit condition, which is called *B*-type resonance<sup>3)</sup>. *B*-type resonance frequency coincides with the electrical anti-resonance frequency. Electro-acoustic conversion efficiency becomes lower at the mechanical resonance under the electrically short-circuit condition, which is called *A*-type resonance<sup>3)</sup>. *A*-type resonance frequency coincides with the electrical series-resonance frequency.

Quality factor  $Q_B$ , temperature rise, capacitance ratio  $C_B/C_f$  and force factor  $A_B$  at the *B*-type resonance frequency have been investigated on a PZT ceramic rectangular bar.



Vibration mode considered here is the fundamental longitudinal mode. Experimental results of  $Q_B$  and temperature rise are illustrated in Fig.5 as functions of vibration velocity  $v_0$ . A-type resonance constants have also been investigated for comparison with B-type constants. Experimental results of  $Q_A$  and temperature rise of the A-type resonance are also shown in Fig.5.

From the figure, it can be recognized that  $Q_B$  is higher than  $Q_A$  over the whole vibration velocity range investigated here: from  $v_0 \approx 0.02$  to about 0.3(m/s), and the difference between  $Q_A$  and  $Q_B$  becomes greater with increasing vibrational velocity. Temperature rise of B-type resonance is less than that of A-type resonance because  $1/Q_B$  is smaller than  $1/Q_A$ . These facts are caused by the presence of dielectric loss and its nonlinearity.

Using  $Q_B$ ,  $C_B/C_f$ ,  $\omega_B$ , in addition, the quality factor  $Q_A$  and the resonance angular-frequency  $\omega_A$  of the A-type resonance which have been obtained prior to the measurement on the B-type resonance, dielectric loss factor  $\tan \delta$  can be given as follows:

$$\tan \delta = C_B/C_f \cdot (1/Q_A - \omega_B/\omega_A \cdot 1/Q_B) \quad (9)$$

In Fig.6, capacitance ratio  $C_B/C_f$ , B-type force factor  $A_B$  and dielectric loss factor  $\tan \delta$  are shown. For comparison,  $\tan \delta_0$  which is directly measured at a sufficiently low frequency (1kHz) is also shown in the figure.  $\tan \delta_0$  includes an elastic loss brought by a quasi-static strain<sup>4)</sup>, therefore it is larger than  $\tan \delta$  in a small vibration velocity.  $C_B/C_f$  and  $A_B$  can be viewed as almost constant over the whole velocity range considered here. However,  $\tan \delta$  has become larger remarkably in the large vibration velocity above about 0.2(m/s).

## §7. Conclusions

First, a method of measuring the vibrational level dependence of the equivalent circuit constants of the piezoelectric transducers has been described. Some experimental results have been also described. This study is available for the design of the piezoelectric devices, such as the ultrasonic motors and the other piezoelectric power devices. In addition, by comparing high-power characteristics on various piezoelectric materials, materials with high performance can be selected.

Secondly, a method of measuring the vibration level dependence of the dielectric loss factor of the piezoelectric transducers has been described. For obtaining the dielectric loss, the equivalent constants both at A-type resonance and at B-type resonance have been measured. From the results, it has been concluded, that  $Q_A < Q_B$  and the difference between them usually become larger with increasing vibration velocity, and temperature rise of B-type resonance is less than that of A-type resonance. In addition, capacitance ratio  $C_B/C_f$  and force factor  $A_B$  of B-type resonance have been shown to be almost constant over the range from  $v_0 \approx 0.02$ (m/s) to about 0.3(m/s). However, dielectric loss factor  $\tan \delta$  has become larger remarkably in the large vibrational velocity above about 0.2(m/s).

## References

- 1) S. Hirose and H. Shimizu: Proc. 1990 Spring Meeting of Acoust. Soc. Jpn. 2-2-2 [in Japanese]
- 2) S. Saito, R. Aoyagi and H. Shimizu: J. Acoust. Soc. Jpn. 33-10 (1977) p. 540 [in Japanese]
- 3) Y. Kikuchi and H. Shimizu: Sci. Rep. Res. Inst. Tohoku Univ. B4-1 (1952) p. 173
- 4) S. Saito and H. Shimizu: Jpn. J. Appl. Phys. Suppl. 24-3 (1985) p. 145

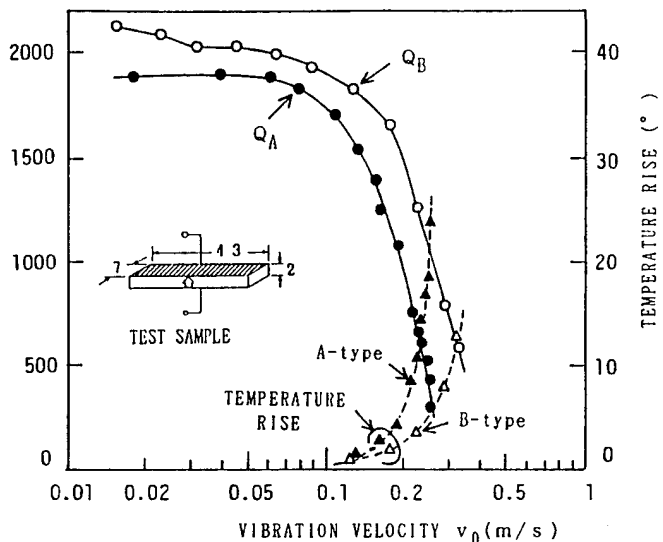


Fig.5 Vibration velocity dependence of the quality factor and temperature rise for both A- and B-type resonances of a PZT ceramic longitudinally vibrating transducer.

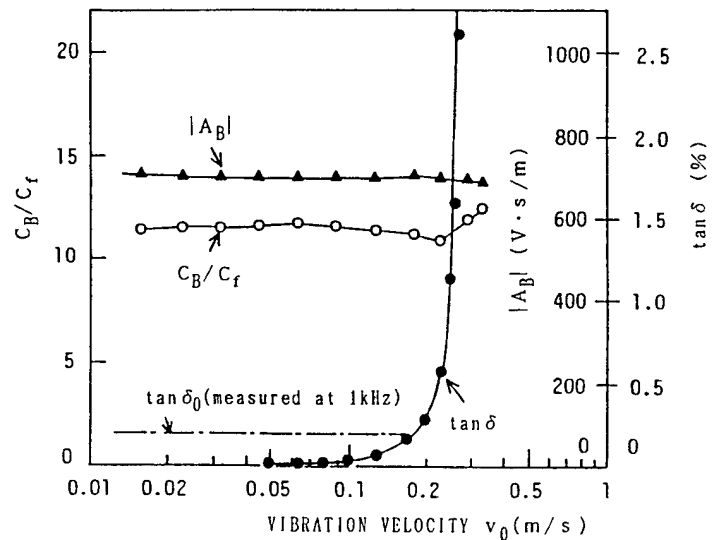


Fig.6 Vibration velocity dependence of the capacitance ratio and force factor for B-type resonance and the dielectric loss factor  $\tan \delta$ .

## Flexi-Distortional Piezoelectric Sensor Results

W. B. Carlson, S. M. Pilgrim, W. A. Schulze, Y. S. Kato, J. M. Frommelt

New York State College of Ceramics, Alfred University, Alfred, NY, USA

**Abstract** -- A longitudinal ("RIBBIE") form of a shear amplification sensor has been tested for amplified  $d_{15}$  response. The mechanically amplified flexi-distortional system may improve the  $d_{hg}$  figure of merit by transferring the compressional stress on the device to a lateral shear on the electroceramic element. This type of amplified system is mechanically classified as distortional and, therefore, without volume change. By transforming the hydrostatic stress to transverse strain, the transverse forces can be used to develop shear strain and activate the  $d_{15}$  coefficient. Electrodes are placed along the sides of the sensing element. Flexi-distortional devices are tested in order to check for the limits of sensitivity in their performance.

### COMPARISON OF $d_h$ PERFORMANCE

The hydrostatic piezoelectric coefficient,  $d_h$ , is determined from applying uniform pressure to all surfaces of the piezoelectric element. Each piezoelectric coefficient governs the charge generated at the electroded surface from the stress applied in each direction. For the monolithic sensor using poled ceramic (conical symmetry) the  $d_h$  coefficient is  $d_{33} + d_{31} + d_{32}$ . For a 1-3 ceramic/polymer composite the objective is to minimize the effect of the  $d_{31}$  and  $d_{32}$  coefficients, thereby causing the  $d_h$  coefficient to approach  $d_{33}$ .

In flexi-distortional (shear) sensors, hydrostatic pressure is redirected and mechanically amplified, thereby creating high lateral internal stresses in the sensor. This lateral stress counters the lateral hydrostatic pressure change. For devices with this internal amplification, the lateral hydrostatic pressure change may, in some cases, be neglected. Overall, there is a positive contribution to the surface charge polarization from the internal stress distribution on the  $d_{15}$  coefficient.

The hydrostatic pressure produces the lateral internal stress,  $-np$ , where the hydrostatic pressure is multiplied by the lateral amplification,  $n$ . This stress is redirected laterally and causes the net lateral stress of  $-np+p$ . The compression and flexural motion in a low angle cap over a lower pressure chamber transmits the stress to the sensing element. The flexi-designs have a greater width than depth, and, therefore, include a further effect for greater force from one direction. The amplification,  $n$ , includes the geometry of the device cap area, the cap slope, and the sensor cross sectional area. In the flexi-distortional design the transverse polarization developed is:

$$P_1 = d_{15}(p-np) \quad (1)$$

After dividing by the pressure change,  $p$ , the hydrostatic piezoelectric coefficient is found. Therefore, for flexi-distortional sensors with large  $n$ ,  $d_h$  is  $nd_{15}$ , or approximately  $n/2 d_{33}$ , when  $d_{15}$  equals  $3/2 d_{33}$ . In flexi-distortional sensors, the amplification,  $n$ , is governed by the sensor shear area. If the shear area is equal to the cross sectional area, then the theoretical  $d_{hg}$  or  $(nd_{15})^2/K_1\epsilon_0$  can be approximately 9/4 greater for the flexi-distortional sensors than for flexi-dilatational sensors. For PZT with  $d_{33}$  equaling 370 pC/N,  $d_{15}$  equaling 550 pC/N, a  $K_3$  equaling 1700, and an  $n$  equaling 3, flexi-distortional figure-of-merit performance is predicted to be  $184,000(10^{-15} \text{ m}^2/\text{N})$ .

### FLEXI-DISTORTIONAL "RIBBIE" MECHANICS

In Figure 1, the force,  $F$ , is applied to the top side of an elliptical tube placed in grooves in an articulated PZT plate. The tube transmits a lateral force to the vertical side members projecting from the plate. The short vertical members represent the sensor elements. These are electroded on the sides and collect charge from the shearing motion of the sensor. The inside of the tube is at a lower pressure because the ends of the tube have been sealed and isolated from the surrounding fluid pressure. A shallower ellipse results in greater amplification of the applied force. The force amplification is simply the ratio of the major to minor axis of the ellipse,  $r$ . The stress transmitted to the ceramic is thus  $r F/A$ , where  $A$  is shear area of the ceramic sensor. If  $F$  is equal to the hydrostatic pressure multiplied by the tube surface area, or  $pA_{cap}$ , then the shear stress acting

on the sensor is  $rpA_{cap}/A$ . The  $rA_{cap}/A$  is the stress amplification factor  $n$ . The polarization is found by multiplying the piezoelectric shear coefficient,  $d_{15}$ , by  $rpA_{cap}/A$ . The elliptical tube and the material stiffness can also be incorporated into the mechanics to give the deformations of the device, and the change of the internal energy.

The amplification mechanism may employ a long plate, or other stiffener rather than an elliptical tube. These designs and numerical stress calculations have previously been described[1]. Each design, however, must be capped near the ends to prevent internal pressurization which would negate the force amplification. For long device lengths this end restraint will not result in significant performance deterioration. Normal piezoelectric coefficients are not activated in these flexi-distortional devices because only side electrodes are employed, and, ideally only shear stress is developed perpendicular to the direction of poling.

### CALCULATION OF FLEXI-DISTORTIONAL DEVICE STRESSES AND POLARIZATIONS

Device stresses may be estimated based upon formula found in strength of materials literature[2]. These stresses can be used to estimate the device polarization, and, to compare with the stress limitations of materials used in the device.

The "ribbie" device may be modeled as a three hinged arch, Figure 2, using thin plates for the cap, and, with hinges at the apex and at the edges above the ceramic. This configuration will amplify the applied pressure,  $p$ , and produce a lateral reaction stress of  $-pL/2t \tan\theta$ . These stresses are then transferred to the sensor element where shear stresses are induced. Shear stresses are partially compensated by lateral pressure from the surrounding fluid. The value of the shear stress can be calculated by multiplying the lateral reaction stress by the ratio of the plate thickness to the sensor width,  $t/w$ . For the tubular configuration tested in this work, the plate slope,  $\tan\theta$ , equals  $1/3$ , plate length equals  $3t$ , sensor width  $w$  equals  $t$ , and height  $h$  equals  $2t$ , this results in an amplification of 9. The high cap slope necessitates reducing this amplification because of significant lateral hydrostatic pressure on the cap. Using the three hinged arch formula for large  $\theta$ , this results in a reduction of the amplification by approximately 10%. The shear stress at the top of the sensor is then  $8p$ .

### INITIAL RESULTS

Bent brass sheet shear sensors, as shown in Figure 2, were tested to check the potential performance of flexi-distortional type sensors. These tests consisted of Berlincourt measurements of the effective  $d_{33}$  response that develops in the "RIBBIE" type device from the amplification of stress on the  $d_{15}$  coefficient. The brass sheet slope was approximately a 1 to 3 ratio, with an effective amplification limited to a theoretical value of 8 as indicated by the above calculations. Previous numerical stress calculations [1] indicate that the actual shear stress is limited to approximately half this value. Therefore, the maximum lateral stress amplification is approximately 4, and the maximum effective  $d_{15}$  coefficient is approximately 4 times the unamplified  $d_{15}$  coefficient for a maximum sensitivity of 2000 pC/N. Actual electrode area limitations result in a 2/3 reduction as calculated from the sensor height to cap width ratio, leading to an overall sensitivity of approximately 1300 pC/N. Several configuration of these shear devices were tested. Initial tests in air have proven that effective  $d_{33}$  responses of  $\sim 1000$  pC/N at 100 hz are possible. Hydrostatic tests were performed at low pressures of less than 8 kPa. These tests yielded  $d_h$  values of  $\sim 100$  pC/N. Frequency response is expected to be lower in shear type devices as compared to the "moonie" type. PZT5-H ceramic with brass sheet were used in all tests.

The amplified  $d_{15}$  measurements can be used to estimate "ribbie"  $d_{hg}$  performance. This is calculated from the theoretical amplification as  $d_{15}$  squared divided by the permittivity. The theoretical performance is then estimated to be  $110,000(10^{-15} \text{ m}^2/\text{N})$  if the amplified  $d_{15}$  is 1300 pC/N. In the hydrostatic tests the actual  $d_h$  results in a performance of

$d_{11}^2$  divided by the permittivity of PZT of 650 ( $10^{-15} \text{ m}^2/\text{N}$ ) is much lower than the estimate of that provided by the above theoretical Berlincourt measurements. Though we are significantly below theoretical expectations, there are many design changes that have been identified which should affect the performance of these sensors.

### CONCLUSIONS

The performance of "RIBBIE" brass sheet shear sensors have been evaluated. Theoretical stress calculations show that they develop a stress amplification of approximately 9. Limitations of electrode surface area produces an effective  $d_{15}$  coefficient of 3 times the unamplified  $d_{15}$ . Hydrostatic tests have been limited, but indicate that shear devices can be constructed and may be practical. The longer geometries may increase the hydrostatic response by eliminating the end clamping due to the end brass plates. Testing of these brass sheet shear devices have led us to conclude that they are feasible for hydrostatic applications, and may improve the manufacturability of composite sensors.

### REFERENCES

1. W. B. Carlson, W. A. Schulze, R. E. Newnham, L. E. Cross, "Flexi-Distortional Piezoelectric Composites," *Ferroelectrics*, in review.
2. R. J. Roark and W. C. Young, "Formulas for Stress and Strain," 5th ed., New York, McGraw-Hill, 1975.

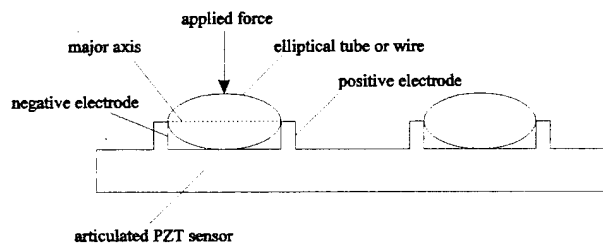


Figure 1. A schematic of the shear sensor depicting placement of the elliptical tube in the grooved PZT to activate the shear response from a compressive load.

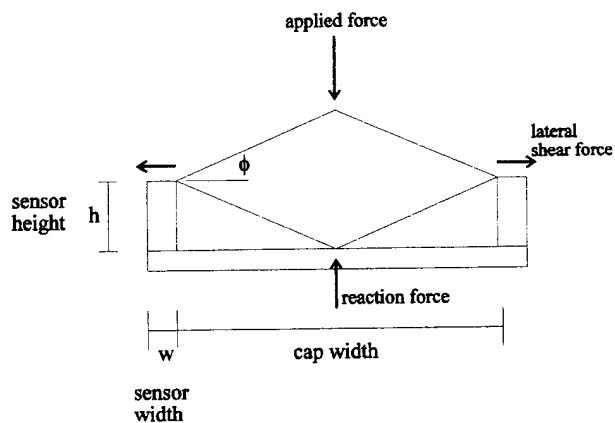


Figure 2. The shear sensor model showing geometry and applied force used for calculating the reaction lateral shear force.



# Poster Session - P5: Photorefractives

# PHOTOREFRACTIVE PROPERTIES OF Cr/Mo CO-DOPED SBN:60

Gary L. Wood, Brian P. Ketchel  
Department of Army  
Army Research Laboratory  
Fort Belvoir, VA 22060-5028

R.R. Neurgaonkar  
Rockwell Science Center  
1049 Camino Dos Rios  
P.O. Box 1085  
Thousand Oaks, CA 91360

**Abstract**—The effect on the photorefractive and optical properties by varying Cr and Mo dopant concentrations equally in co-doped SBN:60 is investigated. We report the effect on the absorption, two-beam coupling, speed of response, and diffraction efficiency. From these measurements the role of the donor and acceptor density is determined.

## Introduction

The doping of photorefractive crystals, and specifically strontium barium niobate ( $\text{Sr}_{1-x}\text{Ba}_x\text{Nb}_2\text{O}_6:1-x$ ), can enhance the photorefractive performance in several ways. Dopants can affect the photorefractive gain, time response, and spectral response, amongst other things. Doping can also increase the absorption, not always a desirable feature for an optical device. Photorefractive optical devices may require particular combinations of gain, speed and absorption [1]. This amount of control requires a good understanding of the role the dopant is playing in the photorefractive effect.

The photorefractive effect requires some mechanism for charge migration in the presence of light. Doping offers a convenient method to provide the necessary charges. By entering the bandgap at an intermediate energy from the valance and conduction band both light generated holes and/or electrons can be generated. One popular model, that fits Ce doped SBN:60 well, has the Fermi level midway between the donor and acceptor level. The acceptor level is then fully compensated with some charges left in the donor level if the donor density is larger than the acceptor density,  $N_D > N_A$ . This simple model involves only two dopant levels, however shallow traps are often present that are very thermally active and compete with light as a mechanism for charge excitation. This causes some of the constants in the two level model to have an intensity dependence. Since the donor and acceptor densities describe photorefractive in SBN:60 control of these densities will control the photorefractive properties of SBN:60. A single dopant, Ce for example, is effective in enhancing the photorefractive properties of SBN, but to date there is no control over  $N_D$  and  $N_A$  with the single dopant. The motivation for co-doping SBN is to achieve some influence over  $N_D$  and  $N_A$  separately. It is believed that Cr will enter the crystal as a donor and Mo as an acceptor. To test this hypothesis we performed various experiments to understand the role of Cr and Mo on  $N_D$  and  $N_A$ .

## Experimental

Four SBN:60 crystals grown by the Czochralski method were used in this study with varying dopant concentrations. Two 0.03% total weight (0.015% Cr/0.015% Mo), and one each of 0.02% and 0.01% total weight also at equal concentrations, 1:1 Cr to Mo. The concentration in weight % here represents the amount of Cr or Mo (in grams) for every 100 g of SBN:60 put into the

starting melt, and assumes the fraction of dopant in the starting materials is the same as the grown crystals. The two 0.03% weight crystals were different in size. One was a thin crystal plate and the other a thicker cube. The cube dimensions of the highest weight dopant to the lowest were; 6.12 mm, 6.2 mm, and 6.4 mm. The crystal plate had the dimensions 6 x 6 x 1.025 mm. All had a pale yellow color with no visible striations. All the crystals were poled in the usual fashion. A cw Ar-ion laser operating at 488 nm was used. Since the gain was measured versus intensity the output power varied from 13 to 86 mW. The Gaussian spot size at the crystal was 1.4 mm half width  $e^{-2}$  maximum. In order to avoid beam fanning the polarization was kept ordinary with respect to the crystals. The absorption of each crystal was measured from the measured transmission and reflectivity. It was found that the absorption increased with intensity for all the crystals. The measured reflectivity did not match the predicted value based on the ordinary index of refraction,  $n_0$ , for the plate and was about 13% off for the 0.02% weight crystal. This is most likely due to poor surface quality.

The photorefractive gain as a function of angle and intensity were measured by the two-beam coupling experiment outlined in reference [2]. The ratio of the input crossing beams was  $\beta = I_{\text{weak}}/I_{\text{strong}} = 0.00178$ . The gain,  $\Gamma$ , was measured with no applied electric field. Since the electro-optic coefficients are positive and the beam fanned to the negative c-axis the charges are predominantly electrons. No coupling was observed with beams bisecting the c-axis so the measured gain is mostly derived from the electro-optic coefficients. Because of the small ratio of  $\beta$  the gain can be fit to the analytical expression in reference [2]. By fitting the gain curves we were able to derive the effective charge density and the electron-hole competition at each dopant level using  $r_{13} = 55$  pm/V and  $n_0 = 2.40$  and  $\epsilon_{33} = 1000\epsilon_0$ , see Table 1. Most likely the intensity dependence in the absorption and the gain is due to the presence of shallow traps.

The diffraction efficiency as a function of decay time was measured with the two-beam coupling experiment by simply blocking the weak beam into the detector and measuring the diffracted beam decay. This method is useful in that it is simple, being automatically Bragg matched, and ensures the erase beam is well characterized. But care needs to be used because it is possible to rewrite the gratings while erasing, which gives a longer decay [3]. We found there is no significant self-enhancement for gain-lengths less than 2, which we were careful to observe. Since we measured the whole Gaussian spatial beam, and the equations for the decay time assume plane waves, the decay time was modified

from a simple exponential to  $\eta(t) = \eta_{H-S} \left[ \frac{\tau}{t} (1 - e^{-t/\tau}) \right]^2$ , where  $\tau$

is the response time [4] and  $\eta_{H-S}$  is the steady-state diffraction formula given by Hong and Saxena [5] when there is gain. By using

the values found from two-beam coupling in the steady-state diffraction formula the theoretical diffraction fit closely to the experimentally measured value. This indicates the phase difference between the intensity grating and the index grating is small since the diffraction efficiency depends on the magnitude of the index change and not only the imaginary part, as the gain does. This is an indication there is no photovoltaic effect present. The time response of the cubes was measured at the angle  $\theta = 7.7^\circ$  to the crystal normal and at the intensity  $I = 0.455 \text{ W/cm}^2$ , see Table 1. The time response as a function of intensity for the 0.03% weight cube was also measured. A good fit to the inverse time response was found by assuming the grating spacing is much larger than the electron transport length and the Debye screening length. The fit also required using a dark decay time of  $\tau_d \sim 4\text{s}$ , including a linear intensity dependence for the acceptor density and using the measured intensity dependence of the absorption.

CRYSTAL	POLARIZATION	MAX. GAIN (cm <sup>-1</sup> )	POWER (mW)	FE	$N_{\text{eff}} \times 10^{16} \text{ (cm}^{-3}\text{)}$	DIFF. EF. $\eta = I_d/I_{\text{thr}}$	DECAY TIME (sec)	$\alpha \text{ (cm}^{-1}\text{)}$
MnM, (Cr/Mo) 0.03%, L = 1.025 mm, 1.1	extraord. pol.	~21	13	0.925	3.27			
	"	~22	45	0.846	4.8			
	"	~23	86	0.824	5.7			
MnM, (Cr/Mo) 0.03%, L = 6.12 mm, 1.1	ord. pol.	~3	13	0.57	2.52	0.00252 Exp	1.23 @ 1 - 0.445 W/cm <sup>2</sup> , 15.4°	1.45 + 0.0231(I/W/cm <sup>2</sup> )
	"	~3.2	45	0.51	3.54	~0.003 Theory	FECA	
	"	~3.3	86	0.48	4.24			
MnM, (Cr/Mo) 0.02%, L = 6.2 mm, 1.1	ord. pol.	~2	13	0.43	2.14	0.001445 Exp	0.826 @ 1 - 0.455 W/cm <sup>2</sup> , 15.4°	1.09 + 0.0224(I/W/cm <sup>2</sup> )
	"	~2.4	45	0.46	2.435	0.00145 Theory	FECA	
	"	~2.6	86	0.47	2.64			
MnM, (Cr/Mo) 0.01%, L = 6.4 mm, 1.1	ord. pol.	2.1	13	0.52	1.50	0.001139	0.675 @ 1 - 0.455 W/cm <sup>2</sup> , 15.4°	0.684 + 0.0261(I/W/cm <sup>2</sup> )
	"	2.4	45	0.5	1.95			
	"	2.5	86	0.49	2.3			

Table 1. Summary of the properties of the four crystals

## Discussion

It is not possible to determine  $N_A$  and  $N_D$  from the data collected unless certain assumptions are made. However, we can determine some features of the dopant concentration on  $N_A$  and  $N_D$  from the data. For instance, Figure 1 shows the measured quantity

$$N_{\text{eff}}(I)/\alpha(I) = \frac{\Phi N_A}{s N_D} \text{ versus the weight \% dopant for three}$$

different intensities [6]. The quantum efficiency is given by,  $\Phi$ , and  $s$  is the absorption cross section. A straight line would indicate that as dopant concentration is increased the donor density increases in the same proportion to the acceptor density. A slight decrease with increasing dopant indicates  $N_A$  is not keeping up with  $N_D$ , but the deviation is small and for the  $2.79 \text{ W/cm}^2$  intensity case the change is barely noticeable. (It is interesting to note the electron-hole competition is most changed with intensity at the 0.03% dopant level which correlates with an increase in the acceptor density). Either the dopants are working as anticipated or the presence of one alone increases both donor and acceptor densities equally. Another quantity of interest is the shown in Figure 2. Here the time response increases (slows down) with dopant concentration. If we ignore the dark decay compared to the intensity decay the time response should depend on the acceptor density alone. Hence the increase shows that  $N_A$  is increasing as we already suspected from Figure 1.

It is planned to repeat Figures 1 and 2 for various weight

concentrations of the Cr dopant alone. If the same general features are observed then the Cr dopant alone is acting in the role of the acceptor and donor and in such a way that both are proportional to the weight percent. If Cr is indeed responsible for the donor alone then the  $N_{\text{eff}}/\alpha$  plot should fall off with increasing dopant concentration. Since  $N_D \propto \text{weight \%}$  if the weight % increases by 2 then  $N_{\text{eff}}/\alpha$  should fall by one half. Also, the time response should not be affected much with increased dopant concentration, being dependent on  $N_A$  alone.

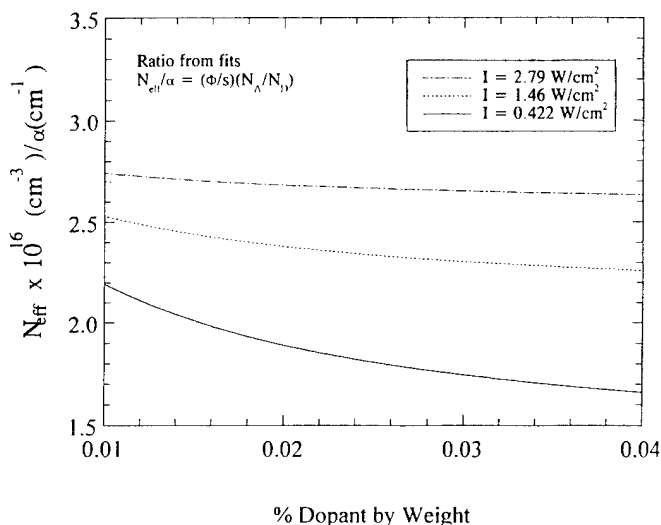


Figure 1. Ratio of  $N_{\text{eff}}/\alpha$  versus % dopant by weight.

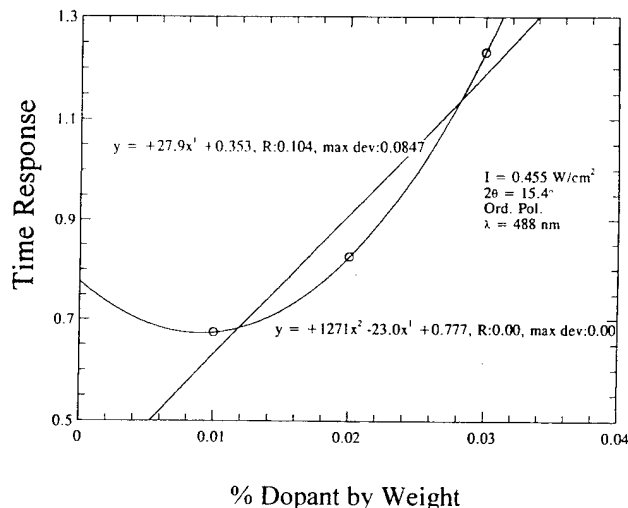


Figure 2. Time response,  $\tau$ , versus % dopant by weight.

## References

- [1] G.L. Wood, W.W. Clark, III, G.J. Salamo, A. Mott, and E.J. Sharp, "Fluence Limiting via Photorefractive Two-Beam Coupling," J. Appl. Phys., vol. 71, 37 (1992).
- [2] G.L. Wood and R.R. Neurgaonkar, "Photorefractive and Optical Properties of Cerium-Doped  $(\text{SrCa})_2\text{NaNb}_5\text{O}_{15}$ ," J. Opt. Soc. Am. B, vol. 11, 1211 (1994).
- [3] J. Otten, A. Ozols, M. Reinfelde, and K.H. Ringhofer, "Selfenhancement in Lithium Niobate," Optics Commun., vol. 72, 175 (1989).
- [4] R. Jaura, T.J. Hall, and P.D. Foote, "Simplified Band Transport Model of the Photorefractive Effect," Opt. Eng., vol. 25, 1068 (1986).
- [5] J.H. Hong and R. Saxena, "Diffraction Efficiency of Volume Holograms Written by Coupled Beams," Opt. Lett., vol. 16, 180 (1991).
- [6] The 0.03% plate had a larger  $N_{\text{eff}}$  than the cube. This difference is most likely due to the different location within the boule each was cut from. This highlights the possible role of oxygen diffusion which was not controlled in this experiment. Consequently, the plate values are not included in Fig's 1 & 2.

# Flux growth of bulk photorefractive barium titanate crystals

M.D. Aggarwal, W.S. Wang and J. Choi  
Department of Physics  
Alabama A&M University, Normal, AL 35762

## ABSTRACT

Single crystals of pure and  $\text{Cr}^{3+}$  doped barium titanate ( $\text{BaTiO}_3$ ) have been grown by top seeded solution growth technique (TSSG). TSSG system consists of a resistance heated super kanthal cylindrical furnace capable of temperatures upto  $1540^\circ\text{C}$  alongwith crystal rotation and pulling arrangement. According to the phase diagram, 65 mol%  $\text{TiO}_2$  is mixed with 35 mol%  $\text{BaO}$  to have a molten flux at  $1460^\circ\text{C}$ . We typically have grown 20-39 g boules from 300 g of melt in a 100 ml platinum crucible. Polished and poled cubes as large as  $15 \times 15 \times 10 \text{ mm}^3$  have been successfully fabricated.

## INTRODUCTION

Barium titanate- $\text{BaTiO}_3$  is one of the most promising electrooptic, photoconductive and photorefractive materials for a variety of applications that include optical phase conjugation, signal processing and for fundamental studies [1-4]. Barium titanate is normally grown by the top seeded solution growth (TSSG). This method combines several advantages of Czochralski technique and solution growth. A novel gradient transport technique and modified "Remeika" technique for  $\text{BaTiO}_3$  crystal growth are also reported [5,6]. The barium titanate crystal growth of high quality and single domain samples, however, is complicated by a sequence of structure phase transitions and its physico-chemical properties. Current efforts at understanding the microscopic origins of photorefractive effect are directed towards improving material sensitivities and decreasing the response time by suitable doping and growing bulk  $\text{BaTiO}_3$  single crystals. A number of pure and  $\text{Cr}^{3+}$  doped  $\text{BaTiO}_3$  single crystals have been grown in our laboratory using the TSSG method. This paper discusses the limiting conditions for  $\text{BaTiO}_3$  single crystal growth. The crystal color and inclusions in our experiment are also described.

## EXPERIMENTAL PROCEDURE

A top seeded solution growth system has been designed and fabricated. This system consists of a resistance heated super Kanthal cylindrical furnace capable of temperatures up to  $1540^\circ\text{C}$  alongwith a crystal rotation and pulling arrangement. The schematic diagram of TSSG system is shown in Fig. 1.

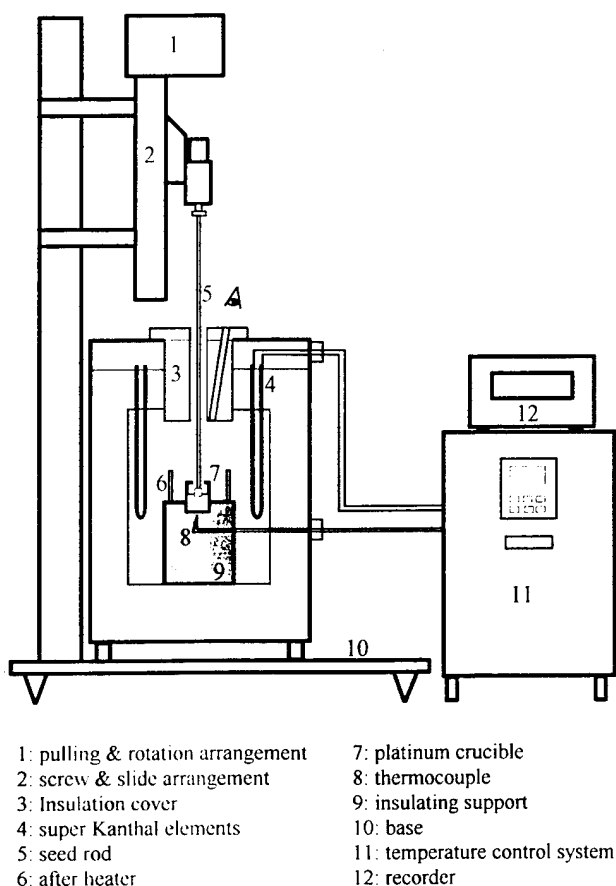


Fig. 1. Schematic diagram of top seeded solution growth system



The starting composition is selected near the eutectic as shown in Fig. 2 [7].

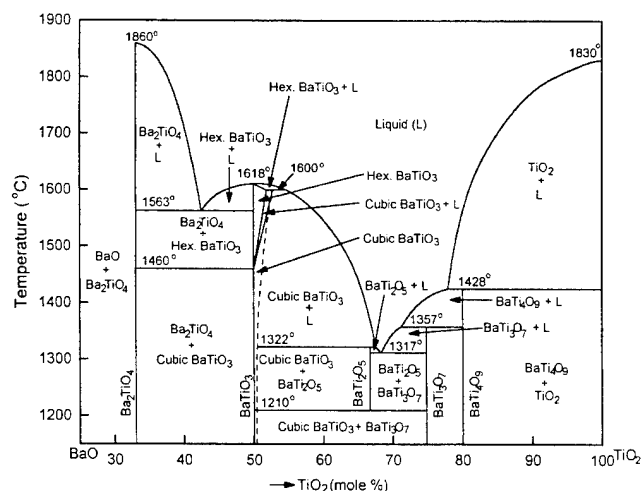


Fig. 2. Equilibrium phase diagram of BaO-TiO<sub>2</sub> system

It can be seen that it may be possible to grow BaTiO<sub>3</sub> crystal from nonstoichiometric melt containing an excess of TiO<sub>2</sub> in the temperature range 1400-1330°C and this technique will avoid crystallization of the hexagonal phase of BaTiO<sub>3</sub>. According to the phase diagram, a starting composition is around 65 mol% TiO<sub>2</sub> + 35 mol% BaO. The melt is contained in a platinum crucible measuring 2 inch in diameter and 2 inch in height most of which is embedded in thermal insulation. Melts are prepared using Johnson-Matthey Puratronic grade BaTiO<sub>3</sub> and TiO<sub>2</sub> powders. In a typical growth run, the melt is soaked for several hours at 1460°C and subsequently cooled down to near 1400°C. The seed orientation is <100> or <001> and then brought in contact with the melt and rotated at 50-60 rpm. After initial homogenization a seed is brought in contact with the melt and slowly pulled at a rate of 0.1 mm/h. The furnace is cooled at a rate of 0.2-0.5°C/h. When the temperature comes close to the eutectic around 1332°C, the grown crystal BaTiO<sub>3</sub> is pulled out of the melt and cooled at 10°C/h. Cooling rate must be very slow (about 1°C/h) while crossing the cubic to tetragonal phase transition near 132°C. We have been able to grow undoped and Cr<sup>3+</sup> doped BaTiO<sub>3</sub> crystal boules weighing 14-39g in 100 cc platinum crucible. A photograph of the few crystals grown in our laboratory is shown in Fig. 3.

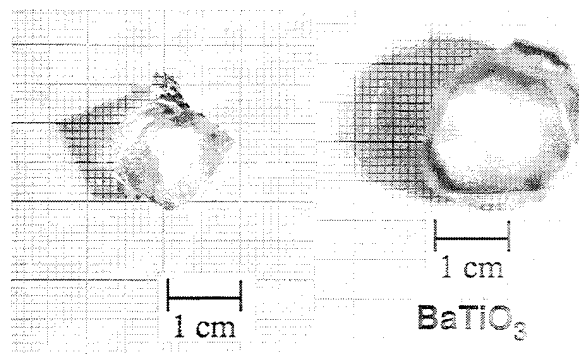


Fig. 3. A photograph of BaTiO<sub>3</sub> crystals grown by top seeded solution growth technique

## RESULTS AND DISCUSSION

### TSSG TECHNIQUE

TSSG technique was originally developed at M.I.T. [8]. Most photorefractive crystals, however, have been grown by this method. Authors deem that there is no essential distinction between Czochralski and TSSG techniques. Some crystals melting incongruently (KNbO<sub>3</sub> etc) can be grown by Czochralski technique below the decomposition temperature [9,10]. The temperature gradient and cooling rate can be changed to induce crystallization. A novel three thermal zone flux method for the growth of BaTiO<sub>3</sub>, KTa<sub>1-x</sub>Nb<sub>x</sub>O<sub>3</sub> and etc is reported [6].

### INCLUSIONS AND COLOR IN BaTiO<sub>3</sub> CRYSTALS

During the BaTiO<sub>3</sub> crystal growth the shape of the crystal-melt interface and pulling rate strongly influence the formation of inclusions. It is well known that the concave interface and high pulling rate are easy to capture inclusions. Moreover, the inclusions induce domains to form. In BaTiO<sub>3</sub>, the 90° domains or twins will form because of inelastic stress from a structural misfit at the phase boundary. 180° domains form to maintain electrical neutrality if the phase boundary velocity is too high and the surface charge density too low [11]. When the composition of starting materials is the same but different melt soaking temperatures are used, the resulting crystals will have different colors. For instance, when the temperature of the melt is lower than 1400°C, BaTiO<sub>3</sub> crystals will show a dark color, but they will be yellowish when the temperature is higher than 1460°C. In addition, as the seed is withdrawn from the melt at a relatively low temperature, then a blue

region will occur around the seed crystal, but the growing crystal will gradually become yellow or even nearly light yellow. The formation mechanism and relation to soaking temperature are being studied now.

#### SEED ORIENTATION AND CRYSTAL GROWTH MORPHOLOGY

The seed orientation  $\langle 001 \rangle$  or  $\langle 110 \rangle$  can be used. For  $\text{BaTiO}_3$  crystal growth along  $\langle 001 \rangle$  direction, the major facets  $\{100\}$  and  $\{110\}$  were observed. However, usually the  $\{100\}$  facets were accompanied by less developed  $\{110\}$  facets. In practice the  $\langle 001 \rangle$  is the preferred seed orientation over  $\langle 110 \rangle$ . The growth rate on (110) faces was greater than that on (001) faces.

Further studies on  $\text{BaTiO}_3$  crystal growth morphology, poling and the photorefractive properties are in progress.

#### ACKNOWLEDGMENTS

The authors express their thanks to Mr Lloyd Sharp for his machine work in the construction of the TSSG system. This work was supported by National Science Foundation Minority Research Center of Excellence through their project HRD-9353548.

#### REFERENCES

- [1] R.S. Cudnay, J. Fousek, M. Egonik, P. Günter, M.H. Garrett and D. Rytz, "Photorefractive and domain gratings in barium titanate" *Appl. Phys. Lett.* 63, pp.3399, 20 Dec 1993.
- [2] P. Günter and J. P. Huignard, "Photorefractive Materials and their applications II", Springer Verlag, Heidelberg, FRG 1988
- [3] Daniel Rytz, Barry A. Wechsler, Mark H. Garrett, Charles C. Nelson and Robert N. Schwartz, "Photorefractive properties of  $\text{BaTiO}_3\text{:Co}$ " *J. Opt Soc Am., B*, 7(12), pp. 2245 December 1990.
- [4] R.N. Schwartz and B.A. Wechsler, "EPR, Optical and Electronic structure studies of photorefractive barium titanate" *J. Am. Ceram. Soc.*, 73(11), pp. 3200, Nov 1990.
- [5] R.C. Bradt and G.S. Ansell, "Growth of Barium titanate single crystals by a modified "Remeika" technique", *Mat. Res. Bull.* 2, pp. 585, April 1967.
- [6] J. Wang, X. Ma, S. Zhang, W.Hu, Z. Zhao, X. Zhang, J. Xu and Q. Guan, "Application of a novel technique for growing  $\text{BaTiO}_3$  and KTN crystals", *Cryst. Res. Technol.*, 28(4), pp. 457 December 1993.
- [7] D.E. Rase and R.J. Roy, "Phase diagram of the  $\text{BaO-TiO}_2$  system" *J. Am Ceram. Soc.*, 38(3), pp102, 1955.
- [8] D. Rytz, B.A. Wechsler, C.C. Nelson and K.W. Kirby, "Top seeded solution growth of  $\text{BaTiO}_3$ ,  $\text{KNbO}_3$ ,  $\text{SrTiO}_3$ ,  $\text{Bi}_{12}\text{TiO}_{20}$  and  $\text{La}_{2-x}\text{Ba}_x\text{CuO}_4$ " *J. Cryst. Growth* 99, pp. 864, 1990.
- [9] W.S. Wang, Q. Zou and Z.H. Geng, "The potassium niobate single crystals grown by the rf heating Czochralski technique", *J. Chinese Silicate Soc.* 10, pp. 406, 1982.
- [10] W.S. Wang, Q. Zou and Z.H. Geng, "Investigation of the color of  $\text{KNbO}_3$  single crystals grown by the rf heating Czochralski technique", *J. Cryst. Growth* 83, pp. 62 January 1987.
- [11] M.H. Garrett, J.Y. Chang, H.P. Jenssen and C. Warde, "A method for poling Barium titanate,  $\text{BaTiO}_3$ " *Ferroelectrics* 120, pp. 167, June 1991.

Masatoshi ADACHI, Zhiming CHEN and Akira KAWABATA

Department of Electronics & Informatics, Faculty of Engineering, Toyama Prefectural University,  
Kosugimachi, Toyama 939-03, Japan

**Abstract** —  $K_3Li_2Nb_5O_{15}$  (KLN) Single crystals have been grown by the rf heating Czochralski technique from a melt with the potassium and lithium enriched composition, 35 mole % of  $K_2CO_3$ , 17.3 mole % of  $Li_2O_3$ , and 47.7 mole % of  $Nb_2O_5$ . Optimum growth conditions were a pulling rate of 1 mm/h and rotation rate of 25 - 30 r.p.m.. The pulling axis was chosen in parallel to the  $[110]$  axis in order to minimize the cracking during the growth. Transparent and pale-yellow crystals up to 10mm in diameter and 20 mm in length were obtained. Dielectric constants  $\epsilon_{11}^T$  and  $\epsilon_{33}^T$  at room temperature were 318 and 106, respectively. the constant  $\epsilon_{33}^T$  showed a marked anomaly at the transition point of  $430^\circ C$ . Pyroelectric constant  $p$  at room temperature was determined as  $80 \mu C/m^2 K$  from the pyroelectric current method. Resistivity  $\rho$  showed a small change at the phase transition temperature. Further, it was found that the addition of small amount of Na to KLN results in more preferable electrooptic and nonlinear-optic behaviors than those of pure KLN.

## INTRODUCTION

Among various ferroelectric materials, a number of ferroelectric niobates having a tetragonal or related orthorhombic tungsten-bronze structure such as  $Ba_2NaNb_5O_{15}$  (BNN),  $(Sr,Ba)Nb_2O_6$  (SBN),  $Ba_{2-x}SrK_{1-y}Na_yNb_5O_{15}$  (BSKNN),  $(Pb,Ba)Nb_2O_6$  (PBN),  $Pb_2KNb_5O_{15}$  (PKN) and this  $K_3Li_2Nb_5O_{15}$  (KLN) have attracted much attention due to their potential applications in electrooptic, nonlinear optic and piezoelectric devices [1-8]. The tungsten-bronze structure is characterized by a framework of  $BO_6$  octahedra sharing the corners with each other, and is represented by general chemical formula  $(A_1)_2(A_2)_4C_4(B_1)_2(B_2)_8O_{30}$  corresponding to the contents of unit cell with an approximate dimension of  $a \times b \times c = 4.0 \times 4.0 \times 12.5 \text{ \AA}$ . One of the tungsten-bronze ferroelectrics, KLN was discovered by Van Uitert et al. in 1967 [6]. A KLN is a typical tetragonal ferroelectric material of completely filled tungsten-bronze structure with a point group  $4mm$ . All the  $A_1$  and  $A_2$  sites are filled with K and all the  $c$  sites are filled with Li. However, detailed phase equilibrium study of the  $K_2O - Li_2O - Nb_2O_5$  ternary system was carried out by Scott et al. [9] and Ikeda et al. [10]. Ferroelectric tungsten-bronze type phase spreads toward the Nb-rich regions where the  $Nb_2O_5$  concentration is 0.51 to 0.55, and the tungsten-bronze phase does not occur with completely filled alkalication sites at the composition  $K_3Li_2Nb_5O_{15}$ . So far, crystal growth of KLN has been successfully attempted by various people for several different purposes [6-13]. However, the growth of these crystals in decent sizes and quality is generally difficult because of complex compounds and high melting temperatures. Nevertheless, the tungsten-bronze materials mentioned above are still attractive and important from applications points of view in the fields of optics and electrooptics in the near future.

In our earlier studies on the KLN tungsten-bronze crystals and their thin films, crystal growth and piezoelectric properties of bulk crystals were reported [7]. The electromechanical coupling factor in KLN were  $k_{15}=0.34$ ,  $k_{31}=0.18$  and  $k_{33}=0.52$ . The growth of single crystal KLN films for optical waveguides fabricated with good epitaxy on various crystal substrates such as tungsten-bronze potassium bismuth niobate (KBN) and sapphire substrates by the epitaxial growth of melting (EGM), the liquid-phase epitaxial

growth (LPE) and the sputtering methods were also reported [14].

In this paper, crystal growth of KLN and Na doped KLN and their properties are described.

## EXPERIMENTAL PROCEDURES

Single crystals of KLN were grown by the Czochralski technique from melts using SEREC 90032 crystal growth system with an ADC system. The raw materials used in this study were  $K_2CO_3$  of 99 %, and  $Li_2CO_3$  and  $Nb_2O_5$  of 99.99 % purity. These oxides were mixed in nonstoichiometric proportion with potassium and lithium enriched composition, 35 mole %  $K_2CO_3$ , 17.3 mole %  $Li_2O$ , and 47.7 mole %  $Nb_2O_5$ . The compounds were weighed out and mixed well by ball-milling in a polyethylene bottle together with methyl alcohol and partially stabilized zirconia balls of 3mm  $\phi$  for 24h. Methyl alcohol was removed by heating. After drying, the powders were calcined at  $900^\circ C$  for 3h. The calcined powders were crushed using a mortar and pestle. The mixture was loaded in the platinum crucible and melted by the rf heating. The crucible was 50 mm in both diameter and height, and was supported in an aluminum oxide crucible. A platinum after-heater was employed to reduce vertical and radial thermal gradients above the melt surface and to minimize heat losses from the crucible. As seed materials, KBN crystals were used because the crystal structures of KLN and KBN are both of the tungsten-bronze type and the melting temperature of KBN is higher by about  $250^\circ C$  than that of KLN. These tungsten-bronze structures and their axes are shown in Fig. 1. In this figure, square  $A_1$ , pentagonal  $A_2$ , octahedral B and triangular C are 12, 15, 6 and 9 coordinated, respectively. The polar axis of tetragonal ferroelectrics is the  $z$  axis. The KBN is orthorhombic on the

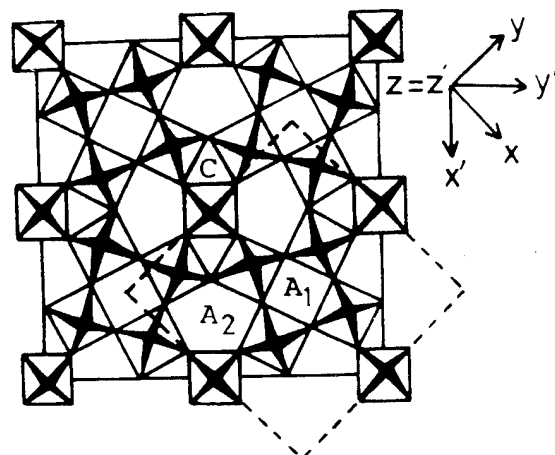


Fig. 1 The tungsten-bronze structure and reference Axes. The (001) projection of the tetragonal lattice is shown by a dashed square.

Table I Fundamental properties of KLN and KBN.

	$K_3Li_2Nb_5O_{15}$	$K_2BiNb_5O_{15}$
Symmetry	Tetragonal	Orthorhombic (Pseudo-tetragonal)
Lattice constant	$a = 12.51 \text{ \AA}$ $c = 3.97 \text{ \AA}$	$a = 17.85 \text{ \AA}$ $a = 7.84 \text{ \AA}$
Curie temperature	430°C	360°C
Dielectric constant	$\epsilon_{11}^T = 318$ $\epsilon_{33}^T = 106$	$\epsilon_{11}^T = 430$ $\epsilon_{33}^T = 500$

contrary to tetragonal in KLN. The coordinate systems (x,y,z) for KLN and (x',y',z') for KBN are compared in Fig. 1 in relation to the crystallographic axes  $a_1$ ,  $a_2$  and  $c$ . The crystallographic and fundamental properties of KLN and KBN are listed in Table I.

X-ray diffraction measurements were performed by means of a diffractometer using Ni filtered  $CuK\alpha$  radiation. Lattice constants  $a$  and  $c$  were calculated using reflection peaks in the  $2\theta=20$  to  $80^\circ$  range. Further the Laue method was used to cut the crystals with the appropriate surface.

The dielectric constants  $\epsilon_{11}$  and  $\epsilon_{33}$  and dielectric loss factor  $\tan \delta$  were measured at 1, 10, 100, and 1,000 kHz using HP 4192A LF impedance analyzer under full program control from room temperature to 600 °C. The pyroelectric constant  $p$  was detected using a YHP 4140B pA meter.

The crystals were poled by the field cooling method under a DC current of about 1.2 mA/cm<sup>2</sup> at temperature of 550 to 350 °C along the [001] axis.

## EXPERIMENTAL RESULTS

Single crystals of KLN could be grown with excess  $K_2CO_3$  and  $Li_2CO_3$  by rf-heating Czochralski method. It has been experienced that while the crystallization rate along the [001] axis is much less than those along any other attempted directions, great difficulties often encountered in obtaining large crystals in this pulling direction, due to the unavoidable occurrences of cracking. Therefore, the pulling axis is chosen in parallel to [100] or [110] axis in order to minimize the cracking during the crystal growth. The crystals obtained are elongated in the lateral direction along the [110] axis and are generally prismatic with clearly defined faces, [001] and [110]. Transparent and pale-yellow crystals up to about 10 mm in diameter and 20 mm in length were obtained. In order to determine the crystal structures of KLN, X-ray diffraction measurements were carried out. The X-ray diffraction analysis revealed that the powders prepared by crushing the crystal are of tungsten-bronze structure as shown in Fig. 2. Lattice constants  $a$  and  $c$  of the KLN crystal obtained by the X-ray diffraction measurement were 3.97 and 15.1 Å, respectively. The values are in good agreement with Bonner's data [11].

The temperature dependences of dielectric constants  $\epsilon_{11}^T$  and  $\epsilon_{33}^T$ , and dielectric loss factor  $\tan \delta$  are shown in Figs. 3(a) and (b). The dielectric constants  $\epsilon_{11}^T$  and  $\epsilon_{33}^T$  at room temperature were 318 and 106, respectively. In Fig. 3(a), the constant  $\epsilon_{33}^T$  at 10, 100 and 1000 kHz shows a marked anomaly at the transition temperature of 430°C and slightly diffuse dielectric property. The  $\tan \delta$  along the [001] axis measured at 1000 kHz is nominally dependent on temperature up to 600 °C. However,  $\tan \delta$  at 10 kHz drastically increases above 450°C. The  $\epsilon_{11}^T$  shows a small anomaly at the phase transition temperature but decreases gradually with increasing temperature as shown in Fig. 3(b). Such temperature behavior and large anisotropy for both  $\epsilon_{11}^T$  and  $\epsilon_{33}^T$  are typical of

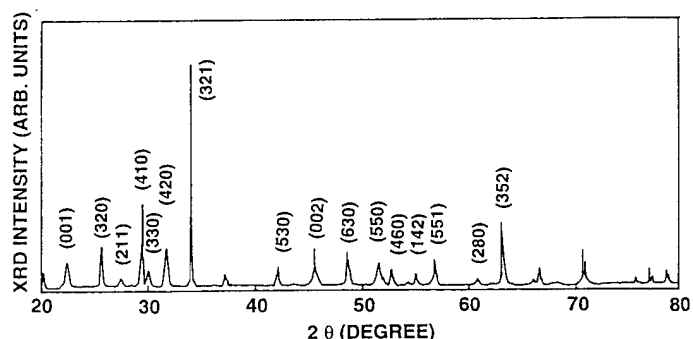
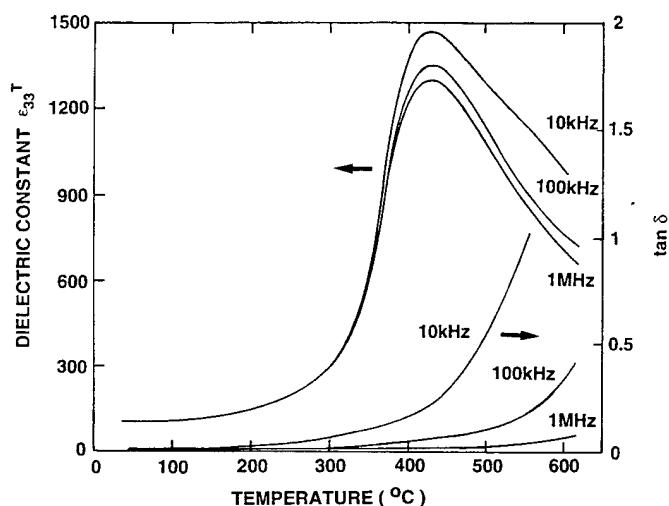
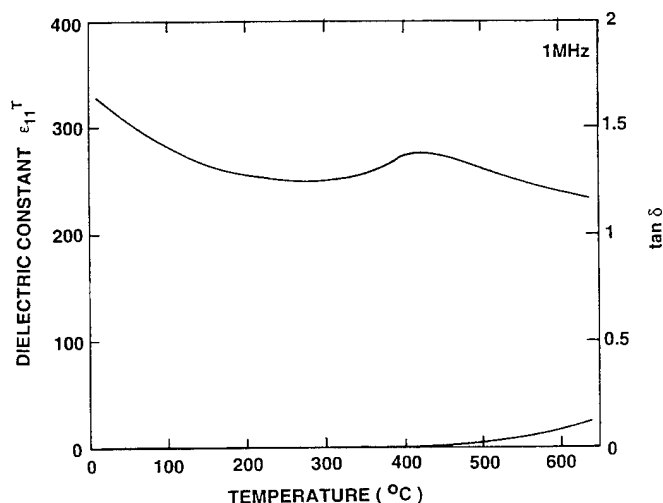


Fig. 2 XRD pattern of KLN powder.

Fig. 3(a) Temperature dependence of dielectric constant  $\epsilon_{33}^T$ .Fig. 3(b) Temperature dependence of dielectric constant  $\epsilon_{11}^T$ .

most tetragonal ferroelectric tungsten-bronzes. Figure 4 shows the resistivity along the [001] axis as a function of temperature around the phase transition temperature. As can be seen from the figure, the electrical resistivity shows an anomaly at the transition temperature depending on applied electrical fields. The pyroelectric constant  $p$  measured by the pyroelectric current method was determined as to be  $80 \mu\text{C}/\text{m}^2\text{K}$  at room temperature.

The reduced half-wave voltage  $v_\pi$  related to the electrooptic coefficient  $r_c$ , and  $r_c$  were determined as 1040 V and  $6 \times 10^{-11} \text{ m/V}$ , respectively, as shown in Table II. The electromechanical, linear electro-optic and nonlinear-optic properties of  $\text{K}_{2.7}\text{Na}_{0.3}\text{Li}_2\text{Nb}_5\text{O}_{15}$  (KNLN) crystals were investigated to clarify the influence of Na doped in KLN. It was found that the electrooptic halfwave voltage ( $v_\pi$ ) relating to the electrooptic constant  $r_c$  for KNLN was reduced to a value of 750 V, much smaller than that for KLN, by adjusting the Na concentration. Further one of the nonlinear-optic coefficients,  $d_{31}$ , of KNLN increased to 1.6 times the value for KLN. Therefore, It is concluded that the addition of small amount of Na to KLN results in more preferable electrooptic and nonlinear-optic behaviors than those of pure KLN. Further study on obtaining large and good quality single crystals of KLN and KNLN is in progress.

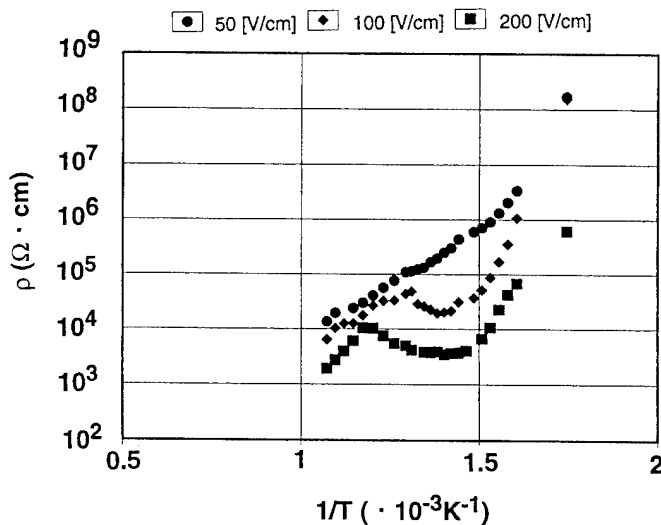


Fig. 4 Temperature dependence of resistivity  $\rho$ .

Table II Properties of KLN and KNLN.

Material	KLN	KNLN
Crystal system	tetragonal	tetragonal
Lattice const. (Å)	$a = 12.51$ $c = 3.97$	$a = 12.56$ $c = 3.98$
Melting temp. (°C)	1050	1100
Curie temp. (°C)	430	350
Dielectric const.	$\epsilon_a = 318$ $\epsilon_c = 106$	$\epsilon_a = 460$ $\epsilon_c = 320$
Refractive index	$n_o = 2.294$ $n_e = 2.156$	
Halfwave voltage (V)	1040	750

## CONCLUSIONS

KLN single crystals have been grown by the rf heating Czochralski technique from a melt with the potassium and lithium enriched composition, 35 mole% of  $\text{K}_2\text{CO}_3$ , 17.3 mole% of  $\text{Li}_2\text{O}_3$ , and 47.7 mole% of  $\text{Nb}_2\text{O}_5$ . Optimum growth conditions were a pulling rate of 1 mm/h and rotation rate of 25-30 r.p.m.. The pulling axis was chosen in parallel to the [110] axis in order to minimize the cracking during the growth. Transparent and pale-yellow single crystal up to 10 mm in diameter and 20 mm in length were obtained. Dielectric constants  $\epsilon_{11}^T$  and  $\epsilon_{33}^T$  at room temperature were 318 and 106, respectively. The  $\epsilon_{33}^T$  showed a marked anomaly at the phase transition temperature of  $430^\circ\text{C}$ , but  $\epsilon_{11}^T$  decreased gradually with increasing temperature. It was concluded that the addition of small amount of Na to KLN results in more preferable electrooptic and nonlinear-optic behaviors than those of pure KLN.

## REFERENCES

- [1] L. G. Ban Uitert, J. J. Rubin, and W. A. Bonner, 'K-1-Growth of  $\text{Ba}_2\text{NaNb}_5\text{O}_{15}$  Single Crystals for Optical Applications,' IEEE J. Quantum Electron. Vol. QE-4, pp. 622-626, 1968.
- [2] R. R. Neurgaonkar, W. F. Hall, J. R. Oliver, W. W. Ho, and W. K. Cory, "Tungsten Bronzes  $\text{Sr}_{1-x}\text{Ba}_x\text{Nb}_2\text{O}_6$ : A Case History of Versatility," Ferroelectrics, Vol. 87, pp. 167-179, 1988.
- [3] W. W. Ho, W. F. Hall and R. R. Neurgaonkar, "Dielectric Properties of Ferroelectric Tungsten Bronze  $\text{Ba}_{2-x}\text{Sr}_x\text{K}_{1-y}\text{Nb}_5\text{O}_{15}$  Crystals at RF and Millimeter Wave Frequencies," Ferroelectrics, Vol. 50, pp. 325-330, 1983.
- [4] M. Adachi, S. G. Sankar, A. S. Bhalla, Z. P. Chang and L. E. Cross, Growth and Dielectric Properties of Lead Barium Niobate Single Crystals and Morphotropic Phase Boundary," Proc. ISAF-6, Bethlehem, PA, pp. 169-171, 1986.
- [5] T. Yamada, "Elastic and Piezoelectric Properties of Lead Potassium Niobate," J. Appl. Phys., Vol. 46, pp. 2894-2898, 1975.
- [6] L. G. van Uitert, S. Singh, H. J. Levinstein, J. E. Geusic and W. A. Bonner, "A New and Stable Nonlinear Optical Material," Appl. Phys., Letters, Vol. 11, pp. 161-163.
- [7] M. Adachi and A. Kawabata, "Elastic and Piezoelectric Properties of Potassium Lithium Niobate (KLN) Crystals," Jpn. J. Appl. Phys., Vol. 17, pp. 1969-1973, 1978.
- [8] R. R. Neurgaonkar, W. K. Cory and J. R. Oliver, "Growth and Properties of Tungsten Bronze  $\text{K}_3\text{Li}_2\text{Nb}_5\text{O}_{15}$  Single Crystals," Mat. Res. Bull., Vol. 24, pp. 1025-1030, 1989.
- [9] A. Scott, E. A. Giess, B. L. Olson, G. Burns, A. W. Smith and D. F. O'Kane, "The Tungsten Bronze Field in the System  $\text{K}_2\text{O}-\text{Li}_2\text{O}-\text{Nb}_2\text{O}_5$ ," Mat., Res., Bull. Vol. 5, pp. 47-56, 1970.
- [10] T. Nagai and T. Ikeda, "Pyroelectric and Optical Properties of Potassium Lithium Niobate," Jpn., J. Appl. Phys., Vol. 12, pp. 199-244.
- [11] W. A. Bonner, W. H. Grodkiewicz and L. G. Van Uitert, "The Growth of  $\text{K}_{0.6}\text{Li}_{0.4}\text{NbO}_3$  Crystals for Electro-Optic and Nonlinear Applications," J. Crystal Growth Vol. 1, pp. 318-319.
- [12] T. Fukuda, H. Hirano and S. Koide, "Growth and Properties of Ferroelectric  $\text{K}_3\text{Li}_2(\text{Ta}_x\text{Nb}_{1-x})_5\text{O}_{15}$ ," J. Crystal Growth Vol. 6, pp. 293-296, 1970.
- [13] S. C. Abrahams, P. B. Jamieson and J. L. Bernstein, "Ferroelectric Tungsten Bronze -Type Crystal Structures. III. Potassium Lithium Niobate  $\text{K}_{(6-x-y)}\text{Li}_{(4+x)}\text{Nb}_{(10+y)}\text{O}_{30}$ ," J. Chem. Phys., Vol 54, pp. 2355-2364.
- [14] M. Adachi, T. Shiosaki and A. Kawabata, "Epitaxial Growth of Potassium Lithium Niobate Single-Crystal Films for Optical-Waveguides," Ferroelectrics Vol. 27, pp. 89-92, 1980.

The Lebedev Physical Institute RAS  
 Leninsky pr.53, Moscow 117924, Russia

S.V.Ivanova

**Abstract** - It was investigated the dependence of the speckle-field in  $\text{Ba}_2\text{NaNb}_5\text{O}_{15}$  crystals in laser beam on the orientation of the crystals, temperature and direction of growing. The different pattern of scattering along the a and c axis make it possible to unambiguously determine the direction of the ferroelectric axis in the crystal, while abrupt change in the nature of scattering with a ferroelectric phase transition makes it possible to determine the Curie point.

## INTRODUCTION

A large number of mixed-oxide composition, possessing ferroelectric properties, crystallize in the tetragonal tungsten bronze structure. The term "tungsten bronze" derives from the metallic potassium tungsten oxide composition which were first demonstrated to have this structure.

In contrast to the tungsten - containing bronzes, the niobate with this structure are generally transparent insulators. This ferroelectrics have been the subject on intensive investigations. The interest to this crystals has been motivated by actual or potential applications of these materials based on their outstanding piezoelectric, electro-optical and nonlinear optical properties [1-5].

Less attention has been given to the understanding of the mechanisms of the structural phase transitions. The ferroelectric tetragonal bronze have a [001] polar axis and transform to a tetragonal centrosymmetric structure above  $T_C$ . In addition an orthorhombic as well as a tetragonal modification of the tungsten bronze structure exists.

Barium sodium niobate,  $\text{Ba}_2\text{NaNb}_5\text{O}_{15}$  (BSN) is at present the best characterized of these compounds though many of its features are still not clear understood.

This crystal undergoes three successive phase transitions on cooling:  
 $4/\text{mmm} \rightarrow 4\text{mm} \rightarrow \text{mm}2 \rightarrow 4\text{mm}$  [6,7].

The highest one at  $585^\circ\text{C}$  is a standard ferroelectric transition with symmetry change from  $4/\text{mmm}$  to  $4\text{mm}$ . This phase contains ferroelectric domains of  $180^\circ$  type which are lying along the c axis. The ferroelectricity is mainly related to the eccentric position of the Niobium atoms in the oxygen octahedra.

The other transition of about  $300^\circ\text{C}$  is ferroelastic with symmetry change from  $4\text{mm}$  to  $\text{mm}2$ . The orthorhombic deformation is related to small displacement of the Barium ions parallel to the [110] direction. The ferroelasticity of the room temperature phase give rise to two orientation of orthorhombic structure. They constitute adjacent ferroelastic domains separated by plane walls with (100) or (110) orientation. Below  $-160^\circ\text{C}$  the domains disappear.

This crystal presents a unique example of a ferroelastic ( $\text{mm}2$ ) phase sandwiched between two phases possessing the same higher point

symmetry.

The room temperature crystal structure of BSN has been studied by Jamieson et al. [8]. It is constituted by framework of oxygen octahedron sharing corners and forming three types of tunnels of different shape and size running along the c direction in which cations are located. The four triangular tunnels remain empty in BSN. The cubic and pentagonal tunnels respectively contain the Na and Ba ions. This structure data on BSN are available only at room temperature.

The existence of incommensurate phases in BSN has been postulated [9] and subsequently confirmed [10]. The static and dynamic characteristics of the incommensurate phases of BSN have been investigated by means of elastic and inelastic neutron scattering between room temperature and  $660^\circ\text{C}$  [11]. Two incommensurate phases were observed on heating from room temperature.

Phase II which is stable up to  $T_{II}=250^\circ\text{C}$  is nearly commensurate, the modulation vector is expressed as

$$k=(a^*+b^*)(1+\delta)/4+c^*/2, \text{ with } \delta=0.01.$$

Phase I is incommensurate with the same direction of modulation and  $\delta$  varies linearly from 0.08 at  $T_{II}$  up to 0.12 at  $T_I$ , about  $288^\circ\text{C}$ ;  $T_{II}$  is discontinues and  $T_I$  is continues.

The modulation consists mainly in a collective shearing of the oxygen octahedra, in which the basis of each octahedron in ab plane is fixed while the oxygen at the upper and lower vertices move parallel to this plane in opposite direction. This alternation along the z axis corresponds to the doubling of periodicity along this direction. The displacement have a predominant component along the a orthorhombic axis which is also parallel to the direction of the modulation. The incommensurate or nearly commensurate modulations, respectively, detected in phases I and II are due to the displacements of the oxygen and also barium atoms at microscopic level [12,13]. The soft mode detected above  $T_I$  consists of the same collective shearing of oxygen octahedra. The modulation wavelength varying significantly in the  $T_I$ - $T_{II}$  temperature range. In the framework of the existing phenomenological theories this variation is associated with a nonsinusoidal character of the modulation, i.e. the presence of discommensurations [11,13,14].

In present work it was investigated the behavior of the laser beam in the crystal having such intricate structure.

## EXPERIMENT AND RESULTS

This work investigated anisotropy of  $90^\circ$ -scattering light in a BSN crystal in a broad temperature range ( $20$ - $600^\circ\text{C}$ ).

Single crystals were grown by Dr.I.I.Naumova and co-workers in the laboratory of the

Department of physics of the Moscow State University using the Czochralski method. Crystals have a composition close to congruent with essentially no growth layers ( $\Delta n = 10^{-5}$ ). The samples  $2 \times 3 \times 5$  mm, oriented in the  $[001]$ ,  $[100]$ , or  $[010]$  directions (tetragonal indices), were placed in a region of constriction of a focused light beam (the length of the constriction was 3 mm and the transverse diameter of the light spot was  $20 \mu\text{m}$ ). The  $\lambda = 514.5$  nm generation line of an argon laser was used as the excitation source. The laser power was varied from 30 to 300 mW. The crystal was mounted in an oven which had two windows that allowed visual observation of the sample. The temperature was measured using a platinum-platinorhodium thermocouple located near the crystal. The focused laser beam was propagated in the crystal perpendicular to the ferroelectric axis and had a polarization direction parallel to this axis. In such a geometry  $90^\circ$ -scattering was observed in the crystal. (Fig.1).

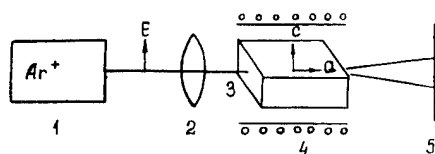


Fig.1. Experimental setup for the observation of  $90^\circ$ -light scattering: 1 - argon laser; 2 - focal lens; 3 - sample; 4 - oven; 5 - screen.

This scattering had a grainy structure in the form of brightly illuminating points both in crystals with zero-orientation (grown in a  $[001]$  direction) and in  $90^\circ$ -orientation (grown in the  $[010]$  direction) (Fig.2a).



Fig.2.  $90^\circ$ -Scattering in BSN crystals at room temperature relative to the orientation of the samples:

- a) the direction of the laser beam is perpendicular to the c axis;
- b) the direction of the laser beam is along the c axis;

In crystals with  $90^\circ$ -orientation the point scattering centers disappear at approximately  $300^\circ\text{C}$  near the second-order phase transition, while in crystal with zero-orientation they are preserved right up to the ferroelectric phase transition (Fig.3a).

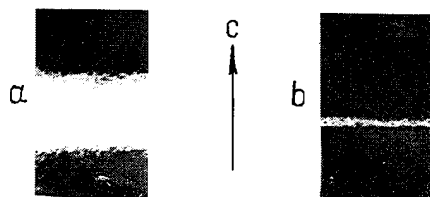


Fig.3.  $90^\circ$ -Scattering in BSN crystal: a) at temperature of  $20^\circ\text{C}$ ; b) at temperature of  $560^\circ\text{C}$ .

The speckle structure disappears also at the propagation of radiation along c-axis (Fig.2b). In these cases the trace of the laser beam presents homogeneous mat thread about five times narrower than the scattering trace with speckle structure.

The described anisotropy of scattering is also characteristic for monodomain BSN crystal and makes it possible to visually identify the direction of the ferroelectric axis. To do this one must find the direction in the crystal in which the laser beam passing through the sample causes scattering in the point centers (Fig.2a,3a). Such an effect is observed when the laser beam is propagated along the a axis in the ac plane. The direction perpendicular to the beam unambiguously determines the direction of the c axis of the crystal. The polarization of the beam in this geometry coincide with the polar axis c.

Near the ferroelectric phase transition the laser beam in the crystal is abruptly narrowed (Fig.3b). The Curie point in ferroelectric crystals is determined from the abrupt change in some sort of physical property (heat capacity, dielectric permittivity, etc.) for ferroelectric with first-order phase transitions. The temperature of the crystal is equal to the Curie temperature at the moment of the abrupt narrowing of the beam and disappearance of the point scattering centers for the zero-orientation crystals.

The described anisotropy of the  $90^\circ$ -scattering of light is observed for multidomain and monodomain BSN crystals.

## CONCLUSION

The behavior of the laser beam in the BSN crystal revealed by this study is following: if the beam was polarized to be an extraordinary ray in the crystal the scattering trace had a speckle structure at the room temperature both in crystals with zero and  $90^\circ$ -orientations. However in the crystal with  $90^\circ$ -orientation the speckle-structure of the beam disappears at about  $300^\circ\text{C}$ ; in crystal with zero-orientation the point scattering centers disappear near the Curie point.

An abrupt change of the scattering laser beam which corresponds to these phase transitions is simultaneously observed on the temperature relation of the elastic scattering of light [15,16].

The origin of this phenomenon is yet not clear.

**Acknowledgments.** The author is grateful to Dr. I.I.Naumova for providing of the crystals and to T.T.Sultanov for preparing photographs and to V.S.Maslov and N.I.Kireeva for optical processing of the crystals.

## REFERENCES

- [1] E.A.Giess, B.A.Scott, G.Burns, D.F.O'Kane and A.Segmuller, "Alkali Strontium-Barium-Lead Niobate systems with a Tungsten Bronze structure: Crystallographic properties and Curie points", *J. Am. Ceram.*, vol.52, pp.276-281, May 1969.
- [2] L.C.Van Uitert, S.Singh, H.J.Levinstein, J.E.Geusic and W.A.Bonner, "A new and stable nonlinear optical material", *J. Am. Ceram.*, vol.11, pp.161-163, May 1967.

- [3] L.C. Van Uitert, H.J. Levinstein, J.J. Rubin, C.D. Capio, E.F. Dearborn and W.A. Bonner, "Some characteristics of Niobates having 'Filled' Tetragonal Tungsten Bronze-like structures", *Mater. Res. Bull.*, vol. 3, pp. 47-58, March 1968.
- [4] S. Singh, D.A. Draegert and J.E. Geusic, "Optical and ferroelectric properties of Barium Sodium Niobate", *Phys. Rev. B*, vol. 2, pp. 2709-2724, October 1970.
- [5] J.E. Geusic, H.J. Levinstein, J.J. Rubin, S. Singh and L.G. Van Uitert, "Nonlinear optical properties of  $\text{Ba}_2\text{NaNb}_5\text{O}_{15}$ ", *Appl. Phys. Letters*, vol. 11, pp. 269-271, September 1967.
- [6] C. Toledano, "Theory of the ferroelastic transition in Barium Sodium Niobate", *Phys. Rev. B*, vol. 12, pp. 943-950, August 1975.
- [7] J. Schneck, J. Primot, R. Von der Muhll and J. Ravez, "New phase transition with increasing symmetry on cooling Barium Sodium Niobate", *Solid State Commun.*, vol. 21, pp. 57-60, January 1977.
- [8] P.B. Jamieson, S.C. Abrahams, J.L. Bernstein, "Ferroelectric Tungsten Bronze type crystal structures: I", *J. Chem. Phys.*, vol. 48, pp. 5048-5057, November 1968.
- [9] J. Schneck, J.C. Toledano, B. Joukoff, F. Denoyer and C. Joffrin, "Neutron and X-ray precession studies of the incommensurate reflections near the  $300^\circ\text{C}$  transition in Barium Sodium Niobate", *Ferroelectrics*, vol. 26, pp. 661-664, 1980.
- [10] J. Schneck and F. Denoyer, "Incommensurate phases in Barium Sodium Niobate", *Phys. Rev. B*, vol. 23, pp. 383-388, January 1981.
- [11] J. Schneck, J.C. Toledano, C. Joffrin, A. Aubree, B. Joukoff and A. Gabelotaud, "Neutron scattering study of the tetragonal-to-incommensurate ferroelastic transition in Barium Sodium Niobate", *Phys. Rev. B*, vol. 25, pp. 1766-1785, February 1982.
- [12] Y. Uesu, T. Fukui, T. Nagasawa, M. Shiwazu, M. Tsukioka, "X-ray dilatometric study of incommensurate-quasi-commensurate phase transition of ferroelectric Barium Sodium Niobate", *Japanese J. Appl. Phys.*, vol. 27, pp. 1167-1177, July 1988.
- [13] G. Van Tandeloo, S. Amelinckx, C. Manolikas, W. Shulin, "The direct observation of 'Discommensurations' in BSN and its homologues", *Phys. Stat. Sol. (a)*, vol. 91, pp. 483-501, October 1985.
- [14] Xiao Qing Pan and Duan Feng, "Direct Observation of Nucleation of Discommensurations in Barium Sodium Niobate", *Phys. Stat. Sol. (a)*, vol. 106, K117-K121, April 1988.
- [15] S.V. Ivanova, I.I. Naumova, T.T. Sultanov, "Anisotropy of light scattering in BSN crystals", *Kratkie Soobshcheniya po Fiske*, vol. 7, pp. 40-42, July 1989.
- [16] S.V. Ivanova, I.I. Naumova, "About the Intensity of Rayleigh and Raman scattering near the ferroelectric phase transition in BSN crystals", *Kratkie Soobshcheniya po Fiske*, vol. 4, pp. 36-39, April 1985.



# Effects of Applied Stress on the Dielectric Properties of PLZT Thin Films

William E. Paradise, F. Wang and G. H. Haertling  
Gilbert C. Robinson Department of Ceramic Engineering  
Clemson University, Clemson, South Carolina 29634-0907

**Abstract** --- The dielectric properties of electrooptic thin films were varied by altering the stresses placed upon the films. Selected thin films in the lanthanum-modified lead zirconate titanate system (PLZT) were produced by using the dip-coating process and applying various stresses. Comparisons were made among thin films under mechanically applied stresses of different magnitude. Properties measured were dielectric constant, saturation polarization, remanent polarization, coercive field and d-spacing. The effects of the applied stresses on the physical and electrical properties of the films are discussed.

## INTRODUCTION

Electrooptic ceramics have been a topic of interest due to the desirable properties they possess. The importance of electrooptic thin films is evident in their many applications ranging from sensors to light modulators.[1] Thin films possess advantages over bulk ceramics such as easier integration with silicon technology, lower operating voltage, higher speed and lower cost which make them more desirable for many devices. The perovskite PLZT system is under current investigation for thin and thick film applications because of their combined dielectric, pyroelectric, piezoelectric and electrooptic properties.

Electrooptic thin films have properties that can vary widely due to their differences in thickness, processing method and substrate type.[2] The effects of applying mechanical stress to electrooptic ceramics, known as strain-biasing, has been used in image storage and display applications.[3] It has also been shown that under compressive stress a transition in ceramics from a rhombohedral to a tetragonal symmetry can occur.[4] It is believed that through the study of these materials, an optimization of their properties can be achieved. In order to understand and optimize thin film electrooptic behavior, the understanding of the correlation between stress and thin-film properties is desirable.

## EXPERIMENTAL PROCEDURE

### Processing

A chemical coprecipitation process was used to produce PLZT acetate precursors.[5] All the elements needed were placed into an acetate form and mixed together. The acetate precursors were chosen primarily for their low cost, insensitivity to moisture and chemical stability. The starting precursors were titanium acetyl acetonate, zirconium acetate, lanthanum acetate and lead subacetate powder. The lead subacetate was mixed into solution by the addition of acetic acid and methanol so that all of the acetate precursors were in a liquid form in order to promote a homogeneous and intimate mixing. Incomplete mixing would produce compositional fluctuations within the thin film's structure.

Thin films were produced by the automatic dip coating process.[6] For thin film production, the acetate solution was diluted with methanol at a 4:1 ratio by weight. This improves solution stability and reduces cracking during heat treatments. The films were dipped onto silver foil substrates, allowed to dry for a minute and then pyrolyzed at 700°C for three minutes. Three compositions (2/55/45, 9/65/35 and 28/0/100) were used, and of

each of these compositions, three film thicknesses were produced. The three films of each composition had 24, 36 and 72 layers and were approximately 1, 2 and 3 microns thick respectively. The films were then electroded for measurement of their dielectric and hysteresis loop properties

### Stressing

To induce a stress within the thin films, the films were placed within a three point bender and flexed as shown in Figure 1a. The applied stress in the films may be correlated to the curvature of the films. The electrical properties can be measured at various stress levels by measuring them at different film curvatures. Compressive versus tensile stress effects on properties are compared simply by taking measurements at concave versus convex curvatures.

### Measurements

The films were electroded with vacuum evaporated copper and measured for dielectric constants, electrical resistivities and hysteresis loops. Capacitance and dissipation factors were measured using an LCR meter at 1 kHz. Resistance was measured using a Keithley electrometer and the hysteresis loops were measured at 1 kHz using a Sawyer-Tower circuit with an oscilloscope readout. The coercive fields and remanent polarizations were calculated for all the films from their hysteresis loops. X-ray diffraction analysis was performed on the thin films using a Scintag XDS 2000 diffractometer with Cu K $\alpha$  radiation at a scan rate of 2 $^\circ$ /min.

The strain induced within the thin films was calculated by Equation 1

$$\text{Strain} = \frac{t}{2R} \quad (1)$$

where  $t$  is the total thickness of the film and substrate, and  $R$  is the radius of curvature of the film.[7] Some assumptions need to be made before this equation can be used though. First, it is assumed that the axes of symmetry lie through the center of the film. Second, the film must have a constant radius of curvature. And third, the substrate must be rigid enough not to plastically deform so as not to relieve any of the stress applied to the film. Radius of curvature can be found by using the following equation

$$(2R-d)*d = L^2 \quad (2)$$

where  $d$  is the deflection of the substrate and film, and  $L$  is the length of the deflection from the center as shown in Figure 1b.[8] The stress is obtained by multiplying the strain value with the Young's modulus of the material. The sign agrees with the convention that it is positive for tension and negative for compression.

A film residing on a rigid substrate of much greater thickness is unable to move freely. Therefore, after the fabrication process, the film is usually strained in a way corresponding to the induced tensile or compressive stress imposed by the substrate.

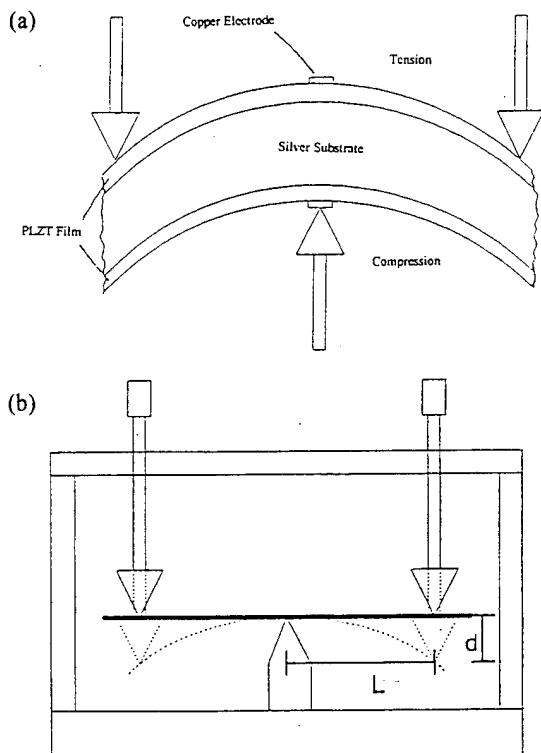


Figure 1. Three point bend showing a) applied stresses and b) measurements needed for the calculation of the radius of curvature.

The substrate should also experience an opposite stress exerted by the film and deform accordingly, which may lead to a distribution or a relaxation of the induced stresses within the film.[9] This effect is neglected here since for the dip coating process the two sides of the substrate are evenly coated and the bending moments from the films on the opposite sides are thus expected to cancel each other.

Should there exist any difference in the thermal expansion behavior between the thin film and the substrate, development of intrinsic stresses within the film during the cooling stage will occur. Since most ferroelectric materials possess large electromechanical coupling effects, the presence of an intrinsic stress in a ferroelectric film will affect its dielectric properties. This intrinsic stress tends to be compressive for PLZT thin films produced on silver substrates due to PLZT's lower thermal expansion than that of the silver substrate. Since it is the changes in properties caused by the addition of applied stresses that is of interest, any induced stresses on the films produced during fabrication are not taken into account within this paper. The effect of the total stress acting on the films is not analyzed, only the effects of the applied portion of the total stress within the films.

## RESULTS AND DISCUSSION

### Dielectric Constant

It is observed from the experiment that the general trend of the dielectric constant for the 2/55/45 composition is to increase with an increasing tensile stress, as shown in Figure 2a. However, the 1  $\mu\text{m}$  films dielectric constant does not continue to increase with added tensile stress. The reasoning for this is not yet fully understood and more research is needed before an accurate assumption can be made. The composition 2/55/45 was chosen for study because it lies near the morphotropic phase boundary in the PLZT system. Since the composition lies near this boundary the

material exhibits both a rhombohedral and a tetragonal symmetry. This phase boundary composition regularly exhibits a ferroelectric memory behavior. As mentioned previously a structural transition can occur within a material under a stress. It is believed that a transition in symmetry may be taking place within the 2/55/45 thin film upon stressing causing the dielectric constant to change.

The 9/65/35 composition is near the paraelectric phase region and tends to have a slim-loop hysteresis with very little memory behavior. The dielectric constant for this composition is observed to be slightly affected by the addition of either a compressive or tensile stress as shown in Figure 2b.

The 28/0/100 composition lies within a cubic region and also tends to exhibit slim-loop properties. This composition showed a slight change in the dielectric constant under different stresses with a maximum being reached when a compressive stress was placed on the film as shown in Figure 2c. The addition of a

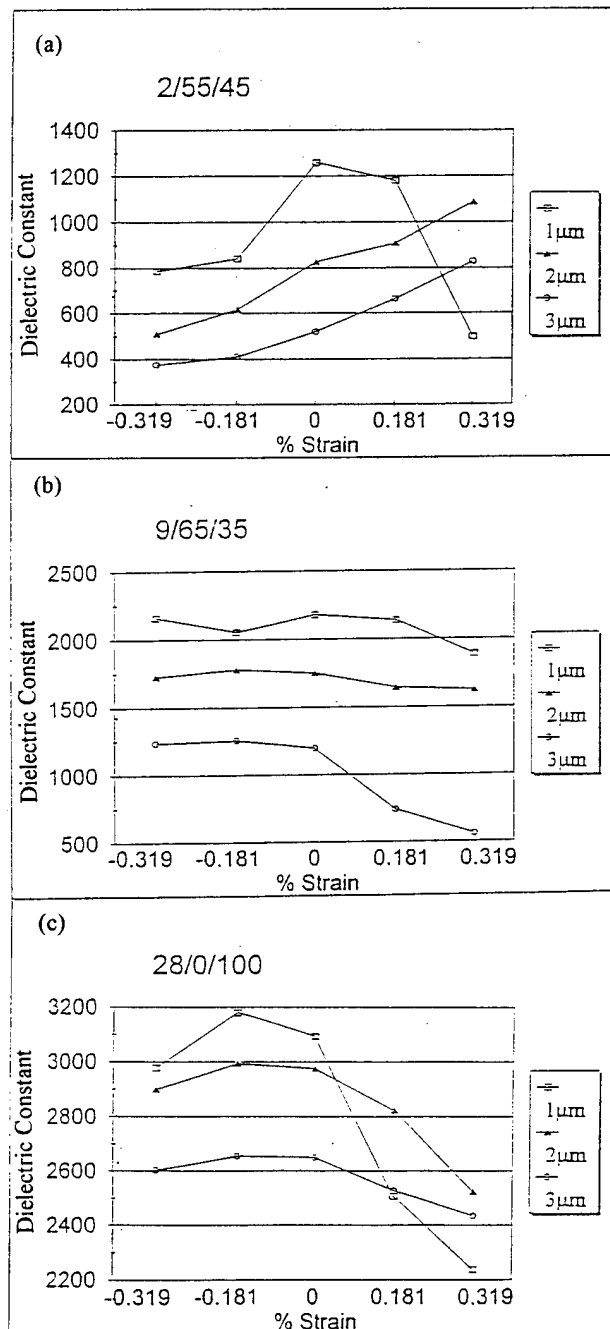


Figure 2. Dielectric constant versus percent strain for a) composition 2/55/45, b) 9/65/35 and c) 28/0/100.

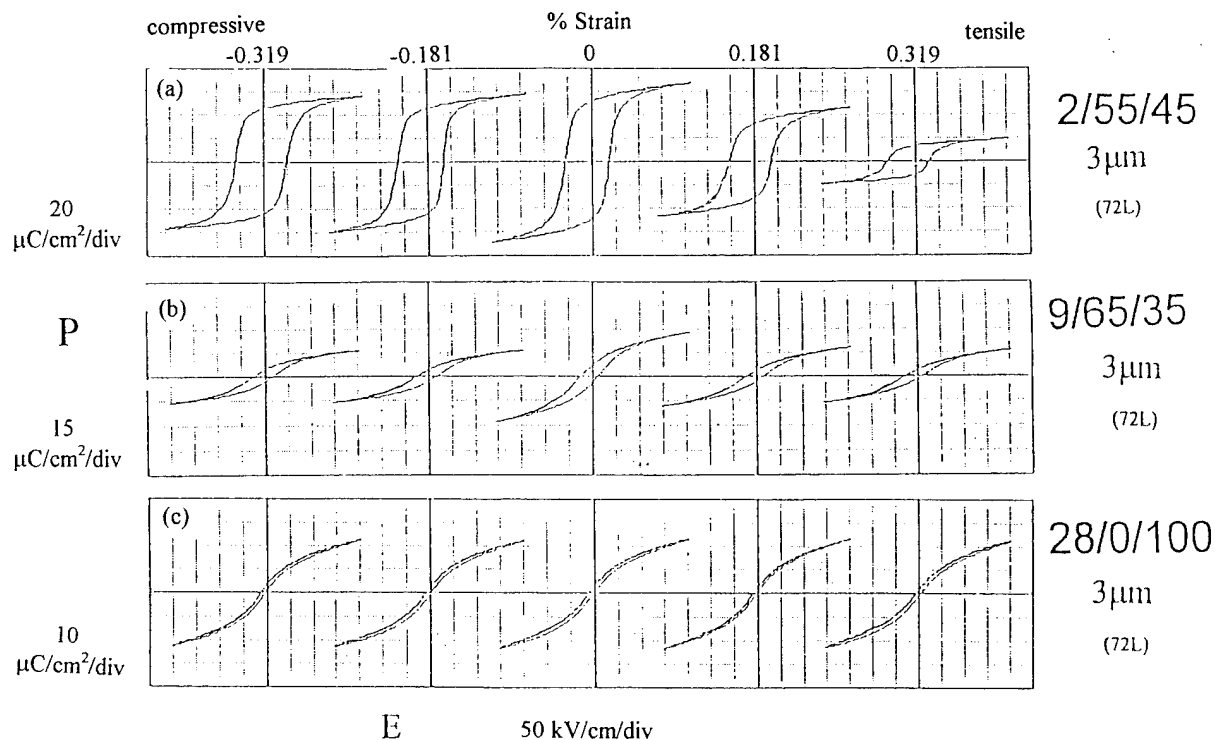


Figure 3. Hysteresis loops at various stresses for a) composition 2/55/45, b) 9/65/35 and c) 28/0/100. The scales for the y-axes are 20, 15 and 10  $\mu\text{C}/\text{cm}^2$  per division, respectively, and the x-axis is 50 kV/cm per division.

further compressive stress caused the dielectric constant to decrease. A decrease was also evident with the addition of a tensile stress.

#### Hysteresis Properties

Both the 9/65/45 and the 28/0/100 showed an increase to some degree in remanent polarization under a compressive stress, but the 2/55/45 thin films had a decrease, as shown in Figure 3. The coercive fields of all the compositions increased under a compressive stress and decreased under tensile. The 28/0/100 thin films did not show much of a change within any of the properties measured. Research on quenched PLZT 9.5/65/35 ceramics showed that internal stresses induced in samples can enhance polar region ordering which would produce a more ferroelectric-like response by the material.[10] This response would produce higher remanent polarizations in quenched samples than in annealed samples. A compressive stress in the thin films will align the domains parallel with the applied electric field, enhancing the ferroelectric properties of the thin films. Tensile stresses will align the domains perpendicular to the applied field and the effect will be a decrease in the ferroelectric properties. The hysteresis properties under tensile stresses correspond to an alignment taking place, but the compressive effects do not follow this convention. The lack of change in the 28/0/100 properties with varying stresses may be related to the composition's pseudo-cubic structure, producing a very stable material with few domains present. Many of the results from this study are not yet fully understood. Most likely is a combination of factors are affecting the properties of the films under the stresses applied. The effects of having the sample clamped during measurement is now being investigated as a possible explanation along with understanding the thermodynamics involved.

#### Lattice Spacing

X-ray diffraction patterns of the 2 $\mu\text{m}$  2/55/45 thin film were taken at different stress levels. In analyzing the lattice spacings of the different levels of applied stress, it was observed that the compressive stress produced slightly larger d-spacings than in the tensile stress. Watanabe et al. [11] proposed that the mechanical stress present in PZT thin films can cause differences in lattice constant between bulk and thin film materials. When a polycrystalline ceramic is deformed in such a way that the strain is uniform over a relatively large distance, the lattice plane spacing in the constituent grains changes from a stress-free value to some new value corresponding to the magnitude of the applied stress. The new spacing is essentially constant from one grain to another for any particular set of planes that are similarly oriented with respect to the stress. A uniform strain over the thin film will cause a shift of the diffraction lines to new  $2\theta$  positions. A smaller lattice constant perpendicular to the film corresponds to a tensile stress. A graph of the (211) d-spacings at the various stress levels is shown in Figure 4. From this figure it can be seen that the d-spacing does decrease from compressive to tensile stress as expected.

#### SUMMARY AND CONCLUSIONS

As anticipated, the properties of the thin films were found to be dependent on the sign and amount of stress applied. A compressive stress on the thin films will align the domains. This aligning will produce slightly larger d-spacings within the material and, if parallel with the applied electric field, will enhance the dielectric properties. It is also believed that the increase in dielectric constant within the 2/55/45 thin films, upon applying a tensile stress, may be caused by a stress induced structural transition. The 28/0/100 composition's properties were less

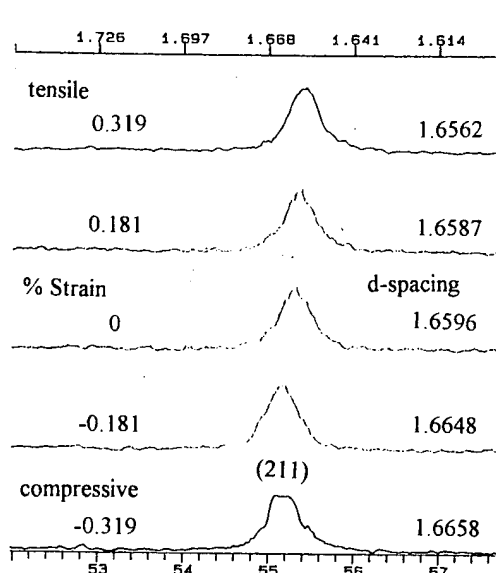


Figure 4. X-ray diffraction patterns of a 2 $\mu$ m PLZT 2/55/45 thin film at various applied stresses.

influence by the applied stresses possibly due to its pseudo-cubic nature.

#### ACKNOWLEDGMENT

This work was supported by ONR under contract number N0014-91-J-1508.

#### REFERENCES

- [1] G. H. Haertling, Engineering Materials Handbook, 1124-30 vol. 4 (Ceramics and Glasses), ASM International, (1991).
- [2] K. D. Preston and G. H. Haertling, "Comparison of Electro-Optic Lead-Lanthanum Zirconate Titanate Films on Crystalline and Glass Substrates," *Appl. Phys. Lett.* **60** [23], 2831-33 (1992).
- [3] Juan R. Maldonado and Allen H. Meitzler, "Strain-Biased Ferroelectric-Photoconductor Image Storage and Display Devices," *Proc. IEEE* **59** [3], 368 (1971).
- [4] A. H. Meitzler and A. H. O'Bryan, Jr., "Ferroelectric Behavior of PLZT Ceramics When Subjected to large Tensile Strains," *Appl. Phys. Lett.* **19** [4], 107 (1971).
- [5] G. H. Haertling, "PLZT Thin Films Prepared From Acetate Precursors," *Ferroelectric* **116**, 51 (1991).
- [6] K. K. Li, "A Study of PLZT Ferroelectric Thin Films Chemically Derived From Acetate Precursors," Ph.D. Thesis, Clemson University, Clemson, SC (1993).
- [7] C. H. Hsueh and A. G. Evans, "Residual Stresses in Metal/Ceramic Bonded Strips," *J. Am. Ceram. Soc.*, [3] 241-8, (1985).
- [8] S. Timoshenko, "Analysis of Bi-Metal Thermostats," *J. Optical Soc. Am.*, [11] 233-56, (1925).
- [9] R. W. Hoffman, Physics of Nonmetallic Thin Films, ed. by C. H. S. Dupuy and A. Cachard, 273-353, Plenum Press, New York (1976).
- [10] W. Y. Gu, E. Furman, A. Bhalla and L. E. Cross, *Electrooptics*, 89, 221 (1989).
- [11] H. Watanabe, T. Mihara and C. A. Paz De Araujo, "Device Effects of Various Zr/Ti Ratios of PZT Thin-Films Prepared by Sol-Gel Method," Proceeding of the 3<sup>rd</sup> International Symposium on Integrated Ferroelectrics, 139-50, 1991.

# Electro-optic Switching behaviour of a Noval Shortpitch Ferroelectric Liquid Crystal Mixture

K.K. Raina and H.J. Coles \*

Thapar Institute of Engineering and Technology,  
Patiala 147 001 (India)

\* Liquid Crystal Group, Schuster Laboratory, The University, Manchester M13 9PL (U.K.)

## ABSTRACT

Electro-optic effects have been studied in a shortpitch ( $p_0 = 0.43 \mu\text{m}$ ), large spontaneous polarization ( $P_s = 90 \text{ nC/cm}^2$ ) ferroelectric liquid crystal mixture. The material in the form of thin films was sandwiched between polyimide coated transparent conducting glass plates. The sample alignment was planar in an electric field without shearing. Disclination loops appeared at low voltages and were then removed at higher voltages to obtain a 'bookshelf' structure which gives higher contrast. This material shows bistability, fast switching times (40  $\mu\text{sec}$  at 8 V/ $\mu\text{m}$ ) and multiplexability. These are useful parameters for the operation of a fast electro-optic liquid crystal display device.

## INTRODUCTION

Ferroelectricity in liquid crystals is a specific property of a chiral smectic C (SmC\*) phase [1]. This phase is characterized by a helical structure, the tilt angle and the spontaneous polarization associated with the helix. The properties of this phase are useful in fast Liquid Crystal Display (LCD) devices because it offers the possibility of fast switching between the permanent polarization of the liquid crystal molecules and the applied electric field. A Surface Stabilized Ferroelectric Liquid Crystal Display (SSFLCD) device was then proposed by Clark and Lagerwall in 1980. This was a major breakthrough in fast responding LCDs as this device showed submicrosecond switching times and bistability [2]. In a SSFLCD device, the helical pitch of the SmC\* material is suppressed by surfaces of the bounding plates, when the pitch is much larger than the cell thickness and this leads to bistability. However, with the advancements in the analysis of switching mechanisms in SSFLC cells, it was found that their electro-optic performance was not as good as anticipated. It was difficult to obtain sufficient bistability, for multiplex driving because the smectic layer structure in a planar cell was not a 'bookshelf' texture but a 'chevron' [3].

Funfschilling and Schadt [4] proposed a Shortpitch Bistable Ferroelectric Liquid Crystal Display (SBFLCD) device and showed experimentally that certain short pitch FLC mixtures do show good bistability, high multiplexing and fast switching times. In short pitch materials, switching takes place in tiny domains and higher contrast can be obtained when the sample is in 'bookshelf' structure. Jakli and Saupe [5] reported a method for obtaining 'bookshelf' textures in homeotropically aligned SBFLC mixtures in the presence of electric field and by shearing of smectic layers. Generation of defect free texture in planar SBFLC cells under electric fields without shearing have been reported by Raina and Coles [6].

In this paper, we shall report on the electro-optic response of a shortpitch ferroelectric mixture. The experimental details and the results have been discussed in the proceeding sections.

## EXPERIMENTAL

### Materials

We have studied the electro-optic behaviour of a Ferroelectric Liquid Crystal mixture FLC 6430 (Roche, Switzerland). This material has a shortpitch ( $p_0 = 0.43 \mu\text{m}$ ), large tilt angle ( $\theta = 27^\circ$ ) and large spontaneous polarization ( $P_s = 90 \text{ nC/cm}^2$ ) measured in 8  $\mu\text{m}$  cell gap at 22°C. A broad ferroelectric phase (SmC\*) is found in this material given by the phase sequence :

$$\text{Crystal} \xrightarrow{-11^\circ\text{C}} \text{SmC}^* \xrightarrow{59^\circ\text{C}} \text{SmA} \xrightarrow{65^\circ\text{C}} \text{Isotropic}$$

## Apparatus

We used polyimide and transparent indium tin oxide (ITO) coated glass cells of 2.5  $\mu\text{m}$  thickness (obtained from EHC, Japan). Investigations were also carried out in 5  $\mu\text{m}$  and 7  $\mu\text{m}$  thin cells (Lucid, UK). Polyimide coating encourages planar alignment of the liquid crystal molecules. Electric fields were applied across conducting tin oxide layers. These cells were filled with FLC mixture at its isotropic temperature and then sealed using NORLAND Optical Sealant. Fig. 1 (a) shows the assembly of a cell filled with liquid crystal mixture. The electro-optic measurements were carried out using an OLYMPUS BH-2 transmission polarizing microscope adapted to give direct sample observations. The sample cell was heated in a thermostatically controlled hot stage LINKAM THM 600. Its temperature could be adjusted in the range of -20 to +600°C with a stability better than 0.1°C. Voltages were applied to the cell using a THURLBY signal generator TG 1304, output amplified by an Electro-Optic Developments LA 10A linear amplifier. A photodiode BPW21PD (signal sensitivity response ~25nsec.) was used and its output was detected on the HP 54501A digitizing oscilloscope. A schematic diagram of our experimental setup is shown in Fig. 1(b).

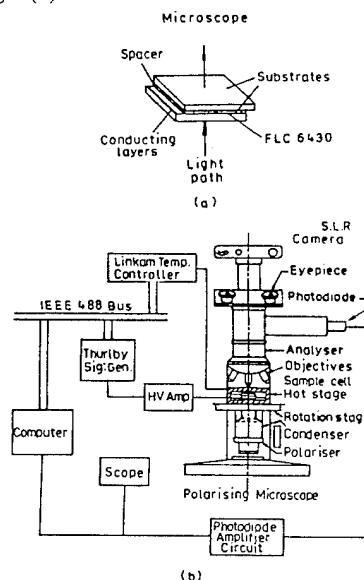


Fig. 1 (a) Assembled sample cell, (b) experimental setup to study electro-optic effects

## RESULTS AND DISCUSSIONS

### Microscopic Observations

The sample cell was first taken to the isotropic phase (above 65°C) and then cooled slowly at the rate of 2°C/min. At isotropic - SmA transition temperature ( $T_{IA}$ ), a polycrystalline texture developed as seen through the microscope with the appearance of stick like 'batonnets', which grew and finally combined with each other to form focal conic texture of SmA phase. To obtain a desired planar alignment in the sample, we applied a low voltage pulse to it across the conducting electrodes at  $T_{IA}$ . Continuous application of the field encourages the planar orientation and a monodomain SmA texture developed in 2.5  $\mu\text{m}$  cell at an extinction position under crossed polarisers. Then the

sample was further cooled to 58°C in the SmC\* phase. At SmA - SmC\* transition temperature ( $T_{AC}^*$ ) textural changes took place with the appearance of helical texture as shown in Fig. 2. At this stage, the extinction position changed by about 3° indicating a shift in the molecular structure. We observed that the helix forms by the growth of stripes which propagate throughout the sample. We suppose that these stripes start from defects and then propagate throughout the cell.

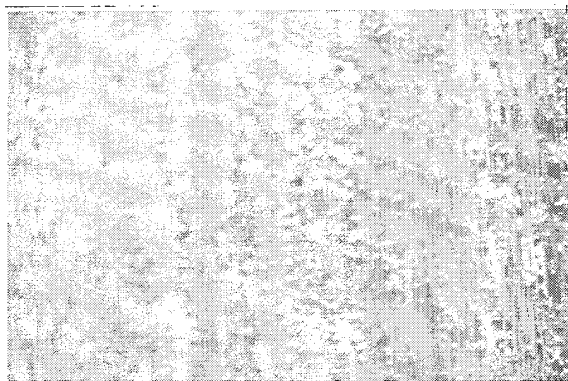


Fig. 2 Texture of the FLC 6430 mixture in SmC\* phase at 58°C under crossed polarizers

#### Threshold Voltage

On applying square wave voltage to the planar cell, we did not notice any optical changes up to the threshold voltage. The helix unwinding threshold depends on field frequency e.g. at 30°C,  $V_{th}$  (15Hz) = 1.9V,  $V_{th}$  (50Hz) = 2.4V,  $V_{th}$  (70Hz) = 2.7V,  $V_{th}$  (100Hz) = 4V and  $V_{th}$  (1kHz) = 12 V. At higher temperatures, the threshold voltage at these frequencies was lower. In thick sample cells, threshold voltage was more than in thin cells thereby indicating the influence of surface forces which also contribute to helix unwinding. (Here the threshold voltage has been taken as the minimum voltage required to unwind the helix of FLC mixture). Above threshold voltage, we noticed the nucleation of new defects. The number of these defect sites depends both on the frequency and amplitude of voltage applied e.g. at 50Hz 0.75 V/μm, disclination loops appeared in the sample. The number of these defect sites was more at 2V/μm but at 8V/μm, we obtained a defect free texture which shows higher contrast. Fig. 3 shows a uniform 'bookshelf' texture of FLC



Fig. 3 Uniform 'bookshelf' texture of the FLC 6430 mixture at 50Hz and voltage amplitude 8V/μm

mixture. The clarity (defect free) in the texture is due to the fact that at higher voltage, we expect a strong interaction between the applied field and the molecular polarization. Thus the minimization of this interaction energy is the driving force for fast switching and re-orientation mechanisms giving rise to clear 'bookshelf' structures at higher voltages.

It was interesting to note colour changes in the sample at different applied voltages e.g. at 0.35 V/μm, sample appeared green, turns red at 0.45V/μm and then pink at 0.8 V/μm. These colour changes were reproducible thereby indicating colour switching phenomena in these materials. The changes might be associated with the deformation in helical stripes and the flow induced by external electric fields giving rise to selective Bragg reflections. At higher voltages (>  $V_{th}$ ) the helix unwinds completely (system gets polarized) and when field was

switched off, it takes several hours and sometimes days until the helical structure reforms completely. This is believed to be memory effect in these materials reminiscent to the properties of ferroelectricity.

#### Switching Responses

The electro-optic responses of the FLC 6430 mixture subjected to a series of bipolar pulses with increasing amplitude is shown in Fig. 4. It is interesting to note the switching behaviour with deformed helix (Fig. 4a, < $V_{th}$ ) and at higher voltage (Fig. 4b, > $V_{th}$ ). We noted the asymmetric behaviour of the switching responses at 30°C which became symmetric at higher temperatures (48°C). This can be explained on the basis of the temperature dependence of the molecular tilt angle  $\theta$  given by

$$\theta = \theta_0 (T - T_{c^*})^\beta$$

Where  $T_{c^*}$  is the  $T_{AC}^*$  temperature and  $\beta$  is the critical exponent ( $\beta = 0.35$ ) e.g. at room temperature,  $\theta = 27^\circ$  which is larger than the optimum value ( $\theta = 22.5^\circ$ ) for the director to switch on the cone of the helix giving rise to asymmetry where as at 48°C,  $\theta = 20^\circ$  only which is well in the range of complete symmetric ferroelectric switching. We noted that the tilt angle in this FLC mixture was independent of the sample thickness. Switching responses indicated bistability in this mixture which is influenced by helix formation, monostability and alignment quality. Because of short pitch, SBFLCDs are sufficiently bistable to allow for virtually infinite multiplexing rates and thus making these FLC mixtures most potential for fast bistable electro-optic liquid crystal display devices.

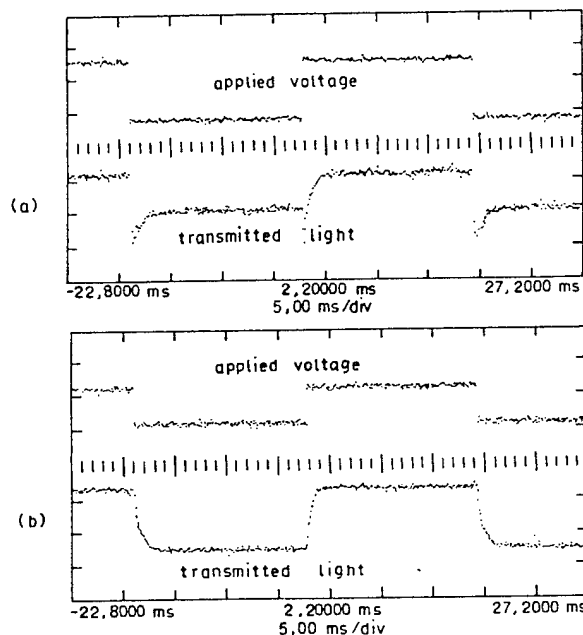


Fig. 4 Oscillograms showing the electro-optic responses of FLC 6430. Switching of the deformed helix at (a) 30°C, (b) 48°C.

#### Response Times

A typical response time characteristics of FLC 6430 mixture as a function of applied voltage at different temperatures is shown in Fig. 5. Here, we define response time as the time required to switch the material from 10 - 90% of its transmission when a voltage pulse is applied to it for a short time (~ 5ms). It is observed that the response time decreases exponentially with increasing voltage and then saturates e.g. at 55°C, the response time decreased from 800 μ sec. at 1V/μ m to 40 μ sec at 8 V/μm and thereafter it saturates. Similarly at 30°C, response time decreases from 650 μ sec at 1.5 V/μm to 40 μ sec at 8 V/μm. But at lower electric field (<1.5 V/μm), the response time increases first. This initial increase in response times at lower voltages and low temperatures might be due to the hindered switching because of the presence of disclination lines and defect inhomogeneities. The switching in

these regions might be delayed due to tiny domain switching and the applied voltage might not be sufficient to switching it completely. At higher temperatures, this effect was not observed possibly due to the

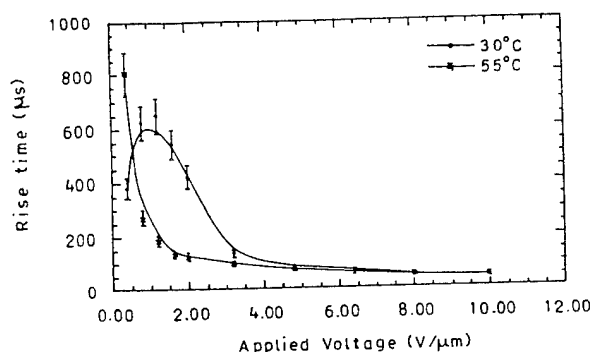


Fig. 5 Rise time as a function of applied voltage for FLC 6430 at different temperatures

pre-transitional effects (near  $T_{AC}^*$ ) which mask the appearance of hindrance mechanism (i.e. fewer disclinations or defects, reduced elastic constants, lower tilt or viscosity, changing pitch etc.) At the moment we do not have an exact explanation for this behaviour, however, this effect has been observed by other research groups as well in low molar mass FLCs.



Fig. 6 Electro-optic switching at 50Hz, 0.4V/μm voltage amplitude. Field is not acting in the texture region

Fig. 6 shows typical microphotograph of the switching in FLC 6430 mixture at 33°C. A low frequency (50Hz) pulse at 0.4 V/μm was sufficient to switch the material from highly defect texture state to a uniform defect free switched state. In the photograph two states have been shown separately before and after the switching. The area where the field has acted is an active region.

#### CONCLUSIONS

A detailed characterization of electro-optic behaviour of short pitch, high spontaneous polarization ferroelectric liquid crystal mixture was performed. Following conclusions have been drawn :

1. 'bookshelf' structures can be generated in planar cells at low frequencies without the shearing of smectic layers. This texture gave a contrast ratio of 80. Thus, the material can be exploited for high contrast displays.
2. the material shows very small values of the threshold voltage. At higher frequencies, the  $V_{th}$  is also higher. This is expected to be due to the electro hydrodynamic instabilities produced in the materials at high frequencies.
3. The electro-optic responses demonstrate asymmetric and symmetric behaviour at low and high temperatures respectively. This indicates the influence of tilt angle on the switching mechanism. More theoretical explanation is needed to understand this phenomena.
4. This material shows sufficient bistability - an important parameter for a working display.

5. voltage dependence of response time shows fast switching at higher voltages. Response time of 40 μsec. was achieved at 8 V/μm. It is also due to the large spontaneous polarization of the molecules. This time can be further reduced under certain controlled conditions like proper cell thickness, nature of the alignment layer and other surface treatments. Efforts are on to reduce this time to a submicrosecond range.

Thus we infer that the new SBFLCD device can be used as a fast electro-optic bistable device. FLC 6430 is an important material to be exploited for device applications in LCD technology. Electroclinic effect near  $T_{AC}^*$  is of great significance and needs to be investigated. We are also in the process of studying this phenomena.

#### ACKNOWLEDGEMENTS

Authors are grateful to Dr. Martin Schadt of Hoffmann La Roche, Switzerland for gifting the FLC 6430 mixture. One of us (KKR) wishes to thank Dr. M.P. Kapoor, Director TIET for constant encouragement. Partial financial support from DST (India) is thankfully acknowledged.

#### REFERENCES

- [1] R.B. Meyer, L.Liebert, L.Strzeleci and P.Keller, "Ferroelectric Liquid Crystals" J.de Phys. (Paris), Vol. 36, PP L69-72 (1975).
- [2] Noel A. Clark and Sven T.Lagerwall "Submicrosecond bistable electro-optic switching in liquid crystal" Appl. Phys. Lett., Vol. 36 PP 899-901 (1980).
- [3] W.J.A.M. Hartmann and A.M.M. Luyckx Smolders "The bistability of the surface stabilized ferroelectric liquid crystal effect in electrically re-oriented chevron structures" J.Appl. Phys., Vol. 67 PP 1253-1261 (1990).
- [4] J.Funfschilling and M.Schadt "Short-Pitch Bistable Ferroelectric LCDs", SID Symp. Digest Vol. 21 PP 106-109 (1990).
- [5] A.Jakli and A. Saupe "Method to obtain uniform bookshelf textures in smectic C\* liquid crystals" Appl. Phys. Lett., Vol. 60 PP 2622-2624 (1992).
- [6] K.K. Raina and H.J. Coles "Electric field generated defect free textures in short pitch ferroelectric smectic C liquid crystal mixture" Europhysics Lett. (Communicated).

# SUSPENDED PARTICLE FLAT PANEL DISPLAYS USING COLLOIDAL PARTICLES

T. Li, T. Kido, and J.H. Adair  
*Department of Materials and Engineering*  
*University of Florida, Gainesville, FL 32611*

## **Abstract**

Electro-optical characteristics of inorganic colloid particles dispersed in organic solvent are discussed as well as its potential applications related to Suspended Particle Displays (SPDs).

## **Historical background**

The study of electro-optical birefringence to determine the size and shape of clay particles can be dated back to the first part of this century [1,2]. In 1943, Donal and Langmuir [2] described using a particle suspension in an electric field as a light valve. In 1968, Marks [3] theorized the interaction of submicron dipoles (anisotropically shaped conductive particles) suspended in a dielectric medium in an electric field by analogy with large dipole antennae used in microwave technology. Since that time several investigations have been conducted with light valves, filters, windows, displays, etc. based on particle suspensions [3,4]. As one of the less well developed display technologies, Suspended Particle Displays have also attracted attention due to their potential as a flat panel display [4].

## **General description of the behaviors of anisotropic colloid particle suspensions under an ac electric field**

Suspensions of anisotropic colloidal particles in dielectric liquid exhibit large, reversible changes in electro-optical and rheological behavior when subjected to an external electric field [1-3,5]. The subject of the current study include electrorheological effect and electro-optical Kerr effect [1,5]. All of these studies are based on the interaction between electrically polarized particles and an applied electric field. The dipoles induced by the electric field may be caused by a number of factors including the ferroelectric nature of the particles, surface polarization of mobile charge groups, double layer polarization, and space charge polarization. Without an electric field, the particles randomly orient due to Brownian movement. In an electric field, the induced dipoles interact with the external field and in some cases also with each other to align the particles in the direction of the applied electric field. The chemical and physical principles leading to the orientation of the particles in an applied electric field have been the subject of a number of investigations. The exact solution can be difficult due

to the complexity of the system and many-body interactions. According to the solution of classical electrodynamics [6] for the isolated sphere, the induced dipole moment,  $\mu$ , is

$$\mu = \alpha E \quad (1)$$

$$\alpha = \epsilon_1 \beta a^3$$

$$\beta = (\epsilon_1 - \epsilon_2) / (\epsilon_2 + 2\epsilon_1)$$

where  $E$  is the applied electric field,  $\epsilon_1$  and  $\epsilon_2$  are the dielectric constant of the dielectric medium and the particle, respectively,  $\alpha$  is polarizability of suspended particles in dielectric medium, and  $a$  is particle radius. Although the solution for anisotropic shapes is more complicated, the general conclusions of this mathematical description still remain; the dipole moment will be enhanced by large difference in the dielectric constants between the particles and dielectric liquid. There are a number of factors which may also affect the alignment of the polarized particles such as the viscosity of the liquid, gravity, and thermal motion of the particles (i.e., Brownian motion). The final position of the suspended particles in a dielectric fluid will depend on a balance of these factors.

## **Suspended particle display and prototype device construction**

Similar to Liquid Crystal Displays (LCDs), Suspended Particle Display (also called Rotatable Dipole Display) is a passive-type display. This means that an external light source is required for operation. The anisotropic colloidal particles, usually platelets or aciculate particles, act as dipoles in the presence of an ac electric field. Application of a high-frequency signal enables the particles to align in the direction of the applied field without electrophoretic motion of the particles in the direction of the electrode of opposite polarity. Since these particles are usually dichroic, the difference in the optical density between the random and aligned state can be quite large. Thus, the portion of the cell which is electrically activated will be colorless (transparent) while the inactivated portion will have the intrinsic color associated with the



materials. A prototype device is shown in Figure 1. Similar to LCDs, a typical SPDs device consists of a cell made by high quality glass with transparent electric conductive layer on the inside of the cell. A thin transparent dielectric layer is on the transparent electrodes to protect the transparent conducting electrodes from destruction due to electrolytic reaction. It also prevents the electrorheological affect and particle aggregation caused by the non-uniform electric field on the boundaries between activated and inactivated portions. Commercial graphite platelets were dispersed in isopropanol. The drive circuit is composed of a function generator and relay-type timer. Optical spectroscopy and a photo-cell were used to characterize the optical spectrum and rise and relaxation time of the device.

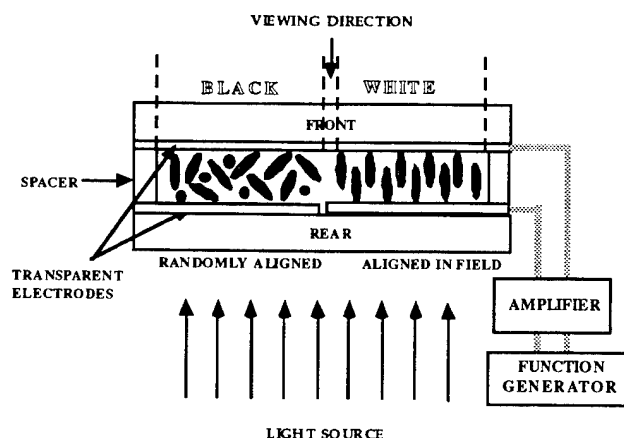


Figure 1. The cross section of the prototype device.

### Electro-optical characteristics of the prototype device

A transmittance spectrum of graphite platelet suspension as a function of frequency of the applied ac voltage pulse is shown in Figure 2. The spectra were collected from 50 kHz to 5000 kHz pulse frequencies. The transmittances of the suspension increase as frequency increase and reach to a maximum response at 500 kHz. This spectra could result from the influence of several factors. According to Marks [3], a critical frequency of ac pules,  $f_c$ , exists at low frequency,

$$f_c = 1/2\tau_f$$

where  $\tau_f$  was defined as a relaxation time factor defined as the characteristic time for an aligned suspension to randomize due to Brownian motion. If the frequency of the ac pulse is equal or less than  $f_c$ , the particles in the suspension will oscillate between partial alignment and randomization. Thus, the transmittance of the suspension is low and fluctuates. If ions are present in the suspension, ion migration in the suspension may also be a factor which influences the transmittance spectrum of the suspension at low

frequencies. An ionic shielding layer will be set up near the induced charges at the end of each dipole. This shield the dipoles from the aligning field, The dipoles then start to randomly orient due to thermal impact and the transmittance decrease. Above 500 kHz, the transmittance of the suspension begin to decrease because the induced charges on the particles can not follow the changes of the high frequency field.

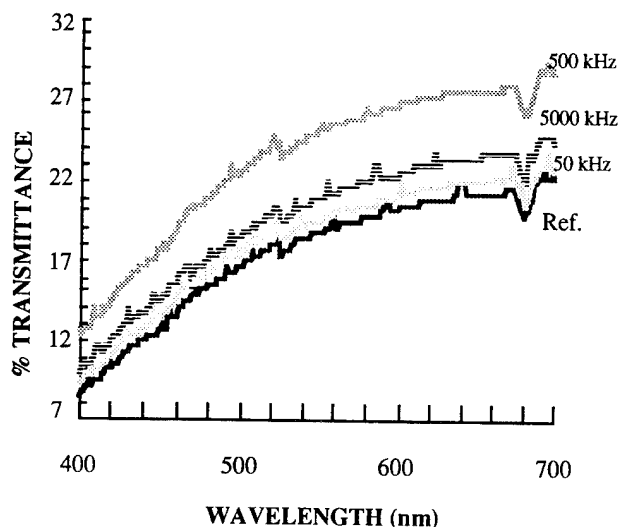


Figure 2. Transmittance spectrum of graphite platelet suspension as a function of the electric field frequency (interelectrode separation:100  $\mu$ m, The applied voltage:30 volts peak-peak).

Unlike liquid crystals there exist a threshold voltage, which in the present context is defined as the voltage corresponding to the transmission light reaching 10% its final value, the transmittance spectrum of graphite platelet suspension vs voltage (Figure 3) shows a logarithmic curve. Insight into the alignment process in our case may lead to the following consideration. When an ac electric field is applied, the induced dipoles will start to align in the direction of the field by overcoming the resistance from the viscosity of solvent and thermal motion. The rate of rotation of

these particles will depend on the relative amount of torque from induced dipole moments over that from the viscosity of solvent and thermal motion. Since dipole moments depend on the size of the particles, we conclude that diffuse changes in the transmittance vs voltage may be caused by the broad size distribution of the graphite particles.

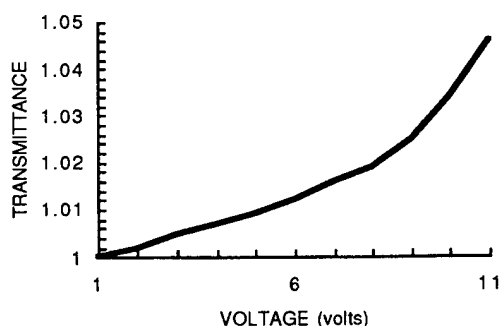


Figure 3. Transmittance spectrum of graphite platelet suspension as a function of the applied voltage (interelectrode separation: 100  $\mu\text{m}$ , field frequency: 500 kHz)

The dynamic behavior of the cell is characterized by three constants: delay time  $\tau_d$ , rise time  $\tau_r$ , and relaxation time  $\tau_f$  (Figure 4). The delay time is defined as the time from the start of the pulse trains to the instant when the transmission of the light reaches 10% of its final value. The rise time is defined as the time duration for the transmission to rise from 10 to 90% of its final value. Similarly, the relaxation time is the time for the transmission to fall from 90 to 10% of its maximum value. These three factors depend upon the size, shape, moment of inertia of the particles, and upon the fluid viscosity, dielectric constant, and density of the liquid phase. It is believed that the main cause for the longer rise and relaxation time for this prototype light valve (Figure 4) may also result from the broad size distribution of the graphite particles as

well as the relatively crude light cell and other electronic components used in the prototype light valve.

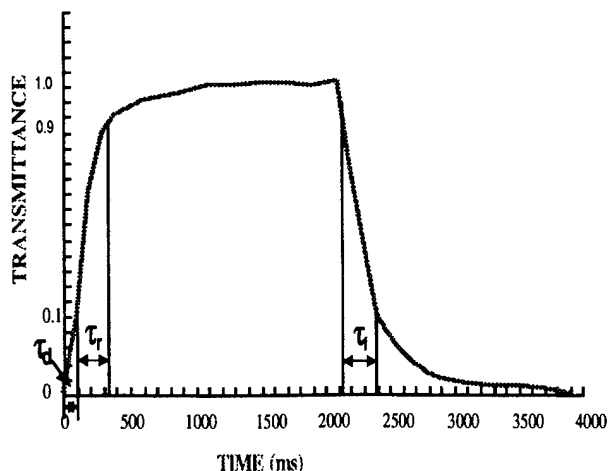


Figure 4. Rising and relaxation time of the graphite platelet suspension (interelectrode separation: 100  $\mu\text{m}$ , pulse frequency: 50kHz).

## Summary

A new prototype device of Suspended Particle Displays has been fabricated by using graphite platelets dispersed in organic solvent. The characteristics of the prototype device are shown in the Table 1.

Table 1. Characteristics Data

Drive voltage	10 - 35 V
Interelectrode Separation	100 $\mu\text{m}$
Response Frequency	50 - 500 kHz
Rise Time	220 ms
Relaxation Time	250 ms
Viewing Angle	Large

As compared with LCDs and other passive displays, SPDs may offer several advantages such as simpler construction, better angle view, and lower cost. The problems remaining are more or less materials related

(i.e., particle dispersion, low contrast, an inherent problem for passive type displays, and lower rise time due to the size of particles and broad size distributions). Thus, the future opportunities of SPDs strongly depend on the continued development of particle synthesis and dispersion.. New types of particles selected or synthesized will improve the device optical spectrum and increase contrast. Better understanding of the solution chemistry of the suspension will help to minimize particle settling and particle aggregation to enhance the response for input signal, and increase device lifetime. Based on our present level of understanding it is believed that Suspended Particle Displays provide an alternative flat panel display technology to conventional displays.

## References

- [1.] A.Kahn and D.R. Lewis, *J. Chem. Phys.*, 801 (1954)
- [2.] J. S. Donal, and D.B. Langmuir, *Proceedings of the I.R.E.* 208 (1943)
- [3.] A.M. Marks, *Applied Optics*, 8, 1397 (1969)
- [4.] R.L. Saxe, R.I. Thompson and M. Forlini, *International Display Research Conference*, 175 (1982)
- [5.] C.F. Zukoski, *Annu. Rev. Mater. Sci.* 23, 45 (1993).
- [6.] J.D.Jackson, *Classical Electrodynamics*, Second Edition John Wiley & Sons, 151 (1975)

# MICROSTRUCTURAL AND OPTICAL PROPERTIES OF POTASSIUM NIOBATE THIN FILMS

Alice F. Chow, Daniel J. Lichtenwalner, Thomas M. Graettinger,  
James R. Busch\*, Orlando Auciello\*\*, and Angus I. Kingon

North Carolina State University, Department of Materials Science and Engineering, Raleigh, NC 27695-7919

\*Battelle Memorial Institute, Columbus, OH 43201-2693

\*\*Also MCNC, Electronics Technology Division, Research Triangle Park, NC 27709-2889

## ABSTRACT

A potassium niobate thin film waveguide is an ideal candidate for producing a compact blue laser source by second harmonic generation. However, good epitaxial quality films are difficult to produce and high optical losses are a continuing problem. A report is presented in this paper on the investigations of the microstructural and optical properties of  $\text{KNbO}_3$  thin films to better understand the origin of optical waveguide losses. Epitaxial, dense  $\text{KNbO}_3$  thin films have been grown on  $\text{MgO}$ ,  $\text{MgAl}_2\text{O}_4$ , and  $\text{KTaO}_3$  substrates by ion-beam sputter deposition. X-ray diffraction, rocking curves, Rutherford backscattering spectroscopy, ion-channelling, field emission scanning electron microscopy, and atomic force microscopy were used to analyze the orientation, epitaxial quality, grain size, and surface roughness of the films. Optical properties including refractive index and optical scattering losses have been characterized by prism-coupling and an optical fiber loss measurement method. The dominant loss mechanism in these film waveguides is discussed. Green light by second harmonic generation has been produced in the transverse and waveguide modes in  $\text{KNbO}_3$  films.

## INTRODUCTION

A short wavelength laser source is necessary to increase the density of present optical recording systems. Green or blue light can be generated from an IR laser by second harmonic generation (SHG) using a nonlinear optical material. Several problems continue to hinder efficient frequency doubling. First, few materials possess high nonlinearity and can be easily phase-matched for the appropriate wavelengths. In addition, bulk crystals that have demonstrated SHG in the blue or green spectral region produce too little power. (At least 5 mW of power is necessary for many practical applications.) [1]

Potassium niobate possesses very high nonlinear constants and one of the highest figures of merit for producing SHG. [2] Also,  $\text{KNbO}_3$  thin films offer field confinement and thus, high conversion efficiency as well as ease of phase-matching by use of normal dispersion. Lithium niobate thin films have demonstrated SHG blue light. However, its bulk nonlinear optical properties are inferior to those of  $\text{KNbO}_3$  and the second harmonic power produced was weak. [3] Ultimately, thin film waveguides will be desired for high power conversion. Nevertheless, high quality  $\text{KNbO}_3$  thin films are difficult to grow due to potassium volatility at the growth temperature. A high degree of epitaxy and defect minimization are necessary for low waveguide losses. Thus, the origin of losses must be pinpointed, and microstructure and film processing must be synergistically controlled.

We report the growth of  $\text{KNbO}_3$  thin films with a high degree of epitaxy, and correlate film microstructures with optical properties. Films were grown by ion-beam sputter deposition. X-ray diffraction (XRD) and x-ray rocking curves were performed to analyze film orientation and grain tilt, respectively. Rutherford backscattering spectroscopy (RBS) revealed film composition information while RBS/channelling detected the grain tilt and misorientation of the films. Substrate and film surface roughnesses were determined by atomic force microscopy (AFM). Field emission scanning electron microscopy displayed the film surface morphology. Refractive indices were calculated from prism-coupling measurements and an optical fiber attachment allowed optical scattering losses to be measured. Highly epitaxial, dense  $\text{KNbO}_3$  thin films have produced green light by SHG in the transverse and waveguide modes.

## ION-BEAM SPUTTER DEPOSITION

Ion-beam sputter deposition was used to produce  $\text{KNbO}_3$  thin films on  $\text{MgO}$  (100),  $\text{MgAl}_2\text{O}_4$  (100), and  $\text{KTaO}_3$  (100) substrates. A computer-controlled, sequential rotating target assembly consists of potassium superoxide ( $\text{KO}_2$ ) and niobium targets that are alternately sputtered by a xenon ion beam. [4] Thus, composition is controlled by programming the ion beam dwell time on each target. Each layer deposited in one rotation of the targets is only 5-10 Å to allow for interdiffusion to form a homogeneous film. The deposition rate is about 10 Å/min. and film growth occurs at 650-700°C. Table 1 summarizes the important sputter deposition parameters.

Table 1. Ion-beam deposition parameters for  $\text{KNbO}_3$  thin film growth.

Beam energy	800 eV
Beam current	15 mA
Xe <sup>+</sup> source gas pressure	$1.4 \times 10^{-4}$ torr
O <sub>2</sub> gas pressure	$2.5 \times 10^{-4}$ torr
Deposition temperature	650-700°C
Deposition rate	10 Å/min.

## MICROSTRUCTURAL PROPERTIES

### Orientation

The d-spacings of the planes parallel to the sample surface can be detected through standard theta-two theta x-ray diffraction.  $\text{KNbO}_3$  films on all substrates under typical growth conditions show a single  $\text{KNbO}_3$  (110) orientation with d-spacings in the range of 4.02-4.04 Å. This corresponds to one of the longer axes of the orthorhombic  $\text{KNbO}_3$  cell. Films deposited at temperatures lower than 600°C often contain additional grain orientations such as the  $\text{KNbO}_3$  (111).

X-ray diffraction rocking curve analysis provides information about the grain tilt of the films. The samples were 'rocked' about the  $\text{KNbO}_3$  [110]. Any misorientation of the film grains will result in detection of planes slightly off the two-theta bragg angle. Figure 1 reveal FWHM values of 0.25, 0.30, and 0.84° on  $\text{KTaO}_3$ ,  $\text{MgAl}_2\text{O}_4$ , and  $\text{MgO}$ , respectively.

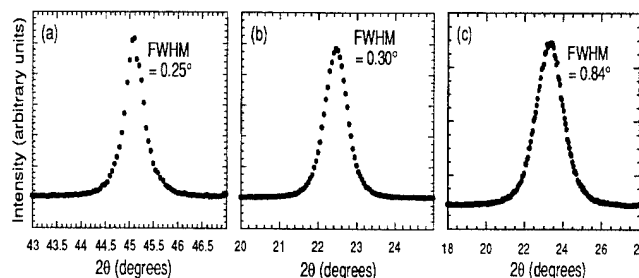


Figure 1. X-ray diffraction rocking curves of  $\text{KNbO}_3$  [110] on (a)  $\text{KTaO}_3$ , (b)  $\text{MgAl}_2\text{O}_4$ , and (c)  $\text{MgO}$  substrates.

### Composition and grain tilt

Rutherford backscattering spectroscopy was used to analyze the composition and thickness of the films.  $\text{KNbO}_3$  films are found to possess K to Nb ratios in the range of 0.60 to 0.90. The potassium deficiency does not seem to affect the bulk properties of the films. For instance, in XRD, only the  $\text{KNbO}_3$  (110) orientation exists and near bulk refractive index values are measured (as discussed later) for all films despite the K deficiency. It is believed that Na atoms arising from impurities in the  $\text{KO}_2$  targets compensate for the K deficiency. A  $\text{KNbO}_3$  film was deposited on a beryllium substrate to allow sodium to be detected in the RBS spectrum without being obscured by the substrate peak. Sodium was found to exist throughout the thickness of the film. Thus, it is likely that Na substitution on the K sub-lattice preserves the integrity of the  $\text{KNbO}_3$  unit cell and further, has the little influence on some film properties such as the refractive index.

RBS/channeling measurements were performed by aligning the beam along the [110] film direction. The amount of scattering from the film would reveal the amount of film misorientation, defects, and other scattering centers. Channelling can only occur if films are of good epitaxial quality. In all cases the film was found to be aligned with the substrate in the perpendicular growth direction as the minimum film channeling direction corresponds to that of the substrate.  $\text{KNbO}_3$  films on  $\text{KTaO}_3$  and spinel substrates displayed the lowest

channeling yields with  $\chi_{\min}$  of only 7% and 9% for the Nb peak, respectively, while  $\text{KNbO}_3$  films on MgO showed a  $\chi_{\min}$  of 18%. A single crystal  $\text{KTaO}_3$  substrate displayed a  $\chi_{\min}$  of 3% which illustrates the high degree of epitaxy of these films. However, films on MgO possess significantly more grain tilt. These results seem to correlate with the XRD rocking curve data shown above.

#### Surface morphology

Field emission scanning electron microscopy was used to characterize the surface microstructure and grain size of the films.  $\text{KNbO}_3$  films on MgO and spinel contained grains of 1000 to 1200 Å in size as shown in Figure 2. Larger grain sizes of ~3000 Å and also 90° oriented domain structures were found for films on  $\text{KTaO}_3$ .

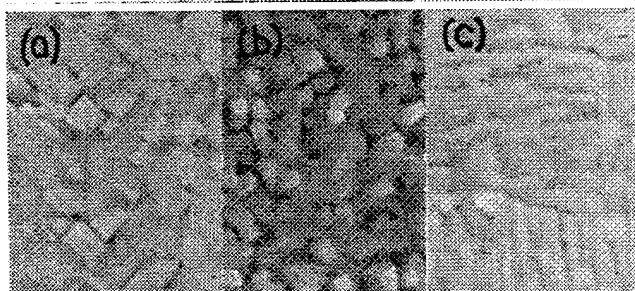


Figure 2. FESEM micrographs of  $\text{KNbO}_3$  on (a) MgO, (b)  $\text{MgAl}_2\text{O}_4$ , and (c)  $\text{KTaO}_3$  substrates

MgO and spinel substrates were purchased from Advanced Composites Materials and Commercial Crystal Systems, respectively. Oak Ridge National Laboratories provided the  $\text{KTaO}_3$  substrates.

Surface roughness of both the films and substrates were analyzed by atomic force microscopy. Substrate surface roughness minimization is key for lowering optical scattering at the interfaces and for optimizing epitaxial film growth. Regions of 5 by 5 microns were scanned for all samples. MgO substrates displayed a root mean square (rms) roughness value of 23 Å with maximum features of 196 Å in height. These periodic large structures are believed to be due to hydroxide formation on the MgO surface. Annealing of the MgO substrates for 14 hours at 1150°C resulted in an rms value of only 13 Å with maximum features of 95 Å. Spinel substrates presented rms values of 14 Å and large features of 270 Å. Upon annealing both the rms and the maximum feature height increased appreciably. The rougher spinel surface can be attributed to either the nature of the more complex spinel structure where several different atomic surfaces are possible, or due to vendor preparation.  $\text{KTaO}_3$  substrates exhibited the lowest surface roughness with an rms of 8 Å and a maximum height of 56 Å. The surface roughness of the  $\text{KNbO}_3$  films were found to be low, with rms values varying from 13 to 37 Å.

#### OPTICAL PROPERTIES

##### Refractive index

The prism coupling technique was used to evaluate the refractive index of the thin films. [5] A He-Ne laser (6328 Å) is focused on a rutile prism clamped to the sample. The beam can be either polarized in the TE (polarized in the plane of the film) or TM (polarized perpendicular to the film) mode. When the propagation constant of the He-Ne beam in the prism matches that of the film, the overlap of the light waves in the airgap between the prism and film allows the light to couple into the film/waveguide. The incident angles which produce coupling conditions are used to calculate the refractive index and thickness of the film. If two coupling angles (two waveguide modes) can be detected, both the thickness and refractive index can be calculated independently. Otherwise, one parameter must be known to calculate the other. Refractive indices measured for all films are 2.21 and 2.28 in the TM (light polarized along  $\text{KNbO}_3$  [110]) and TE modes (light polarized in the film plane), respectively. The bulk refractive index of  $\text{KNbO}_3$  [110] in the TM orientation is 2.222. The refractive indices of the TE modes of our films were measured in two orthogonal propagation directions, but no birefringence was measured, which indicates that 90° domain orientations exist on all substrates. Therefore, the bulk refractive index for the TE modes should reflect an average value between the indices of  $\text{KNbO}_3$  [ $\bar{1}10$ ] and [001], 2.222 and 2.329. Figure 3 displays the  $\text{KNbO}_3$  film refractive indices as a function of composition. Consequently, the fact that the refractive indices fall so close to the bulk values suggest  $\text{KNbO}_3$  films are dense despite the potassium deficiency.

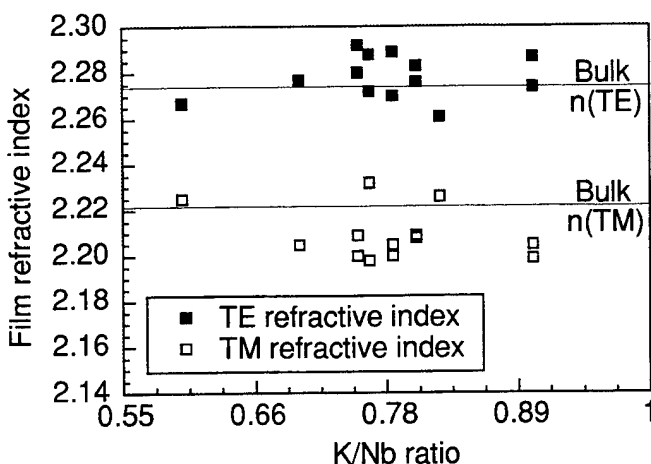


Figure 3. Refractive index of  $\text{KNbO}_3$  (110) measured in the TE and TM modes versus composition

##### Scattering losses

Optical waveguide losses can be measured by analyzing the light streak observed in the film when coupling occurs. Longer light streaks suggest lower scattering losses.  $\text{KNbO}_3$  films on MgO and spinel show higher losses for thick films (>1500 Å) than thinner (~1000 Å) films. Streak lengths of >8 mm can be observed for the latter cases as compared to only 2-3 mm for the thicker films. For our apparatus, losses can only be measured by those films with streak lengths of >5 mm. An optical fiber is mounted on a micrometer that allows movement along the length of the streak. The intensity of the light scattered at the surface of the streak is detected and quantified by a photodiode and connected to a nanovoltmeter. The losses can then be calculated by taking the slope of the  $10\log(I/I_0)$  versus distance along the light streak where  $I$  = intensity of the measurement point and  $I_0$  = initial intensity collected by the first point near the prism. Optical waveguide losses of ~34 dB/cm were found for  $\text{KNbO}_3$  films of ~1100 Å. While even higher losses of >50 dB/cm were detected for thicker (>1500 Å) films.

##### Second harmonic generation

A Nd:YLF laser source with a wavelength of 1.053 μm with ~80psec, 100 MHz pulses under mode-locked operation was used as the source beam for SHG measurements. A harmonic beam splitter transmits the fundamental wavelength to a razor blade beam block, and reflects the second harmonic through a tilted 532 nm bandpass filter onto a ground-glass screen. First,  $\text{KNbO}_3$  samples of thicknesses varying from 4600 to 6500 Å were placed perpendicular to the beam direction. By visual inspection of the screen, strong green light was observed for four samples of  $\text{KNbO}_3$  thin films on both MgO and  $\text{KTaO}_3$  substrates. Currents of only 28 to 30 A (at 30 A, 275 watt/pulse was detected) were necessary to generate strong green light. Saturation of the signal seem to occur at 30 A. A  $\text{KNbO}_3$  sample of ~2400 Å in thickness was then coupled with a 90° rutile prism. A 3-4 mm green light streak was seen in the TM<sub>0</sub> mode using currents of 31 to 33 A.

#### DISCUSSION

Three types of loss mechanisms exist: scattering, absorption, and radiation.[6] However, for dielectric thin films, the predominant contribution to losses are scattering losses. Scattering is subdivided into volume and surface scattering. Surface scattering losses are attributed to both light scattered from the film surface and the film/substrate interface. As the thickness of the film increases, the surface scattering losses decrease for a given coupling angle and arbitrary propagation length. As the mode number increases, the surface scattering will likewise increase, for the number of reflections within the waveguide increases duly. Therefore, properties that affect these losses are film and substrate roughness, and the particular mode or coupling angle.

Volume losses originate from scattering due to imperfections such as point defects, dislocations, and grain boundaries, found in the bulk of the waveguide. Figure 4 illustrates the phenomenon of volume scattering. Our data shows that the optical waveguide losses increase as the thickness of the film increases in the case of  $\text{KNbO}_3$  films on MgO and spinel. This indicates that volume scattering losses are indeed dominating. When the films are just above the thickness

criterion for waveguiding of the first mode, the majority of the field is propagating in the low loss single crystal substrate, and thus, low scattering losses are observed. As the film thickness increases, the amount of the optical field propagating in the film increases, and thus volume losses become a greater proportion of the total losses.

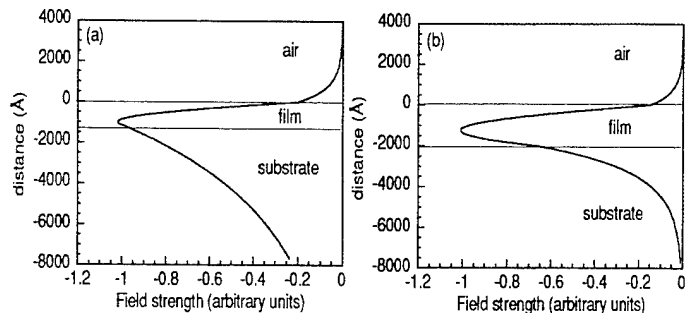


Figure 4. Modal distribution versus distance at the TM=0 mode and wavelength 6328 Å for a KNbO<sub>3</sub> waveguide on MgO substrate for film thickness (a) 1200 Å and (b) 2000 Å

The x-ray diffraction rocking curve and RBS/channeling data show a correlation between lattice mismatch and grain tilt. KNbO<sub>3</sub> films on spinel and KTaO<sub>3</sub>, where a smaller lattice mismatch exists, exhibited less grain tilt as compared to films on MgO. At the deposition temperature, the KNbO<sub>3</sub> film is cubic. Misfit dislocations form to accommodate the lattice mismatch which may result in 'tilts' and 'twists' of the grains. These lattice imperfections can be a significant contributor to bulk scattering. During cooling, the film first transforms to the tetragonal phase at ~435°C. It is during the second transformation to the orthorhombic structure (~225°C) where twin domains may form. The cubic symmetry of the substrates allows the in-plane orientations to be accommodated in any of the four equivalent 90° directions. Light waves travelling in the film will therefore experience refractive index changes as they traverse the twin domains resulting in attenuation. The coarse and fine grain structure as seen in the FESEM micrographs gives additional evidence of the bulk scattering that is occurring in the films.

#### SUMMARY

Epitaxial dense KNbO<sub>3</sub> thin films have been grown on MgO, MgAl<sub>2</sub>O<sub>4</sub>, and KTaO<sub>3</sub> substrates by ion-beam sputter deposition. X-ray diffraction scans show a single KNbO<sub>3</sub> (110) orientation for all films. RBS revealed K to Nb ratios ranging from 0.60 to 0.90. The potassium deficiency of the KNbO<sub>3</sub> films can be explained by sodium incorporation from impurities found in the KO<sub>2</sub> sputtering targets. AFM measurements reveal smooth films when grown on high quality substrate surfaces. Prism coupling measurements show films to possess near bulk TE and TM refractive indices of 2.28 and 2.21, respectively. The optical waveguide losses in the films can be attributed primarily to volume scattering, possibly originating from the coarse and fine grain structure and/or twins formed during structural transformations. KNbO<sub>3</sub> thin films have demonstrated SHG of green light from a Nd:YLF laser source in the transverse and waveguide modes with film thicknesses of 4600-6500 Å and ~2400 Å, respectively. The strong green light seen at low currents and small film thicknesses indicate the high nonlinearity of the KNbO<sub>3</sub> films, the high quality of these KNbO<sub>3</sub> thin films, and the potential for producing a blue laser source.

#### ACKNOWLEDGEMENTS

This research is supported by the Office of Naval Research under Contract No. N0014-91-1307. We thank Dr. N. R. Parikh at University of North Carolina-Chapel Hill for providing the Rutherford backscattering spectroscopy equipment, and Dr. L. A. Boatner at Oak Ridge National Laboratory for supplying the KTaO<sub>3</sub> substrates.

#### REFERENCES

- [1] J. J. E. Reid, M. Ouwerkerk, and L. J. A. M. Beckers, "Potassium Lithium Niobate and its Application to Intercavity Frequency Doubling," *Philips Journal of Research*, vol. 46, nos. 4-5, pp. 199-213, 1992.
- [2] V. G. Dmitriev, G. G. Gurzadyan, and D. N. Nikogosyan, *Handbook of Nonlinear Optical Crystals*. Berlin Heidelberg: Springer-Verlag, 1991.
- [3] G. H. Hewig and K. Jain, "Frequency Doubling in a LiNbO<sub>3</sub> Thin Film Deposited on Sapphire," *J. Appl. Phys.*, 54(1), pp. 57-61, January 1983.
- [4] T. M. Graettinger, S. H. Rou, M. S. Ameen, O. Auciello, and A. I. Kingon, "Electro-optic Characterization of Ion Beam Sputter-Deposited KNbO<sub>3</sub> Thin Films," *Appl. Phys. Lett.*, 58, p.p. 1964-1966, May 1991.
- [5] R. Ulrich and R. Torge, "Measurement of Thin Film Parameters with a Prism Coupler," *Appl. Opt.* 12, p.p. 2901-2908, December 1973.
- [6] R. G. Hunsperger, *Integrated Optics: Theory and Technology*. Berlin Heidelberg: Springer-Verlag, 1991.

# Quantum Size Effects and Nonlinear Optical Properties of ZnS and CdS Semiconductor-doped Silica Glasses Prepared by Sol-Gel Process

Zhao Qingchun, Liu Chunliang, Liu Hongling,  
Zhang Liangying, and Yao Xi

Electronic Materials Research Laboratory(EMRL)  
Xi'an Jiaotong University, Xi'an, 710049, China

## ABSTRACT

Preparation of silica glasses doped with CdS and ZnS microcrystals is presented. The optical absorption spectra and the photoluminescence spectra show that the optical absorption edges and the photoluminescence peaks shift to the higher energy side with decreasing the size of the microcrystals, which exhibit the quantum size effect. The third order optical susceptibilities are measured by degenerate four wave mixing (DFWM) method. The third order optical nonlinearity of the nanocomposites prepared by the sol-gel process is largely enhanced.

## 1. INTRODUCTION

Recently, nanometer-sized semiconductor microcrystals, metal particles, ferroelectric grains and dyes dispersed in a dielectric medium such as porous silica have been receiving a great deal of attention as 0-3 nanocomposites. Because of their large surface-volume ratio and three dimensional confinement of carriers, nanometer-sized particles possess hybrid electronic and optical behaviors that differ from both molecules and bulk, thus these nanocomposites are expected to show a large third-order nonlinearity and very fast response. These nanocomposites can be prepared by various methods of glass fabrication, such as: conventional melt-quenching technique, sputtering, sol-gel process, and so on. Starting from 1990, wet chemical synthesis of silica glasses doped with semiconductor microcrystallites has been explored to generate new or improved nanocomposites.<sup>[3,7]</sup>

Since Jain and Lind (1983) first reported on the highly nonlinear optical properties of CdSSe doped silicate glasses that are commercially available as a cut-off filter, these semiconductor-doped glasses have attracted increasing attention as nonlinear optical materials.<sup>[1,8-10]</sup> Nonlinear

behavior of semiconductor-doped glasses prepared by the sol-gel process make these materials an interesting class for optoelectronics. Takada et.al. reported 8wt% CdS doped gel derived glasses showed  $\chi^{(3)}$  of  $6.3 \times 10^{-7}$  esu under near resonant conditions, i.e. in the vicinity of 460nm.<sup>[13]</sup> Nogami et.al. also reported that in forward degenerate four-wave mixing (FDFWM) experiment, the nonlinearity of 2% CdS doped glass was estimated to be  $1.5 \times 10^{-10}$  esu at 390 nm which corresponds to the band gap energy.<sup>[3]</sup>

In this paper, we studied optical absorption and photoluminescence of the CdS and ZnS doped silica glasses, and the blue shift was investigated in relation to the quantum size effects of CdS and ZnS microcrystals. The third order optical susceptibilities of the CdS and ZnS doped glasses are measured by degenerate four-wave mixing (DFWM) method. The values of  $\chi^{(3)}$  were in range  $10^{-13}$  esu-- $10^{-12}$  esu. Finally, the discussions and conclusions are given.

## 2. QUANTUM SIZE EFFECTS

### 2.1 Preparation and Characterization

CdS and ZnS doped glasses were prepared by sol-gel process and in-situ growth techniques

with  $\text{CdO/SiO}_2$  and  $\text{ZnO/SiO}_2$  gel glasses reacting with  $\text{H}_2\text{S}$  gas.

From X-ray diffraction analysis, these crystals were cubic  $\text{ZnS}$  and hexagonal  $\text{CdS}$  respectively. The size of crystals was determined from broadening of the diffraction lines, using the Scherrer's formula. The mean diameter of the microcrystals were smaller than 10 nm. The Raman spectroscopy confirmed the formation of  $\text{CdS}$  and  $\text{ZnS}$  in these glasses.

## 2.2 Quantum size effects<sup>[2-3,4-7]</sup>

The absorption spectra of  $\text{CdS/SiO}_2$  and  $\text{ZnS/SiO}_2$  semiconductor-doped glasses were showed in Fig.1 and Fig.2, respectively, under different preparation conditions, such as: microcrystal contents, heat treatment times at reaction with  $\text{H}_2\text{S}$  gas. Comparing with the band gaps of  $\text{ZnS}$  and  $\text{CdS}$  bulk crystals, absorption edges shift to a shorter wavelength ( $\text{CdS}$ --520 nm,  $\text{ZnS}$ --350 nm). The Blue shift of energy was found to decrease as the exposure time and temperature to  $\text{H}_2\text{S}$  gas increase.

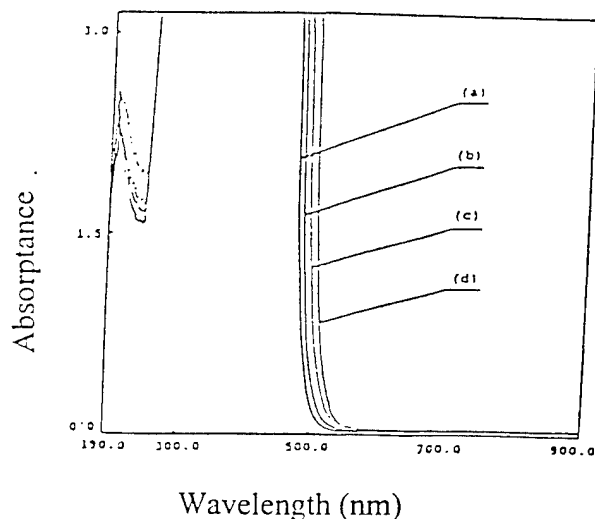


Fig.1 Optical absorption spectra of  $\text{CdS/SiO}_2$  Semiconductor-doped glasses  
(a) 0.5 hr (b) 1 hr (c) 10 hr (d) 48 hr

Fig.3 show the photoluminescence spectra of  $\text{CdS/SiO}_2$  semiconductor-doped glasses with different preparation conditions. The photoluminescence peaks shift to a shorter wavelength with decreasing the crystal size.

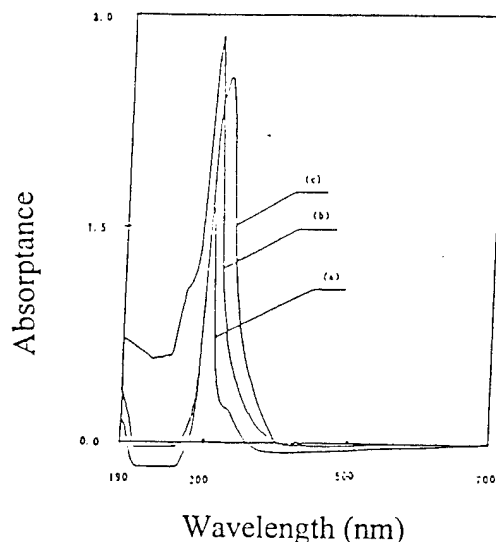


Fig.2 Optical absorption spectra of  $\text{ZnS/SiO}_2$  Semiconductor-doped glasses  
(a) 0.5 wt% (b) 1 wt% (c) 7 wt%

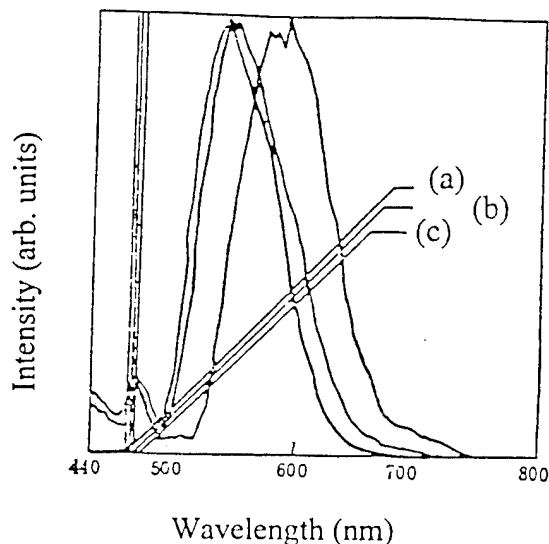


Fig.3 Photoluminescence spectra of  $\text{CdS/SiO}_2$  Semiconductor-doped glasses  
(a) 5 hr (b) 7 hr (c) 48 hr

Above blue shift phenomenon of optical absorption edge and photoluminescence peak indicates that the semiconductor-doped glasses prepared by the sol-gel process exhibit the quantum size effect.

## 3. NONLINEAR OPTICAL PROPERTIES

DFWM method is very popular to measure the third order optical susceptibility of nonlinear

optical materials.<sup>[3,10]</sup> A standard DFWM arrangement is used in this work, it is shown schematically in Fig.4. The Q-switched frequency-doubled Nb:YAG laser operating at 532 nm was used as light source. Typical laser energy used was about 40 mJ in 15 ns pulse duration, pulse repetition rates are of 1-5 Hz. Main beam was polarized by means of a polarization rotator and

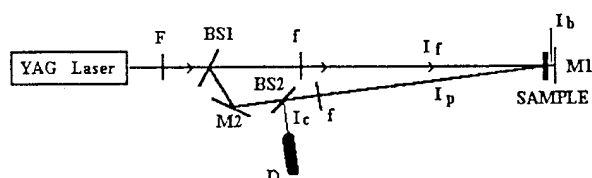


Fig.4 DFWM experimental setup.  
BS1,BS2: Beam splitter; F: Filter;  
f: Focusing lens; D: Detector

focused to 2 mm spot size with its beam waist at the sample by a lens of the focal length of 911 mm. BS1 is a 30% beam splitter used to split off the weak beam from the main beam. 70% of laser output is transmitted through BS1; This power forms the forward pump. BS2 is a 45% beam splitter. Weak beam through mirror M1 and BS2 generated the probe beam. The angle between pump beam and probe beam is about 2 degrees. The backward pump beam is the retroreflection of the forward beam from a mirror M2 immediately behind and in close contact with thin sample or sample cell to insure a maximum temporal overlap of the pulses within the nonlinear medium. All three input beams are linear polarized in the same direction. The conjugate signal beam generated by the mixing process propagates in the reverse direction of the probe beam.

Probe beam is measured by a pyroelectric detector and the phase conjugate reflected beam is detected by a silicon photodiode. In other words, the reflectivity can be directly measured by an energy ratiometer (Laser Precision 7200). The purpose of doing this can reduce the influence of the laser power fluctuation. Furthermore, the measurement was made by taking an average of 10-100 pulses. Attenuators were used to prevent saturation of the photodetector. Pump energy is varied by the aperture.

We have used the DFWM method at identical conditions to measure the nonlinearities of a carbon disulphide ( $\text{CS}_2$ ), which is usually used as standard reference nonlinear material. The value of  $\chi^{(3)}$  for  $\text{CS}_2$  obtained from our experiment is  $(1.7 \pm 0.2) \times 10^{-12}$  esu, which is well consistent with the reported value of  $1.8 \times 10^{-12}$  esu.<sup>[11,12]</sup>

#### 4. RESULTS AND DISCUSSION

After having taken absorption and reflectivity losses into account, We worked at sufficiently low energy fluence to avoid any photodarkening<sup>[8]</sup> of the samples or any saturation. For the samples, we can get the third order nonlinear susceptibility  $\chi^{(3)}$ , which are shown in Table 1. The values of

Table 1  $\chi^{(3)}$  of CdS/SiO<sub>2</sub> and ZnS/SiO<sub>2</sub> semiconductor-doped glasses

Samples	L (mm)	$R \times 10^4$	$\chi^{(3)} \times 10^{12}$
CdS/SiO <sub>2</sub> -1	2.1	1.32	7.0
CdS/SiO <sub>2</sub> -2	2.0	0.0797	1.8
CdS/SiO <sub>2</sub> -3	1.9	0.0158	0.83
CdS/SiO <sub>2</sub> -4	2.2	0.0171	0.78
ZnS/SiO <sub>2</sub> -1	1.5	0.277	3.7
ZnS/SiO <sub>2</sub> -2	1.6	0.287	3.6
ZnS/SiO <sub>2</sub> -3	1.8	0.329	3.5

$\chi^{(3)}$  for the nanocomposites were in range  $10^{-13}$ -- $10^{-12}$  esu, while  $\chi^{(3)}$  of the silica matrix was only about  $10^{-14}$  esu. Thus the third order optical nonlinearity of the porous silica matrix nanocomposites prepared by the sol-gel process is largely enhanced. In other hand, although very high  $\chi^{(3)}$  in the order of  $10^{-7}$  esu have been observable for semiconductor-doped glasses near the absorption edge due to the absorptive resonant effect, the  $\chi^{(3)}$  in the transparent region was even less than our results.

#### 5. CONCLUSIONS

The nonlinear optical properties of both CdS/SiO<sub>2</sub> and ZnS/SiO<sub>2</sub> semiconductor-doped glasses were systematically studied using DFWM



method. The third order optical nonlinearity of the nanocomposites prepared by the sol-gel process is largely enhanced. The blue shifts of absorption edges and photoluminescence peaks exhibit the quantum size effect. Further researches on this work are being under way.

### Acknowledgment

This research was financially supported by the National Advanced Materials Research Project of China.

### REFERENCE

- [1] R. K. Jain and R. C. Lind , "Degenerate four wave mixing in semiconductor-doped glasses", *J. Opt. Soc. Am.* , 73 , 647-53 (1983).
- [2] A. I. Ekimov and A. A. Onushchenko, "Quantum size effects in the optical spectra of semiconductor microcrystals", *Sov. Phys. Semicond.* , 16 , 775-77 (1982).
- [3] M. Nogami, M. Watabe and K. Nagasaka, "Preparation of semiconducting sulfides microcrystalline-doped silica glasses by the sol-gel process", *SPIE Proc. Sol-Gel Optics* , Vol. 1328 , 125-32 (1990).
- [4] N. F. Borrelli , D. W. Hall , H. J. Holland and D. W. Smith , "Quantum confinement effects of semiconducting microcrystallites in glass", *J. Appl. Phys.* , 61 , 5399-409 (1987).
- [5] B. G. Potter , Jr and J. H. Simmons, "Quantum size effects in optical properties of CdS-glass composites", *Phys. Rev.* , 37, 10838-45 (1988).
- [6] A. I. Ekimov , Al. L. Efros and A. A. Onushchenko , "Quantum size effect in semiconductor microcrystals", *Solid State Commun.* , 56, 921-24 (1985).
- [7] N. Tohge , M. Asuka and T. Minami , "Sol-gel preparation and optical properties of silica glasses containing Cd and Zn chalcogenide microcrystals", *J. Non-Cryst. Solids* , 147&148, 652-56 (1992).
- [8] P. Roussignol , D. Ricard , J. Lukasik and C. Flytzanis, "New results on optical phase conjugation in semiconductor-doped glasses", *J. Opt. Soc. Am.* , B4 , 5-12 (1987).
- [9] S. M. Saltiel , B. van Wonterghem and P.M. Rentzepis, "The third order nonlinear susceptibility of semiconductor doped glasses at low power excitation", *Opt. Commun.* , 77 , 59 (1990).
- [10] J. T. Remillard and D. G. Steel , "Narrow nonlinear-optical resonances in CdSSe-doped glass", *Optics Lett.* , 13 , 30-32 (1988).
- [11] A. Yariv , "Phase conjugate optics and real-time holography", *IEEE J. Quantum Electron.* , QE-14 , 650-60 (1978).
- [12] P. Thomas , A. Jares and B. P. Stoicheff , "Nonlinear refractive index and 'DC' Kerr constant of liquid CS<sub>2</sub>", *IEEE J. Quantum Electron.* , QE-10 , 493-94 (1974).
- [13] T. Takada , T. Yano , A. Yasumori , M. Yamane and J. D. Mackenzie , "Preparation of quantum-size CdS-doped Na<sub>2</sub>O-B<sub>2</sub>O-SiO<sub>2</sub> glasses with high nonlinearity ", *J. Non-Cryst. Solids* , 147&148 , 631-635 (1992).

# Poster Session - P6: Pyroelectrics

# Influence of $\gamma$ -ray Irradiation on the Thermochemical Phase Transition in Diethylammoniumtetrachlorocuprate.

V.Kapustianik, S.Sveleba, Ya.Ozhybko, R.Tchukvinskyi, V.Mokryi, V.Soldatov, I.Polovinko\*

Lviv Franko University, Kyrylo & Mefodyi st. 8, Lviv, Ukraine, 290005

\*Kielce Pedagogical University, Lesna st. 17, Kielce, Poland, 25509

**Abstract**—The influence of  $\gamma$ -ray irradiation on the phase transition temperature in  $(\text{NH}_2(\text{C}_2\text{H}_5)_2)_2\text{CuCl}_4$  crystals was investigated. It has been ascertained that irradiation at room temperature leads to increase of transition temperature  $T_1$ . Contrary to this, irradiation just below  $T_1$  is followed by decreasing of transition temperature. Observed effects are connected with breaking of H-bonds and with corresponding change of  $\text{Cu}^{2+}$  ion environment.

## INTRODUCTION.

The crystals of diethylammonium tetrachlorocuprate  $(\text{NH}_2(\text{C}_2\text{H}_5)_2)_2\text{CuCl}_4$  (abbreviatedly DEA- $\text{CuCl}_4$ ) are characterized by availability of thermochemical phase transition. At room temperature the crystal is bright green and changes discontinuously to bright yellow at the phase transition temperature. Several studies of DEA- $\text{CuCl}_4$  have been published, including optical birefringence, spectroscopy [1,2], EPR, NMR and structural investigations at room temperature and in high-temperature phase [3]. At room temperature the compound crystallizes as green needle in the space group  $P2_1/n$  with  $a=7.362$  Å,  $b=15.025$  Å,  $c=45.193$  Å,  $\beta=89.94^\circ$ , and  $z=12$ . One asymmetric unit of the structure contains three tetrahedrally distorted square-planar  $\text{CuCl}_4^{2-}$  ions for a total of 12 isolated copper centers in the unusually large unit cell. All the DEA cations are involved in a strong, two-dimensional N-H...Cl hydrogen bonding net, parallel to the b-c plane, which stabilizes the copper coordination geometry close to square planar [3]. The phase transition temperature is affected by sample purity, particle size, previous history and even relative humidity, making it difficult to define a precise transition temperature. For crystals grown from ethanol solution the phase transition temperature was at  $T_1=323$  K [3]. According to [1] the phase transition is followed by red shift of absorption bands (d-d-transition for copper) averaged by 50 nm due to the change of Cu ion environment from quadratic to tetrahedral. The coordination geometry in the latter case is associated with the existence of only weak cation-chloride hydrogen bonding. According to [3] the high-temperature phase is characterized by two crystallographically inequivalent anions. Both anions show similar flattened tetrahedral geometries and they are distinguishable by their substantially different amplitudes of apparent motion. In the whole the thermochemical phase transition in DEA- $\text{CuCl}_4$  turn out to be surprisingly complex. Structurally, the crystal transforms between two monoclinic unit cells, with three independent  $\text{CuCl}_4^{2-}$  anions in the low-temperature phase and two independent  $\text{CuCl}_4^{2-}$  ions in the high-temperature one. The phase transition is clearly first order in nature based on the lack of any crystallographic relationship between the two phases. No simple structural transformation pathway can be envisioned for converting one phase to the other. To better understanding of this transition nature it would be timely to investigate the influence of  $\gamma$ -ray irradiation on the transition temperature and thermochemical properties.

## EXPERIMENTAL.

The single crystals were grown at room temperature from the aqueous solution of the ammine hydrochloride and cupric chloride dihydrate taken

in the stoichiometric ratio. Obtained samples possess the shape of needles and their orientation was performed similarly to [3]. The thermochemical phase transition was studied by absorption spectroscopy using SF-26 spectrometer. For the temperature investigations the automatic system VRT was employed. As a source of  $\gamma$ -irradiation the  $\text{Ra}^{226}$  was used.

## RESULTS AND DISCUSSION.

Absorption spectroscopy in visible region is the simplest and very informative method of study of phase transition in DEA- $\text{CuCl}_4$ , since this transition is followed by the sharp shift both of fundamental edge and absorption bands corresponding to the d-d-transition of  $\text{Cu}^{2+}$  toward infrared side of spectrum. (Fig.1. curves 1-4). Since the data concerning the spectral properties of DEA- $\text{CuCl}_4$  were reported earlier let us consider in details the influence of  $\gamma$ -ray irradiation on the temperature of phase transition. The measurement of absorption coefficient  $k$  at certain light wave length showed that phase transition in DEA- $\text{CuCl}_4$  manifests considerable temperature hysteresis ( $\Delta T_1=6$  K). More precise value of the hysteresis was obtained at  $\lambda=633.8$  nm, since in this case the sides of hysteresis loop are practically parallel to the coordinate axes (Fig.2. curve 1), contrary to case when  $\lambda=480$  nm, for example.

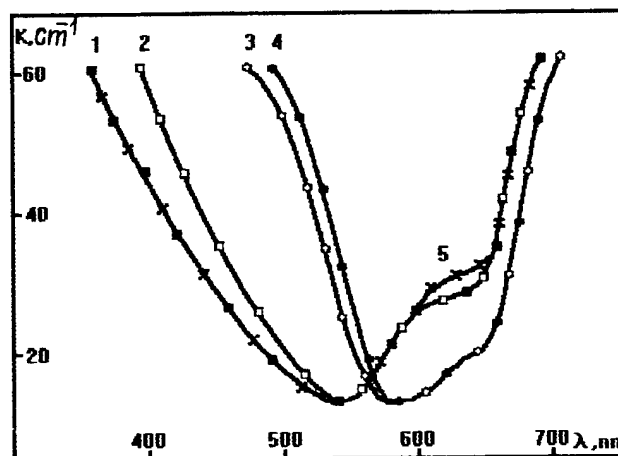


Fig.1. Optical absorption spectra of DEA- $\text{CuCl}_4$  obtained at different temperatures. (1 - 293 K, 2 - 310 K, 3 - 315 K, 4 - 320 K, 5 - 293 K, after irradiation.).

The temperature of transition in the unirradiated sample was  $T_1=311$  K (in heating run). Irradiation at room temperature leads to increasing of  $T_1$  as well as to the deformation of corresponding hysteresis loop. (Fig.2. curves 2-3). The dependence of transition temperature on the dose of irradiation is plotted in Fig.3. It is clearly seen that saturation of effect is observed at  $D=10$  Roentgen. Irradiation at room temperature also manifests itself in strengthening of absorption band at  $\lambda=595$  nm. (Fig.1. curve 5). This band is observed both in high and low temperature phases, but it is more pronounced in latter one. Annealing of

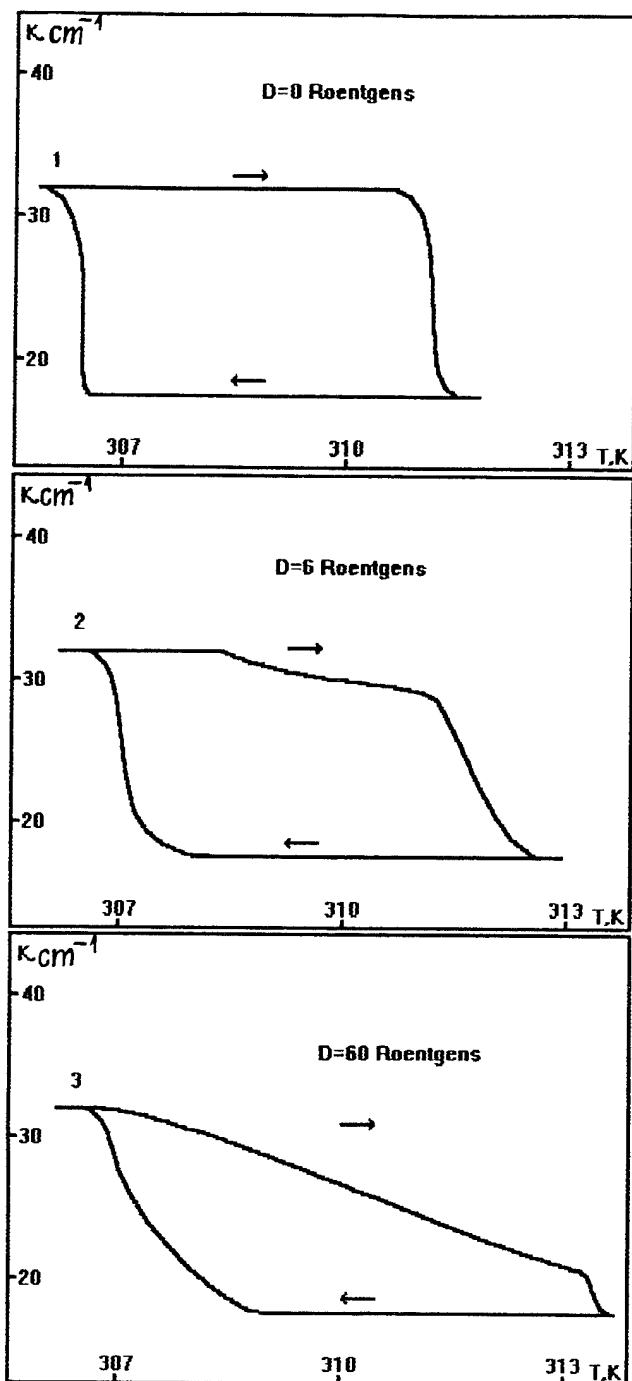


Fig.2. Hysteresis loops of optical absorption of  $\text{DEA-CuCl}_4$  at  $\lambda=633,8$  nm obtained under the influence of different doses of  $\gamma$ -ray irradiation.

the sample at  $T=318$  K during 1 hour leads to the returning of transition temperature to the previous value. However the deformation of hysteresis loop partially remains.

The shift of  $T_1$  value toward high temperatures after irradiation is rather noncharacteristic for ferroelectrics. Under such circumstances it would be very interesting to investigate whether the irradiation at more high temperatures leads to another results. Indeed, irradiation of the sample at 309 K initiates the phase transition at this temperature already through 1s (Fig.4a. the power of irradiation 40 mr/hour). To trigger the phase transition at 308 K at the same power it is necessary near 3s (Fig.4b). Therefore when the irradiation is performed just below the transition temperature, its value is already lowered. In the same time the transition temperature in cooling run remains unchanged and the

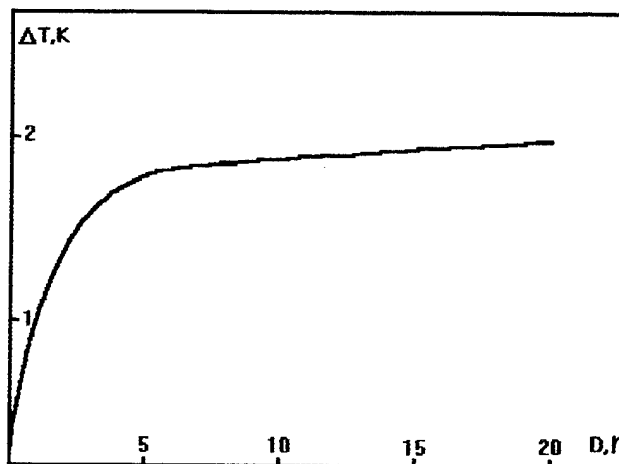


Fig.3. The dependence of the shift of the phase transition temperature on the dose of irradiation.

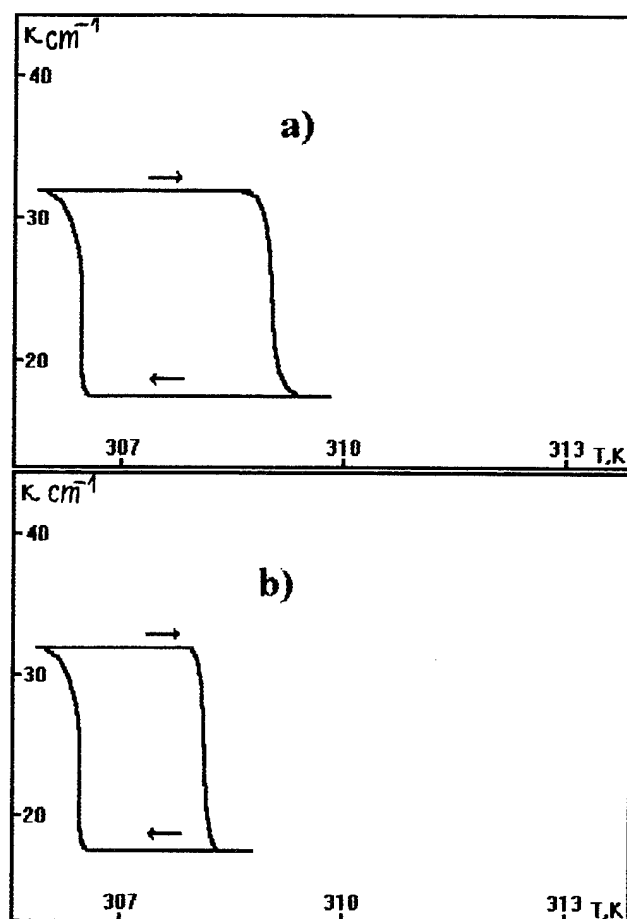


Fig.4. Hysteresis loops of optical absorption of  $\text{DEA-CuCl}_4$  irradiated at 309 K during 1s(a) and at 308 K during 3s(b). Power of  $\gamma$ -ray irradiation 40 mRoentgens/hour.

corresponding hysteresis of phase transition decreases.

To explain such a situation it is necessary to consider the structural position of constituent ions in  $\text{DEA-CuCl}_4$  and special role of hydrogen bonds. In low temperature phase the crystal is characterized by existence of strong hydrogen bond network which stabilizes the  $\text{CuCl}_4^{2-}$  ion in flat geometry. The thermal motion of ions in the high temperature phase leads to weakening of H-bonds and to corresponding relax of three independent  $\text{CuCl}_4^{2-}$  anions of the low-temperature phase toward the electrostatically favored tetrahedral geometry in the high temperature

phase. It is expedient to suppose that  $\gamma$ -irradiation at room temperature causes, firstly, breaking of H-bonds, especially of the most weak ones. After the irradiation the relaxation process proceeds which particularly leads to the reconstruction of H-bond network. However in this case the formation of structure with strong hydrogen bonds characteristic for low temperature phase is predominating. Under such circumstances the possible nuclei of high-temperature phase with weak H-bonds are suppressed and transition temperatures increases.

Such a model correlates with the possibility of existence of supercooled high temperature phase at room temperature during very long time (a few-weeks)[3].

Strengthening of absorption band at 595 nm corresponding to the planar coordination of  $\text{Cu}^{2+}$  also confirms the conclusion drawn above.

Irradiation just below the transition temperature also leads to breaking of H-bonds. However, together with increasing of thermal motions of ions this process triggers the phase transition at lower temperatures.

The  $\gamma$ -irradiation also causes the irreversible change of hysteresis loop, connected, obviously, with breaking of some bonds in diethylammonium. These defects remain in the crystals whereas the network of H-bonds may be reconstructed after annealing and following cooling of the sample into low temperature phase. Remaining defects lead to the eroding of phase transition. The phase transition approaches to the transition of second order. By the way, such a situation is characteristic of the irradiated ferroelectrics.

It must be noted that thermochromic phase transition in  $\text{DEA-CuCl}_4$  may be shifted under the influence of irradiations by quanta of lower energy. Indeed, the irradiation of  $\text{DEA-CuCl}_4$  by powerful beam of ultraviolet light obtained using the deuterium lamp at the temperature just below the phase transition also leads to the lowering of transition temperature. However, the time of irradiation must be in a few orders larger then in the case of  $\gamma$ -irradiation.

#### REFERENCES.

- [1] O.G.Vlokh, M.I.Bublyk, I.I.Polovinko, O.M.Olchova, S.A.Sveleba, and T.M.Sosnovskiy, "Optical Properties of New Ferroelastics  $(\text{NH}_2(\text{C}_2\text{H}_5)_2)_2\text{CuCl}_4$  and  $(\text{NH}_2(\text{C}_2\text{H}_5)_2)_2\text{CoCl}_4$ ", *Pisma v Zhurnal Tiekhnicheskoi Fiziki* vol.16, pp.23-26, August 1990.
- [2] O.G.Vlokh, M.I.Bublyk, I.I.Polovinko, S.A.Sveleba, and T.M.Sosnovskiy, "Temperature Evolution of Absorption Edge in  $(\text{NH}_2(\text{C}_2\text{H}_5)_2)_2\text{CuCl}_4$  Crystal", *Optika i Spektroskopiya*, vol.71, pp.292-293, February 1991.
- [3] D.R.Bloomquist, M.R.Pressprich, and R.D.Willett, "Thermochromism in Copper (II) Halide Salts.4.  $(\text{NH}_2(\text{C}_2\text{H}_5)_2)_2\text{CuCl}_4$ , Structure of the High-Temperature Phase and Physical Characterization of Its Two Phases", *J. Am. Chem. Soc.*, vol.110, pp.7391-7398, 1988.

# Fabration of Pyroelectric Thin Film Ceramics by Tape Casting Method

S. R. Zhang and C. W. Zhong  
University of Electronic Science and Technology of China  
Chengdu, 610054, P. R. China

R. B. Liu, S. W. Lin, C. F. Qu, C. H. Yao and Y. H. Jin  
Shanghai Institute of Ceramics Chinese Academy of Science  
Shanghai, 200050, P. R. China

**Abstract**—The purpose of this research is to obtain the sensitive element of infrared (IR) detector directly by tape casting method. The green tapes of pyroelectric ceramic with the thickness of 100-160  $\mu\text{m}$  were cast from the slurry composed of pyroelectric ceramic powder and an appropriate binder-solvent system. The influence of a special "Sandwich" sintering process on the properties of the monolayer thin film pyroelectric ceramic were investigated. As a result, smooth thin pyroelectric ceramic sheets with relative high density have been got. The dielectric and pyroelectric properties of samples made by tape casting were almost the same as those shaped by dry pressing process. The experiment proves that the tape casting method is a feasible process to make pyroelectric thin film ceramics.

## INTRODUCTION

Pyroelectric ceramics have been widely used as sensitive elements for infrared detector. Generally, the thin ceramic sensitive elements with dimensions of  $3 \times 5 \times 0.08\text{mm}^3$  are processed from pyroelectric ceramic block with complicated cutting and grinding machinery. The utilization ratio of the material is only about 5% due to the waste caused by cutting and grinding process. If the sensitive elements can be prepared directly from pyroelectric ceramic film, the efficiency of manufacturing can be obviously increased and the cost can be greatly reduced.

As well known, the tape casting is a basic process for production of commercial multilayer ceramic capacitors.<sup>[1]</sup> This report presents the results of an attempt to prepare pyroelectric ceramic thin film by application of tape casting method.

## EXPERIMENT

### 1. Preparation of green tape

The flow chart of preparation process of the green tape of pyroelectric ceramic is shown in figure 1.

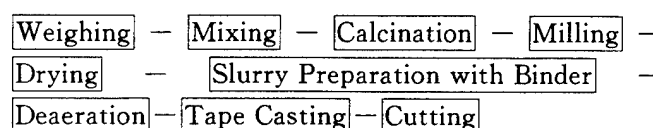


Fig. 1 The flow chart of tape casting process

The ceramic used in this experiment was composed of a strontium doped  $\text{PbZrO}_3\text{-PbNbFeO}_3\text{-PbTiO}_3$  system, which is a newly developed pyroelectric ceramic with good performances.<sup>[2]</sup> The different green tapes with the thickness of 100 $\mu\text{m}$  and 200 $\mu\text{m}$  were prepared. Respecting of high gravity of the ceramic material, an organic binder system with low portion of solvent was used for slurry preparation, which provided better filming ability and avoided defects such as pine hole and cracks on the green tape.

### 2. The sintering of monolayer ceramic film

Before firing, the green tapes were cut into small pieces of  $1.5 \times 1.5$  square millimeters. The burnout of organic substances was carried out at a slow rate of heating until the ceramic film possessed certain mechanical strength. In order to obtain flat ceramic film, a special "Sandwich" sintering method was designed. The green sheets were placed between an alumina pressing cover and an alumina substrate as shown in figure 2.

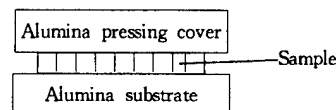


Fig. 2 Schematic illustration of "Sandwich" sintering

After cleaned by ultrasonic, the ceramic films were electroded by vacuum deposited silver, and then polarized in air under an electric field of 4kV/mm in 20 minutes. The volume density was measured by water displacement, and the pyroelectric coefficient was measured by charge integral method.

## RESULTS AND DISCUSSION

### 1. The influence of firing temperature

For green tapes with the thickness of 100 $\mu\text{m}$ , the shrinkage and density depending on firing conditions are shown in table 1.

Table 1 The Dependence of Thickness and Density on Firing Conditions

Sintering Temperature (°C)	1120	1140	1160	1160	1160	1160	1180
Holding Time (min)	30	30	15	20	25	30	30
Thickness ( $\mu\text{m}$ )	62	56	54	54	56	56	60
Density ( $\text{g}/\text{cm}^3$ )	7.16	7.27	7.23	7.43	7.53	7.37	6.97

The proper sintering temperature was mainly determined by thickness shrinkage extent of samples. In addition, it was confirmed by the measurement of volume density.

In the firing process, because the samples directly contacted with alumina substrate and pressing cover, the atmosphere needed to be properly controlled. In the experiment certain amount of ceramic powder was used around the firing samples, which had been proved to be useful for preventing non-stoichiometry.

From the samples sintered by 1160°C/20min, 1160°C/25min and 1160°C/30min, the dielectric and piezoelectric properties were measured. The results are presented as below.

Table 2 Dielectric and Piezoelectric Properties of Ceramic Thin Film

Sintering Condition		1160°C 30min			1160°C 25min			1160°C 20min		
Samples		1	2	3	1	2	3	1	2	3
Before Poling	$\epsilon_r$	396	382	399	396	406	401	362	360	414
	$\tan\delta\%$	3.4	2.5	4.3	1.6	1.1	1.2	6.1	1.4	2.2
After Poling	$\epsilon_r$	296	277	282	313	317	318	317	294	320
	$\tan\delta\%$	1.2	2.9	1.7	0.9	0.9	0.9	2.8	1.4	1.3
$d_{31} \times 10^{-12} \text{C/N}$		58~60			58~60			58~60		

### 2. The pyroelectric properties of ceramic thin film

At twenty four hours after polarization, the pyro-

electric coefficient of the ceramic thin film was measured in the temperature range of 10–74°C. The value of linear pyroelectric coefficient was  $5.0 \times 10^{-4} \text{ cm}^{-2} \text{ K}^{-1}$ .

Several characteristics of the samples made by tape casting was compared with that by dry pressing for the same composition of ceramics in table 3.

Table 3 Properties Comparison of Samples Prepared by Tape Casting and Dry Pressing

	$\epsilon_r$	$\tan\delta\%$	$p$ ( $10^{-4} \text{Cm}^{-1} \text{K}^{-1}$ )	Density $\text{g}/\text{cm}^3$
Tape Casting	315	$\approx 1$	5.0	7.5
Dry Pressing Pressureless Sintering	310	1	5.1	7.6
Dry Pressing Hot Pressing Sintering	320	0.5	5.1	7.8

While it is usually difficult for the thickness of ceramic film to be reduced under 80 $\mu\text{m}$  by the dry pressing process, it is quite easy to obtain ceramic film with thickness less than 60 $\mu\text{m}$  by the tape casting method. Although the dielectric loss of the samples made by tape casting is slightly larger than that of samples made by dry pressing (Hot press sintering), the samples made by tape casting can still remain a high ratio of signal to noise because for a thinner sensitive element the signal responding voltage is higher. Considering the convenience of process, tape casting is a promising way for preparation of pyroelectric thin film ceramic used for IR detector sensitive element.

## ACKNOWLEDGEMENT

One of the authors R. B. Liu is grateful for the support of K. C. Wong Education Foundation, Hong Kong.

## REFERENCE

- [1] L. Sheppard, "Progress Continues in Capacitor Technology," *Amer. Ceram. Soc. Bull.*, vol. 72[3], pp. 45-57, 1993.
- [2] P. C. Osbond and R. W. Whatmore, "Improvements to Pyroelectric Ceramics via Strontium Doping of the Lead Zirconate-Lead Iron Niobium-Lead Titanate," *Ferroelectrics*, vol. 118, pp. 93-101, 1991.

# Dielectric, Piezoelectric, and Pyroelectric Properties of Barium-Modified Lead Magnesium Tantalate-Lead Titanate Ceramics

S.W. Choi and J.M. Jung  
Department of Physics, Dankook University,  
29 Anseodong, Cheonan, Chungnam, Korea

**Abstract** — Dielectric, piezoelectric and pyroelectric properties of relaxor ferroelectrics in the  $0.65\text{Pb}_{1-x}\text{Ba}_x(\text{Mg}_{1/3}\text{Ta}_{2/3})\text{O}_3\text{-}0.35\text{PbTiO}_3$  solid solution series have been investigated. The dielectric constant and loss of ceramic samples were determined. The piezoelectric  $d_{33}$  constant and electromechanical coupling factor were measured for various compositions in the Ba-doping PMT-PT ceramics. The pyroelectric coefficient and spontaneous polarization were measured by the static Byer-Roundy method as a function of temperature. The values of dielectric constant, electromechanical coupling factor and pyroelectric coefficient for Ba-doped PMT-PT are much larger compared to the values observed for the undoped PMT-PT ceramics. Ba-doping also shifted the  $T_c$  downward, approximately  $6^\circ\text{C/mol\%}$  addition of Ba. Further additions of Ba could be used to shift the  $T_c$  downward without significantly changing the dielectric behavior.

## INTRODUCTION

Perovskite lead magnesium Tantalate,  $\text{Pb}(\text{Mg}_{1/3}\text{Ta}_{2/3})\text{O}_3$  (PMT) was first synthesized by Bokov and Myl'nikova.<sup>[1]</sup> The relaxor dielectric maxima at 1 kHz occurs at  $-100^\circ\text{C}$ . However, with the addition of  $\text{PbTiO}_3$  (PT) ( $T_c = 490^\circ\text{C}$ ), the compositions in the PMT-PT solid solution exhibit a morphotropic phase boundary between the rhombohedral and tetragonal phases at about 29 ~ 39 mol% PT.<sup>[2]</sup>

In previous work<sup>[3]</sup> it was reported that the PMT-PT ceramics doped with lanthanum have higher dielectric and pyroelectric constants over those of the undoped PMT-PT compositions. The compositions 0.65PMT-0.35PT with 1 ~ 12 mol% Ba-doping have been selected. The effect of Ba-doping of dielectric, piezoelectric, and pyroelectric properties of 0.65PMT-0.35PT is discussed.

## EXPERIMENT PROCEDURE

Ceramic samples (reagent grade powders) across the 0.65PMT-0.35PT- $x\text{Ba}$  series were prepared using the columbite precursor method.<sup>[4]</sup> The process basically involves the prereaction of  $\text{MgO}$  and  $\text{Ta}_2\text{O}_5$  to form the columbite phase  $\text{MgTa}_2\text{O}_6$  prior to reaction with  $\text{PbCO}_3$ ,  $\text{TiO}_2$  and  $\text{BaCO}_3$ . Upon milling, the various powders were cold pressed to form disks, followed by sintering at  $1250^\circ\text{C}$  for 4 hours in closed alumina crucibles.  $\text{PbZrO}_3$  powder was added to help control Pb stoichiometry in the samples.

The sintered samples were characterized by x-ray diffraction (XRD) to insure phase purity. The grain size was determined of fracture surfaces of the pellets using scanning electron microscopy (SEM).

For the electrical measurement, opposite faces of the samples were coated with sputtered silver electrodes. Temperature dependence of the dielectric constant and loss were measured at various frequencies at the heating rate of  $4^\circ\text{C/min}$  by using an Impedance Analyzer (HP4192A). Piezoelectric properties were measured by the resonance-antiresonance method<sup>[5]</sup> and Berlincourt  $d_{33}$  meter. The pyroelectric coefficient and spontaneous polarization were measured by the static Byer-Roundy method<sup>[6]</sup> as the samples were heated at a rate of  $4^\circ\text{C/min}$  through the phase transition. Prior to the piezoelectric and pyroelectric measurements each sample was poled by applying a DC field of 20 kV/cm at room temperature for 30 min.

## RESULTS AND DISCUSSION

### Physical and Dielectric Properties

Figure 1 shows the SEM fractographs of 0.65PMT-0.35PT- $x\text{Ba}$  ceramics fired at  $850^\circ\text{C}$  and  $1250^\circ\text{C}$  for 4 hours as a function of  $\text{BaCO}_3$  content. It can be seen that the grain sizes were increased about  $4.5\text{ }\mu\text{m}$  to  $9\text{ }\mu\text{m}$  for PMT-PT and PMT-PT-0.01Ba system, respectively. But above 1 mol% of additive the grain sizes decrease. The optimum amount of  $\text{BaCO}_3$  added is about 1 mol% in this research. The resulted densities of the 0.65PMT-0.35PT-0.01Ba ceramics were greater than 95 % of the theoretical value.

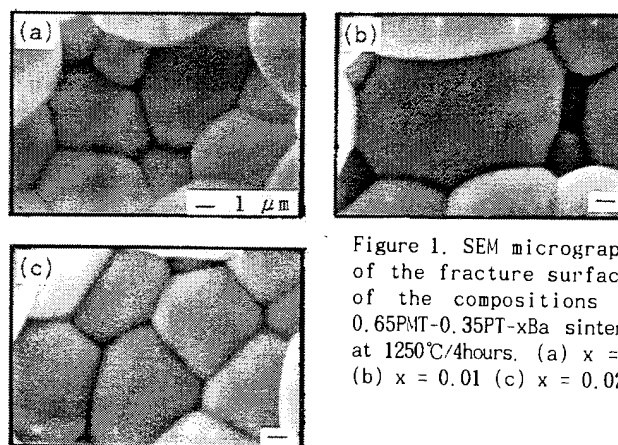


Figure 1. SEM micrographs of the fracture surfaces of the compositions of 0.65PMT-0.35PT- $x\text{Ba}$  sintered at  $1250^\circ\text{C}/4\text{hours}$ . (a)  $x = 0$  (b)  $x = 0.01$  (c)  $x = 0.02$

Figure 2 shows the XRD patterns of 0.65PMT-0.35PT-0.01Ba composition confirming the presence of the perovskite phase. The percentage of perovskite phase was determined by powder x-ray diffraction patterns of calcined and fired ceramics. For all the compositions the amount of perovskite phase is  $< 85\%$  for calcining temperature below  $850^\circ\text{C}$ . Compositions with 1 mol% Ba-doping sintered at  $1250^\circ\text{C}$  showed 100 % perovskite phase (Fig.2).

Figure 3 shows the typical plot of the temperature dependence of dielectric constant and dissipation factor at various frequencies (0.1 to 100 kHz) for composition 0.65PMT-0.35PT-0.01Ba. The  $K$  vs.  $T$  shows the typical relaxor behavior. Dielectric constant vs. temperature behavior at 1 kHz is shown in Figure 4 for various compositions in the 0.65PMT-0.35PT- $x\text{Ba}$ . The addition of  $\text{BaCO}_3$  affects the dielectric properties of 0.65PMT-0.35PT ceramics. The dielectric constant at  $T_c$  increases with additions of Ba up to 5 mol% and then decreases with further additions of Ba (Fig.4), but the temperature range of high-dielectric constant values become still broader. In small concentrations, substitutions modify the ferroelectric properties by controlling grain size and by broadening the Curie peak. Curie peak characteristics, therefore, may be affected by substantial chemical substitution or inhomogeneities which exist in the sintered materials.<sup>[7]</sup> It is found that the room-temperature dielectric constant increased by a factor of about 2 times for 9 mol% barium doping in the 0.65PMT-0.35PT- $x\text{Ba}$  as compared with that of the undoped composition as shown in Fig.4, which is associated with the decrease in  $T_c$  of the PMT-PT ceramics. It is also found that the Ba-doping shifts the phase transition temperature downward.



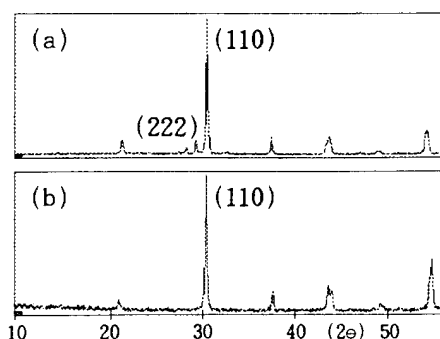


Figure 2. X-ray diffraction patterns of 0.65PMT-0.35PT-0.01Ba. (a) Calcined at 850 °C for 4 hours. (b) Sintered at 1250 °C for 4 hours.

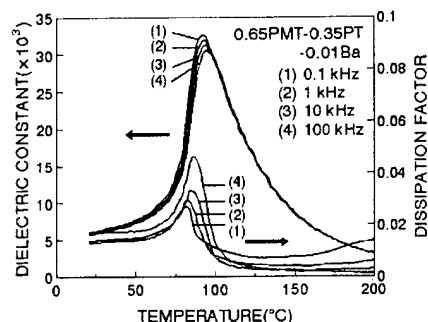


Figure 3. Temperature dependence of dielectric constant and dissipation factor at various frequencies for 0.65PMT-0.35PT-0.01Ba.

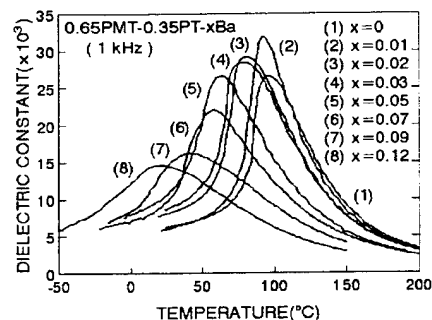


Figure 4. Dielectric constant of 0.65PMT-0.35PT-xBa compositions at varying temperature.

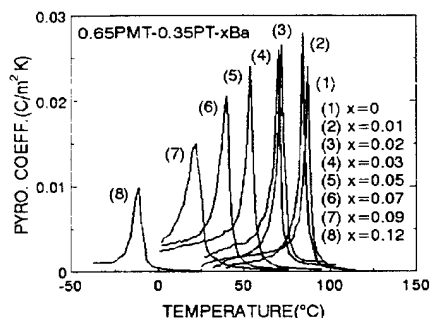


Figure 5. Pyroelectric coefficient of 0.65PMT-0.35PT-xBa compositions at varying temperature.

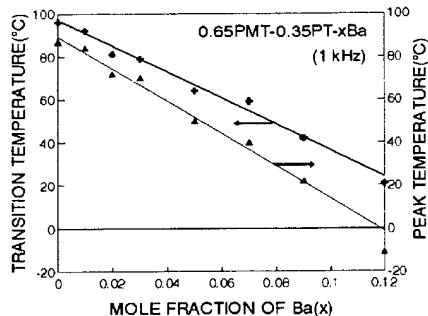


Figure 6. Transition temperature and peak temperature of 0.65PMT-0.35PT-xBa compositions.

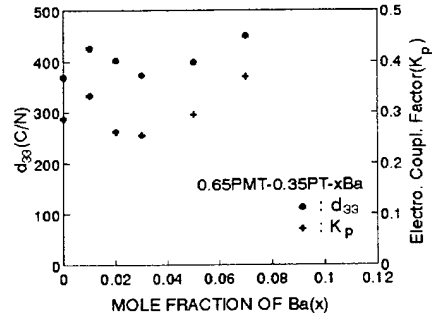


Figure 7. Piezoelectric constant  $d_{33}$  and electromechanical coupling factor  $K_p$  of 0.65PMT-0.35PT-xBa compositions at room temperature.

The transition temperature with mole fraction of Ba in the 0.65PMT-0.35PT-xBa is shown in Fig.6. The transition temperature decreased almost linearly as the amount of Ba in the composition increases, their rates of decrease are about 6 °C/mol%. These shift of the transition temperature by Ba-substitution for Pb may be related to the distribution of ions having different ionic radii in the same sublattice of a complex compound with perovskite structure.<sup>[8]</sup>

#### Pyroelectric and Piezoelectric Properties

Fig.5 shows the pyroelectric coefficient for various compositions in the 0.65PMT-0.35PT-xBa solid solutions as a function of temperature. Pyroelectric coefficient increases with increase of mol% Ba. However, for  $x$  more than  $\sim 0.02$ , the pyroelectric coefficient decreased with  $x$ . Pyroelectric coefficient decreases with increase of mol% Ba similar to that observed in dielectric constant vs. temperature. The peak temperature of pyroelectric coefficient with mole fraction of Ba in the 0.65PMT-0.35PT-xBa is shown in Figure 6. The peak temperature decreases almost linearly as the amount of Ba in the composition increases, their rates of decrease are about 6.5 °C/mol%. Figure 7 shows the piezoelectric constant  $d_{33}$  and electromechanical coupling factor  $K_p$  of the composition 0.65PMT-0.35PT-xBa at room temperature as the mole fraction of Ba. The maximum piezoelectric  $d_{33}$  constant and electromechanical coupling factor  $K_p$  are observed at 7 mol% barium doping. The foregoing composition is in good agreement with those exhibiting maxima in spontaneous polarization.

#### CONCLUSIONS

The barium-modified 0.65PMT-0.35PT ceramics were found to promote densification and grain growth. The dielectric constant of 0.65PMT-0.35PT-xBa ( $x = 0.01$  to 0.03) ceramics

increases considerably with the substitution of Ba. The Curie temperature and peak temperature of pyroelectric coefficient decrease almost linearly with small change of Ba amount, their rates of decrease are about 6 °C and 6.5 °C/mol% addition of Ba, respectively. Pyroelectric coefficient increases with increase of mol% Ba. However, for  $x$  more than  $\sim 0.02$ , the pyroelectric coefficient decreases with  $x$ . The maximum piezoelectric  $d_{33}$  and electromechanical coupling factor  $K_p$  at room temperature are observed at 7 mol% barium doping.

#### ACKNOWLEDGEMENT

This work was supported (in part) by the KOSEF through the SRC of Excellence Program.

#### REFERENCES

- [1] V.A.Bokov and I.E.Myl'nikova, Sov. Phys. Solid State, 2, 2428(1961).
- [2] Y.J.Kim and S.W.Choi, Ferroelectrics, 108, 241(1990).
- [3] Y.J.Kim, S.W.Choi and A.S.Bhalla, to be published in Ferroelectrics.
- [4] S.L.Swartz and T.R.ShROUT, Mat. Res. Bull., 17, 1245(1982).
- [5] Proc. IRE, Inst. Radio Eng., 49, 1161(1961).
- [6] R.L.Byer and C.R.Roundy, Ferroelectrics, 3, 333(1972).
- [7] D.Henning and G.Rosenstein, J. Am. Ceram. Soc., 67, 249(1984).
- [8] G.A.Smolenskii and A.I.Agranovskaya, Sov. Phys. Solid State, 1, 1429(1960).

# Dielectric, Piezoelectric and Pyroelectric Properties of the $\text{Pb}(\text{Mg}_{1/3}\text{Ta}_{2/3})\text{O}_3$ - $\text{PbTiO}_3$ - $\text{PbZrO}_3$ Solid Solution System

H.Y. Weon, Y.J. Kim and S.W. Choi

Department of Physics, Dankook University, 29 Anseodong, Chonan, Chungnam, Korea

**Abstract** — Dielectric, piezoelectric and pyroelectric response of selected compositions from the solid solution system have been investigated as a function of PT and PZ content for composition near the morphotropic phase boundary (PMT-PT). The dielectric constant and loss of poled samples were determined. The piezoelectric  $d_{33}$  constant and electromechanical coupling factor were measured for various composition in the system. The pyroelectric coefficient and spontaneous polarization were measured by the static Byer-Roundy method as a function of temperature. The stability of the perovskite phase was studied as a function of sintering temperature. The transition temperature of the ceramics decreased gradually with the addition of PZ.

## INTRODUCTION

Perovskite lead magnesium tantalate,  $\text{Pb}(\text{Mg}_{1/3}\text{Ta}_{2/3})\text{O}_3$  (PMT) was first synthesized by Bokov and Myl'nikova.<sup>[1]</sup> The relaxor dielectric maxima at 1 kHz occurs at  $-100^\circ\text{C}$ . However, with the addition of  $\text{PbTiO}_3$  (PT) ( $T_c=490^\circ\text{C}$ ), the compositions in the PMT-PT ceramics exhibit a morphotropic phase boundary between the rhombohedral and tetragonal phases at about 29~39 mol% PT.<sup>[2]</sup> In the case of the most of PMT-PT series the transition temperature is above the room temperature. With the addition of  $\text{PbZrO}_3$  (PZ) ( $T_c=230^\circ\text{C}$ ), the transition temperature can be suitably adjusted for the piezoelectric and pyroelectric applications. It was the objective of this work to explore the dielectric, piezoelectric and pyroelectric behavior for PMT-PT-PZ compositions.

## EXPERIMENTAL PROCEDURE

The compositions selected for the present study were of the type  $0.625\text{PMT}-(0.375-x)\text{PT}-x\text{PZ}$  with  $x$  varying between 0 and 0.35. The ceramics were prepared according to the usual sintering technique. Reagent-grade oxide powders of  $\text{PbO}$ ,  $\text{MgO}$ ,  $\text{Ta}_2\text{O}_5$ ,  $\text{TiO}_2$  and  $\text{ZrO}_2$  were used as starting materials. The oxides mixed by ball milling for 15 h were calcined at  $850^\circ\text{C}$  for 4 h. The calcined powders were crushed and ball-milled and pellets  $\approx 10\text{mm}$  in diameter and about  $2\text{mm}$  in thickness were pressed using PVA binder. The pellets were then fired between  $1200^\circ\text{C}$  and  $1325^\circ\text{C}$  for 3 h in sealed alumina crucibles. The percentage of perovskite phase was determined by powder X-ray diffraction patterns of fired ceramics.

The dielectric properties were measured with an Impedance Analyzer (HP 4192A), control unit and its interface. The dielectric constant and loss were measured as a function of temperature at various frequencies between 0.1 and 100 kHz at a temperature rate of  $4^\circ\text{C}/\text{min}$ . The pyroelectric coefficient and spontaneous polarization were measured by the static Byer-Roundy method,<sup>[3]</sup> again at a rate of  $4^\circ\text{C}/\text{min}$ . Piezoelectric  $d_{33}$  constant and electromechanical coupling factor  $k_p$  were measured by using Berlincourt piezo

$d_{33}$  meter and resonance-antiresonance method,<sup>[4]</sup> respectively. Prior to piezoelectric and pyroelectric measurements the specimens were poled by applying a DC field of about 20 kV/cm at room temperature.

## RESULTS AND DISCUSSION

### Sintering and Perovskite Phase

Several compositions in the  $0.625\text{PMT}-(0.375-x)\text{PT}-x\text{PZ}$  system (with  $x=0.00$  to 0.20) were sintered at different temperatures to study the effect of sintering conditions on the amount of perovskite phase. Figure 1 shows the XRD patterns of  $0.625\text{PMT}-0.325\text{PT}-0.05\text{PZ}$  ceramics confirming the presence of the perovskite phase.

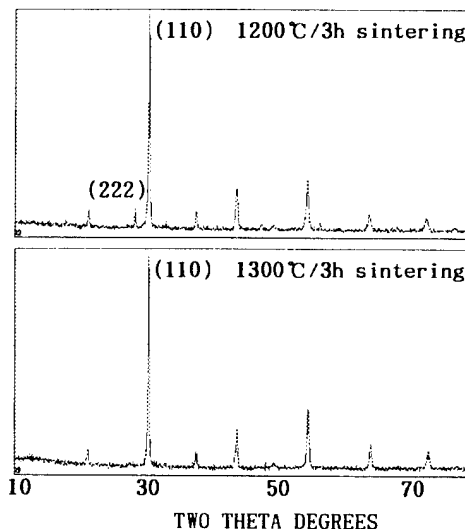


Figure 1. X-ray diffraction patterns for various sintering temperature ( $0.625\text{PMT}-0.325\text{PT}-0.05\text{PZ}$ ).

Figure 2 shows a plot of the percentage of perovskite phase in each composition as a function of sintering temperature. For all the compositions the amount of perovskite phase is  $<85\%$  for sintering temperature below  $1200^\circ\text{C}$ . Compositions with 5 to 20 mol% of PZ, sintered at  $1300^\circ\text{C}$  showed 100% perovskite phase. In all the compositions, a small fraction of pyrochlore phase was observed for sintering above  $1300^\circ\text{C}$ . This behavior is probably due to the loss of  $\text{PbO}$  at high temperatures.

### Dielectric Properties

Figure 3 shows typical plot of the dielectric constant and loss vs. temperature at various frequencies (0.1 to 100 kHz) for  $0.625\text{PMT}-0.325\text{PT}-0.05\text{PZ}$ . The dielectric constant vs. temperature behavior at 1 kHz is shown in Figure 4 for various compositions  $0.625\text{PMT}-(0.375-x)\text{PT}-x\text{PZ}$  ( $0.00 \leq x \leq 0.35$ ). The dielectric constant at  $T_c$  increases with additions of PZ up to 5 mol% and then decreases with further additions of PZ (Figure 4).

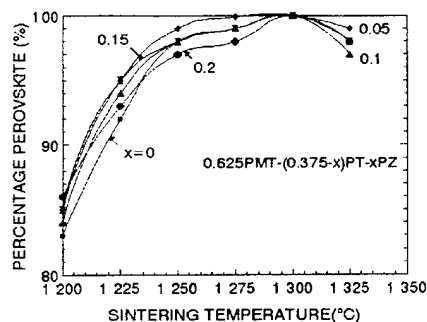


Figure 2. Effect of sintering temperature on percentage of perovskite.

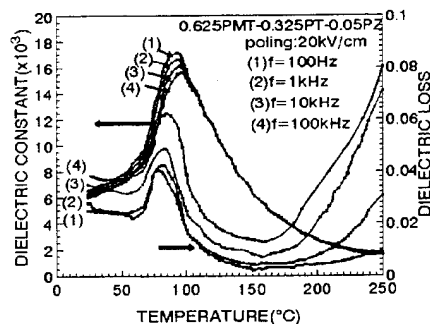


Figure 3. Dielectric constant and loss vs. temperature for different frequencies.

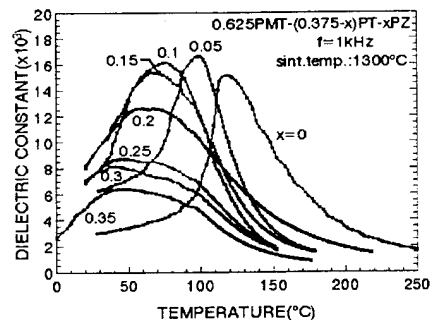


Figure 4. Temperature dependence of dielectric constant (1 kHz) in the 0.625PMT-(0.375-x)PT-xPZ system.

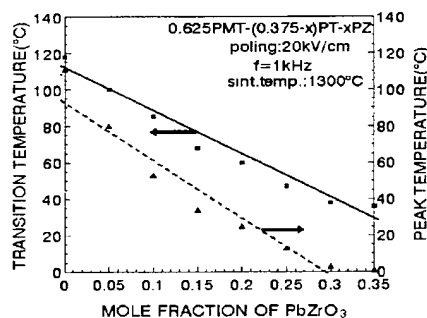


Figure 5. Transition and peak temperature as a function of  $\text{PbZrO}_3$  in the 0.625PMT-(0.375-x)PT-xPZ system.

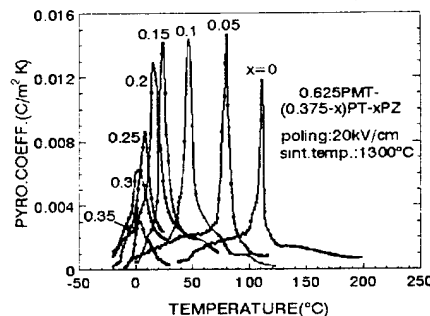


Figure 6. Temperature dependence of pyroelectric coefficient in the 0.625PMT-(0.375-x)PT-xPZ system.

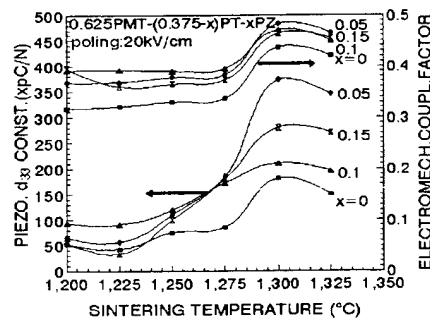


Figure 7. Effect of sintering temperature on piezoelectric  $d_{33}$  constant and electromechanical coupling factor ( $k_p$ ).

In the compositions 0.625PMT-(0.375-x)PT-xPZ, the variation of  $T_c$  with the mole fraction of PZ is shown in Figure 5. The  $T_c$  decreases with increasing PZ, their rates of decrease are about  $2.5^\circ\text{C/mol}\%$ .

#### Pyroelectric and Piezoelectric Properties

Figure 6 shows the pyroelectric coefficient for various compositions in the 0.625PMT-(0.375-x)PT-xPZ as a function of temperature. Pyroelectric coefficient increases with mol% PZ. However, for  $x$  more than  $\sim 0.1$ , the pyroelectric coefficient decreased with  $x$ . The compositions 0.625PMT-(0.375-x)PT-xPZ ( $x = 0.15$  to  $0.20$ ) have their  $T_c$  values near room temperature. The room-temperature pyroelectric coefficient of  $0.014 \text{ (C/m}^2\text{K)}$  is found at the composition  $x=15 \text{ mol}\%$  of PZ content. The peak temperature decreases almost linearly as the amount of PZ in the composition increases, their rates of decrease are about  $3^\circ\text{C/mol}\%$  (Figure 5).

Figure 7 shows the piezoelectric  $d_{33}$  and electromechanical coupling factor  $k_p$  of the composition PMT-PT-xPZ as a function of sintering temperature. The optimum conditions for obtaining samples with improved piezoelectric properties occur at a sintering temperature of  $1300^\circ\text{C}$ . The maximum piezoelectric constant was observed at  $5 \text{ mol}\%$  PZ content.

#### CONCLUSIONS

Compositions with 5 to 20 mol% of PZ, sintered at  $1300^\circ\text{C}$  showed 100% perovskite phase. The dielectric,

pyroelectric and piezoelectric constant were found to improve with increasing sintering temperature up to  $1300^\circ\text{C}$ . The maximum dielectric, pyroelectric and piezoelectric constant were observed at about 5 mol% PZ content. The Curie temperature and peak temperature of pyroelectric coefficient decrease almost linearly as the amount of PZ in the composition increases.

#### ACKNOWLEDGEMENT

This work was supported (in part) by the KOSEF through the SRC of Excellence Program.

#### REFERENCES

- [1] V.A. Bokov and I.E. Myl'nikova, "Ferroelectric Properties of Monocrystals New Perovskite Compounds", Soviet Physics-Solid State, vol. 2 (11), pp.2428-2432, May 1961.
- [2] Y.J. Kim and S.W. Choi, "Dielectric and Pyroelectric Properties in the  $\text{Pb}(\text{Mg}_{1/3}\text{Ta}_{2/3})\text{O}_3$ - $\text{PbTiO}_3$  Solid Solution Ceramics", Ferroelectrics, vol.108, pp.241-246, 1990.
- [3] R.L. Byer and C.R. Roundy, "Pyroelectric Coefficient Direct Measurement Technique and Application to a NSEC Response Time Detector", Ferroelectrics, vol.3, pp.333-338, 1972.
- [4] IRE Standards on Piezoelectric Crystal: Measurement of Piezoelectric Ceramics, Proc. 1961, IRE (Inst. Radio Engrs.), vol.49(7), pp.1161-1169, 1961.

# Dielectric, Piezoelectric, and Pyroelectric Properties of Sr-doped PMT-PT Solid Solution Ceramics

J.M. Jung, Y.H. Park and S.W. Choi  
Department of Physics, Dankook University,  
29 Anseodong, Cheonan, Chungnam, Korea

**Abstract** — Dielectric, piezoelectric and pyroelectric properties of  $0.65(\text{Pb}_{1-x}\text{Sr}_x)(\text{Mg}_{1/3}\text{Ta}_{2/3})\text{O}_3$ - $0.35\text{PbTiO}_3$  ( $0 \leq x \leq 0.12$ ) solid solution near the morphotropic phase boundary (PMT-PT) have been investigated. Dielectric constant and loss of poled ceramic samples were determined. The electromechanical coupling factor and piezoelectric  $d_{33}$  constant were measured for various compositions in the ceramics. The pyroelectric coefficient and spontaneous polarization were measured by the static Byer-Roundy method as a function of temperature. The values of dielectric constant, piezoelectric  $d_{33}$  constant and pyroelectric coefficient for Sr-doped PMT-PT are larger compared to the values observed for undoped PMT-PT ceramics. Transition temperature is continuously shifted to lower temperature with increase of a small amount of  $\text{SrCO}_3$ .

## INTRODUCTION

In 1961 Bokov and Myl'nikova reported the temperature dependence of the dielectric constant, dielectric loss and polarization of  $\text{Pb}(\text{Mg}_{1/3}\text{Ta}_{2/3})\text{O}_3$  (PMT).<sup>[1]</sup> The main feature of dielectric properties of PMT is a broad maximum of dielectric constant at the transition temperature. The relaxor dielectric maxima at 1 kHz occurs at  $-100^\circ\text{C}$ . However, with the addition of  $\text{PbTiO}_3$  (PT) ( $T_c = 490^\circ\text{C}$ ), the compositions in the PMT-PT solid solution exhibit a morphotropic phase boundary at about 29 ~ 39 mol% PT.<sup>[2]</sup> Previously, the effect of  $\text{La}_2\text{O}_3$  additive on the dielectric and pyroelectric properties of the system PMT-PT was studied.<sup>[3]</sup> The effect of Sr-doping of dielectric, piezoelectric and pyroelectric properties of 0.65PMT-0.35PT ceramics is discussed in the present work. The compositions 0.65PMT-0.35PT with 1 ~ 12 mole% Sr-doping have been selected, in accordance with the solid solution phase diagram.<sup>[2]</sup>

## EXPERIMENTAL PROCEDURE

Ceramic samples were prepared by the conventional technique. Reagent-grade oxide powders of  $\text{PbCO}_3$ ,  $\text{TiO}_2$ ,  $\text{Ta}_2\text{O}_5$ ,  $\text{MgO}$  and  $\text{SrCO}_3$  with purity better than 99.8 % were used as starting raw materials. The columbite precursor method by Swartz and Shrout<sup>[4]</sup> for the synthesis of the various composition was used. The sintered samples were characterized by x-ray diffraction to insure phase purity. The grain size was determined on fracture surfaces of pellets using scanning electron microscopy (SEM). Opposite faces of the samples were coated with sputtered silver electrodes.

Dielectric properties were measured with an Impedance Analyzer (HP4192A), control unit and its interface. The dielectric constant and dissipation factor were measured as a function of temperature at various frequencies between 0.1 and 100 kHz at a temperature rate of  $4^\circ\text{C}/\text{min}$ . The pyroelectric coefficient and spontaneous polarization were measured by the static Byer-Roundy method<sup>[5]</sup> as the samples were heated, again at a rate of  $4^\circ\text{C}/\text{min}$ , through the phase transition region. Prior to the dielectric, pyroelectric and piezoelectric measurements the specimens were poled by applying a DC field of 20 kV/cm at room temperature. Piezoelectric  $d_{33}$  was measured by using Berlincourt  $d_{33}$

meter. Electromechanical coupling factor  $K_p$  was measured by using resonance-antiresonance method.<sup>[6]</sup>

## RESULTS AND DISCUSSION

### Grain Size and Density

Modification of the 0.65PMT-0.35PT ceramics by the addition of strontium carbonate has marked beneficial effects on the basic properties of the ceramics. Fig.1 shows the XRD patterns of 0.65PMT-0.35PT-0.02Sr composition confirming the presence of the perovskite phase. As determined by x-ray powder diffraction patterns, less than 1 % pyrochlore phase was detected for the various compositions.

Typical SEM photomicrographs of the fracture surfaces are shown in Fig.2. It is clearly evident that Sr-doped ceramics have larger grain sizes than those of undoped ceramics. As observed, the grain sizes were increased about  $4.5\ \mu\text{m}$  to  $8\ \mu\text{m}$  for PMT-PT and PMT-PT-0.02Sr ceramics, respectively. The resulted densities of the PMT-PT-xSr ceramics were greater than 92 % of the theoretical value. This behavior may be explained by the fact that small amount of Sr acted as a fluxing agent and promoted densification.

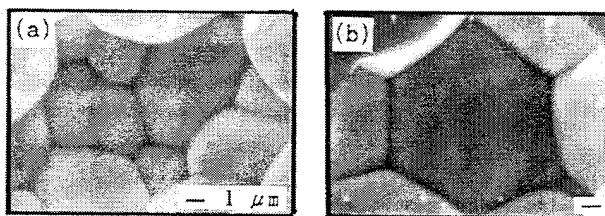


Figure 2. SEM micrographs of the fracture surfaces of the compositions of 0.65PMT-0.35PT-xSr sintered at  $1250^\circ\text{C}$  /4hours. (a)  $x = 0$ , (b)  $x = 0.02$ .

### Dielectric Properties

Fig.3 shows the typical plot of the dielectric constant and loss as a function of temperature and various frequencies for composition 0.65PMT-0.35PT-0.02Sr. The  $K$  vs.  $T$  shows the typical relaxor behavior. The dielectric constant vs. temperature behavior at 1 kHz is shown in Fig.4 for various compositions in the 0.65PMT-0.35PT-xSr ceramics. The values of dielectric constant for Sr-doped PMT-PT are much larger compared to the values observed for the undoped PMT-PT ceramics, specifically, at 2 mol% strontium doping. However, in the region  $x > 0.03$ , the dielectric constant decreases with  $x$ .

The room-temperature dielectric constant of PMT-PT ceramics increases considerably with the substitution of strontium. The room-temperature dielectric constant of 19000 was obtained by substituting 9 mol% Sr. With increasing substitution of Sr for Pb in the base composition, the Curie temperature decreases almost linearly with the amount of substituent, their rates of decrease are about  $9^\circ\text{C}/\text{mol}\%$  (Fig.5). This shift of the Curie temperature by Sr-substitution for Pb may be related to the distribution of ions having different ionic radii in the same sublattice of

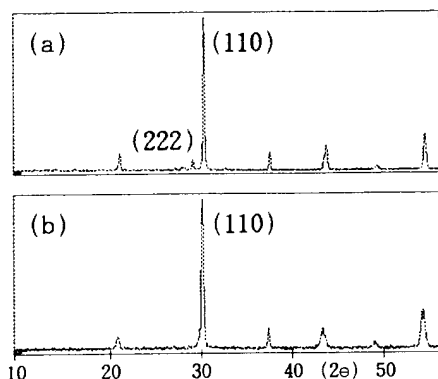


Figure 1. X-ray diffraction patterns of 0.65PMT-0.35PT-0.02Sr.  
(a) Calcined at 850 °C for 4 hours.  
(b) Sintered at 1250 °C for 4 hours.

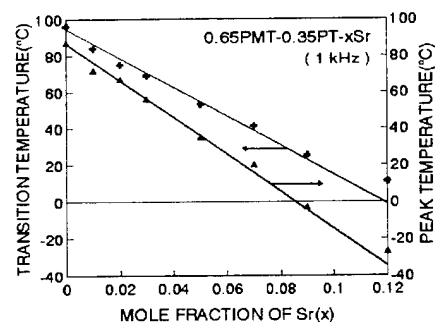


Figure 5. Transition temperature and peak temperature of 0.65PMT-0.35PT-xSr compositions.

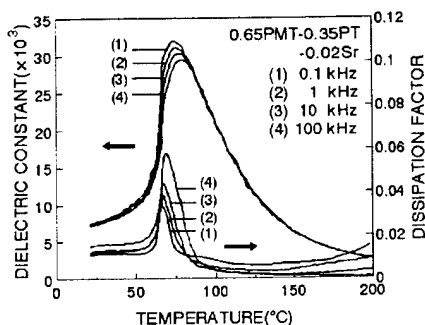


Figure 3. Temperature dependence of dielectric constant and dissipation factor at various frequencies for 0.65PMT-0.35PT-0.02Sr.

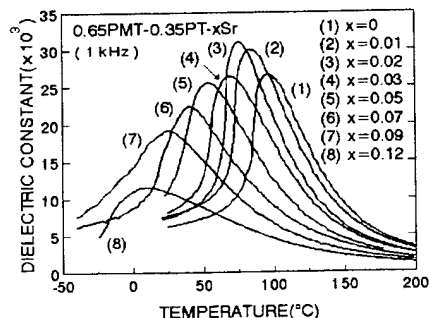


Figure 4. Dielectric constant of 0.65PMT-0.35PT-xSr compositions at varying temperature.

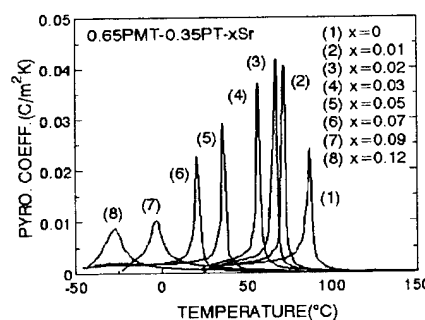


Figure 6. Pyroelectric coefficient of 0.65PMT-0.35PT-xSr compositions at varying temperature.

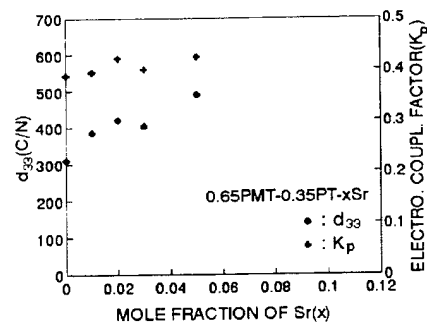


Figure 7. Piezoelectric constant  $d_{33}$  and electromechanical coupling factor  $K_p$  of 0.65PMT-0.35PT-xSr compositions at room temperature.

a complex compound with perovskite structure.<sup>[7]</sup>

#### Pyroelectric and Piezoelectric Properties

Fig.6 shows the pyroelectric coefficients of 0.65PMT-0.35PT-xSr composition with partial replacement of Pb by Sr as a function of temperature. With increase of  $\text{SrCO}_3$  the peak temperature of PMT-PT-xSr ceramics can be suitably adjusted for the room-temperature pyroelectric applications. Pyroelectric coefficient increases with increase of mol% Sr similar to that observed in dielectric constant vs. temperature. However, for  $x$  more than  $\sim 0.03$ , the pyroelectric coefficient decreased with  $x$ . The peak temperature with mole fraction of Sr in the 0.65PMT-0.35PT-xSr is shown in Fig.5. The peak temperature decreases almost linearly as the amount of Sr in the composition increases, their rates of decrease are about 10 °C/mol%.

Fig.7 shows the room-temperature values of piezoelectric  $d_{33}$  and electromechanical coupling factor  $K_p$  of the composition 0.65PMT-0.35PT-xSr as a function of mole fraction of Sr. The maximum piezoelectric  $d_{33}$  and electromechanical coupling factor  $K_p$  are observed at 5 mol% strontium doping. The foregoing composition is in good agreement with those exhibiting maxima in spontaneous polarization.

#### CONCLUSIONS

Substituting small amount of Sr for part of Pb in ceramics 0.65PMT-0.35PT-xSr promoted densification and grain growth. The room-temperature values of dielectric constant and pyroelectric coefficient of 0.65PMT-0.35PT-xSr

ceramics increase considerably with the substitution of Sr. The transition temperature and peak temperature of pyroelectric coefficient decrease almost linearly with the amount of Sr, their rates of decrease are about 9 °C and 10 °C/mol%, respectively. A piezoelectric  $d_{33}$  of 490 C/N and a electromechanical coupling factor  $K_p$  of 0.42 were obtained by substituting 5 mol% Sr.

#### ACKNOWLEDGEMENT

This work was supported (in part) by the KOSEF through the SRC of Excellence Program.

#### REFERENCES

- [1] V.A.Bokov and I.E.Myl'nikova, Sov. Phys. Solid State, 2, 2428(1961).
- [2] Y.J.Kim and S.W.Choi, Ferroelectrics, 108, 241(1990).
- [3] Y.J.Kim, S.W.Choi and A.S.Bhalla, to be published in Ferroelectrics.
- [4] S.L.Swartz and T.R.ShROUT, Mat. Res. Bull, 18, 663(1983).
- [5] R.L.Byer and C.R.Roundy, Ferroelectrics, 3, 333(1972).
- [6] IRE Standards on Piezoelectric Crystal: Measurement of piezoelectric ceramics, proc. 1961, IRE(Inst. Radio Engrs.) 49, 1161(1961).
- [7] G.A.Smolenskii and A.I.Agranovskaya, Sov. Phys. Solid State, 1, 729(1960)

# Series Pyroelectric Ceramics Used for Small Area IR Detector

R.B. Liu S.W. Lin C.F. Qu C.H. Yao Y.H. Jin  
Shanghai Institute of Ceramics, Chinese Academy of sciences  
1295 Ding-Xi Road, Shanghai, 200050, China  
Y.S. Lin Y.R. Zhang  
Kunming Institute of Physics, Kunming, 650223, China

**Abstract**--- Theoretical relationship between the detectivity of small area IR detector with a capacitance compensated preamplifier and the parameters of pyroelectric materials was investigated. The series Sr doped pyroelectric ceramics based on  $\text{PbZrO}_3\text{-PbNbFeO}_3\text{-PbTiO}_3$  system were manufactured. The pyroelectric coefficient ranges of above system are  $4.4\text{-}7.2 \times 10^{-4} \text{Cm}^{-2}\text{K}^{-1}$  and the permittivity ranges are 290-500. Above materials were used to make small area ( $\phi 0.3\text{mm}$ ) IR detector. There is a very good agreement between measured and calculated  $D^*$  values. The highest detectivity  $D^*$  of small area IR detector with the thickness  $0.035\text{mm}$  is  $3 \times 10^8 \text{cmHz}^{1/2}\text{W}^{-1}$ , which shows that this type pyroelectric ceramics had a strong potential to be a good candidate in focal plane thermal imaging arrays application.

## INTRODUCTION

Merits of ferroelectric materials used for pyroelectric IR detector are defined by many reviews in three respect ways:[1][2]

current figure of merit:  $F_I = p/c'$ ; voltage figure of merit:  $F_V = p/c' \cdot \epsilon$ ; and detectivity figure of merit:  $F_D = p/c' \cdot (\epsilon \cdot \tan \delta)^{1/2}$ .

Where:  $c'$  is the volume specific heat capacity;  $p$  is the pyroelectric coefficient;  $\epsilon$  is the permittivity and  $\tan \delta$  is the dielectric loss of the material.

For the current important pyroelectric materials, the merit sequence from high to low are listed below:

$F_I$ : TGS single crystal > modified PZT >  $\text{LiTaO}_3$  single crystal > PVDF polymer;

$F_V$ : TGS single crystal >  $\text{LiTaO}_3$  single crystal > PVDF polymer > modified PZT;

$F_D$ : TGS single crystal >  $\text{LiTaO}_3$  single crystal > modified PZT > PVDF polymer.

$F_V$  and  $F_D$  are mostly used for assessment and for selection of pyroelectric material in the case of single element IR detector.

The ambient temperature operation of pyroelectric effect makes it more competitive with semiconductor devices in thermal imaging application. The recent development in hybrid compact of focal plane arrays and the silicon readout ICs can overcome the problems of thermal diffusion and signal confusion encountered in early pyroelectric vidicons.[3][4][5] The small sensitive area is the character of focal plane arrays comparing to the single element IR detector. So pyroelectric material with high permittivity is needed for matching the input capacitance of read out circuit.

The modified PZT pyroelectric ceramics usually have the high permittivity, but the  $F_V$  and  $F_D$  are relatively lower than that of

pyroelectric crystal groups. In order to decrease the offset of  $F_V$  and  $F_D$  from the high permittivity, We designed a special capacitance compensated preamplifier which can keep the total input capacitance much lower and used to the small area IR detector. So the detectivity of small area detector should be mainly proportional to the pyroelectric coefficient of material although the permittivity may be different. This would be very useful to make use of the pyroelectric ceramics with high pyroelectric coefficient and high permittivity.

In this paper, series Sr doped PZNFT ( $\text{PbZrO}_3\text{-PbNbFeO}_3\text{-PbTiO}_3$ ) pyroelectric ceramics [6] were manufactured and used to make  $\phi 0.3\text{mm}$  IR detector. A great improvement of detectivity were reached both by increasing the pyroelectric coefficient of materials and by means of special capacitance compensated preamplifier.

## DETECTIVITY CALCULATIONS

### Theoretical calculation

The voltage responsivity of a detector can be written as

$$R_V = R_g \cdot \eta \cdot p \cdot \omega \cdot \tau_T / c' \cdot t \cdot (1 + \omega^2 \tau_T^2)^{1/2} (1 + \omega^2 \tau_E^2)^{1/2}$$

Where:  $\eta$ -emittivity;  $R_g$ - input resistance of amplifier;

$$\tau_T = c' \cdot t \cdot A / G_T = C_T / G_T \text{ -thermal time constant,}$$

$$G_T \text{ -heat conductance,}$$

$$\tau_T = 150\text{ms in our calculation,}$$

$$A \text{ -surface area of electrode; } t \text{ -element thickness}$$

$$\omega = 2\pi f; f \text{ -incident power frequency}$$

$$\tau_E = R_g (C_E + C_A); C_E \text{ -element capacitance}$$

$$C_A \text{ -amplifier capacitance}$$

In our experiment, a special capacitance compensated preamplifier was used and  $(C_E + C_A)$  can be kept at a low value ( $C_E + C_A = 0.7\text{pf}$  in our experiment) that leads the  $\tau_E \ll 1\text{s}$ .

The noises included in the calculation are as follows:

$$\text{Thermal noise: } V_T = (4KT R_g \Delta f)^{1/2} / (1 + \omega^2 \tau_T^2)^{1/2}$$

$$\text{Johnson noise: } V_J = (4KT \omega \cdot C_E \tan \delta \Delta f)^{1/2} \cdot R_g / (1 + \omega^2 \tau_T^2)^{1/2}$$

$$\text{voltage noise of preamplifier: } V_A = 1 \times 10^{-8} \text{ V}$$

current noise of preamplifier:

$$V_I = (2q I_{gss} \Delta f)^{1/2} \cdot R_g / (1 + \omega^2 \tau_T^2)^{1/2}$$

$$\Delta f = 1\text{Hz, } I_{gss} = 1 \times 10^{-13} \text{ A}$$

Table 1 Properties of Sr doped PZNFT ceramics and LiTaO<sub>3</sub> crystal

	Sr content mol	p 10 <sup>-4</sup> Cm <sup>-2</sup> K <sup>-1</sup>	ε <sub>r</sub>	tanδ %	c' 10 <sup>6</sup> Jm <sup>-3</sup> K <sup>-1</sup>	F <sub>I</sub> 10 <sup>-10</sup> CmJ <sup>-1</sup>	F <sub>V</sub> m <sup>2</sup> C <sup>-1</sup>	F <sub>D</sub> 10 <sup>-5</sup> Pa <sup>-1/2</sup>
PZNFT	0	4.2	250	0.5	2.5	1.68	0.075	5.05
PZNFTS0	0.01	4.4	290	0.5	2.5	1.76	0.067	4.91
PZNFTS1	0.03	5.1	320	0.5	2.5	2.04	0.072	5.42
PZNFTS2	0.05	7.2	480	0.5	2.5	2.88	0.067	6.25
LiTaO <sub>3</sub>		2.3	47	0.3	3.2	0.71	0.172	6.43

total noise:  $V_N = (V_T^2 + V_J^2 + V_A^2 + V_I^2)^{1/2}$

specific detectivity:  $D^* = A^{1/2} \cdot R_V / V_N$

#### Experiment measurement calculation

The experiment measured values are given by:

$$R_V = V_S / k \cdot w, V_N = V_{NE} / k \cdot \Delta f^{1/2}, D^* = A^{1/2} \cdot R_V / V_N$$

where:  $V_S$ -output signal voltage;  $V_{NE}$ - output noise voltage;

$k$ -amplifier gain;  $w$ - incoming power density ;

$\Delta f$ -measuring frequency bandwidth. ( $\Delta f = 1\text{Hz}$ )

### EXPERIMENTS AND RESULTS

#### Preparation of material and detector

The doping amounts of Sr on PZNFT are 0.01, 0.03 and 0.05 mol respectively. The ceramic powders were fabricated by ordinary processing procedure. Hot pressing sintering was used to sinter the sample. Sintering temperature was 1080 °C for 90 min and pressing pressure was 80kg/cm<sup>2</sup>. The sintered sample were cut and polished to regular slice. Both sides were coated with silver electrode. Poling conditions of the samples were: voltage-4KV/mm; silicon oil temperature- 120°C; time-10min. Pyroelectric coefficient was measured by charge integral method. Measuring frequency for permittivity and loss was 1kHz. The samples used to make detector were pre-poled before thickness reduction processing.

Poled samples were mechanically polished to required thickness. Black Au and NiCr were evaporated on front surface and NiCr was evaporated on back surface. The diameter of the electrode is 0.3mm. Sensitive element was suspended to the fixing pixel. Conducting silver paste was used to fix the conducting wire to preamplifier.

#### Properties of materials and detectors

The properties of Sr doped PZNFT ceramics are listed in table 1. the properties of LiTaO<sub>3</sub> single crystal are also listed in table1 for comparison.

Different sintering conditions were used to sinter the PZNFTS2 samples. The properties difference are shown in table2.

Table 2 Properties dependence of PZNFTS2 on Sintering conditions

Sintering conditions	p 10 <sup>-4</sup> Cm <sup>-2</sup> K <sup>-1</sup>	ε <sub>r</sub>	tanδ %	d <sub>33</sub> 10 <sup>-12</sup> C/N
pressureless sintering	8.8	500	1.8	58
hot-pressing sintering	7.2	480	0.5	65
high temperature annealed after hot-pressing sintering	5.8	430	0.8	72

The pyroelectric coefficient is strongly dependent on the sintering conditions, which may result from the lead evaporation during sintering procedure.

The measured and calculated properties of detector are listed in table3. The properties of LiTaO<sub>3</sub> single crystal detector of same size are also listed in table 3 for comparison.

Table 3 Properties of small area IR detector made of PZNFTS1,2 and LiTaO<sub>3</sub>

materials	t mm	Absorbing Coating	Measured Values		Calculated values	
			R <sub>v</sub> ' (500,10) V/W	D <sup>*</sup> ' (500, 10,1) 10 <sup>8</sup> cmHz <sup>1/2</sup> W <sup>-1</sup>	R <sub>v</sub> (500,10) V/W	D <sup>*</sup> (500,10,1) 10 <sup>8</sup> cmHz <sup>1/2</sup> W <sup>-1</sup>
PZNFTS2	0.073	Black Au	23600	1.7	26000	1.9
	0.035	Black Au	41600	3.0	61000	3.5
PZNFTS1	0.028	NiCr	30500	2.0	37000	2.5
	0.011	Black Au	102700	5.9	123000	6.9
LiTaO <sub>3</sub>	0.028	NiCr	0.9R <sub>v</sub>	0.8D <sup>*</sup>	9800	0.77
	0.011	Black Au	0.9R <sub>v</sub>	0.8D <sup>*</sup>	32700	2.5

## DISCUSSION

The ratio of theoretical calculation  $D^*$  to measured  $D^*$  is larger than 80%, that confirms both the capacitance compensating and increasing pyroelectric coefficient of materials are two effective ways to get high detectivity in small area IR detector. The results also show that the thickness reduction of poled samples by mechanical polishing does not obviously affect the sample's pyroelectric effect. This will make it easier to prepare large area and high density focal plane arrays.

The  $D^*$  values of PZNFTS materials are much higher than that of LiTaO<sub>3</sub> single crystal, although the  $F_D$  merit of the former is lower than that of the latter. The enhancement of  $D^*$  will expand the ceramic single element detector's application range, in which the application of ceramic is limited by low sensitivity. the ceramic materials have a lot of advantages such as the possibility of chemical variation in wide ranges, versatile shaping and the low-cost production. Especially in the application of focal plane arrays, ceramic material will combine the optimization of quality and production. So the major candidate for thermal imaging application is the ceramics. The applicable property of tiny point element of focal plane is at least  $1 \times 10^8 \text{cmHz}^{1/2} \text{W}^{-1}$ . In our experiment, we got  $3 \times 10^8 \text{cmHz}^{1/2} \text{W}^{-1}$  from PZNFTS2 ceramics at the thickness 0.035mm, near the technical acceptable thickness 0.03 mm for focal plane. When PZNFTS2 are used to make focal plane arrays, the necessary substrate will increase the heat dissipation and thus decrease the detectivity. Usually only one third property would be kept from empiricism when substrate is used. So the PZNFTS2 material is hopeful to satisfy the minium requirement for thermal imaging application.

From the trends established in our experiment, it is possible to further enhance the detectivity of small area IR detector. one way is to use the pyroelectric material such as La doped PZT, whose pyroelectric coefficient is even higher than that of PZNFTS2 ceramics; Another way is to use the dielectric operation mode suggested by watton.<sup>[3]</sup> In both cases, the pyroelectric coefficient can reach the range of  $15\text{-}20 \times 10^{-4} \text{Cm}^{-2} \text{K}^{-1}$ .

## SUMMARY

The detectivity of small area IR detector can be enhanced by capacitance compensated preamplifier. When the capacitance compensated preamplifier was used in the small area IR detector, pyroelectric ceramics with higher pyroelectric coefficient will produce higher detectivity although the figure of merit of different ceramics may be similar. PZNFTS2 ceramics is a good candidate for focal plane arrays thermal imaging.

## ACKNOWLEDGEMENT

The author gratefully acknowledges the support of K.C. Wong Education Foundation, Hong Kong.

## REFERENCES

- [1] S.G. Porter, "A Brief Guide to Pyroelectric Detectors", *Ferroelectrics*, Vol.33, pp.193-206,1981.
- [2] S.T. Liu and D. Long, "Pyroelectric Detectors and Materials", *Proceedings of the IEEE*, Vol.66(1), pp.14-26,1978.
- [3] R. Watton and M.A. Todd, "Ferroelectric Ceramics for Infrared Detection", *ELECTROCERAMICS*, British Ceramic Proceedings, No.41, pp.205-217, 1989.
- [4] R.W. Whatmore, " Pyroelectric Ceramics and Devices for Thermal Infrared Red Detection and imaging", *Ferroelectrics*, Vol.118, pp.241-259, 1991.
- [5] M.E. Lines and A.M. Glass, *Principles and Applications of Ferroelectrics and Related Materials*, ch.16 p.573-578, Oxford University Press, 1977.
- [6] P.C. Osbond and R.W. Whatmore, "Improvements to Pyroelectric Ceramics Via Strontium Doping of the Lead Zirconate-Lead Iron Niobium-Lead Titanate", *Ferroelectrics*, Vol.118, pp.93-101,1991.
- [7] E.H. Putley, "The Applications of Pyroelectric Devices", *Ferroelectrics*, Vol.33, PP.207-216,1981.



# Pyroelectric Ceramics with Low Resistivity

R.B. Liu S.W. Lin C.F. Qu C.H. Yao Y.H. Jin  
Shanghai Institute of Ceramics, Chinese Academy of Sciences  
1295 Ding-Xi Road, Shanghai, 200050 China

**Abstract**--- According to the requirement of pyroelectric ceramics used for commercial IR detector without FET gate resistor,  $\text{PbZrO}_3\text{-PbMnSbO}_3\text{-PbTiO}_3$  pyroelectric ceramics with high figure of merit and low resistivity were studied. The resistivity  $\rho$  of above system can be adjusted in the range of  $0.8\text{-}5 \times 10^{11} \Omega\text{cm}$  by further Mn doping. The signal to noise ratio of the detector without gate resistor made by this ceramics can reach the same level of the detector with FET gate resistor. The large size ceramic blocks with good mechanical processing property can be manufactured by pressureless sintering.

## INTRODUCTION

A single element IR detector compacted in TO5 case usually consists of four parts: sensitive element, optical filter, FET and FET gate resistor.<sup>[1]</sup> The idea of eliminating the FET gate resistor by adjusting the sensitive element resistance has been proposed for a long time. The condition is that the resistivity  $\rho$  of pyroelectric ceramics is in the desired range. The input resistance of current FET is about  $1 \times 10^{11} \Omega$ . The resistivity  $\rho$  of pyroelectric ceramics is usually larger than  $1 \times 10^{12} \Omega\text{cm}$ . The element resistance for standard sensitive size ( $1 \times 2 \times 0.08 \text{mm}$ ) is equal to  $0.4(\text{cm}^{-1})\rho$ . In order to eliminate the FET gate resistor and keep good match with FET, it is necessary to decrease the resistivity of pyroelectric ceramics and keep a high figure of merit of pyroelectric ceramics at the same time. The required resistivity for above application is in the range of  $1\text{-}3 \times 10^{11} \Omega\text{cm}$ , and the minimum voltage figure of merit  $F_v = p/c'\epsilon$  should be  $0.07 \text{m}^2\text{C}^{-1}$ .

Where:  $p$  is the pyroelectric coefficient;  $c'$  is the specific heat capacity;  $\epsilon$  is the permittivity.

$\text{U}_3\text{O}_8$  doping is an effective way to decrease the resistivity of PZT ceramics. [2] [3] [4] But there are still problems when this system used for single element detector without gate resistor: (1) temperature stability of detector is not good; (2) the radiative property of  $\text{U}_3\text{O}_8$  raw material is not proper for mass production. [5]

The basic composition of pyroelectric ceramics for commercial single element IR detector is  $\text{PbZrO}_3\text{-PbNbFeO}_3\text{-PbTiO}_3$  (PZNFT). But the resistivity of this system is larger than  $1 \times 10^{12} \Omega\text{cm}$  and hot-pressing sintering is needed to get high density and good mechanical processing property, which increase the cost and needs complicated equipments.

In this paper, We studied the  $\text{PbZrO}_3\text{-PbMnSbO}_3\text{-PbTiO}_3$  (PMSZT) system ceramics, which was used as piezoelectric filter ceramics. [6] High figure of merit was got and the resistivity can be adjusted in the range of  $0.8\text{-}5 \times 10^{11} \Omega\text{cm}$  by further Mn doping. The single element IR detector without gate resistor made of PMSZT can reach the high signal to noise ratio. Large ceramic blocks ( $36 \times 36 \times 18 \text{mm}$ ) with good mechanical processing property were produced by pressureless sintering.

## EXPERIMENTS AND RESULTS

The basic composition is  $\text{APb}(\text{Mn}_{1/3}\text{Sb}_{2/3})\text{O}_3\text{-B}(\text{PbZrO}_3)\text{-C}(\text{PbTiO}_3)$ . The ranges of A,B,C coefficient are:  $A=0.03\text{-}0.15$ ;  $B=0.75\text{-}0.95$ ;  $C=0.05\text{-}0.20$ . First we got the composition range with the relative permittivity  $\epsilon_r$  below 300 shown in table 1. we choosed PMSZT-2 as the middle experiment composition because the resistivity of which is relatively low and the  $F_{1-h}$  phase transition temperature is relatively high. And then we added dopants  $\text{Fe}_2\text{O}_3$ ,  $\text{Cr}_2\text{O}_3$  and  $\text{MnCO}_3$  to adjust resistivity. The resistivity can be changed in the range of  $0.8\text{-}5 \times 10^{11} \Omega\text{cm}$ . We fixed one composition PMSZTA with the resistivity  $2 \times 10^{11} \Omega\text{cm}$ . The property can be repeated in mass production. The properties of which and the comparison with other pyroelectric ceramics are listed in table 2.

The ceramic powders were prepared by ordinary processing procedure. The samples were sintered by pressureless sintering. The pyroelectric coefficient was measured by charge integral method.

Table 1 Dielectric properties of PMSZT system

Samples	$p$ $10^{-4} \text{Cm}^{-2}\text{K}^{-1}$	$\epsilon_r$	$\rho$ $10^{11} \Omega\text{cm}$	$F_{1-h}$ $^\circ\text{C}$	$T_c$ $^\circ\text{C}$
PMSZT-1	2.38	280	>10	78.5	210
PMSZT-2	3.14	210	5-8	71	194
PMSZT-3	3.58	280	>10	63	170
PMSZT-4	4.88	265	>10	50	153

Table 2 Pyroelectric properties of PMSZTA and comparison with other ceramics

Samples	$p$ $10^{-4} \text{Cm}^{-2}\text{K}^{-1}$	$\epsilon_r$	$\rho$ $10^{11} \Omega\text{cm}$	$\tan\delta$ %	$F_v = p/c'\epsilon$ $\text{m}^2\text{C}^{-1}$
PMSZTA	3.8	205	2-2.5	0.3	0.083
PZNFT	4.2	250	>10	0.5	0.075
Japan low $\rho$	3.5	190	1-3	0.5	0.083
Japan high $\rho$	4.0	330	>10	0.5	0.054

The single element IR detectors without FET gate resistor were made by PMSZTA material. The properties of detector are shown in table 3.

Table 3 Detector properties made by different ceramics

	No gate resistor		With gate resistor PZNFT high $\rho$
	PMSZTA	Japan low $\rho$	
Signal (V)	3.6-4.0	4.0	3.5-3.7
Noise (mV)	80-85	80	70-75
S/N	45-50	50	47-52

## DISCUSSION

The sensitive area size is different for different applications. From the single element IR detector  $2\text{mm}^2$  to the focal plane arrays  $0.01\text{mm}^2$ . So for the moment FET input resistance, We need the resistivity of materials changing in the range  $10^9\Omega\text{cm}$  to  $10^{11}\Omega\text{cm}$ .

In our experiment, pressureless sintering were successfully used to sinter large blocks of ceramics. The dielectric loss and mechanical processing property can reach the same level of hot-pressing sintered PZNFT ceramics. This would be very helpful for mass production.

Decreasing of resistivity by Mn doping in  $\text{PbZrO}_3\text{-PbMnSbO}_3\text{-PbTiO}_3$  system is resulted from the aliovalent substituents.<sup>[7]</sup> Lower charge  $\text{Mn}^{3+}$  ions replacing the  $\text{Zr}^{4+}$  and  $\text{Ti}^{4+}$  sites would provide more holes in p-type conductive PZT ceramics, which increases the total conductivity of the ceramics. This is only a simple and direct explanation. A detail study would be carried out in the following work.

## SUMMARY

Extra Mn doping  $\text{PbZrO}_3\text{-PbMnSbO}_3\text{-PbTiO}_3$  system is a very good pyroelectric ceramics used for production of single element IR detector without FET gate resistor by following reasons: (1) They possess high figure of merit and the required low resistivity; (2) High quality large size ceramic block can be produced by pressureless sintering.

## ACKNOWLEDGEMENTS

The author gratefully acknowledges the support of CNNSF under grant 6937707 and the support of K.C. Wong Education Foundation, Hong Kong. The author also thanks the Shanghai Nicera Sensor Company Ltd for the preparation and measurement of the detector and for providing the Japan materials properties.

## REFERENCES

- [1] H.P. Beerman, "Investigation of Pyroelectric Material Characteristics for Improved Infrared Detector Performance", *Infrared Physics*, Vol.15, pp.225-231, 1975.
- [2] A. J. Bell and R.W. Whatmore, "Electrical Conductivity in Uranium Doped, Modified Lead Zirconate Pyroelectric Ceramics", *Ferroelectrics*, Vol. 37, pp.543-546, 1981.
- [3] R. W. Whatmore and A.J. Bell, "Pyroelectric Ceramics in the Lead Zirconate-Lead Titanate- Lead Iron Niobate", *Ferroelectrics*, Vol.35, pp.155-160, 1981.
- [4] R.W. Whatmore, " High Performance, Conducting Pyroelectric Ceramics", *Ferroelectrics*, Vol. 49, pp.201-210, 1983.

- [5] R. B.Liu, "Study on Pyroelectric Ceramics and Composite" Ph.D Thesis, Shanghai Institute of Ceramics, Chinese Academy of Sciences, 1991.
- [6] British Patent, No. 1179170
- [7] A.J. Moulson and J.M. Herbert, *Electroceramics*, New York, Chapman and Hall, ch.6, pp.276-281, 1990.

# PYROELECTRIC AND DIELECTRIC PROPERTIES OF DRY AND MOIST TGS-GELATIN FILMS

V.E. Khutorsky and Sidney B. Lang  
Department of Chemical Engineering  
Ben-Gurion University of the Negev  
84105 Beer Sheva, Israel

## ABSTRACT

TGS-gelatin films have been grown by evaporation of water from a gelatin gel containing a solution of TGS. When this material absorbs water from the atmosphere, it forms a ferroelectric TGS subsystem and a nonferroelectric but highly polarizable dipole subsystem of water absorbed in the intermolecular spaces of gelatin molecules. Moist films have pyroelectric coefficients about four times higher than dried ones. The dielectric properties also change showing the major role played by the orientational polarizability of the water molecules.

## INTRODUCTION

Some recent studies have shown a dramatic effect of moisture on the pyroelectric properties of bone [1, 2]. In physiologically moist bone, the pyroelectric coefficient increased linearly with a bias electric field. A bias field of about  $2 \text{ kV cm}^{-1}$  was sufficient to induce a pyroelectric coefficient about an order of magnitude greater than that observed in ferroelectric ceramics. When the bone was dried with an attendant weight loss of about 10%, the pyroelectric coefficient decreased by about six orders of magnitude. The interpretation was based on the large dipole moment of water. The water in the moist bone is weakly bonded to collagen molecules. It was believed that the water molecules were oriented by the bias electric field creating a high spontaneous polarization. The temperature dependence of this spontaneous polarization caused the large pyroelectric effect. This interpretation was confirmed by the frequency dependencies of the dielectric permittivity and loss tangent which showed an orientational relaxation.

In order to better understand the influence of electric fields on bound water, a material was developed in which the fields were produced by the spontaneous polarization of a ferroelectric component rather than exclusively by external bias fields. Because it was also necessary that the material could absorb water in its bulk, a composite was designed. A composite incorporating triglycine sulfate (TGS) and gelatin could create a material which would both possess ferroelectric properties and absorb water into the intermolecular spaces of the gelatin molecules. TGS is one of the most thoroughly studied ferroelectrics [3, 4]. Gelatin is a biological polymer extracted from bone or other animal tissues [5]. Gelatin is soluble in hot water and at room temperature, forms a soft gel. After it is dried, it becomes a flexible and durable transparent film.

Damjanovic *et al.* have studied composites of triglycerol and gelatin [6-8]. The pyroelectric properties of TGS in polyvinylidene fluoride (PVF<sub>2</sub>) composites were studied by Wang *et al.* [9] and conductivity in the same composites by Amin *et al.* [10].

## EXPERIMENTS

For the preparation of the TGS-gelatin film, a solution of 15 g of deionized water, 0.227 g of sulfuric acid and 0.523 g of glycine was heated to 50-60°C and 0.75 g of Sigma 300 Bloom gelatin was added. The weights of the components were selected in order to produce a 1:1 ratio of TGS to gelatin in the final film. The solution was poured into Petri dishes and gelation occurred. The gel in the dishes was dried either in air or in a vacuum chamber, giving different results. Drying in air occurred slowly taking about two days, whereas vacuum drying required only about two hours. The air-dried films had the form of a number of 2 to 3-mm wide concentric rings which alternately contained or did not contain TGS crystallites. These surrounded a central round region with a diameter of about 1 to 2 cm which did not contain TGS crystallites. The vacuum-dried films had a central round region with a

diameter about half of that of the Petri dishes surrounded by a single annular ring. Both regions contained about 46% TGS, as determined by a chemical sulfur analysis. TGS crystallites were observed in the annular region by means of optical microscopy and x-ray diffraction analysis. No crystallites could be observed in the central region, leading to the conclusion that the TGS there was probably in an amorphous form. The structure of the crystallites was dendritic.

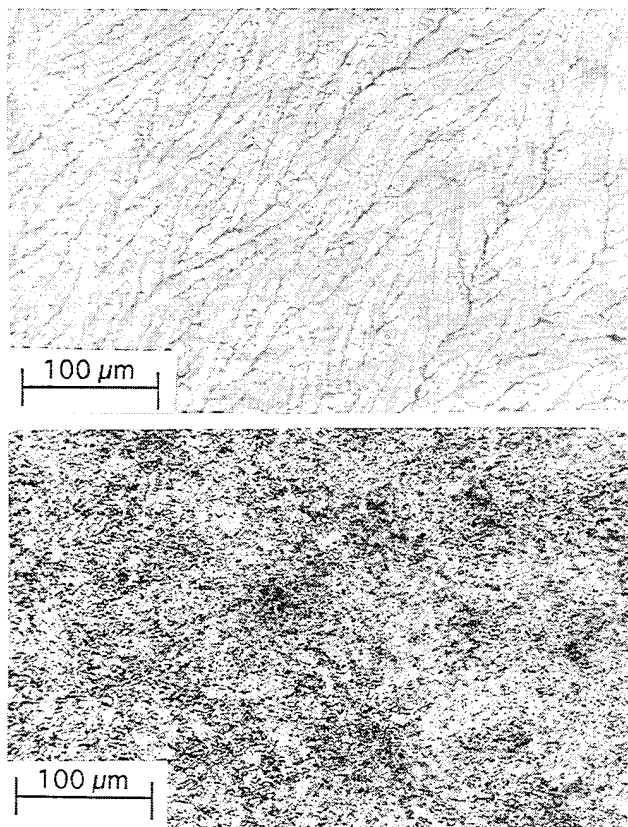
Crystallization in the pattern of concentric rings resembles the phenomenon of Liesegang Rings in gel systems in which chemical reactions take place [11, 12]. It is been shown that the conditions necessary for the formation of Liesegang Rings are the diffusion of the solution components and supersaturation of the solution with the reaction product [13]. There is no chemical reaction in the system described here; however, the evaporation of water causing supersaturation of the TGS is analogous to the production of a supersaturated chemical product. Supersaturation of TGS was evidenced by the dendritic form of the crystallites.

The process for the formation of the rings is as follows. The bottoms of the plastic Petri dishes were not planar, but were convex upwards. This caused nonuniformity in the thickness of the solution layers. The minimal thickness of the layers was usually in the center, with thicker outer portions. As the water evaporated, the thin portions were enriched with TGS and gelatin components more rapidly than were the thick parts, leading to concentration gradients and diffusion. This system is more complicated than the classical Liesegang one because of the drying of the film and the precipitation of the gelatin. An explanation for the absence of TGS crystallites in the central region is that the rate of precipitation of the gelatin exceeded that of the nucleation and growth of TGS crystallites, because of the rapidly decreasing water concentration. This was confirmed by the fact that the thin central regions were much larger in the films which were dried more rapidly in vacuum.

Samples with thicknesses of approximately 50  $\mu\text{m}$  were cut from the annular region of the vacuum-dried films. The dendritic structure of the TGS crystallites is shown in the transmission optical micrographs in Figure 1. The films were stored in air with a 40% relative humidity for a number of hours. During this time, moisture from the atmosphere was absorbed. Silver paint electrodes were applied to both surfaces of the films and black ink was deposited on the electrodes to increase the optical absorptivity.

We measured pyroelectric hysteresis loops (i.e., dependence of pyroelectric coefficient on bias electric field), dielectric permittivity, loss tangent, current-voltage characteristics and the time dependency of the pyroelectric coefficient during the hydration of dried films. The pyroelectric coefficient was determined using the dynamic Chynoweth method [14]. The samples were heated with a 35-mW He-Ne laser beam which was attenuated with a 10% transparency neutral filter. The beam was modulated with a light chopper at 5 Hz. The real (in phase with the laser illumination) and imaginary (in quadrature with the laser illumination) components of the current were recorded and the pyroelectric coefficients were calculated. The measured current is called an alternating current (AC) in this paper rather than a pyroelectric current. The reason is that, although the real part results from pyroelectricity, the imaginary part does not necessarily do so. A detailed description of the experimental equipment and techniques are presented in Khutorsky and Lang [2].

The experimental measurements were made either in vacuum (dry samples) or in air at 40% relative humidity (moist samples). The moist samples contained less than 1% moisture (the sensitivity of the balance did not permit a more exact determination). The bias field dependencies of the real and imaginary components of the AC and the calculated pyroelectric coefficient for moist samples are shown in Fig. 2. The behavior of the real and the imaginary components are

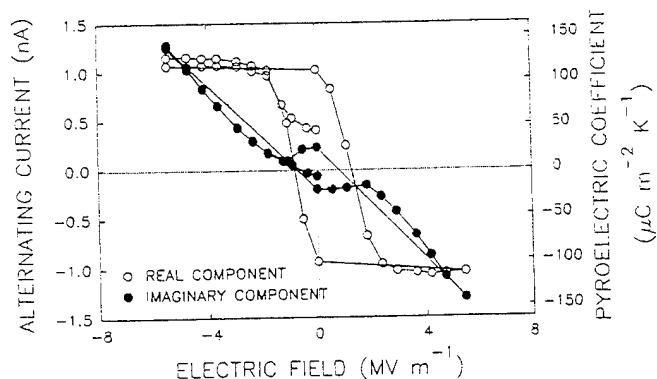


1. Transmission optical micrographs. (upper) annular area with dendritic crystallites, (lower) central area with no crystallites.

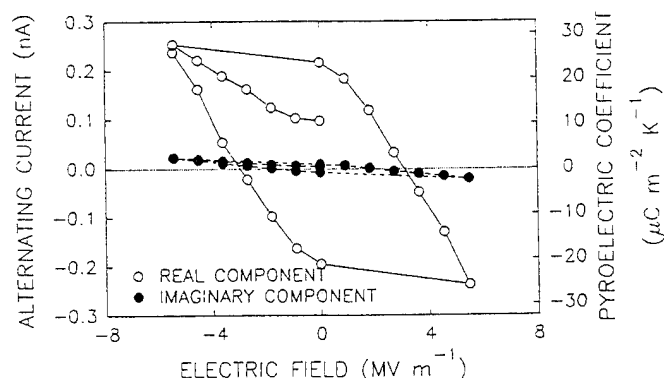
substantially different. The real component is a true pyroelectric hysteresis loop which is very similar in character to a ferroelectric hysteresis loop. The inverted orientation of this loop compared to conventional ones is due to the fact that the pyroelectric coefficient is negative in materials in which the spontaneous polarization decreases with increasing temperature. The magnitude of the pyroelectric coefficient at zero bias is about three times lower than that of pure TGS and about five times higher than that of PVF<sub>2</sub> [4]. The imaginary component of the current does not resemble a hysteresis loop. It was previously shown that the imaginary component can arise from two sources [1, 2]. Nonuniformity of the polarization distribution through the thickness of the film can produce an imaginary component of the current at zero bias field [15, 16]. Another source for an imaginary component is the temperature modulation of the conduction current [2]. This component increases with increase of either conductivity or bias field, and it can also produce a small alternating current of opposite sign after the bias field is turned off. The large magnitude of the imaginary component and the low frequency of thermal modulation suggest that the source of the imaginary component is the modulation of the conduction current.

Moist films were dried in vacuum at either ambient temperature or at 70°C. The AC's reached stable saturation values after 50 hours at ambient conditions or one hour at elevated temperatures, and the weight loss of the film was less than 1%. The bias field dependence of the real and imaginary components and the calculated pyroelectric coefficient for dried films are shown in Fig. 3. The coercive field of the real component has increased and the magnitude of the pyroelectric coefficient has decreased about four to five times compared to the moist films. The imaginary component is now an order of magnitude lower than the real component and 50 times lower than in the moist samples. Both components resemble ferroelectric hysteresis loops. In this case, the conduction current is sufficiently small that its temperature modulation does not produce an alternating current. Thus the imaginary component results from nonuniformity in the polarization distribution.

The conductivity of the samples is strongly dependent upon the moisture content as shown by the current-voltage characteristics in Fig.



2. Bias electric field dependence of real and imaginary components of the AC in moist films and the pyroelectric coefficient calculated for the real component. Imaginary component is due to modulation of conduction current and not pyroelectricity. Laser modulation frequency was 5 Hz. Sample thickness was 55 μm.



3. Bias electric field dependence of real and imaginary components of the AC in dry films and the pyroelectric coefficient calculated for the real component. Imaginary component is due to nonuniformity of the polarization distribution in the film thickness. Laser modulation frequency was 5 Hz. Sample thickness was 55 μm.

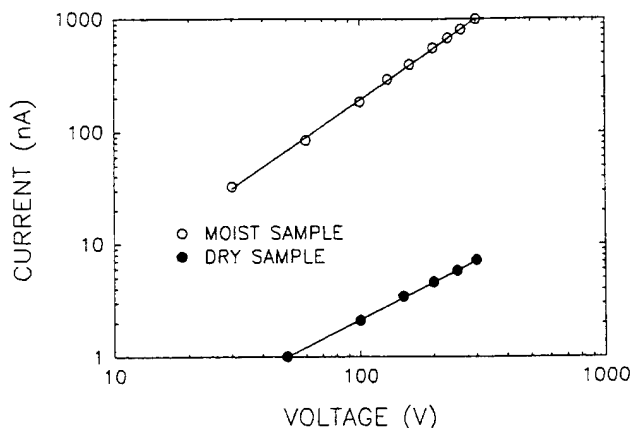
4. The conductivity of the moist sample is about two orders of magnitude higher than that of the dry sample. The current varies linearly with voltage for the dry sample and as the 1.5 power of voltage for the moist sample. The same dependencies were observed for dry and moist bone [1, 2].

A small DC exists in the samples in the absence of a bias electric field. The current was in the range of 0.1-0.2 nA for the case illustrated in Figure 4. When the moisture content of the sample is increased, the currents are initially higher and then decrease slowly with time. These currents are probably discharge currents related to electrochemical phenomena because the samples have metallic electrodes and are virtually solid electrolytes containing moisture and dissolved ions.

Dried samples rehydrate when stored in moist air. Figure 5 shows the AC and pyroelectric coefficient as functions of exposure time to air with a 40% relative humidity. The components reached saturation levels after about 10 to 15 hours and then a small decrease occurred.

## DISCUSSION

The annular region of the TGS-gelatin film is a composite consisting of a polymeric gelatin matrix with TGS crystallites located in empty spaces of the matrix. As the film is cooled during its formation, very long gelatin molecules form a gel containing a dilute TGS solution. As the water is evaporated, the solution reaches saturation and crystallization of TGS occurs. If the process occurs slowly in air, both gelatin and TGS precipitate separately and two phases are formed. When the films are dried rapidly in vacuum, there is insufficient time for separation of two



4. Current-voltage characteristics of moist and dry films.

phases and a homogeneous, but probably non-equilibrium, film is formed.

The long gelatin molecules absorb water which is bonded weakly to the gelatin. The spontaneous polarization of the ferroelectric TGS forms an internal electric field in the bulk of the film. This field creates additional polarization by orienting the large dipole moments of the water molecules. This mechanism differs from that observed in bone where an external bias field was necessary for the water molecule orientation [1, 2]. Thus absorption of the water in the bulk film leads to the development of two polar subsystems, a ferroelectric TGS system and a polarizable water system. Their interaction results in the substantial increase in polarization and pyroelectric coefficient, and the pyroelectric hysteresis loops shown above.

The dielectric measurements confirmed the model of orientational mobility of the water molecules. Figure 6 shows the frequency dependencies of the dielectric permittivity and loss tangent of moist and dry films. The behavior strongly resembles that of bone [1, 2]. The permittivity of the dry films is almost independent of frequency suggesting that non-orientational polarizability forms the major contribution to the dielectric properties. The moist samples have similar high frequency behavior but their permittivities increase by a factor of three as the frequency is lowered. The loss tangents show similar behavior. The frequency dependencies of the moist samples have a Debye-type dispersion with a saturation of the dielectric constant below 5 Hz [17]. This corresponds to a relaxation time of about 0.01 s. Thus the dielectric behavior results from high rotational mobility of the water molecules and a high viscosity opposing their orientation.

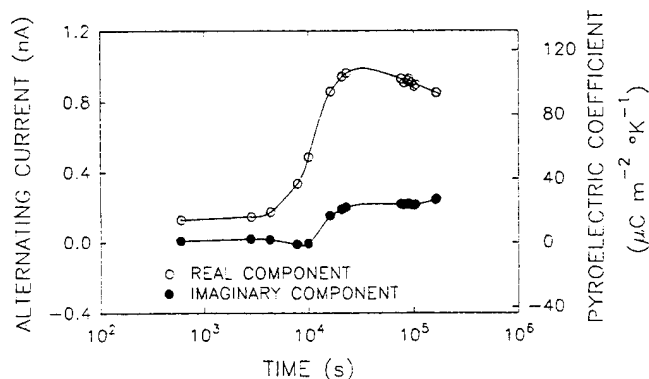
In summary, composite TGS-gelatin films have been grown that are able to absorb water in their bulk. The materials consist of two subsystems: a ferroelectric TGS one and a highly polarizable nonferroelectric system comprised of water absorbed in intermolecular spaces of gelatin. The interaction of these two subsystems in moist films results in a substantial increase in spontaneous polarization and pyroelectric coefficient, and a decrease in coercive field relative to the dry films.

#### ACKNOWLEDGEMENTS

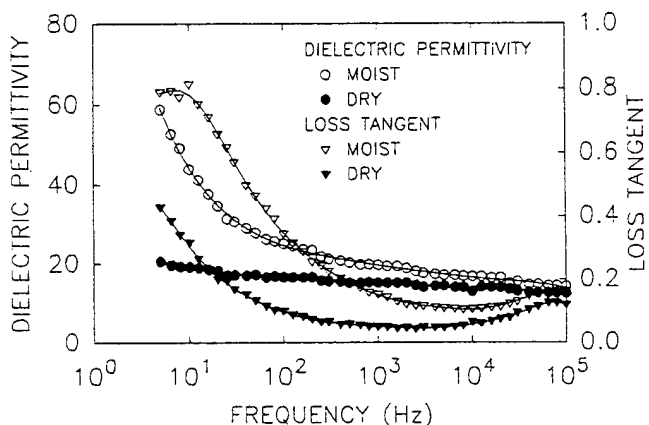
The authors acknowledge with thanks the support of the Israel Ministry of Science and Technology.

#### REFERENCES

- [1] V. Khutorsky and S. B. Lang, "Extremely large electric-field-induced pyroelectric effect in bone," *Ferroelectr. Lett. Sect.*, vol. 15, pp. 153-158, 1993.
- [2] V. Khutorsky and S. B. Lang, "Pyroelectric properties of moist and dry bone," *Electro- and Magnetobiology*, vol. 13, pp. 37-51, In press.
- [3] M. E. Lines and A. M. Glass, *Principles and Applications of Ferroelectrics and Related Materials*. Oxford: Clarendon Press, 1977, pp. 117-126.
- [4] Y. Xu, *Ferroelectric Materials and Their Applications*. Amsterdam: North-Holland, 1991.



5. Time dependency of real and imaginary components of the AC and the pyroelectric coefficient during rehydration of dry films.



6. Frequency dependencies of the dielectric permittivity and loss tangent of moist and dry TGS-gelatin films.

- [5] H. F. Mark, *Encyclopedia of Polymer Science and Engineering*. New York: Wiley, 1985, pp. 488-513.
- [6] D. Damjanovic, A. S. Bhalla and L. E. Cross, "Pyroelectric properties of a new family of synthetic polypeptide polymers," *Ferroelectr. Lett. Sect.*, vol. 11, pp. 117-123, 1990.
- [7] D. Damjanovic, A. S. Bhalla and L. E. Cross, "Pyroelectric properties of synthetic polypeptide films," *Ferroelectrics*, vol. 109, pp. 333-338, 1990.
- [8] D. Damjanovic, A. S. Bhalla and L. E. Cross, "Dielectric and pyroelectric properties of triglycerol-gelatin films," *IEEE Trans. Ultrason. Ferroelectrics Freq. Control*, vol. 38, pp. 630-633, 1991.
- [9] M. Wang, C. S. Fang and H. S. Zhuo, "Study on the pyroelectric properties of TGS-PVDF composites," *Ferroelectrics*, vol. 118, pp. 191-197, 1991.
- [10] M. Amin, L. S. Balloomal, S. A. Khairy, H. M. Osman and S. S. Ibrahim, "Electrical conductivity of ferroelectric-polymer composites," *Ferroelectrics*, vol. 135, pp. 419-429, 1992.
- [11] R. E. Liesegang, "Z. Physik," vol. 23, p. 365, 1897.
- [12] H. K. Henisch, *Crystals in Gels and Liesegang Rings*. Cambridge, UK: Cambridge University Press, 1988.
- [13] Y. B. Zeldovitch, G. I. Barenblatt and R. L. Salganik, "Sov. Phys. Dokl.", vol. 6, p. 869, 1962.
- [14] A. G. Chynoweth, "Dynamic method for measuring the pyroelectric effect with special reference to barium titanate," *J. Appl. Phys.*, vol. 27, pp. 78-84, 1956.
- [15] S. B. Lang, "Laser intensity modulation method (LIMM): Experimental techniques, theory and solution of the integral equations," *Ferroelectrics*, vol. 118, pp. 343-361, 1991.
- [16] N. M. Bezdetny, V. E. Khutorsky and A. K. Zeinaly, "Polarization

distribution in ferroelectrics calculated by regularization method from pyroelectric measurements," Ferroelectrics, vol. 46, pp. 267-273, 1983.

[17] V. V. Daniel, Dielectric Relaxation. London and New York: Academic Press, 1967.

# Inhomogeneity Study of Alanine and Valine-doped TGS Crystal Using Micro-Probe Raman Spectroscopy

B.M.Jin, S.Erdei, and A.S.Bhalla

Materials Research Laboratory, The Pennsylvania State University,  
University Park, PA 16802, U.S.A.

**Abstract** - Micro-probe Raman spectroscopy is used for studying positional inhomogeneity in alanine-doped TGS crystals. 20 data points are measured along the c- and a-axes in b-plane. Several known Raman peaks are observed unchanged, but most other peaks are found to be changed remarkably. The major difference in spectra are found to be related to  $\text{SO}_4$  vibrations. The vibrational frequencies are found to be lowered near the seed position. The most unstable spectra are detected in the vicinity of the seed region.

## INTRODUCTION

Micro-probe Raman spectroscopy (MPRS) has been used for the purpose of property investigation of very narrow, localized regions. In micro-probe Raman scattering, since the incident beam diameter can be controlled to less than 2-3  $\mu\text{m}$ , localized distributions of vibrational modes, which depend on local inhomogeneities, can be studied. This method has successfully been applied to the diamond and other materials thin film for studying the local chemistry of the deposited materials. Many crystals grown from the solution method may have positional inhomogeneities. These inhomogeneities give rise to different and inconsistent electrical and optical properties measurements. This situation is more severe for some specifically doped crystals. We have applied MPRS to study positional inhomogeneity in crystals grown from the 20% alanine and valine-doped TGS solutions. Pure TGS has the disadvantages of easily depoling (since  $T_c \approx 49^\circ\text{C}$ ) and room temperature aging. Alanine doping has been employed to reduce the depoling and the room

temperature aging. Doped crystals most likely have greater positional inhomogeneity than those of the pure ones. Raman studies of pure TGS have been reported<sup>1-6</sup> but there is not much data available for the doped TGS crystals. This may be because the actual incorporated amounts were less than 0.01 mole% and may be positionally inhomogeneous. It was doubtful whether the effects of such a small incorporated amount were detectable. In this paper we report the preliminary result of Raman study on the 20% alanine and valine-doped TGS single crystals.

## EXPERIMENT

Alanine and valine-doped TGS single crystals were grown from the solution by a slow cooling method, starting from the temperature below the transition temperature ( $T_c$ ). A plate perpendicular to the b-axis and nearest to the seed was cut

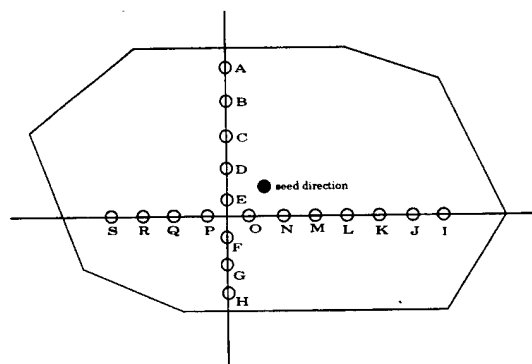


FIGURE 1. Selected data points for the inhomogeneity study of alanine doped TGS b-plate prepared from the crystal section 1cm away from seed position.

(A-H: c-axis direction, I-S: a-axis direction)

from the grown crystal. Wet cloth polishing was performed in order to get good optical quality surfaces. Total of twenty data points were measured: eight points along the c-direction and twelve points along the a-direction in 2mm increments in alanine-doped TGS and similar but smaller data points in valine -doped TGS. (see Fig.1). Ar-ion laser radiation(5145Å) entered the microscope and reflected downward by the beam-splitter to the sample, mounted on a X-Y stage. Focussing is controlled by varying the focal length of the objective, and monitored using a CCD camera. The reflected beam passes through the beam-splitter and double monochromator to the photodetector. Full scan range from 30cm<sup>-1</sup> to 3400cm<sup>-1</sup> with resolution of 0.5 cm<sup>-1</sup> was used for recording the spectra. All experiments were conducted at room temperature. Non-polarized Raman spectra were investigated because interest was confined in the study of inhomogeneity only. Polarized Raman studies and temperature dependency are currently under investigation. A Lorentzian curve fitting method, based on the uncoupled harmonic oscillator model, was followed to analyze the coupled spectra.

## RESULTS AND DISCUSSION

Raman modes are very sensitive to the perfection of the crystal under study. If there are defects or structural mismatches within the crystal, they should be observable in the Raman spectra. In alanine-doped TGS, glycine (I) molecules replaced, causing a structural mismatch. These

imperfections may cause line broadening or shifts in vibrational peak frequencies (see Fig.2.). Figure.2 shows the most unstable Raman spectra observed among the 20 selected measuring points (see Fig.1. for positions). Most of the peaks could not be analyzed due to unstable spectra shapes, although the crystal has good shape. Pure TGS has no Raman active modes between 1800cm<sup>-1</sup> and 2800 cm<sup>-1</sup>,<sup>4</sup> but the spectra of alanine-doped TGS show activity in this range. The observed peaks do not correspond to pure alanine<sup>7</sup>. In the case of point E, all observed vibrations showed abnormal behavior. Point P has a more stable spectra than point at M, implying the structure may be more deformed in that region. Despite this imperfection effect, symmetric and asymmetric CH<sub>2</sub> vibration and N-H stretching modes at 2900 and 3200 cm<sup>-1</sup> are still observed. It is difficult to assign the asymmetric

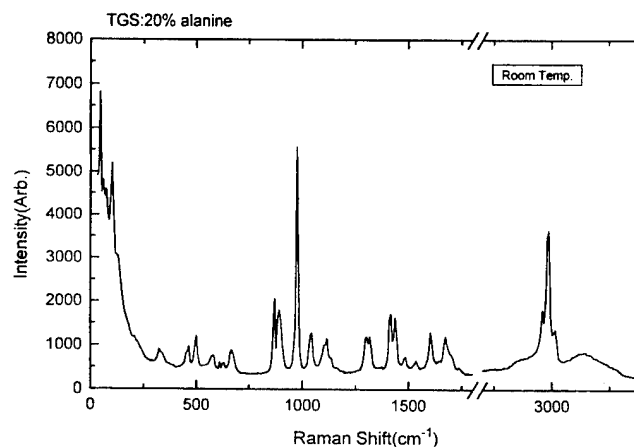


FIGURE 3. Raman spectra of alanine-doped TGS from the good quality area of the crystal(point I).

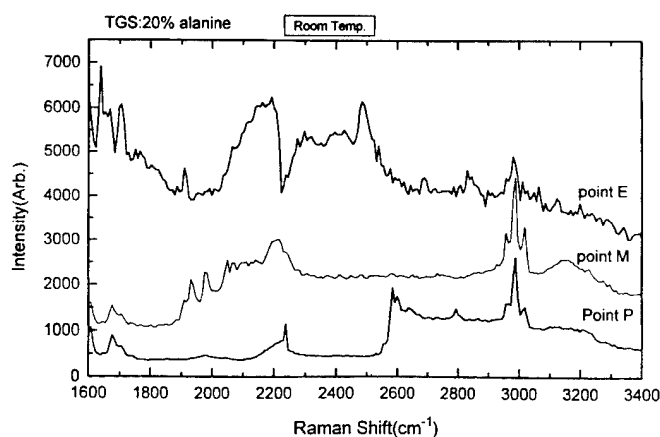


FIGURE 2. Raman spectra recorded from the selected measurement points.

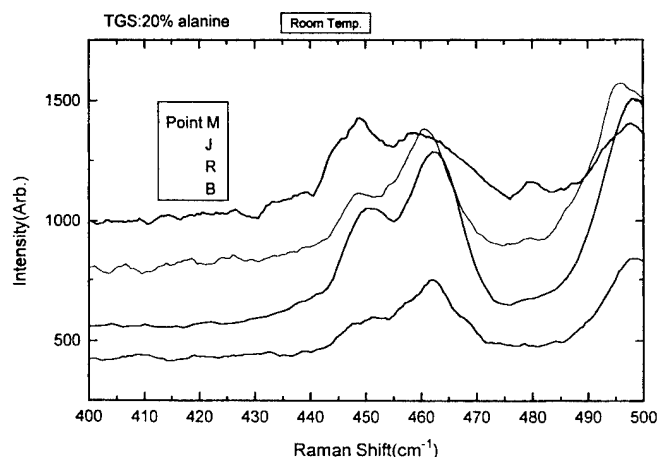


FIGURE 4. Raman spectra of internal SO<sub>4</sub><sup>2-</sup> modes in alanine-doped TGS at different positions.



NH<sub>3</sub> deformation vibration at 1600-1700 cm<sup>-1</sup> for all three measurement positions. The Raman spectra of a non-deformed region (point I) is presented in Fig.3. As expected, there is no peak between 1800cm<sup>-1</sup> and 2800 cm<sup>-1</sup>, but there are several differences between pure and alanine-doped TGS. First, no external librational peaks of SO<sub>4</sub> alone were detected at 170 and 205 cm<sup>-1</sup>, except at the edge of the sample plate(eg, point I,S,H and A), but with very weak intensity, although the glycium/SO<sub>4</sub> vibration below 200cm<sup>-1</sup> is still observable. Second, the C-C bending (deformation) mode located around 330 cm<sup>-1</sup> was split into two frequencies ( 325 and 340 cm<sup>-1</sup> ) through all measuring points, but the spectrum appears strongly coupled and asymmetrical. The splitting tendency is stronger along a-axis than that of c-axis. Galustian et al.<sup>3</sup> and Taurel et al.<sup>2</sup> did not observe this splitting, but Krishnan et al.<sup>1</sup> have observed it. The major differences were found in the vibrational modes related to SO<sub>4</sub> groups. Third, the SO<sub>4</sub>-ν<sub>3</sub> modes at 1092 and 1164 cm<sup>-1</sup> were not observed in alanine-doped TGS crystal. Fourth, the frequency of internal SO<sub>4</sub><sup>2-</sup> modes located at 450 and 463 cm<sup>-1</sup> shifts to lower frequencies, and of the COO' rocking (or bending) mode at 500cm<sup>-1</sup> is observable, depending on measurement positions, as shown in Fig.4. Variation of internal SO<sub>4</sub> mode at 450cm<sup>-1</sup> for all points is presented in Fig.5. The minimum frequency was observed around the seed position along both a and c-

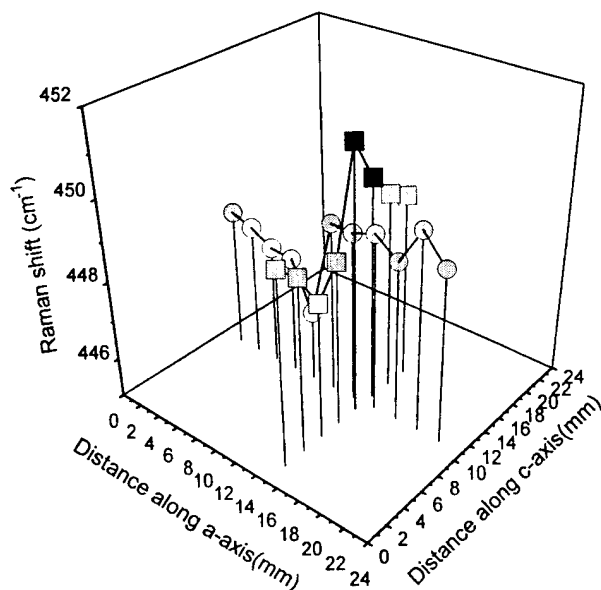


FIGURE 5. Vibrational modes, 450 and 463 cm<sup>-1</sup> variations of the internal SO<sub>4</sub><sup>2-</sup>.

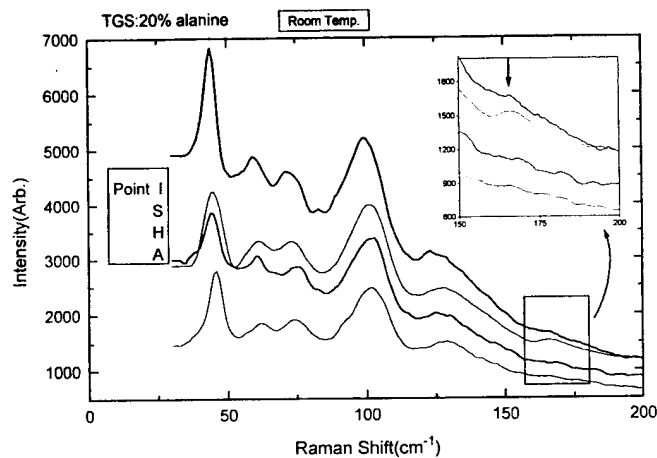


FIGURE 6. Raman spectra of external translational and librational glycium/SO<sub>4</sub> modes in alanine-doped TGS at different positions( see text for mark positions).

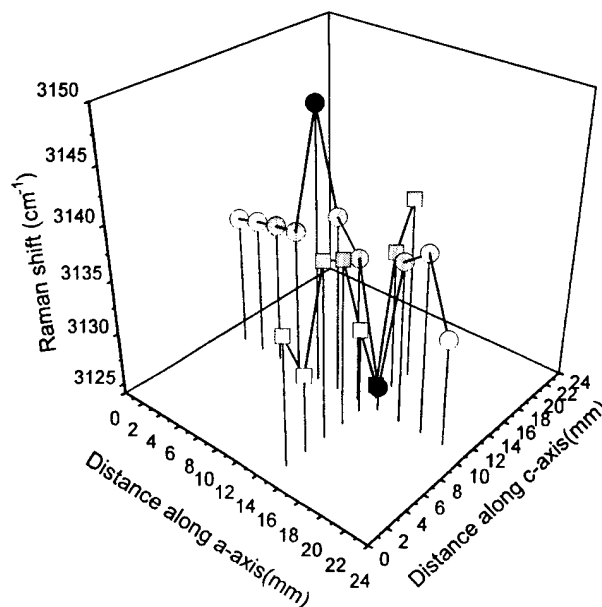


FIGURE 7. N-H stretching vibrational mode 3140 cm<sup>-1</sup> variations as a function of positions.

axes, implying the alanine concentration was highest in center of the crystal. This was also confirmed by investigation of external translational and librational modes of glycine alone (see Fig.6). The most distinct difference is that there are no external glycine translational and librational modes at 170 cm<sup>-1</sup> in alanine-doped TGS, although the external translational and librational modes of glycinum/SO<sub>4</sub>, located below 120 cm<sup>-1</sup> are clearly evident. The 170 cm<sup>-1</sup> vibration is not detected near the seed, but does appear towards the outer part of the crystal. This can be explained as follows: as the

crystal is growing from the TGS seed, pure TGS is more easily incorporated than alanine, so the alanine concentration in solution increases, but the crystal grow faster (① as a result the total surface area also increases, or ② may be as the temperature decreased and the crystal increased the size, the diffusion and incorporation of alanine in the crystal decreased also) than the rate of increase of alanine concentration in the solution, so the real effective alanine concentration inside the crystal is lower at the end of the growth than it is at the beginning. Finally, there are small shifts in symmetric and asymmetric  $\text{CH}_2$  stretching modes located between  $2950\text{--}3100\text{ cm}^{-1}$ , but a great variation of N-H stretching mode depending on measurement positions, as shown in Fig.7. In this figure, point M ( highest measured frequency along the a-axis ) had the most unstable spectra. This tendency is similar in behavior to the one observed for  $\text{SO}_4$  vibration in Fig.5, namely, it has a minimum vibrational frequency around the seed position.

Another attempt was done in the case of 20 mole% of valine doped TGS crystal as the same way like alanine doped ( see Fig.8). Valine is the same chiral molecule but has a bigger molecule than alanine. Therefore there should be different effect in Raman spectra. As expected, we can get a couple of different spectra throughout the whole measured range, but especially we could not observed the librational glycine modes located at  $58$  and  $72\text{ cm}^{-1}$  although we observed in the case of alanine-doped TGS.

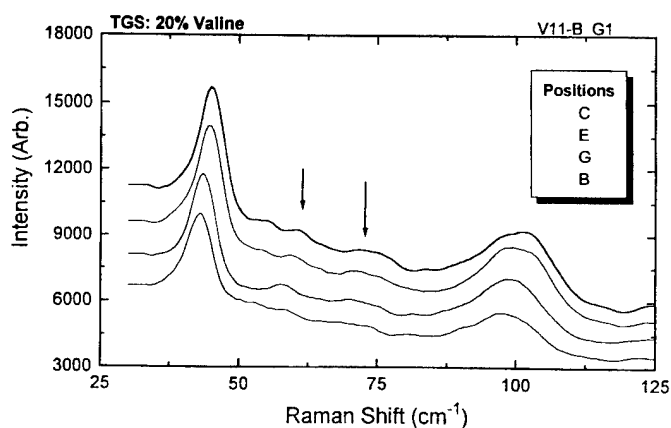


FIGURE 8. Raman spectra of valine 20% doped TGS depending on the positions and showing the depression of librational glycine modes below  $100\text{ cm}^{-1}$ .

## CONCLUSION

In a previous report<sup>8</sup>, determination of the actual alanine and valine contents was unsuccessfully attempted using high performance liquid chromatography (HPLC) method. However electrical measurements (i.e. P-E hysteresis or dielectric constants) show variation in incorporated alanine and valine content within the crystal. Therefore, we tried to confirm this observation using Raman spectroscopy. In this experiment, the effects of alanine and valine on the Raman spectra of TGS was observed. The external  $\text{SO}_4$  vibrations modes at  $170$  and  $205\text{ cm}^{-1}$ ,  $\text{SO}_4 - \nu_1$  vibration at  $1009\text{ cm}^{-1}$  and  $\text{NH}_3$  rocking mode at  $1164\text{ cm}^{-1}$  were not detected because of the compositional variation in alanine doped TGS. In valine doped TGS, librational glycine modes at  $58$  and  $72\text{ cm}^{-1}$  were highly depressed, and it can be implied that bigger molecule can play a more severe damage in internal vibration. Increased crystalline imperfection was found towards the seed point, and the crystal edges have the higher vibrational frequencies than the inside.

## REFERENCES

1. R.S.Krishnan and K.Balasubramian, Proc.Indian Acad. Sci., **A48**, 138 (1958)
2. L.Taurel, E.Pourel and F.Thomassin, Compt. Rend., **246**, 70 (1958)
3. A.Galustian, Spectroscopy Lett., **6**, 347 (1973)
4. V.Winterfeldt and G.Schaack, Ferroelectrics, **15**, 21 (1977)
5. E.Silberman, S.H.Morgan and J.M.Springer, J. Raman Spec., **10**, 248 (1981)
6. Y.Jiarui, L.Gouxian, L.Bing, H.Shifen and W.Huafu, Ferroelectrics, **101**, 251 (1990)
7. L.D.Barron, A.R.Gargaro and L.Hecht, Spectrochimica Acta, **47A**, 1001 (1991)
8. S.Erdei, B.M.Jin, A.S.Bhalla, to be published in Ferroelectrics.

# Pyroelectric Measurements on Various Kinds Doped TGS Single Crystals

B.M.Jin, S.Erdei and A.S.Bhalla

Materials Research Laboratory, The Pennsylvania State University,  
University Park, PA 16802, U.S.A.

**Abstract** - TGS was grown by a slow cooling technique from several kinds of dopants (10 and 20 mole% alanine, 10% alanine +  $\text{LiVO}_3$ , 10% and 20% valine) doped aqueous solution. Temperature dependent pyroelectric coefficient and spontaneous polarization were measured : to study the variation of transition temperature,  $p_{\text{max}}$  at  $T_c$  and room temperature pyroelectric coefficient depending on the dopants and to calculate the figure of merit ( $p/K$ ) with dielectric constant ( $K$ ) measurement. Furthermore, several pieces were selected to investigated the positional inhomogeneities of the same sample. We could not obtain a high figure of merit ( $p/K$ ) in valine doped TGS case because of low temperature dielectric relaxation around  $-10^\circ\text{C}$ , although valine doped TGS has three times higher pyroelectric coefficient ( $p = 1.671 \mu\text{C}/\text{cm}^2\text{K}$ ) at transition temperature ( $T_c$ ).

## INTRODUCTION

The ferroelectric triglycine sulphate  $(\text{NH}_2\text{CH}_2\text{COOH})_3\text{H}_2\text{SO}_4$  (TGS) was initially discovered by Mattias, Miller and Remeila [1] in 1956. Subsequently, TGS single crystals were thoroughly investigated, characterized[2-4] and utilized successfully in pyroelectric detectors[5] and other devices[6-7]. To optimize its performance for practical applications, numerous attempts have been made to prevent depolarization due to its low Curie temperature ( $T_c = 49.5^\circ\text{C}$ ). To achieve this goal, a variety of inorganic dopants have been widely investigated [8-9]. Organic dopants have also been widely investigated[3-4, 10-11]. Partial substitution of glycine with the simple aliphatic amino acid L-alanine, includes high

internal bias fields in LATGS, increasing the spontaneous polarization ( $P_s$ ), transition temperature ( $T_c$ ) and pyroelectric coefficient ( $p$ ), and decreasing the room temperature dielectric constant. These changes are desirable for pyroelectric detectors; however, LATGS crystals possess strong strains, and can easily crack during both crystal growth and subsequent processing. For crack prevention and property enhancement, two general methods have been utilized for development of pyroelectric and infrared detectors. One is utilization of multiple doping; the second method is to find new organic dopants with desirable pyroelectric and mechanical characteristics. In this paper, we are going to present a recent trial for another kind of dopant -- valine : it has a same chiral molecule like an alanine but has a bigger molecule, so it is harder to incorporate into the glycine (I) site than alanine.

## EXPERIMENT

10 and 20 mole% alanine, 10% alanine +  $\text{LiVO}_3$ , 10 and 20% valine doped TGS single crystals were grown by the slow cooling method in water solution. All these crystals were grown below transition temperature. 10% alanine doped and 10% alanine +  $\text{LiVO}_3$  doped crystal has a good quality without any kind of visible cracks. It is very difficult to grow the 20% alanine doped crystal bigger than 3 cm in diameter or without any defects, but the crystal can possess a high internal bias field. 10% and 20% valine doped TGS crystal was also grown. An interesting point is that in the case of valine doping in both percentages, we can grow very high quality of a single crystal without any kind of defect. For determination of the

actual concentration of dopants in crystals, High Pressure Liquid Chromatography (HPLC) (Model 420 Amino Acid Analyzer/Applied Biosystem, USA) was used. (The HPLC measurements were performed courtesy of The Biotechnology Institute at The Pennsylvania State University.) Several sample plates were prepared from the same crystal, but along different parts of b-axis in order to investigate the inhomogeneities of crystal. Before measurement, wet-cloth

polishing was done to make very smooth surface for electrodes. Pyroelectric measurements were performed based on the Byer-Roundy method during heating and cooling runs.

## RESULTS AND DISCUSSION

Pyroelectric coefficient vs. temperature curve for alanine series is shown in Fig.1. 10% alanine + 10%  $\text{LiVO}_3$  doped TGS (designated as L1 sample) has the lowest pyroelectric peak ( $p=0.24 \mu\text{C}/\text{cm}^2\text{K}$ ) at transition temperature. 10% and 20% alanine doped TGS have peak temperatures at  $49.4^\circ\text{C}$ , but  $48.5^\circ\text{C}$  in L1 sample. T3 sample has the highest pyroelectric coefficient ( $p=74.51 \text{ nC}/\text{cm}^2\text{K}$ ) at room temperature. T2 is the nearest position from seed ; from the outside of the seed in 20% alanine doped TGS, T1 and T3 are opposite of each other. 10% alanine doped and L1 samples do not have any kinds of inhomogeneity at different positions, but the 20% alanine doped TGS has a big inhomogeneity (T1, T2 and T3 samples). Therefore, the nearer position from the seed has a more unstable state than the outside positions. For the 10% alanine doped case, there was not that kind of instability. This means that a small amount of impurity does not make any kind of inhomogeneity inside the crystal. Spontaneous polarizations of alanine series were calculated from the pyroelectric coefficient. The result is in Fig.2. As expected from the shape of the pyroelectric coefficient, the L1 sample has the smallest polarization ( $P_s=1.80 \mu\text{C}/\text{cm}^2$ ) at room temperature. A gradual decrease of  $P_s$  beyond the pyroelectric maxima indicates that it possesses the internal bias field ( $E_b$ ), although the exact value can be measured by P-E hysteresis measurement. A quite different situation was observed in valine doped TGS crystal, as shown in Fig.3. Alanine doped TGS showed very diffusive characteristics in dielectric and pyroelectric data, but valine doped TGS showed a very sharp transition in both measurements. U's indicates 10% valine and V's for 20% valine at every different positions. U3a and U3b are on the upper and lower section of the same b-plate, and U6 is opposite of the U3's. V5 is the nearer position from the seed than V9. 10% valine has a higher  $p$  ( $=1.03 \mu\text{C}/\text{cm}^2\text{K}$ ) at  $T_c$  and lower  $p$  ( $=20.03$

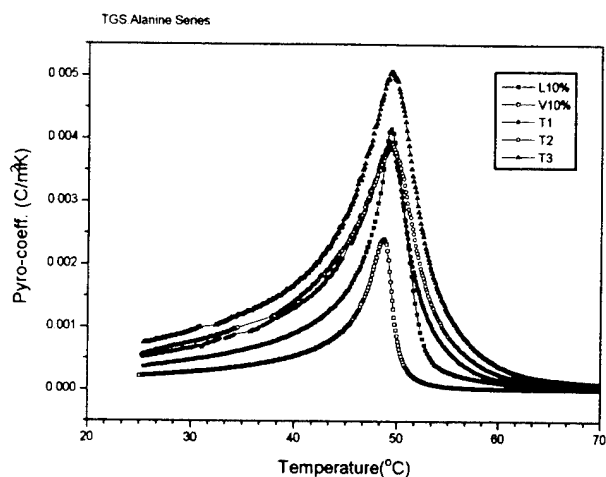


FIGURE 1. Pyroelectric coefficient vs. temperature of different amount of alanine contents. (L10%: alanine 10%, 10%  $\text{LiVO}_3$ : 10% alanine + 10%  $\text{LiVO}_3$  and T1H, T2H, T3H: 20% alanine doped but different positions in same crystal)

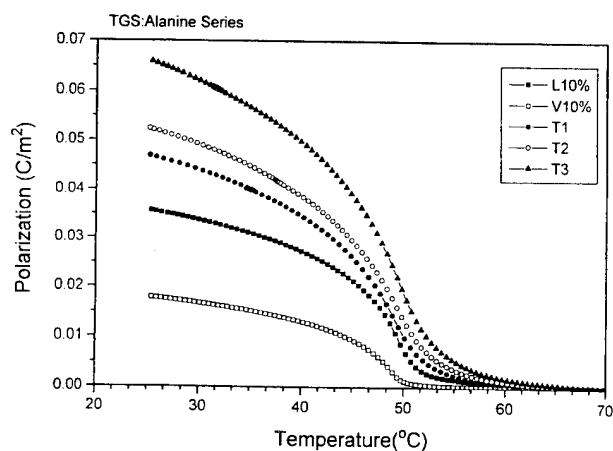


FIGURE 2. Spontaneous polarization vs temperature for alanine doped TGS crystals. T1, T2 and T3 indicate the distance from the seed position along b-axis in 1 cm apart, respectively (see text for more information).

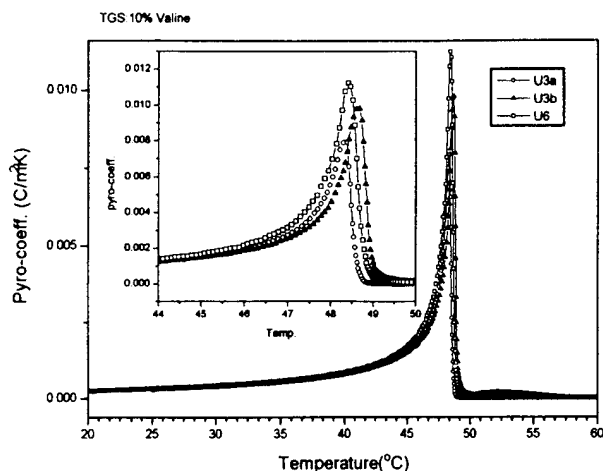


FIGURE 3. Pyroelectric coefficient vs. temperature of 10% valine doped TGS. U's indicates 10% valine and see text for more information. It is clearly seen that the positional inhomogeneity was big in 10% valine doped TGS.

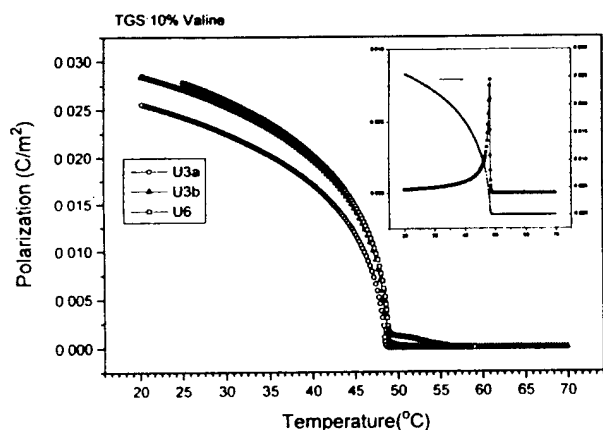


FIGURE 4. Spontaneous polarization vs temperature for 10% valine doped TGS. Inhomogeneity is well profound along c-direction (U3a and U3b)

nC/cm<sup>2</sup>K) at room temperature than alanine. 20% valine doped TGS has roughly two times higher values than 10% valine, but still less than that of 20% alanine doped TGS. Because we tried just 20% of valine only, it is hard to have an exact comparison between alanine and valine. So far, it is clear that alanine has a higher internal bias field and higher pyroelectric coefficient than valine[12] -- this is the direct proof of being a good pyroelectric detector candidate, but it is very difficult to grow high quality and large crystal. Valine doped crystal can be easily grown without any kind of visible crack or defect, although it has a relatively small internal bias field (see Fig.4 -- very small tail beyond T<sub>C</sub>) up to 20 mole%.

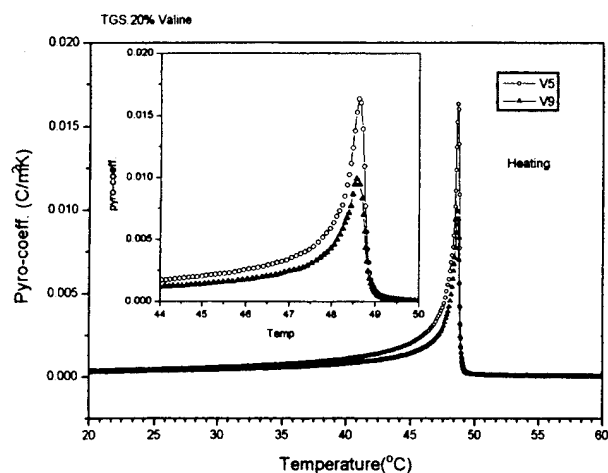


FIGURE 5. Pyroelectric coefficient vs. temperature of 20% valine doped TGS. V's for 20% valine doped TGS. Peak values are different but have same temperatures.

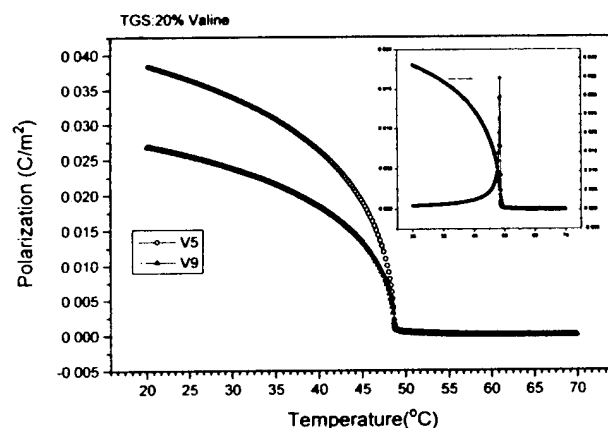


FIGURE 6. Spontaneous polarization vs temperature for 20% valine doped TGS.

Pyroelectric signals are stable in 20% valine doped TGS (Fig.5 & 6) and have peaks at same temperatures in different pieces (V5 and V9). The highest pyroelectric coefficient of valine doped TGS at room temperature is 44.02 nC/cm<sup>2</sup>K. Valine doped TGS has a very small E<sub>b</sub> indicating that the ratio of doping is very small. One more interesting thing is that valine doped TGS has a big anomaly in dielectric constant around -10°C, as shown in Fig.7. Because of this big anomaly, dielectric constant (K) at room temperature is too high and can not get a high figure of merit (p/K), although we can get a reasonable amount of pyroelectric coefficient. This anomaly decreases as the oscillating frequency increases and can not be observed at 100 kHz, which means that it is not related to the phase transition but a relaxational mechanism.

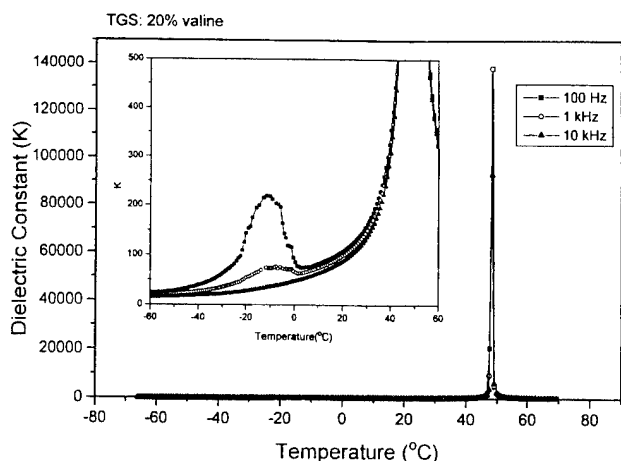


Figure 7. Low temperature dielectric constant measurement showing relaxational behavior at  $-10^{\circ}\text{C}$ . The effect of this relaxation goes up to room temperature causing high dielectric constant at room temperature.

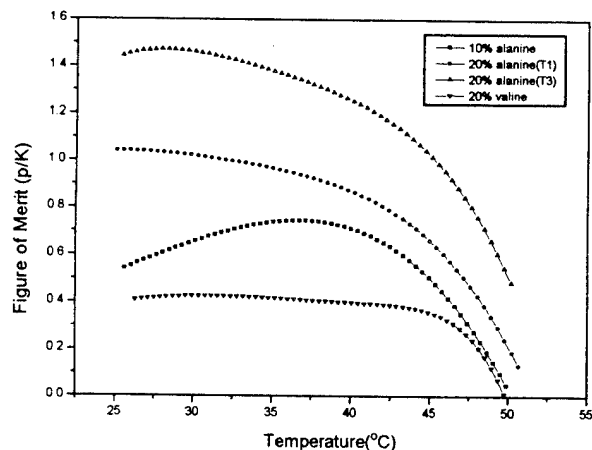


FIGURE 8. Figure of merit (p/K) for various kinds doped TGS. Valine doped TGS has a small p/K, but very flat throughout the ferroelectric phase that means a very stable state.

The resulting figure of merit for various kinds doped TGS is shown in Fig.8. At this moment, it is not clear what kind of mechanism is included to generate this relaxation. After measuring the dielectric spectra in frequency domain, it will be more clearly understandable, and this procedure is now in progress.

#### CONCLUSION

Pyroelectric coefficient measurements were done in several kinds of dopants doped TGS single crystals. Alanine can generate the largest internal bias field but it is hard to grow

good quality and large size of the crystal. Valine has been used to test the effect of glycine (I) substitution effect instead of alanine. Valine has a bigger molecule than alanine, so it is difficult to incorporate into a crystal. The experimental results also show this expectation, but valine has two different and interesting properties. First, 10% valine has a very small internal bias field indicating a small real substitution. And also has a very sharp phase transition in both dielectric and pyroelectric measurement. For the 20% valine case,  $E_b$  is increased, but a good quality of crystal without any defect is still obtained. Second, there was big relaxation phenomena around  $-10^{\circ}\text{C}$ , which is causing the increase of room temperature dielectric constant. We could not observe this relaxation in alanine doped TGS, but every valine doped TGS has this relaxation and this study is in progress.

#### REFERENCES

- [1] B.T.Matthias, C.E.Miller and J.P.Remeika, *Phys. Rev.*, vol.104, pp.849, 1956
- [2] T.F.Conolly and E.S.Truner, *Ferroelectric Materials and Ferroelectricity*. New York: Plenum Press, 1970
- [3] E.T.Keve et al., *Ferroelectrics*, vol.3, pp.39, 1971
- [4] R.B.Lal and A.K.Batra, *Ferroelectrics*, vol.142, pp.51, 1993
- [5] R.W.Whatmore, *Rep. Prog. Phys.*, vol.49, pp.1335, 1993
- [6] J.H.McCusker and S.S.Perman, *IEEE Trans. Electron Devices*, vol.ED-15, pp.182, 1968
- [7] U.Hetzler and P.Wurfel, *Ferroelectrics*, vol.19, pp.15, 1978
- [8] A.S.Bhalla, C.S.Fang, L.E.Cross and Y.Xi, *Ferroelectrics*, vol.54, pp.151, 1984
- [9] C.S.Fang, X.Yao, A.S.Bhalla and L.E.Cross, *Ferroelectrics*, vol.51, pp.9, 1983
- [10] J.Stankowska, A.Czarnecka and G.Kwitowska, *Ferroelectrics*, vol.108, pp.325, 1990
- [11] C.S.Fang, M.Wang, H.S.Zhuo, J.C.Song and K.C.Zhang, *Ferroelectrics*, vol.142, pp.93, 1993
- [12] B.M.Jin, S.Erdei, A.S.Bhalla, "Pyroelectric measurements on various kinds doped TGS Crystals" in Proceeding on the ISAF-9, 1994

# AUTHOR'S INDEX

## AUTHORS INDEX

- ABURATANI, Hideaki, P. 750  
 ADACHI, Masatochi, P. 778  
 ADAIR, J. H., P. 791  
 AGGARWAL, M. D., P. 775  
 AGRAWAL, D. C., P. 108, 454  
 AHMAD, A., P. 111, 762  
 AI, Hua, P. 760  
 ALBERTA, Edward F., P. 245, 249  
 ALDINGER, F., P. 325  
 ALEMANY, C., P. 138  
 ALYOSHIN, Vladimir, P. 499  
 ANDERSEN, B., P. 118  
 ANDERSON, W. A., P. 482  
 ANDERSON, Richard J., P. 681  
 AOKI, Katsuhiro, P. 79  
 AOYAGI, Manabu, P. 766  
 ATSUKI, Tsutomu, P. 408, 450  
 AUCIELLO, O. H., P. 794  
 AUDIGIER, D., P. 383  
 AUDOLY, C., P. 291  
 AURELLE, N., P. 162  
 AZIMI, M.E., P. 39  
 AZUMA, Masamichi, P. 25  
 BAERTLEIN, C. D., P. 523  
 BAKIROV, Azamat, P. 488, 502  
 BALLATO, Arthur, P. 674  
 BALYUNIS, L. E., P. 97  
 BANNO, Hisao, P. 186  
 BAOSONG, Wen, P. 226  
 BATLLO, F., P. 87  
 BATRA, A. K., P. 695  
 BAUER, Francois, P. 333  
 BECKER, A., P. 341  
 BEI, Nianyu, P. 633  
 BEIGE, H., P. 229, 564, 709  
 BELL, A. J., P. 14, 691  
 BENEDETTO, J. M., P. 66  
 BERATAN, Howard, P. 657  
 BERNSTEIN, J. J., P. 495  
 BHALLA, Amar S., P. 245, 249, 273, 279, 607, 636, 821, 825  
 BHANUMATHI, A., P. 154, 269  
 BILODEAU, S. M., P. 687  
 BIRNIE, III, D. P., P. 446  
 BLOCHWITZ, S., P. 229, 709  
 BLOOMFIELD, Philip E., P. 287, 725  
 BONDARENKO, E. I., P. 166, 179  
 BOULTON, J. M., P. 523  
 BREWS, J. R., P. 83  
 BROOK, R. J., P. 562  
 BROOKS, K. G., P. 520  
 BROWN, L. F., P. 337  
 BUSCH, James R., P. 794  
 BUSKIRK, P. C. V., P. 687  
 BUSSE, L., P. 206  
 CAI, Xiukai, P. 601, 604  
 CAO, Wenwu, P. 329  
 CAPURSO, Joseph S., P. 731  
 CARLSON, W. B., P. 770  
 CASAS, L. M., P. 472  
 CASTELLANOS-GUZMAN, A. G., P. 6  
 CASTRO, Francisco, P. 725  
 CHAI, Francis K., P. 83  
 CHAN, H. L. W., P. 194, 198  
 CHANDRAS, Subhas, P. 504  
 CHANG, L. H., P. 482  
 CHATTERJEE, S. N., P. 551  
 CHEN, Deng-Yuan, P. 25  
 CHEN, H. D., P. 495  
 CHEN, H. T., P. 416  
 CHEN, J. L., P. 241, 746  
 CHEN, Y., P. 198  
 CHEN, Zhiming, P. 778  
 CHENG, Hsiu-Fung, P. 59  
 CHENGYU, Song, P. 226  
 CHERNOBABOV, A. I., P. 144  
 CHIN, T. S., P. 115  
 CHING-PRADO, E., P. 108  
 CHO, Kyeong Ho, P. 566, 572  
 CHOI, J., P. 775  
 CHOI, S. W., P. 806, 808, 810  
 CHOW, Alice F., P. 794  
 CHOY, C. L., P. 194, 198  
 CHOY, Tae Goo, P. 617  
 CHU, Sheng-Yuan, P. 743  
 CHUNG, C. W., P. 527  
 CHUNG, Isub, P. 527  
 CHUNG, Su-Jin, P. 265  
 COCKBURN, M. R., P. 597  
 COLE, B., P. 653  
 COLES, H. J., P. 788  
 CORNEJO, I. A., P. 585  
 COUGHLIN, C., P. 182  
 CRAMER, D., P. 755



- CREEDON, Matthew J, P 299.  
 CROSS, L. E., P. 329, 416, 495, 577, 746  
 DAI, Xunhu, P. 361  
 DAMJANOVIC, D., P. 520  
 DANTSIGER, A. Ya., P. 168, 170, 175, 178  
 DAUSCH, D. E., P. 701  
 DEB, Krishnan K., P. 480  
 DERGUNOVA, N. V., P. 170, 175  
 DERIUGINA, N. I., P. 277  
 DESU, Seshu Babu, P. 531  
 DEVLIKANOVA, R. U., P. 170  
 DIESTELHORST, M., P. 564, 709  
 DOBSON, P. J., P. 562  
 DONG, Shuxiang, P. 387, 713, 739  
 DONG, Dunzhuo, P. 19  
 DORMANS, G.J.M., P. 29  
 DOUGHERTY, Joseph P., P. 581  
 DUDKEVICH, V., P. 488, 499, 502  
 DUDKINA, S. I., P. 170, 175  
 DURAN, P., P. 49  
 DURCE, Galen C., P. 633  
 EGAMI, T., P. 43  
 ELKECHAI, O., P. 253  
 ERDEI, S., P. 607, 821  
 EREMKin, V. V., P. 97  
 ETMINAN, S., P. 695  
 EYRAUD, F., P. 383  
 EYRAUD, L., P. 383  
 EYRAUD, P., P. 383  
 FABINY, L., P. 717  
 FAN, Chen-Lung, P. 512  
 FEOKTISTOVA, N. N., P. 190  
 FERNANDEZ, J. F., P. 49  
 FEUILLARD, G., P. 138  
 FIELDING, Jr. J. T., P. 158, 202, 363  
 FLOQUET, N., P. 87  
 FOOTE, M. C., P. 653  
 FORSTER, M., P. 691  
 FOUSEK, Jan, P. 1  
 FRANKE, K., P. 412  
 FRIT, B., P. 257  
 FROMMELT, J. M., P. 769  
 FUIERER, P. A., P. 126  
 FUKUDA, Yukio, P. 79  
 FUNDAUN, I. L., P. 614  
 FURMAN, E., P. 146, 577  
 GACHIGI, K. Wa, P. 353  
 GARG, Ajay, P. 108  
 GASKEY, C. J., P. 416  
 GAVRILYATCHENKO, S. V., P. 168, 170, 175, 178  
 GENG, X., P. 329  
 GESEMANN, H.-J., P. 412  
 GLISSA, N., P. 383  
 GOELLER, Roy M., P. 725  
 GONNARD, P., P. 162, 383  
 GOPALAKRISHNAN, Sodhakar, P. 299  
 GHOSH, P. K., P. 39  
 GRAETTINGER, T.M., P. 794  
 GRIDNEV, S. A., P. 630, 753  
 GRINEVA, L. D., P. 172, 175  
 GROND, W., P. 412  
 GUALTIERI, John G., P. 674  
 GUI, Zhilun, P. 387, 713  
 GUPTA, Vinay, P. 508  
 HABEL, R., P. 229, 709  
 HAERTLING, G. H., P. 146, 313, 390, 701, 781  
 HAJIME, Keibunn, P. 735  
 HALL, D. A., P. 597  
 HANN, Michael J., P. 468  
 HANSON, Charles, P. 657  
 HELLEBRAND, H., P. 755  
 HICKERNELL, F. S., P. 543  
 HIROSE, Seiji, P. 377, 766  
 HIRSCH, M., P. 111  
 HOANG, T., P. 762  
 HOELZER, David, P. 348  
 HOFFMANN, R. C., P. 480  
 HORNING, R., P. 653  
 HOUNG, Boen, P. 214  
 HOWELL, F. L., P. 614  
 HUAN, M. J., P. 585  
 HUANG, J. Y., P. 115  
 HUANG, Weng-Hsing, P. 594  
 HUANG, Y., P. 691  
 HUEBNER, W., P. 101, 122, 130, 134, 150, 206, 512, 581  
 HUH, Min, P. 572  
 ICHINOSE, Noboru, P. 476  
 IGNATIEV, Alex, P. 464  
 IJIMA, Kenji, P. 53  
 IKAWA, E., P. 74  
 IVANOVA, S. V., P. 779  
 IYI, Nobuo, P. 439  
 JACKSON, D. A., P. 480  
 JANAS, V. F., P. 295  
 JANG, E. K., P. 210  
 JANG, S. J., P. 158, 363, 626  
 JIMENEZ, B., P. 138  
 JIN, B. M., P. 273, 279, 607, 821  
 JIN, Y. H., P. 804, 812, 815, 825  
 JOHNSON, B., P. 653  
 JUNG, J. M., P. 806, 810  
 JUNGnickel, B.-J., P. 341  
 KAKIMI, A., P. 62

- KAMISAWA, Akira, P. 345, 450, 547  
 KANCHEROVA, E. T., P. 190  
 KANEKO, Shoji, P. 19  
 KANG, Q., P. 535  
 KAPOOR, Rakesh, P. 633  
 KAPSCH, R. P., P. 564  
 KAPUSTIANIK, V., P. 801  
 KATYAR, R. S., P. 108  
 KATO, Y. S., P. 769  
 KAWABATA, Akira, P. 776  
 KETCHEL, Brian P., P. 771  
 KEWITSCH, Anthony S., P. 719  
 KHUTORSKY, V. E., P. 817  
 KIDO, T., P. 791  
 KIM, H. H., P. 472  
 KIM, I. W., P. 273, 279  
 KIM, J., P. 423  
 KIM, Jeong-Joo, P. 617  
 KIM, J. W., P. 279  
 KIM, Nam Kyoung, P. 591  
 KIM, Shin-Young, P. 617  
 KIM, Tae Hong, P. 617  
 KIM, Y. D., P. 585  
 KIM, Y. J., P. 808  
 KIMURA, Shigeuki, P. 439  
 KINGON, A. I., P. 794  
 KISHAN, Pran, P. 551, 554  
 KITAMURA, Kenji, P. 439  
 KLANCK, Robert, P. 681  
 KLEIN, L. C., P. 427  
 KLEVTSOV, A. N., P. 166, 168  
 KNEER, E. A., P. 446  
 KONDOH, A., P. 399  
 KOROTKOV, L. N., P. 630  
 KOSIK, W. E., P. 70, 431  
 KOSINSKI, John A., P. 674  
 KOTHARI, Deepika, P. 554  
 KOZAKOV, A. T., P. 97  
 KRUPANIDHI, S. B., P. 460  
 KRUSE, P. W., P. 643  
 KUHARUANGRONG, S., P. 559  
 KULKARNI, V. N., P. 454  
 KUWABARA, M., P. 729, 758  
 KWOK, K. W., P. 194  
 KWUAN, S.-I., P. 423  
 LAKEMAN, Charles D. E., P. 404  
 LAL, R. B., P. 695  
 LANCTO, R., P. 372, 622  
 LANDIN, Steven M., P. 468, 585  
 LANG, Sydney B., P. 815  
 LAREAU, R. T., P. 472  
 LARSEN, P.K., P. 29  
 LEE, Hee Young, P. 566, 572, 617  
 LEE, J. K., P. 527  
 LEE, S. H., P. 687  
 LEE, Sungchul, P. 83  
 LEE, W., P. 527  
 LETHIECQ, M., P. 138  
 LI, C. H., P. 115  
 LI, G., P. 146  
 LI, Jia, P. 464  
 LI, Jie-Fang, P. 760  
 LI, Longtu, P. 387, 713, 739  
 LI, T., P. 791  
 LI, X. Y., P. 464  
 LIAW, H. M., P. 543  
 LICHTENWALNER, Daniel J., P. 794  
 LIN, C. H., P. 115  
 LIN, He, P. 464  
 LIN, I. N., P. 59, 261, 491  
 LIN, S. W., P. 804, 812, 815  
 LIN, Y. S., P. 812  
 LIU, Chunliang, P. 797  
 LIU, Donhang, P. 435  
 LIU, Hongling, P. 797  
 LIU, K. S., P. 241, 261, 491  
 LIU, R. B., P. 804, 812, 815  
 LIU, W. G., P. 535  
 LIU, Yun, P. 516  
 LIVNEH, S., P. 295  
 LLOYD, I. K., P. 66  
 LU, P. W., P. 101, 122, 134, 150  
 LU, Yanxia, P. 348  
 LUBITZ, K., P. 755  
 LUGINBUHL, Ph., P. 520  
 LYNCH, Christopher S., P. 357  
 MA, J., P. 687  
 MAALAL, R., P. 257  
 MAGLIONE, M., P. 87  
 MAIWA, Hiroshi, P. 476  
 MAJUMDER, S. B., P. 454  
 MAKAROV, S. D., P. 669  
 MANIER, M., P. 257  
 MANSINGH, A., P. 105, 457, 508, 663  
 MARGOLIN, Aron, P. 488  
 MARKOWSKI, K. A., P. 353, 705  
 MARX, J. G., P. 130  
 MASUDA, H., P. 399  
 MATSUI, Yoshio, P. 439  
 MATSUNAGA, T., P. 729  
 MATSUOKA, H., P. 485  
 MATSUYAMA, E., P. 758  
 McCAULEY, D., P. 353  
 McDONALD, A. G., P. 111

- McKINSTRY, S. Trolier, P. 202, 233  
 McMILLAN, Larry D., P. 25  
 McNULTY, T. F., P. 295  
 MERCURIO, J. P., P. 253, 257  
 MERKLEIN, S., P. 412  
 MESNIER, M., P. 87  
 MEYERS, Jr., R., P. 202  
 MILLAR, C. E., P. 118, 138, 597  
 MIN, Kyung Ki, P. 591  
 MIYASAKA, Y., P. 74  
 MOCHIZUKA, T., P. 399  
 MOHAPATRA, Y. N., P. 454  
 MOKRYI, V., P. 801  
 MOORS, W.G.J., P. 29  
 MORI, K., P. 62  
 MORII, Tohru, P. 394  
 MORIMO, K., P. 729  
 MOSKALYUK, V. A., P. 698  
 MOURE, C., P. 49  
 MUKHERJEE, B. K., P. 390  
 MURAKOMI, Kenji, P. 19  
 MURTHY, K. V. Ramana, P. 283  
 MURTY, S. Narayanan, P. 269, 283  
 MURTY, K. Linga, P. 269  
 NAGAO, Nobuaki, P. 53  
 NAKAMURA, Kiyoshi, P. 222  
 NAKAMURA, Takashi, P. 345, 450, 547  
 NAKAO, Yuichi, P. 345, 450, 547  
 NAM, Hyo-Duk, P. 572  
 NARAYANAN, S., P. 309  
 NARULA, Amarjeet K., P. 443  
 NAUMOV, A. P., P. 170  
 NEURGAONKAR, R. R., P. 594, 633, 681, 719, 771  
 NEWMAN, B. A., P. 337  
 NEWNHAM, R. E., P. 202, 353, 626, 705  
 NGO, E., P. 70, 372, 622  
 NGUYEN, K., P. 653  
 NICHTAWITZ, A., P. 126  
 NIEPCE, J. C., P. 87  
 NIETO, E., P. 49  
 NILES, L. C., P. 495  
 NISHIMURA, Akitoshi, P. 79  
 NIWATSUKINO, Yoshiyuki, P. 735  
 NUMATA, Ken, P. 79  
 O'DAY, M. E., P. 372, 622  
 OGAWA, T., P. 399  
 OGI, Katsumi, P. 408, 450  
 OH, Ki-Young, P. 218, 377  
 OKADA, Nagaya, P. 19  
 OKAMURA, S., P. 62  
 OKAWA, Takashi, P. 367  
 OKAZAKI, Kiyoshi, P. 10, 476  
 OKUDA, Takeo, P. 21  
 ONO, H., P. 74  
 OSBOND, P. C., P. 647  
 OZGUZ, V. H., P. 687  
 OZHIBKO, Ya., P. 801  
 PADMAVATHI, G., P. 269, 283  
 PAN, Wei, P. 713  
 PANDEY, R. K., P. 309  
 PARADISE, William E., P. 781  
 PARDO, L., P. 118, 138  
 PARK, B. C., P. 273  
 PARK, Seung-Eek, 08P. 265  
 PARK, Y. H., P. 801  
 PATEL, A., P. 647  
 PATTNAIK, R. K., P. 611  
 PAUL, O., P. 691  
 PAVLOVA, N. G., P. 630, 753  
 PAYNE, David A., P. 404, 435, 589  
 PAZ DE ARAUJO, C. A., P. 25  
 PEDERSEN, L., P. 138  
 PEI, S. C., P. 115  
 PENG, C.-J., P. 460  
 PEREZ, W., P. 108  
 PERRIAT, P., P. 87  
 PETHYBRIDGE, G. D., P. 562  
 PFEFFER, R. L., P. 472  
 PHANJOUBAM, Sumitra, P. 554  
 PILGRIM, S. M., P. 769  
 PODLESNY, J. C., P. 446  
 POLOVINKO, I., P. 801  
 POPLAVKO, Y. M., P. 698  
 POTTER, B. G., P. 348  
 PRAKASH, Chandra, P. 551, 554  
 PRASAD, N. S., P. 154  
 PRASAD, S. E., P. 762  
 PROBST, I., P. 755  
 PROKOPENKO, Y. V., P. 698  
 QU, C. F., P. 804, 815  
 QUACKENBUSH, E. L., P. 523  
 RACINE, G. A., P. 520  
 RAINA, K. K., 788  
 RAJU, S. Bangar, P. 269  
 RAMAN, V., P. 443  
 RAMESH, R., P. 66  
 RAZUMOVSKAJA, O. N., P. 168, 170, 175  
 REIDMEYER, M. R., P. 206  
 REZNITCHENKO, L. A., 166, 168, 170, 175, 179, 488  
 RICHARD, C., P. 162, 291  
 RICOTE, J., P. 188, 138  
 RINGGARI, E., P. 118  
 RITTENMYER, K., P. 182  
 ROCHE, D., P. 162

- ROEDER, J. F., P. 687  
 ROGOVA, S. P., P. 630, 753  
 ROOIJ, N. F. de, P. 520  
 ROUSH, M. L., P. 66  
 RUMYANTSEV, E. L., P. 669  
 RYSER, P., P. 691  
 SAFARI, A., P. 295, 427  
 SAGAR, D. R., P. 551  
 SAITO, Akiro, P. 719  
 SAITOH, S., P. 399  
 SAKUMA, T., P. 74  
 SALAMO, Gregory J., P. 633, 681, 719  
 SALERNO, D. M., P. 636  
 SAPOZHNIKOV, Lev, P. 449  
 SARMA, B.S., P. 154  
 SARRAZIN, P., P. 87  
 SASAKI, Go, P. 408, 450  
 SATYANARAYANA, Ch. V. V., P. 283  
 SAYER, M., P. 663  
 SCHAEFFER, R., P. 295  
 SCHEINBEIM, J. I., P. 337  
 SCHMIDT, V.H., P. 45, 237  
 SCHNEIDER, G. A., P. 325  
 SCHÖNECKER, H., P. 412  
 SCHRIMPF, R. D., P. 83  
 SCHULZE, Walter A., P. 299, 348, 559, 769  
 SEGEV, Mordechai, P. 719  
 SEM, Irina, P. 499  
 SENGUPTA, L. C., P. 70, 372, 431  
 SENGUPTA, S., P. 70, 431  
 SETTER, N., P. 520  
 SHARMA, H. Basantakumar, P. 457  
 SHARP, Edward J., P. 633, 681, 719  
 SHEINKMAN, M. K., P. 277  
 SHERRIT, S., P. 390  
 SHEVTSOVA, S. I., P. 97  
 SHIBATA, Akira, P. 735  
 SHIKHMAN, V. M., P. 172  
 SHIMIZU, Masaru, P. 303  
 SHIMOOKA, H., P. 729, 758  
 SHIOSAKE, Tadashi, P. 303  
 SHISHIBA, Hideki, P. 735  
 SHORROCKS, N. M., P. 647  
 SHROUT, T. R., P. 158, 363  
 SHUI, Y., P. 329  
 SHUR, V. Ya, P. 669  
 SIDORKIN, A.S., P. 91  
 SINGH, Ramadhar, P. 443, 504  
 SINHA, R. D. P., P. 504  
 SINY, I. G., P. 45  
 SMITH, D., P. 202  
 SMOTRAKOV, V. G. , P. 97  
 SOHN, K. S., P. 472  
 SOLDATOV, V., P. 799  
 SOYAMA, Nobuyuki, P. 408, 450  
 SPIERINGS, G.A.C.M., P. 29  
 SPRUMONT, M., P. 383  
 STADLER, S., P. 614  
 STEIN, M., P. 341  
 STEVENSON, J. W., P. 206  
 STOWELL, S., P. 70, 372, 622  
 SUE, W. R., P. 150  
 SUEMATSU, Hisayoki, P. 439  
 SUGISAWA, Katsuhiko, P. 735  
 SUGIYAMA, O., P. 399  
 SUNDAR, V., P. 353  
 SVELEBA, S., P. 801  
 SVIRIDOV, Evgeny, P. 488, 499, 502  
 SYAMALAMBA, V., P. 283  
 SYRKIN, L. N., P. 190  
 TAHAN, D., P. 427  
 TAKADA, Takahiro, P. 626  
 TAKAHASHI, S., P. 377, 729, 758, 766  
 TAKAO, Fumio, P. 735  
 TAKASU, Hidemi, P. 345, 450, 547  
 TAKAYAMA, Ryouichi, P. 53  
 TAKEDA, Shu-ichi, P. 735  
 TAKEMURA, K., P. 74  
 TAKENAKA, Tadashi, P. 21  
 TAKEUCHI, Takayuki, P. 53  
 TALWAR, P., P. 105  
 TAMAMOTO, T., P. 485  
 TANDON, R. P., P. 105, 443, 504  
 TANIMOTO, Toshio, P. 394  
 TCHUKVINSKYI, R., P. 801  
 TELSIC, S., P. 43  
 TEOWEE, G., P. 446, 523  
 TERABE, Kazuya,, P. 439  
 TIMOFEYEV, V. I., P. 698  
 TING, R. Y., P. 182, 291  
 TING, S. M., P. 295  
 TOKASHIKI, K., P. 74  
 TOMIKAWA, Yoshiro, P. 766  
 TOPOLOV, V. Yu., P. 142, 144  
 TOULOUSE, J., P. 611  
 TOURLOG, Ailie, P. 222  
 TOWE, Terrence W., P. 719  
 TRINATH, K., P. 154  
 TROCCAZ, M., P. 383  
 TROLIER-McKINSTRY, Susan, P. 202, 233  
 TROTTIER, Michael, P. 746  
 TSUKAMOTO, T., P. 62  
 TU, Chi-Shun, P. 45, 237  
 TU, Shun-Lih, P. 491

- TURIK, A. V., P. 142, 144  
 TUTTLE, Bruce, P. 348  
 TWINEY, R. C., P. 647  
 UCHINO, Kenji, P. 218, 319, 377, 743, 750  
 UDAYAKUMAR, K. R., P. 416, 495  
 UEDA, Ichiro, P. 53  
 UHLMANN, D. R., P. 523  
 ULENAERS, M.J.E., P. 29  
 URAKAWA, Y., P. 758  
 VALOT, C. M., P. 87  
 VARMA, S., P. 762  
 VIEHLAND, Dwight, P. 361, 589, 594, 760  
 VOHRA, S. T., P. 717  
 VOLEGOV, V. V., P. 669  
 WAKINO, Kikuo, P. 33  
 WALKER, F. R., P. 295  
 WANG, F., P. 701, 781  
 WANG, Feiling, P. 683  
 WANG, H., P. 182  
 WANG, Sea Fang, P. 581, 626  
 WANG, W. S., P. 773  
 WANG, X. F., P. 134  
 WATANABE, H., P. 74  
 WATTON, R., P. 647  
 WEIHNACHT, M., P. 412  
 WEON, H. Y., P. 808  
 WHATMORE, R. W., P. 647  
 WHEAT, T. A., P. 111, 762  
 WIDERICK, H. D., P. 390  
 WOLFF, A., P. 755  
 WOLNY, W., P. 118  
 WOO, J. W., P. 210  
 WOOD, Gary L., P. 681, 771  
 WU, Naijuan, P. 464  
 WU, T. B., P. 241  
 WU, Xiao-Qing, P. 539  
 WU, Z., P. 636  
 XIE, Kan, P. 464  
 XIONG, Si-Bei, P. 539  
 XU, Z., P. 361, 404, 589, 594  
 XUE, W. R., P. 101, 122, 134  
 YAGI, Y., P. 62  
 YAMADA, Masotoshi, P. 21  
 YAMAMICHI, S., P. 74  
 YAMAMOTO, Hiroshi, P. 735  
 YAMAMOTO, Kohji, P. 394  
 YANG, Cheul-Kee, P. 617  
 YANG, Sheng-Jenn, P. 491  
 YAO, C. H., P. 804, 812, 815  
 YAO, Xi, P. 419, 516, 535, 539, 601, 604, 797  
 YARIV, Amnon, P. 719  
 YARRISON-RICE, Jan M., P. 681  
 YIN, S., P. 636  
 YINMEI, Liu, P. 226  
 YONEZAWA, Tadashi, P. 408, 450  
 YOO, I. K., P. 527, 531  
 YOON, J.-G., P. 423  
 YOSHIKAWA, Shoko, P. 626  
 YOSHIKAWA, Yoshio, P. 95  
 YU, I., P. 210  
 YU, F. T. S., P. 636  
 ZAENTSEV, V. V., P. 630  
 ZAKHAZCHENKO, Irina, P. 499  
 ZHANG, Jinxiu, P. 419  
 ZHANG, Liang-Ying, P. 419, 516, 535, 539, 601, 604, 797  
 ZHANG, Q. M., P. 182, 329, 746  
 ZHANG, S. R., P. 802  
 ZHANG, W. M., P. 134  
 ZHANG, Xiaowen, P. 387, 713, 739  
 ZHANG, Y. R., P. 812  
 ZHAO, F., P. 636  
 ZHAO, Qingchun, P. 794  
 ZHONG, C. W., P. 804  
 ZHONG, Wei, P. 387  
 ZHOU, Qifa, P. 419  
 ZICKGRAF, B., P. 325

# ATTENDEES LIST

## ATTENDEES LIST

Hideaki Aburatani  
Penn State University  
A2 MRL  
University Park, PA 16802

Masatoshi Adachi  
Toyama Prefectural University  
5180 Kurokawa  
Toyama, 939-03  
JAPAN

James H. Adair  
University of Florida  
Gainesville, FL 32611-2066

Mohan D. Aggarwal  
Alabama A&M University  
Dept. of Physics  
Normal, AL 35762

Dinesh C. Agrawal  
Indian Institute of Technology  
Materials Science  
UP., 208016  
INDIA

Aftab Ahmad  
Natural Resources Canada  
405 Rochester St.  
Kiaogi  
CANADA

Frank W. Ainger  
Penn State University  
187 Materials Research  
University Park, PA 16802-4800

Bhanumathi Akella  
Andhra University  
Dept. of Physics  
Warangal  
INDIA

Edward F. Alberta  
Penn State University  
143 Materials Research  
University Park, PA 16802

Sidorkin Alexander  
Voronezh State University  
University Sq. 1  
Voronezh, 394693  
RUSSIA

Xan Alexander  
Advanced Research Projects Agency  
3701 N. Fairfax Dr.  
Arlington, VA 22203-1714

Ahmed Amin  
Texas Instruments  
34 Forest St.  
Attleboro, MA 02703

Dean Anderson  
Motorola  
4800 Alamedon Blvd. NE  
Albuquerque, NM 87113

Pavadee Aungkavattana  
Penn State University  
143 Materials Research  
University Park, PA 16802

Masud Azimi  
Syracuse University  
Department of Electrical  
Syracuse, NY 13244-1240

Richard W. Babbit  
U.S. Army Research Lab.  
Ft. Monmouth, NJ 07703

A. Bakirov  
Rostov State Univ.  
Instt. of Physics  
Rostov-On-Don, 344104  
RUSSIA

Arthur Ballato  
U.S. Army Research Laboratory  
Electronic & Power  
Fort Monmouth, NJ 07703-5601

John Ballato  
Rugers University  
Department of Ceramics  
Piscataway, NJ 08855-0909

Hisao Banno  
NGK Spark Plug Co., Ltd.  
14-18, Takatsuji-cho  
Nagoya  
JAPAN

Francois Batllo  
INTA  
2281 Caffé de Luna  
Santa Clara, CA 95054

Paul F. Baude  
University of Minnesota  
Electrical Engineering  
Minneapolis, MN 55455

Francois Bauer  
Institut Franco-Allemand ISL  
5 Rue Du General  
Saint Louis, MO 68300

Hogd Beige  
Martin-Luther-Universitat  
Fachbeteich Physik  
Halle, 06108  
GERMANY

Uma Belegundu  
Penn State University  
A-11, MRL  
State College, PA 16803

Andrew J. Bell  
EPFL  
Laboratoire De  
Lausanne, 1015  
SWITZERLAND

Michelle R. Bell  
Radiant Technologies  
1009 Bradbury Dr. SE  
Albuquerque, NM 87106

Joseph M. Benedetto  
Army Research Laboratory  
ARSRL-WT-NG  
Adelphi, MD 20783

Howard Beratan  
Texas Instruments  
13532 N. Central Expressway  
Dallas, TX 75265

Steve E. Bernacki  
Raytheon Company  
528 Boston Post Road  
Sudbury, MA 01776

Amar S. Bhalla  
Penn State University  
Materials Research Lab.  
University Park, PA 16802

Mahesh Bhardwai  
Ultran Labs, Inc.  
1020 E. Boal Ave.  
Boalsburg, PA 16827

V. Bheemineni  
MRA Laboratories  
96 Marshall St.  
North Adams, MA 01247

Philip E. Bloomfield  
Drexel University  
Biomedical Engr.  
Philadelphia, PA 19104



Christopher P. Bowen  
Penn State University  
143 MRL  
University Park, PA 16802

Les Bowen  
Materials Systems, Inc.  
53 Hillcrest Road  
Concord, MA 01742

Russell P. Brodeur  
Penn State University  
259 MRL  
University Park, PA 16802

Keith G. Brooks  
Ecole Polytechnique Federale de Lausanne  
Laboratoire de Ceramique  
Lausanne  
SWITZERLAND

Lewis F. Brown  
South Dakota State University  
Dept. of Electrical  
Brookings, SD 57007

David P. Cann  
Penn State University  
152 Materials Res. Lab.  
University Park, PA 16802

James P. Canner  
Murata Electronics  
1900 West College  
State College, PA 16801

Dongmei Cao  
Penn State University  
142 MRI  
University Park, PA 16801

Wenwu Cao  
Penn State University  
164 Materials Research  
University Park, PA 16802

Joseph S. Capusso  
Alfred University  
NYS College of Engr.  
Alfred, NY 14802

Guillermo Castellanos  
Universidad de Guadalajara  
Apdo. Postal 2-638  
Guadalajara, Jalisco 44281  
MEXICO

Antonio B. Catalan  
General Motors Research Lab  
30500 Mound Rd.  
Warren, MI 48090-9055

Francis K. Chai  
University of Arizona  
654 E. Drachmann St.  
Tucson, AZ 85705-7450

Hongju Chang  
Cabot Performance Materials  
County Line Road  
Boyertown, PA 19512

Lin-huang Chang  
State University of New York  
Dept. of Electrical  
Amherst, NY 14260

Ray Chaudhuri  
YTC America, Inc.  
550 Via Alondra  
Camarillo, CA 93012

Deng-Yuan D. Chen  
Ramtron Corp.  
1850 Ramtron Drive  
Colorado Springs, CO 80921

H. Daniel Chen  
Penn State University  
187 Materials Research Lab.  
University Park, PA 16802

Jiayu Chen  
Penn State University  
187 Materials Research  
University Park, PA 16802

Yan Chen  
Penn State University  
142 Materials Research  
University Park, PA 16802

Hsui-Fung Cheng  
National Taiwan Normal University  
Physics Dept.  
TAIWAN

Ana K. Chernakova  
Carnegie Mellon University  
5000 Forbes Ave.  
Pittsburgh, PA 15213

Arthur E. Chiou  
Rockwell Science Center  
1049 Camino Dos Rios  
Thousand Oaks, CA 91360

Yi Chiu  
Carnegie Mellon University  
5000 Forbes Ave.  
Pittsburgh, PA 15213

Kyeong Ho Cho  
Yeung Nam University  
Dept. of Materials  
Kyongsan, 712-749  
SOUTH KOREA

Robert E. Chodelka  
University of Florida  
Dept. of Elect.  
Gainesville, FL 32611-2066

Alice F. Chow  
North Carolina State University  
1001 Capability Dr.  
Raleigh, NC 27695

Dongil Chun  
Ton Yang Central Lab.  
38-1, Jung-Ri  
Yongin-Kun  
SOUTH KOREA

Ilsub Chung  
Samsung Advanced Inst. of Tech.  
P.O. Box 111  
Suwon, 440-600  
SOUTH KOREA

Su Jin Chung  
Seoul National University  
Dept. of Inorganic  
Seoul, 151-742  
SOUTH KOREA

William W. Clark  
U.S. Army Research Laboratory  
AMSRL-EP-ES  
Fort Belvoir, VA 22060-5838

Michael Ronald Cockburn  
University of Manchester/Umist  
12 Birchfields Road  
Longsight, Manchester  
UNITED KINGDOM

William R. Cook  
684 Quilliams Rd.  
Cleveland Hts., OH 44121

Stephen A. Costantino  
Cabot Performance Materials  
County Line Road  
Boyertown, PA 19512

Matthew J. Creedon  
Alfred University  
NYS College of Engr.  
Alfred, NY 14802

L. Eric Cross  
Penn State University  
187 Materials Research  
University Park, PA 16802-4800

J. Thomas Cutchen  
Sandia National Laboratories  
MS 0521  
Albuquerque, NM 87185-0521

David E. Dausch  
Clemson University  
P.O. Box 340907  
Clemson, SC 29634-0907

Gordon O. Dayton  
Vitramon, Inc.  
Box 544  
Bridgeport, CT 06601

N. I. Deriugina  
Ukraine Academy of Science  
Semiconductors Physics  
Kiev, 252028  
UKRAINE

Seshu Desu  
Virginia Tech  
Blacksburg, VA 24061

Sandwip K. Dey  
Arizona State University  
17 ERC  
Tempe, AZ 85287-6006

Martin Diestelhorst  
Martin-Luther University  
Fachbereich Physik/Exp.  
Halle  
GERMANY

Duane Dimos  
Sandia National Labs  
P.O. Box 5800  
Albuquerque, NM 87185

Aydin Dogan  
Penn State University  
249 Materials Research  
University Park, PA 16802

Joseph P. Dougherty  
Penn State University  
144 MRL  
University Park, PA 16802

William C. Drach  
U.S. Army Research Lab, EPSD  
Fort Monmouth, NJ 07724

Joel B. DuBow  
Sarcos Research Corp.  
390 Wakara Way  
Salt Lake City, UT 84112

Dennis Dungan  
General Motors Research Lab.  
30500 Mound Rd.  
Warren, MI 48090

Jeff Eastman  
Argonne National Laboratory  
97000 S. Cass Ave.  
Argonne, IL 60439

Takeshi Egami  
University of Pennsylvania  
3231 Walnut St.  
Philadelphia, PA 19104-6272

Joe T. Evans  
Radiant Technologies, Inc.  
1009 Brandbury Dr. SE  
Albuquerque, NM 87106

James J. Fallon  
Space Sciences Corp.  
10 New King St.  
White Plains, NY 10604

Jose Fernandez  
Penn State University  
Materials Research  
University Park, PA 16802

Joseph T. Fielding  
Penn State University  
249 Materials Research  
University Park, PA 16802

Christopher M. Foster  
Argonne National Laboratory  
Materials Science  
Argonne, IL 60439-4838

Jan Fousek  
Institute of Physics  
Acad. Sci.  
18040 Prague 8  
SLOVAKIA

Jon M. Frommelt  
NYSCC at Alfred University  
2 Pine Street  
Alfred, NY 14802

Paul A. Fuierer  
New Mexico Inst. of Mining & Tech.  
Materials Engineering  
Socorro, NM 87801

Eiichi Fukada  
Kobayashi Inst. Physical Research  
99 Melville Street  
Ontario L9H2A4  
CANADA

Yukio Fukado  
Texas Instruments Japan  
2350 Kibara Mihomura  
Ibaraki, 300-04  
JAPAN

Eugene Furman  
Clemson University  
Dept. of Ceramic Engr.  
Clemson, SC 29634

Mark Garratt  
DeHronic  
60 Harding Ave.  
Dover, NJ 07801

Christopher J. Gaskey  
Penn State University  
107B RUA  
University Park, PA 16802

Xeucang Geng  
Penn State University  
RUA MRL  
University Park, PA 16802

Brady J. Gibbons  
Penn State University  
148 Materials Research  
University Park, PA 16802

Charles D. Glenn  
Consultant  
1610 Manton Ct.  
Campbell, CA 95008

Paul Gonnard  
Institut Nat'l des Science Appliquees  
Lab. Genie Electrique et  
Villeurbanne 69621  
FRANCE

Sudhakar Gopalakrishnan  
Alfred University  
New York State College  
Alfred, NY 14802

Anatoliy V. Gorish  
Rostov Pedagogical University  
344082 Rostov-on-Don  
RUSSIA

Dennis Gaudons  
Piezo Kinetics Inc.  
P.O. Box 756  
Bellefonte, PA 16823

S. A. Gridnev  
Voronezh State Tech. Univ.  
Voronezh, 394062  
RUSSIA

Alexei Gruverman  
National Inst. for Research in  
Inorganic Materials  
Ibaraki, 305  
JAPAN

Peter Gunter  
Nonlinear Optics Laboratory  
Institute of Quantum  
8093 Zurich  
SWITZERLAND

Ruyan Guo  
Penn State University  
108B RUA  
University Park, PA 16802

Raj Gururaja  
Hewlett Packard  
M.S. 0095  
Andover, MA 01810

Gene H. Haertling  
Clemson University  
206 Olin Hall  
Clemson, SC 29634-0907

David Hall  
University of Manchester  
Materials Science Center  
Manchester, MI 7H5

Arvind Halliyal  
California Micro Devices  
215 Topaz Street  
Milpitas, CA 95035

Michael J. Haun  
Colorado School of Mines  
MME Department  
Golden, CO 80401

Mary A. Hendrickson  
U.S. Army Research Laboratory  
Electronics & Power  
Ft. Monmouth, NJ 07703-5601

Aree Herabut  
Rutgers University  
P.O. Box 909  
Piscataway, NJ 08855-0909

Fred Hickernell  
Motorola Inc.  
8201 E. McDowell  
Scottsdale, AZ 85252

Seiji Hirose  
Penn State University  
A10 MRL  
University Park, PA 16802-4801

Yamamoto Hiroshi  
Komatsu Ltd.  
11B Research Unit A  
University Park, PA 16802-4801

Robert C. Hoffman  
Army Research Laboratory  
Dept. of the Army  
Ft. Belvoir, VA 22060-5838

Boen Houn  
Colorado School of Mines  
MME Dept.  
Golden, CO 80401

Wayne Huebner  
University of Mo-Rolla  
222 McNutt Hall  
Rolla, MO 65401

Maria Huffman  
Symetrix Corporation  
5055 Mark Dabbling Blvd.  
Colorado Springs, CO 80921

Noboru Ichinose  
Waseda University  
3-4-1 Ohkubo  
Tokyo, 169  
JAPAN

Kenji Iijima  
Matsushita Electric Industrial Co. Ltd.  
Seika-Cho Hikardai  
Kyoto, 61902  
JAPAN

Victor F. Janas  
Rutgers University  
Ctr. for Ceramics  
Piscataway, NJ 09855-0909

Sei Joo Jang  
Penn State University  
258 Materials Research  
University Park, PA 16802

Byungmoon Jin  
Penn State University  
MRL  
University Park, PA 16801

Man Jung Jong  
Dankook University  
Dept. of Physics  
Changnam, 330-714

B. J. Jungnickel  
Deutsches Kunststoff-Institut  
Schlobgartenstr. 6  
64289 Darmstadt  
GERMANY

Manfred Kahn  
NRL  
Cove 6374  
Washington, DC 20375

Shoji Kaneko  
Shizuoka University  
3-5-1 Johoku  
Shizuoka, 432  
JAPAN

Ram S. Katiyar  
University of Puerto Rico  
P. O. Box 23343  
San Juan, PR 00931-3343

Andrew J. Kennedy  
U. S. Army Research Laboratory  
Attn: AMSRL-EP-EH  
Ft. Belvoir, VA 22060-5838

Brian P. Ketchel  
U. S. Army Research Lab  
10235 Burbeck Road  
Ft. Belvoir, VA 22060-5838

Anthony S. Kewitsch  
Caltech  
128-95  
Pasadena, CA 91125

Hyeong Joon Kim  
Seoul National University  
Dept. of Inorganic  
Seoul, 151-742  
SOUTH KOREA

Hyun H. Kim  
New Jersey Inst. of Technology  
ECE Department  
Newark, NJ 07102

Illwon Kim  
University of Ulsan  
San 29 Mugadong Namgu  
Ulsan, 680-749  
SOUTH KOREA

Jeong Kim  
Seoul National University  
Dept. of Physics  
Seoul, 151-742  
SOUTH KOREA

Nam-Kyoung Kim  
Kyungpook National University  
1370 Sankyuk-Dong  
Taegu, 702-701  
SOUTH KOREA

Namchul Kim  
Penn State University  
259 Intercollege MRL  
University Park, PA 16802

Yangdo Kim  
Colorado School of Mines  
MME Department  
Gordon, CO 80401

Angus I. Kingon  
North Carolina State University  
Raleigh, NC 27695-7919

Lee A. Knauss  
Lehigh University  
Physics Dept.  
Bethlehem, PA 18015

Joohyun Koh  
Penn State University  
Materials REsearch Lab  
University Park, PA 16802

Sridhar Komarneni  
Penn State University  
205 Materials Research  
University Park, PA 16802

Sergey Kramarov  
Rostov Pedagogical University  
344082 Rostov-on-Don  
RUSSIA

Daniel S. Krueger  
University of Missouri-Rolla  
225 McNutt Hall  
Rolla, MO 65401

Saluru B. Krupanidhi  
Penn State University  
206 Materials Research  
University Park, PA 16802

Paul W. Kruse  
Consultant-Infrared Technology  
6828 Oaklawn Avenue  
Edina, MN 55435

Valery D. Kugel  
Tel-Aviv University  
Ramat Aviv  
Tel Aviv 69978  
ISRAEL

Hall Kunkel  
Echo Ultrasound  
R.D. 2, Box 118  
Reedsville, PA 17084

A. Kuprienko  
Rostov Pedagogical Univ.  
B. Sadovaya St. 33  
Rostov-On-Don, 344082  
RUSSIA

Makoto Kuwabara  
Kyushu Inst. of Technology  
1-1 Sensui-cho  
Kitakyushu, 804  
JAPAN

K. W. Kwok  
Hong Kong Polytechnic  
Hung Hom  
Kowloon  
HONG KONG

Sook-Il Kwun  
Seoul National University  
Dept. of Physics  
Seoul, 151-742  
SOUTH KOREA

Ravindra B. Lal  
Alabama A&M University  
Dept. of Physics  
Normal, AL 35762

Steven M. Landin  
Colorado School of Mines  
MME Dept.  
Golden, CO 80401

Sidney B. Lang  
Ben-Gurion University of the Negev  
Dept. of Chemical  
Beer-Sheva 84105  
ISRAEL

Deborah K. Laubscher  
Penn State University  
254 Materials Research  
University Park, PA 16802

Hee Young Lee  
Yeungnam University  
241-1 Dae-Dong  
Kyongsan, 712-749  
SOUTH KOREA

Jong-Myeon Lee  
Tong Yang Central Laboratories  
38-1, Jung-Ri  
Kyungki-Do 449-910  
SOUTH KOREA

Mark R. Leonard  
Rutgers University  
Dept. of Ceramics  
Piscataway, NJ 08855-0907

Guang Li  
Clemson University  
Dept. of Ceramics  
Clemson, SC 29631

Li Li  
Northern Illinois University  
Dept. of Chemistry  
DeKalb, IL 60115

Longtu Li  
Tsinghua University  
Dept. of Materials Science  
Beijing  
CHINA

Tuo Li  
University of Florida  
Dept. of  
Gainesville, FL 32611-2066

Virn Li  
Carnegie Mellon University  
Department of Electrical  
Pittsburgh, PA 15213

Zhuang Li  
Argonne National Laboratory  
MSD Bldg. 212  
Argonne, IL 60439

Kuiming Liang  
Echo Ultrasound  
RR 2, Box 118  
Reedsville, PA 17084-9772

Cheng H. Lin  
National Tsing Hua University  
Dept. of Materials  
Hsinchu  
TAIWAN

I-Nan Lin  
National Tsing Hua University  
Materials Science Center  
Taiwan, 300

Yinmei Lin  
Shanghai Inst. of Ceramics  
Chinese Academy of  
Shanghai, 200050  
CHINA

Donhang Liu  
University of Illinois  
Urbana, IL 61801

Rui-bin Liu  
Shanghai Inst. of Ceramics  
Chinese Academy of  
Shanghai, 200050  
CHINA

S. T. Liu  
Honeywell, Inc.  
12001 State Highway 55  
Plymouth, MN 55441

Yimin Liu  
University of Pittsburgh  
848 Benedum Hall  
Pittsburgh, PA 15261



Philip W. Loveday  
CSIR  
P. O. Box 395  
Pretoria, 0001  
SOUTH AFRICA

Pei-Wen Lu  
Nanjing Institute of Chemical Tech.  
5 Xin MO Far Road  
Jiangsu, 21009  
CHINA

Yanxia Lu  
Alfred University  
NYS College of  
Alfred, NY 14802

Chris Lynch  
University of California  
Dept. of Mechanical  
Santa Barbara, CA 43106

Hiroshi Maiwa  
Shonan Institute of Technology  
1-1-25  
Fujisawa, Kanagawa  
JAPAN

Olga Malyshkina  
Apt. 30, House 2  
Proletarskaja Nab,  
RUSSIA

Abhai Mansingh  
University of Delhi  
Dept. of Physics  
Delhi  
INDIA

Joseph V. Mantese  
General Motors Research & Dev.  
30500 Mound Road  
Warren, MI 48090-9055

Jon-Paul Maria  
Penn State University  
148 Materials Research  
University Park, PA 16802

Kelley A. Markowski  
Penn State University  
249 IRML  
University Park, PA 16802

Jeff Marx  
University of MO-Rolla  
225 McNutt Hall  
Rolla, MO 65401

Daniel E. McCauly  
Penn State University  
A6 Materials Research  
University Park, PA 16802

Raymond C. McGonan  
US ARL  
MSRL-EP-MD  
Ft. Monmouth, NJ 07753

Mark P. McNeal  
Penn State University  
249 IMRL  
University Park, PA 16802

Mohammed Megherhi  
Piezo Kinetics Inc.  
P. O. Box 756  
Bellefonte, PA 16823

Allen H. Meitzler  
Ford Motor Company  
MD-1170, SRL  
Dearborn, MI 48121-2053

Jean-Pierre Mercurio  
LMCTS, URA CNRS 320  
Faculte des Sciences  
Limoges, 87060  
FRANCE

Paul A. Meyer  
Krautkramer-Branson, Inc.  
50 Industrial Park Rd.  
Lewistown, PA 17044

Richard J. Meyer  
Penn State University  
A-2 Materials Research  
University Park, PA 16802

Adolph L. Micheli  
General Motors  
R&D Center  
Warren, MI 48090

Francois Micheron  
Thomson Trt Defense  
BP 55  
Guyancourt Cedex  
FRANCE

Caroline Millar  
Ferroperm A/S  
Mejreskovvej 6  
3490 Kvistgard  
DENMARK

Nai-Ben Ming  
Nanjing University  
National Lab. of Solid  
Nanjing, 210008  
CHINA

Majed S. Mohammed  
General Motors Corp.  
30500 Mound Road  
Warren, MI 48090-9055

Jooho Moon  
University of Florida  
Dept. of  
Gainesville, FL 32611-2066

Jon C. Motton  
Tektronix, Inc.  
P. O. Box 1000  
Wilsonville, OR 97070

Binu Mukherjee  
Royal Military College of Canada  
Kingson  
Ontario, K7K5L0  
CANADA

Maureen L. Mulvihill  
Penn State University  
148 MRL  
University Park, PA 16802

Kenji Murakami  
Shizuoka University  
3-5-1 Johoku  
Shizuoka, 432  
JAPAN

Akira Murata  
Murata Manufacturing Co., Ltd.  
2-26-10 Tenjin  
Kyoto, 617  
JAPAN

S. Narayana Murty  
Andhra University  
2367 India Yeager Road  
West Lafayette, IN 47906

Kaoru Nagamine  
Mitsubishi Materials Corp.  
Shinmaru Bldg. 1-5-1  
Tokyo 100  
JAPAN

Masaya Nagata  
Sharp Corporation  
1211 Ascot Lane  
Blacksburg, VA 24060

Takashi Nakamura  
Rohm Co., Ltd.  
21, Sajin Mizosaki-cho  
Kyoto, 615  
JAPAN

Atsuyuki Nakano  
Penn State University  
109 Materials Research  
University Park, PA 16802

Azar Nazeri  
Naval Research Lab  
Washington, DC 20375

Craig Near  
Morgan Matroc, Inc.  
232 Forbes Road  
Bedford, OH 44146

Ratnakar R. Neurgaonkar  
Rockwell International Science Center  
1049 Camino Dos Rios  
Thousand Oaks, CA 91360

Robert E. Newnham  
Penn State University  
251 MRL  
University Park, PA 16802

Toshio Ogawa  
Shizuoka Inst. of Science of Technology  
2200-2, Toyosawa  
Shizuoka, 437  
JAPAN

Ki-Young Oh  
Penn State University  
156 MRL  
University Park, PA 16802

Takashi Okawa  
Sumitomo Metal Industries, Ltd.  
Electronics Functional  
Amagasaki, Hyogo, 660  
JAPAN

Kiyoshi Okazaki  
Shonan Inst. of Technology  
Tsujido Nishikaigan  
Fujisawa, 251  
JAPAN

John R. Oliver  
Rockwell International Science Center  
1049 Camino Dos Rios  
Thousand Oaks, CA 91360

Michael N. Orr  
University of Arizona  
Dept. of Materials  
Tucson, AZ 85721

Steve P. Ostrander  
Alfred University  
NYS College of  
Alfred, NY 14802

R. Kumar Pandey  
Texas A&M University  
Center for Electronic Materials  
College Station, TX 77843-3128

Rudolf Panholzer  
Naval Postgraduate School  
Code SP/PZ  
Monterey, CA 93943

William E. Paradise  
Clemson University  
Box 7738  
Clemson, SC 29632

Seung Eek Park  
Seoul National University  
Dept. of Inorganic  
Seoul, 151-742  
SOUTH KOREA

Anil Patel  
Gec-Marconi Materials Technology  
Caswell  
Northants, NN12 8EQ  
UNITED KINGDOM

Radha K. Pattnaik  
Lehigh University  
Physics Dept.  
Behlehem, PA 18015

David A. Payne  
University of Illinois  
302 Ceramics  
Urbana, IL 61801

Cheng-Tien Peng  
Penn State University  
AI IMRL  
University Park, PA 16802

Chien-Hsiung Peng  
Ceram, Inc.  
1800 Kraft Drive  
Blacksburg, VA 24060

Leonie M. Peters  
Rutgers University  
c/o Center for Ceramic  
Piscataway, NJ 08901

Guy David Pethybridge  
Oxford University  
Dept. of Materials  
Oxford, OX1 3PH  
UNITED KINGDOMS

Pradeep P. Phule  
University of Pittsburgh  
848 Benedum Hall  
Pittsburgh, PA 15213

Brian M. Pierce  
Hughes Aircraft Co.  
RE/RO2/V518  
Los Angeles, CA 90009-2426

Alain Pignolet  
Penn State University  
224 Materials Research  
University Park, PA 16802

Steven M. Pilgrim  
NY State College of Ceramics  
CES/120 McMahon  
Alfred, NY 14804-1296

Robert C. Pohanka  
U.S. Navy  
Office of Naval Research  
Arlington, VA 22217

Y. M. Poplavko  
Kiev Polytechnic Inst.  
Microelectronics Dept.  
Kiev, 252056  
UKRAINE

Chandra Prakash  
Penn State University  
108 MRL  
University Park, PA 16802

Eswar S. Prasad  
Sensor Technology Limited  
P. O. Box 97  
Collingwood, Ontario, L9Y4K1  
CANADA

Wen Kang Qi  
Penn State University  
160 MRL  
University Park, PA 16802

Kuldeep Kumar Raina  
Thapar Inst. of Engineering & Tech  
School of Basic &  
Patiala, Punjab 147001  
INDIA

Clive A. Randall  
Penn State University  
161 Materials Research  
University Park, PA 16802

Tom Reynolds  
Murata Manufacturing Co., Ltd.  
2-26-10 Tenjin  
Kyoto, 617  
JAPAN

L. A. Reznichenko  
Rostov State University  
Inst. of Physics  
Rostov-On-Don 344104  
RUSSIA

Claude Richard  
Institut Nat'l des Sciences Appliquees  
Lab. Genie Electrique et  
Villeurbanne, 69621  
FRANCE

Jeff Roeder  
Advanced Technology Materials  
7 Commerce Drive  
Danbury, CT 06810

Gil Rosenman  
Tel-Aviv University  
Ramat Aviv, 69978  
Tel Aviv, 69978  
ISRAEL

Debasis Roy  
University of California  
Material Science Program  
Irvine, CA 92717-2575

Ronnen A. Roy  
IBM  
T. J. Watson Research  
Yorktown Heights, NY 10598

Takahashi Sadayuki  
Penn State University  
A12, IMRL  
University Park, PA 16802

Ahmad Safari  
Rutgers University  
Center for Ceramic  
Piscataway, NJ 08855-0909

Yukio Sakabe  
Murata Mfg. Co., Ltd.  
Kyoto  
JAPAN

Greg J. Salamo  
University of Arkansas  
Physics Dept.  
Fayetteville, AR 72701

Etsuro Sawaguchi  
Agne Gijutsu Center  
5-1-25 Minami-Aoyama  
Tokyo, 107  
JAPAN

Robert P. Schaeffer  
Rutgers University  
Center for Ceramic  
Piscataway, NJ 08855-0909

Jim Schloss  
Marsh, Inc.  
707 E. B Street  
Belleville, IL 62222

Hugo Schmidt  
Montana State University  
Dept. of Physics  
Bozeman, MT 59717

Adnreas Schonecker  
Fraunhofer-Inst. fur Keramische  
Technologian U  
Dresden, D-07277  
GERMANY

Norman W. Schubring  
General Motors Corp.  
NAO Research  
Warren, MI 48090

Louise C. Sengupta  
U. S. Army Research Lab  
AMSRL-MA-CA  
Watertown, MA 02172-0001

Somnath Sengupta  
U.S. Army Research lab  
AMSRL-MA-CC-292  
Watertown, MA 02172-0001

Scott R. Sentz  
Channel Industries, Inc.  
839 Ward Drive  
Santa Barbara, CA 93111

Won Choi Seong  
Dankook University  
Dept. of Physics  
Chungnam, 330-714  
SOUTH KOREA

Edgar Seydel  
University of Maryland  
9127 Bridgewater St.  
College Park, MD 20740-4030

Ed J. Sharp  
U.S. Army Research lab  
Ft. Belvoir, VA 22060

M. K. Sheinkman  
Kiev Polytechnic Inst.  
Photoelectronics Dept.  
Kiev, 252056  
UKRAINE

Kim Shin-young  
YOUNGnam University  
Dept. of Material  
Kyongson, 712-749  
KOREA

Yamamichi Shintaro  
NEC Corporation  
4-1-1 Miyazaki  
Kanagawa, 216  
JAPAN

Tadashi Shiosaki  
Kyoto University  
Dept. of  
Kyoto, 606-01  
JAPAN

Harry Shirey  
Piezo Kinetics inc.  
P. O. Box 756  
Bellefonte, PA 16823

Thomas R. Shrout  
Penn State University  
150 MRL  
University Park, PA 16802

V. Ya Shur  
Ural State University  
Ekaterinburg  
RUSSIA

Ian Sidney  
Morgan Matroc-Unilator Division  
Vauxhall Industrial  
Clwyd, LL14 6HY  
UNITED KINGDOM

A. S. Sidorkin  
Voronezh State University  
Voronezh  
SWITZERLAND

David Skatrud  
U. S. Army Research Office  
P. O. Box 12211  
Research Triangle Park, VA 27709

James F. Smith  
Space Sciences Corp.  
10 New King Street  
White Plains, NY 10604

Wallace Arden Smith  
Office of Naval Research  
800 North Quincy Street  
Arlington, VA 22217-5660

Donald M. Smyth  
Lehigh University  
Whitaker lab #5  
Bethlehem, PA 18015

Okamura Soichiro  
Science University of Tokyo  
Dept. of Applied Physics  
Tokyo, 162  
JAPAN

Narayanan Solayappan  
Texas A&M University  
Dept. of Electrical Engineering  
College Station, TX 77843-3128

Nobuyuki Soyama  
Mitsubishi Materials Corporation  
1-297 Kitabukuro-Cho  
Saitama, 330  
JAPAN

Bert Spierings  
Philips Research Labs  
P. O. Box 80.000  
Eindhoven  
THE NETHERLANDS

T. T. Srinivasan  
Rutgers University  
No. Brunswick, NJ 08902

V. Starikov  
Rostov State University  
Inst. of Physics  
Rostov-On-Don, 344104  
RUSSIA

E. C. Subbarao  
Penn State University  
1 MRL  
University Park, PA 16802

V. Sundar  
Penn State University  
249 IMRL  
University Park, PA 16802

Kuharuangrong Sutin  
Alfred University  
NYS College of  
Alfred, NY 14802

Willard H. Sutton  
United Technologies Research Center  
411 Silver Lane  
East Hartford, CT 06108

Danielle M. Tahan  
Rutgers University  
P. O. Box 909  
Piscataway, NJ 08855-0909

Lone-Wen F. Tai  
University of Missouri-Rolla  
222 McNutt  
Rolla, MO 65401

Takahiro Takada  
Sumitomo Metal Industries, Ltd.  
Electronics Components  
Amagasaki, Hyogo, 660  
JAPAN

Yamamoto Takashi  
The National Defence Academy  
Dept. of Electrical Engineering  
Yokosuka, 239  
JAPAN

Tadashi Takenaka  
Science University of Tokyo  
Faculty of Science  
Noda, Chiba-ken, 278  
JAPAN

Tetsuro Tanaka  
2, Yakocho Shimogamo  
Sakyoku, Kyoto, 617  
JAPAN

Toshi Tani  
Toyota CRDL  
Nagakute, Aichi  
480-11  
JAPAN

Toshio Tanimoto  
Shonan Inst. of Technology  
1-1-25  
Kanagawa, 251  
JAPAN

Chutima Tantigate  
Rutgers University  
P.O. Box 909  
Piscataway, NJ 08855

George Taylor  
Princeton Resources  
Box 211  
Princeton, NJ 08542

Kazuya Terabe  
National Inst. for Research  
in Inorganic Materials  
Ibaraki, 305  
JAPAN

Srdan Teslic  
University of Pennsylvania  
3231 Walnut St.  
Philadelphia, PA 19104

Sarita Thakoor  
Jet Propulsion Laboratory  
Mail Stop 303-308  
Pasadena, CA 91109

Robert Y. Ting  
U. S. Naval Research Lab  
P.O. Box 568337  
Orlando, FL 32856-8337

Jean Toulouse  
Lehigh University  
Dept. of Physics  
Bethlehem, PA 18015

Ailie Tourlog  
Tohoku University  
Dept. Electrical Engineering  
Sendai, 980-77  
JAPAN

K. Trinath  
Naval Science & Tech. Lab.  
Visakhapatnam, 530027  
INDIA

Susan Trolier-McKinstry  
Penn State University  
149 MRL  
University Park, PA 16802

A. V. Turik  
Rostov State University  
Dept. of Physics  
Rostov-On-Don, 344104  
RUSSIA

Bruce A. Tuttle  
Sandia National Laboratories  
MS 0607, Dept. 1845  
Albuquerque, NM 87185

Kenji Uchino  
Penn State University  
134 MRL  
University Park, PA 16802

K. R. Udayakumar  
Penn State University  
187 Material Research Lab  
University Park, PA 16802-4801

Peter C. Vanbuskirk  
Advanced Tech. Materials  
7 Commerce Dr.  
Danbury, CT 06816

Dwight D. Viehland  
University of Illinois  
209 Ceramics Bldg.  
Urbana, IL 61801

Suresh Viswanathan  
Alfred University  
120 McMahon Bldg.  
Alfred, NY 14802

Sandeep T. Vohra  
Naval Research Lab  
Code 5670  
Washington, DC 20375

Eve D. Volk  
Seacor Piczo Ceramics  
8 Huntington St.  
Huntington, CT 06484

Kamau WaGachigi  
Penn State University  
A1 Materials Research  
University Park, PA 16802



Kikuo Wakino  
Murata Mfg. Co., Ltd.  
2-26-10, Tenjin  
Kyoto 617  
JAPAN

Jack Bruce Wallace  
University of Western Ontario  
Dept. of Materials Eng.  
London, Ontario, N6A5B9  
CANADA

Jeremy Rex Wallis  
Mattek  
P. O. Box 395  
Pretoria, 0001  
SOUTH AFRICA

Feiling Wang  
Clemson University  
Clemson, SC 29634-0907

Hong Wang  
Penn State University  
187 Materials Research  
University Park, PA 16802-4800

Qing-Ming Wang  
Penn State University  
Materials Research Lab  
University Park, PA 16802

Sea-Fue Wang  
Vitramon, Inc.  
Box 544  
Bridgeport, CT 06601

William L. Warren  
Sandia National Laboratories  
MS 1349  
Albuquerque, NM 87175-1349

Barry A. Wechsler  
Hughes Research Laboratories  
3011 Malibu Canyon  
Malibu, CA 90265

Manfred Weihnacht  
IFW Dresden  
Postfach  
Dresden, 01171  
GERMANY

Tom Wheat  
Natural Resources Canada  
405 Broth St.  
Ottawa, Ontario K1A0G1  
CANADA

John Witham  
Penn State University  
155 Materials Research  
University Park, PA 16802

Dieter Wolf  
Argonne National Lab  
Argonne, IL 60439

Andreas Wolff  
Siemens AG  
Corporate Research  
Munich, 81730  
GERMANY

Wanda Wolny  
Ferroperm  
Hejreskovvej 6  
KD-3490 Kuistgerd  
DENMARK

Gary L. Wood  
U.S. Army  
Army Research Lab  
Ft. Belvoir, VA 22060-5838

Naijuan Wu  
University of Houston  
Space Vacuum Epitaxy  
Houston, TX 77204-5507

Tai-Bor Wu  
National Tsing Hua University  
Dept. Mat. Sci. National  
Hsinchu  
TAIWAN

Yao Xi  
Ziam Jiaotong University  
Zian, 710049  
CHINA

Wan Rong Xue  
University of Mo-Rolla  
222 McNutt Hall  
Rolla, MO 65401

Yohachi Yamashita  
Toshiba Corp.  
R&D Center  
Kawasaki-City, 210  
JAPAN

Dalian Yang  
Penn State University  
142 IMRL  
University Park, PA 16802

Ping Yang  
Sandia National Laboratories  
Albuquerque, NM 87111-0345

Zhou Ye  
Penn State University  
1004 Apt. B  
Anderson, IN 46013

Jong-Gul Yoon  
University of Suwon  
Dept. of Physics  
Hwaseung, Kyng-gi-do  
SOUTH KOREA

Shoko Yoshikawa  
Penn State University  
151 Materials Research  
University Park, PA 16802

Yoshio Yoshikawa  
Nihon University  
Koriyama  
Fukushima, 963  
JAPAN

Insuk Yu  
Seoul National University  
Dept. of Physics  
Seoul, 151-742  
SOUTH KOREA

Nikolai K. Yushin  
A. F. Ioffe Physical Tech. Inst.  
c/o FTIKKS Enterprise  
St. Petersburg, 194021  
RUSSIA

Jiming Zhang  
Advanced Technology Materials  
7 Commerce Drive  
Danbury, CT 06810

Qiming Zhang  
Penn State University  
Materials Research Lab  
University Park, PA 16802

Shuren Zhang  
Shanghai Inst. of Ceramics  
Chinese Academy  
Shanghai, 200050  
CHINA

Feng Zhao  
Penn State University  
Dept. of Electrical Engineering  
University Park, PA 16802

Jian Zhong Zhao  
Penn State University  
RUA 110C  
University Park, PA 16802

Qi Fa Zhou  
Zong Shan University  
Dept. of Physics  
Guang Zhou 510275  
PEOPLES REPUBLIC OF CHINA

Bernhard Zickgraf  
Max-Planck-Institut Metallforschung  
Pulvermetallurgisches  
70569, Stuttgart  
GERMANY